Contents

Contents.. i
Foreword. viii
Committees ix

Planery/Welcome Session **1**

Hadron Accelerator **1**
MOXMA01 – Present Status of J|-|PARC 1
MOXMA02 – Commisioning Experience of SNS 6

Synchroton Light Sources and FELs **11**
MOYMA01 – Overview of Energy|-|Recovery Linacs 11
MOYMA02 – Results from the free|-|electron laser FLASH 16
MOYMA03 – Status and Perspective of XFEL Projects in the World 17

Linear Colliders, Lepton Accelerators and New Acceleration Techniques **18**
MOZMA01 – Report on ILC 18
MOZMA02 – ILC Parameters Rationale and Challenges 19
MOZMA03 – Status of FFAG Developments 21

Accelerator Technology **26**
MOOPMA01 – Challenges in ILC SCRF Technology 26
MOOPMA02 – Overview of Regional Infrastructure for SCRF Development 31
MOOPMA03 – Technological Challanges of ERLs 36
MOOPMA04 – Crab Cavity Development 36
MOOPMA05 – R&D on Vacuum Components for High|-|Current Accelerators 41

Circular Colliders **46**
TUXMA01 – LHC Status 46
TUXMA02 – Record Luminosities at the Tevatron & Future Potentiality 51
TUXMA03 – Next Generation Electron|-|Ion Colliders 56

Synchroton Light Sources and FELs **61**
TUYMA01 – Overview of Synchrotron Radiation Light Sources 61
TUYMA02 – Commissioning of the Indus|-|2 Storage Ring 61
TUYMA03 – Commissioning and Status of the Diamond Storage Ring 66

Beam Dynamics amp; Electromagnetic Fields (Contributory Oral) **71**
TUC2MA02 – Design of the Transfer Lin·10^{-2} for the CTF-3 at CERN 71

Circular Colliders **74**
TUZMA01 – RHIC Status 74
TUZMA02 – Operation for LHC Cryomagnet Tests: Concerns, Challenges & Successful Collaboration . . 84
TUZMA03 – Material Science Challenges for ILC Cavities 89

Beam Dynamics and Electromagnetic Fields **90**
TUZH101 – Coherent Synchrotron Radiation Instabilities and its Effects on Electron Beam Qualities . . . 90
TUZH102 – Ion Instability Issues in Electron Rings 79
TUZH103 – Electron Cloud Experiments, Simulation and Cure 89

Linear Colliders, Lepton Accelerators and New Acceleration Techniques -CO **94**
TUC3MA01 – ILC DR Alternative Lattice Design 94
TUC3MA03 – Ultimate Abilities of Conventional Positron Sources 97

Contributory Oral **100**
TUC3H101 – Optimization Of The BEPCII Lattice With Frequency Map Analysis . . . 100

Poster Sessions **103**
TUPMA001 – New Connection Cryostat to Insert FP420 Proton Tagging Detector in the LHC Ring . . . 103
TUPMA005 – Simulation Study on Bunch Lengthening . . . 106
TUPMA006 – Study on the BEPCII Lattice . . . 109
TUPMA008 – Status of the VEPP|-|4M Electron|-|Positron Collider . . . 112
TUPMA012 – Measurement of Bremsstrahlung Dependent on Stored Beam Current . . . 115
TUPMA014 – State of the SLS Multi|-|bunch Feedback . . . 118
TUPMA015 – Radiation Safety Considerations of the Operation of INDUS|-|1 Synchrotron Radiation Source 121
TUPMA016 – Computation of Wakefields and Impedances for the PETRA III Longitudinal Feedback Cavity 124
TUPMA018 – Compact Hard X|-|Ray Synchrotron Radiation Source with Superconducting Bending Magnets 127
TUPMA020 – Beam Based Alignment and COD Correction for the Siam Photon Source . . . 130
TUPMA022 – Construction Progress of the SSRF Injector . . . 133
TUPMA023 – Project of 2 GeV Synchroton Light Source for the Republic of Kazakhstan . . . 136
TUPMA026 – A Prototype of the SSRF Power Supply Control System . . . 139
TUPMA028 – Status of the Photon Factory . . . 142
TUPMA031 – Development of Trigger and Clock Delay Module with Ultra|-|wide Range and High Precision 145
TUPMA032 – Radiation Safety System for INDUS Accelerator Complex . . . 148
TUPMA034 – Operation Experience of Top|-|up injection at Taiwan Light Source . . . 151
TUPMA035 – SCSS Prototype Accelerator Timing System . . . 154
TUPMA036 – Comparative Studies of Electron Sources for a Free Electron Laser at PSI . . . 157
TUPMA037 – Project of Infrared Storage Ring Free Electron Lasers at AIST . . . 160
TUPMA038 – Start|-|up of an FEL Oscillator from Shot Noise . . . 163
TUPMA039 – Comparison of Codes for Smith|-|Purcell FEL . . . 166
TUPMA042 – Beam Parameters of the SCSS Prototype Accelerator Designed by PARMELA and Comparison with Measured Values . . . 169
TUPMA046 – Future Light Source based on Energy Recovery Linac in Japan . . . 172
TUPMA047 – Development of a Photocathode DC Gun at JAEA|-|ERL . . . 175
TUPMA049 – Development of an Injector to Generate a Very Short Bunch for a Super Coherent Terahertz Light Source Project . . . 178
TUPMA052 – Study on Compact DC Electron Gun using Single Crystal Cathode of LaB6 . . . 181
TUPMA053 – Injection Optimisation for INDUS|-|2 . . . 184
TUPMA056 – Injection of Beam Shaped Locally with Nonlinear Optics . . . 187
TUPMA057 – Physics Design of PAL|-|XFEL Undulator . . . 190
TUPMA058 – Insertion Devices for SESAME . . . 193
TUPMA059 – Beam Dynamics Effects with Insertion Devices for the Proposed 3 GeV Ring in Taiwan . . . 196
TUPMA060 – A Hamiltonian for Wave Length Shifter and its Studies on INDUS|-|1 . . . 199
TUPMA064 – ILC Activity at JINR and Siting in Dubna Region . . . 202
TUPMA066 – Energy Equalization by using S|-|band and X|-|band Accelerator Modules . . . 205
TUPMA067 – New Timing System for the L|-|band Linear Accelerator at Osaka University . . . 208
TUPMA068 – Performance of the Renewed L|-|band Linac and Recent Progress of Development of FEL and SASE at Osaka University . . . 211
TUPMA070 – Progress of RFQ Accelerator at Peking University . . . 214
TUPMA075 – Status of the CTF3 Frequency Multiplication Rings . . . 217
TUPMA076 – Design and Development of Beam Transport Elements for the BARC|-|ECIL Linac . . . 220
TUPMA083 – High Quantum Efficiency Photocathode for RF Guns . . . 223
TUPMA084 – Ions for LHC: Status of the Injector Chain . . . 226
TUPMA085 – LEIR: Towards the Nominal Lead Ion Beam . . . 229
TUPMA088 – High Power RF Testing of a Cell Coupled Drift Tube LINAC Prototype for LINAC4 . . . 232
TUPMA093 – Thermo|-|structural Analysis of 400 KeV Deuteron RFQ Components . . . 235
TUPMA094 – Electron Cooling Rates in FNAL's Recycler Ring . . . 238
TUPMA097 – Characteristics of the Magnetic Channel in the Yoke Hole of K|-|500 Superconducting Cyclotron . . . 241
TUPMA099 – Adiabatic Damping of the Bunch|-|length in the Induction Synchrotron . . . 244
TUPMA102 – Installation and Radiation Maintanance Scenario for J|-|PARC 50 GeV Synchrotron . . . 247

TUPMA105 – Transverse Matching of the SNS Linac Based on Profile Measurements . . . 250
TUPMA108 – Benchmarking of Multiparticle Phase Scan and Acceptance Scan Techniques for the SNS DTL . . . 253
TUPMA109 – Thermal|-|Induced Frequency Detuning of 350 MHz RFQ Structure . . . 256
TUPMA111 – Present Status of J|-|PARC MR Synchrotron . . . 259
TUPMA113 – Design of High Current RF Ion Source for Micromachining Applications . . . 262
TUPMA115 – Simulations of Non-uniform High Density Electronegative Plasma for Optimization of H^- ions and their Extraction . . . 265
TUPMA116 – Periodic Ion Current Burst in 6.4 GHz ECR Source . . . 268
TUPMA119 – Beam Line Design for PEFP User Facility . . . 271
TUPMA122 – High Power Neutron Converter for Low Energy Proton|/|Deuteron Beams: Present Status . 274
TUPMA123 – Electron Acceleration in the Wake Field Excited by 200TW Femto Second Laser in Underdense Plasma . . . 277
TUPMA124 – Multipacting in a Coaxial Cavity . . . 280

Circular Colliders **280**
WEXMA01 – Status of KEKB and Upgrade Plan to SuperKEKB . . . 280
WEXMA02 – The BEPCII: Construction and Initial Commissioning . . . 285

Contributory Oral **290**

Building of International Collaboration for Mega Accelerator Projects **290**
WEYMA01 – International Collaborations in ILC: R & D Issues . . . 290
WEYMA02 – India|-|based Neutrino Observatory |-| Present Status . . . 290
WEYMA03 – Asian Wide Collaboration on Accelerator Sciences . . . 295

Beam Instrumentation and Feedbacks **295**
WEZH101 – Real Time Feedback on Beam Parameters . . . 295
WEZH102 – Beam Instrumentation Experience at ATF . . . 305
WEZH103 – Challenges in ILC Instrumentation . . . 310

Hadron Accelerators **300**
WEZMA01 – Upgrades to the ISIS Spallation Neutron Source . . . 300
WEZMA02 – China Spallation Neutron Source Design . . . 310
WEZMA03 – High Power Proton Accelerator in Korea . . . 315
WEZMA04 – Superconducting Cyclotron Project at VECC . . . 320
WEZMA05 – Status and Plans for the TRIUMF ISAC Facility . . . 325

Contributory Oral **330**
WEC3H101 – Multi|-|bunch Feedback Activities at Photon Factory Advanced Ring . . . 330
WEC3H102 – Fabrication and Performance Test of the Cavity BPM for KEK ATF2 and PAL XFEL . . . 336

Contributory Oral **333**
WEC3MA01 – Experimental Verification of Halo Formation Mechanism of the SNS Front End . . . 333

Poster Sessions **339**
WEPMA002 – A Large Area Scanning Magnet For Homogeneous Irradiation of Targets . . . 339
WEPMA005 – Magnetic Field Calculations of a 10 MeV High Current Compact Cyclotron . . . 342
WEPMA010 – 8 GeV Beam Line Optics Optimization for the Rapid Antiproton Transfers at Fermilab . . . 345
WEPMA011 – Design and Operating Experience of Triode Electron Guns for Industrial Electron Accelerators 348
WEPMA013 – Analysis and Correction of the Measured COD in INDUS|-|2 . . . 351
WEPMA014 – Inhomogenous Field Wien Filter Design . . . 354
WEPMA015 – Characteristics of Beam Extraction System of K500 Superconducting Cyclotron . . . 357
WEPMA022 – Electron Guns and Beamlines in the View of Emittance Compensation . . . 360
WEPMA024 – A General Model of the Resistive Wall Instability in Linear Accelerators . . . 363
WEPMA030 – The Bunch Lengthening due to Electron Cloud in Positron Storage Ring . . . 366
WEPMA035 – Degradation of the Beam passing through Idle Coupled Cavities . . . 369
WEPMA037 – Beam Coupling Impedance Studies of the CSNS Ring . . . 372

WEPMA038 – A Study on the Applicability of Landau Cavity to the 1.2 GeV Booster Synchrotron at Tohoku University . . . 375
WEPMA039 – Effect of Magnetic Field Coupling On INDUS|-|2 Quadrupole Magnets . . . 378
WEPMA044 – Program for the Generation of High|-|Current RFQ . . . 381
WEPMA045 – Study of Space Charge Compensation In LEBT . . . 384
WEPMA048 – Beam Position Monitor at SCSS Prototype Accelerator . . . 387
WEPMA049 – Design of a Stripline Kicker for Tune Measurement in SESAME Storage Ring . . . 390
WEPMA050 – BPM (Beam Position Monitor) in the PAL Linac and BTL . . . 393
WEPMA051 – Development of Wide Band FCT System for Booster Synchrotron of Indus|-|1 & 2 . . . 396
WEPMA054 – Photon Beam Position Monitor with Hydraulic Level System . . . 398
WEPMA058 – Tune and Lifetime Studies at the Australian Synchrotron . . . 401
WEPMA059 – Commissioning of the Australian Synchrotron with Libera EBPPs and Matlab . . . 404
WEPMA060 – Measurements using the X|-|Ray and Optical Diagnostic Beamlines at the Australian Synchrotron . . . 407
WEPMA063 – Diagnostic Supports for Top|-|Up Operation at TLS . . . 410
WEPMA065 – Experience of Beam Diagnostic Systems in Commissioning Stage of Indus|-|2 . . . 413
WEPMA068 – Comparison of the Methods for Beam Energy Spread Measurement at the VEPP|-|4M . . . 416
WEPMA070 – Control of the Multi|-|Bunch Instabilities at TLS . . . 419
WEPMA071 – The Design, Fabrication and Performance Testing of the Analog I|/|Q RF Control System at NSRRC . . . 422
WEPMA073 – Control System based on PCs and PLCs for the L|-|band Linac at Osaka University . . . 425
WEPMA075 – Improvement of Web|-|Based Monitoring of EPICS|-|IOC for PAL Control System . . . 428
WEPMA077 – Monitor and Archive System of Instrumentation . . . 431
WEPMA078 – HTS|-|ECRIS and Low Energy Beam Transport System of the High Current Injector . . . 434
WEPMA080 – Control System for the Bending MPS at PLS Linac . . . 437
WEPMA083 – Design of C|-|band Standing|-|wave Accelerating Structure . . . 440
WEPMA085 – Implementation and Experience of Energy Ramping for Indus|-|2 . . . 443
WEPMA086 – First Experiences with Central Web Based Fault Information System . . . 446
WEPMA087 – Control System for Beam Diagnostic System of Indus|-|2 . . . 449
WEPMA089 – Control and Instrumentation for the VEC Superconducting Cyclotron Cryogen Delivery System . . . 452
WEPMA090 – Status of the Superconducting Insertion Devices Control System at TLS . . . 455
WEPMA096 – Rejuvenation of Linac Control System for TLS . . . 458
WEPMA099 – A New, PXI Bus Based, Pattern Memory System for the Siam Photon Source. . . . 461
WEPMA103 – The Design And Performance of the Prototype Digital Feedback RF Control System For the PLS Storage Ring . . . 464
WEPMA104 – Drive System Instrumentation For VEC SCC Axial|-|Hole Magnetic Field Measurement . . . 467
WEPMA105 – High Power Test of C|-|band Accelerating System for Japanese XFEL Project . . . 470
WEPMA109 – Positron Injector Accelerator and RF System for the ILC . . . 473
WEPMA110 – Development of 100 kW RF Amplifier for Superconducting Cyclotron at VECC . . . 476
WEPMA111 – Mechanical Engineering Challenges in the Development of the FEL at RRCAT . . . 479
WEPMA112 – Thermal Simulations of a Photocathode R. F. Gun . . . 482
WEPMA119 – Control Characteristics of the PEFP RF System . . . 485
WEPMA120 – Development of the Digital RF Control System for the PEFP Proton Accelerator . . . 488
WEPMA122 – Design and Development of 30 MeV, 3 kW RF Electron LINAC . . . 491
WEPMA123 – Comparative Analysis of Blade Tuner Optimization Options for the ILC . . . 494
WEPMA124 – Preliminary Design, Analysis and Manufacturing Aspects of Low Beta 350 MHz Reentrant Superconducting RF Cavity . . . 497
WEPMA132 – Superconducting Niobium Resonator Fabrication And Testing At IUAC . . . 500
WEPMA133 – Evaluation of External Q Using Kroll|-|Yu Method With Microwaves Studio . . . 503
WEPMA135 – Mechanical Analysis and Design of the PEFP Low Beta Cavity . . . 506
WEPMA137 – Design and Simulation of Multibeam Klystron Cavity . . . 509
WEPMA139 – Development of High|-|power Microwave Devices in Toshiba . . . 511
WEPMA140 – Development of C|-|band Multi Beam Sub|-|booster Klystron . . . 514
WEPMA142 – Commissioning and Operational Experience with INDUS|-|2 RF Systems . . . 517
WEPMA143 – High|-|Power, Low|-|Loss, Radial Rf Power Dividers|/|Combiners . . . 520

WEPMA144 – High Power Microwave Generation From Coaxial Virtual Cathode Oscillator 523
WEPMA145 – Development of A 35 Kw Power Amplifier At 350 Mhz For RFQ Accelerator Based Neutron Generator 526

Hadron Accelerators **529**
THXMA02 – Linear Accelerator Designs for the Upgrade of the CERN Proton Injector Complex (Linac4, SPL) 529
THXMA03 – Construction and Commissioning of the HIRFL|-|CSR 534

Accelerator Technology **539**
THYMA01 – Kickers for Injection and Extraction in Damping, Combiner and Storage Rings 539
THYMA02 – Progress in Understanding the High|-|gradient Limitations of Accelerating Structures 544
THYMA03 – Commissioning Experience of Superconducting Radio Frequency Systems for the Taiwan Light Source 549
THYMA04 – Development of Quarter Wave Resonators 554
THYMA05 – Low|-|level RF Control System Design and Architecture 559

Contributory Oral **564**
THC2MA01 – Design of The PEFP Low Beta Cryomodule 564
THC2MA02 – Experiences with the Manufacturing, Testing and Quality Control of Large Number of Superconducting Magnets 567
THC2MA03 – Design of L|-|band Superconducting Cavity for the Energy Recovery Linacs 570

Synchrotron Light Source and FELs **578**
THZMA01 – Status of SOLEIL Project 578
THZMA02 – Status of the Australian Synrotron project 583
THZMA03 – Construction of Shanghai Synchrotron Radiation Facility 593
THZMA04 – Status and Future of Taiwan Light Source 602

Application of Accelerators, Technology Transfer amp; Industrial Relations **573**
THZH101 – Review of Hadron Machines for Cancer Therapy 573
THZH102 – Use of Microbeam at JAEA Takasaki 588
THZH103 – The Progress of Accelerator Mass Spectrometry and their Applications in China 597
THZH104 – Application of Synchrotron Radiation & Neutron Beams to the Study of Nanomaterials and Biomaterials 601

Contributory Oral **607**
THC3MA01 – Operation and Recent Developments at the Siam Photon Source 607
THC3MA02 – SESAME Status 610
THC3MA03 – NSLS|-|II Design: A Novel Approach to Light Source Design 613
THC3MA04 – Status of the Novosibirsk High Power Terahertz FEL 616
THC3MA05 – Bunch Compression using the Transport Line and Short Bunch revolving in NewSUBARU . 619

Contributory Oral **622**
THC3H101 – Status of the Industrial RF|-|accelerators in BINP 622
THC3H102 – Practical Considerations in the Design of a High Current Commercial H|-|minus Cyclotron . 625
THC3H103 – The Compact Induction Circular Accelerator for Radiation Technologies 628

Poster Sessions **631**
THPMA004 – RF Amplifiers and Structures for ISAC|/|TRIUMF 631
THPMA005 – SCSS RF Control Toward 5712 MHz Phase Accuracy of One Degree 634
THPMA008 – Field Measurement Results of the Quadrupole Magnets for ATF2 637
THPMA010 – Structures of Quadrupole Magnet Core 640
THPMA013 – Effect of Eddy Current in Magnetic Lamination on Pulsed Septum Magnet Response 643
THPMA014 – Mechanical Stability of Open|-|type Quadrupole Magnets for a 2.5 GeV SRS (Indus|-|2) . . 646
THPMA015 – Performance of 6 MW Peak, 25kW Average Power Microwave System for 10 MeV, 10 kW Electron LINAC 649
THPMA016 – Median Plane Magnetic Field Mapping for Superconducting Cyclotron (SCC) in VECC . . . 652

THPMA017 – Mathematical Model for Fast and Slow Dumping of K|-|500 Superconducting Cyclotron Magnet 655
THPMA020 – Ideal Coil|-|Shape for Perfect Field in Superconducting Sextupole Magnets 658
THPMA022 – Design of the Proposed 250 Mev Superconducting Cyclotron Magnet 661
THPMA023 – Construction of SSRF Magnet Power Supply System 664
THPMA024 – Implementation of High Precision Magnet Power Supply using the DSP 666
THPMA028 – Regulation Scheme for Precision Magnet Power Supply 669
THPMA032 – Active Filter for Harmonic Mitigation for Magnet Power Supplies of INDUS|-|II 671
THPMA033 – Digital Power Supply Development at the PLS 674
THPMA035 – High Power Modulator For Klystron of Proton Accelerator 677
THPMA036 – Utilizing Multiplier Stack's Reflected Parasitic Capacitance to Achieve ZVS Operation of Resonant Inverter for 750 keV DC Accelerator 677
THPMA039 – 300 kV|/| 6 kW Power Supply System for Self|-|shielded Low Energy DC Accelerator at RRCAT Indore 679
THPMA043 – Development of 3 MeV, 30 kW DC Electron Accelerator at EBC, Kharghar 682
THPMA045 – Analysis and Design of Parallel Resonant Network Power Supply for a Rapid Cycling Synchrotron 685
THPMA046 – Study and Comparison of Reactive Power Compensation Schemes for Air|-|Core Transformer in ELV|-|type DC Accelerators 688
THPMA047 – Stair Current Output Power Supply for Switching Magnet 691
THPMA048 – Study of Vacuum Related Problems During the Energization of K500 Superconducting Cyclotron 694
THPMA050 – Performance of Cryomodule and Cryogenic Network System for the Superconducting Linac at IUAC. Delhi 697
THPMA051 – Cure of Temperature Fluctuations on the Nitrogen|-|cooled Sections of a CESR|-|type SRF Module 700
THPMA056 – Design of the TPS Bending Chamber 703
THPMA058 – Cyclotron RF Structures Leaks, Causes and Repair 706
THPMA059 – The Vacuum System for the SSRF Storage Ring 708
THPMA061 – Numerical study of field errors due to mechanical tolerances in superconducting miniundulators 711
THPMA062 – An APPLE|-|II Type Helical Undulator for SSRF 714
THPMA063 – Energy Stabilization of 2.5 GeV Linac using DeQing 717
THPMA064 – Development of a 200keV Linear Induction Accelerator 720
THPMA065 – Theoretical Analysis of the Recovery Times in Low Pressure Sparkgaps - Positive Ion Diffusion Method 723
THPMA066 – Theoretical Analysis of the Recovery Times In Low Pressure Sparkgaps- Anode Temperature Decay Method 726
THPMA067 – Stability Analysis of a Klystron|-|Modulator for PAL XFEL 729
THPMA070 – Characterisation of Amorphous Magnetic Material with Multiple Pulse Excitation 732
THPMA071 – Study of Insulation Coordination in the Presence of Multiple Dielectric Materials 735
THPMA073 – Artificial Neural Network Calculates Backward Wave Oscillator Parameters Reliably For Pulsed Accelerators 738
THPMA074 – Operational Analysis of Klystron|-|Modulator System for PLS 2.5|-|GeV Electron Linac . . . 740
THPMA076 – Development of the Klystron Modulator using a High|-|voltage Inverter Power Supply 743
THPMA078 – Wideband Current Transformers for the Surveillance of the Beam Extraction Kicker System of the Large Hadron Collider 746
THPMA081 – Precise Positioning of Magnetic Field Centers of Quadrupole Magnets on the Girder 749
THPMA083 – The Magnet Alignment Method For The J|-|PARC Main Ring 752
THPMA084 – A Mechanical Installation Prototype for the SSRF Storage Ring 755
THPMA085 – Mechanical Coupling between the LHC Cryogenic Distribution Line and the Short Straight Section housing the Superconducting Quadrupole. Theoretical Analysis and Experimental Validation 758
THPMA086 – Precise Survey and Alignment of Synchrotron Radiation Source Indus|-|2 761
THPMA087 – Prototype Beam Dump For 10 kW LINAC 764
THPMA088 – Bremsstrahlung Converter For High Power EB Radiation Processing Facility 767
THPMA089 – Studies of Metallic Ion Beams using ECRIS 770

THPMA091 – Air Temperature Analysis and Control Improvement for the Injection Area at TLS 773
THPMA093 – Vibration Evaluation for Utility Instruments and Water Piping System in TLS 776
THPMA094 – SF6 Gas Handling System for 3 MeV, 30 kW Industrial Electron Beam Accelerator at EBC, Kharghar, Navi Mumbai 779
THPMA096 – Installation and Integration of Indus|-|2 782
THPMA100 – Multipacting Study of Linac Prebuncher at CAMD 785
THPMA102 – The Proton and Ion Linear Accelerator ILU|-|9 788
THPMA104 – RF activities of ACCEL Instruments in Asia|-|Pacific 791
THPMA110 – Status of BINP AMS Facility 794
THPMA111 – Target Assembly Design and Neutronics Study for Indian Spallation Neutron Source Using NMTC|/|JAM Code 797
THPMA114 – Activities on the Nuclear Data Measurement at the Pohang Neutron Facility Based on Electron Linac 800
THPMA115 – Present Status of the FFAG Accelerator Complex in KURRI for ADS Study 803
THPMA117 – Design and Fabrication of Arups U6 Undulator at PLS 806
THPMA118 – Electron Accelerator of ELV|-|type and their Worldwide Application 809
THPMA121 – Accelerator Based Applications At BARC|-|TIFR Pelletron Accelerator Facility 812
THPMA123 – Analysis and Evaluation of Gamma and Neutron Dosimetry from 48 MeV 7Li on Natural Cu and its Dose Simulation with MCNP 815
THPMA126 – Beam Optics Design for DC High|-|voltage Accelerator of MW Level 818
THPMA127 – Development of L|-|band Electron Accelerator for Irradiation Source 821
THPMA129 – High Power Industrial Electron Accelerator 824
THPMA130 – Introduction of EPICS in VEC & SCC Control Systems 827
THPMA131 – Indian Participation in LHC, SPL and CTF|-|3 Projects at CERN, Switzerland 829

Linear Colliders, Lepton Accelerators and New Acceleration Techniques **832**
FRXMA01 – Progress of the Laser|-|Plasma Acceleration Research at KERI 832
FRXMA02 – Advances in ERLs and Microwave Superconductivity for Lepton Accelerators, Colliders and Light Sources 835
FRXMA03 – Achievement of ATF and its Future Plans 837

Circular Colliders/Linear Colliders **842**
FRYMA01 – Experiences With The Hera Lepton|-|Proton Collider 842
FRYMA02 – Towards a Multi TeV Linear Collider; Drive Beam Generation with CTF3 847

Application of Accelerators, Technology Transfer amp; Industrial Relations **852**
FRAMA01 – The Accelerator Activities of the EUROTRANS Programme 852

Closing Session **857**
FRBMA01 – Particle Colliders and the Quest for Revealing the Hidden Nature of Space and Time 857

Appendices **859**
List of Authors 859
Institutes List 871

FOREWORD

The 4th Asian Particle Accelerator Conference (APAC 2007) was held at Raja Ramanna Centre for Advanced Technology (RRCAT), Indore, India, from January 29 to February 2, 2007. The conference was organized under the auspices of the Asian Committee for Future Accelerators (ACFA). RRCAT, had kept the laboratory itself as the venue of the meeting, so that there could be a stronger interaction between the conference participants and scientists/engineers of the Centre. RRCAT is the biggest accelerator Centre of India and a home to two synchrotron radiation sources Indus-1, a 450 MeV ring and Indus-2, a 2.5 GeV ring, and a few smaller accelerators for various applications. The Centre has a staff of nearly a thousand scientists, engineers and technicians and roughly half of them are engaged in accelerator related activities. For the organization of the conference, we also received valuable support from Bhabha Atomic Research Centre, Mumbai, Variable Energy Cyclotron Centre, Kolkata, Tata Institute of Fundamental Research, Mumbai, and Inter University Accelerator Centre, New Delhi.

The conference was inaugurated by Dr Anil Kakodkar, Chairman, Atomic Energy Commission, and Secretary, Department of Atomic Energy, of Govt. of India. Dr. V. C Sahni, Director, RRCAT welcomed the participants. The scientific program was organized by the APAC 2007 Scientific Program Committee (SPC) chaired by S. Kotaiah, Project Manager, Indus-2, RRCAT. The conference was spread over four and a half days, including plenary, parallel and poster sessions. There were 45 invited talks, 17 contributed oral presentations and 192 poster presentations on various subjects. We would like to thank all the members of the International Organizing Committee, Scientific Program Committee and Local Organizing Committee for their support, commitment and efforts. The success of the conference owes a lot to their efforts. An industrial exhibition was also arranged during the conference. Various companies both Indian and overseas presented their high technology products and services to the delegates in an informal but professional atmosphere.

The informative invited talks as well as interesting poster papers made APAC07 a very successful event. With valuable help from JACoW members, Editorial Board processed all the technical papers and prepared them for publication on the JACoW web site. The proceedings of this conference is available on the JACoW site (www.jacow.org).

Hosting the conference at RRCAT was a pleasure, since we got in our midst a large number of scientists and engineers who shared their valuable knowledge and experiences in accelerator science and technology. Their scientific and technical insights helped the younger participants learn new ideas, as well as, build friendship.

Last but not the least, our thanks are due to all the participants, particularly our overseas guests, who traveled to Indore to attend the conference and who could also sample a bit of the exotic country that is India!

Dr. V.C. Sahni
APAC 07, Chair

Conference Chair

Swarna Kotaiah (Chairman)	RRCAT, India

Program Committee

Swarna Kotaiah (Chairman)	RRCAT, India
Kazunori Akai	KEK, Japan
Rakesh Kumar Bhandari	VECC, India
Vinod Bharadwaj	SLAC, USA
Caterina Biscari	INFN-LNF, Italy
Swapan Chattopadhyay	TJNAF, USA
June-Rong Chen	NSRRC, Taiwan
Yong-Sub Cho	KAERI, Korea
Vinod Chohan	CERN, Geneva
Jinhyuk Choi	PAL, Korea
Rajani Kanta Choudhury	BARC, India
George Dracoulis	ANU, Australia
Akira Goto	RIKEN, Japan
Hitoshi Hayano	KEK, Japan
Alan Jackson	AS, Australia
S. Kailas	BARC, India
Masanobu Kitamura	Spring-8, Japan
Gwo-Huei Luo	NSRRC, Taiwan
Shekhar Mishra	FNAL, USA
Amiya Kumar Mitra	TRIUMF, Canada
Hasan Padamsee	Cornell University, USA
Carlo Pagani	LASA-INFN, Italy
R.G. Pillai	TIFR, India
Thomas Roser	BNL, USA
Amit Roy	IUAC, India
Tsumoru Shintake	RIKEN, Japan
Gurnam Singh	RRCAT, India
Sudjatmoko	NNEA, Indonesia
Hyyong Suk	KERI, Korea
Tran Duc Thiep	VAST, Vietnam
Thiraphat Vilaithong	CMUniv, Thailand
Marion White	APS-ANL, USA
Yoshishige Yamazaki	KEK, Japan
Yasushige Yano	RIKEN, Japan
Kaoru Yokoya	KEK, Japan
Chuang Zhang	IHEP, Beijing
ZiXiang Zhao	CIAE, China

Local Organizing Committee

Swarna Kotaiah (Chairman)	RRCAT, India
Anil Banerji	RRCAT, India
Suresh Chandra Bapna	RRCAT, India
Pramod V. Bhagwat	BARC, India
Alok Chakrabarti	VECC, India
Tripti Sekhar Datta	IUAC, India
Pravin Fatnani	RRCAT, India
Pundalik Rama Hannurkar	RRCAT, India
Arvind Kumar Jain	RRCAT, India
Satish Chandra Joshi	RRCAT, India
Mangesh Gajanan Karmarkar	RRCAT, India
Srinivas Krishnagopal	RRCAT, India
R.V. Nandedkar	RRCAT, India
Pramod Kumar Nema	BARC, India
Shivanand Shridhar Prabhu	RRCAT, India
M. Pravinkumar	RRCAT, India
Anil Rawat	RRCAT, India
Subimal Saha	VECC, India
Samod Kumar Shukla	RRCAT, India
Gurnam Singh	RRCAT, India
Pitamber Singh	BARC, India

PRESENT STATUS OF J-PARC

F. Naito#, KEK, Tsukuba, Japan

Abstract

Japan Proton Accelerator Research Complex (J-PARC) is the scientific facility with the high-intensity proton accelerator aiming to realize 1 MW class of the beam power. J-PARC is the joint project between High Energy Accelerator Research Organization (KEK) and Japan Atomic Energy Agency (JAEA). The accelerator of J-PARC consists of a 181-MeV linac, a 3-GeV Rapid-Cycle Synchrotron (RCS) and a 50-GeV Main Ring synchrotron (MR). The beam energy of the linac will be extended to 400 MeV from 181 MeV in the near future. As all components of the linac were aligned on the beam line, the beam commissioning has been started in November 2006. Furthermore the excitation test of the aligned magnets in the RCS has also been started. The RCS beam commissioning is scheduled to start in September 2007. Finally the beam commissioning for the 50-GeV synchrotron will be started in May 2008.

INTRODUCTION

Japan Proton Accelerator Research Complex (J-PARC) is the high-intensity proton accelerator facility which was formed by joining together the Neutron Science Project (NSP) of Japan Atomic Energy Agency (JAEA) and the Japan Hadron Facility (JHF) Project of High Energy Accelerator Research Organization (KEK). J-PARC is aiming to realize 1 MW class of the beam power, which was the target value of NSP and JHF. J-PARC has three main purposes; (1) the study of the material science using the strong neutron beam; (2) the nuclear/particle physics using several secondary particle beams which include the neutrino; (3) the experiment of the Accelerator-Driven transmutation System (ADS) for the nuclear waste.

The construction of J-PARC has been started at Tokai campus of JAEA, where is about 130 km north-east of Tokyo. At the present stage, J-PARC consists of the following accelerators:

- a 181-MeV normal-conducting linac (H^- beam: Peak;30mA, Width;500μs, Repetition;25Hz),
- a 3-GeV rapid cycle synchrotron ring (RCS), which provides proton beams at 333μA (1MW), and
- a 50-GeV main synchrotron ring (MR), which provides proton beams of 15μA (0.75MW).

The schematic layout of the facility is shown in figure 1. The design energy of the normal-conducting linac is 400-MeV. However it is limited by the budget problem [1]. The energy recovery of the linac from 181 to 400 MeV is the essential subject to be carried out before the second phase

fujio.naito@kek.jp

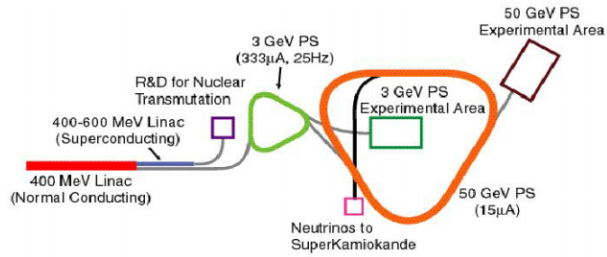

Figure 1: Configuration of J-PARC.

of the project which includes a super-conducting (SC) linac and the ADS. In the second phase the repetition rate of the linac beam is doubled from 25 to 50 Hz. Then one half of the 400-MeV beam from the linac is injected into the RCS, while the other half is further accelerated up to 600 MeV by the SC linac. The 600-MeV beam is transported to the experimental area for the ADS.

The 3-GeV beam from the RCS is mainly used to produce pulsed spallation neutrons and μ-ons for the study of the material and the life sciences.

A part of the beam from the RCS is injected into the 50-GeV synchrotron. The 50-GeV beam is slowly extracted in order to produce the secondary particles for the nuclear/particle physics experiment. It is also fast extracted for the production of the neutrinos, which are sent to the SUPER-KAMIOKANDE detector located 300 km from J-PARC.

The installation of linac has been completed. Thus the linac beam commissioning has been started in November 2006. For the RCS the installation of the components is in progress. In particular, the main magnets have been aligned in the ring. Thus the excitation test of the magnet has been started in December 2006. The linac commissioning and the RCS magnet test are being carried out alternatively. The start time of the beam commissioning of the RCS is scheduled in September 2007. Finally the beam commissioning of the MR will be started in May 2008. The schedule of the J-PARC is shown in figure 2.

LINAC

The linac uses normal-conducting cavities up to 400 MeV, while it uses superconducting cavities (SCC) from 400 to 600 MeV, as shown in figure 3 [1]. The linac is composed of an H^- ion source, an RFQ, a Drift-Tube Linac (DTL), a Separated DTL (SDTL), an Annular Coupled Structure (ACS) linac, an SCC linac and several beam transport lines. All components, except for the ACS and the SCC have been installed in the tunnel. Total number

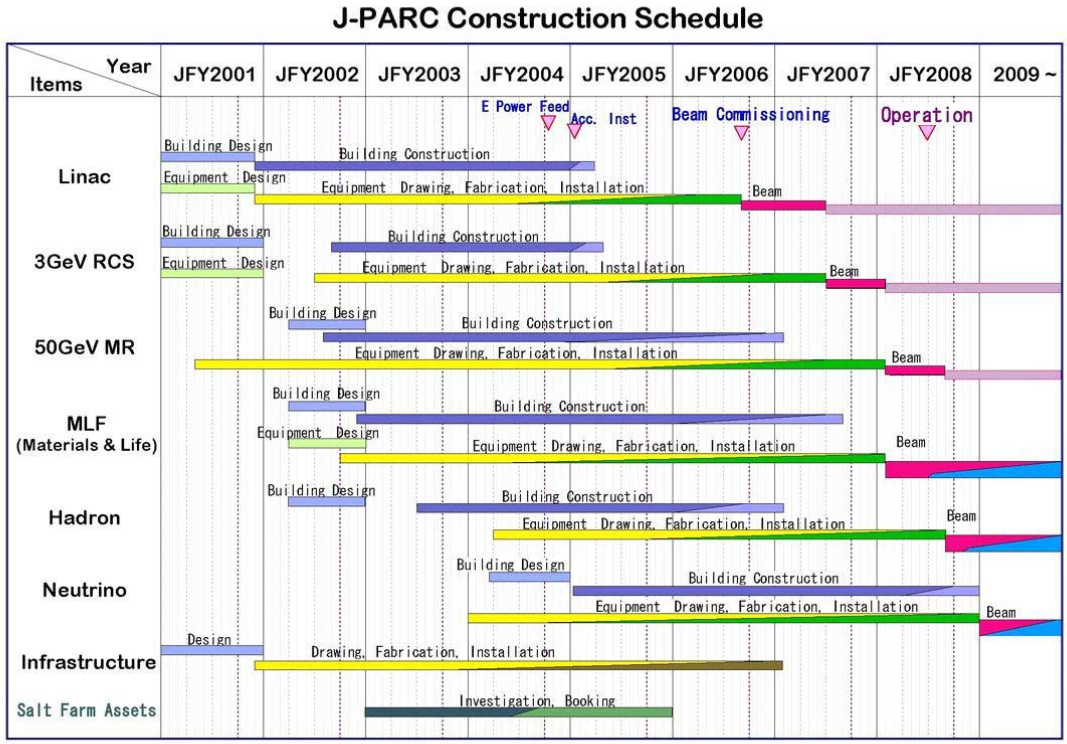

Figure 2: J-PARC Construction Schedule. JFY: Japanese Fiscal Year (It starts April.)

of the DTL and SDTL tank are three and 32, respectively. The SDTL can accelerate the beam up to 191 MeV with 32 tanks. However the last two tanks of them are used as the debunchers in the beam line between the SDTL and the RCS tentatively. As a result, the beam energy is limited to 181 MeV now.

Requirements for the linac up to 400 MeV are summarized as follows;

Current	Average	675 μA
	Peak	50 mA
Pulse	Pulse width	500 μsec
	Chopping ratio	56 %
	RF duty (600 μsec)	3%
Beam	Momentum width	Δp/p = $\pm$0.1% (100%)
	Emittance	3$\sim$5 π mm-mrad (99%)

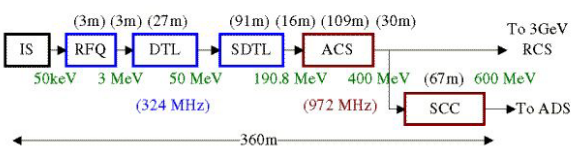

Figure 3: Layout of the proton linac.

H$^-$ ion source

An H$^-$ ion source without cesium has been developed in KEK for JHF project in order to produce a peak current of 30 mA with a pulse length of 500 μsec and a repetition rate of 50 Hz. The extraction voltage of the source is 50 kV.

The H$^-$ ion source has achieved nearly a beam current of 30 mA in maximum with 50 μsec in pulse length and 25 Hz in repetition rate with the filament made of LaB_6. However the study of the source showed that it was very hard to keep the maximum current stable and the filament life was too short for the practical use. Therefore the modification of the H$^-$ ion source is still on going [2].

RFQ

The RFQ has been designed to accelerate 30 mA beam up to 3 MeV with a transmission of more than 90%. The resonance frequency of the RFQ is 324 MHz. The vane is 3 m in length. The contamination of the dipole mode which deflects the beam is minimized by the pi-mode stabilizing loop. The designed performance has been confirmed by the beam study in KEK and the results has been approximately re-confirmed by the beam test in J-PARC in November 2006 [2]. Fine study of the RFQ will be carried out.

MEBT

The 3MeV beam from the RFQ is transferred to the DTL through the MEBT for the matching and diagnostics of the beam. The MEBT consists of the following components:

- 8 quadrupole magnets (Q-mag) with the steering coils,
- two buncher cavities,
- a chopper cavity with two gaps,
- a bending magnet for beam analysis, and
- the beam position monitors in the Q-mags and current transformers.

Figure 4 shows the preliminary data for the chopped beam. The curves show the beam current. Top three lines are the beam current before the chopper. The bottom line shows the chopped beam current. The chopped beam shows the comb pattern. At the moment the rise time of the chopper is slower than that measured at KEK before. Thus we are going to tune the chopper system more.

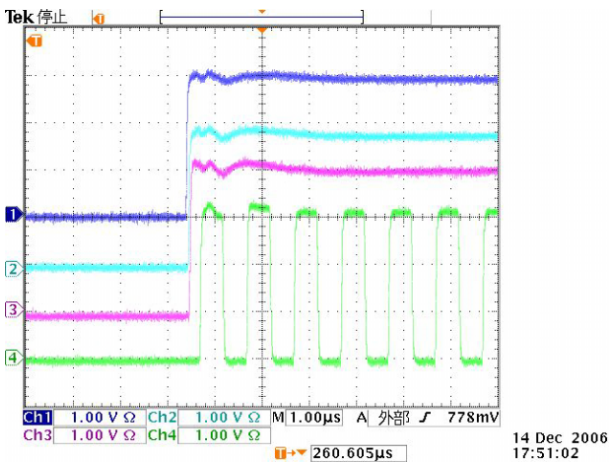

Figure 4: Chopped beam.
Top 3 lines: Output from CTs before the chopper.
Bottom line: Output from CT after the chopper.
(CT: Current Transformer)

DTL

The Alvarez type DTL, which accelerates the H^- beam from 3 MeV to 50 MeV, consists of three independent tanks of which the length is about 9 m. Each tank is composed of three short unit tanks, which are 3 m in length. The resonance frequency of the DTL is 324 MHz. The accelerating field in the tank is stabilized by using the post-couplers.

Since each drift tube (DT) in the DTL accommodates the electromagnetic quadrupole, the DTs have been assembled in the tank very precisely. Maximum deviation of the DT bore center position from the beam axis is approximately less than $\pm 50\mu$m for both x- and y-directions [2]. Overall alignment error of the DT from the beam axis for the DTL section is approximately less than 0.1 mm in x-y plane [3]. The aligned DTL is shown in figure 5.

Figure 5: DTL1,2,3 in the tunnel

As the high-power conditioning of the DTL was completed upto the 1.2 times the desired power level with the repetition rate of 25 Hz and the rf pulse length of 600 μs, the beam commissioning of the DTL has been started in December 2006. The beam accelerated by the DTL-1 (the peak current is 5 mA, the beam pulse width is 20 μs, the repetition rate is 5 Hz, the beam energy 19.7 MeV) passed through the following whole cavities and the beam duct to the beam dump without an observable loss. The initial test was done without the correction of the beam direction by the steering magnet for the DTL and SDTL. It proves that the alignment accuracy of the linac components is sufficiently high. The tuning for DTL-2 and 3 has been roughly carried out. The preliminary result of the phase scan of the DTL-1 is shown in figure 6. The measured data are consistent with the results of the simulation.

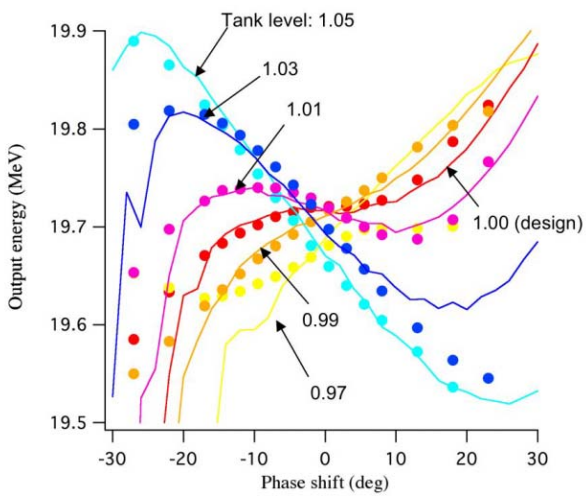

Figure 6: DTL1 phase scan result (Preliminary)
Solid lines are the results of the simulation.
Circles are measured data.

SDTL

The separated DTL (SDTL) has no focusing quadrupole in the drift tube. The doublet quadrupole magnet is set between the adjacent tanks. The resonance frequency is also 324 MHz. It consists of the 32 tanks and it can accelerates the H^- ion beam from 50 to 191 MeV. However the beam energy is limited to 181 MeV because the last two tanks have been installed as the debuncher in the beam line as mentioned above.

The progress of the rf conditioning of the SDTL is relatively slow because the accelerating field of the SDTL is much higher than that of the DTL and one klystron feeds the power to two SDTL tanks. The conditioning status is shown in figure 7. Although the conditioning is not completed, it is possible to accelerate the beam if the pulse length of the beam is short. Therefore the first beam acceleration test to 181 MeV was started with the short pulse beam (5 mA of the peak current, 20 μs of the pulse width and 2.5 Hz of the repetition rate) on January 17, 2007. After the adjustment of the beam monitor system, it has been confirmed that the beam achieved the energy of 181 MeV on January 24, 2007. The test is still continued.

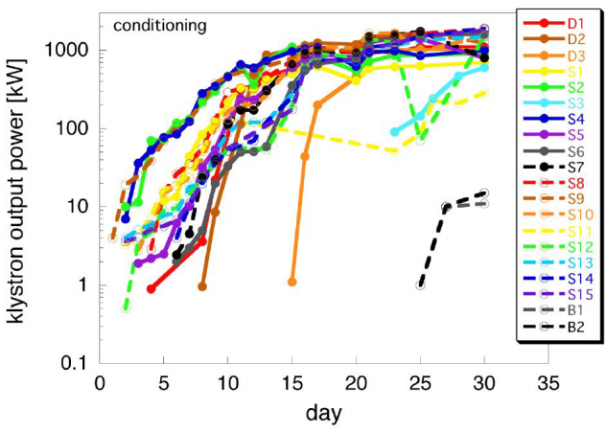

Figure 7: Conditioning history of DTL & SDTL.
D1,2,3: Klystron power for the DTL 1,2 & 3.
Sn (n:integer): power for SDTL(2n-1) & SDTL(2n)
B1,2: Output power for the debuncher 1 & 2.

ACS

J-PARC adopted the Annular Coupled Structure (ACS) as the normal conducting coupled-cavity linac for 191-400 MeV part. The operating frequency is 972 MHz. The 23 modules will be constructed. The ACS has good axial symmetry which is the desirable property for the linac structure. As the result of the many development for the construction, the first practical ACS type debuncher has been assembled and tested by the high-power RF. Figure 8 shows the results of the rf conditioning history of the ACS debuncher [4]. Maximum applied power was 1.2 times the required power. The conditioning has been completed without any trouble.

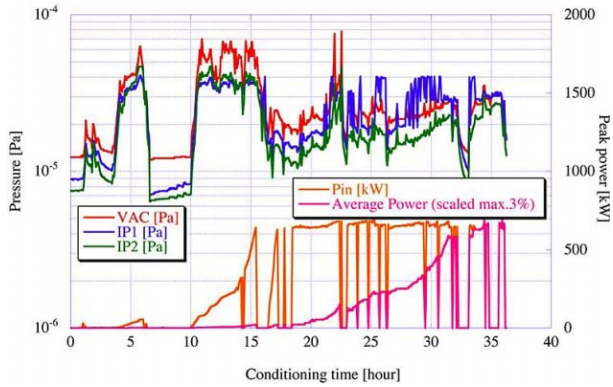

Figure 8: Conditioning history of ACS debuncher.
Upper lines: vacuum level shown in the left ordinate .
Lower lines: Power level. (Orange lines shows the peak power which is denoted in the right ordinate. Pink line show the average power, which is equal to 3% of the value shown in the right ordinate.)

RF system

The 324-MHz high-power pulsed klystron with a modulating anode has been developed for the RFQ, the DTL and the SDTL. Maximum power of 3 MW with the rf pulse width of 600 μsec and 50-Hz repetition rate is required. The results of the high-power test of the klystron achieved the requirements. It is shown in figure 9. The fine tuning of the low-level feed-back system for the klystron is being done with the beam in order to keep the electric field accuracy less than $\pm 1\%$ in amplitude and ± 1 degree in phase.

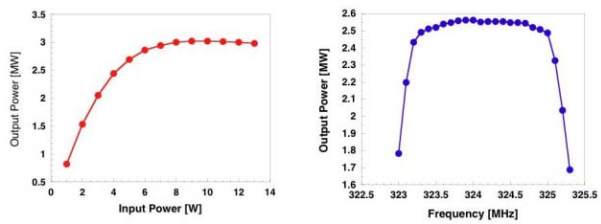

Figure 9: Properties of the 324-MHz klystron.
(Left) Output power vs. input power. (HV=105kV.)
(Right) Frequency dependence of the klystron output.

The development of the 972-MHz modulating-anode klystron for the ACS cavity has been also completed. It was used for the rf-conditioning of the ACS debuncher. The required power for driving the standard ACS cavity is 2.5 MW.

RCS

The status of the rapid cycle synchrotron (RCS) is as follows;

- The dipole, quadrupole and sextupole magnets have been installed with the ceramic beam duct;

- The magnet excitation test has been started;
- A part of the components of the beam injection region has been installed;
- Installation of the RF cavities has been started in January 2007.

The issues for the RCS are concentrated in the injection region. For instance the check of mechanical consistency of each component for the RCS injection region shown in figure 10 is not completed because it is so complicated. Now the consistency is being checked. Furthermore the development of the long-lived beam-stripping foil is the special issue for RCS. Recently the hybrid boron doped carbon foil is found as a candidate of the stripping foil. The test of the foil is being done by irradiation of 650 kV H^- beam accelerated by the Cockcroft-Walton generator in the KEK [5].

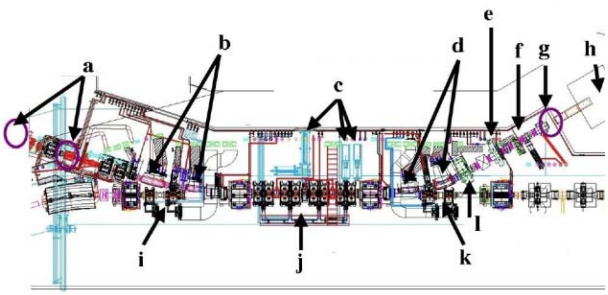

Figure 10: RCS beam injection region.
(a) vertical painting magnet, (b) injection septum magnet, (c) drivers for the stripping foil, (d) septum magnet for H0 dump, (e) vertical steering magnet, (f) horizontal steering magnet, (g) current monitor, (h) dump for H0 beam (H0 dump), (i) painting bump magnet, (j) bump magnet for beam shift, (k) painting bump magnet, (l) Q-magnet for H0 dump

MR

Main tunnel of the MR has been completed [6, 7]. The construction of the experimental area and the beam lines are still continued. In the tunnel, more than half of the (dipole, quadrupole and sextupole) magnets have been installed as shown in figure 11 [8, 9].

For the injection/extraction septum and kicker magnet systems, performance tests are now being carried out intensively. The magnet systems will be installed after that their reliability will be confirmed enough for the practical use.

Some magnetic alloy cores of the RF cavity were seriously damaged under high rf power loading as reported in Ref [10]. The problem is being solved carefully, and long term continuous operation of the cavities is now in progress.

Figure 11: Installed MR magnet.
Blue: Dipole magnet, Yellow: Quadrupole magnet.

CONCLUSION

The beam commissioning of the J-PARC linac has been started in November 2006. The beam accelerated by the DTL has passed through in the following whole equipments (DTLs, SDTLs and magnets) and arrived on the beam dump without the correction by the steering magnet. Although the tuning of the SDTL system is still continued, it has been confirmed that the beam accelerated by the SDTL achieved the energy of 181 MeV. Furthermore the excitation test of the aligned magnet in the RCS tunnel has also been started. For the MR the magnet installation has been started. The beam commissioning for the RCS and the MR is scheduled for September 2007 and May 2008, respectively.

REFERENCES

[1] Y. Yamazaki, "Status of the J-PARC linac, initial results and upgrade plan", Linac04, Lübeck, Germany, 554(2004)

[2] linac group member, private communication

[3] T. Morishita, et. al, "DTL/SDTL installation and alignment of J-PARC linac", (in Japanese) Proc. of 3rd Annual Meeting of Particle Accelerator Society of Japan, Sendai, Japan, 124(2006)

[4] H. Ao, et. al, "High-power test of the first ACS cavity for J-PARCV linac", (in Japanese) Proc. of 3rd Annual Meeting of Particle Accelerator Society of Japan, Sendai, Japan, 376(2006)

[5] I. Sugai and A. Takagi, private communication

[6] H. Kobayashi et al., "Present Status of J-PARC MR-Synchrotron", in this conference.

[7] M. Miyahara et al., "Tunnel Construction for J-PARC MR and Related Issues", in this conference.

[8] M. Yoshioka et al., "Installation and assembling of Accelerator components for J-PARC 50 GeV Synchrotron", in this conference.

[9] M. Shirakata et al., "The Magnet Alignment Method For The J-PARC Main Ring", in this conference.

[10] H. Kobayashi, "Present tatus of the J-PARC accelerator ", Proc. EPAC06 to be published.

COMMISSIONING EXPERIENCE OF SNS*

M.A. Plum representing the beam commissioning team, Spallation Neutron Source,
Oak Ridge National Laboratory, Oak Ridge, TN, U.S.A.

Abstract

The Spallation Neutron Source accelerator complex consists of a 2.5 MeV H^- front-end injector system, a 186 MeV normal-conducting linear accelerator, a 1 GeV superconducting linear accelerator, an accumulator ring, and associated beam transport lines. The linac was commissioned in five discrete runs, starting in 2002 and completed in 2005. The accumulator ring and associated beam transport lines were commissioned in two runs in January-February and April 2006. With the completed commissioning of the SNS accelerator, the facility has begun initial low-power operations. In the course of beam commissioning, most beam performance parameters and beam intensity goals have been achieved at low duty factor. A number of beam dynamics measurements have been performed, including emittance evolution, transverse coupling in the ring, beam instability thresholds, and beam distributions on the target. The commissioning results, achieved beam performance and initial operating experience of the SNS linac will be presented.

INTRODUCTION

The Spallation Neutron Source (SNS) is a short pulse neutron scattering facility located on the campus of the Oak Ridge National Laboratory in Oak Ridge, TN, USA. The construction project was a partnership of six US DOE national laboratories, each of which had responsibility for designing and manufacturing a portion of the facility. At 1.4 MW of proton beam power on target, the SNS will operate at beam powers a factor of eight beyond that which has been previously achieved [1]. The SNS baseline parameters are summarized in Table 1.

Table 1: SNS Design Parameters

Beam Power on Target	1.4 MW
Beam Energy	1.0 GeV
Linac Beam Macropulse Duty Factor	6.0%
Beam Pulse Length	1.0 msec
Repetition Rate	60 Hz
Chopper Beam-On Duty Factor	68%
Peak macropulse H^- current	38 mA
Average Linac H^- current	1.6 mA
Ring accumulation time	1060 turns
Ring bunch intensity	1.5×10^{14}
Ring Space-Charge Tune Spread	0.15
Beam Pulse Length on Target	695 nsec

The SNS accelerator complex [2] consists of a 2.5 MeV H^- injector [3], a 1 GeV linear accelerator [4], an accumulator ring, and associated beam transport lines [5]. The injector (also called the Front-End Systems) consists of an H^- volume ion-source with 50 mA peak current capability [6], a Radio-Frequency Quadrupole and a Medium Energy Beam Transport line for chopping and matching the 2.5 MeV beam to the linac. The linear accelerator consists of a Drift Tube Linac (DTL) with 87 MeV output energy, a Coupled-Cavity Linac (CCL) with 186 MeV output energy, and a Superconducting RF Linac (SCL) with 1 GeV output energy [7]. At full design capability the linac will produce a 1 msec long, 38 mA peak, chopped beam pulse at 60 Hz for accumulation in the ring. The linac beam is transported via the High Energy Beam Transport (HEBT) line to the injection point in the accumulator ring where it is multi-turn charge-exchange injected over 1060 turns and compressed to less than 1 microsecond, reaching an intensity of 1.5×10^{14} protons per pulse. When accumulation is complete the extraction kicker fires during the 250 nsec gap to remove the accumulated beam in a single turn and direct it into the Ring to Target Beam Transport (RTBT) line, which takes the beam to a liquid mercury target. Staged commissioning of the accelerator complex, completed May 2006, was performed in seven discrete beam commissioning runs (shown in Figure 1) which were devoted to commissioning the i) Front-End, ii) Drift Tube Linac Tank 1, iii) Drift Tube Linac Tanks 1-3, iv) Coupled Cavity Linac, v) Superconducting Linac, vi) High-Energy Beam Transport Line and Accumulator Ring, and vii) Ring to Target Beam Transport Line and the mercury target. Table 2 summarizes the main beam commissioning results, comparing beam measurements with design goals. Ramp up to high power operation is now in progress.

LINAC COMMISSIONING

Linac commissioning results have been presented before [8], but for completeness we will provide a brief summary here.

The linac was successfully commissioned in five discrete runs from December 2002 to August 2005. The warm linac commissioning progressed smoothly and measured beam parameters are in good agreement with expectations [3]. RF phase and amplitude set points were determined using two methods (energy degrader / Faraday Cup acceptance scan and phase scan signature matching) that gave consistent results. We now use the phase scan signature matching method exclusively.

The superconducting linac commissioning proceeded much faster than expected. Before commissioning began there was some uncertainty in the algorithms to set the phases of the rf cavities due to concerns with beam loading, but the simple procedure of fitting the time of flight vs. cavity phase with a sinusoidal curve, for 10 mA

* ORNL/SNS is managed by UT-Battelle, LLC, for the U.S. Department of Energy under contract DE-AC05-00OR22725

peak current, 20 μs-long beam pulses, worked very well and the initial tune up was completed in just nine days [8]. For higher peak currents, in addition to feedback control of the cavity amplitude and phase, feed forward has proven essential for achieving the required amplitude and phase regulation in the presence of heavy beam loading. Typical amplitude and phase regulation errors are better than 1% and 1 degree respectively.

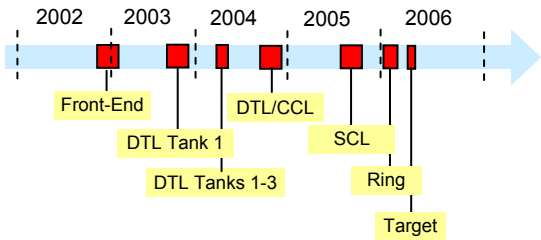

Figure 1: SNS Beam Commissioning Schedule.

Table 2: Beam parameters achieved to date

Parameter	Design	Measured
Linac Transverse Output Emittance [π mm-mrad (rms, norm)]	0.4	0.3 (H) 0.3 (V)
CCL1 Bunch Length [deg]	3	4
Linac Peak Current [mA]	38	>38
Linac Output Energy [MeV]	1000	952
Linac Average Current [mA]	1.6	1.05 (DTL1) 0.007 (SCL)
Linac H^-/ions/pulse	$1.6x10^{14}$	$1.0x10^{14}$
Linac pulse length/rep rate/duty factor [msec/Hz/%]	1.0/60/6.0	1.0/60/5.4 (DTL1) .85/15/.54 (SCL)
Ring intensity	$1.5x10^{14}$	$9.6x10^{13}$
Extracted beam intensity	$1.5x10^{14}$	$9.6x10^{13}$
Beam intensity on target	$1.5x10^{14}$	$5.3x10^{13}$

The linac output energy has ranged between 860 and 950 MeV, depending on the cavity amplitude set points and the number of off-line cavities. At the end of the last running period (Oct – Nov/06) ten of the 81 cavities were off line. One was off line because the tuner range was not set properly to bring the cavity on resonance at the present operating temperature of 4.4 °K. This tuner will be reset during a future maintenance period. The remaining nine cavities were off line due to unexpected signals observed from the higher order mode couplers due to a combination of fundamental power coupling and electron-related or vacuum activity. To be conservative we decided to turn off these cavities until the phenomena are better understood. The SCL has proved to be remarkably robust to changes in cavity amplitudes and the number of off-line cavities, even for up to three consecutive cavities off line.

In December 2006, 60 Hz rf operation was demonstrated for the first time for a full set of four cavities in a cryomodules at 4.4 °K. This was made possible by a recent upgrade to one of the High Voltage Converter Modulators (HVCMs) that provide the high voltage for the klystrons. The other cryomodules will be tested at 60 Hz as the remaining HVCMs are upgraded (expected completion date for the upgrades is May 2007). The maximum repetition rate for beam delivery achieved to date is 15 Hz (the beam power at this time was 60 kW).

Except for the MEBT, where we can use a slit and collector to measure emittance, we use multiple wire scanners to measure the rms emittance and Twiss parameters. In Table 3 we show a comparison between the measured and design transverse emittance for the different parts of the linac.

Table 3: Comparison of measured and expected rms transverse beam emittances. The estimated measurement error is about 20%.

Location	**Measured ε_x, ε_y π-mm-mrad (rms, norm)**	**Design ε_x, ε_y π-mm-mrad (rms, norm)**
MEBT Entrance	0.22, 0.25	0.21
CCL Entrance	0.22, 0.25	0.33
SCL Entrance	0.27, 0.35	0.41
Linac Dump	0.26, 0.27	0.41
HEBT	0.50, 0.37	0.45

RING COMMISSIONING

Much of the ring commissioning was performed using single minipulse injection, where the beam from the ion source is chopped to allow just a single turn (~690 ns bunch length) of beam to be accelerated. For such a beam pulse the power (~12 W) is low enough that beam loss is not a concern, and because beam is injected into the ring with an offset relative to the closed orbit we are able to measure the betatron tune, closed orbit, injection position and angle, magnet polarities and strengths, etc.

The initial stage of the ring commissioning progressed very quickly. In early January, in anticipation of receiving permission to commission the ring, we tuned up the linac to the linac beam dump. On January 12, 2006 we received the final approval from the US Department of Energy to deliver beam from the linac to the ring extraction beam dump. On January 13 we tuned up the 162-m long beam transport line from the linac to the ring injection beam dump. On January 14 we injected single minipulses into the ring, and by January 15 we achieved more than 1000 turns of beam storage. On January 16 we extracted the beam from the ring and directed it to the ring extraction dump 75 m downstream of the ring, and also demonstrated accumulation of seven minipulses. On January 26 we increased the beam intensity to $1.3x10^{13}$ protons per pulse (ppp) to meet our commissioning goal of $>1x10^{13}$ ppp. By the end of the commissioning period

on February 13 we demonstrated accumulation of $1x10^{14}$ ppp of unbunched beam and also made some preliminary measurements of beam instability thresholds (more on this later).

The second ring commissioning period ran from April 8 to May 31. On April 28 we delivered $1.6x10^{13}$ ppp to the spallation target to meet the CD-4 goal needed to successfully mark the end of the construction and initial commissioning of the SNS facility. The entire project was thus completed ahead of schedule and under budget.

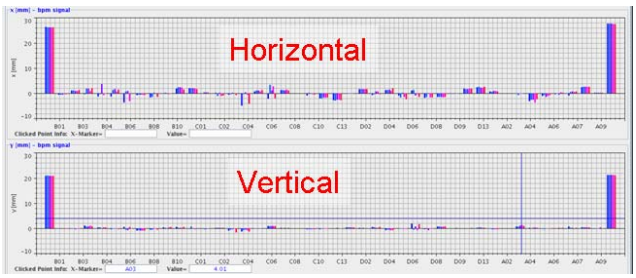

Figure 2: Example of closed orbit in the ring. The large position excursions at the left and right edges of the plot are due to the injection kickers upstream and downstream of these BPMs. For both plots the vertical axis runs from -10 to +30 mm.

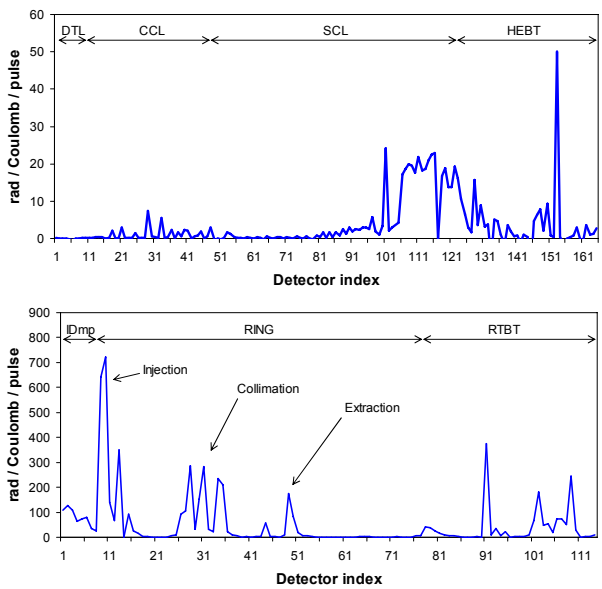

Figure 3: Beam loss monitors in the linac and ring. The beam parameters were 30 kW beam power, 5 Hz, 888 MeV.

During the July and August 2006 running period we began routine beam delivery for neutron production. After the September outage beam delivery resumed for the October – November running period, and the 10 kW administrative limit imposed by the Accelerator Readiness Review process was lifted on 8/Nov/06 (the limit now in place is 100 kW). By the end of November we had separately demonstrated accumulation of $9.6x10^{13}$ ppp and 60 kW of beam power (at 15 Hz) on target, and for routine operations we achieved 30 kW at 5 Hz on target. A typical closed orbit measurement for the ring is shown in Fig. 2, and a typical beam loss profile is shown in Fig. 3.

ISSUES ENCOUNTERED

Ring injection and injection dump beam line

The ring injection section includes four chicane magnets that merge the incoming H^- beam with the circulating proton beam at the charge-exchange stripper foil. These same magnets also direct the H^- beam that misses the foil, and the H^0 beam partially stripped by the foil, to the injection dump beam line. Early in the ring commissioning period we discovered that the nominal chicane magnet set points caused a large (~14 mm) closed orbit distortion and poor beam injection into the ring. This was traced to a design change made in 2000 that had the unintended consequences of the closed orbit offset and also caused large beam losses in the ring injection dump beam line. We were able to adjust the magnet settings to give good injection into the ring and a good closed orbit, but we were not able to simultaneously obtain good transmission of the H^0 and H^- waste beams in the injection dump beam line. A short term solution is now in place where we are using a primary stripper foil that is 5 mm wider and 5 mm taller. This foil fully intercepts the incoming H^- beam so there is little to no H^- beam entering the injection dump beam line. This allows the beam line to be optimized for just a single beam, and reduces the beam loss to levels that should allow us to increase the beam power on target to more than 100 kW.

The mid term solution involves shifting the fourth chicane magnet beam left to place the H^0 and H^- beams in the good field region of the magnet; enlarging the gap of the injection dump septum magnet; adding a C-magnet just downstream of the septum magnet to allow individual control over the H^0 and H^- beam trajectories; and adding a wire scanner profile monitor, a beam position monitor, and a beam current monitor to the diagnostics suite. These modifications should allow the beam power on target to be increased to several hundred kW.

The final solution, needed to raise the beam power to the full 1.4 MW, will depend on the outcome of further modelling and beam measurements. It will likely involve adding a second quadrupole magnet to the injection dump beam line.

Tilted beam on target

A late addition to the target commissioning plan involved mounting a temporary view screen to the face of the neutron spallation target to measure the beam position and distribution on the target. The last permanent beam diagnostic (a harp with three signal wire planes) is 9.5 m upstream of the target, so without the view screen the beam distribution and position would have to be extrapolated based on upstream beam position monitors, wire scanners, the harp, and knowledge of the beam transport. The view screen turned out to be an invaluable

tool during commissioning and operation that survived far longer than expected, and we removed it only when necessary to increase the beam power above 10 kW. An example image is shown in Fig. 4.

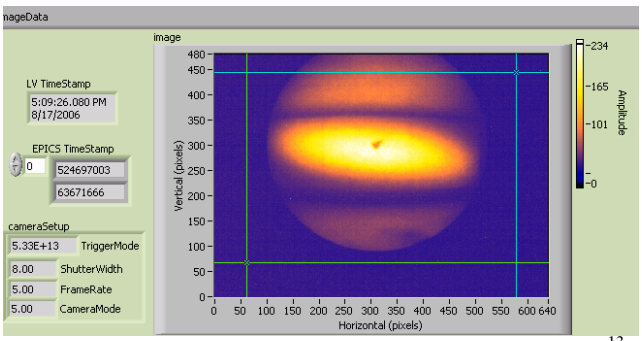

Figure 4: Image from the target view screen, for 5.3×10^{13} ppp extracted from the ring.

The beam distribution on the target shows a slight tilt of ~3 deg. We initially suspected this was due to transverse coupling in the ring, but after further beam measurements and after correcting the coupling we concluded this is not the source of the tilt. We now believe the most likely source is transverse coupling in the ring to target (RTBT) transport beam line, probably due to slight misalignments in the quadrupole magnets. Work is now in progress to develop a beam diagnostic that can be permanently mounted to the target face to provide beam position and distribution information for full power beams. It will be based on light emission, for example from red-hot tungsten wires similar to the SINQ profile monitor [9].

Beam loss

Beam loss is a primary constraint on our ramp up to higher beam power. The high-loss points during 2006 operations are shown in Fig. 3 and in Table 4 along with the highest activation levels (measured at 30 cm five days after the conclusion of 30 kW operations but less than one day after high-intensity beam experiments).

Table 4: Activation measurements at high-beam-loss locations.

Location	**Activation (mrem/h)**
Coupled-cavity linac	8
Ring injection section	20
Injection dump beam line	5
Ring collimation section	32
Ring extraction section	20
Ring-to-target transport line (RTBT)	25

We believe the beam loss in the couple cavity linac (CCL) is due to too few beam position monitors (BPMs) and beam loss monitors (BLMs). The lack of diagnostics made it possible to center the beam at the BPMs and minimize the beam loss at the BLMs, yet still allow substantial beam loss that could not be detected. To alleviate this problem 21 BLMs were added to the CCL in the Dec/06 – Jan/07 outage.

Most of the beam loss in the ring injection section can be explained by beam scattering in the primary and secondary stripper foils. There is also poorly-understood beam loss that occurs 10 m downstream of the primary stripper foil, where there is an aperture reduction. This latter beam loss will be investigated in the near future. The beam loss due to the primary stripper foil is close to nominal but we still expect some additional modest reductions after further beam experiments. We plan to reduce the losses due to the secondary stripper foil by installing a thinner foil. The present secondary foil is 25 mg/cm^2 carbon-carbon, but it is much thicker than necessary. It must only be thick enough to be self supporting.

The beam loss in the ring collimation section is expected since that is intentionally the limiting aperture in the ring. We believe that the majority of the beam loss in the extraction section is due to beam in the gap, caused by poor beam chopping due to the medium energy beam transport chopper that is not yet functional. The beam loss in the RTBT occurs just upstream of the dipole magnet that directs the beam away from the extraction dump and toward the target. We believe this loss is due to a combination of large vertical tails on the beam and a large vertical betatron function at the same place as an aperture reduction. To address this issue we will alter the RTBT quadrupole magnet set points to reduce the betatron function in the vicinity of the aperture reduction and also work to identify the cause of the vertical tails.

HIGH INTENSITY STUDIES

One of the biggest uncertainties in high power operation of the SNS ring is the threshold of the e-p instability, since it is difficult to confidently predict. Early in the ring commissioning period we set up the ring to create conditions most favourable for the onset of instabilities – an unbunched, un-extracted coasting beam with near-zero chromaticity that filled the ring circumference (although the bunchers were turned off, the rf buncher cavities were not shorted, and there may have been some longitudinal structure imposed on the beam due to beam excitation of the cavities). Under these conditions, at the nominal betatron tunes $Q_x = 6.23$, $Q_y = 6.20$, we observed [10] two instabilities. Under certain conditions both instabilities can occur in the same shot, as shown in Fig. 5.

The first instability, observed at 3, 6, and 12 μC beam charge and after storing the beam for several milliseconds, is consistent with an impedance-driven instability due to the extraction kickers. The measured growth rate and frequency spectrum is consistent with our expectations and the threshold is high enough that it

should not interfere with full power 1.4 MW operations under nominal conditions.

The second instability, observed at 4, 8, and 16 μC beam charge, and again after storing the beam for several milliseconds, is consistent with an e-p instability. Although the threshold for nominal operating conditions cannot be directly extrapolated from these measurements, based on similar measurements at PSR [11] we believe that it is unlikely that this instability will interfere with full power operations.

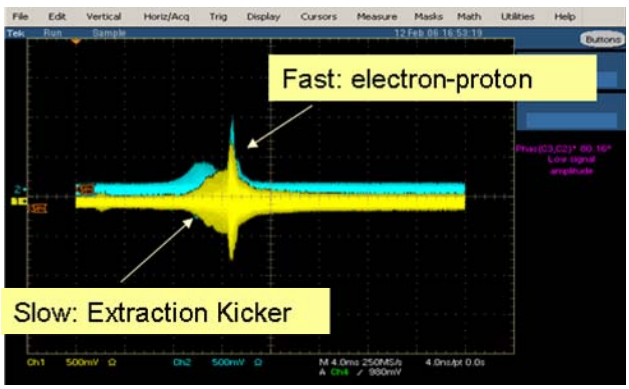

Figure 5: Horizontal (yellow) and vertical (blue) oscillations observed after storing the beam for several milliseconds. Two different instabilities are simultaneously present for this shot.

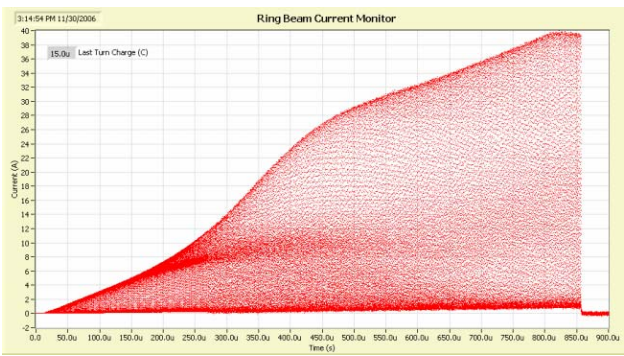

Figure 6: Ring beam current monitor showing accumulation of 9.6×10^{13} ppp.

We observed a third instability after lowering the betatron tune to slightly below the integer ($Q_y \approx Q_y \approx 5.8$) to create conditions favourable for the resistive wall instability. The frequency of this instability is about 191 kHz, as expected, with a growth rate (1.2 msec for 6 μC beam charge) consistent with previous estimates of the impedance of the injection kickers together with the vacuum pipes. As with the other two instabilities, we do not expect this one to interfere with normal operations.

No instabilities have been observed thus far under the normal condition of bunched beam in the ring, and initial indications are that any instabilities under normal conditions will have thresholds high enough that they will not interfere with full-power 1.4 MW operations. In November 2006 we accumulated 9.6×10^{13} ppp (830 turns) of bunched beam and stored it for 1.06 ms (1100 turns) and we did not observe any evidence of a beam instability.

BEAM POWER RAMP UP

So far the SNS has remained on track for the beam power ramp up plan that was set forth in 2002. That plan calls for reaching 3 kW operations in fiscal year (FY) 2006, 50 kW and 150 kW in the first and second halves of FY2007, 800 kW in FY2008, and the final power of 1400 kW in FY2009. The maximum beam power achieved to date is 60 kW at 15 Hz. In this next running period, from mid-January through March 2007, we plan to demonstrate (not necessarily concurrently) 90 kW and 30 Hz.

REFERENCES

[1] C. Prior et al., "ISIS Megawatt Upgrade Plans," PAC 2003, Portland, OR, May 2003, p. 1527.
[2] N. Holtkamp, "Commissioning Highlights of the Spallation Neutron Source," EPAC 2006, Edinburgh, p. 29.
[3] A. Aleksandrov, "Performance of SNS Front End and Warm Linac" LINAC 2006, Knoxville, TN, Aug. 2006.
[4] D. Jeon, "Beam Dynamics in the Spallation Neutron Source Linac," PAC 2003, Portland, OR, May 2003, p. 107.
[5] J. Wei, "Spallation Neutron Source Ring -- Status, Challenges, Issues, and Perspectives," PAC 2003, Portland, OR, May 2003, p. 571.
[6] R.F. Welton et al., PAC 2005, Knoxville, TN, May 2005, p. 472.
[7] I.E. Campisi, "Testing of the SNS Superconducting Cavities and Cryomodules," PAC 2005, Knoxville, TN, May 2005, p. 34.
[8] S. Henderson, "Commissioning and Initial Operating Experience with the SNS 1 GeV Linac" LINAC 2006, Knoxville, TN, Aug. 2006.
[9] R. Dölling et al., "Beam Diagnostics at High Power Proton Beam Lines and Targets at PSI," DIPAC 2005, June 2005, Lyon, p. 228.
[10] V.V. Danilov et al., "Accumulation of High Intensity Beam and First Observations of Instabilities in the SNS Accumulator Ring," ICFA-HB2006, Tsukuba, Japan, May-June 2006.
[11] R. Macek, "Status of the Experimental Studies of the Electron Cloud at the Los Alamos Proton Storage Ring," PAC 2003, Portland, OR, May 2003, p. 3089.

OVERVIEW OF ENERGY-RECOVERY LINACS

R. Hajima# JAEA-ERL, Tokai, Ibaraki 319-1195, Japan

Abstract

Energy-recovery linacs (ERL), which is able to produce a high-power electron beam with high brightness, has been developed for high-power free-electron lasers. Now, ERL is also considered as a future X-ray light source, where coherent X-ray and ultrashort X-ray pulses are realized. In this paper, we overview current R&D status of ERLs in the world, and give a detail description of the ERL light source project in Japan.

INTRODUCTION

An energy-recovery linac (ERL), which is able to generate a high-brightness electron beam with high-average current, has been developed for a driver of high-power free-electron laser. Now, the ERL is expanding its role and contribution to various fields: next-generation X-ray light sources, high-flux gamma-ray sources, colliders for high-energy physics, an electron-cooler for ion beams, etc. World-wide efforts of R&Ds are launching towards such future ERLs.

For an example of ERL, figure 1 shows a 17-MeV ERL-FEL at Japan Atomic Energy Agency (JAEA). The ERL consists of an injector, a merger, a main linac and a return loop. An electron bunch generated by injector is further accelerated by main linac and delivered to the FEL undulator. If we assume a typical conversion efficiency of 1% from the electron energy to the laser energy, the electrons energy of 99% remains unused after the FEL undulator. The energy-recovery is a technique to recycle this unused electron energy to improve the total efficiency of the FEL from the electricity power to the laser power. This recycling of the unused electron energy is possible by decelerating the electrons at the main linac as seen in fig.1. The decelerated electron beam goes to a beam dump. As a result, the energy-recovery technique enable one to accelerate high-power electron beams with small capacity of RF sources.

In the ERL, a fresh electron bunch is injected to a main linac for acceleration at any time, and we can keep an electron beam of small emittance and/or ultrashort pulse duration. This flexible manipulation of transverse and longitudinal dimension of electron bunch is a common feature to linear accelerators, and generation of high-power CW beams is a strong point of storage rings. Thus, the ERL has advantages of linear accelerators and advantages of storage rings simultaneously. Due to these excellent advantages, the energy-recovery linac is now considered as one of the important topics in accelerator science and technology, and a session for ERL has been regularly organized in xPAC since PAC-2003. In this paper, we overview current status of ERLs in the world, and give a detail description of the ERL light source project in Japan.

#hajima.ryoichi@jaea.go.jp

HIGH-POWER FELS

From a historical point view, concept of energy-recovery linac was first proposed for an electron collider in 1965, in which electrons are decelerated for energy recovery after passing an interaction point[1]. However, the ERL technology has been developed for high-power free-electron lasers. In 1980s, experimental attempts for increasing FEL power by energy-recovery linacs were conducted at Los Alamos National Laboratory[2] and Stanford University[3]. These early experiments indeed had a certain impact on ERL development, but they revealed the fact at the same time that the ERL requires sophisticated technology of superconducting accelerator. An energy-recovery linac for practical use was first demonstrated at JLAB IR-demo FEL (Thomas Jefferson National Accelerator Facility) [4], which employed CEBAF-type superconducting cavities. Following this first demonstration of ERL-FEL, two ERL-FELs were built in JAERI (Japan Atomic Energy Research Institute) and BINP (Budker Institute of Nuclear Physics).

In JAERI, a research program towards a high-power free-electron laser started in 1987. In the research program, a 17-MeV superconducting linac was developed and a high-power FEL lasing was demonstrated with the linac[5]. For the further enhancement of the FEL power, the linac was modified into an energy-recovery configuration. Design of the ERL started in 1999, and after a construction period, demonstration of ERL was completed in 2002[6]. In order to make best use of energy-recovery, the injector current has been enlarged with keeping the same RF sources for the main linac. The original injector equipped with two 6 kW solid-state amplifiers have been replaced by two 50 kW IOTs, and the repetition rate of the gun pulser has also been doubled from 10 MHz to 20 MHz. The injector beam current of 10 mA is now available (originally 5 mA) [7]. The FEL power has reached to 0.75 kW with an electron beam of 136 kW (17 MeV, 8 mA). The FEL power is now restricted by energy acceptance of the return loop [8].

The ERL at BINP is a unique facility based on a normal conducting accelerator of 12 MeV operating at 180 MHz. An FEL for high-power THz radiation was developed utilizing this ERL. The first lasing of the FEL was achieved in 2003 and laser power of 20 W has been obtained in THz region[9]. They are also constructing the second FEL with a 40-MeV electron beam, which will be the first multi-turn

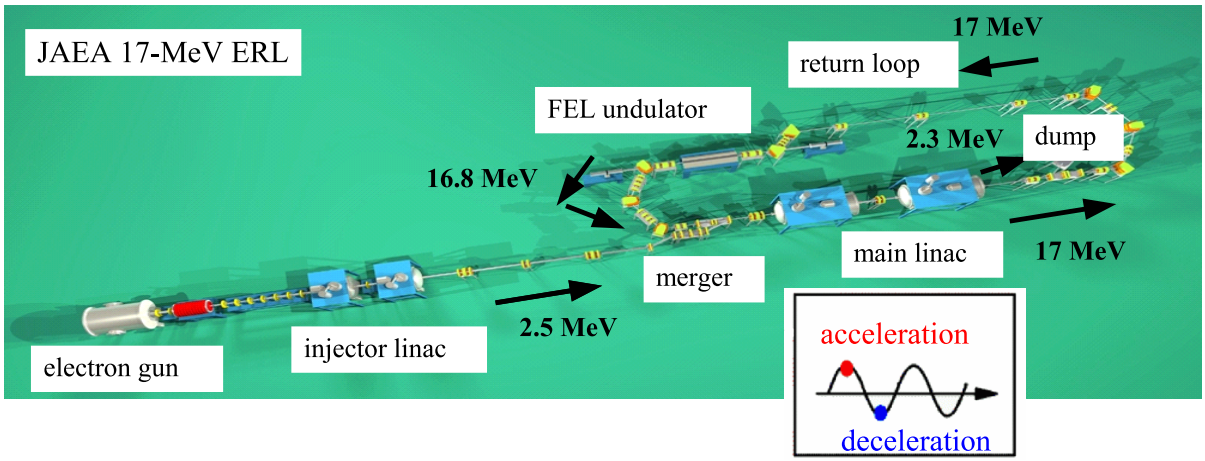

Figure 1: The energy-recovery linac at JAEA.

(4-turn) ERL [10]. These two FELs share the same linac and are installed in a vertical plane and a horizontal plane, respectively.

The IR-demo FEL at JLAB has been upgraded into a 160-MeV ERL, which is called "FEL upgrade". As a result of the upgrade, the electron beam power has been enlarged from 48 MeV, 4.5 mA (IR demo) to 160 MeV, 9.1 mA (FEL upgrade). This enlargement of the beam power has boost up the FEL power [11]. They recently achieved the record of high-power FEL, 14.26 kW at 1.6 μm[12]. Another FEL for UV wavelength is planned to install at the ERL.

From successful operation of these facilities, it has been confirmed that ERL is a suitable device for a high-power FEL. Scalable enlargement of FEL power up to 10 kW level has been clearly demonstrated and further enlargement towards a 100 kW FEL is surely convincing by reinforcement of electron beam power through increasing injector current, increasing electron energy with additional accelerating structures, increasing electron energy with multi-turn configuration.

ERL FOR FUTURE LIGHT SOURCES

The advantages of ERL, high-average current and high-brightness, are also intrinsic properties for future X-ray light sources. The first proposal of ERL light source was given by a group of BINP at the 1st Asian Particle Accelerator Conference, which is "MARS – diffraction limited 4th generation X-ray source"[13]. The term "diffraction limit" means the condition that an electron beam has smaller divergence than the emitted photon beam, and given by $\varepsilon \leq \lambda/4\pi$, where ε is geometrical emittance, λ is radiation wavelength. It is known the geometrical emittance is reduced by linear acceleration, that is adiabatic damping of transverse phase space. If we have an electron beam of normalized emittance $\varepsilon_n = 0.1$ mm-mrad and accelerate the beam to 6 GeV, the beam becomes diffraction limit for hard X-rays of $\lambda = 0.1$ nm.

Diffraction microscopy by using coherent X-rays is now an emerging topic of synchrotron radiation research, because it can be applied to obtain an image of non-crystal material [14]. In an ERL light source with diffraction limited electron beams, the coherent fraction of 10 keV X-ray becomes 20% or more, while the coherent fraction is around 0.1% in the most brilliant beam line of 3rd-generation light sources. Thus, the number of coherent photons in ERL light sources will be increased by two orders of magnitude from existing light sources, and the ERL light sources will promote strongly novel science with coherent X-rays. Figure 2 shows calculated X-ray brilliance for SPring-8 and a future ERL light source, where we assume ERL parameters: electron energy of 6 GeV, geometrical emittance of 8.5 pm, beam current of 100 mA, and electron energy spread of 0.04%. It can be seen the average brilliance is improved by two orders of magnitude in the future ERL light source. This improvement of brilliance corresponds to the increasing of coherent fraction.

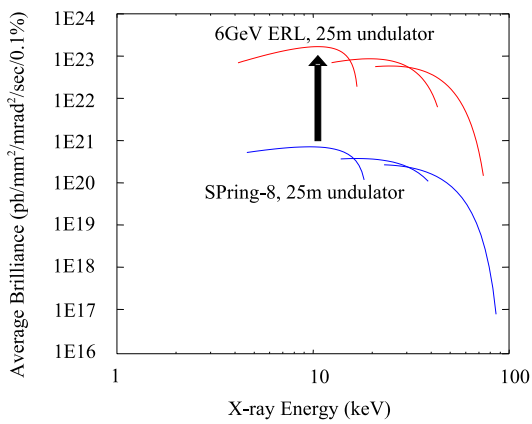

Figure 2: Average X-ray brilliance for SPring-8 and a future 6-GeV ERL.

The ERL light source also drives ultrafast X-ray sci-

ence by utilizing femtosecond electron bunches, which can be generated from a well-established technique of electron bunch compression in a linac or an arc section.

There are three major R&D activities for future ERL light sources in the world, 4GLS at Daresbury, Cornell ERL, and ERL in Japan. In Daresbury, they propose an ERL light source, 4GLS, which consists of a 800 MeV ERL for undulator radiation, an XUV FEL branch, and a 25-35 MeV ERL-FEL for infrared radiation[15]. Now, a 35 MeV ERL is under construction as a prototype to develop technologies relevant to the future ERL light source. Recently, they obtained the first electron beam from a photocathode DC gun [16].

Cornell university has a plan to built a 5 GeV ERL light source utilizing an existing CESR tunnel. They are developing an injector, which fulfills requirements of the future ERL light source, normalized emittance of 0.1 mm-mrad and average current of 100 mA[17].

The status of ERL light source in Japan is described in the following section.

THE ERL LIGHT SOURCE IN JAPAN

In KEK (High Energy Accelerator Organization), a design study of ERL light source was conducted and a report of the design study was published in March, 2003[18], in which a 2.5-5 GeV ERL was proposed as a successor of 2.5-GeV Photon Factory, a 2nd-generation light source.

The FEL Research Group at JAERI, who developed the 17-MeV ERL-FEL, changed its name to ERL Development Group concurrently with the reorganization of two national institutes in Japan, merging of JAERI and JNC (Japan Nuclear Cycle Development Institute) into JAEA (Japan Atomic Energy Agency) in October, 2005. In the midterm plan of JAEA approved by Japan's government (2005-2009), the ERL group is in charge of development of an electron gun for a future ERL light source as well as operation of the 17-MeV ERL-FEL. They also designed a 6-GeV ERL light source[19].

Encouraged by world-wide increasing demands for next-generation light sources, Japanese Society for Synchrotron Radiation Research (JSSRR) set up an ad-hoc committee to discuss next-generation light sources in Japan. The ad-hoc committee for future light sources was headed by Prof. Yoshiyuki Amemiya (Univ. Tokyo) and involved both light source users and accelerator scientists. They started discussion in March 2005, and after several meetings the committee submitted a recommendation in September 2005[20]. The recommendation was finally approved by JSSRR. In the recommendation, they addressed that next generation light source in Japan should contain both an XFEL as an ultimate light source for astonishing progress in specific science and an advanced ring-shaped light source to promote a cutting-edge science in broad area. The latter part of the recommendation was followed by another JSSRR committee, the ad-hoc committee for advanced ring-shaped light sources headed by Prof. Amemiya (from October 2005 to August 2006). The committee concluded that an energy-recovery linac is a most promising candidate for an advanced ring-shaped light source, which will lead us to innovation of synchrotron radiation research in both its quality and quantity, and national-wide research and development for future ERL light sources should be initiated immediately.

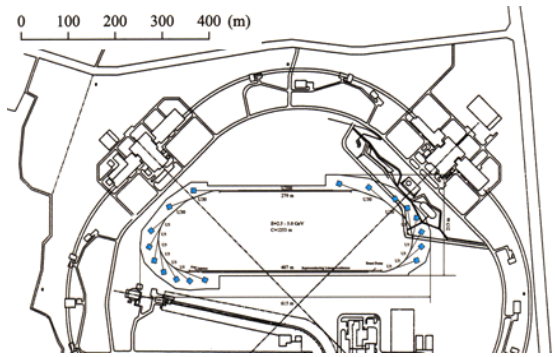

Figure 3: Proposal of a 5-GeV ERL at KEK (Tsukuba campus) presented at the JSSRR public hearing.

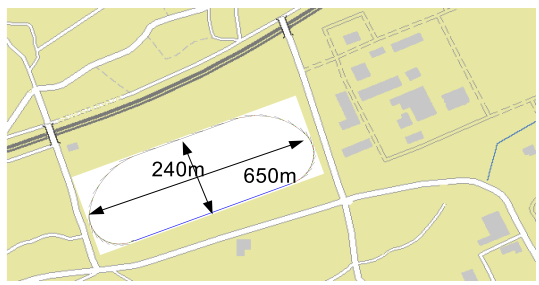

Figure 4: Proposal of a 6-GeV ERL at JAEA (Naka-west campus, former ITER site) presented at the JSSRR public hearing.

During the above critical discussion in JSSRR, they had a public hearing for future light source proposals in Japan. In the hearing at April 12, 2005, four institutes presented their plans, SCSS-XFEL by RIKEN[21], Super-SOR by ISSP[22], 6-GeV ERL by JAEA[19], and KEK presented two plans, 5-GeV ERL[18] and 3-GeV super storage ring. The super storage ring is a storage ring optimized for small emittance, and equipped with crab cavities for generation of femtosecond bunches in a straight section[23], and a set of skewed quadrupoles and a solenoid magnet to generate a round beam in another straight section[24].

In the Photon Factory of KEK, they had discussed the merit of the ERL and the super storage ring in detail. Finally, they concluded that a 5 GeV class ERL should be the most suitable candidate of their future plan to foster cutting-edge experiments, as well as to support a large variety of users' demands from VUV to X-rays[25].

Following the decision of KEK-PF, JAEA and KEK had a negotiation for possible collaboration on the development

of ERL technologies, and reached to the agreement for the collaboration. They signed a memorandum of understanding at March 10, 2006. Thereafter, a joint R&D team has been organized for the development of ERL technologies, and the design study of a future ERL light source. The joint team involves members of KEK, JAEA, ISSP, SPring-8, UVSOR. A high-brightness electron gun[26] and superconducting cavities [27] for the future ERL are under development by the joint team. They plan to build a test facility of 60-200 MeV ERL as a prototype of their future ERL light source of 5 GeV class[28].

SUMMARY

We have overviewed the status of energy-recovery linacs for high-power free-electron lasers and future X-ray light sources. The ERL, which produces high-power electron beams with small emittance and ultrashort pulse duration, is a promising device to realize high-power FELs of 10 kW or more and next-generation X-ray light sources with coherent X-rays and ultrashort X-ray pulses. Extensive R&D efforts towards such future ERLs are now conducted in the world. An electron gun for high-average current and small emittance, and a superconducting cavity for high-average current are critical components for future high-power FELs and next-generation X-ray light sources based on the ERL technology. The details of these technological challenges are given by accompanying papers[29].

Adding to the above applications, there are other proposals to make use of ERLs for high-energy physics. An electron cooler for high-energy ion collider is proposed at BNL/RHIC, where a prototype ERL is under development. It is also possible to use ERLs for electron accelerators of electron-ion colliders. Two proposals, eRHIC at BNL and ELIC at JLAB are under consideration. These applications of ERLs for high-energy physics are described in a separate paper[30].

The author acknowledge the contributions of G. Hoffstaetter, G. Neil, S. Smith, N. Vinokurov, who kindly provided latest information about their ERL projects.

REFERENCES

[1] M. Tigner, Nuovo Cimento 37 (1965) 1228.

[2] D.W. Feldman et al., Nucl. Instr. Meth. A259 (1987) 26.

[3] T.I. Smith et al., Nucl. Instr. Meth. A259 (1987) 1.

[4] G.R. Neil et al., Phys. Rev. Lett. 84 (2000) 662.

[5] N. Nishimori et al., Phys. Rev. Lett. 86 (2001) 5707.

[6] R. Hajima et al., Nucl. Instrum. Meth. A507 (2003) 115.

[7] R. Nagai et al., "Beam Current Doubling of JAEA ERL-FEL", Proc. FEL-2006, p.312 (2006).

[8] N. Nishimori et al., "FEL Oscillation with a High Extraction Efficiency at JAEA ERL FEL", Proc. FEL-2006, p.265 (2006).

[9] E.A. Antokhin et al., Nucl. Instr. Meth. A528 (2004) 15.

[10] V.P. Bolotin et al., Nucl. Instr. Meth. A557 (2006) 23.

[11] G.R. Neil et al., Nucl. Instr. Meth. A557 (2006) 9.

[12] G.R. Neil, private communication.

[13] D.A.Kayran et al. "MARS - A project of the diffraction limited fourth generation X-ray source", Proc. APAC-1998.

[14] . Q. Shen et al., J. Synchrotron Rad. 11 (2004) 432.

[15] J.A. Clarke, "The Conceptual Design of 4GLS at Daresbury Laboratory", Proc. EPAC-2006, p.181.

[16] S. Smith, private communication.

[17] G.H. Hoffstaetter et al., "Status of a Plan for an ERL Extension to CESR", Proc. PAC-2005, p.1928.

[18] "Study Report on the Future Light Source at the Photon Factory – Energy Recovery Linac and Scence Case –", Ed. T. Suwada and A. Iida (2003).

[19] R. Nagai et al., "Linac Optics Optimization for Energy Recovery Linacs", Proc. PAC-2003, p.3443; M. Sawamura et al., "Cost Estimation of an Energy Recovery Linac Light Source", Proc. PAC-2003, p,3449.

[20] "Vision of Future Light Sources in Japan", The Japanese Society for Synchrotron Radiation Research, Sept. 3, 2005.

[21] T. Shintake et al., "Status of Japanese XFEL Project and SCSS Test Accelerator", Proc. FEL-2006, p.33.

[22] N. Nakamura et al., "Design of the Super-SOR Light Source", Proc. EPAC-2004, p.2350.

[23] A. Zholents et al., Nucl. Instr. Meth. A425 (1999) 385.

[24] R. Brinkmann, "Applications of flat to round beam transformation for radiation sources", Proc. EPAC-2002, p.653.

[25] Photon Factory Activity Report 2005, Dec. 2006. `http://pfwww.kek.jp/pfacr/index.html`

[26] R. Hajima et al., "Development of a photocathode DC gun at JAEA-ERL", in these Proceedings.

[27] K. Umemori et al., "Design of L-band superconducting cavity for the energy recovery linacs", in these Proceedings.

[28] T. Kasuga et al., "Future Light Source based on Energy Recovery Linac in Japan", in these Proceedings.

[29] L. Merminga, "Technological challenges of ERL", in these Proceedings; J.R. Delayen et al., "Advances in ERLs and microwave superconductivity for lepton accelerators, colliders and light sources", in these Proceedings.

[30] I. Ben-Zvi, "Next generation electron-ion colliders", in these Proceedings; I. Ben-Zvi et al., Nucl. Instr. Meth. A557 (2006) 28.

PAPER NOT YET RECEIVED

PAPER NOT YET RECEIVED

PAPER NOT YET RECEIVED

PAPER NOT YET RECEIVED

STATUS OF FFAG DEVELOPMENTS

S. Machida, ASTeC, CCLRC Rutherford Appleton Laboratory
Chilton, Didcot, Oxfordshire, OX11 0QX, U.K.

Abstract

Since its revival at KEK in late 1990s, FFAG accelerator draws increasing attentions in many fields including physics experiments, medical, energy, and industrial applications. Construction of prototype machine is going on in Japan and in Europe. We will show status of those activities and accelerator physics issues after some basic of a FFAG accelerator.

INTRODUCTION

What is FFAG?

FFAG stands for Fixed Field Alternating Gradient. Strictly speaking, it only specifies a way of transverse focusing. People, however, usually refer to FFAG focusing accelerator as "FFAG".

A modern synchrotron has Alternating Gradient (AG) focusing. It is sometimes called strong focusing by contrast with weak focusing which uses a magnet with small gradient. Therefore, the primary difference between FFAG and a synchrotron comes from whether magnet field is fixed or ramped.

A synchrotron consists of a dipole to bend a beam and a quadrupole to focus a beam. Bending angle θ and focusing length f of them are,

$$\theta = \frac{BL}{p/e} \quad , \quad (1) \quad \text{and} \quad \frac{1}{f} = \frac{(dB/dx)L}{p/e} \quad , \quad (2)$$

respectively, where L is magnet length and fixed. p is momentum and e is an unit charge. B and (dB/dx) have to be ramped to keep θ and f constant when momentum increases. If they are not ramped, bending radius becomes large to keep the same bending angle and to make an orbit close. In addition, focusing length becomes larger and betatron tune becomes lower.

Fixed field magnets cannot keep bending radius constant for different momenta, but we can make use of the orbit shift to keep betatron tune constant through acceleration. Orbit moves outward and focusing strength is $(dB/dx)L$ so that a magnet with steeper gradient and longer path length outward in principle can keep the betatron tune constant. In terms of bending field profile, it is presented as

$$B_z = B_0 \left(\frac{r}{r_0} \right)^k F(\phi) \quad , \quad (3)$$

where r is radial, ϕ is azimuthal and z is vertical coordinates. F is a function which introduces azimuthal variation. k is called field index. Positive and large k means stronger bending field as the orbit moves outer, which sustain small orbit shift. At the same time, local gradient at the outer orbit is larger so that focusing is stronger.

That type of magnets can focus a beam only in one plane, but not in the other. In order to make an alternating gradient focusing, there are two ways. One is to flip the polarity of magnets alternatively. That changes bending direction as well as sign of focusing. This is called radial sector type FFAG. Another way to make it alternating gradient is to introduce edge focusing for vertical direction in addition to the focusing in the magnet body for horizontal direction. A sharp entrance angle for the all orbits makes the magnet shape spiral. This is called spiral sector type FFAG. Radial sector FFAG tends to be a larger machine compared with spiral one because of reverse bending magnets. It can have higher field index and therefore smaller orbit shift because focusing force comes from magnet body for both directions and can be strong as much as possible. On the other hand, vertical focusing of spiral sector FFAG is limited and that imposes a limit of field index.

What is advantage?

There are several advantages in FFAG compared with other type of machines. Firstly, machine repetition rate can be higher because there is no need to ramp the magnets. Secondly, particles per bunch can be the same or even higher than that of synchrotron because the similar strength of focusing in transverse as well as longitudinal direction is maintained. The larger aperture in horizontal plane even gives more space for particles. Thirdly, output energy can be higher compared with cyclotron because magnet size is smaller.

Beam power of an accelerator is the product of repetition rate, particles per bunch, and output energy. Therefore, compared with a synchrotron and a cyclotron, FFAG can have the potential to be the most powerful accelerator.

There are other advantages. FFAG is not only to be the most powerful accelerator, but with high energy efficiency in terms of beam power out of AC electric power. For example, FFAG with superconducting magnets needs only a power to a beam and the overall efficiency could be very high, which could be well above that of the present accelerators. As an accelerator for accelerator driven transmutation and energy breeder, FFAG has advantage over linac in that respect.

On more technical sides, rf frequency does not have to track magnetic field and horizontal orbit. That eliminates one feedback loop and makes machine operation easier. Also, FFAG has vacuum chamber covering injection to extraction orbits. Although that means physical cross section of the vacuum chamber is larger than that of

synchrotron, it can accommodate momentum spread from injection to extraction.

Why FFAG draws attention NOW?

FFAG was invented in 1950s by Ohkawa [1], Symon [2], and Kolomensky [3], independently. In particular, there was intensive research at Midwestern University Research Associate (MURA) [4]. They made two electron models of radial and spiral FFAG and a bit larger FFAG to show a possibility of colliding beam machine. There seemed no major obstacles to go ahead, but it was just not right time for FFAG. At that time, primary driving force of accelerator development was to obtain as high energy beams as possible, not high intensity beams. Although there have been several activities around the world since MURA was shutdown in 1960s, no serious research and development has been started until recently.

Breakthrough was made at KEK, when Mori and his group constructed a proof of principle FFAG which accelerates a proton beam to 500 keV in late 1990s [5]. The time was ripe for surge of further development. People demand high intensity and high power accelerators for various applications. In particular, a strong community has been already established for neutron scattering, partially because of success of ISIS synchrotron, and muon science. They were talking about a pulsed beam from an accelerator with about MW beam power. Some of high energy physicist explore the possibility of Kaon/Neutrino factory in addition to an energy frontier facility. To make those secondary particles, high intensity proton driver is a must. Although people were (and are) not sure which acceleration scheme was the best to produce high intensity beam, SNS took accelerator complex of linac and storage ring and J-PARC took synchrotron. They are expected to deliver the MW beam in a few years time. FFAG is the third scheme which seems promising from the reason mentioned above.

The study of accelerator driven transmutation system and energy breeder against the world's energy problem is another motivation which drives FFAG development. In those systems, efficient use of electric power in an accelerator is essential as well as high intensity. FFAG is in the spotlight.

Nowadays, accelerator is not only a tool of high energy and nuclear physics, but also for many applications. Medical and industrial usage of accelerator has more cases than physics. Requirements of accelerator in those fields are somewhat different from those in physics experiment. A machine should be easy to operate because a specialist of accelerator may not be always near the machine. For medical application, it should be compact so that it can be fit in a hospital. You may think that accelerator for those applications do not have to be high intensity. However, if high intensity beams become available, it can provide a new technique such as spot scanning in medical treatment. Simple but high intensity potential makes FFAG a good candidate.

At last but not least, FFAG has a potential of accelerating exotic particles such as muons and unstable nuclei. The life time of muons is only 2.2 μs. Conventional scheme of acceleration, except linac, needs more time to complete acceleration. FFAG with high voltage rf seems a feasible option to accelerate muons. It will be discussed more later. The situation of unstable nuclei is similar to muon acceleration. In both cases, the beam emittance in both transverse and longitudinal phase space is huge because they are made as secondary particles. FFAG with large acceptance can accommodate those beams.

RECENT DEVELOPMENT

At KEK

As we have already mentioned, demonstration at KEK opened a new era of FFAG in late 1990s. Although it is not the first time to accelerate particles in FFAG, it had several major achievements. Firstly, it established a whole design procedure using modern tools such as 3D magnetic calculation software and particle tracking. Secondly, new type of an rf cavity with Magnetic Alloy (MA) was installed to have high gradient, wide frequency range and large aperture. It was the first time to accelerate protons with wide range of rf frequency swing. Thirdly, dynamic aperture was compared with tracking and it was shown that it indeed has a large acceptance. Finally, it creates a new community in accelerator research and people start thinking many possible applications using FFAG.

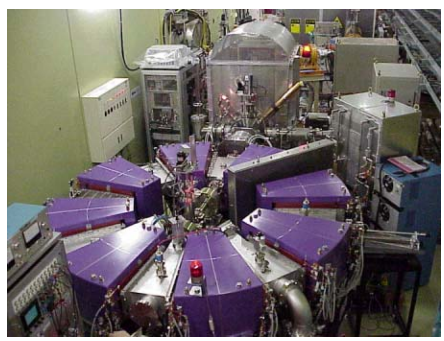

Figure 1: KEK 500 keV model.

One obvious target with FFAG is medical application with high intensity operation and high repetition rate. That makes a new way of shooting, namely spot scanning. Right after the success of small FFAG, Mori and colleague design a prototype of FFAG for medical use. Although the output energy is a bit low, simply because of available space in the lab, 150 MeV proton FFAG was constructed and the beam is extracted with an efficiency of more than 90% in 2005 [6]. The repetition rate of 100 Hz was also demonstrated.

At KURRI

Under Kyoto University, research reactor institute are operated. One of their future plans is to study accelerator driven sub critical reactor system. In particular, they are aiming to obtain the reliable "effective multiplication factor" in the proton energy region between 20 to 150 MeV. The project is called KART. FFAG was chosen as a

promising accelerator for that purpose and the project was approved in 2002 [7]. It consists of three FFAG cascade: 100 keV to 2.5 MeV spiral sector, 2.5 to 20 MeV radial sector and 20 to 150 MeV radial sector FFAG. The third FFAG adopted the similar design of the KEK medical prototype and the second one is a sort of a scaled down model. However, the first stage of FFAG has impressive features such as spiral magnet with 32 distributed trim coil windings to control the field index and induction acceleration unit. By changing field index, momentum at the outer orbit can be controlled keeping the initial momentum constant. With adjusted field strength of the second and third FFAG, the output energy of the accelerator complex can be varied.

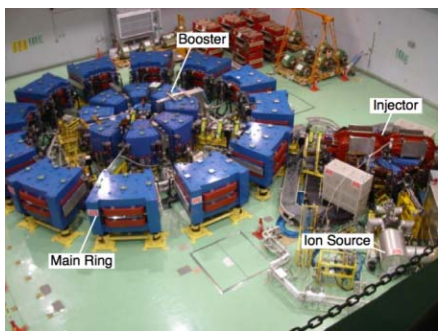

Figure 2: Cascade of three FFAG rings at KURRI [7].

At the moment, a beam is injected into the final FFAG and commissioning of extraction is continued. They are expecting extracted beam and the experiment with the sub critical core and the target for the neutron production pretty soon.

Another project now going on at KURRI is called ERIT, which produces high flux of neutrons for BNCT treatment [8]. An internal target in FFAG produces neutrons, and at the same time, the same target is used as material for ionization “cooling”. The “cooling” actually does not make the emittance smaller, but does suppress the blow up due to scattering. The neutron intensity is supposed to be comparable to that from a nuclear reactor. Although there is no net acceleration, huge momentum acceptance and transverse acceptance of FFAG is a big advantage to circulate a beam whose emittance and momentum spread gradually increase. After about 1,000 turn revolution, the blow up beam is dumped and a new small emittance beam is injected.

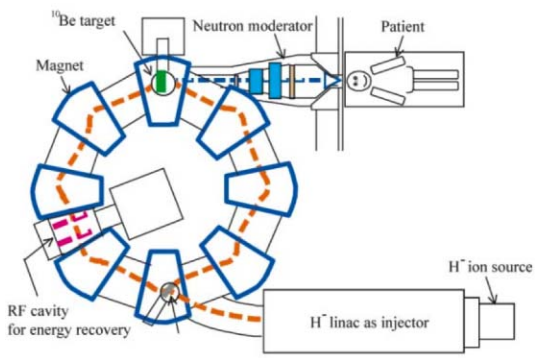

Figure 3: ERIT produces neutron for BNCT.

At Osaka University

Just using a feature of large momentum acceptance, Osaka University is constructing a FFAG for compression of muon momentum spread. This is called PRISM project [9]. Right after the target, muons (or pions) have large momentum spread. Since the time structure should be the same as primary proton beams, a tall muon beam in longitudinal phase space should be created when the proton bunch is shortened. When the tall beam is captured and rotated by a quarter of synchrotron oscillation, the beam becomes long in time and small in momentum. A muon beam stay for 5 turns in the FFAG and extracted. Magnets are ready now and some beam experiments with a few rf cavities are expected soon.

Figure 4: One of PRISM magnet.

At LPSC

RACCAM project is recently approved [10]. According to [10], its goal is, (1) participate to the on-going international collaborations in the field of FFAG and recent concepts of nonscaling FFAG (see the next section) with frames for instance, the neutrino factory, the EMMA project (see the next section also) of an electron model of a muon FFAG accelerator, etc., (2) design, build and experiment a prototype of an FFAG magnet proper to fulfill the requirements of rapid cycling acceleration with relevant momentum and geometrical acceptance, (3) develop the concepts, and show the feasibility, of the application of such FFAG beams to anti-cancer hadron therapy and to researches in radiobiology.

At Daresbury Laboratory

Acceleration of muon in FFAG for neutrino factory was first proposed in Japan [11]. It assumed radial sector type FFAG. Compared with linac and recirculating linear accelerator (RLA), a beam goes through the same rf cavity more times which would make the whole machine cost cheaper because the costly part of the machine is the rf system. The actual design of magnet for muon acceleration seems, however, relatively large because the orbit moves quickly on the low momentum side and the shift becomes less when a beam is accelerated. Although the field profile of Eq. (3) is required to keep the transverse tune constant, it may be an irrelevant requirement for muon acceleration because a muon beam

circulates only for 10 to 20 turns. A beam may not see any effects even if the tune moves and crosses integer and half-integer tune.

A new type of FFAG called nonscaling FFAG was introduced to squeeze the magnet and letting tune move [12]. The conventional type of FFAG is then called scaling type because the orbits corresponding to different momenta are similar and focusing length is scaled to the average radius. Nonscaling FFAG is essentially a synchrotron without ramping magnets. It consists of only dipole and quadrupole magnets and orbit moves outward and tune becomes lower as accelerated. If we make, however, an optics such that dispersion function is minimized, orbit shift can be less than that of scaling one. Neutrino factory based on nonscaling FFAG became the baseline in the recent study as a cost effective scinario [13].

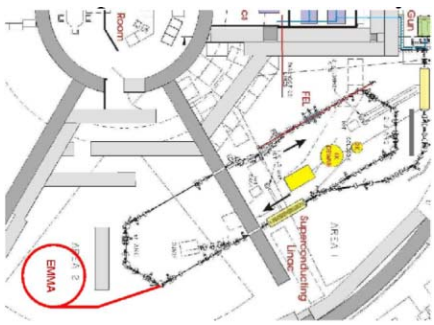

Figure 5: EMMA ring following ERLP machine.

It is, however, hard to convince people that nonscaling FFAG works as we expected. To demonstrate the nonscaling FFAG principle, just as a small FFAG model did at KEK in late 1990s, a low energy electron model was discussed in the community for years and finally Daresbury laboratory hosts the construction project called EMMA [14]. EMMA uses an electron beam from energy recovery linac prototype (ERLP) accelerator and accelerate it from 10 to 20 MeV in about 10 turns. The project will start this year.

ACCELERATOR PHYSICS ISSUES

Nonscaling FFAG and its variety

Idea of nonscaling FFAG makes people think that many variety of optics are possible once we give up the magnetic field profile of Eq. (3). Rees has actually shown that constant tune can be achieved if we have three different kinds of magnets and shape field profile in a proper way [15]. Preliminary results show that the lattice has smaller dynamics aperture than scaling and nonscaling FFAG, partially because of nonlinearity of the profile, so that it may not be applicable to muon beams. Constant tune with smaller orbit shift is, however, attractive and it is a good candidate for proton acceleration with reasonable size of emittance. Another electron model to prove the principle is proposed.

Muon acceleration with constant rf frequency

Either scaling or nonscaling FFAG does not have isochronism so that the frequency of rf cavitiy has to be, in principle, synchronized to the revolution frequency. It is not a problem if the repetition rate is the order of 1 kHz or 10 kHz if we use low Q cavities such as MA loaded one. For muon acceleration, however, the whole cycle is completed only in 10 to 20 turns and it is hard to modulate rf frequency, even though it is not impossible. There are two methods considered, one for each scaling and nonscaling FFAG. For scaling FFAG, rf voltage makes a single rf bucket whose bucket height is more than the momentum range of acceleration. A bunch injected in the bottom part of the rf bucket starts synchrotron oscillation and reaches the top part of the bucket after a half synchrotron period. Such a large bucket can be created with relatively low rf frequency such as 1 to 5 MHz.

Nonscaling FFAG, on the other hand, uses a different method [16]. In the process of lattice optimization, nonscaling FFAG lattice is adjusted such that the transition momentum is in between injection and extraction momenta. Because the particle is already ultra relativistic, entire variation of path length becomes minimum when the transition momentum was chosen in between. Now if we fix the rf frequency a bit higher than the revolution frequency at transition momentum, two stable fixed points appear in the longitudinal phase space: one above injection and the other below extraction momentum. A bunch injection below the first fixed point is now going outside the first bucket to the second one and reaches the final momentum. The rf frequency in this case is 200 MHz.

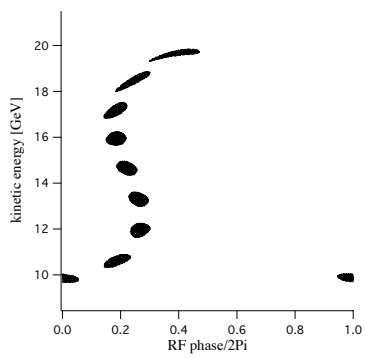

Figure 6: Acceleration outside buckets. One stable fixed points is located at (0, 12.5) and the other at (0.5, 17.5).

Harmonic number jump

There is one possible way of using constant rf frequency in FFAG. If the change of revolution frequency per turn is large enough, a bunch could be captured in a bucket above the current one [17]. The new bucket should have a different harmonic number: it increases if the momentum is above the transition and vice versa. If this scheme works, FFAG can accelerate beams continuously like a cyclotron. It makes the average beam currents even higher. In practice, one has to adjust the energy gain as a

function of momentum. It requires the rf cavity whose field gradient varies in radial direction.

Resonance crossing

Scaling FFAG is supposed to have a constant tune. End fields and mechanical errors of magnets, however, slightly alter the scaling conditions and the tune starts to migrate around the ideal tune. In principle, iteration of 3D field calculation and particle tracking would tell the detailed shape of the end. However, the convergence is not always certain in practice.

If, on the other hand, we know the effects of resonance crossing and the way to correct the driving source, we can allow the tune migration to some extent. The mechanism of resonance crossing was studied with particle trapping model [18]. Since the scaling FFAG has inherent 0^{th} order octupole component, tune shift as a function of amplitude makes isolated islands when a beam cross a resonance. If the crossing occurs adiabatically, the trapped particles are brought to the large amplitude and got lost eventually. The study by Aiba showed the magnitude of adiabaticity to be avoided.

In nonscaling FFAG, there are more concerns about the crossing of linear resonance such as half-integer. Although people believe that it is not harmful if the crossing is fast enough, it is still not clear how fast is enough. Preliminary results show that what happens actually when a beam crosses a linear resonance is mismatch of optics between a cell, nothing like a "resonance" in a conventional sense [19].

Another study on resonance crossing in FFAG deals with space charge. Nonscaling FFAG in principle does not have any nonlinearity so that only linear resonance seems to be a problem. However, when space charge force is not negligible, it excites nonlinear resonance such as octupole and dodecapole. Lee shows that in some case, especially when the tune moves slowly, those space charge induced resonances make a beam blowup which imposes the fundamental limitation on the current in nonscaling FFAG [20]. It also shows how fast the crossing is supposed be to avoid the emittance deterioration.

Time of flight of large amplitude particle

A large emittance beam like muon cannot ignore the time of flight difference coming from transverse amplitude. This affects the energy gain of acceleration outside buckets. Chromaticity correction reduces the difference, but it also introduces nonlinearity and acceptance becomes an issue. It is one of problems to be solved [21].

The work is supported by the UKNF/PPARC under Contract No. 2054.

REFERENCES

[1] T. Ohkawa, Bulletin of Physical Society of Japan, 1953.

[2] K. R. Symon, et. al., "Fixed-Field Alternaing-Gradient particle accelerators", Phys. Rev. Vol. 103, **6**, p. 1837, 1956.

[3] A. A. Kolomensky and A. N. Lebedev, *Theory of Cyclic Accelerators* (North-Holland, Amsterdam, 1966).

[4] F. T. Cole, "O Camelot! A Memoir of the MURA years", http://accelconf.web.cern.ch/AccelConf/c01/cyc 2001/extra/Cole.pdf.

[5] M. Aiba, et. al., "Development of a FFAG proton synchrotron", EPAC'00, Vienna, June2000 p. 581, http://www.jacow.org.

[6] M. Aiba, et. al., "Beam extraction of 150 MeV FFAG", EPAC'06, Edinburgh, June2006, p.1672, http://www.jacow.org.

[7] M. Tanigaki, et. al., "Present status of FFAG accelerators in KURRI for ADS study", *ibid*., p. 2367.

[8] K. Okabe, et. al., "Development of FFAG-ERIT ring", *ibid*., p. 1675.

[9] A. Sato, et. al., "R&D status of the high-intensity monochromatic low-energy muon source: PRISM", *ibid*., p. 2508.

[10] B. Autin, et. al., "The FFAG R&D and medical applications project RACCAM", *ibid*., .p.2308.

[11] S. Machida, "Neutrino factory design based on FFAG", Nulc. Instrum. Methods Phys. Res., Sect. A **503**, 41 (2003).

[12] C. Johnstone, et. al., "Fixed field circular accelerator designs", PAC'99, New York, March1999, p. 3068.

[13] "The Neutrino Factory and Muon Collider Collaboration Study 2-A", http://www.cap.bnl.gov/mumu/study2a/.

[14] R. Edgecock, et. al., "Introduction to the non-scaling electron model FFAG EMMA", NUFACT'05, Frascati, June2005, p.321, http://www.sciencedirect.com.

[15] G. H. Rees, "FFAG studies for Neutrino factory accelerators", *ibid*., p.301.

[16] C. Johnstone, et. al., "FFAGs for rapid acceleration", Nucl. Instrum. Methods Phys. Res., Sect. A 503, 445 (2003).

[17] A. G. Ruggiero, "rf acceleration with harmonic number jump", Phys. Rev. ST Accel. Beams **9**, 100101 (2006).

[18] M. Aiba, "Resonance crossing experiment at a proof of principle fixed field alternating gradient accelerator", Phys. Rev. ST Accel. Beams **9**, 084001 (2006).

[19] S. Machida, "Tracking study of resonance crossing in nonscaling FFAG", FFAG'06, Osaka, Nov2006, http://hadron.kek.jp/FFAG/FFAG06_HP/index.htm.

[20] S. Y. Lee, "fundamental limit of nonscaling Fixed-Field Althernating-Gradient accelerators", Phys. Rev. Letters **97**, 104801 (2006).

[21] S. Machida, "Longitudinal emittance blowup in fixed field alternating gradient muon accelerators", Phys. Rev. ST Accel. Beams **9**, 104002 (2006).

CHALLENGES IN ILC SCRF TECHNOLOGY*

Detlef Reschke#, DESY, D-22603 Hamburg, Germany

Abstract

With a baseline operating gradient of 31,5 MV/m at a Q-value of 10^{10} the superconducting nine-cell cavities of the ILC are a challenging milestone for SRF technology. Worldwide intensive ILC R&D programs are underway or in the planning stage in all three regions of America, Asia and Europe. This paper will give an overview of the main activities in the field of superconducting RF (SCRF) technology.

INTRODUCTION

In 2004 the International Technology Recommendation Panel (ITRP) recommended the choice of superconducting rf technology for a future linear collider. This choice was accepted by ICFA [1], and the first workshop on the International Linear Collider (ILC) was held at KEK in November 2004. During the 2nd ILC Workshop at Snowmass in August 2005 the goal was set to define a baseline configuration, which was published after intense discussions at the GDE (Global Design Effort) meeting at Frascati end of 2005. The Baseline Configuration Document (BCD) is a living document and will evolve following developments in design, costing and successful R&D improvements [2, 3]. In addition to the BCD the Alternative Configuration Document (ACD) describes a number of promising future options in order to gain in performance, cost or risk reduction.

Table 1: Main ILC cavity parameters

ILC parameters:		**BCD (baseline)**	**ACD (alternative)**
Cavity shape		TESLA	Low Loss or Reentrant
Cavity Acceptance Performance	Eacc [MV/m]	35	40
	Q_0	$0{,}8 \cdot 10^{10}$	$0{,}8 \cdot 10^{10}$
Cavity Operation Performance	Eacc [MV/m]	31,5	36
	Q_0	$1{,}0 \cdot 10^{10}$	$1{,}0 \cdot 10^{10}$
Coupler		„TTF type III“	
Cryomodule		„Type IV”	
		8(9) cav. /module	8(9) cav. /module

* We acknowledge the support of the European Community Research Infrastructure Activity under FP6 “Structuring the European Research Area” program (CARE, contract number RII-CT-2003-506395).
#detlef.reschke@desy.de

The ILC is based on 1.3 GHz nine-cell structures of ultrapure Niobium (Fig.1). Table 1 shows some important parameters related to cavity and cryomodule design.

Figure 1: 1.3 GHz 9-cell Niobium cavity of TESLA shape.

CAVITY FUNDAMENTALS

The Q-value of a superconducting cavity is related to the surface resistance R_s by $Q_0 = G / R_s$ with the geometry factor G given only by the geometry of the cavity. For accelerator cavities G is about 270 Ω. As explained in detail in [4], the experimentally observed surface resistance can be described by the BCS-component $R_{BCS}(T, \omega)$, the residual resistance R_{res} determined by preparation and experimental conditions as well as a gradient dependant component $R_s(H)$. One example of the latter is the so-called “Q-slope without field emission”, which appears in electropolished cavities. In order to cure this effect a special bake procedure is applied [5].

At an operating temperature of 2K a well prepared cavity shows a typical Q-value of $2 \cdot 10^{10}$ at low gradient. The Q-value of 10^{10} at the baseline operating gradient requires excellent preparation and experimental conditions resulting in cavities free of additional loss mechanisms like enhanced field emission (see below).

An intensively discussed topic of the last years is the rf critical magnetic field [4] of Niobium. Experimental results indicate a maximum magnetic surface field of (180 – 190) mT at 2 K.

Cavity shape

The shape of the cavity cells determines important characteristics of the accelerator structure as well as fundamental properties of the accelerator (Figure 2, 3) [6]. Here only some cavity related aspects will be discussed. The well-proven TESLA shape used in more than 120 nine-cell structures is the baseline ILC design. It is optimised with respect to cell-to-cell coupling k_{cc} and a low ratio of surface electric field to gradient E_{peak}/E_{acc}. The cell-to cell-coupling of 1.9 % ensures robust tuning properties, good HOM-damping and avoids trapped modes. E_{peak}/E_{acc} of 2.0 is favourable in order to reduce field emission loading. The tilted iris areas allow good wet cleaning and rinsing. The Low-Loss (LL) shape is optimized with respect to a comparable low magnetic surface field to gradient ratio H_p/E_{acc}. This allows about 15% higher gradient for the same magnetic field value.

Drawbacks are the reduced iris diameter, lower cell-to-cell coupling and an 18% higher E_{peak}/E_{acc}. The re-entrant shape (RE) is a compromise with respect to the rf parameters, but the wet cleaning is more difficult. Up to now no nine-cell cavity of this shape exists.

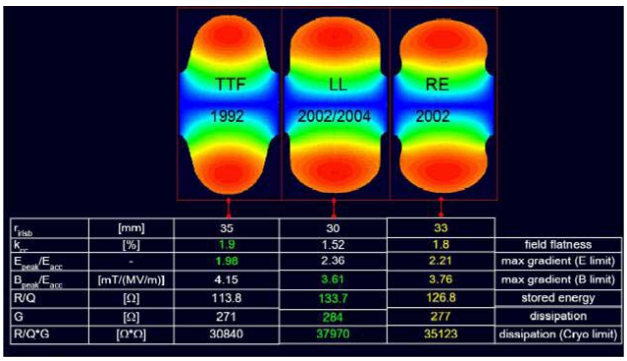

r_{iris}	[mm]	35	30	33	
k_{cc}	[%]	1.9	1.52	1.8	field flatness
E_{peak}/E_{acc}	-	1.98	2.36	2.21	max gradient (E limit)
B_{peak}/E_{acc}	[mT/(MV/m)]	4.15	3.61	3.76	max gradient (B limit)
R/Q	[Ω]	113.8	133.7	126.8	stored energy
G	[Ω]	271	284	277	dissipation
R/Q*G	[Ω*Ω]	30840	37970	35123	dissipation (Cryo limit)

Figure 2: Comparison of cavity shapes.

Figure 3: Reentrant (upper left) and Large Grain TESLA (lower left) single cell cavities; Low-Loss single- and nine-cell cavities (left).

Anomalous loss mechanisms

A detailed description of anomalous loss mechanisms in scrf cavities can be found in [4, 9].

Anomalous loss mechanisms like local thermal breakdown ("quench") or enhanced field emission (responsible for dark currents) often limit the performance of accelerator structures far below their maximum magnetic field limit.

A local thermal breakdown takes place, if the heat load produced by a lossy defect (e.g. a normalconducting particle) cannot be transported to the Helium bath any more. Depending on the heat production and the thermal conductivity at a certain field the surrounding Nb material will exceed the critical temperature T_c and a large surface area becomes normalconducting. As all stored energy is dissipated within about a millisecond, the field breaks together and the cavity quenches.

In order to avoid a quench the Nb material of the cavity needs to be free of lossy defects, and a high thermal conductivity is requested. For the ILC a large amount of such high quality Niobium is necessary with a high reproducibility. Though a number of excellent cavity results (see below) have shown that the required Nb purity is at hand, the industrialization and quality control for app. 20000 cavities still keeps a challenge.

Particles, chemical contaminations like hydrocarbons and surface irregularities have been identified to create field emission [7]. With today's standard preparation procedures, typically field emission loading in well-prepared cavities at 1.3 GHz starts at gradients of (20 – 25) MV/m. No systematic degradation between vertical tests and horizontal system performances is found. Single-cell cavities with their relaxed complexity of necessary components and assembly often achieve gradients far beyond 30 MV/m without field emission. In the last years several 1.3 GHz nine-cell cavities achieved gradients above 35 MV/m both in vertical and horizontal operation. At TTF/FLASH one nine-cell cavity was operated at 35 MV/m with beam [8].

The experience of cavity treatment and handling of the last 20 years leads to the summary, that the quality of surface preparation, final cleaning and dustfree assembly is crucial for field emission free cavities (Figure 4).

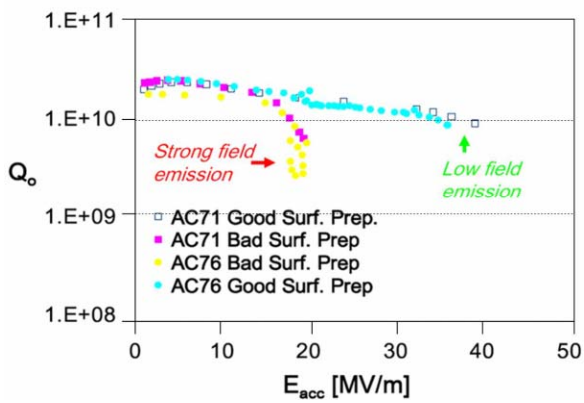

Figure 4: Examples of cavity performance after good and bad preparation procedures.

Preparation techniques

The BCD cavity preparation scheme contains:

- Cleaning after fabrication, mechanical + electrical entrance-check and first tuning
- First electropolishing (EP) (Figure 5) of (120-150) µm in order to remove the damage layer caused

by mechanical stress and deformation. The standard EP mixture contains HF and H_2SO_4 with a volume ratio of 1 : 9 [10].

- 800C firing under defined vacuum conditions in order to release mechanical stress and degas hydrogen
- Final electropolishing of (20 - 50) µm followed by ultra pure water rinsing.
- High Pressure Rinse (HPR) (Figure 6), assembly, HPR for the vertical acceptance test

Details of state-of-the-art cavity preparation is described in [4, 9, 10]

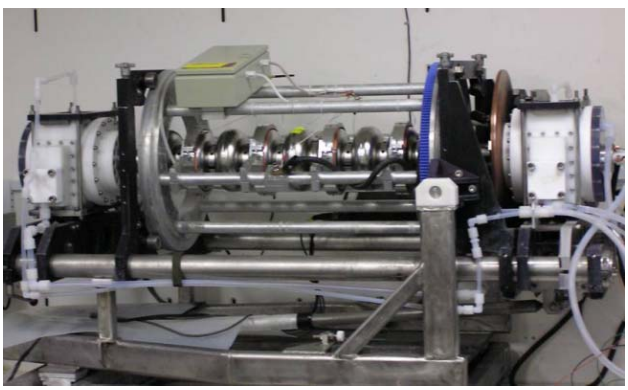

Figure 5: Horizontal EP setup at JLAB.

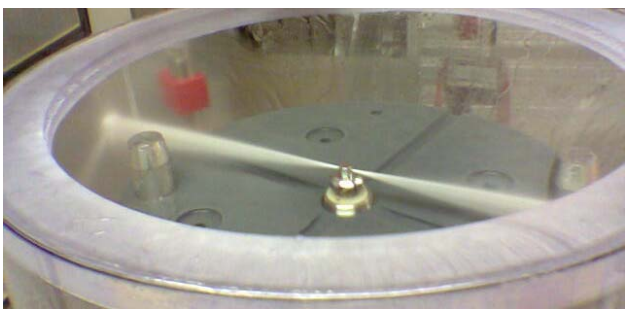

Figure 6: High Pressure Rinsing stand at DESY and Saclay.

R&D ON CAVITIES: S0 TASK FORCE

The mission of the task forces S0 on cavities and S1 on cryomodule (see next chapter) is to provide the information needed for final choice on gradient and exact procedures. It was decided to apply a phased approach to match both, design requirements and cost effort.

The situation before us is:

- The proof-of-principle for (35 – 40) MV/m in nine-cell cavities exists (Figure 7)
- Excellent single cell results of (40 – 50) MV/m show that the baseline preparation techniques are at hand (Figure 7)
- The yield for gradient > 35 MV/m in nine-cell cavities is low

As described above many tests are limited by field emission, some by quench and few by hydrogen Q-disease. The main goal of S0 is to **improve the yield for high gradients.**

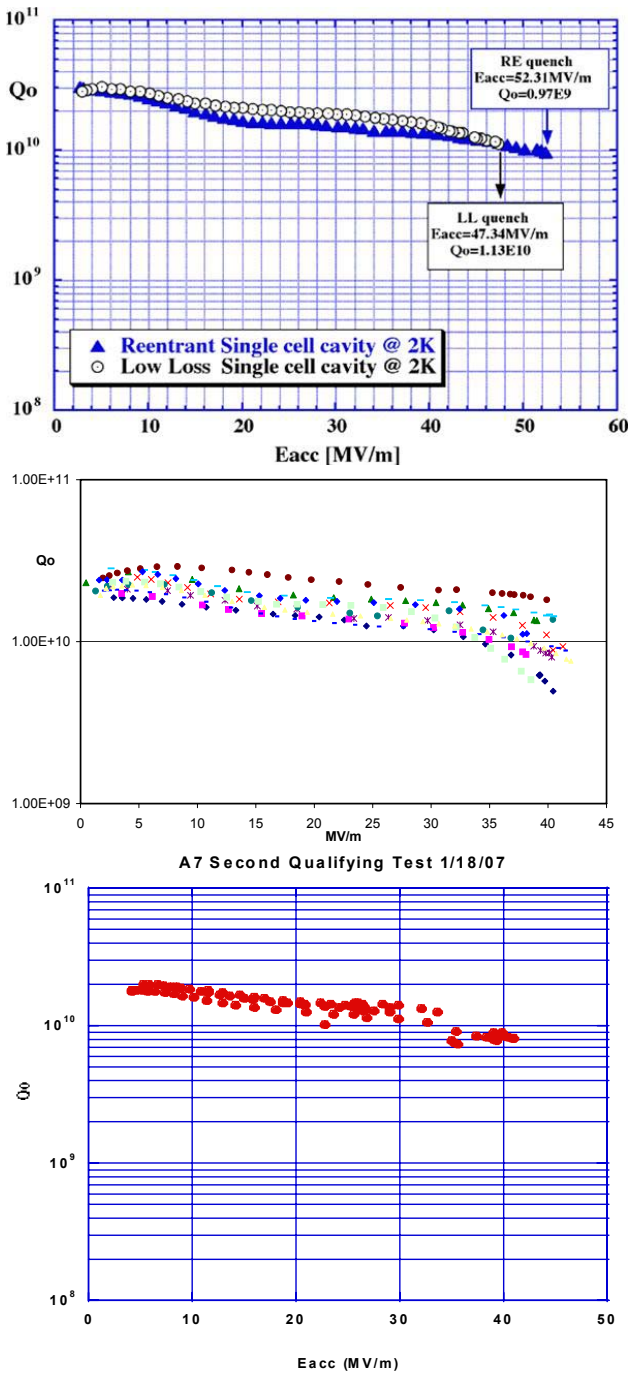

Figure 7: Q(E) performance of RE- and LL-single cells at Cornell/KEK (top); collection of nine- and single-cell results at TTF and CERN/DESY/Saclay collaboration (middle), recent nine-cell result at JLab.

The way to this goal requires the improvement of reproducibility of cavity processing. A yield of 80% in the first test is aimed at. Several R&D programs are launched or participated in parallel to improve fabrication and preparation processes. General topics of investigation are:

i) program on EP and rinsing parameters on single-cell cavities

ii) interregional "tight-loop" experiments on qualified nine-cell cavities in order to define a baseline yield in all regions.
iii) improved quality control by process monitoring (acids, process parameters, water, etc.) and comparison of HPR systems [10]
iv) process monitoring of the assembly procedures
v) improved quality control of the Nb material and during cavity fabrication

The process improvements will be transferred to nine-cell cavities as fast as possible with the goal of a final best recipe. The order of staged batches of 50 nine-cell cavities each are foreseen with aiming for a "final" production and preparation batch with a reproducible gradient of > 35 MV/m in the first or second test.

Valuable input is available from the work of the Tesla Technology Collaboration (TTC). A formal request for collaboration with the TTC is launched. Furthermore the R & D work of the European CARE project, the American SMTF project and of several individual labs is highly valued. Significant benefit is available by synergy effects with the European XFEL project.

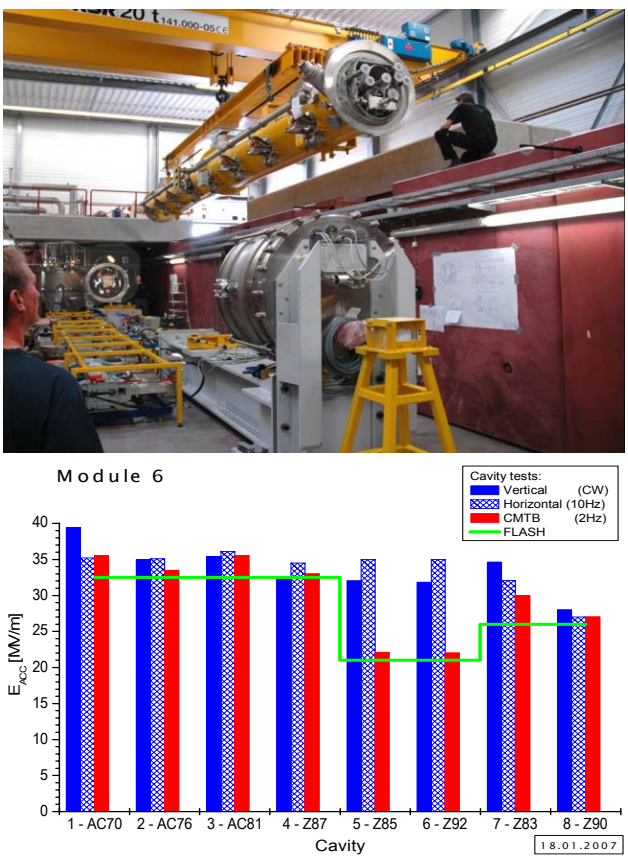

Figure 8: Assembly of the first module to CMTB at DESY (top); gradients of all 8 cavities of module 6 for TTF/FLASH (bottom).

CRYOMODULES: S1 TASK FORCE

An important milestone on the way to the ILC will be the successful test of at least three modules with 31.5 MV/m at $Q_0 = 10^{10}$ operational gradient. These modules shall be fully equipped including fast tuners and other features that could affect gradient performance. Each module should be operated a few weeks under realistic rf and cryo conditions. It is not necessary, that the modules have the final design. Depending on the cavity situation an exchange and re-assembly of cavities is an option.

As an intermediate step a module test with 31.5 MV/m average gradient with accordingly adapted rf distribution may act as a proof-of-existence.

Recently at DESY the Cryo Module Test Bench (CMTB) started its operation with the test of TTF/FLASH module 6 (Figure 8). Though two cavities significantly degraded compared to their fully equipped horizontal test, module 6 was tested successfully including several modes of rf and cryo operation with an average gradient of about 28 MV/m (Figure 8). The reason for the degradation is still unknown. With an adapted rf distribution 4 of 8 cavities will be operated at about 32 MV/m in FLASH.

At KEK as well as at FNAL cryomodule test facilities are close to operation. KEK will test modules with 4 cavities each. Both the BCD TESLA-shape and the ACD Low-Loss shape will be used. The first module assembled and tested at FNAL will be a kit of dressed cavities provided by DESY.

A GLANCE TO ACD

The Alternative Configuration Document is a natural part of the BCD [2]. In most cavity and cryomodule related topics alternatives and long range R&D items are investigated. Examples are listed below:

- Alternative cavity shapes (see above)
- Cavities fabricated of large grain niobium (Figure 3)
- Simplified power coupler designs
- In-situ processing of field emitter by High Peak Power Processing [4]
- Aggressive cost reduction ideas

OUTLOOK

The next near term milestone will be the presentation of the Reference Design Report including a detailed cost estimate in Beijing in Feb 07. It is expected that the European XFEL project with its 1,6 km of superconducting accelerator modules will get its official go ahead in summer 07. In addition to the above mentioned coincident R & D topics, the industrialization of the XFEL will be a reliable technical and cost baseline for the ILC.

In 2007 cryomodule tests will start at KEK and FNAL. The work on nine-cell cavities at DESY, FNAL, JLAB and KEK will be continued. In addition important R & D programs on single-cells, material properties and processing will be continued.

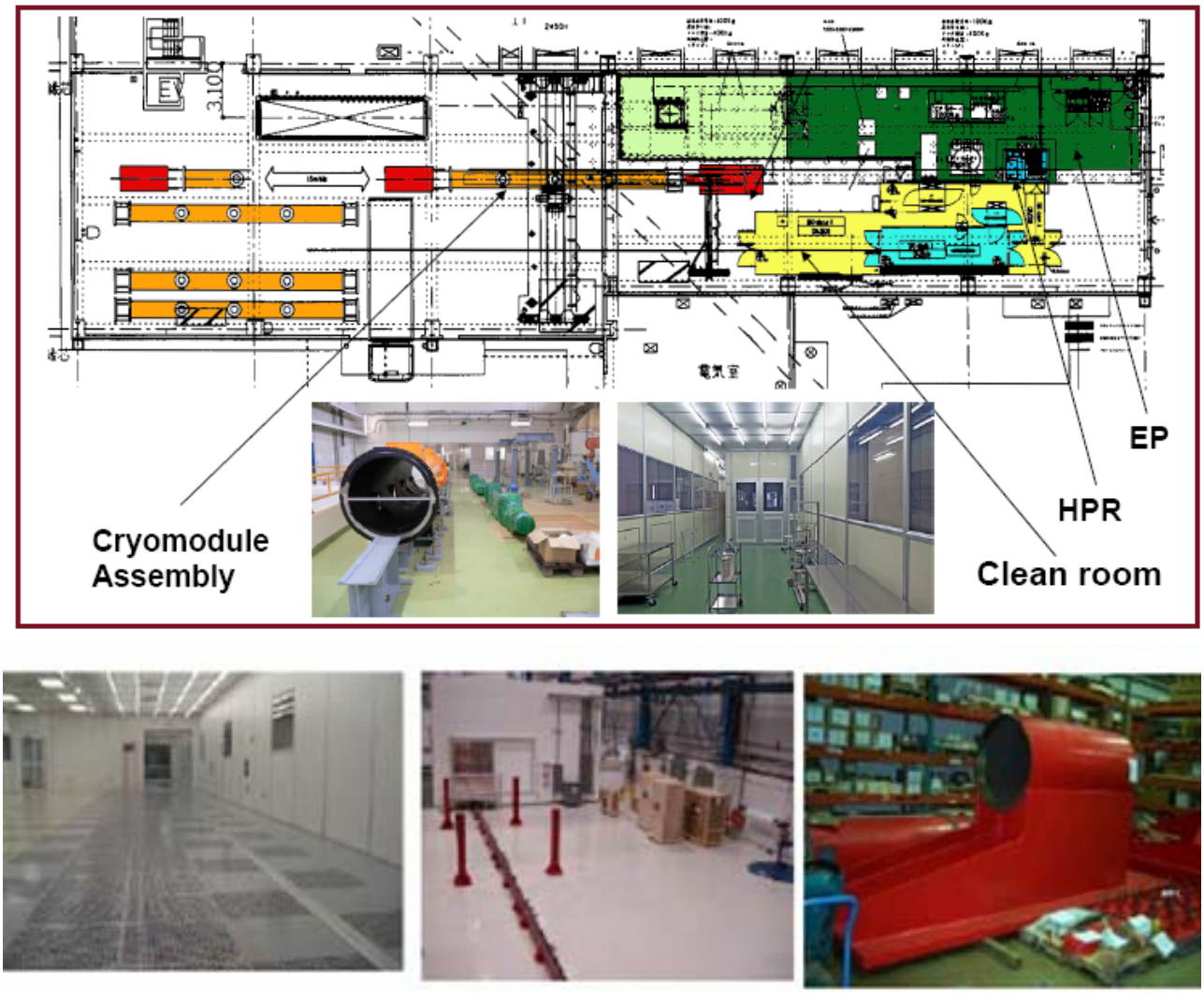

Figure 9: Cryomodule and cleanroom infrastructure at KEK (top) and FNAL (bottom).

ACKNOWLEDGEMENT

I thank all colleagues, who provided me with information, especially H. Hayano, D. Kostin, L. Lilje, J. Mammosser, H. Padamsee, D. Proch and H. Weise

REFERENCES

[1] International Technology Recommendation Panel Report, Sep 2004 http://www.fnal.gov/directorate/icfa/ITRP_Report_Final.pdf
[2] ILC Baseline Configuration Document: http://www.linearcollider.org/wiki/
[3] ILC Global R&D Board; http://www.linearcollider.org/wiki/
[4] H. Padamsee et al., "RF superconductivity for Accelerators", John Wiley & Sons Inc., USA, ISBN 0-471-15432-6, 1998
[5] B. Visentin, "Q-slope at High Gradients: review of Experiments and Theories", Proc of 11th Workshop on RF Superconductivity, DESY, Luebeck, Germany (2003)
[6] ILC Cavity Shapes: http://www.linearcollider.org/wiki/ and http://lcdev.kep.jp/GDE/BCD/64410.CavShape.pdf
[7] D. Reschke, "Field Emission Overview: Cleanliness and Processing", Proc. of the Workshop on "Pushing the Limits of RF Superconductivity", Argonne, USA, ANL-05-10 (2005)
[8] L.Lilje et al. "Achievement of 35 MV/m in the superconducting nine-cell cavities for TESLA ", Nucl. Instr. and Meth. 524 (1-3), (2004), 1
[9] Various Contributions in Proc. of Workshops on RF Superconductivity
[10] P. Michelato, „ High Pressure Rinsing Parameters measurement and Process Optimization", Proc of 12th Workshop on RF Superconductivity, Cornell, USA (2005)

OVERVIEW OF REGIONAL INFRASTRUCTURES FOR SCRF DEVELOPMENT

Carlo Pagani, University of Milano and INFN Milano - LASA, Italy

Abstract

The perspective of building the International Linear Collider, ILC, as a global project based on the SCRF technology, which has been pushed in the last decades mainly in Europe by the TESLA Collaboration, imposed to the other two Regions, America and Asia, the investment of consistent resources to locally develop with industry the capability of handling the "cold" technology. Following the success of TTF at DESY, and before of LEP II at CERN and CEBAF at TJNAF, large dedicated infrastructures are being created at Fermilab and KEK. The new regional infrastructures, together with the existing ones, will form the basis for the realization of a global machine, with a single design and distributed production of the key components. In this paper the importance of the SCRF infrastructures is discussed, and their status and plans are outlined.

INTRODUCTION

Since the early 70s, Superconducting RF, SCRF, has been introduced in the particle accelerator community as a promising technology to efficiently transmit energy to a variety of particle beams.

When a superconductor is exposed to a time varying electromagnetic field the electrons which are not coupled as Cooper pairs lead to energy dissipation in the shallow London penetration depth. Nonetheless it was soon realized that in the practical frequency range of RF accelerators the theoretical surface resistance is order of magnitude lower than in a normal conductor, widely compensating for the required cryogenics and leading to an increase of the overall plug to beam power conversion efficiency [1].

A few laboratories and universities started fundamental investigations and experiments to demonstrate the technical feasibility of SCRF acceleration. Very rapidly the results reached severe technological limitations, mainly due to the modest purity of the superconducting material being used to produce the cavities prototypes. Moreover, to approach the theoretical limits, it also turned out that all the cavity fabrication process and handling were not adequate to preserve the purity of the few tenths of nanometres layer at the cavity surface.

In spite of these limitations, in the middle 80s two major laboratories, TJNAF in US and CERN in Europe, planned to build large accelerators based on SCRF technology. To overcome the limitations faced so far by this technology, an impressive effort was performed in setting up large dedicated infrastructures to define and control the production parameters at the basis of the modest performances.

The construction and operation, in strict collaboration with industry, of hundreds of moderate gradient (5-8 MV/m) cavities at TJNAF for CEBAF [2] and at CERN for LEP II [3] has been the basis for setting a new level of quality control and industrialization. In particular the successful technology transfer was possible because of the large effort dedicated in defining reproducible production parameters making use of the large dedicated infrastructures set up for this specific purpose.

A deeper understanding of the limiting factors contributed then to revise the SCRF technology further, in order to be compatible with the new challenging demands emerging from the High Energy Physics community.

The TESLA challenge to use SCRF as the basic technology for the future TeV e+e- Linear Collider impressed the momentum to move SCRF Technology to a new frontier, opening a new era

- Accelerating fields exceeding 35 MV/m
- Quality factor higher then 10^{10}

As for the past experience, the great success of the TESLA Collaboration was mainly determined by the consistent investment, in term of both resources and experienced persons, in setting up at DESY, the host laboratory, a dedicated infrastructure that was designed to include all the past experience. This infrastructure - called TESLA Test facility, TTF - combined most of the existing know-how and has been the "school" were most of the new SCRF scientists have been formed.

The success of TTF opened the way for a consistent proposal of the TESLA Liner Collider, presented to the International Community in March 2001 [4]. To perform a realistic costing of TESLA, industry has been included in the process, initiating the technology transfer in view of a large scale production. Process parameters defined in the TTF infrastructure went through a deep analysis made by industry for cost estimation and a few suggestions became part of the baseline design.

In August 2004, the ITRP (International Technology Recommendation Panel) unanimous recommendation of basing the next International Linear Collider, ILC, on the TESLA "cold" technology has been the successful end of the TESLA experience, while opening a new era where the SCRF technology is considered the right choice for most of the new accelerator projects.

The TESLA Collaboration achievements, together with the experience on large existing cryogenic infrastructures, brought most of the accelerator community to be confident that SCRF Technology can be reliably applied for a cost effective accelerator design. In fact, at the present technology level, the SCRF is respecting the original promise of being competitive in term of investment cost, while giving better conversion efficiency and lower operating costs.

Since the decision for the TESLA technology, the Global Design Effort, GDE - which was established for

the design and costing of the ILC - is the driving force for the coordination of the worldwide initiative addressed to the regional distribution of the SCRF know-how and its development to the level required for ILC. In this context the new regional infrastructures in construction at Fermilab and KEK are expected to play the central role.

TTF AT DESY

The origin and rationales

In July 1990 the first TESLA Workshop was organized at Cornell by H. Padamsee and U. Amaldi. Two years later the TESLA Collaboration was set up at DESY with the aim of demonstrating that a SCRF-based TeV e^+e^- Linear Collider could have been superior.

The baseline idea was simply that pushing to the limit the niobium SCRF technology, accelerating field up to 50 MV/m could be conceived, with efficiency from plug to beam power much higher than any other NC competitor [9].

Three were the major challenges of this scheme:

- Push the gradient to at least 25 MV/m, at high Q.
- Reduce by a factor of 20 the linac cost per MV.
- Develop the technology for pulsed operation.

Taking advantage of the experience of all the major laboratories investing in this technology, an optimum cavity design was developed and a large infrastructure was set up at DESY, TTF, for the cavity processing and test. Stiffening rings were included in the cavity design to minimize the effect of Lorentz-force detuning in the high power pulsed regime. The major contributions came from CERN, Cornell, DESY, CEA-Saclay and INFN, but important inputs from TJNAF and KEK were essential.

To prove the TESLA concept long cryomodules were required for high filling factor. INFN, supported by FNAL and DESY, developed with the Italian industry a new concept of an eight-cavity cryomodule with outstanding cryogenic efficiency. Module assembling facilities and a shielded area to operate the linac prototype were then included in the TTF Infrastructure.

Infrastructure descriptions

The schematic layout of the TTF infrastructure is presented in Fig.1. It was designed on the basis of the experience from the preceding infrastructures, mainly from CERN, to cover the following four major functions:

- Cavity inspection and processing.
- Cavity test.
- String and module assembly.
- System test in a prototype linac with beam.

The infrastructure design and construction has been performed to control and define all the process parameters in order to optimize the SCRF technology while preparing the required documentation for a smooth technology transfer to industry. A reproducible mass production according to the highest standards in term of QC (Quality Control) and QA (Quality Assurance) was mandatory.

Limiting the short description to the cavity inspection and processing, the most significant steps and apparatus are listed in the following.

- Niobium material inspection with an Eddy-current scanning system to detect major inclusion and forcing producers to a higher level of quality control.
- Inspection laboratory for control and acceptance of the SCRF cavities shapes and EB (Electron Beam) welds by the industry, according to a detailed specified procedure.
- Cavity tuning equipments to reliably converge to a straight tuned cavity, with a flat field distribution.

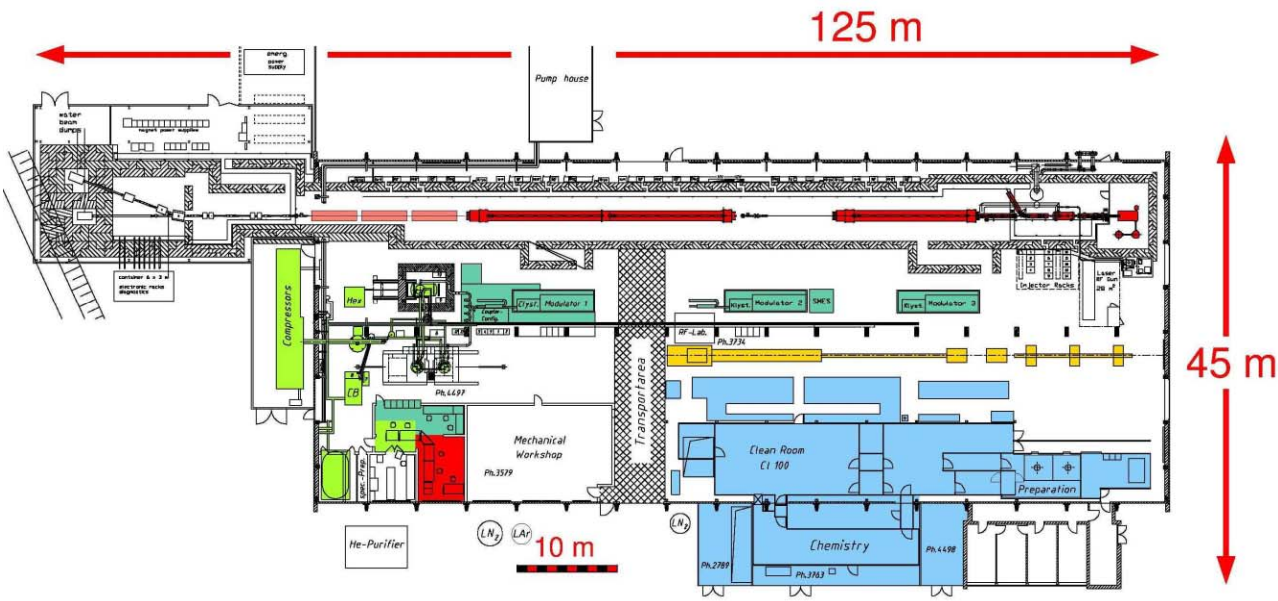

Figure 1: Schematic layout of the TTF original infrastructure at DESY, dedicated to the development of the TESLA SCRF Technology for the realization of an e+e- Linear Collider. The major components are shown in the drawing for size and location wile their short description is given in the text.

- Large class 100 clean room infrastructure for treated cavity preparation, ancillary integration and cavity string assembly. Class 10 areas are also included.
- Closed loop chemical plant connected to the clean room and the ultra high pure (18 MΩ cm) water purifier.
- High pressure ultra pure water rinsing in the clean room area for the subsequent clean drying.
- High temperature vacuum furnaces for hydrogen desorption and stress release (800 °C), and for niobium post-purification for thermal conductivity enhancement (up to 1400 °C).

While not described in this paper, I want to point out that also the other three functions of the infrastructure proved to be essential for setting the SCRF technology. A complex superconducting linac as ILC requires the same level of QA and QC all over the process, which includes cavity tests, ancillary integration, module assembly and linac operation.

Test results and open questions

More than 120 TESLA type cavities have been so far produced by the European industry and have been processed in the TTF infrastructure at DESY. The learning curve has been quite fast, demonstrating the success of the international effort dedicated in the infrastructure design and operation.

Figure 2 shows the vertical test results from the 3rd production batch, i.e. at the end of the learning curve. A very low residual resistance (few nΩ) was measured and the field emission onset was pushed up to around 20 MV/m. The Q drop at high fields was still not cured [5].

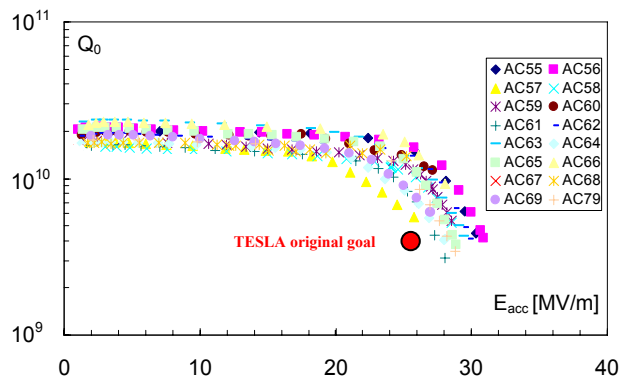

Figure 2: Vertical test results of the TESLA 9-cell cavities from the 3rd production. Standard BCP was applied.

The following steps to approach the physical limits for niobium were mainly determined by the combined introduction of two new ideas originated by the ongoing R&D effort at KEK and CEA-Saclay:

- Electro-polishing (EP) instead of BPC to process the cavity active surface in order to smooth out asperities and improve the effect of HPR [6].
- Moderate temperature baking (100-140 °C) in ultra-high vacuum to re-distribute oxygen in the surface, to mitigate resistive effects [7].

The application of EP raised the onset of field emission, while the moderate temperature baking cured the Q drop. These two very important results from the R&D activity for high gradient were independent but, because of the better quality of the electro-polished surface, baking is simpler and more reproducible for the EP cavities.

Figure 3 shows the tests results of one of the best TESLA EP cavities, as an example of the cure of the Q drop at high field by 120 °C baking. This cavity was electro-polished at DESY in an infrastructure upgrade that was built according to the experience and parameters developed at KEK. The outstanding results of this cavity, AC70, were obtained avoiding the 1400 °C heat treatment, thus giving a proof that the niobium quality has been substantially improved by industry [8].

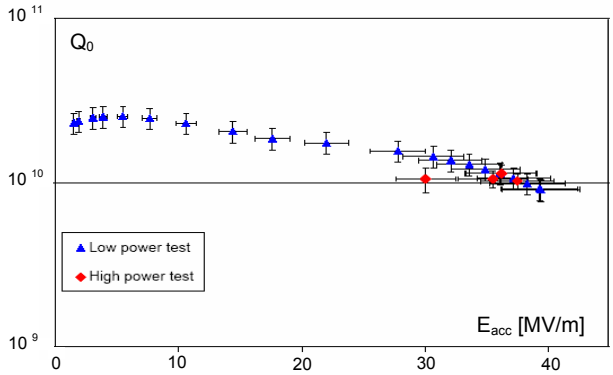

Figure 3: Low and high power tests of AC 70 at DESY.

In spite of the very successful results that have been at the basis of the "cold" decision for the ILC, a lot of work has still to be done for reproducibility. Figure 4 gives an impression of this problem sowing all the TESLA cavity test results. On each cavity several tests have been performed, slightly modifying process parameters.

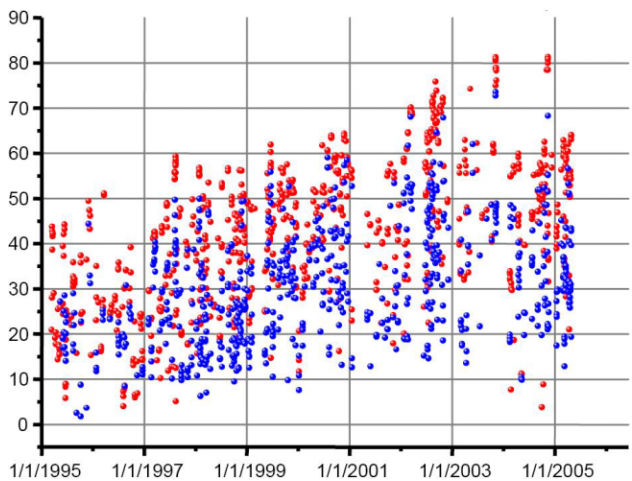

Figure 4: Plot showing the results of all the cavity vertical tests performed in the TTF infrastructure up to mid 2005. Vertical scale is the surface peak electric field [units of MV/m]. For each test the red dot is the maximum field achieved by the cavity and the blue one the field emission onset.

NEW CMTB AT DESY

The decision to transform the TTF linac into a VUV FEL user facility left a limited space for cryomodule test in TTF. Moreover, the preparation phase of the European XFEL was asking for a more continuous availability of tests to define details and gain experience before the construction phase. A new dedicated infrastructure has then been built at DESY, named CMTB (Cryo-Module Test Bench). Commissioning started in mid 2006 and the first complete cryomodule, the so-called #6, has been installed in the following October. The testing program, which includes 10 cool-down / warm-up cycles, is successfully under way in these days.

Figure 5 shows a picture of the CMTB bunker during the installation of the cryomodule #6. By February 2007, 10 cool-down / warm-up cycles will be completed.

Figure 5: CMTB at DESY during the installation of the first cryomodule in October 2006.

Testing a cryomodule in CMTB instead than in TTF turned out to be very efficient. The fact that in the CMTB no beam is available surely limits the completeness of the tests, but conversely CMTB is the right place were the behavior of one complete module, with all the active components installed, can be checked with more diagnostics and in a much shorter time.

SMTF AT FERMILAB

Following the decision of basing the ILC on the TESLA Technology, DOE funded US laboratories to create a large regional SCRF infrastructure at Fermilab, the chemical treatment plants being implemented at ANL to take advantage of the existing facilities and expertise. DESY, INFN and KEK are collaborating to this effort [9].

The new SCRF infrastructure is being located in the Fermilab Meson area. Its mission is going beyond ILC and includes the development of the technology required for a possible high intensity proton linac, also based on SCRF. The sketch of this facility, called SMTF, is presented in Fig. 6 in the version proposed to the DOE for funding.

Limiting the discussion to the ILC related activities, this new regional infrastructure will be including all the functionalities implemented in TTF, apart from chemistry at ANL. The TTF experience is at the basis of the Fermilab design and the technology transfer inside the TESLA Collaboration is being very fruitful.

As for TTF, the ILC Test Area (ILCTA) will include an accelerator called ILCTA_NM. In the first phase, the accelerator will be composed of an electron photo-injector (TTF type) and one ILC RF Unit. An ILC RF unit consists at present of three cryomodules housing 24 cavities powered by a single large klystron and modulator. The electron beam will be provided by an RF gun. The first cryomodule for the ILCTA_NM will be built from a "kit" of parts supplied by DESY and INFN. The kit will include eight fully dressed cavities from DESY and a cold mass built by the Italian industry using the INFN support and drawings. Assembly of the kit will take place at FNAL in the MP9/ICB Cryomodule Assembly Facility. The current schedule envisions this cryomodule to be ready for testing in June 2007. The second cryomodule for the ILCTA_NM will be built using TESLA cavities, processed with US facilities, and housed in a TTF Type III cold mass, produced in Italy by INFN. Coaxial blade tuners will be used for coarse and fast cavity tuning.

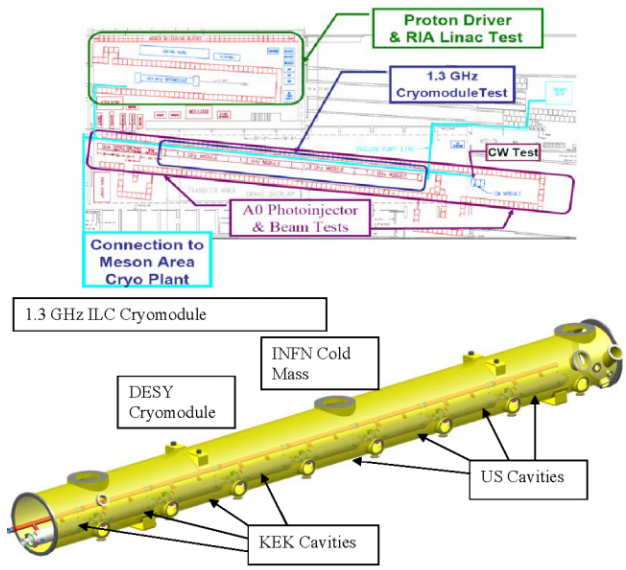

Figure 6: SM&TF Layout Concept at the Fermilab Meson Area, as presented to DOE for funding.

In addition, Fermilab is completing two other test areas: the Vertical Test Facility (VTF) for the testing of "undressed" superconducting cavities at low power, and the Horizontal Test System (HTS) for the high power testing of the "dressed" cavities. These two facilities will be fully operational very soon.

STF AT KEK

The Superconducting Test Facility, STF, under construction at KEK is also similar to TTF. A large dedicated area has been refurnished to allocate the clean room, the module assembly tools and the cryomodule test area with beam. Cavity processing is basically performed in collaboration with industry, following the same scheme successfully applied for TRISTAN. The existing R&D facility, famous for its outstanding achievements, has been partially renewed for research on single-call cavities, support to industry, cavity tumbling and vertical tests [10].

In the first phase, to speed up the learning process, the Type III TESLA cryomodule has been taken as reference for an independent development with industry of two short cryomodules allocating 4 cavities each. These two modules have been recently assembled and tests will start in spring 2007. For the first test just one cavity has been installed in each module, the first of the standard TESLA design and the second of the low losses "Ichiro" type. The status at the time of this conference if presented in Fig. 7.

Figure 7: Installation of the first two short cryomodules in STF at KEK, as in January 2007.

After the experience with the short cryomodules KEK is expected to actively joint Fermilab and INFN in the common development of the Type IV cryomodule that should be the first global prototype for the ILC. The importance of this Japanese strategy is going beyond the national interest. In fact with this strategy KEK could anticipate the system test of different solutions for the cavity design and for their major ancillaries, namely power couplers and tuners. The strong connection with industry is in progress and the participation of other group from Asia is growing, moving the system in the direction of the creation of a fully regional Infrastructure.

OTHER MAJOR INFRASTRUCTURES

Among the many other infrastructures for SCRF development it is worthwhile to quote at least the ones that are substantially contributing on the optimization of the ILC cavity design and processing and/or on the design and test of the cavity major ancillaries. The, although partial, list includes certainly, in alphabetic order CEA-Saclay, Cornell, INFN-LASA, Jefferson Lab and LAL-Orsay.

Through the ILC-GDE a better coordination among the different infrastructures and activities is in progress and the proposal for a second large regional SCRF infrastructure, to be located at CERN, is under discussion for an EU funding request.

CONCLUSIONS

As TESLA in the past, ILC is now leading a consistent worldwide coordinated effort to move the SCRF technology to the level required to build a "cold" Linear Collider, fully fabricated by industry and with the production of the major technologically appealing components distributed among the three Regions (Europe, America and Asia).

In spite of the fact that most of the recent accelerator projects, under construction or being proposed, are extensively using SCRF technology, the TESLA/ILC driven activities are still leading the R&D process for a high quality industrialized product at a moderate cost.

Industry is already producing turn-key reliable systems, including SCRF cavities and cryogenic ancillaries, but their cost and performances are not fully compatible with the requirements for the new large accelerators. The European X-FEL could possibly represent the first large scale applications based on the high gradient technology developed for the Linear Collider. Its realization would represent for Europe the best possible Regional Infrastructure for the ILC.

REFERENCES

[1] H. Padamsee, J. Knobloch and T. Hays, "RF Superconductivity for Accelerators", John Wiley & Sons, 1998.
[2] C. Reece, Proceedings of SRF Workshop 1999, Santa FE, NM, November 1999.
[3] P. Brown et al., Proceedings of SRF Workshop 2001, Tsukuba, Japan, November 2001.
[4] R. Brinkmann, et al. (editors), TESLA - Technical Design Report, volume II. DESY, March 2001. ECFA 2001-209, TESLA Report 2001-23.
[5] B. Aune et al. Phys. Rev. ST-AB, 3(9), September 2000. 092001.
[6] K. Saito et al., Proceedings of SRF Workshop 1997, Abano Terme, Italy, October 1997.
[7] B.Visentin, Proceedings of EPAC 1998, Stockholm, Sweden, May 1998, p. 1885.
[8] L. Lilje et al., Nucl. Inst. Meth., A 524 (1-3); 2004;
[9] S. Mishra, This Conference
[10] H. Hayano, This Conference

PAPER NOT YET RECEIVED

CRAB CAVITY DEVELOPMENT

Y. Morita#, K. Akai, K. Ebihara, T. Furuya, K. Hara, T. Honma, K. Hosoyama, A. Kabe, Y. Kojima, S. Mitsunobu, H. Nakai, K. Nakanishi, M. Ono, Md. M. Rahman* and Y. Yamamoto, KEK, Tsukuba, Ibaraki, Japan
T. Kanekiyo, Hitachi, Ltd., Tsukuba, Ibaraki, Japan
K. Okubo and K. Sennyu, MHI Kobe Shipyard, Japan

Abstract

Two superconducting crab cavities were installed in the KEKB accelerator. The KEKB (KEK B-factory) is a double-ring, asymmetric-energy, high luminosity electron-positron colliding accelerator with a finite angle beam crossing. A purpose of the crab cavities is to deflect the beam-bunches with time-varying RF fields, and to provide the head-on collision at the interaction point (crab crossing scheme). The head-on collision will drastically increase the luminosity. The crab cavity is required to have high RF fields (kick voltage) to provide beam-bunch deflection. The operating mode (crab mode, 509 MHz) is not the lowest order mode (LOM) of the cavity. In order to sufficiently damp the LOM as well as the HOMs for high beam currents in KEKB, a coaxial coupler is attached along the beam pipe. Two crab cavities have been fabricated and tested in a vertical cryostat. The cavities were recently tested with high RF power in cryostats. We have achieved required kick voltage.

INTRODUCTION

The crab crossing was first proposed by R. B. Palmer for linear colliders to increase the luminosity [1]. K. Oide and K. Yokoya suggested that this crossing scheme is applicable for ring colliders such as KEKB [2]. KEKB is a B-meson factory which consists of two storage rings with a finite angle beam crossing at the collision point. One ring is a 3.5 GeV low energy positron ring (LER) and the other is an 8 GeV high energy electron ring (HER) [3]. Main parameters of KEKB are summarized in Table 1. The crab crossing needs an RF deflector which provides transverse kicks for the beam bunches. Consequently, the beam bunches tilt at the interaction point and collide head-on. After the collision, the beam bunches are kicked back by compensating RF deflectors. Fig. 1 shows the crab crossing scheme.

K. Akai invented a beam deflecting RF cavity (Crab Cavity) [4]. His design is the base of the crab cavity for KEKB. This cavity has several unique characteristics. One is a coaxial coupler to damp the lowest order mode (LOM). Another is a not-round cavity cell (squashed cell) for separating unwanted higher order modes (HOMs). The required RF fields are high for KEKB accelerator. The kick voltage is 1.4 MV corresponding to the surface peak electric field of 21 MV/m.

Superconducting cavity is suitable for the high field requirement. To develop superconducting crab cavity, R&D program started in 1994. Using 1/3-scale Nb model cavities, fabrication methods and surface treatments were studied. In 1996 a full-scale Nb prototype cavity was fabricated and tested intensively. We achieved the required kick voltage after several tests. The second prototype cavity was fabricated for a reproducibility check. The cavity exceeded the required voltage and reached almost 3 MV. This cavity was installed in a prototype cryostat for a cool-down test.

In 2003 K. Ohmi suggested the crab crossing would improve the luminosity [5]. Using a beam-beam simulation method, he concluded that the luminosity would increase two times as much as the present one. Two crab cavities were decided to be installed in both KEKB rings. In this scheme there are no compensating crab cavities. The beam bunches wiggle in the ring. The location of crab cavities was chosen at the straight section 1 km away from the collision point, where superconducting accelerating cavities and a large He refrigerator already exist. This scheme helped to reduce the construction costs. Fabrication of two crab cavities started in 2005.

Table 1: Main parameters of KEKB

	LER	HER
Beam Energy (GeV)	3.5	8.0
Beam Current (A)	1.7	1.3
Crossing angle (mrad)	11 x 2	

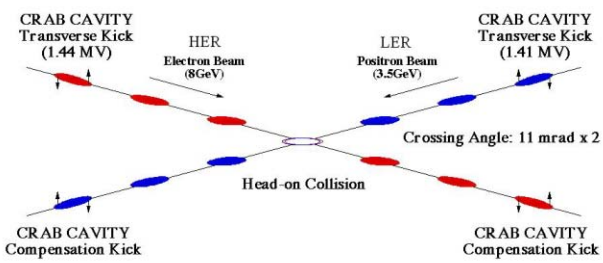

Figure 1: Crab crossing scheme.

CONCEPTUAL DESIGN

The crab cavity is excited with the TM110-like mode (Crab mode, 509 MHz) to kick the beam bunches since this mode has a large R/Q value. However, this mode is not the lowest order mode (LOM). For high current operation, it is important to sufficiently damp the LOM as well as higher order modes (HOMs).

#Yoshiyuki.morita@kek.jp
*present address: Chittagong Univ., Chittagong, Bangladesh

A coaxial coupler is inserted along the beam pipe to damp the LOM. The LOM (TM010-like mode, 410 MHz) propagates in the coaxial coupler as a TEM mode wave then damps at an RF absorber (HOM damper). Other monopole modes can also propagate in the coaxial coupler. On the other hand, the coaxial coupler has a cut-off frequency for the dipole mode. This frequency is set at 600 MHz, which is above the crab mode but below all dipole HOMs. The dipole HOMs also can propagate and damp.

The cavity cell has a not-round structure (squashed cell) to raise the frequency of unwanted parasitic mode such as the other polarization of TM110-like mode above the cut-of frequency.

Attenuation factor of the crab mode in the coaxial coupler is 60 dB/m. A long coupler, 1 m long at least, is required. A stub support supports the long inner conductor of the coupler.

Although the crab mode is below the cut-off of the coaxial coupler, this mode can propagate in the coaxial coupler as a TEM mode if the coupler is misaligned off the central axis. A notch filter is attached on the coaxial coupler to kick back the TEM-coupled crab mode. The RF parameters of the crab cavity are summarized in Table 2. Schematic diagram of the crab cavity is shown in Fig. 2.

Table 2: RF parameters of the crab cavity

fo	509 MHz
R/Q	46.2 Ω
Geometrical Factor	220
Esp/Vkick	13.5 MV/m/MV
Hsp/Vkick	424 Oe/MV
Required Kick Voltage	1.4 MV

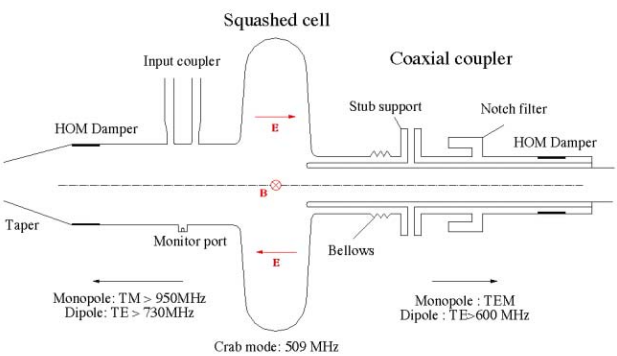

Figure 2: Schematic diagram of the crab cavity.

PROTOTYPE CAVITIES

To realize such a complicated structure of the crab cavity, we established the fabrication method for the squashed cavity cell and surface treatments for high fields [6].

Half cells were hydro-formed from Nb (RRR=180) sheet 5 mm thick and joined by electron beam welding (EBW). Welding seams at the equator of the cell were mechanically grinded. Beam pipes, coupling ports and flanges were also joined by EBW.

The cavity was polished by barrel polishing (100 μm) then electro-polished (EP I, 100 μm). After rinsed with pure water, the cavity was heat treated in a vacuum furnace (700 ^{o}C x 3 hr). Finally the cavity was rinsed by high pressure ultra-pure water rinsing (HPR).

1/3-scale model cavities were fabricated and cold-tested [7]. Then fabrication of full-scale prototype cavities followed. Using the prototype cavity #1, we studied RF performance intensively for high field application. After several modifications of surface treatments, we reached the required surface peak field of 21 MV/m with a Qo value above 10^9 [8].

Fig. 3 shows typical cold test results at 4.2 K. The cavity degraded by a miss-operation of vacuum system. Micro-particles in air contaminated the cavity surface. We tried He processing to this cavity. The RF performance recovered and the peak field exceeded 21 MV/m, however, we observed strong X-ray radiation. After this cold test, cavity was disassembled and rinsed by HPR. The performance recovered completely and no X-rays were observed. HPR is effective to clean up the micro-particles, which may be introduced to the cavity accidentally. The cavity was tested at 2.8 K. The RF fields exceeded 40 MV/m. Lower temperature operation may be an option for high field applications.

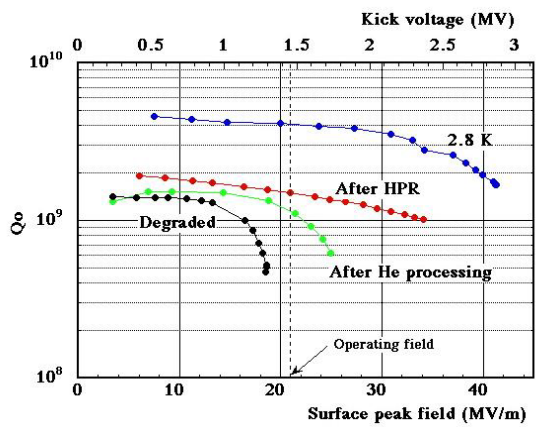

Figure 3: Vertical cold test results after HPR.

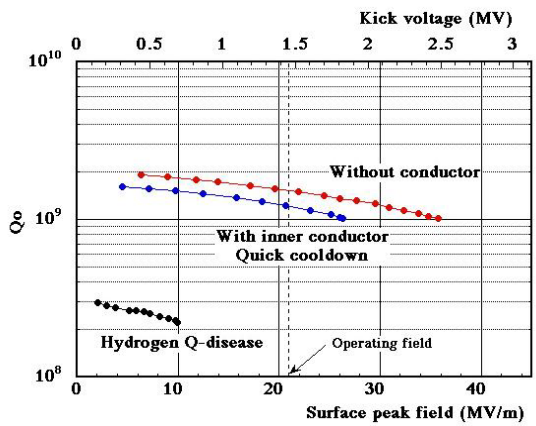

Figure 4: Vertical cold test results with coaxial coupler.

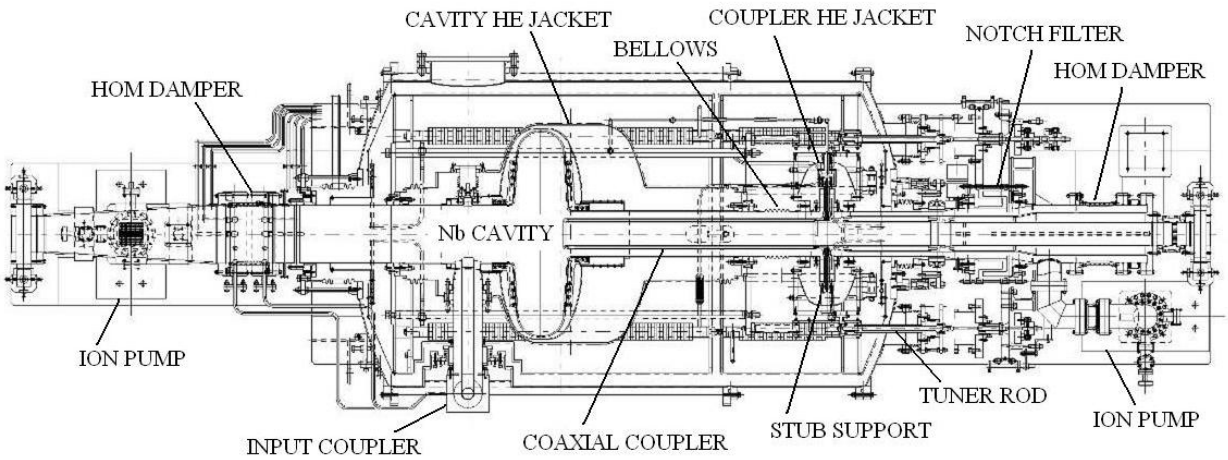

Figure 5: Crab cavity for KEKB (top view).

To test the effect of coaxial coupler, we made a model inner conductor, which is a short version of full size coupler to meet space restrictions of our vertical test stand. Fig. 4 shows cold test results with the inner conductor. At low fields, multipacting was observed around the tip of inner conductor [9]. This type of multipacting was processed in an hour. At the same time serious degradation was observed [10]. This is so-called hydrogen Q-disease of the inner conductor. Nominal surface treatments of the inner conductor involve heat treatment for degassing of hydrogen but we skipped this procedure. As is well known, the hydrogen Q-disease happens if the cavity stays at temperatures around 100 K for several hours. To prevent this disease we cooled down the cavity quickly below 150 K. We achieved the required field even with the coaxial coupler.

The prototype cavity #2 was fabricated for confirmation of our fabrication method. Electro-polishing of 5 μm surface removal (EP II) was added before HPR in standard surface treatments. The cavity exceeded 21 MV/m and reached 35 MV/m. We have established the fabrication method and surface treatments. After the vertical cold tests, this cavity was installed in a prototype cryostat and cooled down to confirm the cool-down procedures.

CRAB CAVITIES FOR KEKB

Engineering designs of the crab cavity for KEKB started in 2004 including a cryostat, coaxial coupler, etc [11]. Fig. 5 shows a cryostat assembly of the HER crab cavity.

Cryostat

We applied a jacket-type He vessel for the squashed cell crab cavity. The jacket is directly welded on stainless steel transition flanges which are connect to the cavity with indium seals. The cavity can be cleaned with HPR without breaking indium seals. The vessel provides 400 L of liquid helium. In the jacket, a permalloy magnetic shield jacket surrounds the cavity. A heater, a liquid helium level sensor, temperature sensors, and PIN diode X-ray sensors are set for monitoring.

The coaxial coupler also has a jacket-type He vessel at the stub support to cool the Nb inner conductor. The inner conductor has a cooling channel which is connected to the He vessel through the cooling path in the stub support. The vessel is connected to the cavity vessel with stainless steel tubes.

Large-size bellows, which is made from Cu-plated stainless steel 240 mm in diameter and 0.2 mm thick, connects the cavity and the coaxial coupler. This bellows is used for adjusting the coupler position for frequency tuning. The bellows has cooling channels at both flanges.

80 K thermal shields made of Al plates and Cu strips surround both jackets. A vacuum vessel made of stainless steel contains this assembly.

Coaxial Coupler

The coaxial coupler consists of three parts. These are a Nb inner conductor and stub support assembly, a tapered section part made of Cu-plated stainless steel, and a notch filter assembly part including a HOM damper. Each part is joined with RF contacts made of BeCu rings.

First the inner conductor part and the tapered section part are connected and installed in the cryostat. Then the notch filter assembly part is connected outside the vacuum vessel.

Frequency Tuner

The resonant frequency of the cavity shifts with displacement of the coaxial coupler by 30 kHz/mm. We use this shift for frequency tuning. The coaxial coupler assembly is connected to a tuning system by tuner rods. The tuner system consists of a main tuner and two sub-tuners. The main tuner is set at the central position of a movable plate to adjust insertion length of the inner conductor, while two sub-tuners are set at both sides of the plate to adjust its alignment. The main tuner consists

of a motor driving jack and a Piezo tuner. One sub-tuner is a motor driving jack and the other is a manual jack.

HOM damper

The HOM damper is a ferrite RF absorber which was developed for the KEKB accelerating damped cavities. The ferrite material is sintered on an inner surface of a copper pipe by the HIP (Hot Isostatic Press) method with 1500 atm and 900 ^{o}C. The size of ferrite material is 120 mm in diameter, 120 mm in length and 4 mm in thickness. Copper tube is wound on the outer surface of the copper pipe for water cooling. One damper is set at the end part of the coaxial coupler and the other is set at the beam pipe. These dampers were RF tested up to 10 kW before installation.

Input coupler

The input coupler is a coaxial-type one which is horizontally inserted into the cavity beam pipe to couple the crab mode. The coupler has a stub support to support the inner conductor. This coupler is required to handle about 100 kW of RF power. The couplers were RF tested up to 200kW before installation.

HIGH POWER TEST

Two crab cavities were fabricated with the same procedure as the prototype cavities. Those cavities were cold tested in a vertical cryostat. Nb inner conductors of the coaxial coupler were also fabricated. The inner conductors were heat treated to prevent hydrogen Q-disease.

The HER crab cavity was first assembled in a clean room and high power tested in July 2006. Several modifications were needed such as the tuner mechanism, limited stroke of the coaxial coupler, etc. After the high power test, the HER crab cavity was disassembled and several modification were done. The tuner rods were replaced by more rigid ones. The large-size bellows, connecting the cavity and coaxial coupler, were made from stainless steel pipe 0.2 mm thick. In the first test, we used bellows made of Cu pipe 0.4 mm thick. This modification made its stroke wider (+/-10 mm). The coaxial coupler part outside the vacuum vessel was set on a movable base for smooth displacement.

The HER crab cavity was tested again in Nov. 2006. The LER crab cavity, which was modified in the same way, was tested in Dec. Details of the high power tests are described below.

Cool-down

The crab cavity was set in a high power test stand and connected to the 8 kW NIKKO helium refrigerator. The refrigerator cooled down the cavity at the rate of 2 K/h to avoid vacuum leakage. The Nb inner conductor of coaxial coupler was also cooled down by adjusting the helium gas flow. During the cool-down, the resonant frequency and shrinkage of the cavity were monitored. The frequency shifted 400 kHz at the end of cool-down.

Tuner Test

After the cool-down, the resonant frequency was adjusted to the operating frequency of 509 MHz by deforming the cavity cell then the tuner adjustment followed. The alignment of the coaxial coupler was set by the sub-tuner by monitoring the RF power leakage at the coaxial coupler. We set the coupler at the position where the RF power leakage is minimized. The main tuner was tested and a frequency shift of 30 kHz/mm was obtained. The main tuner was connected to the tuner feed back system and the resonant frequency was maintained at the operating frequency.

High Power Conditioning

The crab cavity was connected to a 1 MW klystron. Several interlocks were set to protect the cavity. These were vacuum interlocks, an arc sensor at the input coupler, RF power detectors at the coaxial coupler, and a break-down detector of the cavity. We gradually increased the input RF power as the cavity was being processed. Pulse conditioning was used frequently. Fig. 6 shows a conditioning state of the HER crab cavity. We reached 1.4 MV that is the operating voltage of this cavity. After that, the kick voltage slightly degraded because of high vacuum pressure. The pressure was getting higher during the conditioning. We decided to warm the cavity up to 85 K to evacuate condensed gases on the cavity surface. Temperatures and the vacuum pressure during this warm-up are shown in the same figure. We observed hydrogen and nitrogen/carbon mono-oxide out-gassing. We re-cooled the cavity and the vacuum pressure decreased below 10^{-7} Pa. After the evacuation we reached 1.8 MV.

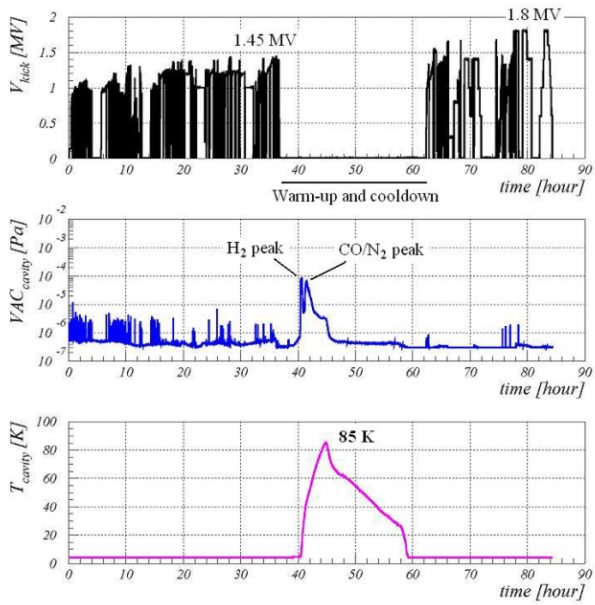

Figure 6: Kick voltage, vacuum pressure and temperature of the HER crab cavity during conditioning.

The LER crab cavity was also conditioned in the same manner. No warm-up of the cavity was needed before we reached 1.8 MV.

The external Q value of the coupler was measured by field decay method. Qext are 1.3 x 10^5 and 2.0 x 10^5 for HER and LER crab cavities, respectively. Those values reasonably agree with the designed one (1.6 x 10^5). We monitored tuner phase during the conditioning. The phase distribution of the HER crab cavity was within 1 degree, which is acceptable for KEKB. On the other hand, that of the LER crab cavity was much larger. We need further investigation.

Qo measurement

RF losses of the cavity were measured calorimetrically at several kick voltages. Heat loads were obtained by adjusting a heater power set in the He jacket so as to keep the liquid He level constant. These heat loads give Qo values. Fig. 7 shows the results for both cavities. Qo measured at the vertical cold tests are shown in the same figure for comparison. These data agree within measurement errors. No significant Qo degradation was observed in these tests.

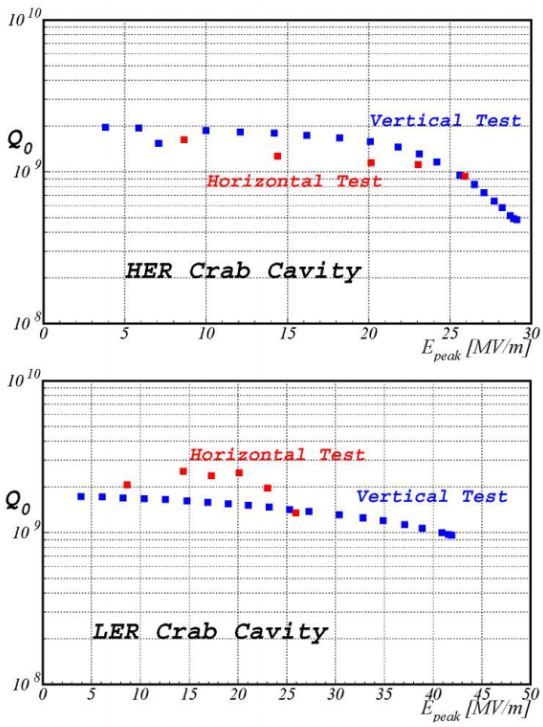

Figure 7: Qo of the HER crab cavity (above) and LER crab cavity (below). Qo obtained in the vertical cold tests are plotted in the same figures.

SUMMARY

The crab cavities for the crab crossing of the KEKB were developed. The fabrication method and surface treatments were intensively studied with prototype cavities. Two crab cavities for KEKB have been fabricated and tested in cryostat. We have achieved the required kick voltage (1.4 MV). Those cavities have been installed in both KEKB rings (Fig. 8). Beam tests will start soon.

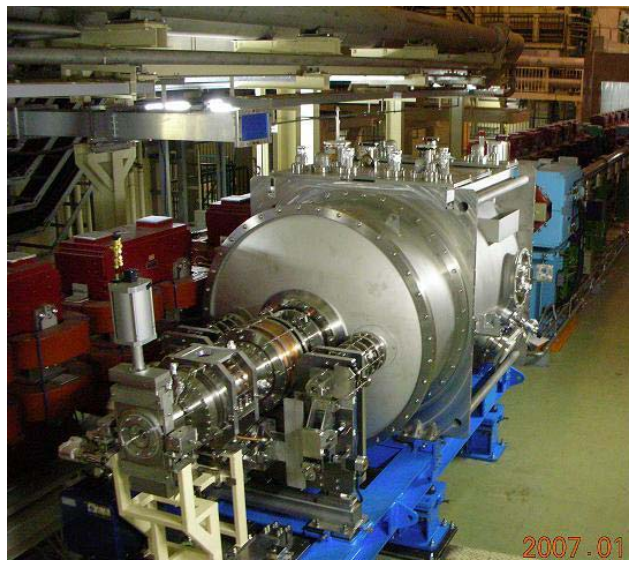

Figure 8: HER crab cavity installed in the KEKB ring.

ACKNOWLEDGEMENT

The authors wish to express their gratitude to Prof. K. Oide for his continuous support.

REFERENCES

[1] R. B. Palmer, SLAC-PUB-4707, 1988.
[2] K. Oide and K. Yokoya, SLAC-PUB-4832, 1989.
[3] KEKB B-factory Design Report, KEK Report 957, June 1995.
[4] K. Akai et al, Proc. of the 15th Int. Conf. on High Energy Accel, 1993, P. 757.
[5] K. Ohmi, presented at 8th KEKB Review Committee, KEK, Japan, Feb. 2003.
[6] K. Hosoyama et al, Proc. of the 8th Workshop on RF Superconductivity, Padova, Italy, 1997, p. 547.
[7] Y. Morita et al, Proc. of the 8th Workshop on RF Superconductivity, Padova, Italy, 1997, p. 540.
[8] H. Nakai et al, Proc. of the 11th Workshop on RF Superconductivity, Lubeck, Germany, 2003.
[9] Y. Morita et al, Proc. of the 11th Workshop on RF Superconductivity, Lubeck, Germany, 2003.
[10] Y. Morita et al, Proc. of the 10th Workshop on RF Superconductivity, KEK, Japan, 2001, p. 403.
[11] K. Hosoyama et al, Proc. of the 12th Workshop on RF Superconductivity, Cornell Univ., USA, 2005.

R&D ON VACUUM COMPONENTS FOR HIGH-CURRENT ACCELERATORS

Y. Suetsugu[#], K. Shibata, H. Hisamatsu, M. Shirai and K. Kanazawa,
KEK, Tsukuba, Japan

Abstract

R&D on various vacuum components adaptable to future high-current accelerators has been continuously progressing at KEK. Copper beam ducts with one or two ante-chambers were designed to dilute the synchrotron radiation (SR) power density, and also to suppress photoelectrons around beams. Inner surfaces with a low secondary electron yield (SEY) were investigated to mitigate electron-cloud formation. Bellows chambers and gate valves with high thermal strength and low beam impedance were developed. A special flange with no gap at the connection point was designed. A novel movable mask (collimator) with low beam impedance was recently proposed. These components have been installed at the KEK B-factory (KEKB), and the performances have been investigated using an intense beam of up to 1.7 A.

INTRODUCTION

In future high-current accelerators, such as Super B-factories, a stored beam current of several amperes and a bunch length of a few mm are required to achieve a luminosity on the order of 1×10^{36} $cm^{-2}s^{-1}$ [1, 2]. These parameters impose very severe challenges to the vacuum system [3, 4]. The beam duct has to manage the synchrotron radiation (SR) power density up to several tens Wmm^{-2}. The vacuum components should have low beam impedance, and be able to stand up against the intense higher order modes (HOM) at the same time. Suppression of the electron cloud instability (ECI) [5] is also a serious problem in a positron ring. These are common key issues not only for a high-current factory machine, but also for the dumping ring (DR) and the collimators of the international linear collider (ILC), and the next generation of SR rings, where a very low emittance is required [6, 7].

R&D on various vacuum components to meet these demands has been progressing at KEK [8-17]. Copper beam ducts with antechambers were designed and manufactured [8, 9]. The antechamber scheme was adopted to deal with the intense SR power and to suppress photoelectrons at the same time. The effects of the inner coatings of NEG materials (Ti, Zr, V) and TiN were studied, which were said to have low secondary electron yields (SEY) [10, 11]. Bellows chambers and gate valves with a comb-type RF-shield were newly developed [12-14]. A special connection flange was designed and examined, which has a small step, or gap, inside, even for a beam duct with antechambers [15]. A movable mask (collimator) with low impedance was recently proposed and the study has just begun [16].

These components have been installed for testing at the KEK B-factory (KEKB) [18, 19]. KEKB is an electron-positron collider with asymmetric energies, and consists of two rings, that is, a 3.5 GeV positron ring (Low Energy Ring, LER) and an 8.0 GeV electron ring (High Energy Ring, HER). The maximum stored beam currents of LER and HER are 1.7 A and 1.4 A at 1389 bunches, respectively. At present, KEKB is the most suitable machine for R&D about future accelerators with high intensities. The R&D is progressing based on various experiences in the vacuum system of KEKB [20, 21]. The concepts of these newly-developed vacuum components and the results of recent studies are reviewed here.

BEAM DUCT

The R&D of vacuum components began with a beam duct with an ante-chamber in 2003 [8, 9]. The beam duct consists of two channels, i.e. a beam channel where a beam circulates, and an SR channel (ante-chamber) aside where synchrotron radiation (SR) passes through. By using the ante-chamber scheme, the maximum power density of SR can be diluted at the side wall. Photoelectrons inside the beam channel, furthermore, are small compared to that of a simple circular duct, which is a big merit for a positron ring to suppress the ECI.

Several kinds of copper beam ducts with ante-chambers have been manufactured, and installed into the KEKB LER. Copper (Oxygen Free Copper, OFC) was adopted for its high thermal strength and good radiation shielding property [20, 21]. The electron beam was used to weld copper to copper. The inner diameter of the beam channel was 94 mm, and the thickness was 6 mm. The depth and the height of the ante-chamber were 65 mm and 15 mm, respectively. The ducts were manufactured using two methods, that is, pressing and forming (cold drawing). A copper beam duct with two ante-chambers is presented in Fig. 1, for example. Two NEG-pump channels were placed at the top and bottom of the ante-chambers.

Beam ducts with one ante-chamber were installed in an arc section of LER. The SR power and the photon density was 3 kW m^{-1} and 8.5×10^{18} photons s^{-1} m^{-1}, respectively, at a beam current of 1 A. The critical energy of SR was 5.8 keV. Beam ducts with two ante-chambers, on the other hand, were installed at a wiggler section, where the SR hits the duct at both sides. The maximum power density and the direct photon density were about 227 Wm^{-1} and 7.5×10^{17} photons m^{-1} s^{-1} at a beam current of 1 A, respectively.

[#]yusuke.suetsugu@kek.jp

Fig. 1 Copper beam duct with two ante-chambers for tests.

The temperatures and vacuum pressures around the ducts were monitored during beam operation up to a beam current of 1.7 A (1389 bunches). Although arcing was observed at a welding part of one model at the beginning of commissioning [8], no problem was found in other models. The temperature of the duct was slightly higher, but almost in agreement with the expectation.

From the view point of ECI, the number of electrons around the beam was measured by an electron monitor [22]. A reduction in the number of photoelectrons by one or two orders of magnitude compared to a simple circular duct was confirmed at a low-current region, less than 0.1 A, where the photoelectrons were dominant [9]. The electron number at a high-current region, such as 1.5 A, was also smaller, but the reduction was only by a factor of 4. This was because the main component of the electron cloud at the region was the secondary electrons, which were generated in a multiplication process by highly charged bunches.

COATING WITH LOW SEY

As described above, secondary electrons play a large part in the formation of an electron cloud at a high-current region. One promising way to suppress the ECI, therefore, is to apply a surface with a low SEY to the inner surface of a beam duct.

The secondary electron and photoelectron yields (SEY and PEY) of the NEG coating and the TiN coating have been studied using KEKB LER [10, 11]. These coatings are said to have a low SEY compared to metals, and the coating processes are well established. Test chambers with the NEG and the TiN coating were first installed at an arc section of the KEKB positron ring. The test chambers have a circular cross section (ϕ94 mm). The thicknesses are about a few micro-metres. The number of electrons around positron bunches was measured up to a beam current of about 1.7 A, and compared with each other.

The electron number of the TiN-coated chamber was clearly smaller than that of the non-coated copper chamber by a factor of 2. The electron number in the case of the NEG-coated chamber, on the other hand, was

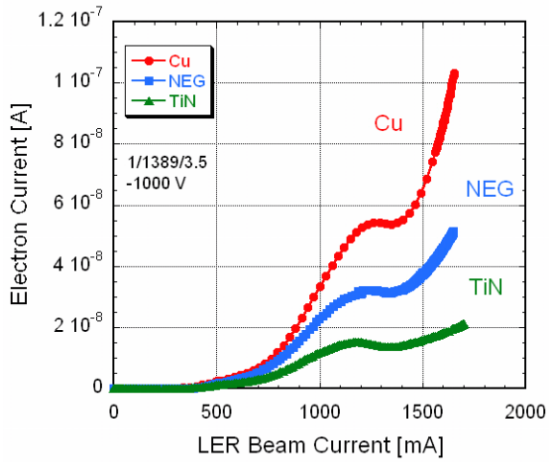

Fig. 2 Measured electron current for copper (Cu), NEG coating (NEG) and TiN coating (TiN) as a function of beam current.

almost the same as that of the copper chamber. Only a small difference was observed at a high current region, around 1. 5 A.

Using a simulation, the maximum SEY (δ_{max}) and the PEY (η_e) of the TiN coating, the NEG coating and the copper were estimated based on the measured electron current. It was found that the TiN coating had an SEY ($\delta_{max} \sim 0.9$) as low as that of the NEG coating ($\delta_{max} \sim 1.0$), but the electron current was clearly smaller than that of the NEG coating, due to its lower η_e (~ 0.14). This study indicated that suppression of photoelectrons is required to make effective use of a surface with a low SEY.

To see the effect of SEY more clearly, similar studies were performed at a straight section of LER, where the direct photon number is less than 1/10 of that at an arc section. The electron number around the beam for the NEG-coated, the TiN-coated and non-coated copper chamber were again measured. The electron numbers for the TiN coating and the NEG coating were about 1/3 and 2/3 of that in the case of the copper chamber, as shown in Fig.2. The difference between the NEG coating and the copper was clear in this case. Assuming almost the same η_e for three cases, the δ_{max} values were again estimated using the previous simulation. Although the study is still in progress, the results are almost consistent with those obtained at the arc section.

BELLOWS CHAMBER AND GATE VALVES

Bellows chambers and gate valves with an RF-shield structure are indispensable to connect beam ducts with one another. The cross section has to fit to that of the beam ducts. The RF-shield should have a uniform inner surface to avoid exciting HOM, reliable electric contact to smoothly flow the beam-induced wall current, and also a high thermal strength.

Bellows chambers and gate valves with a comb-type RF-shield have been developed at KEK [12-14]. A schematic structure of a comb-type RF-shield is shown in

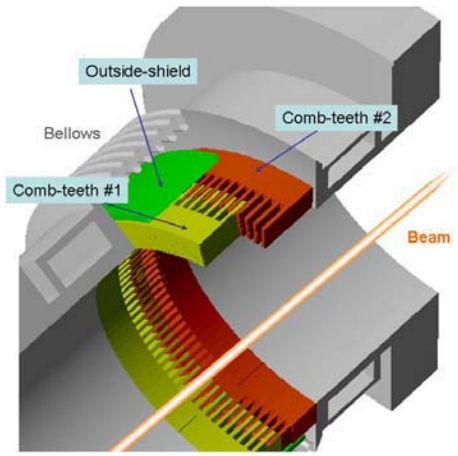

Fig. 3 Conceptual structure of a comb-type RF-shield for a bellows chamber.

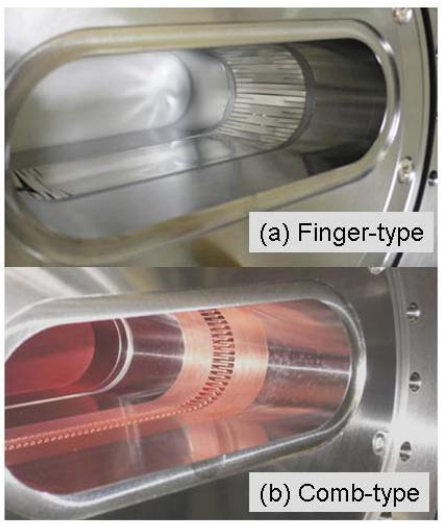

Fig. 4 Inside view of gate valves with (a) finger-type and (b) comb-type RF-shields.

Fig. 3, and an inside view of a gate valve is presented in Fig. 4, for example. The comb-type RF-shield consists of no more than thin fingers, but nested comb teeth. The TE-mode like HOM can hardly go through it. The RF-shield has a lower beam impedance than the conventional finger-type one according to a calculation. The transverse off-set, however, was limited compared to the finger-type.

The first test model of the bellows chamber with this RF-shield was installed in the KEKB LER in 2003. The inner diameter was 94 mm, and the length was 160 mm. The thickness, length and radial thickness of a tooth were 1 mm, 10 mm and 10 mm, respectively. The comb teeth were made of copper.

The temperature of the corrugation of the bellows chamber, which was located just near to the movable mask, decreased to about 1/6 compared to the case of a finger-type RF-shield, from 48°C (ΔT = 23°C) to 29°C (ΔT = 4°C) at a beam current of 1.7 A, for example. No problems, such as discharging, have been observed. The RF-shield was then adopted to bellows chambers with a race-track cross section (150 mm × 50 mm), which were installed in the KEKB HER. A reduction of the temperature by a factor of 3 was again obtained during beam operation.

A simplification of the structure has was tried in parallel. In addition to the comb teeth, the original structure (Ver.0) had small fingers at the back side between overlapped comb-teeth (Back-shield), and a spring-type shield on the outside (Outside-shield), in order to make sure of the shielding for the low-frequency components. A modified model (Ver.2), where the back-shield was omitted from Ver.0, greatly simplified the structure, and has shown no problem up to now.

Bellows chambers with the same cross section to the beam duct with ante-chambers were recently developed, as shown in Fig. 5. A comb-type RF-shield (Ver.2) was adopted for that, since it could smoothly fit to the complicated cross section. The comb-teeth and the cooling channel were OFC. The nominal length of the bellows chamber was 200 mm, and the stroke was ±4 mm.

They were installed in 2004 and revealed no problem up to now. The temperature of the bellows was about 31°C (ΔT = 6°C) at 1.7 A, which was almost the same as that of adjacent circular bellows chambers with a finger-type RF-shield.

R&D to apply the comb-type RF-shield to gate valves has been tried under collaboration with VAT Vakuumventile AG [23]. A big problem in the RF-shield for gate valves was the generation of dust due to abrasion during an open/close motion. The model Ver.2 was thus applied to the gate valves, where bending fingers were used as Outside-shield. The base design of the valve, such as the vacuum sealing mechanism, was the same as the standard one, and only the RF-shield part was modified. The tooth was pure copper, and other parts were stainless-steel (SS304).

The first test model had a diameter of 94 mm and a width of 95 mm, and was installed into the KEKB LER. The temperature at the body decreased from 45 - 37°C (ΔT = 20 - 12°C) to 28°C (ΔT = 3°C) at a beam current of 1.7 A. The decrease of the temperature rise at the body meant a decrease of HOM intruding into the inside. No problem was found in both the temperature and the

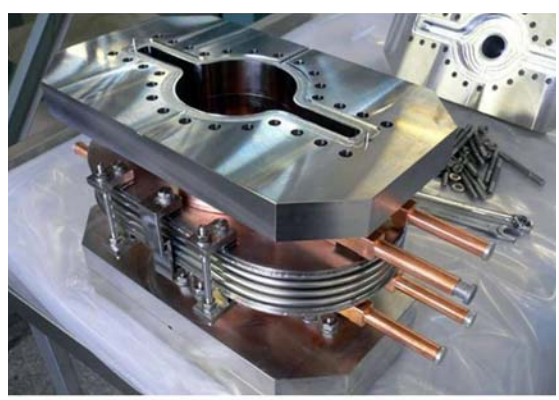

Fig. 5 Bellows chamber for beam ducts with two ante-chambers.

vacuum pressures up to a beam current of 1.8 A. The comb-type RF-shield may be suitable to the gate valve, rather than the bellows chambers, because only expansion and contraction are required, in principle, there.

As a next step, a gate valve with a race-track shape was manufactured and installed into the KEKB HER. The race-track had a width of 150 mm and a height of 50 mm (see Fig. 4). The temperature decreased form 33°C (ΔT = 8°C) to 28°C (ΔT = 3°C) at 1.35 A (1389 bunch). It was interesting that the temperature of a bellows chamber connected to the gate valve also decreased after exchanging the gate valve. This is an indication that the excited HOM decreased upon using the comb-type RF-shield.

CONNECTION FLANGE

Even connection flanges of beam ducts can be a big HOM source, since the number is huge, about 2000 per one ring. Helicoflex sealing is no longer sufficient, although the depth of a gap is about 2 mm [20]. The Helicoflex sealing, furthermore, cannot follow the complicated aperture, such as that of a beam duct with antechambers. The conventional RF-bridge is made of thin metal fingers or metal O-rings [24]. The small fingers may be able to follow the complicated aperture, but a uniform electric contact can hardly be guaranteed.

The MO-type (Matsumoto-Ohtsuka-type) flange used for a connection flange can seal a vacuum at only the inner surface using a copper gasket [15]. The copper gasket also works as a secure RF-bridge, which has no gap or step at the inner surface. The thermal strength of the copper gasket is much higher than that of thin metal fingers or O-rings.

The specially designed MO-type flange was used for the bellows chambers and the beam ducts with antechambers, as also presented in Fig. 1 and Fig. 5. It has a width, a height and a thickness of 320 mm, 190 mm and 30 mm, respectively. The material was stainless-steel 316. A vacuum seal was achieved with a fastening torque of about 16 Nm, which was almost the same as in the case of a standard circular conflate flange with a similar diameter. Baking several times up to 200°C showed no vacuum leak.

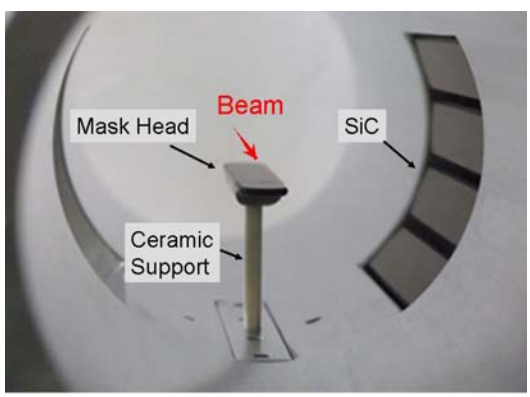

Fig. 6 Inside view of a new-type movable mask (a trial model).

No problem was found up to a beam current of 1.7 A. The temperature of flanges was about 40°C (ΔT = 15°C) at a beam current of 1.7 A. The temperature was almost the same as that of the adjacent standard circular flanges with a metal O-ring.

MOVABLE MASK (COLLIMATOR)

A movable mask (collimator) is a special vacuum component used to cut off spent particles around a nominal beam orbit, and then to decrease the background noise of the particle detector [25, 26]. The movable mask is a key component for high-luminosity machines.

The movable mask has a head (a block of metal with several radiation lengths) just near to the beam orbit. The movable mask, therefore, inherently has a high beam impedance [27]. The loss factors are typically near to 1×10^{12} VC^{-1} at a bunch length of 3 mm. Then, the parasitic loss reaches up to 200 kW, assuming a beam current of 10 A (5000 bunches).

Another problem of the movable mask is damage to the mask head due to direct hitting of the beam, where copper or titanium have usually been used [28]. The beam deposits energy in a narrow area of the head, which can melt it.

Recently, a new structure of a movable mask with low beam impedance was proposed [16]. The mask head is supported by a ceramics rod with a thin and low conductive layer at one side, which can reduce the interference between the mask head and the beam. The mask head is a copper-coated ceramics, which has a higher thermal strength compared to the metals used so far. A HOM absorber (SiC, Silicon Carbide) is prepared just near to the mask head to absorb extra HOM. An inside view of the new structure is presented in Fig. 6.

The RF-properties of the new-type movable mask was examined by simulation codes, such as the MAFIA and the Microwave Studio. The resonant frequencies, the *Q*-factors, the impedances of the trapped modes, and the loss factors were calculated. The growth rates of the coupled bunch instability under the parameters of the KEKB and the Super KEKB were evaluated, and the availability was confirmed. A test model was then manufactured and installed into the KEKB LER this winter. The performance as a movable mask will be tested, as well as the temperatures of the test model and the head, itself, during beam operation this year.

FUTURE PLAN

Following the basic R&D, as described above, a plan to replace the present circular beam ducts at a wiggler section of the KEKB positron ring by beam ducts with ante-chambers is progressing. The wiggler section has a length of about 130 m. The region includes 25 straight ducts (about 3.5 m), 13 Q-duct (ducts for quadrupole magnets, about 1.7 m) with BPM (Beam Position Monitors) and 37 bellows chambers (200 mm). The specification for the beam ducts and the BPM should be matched to those for Super KEKB. The inner surface of

the beam duct will be coated by TiN to reduce the SEY. The replacement can be a final test for an upgrade of KEKB in the future.

The new movable mask will be applied to HER following a beam test at LER. The concept of the "stealth" movable mask can be applied to the clearing electrode for ECI. R&D about the clearing electrode will also begin soon.

ACKNOWLEDGMENT

We would like to thank Professor K. Oide for his continuous encouragement for this study.

REFERENCES

[1] SuperKEKB Task Force, "Letter of Intent for KEK Super B Factory", KEK Report2004-4 (2004).
[2] First LNF Workshop on SuperB, Frascati, Nov. 2005, http://www.lnf.infn.it/conference/superbf05/
[3] J. Seeman, et al. "PEP-II Status and Future Plans ", Proceedings of EPAC'02, 3 -7 June, Paris, p. 434.
[4] Y. Suetsugu, "Vacuum System for High Power Lepton Rings", PAC'03, Portland, 12-16 May, p. 612.
[5] K Oide, "Observations and Cures of Electron-Cloud Effects at The KEKB Low Energy Ring", CERN Report No.SL-2001-003, 2001.
[6] ILC Damping Rings R&D Workshop -ILCDR06, September 26-28, Cornel University, https://wiki.lepp.cornell.edu/ilc/bin/view/Public/DampingRings/ILCDR06/WebHome
[7] C. D. Beard and J. D. A.Smith, "NUMERICAL CALCULATIONS OF COLLIMATOR INSERTIONS", Proceedings of EPAC'06, Edinburgh, June 26 - 30, p. 709.
[8] Y. Suetsugu, K. Kanazawa, K. Shibata, H. Hisamatsu, K. Oide, F. Takasaki, A.E. Bondar, V. Kuzminykh, A. Gorbovsky, R. Dostovalov, K. Sennyu and H. Hara, NIM-PR-A, 538 (2005) 206.
[9] Y. Suetsugu, K. Shibata, H. Hisamatsu, M. Shimamoto, M. Shirai and K. Kanazawa , "R&D on Copper Beam Ducts with Antechambers and Related Vacuum Components", Proceedings of EPAC2006, June 26 - 30, Edinburgh, p.1438.
[10] Y.Suetsugu, K.Kanazawa, K.Shibata, H.Hisamatsu, K.Oide, F.Takasaki, R.V.Dostovalov, A.A.Krasnov, K.V.Zolotarev, E.S.Konstantinov, V.A.Chernov, A.E.Bondar and A.N.Shmakov, NIM-PR-A, 554 (2005) 92.
[11] Y. Suetsugu, K. Kanazawa, K. Shibata and H. Hisamatsu, NIM-PR-A, 556 (2006) 399.
[12] Y. Suetsugu, M. Shirai and K. Shibata, Phys. Rev. Special Topics - Acc. Beams, 6 (2003) 103201.
[13] Y. Suetsugu, M. Shirai, K.Shibata, K. Murata, M. Kaneko, K. Sakamoto, K. Sugisaki and M. Kawahara, NIM-PR-A, 531 (2004) 367.
[14] Y. Suetsugu, K. Kanazawa, N. Ohuchi, K. Shibata, M. Shirai, "APPLICATION OF COMB-TYPE RF SHIELD TO BELLOWS CHAMBERS AND GATE VALVES", Proceedings of PAC2005, May 16-20, Knoxville, p.3203.
[15] Y. Suetsugu, M. Shirai and M. Ohtsuka, J. Vac. Sci. Technol., A23 (2005) 1721.
[16] Y. Suetsugu, K. Shibata, A. Morishige, Y. Suzuki and M. Tsuchiya, Phys. Rev. Special Topics - Acc. Beams, 9 (2006) 103501.
[17] Y. Suetsugu, K. Kanazawa, K. Shibata, N. Ohuchi, H. Hisamatsu, M. Shirai, "R&D STATUS OF VACUUM COMPONENTS FOR THE UPGRADE OF KEKB", Proceedings of PAC2005, May 16-20, Knoxville, p.3256.
[18] K. Akai, et al., Nucl. Instrum. Methods in Phys. Res. A, 499 (2003) 191.
[19] Y. Funakoshi, et al., "KEKB PERFORMANCE" , EPAC2004, 5-10 July, Lucerne, p.707.
[20] K. Kanazawa, S. Kato, Y. Suetsugu, H. Hisamatsu, M. Shimamoto, M. Sato, M. Shirai, Appl. Surf. Sci., 169-170 (2001) 715.
[21] K.Kanazawa, S.Kato, Y.Suetsugu, H.Hisamatsu, M.Shimamoto and M.Shirai, NIM-PR-A, 499 (2003) 66.
[22] Y.Ohnishi, T.Murakami, K.Kanazawa, M.Tanaka and M.Tejima, "Detection of Photoelectron Cloud in Positron Ring at KEKB", www-eng.kek.jp/heacc2001/ProceedingsHP.html.
[23] http://www.vat.ch, home page of VAT Vakuumventile AG.
[24] J.R.Chen and Y.C.Liu, Vacuum, 44 (1993) 545.
[25] Y.Suetsugu, K.Shibata, T.Sanami, T.Kageyama and Y.Takeuchi, Review Sci. Instrum.,74 (2003) 3297.
[26] Y.Suetsugu, T.Kageyama, K.Shibata and T.Sanami, NIM-PR-A, 513 (2003) 465.
[27] Y.Suetsugu, T.Kageyama, Y.Takeuchi and K.Shibata, NIM-PR-A, 533 (2004) 295.
[28] Y.Suetsugu, K.Kanazawa, S.Kato, H.Hisamatsu, M.Shimamoto and M.Shirai, J. Vac. Sci. Technol.A, A21 (2003) 1436.

LHC STATUS

Lyndon Evans, CERN, Geneva, Switzerland

Abstract

The installation of the Large Hadron Collider at CERN is now approaching completion. Almost 1100 of the 1232 main bending magnets are installed and the whole ring will be installed by the end of March 2007. Emphasis is now moving from installation to commissioning, with the cool down of the first of the 8 sectors to liquid helium temperature well underway. In the other sectors, interconnect work is proceeding at a satisfactory pace and will be finished by the end of August. It is foreseen to inject the first beam into the LHC in November with the objective of having first collisions at the injection energy (450 GeV/c) in order to debug the machine and detectors before stopping for the annual winter shutdown. During this time, the detector installation will be finished and the machine will be pushed to full current ready for the first physics run at 7 TeV per beam in 2008.

MACHINE LAYOUT

The LHC is a two-ring superconducting proton-proton collider housed in the 27 km circumference tunnel originally constructed for the Large Electron-Positron collider (LEP), now decommissioned. It is designed to provide proton-proton collisions with unprecedented luminosity (10^{34} cm^{-2} s^{-1}) and a centre-of-mass energy of 14 TeV for the study of rare events such as the production of the Higgs boson if it exists. In order to reach the required energy in the existing tunnel, the dipoles must operate at high field (8.3 T) and therefore have to be cooled in superfluid helium at 1.9 K to increase the critical current of the NbTi conductor to the required value. In addition to p-p operation, the LHC will be able to collide heavy nuclei (Pb-Pb) with a centre-of-mass energy of 1150 TeV (2.76 TeV/U and 7 TeV per charge). By modifying the obsolete antiproton ring (LEAR) into an ion accumulator (LIER) in which electron cooling is applied, the luminosity can reach 10^{27} cm^{-2} s^{-1}.

The basic layout of the LHC is shown in Figure 1. The machine has eight arcs and straight sections approximately 528 m long. Four of the straight sections house the LHC detectors. The two high luminosity detectors, ATLAS and CMS, are located at diametrically opposite straight sections at Points 1 and 5 respectively. The two other detectors (ALICE and LHCb are located at Points 2 and 8, which also contain the injection systems for the two rings.

The other four straight sections contain machine utilities. Points 3 and 7 contain two collimation systems for capturing stray particles. Point 3 is designed to capture off-momentum particles whilst the collimation layout at Point 7 is designed to control the beam halo. Point 4 contains the Radio Frequency superconducting acceleration cavities operating at 400 MHz, twice the frequency of the LHC injector. Finally, Point 6 contains the beam abort systems for the two beams which will allow the beams to be extracted safely and deposited onto external dumps capable of absorbing the considerable stored energy (up to 350 MJ at top energy and intensity).

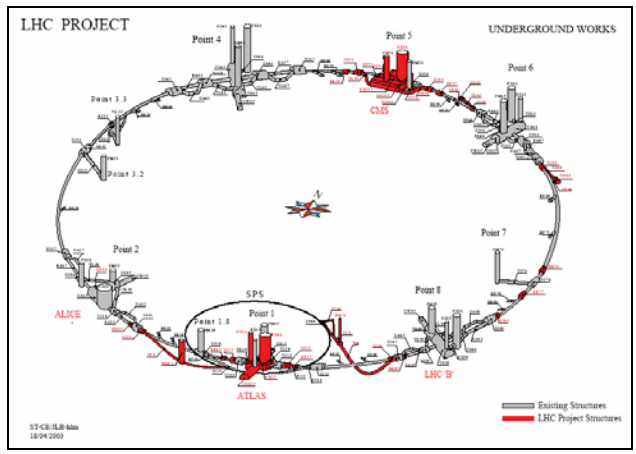

Figure 1: Machine layout.

INSTALLATION AND COMMISSIONING OF MAJOR SYSTEMS

Magnets

The full list of superconducting magnets and their function is shown in Table 1. All magnets have now been delivered. They range from the large 15 m long, 35 ton dipoles to the 11 cm long, 5 kg decapole-octupole correctors inside the dipole cold mass which correct for unwanted multipoles of the dipole field. Half of these correctors (616 units) and half of the sextupole correctors (MCS, 1232 units) were built in India under the supervision of RRCAT. All magnets were tested at 4.2 K at RRCAT before being shipped to the European manufacturers of the dipoles to be integrated into the cold masses.

Figure 2 shows the history of the main dipoles from production to installation. Delivery of all 1232 dipoles (excluding spares) is now complete (top curve). On arrival, the dipoles are inserted into their cryostats and connected to one of the cryogenic test stands (Figure 3), where they are cooled to their operating temperature of 1.8 K. Cold tests include electrical quality assurance and a training campaign where the dipoles are taken above their operational field of 8.3 T. A random sample of about 20 % is used for magnetic measurements in order to check that the correlation between warm measurements at the factories (all dipoles are measured warm) and cold measurements remains good. The cold testing of all magnets has been an enormous effort with the test stations running 24 hours per day, 7 days per week for over 3 years with only one short shutdown per year for maintenance. This would not have been possible without

the contribution of highly qualified personnel from India. Nearly 100 Indian scientists and engineers from 4 different establishments have contributed on a one-year rotational basis.

Table 1: List of superconducting magnets and their function.

Type	Number	Function
MB	1232	Main dipoles
MQ	392	Arc quadrupoles
MBX/MBR	16	Separation and recombination dipoles
MSCB	376	Combined chromaticity and closed orbit correctors
MCS	2464	Sextupole correctors for persistent currents at injection
MCDO	1232	Octupole/decapole correctors for persistent currents at injection
MO	336	Landau damping octupoles
MQT/MQTL	248	Tuning quadrupoles
MCB	190	Orbit correction dipoles
MQM	86	Dispersion suppressor and matching section quadrupoles
MQY	24	Enlarged-aperture quadrupoles in insertions
MQX	32	Low-beta insertion quadrupoles

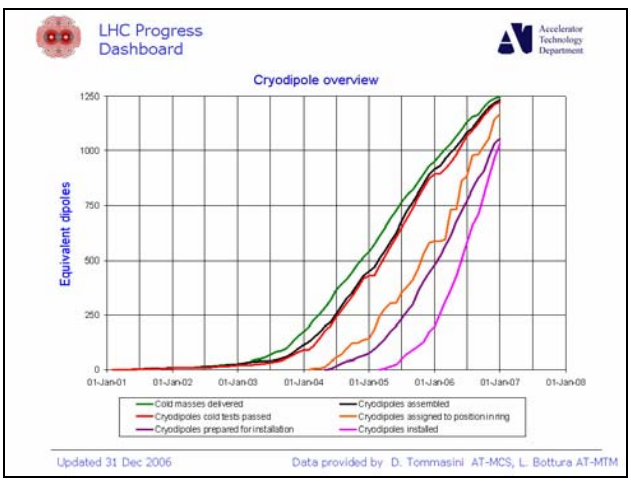

Figure 2: Cryodipole overview.

Once the cold tests are completed, each dipole is assigned a slot in the machine by the Magnet Evaluation Board depending on a number of criteria, one of the most important being the available aperture. The magnets are then prepared for the tunnel (fifth curve), and finally installed (last curve). They are all installed through a single large shaft (Figure 4) and are transported underground to their final location (Figure 5) which can be as much as 15 km from their point of dispatch. They are then transferred from the transport vehicle to their final position (Figure 6). The jacks for aligning the magnets were all made in India. At the time of writing, 1100 of the 1232 dipoles are installed and the whole installation will be finished by the end of March 2007.

The logistics chain for the main quadrupoles is similar to that of the dipoles. The quadrupoles are delivered as Short Straight Sections (SSS) with correctors (MSCB and MO or MQT) produced by other manufacturers already integrated. The SSS are inserted into their cryostats at CERN, which is a much more complicated process than for the dipoles because the SSS are the main interface between the magnets and the cryogenic system. Finally they are individually cold tested before tunnel preparation and installation. Figure 7 shows a similar set of curves as for the dipole. It can be seen that installation will also be complete by March.

Figure 3: Cryogenic test stands.

Figure 4: Lowering of a dipole.

Figure 5: Underground transport.

Figure 6: Magnet transfer.

In addition to the regular arc SSS, there are about 100 special SSS in the matching regions and dispersion suppressors which are integrated into cold masses at CERN from bare quadrupoles and correctors built in industry. Production of all special cold masses is finished. All 32 low-beta quadrupoles (MQX) have been delivered from the USA and Japan.

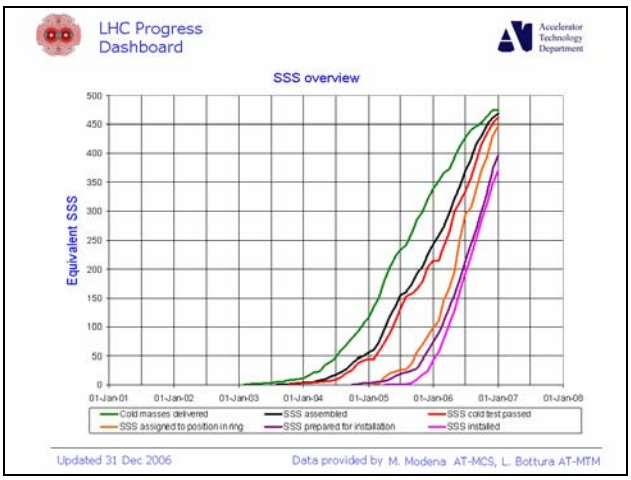

Figure 7: SSS overview.

Finally, one should not forget the very large number of conventional magnets for the LHC and the injection lines manufactured at BINP, IHEP and TRIUMF. For the two beam lines TI2 and TI8, from the SPS to the LHC and for the LHC ring itself, BINP has manufactured 729 magnets of various types. For the injection and dump regions, IHEP has built 60 septum magnets and for the two cleaning insertions, TRIUMF has supervised the construction of 52 two-in-one quadrupoles in Canadian industry.

After installation, the magnets must be interconnected (Figure 8). This is a complex sequence of operations starting with the interconnection of the main and auxiliary busbars followed by an electrical quality assurance. The various lines are then closed with orbital welding machines followed by leak tests. After closure of the external envelope, there is a final pressure and leak test and an electrical quality assurance of the whole octant including the tunnel feed boxes. The last activities before cool down can commence is the “flushing” of the cold masses and cryogenic lines with high pressure helium gas to remove any foreign particles that could interfere with the cryogenic plants.

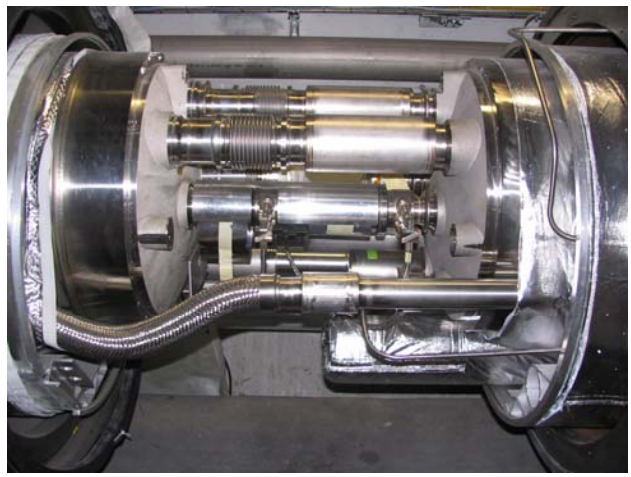

Figure 8: Dipole-dipole interconnect.

At the time of writing, one sector is completely finished and is being cooled down and interconnect work is proceeding in five other sectors in parallel (Figure 9).

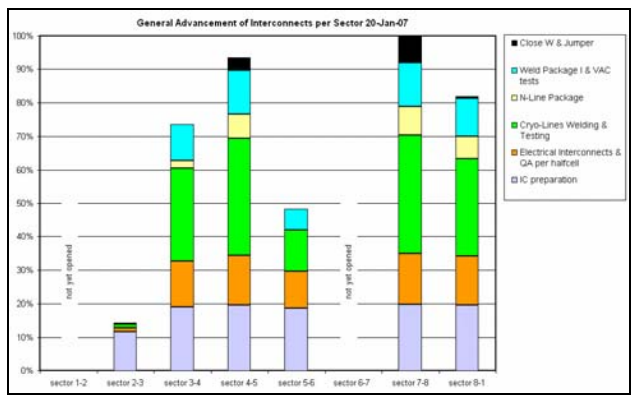

Figure 9: Interconnects status.

Cryogenics

Figure 10 shows a synoptic of the enormous cryogenic system required to cool the LHC. The gas storage, warm compressors and refrigerators are located at the surface. The cold compressors needed to produce the 15 mbar pressure required to reduce the temperature of the helium to 1.9 K are located in underground caverns together with valve boxes which allow a redistribution of cooling capacity between the octants. Finally the tunnel cryogenic distribution line (25 km of complex pipe work) distributes helium around the ring. This distribution line was completed in October 2006, liberating the whole of the tunnel for magnet installation. Commissioning of the whole cryogenic system is now nearing completion and the first octant is being cooled down.

Cooldown begins with 2 weeks of flushing followed by an electrical quality assurance (ELQA) test. In this first cooldown, it has taken 2 weeks to go from ambient to

80 K (Figure 11) after which a second ELQA is done. From 80 K to 4.2 then to 1.9 K takes 1 week.

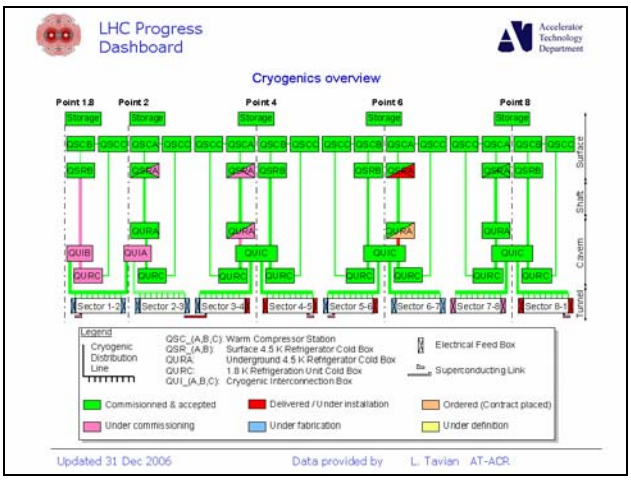

Figure 10: Cryogenic system.

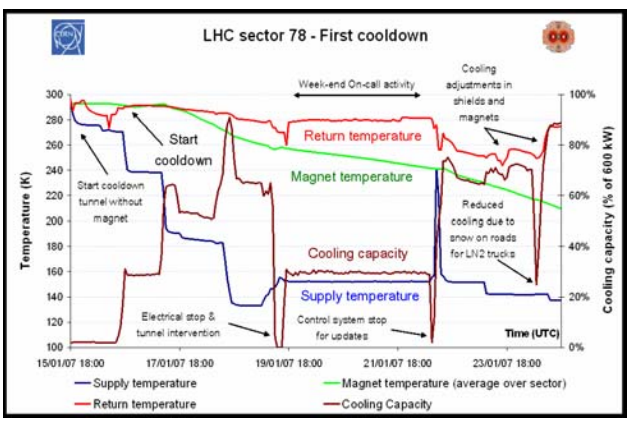

Figure 11: Cooldown.

Radio frequency and transverse feedback

The RF system is located at Point 4. Two independent sets of cavities operating at 400 MHz (twice the frequency of the LHC injector) allow independent control of the two beams. The superconducting cavities are made from copper on which a thin film of a few microns of niobium is sputtered onto the internal surface. Each RF system must provide a maximum voltage of 16 MV. For each beam there are 8 single cell cavities, each providing 2 MV with a conservative gradient of 5.5 MV/m. In fact the cavities have all been conditioned up to 8 MV/m, giving a good safety margin. Each cavity is driven by an individual RF system comprising a 300 kW klystron, coupler, circulator and load (Figure 12). All cavities are now installed (Figure 13) at Point 4 and are being connected to the RF and cryogenic systems.

The LHC transverse feedback system is also located at Point 4. It combines three principal functions: it damps transverse injection errors, prevents transverse dipole mode instabilities and can excite transverse oscillations for beam measurements and cleaning the abort gap. There are four independent systems, one per plane and per ring. The kickers, power amplifiers and supports were provided as a contribution from JINR, Dubna. The system is designed to provide useful gain up to 20 MHz. All kickers are now installed and are being commissioned.

Figure 12: Two 300 kW klystrons with circulators and loads.

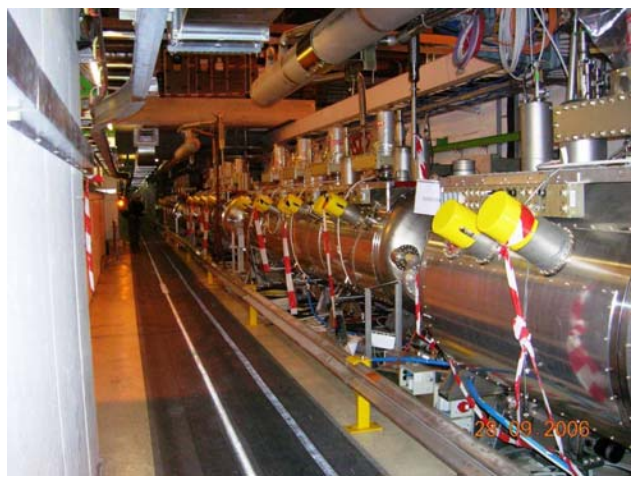

Figure 13: RF cavities at Point 4.

The Power converters

Each of the eight LHC sectors contains one electrical circuit connecting all main bending magnets in series. The main quadrupoles are powered in each sector in two electrical circuits (horizontally focusing (QF) and defocusing (QD)). The power converters for each of these circuits are located in underground galleries, previously used for the LEP klystrons, located close to the even insertion regions. The stored energy in these circuits amounts to 1.2 GJ for the main dipole and 20 MJ for each of the main quadrupole circuits. For the main dipole circuit, an energy extraction system consisting of a high current switch in parallel with an extraction resistor (3*225 mΩ, 220 MJ built at the Institute of High Energy Physics (IHEP) at Protvino) is placed on either side of the arc cryostat. For the quadrupoles only one system is sufficient.

As well as the main dipole and quadrupole circuits, there are many other high current supplies feeding

quadrupoles in the inner triplets and matching sections also located in the underground galleries (968 power converters in total) as well as the low current converters (600 A) for closed orbit correction (752 in total) distributed around the machine in racks underneath the main dipoles.

All 968 high current converters have been delivered and installed as well as 80 % of the orbit corrector supplies. The high current supplies are connected to the tunnel feed boxes with water-cooled cables. First commissioning of the supplies is done with these cables in short circuit in the feed box end so that the supplies see the resistive load of the cables but not the inductive load of the magnets. After all supplies are individually tested in this way, the whole group of supplies (about 50) in a cavern is tested at full current for 24 hours (Figure 14) in order to validate controls, water and air cooling and any problems of overheating due to, for example, bad routing of cable runs. About 60 % of the high power converters have already been tested in this way, and have allowed a number of problems to be resolved before the supplies are connected to their superconducting loads.

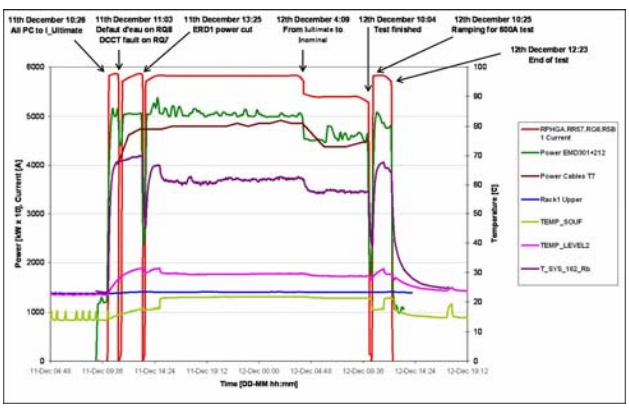

Figure 14: 24-hour run.

There are more than 40 current feed boxes of many different sizes. The largest feed the currents to the main dipoles and quadrupoles as well as retaining the vacuum forces at each end of the arc (Figure 15). The boxes are machined at IHEP and assembled into modules at CERN. A total of 1070 current leads operating between 600 A and 13 kA incorporating a section with high-temperature superconductor are needed. Most of these current leads have been built at the Budker Institute of Nuclear Physics (BINP) in Novosibirsk. Production and installation of these boxes is now proceeding smoothly at the rate required to meet the global installation schedule.

The main magnets are actively protected with quench heaters. If a quench is detected in a magnet, the quench heaters are fired and the power supply is switched off. The quench heater power supplies (a total of 5500 capacitive discharge supplies) have been built in India and assembled at CERN by Indian technicians.

Figure 15: Current feed boxes.

Other systems

Lack of space does not allow the other systems needed to operate the LHC to be treated in any detail. These include injection and extraction systems, collimators, beam instrumentation, vacuum, controls and machine protection. Except for the collimators, which are slightly delayed, installation is proceeding according to schedule. A minimum set of collimators has been defined for the 2007 run. The rest will be installed in the winter shutdown.

CONCLUSIONS

All major hardware procurement for the LHC Project is now complete. Installation of equipment in the tunnel is proceeding smoothly and commissioning of major sub-systems is starting. The first LHC sector (7-8) is complete and cooldown to 1.9 K is proceeding normally.

The schedule is too tight to allow full commissioning of all eight sectors up to the nominal design current corresponding to 7 TeV operation before the 2007-8 winter shutdown. It has therefore been decided that only the first two or three sectors will be fully commissioned in 2007. The remaining sectors will be able to operate safely at their injection level and will allow beams at 450 GeV to circulate in both rings. The RF system will then be activated to capture the beams, hopefully with a good enough lifetime to allow the beams to be brought into collision, providing first events in the detectors. This will be invaluable for early debugging of both the machine and detectors and will give a flying start to a high energy physics run in 2008 once all sectors have been commissioned to nominal current during the shutdown.

ACKNOWLEDGEMENTS

Many people, both inside and outside CERN have been dedicated to this Project. On behalf of my CERN colleagues, and in view of the location of this Conference, I would like to thank our Indian colleagues for their contribution of the highest quality.

RECORD LUMINOSITIES AT THE TEVATRON & FUTURE POTENTIALITY*

S. Werkema#, Fermilab, Batavia, IL 60510, U.S.A.

Abstract

Fermilab Collider Run II has been in progress for nearly six years. During this tine the D0 and CDF experiments have each acquired total integrated luminosities of nearly 2.2 fb^{-1}. Also during this time the peak instantaneous luminosities increased by more than a factor of 25 – from 10 to as high as 270 $\times 10^{30}$ cm^{-2} s^{-1}. An aggressive collider upgrade program continues to make significant progress along side luminosity production operations. This paper will give the status of Tevatron operations and expectations for the remainder of Run II.

PRESENT OPERATIONS

At the present time the Fermilab accelerator complex is providing beam for several high energy physics experiments. In addition to two collider experiments (CDF and D0), proton beam is made available for 120 GeV fixed target experiments and two neutrino experiments (NuMI and MiniBooNE).

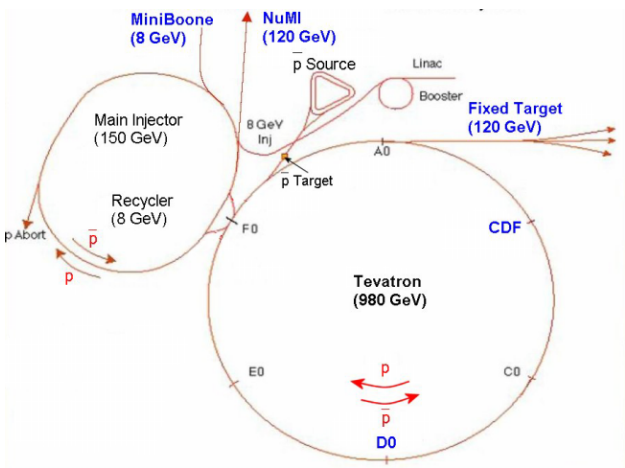

Figure 1: The Fermilab accelerator complex. Four high energy physics programs are supported: collider experiments CDF and D0, NuMI, MiniBooNE, and 120 GeV fixed target experiments.

The layout of the Fermilab accelerator complex and experiments is shown in Figure 1. Protons are accelerated and directed toward their final destination as follows:

- Protons from the Linac are accelerated to 8 GeV in the Booster synchrotron at 15 Hz.
- 4.2×10^{12} protons at 8 GeV are directed to MiniBooNE at a rate of approximately 2.5 Hz [1].
- 8.2×10^{12} protons at 8 GeV are accelerated to 120 GeV in the Main Injector every 2.4 sec for antiproton production.
- 11.5×10^{12} protons at 8 GeV are accelerated to 120 GeV in the Main Injector every 2.4 sec for neutrino production for the NuMI experiment.
- Varying amounts of 8 GeV protons are accelerated to 120 GeV and slow extracted every 61 sec for switchyard fixed target experiments

The contention for protons amongst the various experimental programs places some constraints on the operation of the Tevatron for the collider experiments.

During routine operation the injector chain operates to accumulate antiprotons while a collider store spins in the Tevatron. The average length of a collider store is about 20 hours. After a collider store is terminated a new store is inserted using the newly accumulated antiprotons.

Present and anticipated parameters of the Tevatron collider are given in Table I.

Table 1: Collider Parameters

Parameter	Present†	Upgrade	Units
Peak Luminosity	185	300	10^{30} cm^{-2} s^{-1}
Luminosity Lifetime	8.5	‡	hr
Store hours per week	97	105	hr/wk
Integrated Luminosity	5.1	‡	pb^{-1}/store
Total Run II $\int Ldt$	2.2	7	fb^{-1}
Protons per bunch	250	270	10^9
$\bar{p}$ per bunch	58	127	10^9
Number of bunches	36×36	36×36	
β* at IPs	28	28	cm
$\bar{p}$ stacking rate to Accumulator	17.5	30	10^{10}/hr
$\bar{p}$ stacking rate to Recycler	12.0	‡	10^{10}/hr

† Average values for FY2007
‡ No upgrade goal specified

Antiproton Stacking

Antiproton stacking consists of accelerating 120 GeV protons onto a nickel target disk through a process called slip stacking [2][3]. 8 GeV secondaries are collected off of the target using a high gradient lithium lens. This beam is injected into the Debuncher ring where the 19 nsec bunch structure from the targeted protons is rotated in longitudinal phase space to produce a narrow energy spread. The beam is stochastically cooled for 2.4 sec and transferred to an orbit on the high energy side of the Accumulator ring. The newly injected pulse of antiprotons is moved with RF to an orbit near the central

* Work supported by the U.S. Department of Energy under contract No. DE-AC02-76CH03000
# werkema@fnal.gov

momentum and then stochastically stacked into the core of the stored $\bar{p}$ distribution (see Figure 2).

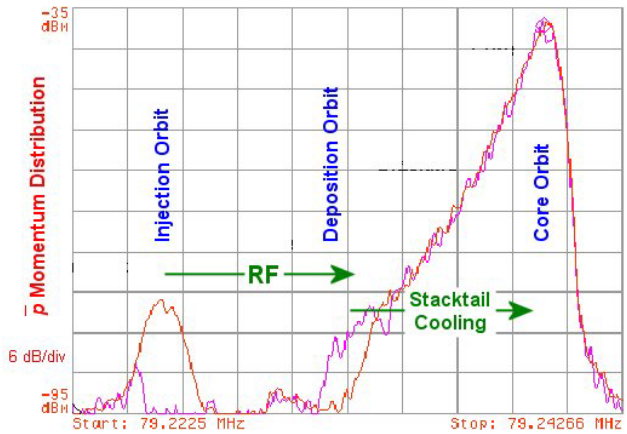

Figure 2: Longitudinal $\bar{p}$ distribution during stacking. The high energy side of the Accumulator is on the left side of the plot, low energy is on the right.

Antiprotons are stacked into the Accumulator in this manner until 60 – 70×10^{10} have been accumulated. The antiproton stack is then transferred to the Recycler Ring. The time between Accumulator to Recycler transfers is approximately 3 to 4 hours.

Loading the Collider

About 20 hours after a collider store has been inserted into the Tevatron the luminosity will have fallen sufficiently low to require a new store. Reloading the Tevatron with a new store is a process that typically takes about two hours.

Reloading the collider consists of the following basic steps:

- Set the Tevatron energy to 150 GeV
- Accelerate 36 proton bunches through the Linac → Booster → Main Injector chain to 150 GeV and inject into the Tevatron.
- Ramp the Tevatron separators to place the proton bunches on helical orbits.
- Accelerate 9 sets of 4 $\bar{p}$ bunches from the Recycler Ring to 150 GeV and inject into the Tevatron.
- Ramp the Tevatron to 980 GeV.
- Ramp the low-β inserts to establish β*.
- RF cog the proton and antiproton bunches into collisions.

Depending on operational exigencies, about 6 to 7 stores are loaded into the Tevatron in this manner each week.

Run II Luminosity History

The performance of the Tevatron collider has improved dramatically since commissioning began in early 2001 (see Figure 3). At the present time the initial luminosity of a collider store is typically 200 – 250 cm^{-2} s^{-1}. The best initial luminosity achieved to date is 277 cm^{-2} s^{-1} on January 18, 2007. This is a factor of 25 better than what was achievable at the beginning of the run. Under good conditions, the collider is presently capable of integrating 40 pb^{-1} per week. A total of 2.2 fb^{-1} has been integrated since the beginning of Run II.

This remarkable improvement has been achieved by a program of sequenced upgrades that were installed during three brief shutdowns and commissioned during collider production running. The progress shown has also occurred despite several significant setbacks as indicated by the several dips in peak luminosity in Figure 3.

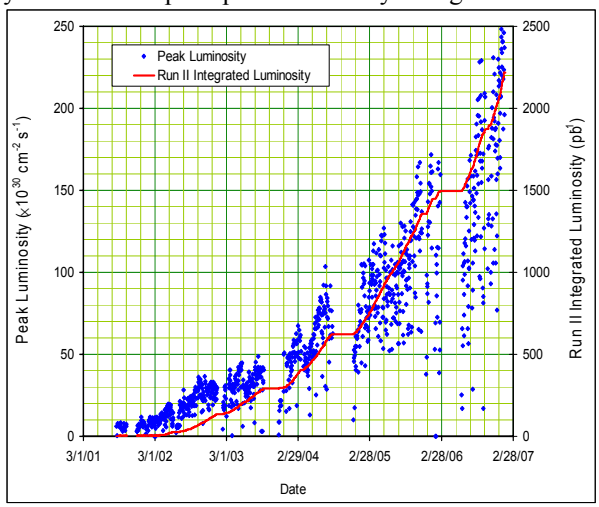

Figure 3: Peak and integrated luminosity versus time since the beginning of Run II.

RECENT PROGRESS

While the focus of this paper is on the recent progress of the upgrade program, the significant milestones of the Run II upgrades project are given in Table 2.

Table 2: Run II Upgrades Milestones

Milestone	Date
Start of Run II commissioning	March 2001
Collider operational	July 2003
Recycler electron cooling operational	July 2005
Slip stacking operational	August 2005
Lower β* from 35 cm to 28 cm	September 2005
Recycler only operations*	October 2005
Tevatron separator upgrade	Spring 2006

* $\bar{p}$ from Recycler only used to load collider

The details of these projects and many earlier accomplishments are documented in references [4][5][6].

Antiproton Production Issues

The antiproton accumulation rate ("stacking" rate) has increased almost two-fold since the beginning of FY 2006. This is due to several factors including:

- Increased beam on target due to slip-stacking
- Completion of the high gradient lithium lens upgrade

- Completion of much of the planned AP2 injection line and Debuncher aperture improvements.

For the first half of Run II the $\bar{p}$ stacking rate remained at an average of about 7×10^{10}/hr. During a shutdown in late 2004 several antiproton source upgrades were installed that increased the apertures of the Debuncher and its injection line. During this same shutdown there were several improvements made to the transfer line between the Accumulator and the Debuncher.

After the recovery from the 2004 shutdown the stacking rate again stagnated at around 10×10^{10}/hr. In late November of 2005 the Tevatron experienced the first if its three magnet failures. The Tevatron down time made the rest of the accelerator complex available for machine studies. The antiproton source took advantage of this time to properly commission the upgrades that were installed during the previous shutdown. The result, as can be seen in Figure 4, was a significant step upward in the $\bar{p}$ stacking rate.

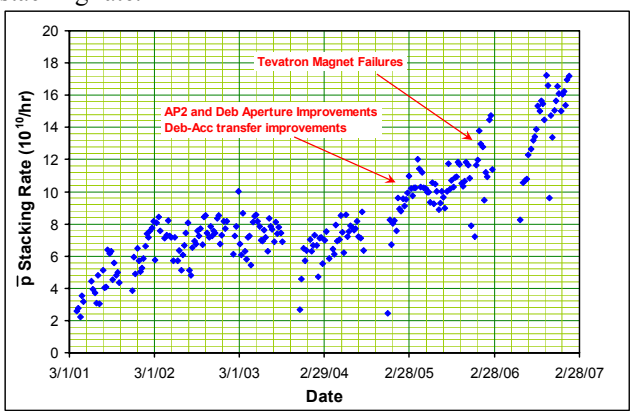

Figure 4: Average weekly stacking rate since the beginning of Run II.

Much of the increase in stacking rate in late 2005 can be attributed to increased proton intensity on the $\bar{p}$ production target due to the commissioning of slip stacking [2][3]. Slip stacking is a method of cogging two proton batches from the Booster into one batch in the Main Injector. The proton intensity on target increased by about 33% by the time slip stacking commissioning was complete.

The increased beam power on the $\bar{p}$ target comes with the complication that the target material is consumed at an increased rate. The target consists of three nickel disks. Approximately 6×10^{18} protons can be targeted on each disk. Thus it takes about 5 weeks to use up one target disk.

A further boost to the antiproton yield was accomplished by the completion of a project to increase the gradient of the lithium collection lens. To date the lens gradient has been raised by about 30%. In conjunction with the gradient increase the study time afforded by the Tevatron failures facilitated a 32% increase in the admittance from the lens through the Debuncher. Figure 5 illustrates the impact of lens gradient on $\bar{p}$ yield. There has been an overall increase in antiproton yield into the Debuncher ring of about 40% due to the combination of aperture and lens gradient improvements.

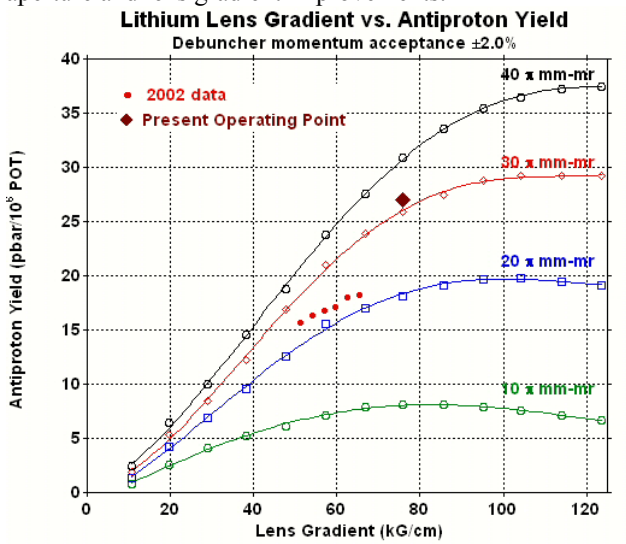

Figure 5: $\bar{p}$ yield versus Li lens gradient for various acceptances. The solid curves are a model, the symbols represent measurements. The 2002 measurement data was taken in the vicinity of the operating point at that time.

The bottleneck for stacking presently resides with the stacktail cooling system in the Accumulator ring. The stacktail cooling must accomplish two tasks in a timely manner for $\bar{p}$ stacking to function properly: (1) it must move beam off of the deposition orbit (see Figure 1) prior to the arrival of the next pulse from the Debuncher, and (2) it must transmit the flux arriving from the deposition orbit to the core at a rate that is sufficient to sustain a high stacking rate. The stacktail cooling system is currently at the limit of its capability in both of these tasks.

The longitudinal $\bar{p}$ distribution in the vicinity of the deposition orbit is highly time dependant – the pulse of deposited beam must transform from its initial shape into nothing in the space of the 2.4 sec stacking cycle time. Any beam left on the deposition orbit is RF phase displaced toward the injection orbit when the next pulse arrives. The rate at which this transformation can occur is proportional to the gain and bandwidth of the stacktail cooling system at the location of the deposition orbit. The gain is limited by system stability. Also, core heating effects and non-linear intermodulation distortion in the traveling wave tubes that drive the stacktail kickers intensify with increasing gain. A modification to the stacktail cooling system that will increase the bandwidth by 20% is presently under development. In addition, the core heating effects have been extensively studied. A scheme to optimize stacktail kicker locations will be implemented soon and is expected to mitigate the core heating somewhat. With these changes we expect the system to be able to clear the deposition orbit sufficiently fast to sustain a stacking rate of 30×10^{10}/hr.

The longitudinal $\bar{p}$ distribution in the stacktail region (the region between the deposition orbit and the core) is a static distribution that increases exponentially as the $\bar{p}$

energy decreases to the energy of the core with a characteristic energy, E_d. The maximum flux, Φ_{max}, through the stacktail is given by:

$$\Phi_{max} = \frac{W^2 \eta E_d}{f_{rev} p \ln\left(\frac{F_{min}}{F_{max}}\right)}$$

where W is the system bandwidth, η is the Accumulator slip factor, f_{rev} is the beam revolution frequency, p is the beam momentum, and F_{min} and F_{max} are the band edges of the stacktail cooling system. Φ_{max} can be increased by increasing the bandwidth, η, and E_d. With the 20% bandwidth improvement mentioned above, Φ_{max} is expected to be very near 30×10^{10}/hr.

Table 1 shows that there is a large difference between the rate at which antiprotons are stacked in the Accumulator and the rate into the Recycler. This is primarily caused by the time required to transfer beam from the Accumulator to the Recycler. This is a process that presently takes about 20 minutes. Hardware, software, and procedural changes are being developed to permit Accumulator to Recycler transfers to take place on event – reducing the time required from 20 minutes to about 30 seconds. We expect these changes to be implemented over the course of the next year.

Tevatron Issues

The early part of fiscal year (FY) 2006 saw three separate major Tevatron magnet failures. Each of these failures was initiated by a "mild" quench. A mild quench is a quench in which the affected magnets warm up by only10-15 °K. The Tevatron has experienced an average of 8 quenches per month since the start of collider production running in the summer of 2003. Ordinarily the recovery time from a mild quench is less than one hour. In these three cases however, the down time ranged from one week to three weeks. The total time lost to the program was about 6 weeks. The damage caused by two of these quenches was determined to be the result of stuck Kautzky pressure relief valves. The particular valve component that caused these two valves to fail was replaced in all (~1200) Tevatron Kautzky valves during the spring 2006 shutdown.

Despite the difficulties, there has been significant improvement in the performance of the Tevatron in recent months. FY 2006 saw the installation of electrostatic separator upgrades, a vastly improved Tevatron beam position monitoring (BPM) system, and a lattice upgrade that facilitated a 25% decrease in the interaction point (IP) β^*.

The separator upgrade project consists of the installation of the addition of additional high voltage (HV) electrostatic separator modules, the installation of polarity reversing switches, and increased HV capacity. The separator improvements that have been installed to date have allowed increased separation of the $\bar{p}$ and p beams at the first parasitic collision points. This significantly mitigates beam-beam effects and resulted in an estimated 20% improvement in integrated luminosity. This improvement is illustrated in Figures 6 and 7.

The Tevatron BPM system underwent a major overhaul. With this upgrade the proton position measurement resolution improved by an order of magnitude (new resolution ≈ 10-25 μm). The new system also allows measurement of the $\bar{p}$ orbits – a capability the previous system did not have. The improved BPM performance has greatly improved the ability to measure and correct the Tevatron lattice [7].

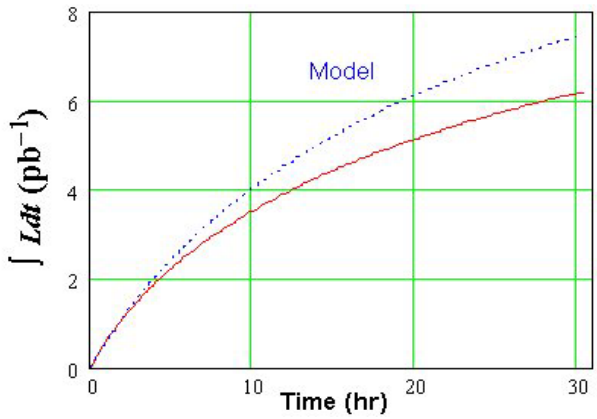

Figure 6: Comparison of a Tevatron luminosity model with data from a collider store *before* the separator upgrade installation. The model does not include beam-beam effects – hence the disparity between the model and the data.

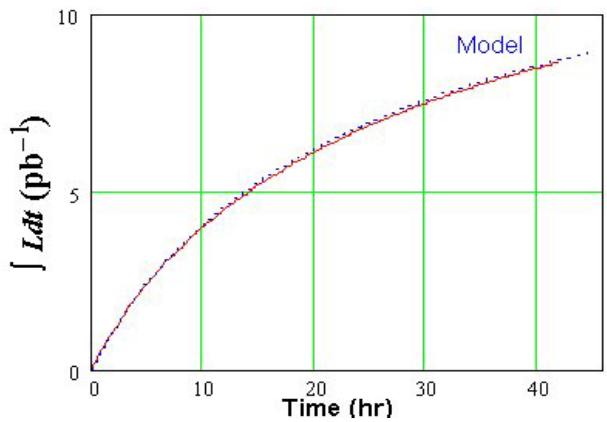

Figure 7: Comparison of the luminosity model with data from a collider store *after* the separator upgrade installation. The model (sans beam-beam) agrees well with the data.

As a consequence of the improved optics measurement capability allowed by the BPM upgrade, new Tevatron optics were developed that permitted a decrease in β^* at the IPs from 35 cm to 28 cm.

The $\bar{p}$ intensity in the Tevatron has reached the level where the proton beam is being driven by the antiproton beam. This problem will become more severe as $\bar{p}$ intensity increases. The solution that is contemplated is a change in the Tevatron working point from the vicinity of 4/7 to the vicinity of 1/2 (see Figure 8). With this change

the Tevatron will accommodate nearly 40% more tune spread; however it will also increase the chromatic lattice functions. This working point change will be implemented after a reconfiguration of the Tevatron's sextupole correction circuits to permit compensation of the anticipated chromatic effects.

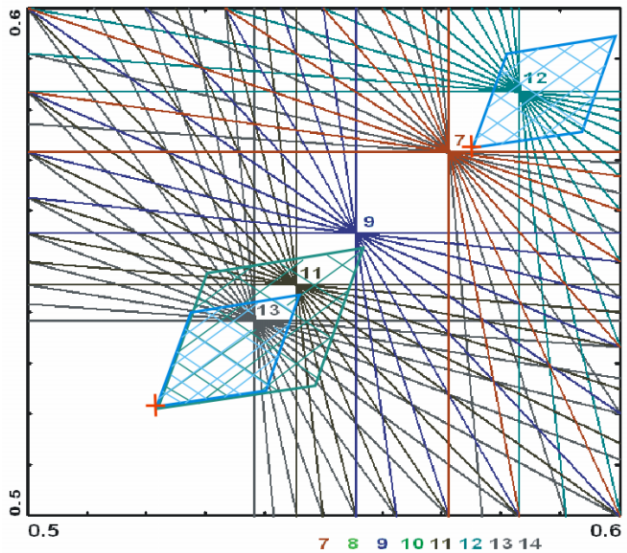

Figure 8: Tevatron tune diagram. The present operating range between 4/7 and 3/5 straddles 12th order resonance lines. The new working point will be near the ½ resonance where there is 40% more operating room.

SUMMARY

Enormous progress has been made in the last two years of Run II operation. The peak luminosity for collider stores has increased by nearly a factor of 2.5. The collider now integrates 30 – 40 pb^{-1} per week. This progress is due to more antiprotons available to the collider as a consequence of the increased $\bar{p}$ stacking rate as well as Tevatron improvements that allow more luminosity to be gained per $\bar{p}$ (β^* reduction) and better store lifetime (separator improvements).

The Run II upgrades project is nearing completion. Over the next year improvements to the stacktail cooling system, further Debuncher cooling and aperture improvements, and further increases in Li lens gradient should permit $\bar{p}$ stacking at a rate of 30×10^{10}/hr. Implementing Accumulator to Recycler transfers on event will increase the overall rate of $\bar{p}$ accumulation in the Recycler. The Tevatron working point change will allow the collider to accommodate the increased $\bar{p}$ brightness.

Run II is projected to end in late 2009. With the present rate of progress, Fermilab is on track to reach a total integrated luminosity of 7 fb^{-1} by that time.

REFERENCES

[1] MiniBooNE Web site, "Progress in Delivering Beam to MiniBooNE" http://www-boone.fnal.gov/publicpages/progress_monitor.html

[2] James MacLachlan, "The Beam Dynamics of Slip Stacking," Fermilab FN-0711, November 2001.

[3] Kiomi Seiya, et.al., "Status of Slip Stackin at Fermilab Main Injector," PAC'05, Knoxville, May 2005, MOPA004.

[4] Vladimir Shiltsev, "Status of Tevatron Collider Run II and Novel Technologies for Luminosity Upgrades," EPAC'04, Lucerne, July 2004, THZCH01.

[5] Dave McGinnis, "Fermilab Tevatron Operational Status," PAC'05, Knoxville, May 2005, MOAA005.

[6] Valeri Lebedev, "Tevatron Operational Status and Possible Lessons for the LHC," EPAC'06, Edinburgh, June 2006, TUXPA01.

[7] Vadim Sajaev, et.al., "Determination of Precise model of a Storage Ring Using Response Matrix Fit: Application to Advanced Photon Source and Tevatron," RuPAC'06, Novosibirsk, September 2006, WEJO03.

NEXT GENERATION ELECTRON-ION COLLIDERS*

Ilan Ben-Zvi**, Collider-Accelerator Department, Brookhaven National Laboratory, U.S.A.

Abstract

The next generation of electron-ion colliders promises very high luminosity, very high degree of polarization in both beams, multiple interaction points (IPs) and large range of energies. It will extend the reach and variety of attainable procresses in High Energy Physics and Nuclear Physics well beyond that provided by the first and only lepton-hadron collider, HERA. Some of these promises are based on new capabilities such as Energy Recovery Linacs (ERLs). We describe plans for these colliders which are under development by various laboratories, and the technology issues that are associated with these applications.

INTRODUCTION

Electron-ion (and positron-ion) collisions have unique properties that make them very valuable for high-energy and nuclear sciences. This was proven over 50 years ago by the seminal work on the form factor of nucleons by Robert Hofstadter which led to a Nobel Prize, and continued with ever increasing energy and luminosity to culminate in the lepton-proton HERA collider [1], providing an unprecedented energy reach, luminosity and lepton polarization. Not surprisingly new questions keep coming up and the need for accelerators with greater reach and greater variety of colliding species is ever present. In particular, the need to study QCD, improve the understanding of the structure and spin structure of hadronic matter, understanding the transition from the deconfined state of free quarks and gluons in the Big Bang to stable hadron matter can be addressed with higher precision in lepton-ion collisions. Hence, the new generation of electron-ion colliders is one of the key instruments to unravel the crucial fundamental physics questions.

Where does one go depends on the science one would like to pursue, and there is no single answer. The interest of nuclear and elementary particle physics span through a very large range of center-of-mass energies and energy ratios, variety of nuclear projectiles (from protons to uranium), use of electrons and positrons, very high luminosity and sometime very high degree of polarization.

In this work I will first outline what the accelerator physics issues are, and then describe three possible future machines which are quite different in approach and maturity of design: eRHIC, ELIC and LHeC.

ISSUES AND TECHNOLOGIES

The luminosity of an electron-ion collider can be written in terms of the fundamental machine limits, the beam-beam parameters and angular acceptance of the IP quads as

$$L = \left(\frac{4\pi\gamma_i\gamma_e}{r_i r_e} \right) \left(\xi_i \xi_e \right) \left(\sigma_i' \sigma_e' \right) f$$

where round beams of the same size are assumed at the IP and subscripts i or e denote ions or electrons. The ξ are the respective beam-beam parameters, r are the classical radii and γ are the relativistic factors, and f the collision frequency. The angular rms spreads σ' at the IP are limited by the aperture of the final focus quadrupoles. Clearly the achievable luminosity scales with the assumed beam-beam parameter and a good understanding of this limit is necessary in any machine.

An ion beam-beam parameter limit of ξ_i=0.015 is supported by the performance of the RHIC, Tevatron and SPS proton colliders. HERA had limited operation to ξ_i ~0.003 to avoid increase of detector background due to beam loss caused by larger beam-beam parameter. The subject of the detector background requires further study. A very slow beam loss with lifetime of about 20 hours can be strongly affected by both the detector and collimation design as well as by electron cooling.

In approaching the design of a new accelerator one has to consider and resolve some of the issues outlined below.

Performance is mostly driven by the potential users of the proposed facility, and include: Richness of the selection of beam species, CM energy, variability of energy and energy-ratio (between the two colliding species), luminosity, polarization, bunch spacing, background, length of IP free of accelerator elements, number of IP's available, prospects of upgradeability and more. All of these affect the utility of the proposed facility to its users, and the users are usually the ones who have to make difficult choices.

Cost is in potential conflict with **performance**; New electron-ion colliders must use to a larger or lesser degree existing facilities in order to reduce the cost and/or improve performance. Of these, the ion machines and their injector-chains are the more expensive elements. Another variable of the cost vs. performance equation is **innovation**. One can use new technical solutions which, if used, can increase performance and/or reduce cost. However, using a new and untried approach may lead to **risk**. This has consequences - reviewers tend to be skeptical of new approaches and the contingency one has to carry influences the cost. Yet, progress requires some risks to be taken. Jawaharlal Nehru said wisely: "The policy of being too cautious is the greatest risk of all". In this paper I will try to portray the different path taken by

* Work done under the auspices of the US Department of Energy.
** ilan@bnl.gov

future electron ion colliders and how innovation/risk dimensions are used to drive performance and cost.

The various issues and technologies of electron-ion colliders were discussed in various dedicated meetings and workshops [2, 3, 4]

Energy Recovery Linac

The idea of using an electron Energy Recovery Linac (ERL) to collide with other leptons is not new [5]. It was more recently proposed in the context of electron-ion colliders [6] and summarized by Merminga [7]. The advantages of the ERL for electron-ion colliders include a higher luminosity, given by the fact that the electron beam is used for the collision only in a single pass and thus withstands a much higher beam-beam parameter.

Round beams, naturally produced in ERLs, are optimal for maximizing the luminosity for a given beam-beam parameter, i.e. they provide for the use of round beams of equal size at the collision point(s). If the electron bunch intensity can always be adjusted to reach the ion beam-beam parameter ξ_i, the luminosity is only limited by the ion beam parameters:

$$L = \gamma_i f \, N_i \frac{\xi_i Z_i}{\beta_i^* r_i}$$

where N_i is the ion bunch intensity, Z_i is the ion charge, β_i^* is the ion beta function at the collision point. Thus, with the ERL, the luminosity can be improved for a given center-of-mass energy by reducing the energy of the electron beam while increasing the energy of the ions.

The ERL delivers a higher polarization than a self-polarizing ring since it can use modern super-lattice GaAs(Cs) photocathodes, which deliver electron spin-polarization between 80% to 90% with good quantum efficiency. In contrast with polarized storage rings imposing many restrictions on the ring geometry and beam energies, an ERL can be easily built with full polarization transparency for the electron beam at all energies. It is easily integrated with multiple electron-hadron interaction points (IPs) and detectors. It does not require spin rotators for longitudinal, radial or transverse polarizations. It has a large energy range at full luminosity and full polarization. Low emittance beams from the ERL make the IP optics simpler, in particular for providing very long "element free" straight sections for the detectors with greatly reduced synchrotron radiation background [8]. It can be upgraded in energy. Multiple-pass ERLs reduce the cost of the machine making it competitive with a storage ring. New single-mode SRF accelerator cavities provide the ERL with the ability to operate at the high currents which may be required in a collider [9]. ERLs are also capable to match the variation of ion bunch frequency at different ion energies.

The main risk in this approach is the availability of a polarized electron source with the necessary high current, an issue that should be resolved with well-focused R&D.

Electron cooling

A critical technology for electron-ion colliders is electron cooling for the ion beam. High-energy electron cooling is a new technology, and so far has been demonstrated only to a relativistic beam factor γ of about 8, while γ of 100 to 150 is necessary in some electron-ion colliders. In addition, cooling of colliding beams has not been done yet and no doubt there will be interesting consequences.

Cooling at the collision energy is needed when the intra-beam scattering (IBS) affects significantly the luminosity lifetime. Thus faster cooling is needed at lower energies or when the ion density is pushed higher to increase the luminosity.

Cooling a dense high energy ion beams is not easy, and requires high charge electron bunches (to make up for the high charge of the ions and overcome IBS) and low emittance (to provide a small angular spread of the electrons). This type of electron beam can be produced only by a linac. Electron cooling at these energies is under extensive investigation and prototyping at BNL [10].

Detector and IP considerations

The demand of a high luminosity ep/eA collider facility, *i.e.* for low β_i^*, drives the installation of focusing machine elements close to the central detector. Interaction region design with machine elements as close as ±1m to the interaction region would significantly limit the achievable detector acceptance. The IP area is of concern to both accelerator physicists and detector physicists. Machine parameters such as bunch separation, crossing angle, location of accelerator elements near the IP, bunch length, synchrotron radiation fan generated by beam separation, beam loss and more affect the detector design and performance. These are critical and challenging requirements. [8].

The eRHIC design provides a machine-element free region of ±3m, and a machine-element free region of approximately ±5 m is possible [11]. ELIC provides ±2m.

In the design of LHeC, a magnet-free space of at least 2.4m was specified in the interaction region to provide sufficient space and acceptance for the experimental detector. [12]

Crossing angle [13] helps with the beam-beam interaction of parasitic collisions and reduces synchrotron radiation problems, but requires fitting high voltage crab cavities into the collider. For eRHIC, the required transverse voltage was calculated in Ref. [8]. Assuming a design similar to the KEKB crab cavity [15] at ωRF ~$2\pi \cdot$200MHz, and β-functions of β^* = 1m and β_{crab} =400m, the transverse voltage for a 250GeV proton beam and 5mrad crab angle is about $V_\perp$ ~15 MV. This is not practical at RHIC. Another important issue for the crab crossing is the very high tolerance imposed on the amplitude and phase stability of the crab cavities [14] by the hadron beams. In the case of ELIC it is estimated that a sub-ppm amplitude stability will be necessary, [16] a very challenging goal.

ELIC

ELIC [17] is a very high luminosity collider designed to provide longitudinally and transversally polarized light ions - p, d, ^{3}He and Li, and unpolarized light to medium ion species. The extremely high design luminosity in this medium energy collider is based on a long list of innovative (but untested) ideas. The use of CEBAF as the injector to a 3-7 GeV, 1-3 A electron ring will provide cost saving. By adding a positron source to CEBAF injector, a positron beam can also be accelerated in CEBAF and accumulated and polarized in same storage ring. An ion accelerator complex will be added, including a 150 GeV, 1 A collider ring with 4 interaction regions. A novel feature is the figure-8 shape of the booster rings, electron collider ring, and the ion collider ring. Although it increases the cost by requiring more bending magnets, such a configuration ameliorates the issue of spin maintenance at acceleration and allows one to arrange desired spin orientation for all light-ion species at all energies.

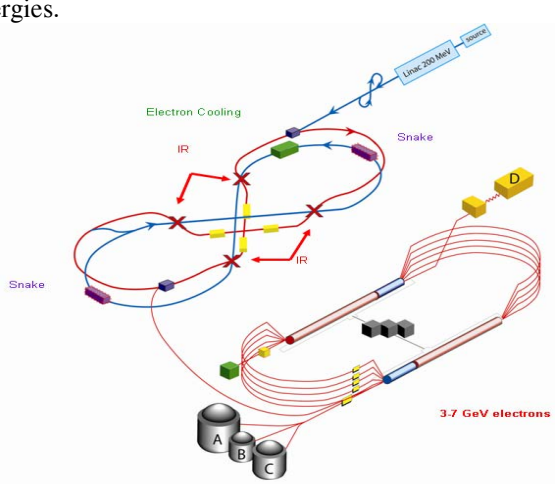

Figure 1: Layout of ELIC.

Another critical component of the ion complex is a 75 MeV ERL-based electron cooler. The high luminosity of ELIC relies on a low emittance and very short (5 mm or less), ion bunches [18,19], which is to be provided by aggressive electron cooling. In order to provide the extremely high current and low emittance for ELIC, the use of a circulator-cooler ring is proposed as a way to accumulate the necessary electron current from a 75 MeV ERL. The very short ion bunches are required for an extremely strong beam focusing at the collision points and crab-crossing of the colliding beams in ELIC. In addition, the luminosity requires an extremely high bunch repetition rate (up to CEBAF's RF frequency of 1.5 GHz).

The short ion bunches provide also for a large synchrotron tune (exceeding the beam-beam tune shift in ELIC case), which presumably eliminates the synchro-betatron non-linear resonances in the beam-beam interaction. Another novel feature of ELIC is the use of flat beams (by lowering the x-y coupling at fixed beam area), which is predicted to reduce the ratio between IBS and electron cooling.

The four IPs of ELIC will have equidistant fractional phase advance, with the expectation of effectively reducing the critical beam-beam tune shift to a value normalized to one IP.

A special spin rotation scheme has been developed to transform the electron spin from vertical in arcs to longitudinal in IPs in a wide energy range, with polarization insensitive to the energy. Self-polarization in arcs supports the injected polarization of electron beam and provides polarization of positron beam.

Table 1: Basic parameters for ELIC.

Parameter	Unit	Value	Value	Value
Beam Energy	GeV	150/7	100/5	30/3
Circumference	km	1.5		
Crossing straights	m	346 x 2		
Bunch collision rate	GHz	1.5		
# of particles/bunch	10^{10}	.4/1.0	.4/1.1	.12/1.7
Beam current	A	1/2.4	1/2.7	.3/4.1
Energy spread, rms	10^{-4}	3		
Bunch length, rms	mm	5		
Beta-star	mm	5		
IP focal parameter	m	6		
Space for detector	m	5		
Extended beam size*	mm	6		
Crab crossing angle	rad	.1	.1	.1
Crab field integral	Tm	.24	.16	.048
Horiz. emit. norm.	μm	1/100	.7/70	.2/43
Vertical emit., norm.	μm	.04/4	.06/6	.2/43
Beam-beam tune shift (vertical) per IP		.01/ .086	.01/ .073	.01/ .007
P sp. charge tune shift		.015	.03	.06
Lumi. per. IP*, 10^{34}	$cm^{-2}s^{-1}$	7.7	5.6	.8
Luminosity lifetime	h	24	24	>24

*)Beam horizontal size in IP focusing triplet

Overcoming space charge at injection is another challenge at ELIC. Stripping injection can be used to stack polarized proton and deuteron beams in the pre-booster after 200 to 400 MeV linac. To minimize the space charge impact on the transverse emittance, a circular painting technique is suggested for stacking. Such a technique was originally proposed for stacking a proton beam in the SNS [20].

The reduction of the 4D emittance growth at stacking 1-3 Amps of light ions is of a critical importance for the effective use of electron cooling in the collider ring, since the initial electron cooling time is determined by the 6D emittance value of the injected ion beam.

eRHIC

RHIC is a high-luminosity ion-ion and polarized protons collider [21]. eRHIC adds an electron accelerator to collide with the RHIC ions [6,22].

eRHIC's preferred design uses a superconducting electron ERL for reasons outlined above, but a more conventional ring-ring version is also under study. R&D on electron cooling, ERL physics, polarized sources, beam-beam studies, head-tail type instability of the proton beam (kink instability), electron beam transverse disruption by the beam-beam interactions, proton beam emittance growth due to fluctuations of electron beam current, electron beam size, and transverse collision offset, cost estimates and other relevant subjects are being carried out by the institutes collaborating on eRHIC.

eRHIC will provide 3-20 GeV polarized electrons and polarized positrons 50-250 GeV polarized protons; 100 GeV/n gold ions and 167 GeV/n polarized 3He ions. The luminosities will be over 10^{33} $cm^{-2}s^{-1}$ for e-p collisions and over 10^{31} $cm^{-2}s^{-1}$ for e-Au collisions. The expected polarization is at least 70% for proton beams and over 80% for electron beams.

The Center-of-Mass Energy (CME) range covered by eRHIC is from 30 to 140 GeV.

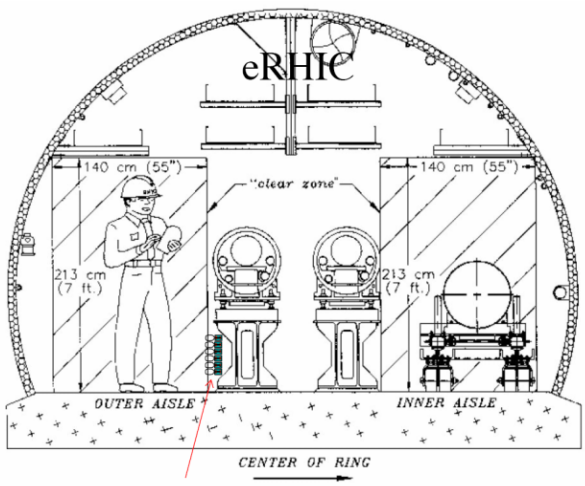

Figure 2: eRHIC's multiple passes in the RHIC tunnel.

The electron beam by-passes the STAR and PHENIX experimental halls. Initial acceleration to the energy of 0.5 GeV is done by the smaller pre-acceleration linac. A 4 GeV ERL is used in a five pass acceleration / deceleration scheme. The two high-energy re-circulating passes of the ERL are sharing the RHIC tunnel with the ion rings, leading to a significant cost saving (see Figure 2). The electron ERL sections are located inside the RHIC tunnel in four of the six available straight sections.

To provide a positron beam, the last ERL turn is closed upon itself to form a storage ring for the positrons. Polarized positrons will be generated through polarized gammas similar to techniques that are being developed for the ILC, cooled in a small cooling ring and accelerated to the desired energy by the linac and stored for collisions. Naturally the luminosity of the positrons will be lower due to the use of a storage ring.

The design parameter tables 2,3 are based on setting the limiting value of the ion beam-beam parameter to ξ_i=0.015, which seems to be realistically achievable, based on the experience of the RHIC operation with polarized proton beams and assuming a dedicated single collision point.

Positrons will collide with the ions while circulating in the storage ring. Because of this the luminosity of positron-ion collisions will be one order of magnitude lower than for electron-ion collisions.

The ERL is based on a 703.75MHz SRF cavity designed for ERL service [23]. The design assumes 20 MeV energy gain per cavity. 200 cavities are used in a 600m long linac (consisting of four 150m long sections that fit in the RHIC straight sections) to provide 4 GeV acceleration in one beam pass. The average luminosity is expected to be about 1/3 of the peak luminosity, leading to a luminosity integral of 530 (580) inverse picobarn per week for the protons (gold) hadrons at the higher energy.

Table 2. eRHIC Parameters for e-p collisions.

	High energy		Low energy	
	p	e	p	e
Energy, GeV	250	20	50	3
Num. of bunches	166		166	
Bunch spacing, ns	71	71	71	71
Particles/bunch, 10^{11}	2	1.2	2.0	1.2
Beam current, mA	420	260	420	260
95% norm. emit, μm	6	115	6	115
Rms emittance, nm,	3.8	0.5	19	3.3
β*, cm	26	200	26	150
Beam-beam parameter	0.015	2.3	0.015	2.3
Rms bunch length, cm	20	0.7	20	1.8
Polarization, %	70	80	70	80
Pk Lumin. 10^{33} $cm^{-2}s^{-1}$	2.6		0.53	

Table 3. eRHIC Parameters for e-Au collisions.

	High energy		Low energy	
	Au	e	Au	e
Energy, GeV/n - GeV	100	20	50	3
Number of bunches	166		166	
Bunch spacing, ns	71	71	71	71
Bunch intensity, 10^{11}	1.1	1.2	1.1	1.2
Beam current, mA	180	260	180	260
95% normal. emit, μm	2.4	115	2.4	115
Rms emittance, nm,	3.7	0.5	7.5	3.3
β*, cm	26	200	26	60
Beam-beam parameter	0.015	1.0	0.015	1.0
Rms bunch length, cm	20	0.7	20	1.8
Polarization, %	0	0	0	0
Pk Lumin. 10^{33} $cm^{-2}s^{-1}$	2.9		1.5	

LHeC

The LHC provides a unique opportunity to probe matter with precision at the shortest length scale, as short as 0.0001 fm with high luminosity. The idea of constructing an electron accelerator at some future time to collide leptons with LHC protons or ion beam (thus making LHeC) has been described in Ref. [12]. This proposed upgrade of LHC to include the possibility of an LHeC is based on rather robust assumptions, fitting a machine not to dissimilar from the LEP design back into the LHC tunnel. The proton beam parameters are taken as the LHC design values. Certainly the expensive piece of hardware is the LHC, although the electron machine at this scale is not cheap. The tentative location of the ep interaction region is shown in Figure 3.

The electron current (and thus bunch charge) is dictated by an assumption on a reasonable power to be available at the CERN site, and is certainly a very sensitive function of the electron beam energy. The current is related to the power and energy through:

$$I_e = 0.351mA \cdot \left(P_{RF} / MW\right) \cdot \left(100GeV / E_e\right)^4$$

With electron energy of 70GeV, 50MW of RF power and SRF cavities, the total beam current is 71 mA.

The luminosity of LHeC is high with conservative beam-beam parameters. That comes as no surprise given its extremely high energies of both projectiles, as can be seen from the expression for the luminosity in terms of the beam-beam parameters.

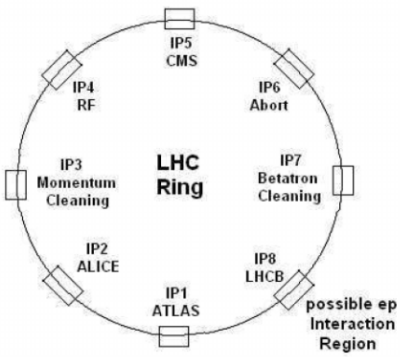

Figure 3. Layout of LHeC.

Table 4. LHeC Parameters for e-p collisions.

Property	Unit	Leptons	Protons
Beam energies	GeV	70	7000
Total beam current	mA	74	544
Particles/bunch	10^{10}	1.04	17.0
Horizontal emittance	nm	7.6	0.501
Vertical emittance	nm	3.8	0.501
Horizontal β* at IP	cm	12.7	180
Vertical β* at IP	cm	7.1	50
Energy loss per turn	GeV	0.707	$6{\cdot}10^{-6}$
Radiated energy	MW	50	0.003
Bunch frequency / spacing	MHz / ns	40 / 25	
Center of mass energy	GeV	1400	
Luminosity	$10^{33}cm^{-2}s^{-1}$	1.1	

SUMMARY

Proposed future electron ion colliders span a wide range of parameters and approaches to risk – innovation – performance – cost trade-offs. What is common to all is the high luminosity. eRHIC is intermediate in CM energy. It is based on an operating ion machine with polarized protons and high luminosity. eRHIC is intermediate in innovation, with the electron ERL as its main innovation, and its main challenge is to demonstrate its polarized electron source.

LHeC has the highest CM energy by far being based on the LHC and LEP. The main shortcoming of LHeC is the absence of proton polarization, and uncertainty with regard to electron polarization. The LHeC design is very conservative and its main challenges are time and budget.

ELIC is limited by its site to lighter ions. In contrast with eRHIC and LHeC, ELIC faces the burden of adding the most expensive part of a lepton-ion collider – the chain of ion machines and has a limited range of ion, but it promises the highest luminosity. In terms of innovation (and attendant risk) ELIC is by far the most innovative design.

Acknowledgements go to: J. Dainton, Y. Derbenev, W. Fisher, V.N. Litvinenko, L. Merminga, C. Montag, P. Newman, E. Pozdeyev, V. Ptitsyn T. Roser and F. Willeke.

REFERENCES

[1] F. Willeke, these proceedings , APAC07, Indore, India.
[2] I. Ben-Zvi and G. H. Hoffstaetter, Summary M5 W.G. on Lepton-Hadron Colliders, Snowmass 2001
[3] http://www.jlab.org/intralab/calendar/archive04/eic/
[4] https://www.bnl.gov/qcdfp/
[5] M. Tigner, Nuovo Cimento 37, 1228-1231 (1965).
[6] I. Ben-Zvi, et al, NIM A463, 94 (2001).
[7] L. Merminga, these proceed., APAC07, Indore, India.
[8] C. Montag et al, Proc. PAC05 and also http://www.bnl.gov/cad/eRhic/Meetings/eRHIC_Talks/RHIC_Plan_Meet/CM_RPM.pdf
[9] E. Pozdeyev, in [4].
[10] I. Ben-Zvi, Proc. EPAC06.
[11] V. Litvinenko et al,, Proc PAC05
[12] J.B. Dainton et al, DESY 06-006, Cockcroft-06-05
[13] R. B. Palmer, SLAC-PUB-4707 (1988)
[14] K. Oide, K. Yokoya, Phys. Rev. A 40, 315, (1989)
[15] K. Hosoyama et al, Proc. SRF05 Cornell University
[16] C. Montag, private communication
[17] Ya. Derbenev et al, Proc. RuPAC 06
[18] Ya. Derbenev et al., ICFA Newsletter, No 30, (2003)
[19] Ya. Derbenev et al., Proc. EPAC04
[20] J.Holmes, et al., Proc PAC05
[21] T. Roser, these proceedings , APAC07, Indore, India.
[22] http://www.sc.doe.gov/Scientific_User_Facilities /History/20-Year-Outlook-screen.pdf
[22] R. Calaga et al, Proceedings, EPAC'04

PAPER NOT YET RECEIVED

COMMISIONING OF THE INDUS-2 STORAGE RING

V.C. Sahni
Raja Ramanna Centre for Advanced Technology (RRCAT), Indore-452 013 &
Bhabha Atomic Research Centre (BARC), Mumbai-400 085

Abstract

An overview of the 2.5 GeV synchrotron radiation source, Indus-2, which has been set up at RRCAT, Indore will be presented with emphasis on commissioning details. The accelerator is used both as a booster and as a storage ring. Using an injection energy of 550MeV, the beam energy has been ramped up to 2.4 GeV. Two beam lines have also been installed, one for x-ray diffraction (XRD) and another for extended x-ray absorption fine structure (EXAFS) studies. To condition the vacuum chamber of the ring, regular operation has been restricted to 2 GeV. To test the XRD beam line, first diffraction pattern from a pyrolitic graphite sample was recorded with bending magnet synchrotron light with ring operating at 2 GeV. Indigenous technological base created in setting up Indus-2 would be used while participating in up coming international accelerator projects.

INTRODUCTION

A programme to build synchrotron radiation sources (SRSs) in the country was started in the eighties by the Department of Atomic Energy. A separate laboratory named Centre for Advanced Technology at Indore was created. The injector accelerators, namely, 20 MeV microtron and a 450-700 MeV booster synchrotron and the first 450 MeV storage ring Indus-1 were commissioned during the 90's. Originally, SRS Indus-2 was planned to be a 2 GeV ring. However, in November 1997, based on the advice of an International Panel, this energy was raised to 2.5 GeV. The design work on the new components, needed for the enhanced energy ring, was started in 1998 along with the civil construction of the building. Development of the prototype components and their large scale manufacture, partly in industry and partly in house, was spread over the next five years. The installation of the different subsystems was taken up from 2003-04 onwards. The complete assembly of Indus-2 & transport line (TL-3) connecting it to booster synchrotron, was finished by early 2005. Thereafter the evacuation of the ring and subsystem commissioning was taken up. By the end of 2005 we had started accumulating electrons in Indus-2 of ~450 MeV energy and the first signatures of the SR from Indus-2 were recorded using a CCD camera mounted over the sighting beam line. Over the past year beam energy ramping experiments were successfully completed, reaching up to 2.4 GeV in stages. In parallel work on building the beam lines for using the SR have also gone on. This paper will concentrate on the progress during the past year and a half. Main developments during the earlier periods have been described before [1].

INDUS ACCELERATOR PROGRAM AT RRCAT

Figure 1 gives a schematic view of the Indus Accelerator Complex and the present status of the machines and the transport lines. A sketch of Indus-2 lattice is given in figure 2 and Table 1 contains the parameters of the ring [1].

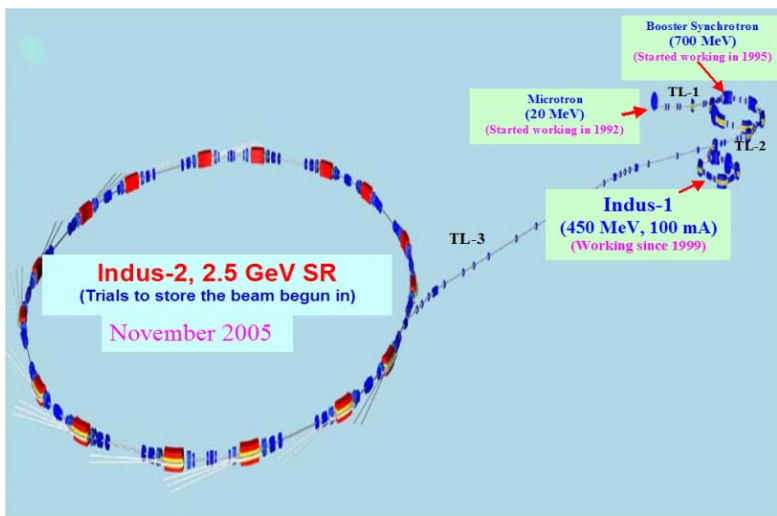

Figure 1: Schematic view of the Indus Accelerator Complex.

Table 1: Parameters of INDUS–2.

Maximum Energy	2.5 GeV
Maximum Current	300 mA
Lattice type	Expanded Chassman Green
Superperiods	8
Circumference	172.4743 m
Bending magnet field	1.502 T
Typical tune points	9.2, 5.2
Beam emittance, ε_x	5.81 x 10^{-8} mrad
ε_y	5.81 x 10^{-9} mrad
Available straight section for insertion devices	5
Maximum straight length available for insertion devices	4.5 m
Beam size σ_x	0.234 mm
(Centre of bending magnet) σ_y	0.237 mm
Beam envelope vacuum	< 1 x 10^{-9} mbar
Beam life-time	12 hrs
RF frequency	505.812 MHz
Critical wave length	1.98 Å (bending magnet)
	0.596 Å (high field wiggler)
Power loss	186.6 kW (bending magnet)

Main subsystems of the ring viz the magnets (dipoles, quadrupoles and sextupoles, septums & kickers) their power supplies, vacuum chambers, RF transmitters, control systems etc were developed at our Centre in Indore. After fabrication, field mapping was done on each of the magnets. Since there was some spread in their measured field profiles (as compared to the design values), we used simulated annealing algorithm to find the optimized locations for the magnets. With the best placement of the magnets in the ring, errors of different magnets compensated one another to obtain good overall performance from the machine. This optimization enabled us to bring down the closed orbit deviations in the electron trajectories by about a factor of 3. Figures 3 shows some of the pictures of Indus –2 inside the tunnel. For more details see [2].

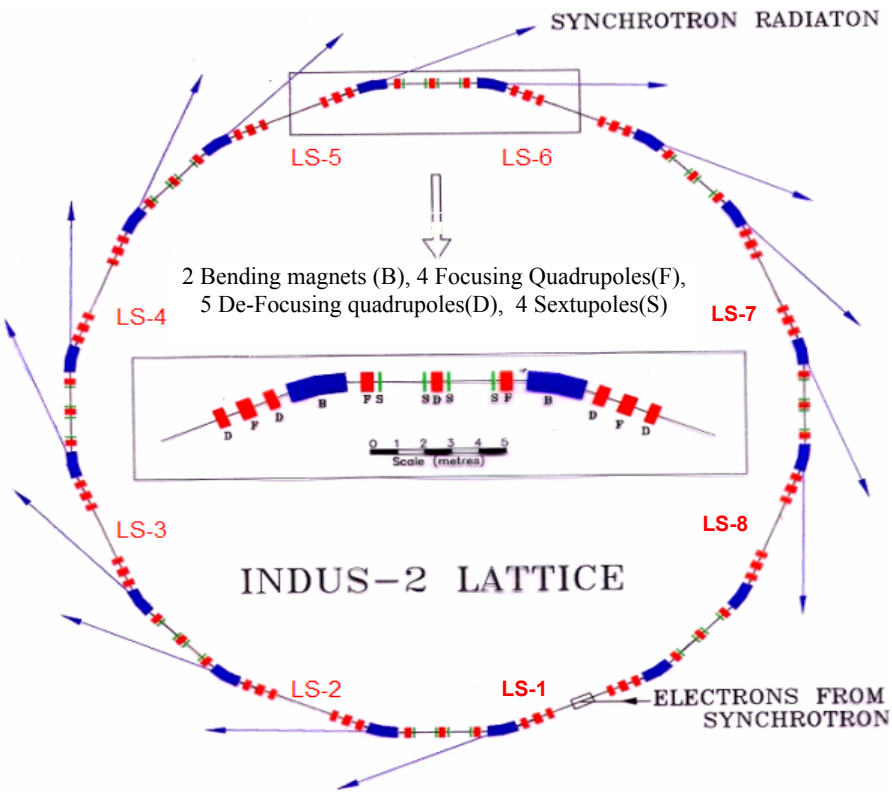

B-Bending magnet; F/D-Focussing / Defocusing quadrupole; S –Sextupole,
LS-1: used for injection; LS-2 to LS-6: for insertion devices. LS-7: Unusable; LS-8: for RF cavities

Figure 2: Indus – 2 lattice & its components.

(a)

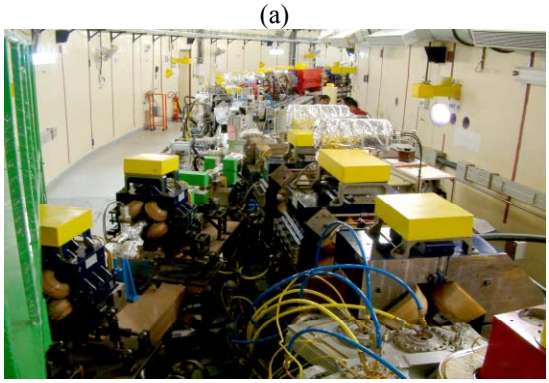

(b)

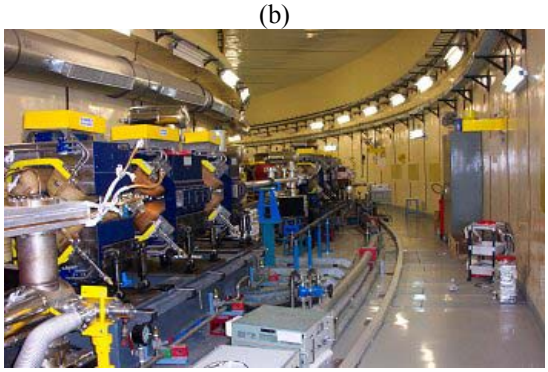

(c)

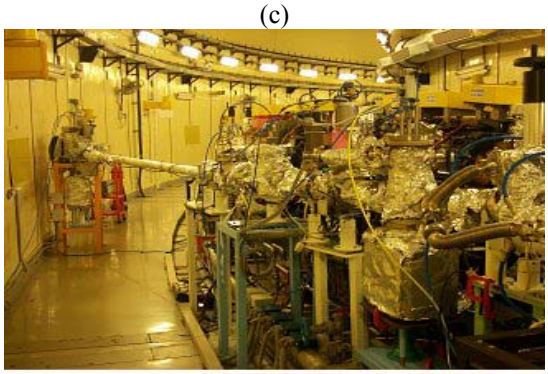

(d)

Figure 3: a) RF Cavities Commissioned in Indus – 2 Ring, b) TL-3 Joining on to Indus-2, c) Long Straight Section Assembly, d) front end of a typical bending magnet beamline as it is linked to Indus-2.

In May 2005 the electron bunches of 450 MeV energy were transported through TL-3, and, as desired by AERB, experiments were conducted to confirm that beam loss was minimal. In August 2005, electrons were injected for the first time into the storage ring and, after optimization of magnetic lattice elements, the beam circulated for four turns (Figure 4), without the kicker and the RF power being turned on [2]. After reaching this milestone, we went through an exhaustive evaluation of various sub-systems, particularly the timing of the kicker magnets and the RF power system. Then in early December 2005, with the kicker magnets and the RF system turned on the beam circulated for ~1 second in the storage ring. The first synchrotron light out of Indus-2 as recorded through the CCD camera mounted on the sighting beam-line on December 2, 2005 as shown in Figure 5.

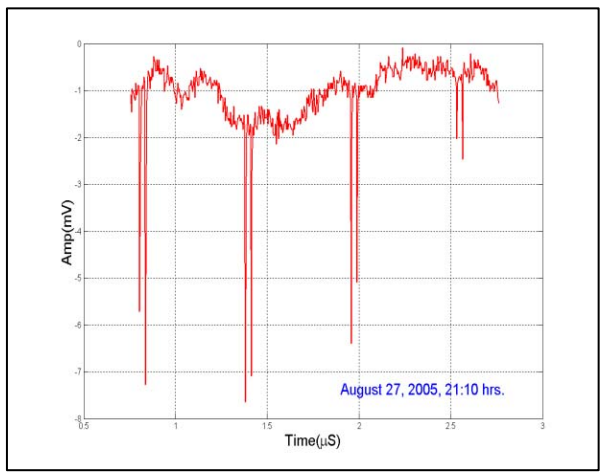

Figure 4: Four turn beam circulation seen on wall current monitor on 27th August, 2005.

Figure 5: First synchrotron light from Indus-2 recorded on Dec. 2, 2005 with CCD camera on sighting beam line.

The beam accumulation experiments were started in January 2006 and first time few mA were stored in mid February 2006. The lattice optimization studies were continued over the next few months and successful energy ramping was achieved in May-June 2006. The data in Figures 6 & 7 shows energy ramping up to 2 GeV and 2.4 GeV respectively. The data in Figure 8 shows the improvement in the vacuum in the ring as a result of the conditioning of the vacuum chambers by the synchrotron radiation and the concomitant increase in the beam life

time with 20 mA of current. In addition to energy ramping experiment we have used steering coils to carry out orbit correction to minimize COD (Figure 9).

While the work on installation and commissioning of the storage ring has been going on, parallel effort is also on towards setting up beam-lines meant for using the synchrotron radiation from Indus-2. Work is going on to build six beam lines of which two, namely, one for x-ray diffraction (XRD) and other for extended x-ray absorption fine structure (EXAFS) studies have been installed.

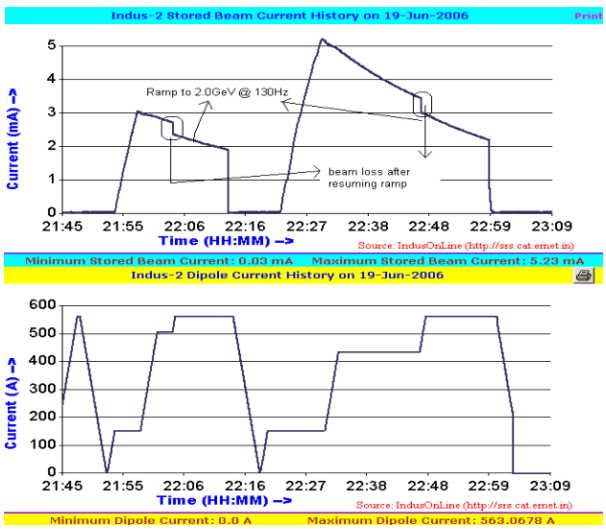

(a) shows current in Indus-2;
(b) shows current in the dipole magnets;
~150 A corresponds to 543 MeV;
~560 Amps corresponds to ~2 GeV

Figure 6: Successful energy ramping to 2 GeV (19/6/2006).

Figure 10 shows a picture of the x-ray diffraction beam-line in the experimental hall and figure 11 shows the first XRD pattern taken with pyrolitic graphite sample. Sadly, in the last quarter of 2006, a bad vacuum leak occurred in Indus-2 and the injectors due to a leak in the bellows. This was the result of large movements of Indus-2 dipole vacuum chambers due to eddy currents generated by power transients and the accompanying Lorentz force acting on the chambers. This problem has since been mitigated using a better arrangement to fasten the vacuum chambers. This has brought about a reduction in the movement of the vacuum chambers to below ~ 2mm (when current in the dipole magnet coils is suddenly turned off from ~550 A level to zero.) which is within the permissible limits of bellows. We also carried out improvements in the booster synchrotron in two ways. One was by replacing the old RF cavity (which had developed some pitting on the internal capacitor plates) with another cavity and other was to attend to better alignment of the extraction septum. The booster synchrotron and Indus-2 were made operational again by mid January 2007. While there has been an overall performance of the system, we have lost a good deal of time in fixing these problems. Some further work was carried out on the installation of PES beam lines and building hutch around the EXAFS beam line. Work is now planned to fine tune current in the steering coils to further bring down the closed orbit deviations (COD) of the beam in the ring. The work on enhancing the infrastructure is also in progress, which will enable us to increase the beam energy to 2.5 GeV in the coming months.

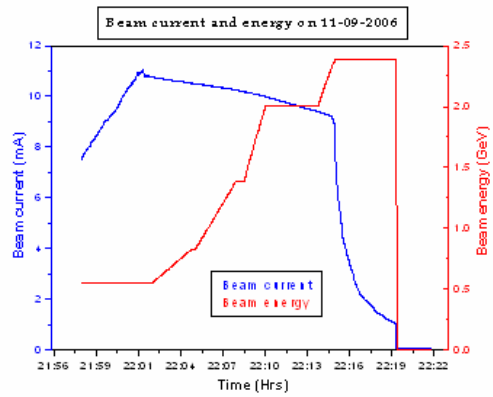

Figure 7: Successful energy ramping to 2.4 GeV.

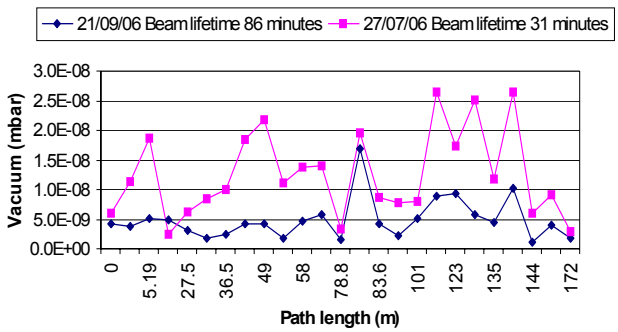

Figure 8: Vacuum in the ring and its influence on beam life time.

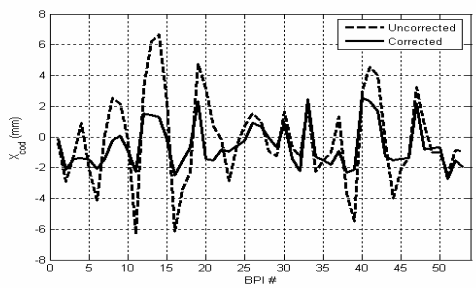

COD	Uncorrected	Corrected
Absolute Max (mm)	6.7	2.75
RMS(mm)	2.9	1.54

Figure 9: Reduction in closed orbit deviation brought about by use of steering coils.

Figure 10: Down stream view of the XRD beamline. The large chamber in picture houses the DCM.

CONCLUDING REMARKS

The paper describes the progress made on synchrotron radiation source Indus-2 which has been set up and commissioned at RRCAT, Indore. In the process of setting up Indus-2, a strong indigenous base has been created in the country. This should come in handy when India participates in up coming international accelerator projects, like, e+ - e- linear colliders, X-FEL, energy recovery linacs, SPL [3] etc. These projects are also of interest to India in so far as they can contribute to development of high intensity proton accelerator. BARC plans are to build Accelerator Driven Sub-critical reactors (ADS) (for details see ref. [4]) for nuclear waste transmutation studies, while RRCAT plans to set up a SNS for condensed matter research. These programmes have a strong overlap with SPL project [3] of CERN. Indian capability would be of value for such programs. A prototype 110kV, 24 A, 700 μsec pulsed modulator for SPL's injector & TL-2 for CTF3 are amongst the elements identified for Indian contribution. It is clear that the accelerator related developments in India have now entered a new phase and in the coming years these will integrate with the world wide efforts in this area.

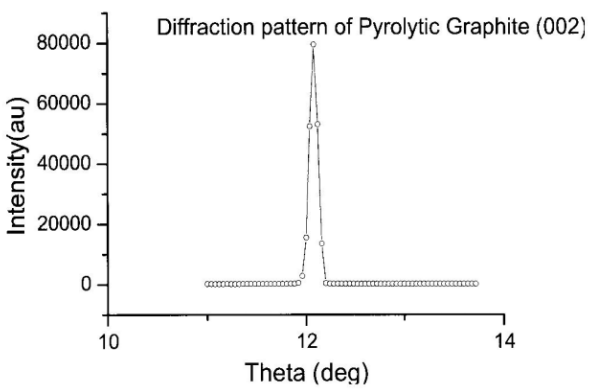

Date : Sept 28, 2006 : Indus-2 beam energy was 2 GeV & current ~4 mA.

Figure 11: First record of the x-ray diffraction with SR from Indus-2 using beam line 12.

ACKNOWLEDGEMENT

The work presented in this talk is the result of the efforts of a very large number of scientists & engineers at RRCAT. It is my pleasure to thank them all for their devoted contributions.

REFERENCES

[1] S. Kotaiah, A. Banerjee, A.G. Bhujle, P. Fatnani, P.R. Hannurkar, M.G. Karmarkar, A.K. Jain, A.M. Kekre, S.S. Prabhu, R.K. Mishra, M. Pravin Kumar, V.C. Sahni, R.S. Shinde, S.K. Shukla and Gurnam Singh, Proceedings of Indian Particle Accelerator Conference, p.65 (2005).

[2] V.C. Sahni, Pramana 67, 225 (2006).

[3] M. Vretenar (For SPL Study group), CERN –PS-2000-059-RF, LINAC2000-TU206, CERN-NUFACT-NOTE-040 (2000), Talk at the 20th International Linac Conference (Linac 2000), Monterey California, 21-25 Aug. 2000, eConf C000821 (2000) TU 2006, Physics/0008142.

[4] P. Singh, Proceedings of Indian Particle Accelerator Conference (InPAC 2005), p25 (2005).

COMMISSIONING AND STATUS OF THE DIAMOND STORAGE RING

R.P. Walker, Diamond Light Source (DLS), Oxfordshire, U.K.,
on behalf of the Diamond Machine Commissioning Team

Abstract

The commissioning of the Diamond storage ring at 3 GeV, as well as the current status and future plans, are described.

INTRODUCTION

The construction phase of Diamond, the UK's new medium-energy 3rd generation synchrotron light source [1,2] concluded at the end of December 2006. Diamond has now entered the operational phase, with first external users starting at the end of January 2007, in line with the original programme. The main parameters of Diamond are given in Table 1.

Table 1: Main parameters of the Diamond storage ring.

Energy	3 GeV
Circumference	561.6 m
Lattice	24-cell DBA
Straight sections	6 x 8 m, 18 x 5 m
RF frequency	500 MHz
Nominal current	300 mA
Nominal rms emittances (H,V)	2.7, 0.03 nm rad
Nominal rms energy spread	0.096 %

This report will concentrate on the recent commissioning of the storage ring at the full energy of 3 GeV which began in September 2006. The earlier commissioning of the 100 MeV linac (August-October 2005) and 3 GeV booster (December 2005 – June 2006), as well as the initial phase of storage ring commissioning (May 2006), were described at EPAC 2006 [2-5].

The first phase of storage ring commissioning took place at 700 MeV, because of the lack of water cooling at that time for both magnets and radiation absorbers. The low energy made commissioning very difficult, however it did prove possible to accumulate a current of 2 mA. Following this period the ring was shut-down for 3 months both to complete the water cooling systems, as well as to install the insertion devices, and further front-ends. By the beginning of September all seven Phase I insertion devices had been installed.

Commissioning at 3 GeV began on the evening of the 4th September 2006. Operation was restricted to outside normal working hours until the radiation shielding had been verified. On the first evening the beam was circulated for 5 turns, with correctors, sextupoles and RF off. The next evening 120 turns were obtained, with sextupoles on. The following evening the RF was turned on and a beam of 2 mA was accumulated. In 3 evenings therefore we had accomplished what had taken a month at 700 MeV, because of calibration, stability and other beam dynamics issues [2].

At that stage the current was deliberately limited at 2 mA until cooling water and interlocks on the radiation absorbers had been fully tested. Two days later this work had been carried out and beam was accumulated up to 10 mA. Another limit was placed at this level since the orbit interlock for protecting the vacuum vessel in case of mis-steered photon beams was not yet in operation. Nevertheless the current was sufficient to allow progress to be made with closed orbit correction and optics optimisation. Once the orbit interlock was operational the current was gradually increased, carefully checking for beam instabilities and monitoring vessel temperatures and vacuum pressures. By the beginning of October, 60 mA had been reached and the target for initial operation of 100 mA was achieved on Nov. 11th. Further progress was limited by the time available for high current operation and RF conditioning, since an increasing amount of time was devoted to beamline commissioning. First light was let into a beamline optics hutch on Oct. 12th, and regular daytime beamline commissioning started on Oct. 23rd.

ACCELERATOR PHYSICS

Closed-orbit

Initial correction of the closed orbit quickly reduced the error to the level of 0.7 mm rms in both planes, but no less. A "beam based alignment" (BBA) was then carried out to determine the offset between the centre of each beam position monitor (BPM) and the magnetic centre of the nearest quadrupole magnet.

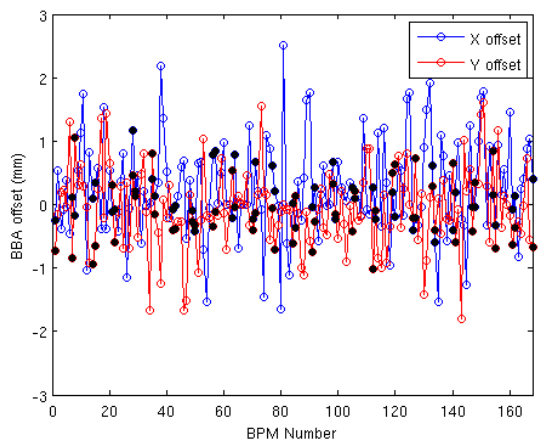

Figure 1: BPM-quadrupole offsets; black dots denote "primary" BPMs.

The Accelerator Toolbox Middlelayer routine "quadcenter" [6] was used for this task. A complete scan of all 168 BPMs required 8 hours. The first measurement did not result in a very accurate determination of the offsets, but nevertheless when the offsets were taken into account the closed orbit could be improved. A further series of iterations was then carried out, each time

reducing the residual closed orbit until an orbit with less than 1 µm deviation at each BPM was able to be produced, using all of the eigenvalues of the response matrix, and all 168 correctors in each plane. Using only 96 correctors, rms orbit errors of 60 µm horizontal and 40 µm vertical could still be achieved, with modest corrector strengths (<0.3 mrad Horiz., <0.15 mrad Vert.), which is further positive evidence for the correctness of the BBA approach.

Fig. 1 shows the final BPM-quadrupole centre offsets. These values might appear quite large, but are not unreasonable given the uncertainty in the mechanical positions of the BPMs as well as the uncertainty of the electrical centres of the BPM pickup blocks, including cable and electronic differences. Some larger errors have been found to be due to variations of cable length within a set of 4, which will be corrected in due course. Fig. 1 shows that the offsets are generally smaller at the "primary" BPMs, which are located on either side of the insertion device straights, but this is probably because of the smaller calibration factor, rather than the better mechanical positioning accuracy.

Following BBA it was discovered that the correctors could be switched off to allow the "bare orbit" to be measured, which gave a result of 4.8 mm rms horizontal and 3.1 mm rms vertical, which is reasonably consistent with the specified quadrupole positioning accuracy.

Closed-orbit Stability

A slow orbit feedback has been implemented at the MATLAB level which currently acts every 5 seconds and maintains the orbit correction at the BPMs to below 0.5 µm rms in both planes. Without the orbit correction, the orbit deviation grows to about 1-2 µm rms within 15 minutes. This orbit stability has also been confirmed through first observations on the XBPMs in the front ends.

The stability of the beam at higher frequencies is of the order of 3-4 µm rms horizontal and 0.8 µm rms vertical when measured at one of the primary BPMs, integrated over the frequency range 0-1 kHz. The major contribution to this is a disturbance at 24.9 Hz. Vibration measurements have detected this both in the ground and on one of the 3 girder types (Girder 1). The second biggest contribution comes from frequencies in the 16-20 Hz range which appear to be associated with resonances in Girders 2 and 3. Where possible the vibration sources will be identified and reduced, the fast-orbit feedback that is under development (see below) should however have no difficulty in combating them.

Linear Optics Optimisation

Measurement and optimisation of the linear optics has benefited greatly from the LOCO program [7]. The first analysis revealed a beta function error of ± 40% in both planes. The first correction reduced this to below 15%, and after a series of iterations, the quadrupole settings calculated by LOCO have reduced this error to less than 1% in both planes, see Fig. 2.

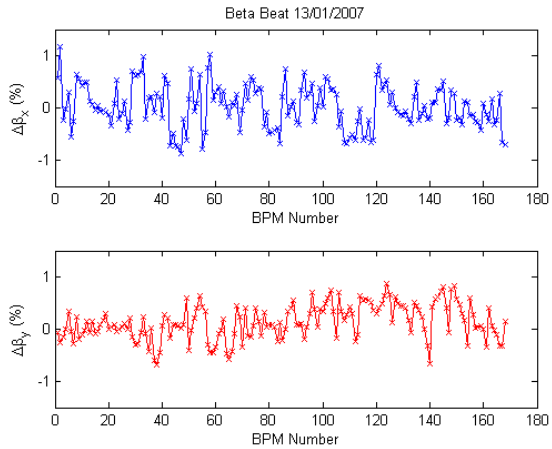

Figure 2: Beta function errors after LOCO correction.

The changes to the quadrupoles required to correct the optics were up to 5% in absolute terms, however, the initial calibration of the magnets was known not to be very accurate. Within magnet types, the relative variations are never larger than 2%, consistent with results found on other machines.

Following LOCO correction the measured dispersion function is also in good agreement with the model.

Emittance, Energy Spread and Coupling

Two X-ray pinhole cameras are located at source points with different lattice functions, so allowing the beam emittances and energy spread to be deduced. Current measurements give a horizontal emittance in the range 2.6-2.8 nm rad and an energy spread of 0.11%, close to the nominal values (see Table 1), given some uncertainty in the knowledge of the optical functions at the two different source points.

LOCO has also been used to correct for linear coupling using the skew-quadrupole correction coils mounted on the sextupole magnets. With skew-quads off, the closest approach of the tunes was $\Delta Q = 0.0067$, which predicts an emittance ratio from betatron coupling at the nominal working point (assuming zero vertical dispersion and a single resonance approximation) of 0.13%. The measured emittance ratio using the X-ray pinhole cameras was 1.3%, indicating that vertical dispersion is dominant. Using the skew-quad correction predicted by LOCO resulted in a very small tune separation of $\Delta Q = 0.0004$ and hence negligible betatron coupling and a measured emittance ratio of 0.17%. It is planned to use the skew-quadrupoles to stabilise the emittance ratio at a fixed value for user operation in the near future.

Instabilities

Multibunch instabilities, both horizontal and vertical, evidenced by the appearance of betatron sidebands around the orbit harmonics in the beam spectrum, became apparent as soon as the stored current began to be increased. In fact, the onset of vertical instability has been observed as low as 17 mA at zero chromaticity, a factor

of 2 lower than the predicted threshold for the resistive wall instability.

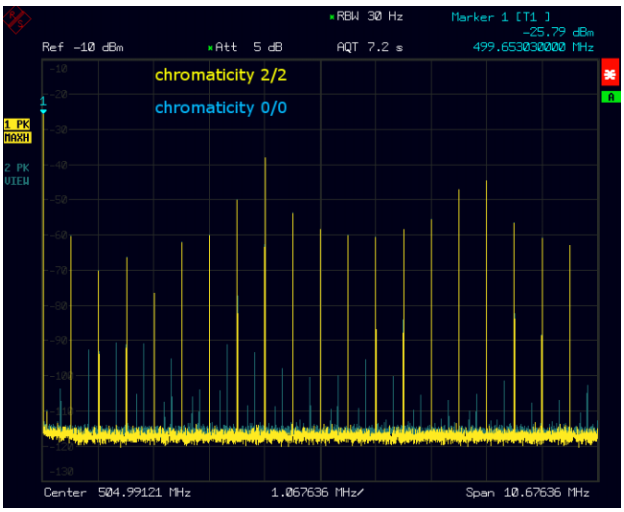

Figure 3: Spectrum analyser signal at 60 mA with zero and +2 chromaticity in both planes and 2/3rd filling. The left-hand-side peak is the RF frequency, one division corresponds to twice the orbit frequency.

The threshold for instability increases as the chromaticity is increased in the relevant plane, but depends also on the percentage filling of the storage ring circumference – uniform filling requires the largest chromaticity to be stable, 1/3rd fill the least, with 2/3rd fill in-between. Fig. 3 shows an example of how positive chromaticity suppresses signs of the resistive wall instability at 60 mA. Currently for operation up to 110 mA with 2/3rd filling a chromaticity ($\Delta Q/\Delta p/p$) of +2 in both planes is sufficient to completely suppress instabilities. Further measurements are planned to characterise the effects of resistive wall and ions, the signatures of which have both been observed under different operating conditions.

Injection Efficiency

Injection efficiency initially was poor, but improved during the process of closed orbit and optics correction. The efficiency (from transfer line exit to stored current) is now typically 85-95%, and is being routinely monitored to determine reproducibility and as an early warning of parameter "drift".

DIAGNOSTICS

All of the diagnostics systems are operational, with the exception only of some in the booster-to-storage ring transfer line. The digital BPM electronics in particular have proved to be extremely valuable during the various phases of commissioning, when the various modes, such as turn-by-turn (for obtaining the initial turns in the ring), slow acquisition (for closed orbit correction) and fast acquisition (for investigating orbit stability and later fast orbit feedback) have been used.

The resolution of the BPM system is well within specification and in line with previous laboratory tests. Beam current dependence has been observed at slightly higher values than expected from the laboratory tests and will have to be studied systematically by correlation with XBPMs and beamline diagnostics.

Pairs of XBPMs in 6 of the front-ends have been installed and calibrated versus insertion device gap. Initial measurements showed a measurement uncertainty of 500 nm for a 100 ms integration time. This means that enough resolution is available to observe beam stability as seen by the beamlines.

INSERTION DEVICES

Seven Phase I insertion devices (IDs) were installed before 3 GeV commissioning began in September and an 8th device (I22) was installed in the Dec./Jan. shutdown. Table 2 summarises the main properties of these devices. The maximum rms phase error refers to the main operating range between 5 and 10 mm gap, and is clearly better in the later devices compared to the first one (I02). All of the insertion devices have been commissioned and are in routine use for beamline commissioning; the in-vacuum devices are currently operating down to the initial minimum gap of 7 mm.

Table 2: Main parameters of the first 8 insertion devices.

Beam -line	ID type	Period (mm)	No. of Periods	Field [T]		Max. phase error (°)
				gap = 5mm	gap = 7mm	
I02	IN-VAC	23	85	0.92	0.70	3.9
I03	IN-VAC	21	94	0.86	0.64	3.1
I04	IN-VAC	23	85	0.92	0.70	2.8
I06	APPLE-II	64	33	0.94T (15 mm)		5.5
I15	SCW	60	24	3.5T		-
I16	IN-VAC	27	73	1.0	0.8	2.3
I18	IN-VAC	27	73	1.0	0.8	2.1
I22	IN-VAC	25	79	0.97	0.75	2.1

The uncorrected closed orbit change as a function of gap is of the order 20-25 μm for the in-vacuum undulators, and 50 μm for HU64. Trim coil settings have been determined as a function of gap (and phase in the case of HU64) and are now set automatically, which results in a residual orbit disturbance of about 1-2 μm rms. The SCW currents have also been adjusted so as to minimise the effect at full field, while the ramp-up of the wiggler field has been corrected to keep the orbit well within the beam position interlock threshold.

No other significant effects on the beam have been observed. The effect on the tunes are small, < 0.001 in the case of the in-vacuum undulators, < 0.004 for HU64 and 0.012 for the SCW. The SCW introduces a beta-beat of 11 %, which so far has not needed to be compensated. No effects on lifetime have so far been observed.

RADIATION PROTECTION

The storage ring tunnel shielding has been progressively verified under both injection and stored beam conditions so as to allow operation by day with unrestricted access around the tunnel enclosure. Currently there is no restriction on access with the ring operating at a current of up to 150 mA. Measured dose rate levels under stored beam conditions have generally been indistinguishable from background. Combined gamma and neutron radiation monitors around the outside of the tunnel will trip the injection if the measured dose rates exceed a set limit, however this has only occurred during the initial stages of commissioning.

RF SYSTEM

The storage ring is currently operating with a single RF cavity: the second cavity developed a leak before 3 GeV commissioning began and is currently under repair. The installed cavity is routinely operated with an accelerating voltage of up to 2 MV, however increasing the beam current above 80 mA has required dedicated conditioning time to overcome vacuum bursts in the vacuum space between the RF window and the cavity, and to condition the coupler between the waveguide and the cavity. The vacuum activity was particularly noticeable at discrete current levels, however the cavity appears to remain conditioned even when operated below the maximum current for extended periods. Additionally, re-conditioning following a complete warm up has been rapid. Other parts of the RF plant are working well, with little down-time. Despite the RF amplifier operating significantly below the specified maximum RF output power, the efficiency of the IOTs remains high. The low-level RF system controls amplitude and phase to within ± 0.1% and 0.1° rms respectively, well within the specification.

VACUUM AND BEAM LIFETIME

At the start of 3 GeV commissioning in September 2006 the storage ring mean static gauge pressure was 4.5 10^{-10} mbar, and the pressure was relatively uniform around the ring apart from the injection straight with an average pressure of 6.5 10^{-9} mbar**.** Apart from 3 ID straights containing NEG-coated Al vessels and the diagnostics straight which had been baked out in-situ, the rest of the stainless-steel vacuum system had only been baked-out in sections prior to assembly on the girders, not in-situ [8].

Conditioning with beam has progressed according to expectations. The dynamic pressure rises have been more or less uniform around the storage ring, with no particular "hot spots". According to RGA scans the residual gas is typically >90% hydrogen without beam and >80% hydrogen with beam.

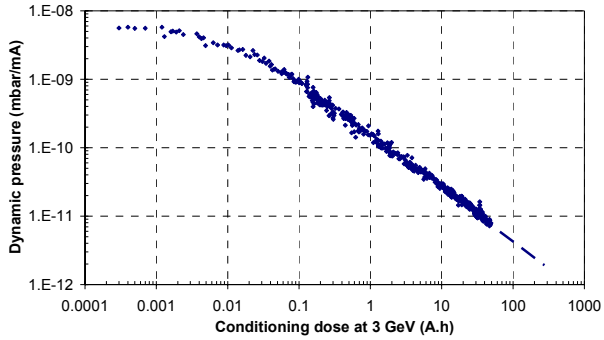

Figure 4: Dynamic vacuum pressure vs. beam dose.

Regarding the in-vacuum undulators, three of the initial five were baked-out in the ring, during which the NEG coated connecting vessels were also baked. The other two with stainless steel connecting vessels were only baked out in the lab. prior to installation. Interestingly, the vacuum performance of these two types is similar, both as regards static and dynamic pressure.

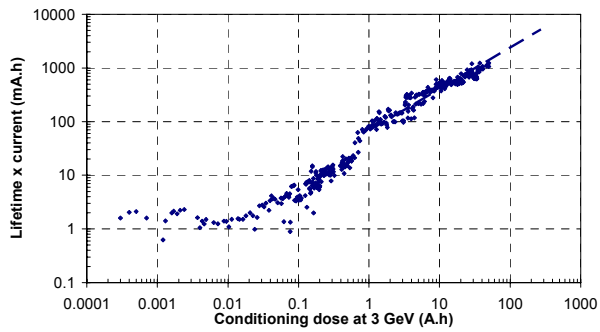

Figure 5: Beam lifetime-current product vs. beam dose.

Fig. 4 shows the average dynamic pressure as a function of beam dose, D, (i.e. integrated current) at 3 GeV which follows a $D^{-0.8}$ law apart from the initial stages of beam conditioning, typical of many other machines. After an accumulated dose of 50 Ah the dynamic pressure is currently 8.0 10^{-12} mbar/mA and the typical static pressure during short periods without beam is 4-5 10^{-10} mbar. After several weeks without stored beam, during a recent maintenance shutdown, the static pressure fell to 3.6 10^{-10} mbar. The static pressure in the injection straight is 2.5 10^{-9} mbar. The graph shows that after further conditioning the target pressure of 10^{-9} mbar at 300 mA after a dose of 100 Ah is close to being met.

Fig. 5 shows the current-lifetime product as a function of beam dose, which continues to increase, consistent with the lifetime being dominated by vacuum pressure. The marked step-change in lifetime around 0.7 Ah coincides with the 3rd beam-based alignment, which allowed the closed orbit to be corrected to <100 µm rms, and the working point to be moved to the nominal one. Lifetimes in excess of 10 h are currently achieved at 100 mA. The data are consistent with achieving the design specification of 10 h lifetime at 300 mA after approximately 100 Ah conditioning.

STATUS AND FUTURE PLANS

The storage ring and injection system are running reliably and providing regular "user beam" from 8 insertion devices, with up to 125 mA beam current, with a slow-orbit feedback in operation. During accelerator physics shifts a maximum of 160 mA has been achieved. The plan for 2007 is to provide at least 3000h of User Mode, in 10 Runs lasting between 2 and 3 weeks. One shutdown period (March/April) will be used to install the second cavity, after which the beam current will be gradually increased to 300 mA. Other shutdowns will be used to install the second module of HU64, two further in-vacuum IDs, and 4 front-ends.

Several upgrades are being developed during 2007 as described below.

Fast Orbit Feedback

A Fast-orbit feedback system is nearing completion. BPM data is transmitted via fast serial links into a series of VME crates where dedicated feedback processors perform the feedback calculations and write the resulting corrector magnet values directly through the VME bus into the power supply controller cards. In this configuration data from all BPMs is available at all locations via multiply redundant links, providing a great resilience against failure.

The current status is that all hardware has been installed, communication of orbits at fast acquisition rate (10,072 measurements per second) is running reliably, the 24 receivers in the power supply racks can record data (up to 100,000 orbits) and all processing tasks (calculation of correction, control loop, communication to power supplies) exist in software, ready for first use. First closure of the loop is expected in February.

Transverse Multibunch Feedback

To avoid the possibility of having to operate with excessively high chromaticity in order to reach 300 mA, and above, with possible negative consequences for lifetime, injection efficiency etc., a transverse multibunch feedback system is being developed, based on the Libera bunch-by-bunch system.

Kicker striplines (SLS-type) and extra pickup buttons are already installed in the diagnostic straight. The bunch-by-bunch feedback processors have been delivered and tested in the lab. The RF front-end has been assembled and tested as a system in the lab, and will be installed in February. First tests of data acquisition will occur in March. Development of the FPGA based feedback algorithm has started, in collaboration with the ESRF, and testing of feedback with beam is expected by mid 2007.

Top-up Injection

Provision of top-up injection has always been part of the design specification for Diamond, and has been taken into account in the design of the linac, booster magnet power supplies, timing system, personnel safety system etc. Detailed attention is now being given to the various studies and tests that need to be carried out e.g. localisation of beam losses with collimators, testing injection with IDs closed, radiation checks, testing safety interlocks etc., as well as safety documentation. It is currently envisaged that top-up will operate in multi-shot, single bunch mode, with injections at a fixed time interval. At 300 mA with 10h lifetime, injection every 2 mins will lead to a 1 mA current stability, which is considered adequate by users.

ACKNOWLEDGEMENTS

It is a pleasure to acknowledge the assistance of G. Portmann (ALS) and J. Safranek (SSRL) in carrying out measurements and data analysis using LOCO.

REFERENCES

[1] "Diamond Synchrotron Light Source: Report of the Design Specification", CCLRC, June 2002
[2] R.P. Walker et al., "Overview of the Status of the Diamond Project", Proc. EPAC 2006, Edinburgh, p. 2718.
[3] C. Christou, "Commissioning of the Diamond Pre-injector Linac", EPAC 2006, p. 3185.
[4] V.C. Kempson et al., "Commissioning of the Booster Synchrotron for the Diamond Light Source", EPAC 2006, p. 3344.
[5] B. Singh et al., "Beam Optic Measurements for the Booster Synchrotron of the Diamond Light Source", EPAC 2006, p. 3347.
[6] G. Portmann, et al., "An Accelerator Control Middle Layer using MATLAB", Proc. PAC 2005, Knoxville, p. 4009.
[7] J. Safranek, Nucl. Instr. Meth. A388 (1997) 27.
J. Safranek et al., "MATLAB based LOCO", SLAC-PUB 9464, (2002).
[8] M.P. Cox et al., "Diamond Light Source Vacuum Systems Commissioning Status", EPAC 2006, p. 3332.

DESIGN OF THE TRANSFER LINE-2 FOR THE CTF-3 AT CERN

Amalendu Sharma, Abdurrahim, A.D. Ghodke, Gurnam Singh
IOAPDD, Raja Ramanna Centre for Advanced Technology, Indore (M.P.)

Abstract

The design of the Transfer Line-2 (TL-2), which will transfer an electron beam from the Combiner Ring (CR) to CLEX area (CLIC experimental area) of CTF-3 (CLIC Test Facility-3) at CERN, is presented in this paper. This line will be used to control the bunch length and Twiss parameters at the entrance to the CLEX area. The line will have a wide tunability of R_{56} parameter, ranging from –0.35m to +0.35m. This has been designed considering the constraints imposed by the building geometry and the magnetic elements to be used. The design optimization of the line has been done up to second order for the entire R_{56} range, keeping T_{566} practically zero and emittance dilution below 10%.

INTRODUCTION

CLIC (Compact Linear Collider) at CERN is based on the new scheme of RF generation at 30 GHz. The RF generation scheme is based on the frequency multiplication and bunch compression of the drive beam. The CTF-3 is to demonstrate the feasibility of such a scheme to provide the 30 GHz RF power source with CLIC nominal peak power and pulse length. The electron beam at nominal energy of 150 MeV after frequency multiplication will be extracted from the Combiner Ring (CR) and it will be transported to CLEX area with required bunch length compression by the TL-2. The general description and layout of the CLIC and CTF-3 can be found in references [1, 2, and 3]. Here in RRCAT, we have carried out the optics design of the TL-2, with required tuning range to handle the bunch length control before delivering the beam in CLEX area. In this paper we have provided the basic theory of bunch length control in the magnetic optics and design of TL-2.

BUNCH LENGTH COMPRESSION

Bunch length compression is possible by establishing the energy time correlation in the bunch by a RF field and then passing it through the magnetic channel to establish the required length energy correlation [4]. When bunch passes through the RF field, the energy time correlation is given by

$$z_1 = z_0 \tag{1}$$

$$\delta_1 = \left(1 - \frac{qV_{RF}}{E_0}\sin\phi_s\right)\delta_0 + \left(\frac{qV_{RF}}{E_0}\cos\phi_s\right)kz_0 \tag{2}$$

Here z gives the longitudinal position of the particle with respect to reference (synchronous) particle. V_{RF}, q, δ and ϕ_s carry their usual meanings. Subscripts 0 and 1 are used for entrance and exit of the cavity. In the approximation used here, it is assumed that cavity has zero length and thus z does not change. The equation 2 can be written as

$$\delta_1 = R_{65}z_0 + R_{66}\delta_0 \tag{3}$$

Here R_{ij} is the element of 6x6 first order transfer matrix. After that the particle passes through the magnetic channel, which has opposite effect of the cavity, i.e. the δ remains unchanged and z is modified. For a magnetic channel, the first order relations can be written down as

$$z_2 = z_1 + R_{56}\delta_1 \tag{4}$$

$$\delta_2 = \delta_1 \tag{5}$$

Z_2 and δ_2 are the longitudinal position and momentum deviation after the magnetic channel. Here R_{56} depends on the dispersion distribution inside the dipole magnets of the magnetic channel. It is given by (in sign convention of MAD-8 [5])

$$R_{56} = -\int \frac{\eta ds}{\rho} \tag{6}$$

Therefore by controlling the dispersion distribution inside the dipole magnets, R_{56} parameter can be controlled and by selecting the proper values of R_{65}, R_{66} and R_{56}, the required bunch length compression can be obtained. Introducing second order terms in the analysis, the equation 4 will be modified as

$$z_2 = z_1 + R_{56}\delta + T_{566}\delta^2 \tag{7}$$

Here T_{ijk}- is the element of the second order transfer matrix. In the present paper we outline the design of the TL-2, which has a wide tuning range of the R_{56} parameter to control the bunch length and in whole tuning range second order term T_{566} is compensated.

OPTICS DESIGN OF THE TL-2

General Layout

The beam parameters of TL-2 are provided in the table-1. The line is to be accommodated in the existing LPI-complex (LEP Pre Injector complex), which has several geometrical constraints and the magnets to be used here to be selected from a stock of already magnets available at CERN. These constraints poses a challenge in the design of the line with such wide tuning range of R_{56} parameter (from -0.35m to +0.35m) with T_{566} corrected to zero and emittance dilution below 10%. The layout of the complete line inside the building is shown in the figure-1. Parameters and numbers of the available magnets are shown in the table-2.

The design of the line can be broken in three modules. Following sections describe the details of each module of this line.

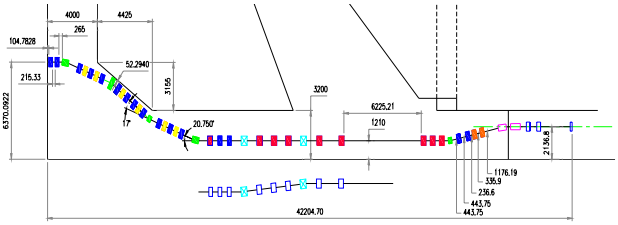

Figure 1: Layout of TL-2

Table 1: Beam parameters of the TL-2

Parameters	@ entrance	@ Exit
Nominal energy (MeV)	150	150
Peak energy (MeV)	300	300
β_x, β_y (m)	8.1, 3.5	4-5, 4-5
α_x, α_y	0.12, 0.31	0.0, 0.0
η_x (m), η'_x	0.0, 0.0	0.0, 0.0
η_y (m), η'_y	0.0, 0.0	0.0, 0.0
ε_x normalized (mm-mrad)	100	110
ε_y normalized (mm-mrad)	100	110
δ in %	1.0	1.0
σ_z (ps)	8.3	1.3

Table 2: Parameters of the available magnets

	Dipole Type-1	Dipole Type-2	Stnd. Quad	Slim Quad	TSL Quad	Sextupole
Mech. length (m)	0.770	0.520	0.592	0.384	0.430	0.350
Mech. width (m)	0.794	0.794	0.819	0.340	0.650	0.420
Effective length (m)	0.518	0.268	0.380	0.300	0.295	0.246
Aperture (mm)	100´45	100´45	184	100	101	167
Strength	1.3 T	1.3 T	5.4 T/m	8 T/m	10.6 T/m	44 T/m2
Number	02	03	26	02	16	12

Module-1

Module-1 of this line is from the extraction septa of the CR to first horizontal dipole magnet. This is an achromat. The septa and the dipole magnet bend the beam in opposite direction and therefore this achromat has an phase advance of 2π in the horizontal plane. The design of this module is governed mainly by the constraints, imposed by the building and the sections of CR in the vicinity of the extraction point. Due to this, the locations for placing the quadrupoles are restricted and all the quadrupoles being operated close to their highest strength result in a rapid rise of β-functions at the exit of this module. All these restrictions lead to a very low flexibility in this module.

Module-2

Module-2 fulfils various requirements of the transfer line. It controls large β-functions, resulting from the module-1 and provides a 6m long dispersion free region for tail clippers. It has a vertical achromat to send the beam 50cm down wards as the LPI-complex and CLEX area have different floor levels. Besides it has a quadrupole triplet for obtaining required Twiss parameters at the entrance of the module-3.

Module-3

Module-3 is the tunable R_{56} arc and a quadrupole doublet for matching the Twiss parameters at the end of the line. The design of this module also is restricted by the existing building geometry. The tunable R_{56} arc of this module has been designed with four dipole magnets and two quadrupole doublets and two quadrupole triplets. The first and last dipole magnets of ±20.75° bend angle form the entrance and exit of this achromatic arc, hence the contribution of these magnets in R_{56} is constant. The other two-dipole magnets, of ±17° bend angle, are used to tune the R_{56} parameter. For tuning the R_{56} in the arc, the quadrupole strength goes very high and thus higher order chromatic terms have larger magnitudes, which require strong sextupoles to compensate them. Therefore the arc has been designed with mirror symmetry to lower down the higher order geometrical aberrations as well as to reduce the number of the power supplies. For obtaining a particular value of R_{56} parameter, dispersion and its derivative at the entrance of the second dipole magnet of the arc are chosen in such a way, so that the dispersion becomes sufficient at the sextupole locations to lower down their strength for correcting the T_{566} parameter. The optimization of this line is done with MAD-8 program, which requires a good starting guess value for solution. To obtain a good starting guess values for the solution, a computer program in C has been written assuming quadrupoles as thin lenses [6]. The lattice function and dispersion at the three extreme values of R_{56} (-0.35m, 0.00 and +0.35m) are shown in the figure-2.

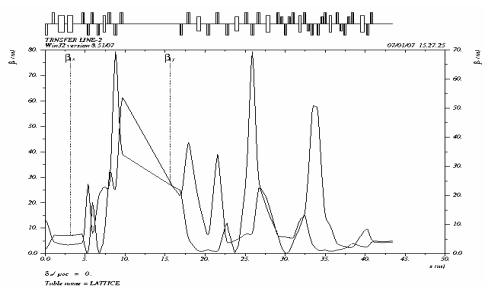

Figure 2a: Lattice function for R_{56} = -0.35m

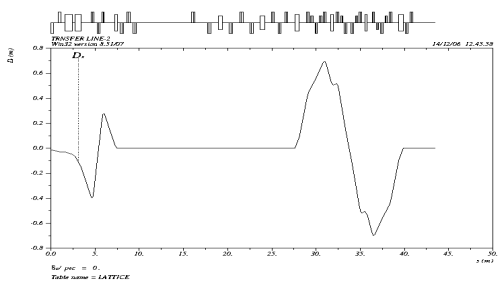

Figure 2b: Dispersion function for R_{56} = -0.35m

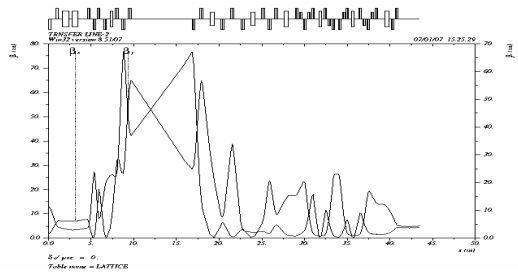

Figure 2c: Lattice functions for R_{56} = 0.00m

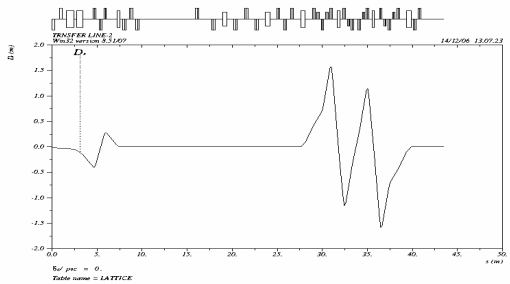

Figure 2d: Dispersion function for R_{56} = 0.00m

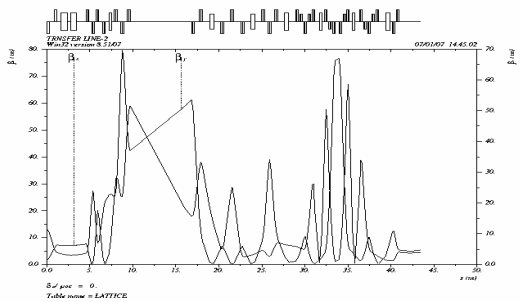

Figure 2e: Lattice functions for R_{56} = +0.35m

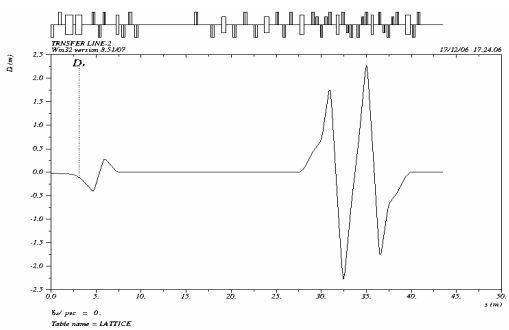

Figure 2f: Dispersion function for R_{56} = +0.35m

For correction of the T_{566} parameter, the six sextupoles, driven by three power supplies are incorporated in the tunable R_{56} arc of the module-3. The complete symmetric optical solution with I-transformer between the sextupoles is not possible in whole tuning range due to matching requirements at the exit. The line has only two quadrupoles at the end for matching the Twiss parameters. Thus for minimizing the phase space distortion due to sextupoles, a distribution of β-functions at the location of the sextupoles with proper phase advance is obtained, so that the sextupolar kicks cancels partially. This distribution is achieved by suitable choice of Twiss parameters at the entrance of the module-3. In this way we are able to improve the situation at R_{56} = 0.00 and -0.35m. The work at other extreme of R_{56} and also improvement in the solutions achieved are in progress. Figure-3 shows the phase space distortion due to sextupoles at the R_{56} = 0.00 and -0.35m.

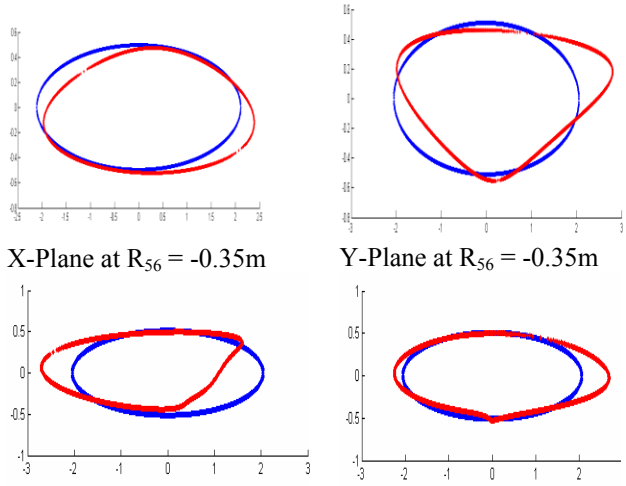

X-Plane at R_{56} = -0.35m Y-Plane at R_{56} = -0.35m

X-Plane at R_{56} = 0.00m Y-Plane at R_{56} = 0.00m

Figure 3: Phase space distortion due to T_{566} correction.

CONCLUSION

Transfer line-2 from the CR extraction point to CLEX area has been designed to achieve with R_{56} varying from -0.35m to +0.35m with constraints due to building layout and choice of magnets. The sextupole scheme is under study.

ACKNOLEDGEMENT

We are thankful to Hans Braun, Gunther Gaschonke and Frank Tecker of CERN for their valuable guidance and feedback on the design of this line. We also thank V. C. Sahni, Director, RRCAT and S. Kotaiah for their continuous encouragement.

REFERENCES

[1] CLIC Study Team, “Proposal for Future CLIC Studies and a New CLIC Test Facility (CTF3)”, CLIC Note 402, CERN/PS 99-047 (LP), July 1999.

[2] Ed. G. Geschonke and A. Ghigo, “CTF3 Design Report”, CTF3 Note 2002-047, CERN/PS 2002-008 (RF), May 2002.

[3] R. Corsini for the CLIC Study Team, “Overview of CLIC and CTF3”, CLIC Note 540, CERN/PS/2002-073, September 2002.

[4] Andy Wolski, “A short introduction to Bunch Compressors for Linear Colliders”, Notes for USPAS Course on Linear Colliders, Santa Barbara, June 2003.

[5] H. Grote and F.C. Iselin, “MAD 8 User Guide”, CERN/SL/90-30(AP), 1990.

[6] Amalendu Sharma, Abdurrahim, A.D.Ghodke and Gurnam Singh, “Preliminary beam optics design of Transfer Line – 2 for CLIC Testing Facility – 3 of CERN”, RRCAT internal report, CAT/ 2006-09.

RHIC STATUS*

Thomas Roser
Brookhaven National Laboratory, Upton, New York 11793-5000, USA

Abstract

As the first hadron accelerator and collider consisting of two independent superconducting rings RHIC has operated with a wide range of beam energies and particle species. Machine operation and performance will be reviewed that includes high luminosity gold-on-gold and copper-on-copper collisions at design beam energy (100 GeV/u), asymmetric deuteron-on-gold collisions as well as high energy polarized proton-proton collisions (100 GeV on 100 GeV) with beam polarization of up to 65%. Plans for future upgrades of RHIC will also be discussed.

THE RHIC FACILITY

With its two independent rings RHIC is a highly flexible collider of hadron beams ranging from colliding intense beams of polarized protons to colliding fully stripped gold ions. The collision of 100 GeV/nucleon gold ions probes the conditions of the early universe by producing extreme conditions where quarks and gluons are predicted to form a new state of matter. Several runs of high luminosity gold-gold collisions as well as comparison runs using proton, deuteron and copper beams have demonstrated that indeed a new state of matter with extreme density is formed in the RHIC gold-gold collisions.

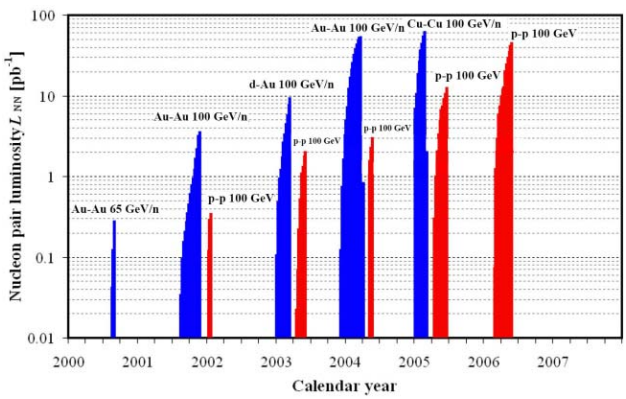

Figure 1: Integrated nucleon-pair luminosity for all the RHIC running modes since start of operation.

The RHIC polarized proton collider has opened up the completely unique physics opportunities of studying spin effects in hadronic reactions at high-luminosity high-energy proton-proton collisions. It allows the study of the spin structure of the proton, in particular the degree of polarization of the gluons and anti-quarks, and also verification of the many well-documented expectations of spin effects in perturbative QCD and parity violation in W and Z production. The RHIC center-of-mass energy range of 200 to 500 GeV is ideal in the sense that it is high enough for perturbative QCD to be applicable and low enough so that the typical momentum fraction of the valence quarks is about 0.1 or larger. This guarantees significant levels of parton polarization.

* Work performed under the auspices of the United States Department of Energy, and with support of RIKEN (Japan) and Renaissance Technologies Corp. (USA)

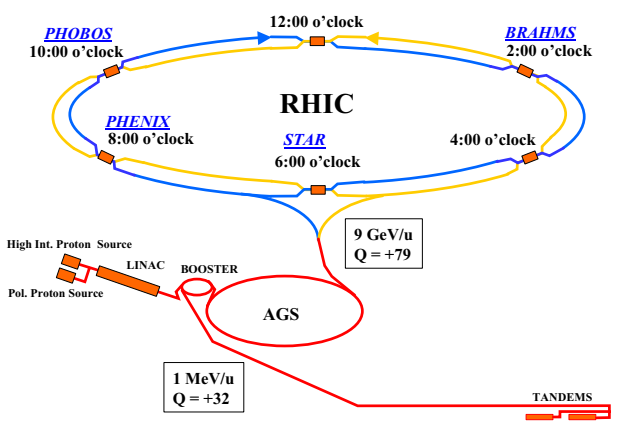

Figure 2: Layout of RHIC and the injector accelerators. The gold ions are stepwise ionized as they are accelerated to RHIC injection energy.

During its first six years of operation RHIC has already exceeded the design parameters for gold-gold collisions, has successfully operated in an asymmetric mode of colliding deuteron on gold with both beams at the same energy per nucleon but, of course, different rigidities, and very successfully completed an additional comparison run of colliding copper beams with record luminosities. In addition, four very successful commissioning and running periods with polarized protons demonstrated the performance of RHIC as a high luminosity polarized collider. For the main part of all these runs RHIC was operating with beam energies of 100 GeV/nucleon - the gold beam design energy. Additional running at lower beam energy was also accomplished during these same running periods again demonstrating the high flexibility of RHIC. Fig. 1 shows, in semi-logarithmic scale the achieved integrated nucleon-pair luminosities for the many modes of operation of RHIC since its start of operation in 2000. Using nucleon-pair luminosity allows the comparison of the different modes properly reflecting the relative statistical relevance of the data samples and also the degree of difficulty in achieving high luminosity.

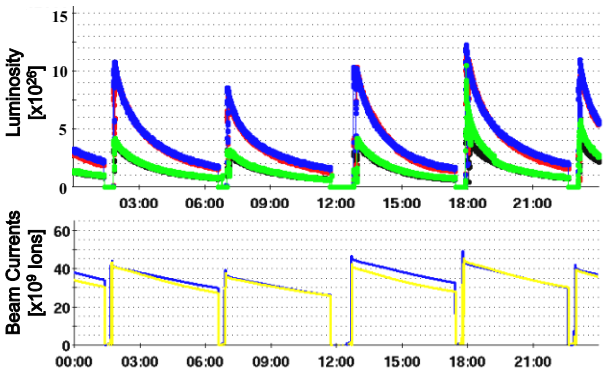

Figure 3: Evolution of the collision rate at the four RHIC detectors and beam currents in the blue and yellow ring during typical stores.

HEAVY ION OPERATION

Gold-Gold Operation Fig. 2 shows the layout of RHIC and the four injector accelerators Tandem, Linac, Booster and AGS. The gold ions are stepwise ionized as they are accelerated to RHIC injection energy, at which point they are fully ionized. The performance of the injector is summarized in Table 1. The Tandem Van de Graaff accelerates Au^{-1} from a sputter source to about 1 MeV/nucleon. The 530 ms long beam pulse is stripped to Au^{+32} and injected into the Booster using horizontal and vertical phase space painting. After acceleration to about 100 MeV/nucleon the beam is stripped to Au^{+77} and transferred to the AGS where it is accelerated to the RHIC injection kinetic energy of 8.6 GeV/nucleon. In the AGS the beam bunches from the Booster are merged to reach the required intensity of about 1×10^9 Au ion per bunch at a longitudinal emittance of 0.3 eVs/nucleon. The final stripping to bare Au^{+79} occurs on the way to RHIC.

RHIC is the first super-conducting, slow ramping accelerator that crosses transition energy during acceleration. At transition energy the spreads of the particle revolution frequency stemming from the spread in velocity and spread in path length cancel exactly and all particles maintain their relative position for a long time. Interaction between particles can then cause instabilities. With pulsed quadrupole power supplies the transition energy is changed quickly during acceleration to effectively jump across it. The dispersion distortion required to change the transition energy is local and the betatron tune shift is corrected in a zero-dispersion region. This scheme allows for up to 1 GeV change in transition energy with very little lattice distortion.

Table 1: RHIC injector performance

Location	RHIC bunch intensity	Efficiency
Tandem	5.4×10^9	
Booster Injection	2.9×10^9	54%
Booster Extraction	2.4×10^9	83%
AGS Injection	1.2×10^9	50%
AGS Extraction	1.1×10^9	92%
Total		20%

The two RHIC rings, labelled blue and yellow, are intersecting at six interaction regions (IR), four of which are occupied by the collider experiments BRAHMS, STAR, PHENIX and PHOBOS. All IRs can operate at a betastar between 2 and 10 m. In two interaction regions (STAR and PHENIX) the quality of the triplet quadrupoles allows further reduction of betastar to 1 m. Typically betastar is 10 m at injection energy for all IRs and is then squeezed during the acceleration cycle first to 5 m at the transition energy, which minimizes its momentum dependence, and then to 1 m for PHENIX and STAR and 3 m for the other experiments at store energy. A typical acceleration cycle consists of filling the blue ring with 56 bunches in groups of 4 bunches, filling the yellow ring in the same way and then simultaneous acceleration of both beams to storage energy. During acceleration the beams are separated vertically by up to 10 mm in the interaction regions to avoid beam losses from the two beams colliding.

Typical stores last about 5 hours. Fig. 3 shows the evolution of the collision rate in the four experiments. The collision rate was measured using identical Zero Degree Calorimeters (ZDC) at all four interaction regions. The ZDC counters detect at least one neutron on each side from mutual Coulomb and nuclear dissociation with a total cross section of about 10 barns. After optimizing longitudinal and transverse steering the peak luminosity at PHENIX and STAR is up to $15 \times 10^{26}\ cm^{-2}\ s^{-1}$ ($5.8 \times 10^{31}\ cm^{-2}\ s^{-1}$ nucleon-pair luminosity) with an average luminosity over the 5 hour store of $4 \times 10^{26}\ cm^{-2}\ s^{-1}$, which is twice the design average luminosity . This corresponds to an initial normalized 95% beam emittance of about $15\pi\ \mu m$ growing to about $40\pi\ \mu m$ at the end of the store. The beam loss and transverse emittance growth during the store is mainly caused by intra-beam scattering, which is particularly important for the fully stripped, highly charged gold beams[1].

The total gold beam intensity was limited mainly by vacuum break-downs in the room temperature sections of the RHIC rings[2]. This pressure rise is associated with the formation of electron clouds, which in turn appear when the bunch peak intensity is high around transition and after bunch compression and when the bunch spacing is small. This situation was greatly improved by installing vacuum pipes with internal coating of non-evaporative getter (NEG) that is properly activated. The resulting residual pressure is 10^{-11} Torr or less. The NEG coating acts as a very effective distributed pump and also suppresses electron cloud formation due to its low secondary electron yield.

The bunch intensity was also limited by a very fast single bunch transverse instability that develops near transition where the chromaticity needs to cross zero. It can be stabilized using octupoles. This instability has a growth rate

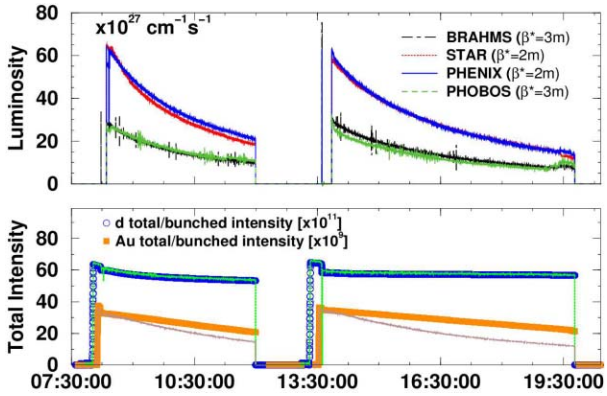

Figure 4: Evolution of the luminosity and beam intensities at the four RHIC detectors during two typical deuteron-gold stores.

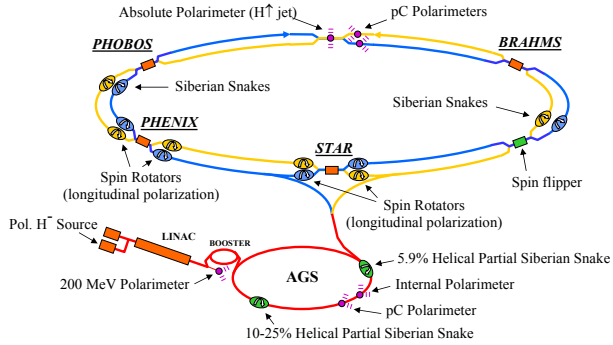

Figure 5: The RHIC accelerator complex with the elements required for the acceleration and collision of polarized protons highlighted.

faster than the synchrotron period and is similar to a beam break-up instability. Recently it was observed that this instability is enhanced by the presence of electron clouds.

The high charge state of the gold ion makes it possible to contemplate stochastic cooling of the 100 GeV/n beam. First tests of equivalent bunched proton beam showed successful logitudinal stochastic cooling of a 100 GeV beam[4]. The full system will be commissioned with gold beam during the next RHIC run.

Deuteron-Gold Operation During Run-3 RHIC was operating for the first time with asymmetric collisions[3]. Colliding 100 GeV/nucleon deuteron beam with 100 GeV/nucleon gold beam will not produce the required temperature to create a new state of matter and therefore serves as an important comparison measurement to the gold-gold collisions. The rigidity of the two beams is different by about 20%, which results in different deflection angles in the beam-combining dipoles on either side of the interaction region. This requires a non-zero angle at the collision point, which slightly reduces the available aperture.

The injection energy into RHIC was also the same for both beams requiring the injector to produce beams with different rigidity. With same energy beams throughout the acceleration cycle in RHIC the effect of beam collisions could be minimized. Typical bunch intensity of the deuteron beam was about 1.2×10^{11} with emittances of about 12 $\pi\mu m$ [norm., 95%] and 0.3 eVs/nucleon. The gold beam parameters were similar to the gold-gold operation described above. The high intensity deuteron beams required careful adjustment of the chromaticity, especially around transition, to avoid transverse instabilities. A peak luminosity of $7 \times 10^{28}\ cm^{-2}\ s^{-1}$ ($3 \times 10^{31}\ cm^{-2}\ s^{-1}$ nucleon-pair luminosity)and store-averaged luminosity of $2 \times 10^{28}\ cm^{-2}\ s^{-1}$ was reached at the IRs with the 2 m betastar. Fig. 4 shows luminosities and beam currents for d-Au collisions. The much shorter beam lifetime of the gold beam clearly demonstrates the stronger effect of intra-beam scattering (IBS) for gold than deuteron beam.

Copper-Copper Operation The collision of copper ions[5], an intermediate size nucleus, served as an additional comparison measurement to determine the minimum energy density needed to create the strongly-coupled quark gluon plasma. The copper beams are expected to be less affected by intra-beam scattering due to the lower charge but this was partially compensated by a significantly higher bunch intensity of 4.5×10^9 ions/bunch available from the Tandem. The higher beam intensity tested new limits for both the fast instability at transition crossing and pressure rise in the warm sections in RHIC. For the latter case the newly installed NEG coated vacuum pipes proved to greatly improve the intensity limits. As a result a new record peak and average nucleon-pair luminosity of $7.9 \times 10^{31}\ cm^{-2}\ s^{-1}$ and $3.2 \times 10^{31}\ cm^{-2}\ s^{-1}$, respectively, was achieved.

POLARIZED PROTON COLLISIONS

Fig. 5 shows the lay-out of the Brookhaven accelerator complex highlighting the components required for polarized beam acceleration. The new 'Optically Pumped Polarized Ion Source'[6] is producing 10^{12} polarized protons per pulse. A single source pulse is captured into a single bunch, which is ample beam intensity to reach the nominal RHIC bunch intensity of 2×10^{11} polarized protons.

In the AGS two partial Siberian snakes are installed. One of them is an iron-based helical dipole[7] that rotates the spin by 11°. A view down the magnet gap is shown in Fig. 6. The other is a superconducting helical dipole that can reach a 3 Tesla field and a spin rotation of up to 45°. Both helical dipoles have the same design with a variable pitch along the length of the magnet to minimize orbit excursions and also to fit into the 3 m available straight sections in the AGS. With the two partial snakes strategically placed with one third of the AGS ring between them all vertical spin resonances can be avoided up to the required RHIC transfer energy of about 25 GeV as long as the vertical betatron

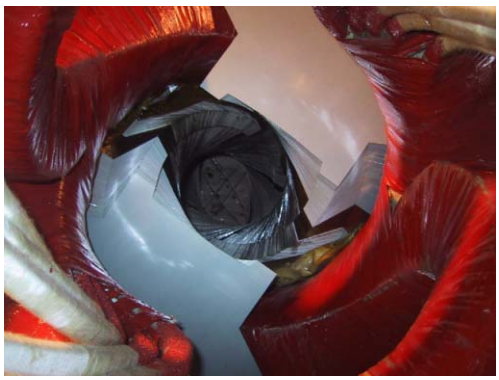

Figure 6: View down the magnet gap of the warm, iron-based helical partial Siberian snake of the AGS.

tune is placed at 8.98, very close to an integer[8]. This was achieved reliably over the whole acceleration cycle. With a 80% polarization from the source 65% polarization was reached at AGS extraction. The remaining polarization loss in the AGS might come from weak spin resonances driven by the horizontal motion of the beam. They could be overcome by moving also the horizontal betatron tune close to an integer.

The full Siberian snakes (two for each ring) and the spin rotators (four for each collider experiment) for RHIC each consist of four 2.4 m long, 4 T helical dipole magnet modules each having a full 360° helical twist. The 9 cm diameter bore of the helical magnets can accommodate 3 cm orbit excursions at injection. Fig. 7 shows the orbit and spin trajectory through a RHIC snake. The super-conducting helical dipoles for both the RHIC snakes and spin-rotators and the superconducting AGS partial snake were constructed at BNL using thin cable placed into helical grooves that have been milled into a thick-walled aluminum cylinder[9].

In addition to maintaining polarization, the accurate measurement of the beam polarization is of great importance. Very small angle elastic scattering in the Coulomb-Nuclear interference region offers the possibility for an analyzing reaction with a high figure-of-merit, which is not expected to be strongly energy dependent[10]. For polarized beam commissioning in RHIC an ultra-thin carbon ribbon is used as an internal target, and the recoil carbon

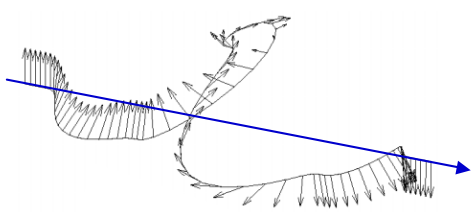

Figure 7: Orbit and spin tracking through the four helical magnets of a Siberian Snake at $\gamma = 25$. The spin tracking shows the reversal of the vertical polarization.

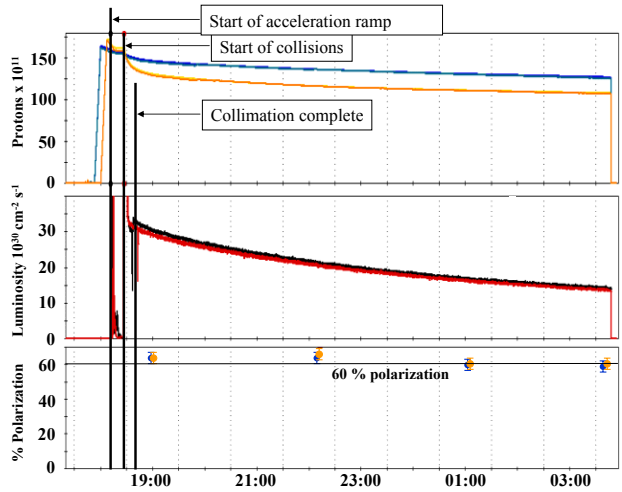

Figure 8: Circulating beam in the blue and yellow ring, luminosity at PHENIX (black) and STAR (red), as well as the measured circulating beam polarization in the blue and yellow RHIC ring (blue(dark) and yellow(light) lines and symbols, respectively) for one typical store.

nuclei are detected to measure both vertical and radial polarization components. The detection of the recoil carbon with silicon detectors using both energy and time-of-flight information shows excellent particle identification. It was demonstrated that this polarimeter can be used to monitor polarization of high energy proton beams in an almost non-destructive manner and that the carbon fiber target could be scanned through the circulating beam to measure polarization profiles. A polarized atomic hydrogen jet was also installed as an internal target for small angle proton-proton scattering which allows the absolute calibration of the beam polarization to better than 5 %.

Fig. 8 shows circulating beam current, luminosity and measured circulating beam polarization of a typical store during last year's run[11]. A peak luminosity of about about 35×10^{30} cm^{-2} s^{-1} was reached. The beam polarization of up to 65% was calibrated at 100 GeV with the absolute polarimeter mentioned above. To preserve beam polarization in RHIC during acceleration and storage the vertical betatron tune had to be controlled to better than 0.005[12] and the orbit had to be corrected to better than 1 mm rms to avoid depolarizing "snake" resonances[13].

More than 20 years after Y. Derbenev and A. Kodratenko[14] made their proposal to use local spin rotators to stabilize polarized beams in high energy rings, it has now been demonstrated that their concept is working flawlessly even in the presence of strong spin resonances at high energy.

A first successful test of polarization survival during acceleration to 250 GeV crossing three very strong spin resonances was performed[15]. A polarization of 45% was measured at 250 GeV using the pC polarimeter calibrated at 100 GeV. It is not expected that the calibration would

change significantly between these two energies, but a more accurate polarization will have to await a calibration measurement with the polarized gas jet performed at 250 GeV. Nevertheless, this preliminary result bodes well for a successful operation of RHIC with polarized 250 GeV proton beams producing collisions at $\sqrt{s} = 500$ GeV with a planned luminosity of up to $1.5 \times 10^{32}\ cm^{-2}\ s^{-1}$.

RHIC UPGRADE PLANS

An initial upgrade of the RHIC luminosity for heavy ion operation by a factor of four beyond design ($2 \times 10^{26}\ cm^{-2}\ s^{-1}$) can be achieved by approximately doubling the number of bunches to 111 (100 ns bunch spacing) and reducing betastar from 2 m to 1 m. As described above the doubling of betastar has already been achieved Routine operation with 100 ns bunch spacing has been demonstrated with proton beams.

Further upgrade of the luminosity requires that the emittance growth from intra-beam scattering is reduced or eliminated. The growth of the beam size due to intra-beam scattering can be overcome by cooling the beams with a high intensity, cold electron beam[16]. To cool the 100 GeV/n gold beam with 10^9 ions per bunch in RHIC a 54 MeV electron beam with an average current of 50 - 100 mA is required. In this case the charge of each electron bunch is about equal to the charge of the ion bunch. The high beam power of about 5 MW of the electron beam makes it necessary to recover the beam energy by decelerating it in a super-conducting linac. Operation of an energy-recovering linac has been successfully demonstrated at JLab with a 160 MeV, 9 mA electron beam.

Table 2 shows the parameters for future RHIC luminosity upgrades for the first stage without electron cooling and then with electron cooling. Electron cooling has the most dramatic effect on the luminosity of gold collisions. However, it also improves operation with polarized protons due to the lower beam emittance.

Table 2: RHIC luminosity upgrade with electron cooling.

Gold-gold	w/o e-cool.	with e-cool.
Beam energy [GeV/n]	100	100
Emittance (95%) [$\pi\mu m$]	15 → 40	15 → 3
Beta function at IR [m]	1.0	1.0 → 0.5
Number of bunches	111	111
Bunch population [10^9]	1	1 → 0.3
Beam-beam param. per IR	0.0016	0.004
Ave. lum. [$10^{26} cm^{-2} s^{-1}$]	8	70
Proton-proton:		
Beam energy [GeV]	250	250
Emittance (95%) [$\pi\mu m$]	20	12
Beta function at IR [m]	1.0	0.5
Number of bunches	112	112
Bunch population [10^{11}]	2	2
Beam-beam param. per IR	0.007	0.012
Ave. lum. [$10^{32} cm^{-2} s^{-1}$]	1.5	5.0

Electron cooling of the high energy, heavy ion beams in RHIC extends beyond presently operating electron cooling facilities in several regards: an electron beam energy that is ten times higher, the use of bunched electron beam accelerated by a linear accelerator, and beam cooling during collider operation. The recombination rate of e^- and Au^{79+} in the cooling section has been estimated to be smaller than the burn-off rate of the heavy ion beams in the collisions, but will be used as a diagnostic for optimizing the cooling performance.

An R&D program has started to develop the critical items of the RHIC electron cooling system. A superconducting rf photo-cathode gun operating at 703.8 MHz is being built to provide the intense and ultra-bright electron beam. A 703.8 MHz super-conducting cavity for the energy-recovering linac has been built and is presently undergoing cleaning. This cavity is capable of accelerating the high intensity electron beam without causing beam-breakup.

ACKNOWLEDGMENT

The highly successful operation of RHIC was made possible by the excellent and dedicated RHIC design, construction, commissioning, and operations teams.

REFERENCES

[1] W. Fischer, Proc. of EPAC 2006, Edinburgh, Scotland, p. 905.

[2] S.Y. Zhang et al., Proc. of EPAC 2006, Edinburgh, Scotland, p. 595.

[3] T. Satogata et al., Proc. of PAC03, Portland, Oregon, p. 1706.

[4] M. Brennan et al.,Proc. of EPAC 2006, Edinburgh, Scotland, p. 2967.

[5] F. Pilat et al., Proc. of PAC05, Knoxville, Tennessee, p. 4281.

[6] J. Alessi et al., Proc. of PAC03, Portland, Oregon, p. 3282.

[7] J. Takano et al., Proc. of PAC05, Knoxville, Tennessee, p. 1003.

[8] H. Huang, Proc. of EPAC 2006, Edinburgh, Scotland, p. 273.

[9] E. Willen et al., Proc. of PAC05, Knoxville, Tennessee, p. 2935.

[10] J. Tojo et al., Phys. Rev. Lett. 89, 052302 (2002).

[11] V. Ptitsyn et al., Proc. of EPAC 2006, Edinburgh, Scotland, p. 592.

[12] P. Cameron et al., Proc. of EPAC 2006, Edinburgh, Scotland, p. 3044.

[13] M. Bai et al., Phys. Rev. Lett. 96, 174801 (2006); M. Bai et al., Proc. of PAC05, Knoxville, Tennessee, p. 2839.

[14] Ya.S. Derbenev and A.M. Kondratenko, Part. Accel. 8, 115 (1978).

[15] M. Bai et al., Phys. Rev. Lett. 96, 174801 (2006); M. Bai et al., "Accelerating Polarized Protons to High Energy", Proc. of SPIN2006, to be published.

[16] I. Ben-Zvi, Proc. of EPAC 2006, Edinburgh, Scotland, p. 940.

OPERATION FOR LHC CRYOMAGNET TESTS: CONCERNS, CHALLENGES & SUCCESSFUL COLLABORATION

V. Chohan , CERN, Geneva, Switzerland

Abstract

The LHC construction phase is coming to a close, with installation work progressing rapidly and beam start-up foreseen by end 2007. For the testing of the 1706 LHC cryomagnets in cryogenic conditions and its successful completion by early 2007, considerable challenges had to be overcome since 2002 to assure certain semi-routine tests operation at CERN. In particular, the majority of staff for tests and measurement purposes was provided by India on a rotating, one-year-stay basis, as part of the CERN-India Collaboration for LHC. This was complemented by some CERN accelerator Operation staff. While only 95 dipoles were tested till 2003, the efforts and innovative ideas coming from the Operation team contributed significantly to the completion of tests of nearly all 1706 magnets by end-2006. These included the improvements and management of the tests work flow as well as the test rates. Amongst these, certain pivotal ideas to stream-line the tests methodology as proposed and implemented successfully by the Indian Associates deserve a special mention. An insight into this as well an overall view of the tests operation will be given, together with an indication of some of the operation-related results from the tests programme.

INTRODUCTION

The Large Hadron Collider (LHC) consists of two interleaved synchrotron rings of 26.7 km circumference, to be installed in the tunnel used previously for the LEP machine [1]. Main elements of these rings are the two-in-one superconducting dipoles and quadrupoles operating in superfluid helium at a temperature of 1.9 K. Cryomagnets include 1232 dipoles (with correctors), 360 Short Straight Sections (SSS) integrated with quadrupoles and higher order poles which are needed for the different accelerator lattice functions and 114 Matching & Dispersion Suppressor region magnets integrated in Special SSS (IR-SSS).

Testing and qualification of the above magnets at cryogenic temperature is a prerequisite to their installation in the LHC tunnel. A superconducting magnet test facility equipped with 12 test benches and the necessary cryogenic infrastructure is operational at SM18 in CERN to perform the power tests and magnetic measurements for qualifying these magnets. Testing of the first series production magnets commenced in ~2001. Since early 2003, the test facility is being operated round the clock to meet the target to complete the testing of all the magnets required for the LHC by December 2006. The construction of all the 12 test benches was completed and the full usage started around June 2004.

The testing and qualification activities of a magnet is intended to verify its cryogenic, mechanical and electrical insulation integrity, qualify the performance of magnet protection systems, train the magnet up to the nominal field or higher so as to minimize training of magnets in the tunnel, characterize the intended magnetic field, accept the magnet based on its quench and training performance and generally, ensure that the magnet meets its design criteria. These may be categorized broadly within the five phases namely, to connect, cool down, cold tests, warm up and to disconnect respectively.

The workforce in the SM18 test facility consists of three teams, with the tests and measurement Operation Team as the major entity supported by the Cryogenics Team and the Magnet Connect/Disconnect Team (called ICS). The Operation Team consists mainly of associates from the Department of Atomic Energy (DAE), India, along with a number of regular CERN employees. The other two teams consist of contract employees from industrial consortia. A CERN team called Equipment Support looks after the improvements, exploitation and the troubleshooting of tests hardware and software on an on-call basis. A sub-team of ICS handles the movement of magnets within the test facility by means of a remotely controlled vehicle named ROCLA. All these teams work in mutual collaboration to complete the magnet tests within the specified time period.

In the massive effort of testing of all 1706 Cryo-magnets in cryogenic conditions within a stringent time frame, considerable challenges had to be overcome since the beginning to arrive at successful completion. This paper presents a brief account of some of the major hurdles encountered in the process and the innovative strategies and techniques that were developed to overcome them. Relevant statistics are presented to highlight the effectiveness of some of these strategies.

CONCERNS & HURDLES

Like any facility of unique requirements, SM18 had also its own characteristic issues, ranging from personnel logistics to infrastructure limitations. Following is a brief account of some of the major issues and challenges that had to be addressed in the routine operation of the facility.

Personnel Logistics Issues: In early 2002, for technical and organizational reasons, the outsourcing of the tests operation was no more an option. Moreover, due to various factors, only 7 non-experienced CERN staff members from accelerator operation could be assigned to run the SM18 test facility. However, for an anticipated round the clock operation of the facility with 12 test benches, a minimum of 4 persons per shift was necessary, thereby demanding minimum staff strength of 24. It was

at this time that DAE, India, offered technical human resources for SM18 operation. India already had a collaboration agreement with CERN since the nineties for the LHC, including a 10 man-year arrangement for tests & measurements during the magnet prototyping phase. Consequently, over 90 qualified personnel from 4 different Indian establishments have participated in magnet testing on a one-year rotational basis. The technical acumen and success of the early batches of Indian Associates lent credence and confidence that the tests activity could be successfully carried out in this manner. The strict, one year rotation was a condition desired by India, leading to the necessity of a large number of persons participating in the programme.

The Indian technical engineers, being not directly related to operation or CERN type of work, had to get familiar with the magnet tests activity before being productive. This essentially necessitated a continuous mentoring program, hence, limiting the number of 'trained staff' at any time. Preparing the work shift schedule with the limited experienced personnel & keep within the CERN rules and regulations was a major hurdle. Arranging proper facilities for the Indian associates to make them 'feel at home' in a foreign land was also an equally challenging task.

Novelty Aspects: Considering that the LHC cryomagnets were unique, they were tested with a research & development mindset by magnet and equipment specialists during the initial phases of SM18 operation. Partially automated test systems (for one magnet at a time) which existed then were considered adequate for usage by the experts. When the Indian and accelerator operation staff took over the running of the facility, the system appeared to be more or less a 'black box' where, not many details of the test systems and test sequences were provided. Testing of the SSS magnets was a challenging task until the end of 2004 while all necessary information got collected and collated; similarly, testing of the special SSS magnets was a grey area even till beginning of 2006; the special SSS magnets have a large variety of structures, types, temperature regimes and their complexity made the collection of all the relevant information required for tests an extremely complex task. Even the role and responsibilities of the Operation Team had to be properly defined during the early phases.

Magnet Qualifying Criteria: During the early phases, each dipole was trained to reach its ultimate field (about 8% above the one required for the LHC), which was a major time consuming activity. Extensive magnetic, special measurements and thermal cycles were carried out in majority of the magnets. Qualification of 'poorly performing' magnets was another laborious task, whereby the magnet was removed from the test bench, fitted with anticryostats and quench location instruments and brought for re-testing at a later date.

Co-ordination of Teams: Language was the biggest obstacle in proper co-ordination of activities of different teams involved in magnet testing. Indian associates who are not conversant with French often found it difficult to verbally communicate with other teams which were exclusively French speaking.

Nature of Industrial Contracts of Other Teams: The nature of consortium contracts was also a hurdle. It had been observed that many times, the work slowed down during the weekends because the contractual working hours of the ICS/ROCLA team got exhausted for the week; magnets were not moved, connected or disconnected. Likewise, lack of suitable technical support in case of malfunctioning of certain systems during outside normal hours was also a factor which affected the overall performance.

Infrastructure Limitations: The test facility in SM18 is organized in 6 clusters of two test benches each, total 12 benches. However, for space and costs reasons, each cluster has a common power converter, one set of data acquisition system and one set of quench heater power supplies, shared by both benches. This means that at any given time, these resources can only be utilized by one of the two benches in a cluster.

The cryogenic infrastructure has limited resources which cannot feed to the simultaneous demand from all the 12 benches. This puts forth a limit on the number of magnets at superconducting temperatures concurrently, the number of training quenches allowed within a specified time period as well as a precise number of magnets using the cryogenic cool-down or warm-up resources [2]. Water resources (to cool down the power converters and other auxiliary systems) are also limited. These constraints necessitate the operation team to optimize all the work by following a complex set of rules and by exercising judicious judgment.

Sometimes due to some imposed factors, the shared resources are blocked. For example, when some special tests were conducted on a magnet, exceptional priority was assigned to this bench, which affected operation on many other benches due to the interlinking of various resources.

The synchronous, cog-wheeling approach foreseen initially [3] was never applied in routine operation because of varying performance of magnets; rather, the 'asynchronous' approach managed by the operation team yielded the desired magnet test rates, aided by the fine trimming of the magnetic and quench performance programmes [4].

EARLY PERFORMANCE

Magnet tests work began in ~2001 with two benches and a limited cryogenic infrastructure. The work environment that existed till late 2002 was not favourable for a time limited and challenging activity like this. Tests were conducted mainly with laboratory type of systems and mobile racks which were not suitable for round the clock operation. The first sets of dipoles consisting of 30 samples from each of the three suppliers (called the pre-series magnets) were required to be tested elaborately with full magnetic measurements and many other extensive tests. In the early phases of testing till end-

2003, due to the lack of readiness of all test benches and cryogenic feed boxes, adequate information, supporting tools and operational experience, only 95 dipoles (including pre-series ones) could be tested [5]. Fig. 1 shows the time required for testing the dipoles during the early stages of 2001-2. With such a low testing rate it would have been impossible to meet the target. Hence, it was imperative to formulate proper throughput strategies and to develop supporting tools for enhancing the throughput; this necessitated an ambitious figure of 16-18 magnet tests per week, higher than anticipated, in order to complete the tests of all magnets by December 2006. This also entailed an extensive study [6] resulting in the application of a selective and reduced magnetic measurement effort.

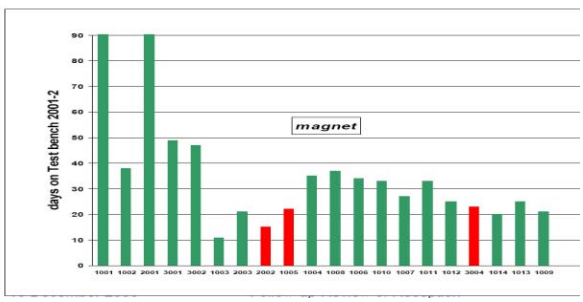

Figure 1: Bench Occupancy during 2001-02.

OPERATIONAL STRATEGIES & TOOLS

In the attempt to overcome the inherent hurdles and to attain maximum throughput, some effective management principles had to be addressed, necessary supporting tools developed, and certain level of operator empowerment had to be efficiently implemented, based on several innovative ideas and techniques. Feedback based on operational experience was given due importance in framing the strategies. Furthermore, the web based network backbone of CERN and computer facilities have been widely used for developing the supporting tools.

Most important innovations and strategies which essentially helped in achieving a high throughput included the introduction of a template based tests approach, web-based tools for tests management, magnet training rules & criteria for 24-hr operator decision taking and empowerment, general and cryogenic priorities handling by the shift crew, thermal cycle criteria and so forth. Some of these relevant points are discussed here in brief.

For the final, smooth operation of the facility with 12 benches, it was necessary to ensure a minimum staff strength of 24 at any time, comprising at least 15 experienced staff; however, the staff strength had to be appropriately adjusted according to the expected departures, arrivals and experience as and when required. This aspect was even further exemplified by the projected work load while the full 12 benches were still under construction on a cluster by cluster basis in 2003-4. To ensure all this, the number of Indian associates inducted into the project at any given time had to be carefully defined and planned, considering the strict one year rotation as well as input of the additional CERN staff during 2005 due to the year long accelerator shutdown. Fig. 2 gives a histogram of the total staff strength during the peak period 2005-6, and depicts the intricacies of manpower management. The staff strength was projected to drop steadily after December 2006, the scheduled deadline for the completion of all tests. Mentoring of newly inducted associates was designed to be an 'on the job' and a continuous process, increasing the number of personnel per shift during the process to ensure that the throughput was not affected.

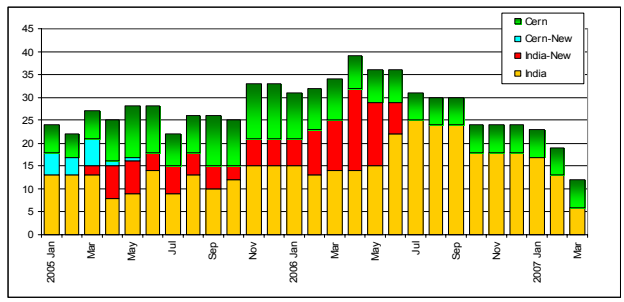

Figure 2: Variation of Operation Staff Strength 2005-6.

Contributions of the Operation Team

On the initiative of the Operation Team, a number of new features to aid the magnet tests had been brought in since mid-2003; the whole process of operation for magnet tests underwent a renaissance from crude manual data logging to a more efficient, sophisticated and highly automated tests management system.

A "To-Do-List" was created, which described the minimum set of tests to be performed on a magnet [7]. The tests were sequentially numbered & prefixed with the nature of tests i.e., "Preparatory test" (PREP) or "Power test" (PT). The "To Do List" approach weaned away the R&D culture in magnet tests and evaluation to a very stable and clear cut approach that could be handled by the Operation Team. Operation methods necessary for conducting each test in the "To-Do-List" were systematically prepared and reviewed to avoid the human errors in magnet testing to the maximum possible extent.

The Magnet Tests Report templates were designed in a manner for ease of use, with operational notes /checklists appended wherever necessary. The flow of tests in the template obeyed the "To-Do-List" to ensure that the tests were carried out systematically, efficiently and in a fail safe, sequential manner.

A new operation web-site was developed where all important documentation like operation methods, manuals, presentations, various template files, troubleshooting procedures, shift-plan & so forth could be obtained with minimum effort. This site immensely helped in easing the training of fresh staff as well as in managing the daily operation activities. The Indian Associates were the exclusive contributors to these very significant & essential documentation production and continual mentoring activities.

A web-based system using HTML & ASP codes called the SM18 Test Management System (SMTMS) was developed with all the data relevant to magnet tests stored in this system [8]. Based on the "To-Do-List", the web-based retrieval from SMTMS permits the automatic generation of the test sequences and reports such as the CDPT (CryoDipole Power Tests, which contains the training history), MAPS (Magnet Appraisal and Performance Sheet, which is a single page tabulation of the goodness of the magnet) and so forth. This enabled a fast, reliable, and error-free generation of crucial data pertaining to the magnet tests. With SMTMS, it is also possible to keep track of times taken for the various phases in magnet tests; all persons directly concerned could keep track of the tests progress from varied geographical locations in CERN & outside [9].

An electronic log-book was implemented using the CERN network backbone in providing web-based applications. Apart from ensuring easy access and usage by all SM18 operation or support personnel, this helped in categorizing and recording the different faults that occurred during the course of magnet testing.

To ensure smooth interaction between the various teams during the different stages of preparation before testing as well as at the end of the tests, a web based tool in the form of an Electronic-Workflow manifest called the e-traveller was created [8],[10]. The interface of this tool with mobile phones alerts and informs relevant teams (via short message service in appropriate languages) about the need for their services on a particular magnet. This helped the Indian associates to overcome the difficulties in verbal communication with the other teams but maintained the work rhythm as well as keeping an automatic record of the tests phases.

In order to attain a high throughput, it was necessary to reduce the number of training quenches per magnet, both from the point of view of limited cryogenic resources as well as the time involved. During 2003, the Operation team had observed that the majority of the magnets cross their nominal field (8.33T or 11850A) in the second ramp (see Fig. 3), whereas not much additional information on the 'goodness' of the magnet was available from the third & higher quenches [11]. Based on this, a new training rule named the 'Two-Quench Rule' was accepted by the magnet experts [4], under which it was recommended to do only two training quenches in each magnet provided it crossed the nominal field with a small margin. Later on, this rule was complemented by the so called 'Three-Quench Rule', under which a magnet is accepted if it crosses a field of 8.6T (12250A) in the third quench even if it had not passed the preceding rule. This strategy drastically reduced the overall cold tests time, thereby resulted in a high throughput. Likewise, the introduction of a Rapid On Bench Thermal Cycle (ROBTC) for magnets with poor performance in the first run was another major step towards reducing the overall magnet test time. These new rules, along with a 24-hr decision taking by the operator on the goodness of the magnet by analyzing the results and using the MAPS, helped in achieving a higher throughput. ROBTC and MAPS are discussed in detail elsewhere [12], [13]. The criteria for arriving at precise MAPS formulation were based on clear-cut rules and magnet specifications as well reviews, e.g. [14].

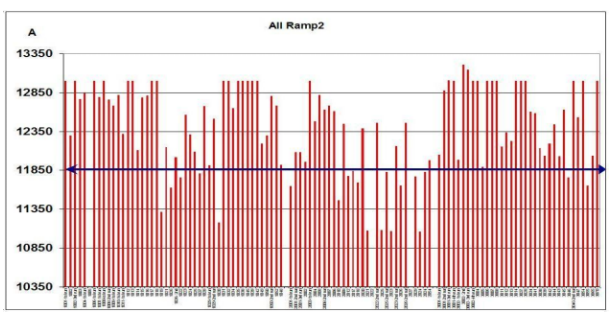

Figure 3: 2nd ramp performance of all dipoles till Dec 03 (each bar corresponds to 2nd ramp current reached).

RESULTS

Fig. 4 depicts the cumulative number of magnet tests, including repeats, since 2002. While the throughput was low till end-2003, it picked up sharply after the introduction of throughput strategies and tools. The plateau regions at the end of each year are due to the annual cryogenic infrastructure shutdown of typically seven weeks.

Fig. 5 gives further details of the magnets tested each year. It segregates the number of dipoles, arc SSS and IR-SSS tested each year, along with the cumulative number of magnets tested in that year. Starting with the meagre 21 magnets tested in 2001-2 and 76 in 2003, 456 magnets were tested in 2004. This count went up to an all time high of 703 magnet tests during 2005. During 2006, 648 magnet tests have been carried out; while this may appear low compared to 2005, it is a remarkable achievement taking into account the fact that the majority of the Special SSS magnets were also tested during 2006. Testing of the Special SSS magnets has been a time consuming activity in logistics & magnet training; each of the 114 magnets needs a special, dedicated to-do-list. Often, each magnet was trained until it reached the ultimate field and elaborate magnetic measurements were also required. [15]. Average repeat rates for the dipole, arc SSS and Special SSS magnets have been around 9%, 12.5% and 12.8% respectively, not counting the repaired

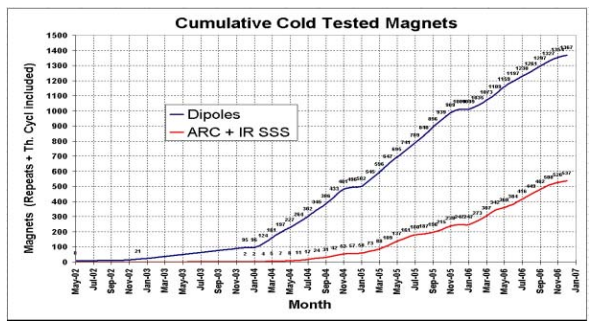

Figure 4: Cumulative Cold Tested Magnets.

and renamed magnets. In addition, ~3% of the dipoles and ~6% of the SSS had to be repaired or rejected after the cold tests. The latter type of issues, observed early in the project, confirmed the need to systematically test all the LHC magnets under cryogenic conditions.

Magnetic measurements were performed on 18.36% of dipoles, 13.32% of arc SSS's and 30.85% of Special SSS's. Often, exceptional tests were performed by the magnet experts on the Special SSS's, needing a considerable amount of time and data analysis.

Period	Dipoles tested (Reqd. Number = 1232)			ARC-SSS + 500 tested (Reqd. Number = 392)			IR-SSS (Reqd.Number = 82)			Total magnets tested
	Fresh	Repeat	Total	Fresh	Repeat	Total	Fresh	Repeat	Total	
Year 2002	21	0	21	0	0	0	0	0	0	21
Year 2003	74	0	74	2	2	2	0	0	0	76
Year 2004	356	45	401	49	3	52	3	0	3	456
Year 2005	468	45	513	148	17	165	20	5	25	703
Year 2006	326	32	358	187	37	224	59	7	66	648
Total	1245	122	1367	386	57	443	82	12	94	1904

Figure 5: Magnets Tested in each Year.

CONCLUDING REMARKS

To complete the tests of all LHC Cryomagnets well in time before LHC beam running in 2007, several innovative ideas, strategies, tools and techniques were introduced and implemented by the Operation Team. The results and statistics of magnet tests underline the significance of them in the successful completion of the tests. While many challenges were met and overcome in operation, delays in magnet delivery issues particularly since mid-2006 remained beyond the control of the Operation Team. Nevertheless, it is expected that all magnet tests for the LHC would be completed by February 2007. The LHC magnet tests operation has also been a singular and very successful example of a large scale collaborative effort in terms of human resources; over 90 persons from India have spent one year each at CERN since 2001 and hence, it remains a unique example in international collaboration of that scale in the particle accelerator domain.

ACKNOWLEDGEMENTS

Acknowledgements are due to all the past & present members of the SM18 Operation Team from DAE-India & AB-Dept, CERN to bring the tests programme to a successful and timely completion. A.Laddha, M.Beachai, S.Malhotra, U.Bhunia, D.Perupayikkad, M.Mascarenhas, S.Sethumadhavan, M.Patil, K.Nair, J.Gore, D.Roy, J.John, S.R.Shimjith from DAE-India and G-H Hemelsoet, E.Veyrunes, K.Priestnall, J.Mazars from CERN AB-Dept contributed significantly to this success. Similarly, the 24-hr operation cryogenic and ICS consortia teams, AT-Dept equipment & mechanical support teams and AB-Dept power on-call teams are acknowledged for their active cooperation. J-P Lamboy, L.Herblin, J. Axensalva, G.D'Angelo, and R.Mompo deserve a particular mention for their help to the Operation Team and dedication to the tests needs.

The direct and indirect support of L. Evans, P. Lebrun & L. Walckiers in helping to overcome the challenges for setting-up and running the SM18 tests facility operation is acknowledged.

The author is thankful to S. Bahuguna, S.R. Shimjith and S. Padmakumar, BARC-DAE, India for their assistance in preparing this paper.

REFERENCES

[1] "LHC Design Report", CERN-2004-003, June 2004

[2] J. Axensalva *et al*., "Cryogenic Infrastructure for Testing LHC Series Superconducting Magnets", Proc. ICEC20, Beijing, May 2004.

[3] J. Axensalva *et al*., "Control System and Operation of the Cryogenic Test Facilities for LHC Series Superconducting Magnets", Proc. ICEC20, Beijing, May 2004.

[4] Ph. Lebrun, private communication, CERN EDMS 811861, CERN, Geneva, January, 2004, http://edms.cern.ch/file/811861/1

[5] V. Chohan *et.al,* "Testing of the LHC magnets in Cryogenic Conditions: Current Experience and Near Future Outlook", Proc. EPAC 2004, Lucerne, Switzerland, July 2004.

[6] L.Bottura, S.Fartoukh *et al*, "A Strategy for sampling the field quality of the LHC Dipoles ", Proc. EPAC 2004, Lucerne, Switzerland, July 2004.

[7] V. Chohan, "Operation before LHC Operation: The SM18 Magnet Tests Facility", Proc. WAO 2005, Fermi National Accelerator Laboratory, USA, May 2005.

[8] G.H. Hemelsoet *et.al,* "Cryogenic Magnet Tests for the LHC: Process Operation using Web-based Tools and Facilities", Proc. ICALEPCS 2005, Geneva, Oct.2005.

[9] V. Chohan, "Testing of the LHC Magnets in Cryogenic Conditions: Operation Challenges, Status and Outlook", Proc. PAC 2005, Tennessee, May 2005.

[10] A. Tovar-Gonzalez *et.al*, "Automatic Management Systems for the Operation of the Cryogenic Test Facilities for LHC Series Superconducting Magnets", Proc.CEC-ICMC, Keystone, Colorado, Aug. 2005.

[11] V. Chohan, "Recent Experience from Operation & Near Future Outlook", Follow-up Review of Reception Tests of Cryomagnets, CERN EDMS 806640, CERN, Geneva, Dec.2003.

[12] S.R.Shimjith *et.al.,*"Rapid On-Bench Thermal Cycle for Testing LHC Cryomagnets: A Review", CERN EDMS 811706.

[13] E. Kandaswamy *et.al.,* "Stripping or Standby – An operational procedure (MAPS) for goodness evaluation of LHC magnets", CERN EDMS 811589.

[14] L.Rossi, "Streamlined series programme", Review of reception tests of LHC cryomagnets", CERN, Geneva, 23 July 2003.

[15] S.Sanfilippo *et.al.,* "Transfer Function of the Quadrupoles and β-Beating", Proc. LHC Project Workshop,Chamonix XV, January 2006.

PAPER NOT YET RECEIVED

PAPER NOT YET RECEIVED

ION INSTABILITY ISSUE IN ELECTRON RINGS*

T.-Y. Lee#, H. S. Kang, J. Choi
Pohang Accelerator Laboratory, San 31, Hyoja-dong, Pohang, Kyungbuk, 790-784 KOREA

Abstract

The fast beam-ion instability attracts interests recently for the International Linear Collider Project. In this paper, we will briefly review and discuss the instability in relation to the ILC project, and we will present a new observation of the instability in the PLS in-vacuum undulator, which shows that the vacuum pressure increase only in a small part of a ring can stimulate the instability.

INTRODUCTION

The so called fast beam-ion instability (FBII) was predicted by simulation and verified later by experiments. FBII is excited by attractive forces between electrons and ions created by passing electrons like other ion-induced instabilities. However, its unique point is that it is excited not by trapped ions but by transient ions; ions that are created by passing electron bunches and cleared by a large gap. Hence there is no periodicity but (approximate) linearity in the interacting ion density. Without trapped electrons, the number of ions that an electron bunch faces is proportional to the number of electrons that are ahead of the electron bunch. Therefore, the number of ions (and the strength of electron-ion interaction) is approximately linear with the position along the electron bunch train. Hence the amplitude of the coherent FBII oscillation grows along the electron bunch train. The difference from the ion trapping is clear. The electron-ion interaction depends also on the electron emittance, especially the vertical one.

The theoretical (and simulational) prediction and description of this picture was firstly given in Ref. [1, 2]. The first experimental observation of FBII was given in Advanced Light Source [3]. With artificially increased pressure and gaps in the bunch train large enough to avoid ion trapping, they observed a factor of 2-3 increase in the vertical beamsize along coherent beam oscillations which increased along the bunch train. Similar experiment was carried out later in Pohang Light Source (PLS) with more visual clarity [4, 5]. Especially, Ref. [5] captured the visual images of FBII with streak camera, which shows clearly the coherent oscillation increasing along the electron bunch train. Also, in the commissioning phase of Canadian Light Source when the vacumm pressure was very high, vertical beamsize blowup was observed, which could be attributed to FBII [6].

Interestingly and accidentally, the strength of FBII is such that it is hardly observed in a currently active electron storage ring of normal operation condition. A few years ago, the B-factory electron ring was considered a candidate for the FBII observation even in the normal operation condition, because of the high electron bunch current. However, FBII turned out to be invisible even in the B-factory. Recently, interests in FBII have been revived because of the future International Linear Collider (ILC) of electron and positron [7]. In ILC, electron beam (and positron beam) will have an extremely low vertical emittance. For that purpose, a damping ring will be constructed. The ILC electron damping ring is considered a strong candidate for the FBII observation, because of its tiny vertical emittance and high bunch current. In this paper, we will review and discuss FBII in relation to the ILC project, and we will present a new observation of FBII in the PLS in-vacuum undulator, which shows that the vacuum pressure increase only in a small part of a ring can stimulate FBII.

FAST BEAM-ION INSTABILITY

A schematic figure of FBII is shown in Fig. 1. The force that stimulates FBII is the attracting linear force between the electron bunch and the ion cloud [8]. The linear force on the n-th electron bunch has the following dependence

$$f_e(n) \propto \frac{\lambda_i(n)}{\sigma_y(\sigma_x+\sigma_y)}, \tag{1}$$

where $\lambda_i(n)$ is the ion density at the position of the n-th electron bunch and σ_x, σ_y are the horizontal and vertical sizes of the electron beam. On the other hand, the linear force on the ions f_i depends on the electron density λ_e instead of λ_i. Because of these linear forces, both electrons and ions oscillate coherently with separate oscillating frequencies. For example, the ion frequency has the dependence of

$$w_i \propto \left[\frac{N}{\sigma_y(\sigma_x+\sigma_y)A}\right]^{1/2}, \tag{2}$$

where N is the number of electrons in a bunch and A is the mass number of the ion. Normally A is that of CO ion.

Obviously λ_i depends on λ_e because ions are created by electrons. Note that $\lambda_i(n)$ is proportional to the vacuum pressure P and the number of electrons from the electron head to the n-th bunch, as described by

$$\lambda_i(n) \propto PNn, \tag{3}$$

where P is the vacuum pressure and N is the number of electrons per bunch. Hence we can rewrite $f_e(n)$ as

$$f_e(n) = K\frac{PNn}{\sigma_y(\sigma_x+\sigma_y)}, \tag{4}$$

* Work supported by the Korean Ministry of Science and Technology
# tylee@postech.ac.kr

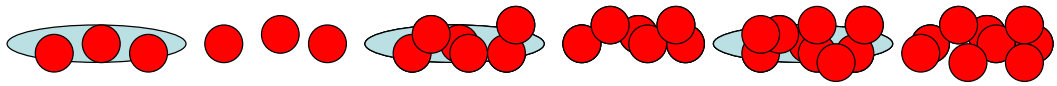

Figure 1: A schematic figure of FBII. A big ellipse represents an electron bunch and small circles represent ions. The number of ions increases along the bunch train.

where K is the overall constant. The FBII growth rate is not linear to $f_e(n)$ but depends on it in a complicated way. However, it is obviously true that the growth rate gets smaller when $f_e(n)$ gets smaller, and vice versa.

Does the bunch separation, L_{sep}, affect on FBII? Yes, it does, although it is not involved in $f_e(n)$. L_{sep} is not the source of ions but a space at which ions are created. The longer L_{sep} is, the longer the ion beam is. Hence the more effective the electron-ion interaction is and the faster the growth rate is. However, a straightforward inclusion of L_{sep} in the theoretical treatment may mislead as in [1], where the growth rate is proportional to $L_{sep}^{1/2}$. But, obviously, it does not mean that the growth rate decreases to 0 as L_{sep} goes to 0. And it does not mean either that the growth rate increases indefinitely as L_{sep} increases continuously. The derivation is valid only for some range of L_{sep}. In reality, the freedom to choose a L_{sep} is not very big. Therefore, assuming L_{sep} is restricted to a narrow range of values, it is possible to ignore the L_{sep} dependence from the discussion.

OBSERVATION OF FBII

It is interesting that FBII is such that it is not observed in any electron storage ring of normal operation condition. It has been observed only when the vacuum pressure was increased order of magnitude-wise. Figure 2 shows the FBII picture at the PLS experiment by the streak camera [5]. The electron beam was composed of 250 bunches and the total current was approximately 170 mA. The streak camera picture in the normal operation condition is shown in (a), and (b) shows the FBII picture taken with the vacuum pumps off. The observed coherent oscillation was that of CO. By turning off the vacuum pumps, the pressure was elevated from 0.16 nTorr to 2.2 nTorr.

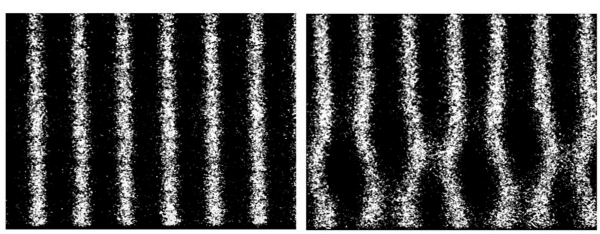

Figure 2: Streak camera images of FBII taken at the PLS experiment. (a) Normal condition (0.16 nTorr). (b) Increased vacuum pressure with ion pumps turned off (2.2 nTorr)

However, a recent experiment at PLS shows that FBII is closer to the observation. In this experiment, vacuum pressure is elevated only in a small portion of the storage ring, in an in-vacuum undulator. One of the PLS undulators is RIVXUN (Revolver In-Vacuum X-ray Undulator) that was designed at SPring 8 [9]. The length of RIVXUN is 1.2 m and the minimum undulator gap is 5 mm. It was found that if the electron beam orbit is distorted when the undulator gap is narrowed, the vacuum pressure of the undulator area is increased up to one order of magnitude. This is because the undulator synchrotron radiation hits the internal undulator wall. We used this situation for an experimental observation of FBII. The experimental setup was like this; we left the orbit distorted and measured the vacuum pressure while narrowing the undulator gap. In this way, it was possible to control the vacuum pressure step by step as shown in Fig. 3.

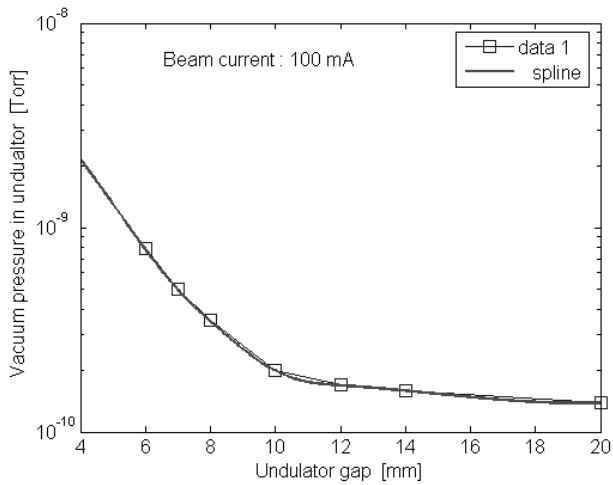

Figure 3: Vacuum pressure measured with varying undulator gap.

Figure 4 shows the streak camera image of the initial stage of FBII. The number of bunches was 350, the undulator gap was 6.4 mm, and the vacuum pressure was approximately 0.6 nTorr. When the undulator gap was lowered further, the oscillation growed and beam loss occurred as shown in Fig. 5. The cause of beam loss is probably the reduced physical aperture. The undulator gap was 5 mm and the vacuum pressure was apprxomately 1.3 nTorr.

The point of this experiment is that the vacuum pressure was higher (5-6 times) only in a small part, approximately 1/300 of the whole ring circumference. The average pressure of the ring would be almost unchanged. But FBII was excited in the small area and sustained in the other

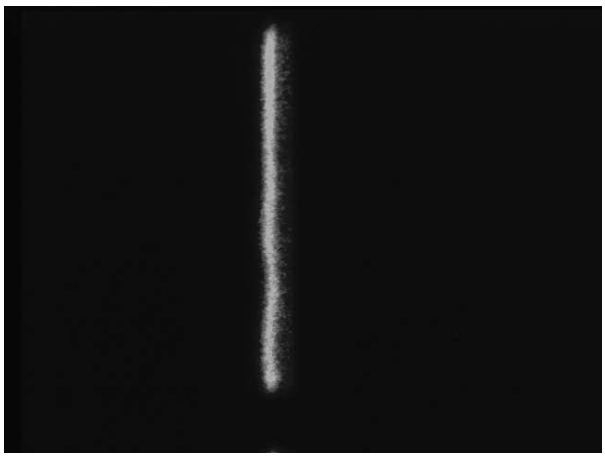

Figure 4: The streak camera image of FBII taken at the new PLS experiment. The undulator gap was 6.4 mm and the vacuum pressure was approximately 0.6 nTorr.

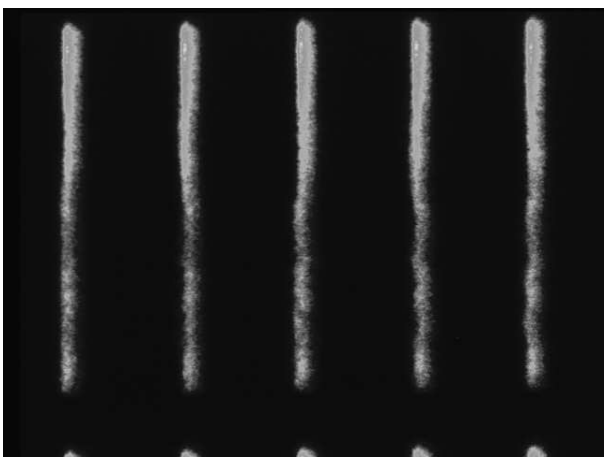

Figure 5: The streak camera image of FBII taken at the new PLS experiment. The undulator gap was 5 mm and the vacuum pressure was approximately 1.3 nTorr.

whole area. This is an important result, because it demonstrates that FBII is potentially more dangerous than previous experiments indicated. We see that the vacuum pressure needs to be homogeneous to suppress FBII effectively. Digital BPM was used to measure the coherent oscillation of FBII as shown in Fig. 6. The digital BPM data in the figure is an average value of all bunches for each turn. Vertical oscillation amplitude of the tail of the bunch train is twice the peak value in the figure. In Fig. 6, coherent oscillation grows until 2500-3500 turns and then damps, and This procedure repeats. The cause of the damping is considered the ion beam blow-up at the saturation of FBII. One turn in PLS is approximately 1 μsec. Hence the growth time in this experiment was around 2-3 msec. The damping time of the PLS storage ring is 8 msec. Future experiments are planned to obtain more quantitative conclusions.

ILC DAMPING RING

The FBII issue is now the main concern of the ILC damping ring. It is one of the key factors of the damping ring design, especially the ring circumference. The central design issue of ILC is to provide the luminosity as high as possible. For the purpose, ILC electron and positron beam must have high bunch current and low emittance. The electron and positron damping rings are supposed to make the electron and positron beam have emittance as low as possible, respectively. However, high bunch current and low emittance bunch train is subject to a possible FBII. As we have seen, FBII has never been observed in a ring of normal vacuum pressure. But the extremely low vertical emittance of ILC damping ring might grow FBII enough to be observed. Therefore, FBII is one of the most serious problems of the electron damping ring and its counterpart for the positron damping ring is the electron cloud effect.

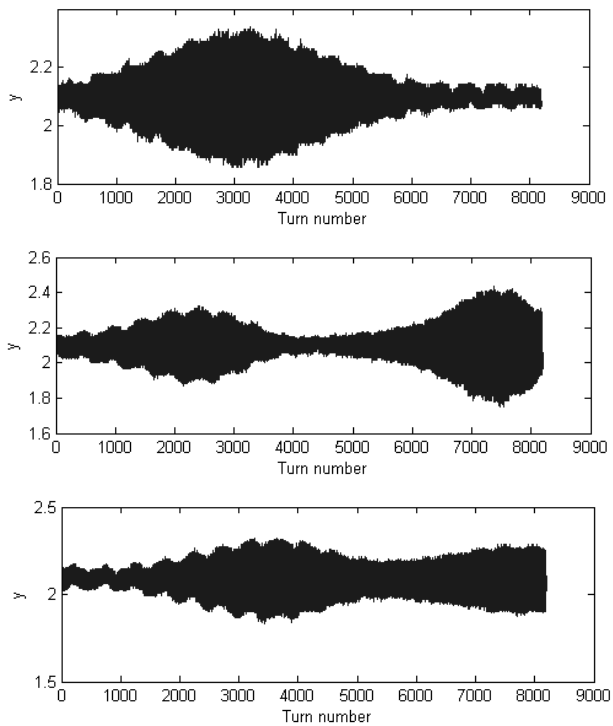

Figure 6: Digital BPM data of FBII. One turn is approximately 1 μsec.

Equation (4) shows how we should design the damping ring not to be affected by FBII. The pressure P should obviously be kept as low as possible and can not be lowered further. The number of electrons in a bunch N can not be lowered significantly because a high luminosity is required. The only parameter that we can handle is the number of bunch n. Since n can range from 1 to a few thousands, it is a very effective tool to control FBII. Even in Fig. 2 of the high vacuum case, the first 1/4 of the bunch train does not show any coherent oscillation. In other words, it is possible not to see FBII if the bunch train is short enough. Hence the electron damping ring should be designed to allow a num-

ber of mini bunch trains with sufficient gap between them to clear ions. Careful simulation study should be done to decide how many bunches are needed in a mini bunch train and how long a gap should be.

SUMMARY

The importance of FBII is determined by the ratio of parameters,

$$\frac{PNn}{\sigma_y(\sigma_x+\sigma_y)}. \quad (5)$$

If this number is big enough, FBII is stimulated. It happens that FBII is not stimulated in the existing electron rings unless the vacuum pressure is elevated deliberately. The new PLS experiment shows that FBII can be stimulated if P is high enough only in a small part of the ring. This is particularly important for ILC damping ring that will have extremely small σ_x and σ_y. To compensate for the low emittance, the number of bunch n should be small enough. Hence the bunch train should be divided into many mini trains and long enough gap between the mini bunch trains.

REFERENCES

[1] T. O. Raubenheimer and F. Zimmermann, Phys. Rev. E 52, 5487 (1995).

[2] T. O. Raubenheimer and F. Zimmermann, Phys. Rev. E 52, 5499 (1995).

[3] J. Bird, A. Chao, S. Heifets, M. Minty, T. O. Raubenheimer, J. Seeman, G. Stupakov, J. Thomson, and F. Zimmermann, Phys. Rev. Lett. 79, 79 (1997).

[4] M. Kwon, J. Y. Huang, T.-Y. Lee, I. S. Ko, Y. H. Chin, H. Fukuma, M. Isawa, K. Ohmi, and M. Tobiyama, Phys. Rev. E 57, 6016 (1998).

[5] J. Y. Huang, M. Kwon, T.-Y. Lee, I. S. Ko, Y. H. Chin, and H. Fukuma, Phys. Rev. Lett. 81, 4388 (1998).

[6] J. C. Bergstrom and J. M. Vogt, Nucl. Instr. and Meth. A 562, 495 (2006).

[7] http://www.linearcollider.org

[8] G. Koshkarev and P. Zenkevich, Particle Accelerators 3, 1 (1972).

[9] Kitamura et al., Nucl. Instr. and Meth. A 467, 110 (2001).

ELECTRON CLOUD EXPERIMENTS, SIMULATION AND CURE*

H. Fukuma#, KEK, Tsukuba, Japan

Abstract

This paper reviews experiments, simulations and mitigation methods of electron cloud effects. A concise review of electron cloud effects was recently given by K. C. Harkay at EPAC06 [1]. Inevitably, several topics in this report overlap with Ref. 1.

INTRODUCTION

Many electrons stay in accelerators. Primary electrons can be produced by synchrotron radiation, lost particles hitting a chamber wall, or by ionization of the residual gas. If the charge of a beam is positive, the primary electrons receive kicks from the beam toward the center of beam chamber and hit the opposite wall, then secondary electrons are produced. Under some operational conditions of machines rapid growth of the electrons known as beam induced multipacting (BIM) [2] can occur. The primary and secondary electrons form a group of the electrons called the electron cloud (EC) which is built up along a bunch train.

In proton rings with long bunches, a large number of electrons are observed at the tail of the bunch due to a mechanism called "trailing edge multipacting" [3, 4]. Before the center of the bunch passes through the EC, all the electrons, i.e. electrons surviving electrons from the last bunch, electrons emitted at the chamber surface by the beam loss and electrons produced by ionization, are trapped in the bunch, and then released at its tail of the bunch. Electrons emitted at the chamber surface between the bunch centre and the tail are not trapped but hit the opposite surface due to the negative slope of the longitudinal beam density. Then amplification of the electrons can occur towards the tail. Trapped electrons and multipacting electrons together result in the large number electrons at the tail.

The EC causes harmful effects on the accelerator performance as discussed below.

OBSERVATIONS AND EXPERIMENTS

Measurements of Electron Yield

A planar retarded field analyzer (RFA) pioneered at APS is widely used to measure the flux and energy distribution of electrons on the chamber wall [5]. Measurements showed that the energy of electrons hitting the wall is very low, typically less than 10 eV. BIM was observed at APS, where the electron yield abnormally increased at the bunch spacing of seven. The result is consistent with a simulation by POSINST [6].

Time resolved measurement by an RFA at PSR showed numerous electrons generated at the tail of the bunch. The measurement led to the discovery of the trailing edge multipacting [3]. The full number of electrons in the beam chamber was measured by an electron sweeper originally designed at PSR. It consists of an RFA and a pulsed electrode which sweeps electrons into the RFA. A large number of electrons, which is approximately equal to that needed to cause the e-p instability, were found in the bunch gap. The long exponential tail of the decay of the electron yield in the gap implies a relatively high secondary emission yield from low energy electrons of 2-5 eV.

Pressure Rise

Electrons hitting the chamber wall desorb molecules on the wall, thereby causing a pressure rise. The pressure increases non-linearly with the beam current if the BIM occurs. In RHIC the number of bunches of the ion beam is limited to about half of the possible number by dynamic pressure rises caused by the EC [7]. The molecular desorption coefficients (MDC) were studied at RHIC [8]. For unbaked stainless steel and assuming CO, the MDC was 0.05. A conditioning effect on the MDC by the beam was observed.

Emission of Secondary Electrons

One of the most important parameters in EC formation is the secondary emission yield (SEY). The secondary electrons are classified into three categories according to their energy spectrum: true secondary electrons, elastically backscattered electrons and rediffused electrons [9]. The SEY as a function of the primary electron energy has a peak δ_{max}, typically 1.5 - 2, around 200-300 eV. As the secondary emission is a surface dependent phenomenon, the SEY depends on the material and is influenced by the surface preparation [10, 11].

A decrease in δ_{max} by electron bombardment is called scrubbing. Scrubbing has been observed in several laboratory measurements [11, 12] and also in-situ at the CERN SPS [13]. After an electron bombardment of 1mC/mm^2, δ_{max} decreased from 1.5 to 1.1 for TiN and from 1.4 to 1.2 for TiZrV [12]. An electron dose of 1mC/mm^2 seems necessary for δ_{max} to decrease below 1.2. A possible mechanism of the scrubbing called graphitization was found by a laboratory measurement at KEK [14]. As-received copper was irradiated by an electron beam of 5 keV. After the irradiation of electrons (total dose of 1 x 10^{20} e-/cm^2), δ_{max} was reduced from 1.85 to 1.02. It was found that a contaminated layer of carbon was changed to graphite which has a low δ_{max}. A further in-situ measurement of the SEY is underway in the KEKB.

*Work supported by JSPS Core University Program.
#hitoshi.fukuma@kek.jp

The SEY at very low energy is important because the energy distribution of the electrons on the wall peaks at very low energy, e.g. below 20 eV for the LHC. At CERN it was found that the SEY approached unity in the limit of zero primary electron energy [15]. A simulation shows that the surface heat load in the LHC is greatly affected by the SEY at low energy [15].

Electron current for a Cu chamber or coated chambers by TiN and NEG material was measured under intense photon irradiation at KEKB [16]. A simulation showed that intense photoelectrons reduce the effect of low SEY on the electron yield. The suppression of the photoelectrons with an antechamber and/or a solenoid is indispensable to make effective use of a low SEY surface.

Instabilities

The transverse coupled bunch instability (CBI) observed at KEK PF in 1995 triggered extensive study of the EC instability [17, 18]. Now instability due to EC is observed in many accelerators.

In BEPC a vertical CBI that can be explained by EC was found in the positron beam after the observation at the PF [19]. The instability was suppressed by increasing the chromaticity. Landau damping is considered to be the main factor of the effect.

In a measurement at KEKB, the mode spectrum of the CBI changed with or without solenoid field, which is a clear evidence of the EC instability [20]. The comparison between the measurement and a simulation shows that 1) with solenoids on, there were no modes which came from the field free region and the dipole region, 2) the lower SEY of 1.0 is favored and 3) the effective solenoid field seems weaker than the nominal field strength, 45 G.

A strong horizontal dipole instability was observed at the positron ring in DAFNE after the long shut down in 2003 [21]. Signatures of the EC effects such as a large positive tune shift and a non-linear pressure rise were observed in the positron ring. The growth time was about 10 μsec which is shorter than the synchrotron period. The unstable mode was -1. Winding solenoids in straight sections did not change the threshold of the instability. The instability is believed to be caused by the EC in the wigglers and the resistive wall impedance.

In RHIC significant EC effects were observed when the bunch spacing was 108 ns [22]. The effects were the fast transverse instability, emittance growth, and beam loss when the beam was accelerated across the transition. The EC effects occurred both in the warm (~30% length) and cold (~70% length) regions.

A beam size blow-up was observed in the positron rings of two B-factories [23, 24]. The blow-up is explained by a single bunch head-tail instability caused by the EC [25]. Multi-bunch operation is necessary to produce the EC. The blow-up was one of the big issues limiting the luminosity at PEPII and still limits the luminosity at KEKB. The blow-up in both rings is greatly suppressed by applying a weak solenoid field in vacuum chambers.

A vertical betatron sideband was found at KEKB [26]. Appearance of the sideband depends on the strength of solenoids and is also associated with loss of luminosity during collision. The threshold where the sideband appears coincides with that of the beam blow-up. The sideband appears to be a signature of the strong head-tail instability due to the EC. The sideband is seen on the upper side of the betatron peak, which suggests that the effective wake function is a focusing wake generated by the pinched EC. Recently simulations by HEADTAIL and PEHTS succeeded in reproducing the sideband when the size of the EC was ten times larger than that of the beam [27].

Betatron Tune Shift

The EC causes a betatron tune shift [28]. The tune shift caused by the EC was observed at several accelerators such as RHIC, DAFNE and KEKB. By measuring the tune shift we can get the information on the density and the lifetime of the EC.

In a recent measurement at KEKB the tune shift of a test bunch which was placed after the end of a bunch train was measured by changing the distance between the train and the test bunch, b_s [29]. The current dependent tune shift (CDTF), defined as the tune shift divided by the bunch current, was positive if b_s was shorter than 10 rf buckets, then changed to the negative if b_s exceeded 10 rf buckets. The change of the sign of the CDTF is not understood yet.

In KEKB when the solenoids were turned on the tune shift by the EC almost disappeared in the horizontal plane but remained in the vertical plane. The reason for the asymmetric contribution of the solenoids is not understood yet [29].

Electron Clouds in Magnets

Spatial and energy distributions of the EC in a dipole were measured by a strip detector originally developed at CERN [30]. The SPS measurement by the strip detector showed two stripes of electrons which had been predicted by the simulation by ECLOUD. The spatial distribution of the EC in a quadrupole measured by the strip detector showed a large electron flux close to the pole tips where the magnetic flux is concentrated [31]. The simulation by CLOUDLAND supports the measurement.

Trapping of the electrons in a quadrupole was found by simulation [32]. It is similar to the plasma trapping in a mirror magnetic field. The trapped electrons could have a long lifetime in train gaps and may affect the bunch coming after the bunch gap.

The electron sweeper was installed in a quadrupole magnet at the PSR. First result showed the long decay time (50-100 μs decay constant) of the EC after beam extraction [33].

At KEK a solenoid of 17 Gauss made of a thin flat cable was installed in 88 quadrupole magnets [34]. If the electrons are generated inside a quadrupole, for example by ionization, the electrons would be trapped and accumulate near the beam. The solenoid may affect the

electrons near the beam where the quadrupole field is very weak. In the measurement no clear effect of the solenoids was found on the sideband, the vertical beam size and the luminosity. The strength of the solenoids might be too weak to remove the electrons near the beam if the electrons are there.

The trapping of the electrons in a quadrupole is being studied also at HCX with 1MeV K^+ beam [35].

MODELING AND SIMULATION

Simulation of the EC effects is usually classified into two categories, the EC buildup and the instability calculation. Programs developed [36] are CLOUDLAND, CSEC, ECLOUD, PEI, POSINST etc. for the EC buildup simulation and ECI, HEADTAIL, PEHT, PEHTS, QUICKPIC etc. for the instability simulation. Here as examples, three codes, CLOUDLAND, PEI and PEHTS are briefly described because the author is somewhat familiar with them.

Electron Cloud Buildup

CLOUDLAND [37] consists of 1) generation of electrons, 2) calculation of kick to electrons by the beam, 3) calculation of kicks to electrons by the space charge force of the EC, 4) movement of electrons in the chamber including magnetic field and 5) generation of secondary electrons on the surface of the chamber.

The kick to the electrons by the beam is given by the Bassetti-Erkine formula. A bunch is divided into several pieces, typically 40, to kick the electron, taking into account the electron movement during kicks [38]. While electrons far from the bunch simply receive a kick, electrons near the bunch oscillate in the bunch field. The space charge force of the EC is obtained from the potential which is a solution of Poisson equation solved by the Particle-In-Cell (PIC) method. The secondary electrons are generated by the Furman and Pivi model [9].

Coupled Bunch Instability

In PEI [18, 39] the EC buildup is calculated in a similar way as described in the previous subsection assuming that the motion of the bunch is not affected by the EC. Then the growth rate of the CBI is calculated in two ways: 1) the wake force method and 2) the tracking method. The wake field is calculated by slightly displacing a bunch in the EC then calculating forces from the perturbed EC. The growth rate is obtained from the usual dispersion relation. The method assumes linearity and superposition of the beam-EC force. In the tracking method, the equations of motion are directly solved numerically. This method is time consuming, but the linearity and the superposition of the wake are not assumed any longer. Fourier transform of the amplitudes of all bunches gives a spectrum of unstable modes.

Single Bunch Instability

In PEHTS [40] the bunch and the EC are modeled as a group of macro particles like in the strong-strong model of the beam-beam force. The bunch is divided into slices. A simple kick and drift integrator is used to integrate the motion of particles. The beam-EC kick is calculated from the electric potential with PIC method. An FFT is applied to solve the potential in order to speed up the calculation. The beam-EC kick is evaluated from the potential on the mesh by interpolation.

Code-to-code Benchmarking

Code-to-code benchmarking is done by international collaboration [41]. For the EC buildup at LHC, the simulated saturation densities differ by a factor 3–4 between codes, the buildup time by even more. The differences are largely explained by the modeling of secondary emission. Sufficient knowledge of the in-situ surface properties is important to obtain reliable results in simulation.

Others

Incoherent emittance growth by the EC below the threshold of coherent instability is found at CERN by simulation [42]. Two mechanisms are identified, 1) a beam particle periodically crossing a resonance and 2) a beam particle periodically crossing a region of the bunch where its motion is linearly unstable. While the former leads to formation of halo, the latter leads to beam-core blow-up. Essentials for both processes are synchrotron motion and incoherent tune shift caused by the pinched EC. For 1), protons at large synchrotron amplitude can cross a resonance back and forward by the synchrotron oscillation, which statistically leads to a beam size growth like diffusion. For 2), the tune shift on the beam axis can be so large that the motion becomes linearly unstable.

Combined phenomenon of beam-beam and beam-EC interactions is proposed [43]. The short-range wake forces due to the EC and the beam-beam interaction may couple and cause a combined phenomenon of complex nature. The effect may lower the threshold current of the blow-up by the EC as shown by the simulation.

The EC can be treated as a bunch to bunch evolution using simple maps, $\rho_{m+1}=a\ \rho_m+b\ \rho_m^2+c\ \rho_m^3$, where ρ_m is electron density before bunch m passes and ρ_{m+1} the electron density after bunch m passed by [44]. Coefficients a, b and c are functions of beam parameters, the chamber geometry and the secondary emission characteristics. They are determined by the EC buildup simulation. "a" is also estimated by an analytic method [45]. As the calculation time of the map is very fast, the map can be a useful tool for the survey of the EC evolution in parameter space, which is time consuming in computer simulations.

CURES

Coatings and Scrubbing

Coating of the chamber surface by materials with low SEY is effective to decrease the electron buildup [10, 11, 12, 14]. Typical coating materials are TiN and NEG

materials such as TiZrV. Application of NEG coating on a large scale has been effective in reducing the EC in RHIC [46]. The scrubbing helps to decrease the SEY further as described before.

Grooved Surface

A grooved surface effectively lowers the SEY both in field free and the magnetic field regions [47, 48]. In the magnetic field, if the electron hits the edge of the groove the secondary electrons execute gyration then hit the wall with low SEY due to their low energy. If the bunch spacing is longer than gyration period, the number of electrons decreases due to successive secondary emission. A grooved surface is not so effective for beams with long bunch length. A calculation shows that the resistive wall impedance is enhanced by a factor of 1.5 for a rectangular groove with a round fin tip [49]. If the region of the BIM is limited such as two stripe regions in a dipole, the area of the grooved surface can be reduced, which decrease the impedance. According to a laboratory test of a triangular grooved surface at SLAC the effective SEY decreased to 1.1 in a TiN coated chamber [12]. A triangular grooved surface in a dipole will be tested in this year at SLAC.

Solenoid

A weak solenoid confines the electrons near the chamber wall. The solenoid is effective in decreasing the electron density especially near the beam. A typical solenoid field is several 10s Gauss because the energy of the electrons is low. A resonant growth of the electrons, which should be avoided, was predicted [50, 51]. The resonance occurs if half of the cyclotron period is equal to the time interval between two consecutive bunches. For example the magnetic field at resonance is 40 G if the bunch spacing is 4 ns. Solenoids cannot be applied in a strong magnetic field.

Clearing Electrode

An electrode is a candidate for clearing the electrons [52]. Unlike the solenoid, the electrode can work in a strong magnetic field. Two types of electrodes are proposed, the multi-wire electrode and the strip line electrode. The multi-wire electrodes are negatively biased. They push electrons to the wall immediately after the electrons are created on the wall. Required voltage is an order of hundred volt because the electron energy is low, typically 5 eV. As the electrodes are located apart from the wall they reduces the physical aperture of the machine and the impedance by the electrodes may be an issue. The design of this type of electrode is in progress at KEK.

The traditional strip line electrode is positively biased to attract the electrons to it. As the gap between the electrode and the chamber can be narrow the strip line electrode may be better in reducing the impedance than the multi-wire electrode. The size of the electrode can be minimized inside magnets because the high density region of the electrons is limited in space. The installation of the prototype of the strip line electrode in PEPII is being discussed. A strip line electrode was proposed for the LHC dipole magnet [53], where the copper electrode coated with TiZrV would also provide distributed high-throughput pumping. Presently strip line electrodes based on a double-layer enamel coating is considered for the new LHC injectors and the CLIC damping ring [64].

Anti-grazing Ridge

Anti-grazing ridges were tested at RHIC. They can largely prevent the shallow angle incidence of the ions. As a result the desorption and production of positive ions due to beam halos can be reduced [54]. Measurements with a proton beam showed that the anti-grazing ridges significantly improved the vacuum performance.

Active Feedback System

A bunch-by-bunch feedback system is effective in suppressing the CBI [55]. The typical damping time is 0.5ms at KEKB.

The e-p instability for long proton bunch machines differs from other instabilities that have been treated by the feedback systems. A proof-of-principle experiment on the long bunch e-p feedback system is in progress at PSR [56]. The bandwidth of the feedback system is 50 - 250 MHz after the BPM. The damp-grow-damp experiment showed a damping rate of the feedback system of 1.75 x 10^4 sec^{-1}.

IMPACT ON UNDER-CONSTRUCTION AND PLANNED ACCELERATORS

In BEPCII the antechamber with TiN coating is adopted in the arc to reduce the primary and secondary electron yields [57]. According to a simulation, the EC density can be reduced to $1.3x10^{11}m^{-3}$ if an antechamber with TiN coating and the photon absorbers at the chamber wall are used. A simulation shows that 1) the threshold electron density of the strong head-tail instability is $9.2\times10^{11}m^{-3}$ which is higher than the expected electron density and 2) the growth time of the CBI is about 4.3 ms which should be damped by the feedback system.

In J-PARC, a TiN film is coated on the inner surface of the duct in order to reduce secondary electron emission in the 3 GeV RCS, while the SUS chambers of the 50 GeV MR are not coated. Simulation shows that Landau damping due to energy spread will cure the instability here [58]. The EC in quadrupole magnets will be studied in the future [58].

In LHC a concern is the heat load to the cryogenic system by the electrons hitting the wall. If δ_{max} exceeds 1.3 the heat load exceeds the available cooling capacity of the beam screen [59, 60]. Beam scrubbing is necessary in order to decrease δ_{max} below 1.3. A simulation including rediffused electrons shows that δ_{max} must be less than 1.2 [61]. The slow emittance growth described earlier is another potential issue [59].

For the ILC damping ring, simulations show that the EC density near the beam is suppressed below instability threshold if the SEY is less than 1.2 and the solenoids are installed in the drift regions [62]. Several mitigation

methods are considered and extensive R&D is planned. In order to study the scrubbing, in-situ measurement of the SEY is planned at PEPII. A rectangular grooved surface in field free region will be tested in PEPII in 2007. A triangular grooved surface and clearing electrodes in a dipole magnet will be fabricated and tested in PEPII in 2007.

SUMMARY

The EC effects have been studied for 40 years. The results contributed to performance improvements of the existing accelerators and to the design of the new accelerators as shown in the recent success of SNS where many EC countermeasures were taken based on design studies [63]. In the author's view the following might be interesting subjects for further study: 1) the slow emittance growth below the threshold of the coherent instability, 2) the density and the distribution of the EC in magnets, 3) the effect of the grooved surface and electrodes on the beam, 4) in-situ measurement of the SEY of technical materials including the scrubbing effect, 5) the active feedback system for a long proton bunch, 6) the understanding of the tune shift caused by the EC and 7) the study of the sideband to obtained the information on the short-range beam-EC interaction.

The author apologizes to those who contributed to the study of the EC but are not mentioned in this report due to a lack of his knowledge.

ACKNOWLEDGMENTS

The author would like to thank J. W. Flanagan, S. Kato, R. Macek, K. Ohmi, M. Pivi, Y. Suetsugu, L. F. Wang and F. Zimmermann for useful comments and information.

REFERENCES

[1] K. C. Harkay, Proc. EPAC2006, 1887 (2006).
[2] O. Gröbner, Proc. PAC1997, 3589 (1998).
[3] R. J. Macek et al., Proc. PAC2001, 688 (2001).
[4] L. Wang et al., PR E 70, 036501 (2004).
[5] K. C. Harkay and R. A. Rosenberg, PRST-AB 6, 34402 (2003).
[6] M. A. Furman et al., Proc. PAC2001, 679 (2001).
[7] W. Fischer, Proc. EPAC2006, 905 (2006).
[8] U. Iriso and W. Fischer, PRST-AB 8, 113201 (2003).
[9] M. A. Furman and M. T. F. Pivi, PRST-AB 5, 124404 (2002).
[10] R. E. Kirby and F. K. King, NIM A 469 (2001) 1.
[11] V. Baglin et al., Proc. EPAC2000, 217 (2000).
[12] F. Le Pimpec et al., NIM A 551 (2005) 187.
[13] J. M. Jimenez et al., Proc. ECLOUD02 17 (2003).
[14] M. Nishiwaki, Thesis, the Graduate Univ. for Advanced Studies, in Japanese (2006).
[15] R. Cimino et al., PRL 93, 14801(2004).
[16] Y. Suetsugu et al., NIM A 554 (2005) 92.
[17] M. Izawa et al., PRL 74, 5044(1995).
[18] K. Ohmi, PRL 75, 1526 (1995).
[19] Z. Y. Guo et al., PRST-AB 5, 124403 (2003).
[20] M. Tobiyama et al., PRST-AB 9, 012801 (2006).
[21] A. Drago et al., DAFNE Technical Note G-67 (2006).
[22] J. Wei et al., Proc. PAC2005, 4087 (2005).
[23] H. Fukuma et al., Proc. EPAC2000, 1122 (2000).
[24] R. L. Holtzapple, SLAC-PUB-9222 (2002).
[25] K. Ohmi and F. Zimmermann, PRL 85, 3821 (2000).
[26] J. W. Flanagan et al., PRL 94, 054801 (2005)
[27] K. Ohmi, talk at ILCDR06 (2006).
[28] K. Ohmi et al., Proc. APAC2001, 445 (2001).
[29] T. Ieiri et al., Proc. EPAC2006, 2101 (2006).
[30] J. M. Jimenez et al., LHC Project Report 634 (2003).
[31] J. M. Jimenez, private communications.
[32] L. F. Wang et al., PR E 66, 36502 (2002).
[33] R. Macek et al., talk at ILCDR06 (2006).
[34] H. Fukuma et al., Proc. EPAC2006, 2901 (2006).
[35] A. Molvik, Proc. HB2006, THAW02 (2006).
[36] See, for example, Proc. ECLOUD02 and ECLOUD04.
[37] L. F. Wang et al., PRST-AB 5, 124402 (2002).
[38] J. S. Berg, LHC Project Note 97 (1997).
[39] S. S. Win et al., PRST-AB 8, 94401 (2005).
[40] K. Ohmi, Proc. PAC2001, 1895 (2001).
[41] E. Benedetto et al., Proc. EPAC2004, 2502 (2004).
[42] E. Benedetto et al., PRL 97, 034801 (2006).
[43] K. Ohmi and A. W. Chao, PRST-AB 5, 101001 (2002).
[44] U. Iriso and S. Peggs, PRST-AB 9, 71002 (2006).
[45] U. Iriso and S. Peggs, Proc. EPAC2006, 357 (2006).
[46] S. Y. Zhang et al., Proc. EPAC06 595 (2006).
[47] G. Stupakov and M. Pivi, Proc. ECLOUD'04, 139 (2004).
[48] L. Wang et al., SLAC-PUB-12001 (2006).
[49] K. Bane and G. Stupakov et al., Proc. EPAC2006, 2961 (2006).
[50] S. Novokhatski and J. Seeman, Proc. PAC2003, 315 (2003).
[51] Y. Cai et al., PRST-AB 7, 24402 (2004).
[52] L. F. Wang et al., Proc. EPAC2006, 1489 (2006).
[53] P. McIntyre and A. Sattarov, Proc. PAC2005, 2971 (2005).
[54] S. Y. Zhang et al., PRST-AB 8, 123201 (2005).
[55] M. Tobiyama and E. Kikutani, PRST-AB 3, 012801 (2000).
[56] R. Macek et al., Proc. HB2006, TUAX04 (2006).
[57] J. Q. Wang et al., Proc. EPAC2004, 2131 (2004).
[58] K. Ohmi and T. Toyama, Proc. HB2006, THAW06 (2006).
[59] F. Zimmermann, "LHC electron-cloud update", LHC MAC, June, 2005.
[60] O. Brüning, Proc. EPAC06, 14 (2006).
[61] M. A. Furman and V. H. Chaplin, PRST-AB 9, 034403 (2006).
[62] M. Pivi, talk at Proc. ILCDR06 (2006).
[63] N. Holtkamp, Proc. EPAC06, 29 (2006).
[64] http://care-hhh.web.cern.ch/CARE-HHH/ECL2/

ILC DR ALTERNATIVE LATTICE DESIGN**

Y. P. Sun*, Key Laboratory of Heavy Ion Physics, Peking University& IHEP, Beijing
J. Gao, IHEP, Beijing; Z. Y. Guo, Key Laboratory of Heavy Ion Physics, Peking University, Beijing

Abstract

The International Linear Collider (ILC) which is based on super-conducting RF acceleration technology requires the damping rings to provide beams with extremely small equilibrium emittances, and large acceptance to ensure good injection efficiency for high emittance, high energy spread beam from the positron source. In order to reduce the cost for ILC damping rings, an alternative lattice which is different from the baseline configuration design has been designed with modified FODO arc cells , and the total quadrupole number has been reduced by half. At the same time, to decrease the total cost involved in constructing access shafts needed to supply power, cryogenics etc. for the wigglers and other systems, the number of wiggler sections is decreased from 8 to 4, and further to 2. This new lattice has been optimised to have a good dynamic aperture. This alternative ILC damping ring lattice design will reduce the cost largely compared with the baseline design.

INTRODUCTION

The International Linear Collider (ILC) damping rings should provide beams with very low natural emittances for the linear collider to reach the required luminosity, and at the same time, the damping rings also need to have a large acceptance to ensure good injection efficiency for high emittance, high energy spread beam from the positron source [1]. Another main design criteria for the damping ring comes from the requirement of providing a long beam pulse of 1 ms containing 2820 bunches (normal parameter set [2]), corresponding to an approximately 300 km long bunch train. To keep the damping ring's circumference reasonable, the bunch train has to be stored in a compressed mode with much smaller bunch spacing than in the linacs. Consequently, each bunch has to be individually injected and ejected. The ring circumference is then determined both by pulse width of the injection and extraction kicker system and electron-cloud (ion) effects. Based on the studies of the various configuration options, the ILC damping ring Baseline Configuration Design (BCD) decides that the positron damping ring should consist of two (roughly circular) rings of approximately 6 km circumference in a single tunnel and the electron damping ring should consist of a single 6 km ring, assuming that the fill pattern allows a sufficient gap for clearing ions [2, 3].

In the ILC damping ring baseline design, a lattice which has a circumference of approximately 6 km using TME arc cells has been used [4]. In this paper, with the aim to reduce the cost of the damping rings, a new lattice with modified FODO arc cells is designed to be an alternative of the baseline design [5]. To decrease the total cost involved in constructing access shafts needed to supply power, cryogenics etc. for the wigglers and other systems, the number of wiggler sections is decreased from 8 to 4, and further to 2.

LINEAR LATTICE DESIGN

There are 120 arc cells in all for a 6 km damping ring, therefore each arc cell provides a bending angle of $\pi/60$ for the beam. The FODO arc cell length is selected as 38.9 m and the phase advance per arc cell is $90^o/90^o$ for the horizontal and vertical betatron motion, respectively. According to Equation 1, the maximum and the minimum value of the beta functions of the FODO arc cell is 66.2 m and 11.4 m, respectively. From Equation 2, the maximum and the minimum horizontal dispersion function is 1.37 m and 1.02 m respectively, which are too large to get a reasonable bunch length of 6 mm.

$$\beta^{\pm} = \frac{L_P(1 \pm \sin\frac{\mu}{2})}{\sin\mu} \qquad (1)$$

$$D^{\pm} = \frac{L_P\phi(1 \pm \frac{1}{2}\sin\frac{\mu}{2})}{4\sin^2\frac{\mu}{2}} \qquad (2)$$

where β^+ and β^- are the maximum and minimum value of the beta functions, D^+ and D^- are the maximum and minimum value of the horizontal dispersion function, L_P is the length of the cell, μ is the phase advance of the cell, and φ is the bending angle in one arc cell, T_o have smaller RMS dispersion value, the length of the drifts that are between the quadrupoles is adjusted and the ultimate value of the two long drifts are 13.7 m and 1.55 m with the maximum and the RMS horizontal dispersion function being 1.15 m and 0.77 m, respectively. The lattice functions in an arc cell are shown in Figure. 1.

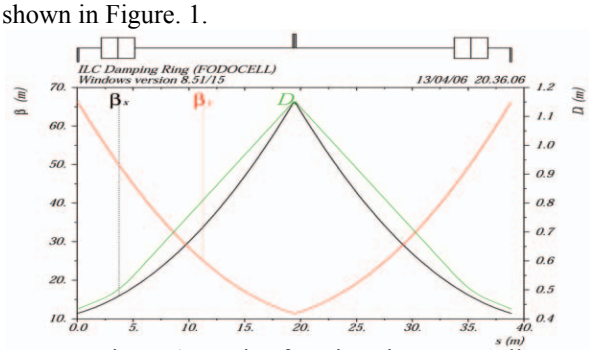

Figure 1: Lattice functions in an arc cell.

* ypsun@ihep.ac.cn
** Supported by the National Natural Science Foundation of China under Grant No 10525525.

The dispersion suppressors match the dispersion function between arc sections and straight sections. There are two kinds of dispersion suppressor insertions. One matches the dispersion function without affecting the alpha and beta functions, and the other suppresses the dispersion function by only modifying the focal length of two quadrupoles, which modifies both the alpha and beta functions. Here we do not use the usual method to make a dispersion suppressor, but insert three quadrupoles into the arc cell to get a dispersion suppressor, as shown in Figure. 2.

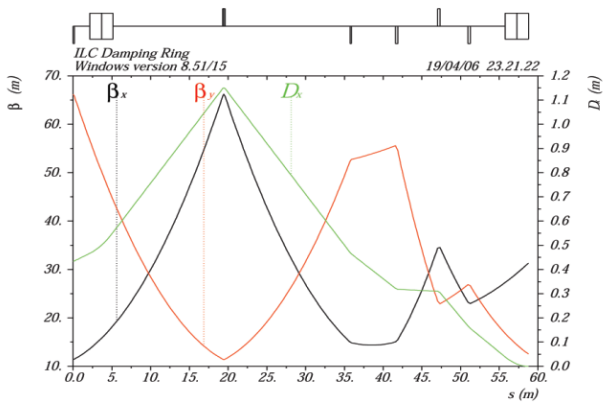

Figure 2: Lattice functions in a dispersion suppressor.

The wiggler/RF cavity sections are kept the same as the original design. The injection and extraction optics are designed to accommodate either of two different types of kickers that are studied at Fermilab: a pulsed kicker system with 6 ns rise time (and longer fall time) and a Fourier kicker, which is shown in Figure 3 [6].

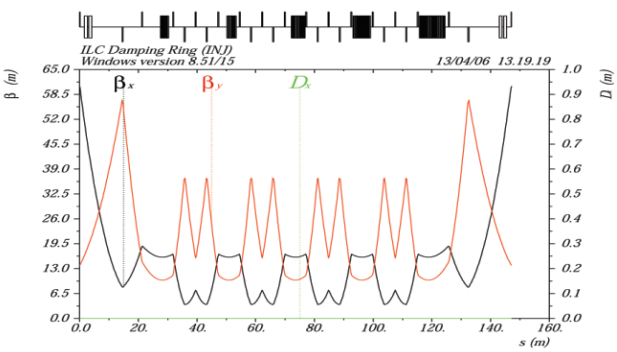

Figure 3: The injection and extraction lattice.

There are totally four long straight sections in the ring. The RF cavities and the wigglers have been installed in two of them. The layout of the ring has been designed with 4-fold symmetry. The lattice functions for the whole ring and the layout of the lattice are shown in Figure 4 and Figure 5 respectively, and the principal lattice parameters are listed in Table. 1.

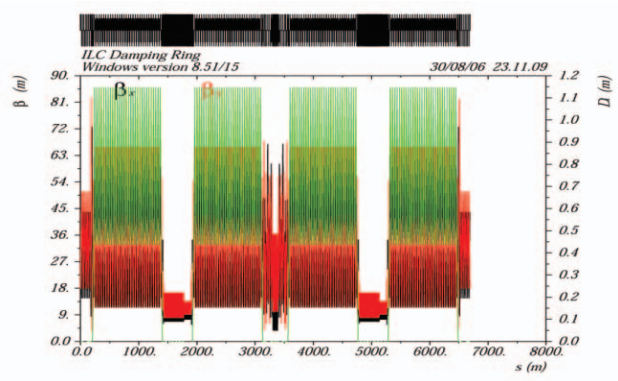

Figure 4: Lattice functions for the whole ring.

Table 1: The principle lattice parameters.

Circumference [m]	6695.057
Harmonic number	14516
Energy [GeV]	5
Arc cell	FODO
Tune	48.35 / 45.32
Natural chromaticity	-59 / -61
Momentum compaction [10^{-4}]	4
Transverse damping time [ms]	25 / 25
Norm. Natural emittance [mm-mrad]	4.2
RF voltage [MV]	46.6
Synchrotron tune	0.093
Synchrotron phase [^{o}]	169.2
RF frequency [MHz]	650
RF acceptance [%]	2.68
Natural bunch length [mm]	5.96
Natural energy spread [10^{-3}]	1.28

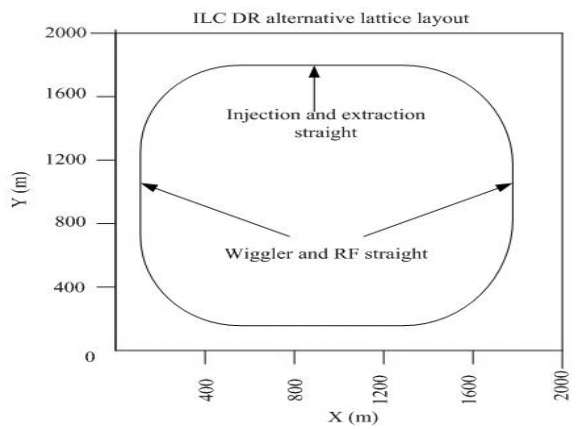

Figure 5: Layout of the DR lattice with 2 wiggler sections.

CHROMATICITY CORRECTION AND FMA RESULTS

Two family sextupoles in the arc cell are used to correct the first order chromaticity to above zero. The phase advance per arc cell is 90^{o}/90^{o} for the horizontal and vertical betatron motion, respectively. There are totally four arc sections and thirty arc cells in each arc section. Therefore, the phase advance per arc section is 15π for both the horizontal and vertical betatron motion. This kind of second order achromat helps to

cancel all driving terms of the third order resonances generated by the sextupoles within each arc section.

In our study it is found that not only the phase advance in the straight section but also the phase advance between the last sextupole in one arc section and the first sextupole in the next arc section are very important. The straight sections are optimized to give a reasonable horizontal phase advance which is near 2π, and a vertical phase advance which is near π.

The position of the two family sextupoles in the arc cell has been adjusted to give a good chromaticity property and a larger dynamic aperture. The variation of tune with momentum spread $\pm 1\%$ is less than 0.06%. After tracking for 1024 turns, the dynamic apertures of both on-momentum and off-momentum particles are obtained, which are shown in Figure 6 [7].

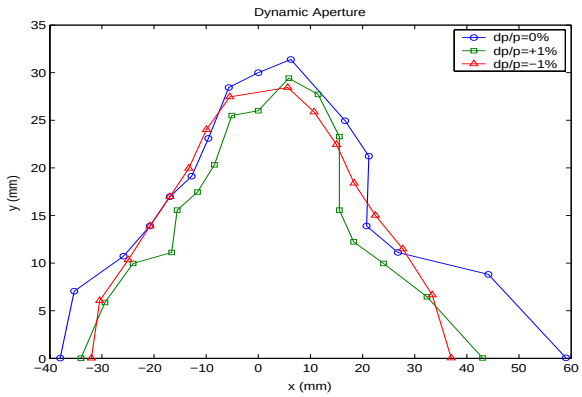

Figure 6: The dynamic aperture with momentum spread up to $\pm 1\%$.

It can be calculated from the injected beam's emittance and the beta functions at the injection point of the ring that the horizontal and vertical bunch sizes of the injected beam are approximately 6.6 mm and 4.2 mm, respectively. It can be seen from Figure. 6 that the dynamic aperture is nine times the vertical injected beam size and seven times the horizontal injected beam size for on-momentum particles. The lattice also gives a good dynamic aperture for off momentum particles.

Frequency map analysis (FMA) is introduced for the demonstration and understanding of the chaotic behavior of a dynamical system. The application to particle accelerator dynamics is done in the case that the motion of a single particle in a storage ring is described in a surface of section of the beam by a symplectic map of dimension 4 or 6 [8]. Here FMA is used to optimize the working points and the dynamic aperture. The optimized result is shown in Figure. 7, where 2500 particles distributed in the range of seven times the injected bunch size are tracked for 1024 turns to do the frequency map analysis on the lattice.

CONCLUSIONS

An alternative damping ring lattice with modified FODO arc cells and only two wiggler sections has been designed to reduce the cost of ILC damping rings. The number of quadrupoles in the whole ring has been decreased by half compared with the original ILC damping ring BCD design. Also the number of access shafts needed to supply power, cryogenics etc. for the wigglers and other systems, is decreased from 8 to 2. The circumference, the equilibrium emittance, the bunch length, the acceptance, the dynamic aperture, and the damping time can fulfill the requirements for the ILC damping ring. The dynamic aperture is large enough with the nonlinear wiggler effects taken into account. Frequency map analysis has been used on this lattice during the optimization of the dynamic apertures by choosing the working point far away from the dangerous resonance lines. Next, the phase advance of the arc cell will be varied to study the lattice with a lower momentum compaction, 2×10^{-4}, which is connected with the requirements of the instability estimation.

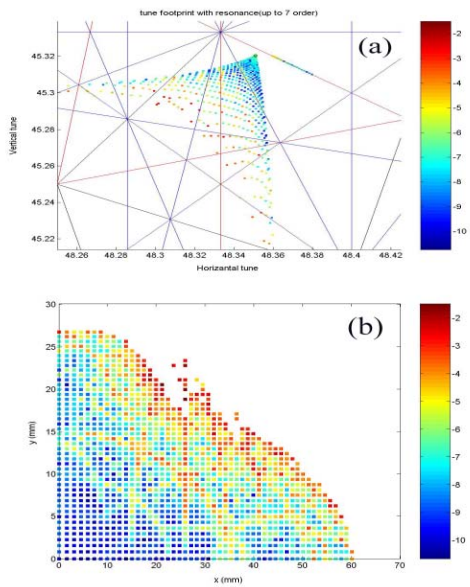

Figure 7: FMA analysis for damping ring DA: (a) footprint; (b) Dynamic aperture with FMA.

REFERENCES

[1] J. Gao, High Energy Physics and Nuclear Physics **30** Supp 156 (2006)
[2] A. Wolski, J. Gao and S. Guiducci, EPAC06 (2006)
[3] ILC BCD 2006 http://www.linearcollider.org/
[4] A. Xiao, Fermilab Technical Report (2004)
[5] Y. P. Sun and J. Gao, High Energy Physics and Nuclear Physics Vol. **30** (12): 1190-1195 (2006)
[6] L. Emery and K. J. Kim, FERMILAB-TM-2272-AD-TD (2004)
[7] A. Terebilo, SLAC-PUB 8732 (2001)
[8] S. Dumas, J. Laskar, Phys. Rev. Lett. **70**, 2975(1993)

ULTIMATE ABILITIES OF CONVENTIONAL POSITRON SOURCES

P. Logachev, M. Avilov, M. Blinov, P. Martyshkin, T. Vsevolozhskaya, Budker INP, Novosibirsk, Russian Federation.

Abstract

Significant increasing of desired luminosity for future e+e- colliders leads to corresponding enlargement of positron production rate. Conventional technology of positron production has not reached yet its technical limits. Experimental study in order to find out these limits for basic subsystems of positron source is presented.

INTRODUCTION

With the advent of first linear accelerators in the middle of last century these machines were used for production and acceleration of positron beams. The first successful acceleration of positron beam was reported from Mark III accelerating system at Stanford [1]. Many linac based e^+ sources were built in subsequent years with significant improvements of beam intensity and quality. But the basic concept of these sources remained practically unchanged [2]. In this concept a high-energy electron beam from driving linear accelerator is focused on a thick target of high Z material, generating an electromagnetic shower in it. A part of shower positrons escapes from the target with a large spread in energy and angles. So only a small fraction of these positrons is guided by magnetic matching device into a following linear accelerator. The first part of this linac is immersed into longitudinal magnetic field of a long solenoid. This field provides transverse focusing for positrons with a large transverse momentum. Quadrupoles mounted on accelerating structure are used downstream of the long solenoid. These quadrupoles have alternating polarity for magnetic field gradient and form so-called FODO structure. A sketch of linac based positron source is shown in Fig. 1.

POSITRON PRODUCTION TARGET

For particular value of driving electron beam energy, an optimum length of positron production target exists [2]. This optimum length corresponds to the maximum of positrons density in the electromagnetic shower as it leaves the target. Space, energy and angle distributions of positrons after the target with an optimum length have a weak dependence upon the energy of primary electron beam within the range from 0.3 GeV up to 30 GeV [3]. This fact makes easier the analysis and comparison of positron sources with different energy of driving electron beam.

Thermal stability of positron production target under the heating energy deposition from the electromagnetic shower is the most important problem. Thermal damage of the target limits the intensity of driving electron beam and, hence, the intensity of secondary positron beam. This damage comes from the excess of mechanical stress limit for solid elements of target assembly.

Driving electron beam may consist of one or few intense and very short bunches usually called as a bunch train, or macro pulse. Driving electron linac produces these macro pulses with some repetition rate. In such a way, the particular time structure of the beam can be varied and depends on the particular application. But for most target designs and driving beam structures the working area for target subsystem can be defined in terms of two parameters. The first parameter is related to negative stress limit reached while the shock wave travels through the solid part of the target assembly (dynamic limit). Intense driving electron bunch or bunch train generates this wave. The second parameter corresponds to the maximum DC power density allowed for particular target design (static limit). Both parameters depends upon the power density in driving electron beam and, hence, upon the electron beam size on the target. However, the positron beam size at the exit of the target with optimum length is practically the same for any diameter of driving beam less than 1 mm. So the optimum driving electron beam transverse size on the target can be fixed at the level of 1 mm (FWHM).

The following time scales can be applied for different processes took place in a short electron bunch interaction with the target: energy deposit (up to 100 ps), time response for temperature (up to few ns) and stress (up to 300 ns). So 100 ns can be chosen as the maximum time duration for the bunch train, which generates shock waves with maximum efficiency. Finally, it is possible to define the first parameter as J=E*N/S, where E is driving electron beam energy in GeV, N is the maximum number of incident electrons in 100 ns time interval, S is the transverse cross section of driving electron beam (mm^2). The second parameter can be defined as DC power (kW) in driving electron beam with 1 mm transverse size on the target. These two parameters form 2-D plot (see Fig.2)

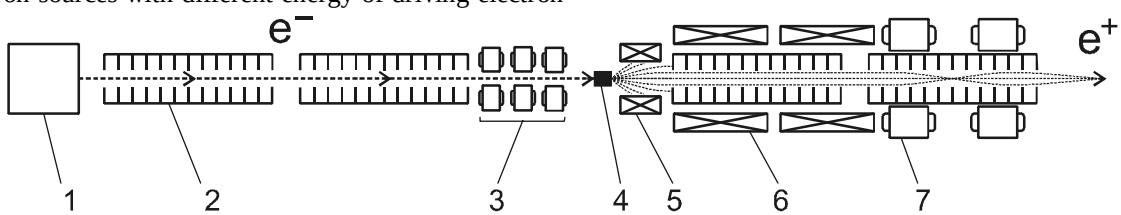

Figure 1: 1 — electron source, 2 — accelerating structure, 3 — focusing triplet, 4 — positron production target, 5 — magnetic matching device, 6 — solenoid, 7 — quadrupole lens.

with different areas available for different kinds of positron production targets. The first kind of target is the stationary solid-state WRe target cooled by water. The second one is rotating WRe target cooled by thermal radiation. And the third one is liquid lead target with BN windows. All calculations were done for 6 GeV energy of driving electron beam.

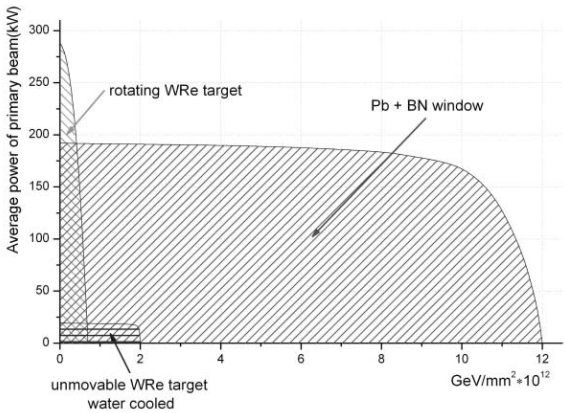

Figure 2: Areas available for different kinds of positron production targets.

Estimations for liquid lead target were performed on the base of experimental data obtained from the prototype of the system, developed in BINP [4]. For rotating WRe target estimations were done using practical experience with prototype of rotating high power target (50 kW in DC) built and successfully tested in BINP in the framework of ISTC Project #2257 [5].

The application area for liquid lead target with BN windows is limited by thermo-mechanical properties of these windows. Open liquid lead jet cannot be used together with high vacuum RF accelerating system. Rotating WRe target cooled by thermal radiation has to operate at the target temperature (around 2000 ºC), at which the mechanical properties of WRe alloy degrade. The maximum practical rotation speed for this kind of targets is limited by the value of 3000 rpm. The vertical scale on Fig. 2 reflects the total DC power in driving electron beam with the energy of 6 GeV. In such a way, the real heating power deposition in the target will be about 5 times less.

MATCHING DEVICE

The transverse size of positron beam at the exit face of the target is significantly smaller than the aperture of the following accelerating structure. Thus there is a possibility to enlarge the positron beam size and reduce the angle spread for positrons. It helps to extend the capture of positrons at least 5 times. This manipulation with positron beam can be done by magnetic focusing lens usually called as matching device. There are three kinds of matching devices that are used in linac based positron sources: Quarter Wave Transformer (QWT), Flux Concentrator (FC), and Lithium Lens (LL)[2]. QWT is a pulsed coil. Positron production target is placed at the entry of this coil. The length and the magnetic field of this coil are adjusted in order to maximize the capture of positrons. Lithium lens has azimuthal magnetic field generated by direct current parallel to the axis of the positron production system. The focusing ability of both QWT and LL is very selective at the initial energy of positrons. From this point of view FC is much better and provides good matching for positrons within wide energy range. This is why FC used in linac based positron sources provides at least double number of positrons in comparison with QWT and LL. FC is the most effective at the maximum magnetic field value of about 10 T. For the best result this high field value should be combined with a good axial symmetry of FC magnetic field. Matching device of FC type, meeting all these conditions, was designed and successfully tested on VEPP-5 Injection complex at BINP [6]. The common feature of all these matching devices is the pulse regime of operation. The time interval of proper magnetic field existance cannot be very long, and bunch train duration must be less than this interval. So the maximum time interval for the magnetic field of a good quality can be chosen as one of key parameters of matching device. Maximum magnetic field value should be the second key parameter. Fig. 3 presents the 2-D plot with areas available for different matching devices. The advantage of Lithium lens is the possibility of operation with long pulse (up to 1 ms).

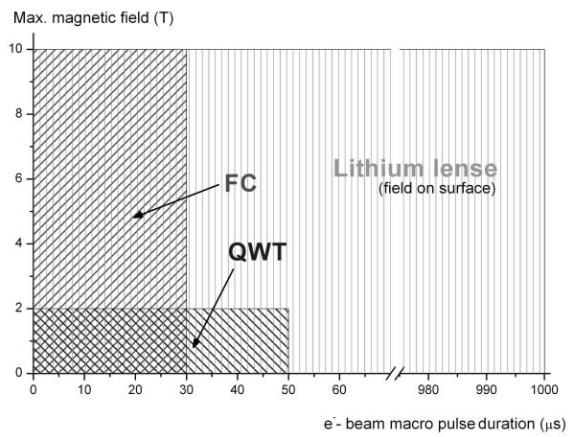

Figure 3: Areas available for different matching devices.

ACCELERATING SYSTEM

Accelerating gradient at the initial part of positron linac affects significantly to the number of accelerated positrons. Fig. 4 shows the dependence of positron capture efficiency upon the value of accelerating gradient. Calculations were done for L-band system (1.3 GHz). Another very important parameter is a macro pulse duration, which is actually restricted by particular frequency. Systems operated at higher frequency have smaller pulse duration and smaller aperture available for positron acceleration. Also maximum positron bunch length suitable for further acceleration should be smaller

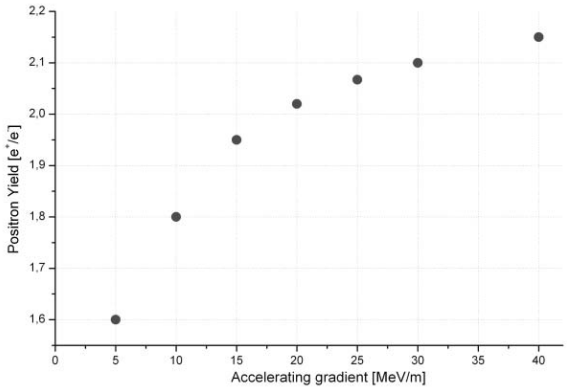

Figure 4: Dependence of positron capture efficiency upon the value of accelerating gradient. Driving e- bunch length 0.3 mm. Acceleration of positrons up to 9 GeV. Different acc. gradient at first 100 MeV only.

for systems with higher frequency. In such a way, moving to higher frequencies one can gain only in accelerating gradient and lose in all other parameters. Thus positron production rate will decrease with frequency rising.

Unfortunately, modern intense positron sources cannot utilise superconducting accelerating structures due to high heating power deposition in the structure body coming from neutron flux and electromagnetic shower. For warm copper structures the high gradient means the high input RF power. So proper powerful klystrons should be available for particular frequency band. Recent development of high power L-band klystrons allows reaching the accelerating gradient of up to 15 MeV/m [7]. It is only twice less than the maximum practical accelerating gradient for S-band (30 MeV/m at 2.8 GHz). The major advantage of L-band system is the operation with long macro pulse (up to 1 ms). Fig. 5 presents the positions of L-band and S-band positron accelerating systems on the accelerating gradient–beam macro pulse duration plot.

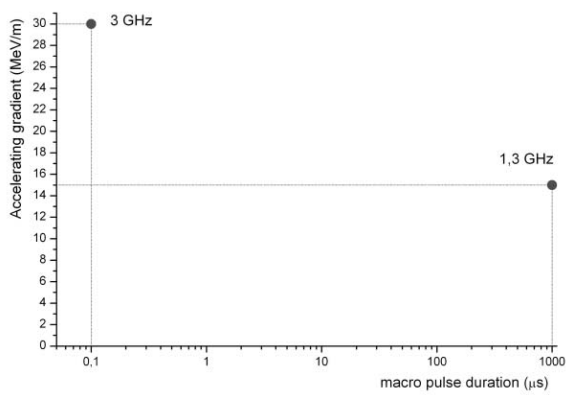

Figure 5: Accelerating gradient vs beam macro pulse duration for L-band and S-band.

CONCLUSION

Existing positron sources, which are in operation, haven't reached yet the limits of their application areas. So significant improvements in some directions are possible in the near future. It may lead to about one order of magnitude increase in positron production rate for best existing installations. Conventional positron production technology still has some reserves for such up-to-date projects as International Linear Collider (ILC) and Super B-factory.

REFERENCES

[1] D. Yount and J. Pine, "Production of Positrons with the Stanford Mark III accelerator," Nucl. Inst. And Meth. 15, hh. 45-50, 1962.

[2] R.Chehab. Positron Sources. Proc. CERN Accelerator School, General Accelerator Physics, Geneva, 1994, p.643.

[3] H.-H. Braun "Positrons for Accelerators", Ph.D. thesis, Zurich University, 1992.

[4] V. Belov, V. Karasyuk, V. Kobets, G. Kraynov, P. Martyshkin, M. Petrichenkov, G. Silvestrov, T. Sokolova, T. Vsevolozhskaya, G. Willewald, A. Bochko, J. Sheppard, V. Bharadwaj, D. Schultz, "Liquid Metal Target for NLC Positron Source", Proceedings of the Particle Accelerator Conference, Chicago, 2001.

[5] O. Alyakrinskiy, M. Avilov, D. Bolkhovityanov, J. Esposito, S. Fadeev, K. Gubin, Ya. Kandiev, A. Korchagin, N. Kot, A. Lavrukhin, N. Lebedev, P. Logatchev, P. Martyshkin, S. Morozov, V. Plokhoi, S. Samarin, S. Shiyankov, A. Starostenko, I. Svyatov and L. Tecchio. High Power Neutron Converter for Low Energy Proton/Deuteron Beams. // Nuclear Instruments and Methods in Physics Research Section A, Vol. 557 Issue 2, 15 February 2006, pp. 403–413.

[6] P.V. Logachev, A. V. Akimov, A. V. Antoshin, P. A. Bak, Yu. M. Boimelshtain, D. Yu. Bolkhovitianov, R. Galimov, S. M. Gurov, E. A. Gusev, N. S. Dikansky, S. N. Klushev, N. Kh. Kot, A. A. Korepanov, I. L. Pivovarov, Yu. I. Semenov, A. N. Skrinsky, A. R. Frolov, A. S. Tsyganov, S. V. Shiyankov "Status of VEPP-5 Injection Complex", Proceedings of the Russian Particle Accelerator Conference, Novosibirsk, 2006.

[7] Juwen Wang "Preliminary Studies of RF Structures for ILC Positron Source", Proceedings of the Workshop on Positron Source for the ILC, Daresbury Lab, April 11-13, 2005.

OPTIMIZATION OF THE BEPCII LATTICE WITH FREQUENCY MAP ANALYSIS*

Y. Jiao#, J.Q. Wang, D.M. Zhou, Q. Qin, G. Xu, S.X. Fang
Institute of High Energy Physics, Beijing 100049, China.

Abstract

The method of frequency map analysis (FMA) is used to analyze and optimize the lattice of the BEPCII storage ring. With the longitudinal oscillation and radiation being considered, both on- and off-momentum frequency maps are studied to have a complete picture of beam dynamics. The synchro-betatron resonances are found to be responsible for one limit of the dynamic aperture, and some efforts are made to reduce the effect of these resonances.

INTRODUCTION

BEPCII is the upgrade project of the Beijing Electron Positron Collider (BEPC) being built at IHEP. To enhance its luminosity, a double-ring design is adopted to house the micro-β scheme and multi-bunch collision. For the colliding beams the design luminosity is 1×10^{33}cm^{-2}s^{-1} optimized at beam energy of 1.89 GeV, which is about two orders higher than that of the BEPC [1]. According to the beam-beam simulations with Cai's code [2] and Zhang's code [3], the working point is chose to be close to the half integer resonance, which thus calls for elaborate analysis and optimization of the beam dynamics.

Frequency map analysis (FMA) is a very useful tool to study the single particle dynamics by constructing a one-to-one relationship between the space of initial conditions (x, y, $x'=y'=0$) and the tune space (Q_x, Q_y) [4]. With this method, we can obtain the dynamic aperture (DA) and the corresponding frequency map (FM) at the same time, and study the effects and features of only one resonance out of others. This method has been used among many light sources (ALS, NSLS, SPEAR3, SOLEIL, ESRF, SSRF, etc) [5-10] and other machines (LHC, SNS) [11, 12]. It is the first time that we systematically apply the FMA to the lattice of the BEPCII storage ring.

The paper is organized as follows. In Sec. 2, we present the FMA results of BEPCII lattices and study the effect of synchro-betatron resonances on the single beam dynamics in detail. Several ways to the optimize the lattices are discussed in Sec. 3. We summarize and conclude our work in Sec. 4.

FMA ON THE BEPCII LATTICES

BEPCII collision mode

The BEPCII lattice loses the 4-fold symmetry of the BEPC, due to the double-ring geometric structure [1]. The vertical beta function at the IP is squeezed by a pair of defocusing superconducting quadrupoles. The dispersion functions are free at the IP, the RF region (outer ring) and the injection point. The beta functions are required to be less than 15 m at the RF cavities in both vertical and horizontal planes and largger than 20 m at the injection point in horizontal plane to save the kicker strength.

A recently designed collision mode lattice [13] with the working point of (6.51, 5.58) is put into analysis using FMA. Table 1 gives the main parameters of the collision mode and the injection mode which will be referred in the following text.

Table 1: Main parameters of the BEPCII lattices

Parameter	Unit	Collision mode	Injection mode
Beam energy	GeV	1.89	1.89
Circumference	m	237.53	237.53
RF voltage	MV	1.5	1.5
$Q_x/Q_y/Q_s$		6.51/5.58/ 0.034	6.58/5.62/ 0.034
Natural chromatity		−10.7/−21.0	−10.5/−12.1
Horizontal natural emittance	nm·rad	141	135
β_x^*/β_y^* (IP)	m	1/0.015	2.8/0.04

For the horizontal working point is much close to the half integer resonance, the nonlinear optimization of the lattice with 4 families of sextupoles by MAD [14], is not perfect. As shown in Fig 1, the average off-momentum DAs with errors (20 random seeds) from SAD [15] are only slightly largger than the required aperture for collision which is $10\sigma_x\times10\sigma_y$ and labeled as the solid square, but smaller than the requirements for injection, i.e., $13.5\sigma_x\times10\sigma_y$, the dashed square. The minimum DAs with errors (among 20 random seeds) for different momentum deviations are even smaller (for more details, refer to [13]).

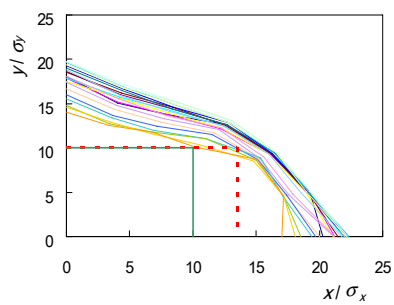

Figure 1: The average DAs with $\Delta p/p \in (-10\sigma_e, 10\sigma_e)$ from SAD, with multipolar magnetic errors[13].

For FMA analysis, tracking is done with AT [16]. Starting from the RF cavity, the particles with different

*Work supported by National Natural Science Foundation of China (10375076)
#jiaoyi@ihep.ac.cn

initial conditions (x_0, y_0, x_0'=y_0'=0, l=0, δ=0 & ±0.006) are tracked for 2000 turns with RF cavity and radiation on. The tunes over the first 1000 turns and the last 1000 turns as well as the diffusion rate of particle motion are computed with the FMA method.

The DAs and FMs are given in Fig. 2. There exists great disparity between the on- and off-momentum DAs and FMs. That is, the off-momentum FMs are not folded like the on-momentum case and the tune footprints cover the range $Q_x \in (6.514, 6.516)$ with a higher diffusion rate or even particle loss. The great disparity can be explained as follows. According to the theory of super-periodic structural resonances analysis (SSRA)[10,17], the horizontal working point is very close to the half integer resonance, which is expected to be a second order super-periodic structural resonance with strong nonlinearity. The chromaticity correction with sextupoles does not have enough effective action range of momentum deviations, leading to a great difference between the on- and off-momentum beam dynamics. The off-momentum beam dynamics could be affected by the synchro-betatron resonance $2Q_x - Q_s = 13$, thus the DA is much smaller than the on-momentum DA especially in vertical plane.

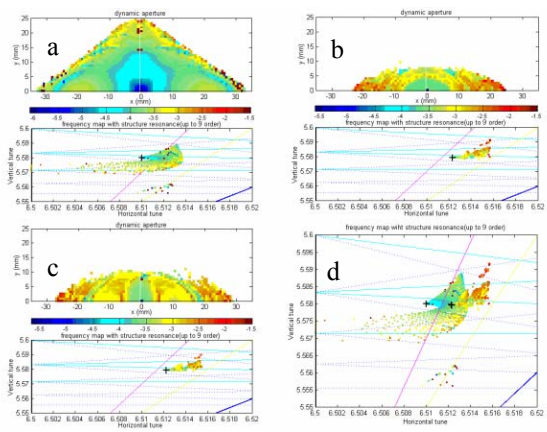

Figure 2: The FMs with $\Delta p/p$=0 (a), −0.006 (b) and 0.006 (c), respectively. (d) shows the FMs of three cases together. The colour scale corresponds to the orbit diffusion from regular (blue) to chaotic (red) motion.

BEPCII injection mode

The injection mode relaxes the constraints on the low vertical beta function at the IP and the working point close to half integer resonance, but calls for larger DA and better beam dynamics. We choose the working point as (6.58, 5.62), which is located in a relatively clean area in tune space.

The tracking (with RF cavity and radiation on) is performed over 2000 turns without errors, with the last 1000 turns being devoted to the diffusion computation. The on- and off-momentum beam dynamics is similar, thus only the on-momentum case is analyzed (Fig 3). The DA is large, namely, $[-30, 45]_{y=0} \times [0, 42]_{x=0}$ mm. From the one-to-one correspondence between the DA and FM, we find that the horizontal DA is limited by the transverse coupling resonance $Q_x - Q_y = 1$. Furthermore, we find the synchro-betatron resonance $2Q_x + 3Q_y + Q_s = 30$ locates at the border of the DA, i.e., it limits the stability area. To confirm the existence of the synchro-betatron resonance, A particle is launched with initial conditions (x, x', y, y', δ, l) = (30mm, 0, 15.5mm, 0.3%, 0) and tracked using AT. The voltage of the RF cavity is the designed value of 1.5 MV. The particle lost in 400 turns, with the coordinates of the particle plotted turn by turn in Fig 4. The vertical amplitudes increase rapidly and exceed the vacuum height as ±26mm. The tunes abstracted from the last 200 turns (Q_x, Q_y, Q_s) = (6.5807, 5.6058, 0.0327) are just on the resonance. For comparison, we make the tracking with the same initial coordinates under two cases: 1) RF cavity and radiation are off; 2) the voltage of the RF cavity is 3 MV (the Q_s will change). Both of the particles are stable.

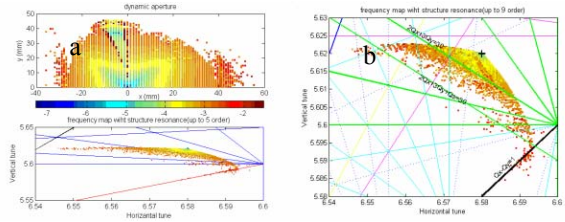

Figure 3: The DA and FM of the injection mode lattice with $\Delta p/p$=0 (a); FMs with $\Delta p/p$=0, ±0.006 together (b).

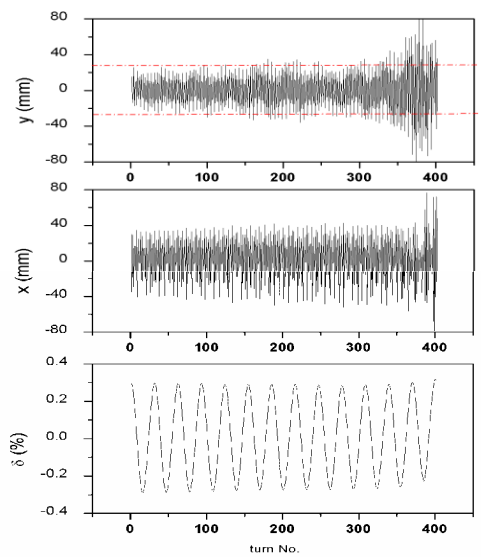

Figure 4: Tracking with longitudinal oscillations and damping. The dashed dot lines indicate the height of the vacuum chamber ±26mm.

OPTIMIZATING THE BEPCII LATTICE

BEPCII collision mode

That we could not move the working point away, or the luminosity will decrease, increases the difficulty of optimization. A big effort is made to find a set of sextupoles with smaller anharmonicities, changing the (dQ_x/dx^2, dQ_x/dy^2, dQ_y/dy^2) from (73, 77, 208) to (70, 68,

198), aiming to make the tunes reach the dangerous resonance at bigger amplitude. As shown in Fig 5(a), the average DAs with errors (20 random seeds) are slightly bigger than that before optimization and satisfy the requirement for beam injection.

Furthermore, we try to reduce the effect of resonance $2Q_x - Q_s = 13$. The growth time of resonance is [18]

$$\frac{1}{\tau} = f_0 \hat{\delta} H = f_0 \hat{\delta} \left| \sum_n k_{sn} D_{xn} \beta_{xn} e^{2i\phi_{xn}} \right|$$

where $\hat{\delta}$ is the energy oscillation amplitude, f_0 is the revolution frequency, k_s, D_x, β_x, ϕ are the integrated sextupole strength, horizontal beta function, horizontal dispersion, and azimuth angle, respectively. We use 9 groups of sextupoles instead of 4 groups and minimize the value of H by fine-tuning sextupole strength. For example, we change the H from 19.7 to 3.1 for $\hat{\delta} = 0.003$. The following tracking using SAD shows that the off-momentum DAs with errors (20 random seeds) have an obvious increase in horizontal plane (see Fig 5(b)).

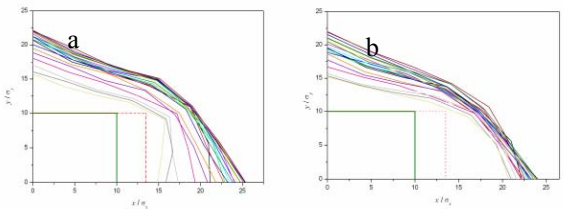

Figure 5: The optimized DAs from SAD with errors and $\Delta p/p \in (-10\sigma_e, 10\sigma_e)$, (a): reduce the anharmonicities, (b): reduce the growth time of the resonance $2Q_x - Q_s = 13$.

BEPCII injection mode

If we keep the tune footprints away from the resonance $2Q_x + 3Q_y + Q_s = 30$ and $Q_x - Q_y = 1$, the limit of the dynamics will vanish and the DA will be larger. Optimizations based on this idea are performed. The working point is moved to (6.57, 5.61), and the amplitude tune shift slope at origin is reduced from $(dQ_x/dx^2)_{x=0}$=760 to 133. As shown in Fig 6, the optimized DA (without errors) increases to be $[-40, 50]_{y=0} \times [0, 45]_{x=0}$ mm. The DA (with errors) obtained with SAD is much bigger than the requirements of the injection mode, which confirms our optimization.

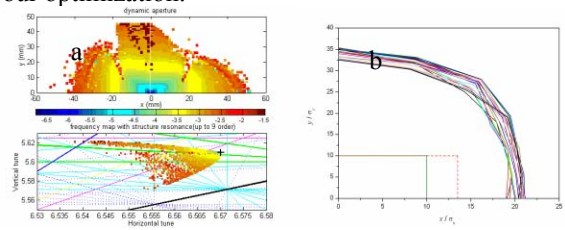

Figure 6: The DA and FM without errors from AT (a); the average DAs with errors and $\Delta p/p \in (-10\sigma_e, 10\sigma_e)$ from SAD (b).

CONCLUSION

The analysis and optimizations of the BEPCII collision and injection modes with FMA are described in this paper. FMA turns out to be a good and effective tool to look into the beam dynamics and the resonance structure in a global way, thus enabling us to avoid dangerous areas in tune space and to further improve the beam dynamics.

The RF cavity and synchrotron radiation are turned on during the tracking, that is, the longitudinal oscillation and the damping process are taken into account. The synchro-betatron resonances may be exited and affected the single particle dynamics. In the case of the BEPCII injection mode lattice with the working point of (6.58, 5.62), such a resonance is responsible for the limit of the DA. When we move the working point away from the resonance, the DA significantly increases.

Compared to the injection mode, the limiting factor for the lattice is more severe, the optimization consequently becomes more complicated and difficult. Reducing the nonlinear anharmonicity terms and minimizing the effect of the synchro-betatron resonance $2Q_x - Q_s = 13$, are proved to be beneficial to the improvement of the beam dynamics.

REFERENCES

[1] IHEP-BEPCII-SB-03-3, 2003.
[2] G. Xu, IHEP-URAP-Note/2005-06, 2005.
[3] Y. Zhang, IHEP Ph. D thesis, 2005.
[4] L. Nadolski and J. Laskar, Phys. Rev. ST Accel. Beams 6, 114801 (2003) .
[5] C. Steier et al, EPAC 2002, pp. 1077, & D. Robin et al, Phys. Rev. Lett. 85, p. 558 (2000).
[6] M. Belgroune et al, EPAC 2002, p. 1229.
[7] Y. Papaphilippou et al, PAC 2003, p. 3189, & Y. Papaphilippou et al, EPAC 2003, p. 2050.
[8] Y. Papaphilippou. PAC 2001, p. 462.
[9] A. Terebilo et al, PAC 1998, p. 1457.
[10] Y. Jiao et al. NIM A 566 (2006) p.270.
[11] Y. Papaphilippou, Phys. Rev. ST Accel. Beams 2, 104001 (1999).
[12] Y. Papaphilippou, PAC2001, p. 462.
[13] Q. Qin, IHEP-AC-AP-Note/ 2006-01, 2006.
[14] MAD code homepage, http:// mad.web.cern.ch/mad/.
[15] SAD code homepage, http://acc-physics.kek.jp/SAD/sad.html.
[16] AT code homepage, http:// www-ssrl.slac.stanford.edu/at /welcome.html.
[17] S. X. Fang, Q. Qin. HEP & NP, 2006, 9: 880.
[18] A. Piwiniski, DESY 93-187 (1993).

NEW CONNECTION CRYOSTAT TO INSERT FP420 PROTON TAGGING DETECTOR IN THE LHC RING

S. Pattalwar CCLRC, Daresbury, UK
T. Colombet, S. Marque, T. Renaglia, D. Swoboda CERN, Geneva, Switzerland
B. Cox, K. Potter, F. Roncarolo Cockcroft Institute and University of Manchester, UK
D. Dattola, INFN, Torino, Italy

Abstract

FP420 is a R&D project to assess the feasibility of installing proton tagging detectors in the region 420m from the interaction points at the LHC. They would function as new sub-detectors at ATLAS/CMS, allowing the measurement of the spatial position and arrival time of outgoing protons emerging intact from the collision. Forward proton tagging in this region is expected to open a new programme of electroweak, QCD and BSM physics.

At present the 420m region is enclosed in a 'connection cryostat' (maintained at 1.9K) that provides continuity for the LHC beam, cryogenic & vacuum services and electrical power circuits through superconducting bus bars. The requirement of near room temperature operation and critical position control close to the beam pipes has made inserting FP420 detectors in this region a very complex task. The currently favoured design calls for the replacement of the connection cryostats with a new ~14m long assembly that will have all the necessary features of the existing connections cryostat as well as the appropriate environment for the operation of the detectors. This paper mainly describes the cryogenic aspects of the new connection cryostat.

INTRODUCTION

The FP420 R&D project [1] is an international collaboration with members from 29 institutes from 10 countries. The aim is to assess the feasibility of installing **F**orward **P**roton Tagging Detectors at **420m** from the interaction points (IP) of the ATLAS and / or CMS experiments at the LHC. The physics potential of forward proton tagging in the 420m region at the LHC has only been fully appreciated within the last few years. By detecting protons that have lost less than 1% of their longitudinal momentum, a rich QCD, electroweak, Higgs and BSM program becomes accessible, with the potential to make measurements which are unique at LHC, and difficult even at a future linear collider.

The drift spaces around 420m from the ATLAS and CMS interaction points are at present enclosed in a 14 m long interconnection cryostat [2] that connects the superconducting arcs and dispersion suppressor regions of the LHC. The cryostat provides continuity not only of the beam pipes held cold at 2K, but also of the isolation vacuum, electrical power, cryogenic circuits and thermal shielding. One of the key challenges for the FP420 experiment is to design a new 14 m section to replace the interconnection cryostat which will allow access to warm beam pipes. In this paper we describe the design concepts of the proposed new connection cryostat.

EXPERIMENTAL REQUIREMENTS

The main requirements of the FP420 experiment are:

- The FP420 detector must be able to reconstruct the tracks of the outgoing protons a few mm away from the beam.
- Silicon pixel detectors [3] must be moved into a position as close to the beam as possible when stable beam conditions are reached.
- Geometry and the materials used for the modified beam pipe must not affect the normal running of the LHC.
- The new design of the cryostat with the detector assembly must ensure the continuity of the existing LHC services as well meet all the necessary criteria for cryogenic performance [4], alignment, transport and commissioning.
- The Si-detectors operate near room temperature whereas the beam pipes are maintained at 1.8K in the current design of the connection cryostat. **Providing a warm access to the beam pipe is a key challenge in designing a new cryostat.**
- The commissioning of the FP420 detectors is being planned during the LHC shutdown in January 2009. Transport, installation, decommissioning & commissioning of the cryostat including the integration of the complete FP420 detector with LHC during the beam shutdown period will be extremely critical.

THE NEW CONNECTION CRYOSTAT

Figure 1 shows the cold mass in the present design of the connection cryostat. Figure 2 shows its cross section. The three bus bars M1, M2 and M3, the two beam pipes V1 and V2 and the heat exchanger line X are all enclosed in a cold mass maintained at 1.9K. Table 1 shows the configurations of the lines in the cryostat

Figure 1: Cold Mass inside the Connection Cryostat.

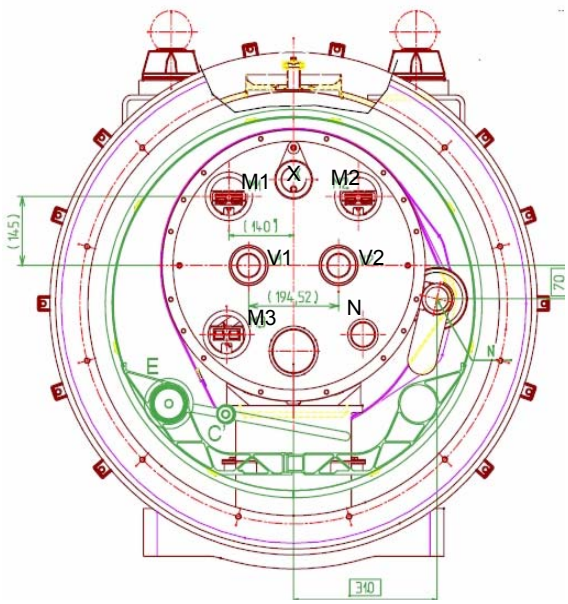

Figure 2: Cross section of the existing connection Cryostat

Table 1: Service in the Cold Mass

Line	T(K)	Dia (mm)
M1, M2,M3 Bus Bars	1.9	80-84
N Aux bus Bars	1.8	50-53
X Heat exchanger	1.8	54-58
E Thermal Shield	50-65	79-86
C Support posts and beam screens	4.6	15-17.2
V1, V2 Helium jackets around beam pipes	1.9	50-53 66-70

The main difficulty in designing a new cryostat is to introduce the 3D Silicon detectors which work near ambient temperature close to the beam pipes which at present are maintained at 1.9K. After several design iterations it was found convenient to split the existing cold mass into two independent cold sections. The upper section contains the heat exchanger (line X) and the lower section contains the rest of the cold services like bus bars in the lines M1, M2, M3 and N. The beam pipes V1 and V2 in the middle are accessible at ambient temperature. Figure 3 shows a 3D sketch of the new proposed cryostat. Figure 4 shows the cross sectional views at the points A, B and C in the figure 3 respectively. Line X assembly is shifted in the horizontal plane to create sufficient space around beam pipes for mounting the silicon detectors. The new beam pipes will be modified to accommodate thin windows with very close proximity to the circulating beam.

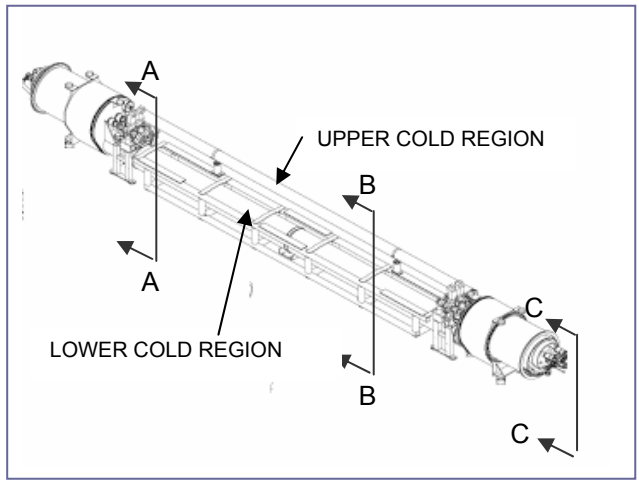

Figure 3: New Connection Cryostat

In order to maintain the compatibility with the connections at the interface between the cryostat and the LHC superconducting magnet it is necessary that the cross section of the new cryostat is identical to that of the existing cryostat. Such a transition (from Figure 4b to 4c) has been achieved inside the shuffling modules at both ends of the cryostat by adapting the design concepts from the ATM modules (Figure 5) [5, 6]. The design of individual components in the transition region is extremely complex but due to the adaptation of the existing designs significant amounts of engineering and design efforts have been saved.

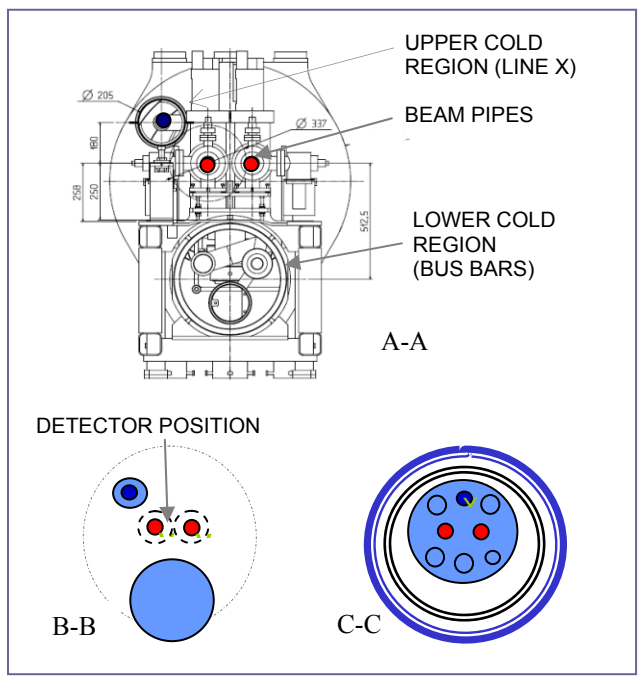

Figure 4: Cross sectional views of the cryostat

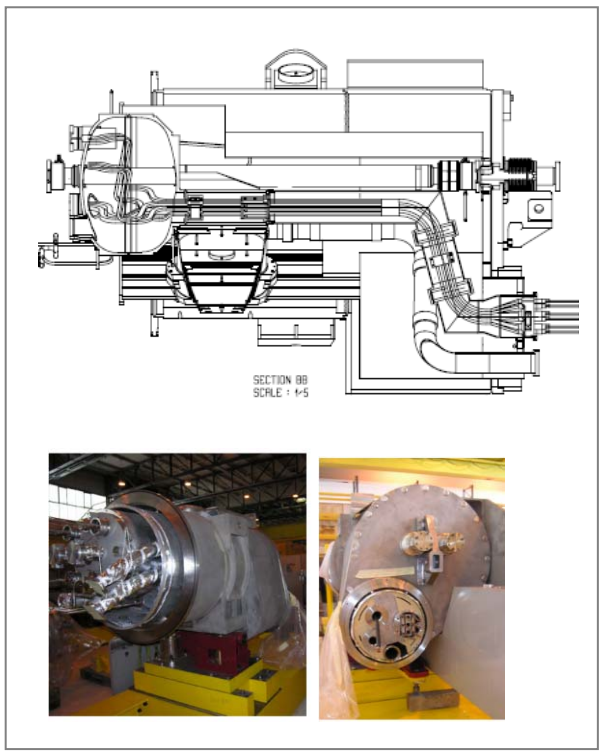

Figure 5: ATM Modules

INTEGRATION WITH THE LHC

The new design now ensures 1:1 replacement with the existing cryostat as well as maintains the continuity of all the services mentioned earlier. A 7.5m long region is available for inserting the Si-detectors in an overall length of 14m. Initial estimates indicate that the overall heat load budget for the new design is lower than those specified for the existing connection cryostat. Detailed calculations will be performed once all the details about the dimensions, tube sizes, material etc. are defined. Due to the limited time available during the beam shutdown period of 3 months the assembly, transport, alignment, commissioning and decommissioning of the cryostats will be extremely critical. Work is in progress [7] to evaluate the necessary sequence of operations for this task.

SUMMARY

FP420 is a R&D project to assess the feasibility of installing proton tagging detectors in the region 420m from the interaction points at the LHC. Key requirement is to create warm access to the beam pipe to insert the silicon pixel detectors as close as possible to the beam. In the proposed design the existing cold mass has been split into two cold regions, upper and lower, with the beam pipes in the middle exposed to ambient temperature. Continuity of all the necessary services and compatibility at the interface between the cryostat and the LHC magnet has been achieved by adapting the design concepts from the ATM module.

The FP420 collaboration expects to have a detailed feasibility and design study to present to the ATLAS and CMS collaborations during 2007, with a possibility of installation and commissioning during the beam shut down in January 2009.

REFERENCES

[1] B. Cox, “FP420 project and the LHC”, AIP conference proceeding 753:103-111, 2005, hep-ph/049144

[2] S. Marque *et al*, “Connection Cryostat for LHC dispersion suppressors (DS)”, LHC Project document No LHC-LE-ES-0001.00 rev 3.2 (EDMS 113854)

[3] C. DaVia, “Radiation hard Silicon detectors lead the way”, CERN Courier 43/1/16, 2003

[4] T. Colombet *et al* “Thermal performance of the LHC connection Cryostat**,** Proceedings of ICEC-21Prague, July 17-20, 2006

[5] T. Colombet, “Use of the ATM for the FP420 Project” LHC Project Document (EDMS 743628)

[6] T. Renaglia, “Utilisation des modules ATM pour le project FP420”LHC Project document No LHC-TS – NOTE 2006-007 (EDMS 771549)

[7] D. Swoboda, “Integration of FP420 into the LHC infrastructure” Presentation at Physics with FP420 Manchester, 10-12 December 2006

SIMULATION STUDY ON BUNCH LENGTHENING

Y. P. Sun#, Key Laboratory of Heavy Ion Physics, Peking University& IHEP, Beijing
J. Gao, IHEP, Beijing; Z. Y. Guo, Key Laboratory of Heavy Ion Physics, Peking University, Beijing

Abstract

The bunch lengthening phenomenon is resulted from one of the most severe single bunch instabilities in electron storage rings. As for BEPCII, controlling the bunch length is the most critical task to fulfil the designed luminosity goal. A new code is developed to calculate the single bunch length and energy spread in storage rings using FORTRAN. In this code, the wake field is calculated using an analytical formula. The bunch length and energy spread under different bunch current are calculated for BEPCII. The tracking results clearly show that the microwave instability threshold is around 65 mA for BEPCII storage ring. The tracking results of this code are in good accordance with those from other codes.

INTRODUCTION

The bunch lengthening phenomenon is resulted from one of the most severe single bunch instabilities in electron storage rings. It is well known that in an electron storage ring an electron will lose energy due to synchrotron radiations. Since this radiation is compensated by the RF cavities in the ring there exists a damping effect on the synchrotron oscillation with the corresponding damping time. The synchrotron radiation energy loss is in the form of randomly emitted photons, and this random quantum excitations together with the previously mentioned synchrotron radiation damping effects result in the single particle equilibrium energy spread and bunch length. The distribution in the normalized time displacement is as a Gaussian with a standard deviation that is equal to the standard deviation of the energy oscillations [1]. It follows that the fluctuating energy oscillations are accompanied by associated fluctuations in the time displacement. And the standard deviation of these fluctuations can be deducted to be (zero current case):

$$\sigma_{l0} = \frac{\alpha_P \overline{R}\, \sigma_{\varepsilon 0}}{\nu_s} \tag{1}$$

where σ_{l0} is the natural bunch length, α_P is the momentum compaction factor, $\sigma_{\varepsilon 0}$ is the natural energy spread and ν_s is the synchrotron tune.

The bunch length is equal to its natural values when the bunch current is low. However, when the bunch current is higher, the bunch length and energy spread increase due to collective effects.

Numerically there are normally three kind of approach to calculate the longitudinal stability of the beam: solving of linearized Vlasov integral equation in frequency domain which has a lot of neutrally stable spurious modes [2]; solving full Vlasov-Fokker-Planck equation in time domain which is slow but accurate [3]; particle tracking with wake fields which is fast but may be noisy [4]. For the macro-particle tracking approach with wake fields, longitudinal single bunch effect is simulated in electron storage rings to study the single bunch lengthening and energy spread. The turn by turn energy and phase deviations of N macro-particles are tracked. The input parameters consist of the usual RF and lattice associated parameters as well as the wake potential. Most of the other codes use the wake potential from the measured or calculated impedance values, but in this code an analytical wake potential is used.

STRUCTURE OF THE CODE

The phase space distribution of the bunch is represented by M randomly chosen test particles which are in Gaussian distribution in both longitudinal position and energy deviation. The turn by turn energy and phase deviations of M macro-particles are tracked as follows: [3]

$$t_m(n) = t_m(n-1) + \frac{\alpha_P T_0}{E_0}\varepsilon_m(n) \tag{2}$$

$$\begin{aligned}\varepsilon_m(n) &= \varepsilon_m(n-1) - \frac{2T_0}{\tau_\varepsilon}\varepsilon_m(n-1) \\ &- U_0\left(1-\cos\left(\omega_{rf}t_m(n-1)\right)\right) - \hat{U}\sin\left(\omega_{rf}t_m(n-1)\right)\sin\phi_s \\ &+ 2\sigma_{\varepsilon 0}\sqrt{\frac{T_0}{\tau_\varepsilon}}R_m(n) + eV_m(n)\end{aligned} \tag{3}$$

where m represents the m[th] test particle, n is the number of the turn, t and ε are the phase and energy deviations, T_0 is the revolutionary time, E_0 is the beam energy, τ_ε is the radiation damping time for energy oscillations, U_0 is the average synchrotron radiation energy loss per turn, $\hat{U}$ is the peak energy gain from RF cavity, ω_{rf} is the angular frequency of the RF cavity, Φ_S is the zero current synchronous phase angle, R_m is a Gaussian distributed random number with mean value equal to 0 and RMS value equal to 1, $\sigma_{\varepsilon 0}$ is the natural energy spread, and V_m is the wake field. In the above equations collective effects are contained in the term of wake field and the wake field gives the effect on particle m from all the particles which precede it in the bunch. Usually the bunch is separated into several bins every sigma. The spectrum of the bunch is gotten by Fourier transformation. Then the wake field is the reverse Fourier transformation of the product of impedance and the bunch spectrum.

The new contribution in this work is the treatment of the wake potential. An analytical expression that describes the wake potential of a storage ring is found to be effective on several storage rings in Ref. [5]. For the convenience of the theoretical treatment in Ref. [5], three

#ypsun@ihep.ac.cn

parameters, i.e., bunch length σ_z, total loss factor $k(\sigma_z)$, and the total inductance $L(\sigma_z)$ are used to describe the total wake potential of the machine.

SIMULATION RESULT ON BEPCII

BEPCII, the upgrading project of the Beijing Electron-Positron Collider (BEPC), has been designed with a luminosity of 10^{33} $cm^{-2}s^{-1}$ at the τ-charm energy region. To reach such a high luminosity, well controlling the bunch length is one of the most critical tasks.

In Figure 1 the dark line shows the longitudinal wake potential of BEPCII storage ring with σ_{z0}=0.0134 m, L=28.89 nH, and $k(\sigma_{z0})$=2.017 V/pC [5,6]; and the light line is the numerical result of MAFIA, where the wake potential of a short Gaussian bunch with 2 mm bunch length as the wake function of the storage ring is calculated (in time domain) [6,7]. The main parameters of the BEPCII storage ring used in this code are from the BEPCII design report [6].

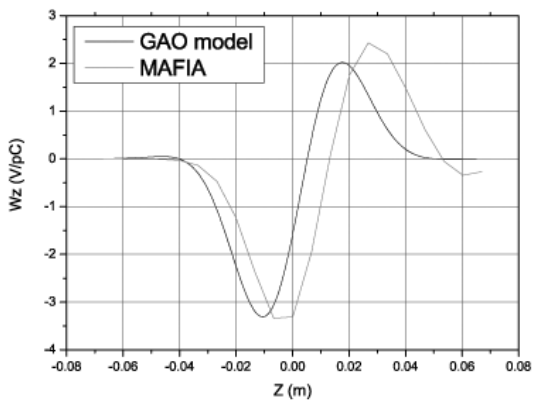

Figure 1: Wake potential for BEPCII storage ring.

First, we should check the convergence of the code without wake field. That means when we do the tracking, we shall take different macro-particle numbers to see if we can get the same result. The initial distribution of the particles is Gaussian in both the energy and time plane. After tracking for 5 longitudinal damping times, and calculating the bunch length and energy spread in each damping time, we can see that without wake field the bunch length and energy spread tend to be around 1.35 cm and 5.19×10^{4}, which are almost the natural bunch length and natural energy spread. This shows that the tracking result of this code is not depending on the number of the macro-particles and this code has a good convergence.

Fifty thousand macro-particles are randomly selected to represent the real electron bunch. The initial distributions in both time and energy are Gaussian with the RMS value equal to the natural bunch length and natural energy spread. When there is no wake field in the tracking process, the tracking results show the natural bunch length and natural energy spread just as predicted by the theory of longitudinal motion, and the electron bunch distribution in both time and energy domain will be kept the same as the initial Gaussian distribution. However, after the wake field is added in, the total longitudinal voltage which is experienced by each electron is distorted, and the distribution of the electron bunch will be influenced. The bunch length will be lengthened accompanied with the bunch current increasing, and at the same time the energy spread will not vary. After the bunch current exceeds a threshold which is called the microwave instability threshold, both the bunch length and the energy spread will be increased significantly and the instability will emerge. The phenomenon is explained by several theories, and confirmed by many experimental and numerical results. The tracking results of this code on BEPCII should confirm this point.

As the microwave instability threshold predicted by the Boussard criteria is 36 mA [6] for BEPCII and at the same time the tracking results of Oide's code show that the threshold is 70 mA for BEPCII, we set the single bunch current from 5 mA to 100 mA in our tracking process.

Tracking these fifty thousand macro-particles for 5 longitudinal damping time, and calculate the bunch length and energy spread in each turn to get the new wake potential for the next turn. The result of single bunch lengthening and energy spread versus single bunch current is shown in Figure 2, where black line and red line are the bunch lengthening and energy spread results of this code; green dots and blue dots are the tracking results of Oide's code [6]. It should be pointed out here that in this code the analytical wake potential is used which is denoted by the dark line in Figure. 1, and in the tracking code of Oide's the MAFIA calculated wake potential is used which is denoted by the light line in Figure. 1.

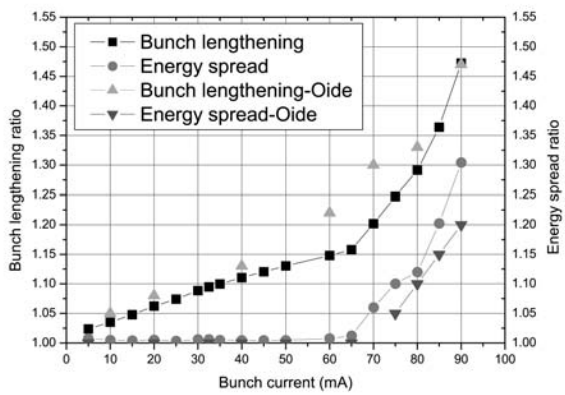

Figure 2: Bunch lengthening and energy spread versus single bunch current.

From Figure 2 we can see that the tracking results of Oide's code show that the microwave instability threshold is 70 mA for BEPCII and the tracking results of this code show that the microwave instability threshold is 65 mA for BEPCII. The little difference of the results is from the difference in wake potential that they used and the computer noise.

The initial and end distribution of the macro-particles at different bunch current are shown in Figure 3, which clearly shows the effect of potential well distortion. The bunch shape is Gaussian at low beam intensities, and it distorts as the beam intensity is increased [8]. One feature of Figure 3 is that the distribution leans forward as the beam intensity increases. This effect comes from the parasitic loss of the beam bunch, and is a consequence of the real (resistive) part of the impedance. As most of the electron storage rings are operated above the transition, the bunch moves forward so that the parasitic energy loss can be compensated by the RF voltage, as shown by the curve of stable phase visa beam current in Figure 4. Another feature of Figure 3 is that the bunch length increases as the beam intensity increases. That is because the bunch shape distortion comes mainly from the imaginary part of the impedance. And the bunch lengthens in Figure 3 is a consequences of the fact that the imaginary part of the impedance seen by the beam is mostly inductive.

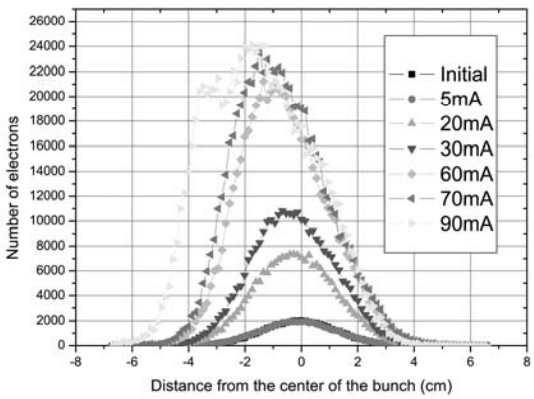

Figure 3: Initial and end distribution of the macro-particles at different bunch current.

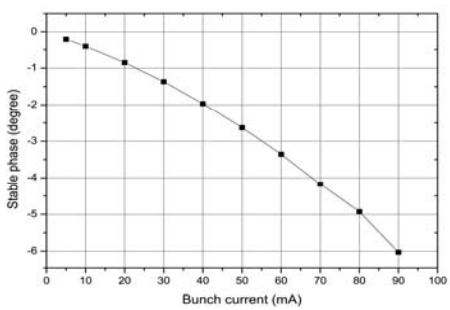

Figure 4: Stable RF phase versus bunch current.

A random electron's phase space is plot for five damping times, which is 80000 turns (For two current case: 5 and 90 mA). The result is shown in Figure 5. From the phase space plot we can see that when the bunch current is higher, the motion of the electrons in the bunch is much more chaotic.

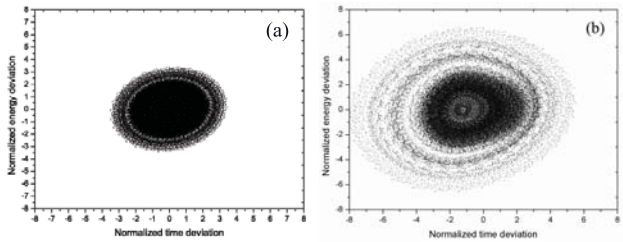

Figure 5: One electron's phase space plot (a): 5 mA case; (b): 90 mA case.

CONCLUSIONS

A new code is developed to simulate the particles' longitudinal phase space motion. First the convergence of this code is checked. The checking result shows that the tracking result of this code is independent on the number of macro-particles. In this code a new expression of the wake potential is used in contrast with the former simulation codes. And simulation results on BEPCII can clearly show the microwave instability threshold and the effect of the potential well distortion, which are in accordance with the other codes' results. Next step we will set up proper longitudinal broadband impedance model for BEPCII and use it in this code to get the new wake potential. The new result will be compared with the result in this paper. And the physical mechanism of the microwave instability and intra-beam scattering should be studied in detail.

REFERENCES

[1] M. Sands, SLAC-121 (1970)
[2] K. Oide and K. Yokoya, KEK-Preprint 10 (1990)
[3] R. Warnock, M. Venturini, and J. Ellison, in Proceedings of EPAC 2002 p. 1589 (2002)
[4] A. Renieri, LNF-76/11(R) Frascati (1976) [5] J. Gao, Nucl. Instrum. Methods, A 491 1-8 (2002)
[6] Institute of High Energy Physics, Design Report of BEPCII (2003)
[7] J. Q. Wang, Private communication (2006)
[8] A. W. Chao, Physics of collective beam instabilities in high energy accelerators (John Willy) (1993)

STUDY ON THE BEPCII LATTICE*

Y. P. Sun#, Key Laboratory of Heavy Ion Physics, Peking University& IHEP, Beijing
J. Gao, IHEP, Beijing; Z. Y. Guo, Key Laboratory of Heavy Ion Physics, Peking University, Beijing

Abstract

BEPCII, the upgrading project of the Beijing Electron-Positron Collider (BEPC), has been designed with a luminosity of 10^{33} cm^{-2}s^{-1} at the τ-charm energy region. According to the beam-beam simulation results, the luminosity of BEPCII with a crossing collision angle of 11 mrad is about 0.50×10^{33} cm^{-2}s^{-1} with the original operation mode at the working point of 6.53/5.58. To increase the operating luminosity of the BEPCII, a low momentum compaction factor (α_P) collision mode has been studied which can increase the luminosity to 0.54×10^{33} cm^{-2}s^{-1}. If the bunch length of the low α_P mode is reduced from 1.5 cm to 1.2 cm, a mode with vertical beta function at IP equal to 1.2 cm could push the luminosity to 0.828×10^{33} cm^{-2}s^{-1} at the working points 6.53/5.56. Also, the BEPCII synchrotron radiation mode is optimized to get a larger dynamic aperture and much more stable tunes.

ON COLLISION LATTICE

BEPCII is an upgrading project of the Beijing Electron-Positron Collider (BEPC), where a new inner ring will be installed inside the old one. The double-ring geometric structure of the BEPCII makes each ring not to be a 4-fold symmetrical structure, though symmetry still exists between the electron and positron rings. Based on several design criteria, a geometric design which satisfies both collision and synchrotron radiation modes requirements is done [1].

From Eq. 1, one can calculate the head-on collison luminosity

$$L(\mathrm{cm^{-2}s^{-1}}) = 2.17\times10^{34}(1+R)\xi_y \frac{E(GeV)k_bI_b(\mathrm{A})}{\beta_y^*(\mathrm{cm})} \quad (1)$$

where $R = \sigma_y^*/\sigma_x^*$ is the beam aspect ratio at the interaction point (IP), ξ_y the vertical beam-beam parameter, E the beam energy, β_y^* the vertical envelope function at IP, k_b the bunch number in each beam and I_b the bunch current.

The beam-beam interaction simulation was carried out with several computer codes, which shows a luminosity reduction in different degrees compared with the designed luminosity. The results from one of the codes show that the luminosity of BEPCII with a crossing collision angle of 11 mrad is about 0.50×10^{33} cm^{-2}s^{-1} with the original operation mode at the working point of 6.53/5.58 [2]. To increase the luminosity of BEPCII, in this paper we will discuss how to adjust the lattice to reach high luminosity. First, the BEPCII lattice is adjusted to reduce the momentum compaction factor α_P while keeping the vertical beta function at 1.5 cm [3]. The corresponding luminosity can be increased to 0.54×10^{33} cm^{-2}s^{-1}. The threshold of microwave instability can be estimated according to the Boussard or the Keil-schnell criteria [4]:

$$I_{th} = \frac{\sqrt{2\pi}\alpha_p \frac{E}{e}\sigma_{e0}{}^2\sigma_{l0}}{R\left|\frac{Z}{n}\right|_{eff}} \quad (2)$$

For low alpha mode, α_P=0.0188, σ_{l0}=1.08 cm, other parameters are the same as in the original mode [1], it can be calculated from Eq. 2 that the threshold of microwave instability will be 34 mA which is much larger than the BEPCII designed single bunch current 9.8 mA.

Secondly, the quadrupoles in the ring are adjusted to give the vertical beta function equaling to 1.2 cm at IP, with the working point kept at 6.53/5.58 [5]. Finally, with the vertical beta function being 1.2 cm at IP, the working point is moved to 6.53/5.56. At the same time, maintaining a low horizontal emittance is very important for gaining a high luminosity.

In the following sections, the matching procedure for the lattice with α_P=0.0188 and β_y^*=1.2cm, the chromaticity correction, and the dynamic aperture tracking results are presented.

As the vertical beta function at IP should be decreased to 1.2 cm, the strength of the quadrupole in the mini-beta insertion should be increased. Here the K1 value of R3OQ1A is kept the same as the original value 1 and the K1 value of R3OQ1B is adjusted from 0.7232 to 0.73. The quadrupoles in region 3 and 4 are adjusted to satisfy other criteria. The quadrupoles in Region 1 and 2 is not changed. In that way the phase advance between kickers and the beta function at the RF cavity are not changed.

The TWISS parameters of the ring are shown in Figure. 1.

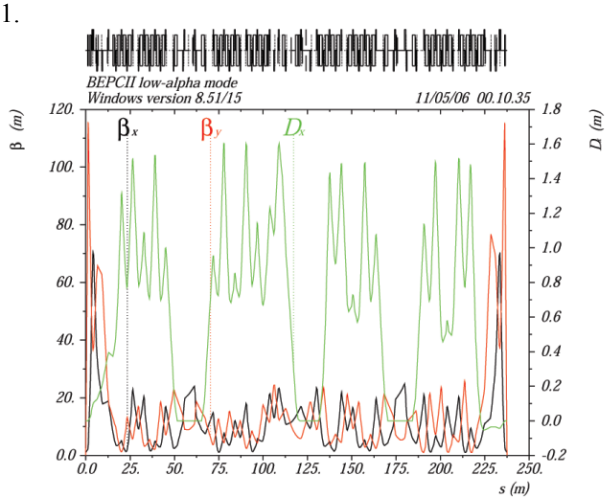

Figure 1: TWISS parameters of the BEPCII high luminosity collision mode

* Supported by the National Natural Science Foundation of China under Grant No 10525525.
# ypsun@ihep.ac.cn

Nine sextupoles in each arc region are used to correct the first order chromaticity from negative values to 1 and the second order chromaticity bigger than 15. The third order chromaticity is also controlled. They are divided into 5 families of defocusing sextupoles (SD) and 4 families of focusing sextupoles (SF). The families of sextuples are set as SD1, SF1, SD2, SF2, SD3, SF3, SD4, SF4, and SD5 from the IP to the injection region in the southern half ring and from the injection region to the RF region in the northern half ring.

The tune variation and beta function variation at IP versus momentum deviation up to ±0.6% are shown in Figure. 2. Tracking for 1024 turns with 10 seeds using SAD [6], the dynamic aperture with all magnets errors is shown in Figure. 3.

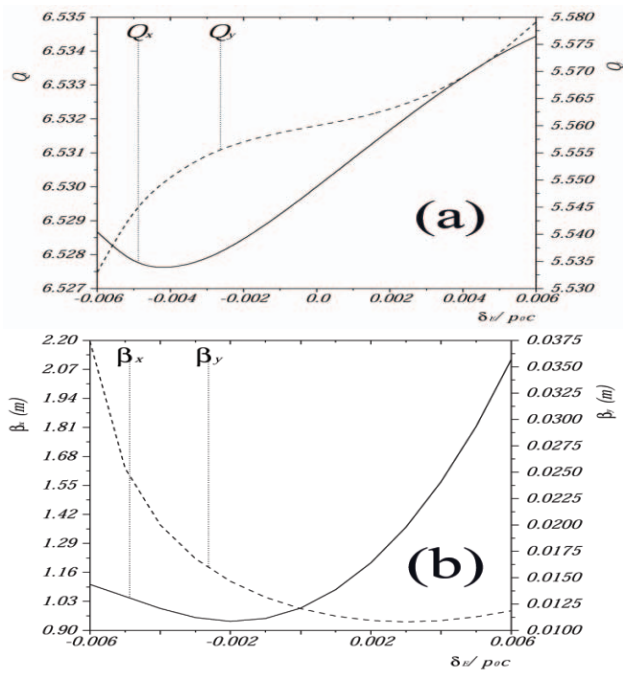

Figure 2: (a) Tunes of the ring vs $\delta p/p$ up to 0.6%; (b) Beta functions at IP vs $\delta p/p$ up to 0.6%.

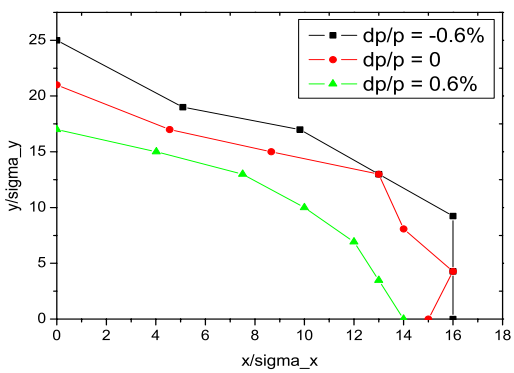

Figure 3: Dynamic aperture calculated using SAD.

ON SYNCHROTRON RADIATION LATTICE

The synchrotron radiation ring is consisted of the two half outer rings of BEPCII. The main parameters of the synchrotron radiation ring are listed as follows: energy 2.5 GeV, circumference 241.13 m, natural chromaticity -8.9/-8.1, tunes 7.28/5.12, horizontal emittance 138 nm.rad, momentum compaction factor 0.015, natural bunch length 0.0117 m, natural energy spread 6.5×10^{-4} [7].

Tracking for 1024 turns using AT (Accelerator Toolbox) [8], the dynamic aperture of BEPCII SR ring is obtained. The results show that the dynamic apertures of off-momentum particles are not good.

Frequency map analysis (FMA) is introduced for the demonstration and understanding of the chaotic behavior of a dynamical system. The application to particle accelerator dynamics is done in the case that the motion of a single particle in a storage ring is described in a surface of section of the beam by a symplectic map of dimension 4 or 6 [9].

Here FMA is performed on the original BEPCII SR lattice, and the results show that the resonance is very severe and the transverse motion is unstable.

Set the horizontal working point in the region (7.2, 7.4) and the vertical working point in the region (5.0, 5.2), the resonance lines up to 6-order are drawn out. From this analysis it can be seen that the working point 7.28/5.12 is on one 5-order resonance line exactly and there are many dangerous sum-resonance lines around this working point. That may be the main reason why the dynamic aperture is not good in this lattice.

For synchrotron radiation use, it is very important to achieve a large dynamic aperture and a stable transverse tune. So the BEPCII SR lattice needs to be optimized to achieve these goals. As the BEPCII SR lattice consists of the two outer half rings of BEPCII lattice and two-fold symmetry exists in the SR lattice, the super periodic structure resonance will be all the integers. So the working point should not be too close to the integer. At the same time the working point should be chosen to be far away from the dangerous resonance lines. Based on these requirements the working point is chosen to be around 7.12/6.3.

In the following sections, we will present the matching procedure for the new lattice, the chromaticity correction, the dynamic aperture tracking results, and the FMA analysis results.

The matching criteria is as follows: (1) The beta functions are less than 30 m and greater than 1 m in the whole ring; (2) The horizontal beta function is greater than 8 m at the position of the injection kickers; (3) The horizontal phase advance is π exactly between the two injection kickers; (4) The vertical beta function in the injection point is greater than 6 m; (5) The beta functions at the RF cavity are less than 15 m; (6) The natural chromaticity should be as small as possible; (7) The

emittance should be as small as possible; (8) Use distributed-dispersion to decrease the emittance.

Following these matching criteria and the requirements for selecting a proper working point, the linear lattice matching [5], chromaticity correction and FMA tracking process are repeated. After optimization the linear lattice is gotten and shown in Figure. 4, where the solid line is the horizontal beta function, the dashed line is the vertical beta function, and the dotted line is the horizontal dispersion function. The main parameters of the new lattice are listed as follows: energy 2.5 GeV, circumference 241.13 m, natural chromaticity -9.0/-8.2, tunes 7.12/6.3, horizontal emittance 145 nm.rad, momentum compaction factor 0.015, natural bunch length 0.0119 m, natural energy spread 6.4×10^{-4}.

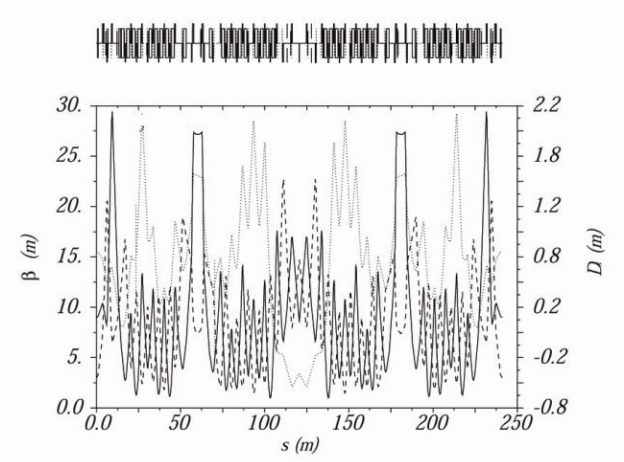

Figure 4: TWISS parameters of the BEPCII synchrotron radiation mode after optimization.

Nine sextupoles in each arc region are used to correct the first order chromaticity from negative values to 1. The second and third order chromaticity is also controlled. These sextupoles are divided into 3 families of defocusing sextupoles (SD) and 2 families of focusing sextupoles (SF). The families of sextuples are set as SD1, SF1, SD2, SF2, SD3, SF2, SD2, SF1, and SD1 from the IP (Interaction Point) to the injection region in the southern half ring and from the injection region to the RF (Radio Frequency) region in the northern half ring.

The tune variation and the beta function variation at IP versus momentum deviation up to 1% are less than 20%. Tracking for 1024 turns using AT [8], the dynamic aperture of the optimized BEPCII SR lattice is obtained. The optimized dynamic apertures of both on-momentum and off-momentum particles are good and they are about 15% to 20% larger in comparison with the original values.

As the nonlinear wiggler effect is not included in the tracking process, we use analytical method to calculate the dynamic aperture of the SR lattice with ideal nonlinear wigglers [10]. The results show that for both on-momentum and off-momentum particles, the dynamic apertures only decrease less than 20% after nonlinear wiggler effect is added in.

Here FMA is performed on this lattice where 2500 on-momentum particles are tracked for 2000 turns, and the result is shown in Figure 5. In this optimized lattice the resonance is not so severe and the transverse tunes are much more stable.

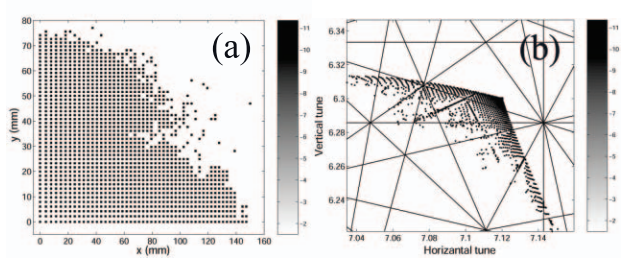

Figure 5: (a): DA with FMA; (b): Footprint on tune space

CONCLUSIONS

A low α_P low β_y^* collision mode for BEPCII has been developed. The aim is to increase the luminosity by reducing the vertical beta function at IP from 1.5 cm to 1.2 cm and to move the working point to high luminosity region. The dynamic aperture is acceptable for collision but still a little small for injection. So the BEPCII ring can be tuned to these modes after the beam has been injected into the ring. For the natural bunch length of 1.08 cm and the vertical beta function of 1.2 cm, the highest luminosity reached is $0.828\times10^{33}cm^{-2}s^{-1}$ at the working point 6.53/5.56 with the assumption that the bunch length can reach 1.2 cm. Higher luminosity possibility is under study. First frequency map analysis (FMA) is performed on the original BEPCII SR lattice. The result shows that the resonance is really severe in that lattice and the transverse motion of the particles is unstable. Then a new SR lattice is designed to get a large dynamic aperture and much more stable transverse motion. The dynamic aperture of the new lattice including nonlinear wiggler effect is calculated to be very good. This new SR lattice can be used in the commissioning stage of BEPCII.

REFERENCES

[1] Design Report of BEPCII (Accelerator Part), unpublished (2003)
[2] G. Xu, Report on IMAC 06 (2006)
[3] Y. P. Sun and J. Gao, HEP&NP S1 (2006)
[4] D. Boussard, CERN Lab II/RF/Int. 75-2, 1975.
[5] H. Grote, and C. Iselin, The MAD Program, CERN/SL/90-13 (AP)
[6] http://acc-physics.kek.jp/SAD/example/
[7] L. M. Chen, BEPC 8th Annual Report p 81 (2003)
[8] A. Terebilo, SLAC-PUB 8732 (2001)
[9] S. Dumas, J. Laskar, Phys. Rev. Lett. 70, 2975 (1993)
[10] J. Gao, Nucl. Instr. And Methods, A 451 545 (2000)

STATUS OF THE VEPP-4M ELECTRON-POSITRON COLLIDER

V. Petrov for the VEPP-4 team
Budker Institute of Nuclear Physics, Novosibirsk, Russia

Abstract

The VEPP-4M electron-positron collider is now operating for high-energy physics experiments in the 1.5-2.0 GeV energy range. The most important of them is precise measurement of the tau-lepton mass at the producing threshold. During all the high-energy physics experiments, absolute calibrations of beam energy by the resonant depolarization method and routine energy monitoring using the Compton back-scattering technique were realized. Monitoring of beam energy spread, which is also important, was implemented using several techniques. To provide the VEPP-4M high performance, some investigation and further development of the machine have been done, the most important results are described.

HIGH-ENERGY PHYSICS EXPERIMENTS

Since 2004, the VEPP-4M electron-positron collider [1] is operating for high-energy physics experiments in the 1.5-2.0 GeV energy range. The most important of them is precise measurement of the τ-lepton mass at the producing threshold. The τ-lepton mass together with the lifetime and the decay probability to $e\bar{\nu}_e\nu_\tau$ can be used to test the $\mu-\tau-$universality principle which is one of the postulates of the Standard Model, the most complete theory describing fundamental properties of matter and elementary particles.

Current situation in the world is as follows: the CLEO-c detector is now operating at the CESR collider with the luminosity of $6 \cdot 10^{31}$ cm^{-2}s^{-1}; the BES experiment is completed not long ago at the BEPC collider with the luminosity of $5 \cdot 10^{30}$ cm^{-2}s^{-1}, new BES-III detector and c-τ factory with the luminosity of 10^{33} cm^{-2}s^{-1} are now under construction.

In the 1.5-2.0 GeV energy range, peak luminosity of the VEPP-4M collider is $2 \cdot 10^{30}$ cm^{-2}s^{-1}. In spite of considerably lower luminosity, the VEPP-4M - KEDR facility have some advantages, the most principal of them are:

- wide energy range of 1.0 - 5.5 GeV in a beam;
- beam energy measurement with record high accuracy of 10^{-6} (2 keV) provided by the resonant depolarization method [2];
- routine monitoring of beam mean energy with the $5 \cdot 10^{-5}$ (100 keV) accuracy and beam energy spread with the 10% accuracy, using the Compton back-scattering method [3];

Fine adjustment of all the facilities included in the VEPP-4 accelerating-storage complex, in parallel with improving of the machine reliability, result in gradual increase of average luminosity, as it is shown in Figure 1. Total luminosity integral collected during the 2004-2006 τ-lepton experiment is about 10 pb^{-1}. Preliminary results of the τ-lepton mass measurement at the VEPP-4 have been reported at the International Conference of High Energy Physics (ICHEP-2006) and international Tau-lepton Workshop (TAU-2006). Accuracy of this τ-lepton mass measurement is the best is the world and exceeds the accuracy reached at the BES and BELLE detectors, as it is shown in Table 1.

Table 1: τ-lepton mass measurements

PDG 2006	$1776.90^{+0.29}_{-0.26}$ MeV
BES 1996	$1776.96^{+0.18}_{-0.21}\ ^{+0.25}_{-0.17}\ (^{+0.31}_{-0.27})$ MeV
BELLE 2006	$1776.77 \pm 0.13 \pm 0.32(\pm 0.35)$ MeV
KEDR 2006	$1776.80^{+0.25}_{-0.23} \pm 0.15\ (^{+0.29}_{-0.27})$ MeV

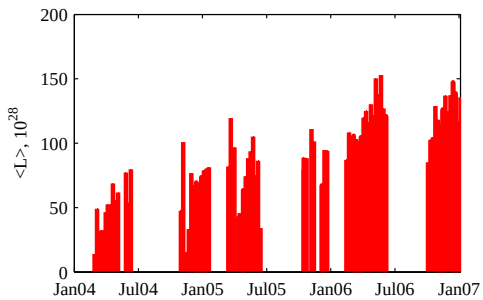

Figure 1: Average luminosity in 2004-2006.

Along with the τ-lepton mass measurement, a series of experiments to improve measurement accuracy of the J/ψ, ψ(2s) and ψ(3770) mesons has been also performed. Measurement accuracy reached in these experiments is 2 times better than the world average value for ψ(2s), and 3 times better for ψ(3770). There are only 5 particle masses (e, p, n, μ, π) measured with better accuracy. Precise measurements of the J/ψ and ψ(2s) meson masses provide the energy scale in the range around 3 GeV which is a basis for accurate determination of masses for all charmed particles. These measurements are also important for the accurate determination of the τ-lepton mass.

For the τ-lepton mass measurement, a procedure of regular particle energy calibration is essential. Absolute energy calibration is realized by the resonant depolarization method, between data collection runs of the KEDR detector. During the runs, routine energy monitoring is carried

out using the Compton back-scattering technique. Energy behavior between the measurements is interpolated using the magnets field measured by a NMR magnetometer, temperature of magnets, tunnel walls, etc. An example of the VEPP-4M measured energy behavior during three successive data collection runs is presented in Figure 2.

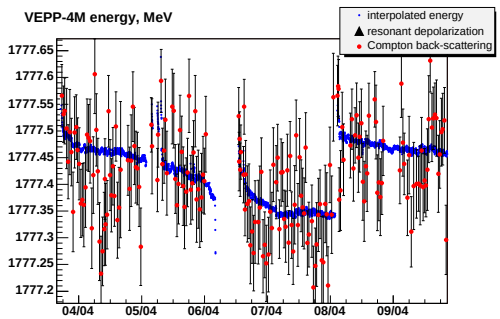

Figure 2: Beam energy monitoring.

ENERGY SPREAD MEASUREMENT

In the experiment of the τ-lepton mass measurement, it is important to know beam energy spread for evaluation of its contribution into the total systematic error of the τ-lepton mass. Routine energy spread monitoring during high-energy physics experimental runs is provided by the Compton back-scattering method, but accuracy of the method now is not better than 15-20%. The energy spread is measured more accurately by scan of the ψ(2s) meson peak, but this procedure is time-consuming and can not be repeated frequently.

Several methods of energy spread measurement are realized at the VEPP-4M [4]. Two methods are based on analysis of chromatic synchro-betatron harmonics of coherent betatron oscillation excited by a short kick. For non-synchronous particles, machine chromaticity introduces a betatron frequency shift. This effect causes beating in the oscillation envelope and synchrotron sideband peaks in the oscillation spectrum. In the first method, the amplitude ratio of synchrotron satellites to the main betatron peak is measured in dependence of chromaticity. Fitting this ratio dependence with the theoretical one gives the energy spread value. In the second method, energy spread is calculated by fitting the measured oscillation envelope with the theoretical curve.

Energy spread was measured using both methods for a set of the VEPP-4M operation modes with different energy and energy spread values. The measurements were done with the small beam current of $10\div50$ μA, when collective effects are negligible. Chromaticity was changed with sextupole magnets and evaluated from the measured betatron tune dependence of the RF frequency. Turn-by-turn beam position was measured using fast photomultiplier tube. Figure 3 shows an example of measured data with the theoretical envelope (upper plot), and its amplitude spectrum with the noticeable synchro-betatron peaks up to 3-rd order (lower plot).

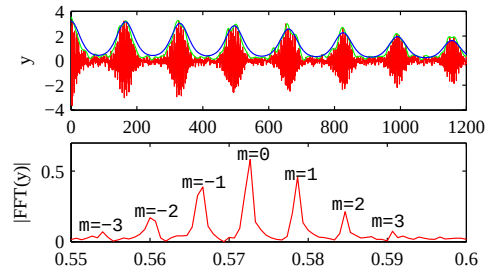

Figure 3: Synchro-betatron oscillation, $\xi_y = 18$.

High-energy physics experiments were performed with the beam current close to beam-beam effects limit of $1.5\div3.5$ mA per bunch, depending on the beam energy. Current dependence of the energy spread was evaluated using measured bunch lengthening and grows of the horizontal bunch size.

Energy spread measurements performed by all three methods conform to results of the J/ψ scan at the 1548 ± 10 MeV energy performed in 2002. There is also a good agreement of these measurements with the 2005-2006 ψ(2s) scan at the 1843 ± 10 MeV energy.

TEMPERATURE MEASUREMENT AND STABILIZATION

Temperature Monitoring System

Specific character of the high-energy physics experiments realized at the VEPP-4M is the high-precision beam energy evaluation required. To a first approximation, beam energy is proportional to the dipole magnetic field integral. On-line monitoring of the magnetic field with 10^{-6} accuracy is realized by nuclear magnetic resonance (NMR) method. But the beam energy also depends on thermal expansion of the magnets and tunnel. For accurate estimation of the beam energy between resonance depolarization calibrations, it became necessary to measure precisely temperature in a lot of locations of the VEPP-4M facility. For this goal, a new system of temperature monitoring is developed [5]. This system is based on High-Precision Digital Thermometers DS1631 with the resolution of $0.0625°$C and absolute accuracy of $0.5°$C in the $0\div70°$C temperature range.

To control the DS1631 sensors and to transfer measured data to the VEPP-4M control system, 32-channel controller was developed in BINP. The controller inquires all the connected sensors every second and writes data to the internal memory. To read/write, store and visualize data of all the controllers installed at the VEPP-4M, a special program runs in a computer included in the VEPP-4M control system. Relay interlock function to prevent overheat is also implemented to the controller, up to 12 solid-state relays can be used in one controller. The control program reads

from and writes to each controller specifications for the relay contact closure then the controller closes relay contacts automatically, if the temperature is out of the specified range.

Thermostabilization of the Magnets

During the high-energy physics experiments, there is not only a demand for high absolute definition of the energy but also for its high stability (better than 10^{-5}). Continuous temperature monitoring shows considerable diurnal and seasonal variations of the VEPP-4M magnets temperature, which cause beam energy variation up to 80 keV/°C. For the VEPP-4M magnets, a double-loop water cooling system is used. The magnets are cooled by circulating distillate which is cooled by service water in a heat exchanger. Temperature of the service water depends on many external factors such as ambient temperature, atmospheric humidity, cooling condition in a cooling tower, etc. All these uncontrollable factors result in quite big diurnal and seasonal variations of the service water temperature.

To stabilize temperature of the VEPP-4M magnets, a system of distillate thermostabilization has been developed. A computer-controlled valve was installed at the service water input of the heat exchanger. Temperature of the distillate and service water is measured permanently by high-precision thermal sensors installed on the heat exchanger input and output. A control program analyzes the data measured and regulates the service water flow and therefore heat-transfer rate. Figure 4 illustrates efficiency of

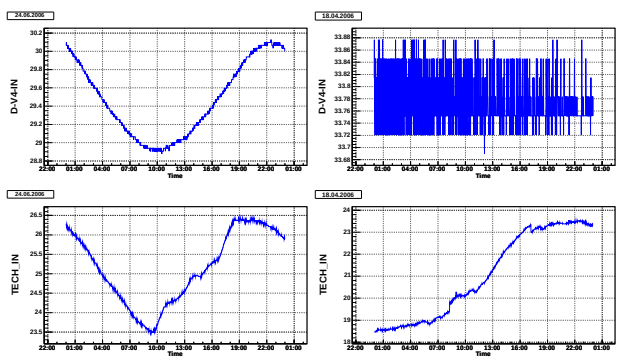

Figure 4: Magnets' distillate thermostabilization.

the system. There are results of one day monitoring of the distillate (upper plots) and the service water (lower plots) temperature. The left pair of plots corresponds to the thermostabilization off, the right one corresponds to the thermostabilization on. One can see that without thermostabilization 3-degree variation of the service water temperature leads to 1.2-degree variation of the distillate temperature, whereas thermostabilization system keeps the distillate temperature stable within 0.1 degree while the service water temperature has 5-degree variation.

Thermostabilization of the RF-cavities

Since 2004, the VEPP-4M collider operates in the $2 \times 2-$bunch mode. It allows us to increase the luminosity, but a problem of longitudinal instability appears. Unstable phase oscillation occurs due to parasitic high-order modes (HOM) of the VEPP-4M RF cavities. This instability is one of the main efficiency decreasing factors, because it reduces luminosity drastically. High-amplitude phase oscillation leads to particle loss and can be dangerous for the KEDR detector.

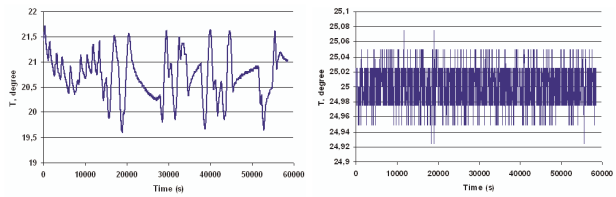

Figure 5: RF-cavities thermostabilization.

Each of 5 RF cavities is equipped by three mechanical remote-controlled HOM suppressors. Fine tuning of these suppressors allows us to find stability regions of longitudinal beam motion. But the cavity temperature variation results in the cavity deformation and then leads to a shift of working conditions away from the stability regions. To stabilize the RF cavity temperature, automatic heaters of cooling water have been developed [6]. Temperature is measured by thermo-sensors with a sensitivity of 10 mV/°C. For each RF cavity, 5 kW flowing water heater is switched on/off by controllable electronic switches. Temperature analysis and power control is provided by a microcontroller.

Using of the thermostabilization system, temperature variation of the RF cavities have been reduced from 5°C down to 0.2°C (see Figure 5). As a consequence, probability of excitation of the phase oscillations has been reduced more than in 100 times.

REFERENCES

[1] http://v4.inp.nsk.su/

[2] V.E.Blinov et al., *Absolute Calibration of Particle Energy at VEPP-4M*, NIM A 494 (2002) 81-85

[3] N.Yu.Muchnoi et al., *Fast and Precise Beam Energy Monitor Based on the Compton Backscattering at the VEPP-4M Collider*, Proc. of EPAC 2006, Edinburgh, 2006

[4] V.A.Kiselev et al., *Beam Energy Spread Measurement at the VEPP-4M Electron-Positron Collider*, Proc. of RuPAC 2006, Novosibirsk, 2006

[5] V.Kaplin, S.Karnaev, I.Morozov, O.Plotnikova, *The Precise Temperature Measurement System of the VEPP-4M Electron-positron Collider*, Proc. of RuPAC 2006, Novosibirsk, 2006

[6] E.G.Miginskaya, I.I.Morozov, V.M.Tsukanov, A.A.Volkov, *Temperature Stabilization of RF-cavities of the VEPP-4M Electron-Positron Facility*, Proc. of RuPAC 2006, Novosibirsk, 2006

MEASUREMENT OF BREMSSTRAHLUNG DEPENDENT ON STORED BEAM CURRENT

Y. Yamamoto

Ritsumeikan University SR Center, Kusatsu, Shiga, Japan

Abstract

Bremsstrahlung was measured as a function of stored beam current using the BGO scintillation spectrometer at the compact superconducting storage ring of Ritsumeikan University. Bremsstrahlung is emitted for collision of stored electrons and residual gas on the beam orbit. Yield of bremsstrahlung depend on stored beam current and residual gas density. We tried to determine gas density on the beam orbit by present measurement.

INTRODUCTION

The compact electron storage ring AURORA, manufactured by Sumitomo Heavy Industries [1], was installed at Ritsumeikan University in 1996 and has been operated successfully since then [2]. It is of the weak focusing type with the simplest lattice composed of a single body superconducting magnet, which produces an axially symmetric strong magnetic field to achieve compactness. The normal operating magnetic field is 3.8 T and the field index is 0.36 at ring energy of 575 MeV. The initial stored beam current is 300 mA in the orbit of 0.5 m in the radius. Table 1 lists the parameters of the injector and the ring. Figure 1 shows the storage ring and beamlines in the experimental hall.

The residual gas density on the beam orbit is very important parameter for storage rings. The pressure in the vacuum chambers is measured by using the vacuum gauge; the base pressure in the vacuum chamber of our storage ring is 1×10^{-8} Pa. On the other hand, the measurement of the pressure on the beam orbit in operation is difficult, because electron beam collide with the vacuum gauge.

We tried to measure bremsstrahlung which was emitted for collision of stored electrons and residual gas on the beam orbit. Yield of bremsstrahlung suggest the density of residual gas.

EXPERIMENTAL SETUP

The maximum energy of bremsstrahlung is 575 MeV to agree with the energy of the stored electron beam. Normal γ-ray survey meters can't measure such high energy bremsstrahlung. We employed BGO (bismuth germanate) scintillation spectrometer (CANBERRA) that could measure ~50 MeV X-ray. Measurement system which was composed by the detector, multichannel analyzer (ASA-100 CANBERRA) and PC was constructed behind the beam extraction port BL-16 at the atmosphere.

Partial pressure in the vacuum chamber was measured by the partial pressure vacuum gauge (M-066QG, ANELVA) and electron beam size was measured by the SR interferometer [3] and the conventional profile monitor. Figure 2 shows schematically the structure of measurement system.

Table 1: Parameters of the injector and storage ring

Injector parameters	
Energy	150 MeV
Repetition	10 Hz
Peak current	1 mA
Pulse width	2 μs

Storage ring parameters	
Energy	575 MeV
Stored current	300 mA
Circumference	3.14 m
Radius of curvature	0.5 m
Field strength	3.8 T
RF frequency	190.86 MHz
Number of cavities	1
Harmonic number	2
Critical energy of radiation	844 eV
Vertical beam size(σ)	0.14 mm
Horizontal beam size(σ)	1.2 mm
Beam lifetime	300 min

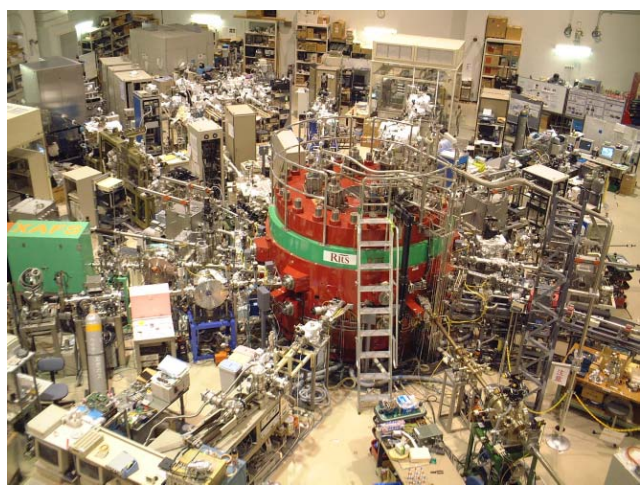

Figure 1: Photograph showing the storage ring and beamlines in the experimental hall.

y-yama@st.ritsumei.ac.jp

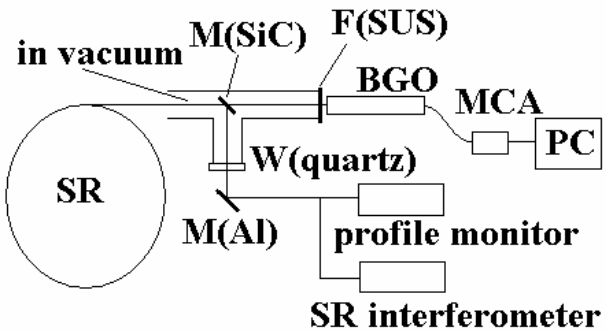

Figure 2: Structure of the bremsstrahlung measurement system at BL-16. M(SiC): silicon carbide mirror in vacuum; M(Al): aluminium mirror in atmosphere; W(quartz): quartz view window; F(SUS): SUS blank flange.

RESULTS AND DISCUSSION

Dependence on the beam current

Figure 3 shows the energy spectrum of bremsstrahlung for beam energy of 575 MeV and beam current of 200mA. Intensity of γ-ray from capture of neutron is negligible low. Normalized integral counts of bremsstrahlung with the photon energy of 3-30 MeV were plotted with open diamonds as a function of the beam current in figure 3. Partial pressures except for hydrogen were less than 1% and vertical beam sizes were about 11μm for each measurements of bremsstrahlung.

Counts of bremsstrahlung (Y_{brem}) are given by

$$Y_{brem} = \sigma_{brem} \cdot I \cdot \rho \quad (1)$$

where σ_{brem} is bremsstrahlung cross section [4], I is beam current and ρ is density of gas on the beam orbit. Plotted points in fig. 4 give ρ depended on the beam current because the vertical axis mean ρ from next equation.

$$Y_{brem} / I \propto \rho(I) \quad (2)$$

Assuming that $\rho(I)$ was given by equation (3), we tried to fit $\rho(I)$.

$$\rho(I) = \rho_o \cdot I^{1-\Delta} + \rho_b \quad (3)$$

Where $\rho_o \cdot I^{1-\Delta}$ is density of gas induced by synchrotron radiation and ρ_b is gas density given by base vacuum in chamber. Gas density $\rho(I)$ is not linear for beam current I, Δ is ~0.2 in beat fit (curve in fig. 4). This physical meaning is not yet clear at the moment.

According to obtained best fitting, density of gas at beam current of 300 mA in normal operation is about 100 times as large as in no operation. The base pressure in no operation in the vacuum chamber is 1×10^{-8} Pa. Hence, pressure on beam orbit is $\sim 1\times10^{-6}$ Pa in normal operation. We reported for the lifetime of gas scattering in the previous paper [5]. The pressure to calculate from this gas scattering lifetime is $\sim 2\times10^{-6}$ Pa.

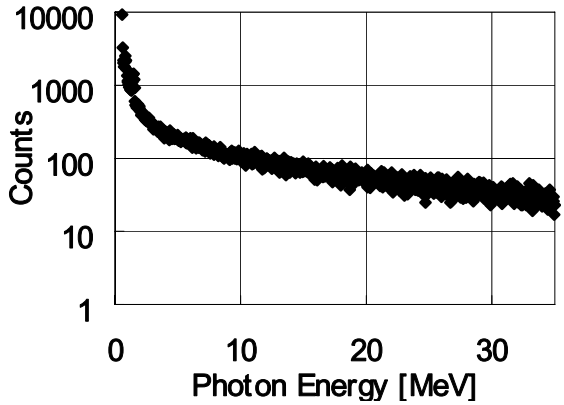

Figure 3: Observed bremsstrahlung spectrum by BGO scintillation spectrometer at the BL-16. Stored electron beam energy is 575 MeV and beam current is 200 mA.

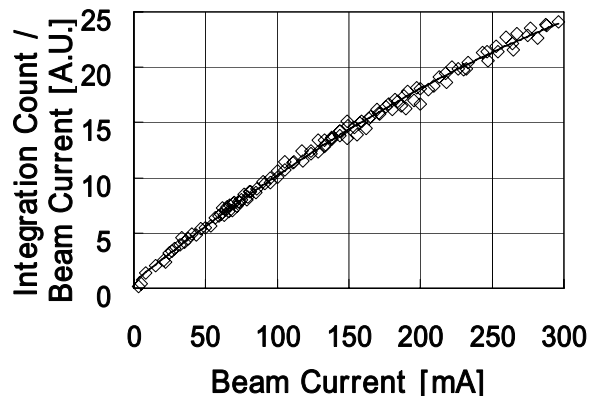

Figure 4: Yield of bremsstrahlung as a function of the beam current. Open diamonds are normalized integral counts of bremsstrahlung with the energy of 3-30 MeV. Solid curve is fitting result.

Dependence on the vertical beam size

We measured bremsstrahlung for various vertical beam sizes at low beam current. The beam size was controlled by RF-KO. Figure 5 shows counts of bremsstrahlung as a function of the vertical beam sizes.

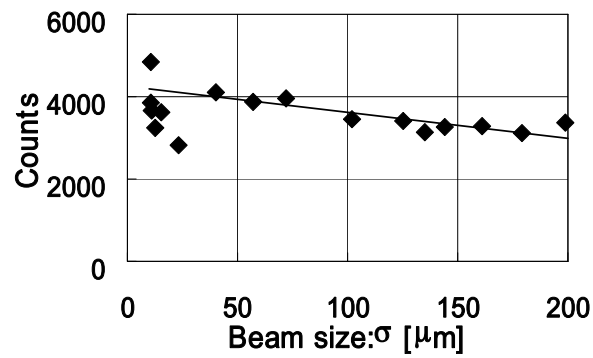

Figure 5: Yield of bremsstrahlung as a function of the vertical beam size. Beam current is about 60 mA. Solid line is linear approximation.

The vertical divergences of electron beam depend on the vertical beam size. This effect is negligible low in our measurements. The divergence for the biggest beam size (~200 μm) in our measurement is less than 1 mrad. The diameter of BGO scintillation detector is 50 mm. This detector was set at a length of about 3 m from light emitting point.

Counts of bremsstrahlung depend on the vertical beam sizes weakly according to figure 5. It is cause of this dependence that ions crowd on the electron beam orbit because of ion-trapping effect. The distribution of trapped ions and residual gas is broader than distribution of electrons in bunches, because the density of electrons in bunches is linear for the vertical beam size and horizontal beam size is constant. The dependence for vertical beam size is not simple. Significant dip is in beam size of 20 μm in fig. 5.

ACKNOWLEDGEMENTS

We would like to thank Mr. M. Inoue, Mr. S. Okada, Mr. N. Kurosawa and Mr. T. Yoshino for their aid in data collection.

REFERENCES

[1] N. Takahashi, Nucl. Instrum. Methods Phys. Res. A **24/25**, 425 (1987).
[2] H. Iwasaki, Y. Nakayama, K. Ozutsumi, Y. Yamamoto, Y. Tokunaga, H. Saisho, T. Matsubara, and S. Ikeda, J. Synchrotron Radiation **5**, 1162 (1998).
[3] Y. Yamamoto, I. Sakai, T. Mitsuhashi, D. Amano and H. Iwasaki, Nucl. Instrum. Methods Phys. Res. A **467-468**, 921 (2001).
[4] H. W. Koch and J. W. Motz, Reviews of Modern Physics, **31** (1959) 920
[5] I. Sakai, Y. Yamamoto, T. Mitsuhashi, D. Amano and H. Iwasaki, Nucl. Instrum. Methods Phys. Res. A **480**, 373 (2002).

STATE OF THE SLS MULTI BUNCH FEEDBACKS

M.Dehler[#], G. Marinkovic, R.Kramert, P.Pollet, T.Schilcher,
Paul Scherrer Institut, CH-5232 Villigen PSI, Switzerland

Abstract

In order to control coupled bunch oscillations in the SLS storage ring, feedback systems for all three planes were foreseen, which are realized as fully digital bunch by bunch systems. With the development of dedicated ADC and DAC boards, the feedbacks could be commissioned. Important parts of the computations for the transverse planes were implemented into the FPGA, making the DSPs originally planned to be used obsolete and allowing for an extremely low latency time of 300 ns. The systems give a larger freedom of choice for the beam optics and also lead to a better closure of the injection bump during top up mode. At present, systems for all planes have been commissioned and are in routine service.

INTRODUCTION

The Swiss Light Source (SLS) is a 2.4 GeV synchrotron light source at the Paul Scherrer Institut. As in other high current electron rings, coupled bunch instabilities can show up due to either resistive wakes and residual ions in the transverse case or due to higher order modes in the longitudinal plane.

Until now, transverse stability was obtained by a high chromaticity beam optics and by an inhomogeneous fill pattern in the ring. An additional contribution toward stable operation was obtained via Landau damping of a superconducting third harmonic cavity[1]. In order to have a higher flexibility in beam optics and a better performance in the longitudinal case, bunch by bunch feedback systems have been developed over the past years and commissioned in 2006. First, a technical overview of the systems is given, before preliminary results in operation are shown.

FEEDBACK SYSTEMS

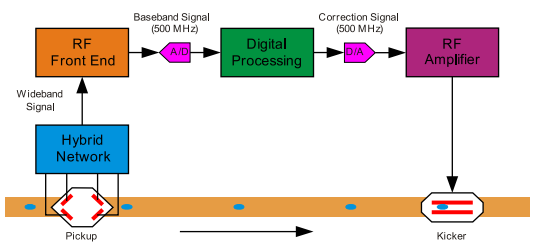

Figure 1: Functional blocks of a transverse bunch by bunch feedback system

[#]e-mail: Micha.Dehler@psi.ch

Energy	2.4 GeV
RF frequency	499.65 MHz
Harmonic number	480
Transverse	
Tunes β_x, β_y	0.43/0.73
Damping time	9.0 msec
Kicker shunt impedance	14.5/20.0 kΩ
Installed amplifier power	500 W
Filter	IIR/8 tap FIR
Longitudinal	
Synchrotron tune ν_s	$1.9 \cdot 10^{-3} - 4.8 \cdot 10^{-3}$
Damping time	15.0 msec
Kicker shunt impedance	1.5 kΩ
Installed amplifier power	250 W
Filter	IIR/16 tap FIR

Table 1: System parameters

The functional blocks of the system are shown in Figure 1. The feedback is a wide band system able to correct the positions of individual bunches, spaced 2 ns apart. Signals coming from button type pickups pass a passive hybrid network, where sum signals used for the longitudinal plane respectively difference signals for the transverse system are generated. The signals are fed into an RF front end [2] from Instrumentation Technologies mixing down the transverse signals and running a phase detection on the sum to obtain the longitudinal position. A digital system running at around 500 MS/s, consisting of an ADC, the digital filter and DAC creates the analog correction signal. Transversally, the signals are fed to the beam directly via broad band power amplifiers and strip line kickers. For the longitudinal plane, a single side band modulator mixes the signals up into the 1.25-1.5 GHz range, where they are amplified and fed to a longitudinal kicker. The analog parts have already been described in [3] and [4], hence we will concentrate on the description of the digital part.

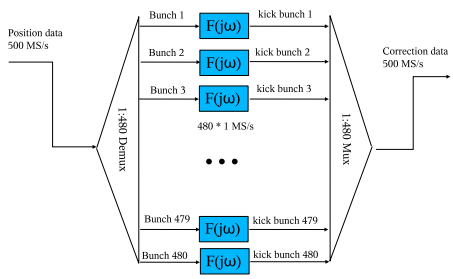

Figure 2: Data flux in the digital filter

Originally it was planned to do the calculation of the correction kicks with the help of digital signal processors [3]. But at the time of development of the new ADC and DAC firmware (basic description in [5]), it turned out, that the FPGA was able to manage the data flux with enough processing reserves to integrate the digital filter algorithm.

As the name bunch by bunch feedback implies, the incoming position data is demultiplexed into 480 (the number of bunches in the SLS storage ring) data streams,each at approximately 1 MS/s and each containing the positions of one individual bunch. These get processed by dedicated filters and all streams multiplexed into a 500 MS/s signal suitable for reconversion into the analog domain by the DAC.

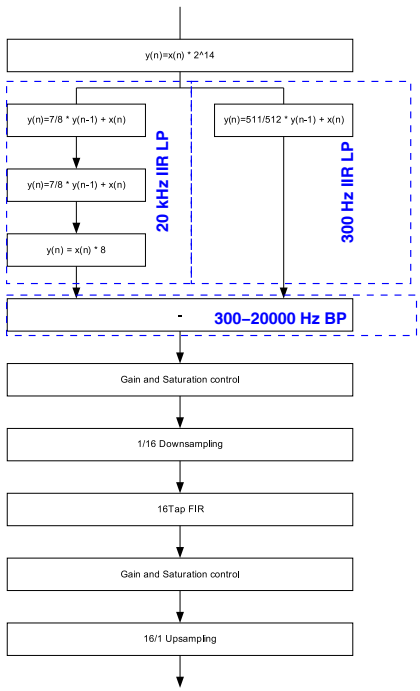

Figure 3: Longitudinal feedback filter setup for individual bunches

Figure 3 shows the processing of the individual bunch data in the longitudinal plane. After normalizing the data, the stream is split and sent into two IIR low pass filters. Subtracting both gives a band pass limited signal from 300-20000 Hz (Fig. 4), where the common mode as well as high frequency perturbations coming from the betatron tunes have been suppressed. Only the synchronous frequencies between 2 and 5 kHz will pass with negligible amplitude and phase variations. Apart from suppressing unwanted signal components, the big advantage of this approach is the additional averaging due to the reduced bandwidth. With a nominal data width of 8 bits coming from the ADC, we observed an effective resolution of 13 bits in laboratory measurements.

After a gain adjustment to minimize rounding errors in the following stages, the data stream is down-sampled by a factor 16 and then sent through a configurable FIR filter with 16 taps. A second gain adjustment and a 16:1 up-

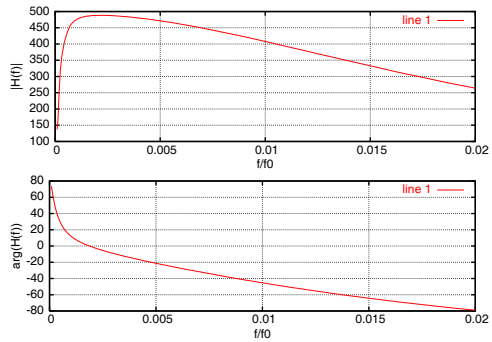

Figure 4: Characteristics of introductory IIR filter used in the longitudinal feedback

sampling stage complete the data processing.

For the transverse signals the processing is similar with the following differences. The preprocessing consists of a IIR high pass cutting the common mode as well as low frequency signals up to 20 kHz. Down- and up-sampling stages have been eliminated and the user defined FIR filter has eight taps.

COMMISSIONING RESULTS

Longitudinal

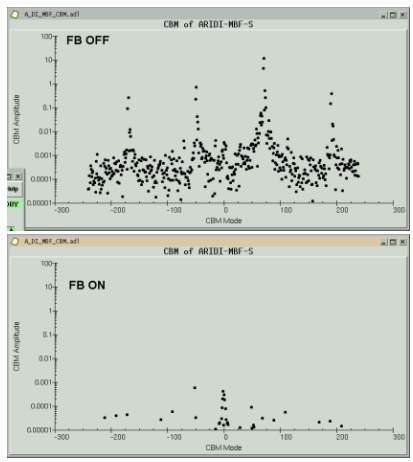

Figure 5: Screen shots of longitudinal CBM spectra without (upper) and with feedback (lower)

The presence of the third harmonic cavity (3HC) in the SLS storage ring [1] poses a special challenge in setting up a bunch by bunch feedback. As the ring is filled, more voltage gets induced in the 3HC with increasing beam current and the synchrotron tune goes from 4.5 kHz down to approximately 2 kHz. Whereas this could be compensated for by simultaneously adjusting the filter coefficients of the feedback, there is also a second effect. As we get to the onset of an instability, the longitudinal oscillation changes the beam spectrum so, that less voltage gets induced into the 3HC. The stabilization effect by the cavity goes down, the

instability gets stronger, we get even less voltage etc. until we end up with a wildly oscillating beam and a strongly increased synchrotron tune.

Optimizing the digital filter settings just for the synchrotron tune of the stable beam becomes counterproductive. As the instability shows up, the tune moves off the optimized value. Capturing an instable beam may be impossible, since the synchrotron tune is far off and the feedback rather inefficient. At present, we are working with rather wide band filters to cope with these effects, but development work is still going on.

Screen shots of the longitudinal coupled bunch mode spectra are shown in Figure 5. In the spectrum without feedback one sees clearly the big modes induced by higher order modes in the main RF cavities. With running feedback, these are reduced by several orders of magnitude and no more visible to the beam line users.

Transverse

Depending on the actual pressure profile in the vacuum system, which can change due to new vacuum chambers being built into the storage ring, we may see coupled bunch modes in both planes due to ion instabilities. Resistive wall instabilities are presently suppressed by employing an increased chromaticity.

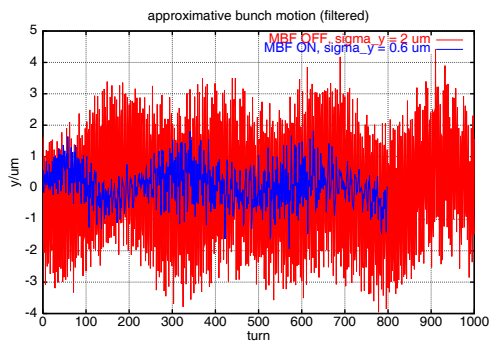

Figure 6: Vertical bunch motion at nominal chromaticity with and without feedback

Having the chromaticity reduced to the nominal value, the beam starts to oscillate as shown in Figure 6. The rms amplitude of 2 μm is to be compared with the vertical beam size of 10 μm and is already visible for the beam lines. Switching on the feedback reduces this to a value of 0.6 μm, which is already at the resolution limit of the system.

The feedbacks actually act on all beam jitters and reduce the damping time needed until the beam reaches its equilibrium. An important source is jitter introduced by the injection kickers. Whereas the horizontal jitter has been mostly eliminated by careful tuning of the kicker strength, one still sees a vertical kick. The vertical kick and subsequent oscillation is seen by the beam lines as an enlarged beam with a corresponding reduced photon flux density. Figure 7 shows the vertical beam size as measured via a synchrotron radiation monitor versus the time after injection. Without feedback the beam increases from an equilibrium size of 14 μm to a value of 35 μm. 15 milliseconds are required for the beam size to come back. With running feedback, the beam size only increases to 23 μm and needs only 10 milliseconds to damp down. Since the beam lines are working with longer shutter times, the drop in photon flux is no more visible. Gating the experimental data acquisition during injection is no more necessary.

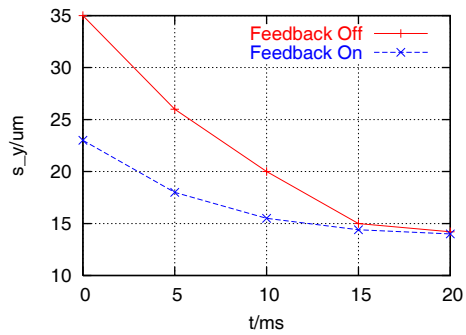

Figure 7: Vertical beam size as seen by synchrotron radiation monitor versus time after injection (Camera shutter time 250 μs/turns, beam current 190 mA

As mentioned, the effects are much less pronounced horizontally. At injection, we see beam sizes of 58.5 μm (feedback off) versus 58.1 μm (feedback on) compared to an equilibrium value of 57.5 μm.

SUMMARY

For the control of coupled bunch instabilities at the SLS storage ring, feedback systems for all three planes have been commissioned and put into operation. These are bunch by bunch systems running digital filters on all individual bunches. The real time data processing using high performance FPGAs has a low latency of the whole system of 300 ns and allows for more sophisticated filter algorithms increasing the resolution of the systems. Apart from the stabilization purposes, they give full diagnostics of individual bunches and help to eliminate transient beam jitters occurring at injection.

REFERENCES

[1] M. Pedrozzi et al., "SLS operational performance with third harmonic superconducting system", Proc. of the 11th workshop on RF Superconductivity SRF2003, Hamburg, Germany, September 2003.

[2] Instrumention Technologies d.o.o. `http://www.i-tech.si`

[3] D. Bulfone et al, "The ELETTRA Digital Multi-Bunch Feedback Systems", Proc. of EPAC 2002, Paris, France, June 2002.

[4] M. Dehler, "Kicker design for the ELETTRA/SLS longitudinal feedback", Proc. of EPAC 2002, Paris, France, June 2002.

[5] M.Dehler et al, "Capabilities of the ELETTRA/SLS Multi Bunch Feedback Electronics" Proc. of the 6th European Workshop on Beam Diagnostics and Instrumentation for Particle Accelerators (DIPAC) 2003, Mainz, Germany, May 2003.

RADIATION SAFETY CONSIDEREATIONS OF THE OPERATION OF INDUS-1 SYNCHROTRON RADIATION SOURCE

G. Haridas, M.K. Nayak, Vipin Dev, Dimple Verma, K.K. Thakkar,
Health Physics Unit, Raja Ramanna Centre for Advanced Technology, Indore, India 452 013
P.K. Sarkar, D.N. Sharma
Radiation Safety Systems Division, Bhabha Atomic Research Centre, Mumbai 400085

Abstract

Radiological safety aspects of the operation of the electron storage ring, Indus-1 (450 MeV, 100 mA) is described in the paper. The ring is provided with a modular hybrid shielding comprising of mild steel and lead through which synchrotron radiation (SR) beam lines pass out. During the commissioning phase several radiation protection problems like streaming of high-energy bremsstrahlung x-rays through front ends of SR beam lines, shield joints, its detection and containment were encountered. Experimental measurements on the response of conventional radiation monitors with respect to water phantom were carried out to evaluate the dose build up factors in the streaming high-energy radiation field. The studies lead to the deduction of correction factors for the monitors for use in Indus-1. Improvement in monitor response on account of spectral degradation through shield and radiation levels during accidental beam loss are other problems, which are evaluated. Details of the radiation protection programme, radiation physics studies, the current status of radiation levels and access control are presented.

INTRODUCTION

Indus-1 is a 450 MeV electron storage ring [1] operated at Centre For Advanced Technology, India, giving rise to synchrotron radiation with a critical wavelength of $61A^0$ (202 eV). It has a circumference of 18.96 m with four bending dipole magnets from which synchrotron radiation is tapped through front ends and has five beam lines for different types of experiments like reflectivity, photoelectron spectroscopy etc. [2]. Bremsstrahlung x-ray photons form the major radiation hazard at intermediate energy electron storage rings like Indus-1. These photons have a continuous energy spectrum, whose maximum energy extends up to the energy of electrons in the ring. During commissioning of the storage ring, several radiation safety problems in regard to high-energy photons were encountered. For installation and commissioning of synchrotron radiation beam lines, modular hybrid shielding [3], comprising of lead and iron was installed, with a total thickness of 160 mm (80 mm lead + 80 mm iron). This modification has left shield joints and penetrations at some locations through which bremsstrahlung x-rays, produced as a result of interaction of electrons, with accelerator structures, mainly vacuum envelopes and residual gas molecules [4], streamed out to accessible areas. For proper monitoring of these high-energy photons no radiation monitors are commercially available. However, Victoreen survey meter, model 450 P (which is a pressurized ion chamber based survey meter) was used with water phantom to study its adequacy for radiation monitoring in such high-energy photon fields, experimentally. It was found that the dose rate builds up to certain thickness of water and reduces. From the measurements dose equivalent build up factor was found out. Build up factors were also calculated from Monte-Carlo calculations carried out using the code EGSnrc [5] and was found to be in good agreement with measurements. To see the spectral degradation of bremsstrahlung photons on account of radiation shield and adequacy of radiation monitors behind thick shields, photon spectrum measurements were carried out with a 50.8 mm X 50.8 mm BGO detector in the direct and transmitted photon field (through shield) from the storage ring. The transmitted spectrum showed spectral degradation and indicated good response by radiation monitors. Radiation levels around the storage ring during accidental beam loss due to different reasons like tripping of dipole, RF etc also were evaluated.

RADIATION MEASUREMENTS

Measurements of radiation dose with conventional instruments gave underestimation in streaming high energy photon field as dose was found to build up when measured with respect to different thickness of water phantom. The depth dose measured at two different locations (one at a front end in the accessible area and another near a bending magnet within the shielded enclosure) around Indus-1 is reproduced [6] in Fig 1. Monte Carlo calculations on the dose build up factors in water due to different incident bremsstrahlung photon spectra (obtained from semi-infinite copper slabs of different thickness on 450 MeV electron bombardment using EGS-4) gave comparable results with experimental values.

Fig 2 shows the average energy of the incident spectra and the respective the build up factors obtained in water when plotted as a function of the thickness of water where the maximum dose occurred (designated as shower maximum, X_{max}).

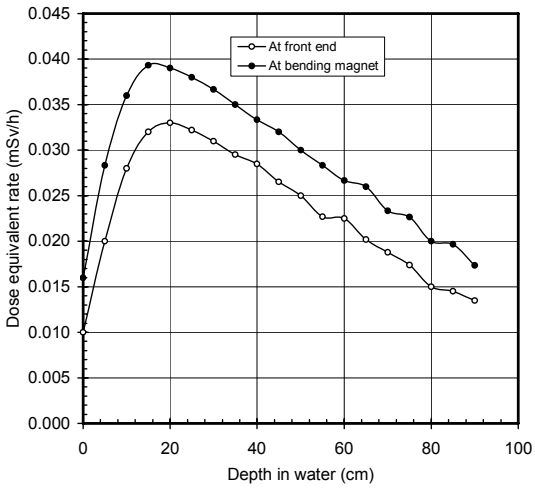

Figure 1: Depth dose measured at front end and near bending magnet around Indus-1

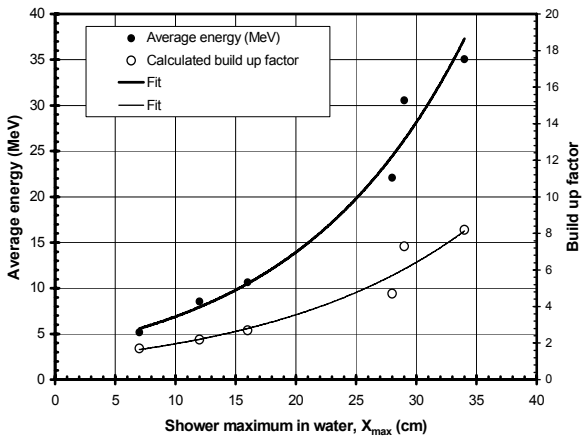

Figure 2: Average energy of the incident photon spectrum and the corresponding build up factors calculated for water phantom

From the studies a fit for the dose build up factor obtained is given below.

$$BF = 1.08 \exp\left(\frac{X_{\max}}{16.9}\right)$$

Using the fit dose build up factor at a depth of 30 cm (size of a human body) is found out to be 6.4, which is used as a conservative correction factor for radiation monitors for use in Indus-1.

Also the depth at which the maximum dose occurs, X_{max} as a function of the average energy assumes the form

$$X_{\max} = 14.29 \ln\left(\frac{E_{avg}}{3.41}\right)$$

which says that for an average energy ≤ 3.41 MeV, no build up takes place.

SPECTRUM MEASUREMENTS

In order to see the effect of spectral degradation on account of shield, and the subsequent response of the survey meter, spectrum measurement was done using a 50.8 mm x 50.8 mm BGO (Bismuth Germanate) detector and an 8KMCA in the direct and transmitted radiation field from the storage ring. It was possible to get an energy range from 300 keV to 12 MeV with the set up. As high-energy calibration was not possible beyond 2.7 MeV (^{24}Na) it was assumed to be linear up to 12 MeV.
For the measurement in the direct photon field, a through hole on the hybrid shielding wall, at the median plane of the storage ring, was used and for the transmitted field, 80 mm of lead was inserted in the hole. The spectra obtained in both the cases during the storage mode of operation of the ring are presented in Fig 3.

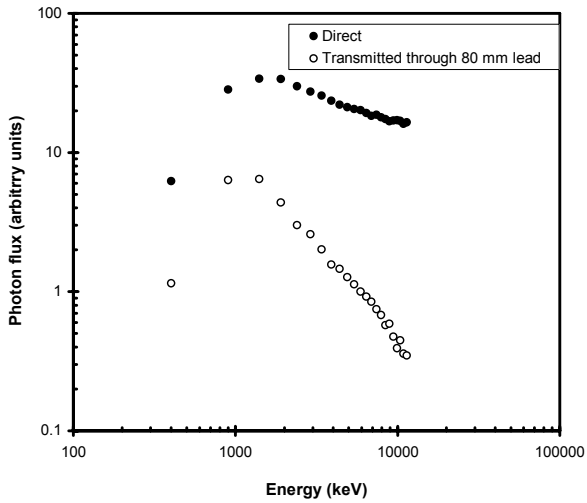

Figure 3: Direct and transmitted photon spectra measured around Indus-1

The spectral degradation was clearly evident from the transmitted spectra. The average energy of the transmitted spectrum worked out to be 3.3 MeV, and hence no dose build up is expected to take place, which is verified experimentally. Therefore the response of radiation monitors need not be corrected outside the hybrid radiation shielding of Indus-1 storage ring.

RADIATION LEVEL DURING NORMAL OPERATION

Radiation level during the normal operation of injection as well as storage at the design current of 100 mA at 450 MeV was found to be well within permissible dose limits recommended by International Commission on Radiological Protection (ICRP). Radiation level measured outside the shielding, in accessible areas is about 0.5 μSv/h. Victoreen survey meter 450P was used for photon radiation survey and pressurized ion chamber based pulsed x-ray monitor developed in house is used for area radiation monitoring. Photo- neutron dose rate is

found to be negligible. Neutron monitoring is done with Rem-meter. No sky shine problem was observed. Maximum induced activity found at Indus-1 accelerator complex was 2 μSv/h, at injection septum of booster synchrotron. No measurable activity in cooling water or in air was observed.

RADIATION LEVEL DURING ACCIDENTAL BEAM LOSS

During the condition of beam storage in the ring, there are chances of beam getting killed due to several reasons, due to which occupational workers out side the shielding may receive some dose. The possible reasons of beam killing identified are tripping of a) Bending dipole magnet b) Quadrupole Magnet and c) Radio Frequency to accelerating cavity. An experiment was carried out to evaluate the radiation level around the ring during the accidental beam loss.

For the present experiment, electron beam at 450 MeV was accumulated up to 100 mA and the dosimeters (Direct Reading Pocket Dosimeters) were placed within and outside the radiation shielding covering the $3/4^{th}$ circumference of the ring excluding the injection section. Then the beam was suddenly killed either by dipole tripping, quadrupole tripping or by RF tripping. Each type of accidental loss mentioned was experimentally simulated four times and the dose per event (maximum dose per killing) is found out. It was observed that in case of dipole trip and RF trip the radiation level around the ring is almost uniformly distributed (maximum up to 0.4 mSv/event) whereas in the case of quadrupole trip high radiation level was recorded at a location near bending magnet –3 (maximum up to 7.5 mSv/event), indicating a localized beam loss. However, dose recorded outside the hybrid shielding, in accessible areas was negligible in all the three cases.

RADIATION SAFETY SYSTEMS

Various radiation safety systems like search & scram, door interlocks, area radiation monitoring, shielding, audio-visual warning systems and public address systems are provided within the accelerator complex. The radiation safety systems have undergone modifications based on operational experiences from time to time and now optimised. Details of the radiation safety systems can be found in literature [7]

CONCLUSION

Commissioning and operation of the synchrotron radiation source Indus-1 has indicated several radiation protection problems, mainly streaming of high-energy photons through shield joints front ends. The streaming locations were identified and shielded subsequently. Conventional radiation monitors which have an energy response up to few MeV was found to be inadequate for correct measurement of radiation dose in high energy streaming photon fields. Studies indicated that radiation dose builds up within a water phantom up to few tens of centimeters. Systematic studies on the dose build up at two locations together with Monte Carlo calculations suggest a high-energy response correction factor of 6.4 for radiation monitors within the shielded enclosures and in streaming high-energy photon fields from Indus-1. Radiation levels in accessible areas during normal operating condition were found to be within permissible limits. Radiation level outside the shielding due to accidental beam loss of 100 mA stored beam current was found to be negligible. The radiation safety systems provided was found to be adequate with the result that no unusual occurrences have occurred till date.

ACKNOWLEDGEMENTS

The authors express sincere thanks to Mr. H.S. Kushwaha, Director, Health & Safety Env. Group, BARC for his guidance in this work. The support by Dr. V.C. Sahni, Director, RRCAT & Mr. S. Kotaiah, Project Manager, Indus-2 is here by acknowledged. The co-operation by Mr. Gurnam Singh, Head, IOAPDD, RRCAT and his team members is remembered with gratitude. The technical help provided by Dr. S. Krishnamachari & Dr. S. Anil Kumar, RSSD, BARC in spectrum measurement is acknowledged.

REFERENCES

[1] D.Angal-Kalinin, A. Banerjee, P.R. Hannurkar, M.G.Karmakar, S.Kotaiah, S.P. Maskar, P.K. Nema, S.S. Prabhu, M. Pravin kumar, S.S. Ramamurthi, S.K. Sukla, G. Singh, H.C. Soni & B.J. Vaidya "Synchrotron Radiation source Indus-1" Current Science, Vol.82 (3) (2002) p.283.

[2] R.V. Nandedkar "Beam lines on Indian Synchrotron Radiation Source Indus-1" Current Science, Vol.82 (3) (2002) p.291.

[3] Sanjay Chouksey, R.G. Marathe, R.K. Sahu & Gurnam Singh "Radiation Shielding for Indus-1 Storage Ring" Radiation Protection and Environment, Vol.23 (4) (2000) p.288.

[4] A.Rindi "Gas bremsstrahlung from electron storage rings" Health Physics 42 (2) (1982) p.187.

[5] D.W.O.Rogers et.al NRC user codes for EGSnrc. NRCC Report PIRS-702 (Rev.B), (2003)

[6] Haridas.G. Nair, M.K. Nayak, Vipin Dev, K.K.Thakker P.K. Sarkar & D.N. Sharma "Dose build up correction for radiation monitors in high – energy bremsstrahlung photon radiation fields" Radiation Protection Dosimetry 118 (3) p.233

[7] R.G. Marathe, Yogendra Sheth, G. Haridas, K.K.Thakkar and Gurnam Singh "Radiation Safety Systems for Indus-1" Radiation Protection and Environment Vol 23(4) (2000) p.294

COMPUTATION OF WAKEFIELDS AND IMPEDANCES FOR THE PETRA III LONGITUDINAL FEEDBACK CAVITY

A.K. Bandyopadhyay *, A. Joestingmeier, A.S. Omar ,
Otto-Von-Guericke University, Magdeburg, Germany.
K. Balewski, R. Wanzenberg, DESY, Hamburg, Germany.

Abstract

At DESY the existing PETRA II storage ring will be converted into a 3rd generation synchrotron radiation source, called PETRA III. The total beam current is limited by coupled bunch instabilities which are mainly driven by the parasitic modes of the RF cavities. It is planned to use longitudinal and transverse feedback systems to achieve the design current of 100 mA. Eight single cell feedback cavities will be installed into the PETRA III ring to damp the coupled bunch longitudinal phase oscillations. It is important to know the contribution of the feedback cavity to the impedance budget of PETRA III. In this article, the wake and impedance computation results, using the loss and kick parameters, will be reported. The computer codes MAFIA and Microwave Studio have been used to compute the electromagnetic fields.

INTRODUCTION

PETRA III

Beginning in mid 2007, the PETRA storage ring will be converted into a 3rd generation light source, PETRA III [1]. The planned facility aims for a very high brilliance of about 10^{21} photons /sec /0.1% BW /mm^2 /mrad^2 using a low emittance (1 nm rad) beam with an energy of 6 GeV and a total electron or positron design current of 100 mA. It is essential to use powerful feedback systems to prevent coupled bunch instabilities which are mainly driven by parasitic modes of the 500 MHz RF cavities. Eight single cell cavities will be installed to provide the required damping of $1/\tau = 800$ Hz. The cavity design has been adopted from the SLS [2] and DAFNE [3] overdamped feedback cavity designs. The cavities will be operated at a frequency of about 1375 MHz. The cavities are necessary to prevent longitudinal coupled bunch instabilities but are a potential source of higher order modes and wakefields which may cause beam instabilities. The impedance of the feedback cavities, investigated by numerical methods, are presented here.

Wakefields and potentials

The electromagnetic fields excited by a charged particle traversing any discontinuity in the beam pipe are called wakefields. The integrated effects of these fields over a given path length of a trailing charge gives rise to longitudinal and transverse wake potentials [4, 5]. The wake potential of a point charge q_1 is defined as:

$$\mathbf{W}^{\delta}(\mathbf{r},s) = \frac{1}{q_1}\int [\mathbf{E}(r,z,t) + c_0\mathbf{e}_z \times \mathbf{B}(r,z,t)]_{t=\frac{z+s}{c_0}} dz \tag{1}$$

where $\mathbf{E}$ and $\mathbf{B}$ are the electric and magnetic field excited by the charge q_1 at the longitudinal position $z = c_0 t$, $\mathbf{r}$ is the radial offset of the charge q_1 and the test charge, c_0 is the velocity of light in vacuum, s denotes the distance between the exciting charge and the test charge in the bunch coordinate system and $\mathbf{e}_z$ is the unit vector along the z-direction (Fig. 1). The wake potential $W(s)$ due to a charge distribution can be obtained as the convolution of the point charge wake potential with the line charge density. The loss parameter $(k_{\|})$, kick parameter $(k_{\perp})$ and the $k(1)$ parameters are defined according to the equations:

$$k_{\|} = \int_{-\infty}^{\infty} \lambda(s) W_{\|}(s) ds \tag{2}$$

$$k_{\perp} = \int_{-\infty}^{\infty} \lambda(s) W_{\perp}(s) ds \tag{3}$$

$$k(1) = \int_{-\infty}^{\infty} \frac{d\lambda(s)}{ds} W_{\|}(s) ds \tag{4}$$

where $\lambda(s)$ is the charge density and $W_{\|}(s)$ and $W_{\perp}(s)$ are the longitudinal and transverse wake potentials as functions of the bunch coordinate s. The loss parameter $(k_{\|})$ can be used to estimate the total energy loss of the beam, while the kick parameter $(k_{\perp})$ and $k(1)$ parameters are used to estimate the coherent tune shifts of the lowest order coupled bunch modes in the transverse and longitudinal planes.

The frequency domain description of the wakes are represented by the impedances, which are defined as the Fourier transforms of the wake potentials. The longitudinal

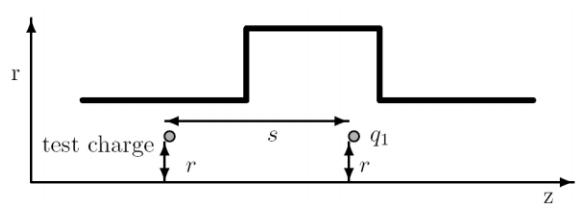

Figure 1: A charge q_1 and the test charge traversing a discontinuity in the beam pipe.

* ayan.bandyopadhyay@et.uni-magdeburg.de

($Z_\parallel$) and transverse impedances ($Z_\perp$) are defined as

$$Z_\parallel(\omega) = \frac{1}{c_0}\int_{-\infty}^{\infty} W_\parallel(s) e^{-\frac{i\omega s}{c_0}}\, ds \quad (5)$$

$$Z_\perp(\omega) = \frac{-i}{c_0}\int_{-\infty}^{\infty} W_\perp(s) e^{-\frac{i\omega s}{c_0}}\, ds. \quad (6)$$

SIMULATION RESULTS

Kicker geometry

One quarter of the PETRA III longitudinal feedback cavity is shown in Fig. 2. Four of the total eight coaxial ports, two waveguide ports (beam pipe), the relevant coordinate system and ports designation used for the simulations can be seen in the figure. Due to the geometrical symmetry of the cavity, only one quarter of it has been modeled for the electromagnetic simulations with Microwave Studio and MAFIA [6, 7].

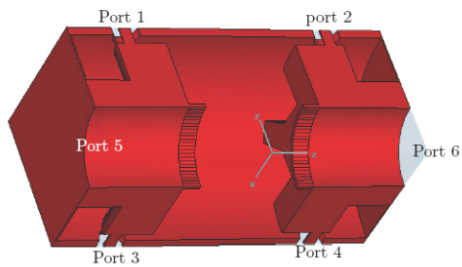

Figure 2: One quarter of the longitudinal feedback cavity as modeled for the simulations.

Scattering parameters

The resonant frequency of the TM_{010} like mode, which is the operating mode of the cavity, was computed as 1.3079 GHz with the MAFIA eigenmode solver. The scattering parameters have been computed covering the operating band of the cavity. Port 1 has been used for the excitation, keeping the other ports terminated with their corresponding wave impedances. As the cutoff frequency of the beam pipe (2.92 GHz for the TE modes and 3.82 GHz for the TM modes) is well above the operating band frequency, the beam pipe terminations have almost no influences on the scattering parameters. This point has been confirmed by simulations with matched terminations and short circuits at the beam pipe ports. The amplitudes of the reflection coefficient at port 1 and the transmission coefficient from port 1 to port 2 computed with MAFIA and Microwave Studio are shown in Figs. 3 and 4 respectively. The agreement between the results computed with MAFIA and Microwave Studio confirms the consistency in modeling and meshing of the structure with both codes.

Wakes and impedances

The longitudinal wakefields has been calculated with the MAFIA time domain solver. For the simulations a Gaussian charge distribution with an rms bunch length (σ_z) of 10 mm and a total charge of 1 C was used, which traversed

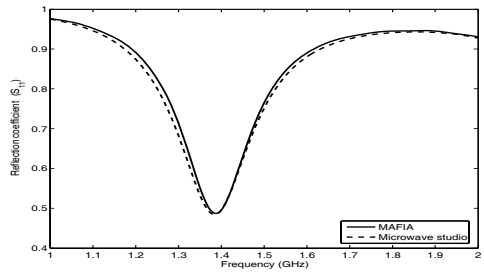

Figure 3: Amplitude of the reflection coefficient (S_{11}) at port 1 versus frequency.

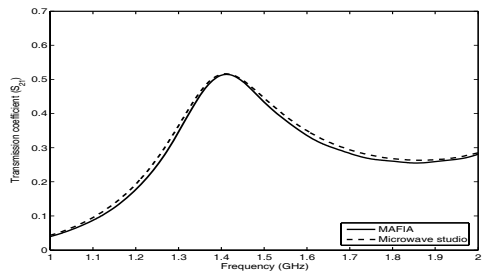

Figure 4: Amplitude of the transmission coefficient (s_{21}) from port 1 to port 2 versus frequency.

the feedback cavity on the z-axis. The longitudinal wake and the bunch charge density along the bunch coordinate are shown in Fig. 5. The longitudinal loss parameter and the $k(1)$ parameters were computed according to equations (2) and (4) as -4.6997×10^{11} V/C and 1.7489×10^{13} V/(C m), respectively.

A discrete Fourier transform (DFT) has been applied to obtain the impedances of the cavity. Fig. 6 shows the longitudinal impedance spectrum normalized to the bunch spectrum. Below the cutoff frequency of the beam pipe, sharp impedance peaks corresponding to the resonant modes of the cavity are present. The first impedance peak (which corresponds to the operating mode of the cavity) appears to be at 1.379 GHz. This frequency is higher than the computed resonant frequency of the operating mode at 1.3079 GHz since the coaxial waveguide ports were shorted for the eigenvalue computations but matched with a matched waveguide impedance for the time domain computation. In addition to the impedance peak due to the fundamental cavity mode, the presence of another peak around 2.28 GHz

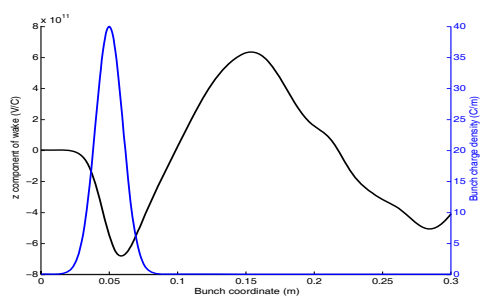

Figure 5: Longitudinal (z) component of the wake for PETRA III feedback cavity and the bunch charge distribution along the bunch coordinate.

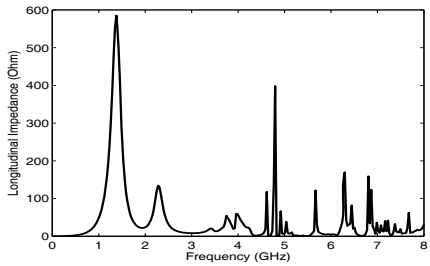

Figure 6: Longitudinal impedance versus frequency for the longitudinal feedback cavity.

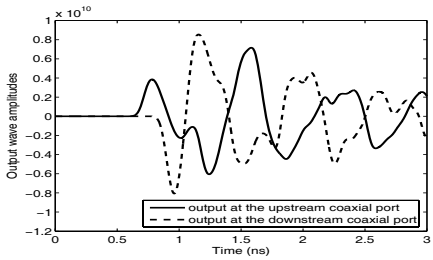

Figure 7: Output wave amplitudes at the upstream and downstream coaxial ports during the on axis wakefield computations.

can be noticed. The output wave amplitudes recorded at the upstream and downstream coaxial ports (ports 1 and 2, respectively) are shown in Fig. 7. Due to the symmetry of the cavity, the output signals recorded at ports 3 and 4 are exactly the same as those recorded at ports 1 and 2.

The transverse kick parameters and impedances have been computed considering one quarter of the cavity and combining the wake computation results with different boundary conditions at the x-z plane. Fig. 8 shows the transverse wakes normalized to the beam offset. Also for the transverse wake computations, all the coaxial ports have been terminated with matched loads. The transverse impedance normalized to the beam offset is shown in Fig. 9. The longitudinal loss parameter and the $k(1)$ parameter have been computed according to equations (2) and (4) for a 2 mm y-offset beam as -4.7400×10^{11} V/C and 1.7195×10^{13} V/(C m), respectively. The corresponding transverse kick parameter (equation 3) normalized to the beam offset is 1.3150×10^{13} V/(C m). All the computed loss and kick parameters for the feedback cavity are summarized in Table 1. Due to the geometrical symmetry of the cavity the vertical and horizontal impedances and hence also the kick and loss parameters are identical.

SUMMARY

The longitudinal and transverse wakefields, corresponding impedances, and loss and kick parameters for the PETRA III longitudinal feedback cavity have been computed with the MAFIA code. The scattering parameters of the cavity in the operating frequency band has been calculated with MAFIA and Microwave Studio codes.

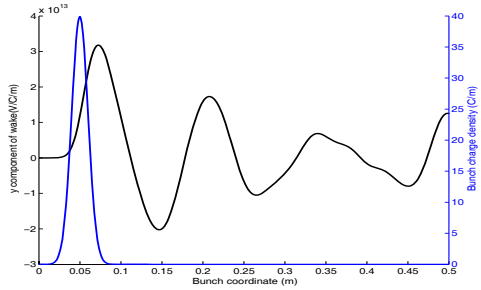

Figure 8: Transverse (y) wake normalized to the beam offset.

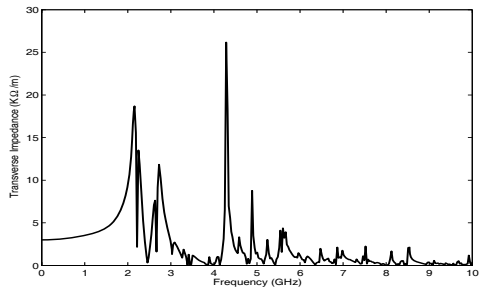

Figure 9: Transverse (y) impedance normalized to the beam offset.

Table 1: The loss and kick parameters for the PETRA III longitudinal feedback cavity with nose cones.

Longitudinal loss parameter [V/C]	$k(1)$ parameter [V/(C m)]	Transverse kick parameter [V/(C m)]
-4.6997×10^{11}	1.7489×10^{13}	n.a.
-4.7400×10^{11} (offset=2.0 mm)	1.7195×10^{13} (offset=2.0 mm)	1.3150×10^{13}

REFERENCES

[1] K. Balewski et. al., Eds., "PETRA III: A low emittance synchrotron radiation source," Technical Design Report, DESY 2004-035, Feb. 2004.

[2] M. Dehler, "Kicker design for the ELETTRA/SLS longitudinal multi-bunch feedback," in *8th European Particle Accelerator Conference (EPAC)*, (Paris, France), pp. 2070–2072, 2002.

[3] R. Boni, A. Gallo, A. Ghigo, F. Marcellini, M. Serio, and M. Zobov, "A waveguide overloaded cavity as longitudinal kicker for the dafne bunch-by-bunch feedback system," *Particle Accelerators*, vol. 52, pp. 95–113, 1996.

[4] B. W. Zotter and S. Kheifets, *Impedances And Wakes In High Energy Particle Accelerators*. London: World Scientific Publishing Co. Pvt. Ltd, 1998.

[5] T. Weiland and R. Wanzenberg, "Wake fields and impedances." Joint US-CERN particle accelerator school, Hilton Head Island, SC, USA, November 1990. Edited by M. Dienes, M. Month and S. Turner.

[6] "CST Microwave Studio." Version 5, March 2005. CST GmbH.

[7] "MAFIA." Release 4, Nov 2004. CST GmbH.

COMPACT HARD X-RAY SYNCHROTRON RADIATION SOURCE WITH SUPERCONDUCTING BENDING MAGNETS

E.I. Antokhin, A.A. Gvozdev, G.N.Kulipanov, P.V. Logachev, N.A. Mezentsev, V.E.Panchenko, A.V. Philipchenko, Y.V. Rakshun, A.V. Utkin, N.A. Vinokurov, K.V. Zolotarev*,
Budker Institute of Nuclear Physics, 630090, Novosibirsk, Russia

Abstract

Synchrotron radiation (SR) with relatively hard spectrum (up to 50 keV) is necessary for realization many modern X-ray analytical methods. These methods can be effectively used in industrial and medical applications, in universities and scientific centers. So, the task of developing of compact source of hard synchrotron radiation is very perspective. Budker INP has a big experience for developing and fabrication of high field superconducting insertion devices for different SR centers. In frame of this activity a superconducting bending magnet with field up to 9.6 T was fabricated for BESSY-II and commissioned in 2004. This magnet also became a prototype for compact hard SR source. A project of such storage ring is under developing in Budker INP now. This design fixed beam energy to 1.2 GeV, ring circumference about 56 m. Estimated horizontal equilibrium emittance will better near 10 nm. This report includes a detailed description of main parameters and magnetic structure of designed storage ring as well as preliminary design of injector system and beamline layout.

INTRODUCTION

Development of compact and low-cost SR sources of hard (up to 50 keV) X-rays is an actual task for further application of the advanced X-ray methods in industry, medical centers, hospitals, small scientific centers and universities. Application of superconductive bending magnets allows solving this task with relatively small electron beam energies in a storage ring. Economically, a high cost of the magnetic system of such a storage ring can be compensated by cheaper injector, RF and protection systems and abrupt decrease of expenses for construction of the infrastructure of the complex. Low beam energy simplifies reduction of the emittance value and permits increasing spectral brightness of the source as compared with a high-energy storage ring with a magnetic system of a similar type.

The concept of compact SR source using superconducting magnets has been realized in different projects (AURORA, NIJI-3, SXLS, Helios, Super-ALIS etc.) (see [1, 2]) in the 1990s. However, these projects were aimed at generation of VUV and soft X-rays, which did not allow using such installations for research in the hard X-ray region.

In 1992 a prototype of superconducting bending magnet with a working field of 6 Tesla was fabricated and successfully tested at Budker INP. It was decided to organize manufacture of such bending magnets for future creation of compact SR sources consisting of superconducting and conventional bending magnets [3, 4]. Unfortunately, these projects were not realized because of serious problems in Russian economics at that time.

In 2001 a project for design and fabrication of a 9 Tesla superconductive bending magnet (Superbend) was started in the framework of collaboration between Budker INP and BESSY. In 2003 the Superbend was successfully tested and a field of 9.37 Tesla was obtained. After some work to minimize heat inleak in the cryostat and to reduce liquid helium consumption, the magnet was successfully commissioned at the BESSY site. The maximal field value of 9.6 T was achieved in 2004 during site acceptance testes at BESSY [5].

The successful commissioning of the superconducting bending magnet confirmed reliability of the BINP technology and allowed creation of a compact SR source of hard X-rays on the basis of such magnets. This project was started at Budker INP in 2006.

Besides, Siberian Synchrotron Radiation Center (SSRC) at Budker INP unites a lot of SR users from Siberian Branch of Russian Academy of Science and from other organizations. SSRC has good experience in organization of large user communities, and has the infrastructure required for research [6]. But the main problem of SSRC is the absence of a specialized SR source. This project can be considered as a way of noticeable up-grade of this center. Thus, development of such compact and bright SR source is really a very actual task.

POSSIBLE SCHEME OF COMPACT STORAGE RING

To show realizability of all the above-mentioned ideas, a scheme of such a system was suggested. Main parameters of the complex are sumarized in Table 1 and general view is presented in Figure 1. The ring perimeter is 56 m, and a 17 × 22 m hall can accommodate such storage ring. This variant allows organization of as many as 18 channels for hard spectrum SR extraction and of a rather large amount of channels for the soft X-radiation.

*Zolotarev@inp.nsk.su

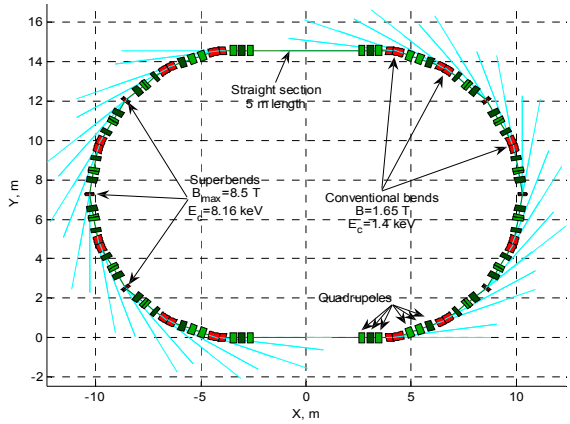

Figure 1: Possible schemes of compact SR source.

Table 1: Main parameters of a compact storage ring – SR source (requirements).

Parameter	Value
Electron energy	1.2 GeV
Critical energy of SR quanta	8.16 keV for SR from superconductive magnets (8.5 T) 1.6 keV for SR beams from normal magnets (1.65 T)
Number of bending magnets	6 superconductive magnets 12 conventional magnets
Number of SR beamline	18 with hard X-ray spectrum 6-10 with soft X-ray and VUV spectrum
Beam phase-space volume	10 nm·rad
Beam current	800 to 1000 mA
Beam lifetime	8 to 10 hours
Orbit perimeter	< 60 m
Size of a hall for the storage ring facility	17 × 22 m (without the space required for users' stations)

Fig.2 presents the optical functions of the suggested scheme. Magnets and quadrupole lenses are arranged in accordance with the theoretical minimal emittance (TME) lattice requirement, as far as it is possible for such compact lattice. The structure has a racetrack shape and consists of two arcs and two 5-m long straight sections. Each of the arcs includes 3 Superbends and 6 conventional bends. Bending angles in all the magnets are the same and equal 20º. The edge arc bends work as dispersion suspensors; they provide zero dispersion in the straight section. The Superbends are separated with conventional magnets, to prevent intersection of beamlines from a Superbend with the cryostat of next one.

The computed horizontal beam emittance is 11 nm rad. Thus, this facility can be classified like the most compact among the 3rd generation SR sources.

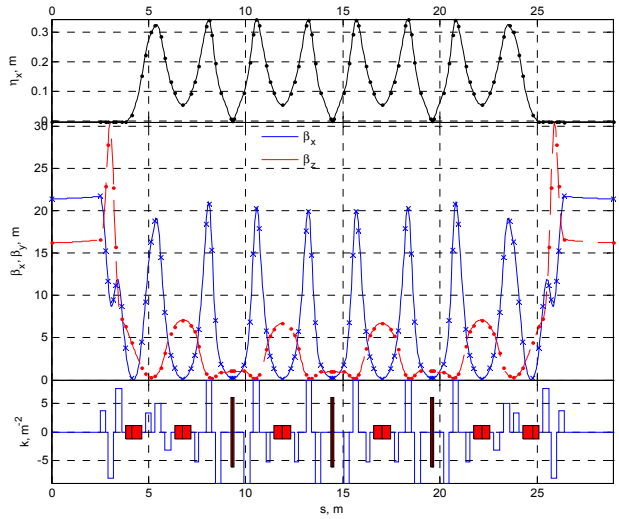

Figure 2: Optical functions in one superperiod of a compact SR source.

Of course, this design is only a first proposal and covers only the stage of linear optimization of lattice optics. A lot of problems of nonlinear beam dynamic are complicating implementation of this scheme. But this example shows the main direction for design optimization.

Since bending angles in the magnets are big enough, several beamlines can be extended from one magnet, three beamlines in this design. In this case, the central beamline takes SR from the center of the Superbend, where the magnetic field is maximal. The angle between neighbor beamlines is 5º, which provides enough space for users. Since the field at irradiation points in side channels is about 8 T, spectral parameters of SR of these beamlines do not differ much from those of the central one. The same angle was selected for beamlines from the normal conducting magnets.

BRIEF SUBSYSTEMS DESCRIPTION

Other subsystems of this facility can be built in accordance with standard Budker INP approaches and technologies. Most of these components already have working prototypes and thus can be used after small modifications.

The injector system will include a 150 MeV linac and a booster synchrotron for full energy (1.2 GeV) injection.

A special electron and positron source as an universal injector facility was created and commissioned at BINP [7]. The fist section of this facility can be used in the current project as an initial electron beam source. It contains two sections of the linear accelerator structure that can accelerate electron bunches up to 150 MeV. All parameters of this linac meet the booster injection requirement, so it was decided to use this system.

The booster takes the electron beam from the linac and accelerates it up to 1.2 GeV, for full energy injection into the main ring. The booster will be similar in design to the booster produced at BINP for Duke University (North Carolina, USA) [8].

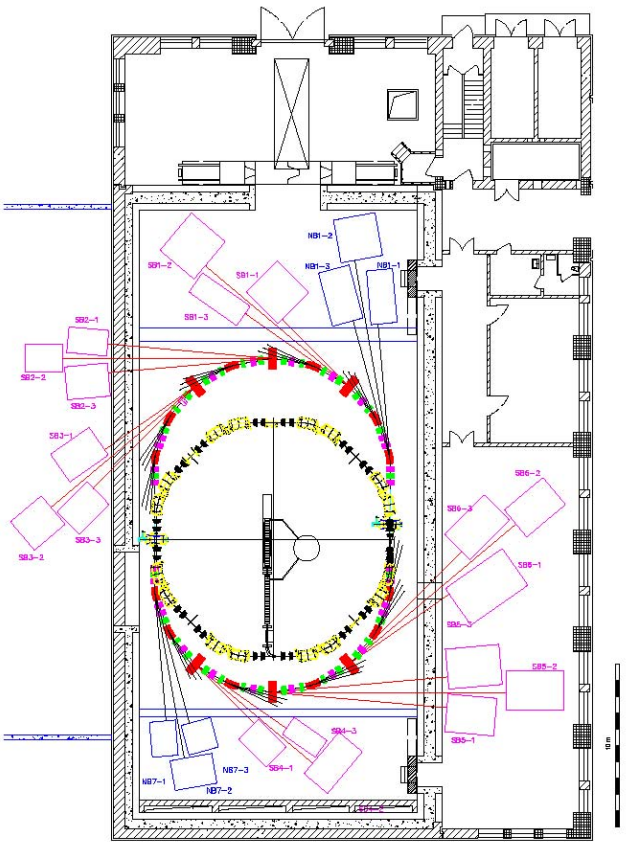

Figure 3: General layout of compact SR source facility, SR beamlines and experimental stations.

Standard RF cavities used at Budker INP, with high order mode suppression and a frequency of 180 MHz, will be installed in the booster and main ring. In spite of big dimensions of the system, relatively long bunches formed by this cavities will help to decrease intrabeam scattering and to increase the beam life time.

The facility will be located in an already existing building of Budker BINP. Figure 3 shows a possible layout of the injector system, storage ring, beamlines and experimental stations for users. A median plane of booster synchrotron and linac will be located in 1 m lower than mediam plane of main ring. This building is being reconstructed now. Some stations will be placed in a building extension to be created later.

Altogether 18 experimental stations will be installed on beamlines from the Superbends. They will use SR in the hard X-ray region. The most popular X-ray research techniques will be presented, XAFS, XRD, and XRF among them. Also 6 beamlines will use SR from the conventional bends. Thus, some research techniques in the soft X-ray and VUV regions will also be implemented.

CONCLUSIONS

Modern technology for fabrication of superconductive bending magnets can be effectively used to create a compact SR source with hard X-ray spectrum. The relatively small beam energy of such storage ring simplifies meeting a number of important requirements for biological protection, injection system and emittance minimization.

BINP has great experience in development and creation of different accelerators. All necessary technologies for fabrication of this facility and all components are also available. Thus, such compact SR source really can be created.

Since SSRC really needs a specialized SR source, the decision for development of such source was taken at BINP. This source should cover large part of SR user needs in the hard and soft X-ray ranges.

A detailed project of this source is under development now. Prototypes of some critical components can be fabricated next year.

It is possible to suppose that the facility will be commissioned in the end of 2010.

REFERENCES

[1] Y.Tsutsui, K.Emura, F.Miura,H.Takada, T.Tomimasu, "The Superconducting Compact Storage Ring NIJI-III", in Processing of PAC 1991, pp. 2655-2657.

[2] Hiromitsu Nakabushi, Superconducting Compact SR Source AURORA for X-ray Lithography, processing of EPAC-92, pp.206-208.

[3] L.G.Morgunov, Development of compact storage rings at Siberia-SM, Synchrotron Radiation News, Nov./Dec. 1990.

[4] G.N.Kulipanov, N.A.Mezentsev, L.G.Morgunov, et al, Development of supercunducting compact storage rings for technical purposes in the USSR, Proceedings of the 4th International Conference Synchrotron Radiation Instrumentation, 15-19 July 1991, Chester, UK, p.731-736

[5] A.M. Batrakov, S.V. Khruschev, D. Kraemer, G.N. Kulipanov, V.H. Lev, N.A. ,et al, "Nine tesla superconducting bending magnet for BESSY-II", NIMA A 543 (2005), pp.35–41.

[6] A.I. Ancharov, V.B. Baryshev, V.A. Chernov, A.N. Gentselev, B.G. Goldenberg, D.I. Kochubei, V.N. Korchuganov, G.N. Kulipanov, M.V. Kuzin, E.B. Levichev et al., Status of the Siberian synchrotron radiation center NIMA A 543 (2005), pp.35–41.

[7] "Status of Work on the VEPP-5 Injection Complex", M.S.Avilov, A.V.Akimov, A.V.Antoshin, et al. Atomic Energy, Volume 94, Number 1

[8] S.F.Mikhailov, V.N.Litvinenko, P.Morcombe, G.Swift, N.A.Vinokurov, N.G.Gavrilov, Yu.G.Matveev, D.A.Shvedov, “Project of Booster Synchrotron for Duke FEL storage ring”, Proc. of the 2001 Part. Acc. Conf., Chicago, 2001, p. 3525-3527.

BEAM BASED ALIGNMENT AND COD CORRECTION FOR THE SIAM PHOTON SOURCE

S. Rugmai[#], NSRC and Suranaree University of Technology, Nakhon Ratchasima, Thailand.
C. Kwankasem, P. Sudmuang, and P. Klysubun, NSRC, Nakhon Ratchasima, Thailand.

Abstract

The first systematic Beam based Alignment (BBA) and COD correction attempt for the Siam Photon Source (SPS) has been performed. Automated measurements were carried out using Matlab OPC Toolbox, interfacing to the accelerator control system. Calculations of theoretical parameters were performed with Accelerator Toolbox via Matlab interface. Since the Beam Position Monitors (BPMs) were not properly calibrated beam based calibrations were carried out. Preliminary calibration factors for each BPM were obtained by normalizing BPM signals to modelled corrector magnet responses. Measurements of offsets between BPM and quadrupole centers were performed by quadratic fitting for minima of orbit response to changes of quadrupole strengths. The resulting offsets were superimposed to the BPM readings. COD correction was then performed.

INTRODUCTION

The Siam Photon Source (SPS) has been in operation with currently three beamlines completed and opened for users. The machine performance has constantly been improved, including the recent energy upgrade from 1 to 1.2 GeV [1]. However, proper correction of the closed orbit has not been carried out. Many obstacles contribute to the difficulties for carrying out the COD correction. In the past, the machine control system lacked a good user interface system to enable fast and reliable beam measurements. This major obstacle has been solved by installation of Matlab OPC Toolbox to enable real time interface and programming via Matlab [2]. A project for proper COD correction and orbit stabilization has then been under way. Results of beam based BPM calibration, beam based alignment (BBA) measurements and COD correction are presented in this report.

BEAM BASED BPM CALIBRATION

The SPS contains 16 horizontal and 12 vertical corrector magnets, 28 quadrupole magnets and 20 BPMs. It is unfortunate that the BPMs of the SPS were not properly calibrated prior to installation. Dismantling the BPMs for recalibration at this stage is not a preferable option. It was therefore decided that a beam based calibration should be attempted. The calibration was carried out by calibrating the measured orbit responses to the theoretical values, i.e.

$$\Delta = \frac{\theta\sqrt{\beta_i \beta_j}}{2\sin \pi\nu} \cos\left(\left|\mu_i - \mu_j\right| - \nu\pi\right), \qquad (1)$$

where θ is the corrector kick angle, β the beta function, μ the phase advance, ν the betatron tune, and where the subscript i and j indicate the values at the BPM and the corrector positions, respectively. This calibration method therefore relies on the knowledge for corrector magnet characteristics and the theoretical model of the storage ring. The corrector magnets were accurately measured for the B-I slope and effective magnetic lengths [3]. The storage ring theoretical model was obtained by fitting the measured beta function and betatron tunes [4]. From the measured beta functions the four-fold symmetry of the ring is reasonably reproduced. For simplicity, the symmetry was therefore kept in the fitted model. The measured and fitted beta functions are shown in Figure 1. The model is used in Accelerator Toolbox [5] for calculations.

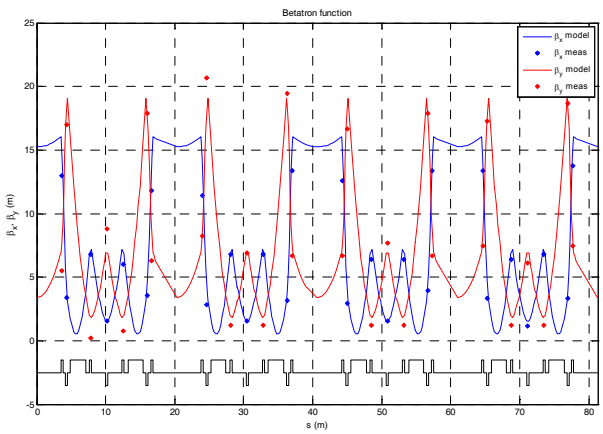

Figure 1: Measured and modelled beta functions

Even though this will contribute some errors to the calibration it is expected that the results should be good enough for preliminary COD correction. Moreover, it is hoped that this should at least give a reasonable working system to perform a more systematic refinement such as that using LOCO [6].

Automated measurements of the response matrix were carried out by varying corrector currents and measuring orbit responses. The calibration factors in the horizontal and vertical planes for each BPM were then calculated by averaging the ratios between the model and measured responses for all corrector magnets. The final calibration factors for horizontal and vertical planes were then obtained by averaging the factors obtained for all BPMs

[#]supagorn@nsrc.or.th

in each plane. The results gave the calibration factors of 17.40 in the horizontal and 51.80 in the vertical planes. These calibration factors are then set to the control system for BPM readings.

BPM OFFSET MEASUREMENTS

A Matlab program has been written for automated BPM offset measurements, using OPC Toolbox for interfacing with the machine control system. The offset between the electrical center of a BPM and the magnetic center of an adjacent quadrupole is determined from the position where orbit response to a change in the quadrupole current is minimum. The method carried out at the ALS [7] is adopted here. Firstly, a target BPM is chosen together with the adjacent quadrupole. Next, the program chooses the theoretically most effective corrector at that quadrupole position. The beam orbit inside the quadrupole is then moved to a certain position by setting the current of the chosen corrector, after which the beam position from the BPM signal is recorded. The quadrupole trim coil current is then varied (by ±3 A) and the beam position in all the 20 BPMs are recorded. The merit function is then calculated by

$$M(I_C) = \sum_{i=1}^{20} \left(\Delta_i^+ - \Delta_i^-\right)^2 , \qquad (2)$$

where $M(I_C)$ indicates the merit function being the function of corrector current, Δ^+ and Δ^- are the orbit responses for positive and negative changes of the quadrupole trim coil current, respectively, and where the subscript i indicate the BPM number. The corrector current is then changed again to move and record the beam orbit. The procedure for calculating the merit function is then repeated. Since the orbit response to the change in quadrupole current is linear with the beam position in the quadrupole this merit function is therefore quadratically dependent on the corrector current. The whole procedure is repeated until a parabola is obtained for the merit function. A quadratic fit is then performed to obtain the parabola minimum. The minimum of $M(I_C)$ therefore indicates the corrector current where the beam position in the quadrupole gives minimal response to changes in qudrupole strength. This position is therefore taken as a quadrupole magnetic center. The beam position inside the BPM at this orbit can then be interpolated from the linear dependence of the BPM signal to the corrector current. This value of beam position inside the BPM is therefore the required BPM electrical offset regarding to the quadrupole magnetic center.

An example of the user interface panel for the offset measurement is shown in Figure 2. Twenty BPM readings were averaged for each orbit during the measurement. Results of the measured offsets are shown in Figure 3. It was found that some of the offsets are quite large. Values for mechanical offsets from misalignments measured during the previous shutdown are also shown for comparison. It is seen that the mechanical misalignments contribute very little to the BPM offset. The measured offsets are therefore believed to be real, to within the measurement errors. These measured offsets are compensated prior to COD correction.

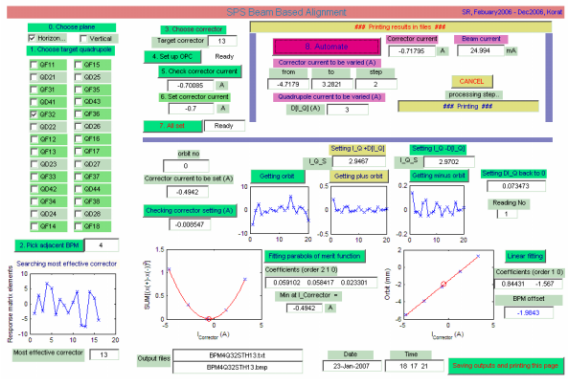

Figure 2: User interface panel for BPM offset measurement code

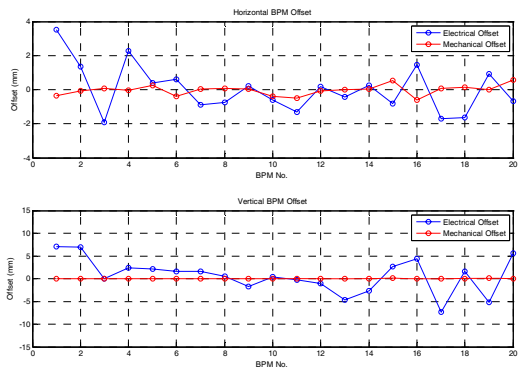

Figure 3: Results of BPM offset measurements. Measured offset from mechanical misalignments are also shown for comparison.

COD CORRECTION

Preliminary COD corrections were performed at the beam energy of 1.2 GeV by solving the matrix equation,

$$\mathbf{A}\cdot\boldsymbol{\theta} + \mathbf{b} = 0 , \qquad (3)$$

where $\mathbf{A}$ is the orbit response matrix and $\mathbf{b}$ the column matrix for BPM readings. The solution $\boldsymbol{\theta}$ is the column matrix for the required corrector kick angles to correct the COD. The above equation was solved using Singular Value Decomposition (SVD). The solution was then superimposed on the corrector settings for COD correction. It was found that the correction was able to reduce the RMS of the COD by approximately 87% (horizontal) and 58% (vertical) of the uncorrected orbit. The RMS of the residual COD is approximately 0.4 mm (horizontal) and 0.8 mm (vertical). The CODs before and after the correction are shown in Figure 4. This COD correction result is now temporarily used during the beam service by

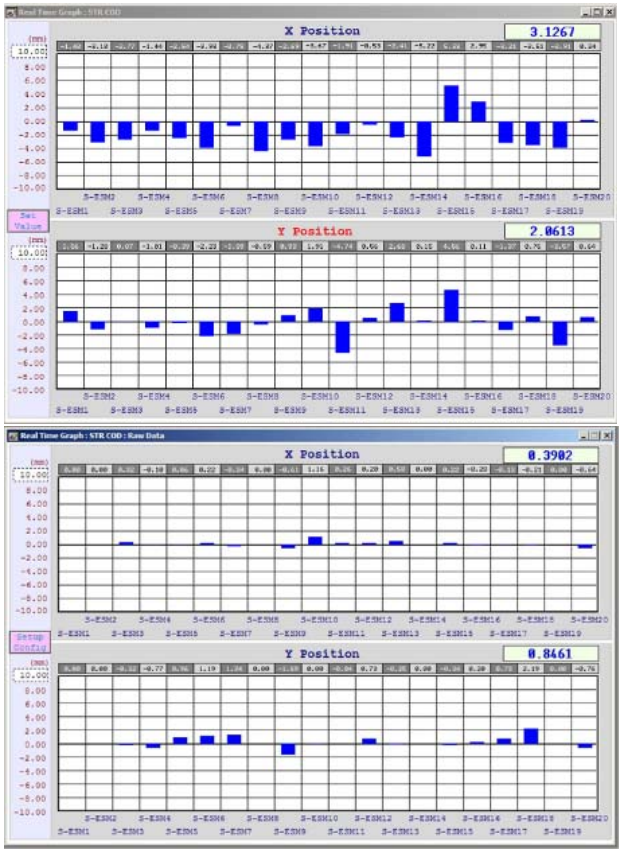

Figure 4: COD before and after COD correction.

scaling down the obtained corrector currents to 1 GeV injection energy. It is expected that there may be many parameters contributing to the difficulties in correcting the residual COD. In addition to calibration errors there also appear to be large noises in the BPM signals. Reproducibility of the COD correction is, however, good enough for the beam service at this stage. Works on BPM noise analyses and reduction, together with better calibration and more accurate offset measurements to improve the efficiency and reproducibility of COD correction are now underway. Systematic response matrix analyses using LOCO [6] is also being carried out.

CONCLUSION

Beam-based calibration of BPMs in the SPS has been carried out. The measured response matrix was calibrated to the model obtained from beta function and betatron tune fitting. The calibration factors for horizontal and vertical planes were obtained by averaging of the response ratios for all corrector magnets and BPMs. The BPM-Quadrupole offsets were then measured with Matlab programming interfacing via OPC Toolbox. The measured offsets were compensated prior to COD correction. The COD correction was performed by solving the response matrix equation using SVD. The result was able to reduce the COD by approximately 87% in the horizontal and 58% in for vertical plane.

ACKNOWLEDGEMENT

The authors would like to thank accelerator division staff for their contribution to this work.

REFERENCES

[1] S. Rugmai *et. al*., “Energy Upgrade of the Siam Photon Source”, AIP Proceedings **879**(2007)58.

[2] P. Klysubun and C. Netsai, “Development of Matlab-based Data Logging System at the Siam Photon Source”, EPAC’06.

[3] S. Prawanta *et. al.*, “Magnetic Field Measurement of Storage Ring Steering Magnets”, NSRC Technical Note NSRC-TN-2004/20.

[4] C. Kwankasem, “Measurement Results of Beta Functions and Dispersion Functions”, NSRC Technical Note NSRC-TN-2006/02.

[5] A. Terebilo, “Accelerator Toolbox for Matlab”, SLAC-PUB-8732(2001).

[6] J. Safranek, *Experimental Determination of Storage Ring Optics Using Orbit Response Measurements*, Nuc. Inst. & Meth. in Phy. Res. A,” 388 (1997) 27-36.

[7] G. Portmann, D. Robin and L. Schachinger, *Automated Beam Based Alignment of the ALS Quadrupoles*, PAC’95.

CONSTRUCTION PROGRESS OF THE SSRF INJECTOR

D.M. Li, M.H. Zhao, H.H. Li, Z.Q. Shen, Z.T. Zhao
Shanghai Institute of Applied Physics, Shanghai 201800, P.R. China

Abstract

Shanghai Synchrotron Radiation Facility (SSRF) is a third generation synchrotron radiation source facility under construction. To meet full energy top-up injection requirements of 3.5GeV storage ring, the injector of SSRF was designed which consists of an 150 MeV linac, a two super-period 28 cells FODO type booster and two transport lines (LT and HT). The cycle rate of the booster is 1 or 2 Hz.

In this paper, the brief description of SSRF injector design, and the progress of construction of the linac, booster and transport lines are described.

INTRODUCTION

As a third generation synchrotron radiation source facility, the SSRF storage ring calls for a 3.5GeV full energy injector, a top-up injection is also demanded [1]. After the SSRF project was approved in 2004 [2], the SSRF injector was redesigned to satisfy these new demands, a new detailed scheme of SSRF injector was carried out [3]. In the finally scheme, the SSRF injector is comprised of a dedicated 150MeV linac, a two-fold 28 cells booster and two beam transport lines. The high reliable linac is used as the pre-injector to meet the requirements of the booster injection. Figure 1 shows the schematic layout of SSRF injector.

The injection cycle rate has been fixed to 2 Hz. With this cycle rate and single bunch of 1nC charge, the booster can smoothly perform normal injections and continuous top-up injections. To speed up the commissioning of storage ring, the multi-bunch mode of the injector is also included in the renewed design, which produces maximal 150 bunches occupying a total time of 300ns.

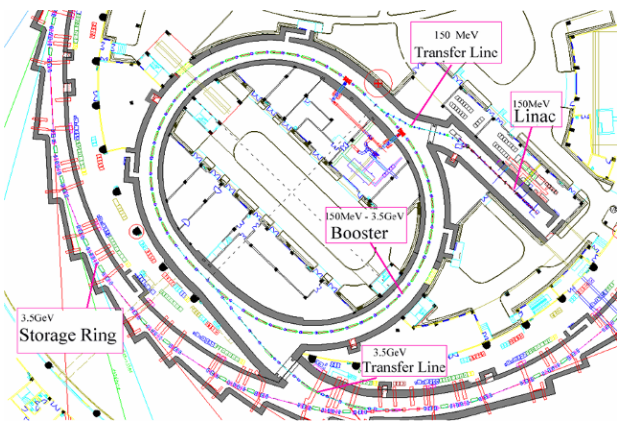

Figure 1: Schematic layout of SSRF injector

SSRF was started construction in the end of 2004. The beam commissioning will be completed in April, 2008 according to the schedule. The building construction has been basically finished. The linac installation was started in November, 2006, and the beam commissioning will be started in April, 2007. The Booster will start commissioning before October, 2007. Up to now, most of on-line installing components, power supplies, and instruments are under manufacture or purchasing for the SSRF booster and transport lines.

LINAC

The 150MeV linac is used as the pre-injector of 3.5GeV booster, which consists of four 3m long constant gradient accelerating sections and an injection section. A thermionic cathode electron gun, a 499.65MHz sub-harmonic buncher and a 2998MHz buncher, compose the linac injector section. The main beam parameters of the linac are listed in Table 1.

Table 1: The main parameters of linac

Nominal energy (MeV)	150
Repetition Rate (Hz)	1~5
Beam charge (nC)	
Single-bunch	1
Multi-bunch,	3~5
Pulse to pulse energy stability	0.25%
Relative energy spread	0.5% (rms)
Normalized Emittance (mm.mrad)	<100
Rf Frequency (MHz)	2998

The buncher and four accelerating structures are powered by two 45MW klystrons, each is driven by a 1kW solid-state amplifier. The pre-buncher is driven by a 500MHz r.f. amplifier.

Manufacture and test of all linac components have almost been finished. Mechanical and electrical installation are close to be completed. The beam commissioning will begin from April 2007. Figure 2 shows the progress of linac installation

BOOSTER AND TRANSPORT LINE

The SSRF booster performs as a synchrotron to accelerate the electrons from the linac energy of 150MeV to the storage ring energy of 3.5GeV. To achieve the emittance demands of top-up injection, the design of booster has been carefully optimized: 1) A reasonable low nature emittance and a relative large dynamic aperture. 2) Keeping bending magnet field strength at about 0.8T to limit the energy loss per turn and therefore cut down the scale and cost of RF system. 3) The booster is seated in an independent tunnel for the convenience in commissioning and maintenance.

Figure 2: Progress of SSRF linac installation

The circumference of the SSRF booster, comprising of 28 cells, is 180.0 m. The nature emittance is about 100 nm·rad. The layout of one standard cell of booster is shown in Figure 3. The beta functions for one super-period are shown in Figure 4. Table 2 and Table 3 summarize the main parameters and magnet parameters of SSRF booster.

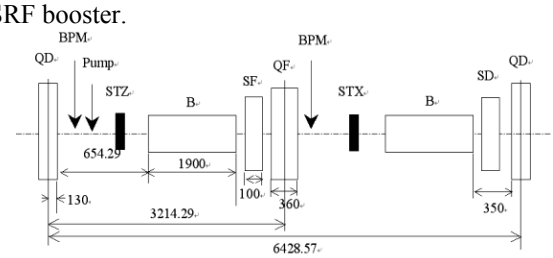

Figure 3: Schematic diagram for one cell

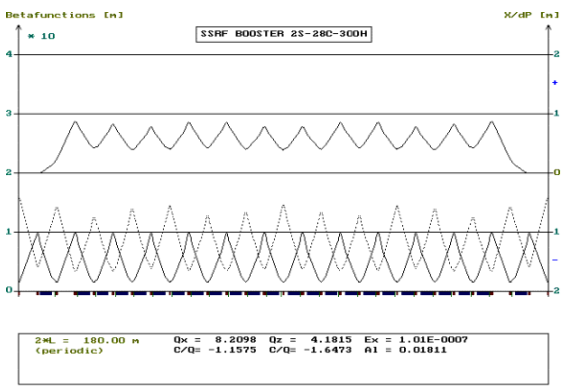

Figure 4: β-function and dispersion of booster

Table 2: Main parameters of the SSRF booster.

Parameters item		Unit	Value
Injection energy		GeV	0.15
Extraction energy		GeV	3.5
Beam current	Single bunch	nC	1
	Multi-bunch	mA	<15
Cycle rate		Hz	2
Circumference		m	180
Harmonic number			300
Super-period number			2
Cell number			28
Natural emittance at 3.5 GeV		nmrad	101
Energy loss per turn(3.5GeV)		MeV	0.915
Cell length		m	6.4286
Betatron tune, ν_H /ν_V			8.2/4.18
Natural chromaticity,ξ_H/ξ_V			-9.50/-6.89
Max. β function,β_H/β_V		m	10.0/16.0
Max. dispersion D_H		m	0.878
Nature Momentum spread			7.8×10^{-4}
Momentum compaction,α_P			0.018
Damping time, τH/τV/τL		ms	4.8/4.6/2.3
RF Frequency		MHz	499.65
RF Cavity (5 cells cavity)			2
Required RF voltage V_0		MV	1.74
Synchrotron tune, f_Z			0.0191

Table 3: Magnet parameters of the SSRF booster.

Bending magnet	
Number	48
Magnetic length (m)	1.9
Max. dipole field (T)	0.804
Gap height (mm)	32
Quadrupole magnet	
Number of QF, QD	28, 28
Magnetic length (m), QF/QD	0.36/0.26
Max. gradient (T/m), QF/QD	15.94/-15.64
Aperture radius (mm)	30
Sextupole magnet	
Number of SF, SD	22, 26
Magnetic length (m)	0.10
Max. gradient, SF/SD, (T/m^2)	109/-102
Aperture radius (mm)	30

The booster injection system consists of a septum and a fast kicker. The extraction system is comprised of a fast kicker, three bump magnets, a thin septum and a thick septum. The schematic layout and beam envelops of the injection and extraction are shown in Figure 5 and Figure 6 respectively.

The SSRF booster will use the biased sinusoidal wave as the dipoles magnetic field ramping curve, and the ramping curve of quadrupoles must trace the dipoles with precision of 0.1%.

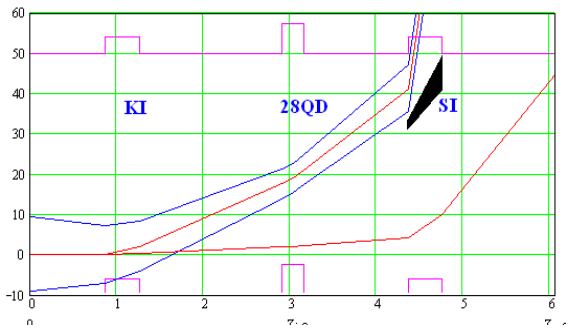

Figure 5: Schematic layout of booster injection

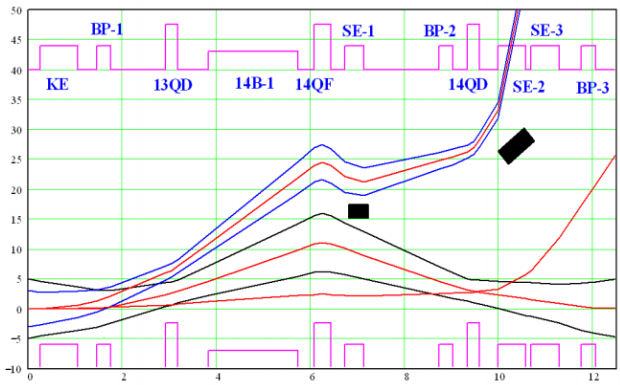

Figure 6: Schematic layout of booster extraction

Schematic layouts of magnets and diagnostic components for the low energy beam transport line (LT) and high energy beam transport line (HT) are shown in Figure 7 and Figure 8.

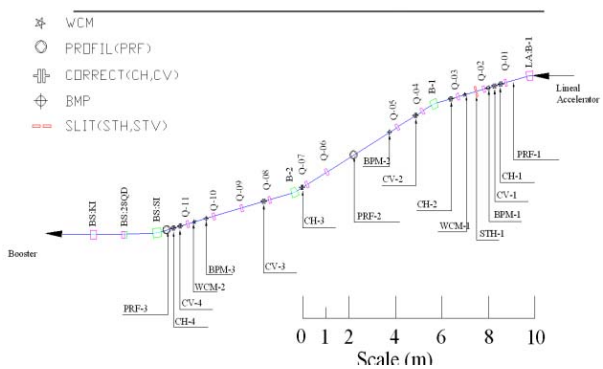

Figure 7: Schematic layout of LT

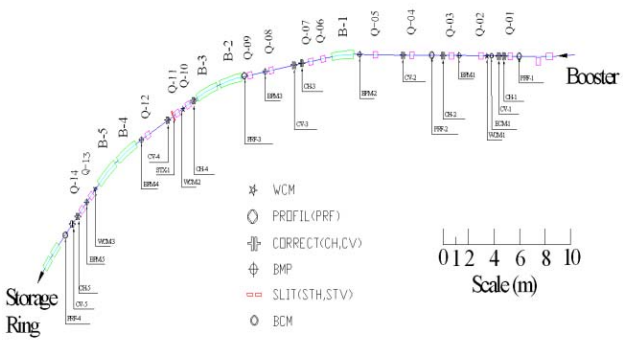

Figure 8: Schematic layout of HT

The prototype of key devices, such as dipole magnet, 2Hz dynamic dipole power supply, kicker and septum, fast pulse generators etc., have been developed and tested. Most of online devices are in the mass productions.

The installation of utilities in booster tunnel and technical halls was already started from January, 2007. In the meantime the pre-installation of booster cells was also started, and cells installation into tunnel will be started from April 2007.

Figure 9 and Figure 10 show some progress of SSRF booster.

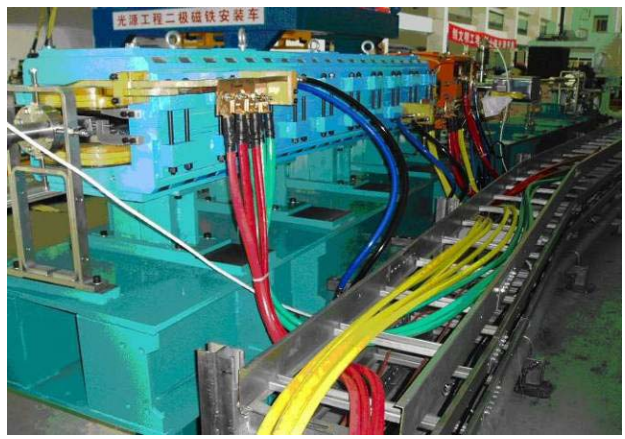

Figure 9: Test installation of a booster standard cell

Figure 10: Utilities installation in Booster tunnel

REFERENCES

[1] Z.T. Zhao, Construction of Shanghai Synchrotron Radiation Facility, These proceedings.

[2] Z.T. Zhao, H.J. Xu, Progress of the Shanghai Synchrotron Radiation Facility, proceedings of APAC 2004, Gyeongju, Korea.

[3] D.M. Li, Q.Gu, Z.T.Zhao, The New Scheme of SSRF Injector, proceedings of APAC 2004, Gyeongju, Korea.

PROJECT OF 2 GeV SYNCHROTRON LIGHT SOURCE FOR THE REPUBLIC OF KAZAKHSTAN

K. Kadyrzhanov, S. Lysukhin, INP, Almaty, Kazakhstan
E. Antokhin, K. Zolotarev, N. Mezentsev, G. Kulipanov, A. Philipchenko, V.Panchenko, A. Utkin
BINP, Novosibirsk, 630090, Russia.

Abstract

Applications of synchrotron radiation (SR) are very popular for last time in many research fields. Thus a developing of compact source for generation of hard X-ray synchrotron radiation is very actual task. The goal of this work is a developing project of SR source for Republic of Kazakhstan. This storage ring mainly dedicated for performing the high sensitive X-ray fluorescence analysis of different natural samples to be used for ore exploration, ore processing and metallurgy . But implementations of other popular techniques applied for research and education with using synchrotron radiation (XAFS, XRD, etc) are also possible. This report includes a detailed description of main parameters and magnetic structure of designed storage ring as well as preliminary design of injector system.

INTRODUCTION

The growth of Kazakhstan industry demands the developing modern methods of element analyses for ore exploration and processing. In order with traditional for XRF "light" elements Z<30 (Ti, Cr, Mn, Co, Ni, Cu, Zn) there is necessity to have express and precision methods of determination Nb, Mo, Pd, Ag, Cd, In, Sn (41<Z<50) and Hf, Ta, W, Re, Pt, Au, Th, U (Z>70), that requires hard X-ray radiation with the photon energy up to100 KeV.

To provide this requirement the electron beam working energy is planed to be 2 GeV and hard X-ray flux is possible due to using superconducting bending magnet with maximal field value up to 8.5 Tesla. Thus critical photon energy for chosen energy and magnetic field values is 20 keV, that enough for fluorescence analysis of U by studying L and K-series [1].

Horizontal equilibrium emittance should correspond to the modern synchrotron light sources of 3rd generation, but with circumference of moderate size, providing moderate capital and operation cost. Moreover the number of SR channels for XRF analysis and other synchrotron radiation techniques should be as large as possible.

LATTICE CHOICE

Based on above demands and considerations we chose the emmitance as about 10 nmrad as desired target and tried to find the appropriate lattice.

Background

The well-known formula for theoretical minimum emittance is as follows:

$$\varepsilon_x = \frac{C_q\gamma^2}{J_x}\frac{\oint \frac{\mathcal{H}(s)}{\rho^3(s)}ds}{\oint \frac{ds}{\rho^2(s)}} = \frac{C_q\gamma^2}{J_x}\frac{I_5}{I_2} = \frac{C_q\gamma^2}{J_x}A \qquad (1)$$

where A is part concerning integration, C_q=3.84·10 $^{-13}$ m·rads, γ is relativistic factor, ρ is bending radius, θ is bending angle, J_X is damping coefficient.

Integrating over all dipole magnets within the cell and assuming that dipole field is isomagnetic (i.e. magnets have constant radius) one can rewrite A from (1) as [2]:

$$A = \frac{\sum_i \frac{\int_{L_i}\mathcal{H}\,ds}{\rho_i^3}}{\sum_j \frac{L_j}{\rho_j^2}} = \frac{\sum_i \frac{\int_{L_i}\mathcal{H}\,ds}{\rho_i^3}}{\sum_j \frac{\theta_j}{\rho_j}} \qquad (2)$$

If for dipole magnets the values of optical functions satisfy the conditions for theoretical minimum emittance, then [3]:

$$\frac{\langle\mathcal{H}\rangle_{\min}}{\rho} = K\theta^3 \qquad (3)$$

where $K = \frac{1}{12\sqrt{15}}$ for central magnet and $K = \frac{1}{4\sqrt{15}}$ for side magnet (dispersion matching cells).

Then equation (2) can be written as:

$$A = \frac{\sum_i \frac{\langle\mathcal{H}\rangle L_i}{\rho_i^3}}{\sum_j \theta_j/\rho_j} = \frac{\sum_i \frac{K_i\theta_i^4}{\rho_i}}{\sum_j \theta_j/\rho_j} = \frac{\sum_i K_i\theta_i^4\langle B_i\rangle}{\sum_j \theta_j\langle B_j\rangle} \qquad (4)$$

where $\langle B_i\rangle$ is mean magnetic field value over magnet of *i*-th type.

Equation (4) allows performing the estimation of theoretical minimum emittance for different lattice types, consisting of different dipole bend magnets.

Taking into account the necessary of using superconducting magnet for hard X-ray generation the appropriate lattice type seems TBA cell with superconducting bend magnet (superbend) as central magnet and 2 conventional "warm" dipole magnets as side magnets.

For TBA case with different central and side magnets formula (4) can be rewritten as:

$$A = \frac{1}{12\sqrt{15}} \frac{\theta_c^4 \langle B_c \rangle + 2 \cdot 3 \cdot \theta_s^4 \langle B_s \rangle}{\theta_c \langle B_c \rangle + 2 \cdot \theta_s \langle B_s \rangle} \quad (5)$$

where indexes c and s denote central and side magnets correspondently.

In 2004 BINP fabricated a 9 Tesla Superbend for BESSY-II storage ring (Berlin, Germany). This magnet can be a prototype for current project. Some design details will be discussed later, but a typical field integral value of this magnet (about 1.6 T m) can be used for choice of bending angle for 2 GeV electron beam. The theoretical minimum emittance in that case is equal to 8.2 nmrad for 20^0 bending angle of each magnet according Eq. 5. In next sections the more detail description of accelerator storage ring lattice based on TBA cell is done.

TBA lattice with non-zero dispersion

The major parameters of TBA lattice with 6 cells are given in Table 1.

Table 1: Lattice parameters

Energy (GeV)	2
Circumference (m)	135
Beam current (mA)	500
Horizontal emittance (nmrad)	6
Number of cells	8
Superbend/"Warm" dipole field (T)	8.5/1.6
Superbend/"Warm" dipole bend angle (deg.)	10/17.5
Number of straights	8
Full length of straights (m)	42
Betatron tune (horiz; vert)	4.69; 2.62
Natural chromaticity (horiz; vert)	-23.9; -4.2

The layout of the lattice cell and plot of the beta and dispersion functions are shown in figure 1. Both the horizontal beta function and dispersion are symmetric within the superbend and conventional dipole magnets, reaching the minimum at their centers. The dispersion at straight section is non zero and has value of about 0.4 m. The emittance value generated on superbend magnet is about 20% of its value on normal conducting dipole. The corresponding electron beam size at magnet center is 25 μm, that provides good radiation source properties.

Note that since the bending angle is large enough as 20^0 it is possible to organise 4 synchrotron radiation channels from each superbend without problems related to space issue. So the total amount of proposed 24 keV critical photon energy SR channels for this storage ring structure is assumed to be 24.

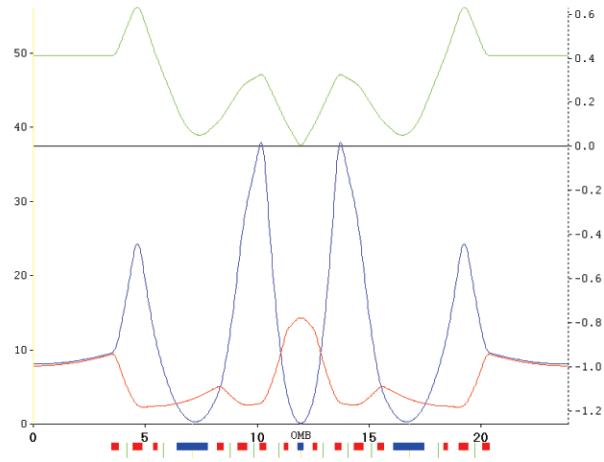

Figure 1: Lattice functions and cell layout (blue is horizontal beta, red is vertical beta, top plot is dispersion).

TBA lattice with zero dispersion

Lattice functions for zero dispersion at straights are presented in figure 2. The lattice layout is left the same as previous one, but values of gradient of quadrupoles are correspondingly changed. The emittance grows in this case to 29 nmrad. Although emittance value becomes essentially larger it is possible at zero dispersion mode to install damping wigglers into 7 m long straights to reduce emittance value. The ways of emittance reducing for zero dispersion regime is subject for further studying.

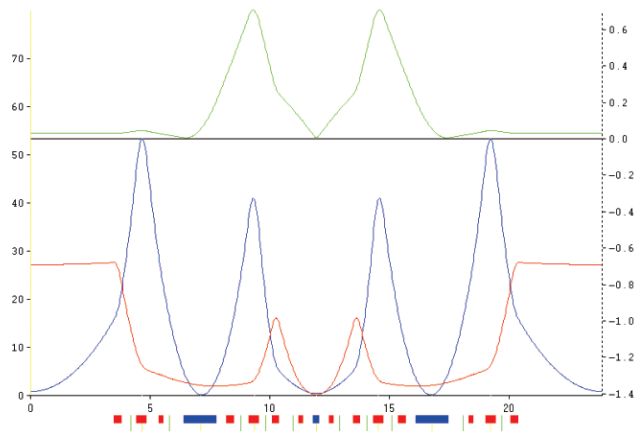

Figure 2: Lattice functions for zero dispersion mode (blue is horizontal beta, red is vertical beta, top plot is dispersion).

9 T SUPERBEND MAGNET

The design of central dipole magnet for TBA cell is based on 9 Tesla superconducting bending magnet constructed for BESSY-2 storage ring [4]. The general parameters of 9 T superbend is summarised in Table 2.

Table 2: Parameters of superbend magnet.

Vertical/horizontal aperture (mm)	30/75
Pole gap (mm)	46
Operating magnetic field (T) Maximum magnetic field (T)	3.3-8.5 9.6
Coil material	Nb_3Sn, NbTi
Current in coil for 8.5 T (A)	264
Ramping time 0-7 T/0-9 T (min)	<5/<15
Eff. Magnetic length along beam (m)	0.1777
Bending angle (deg.)	11.25 (for 1.9 GeV)
Stored energy for 8.5 T (kJ)	180

Superbend magnet consists of 2 superconducting coils assembled above and below of vacuum chamber. The coil consists of five sections winding around magnetic steel core. The first and second sections are wound from Nb_3Sn wire and third section is from NbTi wire. The forth NbTi section is used for correction. The magnetic steel pole has a shimming notch to obtain necessary transverse field homogeneity. The magnet implies the magnetic steel yoke, so the fridge magnetic fields are very low. Figure 3 presents the drawing and picture of the superbend magnet.

Figure 3: General view and picture of 9 T superbend magnet.

OTHER SYSTEMS

Here we briefly discuss the key components of accelerator complex, which are assumed to be produced from state-of-art systems, i.e. previously developed and manufactured at BINP. The electron linac is planed as having energy of 100 MeV. The booster synchrotron should satisfy the following specification:

- full energy injection
- repetition rate 1-3 Hz.

The magnetic elements and support structures of main storage ring are planed to be produced the same as ones designed and produced for Swiss Light Source by BINP. RF system can be standard BINP's 180 MHz system with high order mode suppression.

SYNCHROTRON RADIATION OUTPUT

Figure 4 shows the photon spectrum from 9 T superbend magnet for 2 GeV electron energy and 500 mA current. 24 synchrotron radiation channels with such spectrum will be used for XRF analysis performing for purposes of ore exploration and processing as well as for other applications utilising hard X-ray radiation.

The developed storage ring lattice allows to accommodate up to 6 straights, length of each can be up to 7 m. These straights may be used for installation of different type undulators and wigglers.

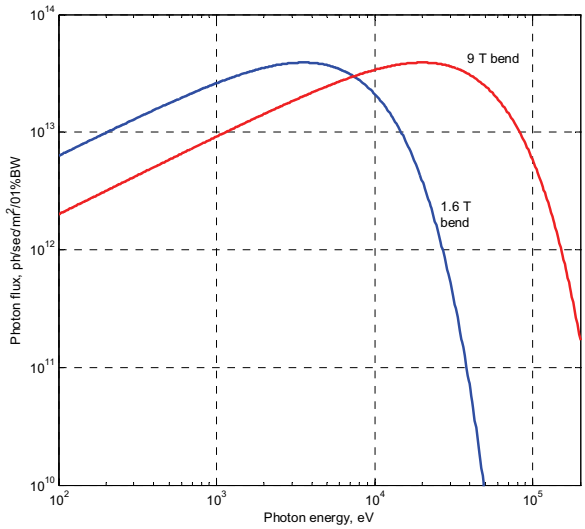

Figure 4: Synchrotron radiation spectrum from 9 T superbend magnet, E=2 GeV, I=500 mA.

CONCLUSION

The designed storage ring satisfies requirements imposed for modern 3rd generation light sources. Otherwise one seems to be economical and compact due to employing superconducting 9 Tesla bend magnets and standard key accelerator systems, developed at Budker INP. The main application of this light source is fluorescence analysis for ore and mettalurgy industry with hard X-rays from superbend. But the other widely used techniques like EXAFS, X-ray diffraction, microscopy, tomography, etc. also can be provided with recent light source design aiming the variety of research, industrial and educational purposes.

REFERENCES

[1] X-ray Data Booklet, http://xdb.lbl.gov
[2] A. Ropert, CERN Accelerator School, Lattices and Emittances, 1996, CERN 98-4, p.100
[3] L. C. Teng, Minimum emittace lattice for synchrotron radiation storage rings, ANL/FNAL, 1985, p.15
[4] S.V. Khruschev et al, 9 Tesla superbend for BESSY-2, proceedings of APAC 04, S. Korea, 2004.

A PROTOTYPE OF THE SSRF POWER SUPPLY CONTROL SYSTEM

J.G. Ding, H.J. Zhu, H. Zhao, L.R. Shen,
Shanghai Institute of Applied Physics, Shanghai 201800, P.R. China

Abstract

The Shanghai Synchrotron Radiation Facility (SSRF) is a third generation, 3.5GeV synchrotron light source currently being constructed at the Shanghai Institute of Applied Physics (SINAP) in Shanghai, China. There will be over 700 magnet power supplies (PS) in the Storage Ring, Booster, Linac and Transport Lines. According to the requirement of control precision, reliability and stability of the magnet power supplies, we decided to use PSI-designed digital PS control system [1][2][3] for PS control, that typical resolution reaches 1ppm and long term stability and reproducibility is better than 30ppm. Each PS has a local digital controller for a digital regulation loop and a optical point-to-point link to the VME level. The low-level EPICS [4] interface is identical for all power supplies. The VME-based front-end consists of a Single Board Computer (SBC), IP carriers and Industry Pack (IP) I/O modules. A prototype of the PS control system has been setup and tested at SINAP. Control and monitoring of the prototype has been implemented with EPICS. This paper describes the development of the prototype and the progress of the power supply control system and discusses our future plan.

OVERVIEW

The SSRF design requires a large number of magnet power supplies with a wide power range and a variety of different features. Power supplies should work with high performance of precision, stability and flexibility. The PSI (Paul Scherrer Institut, Switzerland) developed digital power supply control system was chosen as the front-end of the power supplies after investigating the control solution of the domestic and foreign labs.

The digital PS is a fully digital controlled, uniform solution for all magnet PS. It consists of two parts: a digital Power Supply Controller (PSC) and a VME 64x based system. The overall control system architecture is shown in figure 1.

One PS controller contains a pair of DSP controller card and an ADC card connected through a backplane. They executes digital regulation loop for PS. Each PS controller has two communication links to the outside. A RS232 link connects the PS controller with a Personal Computer for the local operations and system configuration. A point-to-point optical fiber link connects the PS controller with an IP module hosted on a VME carrier board for the remote control. Plastic Optic Fiber is used for the optical link. The optical communication is controlled by a FPGA on the both ends: on the DSP card and on the IP module. Each controller also has an additional optical trigger input. The trigger input is used to start a programmable current waveform.

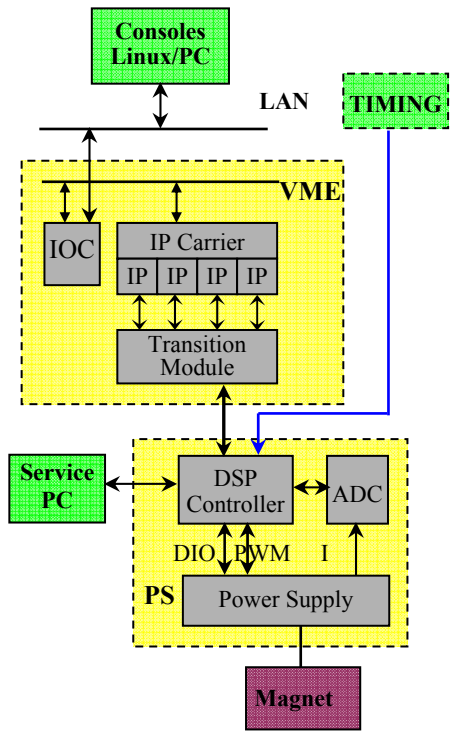

Figure 1: The PS control system architecture

The IP board is designed by PSI particularly for the solution. One IP module can serve two power supplies, each with one bidirectional 5MHz link. Four IP modules fit on an IP carrier VME card. Thus control density of eight PS per VME card can be reached. The throughput of each link reaches 10K float value frames per second.

The VME system is used as an EPICS Input/Output controller (IOC) to access the readable/writable registers of the PS controllers. IOC executes process control for power supplies by the EPICS runtime databases. The Linux/PC consoles run EPICS Channel Access (CA) clients to control/monitor the IOC execution.

SYSTEM SETUP

For SSRF project, our control platform is EPICS. The IOC for PS control is a VME 64x based system. Two kinds of SBC boards of PowerPC 74xx family have been evaluated to be used: Motorola 5500 and GE 7050. The IP carrier we use is SBS VIPC 664-ET. A Transition Module (TM) is used for the rear I/O of the carrier to connect the control system and the power supply and also executes optical/electrical signal conversion between them.

PS controllers, IP and TM boards are purchased from Diamond Light Source Ltd. Prototype power supplies together with backplanes are made by domestic factories. Control parameters of the PS controllers, such as PID algorithm parameters, maximum/minimum current limits, and digital input/output masks, etc., are configured by the SSRF Power Supply Group.

The VME based control system has been setup. Figure 2 is configuration of our VME based system. It is comprised of a 21-slot VME 64x crate with a Motorola 5500 SBC, seven IP carrier cards and seven TM modules. The first six IP carriers each has four IP boards installed, and the seventh has only one. Therefore our setup can control 50 sets of power supplies.

Figure 2: The prototype system configuration

A laptop computer is used for vxWorks/EPICS development. The laptop running Windows XP with Tornado 2.2.1 and vxWorks 5.5.1 installation performs functions to build vxWorks boot ROM and loadable image, compile EPICS base and EPICS applications for the PPC 5500 BSP target. The IOC runs vxWorks kernel, EPICS iocCore and applications these are download from the laptop when IOC is booted or reset. A desktop PC is used as a console running Linux with EPICS base and extensions installation.

SOFTWARE

The software functionality is organized in layers as shown in figure 3.

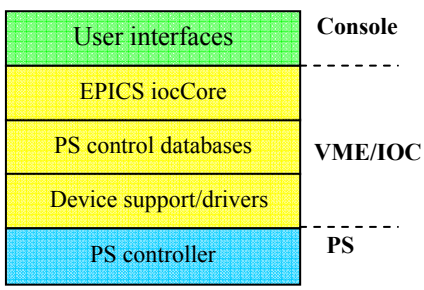

Figure 3: The PS control software scheme

PS Controller Software

The regulation loop and control of fast current waveform is handled by the PS controller. Software has already been written in the Flash EEPROM before PS controllers are shipped. Software is identical for all PS controllers and only differs by control parameters.

VME/IOC Software

For the IOC software, EPICS base 3.14.8.2 is used. The PS control EPICS device support/driver was transferred from Swiss Light Source that is also identical for all PS. The original version of device driver was run on EPICS base 3.13.x. To run the driver on the EPICS core of 3.14.8.2, some modifications have been made.

For the EPICS runtime database, we have developed two database templates for PS control: a standard template for PS basic control functions and a waveform template for current waveform download/upload. The standard template is used for all Linac, Booster, Transfer Lines and Storage Ring power supplies. The waveform template is only for the energy ramping power supplies of the Booster. The two templates have a total of more than 100 records. Some of the records are directly connected to the communication registers of the PS controller. The others are soft records for extra features, like initialization after IOC is booted or rebooted and hysteresis handling. Besides of the parameters like the switch, set and read-back the current, and the status of the power supply, there are parameters for PS fault diagnostic. Further more, there are some channels for diagnostics of the optical link. The database for each individual power supply is generated from the templates when IOC is booted by its PS name and other macro substitutions.

Console Software

The operator interface for magnet control is implemented with EDM. EDM is an EPICS GUI "display manager" tool to edit and execute controls to access process variable in IOCs. EDM screens are developed on Linux/PC platforms. Some application programs like routines for waveform download and upload from PS controller have been developed and already available. These applications are embedded in the EDM screens using the Shell control.

TEST RESULTS

The system described above has been tested with the prototype power supplies at SSRF. With up to 50 PS databases, more than 5,000 records loaded, VME/IOC works fine. For long time test over 50 hours, there was no any error noted. EDM screens, waveform download/ upload programs have been tested with the prototype control system. Features of IOC initialization and automatic/manually hysteresis handling also have been tested.

SUMMARY

There will be 608 power supplies used in SSRF project with fast corrector power supplies excluded. These power supplies will be controlled by 27 IOCs. It is estimated there are nearly 60K channels to be controlled in the power supply control system.

Besides, there are 40 common DC converters distributed in 20 PS stations along the storage ring. They are locally controlled by OMRON PLCs and connected to Local Area Network. We will use a soft IOC to control them via Ethernet communication.

The prototype power supply control system has demonstrated good performance of the digital PS solution. More tests will be done for runtime databases. Presently screens to meet physics requirements and screens of engineer levels have started to design. They will be in tree-layered structure, expanded from primary templates with macro-substitutions at runtime.

In addition, compared performance of Motorola 5500 to GE 7050, both are compatible in application layer, but the latter have shown higher performance and cost-efficiency. So GE 7050 will be used as IOCs for power supply control of the storage ring.

SSRF will begin beam commissioning at April, 2007. So the control system will be available before then.

ACKNOWLEDGEMENT

We are grateful to Kiman Ha of PAL, Korea, F.Jenni, T.Korhonen and A.Luedeke of PSI, Switzerland, and T.Dobbing of DLS, Britain for their kindly help and support to our work.

REFERENCES

[1] F.Jenni, L.Tanner, “Digital Control for Highest Precision Accelerator Power Supplies”, PAC’01, Chicago, May 2001.

[2] A.Ludeke, “Application of Digital Regulated Power Supplies for Magnet Control at the Swiss Light Source”, ICALEPS’01, California, 2001.

[3] L.Tanner, “Digital Power Supply Control System Technical Manual (Draft Version)”, Paul Scherrer Institut, Switzerland, Feb., 2005.

[4] Epics home page: http://www.aps.anl.gov/epics

STATUS OF THE PHOTON FACTORY

S. Sakanaka, S. Asaoka, W. X. Cheng, K. Haga, K. Harada, T. Honda, M. Izawa, T. Kasuga, Y. Kobayashi, H. Maezawa, A. Mishina, T. Mitsuhashi, T. Miyajima, H. Miyauchi, S. Nagahashi, T. Nogami, T. Obina, C.O. Pak, H. Sasaki, Y. Sato, T. Shioya, M. Tadano, T. Takahashi, Y. Tanimoto, K. Tsuchiya, T. Uchiyama, A. Ueda, K. Umemori, and S. Yamamoto
Institute of Materials Structure Science (IMSS), KEK, 1-1 Oho, Tsukuba, Ibaraki 305-0801, Japan
T. Ieiri, S. Isagawa, T. Kageyama, M. Kikuchi, K. Kudo, T. T. Nakamura, H. Nakanishi, K. Oide, M. Ono, T. Ozaki, H. Sakai, Y. Sakamoto, S. Takasaki, M. Tejima, and S. Yoshimoto
Accelerator Laboratory, KEK, 1-1 Oho, Tsukuba, Ibaraki 305-0801, Japan

Abstract

The present status of two synchrotron light sources, the PF and the PF-AR storage rings at KEK, is presented. An upgrade project of the PF storage ring was successfully completed in 2005. Through this upgrade, four short-straight sections were newly created, and ten existing straight sections were extended. Two short-gap undulators were then installed in the new sections, and were commissioned. Further improvements, including a top-up operation, are in progress. The other PF-AR is a unique single-bunch hard X-ray source. During 2005-2006, two in-vacuum undulators were successfully commissioned.

INTRODUCTION

The High Energy Accelerator Research Organization (KEK) manages two synchrotron light sources [1], the Photon Factory (PF) storage ring and the Photon Factory Advanced Ring (PF-AR). The principal parameters of both rings are shown in Table 1. The 2.5-GeV PF storage ring was commissioned in 1982 as one of the major synchrotron radiation (SR) sources in the world, and it has been operated very well. The PF ring has been upgraded three times (see Table 2). Through the series of upgrades, the PF ring has become competitive [2] with other intermediate-energy third-generation light sources. We report in the next section the latest upgrade, the recommissioning, and the prospect for further improvements. The other 6.5-GeV PF-AR (see Table 3), initially named the TRISTAN Accumulator Ring, was commissioned in 1984 as a booster for the TRISTAN 30-GeV e^+e^- collider. It was converted to a dedicated SR source in 1998, and was largely upgraded in 2001. The third section describes recent improvements and operational status of the PF-AR

PF STORAGE RING

Upgrade

We carried out an upgrade project [3, 4] of the PF storage ring from March to September, 2005. This project aims at creating more space for advanced insertion devices. We refurbished the magnet lattice of about two-thirds of the ring as shown in Fig. 1. This upgrade resulted in creation of four short-straight sections of 1.4 m each, as well as extension of existing 10 straight sections.

Table 1: Principal parameters of the PF and the PF-AR storage rings.

	PF	PF-AR
Beam energy	2.5 GeV	6.5 GeV
Circumference	187 m	377 m
Natural emittance	35 nm·rad	293 nm·rad
RF frequency	500.1 MHz	508.6 MHz
Energy loss per turn	0.4 MeV	6.66 MeV
Injection energy	2.5 GeV	3 GeV
Typical number of bunches	280	1
Initial stored current	450 mA	60 mA
Beam lifetime (at initial cur.)	30-40 hrs	15-20 hrs
Number of insertion devices	9	6

Table 2: Brief history of the PF storage ring.

Year	Event
1982	Commissioned.
1986	Upgraded to lower emittance (460 → 130 nm·rad).
1997	Upgraded to lower emittance (130 → 36 nm·rad).
2005	Upgraded (extensions in straight sections) [3, 4].

Table 3: Brief history of the PF-AR.

Year	Event
1984	Commissioned as the TRISTAN injector.
1986	Parasitic SR usage started.
1998	Converted to a dedicated light source.
2001	Upgraded (beam current and lifetime) [5].

In these sections, we replaced quadrupole magnets to thinner ones, and moved them closer to bending magnets. We also renewed the beam ducts in these sections [6], and reconstructed thirteen beamline front-ends [7] so that we accommodated them both to the new lattice and to coming new IDs. We also reinforced septum magnets for injection, renewed our control system to an EPICS

(Experimental Physics and Industrial Control System)-based one [8], and installed a transverse bunch-by-bunch feedback system [9].

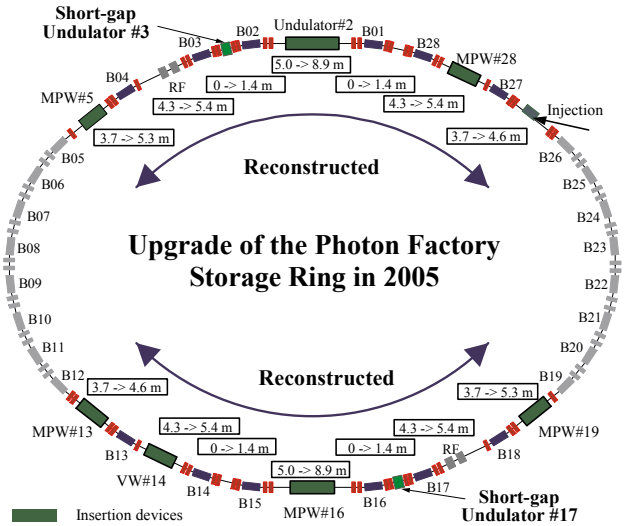

Figure 1: Upgrade of the PF storage ring in 2005.

Recommissioning

The PF storage ring was recommissioned on September 20, 2005. We could successfully store the beams within five days, and could achieve a target beam current of 450 mA on September 30. After vacuum conditioning with beams, user operations resumed on October 18, 2005. From November 22, we reduced a frequency of injections from three to two times a day due to an improvement in the beam lifetime. The progress in vacuum conditioning after the recommissioning is reported in [6].

New Insertion Devices

In the newly created short-straight sections, we installed two short-period short-gap undulators, SGU#17 [10] and SGU#3, of in-vacuum type. The first short-gap undulator, SGU#17, has a period length of 16 mm, a number of periods of 29, and a maximum magnetic field of 0.92 T at a magnet gap of 4 mm, respectively. The other SGU#3 has very similar parameters but a different period length of 18 mm. The brilliance of the undulator radiation from the SGU#17 is shown in Fig. 2. These short-gap undulators can provide brilliant hard X-rays of up to 15 keV using up to the seventh-harmonic radiation at the beam energy of 2.5 GeV. To this end, the field errors of these undulators were corrected very carefully. In order to achieve very short magnet gaps, the vertical betatron function was squeezed to 0.4 m at the center of the undulator. The SGU#17 was successfully commissioned in October, 2005, and then, it has been operated very well with a minimum gap of 4 mm. The other SGU#3 was installed in the summer of 2006, and it was commissioned in October, 2006.

Operational Status and Accelerator Study

We annually operated the PF storage ring for about 5,000 hours during the last six years except in 2005.

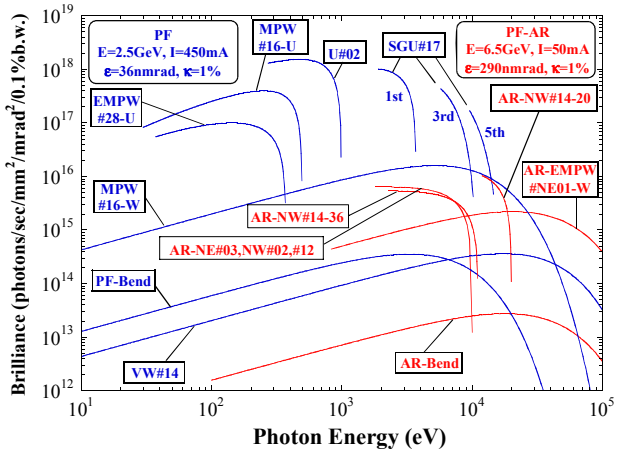

Figure 2: Brilliance of the synchrotron radiation available at the PF (blue traces) and the PF-AR (red) storage rings.

Approximately 16-19% of the operation time was used for accelerator study and tune-up. Failure time was about 0.5% of the total time during past four years. Detail operational statistics were summarized in [1].

We have currently 22 beamlines (BLs) for users including nine BLs from insertion devices (IDs). The number of registered users of the Photon Factory surpasses 2,500, and annual visits for experiments are 23,000 persons·days.

We have actively carried out accelerator physics studies. For example, the determination of non-linear resonance parameters [11], the development of various unique SR monitors [12], and the observation of quadrupolar tune shifts [13], are worthy of special mention.

Developments in Progress

Taking full advantage of the straight-section upgrade, we plan to renovate some conventional IDs to advanced ones. As the first step of this strategy, we plan to install a fast-switching elliptically-polarizing source in an 8.9-m straight section, while retiring a multipole wiggler, MPW#16. This device [14] will comprise a pair of APPLE-type undulators in tandem, and a fast orbit-bump system for selecting one of the photon beams from two undulators. One of the undulators is under construction.

A top-up operation project of the PF ring is underway. To share the injector beams with the KEK B-factory, the 8-GeV injector linac will be improved so that it can change an electron-beam energy from pulse to pulse, and can deliver the beams to the PF and the KEKB nearly simultaneously. We have remodelled our beam-transport line, and optimized an injection bump for minimizing coherent beam oscillations. After some remaining works, the top-up operation will be realized step by step.

PF-AR

Outline

The PF-AR is a unique 6.5-GeV “single bunch” light source which can provide high-flux hard X-ray pulses. High beam currents of up to 60 mA with a single bunch

allow us to reconcile pulse X-ray experiments with the other experiments requiring high-flux X-rays. A layout of the PF-AR is shown in Fig. 3. There are seven beamlines including five BLs from IDs. The PF-AR is a pioneer facility where the first in-vacuum undulator [15] was developed. Since then, we have installed five in-vacuum undulators in the PF-AR for hard X-ray production.

The PF-AR was largely upgraded [5] in 2001, where all vacuum chambers were replaced, and many other improvements were carried out. This upgrade resulted in high beam currents and long beam lifetime (15-20 hrs) of today.

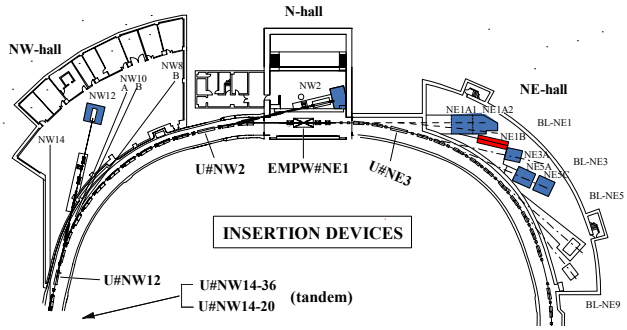

Figure 3: Layout of the PF-AR. A part of the ring, where the beamlines are located, is shown.

Operational Status

We annually operated the PF-AR about 5,000 hours after the upgrade in 2001. The total operation time in FY2005 was 5,328 hours, where an interruption of operations was 1.2% of total time. Under usual operations, the beams were injected twice a day, while we sometimes provided special two-bunch, 5-GeV operations for clinical users.

New Insertion Devices

Funded by the ERATO Non-Equilibrium Dynamics Project, two in-vacuum undulators [16], U#NW14-36 and U#NW14-20, were installed in the summers of 2005 and 2006, respectively, for the beamline AR-NW14A. These undulators were designed for time-resolved X-ray diffraction experiments and for XAFS experiments. They were installed in the same west straight-section in tandem, and are used exclusively. The former undulator, U#NW14-36, has a period length of 36 mm and a number of periods of 79, and it can provide wide-energy photons of 5-25 keV with up to the fifth harmonic radiation. The other U#NW14-20 has a period of 20 mm and 75 periods, and it can provide photons of 13-18 keV with the first harmonic. The brilliance of SR from these undulators is shown in Fig. 2. These undulators were successfully commissioned in the autumns of 2005 and 2006, respectively.

Accelerator Study

A novel beam-injection scheme [17] using a pulsed quadrupole magnet, instead of using several kicker magnets, was proposed. This scheme was successfully demonstrated at the PF-AR.

FUTURE PROJECT

We had a series of intensive discussions with user scientists and with other accelerator scientists in Japan about how the future Photon Factory should be. We came to a conclusion that we should immediately start R&D for the future light source which is based on the Energy Recovery Linac (ERL). In April 2006, KEK formed an inter-departmental “ERL project office”, and started R&D for the ERL-based future light source. The future project of the Photon Factory is described in [18].

CONCLUSIONS

The upgrade of the PF storage ring was successfully completed in 2005. This resulted in the creation of much available space for new insertion devices, and for renovating old IDs to advanced ones. Two short-gap undulators were newly installed, and were commissioned successfully. Through the series of upgrades, the PF storage ring has become competitive to other intermediate-energy third-generation sources. The delivered user hours and the reliability of operations are comparable to the best of its class in the world [2].

The other 6.5-GeV PF-AR has annually been operated for about 5,000 hours with high reliability. Two in-vacuum undulators were commissioned during 2005-2006.

ACKNOWLEDGMENT

We would like to thank the staff of the Accelerator Division III for their efforts to improve the KEK linac.

REFERENCES

[1] Photon Factory Activity Report 2005. http://pfwww.kek.jp/pfacr/index.html
[2] Photon Factory Review 2006. http://pfwww.kek.jp/hyoka05/reviewreport.pdf
[3] T. Honda *et al.*, EPAC’06, p. 3365.
[4] T. Honda *et al.*, Proc. SRI2006, Daegu, Korea, 2006 (to be published).
[5] For example, T. Miyajima *et al.*, PAC2003, p. 860.
[6] Y. Tanimoto *et al.*, EPAC’06, p. 3371.
[7] H. Miyauchi *et al.*, Proc. SRI2006 (to be published).
[8] T. Obina *et al.*, Proc. SRI2006 (to be published).
[9] W. X. Cheng *et al.*, EPAC’06, p. 3009.
[10] S. Yamamoto *et al.*, Proc. SRI2006 (to be published).
[11] T. Miyajima *et al.*, Jpn. J. Appl. Phys. **44** (2005) 2006.
[12] For example, T. Mitsuhashi, Proc. DIPAC2005, p. 7.
[13] S. Sakanaka *et al.*, Phys. Rev. ST-AB **8** (2005) 042801.
[14] K. Ito *et al.* (ed.), KEK Internal 2005-7, pp. 39-45 [in Japanese].
[15] S. Yamamoto *et al.*, Rev. Sci. Instrum. **63** (1992) 400.
[16] S. Yamamoto *et al.*, Proc. SRI2006 (to be published).
[17] K. Harada *et al.*, PAC2005, p. 1517.
[18] T. Kasuga *et al.*, in these proceedings.

DEVELOPMENT OF TRIGGER AND CLOCK DELAY MODULE WITH ULTRA-WIDE RANGE AND HIGH PRECISION *

T. Ohshima#, Y. Fukuyama, J. Kim, JASRI/SPring-8, Hyogo, Japan,

Y. Tanaka, RIKEN SPring-8 Center, Hyogo, Japan,

E. Nonoshita, H. Sengoku, Candox Systems Inc., Saitama, Japan

Abstract

Pump and probe experiments using short pulse lasers and synchrotron radiations require precise timing relation between the laser pulse and the RF reference signal of the accelerator. The pulse laser needs clock signal for a mode-locked laser and trigger signal for a regenerative amplifier. The delay time of these two signals were usually adjusted by using a mechanical phase shifter or a cable delay. They have disadvantages of short tuning range or discontinuity in the clock signal. We developed a new delay system, which can continuously change the delay time with the range over 200 ns and the precision better than 3 ps. The key point of the system is combination of an IQ modulator and a synchronous counter. The IQ modulator can change the phase of the RF signal with infinite amount with high precision in ether positive or negative direction. The phase-modulated RF signal is fed to a frequency divider and its output is used for the clock signal of the mode-locked laser. The signal is also fed to the synchronous counter and its output is used for the trigger of the regenerative amplifier. The effectiveness of this system was confirmed by an experiment carried out at the SPring-8. Composition of the delay system, performance and its applications are described in the paper.

INTRODUCTION

The SPring-8 is one of the 3rd generation X-ray source facilities. One of outstanding features of the SPring-8 is its flexible time structure. The FWHM of the X-ray pulse width is about 40 ps. The interval of the pulses can be changed from 2 ns to 600 ns by using a various filling patterns. The interval can be increased of the order of millisecond by using a high-speed mechanical shutter (X-ray Pulse Selector: XPS). Using this feature, time resolved experiments, such as nuclear magnetic resonance, pump and probe experiments are carried out at the SPring-8. In the pump and probe experiments a time evolution of the excited state of material pumped by a laser light (or X-ray) is measured by probing X-ray (or laser light) by changing the irradiation timing of pumping light. In the experiments we need following signals:

a) Clock signal for a mode-locked laser whose frequency is 84.76 MHz, which is one-sixth of the RF reference frequency of 508.58MHz.

b) Trigger signal for a regenerative amplifier with, for example, 949Hz repetition rate.

c) Trigger signal for a XPS with same repetition rate as b).

All these signals should be precisely synchronized to the timing of the X-ray. And the clock signal of a) should be continuous to avoid frequency jump of the mode-locked laser. Because the X-rays are generated from the electron bunches stored in the ring, and the timing of the electron bunches are determined by the acceleration RF system, the signals for the laser can be generated from the RF reference signal. Usually mechanical delay modules such as trombones or cable delays are used to change the clock timing. But they have disadvantages: the trombone has a short tuning range, and the cable delay has a discontinuity when the delay length is changed using RF switches.

To achieve the large delay range with high precision without discontinuity, we developed a new timing system. It consists from a phase delay with infinite tuning range and a synchronous counter. Detail of the composition of the system and its performance are shown below.

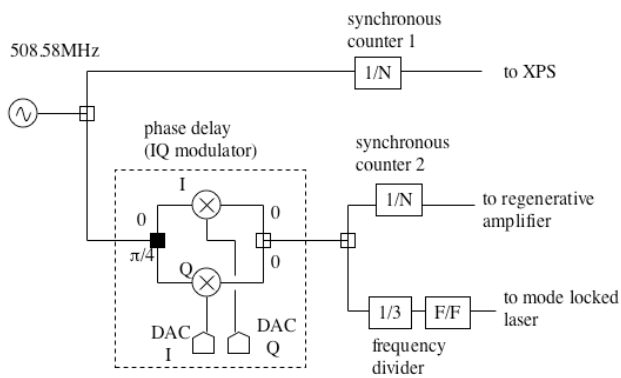

Fig. 1. Schematic diagram of the trigger and clock delay system.

COMPOSITION OF TRIGGER AND CLOCK DELAY SYSTEM

The trigger and clock delay system is composed by a phase delay and a synchronous counter. Fig. 1 shows the schematic view of the trigger and clock delay system. The 508.58MHz-RF reference signal is divided into two. One is fed to a synchronous counter No. 1 to generate a trigger signal for the XPS. The timing of the signal is adjusted to synchronize that of X-ray pulse. The other reference signal is fed to a phase shifter to make a delayed reference signal. The delayed signal is divided into two. One is fed

* This work was supported by CREST, Japan Science and Technology Agency.

ohshima@spring8.or.jp

to a frequency divider to generate a clock signal for the mode-locked laser. The other delayed signal is fed to a synchronous counter No. 2 whose output is used for triggering the regenerative amplifier.

The timing of the laser pulse can be changed by changing the amount of the phase delay. If the phase delay is increased by π/4 using this phase shifter, the phase of the clock for the mode locked laser and the pulse timing from the counter No. 2 is delayed in 0.5 ns. If the phase delay is decreased, the timing is made earlier. In case of phase rotation of θ that is over 2π, there is no difference between θ and θ - 2π in the RF property of the 508.58MHz signal. But they make big difference by combining the phase shifter with the counters. The delay time of the counter can be changed much longer than the clock period of 2 ns if the phase angle is rotated in multi-turn. For example, the phase rotation of 100 turns corresponds to the delay time of 200 ns.

We use an IQ modulator as the phase shifter. The reference signal is divided to an in-phase signal (I) and quadrature signal (Q), which has π/4 phase delay relative to the I signal. Both signals are fed to the mixers. The control voltages of the mixers are set to give an aimed phase angle using DACs. The outputs of the mixers are combined in-phase and delayed reference signal is obtained. This phase can be increased or decreased smoothly, and infinitely. The phase angle is determined by the amplitudes of the control voltages from the DACs and its precision is not affected by the amount of the phase rotation. This means the precision is kept constant even if the phase rotation is very large.

We use a HMC495 made by Hittite Microwave Corporation as an IQ phase modulator. The working frequency is 0.25GHz to 3.8GHz. The control signals to the modulator are fed from a SR245 made by Stanford Research Systems that has 13-bits DACs. We use a 17K32 made by Digitex Lab. Co., Ltd as the synchronous counter, which can count up to 30bits with 508MHz clock. Two parameters N and M are set to this counter. N determines the number of the frequency division. M determines the delay time in a step of the clock period.

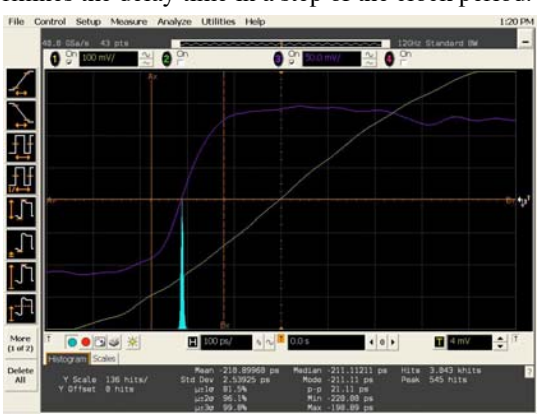

Fig. 2. The screen of the oscilloscope that measured the jitter for the 508.58MHz reference clock (red line) and the output from the IQ modulator (blue line).

PERFORMANCE TEST

We measured the jitter of the output from the IQ modulator relative to the zero cross timing of the 508.58MHz reference clock using an oscilloscope DSO81204B (Agilent). Fig. 2 shows the copy of the screen of the oscilloscope. The root mean square of the jitter was 2.5 ps. Then we fed the delayed reference signal to the synchronous counter. The measured r. m. s. jitter was 2.8ps. The increase of the jitter came from the counter and not from the IQ modulator, because the jitter was not change even if the reference signal was directly fed to the counter. These values include the jitter of the oscilloscope. So the actual jitter of the delay system is less than these values.

In order to determine the precision of synchronization of the timing system in an actual experiment with synchrotron radiation, we carried out pump-probe measurements at the BL40 in the SPring-8 [1]. A lattice constant of a high-purity GaAs crystal was changed when it was irradiated with a strong laser pulse. The slight shift of Bragg angle of the crystal was measured using the diffracted X-ray intensity monitored by an avalanche photo diode (APD). Fig. 3 shows the experimental setup. The strength of the output signal from the APD was measured as a function of the interval between the laser pulse and the X-ray pulse. The interval was changed from -5 ns to 200 ns with a step of 10 ps. The speed of the phase rotation of the IQ modulator was enough lower than the response frequency of the phase lock loop in the mode-locked laser to avoid the frequency jump. Fig. 4 shows the measured intensity of the APD. The precision of synchronization between the laser pulse and the X-ray pulse was determined to be 8.40 ps from this data using deconvolution analysis. This high precision implies that the time response of shorter than 40 ps (SR pulse duration) is measurable. It also demonstrates the benefit of the top-up operation that enables the bunch current almost constant.

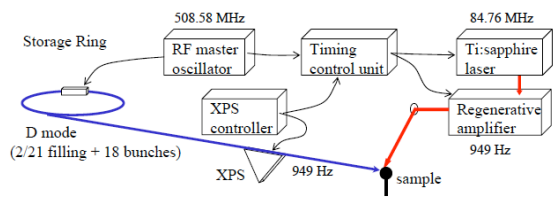

Fig. 3. The setup of the pump and probe experiment.

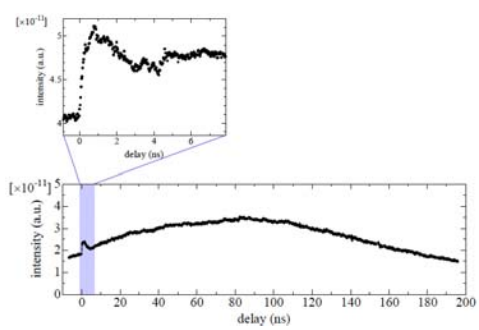

Fig. 4. The output intensity from the APD as a function of the interval between pumping laser and the X-ray pulse.

In the actual experiments, the timing of the X-ray pulse is not constant relative to the RF reference signal and is affected by the gap positions of the insertion devices, the RF acceleration voltages, the filling patterns and so on. So, at the SPring-8, the averaged synchronous phase angle is monitored every one second using a phase detector. It measures the phase difference between the 508.58MHz reference signal and the pickup signal from the button electrode. Fig. 5 shows a trend graph of the averaged synchronous phase angle for 24 hours. The figure also shows the gap positions for some insertion devices. We can see a clear dependence of the synchronous phase on the gap positions. The synchronous phase angles of all buckets are also measured using a high-speed oscilloscope every one minute [2]. Fig. 6 shows an example of the current and the synchronous phase angle of the bunch as a function of the bucket address. The filling pattern is eighteens single bunches with 1.5 mA bunch current and 116 bunch-train that carries the charge corresponding to 73 mA. The RF voltage in the acceleration cavity is reduced as the bunch train passes through because of its high beam loading, and the voltage is recovered gradually during the passage of the single bunches where beam loading is small. Measured synchronous phase angles are stored in a database and by using them the SR users can make compensation to their experimental data.

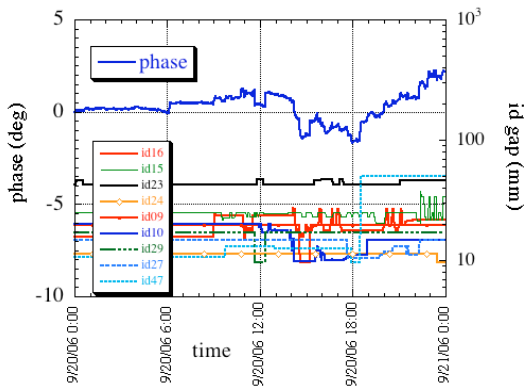

Fig. 5. The averaged synchronous phase angle and the gap positions of insertion devices.

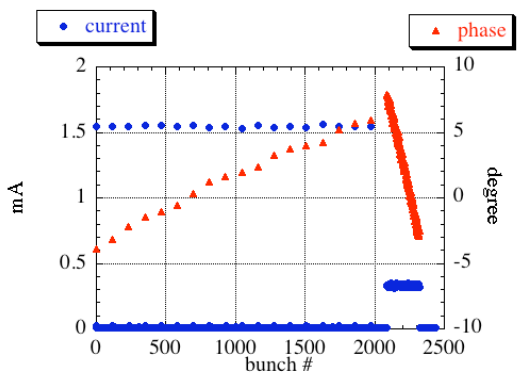

Fig. 6. The current (circle) and the synchronous phase angle (triangle) for the electron bunch as a function of the bucket address.

NEW TIMING MODULE

We are now under fabrication of a module that has all timing function in it by Candox Systems. Inc. The front panel of the module is shown in Fig. 7. The size is 19" wide and 2U height. The input frequency range is from 250 MHz to 800 MHz. The frequency-dividing ratio for laser clock can be selected from even integer of 2 to 512. The synchronous counter for laser amplifier is 32bit. The key components such as IQ modulator, high-speed logic circuits are mounted on a temperature controlled plate. For an application in FEL experiments, this module accepts an external reset signal for counters. The remote control is done with TCP/IP through Ethernet. Its first module will be delivered on March this year and test of the module will be done very soon.

Fig. 7. The front view of the newly developing delay module.

SUMMARY

We developed a trigger and clock delay system used for pump and probe experiments carried out at synchrotron radiation facility. It has a large tuning range of more than 200ns, and high precision of less than 3 ps. It consists of a IQ modulator and synchronous counters. The IQ modulator can be change the signal phase in a wide range over the clock period of 2 ns without degrading its timing precision. The performance was checked by a pump and probe experiment using a GaAs crystal at the SPring-8. The result showed the good time precision of less than 8 ps, which is shorter than the FWHM of the X-ray pulse of 40 ps. This also indicates a high precision and stability of the timing system, and the time structure of the electron bunch is almost constant. The timing system developed here can be used for many applications. The system can be used for laser timing control for SR experiments or FEL experiments, trigger signals for pulse magnets of accelerator and so on. A new delay module is under fabrication, which include all timing functions in 19" width and 2U height.

ACKNOWLEDGEMENTS

The authors thank to all members of CREST team for their support in performing the experiments. They also thank to Dr Y. Otake, RIKEN for his helpful information on IQ modulator.

REFERENCES

[1] Y. Fukuyama, et. al., The 1st Workshop of the Asia/Oceania Forum for Synchrotron Radiation Research, Tsukuba, Japan, November 2006, p.48.

[2] T. Ohshima, A. Yamashita and M. Yoshioka, "Beam phase measurement of stored bunch," EPAC2006, Edinburgh, June 2006, p. 1133.

RADIATION SAFETY SYSTEM FOR INDUS ACCELERATOR COMPLEX

R.G.Marathe, D.S.Thakur, Vimal Bhatnagar, R.K.Gupta, K.K.Thakkar, P.Fatnani and Gurnam Singh,
Raja Ramanna Centre for Advanced Technology, Indore, INDIA

Abstract

Ionizing radiation emitted from the accelerators of Indus facility and similar facilities is a major occupational hazard. Therefore, a Radiation Safety System (RSS) is installed at Indus facility as a mandatory feature. The essential constituents of the RSS are: Shielding structure, erected as a part of the building, for protecting the personnel from ionizing radiation; Protection system for ensuring that nobody is inside the shielded area when the facility is in operation and detection and monitoring of the radiation levels inside & outside the shielded area. This paper deals mainly with the later two parts. The Protection and Monitoring systems were set-up in stages, first, for microtron and booster synchrotron, followed by that for Indus-1 ring. For Indus-2, it was commissioned in July 2005. These systems were then integrated and have been performing as intended. This paper presents the integrated radiation safety system of Indus Accelerator Complex with emphasis to the features of Indus-2 RSS.

INTRODUCTION

Indus Accelerator Complex is the first synchrotron radiation facility in India, located at Raja Ramanna Centre for Advanced Technology, Indore. It consists of a 450 MeV electron storage ring Indus–1 and 550-2500 MeV booster-cum-storage ring Indus-2. A common injector system that feeds these rings consists of a 20 MeV microtron & a 450-600 MeV booster synchrotron. All these accelerators produce intense ionizing radiation due to gradual or accidental loss of high-energy electrons in these machines. A Radiation Safety System (RSS) has been installed at this Complex to protect the personnel from this harmful radiation as a mandatory pre-requisite. Shielding structures made of thick concrete walls and roofs, form part of the Complex-building and enclose these four machines to contain the harmful radiation. The objectives of RSS are to:

- Prohibit any radiation producing activity in a shielded area till it is accessible;
- Prompt and ensure evacuation of shielded areas;
- Permit operation of accelerator / systems only after the respective area is searched and locked;
- Terminate the operation if trapping of a person is annunciated from a locked shielded area or access to such an area is attempted;
- Display the status of operation and access restrictions;
- Monitor, regulate and record the access of personnel to machine areas;
- Monitor, record and display radiation fields in the Complex and annunciate high radiation levels.

The RSS mainly consists of a hard-wired, relay-logic based Protection System and Ion-chamber-based Radiation Monitoring System to achieve these objectives.

DESCRIPTION OF RSS

The shielding structures around the machines mark the boundaries in reference to which we have set-up our RSS. The entire Complex has been divided into three zones as follows:

ZONE#1: Normal occupancy area, e.g. Foyer, offices, sitting rooms, labs – Without any monitoring of radiation field/ dose to personnel,

ZONE#2: Controlled / Restricted entry area, e.g. Experimental Areas, RF system areas, Magnet P/S areas. – With continuous monitoring of radiation field and dose to the personnel,

ZONE#3: Shielded Areas, inaccessible during operation / entry-restricted during shutdown, e.g. Microtron and Booster hall, Indus-1 hall, Indus-2 tunnel, Transport line tunnel – with continuous monitoring of radiation field & dose to personnel.

The main constituents of RSS are

- Protection System
- Radiation Monitoring System
- Access Control System
- Closed Circuit TV Surveillance System
- Moving Message Display System
- Public Address System

Protection System

This is a relay-based system and operates with 24 V dc supply. It has three parts, one for each of the three machine areas namely, Microtron & Booster, Indus-1 ring and Indus-2 ring. Each part is comprised of Search & Scram switches, door interlocks, flashing lamps, siren, key-interlocks and a central Safety Interlock Unit. Search switches are located around the machine in each of these areas. Search of each area is carried out while actuating these switches sequentially. Along with the search switches, scram switches are also provided which can be actuated to stop machine operation if needed. All access doors of these areas are fitted with limit switches interlocked with the search logic. Flashing lamps and siren are provided for audio-visual annunciation of access prohibition for machine areas. These field devices are connected to the Safety Interlock Unit of the respective machine area, which ensures that machine operation is allowed only when all the device interlocks are cleared. For Microtron and Booster ring area this system was commissioned in 1994 and for Indus-1, in 1999. These have been modified and improved since then. The system for Indus-2 is more spread-out and therefore more

complex. It has an intermediate stage, namely RSS station, for local integration of logic. Indus-2 machine area is divided in four parts and field devices of each part are connected to an RSS station. These four RSS stations are in turn connected to Indus-2 Safety Interlock Unit kept in Indus Control room. In addition to the devices listed earlier, in Indus-2, a PULL CORD is also provided along the outer wall as a scram device, which, if pulled down, stops beam transport to Indus-2. The status of Protection system is indicated in the Control Room on the Safety Interlock Units. For Indus-2, the status is also sent to control room via a data acquisition system for display on a computer console. The block-diagram shows this.

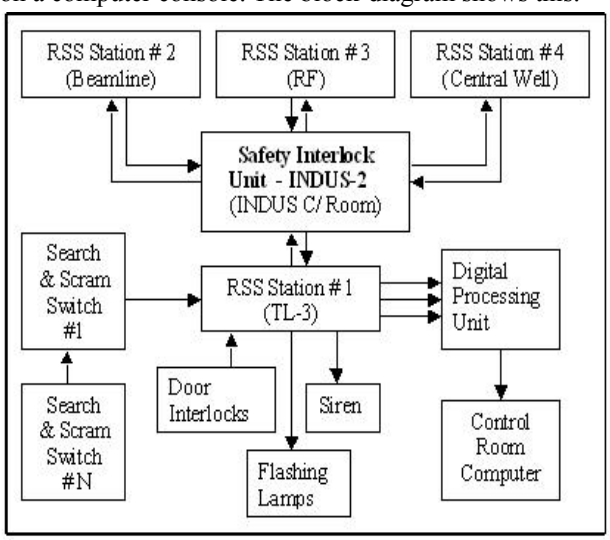

Figure 1: Block-diagram of INDUS-2 Protection System.

The Protection System also integrates features of these three parts and facilitates selection of operation modes for switching the electron beam injection between Indus-1 and Indus-2. It controls a switching magnet and a Beam-Shutter provided in the beam transport line that leads electron beam to the storage rings for ensuring radiation safety in an occupied machine area, while the other machine is in operation.

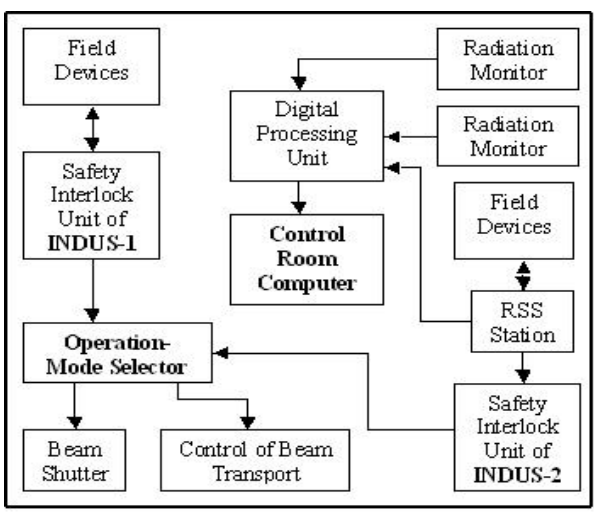

Figure 2: Block-diagram of Protection & Radiation Monitoring System.

Radiation Monitoring System

The unwanted hazardous radiation around electron accelerators is mainly bremsstrahlung radiation. Its high energy and pulsed nature make its detection and estimation difficult. However, in the experimental area around a storage ring, it is possible to measure this radiation using integrating detectors, because the beam storage and shielding structure smoothens the pulsed nature and reduce its energy. We have installed Ion-chamber-based radiation monitors at Indus Complex. High-range monitors having small SS ion-chambers are used as Beam-Loss Monitors near the machines (Zone#3), while low-range monitors having large SS and Al ion-chambers are used in the experimental halls and other occupied areas (Zone#2). Few high-sensitivity Environment monitors are placed in Zone#1 and around the complex. Neutron monitors are also installed to estimate of photo-neutron radiation. These monitors have been supplied by ECIL, Hyderabad and Electronic Division, BARC, Mumbai. All these monitors are provided with local high-radiation alarm and are connected to a computer in the control room, as shown, via a data acquisition system developed by Control Section of RRCAT.

Table 1: Details of Radiation Monitors.

Para-meters	Indus-1 Area radiation monitor	Indus-2 Area radiation monitor	Indus-2 Environ. radiation monitor	Indus-2 Beam Loss monitor
Detector	Ion chamber	Ion chamber	Ion chamber	Ion chamber
Gamma sensitivity	4 pA / mR/hr	12 pA/ mR/hr	18 pA/ mR/hr	25 pA/ R/hr
Sensitive volume	5 litre	25 litre	7 litre	20 cc
Energy range	300 keV -3 MeV	100 keV – 3 MeV	100 keV -3 MeV	300keV -3 MeV
Chamber wall	SS (2 mm)	Al (4 mm)	SS (4 mm)	SS 304L (1.5 mm)
Detector gas	Argon	Nitrogen	Argon	Argon
Pressure	150 psi	85 psi	100 psi	300 psi
Dose range	100 µR/h to 10 R/h	20 µR/h to 100mR/h	5 to 100 µR/h 0.1 to 10 mR/h	0.1 to 10 R/h 10 to 1000 R/h

Access Control System

Motorised tube-stile and turnstile gates are installed at all the entrances to Zone#3 of Indus-2 and at the entrance of Indus-1 hall. These gates are operated with electronic I-cards. These cards are issued to personnel authorised by the Operation-in-charge. The information of I-cards is recorded in a computer at control room when the gates are operated. The recorded data indicates the presence of personnel in the restricted zones. In the event of a fire accident, all these gates are released automatically for manual opening.

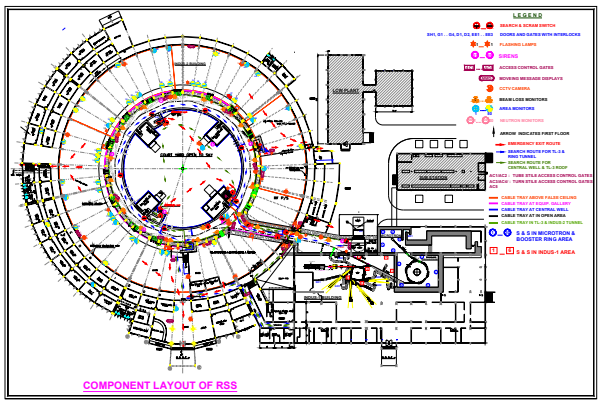

Figure 3: Layout of Radiation Safety System components in INDUS Accelerator Complex.

CCTV, Message Display and PA Systems

These systems are provided as a link between the operation staff and other personnel and aid greatly to the radiation safety in the complex. The CCTV system has colour-CCD cameras with motorized zoom lens and pan and tilt units connected to video monitors at control room and security post. The operation crew at Control Room visually monitors all the Zone #3 and Zone #2 areas before and during machine operation to detect any entrapment of personnel and accident in the machine areas. The Public Address System is used extensively for announcement before start-up of operation and also during testing of various systems to avoid accidents. Moving Message displays are provided in the machine areas and experimental areas to inform the personnel about the machine status and emergencies.

MODIFICATIONS AND PERFORMANCE

The radiation safety system of Indus has been modified and upgraded during past years. For the Injector system, trapped-key type kori-lock system was added. At Indus-1, changes were done to take care of the alterations done in the shielding while setting-up beam lines and to segment the search process. Kori-lock system and turnstile gate were also added. For Indus-2, distributed architecture was employed for the Protection system. It is segmented to quickly locate the place of breach of any interlock and failure of any field device.

A radiation safety system is a statutory requirement as per the regulatory rules and we were required to install this system for each machine before the commissioning trials could commence. Very reliable and consistent performance of RSS has played key role in the commissioning and regular operation of microtron, booster ring, Indus-1 and Indus-2. Provision has been made for bypassing the interlocks if the system fails (partly or completely) and an administrative procedure is also defined for this. However, such situations have arisen rarely during the past years.

CONCLUDING REMARKS AND FUTURE

The key feature of any safety system is its simplicity and reliability. Therefore we have used simple relay logic and hard-wired system for the Protection system, which is the heart of our RSS. This has kept the cost low and maintenance easy. Radiation detection and measurement is also done totally with analogue systems. The digital part is used only for display and annunciation. However, we now plan to replace the Protection system with PLC based system and use standard modules to build the system. Some development work for better estimation of radiation levels will also be taken up.

ACKNOWLEDGEMENT

The authors acknowledge the untiring efforts by Shri A.D.Kherde who carried out the fabrication, assembly and testing of all the modules of Protection system and Shri P.Haridas, who tested and installed Radiation Monitoring system. The contribution by S/Shri Anil Kumar, N.K.Chakraborty J.Azhakuvelavan and Vinay Kumar towards testing, installation and commissioning of the Indus-2 RS system is highly acknowledged

The authors are grateful to Dr V.C.Sahni, Director, RRCAT and Shri S.Kotaiah, Project Manager, Indus-2 for their guidance, support and constant encouragement.

REFERENCES

[1] RRCAT Internal Report, “Minutes of the meeting of Working Group for Indus-1 & 2 Radiation Safety System - RSS Design details”, June 2002.

[2] R.G.Marathe et al., “Instrumentation for Radiation Safety System of Indus-1”, Radiation Protection and Environment, Vol. 23, No.4, 2000.

[3] Technical Report of Synchrotron Radiation Source Indus-2, September 1998, Raja Ramanna Centre for Advanced Technology, Indore.

OPERATION EXPERIENCE OF TOP-UP INJECTION AT TAIWAN LIGHT SOURCE

G.H. Luo, H.P. Chang, C.T. Chen, Jenny Chen, J.R. Chen, C.C. Kuo
Keng S. Liang, Y.C. Liu, R.J. Sheu and D.J. Wang
National Synchrotron Radiation Research Center, No. 101, Hsin-Ann Road, Hsinchu, Taiwan

Abstract

The storage ring of Taiwan Light Source (TLS) has one Superconducting (SC) cavity, one SC wavelength shifter, and two SC wigglers installed during last two years. The operation mode was also upgraded to have the capability of top-up injection. Top-up is an operation mode in which the beam current is maintained above certain level by frequent injections in the storage ring. The current stability maintains in the range of 10^{-3} for long period of operation. It provides constant thermal loading on all components in the storage ring and the optics components of beamlines, as well as constant signal to the beam position monitor. The top-up injection is a routine operation mode during user shifts at TLS. Statistics and operation experience with superconducting devices will be discussed in this paper.

INTRODUCTION

The Taiwan Light Source (TLS) was designed to provide 200 mA, 1.3 GeV electron beam to generate photon source for academic and industrial research scientists. The storage ring is a six-fold symmetry Triple-Bend-Archomat (TBA) lattice with six straight sections. Four of the straight sections are occupied by conventional normal-conducting insertion-devices, U9, U5, W20 and Elliptical Polarized Undulator EPU5.6.

The strong demanding of synchrotron light in x-ray regime made the beam physicists to reduce the engineering margin and pushing the beam energy to 1.5 GeV and squeeze the space at injection and RF sections to accommodate super-conducting high-field insertion devices. A 3-poles and 5.3 Tesla superconducting wavelength shifter was installed at downstream of the injection kicker #3 to provide high photon flux in x-ray regime. One 29-poles and 3.5 Tesla superconducting multipoles wiggler was installed at the RF straight section next to the Super-conducting RF (SRF) cavity to generate high flux x-ray.

It was also a strong demand to increase the photon flux and reduce the photon fluctuation due to the Higher-Order-Modes (HOM) excitation from Dories cavity. An SRF cavity was installed to replace two Doris cavities at the end of 2004. The SRF cavity was designed to be a HOM free cavity and had the capability to provide 8 MV/m accelerating gradient with power handling capability up to 200 kW. The SRF cavity extends large flexibility for tuning the cavity to optimise the operation parameters. Figure 1. shows the schematic layout and timeline of the TLS facility.

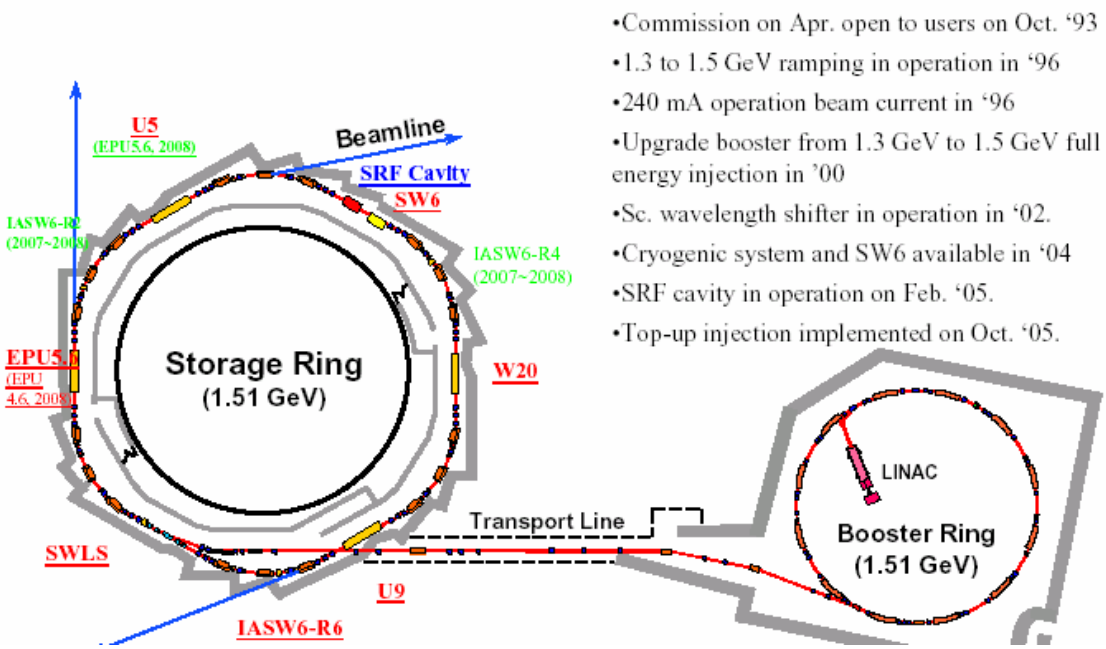

Figure 1. Schematic layout and timeline of the accelerator facility of Taiwan Light Source

There were several top-up injection experiments carried out at TLS [1] since 1995. The operation conditions of storage ring and injector were modified at various stages, e.g. energy ramping at storage ring, adding strong field insertion device and separated injection and user's working point, which made the top-up operation impractical at TLS.

The Advanced Photon Sources [2,3], Swiss Light Source [4] and SPring-8 [5] have demonstrated a successful operation in partial or full time with top-up mode for the third generation light source in recent years. A task force was formed to tackle the technical challenges and obstacles at NSRRC.

STORAGE RING AND STATISTICS OF OPERATION

Demanding of lower emittance, small gap insertion device and doubling the stored beam current made the beam physicists re-evaluate the feasibility of top-up operation at TLS. In normal operation before 2003, the injection working point was different from the user's working point at TLS. Merge the injection and operation lattices are the first step to reach the goal.

Two modes, fixed current bin and fixed time interval, of top-up injection were evaluated during accelerator development period. The chosen of stored beam current bin as key parameter means system will trig injection as stored current lower than a specified value. The injection will cease as the stored current higher than a specified value. In considering the user's data acquisition convenience, the top-up injection was chosen to be in fixed time interval. The injection is synchronized with Network Time Server every minute such that the user can gate out the disturbed data points, if there is any.

During the normal operation, the injection time interval was set to every 60 seconds. The maximum stored beam current was limited to 302 mA. The recorded current bin is ~1.2 mA. Figure 2 shows top-up operation at 350 mA during one section of accelerator development. The stored current variation is less than ± 0.2%.

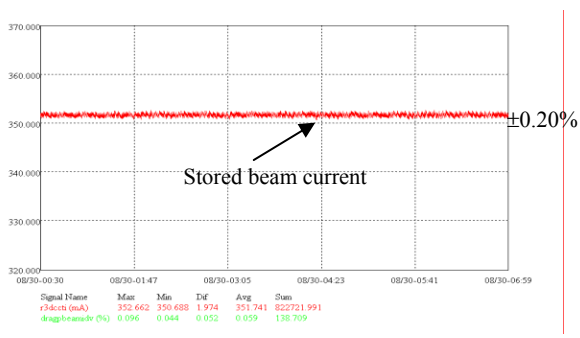

Figure 2. Top-up operation at 350 mA, the injection interval is set to every 60 seconds.

With the help of longitudinal and transverse feedback system, the beam stability measured by a 50 um pinhole detector shows a very stable photo-current during users shift. About 95% of the users beam time has $\delta I/I_0$ ratio better than 0.1%. The operation current was then increased to 400 mA. The transverse feedback system and SRF system are functioned as expected to suppress the instability and provide enough power to the stored beam during accelerator development time. To leave some engineering margins, the target operation current is set to 350 mA in coming year. Figure 3 shows the photon stability, 90% of time has $\delta I/I_0 < 0.07\%$, which was measured by one of diagnostics beamline during the 350 mA top-up operation.

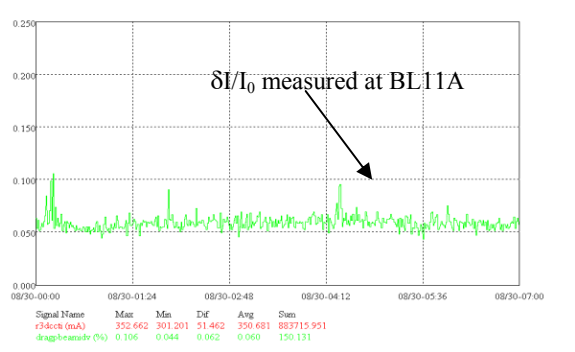

Figure 3. Photon stability measured by one of diagnostic beamline during 350 mA top-up operation.

From simulation, we understand that the transverse acceptance and time jitter of injection components are the key factors that affect the injection efficiency and filling pattern. By using a double trigger method in thyratron tube of the kickers, the jitters from injection bump reduced from ±10 ns to ±1 ns. This greatly improved the tuning of the injection process. The matching condition of injection components, jitter and amplitude, has been optimised to minimize the effect on filling patterns and maximize the injection efficiency. After very frequent injections, we can keep a reproducible filling pattern. However, we still found infrequent beam loss during the first year of top-up injection. The monthly statistics of unexpected beam loss number is shown in Figure 4. The major contributors of unexpected loss mainly came from kickers, SRF and noises during injection. The quality control of kickers system is under evaluation in order to reduce the number of unexpected beam loss. The fine tune of SRF feedback loops and preventing injection noises getting into interlock system is under way to have better tolerance in operation. The final target is to reach mean-time-between-failure better than 80 hours as short term goal. The statistics of scheduled, delivered and availability ratio in 14 years of TLS operation is shown in Fig. 5.

The beneficial of the constant stored beam in a storage ring is very obvious. The thermal gradient and deformation in time domain of top-up operation of optical components along the beam line can be minimized. The thermal expansion and contraction of girder and supporting structure along the storage ring chamber can be minimized either. This will help in the orbit control and also stabilize the launching condition of photons from

the source. Figure 6 shows the absolute displacement of Beam Position Monitor (BPM) relative to the ground. In decay mode, the stored beam current decayed from 200 mA to 100 mA, the position displacement of BPM can be as large as 15 μm in horizontal direction and 5 μm in vertical direction. However, in top-up mode the displacement of the BPM relative to the ground can be reduced to within sub-micron meter range as shown in Fig. 6.

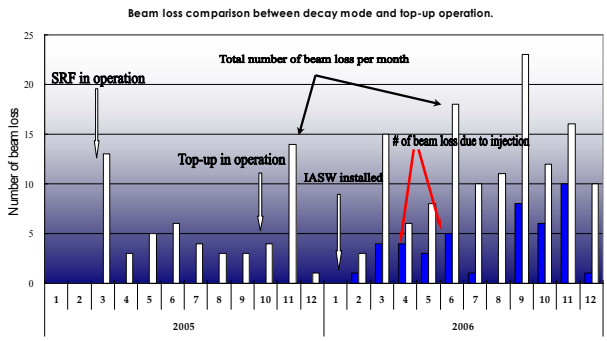

Figure 4. The statistics of unexpected beam loss before-and-after the top-up operation.

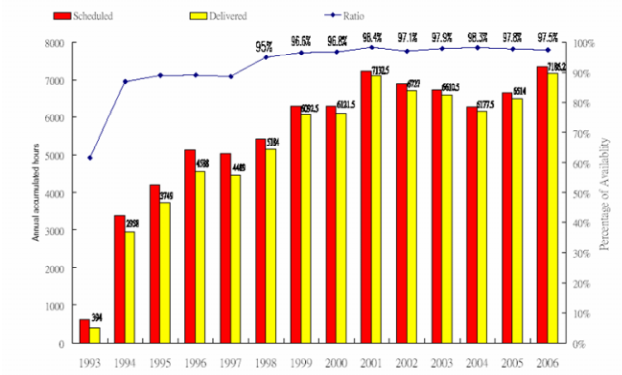

Figure 5. Statistics of scheduled, delivered and the availability ratio in 14 years of TLS operation.

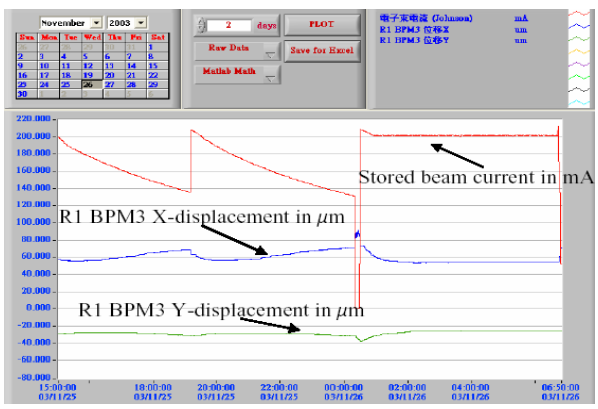

Figure 6. Recorded absolute position displacement in vertical and horizontal directions of BPM during decay and top-up mode.

RAIDIOLOGICAL CONSIDERATIONS

It is the first priority to keep the experimental area as a non-radiation controlled working environment. The basic design parameters of shield wall are according to the specification of Design Handbook [6] which was targeted to operate at beam energy of 1.3 GeV and maximum current of 400 mA in storage ring. The shielding wall was enhanced along the storage ring especially at the injection section. The exclusion zones of beamlines' front-end have been extended outward to keep the radiation dosage under controllable range. Additional radiation safety interlock systems, e.g. integrated dosage meters and dipole current margin, were implemented to abort the injection, if accumulated dosage or injection period excess the specified value.

Through devoted effort from NSRRC staff, the trip-off numbers due to radiation interlock is minimized during the test period of the third quarter of 2005. Not a single interrupt of top-up operation has been recorded due to excessive radiation dose since the machine start up in 2006. All the surveillance results and the TLD readings of the staff and users in NSRRC demonstrate that the radiological impact to personnel and environment due to top-up operation is well controlled and over-estimated at the beginning of the project.

SUMMARY

To reach the ultimate goal of third generation light source, TLS has prepared all the necessary steps to provide top-up operation mode to the users. The top-up mode provided the best thermal solution to the beamlines' optical components and locked the launching condition of the synchrotron light to users. Top-up injection also extends the new opportunities in probing better operation condition, for example lower the emittance, lower the gap of insertion device and increasing the bunch current without worrying the impact of beam lifetime. The top-up mode is routinely operated with SRF and three superconducting insertion devices successfully at TLS. It lays a solid foundation for the construction of a new 3~3.3 GeV Taiwan Photon Source.

REFERENCES

[1] T.S. Ueng, et al., "Topping Up Experiments at SRRC, "EPAC'96, 1996.
[2] L. Emery and M. Borland, " Upgrade Opportunities at the Advance Photon Source Made Possible by Top-Up Operations,"EPAC'02, Paris, 2002, p.218.
[3] L. Emery, M. Borland "Top-Up Operation Experience at the Advance Photon Source," PAC'99, 1999, New York, p. 200.
[4] A. Ludeke, M. Munoz, "Top-up Operation Experience at the Swiss Light Source," EPAC'02, 2002, Paris, p.721.
[5] H. Tanaka, et.al. "Top-up Operation at Spring-8," EPAC'04, 2004, Lucerne, p. 222.
[6] SRRC Design Handbook

SCSS PROTOTYPE ACCELERATOR TIMING SYSTEM

N. Hosoda, T. Ohata, T. Ohshima, JASRI/SPring-8, 1-1-1, Kouto, Sayo, Hyogo, 679-5198, Japan
H. Maesaka, Y. Otake, RIKEN/SPring-8, 1-1-1, Kouto, Sayo, Hyogo, 679-5148, Japan

Abstract

The 250 MeV SPring-8 Compact SASE-FEL Source (SCSS) prototype accelerator (SPA) was constructed. We observed the first amplification of light from the undulator at a 49 nm wavelength in June, 2006. We set our target time jitter of the system to be less than 1 ps. To achieve this, new timing devices, such as a master trigger unit (MTU), a master trigger distribution unit, a trigger delay unit (TDU), and a level converter unit, were developed. Reference clocks of 238 MHz and 5712 MHz RF are delivered to timing modules distributed along the accelerator. The MTU generates a master trigger synchronized both to the 60 Hz AC line and to the 238 MHz reference clock with a repetition rate of 1 Hz to 60 Hz. The TDU is an 8-ch 24-bit delay counter used to generate delayed signals from the master trigger for each component. The TDU uses 238 MHz RF as a counter clock and 5712 MHz RF to recover the time jitter. A measured jitter of 0.71 ps in standard deviation was achieved in the TDU. We measured the jitter between the arriving time of an electron beam to a monitor and a 5712 MHz RF; it was 0.34 ps. This demonstrates good stability of the timing system and the RF system of the SPA.

INTRODUCTION

The SPring-8 Compact SASE-FEL Source (SCSS) project is in progress. The 250 MeV SCSS prototype accelerator (SPA) was constructed to verify the feasibility of the source. The total length of the SPA is 60 m. We observed the first amplification of 49 nm light in June, 2006 [1].

The main acceleration radio frequency of the SPA is 5712 MHz (C-band). Three sub-harmonic frequencies of 238 MHz, 476 MHz, and 2856 MHz (S-band) are also used to compress the electron bunch length from 1ns to 1 ps before injecting to the main accelerator. All components around the facility of an electron gun, accelerator, insertion devices, and experimental apparatuses should be driven synchronously with the repetition rate from 1 Hz to 60 Hz using a 5712 MHz RF clock generated at a single source to obtain stable coherent light as the result of a stable electron beam. The distribution of stable 5712 MHz RF is one of the key technologies of the system [2]. We developed the timing system of the SPA, since the time jitter of the system was less than 1ps. This comes from a phase jitter of about 1 degree of 5712 MHz RF, which corresponds to a beam energy jitter requirement of 10^{-4} to generate and amplify 60 nm light at the SPA [3].

In this paper, we describe the timing system of the SPA.

TIMING SYSTEM

Overview

Figure 1 shows a schematic of the system. A newly developed master oscillator having a low noise characteristic generates a 5712 MHz RF. In addition, it generates a 238 MHz RF dividing the 5712 MHz RF. Ten W CW amplifiers amplify these RF signals to compensate for any cable loss in the distribution. Coaxial cables of HF-15D are used to distribute the RF signals in the SPA, because the maximum cable length is only 30 m. Its temperature coefficient is 5 ppm/K. We do not yet apply a dedicated feedback circuit to stabilize the electrical length of the cables, but no problem has occurred.

Trigger signals are needed for most equipment around the machine, for example, electron beam generation, single bunch formation, acceleration, and monitoring. To prepare the required timing triggers, we developed a trigger distribution system. A master trigger unit (MTU) generates a pulse signal, which is the master trigger of the whole operation sequence of the accelerator. Four trigger distribution units are used to distribute the master trigger. We adopted LVDS (low voltage differential signaling) for the signal transmission. Each trigger distribution unit is connected in series with 100 Ω twisted-pair cables to reduce the noise influence. Trigger delay units (TDU) receive the master trigger from the trigger distribution

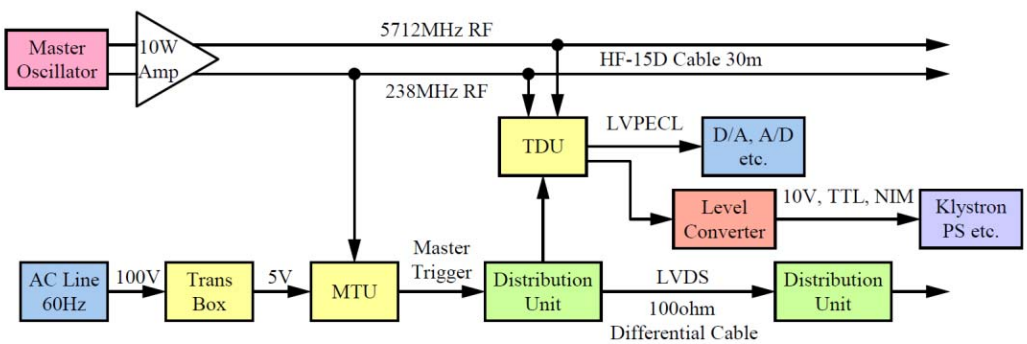

Figure 1: Schematic of the SPA timing system.

unit. The TDU generates eight delayed signals driven by the master trigger. The nine TDUs are used in seven 19-inch racks located in the klystron gallery.

The output voltage level of the TDU is LVPECL to suppress the jitter. D/A and A/D converter units, which have been newly developed for manipulating the IQ modulators/demodulators of the RF low-level systems, beam position monitors, and beam current monitors, have the same level of LVPECL at their trigger inputs. We can directly connect the output signals of the TDU to these units. However, some high-voltage power supplies used in noisy environments and off-the-shelf equipment, such as the klystron power supplies, the fast high-voltage pulser for the beam deflector, and cameras require 0-10 V, NIM or TTL level signals. To provide these signals, we developed a level converter unit.

Master trigger unit

The operation cycle of the SPA is from 1Hz to 60 Hz, because the master trigger is required to synchronize by a 60 Hz AC line for stable operation of the high-voltage power supplies for the klystron and the gun modulators. In addition, it is required to synchronize by a 238 MHz RF for stable acceleration of the electron beam.

Figure 2 shows a block diagram of the MTU. The input signals of the MTU are a 238 MHz RF, a 60 Hz AC line clock, and a 60 Hz RF clock from an arbitrary source. The output signal is a master trigger having the LVPECL level. A DSUB 9-in connector on the MTU panel is for the AC line clock and SMA connectors are for the other signals mentioned above.

The MTU has a FPGA of Altera Stratix EP1S10, which runs with the 238 MHz clock. The two 60 Hz clocks are selected in the FPGA, and then the selected clock is divided so as to generate a defined operation cycle. The output clock from the FPGA and a 238 MHz clock are entered into a final-stage D flip-flop of ON Semiconductor NBSG53A. This is a high-performance Silicon Germanium product having a maximum operation clock speed of 8 GHz. The master trigger in the MTU is resynchronized by the 238 MHz clock in the D flip-flop and the pulse jitter is reduced.

We designed MTU as a VME module to control it via the computer network. The MADOCA control system, which was developed for an accelerator complex at SPring-8, was used to reduce the development time and to integrate the SPA to the complex easily.

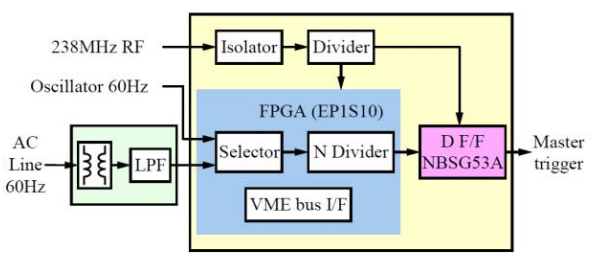

Figure 2: Block diagram of the MTU and the transformer box.

5712 MHz synchronous trigger delay unit

A block diagram of the TDU is shown in Fig. 3. The input signals are a master trigger, a 238 MHz RF, a 5712 MHz RF, and eight inhibit logic signals to stop the signal output. The output signals are eight delayed signals. The connectors of the TDU are a high-density DSUB 25-pin for logic signals and SMAs for others. The TDU is also a VME module.

The TDU consist of two boards. The first board generates delayed signals by using a FPGA, which is the same chip as that used in the MTU. The FPGA has a function of a 238-MHz 24-bit delay counter, which is able to delay by about 70.5 ms. The width of the output signal is defined by a 15-bit counter. The FPGA can suppress the output of the delayed signals by hardware inhibit signals, or a software command.

We designed a second board of the TDU, to which it synchronizes the delayed signals to the 5712 MHz clock so as to reduce the jitter and to achieve jitter of less than 1 ps. This can be done by the same D flip-flop, which is used in the MTU. First, the delayed signal of the FPGA output synchronizes by a 238 MHz clock using the D flip-flop. Because if the jitter of the signal exceeds 175 ps, which is one cycle of 5712 MHz, then the final delayed signal may jump every 175 ps step, depending on the conditions. Then, after 238 MHz clock synchronization, the delayed signal synchronizes by 5712 MHz clock at the final stage D flip-flop of the second board. The second board is installed into an aluminum box to isolate it from any electromagnetic influence. This box also contains the function of temperature control with a heater and a thermo sensor. The temperature control system suppresses the time drift of the signals. The first and second boards are connected with semi-rigid coaxial cables.

We estimated the jitter of the TDU to be 0.8 ps in a calculation, when designing the TDU. Figure 4 shows the measured jitter of each channel output of a TDU at room temperature. An Agilent DSO81204B, which is a 12 GHz bandwidth real-time oscilloscope having up to a 40 GSa/s sample rate, was used for measurements. The standard deviation of the jitter was 0.71 ps, which is below the

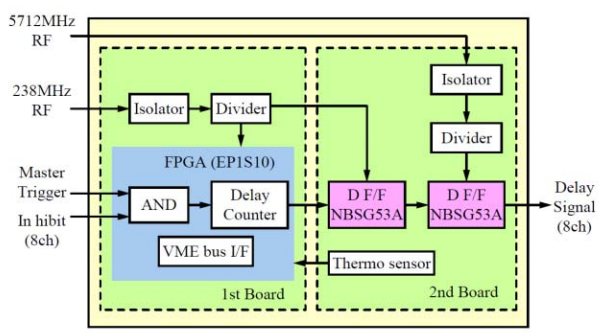

Figure 3: Block diagram of the TDU.

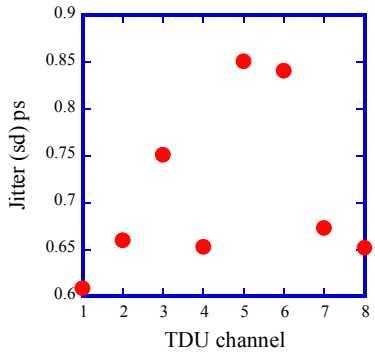

Figure 4: Measured jitter of each channel output of the TDU at room temperature.

estimated value.

TIMING STABILIZATION OF A BEAM CUT OUT BY A BEAM DEFLECTOR

One of the important technologies using in the SPA, which is different than other X-FEL projects using an RF gun, is a thermionic electron gun that generates a 500-kV 2-μs pulse beam. The 1 ns beam is cut out from the 2 μs pulse beam with a beam deflector and a fast high-voltage pulser. Stabilizing this 1 ns beam timing against the acceleration RF phase is essential for stable amplification of light.

The beam timing at the deflector is mainly changed by the effect of an ambient temperature change. The operation of the SPA starts in the morning and stops in the evening, every day. Because of this operation, the temperature of the equipment especially drifts during a few hours after start-up in the morning. For example, the daily variation of the temperature was 1.2 degree C and the drift of the trigger timing of the deflector was 46 ps, according as the temperature.

We employed a beam-deflector timing stabilization system to correct for any long-term drift. We inserted a delay line between the output of the TDU and the trigger input of the fast high-voltage pulser. The delay line had a 2000 ps range and a 1 ps resolution. It was controlled using a stepper motor. A schematic diagram of the system is shown in Fig. 5. The deviated delay time of the pulse signal, which passed through the beam deflector, relative to another output from the TDU, was measured using a time interval counter SR620 made by Stanford Research Systems. Next, the correction value was calculated using the PID method on the workstation. The deviated delay time of the signal was then cured by changing the delay line setting.

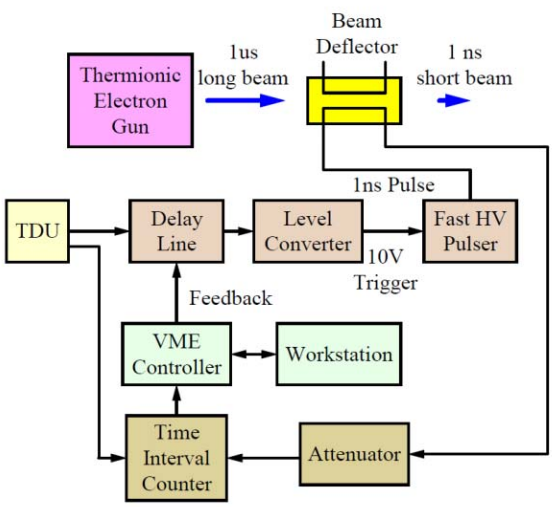

Figure.5: Schematic diagram of the beam-deflector timing stabilization system.

CONCLUSION

We measured the time jitter between a 250 MeV electron beam and a 5712 MHz RF. The beam timing was measured using a signal from a reference cavity of a beam-position monitor. The resonance frequency of the cavity was 4760 MHz. The first zero-cross timing of the output from the cavity was used for the trigger of the oscilloscope DSO81204B, and the jitter of the reference 5712 MHz RF signal was measured. The jitter was 0.85 ps. The triggering jitter of the oscilloscope was also measured, and was 0.78 ps. From these values, we obtained 0.34 ps as the jitter of the arriving time of the beam relative to the reference 5712 MHz RF. The jitter between a beam and a delayed signal of the TDU was 0.86 ps, which was not better jitter than that of the beam arrival timing, but is less than our target of 1 ps. As a result, we obtained a 0.06% (peak to peak) beam energy stability. This satisfies the requirement of the system and demonstrates good stability of the SPA.

We successfully constructed the timing system of the SPA, and observed amplification of 49 nm light. Some user experiments using the SPA are being planned for autumn of this year.

In the case of the 8 GeV SCSS project, the timing system spreads in 800 m distance. We are developing an optic fiber system to distribute the RF and the trigger signals. We will install the new timing system to the SPA and check its performance.

REFERENCES

[1] T. Shintake et al., “First Lasing at SCSS”, FEL06, Berlin Germany, August 2006.
[2] Y. Otake et al., “SCSS rf control toward a 5712 MHz phase accuracy of one degree”, APAC07, Indore India, January 2007.
[3] Y. Otake et al., “Sub-pico-second trigger system for the SCSS prototype accelerator”, FEL06, Berlin Germany, August 2006.

COMPARATIVE STUDIES OF ELECTRON SOURCES FOR A FREE ELECTRON LASER AT PSI

M.Dehler*, A. Anghel
Paul Scherrer Institut, CH-5232 Villigen PSI, Switzerland

Abstract

Within the scope of the low emittance gun project (LEG) at PSI, research is conducted into the development of a high brightness electron source suitable for compact, short wavelength free electron lasers. The gun, supposed to generate up to 5.5 Amperes of beam current, consists of a pulsed DC diode followed by a 1 1/2 cell RF gun. Using specialized codes, the performance of field emitter arrays is evaluated assuming realistic geometries. As an alternative, we examine the performance of conventional photo emission using copper cathodes, which we compare to that of field emitter arrays.

INTRODUCTION

High brilliance electron sources are an essential ingredient for a compact free electron laser in the Angstrom wavelength region. Their low emittance simultaneously reduces the required beam energy and saturation length for the lasing process, decreasing the cost and size of such a facility.

A study at the Paul Scherrer Institut (PSI)[1] focuses on developing suitable technologies toward a low emittance gun (LEG). We see double gated field emitter arrays as an option for a electron source with a strongly reduced initial thermal emittance, the objective being a current of 5.5 A with a slice emittance of 50 nm rad. Development of a suitable emitter is under way at PSI's laboratory for micro- and nanostructures (LMN)[2]. To avoid space charge forces destroying the emittance, fast acceleration in a pulsed DC diode gun running at high gradients up to 250 MV/m is a second focal point of research.

To simulate these devices with the required accuracy, special codes and techniques have been developed[3]. Special care has been exercised in modeling all real world effects using a realistic initial phase space distribution including also inhomogeneities in the emission density. In the following, we give an overview of current results. For comparison, similar simulations have been performed assuming emission from a copper cathode.

FIELD EMISSION CATHODES

Also known as Fowler-Nordheim tunneling, field emission is a form of quantum tunneling in which electrons pass through a barrier in the presence of a high electric field [4]. Being a cold emission process, it is seen as a possible alternative to photo emission, the advantages being a more simple, robust setup and the potential for a higher brightness.

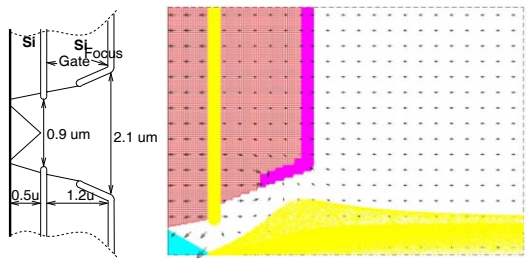

Figure 1: Geometry of double gated field emitter with beam trajectories ($I_b = 0.5mA$).

To create the required current, micron sized field emission tips are grouped into arrays, typically with a gate creating the necessary field to extract the electrons. The beamlet out of a tip will diverge strongly due to field forces and space charge effects resulting in a large emittance. A double gated geometry as in fig. 1, where the second gate acts as an electrostatic lens, avoids that in minimizing the transverse momentum spread.

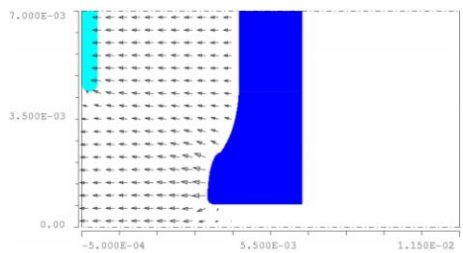

Figure 2: Gun geometry in cylindric coordinates together with accelerating field.

Parameterizing the phase space of the individual tip, we compute the beam dynamics in the pulsed DC gun[6]. The geometry is shown in Figure 2. The nominal accelerating gradient is 250 MV/m. Optimizing the cathode layout resulted in a cylindrical array of emission tips with a diameter of 500 μm. Figure 3 shows, how the slice emittance evolves from emission at the cathode ($z = -0.5mm$) to the drift following the anode. The emittance is dominated by the initial momentum spread of the individual beamlets. If, as in the second trace in Figure 3, we assume an ideal emitter geometry producing a zero emittance and divergence beamlet, a much better total performance with an emittance value of 23 nm rad could be obtained. So, optimizing the initial momentum spread of the emitted electrons further is of high interest.

* e-mail: Micha.Dehler@psi.ch

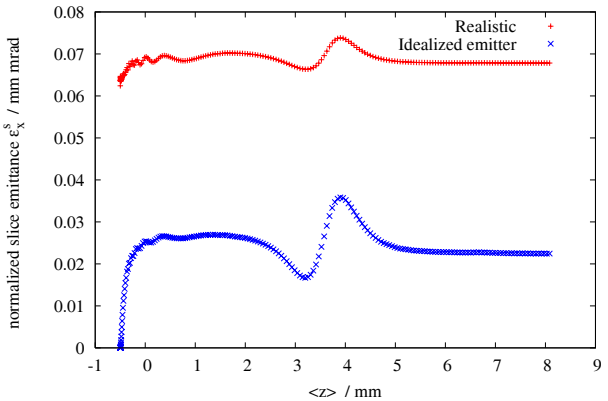

Figure 3: Evolution of slice emittance for homogeneous field emitter array ($E_{acc} = 250MV/m$). Upper trace uses phases space computed from geometry in fig. 1, lower trace assumes ideal emitter with zero initial momentum spread.

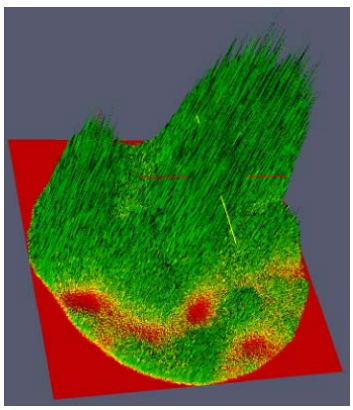

Figure 4: Stochastic transverse charge distribution at the exit of the gun ($\beta = 1, \zeta = 15\mu m$)

Typical field emitter arrays are subject to strong variations in the tip to tip emission current. We hope to be able to reduce that by advanced conditioning techniques, as discussed for example in [7]. Nonetheless, we cannot hope to eliminate the problem completely and any realistic simulation should take account of that. As a model, we assume a stochastic distribution of the field enhancement factors of the individual tips with mean $< \beta >$, a standard deviation σ and a spatial correlation length ζ. Inserting it into the Fowler Nordheim equation, we obtain the current distribution used in the gun simulation. Figure 4 shows an example. As can be seen in Table 1, an inhomogeneous field enhancement distribution has a relatively small influence on the emittance, as long as it is spatially uncorrelated. In this case, the voltage of the focusing gate is no more perfectly matched to the tip currents, which leads to increased momentum spread of the emitted electrons. The initial emittance is increased, but still inhomogeneities in transverse charge distribution are very localized, so that the amount of additional nonlinear space charge forces stay limited. Dangerous are any spatial correlations. These lead to macroscopic space charge forces and result in emittance growth in the gun.

Table 1: Slice emittance in nm rad in the bunch center. (Average field enhancement $< \beta >= 10$, σ standard deviation of β, ζ correlation length in μm)

σ	ζ	min(ϵ)	$< \epsilon >$	max(ϵ)
0.0	0.0	68.0	68.0	68.0
1.0	0.0	96.7	98.9	103.1
1.0	15.0	256.1	373.0	469.4
1.0	50.0	47.1	284.2	474.4
2.0	0.0	169.7	175.0	183.6
2.0	15.0	372.4	419.3	458.0
2.0	50.0	246.4	403.3	572.6

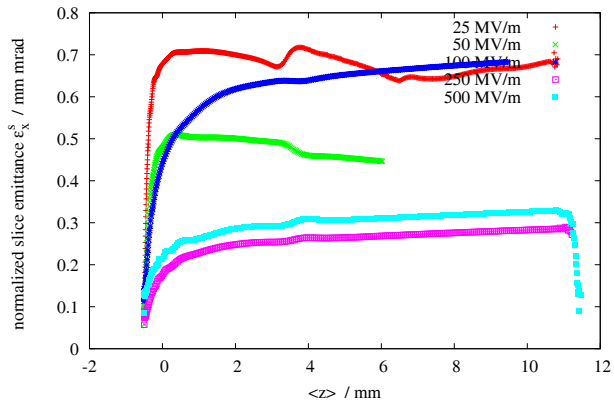

Figure 5: Evolution of slice emittance for an inhomogeneous field emitter array ($\sigma = 2$, $\zeta = 50\mu m$) for various accelerating gradients. The initial current densities have different distributions (but same stochastic momenta) and are not perfectly comparable.

As space charge effects are relatively minor in the homogeneous case, lowering the accelerating gradient only has small effects on the emittance. The situation looks quite different, if one includes inhomogeneities. Here space charge dominates the emittance growth and high gradients help to avoid major deteriorations. Fig. 5 shows results from runs with different gradients. When comparing the traces, one should keep in mind, that the initial current densities had the same stochastic momenta,but differed in their actual distributions generated, so that we cannot do an exact comparison. Nonetheless, it is clearly visible, that for gradients below 250 MV/m, we get strong space charge effects. In conclusion, elevated gradients are an interesting tool to compensate for higher tolerances of the field emitter array.

PHOTO EMISSION

For comparison purposes, we present computations with the 2 1/2 particle in cell module MAFIA TS2[8] using a photo emission model. As in the last section, the diode

geometry is that of fig. 2. We assume photo emission by a laser with a wave length of 260 nm from a smooth copper cathode of diameter 500 μm. The laser pulse has a flat top shape of 40 ps length generating the design current of 5.5 A.

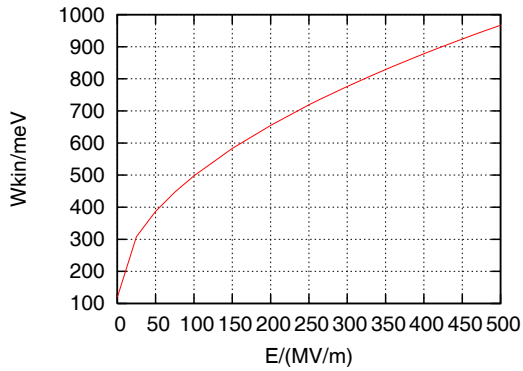

Figure 6: Initial momentum spread at cathode versus accelerating gradient

The transverse current density is taken to be homogeneous. As the accelerating gradient increases, the effective work function at the cathode surface is lowered due to the Schottky effect and, due to the difference between the energy of the laser photons and the work function, we have to assume a larger initial momentum spread of the emitted electrons (Fig. 6).

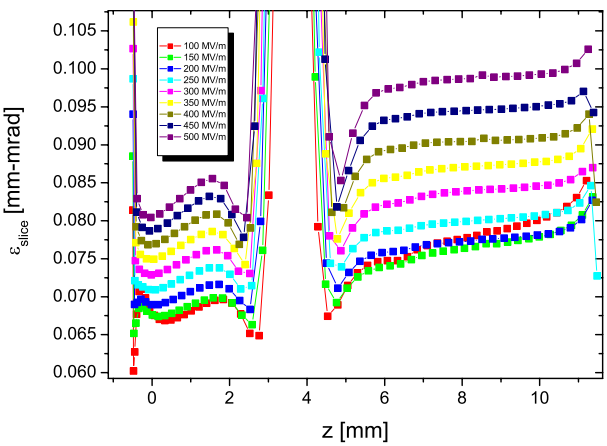

Figure 7: Emittance of center slice of 40 ps bunch for various gradients.

Fig. 7 shows in fine resolution the emittance of the center slice in the beam, as the bunch gets accelerated through the gun. Of special interest is the variation of the final slice emittance as a function of the gradient. For low fields, the initial (thermal) emittance is low because electrons are emitted with low kinetic energy. But there is not enough acceleration and the emittance grows due to dominating space charge effects. For high gradients, emitted electrons are immediately accelerated but the initial thermal emittance is starting to dominate. At 150 MV/m, both effects balance out, so that a theoretical minimum of 75 nm rad is reached.

An open question is the influence of inhomogeneities either in the transverse current distribution or ripples of the emitted current on the optimum gradient and the minimum emittance. Further simulations are under way to clarify these points.

DISCUSSION

We present simulation results for a field emitter based electron source. Using the realistic emitter geometry and assuming a perfect homogeneity of the emitter array, a slice emittance below 70 nm rad can be obtained for the design current of 5.5 A. This value is mainly determined by nonlinear optical effects in the individual emitter and emittance growth in the diode. Inhomogeneities lead to deteriorations, which are most pronounced, if their spatial distribution lead to increased space charge effects. As we go up in gradient, the beam gets accelerated early into relativistic velocities and becomes more tolerant to imperfections in its initial distribution.

Under idealized assumptions, photo emission can reach similar levels of performance. In terms of sensitivity to transverse inhomogeneities, we expect a similar behavior as for field emission cathodes. Additional deteriorations may come from current ripples due to spikes in the incoming laser pulse creating short range wake fields.

REFERENCES

[1] K. Li et al., “Low Emittance X-FEL Development”, Proc. 2005 Free-Electron Laser Conference (FEL2005), Stanford (CA), USA

[2] E. Kirk et al., “Development of all-metal Field Emitter Arrays for high Current Applications”, to be published in Proc. Eighth IEEE International Vacuum Electronics Conference (IVEC2007), Kitakyushu, Japan, May 2007.

[3] A. E. Candel, M. Dehler, M. Troyer, “A massively parallel particle in cell code for the simulation of field emitter based electron source”, NIM A A 558, pp. 154-158 (2006)

[4] R. H. Fowler, L. Nordheim, “Electron Emission in Intense Electric Fields”, Proc. Royal Society of London. Series A, Vol. 119, No. 781 (May 1, 1928), pp. 173-181

[5] M. Dehler, “Design and Modeling of Field-Emitter Arrays for a High Brilliance Electron Source”, Proc. 9th International Computational Accelerator Physics Conference, Chamonix, France, October 2006

[6] M. Dehler, A. E. Candel, E. Gjonaj, “Full scale simulation of a field-emitter arrays based electron source for free electron lasers”, J. Vac. Sci. Technol. B 24 (2), pp. 892-897 (2006)

[7] Schwoebel, P.R. Spindt, C.A. Holland, C.E, “High current, high current density field emitter array cathodes,” Technical Digest of the 17th International Vacuum Nanoelectronics Conference, (2004), ISBN: 0-7803-8397-4

[8] MAFIA 4, Computer Simulation Technology, Darmstadt `http://www.cst.de`

PROJECT OF INFRARED STORAGE RING FREE ELECTRON LASERS AT AIST

N Sei#, K. Yamada, H. Ogawa, M. Yasumoto
National Institute of Advanced Industrial Science and Technology, 1-1-1 Umezono, Tsukuba, Ibaraki 305-8568, Japan

Abstract

Development of free electron lasers (FELs) with a compact storage ring NIJI-IV in the near and middle infrared regions is planned in National Institute of Advanced Industrial Science and Technology (AIST). Infrared FELs with a linear accelerator have been already developed and used for various applications in many FEL facilities. However, there is no storage ring FEL (SRFEL) which can oscillate in those regions widely. Although an SRFEL is inferior to a linear accelerator FEL in an average power, it has an extremely stable wavelength and its spectrum line width is as narrow as that of a monochromatic light in a synchrotron radiation facility. The optical klystron ETLOK-III for the infrared FEL has been already installed in the NIJI-IV, and the spontaneous emission from the ETLOK-III has been measured. New optical cavity chambers which could suppress low-frequency vibrations are designed. They will be installed in the NIJI-IV in February. An infrared SRFEL will be achieved by the end of this year.

INTRODUCTION

Oscillations of free electron lasers (FELs) have been developed with a compact storage ring NIJI-IV in National Institute of Advanced Industrial Science and Technology (AIST). The first lasing was achieved at wavelengths of 595 and 488 nm in 1992 [1]. Improvements of the electron-beam qualities in the NIJI-IV have been advanced for shortening FEL wavelength. The wavelength of 212 nm, at which an FEL oscillation was achieved with the NIJI-IV, was the record for the shortest wavelength of FELs in 1998 [2]. The wavelength of the NIJI-IV FEL was down to 198 nm in 2003 [3], and the NIJI-IV FEL reached to the VUV region. FELs in the deep UV and VUV regions are suitable as an intense light source to observe chemical reactions which are occurred on the surface of transition-metals because the work function of the transition-metals lays around 5 eV. Then, experiments of photoelectron emission microscopy with the NIJI-IV FELs have been developed, and catalytic CO oxidation on Palladium surface was observed with video-rate time resolution [4]. FEL experiments for further shortening the wavelength below 195 nm are being carried out.

A new challenge to enhance the region of the NIJI-IV FEL wavelength has been advanced. A new optical klystron ETLOK-III, which was designed for the infrared FEL oscillations in a wavelength region of 1-10 μm, was installed in a long straight section of the NIJI-IV in 2004 [5]. Although many infrared FEL facilities based on linear accelerators are operating, no SRFEL has been achieved in the wide infrared region. Generally, an SRFEL has the advantage of a narrow spectrum line width and stability of the lasing wavelength compare with a linear accelerator FEL. It can be used as well as synchrotron radiation passed a monochromator. The average power of the synchrotron radiation in an infrared beam line is about 10 μW at most. Then the SRFEL can be expected as a light source which is more intense than the synchrotron radiation. The output power which is our target is 1 mW. Spectra of spontaneous emission from the ETLOK-III have been already observed in the visible and near-infrared regions. New optical cavity chambers for adjusting positions and rotations of the cavity mirrors will be installed in the both ends of the long straight section in February. In this article, we explain the recent status of the development of the infrared SRFEL with the NIJI-IV.

INSERTION DEVICE

The insertion device for the infrared FEL oscillations, optical klystron ETLOK-III, has two 1.4 m undulator sections and a 72 cm dispersive section [6]. Figure 1 illustrates outline of the magnet arrangement of the ETLOK-III. Gap of the undulator section can be changed between 36 and 150 mm, and number of the periods in one undulator section is 7. The maximum K value is estimated to be 10.4 from the observed spontaneous emission spectra. Gap of the dispersive section can be changed between 42 and 188 mm. Because the magnets in the dispersive section are inserted between two tables which fix the magnets of the undulator sections, the gap of the dispersive section cannot be opened from the gap of the undulator sections over 38 mm. The dispersive section is so long that the electron beam with comparatively low energy meanders greatly in it. The electron beam passes in magnetic field of the dispersive section which is not uniform in the horizontal direction. Then the electron beam is kicked in the dispersive section and comes off the central axis of the ETLOK-III. The kick force becomes stronger as the gap of the dispersive section becomes smaller. The minimum dispersive gap at which the electron beam could be stored in the NIJI-IV was 80 mm. To cancel the kick force, we attached 5 mm iron plates to shunt magnetic field of the both end magnets in the dispersive section with a couple of 3 mm

#Sei.n@aist.go.jp

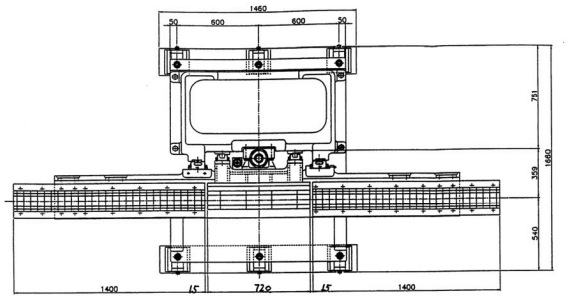

Figure 1: Schematic view of the optical klystron ETLOK-III.

thickness coils. The plate can be shifted on the side of the end magnet in the dispersive section. We will investigate the effect of the plates on the electron-beam trajectory soon.

OBSERVED SPONTANEOUS EMISSIONS

Spectra of the spontaneous emission from the ETLOK-III were measured with a photodiode array attached to a monochromator [5]. The resolution of this measurement system was estimated to be about 0.2 nm. Because the dispersive section has a parabolic distribution of magnetic field in the horizontal direction, precise adjustment of the electron-beam orbit is necessary to obtain a large modulation factor for the spontaneous emission. Figure 2 shows a spectrum of spontaneous emission with the undulator gap of 140 mm and the dispersive gap of 170 mm. The resonant wavelength measured in this condition was about 480 nm, and it was agreement with the wavelength estimated from the measurement of magnetic field in the ETLOK-III. The energy spread of the electron bunch can be estimated from the modulation factor of the spontaneous emission spectrum [7]. Taking the resolution of the measurement system into consideration, the energy spread was evaluated to be 2.7×10^{-4} in the undulator gap of 140 mm. This value was good agreement with the natural energy spread of 2.6×10^{-4}.

We could observe spectra of the higher harmonic emission in the UV and the visible regions. Figure 3 shows a spectrum of the third harmonic emission with the undulator gap of 100 mm and the dispersive gap of 130 mm. The resonant wavelength measured in this condition was about 1.42μm, so that it was about 2.2% longer than the wavelength estimated from the measurement of magnetic field in the ETLOK-III. The energy spread evaluated from the spontaneous emission was about 3.1×10^{-4}. Generally, further precise adjustment of the electron-beam orbit is demanded for the higher harmonics. The overestimation for the energy spread would be caused by the misalignment of the electron-beam orbit and/or the kick force in the dispersive section.

The maximum FEL gain is estimated to be over 2% at the electron-beam current of 15 mA in the visible and near-infrared regions. The maximum FEL gain for the third harmonics would be over 6% in the visible region due to rather large N_d, which is a number of periods of the

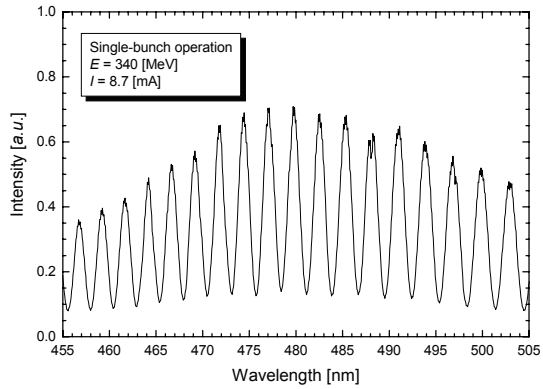

Figure 2: Spectrum of the fundamental emission from the TLOK-III with g_u (undulator gap) = 140 and g_d (dispersive gap) = 170 mm.

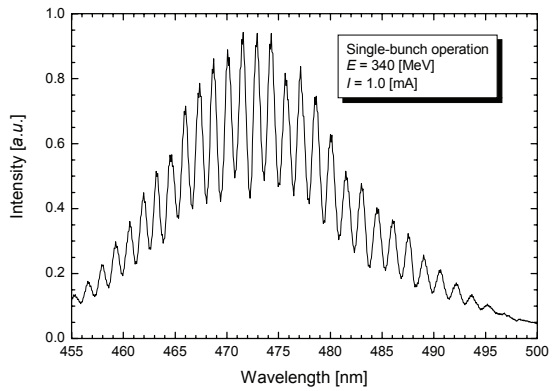

Figure 3: Spectrum of the third harmonics emission from the ETLOK-III with g_u = 100 and g_d = 130 mm.

FEL wavelength passing over an electron in the dispersive section. Because high-reflection mirrors of 99.8% or more are available in those regions [5], it will be easy to realize FEL oscillations after installation of optical cavity chambers in the both ends of the long straight section.

DESIGN OF OPTICAL CAVITY CHAMBER

Stable optical cavity chambers in which cavity mirrors are mounted are necessary to obtain stable cw oscillations in the SRFELs. When longitudinal overlapping between an electron beam and an optical pulse are insufficient, micropulses of the SRFELs form macro-temporal pulses, and cause unstable cw lasing. Not only the intensity of the SRFELs but also the pulse width and the spectral line width are unstable [8]. When the longitudinal overlapping is almost perfect, a cw lasing with the extremely steady line width was observed with the ETLOK-II in the UV NIJI-IV FEL as shown Fig. 4. A threshold detuning length where the steady cw lasing appears depends on the effective FEL gain. In the case that the FEL gain is larger enough than the cavity loss, the threshold detuning length is about 0.5 μm for the UV NIJI-IV FEL. Then, it is

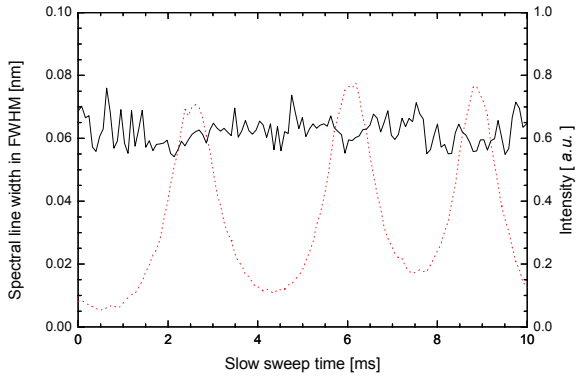

Figure 4: Evolution of the spectral line width of the SRFEL micropulse measured at the electron-beam current of 19 mA and the wavelength of 300 nm in the nearly perfect longitudinal overlapping. The micropulse intensity is also shown in the dotted line for comparison.

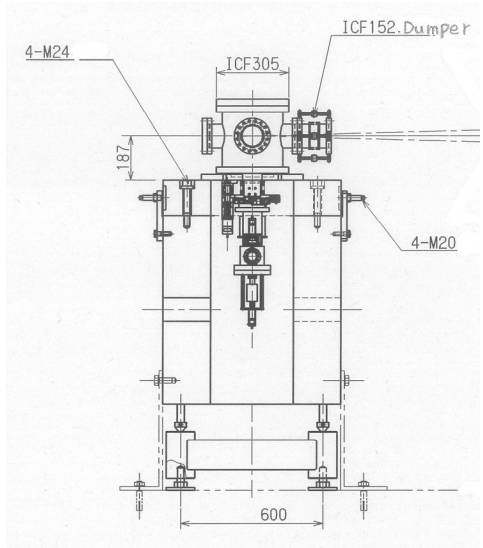

Figure 5: Overview of the new optical cavity chamber.

necessary to suppress amplitude of vibrations on the new optical cavity chambers for the infrared FELs within 0.5μm.

In order to estimate the vibrations on the optical cavity chambers, we measured vibration spectra with an accelerometer (Akashi AVT103) where the optical cavity chambers will be set up. Generally vibrations in the low frequency have large amplitude. There were some peaks around the frequency of 3 Hz in the vibration spectrum, and the maximum amplitude in those peaks was about 0.4 μm. Then, we adopted granite with the weight of about 1 ton as a stand to suppress the low-frequency vibrations. A vibration dumper which was able to intercept the low-frequency vibrations from the storage ring NIJI-IV was installed between the bending magnet chamber and the optical cavity chamber. Overview of the optical cavity chamber is illustrated in Fig. 5. The amplitude of vibrations at the cavity mirror will be controlled within 0.5 μm by these devices.

An optical cavity mirror holder, which is installed in the optical cavity chamber, can be controlled by stepping motors for three-axis positioning and two-tilt angles perpendicular to the optical axis. The nominal resolutions for the position on the optical axis and the tilt angles are 0.1 μm and 5 μrad, respectively. The mirror hold contains two remotely inter-changeable mirrors of up to 51 mm diameter. Effective diameter of the cavity mirror is 46 mm, so that a diffraction loss at the cavity mirrors will be negligible small in a wavelength region below 10 μm. The new optical mirror chambers for the infrared FEL will be installed in the NIJI-IV FEL system in February.

CONCLUSIONS

An active project to develop the first storage ring FEL in the near and middle infrared regions has been described. The optical klystron ETLOK-III was installed in the storage ring NIJI-IV for infrared FEL oscillations. The spectra of the spontaneous emission from the ETLOK-III were measured in the visible and the near-infrared regions. It was expected that the maximum FEL gain in those regions was over 2%. In order to obtain stable cw lasing, new optical cavity chambers for the infrared SRFEL were designed. The optical mirror holder can be precisely controlled by stepping motors for three-axis positioning and two-tilt angles perpendicular to the optical axis. The mirror chambers will be installed in the NIJI-IV FEL system in February. The first lasing with this system in the infrared region will be achieved by the end of this year.

ACKNOWLEDGEMENTS

This work was supported by the Budget for Nuclear Research of the Ministry of Education, Culture, Sports, Science and Technology of Japan.

REFERENCES

[1] T. Yamazaki *et al.*: Nucl. Inst. and Meth. **A331** (1993) 27.
[2] K. Yamada *et al.*: Nucl. Inst. and Meth **A429** (1999) 159.
[3] K. Yamada *et al.*: Nucl. Inst. and Meth **A528** (2004) 268.
[4] H. Ogawa *et al.*: Proc. 26th Free Electron Lasers Conf., Trieste, Italy 2004 p258.
[5] N. Sei *et al.*: Proc. 26th Free Electron Lasers Conf., Trieste, Italy 2004 p258.
[6] N. Sei *et al.*: Jpn. J. Appl. Phys. **41** (2002) 1595.
[7] N. Sei *et al.*: Jpn. J. Appl. Phys. **42** (2003) 5848.
[8] N. Sei *et al.*: submitted to Jpn. J. Appl. Phys.

START-UP OF FEL OSCILLATOR FROM SHOT NOISE

V. Kumar*, S. Krishnagopal, RRCAT, Indore, M.P. 452013, India
W.M. Fawley, LBNL, Berkeley, CA 94720, USA

Abstract

In free-electron laser (FEL) oscillators, as in self-amplified spontaneous emission (SASE) FELs, the build-up of cavity power starts from shot noise resulting from the discreteness of electronic charge. It is important to do the start-up analysis for the build-up of cavity power in order to fix the macropulse width from the electron accelerator such that the system reaches saturation. In this paper, we use the time-dependent simulation code GINGER[1] to perform this analysis. We present results of this analysis for the parameters of the Compact Ultrafast TErahertz FEL (CUTE-FEL) [2] being built at RRCAT.

INTRODUCTION

In an FEL oscillator driven by a pulsed radio-frequency linear accelerator, the growth of radiation starts from the noise present in the electron microbunches and gets further amplified in multiple passes, over the duration of the electron macropulse. The radiation power in the FEL cavity must saturate early enough such that one gets a temporally clean, usable radiation pulse for a significant portion of the electron macropulse. In this context, it is important to perform the start-up analysis while designing an FEL oscillator, as has been emphasized by many authors [3-9].

For typical oscillator parameters, quantum effects can be neglected [5,8] and the build-up of radiation starts from classical shot noise. Including the shot noise in the analysis of the interaction of an electron bunch with the radiation field in an FEL oscillator poses several challenges. First, the discreteness of charge has to be taken into account correctly, since the shot noise essentially results from this. Second, one has to include the broad bandwidth of radiation while studying the evolution of shot noise. This typically necessitates the use of time-dependent codes.

There have been earlier attempts to address these issues for FEL oscillators. Sprangle *et al.* [3,4] have studied the start-up process in FEL oscillators analytically, including the discrete nature of electrons, multiple radiation frequencies and finite pulse structure. The analysis, however, ignores the important non-linear effects and warm beam effects, and the three-dimensional effects are included only heuristically in terms of filling factors. Kuruma et al. [6] have studied the problem numerically using a one-dimensional, multi-frequency code where they have simulated the evolution of shot noise. Here also, three-dimensional effects have been ignored. In this paper, we simulate the start-up from shot noise of an FEL oscillator using the polychromatic FEL code GINGER [1] which takes three-dimensional effects into account. In the next section, we discuss the details of simulations that we have performed for CUTE-FEL being developed at RRCAT. The results are discussed in the following section and finally we present some conclusions.

* vinit@cat.ernet.in

NUMERICAL SIMULATION

For simulating the start-up from shot noise, we have used the FEL code GINGER [1], a multidimensional [full 3D for macroparticle and 2D $(r-z)$ for radiation], time-dependent code to simulate FEL interaction in single-pass amplifier as well as oscillator configurations. GINGER utilizes the KMR [10] wiggle-period-averaged electron-radiation interaction equations and the slowly-varying envelope approximation (SVEA) in both time and space for radiation propagation. For propagation outside the undulator for oscillator problems, the code uses a Huygens integral method. Shot noise is modeled by giving a controlled amount of randomness to the initial longitudinal phases of macroparticles; the algorithm [11] generates the statistically-correct shot noise at the fundamental as well as at harmonics.

The design parameters of CUTE-FEL are given in Table 1. For the simulations reported here, we have used γ = 20.53, where γ is the electron energy in unit of its rest mass energy. We had earlier done the time-independent simulation of CUTE-FEL using the code TDAOSC [12] which is an oscillator version of the code TDA [13]. For the parameters mentioned in Table 1, we had obtained a single pass, small signal gain (≡ssg) of 88%, saturated cavity power of 9 MW and hole out-coupled power of 0.65 MW. TDAOSC models the hole outcoupling in the mirror and the optimum hole radius was found to be 2 mm. The resonator parameters were also optimized using TDAOSC. The round trip radiation loss was calculated to be 15%, of which 7.5% was due to hole outcoupling, 2.5% due to mirror reflectivity, and 5% due to diffraction loss. Because GINGER does not model hole out-coupling, we instead put a total of 10% loss mirror reflectivity. This value includes a 7.5% loss from hole out-coupling and 2.5% from the actual mirror reflectivity. Note that GINGER does include diffraction and refraction effects.

We first performed time-independent simulation using GINGER in order to verify our old results and obtain a single pass ssg of 90% and saturated cavity power of 8.3 MW. Assuming 7.5% out-coupling, the out-coupled power becomes 0.62 MW. These numbers agree quite well with earlier results of Ref. 12. We then proceeded with time-dependent oscillator simulations adopting a Gaussian longitudinal electron beam profile with a rms width of 4 ps and peak current of 20 A ($Q = 0.2$ nC). The longitudinal slice

Table 1: CUTE-FEL design parameters

Electron beam energy (E)	10 MeV
Peak beam current (I)	20 A
RMS energy spread (σ_γ/γ)	0.5%
RMS normalised emittance	30 π mm-mrad
RMS pulse width (σ_z)	1.2 mm
Micropulse rep. rate	36.62 MHz.
RMS e-beam size (σ_x, σ_y)	0.65 mm, 2.00 mm
Electron macropulse width	8 μs
Undulator period (λ_u)	50 mm
Peak und. parameter (K)	0.8
Undulator length ($N_u\lambda_u$)	2.5 m
Undulator gap	35 mm
Beam pipe diameter	28 mm (ID)
Radiation wavelength (λ_R)	80 μm
Optical cavity length	4.1 m
Location of down. mirror	65 cm from und. exit
Location of up. mirror	95 cm from und. entr.
Mirror radii of curvature	2.25 m (d), 2.5 m (u)
Mirror reflectivity (power)	99%
Hole radius in down. mirror	2 mm

spacing was two radiation wavelengths. In the next section, we discuss the results of the time-dependent simulation.

RESULTS

We have studied the variation in the single pass ssg with cavity detuning ΔL_c. As is well known, there is no gain at zero cavity detuning and one must reduce the cavity length slightly in order to get positive gain [14]. Fig. 1 shows the net round trip gain as a function of cavity detuning from the synchronized cavity length 4.1 m. We find that maximum gain occurs for $\Delta L_c \approx 80\mu$m with a net round trip gain of 21%, equivalent to gain in the undulator of 36%. In the time-independent simulation, where the pulse structure and the slippage were ignored, the maximum ssg was 90%. One can also use the following analytical formula of Dattoli et al. [15] to predict the effects of finite pulse width:

$$g = \frac{g_0}{1 + \frac{1}{3}\mu_c}, \qquad (1)$$

where g and g_0 are the ssg with and without finite pulse effect respectively, $\mu_c = N_u\lambda_R/\sigma_z$, N_u is the number of undulator periods, λ_R is the radiation wavelength and σ_z is the rms electron pulse length. Using the above formula, the ssg after including the time-dependent effect is obtained to be 42%. This agrees well with GINGER calculation.

Figure 2 displays the evolution of power spectrum where one sees that the initially broad band noise evolves to a sharper spectrum - unlike in the case of SASE, where the spectrum remains noisy. This occurs both from detuning and slippage effects and because the cavity preferentially filters out modes other than the fundamental cavity mode.

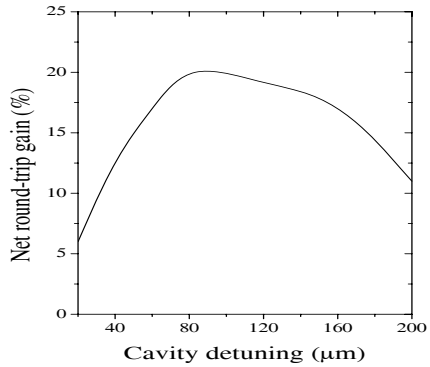

Figure 1: Net round-trip gain as a function of cavity detuning.

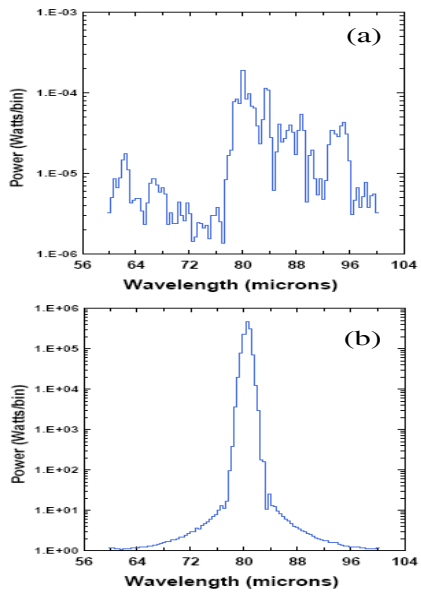

Figure 2: Power spectrum of the output signal after (a) first pass, and after (b) saturation.

Figure 3 shows the evolution of cavity power from shot noise for ΔL_c = 80 μm. The cavity power saturates in around 135 passes. Since round trip time in this cavity is 27.3 ns, this means the start-up time is around 3.7 μs. It is interesting to compare the start-up time in FEL oscillator with saturation length in a SASE FEL. Here, the net round trip gain is 21% which means that power gets e-folded in around 5.25 passes. Hence, 135 passes is around 26 gain lengths. This is simular to growth of power in SASE FELs where it typically takes 20-30 power gain lengths for saturation [16]. Fig. 4 shows the variation in start-up time with ΔL_c. We have verified that at other detuning values the number of passes required for saturation is also equivalent to around 25 power gain lengths.

The variation of total energy in the out-coupled micropulse at saturatation as a function of ΔL_c is shown in

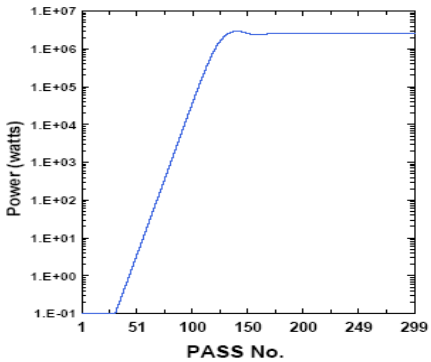

Figure 3: Average cavity power as a function of pass number. The power is averaged over the electron beam duration of 24 ps.

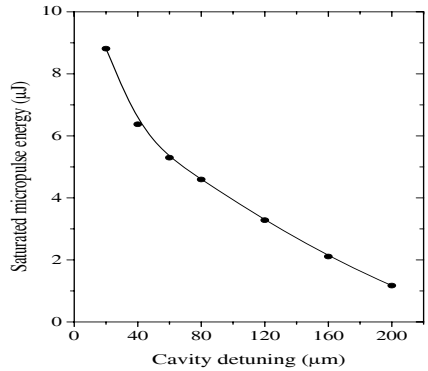

Figure 5: Variation of micropulse energy in the out-coupled pulse as a function of cavity detuning.

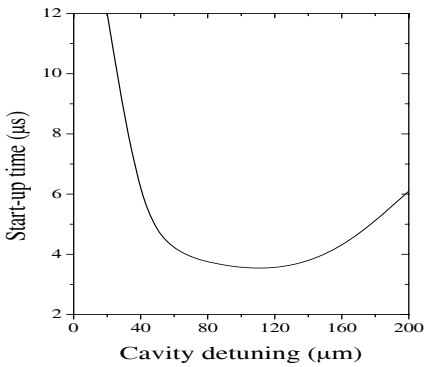

Figure 4: The variation of start-up time with cavity detuning.

Fig. 5. We find that as ΔL_c increases, the micropulse energy decreases. At lower detuning, the micropulse energy at saturation is large, but since gain is small, the start-up time will also be large. As is well known, at higher detuning where the small signal gain may be larger, the saturated power is smaller [14]. The 8-μs electron macropulse width for RRCAT FEL corresponds to 300 passes. At lower cavity detuning values, it may then be difficult for the FEL to saturate. We therefore plan to operate around a cavity detuning of 80 μm.

CONCLUSIONS

We have performed multidimensional, time-dependent simulations of start-up of the CUTE-FEL oscillator from shot noise including the effects of detuning, and outcoupling. We determined the start-up time for the design parameters is around 3.7 μs. Furthermore, the number of passes required for the FEL to saturate is equivalent to 25 gain lengths, similar to single pass, SASE FELs.

REFERENCES

[1] W. Fawley, *A user Manual for GINGER and Its Post-Processor XPLOTGIN*, LBNL-49625-Rev. I ed., Lawrence Berkley National Laboratory (2004).

[2] S. Krishnagopal et al., Proceedings of FEL conference (2006) 496.

[3] P. Sprangle, C. M. Tang and I. Bernstein, Phys. Rev. Lett. 50 (1983) 1775.

[4] P. Sprangle, C. M. Tang and I. Bernstein, Nucl. Instr. and Meth. A 237 (1985) 41.

[5] S. Benson, J. M. J. Madey, Nucl. Instr. and Meth. A 237 (1985) 55.

[6] W. B. Colson, Nucl. Instr. and Meth. A 296 (1990) 348.

[7] S. Kuruma et al.,Nucl. Instr. and Meth. A 331 (1993) 421.

[8] W. S. Graves, Nucl. Instr. and Meth. A 393 (1997) 210.

[9] Z. Dong et al., Nucl. Instr. and Meth. A 475 (2001) 187.

[10] N.M. Kroll, P.L. Morton, and M.R. Rosenbluth, IEEE J. Quantum Elec. QE-17, (1981) 1436.

[11] W.M. Fawley, PRST-AB 5 (2002) 070701.

[12] S. Krishnagopal et al., Nucl. Instr. and Meth. A 318 (1992) 661.

[13] T. M. Tran, J. S. Wurtele, Computer Phys. Commun. 54 (1989) 263.

[14] D. Oepts, in: J. Chen et al. (Eds.), *Development and Application of Free Electron Lasers*, Beijing, China; Proceedings of the CCAST symposium (Gordon and Beach, 1997).

[15] G. Dattoli et al., Opt. Commun. 35 (1980) 407.

[16] K.-J. Kim, Nucl. Instr. and Meth. A 250 (1986) 396.

COMPARISON OF CODES FOR SMITH-PURCELL FEL *

Vinit Kumar#, RRCAT, Indore, M.P. 452013, India
Kwang-Je Kim, ANL, Argonne, IL 60439, USA
Dazhi Li, ILT, Suita, Osaka 565-0871, Japan

Abstract

Smith-Purcell (SP) free-electron lasers (FELs) using low energy electron beam are being seen as attractive option for a compact source of coherent terahertz radiation. Recently, Kumar and Kim [1] have performed numerical simulation of SP-FELs based on a computer code using Maxwell-Lorentz equations. Li et al. [2,3], and Donohue et al. [4] have performed calculations using particle in cell (PIC) codes. In this paper, we present a comparison of these methods and compare results obtained using different codes.

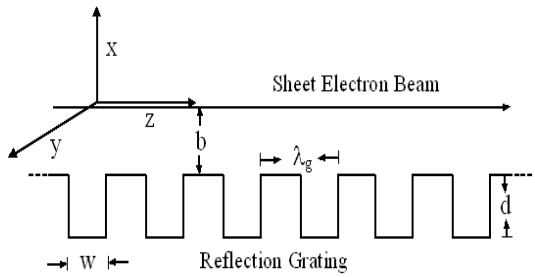

Figure 1: Schematic of an SP-FEL using a sheet electron beam. The sheet electron beam is in the plane x = 0.

INTRODUCTION

Recently, there has been a lot of interest in the analysis and simulation of Smith-Purcell (SP) free-electron laser (FEL) [1-6]. The possibility of a SP-FEL based on low energy electron beam is seen as an attractive option for compact terahertz (THz) source of coherent radiation. The SP-FEL is a backward wave oscillator (BWO) for low energy electron beam [1,5]. In a BWO, like any oscillator system, the electron beam current needs to be higher than a threshold value, known as the start current, in order to produce coherent electromagnetic oscillation. If the electron beam current is higher than the start current, the coherent electromagnetic oscillations start growing and then saturate due to nonlinearity. In order to build such a device, it is important to study the start current and the saturation behaviour of SP-FEL. Kumar and Kim [1] have performed an analysis and numerical simulation of a SP-FEL system using Maxwell-Lorentz equations, where they have studied the growth of power, the efficiency at saturation and the start current in a SP-FEL. Li et al. [2] and Donohue et al. [4] have performed a more detailed 2D simulation of a SP-FEL system using a computer code MAGIC [7] which is a particle in cell (PIC) code. In Ref. 3, Li et al. have performed three-dimensional simulation of SP-FEL system using MAGIC. A natural question then arises that how do these different codes compare with each other. In this paper, we present a comparison of the results obtained using different computer codes for simulating a SP-FEL. We find that the results of the fast, 2-D simulation using Maxwell-Lorentz equation developed in Ref. 1 agree well with other more elaborate simulations.

In the next section, we discuss the numerical simulation and calculations that we have performed based on Maxwell-Lorentz equations. We then discuss the comparison of results obtained using this approach with the already published results [2-4] obtained using PIC code in the following section and conclude.

DETAILS OF MAXWELL-LORENTZ SIMULATION

We start with a brief description of the SP-FEL system. Figure 1 shows the schematic of the SP-FEL setup. We assume the system to have translational invariance in the y-direction and hence ours is a 2D analysis. We assume a sheet electron beam which travels with a speed βc along the z-axis, at a height b above the grating of length L, having grooves of depth d, width w and period λ_g. Here, c is the speed of light in vacuum.

In a SP-FEL, the electron beam interacts with the co-propagating surface electromagnetic mode supported by the grating. As shown in Refs. 1 and 5, the co-propagating surface mode has a group velocity in the direction opposite to the electron beam for low electron beam energy. The backward surface mode supported by the grating is a linear combination of infinite number of Floquet-Bloch harmonics having the z-component of propagation vectors differing from each other by an integral multiple of k_g, where $k_g = 2\pi/\lambda_g$. The y-component H_y of the magnetic field of the backward surface mode can be written as $\sum A_n \exp(ik_0 z + ink_g z - \Gamma_n x - i\omega t)$, where the summation is implied over all n from -∞ to +∞ [1]. Here, ω is the frequency, $k_0 = \omega/c\beta$ is the propagation vector of the backward surface mode and $\Gamma_n = \sqrt{(k_0 + nk_g)^2 - \omega^2/c^2}$. The zeroth-order component of this mode has the longitudinal electric field given by $E_0(z,t)\exp(ik_0 z - i\omega t)$ at $x = 0$. The amplitude of all other components of the backward surface mode have to maintain a fixed ratio with the amplitude of the zeroth-order component such that the elec-

* Work supported by U.S. Department of Energy, Office of Basic Energy Sciences, under Contract No. W-31-109-ENG-38.
#vinit@cat.ernet.in

tromagnetic field satisfies the required boundary conditions at the grating surface. Hence, as the zeroth-order component of the surface mode evolves due to interaction with co-propagating electron beam, the amplitude of all other components also evolve proportionately.

The evolution of the backward surface mode due to interaction with the co-propagating electron beam can be described using following Maxwell-Lorentz equations [1].

$$\frac{\partial \mathcal{E}}{\partial \tau} - \frac{\partial \mathcal{E}}{\partial \zeta} = -\mathcal{J}\langle e^{-i\psi}\rangle, \quad (1)$$

$$\frac{\partial \eta_i}{\partial \zeta} = (\mathcal{E} + \mathcal{E}_{sc})e^{i\psi_i} + c.c., \quad (2)$$

$$\frac{\partial \psi_i}{\partial \zeta} = \eta_i, \quad (3)$$

$$\mathcal{E}_{sc} = i\frac{\mathcal{J}}{\chi L}(\chi_1 - e^{2\Gamma_0 b})\langle e^{-i\psi}\rangle, \quad (4)$$

where, the notations used are described in Ref. 1. Here, $\mathcal{E}$ is the dimensionless electric field, $\mathcal{E}_{sc}$ is the dimensionless space charge field, $\mathcal{J}$ is the dimensionless beam current, τ is the dimensionless time, $\zeta = z/L$ is the normalised distance along the grating, ψ_i is the phase of i^{th} electron, η_i is the dimensionless relative energy of the i^{th} electron and χ and χ_1 are related to the singularity associated with the surface mode as defined in Ref. 1. The formula for conversion from E_0 to $\mathcal{E}$ is the following

$$\mathcal{E} = \frac{4\pi}{I_A Z_0}\frac{kL^2}{\beta^2\gamma^3}E_0, \quad (5)$$

where Z_0 = 377 Ω is the characteristic impedance of free space, I_A = 17 kA is the Alfvén current and γ is the electron energy in the unit of its rest mass energy.

Eqs (1-4) can be used to perform 2D simulation of the SP-FEL. For given grating parameters and electron beam parameters, one has to first evaluate the resonant wavelength $\lambda = 2\pi c/\omega$, the group velocity v_g of the surface mode in the backward direction and the parameters χ and χ_1 as per the procedure described in Ref. 1. We then proceed for numerical solution of Eqs. (1-4) for which we use the approach used by Ginzburg et al. [8] and later also by Levush et al. [9] for BWO. The electron dynamics equations for a given field distribution along the interaction region are solved by the predictor-corrector method. Then, knowing the modified electron distribution in phase space, the field distribution at the next time step is obtained by solving the partial differential equations (Eq. 1) by the finite difference method. The method is stable for $\Delta\tau < \Delta\zeta$. Here, $\Delta\tau$ and $\Delta\zeta$ are the step sizes in τ and ζ respectively, used in the finite difference method. For initializing the electron beam in phase space, we simulate the shot noise using the algorithm given by Penman and McNeil [10], which is commonly used in FEL codes. In our simulation, we have used 1024 test particles and the step sizes are $\Delta\tau$ = 0.01 and $\Delta\zeta$ = 0.02. We have checked for the convergence of the solution with these simulation parameters. One can analyse the growth of power in the backward surface mode and thus study the saturated electric and magnetic field in the surface mode as well as the start current using this simulation [1].

Once the dimensionless electric field $\mathcal{E}$ at the location of the sheet beam is known using this simulation, one can calculate the amplitude of the total electric and magnetic field in the surface mode. The total magnetic field at the grating surface and the total electric field at the location of the sheet beam are given by the following expressions

$$H_y(x = -b, z, t) = \frac{I_A}{4\pi}\frac{\beta^4\gamma^4}{kL^2}e^{\Gamma_0 b}\mathcal{E}\mathcal{T}_1, \quad (6)$$

$$E_z(x = 0, z, t) = Z_0\frac{I_A}{4\pi}\frac{\beta^3\gamma^3}{kL^2}\mathcal{E}\mathcal{T}_2, \quad (7)$$

where $\mathcal{T}_1$ and $\mathcal{T}_2$ are given by the following series

$$\mathcal{T}_1 = \sum_{n=-\infty}^{n=+\infty}\frac{A_n}{A_0}e^{(ik_0 z + ink_g z - i\omega t)}, \quad (8)$$

$$\mathcal{T}_2 = \sum_{n=-\infty}^{n=+\infty}\frac{\Gamma_n}{\Gamma_0}\frac{A_n}{A_0}\frac{e^{-\Gamma_n b}}{e^{-\Gamma_0 b}}e^{(ik_0 z + ink_g z - i\omega t)}. \quad (9)$$

Note that the coefficients A_n/A_0 for given grating parameters and the phase velocity of the surface mode can be calculated by satisfying the boundary conditions at the grating surface [1,5].

Eqs. (1-4) can be solved analytically in the linear regime and we can derive the following expression for the start current density [1]

$$\frac{dI_s}{dy} = 7.68\frac{I_A}{2\pi\chi}\frac{\beta^4\gamma^4}{kL^3}e^{2\Gamma_0 b}. \quad (10)$$

In the next section, we will use the numerical simulation based on Eqs. (1-4) and then calculate the total electromagnetic field at saturation and the start current using Eqs. (6-10) to compare with results obtained using PIC simulations.

COMPARISON WITH PIC SIMULATIONS

A more powerful, but computer intensive approach to simulate a SP-FEL is to use a PIC code. Donohue et al. [4] and Li et al. [2,3] have recently used a commercially available code MAGIC [7] to perform 2D/3D simulation of SP-FEL. MAGIC is an electromagnetic PIC code, i.e., a finte-difference, time domain code for simulating plasma physics processes. The full set of Maxwell's time-dependent equation is solved to obtain electromagnetic fields. Similarly, the complete Lorentz force equation is solved to obtain relativistic particle trajectories, and the continuity equation is solved to provide current and charge densities for Maxwell's equations.

First, we compare our results for parameters discussed by Donohue et al. in Ref. 4. They have performed 2D simulation using a sheet electron beam. The parameters used are: beam energy = 50 keV, dI/dy = 1000 A/m, λ_g

= 173 μm, d = 100 μm, w = 62 μm, N = 35 and B_z = 2 T. Here, N is the number of grating periods and B_z is external magnetic field used for guiding. The beam thickness is the x direction is taken to be 20 μm and the edge of the beam is taken to be at a height of 20 μm from the grating top surface. With these parameters, the amplitude $|B_y|$ of the total magnetic field at the grating top surface ($x = -b$) in the surface mode at saturation has been obtained to be 0.01 T in Ref. 4 using 2D MAGIC simulation. In our model, since we take a sheet beam of zero thickness, we choose the equivalent height b of the sheet beam from the grating top surface to be 30 μm. For these parameters, we obtain λ = 631 μm, v_g/c = 0.39, χ = 28 per cm and χ_1 = 1.9. We have then run the simulation based on Maxwell-Lorentz equation discussed in the previous section using these parameters and find that at saturation, the amplitude $|\mathcal{E}|$ of dimensionless electric field is 5.34. Next, by solving the boundary value problem at the grating surface [1,5], we evaluated the coefficients in the surface mode as A_2/A_0 = -0.14 + i 0.175, A_1/A_0 = 1.31 + i 2.74 and A_{-1}/A_0 = -0.09 - i 0.18. We find that other coefficients are very small and not significant. Putting these coefficients in the series in Eq. (8), we find that peak value of $|\mathcal{T}_1|$ is 4.41. Putting all these in Eq. (6), we evaluate the amplitude of $|H_y|$ at saturation to be 7.13 $\times$ 10^3 A/m which gives us $|B_y|$ = 0.009 T. This agrees quite well with the result obtained using MAGIC.

Next, we compare our results with those obtained by Li et al. in Ref. 2. Here, they have used electron beam energy = 40 keV and the same grating parameters as in the previous example except that N = 50. They have used the electron beam thickness in the x direction as 24 μm and the height of the edge of the electron beam from the grating top surface as 34 μm. For these parameters they obtain the start current density as 600 A/m. In this case, we obtain λ = 663.67 μm and χ = 15 per cm. Assuming an equivalent b = 46 μm in our sheet beam model and using Eq. (10), we obtain start current density as 520 A/m. This is around 13% smaller than the value obtained using MAGIC.

Finally, we compare our results with 3D MAGIC simulations reported recently by Li et al. in Ref. 3. Here, they have used electron beam energy = 100 keV, I = 0.8 A, λ_g = 2 cm, d = 1 cm, w = 1 cm, N = 46 and B_z = 2 T. A cylindrical electron beam of radius 2.5 mm is assumed and the edge of the beam is taken to be at a height of 2 mm from the grating top surface. For simulating this case, we take b = 4.5 mm in our sheet beam model. We obtain λ = 64.55 mm, v_g/c = 0.16, χ = 1.21 per cm and χ_1 = 5.5 for this case. Using Eq. (10), we find that dI_s/dy = 1.6 A/m for these parameters. Li et. al. have studied the growth of electromagnetic oscillation for this case using MAGIC and obtain the start current to be 0.5 A. Note that since our analysis is 2D, we can calculate the start current density dI_s/dy and not the total start current I_s. If the width of the surface mode in y direction is Δy, the start current $I_s = dI_s/dy \times \Delta y$. The width of the mode Δy is an unknown parameter in our 2D analysis and can be calculated only in a 3D analysis. However, here we can evaluate the equivalent Δy by dividing the start current obtained using MAGIC by start current density obtained using our 2D analysis. This way, we obtain the equivalent Δy = 25 cm for this case. Hence, the equivalent surface current density for the beam current of 0.8 A is 3.2 A/m in our 2D simulation. For these parameters, we have performed the numerical simulation based on Maxwell-Lorentz equations and find that $|\mathcal{E}|$ = 4.39 at saturation. Next, in order to evaluate the amplitude $|E_z|$ of the total electric field in the surface mode at the location of the electron beam ($x = 0$) using Eq. (7), we need to evaluate the series in Eq. (9). We find that all the terms except n = 1 and 0 can be neglected in the series and $A_1/A_0 = i$ 1.53. Hence, we find the peak value of $|\mathcal{T}_2|$ to be 2.25. Putting these numbers in Eq. (7), we obtain $|E_z|$ = 1.7 $\times 10^4$ V/m which compares well with 1.45 $\times 10^4$ V/m as obtained using MAGIC.

CONCLUSIONS

We have compared the results of 2D simulation of SP-FEL using Maxwell-Lorentz equation with 2D/3D MAGIC simulations and found the comparison to be good. Simulations based on Maxwell-Lorentz equation are fast and the reported simulations typically take few tens of minutes whereas the MAGIC simulations take longer time. 3D MAGIC simulations reported here typically take several days. We plan to perform detailed 3D MAGIC simulations in future to study the 3D mode size and structure.

REFERENCES

[1] V. Kumar and K.-J. Kim, Phys. Rev. E 73 (2006) 026501.

[2] D. Li et al., Phys. Rev. ST Accel. Beams, 9 (2006) 040701.

[3] D. Li et al., Proceedings of FEL conference, (2006) 439.

[4] J. T. Donohue and J. Gardelle, Phys. Rev. ST Accel. Beams, 9 (2006) 060701.

[5] H. L. Andrews and C. A. Brau, Phys. Rev. ST Accel. Beams, 7 (2004) 070701.

[6] H. L. Andrews et al., Phys. Rev. ST Accel. Beams, 8 (2005) 050703.

[7] D. Smithe and T. M. Abu-Elfadi, Comput. Phys. Commun. 95 (1997) 106.

[8] N. S. Gingburg, S. P. Kuznetov, and T. N. Fedoseeva, Sov. Radiophys. Electron., 21 (1979) 728.

[9] B. Levush et al., IEEE Trans. Plasma Sci. 20, (1992) 263.

[10] C. Penman and B. W. J. McNeil, Opt. Commun. 90 (1992) 82.

BEAM PARAMETERS OF THE SCSS PROTOTYPE ACCELERATOR DESIGNED BY PARMELA AND COMPARISON WITH THE MEASURED VALUES

Toru Hara*, Hideo Kitamura, Tsumoru Shintake, Hitoshi Tanaka, Kazuaki Togawa
RIKEN/XFEL, 1-1-1 Kouto, Sayo-cho, Sayo-gun, Hyogo 679-5148, Japan
Takanori Tanikawa
University of Hyogo, 3-2-1 Kouto, Kamigori-cho, Ako-gun, Hyogo 678-1297, JAPAN

Abstract

The 250 MeV prototype facility of the X-FEL project at SPring-8 was constructed in Octorber 2005 and the machine commissioning was started in May 2006. One month later, we have succeeded in confirming the amplification of synchrotron radiation. The electron beam parameters, such as peak currents and emittances, have been designed and estimated using PARMELA. In contrast to other X-FEL projects, the SCSS injector uses a thermionic pulsed electron gun. Compared with RF photocathode guns, a thermionic gun is stable and easy to handle. Its peak current, however, is smaller and compression of an electron bunch is necessary at the early stage of a low beam energy injector. In this report, we compare the simulation and the measured beam parameters, such as the bunch length and the projected emittance, on the SCSS prototype accelerator. The measured values, after the bunch compression process and the emittance degradation due to space charge, show fairly good agreement with the simulation.

INTRODUCTION

The SPring-8 Compact SASE Source (SCSS) prototype facility was constructed in 2005 as a test bench of the X-FEL project aiming at the lasing wavelength less than 0.1 nm [1]. One of the unique features of the project is the use of a thermionic pulsed electron gun instead of a laser photo-cathod RF gun. In order to reduce the initial beam emittance, a single crystal CeB_6 (ϕ 3 mm) is used as a cathode and a high pulsed voltage of 500 kV is applied to the anode to extract the electron beam [2]. The thermionic gun has clear advantages such as stable operation and easy maintenance, however, its peak current is smaller compared with that of photo-cathode guns. As a result, electron bunch compression is necessary at the low beam energy section ($\leq$ 1 MeV) of the accelerator.

Fig. 1 shows a schematic layout of the SCSS prototype accelerator. A fast deflector is installed just after the electron gun, and an 1 ns electron bunch is sliced out from a μsec electron beam of 1 A from the gun cathode. At the same time, the periphery of the electron beam, which is emitted from the cathode edge, is removed by a pinhole (ϕ 5 mm). Then the 1 ns electron bunch is compressed by a velocity bunching scheme using a 238 MHz, 476 MHz and S-band APS cavities. The peak current is reached about 80 A after the S-band traveling wave tube with the beam energy of 40 MeV. At this point, the beam parameters are similar to those of the RF photocathode guns. Then the electron bunch is further compressed in a magnetic bunch compressor (BC), and accelerated up to the 250 MeV nominal energy using C-band accelerators.

Since the slice emittance and the peak current, which are the most important parameters for the FEL operation, does not change significantly in the C-band main accelerator, the key of the parameter design is how to obtain a large peak current without degrading the gun emittance at the BC end.

* toru@spring8.or.jp

BEAM PARAMETER DESIGN WITH PARMELA

Initial Conditions

Since PARMELA can not treat a DC electron gun, 500 keV energy is immediately given to the electrons at the start, and no DC acceleration process between the cathode and anode is considered in the simulation. The bunch length and normalized emittance at the gun cathode are assumed to be 1 ns and 0.5 π mm-mrad respectively. In order to focus the electron beam, magnetic lens are used in the prototype accelerator for the beam energy below 1 MeV. The initial beam size and divergence at the cathode are determined so that the simulation reproduces the measured sizes at three locations of the injector section ((a), (b) and (c) in Fig. 1) as a function of the focusing strength. Fig. 2 shows the simulated and measured beam sizes at these locations as a function of the magnetic lens current.

Bunch Compression

The emittance degradation of the SCSS prototype accelerator is mainly due to the space charge effect at the low energy injector section. The focusing strength and the RF parameters should be chosen so as to keep the uniform transverse electron beam profile from the gun cathode during the velocity bunching process. In other words, the nonlinear divergence coming from the space charge effect should be minimized to avoid the slice emittance degradation. The optimized beam energies and peak currents along the accelerator are shown in Fig. 1.

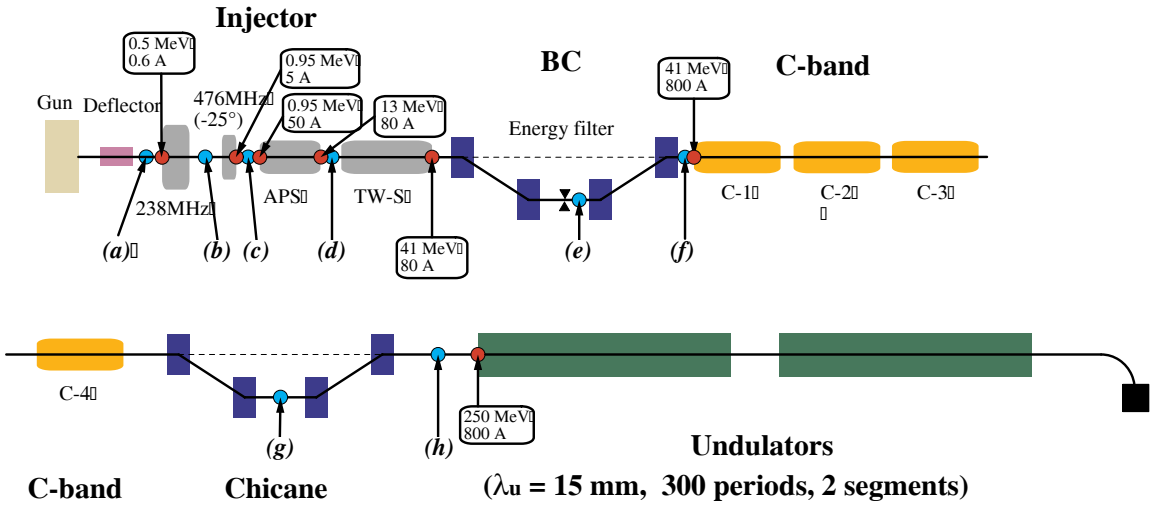

Figure 1: Layout of the SCSS prototype accelerator.

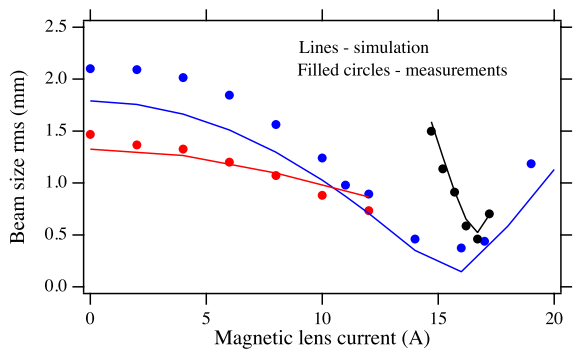

Figure 2: Comparison of the beam sizes between the measurements (filled circles) and the simulation (lines). The figure shows the beam sizes at three locations (a)-black, (b)-blue and (c)-red in Fig. 1 as a function of the focusing strength of neighboring magnetic lens.

In order to verify the velocity bunching process, a microwave spectrometer was used to estimate the bunch length [3]. The microwave spectrometer measures coherent radiation power of specific spectral regions generated from the electron bunch passing through a fluorescent screen. Since the coherent radiation power is increased for a shorter bunch length and a higher peak current, the RF phase of the maximum compression at the observation point, where the bunch length becomes the minimum, can be found. Beyond the RF phase of the maximum compression, the bunch length increases again, so called overbunching.

Fig. 3 is the measured variation of the bunch length at two different locations ((c) and (d) in Fig. 1) as a function of the 476 MHz cavity RF phase. The S-band APS cavity was switched off at the time of measurement. By comparing the RF phases of the maximum bunch compression between the measurements and simulation in Fig. 3, it is confirmed that the electron bunch is compressed as expected. For the FEL operation, the phase of 476 MHz cavity is set at $-25°$ corresponding to the maximum bunching point in the S-band APS tube, and the velocity bunching is stopped before overbunching due to the beam acceleration in the APS.

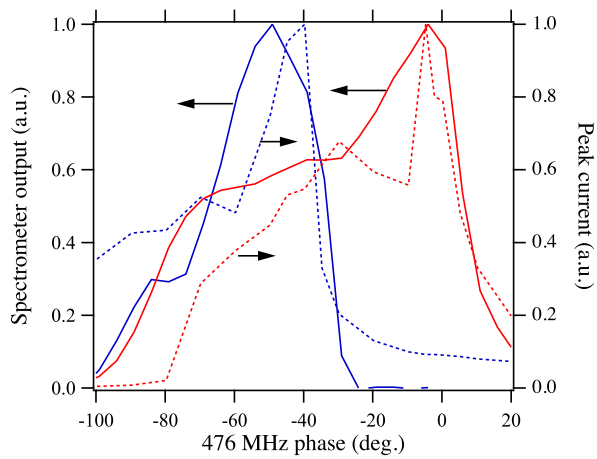

Figure 3: Relative change of the bunch length measured by a microwave spectrometer (solid lines) and the peak current calculated with PARMELA (dotted lines) as a function of the RF phase of the 476 MHz cavity. Left peaks (blue lines) corresponds to the location just before the S-band APS ((c) in Fig. 1), and right peaks (red lines) after the APS ((d) in Fig. 1). 0° is the crest phase of the 476 MHz RF (maximum acceleration).

The final bunch length after the BC is measured using dispersion of the chicane and energy chirp given by the last two C-band tubes. When putting the electron bunch at zero-cross phase of the C-band RF, the amount of energy

chirp inside the bunch is roughly proportional to the bunch length. This energy chirp is converted into the increase of the horizontal beam size at the middle of the chicane ((g) in Fig. 1), where the dispersion is not zero. From this, the bunch length can be roughly estimated. The result of the measurement was about 1.1 ps (full width) and it is slightly longer than the simulated value 0.7 ps (full width).

We also tried to measure the bunch length with a streak camera using OTR (Optical Transition Radiation) from a gold mirror. The obtained value was about 2 ps (RMS). The discrepancy thought to be the chromatic aberration of the transport line between the OTR screen and the streak camera, which is about 8 m.

Emittance and Beam Size

The transverse electron beam profiles were measured at various locations along the accelerator using fluorescent and OTR screens. Fig. 4 is an example of the beam sizes measured and simulated at the middle of the BC ((e) in Fig. 1). The measured beam size is slightly larger due to the thickness of the fluorescent screen (1 mm).

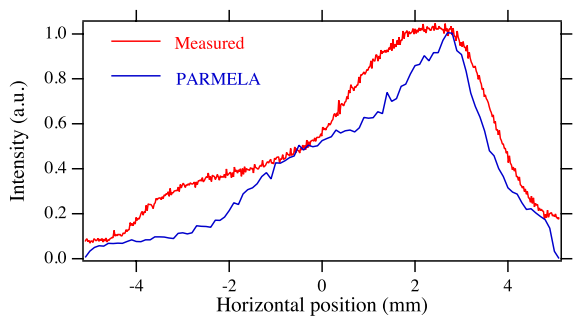

Figure 4: The horizontal beam profiles measured (red) and simulated (blue) at the middle of the BC ((e) in Fig. 1).

Table 1: Comparison of the projected emittances between the Q-magnet scan measurements and the PARMELA simulation

Location	**Measurement (mm-mrad)**	**Simulation (mm-mrad)**
End of BC (f) in Fig. 1	$\varepsilon_x \approx 3\pi$ $\varepsilon_y \approx 3\pi$	$\varepsilon_x = 2.8\pi$ $\varepsilon_y = 2.6\pi$
Before undulator (h) in Fig. 1	$\varepsilon_x \approx 4\pi$ $\varepsilon_y \approx 2\pi$	$\varepsilon_x = 2.3\pi$ $\varepsilon_x = 2.3\pi$

Since the slice emittance can not be directly measured at the moment, the projected emittance was measured using a Q-magnet scan method. Table 1 compares the measured and simulated projected emittances at two locations of the accelerator, the end of the BC ((f) in Fig. 1) and just before the undulator ((h) in Fig. 1). Considering the measurement errors, the measurement and the simulation are in good agreement.

Fig. 5 is the slice emittance and longitudinal profile of the electron bunch just before the undulator obtained from the simulation. The measured brightness of the electron beam, which was estimated from the FEL gain dependence on the bunch charge and the undulator K parameter, is between $240 \sim 310 A/\pi^2 mm^2 mrad^2$, and the design value ($200 A/\pi^2 mm^2 mrad^2$) is expected to be achieved in the prototype accelerator [4].

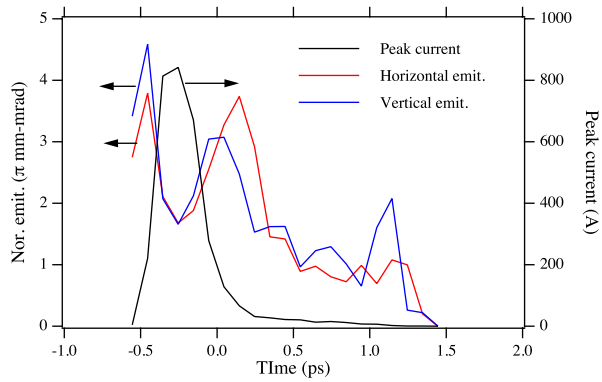

Figure 5: Longitudinal electron bunch profile and slice emittances just before the undulator ((h) in Fig. 1) expected by the PARMELA simulation.

SUMMARY

Though the electron beam simulation carried out using PARMELA does not include Coherent Synchrotron Radiation (CSR) effect at the bending magnets, the results of the simulation reproduce well the measured beam parameters. Particularly, the measurement and the simulation show a fairly good agreement in the bunch compression process and the space charge effect at the low energy section. It is an important step toward the construction of the XFEL facility that the design parameters of the electron beam were achieved in the prototype accelerator.

REFERENCES

[1] http://www-xfel.spring8.or.jp

[2] K. Togawa, et al., "Emittance Measurement on the CeB6 Electron Gun for the SPring-8 Compact SASE Source", Proceedings of the FEL Conference 2004, pp. 351-354, URL: http://www.JACoW.org.

[3] H. Maesaka, et al., "Development of the Microwave Spectrometer for the Bunch Length Measurement Using Coherent Synchrotron Radiation at the SCSS Prototype Accelerator", Proceedings of the 3rd Annual Meeting of Particle Accelerator Society of Japan, August 2006, Sendai, Japan, pp. 328-330.

[4] Hitoshi Tanaka, et al., "Low Emittance Injector at SCSS", Proceedings of the FEL Conference 2006, Berlin, Germany, pp. 769-776.

FUTURE LIGHT SOURCE BASED ON ENERGY RECOVERY LINAC IN JAPAN

Toshio Kasuga, Takaaki Furuya, Hiroshi Kawata, Yukinori Kobayashi, Shogo Sakanaka, and Kotaro Satoh
High Energy Accelerator Research Organization (KEK), Tsukuba, Ibaraki 305-0801, Japan
Norio Nakamura
Institute for Solid State Physics (ISSP), University of Tokyo, Kashiwa, Chiba 277-8581, Japan
Ryoichi Hajima
Japan Atomic Energy Agency (JAEA), Tokai, Naka, Ibaraki 319-1195, Japan

Abstract

After extensive discussions on the future light source of the Photon Factory at the High Energy Accelerator Research Organization (KEK), it has been concluded that a 5 GeV energy recovery linac (ERL) should be the most suitable candidate to foster cutting-edge experiments, as well as to support a large variety of user needs from VUV to X-rays. On the other hand, the Japan Atomic Energy Agency (JAEA), which has built a low energy (17 MeV) ERL, also proposed another 5-6 GeV ERL as a light source. These two institutes, with a participation of some members of the Institute for Solid State Physics (ISSP) of the University of Tokyo, agreed to promote an ERL-based next-generation synchrotron light source in Japan. Before constructing a 5 GeV ERL, it is necessary to develop several critical components, such as an electron gun and superconducting accelerating structures, and to prove their performance. To this end, we plan to construct a test ERL of 200-MeV class at the KEK site. An R&D team for the test ERL is going to be organized in collaboration with accelerator scientists from the other facilities, the UVSOR and the SPring-8.

INTRODUCTION

We have been investigating the feasibility of an energy recovery linac (ERL) as a light source for several years [1-3]. After the discussions on the future light source of the Photon Factory, it has been concluded that a 5 GeV class ERL should be the most suitable candidate to foster cutting-edge experiments, as well as to support a large variety of user needs from VUV to X-rays [4]. A conceptual layout of a 5 GeV ERL, proposed in the feasibility study, is shown in Fig. 1. The principal parameters are also shown in Table 1 [1]. In order to realize this kind of light source, the development of many components that compose the light source is necessary. Investigations into the beam dynamics issues, for example, the energy recovery in rf cavities, the stability of the beams, the conservation of normalized emittance, etc., are also essential. Therefore, construction of a test ERL seems to be inevitable. Both the design concept and the key technologies will be demonstrated by the test ERL. An R&D team for the test ERL is going to be organized in collaboration with accelerator scientists from KEK, JAEA, ISSP, UVSOR and SPring-8. We are planning to construct a 200-MeV class ERL, and to substantiate the principle of the ERL within several years. The principal parameters of the test ERL are also shown in Table 1.

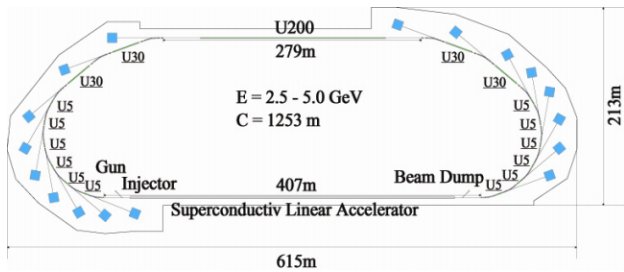

Figure 1: Conceptual layout of 5GeV ERL.

Table 1: Principal parameters of the future light source and the prototype.

	Future LS	Test ERL	
Beam energy	2.5-5.0	0.06-0.2	GeV
Injection energy	5-10	5-10	MeV
Circumference	1253	68.8	m
Beam current (Max.)	100	100	mA
Normalized emittance	0.1-1	0.1-1	mm·mrad
Energy spread (rms)	5	-	E-5
Bunch length	1-0.1	1-0.1	ps
RF frequency	1.3	1.3	GHz
Accelerating gradient	10-20	10-20	MV/m

DEVELOPMENT OF A PHOTOCATHODE DC GUN

The combination of a DC gun and a photocathode should be an optimum electron source, which fulfils the requirement of ERL light sources: electron beams of high-average current and ultra-small emittance. To demonstrate the ERL-quality electron beams, we are developing a photocathode DC gun at JAEA. The gun consists of a main chamber for DC electrodes, an NEA surface preparation chamber, and a load-lock system for transporting a photocathode between these chambers. A ceramic insulator of the gun and a high voltage stack of 250 kV-50mA power supply are located side-by-side in a pressure vessel, holding 2-atm SF6. A high-voltage test without a beam load has been completed successfully, and assembling of the load-lock system is in progress. We are proposing a superlattice semiconductor for the

photocathode, which realizes high-quantum efficiency and small thermal emittance simultaneously [5]. As the first step of the photocathode development, we have fabricated several types of bulk samples, which are GaAs and AlGaAs with different content of aluminum. Measurements of quantum efficiency and life-time of these samples have indicated that AlGaAs has larger quantum efficiency and longer life-time than GaAs. Detail experimental results of photocathode and status of DC gun are presented in an accompanying paper [6].

LATTICE AND BEAM DYNAMICS ISSUES OF THE TEST ERL

In order to prove successful operations of key components, as well as to verify our predictions of accelerator physics issues, we plan to construct a test ERL. The test ERL will comprise a DC photoinjector, a superconducting (SC) injector linac, one or two cryomodules for the main linac, a return loop and a beam dump. An injection energy will initially be 5 MeV, and will be upgraded up to 10-15 MeV. The maximum beam energy will be 60-200 MeV, depending on the number of superconducting cavities in the main linac and on their accelerating gradient (15-20 MV/m). The maximum beam current of 100 mA is anticipated.

An injector design [7], made by the JAEA group, was adopted for our starting point. The design is made up of a 500-kV DC photocathode gun, two solenoids, (temporarily) five three-cell cavities, some quadrupoles and a three-dipole merger. Normalized emittances were predicted to be approximately 1 and 0.1 mm·mrad under bunch charges of 77 and 7.7 pC, respectively, at the end of the merger. Further optimization of this design is underway.

To prove successful operations of SC cavities for the main linac under high beam currents, as well as to verify some predictions of accelerator physics issues, a return loop is necessary. Figure 2 shows our current design. A triple-bend achromat (TBA) lattice was adopted for two arcs because similar lattice will be adopted to our practical 5-GeV ERL. Two cryomodules will finally be installed in one of the straight sections, and a test undulator will be installed in the other straight section in order to evaluate the quality and the stability of emitted photon beams. Figure 3 shows typical optical functions calculated with a computer code SAD.

At a typical rms bunch length of 1 ps under usual beam circulations, an intense CSR (approximately 85 keV/turn at a beam energy of 200 MeV) will be emitted along the arcs. The beam optics should then be optimized so that small beam emittances can be preserved under the CSR. Under the other bunch compression mode, there are such important issues as i) control of R_{56}, T_{566}, and higher terms for achieving shortest bunches, and ii) minimizing emittance growth under more intense CSR. The optimization of beam optics under both operations is underway.

We are also investigating some potential problems under ERL operations such as a beam breakup instability due to cavity HOMs, a resistive-wall beam breakup instability, and an ion trapping.

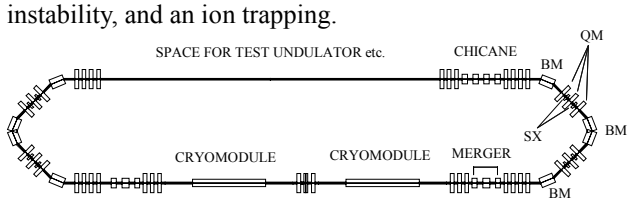

Figure 2: A prototype design of the return loop for the test ERL.

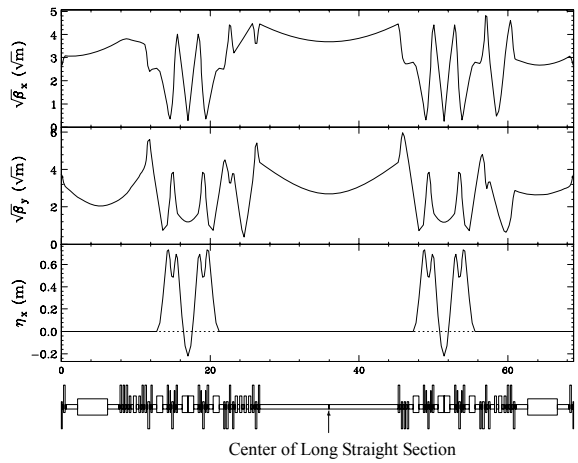

Figure 3: Typical optical functions along the return loop. Periodic condition was assumed.

DEVELOPMENT OF ACCELERATING STRUCTURES

Two kinds of 1.3 GHz superconducting (SC) linacs are under investigation, i.e., the injector linac and the main linac. The choice of 1.3 GHz allows us to use the SC cavity technology that has been developed for a linear collider [8].

Injector Linac

At a total rf voltage of 10 MV, the injector linac delivers the RF power of 1 MW to the beam of 100 mA in CW mode. Therefore, the most difficulty of the injector linac is the power couplers. To reduce the power of each coupler, a couple of SC cavities of 2 or 3 cell structure with double input couplers is considered as a candidate of the injector linac. Cavity design and fabrication of a prototype cavity will be started soon.

Main Linac

A nine-cell structure with sufficiently damped HOM has been optimized to achieve a stable accelerating gradient of 15-20 MV/m under the beam of 100 mA. A large iris diameter of the cells and large beam pipes on both ends can propagate out the HOMs from the cavity to the absorbers, which is the way that has been successfully used in KEKB SC cavity [9]. Furthermore, an eccentric-fluted beam pipe has been proposed and adopted so as to take out the quadrupole modes [10]. Figure 4 shows the cavity with absorbers on both ends. A Cu-model and a

full scale Nb cavities are under fabrication. Geometrical parameters of the cavity are listed in Table 2.

Figure 4: A nine-cell cavity for the main linac. HOM absorbers are on both sides.

Table 2: Geometrical parameters of the 9-cell cavity.

Frequency	1.3	GHz
Structure	9	cells
Iris diameter	80	mm
Dia. of beam pipes	100, 120	mm
R/Q	897	Ohms
Geometrical factor	289	Ohms
E_{sp}/E_{acc}	3.0	
H_{sp}/E_{acc}	42.5	Oe/(MV/m)

SITE

We have been planning to construct the test ERL in the experimental hall which has been used for the cold neutron science at the KEK Tsukuba campus [4]. However, in the design study, we found that the hall is not large enough to house a 200-MeV class machine. It is almost impossible to equip VUV beamlines around it, and furthermore it is difficult to construct sufficient radiation shields. In the meanwhile, the KEK 12-GeV Proton Synchrotron (PS) was closed, and the research using the PS is moving to the J-PARC project. In the near future, the experimental halls around the PS will be available for new activities of KEK. We are now discussing the possibility to change the site for the test ERL. Figure 5 shows a temporary layout of the test ERL which is fit to the east experimental hall of the PS.

SCHEDULE

A short sketch of the development schedule of the test ERL is shown in Table 3.

Table3: Timetable of development of the test ERL.

2006	"ERL Project Office" started. Design study, R&D (SC RF cavity, Gun).
2007	Design study and R&D for SC RF cavity, a gun, beam diagnostics etc.
2008	Fabrication/Test of components. Cryogenic system.
2009	Installation (in east experimental hall of PS ?).
2010	Commissioning, machine development.
2011	Operation, machine development. Construction of 5GeV ERL.

ACKNOWLEDGMENT

We would like to acknowledge the contributions of members of an ERL development team, consisting of the staff from KEK, JAEA, ISSP, UVSOR, and SPring-8.

REFERENCES

[1] Study Report on the Future Light Source at the Photon Factory —Energy Recovery Linac and Science Case—, March 2003 [in Japanese].
[2] K. Yokoya, "ERL Project at KEK", invited talk at APAC04.
[3] M. Shimada *et al.*, Proc. EPAC06, p. 190.
[4] Photon Factory Activity Report 2005, Dec. 2006. http://pfwww.kek.jp/pfacr/index.html
[5] T. Rao *et al.*, Nucl. Instr. Meth. **A557** (2006) 124-130.
[6] R. Hajima *et al.*, in these proceedings.
[7] R. Hajima and R. Nagai, Nucl. Instrum. Methods **A557** (2006) 103.
[8] http://www.desy.de/~teslatdr/tdr_web/pages/
[9] T. Furuya *et al.*, Proc. 11th Workshop on RF Superconductivity, DESY, 8-12 September, 2003.
[10] K. Umemori *et al.*, in these proceedings.

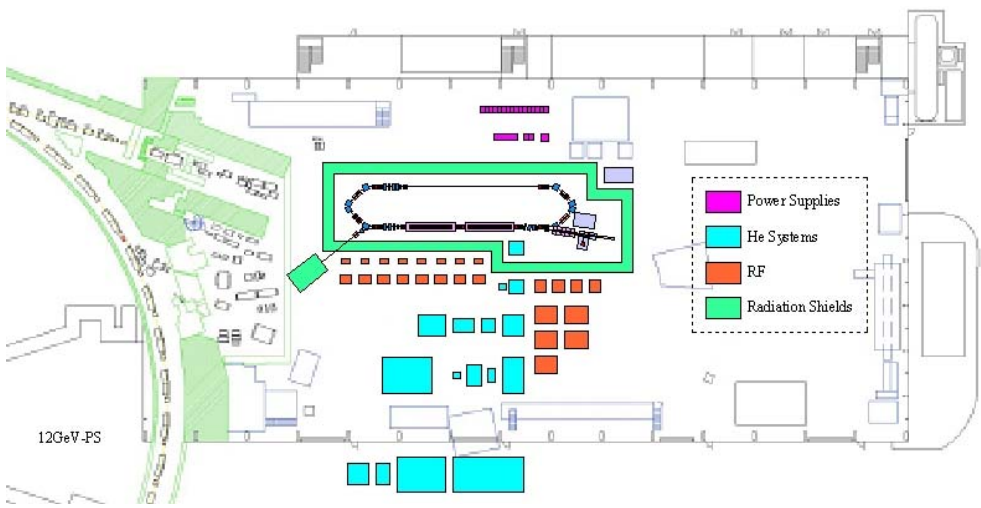

Figure 5: A temporary layout of the test ERL which is fit to the East Experimental Hall of the 12-GeV PS.

DEVELOPMENT OF A PHOTOCATHODE DC GUN AT JAEA-ERL

R. Hajima#, T. Nishitani, H. Iijima, R. Nagai, N. Nishimori
JAEA-ERL, Tokai, Ibaraki 319-1195, Japan

Abstract

An electron gun producing an e-beam with high-brightness and high-average current is a key component to realize a next-generation X-ray light source based on an energy-recovery linac (ERL). In JAEA, we are developing a photocathode DC gun for a future ERL light source. The DC gun is operated at 250 kV and 50 mA at maximum, and equipped with a load-lock chamber for cathode preparation. In order to keep small emittance at high current operation, we adopt new type of semiconductor photocathode such as AlGaAs and superlattice. In this paper, we present the status of the gun development and future plans towards the ERL test facility to construct in collaboration with KEK and other institutes.

INTRODUCTION

In JAEA (Japan Atomic Energy Agency), we have conducted a research program for a high-power free-electron laser since 1987. As a part of the research program, an energy-recovery linac (ERL) has been commissioned. The design study of the ERL was started in 1999[1]. After one-year construction period we made first demonstration of energy-recovery operation in 2002[2]. The ERL consists of a 250 kV DC gun with thermionic cathode, 2.5 MeV injector, an ERL loop for 17 MeV electrons, and an FEL undulator. The FEL wavelength is around 20 μm [3]. The ERL also generate strong radiation in millimeter wavelength region by coherent synchrotron radiation from a bending magnet[4].

Following the successful demonstration of ERLs at JAEA and Jefferson laboratory[5], several new proposal of ERLs have been suggested. Since the energy-recovery linac provides a versatile technology to generate a high-brightness electron beam of high-average current, it can be applied to various kinds of accelerators. Next-generation X-ray light source is one of the most promising direction for the future ERL development. We can produce X-rays with excellent coherence and/or ultrashort pulse duration, if we employ an energy-recovery linac equipped with a high-brightness injector such as a photocathode gun. In Cornell university, a 5 GeV ERL light source is proposed as a successor of CESR, and an injector for the ERL is under development[6]. Research and development towards next-generation light source based on an 800 MeV ERL is carried out at Daresbury[7].

In Japan, KEK and JAEA had proposed each own 5-6 GeV ERL project for a future light source independently. These two institute, however, agreed to unite their projects into a single form in March 2006. We are now working together to construct an ERL test facility at KEK site to resolve technical and physical challenges[8]. In the joint project, JAEA is mainly responsible for the gun development and KEK has charge of superconducting cavities[9].

In this paper, we present the status of electron gun development for the future ERL light source in Japan.

hajima.ryoichi@jaea.go.jp

ELECTRON GUN FOR ERL LIGHT SOURCES

Next-generation light source based on the ERL technology provides an evolutionary path of X-ray science, because the ERL generates coherent X-rays and femtosecond X-rays which are difficult to obtain in existing storage rings. When the divergence of an electron beam is smaller than the intrinsic divergence of an X-ray, a large part of undulator radiation becomes coherent, and this criteria is called "diffraction limit" and given by $\varepsilon < \lambda/4\pi$, where ε is geometrical rms emittance and λ is X-ray wavelength. In order to satisfy the diffraction limit for 1 Å X-rays, emittance should be less than 8 pm-rad, which corresponds to normalized rms emittance of $\sim$0.1 mm-mrad at 5 GeV. Average current of an ERL light source should be as large as 100 mA to obtain X-rays of flux comparable to 3rd-generation light sources. Thus, the requirements of an electron gun for a future ERL light source are average current of 100 mA and normalized rms emittance of 0.1 mm-mrad.

Developing an electron gun to satisfy the above requirement is a serious matter. Photocathode RF guns have been studied for high-brightness electron beams and normalized rms emittance is approaching to a value of 1 mm-mrad [10]. Recently, a DC gun with a thermionic cathode generating an electron beam of 1.1 mm-mrad was built for an XFEL[11]. These guns, however, are designed for pulsed operation with small duty cycle. The gun of JAEA-ERL is compatible with 10-mA CW operation but has rather large emittance, 13 mm-mrad, due to its gridded thermionic cathode[13].

The only candidate for the future ERL light source is the combination of a DC gun and semiconductor cathode with negative electron affinity (NEA) surface. Since GaAs with NEA surface is able to emit photo-electrons by visible lasers, it is an optimum electron source for generating high-average current. An NEA cathode can be installed only at DC guns, because stable operation of an NEA surface requires ultra-high vacuum, typically 10^{-9} Pa. A DC gun with NEA cathode has been employed at the JLAB ERL, where average current of 9 mA and normalized emittance

of 10 mm-mrad have been obtained[14]. Similar electron guns are also used for generating polarized electrons. In the studies on a polarized electron source, emittance of 0.1 mm-mrad has been demonstrated with small average current, 1 nA$\sim$ 1μA [15][16].

We consider that an electron gun for future ERL light sources can be realized by improving existing technologies of DC guns and NEA photocathodes.

STRATEGY OF GUN DEVELOPMENT

In order to develop an electron gun which fulfills the requirements of future ERL light sources, 100 mA and 0.1 mm-mrad, we have launched two apparatus: a photocathode test bench and a 250-kV DC gun.

Since the performance of electron guns depends much on their photocathode, improvement of semiconductor photocathode is the main task in the gun development. For this purpose, we have assembled the photocathode test bench consisting of an old MBE chamber and a mode-locked Ti:sapphire laser. The chamber reaches ultra-high vacuum $\sim 3 \times 10^{-9}$ Pa, which is enough to activate an NEA surface. Quantum efficiency of a photocathode can be measured as a function of injection laser photon energy by using the Ti:sapphire laser and other auxiliary lasers. In the test bench, beam current is limited at a few μA because of available extraction voltage $\leq$1 kV. This small current and low voltage operation makes it difficult to estimate cathode life time in a practical situation. This is because ionization rate of residual gas by electron beam is a strong function of electron energy and degradation of NEA surface due to ion back-bombardment shows quite different behavior depending on DC voltage and field. However, we can compare performance of various cathodes with respect to their relative life time at the test bench.

We decided to construct a 250-kV, 50-mA DC gun for the demonstration of high-brightness and high-average current beams under more practical conditions than the test bench. Although simulation studies predict normalized emittance of 0.1 mm-mrad is obtained at gun voltage higher than 500 kV[17] [18], we chose a rather low voltage gun, 250 kV, which can be assembled by making best use of spare components available at JAEA-ERL. In the DC gun, we will explore the performance of newly developed photocathode under high-average current and high voltage condition as well as beam diagnosis at the downstream.

PHOTOCATHODE

There are two sources of initial emittance at semiconductor photocathodes. One is thermal motion of electrons which reflects the cathode temperature, and the other is residual energy of photo-excited electrons with respect to the potential of the conduction band. Although the latter is partially compensated during electron diffusion to the surface, the compensation works little for electrons generated near the surface. In previous experiments with polarized electron sources clearly showed the above physics, and initial emittance equivalent to thermal motion at room temperature is only available when the laser photon energy tunes to the band gap energy[15] [16].

Quantum efficiency of NEA semiconductor is proportional to density of state of conduction band and shows a monotonically increasing function of injection photon energy. Operation of high-average current requires electron excitation by photon energy larger than the band gap energy. This behavior of quantum efficiency is incompatible with the criteria for small initial emittance.

We have suggested that the incompatible properties, small emittance and large quantum efficiency, can be obtained concurrently by using a superlattice semiconductor instead of conventional bulk cathodes[19]. In order to promote this strategy, we made a series of experiments with bulk GaAs and bulk AlGaAs, in which quantum efficiency and life time of different cathodes were measured to confirm the predicted relation between the performance of photocathodes and their band structure. From the measurements, it was found that AlGaAs has two times larger quantum efficiency and more than 10 times longer life than GaAs[20]. The large quantum efficiency in AlGaAs is due to its band gap energy 1.79 eV, which is larger than GaAs, 1.42 eV. We can also attribute the improvement of life to the difference of electron affinity, 4.1 eV for AlGaAs and 3.8 eV for GaAs, because the smaller electron affinity results in the lower vacuum potential, i.e. the larger negative electron affinity. As a result of the measurements, we have confirmed that performance of NEA cathode is controllable by tuning the band structure.

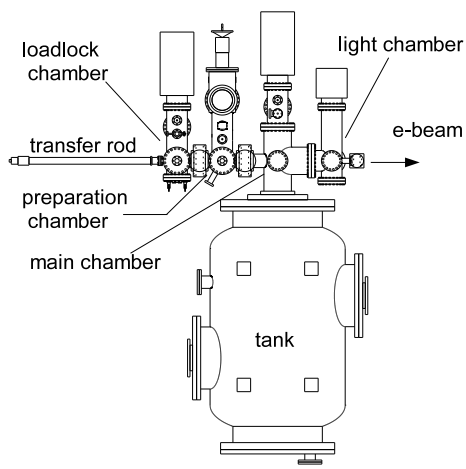

Figure 1: Top-view of the 250-kV, 50-mA gun.

250-KV DC GUN

Figure 1 shows layout of the 250-kV, 50-mA DC gun under construction. A high-voltage generator of Cockcroft-Walton circuit and a ceramic colum are installed in the tank filled with SF_6 gas, and the high-voltage terminal is con-

necting to a cathode block in the main chamber. In the preparation chamber, a photocathode surface is activated by cesium and oxygen to turn it into the NEA state. A laser light is introduced from the bottom of the light chamber, and an electron beam is extracted to the right side.

A high-voltage test without a beam load was completed [20], and further assembling of vacuum chambers is underway. The first beam extraction is expected around summer of 2007.

We are also designing beam transport and diagnostic systems for the 250-keV beam. A solenoid magnet will be installed at $z = 0.25$ m for emittance compensation and beam focusing at the down stream. The solenoid has a bucking coil to compensate magnetic field at the cathode surface. The beam emittance will be measured by double slit technique. Figure 2 is a result of PARMELA[21] simulations for a 250-keV electron beam, where we assume the initial bunch has uniform distribution of 2 mm in diameter for a 77-pC bunch, and 0.6 mm for a 7.7-pC bunch, and Gaussian distribution, $\sigma_t = 14$ ps, in longitudinal direction, electron temperature at the cathode is 30 meV. In fig.2, normalized rms emittance has the minimum value of 0.57 mm-mrad for a 77-pC bunch, and 0.15 mm-mrad for 7.7 pC. The trend of emittance in fig.2 shows somewhat different behavior from well-known emittance dilution by space charge force and its compensation by solenoid magnet, because the electron bunch does not keep its initial temporal profile, rms bunch length at $z = 2.2$ m is 66 ps for 77 pC and 29 ps for 7.7 pC.

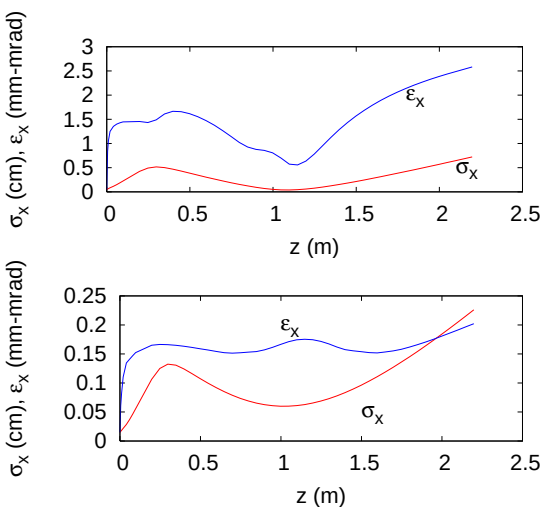

Figure 2: PARMELA simulation: Beam envelope and normalized rms emittance of a 250-keV, 77-pC bunch (top) and 7.7-pC (bottom). The cathode is located at $z = 0$ and the solenoid is installed at $z = 0.25$ m.

SUMMARY AND FUTURE PLANS

In JAEA-ERL, we are developing a photocathode DC gun for future ERL light source. Studies at the photocathode test bench have revealed that AlGaAs has higher quantum efficiency and longer life time than GaAs. The better performance of AlGaAs agrees with the theorical prospect that the larger band gap gives the larger quantum efficiency, and the larger electron affinity results in the longer cathode life. We continue further improvement of photocathode including superlattice structure. The 250-kV DC gun is under assembling and the first beam is expected around summer of 2007.

The outcome from the photocathode test bench and the 250-kV gun will be succeeded by a 500-kV gun for the ERL test facility which is to be constructed at KEK site. As for a drive laser for the photocathode gun, we plan to develop a fiber laser system.

The authors would like to acknowledge the contribution of Profs. Y. Takeda, M. Tabuchi for preparing AlGaAs and GaAs photocathodes under a collaboration program between JAEA and Nagoya University. This work was supported in part by MEXT KAKENHI (18740253).

REFERENCES

[1] R. Hajima et al., Nucl. Instrum. Meth. A445 (2000) 384.

[2] R. Hajima et al., Nucl. Instrum. Meth. A507 (2003) 115.

[3] N. Nishimori et al., Proc. FEL-2006, p.265.

[4] R. Hajima et al., Proc. FEL-2005, p.301.

[5] G.R. Neil et al., Phys. Rev. Lett. 84 (2000) 662.

[6] G.H. Hoffstaetter et al., Proc. PAC-2005, p.1928.

[7] J.A. Clarke, Proc. EPAC-2006, p.181.

[8] T. Kasuga et al., "Future Light Source based on Energy Recovery Linac in Japan", in these proceedings.

[9] K. Umemori et al., "Design of L-band superconducting cavity for the energy recovery linacs", in these proceedings.

[10] J. Yang et al., J. App. Phys. 92 (2002) 1608-1612.

[11] K. Togawa et al., Proc. FEL-2004, p.351.

[12] D.A. Kayran et al., Proc. RuPAC-2004, p.360.

[13] N. Nishimori et al., Proc. EPAC-2000, p.1672.

[14] C. Hernandez-Garcia et al., Proc. FEL-2004, p.558.

[15] N. Yamamoto et al., "Initial Beam Emittance Measurements for Electron Gun with NEA-GaAs type Photocathodes", Proc. 3rd Annual Meeting of Acc. Society of Japan (2006) p.169 (in Japanese).

[16] B M. Dunham et al., Proc. PAC-1995, p.1030.

[17] R. Hajima and R. Nagai, Nucl. Instrum. Meth. A557 (2006) 103.

[18] I.V. Bazarov et al., Phys. Rev. ST Accel. Beams 8 (2005) 034202.

[19] T. Rao et al., Nucl. Instrum. Meth. A557 (2006) 124.

[20] T. Nishitani et al., Proc. FEL-2006, p.319.

[21] L.M. Young, J. H. Billen, "PARMELA User's Manual", LA-UR-96-1835 2005 (version 3.40).

DEVELOPMENT OF AN INJECTOR TO GENERATE A VERY SHORT BUNCH FOR A SUPER COHERENT TERAHERZ LIGHT SOURCE PROJECT*

T. Tanaka#, T. Muto, F. Hinode, M. Kawai, K. Nanbu, K. Kasamsook, K. Akiyama, M. Yasuda and H. Hama, Laboratory of Nuclear Science, Tohoku University, 1-2-1 Mikamine, Taihaku-ku, Sendai, 982-0826, Japan
H. Tanaka, N. Kumagai, RIKEN/Spring-8, 1-1-1 Koto, Sayo-cho Sayo-gun, Hyogo- pref. 679-5198, Japan

Abstract

A project to develop a coherent Teraherz (THz) light source is in progress at Laboratory of Nuclear Science, Tohoku University. The coherent synchrotron light in the THz region is emitted from electron bunches with a very short bunch less than 100 fs (rms) generated by a thermionic RF gun and a sophisticated bunch compressor. As an injector for the linac, we have developed an independently tunable cells (ITC) RF gun and a magnetic bunch compressor which consists of a triple-bend achromat (TBA) lattice. As a result of simulation of the injector, we have obtained a very short bunch length of ~ 40 fs (rms). Results of low power tests of the ITC-RF gun and the tracking simulation of the bunch compressor will be presented in this proceeding.

INTRODUCTION

For a coherent Teraherz (THz) light source project employing an isochronous ring [1], a very short bunch less than 100 fs (rms) is required as an injected beam. A thermionic ITC-RF gun and a bunch compressor with a TBA lattice have been studied as the injector for the linac [2]. The thermionic RF gun can generate a macropulse with μs order which is an advantage for generating high average power of the radiation. Longitudinal phase space distribution can be manipulated in the ITC-RF gun so that the bunch length can be compressed effectively at the downstream of the gun. This gun can also generate a low emittance beam compared with a conventional dispenser cathode DC gun. Since the designed bunch compressor can vary R_{56} and the higher order term of the dispersion function, the bunch compression is able to be optimized even the initial longitudinal phase space distributions is changed.

GENERATION OF VERY SHORT BUNCH

Design of a thermionic RF gun

Taking the circumference of the isochronous ring (~ 150 ns) and the filling time of the gun assumed 0.3 μs into account, the macropulse duration of the injector has been chosen to be around 1.5 μs, which is possibly an advantage for avoiding back-bombardment effect [3]. The bunch charge should be as large as possible. The momentum deviation of the injected beam for the ring should be the order of 10^{-4} to have the beam turns the ring many times without bunch lengthening. Consequently the momentum acceptance of the injector part is required to be at least 10^{-2} because the beam is accelerated from 2 MeV to 200 MeV in the linac. Normalized rms emittance of the beam has to be very small less than 2 π mm mrad because the path length difference due to the betatron oscillation should be reduced. As a cathode material, a small single crystal of LaB_6 with a diameter 1.75 mm has been chosen. This cathode has a higher current density than that of conventional dispenser cathodes. The normalized emittance can achieve a small value because of the small area of the surface. According to a simulation study, the small cathode is also effective to reduce back-bombardment effect because the beam size of backstreaming electrons is larger than the area of the cathode [4]. To control an electron distribution in the longitudinal phase space, we employed independent two cells, which don't couple with each other. Parameters of the gun are listed in Table 1.

Table 1: Design parameters of ITC-RF gun

RF frequency	2,856 MHz (S-band)
Cathode material	LaB_6
Current density @ cathode	100 A/cm^2
Cathode diameter	1.75 mm
Number of cells	2
Feeding total power	~ 5 MW
E_{total} @ exit of gun	~ 2 MeV
Bunch length (rms)	~ 100 fs
Bunch charge	~ several tens pC
$\varepsilon_{norm.\ rms}$	< 2 π mm mrad
$\Delta p/p$	< 2 %
Macropulse duration	1.5 μs
Filling time	0.3 μs

Study of the beam dynamics in the ITC-RF gun has been done by using a 3D FDTD PIC code [4]. We had to find out an appropriate distance between the cells and the strength of the accelerating field in each cell, because the longitudinal phase space strongly depends on these parameters. A 2D code: SUPERFISH [5] has been used to determine the radius of cells so as to resonant frequencies become 2856 MHz. The iris radius between cells has been

*Work supported by the Grants-in-Aid of Japan Society for the Promotion of Science, contract No. 17360035.
#takumi@lns.tohoku.ac.jp

also determined by the code to make the coupling between cells negligible. The gun will be operated at the π-mode-like basically.

The gun has three degrees of freedom to control: the field strength of 1st cell E_1, the field strength of 2nd cell E_2 and relative phase between cells Δθ. To compress a bunch length effectively by a magnetic bunch compressor located at the downstream of the gun, we have searched an optimum operating point of the gun to generate a beam with a linear distribution in the longitudinal phase space. As a result of optimization, E_1 was fixed around 25 MV/m because the head of emitted electrons from a cathode must arrive at the middle point of between cells on time of a half RF cycle. Using optimized parameters (E_1, E_2) = (25, 50) MV/m, longitudinal phase spaces at exit of this gun for different values of Δθ are shown in Fig. 1.

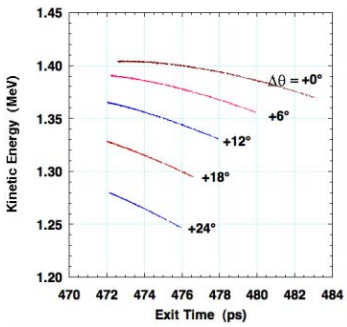

Fig. 1: longitudinal phase space. Δθ is a variable in this simulation. (E_1, E_2) = (25, 50) MV/m. $\Delta p/p_{max}$ = 2 %.

As shown in Fig. 1, a linearity of phase space distributions depends on the Δθ, and then we can manipulate it.

The normalized rms emittances less than 1 π mm mrad obtained by the simulation satisfy the designed. The bunch charge of this beam with momentum width $\Delta p/p$ = 2 % is about 30 pC which almost satisfies the design value.

Measurement basic parameters of the ITC-RF gun

A prototype of the ITC-RF gun has been manufactured as shown in Fig. 2.

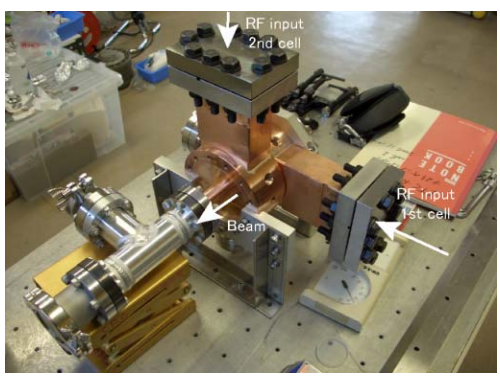

Fig. 2: An overview photo of the manufactured gun.

Some basic parameters of the gun has been measured by using a network analyzer (Agilent 8753ES). Resonant frequencies of both cells, two coupling coefficients β between RF input port and cell, and Q values have been measured at several conditions. The temperature around the gun has been kept at 21℃ within accuracy of 1℃ during the measurement. Measured resonant frequencies are (f_1, f_2) = (2810.8, 2821.3) MHz, where f_1 and f_2 represent frequencies of the 1st cell and the 2nd cell respectively. The measured frequencies are lower than a designed value of 2856 MHz. Calculating the resonant frequencies by 3D codes, an FDTD code or MW-STUDIO [6], it became clear that those are decreased by adding RF input ports and vacuum ports to. There are some methods to adjust resonant frequencies. Operating temperature of this gun changes the frequencies. Another way is changing inner wall shape by bolting down the outer wall. There are six holes to bolt down the outer wall for each cell. The first method is used to have the frequencies become down mainly by rising temperature from 21℃ to 50℃. Frequency change has been measured as a function of the temperature, which is summarized in Table. 2.

Table 2: Response rates of resonant frequencies to the temperature

df/dT	Measured value [kHz/K]	Calculated value [kHz/K]
1st cell: df_1/dT	-46.9	-37.9
2nd cell: df_2/dT	-45.9	-48.0

In SUPERFISH calculation in Table 2, it was assumed that the geometrical change caused is only the cavity diameter. The measured value of df_2/dT is in good agreement with the calculated value. The measured value of the 1st cell is different from the calculated value compared with the 2nd cell. Because the geometry of the 1st cell is not perfectly pill-box shape, the frequency response depends on not only the diameter but also the other geometrical lengths.

By using the second method, bolting down the outer wall of each cell, each resonant frequency can shift to 2815.5 MHz and 2825.3 MHz respectively. Both resonant frequencies were increased by 5 MHz higher than before. As a result, the adjustable range of frequency is from -1.5 MHz to +5.0 MHz around the target frequencies. It is important to estimate the amount of frequency shift by adding RF input ports and vacuum ports to axially symmetrical cavities. A measured strength of RF coupling between 1st cell and 2nd cell is negligible small. Measured parameters are summarized in Table 3.

From measured beta in Table 3, the filling times of each cell are 0.34 μs and 0.24 μs respectively. The acceptable macropulse duration for the THz ring is about 150 ns. Consequently macropulse duration of 1.5 μs is long enough to generate 150 ns flat top.

Table 3: Measured values in low power tests and calculated parameters using SUPERFISH

parameter	Measured value	Calculated value
f_1 [MHz]	2810.81	2856.0
f_2 [MHz]	2825.36	2856.0
β_1	2.3	—
β_2	3.4	—
Q_1	9984	13000
Q_2	9600	12500

Magnetic bunch compressor

Beam has to be compressed from several ps to less than 100 fs at the downstream of the gun by the magnetic bunch compressor. Magnetic bunch compression employs path difference for particles at different momenta in a dipole magnetic field. In case of the ITC-RF gun, momentum deviation makes a considerable difference of velocity for each particle because of the low beam energy around 2 MeV. As a magnetic compressor, a TBA transport has been adopted. In addition the bunch compressor can vary the higher order term of the dispersion function by using one family of sextupole magnet to manipulate nonlinear longitudinal phase space distribution. An element in the transport matrix R_{56} is varied by changing a dispersion function of the 2nd bending magnet. The designed optics is shown in Fig. 3.

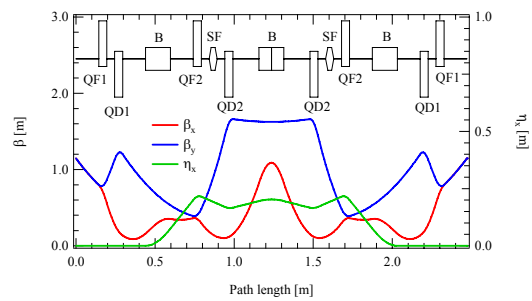

Fig. 3: TBA optics. Left axis is for beta functions. Right axis is for dispersion function.

Each bending angle is 60 degree. Total bending angle of the lattice is 180 degree. This lattice has four families of quadrupole as shown in Fig. 3 which are specified two purposes mainly. The dispersion function at the 2nd bending magnet is controlled by quadrupole magnets between bending magnets to change the R_{56}. The other quadrupole magnets are used for matching of horizontal and vertical Twiss parameters at exit and reducing the beta function in bending magnets. In order to estimate a bunch compression, a particle distribution of Fig. 1 ($\Delta\theta$ = 18 deg.) has been used. Designing of optics and tracking simulation have been done by using SAD code [7]. The results of the longitudinal phase spaces and the particle time distributions at a optimum operating point are shown in Fig. 4.

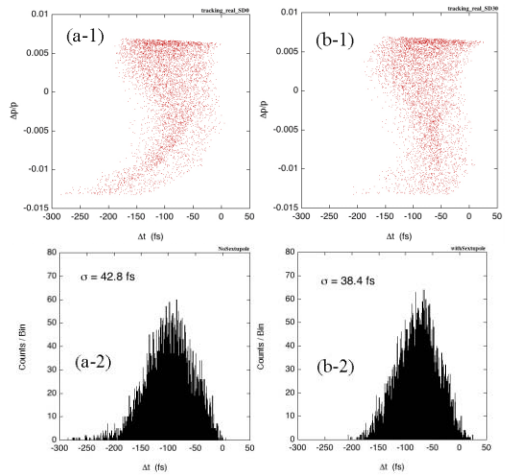

Fig. 4: longitudinal phase spaces of a compressed beam and its time distributions. (a-1) compressed beam with sextupole off, (b-1) compressed beam with sextupole on, (a-2) time distribution of (a-1), (b-2) time distribution of (b-1).

As shown in Fig. 4, the compressed bunch lengths are 42.8 fs (rms) with sextupole off and 38.4 (rms) fs with sextupole on. In the case of sextupole on, the higher order term of dispersion function can be compensated.

SUMMARY

A prototype of the ITC-RF gun has been manufactured, and some basic parameters were measured. The measured resonant frequencies of this gun are lower than the designed values. Therefore, it is important to estimate the amount of frequency shift caused by adding RF input ports and vacuum ports with using 3D code.

The bunch compressor has been designed to compress a beam from the gun. This transport has been designed as it can adjust the R_{56} and higher order of dispersion function to deal with various longitudinal phase space distributions. As a result of beam tracking, this transport can achieve a very short bunch length until 38.4 fs (rms) which is much shorter than the target value 100 fs (rms).

As an injector of the THz ring, the ITC-RF gun and the bunch compressor may have a possibility to generate a very short bunch.

REFERENCES

[1] H. Hama, et al., New Journal of Physics 8 (2006) 292
[2] T. Tanaka, et al., Proc. of the 28th International FEL Conf., Berlin Germany, pp. 371.
[3] C.B. McKee and J.M.J. Madey, Nucl. Instr. and Meth. A 296 (1990) 716.
[4] H. Hama, et al., Nucl. Instr. and Meth. A 528 (2004) 371.
[5] http://laacg1.lanl.gov/laacg/services/download_sf.phtml
[6] http://www.cst.com/Content/Products/MWS/Overview.aspx
[7] http://acc-physics.kek.jp/SAD/sad.htm

STUDY ON COMPACT DC ELECTRON GUN USING SINGLE CRYSTAL CATHODE OF LaB_6*

K. Kasamsook#, K. Nanbu, M. Kawai ,K. Akiyama, F. Hinode, T. Muto , T. Tanaka, M. Yasuda, H. Hama
Laboratory of Nuclear Science, Tohoku University,
1-2-1 Mikamine, Taihaku-ku, Sendai 982-0826, Japan

Abstract

A novel, compact DC gun has been developed and is currently on a test bed at LNS. Applying 50 kV high voltage for the gun, it is expected to supply a high brightness beam which the beam current of 300 mA and the variable pulse duration from 1 to 5 μsec. In addition, a floating bias voltage can be applied between the cathode and the wehnelt to manipulate electric field near cathode surface. In order to produce lower emittance beam, the size of thermionic cathode should be very small, but the cathode should be higher current density. Consequently we have chosen single crystal LaB_6 as the thermionic cathode, which can provide higher current density with good homogeneity electron emission. The design parameters and initial operating experience of the DC gun are discussed. This DC gun will be used for Smith-Purcell FEL [1], advanced accelerator researches and other experiments.

INTRODUCTION

Recently, electron guns with high brightness are of great interest to achieve many applications in the field of electron beam technology such as Smith-Purcell FEL , for example. The low emittance DC electron gun at LNS is one of the candidates. The prominent point of this DC electron gun has no grid which would degrade beam emittance. The cathode is made of a single crystal material with the low work function, and heated to higher for producing electrons. We have chosen a low applying voltage (50 kV) to reduce the size of the entire system. The schematic diagram of DC gun power supply is shown in Fig.1. In spite of such low voltage, the emittance can be reduced to very small because of a very short distance between the cathode and the anode, and the bias voltage apply between wehnelt and cathode can manipulate the beam property. In order to produce low emittance beam, the cathode size should be small, so that the higher current density is required. Such high current density can be realized by some cathode materials such as single crystal LaB_6 or CeB_6 [2,3]. The design parameters and the drawing of the low emittance DC electron gun with solenoid lens are shown in Table 1 and Fig.2, respectively.

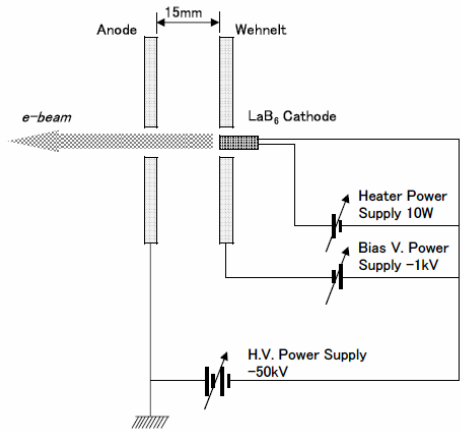

Figure 1: The schematic diagram of DC gun power supply.

Table 1: Design parameters of electron gun.

Beam energy	50 keV (Max.)
Peak current	>300 mA
Pulse width (FWHM)	1-5 μsec
Repetition rate	50 pps
Normalized emittance	<10 π mm mrad.
Normalized thermal emittance	0.25 π mm mrad* *theoretical
Cathode diameter	1.75 mm.

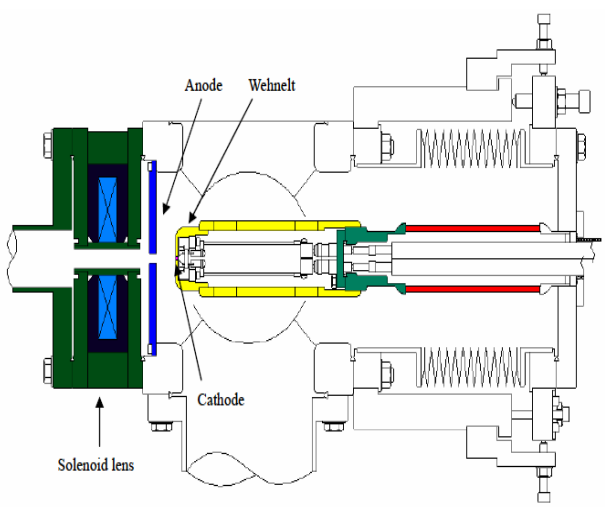

Figure 2: The low emittance DC electron gun.

*Work supported by KEK grant for accelerator science.
#kasam@lns.tohoku.ac.jp

DC GUN DEVELOPMENT

LaB_6 cathode

The thermal limit of normalized rms emittance of electrons emitted from a hot cathode is given by equation (1):

$$\varepsilon_{\mathrm{n,rms}} = \frac{r_c}{2}\sqrt{\frac{k_B T}{m_o c^2}} \quad , \qquad (1)$$

where r_C is the cathode radius, k_B is Boltzmann constant, m_0 is electron rest mass and T is the cathode absolute temperature. From the above relation, in order to obtain the small emittance less than 1 π mm mrad, the diameter of the cathode must be in the range of a few mm. On the other hand, high emission density is required to produce a several hundred miliampere peak current from the small surface. The LaB_6 can emit such an intense current over the long lifetime. A single crystal is preferable for obtaining low emittance because of its extremely flat surface with low porosity after surface material evaporation. The emission density is much more uniform because the crystal orientation is the same over the whole surface. So, we decided to use a single-crystal LaB_6 cathode with a flat crystal surface shown in Fig. 3.

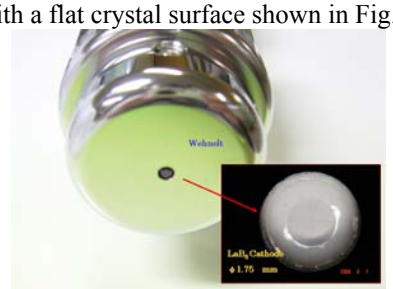

Figure 3: The assembly of single-crystal LaB_6 cathode.

Gun High Voltage

The high voltage power supply was tested by loading with the electron gun. The beam current was measured by the Faraday plate. The cathode was heated up to ~1900 K by applying 10 W of heater power and the DC pulsed current, 1.5 A, was measured in the test chamber. Fig. 4 shows the measured waveforms of the accelerating voltage and beam current. Up to now, the cathode has been operated for 4000 hours without failure.

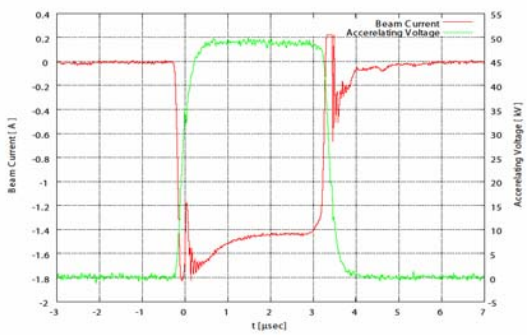

Figure 4: The measured waveforms of the accelerating voltage and beam current.

Gun simulation

We developed the 3 dimensional self-developed code. The simulation showed the small value of normalized emittance. The result of electron beam extraction and normalized emittance with bias voltage of 600 V is shown in Fig. 5 (above), and the macro-particle distribution and phase space distribution at the end point are shown as well (below).

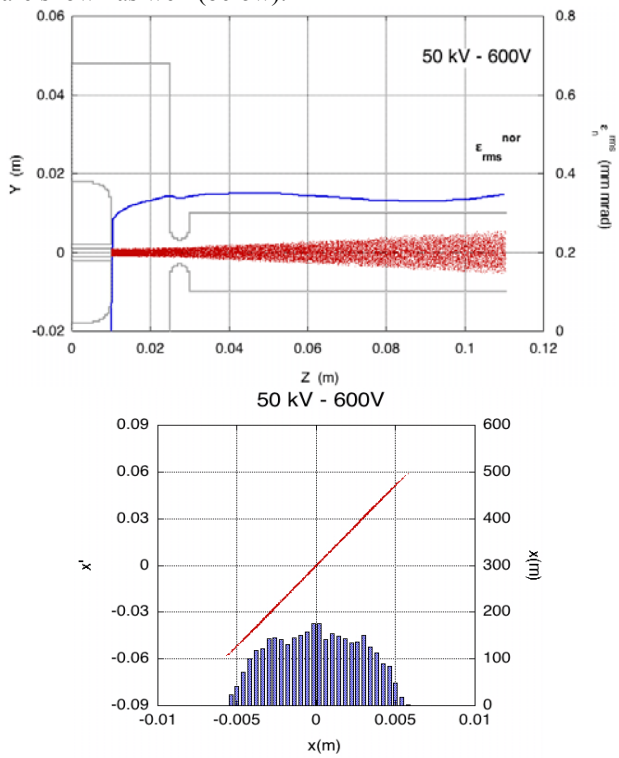

Figure 5: An electron beam extraction and normalized emittance of 300 mA (above) and the macro-particle distribution including phase space distribution (below) at the end point according to a simulation.

In the simulation, we applied bias voltage of 600 V between wehnelt and cathode to manipulate the electric field around the cathode surface. The result shows that we can manipulate the equipotential line near the cathode surface by adjusting the special bias voltage to optimize the extracted beam emittance [4]. An extremely low emittance less than 1 π mm mrad is obtained by the simulation.

MEASUREMENT RESULTS

We measured gun characteristics at the test bench. The first measurement of the LaB_6 gun is V-I characteristics. The measurement was done for various cathode temperatures, which is shown in Fig. 6. From V-I characteristic curve, our gun should be operated at 1800 K in temperature limited region to avoid the space charge effect from high emission current. In this region, the beam current is dominated by Schottky effect rather than Child's law. Accordingly, the slope of the current-voltage curve becomes very smooth.

We have deduced the work function of LaB_6 cathode by measuring the thermal emission current varying the cathode temperature. In the ideal case Richardson-Dashman's formula shows the emission current density given by equation (2)

$$J = 120.4T^2 \exp(-\phi'/k_B T) \quad , \qquad (2)$$

where J is emission current density, T is cathode temperature , k_B is Boltzmann constant, and ϕ' is effective work function, respectively. From equation (2), we can calculate the work function of LaB_6 cathode to be 2.4 eV. This measured value is not far from the previous value [5].

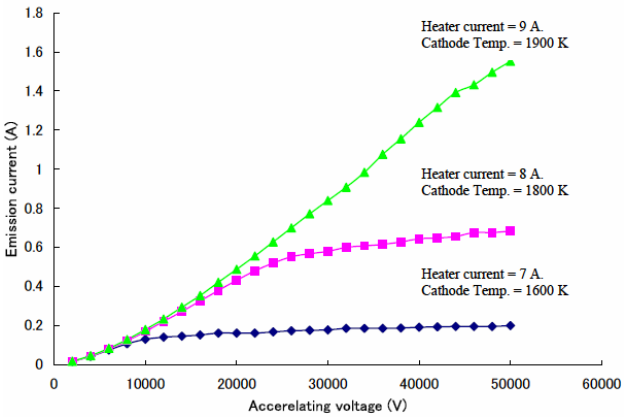

Figure 6: Current-voltage characteristic curve of the LaB_6 gun.

One of the most important characteristics of an electron gun is its perveance (P) express by equation (3)

$$P = \frac{I}{V^{3/2}} \quad , \qquad (3)$$

where I is the beam current and V is the anode potential with respect to the cathode. For guns with flat cathodes, current density inhomogeneity becomes large when the perveance is high value. However, electron beams with higher perveance are needed in number of applications where charge or current density is a key parameter. From curve fitting function, we can obtain 0.155 $\mu A/V^{3/2}$. This result shows that this DC gun has high emission current density.

In order to focus the beam and to compensate space-charge blow-up the DC solenoid lens has been designed and installed downstream of the anode structure. The solenoid is capable of delivering high magnetic field strength on axis. Through proper tuning of the solenoid current beam focus can be produced at any location within the diagnostic module which is built around a 104 mm long drift section behind the solenoid magnet. We can achieve the minimum beam size diameter of 1.6 mm at solenoid current 2.5 A. The beam profile at plastic scintillator [EJJEN TECHNOLOGY, EJ-212] is shown in Fig. 7. Fig. 8 shows the effect of solenoid current that induces the magnetic field strength to confine the electron beam.

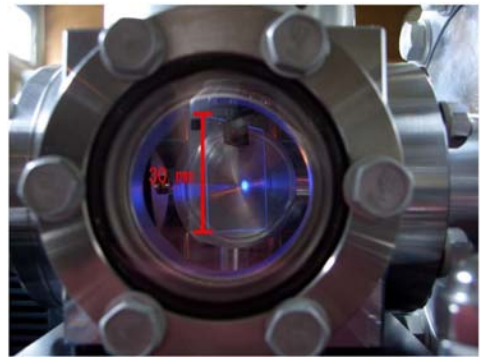

Figure 7: The beam profile at 45 kV confined by solenoid current 2.5 A.

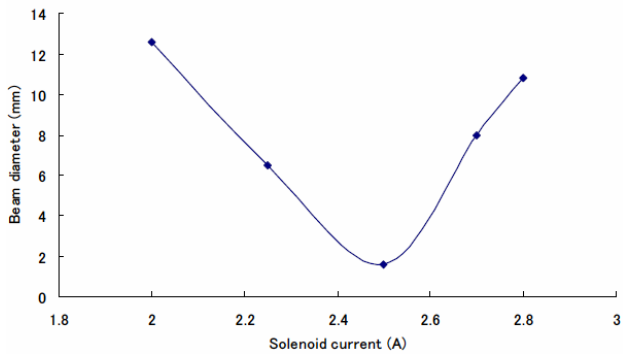

Figure 8: The beam diameter plotted as a function of solenoid current.

SUMMARY

At the present the DC gun has been examined on a test stand, and characteristics of the extracted beam from the gun are measured. The simulation shows that a fairy simple and compact system have a capability to fulfil the design goals.The measurement results show high emission current density of DC gun with LaB_6 cathode ,and we can also control the beam size at downstream of gun exit by solenoid lens. As the next step, we are planning to measure other beam parameters including the beam emittance.

REFERENCES

[1] K. Kim et al., Nucl. Instr. And Meth. A 475 (2001) 158.
[2] H. Kobayashi et al., Emittance Mearsurement for High-Brightness Electron Guns, 1992 Linear Accelerator Conf., Ottawa, Canada, August 1992.
[3] K. Togawa et al., "CeB_6 Electron Gun for the Soft X-ray FEL Project at Spring-8",FEL2003, Tsukuba, Japan, September 2003.
[4] K. Kasamsook et al., "A Compact Low Emittance DC Gun Employing Single Crystal Cathode of LaB_6",FEL2006, Berlin, Germany, August 2006.
[5] G. I. Kuznetsov at al., Physica Scripta. vol. T71 (1997) 130.

INJECTION OPTIMISATION FOR INDUS-2

Ali Akbar Fakhri* and Gurnam Singh
Raja Ramana Centre for Advanced Technology, Post - CAT, Indore – 452 013

Abstract

In this paper commissioning experience of injection into INDUS-2, a 2.5 GeV synchrotron radiation source is discussed. In initial stage commissioning, partial beam loss was observed. In this context effect of various injection errors such as mismatch between pulse widths, jitter and magnetic field stability of kickers on injected and stored beam are studied [(1)]. A brief summary of the results is presented. After reducing jitter and fine adjustments of timings of kicker power supplies, partial beam loss reduced significantly.

INTRODUCTION

A multi turn injection scheme employing a compensated bump generated by four kickers has been chosen for beam injection into INDUS-2. The injector for this ring is a synchrotron with peak energy of 450-550 MeV. The synchrotron provides two bunches each one around 1ns long and separated from each other by nearly 30ns, at the required energy at a repetition rate of 1 Hz. After injecting several pulses at 450-550 MeV, the beam is accelerated to 2.5 GeV by slowly increasing the magnetic field of the bending magnets. The injection is carried out in the radial plane from the outer side of the ring by using a compensated bump generated by four kicker magnets. The Indus-2 storage ring has kicker magnets k1 to k4, placed symmetrically in a 4.5m-long straight section. The straight section part containing injection kickers is free from quadrupoles, so the deflection bump is independent of the machine optics

BEAM INJECTION

Since the synchrotron routinely delivers a beam to Indus-1 at 450 MeV, initial attempts were made to inject the beam in Indus-2 at this energy. To reduce the residual betatron oscillation of the injected beam as well as stored beam, it was decided to move septum chamber towards the beam orbit by 8 mm. By looking the beam position at BPM-1(just after up stream kicker magnet), BPM-3(located at achromat section) and just after one turn (at septum BPM) proper optimisation of position and angle was carried out by changing thick and thin septum currents. After this optimisation 2.ms Fig.1)beam rotation was observed. Further optimising RF frequency, kicker strength and time delays the beam survival time of more than 1 second was achieved. At 450 MeV beam energy the damping time in horizontal plane is 810 ms, this being comparable to the synchrotron repetition rate, the injected beam oscillations are not fully damped when the next pulse is injected into the ring. So it was decided to inject the beam at a higher energy. The energy in the synchrotron was then ramped to 550 MeV and the beam at this energy was extracted for injection into Indus-2. At this energy the damping time is 444 ms, therefore, the beam is fully damped when the next pulse arrives after one second. Once the beam was stored for full injection cycle the kickers were adjusted to allow the beam accumulation. At this stage, it was very important to adjust the timing of the kicker pulses. Much time and efforts were spent to ensure that the stored beam traversed kickers at the proper time. Further optimisation is carried out by optimising beta functions at the end of TL-3, in which beta function is reduced from 14m to 8m, with this exercise a small beam spot on the last BPM of TL-3 and BPM 1 of Indus 2 was observed.

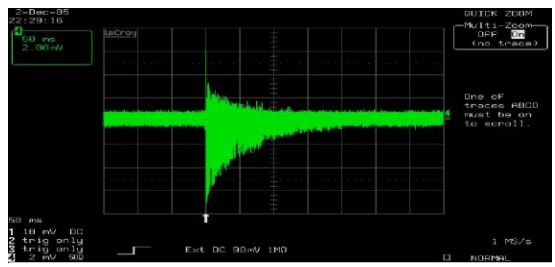

Figure 1: WCM signal indication of survival of the beam up to 200 ms.

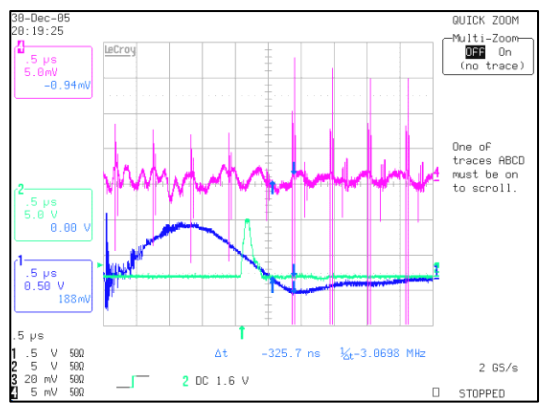

Figure 2: Beam storage to more than 1 second beam crosses injection kicker after 1 second.

In initial stage at time of injection, partial beam loss was observed. The loss was attributed to the following reasons associated with injection kickers namely 1) Magnetic field stability 2) Mismatch between pulse widths 3) Jitter. Initially effects of these errors were observed by looking at the synchrotron light monitor, which is located far away from the injection sections. Due to various injection errors, in the SLM beam spot variation was observed. A theoretical study of the effect of these errors is discussed in this paper.

* fakhri@cat.ernet.in

INJECTION ERRORS

The bump strength (B) and the location of the septum from the designed orbit (L_s) can be approximately calculated from the following relation[1]

$$B = 4\sigma_{xi} + S_{sc} + S_t$$

$$L_s = B + 4\sigma_{xs} + S_c + S_{res}$$

Where, σ_{xi}: Beam size of the injected beam, σ_{xs} : Beam size of the stored beam, septum clearance S_c =2.0mm; septum thickness S_t =3.0mm, $S_{Residuals}$: residual oscillation of stored beam which is arising due to nonclosure of the bump, injected beam emittance ε_{xi} = 2.35*10-07mrad and stored beam emittance ε_{xs} = 2.5*10-08mrad are respectively at 550MeV. The value of ε_{xs} has been arrived at by taking into consideration a blow-up of emittance due to intrabeam scattering and bunch lengthening due to single bunch instabilities[2], for the injected beam also a blow-up factor of two (2) has been assumed. If bump strength is reduced then it will increase the injected beam oscillation ($I_{Residual}$). In the case of Indus-2, above relations are only guidelines not exact due to sinusoidal nature of the kicker pulse having a slow fall time (1.6μS). In multi bunch-filling mode, injection kicker will be energized according to synchronize pulse. To simulate it, stored beam is tracked according to bunch filling pattern. Tracking studies have been carried out with the computer code RACETRACK[3]. To accommodate injection errors computer code RACETRACK has been modified. In studies, both bunches (coming from the synchrotron) are tracked. Here results are presented for design (9.3,5.2) & moderate optics[4] B(II) (9.3,6.2) for accepting 1.5 sigma of injected beam. In these calculations inner side of septum location is fixed at 15.0mm from design orbit.

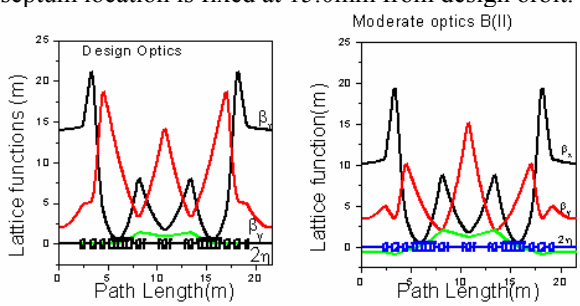

Figure 3: Lattice functions for design and moderate optics.

Effect of Magnetic Field Stability

To show its effect, injected and stored bunches are tracked with various combination of peak field stability according to measured data peak field stability is in the range of ($\Delta B/B = \pm 1*10^{-3}$). Its result shows that septum clearance is reduced by 0.5mm.

Mismatch between Pulse Widths

The four kicker pulse lengths are not identical; they differ from each other, as shown in the table-1. Mismatch between pulse widths leads to extra residual betatron oscillation.

Table 1: Measured Pulse Length of the Kickers

Kicker magnet	T_R(μs)	T_F(μs)
K1	1.3	1.53
K2	1.27	1.53
K3	1.29	1.60
K4	1.29	1.60

There are following four possibilities to minimize these effects, i.e. either starting point of all the four kickers are matched (Case A) or peak point of all the four kickers are matched (Case B) or downstream kickers are energised earlier then the upstream kickers (Case C), or the upstream kickers are energised earlier than the downstream kickers (Case D). From simulation of beam tracking for the four cases, maximum oscillation at septum location for both the injected and stored bunches at design & moderate optics B(II) are tabulated.

Table 2: For Design Optics

Case	$I_{Residual}$ (mm)	$S_{Residual}$ (mm)
Ideal	11.73	0.0
Case A	12.00	0.53
Case B	14.38	2.24
Case C	13.63	5.16
Case D	14.10	2.10

Table 3: For Moderate Optics

Case	$I_{Residual}$ (mm)	$S_{Residual}$ (mm)
Ideal	12.90	0.0
Case A	13.20	0.08
Case B	14.65	1.34
Case C	12.03	2.61
Case D	14.36	1.15

The above table clearly indicates effect of mismatch between pulse widths can be significantly reduced by matching the starting point of the kickers.

Jitter

Effect of jitter is very severe in comparison to any other errors. The effect of jitter will further detoriate injection efficiency. In table-2 effect of jitters for case (A) are tabulated.

Table 4: For Design Optics

Jitter (ns)	$I_{Residual}$ (mm)	$S_{Residual}$ (mm)
2	12.55	1.33
7	13.96	3.81
12	15.38	6.29

Table5: For Moderate Optics

Jitter (ns)	$I_{Residual}$ (mm)	$S_{Residual}$ (mm)
2	13.49	0.65
7	14.24	2.10
12	15.14	3.56

The tracking results indicate that for design optics, it is very difficult to inject the beam having jitter in the range of ±12nS. The deflection errors caused by jitters between k1 & k2 and between k3 & k4 are mainly responsible for it.

INJECTION OPTIMISATION

Initially effect of injection errors is minimized by reducing bump strength, and by optimising time delay between injection kickers at design optics. The results show that if kicker pulse widths have different pulse width then in this case it is better to match the starting point of kickers in comparison to peak matching. The bump strength reduction will lead additional oscillation in the stored beam as well as injected beam. To obtain a better solution it was decided to reduce kicker jitters from ±12ns to ±7ns.To increase the injection efficiency it is better to use moderate optics. In fig4, .5 & 6 for moderate optics B(II) tracking results are plotted for injected beam & stored beam having no jitter, jitter of 12ns and 7ns. These results indicate that for 7ns jitter, stored beam remain well separated from the septum magnet in comparison to 12 ns jitter. After reducing jitter and by using moderate optics partial beam loss was significantly reduced. In the longitudinal plane energy acceptance is small, the reason may be that the Indus-2 RF frequency is higher as the dipole current at injection is higher than the design current. Determination of correct RF frequency is expected to increase the energy acceptance in longitudinal plane as well as in the horizontal plane.

CONCLUSIONS

To increase injection efficiency into Indus-2, mismatch between kicker pulses and its jitter have to be further reduced. Further optimisation has to be carried out by optimising Indus-2 dipole current, RF frequency, RF voltage and by reducing closed orbit distortion. Injecting the beam at higher energy can also increase the injection efficiency, as in this case damping time of the injected beam is reduced

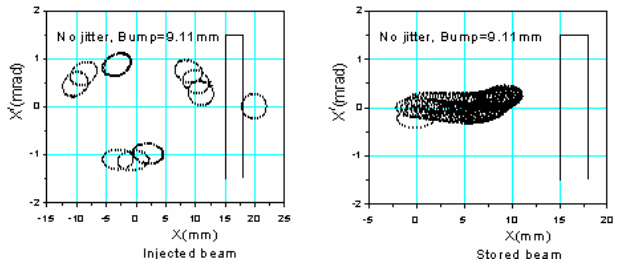

Figure 4: Injected and stored beam oscillations for an ideal case.

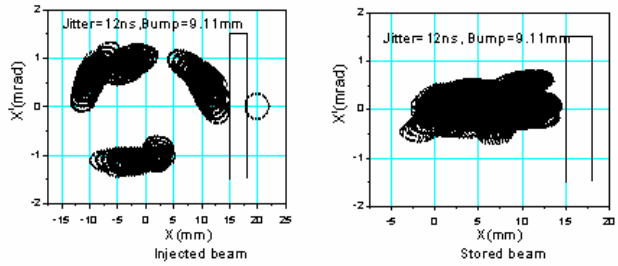

Figure 5: Effect of 12ns jitters in timing of kickers on injected beam and stored beam oscillations.

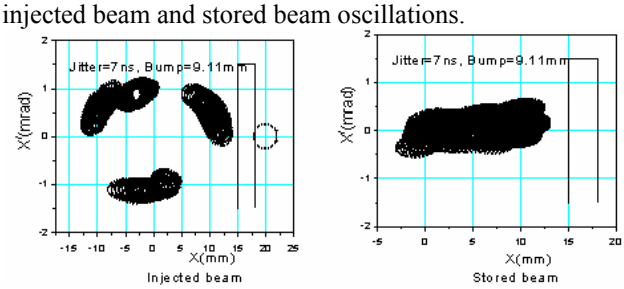

Figure 6: Effect of 7ns jitters in timing of kickers on injected beam and stored beam oscillations.

REFERENCES

[1] Ali Akbar Fakhri et.al, “Injection schemes for Indus-2 commissioning”, RRCAT/2006-16.

[2] D.Angal Kalinin & G. Singh “Single bunch instabilities and beam lifetime in Indus-2” CAT/2000-11

[3] A.Wrulich, "RACETRACK; A computer code for the simulation of nonlinear article motion in accelerators", DESY 84-026 (1984)

[4] Ali Akbar Fakhri et. al. “Optics for commissioning and routine operation of Indus-2”,CAT/2005-15

INJECTION OF BEAM SHAPED LOCALLY WITH NONLINEAR OPTICS*

Chun-xi Wang#, ANL, Argonne, IL 60439, USA

Abstract

We discuss nonlinear beam shaping by octupole and sextupole to fold the tails of a Gaussian beam into its core, for the purpose of improving betatron injection in storage rings by significantly reducing the beam width at the injection septum and thus reducing beam centroid offset from the stored beam. Necessary conditions as well as challenges for such nonlinear injections are explored.

INTRODUCTION

Injection is an important (yet often problematic) process in circular accelerators. Usually fast and strong kicks are used to merge the incoming beam with the stored beam (noticeable exceptions are charge-exchange H^- injection with a stripping foil and International Linear Collider damping ring injection where no stored beam exists during injection). Due to Liouville's theorem, certain phase-space separation of the incoming and stored beams are unavoidable. Here we consider the transverse injection scheme where the two beams are separated in the transverse phase space, say the horizontal plane. This injection scheme is commonly used in lepton machines where the two separated beams can be radiation damped into one. It is important to minimize the phase-space separation so that both beams can stay within the acceptance of the circular machine. This becomes more and more critical in modern storage-ring-based light sources such as the Advanced Photon Source, where acceptance is sacrificed for small emittance and narrow-gap insertion devices. On the other hand, the sizes of the stored and injected beams as well as the physical existence of a (septum) kicker requires certain clearance from the beams and thus limits the minimum separation reachable by the two beams. Therefore, the area close to the septum becomes the bottleneck of the injection process, which may result in demanding requirements for the kicker and incoming beam emittance. This note will explore possibilities to ease this bottleneck by properly folding the long tails of the Gaussian phase-space distribution of an incoming beam locally with nonlinear optics such that the incoming beam can come much closer to the septum and the stored beam.

NONLINEAR BEAM SHAPING

It is well-known that octupoles can be used to fold the tails of a Gaussian beam onto its core and make a more uniform distribution with sharper edges [1-4]. This technique is commonly used to make uniform illumination on targets. There are also proposals of using octupole beam shaping in linear colliders to make a cylindrical beam lens for final focusing or to make a nonlinear collimation system. To explore nonlinear beam shaping for injection purposes, we consider using a sextupole ($n = 2$) or octupole ($n = 3$).

To simplify the discussion we assume the nonlinear element is thin and write the beam transport from the nonlinear element to the injection point as

$$\begin{bmatrix} x \\ p \end{bmatrix} = R \begin{bmatrix} x_0 \\ p_0 \end{bmatrix} + kR \begin{bmatrix} 0 \\ x_0^n \end{bmatrix}, \qquad (1)$$

where R is the linear transfer matrix between the initial and final phase-space points $\{x_0, p_0\}$ and $\{x, p\}$, respectively; and k is the integrated strength of the nonlinear element. Using the Twiss parameters at the ends and the phase-advance Δ between them, the R-matrix can be written in the well-known form

$$R = \begin{bmatrix} \sqrt{\beta} & 0 \\ -\frac{\alpha}{\sqrt{\beta}} & \frac{1}{\sqrt{\beta}} \end{bmatrix} \begin{bmatrix} \cos\Delta & \sin\Delta \\ -\sin\Delta & \cos\Delta \end{bmatrix} \begin{bmatrix} \frac{1}{\sqrt{\beta_0}} & 0 \\ \frac{\alpha_0}{\sqrt{\beta_0}} & \sqrt{\beta_0} \end{bmatrix}. \qquad (2)$$

Since our main concern is the transverse dimension of the beam at the injection point, we express the transverse position as

$$x = \sqrt{2\beta J_0}\,[\cos(\theta_0 + \Delta) + 2\,\bar{a}\sin\Delta\cos^n\theta_0], \qquad (3)$$

where J_0 and θ_0 are the action-angle variables in the initial phase space and the parameter $\bar{a} \equiv 2^{\frac{n-3}{2}} k\, \beta_0^{\frac{n+1}{2}}\, J_0^{\frac{n-1}{2}}$. Our focus is on the beam edge given by the 3σ contour with $J_0 = 9\epsilon/2$, where ϵ is the emittance of injected beam. The first term yields the unperturbed position and the second term gives the correction due to the nonlinear kick. For a given $\bar{a}$, extreme position x_m will be reached when $\partial_{\theta_0} x = \partial_\Delta x = 0$, i.e.,

$$\begin{aligned} \sin(\theta_0 + \Delta) &= -2\bar{a}\sin\Delta\ n\cos^{n-1}\theta_0 \sin\theta_0 \\ &= \ 2\bar{a}\cos\Delta\ \cos^n\theta_0. \end{aligned} \qquad (4)$$

Let θ_m and Δ_m be a solution set, then we have the condition $\cos(\theta_m + \Delta_m) = -(n+1)\sin\theta_m \sin\Delta_m$ and the extreme value

$$x_m = \sqrt{2\beta J_0}[-(n+1)\sin\theta_m + 2\bar{a}\cos^n\theta_m]\sin\Delta_m. \qquad (5)$$

Therefore, it is desirable to have the phase advance Δ_m close to a multiple of π (note that there is no solution for $\Delta_m = \text{integer} \cdot \pi$). A more geometric view of this is that, under such a condition, the peaks of the two terms in Eq. (3)

* Work supported by U.S. Department of Energy, Office of Science, Office of Basic Energy Sciences, under Contract No. DE-AC02-06CH11357.

wangcx@aps.anl.gov; http://www.aps.anl.gov/~wangcx

are synchronized for more effective cancellation. Because of this and an important reason discussed below, it is preferable to choose a phase advance Δ close to but less than π.

With a phase advance $\Delta \simeq \pi$, the transverse position becomes

$$x \simeq \sqrt{2\beta J_0}\,[-\cos\theta_0 + 2\,\bar{a}\sin\Delta\cos^n\theta_0]\,. \qquad (6)$$

For a sextupole, Eq. (6) can be written as

$$x^{\rm sex} = \sqrt{2\beta J_0}\,2\bar{a}\sin\Delta\left[\left(\cos\theta_0 - \frac{1}{4\bar{a}\sin\Delta}\right)^2 - \left(\frac{1}{4\bar{a}\sin\Delta}\right)^2\right]. \qquad (7)$$

Note that the mapping due to a sextupole is asymmetric. The last term in the above equation gives the minimum width $\sqrt{2\beta J_0}/|8\bar{a}\sin\Delta|$ provided that $4\bar{a}\sin\Delta \geq 1$. If we choose $\bar{a}\sin\Delta = \pm 1/2$, a beam will be compressed by a factor of 4 on one side while enlarged by a factor of 2 on the other side. For an octupole, Eq. (6) has the extreme values

$$x_{m1} = \pm\sqrt{2\beta J_0}\,(1 - 2\,\bar{a}\sin\Delta), \qquad (8)$$

$$x_{m2} = \pm\sqrt{2\beta J_0}\,\sqrt{\frac{4}{27}\frac{1}{2\bar{a}\sin\Delta}}, \qquad (9)$$

at $\theta_0 = \text{integer}\cdot\pi$ and $\cos^2\theta_0 = 1/6\,\bar{a}\sin\Delta$, respectively. Setting $|x_{m1}| = |x_{m2}|$ yields the optimum solution

$$x^{\rm oct}_{\rm opt} = \sqrt{2\beta J_0}\,\frac{\cos(3\theta_0)}{3}, \quad \text{with } \bar{a}\sin\Delta = \frac{2}{3}, \qquad (10)$$

where a factor 3 reduction in amplitude can be obtained, which is consistent with [5].

SYMMETRIC FOLDING BY OCTUPOLE

To illustrate the beam shaping effects, we show some examples with the parameters $\beta = \beta_0 = 20\,m$, $\alpha = \alpha_0 = 0$, $\epsilon = 90\,nmrad$, which are close to the injected beam parameters at the final septum kicker in the Advanced Photon Source. Two cases are shown here. One with a phase advance $\Delta = 0.98\pi$, and $k = 6.55\times10^4\,m^{-3}$, which gives $\bar{a}\sin\Delta \simeq 2/3$ for 3σ contour. The other with a phase advance $\Delta = 0.9\pi$, and $k = 1.2\times10^4\,m^{-3}$, which gives $\bar{a}\sin\Delta = 0.6$. In Fig. 1a and Fig. 1b the phase-space contours are plotted for the two cases together with the 3σ-contours for the original beam and a Gaussian beam with 3 times smaller emittance. In Fig. 1c beam distributions across the axis are plotted for the two cases together with the original distribution as well as an unshaped distribution with a 3 times smaller emittance. Clearly octupole beam-shaping is symmetric, which is important for many applications (and thus more commonly used than sextupoles).

ASYMMETRIC FOLDING BY SEXTUPOLE

Similar to the octupole examples above, Fig. 2 shows beam shaping with a sextupole. For the $\Delta = 0.98\pi$ example, a sextupole with $k = 200\,m^{-2}$ ($\bar{a}\sin\Delta \simeq 0.5$) is used. For the $\Delta = 0.9\pi$ example, a sextupole with $k = 27\,m^{-2}$ ($\bar{a}\sin\Delta \simeq 0.34$) is used. Unlike using an octupole, sextupole beam shaping is asymmetric. It can effectively fold one side of the Gaussian tail back into its core, but on the other side, the tail becomes longer. Since the main congestion during injection is only on the side close to the septum, sextupole beam shaping can be used to ease injection. Note that the minimum width in Fig. 2c is smaller than that in Fig. 1c.

The illustrations in Figs. 1 and 2 demonstrate that an octupole or sextupole can effectively fold the Gaussian tail back into its core and significantly reduce the effective beam width. For the moderately shaped beams in Figs. 1b and 2b, it is equivalent to reducing the injected beam emittance threefold, while the required field strengths are feasible.

LOCALIZING NONLINEAR DISTORTION

Although nonlinear beam shaping can significantly reduce beam width and thus ease the injection bottleneck around the final septum, overall the beam will occupy a much larger phase-space area after strong nonlinear distortions. Therefore, it is important to make such a distortion as local as possible. An obvious solution is to compensate the initial kick with another nonlinear kick after a π phase advance. If the Twiss parameters at both kicks are the same, we have the common "-I" correction where kicks of the same strength will cancel each other and leave no nonlinear effects afterward. However, the map between the opposite kicks does not have to be a "-I" transformer, as long as it is linear with a π phase advance. Under such conditions, the beam at the compensating element (with Twiss parameters β_c and α_c) is given by

$$\begin{bmatrix} x \\ p \end{bmatrix} = -\begin{bmatrix} \sqrt{\beta_c/\beta_0} & 0 \\ \frac{\alpha_0-\alpha_c}{\sqrt{\beta_c\beta_0}} & \sqrt{\beta_0/\beta_c} \end{bmatrix}\begin{bmatrix} x_0 \\ p_0 \end{bmatrix} - k\sqrt{\frac{\beta_0}{\beta_c}}\begin{bmatrix} 0 \\ x_0^n \end{bmatrix}, \qquad (11)$$

thus, a compensating kick of strength

$$\bar{k} = \left(\frac{\beta_0}{\beta_c}\right)^{\frac{n+1}{2}} k \qquad (12)$$

will remove the nonlinear term. The β-factor could be used to reduce the strength of the compensating nonlinear element that is located inside the storage ring. For example, $\beta_c = 30\,m$ will reduce the compensating sextupole strength from $k = 27$ in Fig. 2b to $\bar{k} = 15$.

As we discussed before, the phase advance between the beam-shaping element to the injection point is close to but less than π, thus the compensating nonlinear element will be fairly close to the injection point with a small phase advance between to make up the difference from π. Therefore, the storage ring will see little of the nonlinear manipulation of the injected beam. However, the compensating nonlinear element in the storage ring will usually be strong and need certain upstream nonlinear elements in the ring

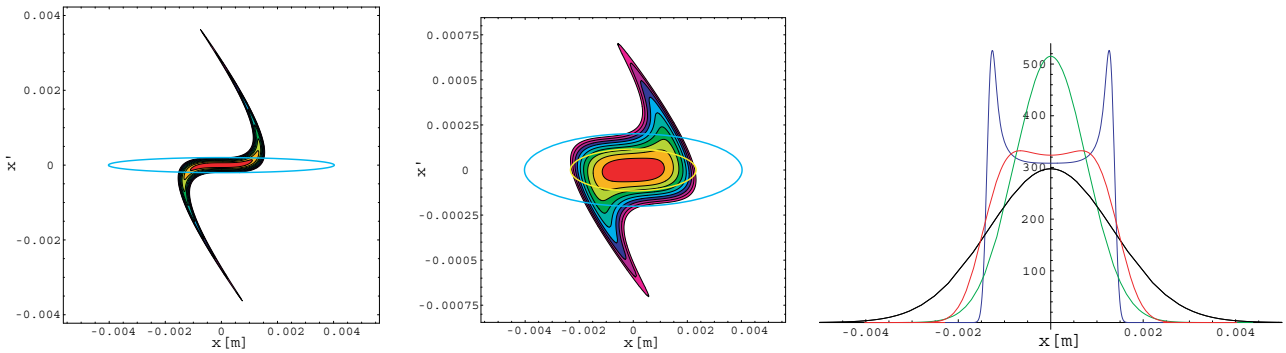

(a) $\Delta = 0.98\pi$, $\bar{a}\sin\Delta \simeq 2/3$ (b) $\Delta = 0.9\pi$, $\bar{a}\sin\Delta \simeq 0.6$ (c) beam distributions across the axis

Figure 1: Illustration of octupole beam shaping: (a) contour plots of phase-space distributions, up to 3σ contour for a shaped beam and 3σ contour only for the original beam; (b) similar to (a) but with additional 3σ contour (yellow) of a three times smaller emittance; (c) beam distributions across the axis for the original beam (black), shaped beam (blue) with $\Delta = 0.98\pi$, shaped beam (red) with $\Delta = 0.9\pi$, and unshaped beam (green) with a three times smaller emittance.

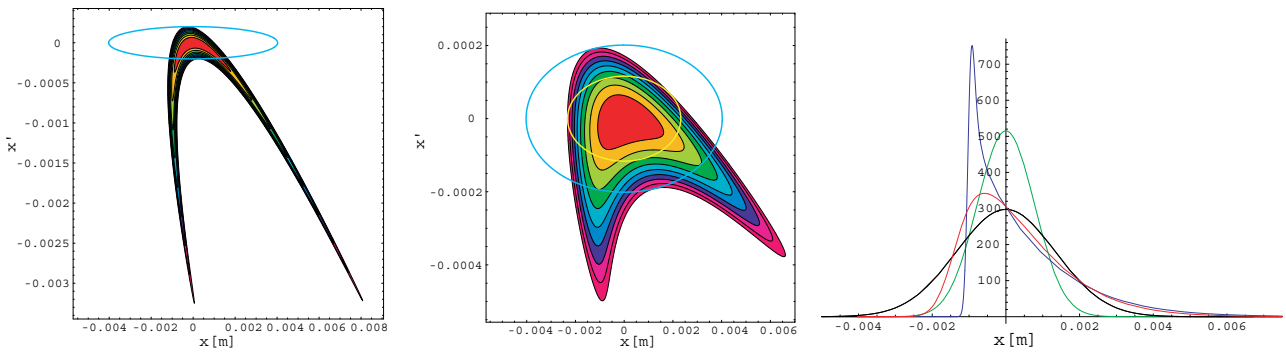

(a) $\Delta = 0.98\pi$, $\bar{a}\sin\Delta \simeq 1/2$ (b) $\Delta = 0.9\pi$, $\bar{a}\sin\Delta \simeq 0.34$ (c) beam distributions across the axis

Figure 2: Illustration of sextupole beam shaping. See the caption of Fig. 1 for explanation.

to reduce its effect on the stored beam such that most of the ring will be sufficiently linear with adequate dynamic aperture. Though nontrivial, it seems possible to accommodate such a nonlinear injection in a storage ring, especially in new designs (whether it is worthwhile is another issue). Note that the strength of the compensating element can be somewhat smaller than $\bar{k}$, because non-perfect correction will only leave a small amount of nonlinear distortion in the injected beam, which is tolerable in the ring. As an example, Fig. 3 plots the phase space after a compensating sextupole with only half the $\bar{k}$ required by Eq. (12). Another possibility is to cut off the nonlinear tails before injection by collimation. Further feasibility study is necessary, including the effects of possible centroid offsets in the compensating element.

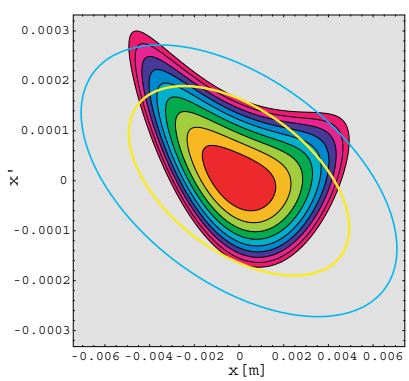

Figure 3: Phase-space contours after an incomplete compensation with half of the required strength. Inner (outer) ellipse is the undistorted 3σ (4.3σ) contour.

REFERENCES

[1] P.F. Meads, Jr., "A nonlinear lens system to smooth the intensity distribution of a Gaussian beam," PAC'83, p. 2838.

[2] A. W. Chao and M. Tigner, *Handbook of Accelerator Physics and Engineering*, World Scientific Publishing Co. Pte. Ltd., 1998.

[3] F. Meot, T. Aniel, Phys. Rev. ST-AB **3**, 103501 (2000).

[4] D. Varentsov, I.M. Tkachenko, and D.H.H. Hoffmann, Phys. Rev. E **71**, 066501 (2005).

[5] R. Brinkmann, P. Raimondi, A. Seryi, "Halo reduction by means of non linear optical elements in the NLC final focus system," PAC'01, p. 3828 (2001).

PHYSICS DESIGN OF PAL-XFEL UNDULATOR*

D.E.Kim#, K.H.Park, J.S.Oh, C.W.Chung, and I.S.Ko, PAL, POSTECH, Korea.

Abstract

Pohang Accelerator Laboratory(PAL) is planning a 0.3 nm – 0.45 nm SASE (Self Amplification of Spontaneous Emission) XFEL based on 3.7 GeV linear accelerator. It is targeting utilization of 0.1 nm X-ray radiation using the 3rd harmonic FEL radiation. With 3.7 GeV electron beam energy, achieving 0.3 nm fundamental FEL lazing is very challenging and it requires very low emittance electron beam with minimum energy spread. It also requires small period undulator with very small gap. In this context, application of SPring8 type in vacuum undulator is seriously considered. This reflects the experiences from SPring8 SCSS project. In this report, the physics design efforts of the undulator is described. The periodic parts are optimized to achieve the highest field with other requirements. The end structures were designed to be asymmetric along the beam direction to ensure systematic zero 1st field integral. The thickness of the last magnets were adjusted to minimize the transition distance to the fully developed periodic field. The final design features 4 mm minimum pole gap, 15 mm period, peak effective field of 1.09 Tesla.

INTRODUCTION

Pohang Accelerator Laboratory (PAL) is planning to build a X-ray FEL based on SASE (self amplified spontaneous emission) process[1]. The machine is named as PAL-XFEL and will utilize the upgrade inject linac for PLS (Pohang Light Source) electron storage ring. Current electron beam energy of the linac is 2.5 GeV and it needs to be upgraded to at least 3.7 GeV for 0.3 nm FEL radiation. The SASE XFEL offers unprecedented opportunity for X-ray users. SASE XFEL radiation is supposed to be at least ten orders of magnitude brighter than the 3rd generation synchrotron light sources. The SASE XFEL is transversely coherent and the pulse length is very short, femto-second level, which also privides users with chances for new scientific research.

On the other hand, the SASE XFE is quite a scientific challenge, as is well known; the generation of an extremely low emittance electron beam through a photo-cathode RF gun, bunch compression to an extremely short length, maintaining the low emittance to the end of the linac, and keeping the beam orbit as straight as possible in the undulator. The PAL-XFEL adds a few more scientific difficulties because it is targeting relatively short radiation wavelength (0.3 nm) with lower electron beam energy (3.7 GeV). Therefore, the PAL-XFEL requires very short period undulator with minimum possible gap. This implies the use of in Vacuum undulator developed at SPring8 is essential to the project. In this paper, the magnetic design of the periodic part, the magnetic design of the end part and other physics requirement of the PAL-XFEL undulator will be described. The major design parameters of the PAL-XFEL are summarized in Table 1.

Table 1: Major design parameters of PAL-XFEL

Beam Parameters	**Value**	**Unit**
Electron energy	3.7	GeV
Peak current	3	kA
Normalized slice emittance	1	mm mrad
RMS slice energy spread	0.02	%
Full bunch duration	270	fs
SASE FEL Parameters		
Radiation wavelength	0.3	nm
FEL parameter ρ	5.7×10^{-4}	
Peak brightness	1×10^{32}	pts/sec/m m^2/$mrad^2$/ 0.1%BW
Pulses repetition rate (Max.)	60	Hz
1-D gain length	1.2	m
Saturation length, L_{sat}	45	m

MAGNETIC FIELD REQUIREMENTS

A few kinds of technologies are considered for SASE XFEL undulators. For higher magnetic field at smaller magnetic period, superconducting (SC) undulator looks promising. But they believe that the technology is not mature and there is higher risk factor that hinders many laboratories to adopt SC technologies for SASE-FEL undulator. Helical undulator has advantage in getting polarized radiation with shorter saturation undulator length. But it has difficulty in manufacturing and error control. Therefore, many laboratories prefer Halbach type hybrid undulator or PPM (Pure Permanent Magnet) type undulator which can be in vacuum or out vacuum type. A lot of experiences are accumulated in this kind of planar undulator for error control and tuning procedures. It achieves comparatively higher flux density and it is believed that the tight SASE-XFEL undulator requirements can be met.

The basic magnetic structure of the undulator will be a Halbach type hybrid structure that use strong rare earth high performance magnets and ferromagnetic poles. This type can produce higher flux density and the field is mostly dominated by the mechanical manufacturing accuracy instead of less controllable material property of the magnets. Due to these advantages, the ambitious EURO-XFEL at DESY, SLAC LCLS (Linac Coherent Light Source) and SCSS at SPring8 projects are planning to use the Halbach hybrid type undulator.

*Work supported the Korean Ministry of Science and Technology and POSCO.
#dekim@postech.ac.kr

Vanadium permendur is popular for ferromagnetic pole due to its higher saturation. For rare earth magnetic material, higher remanence and higher coercivity is required. Higher remanence is important for higher undulator field. Higher coercivity is preferable for stronger resistance to the radiation damage. Experimental studies show that higher coercivity is very helpful for less degradation in magnetic performance after electron iradiation[2]. A good compromise would be Neomax35VH class permanent magnets. remanence of 1.17 T to 1.26 T and coercivity of 11.0 kOe to 12.0 kOe. The intrinsic coercivity reaches up to 25 kOe meaning high resistance to demagnetization.

PERIODIC MAGNETIC STRUCTURE

The key features of PAL SASE-XFEL can be summarized as achieving most promising 0.3 nm wavelength FEL radiation using lower e-beam energy. To achieve this goal, all parameters set to be very aggressive. For undulators, achieving smallest possible magnetic gap is helpful in achieving smallest possible undulator period. Therefore, PAL-XFEL undulator system will positively use IVUN which is actively developed and used by SPring8 ID team. Since the advent of SPring8's success in implementing IVUN in their storage ring, the adoption of IVUN in synchrotron radiation sources have been becoming popular in all major synchrotron radiation laboratories. The IVUN technologies are well established by SPring8 and SSM(Sumitomo Special Metals) Inc. This strategy that uses well established commercialized undulator can reduce risks and speed up the development period. In this context, we mostly concentrate in the physics design of magnetic structures and the detailed mechanical engineering should be elaborated with eligible undulator supplier. In this report, the undulator which will be used for 0.3 nm SASE-XFEL with 4 mm magnetic gap and 15mm magnetic period will be treated.

To estimate the minimum undulator pole width, we need to know the required transverse roll-off. Pierce parameter is a key parameter in FEL theory and it determines the gain length and the spectral bandwidth. And it naturally gives requirements for undulator field accuracy. For 0.3 nm PAL SASE-XFEL case, the undulator period is 15 mm and $\rho \approx 4.3\times10^{-4}$.

The transverse uniformity of the field should satisfy $\Delta B_z / B_z(x=0) \le \rho$ for sufficient wide range. Although the rms e-beam radius is about $r \approx 36\mu m$, we require good field region of ±1 mm for expected operating magnetic gap of 4 mm~6 mm. This redundancy will alleviate alignment requirements and other tolerances with small increase in pole width. The maximum gap is set to 6 mm arbitrarily as the upper limit of the operation since the field will be small for gap larger than 6 mm and there will be no chance of saturated SASE-FEL lasing.

To estimate the required pole width, the transverse roll-off is calculated using ANSYS[3] while varying the pole width with 15 mm period and 6 mm maximum operating gap. From the calculation, it is seen that we can safely achieve required tolerance of $\Delta B / B_0 < 1.0\times10^{-4}$ for ±4 mm at pole width of 30 mm. The pole width 30mm is good enough allowing wide good field region. To optimize the pole thickness, the effective peak field is calculated while varying the pole thickness. The pole height was set to 25 mm with sufficient overhang. The effective peak field is calculated from the fourier component along the longitudinal direction. The maximum effective field occurs when the pole thickness is 2.4 mm. From this pole thickness can be preliminarily decided to be 2.4 mm. Same kind of calculation is repeated while varying the pole height. The block size is also increased to maintain constant vertical overhang of 4 mm. For pole height larger than 20 mm, the increase of the effective peak field slows down rapidly suggesting 25 mm pole height is reasonable first estimate for the pole height. Therefore, the final magnetic geometry for periodic part could be described as 30 mm pole width, 25 mm pole height, 2.40 mm pole thickness. The magnet is 38 mm wide and 29 mm high and 5.10 mm thick.

Table 2: Major parameters of SASE-XFEL Undulator. The effective peak field at 4 mm is slightly higher than the target field (B_0=1.0573, K_{eff}=1.4812). This difference can be used as a engineering margin.

Parameter	Value
Pole Gap (nominal)	4 mm
Period	15.00 mm
Pole Dimension (W × H × T)	30 × 25 × 2.40 mm^3
Magnet Dimensions (W × H × T)	38 × 29 × 5.10 mm^3
Effective Peak Field (B_{eff})	1.0917 Tesla
Undulator Magnetic Length (L_{und})	4500 mm
Effective K value (K_{eff})	1.529
Fundamental photon energy	3.996 keV
Fundamental photon wavelength	0.310 nm

MAGNETIC STRUCTURES AT THE TRANSITION REGION

To achieve maximum number of periodic field, the undulators need to reach the periodic field with minimum possible transition from the ends. A number of different schemes have been used in the past for this purpose. K Halbach calculated the correct excitation pattern for the transition poles that results zero offset. The scheme involves adjusting the strength of a few poles near the ends. APS[4] and LCLS undulator uses a pole recess and partial strength magnet for the last magnet. SPring8 uses a longitudinal gap for last magnet for smallest undulator orbit offset. ESRF has their own unique and smart transition sequence[5]. In our case, we modify APS scheme and try to use a recess in the last pole and thinner last magnet. This thinner magnet can avoid the difficult process of partial demagnetization of magnet block. And an asymmetric undulator configuration that have even number of poles are selected. In this scheme, the first pole and the end pole has different polarity and the residual field integral is systematically zero. A small residual field

integral may exist that may result from manufacturing errors. These kinds of small errors are usually well manageable. This concept can reach the periodic field with shorter transition length and it is geometrically simple, and does not need flux shunts. The geometry of the end transition sequences are determined by varying the thickness of the last magnet, ad the recess of the past pole. Varying the 2 parameters, the optimal geometries are optimized that results minimum orbit drift in the undulator for the operating gap range. The transition parts are simulated using RADIA[6,7]. Simulating the whole undulator is unpractical due to the limited computer resources. As a compromise, only 20 periods are calculated. Since integral contribution from the periodic part cancel each other, this 20 period modelling is not bad to estimate the orbit drift from the transition sequences. The typical calculated field profile, and orbit are shown in Fig 1 and Fig 2, respectively. It can be seen that the field is approaching to the periodic part in a minimum distance. In our case, the field is odd in z direction and the field is asymmetric. It is seen that the average slope in the body of the undulator is nearly zero and the residual offset is practically zero.

SUMMARY

In this report, the design efforts for the undulator for PAL-XFEL are summarized. The undulator has 15mm period with 4 mm minimum gap. The periodic magnetic structures are optimized and the details of the transition parts are elaborated. In the calculation, the RADIA code developed from ESRF, and ANSYS are mostly used. The major parameters are summarized in Table 1. Since the geometries are not implemented completely (tolerances etc) and the magnetic properties are approximate, there might be small differences between the calculation and the reality. This can results an error but the difference will be small. Our experiences show that the peak field agrees within 1% of the calculated values. Also these differences might show somewhat different behaviour in the gap dependence of the residual field. But hopefully, the final undulator after tuning the minor differences will agree with design and will meet all the design requirements.

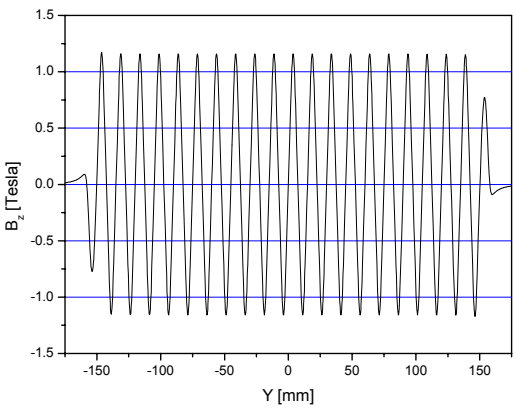

Figure 1: The calculated field profile.

REFERENCES

[1] T-Y.Lee et al.,"Design and Physics Issues of the PAL-XFEL", Journal of the Korean Physical Society, 48(4), (2006)791.
[2] T.Bizen, et al., "Demagnetization of undulator magnets irradiated high energy electrons", Nucl. Inst. & Meth. A 467, (2001)185.
[3] http://www.ansys.com
[4] Vasserman, E.R. Moog, "A Passive scheme for ID end correction", Rev. Sci. Instrum. 66(2), (1995)1943.
[5] J.Chavanne, P. Elleaume, P.V.Vaerenbergh, "End Field Structures for Linear/Helical Insertion Devices", PAC'99, New York, 1999, p. 2665.
[6] P.Elleaume, O. Chubar, J. Chavanne, "Computing 3D Magnetic Fields from Insertion Devices", IEEE, (1998) 350.
[7] http://www.esrf.fr/machine/groups/insertion_devices/Codes/Radia/Radia.html

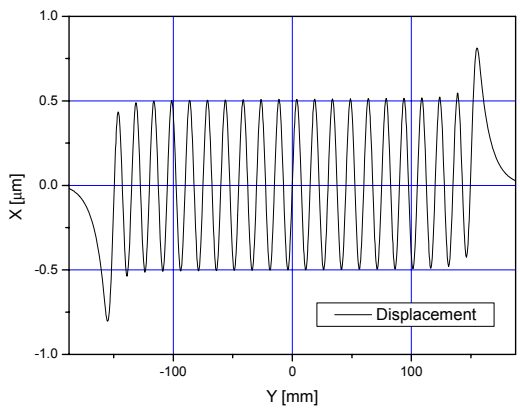

Figure 2: The calculated orbit based on the calculated field profile.

INSERTION DEVICES FOR SESAME

Hamed Tarawneh, Geatano Vignola
SESAME, c/o UNESCO Amman Office, P.O. Box 2270, Amman 11181, Jordan

Abstract

The Phase-I SESAME beamlines have been defined by the scientific research programme of the SESAME users and Insertion Devices (IDs) will be the primary photon sources. It foresees two planar wigglers dedicated for WAFS/XRF and powder diffraction beamlines covering spectral range of 3-30 keV and 3-25 keV respectively, one elliptically polarizing undulator dedicated for Photo-absorption spectroscopy that covers a spectral range of 0.1-1 keV, one undulator dedicated for material science that covers 8-12 keV, one In-vacuum undulator dedicated for MAD protein crystallography covering 5-15 keV and two IR ports from a bending magnet dedicated for IR Spectromicroscopy covering 0.01-1eV. This paper describes the proposed designs for the first two devices and their effects on the SESAME lattice [1].

INTRODUCTION

SESAME is a third generation synchrotron light source, with an electron beam energy of 2.5 GeV and 400 mA beam current, located in Allan, Jordan. The SESAME storage ring is optimized for the use of Insertion Devices (IDs) and can allocate up to 12 IDs which will serve the SESAME users community. In this note, the magnetic design for two IDs, Hybrid Multipole Wiggler (HMW) and an Elliptically Polarizing Undulator (EPU), suitable for the Phase-I beamlines of SESAME will be presented.

Both devices fulfill the electron beam stay clear requirements defined by the SESAME lattice leading to an acceptable vacuum lifetime. The beam lifetime is an important issue for the 2.5 GeV SESAME storage ring since the injection energy is 800 MeV and top-up injection will be implemented in a second stage.

The magnetic design and optimization of the two IDs was done using the computer codes Radia [2] and FEMM [3] whereas the characteristics of the output photons are studied with the SPECTRA code [4]. The effects of the IDs on the electron beam were studied numerically using the particle tracking code BETA [5].

EPU UNDULATOR

The Apple-II type helical undulator [6] has been chosen to provide high flux circularly polarized radiation in the soft X-ray spectral range. This magnet will operate out of vacuum with minimum magnetic gap of 13 mm, period length of 60 mm and 28 periods. This satisfies a stay clear aperture 8.5 mm for an ID length of about 2 m [1] and fundamental photon energy of elliptically polarized light less than 100 eV at the minimum undulator gap.

In this undulator, NdFeB magnet blocks with a remanent field B_r= 1.22 T and a relative permeability of 1.05 parallel to and 1.17 perpendicular to the easy axis of the blocks are used. The blocks have a thickness of ¼ period and 40 mm × 40mm cross section with 5 mm × 5mm cuts needed to clamp the blocks in the holders.

The magnet structure has four sub-assemblies, two above and two below the beam axis. By moving the sub-assemblies longitudinally relative to each other, the relative strength of the transverse components of the magnetic field is altered leading to change in the polarization of the emitted radiation. Only the helical mode of operation has been considered where horizontal, vertical and elliptical polarized light can be obtained.

An asymmetric layout has been adopted for the SESAME EPU, i.e. the vertical magnetic field has the same polarities at the entrance and exit of the magnet, with the end sections of the Elettra type [7]. The achieved magnetic flux densities for the three modes of operation as a function of the undulator gap and phase are shown in Fig. 1. Tab. 1 summarizes the main magnetic properties of the SESAME EPU at minimum gap.

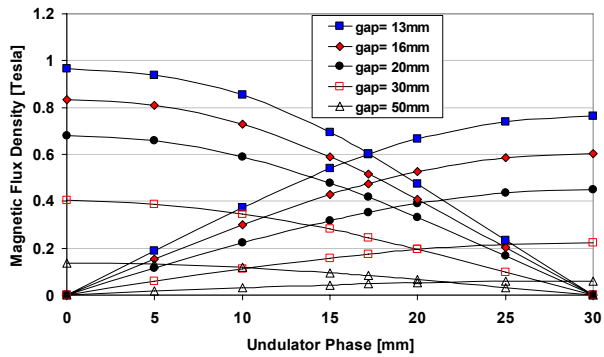

Figure 1: On-axis magnetic flux densities of the SESAME EPU undulator at different gaps and phases.

Table 1: Flux densities, K-values and minimum photon energies at minimum gap of 13 mm.

Undulator Phase	B_x [T]	B_z [T]	K-value	Ph Energy [eV]
Horizontal. 0mm	-	0.97	5.44	62
Circular 17.2mm	0.60	0.60	3.36	79
Vertical 30mm	0.76	-	4.26	98

HMW WIGGLER

The HMW will provide photon energies from 3-25 keV, which are defined by the scientific case of the SESAME. The HMW is a hybrid device with period length of 160 mm, a minimum gap of 14.5 mm, maximum flux density of 2.10 Tesla and total magnetic length of 3.092 m.

The magnet configuration consists of NdFeB magnet blocks with B_r= 1.3 T to produce the magnetic field and Vanadium Permendur material is chosen for the pole

pieces to increase the effective magnetic field and channel it to create a high peak field on the electron beam trajectory. The main parameters of the SESAME HMW wiggler magnet are shown in Tab. 2.

Table 2. Design parameters of the SESAME HMW.

Period length, mm	160
Peak Field, Tesla	2.10
The deflection parameters {K}	31.37
Minimum gap, mm	14.5
Number of periods	19
Total length, m	3.092
Total number of full-size poles	78
Total number of full-size PM block	80
Main PM block dimensions [mm^3]	140×52×100
End PM block dimensions [mm^3]	140×26×100
Main pole dimensions [mm^3]	100×28×80
End pole dimensions [mm^3]	100×14×66

The pole width has been optimized to reduce the transverse roll-off of the achieved magnetic field, as shown in Fig. 2.

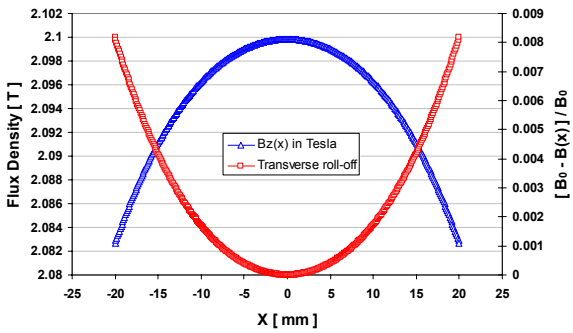

Figure 2: Transverse roll-off as a percentage of the on-axis peak flux at minimum gap.

The end section is half in length for the PM block and the pole. An extensive 3D calculation shows that the height of the end pole is 14 mm less than the full-size pole to give minimum field integrals. The first and second vertical field integrals are shown in Fig. 3.

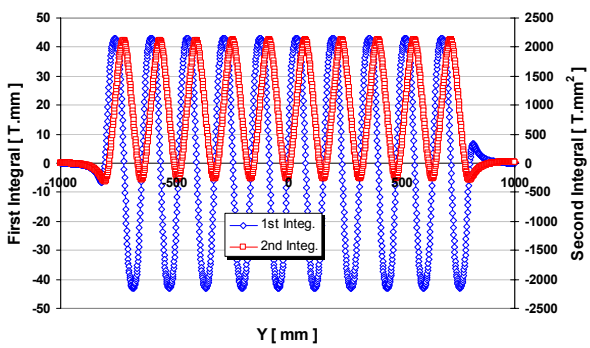

Figure 3: Field integrals of the HMP wiggler.

EFFECT ON SESAME LATTICE

In the BETA code any insertion device can be described by interpolation tables which provide an angular kick as a function of the coordinates of the particle passing through that element, i.e. mapped insertion device [5]. Such a map has been generated for both IDs and used for tracking particles, within the map, to investigate the effect of the higher order multipoles on the dynamic aperture of the SESAME lattice. The map has a finite size, ±30 mm in x-axis and ±5 mm in z-axis, which is considered as a physical limitation in the BETA code. Tracking the particles for 500 turns within this map (aperture) for both devices has not lead to significant reduction in the dynamic aperture of the SESAME lattice, see Fig. 4 and Fig. 5.

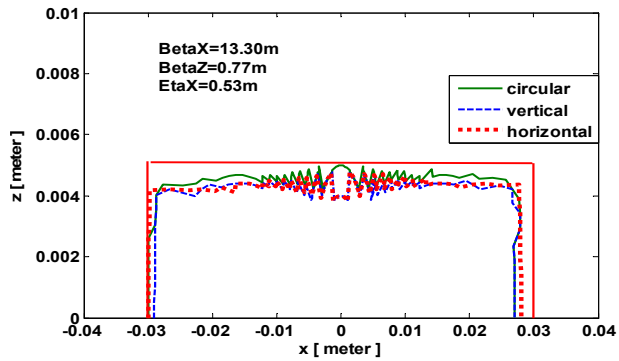

Figure 4: Dynamic aperture for the SESAME lattice with the mapped EPU magnet engaged at different phases.

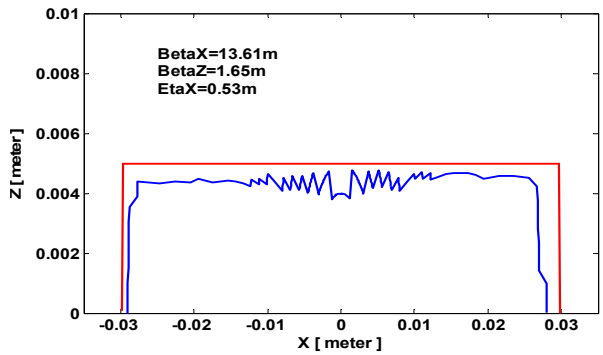

Figure 5: Dynamic aperture for the SESAME lattice with the mapped HMP wiggler engaged.

PHOTON OUTPUT

The magnetic field model has been used to calculate the synchrotron radiation output from both devices using the SPECTRA code [4]. The broadening of the peaks due to emittance and electron beam energy spread are included in the calculations. Fig. 6, 7 and 8 show the brilliance of the SESAME EPU for all modes of operation. The overlap between the first four harmonics is very good for the horizontal and the vertical modes of operation.

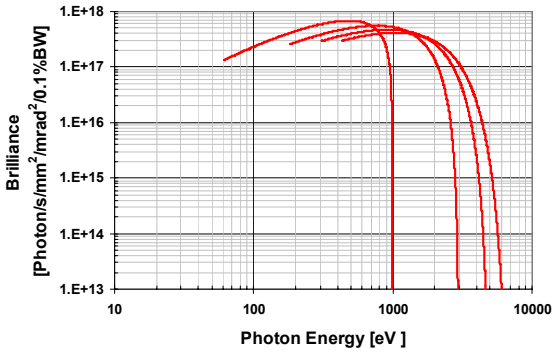

Figure 6: EPU brilliance for horizontal polarization.

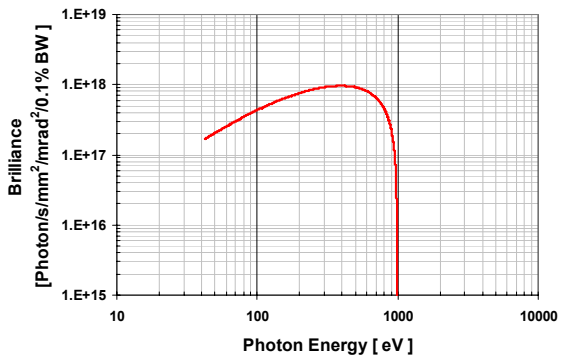

Figure 7: EPU brilliance for circular polarization.

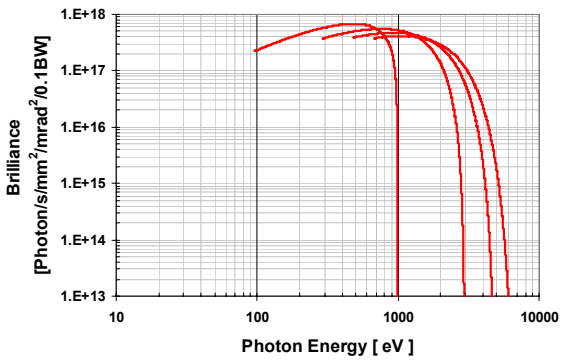

Figure 8: EPU brilliance for vertical polarization.

The HMW wiggler magnet will be housed in a long straight section of the SESAME lattice [1]. The criterion for the useful photon energy range has been chosen such that the flux densities are within 10% of their maximum value. Tab. 3 shows the predicted output photons from the HMW wiggler magnet. The photon flux density is shown in Figure 9.

Table 3: Parameters of the output photons of the SESAME HMP wiggler

Beam Energy Loss, keV	53.0
Total Radiated Power, kW	21.2
Critical Photon Energy , keV	8.73 (6.17)
Maximum Flux density	1.80×10^{15}
Useful Energy Range (10 % of max. flux density)	0.1-40 keV

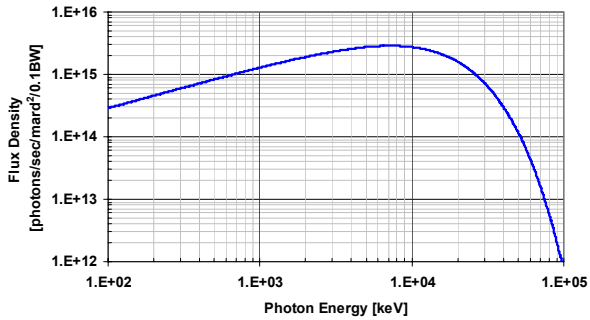

Figure 9: Photon flux density of the HMW wiggler magnet at 400 mA.

CONCLUSIONS

The designs of an elliptically polarizing undulator and a hybrid multipole wiggler have been presented. Both devices satisfy the demands of the SESAME user communities and have very low residual field integrals.
The dynamic aperture of the SESAME lattice has not suffered severe reduction due to the inclusion of both devices and the effect on the emittance and energy spread is negligible.
Further works on the optimization of the support system to achieve minimum deflection of magnet girder and power loading on the vacuum chamber are in progress for both devices.

REFERENCES

[1] G. Vignola, M. Attal, " SESAME Lattice", Technical Note: O-1, December 21, 2004, Amman, Jordan.
[2] http://www.esrf.fr/Accelerators/Groups/Insertion Devices/Software/Radia
[3] http://femm.foster-miller.net/
[4] http://radiant.harima.riken.go.jp/spectra/index.html.
[5] L. Farvacque, et. al. "BETA users' guide", Grenoble, France, 3rd edition, July 2001.
[6] Sasaki, "Analysis for a planar variably-polarizing undulator", Nuclear Instruments and Method in Physics Research A, NIMA 347, 1994.
[7] B. Diviacco, et. al. "Development of elliptical undulator for Elettra", Proceedings of EPAC'00, Vienna, Austria.

BEAM DYNAMICS EFFECTS WITH INSERTION DEVICES FOR THE PROPOSED 3 GEV RING IN TAIWAN

H. C. Chao*, C. C. Kuo,
NSRRC, Hsinchu 30076, Taiwan, R. O. C.
S. Y. Lee
Department of Physics, Indiana Univeristy, Bloomington, Indiana, 47405, USA

Abstract

The effects of insertion devices on beam dynamics of storage rings were studied. We will focus on the changes of the emittance and the energy spread in the presence of insertion devices. Formulas for the beam emittance and the energy spread with insertion devices are also derived, in which an intrinsic parameter depending on the design of the lattice is introduced in the calculations. Simulation results and comparisons of achromatic and non-achromatic cases in the proposed 3 GeV synchrotron radiation light source in Taiwan are shown.

INTRODUCTION

A new 3 GeV third generation synchrotron radiation light source is proposed by National Synchrotron Radiation Research Center (NSRRC) in Taiwan[1]. The circumference of the storage ring is 486 m with natural emittance 1.7 nm-rad for non-achromatic case and 5.2 nm-rad for achromatic case. The twiss functions of non-achromatic case are shown in Figure 1. The lattice has a structure of 24 cells of DBA with 6-fold symmetry. It has 24 straights including 6 long straights (10.9 m) and 18 standard straights (5.8 m) for injection or insertion devices (IDs).

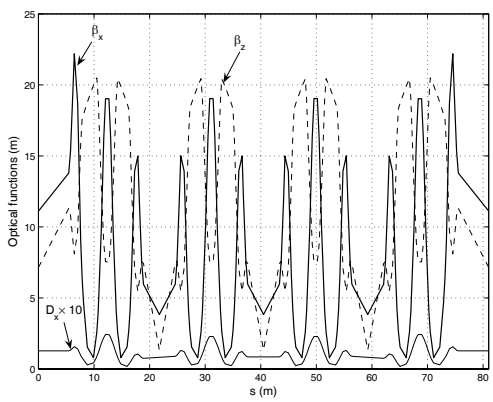

Figure 1: Optical functions of one superperiod (non-achromat lattice)

IDs are often used to produce partial coherient light or to shift energy ranges of synchrotron radiation light source. In the meanwhile, they bring some effects on electron beam parameters. First consider the synchrotron radiation integrals defined by

$$I_2 = \oint \frac{1}{\rho^2} ds \tag{1}$$

$$I_3 = \oint \frac{1}{|\rho|^3} ds \tag{2}$$

$$I_4 = \oint \frac{D_x}{\rho}(\frac{1}{\rho^2} + 2K) ds \tag{3}$$

$$I_5 = \oint \frac{\mathcal{H}}{|\rho|^3} ds, \text{ where } \mathcal{H} = \frac{D_x^2 + (\alpha_x D_x + \beta_x D_x')^2}{\beta_x} \tag{4}$$

The integrals are taken over the whole ring. K is the focusing function. β_x is the horizontal betatron amplitude funcion and $\alpha = -\beta_x'/2$. D_x is the horizontal dispersion function and D_x' is its differential.

Some important parameters of beam dynamics can be characterized by synchrotron radiation integrals.

- Energy loss per turn

$$U_0 = C_\gamma \frac{\beta^3}{2\pi} E^4 I_2 \approx \frac{C_\gamma E^4 I_2}{2\pi} \tag{5}$$

$$C_\gamma = \frac{4\pi}{3} \frac{r_0}{(mc^2)^3} = 8.85 \times 10^{-5} \text{ m/(GeV)}^3$$

- Energy spread

$$(\frac{\sigma_E}{E})^2 = C_q \gamma^2 \frac{I_3}{2I_2 + I_4} \tag{6}$$

$$C_q = \frac{55}{32\sqrt{3}} \frac{\hbar}{mc} = 3.83 \times 10^{-13} \text{ m}$$

- Natural emittance

$$\varepsilon_{x0} = C_q \gamma^2 \frac{I_5}{I_2 - I_4}\,, \tag{7}$$

where r_0 and m are the radius and the mass of the particle (here electron); γ is the Lorentz factor; c is the speed of light in vaccum; E is the particle energy; and $\hbar$ is Planck's constant.

EFFECTS OF INSERTION DEVICES

Adding IDs brings additional magnitudes of synchrotron radiation integrals. Taking this effect into account the

* hjjhao@nsrrc.org.tw

following relations can be derived.

$$\Delta U_w = \frac{C_\gamma E^4 \Delta I_2}{2\pi} \tag{8}$$

$$\sigma_E = \sigma_E^0 \sqrt{\frac{1+\frac{\Delta I_3}{I_3^0}}{1+\frac{2\Delta I_2+\Delta I_4}{2I_2^0+I_4^0}}} \tag{9}$$

$$\varepsilon_x = \varepsilon_x^0 \left(\frac{1+\frac{\Delta I_5}{I_5^0}}{1+\frac{\Delta I_2-\Delta I_4}{I_2^0-I_4^0}}\right), \tag{10}$$

where the superscript 0 denotes that the value is evaluated for the case of no IDs added. There is no approximation made so far. For separate function accelerators, we can omit I_4 because I_4 is much smaller than I_2. Similarly ΔI_4 is also small.

From the definition of synchrotron radiation integrals, the following relations holds: $I_2^0 = \frac{2\pi}{\rho_0}$ and $I_3^0 = \frac{2\pi}{\rho_0^2}$, where ρ_0 is the bending radius of dipole magnets with field strength B_0. For the integral $I_5^0 = \oint \frac{\mathcal{H}}{|\rho|^3} ds$, $\frac{1}{\rho}$ is nonzero only in dipole magnets and we can tear the integral into a product of total dipole length and the averaged $\mathcal{H}$ in the dipole magnets.

$$I_5^0 = \oint_{\text{dipoles}} \frac{\mathcal{H}(s)}{|\rho_0|^3} ds = \frac{1}{\rho_0^3} \times 2\pi\rho_0 \langle\mathcal{H}\rangle = \frac{2\pi}{\rho_0^2}\langle\mathcal{H}\rangle\,, \tag{11}$$

where the bracket denotes the average operator only in the dipole magnets. The $\langle\mathcal{H}\rangle$ can be evaluated by equation (7)

$$\varepsilon_{x0} \approx C_q\gamma^2 \frac{I_5}{I_2} = C_q\gamma^2 \frac{2\pi\langle\mathcal{H}\rangle/\rho_0^2}{2\pi/\rho_0} = C_q\gamma^2 \frac{\langle\mathcal{H}\rangle}{\rho_0} \tag{12}$$

if we know the natural emittance of the lattice.

Now we try to estimate the perturbed quantities ΔI_2, ΔI_3, and ΔI_5. Suppose B_w is the peak field, λ_w is the period length, and N is the number of periods of the ID. The length of the ID is therefore $L_w = N\lambda_w$. A simple model of magnetic field of the ID can be written as

$$B_z(s) = B_w \cos(\frac{2\pi s}{\lambda_w}) \tag{13}$$

Let ρ_w be the bending radius corresponding to the B_w, ρ is also a function of s.

$$\frac{1}{\rho(s)} = \frac{1}{\rho_w}\cos(\frac{2\pi s}{\lambda_w}) \tag{14}$$

ΔI_2 and ΔI_3 are independent of the dispersion function and can be evaluated through (1) and (2) directly by changing the range of the integral from the overall ring to only the range of that ID.

$$\begin{aligned}\Delta I_2 &= N\int_0^{\lambda_w} \frac{1}{\rho^2} ds = \frac{N}{\rho_w^2}\int_0^{\lambda_w} \cos^2(\frac{2\pi s}{\lambda_w}) ds \\ &= \frac{\lambda_w N}{2\rho_w^2} = \frac{L_w}{2\rho_w^2}\end{aligned} \tag{15}$$

$$\begin{aligned}\Delta I_3 &= N\int_0^{\lambda_w} \frac{1}{|\rho|^3} ds = \frac{N}{\rho_w^3}\int_0^{\lambda_w} |\cos(\frac{2\pi s}{\lambda_w})|^3 ds \\ &= \frac{4}{3\pi}\frac{\lambda_w N}{\rho_w^3} = \frac{4L_w}{3\pi\rho_w^3}\end{aligned} \tag{16}$$

The change of $\mathcal{H}$-function due to the ID is small. $\mathcal{H}$ keeps nearly a constant in the range of ID and can be carried outside the integral

$$\begin{aligned}\Delta I_5 &= \int_w \frac{\mathcal{H}}{|\rho|^3} ds = \frac{1}{\rho_w^3}\int_w \mathcal{H}(s)|\cos^3(\frac{2\pi s}{\lambda_w})| ds \\ &= \frac{\hat{\mathcal{H}}}{\rho_w^3}\int_w |\cos^3(\frac{2\pi s}{\lambda_w})| ds = \frac{4\hat{\mathcal{H}} L_w}{3\pi\rho_w^3}\,,\end{aligned} \tag{17}$$

where $\hat{\mathcal{H}}$ is the $\mathcal{H}$ value in straight section without IDs.

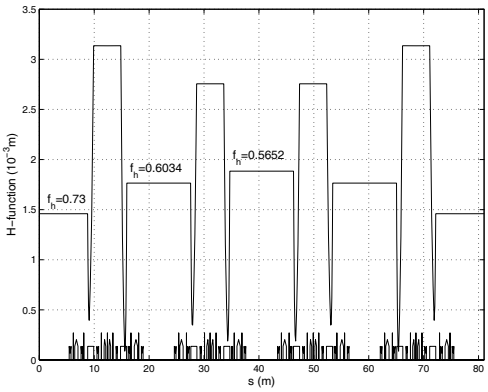

Figure 2: $\mathcal{H}$-function of one superperiod (non-achromat lattice)

Defining f_h by $\langle\mathcal{H}\rangle = f_h\hat{\mathcal{H}}$, f_h is a factor depending on the design of the lattice and the position of IDs. Figure 2 shows the $\mathcal{H}$-function of one superperiod of the non-achromat lattice calculated by MAD. The value of f_h at three kinds of straights are 0.7300, 0.6034, 0.5652, respectively. Putting equations (15-10) into equations (8-10), we get the final formulas for non-achromat lattices.

$$\Delta U_w = \frac{C_\gamma E^4 L_w}{4\pi\rho_w^2} \tag{18}$$

$$\sigma_E = \sigma_E^0 \sqrt{\frac{1+\frac{2L_w\rho_0^2}{3\pi^2\rho_w^3}}{1+\frac{L_w\rho_0}{4\pi\rho_w^2}}} \tag{19}$$

$$\varepsilon_x = \varepsilon_x^0 \left(\frac{1+\frac{2L_w\rho_0^2}{3\pi^2 f_h\rho_w^3}}{1+\frac{L_w\rho_0}{4\pi\rho_w^2}}\right) \tag{20}$$

One should note that the emittance will decrease slightly for $B_w < \frac{3\pi f_h B_0}{8}$ and grow rapidly when $B_w \geq \frac{3\pi f_h B_0}{8}$. Similary case for the energy spread where the critical field $B_w = \frac{3\pi B_0}{8}$.

For achromat lattices, the dispersion function vanishes in straight sections and the perturbed dispersion function caused by the ID itself is small and can be omitted. Therefore ΔI_5 is approximately zero by definition and the equation of the emittance change can be written as

$$\varepsilon_x = \varepsilon_x^0 \left(\frac{1}{1+\frac{\Delta I_2}{I_2}}\right) = \varepsilon_x^0 \left(\frac{1}{1+\frac{L_w\rho_0}{4\pi\rho_w^2}}\right) \tag{21}$$

For more than one IDs, the total effects on the synchrotron integrals are accumulated from the contribution of each ID individually. The change of the energy spread and the emittance can be generalized as

$$\sigma_E = \sigma_E^0 \sqrt{\frac{1+\sum_w \frac{2L_w\rho_0^2}{3\pi^2\rho_w^3}}{1+\sum_w \frac{L_w\rho_0}{4\pi\rho_w^2}}} \tag{22}$$

$$\varepsilon_x = \varepsilon_x^0 \left(\frac{1+\sum_w \frac{2L_w\rho_0^2}{3\pi^2 f_{h,w}\rho_w^3}}{1+\sum_w \frac{L_w\rho_0}{4\pi\rho_w^2}} \right) \tag{23}$$

For ideal helical undulators, $\Delta I_2 = \frac{L_w}{\rho_w^2}$, $\Delta I_3 = \frac{L_w}{\rho_w^3}$, and $\Delta I_5 = \frac{\hat{\mathcal{H}} L_w}{\rho_w^3}$. The two equations above can be modified as

$$\sigma_E = \sigma_E^0 \sqrt{\frac{1+\sum_w \frac{L_w\rho_0^2}{4\pi\rho_w^3}}{1+\sum_w \frac{L_w\rho_0}{4\pi\rho_w^2}}} \tag{24}$$

$$\varepsilon_x = \varepsilon_x^0 \left(\frac{1+\sum_w \frac{L_w\rho_0^2}{4\pi f_{h,w}\rho_w^3}}{1+\sum_w \frac{L_w\rho_0}{4\pi\rho_w^2}} \right) \tag{25}$$

RESULTS AND DISCUSSIONS

The parameters of the IDs proposed by NSRRC are listed in Table 1. During the simulation only vertical field components are considered for the elliptically polarizing undulators. Randomly distributing all the IDs in the ring as shown in Figure 3, good agreements of the results of ID effects calculated by MAD and predicted by this formula are shown in Table 2.

Table 1: Parameters of IDs of TPS

ID Name	Length (m)	Peak Field (Bz/Bx) (Tesla)	Num of ID
EPU10	3.7	1.0	1
EPU7	3.6	1.0/0.77	2
SW6	2.0	3.5	1
EPU6	3.7	0.9/0.7	2
EPU4.6	3.7	0.76/0.49	2
IVU2.8	3.7	0.9	10
SU1.5	2.0	1.4	1
CU1.8	3.7	1.29	4

Take a look at equation (21) for achromatic case, it can be rewritten as $\varepsilon_x = \varepsilon_x^0 \left(\frac{1}{1+\frac{\Delta U_w}{U_0}} \right)$ by equations (6) and (8). The theorical minimal emittance of DBA lattice is 3 times larger than that of DB lattice. To reduce the emittance by a factor of 3, the required radiated energy from IDs (ΔU_w) must be twice than the energy radiated from the dipole (U_0, here is 0.8598 MeV/turn). But the total energy loss is too high for the rf cavity to compensate. The dipole field must be designed to be weaker so that the rf voltage be in a resonable range. On the other hand, strong bending dipole fields are preferred to hold the growth of the emittance for non-achromatic case because the emittance grows when $B_w \geq \frac{3\pi f_h B_0}{8}$.

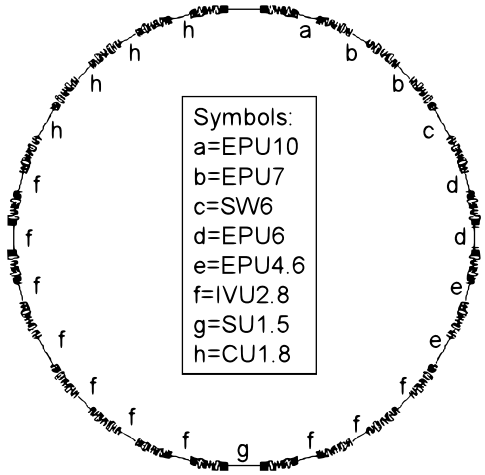

Figure 3: The locations of IDs

Table 2: Comparison of Effects of IDs on Beam Dynamics calculated by MAD8 and by the formula (non-achromat lattice)

ID Name	Relative Energy Spread (10^{-4})		Emittance (nm-rad)	
	MAD8	Formula	MAD8	Formula
w/o ID	8.8598	8.8598	1.6748	1.6748
EPU10	8.8294	8.8291	1.6818	1.6821
EPU7	8.8011	8.8006	1.6915	1.6920
SW6	9.7174	9.7392	2.2394	2.2392
EPU6	8.7996	8.7991	1.6808	1.6811
EPU4.6	8.8040	8.8036	1.6664	1.6665
IVU2.8	8.5919	8.5911	1.6924	1.6933
SU1.5	8.8595	8.8596	1.6903	1.6904
CU1.7	8.8092	8.8094	1.7881	1.7889
ALL ID	9.1251	9.1403	2.1758	2.1770

Under the situation of all proposed IDs installed, the total energy lost from all IDs are 0.5914 MeV per turn and the energy spread is 0.0914%. The natural emittance for non-achromatic and achromatic cases are 2.1770 and 3.1122 nm-rad respectively. For non-achromatic case the presence of dispersion in straights must be taken in account.

The two dimensional effective emittance is defined by $\varepsilon_{\text{eff}} = \sqrt{\varepsilon_x^2 + H\sigma_\delta^2\varepsilon_x}$, where σ_δ represents the relative energy spread $\frac{\sigma_E}{E}$. The effective emittance at three kinds of straights are respectively 2.7189, 2.8194, and 2.8576 nm-rad, which are smaller than 3.1122 nm-rad of the achromat lattice.

ACKNOWLEDGEMENTS

The authors would like to thank the colleagues of the beam dynamics group of NSRRC for their assistance.

REFERENCES

[1] See "NSRRC TPS Proposal".

[2] S. Y. Lee, "Accelerator Physics", World Scientific, 2004.

A HAMILTONIAN FOR WAVE LENGTH SHIFTER AND ITS STUDIES ON INDUS-1

Ali Akbar Fakhri*, and Gurnam Singh
Raja Ramanna Centre for Advanced Technology, Post - CAT, Indore – 452 013

Abstract

The INDUS-1 is a 450 MeV synchrotron radiation source for the production of VUV radiation. In order to produce the radiation of shorter wavelengths (λ_c = 31 A^o), a superconducting wavelength shifter (WLS) with peak field of 3T is being considered for Indus-1. In this paper, L. Smith's Hamiltonian for Halbach's magnetic field model has been re-derived to estimate focussing component under the compensated electron beam trajectory transformation. Various linear compensation schemes are presented to minimize the linear effects of WLS and its effects on machine operation are also theoretically studied.

INTRODUCTION

It is well known that an insertion device perturbs [2,3] the motion of an electron in storage rings. It produces the linear and non-linear beam dynamics effects. In the case of the WLS nonlinear contribution would be small but due to its linear effect, linear optics will be distorted and it will disturb the nonlinear optics of the ring. So it is necessary to predict precisely quadrupole component for WLS. For this purpose, Hamiltonian for WLS has been rederived for compensated electron bump trajectory transformation and its effects on Indus-1 machine operation are studied theoretically.

A HAMILTOINAN FOR WAVELENGTH SHIFTER

Magnetic Field

The components of the transverse magnetic field in a WLS with finite pole width may be obtained from Halbach's[1] expression.

$$B_x = \frac{k_{mx}}{k_{my}} B_m \sinh k_{mx}x \sinh k_{my}y \sin k_m(z-c_m)$$

$$B_y = B_m \cosh k_{mx}x \cosh k_{my}y \sin k_m(z-c_m)$$

$$B_z = -\frac{k_m}{k_{my}} B_m \cosh k_{mx}x \sinh k_{my}y \cos k_m(z-c_m)$$

$$k_{mx}^2 + k_{my}^2 = k_m^2 = (\pi/d_m)^2$$

If k_{mx}^2 is small then $k_{my}^2 \sim k_m^2 \sim (\frac{\pi}{d_m})^2$ and $B_1 = B_3 = -\frac{B_2 d_2}{2d_1}$

Where subscripts m denotes pole number 1,2, 3, B_m is used to denote peak magnetic field, d_m is used to represent corresponding pole length and c_m denotes phase adjustment (c_1=0, c_2=d_1 c_3=d_1 +d_2) for different pole. In present case d_1= d_2= d_3 & $k_{x1} = k_{x2}$. B_2 is the its' peak magnetic field and x, y and z are horizontal, vertical and beam directions respectively.

Electron beam trajectory

The equation of motion for the first pole in the horizontal plane, with coshk_xx~1and y=0. is :

$$\frac{d^2x}{ds^2} = \frac{B_2}{2B\rho} \sin k(s-c_1)$$

Where ρ =radius of curvature in the field B and ds = vdt
The first integral of equation is

$$\frac{dx}{ds} = -\frac{B_2}{2kB\rho}\left[\cos k(s-c_1) - 1\right]$$

By using the relation $z_e^{'2} = 1 - x_e^{/2} \sim 1$
After second integration

$$x = -\frac{B_2}{2kB\rho}\left[\frac{\sin k(s-c_1)}{k} - s\right]$$

Similarly for the second pole and third pole, we can write

$$x = \frac{B_2}{k_2 B\rho}\left[\frac{\sin k(s-c_2)}{k} + \frac{d}{2}\right]$$

$$x = -\frac{B_2}{2kB\rho}\left[\frac{\sin k(s-c_3)}{k} + s - 3d\right]$$

In above equations on right hand side second additional term is due to compensated electron bump trajectory.

A Hamiltonian for Betatron motion

The Hamiltonian of the motion of an electron under above magnetic field[2] can be written as,

$$H = \frac{1}{2}\left[p_z^2 + (p_x - A_x \cos k_m(z-c_m))^2 + (p_y - A_y \cos k_m(z-c_m))^2\right]$$

Where: $A_{mx} = -\frac{B_m}{k_m B\rho} \cosh k_{mx}x \cosh k_{my}y$

$$A_{my} = \frac{B_m k_{mx}}{k_{my}} \frac{\sinh k_{mx}x \sinh k_{my}y}{k_m B\rho}$$

A canonical transformation is required to change variables from (x, y, z) to (x_β, y_β, s) where s is distance along the equilibrium orbit, x_β is a displacement in the (x, z) plane perpendicular to the equilibrium orbit and $y_\beta = y$ is vertical displacement from the equilibrium orbit. Transformation between variables for first pole, second pole and third pole can be written as

$$x = x_e + z_e^{/} x_\beta = x_e - \frac{B_2}{2kB\rho}\left[\frac{\sin k(s-c_1)}{k} - s\right] \sim x - a_1$$

$$z = s - x_e^{'} x_\beta = s - x_e^{/} \frac{B_2}{2kB\rho}\left[\frac{\sin k(s-c_1)}{k} - s\right] \sim s$$

* fakhri@cat.ernet.in

For the second pole

$$x \sim x_e + \frac{B_2}{kB\rho}\left[\frac{\sin k(s-c_2)}{k} + \frac{d}{2}\right] \sim x_e - a_2$$

$$z = s - \frac{B_2}{kB\rho}\left[\frac{\sin k(s-c_2)}{k} + \frac{d}{2}\right] x_e^{'} \sim s$$

For the third pole

$$x \sim x_e - \frac{B_2}{2kB\rho}\left[\frac{\sin k(s-c_3)}{k} + s - 3d\right] \sim x_e - a_3$$

$$z = z_e - \frac{B_2}{2kB\rho}\left[\frac{\sin k(s-c_3)}{k} + s - 2.d_1 - d2\right] x_e^{'} \sim s$$

Where

$$a_1 = \frac{B_2}{2kB\rho}\left[\frac{\sin k(s-c_1)}{k} - s\right], a_2 = -\frac{B_2}{kB\rho}\left[\frac{\sin k(s-c_2)}{k} + \frac{d}{2}\right]$$

$$\& \quad a_3 = \frac{B_2}{2kB\rho}\left[\frac{\sin k(s-c_3)}{k} + s - 3d\right]$$

and the canonical momentum transformation can be written as

$$p_x = z_e^{'} p_{x_\beta} + \frac{x_e^{/}}{(1+\Omega x_\beta)} p_s$$

$$p_z = \frac{z_e^{/}}{(1+\Omega x_\beta)} p_s - x_e^{/} p_{x_\beta}$$

$$p_y = p_{y_\beta}$$

After transformation, Hamiltonian, the betatron equations of motion can be obtained by Hamiltonian' s equations.

$$x'' = -\frac{B^2{}_m k_{mx}^2}{2k_m{}^2 B^2 \rho^2}\left[(x-a_m) + \frac{1}{3}k_{mx}^2(x-a_m)^3 + k_{my}^2(x-a_m)y^2 - \frac{1}{2}k_{mx}^2(x-a_m)y^2\right]$$

$$+\frac{B_m \sin k_m(s-c_m)}{B\rho}\left[\begin{array}{l}\frac{k_{my}^2 y^2}{2} + \frac{k_{my}^4 y^4}{24} + \frac{k_{mx}^2(x-a_m)^2}{2} + \frac{k_{mx}^2 k_{my}^2 (x-a_m)^2 y^2}{4} \\ + \frac{k_{mx}^4 (x-a_m)^4}{24}\end{array}\right]$$

$$+\frac{B_m \cos k_m(s-c_m)}{k_m B\rho} yy' k_{mx}^2\left[a_m + \frac{k_{my}^2 y^2}{6} + \frac{k_{mx}^2(x-a_m)^2}{2}\right]$$

$$y'' = -\frac{B^2{}_m k_{my}^2}{2k_m^2 B^2 \rho^2}\left[\begin{array}{l} y + k_{mx}^2(x-a_m)^2 y + \frac{1}{3}k_{mx}^4 y(x-a_m)^3 \\ + \frac{1}{6}k_{my}^2 y^3\end{array}\right]$$

$$-\frac{B_m \cos k_m(s-c_m) k_{my}^2 yx'}{k_m B\rho}\left[1 + \frac{1}{2}k_{my}^2 y + \frac{1}{2}k_{mx}^2(x-a_m)^2\right]$$

$$-\frac{B_m \sin k_m(s-c_m)}{B\rho} k_{mx}^2 y\left[\begin{array}{l}(x-a_m) + \frac{1}{6}k_{my}^2(x-a_m)y^3 \\ + \frac{1}{6}k_{mx}^4(x-a_m)^3 y\end{array}\right]$$

In averaging procedure sin(k_ms) and cos(k_ms) term are retained due to compensated electron bump trajectory After averaging the electron trajectory in combination with different magnetic field component gives net linear and non-linear effect. There is a linear effect, which is equivalent to that of a horizontally and vertically focusing quadrupole, whose strengths are given by,

$$x'' = -\frac{3}{4}\frac{B_m^2 k_{mx}^2}{(B\rho)^2 k_m{}^2} x - \frac{5}{4}\frac{B_m^2}{(B\rho)^2}\frac{k_{mx}^2}{k_m^2} x$$

$$y'' = -\frac{3}{4}\frac{B_m^2 k_{my}^2}{(B\rho)^2 k_m{}^2} y + \frac{5}{4}\frac{B_m^2}{(B\rho)^2}\frac{k_{mx}^2}{k_m^2} y$$

The term in k_x is due to collapse of the field in x direction due to finite width of magnetic poles and first term in k_y is due to the edge focusing of the magnet. In the case of k_x^2=0.0, WLS will act as a focussing device in the vertical plane and oscillating sin & cos term in the Hamiltonian will not give any contribution to the quadrupole component. If WLS has finite coupling then oscillating term in the hamiltoinian cannot be neglected and orbit offset in the sextupole component will give quadrupole component in addition to the edge focussing. This shows that for WLS, coupling coefficients are very stringent. In the equation second term represents the quadrupole component, which arises due to orbit offset in the sextupole component.

STUDIES FOR INDUS-1

In Indus-1, WLS can be operated in two options: a) It is switched on after injection. b) It is kept on during injection. Since, beam lifetime is short, therefore second option is preferred. The parameters of WLS are B = 3T, number of poles (n) =3, total magnetic length =0.54m. Further effects of coupling are studied by introducing coupling $(k_x/k_y)^2$ = -0.03. A series of hard-edged rectangular magnets was used to model the horizontal & vertical focussing caused by the WLS. In horizontal plane focussing due to finite k_x is modelled by defining field index into the dipole. The linear as well as non-linear effects are proportional to β_y at its location and inversely proportional to the square of beam energy. In Indus-1, β_y at WLS is small (0.7m – 1.2m), but due to its low energy, its linear effects are significant, however non-linear effects of WLS will not be stringent. In this paper a study, has been carried out for present operating tune point (1.69, 1.28).

Linear effect compensation

It is required to correct both tunes and β-asymmetries for smooth operation. The various options of compensations such as local beta/global tunes, global beta and tunes using 8 and 16 QMs were studied using computer program BURHANI [5] it is found that it is not possible to compensate both simultaneously. The β-asymmetries can be compensated completely by α -matching, except in region of the device using QF and QD families of quadrupoles placed in the neighbourhood of WLS. But it changes the linear tunes by a large amount. Therefore, the scheme in which first α-matching are done by using neighbouring QF and QD families and then linear tunes are compensated globally with remaining families of QF and QD was studied (fig.1 & 2). It offers a promising solution. The vertical β-asymmetries is corrected from 49% to 21 % and are reduced proportionally further if tunes are corrected partially. This scheme can help to achieve acceptable level of linear distortions for operation of WLS in a real machine. It is noted that only tunes correction is not a good solution as it leaves the large β-asymmetries.

Table 1: β-asymmetry correction results

	$\Delta\nu_X$	$\Delta\nu_Y$	$(\delta\beta/\beta)_{xrms}$	$(\delta\beta/\beta)_{yrms}$
Before correction	-0.02	0.06	10.39	27.47
Only Tune	0.0	0.0	9.36	27.47
α matching. & Tune	0.0	0.0	6.78	23.87
α matching &partial tune	-0.02	0.09	5.24	20.48

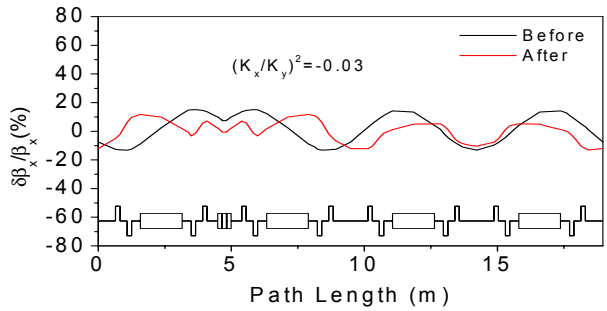

Figure 1

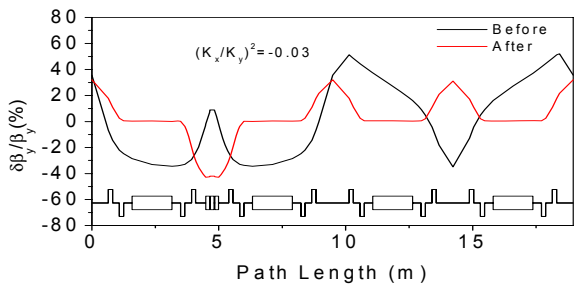

Figure 2

Dynamic aperture

In the presence of WLS, dynamic aperture is reduced mainly due to its linear effects. In the fig .3 dynamic apertures are plotted for on momentum particle after 100,000 turns for a finite k_x. It indicates that after α-matching and globally tunes correction; dynamic aperture improves in vertical plane by 33% and in horizontal plane by 18%. In comparison to only global tune correction. In both cases, dynamic aperture shrinks in comparison to the ideal lattice.

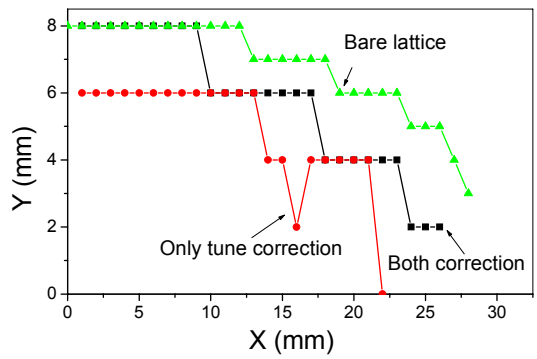

Figure 3

Injection simulation

In the Indus –1, one-kicker horizontal multi-turn injection scheme is adopted. In this scheme, the septum and kicker magnets are located at symmetry points of the ring and diametrically opposite to each other so that maximum of orbit bump (X_{bump}) parallel to the design orbit can be produced at the exit of the septum magnet. As a result, residual betatron oscillation will propagate all over the ring. So if injection is carried out in the presence of the WLS (having finite K_x), then β-asymmetries in the horizontal plane will deteriorate the injection efficiency. At the septum location (located at 21mm from design orbit) maximum oscillation amplitude of injected and stored bunches are tabulated in table 2 for the bare lattice, after tune correction and after both α-matching and globally tune correction. For above calculation 16mm orbit bump is produced using a single kicker magnet.

Table 2: Max. Beam oscillation at septum location

	Injected	stored
Bare lattice	16.85	16.8
Tune correction	18.07	15.8
α matching & Globally tune	16.63	17.43

The above results indicate that injection is possible in all cases; its injection efficiency may be poor. If injection or dynamic apertures are still not sufficient then after α matching, tune correction can be done partially, so that β-asymmetries are reduced to acceptable levels.

CONCLUSIONS

The Hamiltonian for the WLS gives an extra term for the quadrupole component, which arises due to orbit offset in sextupole magnet. To operate WLS in INDUS-1, local β correction/ partial or total global tunes correction may be required. It requires two additional power supplies for the independent variations of QF and QD families nearest to the WLS.

REFERENCES:

[1] G. Singh, et al "Commissioning status of Indus-1 SR facility" Indian Journal of Pure and Applied Physics Vol. 39 1-2; 1-2 pp. 96-103 (2001)

[2] Lloyd Smith, "Effects of wigglers and undulators on beam dynamics", Report No. LBL-21391, ESG-18 (1986)

[3] K. Halbach, "Fields of undulators and wigglers," NIM (187), pp109-177 (1981).

[4] Ali Akbar Fakhri, et al "A Hamiltonian for wave length shifter and its effect on Indus-1" CAT/2004-23

[5] A. A. Fakhri et.al. "The effects of insertion devices on betatron functions and linear betatron tunes and method of their correction for the storage ring INDUS-2," Report no. CAT/98-6

ILC ACTIVITY AT JINR AND SITING IN DUBNA REGION

Yu.Budagov, Yu.Denisov, I.Meshkov, G.Shirkov, A.Sissakian, G.Trubnikov[#].
Joint Institute for Nuclear Research, Dubna, 141980, Russia

Abstract

JINR actively participates in ILC project. JINR physicists are taking part in several fields of activity in ILC: works on photo injector prototype, participation in design and construction of cryomodules, laser metrology, etc. Moreover Joint Institute is officially approved candidate for possible hosting of ILC in the region near Dubna. International intergovernmental status of JINR, comfortable location of site, well developed infrastructure, geological, climate and relief conditions may become powerful advantages of Dubna siting among other proposals of ILC location. All above mentioned topics are discussed in the presented report.

INTRODUCTION

Prominent achievements of the fundamental science form the material and technical basis of the modern civilization. The crucial role here belongs to the elementary particle physics. Its main discoveries and laws are the result of complicated experiments, many of which have been carried out on beams of the elementary particle accelerators.

Expressing the undivided opinion of many leading scientists of the present time, the International Committee for Future Accelerators (ICFA) and the International Union of Pure and Applied Physics (IUPAP) declared about the major decision to join efforts of world scientific centers in construction of the advanced accelerating complex – the International Linear Collider (ILC) [1].

The unprecedented task of the ILC is to provide measurements in the field of elementary particle physics at the unprecedented accuracy in the wide region of maximally high energies of colliding particles (electrons and positrons). The possibility of energy variation (in the system of the center of mass of colliding particles from 500 to 1000 GeV) is of key importance to provide the maximal accuracy of measurements.

Today the ILC project is seen as a completely international scientific project, which must be developed, financed, governed, maintained and exploited in the framework of the wide international scientific cooperation organized properly.

The following main parameters of the facility are recommended at the international meeting in Snowmass. The luminosity at the energy of electrons 500 GeV is $2 * 10^{34}$ cm^2 s^{-1}. For a 500 GeV facility based on the resonator of the TESLA type the maximal acceleration rate of all the 20000 resonators must be 35 MV/m and operating gradient – 31.5 MV/m at the length of each of two linear accelerators 10.6 km. At the subsequent increase of energy up to 1 TeV the resonators having the maximal gradient 40 MV/m and operating gradient 36 MV/m are recommended, which will lead to the increase of length for 9.3 km of each of two linear accelerators (Fig.1). In this case, the total length of two linear accelerators will be about 40 km and the length of the whole facility (total tunnel length) – about 50 km.

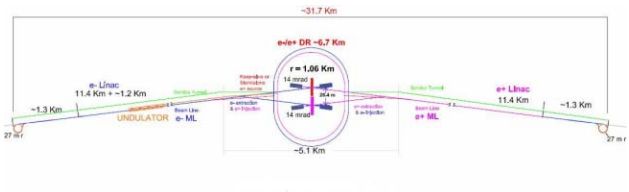

Figure 1. Schematic layout of the 500 GeV machine

PROJECT ORGANIZATION

Organization and scale of the works to construct the ILC accelerator are unprecedented. Wide interstate relations at every stage of the project realization will allow the participants to use mutually the best scientific and technological achievements in their countries. Involvement of scientists and specialists from the Russian Federation (RF), JINR and its Member States in a high-tech project of the accelerator construction of such scale will contribute to accelerated development of advanced technologies in these countries and, first of all, in Russia. By now scientific, technological and organizational development in the framework of the ILC project has started. In accordance with the schedule, the basic and alternative configurations of the facility have been formulated at the end of 2005. As a result, the Baseline Configuration Document (BCD) has been prepared. On the basis of this document in the course of 2006 the designing is carried out, the cost is estimated and the physical program of investigations at ILC is formed. The accelerator project is worked up by scientists and specialists from leading research centers and engineering companies of America, Asia, Europe, including Russian Institutes and JINR in Dubna.

COST OF THE PROJECT

Currently, cost of the full-scale ILC project is estimated about 8-9 B$, by the GDE. The estimate is performed for the ILC length of 50 km and is obtained by the extrapolation of the approximate cost of the TESLA collider, 33 km long, (Germany). The cost of experimental installations is not included here. Expenses for labor resources are not taken into account either, since they are proposed to be covered by the organizations participating in the project. The given estimate will be corrected after preparation of the BCD document, which will make the ILC parameters clearer.

By the GSPI (Moscow) specialist estimate, in case of placing the accelerator in the vicinity of Dubna, the total cost of building and assembly works of underground and

overground facilities of the main construction will be 2.3 B$, according to the summary estimated calculation in prices of 2006. This cost includes the cost of tunnel construction of the linear accelerator itself and all of its technological systems and shafts about 1 B$.

The cost of power supply objects, which are necessary to erect in order to provide the electric power from the power supply sources at a reduced rate is 170 M$.

According to the preliminary plans, the country interested in the ILC construction on its territory finances no less than 30 % of the project realization cost.

LOCATION

The contemporary international scientific community has shown a considerable interest to the initiative to construct ILC in Russia, in Dubna, where JINR has essential benefits and privileges as an International Intergovernmental Organization and has a unique experience of organization and successful realization of large-scale research projects based on wide cooperation of scientific centers and industrial enterprises of many countries. The main advantages of the ILC construction in Dubna are as follows:

1. The presence of JINR as a basic scientific and organizational structure. JINR is an international intergovernmental organization, which includes 18 Member States and 4 States, which are associated members. The agreement between the Russian government and JINR on the special status of the scientific organization has been put into effect by the Federal Law from January 2000;

2. Experienced personal of JINR in accelerators, cryogenics, power supplies and etc. Infrastructure and workshops of JINR on the first stage of ILC project realization;

3. A good position in the European region. The town Dubna provides with all the necessary means of transport to deliver all kinds of the equipment of the accelerator itself and its technological systems: highways, railways, waterways (through Volga river to Black sea, Baltic sea, Polar ocean). The international airport «Sheremetyevo» is situated at the distance of 100 km from Dubna;

4. The location in Dubna of the "Dubna" Satellite Communications Center (SCC), a unique center, according to the world standards. The Center is a branch of the Federal "Russian Satellite Communications Company", the largest satellite communications operator in Russia. The "Dubna" SCC closely collaborates with JINR. SCC is equipped by powerful fiber-optic channels providing the communication of information flows without distortions at the processing of scientific data received from accelerators of leading scientific centers throughout the world (CERN, FNAL, BNL, DESY, etc.).

5. The presence of up-to-date network and data-processing infrastructure in JINR and Dubna. In the course of 2003-2004 in JINR and the town the optical cables for data communication with the speed 1 Gbit/s were built. This formed a basis to create and start the Dubna-Moscow communication channel of 2.5 Gbit/s in 2005. In order to provide the effective participation of JINR in international and national projects in the framework of this channel a segment with carrying capacity 1 Gbit/s was formed. The adequate development of external channels and networks of JINR and the town is planned: extension of the Dubna-Moscow channel up to 40 Gbit/s, extension of the international segment in the framework of the projects GEANT2, GLORIAD, increase of the carrying capacity of the channels up to 100 Gbit/s.

6. A Special Economic Zone (industrial + scientific) in the Dubna region (Edict of Russian Government, Dec. 2005), provides unique conditions in taxes and custom regulations.

A positive reaction was received in preliminary discussions with the interested governmental persons and organizations in Russia.

The area is thinly populated, the path of the accelerator traverses 2 small settlements and a railway with light traffic between Taldom and Kimry. Possible "line" crosses only the railway to Savelovo (of low utilization) and the River Hotcha with a very small flow rate (Fig.2).

There are no any national parks, biological reservations, any religious and historical places an the planned area. There are no new projects planned to develop on the allocated territory.

It possible to avoid purchasing land and get the development area for free use without time-limit; like that has been done for the international intergovernmental organization JINR by the existing agreement between the JINR and the Government of the Russian Federation.

The climate is temperate-continental. The mean annual rainfall is 783 mm. The mean wind speed is 3.2 m/s. According to the climatic parameters, the territory of Dubna is considered to be comfortable.

The northern part of Moscow region and the neighboring regions have a developed system of objects of generation and transmission of electrical energy. There are first-rate generating stations: the Konakovo EPS (electric power station, ~30 km from Dubna) and the Udomlia APP (atomic power plant, ~100 km from Dubna). Two trunk transmission lines with the voltage 220 kV and 500 kV pass through the territory of Dubna. The investigation of possibilities of the power supply for the accelerator and its infrastructure with the total power up to 300 MW gives the following variant: Construction of the power line-220 kV, 35÷40 km long, directly from the center of generation – the Konakovo EPS to the Central Experimental Zone of the accelerator with a head step-down substations 220/110 kV. It will require the investment in larger amount but the cost of power obtained directly from the centers of generation will be lower for 40÷50 % (from 0.05$ per 1kWh down to 0.02-0.03 $ per 1kWh in prices of 2006).

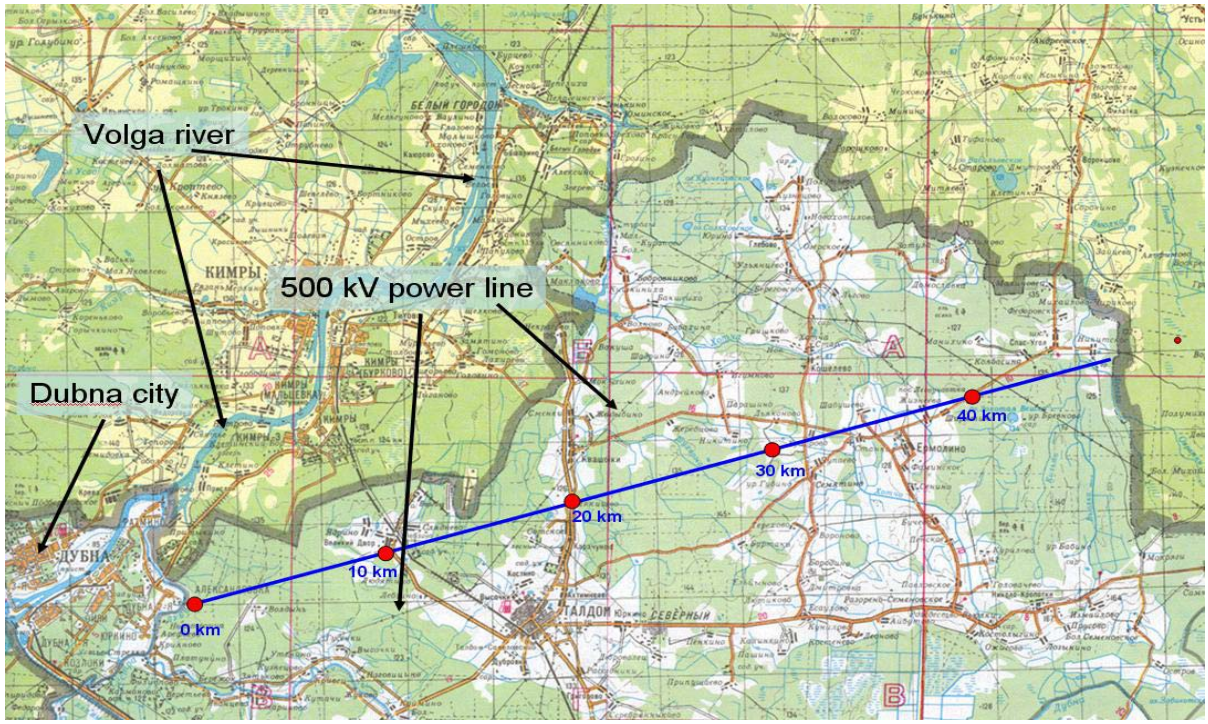

Figure 2. Planned location for ILC near Dubna, Moscow region.

GEOLOGY AND RELIEF

The area of the proposed location of the accelerator is situated within the Upper Volga lowland. The characteristic feature of this territory is the uniformity, monolithic character of the surface. The existing rises of the relief in the form of single hills and ridges have smoothed shapes, soft outlines and small excesses. The territory of the area is waterlogged. The absolute marks of the surface range from 125 to 135 m with regard to the level of the Baltic Sea. The difference of surface marks is in the range of 10 m only on the base of 50 km.

This area is situated within the Russian plate – a part of the Eastern European ancient platform – a stable, steady structural element of the earth's crust.

The Russian plate, like all the other plates, has a well-defined double-tier structure. The lower tier or structural floor is formed by the ancient – lower Proterozoic and Archaean strata of metamorphic and abyssal rocks, which are more than 1.7 billion of years old. All these strata are welded into a single tough body – the foundation of the platform. The area of the ILC accelerator is located in the southern part of a very gently sloping saucer-shaped structure – the Moscovian syneclise. Alluvial deposits i.e. fine water-saturated sands, 1-5 m of thickness. Below one can find semisolid drift clay of the Moscovian glaciation with exception of detritus and igneous rocks. The thickness of moraine deposits is 30-40 m.

The ILC linear accelerator is proposed to be placed in the drift clay at the depth of 20 m with the idea that below the tunnel there should be impermeable soil preventing from the underlying groundwater inrush. It is possible to construct tunnels using tunnel shields with a simultaneous wall timbering by tubing or false work concreting. Standard tunnel shields in the drift clay provide for daily speed of the drilling progress specified by the project of the accelerator - it is needed approximately 2.5 years.

CONCLUSION

Initiative in the decision of question of the ILC siting in Dubna could take jointly with JINR the leading European accelerator centers (DESY, CERN, INFN, and some others), and also Russian Academy of Science and Budker INP firstly, Kurchatov RSC, Lebedev Ph. Institute, ITEP, INR RAS, MSU as well as some other organizations and institutions. Such an offer obviously would get an approvement from all sides of international community, if at the first stage of the project the main part of funding will take European countries and Russia. Of course it doesn't limit but assumes wide collaboration with other institutes and their countries.

Realization of such a widescaled project namely in Dubna will let Russia to become in a perspective future by a leader and center of attraction for scientists from Russia and neighbor countries. Another obvious factor is an attraction of significant investments and financial resources at all stages of the project including further exploitation of the new accelerator center during long years. Creation of ILC accelerator complex in a mentioned format of international collaboration will raise prestige of the fundamental science in a total and the role of Russia as one of the world leader.

REFERENCES

[1] International Linear Collider GDE official page, http://www.linearcollider.org

ENERGY EQUALIZATION BY USING S-BAND AND X-BAND ACCELERATOR MODULES

Kazue Yokoyama#, Takuya Kamitani
Accelerator Laboratory, High Energy Accelerator Research Organization (KEK),
1-1 Oho, Tsukuba, Ibaraki 305-0801, Japan

Abstract

To reduce the beam loss and to restrict the expanse of the bunch length of the positron beam from the KEKB injector, an energy spread of ± 0.25% or less is required for the beam-transport (BT) line of the KEKB ring [1]. Generally, a positron beam has a large energy spread because the original bunch length is large and all positrons do not see the same accelerating field. Thus, an energy compression system (ECS) that consists of a magnetic chicane and two 2-m S-band accelerating structures was implemented at the end of the linac and has been used, but it has a demerit that the beam bunch is lengthened [2]. In this paper, we propose a new method to suppress the energy spread without enlarging the bunch length. This method utilizes superimposed acceleration of the S-band modules and X-band modules.

ENERGY COMPRESSION BY USING DIFFERENT FREQUENCY

A large energy spread of a positron beam is due to a position dependence of the energy gain. Assuming that the energy gain of beam particles riding on the rf wave crest is to be E_{e+} at the end of the linac, the total energy gain of the linac can be approximately expressed as

$$E_{total\ gain} = E_{e^+}\cos(2\pi\frac{z}{\lambda_s}) \quad (1),$$

where z is the distance from the centre of the bunch and λ_s is the wavelength of the S-band frequency. Equation (1) signifies that a large energy spread of the positron beam is due to a position dependence of the energy gain, considering that its original bunch length is large. Therefore, the positrons away from the centre bunch require a higher electric field to compensate for the energy variation. A correction function can be obtained by the Taylor expansion up to the 2nd order; it is proportional to the square of z, as follows:

$$E_{equalizer} = E_{e^+} - E_{e^+}\cos(2\pi\frac{z}{\lambda_s}) \approx \frac{1}{2}E_{e^+}(2\pi\frac{z}{\lambda_s})^2 \quad (2)$$

The correction function, which is proportional to the square of z, can be realized by superimposing a different frequency of the same energy gain as the S-band. It can be expressed as

$$\begin{aligned} E_{equalizer} &= \Delta E\cos(2\pi\frac{z}{\lambda_s}) - \Delta E\cos(2\pi\frac{z}{\lambda_a}) \\ &= \Delta E\cos(2\pi\frac{z}{\lambda_s}) - \Delta E\cos(2\pi\frac{z}{\lambda_s}\times k) \\ &\approx \Delta E\times\frac{1}{2}(2\pi\frac{z}{\lambda_s})^2(k^2-1) \end{aligned} \quad (3),$$

where λ_a is the wavelength of the rf frequency, which we try to use, also $\lambda_s = k\ \lambda_a$. To compensate for energy variation up to the 2nd order, an acceleration of

$$\Delta E = \frac{E_{e^+}}{k^2-1} \quad (4)$$

is required from Eq. (2) and Eq. (3).

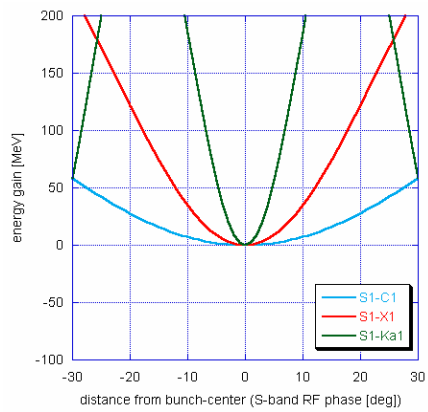

Figure 1: Comparison of the correction functions for three different frequencies with same energy, ΔE.
The legends of S1-C1, S1-X1 and S1-Ka stand for C-band (k = 2), X-band (k = 4) and Ka-band (k = 10), which are innovated for compensation, respectively.

Figure 1 shows that energy gain depending on the rf frequency which supplies the accelerating electric field when the correction function is obtained with the same energy, ΔE = 160 MeV corresponds to the energy of an accelerator module of the KEKB injector. This shows that a higher frequency is more effective for compensation than a lower frequency when comparing it with the same energy of the energy correction. For example, an energy of about 1166 MeV from the C-band (k = 2) module is required to compensate for a 3.5 GeV positron at the KEKB injector, while it is achieved by an energy of only about 233 MeV from the X-band (k = 4) module. Thus, in this method, innovating X-band modules is more practical than the C-band modules for savings in both cost and space. In addition, the aperture of a X-band accelerating structure is one 4th the size of the S-band accelerating

Kazue.Yokoyama@kek.jp

structure, but the beam loss can be reduced by providing some focus coil. On the other hand, a correction of the higher order should be dealt with in the case of a higher frequency, as can be expected from Fig. 1.

SIMULATION AND RESULT

Performance of this energy-spread compensation scheme using S-band and X-band modules was evaluated by particle simulation in longitudinal phase space and was compared with that of the present ECS scheme.

Simulation

The beam energy distribution is calculated and simulations are based on Eq. (5) below, assuming that the particles are transferred from the focus system with a Gaussian distribution.

$$E_{total\ gain} = \sum_{i=1}^{n} E_i \cos(2\pi \frac{z_j}{\lambda_s} + \varphi_i) \qquad (5),$$

where z_j is the particle position which respect to the bunch center, E_i is the energy gain of the S-band modules and φ_i is the accelerating rf phase.

The initial particles have 11 MeV of centre energy (1 σ ~ 2 MeV), 20 ps (FWHM) of bunch length and the number of particles is 10^4 for simulations. The particles are accelerated to the end of the linac with 25 S-band modules almost on their crest phases except for four center energy adjusting modules. Typical energy gain by an S-band module is 160 MeV.

Energy Compression System

In the KEKB injector, an energy compression system was implemented at the end of the linac to reduce the energy spread of the positrons from the linac by a factor of 1/2, to meet the energy acceptance of the BT line and the low-energy ring. The ECS is a phase space rotator which consists of a magnetic chicane by six bending magnets and two 2-m S-band accelerating structures. In the chicane, higher energy particles are forced to negotiate a longer path length than lower energy particles; particles of different energies traverse different path lengths. Thus, the path-length difference rearranges the relative longitudinal position of the particles in the bunch in correlation to their energies. After the chicane, the accelerating structures compensate the energy difference by dependence of energy gain on the positions of the particles riding on the rf wave. Figure 2 shows the particle distribution in the bunch (a) upstream of the ECS (at the end of the linac) and (b) downstream of the ECS. As Fig. 2(b) indicates, the bunch length is expanded through the ECS. In reality, the energy spread is also restricted by the diameter of the beam duct in the bending magnets which is limited by an energy acceptance of the ECS itself. Hence, beam loss by this acceptance is taken into account. Figure 3 shows the energy distribution in the bunch (a) upstream of the ECS and (b) downstream of the ECS. From this simulation, the ratio of a particle in the energy acceptance (± 0.25%) at the end of the linac to the initial particle is 44.2% and is improved to 74.1%, owing to the ECS. Since the acceptance of the bunch length is ± 6 mm (~ ± 2 σ) the ratio of an adequate particle ends up to be 65.2%.

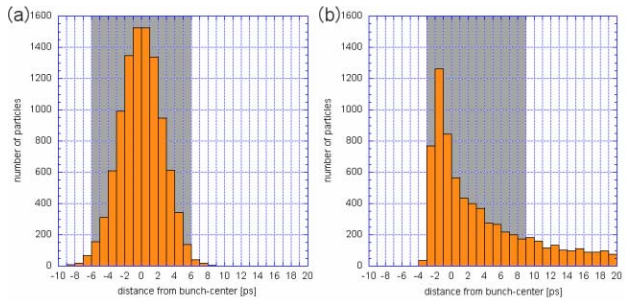

Figure 2: Longitudinal distribution of particles in the bunch. (a) upstream (at the end of linac) and (b) downstream of the ECS. The shaded region indicates the longitudinal acceptance of ± 6mm.

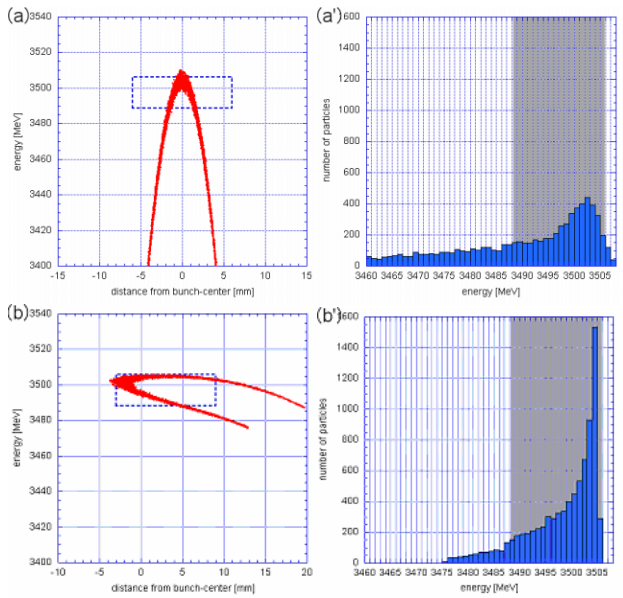

Figure 3: Phase space and energy distributions.
(a), (a′) upstream; (b) , (b′) downstream of the ECS. The dotted box region and the shaded region indicate the energy and the longitudinal acceptance of ± 0.25 % and ± 6mm, respectively.

Energy Equalization by Using an Accelerating Field of the S-band and the X-band

In this new scheme, cosine-like beam energy variation is equalized by using accelerating modules of different frequencies in the previous section. The advantage of this method is that the beam energy can be made uniform with the bunch length unchanged. We estimate the effect of a energy compression by simulations. The present KEKB injector accelerates positron beams up to 3.5 GeV with the S-band modules. For the energy equalization, the required energy gain of a X-band module is 233 MeV, from Eq. (4). The same energy gain is also required for additional S-band modules for energy equalization. A correction function is obtained by superimposing a

deceleration by X-band modules and an acceleration by S-band modules.

Figure 4 shows the energy distribution obtained by using an energy compensation at the end of the linac. At the end of the linac, particles remaining in an acceptance of ± 0.25 are 44.2%, as shown in Fig. 3(a), but it improves to 92.6% with compensation, as shown in Fig. 4. This result shows that the compensation system (92.6%) can more capture particles than the ECS (65.2%).

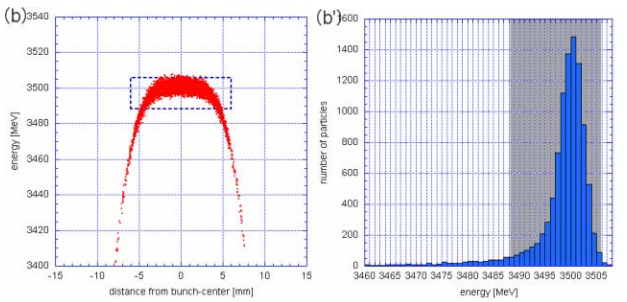

Figure 4: Phase space and energy distributions with the energy equalization by the S-band and the X-band accelerator modules. Jitter effects are not included.

Effect of RF Jitter

The effect of jitter, which originates in the accelerating rf source, must be considered in this method. The energy fluctuation is caused by the phase, power and timing jitter of devices, such as a thyratron, a klystron and an electron gun. These jitter effects can be approximately estimated from Eq. (5) by introducing a phase fluctuation, φ_i, from each sub-booster and klystron, a power fluctuation, E_i, from each klystron, and a timing jitter from the bunching section. In this simulation, suppose that the phase fluctuation is ± 0.1% and ± 0.63 ° for the sub-boosters and klystrons, respectively, the power fluctuation of the klystrons is ± 0.375% [5], and the timing jitter from the injection section is ± 1 ps. Each jitter is set in the simulation as a random number. Since jitters of the X-band module is not well known, they are assumed to be same as the S-band module at first. The simulation result is the average value of 25 sets of simulations. From the simulation, particle counts of about 3% are decreased in jitter compared with no jitter as for the case of the ECS scheme (62.0%), as shown in Fig. 5(a). In energy compensation with X-band modules, the particle counts of about 5% is decreased with jitter (87.4%) compared with no jitter. This result shows that energy compensation induces 1.7-times the jitter, as that of the ECS scheme. Another cases that jitters of the X-band module is assumed to be four-times as the S-band module, the particles remaining in the acceptance are reduced to 76.5%, as shown in Fig. 5(b). It is found that timing jitter in the X-band is the most serious issue for this compensation scheme.

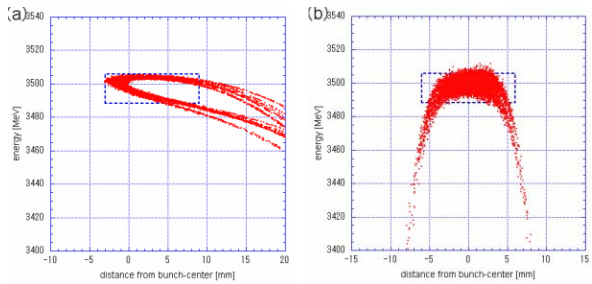

Figure 5: Examples of the energy distribution in a bunch while considering rf jitter. (a) used by only S-band modules and downstream the ECS (62.0%); (b) used by X-band modules that timing jitter is four-times as the S-band modules for compensation (76.5%).

CONCLUSION

It is shown that the superimposed acceleration of the S-band and the X-band modules can improve the energy spread of a positron beam more effective than the present ECS. To demonstrate a performance of this scheme with the existing equipments, we are planning an experiment by using the superimposed acceleration of the S-band and the existing C-band modules at the present KEKB injector instead of the X-band modules.

REFERENCES

[1] KEKB B-Factory Design Report, KEK Report 95-7, (1995) pp12-27 - 12-31.

[2] Y. Ogawa, et al., "Commissioning of the KEKB Linac", Proceedings of the linac98, Chicago, USA, August 23 - 28, (1998) pp711 - 715.

[3] T. Higo et al., "High Gradient Study at KEK on X-band Accelerator Structure for Linear Collider", Proceedings of PAC 2005, Knoxville, Tennessee, USA, May 16-20, (2005) pp1162-1164.

[4] L. Rinolfi and T. Kamitani, "The CLIC Positron Production Scheme" Proceedings of LINAC2002, Gyeongju, Korea, August 19 – 23, (2002) pp94- 96.

[5] S. Michizono et al., "Output RF Phases from the S-band Klystrons used in the KEKB Linac", Proceedings of EPAC2000, Center Viennap, Austria, June 26-30, (2000) pp2084-2086.

NEW TIMING SYSTEM FOR THE L-BAND LINEAR ACCELERATOR AT OSAKA UNIVERSITY

Shigeru Kashiwagi*, Goro Isoyama, Ryukou Kato, Shoji Suemine
ISIR, Osaka University, 8-1 Mihogaoka, Ibaraki, Osaka 567-0047, Japan
Takao Asaka, Yoshitaka Kawashima
SPring-8, 1-1-1, Kouto, Mikazuki, Sayo-gun, Hyogo 679-5198, Japan

Abstract

A highly precise and flexible timing system has been developed for the L-band linac at ISIR, Osaka University. It provides four RF signals and several timing signals for operation of the linac and for experiments with the linac. In order to realize long-term stability of the timing system and hence operation of the linac, a rubidium atomic clock producing a 10 MHz RF signal with the fractional stability of 10^{-15} is used as a time base for the synthesizer used as a master oscillator for generating the acceleration frequency of 1300 MHz. The 1300 MHz signal from the master oscillator is directly counted to produce the four RF signals and the clock signal of the timing system at 27 MHz. The master timing signals for linac operation is taken from the AC line frequency and it is precisely synchronized with the 27MHz clock signal. To make an arbitrary delayed timing signal, a standard digital delay generator is used to make a gate signal for a GaAs RF switch, with which one of the 27MHz clock pulses is sliced out to generate the delay timing signal. Any timing signal can be made in an interval of 37 ns and the timing jitter of the delayed signal is achieved to be as small as 2 ps (rms).

INTRODUCTION

The L-band electron linear accelerator is used for studies on nanotechnology and beam science as well as for basic studies in the related fields at the Radiation Laboratory of the Institute of Scientific and Industrial Research (ISIR), Osaka University. The L-band linac can produce electron beams of different time structures, like a single-bunch, multi-bunch with 9.1 ns spacing and so on, corresponding to various beam experiments. The high intensity single-bunch beam is the most characteristic beam of this L-band linac and it is very useful for radiation chemistry studies by means of pulse radiolysis in the time range down to sub-picoseconds [1,2] and basic study of Self-Amplified Spontaneous Emission (SASE) in the far-infrared region [3,4].

The timing system of the linac plays a very important role in generating a high quality and stable electron beam. Timing jitter between a trigger signal for the electron gun and a reference RF signal of accelerator system directly affects the stability of the electron beam in terms of intensity and energy. Experiments using the L-band linac require synchronized trigger pulse for their data acquisition, and RF signals for laser oscillator. In order to enhance the stability of the linac, we have developed a new highly precise and flexible timing system for the L-band linac at ISIR, Osaka University.

*shigeruk@sanken.osaka-u.ac.jp

CONFIGURATION OF L-BAND LINAC AND LASER SYSTEM

The fundamental accelerating frequency of the L-band linac at ISIR is 1300 MHz. The linac has been optimized for generating the high-intensity single-bunch beam. The L-band linac is consisted of a high-current triode electron gun, three stage sub-harmonic bunchers (two operate at 108 MHz, which is a 12^{th} subharmonic of the fundamental frequency and one at 216 MHz, a 6^{th} of 1.3GHz), two fundamental traversing wave bunchers and 3m-long main accelerating structure. The SHB system is used mainly for single-bunch operation. The timing system is required to generate three RF signals for these RF components.

Two grid pulser circuits of the electron gun are used for generating single-bunch and multi-bunch beam. The trigger pulse for the gun grid has to be synchronized with RF signals precisely. In single-bunch operation, one trigger pulse for the gun grid with 120V height and 50ns duration is distributed from the timing system. In multi-bunch operation, two triggers for a start and a stop of pulse are necessary to decide the pulse length of multi-bunch beam in the grid pulser circuit. The trigger pulse for single-bunch and the start trigger of multi-bunch generation are common, and the input trigger pulse for the trigger circuit of the gun is switched by operation mode of the linac.

The femtosecond laser system for picosecond pulse radiolysis experiment consists of a CW green laser, a femtosecond Ti:sapphire laser operated at 81 MHz, Nd: YLF laser with a regenerative amplifier operated at 960 Hz, an optical parametric amplifier (OPA) and pulse generator. Thus, the laser system requires 81 MHz RF signal and 960 Hz and 60Hz trigger pulses to the timing system of the linac.

NEW SYNCHRONOUS TIMING SYSTEM

To achieve the stable and precise synchronization between RF signals and trigger pulses for the accelerator system, the timing system has been replaced with a new one. The new timing system of the linac comprises of a master RF part and a synchronous timing part. It provides four synchronous RF signals and a 27 MHz clock signal as well as various timing signals for operation of the linac and for the experiments. Fig. 1 shows a block diagram of new timing system for the L-band linac.

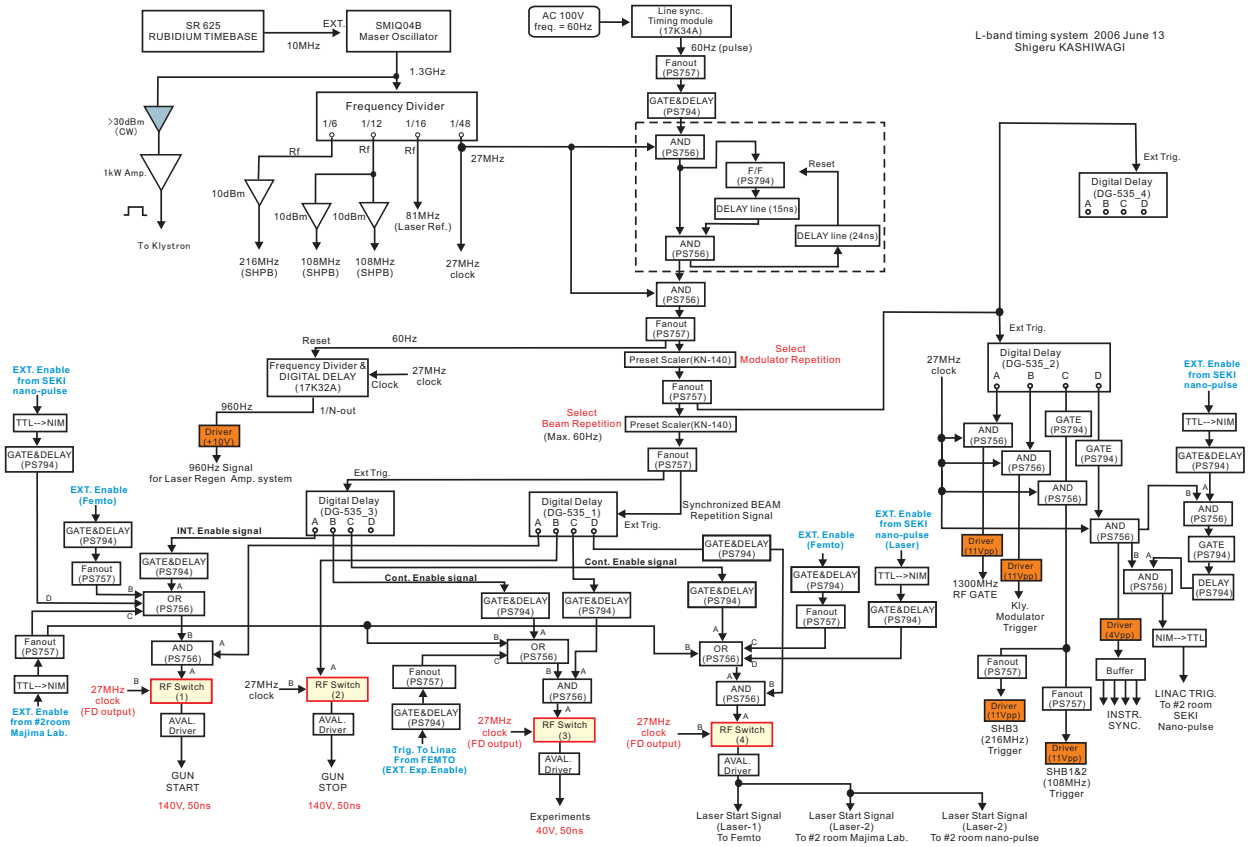

Figure 1: Block diagram of the new timing system for the L-band linac at ISIR, Osaka University.

Master RF part

In new timing system, some necessarily harmonic frequencies for the linac operation are produced by dividing a master frequency of 1300 MHz, because the phase fluctuation of the dividing frequency is much smaller than the multiplied one [5]. The master RF of 1300 MHz is generated by a frequency synthesizer (Rohde & Schwarz: SMIQ04B) and a rubidium atomic clock producing 10 MHz RF signal is used as an external time base for the frequency synthesizer to realize long term stability. The 1300 MHz RF signal is directly counted and frequency-divided using ripple counter circuit to produce RF signals of a 6th and 12th sub-harmonics at 108 MHz and 216 MHz, and a 16th sub-harmonic at 81 MHz together with the NIM-level clock signal of a 48th sub-harmonic signal at 27 MHz. Band-pass filters are introduced at the frequency divider output to suppress the higher and lower harmonic frequencies. These generated RF signals are distributed to each component or RF amplifier. The synchronized 27MHz clock pulses are used as timing step of trigger pulses.

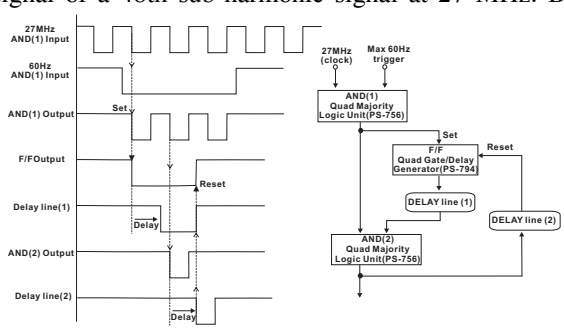

Figure 2: Timing chart and block diagram of synchronizing system using a logic circuit (Phillips-756) and flip-flop circuit (Phillips-794).

Synchronous timing part

The synchronous timing part was fabricated using commercially available components and devices, such as standard NIM logic modules and digital delay generators, so that it is flexible for future expansion and development. The linac must be operated synchronously with the AC line frequency, which is 60 Hz in the western half of Japan, and the maximum repetition rate of the linac operation is also 60 Hz. In the synchronous timing part, the start signal is produced from the AC line voltage synchronized with the 27 MHz clock signal. Fig. 2 shows the timing chart and block diagram of synchronizing system using standard NIM modules and delay lines. The repetition rates of RF pulses and the beam are determined with two preset counter modules respectively. The 960 Hz clock is generated using synchronous universal counter, which counts the 27 MHz clock and divides the clock frequency [6].

To make an arbitrary delayed timing signal, the start signal is sent to standard digital delay generator (Stanford Research Systems: DG535) as the external trigger and it produces preset delayed signals. One of their delayed signals is used for producing a gate signal to slice out one of the 27 MHz clock pulses. Since the gun (start and stop),

the experimental and the laser triggers, have to be synchronized with the reference RF signal precisely, we therefore use a fast GaAs RF switch (Mini-Circuits: ZASWA-2-50-DR) to slice out the timing pulses from the 27MHz clock. The fast RF switch is a passive device, thus the time jitter of the sliced out timing pulse is determined by stability of the clock. This is expected to be shorter than a few ps. To make other trigger pulses, such as the klystron modulator trigger, the delayed signals are made to be coincident with the 27 MHz clock using a logic module. The time jitter of the logic module is expected to be about 5 ps. Thus, any timing signal can be generated at an integer multiple of 37 ns, which is a period of 27 MHz clock.

Avalanche pulser

The avalanche pulser circuit is used to make high voltage pulse with less than a nanosecond rise time at the output part of the timing system. The timing jitter of the arbitrary delayed timing signal for triggering each component is mainly determined by a time jitter of the avalanche pulser. The required avalanche pulser outputs are 140 V and 50 V for the Gun-Start/Stop trigger and the Experimental/Laser triggers, respectively. The synchronized timing pulse is applied to the avalanche pulser circuit as a trigger. The time jitter of avalanche pulser is strongly dependent on the leading-edge of the drive pulse for the avalanche transistor. To get good leading-edge of the drive pulse, a transistor is used as a pre-amplifier with gain 5 and an emitter follower circuit is used for the last pre-amplifying stage to provide low output impedance. In this circuit, two transistors are used to provide the drive pulse with good leading-edge for avalanche transistor. The timing jitter of this circuit was smaller than that of the circuit, which uses only one transistor in emitter ground circuit.

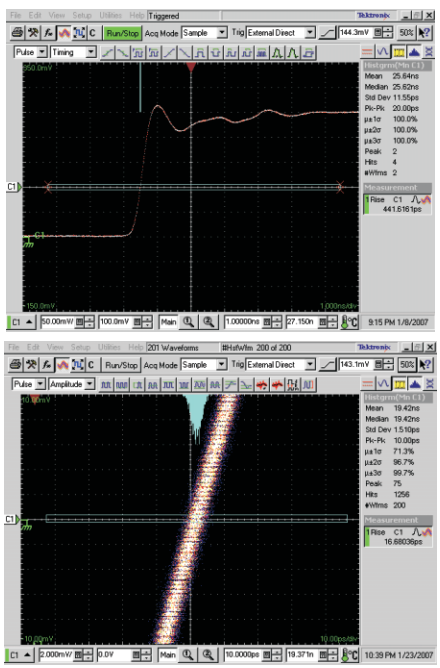

Figure 3: Measured leading-edge and timing jitter of 50 V trigger pulse. The rise time of one was 0.44 ns and the timing jitter was 1.51 ps (rms) and 10.0 ps (pk-pk) in 1 hour measurement.

TIMING JITTER MEASUREMENT AND RESULT

The timing jitter measurement have been performed for the produced subharmonic RF signals and the synchronous trigger pulses relative to the master reference RF of 1300 MHz using the Tektronix Communication Analyzer (Tektronix CSA8000B with 80E03 sampling module). In the measurement, the subharmonic RF signals or the timing pulses are used as a trigger of the oscilloscope. Absolute timing jitters of subharmonic frequencies relative to the master reference RF are approximately 1.3-1.5 ps (rms) and the jitter of 27 MHz clock was 0.96 ps (rms). To make the jitter smaller, we will use narrow band-pass crystal filter for subharmonic RF signals to suppress the phase noise.

A rise-time (10-90%) of amplified trigger pulse was also measured using the sampling module with 20 GHz frequency bandwidth. The measured leading-edge of the 50V trigger pulse with 46 dB attenuator is shown in Fig. 3 (upper) and the rise-time of the 140 and 50 V trigger pulses were 1.86 ns and 0.44 ns, respectively. Absolute timing jitter (rms) of trigger pulses relative to the master RF were 2.7 ps (pk-pk = 16.4 ps) and 1.5 ps (pk-pk = 10.0 ps) in 1 hour measurement, respectively.

SUMMARY

The new highly precise and flexible timing system has been developed for the L-band linac and now it is used in real beam operation. Performance of new timing system improved than a former one. In the timing jitter measurement, the jitter of the 50 V trigger pulse relative to the master reference RF was 1.5 ps, before installation of new timing system it was about 5 ps. About other signals, the performance improved than before.

REFERENCES

[1] A. Saeki, T. Kozawa, S. Kashiwagi, K. Okamoto, G. Isoyama, Y. Yoshida and S. Tagawa, Nucl. Instr. and Meth. A 546 (2005) 627.
[2] T. Kozawa, Y. Mizutani, K. Yokoyama, S. Okuda, S. Tagawa, Nucl. Instr. and Meth. A 429 (1999) 471.
[3] R. Kato, M. Fujimoto, T. Igo, S. Isaka, T. Onishi, S. Furukawa, S. Okuda, S. Suemine, G. Isoyama, Nucl. Instr. and Meth. A 507 (2003) 409.
[4] R. Kato, R. A. V. Kumar, T. Okita, S. Kondo, T. Igo, T. Konishi, S. Okuda, S. Suemine, G. Isoyama, Nucl. Instr. and Meth. A 445 (2000) 164.
[5] M.Sawamura, E. J. Minehara, R. Nagai, M.Sugimoto, M. Takao, R. Kato, N. Kikuzawa, M. Ohkubo, Nucl. Instr. and Meth. A 358 (1995) ABS 73-74.
[6] H. Suzuki, H. Ego, M. Hara, T. Hori, Y. Kawashima, Y. Ohashi, T. Ohshima, N. Tani, H. Yonehara, Nucl. Instr. and Meth. A 431 (1999) 249.

PAPER NOT YET RECEIVED

PROGRESS OF RFQ ACCELERATORS AT PEKING UNIVERSITY*

C.E.Chen Z.Y.Guo J.X.Fang Y.R.Lu X.Q.Yan K.Zhu S.X.Peng Z.Wang C.Zhang
S.L.Gao J.F.Guo W.G.Li Z.Z.Song J.X.Yu M.L.Yu
IHIP, School of Physics, Peking University, Beijing 100871, P.R.China

Abstract

The progress of two RFQ accelerators at Peking University is presented: one is Separated Function RFQ (SFRFQ), which separates the focusing and acceleration of traditional RFQ to get higher acceleration efficiency. The first prototype of the SFRFQ is designed to accelerate O^+ from 1MeV to 1.5MeV and used as a postaccelerator for ISR RFQ-1000 (Integral Split Ring) [1]. The other is high current deuteron 201.25MHz RFQ, it will accelerate 50mA D+ beam to 2MeV with a duty cycle of 10%. The design study of SFRFQ and high current Deuteron RFQ accelerator are outlined.

INTRODUCTION

The RFQ accelerators are extensively used to accelerate low energetic heavy ions and proton nowadays. Accelerator Driven Subcritical system (ADS), Spallation Neutron Source and other applications drive the RFQ developing towards high average beam power [2-4]. The RFQ team at Peking University has been engaged in developing RFQ technology since 1980s. A 300keV heavy ion Integrated Split-ring Resonator RFQ (ISR RFQ-300) with the mini-vane electrodes was constructed and put into operation in 1994[5]. Based on these experiences, A 1MeV heavy ion ISR RFQ was completed and run successfully in 2000[6]. The experiment [7] and simulation [8] for simultaneous acceleration of both positive and negative ions were realized.

To increase accelerating efficiency, a new accelerator structure, Separated Function RFQ (SFRFQ), has been proposed and investigated. It separates the transverse field for the focusing and axial component for ion acceleration by inserting a series of periodical gaps [9-12]. In order to explore the feasibilities of SFRFQ, a prototype is going to be manufactured. A match section between 1MeV RFQ and SFRFQ is designed for the transverse emittance matching. Meanwhile to upgrade the beam current to mA for ISR RFQ-1000, a new designed ECR ion source for this accelerator has been developed in the last two years [13].

A high power Deuteron RFQ accelerator has been launched for neutron radiography. The beam dynamics has been studied in detail and improved by equipartition method[14-16]. The RFQ structure, mechanical and cooling system design have been investigated.

*Supported by NSFC (Contract No.10455001)
Email: chenje@pku.edu.cn

SFRFQ

SFRFQ is an accelerating structure which is suitable for accelerating middle energy beam [10]. A SFRFQ prototype is being constructed to explore its feasibilities, which compose an accelerating system with ISR-1000. The whole system include ECR ion source, LEBT, ISR1000, match section and SFRFQ. Figure 1 gives the sketch map. Figure 2 shows SFRFQ's structure schematically, where diaphragms were mounted onto the electrodes.

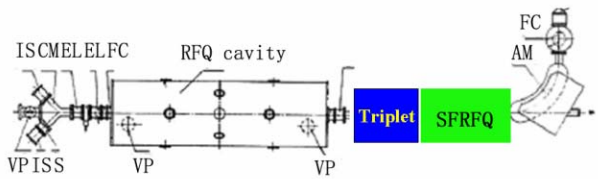

Fig. 1: Accelerating system composed by ISR-1000 and SFRFQ

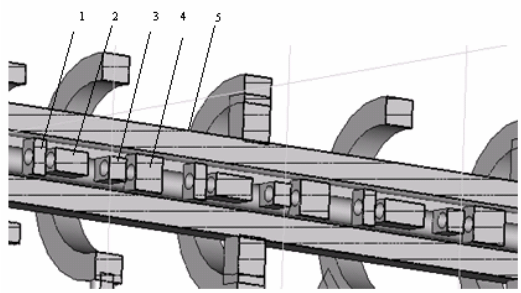

Fig. 2: Schematic view of the SFRFQ 1,2,3&4 diaphragm, 5 electrode

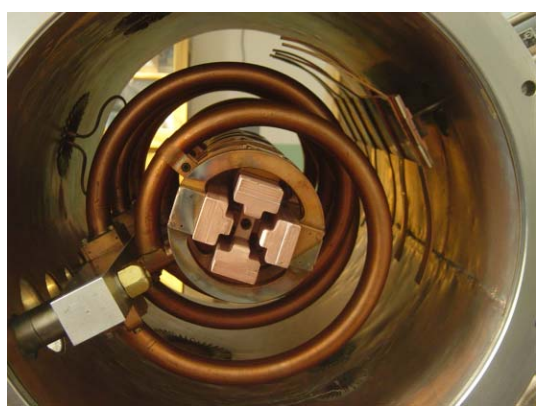

Fig. 3: Power test model of SFRFQ

The beam dynamics of the SFRFQ is being investigated by self-developed code. The longitudinal electric field and its RF property were simulated by Microwave Studio(MWS). Based on the simulations, an optimized design of SFRFQ structure was completed to improve RF efficiency, and to get better mechanical performance, etc[12]. Figure 3 shows the SFRFQ cavity that is especially designed to investigate the longitudinal field distributions and to do RF conditioning and its intervane voltage measurements.

The longitudinal field distribution was measured by perturbation method and Angilent Network Analyzer. The measured results are consistent with the simulated field distribution (shown in Figure 4). It is remarkable here that the field between two neighbouring higher peaks is actually inverse field. It will decrease the effective energy gain in SFRFQ, but RF quadruple field provides additional transverse focusing. The high power RF test shows that gap or intervane voltage can reach to 79kV when RF amplifier delivers 35kW peak power (shown in Figure 5).

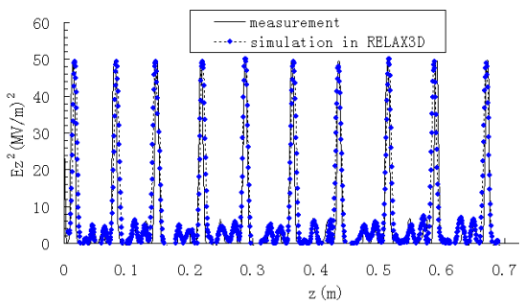

Fig. 4: The measured and simulated electrical field distribution

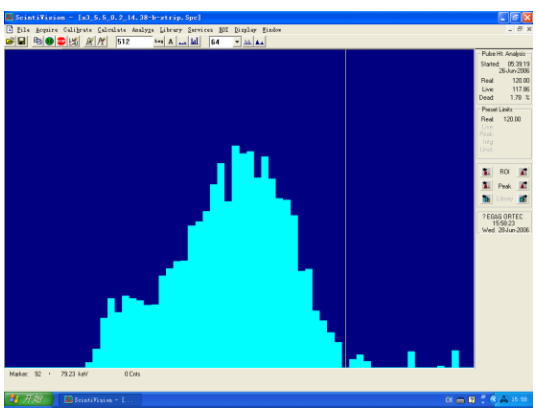

Fig. 5: Roentgen spectrum of the model cavity at RF power 35kW, which showed a gap voltage of 79kV

The 1MeV RFQ, working as injector of SFRFQ, is upgraded. An ECR ion source with extracting voltage of 22kV and a new LEBT have been designed and tested. The peak current of extracted O^+ beam reached 5 mA with duty factor 1/6 and pulse duration 1ms. Figure 6 shows the new ECR ion source for 1MeV RFQ. To realize the beam matching from 1MeV ISR RFQ-1000 to SFRFQ cavity, a match section with triplet magnetic quadruples has been designed and is under construction.

Fig. 6: New ECR ion source

DEUTERON RFQ

Meanwhile a high current and high duty factor deuteron RFQ has been designed for neutron generator. It will accelerate D^+ from 50keV to 2MeV with 10% duty factor and operating frequency 201.25MHz. The RF amplifier using Thomson tetrode TH781 could deliver RF peak power 400kW[17]. In order to avoid cavity radioactivity by D-D reaction, the beam transmission efficiency is designed over 90% while the energy of most lost deuterons is below 100keV[14]. And the beam dynamics design has been further improved by equipartitioned design method [15]. Table 1 lists the principal parameters of deuteron RFQ accelerator.

Table 1: The Deuteron RFQ parameters

Input energy/keV	50
Output energy/MeV	2.0
Beam current/mA	50.
Frequency/MHz	201.25
Electrodes voltage/kV	74
RFQ length/mm	2700.
Accelerating cells	181
Max modulation	1.8
Aperture radius/mm	3.78
Transmission	93.6%
Kilpatric	<2.0

In RF structure design, the influence of electrodes' shape on RF loss has been investigated by simulation. The effects of distance, height and width of stem have also been investigated. RF loss of the whole RFQ structure can be reduced to about 270kW by optimizing above parameters[18]. The dipole component of quadruple field has been reduced to 4% by adjusting the slope of stem centre part [19]. The tuning blocks were inserted to RFQ structure and fixed between two neighbouring stems. It behaves as a volume tuner, which will tune the cavity resonant frequency and the longitudinal field distribution more flat [20]. Figure 7 gives the simulation results.

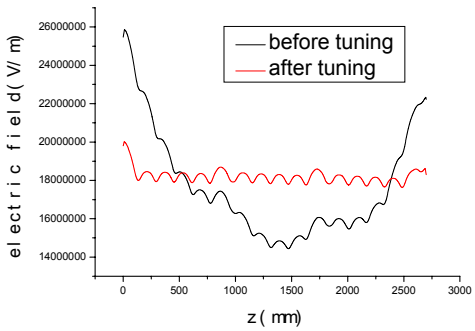

Fig. 7: Simulation results of tuning field

The 80kW pressured water cooling system of the RFQ has been designed and run successfully. The thermal analysis of inner cavity structure has been carried out based on RF power consumptions of different parts. Figure 8 shows the cooling channel sketch and temperature distribution of a stem. From the analysis, the temperature raise and deflection of RFQ structure is acceptable[21]. 400kW RF amplifier with 781 tetrode has been tested successfully with 1% up to 8% duty factor and repetition frequency of 100Hz[22].

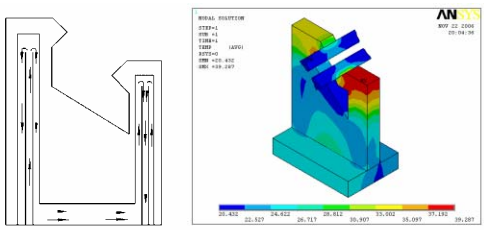

Fig. 8: Cooling channel sketch and temperature distribution

CONCLUSION

The structure of SFRFQ was optimized. The longitudinal field distribution was measured and RF power experiments were carried out with a SFRFQ model. Experiments show the measured results agree with the simulated results. Also the structure can be operated on designed electrode voltage without sparking. The injector of SFRFQ is being upgraded, which includes a new designed ECR ion source, LEBT, 1MeV RFQ and a matching section.

The preliminary design of deuteron RFQ is figured out. The beam dynamics simulation, RF cavity design, RF tuning and cooling system design have been completed. The design objectives, such as relative high beam transmission efficiency, short RFQ length and low power loss and so on, have been realized.

REFERENCES

[1] Y.R. Lu, et al, NIMA, 2003, A515 (3): 394-401.
[2] I.M.Kapchinskij, V.A.Teplyakov, Prib.Tekh.Eksp., 1970,(4),P19
[3] A.Ratti, et al., Proceedings of EPAC 2000, P495
[4] H.V.Smith, et al., Proceedings of EPAC 2000, P969
[5] J.X.Fang, C.E.Chen et al., IEEE NS-32(1985)P2981.
[6] C.E.Chen, J.X.Fang et al., Proceedings of EPAC 2000, P1850
[7] X.T.Ren, Y.R.Lu, J.X.Yu, et al, , High energy physics and nuclear physics, Vol.24, No.4,2000, P.347-351
[8] X.Q.Yan, et al., Phy. Rev. ST Accel. Beams 9, (2006)020201
[9] C.E.Chen, et al., Progress on Natural Science, Vol. 12, No.1,23, 2002
[10] X.Q.Yan, et al., Bulletin of China Academic Journal, Vol.7, No.11, 1441,2001
[11] C.E.Chen, et al., Proceedings of APAC 2004, P595
[12] Z.Wang, et al., Acta Physica Sinica, Vol.55, No.11, 2006, P5575
[13] Z.Z.Song, et al., Rev. Sci. Instrum. 77, 03A305 (2006)
[14] C.Zhang, et al. Phy Rev. ST Accel. Beams 7, (2004) 100101
[15] X.Q.Yan, et al., Proceedings of EPAC 2006
[16] Z.Y.Guo, et al., Proceedings of Linac 2006
[17] Y.R.Lu, et al., Proceedings of Linac 2006
[18] K.Zhu, et al., HEP&NP, 2005, 29(5), P512
[19] H.Podlech, et al., Proceedings of EPAC, 2002, Paris, France. P942
[20] A.Schempp, et al., Proceedings of Linac, 2004.
[21] K.Zhu, et al., HEP&NP, 2005,29(8),P797
[22] Y.R.Lu, et al., Proceeding of Linac 2006

STATUS OF THE CTF3 FREQUENCY MULTIPLICATION RINGS

A. Ghigo*, C. Biscari*, R. Corsini, S. Doebert, G.Geschonke, F. Marcellini*, L.Rinolfi,
M.Serio, A. Stella*, F. Tecker, P. Urschütz
CERN, Geneva, Switzerland. *INFN-LNF, Frascati, Italy

Abstract

The CLIC Test Facility (CTF3) is in construction at CERN by an international collaboration to demonstrate the feasibility of the two beam acceleration scheme at the CLIC parameters. The drive beam of CTF3 is accelerated by a fully loaded Linac that generates a long bunch train and two rings that provide the high current and bunch frequency multiplication by interleaving bunch trains. The status of the commissioning of the first ring (Delay Loop) and of the transfer lines are reported together with the installation of the second ring (Combiner Ring).

INTRODUCTION

The Compact LInear Collider (CLIC) Test Facility project [1,2] has the aim to demonstrate the feasibility of a 3 TeV electron-positron linear collider with reasonable length and cost using the dual beam accelerator scheme [3,4,5]. The layout is shown in Figure 1.

The two main characteristics of the CLIC accelerators are:

- the high accelerating gradient (>100MV/m) in high frequency RF accelerating cavities
- the production of high RF power by extracting power from a low energy high intensity electron beam, the Drive Beam, manipulated in order to create the appropriate time structure.

An international collaboration has been set to develop the CTF3 project with the following participating Institutes: Ankara Un. (Turkey); BINP, JNR, IAP (Russia); CCLRC-RAL (UK); CERN; CIEMAT, UPC, IFC (Spain); DAPNIA, LAL, LAPP, LURE (France); HIP (Finland); INFN-LNF (Italy); KEK (Japan); LLBL, LBL, NW Un., SLAC (USA); PSI (Switzerland); RRCAT (India); Uppsala Un.(Sweden) Incoming partners are Pakistan, Iran, Cockroft Inst., J.Adams Inst., JLAB, EPFL, INFN-Mi.

CTF3 is based at CERN in the building that hosted the LEP pre-injector complex, whose hardware and infrastructure are largely reused. Drive Beam is generated by a fully loaded Linac, 70 m long, followed by two rings in which the beam manipulation is performed: the Delay Loop (DL) 42 m long and the Combiner Ring (CR) 84 m long.

The drive Linac operates at 3 GHz and produces electron beam pulse trains at the energy of 150 MeV with a 1.4 μsec pulselength and 3.5A current at 1.5 GHz bunch frequency. The Linac RF power is transferred to the electron beam and an efficiency of 94% has been measured.

A RF power production station has been also installed, halfway along the linac, to test the RF power extraction structures (PETS). The electron beam is alternatively extracted in a dog-leg line and is sent to the PETS: the 30 GHz power extracted is transferred through 30 GHz waveguide to an external laboratory where the accelerating structures are conditioned and tested.

In the frequency multiplication system successive trains of bunches coming from the Linac are interleaved in the two rings by injecting with RF deflectors.

The time structure necessary for the recombination process is produced in the injector: a high current thermoionic electron gun is followed by three sub-harmonic buncher cavities at 1.5 GHz and 3 GHz bunching system. The sub-harmonic cavities and their sources are wide-band system and allow fast phase shift along the bunch train. The 1.5 GHz electron pulse, 1.4 μsec long, is composed by up to 10 sub trains in which the phase is shifted by 180.

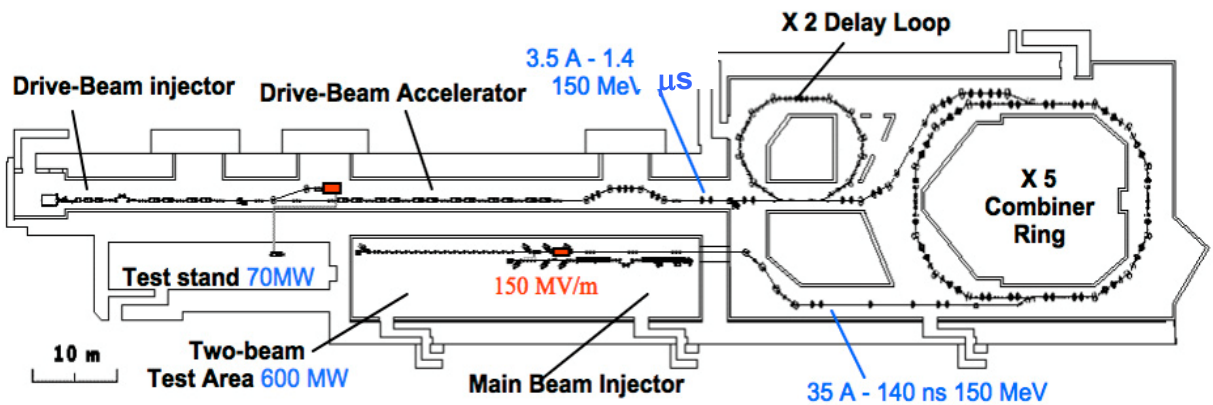

Figure1: CLIC Test Facility accelerator and building layout.

At the entrance of the Delay Loop a 1.5 GHz RF deflector kicks bunches of the train that have the right phase (even) to be injected in the ring and kicks off the bunches with opposite phase (odd) [6].

The length of the ring is exactly a multiple of the RF period in order to receive the exit kick at the deflector and to interleave even and odd bunches of the successive trains.

At DL exit a series of electron pulses, with doubled current, 140 nsec long with frequency of 3 GHz and empty space of 140 ns duration are created (see Figure 1) ready for multiple combination in the second ring.

In the Combiner Ring, the successive trains of bunches are injected with funnelling technique up to a number of five. Twin 3 GHz RF deflectors are used to correct the injection angle of the incoming beam and to kick on a closed bump the previous injected trains. The length of the Combiner Ring can be fine adjusted to permit bunches to pass in the RF deflectors with the right phase.

Fine tuning of the path length is assured by local deformation of the beam trajectory performed using a compensate three pole wiggler: this idea has been successfully tested in the Delay Loop.

DELAY LOOP

The installation of the Delay Loop started early 2005 and before the 2005 CERN winter shut-down the first beam passed in the ring with 90 % of transport efficiency.

Between March and May 2006 the commissioning continued sharing the operation time with the 30 GHz RF power production and accelerating cavities tests. The injection with the 1.5 GHz RF deflector has been proved at the energy of 100 MeV and the bunch recombination process demonstrated up to the nominal current and pulselength values

Horizontal and vertical emittances have been measured in different location along the linac and at the chicane exit to match the optical function. Quadrupole scan methods has been used observing the beam transverse dimensions on carbon OTR screen via large aperture optics CCD camera.

Pulselength and longitudinal structure of the trains have been measured with a streak camera collecting the synchrotron radiation produced in the DL bending magnet through glass windows and the OTR radiation.

A measurement at the RF deflector location has been also performed passing the electron bunches in the RF deflector zero crossing phase: the head and the tail of the bunch are deflected in opposite direction and observing the transverse dimension on a OTR screen the pulselength has been measured with one picosecond resolution.

After the orbit correction the dispersion function has been measured by scaling the quadrupoles currents and measuring the beam trajectory.

In Figure 2 the beam currents, measured at Linac end, in the DL and after the recombination at the DL output are reported

Detailed description of the commissioning phase has been reported in the EPAC06 conference [7].

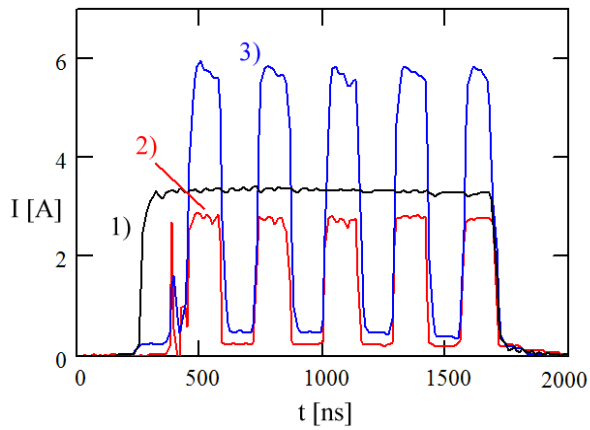

Figure 2: Beam current as a function of time, measured: 1) before the delay loop 2) in the loop 3) after the loop, showing the final recombination in five 140 ns pulses.

COMBINER RING

The design of the Combiner Ring must fulfil the Drive Beam requirements of producing short bunches equally spaced at the RF power production frequency after the recombination process in order to have the maximum power extraction efficiency in the PETS. The beam energy spread must be as small as possible and the machine lattice has to be isochronous in order to avoid lengthening of bunches. The energy loss must be small to avoid different bunch spacing for the trains that perform different number of turns in the ring.

To reduce the contribution of the Coherent Synchrotron Radiation (CSR), due to the short bunch, a magnetic chicane that can vary the bunch length on a wide range has been placed at the Linac end

Vacuum chambers

All the vacuum components of the DL and CR are designed to have very low coupling impedance to minimize the energy loss and energy spread in the beam. The bending magnet vacuum chambers have racetrack inner shape and are realized with aluminium alloy.

Each chamber is manufactured from two plates of aluminium machined under controlled environment condition and then welded together along the equatorial plane. Also the straight chambers have the same shape with exception of part of the injection and extraction region.

The bellows are RF shielded with copper sliding contacts and the pump ports are RF shielded using screen with hidden slots directly machined on the chamber wall and surrounded by an antechamber where the vacuum pump is connected.

The construction of transfer line and CR vacuum chamber components have started in summer 2006 and largest part has been produced by Italian firms.

Beam Position Monitor

The DL and CR Beam Position Monitors with racetrack shape (BPI) have a stay clear aperture of 90x37mm^2. This monitor works in principle as a transformer excited by the beam, representing a single turn primary loop, whose four secondary windings surround toroidal ferrite cores placed in correspondence of a vacuum chamber ceramic gap. The beam current acts as a winding that drives magnetic flux in the core, inducing a voltage signal in the secondary windings.The beam image current, diverted to the four strip placed outside a ceramic gap and short circuited to the two ends of the metallic vacuum chamber, is picked up through the small ferrite core transformers (FerroxCube 4C65) placed at the end of each strip and providing signals whose amplitude is beam position dependent. The striplines are surrounded by ferrite (Ferroperm Magnetics *PERMAX* n°56) to improve the low frequency response. Such ferrites are lossy at high frequencies and damp unwanted resonances of the external metallic shield.

In the combiner ring BPIs the ratio of the small transformers and the signal load impedance has been reduced, to increase the low frequency response of the device providing a lower cut-off frequency below 50 KHz.

TL1-Transfer line commissioning

The transfer line between the DL and CR (TL1), including the injection straight of the CR, has been installed and commissioned in autumn 2006.

The beam trajectory and transport efficiency in the transfer line and Combiner Ring injection section has been measured by means of 11 BPI as shown in Figure 3.

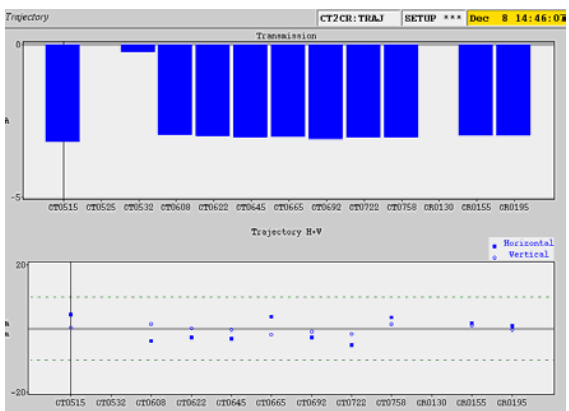

Figure 3: electron beam trajectory and transport efficiency in TL1 and CR injection.

A diagnostic station has been placed in front of the auxiliary port of the first CR dipole vacuum chamber to measure with an OTR monitor the beam profile and emittance. The beam transverse distribution is shown in Figure 4.

In February this year the Combiner Ring vacuum chamber will be installed; all the components are ready except the BPI that are in preparation at the Frascati Labs.

The installation of the missing BPI is foreseen for March this year in order be ready for the commissioning at the end of CERN winter shut down.

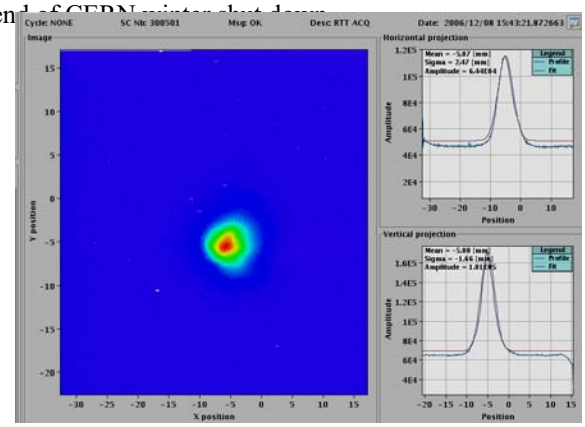

Figure 4: electron beam tranverse shape observed after CR injection.

CONCLUSIONS

The CLIC Test Facility CTF3 is a developing project in which the commissioning phases follow the installation of the different machine that compose the project.

The CTF3 international collaboration aims to demonstrate the CLIC feasibility before 2010. The construction of the Drive Beam has been advanced in stages and the Linac, the transfer lines and the Delay Loop have been successfully commissioned. The final commissioning of the frequency multiplication rings is foreseen in 2007.

REFERENCES

[1] G.Geschonke, A.Ghigo (ed.), "CTF3 Design Report", CERN/PS 2002-008(RF), LNF-02/008 (IR).

[2] A. Ghigo for the CLIC Collaboration, "CLIC feasibility study at CTF3" Proceedings of EPAC'06, Edimburgh, June 2006

[3] J.P.Delahaye for CLIC team, "The CLIC study of a multi-TeV e^+e^- linear colliders", Proc. PAC99 New York, USA.

[4] G.Guignard (ed.), "A 3 TeV e+e- linear collider based on CLIC technology", CERN 2000-008 and R.Corsini (ed.) "The CLIC power source" CERN Yellow Report 99-06.

[5] H.H. Braun for CLIC team "CLIC progress towards multi-TeV linear colliders", Proceedings of PAC 2005, Knoxville.

[6] F. Marcellini et al., "The RF deflector for the CTF3 Delay Loop" Proceedings of EPAC'06, Edimburgh, June 2006

[7] C. Corsini et al."Commissioning status of the CTF3 Delay Loop", Proceedings of EPAC'06, Edimburgh, June 2006

[8] D. Alesini et al. "RF beam deflector for CTF3 combiner ring", Proceedings of EPAC 2002, Paris, France.

DESIGN AND DEVELOPMENT OF BEAM TRANPORT ELEMENTS FOR BARC-ECIL LINAC

P. Roychowdhury, P. Jain, D.P. Chakravarthy, K. C. Mittal, and A. K. Ray
Accelerator and Pulse Power Division
Bhabha Atomic Research Centre, Mumbai- 400 085

Abstract

A 10 MeV, 2 kW RF electron linac is under development for cargo scanning. It consists of electron gun, RF linac structure, solenoid focusing magnets, steering magnet, beam diagnostics and x-ray target. To obtain properly resolved x-ray images, a beam diameter of 2mm is required at the target. Since the beam diameter at the target is critical; the transverse beam optics of the whole RF accelerator from gun end to the target has been simulated by solving the beam envelope equation. The envelope equation has been solved using Runga Kutta method consisting of external focusing field, RF field, space charge field and emittance. Various combinations of solenoid magnet focusing have been studied. It has been found that two solenoid magnets in the gun region and one after the linac region are sufficient to transport the beam and focus to a diameter of 2mm at the target. Based on these studies three solenoid magnets have been designed and fabricated.

INTRODUCTION

The industrial linacs are now making a major contribution to cargo inspection for manifest verification. This kind of system can easily inspect the contraband goods hidden in high density materials or fully loaded containers/ vehicles and show high quality scanning images. A 10 MeV, 10 kW RF linac for industrial application [1] has been installed at electron beam centre (EBC), Kharghar, Navi Mumbai and commissioned with 10 MeV, 15 mA, 10 μs pulse at 100 Hz PRF. The system consists of LaB_6 based electron gun injected into a standing wave on-axis coupled cavity linac, which accelerate the beam to energy of 10 MeV. A 2856 MHz, 3.5 MW Klystron based RF power source has been used to established the required electric field inside the linac. A similar system with x-ray target is under development at ECIL, Hyderabad for cargo scanning. This linac as a radiation source will be situated in a shielded room with concrete walls.

The electron gun of the linac produces electron beam of 50 keV, 10 μs, 100 Hz with maximum peak current ~1A. The beam is then focused by two solenoid magnetic lenses S1 and S2 and enters in the standing wave linac section L. In the drift section D1, a beam current transformer is incorporated to measure the gun current. The beam after coming out of linac hits the tantalum target T located beyond one meter concrete wall and produces x -radiation. A second beam current transformer is located in the drift region D3 to measure the beam current from the linac. A solenoid magnetic lens S3 is employed in front of the target to focus the accelerated beam to 2mm diameter.

THE ENVELOPE EQUATION

The generalized paraxial rms beam envelope equation for a cylindrically symmetric system which explicitly includes the effects of rf acceleration and external focusing is given as [2]

$$\mathbf{A'' + [\{\gamma'^{2}(\gamma^2 + 2)\}/ 4\beta^4\gamma^4 + K_{r,rf} + K_{r,B}]\, A - \beta\gamma Q/ A - \varepsilon_n/ A^3 = 0} \qquad (1)$$

where, $K_{r,rf} = 1/8\ (e\ E_0/\ \beta\gamma m_0c^2)^2$ is the rf focusing strength, $K_{r,B} = (eB_z(z) / \beta\gamma m_0c)^2$ is the solenoidal focusing strength and for the standing-wave accelerating structure, $\gamma' \approx e\ E_0\ /2mc^2$. The normalized rms beam size $A = \sigma_r(\beta\gamma)^{1/2}$, the normalized rms emittance $\varepsilon_n = \beta\gamma\varepsilon$, and the perveance of the beam $Q = I/\beta^3\gamma^3\ I_0$, with $I_0 = ec/r_e \approx 17$ kA for electrons. The input beam parameters of the 50 keV beam from the electron gun are the following: r = 5 mm, r' = 25 mrad, and I = 100 mA. The average accelerating gradient E_0 = 12 MV/m.

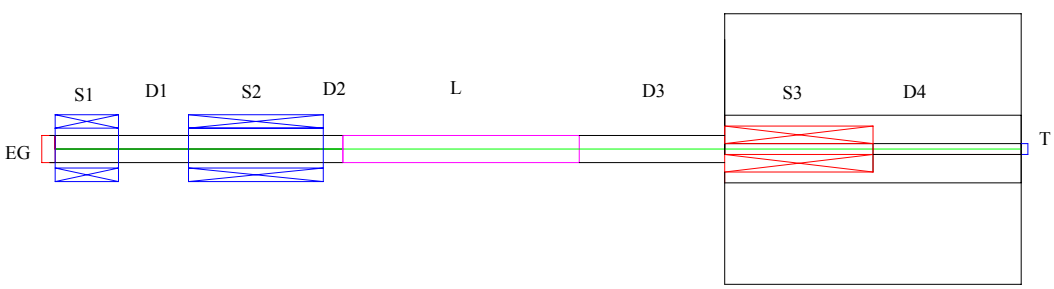

Figure 1: Schematic of beam transport elements: EG-Electron Gun, S-Solenoids, D-Drifts, L-Linac, T-Target.

The beam envelope for the beam line elements in Fig.1 consisting of Electron Gun EG, Solenoid S1, Drift D1, Solenoid S2, Drift D2, Linac L, Drift D3, Solenoid S3, Drift D4, and Target T is shown in Fig. 2. Here, the axial magnetic field $B_z(z)$ for the solenoids S1, S2 and S3 are shown in Figs. 3 and 4. With these input parameters the second order ordinary differential equation (1) has been solved using Runga-Kutta method after reducing to two first order equations. Various combinations of magnetic fields in the solenoids have been studied and it has been found that for the magnetic field configurations in Figs. 3 and 4, the optimum beam transport has been obtained. The 5 mm radius beam from the electron gun EG is focused to 2.4 mm radius by two solenoids S1 and S2 at the linac entrance. The beam in the linac region is focused by accelerating rf field to a radius of 4.2 mm at the linac exit. The beam is then focused by solenoid S3 to a diameter less than 1mm at the target.

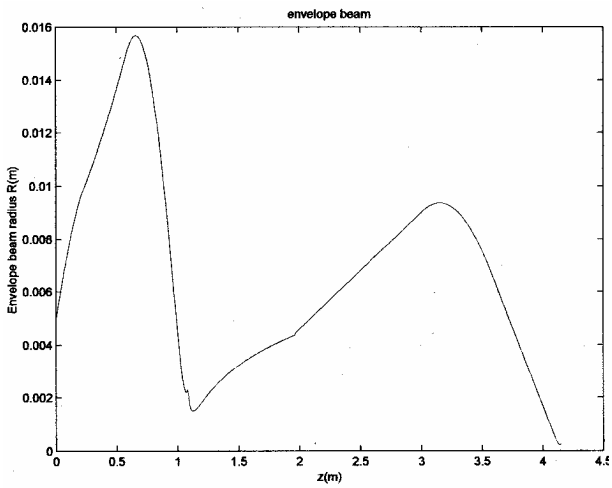

Figure 2: Beam envelope from EG to T: S1 (0<z<0.235), D1 (0.235<z<0.585), S2(0.585<z<0.995), D2 (0.995<z<1.087), L(1.087<z<1.964), D3 (1.964<z<3.014), S3 (3.014<z<3.564), D4 (3.564<z<4.15).

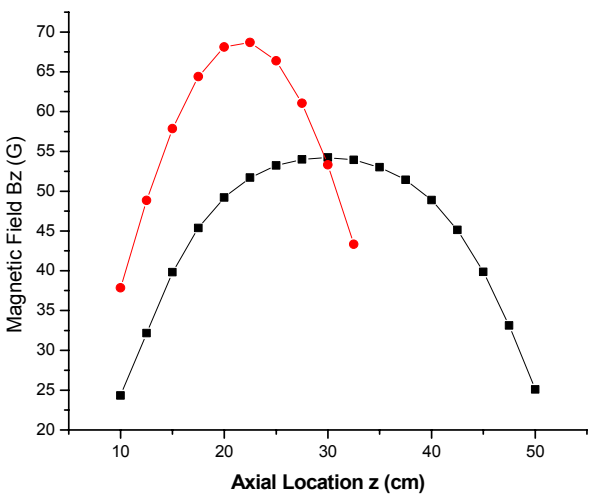

Figure 3: Axial field B_z versus z for S1 (•) and S2 (▪).

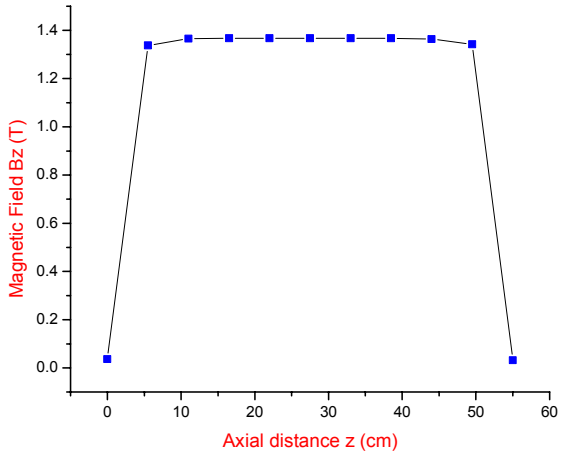

Figure 4: Axial field B_z versus z for S3 (▪).

SOLENOID MAGNETS

The solenoid magnets S1, S2 and S3 have been designed using POISSON code [3]. The field contour for S1 is shown in Fig. 5. The axial magnetic field variation B_z with distance z for S1, S2 and S3 are shown in Fig. 3 and 4.

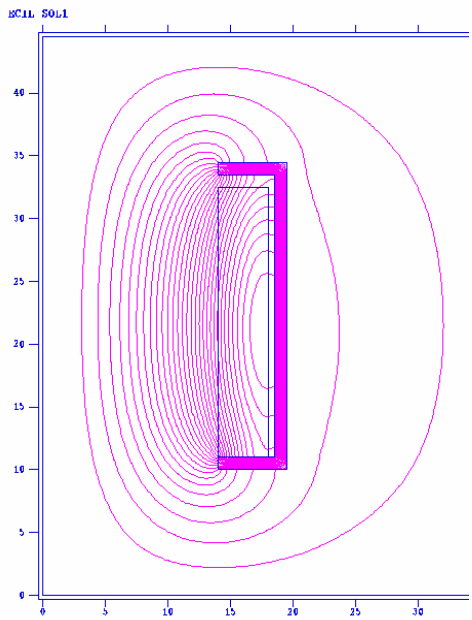

Figure 5: Field contour for solenoid S1.

The design parameters for the solenoids S1, S2 and S3 are shown in table 1. The solenoids coils after winding are baked for moisture removal and then vacuum impregnated in epoxy. The yoke materials for the solenoid magnet are low carbon steel grade-1010. The solenoid magnet S3 and its power supply have been fabricated by M/s Danfysik, Denmark.

Table1: Parameters of Solenoid Magnet

Sl. No.	S1	S2	S3
Inner Dia. (mm) Outer Dia. (mm) Length (mm) Max. field (G)	280 360 215 200	230 310 400 200	40 170 550 2000
Conductor size (mm) Resistance (Ω) Voltage drop (V) Power (kW)	1.5 x 5 0.99 9.9 0.1	1.5 x 5 0.89 8.9 0.09	5 x 5 0.198 21.3 2.2
No. of cooling circuit Pressure drop (bar) Flow rate (lit/min.) ΔT (^{0}C)			4 5 0.5 0.49

BEAM CURRENT MEASUREMENT

The beam current will be measured at two locations, one after the electron gun in the drift region D1 and the other at the exit of the linac in the drift region D3. Two Beam Current Transformers (BCT's) procured from M/s Bergoz Instrumentation, France, will be used to measure the beam current. The transformers have been specially designed to be mounted inside the vacuum chamber. Two alumina (>99.8% purity) casing have been fabricated to mount the BCT's. Signals from the BCT's are brought out of the vacuum using Kapton insulated UHV grade coaxial cable and a ceramic to metal brazed double shielded BNC vacuum feedthrough. The BCT with ceramic casing is shown in Fig. 6.

Figure 6: BCT and alumina enclosure

The signals obtained from the BCT's installed in the beam line of the Industrial RF linac at EBC, Kharghar is shown in Fig 7 and 8. Fig. 7 shows the electron gun current waveform (bottom trace) of 400 mA, 10 μs flat peak obtained at 50 kV (top trace). The current wave form from the exit of the linac is shown in Fig. 8 with the peak current measuring 15 mA.

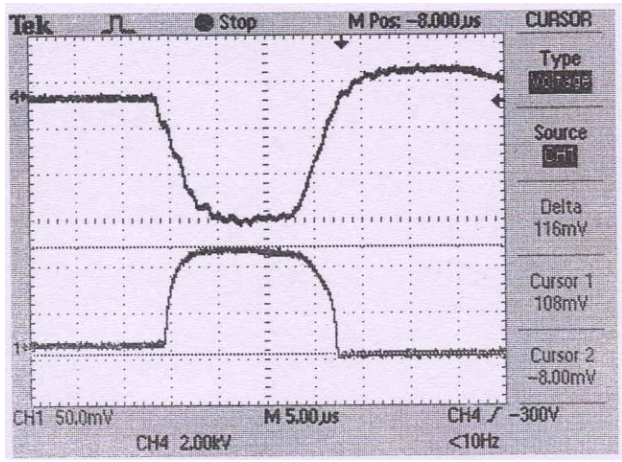

Figure 7: Voltage and current waveform of the electron gun measured using a divider and a FCT.

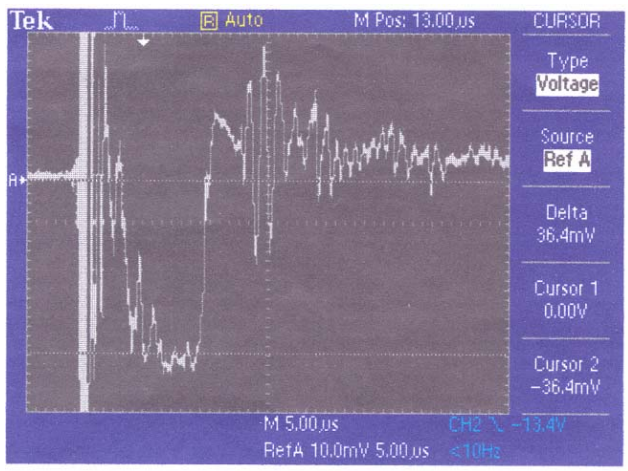

Figure 8: BCT signal for the beam current at the linac exit.

CONCLUSION

The transport of the electron beam from gun end to the x-ray target has been simulated by solving beam envelope equation consisting of external focusing field, RF field, space charge field and emittance. It has been found that two solenoid magnets in the gun region and one after the linac region are sufficient to transport the beam and focus to a diameter of 2mm at the target. Based on these studies three solenoid magnets have been designed and fabricated. Also to measure the beam current in the gun region and at the linac exit two BCT's have been procured.

REFERENCES

[1] V.T. Nimje et. al., "Present status of 10 MeV, 10 kW Industrial RF electron linac", InPAC-06, Mumbai, Nov. 2006, p - 171.
[2] J. D. Lawson, The Physics of Charge-Particle Beams, 2nd ed. (Oxford University Press, New York, 1988).
[3] http://laacg.lanl.gov.

HIGH QUANTUM EFFICIENCY PHOTOCATHODES FOR RF GUNS*

D. Sertore#, P. Michelato, L. Monaco, C. Pagani, INFN Milano - LASA, Segrate (MI), Italy
F. Stephan, DESY-Zeuthen, Zeuthen, Germany
S. Schreiber, DESY, Hamburg, Germany.

Abstract

High Quantum Efficiency Photocathodes are nowadays routinely used as electron sources for laser driven RF guns. In this paper, we review the production, characterization and operation performances of the Cs_2Te photocathodes prepared at INFN Milano – LASA and operated at DESY for the FLASH and PITZ photoinjectors.

INTRODUCTION

Since the 90s, INFN Milano is involved in the study of the growth process of photocathodes based on alkali antimonide and more recently alkali telluride. The figure of merit for the photocathode characterization are the operative lifetime, the achievable current density, the extracted charge, the dark current, the sensitivity to gas exposition, the Quantum Efficiency (QE), and the uniformity of the cathode sensitive layer response.

The growth process was studied applying surface science techniques like XPS (X-ray Photoelectron Spectroscopy) and AES (Auger Electron Spectroscopy) [1]. We applied the same techniques also for investigating the response to gas exposition.

Since 1998, INFN Milano is in charge of the production of the photocathodes for TTF, now FLASH. From the year 2000, we have also responsibility for the production of the photocathodes for the PITZ facility. In the production process, we apply the knowledge gathered in previous years of R&D activities. Up to now, none of the cathodes has shown any limitation in the extracted charge, even after long periods of usage. The main reason to change cathodes during the gun operation is the growth of dark current to high values. Since the start-up of the cathode delivery, we have collected many parameters that characterize both the plug preparation and the growing process. In the following section we briefly review the preparation, characterization and operational performances of the cathodes, from their deposition at INFN Milano-LASA to their use at FLASH and PITZ.

PHOTOCATODES PRODUCTION

The Preparation System

The preparation system consists of a UHV chamber whose base pressure is few 10^{-10} mbar (low 10^{-9} mbar during cathode growing). A CF63 sapphire viewport allows the cathode illumination for photocurrent measurements. The sources for Te and Cs evaporation are hosted on a frame that holds up to 6 sources. The Te sources are made from pure Tellurium (99.9999 %). Cs is evaporated from SAES® sources based on Cesium chromate. A circular masking system, placed in front of the cathode, shapes the round active layer (Φ= 5 mm) and assures its centering on the plug. The cathodes are loaded in the transport box and moved into the chamber by a magnetic-coupled manipulator. The box is then sent to FLASH or PITZ maintaining the UHV condition at all times.

The Coating Growth Procedure

The cathode plug is made out of pure Molybdenum with a 16 mm front surface diameter. The surface is cleaned and polished to optical quality with an automated lapping procedure. In addition to normal cleaning, some cathodes have been cleaned with a buffered chemical polishing method (BCP) or with electro-polishing (EP). Thin films of Tellurium and Cesium are then deposited in UHV condition. Tellurium and Cesium react to produce Cs_2Te. During the evaporation, the plug is heated to 120 °C. First, a thin layer of 10 nm of Tellurium is produced, and then Cesium is evaporated at a rate of 1 nm/min. The film is illuminated with UV light (λ=254 nm) of a Hg lamp to monitor the quantum efficiency. The evaporation is stopped, when the QE is at maximum. The final photoemissive layer thickness is some tens of nanometers.

For special purposes, we produce also KCsTe photocathodes that have higher QE then Cs_2Te but shorter lifetime. After the preparation, the plug is heated to 120 °C for the deposition of a 10 nm layer of Te. The temperature is then risen to 150 °C for a K layer deposition. Also in this case we use UV light from an Hg lamp to monitor the quantum efficiency. Once the maximum of the photocurrent arrives, the plug is cooled down to 120 °C for the final Cs layer deposition, until the maximum QE value is reached.

Some Statistics on Produced Cathodes

So far we have produced 51 Cs_2Te photocathodes and 2 KCsTe. 37 Cs_2Te photocathodes have been delivered to FLASH and 14 to PITZ. The overall number of uncoated Mo plugs delivered to different labs is 28 (11 to FLASH and 17 to PITZ). They are used for gun conditioning and dark current measurements.

Fig. 1 reports a summary of the QE measured at LASA for the whole photocathode production. Green dots are QE measurement before the shipment and the magenta ones after their use in the gun and return to LASA from the different labs. These data are available on-line from the Web interface to a database [2]

*Work supported by the European Community, contract number RII3-CT-2004-506008
#Daniele.Sertore@mi.infn.it

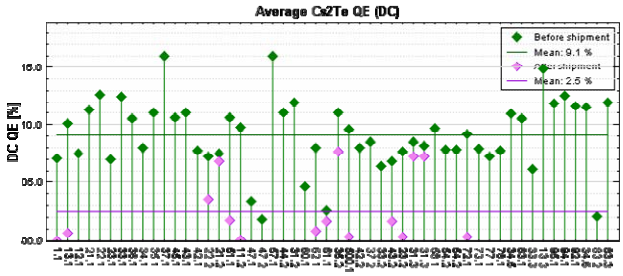

Figure 1: QE of the Cs_2Te photocathodes produced at LASA before and after their use at FLASH and PITZ.

PHOTOCATODES CHARACTERIZATION

After production, the photocathodes are qualified by measuring their QE uniformity over the active layer, taking pictures and measuring their spectral response.

A typical QE map over the cathode area (Φ = 5mm) is reported in Fig. 2. The UV beam (λ=254 nm) was focused onto a small spot (Φ = 1 mm). A well defined area corresponding to the active layer with QE uniformity within 10 % can be clearly seen. Similar uniformities are achieved for larger diameter active layers as well.

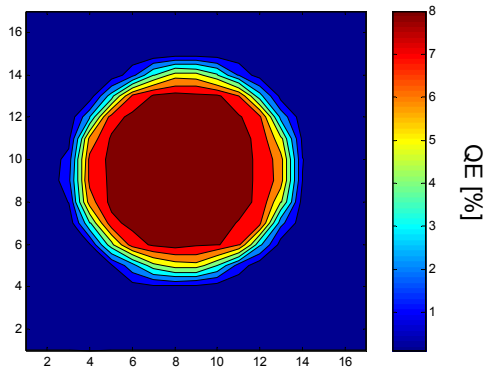

Figure 2: QE map of a typical photocathodes measured at λ=254 nm. Each tick represents 0.5 mm.

The spectral response is useful to study aging effect and to determine the physical properties that are helpful for modeling the photoemission process and estimate the thermal emittance. Fig. 3 shows a typical response for a Cs_2Te photocathodes.

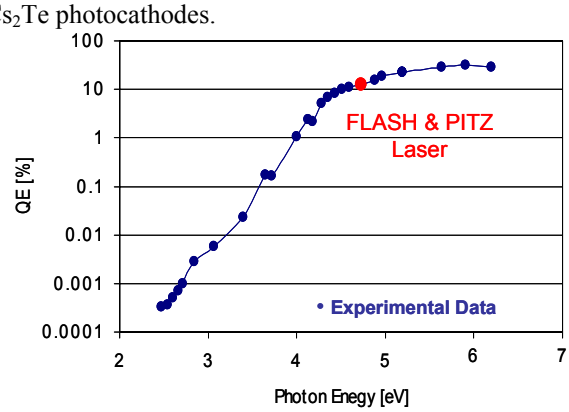

Figure 3: Spectral response of a typical Cs_2Te photocathode. The red dot represents the QE value at the photon energy of the laser used at the photoinjectors.

PHOTOCATODES PERFORMANCES DURING OPERATION

After production, the cathodes are loaded in the transport chamber that typically contains 2 cathode plugs with a Cs_2Te film, one blank plug, and one plug with a scintillator. If required, the blank cathode can be used for RF conditioning of the gun; the scintillator eases the alignment of the UV laser beam onto the cathode.

The FLASH L-band 1 1/2-cell RF gun is operated with a 5MW 1.3GHz klystron. With a forward RF power of 3.2MW, a gradient of 42MV/m on the cathode surface is achieved on crest. The repetition rate is up to 10 Hz, FLASH presently runs with 5 Hz. The gun is operated with various RF pulse lengths from 70 µs to 900 µs depending on the requirements on the beam. To reduce dark current, the RF pulse length is always minimized.

At PITZ a similar configuration is used but the L-band gun is operated with a 10 MW klystron aiming to reach 60 MV/m on the cathode surface.

During operation in both photoinjectors, the main parameters we are interested in are quantum efficiency and dark current but also secondary emission [3] and multipacting effect [4] have been studied.

Quantum Efficiency

Given a constant charge output from the gun, the quantum efficiency determines the laser pulse energy. The two main effects that influence QE are the aging and the effect of cathode operation in a high electric field region.
At FLASH, an automated procedure has been set-up to frequently monitor the QE during operation [5]. We record, with a calibrated toroid (± 1%), the emitted charge versus the laser energy measured with a calibrated joulemeter (Molectron ± 5%). The charge increases linearly with the laser energy until space charge effects lead to a saturation of the emitted charge. The QE is calculated from a straight line fit to the linear part. The relative and systematic error of the measurements presented here are in the order of 20 %. The systematic error is mainly due to the uncertainty of identifying the linear part for the fit and due to the cross-calibration of the laser pulse energy monitor with the energy measured in front of the vacuum window (see fig. 4).

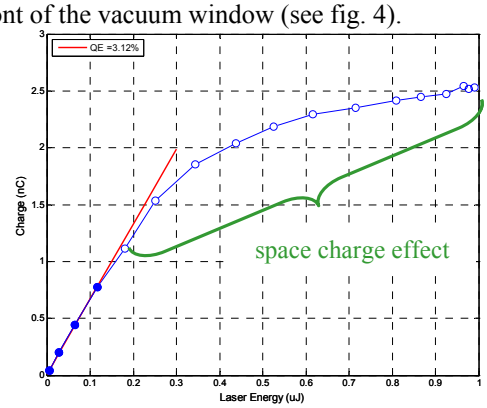

Figure 4: typical measurement of charge vs. laser energy at λ=262 nm. The QE is calculated considering the linear dependence of the extracted charge from the laser energy.

The aging effect has been valuated taking different QE measurements during the operative lifetime of several cathodes. Different phenomena affect the QE aging. In particular, long pulse operation (900 μs) and ion back bombardment play a critical role. Fig. 5 shows the behavior of cathode 78.1.

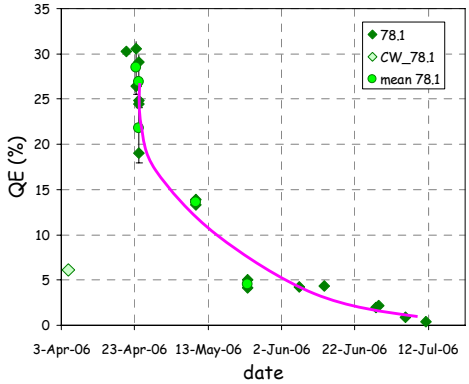

Figure 5: QE aging of cathode 78.1.

As mentioned before, also the analysis of the high electric field influence on the QE is important mainly for its impact on the thermal emittance that plays a key role for the future high brightness electron sources.

To extrapolate the field enhancement factor, we have studied the charge versus laser energy curve. We have model the curve, including different effects like laser spot shape, field enhancement, space charge and a typical example is reported in Fig. 6.

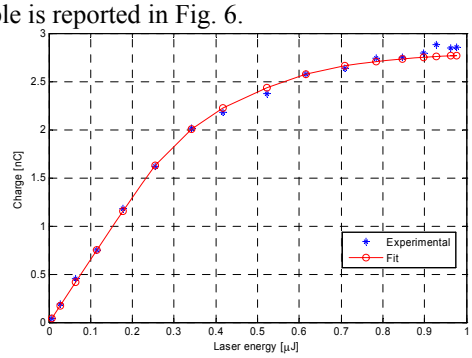

Figure 6: Analysis of the charge versus laser energy taking into account for example space charge, field enhancement and laser spot shape.

Dark Current

Dark current emission is one of the limiting factors in the operation of RF gun-based linear accelerators, due to possible activation and damage of accelerator components and the possibility of inducing quenches in superconducting cavities. The presented data are available from the Web interface of the database [2]. We present here a summary of the data collected in many years of operation and an attempt to identify the dark current source by its modeling.

Fig. 7 shows the dark current trend at PITZ for several photocathodes and three different guns. A main trend to notice is the decrease of dark current during each gun operation. This effect is more pronounced for PITZ-G1 and PITZ-G3 and can be explained as an effect of the gun cavity conditioning. Further explanation has been presented at EPAC06 [6].

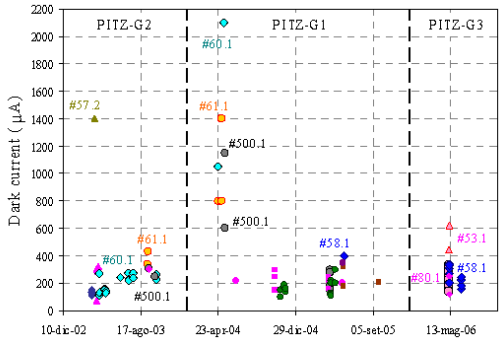

Figure 7: Dark current trend at PITZ from 2002 to 2006.

In order to identify the source of the dark current in the region of the cathode/gun backplane, we have set-up a model that assume a source of dark current in the transition region cathode/gun. Fig. 8 shows the image taken on a screen (left) and simulated (right). The reproduced flares structure is due to the combined effect of dark current energy spread and chromatic effect of the solenoidal field in which the emitted electron flight.

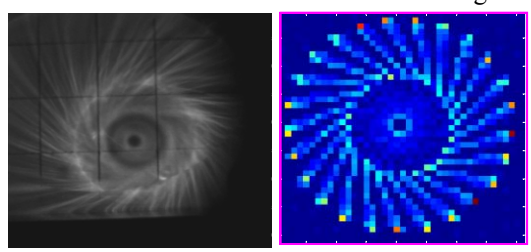

Figure 8: Comparison between screen and simulated dark current (not proper scaled).

CONCLUSIONS

In this paper, we have reviewed the complete photocathode process from the production at INFN Milano–LASA to their use in the FLASH and PITZ photoinjectors. We have consider mainly QE and dark current that up to now are the limiting factor in assuring a very long operational lifetime of the photocathode, today limited to about 90 days.

REFERENCES

[1] A. di Bona et al., “Auger and x-ray photoemission spectroscopy on Cs2Te photocathodes”, J. App.Phys. 80(5), 1 Sept. 1996.
[2] http://wwwlasa.mi.infn.it/ttfcathodes/
[3] J.H. Han et al., “Emission mechanism in a photocathode rf gun”, PAC05, Knoxville, USA.
[4] J.H. Han et al., “Dark Current and multipacting in the photocathode rf guns at PITZ”, PAC05, Knoxville, USA.
[5] D. Sertore et al.,”High QE photocathodes at FLASH”, EPAC06, Edinburgh,
[6] L. Monaco et al.,”Dark Current investigation of FLASH and PITZ rf guns”, EPAC06, Edinburgh, UK.

IONS FOR LHC: STATUS OF THE INJECTOR CHAIN

D. Manglunki, A. Beuret, J. Borburgh, Ch. Carli, M. Chanel, L. Dumas, T. Fowler, M. Gourber-Pace, S. Hancock, M. Hourican, J.M. Jowett, D. Kuchler, E. Mahner, M. Martini, S. Maury, S. Pasinelli, U. Raich, A. Rey, J.-P. Royer, R. Scrivens, L. Sermeus, G. Tranquille, J.-L. Vallet, B. Vandorpe

CERN, Geneva, Switzerland.

Abstract

The LHC will, in addition to proton runs, be operated with Pb ions and provide collisions at energies of 5.5 TeV per nucleon pair, i.e. more than 1.1 PeV per event, to experiments. The transformation of CERN's ion injector complex (Linac3-LEIR-PS-SPS) to allow collision of ions in LHC in 2008 is well under way. The status of these modifications and the latest results of commissioning will be presented. The remaining challenges are reviewed.

INTRODUCTION

The commissioning of the new ion injection chain for the LHC is advancing in stages, as planned [1]. After the successful first operation of the Low Energy Ion Ring (LEIR) in 2005 [2], the Proton Synchrotron (PS) has now been commissioned with the ion beam.

This paper summarizes the operation in 2006 of all the machines involved in the ion injection chain, except for LEIR which is described in a separate paper [3]. Most of the work presented here was achieved while the machines operated in parallel.

SOURCE AND LINAC 3

In 2006 the Grenoble Test Source for LHC was running most of the time for the commissioning of the LEIR and the PS with lead. During this time the source provided ~100 eμA of Pb^{27+} and Linac 3 gave more than 20 eμA of Pb^{54+}. The beam was stable and the source required very little retuning. Besides beam delivered for LEIR and PS commissioning, studies of the source biased disc were made [4] and the extraction and acceleration of Pb^{29+} was tested. With a similar ion current out of the Linac, Pb^{29+} has the advantage of lower RF fields in the tanks, which reduces the x-ray emission.

PROTON SYNCHROTRON

Beside acceleration, the role of the PS is to adapt the beam from LEIR according to a variety of constraints imposed by the downstream machines. Notably, it is the PS machine that imposes the bunch spacing required by LHC experiments, while the bunch length and repetition frequency at PS ejection must lie within the narrow ranges acceptable by the rf system of the SPS. In the nominal scheme, this requires complex rf gymnastics [5] to be performed at an intermediate energy in the PS cycle. In order to minimize the risk to beam lifetime, the intermediate plateau was chosen close to the highest energy consistent with the frequency range of the cavities performing the gymnastics.

The aim of the commissioning period was to make sure the PS would be able to deliver the "Early beam"; the achieved performance is summarized and compared with the design values, in table 1. However, a lot of time and effort was invested to prepare the "Nominal Beam", in order to identify potential problems and devise solutions [6].

Table 1: Performance of the Early Beam. Transverse emittances are given as normalised RMS values: $\varepsilon^{*}_{H,V} = \sqrt{\gamma^2 - 1}\,\sigma^2_{H,V} / \beta_{H,V}$

	Design	Achieved
N [E8 ions/bunch]	1.20	1.1
ε^*_H [μm]	1.00	0.85
ε^*_V [μm]	1.00	0.73
$\varepsilon_{//}$ [eVs/u]	0.05	0.03
τ_B [ns]	3.9	3.0

First injection into PS ring

In order to inject ions from LEIR into the PS, the new septum in its refurbished tank and kicker previously used for antiproton transfer from PS to LEAR, are complemented by a 2-dipole bump in order to cope with the higher magnetic rigidity of the Pb^{54+} beam [5]. The first injections took place on a flat cycle to study the beam behaviour at low energy. The lower limit for the beam lifetime was measured and exceeded 700 ms, confirming the excellent quality of the vacuum in the PS.

LEIR to PS transfer line matching

The transverse matching of the beam delivered has been measured with three secondary emission profile monitors (SEM) installed in the PS. One should note that due to imperfections (one vertical monitor "blind" at the center), the vertical trajectory had to be distorted strongly for the vertical measurement. The dispersion has been determined by measuring the beam position as a function of the momentum offset and the betatron functions and emittances from the beam sizes.

During a first measurement campaign, good betatron matching, but a significant (even though acceptable in terms of induced emittance blow-up) dispersion mismatch has been observed.

Based on the first measurement, a new setting of the transfer line has been implemented and investigated

during a second measurement campaign. Almost perfect matching (betatron functions and dispersion) has been found for the horizontal phase space. A relatively large betatron mismatch has been found in the vertical phase space. The poor result in the vertical phase space may be an artefact induced by the trajectory perturbation (to shift the beam to a working region of the SEM).

RF aspects

In the early scheme, a single bunch is delivered by LEIR, captured on h=16 in the PS and accelerated without gymnastics through transition to top energy, where it is rebucketed on h=169 to reduce the bunch length below 4 ns in order to fit into a 200 MHz bucket in the SPS. Figure 1 shows such a bunch, inside specification, immediately prior to extraction from the PS. The main problems encountered in the PS were a lack of sensitivity of the radial loop at low energy and insufficient accuracy of the raw frequency programme at high energy due to the proximity of transition to the flat-top. The former must await a shutdown for a definitive solution, while the later was cured by the introduction of a frequency trim function.

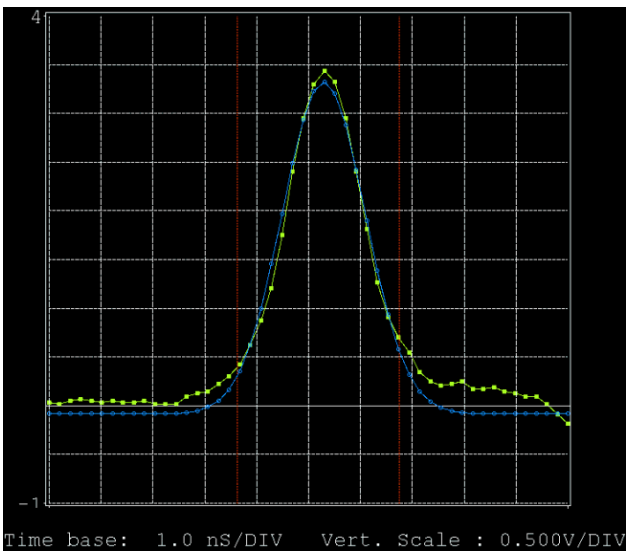

Figure 1: 4ns long Pb54+ bunch from Early Beam, immediately prior to extraction from the PS.

In the nominal scheme, two bunches are delivered by LEIR, are captured on h=16 and, after a series of quasi-adiabatic harmonic changes - including a splitting step - to h=24, four bunches arrive on the flat-top where they are rebucketed on h=169. There was insufficient beam time in 2006 to do much more than debug the rf gymnastics, but four bunches have already been obtained at the end of the intermediate plateau.

Both schemes involve coarse (at h=1) and fine (at h=9) synchronisation steps to lock the PS onto the waiting SPS. This was achieved for the early beam by simulating the SPS reference source.

Transition crossing

The ion beam crosses the transition at a kinetic energy of 4.8 GeV/u (γ_t=6.12). Although neither longitudinal nor transverse microwave instabilities are expected close to the transition at the intensities required for the LHC ion runs, the available gamma-transition jump system will be used for safety, albeit at reduced strength (i.e. identical quadrupole current): due to the 72.2 T.m beam rigidity of lead ions at transition, a maximum transition jump value of only 0.1 can be achieved, instead of the unity transition jump feasible for protons which cross transition at a beam rigidity of 18.9 T.m.

PS to SPS transfer line matching

Pb^{54+} ion bunches have been ejected at 5.88 GeV/u from the PS and stripped to Pb^{82+} in the TT2 transfer line to SPS. A low-β insertion has been implemented to minimise multiple scattering emittance growth through the stripping foil. To this end, four new quadrupoles were added and the first quadrupole of the two TT2 quadrupole strings had to be powered individually to complete the matching [7]. 13 quadrupoles are now available to tune the low-β ion optics instead of 7 used so far to match the proton optics. After the low-β insertion has been put in operation, the emittance blow-up due to multiple Coulomb scattering has been kept within the emittance budget with a comfortable safety margin as shown in the measurement results. In addition, new extraction optics were tried, with one of the kick enhancement quadrupoles off (QKE58). Table 2 shows, for various optics, the expected normalized RMS emittance blow-ups due to multiple Coulomb scattering in a 0.8 mm thick aluminium stripping foil calculated with the formula

$$\Delta\varepsilon_{H,V} = \frac{\sqrt{\gamma^2 - 1}}{2}\beta_{H,V}\left\langle\theta^2\right\rangle$$

where $<\theta^2>$ is the RMS multiple scattering angle. At the time of the commissioning, one matching quadrupole (labelled QFO205) out of the 13 was equipped with a power converter delivering a maximum current (400 A) below the value required for the nominal low-β optics. A temporary, constrained, low-β optics had to be implemented.

The emittance and optics were measured both with this constrained low-β optics and with the regular optics, with the stripping foil positions both “In” and “Out”. The measured normalized RMS emittances are shown in Table 3 from which the normalized RMS emittance blow-ups due to the stripping process are derived.

Tables 2 and 3 show quite a good agreement between the calculated and measured emittance growth for the constrained low-β optics. However the measured emittance growth for the regular optics is about 36% higher than the calculated one.

Table 2: Values of envelope function β and normalised RMS emittance growth due to mismatch, calculated with various TT2 optics; PS ejection optics with kick enhancement quadrupole (QKE58) on/off

Optics	β_H m	β_V m	$\Delta\varepsilon^*_H$ μm	$\Delta\varepsilon^*_V$ μm
Nominal low-β (QFO205=437 A, QKE on)	5.0	4.4	0.07	0.06
Restricted low-β (QFO205=400 A, QKE on)	8.1	5.6	0.11	0.08
Restricted low-β (QFO205=330 A, QKE on)	8.9	8.1	0.13	0.11
Restricted low-β (QFO205=330 A, QKE off)	10.2	6.9	0.14	0.10
Regular β (QFO205=156 A, QKE on)	23.6	22.1	0.33	0.31

Table 3: Blow-up of normalised RMS transverse emittances due to stripper, respectively measured with low-β and regular TT2 optics; PS extraction optics with QKE58 on.

	Stripper position	ε^*_H μm	ε^*_V μm	$\Delta\varepsilon^*_H$ μm	$\Delta\varepsilon^*_V$ μm
Low-β optics	Out	0.34	0.34	0.12	0.09
	In	0.46	0.43		
Regular optics	Out	0.40	0.33	0.45	0.43
	In	0.85	0.76		

Transfer to the SPS front porch

This part of the programme had never been planned beforehand but as a few hours of dedicated machine development time were still available, it was decided to try and bring the beam down the whole PS-to-SPS transfer line. Currents were set up according to the nominal optics used for the LHC proton beam, scaled to the lower magnetic rigidity of the lead ion beam. Although no instrumentation was available in the middle of the line, without any further adjustment, beam was immediately observed on the last screen, just upstream from the SPS injection septum! This has been made possible by the new LHC Software Architecture (LSA) in function at the SPS [8], and the fact that the operations teams for all the accelerators now work in a single control room, the CERN Control Centre (CCC), allowing for a much more efficient collaboration between them [9].

WHAT NEXT?

The next steps we hope to achieve in 2007 are:

- Installation of new power supplies in the PS-SPS transfer line, allowing the implementation of the full low-beta scheme.
- Injection of the Early Beam in the SPS, followed by acceleration and extraction.
- Production of the Nominal Beam in LEIR and PS
- Study of the behaviour of the ion bunches on the SPS injection flat bottom (intra-beam scattering and Laslett tune shift), in order to test the expectation that no further complicated RF manipulations will be necessary for the Nominal Beam in the SPS [10,11]

CONCLUSION

- The source, LINAC 3, LEIR and PS are practically ready to supply the Early Beam, and the LHC ion injection chain is on schedule.
- Although some power supplies still need upgrading, the low-β scheme at the stripper was validated with lower currents.
- Last minute transfer of the lead ion beam to the SPS front porch proved to be a successful test for the LHC Software Architecture and the CCC.
- Fine tuning of the RF manipulations needed for the Nominal Beam will need more machine development time in 2007.

REFERENCES

[1] S. Maury, “I-LHC project overview and status”, Proc LHC Project Workshop (Chamonix XV), Divonne, January 2006.
[2] P. Belochitskii et al, “LEIR commissioning”, Proc. EPAC’06, Edinburgh, June 2006.
[3] M. Chanel et al, “LEIR: towards the nominal lead ion beam”, this conference.
[4] L. Dumas et al, “Operation of the GTS-LHC Source for the Hadron Injector at CERN”, Proc. ECRIS'06, Lanzhou, China, 2006.
[5] M. Benedikt et al (ed), “The LHC design report Vol IIII”, chap 37, CERN-2004-003.
[6] A. Beuret et al, “The LHC Lead injector chain”, Proc EPAC’04, Lucern, , July 2004.
[7] M. Martini, “Status of what has been and what has to be done on PS & Transfer Lines”, Proc LHC Project Workshop (Chamonix XII), Chamonix, March 2003.
[8] M. Albert et al, “LHC Software Architecture: TI8 Commissioning”, LHC Project Note 368.
[9] D. Manglunki, “The CCC Project”, Proc LHC Project Workshop (Chamonix XIII), Chamonix, January 2004.
[10] D. Manglunki, “Status of what has been and what has to be done on SPS”, Proc LHC Project Workshop (Chamonix XII), Chamonix, March 2003.
[11] H. Burkhardt et al , “Investigation of Space Charge Effects and Intrabeam Scattering for Lead Ions in the SPS”, Proc EPAC’04, Lucern, July 2004.

LEIR: TOWARDS THE NOMINAL LEAD ION BEAM

M. Chanel, M.E Angoletta, V. Baggiolini, P. Belochitskii, A.Beuret, A. Blas, J. Borburgh, C. Carli, K. Cornelis, T. Fowler, M. Gourber-Pace, S. Hancock, C.E. Hill, M. Hourican, D. Kuchler, E. Mahner, D. Manglunki, S. Maury, M. Paoluzzi, S. Pasinelli, J. Pasternak, U. Raich, F. Roncarolo, C. Rossi, J.P. Royer, M. Royer, R. Scrivens, L. Sermeus, G. Tranquille, M. Vretenar,

CERN, Geneva, Switzerland.

Abstract

The Low Energy Ion Ring (LEIR) is a central piece for LHC ion operation at CERN, transforming long Linac3 pulses into high density bunches needed for LHC. The first phase of LEIR commissioning successfully attained its goal of providing the so-called "early ion beam" (one bunch of 2.25 10^8 Lead ions) needed for the first LHC ion runs with reduced luminosity. Studies in view of generating the beam needed for nominal ion operation (2 bunches of 4.5 10^8 ions in LEIR) were carried out in parallel with the setting-up of the early beam in the accelerators further downstream in the LHC injector chain. The main characteristics of the machine using a new state of the art electron cooler are discussed together with the latest results.

INTRODUCTION

The LHC [1,2], presently in construction at CERN will, in addition to proton operation, provide Pb ion collisions. The ion accelerator chain existing before the LHC era was by far not sufficient to provide the ion beams needed. The most fundamental upgrade of this ion accelerator chain [3-5] was the addition of the Low Energy Ion Ring. The role of this small accumulator ring, equipped with a new state-of-the-art electron cooler (built by BINP-Novosibirsk), is to convert several (200 μs) long Linac pulses into short high brilliance bunches needed for LHC ion operation.

Since nominal LHC ion operation is very demanding for both the LHC and the injector chain, first LHC ion operation will take place with a lower luminosity and less bunches using the so-called "early scheme" [3-5]. During the LEIR commissioning [6-9], the beam for this early scheme has been produced and transported to the PS injection region. The goal of the first LEIR operation run during last fall was to send the early beam to the PS to commission it[10], and to explore the way to the nominal beam in LEIR.

THE "EARLY SCHEME"

In LEIR, the simple "early scheme" consists in accumulating 2.2 10^8 lead ions(54+), bunching this beam on h=1, accelerating it from 4.2 to 72 MeV/n and sending it to the PS (Figure 1).The main results of this run are:

- The Ion Source performance was significantly improved such that LEIR received regularly, from the Linac3, an intensity of 22 eμA or more.
- Only one shot was needed to produce the early beam. The beam was cooled, accelerated on a cycle of 2.4 s and extracted toward the PS without particular difficulties.

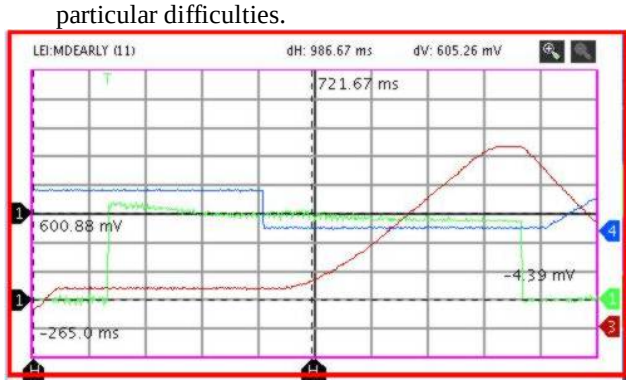

Figure 1: The "early ion beam" in LEIR (200ms/div). The red trace is the main bending field, the green trace is the beam current (8 10^7 ions/div), the blue trace is the electron cooling cathode voltage which is reduced just before the ramp.

- The injection efficiency was strongly influenced by shot to shot trajectory fluctuations in the injection line. This has been caused by stray fields generated by pulsed magnets (PS ring and ejection line). Magnetic shielding will be implemented to cure the problem during the present machine shut down.
- The new fully digital RF system was for the first time used in operation (see below). It performs very well and reliably apart from a fault related to commissioning the system.
- The normalised transverse emittances measured along the transfer line to the PS by the 3 profiles method (3 secondary emission grids distant by about 60 degrees phase advance) were found to be about 0.3 μm. The longitudinal emittance is ε_l<0.02 eVs/n. All these measurements are well within specifications.
- The availability of the beam for the PS commissioning was about 78%. The stops were mainly due to 3 faults; delay of the start-up by a vacuum leak in the electron cooler; a general stop of the power network at CERN; an error introduced in the RF digital system while commissioning a voltage loop in parallel to sending beam to the PS.

THE "NOMINAL SCHEME"

In LEIR, the so-called nominal scheme" consists in accumulating 9 10^8 lead ions (54+), bunching this beam on h=2, accelerating and sending it toward the PS. The main issues are: i) to accumulate in less than 1.6 s the number of particles needed by applying 4 or 5 successive sequences of multi-turn injection and cooling, ii) to maintain a sufficiently low pressure, good vacuum quality and, in turn, a low beam loss rate during operation[11-12], iii) to cool the beam to very small normalised emittances ($\varepsilon_{h,v}$<0.7 μm, ε_l<0.1eVs) leading to a strong space charge and Intra-Beam Scattering (IBS) regimes at the beginning of acceleration. The results (Figure 2) obtained and the remaining questions are:

- Careful adjustments of the injection and cooling settings allowed reducing the cooling time to 300ms. Thus five injections could be accumulated. The nominal intensity has been available at the end of the accumulation. Due to losses during the ramp, about 80% of the nominal intensity could be ejected and transferred towards the PS.

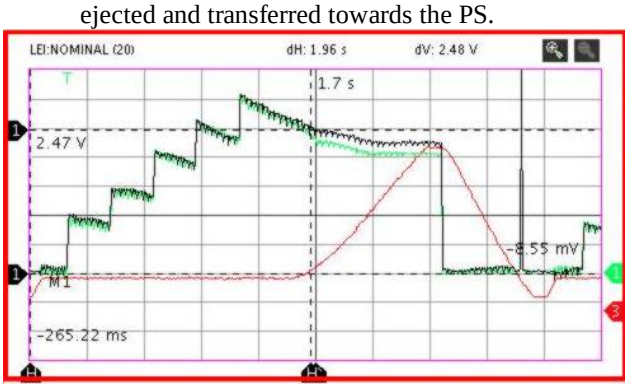

Figure 2 : The "nominal beam" in LEIR(400ms/div). The red trace is the main bending field, the green and black traces are the beam current with 5 injections (1.9 10^8 ions/div). Note the increased losses rate after each injection. About 9 10^8 ions are present before acceleration and more than 7 10^8 remain at extraction.

- The increased Linac3 current to above 22 eμA most of the time allows to accumulate the number of lead ions needed. A further increase of the Linac 3 current, bringing it closer to the design value (50 eμA) will help obtaining the "nominal beam".
- The upgrade of the vacuum system allowed increasing the beam lifetime beyond 10 s. No significant improvement was observed with scrubbing. A slightly hollow beam of the electron cooler improved the lifetime to some extent. Nevertheless up to 1.7 10^9 ions has been accumulated by continuous injection sequences in less than 6 s. The beginning of acceleration where space charge effects are strong is still a concern as frequently large losses appear. A better understanding of the strong transverse oscillations observed in this part of the cycle is needed.
- The two bunches were extracted and sent to the PS without too many problems. Unfortunately, we were not able to measure the emittances in the transfer line due to problems with the secondary emission monitors in the ejection line.

MULTITURN INJECTION

The long pulse (200μs i.e. 70 revolutions in LEIR) from the Linac3 is injected with stacking in the horizontal, vertical (by an inclined electrostatic septum), and longitudinal (by energy ramping) phase spaces, with about 50% injection efficiency (Figure 3). A possible improvement is a further increase of the injection efficiency to reduce the vacuum deterioration around the electrostatic septum.

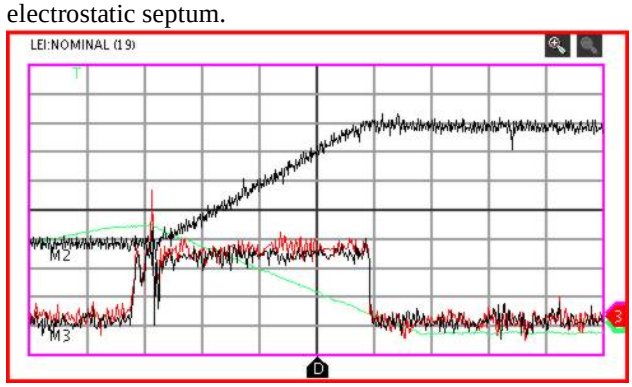

Figure 3: A typical multiturn injection in LEIR (50μs/div). The green trace is the current of one of the 4 orbit bumpers, the red and black close traces are the injection current (10 μA/div) and the black ramping trace is the accumulated current (270 μA/div).

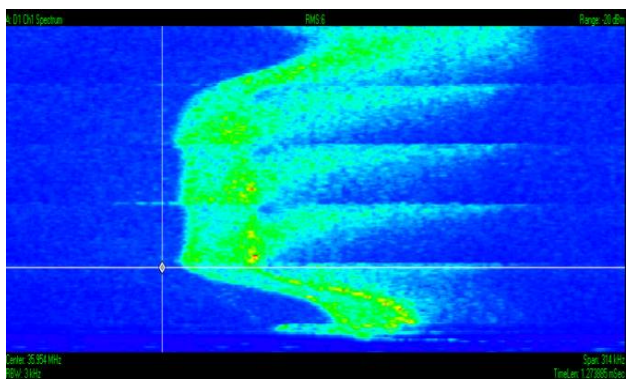

Figure 4: Spectrogram of the momentum cooling during stacking on the injection front porch. The vertical and horizontal axis denote time (1.6 s total from top to bottom); and momentum spread (1% full scale) respectively. There are 5 injections-cooling stacking sequences every 300ms

ELECTRON COOLING

The new state of the art electron cooling device [9] has been run with a current of 200 mA, an adiabatic expansion (about a factor 2.6) to adjust the electron beam to the ion beam dimension. A slightly hollow electron beam distribution turned to be the best compromise between a fast cooling (in 0.3 s) and minimal

recombination rate between the circulating ions and the electrons of electron beam (Figure 4).

ALL DIGITAL LOW LEVEL RF

LEIR is the first CERN circular machine equipped with an all-digital low-level RF (LLRF) system [14]. This is a modular system composed of custom VME motherboards and daughter cards which use floating-point Digital Signal Processors and Field Programmable Gate Arrays. Input signals (cavity gap returns, transversal and longitudinal pick-ups, PS RF reference) are digitally down converted to base band and their in phase and quadrature components are used for the beam control loops. Digital up-conversion allows cavity control and RF train generation. A width-modulated clock phase-synchronizes all the synthesizers and receivers located on the daughter cards with a revolution tag

The LLRF system captures and accelerates the beam at harmonic $h = 1$ or $h = 2$, and synchronize the bunch(es) in frequency and phase with the PS machine prior to extraction. Frequency program, steering, beam phase, radial and synchronization loops are implemented in full Pulse-to-Pulse Modulation fashion; all beam control parameters are user-controllable. Extensive online diagnostics is also available; Figure 5 shows the cavity-to-beam phase φ and the magnetic field measured by the system as a function of the time within a cycle.

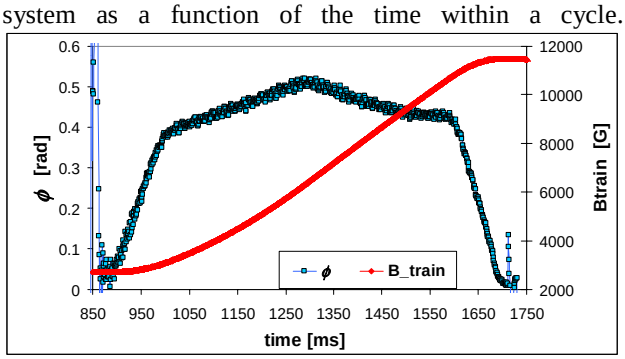

Figure 5: Cavity-to-beam phase φ and magnetic field measured by the LLRF system as a function of cycle time.

The non-tunable, large-bandwidth (0.35–5 MHz) cavities are based on the Finemet® high-permeability magnetic alloy [15]. The LLRF system short-circuits a cavity when no voltage is applied to it. This reduces the effective impedance seen by the coasting beam. During the 2006 LEIR run, the LLRF system has controlled cavity voltage and phase in a feed-forward fashion, over the required 60 dB dynamic range. During the 2007 run a dual harmonic cavity servo-loop will flatten the bunch(es) to reduce the transverse space charge tune shift. It will also minimise the cavity impedance at frequencies $h\ f_{rev}$ and $2{\cdot}h\ f_{rev}$, where f_{rev} is the revolution frequency and h the main harmonic.

CONCLUSION

The "early beam" has been produced in LEIR. In addition, the "nominal beam" is in good progress as 80% of the desired intensity was extracted towards the PS. Further studies will focus on: i) losses at high intensity, ii) to improve the intensity reproducibility and iii) make the operation easier by improving the beam measurements software.

REFERENCES

[1] O. Brüning et al. (eds), "LHC design report" Vol. 1, CERN-2004-003.
[2] O. Brüning, "LHC progress and commissioning plans", Proceeding of EPAC06, Edinburgh
[3] M. Benedikt et al. (eds), "LHC design report", Chapters 21 and 32 to 38 of Vol. 3, CERN-2004-003.
[4] A. Beuret et al., "The LHC lead injector chain", Proceedings of EPAC 2004, Lucerne 2004.
[5] M.E. Angoletta et. al., "Ions for LHC: Physics and Engineering Challenges", Proceedings of PAC05, Knoxville, 2005.
[6] C. Carli et al, LEIR Commissioning, Proceeding of EPAC06, Edinburgh
[7] F. Roncarolo, C. Carli, M. Chanel, L. Dumas, R. Scrivens, "Design and Validation with Measurements of the LEIR Injection Line", Proceeding of EPAC06, Edinburgh
[8] P. Beloshitsky, C. Carli, M. Chanel, J. Pasternak, "LEIR Lattice", Proceeding of EPAC06, Edinburg
[9] A. Bubley, V. Parkhomchuk, V. Prieto, R. Sautier, G. Tranquille, "LEIR Electron Cooler Status", Proceeding of EPAC06, Edinburgh
[10] D. Manglunki et al, 'Ions for LHC: Status of the Injector Chain", this conference.
[11] J. Bosser, C. Carli, M. Chanel, C. Hill, A. Lombardi, R. Maccaferri, S. Maury, D. Möhl, G. Molinari, S. Rossi, E. Tanke, G. Tranquille, M. Vretenar, "Experimental Investigation of Electron Cooling and Stacking of Lead Ions in a Low Energy Accumulation Ring", Particle Accelerators, Vol. 63, pp171-210,1999
[12] E. Mahner, J. Hansen, D. Kuchler, M. Malabaila, M. Taborelli, "Ion-stimulated gas desorption yields of coated (Au, Ag, Pd) stainless steel vacuum chambers irradiated with 4.2 MeV/u Lead Ions", Physical Review Special Topics – Accelerators and Beams 8, 053201 (2005)
[13] J. Pasternak, C. Bal, C. Carli, M. Chanel, E. Mahner, "A Collimation Scheme For Ions Changing Charge State in the LEIR Ring", Proceedings of PAC05, Knoxville, 2005.
[14] M.E. Angoletta et al., "Beam Tests of a New Digital Beam Control System for the CERN LEIR" Accelerator, PAC05, Knoxville, 2005, p 1649-1651.
[15] R. Garoby et al., "The LEIR RF System", PAC05, Knoxville, 2005, p 1619-1621.

HIGH POWER RF TESTING OF A CELL COUPLED DRIFT TUBE LINAC PROTOTYPE FOR LINAC4

M. Vretenar, Y. Cuvet, F. Gerigk, J. Marques Balula, M. Pasini, CERN, Geneva, Switzerland

Abstract

A Cell-Coupled Drift Tube Linac (CCDTL) accelerating structure at 352 MHz has been adopted for the energy range 40 to 90 MeV of Linac4, the new 160 MeV injector linac for the CERN accelerator complex. With regard to a conventional DTL in this energy range this structure presents the advantages of lower construction cost and easier access, cooling and alignment of the focusing quadrupoles placed between tanks.

A full-scale high-power prototype representing 1/3 of a complete module has been designed and built at CERN. It is fed by a waveguide input coupler of novel conception.

This paper summarizes the main mechanical features of the prototype and reports the RF tuning procedure and the results of high-power RF testing.

THE CCDTL PROTOTYPE

A CCDTL module, in the geometry adopted for Linac4 [1], consists of three DTL-type tanks containing two drift tubes each, connected by off-axis coupling cells. Between tanks are placed electromagnetic quadrupoles and diagnostic equiment whose installation, alignment and access is greatly simplified with respect to a DTL. The module resonates at 352 MHz in the $\pi/2$ mode, leaving the couping cells unexcited. Figure 1 shows an open 3D view of a module, together with its support and the short-circuited WR2300 waveguide coupled to the central tank.

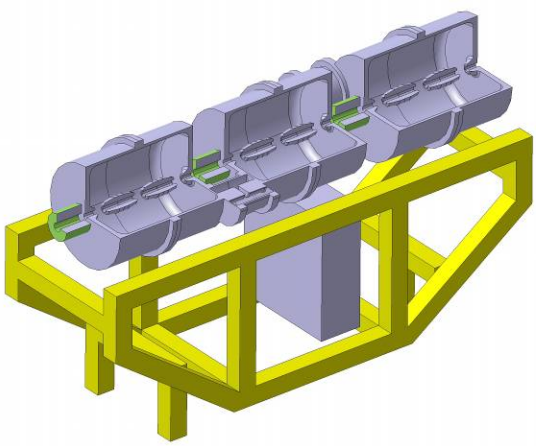

Figure 1: open view of a CCDTL module.

A CCDTL prototype consisting of two half accelerating cells connected by a coupling cell (Fig. 2) has been recently designed and built [2]. The chosen geometry is the smallest presenting the same electric field and thermal distribution as the final CCDTL structure. The half-tanks are made of copper-plated stainless steel, with cooling channels directly machined in the external part of the tank cylinder. Each half-tank contains a drift tube made in copper and cooled via the supporting stem. The half-tanks are connected via coupling slots to a coupling cell and are closed by disc covers, to provide the correct boundary conditions for the electric fields. In the final CCDTL configuration, two half-tanks are connected to form a complete tank. Vacuum and RF tightness between half tanks and covers and between the coupling cell elements are provided by "Helicoflex" type contacts. The end walls are EB welded to the tank cylinder, as well as the coupling cell end wall. Table 1 summarises the geometrical dimension of the prototype cavity.

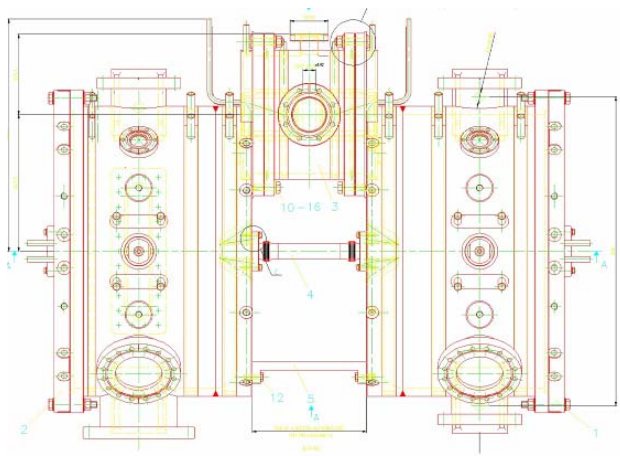

Figure 2: View from top of the CCDTL prototype. The coupling cell is off-axis; the quadrupole is replaced by a tube.

Each accelerating cell is equipped with two ports for tuners and one port for vacuum pumping. One of the accelerating cells has the port for the waveguide input coupler. The coupling cell is equipped with two tuning ports. All cells have a RF pickup port. Figures 3 and 4 show the prototype at different stages of its assembly.

Table 1: Geometrical dimension of the accelerating and coupling cell of the CCDTL prototype.

Accelerating tank diameter	495 mm
Drift tube diameter	85 mm
Full bore aperture	28 mm
Half accelerating cell length	302.5 mm
Gap length	49.05 mm
Coupling cell length	240 mm
Coupling cell nose diameter	93 mm
Coupling cell diameter	233 mm
Coupling cell gap	22.8 mm

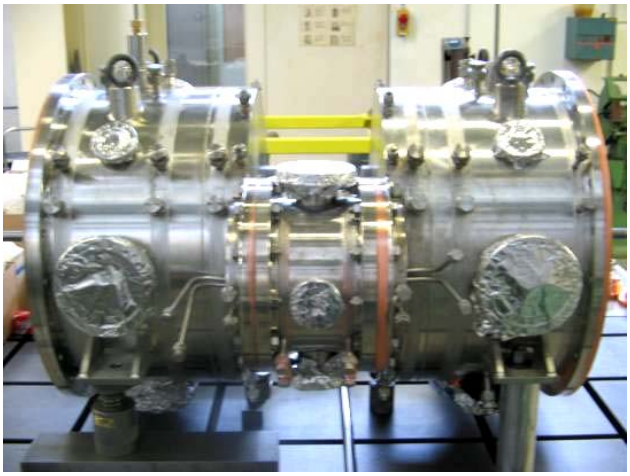

Figure 3: CCDTL during assembly in the workshop.

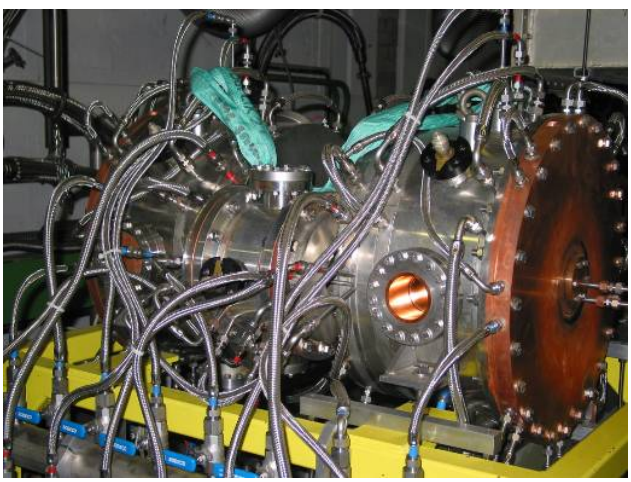

Figure 4: CCDTL cavity assembled, tuned, vacuum tested and with cooling system connected.

RF TUNING PROCEDURE

For the low-level measurements the cavity was first assembled without the waveguide coupler and preliminary measurements were made to characterise each cell. In order to measure the frequency and Q-value of an individual cell, the remaining cells were detuned by insertion of a metallic bar in the beam aperture, or in case of the coupling cell by short-circuiting the gap with a spring contact.

Next step was to tune to 352.2 MHz the frequency of each of the three cells constituting the resonator, by means of piston tuners and of end caps inserted via the central aperture in the end covers. After this adjustment, the input waveguide coupler was mounted and matched to the waveguide impedance. The half-height WR2300 waveguide from the RF generator is terminated into a movable short-circuit (a sliding plate) at $\lambda/4$ distance from an iris that couples the waveguide to the resonator. By moving the short-circuit plate, the voltage on the iris can be varied, allowing to change the coupling between waveguide and resonator until the critical coupling, corresponding to zero reflected power, is achieved. The coupling factor $\beta \equiv P_{ext}/P_{cav} = Q_0/Q_{ext}$ was measured for different short-circuit positions and the measured data is reported in Fig. 5. The curve follows the sinusoidal variation predicted by theory, allowing for a maximum coupling of 1.04, above critical coupling. Finally the cavity was accurately tuned to the design frequency, and frequency, Q-values and bead-pull measurements of electric field on axis were taken. The results are reported in Table 2 and Fig. 6. The asymmetry between electric field in the inner and outer gaps is typical of the CCDTL and taken into account in beam dynamics simulations.

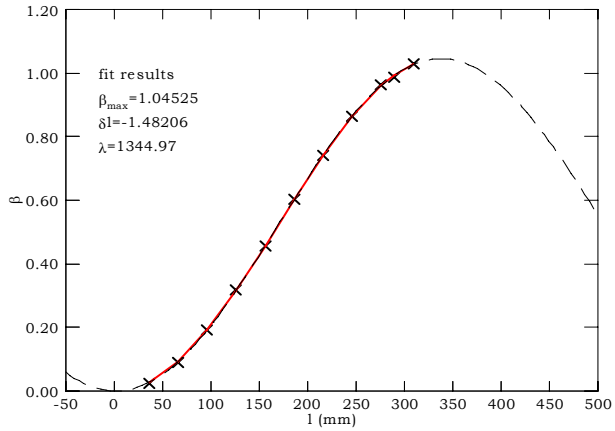

Figure 5: Coupling coefficient as a function of short-circuiting plate position.

Table 2: Results of the low-power measurements.

	Freq. (MHz)	Q_0
0-mode	350.686	
π/2-mode	352.187	22700
π-mode	353.725	
k (coupling bw. cells)	0.88%	
Field Flatness error	<1%	

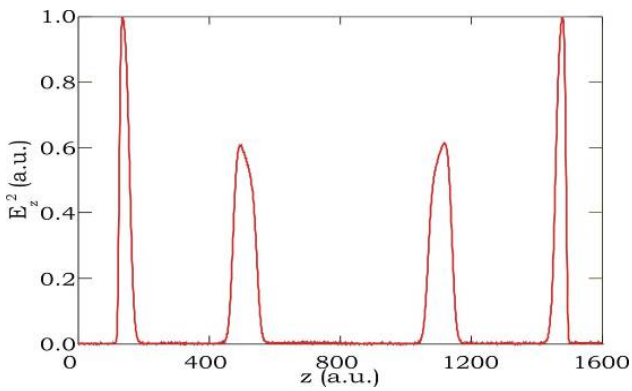

Figure 6: Bead-pull measurement.

Particular effort has been devoted to understanding the reason for the low Q-value (65% of the theoretical one) measured. Computer simulations indicate that this is due to the fact that the grooves housing the vacuum (and RF) joints were not copper-plated. After the first round of high-power tests, it is foreseen to open the half-tanks and apply local plating on the groove surfaces, in order to improve the Q-value.

HIGH POWER MEASUREMENTS

High-power tests started in September 2006. The power source was a LEP-type klystron (1 MW, CW), fed by a power supply that is presently limited to 58 kV. The RF power out of the klystron is therefore restricted to about 300 kW. For the tests the klystron RF input was pulsed, in order to obtain the required duty cycle. A calibrated directional coupler measured the forward power. The cavity voltage was measured at the two pick-ups in the half-tanks. A set of thermocouples was installed to monitor the temperature during the test. The vacuum in the prototype was of the order of 10^{-8} mbar. Figure 7 shows the prototype connected to the klystron waveguide. The circular RF window, inserted in the last section of waveguide, is visible in the front.

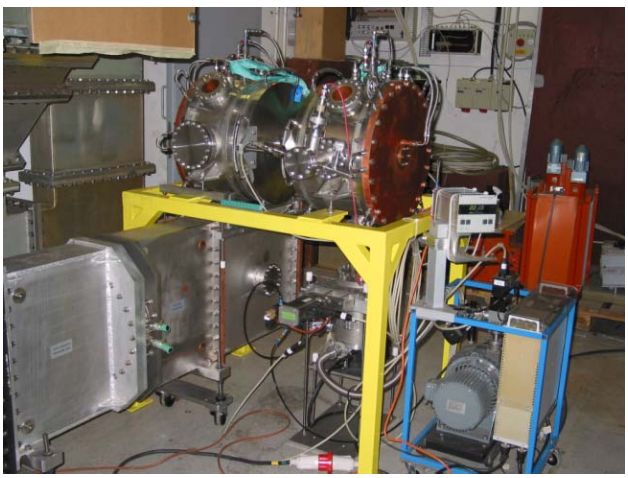

Figure 7: The prototype at the high-power test stand.

The initial conditioning of the cavity went almost unnoticed. Using a 100 μs long pulse at a repetition frequency of 5 Hz (higher than the Linac4 repetition frequency of 2 Hz), within few hours it was possible to reach in the cavity the maximum power delivered by the klystron, and no multipactoring was observed during the conditioning process. The corresponding gradient in the cavity was E_0 = 4 MV/m, slightly above the maximum gradient foreseen in the Linac4 CCDTL design.

In the continuation of the test it was observed that at high power levels the frequency of the cavity was continuously drifting. The thermal measurements showed an abnormal heating of one of the two drift tubes, and a water test indicated that the cooling circuit inside the tube was blocked. As a consequence, it was not possible to increase the repetition rate up to the SPL value of 50 Hz, as was foreseen in the original plan. After this series of high-power tests, the drift tube will be dismounted, the cooling will be repaired and the tests will resume.

Finally, the prototype was extensively measured at the Linac4 limiting operating mode, corresponding to 2 Hz repetition rate and 500 μs pulse length. With a reduced cooling of the drift tubes, the frequency was stable. The maximum RF power measured at the cavity input was 305 kW, corresponding to an effective voltage of 1.1 MV and a peak field on the drift tube of 32.4 MV/m (1.76 Kilpatrick). The mean electric field inside the cavity was E_0= 4 MV/m, calculated for a length of 306.4 mm. The present CCDTL design foresees a mean electric field ranging between 2.8 and 3.9 MV/m. The maximum gradient achieved during the tests, limited by the klystron power supply, was about 2% higher than the maximum CCDTL gradient foreseen for Linac4 operation.

Figure 8 shows a plot of the power level in the cavity measured at the input directional coupler (forward power) and at the output pick-up in one of the half-tanks. The two measured powers are identical over all the measurement range, indicating that no dark current was present during the test and hence that the voltage was still far from the breakdown limit [3].

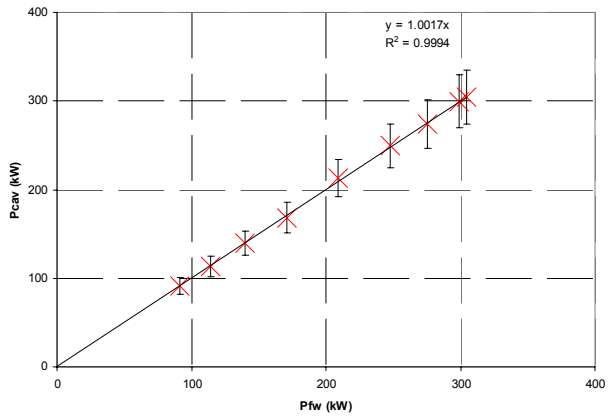

Figure 8: Power in the cavity vs. Power forward from the klystron.

The tests have now been temporarily interrupted to allow the repair of the drift tube cooling channels. During the time required for the repair, the test stand measurement equipment will be improved and the two end covers will be copper plated, in order to improve the Q-value.

ACKNOWLEDGEMENTS

The authors wish to thank the CERN workshops and V. Bretin for their support in constructing and debugging the prototype and O. Brunner and P. Maesen for their help in setting up the test stand. We acknowledge the support of the European Community-Research Infrastructure Activity under the FP6 “Structuring the European Research Area” Program (CARE, Contract No. RII3-CT-2003-506395).

REFERENCES

[1] F. Gerigk, M. Vretenar (eds.), “Linac4 Technical Design Report”, CERN-AB-2006-084 ABP/RF.
[2] M. Vretenar, Y. Cuvet, J. Genest, C. Völlinger, F. Gerigk, “Development of a 352 MHz Cell Coupled Drift Tube Linac Prototype”, LINAC 2004, Lübeck.
[3] M. Vretenar, “Field emission measurements on RFQ2 and recalibration of the vane voltage”, PS/RF/Note 97-11.

THERMO-STRUCTURAL ANALYSIS OF 400 KEV DEUTERON RFQ COMPONENTS

Piyush Jain#,Vlsrao. Sista, Rajesh Kumar, P. K. Nema, P.Singh
Bhabha Atomic Research Center, Mumbai-400085, India

Abstract

In this paper we are presenting Thermo-structural analysis of 400KeV, 1mA RFQ components i.e. RF Coupler, Tuner and Vacuum port. This investigation will help us to design local cooling schemes for these components. Parametric studies are also included in this paper. Feasible cooling schemes which meet cooling requirements of components will also be shown.

INTRODUCTION

The renewed interest in Accclerator Driven Systems (ADS) has spurred tremendous interest in developing high intensity proton accelerators, and has set challenging demands in terms of delivering high current (~ tens of mA) and high energy ($\geq$1 GeV) required for the spallation process. In Indian context, ADS will be used for the utilization of thorium resources for the energy production. In view of the importance of ADS, a project to design and build a 20 MeV, 30 mA CW proton accelerator (LEHIPA) as an injector to 1 GeV Linac has been initiated.

The LEHIPA mainly consists of a 50 keV ECR ion source, Low Energy Beam Transport (LEBT) line, 3 MeV Radio Frequency Quadrupole (RFQ) accelerator, Medium Energy Beam Transport (MEBT) line and a 20 MeV Drift tube Linac (DTL). 400 KeV, 1mA prototype deuteron RFQ will be build in order to understand the accelerator technologies required for LEHIPA project mainly regarding handling of very large RF power at 350 MHz. This RFQ will be utilized to replace 14 MeV neutron generator presently working at BARC.

RFQ will be made of OFHC copper. Because of the surface resistance offered by RFQ materials a portion of RF power gets dissipated in cavity itself. Average thermal load resulting from the RF power for the 400 keV RFQ is 68 KW. Main Coolant channels [1] have been designed to take care of this dissipated power. But these Main Coolant channels are not capable of eliminating potential Hot-Spot in RFQ components i.e. RF Coupler, Tuner, and Vacuum Port. Hence, Local Cooling of these components is required.

THERMO-STRUCTURAL ANALYSIS

Analysis is performed with help of FEM code 'ANSYS'. Modelling is done in ANSYS itself, this will facilitate easy remodelling. Investigation of temperature rise can be carried out with Thermal analysis, and deformation and stress pattern can be investigated with help of structural analysis. But in our case results of thermal analysis affect loading conditions in structural analysis, so coupling of thermal and structural filed is done. In Thermal analysis load is Heat flux, which is applied on mesh nodes by importing heat flux files from physics design calculations. 30% extra Heat Flux is added for safety margin. After performing thermal analysis elements are switched to structural elements while keeping model, material, mesh pattern unchanged. Now, temperature at nodes of mesh (which works as structural load) is imported from thermal analysis result file. Other boundary conditions like symmetricity, restriction of movement on flange are also applied. In following discussions h denotes Convective Heat Transfer Coefficient (in SI units) and Temperature is in Celsius. All the temperature profiles are shown on half-symmetric model.

RF Coupler

Co-axial type of coupler [2] has been chosen for this RFQ. Coaxial coupler mainly consists of Inner conductor, Outer Conductor, Ceramic window, Loop and Flange. Power dissipation in each coupler is 1.2 KW and peak Heat Flux is 35 W/cm^2.

Analysis without local cooling channel shows that temperature of loop and nearby portions may rise up to melting point of OFHC copper. Hence, local cooling scheme has been designed based on temperature profile which we got without local cooling channels. Inner conductor will be cooled by coaxial coolant channel. Outer conductor will be cooled with help of jacket from outside. Analysis shows that portion of outer conductor which penetrates inside RFQ is not required to cool locally; still temperature rise may be kept in check. Inner cooling channel and cooling jacket is shown in Figure 1. Temperature profile (with deformations) with this kind of cooling scheme is shown below in Figure 2. In this case, convection heat transfer coefficient (h) is 15000 with coolant temperature 16^{O}C.

piyushj@barc..gov.in

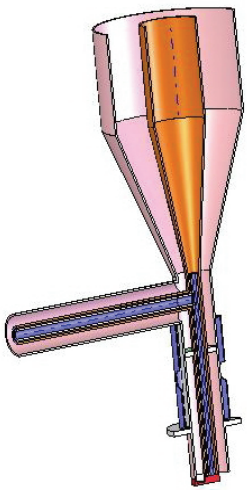

Figure 1: Cooling Scheme.

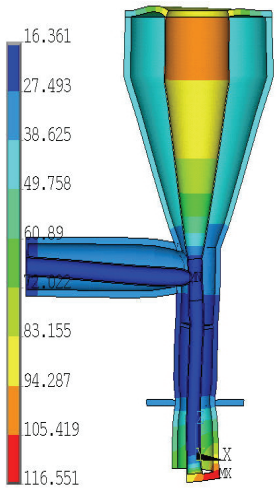

Figure 2:Temperature Profile.

Maximum temperature rise is in loop and nearby portions on outer conductor. To minimize temperature parametric study has been carried out. Thickness of outer conductor has been increased (inner diameter of outer conductor is fixed by physics design) to maximum possible value while space constraints are kept in mind. Increased thickness of outer conductor facilitates cooling of loop by decreasing conduction resistance. Maximum deformation found is .64e-04m. Joint between Ceramic window and conductors was area of concern because of difference in thermal expansion characteristic of OFHC and Ceramic. But thermal gradient on ceramic plate and nearby zone is negligible. So, ceramic window will remain intact to conductors during RFQ operation.

Results of parametric studies are shown below:

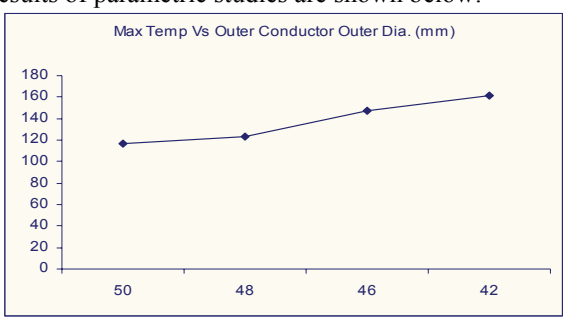

Figure 3: Max. Temp. Vs Outer Conductor Outer Dia.

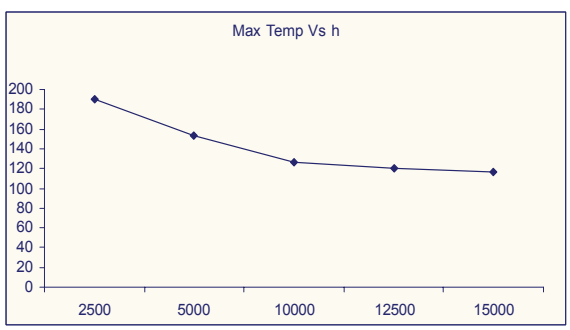

Figure 4: Max. Temp. Vs h.

With increase in h, maximum temperature in coupler body reduces. Temperature in loop is above 100 ^{O}C. So, h must be maximised but erosion of conductors because of high coolant flow will be the limiting factor.

Tuner

In order to correct the frequency slug type tuners will be used. Maximum 10 mm penetration [3] of tuner in RFQ cavity is allowed by physics design .In this case power dissipation per coupler is 800 W. Maximum heat flux is 25 W/cm^2 .Temperature rise without cooling is up to 1100 ^{O}C. Hence, local cooling channels are required. Resulting temperature profile, when h is 5000 and Inlet coolant temperature is 30 ^{O}C, is shown below in Figure 5. Pick-up loop will be incorporated in Tuner. Detailed design of pick-up loop is in progress. Coolant channels are made in such a way that central portion of tuner is left unused for pickup loop.

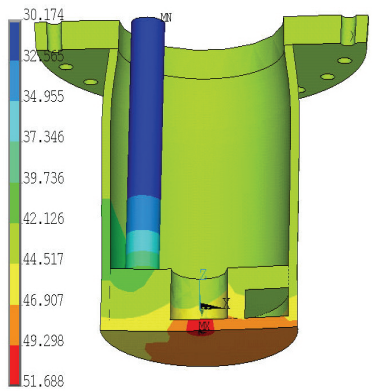

Figure 5: Temperature Profile.

Because of easy accessibility of coolant to the areas of high heat flux temperature rise is relatively lower. Hence, cooling requirement is not stringent in case of tuner. Relatively lower coolant flows with higher inlet temperature are acceptable in case of tuner.

Result of parametric study is shown below:

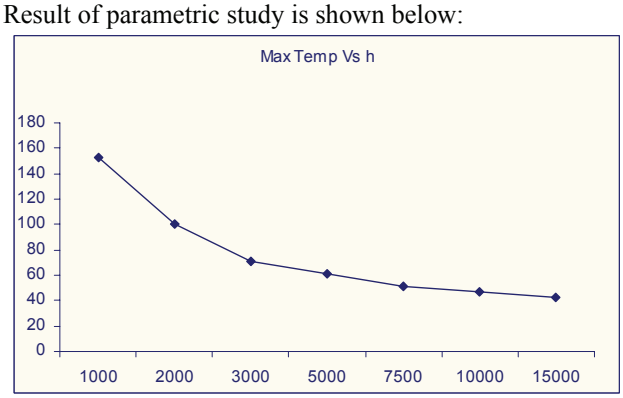

Figure 6: Max. Temp. Vs h.

From figure above it can be noted that even at lower h=5000 maximum temperature is sufficiently low.

Vacuum Port

Total power dissipated on vacuum port surface is 400W. Maximum heat flux is 35W/cm^2. Temperature rises up to 900 ^{O}C when there is no local cooling of vacuum port. Coolant path is shown in Figure 7. With h=2500 and 30 ^{O}C inlet coolant temperature profile is shown in Figure 8. Maximum Deformation found is .9e-04m.

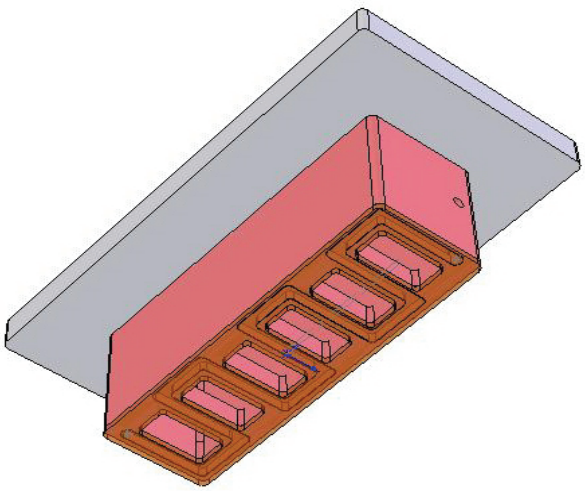

Figure7: Coolant Path.

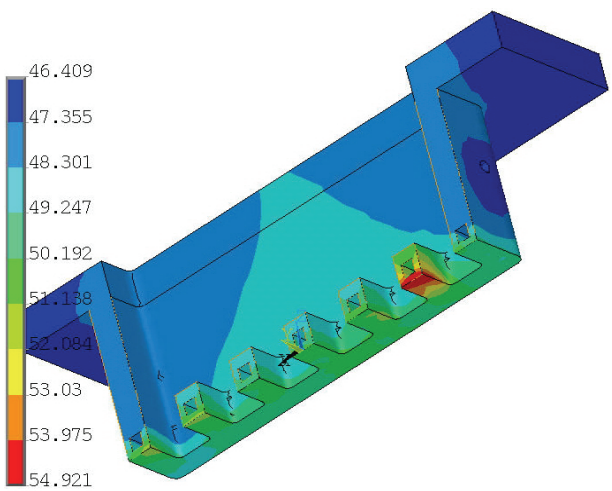

Figure 8: Temperature Profile.

Result of parametric study is shown below:

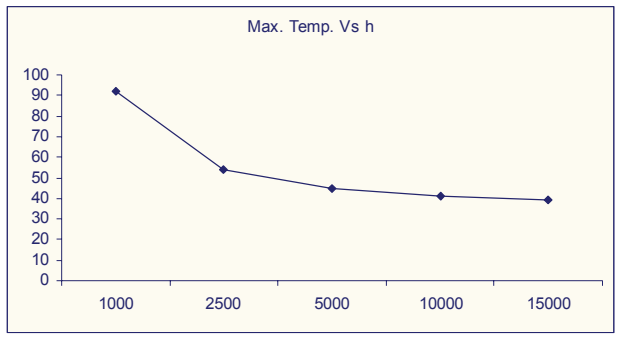

Figure 9: Max. Temp. Vs h.

ACKNOWLEDGEMENT

We acknowledge Dr. S. Kailas and R.K. Chaudhury for their support and Mr. M. Aslam for his suggestions.

CONCLUSION

As analyses suggest, local cooling of Vacuum-Port, Tuner and RF port is essential for safe operation of RFQ. Cooling requirements for Vacuum Port and Tuner are not stringent. Hence, lower coolant flow at room temperature will suffice. But temperatures in RF port must be minimised by utilising relatively higher coolant flow rate at lower inlet temperature.

REFERENCES

[1] Vishnu Verma, R.K. Singh, A. K. Ghosh, H.S. Kushwaha “Thermal and Stress Analysis of CW-RFQ for Accelerator Driven Sub-Critical Reactor System”, ICRAHT-2006.

[2] Rajesh Kumar, S.V.L.S. Rao, P. Singh "RF Design of High Power Couplers for ADS”, InPAC, 2006, Pg347".

[3] Shweta Roy, Rajni Pande, T. Basak “Design of Tuner for the 400KeV Deuteron RFQ”, InPAC, 2006, Pg209.

ELECTRON COOLING RATES IN FNAL'S RECYCLER RING *

A. Shemyakin # and L.R. Prost
FNAL, Batavia, IL 60510, USA

Abstract

A 0.1-0.5 A, 4.3 MeV DC electron beam provides cooling of 8 GeV antiprotons in Fermilab's Recycler storage ring. The paper presents cooling rate formulas derived in the framework of a simple non-magnetized model and compares them with measurements.

INTRODUCTION

Since the first cooling demonstration in 2005 [1], the Recycler Electron Cooler (REC) is used for storing and preparing antiproton bunches for every Tevatron store. To understand and improve the cooling process, dedicated cooling measurements of two types are performed.

In drag rate measurements [2], a low-intensity, coasting antiproton beam is first deeply cooled. Then the electron energy is changed by a jump, and the evolution of the average antiproton momentum is analyzed.

In the measurements of the second type, an antiproton beam with a Gaussian velocity distribution is kept between barrier buckets at a constant length. After turning the electron beam on, the initial derivatives of the momentum spread and transverse emittance are recorded.

In this paper, we compare results of these measurements with a non- magnetized model.

COOLING MODEL

The REC employs a weak 105 G longitudinal magnetic field to focus the electron beam in the cooling section. The simplest model to estimate the cooling rates of the antiproton beam is as follows:

1. The influence of the magnetic field on the cooling dynamics is neglected (so-called non-magnetized cooling).
2. The electron beam properties are assumed to be the same along the cooling section and across the beam.
3. The angle and momentum distributions of both electron and antiproton beams are Gaussian.
4. Variation of the Coulomb logarithm L_c over the range of relative velocities is neglected, and it is taken out of the cooling force integral.
5. For both beams, velocity spreads in *x* and *y* directions are equal in the cooling section.
6. The antiproton beam is assumed to be coasting, i.e. effects of RF barriers are neglected.
7. Antiproton motion in all three directions is uncoupled.

Cooling force

Under these assumptions, the formula for the non-magnetized cooling force [3] can be reduced to a one-dimensional integral [4] (similar to what is called "Binney's formula" in [5]):

$$F_{b_xi}(\vec{V}_p) = -A\cdot\frac{\partial}{\partial V_{xi}}U(V_{px},V_{py},V_{pz}),\ A = 4\pi\cdot m_e r_e^2 c^4 n_{eb}\eta\cdot L_c$$

$$U(V_{px},V_{pz},V_{pz}) = \frac{2}{\sqrt{\pi}}\cdot\int_0^\infty dt\frac{\exp\left(-\frac{t^2V_{px}^{\ 2}}{1+2\cdot\sigma_{ex}^2t^2}-\frac{t^2V_{py}^{\ 2}}{1+2\cdot\sigma_{ey}^2t^2}-\frac{t^2V_{pz}^{\ 2}}{1+2\cdot\sigma_{ez}^2t^2}\right)}{\sqrt{\left(1+2\cdot\sigma_{ex}^2t^2\right)\left(1+2\cdot\sigma_{ey}^2t^2\right)\left(1+2\cdot\sigma_{ez}^2t^2\right)}} \quad (1)$$

where F_{b_xi} , V_{pxi}, and σ_{exi} are the *xi* components of the cooling force, antiproton velocity, and electron r.m.s. velocity spread, correspondingly; n_{eb} is the electron density, m_e is the electron mass, r_e is the classical electron radius, c is the speed of light, η is the portion of the ring occupied by the cooling section. All values are in the beam frame.

Cooling rates

The beam-frame longitudinal cooling rate is derived by averaging the cooling force power over the antiproton velocity distribution $f_p(\vec{V}_p)$ [6]:

$$M_p\frac{d\sigma_{pz}}{dt_b}\sigma_{pz} = \int F_{b_z}V_{pz}f_p(\vec{V}_p)\,d\vec{V}_p = \sqrt{\frac{2}{\pi}}\frac{A\cdot\sigma_{pz}^{\ 2}\cdot f_{long}(\alpha)}{\sqrt{\sigma_{ez}^{\ 2}+\sigma_{pz}^{\ 2}}(\sigma_{ex}^{\ 2}+\sigma_{px}^{\ 2})},$$
$$f_{long}(\alpha) = \frac{1-\sqrt{\frac{\alpha}{1-\alpha}}\cdot\arccos(\sqrt{\alpha})}{1-\alpha},\quad \alpha = \frac{\sigma_{ez}^{\ 2}+\sigma_{pz}^{\ 2}}{\sigma_{ex}^{\ 2}+\sigma_{px}^{\ 2}}, \quad (2)$$

where M_p is the proton mass, σ_{pxi} is the *xi* component of the antiproton r.m.s. velocity spread, and the case where $\sigma_{ex}=\sigma_{ey},\sigma_{px}=\sigma_{py}$ is considered. Eq. (2) is valid for $\alpha<1$. This is typical for the REC parameters and will further be assumed in this paper. When $\alpha>1$, the result is expressed through $\cosh^{-1}(\sqrt{\alpha})$. In the lab frame, the time derivative of the momentum r.m.s. spread δp is calculated as

$$\dot{\delta p} \equiv \frac{\delta p}{\tau_{long}} \equiv \frac{d}{dt_l}\delta p = \frac{d\sigma_{pz}}{dt_b}M_p\,. \quad (3)$$

A similar integration for the transverse velocity gives

$$\frac{d}{dt_b}\left(\sigma_{px}^2\right) = \sqrt{\frac{2}{\pi}}\frac{A\cdot\sigma_{px}^2\cdot f_{tr}(\alpha)}{M_p(\sigma_{ex}^{\ 2}+\sigma_{px}^{\ 2})^{3/2}},$$
$$f_{tr}(\alpha) = \frac{\arccos\sqrt{\alpha}-\sqrt{\alpha(1-\alpha)}}{2(1-\alpha)^{3/2}}\,. \quad (4)$$

Eq. (4) takes into account a decrease of the cooling rate by a factor of 2 due to averaging over the betatron phases. Transition to the lab frame gives the expression for the time derivative of the transverse emittance:

$$\tau_{tr}^{-1} \equiv \frac{1}{\varepsilon}\frac{d\varepsilon}{dt_l} = \sqrt{\frac{2}{\pi}}\frac{A\cdot f_{tr}(\alpha)}{\gamma M_p(\sigma_{ex}^{\ 2}+\sigma_{px}^{\ 2})^{3/2}} \quad (5)$$

* FNAL is operated by Fermi Research Alliance, LLC under Contract No. DE-AC02-07CH11359 with the United States Department of Energy.
# shemyakin@fnal.gov

Note that the antiproton transverse velocities enter Eq. (3) and (5) only by being summed in squares with the transverse electron velocities. For REC operational parameters, typical velocity spreads in units of 10^7 cm/s are as follows: σ_{px} ~0.7–2, σ_{pz} ~0.7–1.5, σ_{ex} ~5, σ_{pz} ~0.2. For this range $\alpha << 1$, $\sigma_{ex}^2 >> \sigma_{pz}^2 >> \sigma_{ez}^2$ and Eq. (2)-(5) predict that the time derivative of the momentum spread and the logarithmic time derivative of the transverse emittance vary by less than by ±15%. The ratio of longitudinal and transverse cooling times τ_{long}/τ_{tr} from Eq. (3) and (5), which is a function of the single parameter α, is much less than 1.

Drag rate

In the drag rate measurements, the temporal evolution of the average antiproton momentum deviation $\bar{p} = \bar{P} - P_0$ is recorded after a change of the electron momentum to some value p_e. Here $\bar{P}$ and P_0 are the average and nominal momenta, correspondingly. To compare the rate $\dot{\bar{p}}$ with the model, the cooling force of Eq. (1) is integrated over a Gaussian antiproton velocity distribution and is transformed into the lab frame. Integration over transverse velocities yields to a compact formula [6]:

$$F_{lz}(\Delta p) = -F_0 \cdot \int_0^{\Delta p / p1} du \frac{e^{-u^2} u^2}{u^2 + \left(\frac{\Delta p}{p2}\right)^2} \qquad (6)$$

where $\Delta p = p - p_0$ is the offset of the antiproton momentum with respect to its new equilibrium value $p_0 = p_e \frac{M_p}{m_e}$, and

$$F_0 = \frac{n_{el}}{\vartheta_t^2} \cdot \frac{2}{\sqrt{\pi}} \cdot \frac{4\pi \cdot m_e r_e^2 c^2 \eta \cdot L_c}{\gamma^3 \beta^2},\ p1 = \delta W_e \cdot \sqrt{2} \frac{M_p}{\beta m_e c},$$

$$p2 = \vartheta_t \cdot \sqrt{2}\, \gamma^2 \beta c M_p,\ \vartheta_t = \frac{1}{\gamma \beta c} \sqrt{\sigma_{ex}^2 + \sigma_{px}^2 - \sigma_{ez}^2},$$

$\vartheta_e = \frac{\sigma_{ex}}{\gamma \beta c}$ - 1D electron r.m.s. angle in the cooling section,

$\delta W_e = p_e \sigma_{ez}$ - r.m.s. ripple of the electron energy,

$n_{el} = \gamma\, n_{eb} = \frac{j_e}{\beta c}$ - electron density in the lab frame,

γ and β are the Lorentz- factors, and j_e is the electron current density. For a small momentum spread δp, averaging of the cooling force over the antiproton momentum distribution can be done by expanding the force near the average momentum offset:

$$\dot{\bar{p}} = \overline{F_{lz}(\Delta p)} \approx F_{lz}\left(\overline{\Delta p}\right) + F''_{lz}\left(\overline{\Delta p}\right) \cdot \frac{\delta p^2}{2}. \qquad (7)$$

Expansion (7) is converging when the contribution of the term with the second derivative is small. Therefore, an interpretation of a drag rate as a longitudinal cooling force, $\dot{\bar{p}} \approx F_{lz}\left(\overline{\Delta p}\right)$, is valid when

$$\delta p^2 << \frac{2F_{lz}(\bar{p})}{F''_{lz}(\bar{p})}. \qquad (8)$$

A typical behavior of the second-derivative term $F''_{lz}\left(\overline{\Delta p}\right) \cdot \frac{\delta p^2}{2}$ is shown in Fig.1.

DRAG RATE MEASUREMENTS

In the drag rate measurements, usually only the initial slope $\dot{\bar{p}}$ immediately after the energy jump is used (see a detailed description in Ref. [7]). To provide enough information for fitting the curve $F_{lz}(\Delta p)$, the measurement is repeated at different jump amplitudes. In Ref. [7] these data were fitted to an approximation of Eq.(1) assuming zero transverse antiproton velocities. Fitting of the same data to Eq.(6) gives very similar values of the electron beam parameters θ_e, δW_e and j_e (Fig.1). It is related to the fact that antiproton transverse velocities enter Eq. (6) only through θ_t dominated by electron angles. Fig.1 shows that the condition of Eq. (8) was always fulfilled in these measurements.

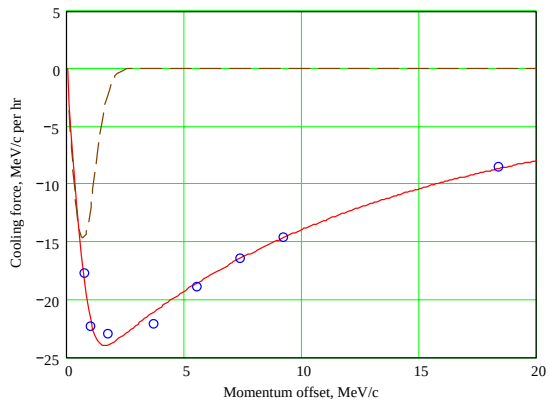

Figure 1. Drag rates measured on February 6, 2006 (blue circles). N_p = 3.5·10^{10} antiprotons, transverse emittance (95%, normalized, measured with a Schottky pickup) is $\varepsilon \approx$ 1.5π mm·mrad, initial momentum spread δp = 0.2 MeV/c, electron beam current I_e = 0.1 A. The red solid line represents Eq. (6) at δW_e = 370eV, θ_e = 0.2 mrad and j_e = 1.3 A/cm^2. Contribution of the second derivative term is shown by the dashed brown line (for presentation purpose, it is negated and shown for δp = 1 MeV/c). L_c = 10.

In addition, drag rate measurements were performed at a fixed amplitude of the energy jump while varying the electron beam current (Fig.2). The various data sets represent successive adjustments to the cooler, going from improving the alignment of the electron and antiproton beam trajectories after recalibration of the beam position monitors in the cooling section, to a novel beam-based alignment procedure of the cooling section magnetic field, to a new iteration of focusing setting optimization. Each time, the drag force increased, in particular for high beam

currents and most notably for I_e = 300 mA. However, the reason for the drop at I_e = 400 mA is still unclear.

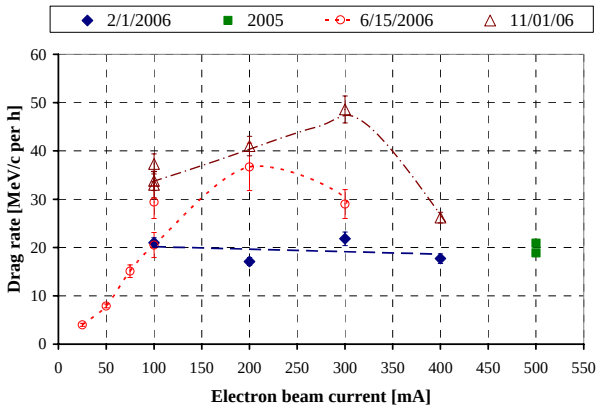

Figure 2. Drag rate (negated) as a function of the beam current. In all cases, the electron energy jump is 2 keV.

COOLING RATE MEASUREMENTS

An example of a cooling rate measurement is shown in Fig.3. An antiproton beam, kept between barrier buckets, is initially cooled only using the stochastic cooling system in order to create a velocity distribution close to Gaussian in all directions. The beam's momentum distribution is measured by a Schottky pickup, and the transverse distributions are measured with flying wires (FW). After turning off stochastic cooling, the antiproton beam is let diffuse. Then the electron beam is turned on. The difference of the slopes in the time of electron cooling and during diffusion is considered a measure of the cooling rate.

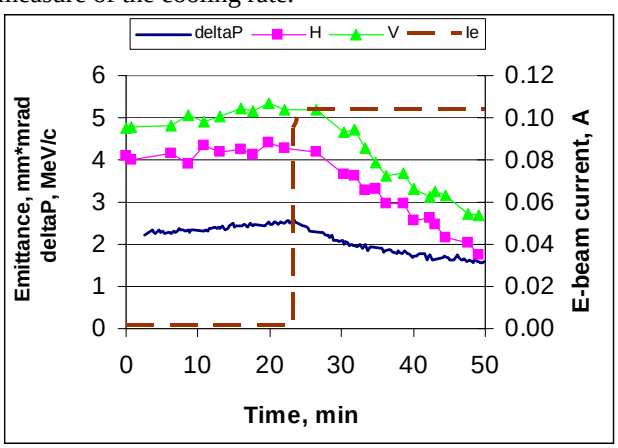

Figure 3. Cooling rate measurement (Dec 20, 2006). The beam length is 8.7 μs, N_p = 50·10^{10}. The dashed brown line represents the electron beam current. H and V show the horizontal and vertical emittance (95%, norm., FW), respectively, and deltaP represents the r.m.s. momentum spread δp. The measured cooling rates are 8 (H), 11 (V) mm·mrad/hr, and 4.6 MeV/c per hr (δp), and corresponding cooling times are 0.52, 0.48, and 0.55 hours.

To compare the results with the model, the electron beam parameters found with the drag rate measurements shown in Fig.1 are fed into Eq. (2)-(5). The measured cooling rates are found to be consistently 2–3 times low for the longitudinal rate and high by a similar factor for the transverse rates. This results in τ_{long}/τ_{tr} ~1, which is also in disagreement with the model. So far no conclusive explanation for this discrepancy has been found. Several areas are looked into for hints:

- Instrumentation inconsistencies. For example, the transverse cooling rate recorded with a Schottky monitor is always significantly lower than the rate measured with flying wires [8].
- Heating mechanisms, including IBS.
- Dependence of the cooling rates on the antiproton emittance. Note that the drag force is always measured at a low emittance.
- Mechanisms of redistribution of the cooling rates, possibly similar to the one described in Ref. [9].
- Effect of the magnetic field on the cooling dynamics.

SUMMARY

1. In the framework of a simple model assuming Gaussian velocity distributions for the antiproton beam, formulas for electron cooling rates are expressed with elementary functions.
2. We find a significant disagreement (2-3 times) between measured cooling rates and predictions from our simple model combined with parameters fitted from the drag rate measurements.

ACKNOWLEDGMENTS

Authors are thankful to A. Burov, V. Lebedev, and S. Nagaitsev for many useful discussions. We acknowledge the participation of A. Fedotov and A. Sidorin in some of the measurements shown and the help from D. Broemmelsiek and M. Hu with instrumentation.

REFERENCES

[1] S. Nagaitsev *et al.*, Phys. Rev. Lett. **96**, 044801 (2006)
[2] H. Danared *et al.*, Phys. Rev. Lett. **72** (1994) 3775
[3] Ya.S. Derbenev and A.N. Skrinsky, Particle Accelerators **8** (1977) 1
[4] V. Lebedev, private communication
[5] I.N.Meshkov *et al.*, Physics guide of BETACOOL code, v.1.1, BNL note C-A/AP#262, p. 17
[6] A. Shemyakin, FERMILAB-TM-2374-AD
[7] L.Prost *et al.*, Proc. of HB2006, Tsukuba, Japan, May 29-June 2, 2006, WEAY02
[8] L.Prost *et al.*, Proc. of RuPAC'06, Novosibirsk, September 10-14, 2006, WEBO02
[9] M. Beutelspacher *et al.*, Proc. of EPAC'00, Vienna, 26-30 June 2000, p. 530

CHARACTERISTICS OF THE MAGNETIC CHANNEL IN THE YOKE HOLE OF K500 SUPERCONDUCTING CYCLOTRON

J. Pradhan, U Bhunia, J Debnath, S Paul, Z A Naseer, A Dutta, S Bhattacharya,MK Dey, C Mallik and RK Bhandari,
Variable Energy Cyclotron Centre, I/AF, Bidhan Nagar, Kolkata-700 064,INDIA

Abstract

The detail magnetic field measurement of K-500 superconducting cyclotron has been carried out. The last magnetic channel of the extraction system placed in the yoke hole of the cyclotron before external beam line is active, unlike others, which are all passive. This channel comprises a coil and a special shaped iron to produce both quadrupole and dipole field for focussing and radially aligning the different ion species coming out from the cyclotron, with the external beam transport line. The magnetic field inside the channel along with the outside stray field has been measured for different channel currents as well as main magnet excitations. A 3-D model of the full magnet is constructed using magneto- static code RADIA [2] to simulate the yoke field. This paper reports the comparative study of measured and calculated field and studies the trajectories for the representative ions through the stray field calculated from the model. The later being used to locate the starting point (or matching point) for the external beam transport line.

INTRODUCTION

The main magnet of K-500 superconducting cyclotron (SCC) consist of two coils (α coil and β coil), which has been excited to different measurement grid points and detail field mapping is carried out. The last magnetic channel of the extraction system is located in the yoke hole and is active unlike others, which are all passive. This channel is used to focus the beam radially as it passes through the yoke and also help to align the beam with the central trajectory of the external beam line. The magnetic field can be changed by varying channel current in both positive and negative direction, depending on the requirement of different ion species. The channel consists of ten pancake coils made up of 6mm × 6 mm hollow copper conductor. Its tapered iron pole piece (as shown in fig. 2) produces constant gradient field. The uniformity of the field gradient is maintained to avoid the deterioration of the exit beam quality. The detail design studies have been published elsewhere [1]. This paper reports the results of field measurement inside the channel and its comparison with the results of 3-Dimensional magneto-static code RADIA [2]. Particles with different charge to mass ratio and final energy have different trajectories along the extraction path. So the particle tracking for different representative ions is performed to locate the matching point of the external beam transport line.

MEASUREMENT SCHEME

The magnet was mapped using a special zig, which is inserted inside the channel. The field is measured with the help of transverse hall probes and F W Bell make gauss meter. The measurements are performed under three main coil excitations: I_α / I_β= 300 A/300 A; I_α / I_β= 575 A/75 A; and I_α / I_β= 459 A/471 A. The channel current is varied from 0A to 300A in both positive and negative direction. Fields have been measured on a rectangular grid aligned with channel, having long dimension (+z) pointing in the direction of the beam. In the transverse direction (x), there were three points for each z, measured at –8mm, 0, +8 mm from the centre of zig. The measurement step is 0.5 inch along z direction. The stray magnetic field outside the main magnet is also measured up to about 5 m from the yoke.

FIELD SIMULATION AND RESULTS

This active magnetic channel is situated in the yoke hole and it is necessary to generate the yoke field for estimating the actual field inside the channel and compare it with the experimentally measured data. A complete 3-D model of K-500 SCC main magnet is made with the help of code RADIA. This is three sector cyclotron having mirror symmetry about its median plane. The median plane view of the magnet along with channel in the yoke hole is shown in figure 1.

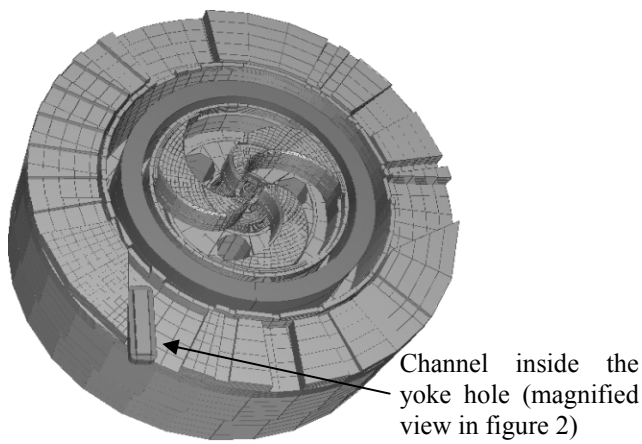

Figure 1. Median plane view of main magnet of K-500 Superconducting Cyclotron (SCC)

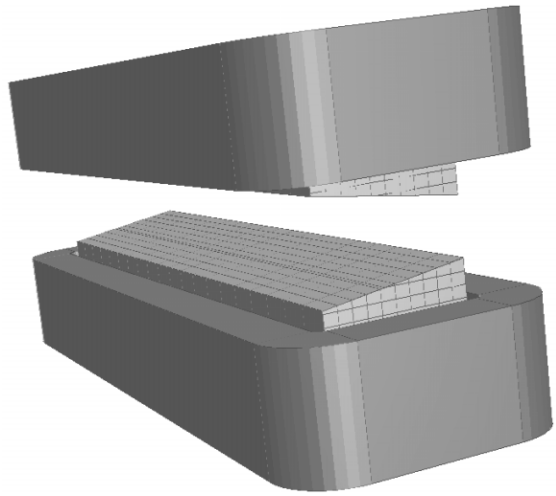

Figure 2. Magnified view of the magnetic channel

This model is also used to generate field in the extraction region, which is otherwise difficult to measure. The comparison is made using some scaling with measured data (accelerator and extraction region) and shows reasonable good agreement, in spite of various computational limitations like block sizes, material property and so on. The data in the yoke hole with channel and stray field outside are discussed here. The longitudinal field along the length of the channel with the channel centre at Z=0 is shown in figure 3.The stray field outside the yoke of main magnet is shown up to 20 inches from the channel centre. Similarly the increase of field gradient with the channel central field is compared and shown in figure 4. Moreover the deviation of calculated field gradient from measured data is more than 10% in higher field. This is possibility due to the saturation of iron in higher field besides others. The measured central field (Bc) inside the channel at zero channel current for four different excitations of the main coil increases linearly with the current and is in good agreement with the calculation as shown in figure 5.

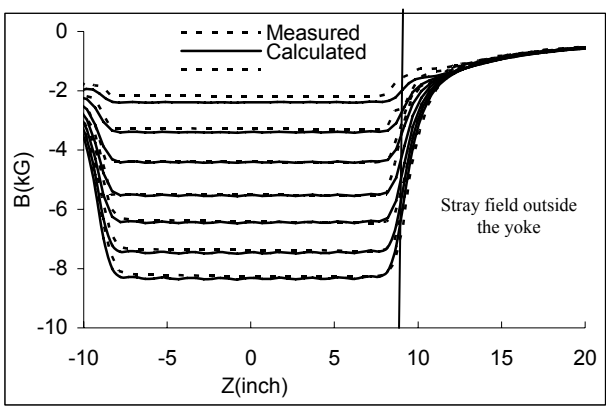

Figure 3. Longitudinal field inside the channel

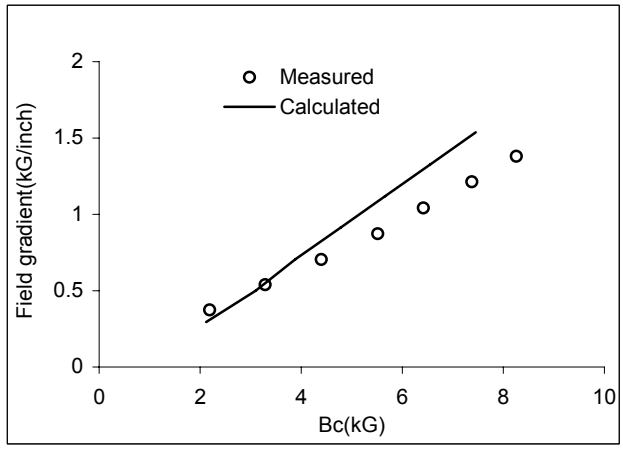

Figure 4. Field gradient at different field (Bc)

The comparison between the measured data and the calculated results using some scaling is made in order to confirm the reliability of the simulated model. It will be used for extrapolation to higher excitation where we are unable to take data. Still the calculation shows some deviation, which can be improved further.

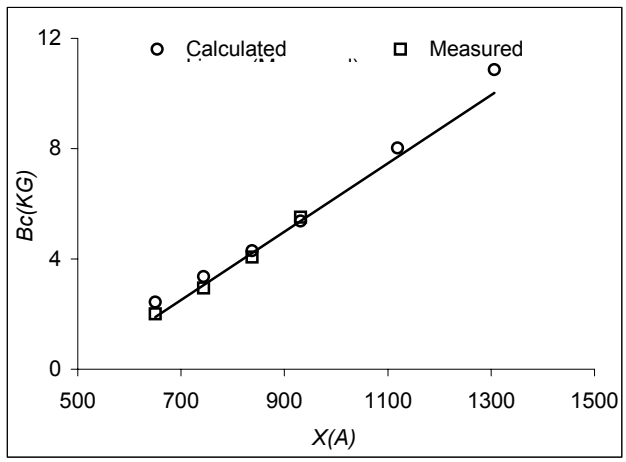

Figure 5. Central field (Bc) at zero channel current for different main coil excitation, where $X=I_\alpha+I_\beta$ & $Y=(7\times I_\alpha-3\times I_\beta-800)/3=333.33$

PARTICLE TRACKING

It is necessary to bring the central trajectory of different beams coming out of the cyclotron to be aligned with central axis of the external beam line. So the trajectories of the representative ions covering the operating region of K-500 cyclotron are studied. There is a slit located just before the channel. The beam is tracked from the slit to some distance beyond the yoke through the field obtained from the RADIA calculation and by running computer routines, which integrates the equations of motion. It is found that by tuning the available channel currents, all the particles could be

forced to deflect through a common point. Just one steering magnet at that point is needed to align all the beams along the successive external beam transfer line.

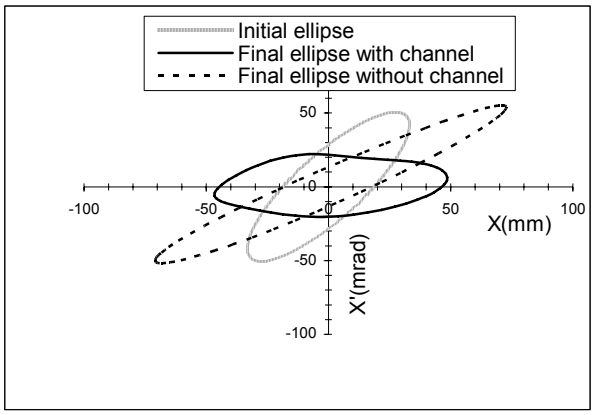

Figure 6. Radial phase space ellipse at the entrance and at the exit from the channel for the ion Z/A=0.25 and T/A=30MeV/n

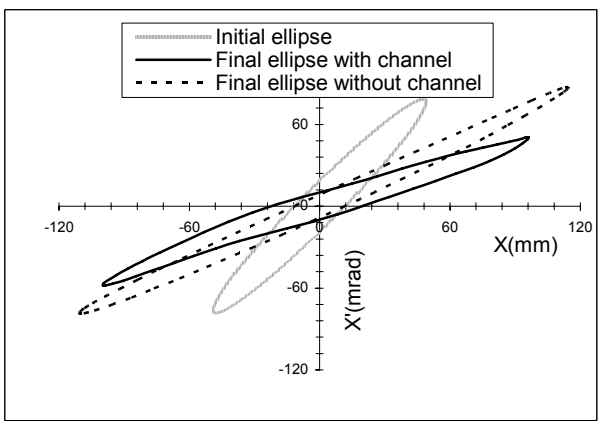

Figure 7. Radial phase space ellipse at the entrance and at the exit from the channel for the ion Z/A=0.5 and T/A=56MeV/n

Phase space ellipse is tracked through the yoke traversal path for different ion species. The initial phase space ellipse at the slit location is obtained from the detail beam dynamics calculation, which is discussed elsewhere [3]. Results of radial phase space (area ~ 950 π mm-mrad) at the entrance of the slit and the exit from the yoke for the two cases with and without magnetic channel inside the yoke hole is presented in figure 6 and figure 7 respectively. A focusing effect is evident from the figures, in presence of channel in the yoke hole with relatively small divergence and beam size, which do not pose any problem for the successive beam handling.

CONCLUSION

The comparison between the RADIA simulations and measured data was made to know whether the code can be use to generate field data, where the measurements are not performed. It is found that with proper use of scaling function and of course with further development, the code can be used to serve the purpose. The study of particle tracking of all the ion species yield the common point for all the beams and one steering magnet at that point is needed to align all the beams along the successive external beam transfer line. Because of relatively small divergences and beam sizes, at the exit of the channel it will not be any problem for successive beam handling.

ACKNOWLEDGEMENTS

The authors would like to thank all the colleagues of the field measurement team for their support and co-operation. Their contribution led to the successful completion of the magnetic field measurement.

REFERENCES

[1] J Pradhan et al., “Design of Active Magnetic Channel M9 for the Extraction System of VECC K-500 Superconducting Cyclotron”,Presented in InPAC-2003 at RRCAT, Indore.

[2] RADIA Technical Reference Manual ESRF, Grenoble, France

[3] S Paul et al., “ Characteristics of Beam Extraction System of K-500 Superconducting Cyclotron” presenting in APAC-2007 at RRCAT, Indore.

ADIABATIC DAMPING OF THE BUNCH-LENGTH IN THE INDUCTION SYNCHROTRON

Tanuja Dixit#, The Graduate University for Advanced Studies, Hayama, Miura, Kanagawa 240-0193, Japan
Yoshito Shimosaki, Ken Takayama, Accelerator Laboratory, High Energy Accelerator Research Organization (KEK), 1-1 Oho, Tsukuba, Ibaraki, 305-0801, Japan

Abstract

It was observed that a bunch-length shrunk with acceleration in the Induction Synchrotron (IS) experiment, where a single proton-bunch injected from the 500 MeV Booster was accelerated to 6 GeV in the KEK-PS. A novel technique capable of quantitatively predicting the adiabatic phenomenon of bunch shortening has been developed, based on a hypothesis that the particle oscillation amplitude varies inversely proportional to the square root of its oscillation frequency. The experimental result and analytical prediction is in good agreement with each other.

INTRODUCTION

The induction acceleration experiment was carried out using the KEK 12 GeV proton synchrotron (12GeV-PS) in a series of experiments to demonstrate a proof of principle of the IS [1], the schematics of which is shown in Fig. 1. Details of the experiments have been described in the literatures [2,3,4].

A specific property of the functional separation of acceleration and confinement in the IS allows us to control the beam size through the entire period of acceleration. However, the accelerated beam bunch is subjected to adiabatic damping, as seen in the conventional RF synchrotron. It is quite important to know how the bunch size evolves through the entire acceleration in the IS and what factors dominantly determine the bunch size. A theoretical approach to predict the temporal evolution of the bunch size is developed. After the approach is carefully justified by comparing with computer simulations, the theoretical prediction is compared with the experimental results. Last we will discuss how this theoretical approach can provide a useful tool to estimate a temporal evolution of the bunch size associated with adiabatic changes in the external parameters, such as the barrier voltage amplitude and a time-interval between barrier voltages.

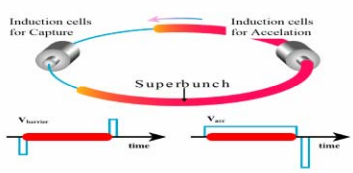

Figure 1: Schematic view of the Induction Synchrotron

#tanuja@www-accps.kek.jp

EXPERIMENTAL RESULTS

The bunch profile which was monitored by the wall current monitor, was recorded every 33 msec from the injection to the end of acceleration. Experimental results through the entire acceleration period are plotted for typical four shots in Fig. 3, where the bunch size is defined as a width measured at 5% of the peak height. From Fig. 3, we can clearly identify four regions: At the injection (I), the bunch width is 100 nsec but it quickly increases to ~ 400 nsec because of mismatching to the barrier bucket [3]. Tumbling of the bunch in the phase space and the succeeding filamentation are apparent there, leading to a long bunch width. In the remaining minimal field region (II) before acceleration, the bunch size is almost constant. This implies good matching with the barrier bucket shape throughout the region. The initial acceleration region (III) is characterized by serious beam loss as shown in Fig. 2. Quick shrinking of the beam size is caused by the beam loss in addition to damping associated with acceleration. The reason of beam loss is not fully understood, although it is speculated that the control of the trigger pulse density is not enough at this transient region. There is no beam loss in the constant acceleration region (IV). A steady state damping is clear. Near the end of acceleration region, the bunch width is almost constant. We will discuss more about this region hereafter.

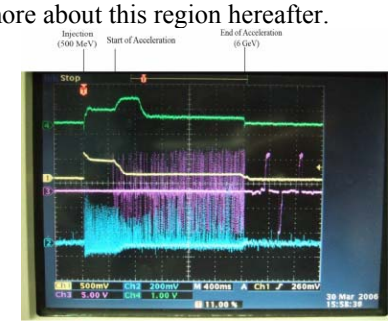

Figure 2: Experimental results. From top to bottom, ΔR signal, beam current, acceleration voltage pulses, and bunch signal

THEORY

To develop the theory, we set a hypothesis that the phase oscillation evolves such that the instantaneous oscillation amplitude is inversely proportional to the square root of the phase oscillation frequency. This hypothesis is originated from an analogy of the WKB solution for a harmonic oscillator with slowly varying

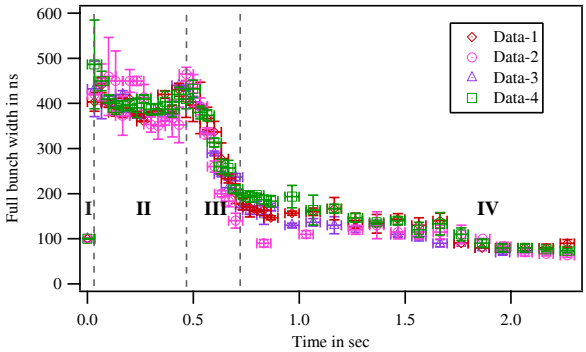

Figure 3: Evolution of the bunch length in time.

parameters. Note that the phase motion of a particle trapped in the barrier voltages strongly depends on the oscillation amplitude; in this sense, the motion is a nonlinear motion. The hypothesis has been justified by comparing the prediction from the hypothesis with computer simulations assuming completely same parameters to characterize the motion in reference [5]. Here, an analytical formula to give the temporal evolution of the oscillation amplitude, which represents an outer bunch-edge, is briefly introduced below.

For simplicity, the induction cells for acceleration and confinement are represented by a single device in the present acceleration model. Two dynamical variables of energy E and phase ϕ are used. The former is the total energy of a particle. The latter is defined by $\omega_s t$, where ω_s is the angular revolution frequency of the ideal particle (synchronous particle) and t is time. Note that the synchronous particle is always accelerated with the designed acceleration voltage V_{ac}, which is uniquely determined by the magnetic ramping pattern of accelerator in terms of $\rho C_0 dB/dt$, where ρ is the bending radius, C_0 is the machine circumference, and B is the magnetic flux density. Its dynamical variable has a subscript "s". These dynamical variables are measured right before entering the above representative acceleration device. Introducing $W = \Delta E/\omega_s$ and ($\Delta E = E - E_s$), changes in W and ϕ per turn can be given by

$$\begin{cases} \dfrac{dW}{dt} = \dfrac{e\left[V(\phi) - V_{ac}\right]}{2\pi} \\ \dfrac{d\phi}{dt} = \dfrac{\omega_s^2 \eta}{(\beta_s)^2 E_s} W \end{cases}, \quad (1)$$

where e is the unit charge, $V(\phi)$ is the induction voltage seen by a particle, $V(\phi) = V_{bb} + V_{ac}$, η is the slippage factor defined by $1/\gamma_T^2 - 1/\gamma_s^2$ (γ_T is the transition gamma of the accelerator ring) and β and γ are the relativistic beta and gamma, respectively. We assume the barrier voltages V_{bb} with a trapezoidal profile as depicted in Fig. 4a. As the parameters of η, β_s, γ_s, E_s, and ω_s can be regarded as constant for a short time period of the single synchrotron period, the orbit in the phase space is closed; it is nothing but the contour derived from the Hamiltonian, which mimics the barrier bucket shape as depicted in Fig. 4b. The motion in the barrier bucket is qualitatively divided into three regions: (I) focusing in the linear potential, (II) focusing in the parabolic potential, and (III) drift in the null voltage region. It is noted that the motion in region (I) and (II) is subject to adiabatic damping. In addition, it is emphasized that the exact solution throughout the region is known for the above short time period.

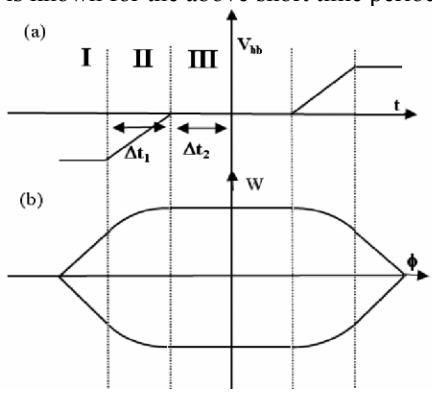

Figure 4: (a) Barrier voltage profile with three distinct regions and peak height of V_0. (b) Typical trajectory in the phase space

To analyze the temporal evolution of this oscillation amplitude associated with acceleration, we start from the canonical Eq. (1). From Eq. (1), we have the second-order differential equation with respect to ϕ,

$$\frac{d^2\phi}{dt^2} - \frac{(dA/dt)}{A(t)} \cdot \frac{d\phi}{dt} + \frac{eV_{bb}(\phi)A(t)}{2\pi} = 0, \quad (2)$$

where the abbreviation $A(t) = |\eta| \omega_s^2 / \beta_s E_s$ is used. A temporal change in the phase of an individual particle is governed by Eq. (2). Since the parameters in this equation include all information associated with acceleration, its solution can tell us what happens in the phase motion through the entire acceleration period. To eliminate the damping term, a new variable $u(t) = \phi(t)/v(t)$ is introduced. When $v(t) = A^{1/2}$, Eq.(2) reduces to

$$\frac{d^2u}{dt^2} + \left[\frac{d^2A/dt^2}{2A(t)} - \frac{3}{4} \frac{(dA/dt)^2}{A^2(t)} \right] \cdot u(t) + B(t) = 0, \quad (3)$$

where $B(t) = eV_{bb}(\phi)A^{1/2}/2\pi$. Since $A(t)$ is a slowly varying function of time, its first-order and second-order time-derivatives are small. Accordingly, the second term in the left-hand side of Eq. (3) can be ignored in the further derivation. We arrive at a final form of the phase oscillation equation that must be substantially solved, $d^2u/dt^2 = -B(t)$. The restoring force $B(t)$ can be assumed to be constant during a single synchrotron oscillation period T, which is much shorter than $1/(dA/dt)/A$. In addition, the synchrotron oscillation is symmetric in the phase space, as depicted in Fig. 4b. If we obtain exact solutions in three regions of I, II, and III in Fig.4a, the synchrotron frequency $\Omega_s = 2\pi/T$ is written in an analytic form [5]. From the hypothesis, the instantaneous amplitude of the phase, $\langle\phi\rangle$, is given by

$$\langle\phi\rangle = C \frac{\sqrt{A}}{\sqrt{\Omega_s}}, \quad (4)$$

where C is a constant coefficient determined from the initial condition. Introducing the instantaneous oscillation amplitude in time $<\tau>=<\phi>/\omega_s$ and substituting the analytic form into Eq. (4), we obtain

$$\langle\tau\rangle^2 = C^2\sqrt{\frac{8\eta\Delta t_1}{\pi\omega_s eV_{bb}\beta_s^2 E_s}}\left\{\sqrt{\frac{2}{\Delta t_1}\left\{\langle\tau\rangle-(\Delta t_1+\Delta t_2)\right\}}+\sin^{-1}\left[\frac{\Delta t_1}{\sqrt{\Delta t_1^2+2\Delta t_1\left\{\langle\tau\rangle-(\Delta t_1+\Delta t_2)\right\}}}\right]+\frac{\Delta t_2}{\sqrt{\Delta t_1^2+2\Delta t_1\left\{\langle\tau\rangle-(\Delta t_1+\Delta t_2)\right\}}}\right\} \quad (5)$$

Equation (5) is a transcendent function of $<\tau>$. Note that the equation includes information about the initial condition of an individual particle through the term of C, the barrier conditions of V_0, Δt_1, and Δt_2, and the parameters of ω_s, β_s, E_s, and η uniquely determined for a fixed accelerator. By solving Eq. (5), we can obtain the temporal evolution of the oscillation amplitude in time associated with the acceleration.

Here, we have to pay our attention on an important feature in the adiabatic damping of the synchrotron oscillation. If the barrier condition is maintained to be a constant, a particle, the oscillation amplitude of which has initially extended to the flat barrier region (I), will fall in the linear barrier region (II) as a result of the adiabatic damping. In this situation, Eq. (5) becomes invalid. Beyond the boundary between the linear and quadratic potentials, the analytical form for the synchrotron oscillation changes. The instantaneous oscillation amplitude in time must satisfy the following relationship,

$$\langle\tau\rangle^2 = C^2\sqrt{\frac{8\eta\Delta t_1}{\pi\omega_s eV_{bb}\beta_s^2 E_s}}\left\{\frac{\pi}{2}+\frac{\Delta t_2}{\left[\langle\tau\rangle-\Delta t_2\right]}\right\}, \quad (6)$$

where C is determined from the boundary condition. Consequently, Eq. (5) and Eq. (6) gives the oscillation amplitude in the regions where $<\tau> > (\Delta t_1+\Delta t_2)$ and $<\tau> < (\Delta t_1+\Delta t_2)$, respectively. These two solutions should be connected at $<\tau> = (\Delta t_1+\Delta t_2)$.

The present result has been obtained assuming the trapezoidal profile of the barrier voltage. It is straightforward to know the temporal evolution of the oscillation amplitude $<\tau>$ for more extreme profiles, such as a rectangular profile ($\Delta t_1=0$), a short profile ($\Delta t_2=0$), and a discrete profile ($\Delta t_1=\Delta t_2=0$). For the rectangular profile,

$$\langle\tau\rangle^2 = C^2\sqrt{\frac{8\eta}{\pi\omega_s eV_{bb}\beta_s^2 E_s}}\left\{\sqrt{2\left(\langle\tau\rangle-\Delta t_2\right)}+\frac{\Delta t_2}{\sqrt{2\left(\langle\tau\rangle-\Delta t_2\right)}}\right\} \quad (7)$$

This form mostly suggests a particular feature of the adiabatic damping in the induction synchrotron, which can be distinguished from that in RF synchrotrons. A solution of Eq. (7) is always written in terms of $<\tau>=g(t,\Delta t_2)+\Delta t_2$, where $g(t,\Delta t_2)$ is a slowly varying function of t and is subjected to adiabatic damping and gradually becomes smaller. Since the isolated offset term of Δt_2 is controllable, the oscillation amplitude can be maintained in a well controlled manner throughout the acceleration, as expected.

COMPARISON WITH EXPERIMENTAL RESULTS

Experimental results and analytical predictions can be compared only after loss at the beginning of acceleration, i.e. from 0.633 sec from injection as shown in Fig. 3. From this time onwards bunch shrinking can be attributed only to adiabatic damping. Assuming an initial bunch length of 190 nsec, which was taken from the experimental result at t=0.633 sec, the theoretical prediction is plotted in Fig. 5. We can see that both are in fairly good agreement.

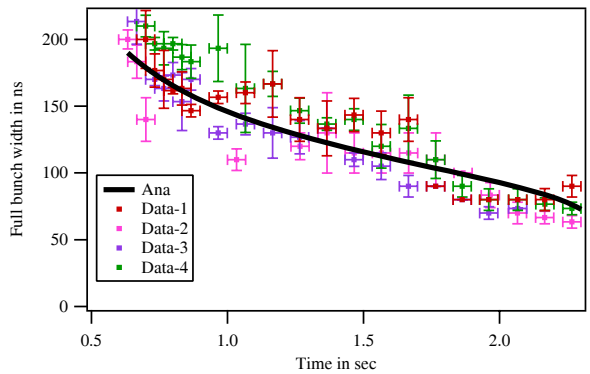

Figure 5: Comparison between the experimental results and theoretical predictions after 0.633 sec from injection.

SUMMARY

A novel theory to estimate adiabatic damping phenomenon in the induction synchrotron has been presented. The theory is based on an analogy of the WKB solution for a harmonic oscillator, the parameters of which slowly vary in time. It has turned out that the theory can quantitatively explain the experimental results. In RF synchrotrons the bunch size infinitely shrinks beyond transition energy. We know that this is intrinsic feature in the RF synchrotrons. However, this is not the case in an induction synchrotron. The bunch-length in an induction synchrotron is mainly determined with the time duration between barrier voltages as expected. This fact has been proven mathematically.

The present research has been supported by a Grant-In-Aid for Creative Scientific Research (KAKENHI 15GS0217).

REFERENCES

[1] K.Takayama and J.Kishiro, *Nucl. Inst. Meth. in Phys. Res.* A 451, 304-317 (2000).
[2] K.Takayama *et al.*, *Phys. Rev. Lett.* 94, 144801-4 (2005).
[3] K.Torikai *et al.*, KEK Preprint 2005-80 (2005), submitted for publication.
[4] K.Takayama et al., "Experimental Demonstration of the Induction Synchrotron", *Phys. Rev. Lett.* Feb. issue (2007).
[5] T.Dixit, Y.Shimosaki, and K.Takayama, submitted for publication (2007).

INSTALLATION AND RADIATION MAINTENANCE SCENARIO FOR J-PARC 50 GEV SYNCHROTRON

M. Yoshioka, T. Fujino, H. Kobayashi, Y. Hori, K. Ishii, T. Kubo, H. Matsumoto, T. Oogoe, Y. Saito, Y. Sato, M. Shimamoto, Y. Takeuchi, M. J. Shirakata, M. Uota, Y. Watanabe
KEK, 1-1 Oho, Tsukuba, Ibaraki, Japan
M. Hosokawa, THK CO., LTD., 2-2-7 Sasano-cho, Hitachinaka, Ibaraki, Japan
Y. Kuniyasu, Mitsubishi Electric System & Service Co., LTD.,
2-8-8 Umezono, Tsukuba, Ibaraki, Japan
H. Oki, KDC Engineering Co., LTD., 1-58-4 Yayoi-cho, Nakano-ku, Tokyo, Japan

Abstract

This paper describes the installation of the accelerator components and the installation schedule for the 50 GeV J-PARC Synchrotron and the maintenance scenario for the handling of radioactive components.

INTRODUCTION

J-PARC is a high intensity proton synchrotron, which KEK and JAEA are jointly constructing at Tokai [1,2]. The accelerator is composed of a 181 MeV linac, a 3 GeV Rapid Cycling Synchrotron (25Hz, RCS), and a 50 GeV Slow Cycling Synchrotron (0.3Hz, MR) which has a circumference of 1568 m. The RCS primarily provides a 1 MW proton beam to a material and life science experimental facility. The MR receives part of the RCS beam (~5%) through the beam transport line (BT), which is 220 m long; after the MR accelerates it to the maximum 50 GeV, the extracted beam with an intensity of 750 kW is sent to two experimental facilities. Fast extraction delivers a beam for the long base line neutrino experiment T2K, slow extraction is used for the Hadron experiment. This paper describes the installation of accelerator components for the MR and a maintenance scenario for the handling of radioactive components.

Beam loss is the major factor which limits the operation of J-PARC. Once accelerator components become highly activated by any lost beam, it becomes very difficult to maintain components in the area. Our experience with KEK's 12 GeV proton synchrotron (PS), which was decommissioned in March last year, has shown us that the radiation exposure to workers would exceed the permissible level unless the radioactivity at the location where the workers would be is less than 0.5 mSv/h. The beam intensity of the PS was 5 kW, which is less than 1% of the J-PARC design, but beam losses sometimes reached 500 W, producing radiation levels exceeded 10 mSv/h in the immediate area. For the J-PARC MR, the expectation is that the beam losses should concentrate in the five areas shown in Figure 1 and that the beam loss everywhere outside these five areas should be at less than 0.5 W/m. According we designed the aperture of MR carefully considering this scenario. In order to cut the beam halo locally, there will be two collimator systems [3], one upstream in the BT and one in the MR. Septum magnets for beam injection and extraction are the most critical MR components in this regard. Necessarily the septum magnets aperture is ultimately a trade-off where electromagnetic and mechanical requirements are compromised, and we have to accept a certain amount of beam loss. Given that, we have worked out a safe and yet practical maintenance scenario for possible required replacement of the units comprising the two collimators, the beam injection, slow extraction, and fast extraction systems.

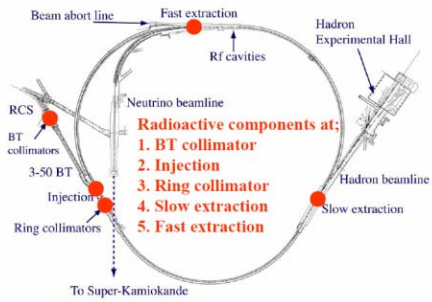

Figure 1: Location of radioactive components

INSTALLATION OF MAGNETS

Installation

The BT and MR magnet quantities and weights are shown in Table 1.

Table 1: BT and MR magnets

	Type of Magnet	Qty.	Weight (ton)
MR	Dipole	96	33
	Quadrupole	216	10~15
	Sextupole	72	2
	Resonant Sextupole	8	2
	Corrector dipole	186	0.3
BT	Pulse dipole	1	16
	Horizontal dipole	3	14~18
	Vertical dipole	2	4.5
	Quadrupole	38	3.5~5.5
	Corrector dipole	14	0.75

The floor level of the accelerator tunnel is excavated ~11 m below the ground surface. Magnets are unloaded at a carry-in vertical shaft by crane and conveyed to the accelerator tunnel by truck. The BT has a crane which is used to install the magnets in the accelerator tunnel. The two straight sections for fast and slow extraction in the

MR also have cranes, but there are no other cranes in the MR. As seen in Figure 2, we used an air floatation transport systems of custom design (the air pallet) to transport and install the bending and focusing magnets which weigh 10~33 tons each. After the magnets are transported to their predefined locations, the bed of the air pallet which holds the magnets is separated from the moving transport part. Finally the magnets are moved on to the beam line and positioned manually. A conventional truck and temporary crane were used to transport and install small correction magnets and other parts. The interior cross section of the standard parts of the tunnel is 5 m wide and 3.5 m high which provides adequate workspace. By now we have almost finished installing magnets everywhere except in the straight sections. We will concurrently be installing cables, completing the vacuum and beam diagnostic systems, and connecting cooling water to the magnets. We will start installing beam injection, fast beam extraction, and the RF acceleration system in September 2007, and finish most of the installation work by the end of November 2007. Off-beam commissioning will start in December 2007, and MR beam commissioning will begin in May 2008. The slow extraction system, however, is scheduled to be installed between July and September 2008.

Figure 2: air float transportation system

Uneven Settlement of Accelerator Tunnel Floor

Two problems have arisen because we are installing magnets as soon as possible after civil construction is completed for each tunnel section; this is necessary to meet J-PARC's overall construction schedule. One problem is the difficulty of managing and scheduling concurrent operations, and the other is the large and uneven settlement of the floor level [4]. Settling of up to a maximum of 40 mm has occurred in places, and there is no sign of stabilization yet. We can solve the first problem through our own effort, but we have no solution for the second but to wait until the ground finally compacts solidly. The subsurface at the site is composed of mudstones, and the topology of both the bedrock and the terrain above are complicated because the work of the rivers that formed the complicated subsurface terrain during the past hundred thousand years is buried. Currently we are adjusting the magnet alignment only as much as needed to connect the vacuum ducts, but we will need to redo the magnet setting and do precise alignment before the beam commissioning which is scheduled to start in May 2008.

MAINTENANCE SCENARIO FOR RADIOACTIVE COMPONENTS

General Description

We need to make the septum magnets replaceable in order to upgrade beam performance, to decrease beam loss, and to improve reliability. However, direct hands-on manual maintenance work may be out of the question because of residual radiation, such as when a septum magnet fails to operate properly. In such a case, workers would have to remain several meters away from the septum magnet in order to decrease their radiation exposure all the while somehow detaching and extracting the magnet from the beam line quickly. The procedure would involve first detaching vacuum flanges, disconnecting the cooling water plumbing and electrical cables, and finally moving the magnet away to where it could be dismantled and worked on. In this paper, we will focus on our concept for detaching the vacuum flange and uninstalling the magnet, as both of these have a large impact on the magnet design.

Vacuum flange and semi-remote handling

To reduce the time required working with the flanges, in cooperation with Cefilac we decided to chose a large aperture quick-disconnect ISO 1609 compliant vacuum flange system. We also selected the Cefilac Helicoflex-delta type for the vacuum seal because its compressive force requirement is small. This Cefilac product line offers several flange apertures ranging from 180 mm to 450 mm. Here, we will describe the common mechanism necessary for semi-remote handling. We focus on the bellows and flange components in the vacuum system. The procedure for disconnecting the vacuum connection is divided into two steps of (a) loosening the chain clamp which releases the flange and (b) compressing the bellows to open a gap between the two flange surfaces of more than 15 mm.

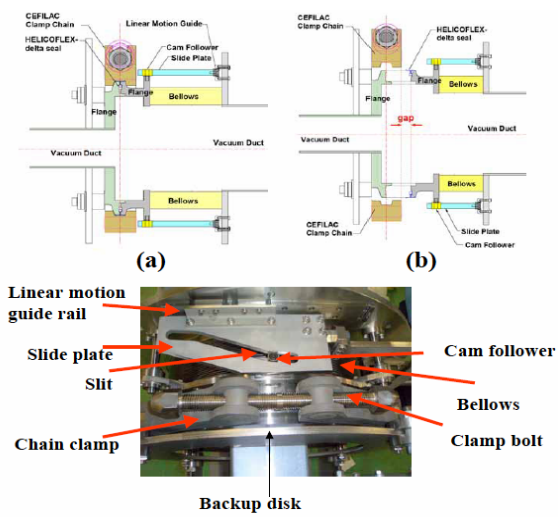

Figure 3: Semi-remote handling vacuum flange(a) Loosen the chain clamp, (b) compress the bellows

As shown in Figure 3, the chain clamp is attached to the backup disk. Depending on the magnet type and where it is situated, the backup disk may be fixed to the vacuum duct, to the magnet itself, or be supported on an independent stand. As the clamp bolts are loosened, the clearance about the flange opens evenly because of a spring set inside the clamp. The clamp bolts can be loosened using a special tool from a position several meters away from the magnet. The other half of the flange is welded to the bellows. Two cam followers are affixed above and below the bellows on the flange side. The linear motion guide rail is fixed perpendicular to the beam axis. One can push the slide plate, which is mounted on the rail, using another long special tool. The plate has a slit at 30 degrees against the right angle of the beam axis, and the cam follower moves inside the slit in the direction of the beam. This allows the bellows to be compressed along to the direction of the beam. Roughly reverse steps are required to reconnect the flange; the flange has a self-aligning design to allow mating the connection even if the original flange centers are off by up to 1.5 mm. Because the guide rail needs a lubricant agent, its radiation resistance is an important design criterion. We have selected a lubricant agent which should have enough radiation hardness.

Detaching magnets and reinstalling them

Next we move on to describe the scenario for moving the magnet away after detaching the vacuum flanges, cooling water, and various cables which tie it to the beam line. We originally planned to use the same air pallet built for the magnet installation but we then concluded that it was not suitable for providing the stable and precise control needed because the distance between the two flange surfaces may be only 15 mm at minimum. Therefore we have worked out an alternatively method. After installing a linear motion guide rail perpendicular to the beam on the tunnel floor, we place the septum magnets and the support table on the linear motion guide rail. In the initial installment, the rail, support table, and septum magnets are fixed after they are aligned to the necessary precision. Locating brackets have a structure that allows for easy detachment by semi-remote handling, making it possible to move the support table and septum magnets perpendicular to the beam line with a small amount of force. Once they come out of the line, they are loaded on a truck using the setup or temporary crane and transported outside through the tunnel. A general purpose truck is sufficient for this. We are currently examining this mechanism for septum magnets for fast beam extraction. Originally developed for a group of final focusing magnets at the collision point of KEKB [5], this method has been used some dozen times during the past ten years without any trouble. In addition, it has location reproducibility that is less than 20 μm, and we can safely say that it is an established technology.

For installing an entirely new septum magnet, away from the hot area we would build up a mock-up simulating the actual beam line and where the new septum magnet could be a pre-aligned. After that, it could be transported to the accelerator tunnel, and installed on the beam line using the semi-remote procedure.

SUMMARY

We are installing accelerator components to prepare for pre-beam commissioning scheduled to start in December 2007. Installation of magnets will finish soon and the installation of cables, vacuum and beam diagnostic systems, and cooling water connections will go on at a quick tempo. Except for the slow beam extraction system, we will start installing RF acceleration, beam injection and fast beam extraction systems in September 2007.

Installation of accelerator components has been carried out concurrently with the civil construction and uneven foundation settlement remains an issue because of the site ground characteristics. It will be necessary to correct and realign to the required alignment precision before the beam commissioning can begin.

The basic idea of maintenance scenario is to localize areas that might become highly activated by using collimator systems in the BT and MR. Since septum magnets for beam injection and extraction are critical components for the reliable operation of J-PARC and yet have to be where beam loss is inevitable, they should be replaceable. Accordingly a semi-remote handling vacuum flange system has been developed. Septum magnets will be mounted on a linear motion guide rail, which is set on the tunnel floor perpendicular to the beam line. The guide rail will allow smoothly transitioning in and out of the beam line the magnets for beam injection and the two beam extraction systems.

ACKNOWLEDGMENT

This paper describes work done in part by the accelerator team of J-PARC. We have consulted closely with the groups doing remote handling for J-PARC's T2K and Hadron experiments. We also appreciate and profited from exchanging very informative ideas with Dr. N. Holtkamp and the Group of Dr. G. Murdock of SNS (ORNL), and Dr. P. Gear of ISIS (RAL).

REFERENCES

[1] T. Koseki et al., "Present Status of J-PARC MR Synchrotron", This conference,
[2] F. Naito, "Present Status of J-PARC", This conference
[3] M. J. Shirakata et al., Proc. of EPAC'06 Edinburgh, Scotland, June 2006, p. 1148,
[4] M. J. Shirakata et al., "The Magnet Alignment Method for the J-PARC Main Ring", This conference,
[5] K. Kanazawa et al., "The Interaction Region of KEKB", Nuclear Instruments and Methods in Physics Research Section A, Vol. 499, Issue 1, 21 February 2003, p. 75

TRANSVERSE MATCHING OF THE SNS LINAC BASED ON PROFILE MEASUREMENTS*

Dong-o Jeon# and Paul Chu, Oak Ridge National Laboratory, Oak Ridge, TN37831, U.S.A.

Abstract

For a high intensity linac such as the SNS linac, it matters to match adequately to minimize the beam mismatch and potential beam loss. The technique of doing the matching using the wire-scanners in series was employed [1]. It was verified that matching was improved through the matching technique based on the beam profile measurements from wire-scanners in series.

INTRODUCTION

The Spallation Neutron Source (SNS) accelerator system is designed to accelerate intense proton beams to energy of 1-GeV, delivering more than 1.4 MW of beam power to the neutron production target [2]. Being a high intensity linac, a primary concern is potential damage and radio activation of accelerator components resulting from uncontrolled beam losses. A major source of loss is beam halo that intercepts the bore of the linac. It is important to accomplish adequate level of transverse matching between sections of linac.

When emittance measurement device is available, minimization of rms emittance proves to be effective in doing the matching as for the SNS DTL (Drift Tube Linac) tank 1 commissioning [3,4].

Alternatively wire-scanners installed in series can be used to do the matching [1]. For the purpose of transversely matching between two different structures of the SNS linac, four wire-scanners are installed in series. During the beam commissioning runs, the matching technique based on beam profile measurements was tested and the results are presented here.

MATCHING SCL TO HEBT

We applied the technique based on profile measurements to matching the Superconducting Linac (SCL) to the High Energy Beam Transport (HEBT). We performed a Gaussian fit to the measured beam profile and obtained its beam size σ. By fitting the beam envelope from the Trace3D code to the wire-scanner profile data, we obtained the input beam Courant-Snyder parameters β and α, and the beam emittance ε, as shown in Fig. 1. Table 1 lists the incoming beam parameters determined above. The solid circles in Figs. 1 and 2 represent the beam profile data from the wire-scanners in the HEBT and the solid lines represent simulated beam profile obtained from the Trace3D code. It should be noted that there is a mild oscillation in the beam core before the beam enters HEBT at Z=8x10^4 [mm]. The blue color represents the x beam size and the red the y beam size. HEBT starts from 8x10^4 mm in the figure and the upstream of that point is the SCL.

With the beam parameters of the incoming beam determined, the matching quadrupoles are optimized using the Trace3D code to do the matching. When the matching routine completes the matching, we change the matching quadrupoles as suggested and subsequent wire-scanner measurement is done as shown in Fig. 2.

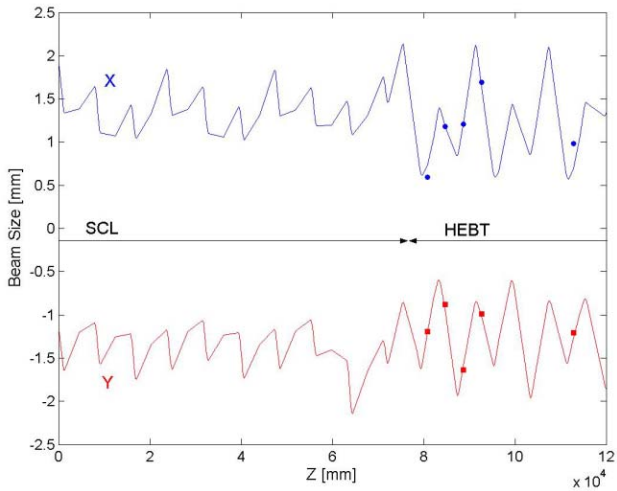

Figure 1: Plots of beam profiles before matching SCL to HEBT. Solid lines are plots of beam size σ [mm] from the Trace3D program and solid circles are wire-scanner measurement data.

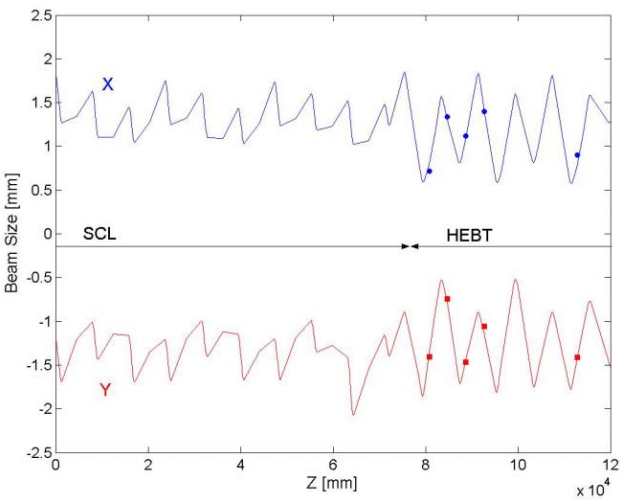

Figure 2: Plots of beam profiles after matching SCL to HEBT. Solid lines are plots of beam size σ [mm] from the Trace3D program and solid circles are wire-scanner measurement data.

* SNS is managed by UT-Battelle, LLC, under contract DE-AC05-00OR22725 for the U.S. Department of Energy.
#jeond@ornl.gov

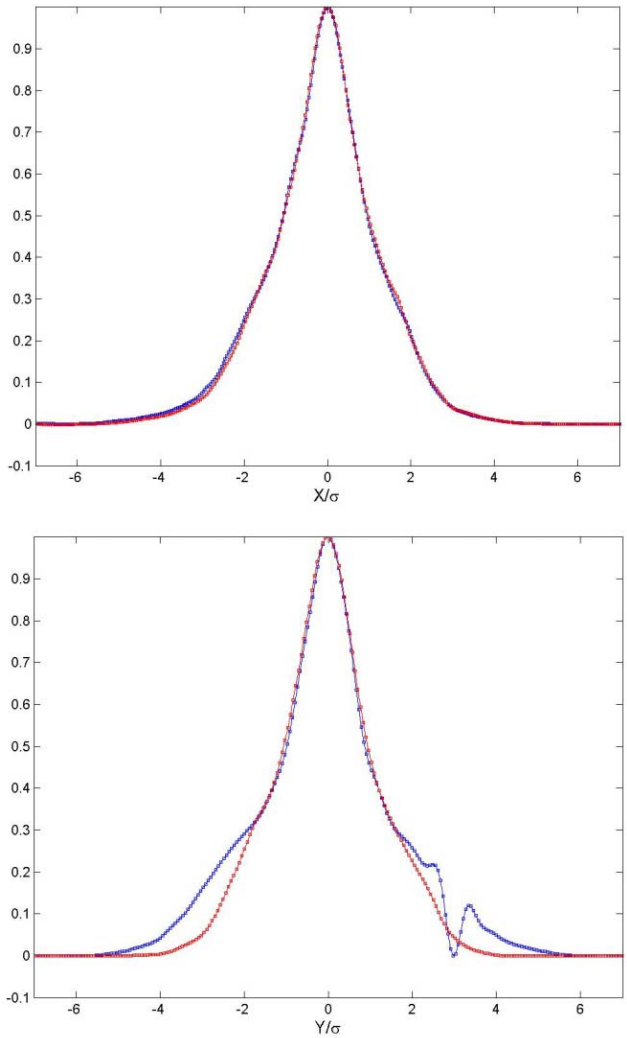

Figure 3: Plots of beam profiles in X plane (upper plot) and Y plane (lower plots). Blue lines are profiles before the matching and red ones after the matching. Reduction in tail is observed in Y plane, while there is little change to the tail in X plane.

Figure 3 illustrates the beam profile change before and after the matching is performed. Reduction in beam tail is observed in Y plane. The glitch in the blue curve of the lower plot is due to the missing beam pulse during the scanning. Further study and measurements will be conducted during coming beam operations.

Table 1: Input beam parameters

	X plane	**Y plane**
ε [mm-mrad]	0.326	0.345
β [m]	16.05	6.36
α	-1.49	0.112

Table 1 lists the input beam parameters at Z=0 in Figs. 1 and 2. ε_x=0.343 and ε_y=0.351 are the normalized rms emittance [mm mrad] of the equivalent uniform beam distribution having the same rms beam size as the beam profile.

MATCHING DTL TO CCL

The same technique was applied to matching the Drift Tube Linac (DTL) to the Coupled Cavity Linac (CCL). At the end of DTL, the proton beam energy is 86.6 MeV. Figure 4 shows the data before the matching and Fig. 5 the data after the matching. The solid circles in Figs. 4 and 5 represent profile measurements in CCL module 1 and 2. The first four wire-scanners were used by the matching routine. It should be noted that the third wire in x plane was malfunctioning as indicated in the figure. Again the blue color represents the x beam size and the red the y beam size. It is clear that the matching in x plane is improved significantly whereas a slight degradation is observed in y plane. We observe an overall improvement in matching.

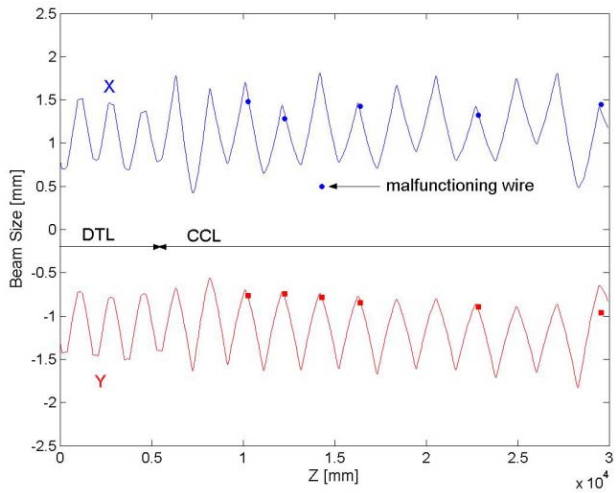

Figure 4: Plots of beam profiles before matching DTL to CCL. Solid lines are plots of beam size σ [mm] from the Trace3D program and solid circles are wire-scanner profile data.

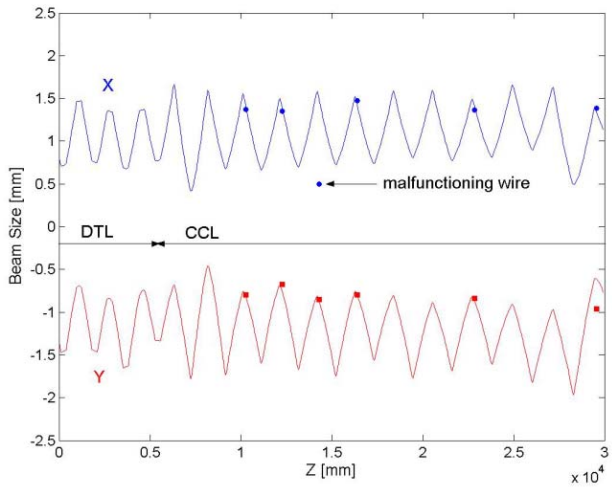

Figure 5: Plots of beam profiles after matching DTL to CCL. Solid lines are plots of beam size σ [mm] from the

Trace3D program and solid circles are wire-scanner profile data.

CONCLUSION

A study of transverse matching of the SNS linac was performed. Positive results were obtained showing that the matching is improved. Further matching study will be conducted for other sections of the SNS linac.

REFERENCES

[1] Dong-o Jeon and J. Stovall, J. Proc. of the 2003 Part. Accel. Conf. (Portland, 2003), p. 2652.
[2] J. Wei et al, Proc. of the 2001 Part. Accel. Conf. (Chicago, 2001), p. 319.
[3] D. Jeon et al, Proc. of the 2004 European Part. Accel. Conf. (Lucerne, Switzerland, 2004), p. 1536.
[4] D. Jeon and J. Stovall, Proc. of the 2003 Part. Accel. Conf. (Portland, 2003), p. 2652.

BENCHMARKING OF MULTIPARTICLE PHASE SCAN AND ACCEPTANCE SCAN TECHNIQUES FOR THE SNS DTL*

Dong-o Jeon#, Oak Ridge National Laboratory, Oak Ridge, TN 37831, U.S.A

Abstract

It is important to bring the cavity rf field amplitude and phase to the design for a high intensity linac such as the Spallation Neutron Source (SNS) linac. A few techniques are available such as the acceptance scan and multiparticle phase scan for tuning the Drift Tube Linac (DTL). During the SNS linac commissioning, tuning of cavities was conducted using the acceptance scan and phase scan technique based on multiparticle simulations. The two techniques are benchmarked.

INTRODUCTION

The Spallation Neutron Source (SNS) accelerator system is designed to accelerate intense proton beams to energy of 1-GeV, delivering more than 1.4 MW of beam power to the neutron production target [1]. The design peak current in the linac is 38mA and the macropulse average current is 26mA due to chopping.

Being a high intensity linac, it is crucial to minimize the machine activation induced by beam loss. Finding the right rf set-point can minimize longitudinal halo formation. Because bunch length is relatively long for the DTL, multiparticle tracking is important to accurately simulate the behavior of beam through each tank.

A few techniques for setting rf set-points were studied in depth in the past [2]. In this paper, we describe and compare the results of two techniques used for tuning the DTL, namely, phase scan using BPMs and acceptance scan using Energy Degrader and Faraday Cup (ED/FC). Experimental data were compared with the multi-particle simulations using the PARMILA code [3]. For general SNS linac commissioning results, please refer to [4].

MULTIPARTICLE PHASE SCAN

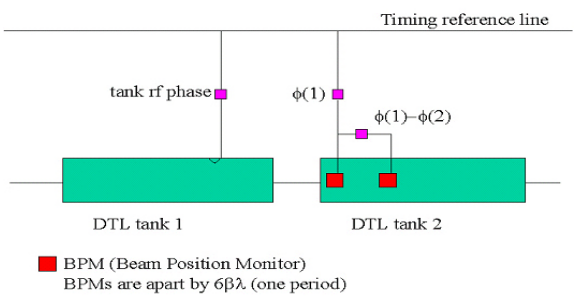

Figure 1: Schematic plot of phase scan with two down-stream BPMs.

The schematic plot of the Phase Scan is in Fig. 1. The two down-stream BPMs of, say, DTL tank 1 are inside DTL tank 2. They are 6βλ apart (a complete period). Phase advance plays an important role in this technique and is a function of tank rf amplitude and the offset from the design rf phase.

Phase Scans were performed using two down-stream BPMs during the SNS linac beam commissioning. The cavity field amplitude, cavity field phase and beam energy are varied to best match the measured values. The simulation is based on multiparticle tracking because bunch is relatively long for DTL tanks 1, 2 and 3.

Phase scan was performed for the DTL tank 1 and the data are shown in Fig. 2. Lines with circles represent the measurement data showing the difference of two BPM phase data ϕ(1)−ϕ(2). Solid lines are Parmila simulations. The agreement between the measurement and simulation is excellent. The rf set-point obtained from this phase scan is (A, ϕ)=(0.179, -125.5°). Here, A is the Low Level RF amplitude and ϕ the LLRF phase. The incoming beam has an energy deviation of –0.0265 MeV from 2.5MeV, that is –1.060 %.

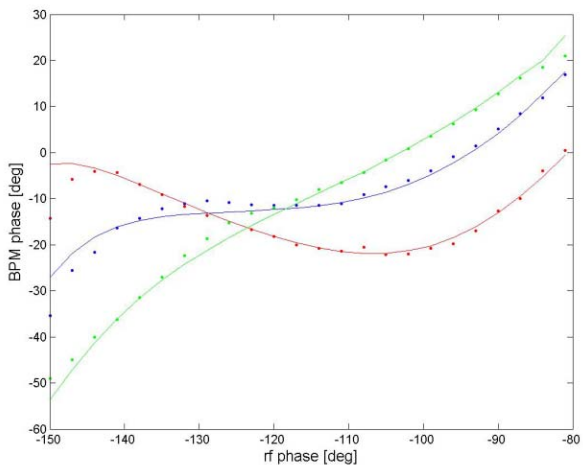

Figure 2: Plots of DTL tank 1 phase scan. Plotted are experimental data (solid lines with circles) and simulation results (solid lines) for three different rf amplitudes.

Phase scan was also performed for the DTL tank 2. The obtained rf set-point is (A, ϕ)=(0.483, 166.5°). The incoming beam has an energy deviation of –0.0236 MeV from 7.523MeV, that is –0.314 %. The plotted data in Fig. 3 are also the phase difference of two BPMs phase data. Now the agreement between the measurement and simulation becomes better.

* SNS is managed by UT-Battelle, LLC, under contract DE-AC05-00OR22725 for the U.S. Department of Energy.
#jeond@ornl.gov

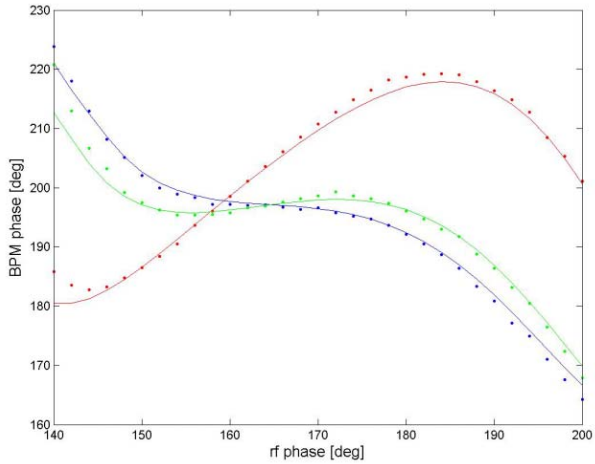

Figure 3: Plots of DTL tank 2 phase scan. Plotted are experimental data (solid lines with circles) and simulation results (solid lines) for three different rf amplitudes.

Phase scan was performed for the DTL tank 3, showing that the rf set-point is (A, ϕ)=(0.490, 105.0°). The incoming beam has an energy deviation of 0.0579 MeV from 22.885MeV, that is 0.254 %. In Fig. 4, the phase difference of two BPMs is plotted.

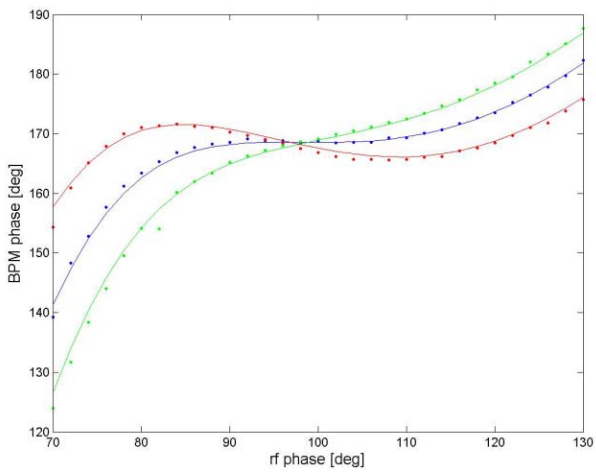

Figure 4: Plots of DTL tank 3 phase scan. Plotted are experimental data (solid lines with circles) and simulation results (solid lines) for three different rf amplitudes.

BENCHMARKING WITH ACCEPTANCE SCAN

Another widely used method for rf set-point is the acceptance scan with the Energy Degrader and Faraday Cup (ED/FC). This is also called phase scan. The absorber removes low energy tail of beam bunch and the surviving beam is collected using the Faraday Cup. A schematic plot of this scheme is shown in Fig. 5.

This technique was widely used in the early commissioning of the SNS DTL. One of the virtues is its simplicity and ease of use. For more reliable and accurate rf set-point, Phase Scan is preferred.

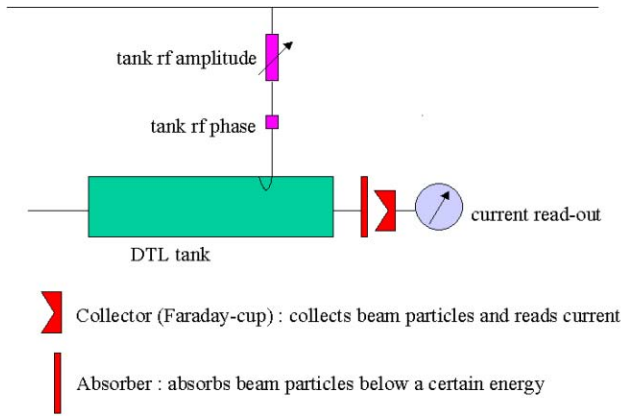

Figure 5: Schematic drawing of acceptance scan with the absorber and collector.

For benchmarking two techniques, acceptance scan was performed for DTL tank 1 to 3 under the identical machine conditions. Figure 6 shows the result of DTL tank 1 acceptance scan, which resulted in an rf set-point of (A, ϕ)=(0.176, -124.6°). Figure 7 shows the result of DTL tank 2 acceptance scan, which resulted in an rf set-point of (A, ϕ)=(0.484, 168.0°). Figure 8 shows the result of DTL tank 3 acceptance scan, which resulted in an rf set-point of (A, ϕ)=(0.494, 104.7°).

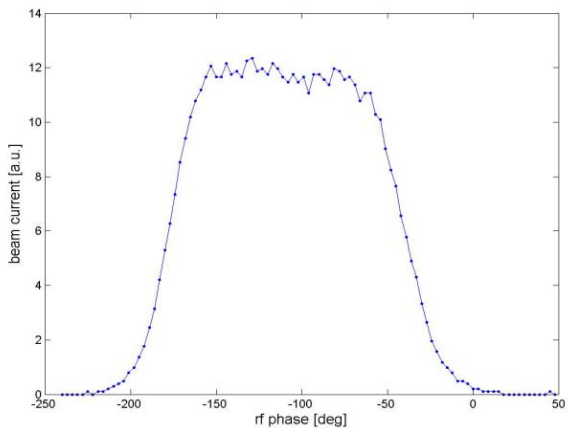

Figure 6: Plot of DTL tank 1 acceptance scan.

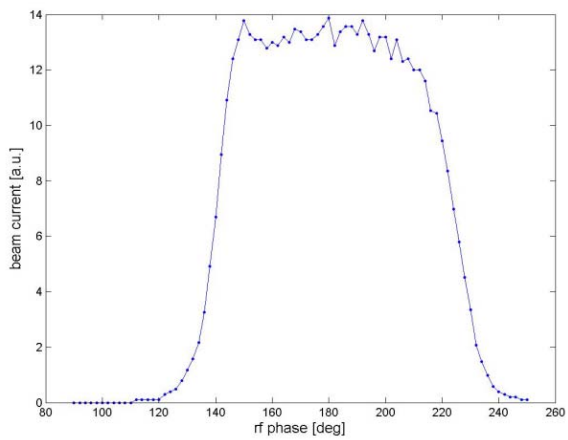

Figure 7: Plot of DTL tank 2 acceptance scan.

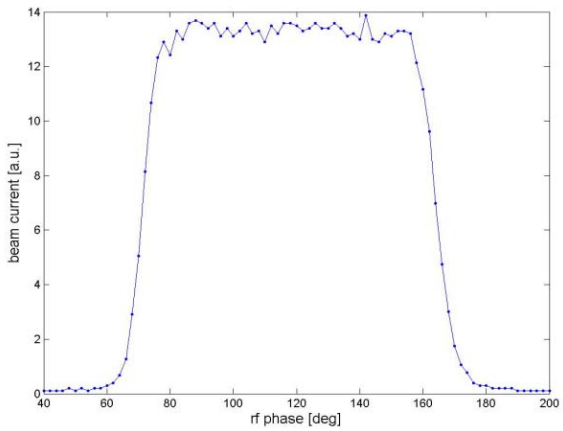

Figure 8: Plot of DTL tank 3 acceptance scan.

Table I summarizes the benchmarking results of the Phase Scan and the Acceptance Scan for the DTL tank 1 to 3. The rf amplitude of the tank predicted by both techniques differ at most by 1.7% and the rf phase by 1.5°. This is an excellent agreement demonstrating the consistency in the analysis of both techniques. DTL tank 1 is deemed to be the most sensitive tank of all. Further analysis is under way for other DTL tanks.

Table 1: rf set-point from PS and AS

	Phase Scan	**Acceptance Scan**
DTL 1	(0.179, -125.5°)	(0.176, -124.9°)
DTL 2	(0.483, 166.5°)	(0.484, 168.0°)
DTL 3	(0.490, 105.0°)	(0.494, 104.7°)

CONCLUSION

Preliminary comparison was made between the Phase Scan and the Acceptance Scan. Both techniques resort to multiparticle tracking with space charge force for the analysis of the measurement data. Tuning results show an excellent agreement for DTL tank 1. At low beam energy for the SNS linac, the longitudinal bunch size is relatively long and multiparticle tracking can guarantee the accuracy of phase scan or acceptance scan simulation. More studies will be conducted during the next commissioning runs. For more accurate rf set-point, the Phase Scan technique is preferred.

REFERENCES

[1] J. Wei et al, Proceedings of the 2001 Part. Accel. Conf. (Chicago, 2001), p. 319.
[2] D. Jeon et al, Proceedings of the 2002 LINAC Conf. (Gyeongju, Korea, 2002), p. 368.
[3] H. Takeda and J. Stovall, Proceedings of the 1995 Part. Accel. Conf. (Dallas, Texas), p. 2364.
[4] S. Henderson et al, Proc. of the 2004 European Part. Accel. Conf. (Lucerne, Switzerland, 2004), p. 1524.

THERMAL-INDUCED FREQUENCY DETUNING OF 350 MHz RFQ STRUCTURE

N. K. Sharma, S. C. Joshi, N. Kumar
Raja Ramanna Centre for Advanced Technology, Indore 452013, INDIA

Abstract

A 350 MHz, 4.5 MeV RFQ structure is being developed for high power Proton Linac for Indian SNS. RFQ structure operated at higher duty factor will be subjected to thermal deformations and hence the detuning of resonating structure due to RF induced heating. A detailed Thermal-Structural-Electromagnetic sequential analysis of RFQ has been performed using Multi-physics ANSYS (Finite Element Analysis Software). A cooling scheme has been designed for efficient heat removal from the structure to minimize the thermal induced frequency shift. During analysis the parameters such as cooling water flow rate and bulk water temperatures are varied to study their effect on temperature distribution and associated frequency variation. The frequency shift is found highly sensitive to vane tip cooling parameters.

RFQ FOR LOW ENERGY H⁻ ION LINAC

A 350 MHz integrated vane type RFQ structure has been selected for accelerating proton/H- ion from the ion source to 3- 4.5 MeV. The operating frequency 350 MHz is selected on the basis of available RF power sources. Higher output energy from RFQ like 4.5 MeV is preferred from the injection point of view into the following linac structures like DTL/ low beta SC cavities. An intervane voltage of 65 kV is selected for the high duty operation of RFQ. While lower inter-vane voltage in RFQ reduces the power dissipation per unit length in the structure, however it results in increased length of RFQ structure.

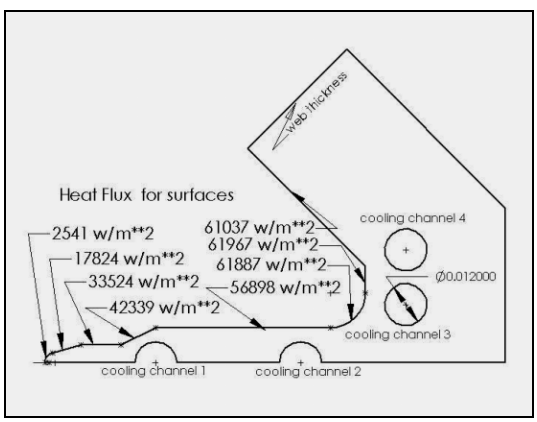

Figure 1: RFQ geometry with heat flux

COUPLED FIELD ANALYSIS OF RFQ

The RFQ cavity structure has been designed using SUPERFISH for the inter-vane voltage of 65 kV. The total power loss in the RFQ structure is 539 kW. Figure 1 shows the surface heat flux in RFQ. The power loss for the thermal analysis has been considered 50% more than the power loss calculated by SUPERFISH to compensate for the deviation in ideal surface conditions, theoretical electrical conductivity and joints etc. The material for the construction of RFQ is OFHC copper. The RFQ cavity has been analyzed using FEA software ANSYS considering six cooling channels per quadrant of RFQ cavity. Thermal analysis of RFQ has been performed to remove the RF induced heat from the structure The circular shape, 12 mm diameter of cooling channel is selected due to ease in machining. The relative locations of remaining five channels were determined by parametric thermal design optimization. Parametric studies are performed to evaluate the effect of cooling water flow rate and cooling water bulk temperature and their effect temperature distribution are shown in the figures.

Thermal-Structural-Electromagnetic sequential Analysis of RFQ

Thermal-structural-electromagnetic sequential analysis has been performed to evaluate the thermal induced frequency shift of RFQ structure. The RFQ geometry is modeled by using Plane 2D elements for OFHC Copper walls and a corresponding MESH 200 unsolved elements for cavity space. The temperature distribution obtained from the thermal analysis was taken as an input for the structural analysis. The displacement constraints were applied such that the RFQ structure is free to expand in the radial direction. The deformation due to self weight of the structure is also incorporated in the analysis. During thermal and structural analysis the MESH 200 elements act as a dummy element. The high frequency electromagnetic analysis is performed for resultant deformed cavity to evaluate the thermal induced detuning of the structure. During HF electromagnetic analysis, the unsolved MESH200 elements are converted into corresponding high frequency elements. Various multiple iterative ANSYS macros have been incorporated in the sequential analysis to evaluate the effect of cooling channel flow rate and bulk water temperature on resonating frequency. Figure 3 and Figure 4 shows the effect of flow rate and bulk water temperature in various cooling channels on temperature rise in RFQ.

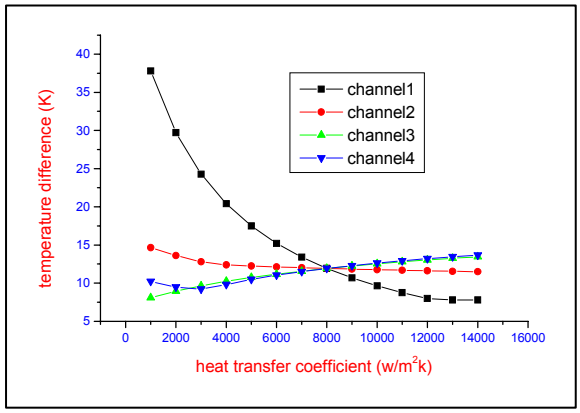

Figure 2: Effect of cooling channel flow rate on Temperature rise

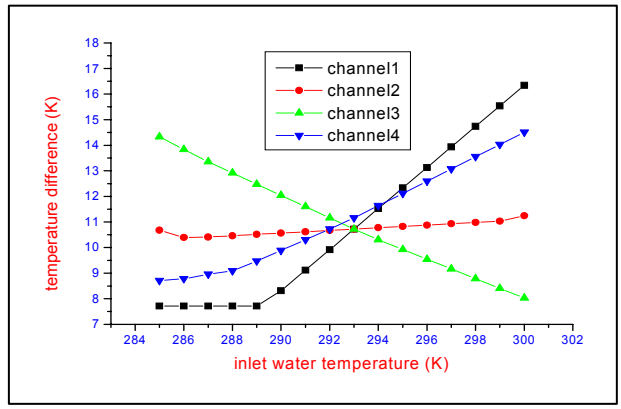

Figure 3: Effect of cooling channel bulk water temperature on Temperature rise in RFQ

Effect of cooling water flow rate on resonating frequency

To study the effect of cooling water flow rate on frequency shift, the heat transfer coeff in one of the cooling channel is varied from 2000 -12000 W/m*mK, while all other parameters are kept constant. The analysis is performed by varying the flow rate in each channel one by one and the frequency shift is evaluated. It is observed from the analysis that increase in flow rate of vane tip cooling channel increases the resonating frequency whereas frequency decreases with an increase in flow rate of web cooling channels. It is also seen that frequency sensitivity is highest for the cooling channel nearest to the vane tip as sown in Figure 4.

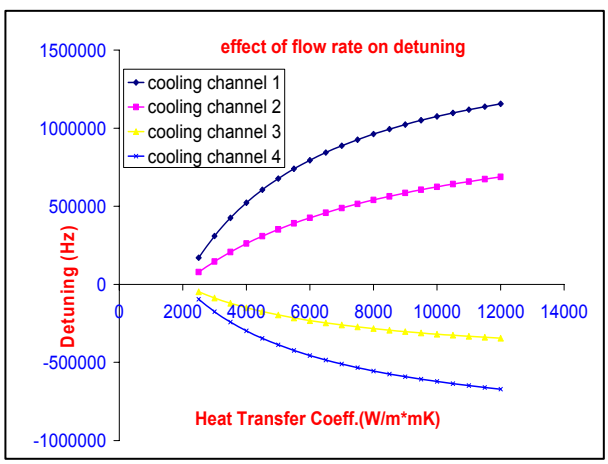

Figure 4: Effect of cooling channel flow rate on thermal induced frequency shift.

Effect of bulk water temperature on frequency shift

To study the effect of bulk water temp on frequency shift, the bulk water temp of each channel is varied one by one from 288K to 300K, while all other parameters are kept constant. It is seen that increase in bulk water temperature of vane tip cooling channels decreases the resonating frequency whereas frequency increases with increase in web cooling channels bulk water temperature. The sensitivity for the vane tip cooling channel is maximum for thermal induced detuning. The structure is detuned about –17 kHz and –8.2 kHz with 1K rise in bulk water temperature of vane tip cooling channels and the frequency shifts about +6.5 kHz and +12 kHz with web cooling channels bulk water temperature. The variation of frequency shift with bulk water temperature is found linear in nature as shown in Figure 5.

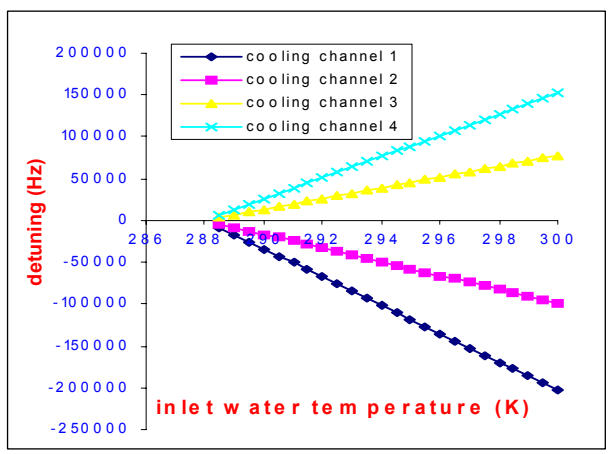

Figure 5: Effect of cooling channel inlet water temperature on thermal induced frequency shift.

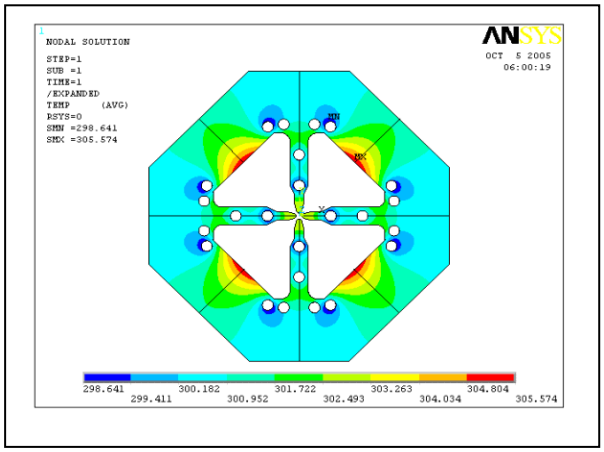

Figure 6: Optimized RFQ structure to minimize thermal induced detuning
Web thickness = 70 mm
V1 = 3.5 m/s T1= 288 K V2=3.5m/s T2=288 K
V3 = 1.4 m/s T3= 300 K V4=3.0 m/s T4=288 K

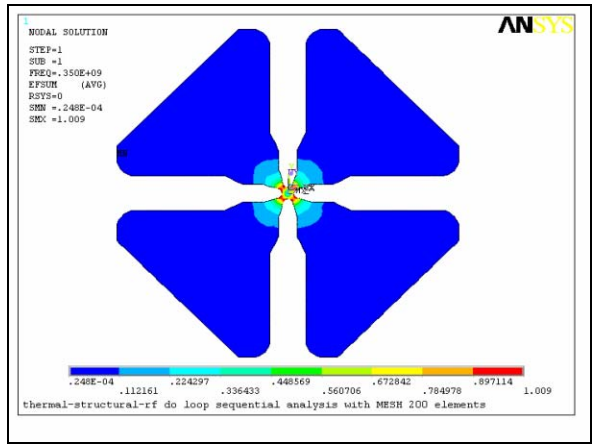

Figure 7: Electric field plot of the final optimized cavity. Frequency of undeformed cavity is 349.202 MHz and the frequency of deformed cavity is 349.536MHz giving detuning of 334.293 KHz.

CONCLUSIONS

A sequential analysis has been carried out for a proposed 350 MHz RFQ geometry with various cooling parameters, scaled up heat flux from SUPERFISH analysis and suitable structure constraints. Results obtained from the structure analysis were taken as input to the high frequency analysis for estimation of thermal induced frequency detuning. The frequency sensitivity of resonating structure with cooling water flow rate and bulk water temperature has been investigated. It is inferred from the results that the cooling water flow rate and bulk water temperature in the cooling channels 1& 2 located near the RFQ vane tip has opposite effect on frequency detuning of RFQ structure as compared to their variation in cooling channels 3 & 4 located in the RFQ wall. The data obtained from the variation of cooling parameters will be utilized for the fine frequency control of the resonant cavity during high power operation.

REFERENCES

[1] N.K.Sharma, S.C.Joshi, N.Kumar and S.Raghvendra, "Optimisation of cooling circuit for 350 MHz 4.5 MeV RFQ for proposed high power Linac", INPAC-2005, March 2005, VECC, Kolkata.

[2] S.C. Joshi, N. Sharma, N. Kumar, S. Raghvendra, S.A. Pande, G.V. Kane. 3D Thermal-Fluid Coupled Analysis for 350 MHz RFQ for Indian SNS Programme" APAC-2004, March 2004, Gyeongju, Korea

[3] S. C. Joshi, et al., "Engineering Design & Analysis of 350 MHz, 4.4 MeV RFQ for proposed Low Energy part of High Power Proton Linac," InPAC-2003, February 2003, CAT, Indore

[4] S.C.Joshi et al, "Prototype Engineering design of 350 MHz RFQ for proposed Proton Linac for Indian ADS programme", LINAC 2002, Gyeongju, Korea

PRESENT STATUS OF J-PARC MR SYNCHROTRON

T. Koseki[#,A)], H. Kobayashi [A)], M. Yoshioka [A)], H. Matsumoto [A)] and J-PARC MR Group [A),B)]
[A)]Accelerator Laboratory, KEK, Tsukuba, Japan
[B)]JAEA, Tokai, Japan

Abstract

The J-PARC (Japan Proton Accelerator Research Complex) is a joint project of High Energy Accelerator Research Organization (KEK) and Japan Atomic Energy Agency (JAEA). Presented in this paper is a recent status of a 50-GeV slow cycling main ring synchrotron (MR) of J-PARC. Installation and performance test of accelerator components are now in progress. Beam commissioning of the MR is scheduled to start in May 2008.

INTRODUCTION

The J-PARC facility consists of a 400-MeV linac, a 3.0-GeV rapid cycling synchrotron (RCS), a 50-GeV slow cycling main ring synchrotron (MR) [1, 2] and related experimental facilities for use in various fields of science and technology. The RCS will provide a 3.0-GeV, 1-MW proton beam to neutron and muon targets in the Materials and Life Science Experimental Facility (MLF). The MR will provide a 50-GeV, 0.75-MW proton beam to the Hadron Beam Facility (HD) and a neutrino production target in the Neutrino Facility.

The J-PARC project is being promoted in two phases. The facilities mentioned above are constructed in Phase I. However, the maximum beam energy of the MR is 40 GeV in Phase I because of flywheel electric power system will be ready for only Phase II. Furthermore the Linac starts with a beam energy of 181 MeV, then the beam power of the RCS will be limited to 0.6 MW in maximum.

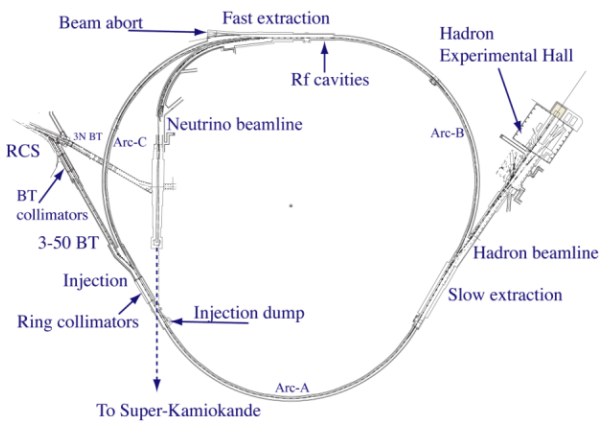

Figure 1: Plan view of MR and experimental facilities.

Figure 1 shows a plan view of the MR and the experimental facilities. The MR has an imaginary transition lattice structure to avoid transition crossing during acceleration. It has a three-fold symmetry and a circumference of 1567.5 m. Three dispersion-free 116-m long straight sections are dedicated to "injection and beam collimators", "fast extraction and rf system", and "slow extraction". The slow extraction beam is delivered to the HD experimental Hall for particle and nuclear physics experiments. The fast extraction beam is delivered to the neutrino production target. The produced neutrino beam is sent to Super-Kamiokande, a large water Cherenkov detector, located 300 km west for long baseline neutrino oscillation experiment. The main parameters of the MR are summarized in Table 1.

Table 1: Main Parameters of MR.

Circumference [m]	1567.5
Superperiodicity	3
Repetition rate [Hz]	~ 0.3
Injection Energy [GeV]	3.0
Extraction Energy [GeV]	30/40(Phase I), 50 (Phase II)
Harmonic number	9
Number of bunches	8
Transition γ	j31.7
Typical tune	22.4, 20.8
Transverse emittance at inj. [πmm-mrad]	54
Transverse emittance at ext.[πmm-mrad]	10(at 30 GeV) 6.1(at 50GeV)
Rf frequency [MHz]	1.67 – 1.72

Beam commissioning is started from the upstream accelerators while the construction of the downstream accelerators and experimental facilities is in progress. The construction of the linac has been completed and beam commissioning started in November 2006. Recently, we have achieved beam acceleration up to the nominal beam energy of 181 MeV [3]. The construction of the RCS will be completed in April 2007. The beam commissioning of the RCS is scheduled to start in this September.

For the MR, civil construction of the accelerator tunnel has been completed at the November 2006. Installation of the accelerator components is now in progress.

CONSTRUCTION STATUS

The MR lattice requires 96 dipoles, 216 quadrupoles with eleven families, 72 sextupoles with three families. The MR also has eight sextupoles with two families to excite the third order resonance for the slow extraction. The mass production and magnetic field measurement of

[#]tadashi.koseki@kek.jp

all these magnets have been completed [4]. More than 80 % of the magnets have been installed in the MR ring tunnel and aligned by the end of 2006 [5,6]. In addition, the MR has 186 steerings. Most of the steerings have been manufactured and delivered to the J-PARC cite.

For vacuum system, about 30 % of beam ducts in both the Arc-B, and Arc-s sections have been connected. A vacuum evacuation test is now well underway. Figure 2 shows the installed magnets and vacuum components in the Arc-B section.

The MR has 186 BPMs. Each BPM has a diagonal cut electrostatic pickup [7]. The position calibration of all the BPMs has been completed already. The position accuracy less than ±0.1 mm was achieved using the wire method. So far, about half of the BPMs have been installed.

Figure 2: Magnets and beam duct in the MR ring tunnel. The vacuum evacuation test is in progress.

For 3-50 BT, the beam transport line from the RCS to the MR, installation of 80 % of the magnets, and beam collimators has been completed. Beam ducts and BPMs are now being installed well.

PERFORMANCE TEST OF ACCELERATOR COMPONENTS

Injection and extraction devices

All the injection and extraction devices except for the slow extraction system have been fabricated and delivered to KEK/JAEA. Performance test of them is being carried out. Each device will be installed in the ring tunnel after the good reliability is confirmed.

The fast extraction section has six septum magnets (S1, S2, S30-S33). Each septum magnet is bipolar system and can extract the beam both inward and outward of the ring. They correspond to the neutrino beamline and the abort beamline, respectively. Figure 3 shows the septum magnets installed in an experimental hall for the performance test. Magnetic field in the extraction beam side and leakage field in the circulating beam side are being measured for all the septum magnets. In addition, vibration measurements of coil and beam duct are being carried out. We are also planning long-term continuous operation for about 1000 hrs. For the power supply of the septum magnets, EPICS based control system, the same scheme of the MR control system, has been built and being operated successfully. The fast extraction section is one of five areas in which the beam loss should be localized in the MR. Radiation maintenance scenario of the septum magnets is also investigated vigorously [5]. Installation of the septum magnets will be started in September 2007.

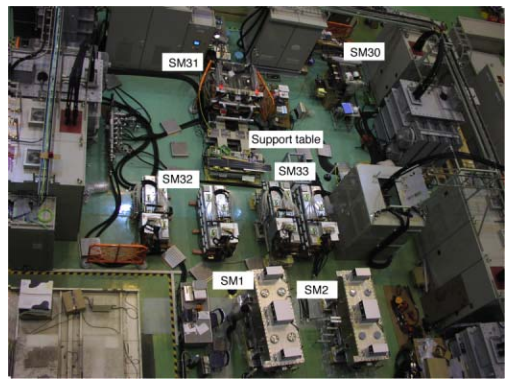

Figure 3: Fast-extraction septum magnets. SM31 is under testing.

Extracted beam from the RCS is switched to the MR and to the MLF by a pulse bending magnet. The requirements to magnetic field of the magnet are rise/fall time of less than 40 msec and flatness of 5×10^{-4} during the injection period of the MR. Since the magnetic field pattern is deteriorated due to the effect of eddy current on magnet end-plates, some correction schemes are necessary to achieve the requirements. We have already reported a method to compensate the eddy current effect by attaching phase advance-circuits to the magnet in parallel [8]. Recently, a new method has also been developed and tested. A field correction pattern to compensate the eddy current effect is made using pattern memory unit. The correction pattern is superimposed on the pattern input of feedback control loop of the power supply. By the new method, the measured rise time and flatness are improved sufficiently and satisfy the requirements. The pulse bending magnet will be installed in April 2007.

For the other devices, such as injection kicker/septum magnets, injection-dump kicker/septum magnets and fast extraction kicker magnets, their performances are being tested now in detail.

For the slow extraction system, detailed design of the components, electrostatic septum, septum magnets, bump magnets is in progress. They will be ordered and fabricated in Japanese fiscal year 2007.

MA Loaded RF Cavity

A high gradient rf cavity using magnetic alloy (MA) cores has been developed for the RCS and MR [9]. The maximum accelerating voltages required for the RCS and MR are 450 kV and 280 kV, respectively. In order to obtained the voltages, field gradient larger than 20 kV/m is necessary.

In 2006, we have improved the manufacturing process of the MA cores to increase reliability of operation [10,11]. As already reported [2], we observed some damages on the MA cores in test operation with 25 kV/m. Detailed study shows it is reasonable to assume that the core was damaged by electric field and that the damages occurred due to poor insulation between the MA layers. We have investigated the manufacturing process of the core and improved the winding process so as not to decrease a DC resistance of the core. By this improvement, impedance of the cores is increased about 10 %. Another improvement is a treatment of cut core surface. In the MR, the MA cores are loaded to the cavity with cut-core configuration. The core is cut by water jet and then the cut surfaces are polished. In order to improve surface quality, we adopt diamond polishing. The core surfaces are polished with fine diamond powder without any oils and acids.

Figure 4 shows the cavities under long-term operation for test of the cut-cores. The cut-cores, which manufactured by the improved processes, are installed on the accelerating gap side. So far six cores have been tested for 2000 hrs and 12 cores for 1000 hrs without any serious troubles. These cores are now ready to install. Installation of the cavity is planned to start in September 2007.

Figure 4: The cut-core loaded cavities under long-term continuous operation with nominal voltage of 15 kV/gap and 60 % duty.

Magnet power supplies

Performance test of steering power supplies has been carried out. Required tracking error of less than 0.1 % was obtained with 4 msec-step pattern control. Electric and magnetic noises due to the steering system were also investigated. Recently, performance test of quadrupole power supplies has been started.

BEAM COMMISSIONING PLAN

All the components will be installed in the MR tunnel by December 2007 except for the slow extraction components. At first, we will start the off-beam commissioning. All the components should be online and ready to start the beam operation in this stage. After that, we will start the beam commissioning in May 2008. In order to allow hands-on maintenance of the hardware components, beam loss should be controlled as low as reasonably achievable. The maximum beam loss at the regular zones (not hot zones) is assumed to be less than 0.5 W/m [5]. Then we adopt the following approaches for the beam commissioning; 1) the beam tuning is started with very low intensity to minimize the activation of the components. 2) beam transport to a proper beam dump should be established at first, and then fine tuning is performed.

Beam commissioning of the MR is divided into three stages [12]. The first stage is from May to June 2008. Beam transportation through the 3-50 BT, beam Injection, establishing closed orbit, and beam acceleration will be studied. From July 2008, the MR will be shutdown, and we will install the slow extraction devices. In addition, installation of superconducting magnets of the Neutrino beamline will be started. The second stage of the beam commissioning is scheduled from Nov. 2008 to Jan. 2009 although the schedule is not completely fixed yet. In this stage, slow extraction system and beam transport to the hadron beamline will be commissioned. The third stage is scheduled to start from April 2009. Commissioning of the neutrino beamline will start in this stage.

SUMMARY

The construction of the MR is now under way. The off beam commissioning is scheduled to start from December 2007 and beam commissioning from May 2008.

REFERENCES

[1] "Accelerator Technical Design Report for J-PARC", KEK-Report 2002-13 and JAERI-Tech 2003-044.
[2] H. Kobayashi, "Present Status of the J-PARC Accelerator", EPAC 2006, to be published.
[3] F. Naito, in these proceedings.
[4] K. Niki, *et al.*, "Results of Field Measurements for J-PARC Main Ring Magnets", EPAC 2006, to be published.
[5] M. Yoshioka *et al.*, "Installation and Assembling of Accelerator Components for J-PARC 50 GeV Synchrotron", in these proceedings.
[6] M. Shirakata *et al.*, "The Magnet Alignment Method for the J-PARC Main Ring", in these proceedings.
[7] T. Toyama *et al.*, "Beam Position Monitor for the J-PARC Main Ring Synchrotron", DIPAC 2005, p. 271.
[8] K. Koseki *et al.*, "Pulsed Bending Magnet of the J-PARC MR", EPAC 2006, to be published.
[9] C. Ohmori *et al.*, "High Field Gradient Cavity for JAERI-KEK Joint Project", EPAC 2002, p. 257.
[10] M. Yoshii *et al.*, "New Cutting Scheme of Magnetic Alloy Cores for J-PARC Synchrotrons", EPAC 2006, to be published.
[11] M. Yamamoto *et al.*, "High Power Test of MA Cavity for J-PARC RCS", EPAC 2006, to be published.
[12] T. Koseki *et al.*, "Commissioning Scenarios for the J-PARC Accelerator Complex", HB2006, to be published.

DESIGN OF HIGH CURRENT RF ION SOURCE FOR MICROMACHINING APPLICATIONS

P.Y. Nabhiraj, Ranjini Menon, C. Mallik, R.K. Bhandari
Variable Energy Cyclotron Centre, 1/AF, Bidhan Nagar, Kolkata, India
G. Mohan Rao, S. Mohan
Department of Instrumentation, Indian Institute of Science, Bangalore, India

Abstract

Liquid Metal Ion Source (LMIS) and Gas Field Emission Ion Source (GFEIS) are the major ones in micromachining applications so far. They have limitations of contaminations and low throughput. Plasma based ion sources can produce heavier ions for higher throughput, lighter ions for fabrication of higher resolution structures, ions for doping, ion assisted direct writing of metallic, oxide, nitride and carbide layers and lines. Considering wide range of applications, a 13.56 MHz inductive coupled plasma (ICP) ion source for producing high brightness ion beams with very low energy spread has been developed. It is a very compact ion source with external helical antenna wound around a 30 mm quartz tube. 1 mA of Argon and 0.5 mA of proton ion beams have been extracted from 2 mm dia aperture in plasma electrode at 4.0 kV extraction potential and ~200W of RF power. Using LabView software an automated plasma diagnostic system has been designed and used to measure the plasma parameters. Retarding Field Analyser (RFA) has been designed and developed for ion energy spread measurements. This paper describes the features of the ion source, ion beams produced, some results of the plasma diagnostics.

INTRODUCTION

Ions in keV energies when incident on solid surface produce several effects such as sputtering of target atoms, secondary electron emission, inducing chemical reactions, creation of defects, implantation of ions and altering the surface properties. Some of these effects are put into use in the field of micro electro mechanical system (MEMS)/ nano electro mechanical system (NEMS) and semiconductor device manufacturing. The conventional lithographic techniques using UV, electron beam, X-rays have reached the limitations. Ion beams are most suitable to overcome these limitations as they have least proximity effect due to their low scattering and absence of diffraction effects. During 1950's Feynman [1] in his visionary speech proposed to use FIB for creation of structure of nanometer sizes. With the use of ion beams for the processes, resist can be avoided and the ion doses and energies can be varied accurately making them versatile in many applications. Development of liquid metal ion sources (LMIS) producing typical semiconductor dopants, broadened the field of applications [2], [3]. In case of resist based lithography, resists have higher sensitivity for ion beams facilitating higher throughput. Conventional LMIS has many limitations like, production of ion beams of a fewer elements, shorter life time of the source etc. Gaseous field ion source can give stable beam for longer time. But technology is cumbersome due to the involvement of cryogenics. The other problem using LMIS is that these metallic ions get trapped in the target producing impurities in the deposited films. To overcome the limitation of LMIS, Inductive Coupled Plasma (ICP) based ion sources are being developed for focused ion beam applications. These ion sources can produce ion beams of all the typical dopants for semiconductor fabrication applications and heavy gaseous ion beams for micromachining applications. A mini ICP with external helical coil, measuring 30 mm in diameter has been developed for this application. Small volume ICP source can produce very high density plasma at low powers. ICP based gaseous ion sources are one of the excellent tools to grow thin films of practically any materials with least contamination.

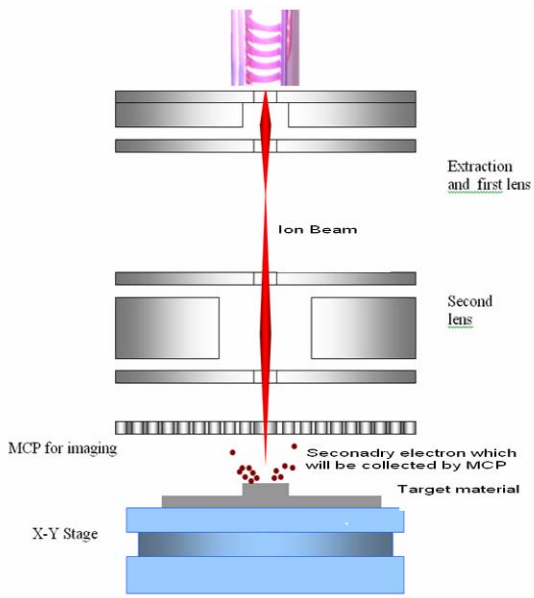

Figure 1: Schematic of focused ion beam system.

Fig 1. shows the schematic of focused ion beam (FIB) systems with the inductive coupled plasma ion source. This set up is being designed for micromachining applications in the micro and sub-micro scales. Typical FIB column consists of ion source, extraction system, focusing elements, ion beam scanning and blanking systems, micro channel plates for ion and secondary electron detection for real-time imaging of the surface by

ion beam scanning and the precision x-y-z stage for positioning the specimen.

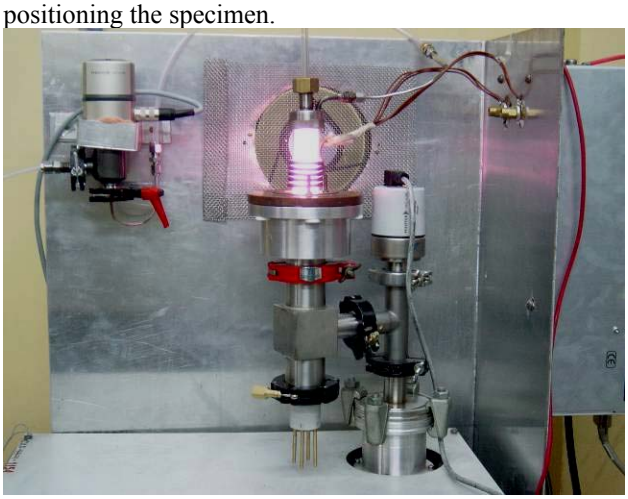

Figure 2: ICP ion source operating with 100W of RF power at 0.01 torr pressure.

Inductive Coupled Plasma Ion Source

Inductive coupled plasma source with external helical coil is chosen to be the ion source for micromachining applications as this can produce ion beams of various species with high intensity and the low energy spread. External helical coil is chosen to reduce the capacitive coupled discharge effect thereby reducing the ion energy spread. The plasma chamber is made of quartz tube of 30 mm diameter and 70 mm height. Top of the tube is connected with the gas feed system where fine gas control is done through motorised needle valve. Inductive coupling coil is made of 5 turns of water cooled hallow copper tube having R=0.7Ω and L=1μH. This is connected through the impedance matching network made by two 250 pf vacuum variable capacitors to the 13.56 MHz 1.2 KW RF power generator (Dressler make). Fig 2. shows the setup with the argon plasma operating at 0.01 torr of pressure. For producing the submicron size ion beams, the brightness of the ion source should be high. Brightness of an ion source depends on the plasma parameters such as n_e, n_i, T_e, V_p that are measured by using self compensated single Langmuir probe [7] and the double Langmuir probe. The results by single probe measurement are influenced by plasma potential oscillations at 13.56 MHz, higher current drain and the RF pick up by the measuring equipments. Use of double Langmuir probe overcomes the problems of single probe measurements with some limitations [8]. Experimental results of double probe are discussed in the following sections, which are approximately same as the single probe measurements that were carried out earlier.

Plasma Diagnostics by Double Langmuir Probe

Fig 3 describes the schematic of double Langmuir probe measurement system. Double probe is made in-house by sealing the tungsten wire of 0.25 mm diameter in the glass tube and protruding 10 mm into the plasma. Keithley pico-ammeter with voltage source (Model 6487) is used for the measurements. This is controlled by computer through serial port of meter. Acquired data is automatically analysed by using LabView application. Sufficient filters are introduced to eliminate RF pickup. Fig 4. shows the typical double probe characteristics acquired with argon plasma at 0.01 Torr and 100W of RF power. Double probe characteristics are obtained at different RF power levels at fixed gas pressure. It is found that electron temperature increases with increase in RF power. Electron temperatures of 5, 7.8, 12.5 eV are calculated from probe characteristics obtained with 50, 80 and 100W of RF powers respectively. Following the calculation in ref. [5] and assuming the ion temperature is equal to gas temperature which is about 1000^0 K. [6], for the graph shown in fig 4, the ion density is about $2x10^{18}/m^3$.

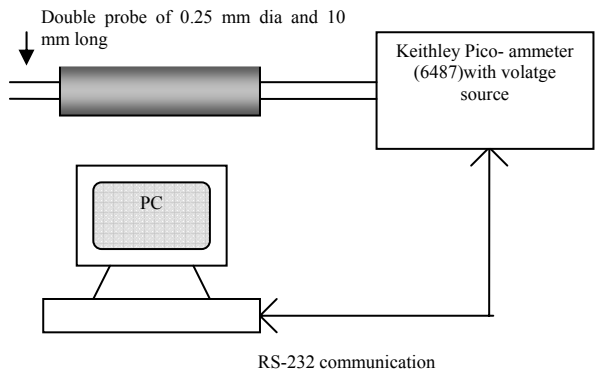

Figure 3: Schematic double probe measurement system.

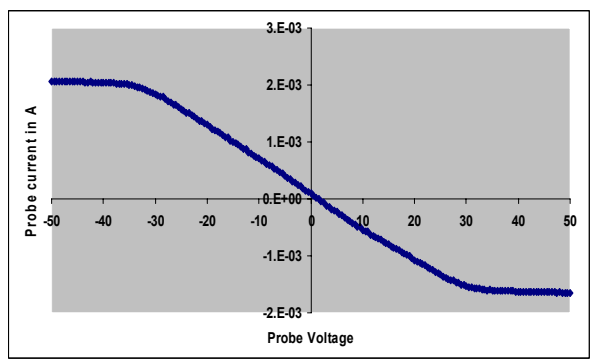

Figure 4: Typical double probe characteristics of argon plasma at 0.01 torr pressure and 100W RF power.

The single probe analysis carried out earlier with similar plasma conditions show that T_e= 6eV-12eV and n_i= 1 to $9x10^{17}/m^3$

Ion Energy Spread Studies by Retarding Field Analyser

Ion energy spread is the most important factor in developing the submicron ion beams. It is seen that 1eV ion energy spread produces around 4 micrometer diameter ion beam for the geometry described in [4] for the ion energy of 3 KeV. It is desirable to have as less as possible ion energy spread from the ion source to have

least chromatic aberration contribution in the ion beam spot size. An effort has been made to measure the ion energy distribution by using multigrid retarding field analyser (RFA). RFA has been developed in-house. A special grid fabrication system has been developed. The grids are made by soldering 50 micron gold coated tungsten wire onto the copper ring of 30 mm ID, 40 mm OD and 2 mm thick. Wire to wire distance is 310 microns providing around 66% transparency. Wires are wound using a zig having 80 turns per inch pitch and having facility for alignment of the wires. Plasma electrode has 2 mm dia aperture. All electrodes are spaced 1.7 mm apart by Teflon spacers and assembled in Teflon housing.

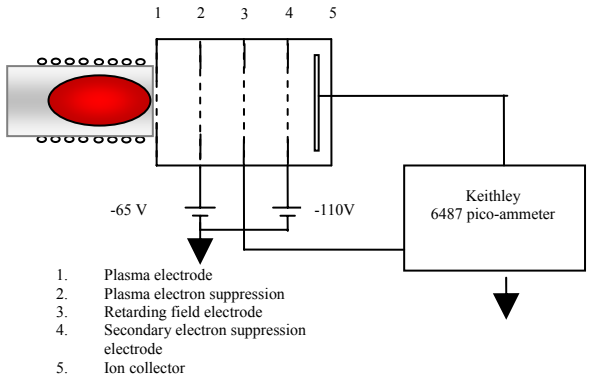

Figure 5: Schematic of retarding field analysis system.

First grid shown in the fig 5 is biased to -65V. for a maxwellian energy distribution at $T_e \sim 5eV$ > 99% of plasma-born electrons are suppressed by -65V on the grid number 2. Grid number 3 is connected to the variable bipolar supply of the Keithley pico-ammeter (6487 model). Fourth grid is biased to -110 V to ensure good suppression of secondary electrons from the collector. Fig 6. shows the typical plot of ion beam current with retarding field voltage. Differentiation of the plot gives the ion energy distribution. This graph was obtained for argon plasma at 100W of Rf power and 0.01 torr pressure. From these plots the energy spread is calculated to be about 10 eV. The real ion energy spread is less than 10eV as lens effect of the grids contributes to the ion energy spread significantly. It needs more investigation with proper grids and grids spacing to get more accurate results.

Beams Developed

Various ion beams have been developed using the above described ICP ion source. Plasma electrode having 2 mm diameter aperture is floated at extraction potential and the second electrode at 5 mm is grounded. Various ion beams were optimised with different powers but with same extraction voltage of 4 kV. Proton, Oxygen, Nitrogen, Argon ion beams of 1, 2, 1.5, 2.2 mA respectively have been extracted. Fig 7. shows the comparison of theoretical (Child Langmuir relation) and experimentally extracted argon ion current density from at 0.01 Torr pressure and 100W of RF power. At higher extraction voltages the experimental values are approximately same as theoretical values.

$$j_v := 4 \cdot \varepsilon_0 \cdot \sqrt{2 \cdot \frac{q}{m}} \cdot \frac{(v)^{\frac{3}{2}}}{d^2}$$

Where J_v is the current density, v = extraction voltage and d is distance between the plasma electrode and the extraction electrode. Efforts are being put to reduce the ion energy spread and increase the extracted current.

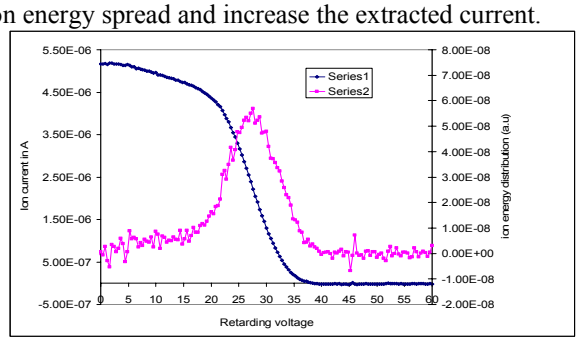

Figure 6: RFA characteristics and ion energy distribution from argon plasma at 100W and 0.01 Torr pressure.

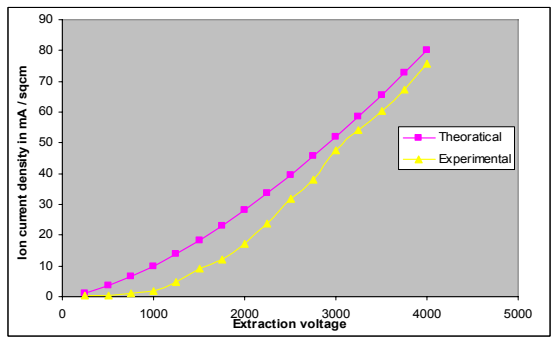

Figure 7: Comparison of theoretical and experimental extracted ion beam current density.

REFERENCES

[1] R.P. Feynman, There's Plenty of Room at the Bottom –An Invitation to Enter a New Field of Physics, 1959,http://www.zyvex.com/nanotech/feynman.html
[2] Shinji Nagamachi et.al. Rev. Sci. Instrum. 67 (6), June (1996), 2351
[3] J.H. Daniel D.F. Moore Sensors and Actuators 73 (1999), 201.
[4] P.Y. Nabhiraj et al. " Design of compact low energy ion beam focusing column for plasma based FIB system". Proc. InPAC-2006, Mumbai. Nov 1-4, (2006) 211.
[5] E.O. Johnson and L Malter " floating double probe method .." Phys. Rev Vol 80, No 1 1950 P -58.
[6] Alexander A. et al. " Sensor for monitoring plasma parameters" Proc. SPIE Vol 5339, P 415.
[7] K. Ranjini et al. " Development of Langmuir probe diagnostic system for 13.56 MHz plasma source". Proc. InPAC-2006, Mumbai. Nov 1-4, (2006). 237
[8] B.M. Annaratone et al. " On the use of double probe in RF discharges"

SIMULATION OF NON-UNIFORM HIGH DENSITY ELECTRONEGATIVE PLASMA FOR OPTIMIZATION OF H$^-$ ION AND THEIR EXTRACTION

Ajeet Kumar* , V. K. Senecha and S. Kotaiah, Power Supply Division, RRCAT, Indore, India-452013

Abstract

Numerical simulations of radio frequency multi-cusp volume type H^- ion source have been performed under non-uniform electronegative plasma equilibrium conditions in order to understand the physics of formation of various ion species (H^+, H^-, e^- etc.) and for optimization of H$^-$ ion formation and extraction. Coupled momentum balance equations along with continuity equations were solved in a cylindrical geometry to obtain the density profile of various ion species. The relevant cross-section data available in the literature as a function of temperature has been used in the computation. The hydrodynamic model of plasma in equilibrium with background neutral gas has been used. Low degree of ionization ($\approx 1\%$) has been assumed. The collision less sheath formation, penetration of electric and magnetic field and power requirment to sustain the plasma has been worked out numerically. An effort has been made to give a self-consistent numerical scheme for the solution of inductively coupled plasma(ICP) in equilibrium, and the results obtained have been presented.

INTRODUCTION

In order to meet the high current requirement of H^- ion for spallation neutron source, which is being proposed to be developed at RRCAT, a detailed theoretical investigation of H^- ion source has been carried out. The fluid model has been applied by various authors, to study various aspects of ion source [1, 2, 4]. In our numerical model we have retained the inertial derivative term. The effective collision frequency of electron and RF field frequency has been computed assuming Maxwellian velocity distribution. This was crucial because the discharge is assumed to be operated at 13.56 MHz, and typical plasma parameters are such that, neither high frequency nor the dc limit will be suitable. At this frequency it is safe to assume that electron respond to RF field while ions respond to the average field.

STEADY STATE FLUID MODEL

The steady state equilibrium of different species in the RF field implies the average value of different measurable parameter over several RF cycles remain unchanged. We have numerically solved the steady state equlibrium values in cylindrical geometry for H^+, H^-, e^- species in H$^-$ ion source. It is assumed that the background hydrogen molecular density to be uniform, depending only on the pressure of the plasma chamber. The particle balance equation in the steady state for i^{th} species is:

$$\vec{\nabla} \cdot \vec{\Gamma}_i = (G - L)_i \tag{1}$$

where $\vec{\Gamma}_i$ is the flux of the i^{th} species and G and L are the gain and the loss term of the i^{th} species. It has been evaluated from the cross-section data [2]. The flux of the i^{th} species is given by $\vec{\Gamma}_i = n_i \vec{u}_i$, where n_i is the density and $\vec{u}_i$ is the diffusion velocity. The momentum balance equation in steady state for i^{th} species is written as:

$$m_i n_i (\vec{u}_i \cdot \vec{\nabla}) \vec{u}_i = -\vec{\nabla} P_i - e n_i \vec{\nabla} \phi + e n_i \mu \vec{u}_i \times \vec{H} - f_i \vec{u}_i \tag{2}$$

Where ϕ is electric potential. For neutral species the forces due to electric and magnetic field would be absent. Here f_i is the effective coefficient of frictional force on i^{th} species assumed to be proportional to diffusion velocity. It arises due to loss of momentum in the collisions with background molecules and in the creation and distruction of the species inside the plasma. It can also be evaluated using cross-section data and collision frequencies.

Plasma eqilibrium in RF field

The discharge is assumed to be created by inductive coupling of RF power through antenna coil wound over cylidrical ceramic chamber. Cylindrical co-ordinate system has been used with $\hat{z}$ axis coinciding with the antenna axis. Due to cylindrical symmetry any variation in the $\hat{\theta}$ direction has been ignored. The z variation in the plasma has been ignored which is a good approximation if $Z >> R$ or in the mid plane of the plasma cylinder. Hence we can write:

$$\vec{H} = H(r,t)\hat{z} \tag{3}$$

$$\vec{E} = E_r(r,t)\hat{r} + E_\theta(r,t)\hat{\theta} \tag{4}$$

$$\vec{u}_i = \tilde{u}_{ir}(r,t)\hat{r} + \tilde{u}_{i\theta}(r,t)\hat{\theta} \tag{5}$$

$$n_i = n_i(r,t) \tag{6}$$

Where $\vec{u}_i$ and n_i are the velocity and density of the i^{th} species respectively. The presence of Magnetic field in the ICP cannot be ignored altogether. Neglecting screening effect, it can be shown that the $\frac{F_{mag}}{F_{elec}} \approx \frac{R(Plasma\ Radius)\, w(rad/sec)}{V_t(Thermal\ velocity)}$ where w is RF frequency. Typically for H^- ion source the, electron temperature is $5\,eV$ and the ion temperature is $\approx 0.5\,eV$. Hence magnetic field has been ignored in the momentum balance of heavy ions while it has been considered in the momentum balance of electron. From the $\hat{\theta}$ component of the momentum balance of electron, writing $E_\theta(r,t) =$

* ajeet@cat.ernet.in

$\mathrm{Re}[\tilde{E}_\theta(r)e^{iwt}]$, $H(r,t) = \mathrm{Re}[\tilde{H}(r,t)e^{iwt}]$ and $\tilde{u}_{e\theta}(r,t) = \mathrm{Re}[u_{e\theta}e^{iwt}]$, and after neglecting u_r/r in comparision with ν_{ef} we get:

$$u_{e\theta} = \frac{-e(\tilde{E}_\theta - u_{er}\mu\tilde{B})}{m_e(\nu_{ef} + i\omega_{ef})} \tag{7}$$

Define $f_e = m_e n_e \nu_{ef}$. Here ν_{ef} is the effective collision frequency and the $w_{ef}$is the effective RF frequency. They have been evaluated over the Maxwellian energy distribution $f(\varepsilon)$ as:

$$\frac{1}{v_{ef} + j\omega_{ef}} = \int_0^\infty \frac{\varepsilon^{3/2}}{v_e(\varepsilon) + j\omega} \frac{df}{d\varepsilon} d\varepsilon \tag{8}$$

In the steady state equilibrium condition we are only concerned with the radial variation of the density and the diffusion velocity of the electron, averaged over several RF cycle. This,along with the assumption of isothermal plasma, the $\hat{r}$ component of momentum balance gives:

$$u_r(r)\frac{du_r(r)}{dr} = -\frac{e}{m_e}E_r(r) - \frac{eT_e}{n_e(r)m_e}\frac{dn_e(r)}{dr} - \nu_{ef}u_e(r) \tag{9}$$

where $E(r) = < E(r,t) >_t$, $n_e(r) = < n_e(r,t) >_t$ and $u_e(r) = < \tilde{u}_e(r,t) >_t$. Similarly the momentum balance for positive ions in isothermal plasma equilibrium condition is written as:

$$u_+(r)\frac{du_+(r)}{dr} = \frac{e}{m_+}E_r(r) - \frac{eT_+}{n_+(r)m_+}\frac{dn_+(r)}{dr} - \nu_{+f}u_+(r) \tag{10}$$

here the ν_{+f} is the effective collision frequency defined for positive ions in terms of frictional force ($f_+ \approx \nu_n n_+ + < \sigma v >_{iz} n_e n_{H_2} + < \sigma v >_{mn} n_{H^-} n_{H^+}$). The $< \sigma v >$ are different reaction rates, which has been obtained from reference [2]. The continuty equation for the positive ion:

$$\frac{1}{r}\frac{d(ru_+n_+)}{dr} = (G - L)_+ \tag{11}$$

where $(G-L)_+ \approx < \sigma v >_{iz} n_e n_{H_2} - < \sigma v >_{mn} n_- n_+$. Thus to close the equation (10) and (11) for H^+ species we assume H^- and e^- are in Boltzmann quilibrium with electric potential i.e. $n_- = n_{-(r=0)}e^{\phi/T_-}$ and $n_e = n_{e(r=0)}e^{\phi/T_e}$. And quasi neutrality condition $n_+ = n_e + n_e$ to be valid. The modified Bohm velocity ($u_B = \sqrt{\frac{eT_e}{m_+}\left(\frac{1+\alpha_s}{1+\gamma_-\alpha_s} + \frac{1}{\gamma_+}\right)}$), determines the diffusion velocity of the positive ion at the sheath edge. Here $\gamma_+ = \frac{T_e}{T_+}, \gamma_- = \frac{T_e}{T_-}$ and $\alpha_s = \frac{n_{s-}}{n_{se}}$, where n_{s-} and n_{se} are the H^- density to electron density at the sheath edge. The extracted H^- current to electron current ratio can be related in a simple way using thermal flux model as $\frac{I_-}{I_e} = \frac{n_-}{n_e}\sqrt{\frac{T_- m_e}{T_e m_-}}$.

Sheath formation

A simplistic picture of collisionless sheath has been worked out. With the assumption that H^- to electron density ratio is very small, and by balancing flux and energy we get [4]:

$$\frac{1}{r}\frac{d^2(r\phi)}{dr^2} = \frac{en_{se}}{\varepsilon_o}\left(e^{(\phi/T_e)} - \frac{1}{\sqrt{1 - \phi/\varepsilon_s}}\right) \tag{12}$$

With the knowledge of n_{se} and $\frac{d\phi}{dr}$ at the beginning of the sheath, above equation has been numerically solved for ϕ.

RF Power coupling

With the plasma parameter close to high density discharge, we can ignore the capacitve couping of RF power to the plasma. The Power is transfered from RF electric field to the plasma electron, which essentially carry the RF discharge current. The presence of magnetic field and non uniformity in the plasma density renders the Maxwells quation analytically non-solvable. We resort to numerical solution. Since plasma frequency(w_{pe})>>RF frequency, it can be safely assumed that the displacement current is negligible compared to conduction current. Hence from Maxwells equation

$$\frac{d\tilde{H}_z}{dr} = -\frac{\omega_{pe}^2\varepsilon_o}{v_{ef} + j\omega_{ef}}\tilde{E}_\theta + \frac{\omega_{pe}^2\varepsilon_o u_r \mu \tilde{H}_z}{v_{ef} + j\omega_{ef}} \tag{13}$$

$$\frac{1}{r}\frac{d(r\tilde{E}_\theta)}{dr} = -j\mu\omega\tilde{H}_z \tag{14}$$

Using above two equations, we can solve for $\tilde{E}_\theta$ and $\tilde{H}$ with boundary condition, $E_\theta(r=0) = 0$ and $H(r=R) = Ho \approx NI_{RF}$. Where N is the number of turn of RF antenna per unit length and I_{RF} is the RF current. Using complex Poynting theorem, the time average power flowing into the plasma chamber can be calculated.

IMPLEMENTED NUMERICAL SCHEME

The radius of the plasma chamber has been discretized in equal intervals. The j is the index, which runs from 0 to n, and n can be varied to increase the accuracy of the solution. At $r = 0$, we assumed the value of n_i and u_i be known for all species. With this convention the continuity equation and the momentum balance for n_i gives respectively.

$$n_j u_j = \Gamma_j = \frac{r_{j-2}\Gamma_{j-2} + (G-L)_{j-1}r_{j-1}2\Delta r}{r_j} \tag{15}$$

$$\frac{u_j - u_{j-1}}{\Delta r} + \frac{e}{mn_j u_j}T\frac{n_j - n_{j-1}}{\Delta r} + \frac{e}{mu_j}\frac{\phi_j - \phi_{j-1}}{\Delta r} + v_{efj} = 0 \tag{16}$$

Using (16) and (17) to eliminate u_i and solving for ϕ_j:

$$\phi_j = \phi_{j-1} - \left[\frac{1}{n_j^2}\left(\frac{m_+\Gamma_i^2 + f_j\Delta r\Gamma_i}{e}\right) - \frac{1}{n_j}\left(T_i n_{j-1} + \frac{m_+ u_{j-1}\Gamma_i}{e}\right) + T_i\right] \tag{17}$$

Now substituting the values of ϕ_j in the charge balance equation one can iteratively solve for n_j. Special care

should be taken at $j = 1$. Momentum balance gives $n_1 = n_0$ for all species and the continuity equation gives $n_i u_i = (G-L)_i \Delta r/2$. Using this scheme, we compute the value of n and u as a function of r and stop when u = Bohm velocity. We use particle and energy balance as check on the accuracy of the solution [1, 3]. If above criteria are not satisfied within the set accuracy limit, then program will adjust the parameter T_e and $n_e(r = 0)$ in such a way that it leads closer to the real solution. The integral involved in computing energy balance has been calculated numerically.

RESULT AND DISCUSSION

From Figure 1, it is evident that the different species shows maxima at the center of the chamber. This is because the loss due to diffusion is minimum in the central region. The density of the charged species changes sharply

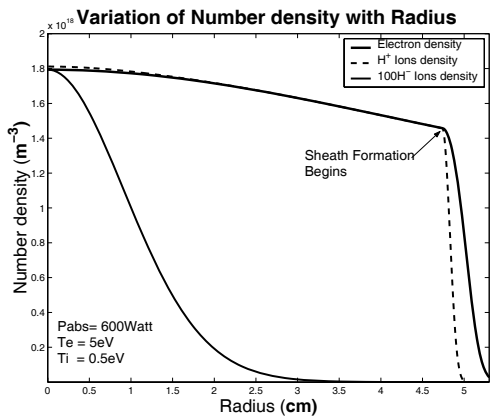

Figure 1: Density Profile of Different species

at the onset of the sheath formation. It is also clear that the density of the H^- ion become insignificant in the sheath region. Hence in the sheath region, the ion flux is essentially balanced by the electron flux and the quasi-neutrality is no longer valid. Within the plasma region, the H^- ion

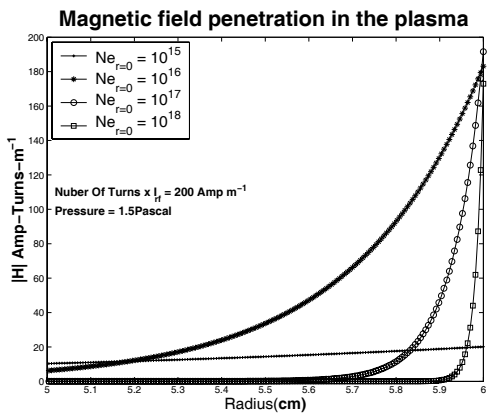

Figure 2: Profile of Magnetic field inside the plasma.

density decreases sharply towards the presheath edge, this is possibly because electron and H^+ gain enough energy due to acceleration in the presheath potential, that it strips out an extra electron attached to the H^- ion. For computing penetration of electric and magnetic field in the plasma, the product of number of turns of RF antenna and RF current ($N \times I_{RF}$) is taken as input to the program.From the Figure 2 and Figure 3, it is clear that as the density of electron decreases the electric and magnetic field pnetrates to a greater depth inside the plasma. The electric field decreases sharply for the low electron density. Thus there is crossover of electric field when we go from low electron density to high electron density. Such result has also been reported by experimental measurment [5]. The overall nu-

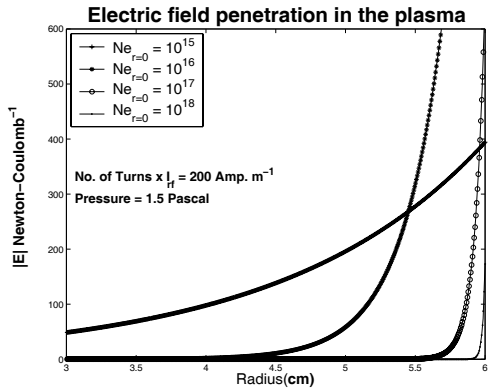

Figure 3: Profile of electric field inside the plasma.

merical scheme seems quite suitable for the simulation of the steady state equlibrium plasma of H^- ion source and are improved over uniform density model [3]. The other qualitative features are in good agreement with the experimental results of RF driven H^- ion source.In future work the sheath formation will be more accurately worked out considering collisional process. Further surface effect will be taken into account appropriately.

REFERENCES

[1] A.J.Lichtenberg, V.Vahedi, M.A.Lieberman and T.Rognlien. "Modelling of electronegative plasma discharge", J. Appl. Phys 75(5), 1 March 1994

[2] M.Bandyopadhya, Ph.D Dissertation,"studies of an inductively coupled negative hydrogen radio frequency source through simulation and experiment", Max Plank Institute for plasma physics, 2004

[3] Ajeet Kumar, V.K.Senecha and S. Kotaiah,"Computer simulation to design H^- Ion source", Indian Particle Accelarator conference Proceedings 2006, page number 227

[4] Michael A. Liberman and Allan J. Lichtenberg,"Principal of Plasma Discharge and Material Processing",Publisher: John Wiley and sons, 1994

[5] R. Piejak, V.Godyak and B.Alexandrovich. "Magnetic field distribution measurment in a low- pressure inductive discharge" J. Appl. Phys, 78(9), 1 Nov. 1995

PERIODIC ION CURRENT BURST IN 6.4 GHZ ECR SOURCE

G.S. Taki#, P.R. Sarma, R.K. Bhandari, Variable Energy Cyclotron Centre, Kolkata, India
A.G. Drentje, Kernfysisch Versneller Instituut, Groningen, The Netherlands
T. Nakagawa, Institute of Physical and Chemical Research (RIKEN), Wakoshi, Japan
P.K. Ray, Bengal Engineering and Science University, Howrah, India

Abstract

We studied the enhancement in extracted ion current in the 6.4 GHz ECR ion source at VECC, Kolkata by inserting a negatively biased disc. In addition to the expected increase in current, we observed a sudden jump in the current at some low bias voltage. We recently measured and analyzed the time spectra of high charge state ion current for neon to understand the origin of the jump. It revealed the presence of a burst frequency in kilohertz range. This frequency shows a synchronous jump with the ion current and also a good linear correlation with it. This may signify that current per burst is a constant factor ; higher current means that there are more number of bursts.

INTRODUCTION

Various techniques are employed for enhancing the extracted beam current from Electron Cyclotron Resonance (ECR) ion sources. The most common method is to add a lighter gas to the sample gas in order to reduce the ion temperature thereby increasing the retaining time and thus the ion current [1]. Another approach is to supply low temperature electrons to the main stage plasma. In this process the plasma becomes more stable, as a result of which the ion confinement time increases. Wall coating [2], use of an electron emitter [3], and the insertion of a biased disc [4-6] are the cold electron supplying techniques.

The use of biased disc in ECR sources was first demonstrated by Melin et al. [4]. In recent years, this technique has become the most popular method of increasing the extracted ion current from an ECR ion source. Melin [4] and Gammino et al. [7] systematically studied the improvement in ion current by biased probes. The improvement was thought to be due to an increase in the electron density with the application of a negative potential. D. Meyer [8] suggested that when negative potential is applied on the disc, the plasma potential decreases making the ECR plasma more stable. As a result, high charge state production increases. Tarvainen et al. [9] and Mironov et al. [10] made measurements on the plasma potential and found that it decreased when the negative potential at the biased disk was increased.

In order to study the performance of the biased disc systematically we made measurements on the extracted ion current by varying the disc bias potential [11,12]. The modification undertaken on the vacuum system allowed the source to sustain a base pressure of 6×10-8 Torr on the injection side. The measurements showed that as the negative bias potential was increased, the extracted ion current for any species showed a small decrease and then at a small negative potential it jumped to a high value. As the potential was further increased, the ion current also increased and saturated at a large bias potential.

Fig.1. shows typical results of the measurement on ions of various charge states. It is to be noted that the potential at which the current abruptly jumps is the same for all species. Another interesting feature is that for H^+ the ion current jumps to a lower value.

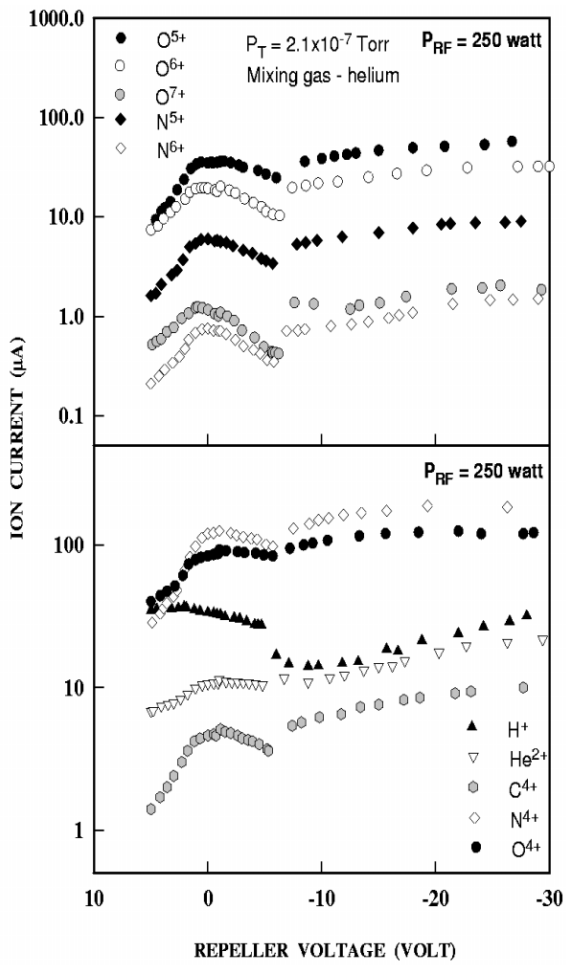

Figure 1: Variation of ion current with bias voltage.

gstaki@veccal.ernet.in

EXPERIMENT

In order to understand the origin of jump we investigated the time spectra of the extracted ion current. A Faraday cup, located beyond the 900 analyzing magnet, was used for measuring the ion current. In this arrangement we could measure the spectra for individual analyzed ion species. The output of the Faraday cup was fed to a 200 MHz Tektronix storage oscilloscope which stored data at intervals of 0.01 ms. Duration of each measurement was 100 ms allowing us to collect 10000 data points in each spectra.

Fast Fourier analysis was performed on the spectra using the MATLAB software. Fig.2 shows a typical time spectrum of Ne^{6+}. Figs.3 show the Fourier spectra before and after the jump in Ne^{7+} ion current.

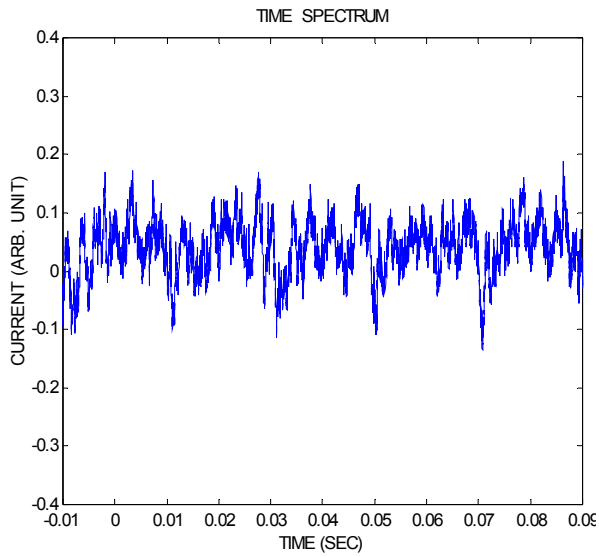

Figure 2: Typical time spectrum for Ne^{6+} with no bias. DISCussions

The time spectra were Fourier analyzed for a number of applied bias voltages. Presence of a frequency peak different from the usual 50 Hz noise were revealed in all the cases. With no disc bias the frequency was around 300 Hz. As the negative bias voltage was increased, the current showed a marginal decrease and showed an abrupt jump at a small negative voltage (-2.5V) (Fig.4). The frequency also showed a simultaneous abrupt change. It increased to a value of about 1170 Hz. Thereafter both the current and the frequency remained essentially constant.

Fig.5 plots the frequency as a function of the extracted ion current. The general trend is that the frequency increases as the current increases. In fact the plot shows a good linear correlation between the frequency and the current. The statistical correlation coefficient comes out to be 0.85. The presence of a frequency peak in the Fourier spectra means that a large portion of the ions come out of the source in periodical bursts. If we subtract the minimum ion current (just before the jump) then the frequency-current plot becomes a straight line passing through the origin. Thus one can see two parts of the current. The minimum part is constant part whereas the other part is frequency dependant.

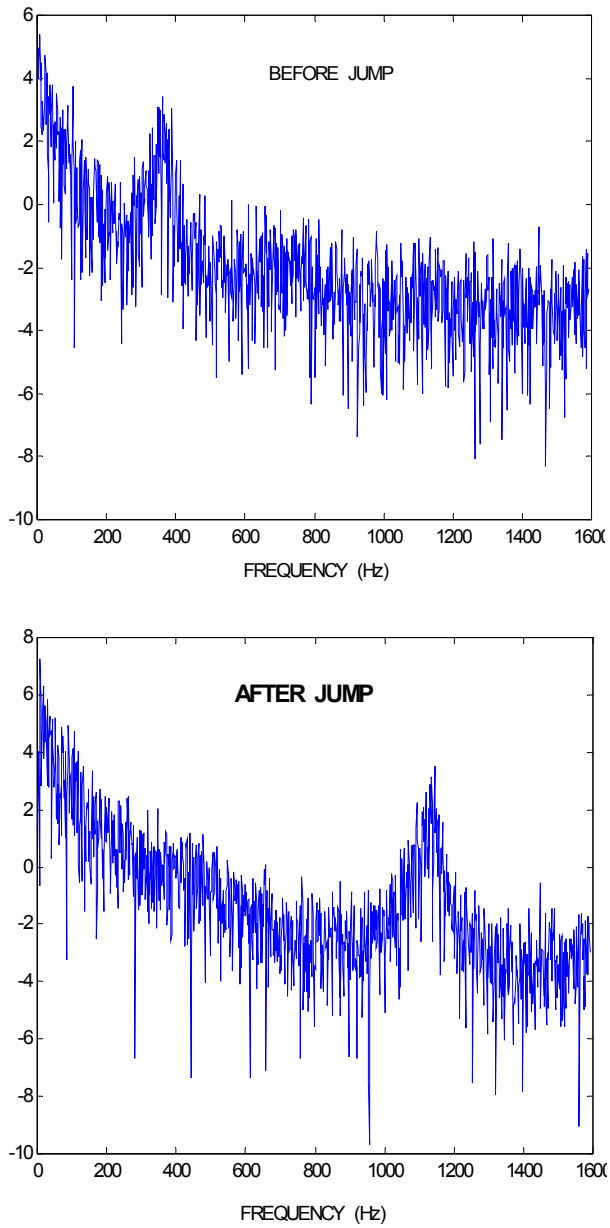

Figure 3: Fourier spectra of the ion current. The burst frequency changes with the applied bias voltage.

At saturation, the frequency dependant part gives the major contribution to the ion current. The fact that the ion current (I-Imin) is proportional to the burst frequency, then simply means that the more the number of bursts per unit time, the more is the current. It also says that the current per burst is a constant factor. Thus increasing the burst frequency by some means appears to be the key factor in increasing the extracted ion current. We have measured the time spectra and done the analysis for Ne^{7+} also. In this case also we have obtained similar results.

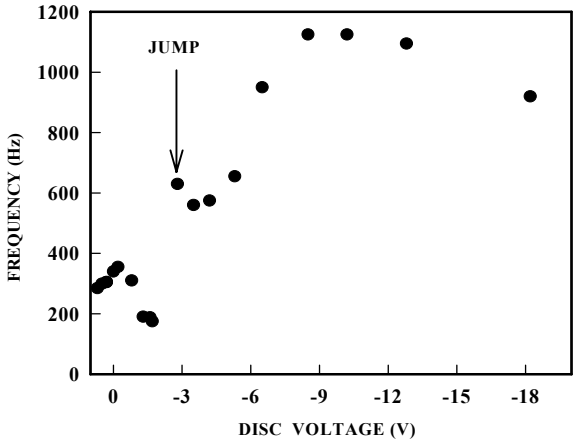

Figure 4: Jump in the burst frequency (Ne^{7+})

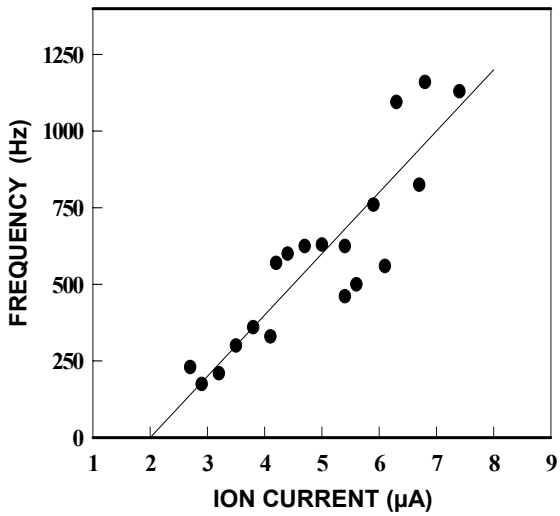

Figure 5: Correlation between the burst frequency and the ion current.

R.C. Garner et al. showed that the ions and electrons in a microwave generated plasma, show a burst in the kilo-Hertz frequency range. They observed [13-15] that a mirror confined plasma, which is inherently anisotropic when the electrons are heated to energies greater than the plasma potential, may be whistler unstable. The whistler instability means an electron micro-instability which is driven by the temperature anisotropy of the electron velocity space distribution. This whistler instability is driven by the warm electron component (~ 2 keV). Unstable rf emission in a regime near the electron cyclotron resonance frequency (0.7fce to fce) has been obtained in the mirror-confined ECR heated plasma. This rf emission associated with the micro-instability occurs in fairly regular burst with a fixed burst time. The energy per burst was found to maintain a constant value. It was also experimentally observed by them that the rf emission burst correlates with the electron end-loss burst as well as burst of ion end-loss.

The periodicity of the burst depends upon the mid-plane magnetic field and the operating pressure. Whistler B occurs at lower operating pressure (<5×10-7 Torr) and whistler B and C both exist at marginally high operating pressure (7×10-7 to 2×10-6 Torr). In case of whistler B the end losses are along the axis.

Garner quoted a value of 5×10-6 J per burst in their 10 GHz ECR device. In our 6.4 GHz source, the total ion current is about 400 μA. Taking a value of 30 eV for the energy per ion and a measured burst frequency of 1.2 kHz, the overall energy per burst comes out to be about 3×10-5 J. This is of the same order of magnitude as that obtained by Garner. So it may be surmised that the periodic current bursts observed in our experiment is of similar origin to that discussed by Garner. Further experiments with a bias voltage modulated by kilo-Hertz ac component may be of interest.

REFERENCES

[1] A.G. Drentje, Rev. Sci. Instr. 74 (2003) 2631.
[2] C.M. Lyneis, Proc. 8th Int. Workshop on ECR Ion Sources, 1987, Ed. J. Parker, NSCL Reports, MSUCP, p.42
[3] Z.Q. Xie and C.M. Lyneis, Proc. 11th Int. Workshop on ECR Ion Sources, Groningen, 1993, Ed. A.G. Drentje, KVI Report-996, p.106.
[4] G. Melin et al. Proc. 10th Int. Workshop on ECR Ion Sources, Knoxville,1990, Ed. F.W. Meyer and M.I. Kirkpatrik, Oakridge report, Conf-9011136, p.1.
[5] S. Biri, T. Nakagawa, M. Kidera, L. Kenez, A. Valek, and Y. Yano, Proc. 14th Int. Workshop on ECR Ion Sources, CERN, Geneva,1999.
[6] A.G. Drentje, A. Kitagawa, M. Muramatsu, H. Ogawa and Y. Sakamoto, Rev. Sci. Instr. 75 (2004)1399.
[7] S. Gammino, J. Sijbring and A.G. Drentje , Rev. Sci. Instr. 63 (1992)2872.
[8] D. Meyer, D.O. Bolshukhin, I.P. Vinogradov and K. Wiesemann, Proc. 12th Int. Workshop on ECR Ion Sources, 1995, (RIKEN, Japan), Ed. M. Sekiguchi and T. Nakagawa, INS, Tokyo, report INS-J-182, p.34
[9] O. Tarvainen, P. Suominen and H. Koivisto, Rev. Sci. Instr. 75 (2004)3138
[10] V. Mironov et al. Rev. Sci. Instr. 73, 623 (2002).
[11] G.S. Taki, R.K. Bhandari and D.K. Bose, Proc. DAE Symp. on Nucl. Phys. (Bombay, India) 35B (1992)468.
[12] G.S. Taki, P.R. Sarma, D.K. Chakraborty, R.K. Bhandari, P.K. Ray and A.G. Drentje, Rev. Sci. Instr. 77 (2006)03A310.
[13] R.C. Garner, M.E. Mauell, S.A. Hokin, R.S. Post and D.L. Smatlak, Phys. Rev. Lett. 59 (1987)1821.
[14] R.C. Garner, M.E. Mauell, S.A. Hokin, R.S. Post and D.L. Smatlak, Phys. Fluids, B2 (1990)242.
[15] A. Girard, Rev. Sci. Instr. 63 (1992)267.

BEAM LINE DESIGN FOR PEFP USER FACILITY*

Y.S. Cho#, B.C. Chung, K.Y. Kim, Y.H. Kim, K.R. Kim, Y.Y. Lee, B.H. Choi, Proton Engineering Frontier Project, Korea Atomic Energy Research Institute, Daejeon 305-353, Korea.

Abstract

In the Proton Engineering Frontier Project (PEFP), 20MeV and 100MeV proton beams from a 100MeV proton linear accelerator [1] will be supplied to users for beam applications. The basic lattice for beam transport line will be FODO from the linac to the targets. Dipole magnets exited with shaped AC currents will distribute the beam from the linac to five targets simultaneously. To provide flexibilities of irradiation conditions for users from many application fields, we design beam lines to the targets with wide or focused, external or in-vacuum, and horizontal or vertical beams. The details of the beam line design will be reported.

INTRODUCTION

The main concept of the PEFP proton beam facility is that a high power proton accelerator supplies proton beam to many users simultaneously. This concept can be compared with a facility with many low power proton accelerators for many users. Based on the user demand survey for proton beam applications, we have chosen a facility with a high power accelerator. There are many types of proton accelerator for proton beam applications, such as cyclotron, synchrotron, and linac. Because the capability of high beam power is the most important feature, we have decided to choose a linac for the main accelerator of the facility. Figure 1 shows the schematic diagram of the PEFP user beam line.

Proton beams of 100MeV and 20MeV will be extracted and distributed to maximum five users simultaneously by AC magnets with a programmable current power supply. We will control the beam energy stepwise with RF ON/OFF of each DTL tank. To control the beam energy continuously, we will put energy degraders and energy filters in the beam lines for special applications.

BEAM LINE REQURIEMENTS

The surveys for proton beam demand from many application fields, such as nano-technology (NT), bio-technology (BT), space technology (ST), and radio-isotope production, have been done through the homepage (http://www.komac.re.kr) and the user program from 2003 to 2006. From these activities, we have selected the common requirements for many applications and have summarized the beam line requirements for 10 beam lines of 100MeV and 20MeV, which are shown in Table 1 and 2. In the selection process, we have put more weighting to high beam power applications, which will be main applications in this facility.

Table 1: 100MeV beam line requirements

Beam Line No.	Energy	Avg. Current	Irradiation Condition	Max. Target Size
BL100	100MeV	~1.8mA	Horizontal Vacuum	Beam Dump
BL101	33,45,57, 69,80,92, 103MeV	30~ 300μA	Horizontal Vacuum	100mm
BL102	20~ 103MeV	~10μA (10nA)	Vertical External	300mm
BL103	20~ 103MeV	30~ 300μA	Horizontal External	300mm
BL104	20~ 103MeV	10nA ~10μA	Horizontal External	300mm
BL105	103MeV	30~ 300μA	Horizontal Vacuum	100mm

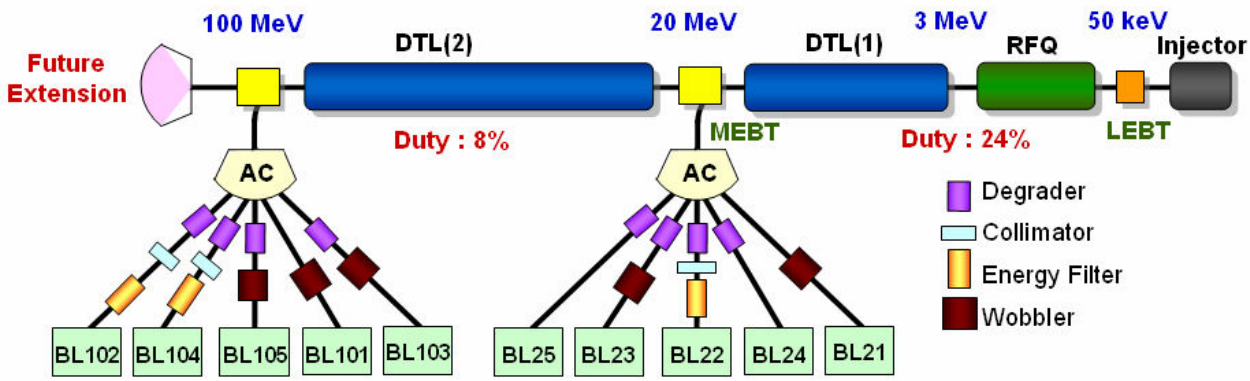

Figure 1: Schematic diagram of PEFP user beam line.

*Work supported by the 21C Frontier R&D program in Ministry of Science and Technology of the Korean Government
#choys@kaeri.re.kr

Table 2: 20MeV Beam Line Requirements.

Beam Line No.	Energy	Avg. Current	Irradiation Condition	Max. Target Size
BL20	20MeV	~4.8mA	Horizontal Vacuum	-
BL21	20MeV	120μA ~1.2mA	Horizontal Vacuum	100mm
BL22	3~20MeV	10nA ~60μA	Vertical External	300mm
BL23	3~20MeV	60μA ~1.2mA	Horizontal External	300mm
BL24	20MeV	120μA ~1.2mA	Horizontal Vacuum	100mm
BL25	20MeV	120μA ~1.2mA	Horizontal Vacuum	300mm

BEAM LINES

Table 3 shows the beam parameters from the proton linac, which consists of a 50 keV proton injector, a 3 MeV RFQ, and a 20 MeV DTL [2], and a 100MeV DTL as shown in Figure 1. The average beam current is enough to supply the beams to 5 beam lines simultaneously.

Table 3: Beam Parameters.

Energy (MeV)	20	100
Energy spread (%)	< 1%	< 1%
Peak current (mA)	1~20	1~20
Max. beam duty (%)	24	8
Average beam current (mA)	0.1~4.8	0.1~1.6
Pulse width (ms)	0.1~2	0.1~1.33
Max. repetition rate (Hz)	120	60
Max. beam power (kW)	96	160

With the beam line requirements, we have arranged target rooms for beam applications on the experimental hall, which was be 50m wide and 150m long. Figure 2 shows the layout of 20MeV beam lines.

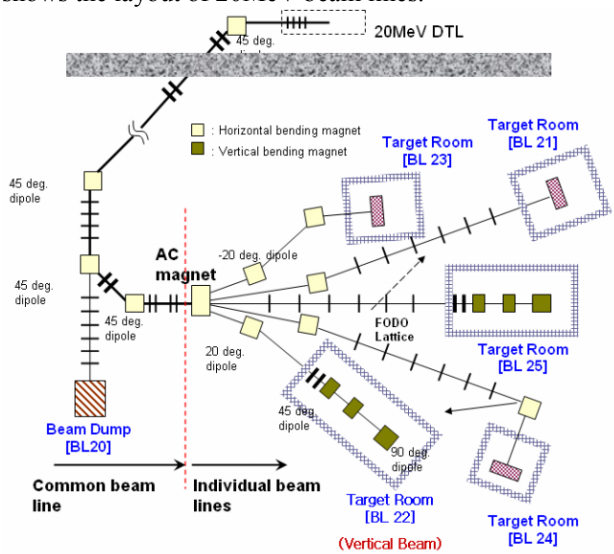

Figure 2: Layout of 20MeV Beam Lines.

A 20MeV proton beam from the Drift Tube Linac (DTL) is transported with bending magnets and quadrupole magnets from linac tunnel to experimental hall. The first bending magnet for the user beam line is located between two buncher cavities of medium energy beam transport (MEBT) [3] at the end of the 20MeV Linac. The basic lattice of the beam transport line is FODO, and the all bends are achromatic.

Figure 3 is an example of the beam optics calculation from the 20MeV Linac to target room #25 with TRACE-3D [4].

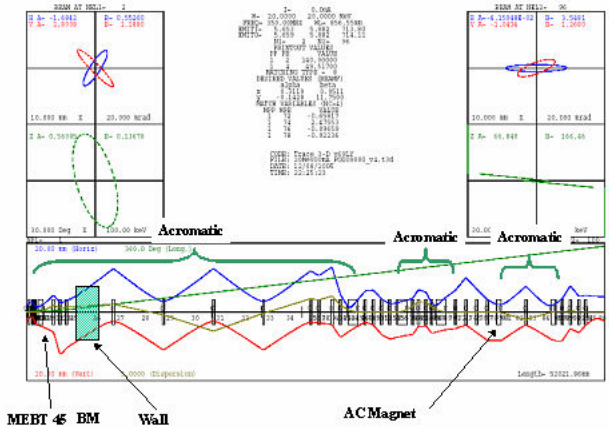

Figure 3: Beam Optics of BL25.

For 100MeV beam lines, the schematic layout is almost same with the 20MeV beam lines. A 100MeV beam is transported through long transport line with doublet lattice from the 100MeV DTL. Figure 4 shows the beam optics from the linac to the target room #102.

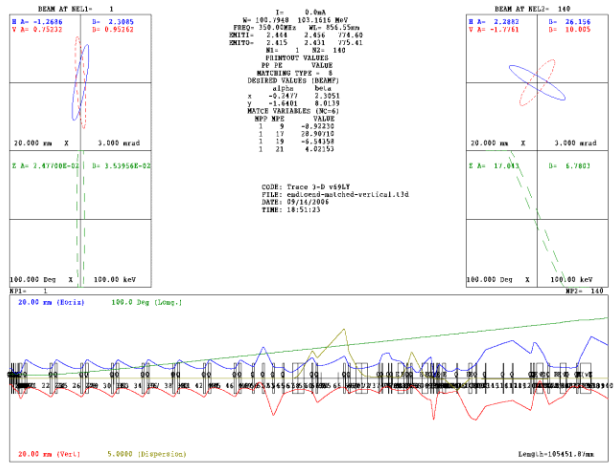

Figure 4: Beam Optics of BL102.

BEAM LINE COMPONENT R&D

In the concept of the user facility, AC magnets are important components. We are designing the AC magnet, as shown in Figure 5. The AC magnet will be excited

with a programmable current power supply, which is synchronized with linac beam pulses.

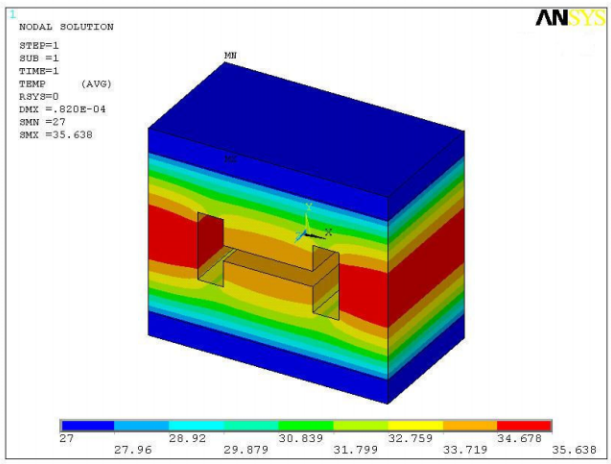

Figure 5: Thermal Analysis of AC Magnet.

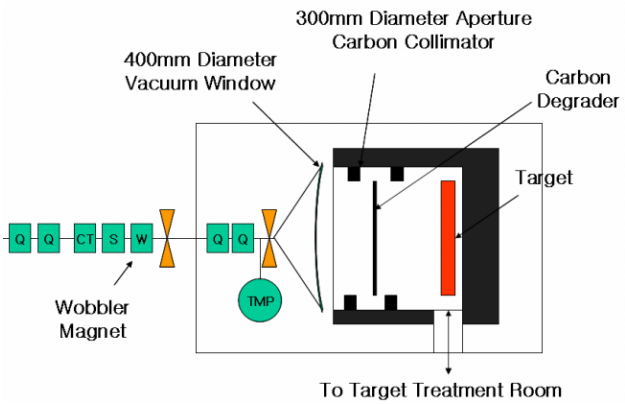

Figure 6: Target Room for external beam with large area

An important requirement in the beam lines is external beam, which requires beam windows. It is not easy to design high power beam window with large area because of thermal load for low energy and radiation damage for high energy. Magnets for beam irradiation, such as wobbler magnet, scanning magnet, and large aperture quadrupole magnet, are also important to utilize high current proton beam efficiently for applications, which require uniform irradiation on the target, as shown in Figure 6. The R&D for target rooms is started.

SUMMARY

20MeV and 100MeV proton beams from a 100MeV proton linear accelerator will be supplied to users for beam applications. From the results of user demand survey, beam line requirements have been prepared. With the requirements, the layout of the experimental hall was developed as shown in Figure 7. The R&D for beam line components, such as AC magnets, is on-going. The construction will start in 2007, and the operation will start in 2011.

REFERENCES

[1] Yong-Sub Cho, *et al.*, "100 MeV High-Duty-Factor Proton Linac Development at KAERI," LINAC'06, Knoxville, to be published.

[2] Hyeok-Jung Kwon, *et al.*, "Test results of the PEFP 20 MeV Proton Accelerator," LINAC'06, Knoxville, to be published.

[3] Ji-Ho Jang, *et al.*, "Design of the PEFP MEBT," PAC'04, Knoxville, Tennessee, USA 2004.

[4] K.R. Crandall and D.P. Rusthoi, "TRACE 3-D Documentation," LA-UR-97-886.

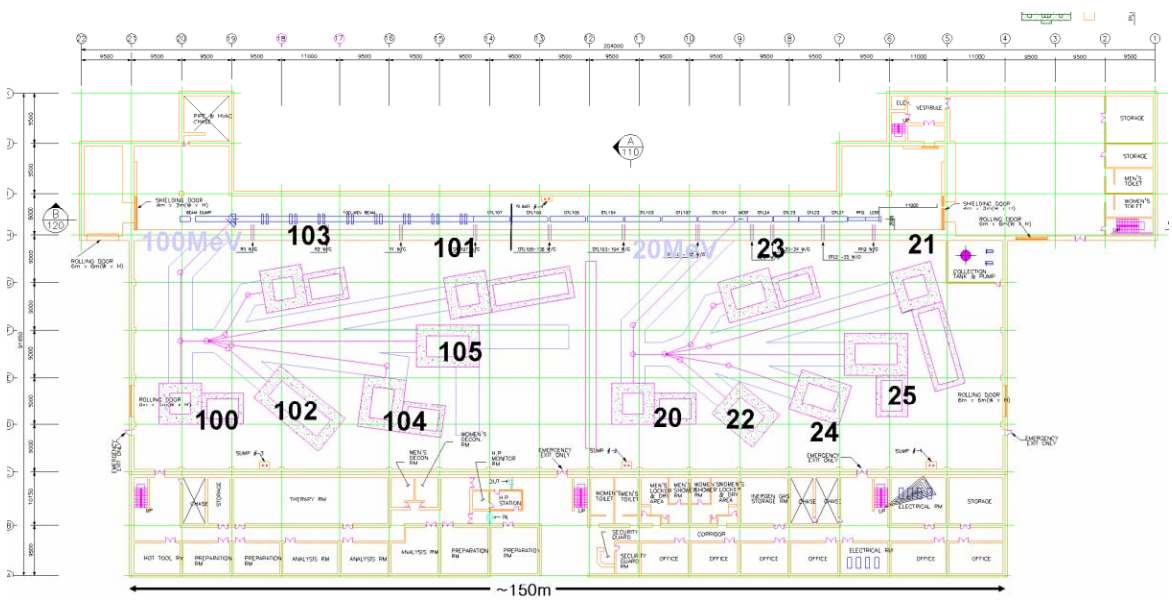

Figure 7: PEFP Experimental Hall with user beam lines.

HIGH POWER NEUTRON CONVERTER FOR LOW ENERGY PROTON/DEUTERON BEAMS: PRESENT STATUS*

A.Antoshin, M.Avilov, D.Bolkhovityanov, S.Fadeev, K.Gubin, N.Lebedev, P.Logachev, P.Martyshkin, S.Shiyankov, BINP, Novosibirsk, Russia,
L.Tecchio, INFN-LNL, Legnaro, Italy.

Abstract

In BINP, Russia, the high temperature neutron target for SPES project (INFN-LNL, Italy) is proposed. The target is designed to produce up to 10^{14} neutron per second within the energy range of several MeV under irradiation by proton/deuteron beam of power up to 200 kW. By now, the target prototype is successfully tested. The development of liquid metal driving system and target general design is started. This paper describes the design of the target and the target prototype as well as the results of prototype tests under high-power electron beam.

Special attention is paid to the carbon material with high content of ^{13}C isotope. The material is produced in accordance with the original technology and is used for manufacturing the converter irradiated with the proton beam.

INTRODUCTION

In the framework of the European program, to define a second generation Radioactive Ion Beam (RIB) facility, the Legnaro National Laboratories (LNL) are proposing the construction in the next years of a specialized national facility for RIB originated by fission fragments produced by fast neutrons (SPES) [1]. Protons/deuterons of 40 MeV and 150 kW will produce in a converter about 10^{14} neutrons per second centered at around 14 MeV that will induce fission in a suitable fissile target, with the aim of 10^{13} fission per second at least.

The neutron energy distribution, the target size and its constituents are the most important parameters to be investigated in order to maximize the efficiency for RIB production. A few different methods for producing fast neutrons and their induced fissions following the (p,xn) or (d,xn) reactions on different materials were investigated.

Designing the SPES facility, simulations of neutron spectra for several beam converter materials/configurations have been performed with the MCNPx [2] and the PRIZMA [3] codes. Furthermore, the isotopic distributions are evaluated combining the MCNPx with the code SP-FISPACT2001 [4] that allows the neutron transport below 20 MeV. The simulations performed were compared with experimental angular distributions measured at energies of 20, 40, 50 and 90 MeV for ^{12}C, ^{13}C and beryllium converters.

Results of simulations show the difference of neutron yield between different converter material are not critical, optimal target construction is more important. Calculated neutron angle-energy distributions allowed to estimate the different isotopes production and radiation shielding, to propose and optimize the full target system assemblage (see fig.1).

The design of the converter and its prototype and the results of the prototype tests are discussed in detail in the following paper.

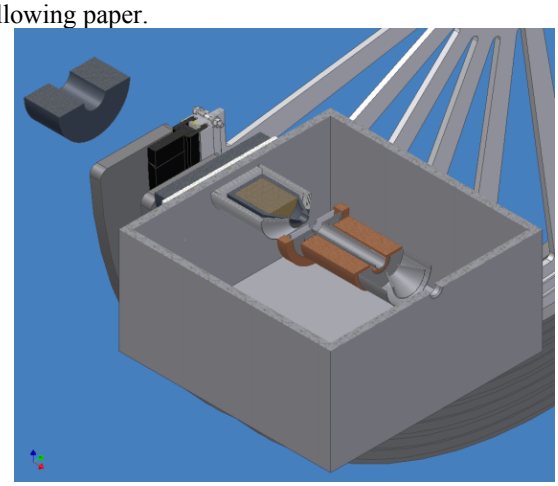

Figure 1: Layout of the SPES target system. Left to right: protecting collimator, neutron converter inside the cooling panels, fission target, ion source.

CONVERTERS AND PROTOTYPE DESIGN

The proposed target design [5] comprises the carbon converter assembled with plates, which are mounted on rotating metal disk (see fig.1). The converter material considered is ^{13}C (for proton beam) and natural carbon (for deuteron beam), both under graphite form with thickness of 10 mm, suitable to stop full beam inside it. The diameters of the wheel and of the rotating shaft are close to 100 cm and 5 cm, respectively. The thermal power deposited in the converter material is dissipated only by thermal radiation. Heat removal from vacuum chamber is carried out by water circulating inside aluminum cooling channels fixed to the chamber's walls. Before the converter a collimator acts as a beam position monitor. Beyond the converter, a graphite plate serves to survey and monitoring eventual damages of the converter and, at the same time, protects the vacuum chamber from primary beam.

The converter prototype is described in detail in paper [6]. It is scaled to 1/3 of the real power (50 kW) by reducing its dimensions and limited to 20 MeV equivalent proton beam energy to match the energy and power of the electron accelerator used to perform experimental tests. All construction is assembled inside the special cooled vacuum chamber. The rotation of prototype is carried out

by an electrical motor by means of a ferromagnetic rotary feedthrough.

The most important thing is to investigate the converter parameters as follows: maximum operating temperature and thermo-mechanical stress distributions inside the converter itself; mechanical stress due to the rotation is far less than thermal one. During regular operation converter can reach the temperature up to 2000^0C for effective cooling, and temperature gradients up to 100^0C/mm (see fig.2).

Main purposes of the tests were the examinations of the basic physical and technical solutions proposed for the target:

- To clear up the possibility of converter design to dissipate the beam power, and its reliability;
- To test the cooling channels aimed to accept and remove the heat power;
- To check up the calculations of prototype operation conditions;
- To check up the converter made of 13C-based material under the regular operational conditions.

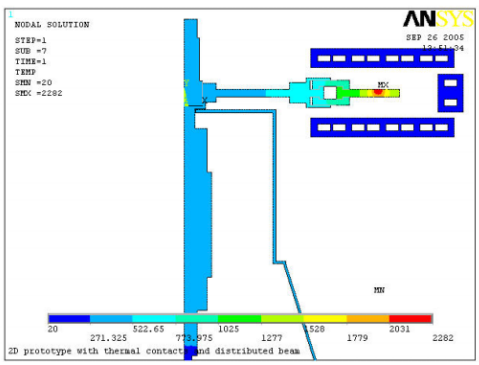

Figure 2 : Temperature distribution (°C) of prototype in regular regime as calculated by ANSYS code.

^{13}C BASED MATERIAL

The material with high content of ^{13}C isotope is not commercially available. In the framework of our project the development of this material was initiated in NIIGrafit, Moscow. Technology is based on the process of MPG-brand graphites production: crushing and sizing of the ^{13}C powder; mixing the components with the phenolformaldegid resin (binder) and urotropin (catalyst); compacting, burning and graphitization. Unfortunately, a few quantity of ^{13}C powder does not permit to perform complex investigation of material properties, but we can obtain material close to industrial graphites (see tab.1). This material stands any mechanical treatment.

Table 1: properties of the ^{13}C-based carbon material.

Properties	1.23 g/cm^3	1.45 g/cm^3
Compression strength, $\sigma_{compr.}$, MPa	29.2	62.6
Heat conductivity at 25°C, λ, W/m ·K	8.5	15.2
Linear heat expansion factor, α, 1/deg.	$3.8\cdot10^{-6}$	$4.3\cdot10^{-6}$
Specific electrical resistance, ρ, μOhm ·m	78.3	51.5

TESTS OF PROTOTYPE

Test of prototype includes the distributed volume heating of prototype converter by the high power electron beam of ELV-6 accelerator [7] with energy 1.4 MeV, diameter over 7 mm, power up to 70 kW. View of prototype installation is shown on the fig.3. During experiment the beam position, current and effective size (by the linear scanning along the prototype diameter) were controlled. The main measured parameters were: graphite converter temperature distribution, temperatures of the metal parts of prototype, heat power accepted by the cooling channels, beam and rotation parameters.

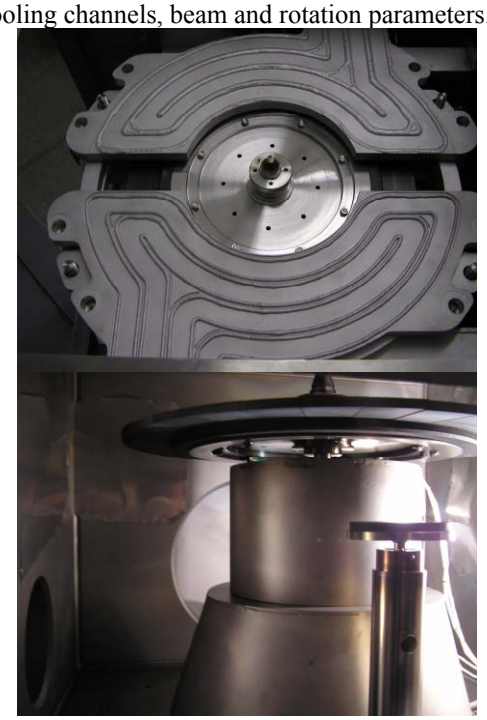

Figure 3 : View of prototype.

The main experimental results are:

- Temperature distribution over the converter's plates under different beam power (20 to 70 kW) and size (7 to 26 mm) corresponds to calculated one;
- Temperatures of the metal elements in the stable regular regime are in good agreement with calculations;
- Total beam power is successfully accepted by the cooling channels within the accuracy of the measurements;
- The assembly with the usual graphite is successfully stood under regular (50 kW power and 8 mm of beam size) regime for more than 70 h, and short time under high power (70 kW, 8 mm) regime;
- The assembly with the 13C-based material is successfully tested under regular (50 kW, 8 mm) regime;

- Studies of carbon materials before and after test did not observe any changes of its structures and properties;
- Prototype operating parameters during the tests were stable and repeatable.

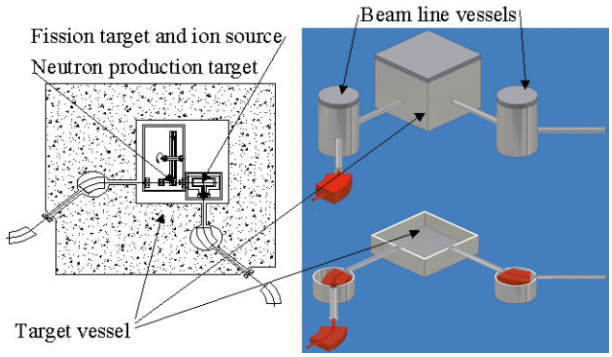

Figure 4 : Schematic view of target area vacuum chamber design.

Figure 5 : The parts of liquid lead cogwheel pump.

Authors would like to thank I.Bubnenkov and A.Sorokin (NIIGrafit, Moscow) for the ^{13}C material creation.

CONCLUSION

Nowadays the performed R&D represents efficiency of proposed decisions for neutron target:

- Construction of the target was produced and tested with the high-power electron beam;
- New experimental 13C based material was created and tested;
- Neutron angle-energy distribution and radionuclides production were calculated, biological shielding was estimated.

Next steps of the target are started. It is: .

- ***Design of the target system as the single complete unit***. The basic principles arise from the radiation safety: the neutron target, the fission target and the ion source are mounted on common concrete foundation inside large stainless steel vacuum chamber; bending magnets are desired for both beams in order to stop the direct neutron flux coming through beam line aperture; neutron production target and fission target with ion source must be separated one from the other, the space between the neutron production target and the fission target should not exceed 50 mm; replacement of units must be done with the remote handling.
- ***Development of the target rotation driving system.*** Hard operating conditions (high temperature, vacuum, extremely high radiation) do not allow the use of conventional mechanical units. Of possible variants is the use of liquid metal driving system. The main elements of the system are liquid metal pump and the reverse to it liquid metal motor, liquid metal sliding bearings. This approach is under the test now in Budker INP (liquid lead positron production target development in the framework of ILC collaboration). Cogwheel pump for liquid lead was successfully tested at BINP for more than 10000 h in continuous regime.

REFERENCES

[1] L.Tecchio et. al. “Project of a Next-generation ISOL Facility for Exotic Beams at LNL”. EPAC2000, June 25-30 2000, Vienna.

[2] Laurie S. Waters, Editor: ‘MCNPXTM User’s Manual’, Version 2.1.5, TPO-E83-G-UG-X-00001, November 14, 1999 (http://mcnpx.lanl.gov/).

[3] V.V. Plokhoi et al.; Monte Carlo Simulation by PRIZMA Code of Neutron Production in Be, Li, B and C Targets Irradiated with 10 MeV Proton Beam, Workshop on Neutron and RIB Production Targets, Legnaro July 23-27, 2001,edited by P.V. Logatchev and L.B. Tecchio, SPES-03 (2001), p. 15.

[4] R.A. Forrest and J-Ch. Sublet; “FISPACT-2001: User manual”, EURATOM/UKAEA Fusion Association, Culham Science Centre, Abingdon, Oxford-shire OX14 3DB, UK, March 2001.

[5] O.Alyakrinskiy, et. al. “High power neutron converter for low energy proton/deuteron beams”. Nuclear Instruments and Methods in Physics Research Section A: Accelerators, Spectrometers, Detectors and Associated Equipment, 2006, Vol.557, Iss.2, pp. 403-413.

[6] M.Avilov, et al. “Prototype of high temperature intense neutron target”, Proc. of third Asian Particle Accelerator Conference to be held in March 22-26, 2004 at Gyeongju, Korea.

[7] R.A. Salimov et. al. “DC High Power Electron Accelerators of ELV-series: Status, Development, Applications”. Radiation Physics and Chemistry, 2000, Vol.57, Iss. 3-6, pp. 661-665.

ELECTRON ACCELERATION IN THE WAKE FIELD EXCITED BY 200TW FEMTO SECOND LASER IN UNDERDENSE PLASMA

R. Taki[a], W. M. An[b], Y. Q. Gu[c], Y. Guo[c], W. Hong[c], J. F. Hua[b], W. H. Huang[b], C. Y. Jiao[c], T. Kameshima[a], S. Kurokawa[ad], Y. Z. Lin[c], H. J. Liu[c], K. Nakajima[ad], H. S. Peng[c], L. Sun[c], C. M. Tang[c], C. X. Tang[b], X. D. Wang[c], X. D. Wang[e], T. S. Wen[c], X. L. Wen[c], Y. C. Wu[c], B. H. Zhang[c], K. N. Zhou[c] and Q. H. Zhu[c]

[a]Department of Accelerator Science, Graduate University for Advanced Studies, 1-1 Oho, Ibaraki 305-0801, Japan

[b]Department of Engineering Physics, Tsinghua University, Beijing 100084, P.R.China

[c]Laser Fusion Research Center, China Academy of Engineering Physics, Mianyang, Sichuan 621900, P.R. China

[d]High Energy Accelerator Research Organization, 1-1 Oho, Ibaraki 305-0801, Japan

[e]University of Southern California, Los Angeles, California 90089-0484, USA

Abstract

Laser-plasma acceleration experiment has been carried out using 200TW, 30fs Ti:Sapphire laser pulses focused on helium gas-jets with F/8.75 optics. Intense mono-energetic electron beams have been produced by controlling plasma length and density precisely. Energy spectral oscillations of accelerated electrons in respect to ejection angle have been also observed. Measurement of images from Thomson scattering and fluorescence side scattering from plasma indicate highly relativistic effects such as a long self-channeling and filamentation. It seems that these nonlinear phenomena strongly disturb high energy gain acceleration and high quality beam generation.

INTRODUCTION

Wake-field acceleration including plasma beat wave, plasma wake-field and laser wake-field acceleration has been studied to take advantage of high acceleration gradient which promises a compact accelerator. Recently good quality and high energy electrons have been demonstrated based on laser wake-field acceleration [1-3]. The recent development of laser technology enables us to use ultra-high power and short pulse lasers which can excite a large amplitude plasma wave. Electron motion in large amplitude plasma is involved in nonlinear dynamics. It has been studied theoretically and in particle-in-cell simulations [4,5], however, not well demonstrated experimentally yet. Here we present the results of electron acceleration in the nonlinear plasma wave excited by 200 TW femto second pulses.

EXPERIMENTAL SETUP

The experiment was performed with Ti:Sapphire laser system "SILEX-1" at CAEP [6]. The laser pulses of 800 nm wave length and 30 fs duration with 4 - 8.3 J were focused with F/8.75 optics onto helium gas-jets. The laser spot radius, w_0, was 12 μm, which yields peak intensity up to 1.8 – 3.8×10^{19} W/cm^2 and the laser strength parameter, a_0, up to 2.9 – 3.8 on assumption that the energy concentration is 30%. The laser was polarized in horizontal axis. The experimental setup for electron energy measurements is shown in Fig. 1. Thomson scattering images from plasma were recorded by a charge-coupled device, CCD, camera (CCD1) which was set on top of a gas-jet applying a band-pass filter with the wave range of 800 nm ± 10 nm in front of the CCD camera. Fluorescence side scattering images were also monitored by a CCD camera (CCD2) followed by a band-pass filter with the wave range of 400 nm ± 10 nm. Accelerated electrons were momentum analyzed using a permanent magnet, a phosphor screen, DRZ, placed just after the exit of the magnet, and a CCD camera (CCD3). Backward Raman scattering was measured by an optical multi-channel analyzer (OMA) system.

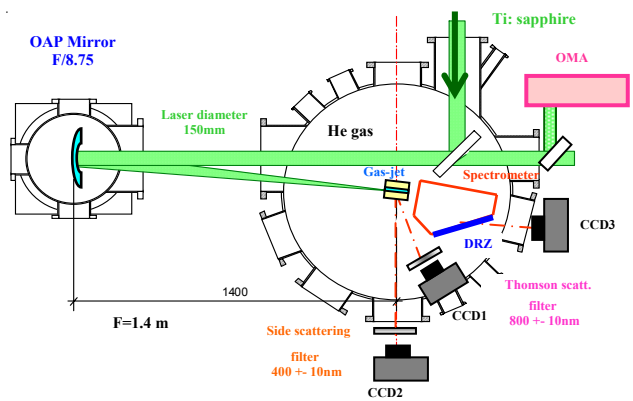

Figure 1: Schematic layout of the experimental setup for electron energy measurements.

Helium gas-get nozzles

We used two kinds of nozzles shown in Fig. 2(a) and (b) to adjust the plasma lengths. The nozzle in (a) is a supersonic Laval nozzle [7] which has a rectangular slit

10 mm in length and 1.2 mm in width. The nozzle in (b) is a conical nozzle which has a ϕ5 mm aperture at exit and a ϕ1 mm aperture at entrance. The nozzle in (a) was set in such a way the main laser went through the 10 mm side of the slit in order to produce longer plasma channels.

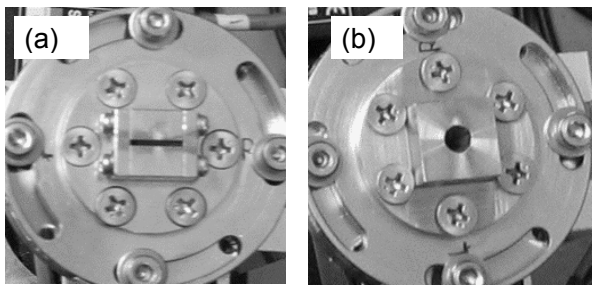

Figure 2: (a) Supersonic Laval nozzle with a slit 10 mm in length and 1.2 mm in width. (b) ϕ5 mm conical nozzle.

RESULTS

Electron acceleration with Laval nozzle

High intense electron beam was generated when the laser power was 202 TW, a_0 = 3.5, and plasma density was approximately $1\times10^{19}/cm^3$. The energy spectrum is shown in Fig. 3. The peak energy is 34 MeV. The spectrum has three lines which are separated vertically from each other. The upper and middle lines in the spectrum bend down as the energy becomes higher. At the end of these lines, there are two high mono-energy parts at 131 MeV as shown in Fig.3 (b). Figure 4(a) and (b) show Thomson scattering and fluorescence side scattering images, respectively. The laser was injected from the left side of the figures. In Fig. 4(a), a discontinuous bright line having a fine spot structure reaches to 4.7 mm long. This image shows a long self-channeling of laser in plasma involving relativistic focusing and ponderomotive channeling [8]. In Fig. 4(b), there is a thin bright line in the middle of a channel. This line is cased by second harmonic Thomson scattering of laser due to 8 figure motion of electron in the plasma [9]. The surrounding light is caused by the recombination of plasma.

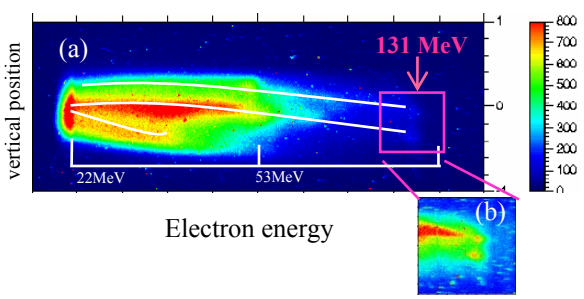

Figure 3: (a) Electron energy spectrum with 202 TW laser power, a0 = 3.5 and plasma density around $1\times10^{19}/cm^3$. (b) Close up view of two high mono-energy parts at 131 MeV.

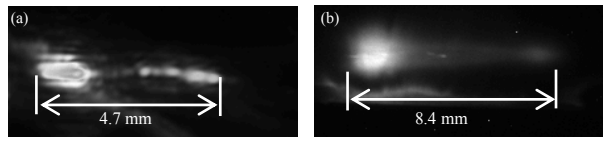

Figure 4: (a) Image of Thomson scattering from plasma. A discontinuous bright line with fine structures reaches to 4.7 mm long. (b) Image of fluorescence side scattering.

Filamentation

In addition to a long self-channeling, we observed a non linear phenomenon, filamentation [10], in Thomson scattering images when we used the supersonic laval nozzle. These images are shown in Figs. 5(a) and (b). The channels divide into two or more. In most cases when filamentaions occurred, electrons were not observed. Moreover, from the fluorescence side scattering image (not shown here) , we have found that laser propagations are shorter than those with electron. Non linear phenomena such as filamentation seem strongly disturb electron acceleration.

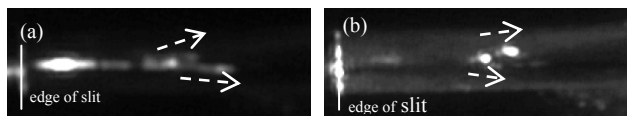

Figure 5: (a), (b) Thomson scattering images showing filamentations. The channels divide into two. The arrows are for eye-guide.

Electron acceleration with conical nozzle

To avoid filamentations and channel deflections, we optimized the plasma length using the conical nozzle shown in Fig. 2(b). In the condition that the laser axis passed through 4.5 mm long above the conical nozzle with 195 TW laser power, a_0 = 3.5 and plasma density of around $1\times10^{19}/cm^3$, mono-energetic electron beam was produced. The energy spectrum is shown in Figure 6. The mono-energetic part forms a Gaussian centred at 52.3 MeV with an energy spread of 6.3 MeV FWHM. Beam divergence is estimated to be 0.33 degrees FWHM from 3.3 mm vertical spot size on DRZ and 28 cm path length. Figure 7(a) and (b) show Thomson scattering and fluorescence side scattering images on this shot. Self-channeling continues 1.9 mm long in plasma, which implies the field gradient of 27GeV/m.

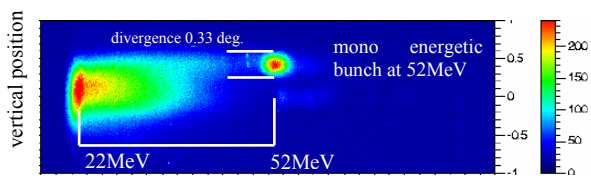

Figure 6: Electron energy spectrum with 195 TW laser power, a_0 = 3.5, and plasma density of around $1\times10^{19}/cm^3$.

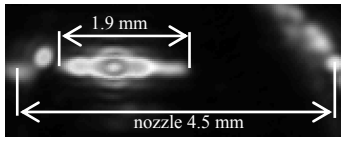

Figure 7: Image of Thomson scattering from plasma.

Energy spectrum oscillation

Figure 8 shows a electron spectrum obtained using the same conical nozzle. The laser power at this show is 224 TW and a_0 is 3.7. Vertical oscillation of electron position is clearly seen. This vertical (transverse) motion is due to wiggle trajectory of electrons in the plasma [5]. Figure 9 shows the same energy spectrum integrated over the vertical position. At this shot, electrons have been accelerated up to more than 150 MeV.

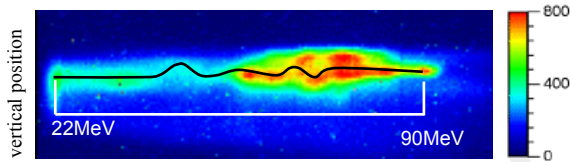

Figure 8: Electron energy spectrum with 224 TW laser power, a0 = 3.7, and plasma density of around $1\times10^{19}/cm^3$.

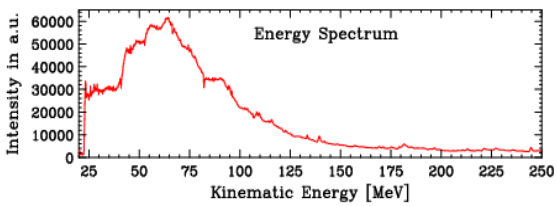

Figure 9: Electron energy spectrum with 195 TW laser power, a0 = 3.5, and plasma density of around $1\times10^{19}/cm^3$.

CONCLUSION

The laser-plasma accelerator experiment in the range of 200TW femto second pulses has been demonstrated. 52 MeV mono-energetic electron beam has been obtained controlling the plasma length and plasma density. Non-linear phenomena of laser plasma interaction, such as a long self-channeling, filamentation have been seen. Electron transverse oscillations are also measured. Filamentations may disturb the acceleration of electrons. A further analysis is in progress.

ACKNOWLEDGMENTS

This work was supported by the Japan Society for the Promotion of Science under the CORE UNIVERSITY program on accelerator science and by the Japan Science and Technology Agency under the China-Japan-Korea Tri-Lateral Cooperation Project on Intense Lasers. The authors gratefully acknowledge the support of the staff of the Laser Fusion Research Center, China Academy of Engineering Physics.

REFERENCES

[1] C. G. R. Geddes, C. Toth, J. van Tilborg, E. Esarey, C. B. Schroeder, D. Bruhwiler, C. Nieter, J. Cary, and W. P. Leemans, Nature 431, 538 (2004).

[2] J. Faure, Y. Glinec, A. Pukhov, S. Kisetev, S. Gordienko, E. Lefebvre, J. P. Rousseau, F. Burgy, and V. Malka, Nature 431, 541 (2004).

[3] S. P. D. Mangles, C. D. Murphy, Z. Najmudin et al., Nature 431, 535 (2004).

[4] P. Sprangle, E. Esarey, and A. Ting, Phys. Rev. A 41,4463(1990).

[5] Sergei V. Bulanov, Mitsuru Yamagiwa, Timur Zh. Esrkepov, James K. Koga, Masaki Kando, Yutaka Ueshima, and Kanji Saito, Phys. Plasma 12, 073103 (2005).

[6] H. S. Peng, X. J. Huang, Q. H. Zhu et al., Proceedings of SPIE 5627, 1 (2005).

[7] T. Hosokai, K. Kinoshita, T. Watanabe et al., Proceedings of EPAC 981(2002), Paris, France.

[8] B. Hafizi, A. Tingm P. Sprangle, and R. F. Hubbard, Phys. Rev. E 62, 4120 (2000).

[9] E. Esarey, S. K. Ride, and P. Sprangle, Phys. Rev. E 48, 3003 (1993).

[10] P. E. Young, H. A. Baldis, R. P. Drake, E. M. Cambell, and K. G. Estabrook, Phys. Rev. Lett. 61, 2336 (1998).

PAPER NOT YET RECEIVED

STATUS OF KEKB AND UPGRADE PLAN TO SUPERKEKB

Mi. Yoshida#, T. Agoh, K. Akai, M. Akemoto, A. Akiyama, M. Arinaga, K. Ebihara, K. Egawa, A. Enomoto, J. Flanagan, S. Fukuda, H. Fukuma, Y. Funakoshi, K. Furukawa, T. Furuya, J. Haba, K. Hara, T. Higo, S. Hiramatsu, H. Hisamatsu, H. Honma, T. Honma, T. Ieiri, N. Iida, H. Ikeda, M. Ikeda, S. Inagaki, S. Isagawa, H. Ishii, A. Kabe, E. Kadokura, T. Kageyama, K. Kakihara, E. Kako, S. Kamada, T. Kamitani, K. Kanazawa, H. Katagiri, S. Kato, T. Kawamoto, S. Kazakov, M. Kikuchi, E. Kikutani, H. Koiso, Y. Kojima, I. Komada, T. Kubo, K. Kudo, N. Kudo, K. Marutsuka, M. Masuzawa, S. Matsumoto, T. Matsumoto, S. Michizono, K. Mikawa, T. Mimashi, S. Mitsunobu, K. Mori, A. Morita, Y. Morita, H. Nakai, H. Nakajima, T. T. Nakamura, H. Nakanishi, K. Nakanishi, K. Nakao, H. Nakayama, S. Ninomiya, Y. Ogawa, K. Ohmi, S. Ohsawa, Y. Ohsawa, Y. Ohnishi, N. Ohuchi, K. Oide, M. Ono, T. Ozaki, K. Saito, H. Sakai, Y. Sakamoto, M. Sato, M. Satoh, K. Shibata, T. Shidara, M. Shirai, A. Shirakawa, T. Sueno, M. Suetake, Y. Suetsugu, R. Sugahara, T. Sugimura, T. Suwada, S. Takano, S. Takasaki, T. Takenaka, Y. Takeuchi, M. Tawada, M. Tejima, M. Tobiyama, N. Tokuda, S. Uehara, S. Uno, N. Yamamoto, Y. Yamamoto, Y. Yano, K. Yokoyama, Ma. Yoshida, S. Yoshimoto, K. Yoshino
KEK, Tsukuba, Ibaraki 305-0801, Japan

Abstract

KEKB is an electron-positron two-ring collider for the leading B meson factory. It consists of an 8 GeV electron ring (HER) and a 3.5 GeV positron ring (LER) and their injector linac. It has been operated since December 1998, and has recently marked the peak luminosity of 17.12 /nb/s. This peak luminosity is obtained under the crab-ready beam optics having the robust operating condition by some efforts to solve the optics problems. We are aiming more luminosity improvement after the crab cavity installation. Further the major upgrade plan for SuperKEKB is expected to achieve 400 /nb/s keeping the baseline of the original proposal. This paper describes the recent status of KEKB and upgrade plans for SuperKEKB.

OVERVIEW

The 8 GeV electron and 3.5 GeV positron rings are built in the 3 km-long TRISTAN tunnel. This collider aims to make a detailed study of the B-meson. Especially the CP violation effects are measured in its decay. The energy difference between the electron and positron beams gives a boost to the produced B-meson pairs. This boost makes it possible to measure the time dependent features of B-meson decay due to the large CP asymmetry predicted in B-meson system.

Since the construction of KEKB started in 1994 and the first event was observed by Belle detector in June 1999, the KEKB continuously accumulate its integrated luminosity for 7 years. Figure 1 shows 7-year's history of the KEKB luminosity and beam currents. The KEKB has recently marked the peak luminosity of 17.12 /nb/s (= 1.712×10^{34} /cm^2/s) which is 70 % higher luminosity than the designed peak luminosity of 10 /nb/s. Not only the peak but also the integrated luminosity of 710 /fb has been accumulated with the peak increasement of 1.232 /fb/day which is obtained in the continuous injection mode operated after 2004.

#mitsuhiro.yoshida@kek.jp

RECENT STATUS OF KEKB

The recent status of KEKB mainly in 2006 is summarized. A status report before this was written in the previous report [1, 2]. Table 1 shows present machine parameters of KEKB compared with those of about one year ago and the design parameter. The performance progress in the past one year is not very remarkable compared with earlier years. We describe the recent status of KEKB including causes of the present performance limitations.

Table 1: Machine parameters of KEKB

	Design		**Dec. 2005**		**Dec. 2006**	
	LER	HER	LER	HER	LER	HER
Energy [GeV]	3.5	8.0				
Circumference [m]	3016.26				3016	
I_{beam} [mA]	2600	1100	1719	1347	1662	1340
# of bunches	5000		1388		1388	
I_{bunch} [mA]	0.52	0.22	1.23	0.97	1.20	0.965
Bunch Spacing [m]	0.59		1.8 - 2.4		2.1	
Emittance [nm]	18	18	18	24	18	24
β_x^* [cm]	33	33	59	56	59	56
β_y^* [cm]	1.0	1.0	0.65	0.62	0.65	0.59
Ver. Size@IP [μm]	1.9	1.9	2.1	2.1	1.9	1.9
RF Voltege [MV]					8.0	15.0
ν_x	45.52	47.52	45.506	44.512	45.505	44.509
ν_y	46.08	43.08	43.531	41.578	43.534	41.565
ξ_x	0.039	0.039	0.117	0.073	0.117	0.070
ξ_y	0.052	0.052	0.096	0.055	0.105	0.056
Lifetime [min.@mA]			135@ 1719	222@ 1347	110@ 1600	180@ 1340
Luminosity [/nb/s]	10		16.27		17.12	
Lum/day [/fb]	~ 0.6		1.183		1.232	
Lum/7 days [/fb]	-		7.358		7.809	
Lum/30 days [/fb]	-		29.018		30.21	

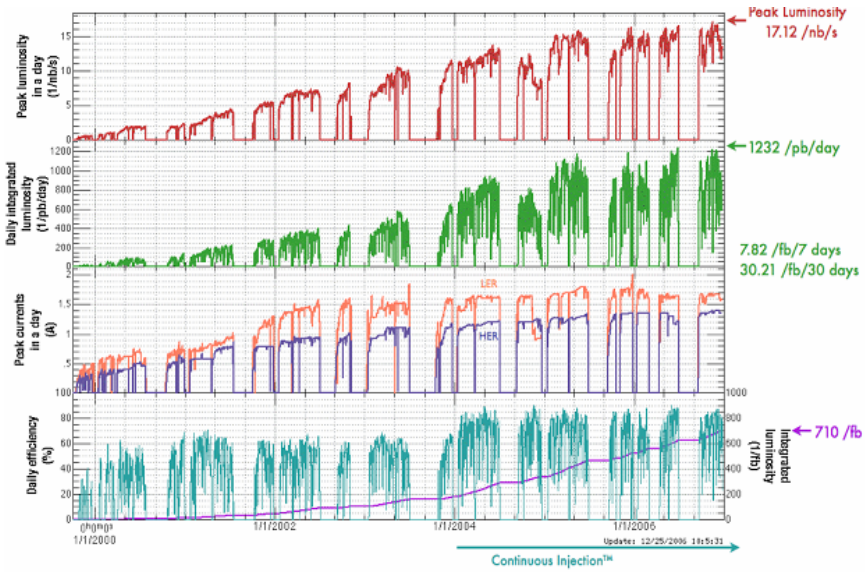

Figure 1: History of KEKB (Oct. 1999 – Dec. 2006).

Beam parameter modifications for luminosity

The luminosity for the ring collider is given as

$$L \approx \frac{\gamma\pm}{2er_e}\frac{I\pm\xi_y\pm}{\beta_y^*}\frac{R_L}{R_y} \qquad (1)$$

Higher currents $I\pm$, larger vertical beam-beam parameter ξ_y, and smaller β_y^* are necessary to obtain higher luminosity. R_L, and R_y are reduction factors of the luminosity and ξ_y, respectively, due to the hour-glass effect and the finite crossing angle (22 mrad at KEKB). The ratio R_L / R_y is close to unity when the bunch length σ_z is well smaller than β_y^*.

The beam parameters are summarized in Table 1. In actual parameters of HER, $I_$ and $\xi_y_$ are a little larger, and $\beta_y^*_$ is much smaller than design values. Consequently, the luminosity reaches to 1.71 times higher than the design value.

Bunch spacing and effects of electron clouds

The averaged bunch spacing is 3.5 rf buckets at present KEKB, while in the original design we planed to fill all RF buckets except for the abort gap. The longer bunch spacing causes larger bunch currents which generate higher HOM heating power. And the HOM power is one of the present limitations of the stored beam currents. It is desirable to increase the number of bunches and decrease HOM power from the viewpoint of hardware protection against the high beam currents.

Since the beginning of KEKB, effects of electron clouds have been strictly limiting the KEKB performance. To solve their effects, more than 95 % of the drift space in the LER ring, which is equivalent to 75 % of the total circumference, is covered by solenoid fields of higher than 20 Gauss. The blow-up of the vertical beam size in the LER ring has been suppressed after the installation of solenoid coils, and the luminosity saturation at high current is reduced in the present bunch spacing of 3.5 rf buckets.

However, even with the solenoid coils, the evidences of the effects of the electron clouds are observed. The most direct evidence of the effects is vertical betatron sidebands appeared in the transverse beam spectra of the positron bunches [3]. The sidebands seem to be signals of the fast head-tail instability due to short-range wake fields within the electron clouds. In case of the only positron single beam, a beam size blow-up was observed associated with the upper sidebands above a threshold beam current of the instability. With the collisions of the electron and positron beams, the luminosity saturation was observed at the condition of the LER beam current of higher than approximately 1700 mA and the HER beam current fixed to around 1300 mA. Further in the measurement of bunch-by-bunch luminosity, the degradation of the luminosity was also observed for the bunches after the shorter bunch spacing.

From these observations, it seems that the degradation in the specific luminosity depending on the bunch spacing is originated from the effects of the electron clouds. The remaining problem is where in the ring do the electron clouds exist. In the summer shutdown 2005, we installed solenoid coils in the inside of 88 quadrupolemagnets out of 461. However, we observed no effects of these additional solenoids on the luminosity. And in this winter shutdown, we installed the ante-chamber in the drift space with high synchrotron radiation density following after the wiggler section.

Sextupole tuning

We observed that the sextupole tuning occasionally increased the luminosity after the luminosity was saturated by tuning the betatron tunes and the beam optical parameters between the two beams, such as a beam orbit offset at the IP, a vertical crossing angle, beam x-y coupling parameters at the IP, collision timing, waist

points. Recently new sextupole tuning panel was developed to tune with toggling the constraints of the tilt at the IP. After new sextupole tuning was optimized, it makes possible to reach the lower horizontal betatron tune of the HER ring of 0.509, and the luminosity becomes approximately 5 % higher than before.

Betatron tune

The horizontal betatron tune ν_x is one of the most important parameters to achieve high luminosity at KEKB. When ν_x is coming closer to a half-integer resonance, the luminosity is being significantly improved. The present values of the fractional part of ν_x are 0.506(LER) and 0.509(HER). The merit of ν_x closer to the half-integer is larger dynamic emittance which should decrease effective beam-beam parameter and then should improve the luminosity. Recent beam-beam simulations reproduce well this tune dependence. The simulations say that the luminosity will be much improved by getting ν_x close to the half-integer in HER same as in LER. In HER, however, the synchro-betatron resonance $2\nu_x + \nu_s =$ integer is much stronger than in LER, so stable operation at lower ν_x is difficult. Optimization of beam parameters is planed to avoid the synchro-betatron resonance to make better chromaticity correction to weaken effects of the resonance and changing the synchrotron tune by adjusting.

Lower Emittance

The beam-beam simulation predicts the higher luminosity in the lower emittance operation. We changed the optics settings for the low emittance operation only for the LER ring in this October. However the beam abort due to the horizontal beam oscillation was frequently occured, and we cannot confirm the effect of the lower emittance operation.

Horizontal beta function

The horizontal beta function β_x^* is once reduced from 59 cm and 56 cm for the LER and HER ring respectively to 50 cm for both rings. Although it aims to obtain the higher luminosity, the betatron tunes of LER ν_y and HER ν_x cannot reach to the previous values due to the short beam lifetime. Thus we cannot distinguish whether this is effective or not.

PLANS FOR 2007

The plans for 2007 to improve the KEKB luminosity against the present luminosity limitations are described.

Crab cavity

The choice of a finite beam crossing angle in the horizontal plane at the IP, 22 mrad, is a notable feature of KEKB. This scheme eliminates parasitic collisions and makes it much easier to optimize the lattice near IP for two beams of different energies, and reduce the beam background to the Belle detector. Currently the finite crossing angle causes the degradation of the beam-beam parameter.

To recover this degradation due to the crossing angle, The crab cavity was developed to rotate the beams to provide head-on collision. Figure 2 shows the crab crossing scheme. Simulations [4] predict that head-on collision may bring the larger beam-beam parameter of ξ_y = 0.19, which means that the luminosity may be doubled.

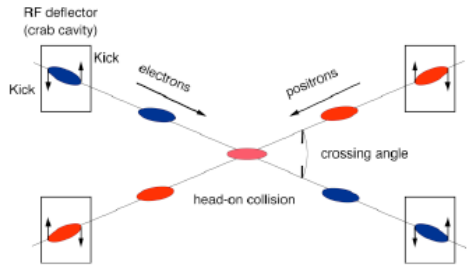

Figure 2: Schematic view of the crab-crossing scheme.

Figure 3: Installed crab cavity.

In this winter shutdown, the crab cavity was installed. Figure 3 shows the photo of the installed crab cavity. On the contrary of the original plan, only one cavity in each ring was installed. Though the crabbing orbit propagates over the rings, any problem has not yet been pointed out.

We already succeeded to operate for the optics which meets conditions required for realizing the crab crossing scheme. The conditions are horizontal phase advances from the crab cavities and IP, large horizontal beta functions at the crab cavities and horizontal phase advances from SR monitors to IP. The last condition is required to measure the crab angle with streak camera systems. Thus we can just start the beam commissioning with the crab cavity.

Higher current

A further increase of the KEKB luminosity depends on mitigating the electron-cloud in LER, more beam current in HER. The drift space of the LER ring is almost covered by solenoid fields to reduce the electron-cloud. To find and reduce the remaining electron-cloud, the ante-chambers is locally installed to the arc section after the

wiggler section. On the other hand, there is a clear tendency to improve luminosity by a further increase of the HER beam current. For this purpose, one more RF station for the ARES cavity in HER was installed during the summer shutdown in 2005, since the HER beam current was limited by available RF power. With this new RF station, the target HER beam current was 1500mA. However, troubles with vacuum bellows at the level of 1350mA are frequently occured. These troubles are caused by the lost of the spring finger contact of vacuum bellows due to the horizontal deformations. The vacuum bellows will be replaced to newly developed comb-type bellows according to the budget.

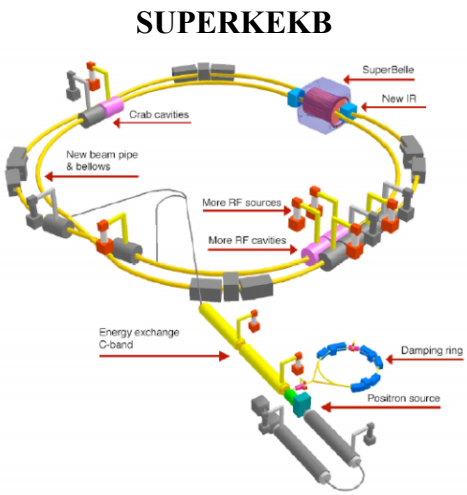

Figure 4: Schematic layout of SuperKEKB.

Table 2: Machine parameters of SuperKEKB compared with KEKB

	KEKB Design		KEKB Dec. 2006		SuperKEKB	
	LER	HER	LER	HER	LER	HER
Energy [GeV]	3.5	8.0			3.5	8.0
Circumference [m]	3016.26					
I_{beam} [mA]	2600	1100	1662	1340	9400	4100
# of bunches	5000		1388		5000	
I_{bunch} [mA]	0.52	0.22	1.20	0.965	1.88	0.82
Bunch Spacing [m]	0.59		2.1		0.59	
Emittance [nm]	18	18	18	24	24	
β_x^* [cm]	33	33	59	56	20	
β_y^* [cm]	1.0	1.0	0.65	0.59	0.3	
Ver. Size@IP [μm]	1.9	1.9	1.9	1.9	0.73	
ξ_x	0.039	0.039	0.117	0.070	0.152	
ξ_y	0.052	0.052	0.105	0.056	0.215	
Luminosity [/nb/s]	10		17.12		400 (~ 800)	

SuperKEKB is an upgrade to the KEKB machine. Figure 4 shows the schematic layout of SuperKEKB. Table 2 shows the machine parameters of SuperKEKB compared with KEKB in order to achieve over 20 times higher luminosity (400 /nb/s). Smaller β_y^* (3 mm), larger ξ_y (0.19) and higher currents (9.4 A in LER and 4.1 A in HER) are pursued. Further it is based on the crab crossing scheme which will be tested in recent upgrade of KEKB. Existing resources such as tunnel, facilities, magnets, power supplies will be reused as much as possible. The present 509 MHz RF system will be reused, but with twice the number of RF stations. It will also be necessary to reinforce the HOM dampers and further increase the stored energy of the cavities to store much higher beam currents. According to another recent simulations, the luminosity of SuperKEKB exceeds 800 /nb/s at beam currents of 10.1 A in LER and 4.4 A in HER [5].

KEKB Ring Upgrade

Items to be upgraded for KEKB rings are as followings.

(1) New IR with redesigned final quadrupoles and compensation solenoids.

The superconducting final focusing quadrupole magnets (QCS) should be moved toward the IP in order to squeeze the vertical beta function at the IP. To conserve the detector region and to move both QCS's toward the IP for the IR layout, we make the compensation solenoids overlaid on the QCS in the longitudinal direction.

(2) New beam pipes and bellows.

The main issues arise from the intense synchrotron radiation (SR) due to the large beam current. In order to cure the heating from SR and/or the effect of the photoelectron cloud, an ante-chamber scheme will be used. The ante-chamber consists of a beam channel and an SR channel. The beam goes through the beam channel and the SR passes through to the SR channel. The SR is absorbed by a photon stop inside the SR channel. Also we have to replace to the newly developed comb-type bellows for high current beam.

(3) More rf systems with improved ARES cavities, couplers, and HOM absorbers of superconducting cavities.

The present 509 MHz RF system for KEKB employs two types of the damped cavities: a normal conducting cavity (NC) coupled with an energy storage cavity (ARES) and a single-cell superconducting damped cavity (SCC). We will increase the number of ARES cavities from 32 to 40 and SC cavities from 8 to 12. The modification to the RF units at Super KEKB is that one 508 MHz 1 MW CW klystron feeds power to one ARES cavity, as opposed to two ARES cavities which is the current scheme at KEKB. The RF unit is one to one for the SC cavities. Therefore, the total number of RF units increases from 24 to 52, including the klystrons, power supplies, high power system and control system. Also the damper structure and the dummy load should be much improved for the high current.

(4) Reinforced cooling system.

The total power loss at Super KEKB is 83.4 MW, which is three-times larger than at KEKB. If we give up on wigglers in LER, the total power loss becomes 66.5 MW. This number is twice that of KEKB. However, we obtain a simulation result that the luminosity is degraded as the damping time increases. The cooling system must

be upgraded for Super KEKB whether wigglers exist or not.

Linac Upgrade

The KEKB injector linac is also planned to upgrade as following items.

(1) Exchange of beam energy

The C-band accelerating structure and the 1.0 GeV damping ring are planned to aim for the efficient injection and to cure the electron cloud problem. The KEKB injector linac has provided 8 GeV electrons and 3.5 GeV positrons to inject those rings directly. In the SuperKEKB project, energy exchange of beams has an important role to escape the influence of electron clouds for the positron ring (LER). To exchange the beam energy of the LER and the HER, the energy of a positron beam has to be raised from 3.5 GeV to 8 GeV However the acceleration length after generating positrons is restricted because a positron is a secondary particle. One of solutions is to double an acceleration field. Thus the C-band (5712 MHz) accelerating unit [6] has been developed to obtain the higher acceleration field over 40 MV/m. Figure 5 shows the layout of one layout of the upgrade plans using the C-band accelerating units. In this layout, three sectors are replaced to the C-band accelerating units. A C-band accelerating unit consists of one 50 MW klystron and four accelerating structures. And a sector consists of 16 accelerating units whose klystron RF inputs are driven by a 150 kW sub-booster klystron.

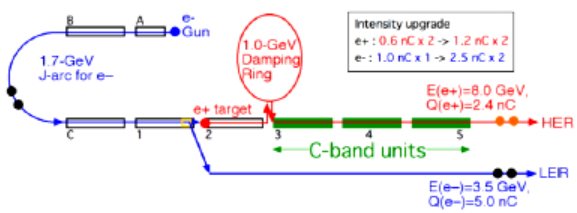

Figure 5: Layout of the linac upgrade for SuperKEKB.

(2) Fast beam mode switch

The KEKB injector linac has to inject 8 GeV electrons and 3.5 GeV positrons to KEKB ring, 2.5 GeV electron to PF ring and PF-AR ring. The multiple beam modes are currently switched at intervals of five minutes. It takes 30 seconds to switch the beam mode and the repetition of the bunched beam is usually only 10 pps inspite of the maximum repetition of 50 pps. In the present condition, the continuous injection can be performed for either LER or HER at once and the injection for KEKB is stopped when the injection for PF or PF-AR is required. Thus the upgrade for the fast beam mode switch is advanced [7]. The upgrade items for the fast beam mode switch are the construction of the new PF BT-line to bypass the ECS magnet, the fast low-level rf phase switch, the installation of the pulse bend and the positron target with a electron bypass hole.

(3) Multi bunch acceleration

The KEKB injector linac is usually operated to accelerate only two 10 nC electron bunches to generate positron, since more bunch cannot be equalized the beam energy using the conventional pulse compressor (SLED) and the simple phase modulation. We tested some way to accelerate more bunches without any modification of high power RF distribution [8]. One way to realize the multi-bunch acceleration is compensating the beam loading. This beam loading compensation method is usually realized by combining the output power of two or more klystrons. However our linac system consists of one 50 MW klystron in one acceleration unit, and eight klystrons are driven by a 100kW klystron. One way to realize the beam loading compensation in our linac is using the amplitude modulation of the klystron. This is realized using the I-Q modulation of the low level RF considering the non-linear characteristics of the total amplification system including klystrons.

Consideration for higher luminosity

Recently, a novel colliding scheme, the long bunch and the crab waist, was proposed [9]. It is an horizontal dependent vertical focus at the IP, which is generated by a pair of sextupole magnets. This scheme may allow beams with a very small horizontal size and a relatively long bunch length to collide at a large finite angle crossing with a small β_y^*. The relatively long bunch length is also attractive from the view point of the CSR and HOM power. Extensive simulation work is progressing to study the possibility to apply this scheme to the present factories or Super-factories.

REFERENCES

[1] H. Koiso *et al.*, "KEKB and SuperKEKB", Proceedings of APAC'04, Gyeongju, Korea, March 2004, p. 490.
[2] Y. Funakoshi *et al.*, "Recent Progress at KEKB", Proceedings of EPAC'06, Edingurgh, Scotland, June 2006, p. 610.
[3] J. W. Flanagan *et al.*, "Observation of Vertical Betatron Sideband due to Electron Clouds in the KEKB", Phys. Rev. Lett. 94, 054801 (2005).
[4] K. Ohmi et al., "Study of beam-beam interactions with/without crossing angle", Proceedings of PAC'03, SLAC, May 2003.
[5] K. Ohmi *et al.*, "Crab crossing and crab waist at super KEKB", SuperB workshop, SLAC, June 2006.
[6] T. Kamitani et al., "Development of C-band accelerating section for SuperKEKB", Proceedings of LINAC 2004, Lubeck, Germany, August, 2004.
[7] M. Satoh *et al.*, "The KEK Injector Upgrade for the Fast Beam-Mode Switch", Proceedings of EPAC'06, Edinburgh, Scotland, June 2006, p. 855.
[8] M. Yoshida *et al.*, "Study on High-Current Multi-Bunch Beam Acceleration for KEKB Injector LINAC", Proceedings of LINAC'06, Knoxville, USA, August 2006.
[9] P. Raimondi, SuperB Meeting, Fraxcati, March 2006.

THE BEPCII: CONSTRUCTION AND INITIAL COMMISSIONING

C. Zhang and Q.Qin for the BEPCII Team, IHEP, CAS, P.O.Box 918, Beijing 100049, China

Abstract

The BEPCII, as a natural extension of the BEPC (Beijing Electron-Positron Collider), is a double ring e-e+ collider and a synchrotron radiation (SR) source with its outer ring, or SR ring. As an e-e+ collider, the BEPCII will operate in the beam energy region of 1-2.1 GeV with design luminosity of 1×1033cm-2s-1 at 1.89 GeV. As a light source, the SR ring operates at the beam energy of 2.5 GeV with the design intensity of 250 mA. The project started construction in the beginning of 2004. The upgrade of the injector linac completed in late 2004. The BEPC ring dismount started in July 2005. Installation of the storage ring components except the superconducting (SC) insertion magnets completed in early November, 2006. The improvement of the cryogenics of SC megnets is in progress. The commissioning of the SR ring with conventional magnets in the interaction region (IR) started on Nov. 13 and the first electron beam stored on Nov. 18. The BEPCII has been operating for SR users since Dec. 25, 2006 at 2.5 GeV with the peak beam current of 100-150 mA. The beam lifetime increases steadily and reached about 7 h at beam current of 80 mA with an accumulated beam dose of 45A·h. This paper provides an overview of the construction and initial commissioning of the BEPCII.

GENERAL DESCRIPTION

The BEPCII serves the purposes of both high energy physics experiments and synchrotron radiation applications. The details of the BEPCII design can be found in its design report [1]. The goals of the BEPCII are shown in Table 1.

Table 1: The design goals of the BEPCII

Beam energy	1–2.0 GEV
Optimum energy	1.89 GEV
Luminosity	1×10^{33} cm^{-2}s^{-1} @189 GeV
Linac injector	Full energy inj.: 1.55–1.89GeV Positron inj. rate ≥50 mA/min
Dedicated SR	250 mA @ 2.5 GeV

Serving as a collider, the BEPCII will operate in the beam energy region of 1.0-2.1 GeV so that its physical potential in τ-charm range is preserved. The design of the BEPCII aims at a high luminosity. The luminosity of an e^+-e^- collider is expressed as

$$L(\mathrm{cm}^{-2}\mathrm{s}^{-1}) = 2.17\times10^{34}(1+r)\xi_y \frac{E(GeV)k_b I_b(\mathrm{A})}{\beta_y^*(\mathrm{cm})}, \quad (1)$$

where $r=\sigma_y^*/\sigma_x^*$ is the beam aspect ratio at the interaction point (IP), ξ_y the vertical beam-beam parameter, β_y^* the vertical β-function at IP, k_b bunch number in each beam and I_b the bunch current. The strategy for the BEPCII to reach the design luminosity is to apply multi-bunch collisions (k_b=93) with double rings and micro-β at IP with short bunches whose length is compatible to the β_y^* value. The layout and installed double-ring accelerator units in the BEPCII tunnel are shown in Fig. 1.

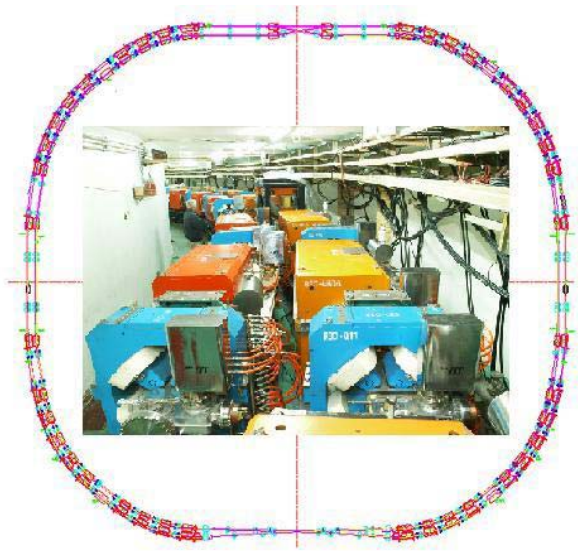

Figure 1: Layout and installed double-ring units.

The inner ring and the outer ring cross each other in the northern and southern IP's. The horizontal crossing angle between two beams at the southern IP, where the detector locates, is 11mrad×2 to meet the requirement of sufficient separation but no significant degradation to the luminosity. While in the northern crossing region, the two beams cross horizontally and a vertical bump is used to separate two beams, so that the optics of the two rings can be symmetric. For the dedicated synchrotron radiation operation of the BEPCII, electron beams circulate in the outer ring with a pair of horizontal bending coils in SC magnets serving this purpose and in the northern IP a bypass is designed to connect two halves of the outer ring. The machine physics issues are intensively studied [2].

The milestones of the BEPCII are as follows:

January 2004	Construction started
May. 4, 2004	Dismount of 8 linac sections started
Dec. 1, 2004	Linac delivered e^- beams for BEPC
Mar. 19, 2005	First e^+ beam of 50mA obtained
July 4, 2005	BEPC ring dismount started
Mar. 2, 2006	BEPCII ring installation started
Nov. 13, 2006	BEPCII ring commissioning started
Nov. 18, 2006	First e^- beam stored in the ring
Dec. 25, 2006	Beams with 2.5 GeV, ~100 mA, ~3h lifetime provided for SR users

Table 2: Main Parameters of the BEPCII.

Parameters	Unit	Collision	SR
Energy	GeV	1.89	2.5
Circumference	m	237.53	241.13
RF frequency	MHz	499.8	499.8
RF voltage	MV	1.5	1.5~3.0
Beam emittance	nm·rad	144	120
Bunch number		93	200-300
Beam current per ring	A	0.91	0.25
Injection energy	GeV	1.89	1.89
β function at IP	m	1/0.015	–
Crossing angle	mrad	11× 2	–
Beam-beam Parameter		0.04	–
Luminosity	$cm^{-2}s^{-1}$	1.0×10^{33}	–

THE INJECTOR LINAC

The BEPC injector is a 202-meter electron/positron linac with 16 RF power sources and 56 S-band RF structures. The BEPCII requires the injector in two aspects. One is the full energy of e^+ and e^- beams injected into the storage rings, i.e. $E_{inj} \geq 1.89$ GeV; the other is e^+ injection rate ≥ 50 mA/min. To realize the full energy top-off injection up to 1.89 GeV, the klystrons are replaced with the new 45-50 MW ones and the modulators upgraded with new pulse transformer oil tank assembly, PFN's, thyratrons, charging choke and DC power supplies. In order to compensate the RF phase drift due to various factors, an RF phasing system is developed.

The technical measures taken for increasing positron intensity in the BEPCII injector can be summarised as following: to increase the e^- beam current on e^+ target from 2.5A to 6A, the repetition rate from 12.5Hz to 50Hz, the bombarding energy for e^+ from 140MeV to 240MeV; to develop a new positron source to increase the yield from 1.4% to 2.7%, and to apply two-bunch injection scheme. Though the pulse length reduced from 2.5 ns to 1ns, the total gain factor of the e^+ intensity can be about 20 times higher than the BEPC. The new developed positron source is pictured in the Fig. 2.

Figure 2: The new developed positron source.

All the new hardware subsystems, including the electron gun, the 40MeV pre-injector, the 200MeV booster section and the positron source of the linac were installed in the summer 2004 after dismounting the old devices. Figure 3 shows the BEPCII linac injector.

Figure 3: The BEPCII linac injector.

It took less than one month to start up the machine and process the new systems before the linac provided electron beams for the dedicated SR operation of the BEPC storage ring starting from the beginning of the December 2004. The commissioning of the linac for e^+ beam has been carried out during the machine studies. The first e^+ beam of 50mA was obtained at the linac end on March 19, 2005. The e^- beam current output from the gun is ~10A, and ~6A at the positron converter target which is the same as simulation. All of the 16 RF power sources were rebuilt, and stably work at 50pps. The new control and beam instrumentation systems make the machine commissioning and operation more convenient. The performance of the linac is listed in Table 3, showing that its design specification is reached.

Table 3: The results of the linac commissioning.

	Unit		Measured	Design
Energy	GeV		1.89	1.89
Beam current	mA	e^+	61	40
		e^-	>500	500
Emittance	mm·mr	e^+	0.4	0.4
		e^-	0.09	0.1
Energy spread	%	e^+	-	0.5
		e^-	0.5	0.5
Repetition rate	Hz		50	50
Pulse length	ns		1.0	1.0

The linac is now well operated for e injection in the SR operation with the beam orbit and beam energy stabilities better than ±0.1mm and ±0.1%, respectively, shown in Fig. 4.

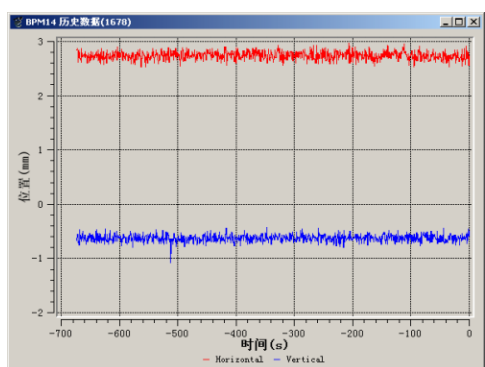

Figure 4: Beam orbit stability in the linac operation.

THE STORGE RINGS

RF system

The SC RF cavities are chosen for its advantage of large accelerating gradient and well-damped HOMs. Two SC cavities are installed in the BEPCII with one cavity in each ring to provide necessary RF voltage of 1.5 MV. Each cavity is powered with a 250 kW klystrons. The horizontal high power test gives the Q values of 5.4×10^8 and 9.6×10^8 at V_{rf}=2 MV for the west and east cavities, higher than the design values of 5×10^8 at 2 MV. Figure 5 pictures the cavity in installation.

Figure 5: A superconducting cavity in installation.

Magnets and power supplies

The BEPCII will reuse 44 BEPC bends and 28 quads. There are 267 new magnets, including 48 bends, 89 quads, 72 sextupoles, 4 skew quads and 54 dipole correctors, need to be produced. Most magnets were fabricated in the IHEP workshop. The magnets were measured with both rotating coils and straight wires. The results are in agreement each others within 10-3. Figure 6 pictures a quadrupole magnet with rotating coil measurement. There are 1 electric and 3 permanent wigglers in the storage rings serving as SR wavelength shifters. Among the 3 permanent wigglers, two are out-vacuum and one in-vacuum.

Figure 6: A quadrupole magnet in measurement.

To provide required flexibility for BEPCII operation with various modes, each arc quadruple is excited with an independent power supply. There are all together 345 power supplies in the storage rings. The power supplies have been installed, connected to the magnets and tested. Their current stability is better than 1×10^{-4}.

Injection Kickers

In order to meet the challenges both on the filed uniformity and low coupling impedance, a modified slotted pipe kicker has been developed with the coating strips on ceramic bar instead of metallic plates as the beam image current return paths. With the careful design and manufacture, the measured field uniformity is better than ± 1% in the central plane, ± 2% in y=5mm plane, ± 5% in y=10mm plane, shown in Figure 7.

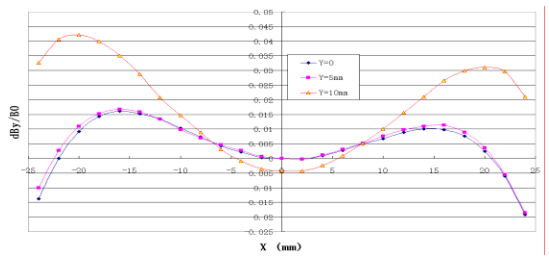

Figure 7: Measured field uniformity of a kicker.

Vacuum System

The BEPCII imposes two challenges to the vacuum system, one is the vacuum pressure, and the other is the impedance. The design dynamic vacuum pressure are 8×10-9 Torr in the arc and 5×10-10 Torr in the IR. Antechambers are chosen for both e+ and e- rings. For the e+ ring, the inner surface of the beam pipe in the arc is coated with TiN in order to reduce the secondary electron yield (SEY). Measurement results show that the maximum SEY is 1.6-1.9 after the coating, seen in Fig. 8.

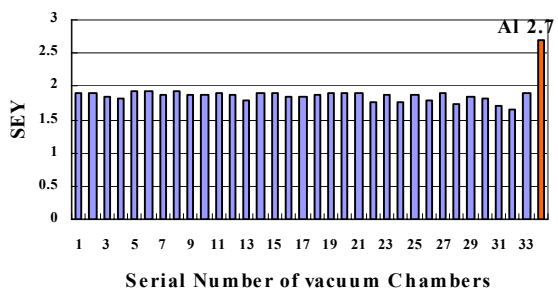

Figure 8: measured SEY of TiN-coated chambers.

IR and SC Insertion Magnets [3]

The IR has to accommodate competing and conflicting requirements from the accelerator and the detector. Many types of equipment including magnets, beam diagnostic instruments, masks, vacuum pumps, and the BESIII detector must co-exist in a crowded space. A special pair of superconducting magnets (SCQ's) is placed in the IR. Each SCQ consists of a main and a skew quadrupoles, 3 compensation solenoids and a dipole coils, to squeeze the β function at IP, compensating the detector solenoid and to serve as the bridge connecting outer ring for SR operation, respectively. The SCQ's were produced and will be measured when the cryogenics is ready. Some special warm bore magnets in IR such as septum bending magnet and two-in-one quadrupoles have been manufactured, tested and installed. The magnetic field measurement re-

sults confirm the design. Figure 9 shows two SCQ's and some warm magnets installed in the IR.

Figure 9: SCQ's and some warm magnets installed in IR.

Instrumentation and Control

The instrumentation system consists of 136 beam position monitors (BPM's), 2 DCCT's, 2 bunch current monitors and 2 synchrotron radiation monitors. Transverse feedback systems are equipped in order to damp beam instabilities. The control system is based on the EPICS environment, providing a friendly man-machine interface for operators. The instrumentation and control systems have been examined during the commissioning.

Cryogenics system

The BEPCII cryogenics system is composed of four sub-systems: the central cryogenic plant and three satellite cryogenic systems for the RF cavities, the SCQ magnets, and the SSM detector solenoid. Two 500W refrigerators serve the purpose to cool the SC devices at 4.5K, one for the cavities and another for the magnets. The cavity side cryogenics has been in normal operation, while the magnet part is being improved to solve the problem of the control Dewar, valve boxes and current leads.

COMMISSIONING AND OPERATION

The operation of the BEPC completed on July 4, 2005, and then dismount of the old ring started. After 16 months' hard work, the storage ring installation was finished in early November 2006 except the cryogenics of the magnets. It was decided to install conventional magnets in the IR to start storage ring commissioning and SR operation. In the meantime, the improvement of the cryogenics system and measurement of the SC magnets are being carried out at the BESIII off-line position. Figure 10 shows the IR with conventional magnets and Table 4 gives some results of the SR ring commissioning.

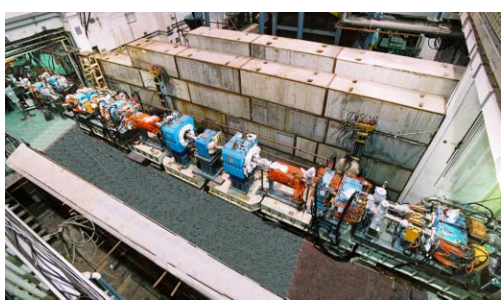

Figure 10: IR with conventional magnets.

Table 4: Some results of the SR ring commissioning.

Parameters	Unit	Measured	Design
Operation Energy	GeV	2.5	2.5
Injection energy	GeV	1.89	1.89
Circumference	m	241.127	241.130
RF voltage	MV	1.5	1.5~3.0
Tunes ($\nu_x/\nu_y/\nu_s$)		7.27/5.40/ 0.0242	7.27/5.37/ 0.0249
Bunch number		~100	200-300
Beam current	mA	200	250

The commissioning of the storage ring started on Nov. 13, 2006. One turn beam signal was observed with a beam position monitor on the first day. In the early morning of Nov. 18, circulating beams without RF and stored beams with RF were obtained, seen in Fig. 11. Figure 12 exhibits the beam image with the SR monitor.

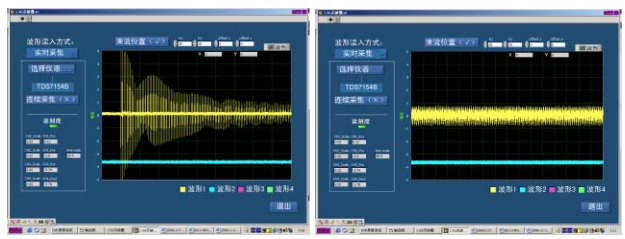

Figure 11: Circulating & stored beam with a BPM.

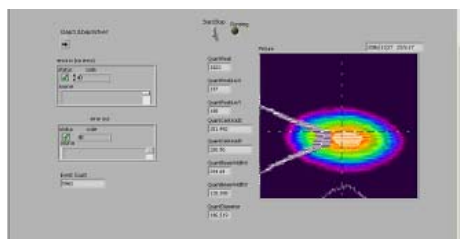

Figure 12: Beam image signal with the SR monitor.

The hardware systems were tested and debugged during the commissioning. It took a few days to calibrate the power supplies with a larger current range to reduce magnet setting errors at low field. Misconnection of some corrector power supplies was found and amended; cables of the BPM's were re-calibrated; and some "bad" BPM's, judged by the 3-button check, were disabled. The orbit correction with transfer functions was performed. The residual rms orbit distortion after correction is reduced to 0.42mm and 0.27mm on the horizontal and vertical planes, respectively, shown in Figure 13.

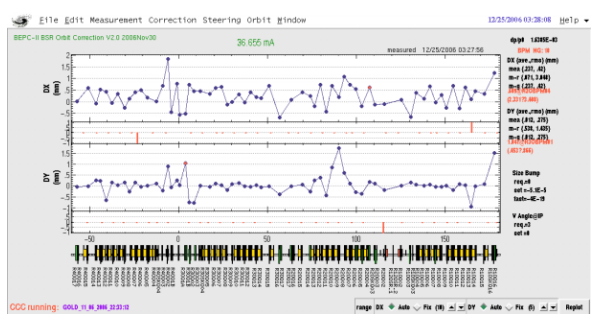

Figure 13: Residual orbit distortion after correction.

Twiss parameters were measured and compared to the designed values. The results are displayed in Fig. 14 and Fig. 15. It can be seen from Figure 14 that the measured β-functions agree to the designed values within about 5% after correction with response matrix method. Figure 15 shows that the measured dispersion agreed well with the design values within 0.1-0.2 m.

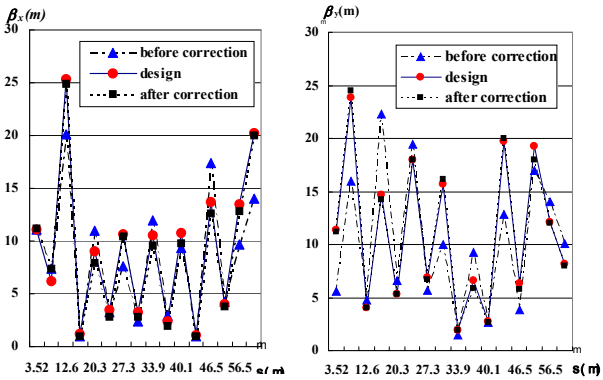

Figure 14: Measured and designed β-functions.

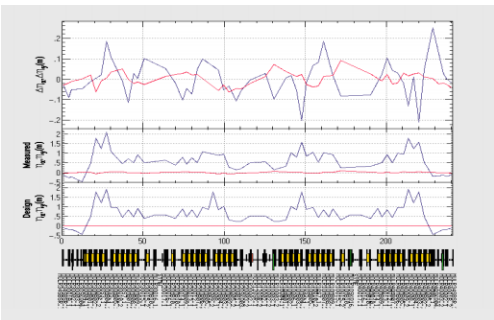

Figure 15: Measured and designed η-function.

Maximum beam current at 1.55 GeV and 1.89 GeV reached 250 mA with no limit indicated. By improving the vacuum pressure along with the accumulation of beam dose, beam lifetime increases smoothly. Figure 16 demonstrates how the SR cleaning improves vacuum pressure and then the beam lifetime. The beam lifetime gets to 7 hours at beam current of 80 mA when beam dose accumulated to 45 A·h.

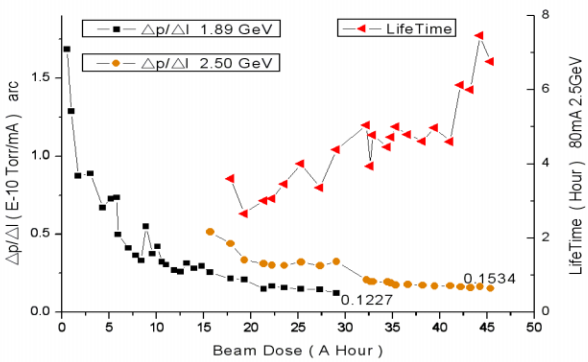

Figure 16: Vacuum and beam lifetime vs. beam dose.

The commissioning together with SR beam lines was carried out with local orbit adjustment. Beams have been provided for SR users since Dec. 25, 2006, when beam current was about 100 mA with a lifetime around 3 h at 2.5 GeV. Since then, the performance has been improving continuously. Now, the peak beam current reaches 150 mA at 2.5 GeV with a lifetime about 4 h and three fills a day. Fig. 17 displays beam current and lifetime in a day.

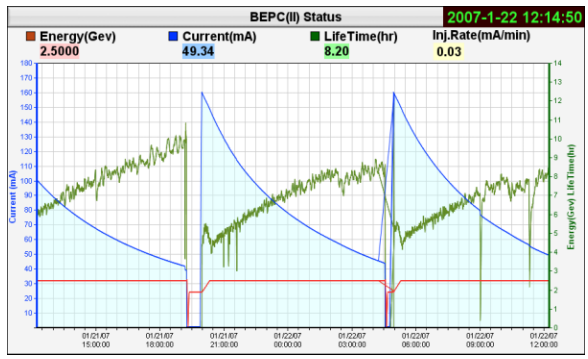

Figure 17: Beam current and lifetime in a day.

About 80 SR experiments were carried out by users with 9 beamlines. As an example, Figure 18 exhibits the protein sm424 in serine degradation pathway of the structural genome of streptococcus mutans during the recent BEPCII operation.

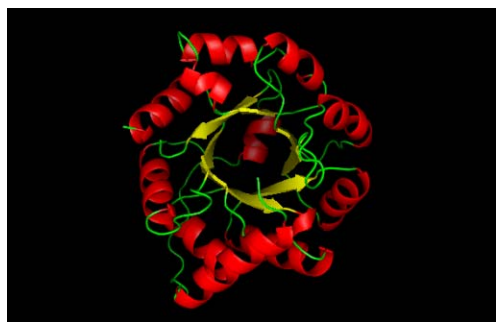

Figure 18: An example of the SR Users' experiments.

PLAN AND SCHEDULE

The first round SR operation will be ended on Feb. 1, 2007. Commissioning for the ēring, the e+ ring and e+-e collision will be followed. The second round SR operation of one month will be arranged in June. The SCQ's tested in the off-line position during the commissioning should be ready for installation in July. After the SCQ's are installed, the BEPCII commissioning will be continued. The information of the BESIII detector can be found in the reference [3]. It is expected that the luminosity would be high enough for the BESIII detector to start up by the end of 2007.

REFERENCES

[1] BEPCII Group, BEPCII Design Report, IHEP-Proceedings, Aug. 2001.
[2] G. Xu, et al, Proceedings of EPAC 2004, July 2004.
[3] Y.Z.Wu, et al, Proceedings of EPAC 2006, June 2006.
[4] Y.F.Wang, International Journal of Modern Physics A, Vol.21(2006),5371-5381.

PAPER NOT YET RECEIVED

THE INDIA BASED NEUTRINO OBSERVATORY - PRESENT STATUS

V. M. Datar* (on behalf of the INO collaboration), NPD, BARC, Mumbai - 400085, INDIA

Abstract

The current status of the India based Neutrino Observatory (INO) is summarized. The two major physics goals are (a) unambiguous demonstration of neutrino oscillation and a more precise measurement of the associated neutrino parameters and (b) to search for matter effects in neutrino oscillation, using the charge identification capability of the magnetized iron calorimeter, which would help determine the sign of one pair of neutrino mass differences. The status of the 1 m^3 prototype iron calorimetric detector, the design of the 50 kton magnet, the experience with resistive plate chambers used for tracking the charged particles produced in neutrino-iron interactions and the planned electronics and data acquisition system will be presented.

INTRODUCTION

The neutrino was invented by Pauli [1] in 1930 to resolve the energy-momentum conservation and spin-statistics crisis in beta decay. The first evidence of the existence of the electron (anti)neutrino was provided in a pioneering reactor experiment [2]. This was followed by the discovery of the muon neutrino and, much later, the tau neutrino [3]. The helicity of the neutrino was shown [4] to be -1 $\pm$ 0.3 in agreement with the two component neutrino theory. An upper limit of the anti-neutrino mass was set at about 55 eV/c^2 through a careful measurement of the beta spectrum in tritium decay near the end point [5]. After unsuccessfully searching for neutrinos at a reactor (which is a copious source of *anti*neutrinos) [6] Davis used the radiochemical detection technique, involving the separation of ^{37}Ar from 600 tons of the cleaning fluid C_2Cl_4 containing ^{37}Cl, to measure neutrinos produced in nuclear reactions, and beta decays of the unstable nuclei produced thereby, in the hot core of the sun [7]. The roughly threefold shortage came to be known as the solar neutrino problem [8]. One of the explanations proposed to explain this shortfall was that the electron neutrinos produced in the solar interior change into another type (flavour) of neutrino, which is not measurable by the ^{37}Cl based detector. This chameleon like behaviour, known as neutrino oscillation, was first proposed by Pontecorvo [9]. The solar neutrino problem was resolved in a definitive manner by the Sudbury Neutrino Observatory experiment [10] using 1 kton of heavy water. Charged current interactions measured the electron neutrinos while neutral current events measured all neutrinos, irrespective of their type or flavour (ν_e, ν_μ, ν_τ). The shortfall in the ν_e flux was recovered in the flux of $\nu_\mu + \nu_\tau$.

* datar@barc.gov.in

Table 1: Best values of neutrino parameters.

Parameter	Exp. value (1σ)
Δ^2_{21}	$(7.9\pm0.4)\times10^{-5}$ eV^2
Δ^2_{23}	$\pm2.4\pm0.2\times10^{-3}$ eV^2
θ_{12}	$34.1^\circ\ ^{+1.6^\circ}_{-1.2^\circ}$
θ_{23}	$41.6^\circ\ ^{+5.7^\circ}_{-2.9^\circ}$
θ_{13}	$<8^\circ$

An equally intriguing problem resulted from the detailed measurements of atmospheric neutrinos. The IMB [11] and Kamiokande [12] collaborations found an anomalous ν_μ/ν_e ratio as a function of zenith angle. This ratio is expected to be close to 2, for high energy neutrinos, and the same for all directions in the absence of oscillations. If ν_μ oscillates into ν_τ the above ratio would be 2 for down going neutrinos but smaller than 2 for upgoing neutrinos. SuperKamiokande provided the first definitive results [13] which showed that neutrinos oscillate and therefore possess a small mass. It may be mentioned that atmospheric neutrinos were first detected at Kolar Gold Fields by an Indian team, just ahead of an experiment led by Reines in a South African mine [14].

The above mentioned, as well as a few more, key experiments have led to a dramatic change in our understanding of neutrinos and cannot be understood within the hitherto successful standard model of high energy physics. The widely accepted explanation of the experimental observations is that neutrinos switch identities, or oscillate into other flavours, as they propagate. This can occur if the flavour eigenstates (electron, muon and tau) are not simultaneously mass eigenstates (m_1, m_2, m_3). In general these two bases are connected by a unitary matrix. For 3 active flavours there are 7 independent parameters *viz.* the 3 mass parameters, 3 mixing angles θ_{12}, θ_{13}, θ_{23} and δ_{CP}. If the neutrino is its own (Majorana) antiparticle there are two additional phases which, however, would not be observable in ν-oscillation experiments. Table 1 lists the presently known experimental values [15]. Here Δm^2_{ij} is defined as m^2_i-m^2_j.

There are several experiments planned in the near future which will improve the precision further and might even throw up unexpected results. Neutrinos are providing us the first clues to physics beyond the standard model and their study is expected to provide even more surprises. With a view of reentering this exciting area an initiative has been taken to set up an underground laboratory in India. One of the main experiments is aimed at making precision

measurements on atmospheric neutrinos using a large iron calorimetric (ICAL) detector.

Two other important problems in neutrino physics should be mentioned. The first of these is that we do not yet know whether the neutrino is its own antiparticle (Majorana) or not (Dirac). A definitive measurement confirming or disproving the claim [16] of observing neutrinoless double beta decay (DBD) (which, if true, makes the neutrino a Majorana particle) would be crucial. Moreover, if the neutrino is a Majorana particle, the rate of 0ν DBD can be related to its absolute mass. The second important problem is to measure the absolute mass of the neutrino irrespective of whether it is a Majorana or Dirac particle. Presently the upper limit derived from a beta spectral measurement of tritium is 2.2 eV/c^2 [17] and there are plans to search for a mass down to about 0.2 eV/c^2 [18].

MAJOR PHYSICS GOALS OF ICAL

The major physics issues and questions that the ICAL detector will address are: (1) Observation of oscillatory pattern of muon neutrino flux with L/E and a precise measurement of neutrino oscillation parameters. (2) Search for matter effects leading to a determination of the sign of Δm^2_{23}. This depends crucially on the magnitude of θ_{13} which will be determined by other ongoing/planned experiments. (3) Whether θ_{23} is 45°; else determine whether $<$ or $>$45° (octant ambiguity). (4) Measure leptonic CP phase δ_{CP}, if θ_{13} is non-zero. Item no.2 can be studied using atmospheric neutrinos provided θ_{13} is $>$ about 5°. The sensitivity to the ordering of the neutrino masses arises as follows. The $\nu_\mu - \nu_\tau$ and $\nu_\tau - \nu_e$ mixing changes, through the $\nu_e - e$ charged current interaction, both the mass and the mixing angle from their vacuum values to those in the presence of matter. The sign of the contribution to each of these is opposite for neutrino and antineutrino for a given Δ_{32}. For the opposite sign of Δ_{32} these contributions change sign allowing a discrimination between the the normal ($\Delta m^2_{32} > 0$) and inverted ($\Delta m^2_{32} < 0$) hierarchies. At a later stage this and items 3 and 4 could be studied even better with an accelerator produced neutrino beam and neutrino factory, respectively.

CHOICE OF DETECTOR AND SITE

The ideal neutrino detector should have as low a threshold as possible possibly sub-MeV if it should be sensitive to geo, nuclear reactor, solar, supernovae and atmospheric neutrinos. Keeping in mind the physics reach of a potential detector, the technical capability of our R&D and that of our industry, feasibility of fabrication and assembly of subsystems of the detector and the time required to make it while being competitive internationally, a large magnetized iron calorimeter (ICAL) measuring atmospheric neutrinos seemed to be the best option. A low energy threshold ICAL detector using thin iron sheets as the target material for neutrinos would increase its dimensions while the use of very thick iron plates would increase that threshold. While the choice of 6 cm iron plates in ICAL results in an energy threshold of a few hundred MeV atmospheric and accelerator produced muon neutrinos can be studied fruitfully while keeping its size reasonable. A proposal [19] for a similar detector, called MONOLITH, was made by an Italian group but was not funded. The need for such a detector with its inherent charge discrimination capability, allowing it to distinguish between μ^+ and μ^- produced through charged current interaction of ν_μ and $\bar{\nu}_\mu$, respectively, was stressed in a recent APS study [20]. Such a detector is complementary to the water Cerenkov detectors such as SuperKamiokande and smaller magnetized iron calorimetric detectors measuring neutrinos produced at accelerators at relatively short baselines, such as the MINOS experiment[21].

A magnetized iron calorimeter is an attractive option if charge identification of the muons following a charged current interaction with the target nucleus is necessary. A magnetic field of about a tesla can be rather easily obtained, using a suitably configured DC current carrying coil for excitation, in soft iron or steel with low carbon content. It is available in large quantities and is reasonably cheap.

A reasonably precise measurement of the energy-momentum of the interacting atmospheric neutrino is required to measure L/E on an event by event basis. This can be done through by tracking the charged muon, produced via the charged current neutrino-nucleus interaction, by many layers of a position sensitive detector. The directional information, up or down going, can be obtained for muons which may or may not stop in ICAL through a fast time (sequence) measurement of the individual detectors. The total area required to be covered is about 10^5 m^2. Of the two possibilities *viz.* gas detectors operated in the avalanche or streamer mode and plastic scintillators with fibre readout, a choice of the former was made. Among the various options in gas detectors the resistive plate chamber (RPC) seems to be a good choice due to its good position and time resolution, ease of construction in large numbers, ruggedness, low cost/unit area, and operational experience in other large experiments. The R&D work on the glass RPC detector including the associated subsystems involving gas circulation, electronics and data acquisition is ongoing.

In consultation with the Geological Survey of India two possible sites for INO were identified, one at Rammam near Darjeeling in West Bengal and another at PUSHEP, Masinagudi, near the foothills of the Nilgiris in Tamilnadu. Two teams made an in depth study of the advantages and shortcomings of each site. A site selection committee consisting of physicists, a civil engineer and geologists was formed. Criteria were framed to decide the suitability in terms of depth, seismicity, proximity to industrial centres, access by road etc. This committee looked into all aspects and recommended, unanimously, that Masinagudi was the preferred site for INO.

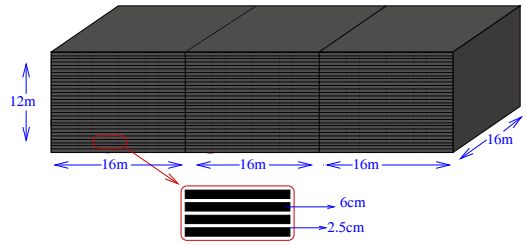

Figure 1: Schematic view of the 50 kton iron calorimeter detector consisting of 3 modules each having 140 layers of iron plates.

ICAL AND SUBSYSTEMS

The conceptual design of ICAL has been made and has a modular structure. Each module weighing 16 kton has a size of 16 m×16 m×12 m and comprises of 140 layers of a unit cell consisting of a 6 cm thick soft iron/low carbon steel plate and a 2.5 cm layer of a X-Y position sensitive resistive plate chamber (RPC). The magnetic field generated with the help of two sets of DC-current carrying coils will be $\sim$ 1 tesla. A schematic of the 50 kton detector is shown in Fig. 1.

Some more details of each of the subsystems including the present status are given in the following sections.

Magnet

The main design criteria for the ICAL magnet were piecewise field uniformity, modularity, optimum copper-to-steel ratio and access for maintenance. A preliminary design of the 16 kton module has been made including a finite element calculation of the magnetic field, using the commercial software Magnet 6.0 [22], for a few configurations of the current carrying coils. Based on these calculations the presently preferred configuration was arrived at. More details may be found in Ref.[23].

Resistive plate chamber

The resistive plate chamber consisting of two glass plates 2 m×2 m area and 2 mm thick separated by an insulating spacer of 2 mm will be used. This choice of glass, as opposed to bakelite, was based on considerations such as cost, availability, ease of construction and suitability for an underground experiment involving low event rates. Most of the R&D work has been carried out using RPCs 30 cm×30 cm in size but a few chambers of a larger size (1.2 m×0.9 m) have also been made. The gas mixing and circulation system has been developed in collaboration with a local vendor and, apart from a few teething problems, has performed quite satisfactorily. Similarly vendors for the conductive coating on the outer walls for applying the high voltage, polycarbonate spacers and buttons and gas inlet/outlet connections have been identified.

A test stack with 10 small sized RPCs (30 cm×30 cm) was set up at the RPC laboratory at TIFR and used to track cosmic muons. The trigger was provided by plastic strip scintillator detectors placed above and below the RPC stack. Fig. 2 shows a picture of the setup. The RPCs have

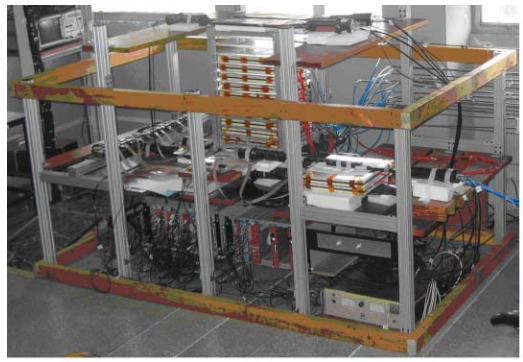

Figure 2: Muon tracking setup using RPC stack.

been operated in the streamer mode, with a gas mixture of HF134a:Ar:isobutane of 62:30:8, or in the avalanche mode with HF134a:isobutane of 95.5:4.5. The electronic pulse following a minimum ionizing particle traversing the RPC is a few hundred mV across a 50Ω load when operated in the streamer mode, while the corresponding figure for the avalanche mode is between 1-5 mV. While the streamer mode of operation simplifies the electronics, since the pulse can directly trigger a fast timing discriminator, the counters have not functioned in this mode for periods beyond about a month. The reason could be the formation of HF in the presence of moisture as an impurity in the detector gas. On the other hand two RPCs have been operating with individual efficiencies of 75-85% in the avalanche mode for a period of more than 1 year. Both these counters have dimensions of about 30 cm×40 cm and have been made from Japanese float glass. The problem of short lifetimes of RPCs [24] using local float glass could be because of some critical parameters and is being addressed through measurements of chemical composition, surface roughness as probed by reflectivity and atomic force microscopy etc.

Gas mixing and distribution system

A 4-gas mixing and distribution unit suitable for the test bench as well as for the prototype 1 m^3 detector was designed and developed locally (see Fig. 3). It can supply gas at slightly above 1 bar to 16 detectors and can be operated in a continuous flow mode. The important features of this system are an input gas purifier (to remove oil and moisture traces) and 2 μm dust filters, a gas mixing system using mass flow controllers, flow sensors and monitors, moisture monitor, safety bubblers on individual gas lines to prevent excess-pressure in the RPCs, isolation bubblers using low vapour pressure silicone oil preventing air, into which the gas is vented, from back diffusing into the RPC, an exhaust manifold and a remote control and monitoring system with a PC interface.

Figure 3: Front view of the 4-component gas mixing unit with 16 output channels.

The designing of a closed loop gas system for the 50 kton detector has been initiated. The system would be capable of mixing upto 4 gases, have a purification column to remove trace amounts of moisture and detector gas breakdown products, gas manifolds, flow controllers (mass flow controllers and impedances), sensors for measurement of various gas parameters such as flow, temperature, pressure, humidity etc and their logging in PC based readout and acquisition system.

Electronics and data acquisition system

The passage of a minimum ionizing particle induces a voltage pulse on the corresponding X- and Y- pickup strips. This pulse (with or without amplification, depending on whether the RPC is operated in the avalanche or streamer modes) goes to a fast timing discriminator (TD) located at the end of the strip. The logic output of the TD is then used to tag the strip which was 'hit' and also given to a multiplexed TDC for recording the time information. An FPGA based trigger module fabricated in-house recording the hit pattern and multiplexing will be used in the prototype detector tests. A multi-level programmable trigger generator with physics motivated trigger logic will be used to initiate data recording. The data acquisition system (DAQ) will be based on the VME standard and will be linked to PCs with the Linux OS. More details may be found in the Ref.[23]. The present plan is to use a scaled up version of this system but experience with the 1 m^3 prototype detector should provide inputs for the ICAL detector electronics and DAQ.

ICAL prototype

A detector on the scale of ICAL has never been built in the country before. It is therefore prudent to build a smaller version and gain experience with the various subsystems and make course corrections on the way towards the design and fabrication of the 50 kton detector. The INO collaboration decided to build a ∼2.6 m × 2.8 m × 2.5 m ICAL prototype detector. This detector will track cosmic ray muons.

SIMULATION OF ICAL

The simulation of the 50 kton ICAL has been done in 3 steps. Firstly, the detector geometry was defined using the GEANT [25] detector simulation software from the CERN library. Neutrino events were generated using NUANCE [26]. Finally the simulated data was used to reconstruct particle tracks and their energy-momentum. The data can now be projected for analysis and visualization. A sample

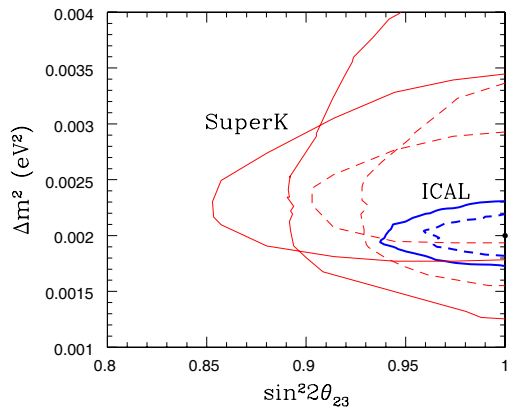

Figure 4: Allowed parameter space from a 300 kton.yr ICAL simulation using fully contained CC muon events (dashed-90% CL, full-99%CL) compared with SK results. The input parameters used in the simulation are indicated by the dot in the figure.

plot is shown in Fig. 4 which compares the allowed region in θ_{23}-Δm^2_{23} space from ICAL simulations with SK results [27].

TRAINING PEOPLE FOR INO

There is a need to develop expertise among the younger group of people who will be associated with the INO project for the next 10 years or more. This will also provide a strong base for future high energy projects both national and international. Various ideas are discussed in the INO Project report such as the formation of an INO School modelled on the lines of the successful BARC Training School, direct recruitment of physicists and engineers and instituting INO Fellowships at selected universities, engineering colleges, NIITs and IITs. A modest beginning in the first mentioned approach has been made this year. A 4 week intensive program involving about a dozen students and recently recruited staff (with a physics background) doing INO related work at the various centres was completed in April-May of 2006. The theoretical component was organized and conducted by HRI, Allahabad while the experimental portion took place at VECC, Kolkata. The feedback was good and hence encouraging.

ESTIMATED COST AND TIME

The INO project has been put up through the Mega-sciences Committee of the Department of Atomic Energy for the 11th five-year plan. The INO project report [23] has most of the details as of May 2006. The total projected cost is Rs. 670 crores over 2 plan periods. About half of this estimated budget is for the low carbon steel for the 100 kton magnet.

The detailed project report (DPR) for the site and associated infrastructure, including that necessary for the underground and overground laboratories, is being prepared by the TNEB (Tamilnadu Electricity Board) engineering team. This contract was given by an Engineering Task Force set by Chairman, DAE. This DPR is expected to be ready by the end of the 10th plan period. A similar DPR will be prepared by a team of scientists and engineers for the ICAL.

An approximate timeline is that the first phase, involving the setting up of the 50 kton detector, should be completed 5 years from the time of financial sanction. By then other experiments such as double-CHOOZ would have measured or put an upper limit on θ_{13}. If this parameter, which is crucial to the existence of matter effects that would be measurable by ICAL, is not too small the next phase of adding additional modules totalling 50 kton would be undertaken. The construction time should be smaller for the second phase, perhaps $\sim$ 3 years. Efforts are also being made to seek international participation in this experiment. If such collaborations materialize also with accelerator based groups the possibility of doing long baseline neutrino measurements, with much higher sensitivity to some of the neutrino parameters, might become a reality.

PRESENT STATUS OF INO

An interim report of the INO project was presented in May 2005 to the Chairman, DAE. Another presentation was made to the Scientific Advisory Committee to the Prime Minister in September, 2005. It was well received and a specific suggestion made to get it peer reviewed by international experts. The report was sent to seven distinguished scientists including six internationally well known experts in neutrino physics and one from India. The reports are generally very positive. Most referees have urged speedy construction in view of potential competition and another has expressed concern about the availability of adequate human resources. In any case, the collaboration is seeking a stronger participation, both national and international. The INO project is also one of the two mega-projects identified by the high energy physics community in the DAE-DST Roadmap meeting for high energy, nuclear and astro-physics held in April, 2006 at HBCSE, Mumbai. The INO collaboration looks forward to formal financial sanction by the Planning Commission and the Govt. of India by the 2nd half of next year.

REFERENCES

[1] W. Pauli, letter to participants of workshop at Tubingen (1930).

[2] C.L. Cowan and F. Reines, Science **124**, 103 (1956).

[3] G. Danby *et al.*, Phys. Rev. Lett. **9**, 36 (1962); K. Kodama *et al.* (DONUT collaboration), Phys. Lett. **B 504**, 218 (2001).

[4] M. Goldhaber, L. Grodzins and A.W. Sunyar, Phys. Rev. **109**, 1015 (1958).

[5] K.E. Bergkvist, Nucl. Phys. **B 39**, 317 (1972).

[6] R. Davis, Phys. Rev. **97**, 766 (1955); *ibid* Bull. Am. Phys. Soc., Washington meeting (1959).

[7] R. Davis, 2002 Physics Nobel prize lecture and references therein (http://nobelprize.org).

[8] J.N. Bahcall, arXiv:physics/0411190 (2004).

[9] B. Pontecorvo, Zh. Eksp. Teor. Fiz. **33** (1957) 549; *ibid* **53** (1967) 1717.

[10] Q. R. Ahmad *et al.*, Phys. Rev. Lett. **87**, 071301 (2001); ibid **89**, 011301 (2002); ibid **92**, 181301 (2004).

[11] T.J. Haines *et al.*, Phys. Rev. Lett. **57**, 1562 (1986); D. Casper *et al.*, Phys. Rev. Lett. **66**, 2561 (1991).

[12] K.S. Hirata *et al.*, Phys. Lett. **B 205**, 416 (1988); *ibid* **B 335**, 237 (1994).

[13] S. Fukuda *et al.*, Phys. Rev. Lett. **81**, 1562 (1998); *ibid.* **82**, 2644 (1999); *ibid.* **85**, 3999-4003 (2000).

[14] C.V. Achar *et al.*, Phys. Lett. **18**, 196 (1965); *ibid.* **19** 78 (1965); F. Reines *et al.*, Phys. Rev. Lett. **15**, 429 (1965).

[15] G.L. Fogli, E. Lisi, A. Marrone, A. Palazzo and A.M. Rotunno, arXiv:hep-ph/0506307

[16] H.V. Klapdor-Kleingrothaus, I.V. Krivosheina, A. Dietz and O. Chkvorets, Phys. Lett. **B 586**, 198 (2004).

[17] V.M. Lobashev *et al.*, Nucl. Phys. **A 719**, 153 (2004); C. Kraus *et al.*, Eur. Phys. J. C **40**, 447 (2005).

[18] KATRIN collaboration, A. Osipowicz *et al.*, hep-ex/0109033; L. Bornschein, Nucl. Phys. **A 752**, 14c (2005).

[19] N. Y. Agafonova *et al.*, *MONOLITH: A massive magnetized iron detector for neutrino oscillation studies,* LNGS-P26-2000; http://castore.mi.infn.it/∼monolith/ .

[20] APS Multidivisional Neutrino Study - Joint Study on the Future of Neutrino Physics: The Neutrino Matrix (Nov., 2004).

[21] D.A. Petyt, seminar at Fermi Lab, 30 March 2006, http://www-numi.fnal.gov/talks/results06.html.

[22] Magnet 6.0 finite element electromagnet software from Infolytica, Canada.

[23] INO Project Report 2006 INO/2006/01, on the web as http://www.imsc.res.in/∼ino/OpenReports/INOReport.pdf

[24] S.S. Bhide *et al.*, Nucl. Phys. **B 158**, 195 (2006).

[25] GEANT, CERN Program Library W5013 (http://wwwasd.web.cern.ch/wwwasd/geant/).

[26] The NUANCE Neutrino Generator, D. Casper, Nucl. Phys. Proc. Suppl. **112**, 161 (2002).

[27] Y. Ashie *et al.*, [Super-Kamiokande Collaboration], Phys. Rev. **D 71**, 112005 (2005).

PAPER NOT YET RECEIVED

REAL-TIME FEEDBACK ON BEAM PARAMETERS

Ralph J. Steinhagen (CERN, Geneva, Switzerland)

Abstract

Traditionally, tight beam parameter stability requirements were most pronounced for light sources and lepton colliders but have now become increasingly important for present and future hadron accelerator operation, not only for performance but also for reasons of machine protection, as recent improvements have led to significantly increased stored beam energies.

In the latest generation machines, performance depends critically on the stability of the beam. In order to counteract disturbances due to magnetic imperfections, misalignments, ground motion, temperature changes and other dynamic effects, fully automated control of the key beam parameters – orbit, tune, coupling, chromaticity and energy – becomes an increasingly important aspect of accelerator operation.

This contribution presents an overview of beam-based feedback systems, their architecture, performance limitations and design choices involved.

INTRODUCTION

With respect to beam-based feedback systems, the wide range of accelerators can be grouped roughly into synchrotron light sources, lepton and hadron colliders that are distinct in their requirements of number and type of feedbacks deployed.

The requirements on beam stability in synchrotron light sources are determined by the quality and properties of the photon beam seen by experiments. Depending on the time scale of the experiment's data integration and perturbation frequency, movements of the beam centroid may either "smear out" the effective emittance, which has a deteriorating effect on the photon beam quality, or lead to an increase of measurement noise. Due to synchrotron radiation, the beam emittance is usually much smaller in the vertical plane. To preserve and minimise the effective emittance, nearly all light sources deploy fast orbit and energy feedbacks. These minimise transverse beam movements, spurious dispersion by centering the beam in the quadrupoles and maintain a stable vertical orbit inside the sextupoles that would otherwise give rise to emittance coupling. A summary and overview of beam stability requirements and stabilisation in synchrotron light source can be found in [1–4].

The beam stability requirements in lepton and present hadron colliders are driven by luminosity optimisation inside the experimental insertions. They favour, similar to light sources, small emittance and stable beam overlap at the interaction point ([5–7]). In addition to orbit feedbacks, tune feedbacks are often also deployed ([8, 9]) to stabilise the beam during acceleration and to avoid resonances that may cause increased particle loss.

Recent improvements in hadron colliders lead to significantly larger stored beam energies which require an excellent control of particle losses inside a superconducting machine. In case of the LHC, the energy stored in the beam is sufficient to quench all magnets and cause serious damage [10]. Thus, most requirements on key beam parameters in superconducting hadron colliders strongly depend on the capability to control particle losses inside the accelerator. In the case of the LHC, the Cleaning System has the tightest constraints on the orbit and requires a stability better than $25\,\mu\mathrm{m}$ during nominal operation at the location of the collimators [11, 12]. Other requirements range from 0.5-0.2 mm r.m.s. for global stabilisation down to $10\,\mu\mathrm{m}$ for physics analysis improvements in the TOTEM experiment [13].

In contrast to lepton machines that require tune stability in the order of $\delta Q \approx 10^{-2} \ldots 10^{-3}$ to avoid up to 4th order resonances, synchrotron radiation damping is negligible in hadron colliders. In order to provide sufficient beam lifetime, resonances of up to the 12th order have to be avoided [14]. The corresponding tune stability δQ is thus required to be better than 0.001 at the LHC. The chromaticity has to be controlled within $Q' \approx 2 \pm 1$, while the uncorrected chromaticity changes are expected to exceed more than 100 units within a few hundred seconds after the start of the ramp [14].

PARAMETER STABILITY

The wide range of perturbation sources that may affect orbit, tune, coupling, chromaticity and energy can be grouped into:

1. Environmental sources, driven by temperature and pressure changes, ground motion, tides and noise induced by human activity which are mostly propagated through quadrupoles and their girders onto the beam,

2. Machine-inherent sources, such as the decay and snap-back of magnet multipoles, cooling liquid flow, vibration of pumps and ventilation, eddy currents and changes of machine optics (final focus),

3. Machine element failures, which are mainly important for large machines such as the LHC where the single circuit failure out of more than 1300 corrector circuits is non-negligible during regular operation.

Their time scale ranges usually from long-term (month to days) over medium term (days to hours) down to short term

(hours to milliseconds). Beam-based feedbacks can contribute and improve beam parameter stability for perturbations on slow to medium time scales but are ultimately limited by thermal drifts, noise and systematics of corrector circuits and beam instrumentation [15]. The sensitivity to thermal drifts in 3^{rd} generation light sources lead to a rigorous stabilisation of not only the orbit but also the temperature of the experimental hall, tunnel, cooling water, and vacuum chamber to a level of about $\pm 0.1\,^{\mathrm{O}}\mathrm{C}$ [16]. The quest for temperature stabilisation leads also to 'top-up' operation that maintains a constant beam current and thus constant heat load inside the tunnel [1, 2].

FEEDBACK CONTROL DESIGN

In case of low-order beam parameters – orbit, tune, coupling, chromaticity and energy – the effect of individual corrector circuits is, for most accelerators, sufficiently linear and can be cast into matrices. In the case of the orbit, for example, one can write

$$\Delta \underline{z}(t) = \mathbf{R} \cdot \underline{\delta}(t) \tag{1}$$

with $\Delta \underline{z} = (z_1, \ldots, z_m)^T$ holding the readings of m beam position monitors (BPMs) and $\underline{\delta} = (\delta_1, \ldots, \delta_n)^T$ holding the strengths of n dipole corrector circuits (CODs) and the matrix elements R_{ij} describing the response of the i-th BPM to the j-th COD circuit.

The external perturbations, corrector circuit strengths $\underline{\delta}(t)$ and thus the beam parameters themselves are usually a function of time. Many feedback designs on beam parameters decouple the control into what is further referred to as *space* and *time domain* which makes the choice of parameter correction strategy and the controller adjusting the temporal behaviour of the corrector circuits more flexible, particularly in the presence of element failures that require quick adjustments of the feedback controller and response matrices.

Space Domain

The parameter control in space domain establishes corrector circuit strengths $\underline{\delta}_{ss} = \lim_{t\to\infty} (\delta_1(t), \ldots, \delta_n(t))^T$ that for steady-state perturbations minimises the residual r of

$$r = \left\| \underline{z}_{ref} - \underline{z}_{actual} \right\|_2 = \left\| \mathbf{R} \cdot \underline{\delta}_{ss} \right\|_2 < \epsilon \tag{2}$$

with $\mathbf{R}$ the beam response matrix, $\underline{z}_{ref}$ the reference and $\underline{z}_{actual}$ the measured parameter. The two-norm (or r.m.s.) of the parameter vector is defined as $\|\underline{x}\|_2 = \frac{1}{N}\sqrt{\sum_{i=0}^{N} x_i^2}$ with x_i being the individual vector entry and N the total number of entries.

The control in space domain consists essentially of the inversion of the beam response matrices. Singular-Value-Decomposition (SVD) is one of the most popular and widely used inversion algorithms ([1–3]) and a generalisation of the Jacobi matrix eigenvalue decomposition to the general case of non-square matrices [17, 18]. As shown in [17], any matrix $\mathbf{R} \in \mathbb{R}^{m\times n}$ with $m \geq n$ can be decomposed into

$$\mathbf{R} = \mathbf{U} \cdot \lambda \cdot \mathbf{V}^T \tag{3}$$

with $\mathbf{U} \in \mathbb{R}^{m\times n}$ being a dense unitary matrix, $\lambda = diag(\lambda_1, \ldots, \lambda_n)$ a diagonal matrix holding the eigenvalues of $\mathbf{R}$, and $\mathbf{V} \in \mathbb{R}^{n\times n}$ an orthogonal matrix containing the eigenvectors of $\mathbf{R}$ in its columns.

Depending on the device layout and lattice parameters, equation 1 may contain singularities that can, using SVD, be identified by eigenvalues close or equal to zero. The SVD can be used to compute a so-called *pseudo-inverse* response matrix $\tilde{\mathbf{R}}^{-1}$ that relates the required steady-state circuit strengths $\underline{\delta}_{ss}$ to the measured orbit error $\Delta\underline{z}$:

$$\underline{\delta}_{ss} = \mathbf{V} \cdot \tilde{\lambda}^{-1} \cdot \mathbf{U}^T \cdot \Delta\underline{z} = \tilde{\mathbf{R}}^{-1} \cdot \Delta\underline{z} \tag{4}$$

Possible singularities are removed by setting the inverse of singular eigenvalues to zero. The number of eigenvalues used for the inversion defines the trade-off between precision and robustness of the correction: A higher number of eigenvalues provides a better convergence but at the same time tends to be more prone to spurious parameter readings and noise.

In case the true accelerator response differs from the one used during the design of the parameter control, the correction error gradient $\underline{\delta}_s s$ may point off the true minimum, as illustrated in Figure 1. It is visible that independent of the

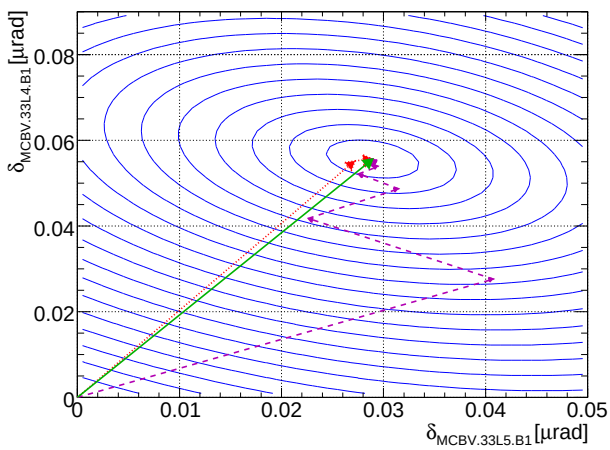

Figure 1: SVD residual contour: The perfect correction (solid green), the correction with optics error (dotted red) and COD calibration errors (dashed violet) are indicated. The contour lines correspond to constant values of the residual orbit error r. The correction is based on a regular FODO lattice (LHC arc) and shows the projection of two selected COD settings.

type of error, the corrections converge to the same steady-state setting. However, depending on the errors the convergence speed can vary between one (perfect) and about seven iterations (20% COD calibration errors).

In most digital approximations, analogue systems are sampled at least 10 times higher than the analogue bandwidth. Since the deteriorating effect due to beam response

matrix uncertainties can be mitigated through a higher sampling frequency, it is usually favourable to sample much higher than a factor of 10. In case of synchrotron light sources, typical sampling to bandwidth ratios are about 40 or more [1–3].

Time Domain

A simple loop block diagram consisting of a single-input-single-output (SISO) process $G(s)$ and controller $D(s)$ is shown in Figure 2. The stability and sensitivity

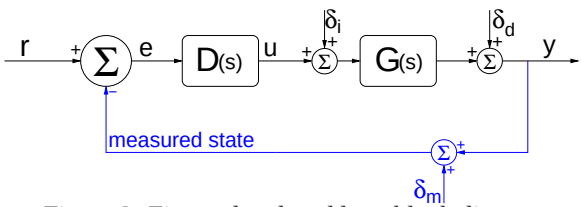

Figure 2: First order closed loop block diagram

to perturbations and noise is defined by the following functions

$$T(s) := \frac{y}{r} = \frac{D(s)G(s)}{1+D(s)G(s)} \quad (5)$$

$$S_d(s) := \frac{y}{\delta_d} = \frac{1}{1+D(s)G(s)} \quad (6)$$

$$S_i(s) := \frac{y}{\delta_i} = \frac{G(s)}{1+D(s)G(s)} \quad (7)$$

$$S_u(s) := \frac{u}{\delta_d} = \frac{D(s)}{1+D(s)G(s)} \quad (8)$$

where $T(s)$ is the complementary (nominal) transfer function, $S_d(s)$ the *nominal sensitivity* defining the loop disturbance rejection, $S_i(s)$ the *input-disturbance sensitivity* and $S_u(s)$ the *control sensitivity*. The state variable is indicated in Figure 2. The sensitivity to measurement noise is equal to the nominal transfer function T_0.

Classic feedback designs rely on the discussion of denominator zeros in equation 5 and 6 while keeping constraints such as required bandwidth, minimisation of overshoot, limits on the maximum possible excitation signal and robustness with respect to model and measurement errors. For ideal processes, this yields adequate controller designs but often falls short in providing a simple comprehensive method for estimating and modifying the loop sensitivity (robustness) in the presence of process uncertainties, non-linearities and noise.

This paper focuses on Youla's affine parameterisation method for optimal controllers, which is based on the analytic process inversion, first introduced in [19]. For an open-loop stable process $G(s)$, the nominal closed-loop transfer function is stable if and only if $Q(s)$ is an arbitrary stable proper transfer function and $D(s)$ parameterised as:

$$D(s) = \frac{Q(s)}{1-Q(s)G(s)} \quad (9)$$

The stability of the closed loop system follows immediately out of the above definition if inserted into equations 5 to 8. The sensitivity functions in the $Q(s)$ form are given as:

$$T(s) = Q(s)G(s) \quad (10)$$

$$S_d(s) = 1-Q(s)G(s) \quad (11)$$

$$S_i(s) = (1-Q(s)G(s))G(s) \quad (12)$$

$$S_u(s) = Q(s) \quad (13)$$

Assuming $G(s)$ is stable, the only requirement for closed loop stability is for $Q(s)$ to be stable. The strength of this method is the explicit controller design with respect to required closed loop performance, as visible in equation 10, and required stability (equations 11 to 13). Equations 10 and 11 are complementary and illustrate the intrinsic limiting trade-off of feedbacks that either have a good disturbance rejection or are robust with respect to noise. The ultimate limit is thus rather defined by the bandwidth and noise performance of the corrector circuits and beam measurements than by the feedback loop design itself. Systematic and thorough analysis of involved beam instrumentation and corrector circuits are thus essential for achieving best beam parameter stabilisation.

The design formalism can be demonstrated using a simple first order system $G_0(s) = \frac{K_0}{\tau \cdot s+1}$ with open-loop gain K_0 and time constant τ. A common controller design ansatz is to write $Q(s)$ as

$$Q(s) = F_Q(s) \cdot G_0^i(s) \quad (14)$$

with $F_Q(s)$ a trade-off function and $G_0^i(s)$ the pseudo-inverse of the process. Since G_0 does not contain any unstable zeros, the pseudo-inverse equals the inverse and is given by $G_0^i(s) := [G_0(s)]^{-1} = \frac{\tau \cdot s+1}{K_0}$. $Q(s)$. In order for $D(s)$ to be biproper, $F_Q(s)$ must have a degree of one and can be written as:

$$F_Q(s) = \frac{1}{\alpha s+1} \quad (15)$$

Inserting equation 14 into Youla's controller parameterisation equation 9 yields the following controller

$$D(s) = \frac{\tau}{K_0\alpha} + \frac{1}{K_0\alpha s} = K_p + K_i \cdot \frac{1}{s} \quad (16)$$

which shows a a simple PI controller structure with proportional gains K_p and integral gain K_i. Inserting equation 14 into equation 10 yields

$$T_0(s) = F_Q(s) \quad (17)$$

that the closed loop response is essentially determined by the choice of trade-off function $F_Q(s)$ and that the closed loop bandwidth is proportional to the parameter $1/\alpha$. This can be used to tune the closed loop between: high disturbance rejection but high sensitivity to measurement noise (small α) and low noise sensitivity but low disturbance rejection (large α) depending on the operational scenario.

The maximum possible closed loop bandwidth is limited by the excitation, as described by equation 13. In case of power converters, for example, the excitation is limited by the maximum available voltage.

The same method can be extended to open-loop unstable and multi-input-multi-output (MIMO) systems [19]. Real life feedbacks may contain significant delays λ (due to e.g. data transmission, data processing etc.) and non-linearities $G_{NL}(s)$, due to e.g. saturation and rate limits of the corrector circuits' power supplies. The modified process can be written, for example as:

$$G(s) = G_0(s) \cdot e^{-\lambda s} G_{NL}(s) \tag{18}$$

Using the same pseudo-inverse $G_0^i(s)$ as for the above example and inserting equation 14 into equation 9 yields a controller parameterisation $D_{NL}(s)$ including a classic Smith-Predictor and anti-windup paths, discussed in more detail in [20, 21]. Inserting equation 14 including the delay and non-linearities into equation 10 yields the following closed loop transfer function:

$$T(s) = F_Q(s) \cdot e^{-\lambda s} G_{NL}(s) \tag{19}$$

Similar to the linear case discussed above, the closed loop is essentially defined by the function $F_Q(s)$ that within limits can be chosen arbitrarily based on the required disturbance rejection and robustness during possibly different operational scenarios (gain-scheduling). Further information and a review on Youla's parameterisation can be found in [21, 22].

DEPENDABILITIES AND CROSS-TALK

In many accelerators, beam-based feedbacks are usually established and designed one by one, and often, little effort is put into the study of cross-dependency and decoupling of these loops. However, for robust and reliable control it is necessary to address possible cross-constraints, cross-talk and coupling between several simultaneous and possible nested loops already in the design stage.

A typical cross-dependency is intrinsic to the stability requirements on orbit and tune: though tight constraints on orbit excursion to micrometre level are beneficial to minimise feed-down effects and beam life-time, it also imposes constraints on other feedbacks such as tune and chromaticity, the measurements of which rely on transverse excitations and momentum modulation. In the case of the LHC, the tight constraints lead to the development of a robust diode-based tune measurement technique that is capable of detecting nanometre scale beam oscillations ([23]) and that enables a tune and coupling phase-locked-loop (PLL) that can operate with transverse excitation levels below $1\,\mu\mathrm{m}$ [24, 25].

Another possible cross-dependency is given by coupling due to the beam response itself. As described in [26], a robust and reliable tune PLL requires also the measurement and control of global coupling. Classic tune PLL designs ([8,9]) often model the PLL as a first order process defined by the phase detector's filter time constant and open loop gain K_0 that depends on the angle of the phase slope at the location of the tune resonance. In the presence of varying chromaticity, the open loop gains K_0 and thus the optimal controller parameter are functions of chromaticity itself. Using linear control design only, this cross-dependence implies either a controller design that is optimal for large chromaticities, which becomes sensitive to noise and unstable for low values of chromaticity, or a controller design that is optimal for small chromaticities but lags behind the real tune for large values of chromaticity [24, 27].

A more complex example for inter-loop coupling can be illustrated by the LHC, which requires a simultaneous control of orbit, tune, coupling, chromaticity and energy. The forseen nested control scheme for chromaticity, tune and coupling is shown in Figure 3. The tune PLL is the innermost loop measuring the global tunes and coupling parameters. The loop is first nested within the loop that measures and controls the chromaticity and is then surrounded by the feedback loop controlling the global tunes and coupling. The decoupling is obtained by choosing gradually reduced bandwidths for the tune PLL ($f_{bw} \approx 8\,\mathrm{Hz}$), chromaticity ($f_{bw} \approx 1\,\mathrm{Hz}$) and tune feedback ($f_{bw} < 1\,\mathrm{Hz}$). This nesting hierarchy is required in particular to eliminate the cross-talk between tune and chromaticity feedback, as the tune feedback would otherwise minimise the momentum-driven modulation as well as tune modulation and thus compromise the chromaticity measurement.

In addition, cross-talk is introduced between the chromaticity and orbit/energy feedback through the dispersion orbit that is driven by the momentum modulation required by the chromaticity feedback. In order to minimise this cross-dependence, the foreseen LHC orbit feedback filters and separates the dispersion orbit from the measured closed orbit prior to performing any orbit correction.

CONCLUSIONS

Beam-based feedbacks can contribute and improve beam parameter stability for perturbations on slow to medium time scales but are ultimately limited by thermal drifts, noise and systematics of involved devices on long time scales from days to months. Systematic and thorough analysis of involved beam instrumentation and corrector circuits are thus essential for achieving best beam parameter stabilisation.

The use of imperfect design beam response does not necessarily affect the precision of the correction but may lead to a reduction of effective feedback bandwidth. This effect can be mitigated by higher sampling frequencies which are usually in the order of 40 times higher than the desired feedback bandwidth.

Youla's affine parameterisation provides a simple yet powerful design tool for optimal adaptive non-linear control. Its strength is the explicit controller representation that enables an unobscured feedback design with respect

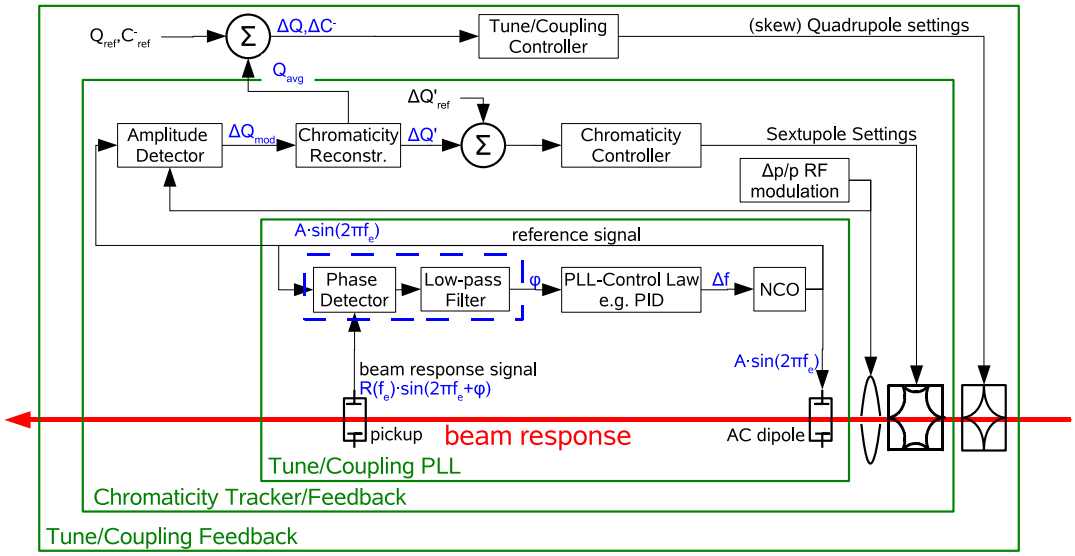

Figure 3: Nested loop scheme required for a coherent control of tune, coupling and chromaticity.

to closed loop robustness (noise insensitivity) and steering precision. It can further be used to design controllers with adaptive gains that are scheduled depending on the requirements of the applicable operational scenario.

It is advisable to address the incorporation of cross-constraints and coupling of multiple simultaneous nested loops early at the design stage as well as design feedbacks as an ensemble.

REFERENCES

[1] PSI, Proceeding of "3rd International Workshop on Beam Orbit stabilization", 2004, http://iwbs2004.web.psi.ch/

[2] M. Böge, "Achieving Sub-micron Stability in Light Sources", EPAC'04, Lucerme, Switzerland, 2004

[3] G Decker, "Beam Stability in Synchrotron Light Sources", DIPAC'05, Lyon, France, 2005

[4] R. Hettel, "Beam Stability Issues at Light Sources", 25th ICFA Adv. Beam Dyn. WS., Shanghai, 2002

[5] M. Masuzawa et al. "IP orbital feedback for collision tuning at KEKB", EPAC'00, p. 1211, 2000

[6] J. Wenninger, "Slow BPM Based LEP Orbit Feebdack Control", private communication

[7] L. Hendrickson et al., "Slow Orbit Feedback System for PEP-II", EPAC'00, Vienna, Austria, 2000.

[8] O. Berrig et al., "The Q-Loop: A Function Driven Feedback System for the Betatron Tunes During the LEP Energy Ramp",CERN SL-98-039, 1998

[9] A.Fisher et al., "Tune Feedback in PEP-II",SLAC-PUB-10230, 2003

[10] "Damage levels - Comparison of Experiment and simulation", Chamonix XIV and PAC'05, Knoxville/TN, 2005

[11] R. Assmann, "Collimation and Cleaning: Could this limit the LHC Performance?", CERN, Chamonix XII, 2003

[12] S. Redaelli, "LHC aperture and commissioning of the Collimation System", CERN, Chamonix XIV, 2005

[13] TOTEM collaboration, "Technical Design Report", CERN-LHCC-2004-002, p. 21 ff., 2004

[14] S. Fartoukh, O. BrÃ¼ning, "Field Quality Specification for the LHC Main Dipole Magnets", LHC Project Report 501

[15] R. Assmann et al., "Non-Linearities in the Response of Beam Position Monitors", AIP 546, Boston, MA, 2000, pp. 267-274, CERN-SL-2000-055-BI

[16] T.Schilcher, "Commissioning and Operation of the SLS Fast Orbit Feedback", EPAC'04, Lucerne/Switzerland, 2004

[17] G. Golub and C. Reinsch, "Handbook for automatic computation II, Linear Algebra", Springer, NY, 1971

[18] K.G.J. Jacobi, "Über ein leichtes Verfahren, die in der Theorie der Säcularstörungen [..]", Crelle's Journal, 1846, 30 p. 51-94, 97-144

[19] D. C. Youla et al., "Modern Wiener-Hopf Design of Optimal Controllers", IEEE Trans. on Automatic Control,1976, Vol. 21-1,pp. 3-13 & 319-338

[20] O. Smith, "Feedback Control Systems", McGraw-Hill, 1958

[21] Goodwin, Graebe, Salgado, "Control System Design", Prentice Hall, 2000

[22] B. Anderson, "From Youla-Kucera to Identification, Adaptive and Non-linear Control", Automatica, 1998, Vol. 34, No. 12, pp. 1485-1506

[23] M.Gasior, R.Jones, "The principle and first results of betatron tune measurement by direct diode detection", CERN-LHC-Project-Report-853

[24] R.J.Steinhagen, "First Results of the PLL Tune Tracking in the SPS", Tune Feedback Final Design Review, BNL, $www.agsrhichome.bnl.gov/LARP/061024_TF_FDR$

[25] R.Steinhagen et al., "The LHC Phase-Locked-Loop for Continuous Tune Measurement - Prototype tests at the CERN-SPS", tbp. at PAC'07, 2007

[26] R. Jones et al., "Towards a Robust Phase Locked Loop Tune Feedback System", DIPAC'05, Lyon, France, 2005

[27] R.J. Steinhagen et al., "Influence of Varying Chromaticity on Robustness of the LHC Tune PLL and its Application for Continuous Chromaticity Measurement.", tbp. at PAC'07, 2007

BEAM INSTRUMENTATION EXPERIENCE AT ATF*

Yosuke Honda, High Energy Accelerator Research Organization (KEK), Tsukuba, Japan
ATF International Collaboration

Abstract

With its low-emittance stable electron beam, ATF in KEK has been an unique facility to develop various beam instruments. This paper reviews some of those devices that are used in the operation, were tested in the past, and being under development.

INTRODUCTION

Accelerator Test Facility (ATF) in KEK is a test accelerator to produce a high quality electron beam required in ILC. It consists of an injector linac, a damping ring (DR) and an extraction line. Beam energy is 1.3 GeV, nominal beam charge is 1×10^{10} e/bunch, and pulse repetition rate is 1.56 Hz in the usual operation. There are three types of operational modes, a single bunch mode, a multi-bunch mode of 20-bunches with 2.8 nsec bunch spacing, and a 3-bunches mode with 150 nsec spacing.

The damping ring reduces transverse emittances of the beam down to 1.5 nm·rad and 6 pm·rad in horizontal and in vertical plane, respectively ([1]). Emittance tuning procedures are routinely performed applying corrections to reduce dispersions and couplings based on beam orbit measurements around the DR. The emittance realized in the DR can be measured by three types of monitors, SR-interferometer, X-ray SR imaging monitor and Laserwire monitor. The typical dimensions of the damped beam are 100 μm in horizontal, 10 μm in vertical, and 8 mm in longitudinal.

After beam reaches to the equilibrium in the DR, it is kicked out to the extraction line. The emittance in the extraction line is measured with wire-scanners. The extracted low-emittance beam has been useful to test various devices, such as cavity BPMs, laser-wire, ODR, OTR and fast feedback system (FONT). Recently, most of the beam operation shifts are devoted for development works of these new instruments.

It is scheduled to extend the extraction line for building a test beam line for ILC final focus (ATF2 [2]). Its construction will start in the summer of 2007. Monitors to be used in ATF2 are also being tested.

This article reviews development works of various instruments in ATF. In the following, the instruments are categorized into four sections, beam position monitors, beam size monitors, bunch length monitors, and beam control.

* Work supported by "Grant-In-Aid for Creative Scientific Research of JSPS (KAKENHI 17GS0210)"

BEAM POSITION MONITORS

Beam position is the most essential information. Single shot pick-up BPMs are used for usual operation. Recently, lots of works were done on cavity BPMs using the extracted beam. In the new beam line of ATF2, cavity BPMs will be used as main monitors for operation.

Pick-up BPM

The diameter of the beam duct is 24 mm in the most part of the beam line. Button type pick-ups are used in the DR, and strip-lines are used in the linac and in the extraction line. In order to quickly measure beam positions in shot-by-shot basis, a single-shot wide-band detection system was developed. The band width of the processor reaches up to 1 GHz, which almost covers the spectrum of the signal after transported to the outside of the tunnel. Bi-polar signals from pick-ups are clipped into uni-polar signals with a diode detector, then they are recorded by 14 bit charge sensitive ADCs. Each channel of the processors was calibrated using a dummy pulse distributed to all channels at the same time. The resolution reaches to 2 μm at 10^{10} e/bunch beam intensity.

Damping ring BPM upgrade

In order to realize further small vertical emittance, tests to improve the DR BPM by replacing it to a narrow-band system have started. Heterodyne receivers following narrow-band BPFs are installed closely to the pick-ups. On board processors with digital waveform recorders process signals of every beam revolutions. It is expected to have 100 nm resolution with 500 nm accuracy in a machine cycle.

Cavity BPM

Electro-magnetic modes in a cavity-like structure on beam ducts are excited by the beam passage. Among the various resonant modes, transverse dipole modes are useful to measure the beam positions because their field strength are proportional to the product of beam charge and the beam offset with respect to the electrical center. The beam signal is read out through a selective coupler which couples only with the dipole mode. Its strong and narrow-band signal enables us to measure the beam position with $\sim$nano-metre resolution. Mechanical rigidness and reliability of the electric center are also advantages of cavity BPMs. This types of BPMs are expected to play important roles in ATF2 and future accelerators.

Signal strength depends on the choice of cavity frequency. Considering the relatively long bunch length, C-band frequency was estimated to be the most sensitive in our case. All types of cavity BPM developed in ATF use 5.7∼6.5 GHz.

nano-BPM Three-BPM method is an usual technique to study very high resolution BPMs. A triplet of BPM are supported by a rigid frame so that the relative position of the three to be mechanically stable. Because of the very high resolution, the measurable range of the BPM is limited. A precise mover system is needed to align the BPMs in a straight line within 10 μm. Two of the three are used to monitor the beam orbit and they predict the beam position at the remaining BPM. Comparing the actual measurement with the prediction, resolution of the BPM can be estimated. Two sets of BPM triplet systems have been developed in the extraction line. Figure 1 is the one with parallel-link movers (upstream). A fast digital waveform recorder samples the down-converted BPM signals. Using an analysis procedure of fitting or digital down-conversion, the data is converted to beam positions. The other one (downstream) has active stabilization movers using sensors with optical interferometers. As for the electronics, this system uses a fast analogue electronics which directly rectifies the signal into beam positions. Figure 2 shows the data taken by the latter system. Calibrating the scale by moving one of the BPM with known amount, the residual between the measurement and prediction can be estimated. Both of the systems have proved position resolutions smaller than 20 nm. ([3]).

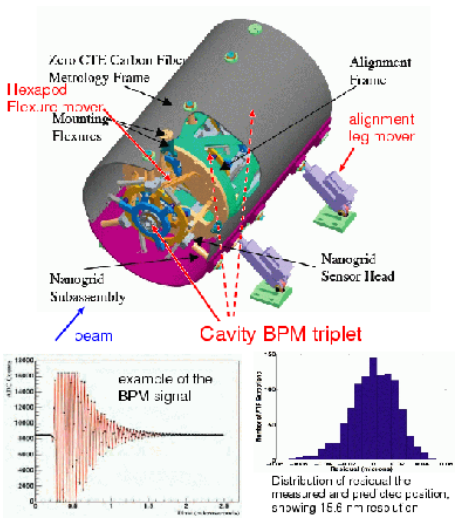

Figure 1: nano-BPM triplet system in the upstream.

ATF2-BPM Reliable beam position control within a few μm accuracy is required along the final focus beam line of ILC and ATF2. Figure 3 is the cavity BPM to be attached on quadrupole magnets of ATF2 ([4]). It is a cylindrical cavity read out from four symmetric ports of waveguides

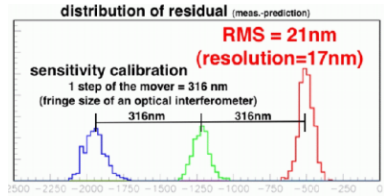

Figure 2: Result of the system in the downstream.

coupled with slots. The front end electronics to down-convert the signal into 20 MHz is also developed. An on-line calibration/analysis system to extract beam positions has been developing.

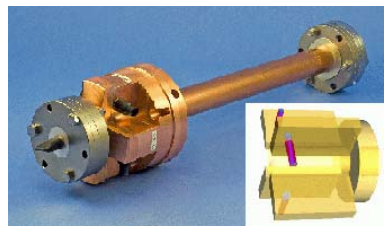

Figure 3: ATF2-BPM.

IP-BPM One of the major goals of ATF2 is to demonstrate stabilization of the beam position at the focal point (the virtual interaction point, IP) within a few nanometer. An ultimately high resolution cavity BPM located at the IP (IP-BPM) is necessary to prove it. Due to the special beam optics at the IP, several special considerations were needed in designing IP-BPM. To reduce the signal originated by the angle of the beam orbit, the length of the cavity in the beam direction was shorten compared with other cavity BPMs. To be free from cross-coupling between the dipole modes of different directions, the cavity has a rectangular shape with dipole mode frequencies 714 MHz apart. Tests in the extraction line has started recently (Figure 4).

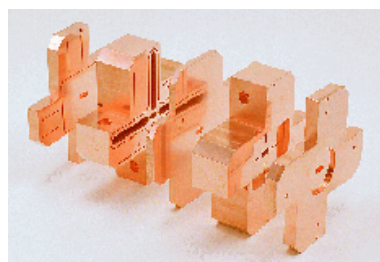

Figure 4: Structure of IP-BPM.

BEAM SIZE MONITORS

Beam size measurements are important to estimate transverse emittances. High resolution beam size monitors are needed especially for the vertical beam size. To separately

measure bunches in the multi-bunch beam, the monitors have to have a good time resolution.

X-ray SR Monitor

Imaging its source point on a screen, synchrotron radiation (SR) can be used to measure the beam profile. Since the beam size in the arc sections of the DR is too small to image with a visible light due to the diffraction limit, we have developed an X-ray optical system as shown in Figure 5 ([5]). SR from a bending magnet is first reflected by a monochromator of Si crystal to choose 3.24 keV X-ray, then transported through a magnification optics which consists of two Fresnel Zone Plates (FZP). It was designed to realize a $\times 20$ magnified image of the source on an X-ray CCD camera. This monitor can measure beam size as small as 5 μm with 1 μm resolution, and is now routinely used in beam operation.

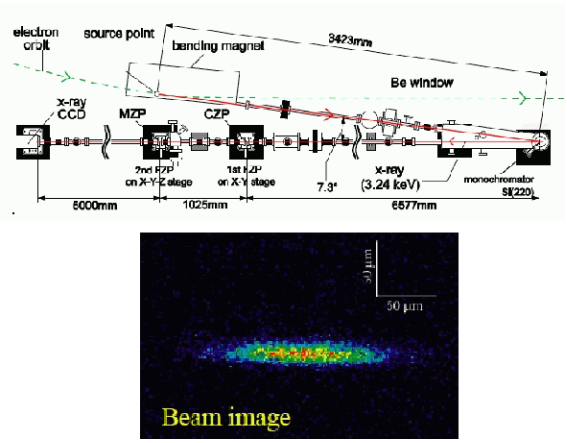

Figure 5: X-ray SR Imaging system.

SR Interferometer

Spatial coherence of SR can be used to estimate its source size. SR of visible light region is transported to a double-slit interferometer as explained in Figure 6 ([6]). Visibility of the interferogram is a good measure to tell the beam size, the smaller is the beam size, the larger is the visibility. This monitor can measure 5 μm beam size with a carefully tuned system.

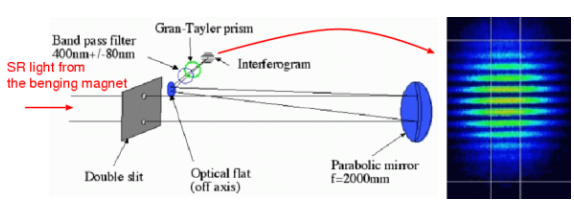

Figure 6: SR Interferometer system

Laserwire monitor

To reliably measure beam emittances in DR, a direct way to measure the beam size was developed ([7]). This monitor uses a thin laser beam to scan the electron beam in the transverse direction. Compton scattering produces gamma rays in the forward direction of the electron beam. Since the flux of the gamma ray is proportional to the convolution of the beam profile and the laser profile, the beam profile can be obtained by scanning the laser across the beam. To be able to measure a small beam size, laser beam has to be well focused. A cw laser of 532 nm wavelength is injected into a high finesse optical cavity of nearly concentric configuration to stably realize such a small spot while enhancing the effective laser power by $\sim$1000 times. By identifying the bunch number with the incoming timing of the scattered gamma rays, this monitor can separately measure each bunch of the multi-bunch beam at the same time. This monitor can measure 5μm beam size with a good accuracy since the laser spot size is known precisely. Since it takes $\sim$5 minutes to complete a scan, accurate beam orbit monitoring to remove the effects of beam position drift is necessary to further improve the system.

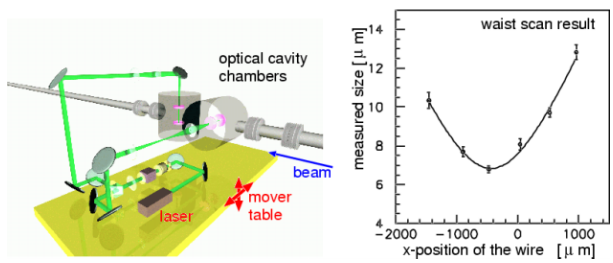

Figure 7: Laserwire system in the DR

Laser-wire system in the extraction line

To apply the laser wire technique in a single path beam line, a different approach of laser system has been developing in the extraction line ([8]). A laser beam is focused with a specially designed lens system to have a $\sim\mu$m spot size, and is used to scan across the electron beam. To obtain enough signal in single collision, a pulsed laser of high peak power is necessary. Timing system is also important to establish a stable collision. Because this is a non-invasive method to measure the beam and a laser target is never damaged by high intensity electron beams, laserwires are expected to become main beam size monitors in ILC. The collision chamber shown in Figure 8 has been installed and tests are underway. Figure 9 is an example of the beam measurement.

Wire scanners

The emittances of the extracted beam are usually measured by a wire scanner system. Tungsten wires of 10 μm diameter are installed in horizontal, vertical, 45 degree and

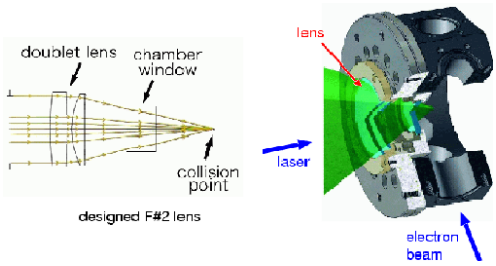

Figure 8: Lens and the collision chamber of the laser-wire system.

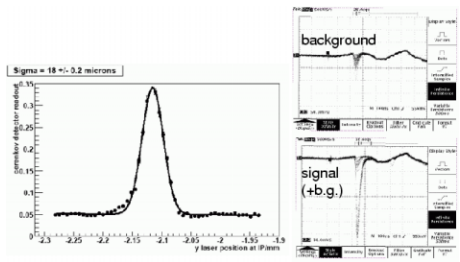

Figure 9: Example of test data by the laser-wire system.

10 degree direction in a scanning system ([9]). The horizontal (vertical) wires are used to measure the vertical (horizontal) beam size, and the angled wires to estimate the beam tilt. An air-Cherenkov detector placed downstream measures the flux of the gamma ray produced in the collision of the wire and the beam. There are 5 sets of the wire scanners in the dispersion-free section of the line to calculate emittances by measuring development of the beam size along the phase advance. Although it can measure beam size as small as 3 μm, the resolution of the emittance measurement is limited by residual dispersions in the extraction line.

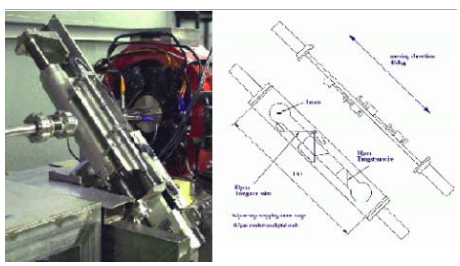

Figure 10: Wire scanner system

OTR monitor

A beam profile monitor to be able to measure beam spots as small as 5 μm with the optical transition radiation (OTR) was developed in the extraction line. Radiation of visible light is emitted from a polished plane of a beryllium target. In order to image the radiation that has an opening angle of $\sim 1/\gamma$ without aberrations, a high NA lens system to magnify the source image is needed. Although it successfully proved the expected resolution, the target could not tolerate the high intensity beam for a long enough time.

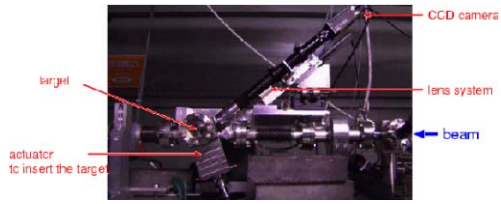

Figure 11: OTR monitor.

ODR monitor

A beam size monitor based on the optical diffraction radiation (ODR) has been developed in the extraction line ([10]). ODR is a kind of wake-fields generated by a passage of a beam near a conductive object. A metal plate with a slit is installed in the beam line with 45 degree angle to the beam. When an electron beam passes through the slit, radiations of visible light are emitted toward perpendicular direction of the beam from both edges of the slit. They generate an interference pattern of double peak in its angular distribution as shown in Figure 12. The beam size can be estimated from the contrast of the pattern. A low-noise cooled CCD camera detects the image of the radiation shot by shot. This monitor can measure beam size as small as 15 μm. Flatness of the target, controlling beam position in the slit, and shielding the background of synchrotron lights from magnets in the upstream are important to do a reliable measurement.

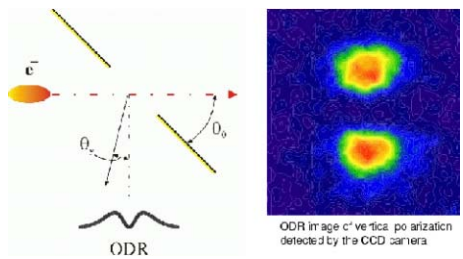

Figure 12: ODR system.

BUNCH LENGTH MONITORS

Bunch length and longitudinal motion of bunches are useful to investigate impedance and instabilities in the DR. The injected bunch length from the linac of 10 psec is lengthened to $\sim$25 psec in the equilibrium of the DR.

SR measurement with a streak camera

Time structure of electron bunch is imprinted in the time structure of the SR. SR light from a bending magnet of the DR is transported to a streak camera. It converts the light into photo-electrons, and projects the time axis into

a transverse profile as an image. This system is also used to measure longitudinal motion of the bunch circulating in the DR with a synchronized scanning setup to the beam revolution.

Pulsed laser system

Using the technique of the optical cavity developed for the laserwire monitor, an optical cavity for a mode-locked pulse laser of 357 MHz was developed and installed in the same way as the laserwire. Since the round-trip time of the optical cavity is made exactly the same as the bucket spacing, timing of the laser can be synchronized to the DR bunches. The shorter pulse length (∼7 psec) of the laser than the electron beam enables us to obtain longitudinal bunch shape by scanning the relative phase between the beam and the laser.

CSR monitor

Short bunched beams in the first few turns after DR injection emit a coherent synchrotron radiation (CSR) of THz region (shown in Figure 13). In order to study the properties of CSR a transport line for the radiation and a schottky barrier diode detector is installed at the end of the straight line of the DR. Since the strength of the coherent radiation strongly depends on the peak intensity of the bunch, it might become a good tool to check the bunch length of the incoming beam.

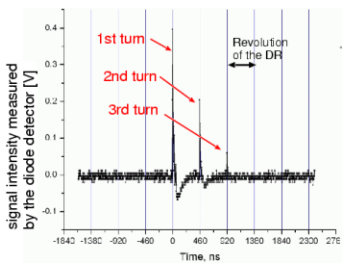

Figure 13: CSR signal in the first few turns in the DR.

Energy spread monitor

The beam energy spread is converted to the beam size at a high dispersion location. There is a screen monitor of phosphor plate at a designed high dispersion region of the extraction line where the horizontal beam size is dominated by the dispersion effect. Energy spread monitor has been a useful tool to measure the strength of the intra-beam scattering (IBS). The larger the energy spread, the stronger the IBS (*i.e.* the smaller the vertical emittance).

BEAM CONTROL

Not only measuring the beam, but also acting on it is important to realize a high quality beam. Works to develop the feedback/feedforward system are underway in the extraction line.

FONT

In order to realize stable beam collision in ILC and stabilization in the virtual IP of ATF2, a beam position feedback/feedforward system has been developing. It consists of a strip-line BPM, a fast BPM processor board, and a strip-line kicker to give a correction on the beam orbit.

FONT3 At the first stage of this experiment in ATF, we developed the system for the multi-bunch beam of 20-bunches train ([11]). Developing a fast analogue BPM processor, a feedback system with small total latency (23 nsec) was realized. It demonstrated stabilizing the beam position of the later part of the train using the measurement in the first part of it (Figure 14).

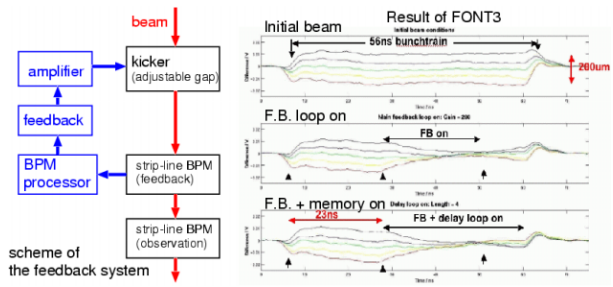

Figure 14: Result of FONT3.

FONT4 Since the bunch spacing specified for ILC is ∼300 nsec, the very fast BPM processor is not necessary. Given time is long enough to design the system with a digital processors which should have more redundancies. A processor board using a Field Programmable Gate Array (FPGA) has been developed for the tests with 3-bunches mode in ATF.

SUMMARY

Development of beam monitors has been an important theme to realize the high quality beam in the ATF. Lots of beam instrumentation works have been done with its international collaboration.

REFERENCES

[1] Y. Honda *et al.*, Phys. Rev. Lett. 92, 054802 (2004).
[2] "ATF2 Proposal", KEK Report 2005-2.
[3] S. Walston *et al.*, Proc. of EPAC06, Edinburgh (2006) p1256.
[4] J-Y. Huang *et al.*, Proc. of APAC07.
[5] H. Sakai *et al.*, Proc. of EPAC06, Edinburgh (2006) p2784.
[6] T. Naito *et al.*, Phys. Rev. ST-AB (2006) 122802.
[7] Y. Honda *et al.*, Nucl. Instr. Meth. A538 (2005) p100.
[8] S. Boogert *et al.*, Proc. of EPAC06, Edinburgh (2006) p738.
[9] H. Hayano, Proc. of Int. Linac Conf., Monterey (2000) p146.
[10] P. Karataev *et al.*, Nucl. Instr. Meth. B227 (2005) p158.
[11] P Burrows *et al.*, Proc. of EPAC06, Edinburgh (2006) p852.

PAPER NOT YET RECEIVED

UPGRADES TO THE ISIS SPALLATION NEUTRON SOURCE

C.R. Prior, CCLRC Rutherford Appleton Laboratory, Chilton, Didcot, Oxon, U.K.

Abstract

With studies of a European Spallation Source (ESS) suspended and high-level discussions taking place over the future of neutrons in Europe, efforts are being made to ensure the sustained success of ISIS well into the foreseeable future. Recent developments include upgrading the injector by replacing the Cockcroft Walton with an RFQ, and installation of a new dual harmonic RF system that should eventually enable up to 50% more protons to be accelerated in the ring. A programme of ion source development also aims at improved reliability, enhanced beam current and longer life-time. This promise of more beam power has led to construction of a second target station providing users with additional experimental facilities starting in October 2008. In the longer term, ideas are forming either for a new high intensity proton driver or for a phased development of ISIS to the 5 MW level. As an alternative to generating neutrons, such a machine might also be part of a neutrino factory, a complex of accelerators generating neutrinos from muon decay. This paper describes these activities and identifies their relative importance on an international development scale.

INTRODUCTION

At the heart of the ISIS facility at the Rutherford Appleton Laboratory (RAL) in the United Kingdom is a set of accelerators that together form an extremely robust, reliable and stable machine. The ISIS source celebrated its twentieth anniversary of neutron production in 2004, and with a proton beam output of 0.16 MW has held the accolade of the world's most powerful pulsed proton source for a number of years. Much high quality research has been carried out, with important developments over a range of topics relating to physical and biological sciences. Operational experience and technological progress have provided valuable guidance for studies towards future accelerator-based neutron sources. ISIS is increasingly seen as a benchmark not only for neutron production but also as a starting point for a high power proton accelerator. Many of the ideas behind its design have had a bearing on the US spallation neutron source (SNS), the Japanese high intensity accelerator facility (J-PARC), and spallation neutron facilities proposed for Europe, China and India.

However ISIS is now an elderly machine. Its purported successor - a new European Spallation source (ESS) [1] - was developed between 1990-2002, and discussions over its construction continue at a high level but no decision has yet been reached. Given the high demand for neutrons in Europe, it is important in the first instance to ensure that ISIS continues to run reliably at its present level. At the same time there is a need to look towards the future. A relatively modest upgrade seems feasible in the medium term, and regardless of whether ESS is or is not built, ways to increase the beam power to at least 1 MW and possibly as high as 5 MW are being explored.

ISIS

The ISIS accelerating system (Figure 1) is based on a 70 MeV H^- linac injecting via an Al_2O_3 stripping foil into an 800 MeV, 50 Hz proton synchrotron. Between 5 and 10% of the injected beam is lost during trapping and initial acceleration. Each pulse consists of two bunches of about 120 ns duration, directed onto a tantalum-clad tungsten target, where a variety of experiments are carried out for condensed matter research.

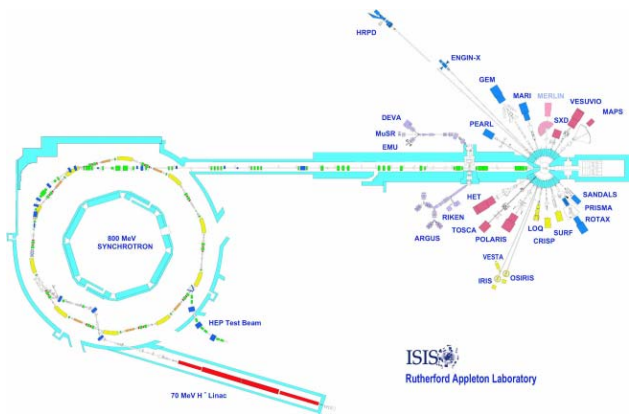

Figure 1: The ISIS Spallation Neutron Source

In its present configuration, the machine is limited by space charge to an intensity of 2.5×10^{13} protons per pulse, but a programme of development aims to increase this by perhaps as much as 50% at relatively modest cost. The key to this was identified in an earlier study [2] and involves a combination of $h = 2$ and $h = 4$ RF cavities. By carefully balancing parameters, stable areas of longitudinal phase space can be increased, allowing more beam to be injected without change in either the peak bunch current or the transverse tune shift. It is important to keep beam loss as small as possible, which is achieved by modulating the peak voltages during the accelerating cycle and controlling the relative phases between the RF harmonics in a specific way The new cavities were installed in

the summer of 2004. At the same time the opportunity was taken to upgrade the 70 MeV linac, parts of which dated back to ISIS's predecessor on the site, the old NIMROD accelerator. The ion source was updated and the ageing Cockcroft-Walton injector was replaced with a radio-frequency quadrupole (RFQ) constructed at the University of Frankfurt. The RFQ operates at 202.5 MHz and delivers H^- micro-bunches at 665 keV. Some initial problems over alignment and the need to optimise the upgraded linear accelerating system have led to standard operation falling in the last two years to around the 140 kW level (180 μA). However machine runs in November 2006 have seen extremely promising performance. With only two of the four $h = 4$ cavities in operation and the $h = 2$ cavities still at the original production settings, over 200 μA of beam current have been accelerated, with 97% transmission, the highest ever achieved. These results suggest that with the full dual harmonic system operating under the theoretical, optimised settings, predicted loss of around 0.5% and beam powers up to 0.24 MW (300 μA) can become a reality.

In order to accommodate the increased power, a second target station (TS2) is being built. It will operate at 10 Hz, taking one pulse in five from the existing 50 Hz target (TS1). TS2 is designed for low beam power, 48 kW, receiving about 60 μA of the ISIS beam current. The cost of the project is in the region of £140 m[1], and construction involved the removal of part of a hill on the western edge of the laboratory. The building was finished in October 2006. In the centre, the monolithic core - a huge steel structure housing a tungsten target 6 cm wide by 30 cm long surrounded by 5.5 m of shielding - is taking shape. The beamline from ISIS is currently being installed and October 2007 should see the first beam on target. The experimental programme is due to start in 2008 and the enhanced cold neutron flux is expected to lead to breakthroughs on next generation materials for super-fast computers, data storage, sensors, pharmaceutical and medical applications, materials processing, catalysis, biotechnology and clean energy technology. An aerial view of the new facility with a schematic layout superimposed is shown in Figure 2.

Figure 2: Aerial view of ISIS showing the new extracted proton beamline and the building for Target Station 2.

GENERIC ACCELERATOR R&D

Ideas for upgrading the facility to the megawatt level stem from work on the ESS and studies in the U.K. for proton drivers for a neutrino factory (NF).[2] High power proton machines for either purpose have to confront design goals well beyond anything ISIS has achieved, most importantly the need at high beam powers and intensities for an extremely low loss system. Elaborate collimation schemes need to be incorporated and special features included, such as fast beam choppers in the low energy stages of the linacs and achromatic arcs in the transfer lines from the linacs to the rings. Choppers are used to create gaps in the linac micro-bunch train so as to enable bunches to be trapped in stable regions of phase space in the accumulator/storage rings. A balance needs to be maintained between many parameters, with trade-offs between, for example, the ring injection period and the linac current. Charge exchange injection is the only practical way of reaching the desired intensities, and, in order to control stripping foil heating, the injection time need to be limited and this means a higher current from the linac.

Front-End Test Stand

Bearing this in mind, among the most challenging R&D aspects are development of an H^- ion source and the fast beam chopper. A long-standing aim at RAL has been the construction of a linac front-end test stand to demonstrate the feasibility of the low energy stages needed for a high power proton facility. This is now being realised. Because of synergies with other projects, parameters are not tied to any one proposal and funding is from a variety of bodies, including the U.K. research councils and the European Union Framework 6 CARE/HIPPI programme. The basic layout of the test-stand, shown in Figure 3, links an H^- ion source, a low energy beam transport system (LEBT), a radio-frequency quadrupole linac (RFQ), a fast beam chopper and transport system (MEBT), and a comprehensive system of diagnostic equipment. Modifications to the ISIS Penning source aim for a current of 60–70 mA, a normalised rms emittance of 0.2 π mm.mrad and a duty cycle of up to 10%. The work is already well on target. A combination of electromagnetic and thermodynamic modelling has provided insight into thermal properties and enabled discharge pulses of up to 1.8 ms to be achieved. Further experimentation has enabled the design current to be

[1] U.K. £1≈ U.S.$2 at January 2007 rates.

[2] A neutrino factory uses a 4-5 MW proton driver to generate a secondary muon beam. The muons are accelerated rapidly and stored before they decay to give intense streams of neutrinos that are directed at distant detectors.

met. Now emittance measurements and studies are underway. Much remains to be done to realise a fully operational, long-lifetime source, but the present design is probably the best of its kind available today.

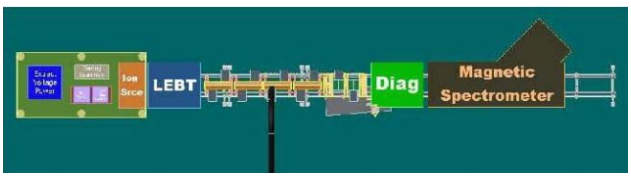

Figure 3: The Front-End Test Stand at RAL

From the ion source, the beam will be matched by a Low Energy Beam Transport system (LEBT), into an RFQ; then bunched and accelerated to 3 MeV. A magnetic LEBT with three solenoids has been identified as preferable to the operating ISIS electrostatic scheme. Design of the FETS RFQ has followed lengthy discussions over the choice of RF frequency. Taking into account global needs and the availability of hardware, a system based on 324 MHz has been chosen. This is the J-PARC frequency, and a 3 MW klystron, developed by Toshiba, has been ordered and recently delivered to RAL. Work is in progress to compare designs of high duty-cycle 324 MHz 4-rod and 4-vane RFQs. The 4-vane model promises a higher Q-value and a much lower RF requirement, and will therefore be the likely choice. A cold model has been manufactured in aluminium to test machineability, and a simple copper structure has been produced to study the brazing process. A bead-pull measuring system has been built to evaluate the field distribution and test readings against theoretical electrodynamic modelling. Parallel beam dynamics simulations, carried out on the RFQ cavity and cold model designs, suggest a transmission as high as 94%.

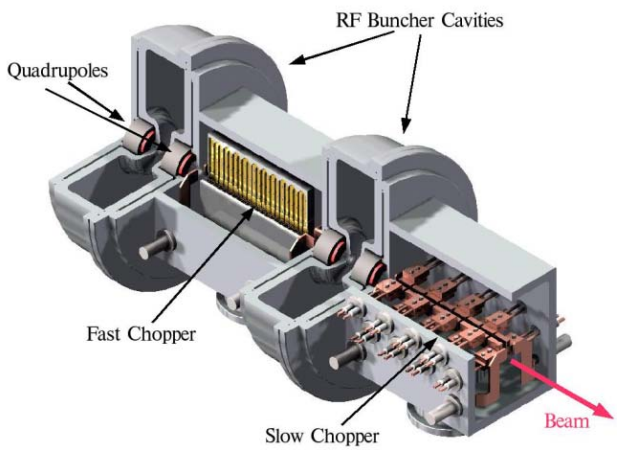

Figure 4: RAL Fast Beam Chopper

The fast beam chopper [3] which follows is one of the most crucial and important components of the structure for successful operation of a robust, low-loss machine. As FETS is seen as a generic accelerator R&D project, it has to show flexibility to meet a variety of needs. The chopper can be required to create gaps in the bunch train from the order of a few to a few hundred nanoseconds. For the ESS, for example, the chopper has to deflect about 72 micro-bunches from every 240 at the ring revolution frequency of 1.24 MHz. Many years of work have crystallised into a combined slow-fast structure. At 324 MHz, the gap between micro-bunches is of the order of 2.5 ns; and a deflecting electric field has to rise within this gap to kick the following bunches cleanly to a beam dump. A fast modular pulser has been developed that achieves < 2 ns rise time with a 15 ns flat top at ± 1.45 kV, which is sufficient to deflect 3-4 microbunches. This creates a longer gap for a slow-rise, long duration field that deflects the rest. A module is shown in Figure 4. The slow pulse generator has reached an amplitude of ± 6.0 kV with a duration of 0.2-100 μs; all specifications have been met apart from the required duty factor.

H^- Linac

The general aim of the EU CARE/HIPPI package [4], which partly funds work on FETS, is to explore accelerating structures for hadrons up to 200 MeV. The motivation is the likely construction of a new linac (Linac4) at CERN and proposals for an 180 MeV linac at RAL [5]. Both designs are similar and a schematic drawing of the U.K. layout is shown in Figure 5. FETS will be used for the front-end; then a drift-tube linac (DTL) will accelerate the beam to 90 MeV at 324 MHz. The DTL has 4 tanks, using one Toshiba klystron per tank. The remainder of the structure has a a triple frequency jump to 972 MHz leading into a side-coupled linac (SCL).

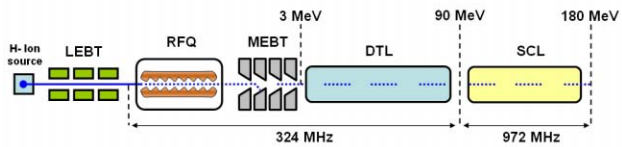

Figure 5: Structure of the 180 MeV H^- linac

The linac stems partly from earlier ESS studies and partly from work on a neutrino factory. The RAL group has designed high intensity proton drivers at energies of 5, 8, 10, 15 and 30 GeV [6], all of which include booster synchrotrons fed from the same linac design. The argument for such a low energy relates to the need for very short proton bunches ($\sim$1 ns) and theory suggests that a small longitudinal emittance is best achieved by accumulating the beam at about 200 MeV. Studies of accelerating structures within HIPPI are therefore an important part of the U.K.'s NF programme as well as of interest for neutron sources.

IDEAS FOR ISIS UPGRADES

By the end of 2007, ISIS should have new and upgraded equipment in place to raise the operating current to 250-

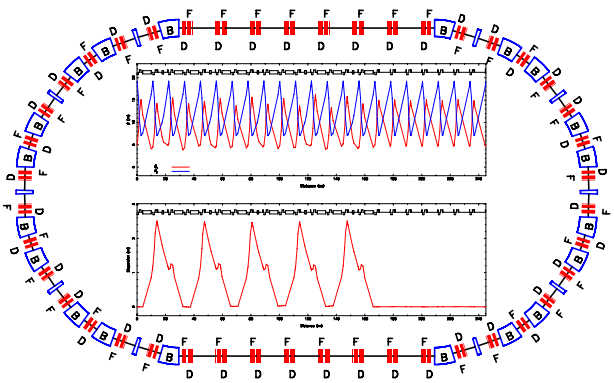

Figure 6: Details of the racetrack synchrotron

300 μA (200-240 kW of beam power). Beyond this, the only practical method of increasing the power of the facility is by raising the energy through the addition of a second ring. A synchrotron with a racetrack lattice structure has been devised with a mean radius of 78 m, three times the 26 m of the present ISIS synchrotron. ISIS's two bunches, each with an intensity of 1.9×10^{13} protons, would go straight into this ring via bucket to bucket transfer at $h = 6$. Accelerating to 3 GeV would provide an approximate four-fold increase in energy and take the beam to the MW level of power.

Details of the ring, including optical parameters and magnetic specifications (see Figure 6), were given in [7]. Using a magnetic dipole field variation of the form

$$B(t) = B_0 - B_1 \cos 2\pi f t + B_2 \sin 4\pi f t, \quad B_2 = \frac{B_1}{4\sqrt{2}}$$

minimises the maximum value of $\dot{B}$ during the cycle and reduces the total RF voltage in the ring by about 30%. With this scheme, at $f = 50$ Hz repetition rate, it takes ~570 kV to take the full ISIS pulse from 0.8 to 3 GeV in just under 12 ms. The final bunches are ~72 ns in duration (compared with the current figure of ~120 ns) with a momentum spread of $\pm 3 \times 10^{-3}$.

The advantages of this approach are that: space charge is reduced at 800 MeV; the present ring gives a well-defined beam and enables fast injection into matched RF buckets; and beam losses should be very low. It also provides many opportunities for further developments to higher beam power.

In this mode of operation, the machine would be used as a a spallation neutron source. However, the possibility exists of operating at $f = 16.7$ Hz and accelerating only one pulse in three from ISIS (the others being discarded) to 8 GeV over 30 ms. The aim would be experimental tests of bunch compression to ~1 ns (rms) for the neutrino factory. Pion target tests could also be undertaken along with investigations of a prototype pion decay/muon capture channel.

Unfortunately, ISIS's existing target, TS1, is limited by its methane moderator to about 0.25 M, so adding a synchrotron would involve the additional expense of a new,

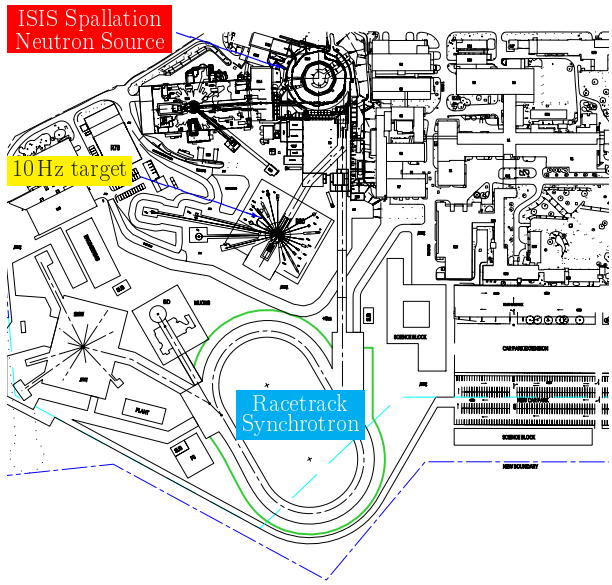

Figure 7: ISIS with the addition of a 3 GeV racetrack synchrotron

third, target. A possible layout, including both a neutron and a muon target, is show in Figure 7. Note that construction would require removal of the rest of the hill that has already been excavated for TS2. The need for a new target for almost any acceptable power upgrade means an underlying cost of at least the £140 m of TS2, and the total would inevitably reach the order of a few hundred million U.K. pounds.

A more modest upgrade, though because of the additional target cost it hardly seems economically worthwhile, would be to replace the existing 70 MeV linac with the new 180 MeV design. At this energy, space charge levels at injection are halved, the number of particles in a bunch could be doubled to about 3.8×10^{13}, and initial studies suggest that the synchrotron could output ~0.4 MW of beam power. The smaller energy sweep in the synchrotrons would also allow the machine to operate at the higher repetition rate of 65 Hz with the same peak dB/dt. This would give about $\frac{1}{2}$ MW beam power.

An alternative way of reaching $\frac{1}{2}$ MW would be to build an additional 800 MeV ring on top of the existing synchrotron in the ISIS tunnel. Injected from the same linac, two additional bunches of $\sim 1.9 \times 10^{13}$ could be accelerated, giving four on target at 50 Hz. Adding the new 180 MeV injector would increase the bunch intensity and take this nearer to 1 MW. However there would be practical difficulties in installing a second ring among the paraphernalia of the first.

For higher beam powers, options are to use the 180 MeV injector and add the 3 GeV synchrotron to ISIS. This would get nearer 2 MW. Nevertheless, only two of the six racetrack buckets would be filled. Building the second 800 MeV ring would double the number of bunches and fill four buckets for up to 4 MW. A higher energy of 4 GeV

could also be conceived to reach a goal of 5 MW, but this target is heavily reliant on success at every step.

The upgrade route identified in [7] uses the racetrack synchrotron but, instead of ISIS, has a new 1.2 GeV booster. This would be detached from ISIS, which could continue in its present form until the new machine came on line. The booster comprises the 180 MeV linac injecting into two stacked rapid cycling synchrotrons (RCS) of mean radius 39 m, operating at 50 Hz and optimised for low loss charge-exchange injection. One ring would be filled immediately after the other, each with three bunches of 1.7×10^{13} protons, and all six bunches would be fed into one of two stacked racetrack synchrotrons operating at 25 Hz. The racetracks would be extracted on alternate half-cycles, restoring the operating repetition rate of 50 Hz on target (Figure 8). The original idea was that this would provide an enhanced neutron source at 3 GeV, but could also be built for 6 GeV at which energy the bunches could be compressed to 1 ns and used as a 5 MW driver for a neutrino factory.

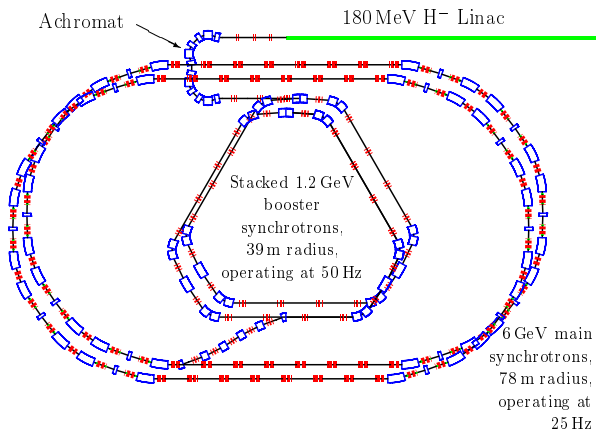

Figure 8: A stand-alone 4-5 MW proton driver

If the (possibly impractical) suggestion of combining neutrons with neutrinos is dropped, a simpler ring, designed specifically for neutrons, could be used. For example, half the beam from ISIS (after the present upgrade and TS2 is operating) could be accelerated in a "neutron optimised" ring (NO) of radius 52 m (twice ISIS's radius) at 25 Hz to 3.5 GeV. This would put $\frac{1}{2}$ MW on a new target (TS3) and 0.12 MW to TS1 and TS2. This could be doubled by adding an 800 MeV storage ring on top of the NO-ring to hold two bunches from ISIS for 20 ms pending arrival of the next two; then four bunches could be accelerated to 3.5 GeV. This would give four bunches on target at 25 Hz. The alternative, to make the storage ring into a second RCS, the two being extracted on alternate half cycles, would give the same beam power with two bunches per pulse at 50 Hz. Further increases could be achieved by using the 180 MeV injector to increase the number of protons per bunch and a second synchrotron in the ISIS tunnel to double the number of bunches, along the lines described above.

Other possibilities are effectively new machines separate from ISIS. For example, the ESS could finally be constructed as detailed in the baseline-design document. Alternatively older ideas based on an 800 MeV linac injecting into a 3.5 GeV RCS could be re-visited. An even older suggestion, driven by the neurtino community and undergoing a revival because of advances in technology, would involve a linac and a fixed-field alternating gradient accelerator (FFAG).

SUMMARY

Many suggestions, with varying degrees of practicality, have been described above for upgrades to the ISIS spallation neutron source. However it should be made clear that there is no formal programme of development beyond the present dual harmonic installation and construction of TS2. The U.K.'s strategy is to support appropriate investment in the existing accelerators, targets and instruments, and to explore in an international context opportunities for a second-generation neutron source for Europe. The U.K. has the potential to build a megawatt-class spallation source through the upgrade of ISIS but has deferred planning of any specific option until the outcome of wider discussions of European plans is known.

ACKNOWLEDGMENT

Grateful acknowledgements are due to members of the ISIS upgrade team, especially C.M. Warsop, who identified a coordinated structure amongst a myriad of ideas.

REFERENCES

[1] The ESS Project Volume III: Technical Report, 2002; http://www.ess-europe.de.

[2] C.R. Prior: "Study of Dual Harmonic Acceleration in ISIS", Proceedings of XIIth International Collaboration on Advanced Neutron Sources, ICANS-XII, Abingdon, U.K., May 1993.

[3] M.A. Clarke-Gayther: "A Fast Chopper for the ESS 2.5 MeV Beam Transport Line", Proceedings of the 8th European Particle Accelerator Conference, EPAC'02, Paris, June 2002.

[4] http://mgt-hippi.web.cern.ch/mgt-hippi/

[5] F. Gerigk: "A New 180 MeV H⁻ Linac for Upgrades of ISIS", Proceedings of the 9th European Particle Accelerator Conference, EPAC'04, Lucerne, Switzerland, July 2004.

[6] C.R. Prior and G.H. Rees: "Synchrotron-based Proton Drivers for a Neutrino Factory", Proceedings of the 7th European Particle Accelerator Conference, EPAC'00, Vienna, June 2000.

[7] C.R. Prior et al: "ISIS Megawatt Upgrade Plans", Proceedings of the US Particle Accelerator Conference, PAC03, Portland, Oregon, May 2003.

CHINA SPALLATION NEUTRON SOURCE DESIGN*

J. Wei†[3,1], S.-X. Fang[1], J. Feng[2], S.-N. Fu[1], H.-F. Ouyang[1], Q. Qin[1], H.-M. Qu[1], J.-Y. Tang[1], F.-W. Wang[2], S. Wang[1], Z.-X. Xu[1], Q.-W. Yan[2], J. Zhang[2], Z. Zhang[2]
for the China Spallation Neutron Source (CSNS) teams
Institute of High Energy Physics, China[1]; Institute of Physics, China[2];
Brookhaven National Laboratory, USA[3]

Abstract

The China Spallation Neutron Source (CSNS) is an accelerator-based high-power project currently in preparation under the direction of the Chinese Academy of Sciences (CAS). The complex is based on an H^- linear accelerator, a rapid cycling proton synchrotron accelerating the beam to 1.6 GeV, a solid tungsten target station, and five initial instruments for spallation neutron applications. The facility will operate at 25 Hz repetition rate with a phase-I beam power of about 120 kW. The major challenge is to build a robust and reliable user's facility with upgrade potential at a fractional of "world standard" cost.

INTRODUCTION

There exist three classes of high-power spallation neutron facilities[1, 2]: continuous-wave (CW) facilities driven by high energy, high intensity cyclotrons or linacs (e.g. the operating SINQ isochronous-cyclotron at PSI with a beam power of 1.2 MW at 590 MeV [3]); long-pulse (ms) facilities driven by high energy, high intensity linacs (e.g. the operated LAMPF proton linac with a beam power of 1 MW at 800 MeV [4] and the PEFP under construction in Korea with a high-duty 100 MeV linac [5]); and short (μs) pulse facilities driven by a combination of high intensity linacs and rings, as shown in Fig. 1 [4, 6, 7, 2]. Among the short-pulse facilities are two types of accelerator layout: a full-energy linac followed by an accumulator (e.g. the operating LANSCE linac and PSR with a beam power of 80 kW at 800 MeV [4] and the SNS project just commissioned at ORNL with a 1 GeV superconducting (SC) RF linac and an accumulator [8]) and a partial-energy linac followed by a rapid cycling synchrotron (RCS) (e.g. the operating ISIS facility at RAL with a beam power of 160 kW from a 70 MeV linac and a 800 MeV synchrotron [9] and the J-PARC under construction in Japan with a 400 MeV linac and 3 GeV and 50 GeV synchrotrons [10]).

CSNS is an accelerator-based short-pulse facility with a partial-energy linac followed by a RCS. CSNS provides a multidisciplinary platform for scientific research and applications by national institutions, universities, and industries [12, 13, 14]. The high-flux pulsed neutrons from CSNS will compliment cw neutrons from nuclear reactors and synchrotron lights from synchrotron radiation facilities. Strongly advocated by the users groups, the CSNS project was approved by the Chinese central government in 2005.

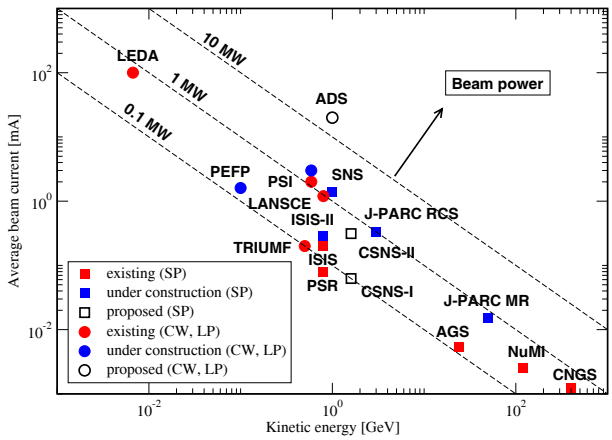

Figure 1: Accelerators at the power frontier (short pulse SP, long pulse LP, continuous wave CW).

As shown in Fig. 1 and Table 1, the CSNS accelerator is designed to deliver a beam power of 120 kW with the upgrade capability of up to 500 kW by raising the linac output energy and increasing the beam intensity.

Table 1: CSNS accelerator primary parameters.

Project Phase	**I**	**II**	**II'**
Beam power on target [kW]	120	240	500
Proton energy on target [GeV]	1.6	1.6	1.6
Average beam current [μA]	76	151	315
Pulse repetition rate [Hz]	25	25	25
Proton per pulse on target [10^{13}]	1.9	3.8	7.8
Pulse length on target [ns]	<400	<400	<400
Linac output energy [MeV]	81	134	230
Ion source/linac length [m]	50	76	86
Linac RF frequency [MHz]	324	324	324
Macropulse ave. current [mA]	15	30	40
Macropulse duty factor [%]	1.1	1.1	1.7
LRBT length [m]	142	116	106
Synchrotron circumference [m]	230.8	230.8	230.8
Ring filling time [ms]	0.42	0.42	0.68
Ring RF frequency [MHz]	1.0-2.4	1.3-2.4	1.6-2.4
Max. uncontr. beam loss [W/m]	1	1	1
Target material	tungsten		
Moderators	H_2O, CH_4, H_2		
Number of spectrometers	5	18	>18

* Work performed under the auspices of the Chinese Academy of Sciences (CAS) and the U.S. Department of Energy.
† weijie@ihep.ac.cn and jwei@bnl.gov

Figure 2: Artist's layout of the CSNS complex.

The CSNS complex operates at a repetition rate of 25 Hz producing spallation neutrons by striking the metal target with proton beams. Initially, the H^- beam is produced from the ion source, and then pre-chopped and transported through the LEBT. The beam is then bunched and accelerated through the RFQ at a RF frequency of 324 MHz. The MEBT accepts the 3 MeV beam from the RFQ, further chops the beam to the ring RF period, and matches the beam to the DTL. At phase I of the project, the DTL accelerates the beam to 81 MeV. The LRBT transport contains empty drift spaces for future addition of linac modules (DTL or superconducting RF) for the linac energy and beam power upgrade. Upon collimation in both the transverse and longitudinal directions in the LRBT, the H^- beam is stripped of the electrons and injected by phase-space painting into the RCS ring. The ring accumulates and then accelerates the proton beam to 1.6 GeV. The beam is extracted in a single turn and delivered to the target through the RTBT transport (Fig. 2, [12]). Upon striking the solid tungsten target, each proton produces 20 to 30 neutrons through spallation process. These neutrons are slowed down to the desired energies through three types of moderators (H_2O, liquid CH_4, and liquid H_2) for neutron scattering experiments.

Financially, the project must fit in China's present economical condition with a cost of about 1.5 billion Chinese Yuan (CNY) (about US$0.2 B). This limits the initial beam power to about 120 kW. On the other hand, we strive to reserve the upgrade potential up to 500 kW so that the facility is competitive in future. Since this is the first high-intensity proton machine in China, we intend to adopt mature technology as much as possible.

The CSNS complex is planned to be built at Dongguan, Guangdong province in southern China. Due to limited initial funding, prototype R&D on key accelerator components is staged in two periods. With the initial funds of about 30 million CNY (about US$4M), we started period-I design, prototyping and testing of some major components of the accelerator system (a section of the DTL tank, two RCS magnets, a set of RCS dipole power supply, a RCS RF cavity, and a set of RCS ceramic vacuum ducts), the target system (target body, moderator and cooling system, decouple and poison), and the instrument system (background chopper, neutron guide, neutron detector). Project construction is expected to start in 2008 for a period of about 5 years.

Among physical, technical, and managerial challenges facing the project, the primary challenges are to complete the project as a first quality, reliable user's facility with a fraction of the "world standard" cost, and to reserve upgrade potential for future developments. To meet these challenges, we must keep the final component fabrication domestic as much as possible taking advantage of the relatively low labor cost, and seek worldwide collaborations for advanced technology.

ACCELERATOR SYSTEMS

The design of the accelerator complex is based on the experience at accelerator facilities including ISIS, PSR, SNS, J-PARC, the BNL AGS/Booster (Fig. 1), and the Beijing Electron Positron Collider (BEPC), and project proposals including the AUSTRON [15] and the ESS [16].

The initial H^- ion source needs to provide 0.5 ms long, 25 mA peak current, $0.2\pi\mu$m emittance ($\epsilon_{N,rms}$) pulses at 25 Hz to 50 keV energy for phase I. Two types of ion sources are considered best candidates for their favorable cost and reliability performance: the ISIS-type Penning surface source [17], and the DESY/modified-SNS-type RF driven source with external antenna [18, 19]. Owing to the kind support from the ISIS, we started to build the ISIS-type H^- Penning source body to be initially tested at ISIS. A pre-chopper in the LEBT is designed to chop the beam macropulse at a 50% ratio at the ring injection revolution period.

Originally, the RF frequency of the linac was 352 MHz based on available cw klystron and waveguide equipment assisted by CERN. However, the pulsed feature of the beam demands a linac RF source of higher peak power for efficiency. The RF frequency for the linac is thus changed to 324 MHz, the same as that of J-PARC so that the same klystron can be used for the RFQ and DTL. This frequency also gives a reasonable room for the EM quadrupole inside the drift tube.

The four-vane RFQ is similar to the one previously developed at IHEP for the Accelerator Driven Sub-critical (ADS) program [20] (Fig. 3). In comparison, the input energy is lowered to 50 keV to ease chopping. Space is reserved in the Medium Energy Beam Transport (MEBT) to house both the secondary chopper and beam halo scraper for phase II and beyond when the beam intensity is higher.

The DTL accelerates the 3 MeV beam from the RFQ to 81 MeV ([21]). Each of the four tanks consumes about the same amount of RF power (cavity RF power of 1.5 MW, total RF power of 2.0 MW). To reach a high effective shunt impedance, we vary the cell shape with β stepwise while keeping the maximum surface field below 1.3 times the Kilpatrick limit. J-PARC type EM quadrupoles made of electroformed hollow coils are used [22].

Five sets of power sources are used to power the RFQ and four DTL tanks. At 324 MHz RF frequency and 2.5 MW peak power, the Toshiba E3740A klystron is one of the candidates [23]. An ac series resonance high-voltage

Figure 3: The 3.5 MeV, ADS RFQ under commissioning at IHEP, China. The first proton beam was injected from the ECR ion source and successfully extracted with a transmission efficiency of about 92% on a proton beam of 43 mA peak current. The beam duty factor reached 6% with beam of 1.2 ms pulse length running at 50 Hz.

power supply is under development for the klystrons avoiding step-up high voltage transformers and multiphase high voltage rectifiers [24].

The Linac to Ring Beam Transport (LRBT) serves several functions [25]. The debuncher located at a distance from the end of linac reduces energy deviation and fluctuation. The 45° bend facilitates momentum collimation of possible beam halo and tail in the longitudinal direction. Three sets of scrapers provide collimation in the transverse directions. Finally, the beam is matched to phase-space parameters for ring injection downstream of the 45° anti-bend. The 45° bends sufficiently isolate the ring from the linac so that construction or maintenance may be performed on the ring while the beam is present in the linac. The bend also provides outlets of the linac beam for future applications.

Fig. 4 shows the layout of the RCS ring. A four-fold symmetric lattice is favored over three-fold to separate injection, collimation, and extraction to different straights. The ring adopts a hybrid lattice with missing-dipole FODO arcs and doublet straights (Fig. 5 [27, 28]). The dispersion is suppressed by using two groups of 3 half-cells (with 90° horizontal phase advance per cell) located on each side of a missing-dipole half-cell [28]. The long (one 9 m and two 6 m uninterrupted drifts per straight) dispersion-free straights facilitate injection [29], extraction [29], and transverse collimation. The FODO arcs allow easy lattice optics correction. The 4 m gap created by the missing dipole near the maximum dispersion location allow efficient longitudinal collimation [28].

The transverse acceptance is $350\pi\mu$m at the collimator and ring extraction channel, and $540\pi\mu$m elsewhere in the ring. The expected space-charge tune spread is about 0.2 for a beam of $320\pi\mu$m emittance. The momentum acceptance in $\Delta p/p$ is $\pm 1\%$ at the longitudinal collimator, and

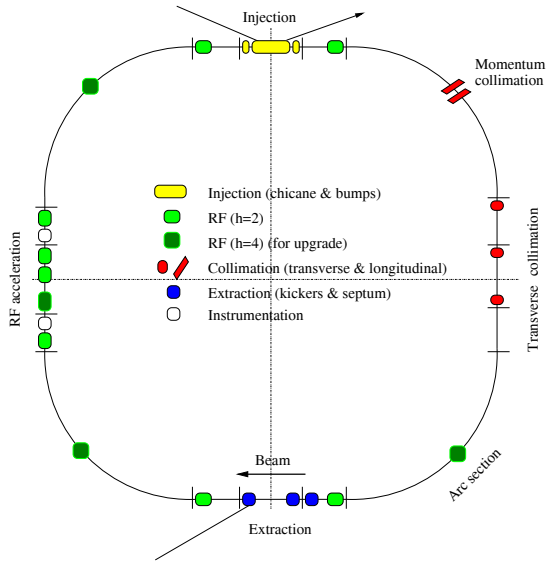

Figure 4: Functional layout of the CSNS RCS ring.

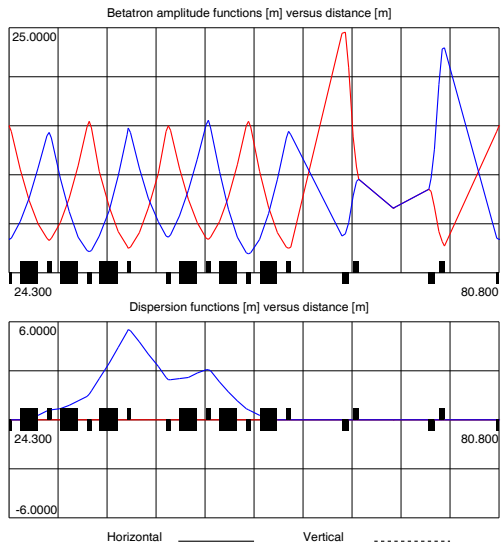

Figure 5: CSNS synchrotron lattice functions in one superperiod. The ring has a periodicity of 4.

$\pm 1.5\%$ elsewhere for a beam of $320\pi\mu$m emittance [30].

The acceleration is performed by 8 RF cavities with maximum total voltage of 165 kV per turn at harmonic $h = 2$. The main dipole field varies from 0.16 to 0.98 T. The bunching factor varies from 0.38 at injection to 0.12 at extraction. Chopping at 50% rate significantly reduces the expected beam loss occurring mostly during initial ramping. Space is reserved to house the second harmonic ($h = 4$) RF cavities to increase the bunching factor allowing a higher total beam intensity (Fig. 4).

The ring contains 24 main dipoles, 48 quadrupoles, 16 sextupoles, 32 trim quadrupoles, 32 multi-coil correctors, and injection and extraction magnets. With a high field (maximum dipole field of 0.98 T) and large aperture (dipole gap height of 178 mm and quadrupole pole radius from 209

to 308 mm) main magnet prototyping is in progress starting with J-PARC type stranded aluminum wires fabricated by domestic vendors. So far, three domestic vendors have successfully fabricated RCS dipole magnet coils made of such wires (Fig. 6). This type of coil will be used for the prototype ring dipole magnet. For the ring quadrupole magnet, we pursue in parallel designs with stranded aluminum wires and with four-piece hollow-conductor copper wires. A comparison will be made to determine the most robust and cost effective quadrupole magnet design.

Figure 6: One of the first prototypes of the J-PARC type stranded magnet coil fabricated by a vendor in China.

The ring main magnets are powered by a family of dipole and 8 families of quadrupole power supplies arranged in parallel groups with multimesh White circuits operating at 25 Hz resonance [31]. The demand for stability and matching is high (THD $<0.02\%$, stability $<0.1\%$). The trim quadrupoles and correctors are expected to play important roles in orbit and tune controls during the ramp cycle [26]. The sextupoles are dc powered for chromatic correction mainly at injection.

The ring RF system uses ferrite-loaded cavities to meet phase I ($h = 2$) requirements [32]. The design gradient is about 10 kV/m. Test stands are set up to measure the ferrite properties under the dynamic ramp cycle.

Ceramic ducts are chosen for the ring vacuum chambers under magnets to alleviate heating and field distortion caused by the eddy current, and to resist the impact of possible high-power beam loss. Both ISIS-type glass joint and J-PARC type metallic brazing are under study to form long, curved, large-bore ducts. Detachable, external metal-stripe wrappings are considered for the RF shielding, and all inner surfaces (ceramic, metal, and ferrite) are to be coated with TiN to reduce secondary electron emission yield [2].

The injection adopts SNS-type scheme with phase-space painting using 4 shift dipoles and 8 painting bump magnets [29, 33]. For simplicity, we consider using dc shift dipoles instead of 25 Hz ac. The beam-dynamics impact of the closed bump with its amplitude reducing with energy ramping is expected to be small. Excessive foil hits are avoided by displacing the orbit from the corner-located foil immediately upon the injection completion using the painting bumps powered by IGBT-based programmable supplies.

The extraction adopts SNS-type single-turn extraction with vertical kicking and horizontal bending. The kicker system consists of lumped, in-vacuum ferrite modules powered by dual PFN charging supplies. The Lambertson-type septum avoids possible damage caused by beam loss on the magnet coil.

For beam diagnostics we plan a suite of instruments similar to those of SNS, starting with allocating space and specifying accelerator-physics requirements. For accelerator controls, machine protection, and commissioning applications we build from the experience of BEPC/BEPCII and SNS projects (adopting EPICS, XAL, PSI/PSC control, static and dynamic databases, etc.).

TARGET SYSTEMS

With a design beam power of about 200 kW, CSNS uses a heavy water-cooled tungsten plat target surrounded by a beryllium-iron reflector, three wing-moderators (decoupled water at the room temperature, coupled hydrogen at 20 K and decoupled-poisoned methane at 100 K), bulk shields and neutron-scattering facilities, as shown in Fig. 7 [35]. Proton pulses from the accelerator impinge on the target, and the resulting spallation process produces large quantities of fast neutrons. The moderators slow these neutrons down to energies suitable for neutron scattering. 18 ports with vertical steel shutters are designed in the iron-heavy-concrete shielding passing neutrons for the instruments. A trolley system is designed to move the target vessel out of the main shielding for maintenance.

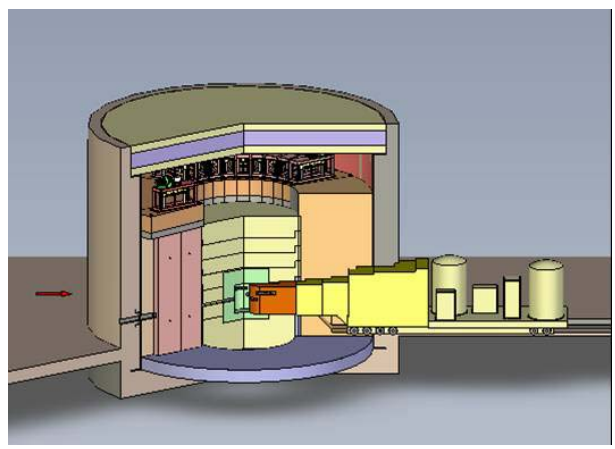

Figure 7: CSNS target station layout.

Tungsten is a proven target material for a facility with beam power of 100 to 200 kW. However, cladding with tantalum is necessary due to material brittleness caused by radiation damage and corrosion by heavy water coolant. Cladding using hot isostatic press and plasma spraying methods are attempted. Meanwhile, we study tungsten-rhenium alloy as alternative target material. Such alloy still has high charge state and mass density to provide a high neutron flux, and yet is expected to be resistant to radiation and thermal damage [36].

INSTRUMENT SYSTEMS

As shown in Fig. 8, so far 17 neutron scattering instruments are selected according to user demands and mod-

erator specifications: 6 powder neutron diffractometers, a single crystal diffractometer, a small angle neutron scattering diffractometer, two reflectometers, three direct geometry inelastic neutron scattering spectrometers, and four reversal geometry inelastic neutron scattering spectrometers [37]. The remaining beam line from liquid hydrogen moderator is reserved for basic neutron physics and/or neutron radiography. Among these 18 instruments, five day-one instruments are supported by the limited project funds: a high intensity diffractometer, a high resolution diffractometer, a broad Q-range small angle diffractometer, a multi-purpose reflectometer, and a direct geometric inelastic spectrometer.

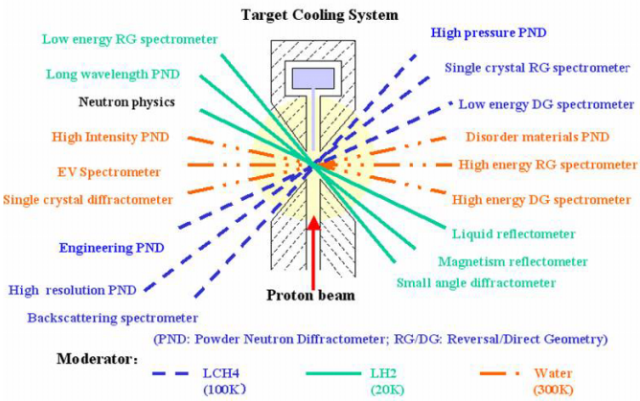

Figure 8: CSNS instrument layout.

FUTURE OUTLOOK

The CSNS is designed to provide beam power up to 500 kW in phased stages capable of supporting one or more target stations. Power upgrade depends crucially on maintaining low uncontrolled beam loss. The upgrade beyond phase I will mainly be realized by raising the linac energy to allow a higher beam intensity under the same ring space-charge limit, and by adding the second harmonic RF to increase the bunching factor in the ring.

It is possible for CSNS to serve multiple purposes including serving as a test facility for the ADS (ADTF). Fig. 9 shows a possible layout with ADTF receiving test beams from the CSNS linac, CSNS ring, and a dedicated high-duty linac. Extension of the linac provides higher power, while extension of the ring yields higher energies.

We thank colleagues and friends around the world for their generous help on the CSNS project.

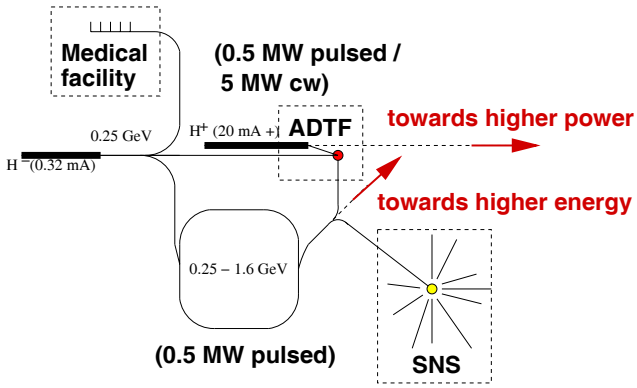

Figure 9: Possible CSNS upgrades towards higher power, higher energy, and multipurpose.

REFERENCES

[1] *Handbook of Accelerator Physics and Engineering*, ed. A. Chao and M. Tigner (World Scientific, Singapore, 2006)
[2] J. Wei, Rev. Mod. Phys. **75** (2003) 1383; J. Wei et al, PRST-AB, **3** (1999) 080101
[3] G.S. Bauer et al, PAC (1997) 3785
[4] ICANS XII (1993), RAL Proc. 94-025; ICANS XIII (1995), PSI Proc. 95-02
[5] B.-H. Choi, APAC (2004) 231
[6] G.H. Rees, PAC (1993) 731
[7] P. Bryant, PAC (1995) 322
[8] N. Holtkamp, EPAC (2006) 29
[9] I.S.K. Gardner, EPAC (1994) 3
[10] JAERI-Tech 2003-044, KEK Report 2002-13 (2003)
[11] I.S.K. Gardner et al, PAC 97 (1997) 988
[12] IHEP Report IHEP-CSNS-Report/2004-01E (2004)
[13] S.-X. Fang et al, J. Korean Phys. Soc. **48**(4) (2006) S697
[14] J. Zhang, Q.W. Yan, C. Zhuang et al, J. Neutron Research 13, 11 (2005)
[15] P.J. Bryant, et al. eds., *AUSTRON Feasibility Study* (1994)
[16] *The European Spallation Source Project Technical Report* (ESS Council, 2002)
[17] R. Sidlow et al, EPAC (1996) THP084L; G.E. Derevyankin, V.G. Dudnikov, AIP Conf. Proc. No. 111 (New York, 1984) 376; D.C. Faircloth et al, PAC (2005) 1910
[18] J. Peters, LINAC (1996) 199
[19] R. Keller et al, PAC (2001) 70; R.F. Welton et al, PAC (2005) 472
[20] S.-N. Fu et al, J. Korean Phys. Soc. **48**(4) (2006) S806
[21] S. Fu et al, LINAC (2006, to be published)
[22] H. Ino et al, LINAC (2000) 1015; K. Yoshino et al, LINAC (2000) 569; F. Naito et al, LINAC (2002) 361
[23] Toshiba Elec. Tubes Dev. Co. Ltd., www.toshiba-tetd.co.jp
[24] J. Li, Z. Zhang, et al, CSNS Tech. note (2006)
[25] J.-Y. Tang et al, EPAC (2006) 1780
[26] C.M. Warsop, AIP Conf. Proc. 448 (New York, 1998) 104
[27] S. Wang et al, EPAC (2006) 1996
[28] J. Wei et al, EPAC (2006) 2074
[29] J.-Y. Tang et al, EPAC (2006) 1783; 1777
[30] N. Wang, Q. Qin, these proceedings
[31] X. Qi, Ph. D. dissertation, IHEP, CAS (2006)
[32] H. Sun, W.L. Huang, et al, Tech. note BSNS/ACC-RR-343-01 (2006)
[33] J. Qiu et al, EPAC (2006) 1774
[34] L. Young, PAC (1993) 3136
[35] Q.W. Yan, W. Yin, B.L. Yu, ICANS (2003) 25
[36] X.J. Jia, Q.W. Yan, 8th Intern. Workshop on Spallation Materials and Technology (2006, Taos, NM, USA)
[37] F.W. Wang, P.L. Zhang, Q.W. Yan, ICANS (2003) 345; F. W. Wang, et al., ICANS (2005) 968

HIGH POWER PROTON ACCELERATOR IN KOREA*

Byung-Ho Choi, Jun Yeon Kim, Kye Ryung Kim, Hyeok-Jung Kwon, Ji-Ho Jang, Kui Young Kim, Jae Won Park, Sun An, Byungchul Chung, Yong Young Lee and Yong-Sub Cho#
PEFP, Korea Atomic Energy Research Institute
P.O.Box 105, Yueong, Daejeon 305-353, Republic of Korea

Abstract

A high power proton accelerator project, Proton Engineering Frontier Project (PEFP), as one of the 21C Frontier Projects promoted by Korean Government, has the goals to develop a 100 MeV high current proton linear accelerator and the user programs for its beam utilization and industrial applications. The upstream part of the 100 MeV linac, the 20 MeV linac, was successfully developed and tested. The rest part of the accelerator and beam lines and user facilities are under development, and also the site preparation and construction works are in progress. In parallel, proton beam utilizations and accelerator application technologies have been extensively studied and developed. In this paper, the status and the future plan of the project, including beam test results of the 20 MeV linac, site preparation and construction works, and development of proton beam utilization and user program are presented.

INTRODUCTION

A high-power proton accelerator (HPPA) can produce intense beams of protons and secondary particles, such as neutrons, radioisotopes, mesons, and neutrinos. Such intense beams provide us with the practical and efficient means to realize quantum engineering. High-current proton beams with low energy (< 10 MeV) are useful in industrial and defense applications, such as ion-cutting, power semiconductors, mine detection, boron neutron capture therapy, and neutron radiography. Low-current proton beams with moderate energy (10–250 MeV) are valuable in biological and medical researches and applications, for example, mutations of plants and micro-organisms, proton and neutron therapy, and radioisotope production. High-power proton beams with energies around 1 GeV are widely utilized in spallation neutron sources, radioisotope beam facilities, nuclear and high-energy physics experiments, and accelerator-driven systems.

The PEFP was launched by the Korean government in 2002 to realize potential applications of the intense proton beams. Its primary goal in the first stage is to develop a high-current proton linear accelerator to supply 100 MeV, 20 mA proton beams and to construct beam line facilities, with which the users can access the proton beams with wide ranges of energies and currents for their research and development programs [1]. In addition, the PEFP accelerator can be exploited as a proton driver for various applications in the low- to medium-energy range, or an injector for a high-energy proton machine in the next stage of development.

* This work was supported by the 21C Frontier R&D program in Ministry of Science and Technology (MOST) of the Korean Government.
# choys@kaeri.re.kr

ACCELERATOR DEVELOPMENT

We have successfully developed a 20 MeV proton linac in the first phase of the project, which consists of a 50 keV proton injector, a 3 MeV RFQ, and a 20 MeV drift tube linac (DTL). In the second phase, we will develop the high energy part of the PEFP 100 MeV linac and beam line facilities which supply the users with the low and medium energy proton beams. Two user facilities are to be installed to utilize the 20 MeV and 100 MeV proton beams at the end of the 20 MeV and 100 MeV accelerating structures, respectively. The schematics of the PEFP linac and beam line facilities are illustrated in Fig. 1. Some characteristic parameters of the accelerator are given in Table 1 [2].

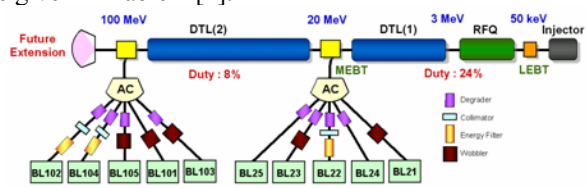

Figure 1: Schematics of the PEFP 100 MeV linac and beam line facilities.

Table 1: Characteristics of the PEFP accelerator.

Energy (MeV)	20	100
Energy spread (%)	< 1%	< 1%
Peak current (mA)	1~20	1~20
Max. beam duty (%)	24	8
Average beam current (mA)	0.1~4.8	0.1~1.6
Pulse width (ms)	0.1~2	0.1~1.33
Max. repetition rate (Hz)	120	60
Max. beam power (kW)	96	160

The injector consists of a duoplasmatron H^+ ion source and a low-energy beam transport (LEBT). The extracted beam current from the source reached up to 50 mA at a voltage of 50 kV. The extracted beam has the normalized emittance of 0.2 π mm-mrad with the proton fraction more than 80%. To achieve a pulsed operation, a high-voltage switch is installed, of which rising and falling times are less than 50 ns, respectively [3]. The LEBT consists of two solenoid magnets, which focus the protons and filter the H_2^+ ions, and two steering magnets which control the beam position at the entrance of the RFQ.

The PEFP RFQ is designed to accelerate the proton beam from 50 keV to 3 MeV with the 4 vane structure [4]. The entire structure is separated into two segments which are resonantly coupled for the field stabilization. The RF power is fed into the cavity through two iris couplers in the third section. Some design specifications of the PEFP RFQ are summarized in Table 2.

Table 2: Characteristics of the PEFP 3 MeV RFQ.

Frequency	350 MHz
Input / Output energy	50 keV / 3 MeV
Transmission rate	98.3 %
Length	326.64 cm
Peak surface field	1.8 Kilpatrick
Output emittance (normalized rms)	0.22 π mm-mrad 0.11 π deg-MeV
Type	4-vane type resonant coupling

Figure 2: The PEFP 3 MeV RFQ.

The PEFP RFQ (see Fig. 2) was successfully fabricated and tuned. The high-power RF test shows that the stable power level reaches about 440 kW, 110% of the required level after baking its RF window and modifying the power coupler. Figure 3 shows a beam test result with the peak current of 3 mA, measured by a current transformer at the RFQ exit. The transmission rate was measured to be more than 98%.

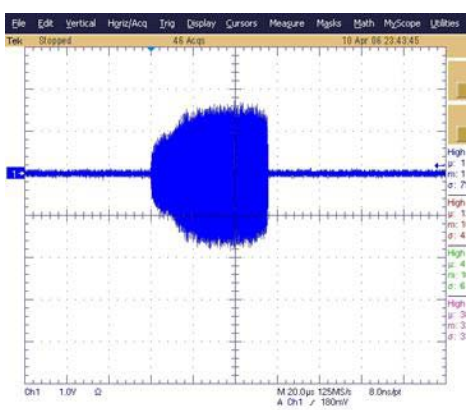

Figure 3: The output beam current of the PEFP RFQ. The horizontal scale is 1 μs/div. and the vertical is 2 mA/div.

Figure 4:The PEFP 20 MeV DTL.

The PEFP 20 MeV DTL, shown in Fig. 4, consisting of four tanks, is designed and fabricated to accelerate the proton beam from 3 MeV to 20 MeV with the maximum peak current of 20 mA and the maximum duty of 24% to meet the user demands. One of its unique design features is that a klystron supplies the RF power into the four tanks to efficiently utilize a 1 MW CW klystron [5]. The RF system for the 20 MeV DTL, including a klystron, circulator, and power dividers, was constructed and tested. The klystron was tested up to 600 kW power. Figure 5 shows a beam test result with 1 mA peak current measured by the current transformers at the entrance and the exit of the 20 MeV DTL. The beam transmission rate was measured to be nearly 100% [6].

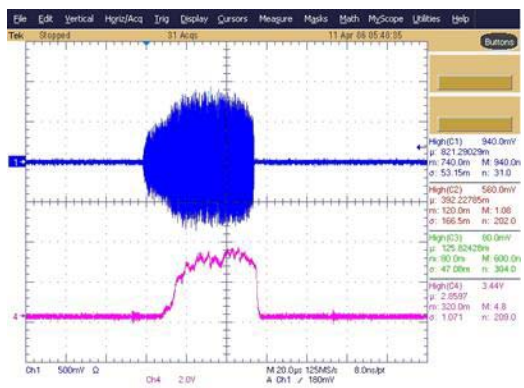

Figure 5: The beam currents measured at the entrance (upper plot) and the exit (bottom plot) of the 20 MeV DTL. The vertical scale is 0.5 mA/div. and the horizontal is 20 μs/div.).

By far, we have performed a limited beam test with low beam currents and short pulses simply because of the inadequate radiation shielding environment. We are planning to perform the full power test, and measure the energy and the emittance of the output beam as soon as the national radiation safety authority licenses the full power operation.

We have redesigned the high energy part of the PEFP 100 MeV accelerator by reducing the maximum beam duty to 8% from 24% in consideration of the user demands. Therefore, the PEFP 100 MeV accelerator has

two largely different DTL structures and operation conditions: the low energy part (up to 20 MeV) is called as DTL-1 and the high energy part covering from 20 MeV to 100 MeV is called DTL-2. Table 3 compares the design specifications of DTL-1 and DTL-2. The noticeable differences are the accelerating field gradients, electromagnet types, RF operation modes, and RF system configurations. The fabrication of DTL-2 tanks is in progress [6]. The design of electromagnetic quadrupole magnet using a hollow conducting copper coil is completed and prototyping is in progress.

Table 3: Specifications of the PEFP DTL-1 and DTL-2.

Parameters	DTL-1	DTL-2
Resonant frequency	350 MHz	
Klystron operation	DC	Pulse
Beam operation	Pulse	Pulse
Max. peak current	20 mA	
Max. pulse width	2 ms	1.33 ms
Max. repetition rate	120 Hz	60 Hz
Max. beam duty	24%	8%
Max. average current	4.8 mA	1.6 mA

BEAM LINES AND USER FACILITIES

One of the important goals of the project is to develop the beam lines and user facilities. To meet the user demands as much as possible, the PEFP focuses on efficient utilizations of the proton beams, to supply various protons with different conditions, to provide multi-users with the plenty of protons, and to achieve cheaper proton beams compared to other facilities such as cyclotrons and synchrotrons.

In order to provide wide ranges of beam energies, currents and beam time, it is essential to extract a low energy beam of 20 MeV and a medium energy beam of 100 MeV, and to distribute the beams to the multi beam lines simultaneously. Figure 6 shows the schematics of the PEFP 20 MeV beam lines and user facilities, in which the proton beams are extracted by using a 45° bending magnets and transported through a common beam line up to a beam distribution system with a programmable AC magnet which distributes the proton beams into maximum five individual beam lines. The 100 MeV beam lines and user facilities have the similar structure. Each beam line has a degrading and filtering system to control beam energy, a collimator to control flux, and a scanning system to make a uniform irradiation possible for large area applications.

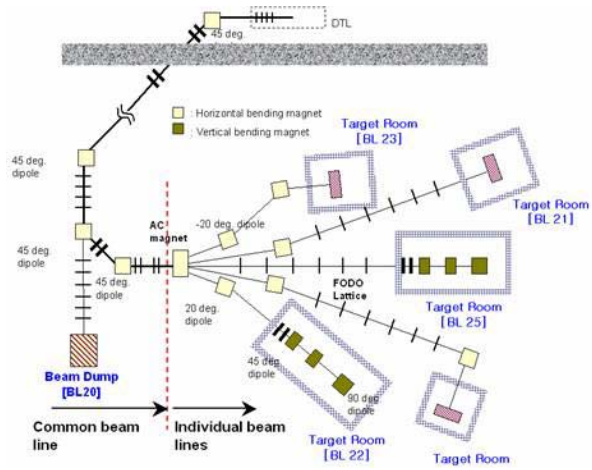

Figure 6: The PEFP 20 MeV beam line facility.

Implementing the 20 MeV beam extraction magnet requires relatively large space between the DTL-1 and DTL-2, which raise the beam matching issue between them. To resolve the problem, we implement a medium energy beam transport (MEBT) system with two small buncher cavities between which the beam extraction magnet is placed. Each cavity has three cells with four quadrupole magnets [7]. The quadrupole magnets in the cavity are used for transverse matching and RF for the longitudinal matching between the DTL-1 and DTL-2. Figure 7 shows the schematic plot of the MEBT and the matching calculated by TRACE-3D [8].

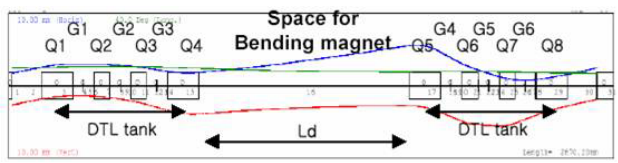

Figure 7: Beam matching in the PEFP MEBT system.

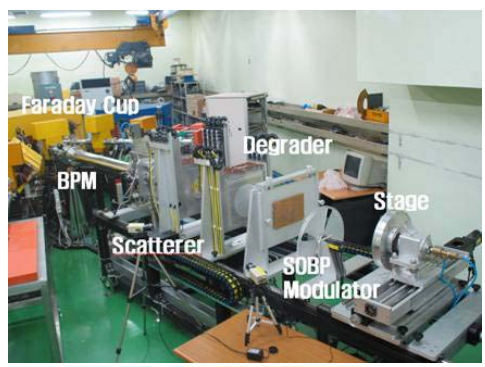

Figure 8: 45 MeV proton beam line at KIRAMS.

To support on-going user programs, and to develop and test the beam line components, a test beam line has been developed and installed in the MC-50 cyclotron located at KIRAMS as shown in Fig. 8. The test beam line currently supports a wide range of user programs.

CONSTRUCTION WORKS

The project host site was selected, in January 2006, to be *Gyeongju* city located in the south-eastern part of Korea. Since then, detailed geological surveys of the site and site plan have been completed. Based upon these, facility layout, site improvement and access road are under engineering.

General arrangements of the accelerator and beam application buildings are completed along with setting up interface requirements for utility design of conventional facilities as shown in Figure 9. The architectural works of conventional facilities are under way.

Figure 9: Bird's eye view of the PEFP research center.

This work is to build up facilities to supply the research center with electric power, water and other kinds of utilities from outward sources. Gyeongju local government is planning for this in cooperation with the PEFP. The construction schedule of the PEFP research center is given in Figure 10.

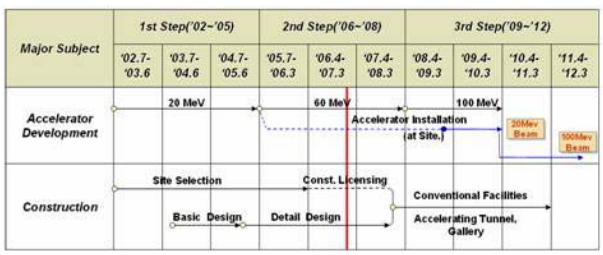

Figure 10: Projected construction schedule of the accelerator center.

THE USER PROGRAMS

The PEFP has supported its user programs to develop new research fields using proton beams, to promote basic researches on proton beam utilization, to reflect the user demands of the PEFP facility design, and to expand the beam user community in Korea. The PEFP user program supports five subprograms in the study and development of utilization and applications of the proton beams at low and medium energies using the available domestic and foreign proton facilities in the U.S.A., Japan, and EU. Under the programs, there are 23 basic research projects using proton or neutron beams in the wide range of leading research fields as summarized in Table 4.

Some of the user programs have produced promising results. One useful industrial application of low-energy proton beams is to produce power semiconductors with fast switching characteristics through charge carrier lifetime control. This can be realized by proton beam irradiation of the p-n junctions of power semiconductors. After proton beam irradiation, the switching speed of a fast recovery diode improves by more than five times.

Table 4: Active research fields by using proton beams.

Nano-technology	Ion-cutting, Nano-particle shaping & fabrication, Carbon nano-tube, Nano-machining
Bio-technology	Mutations of plants, Mutations of micro-organisms
Space-technology	Radiation hard electronic device, Radiation effect on materials
Information technology	High power semiconductor, Semiconductor manufacturing R&D, Proton beam lithography
Medical research	Low energy proton therapy, Biological radiation effects, New RI production R&D
Material science	Proton irradiation effects, Gemstone coloring
Nuclear & particle physics	Detector R&D, Nuclear data

Proton beams are useful for cutting hard materials into thin films on the nanoscale. When a constant energy proton beam is irradiated onto a silicon wafer, they penetrate the silicon wafer and are deposited within a certain range, creating a weak layer in silicon which can be easily split into a very thin film. This can be an effective method to fabricate silicon-on-insulator wafers.

The structure of DNA can be changed by the proton beam irradiation through energy transfer processes. New genetic resources can be formed by such mutations. Two application studies are under way: one is concerned with the mutation of plants, such as vegetables and flowers, and the other with of micro-organisms, such as escherichia coli for producing plastics, such as polyhydroxybutyrate.

Protons beams of moderate energy can reproduce the radiation environment in space and then are used to study the radiation effects on silicon-based electronic device and materials of a spacecraft. We have several projects investigating the radiation effects on the silicon-based electronic components. A project recently discovered a very interesting property of CNT-based transistor via proton irradiation experiments, which shows a consistent radiation harness of the CNT under wildly varying the radiation conditions [9]. Recently, a user program discovered a key mechanism of the ferromagnetism of graphite by irradiating high energy proton beams [10].

Proton beam irradiation and subsequent annealing modify the optical properties of gemstones, such as diamond and ruby; for examples, such processing changed the diamond color from white to purple and

decolorized ruby by probably interacting the impurities and the defects.

THE EXTENSION PLANS

We are drawing a post-PEFP plan to extend the accelerator capability and its utilization scopes in reflection of user demands and future trends of HPPA. Active research fields in Korea, which require a HPPA, are nuclear and high-energy physics facility, spallation neutron source, radioisotopes and medical research facility, accelerator driven system research facility, etc. As an option study, we have focused on radioisotope production and medical research facility, and spallation neutron source.

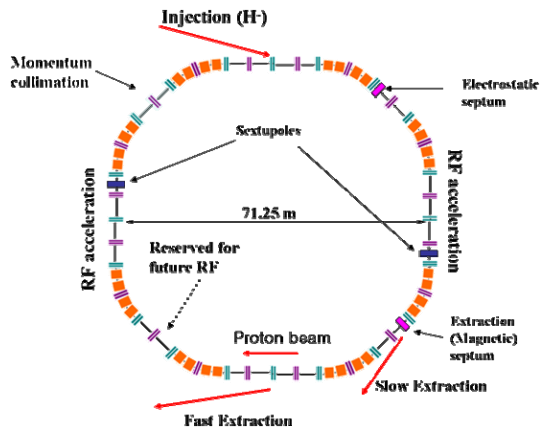

Figure 11: Conceptual design of the proposed RCS.

Table 5: Proposed machine parameters

Rapid cycling synchrotron	
Beam power	44-800 kW
Injection energy	0.1-0.2 GeV
Extraction energy	1-2 GeV
Repetition rate	15-60 Hz
Injector	
Beam energy	100-200 MeV
Beam current	20-40 mA
Duty	8-10 %

A rapid cycling synchrotron (RCS) with the extraction energy 1-2 GeV and injection energy 0.1-0.2 GeV would be an optimal machine to support both the spallation neutron source and radioisotope production and medical research facility. We have designed an RCS, as shown in Fig. 11, with some parameters summarized Table 5. The proposed machine has unique features of the fast extraction for the spallation neutron source application and the slow extraction for the radioisotope productions and medical applications. In addition, the RCS is designed to have upgrade option of the beam power from 44 kW to 800 kW step by step. A superconducting cavity linac is considered as an option for the high energy part of the 200 MeV injector of the RCS [11].

CONCLUSIONS

The PEFP launched by the Korean government in 2002 has the goals to develop a 100 MeV proton linear accelerator and the user programs to utilize the proton beams. A 20 MeV linac, the upstream part of the PEFP 100 MeV proton linac, has been successfully developed and integrated, including its low level RF control and beam diagnostic systems. The high energy part the accelerator, beam lines and user facilities are under development.

The site preparation and construction works are in progress in cooperation with the local government of Gyeongju city to start the ground-breaking and construction in 2007. The design of the accelerator building and conventional facilities are under way.

In parallel, the PEFP user program supports 23 projects to foster and widen the proton beam utilization and application. A beam line facility with a 50 MeV cyclotron at KIRAMS was set up to support the on-going user programs. Some of the user programs have produced promising results which show a great potential of utilizations and applications with proton beam irradiation.

REFERENCES

[1] Byung-Ho Choi, Kye Ryung Kim, Jun Yeon Kim and Yong-Sub Cho, J. of Biomedical Nanotechnology, 2 (2006) 94.
[2] Yong-Sub Cho, *et al.*, "100 MeV High-Duty-Factor Proton Linac Development at KAERI," LINAC'06, Knoxville, to be published.
[3] Yong-Sub Cho and Kui Young Kim, J. Korean Phys. Soc. 48 (2006) 721.
[4] Hyeok-Jung Kwon, *et al.*, "Characteristics of the PEFP 3 MeV RFQ," EPAC'06, Edinburgh, 2006, p.1334.
[5] Han-Sung Kim, *et al.*, "RF Characteristics of the PEFP DTL," EPAC'06, Edinburgh, 2006, p.1331.
[6] Hyeok-Jung Kwon, *et al.*, "Test results of the PEFP 20 MeV Proton Accelerator," LINAC'06, Knoxville, to be published.
[7] Ji-Ho Jang, *et al.*, "Design of the PEFP MEBT," PAC'04, Knoxville, Tennessee, USA 2004.
[8] K.R. Crandall and D.P. Rusthoi, "TRACE 3-D Documentation," LA-UR-97-886.
[9] Woong-Ki Lee, *et al.*, Nanotechnology, 17 (2006) 5675.
[10] Kyu Won Lee and Cheol Eui Lee, Phys. Rev. Lett., 97 (2006) 137206.
[11] Sun An, Y. S. Cho and B. H. Choi, "Design of the PEFP Low Beta Cryomodule", APAC2007, Indore, India, 2007

SUPERCONDUCTING CYCLOTRON PROJECT AT VECC

Rakesh Kumar Bhandari (for the VECC Staff)
Variable Energy Cyclotron Centre, I/AF Bidhan Nagar, Kolkata-700 064, India

Abstract

Construction of the K-500 superconducting cyclotron at Kolkata is now in final stages. The main magnet was operated satisfactorily for almost one year during 2005-2006. The coil was continuously kept cooled at 4.5K temperature during the entire period. Extensive magnetic field measurements were done for correction of the imperfections, centering of the main coil, calculation of operational settings, calculation of extraction trajectory etc. Subsequently, in April 2006 the coil has been warmed up to facilitate assembly of other systems of the machine. All major systems have been fabricated and the assembly is currently going on. We plan to start the commissioning tests later in the year 2007. In this paper our experience with the operation of the main superconducting magnet and magnetic field measurements will be discussed. Developmental highlights of various systems will be briefly presented.

INTRODUCTION

The main magnet of the superconducting cyclotron is designed to operate at about 800A current in each α as well as β coil producing a maximum of about 6T magnetic field [1]. The main magnet iron structure, weighing about 80 tonnes, along with superconducting coil and cryostat had been installed at the new cyclotron building in later part of 2004. The liquid He plant, cryogenic delivery system, power supplies and the control systems were successfully commissioned. The magnet was cooled down to liquid He temperature and energised first time in the early 2005.

In the subsequent months, the magnet was operated satisfactorily for almost one year. The coil was continuously kept cooled at 4.5 K temperature during the entire period. Extensive magnetic field measurements were done for correction of the manufacturing defects and assembly errors in the iron structure, centering of the main coil, calculation of operational settings, calculation of extraction trajectory etc. After completion of magnetic field measurement activity in April 2006, the coil was warmed up to facilitate assembly of the RF system and other major systems of the machine. All major components of the RF system have been fabricated and the assembly work is currently going on. The installation of ECR ion source has been started. Installation work of injection beam line has also started.

INSTALLATION AND COMMISSIONING OF DIFFERENT SYSTEMS

The superconducting magnet along with cryogenic delivery system (fig. 1) and other related subsystems was installed by early 2005 [1]. The low carbon iron frame and the annular cryostat, housing Nb-Ti superconducting coil, were assembled and aligned concentrically. The coil is suspended inside the cryostat by nine glass epoxy support links - 6 vertical and 3 radial. The tensile forces on the support links are monitored by strain-gauged-studs. The 200W (at 4.5K) helium refrigerator/liquefier had already been installed alongside the cyclotron building. The transfer lines along with valves, manifolds and sensors have been installed connecting the cold box and nitrogen delivery system to the cryostat. The control system based on industrial PLC and HMI software was commissioned. A turbo-molecular pump, backed by scroll pump, maintains ~10^{-6} mbar pressure in the cryostat outer vacuum chamber. Two 1000A, 20V power supplies with 10-ppm stability for the main coil along with dump resistors and control software have been installed. The magnetic field measurement setup that uses optical encoders for accurate position measurement and stepper and smart motor driver for the search coil was also installed and tested thoroughly.

Figure 1: Main magnet with cryogenic delivery system.

Cooling of the Coil and Cryostat

The moisture level in the liquid helium chamber was reduced below 10 ppm, before starting the cool down process, by repetitive evacuation and purging with pure helium gas and heating the coil with 5A current. Then the temperature was brought down by sending cold helium gas from the plant to the cryostat. Initially, the liquid nitrogen flow to the radiation shield was not available. Still the liquid helium plant was capable enough to cool

the coil to 4.5K and to immerse it with liquid helium (fig. 2). Subsequently, the liquid nitrogen flow to the shield was provided. Some leaks were detected on the current lead bellows during cooling down and those were fixed.

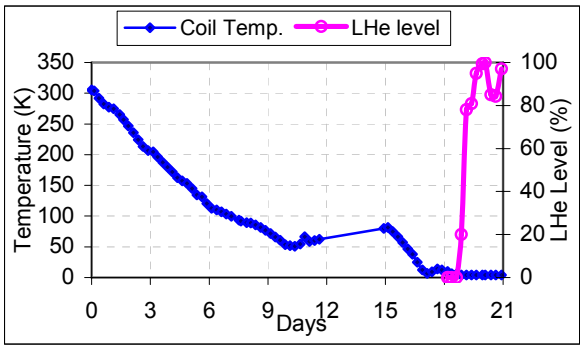

Figure 2: Coil temperature and liquid He level vs. time during the cool down.

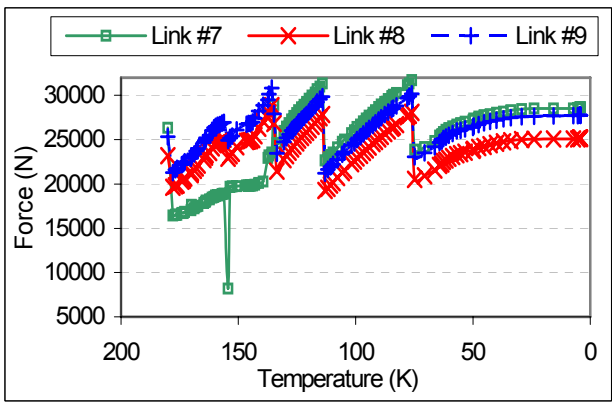

Figure 3: Radial support link forces during cool down.

During the cool down, the radial support link forces were adjusted to keep the forces within safe limits. At 154.4K temperature, the safety nut of the link #7 happened to share the entire load instead of the strain gauge stud due to a human error. This is indicated as a sharp dip in fig. 3. Liquid He boil-off measurement was carried out to find out the cryostat heat load (≈23W).

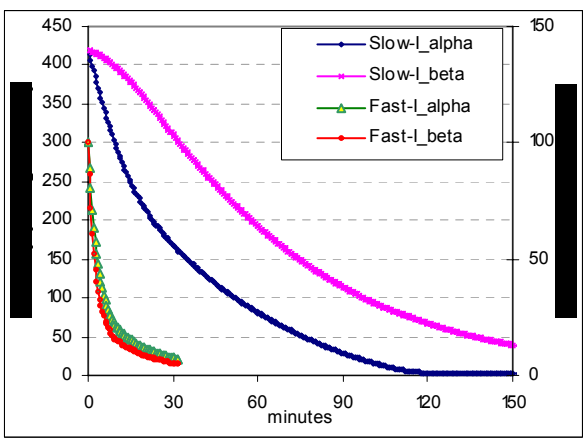

Figure 4: Slow-dump and fast-dump decay curves.

Magnet Excitation

After stabilizing the required liquid helium level in the cryostat for a couple of weeks, the magnet excitation was initiated. All the safety interlock systems were tested by forcing the coil current decay through slow and fast dump resistors (fig. 4). Several iterations were required for coil the centering process and adjustment of plant parameters before reaching 550A current and 4.8T magnetic field at 33 cm radius in the hill region (fig. 5).

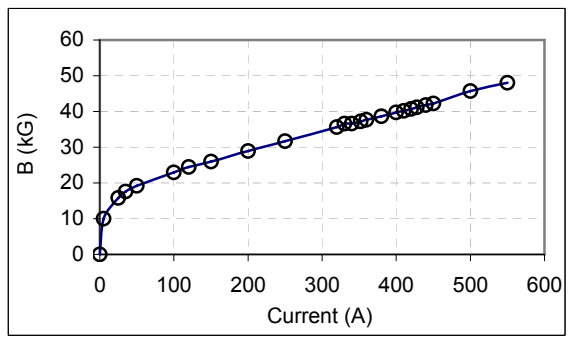

Figure 5: Magnetic field at 33 cm radius in hill region.

Coil Centering

The coil experiences position and current dependent force that was observed as change in the radial support link force. The coil needs to be moved to a position where the coil axis matches with the magnetic axis of symmetry. At this position, the forces on the radial support links decrease monotonically with current due to expansion of the coil in response to the magnetic hoop stresses as shown in fig. 6.

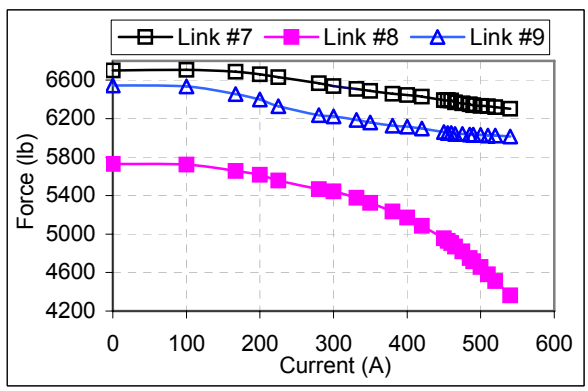

Figure 6: Radial support link forces vs. coil current.

Magnetic Field Measurements

Extensive magnetic field mapping has been done at different main coil excitations. The field has been measured with a search coil and NMR (for calibration) set up, with linear and angular positioning accuracy of 10 μm and 0.5 arc-seconds, respectively. The required field uniformity to lock the NMR signal was found at the centre of the magnet and near the RF holes in the valley region as shown by contour plots with 10 G step in figure 7 a & b.

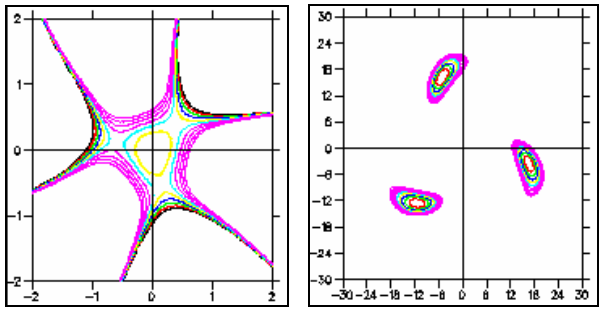

Figure 7: (a) Contour plots of magnetic field at the centre, (b) contour plots near the three RF holes showing the uniform field regions where NMR signal locked.

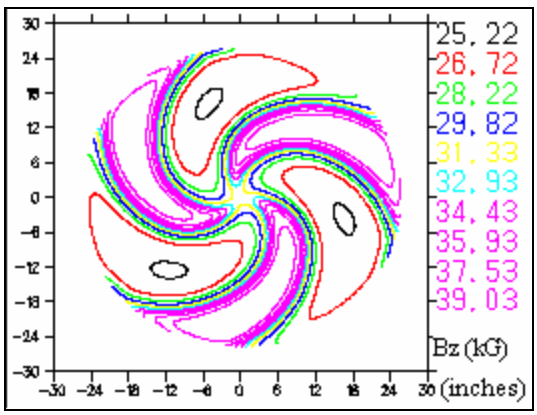

Figure 8: Isogauss contour plot of the measured field.

Three-fold symmetry dominated magnetic field is characteristic feature of the three-sector geometry of our superconducting cyclotron magnet as shown in fig. 8. Deviation from perfect three-fold symmetry arises out of manufacturing and assembly errors, as shown by the contour plot of all error harmonics in fig. 9.

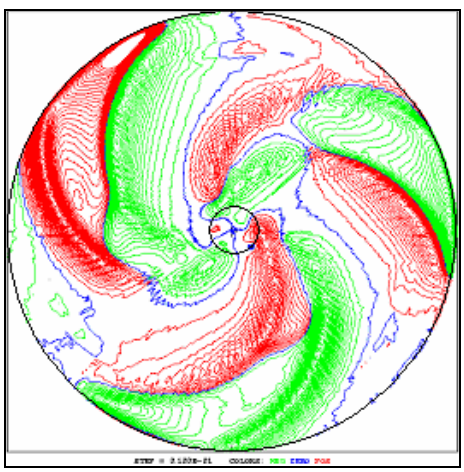

Figure 9: Error harmonics other than 3rd harmonic and those multiple of 3.

Average Field Correction

The radial distribution of the average field (B_{av}) for different current settings (I_α, I_β) is shown in fig 10. Iron shims were added to remove unwanted dips in the average iron field at about 4", 7" and 14" radii (fig. 11). The positions of these shims are shown in fig. 12.

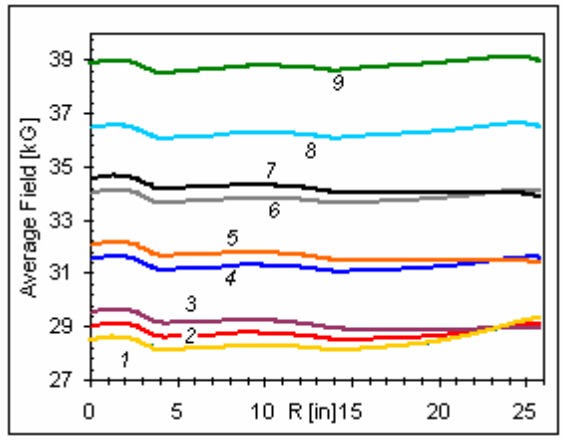

Figure 10: Average field for following main coil excitations (I_{alpha}, I_{beta}). 1: (475, 175), 2: (425, 225), 3: (375, 275), 4: (453, 290), 5: (403, 340), 6: (481, 356), 7: (509, 422), 8: (459, 472), 9: (537, 487).

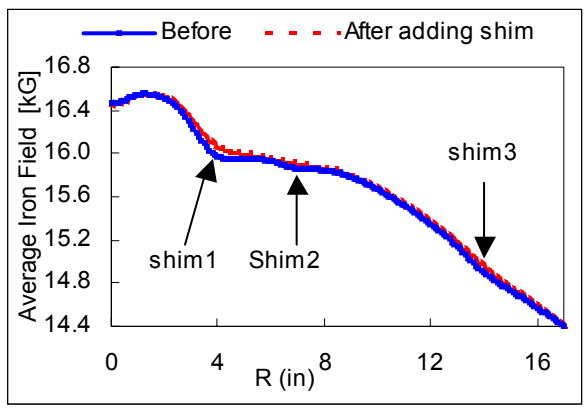

Figure 11: Correction of errors in the average field.

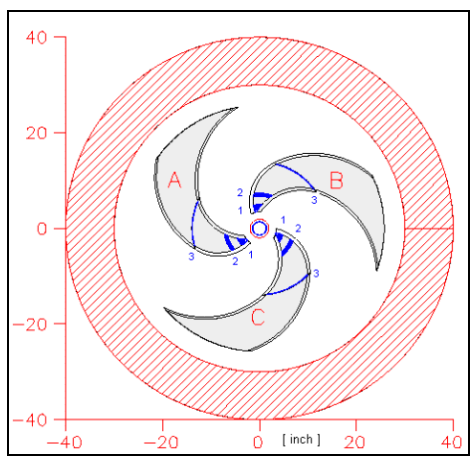

Figure 12: Shim positions for B_{av} correction (dark strips).

First Harmonic Correction

Minimization of 1st harmonic component in the field is one of the most important motives of the field measurement activity. The radial distributions of 1st harmonic component at different stages of corrections are

shown in fig. 13 as Map1, Map2 and Map3. The 1st harmonic amplitude and phase distribution were carefully investigated to determine the size and position of the iron shims. One of the observations was the movement of the pole-tips when magnet was excited. Culprits were faulty bolts. It was detected by the measurements and were replaced with some difficulty. The final positions of the shims are shown in fig. 14. We could limit the 1st harmonic component to within 7 gauss near the extraction radius, which can be adequately handled during the beam extraction process with the help of the trim coil #13.

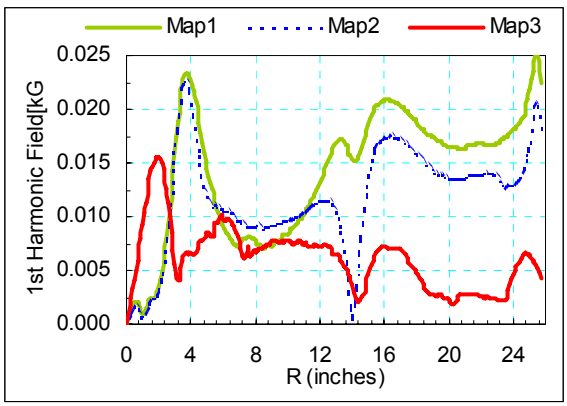

Figure 13: Minimization of 1st harmonic in the main field.

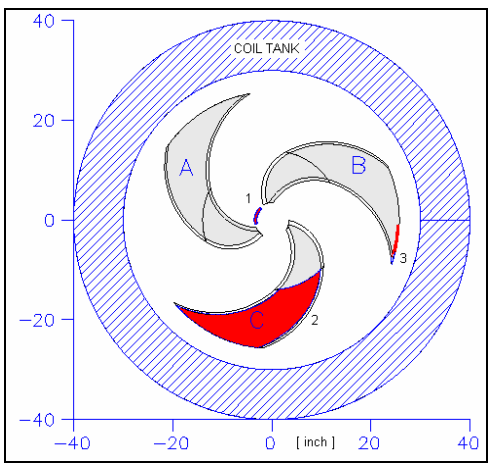

Figure 14: Shim positions for 1st harmonic correction.

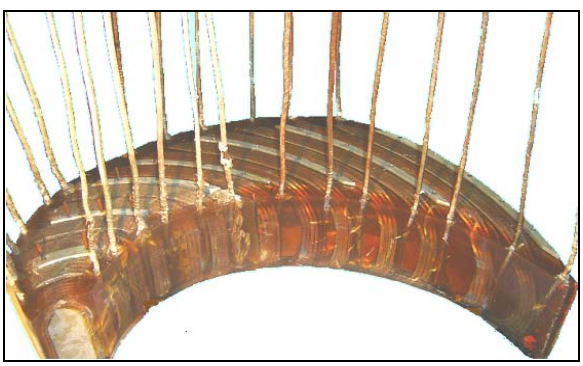

Figure 15: Trim coils placed on the pole tip.

Trim coils

After completion of the magnetic field measurements, the magnet has been disassembled to install the trim coils, RF resonators and other systems. There are 13 epoxy potted trim coils wound on each pole tip as shown in the fig. 15. The trim coil assembly work has been completed.

Installation of RF System

All the three RF amplifiers have been installed in the cyclotron vault and tested. Fig. 16 shows the Q-value of one of the amplifier cavities measured using a vector network analyser.

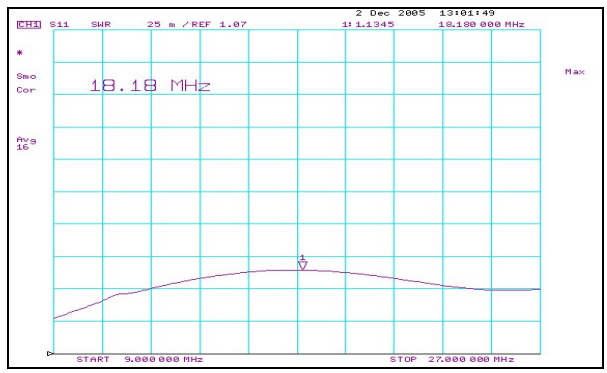

Figure 16: Loaded Q is >100 in the entire frequency range of 9–27 MHz, indicating at least 20dB harmonic rejection.

A significant part of the RF resonator system has been assembled on the bench and final assembly work in the cyclotron is in progress. Figs. 17 to 20 show important parts of the RF amplifier and resonator system. The RF liners are also undergoing vacuum and hydraulic tests. We expect to complete the assembly of the entire RF cavity very soon. The commissioning of the RF system is expected to start by mid 2007.

Figure 17: Assembly of screen bypass capacitor with tetrode tube (left) and upper half of one of the three dees (right).

Other Systems

The cryopanels for cyclotron main vacuum chamber are in the final stages of fabrication. The cryogenic delivery system for the cryopanels is presently being installed in the cyclotron vault.

Figure 18: Sliding short assembly with Be-Cu contact fingers.

Figure 19: One of the six RF resonators being assembled at VECC.

Figure 20: RF liner assemblies ready for installation.

Injection and Extraction Beam Lines

The ECR ion source is being installed in the high bay of the superconducting cyclotron building. Most of the components of the injection beam line are also ready for installation. Fig. 21 shows the injection scheme with two ECR ion sources. Layout of the external beam lines is shown in fig. 22.

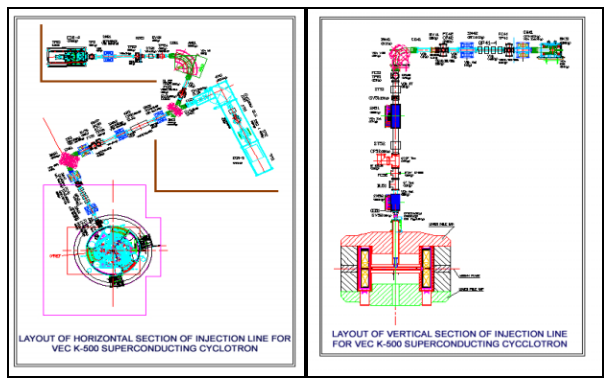

Figure 21: Horizontal and vertical views of the injection beam lines with two ECR sources.

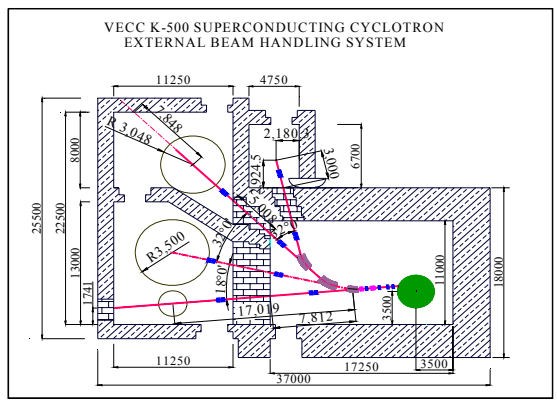

Figure 22: External beam lines layout for the VECC superconducting cyclotron. There are three beam lines for nuclear physics and one for irradiation experiments.

CONCLUSIONS

Most important component of the cyclotron i.e. the superconducting magnet has already been commissioned. Other systems are currently being assembled. Commissioning tests will start before the end of 2007.

ACKNOWLEDGEMENT

Construction of the superconducting cyclotron is a combined effort of several dedicated scientists, engineers and administrative staffs of the Centre. Their contributions are gratefully acknowledged.

REFERENCES

[1] R. K. Bhandari, "Status of the K-500 Superconducting Cyclotron", Proc. of Indian Particle Accelerator Conference (InPAC-2005), Kolkata, March 1-5, 2005, p. 1.

STATUS AND PLANS FOR THE TRIUMF ISAC FACILITY

P. W. Schmor, TRIUMF, Vancouver, Canada

Abstract

The TRIUMF 500 MeV cyclotron provides up to 100 μA of protons for the production of exotic beams, primarily via spallation in a thick target, at ISAC. The cyclotron is being upgraded and refurbished to meet the ISAC requirements for reliability and stability. The ISAC (Isotope Separator and Accelerator) at TRIUMF uses the ISOL (On Line Isotope Separator) technique to provide mass-separated isotopes at energies up to 60 keV for low-energy experiments. For higher energies, the ion beam is transported at 2 keV/u, injected into a room temperature RFQ Linac and then into a five-tank drift tube linac that provides variable-energy accelerated exotic-beams from 0.15 to 1.8 MeV/u for nuclear astrophysics experiments. The first stage of a Linac using super conducting rf cavities has been recently commissioned to increase the energy to 4.0 MeV/u for A/q = 7. In January, 2007 a $_{11}$Li beam was accelerated to an energy of 3.6 MeV/u for the first experiment in the ISAC II experimental hall. Additional super conducting rf cavities will be added to the linac chain to permit a further increase in the maximum energy of the exotic beams to 6.6 MeV/u by 2010. An ECR-based charge state booster is also being added in front of the RFQ to increase the available mass range of the accelerated isotopes from 30 to about 150. A second proton beam line and new target station for target and ion source development have been proposed for ISAC. In the future this new target station could be used as an independent simultaneous source of exotic beams for the experimental program.

INTRODUCTION

There are two main techniques for creating these exotic beams, namely, the fragmentation method and the ISOL method. At TRIUMF the ISOL approach is used. ISOL type facilities typically use a light-ion driver-accelerator to produce a variety of isotopes in a target. At TRIUMF the driver is an H-, 500 MeV, cyclotron that has been shown to have the capability of accelerating over 400 μA to 500 MeV. The TRIUMF cyclotron can simultaneously extract multiple independent proton beams into different locations. The transport beamline from the cyclotron to the target area in ISAC is shielded for a maximum current of 100 μA of 500 MeV protons on a thick target where the exotic isotopes are created & ionized.

The extracted beam is transported through a beamline with electrostatic focusing and steering elements. The electrostatic approach allows isotopes with adequate intensities to be used for tuning purposes and then, to adjust only the mass selecting system to the low flux isotopes. These fluxes cannot be, in general, observed on the normal beam diagnostic elements. However, with the electrostatic focusing elements, the beamline tune is not sensitive to the mass, only to the beam energy and that is kept constant. Therefore the low intensity isotope can be transported through the line without needing to readjust the beam optics elements and requires only a minimum of low intensity diagnostics for optimizing the transport efficiency to the experimental target. An off line ion source (OLIS) is used to provide stable beams for commissioning beamlines, accelerators, setting up tunes and experimental calibrations. The required beam quality, the beam intensity, the beam energy and the momentum spread of the accelerated exotics depend on the particular experiment. For ISAC I the user input led to a continuously variable energy from 0.15 to 1.5 MeV/u for isotopes having an A/q ≤ 30. Recently ISAC II was added with super conducting linac to increase the energy of the isotopes. The accelerator layout is shown in figure 1.

The production of exotic isotopes in an ISOL target depends on a number of variables such as driver beam-current & energy, nuclear cross-section for production, target material and target thickness. The observed yield of a particular exotic isotope also depends on the half-life of the isotope, the time that it takes the isotope to leave the target and reach the ion source, and the efficiency for ionization in the ion source. The time required to reach the ion source following production depends on material properties that are temperature dependent. The observed exotic flux from an ISOL target varies non-linearly with the proton beam current because of changes in the target temperature and factors such as radiation induced diffusion. Enhanced variations of the exotic beam flux compared to the proton beam current variations, introduce difficulties for both the experimenter and the accelerator operator. To minimize these problems it is necessary to require beam size, beam position, beam profile and beam current stability tolerances on the proton beam from the driver accelerator. In addition each accelerator event that causes an interruption in beam delivery results in an even longer interruption to the delivery of exotic ions. The target temperature at high beam powers is primarily determined by the driver beam power. The time to restore the equilibrium operating temperature in the target when the beam is restored to the operating level exceeds the time for the temperature to drop to unusable levels when a short beam interruption occurs. Consequently it has become important to monitor, analyze, and take actions to reduce the mechanisms causing the beam interruptions and beam instabilities.

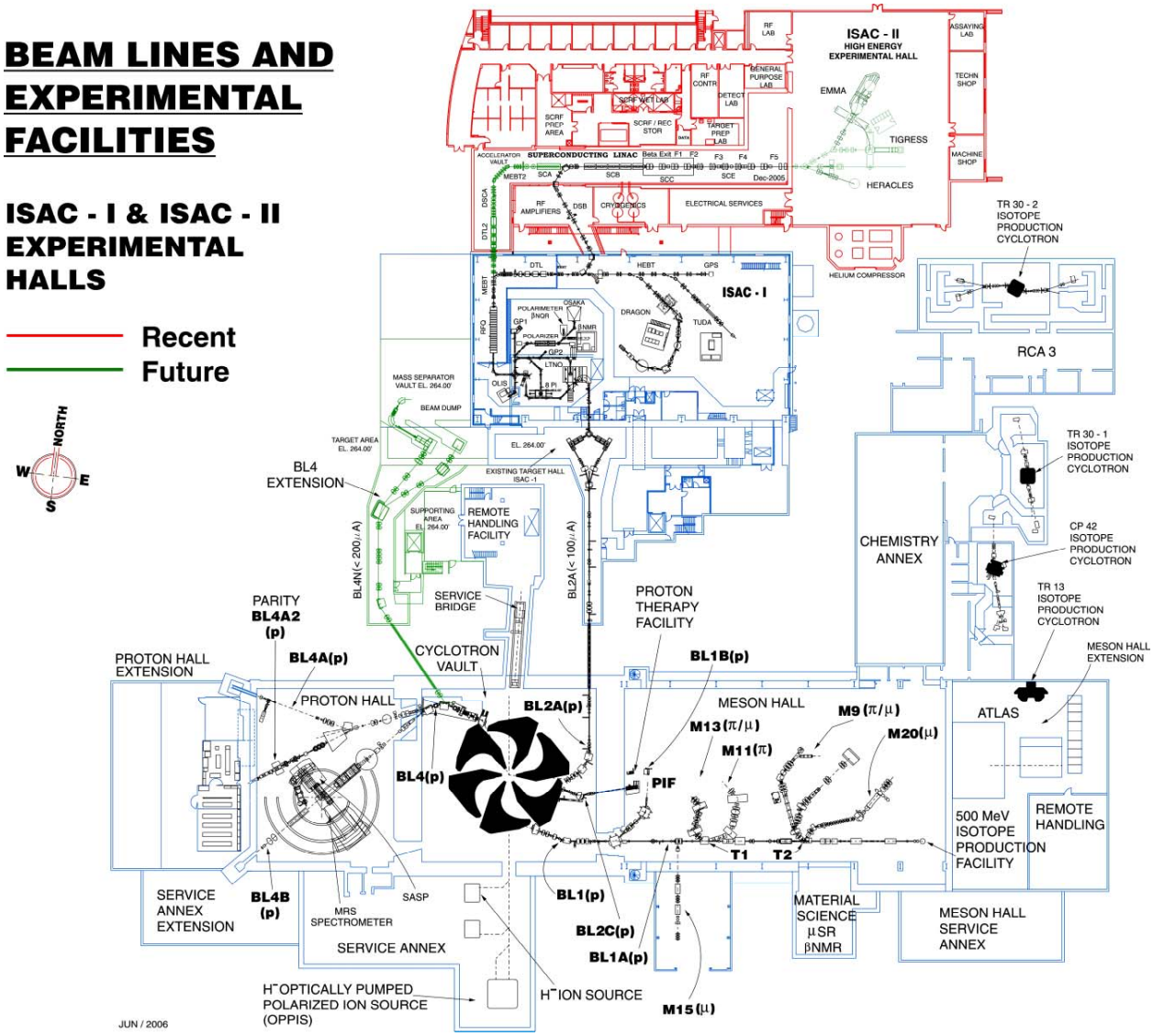

Figure 1: A schematic layout of the TRIUMF facility. The red lines indicate the building envelop for the ISAC II civil construction. The green lines labeled as BL4 extension, indicate the proposed building envelop for the proposed new high power target test facility. The ISAC II high beta cryomodules have been omitted in the schematic. Instead the HEBT beamline to the experimental hall is shown after completion of medium beta cryomodule installation in 2006.

CYCLOTRON DRIVER

A cyclotron refurbishment program was initiated to replace selected unreliable cyclotron components & to allow higher current operation. The cyclotron vacuum is being improved to reduce activation from stripping by residual gas molecules in the cyclotron vacuum chamber. Beam dynamics studies have focused on understanding the sources of the beam instabilities and on increasing the 'head-room' for the current of the circulating beam in the cyclotron. Diagnostics and feedback have been added to monitor and improve the beam stability on the ISAC targets. The cyclotron current extracted for the ISAC target is stabilized, though feedback from a non-intercepting current monitor, by varying the duty cycle with a 1 kHz pulser. Collimators & halo monitors are being used to ensure the beam size is maintained throughout the operation.

ISAC TARGETS & ION SOURCES

The exotic isotopes created in the target material are transferred by effusion and diffusion processes to an adjacent ion source where the isotopes are ionized, extracted and formed into an ion beam. The isotope production target material is located in a tube (2 cm diameter and up

to 20 cm long) and the material composition varies depending on the particular isotopes that are being optimized. The target and ion source can be biased up to a voltage of 60 keV. Target configurations have been developed that allow extended operation at the full 50 kW beam power.

Isotopes are ionized at ISAC by three different types of ion sources; a thermal (surface) ion source, a resonant laser ion source and a FEBIAD (forced electron beam induced arc discharge) ion source. Each of these ion sources is capable of operating for many weeks with high power targets. An ECRIS (electron cyclotron resonance ion source), based on a 2.45 GHz design from GANIL, has been modified for operation at 6 GHz and is being tested on a test stand.

Two ion sources are being presently used to provide stable beams from an off line ion source (OLIS). There is a need to add a more universal ion source to meet these needs and super-nanogan ECRIS has been acquired for this purpose. Proposals have suggested that OLIS might even be useful for longer lived isotopes that were produced by one of the other four cyclotrons on site and delivered to the OLIS ion source in gas bottles after chemical separation.

ISAC I

Although the ISAC I accelerators were initially designed for a maximum energy of 1.5 Mev/u for beams having a $A/q \leq 30$ ratio, isotopes have been accelerated from the injection energy of 2 keV/u up to a maximum energy of 1.8 MeV/u. The accelerating system consists of a multi-harmonic pre-buncher, a cw RFQ, a medium energy beam transport (MEBT) section, an electron stripper, a re-buncher and a cw drift tube linac. The pre-buncher provides a pseudo saw tooth velocity profile at a fundamental frequency of 11.8 MHz, thereby providing approximately 86 nS between beam buckets. Bunched beam from the pre-buncher fills every third bucket of the 35 MHz, cw, 8 m long, split-ring, RFQ. The singly-charged beam out of the RFQ, at energy 0.15 Mev/u, is focused (transversely and longitudinally) and stripped to a higher charge state in the medium energy beam transport line (MEBT). The MEBT has a 106 MHz bunch rotator to provide a time focused beam at the stripper and a dual frequency rf chopper to select cleanly separated rf bunches separated by either 85 or 107 ns. The stripped beam is magnetically bent through 90 by two 45 dipoles where silts are used to select only those isotopes having a chosen A/q ($3 \leq A/q \leq 6$) and re-bunched prior to injection into the first tank of the DTL. The DTL provides a beam that can be continuously varied in energy from 0.15 to 1.8 MeV/u. The DTL is a separated-function structure with five DTL tanks, each operating at 0° synchronous phase, with magnetic triplets located between each tank and three split-ring, three-gap bunchers located between tanks 2,3, and 4. As the DTL system operates cw at 106 MHz, only 1 in 9 rf buckets are nominally filled (beam bursts are at the pre-buncher fundamental frequency). Two additional bunchers are located in the high-energy beam transport (HEBT) beam line prior to the experimental stations to optimize the longitudinal timing at the experiments. For bunching the lower beta beams an 11.8 MHz triple-gap structure is used and a 35.4 MHz spiral buncher is used for bunching the higher beta beams. This accelerator has provided a wide range of isotopes over the full energy range to the experimental stations for the past six years.

ISAC II

The ISAC I facility has been accelerating radioactive ions (with $q = 1$ and $m = 30$) up to 1.8 MeV/u. ISAC II will increase both the possible mass to at least $m = 150$ and the energy to 6.5 MeV/u.

The ISAC II LINAC has been described at previous conferences[1,2]. Briefly the completed system will include a cw DTL to increase the energy of the beam from the RFQ to 400 keV/u before stripping to a higher charge state. A superconducting linac with cavities designed for $\beta_o = 4.2\%$ (8 low beta cavities at 70.7 MHz), 5.7% (8 medium beta cavities at 106 MHz), 7.1% (12 medium beta cavities at 106MHz) and 10.4% (20 high beta cavities at 141 MHz). The design fields for these cavities are specified to achieve the ISAC II design energy (6.5 MeV/u) for $A/q = 6$. Solenoids are located between groups of cavities for transverse focusing and to enhance multi-charge acceleration when strippers are used. The medium beta section of the superconducting linac is composed of five cryomodules with each cryomodule consisting of four bulk niobium quarter wave cavities for accleleration and one superconducting solenoid for periodic transverse focusing. The cavities each produce about 1 MV of accelerating voltage. The top assembly of an ISAC II cryomodule is shown in Figure 2.

Although heavier masses are being produced in the targets and extracted from the ion sources, the high-pressure conditions near the ion sources permit only singly ionized ions to be extracted at reasonable intensities. These heavier masses could be accelerated if their charge state was increased to within the required A/q. In order for experimenters to reach the Coulomb barrier for masses up to $A = 150$, it is necessary to increase both the length of the ISAC accelerating system and the maximum mass that can be accelerated. To increase the maximum mass of ions accelerated by the RFQ, a 1+ to n+ charge state booster (CSB) is required. The installation of an ECR-based charge-state-booster in ISAC, in 2008, will allow the acceleration of all masses to 0.15 MeV/u.

A plan to achieve the ISAC II specifications in a phased approach is being followed in a way that allows experiments to begin prior to completion of the full accelerator capability. In the first phase, at the end of 2006, the accelerator has 20 medium-beta superconducting cavities that bring the beam to 4.0 MeV/u for $A/q = 7$ and, of course, somewhat higher for isotopes that can be charge-boosted to a lower A/q (9 MeV/u for $A/q = 2$). At this energy a number of experimenters have approved experi-

mental proposals and are waiting to begin data taking. By the end of 2009, on completion of the second phase, 20 more cavities (high-beta) will be added to bring the final energy up to 6.6 MeV/u (for A/q = 7). The accelerator layout is shown in figure 3.

In a later addition, ISAC I would be extended from the RFQ to a new DTL in ISAC II, that would allow acceleration of the beams from the RFQ to 0.4 keV/u. This would provide an alternative for accelerating elements that are not efficiently charge-boosted and require additional stripping before acceleration in the superconducting ISAC II linac. A short superconducting low beta section would be added to bring the energy up to the 1.5 MeV/u required for injection into the medium beta superconducting linac.

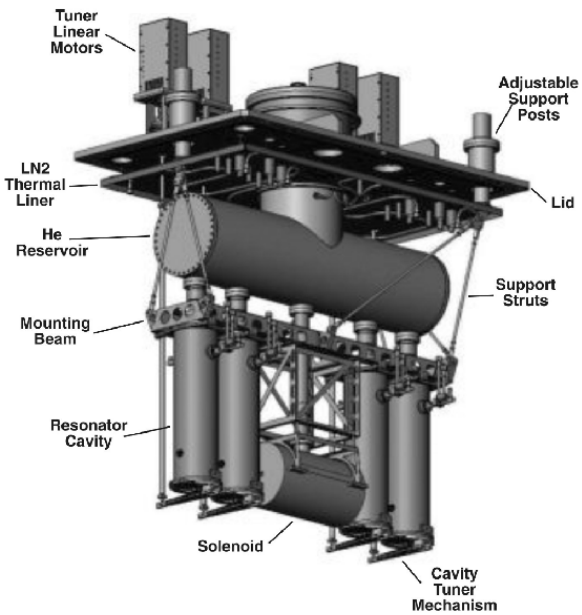

Figure 2: Component layout for each of the five medium beta cryomodules installed and operating in the ISAC II accelerator.

The first stable beam acceleration through all 20 cavities occurred on April 08, 2006 when 12C3+ was accelerated to 6.3 MeV/u within the accelerator vault during the accelerator commissioning. Subsequently a variety of other stable beams with different A/q values have been commissioned. The measured average gradient is 7.2 MeV/u resulting in final energies of 10.8 MeV/u (4He2+), 6.8 MeV/u (4He1+, 12C3+, 20Ne5+, 40Ca10+) and 5.5 MeV/u (22Ne4+) with transmissions exceeding 90%.[3]

CSB (CHARGE STATE BOOSTER)

The CSB for ISAC is a Phoenix based ECRIS. TRIUMF has collaborated with ISN, Grenoble on its further development. The ECRIS has been assembled on an extension of an existing ion source test stand where its performance is being measured and optimized. The CSB booster will be installed in the mass separator pit at the target level, downstream of the mass separator, in the January 2008. The low energy beam transport structure to allow the beam to go through the CSB is being installed this year (2007).

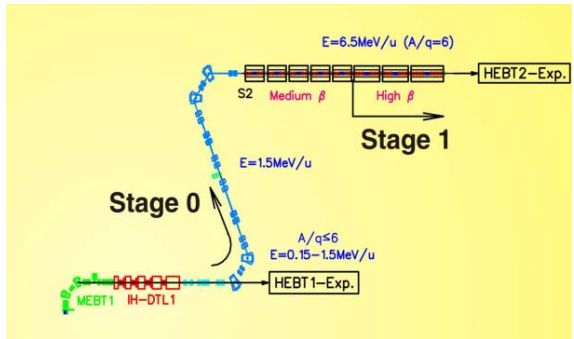

Figure 3: The accelerator layout at ISAC II. Stage 0 which includes the medium beta superconducting section is operational. Stage 1 which adds 20 high beta cavities is scheduled to be completed in 2009.

ISAC II OPERATION

A major milestone at TRIUMF was achieved on January 5, 2007 when an accelerated radioactive beam, 11Li was delivered from the ISAC II accelerator to the first experiment in the ISAC II experimental hall. The beam was transported to the MAYA experimental setup and within two hours data taking commenced. The MAYA equipment was brought to TRIUMF from the GANIL laboratory in France to study the outer skin structure of the exotic nucleus 11Li. The medium beta cryomodules in the ISAC II accelerator adds 20 million volts of accelerating voltage to the existing ISAC accelerator chain. For the MAYA experiment, only 11 of the 20 available cavities were needed to accelerate the beam to the required experimental energy of 39.6 MeV.

FUTURE PLANS

High power target development and the experimental program compete for the same beam time from ISAC. Target development scheduling requires a substantial overhead and is inconsistent with the beam reliability demanded by the user community. Experience has shown that high power target development must be done on line with proton beam. Therefore to maintain a viable experimental program, TRIUMF has decided that it is necessary to build a dedicated target development facility. A rarely used (recently) extraction port could be upgraded for high current operation and a beam line constructed to a new target hall in ISAC, capable of operating at the nominal 100 kW. The facility would include the ISAC style target station modules, a mass separator and yield station. The facility would make use of the existing remote-handling capability, the existing nuclear exhaust system and the existing hot cells. It would operate independently of the other cyclotron beam lines and therefore target development could be carried out simultaneously

with the ISAC experimental program. The expansion would be done in a manner that in the future when the target development facility is not being used for target development a second RIB beam could be transported to any of the ISAC experimental stations. This would permit the facility to operate multiple RIB experiments simultaneously. A potential layout for this new facility is shown in figure 4.

SUMMARY

The accomplishments described in this paper were realized by a team effort. Without presenting the many names individually, I must nevertheless acknowledge them for these achievements.

The success of a facility is ultimately measured by its science output. The nuclear physics experimental facility has attracted experimental groups internationally because of its unique capabilities. Experimental groups are acquiring and setting up the apparatus needed for the ISAC II science program. The three major facilities will include TIGRESS (a high efficiency gamma array), HERACLES, EMMA (a recoil mass spectrometer) and a general purpose station which presently accommodates the MAYA detector.

REFERENCES

[1] R.E. Laxdal, "ISAC-I and ISAC-II at TRIUMF: Achieved Performance and New Construction", Proceedings of LINAC 2002, Gyeongju, Korea, p. 296.

[2] G. Dutto, "Recent Progress at TRIUMF", Proceedings of APAC 2004, Gyeongju, Korea, p. 544.

[3] R. E. Laxdal et al; "Commissioning of the ISAC-II heavy Ion Linac at TRIUMF", Proceedings of EPAC06, Edinburgh, Scotland, p. 1556

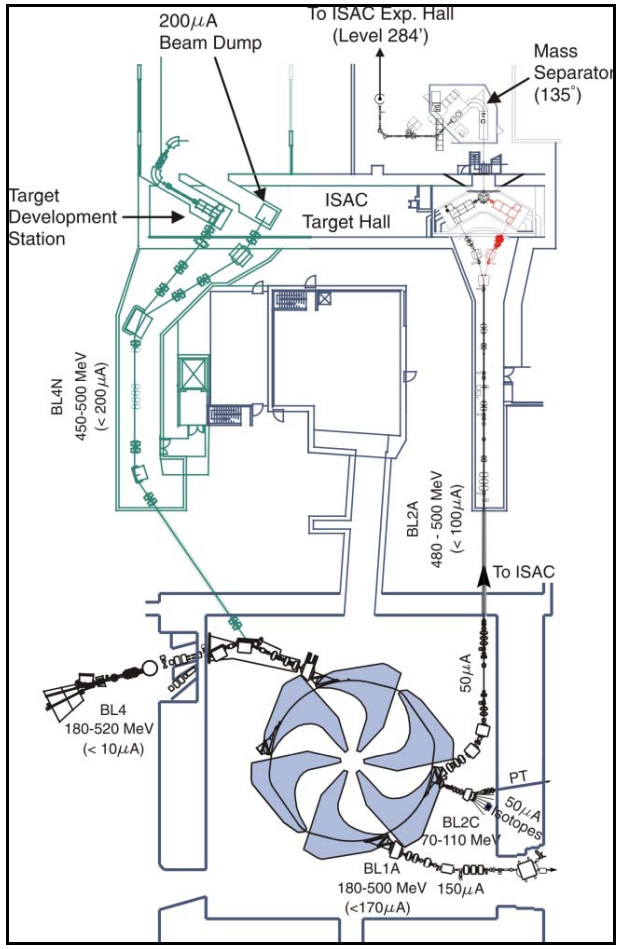

Figure 4: The BL4 cyclotron extraction port will be used to provide beams for high target development in an underground expansion of the ISAC target hall (shown in green).

MULTI-BUNCH FEEDBACK ACTIVITIES AT PHOTON FACTORY ADVANCED RING

Weixing Cheng, Takashi Obina
Photon Factory, Institute of Materials Structure Science (IMSS),
High Energy Accelerator Research Organization (KEK),
1-1 Oho, Tsukuba, Ibaraki 305-0801, Japan

Abstract

The photon factory advanced ring (PF-AR) is a dedicated single bunch light source operating at KEK, normally it's operated at 6.5 GeV with 60mA injection beam current. However, there has some users' experiment require multi-bunch operation for high intensity x-ray beams. The old transverse damping system can suppress only one (or two) bunches, new multi-bunch feedback system has been successfully tested to a maximum of 64 bunches.

Both analog and digital transverse feedback loop has been tested at AR to store multi-bunches. For analog feedback control loop, long cables are used to delay the bunch position error signal from BPM buttons. Betatron phase advance between stripline kicker and BPM are well selected to be around 90 deg. A digital feedback loop based on FPGA evaluation board has been successfully operation, which include two ADCs, one Virtex4 FPGA chip and two 14 bit DACs. Bunch position error signal sampled by ADC, filtered by 10-tap FIR filter implemented in FPGA and send to DAC output for correction. Phase shifter in the FIR filter can be adjusted depend on the kicker and BPM betatron phase advance, FIR filter will also cut the DC components and pass through the betatron oscillation signal which increase the system dynamic range a lot. Digital delay can also be implemented inside FPGA instead of long cable delays.

Maximum beam current of 97mA has been achieved for several bunches' storage, betatron oscillation of the stored beam can be suppressed well.

INTRODUCTION

The PF-AR is a dedicated single bunch ring, injection beam current of 60mA with a typical lifetime of 15 hours has been achieved. Some user's experiment need more high intensity x-ray radiation, one example is clinical application at 5.0 GeV mode[1], for this reason, multi-bunch injection and storage has been tested at PF-AR.

There has injection threshold around 20mA even for single bunch injection at PF-AR, feedback damper system is needed to suppress the injection oscillation, as well as stored beam betatron oscillation. The old transverse damping system has been operated in PF-AR for more than 20 years, key component of the damper system is such a called BOD (Bunch Oscillation Detector[2]), which can detect and damp one bunch oscillation. There has two such kind of BOD detection circuits available, that means it's possible to store 2 bunches. For more bunches injection and storage, new feedback systems is required, benefits of highly developed digital technology makes it possible to implement the required feedback control loop relatively simple in these days. Compared to digital feedback control, analog control suppress the beam oscillation in a more direct way, there has many good review paper for feedback control.[3,4] Both analog and digital feedback loop has been successfully tested for multi-bunch injection and storage. Table 1 list the main parameters of PF-AR feedback system.

Table 1: Parameters of PF-AR Feedback System.

Beam Energy	6.5 GeV/ 5 GeV
Injection Energy	3.0 GeV
RF frequency	508.57 MHz
Harmonic Number	640
Circumference	377.26 m
Revolution frequency	795 kHz
Qx/Qy/Qs	10.15/10.21/0.03
Emittance	294 nm.rad
BPM SW20 βx/βy	13.6527/2.43916 m
Kicker βx/βy	3.81227/12.1319 m
BPM->Kicker ΔΦx/ΔΦy	9.73924/9.73916
Kicker length	1300 mm
Kicker shunt impedance	>100 kOhm @20MHz

FEEDBACK IMPLEMENTATION

For analog feedback system, it's convenient to use two BPMs to detect bunch position signal. Two BPMs vector sum can produce arbitrary phase advance between BPM and kicker. Figure 1 shows the betatron phase relations of BPMs and kicker. During the machine study at PF-AR, to make the RF electronics simple, only one BPM signal is used to detect the betatron position oscillation, phase advance from the BPM to kicker is well selected to be around 90/270 deg, which means the fractional part of BPM-> kicker phase advance should be near 0.25 or 0.75, BPM SW20 can fulfill it in both vertical and horizontal plane as shown in Table 1.

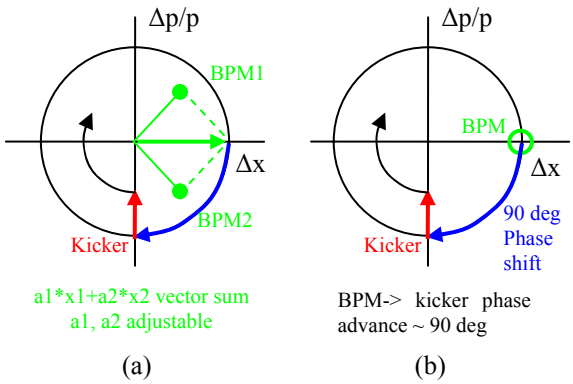

Figure 1: Phase relations between BPMs and kicker in analog feedback.

To realize one-turn delay from BPM to kicker, additional 160m low-loss cable is needed besides the cables between ring tunnel and local control station. Such a long cable and analog loop has some disadvantages, for example close orbit change will decrease the system dynamic range a lot. One solution is adopting analog 2-tap filter to cut the DC orbit offset and revolution harmonics, however another one-turn delay cable is needed and cable length varies depends on the environment temperature, that will generate one-turn delay errors and decrease the 2-tap filter performance; another solution is adopt feedback loop to cancel the closed orbit change, for example, gain of each button-channels can be adjusted depends on the COD offset. In this way, it's possible to compensate the COD influence, however, the system becomes complicated. Long cable attenuation is another problem, which will decrease the signal-to-noise ratio too.

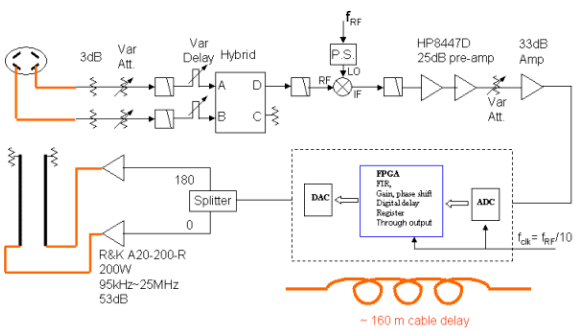

Figure 2: Multi-bunch transverse feedback for PF-AR.

Reliable solution for these analog feedback disadvantages is using digital filter. As the FPGA (Field Programmable Gate Array) technology developing, more and more accelerator diagnostic and control systems have used FPGA chips [5]. A digital feedback loop based on FPGA evaluation board has been successfully operation at PF-AR, the evaluation board includes 2 channels 105MSPS 14 bit ADC, Xilinx Virtex4 XC4VSX35 FPGA chip and 2 channels 14 bit DAC. As shown in Figure 2, bunch position error signal sampled by ADC, filtered by 10-tap FIR filter implemented in FPGA and send to DAC output for correction. Phase shift in the FIR filter can be adjusted depending on betatron phase advance from BPM to kicker, FIR filter will also cut the DC components and pass through the betatron oscillation signal, which increase the system dynamic range. Digital delay can be easily implemented inside FPGA instead of long cable delays. In Fig. 2, ADC+FPGA+DAC inside the dashed box is implemented in the evaluation board, which can be replaced by 160m long cable (8-D low loss) shown as brown line in the drawing.

System Generator[6] from Xilinx is a powerful toolbox for DSP design and implementation into FPGA chips. Combined with MATLAB/Simulink, System Generator can generate the model including FIR filters and digital delay, ISE[6] project can be produced from it. For non-experts of HDL (Hardware Description Language) programmer, System Generator is an easy to use toolbox which makes you possible to realise the design within one hour. Generated bit file can be downloaded through JTAG cable.

For ADC, FPGA and DAC processing clock, it's possible to handle maximum sampling rate of 105 MSPS, however, the main component who limit the system bandwidth is high power amplifier. There has 25MHz 200W amplifier available which can feedback about 64 bunches even fill in PF-AR ring. In this case, ADC and FPGA processing clock is divided by 10 from RF frequency. Latency from ADC to DAC output is about 534ns, which makes it possible to feedback within one turn even considering the cables between tunnel and local station. 10-tap FIR filter implemented with simple MAC (Multiplier-Accumulator) operation passes horizontal betatron oscillation component, DC and revolution harmonic are well suppressed, a typical measured FIR filter response is shown in Fig. 3.

Figure 3: 10-tap FIR filter frequency response used in PF-AR multi-bunch feedback. (Blue line – amplitude response; red line – phase response).

PERFORMANCE

With the analog and digital control loop, several machine studies have been going on at PF-AR, maximum beam current of 97mA has been achieved for multi-bunch injection and storage.

Figure 4 shows the filling pattern of 16 bunches in AR ring using analog feedback, BPM spectrum getting from real-time spectrum analyzer gives the betatron oscillation information with feedback ON and OFF.

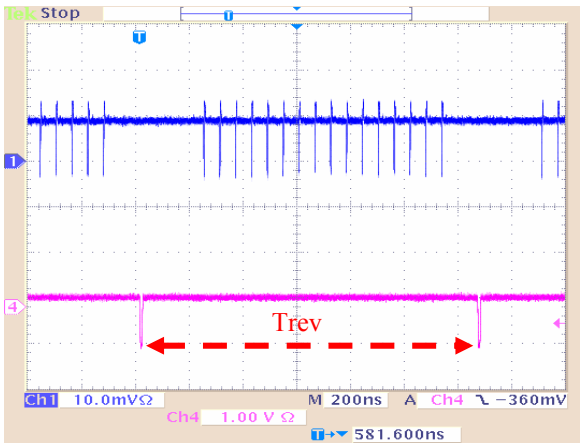

(a)

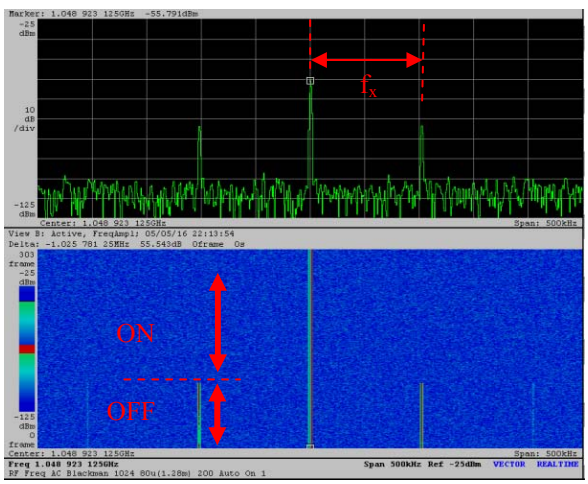

(b)

Figure 4: (a). Sixteen bunches filled in AR ring, CH1 is BPM button signal, CH4 is revolution frequency of the ring; (b). BPM spectrum with feedback ON/OFF, while feedback turns off, the horizontal sideband appears clearly. (Centre frequency: 1.048923125 GHz, SPAN: 500 kHz).

Digital feedback control loop based on the FPGA evaluation board has been tested in PF-AR. A typical filling pattern getting in AR's machine study is shown in Fig. 5. In the oscilloscope screen capture, 3 bunches were stored, labelled bunch #1, #2, #3, CH1 is the BPM diagonal buttons delta signal, oscillation can be observed while the feedback is OFF, CH2 is stripline kicker upstream signal, CH3 is the revolution frequency. Since bunch #3 is under injection, the oscillation is larger compared with other two bunches.

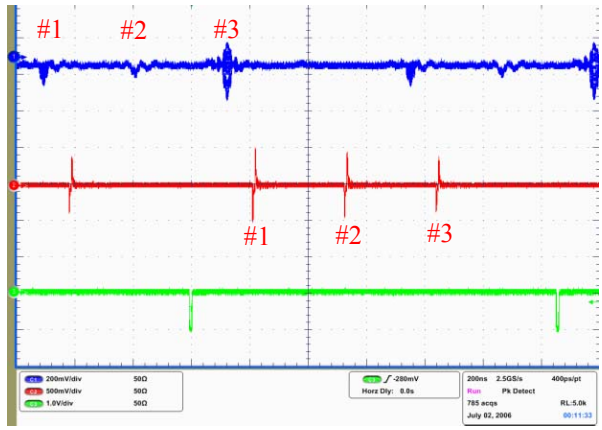

Figure 5: Filling of 3 bunches in AR ring using digital feedback loop. (I ~ 60mA).

Injection damping can be achieved to be less than 1ms using the feedback system, however blow up phenomena has been observed after several ms to several tens ms. This phenomena had been analyzed before by Dr. Minagawa[7] as a saw-tooth instability. From BOD output, same blow up phenomena has been observed. While blow up happens, it's very hard to injection any more, the reason for this blow up phenomena seems related to longitudinal instabilities, which is not clarified yet.

SUMMARY

Using multi-bunch feedback, 16 bunches (64 bunches maximum) has been successful stored with a maximum beam current large than 90mA. Blow up phenomena was observed for several bunches' injection, while this blow up happens, it's very hard to injection the beam. Future work will try to solve this problem and increase the beam lifetime for multi-bunch operation.

REFERENCES

[1] T.Miyajima et al., "Operation and Recent Developments of the Photon Factory Advanced Ring", PAC2005 Proceeding, pp. 2845-2847, Knoxville, May 2005.
[2] P.L. Pellegrin, "T.A.R Bunch Oscillation Detector", TRISTAN Design Note, TN-82-011, 1982.
[3] G.Lambertson, "Beam Bunch Feedback", 1994 US-CERN-Japan Joint Accelerator School, Maui, HI, Nov. 1994.
[4] M.Tobiyama, "Beam Feedback Systems", JAS2000.
[5] Weixing Cheng et al. "Bunch-by-bunch Feedback for the Photon Factory Storage Ring", EPAC 2006.
[6] http://www.xilinx.com/ise/
[7] Y.Minagawa et al, "Transverse Sawtooth Instability Observed in Photon Factory Advanced Ring", PAC2003 Proceeding, pp. 3080.

FABRICATION AND PERFORMANCE TEST OF THE CAVITY BPM FOR KEK ATF2 AND PAL XFEL*

J. Y. Huang#, S. H. Kim, Y. J. Park, W. H. Hwang, S. J. Park, *PAL, KOREA*
Y. Honda, H. Inoue, T. Tauchi, J. Urakawa, *KEK, Japan*
M. Ross, *FNAL, USA*

Abstract

A high-resolution beam position monitor (BPM) based on a pill-box type microwave cavity has been developed for the accurate beam position measurement in the KEK-ATF2. Based on the prototype cavity BPM designed in the KEK, the cavity structure and the isolation between horizontal and vertical modes are further improved by the collaboration between KEK, SLAC and PAL. The resonant frequency of the cavity and the isolation between horizontal and vertical modes can be tuned efficiently using tuning pins brazed on the cavity rim instead of the conventional tuning plunger. Offset between electrical and mechanical centers could be reduced by tuning within +/- 5 um, the isolation tuned better than 50 dB, and the 100 nm resolution of the cavity BPM has been proved through the beam tests in the ATF extraction beamline. Technical design considerations, fabrication, and test results of the cavity BPM are described in this paper.

INTRODUCTION

In the next generation linear accelerators like the International Linear Collider (ILC)[1] and the X-ray Free Electron Laser (XFEL)[2,3], precise beam trajectory control as well as the beam-based accelerator alignment are very important for achieving nanometer-sized beams at the interaction point (IP) of the ILC or keeping the orbit stability better than a few micrometers in the XFEL for the stable FEL amplification along the undulator. A Resolution as good as 100 nanometers and a long-term stability within a few micrometers are required for the beam position monitors (BPM). Although BPMs with pickup electrodes or striplines have been improved for a better resolution, it has been limited to a few micrometers. For the ultra-short, high peak current bunches, a pill-box type cavity BPM has been considered as a promising candidate providing higher electrical sensitivity and mechanical stability. In a cavity BPM, a beam with a position offset from the electrical center excites large signal of TM110 transverse dipole mode. This signal is coupled to a waveguide through a coupling slot, and then picked up with a pickup electrode positioned at the waveguide wall.

The KEK-ATF2 [4] is an advanced accelerator test facility being built by extending the extraction beamline of the existing ATF to test advanced beam diagnostic systems and beam dynamics required for the final focus area of the ILC.

Three prototype cavity BPM have been developed and fabricated for the KEK-ATF2. With the successful results from beam tests done in the ATF, 11 cavity BPMs have been produced. The remaining 28 cavity BPMs are being fabricated by the PAL and will be installed in the KEK-ATF2.

PROTOTYPE DESIGN AND FABRICATION

Design of the cavity and waveguide structure of the cavity has been done in the KEK with computer simulation codes, and a prototype cavity BPM was fabricated and tested in the KEK-ATF by Y. Honda. A C-band cavity tuned at 6.426-GHz TM110 dipole mode was selected as the pickup cavity. Mechanical and electrical design parameters of the cavity BPM are summarized in the Table 1 [5].

Table 1. Design parameters of the cavity BPM

Tuned frequency	6.426 GHz
Resolution	100 nm
Dynamic range	500 um
Isolation (x/y)	< -30 dB
Q_0	> 5000
Offset of e-center	< 10 um
Coupling	> 0.3

Offset of the beam excites TM110 transverse magnetic mode in the cavity and the signal is coupled to the electrical pickups in the waveguide through four 1.5 x 13 mm^2 rectangular coupling slots. (See Fig. 1) Waveguide structure was optimized to reduce reflections, to increase coupling, and to reject common modes.

Two variations of the prototype cavity BPMs - a perfect cylindrical cavity, and a cavity with two dents on the symmetrical positions along the inner rim of the cavity to enhance the mode separation - are fabricated and tested for comparison of isolation between horizontal and vertical modes. Fig. 1(a) shows the schematic for the two types of the prototypes. Pair of 0.1-mm dents made with 6-mm milling drill (cavity diameter = 53.822 mm) on the inner surface of cavity rim has given resonance frequency shift of 500 kHz.

The effects of machining errors and deformations of the cavity components are tested before the final design. The 1- mm thick septum for the coupling slot between the cavity and the waveguide was found to be deformed during brazing, so the thickness was increased to 1.5 mm. For the compensation of the mechanical error of the cavity, four tuning pins are brazed into the recess of cavity body on the diagonal positions of the cavity. Tuning pins can push or pull cavity wall slightly for the compensation and cancellation of the mechanical errors,

such as volume and symmetry of the cavity. Fig. 1 shows the schematic of the cavity with and without dents.

Machining accuracies are tightly controlled during machining using special jigs. Surface roughness of the cavity wall is better than R_{max}< 0.8 um by using diamond tools. Overall errors of the prototype cavity measured with 3-dimensional profiler were kept within 10 um.

Brazing procedure has been also investigated through trial and errors before the final brazing finding out optimum thickness of brazing alloys and appropriate shape of brazing alloy slots to reduce spill-out of the brazing alloy. All of the cavity BPM parts are brazed at the same time with a special brazing jig to reduce deformations which can occur during multiple brazing processes. Brazing temperature is chosen to be 720 C as the signal pickup feedthrus had been brazed at 780 C.

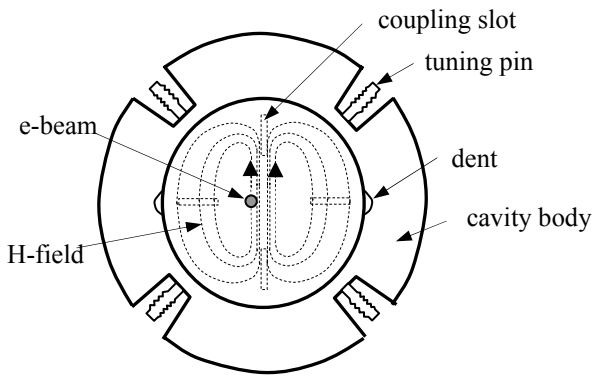

(a)

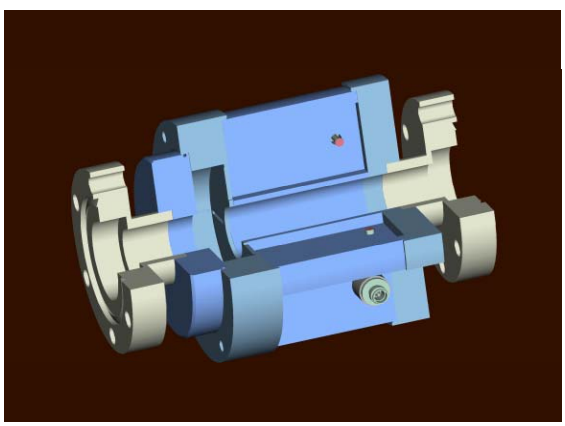

(b)

Figure 1: Schematics of cavity BPM. a) Cross-sectional view the cavity across the beam path showing tuning pins and coupling slots. Dents are carved for the test only. b) Computer aided assembly drawing of the cavity BPM.

MEASUREMENTS

Mechanical Measurements

Mechanical dimensions of all parts are measured with precision 3-D profiler before brazing. Fig. 2(a) shows a cavity body being set up on the 3-D profiler for the measurements. Mechanical errors of all the components come within 10 um, well below the design requirement of 20 um. Table 2 summarizes the test results.

Figure 2(a): A cavity body set up on the 3-D profiler for the dimensional check. b) A cavity BPM assembled in a tightening jig for the microwave measurements before brazing.

Microwave Measurements

Resonance frequency, reflection and transmission of the cavity ports are measured with the HP8510C network analyzer before and after brazing. The resonance frequency has increased 1 ~ 2 MHz after brazing, and further increased by 2 MHz when the cavity was evacuated. The cavity frequency was tuned up with an increase of 1.3 MHz in average. From this result, the cavity size will be 18 um reduced for the final production of 28 cavity BPMs. Quality factor of the cavity is better than 5000.

Mechanical and electrical center of the cavity has been measured by an antenna setup invented by H. Inoue in KEK. The offset came within 5 um accuracy well below the requirement of < 10 um.

Table 2. Results of the mechanical and microwave measurements for production model.

Parameters	Before brazing	After brazing		Design Value
		Before tuning	After tuning	
Frequency (GHz)	6.42158	6.42418	6.42548	6.42600
Isolation (dB)	23.7	25	46.6	> 30
Q_L	random	> 5000	6025	> 5000
Coupling	-	-	0.36	> 0.3
Offset (um)	-	< 5	< 5	< 10

Isolation between x-y planes is very important to achieve position resolution of 100 nm. The requirement of isolation < -30 dB was not easy without tuning mechanism for both with-dent and without-dent model. Using the tuning screws, the frequency can be adjusted accurately and the isolation could be controlled better

than -50 dB. Tuning range of the cavity is as large as +/- 3 MHz.

Beam Test at ATF

One of the prototype BPMs was selected to be installed in the ATF extraction beamline for the test of sensitivity and isolation. Fig. 3 shows the signal detection circuit connected with BPM pickup and the beam signal from a single pass of a beam bunch. Real beam position was checked with two stripline BPMs installed upstream and downstream of the test cavity BPM. Beam intensity was 0.8 x 10^{10} e/bunch when measured with an integrating current transformer (ICT) installed at the end of the extraction beamline. Nominal ATF bunch length is 8 mm.

Sensitivity of the cavity BPM was measured to be 0.8 V/mm when the two port signals are combined as shown in Fig. 3. Isolation was better than 40 dB with real beam measurements. [6]

By comparing the correlation between output signals from two opposite ports of the cavity, the 100 nm resolution of position measurement was proved within the dynamic range of +/- 50 um. [7]

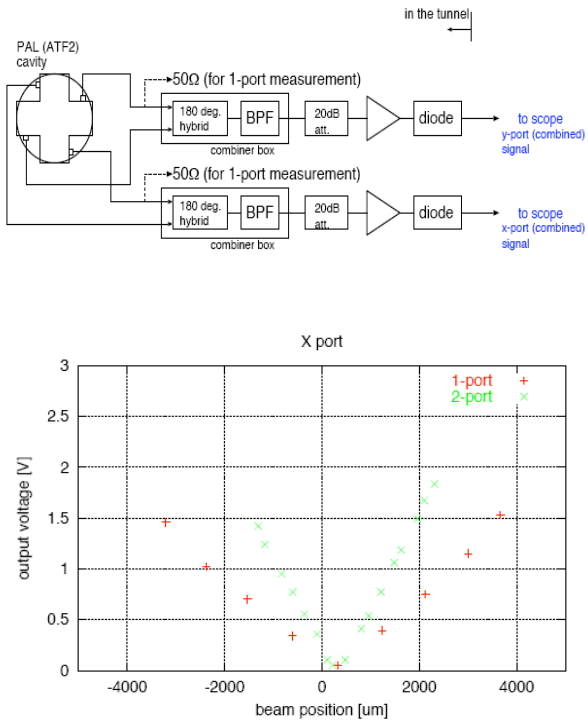

Figure 3: Signal detection circuit (top) and the sensitivity of cavity BPM (bottom) showing ~ 0.8 V/mm. Dashed lines are drawn for the guide over the 2-port data points (x). Quoted from Ref.[6].

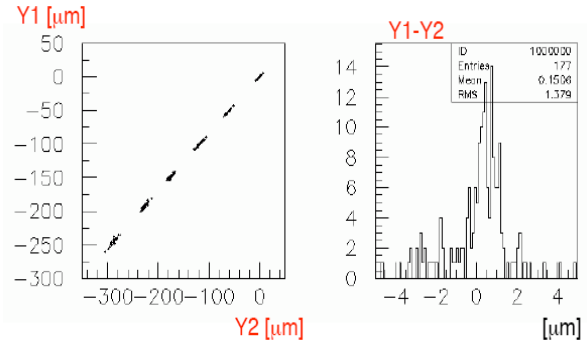

Figure 4: Comparison of two port signals (a), and the analysis of data shows 100nm rms resolution (b). Quoted from Ref. [7]

SUMMARY

Cavity BPMs are fabricated in PAL according to the KEK design. Errors in machining and brazing brought errors in the resonance frequency and isolation of the cavity. Resonance frequency of the cavity has increased slightly after the brazing. When the cavity is evacuated, the frequency further increases by 2 MHz. Four tuning screws positioned diagonally on the rim of the cavity could tune the cavity frequency and the x-y isolation well within the design parameters of the cavity. Overall design performance was proved through mechanical test, microwave test, and the beam test in the KEK-ATF.

REFERENCES

* Work supported by MOST, Korea, and KEK, Japan
# huang@postech.ac.kr

[1] For the overview on ILC project, refer to the website http://www.linearcollider.org/cms/

[2] LCLS Conceptual design Report, SLAC-R-593 (2002).

[3] XFEL Technical Design Report, DESY-2006-097.

[4] ATF2 Proposal, KEK Report 2005-2.

[5] Y. Honda, "Summary of Requirements on QBPM in the ATF2 ", Internal Technical Note, KEK, Jan. 2006.

[6] Y. Honda, et. al, "Beam Test of Prototype BPM after Tuning" , Internal Technical Note, KEK, Dec. 2005.

[7] Y. Honda, "Beam Test of ATF2 QBPM Electronics", Internal Technical Note, KEK, Apr. 2006.

EXPERIMENTAL VERIFICATION OF HALO FORMATION MECHANISM OF THE SNS FRONT END*

Dong-o Jeon#, Oak Ridge National Laboratory, Oak Ridge, TN37831, USA

Abstract

A series of emittance measurements were performed at the end of Drift Tube Linac tank 1 of the Spallation Neutron Source to verify experimentally the previously proposed halo generation mechanism and its mitigation schemes [1]. The emittance measurements clearly showed a visible reduction in the halo as well as a significant reduction in the rms emittance when the proposed round beam optics is employed. This confirms experimentally the new halo generation mechanism.

INTRODUCTION

The Spallation Neutron Source (SNS) accelerator system is designed to accelerate intense proton beams to energy of 1-GeV, delivering more than 1.4 MW (upgradeable to 2 MW) of beam power to the neutron production target [2]. The peak current in the linac is 38mA and the macropulse average current is 26mA due to chopping. The SNS linac has the following structure; ion source, LEBT (Low-Energy Beam-Transport), RFQ (Radio-Frequency Quadrupole), MEBT (Medium-Energy Beam-Transport), DTL (Drift Tube Linac), CCL (Coupled Cavity Linac), and SCL (SuperConducting Linac). A primary concern is potential damage and radio activation of accelerator components resulting from uncontrolled beam losses. A major source of loss is beam halo that intercepts the bore of the linac.

The uncertainty in the initial matching condition is Beam dynamics simulations of the SNS linac showed that the beam halo develops at low energy, but some halo particles survive acceleration to higher energies before being lost primarily on the CCL bore. This particle loss at higher energies results in radio activation of the CCL. In order to find ways to mitigate this halo related beam loss, studies were conducted to identify the sources and mechanism of halo formation. It turns out that the MEBT is the largest contributor to Front End (FE) halo generation in the SNS linac.

A new halo generation mechanism was reported in the non-periodic lattices such as the SNS linac MEBT (Medium-Energy Beam-Transport between RFQ and DTL) [1]. It was found that the nonlinear space charge force resulting from large transverse beam eccentricity ~2:1 in the ~1.6-m-long MEBT chopper section shown in the upper plot of Fig. 1 is responsible for halo formation. This MEBT optics is called as "nominal optics". As a result, the beam distribution, based on the Front End emittance measurements and multiparticle simulation studies, develops halo that leads to beam loss and radio activation of the SNS linac. Designing lattices with transverse beam eccentricity close to 1:1 as shown in the bottom plot of Fig. 1 suppresses this kind of halo generation. This optics is called as "round beam optics". Multiparticle simulations show that the rms emittance in both planes and halo are reduced significantly when the round beam optics is employed. Modifying the MEBT optics and introducing adjustable collimators in the MEBT significantly reduced beam losses in the CCL, which is a preferred scheme for mitigating halo. For the details, please refer to the previous study [1].

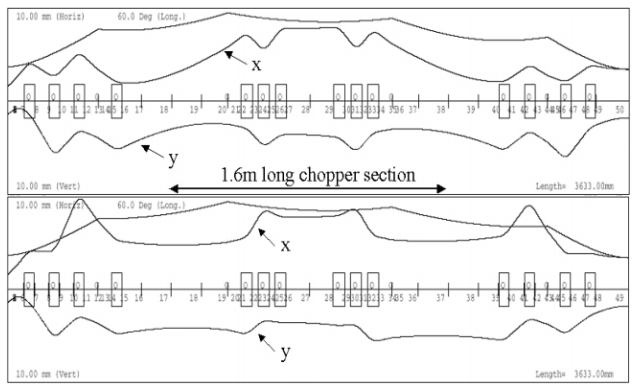

Figure 1: MEBT beam profiles obtained from Trace3D for the "nominal optics" at the top and for the "round beam optics" at the bottom employed for the emittance measurements. The beam is going from left to right.

A series of measurements were conducted to verify the effectiveness of the proposed halo mitigation scheme. One set of measurements was dedicated to see if the proposed round beam optics reduces halo and rms emittance. Round beam optics was adopted with transverse beam eccentricity close to 1:1 as shown in the bottom plot of Fig. 1. Matching was performed prior to measurements by minimizing the rms emittance in both planes. The other set was dedicated to see the effectiveness of the halo collimation in MEBT. For the DTL tank 1 commissioning, dedicated "Diagnostics-plate" [3] is attached at the end of DTL tank 1. There are horizontal and vertical emittance slits and harps installed for the emittance measurements, enabling emittance measurements in both planes. The arrows indicate the horizontal slit and harp.

* SNS is managed by UT-Battelle, LLC, under contract DE-AC05-00OR22725 for the U.S. Department of Energy.
#jeond@ornl.gov

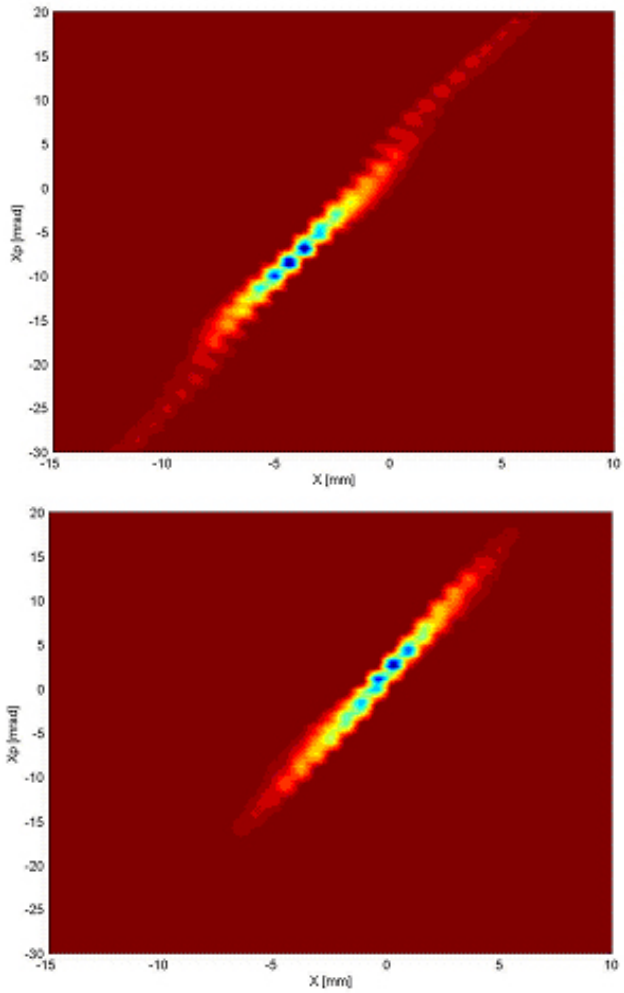

Figure 2: Horizontal emittance plots of the nominal MEBT optics (the top plot) and the round beam optics (the bottom plot). The halo is visibly reduced. The rms emittance is reduced from 0.454 mm-mrad to 0.289 mm-mrad with 0% threshold.

Figure 2 shows the results of horizontal emittance measurements for two different MEBT optics; one is the nominal optics and the other the round beam optics. Compared with the nominal MEBT optics, the halo is visibly reduced and the rms emittance is significantly reduced from 0.454 mm-mrad to 0.289 mm-mrad when the proposed round beam optics is employed. Because there is one electromaget quadrupole between the downstream end of DTL tank 1 and the emittance slits, the beam is rather stretched out in horizontal plane. The results of the vertical emittance measurements are shown in Fig. 3. Again visible reduction in the halo should be noted. The rms emittance is reduced from 0.472 mm-mrad to 0.306 mm-mrad.

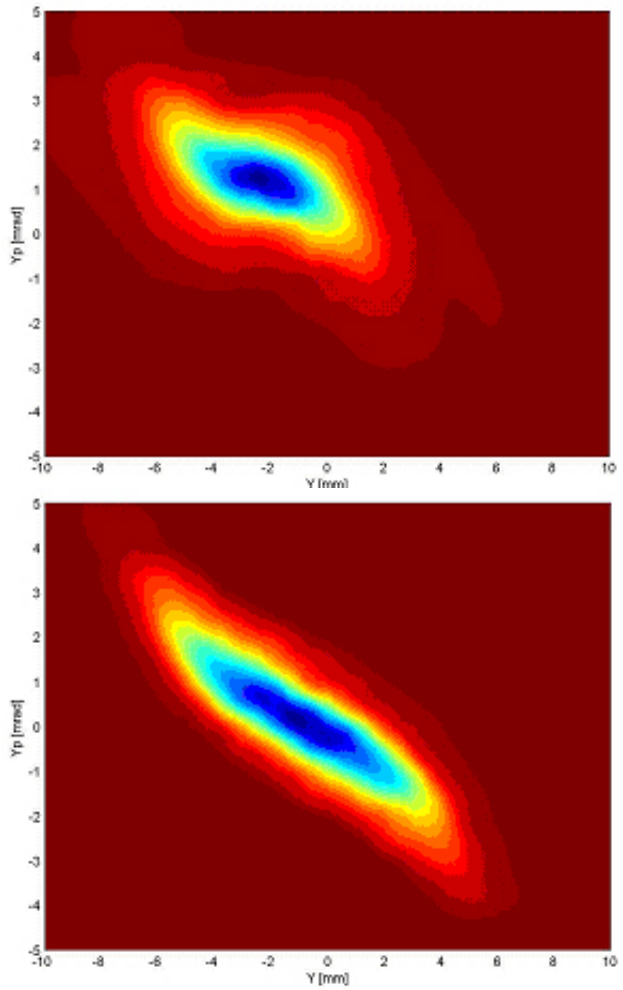

Figure 3: Vertical emittance plots of the nominal MEBT optics (the top plot) and the round beam optics (the bottom plot). The halo is substantially reduced. The rms emittance also is reduced from 0.472 mm-mrad to 0.306 mm-mrad with 0% threshold.

The ratio ε (round beam optics) / ε (nominal optics) of measurement results are consistent with the multiparticle simulations using the Parmila code [4].

Plots of beam distributions obtained from the simulation are shown in Fig. 4. The upper plots are beam distributions when the nominal MEBT optics is used and the lower plots when the round beam optics is used. The model predicts that the extended halo in the horizontal plane for the nominal optics disappears when the round beam optics is used, just like the measurement results in Fig. 3. The model also predicts that the rms emittance in both planes is reduced significantly when the round beam optics is employed instead. The ratio of ε_x (round beam optics) / ε_x (nominal optics) = 64% for the measurement and 74% for the simulation. Likewise ε_y (round beam optics) / ε_y (nominal optics) = 65% for the measurement and 91% for the simulation.

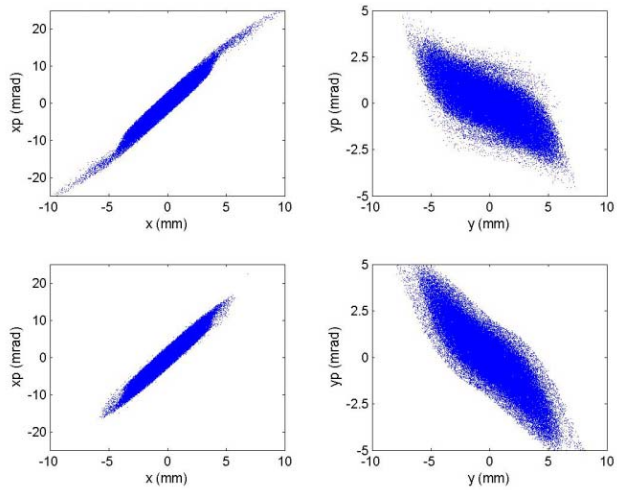

Figure 4: Plots of simulated beam distributions. Upper plots are obtained using the nominal MEBT optics and lower plots using the round beam MEBT optics. Reduction in halo is visible in both planes.

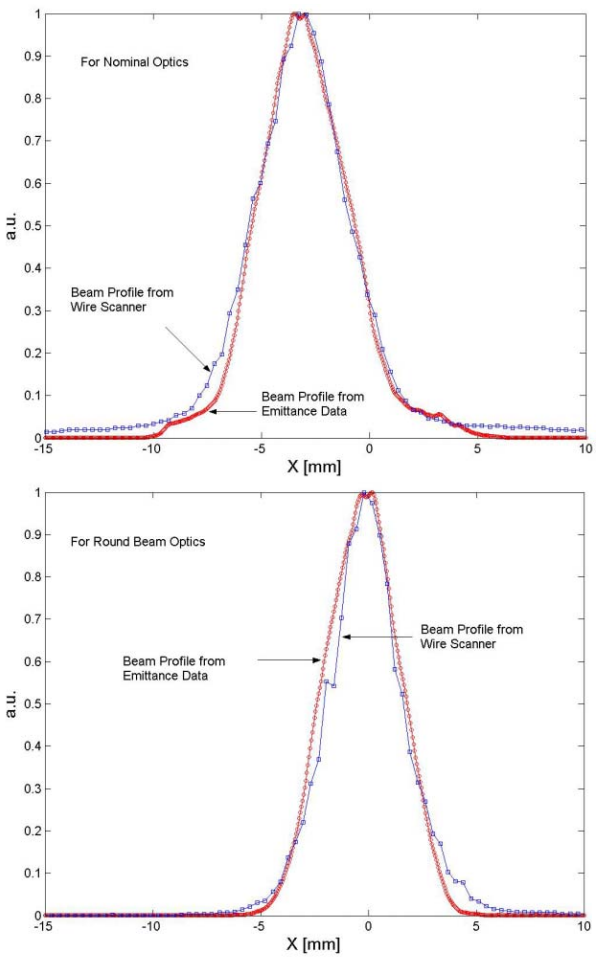

Figure 5: Plots of horizontal beam profile for two different optics sets. The top plot is for the nominal optics and the bottom for the round beam optics. Beam profile plots were obtained from the emittance data and wire scanner data. Wire-scanner seems to overestimate the tail at low intensity.

A comparison was made between the emittance data and raw wire scanner profile data. The beam profiles from the emittance data were consistent with the wire scanner beam profiles, as expected. The core of beam profiles obtained from the emittance data agrees well with the core wire scanner beam profiles for the two different sets of optics, as shown in Fig. 5. However, it is interesting to note that wire scanner seems to overestimate the beam tail compared with the profile obtained from the emittance data.

CONCLUSION

A series of emittance measurements verified the halo formation mechanism in MEBT of the SNS linac previously predicted through simulation studies [1]. Emittance measurements confirmed significant reduction both in the rms emittance and in the halo when the round beam MEBT optics is employed as predicted. This also serves as a valuable benchmarking of space charge codes demonstrating that measurements results are quite consistent with the simulation.

REFERENCES

[1] D. Jeon et al, Phys. Rev. ST Accel. Beams **5**, 094201 (2002).
[2] J. Wei et al, Proc. of the 2001 Part. Accel. Conf. (Chicago, 2001), p. 319.
[3] M. Plum et al, Proceedings of the 2001 Part. Accel. Conf. (Chicago, 2001), p. 2374.
[4] H. Takeda, Parmila code, Los Alamos National Laboratory.

A LARGE AREA SCANNING MAGNET FOR HOMOGENOUS IRRADIATION OF TARGETS

A.Mandal, G.Rodrigues, S.K.Suman and Rajesh Kumar
Inter University Accelerator Centre, New Delhi-110067

Abstract

The scanner is an important tool for accelerator based material science research. For high energy (~100 MeV) ion beam scanner has to be magnetic one. Major problem faced with magnetic scanner is its high inductance which causes large impedance to the a.c. power supply used to energise the magnet. We have designed a magnetic scanner keeping attention to minimise its inductance. The scanner is composed of two independent H-type dipole magnets which are fed by saw tooth pulses. It can scan over an area of 50 mm x 50 mm at a distance of 3 metre. The power supplies for this scanner have also been designed. These are bipolar, wideband, high speed amplifiers that can reproduce complex waveform without any distortion. The ratings are 60 V, 50 A operating at 50 Hz for x-scanner and 5V, 70A at 0.2 Hz for y-scanner.

INTRODUCTION

Beam Scanner is an important tool in Accelerator based research in Material Science in the scientific laboratory as well as in industry. It helps in scanning ion beam over a large area of the sample in a considerably less time, thus saving a lot of costly beam time which in turn helps in reducing price of the product in the industry. The scanner used in the low energy accelerator is electrostatic whereas it is magnetic in the high energy end. We have developed a magnetic scanner for homogenous irradiation of samples in material science beam line in beam hall – II of 15 UD pelletron [1]. The problem encountered in magnetic scanner is the high inductive impedance of the magnet which poses great problem in developing suitable power supply for energising the magnet. Keeping this in view we have made the design criteria of the magnet to have low inductance ~ 4mH. We have also developed suitable power supply for the magnet. The following sections describe the design of the magnet and power supply.

DESIGN OF THE MAGNET

The scanning magnet has been designed with the following beam and geometrical specifications:

ME/Z^2 for the beam = 400 a.m.u.MeV where M is mass in a.m.u and E, the energy in MeV and Z is charge state of the ion. L, the distance of the target from the magnet = 3 metre and scanning area = 50 mm x50 mm

To reduce the indutance we have considered two separate H-shaped magnets for scanning in horizontal (X) and vertical (Y) planes. The first dipole is for scanning in Y-plane and the second one for X-plane. The ratio of operating frequency for X and Y magnets is 100: 1. Since operating frequency for X is large compared to Y magnet, the length of X magnet has been increased compared to Y-magnet to have same scanning length in both planes at reduced current. The linear deflection of the beam by a dipole magnet of magnetic field B at a distance L is given by the formula:

$$D\ (mm) = 6950\ L \int B\ dl / (ME/z^2)^{0.5}$$

For a deflection of 25 mm at a distance of 3 metres, $\int B.dl$ = 0.02398 T.m. Taking the effective length of the x-magnet 0.2 m we get B =0.12 T. Ampere-turn is calculated using the formula $NI = Bg/\mu$ where g is the pole-gap and μ is the permeability of the air medium. Taking pole gap 53 mm, NI comes out to be 4774. If we take I= 50 A, N=96. Hence the number of turns per pole is 48. Taking the effective length for y magnet as 0.125 m, B turns out to be 0.19T. This is achieved by energising it at a current of 75 A for N = 96. The physical design specifications of the magnet is given below:

Pole gap	53 mm
Physical length (mm)	175(x magnet), 100 (y magnet)
Pole width	100 mm
Pole height	60 mm
Turns/coil	48
DC resistance	25 mili-ohm/coil
Inductance	~ 4 mH (2-coils)
Impedance	~ 1.2 ohm at 50Hz
Current	50 A (x), 75 A (y)
Voltage	60 V (x), 5 V (y)
Power	3 KW (x), 0.4 KW (y)

The schematic design of the magnet is shown below.

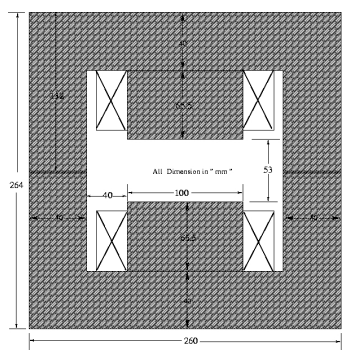

Figure 1: Schematic design of the magnet

The magnet has been fabricated by local vendor in Delhi. It has been tested with DC power supply. The excitation curve and axial field mapping are shown in figure 2 and 3 respectively.

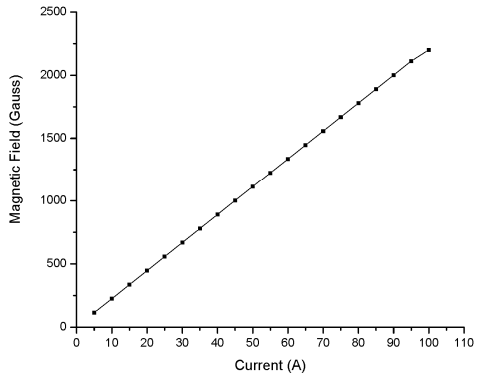

Figure 2: Excitation curve

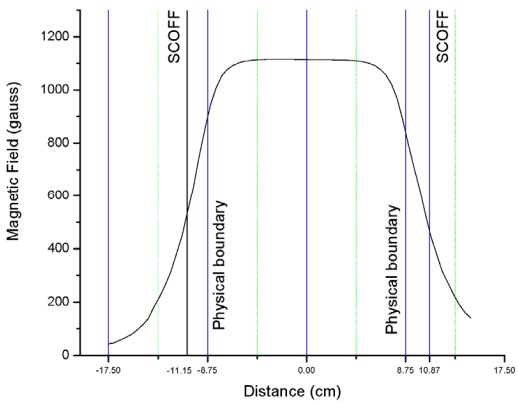

Figure 3: Axial field distribution

POWER SUPPLY

Scanner magnet power supply is basically an amplifier with considerable bandwidth which provides current regulated triangular wave output to magnet (inductive loads) corresponding to triangular wave input. The power supply works on a linear series pass technique. A group of complimentary transistors have been used in push pull configuration at output stage (series pass element) to get the bipolar output, which is driven by high gain error amplifier for achieving wide signal bandwidth and rapid output slewing. A special technique has been used in the regulation (figure 4) for achieving a cross-over distortion free output, foldback type limit for both output voltage and current. As shown in the schematic of regulation technique, the control circuit has mainly two loops viz., quiescent current loops and regulation loops. The quiescent current control circuit keeps a constant current flowing through push-pull stage, regardless of the load condition and direction of load current for getting a crossover distortion free output. While the outer feedback control loop is for output regulation, where output feedback signal is compared with reference at the input of error amplifier. The resulting error signal drives push-pull stage and regulates output. Six identical high gain error amplifiers are used in the regulation system. Four error amplifiers are for foldback limit and remaining two for output regulation. Both voltage as well as current regulation has been provided in the circuit. Whenever power supply is in voltage regulation, the current control will simultaneously work for foldback limit and vice versa. The specifications of the power supply is give below.

Specifications:

- Output current range : ±(0-50A)
- Output voltage range : ±(0-60V)
- Scanning frequency range : 0.4 - 50Hz
- Input voltage : 415V, 3 phase

Features:

- CAMAC / Local operation.
- Voltage and current regulation with foldback output limit.
- Back e.m.f protection.
- True regulated triangular wave output without crossover distortion.
- Necessary safety interlock to put-off load current if either interlock fails.
- Status indication of power supply on front panel as well as for CAMAC.

The block diagram of the power supply is shown in figure 5. The power supply has been tested with the magnet. The output waveform is shown in the figure 6.

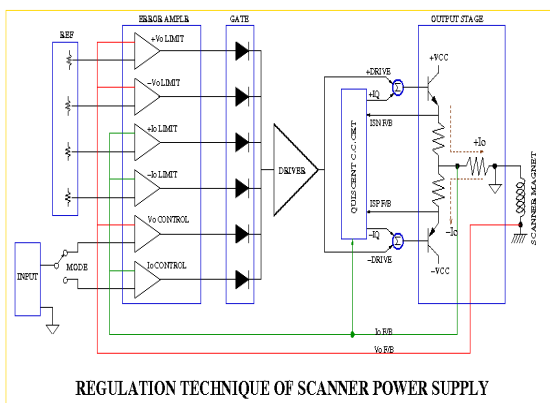

Figure 4: Schematic of regulation technique

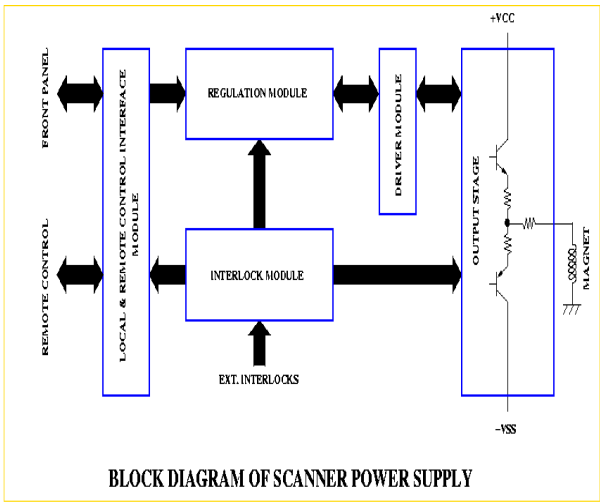

Figure 5: Block diagram of the power supply

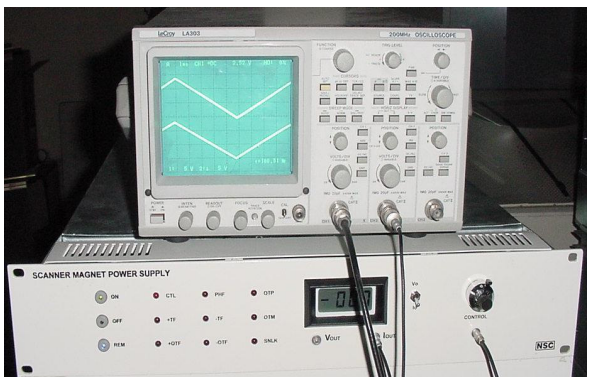

Figure 6: Output waveform with magnet as load

REFERENCES

[1] D.Kanjilal, S.Chopra, M.M. Narayanan, Indira S. Iyer, V.Jha, R.Joshi and S.K.Datta, Nucl.Instrum. Methods A 328 97 (1993)

MAGNETIC FIELD CALCULATIONS OF A 10 MEV HIGH CURRENT COMPACT CYCLOTRON

V. S. Pandit#, P. Sing Babu, A. Goswami and P. R. Sarma
Variable Energy Cyclotron Centre, 1- AF, Bidhannagar, Kolkata, India

Abstract

In this paper we present the design study of the main magnet of the 10 MeV compact cyclotron. The preliminary dimensions of the magnet and the properties of the equilibrium orbits were first obtained using hard edge approximation. The primary size of the magnet was estimated using two-dimensional POISSON code. Finally a 3D code was utilized for the field optimization. The profile of magnet sectors was optimized based on the computed results to get the desired values of isochronous field and the betatron tunes.

INTRODUCTION

Under the ADS development programme of the DAE, a 10MeV, 5-10mA compact radial sector proton cyclotron, is being developed at VECC in Kolkata [1, 2]. A 2.45 GHz microwave ion source will produce ~30mA of proton beam at 100keV. The extracted beam will be first collimated using slits and then it will be bunched using a sinusoidal buncher. It will be injected axially in the central region of the cyclotron where a spiral inflector will place the beam on the proper orbit. Two delta type resonators, each having ~ 45 degree angle located in the opposite valleys, will be used for providing acceleration to the beam. Finally, this beam will be extracted using an electrostatic deflecting channel. The main aim of this project is to study and settle various physics and technological issues associated with the production, bunching, acceleration, injection, extraction, etc. of the high intensity beams.

In our design there are four magnet sectors. We have tried to keep a maximum magnetic field of 1.5T at the hill centre, and an average magnetic field of 0.689T, which correspond to a particle revolution frequency of 10.5MHz for proton. The hill gap is 4 cm and the valley gap is 64 cm, same as the distance between the upper and lower return yokes. For the injection system, one hole is provided at the center. We have provided four holes in the four valleys, two of them will be used for vacuum pumps and the rest two will be used for the RF cavities vertically. Apart from using a high dee voltage, we have chosen a low average magnetic field and hence a large extraction radius of ~65 cm for 10 MeV cyclotron to have a reasonable turn separation at the extraction radius. Though this method increases the cost of the cyclotron, it gives more flexibility and a clear advantage for injection and extraction. The harmonic mode h of operation is equal to 4. The magnet design combines the advantages of solid pole cyclotron and separated sector cyclotron. A high flutter provides strong focusing in the vertical direction. The main idea was to provide the vertical betatron tune > 0.5 at all radii. This is necessary for handling the beam space charge defocusing force at the average beam current of ~ 5mA. In order to meet the isochronism, the shaping of the azimuthally averaged magnetic field was done with the help of varying the sector angular width along the radius.

The primary size of the magnet was estimated using two-dimensional code. Finally a 3D code was utilized for the field calculation and optimization. The profile of magnet sectors was optimized based on the computed results to get the desired values of isochronous field and the betatron tunes.

#pandit@veccal.ernet.in

CYCLOTRON PARAMETERS

The conceptual dimensions of the magnet and the properties of the equilibrium orbits (EO) were first determined by a computer code based on hard edge approximation and matrix method [3, 4]. Here we outline the procedure briefly. Details are given in reference [5]. For an N sector cyclotron with magnetic fields B_H and B_V in the hill and valley respectively, the angles of turning of orbits η and ξ can be given as

$$\eta = \frac{B_H B_V}{B_H - B_V} \cdot \frac{2\pi}{N} \cdot \left(\frac{1}{B_V} - \frac{1}{\gamma B_0} \right), \quad \xi = \frac{2\pi}{N} - \eta \qquad (1)$$

where γ is the usual relativistic term and B_0 is the central magnetic filed. One can easily obtain the angular widths of the hill and valley η_0 and ξ_0 on an equilibrium orbit for a given energy by solving

$$\cot\left(\frac{\eta_0}{2}\right) = \cot\left(\frac{\pi}{N}\right) + \frac{B_H}{B_V}\left(\cot\left(\frac{\eta}{2}\right) - \cot\left(\frac{\pi}{N}\right) \right),$$

$$\xi_0 = \frac{2\pi}{N} - \eta_0 \qquad (2)$$

In order to calculate betatron tunes we need entry and exit angles to the hill (which becomes the exit and entry angles for the valley), which are given by

$$\phi_1 = \varepsilon_1 + \frac{\eta - \eta_0}{2}, \quad \phi_2 = \varepsilon_2 - \frac{\eta - \eta_0}{2}$$

$$\tan \varepsilon_2 = \tan \varepsilon_1 + R \cdot \frac{d\eta_0}{d\gamma} \cdot \frac{d\gamma}{dR} \qquad (3)$$

Here ε_1 is the spiral angle at the entry of the hill, which is zero in the present case. The effective spiral angle ε_2 at the exit of the hill includes spiral angle as well as flaring effect [4]. We have used the well-known matrix method to estimate the betatron tunes. Here hills and valleys are treated as bending magnets of lengths $\eta\rho_H$ and $\xi\rho_V$ having focusing strengths of $1/\rho_H$ and $1/\rho_V$, ρ_H and ρ_V being the radius of curvature in the hill and valley respectively. The

flaring and the edge effects are introduced by using thin lens matrices at each hill-valley boundary. Since the vertical focusing frequency is quite sensitive to the fringe field at the hill-valley boundary, we have modified the classical hard edge formula to include the soft edge effect. The radial and vertical betatron tunes υ_r and υ_z can be easily obtained from:

$$\upsilon_r = \frac{N}{2\pi}\cos^{-1}\left[\tfrac{1}{2}Tr(\mathbf{V_R}\cdot\mathbf{H_R})\right]$$

$$\upsilon_z = \frac{N}{2\pi}\cos^{-1}\left[\tfrac{1}{2}Tr(\mathbf{V}_V\cdot\mathbf{H}_V)\right]$$

Here $\mathbf{H_R}$, $\mathbf{H_V}$ and $\mathbf{V_R}$, $\mathbf{V_V}$ are the transfer matrices for horizontal and vertical motions in the hill and valley respectively. We have obtained the initial shape of the magnet and properties of the equilibrium orbit using an iterative process. Care has been taken to keep betatron tunes υ_r and υ_z sufficiently away from the resonance.

MAGNET DESIGN

A 3D computer code was used to calculate and achieve the isochronous magnetic field. Fig. 1 shows the model of the magnet. In order to improve the accuracy we have used one eighth model and divided the hill in several parts to give different mesh sizes appropriate with the dimension i.e., smaller mesh sizes at lower radii. One of the most difficult problems to solve was the shaping of the magnetic field in the central region. In our case the height of the spiral inflector is ~10cm (100 keV injection energy), which requires a reasonably large space and, therefore, a careful optimisation of the central plug was needed. The required isochronous field within the tolerances was obtained after several iterations by shimming the angular width of the hill as a function of radius as shown in Fig. 2. Initially the sector radius was chosen to be equal to the extraction radius plus one pole gap, however, during the iteration it was modified to provide good field region up to the final closed EO.

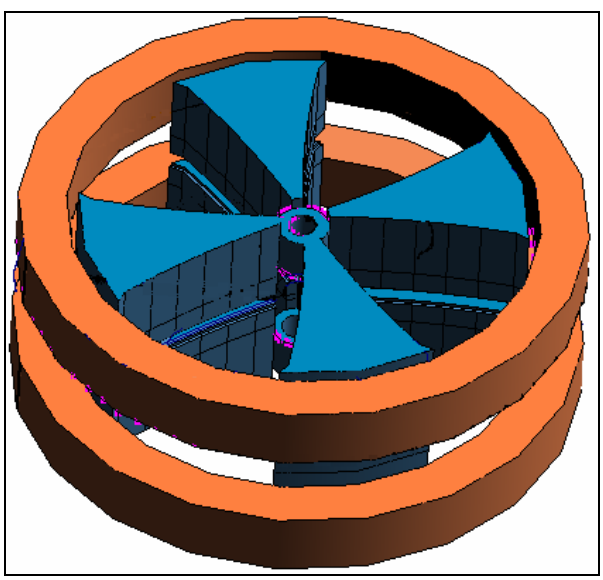

Figure 1: Model of the magnet used for field calculation.

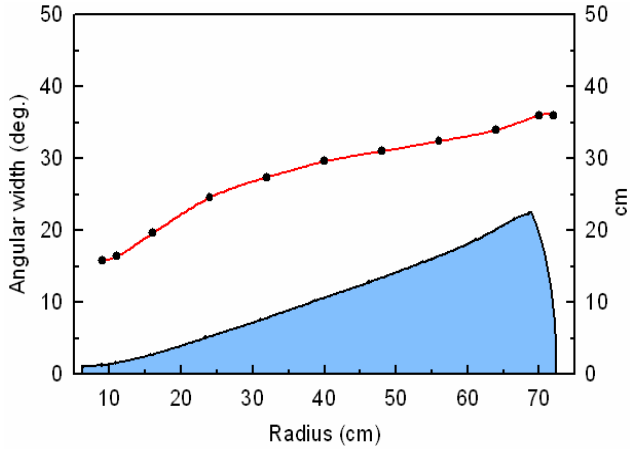

Figure 2: Optimized angular width of the sector as a function of radius and a half model of the hill.

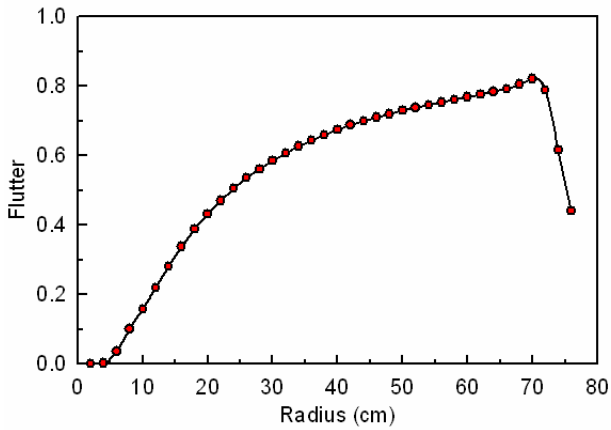

Figure 3: Flutter as a function of the radius.

Table 1: Optimized parameters of the magnet

Injection energy	100 keV
Final energy	10 MeV
Number of sectors	4
Hill gap	40 mm
Valley gap	640 mm
Sector angular width	16-34 deg
Hill field at extraction	1.5 T
Valley field at extraction	0.15 T
Extraction radius	65 cm
Pole radius	72 cm
Ampere turns	315 × 200
Iron weight	25 ton

ORBIT PROPERTIES

The properties of the equilibrium orbit i.e., the radial and axial tunes, frequency error, integrated phase shift, and average magnetic field etc. were optimized after several iterations using the equilibrium orbit program GENSPEO [6]. Fig. 3 shows the variation of calculated flutter with radius whereas Table 1 presents the optimized important parameters of the magnet. All the EO calculations were done at energy intervals of 200 keV

starting from 100 keV. Fig. 4 presents the frequency error Ω(ω) between the calculated field and the isochroous field as function of radius whereas Fig. 5 shows the integrated phase shift. The analysis shows that the phase excursion in the entire region is limited within ± 10deg. The radial and axial betatron tunes are plotted in Fig. 6 and compared with those of the analytical calculations.

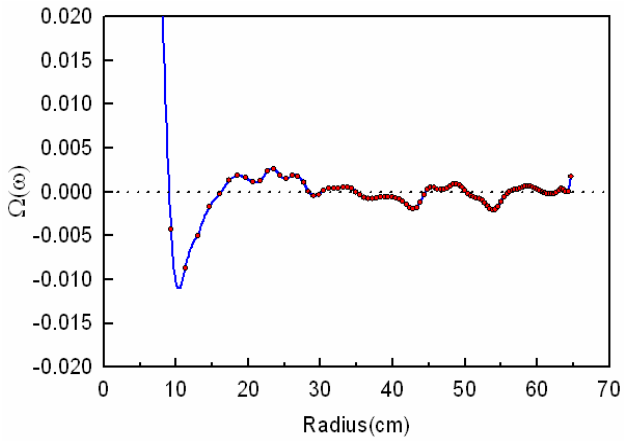

Figure 4: Variation of frequency error $\Omega(\omega) = (\omega_0-\omega)/\omega$ as a function of the radius.

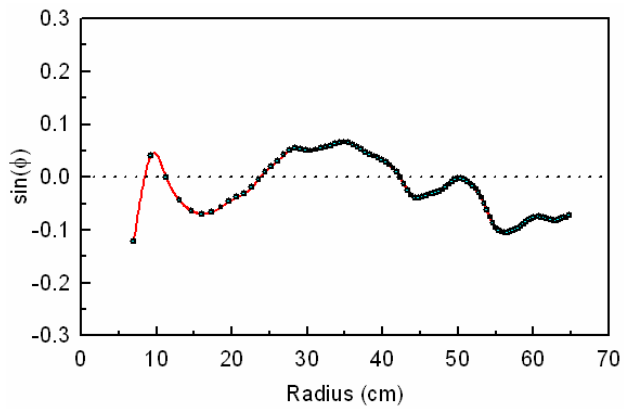

Figure 5: Variation of integrated phase shift with radius. The phase excursion during the entire region is within reasonable limit of ± 10deg.

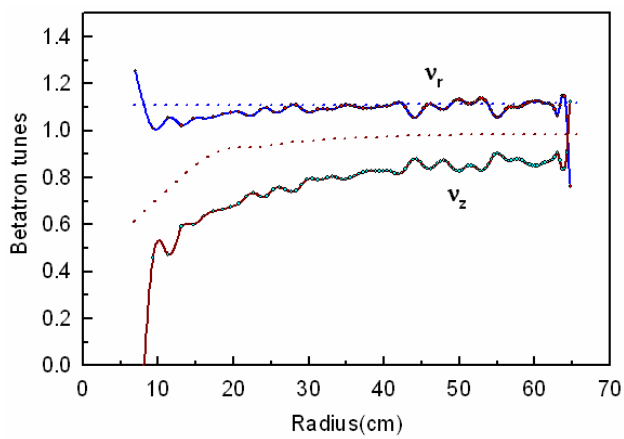

Figure 6: Variation of radial and axial betatron tunes with radius. Dotted curves represent the analytical results.

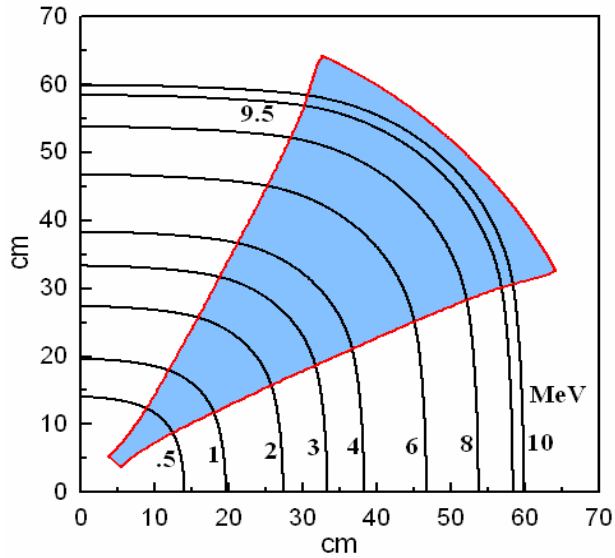

Figure 7: Equilibrium orbits for different energies. The separation between the last two orbits is ~1.8 cm.

CONCLUSION

In this work we have presented the modelling of the magnet and 3D calculations of the magnetic field of the 10 MeV compact cyclotron. The 3D magnetic field calculation has been found to be utmost useful for the optimisation of the hill shape near the central part. The detailed interpretations of the results and further detail modelling, particularly in the central region, are in progress. Studies related to the design optimization of the RF system are in progress.

REFERENCES

[1] V. S. Pandit, "Development of ion source and injection system for high current compact cyclotron" Indian Particle Accelerator Conference InPAC-05 (2005) 13

[2] V. S. Pandit, "Beam dynamics studies of a high current compact cyclotron" Indian Particle Accelerator Conference InPAC-06 (2006) 20

[3] J. R. Richardson, "Sector Focusing Cyclotrons", Progress in Nuclear Techniques & Instrumentations, Vol. 1, North Holland (1965)

[4] J. J. Livingood, "Principle of Cyclic Particle Accelerators", D. Van Nostrand Comp. (1961)

[5] A. Goswami, P. Sing Babu and V. S. Pandit, "Behaviour of space charge dominated beam in a high current compact cyclotron"' Nuclear Instruments and Methods A 562 (2006) 34.

[6] M. M. Gordon, "Computation of Closed Orbits and Basic Focusing Properties for Sector-focused cyclotrons and the Design of "Cyclops", Particle Accelerators, 16 (1984), pp. 39-62.

8 GEV BEAM LINE OPTICS OPTIMIZATION FOR THE RAPID ANTIPROTON TRANSFERS AT FERMILAB*.

V. Nagaslaev#, V. Lebedev, J.Morgan, D.Vander Meulen
Fermilab, PO Box 500, Batavia IL 60510, USA

Abstract

Tevatron Run-II upgrade requires a significant increase of the efficiency and speed of the antiproton transfers from the Accumulator to the Recycler. The goal for the total transfer time is challenging a reduction from 1 hour down to a few minutes. Here we discuss the beam line optics aspects of this project. Results of lattice measurements and optimization are analyzed in terms of transport efficiency and stability.

INTRODUCTION

The transport of antiprotons between the Accumulator and Recycler involves 3 machines and 5 beam lines. The total length of the beam lines is over 1 km and each machine performs RF manipulations with the beam on its way. Because some of the beam lines are also used for transfers at 120GeV and 150GeV in addition to 8GeV, an initial tune up is made with the reverse proton beam prior to transporting antiprotons. The antiproton beam is sent from the Accumulator in multiple transfers, usually 5 or 6. A 2.5 MHz H=4 RF system (ARF4) is used to bunch a portion of the stack and accelerate it to the injection/extraction orbit about 140 MeV away. The extraction kicker (EKIK) then kicks this portion into the 8GeV transport line. This beam passes through the AP3, AP1, P2 and P1 beam lines on its way to the Main Injector. Main Injector RF synchronously captures the beam and decelerates it by about 40 MeV to match the Recycler ring energy.

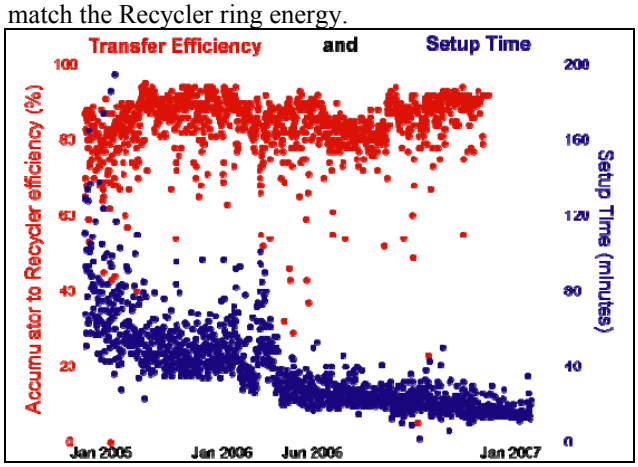

Figure 1. Accumulator to Recycler transfer efficiency and the shot set up time in 2005 through 2007. Transfer efficiency data is unavailable for the past few months but is thought to be near the historic best.

Antiprotons are then transported to the Recycler through the R22 beam line. Recycler RF forms barrier buckets to isolate the injected beam and pre-cool it before merging with the main antiproton stack. In the transfer process (shots) each machine is changing its state and mode of operation synchronously with others. The most complex transformation takes place in the Accumulator ring. It has to change from pbar accumulation (stacking) mode, where it injects antiprotons from the Debuncher and stochastically cools them into the dense core, to the transport (unstacking) mode. This process historically involved manipulation of thousands devices. Factoring in cooling the core down before the transfers, the whole process used to take more than an hour prior to 2006.

STEPS TO EFFICIENT TRANSFERS

In order to maximize the rapid transfer efficiency good beam orbit control is required. Beam line lattice functions should be well matched to the optics of the downstream machine to avoid emittance dilution. Effective apertures should be maximized, achieved by the lattice optimization and proper beam steering. A number of hardware upgrades are needed in order to meet the goals of rapid transfers.

Magnet ramping

In 2003 the optics of the beam line was modified in order to avoid changing polarity on some magnets when switching between 120GeV and 8GeV beam line power supplies. This facilitated a faster transition between modes and improved the reproducibility of magnetic fields. The 2 sets of power supplies were originally used to improve power supply regulation. The next step is to avoid switching between power supplies. AP1 line is now being converted to single power supply operation with installation of waveform generating cards. The P1 and P2 beam lines already ramp and the AP3 beam line is dedicated to 8GeV operation.

BPM upgrade

An upgrade of the beam line Beam Position Monitor (BPM) system has been recently completed. New advanced system allows taking data at both 53 MHz (protons) and 2.5 MHz (pbars) for all transfer modes in real time. In particular it has made it possible to take good quality orbit data during antiproton transfers which have many advantages.

MI dampers

There is a transverse narrowband damper system in the Main Injector used for damping oscillations in proton beams arriving from the Booster. Switches have been installed in this system to make them bi-directional, so

** Work supported by FRA, LLC under Contract No. DE-AC02-07CH11359 with the United States Department of Energy.
#vnagasl@fnal.gov

that they can be used for fast damping of antiproton injection oscillations in wideband mode. Installation and commissioning of the new control cards is expected to be completed in February 2007.

ARF4 modifications

Some beam loss on antiproton transfers takes place because the extraction kicker does not have a sufficiently fast rise time (it was originally designed for single bunch transfers). The leading and trailing particles in the 4 bunch train get too little and too much kick respectively. Since it is impractical to build and install a new high vacuum kicker tank in the time remaining in Run II, bunch shortening and other alternative extraction methods were considered. The simplest approach has already been implemented. The ARF4 voltage has been increased by more than a factor of 2 during antiproton transfers, resulting in shorter bunches and improved efficiency. Further modifications to ARF4 have been recently proposed to double the voltage again and, further reduce the bunch width. Since the momentum spread of the beam will grow with each increase in voltage, the beam line apertures in dispersive locations may need optimization to prevent scraping.

ORBIT CONTROL AND LATTICE MATCHING

Orbit control and lattice optimization are the key elements for achieving the best transfer efficiency. The lattice design should ensure maximum beam line aperture and the orbit should be steered to the center of that aperture. The centered orbit has been defined using quadrupole centering and local orbit bumps. This orbit has been recorded as the "reference" orbit and the normal orbit is kept as close as possible to the reference. Based on the ongoing studies and observations the reference orbit may be updated to improve aperture.

Figure 2 shows the beam size envelopes calculated with the OptiM program throughout the line for the beam with an unnormalized emittance of 1 π·mm·mrad.

The tightest horizontal aperture is located in the Accumulator extraction Lambertson magnet. In the lattice design the horizontal beta function is minimized in this location. But it is still important to carefully control the orbit in this region. In addition to the tight aperture, due to the substantial non-uniformity of the field in this magnet there is a strong skew-sextupole component which causes coupling for a horizontally displaced beam.

Currently orbit checks are carried out with reverse proton beam before every set of antiproton transfers. If necessary, orbit corrections are applied in the beam line (usually only needed once every few days). Another application then checks for injection oscillations of the proton beam in the Accumulator. Once orbit and closure are verified and corrected, operation proceeds to the shots. Kicker voltages are adjusted to compensate for the differing electric field effects on the protons and antiprotons. An offset is required on several trims to compensate for small trajectory differences between the protons and antiprotons. These corrections have been found empirically. Once the beam line tune up has been completed, orbit oscillations on the antiproton transfers are typically quite small, generally less than 0.5mm. When they are larger, closure corrections at the end of the beam line are applied by the BLT application (Beam Line Tuning) in the Main Injector. It is anticipated also that a new orbit control application will be used to calculate and apply corrections to the beam line orbit after each antiproton transfer. Such an application has been developed for the 120 GeV transport and proved to be very successful. With the improved tools and the addition of transverse injection dampers in Main Injector, the need for a routine reverse proton beam line tune up and orbit closure will be eliminated.

Lattice matching

The lattice design of the AP3-P1 8 GeV transfer lines has been greatly improved. Lattice improvements were part of the Run-IIb upgrade plan [1] and featured

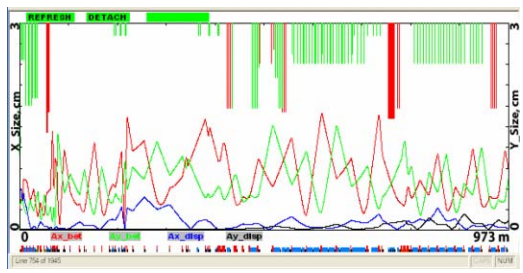

Figure 2. Beam size envelopes in the 8 GeV antiproton transport between the Accumulator and Main Injector. Red and green lines represent horizontal and vertical beam size at 95%, respectively. Vertical red and green bars in the upper part of the plot indicate the aperture limits.

substantially lower beta-functions, which resulted in more aperture room. The new lattice resulted in magnet polarities being the same for both 8 GeV and 120 GeV modes of operation. Better matching of the horizontal dispersion was also achieved. However, matching the vertical dispersion function has proven more difficult, requiring the rewiring of blocks of quadrupole groups that are bussed together. This work is planned as a future upgrade.

Lattice functions are determined using the differential orbit method [2]. Figure 3 shows a set of 4 differential orbits: 2 in the horizontal plane and 2 in the vertical plane. With the single corrector bumps separated by π/2 in betatron phase, these data sets provide enough information to fully determine all the corrections to the quadrupole designed strengths.

These corrections are found by varying all focusing elements to fit the orbit data with the calculated trajectories. Until very recently measurement of the lattice functions in the beam line could only be carried out using reverse protons from the Main Injector. This allowed a variety of intensities and frequent beam pulses. The

disadvantage of this method was that the orbit variations could not be seen beyond the beam line, so it was not possible to reliably determine the errors in the few last quadrupoles of the line. This problem has been resolved with the new 2.5 MHz BPM system upgrade, mentioned above. With the differential orbits recorded with an antiproton beam moving in the opposite direction, those missing quadrupole corrections can be easily found. Correction to the quad EQ2 quadrupole gradient was found to be around 1% which makes quite significant change of the beta-functions in the antiproton direction, as it is shown in Figure 4.

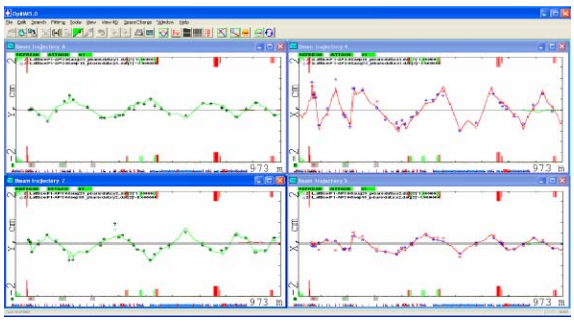

Figure 3. Four differential orbits taken with antiprotons.

Figure 4. Top and bottom plots show the change in the beta-functions (red trace – horizontal, green - vertical) in pbar direction when EQ2 quad strength is changed by 1%.

With the new measurements of the lattice functions using antiprotons, optics corrections were calculated and implemented to match the Accumulator, beam line and Main Injector. Figure 5 presents data taken with the Main Injector Ionization Profile Monitor (IPM) on the beam size turn-by-turn oscillations. Substantial oscillations in the September 29 data (blue traces) indicate an optics mismatch and transverse quadrupole oscillations of the beam size at double betatron frequency.

These oscillations eventually lead to beam emittance dilution and larger beam size, which causes losses and poor lifetime of the injected beam in the final destination-the Recycler ring. Making the optics match eliminated the beam emittance blow up and resulted in the overall transfer efficiency improvement in the end of October 2006, as it is shown in the Figure 1.

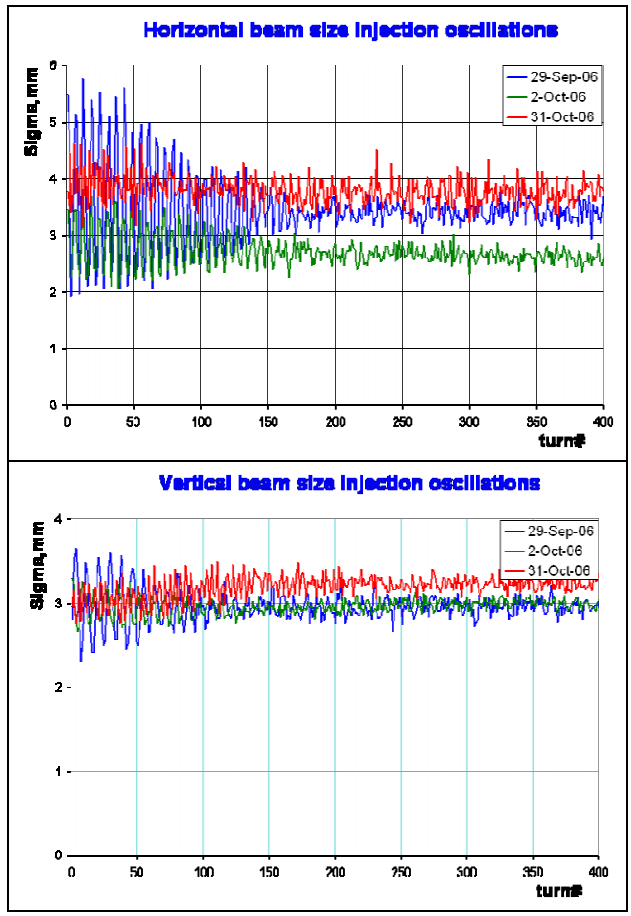

Figure 5. Main Injector IPM measurements of the transverse beam size oscillations at injection. Top and bottom plots show horizontal and vertical oscillations, correspondingly, before the optics matching (blue), after first correction (green) and after second correction (red).

CONCLUSIONS AND CURRENT PLANS

Substantial progress has been made towards fast, stable and efficient antiproton transport between the Accumulator and Recycler. While the total shot time has been reduced down to 15 minutes transfer efficiency has been maintained at the 95% level. Better dispersion matching still needs to be implemented. Orbit control application and Main Injector wideband dampers are expected to be completed soon in preparation for the elimination of the reverse proton tune up. Optics matching of the AP3-P1 line to the Main Injector has helped to maintain good antiproton transfer efficiency. The similar effort is now underway to improve optics of the R22 line between Main Injector and Recycler rings.

REFERENCES

[1] Run-IIb plans. http://www-bd.fnal.gov/doereview02/RunIIBTDR.pdf

[2] V.Lebedev et al., Measurement and correction of linear optics and coupling at Tevatron complex. ICAP-04, St. Petersburg; NIM A558 (2006), p299.

DESIGN AND OPERATING EXPERIENCE OF TRIODE ELECTRON GUNS FOR INDUSTRIAL ELECTRON ACCELERATORS

Arvind Jain, A.R.Chindarkar, K.C.Mittal
Accelerator and Pulse Power Division, Bhabha Atomic Research Centre, Mumbai 400 085
arvjain@ barc.gov.in

Abstract

The Accelerator and Pulse Power Division of BARC is presently constructing three industrial electron accelerators for radiation applications. a) a 500keV, 10 KW Cockcroft-Walton accelerator b) a 10MeV , 10kW electron linac and c) a 3MeV, 30kW DC machine. While the DC machines require an almost parallel beam with less than 1.0 degree divergence, the RF linac gun requires a 50keV, 2 ampere pulsed beam of low emittance. Using relativistic electron optics, including space charge effects, very simple triode gun designs with flat cathode, grid and anode apertures which fulfil these requirements and are easy to fabricate experimentally are described. Our operating experience with these guns are also described.

INTRODUCTION

The Accelerator and Pulse Power Division of BARC is presently constructing three industrial electron accelerators for radiation applications. a) a 500 keV, 10kW Cockcroft-Walton accelerator b) a 10 MeV , 10 KW electron linac and c) a 3 MeV, 30 KW DC machine. These accelerators, for irradiation purposes, require electron guns with special requirements. The two DC machines require an almost parallel beam with less than 1.0 degree divergence from the gun to enable the beam to drift through the accelerating modules. The linac requires a 50 to 80 keV , 1 to 3 ampere pulsed beam with a duty cycle of 0.1% . In this case a normalized emittance of the electron beam less than 100π mm mR MeV/c is required. Using relativistic electron optics, including space charge effects, very simple gun designs are presented which fulfill these requirements. A triode gun, having a flat cathode and parallel discs with apertures for the grid and anode have been used in the designs. The electron trajectories have been obtained using the SLAC gun design code EGUN [1].

GUN DESIGN

The triode gun is shown schematically in Fig.1. In the figure, C is the flat cathode, G the grid and A the anode. The diameter of the grid aperture is D_g and that of the anode is A_g. 'g' is the distance between the cathode and grid and 'a' the distance between the grid and the anode. The thickness of the grid and anode are t_g and t_a respectively. These parameters completely define the gun. All three, viz. the cathode, grid and the anode are separated by insulators and can take independent potentials.

Different values were tried in the program EGUN for the grid aperture D_g and the anode aperture A_g , the cathode-grid spacing 'g' and the grid-anode spacing 'a' in the program [2]. The electron beam profile obtained if the correct parameters are not used in the design is shown in Fig.1(a). By trial and error, the correct geometry has been obtained which results in a parallel beam as shown in Fig.1(b).

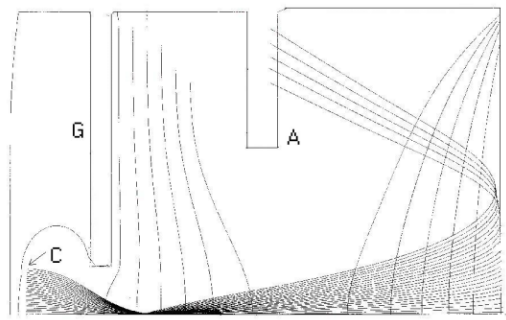

Figure 1(a): The effect on the electron trajectories if the proper apertures are not used.

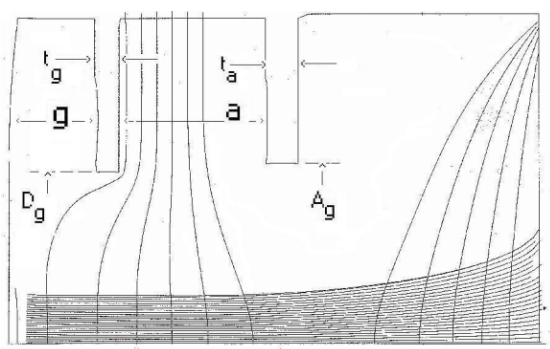

Figure 1(b): With the proper parameters, a parallel beam is obtained.

In our DC machines, the electron gun is followed by the NEC (National Electrostatic Corporation) accelerating tube section. The first three accelerating electrodes of the NEC accelerating tube were included in the EGUN program to see their effect on the electron trajectories. The first three electrodes were given potentials of +13kV, +33kV, and +53kV respectively . The results are shown in Fig.2(a).

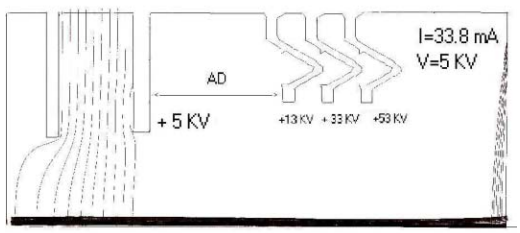

Figure 2(a): The first 3 accelerating electrodes are introduced in Fig.1(b),

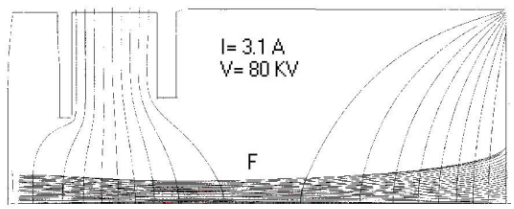

Figure 2(b): the gun geometry and electron trajectories for the linac gun.

Table 1: Parameters obtained in the triode gun design. (All dimensions in mm)

	For DC machines	For Electron Linac
Diameter of grid aperture, D_g	31.0	27.64
Diameter of anode aperture, A_g	34.0	34.14
cathode grid spacing, g	7.5	8.13
grid anode spacing ,a	13.8	13.82
grid thickness, t_g	3.0	2.44
anode thickness, t_a	5.0	3.25

The distance "AD" between the anode and the first accelerating electrode has been adjusted in the program so that the parallel nature of the electron beam obtained in the earlier design is not disturbed by the accelerating electrodes although the beam profile is not very sensitive to this parameter. The beam current from the gun can be controlled either by decreasing the heater power or by giving a negative bias on the grid G. For example, with a grid bias of -600V, the beam current can be reduced from 33.8mA to 16.61mA. The design obtained has been used for the 3 MeV machine also. In this case, the length of the accelerating columns is six times longer, and the requirement of a parallel or weakly focused beam becomes essential. The final design of the gun is given in Table 1.

For the linac gun, the beam characteristics required are different. A pulsed gun is required to deliver a 3 ampere peak current at about 80 KV with a duty cycle of 0.1%. The emittance of the gun required is less than 100 π mm mR MeV/c. A simple triode gun design was obtained as shown in Fig.2(b) and the parameters of this design are listed in Table 1.

EXPERIMENTAL RESULTS AND OUR OPERATING EXPERIENCE

The DC electron gun shown in Fig.1(b) was fabricated with the geometrical parameters in Table 1. The cathode used was a flat LaB_6 pellet of diameter 10 mm having a thickness of 1 mm [3]. With a heater power of 180 watts, the gun gave a current of 30 mA for a anode voltage of 6KV. The emittance was measured by placing concentric rings of decreasing aperture at a distance of 10 cm. from the anode. The beam was found to be almost parallel, as expected.

The RF electron gun shown in Fig.2(b) was fabricated according to Table 1.Again, the cathode was a flat LaB_6 pellet with a diameter of 10 mm and thickness 1 mm.[4] The pellet is housed in a rhenium cup and is housed in a cylindrical tantalum heat shield of 25 mm diameter. The heater coil is made up of a tungsten wire of 0.5 mm diameter also housed in a tantalum heat shield and placed close to the LaB_6 pellet. The grid and anode electrodes are made of stainless steel. With a heater power of 400 watts, (23.5V, 17A), the gun gave a peak current of 1.4A for an anode voltage of of 50 kV. The voltage was applied at a pulse rate of 400 pulses per second with a pulse width of 10 microseconds. Using the $V^{3/2}$ law, this current will scale to 2.83A at 80keV, which is close to the design value of 3.1A obtained in the computer program. The beam emittance was measured by measuring the beam diameter and divergence with the help of a segmented graphite faraday cup placed at a distance of 15cms from the anode. The emittance measured is 57mm mR MeV/c. The anode current is less than 6% of the beam current. This current is mainly due to the low energy electrons, back-scattered electrons from the faraday cup and secondary electrons. This current will reduce when the beam is injected into the linac cavity because the faraday cup will not be in the path of the beam.

CONCLUSIONS

Simple triode gun designs have been obtained for industrial electron accelerators. These guns use flat LaB_6 cathodes, parallel discs with apertures for the grid and anode, and are easy to fabricate experimentally. Our operating experience with the guns are described. The experimental results agree well with the computer calculations. The parameters of the guns are listed, and with proper scaling, the gun designs can be used for other electron machines where similar beam characteristics are required.

REFERENCES

[1] W.B. Herrmannsfeldt, Electron Trajectory Program SLAC-166., Sept. 1973.

[2] Arvind Jain, A.R.Chindarkar, B.N.Karkera, K.C.Mittal, A.S.Paithankar, R.C.Sethi and P.H.Ron, Indian J.Phys.73S (2), 69-71 (1999).
[3] A.R.Chindarkar, K.C.Mittal, A.S.Paithankar, J.A.Gokhale, G.VenuGopal and Arvind Jain, PATPAA conference, 1996, An electron gun for 500 keV industrial accelerator using LaB6 cathode.
[4] A.R.Chindarkar , et al., Intl. Sym. On Discharge and Elec. Inst. In Vacuum, June30-July5, 2002, Tours, France.

ANALYSIS AND CORRECTION OF THE MEASURED COD IN INDUS-2

Riyasat Husain#, A.D.Ghodke and Gurnam Singh
Raja Ramanna Centre for Advanced Technology, Indore-452013(MP) INDIA

Abstract

In Indus-2 there are 56 button type beam position monitors (BPMs), 48 horizontal and 40 vertical corrector magnets. The measured orbit has been fitted by effective quadrupole misalignments by using SVD of the response matrix generated between BPMs and the quadrupole misalignments in the model obtained by setting the magnet strengths as per the current set in the magnets. We present the global orbit correction algorithm developed for minimizing the orbit. The preliminary result for the orbit correction, at injection energy, in horizontal plane using best orbit correctors identified by an SVD of the response matrix is presented.

INTRODUCTION

The synchrotron light sources are characterized by low emittance of the electron beam and high brightness of the photon beams radiated from dipoles and insertion devices. Indus-2 is a 2.5GeV synchrotron radiation source with expanded Chasman Green lattice. The source consists of 8 unit cells; one unit cell contains 2 dipoles, 9 quadrupoles and four sextupoles. There are 7 beam position monitors (BPMs), 6 horizontal and 5 vertical corrector magnets in each cell for orbit measurement and its correction. One unit cell is shown in figure (1). The ring comprises of 72 quadrupoles divided into five families of quadrupole magnets. The closed orbit results from field errors and the errors arising from magnetic element positioning. The most severe effects come from misalignment of quadrupole magnets, where the resulting dipole field is proportional to both gradient and alignment errors. Indus-2 ring is being commissioned and measurement and correction of the beam dynamics parameters such as closed orbit distortion, tune, chromaticity etc. are being done. In this paper we describe the COD correction algorithms and its measurement and correction.

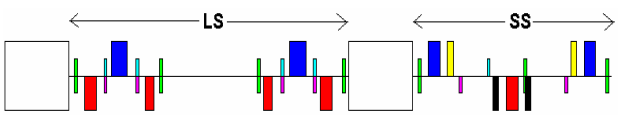

Figure 1: One unit cell of Indus-2 ring: Rectangles: empty-dipoles; blue-focusing quadrupoles; red-defocusing quadrupoles; yellow-focussing sextupoles; black-defocusing sextupoles; green-beam position monitors; magenta-horizontal corrector magnets and cyan-vertical corrector magnets. LS and SS stand for long straight section and short straight section.

#riyasat@cat.ernet.in

The measured orbit has been fitted by effective quadrupole misalignments by singular value decomposition (SVD) of the response matrix generated between BPMs and the quadrupole misalignments in the model obtained by setting the magnet strengths as per the current set in the magnets. We present the global orbit correction algorithm developed for minimizing and controlling the orbit. The preliminary result for the orbit correction, at injection energy, in horizontal plane using most effective correctors identified by SVD of the response matrix is presented.

ALGORITHM

Considering M BPMs and N correctors used for closed orbit correction in the storage ring, the response matrix Rij corresponding to the beam motion at the ith BPM per unit angle of kick by the jth corrector is given by

$$R_{ij} = \frac{\sqrt{\beta_i \beta_j}}{2\sin(\pi\upsilon)} \cos\left(\left|\varphi_i - \varphi_j\right| - \pi\upsilon\right) \quad (1)$$

where (β_i, φ_i), and (β_j, φ_j) are the beta function and phase advance at BPM and corrector locations, ν is the betatron tune.

The solution of the problem of the system of simultaneous linear equations between BPMs and the correctors is to effectively find out the inverse of the response matrix, R^{-1}. By SVD, the response matrix R can be decomposed into U, S, V [2]

$$R = U \times W \times V^T \quad (2)$$

Where *U* is an *MxM* unitary matrix (*UUT = UTU = 1*) and *V* is an *NxN* unitary matrix (*VT V= VTV = 1*), *W* is an *MxN* diagonal matrix with positive or zero. We call these diagonal elements $W_n(\geq 0, 1 \leq n \leq \min(M,N))$ the eigenvalues, which represent the coupling efficiency between the BPMs and correctors. The matrix R is singular if any of the eigen values are equal to zero. The R^{-1} can be calculated as

$$R^{-1} = V \times (W_{inv}) \times U^T \quad (3)$$

Here, W_{inv} is a diagonal matrix of dimension NxM and the elements are given by

$$W_{inv} = q_{\min(i,j)} \delta_{ij} \quad (4)$$

with

$$q_n = \begin{cases} 0, w_n \le \varepsilon w_{\max} \\ \dfrac{1}{w_n}, otherwise \end{cases} \quad (1 \le n \le \min(M,N)) \qquad (5)$$

where ε is the singularity rejection parameter in the range [0,l]. This parameter is determined primarily by the orbit correction needs and the corrector strength limits. Zero q_n's correspond to decoupled channels which do not contribute to orbit correction.

When ε = 0, all the non-zero eigen values are retained and the most accurate correction will result. However, this will require very robust power supplies for the correctors. On the other hand, if ε = 1, R^{-1} is a null matrix and there will be no orbit correction. Usually, ε is set to the smallest value such that none of the power supplies saturates.

SIMULATION

The singular values in descending order of the model response matrix obtained with all 56 BPMs and 48 correctors in horizontal plane are shown in figure (2). The large decrease at # 32 indicates that 16 of the correctors are redundant and therefore do not contribute much to orbit correction. These correctors have the smallest values of the function

$$E(j) = \sum_n w_n V_{jn}, \qquad (1 \le j \le 48) \qquad (6)$$

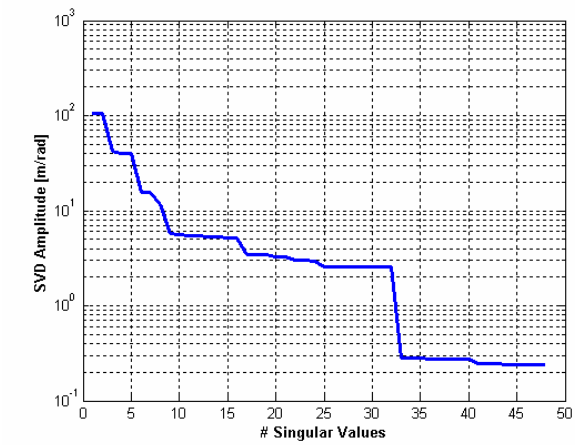

Figure 2: Singular value decomposition in horizontal plane of the model response matrix [9.3, 6.2].

In figure (3), the function E is plotted with number of correctors. It can be seen that 16 correctors having larger amplitude of E are most effective in correcting the COD. We simulate the closed orbit in the ring at presently working tune (9.3, 6.2) assuming rms misalignments of all quadrupole magnets by 0.2mm terminated at 3σ. The effect of singular values on orbit correction is shown in figure (4). The COD correction with 8, 16, 32 most effective correctors and all 48 correctors is shown in figure (5). It can be inferred that there is not much gain in orbit correction by all 48 corrector magnets as compared to the correction by 32 magnets.

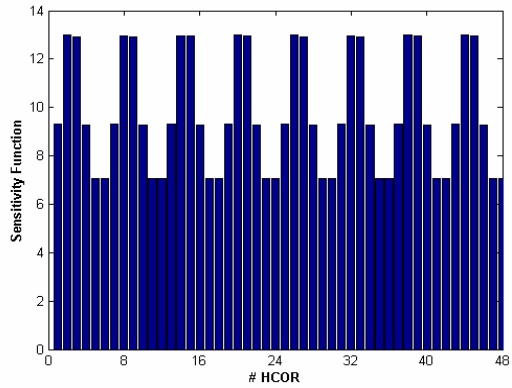

Figure 3: Sensitivity function for the horizontal corrector magnets for model response matrix [9.3, 6.2].

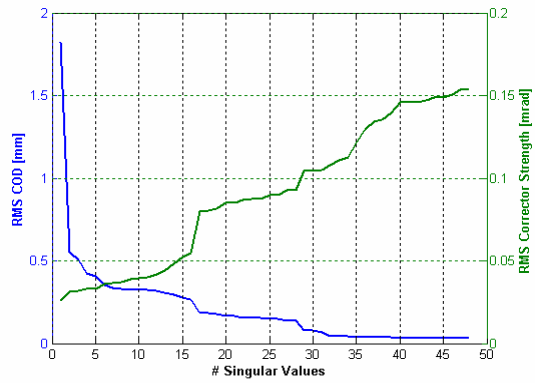

Figure 4: Effect of singular values on closed orbit correction in horizontal plane generated with 0.2mm rms random (seed-123456) misalignment of all Quadrupoles terminated at 3σ.

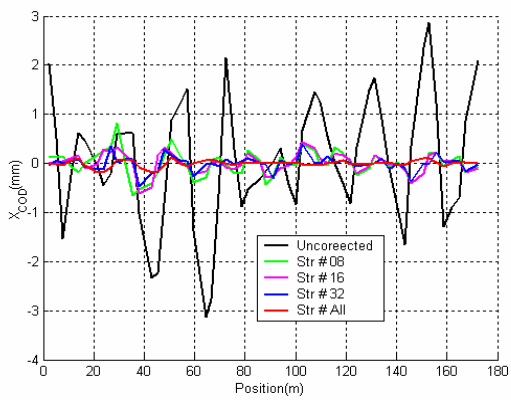

Figure 5: Orbit correction with the ideal lattice response matrix in horizontal plane.

MEASUREMENT AND ANALYSIS

The theoretical betatron tunes estimated by considering magnetic field as per the set current in the magnets are (9.31, 6.14). The response matrix was generated with this model and compared with the measured response. The

result for one of measured changes in COD due to 1A current in the corrector magnet is shown in figure (6). This show an agreement between model and measured response in horizontal plane while there is a small deviation in vertical plane. This effect may be attributed to the change in tune in vertical plane or due to the calibration error of the integrated magnetic field data of vertical corrector magnet. The FFT analysis of the measured COD in horizontal and vertical planes show the peak at 9th and 6th harmonics which confirm the integer part of the set betatron tune [3,4].

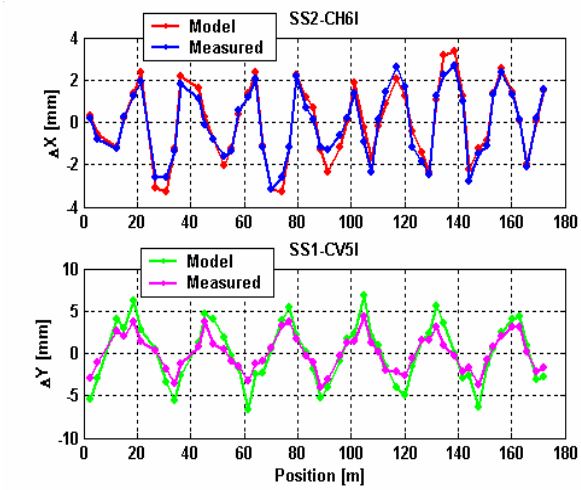

Figure 6: The measured and model response with 1.0A current in corrector magnets in both the planes.

The measured COD has been fitted, as shown in figure (7), with the quadrupole misalignments by SVD of the response matrix constructed by the COD change at BPMs per unit change of misalignments. The effective misalignments so obtained may not be the actual misalignments but give information about the magnitude of the misalignments. To get actual misalignments one should change the tune and recalculate the misalignments.

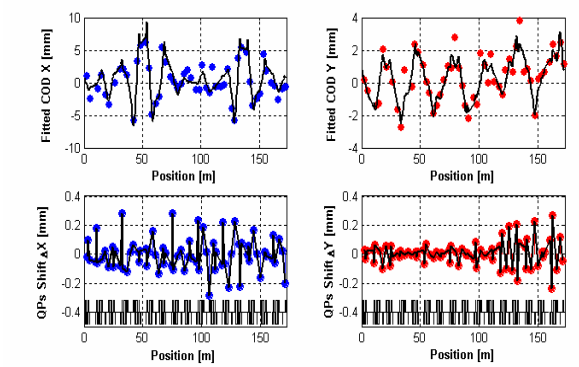

Figure 7: The COD fit with the effective misalignments of the quadrupoles.

The measured COD has been corrected in horizontal plane at the injection energy 550MeV. In the first trial of orbit correction, out of 48 correctors 16 were identified as the most effective correctors by SVD of the model response matrix. The measured and corrected closed orbit with these 16 correctors is shown in figure (8) together with the measured COD in vertical plane. In the first iteration of orbit correction, the maximum and rms COD has been reduced to 2.5mm and 1.3mm from 6.7mm and 2.9mm respectively [3]. Further improvement in orbit correction will be tried. The correction in vertical plane is yet to be attempted.

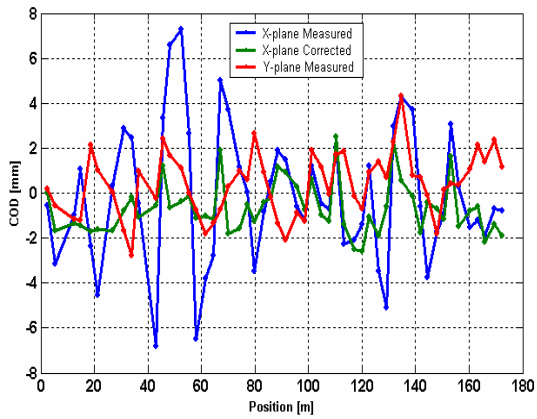

Figure 8: Measured COD in horizontal and vertical plane and corrected orbit in horizontal plane at 550MeV.

CONCLUSION

The closed orbit response matrix has been measured and found to be in agreement with the model response matrix in horizontal plane. The COD correction in horizontal plane has been done using 16 corrector magnets and further improvement in correction will be tried.

ACKNOWLEDGEMENT

Authors would like to thank Beam Diagnostics Section for their help in taking measurements.

REFERENCES

[1] G.Singh, G.K.Sahoo, D.Angel, B.Singh, A.D.Ghodke and P.Kant, "Synchrotron Radiation Source Indus-2", Indian Journal of Applied Physics, Vol. 35, 1 (1997) 183-192.

[2] Y. Chung, G. Decker and K. Evans Jr., "Closed Orbit Correction Using Singular Value Decomposition of the Response Matrix", PAC 1993.

[3] A.D.Ghodke et al.,"Progress in Commissioning of Indus-2", ICFA, Beam Dynamics Newsletter -41, 77-95.

[4] T.A.Puntambekar et al., "Experience of Beam Diagnostic Systems in Commissioning Stage of Indus-2" These Proceedings.

INHOMOGENOUS FIELD WIEN FILTER DESIGN

Puneet Jain [#] , P. Roychowdhury, D. P. Chakravarthy, Asish K. Ray
Accelerator and Pulse Power Division, BARC, Mumbai 400085, INDIA

Abstract

The Wien velocity filter is a useful device that transports pure proton fraction from high-power ECR proton source to the RFQ. It is a deflecting device, which has crossed electrostatic, and magnetostatic fields. Both fields are perpendicular to the beam trajectory that deflects and eliminates the undesired species of ions from the main beam. A tilted-pole Wien filter [1] surpasses the classical parallel-rectangular-poles Wien filter in performance as the former eliminates the astigmatism. The present paper describes the design of an inhomogeneous field Wien filter where the equations of motion are developed and solved up to a second-order approximation for a paraxial ion beam inside an E×B mass separator without considering the space charge effects.

INTRODUCTION

A high current low emittance ECR proton source is being developed at Accelerator and Pulse Power Division (APPD), Bhabha Atomic Research Centre (BARC) for Accelerator Driven sub critical Systems (ADS) applications [2]. This source (50 keV, 30 mA) will be an injector to 3 MeV RFQ, a subsequent accelerating structure. The beam coming out of the source [3] may contain molecular hydrogen ions (H_2^+) species besides pure proton (H^+). It is desired to have more than 80% of proton fraction before it reaches RFQ. To remove the undesired species of molecular hydrogen ions, a device viz. Wien filter is used. The protons and molecular hydrogen ions in the beam have same energy (50 keV) but owing to different masses, have different velocities. The Wien filter removes the undesired molecular hydrogen ions species and hence this device is also called mass separator or Wien velocity filter (WVF). The WVF is a mass-dispersive electromagnetic optical device, having mutually perpendicular electrostatic and magnetostatic fields both being transverse to the direction of the charged particle beam. An appropriate choice of the separator's electric (E) and magnetic (B) field strengths, deflection forces sets up inside the device, which in turn cancel out for the desired beam species having axial velocity v = E/B. A classical WVF [4] consists of rectangular-parallel surfaces of electrodes and magnetic poles respectively (Figure 1). Along with spatial dispersion, the forces inside E×B separators also cause focusing of the beam. This focusing is not axisymmetric and astigmatism is introduced into the undeflected beam. A circular beam emerges out as an elliptical one out of the classical separator. This paper discusses how the astigmatism is removed up to a certain limit by introducing field gradients both in E and B.

[#] Email : pun12j@yahoo.co.in

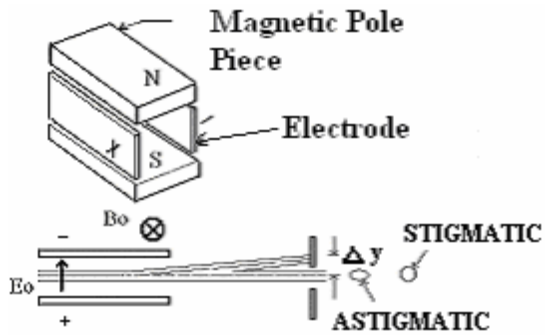

Figure 1: Schematic of classical Wien Filter

ELECTRODES GEOMETRY

We shall be using right-handed Cartesian coordinate system as shown in Figure 2.

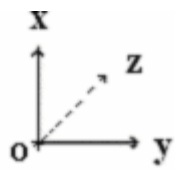

Figure 2: Coordinate system used in our analysis

For a parallel plate capacitor, one needs to choose electrodes profile as constant y lines. Obviously constant x lines shall be the electric field lines. To get an electric field gradient symmetric to y-axis we make a complex plane transformation given by w = Sin (ζ), where w (u, v) = u (x, y) + i v (x, y) and ζ (x, y) = x + i y. The equipotential curves are given by v = Cos (x) Sinh (y) and the orthogonal curves u = Sin (x) Cosh (y) shall be the corresponding field lines (Figure 3). The electrodes geometry shall therefore be according to constant v curves.

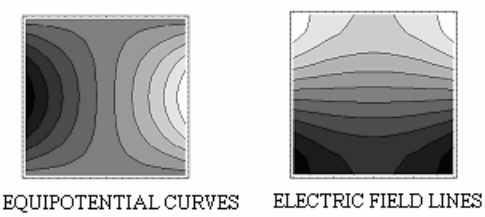

Figure 3: Electrodes profile (left figure) and the electric field lines (right figure)

MAGNETIC POLES GEOMETRY

The magnetic field used in the WVF should have a quadrupole component also besides a dipole. Such a configuration can be conceived by using tilted magnetic

poles as shown in Figure 4. This field configuration is such that it gives a focusing Lorentz force for a diverging beam and a defocusing Lorentz force for a converging beam. Thus stability requirement of the beam is also maintained.

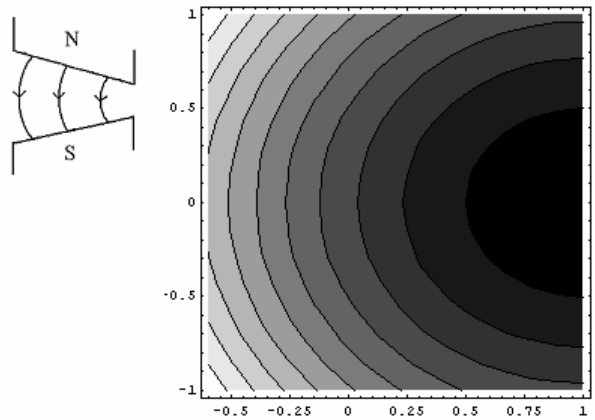

Figure 4: Schematic of Magnet pole pieces (left figure) and the corresponding magnetic field lines (right figure)

EQUATIONS OF MOTION

The following assumptions were made before setting up the equations of motion.

Assumptions

- The effect of space charge has been neglected. The formalism is developed for a single charged particle.
- The fields have no components or variations in the z direction. Employing shorting rings can reduce the width of the axial fringe fields at the entrance and exit of the separator.
- The natural length scale to which transverse displacements are compared, r_0, is the cyclotron radius m_0v_0/eB_0 of a particle of velocity v_0, in a magnetic field B_0. A second expression for r_0, found by evoking the balance condition $E_0 = v_0B_0$, is $r_0=2V_0/E_0$

eV_0 is the kinetic energy of the beam due to the extractor potential. In a paraxial approximation, the terms up to second order viz. $(x/r_0)^2$, $(y/r_0)^2$, (xy/r_0^2) are retained.

E and B fields

Following the coordinate system as shown in figure 2, the E and B fields can be written as:

$$E_x = - E_0 (xy/r_0^2)$$

$$E_y = E_0 [1 + ½ (x/r_0)^2 + ½ (y/r_0)^2]$$

$$B_x = - B_0 [1 - ½ (y/r_0)]$$

$$B_y = ½ B_0 (y/r_0)$$

$$v_z = v_0 [1 + y/r_0 + ½ (x/r_0)^2 + ½ xy/r_0^2]$$

From the Lorentz equation, $m_0\mathbf{a} = e(\mathbf{E_0} + \mathbf{v_0} \times \mathbf{B_0})$ we get the following equations of motion in x and y directions:

$$(d^2/dt^2)\, x = - ½ (ev_0B_0/m_0r_0)\, x – ½ (ev_0B_0/m_0r_0^2)\, 3xy$$

$$(d^2/dt^2)\, y = - ½ (ev_0B_0/m_0r_0)\, y – ½ (\, ev_0B_0/m_0r_0^2)\, xy$$

Noting the fact that $d^2/dt^2 = v_0^2\, (d^2/dz^2)$, the same may be rewritten as:

$$(d^2/dz^2)\, x = - ½ (eB_0/m_0\, v_0)^2\, x – ½ (eB_0/m_0\, v_0)^2\, (3xy/r_0) \quad \text{…….. (1)}$$

$$(d^2/dz^2)\, y = - ½ (eB_0/m_0\, v_0)^2\, y – ½ (eB_0/m_0\, v_0)^2\, (xy/r_0) \quad \text{…….. (2)}$$

The above-mentioned pair of equations [eqn. (1) and eqn. (2)] is a coupled oscillator problem.

Solutions

For a 50 keV proton beam $v_0 = 3.0 \times 10^6$ m/s. For a weak separator the typical value of the focal length is ~ 100 cm, and cyclotron radius r_0 ~ 25 cm. The corresponding values of fields are: E_0 ~ 4 kV/cm and B_0 ~ 0.133 T

Plugging these numbers back in the equations (1) and (2), we get

$$(d^2/dz^2)\, x = - 8.5\, x – 102\, xy \quad \text{…….. (1a)}$$

$$(d^2/dz^2)\, y = - 8.5\, y – 34\, xy \quad \text{…….. (2a)}$$

It is clearly seen that the focusing forces strengths are same in both the transverse directions. Thus astigmatic problem is resolved. An interesting feature to be noted is that the coupling term is stronger than the focusing strengths.

If we denote $(d/dz)\, x = x'$ and likewise for other variables then it may be further expressed as:

$$x'' = - C\, x – 4.24\, C^{3/2}\, xy \quad \text{…….. (1b)}$$

$$y'' = - C\, y – 1.41\, C^{3/2}\, xy \quad \text{…….. (2b)}$$

where $C = ½ (eB_0/m_0\, v_0)^2 = 8.5\ m^{-2}$ corresponding to the same values chosen previously.

The proton beam emerging from the final extractor electrode is expected to have 8 mm diameter and 0.2 pi mm-mrad emittance.

To solve the second order coupled ordinary differential equations the following initial conditions were chosen:

$$x\,(0) = 4 \text{ mm}, \; x'(0) = 40 \text{ mrad}, \text{ and,}$$

$$y\,(0) = 4 \text{ mm}, \; y'(0) = 40 \text{ mrad}$$

ANALYSIS OF SOLUTIONS

The phase space plot between x vs. x'and y vs. y' for C=8.5 is shown in Figure 5. The phase space plot is closed and hence the stable solutions exist.

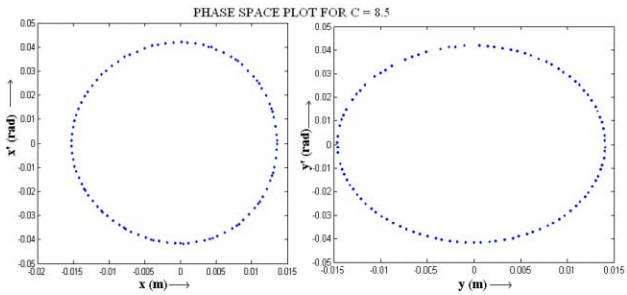

Figure 5: Phase space plots in x and y planes for C =8.5 m^{-2}

Next we examine the range of E_0 and B_0 that gives the stable solutions maintaining the Wien filter condition viz. $E_0 = v_0B_0$. Since v_0 is fixed for a given beam, we therefore need to consider only one variable say B_0.

As $B_0 \propto \sqrt{C}$, we shall see the solutions in phase space with C as a variable parameter. It is evident from the equations of motion (equations 1b and 2b) that as the parameter C is decreased there is no problem in the stability of the solutions but the focal length increases as $f \propto C^{-1}$. This will increase the length of the beam line and hence the cost of the system goes up. We therefore examine the stability of the solutions with increased values of C. The phase space plot between x vs. x'and y vs. y' for C increased to ten times of its actual value. (Figure 6)

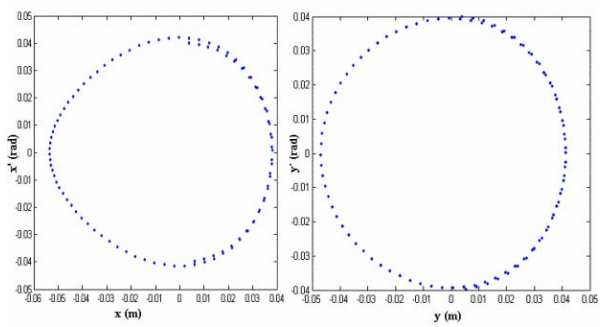

Figure 6: Phase space plots in x and y planes for C =85 m^{-2}

The ten times value of C corresponds to approximately thrice the value of B_0. The phase space plot in x-x' plane shows that the motion is slightly unbounded. The motion in y-y' plane, however, remains bounded.

Further increasing C to say fifteen times (corresponding to approximately four times B_0) the phase space plot in y-y' plane shows that the motion is slightly unbounded, however in x-x' plane the motion is completely unbounded. (figure 7)

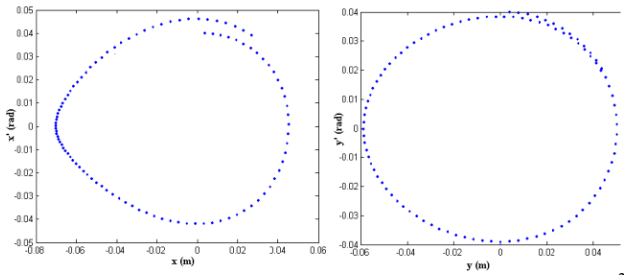

Figure 7: Phase space plots in x and y planes for C =127.5m^{-2}

The equations of motion can also be expressed by an effective Hamiltonian with nonlinear terms as:

$$d/dz\,(C\,x^2 + x'^2 + 12\,C\,x^2y) - 12\,C\,x^2y' = 0$$

$$d/dz\,(C\,y^2 + y'^2 + 4\,C\,y^2x) - 4\,C\,y^2x' = 0$$

The nonlinear terms viz. x^2y' and y^2x' have the same effect as the Hamiltonian given by:

$$H(x,x',y,y') = C(x^2 + y^2) + (x'^2 + y'^2) + (12C\,x^2y + 4C\,y^2x)$$

With this Hamiltonian, one can further explore the beam dynamics.

CONCLUSIONS

- Inhomogeneity in electric and magnetic fields does help in removing astigmatism problem.
- Coupling terms appear only due to inhomogeneous characteristics of electric and magnetic fields.
- To achieve focusing at relatively smaller lengths, the electric and magnetic fields should be large, however at large values, the solutions do not remain stable. For our system (50 keV proton beam) there is a bound on minimum focal length, which is $f \geq 10$ cm.

The authors wish to thank Mr. Zafar Ahmed, Dr. S.R. Jain and Mr. S.C.L. Shrivastava, Nuclear Physics Division, BARC for having technical discussions on the subject.

REFERENCES

[1] E. Leal-Quiros and M.A. Prelas, "New tilted-poles Wien filter with enhanced performance", Review of Scientific Instruments **60** (3), March 1989

[2] P. Roychowdhury et al., "Status and development of ECR proton source at BARC", Indian Particle Accelerator Conference (INPAC 2005), March 1-5, 2005, Kolkata, India

[3] P. Roychowdhury et al., "Design and development of high current ECR proton source at BARC" Indian Particle Accelerator Conference (INPAC 2006), November 1-4, 2006, Mumbai, India

[4] L. Wahlin, "The Colutron, a zero deflection isotope separator", Nuclear Instruments Methods **27**, 55 (1964)

CHARACTERISTICS OF BEAM EXTRACTION SYSTEM OF K500 SUPERCONDUCTING CYCLOTRON

S. Paul[#], J. Debnath, M.K. Dey, J. Pradhan, A. Dutta, C. Mallik, R. K. Bhandari
Variable Energy Cyclotron Centre, 1/AF Bidhannagar, Kolkata 700 064

Abstract

Extensive Magnetic Field measurement of the K500 Superconducting Cyclotron has been completed. In this paper we report the beam dynamical calculations along the extraction system based on the measured magnetic field data. The beam matching to the external beam transport system, for different ion species spanning the operating region is also explored.

INTRODUCTION

The K500 Superconducting Cyclotron at VECC, Kolkata uses 2 electrostatic deflectors, 8 passive magnetic channels and 1 active magnetic channel as its extraction elements [1]. Except for the active magnetic channel, all the other elements are radially movable, typically by ± 0.25 inches around a centre position. Th is maneuverability is due to the fact that not all the ions spanning the operating region of the cyclotron will have the same optimum beam extraction radius. Though it is possible that by adjusting the position and electric field of the electrostatic deflectors only, one can guide the extracted trajectories along a fixed common path, it is extremely difficult given the azimuthal length of the extraction path (~330^0), the total number of extraction elements involved, and the large variations in orbit scalloping across the anticipated range of magnetic fields. During the magnetic field mapping exercise, the magnetic field and magnetic field gradient along the extraction path has been measured both in the absence and presence of the magnetic channels at its central position, at different main magnet excitations, using a specially designed flexible zig and hall sensors.

The extraction elements

The different parameter of the extraction elements that affects the beam behaviour is listed in Table 1. For the deflectors, the septum to electrode gap is set to 6mm and the maximum voltage is set at 100 kV. To compensate the field perturbation effects of the magnetic channels on the inner orbits, 2 compensating bars (C_1 and C_2) are used, whose locations are also enlisted. C_1 compensates the effect of M_1 while C_2 compensates the overall effect of the remaining magnetic channels. The entries in Table 1. are as follows:

θ_i , θ_f : Initial and final azimuth of the element listed,
R_i , R_f : Average central ray radius at the initial and final azimuth of each element,
B : Magnetic field for the element
$\delta B/\delta x$: Gradients for the element.

Table 1: Extraction element's parameter

Element	θ_i (deg.)	θ_f (deg.)	R_i (in)	R_f (in)	B (kG)	$\delta B/\delta x$ (kG/in)
E_1	-23	32	26.6	26.93	-	-
E_2	94	137	27.1	27.68	-	-
M_1	140	153	27.7	27.76	1.14	8.3
M_2	200	206	28.28	28.39	1.14	8.3
M_3	226	232	28.89	29.08	1.04	13.3
M_4	236	242	29.21	29.44	1.04	13.3
M_5	256	262	30.09	30.46	1.04	13.3
M_6	266	272	30.75	31.24	1.04	13.3
M_7	276	282	31.62	32.31	1.14	8.3
M_8	286	292	32.88	33.95	0.96	11.6
C_1	320	334	27.75	27.75	-	-
C_2	46	58	28.95	28.95	-	-

SYSTEM CHARACTERISTICS

Figure 1. shows a plot of the magnetic field and radial gradient ($\delta B/\delta x$) across a typical magnetic channel. The field and the gradient is constant within ± 5 % across the beam width (~ ± 0.15 inch) and is therefore quite sufficient.

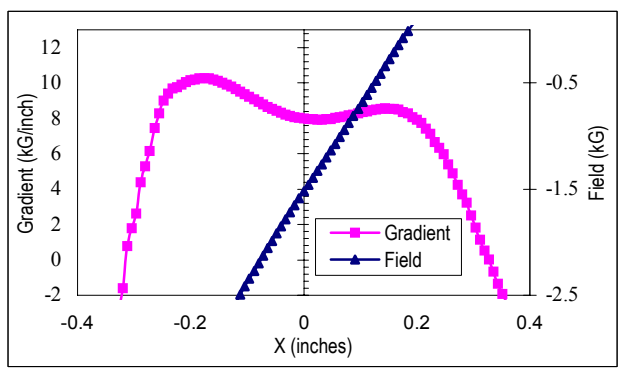

Figure 1: Field and gradient across a magnetic channel.

The properties of beams from the K-500 Superconducting Cyclotron were calculated by the ray-tracing method. In this calculation, the effect of the magnetic channels were included using the result of the magnetic field measurement. Three different species (Table 2.) spanning the operating-region of the cyclotron

[#]spaul@veccal.ernet.in

were chosen such that they correspond to different level of cental main magnetic field (B_0) of the cyclotron.

Table 2 : Beam Characteristics of investigated ions

Q/A	T/A (MeV/A)	B_o (kG)	E_{def} (kV/cm)	R_{def} (inch)
0.5	56.0	31.08	105.5	26.32
0.25	20.0	38.35	64.6	26.29
0.25	30.0	46.50	118.0	26.26

The trajectories of these 3 species are shown in Figure 2. on a Cartesian (R,θ) plot. The effects of the different scalloping of the orbits are quite evident.

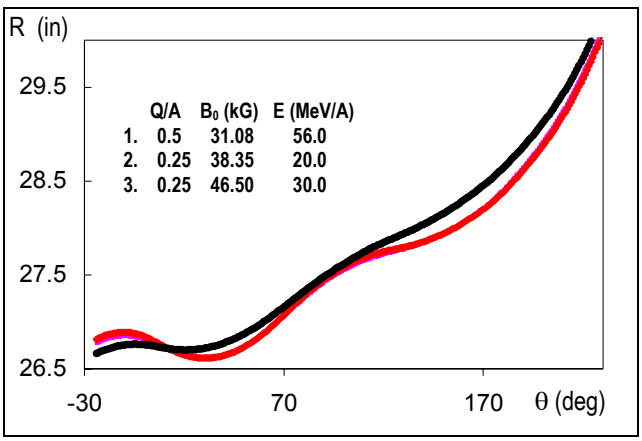

Figure 2: Extraction trajectories on Cartesian (R,θ) Plot.

The radial and angular dispersion of the extracted beam generated by the energy spread in the beam itself is also an important characteristic of the extraction system and has to be known while designing the optics of the external beam handling system. These effects have been calculated up to the slit (@ R = 44.4", θ = 317.5°) placed before the active magnetic channel (M_9) by ray-tracing beams corresponding to energy spreads of $\Delta E/E = \pm 0.1\%$ around the reference particle. These calculations are made by starting with the appropriate non-monochromatic phase space ellipse at the entrance of the first electrostatic deflector, and are therefore fully consistent. Table 3. lists the dispersive effects of the 3 species at M_9 slit in terms of R_{16} and R_{26}, namely the radial and angular dispersion respectively, as defined in the beam transfer code TRANSPORT [2], i.e. cm (or mrad) per percent of momentum spread.

Table 3: Dispersion parameters of investigated beams

Q/A	T/A (MeV/A)	R_{16} (cm/%Δp/p)	R_{26} (mrad/%Δp/p)
0.5	56.0	-6.45	-67.29
0.25	20.0	6.59	59.82
0.25	30.0	5.79	32.31

The radial and axial phase space ellipses of the different beam species obtained by tracking the corresponding eigen ellipses from the deflector entry to the M_9 slit passing through the extraction path were also investigated. The radial and axial ellipses obtained for 2 such species are shown in Figure 3 and 4.

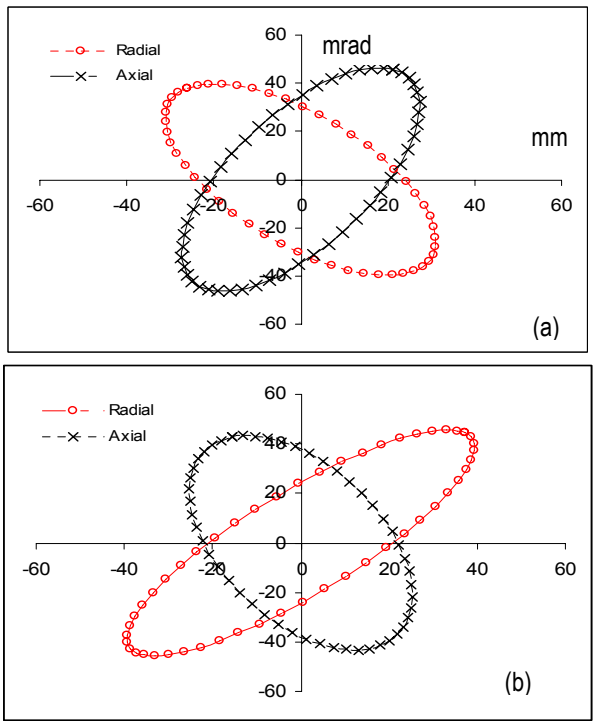

Figure 3: Phase space ellipse at (a) deflector entry (b) M_9 Slit for ions with Q/A=0.25, T/A=20 MeV/n, Bo=38.3 kG.

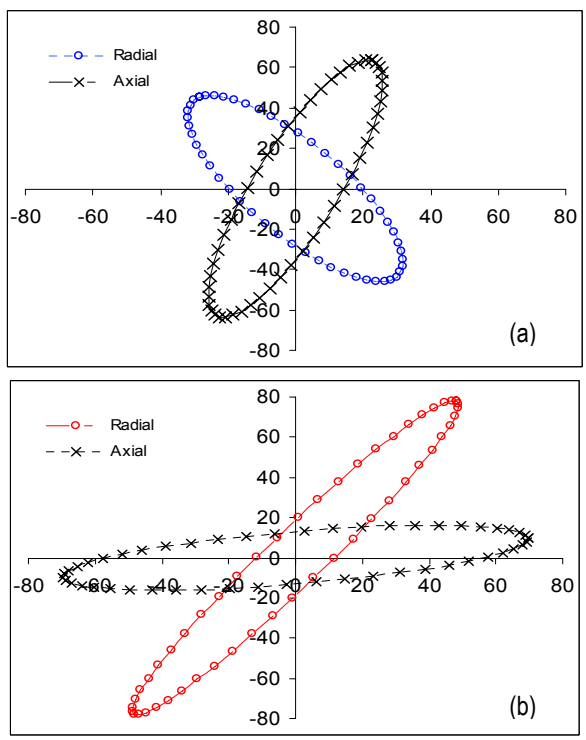

Figure 4: Phase space ellipse at (a) deflector entry (b) M_9 Slit for ions with Q/A=0.5, T/A=56 MeV/n, Bo=31.08 kG.

The initial ellipse is obtained by running the equilibrium orbit code GENSPE [3] in the main magnetic field of the cyclotron and the emittance is taken as 0.04 square inches.

REMARKS

The calculation and characteristics of the extraction system of K-500 Superconducting Cyclotron that has been reported in this paper covers up to the slit before the active magnetic channel (M_9). The subsequent tracking of the beams through the yoke field and M_9 has also been carried out and reported in this conference [4].

REFERENCES

[1] S. Paul, et.al , "Simulation Study of the Extraction System of K500 Superconducting Cyclotron in VECC, Kolkata", presented in InPAC'05 (2005).

[2] K.L.Brown, D.C.Carey, Ch. Iselin & F. Rothacker, "TRANSPORT, A Computer Program for Designing Charged Particle Beam Transport Systems", Yellow Reports, CERN 73 – 16 (1973) & CERN 80 – 04 (1980).

[3] M.M.Gordon, "Computation of closed orbits and basic focussing properties for sector-focussed cyclotrons and the design of CYCLOPS",Particle Accelerators, 1984, Vol. 16, p 39 – 62.

[4] J. Pradhan, et. al, "Characteristics of the magnetic channel in the yoke hole of K500 SCC", Presented in this conference.

ELECTRON GUNS AND BEAMLINES IN THE VIEW OF EMITTANCE COMPENSATION

S. V. Miginsky#, Budker INP, Novosibirsk, Russia

Abstract

Space charge effect is ever of fundamental importance for low-energy parts of accelerators. Simple and robust estimations of the emittance degradation in various electron guns were obtained analytically and numerically. Nonuniform longitudinal and transverse distribution of current and the effect of gun electrodes were taken into account. The parameters of optimal beamlines for emittance compensation were estimated.

INTRODUCTION

Emittance compensation technique has been mentioned first probably in [1]. It was explained and developed further in [2] and other papers. The two basic effects, caused by the longitudinal nonuniformity of charge density and the transverse one, and their combination in uniform and nonuniform beamlines were considered in [3] and [4], also with accelerating and bunching. The main results of the two latter works is that the charge phase advance through the beamline should be $2n\pi$ (n is integer) and the focusing should be optimal. Then the normalized emittance dilution is well estimated as

$$\varepsilon_n \cong \xi r \sqrt{\frac{I}{I_0 \beta\gamma}}, \qquad (1)$$

where r is the rms size of the beam at the entrance; I is the peak current; $I_0 = 4\pi \cdot mc^2 / Z_0 |e|$, ≈ 17.045 kA for electrons; $\beta = v/c$; $\gamma = 1/\sqrt{1-\beta^2}$; v is the longitudinal velocity; and ξ is the dimensionless coefficient depended on the type of the beamline.

In this paper we consider electron guns in the same view. We take into account only macroscopic space charge effect and neglect thermal and grid emittance. There are at least three significant differences from the previous cases:

- Metallic electrodes always exist near the emitter. Its charge depends on the one of the beam and generates comparable fields.
- A bunch ever starts at very low energy, so its velocity and length are small enough. If the length of a bunch in the moving frame is comparable to or less than its radius, the interaction between its slices can't be neglected.
- The head and the tail of a bunch are in different conditions. If we consider them at the same position, the bunch will have lower energy in the first case and the transverse force will be smaller due to nonlocal interaction.

We use a steady-state code that takes into account the first effect, but not the two others.

#S.V.Miginsky@inp.nsk.su

EMITTANCE DILUTION IN GUNS

Phenomena and Basic Scaling

If the emitter is round and the beam is homogeneous and stationary, the gun geometry can be optimized so that the space charge effect doesn't affect the emittance, as in the well known Pierce gun [5]. If the beam is not uniform in the longitudinal direction, the transverse phase portraits of its slices differ and their emittances are not equal to zero. Let's consider these phenomena and estimate the total emittance.

Particle motion in the same gun is similar if its voltage and current meet Child-Langmuir law $I \propto U^{3/2}$. In this case the emittance (not normalized!) doesn't depend on the current. The quality factor of a gun

$$\frac{\varepsilon}{r\sqrt{\dfrac{I}{I_0(\beta\gamma)^3}}} \equiv \frac{\varepsilon}{r\sqrt{j}}, \qquad (2)$$

where r is the emitter radius, also doesn't depend on the current. At the same time, brightness $I/\varepsilon_n^2 \propto \sqrt{U}$. If all the dimensions of a gun are changed proportionally, its quality factor preserves while its brightness is $\propto \sqrt{U}/r^2$. Thus, one should find the quality factor and the optimal compensation beamline for any gun.

Charge Amplitude and Phase

Consider round beams and small deviations δ from the principal trajectories in the transverse phase space as in [3] and [4]. Then the motion is described by a second order differential equation with variable coefficients and a transform matrix exists for each beamline

$$\begin{pmatrix} \delta \\ \delta' \end{pmatrix} = \begin{pmatrix} C & S \\ C' & S' \end{pmatrix} \cdot \begin{pmatrix} \delta_0 \\ \delta_0' \end{pmatrix}. \qquad (3)$$

$\delta' = 0$ (see [3] (3)) at the emitter and we should zero it at some point after the gun to minimize the emittance. Thus, only C and C' are significant in our case and one can define the charge phase advance as

$$\varphi = \arctan\left(\frac{-C'x}{C\sqrt{j}}\right), \qquad (4)$$

where x is the rms-size of a slice. The quadrant should be taken so that the signs of $\cos\varphi$ and $-\sin\varphi$ coincide to ones of C and C' respectively. This definition possesses a critical property: if a uniform beamline with the phase advance $\pi - \varphi$ and x, j, and $\beta\gamma$ equal to ones at the exit of an arbitrary beamline with the phase advance φ, the total phase advance is π.

$$\begin{pmatrix} \cos(\pi-\varphi) & \frac{x}{\sqrt{j}}\sin(\pi-\varphi) \\ -\frac{\sqrt{j}}{x}\sin(\pi-\varphi) & \cos(\pi-\varphi) \end{pmatrix} \cdot \begin{pmatrix} a\cos\varphi & * \\ -a\frac{\sqrt{j}}{x}\sin\varphi & * \end{pmatrix} = \begin{pmatrix} -a & * \\ 0 & * \end{pmatrix}$$

The same situation occurs with 2π. Then one can define the relative charge amplitude as

$$a = \sqrt{C'^2 + \left(C\sqrt{j}/x\right)^2} \,. \tag{5}$$

Basic Gun

A diode gun similar to used in [6] has been simulated first. Its geometry is shown in fig. 1. The emitter radius was 5 mm, the distance between the electrodes was 123 mm, while the beam was observed at 200 mm from the cathode. The optimal current was 2 A at 300 kV. SAM simulation code [7] was used to calculate beam motion in the gun. As usually for emittance compensation, a bunch has been divided by slices, and each slice was considered independently as a steady-state beam. The current density at the cathode was always homogeneous.

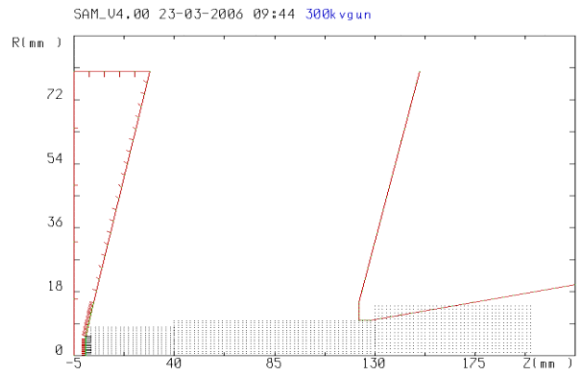

Figure 1: The geometry of the basic gun, red solid lines are electrodes.

The calculated beam parameters depending on the beam current are depicted in fig. 2. They were calculated by the following formulae:

$$x = \sqrt{< x^2 >},$$
$$x' = < xx' > / \sqrt{< x^2 >}, \tag{6}$$
$$\varepsilon = \sqrt{< x^2 >< x'^2 > - < xx' >^2}\,.$$

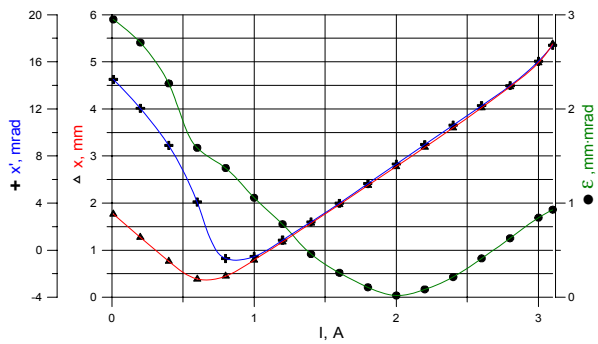

Figure 2: Beam parameters vs. beam current: rms-size, its derivative and emittance.

Let's calculate the charge phase and the relative charge amplitude from these data now. The beam size at the cathode preserves, but its "proportional" size $x \propto \sqrt{I}$ [3], so that

$$\frac{\partial x}{\partial I} = \frac{1}{2}\frac{x}{I}\,. \tag{7}$$

Than the initial charge vibration amplitude is

$$\delta x = -\delta I \frac{\partial x}{\partial I} = -\frac{1}{2} x \frac{\delta I}{I} \;\Rightarrow\; \frac{\partial \delta_0}{\partial I} = -\frac{1}{2I}\,. \tag{8}$$

The deviation from the "proportional" trajectory at the gun exit is

$$\delta = \frac{\delta x - \frac{1}{2} x \frac{\delta I}{I}}{x} = \left(\frac{1}{x}\frac{\partial x}{\partial I} - \frac{1}{2I}\right)\delta I \;\Rightarrow\; \frac{\partial \delta}{\partial I} = \frac{1}{x}\frac{\partial x}{\partial I} - \frac{1}{2I}\,, \tag{9}$$

and its derivative by the longitudinal coordinate is

$$\delta' \equiv \left(\frac{\delta x}{x}\right)' = \frac{\delta x'}{x} - x'\frac{\delta x}{x^2} \;\Rightarrow\; \frac{\partial \delta'}{\partial I} = \frac{1}{x}\frac{\partial x'}{\partial I} - \frac{x'}{x^2}\frac{\partial x}{\partial I}\,. \tag{10}$$

The significant matrix elements are

$$C \propto \frac{\partial \delta}{\partial I}, C' \propto \frac{\partial \delta'}{\partial I}\,, \tag{11}$$

and the charge phase at the gun exit is

$$\varphi = \arctan\left(\frac{-C'x}{C\sqrt{j}}\right) = \arctan\left(\frac{\frac{\partial x'}{\partial I} - \frac{x'}{x}\frac{\partial x}{\partial I}}{\left(\frac{1}{2I} - \frac{1}{x}\frac{\partial x}{\partial I}\right)\sqrt{j}}\right)\,. \tag{12}$$

To calculate the relative charge amplitude one should compare $\partial\delta/\partial I$ with the same derivative for a beam starting at the same point with fixed initial conditions, that is $\partial\delta/\partial I = -1/2I$ and $\partial\delta'/\partial I = -1/2I \cdot \sqrt{j}/x$. The root of the sum of the squares of these ratios gives the relative amplitude:

$$A = \sqrt{\left(\frac{2I}{x}\frac{\partial x}{\partial I} - 1\right)^2 + j\left(2I\left(\frac{\partial x'}{\partial I} - \frac{x'}{x}\frac{\partial x}{\partial I}\right)\right)^2}\,. \tag{13}$$

The dependencies of the phase and the amplitude on the current for the mentioned gun are shown in fig. 3.

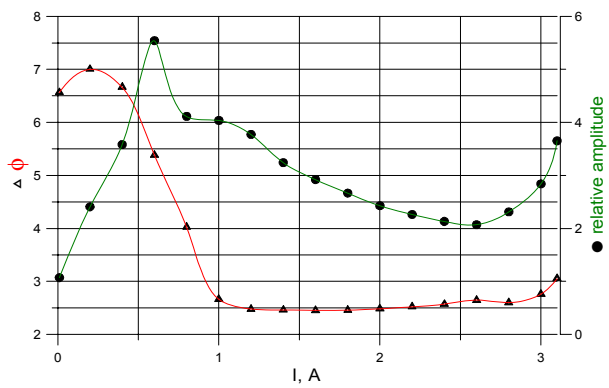

Figure 3: Charge phase and relative amplitude vs. beam current.

It is seen that the phase is almost constant within current limits from 1 to 3 A and its value is ≈ 2.5 ≈ 0.8π. Thus, if an ideal uniform beamline (where the phase advance doesn't depend on the amplitude) with the phase advance ≈ 1.2π is placed after the gun, one should expect the

minimal emittance. The following questions are still left: (i) what peak current of a bunch gives the minimum emittance in this system, (ii) which slice should be matched to the compensation beamline, and (iii) what is the optimal phase advance of the latter. The dependencies of the non-compensated emittance and the $\varepsilon/\sqrt{j}$ (r = const) on the peak current of a Gaussian bunch are shown in fig. 4. The compensated values one can find in fig. 5.

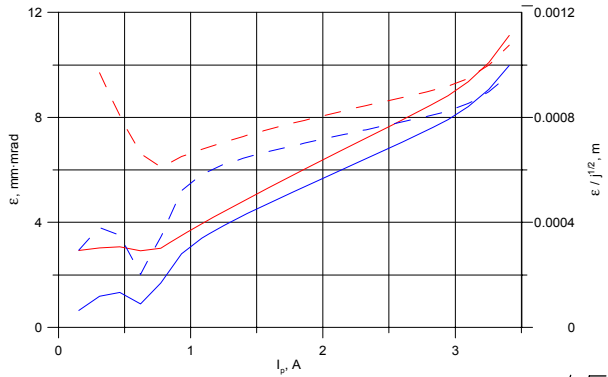

Figure 4: Non-compensated emittance (solid) and $\varepsilon/\sqrt{j}$ (dashed) vs. peak current of Gaussian bunch. Upper (red) curves take slice emittances into account.

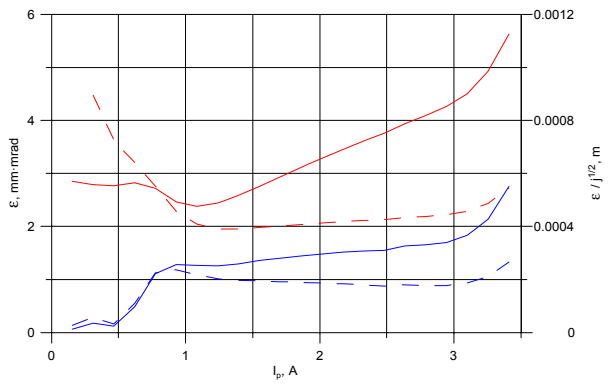

Figure 5: Compensated emittance (solid) and quality factor (dashed) vs. peak current of Gaussian bunch. Upper (red) curves take slice emittances into account.

One can see that $\varepsilon/\sqrt{j}$ in this case is almost independent on the current and equals $\approx 2\cdot10^{-4}$ m without slice emittances and $\approx 4\cdot10^{-4}$ m with them. A non-ideal compensation beamline increases the quality factor by ([3]: (5), (15), Table 1)

$$0.023\frac{x_1}{x}a^3\frac{\varphi}{2\pi}\approx 0.27\,. \qquad (14)$$

Thus $\varepsilon/\sqrt{j}$ will be $\approx 4\cdot10^{-4} + 0.27\cdot2.5\cdot10^{-3} \approx 1\cdot10^{-3}$ m.

Other Guns

Four other guns have been simulated in the same way to investigate the influence of the gun geometry. The emitter radius was the same while the length was varied. The electrodes were shaped to make perfect electric field. Additional electrodes were added to the guns "Short 2" and "Long 2" to equalize their perveance to the primary one. The optimal current in all the cases was ≈ 2 A. The results are placed in table 1. The values in parentheses in the second column mean the observation points. The last column considers the slice emittances.

Table 1: Guns parameters

Gun	Length, mm	U, kV	φ	$\varepsilon/\sqrt{j}$, m	$\varepsilon/\sqrt{j}$ (slices), m
Basic	123 (200)	300	2.5	$2\cdot10^{-4}$	$4\cdot10^{-4}$
Short	61.5 (100)	150	2.2	$7.5\cdot10^{-5}$	$4.8\cdot10^{-4}$
Short 2	61.5 (100)	300	2	$2.5\cdot10^{-4}$	$5\cdot10^{-4}$
Long	246 (400)	850	2.5	$4\cdot10^{-4}$	$5.4\cdot10^{-4}$
Long 2	246 (400)	300	3.1	$1.2\cdot10^{-4}$	$4.6\cdot10^{-4}$

One can see the charge phase is ever 2.5±0.5 and $\varepsilon/\sqrt{j} = (4.7\pm0.7)\cdot10^{-4}$ m.

CONCLUSIONS

- Emittance compensation applied to an electron gun always improves emittance by several times.
- The expected compensated normalized emittance of a well-designed gun with an ideal compensation beamline is

$$\varepsilon_n \approx 0.2x_e\sqrt{\frac{I}{I_0\beta\gamma}} = 0.1r_e\sqrt{\frac{I}{I_0\beta\gamma}}\,, \qquad (15)$$

  where r_e is the emitter radius and x_e is the rms beam size at the emitter.
- A non-ideal optimal compensation beamline worsens this value to

$$\varepsilon_n \approx 0.45x_e\sqrt{\frac{I}{I_0\beta\gamma}} = 0.225r_e\sqrt{\frac{I}{I_0\beta\gamma}}\,. \qquad (16)$$

- The charge phase advance of the compensation beamline should be 1.05…1.35π.
- The compensation beamline should be matched to the 0.5…0.75 of the peak current.

REFERENCES

[1] B.E.Carlsten. NIM **A 285** (1989) 313.
[2] L.Serafini, J.B.Rosenzweig. Phys. Rev. **E 55** (1997) 7565.
[3] S.V.Miginsky. Minimization of Space Charge Effect. XVI International Synchrotron Radiation Conference SR-2006 (Proc. to be published in NIM).
[4] S.V.Miginsky. Optimal Beamlines for Beams with Space Charge Effect. RuPAC 2006.
[5] J. R. Pierce, Theory and Design of Electron Beams, Van Nostrand, Princeton, New Jersey, 1954.
[6] S.V.Miginsky, V.V.Anashin, V.S.Arbuzov, et al. Status of a 2-MeV CW RF injector for the Novosibirsk high-power FEL. APAC 2001, Proc.: 82.
[7] M.A. Tiunov, B.M. Fomel and V.P. Yakovlev. SAM – an Interactive Code for Evaluation of Electron Guns, Budker INP prepr. 96-11, Novosibirsk, 1996.

A GENERAL MODEL OF THE RESISTIVE WALL INSTABILITY IN LINEAR ACCELERATORS *

J. R. Delayen#, Thomas Jefferson National Accelerator Facility, Newport News, VA 23606, USA
and Old Dominion University, Norfolk, VA 23529, USA
Juhao Wu, Stanford Linear Accelerator Center, Menlo Park, CA 94025, USA

Abstract

A general model for wakefield-generated instabilities in linear accelerators, originally developed for cumulative beam breakup [1], is applied to the resistive wall instability. The general solution for various bunch charge distributions and application to various accelerator configurations are presented.

INTRODUCTION

The beam breakup instability caused by the resistive wall impedance has been studied for the cases of a uniform single bunch and of a point-like bunch train [2] in the asymptotic limit of strong coupling. However, in the final focus of a linear collider or in light sources, the beam current profile is typically non uniform and the coupling, while not negligible, is relatively modest. The formalism developed previously for cumulative beam breakup [1] is applied here to investigate the resistive wall instability for arbitrary beam current profile and arbitrary strength of the wake field

FORMULATION AND SOLUTION

In a continuum approximation, the transverse motion of a relativistic beam under the influence of focusing and transverse wakefield can be modeled by [1]

$$\left[\frac{1}{\gamma}\frac{\partial}{\partial s}\left(\gamma\frac{\partial}{\partial s}\right)+\kappa^2\right] x(s,\zeta) = \varepsilon\int_0^{\zeta} d\zeta_1\, w(\zeta-\zeta_1)F(\zeta_1)x(s,\zeta_1) \tag{1}$$

where γ is the usual energy parameter; s is the distance from the front of the accelerator; κ is the focusing wave number; $\zeta = t - s/c$, is the time measured after the arrival of the head of the beam at location s; $F(\zeta) = I(\zeta)/\bar{I}$, the current form factor, is the instantaneous current divided by the average current; $w(\zeta)$ is the wake function; ε is the coupling strength between the beam and the deflecting field, and includes properties of the beam and the transport channel. If the wakefield source is the resistive-wall of a cylindrical pipe, then the long-range wake field is [3]

$$W(\tau) = \frac{\varepsilon}{\sqrt{\tau}}, \tag{2}$$

where

$$\varepsilon = (4c^2\bar{I})/(c\gamma b^3 I_A)\sqrt{\varepsilon_0/\pi\sigma_c}\ . \tag{3}$$

In the above expression, c is the speed of light, γ is the Lorentz factor, b is the radius of the pipe, $I_A = 17{,}045$ Amp is the Alfven current, ε_0 is the vacuum permittivity and σ_c is the pipe conductivity. With this definition we have

$$w(\zeta) = \zeta^{-1/2} \quad \text{for} \quad \zeta > 0\,. \tag{4}$$

While Eq. (1) assumes a perfectly aligned accelerator, misalignment of the cavities and focusing elements can also be included in the following analysis in a straightforward fashion [1].

Without loss of generality, we will assume a coasting beam. As shown in [1], the analytical results can be extended to an accelerated beam by suitable coordinate and variable transformations. We will also assume that the beam is injected parallel to the axis with a time-independent offset x_0. Under these assumptions, the equation of motion becomes [1]

$$\frac{\partial^2}{\partial s^2}x(s,\zeta)+\kappa^2 x(s,\zeta) = \varepsilon\int_0^{\zeta} d\zeta_1\, w(\zeta-\zeta_1)\,F(\zeta_1)x(s,\zeta_1). \tag{5}$$

and the solution is

$$x(s,\zeta) = x_0\sum_{n=0}^{\infty}\varepsilon^n\, h_n(\zeta)\, j_n(\kappa,s)\,, \tag{6}$$

with

$$h_0(\zeta) = 1; \qquad h_{n+1}(\zeta) = \int_0^{\zeta} d\zeta_1\, w(\zeta-\zeta_1)\,F(\zeta_1)$$
$$j_n(\kappa,s) = \frac{1}{n!}\left(\frac{s}{2\kappa}\right)^n\sqrt{\frac{\pi\kappa s}{2}}J_{n-1/2}(\kappa s) \tag{7}$$

Once the profile of the charge distribution in the bunch is determined, the functions $h_n(\zeta)$ can be calculated and then the shape and position of the bunch at any location s determined form Eqs. (6) and (7).

UNIFORM CHARGE DISTRIBUTION

In the case of a uniform charge distribution, the functions $h_n(\zeta)$ can be calculated in closed form and are

*Authored in part by Jefferson Science Associates, LLC under U.S. DOE Contract No. DE-AC05-06OR23177 (JRD) and supported in part by U.S. DOE Contract No. DE-AC03-76SF00515 (JW). The U.S. Government retains a non-exclusive, paid-up, irrevocable, world-wide license to publish or reproduce this manuscript for U.S. Government purposes.

#delayen@jlab.org

$$h_n(\zeta) = \frac{[\pi\zeta]^{n/2}}{\Gamma(\frac{n}{2}+1)}. \quad (8)$$

If the coupling constant ε is small only a few terms in the series are sufficient and the bunch shape is given by

$$\frac{x(s,\zeta)}{x_0} = 1 + \varepsilon s^2 \zeta^{1/2} + \frac{\pi}{24}\left(\varepsilon s^2 \zeta^{1/2}\right)^2 + \frac{\pi}{540}\left(\varepsilon s^2 \zeta^{1/2}\right)^3 + ... \quad (9)$$

in the absence of focusing, and by

$$\frac{x(s,\zeta)}{x_0} = \cos\kappa s\left[1 - \frac{\pi}{8}\left(\frac{\varepsilon s \zeta^{1/2}}{\kappa}\right)^2 + \frac{\pi^2}{768}\left(\frac{\varepsilon s \zeta^{1/2}}{\kappa}\right)^4 + ...\right] + \sin\kappa s\left[\frac{\varepsilon s \zeta^{1/2}}{\kappa} - \frac{\pi}{36}\left(\frac{\varepsilon s \zeta^{1/2}}{\kappa}\right)^3 + ...\right] \quad (10)$$

in the presence of focusing.

If the coupling is strong, then the displacement can be evaluated by the method of steepest descent and is given by

$$\frac{x(s,\zeta)}{x_0} \sim \frac{1}{\sqrt{2\pi}} X^{-1/10} \exp\left(X^{1/5}\right)$$
$$X = \left(\frac{5}{2}\right)^5 \frac{\pi\varepsilon^2 s^4 \zeta}{8} \quad (11)$$

in the absence of focusing and by

$$\frac{x(s,\zeta)}{x_0} \sim \frac{X^{-1/6}}{\sqrt{2\pi}} \exp\left(X^{1/3}\right)\cos\left(\kappa s + \frac{\pi}{6} - \sqrt{3}X^{1/3}\right)$$
$$X = \left(\frac{3}{4}\right)^3 \frac{\pi\varepsilon^2 s^2 \zeta}{2\kappa^2} \quad (12)$$

in the presence of focusing.

NONUNIFORM CHARGE DISTRIBUTION

Parabolic charge distribution

In the case of a single bunch of length ζ_b with a parabolic current distribution, the current distribution is of the form

$$F(\zeta) = \alpha\left(\frac{\zeta}{\zeta_b} - \frac{1}{2}\right)^2 + 1 - \frac{\alpha}{2}, \quad (13)$$

where α is a free parameter that is used to model the shape of the current distribution. In this case the functions $h_n(\zeta)$ cannot be obtained in closed form but can be calculated to arbitrary order through the recursion relations (7). The usual parabolic shape is obtained with $\alpha = -6$ which, together with the first functions $h_n(\zeta)$ is shown in Fig. 1. In certain circumstances, such as light sources, the charge is concentrated at the head and tail of the bunch, which can be modeled by $\alpha > 0$ as shown in Fig. 2.

Gaussian charge distribution

The form factor of a gaussian bunch truncated at $\pm 2\sigma$ can accurately be modeled by

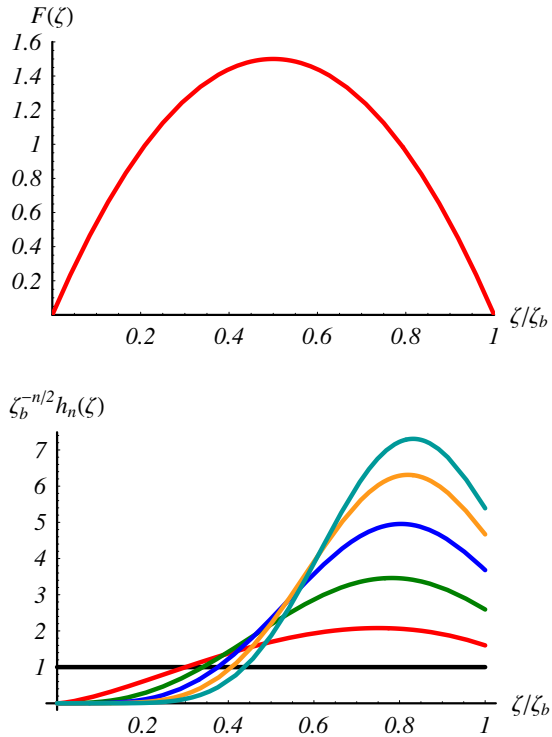

Fig. 1: Parabolic charge distribution from Eq. (13) with $\alpha = -6$ and functions $h_0(\zeta)$ to $h_6(\zeta)$.

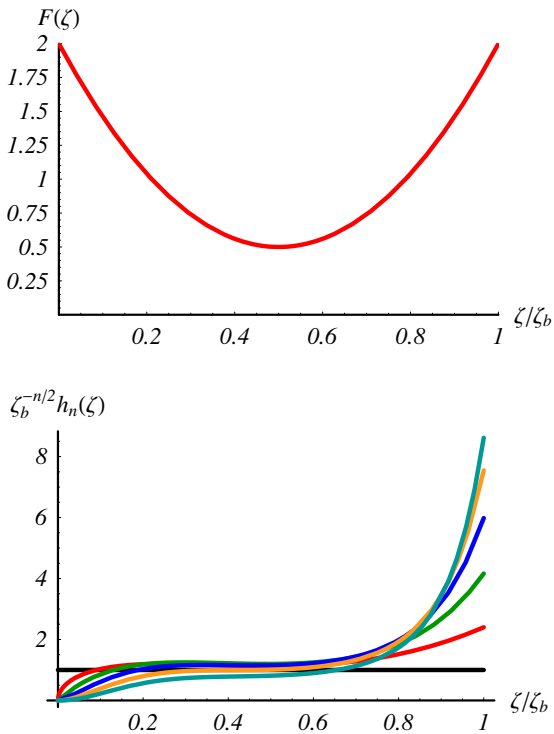

Fig. 2: Parabolic charge distribution from Eq. (13) with $\alpha = 6$ and functions $h_0(\zeta)$ to $h_6(\zeta)$.

$$F(\zeta)=\frac{5}{3}\left[1-\frac{168}{25}\left(\frac{\zeta}{\zeta_b}-\frac{1}{2}\right)^2+\frac{64}{5}\left(\frac{\zeta}{\zeta_b}-\frac{1}{2}\right)^4\right] \quad .(14)$$

Such a charge distribution and the associated functions $h_n(\zeta)$ are shown in Fig. 3.

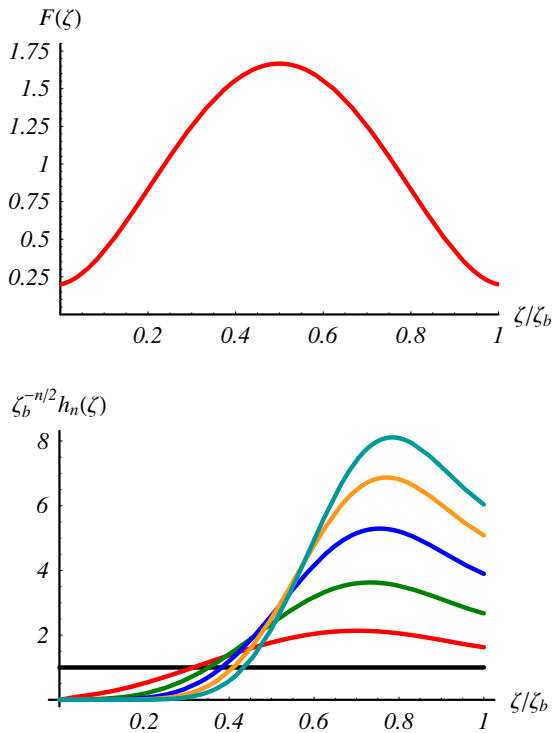

Fig. 3: Gaussian charge distribution from Eq. (14) and functions $h_0(\zeta)$ to $h_6(\zeta)$.

APPLICATIONS

The displacement and distortion of the bunch as it travels along the beam line under the influence of the resistive wall wakefield given by Eq. (6) is of the form

$$x(s,\zeta)=x_0\mathbf{A}(s,\zeta;\varepsilon)\,. \qquad (15)$$

Table 1: Parameters representative of LCLS and ILC.

	LCLS	ILC
Bunch duration (ps)	.077	1
Pipe radius (cm)	0.3	2
Pipe length (m)	150	300
Conductivity ($10^7\Omega^{-1}m^{-1}$)	6	3.47
κ (m^{-1})	1/18	1/12500
Bunch charge (pC)	1	3.2
ε	104	$6.5\ 10^{-3}$

If focusing is present, then it can be separated in two parts:

$$\mathbf{A}(s,\zeta;\varepsilon)=\mathbf{A}_c(s,\zeta;\varepsilon)\cos\kappa s+\mathbf{A}_s(s,\zeta;\varepsilon)\sin\kappa s\,. \quad (16)$$

As examples of the application of these results to various accelerator configurations, Fig. 3 shows the functions $\mathbf{A}_c(s,\zeta;\varepsilon)$ and $\mathbf{A}_s(s,\zeta;\varepsilon)$ for LCLS with charge distribution of Fig. 2 and $\mathbf{A}(s,\zeta;\varepsilon)$ for ILC with charge distribution of Fig. 1. Typical parameters for these two accelerators are shown in Table 1.

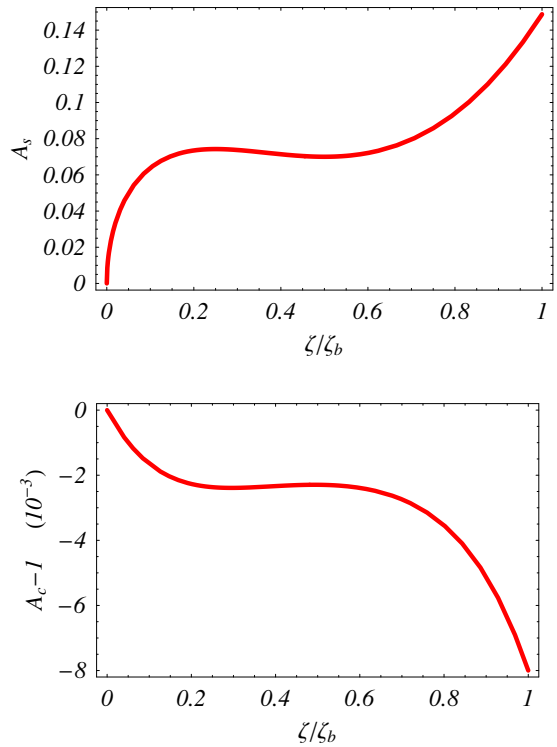

Fig. 4: Profile of an LCLS bunch assuming the charge distribution of Fig. 2.

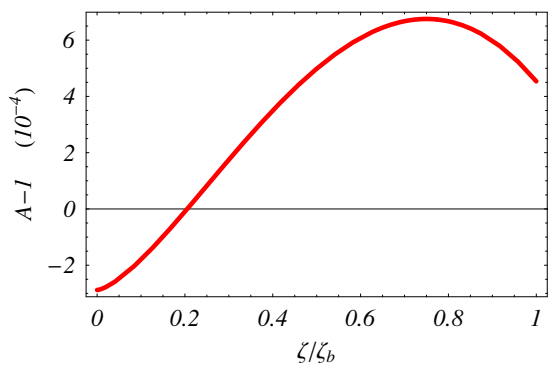

Fig. 5: Profile of an ILC bunch assuming the charge distribution of Fig. 1.

REFERENCES

[1] J. R. Delayen, Phys. Rev. ST Accel. Beams **6**, 084402 (2003); **7**, 074402 (2004); **8**, 024402 (2005).
[2] J.-M. Wang and J. Wu, PRST AB **7**, 034402 (2004).
[3] A. W. Chao, Physics of Collective Beam Instabilities in High Energy Accelerators, (John Willey and Sons, New York, 1993).

THE BUNCH LENGTHENING DUE TO ELECTRON CLOUD IN POSITRON STORAGE RING*

Y. D. Liu#
Institute of High Energy Physics, CAS, P.O. Box 918, 100049, Beijing, China

Abstract

The electron cloud generates not only the transverse wake field but also the longitudinal wake field. The mechanism of the bunch lengthening due to longitudinal wake produced by the electron cloud in the positron storage ring is analyzed. The longitudinal field, which depends on the density of the electron cloud in the storage ring, arises from the accumulation of the electrons near to the centre of the bunch during the bunch passage. Based on the longitudinal wake field, tracking method is used to simulate variation of the bunch longitudinal profile in different electron cloud density. According to simulation, the longitudinal action on the bunch from electron cloud is the same as the potential-well distortion to shift the bunch distribution and give a rise to the bunch deformation.

INTRODUCTION

The electron cloud accumulated in the vacuum chamber is usually associated with the transverse coupled bunch instability and bunch blow up. Experimental studies and numerical simulation have been developed for these phenomena [1]. In fact, electron cloud interacts with a positron bunch not only in transverse direction. Longitudinal instability was first discussed by G. Rumolo and F. Zimmermann as a single bunch effect, such as bunch lengthening [2]. The accurate simulation on the longitudinal interaction between electron cloud and the bunch need a fully self-consistent three dimensional plasma particle in cell model to solve Maxwell's equation as code OSIRIS which will spend much longer time [3]. In this paper, a simplified 2D approach is use to estimate the longitudinal electron cloud wake excited by a bunch passing through the electron cloud. Based on the longitudinal wake field, tracking method is used to simulate variation of the bunch longitudinal profile due to electron cloud.

PHYSICAL MODEL FOR THE LONGITUDINAL WAKE

During the passage of a bunch through the electron cloud, the electrons are attracted by the beam electric field and accumulate around the positron beam. The positron bunches have to lose some mount of their kinetic energy to build the electron cloud during the interaction with the electrons. The energy variation inside the bunch can be seen as a longitudinal wake. The bunch particles have an additional energy spread due to the longitudinal wake from the electron cloud. The electromagnetic field of the electron cloud can drive from the Maxwell equations as following formula [4]

$$\nabla \cdot \vec{E} = \frac{\rho}{\varepsilon_0} \tag{1}$$

$$\nabla \times \vec{H} = \vec{j} + \varepsilon_0 \frac{\partial \vec{E}}{\partial t} \tag{2}$$

$$\nabla \times \vec{E} = -\mu_0 \frac{\partial \vec{H}}{\partial t} \tag{3}$$

where ρ and $\vec{j}$ are the charge density and current density of the electron cloud, respectively. Here, ρ, $\vec{j}$, $\vec{E}$, $\vec{H}$ are the function of time t during the bunch passing. For azimuthally symmetrical fields and the assumption that the electron cloud has a periodic structure, the equations can be expressed as

$$\frac{1}{r}\frac{\partial}{\partial r}(rE_r) - \frac{\partial E_z}{c\partial \tau} = \frac{\rho}{\varepsilon_0}, \tag{4}$$

$$\frac{\partial H_\theta}{c\partial \tau} = j_r + \varepsilon_0 \frac{\partial E_r}{\partial \tau}, \tag{5}$$

$$-\frac{\partial E_r}{c\partial \tau} - \frac{\partial E_z}{\partial r} = -\mu_0 \frac{\partial H_\theta}{\partial \tau}, \tag{6}$$

where $\tau = z/c$, is the time difference to synchrotron particles. According to the relation $Z_0 = \frac{1}{\varepsilon_0 c} = 120\pi\Omega$, the integration in the radial direction and the boundary condition $E_z(r=a,\tau)=0$, the longitudinal electric field of the electron cloud is expressed as,

$$E_z = Z_0 \int_r^a j_r dr, \tag{7}$$

where Z_0 the impedance in free space and j_r is transverse current density of electron cloud.

As an example of BEPCII, assuming the bunch current is 9.8mA and central density of the electron cloud is $1.0\text{x}10^{13}\text{m}^{-3}$, the bunch longitudinal distribution and its electric field caused by electron cloud is shown in Figure 1.

From Figure 1, the longitudinal electric field is much smaller than the transverse filed which is on the order of 10^4 V/m [5]. During the passage of a positron bunch the transverse distribution of the electron cloud also has some significant change as displayed in Figure 2.

*Work supported by National Natural Science Foundation of China (10605032)
#liuyd@mail.ihep.ac.cn

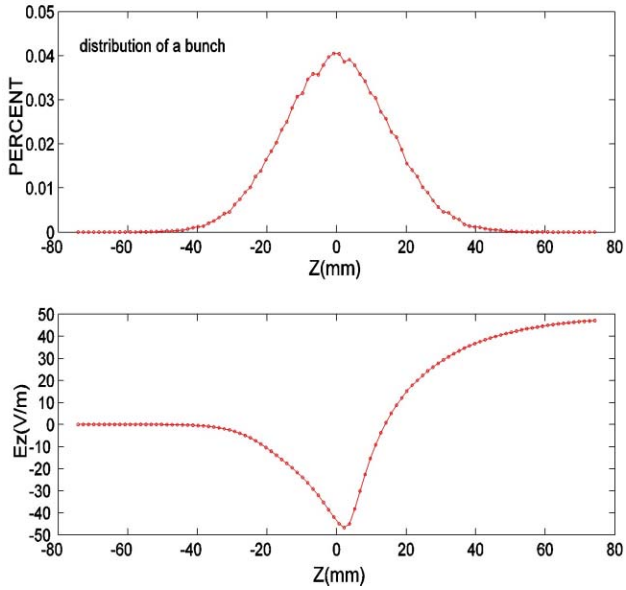

Figure 1: Longitudinal profile of a bunch and its electric field

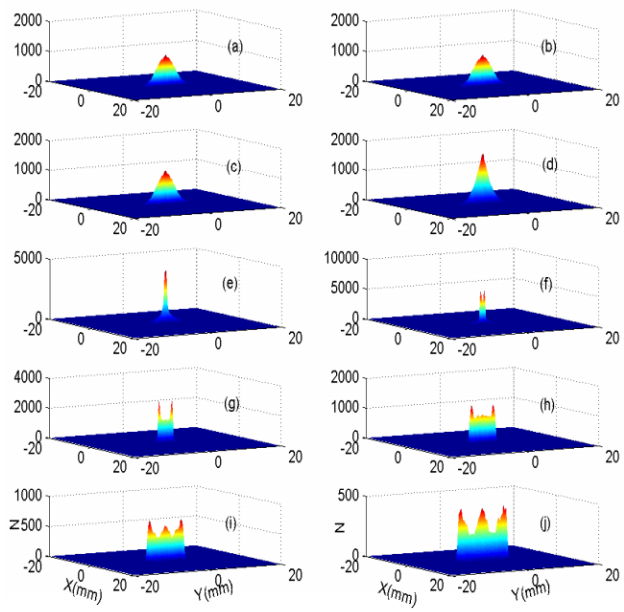

Figure 2: The distribution of the electron cloud during the passage of a positron bunch

During the time of a positron bunch passing through the electron cloud, the electrons in the cloud are moving toward to the centre of the beam orbit and then moving back to the walls of vacuum chamber. So the sign of electric field is different. The head particles of the bunch lose energy but the tail particles get additional energy from the electron cloud.

BUNCH LENGTHENING CAUSED BY THE LONGITUDINAL WAKE

The bunch length and energy spread varied due to the longitudinal wake caused by the electron cloud. The longitudinal interaction between bunch and electron cloud depends on the bunch current and density of electron cloud. A normal method to simulate the process of bunch lengthening is to track the motions of many macro-particles presenting the bunch. The motion of macro-particles is described in the longitudinal phase by [6]

$$z_i(n) = z_i(n-1) + \frac{\alpha c T_0}{E}\varepsilon_i(n) \tag{8}$$

$$\varepsilon_i(n) = \varepsilon_i(n-1) - \frac{2T_0}{\tau_\varepsilon}\varepsilon_i(n-1) + 2\sigma_{\varepsilon 0}\sqrt{\frac{T_0}{\tau_\varepsilon}}R_i(n) - U_0 + V\cos(\phi_s + \frac{2\pi h}{C}z_i(n)) + V_i[z_i(n))]. \tag{9}$$

where $\varepsilon_i(n)$ and $z_i(n)$ are the energy and position coordinates of the i[th] particle after n revolutions in the storage ring. T_0 is the revolution period; τ_ε the damping time; U_0 the energy lost per turn; ϕ_s the synchronous phase; h the harmonic number; C the ring circumference; E the bunch energy; α the momentum compaction factor; $\sigma_{\varepsilon 0}$ the natural energy spread; R_i a random number obtained from a normal distribution with mean 0 and RMS 1. The wake potential V_i caused by the electron cloud depends on the longitudinal electric field of E_z .

In the simulations 10^6 macro-particles are tracked over 6 longitudinal damping times and the bunch length are calculated by averaging particle positions in the last damping time. For BEPCII, positron bunch current 9.8mA, bunch natural length 13.53mm, the longitudinal electric field and the tracking result for bunch length in different electron cloud density are shown in Figure3 and Figure 4.

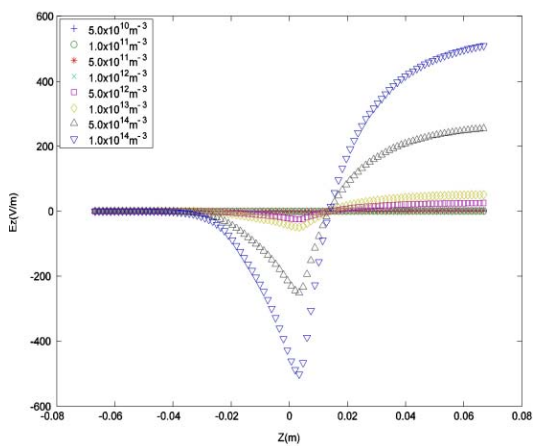

Figure 3: Longitudinal electric fields in different electron cloud density

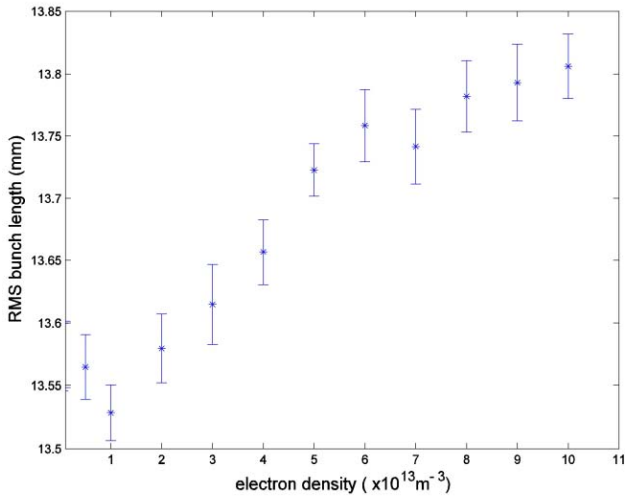

Figure 4: Bunch length in different electron density

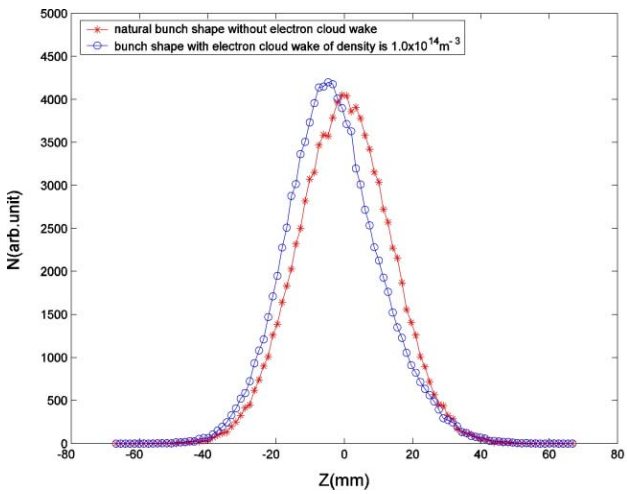

Figure 5: The longitudinal distortion of bunch shape due to electron cloud

According to the simulation results for bunch length in different electron cloud density, the electric field due to electron cloud can lead to the bunch lengthening. The bunch initial Gaussian distribution is shifted slightly in the forward direction for compensating the additional energy loss to the electron cloud. The longitudinal action between electron cloud and bunch can be seen as an electron cloud potential well which cause the possible bunch distortion.

CONCLUSION

The longitudinal electric field due to electron cloud is analyzed and simulated in the paper. The longitudinal effect of electron cloud serves as a potential well to interact the dynamics of bunch particles. By tracking methods to simulate the bunch length in different electron cloud density, results show that the bunch lengthening caused by the electron cloud density $1.0x10^{14}m^{-3}$, is just 2.0% comparing to the natural bunch length. Its effect appears to be negligible for BEPCII.

ACKNOWLEDGEMENTS

The author is grateful for the discussion with Prof. Guo and Dr. Qin. The suggestion from the members of accelerator physics group in BEPC is very helpful for the work.

REFERENCES

[1] K. Ohmi, F. Zimmermann, “Head-tail Instability caused by Electron Cloud in Positron Storing Rings”, Phys. Rev. Lett. 85, 3821(2000).

[2] G. Rumolo, F. Zimmermann, “Electron Cloud Simulations: Beam Instabilities and Wake Fields”, Proceedings of ECLOUD’02, 147–154, CERN, Geneva, 2002.

[3] A. Z. Ghalam, T. Katsouleas., et al., “Three-dimensional continuous modeling of beam-electron cloud interaction: Comparison with analytic models and predictions for the present and future circular machines”, Phys. Plasma, Vol 13, 056710(2006).

[4] A. Novokhatski, J. Seeman, “Simulation of electron cloud multipacting in solenoidal magnetic field”, SLAC-PUB-10327.

[5] LIU Yu-Dong, GUO Zhi-Yuan., et al., “The Electron Cloud Instability Simulation Studies for BEPCII”, HEP & NP, 2004, 28(11), 1222(2004).

[6] R. Siemann, "Computer Simulation of Bunch Lengthening in SPEAR", NIM 203 (1982).

DEGRADATION OF THE BEAM PASSING THROUGH IDLE COUPLED CAVITIES

Y. Shobuda, JAEA, Tokai_mura, Ibaraki, Japan
S. Machida, CCLRC/RAL/ASTeC, Chilton, Didcot, Oxon, U.K.

Abstract

Effects of wake fields on a high intensity proton beam are studied, when it passes through idle coupled cavities (The same number of modes as that of gaps that compose of the cavities build up.). Since the cavities are designed for an accelerated beam, the shunt impedance for the respective mode is different from the designed value, when the beam is not accelerated. This change of shunt impedances reduces the detuning effects in the sense of the reduction of the beam degradation.

INTRODUCTION

J-PARC (Japan Proton Accelerator Research Complex) is composed of linac, 3GeV RCS (Rapid Cycling Synchrotron) and Main ring [1]. In the first stage, 181[MeV], 30[mA] proton beam will be injected into RCS. In the upgraded J-PARC, it is planned that 400[MeV], 50[mA] proton beam will be injected into RCS through ACS (Annular Coupled Structure linac).

Before we inject the beam into RCS in case of the upgraded J-PARC, it is necessary to investigate the beam degradation due to the idle ACS, because RCS in J-PARC requests the momentum spread should be below 0.1%[1] before injection. It is not clear that we can reduce the beam degradation, especially when the chopped beam is injected into the cavity, by selecting the most appropriate frequency of the cavity, because the coupling effects between gaps (the shunt impedance for the non-accelerated beam is different from the designed value, because the ACS is designed for the accelerated beam.) is not negligible for the proton beam.

Further, as our commissioning, it is necessary to let beam pass through idle cavities, in order to adjust parameters of the accelerator. Tuning phase and amplitude of the powered cavity is one of the important processes at the commissioning of linac. The scheme of measurements of TOF (time of flight) is sometimes used for this purpose. Since many cavities exist between monitors for the measurements, it is severer the measurement of TOF as the intensity of beam becomes higher. Under this situation, it is important to investigate wake field effects on the beam quality [2].

In section 2, we consider the situation that the 181[MeV], 30[mA] chopped beam passes through the idle ACS. In section 3, we discuss the possibility of the correction scheme of TOF. Conclusions follow in section 4.

THE BEAM DEGRADATION

In the upgraded J-PARC, it is planned that 400[MeV], 50[mA] proton beam will be injected into RCS through ACS. The ACS is composed of 42 cavities. One cavity is composed of N_g=17 gaps [3]. Parameters for the ACS were already calculated by M. Ikegami: the shunt impedance ZT^2=41.223[MΩ/m], the quality factor Q=20300 and the frequency of the cavity $f_{\pi/2}$=972[MHz] [3].

Let us consider the situation that 181[MeV], 30[mA] chopped beam described in Fig.1 passes through the idle ACS. J-PARC RCS condition requires the momentum spread should be below 0.1%[1] before injection. It is not clear that we can reduce the momentum (energy) spread by selecting the most appropriate frequency of the idle cavities, because the coupling effects between gaps are not negligible for proton beam. Further, the chopped beam has many intrinsic frequencies.

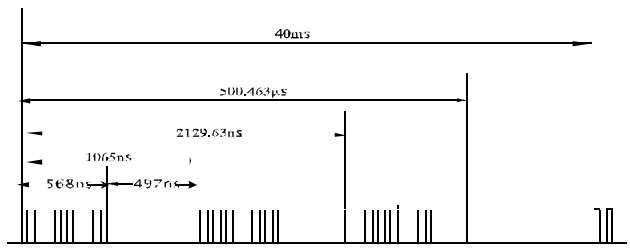

Figure 1: The chopped beam at J-PARC is described. Time period of the smallest pulse is 324[MHz]. The time period of the bunch (1065[ns]) corresponds to 0.93[MHz]. The interval of bunches is fluctuating around 1065[ns] (typically ~3[ns]). The repetition rate of the beam is 25[Hz].

Let us explain how to calculate frequencies and the shunt impedance of the coupled cavity when beam is not accelerated. When ACS has only one tuner, Brillouin curve for the detuned cavity is obtained by solving

$$D_{N_g}=\begin{vmatrix} i\left(\frac{\omega}{2\pi f_{\pi/2}}-\frac{2\pi f_{\pi/2}}{\omega}\right) & i\frac{\kappa}{2} & \cdots & 0 \\ i\frac{\kappa}{2} & i\left(\frac{\omega}{2\pi f_{\pi/2}}-\frac{2\pi f_{\pi/2}}{\omega}\right) & \cdots & \vdots \\ \vdots & \vdots & \ddots & i\frac{\kappa}{2} \\ 0 & \cdots & i\frac{\kappa}{2} & i\left(\frac{\omega}{2\pi f_{\pi/2}}-\frac{2\pi f_{\pi/2}}{\omega}\right) \end{vmatrix}=0, \qquad (1)$$

where the only ($(N_g+1)/2$, $(N_g+1)/2$) component of D_{Ng} is replaced by $i(\omega/2\pi(f_{\pi/2}+df)-2\pi(f_{\pi/2}+df)/\omega)$ and df is the amount of detuned frequency (D_{Ng} is the determinant of N_g*N_g.)[4]. Here κ=0.055 [5] is the coupling constant. One of detuned cases is represented in Fig.2. The frequency f_k is changed only when the mode index (k) is odd. We approximately reproduce the well-known Brillouin curve formula:

$$f_k = f_{\frac{\pi}{2}}\left(1-\frac{\kappa}{2}\cos\left[k\frac{\pi}{N_g+1}\right]\right), \qquad (2)$$

if κ is negligibly small and df=0, where k runs from 1 to N_g (k=9 is the accelerating mode.).

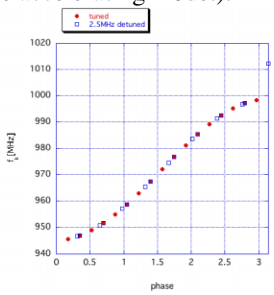

Figure 2: Brillouin curve of the detuned cavity. Blue square represents the case that the π/2 mode is 2.5[MHz] detuned. Detuning effects change the frequency f_k, only when k is odd. Horizontal axis is the argument of cos in Eq.(2). Vertical axis is the frequency for the respective mode.

We calculate the shunt impedance for the non-accelerated beam, using the designed shunt impedance R^m[3](which means that for the accelerated beam), where m is the cavity index. Here we assume that the voltage of i-th gap in the m-th cavity for mode k is represented as

$$V_i^m = V_0^m \cos\left[2\pi f_k t - i\frac{\pi k}{(N_g+1)/2}\right], \quad (3)$$

where m runs from 1 to 42, i runs from 0 to N_g-1. Thus, we obtain the shunt impedance for the non-accelerated beam:

$$\sum_{i=0}^{N_g-1}\frac{R_m}{N_g}\cos\left[i\pi\left(\frac{\beta_m}{\beta}\frac{f_k}{f_{\pi/2}}-\frac{k}{(N_g+1)/2}\right)\right], \quad (4)$$

where β is the actual velocity of the beam and β_m is the designed β. When the particle were accelerated in π/2 mode, the argument of cos in Eq.(4) would be 0. Therefore, this shunt impedance reproduces the designed shunt impedance (R^m). According to Eq.(4), the shunt impedances for k=9,10,11 behave like those in Fig.3. The shunt impedance for the respective mode equally contributes on the effective shunt impedance of the linac. The shunt impedance for k=9 contributes on the first part, that for k=10 does on the middle part, and that for k=11 does on the final part of the linac.

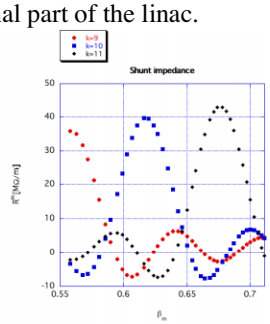

Figure 3: The shunt impedances for k=9,10,11 along the linac. The shunt impedance for the respective mode equally contributes on the effective shunt impedance of the linac.

The effective shunt impedance ($ZT^2(\beta)$) for the linac is given by taking an average of Eq.(4), then,

$$ZT^2(\beta) = \frac{\sum_{m=1}^{42}\frac{N_g\beta_m c}{2f_{\pi/2}}\sum_{i=0}^{16}\frac{R_m}{N_g}\cos\left[i\pi\left(\frac{\beta_m}{\beta}\frac{f_k}{f_{\pi/2}}-\frac{k}{(N_g+1)/2}\right)\right]}{\sum_{m=1}^{42}\frac{N_g\beta_m c}{2f_{\pi/2}}}. \quad (5)$$

$ZT^2(\beta)$ is 4.29[MΩ/m] for k=9, that 8.84[MΩ/m] for k=10 and that 12.87[MΩ/m] for k=11. Since the designed effective shunt impedance for the accelerating mode was 41.223[MΩ/m], $ZT^2(\beta)$ for this mode becomes 1/10 times smaller, while $ZT^2(\beta)$ for k=10, k=11 are increasing.

The energy loss and energy spread of the beam are expressed in Fig.4 when the beam passes through the idle ACS. The energy loss is reduced by detuning effects indeed, while the effect on the energy spread is not so drastic. There are peaks in both figures in Fig.4. These peaks correspond to intrinsic frequencies of the beam. The beam profile for df=1.94[MHz], which is the most appropriate frequency, is represented in Fig.5. Transient effects are significant. It is found that the beam has an onion structure due to multi-wake effects.

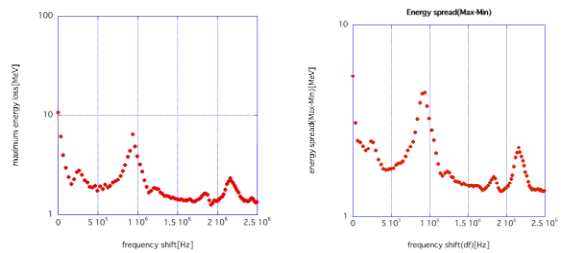

Figure 4: The energy loss and energy spread of the beam for the detuned frequency of cavity. The energy loss can be 1.27[MeV] and the energy spread can 1.34[MeV] at df=1.94[MHz].

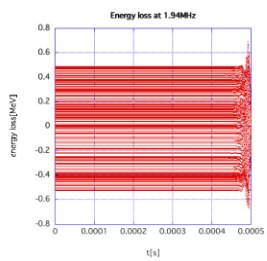

Figure 5: The beam profile at df=1.94[MHz]. The right hand side is earlier along the time axis. It is found that the beam has an onion structure due to multi-wake effects.

THE CORRECTION SCHEME OF TOF

Let us consider the situation that the 30[mA], β=0.532007, 324[MHz] beam passes through idle cavities (the beam has no multi-intrinsic frequencies in this case.) in order to tune the phase and amplitude of another powered cavity. Here we assume that the idle cavities exist between monitors.

In this situation, we measure the TOF and evaluate the beam energy. Since the wake field effect is so serious that

the TOF is modulated when the beam passes through the idle cavities. We take into account the modulation of pulse interval due to wake field effects. The energy loss of the beam ΔE due to wake field effects can be calculated, and the results are described in the right figure of Fig.6 where df=2[MHz]. The TOF under the influence of the wake field is described in the left figure of Fig.6. Since the TOF for the final particle is 442.73[ns], we can calculate β=L/t/c=0.531941 where L=70.65[m]. In this calculation the detuned cavity space is assumed to be the drift space. This value is -0.012% different from the original β(=0.532007) due to wake field effects.

In order to do fine tuning, we had better correct this TOF. When the following relation is satisfied:

$$\frac{mc^2}{\sqrt{1-L^2/\left(c^2(t-\Delta t)^2\right)}}-\Delta E \approx \frac{mc^2}{\sqrt{1-L^2/\left(c^2t^2\right)}}, \qquad (6)$$

Δt can be approximately written as,

$$\Delta t \approx \frac{t^3c^2}{L^2mc^2}\left(1-\frac{L^2}{c^2t^2}\right)\Delta E, \qquad (7)$$

where t-Δt is the corrected TOF, while t is the measured TOF. We can correct the TOF, when we know the ΔE in advance. According to the right figure of Fig.6, we find that the asymptotic value of ΔE=0.06526[MeV]. Then, we obtain Δt =73.2[ps] by Eq.(7). Using this Δt, β=L/(t-Δt)/c=0.532029. This value coincides with the original β with 0.004% accuracy. Thus, this correction scheme is useful to reproduce the original β.

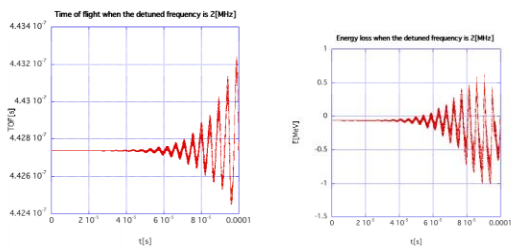

Figure 6: The left figure describes the TOF when the beam passes through the idle cavities. The right figure does the energy loss due to wake effects. The passing length L=70.65[m].

CONCLUSIONS

We investigate the influence of the wake field on the high intensity proton beam passing through detuned cavities. In particular, we have to notice the limitation of the reduction of the beam degradation due to the detuning effects, when the chopped beam passes through the cavity. The energy spread cannot be drastically reduced by the detuning effect, especially when the beam has multi intrinsic frequencies, because there are many resonance points along the detuned frequency axis. There are multi-peaks in the figure of the energy spread along the detuned frequency, which means that the allowed region is restricted.

We should notice coupling effects of the cavities, when we detune the frequency of them. There build up the same number of frequencies as the number of gaps in the coupled cavity. When the beam passes through detuned coupled cavities, the shunt impedance for this case is different from the designed shunt impedance. The coupling effects can reduce the shunt impedance for the accelerating mode, while shunt impedances for the other modes may become larger. This is because the behavior of the shunt impedance for the designed β_m is different for respective mode. Thus, we should beware of the limitation of the reduction of the beam degradation due to these coupling effects.

We also study the correction scheme of the TOF by subtracting the wake field effect from the beam, for tuning the phase and amplitude of another powered cavities. By knowing the deceleration energy of the beam due to the wake field effects, we can obtain the corrected TOF and evaluate the original energy of the beam.

ACKNOWLEDGEMENTS

The authors thank Y. Yamazaki, K. Yokoya, M. Ikegami, Y. Iwashita, K. Ohmi, T.Toyama, J. Kishiro, F. Noda, A. Ueno and T. Kato for discussions. The authors also thank the member of J-PARC project at JAEA/KEK.

REFERENCES

[1] Y.Yamazaki, Accelerator Technical Design Report for J-PARC, KEK Report 2002-13,JAERI-Tech 20003-044

[2] A. W. Chao, Physics of collective beam instabilities in high energy accelerators, New York, Wiley, (1993)

[3] M. Ikegami, Fundamental beam dynamics design of an Annular Coupled Structure Linac for KEK/JAERI Joint Project, 2002.

[4] Y. Yamazaki, Analysis of a Standing-Wave Accelerating Structure Based on a Coupled-Resonator Model, KEK Report 99-2, 1999.

[5] M. Ikegami, private communications.

BEAM COUPLING IMPEDANCE STUDIES OF THE CSNS RING

N. Wang*, Q. Qin
Institute of High Energy Physics, Beijing 10049, P. R. China

Abstract

The China Spallation Neutron Source (CSNS) is a high intensity proton accelerator with an injection energy of 80 MeV. The knowledge of the impedance in the vacuum chamber is necessary for optimizing the beam performance. In this paper, the longitudinal and transverse coupling impedances of the CSNS Rapid Cycling Synchrotron (RCS) are estimated.

INTRODUCTION

The CSNS is comprised of an 80 MeV Linac and a 1.6 GeV RCS ring [1]. Two bunches of 1.88×10^{13} protons are accelerated in the ring with a repetition frequency of 25 Hz. Many elements installed in the ring will cause beam instability via coupling impedance. Impedance from sources, such as space charge, vacuum wall and vacuum components, is calculated with analytical formulae. Impedance of other devices such as kicker magnets and RF cavities are difficult to calculate and should be measured. The results have been derived according to their preliminary design, rather than the impedance threshold given by the beam instability criterion. For further study, we will calculate the beam current threshold based on the impedance budget obtained, and then re-evaluate the impedance according to the stability criterion. This iteration will compromise the requirements of mechanical design for each vacuum component under an acceptable beam instability effect.

The main parameters of the CSNS/RCS are shown in Table 1.

Table 1: CSNS/RCS ring parameters

Circumference	m	230.8
Inj./Ext. energy	GeV	0.08/1.6
Repetition rate	Hz	25
Beam power	kW	120
Average Current	mA	63
RF harmonics		2
Trans. acceptance	πμm·rad	540

COUPLING IMPEDANCE

Transverse and longitudinal coupling impedance are calculated analytically for both injection and extraction energies.

Space Charge

The transverse space charge impedance for a round beam of radius a in a round pipe of radius b is given by

$$Z_{\perp} = -j\frac{Z_0 R}{\beta^2\gamma^2}\left(\frac{1}{a^2}-\frac{1}{b^2}\right), \quad (1)$$

where Z_0 = 377 Ω, $\beta = v/c$, γ is the Lorentz factor, and $2\pi R$ is the accelerator circumference. The longitudinal space charge impedance under the same condition is

$$\frac{Z_{//}}{n} = -j\frac{Z_0}{2\beta\gamma^2}\left[1+2\ln\frac{b}{a}\right], \quad (2)$$

where $n = \omega/\omega_0$ and ω_0 is the revolution frequency.

Chambers in the dipole magnets will be designed to have racetrack cross-sections. They are taken as rectangular chambers in calculation for simplicity. The space charge impedance for a rectangular beam pipe is given as [2]

$$Z_{H,V}(\omega) = -j\frac{Z_0 R}{\beta^2\gamma^2}\left[\frac{1}{a^2}-\frac{8}{h^2}\left(\xi_1^{H,V}-\varepsilon_1^{H,V}\right)\right],$$
$$\frac{Z_{//}(\omega)}{n} = -j\frac{Z_0}{2\beta\gamma^2}\left[1+2\ln\left(\frac{2h}{\pi a}\tanh\left(\frac{\pi w}{2h}\right)\right)\right], \quad (3)$$

where w and h stand for width and height of the chamber, and $\xi_1^{H,V}$ and $\varepsilon_1^{H,V}$ are electric image coefficients. For the CSNS/RCS ring, the space charge impedance are $Z_{//}/n$ = $-j$ 792 Ω, $Z_{\perp x}$ = $-j$ 17.5 MΩ/m and $Z_{\perp y}$ = $-j$ 9.5 MΩ/m at 80 MeV, and $Z_{//}/n$ = $-j$ 102.8 Ω, $Z_{\perp x}$ = $-j$ 4.7 MΩ/m and $Z_{\perp y}$ = $-j$ 4.5 MΩ/m at 1.6 GeV. It plays a dominant role in the whole impedance.

Resistive Wall

The RF shielded ceramic chambers will be chosen in the dipoles and quadrupoles due to the rapid field variation, and stainless steel (or titanium) chambers could be at the field free regions.

We choose ~ 0.5 mm in thickness and 5 mm in width copper stripes as the RF shield. The selection of the thickness of the copper stripes compromises the shielding efficiency and the ohmic loss due to eddy current.

A quick disconnect Ti flange will be welded to a sleeve attached to the ceramic segment by metal and brazing. Beam chambers in the straight sections, the vacuum chambers for steering magnets, DC bumpers, and extraction septum, are stainless steel pipes. They present an important portion for the resistive wall impedance due to its low conductivity [3].

For a round beam pipe, whose skin depth is small compared to the thickness of the vacuum chamber, the resistive wall impedance is [4]

$$Z_{//}(\omega) = (1+j\,\mathrm{sgn}(\omega))\frac{l}{2\pi b\sigma\delta},$$
$$Z_{\perp}(\omega) \approx 2cZ_{//}(\omega)/(\omega b^2), \quad (4)$$

where we have introduced the skin depth at ω

*wangn@ihep.ac.cn

$$\delta = \sqrt{\frac{2}{\mu_0 \sigma \omega}} \ , \qquad (5)$$

and σ is the conductivity. The resistive wall impedance is usually the dominant contribution of the transverse impedance at low frequencies.

The resistive wall impedance of the rectangular chamber with a width w and a height h can be represented by [2]

$$Z_{//}(\omega) = (1+j)\left(\frac{l}{\pi h \sigma \delta}\right) F\left(0, \frac{w}{h}\right), \text{ and}$$

$$Z_{V,H}(\omega) = (1+j)\frac{cl}{\pi \sigma \omega \delta}\left(\frac{2}{h}\right)^3 F_{V,H}\left(0, \frac{w}{h}\right), \qquad (6)$$

where the first parts are the resistive wall impedance of a circular beam pipe of a radius $h/2$ with the beam at the centre. F (0, w/h) and $F_{V,H}$ (0, w/h) are form factors determined by the width to height ratio w/h. For the CSNS case $w/h \sim 1.57$, then we have $F \sim 0.35$, $F_H \sim 0.4$, and $F_V \sim 0.825$.

The resistive wall impedance of the CSNS/RCS is $Z_{//}/n = 1.2(1+j)/n^{1/2}$ Ω, $Z_{\perp x} = 25.6(1+j)/n^{1/2}$ kΩ/m and $Z_{\perp y} = 26.5(1+j)/n^{1/2}$ kΩ/m at 80 MeV, while $Z_{//}/n = 1.8(1+j)/n^{1/2}$ Ω, $Z_{\perp x} = 16.6(1+j)/n^{1/2}$ kΩ/m and $Z_{\perp y} = 17.2(1+j)/n^{1/2}$ kΩ/m at 1.6 GeV.

The inner surface of the ceramic chamber will be coated with a 10 nm ~ 15 nm in thickness TiN to suppress secondary electron emission. This part of impedance is calculated by [5]

$$\mathrm{Im}\left(\frac{Z_{//}}{n}\right)_{Ceramic-TiN} = -Z_0 \frac{\varepsilon_r \beta^2 - 1}{\varepsilon_r \beta} \ln\frac{d}{b}\frac{l}{C},$$

$$\mathrm{Re}\left(\frac{Z_{//}}{n}\right)_{Ceramic-TiN} = 2Z_0 \left(\frac{\varepsilon_r \beta^2 - 1}{\varepsilon_r \beta} \ln\frac{d}{b}\right)^2 \frac{bt}{\delta_0^2} n \frac{l}{C},$$

$$\text{and } (Z_\perp)_{Ceramic-TiN} = \frac{2R}{b^2 \beta}\left(\frac{Z_{//}}{n}\right)_{Ceramic-TiN}, \qquad (7)$$

where ε_r is the relative dielectric constant ~ 10, δ_0 the skin depth of TiN at the revolutionary frequency. The results for the CSNS/RCS are $Z_{//}/n = j2.3+0.001n$ Ω and $Z_\perp = j44.9+0.2n$ kΩ/m at 80 MeV, $Z_{//}/n = j14.4+0.1n$ Ω and $Z_\perp = j\ 117.6+0.8\ n$ kΩ/m at 1.6 GeV, respectively.

RF gap

The CSNS RF system of the ring consists of eight stations and each station has two RF gaps. The impedance is divided into two parts: one from the inner copper duct which has the property of resistive wall, and the other from the cavity gap itself.

The cavity gap can be treated as a small cavity. It is only a few centimetres long so the transverse impedance could be negligible. The longitudinal impedance is calculated with the code ABCI [6]. The calculation results are shown in Fig.1. The real part is negligible compared to the imaginary part. The impedance is mostly inductive with a value of $Z_{//}/n = j\ 8.35\times10^{-3}$ Ω at 80 MeV and $Z_{//}/n = j\ 0.02$ Ω at 1.6 GeV.

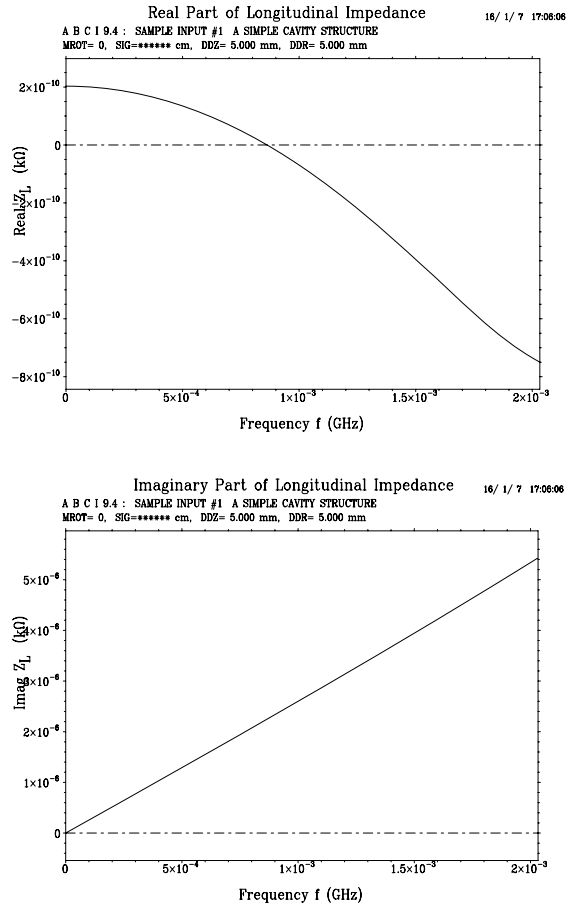

Figure1: Real and imaginary parts of the longitudinal impedance of the RF gap

Extraction Kicker Magnet

The CSNS adopts Lambertson magnets to extract the beam from the RCS ring. Five kicker magnets will be installed in the extraction straight section. The kickers will be designed as window frame magnets.

The transverse impedance of these kickers is modeled as a cylindrical ferrite shell inside a perfectly conducting pipe, yielding the transverse impedance as [7]

$$Z_\perp = \frac{c\omega\mu_0^2 l^2}{4a^2 Z_k}, \qquad (8)$$

where l is the magnet length, $2a$ the inner height, and $Z_k = j\omega L + Z_g$ with L the magnet inductance, and Z_g the termination impedance.

The magnet inductance of window frame magnet unit is calculated with $L = \mu_0 bl/a$. And the winding termination of each unit is 25 Ω. The transverse impedance of the total five kickers is shown in Fig. 2. The real part of the impedance is peaked at a frequency of 24MHz with a peak value of $Z_\perp = 24$ kΩ/m.

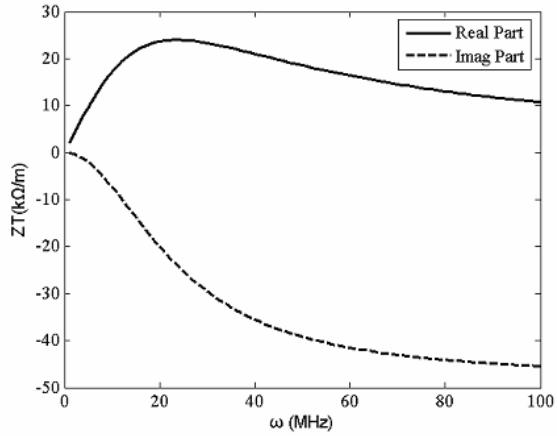

Figure 2: Transverse impedance of the extraction kickers.

The longitudinal impedance can be expressed as

$$\frac{Z_{//}}{n} = j\omega_0 L\,, \tag{9}$$

where L is the inductance of the ferrite ring. We will put copper sheets of a thickness δ_{Copper}= 1 mm in the ferrite core to reduce the massive ferrite loss, so the corresponding leakage inductance is estimated as [8],

$$L = 2\frac{\mu_0 l}{2\pi}\ln\frac{\pi a}{2\delta_{Copper}}. \tag{10}$$

The longitudinal impedance is $Z_{//}/n = j16.5\ \Omega$ at the energy of 80MeV and $Z_{//}/n = j39\Omega$ at the energy of 1.6 GeV.

Pipe Transitions

The detailed structure of pipe transition between chambers has not been decided yet. Steps are used in this budget, which yield greater impedance than smooth transitions. The difference between a step-up and a step-down is negligible. The impedance of a step with transition height h is given as

$$\frac{Z_{//}}{n} = j\omega_0\frac{Z_0 h^2}{4\pi^2 bc}\left(2\ln\frac{2\pi b}{h}+1\right),$$
$$Z_{\perp} = \frac{2R}{b^2\beta}\frac{Z_{//}}{n}. \tag{11}$$

The total longitudinal impedance is $Z_{//}/n = j\ 0.27\ \Omega$ at 80 MeV and $Z_{//}/n = j0.64\Omega$ at 1.6 GeV, while the transverse impedance is $Z_{\perp} = j\ 55$ kΩ/m.

Collimators

There will be one primary and three secondary transverse collimators, and two longitudinal collimators in the RCS ring. A simplified model of collimator is considered, which consists of a resistive wall with a smaller radius and the steps as well.

The impedance of the collimator steps is $Z_{//}/n = j\ 0.1\ \Omega$ and $Z_{\perp} = j\ 16$ kΩ/m at 80 MeV, $Z_{//}/n = j\ 0.47\ \Omega$ and $Z_{\perp} = j\ 16$ kΩ/m at 1.6 GeV, respectively.

The impedances for injection and extraction energies at frequency below 10MHz are summarized in Table 2 and 3.

Table 2: Coupling Impedance at 80 GeV

	$Z_{//}/n$ (Ω)	$Z_{\perp}$(kΩ/m)
Space charge	$-j$ 792	$-j$ 17500 (H)
		$-j$ 9539 (V)
Resistive wall	$1.2(1+j)/n^{1/2}$	$25.6(1+j)/n^{1/2}$ (H)
		$26.5(1+j)/n^{1/2}$ (V)
ceramic+TiN	$j2.3+0.001n$	$j44.9+0.2n$
RF gaps	j 0.13	
Ext. kickers	j 16.5	$j7.3+17.2$
Pipe transitions	j 0.27	j 55
Collimators	j 0.1	j 16

Table 3: Coupling Impedance at 1.6 GeV

	$Z_{//}/n$ (Ω)	$Z_{\perp}$(kΩ/m)
Space charge	$-j$ 102.8	$-j$ 4713 (H)
		$-j$ 4489 (V)
Resistive wall	$1.8(1+j)/n^{1/2}$	$16.6(1+j)/n^{1/2}$ (H)
		$17.2(1+j)/n^{1/2}$ (V)
ceramic+TiN	$j14.4+0.1n$	$j117.6+0.8n$
RF gaps	j 0.32	
Ext. kickers	j 39	$j7.3+17.2$
Pipe transitions	j 0.64	j 55
Collimators	j 0.47	j 16

SUMMARY

The coupling impedances of the components of the RCS ring are obtained according to their preliminary design. Structures of some elements such as bellows, ports, BPMs, valves, etc. are not yet decided, and further evaluation is needed.

The impedance measurement is needed to confirm calculation and stability needs further consideration.

ACKNOWLEDGEMENTS

The authors would like to thank Prof. Y. H. Chin from KEK and J. Wei, J. Y. Tang, S. Wang, D. M. Zhou, W. Kang from IHEP for their valuable discussion and support.

REFERENCES

[1] CSNS Conceptual Design Report (IHEP, 2005).
[2] K. Y. Ng, Particle Accelerators 16, 1984
[3] J. Y. Tang, private communication
[4] A. Chao, "Physics of Collective Beam Instabilities in High Energy Accelerators", John Wiley and Sons, 1993, and references therein.
[5] Y. H. Chin, ATAC 2005
[6] Y. H. Chin, LBL-35258, 1994
[7] G. Nassibian and F. Sacherer, NIM, 159, 21 (1979).
[8] G. Lambertson, Workshop on RHIC Performance, March, 1988.

A STUDY ON THE APPLICABILITY OF LANDAU CAVITY TO THE 1.2GeV BOOSTER SYNCHROTRON AT TOHOKU UNIVERSITY*

F. Hinode #, K. Akiyama, H. Hama, M. Kawai, K. Kasamsook, A. Kurihara, T. Muto, K. Nanbu, Y. Shibasaki, S. Takahashi, T. Tanaka, M. Yasuda
Laboratory of Nuclear Science, Tohoku University, Sendai 982-0826, Japan

Abstract

A 1.2 GeV Stretcher-Booster (STB) ring at Laboratory of Nuclear Science (LNS), Tohoku University, has been mainly operated for experiments of nuclear physics. One of the many issues limiting performance of the STB ring is supposed to be strong longitudinal coupled-bunch instability. In order to suppress the instability, applicability of a third-harmonic Landau cavity has been studied. The 1.5 GHz harmonic cavity was manufactured and installed in the ring. As a preliminary result of the beam test, it was turned out that the very strong signal of collective synchrotron oscillation was able to damp drastically depending on tuning angle of the harmonic cavity. Present status of the STB and the first test result of beam operation with harmonic cavity are described in the paper.

INTRODUCTION

In these years, the STB ring has been mainly operated in the booster-storage mode in which the high energy gamma-ray beam generated via bremsstrahlung from internal target wire has been utilized for experiments of nuclear physics [1]. The STB ring had been designed and constructed so as to have functions of: 1) pulse-beam stretcher [2], and 2) booster ring as an injector for a light source project [3]. The main parameters of the ring are listed in table 1. The STB is not the light source ring but also has storage ring-like function. Although the stored beam current is sufficient level (~15 mA) in the present operation for the nuclear physics user, it has still continued to increase the stored current toward the future application such as light source. The injected beam from linac is ramped up to variable top energy (1.2 GeV max.) during about 1 sec. The flat top time is also variable. The injection energy is not high enough (150 or 200 MeV), so that radiation damping time is much long (~ 1 s in the longitudinal direction). Although the injector linac provides sufficient beam current without beam stacking, circulating beam current decays rapidly due to instabilities before the beam reaches the top energy. One of the main causes of the beam current limitation might be supposed due to strong coupled-bunch instability because any care for the ring impedances had not been taken. Actually very strong synchrotron oscillation signal have been observed around 3.6 GHz. Since the main rf cavity itself does not have adequate HOM in such frequency region, any other possibility for the narrow band impedance source has been investigated. On the other hand, Landau cavity might be effective in order to suppress the instability. It is also supposed that the Landau cavity can improve the beam lifetime by increasing the bunch length. This approach is successfully employed in many light sources such as MAX-II, ALS and BESSY-II so far [4-6]. This technique is getting well established, but there may still remain difficulty and/or less knowledge in low energy ring where the radiation damping is very weak. Especially in the booster ring with large energy deviation from injection to flat top, to study the effect of the harmonic cavity seems to be interesting for longitudinal beam dynamics.

Table 1: The main parameters of STB ring

Lattice type	Chasman-Green
Superperiodicity	4
Circumference	49.7 m
Maximum energy	1.2 GeV
Injection energy	0.2 or 0.15 GeV
Betatron tune (ν_x,ν_y)	(3.22, 1.15)
Chromaticity (ξ_x,ξ_y)	(~ -5.5, ~ -4.7)
RF frequency	500.14 MHz
RF voltage	140 kV
Harmonics	83
Natural emittance	170 nmrad (@ 1.2 GeV)
Momentum compaction	0.0378

HIGHER HARMONIC CAVITY FOR STB

Among some choices we decided to test the normal-conducting passive third harmonic cavity because of that simplicity and easier understanding of beam dynamics. The tentative target was set to 100 mA for the design of higher harmonic cavity. The parameters of the cavity are listed in table 2.

Table 2: Parameters of the harmonic cavity (measured)

Frequency (@0mm,30˚C)	1499.1		MHz
Frequency range (tuner position)	+11.4 -1.2	(+25 mm) (-15 mm)	MHz
Pickup probe coupling	-30		dB
Loaded Q	22,270		
Shunt impedance*	3.8		MΩ

* Rsh =V^2/P : calculated value assuming R/Q by SUPERFISH

For the full energy operation, analytic modeling and simulations were first performed without consideration of HOMs in the rf cavities [7]. This allows the study of Robinson instabilities and coupled-bunch instabilities

* Work supported by the Grants-in-Aid of Japan Society for the Promotion of Science, contract No. 16560040
# hinode@lns.tohoku.ac.jp

excited by the fundamental modes of the rf cavities. The methods are described in the references [8, 9]. The modeling and simulations were then repeated with a HOM included. The results show that if three harmonic cavities are used, near-optimal bunch-lengthening may be obtained at the maximum ring current of 100 mA. The results also show that a single passive harmonic cavity will not provide sufficient voltage for optimal bunch-lengthening. For injection energy of 200 MeV, almost same analysis were performed and showed that increased energy spread from the instability or lost macro-particles occurred for nearly all currents and tuning angles. This analysis didn't include intrabeam scattering, so that they may be less accurate for low-energy operation than full-energy. Furthermore, there are a lot of impedance sources in the STB as mentioned before, thus it is difficult to estimate beam behaviour precisely.

As the first step of the study with passive higher harmonic cavity, we decided to prepare one harmonic cavity and try the beam test in the STB. The cavity was designed as a single cell pillbox type and manufactured by Toshiba Co. Ltd., which is shown in Fig. 1. Although the beam pipe diameter should be large enough so as to maintain the physical aperture, it has 40 mm in diameter to keep sufficiently high shunt impedance. To realize a tuner parking option, two tuner ports are prepared; one is used for a movable and the other for fixed one. The fixed tuner port might be used for an input port as a future option. The movable tuner can change the resonant frequency within two times of the revolution frequency. The cavity parameters in table 2 are measured ones, which are almost the same as designed values.

Figure 1: The third harmonic cavity.

BEAM TEST

Figure 2 shows observed beam spectrums for 1.2 GeV operations, which are obtained by a BPM located at dispersive section. Very strong synchrotron signal is clearly seen only at 3.6 GHz. Since there seems to be no HOM in such frequency region in the main cavity as mentioned earlier, other impedance source might cause this instability. Actually, obvious dependence on this synchrotron oscillation signal is not seen even some variations such as main cavity temperature, tuning angle and beam orbit. This instability has a threshold at 8.5 mA as shown in Fig. 3. As a possible source, it might be considered that the main cavity forms a resonator with beam ducts, which have sudden transitions of the shapes in their connections.

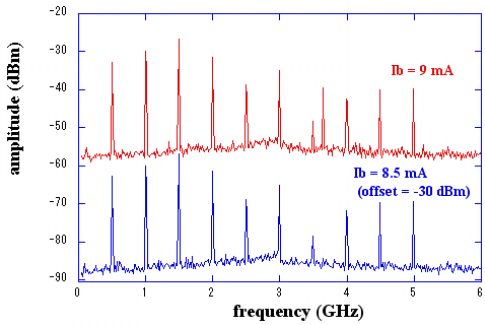

Figure 2: Observed beam spectrum by BPM located at dispersive section.

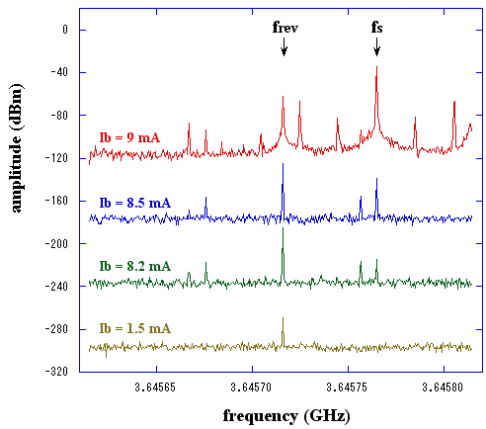

Figure 3: Observed beam spectrum (expanded around 3.6 GHz) as varying beam current. Each spectrum for lower current than 9 mA has some offset for ease to see.

In such circumstances, the harmonic cavity was installed. Figure 4 shows excited power in the cavity with respect to the tuner position. The positive implies that tuner moves toward the cavity center. The corresponding tuning angle is also shown in Fig. 4, which is defined by $\tan\psi = 2Q_L(\omega_{HC} - 3\omega_{RF})/\omega_{HC}$, where ω_{HC} and ω_{RF} are resonant frequencies of the harmonic and main cavity, respectively. Since the beam current is quite small, the excited power is also very small except for the on-resonance region.

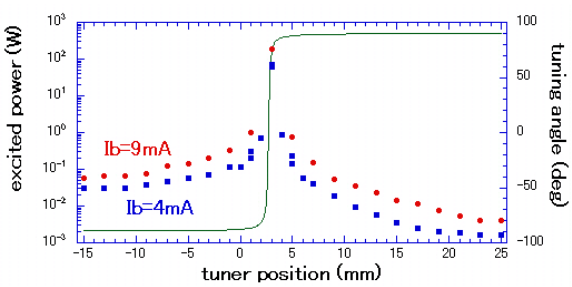

Figure 4: Excited power in the harmonic cavity for beam current of 9 and 4 mA. The tuning angle corresponding to the tuner position is also shown (solid line).

Figure 5 shows an image of the intensity of beam spectrum with respect to the tuner position. A stable region was observed around the tuner position of -10mm, where the intensity of revolution signal is not changed but synchrotron oscillation signal is drastically damped. At the 0 deg. of tuning angle (+3mm position), significant beam loss was also observed. Since the synchrotron frequency is not changed except for $\psi \sim 0$ deg., significant voltage is not induced in the harmonic cavity. It has not been well understood yet that the instability can be damped in spite of such small excited voltage. As a possible reason, HOM in the harmonic cavity might be considered. A model analysis should be done continuing the beam study whether the HOM is the cause or not.

A summary of the stable and unstable region against the coupled-bunch instability is shown in Fig. 6 for various beam currents. At the tuner position of +15mm which corresponds to $\omega_{HC} = 3\omega_{RF} + \omega_{rev}$, there is a narrow stable band, where the synchrotron amplitude is damped but beam become unstable and lost as increasing beam current.

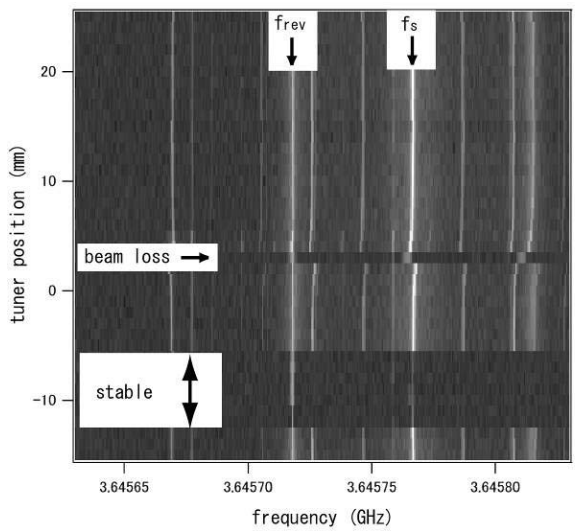

Figure 5: Image plot of intensity of beam spectrum. The image intensity increases from black to white.

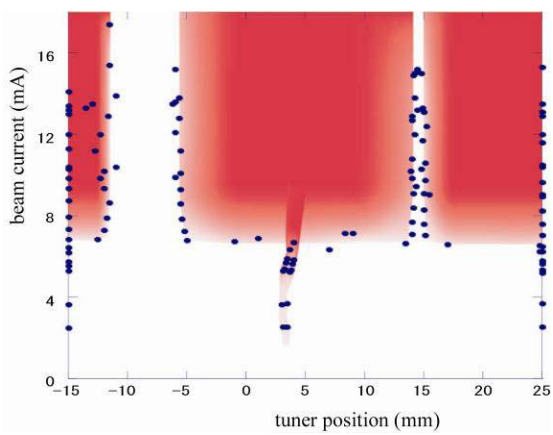

Figure 6: Stable region against coupled-bunch instability. White (Red) shows stable (unstable) region. Plots are observed points, which divide the two regions.

CONCLUSION

As the first step of the study with passive higher harmonic cavity, one harmonic cavity was manufactured and tested in the STB. The very strong synchrotron oscillation signal due to the coupled-bunch instability was drastically damped by the harmonic cavity at a specific tuning angle. However, this is not clearly understood, since any significant voltage is never excited in the harmonic cavity because of the large tuning angle. This will be made more clear using model analysis. For the lower energy operation the cavity effect might be also interesting, but any obvious improvements has not been seen yet.

ACKNOWLEDGEMENT

We would like to acknowledge R. A. Bosch of SRC, University of Wisconsin-Madison for the invaluable support in model analysis.

REFERENCES

[1] F. Hinode, H. Hama, M. Kawai, A. Kurihara, A. Miyamoto, M. Mutoh, M. Nanao, Y. Shibasaki, K. Shinto, S. Takahashi, T. Tanaka, Proceedings of 2005 Particle Accelerator Conference, Knoxville, p 2458.

[2] A. Miyamoto, F. Hinode, M. Kawai, K. Shinto, T. Tanaka, H. Hama, Proceedings of 2005 Particle Accelerator Conference, Knoxville, p 1892.

[3] H. Hama, F. Hinode, K. Shinto, A. Miyamoto, T. Tanaka, Nucl. Instr. and Meth. A 528 (2004) 571.

[4] M. Georgsson, Å. Andersson, M. Eriksson, Nucl. Instr. and Meth. A 416 (1998) 465.

[5] J. M. Byrd, S. De Santis, M. Georgsson, G. Stover, J. D. Fox, D. Teytelman, Nucl. Instr. and Meth. A 455 (2000) 271.

[6] M. Georgsson, W. Anders, D. Krämer, J. M. Byrd, Nucl. Instr. and Meth. A 469 (2001) 373.

[7] R. A. Bosch, (private communication).

[8] R. A. Bosch, Phys. Rev. ST Accel. Beams 8, 084401 (2005).

[9] R. A. Bosch, K. J. Kleman and J. J. Bisognano, Phys. Rev. ST Accel. Beams 4, 074401 (2001).

EFFECT OF MAGNETIC FIELD COUPLING ON INDUS-2 QUADRUPOLE MAGNETS

G Sinha, A. Kumar, A. K. Mishra and Gurnam Singh
IOAPDD, Raja Ramanna Centre for Advanced Technology, Indore-452013

Abstract

The distances between the magnets in the Indus-2, are small and as a result, the magnetic field of one magnet may affect the fields of the adjacent magnets. Therefore, it is important to find out the effect of mutual coupling between magnets in the actual condition in the ring and the ways to overcome this problem. In this paper, we will discuss how the field quality of quadrupole magnets (QP) in the ring is affected when accompanied by various corrector dipole magnets (CDP)(vertical and horizontal) and sextupole magnets (SP). Variations of integrated quadrupole field strength in presence of CDPs are measured at various field excitations and also by varying the distance between the magnets using a rotating coil. Experimental results are compared with the results obtained from 3D simulations. Possibilities of studying the interference effect by scanning the field by a Hall probe, is explored. Dependence of field interference on the distance between magnets, pole gap and the steel length are studied. Effects of the adjacent magnets on the higher order multipole of QP are also examined.

INTRODUCTION

Double Bend Achromat Indus-2 lattice consists of eight super periods each having two dipole bending magnets, four focusing and five defocusing QPs and four SPs and seven CDPs (used for closed orbit correction). There are total 72 QPs in the ring. These are divided in five different categories named as Q1, Q2, Q3, Q4 and Q5. All of these magnets have the same maximum gradient of 16 T/m. and same bore diameter of 85 mm and same cross section. Steel lengths of the Q1, Q2, Q3, Q4 and Q5 magnets are 262.5, 512.5, 362.5, 362.5 and 362.5 mm, respectively. There are two quadrupole triplets (Q1, Q2 and Q3) for the adjustment of beam sizes in the long straight section (LSS) and four CDPs are placed in between them (Figure 1). The achromat section consists of a triplet QP having two Q4s and one Q5 and four SPs and three CDPs. The distance (steel edge to steel edge) between a QP and a CDP vary from 176.25 mm to 383.75 mm in the LSS. In the achromat section, SP is placed as close as 195.75 mm from QP. It is clear that the fringe field of a QP is extended beyond the location of the adjacent magnets.

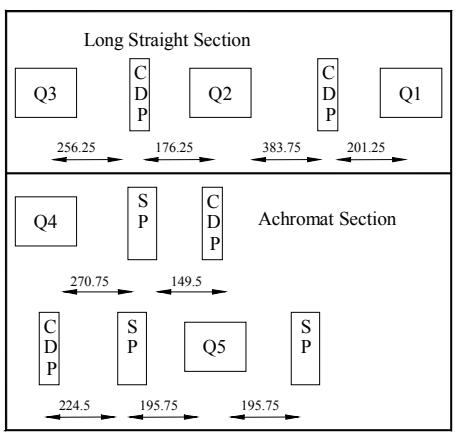

Figure 1: Block diagram of the portion of the unit cell where field interference between various magnets can occur. Distances are in mm.

EXPERIMENTAL RESULTS

Integrated QP field strength is measured at a reference radius of 32mm using a rotating coil system [1]. Around 150 A current in QP produces required maximum field gradient of 16 T/m. To find the effect of the adjacent CDP on a QP, the current in Q1 is fixed at 150A and the distances between them are varied from 135 mm to 460 mm. In the first case there is no current in the CDP. Then the same experiment is repeated while the current in the CDP is set to 10 A to check whether the field interference depends on the field excitation of the CDP. The integrated quadrupole field strength (B_2.L) of Q1 (steel length is

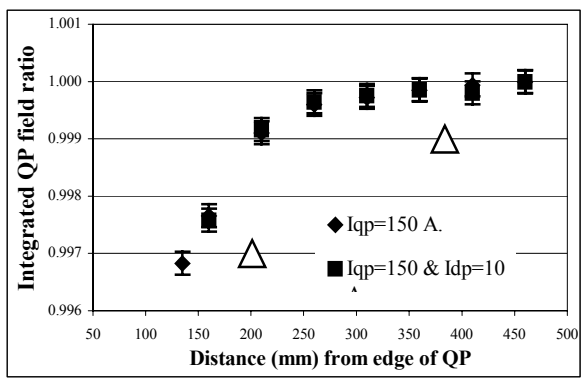

Figure 2: Variation of the ratio of the measured integrated quadrupole gradient, to the nominal gradient, with distance between the quadrupole (Q1) and the CDP. In one case current in QP is 150 A. and no current in CDP. Other case QP and CDP are having 150 A and 10 A currents, respectively. Open triangles indicate the minimum and the maximum distances in the ring.

262.5 mm) reduces by 0.18% and 0.0085% from its nominal value when the CDP is at a distance of 176 and 384 mm, respectively. Reduction of the field strength varies inversely with the third power of the distance between them (1/dist.^{3}). No additional change is observed when the CDP is powered by 10A within the experimental accuracy (Fig.2). Therefore, the reduction of B_2.L is independent of the field excitation of the CDP. This finding is in agreement with the simulation results obtained by others [2].

To check the variation of the field with the excitation current of the QP, position of the CDP is fixed at two different distances and the currents in QP are varied. Figure 3 shows that the reduction of B_2.L remains almost constant within the experimental accuracy, with the excitation of QP at two different distances.

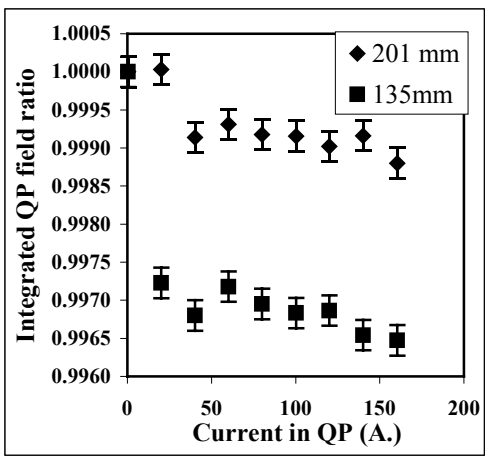

Figure 3: Variation of the ratio of the measured integrated quadrupole gradient to the nominal gradient with the quadrupole (Q1) current in presence of CDP at two different distances 201 and 135mm.

Therefore, the variation of the field also does not depend much on the excitation of the QP [3]. No significant

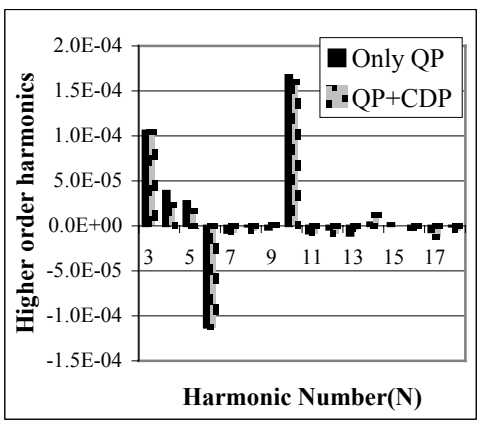

Figure 4: Higher order harmonics normalized with respect to the main quadrupole ($NB_nR^{n-2}/2B_2$) component. In one case CDP is placed at 201 mm away from the edge of the QP and the other with out CDP, i.e., QP stands alone.

effect on the higher order harmonics of QP from the magnetic field coupling is observed [3]. All the higher order harmonics are of the order of 10^{-4} or less (Figure 4).

Experiment is done by fixing the QP current at different values (30, 60, 100, 140 and 160 A) and then by varying the current in a SP. No significant change in B_2.L is observed in presence of SP at a distance of 265 mm and also with the excitation of SP. All the values are with in the experimental accuracy (± 3x 10^{-4}).

SIMULATION RESULTS

Simulation studies have been done using OPERA-3D[4] to understand the experimental results. Simulations have been done for a QP (Q1) alone and by placing a CDP at various distances 135, 201, 260 and 410 mm, respectively from the edge of the QP and then the difference of field from the nominal value was taken. Current in QP was set to 150 A, which produced integrated quadrupole field strength of 4.818 T.

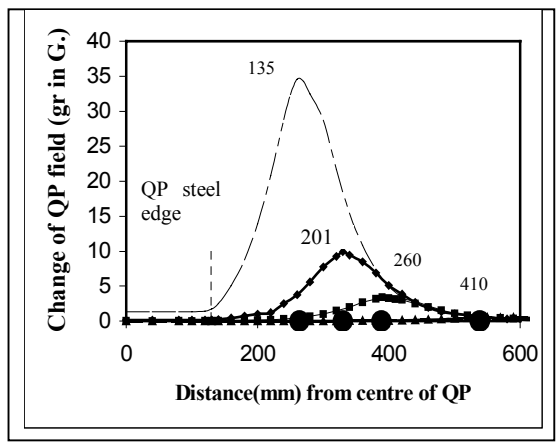

Figure 5: Plot of the difference of the simulated QP field component b_2 (gr) (between the case when QP stands alone and accompanied by CDP) against the distance from the center of QP. Dots on the X-axis indicate the position of the starting point of the CDP.

Magnetic field can be expressed as $B_y + iB_x = -\sum n(iA_n + B_n)(x+iy)^{n-1}$ where, A_n and B_n are the skew and normal components for 2n pole fields. Measuring the field on a circle of radius 0.032m and by doing FFT the QP field strength b_2 ($2B_2r$= gr) was found out. The differences of b_2, in Figure 5, starts' arising at the edge of the QP and become maximum near the point where the steel of the CDP starts (dots on the X-axis) and then it falls down symmetrically about the peak at all distances. Area under the curve, in each case, is the measure of the interference between the magnets. By knowing the total integrated quadrupole field strength in absence of nearby magnets and the difference in presence of CDP in each case, percentage changes are calculated which are in good agreement with the experimental results.

Figure 5 depicts an interesting point. When the distance of CDP is more than twice of the bore diameter (2d) of QP (for example at 201 mm) b_2 remains mostly

constant throughout the steel length of the QP (Δb_2=0). It starts changing near the edge of the QP steel. However, if the distance is lower than 2d (at 135 mm) b_2 at the center also reduces. Δb_2 remains constant (not zero) throughout the length of QP and starts increasing near the edge, peaks near the starting point of CDP and then fall down as observed for larger distance. Therefore, if the adjacent magnet is placed closer to the QP it will affect the field even at the center of QP and the coupling will be stronger. In that case the change will also depend on the length of the QP. However, in Indus-2 ring magnet separations are more than twice of the bore diameter of QP. Therefore, in experimental data reduction of QP field strength is found independent of QP steel length (total change, not the percentage change). Experimental results on Q3 and Q1 showed same reduction of strength. So, the findings of Q1 have been used to calculate field reduction of other QPs.

A rotating coil measurement does not provide detailed of the field reduction because it provides an integrated value. Therefore, there is a need to do point by point measurement. It is possible to find the value of b_2 at different distances in case of simulation, which helps in better understanding the experimental results. b_2 can be obtained by taking Fourier transformation of the field measured on a circle at any distance. This is also found that the reduction QP field strength does not depend on the width of the CDP. This is because Δb_2 shows peak near the point where the steel of the CDP starts but not much variation through out the length of the CDP.

We tried to observe the variation of the vertical component of the field (B_y) at 32 mm distance from the center of QP along the length of the magnet from the simulation results. Figure 6 shows the difference of B_y

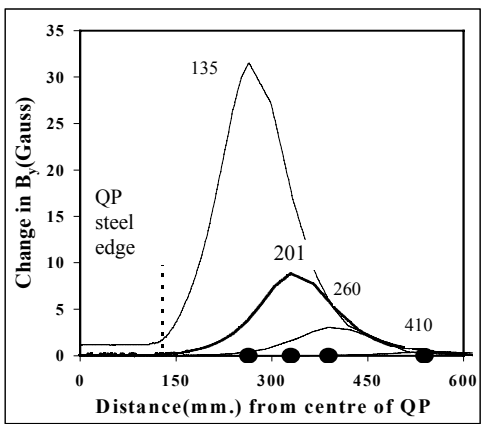

Figure 6: This is a similar plot as in figure 5. Here instead of Δb_2 the difference of the vertical component of the field (ΔB_y) at 32 mm, from the center of the QP, along the length of the magnet is plotted. This variation is very similar to that of Δb_2.

when a QP stands alone and accompanied by a CDP at various distances (135, 201, 260 and 410 mm from the edge of the QP). It also depicts the similar picture of the variation of Δb_2. This indicates that it is possible to understand qualitatively the coupling behaviour between magnets by scanning the magnetic field along the length using Hall probe. The percentage change of effective length of QP when the CDP placed at distances 135, 201, 260 and 410 mm from the edge of the QP are 0.27, 0.085, 0.032 and 0.004, respectively. Though the values of these changes are slightly less than that of b_2, it shows similar trend. Therefore, in some cases if the rotating coil measurement is not possible a simple Hall probe scanning can provide useful information about the magnetic field coupling.

CONCLUSION

In presence of the accompanying magnet in the ring the quadrupole field strength of Q1, Q2 and Q3 type of QPs are reduced by 0.098, 0.096 and 0.024 %, respectively. Proper excitation curve should be used for various QPs depending its position in the ring to overcome the field interference effect. The interference of the fields between a QP and a CDP does not depend on steel length of the QP and the excitations of both the magnets. Reduction of the field strength varies inversely with the third power of the distance between them ($1/dist.^3$). The presence of the steel block of the CDP distorts the fringe field of the QP and causes the reduction of quadrupole field strength. No significant effect on the higher order harmonics of QP from the magnetic field coupling is observed.

ACKNOWLEDGMENT

One of the authors is indebted to Dr. W. Meng for useful discussion on simulation. Help provided by K. Sreeramlu, P. K. Kulshreshtha, and Laxman singh during measurement are gratefully acknowledged.

REFERENCES

[1] Danfysik Model 692 User Manual, Danfysik.
[2] Y. Papaphilippou, Y.Y Lee and W. Meng, Particle Accelerator Conference, 2001, P. 1667.
[3] K. Egawa and M. Masuzawa, Particle Accelerator Conference, 1999, P. 3354.
[4] OPERA-3d user guide, Vector Fields Limited, U.K

PROGRAM FOR THE GENERATION OF HIGH CURRENT RFQ

Vlsrao.Sista#, S.C.L. Srivastava, T.Basak, Rajni Pande, Shweta Roy and P.Singh
Bhabha Atomic Research Centre, Mumbai-400085, India

Abstract

In general design of the linear accelerators, the beam dynamics parameters are calculated from data describing the accelerator structure. In this approach, the desired phase advances (beam dynamics parameters) are obtained after several iterations of structure parameters. A program has been written for the generation of RFQ Linac, which is based on choosing the zero current transverse and longitudinal phase advances. Given the zero current transverse and longitudinal phase advances, the structure parameters are calculated using the analytical formulae. In this paper, we discuss the design of the high current RFQ using this procedure and compare it with the ones obtained from the standard codes.

INTRODUCTION

The renewed interest in Accclerator Driven Systems (ADS) has spurred tremendous interest in developing high intensity proton accelerators, and set challenging demands in terms of delivering high current (~ tens of mA) and high energy ($\geq$1 GeV) required for the spallation process. In Indian context, ADS will be used for the utilization of thorium resources for the energy production. In view of the importance of ADS, a project to design and build a 20 MeV, 30 mA CW proton accelerator (LEHIPA) as an injector to 1 GeV Linac has been initiated.

The LEHIPA [1] mainly consists of a 50 keV ECR ion source, Low Energy Beam Transport (LEBT) line, 3 MeV Radio Frequency Quadrupole (RFQ) accelerator, Medium Energy Beam Transport (MEBT) line and a 20 MeV Drift tube Linac (DTL).

The Linac for the ADS system requires extremely low beam loss in order to allow hands-on maintenance. It has also been studied that if the beam is not in thermal equilibrium, the equipartitioning process caused by the strong coupling between the transverse and longitudinal motions can lead to emittance growth [2] and halo formation [3,4]. Hence we have studied ability of the RFQ to prepare an equipartitioned beam. The choice of the phase advances per focusing period (with, without space charge) of the transverse (σ_t,σ_{0t}) and longitudinal (σ_l,σ_{0l}) oscillations are crucial for the design of high current accelerators. These parameters not only determine the motion stability but also the emittance growths and the halo formation which can produce undesirable beam losses in high current accelerators. The zero current phase advance parameters (σ_{0t} and σ_{0l}) determine the structure parameters. A program has been written for the generation of RFQ by choosing the phase advances at the end of the gentle buncher.

#vlsrao.sista@gmail.com

DESIGN STRATEGY

An equipartitioned beam has equal transverse and longitudinal temperatures,T_l=T_t. Theoretically, for a matched bunch in a smooth-focusing system, the temperatures can be related to the rms beam widths and normalized rms emittances [5].

$$\frac{T_l}{T_t} = \frac{\varepsilon_{\ln}^2}{\varepsilon_{tn}^2} \cdot \frac{a^2}{(\gamma b)^2} \tag{1}$$

Where ε_{tn}, $\varepsilon_{\ln}$ denotes the full (100%) normalized emittance of a uniform beam distribution, a and b corresponds to full beam radii in the transverse and longitudinal directions respectively, γ is the relativistic factor. From the envelope equations the full current phase advances (σ_t, σ_l) are given by

$$\sigma_t = \frac{\varepsilon_{tn}\lambda}{a^2\gamma} \tag{2}$$

$$\sigma_l = \frac{\varepsilon_{\ln}\lambda}{b^2\gamma^3} \tag{3}$$

where λ is the wavelength.

From the smooth approximation theory the phase advances with space charge for the uniformly ellipsoidal beam bunch are related to the external focusing forces in the form of:

$$\sigma_t^2 = \sigma_{0t}^2 - \frac{Q(1-ff)}{2a^2b} \tag{4}$$

$$\sigma_l^2 = \sigma_{0l}^2 - \frac{Qff}{a^2b} \tag{5}$$

where the bunch form factor *ff* is a function of γb/a [6] when $0.85 \leq \gamma b/a \leq 5$ then *ff*=a/3γb, and $Q = \frac{3Z_0 qI\lambda^3}{4\pi m_0 c^2 \gamma^3}$ with Z_0=377Ω

The Q parameter is then fixed by the choice of the beam current, I, the particle rest mass (m_oc^2), charge, and energy (W) and the operating frequency of the system.

For the equipartitioned beam the ratio of the transverse and longitudinal temperatures should be equal to one.

From Eq. (1) we get $\frac{\varepsilon_{ln}}{\varepsilon_{tn}} = \frac{\gamma b}{a}$ and therefore by choosing the ratio of $\frac{\varepsilon_{ln}}{\varepsilon_{tn}}$ and from the equations (2)-(5) we can calculate the beam sizes as function of zero current phase advances. The zero current phase advances are chosen based on the following constraints in order to avoid envelope instabilities, resonances and space charge limits [7]

$\sigma_{0t}, \sigma_{0l} \leq 90^0$
$\sigma_t/\sigma_l \neq$ n or 1/n (where n is integer)
σ_t/σ_{ot} , $\sigma_l/\sigma_{ol} > 0.4$

The next step is to determine the accelerator parameters which give the chosen phase advances and this choice should lead to a physically realizable design.

RFQ DESIGN

We have adopted the conventional philosophy, where RFQ is divided in to four sections namely RMS, Shaper, Gentle Buncher (GB) and accelerator. The parameters of the RFQ accelerator at the end of the GB section are calculated according to the basic formulae [8].

Accelerator section parameters

In accelerator design we kept the acceleration efficiency (A) and synchronous phase (φ_s) constant, so $\sigma_{0l} \propto \beta_s^{-1}$. In order to keep the ratio of the beam sizes constant to have a equipartitioned RFQ, σ_{0t} has been varied with βs. From the values of σ_{0t} and σ_{0l} the aperture (a) and modulation (m) are calculated as a function of energy.

Gentle Buncher parameters

The calculation of this section follows the K-T approach [9], where σ_{0l} and spatial length of the bunch Z_b are kept constant all along the GB section.

Shaper parameters

We have employed two different ways for the generation of shaper section.

a) The accelerator parameters modulation (m), aperture (a) and φ_s are varied linearly with the energy.
b) The focusing factor (B), φ_s, modulation (m) are varied linearly to the final values with the energy of the beam.

The shaper length has to be calculated in such a way that the energy gain in the shaper should be equal to the required energy gain at the end of the shaper.

NUMERICAL SIMULATIONS

The parameters of 3 MeV, 30 mA proton RFQ are generated by choosing the ratio $\frac{\varepsilon_{ln}}{\varepsilon_{tn}}$=1.3. The parameters are chosen in such a way to keep the peak surface field below 1.8 times kilpatrick limit all along the structure. In this design, the value of ρ/r_0=0.93 is kept constant along the RFQ, where ρ is the transverse radius of curvature and r_0 is average aperture radius. The parameters of the RFQ are shown in the Fig. 1 and enumerated in Table 1.

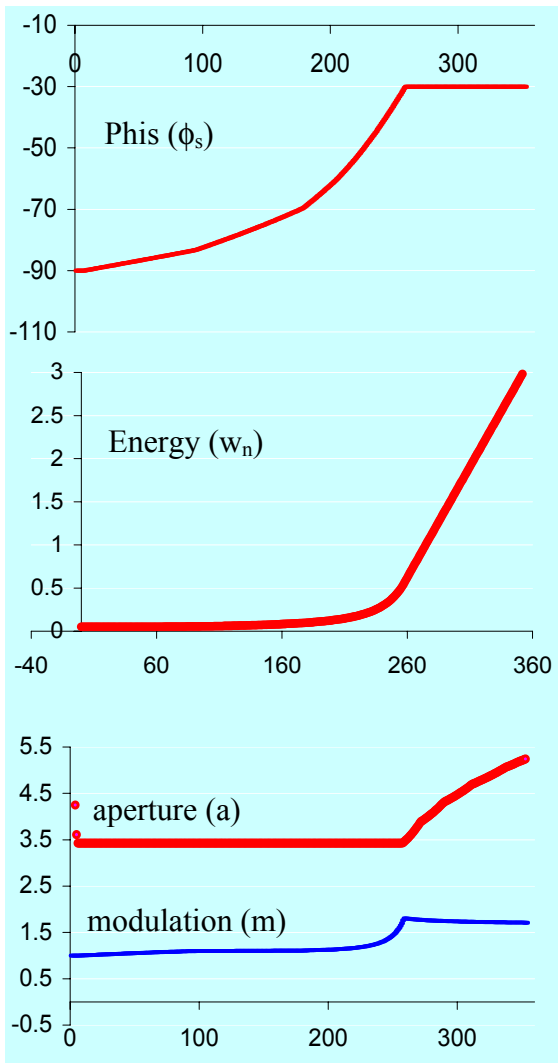

Figure 1: RFQ parameters (φ_s,W_n,m,a) vs cell number.

Numerical simulations of the beam dynamics have been performed with program LIDOS [10]. The variation of the longitudinal and transverse oscillation frequency along the length of the RFQ is shown in Fig 2. The initial particle distribution is waterbag in the transverse direction, with a normalized rms emittance of 0.02 π cm-mrad. It has been observed that the transverse emittance growth ($\varepsilon_{out}/\varepsilon_{in}$) is equal to one at the end of the RFQ. The

variation of transverse emittance along the RFQ is shown in Fig 3. The transmission is more than 97%. The transverse zero current phase advance σ_{0t} is varied from 29.6° at the beginning of the shaper to about 12.7° at the end of the RFQ. The variation of the structure parameters by choosing the different ratios of $\frac{\varepsilon_{ln}}{\varepsilon_{tn}}$ has to be studied.

Table 1: Design parameters of RFQ

Parameter	Value
Input energy	50 keV
Output energy	3.0 MeV
Frequency	352.21 MHz
Intervane voltage	80.14 kV
Peak surface field	32.8 MV/m
Length	4.0 m
i/o transverse emittance	0.02/0.0204 cm-mrad
Output long. Emittance	0.037 cm-mrad

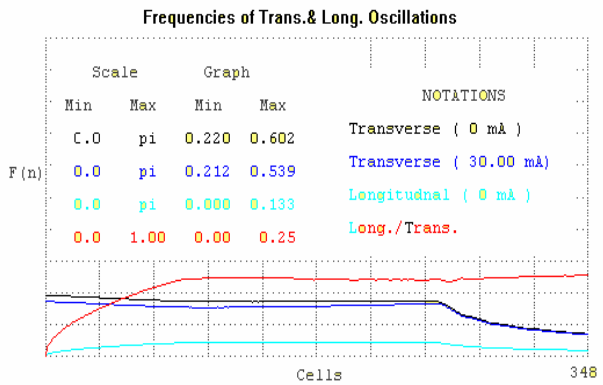

Figure 2: Logitudinal & Transverse oscillations vs cell number.

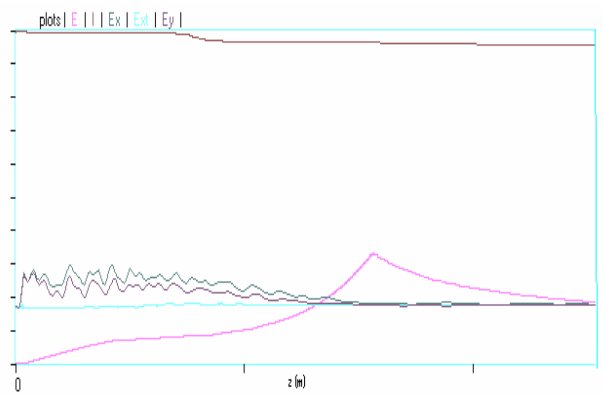

Figure 3: Transverse emittance vs z

CONCLUSIONS

The equipartitioning design procedure of RFQ linacs has been presented and it has been observed that this method can decrease the emittance growth. One of the main advantages with equipartitioned scheme is matching between the RFQ and DTL structures. Since the r_0 is increased in the accelerator section, the ρ has varied along the structure. So the fabrication of the vanes has to be done with ball & mill cutting tool.

ACKNOWLEDGEMENT

We thank Drs. S. Kailas and R.K. Choudhury for their support and Mr. Piyush Jain for his help in calculations and useful discussions.

REFERENCES

[1] P. Singh, "Status of the LEHIPA Project at BARC", InPAC-2006, p 50.
[2] Hofmann, "Transport and focusing of high-intensity unneutralized beams". Applied charged particle optics, part C, A. Septier, Academic Press, 1993
[3] J-M Lagniel, "Chaotic behaviour induced by space charge" EPAC 94
[4] J-M Lagniel and A. Piquemal, "On the dynamics of space-charge dominated beams", LINAC94 conf. proc.
[5] R.A. Jameson, "Equipartitioning in linear accelerators" Proc. 1981 Linac Conf., Santa Fe.
[6] A.D. Vlasov, "Theory of linear accelerators", Israel Progr. For Scientific Translations, Wiener Bindery Ltd., 1968.
[7] M. Reiser, "Theory and Design of Charged Particle Beams" (John Wiley & Sons, New York) 1994.
[8] Jean-Michel Lagniel, "Tools for the Design of High-Current Linacs" Proc. 1994 Linac Conf., Tsukuba, Japan.
[9] I. M. Kapchinskiy and V.A. Tepliakov, Prib. Tekh. Eksp. 4, 17-19 (1970)
[10] LIDOS, A Computer Code for Beam Dynamics of RFQ Linac, Version 1.1.

STUDY OF SPACE CHARGE COMPENSATION IN LEBT

S.C.L.Srivastava#, Vlsrao.Sista, Rajni Pande, Shweta Roy, T. Basak and P.Singh
Bhabha Atomic Research Centre, Mumbai-400085, India.

Abstract

A 20 MeV, 30 mA CW proton accelerator is being built in BARC which consists of 50 keV ECR ion-source, LEBT, 3 MeV RFQ, MEBT and 20 MeV DTL. In designing low energy beam transport (LEBT) line, which matches the beam from ion-source to RFQ, the expansion of the proton beam is a severe problem. As the energy of the beam is 50 keV, Coulomb repulsion is enormous and for minimization of this repulsion, space charge compensation is done. To simulate the beam dynamics part, a PIC code is written, which allows beam of different distributions like KV, Parabolic and Waterbag. This is an electrostatic code, which can also take care of external magnetic fields. A Monte Carlo collision scheme is being implemented for the ionization of the background gas. In this paper, we are presenting the simulation of space charge compensation of the 30 mA proton beam at 50 keV.

INTRODUCTION

Newly proposed accelerators with application to nuclear waste transmutation, subcritical nuclear reactors, neutron spallation sources require high intensity linacs. A 20 MeV, 30 mA CW proton accelerator is being built in BARC which consists of 50 keV ECR ion-source, LEBT, 3 MeV RFQ, MEBT and 20 MeV DTL [1]. In the low energy section of such accelerators beams of tens of mA are strongly subjected to the Coulombian repulsion. The transport of such space-charge dominated beams are challenging task because of the same reason. Apart from applying the usual magnetic fields based structure for focussing; the method of space-charge neutralization has also been tried for the same. In this process, a gas is introduced in the beam pipe, which gets ionized by the beam. The produced electrons are trapped in the beam potential and reduce the repulsive space charge forces. A better understanding of the kinetics of the process will make it more efficient and may find different application in other fields. To study this kind of situation, we need to solve the full Poisson-Vlasov model including the different kind of collisions. This makes PIC-MCC simulation technique as a competitive candidate.

BASICS OF A PARTICLE-IN-CELL/ MONTE CARLO MODEL

In the PIC method, so-called ‘‘superparticles’’ move in the simulation region through an artificial grid on a timestep basis. Each of these superparticles represents typically about 10^8 real particles. Only charged particles are simulated with these superparticles; neutrals are assumed to form a continuum. In the beginning of the simulation, every charged particle is assigned to a specific position on the grid, leading to a self-generated electric field. The particles move in response to both the applied and self-generated fields, according to Newton’s laws. This gives rise to new positions for the particles, changing the self-generated field, and hence changing the force acting on the particles. Mathematically, this is done every timestep by first *weighting* the positions of the particles to the grid, yielding the charge densities on the grid points. The potential and electric field on the grid points are then determined from the calculated charges, by Poisson’s equation. A weighting procedure is applied again, to obtain the forces on the positions of the particles from the previously obtained field on the grid points. From the force on the positions of the particles, first, the velocity of every particle is calculated and, from the velocity, the position is determined, using a leap-frog algorithm [2]. After the particles are placed in their positions, a Monte Carlo algorithm is used to simulate collisions between particles. This procedure is repeated for many timesteps, until convergence is reached.

In the MC module, a random number between 0 and 1 is chosen to determine for every particle whether a collision occurs or not. If a collision takes place, a second random number is generated to determine the collision type. The energy and direction of the particles after the collision are determined, depending on the collision type, again using random numbers. We make use of the ‘‘null-collision’’ method [3]. In this approach, a fictitious collision process (null-collision) is introduced, with a collision frequency such that when it is added to the sum of the collision frequencies of the real collision processes, a constant total collision frequency over position and energy is obtained. In this way, the maximum fraction of the total number of particles in the simulation that undergo a collision (either a real or a null collision) during a timestep Δt, is given by

$$P_{null} = 1 - \exp(-\nu' \Delta t) \tag{1}$$

where

$$\nu' = \max_{x,E}(n_t \sigma_T \nu) \tag{2}$$

In Eq.(2), x denotes the position, E is the energy of the incident particle, n_t is the density of target particles at particle position, σ_T is the total cross section for every species and ν is the velocity of the incident particle. Typically the target particles are assumed to be uniformly

shashics@barc.gov.in

distributed in the system as a background species with a constant n_t. However, in the case of electron-ion collision n_t is also a function of position. The more details of PIC-MC are discussed by Vahedi [3].

PIC- MCC MODEL FOR SPACE-CHARGE COMPENSATION OF CW H^+ BEAM

To simulate the process, a 2D(x-y) PIC-MCC code is being developed which will be able to do the beam dynamics of the CW beam in a system consisting of drift space, solenoid and quadrupoles with or without presence of neutralizing gas. The very first need of a PIC code is to get different particle distributions, to represent the beam. These simulations are highly dependent on the representation of the beam in phase space, which necessitates the generation of distributions in accordance to different models like KV, Waterbag, parabolic and Gaussian normally used in the literature.

Phase space distributions

Consider the distributions in 4Dphase space (x, x′, y, y′) as n(x, x′, y, y′) = dN/dxdx′dydy′ which depends on total emittance ε:

$$n(x, x', y, y') = n(\varepsilon)$$
$$\varepsilon = A_x^2 + cA_y^2 \quad (3)$$

Where

$$A_x^2 = \left(\sqrt{\beta_x}\,x' + \frac{\alpha_x x}{\sqrt{\beta_x}}\right)^2 + \left(\frac{x}{\sqrt{\beta_x}}\right)^2 \quad (4)$$

$$A_y^2 = \left(\sqrt{\beta_y}\,y' + \frac{\alpha_y y}{\sqrt{\beta_y}}\right)^2 + \left(\frac{y}{\sqrt{\beta_y}}\right)^2$$

c is ratio of emittances in x and y plane [4].

The equation ε = const describes a hyperellipsoid surface in phase space x, x′, y, y′. As distribution function depends on ε, the phase space density, n, will be constant on one hyperellipsoid surface while it will vary from one surface to another. A numerical algorithm is written to generate the different distribution like KV, Waterbag and parabolic [5]. The projections of the different distributions on (x, x′) are shown below-

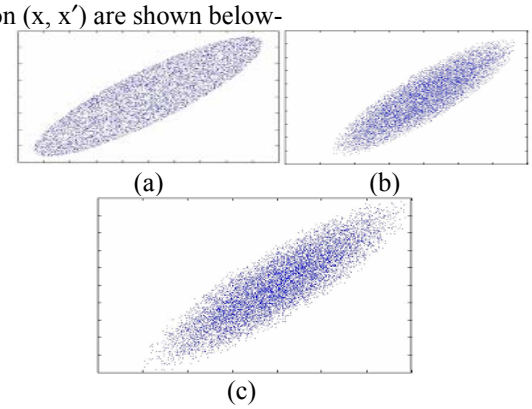

Figure 1: Projections of 4D phase space distributions on (x, x′) plane.(a) KV (b) Waterbag (c) Parabolic

Poisson Solver

As the particles are in non-relativistic regime, we need not to solve the full wave-equation. This provides enough reason to write an electrostatic PIC code rather than attempting for an electromagnetic one. To find the potential and in turn the electric field, we need to solve the Poisson equation. We have used the direct method to solve the Poisson equation. This method is called spectral method, since it involves the expansion of potential and source terms as truncated Fourier series. In one direction, the boundary conditions may be Diritchlet or Neumann boundary condition while in the other direction the provision is for mixed boundary conditions.

$$\alpha_l u(x,y) + \beta_l \frac{\partial u(x,y)}{\partial x} = \gamma_l(y) \quad (5)$$

at $x = x_l$ and

$$\alpha_h u(x,y) + \beta_h \frac{\partial u(x,y)}{\partial x} = \gamma_h(y) \quad (6)$$

at $x = x_h$.

$$u(x,0) = u(x,l) = 0$$
$$or \quad (7)$$
$$\frac{\partial u(x,y=0)}{\partial y} = \frac{\partial u(x,y=l)}{\partial y} = 0$$

Integrator of particle trajectories

In the most general case of integration of particle trajectories in this code are done in following steps-

- In the first stage, the particle performs a half step acceleration in the electric field
- After that, the vector of the particle velocity accomplishes rotation in the magnetic field, utilizing the Boris scheme.
- In the third stage, the particle performs again half step acceleration in electric field (if applicable MC module will take over).
- And at the final stage particles are advanced with this velocity.

Now let's consider the different component of the lattice.

Drift

In drift, magnetic field and external electric field are absent so the particle moves in its own self field.

Solenoid

In case of solenoids, focussing fringe fields are calculated upto the linear terms and given by following.

$$B_r = -\frac{r'}{2} B'(z) \quad (8)$$

This term is responsible for the end effects of the solenoid which otherwise have flat magnetic field profile. In our PIC code, we have implemented it at the beginning and end points. This model is known as hard edge model of solenoids.

Quadrupole

The fields of quadrupoles are given by the following equation-

$$B_x = B_0 \frac{x}{a}, B_y = B_0 \frac{y}{a} \quad (9)$$

The particles trajectories are evaluated in the above prescribed manner.

We have completed the implementation till this point in code and results are described in the next section. The MC module is still under development. However, the methodology has been worked out and in brief, it is discussed below.

In the beginning, we will start with the ionization process only. The ionization cross-section of various gases by proton at different energies can be described by the empirical scaling law [4]. As we are interested in the detail kinetics of the space charge compensation process the ionization by energetic electrons will also be taken care of. This requires the energy and angular distribution of produced electron in the ionization process by proton. There are number of experimental data available and we are making use of that by fitting some empirical formulas.

RESULTS

As we have stated earlier that PIC part of this code has already been implemented. We have used this code to simulate the low energy beam transport section for the 20 MeV, 30 mA proton accelerator being built in BARC. A comparison between the parameters obtained by TRACE2D and our code is presented.

Table 1:LEBT Parameters

ELEMENT	LENGTH	STRENGTH
Drift	60 cm	
Solenoid	30 cm	1.903 kG
Drift	50 cm	
Solenoid	30 cm	2.113 kG
Drift	15 cm	
Total Length	185 cm	

The LEBT is designed using TRACE2D with the following input Twiss parameters [6], $\varepsilon = 0.02\pi$ cm mrad, $\beta_x=\beta_y=24.768$ cm/rad, $\gamma_x=\gamma_y=0.171$ rad/cm and $\alpha_x=\alpha_y=-1.8$. The output parameters are found to be as $\varepsilon = 0.02\pi$ cm mrad, $\alpha_x=\alpha_y= 1.8$, $\beta_x=\beta_y=6.43$ cm/rad. As TRACE2D is a envelope tracking code, so constant emittance is obvious. With the same input and lattice when we tried with our code, we got the output values as $\varepsilon = 0.0225\pi$ cm mrad, $\alpha_x=1.834$, $\alpha_y=1.90$, $\beta_x=6.61$ cm/rad, $\beta_y=6.87$ cm/rad. The particle trajectories are shown in the Fig.2

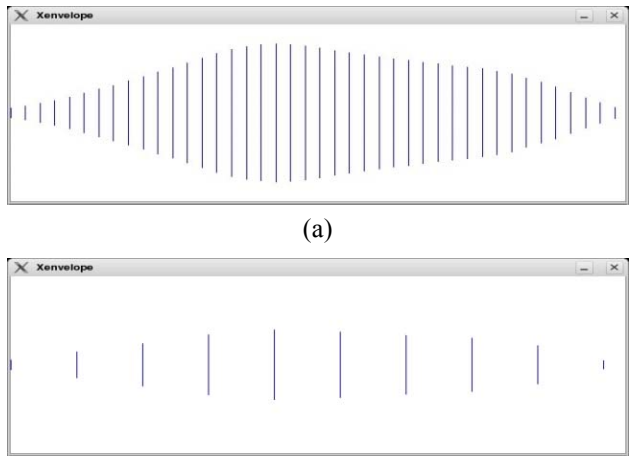

(a)

(b)

Figure 2: The trajectories of particle through LEBT line for (a) 30 mA, (b) 3 mA.

We also tried to see the maximum beam size as a function of space charge compensation (reduced current). We found that with 90% compensation the maximum beam size reduces from 6.1 cm to 3.40 cm.

CONCLUSION

The development of PIC part of the code is already completed and results has been compared with TRACE2D calculations and also in some cases solving analytical KV equation. The results are in good agreement. The difference in some cases is expected as ours is a PIC code while others are envelope tracking codes. The MC module implementation is in progress.

REFERENCES

[1] P. Singh, "Status of the LEHIPA Project at BARC", InPAC-2006, p 50.
[2] C.K. Birdsall and A.B. Langdon, "Plasma Physics via Computer Simulation" (IOP, Bristol) 1991.
[3] V.Vahedi and M. Surendra, Comput. Phys. Commun, **87**, 179(1995).
[4] M. Reiser, "Theory and Design of Charged Particle Beams" (John Wiley & Sons, New York) 1994.
[5] S.C.L. Srivastava, S.V.L.S. Rao, P. Singh, "Generation of different particle distributions in 4d phase space", InPAC-2006, p 209.
[6] Rajni Pande *et al.,* "Effect of Space Charge Compensation on LEBT Design", Proc. DAE Symp. Nucl. Phys.(India), 46(B), 466(2003).

BEAM POSITION MONITOR AT THE SCSS PROTOTYPE ACCELERATOR

H. Maesaka#, Y. Otake, K. Togawa, T. Shintake, RIKEN/SPring-8, Kouto, Sayo, Hyogo, Japan,
H. Ego, T. Fukui, N. Hosoda, T. Ohshima, JASRI/SPring-8, Kouto, Sayo, Hyogo, Japan

Abstract

This paper presents the design and the performance of the beam position monitor (BPM) in the prototype accelerator of the X-ray free electron laser (XFEL) project at SPring-8. An RF cavity-type BPM has been developed, since it has the capability to achieve the required position resolution, which is less than 1 μm. The TM110 mode of a beam-induced field is extracted and its amplitude and phase yield the beam position. Conversion coefficients were determined by beam-based calibration. The position resolution was also evaluated by a beam-based method. The preliminary result was obtained to be approximately 5 μm, or better. This result is sufficient for tuning the beam of the prototype accelerator to generate the vacuum ultraviolet (VUV) FEL, and a FEL amplification has been observed. However, XFEL requires better resolution. Therefore, we are planning to perform more precise measurements and to develop a new detection circuit.

INTRODUCTION

The XFEL project, SCSS (SPring-8 compact SASE[!] source) [1], is in progress, and the prototype accelerator [2] is in operation. One of the most important subjects to produce XFEL is that the electron beam must overlap with the radiated X-ray throughout the undulator section. The position difference between the beam and the X-rays is required to be less than 4 μm [3]. Therefore, the resolution of the BPM is necessary to be less than 1 μm. The cavity type RF-BPM has a capability to achieve the required performance, since past experiments, such as Ref. [4], showed resolutions of a few tens of nanometers. Another advantage is that the agreement between the electrical center and the mechanical center is fine, since the cylindrical shape of the RF-BPM enables a precise lathe process. We describe the design and the performance of the RF-BPM used at the prototype accelerator.

MEASUREMENT PRINCIPLE

Suppose that there is a cylindrical RF cavity in a beam line. When a short bunch of charged particles passes through the cavity, it excites electromagnetic oscillations resonating with the cavity. Since the electric field of a dipole mode, such as TM110, linearly varies with the transverse offset near the cavity axis, the amplitude of the beam-induced field strongly depends on the beam position. On the other hand, the electric field of a monopole mode, such as TM010, has axis symmetry at the cavity center. Accordingly, the amplitude is almost independent of the beam position, and is sensitive to only the beam charge. Thus, dipole modes are available for beam-position measurements. Since the TM110 dipole mode is the lowest order, we consider this mode hereafter.

The complex amplitude of the TM110 frequency is expressed as [5]

$$V_{RF} = A_1 qy + iA_2 qy' + iA_3 q + V_N . \quad (1)$$

Descriptions of each term are:

- $A_1 qy$: Beam position signal. The amplitude is proportional to the beam displacement, y, and the beam charge, q.
- $iA_2 qy'$: Beam angle signal, which is induced by the beam angle, y'. The phase is 90 degrees different from the first term, which is the reason why the imaginary unit i is multiplied.
- $iA_3 q$: Contamination from the tail components of the frequency distribution of monopole modes. Even if the eigenfrequency is different, the finite Q value causes a measurable effect on the TM110 frequency. The phase of this term is also 90 degrees apart from the first term.
- V_N: The other components, such as thermal noise.

Here, A_1, A_2 and A_3 are proportionality coefficients. Thus, we can obtain the beam position when we know the amplitude and the phase of the TM110 signal together with the beam charge. To measure the charge, it is effective to prepare another TM010 cavity whose resonant frequency is the same as that of the TM110 cavity. In this case, the TM010 cavity provides a phase reference of the TM110 signal in addition to charge information.

HARDWARE SETUP

The drawing of the RF-BPM installed in the prototype accelerator is shown in Figure 1. The RF-BPM consists of two cavities, a position-detection cavity (TM110) and a reference cavity (TM010). The resonant frequency is

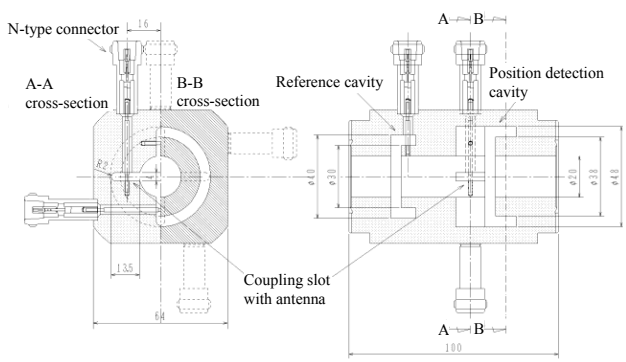

Figure 1: Drawing of the RF-BPM.

#maesaka@spring8.or.jp

[!]Self Amplification of Spontaneous Emission

4760 MHz for both cavities. Although the acceleration frequency is 5712 MHz, the BPM frequency is intentionally shifted so as to avoid any background from the dark current synchronized to the acceleration RF. The position-detection cavity has four coupling slots with antennas, two for x direction and the others for y direction. The slot is designed to couple with the TM110 mode selectively and to be insensitive to the TM010 mode. The loaded Q factor is approximately 100. The voltage of the signal into a 50 ohm cable is calculated to be 16 mV/nC/μm [1].

Figure 2 shows a photograph of the RF-BPM system. The RF-BPM cavity is mounted on the XY stage so that the BPM center can be adjusted to the radiated photon path. A removable iris is attached to the RF-BPM for precise alignment using a HeNe laser [1]. The RF-BPM system is installed on a stable support made of cordierite ceramics. These alignment components are designed to achieve a position accuracy of 4 μm.

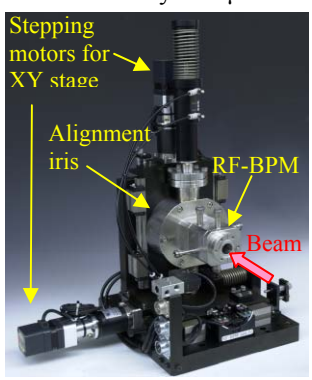

Figure 2: Photograph of the RF-BPM system.

The RF-BPM has three outputs: two from the position-detection cavity (X and Y) and the other from the reference cavity. The signal of each channel is processed by an electric circuit (Figure 3). The raw signal is mixed down to 476 MHz by a heterodyne method and fed into two sections. One is a log amplifier to obtain the logarithm characteristic of the amplitude, and the other is the phase detector after a 100 ns delay line. The amplitude and phase are finally merged with a solid-state switch and recorded with a VME waveform digitizer (ADC) [1,6]. The switch is turned to the log amplifier by default. When a sufficiently large RF amplitude is detected, the switch is flipped to the phase detector. Therefore, one digitizer channel can read out both the amplitude and the phase. By using a log amplifier, the dynamic range is extended to 80 dB and a small signal is magnified to maximize the position resolution around the BPM center.

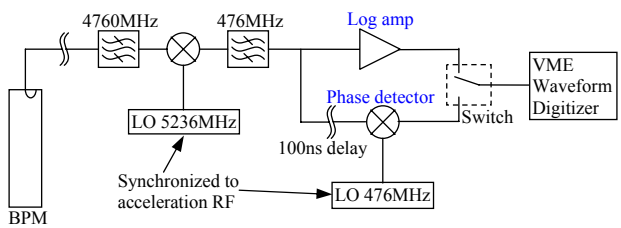

Figure 3: Detection circuit of the RF-BPM signal.

MEASUREMENTS

The amplitude and the phase of a BPM signal are obtained as two sampled voltages from ADC. The absolute value of the beam position is calculated by

$$|y| = \alpha \exp[\beta(V_y - V_q)], \quad (2)$$

where V_y and V_q are amplitude data of the position-detection cavity and the reference cavity, respectively, and α and β are conversion coefficients. The exponential representation comes from logarithmic compression by the detection circuit. The beam charge is normalized by subtracting V_q from V_y. The sign of y is determined by the phase signal, since the phase is inverted by 180 degrees, depending on the sign, as shown later in Figure 4 (b).

Calibration

The conversion factors in Eq. 2 were determined by a beam-based calibration. During data taking, the beam was kept unchanged and the XY stage was moved. The calibration procedure was as follows:

1. Move the XY stage to the origin.
2. Adjust the beam trajectory to the BPM center by using corrector magnets. This is done by looking for the point that the BPM signal is minimized.
3. Move the XY stage by 0.1mm step, and take 100 events for each step.
4. Fit Eq. 2 to the amplitude data.

When the BPM calibration was carried out, the beam energy was 250 MeV and the beam charge was 0.2 nC. The calibration data are shown in Figure 4. The amplitude was properly fitted by Eq. 2. The phase data indicates that the phase flipped by 180 degrees at 0.0mm. Thus, the calibration was appropriately done.

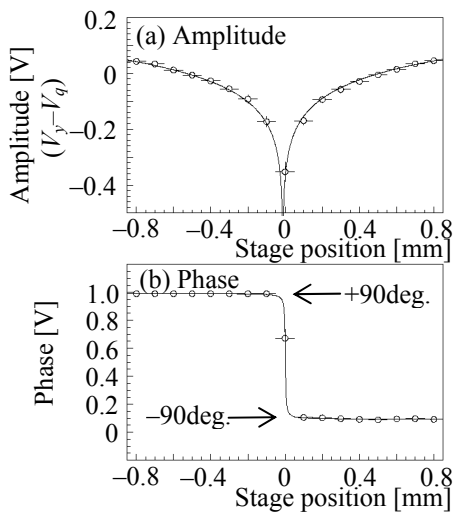

Figure 4: Fit results of the calibration data, (a) the amplitude data after beam charge correction and (b) the phase data.

Resolution measurement

The position resolution can be measured by using three adjacent RF-BPMs. The first and third BPMs determine the expected position at the second BPM, assuming the straight trajectory. The position resolution is obtained from the residual, which is the difference between the detected position of the second BPM and the expectation.

We used four BPMs (called A, B, C and D) in the undulator section, as illustrated in Figure 5. The resolution of B (C) was evaluated from A–C (B–D). More than 1000 beam shots were acquired for several minutes. During data taking, electromagnets between BPMs were turned off and the gap of the undulator was fully opened to minimize the magnetic field. The beam energy, charge and profile width were 250 MeV, 0.2 nC and 0.3 mm RMS, respectively.

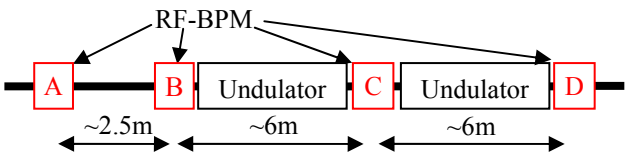

Figure 5: Arrangement of RF-BPMs in the undulator section of the prototype accelerator.

The residual distributions of BPM B are shown in Figure 6. The width of the residual distribution is proportional to the BPM resolution. Under the assumption that the resolutions of three relevant BPMs are the same, the position resolution can be calculated. If BPMs are arranged at even intervals, for example, the position resolution, σ_{BPM}, is

$$\sigma_{BPM} = \sqrt{2/3} \cdot \sigma_{res}, \qquad (3)$$

where σ_{res} is the standard deviation of the residual distribution. Analysis results are summarized in Table 1. The resolution was approximately 5 μm, or better.

Discussion

As a result of beam tuning with RF-BPMs, VUV-FEL amplification in the wavelength region of 40–60nm was

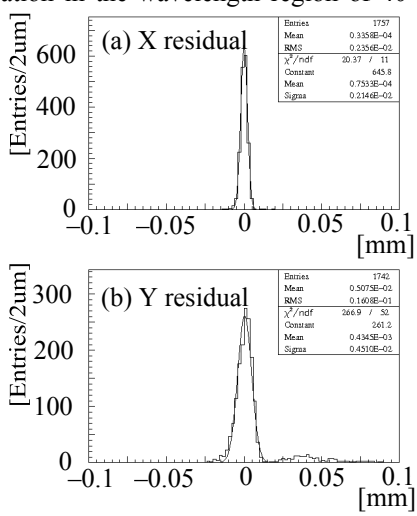

Figure 6: Residual distributions of BPM B for (a) the x-direction and (b) the y-direction.

Table 1: Results of the resolution measurement.

BPM	X resolution [μm]	Y resolution [μm]
B	1.7	3.6
C	5.2	4.9

observed [7]. Thus, the performance is sufficient for the prototype accelerator.

However, the measured resolution is not as good as the design value, which is the requirement of XFEL, less than 1 μm. Since there are undulators and other components between the BPMs, the beam trajectory is not exactly straight due to unignorable magnetic fields. This is thought to be the main reason for the deterioration.

SUMMARY AND FUTURE PLAN

To achieve a precise alignment of the beam trajectory required by XFEL, the RF-BPM was designed and installed in the prototype accelerator. Beam-based calibration was appropriately achieved. The preliminary position resolution was obtained to be approximately 5 μm, or better. This is sufficient for VUV-FEL amplification in the prototype accelerator. Since the data was taken over 1000 beam shots, we may conclude that beam line components in the undulator section were sufficiently stable during data taking, *i.e.* no vibration nor power supply jittering.

However, XFEL requires better resolution. Therefore, we are planning to prepare a BPM triplet to perform more precise resolution measurements. In addition, we are developing a new detection circuit. The present circuit is not effective to distinguish the beam position signal from contaminations of the beam angle and monopole modes, because the recorded amplitude is the sum of these signals. Therefore, an IQ demodulator is used for the new circuit, since it separates the position signal (in-phase) from contaminations (quadrature), by definition.

ACKNOWLEDGEMENTS

The authors give thanks to S. Kojima and K. Kase for their special efforts in the mechanical design. The authors also acknowledge the SCSS group members for their helpful support during installation and beam operation.

REFERENCES

[1] SCSS XFEL Conceptual Design Report (2005).
[2] T. Shintake *et al.*, "Status of The SCSS Test Accelerator and XFEL Project in Japan", Proc. EPAC 2006.
[3] T. Tanaka *et al.*, Nucl. Instrum. Meth. **A 528**, 172 (2004).
[4] T. Slaton *et al.*, "Development of Nanometer Resolution C-band Radio Frequency Beam Position Monitor in The Final Focus Test Beam", SLAC-PUB-7921 (1998); V. Vogel *et al.*, "Performance of a Nanometer Resolution Beam Position Monitor System", UCRL-CONF-216283 (2005).
[5] T. Shintake, "Development of Nanometer Resolution RF-BPMs", Proc. HEAC 1999.
[6] T. Fukui *et al.*, "A Development of High-speed A/D and D/A VME Boards for a Low Level RF System of SCSS", Proc. ICALEPCS 2005.
[7] T. Shintake *et al.*, "First Lasing at SCSS", Proc. FEL 2006.

DESIGN OF A STRIPLINE KICKER FOR TUNE MEASUREMENT IN SESAME STORAGE RING

Seadat Varnasseri#
SESAME, c/o UNESCO Amman Office, P.O. Box 2270

Abstract

In this paper the SESAME* storage ring tune measurement system is described. Travelling wave electrodes are commonly used in synchrotron light sources as a tool for both excitation and beam sensing for tune measurement. Normal longitudinally symmetric stripline has a positive sine wave response in the frequency domain. An exponentially tapered stripline has a constant coupling impedance versus frequency and better frequency response, but complicated in manufacturing. In this paper the design of stripline kicker for the purpose of tune measurement in the SESAME storage ring is reported.

INTRODUCTION

In SESAME the electrons are injected from a 20 MeV microtron into a 800 MeV booster synchrotron, with a repetition rate of 1 Hz. The 800 MeV beam is transported through the transfer line to the main storage ring and after accumulation, accelerated to 2.5 GeV[1,2]. During the normal operation , injection and ramping period in the storage ring, the betatron and synchrotron tunes in the storage ring will be measured frequently. The tune as well as time structure measurements could be done with the kicker-pickup striplines combination.

HARDWARE DESCRIPTION

Betatron and synchrotron motion in circular machines is usually incoherent, except in presence of an instability, therefore their values can not be easily measured. In order to make the measurement of the tunes, it is necessary to make the motion coherent by exciting the beam at the proper frequency. At SESAME storage ring the betatron tune measurement is performed by exciting the beam externally in the horizontal and vertical planes simultaneously through a stripline as a shaker and detect the excitation by another stripline as a detector. The main components for tune measurement in the storage ring consist of stripline shaker, stripline detector, low frequency voltage amplifier, network analyzer and the associated electronics for the detector. Figure.1 shows a simplified block diagram of the storage ring tune measurement. The overall tune monitoring system provides the capability of monitoring the storage ring tunes, ν_x and ν_y during ramping and stored beam operation.

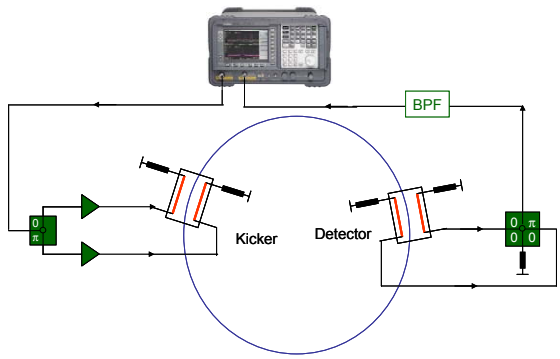

Figure 1: Simplified block diagram for tune measurement.

The horizontal/vertical tunes and other related parameters are given in Table1.

Table 1. Various tune related parameters

Injection Energy (GeV)	0.8
Stored Beam Energy (GeV)	2.5
RF frequency (MHz)	499.654
Revolution Frequency (MHz)	2.25
ν_x	7.23
ν_y	6.19
Fractional Tunes (kHz)	
$\Delta\nu_x$	517
$\Delta\nu_y$	427

STRIPLINE DESIGN

To simplify the design and minimize the manufacturing and development costs, two striplines with the same mechanical structure and dimensions will be used. One stripline for the excitation of the beam as the shaker and the other as the pickup to detect the excitation resonances. The stripline has four strips, one pair in each plane. For horizontal betatron tune (in order to measure directly the displacement relatively to the centre), the left pair of strips will be 180^0 out of phase with the right pair, and for y-tune the top and bottom pair will be out of phase. The strip has N-type vacuum feed through at the end and has a length of 150 mm. By a suitable choice of the ratio between the strip width and distance from the wall, the characteristic impedance is made 50 Ω [3]. The possibility of a design by means of using exponentially tapered strips in order to have smooth frequency domain response also has been investigated, but the difficulties come into the mechanical dimensions which makes extra cost. However the initial design was based on a pipe radius of 35mm, but due to the problems of radiation

s.varnasseri@unesco.org.jo

* Synchrotron-light for Experimental Science and Applications in the Middle East is an independent intergovernmental organization developed under the auspices of UNESCO It involves at present the following member states: Bahrain, Cyprus, Egypt, Israel, Jordan, Pakistan, Palestinian Authority and Turkey. Iran is in the process of finalizing its formal membership.

and wall heating absorption, the final design is based on the pipe radius of 52 mm. The width of strip is 23.75 mm and the covering angle for each strip is 29.6^0. The thickness and the distance from the wall are 2 mm and 5 mm respectively (see Fig. 2).

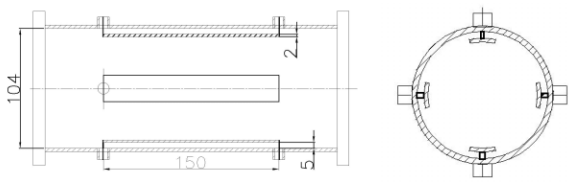

Figure 2: Schematic of stripline side view and cross section.

FREQUENCY RESPONSE AND SPECIFICATION [4,5]

Electromagnetic analysis in 2D and 3D has been performed by the SUPERFISH and ANSYS codes. Figure.3 shows the cross section , electric and magnetic field lines of the TEM deflecting mode. The polarity of the strips pair is opposite by means of 180º phase difference, and the particle beam travels in the opposite direction with respect to the TEM wave.

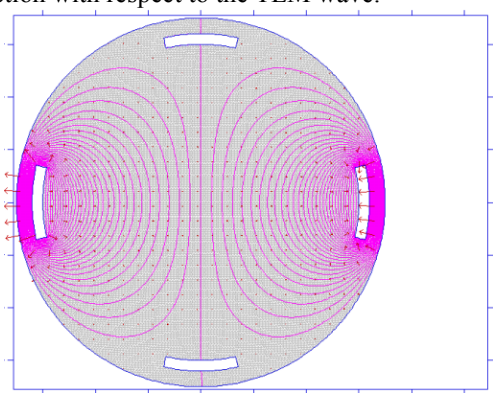

Figure 3: Full cross section of the stripline and EM field lines.

The geometry of stripline in 2D has been selected in order to give a 50 Ω rf impedance for the whole structure. The stripline frequency response up to 3 GHz has been analyzed and the transfer impedance is shown in Fig.4.

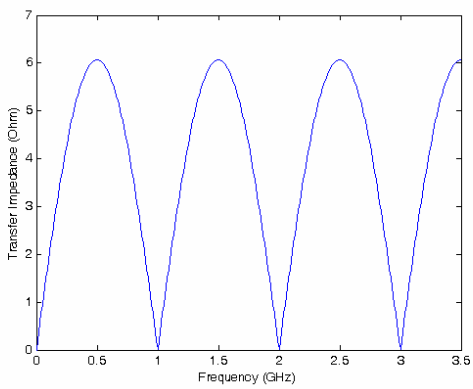

Figure 4: Stripline frequency response

The length of the strip is such that the transfer impedance is maximum at odd harmonics of storage ring rf frequency.

TRANSVERSE IMPEDANCE

However the effects of wake fields for the stripline is ignorable, since there is no HOM trapped in the structure, but in order to have a clear idea about the magnitude of the first mode of transverse dipole wake field impedance, the imaginary and real part of transverse wake fields are shown in Fig.5-6. The analysis is based on the analytical and numerical models given in [6].

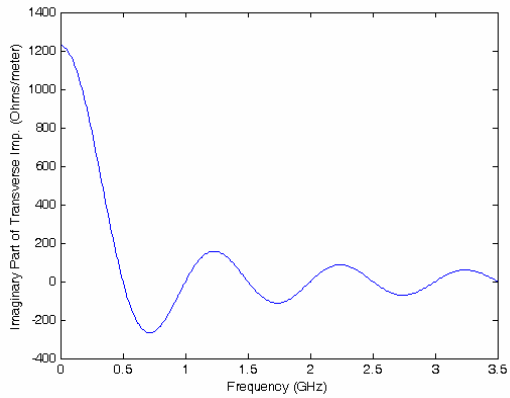

Figure 5: Imaginary part of transverse impedance vs. frequency.

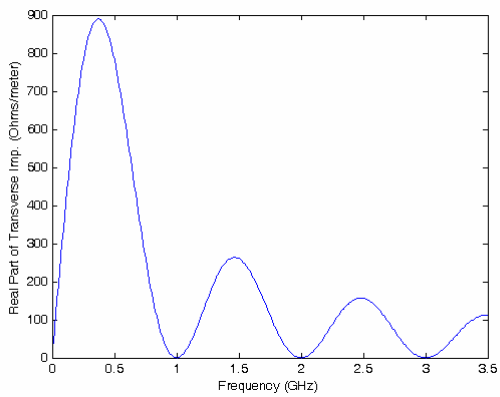

Figure 6: Real part of transverse impedance vs. frequency.

ELECTRICAL MODEL

The equivalent circuit for the terminated transmission line detector is shown in Fig.7. The problem is simplified by assuming that the velocity of the wall current is equal to the velocity of the beam, which is approximately true in the absence of dielectrics and/or magnetic materials for relativistic beams [7]. R_L, R_R, are the loads at two sides of stripline, Z_0 is the stripline characteristic impedance and i_w is the induced current. In our case $R_L=Z_0=50$ Ω and $R_R=0$.

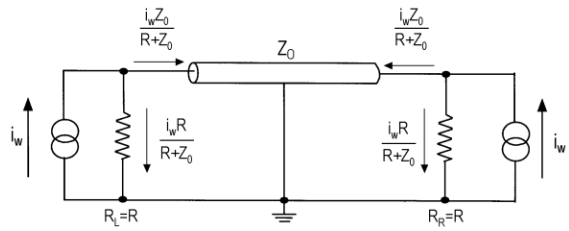

Figure. 7: Equivalent circuit for the stripline as a transmission line.

The time domain response of the stripline to a short bunch (shorter than the stripline length l) is a pulse doublet. The second pulse has the opposite polarity of the first pulse with a time delay of 2l/c. In a time period of λ/4c , the total voltage appearing across R_L is calculated by:

$$V_{RL} = \frac{i_w}{2}(1 - e^{-j2wt})R \qquad (1)$$

It is essential that the tune measurement process should not disturb the photon beam experiments. This is accomplished by keeping transverse beam motion below a few microns. As a result a power of 10 dBm will be sufficient in order to excite a few micron the stored beam at full energy.

CONCLUSION

Different types of striplines have been studied, considering the manufacturing and development point of views. Exponentially tapered and slot-coupled pick up due to the difficulties in manufacturing were not selected for the purpose of tune measurement in SESAME storage ring. As a result the normal symmetric pick up has been selected to be the proposed stripline for the storage ring and the design is based on the latter type.

REFERENCES

[1] G. Vignola et al "SESAME status" APAC 2007, India
[2] G. Vignola, M. Attal "SESAME lattice" Tech note. O-1, Dec 2004
[3] M. Serio "Transverse betatron tune measurement" Joint US-CERN School on particle accelerators, Oct. 1998
[4] L. Palumbo "Wake fields and impedance" INFN pub. Sep. 1994, Italy
[5] J. Hinkson, K. Rex "A wide band slot-coupled beam sensing electrode for the advanced light source" PAC 1991, US
[6] B.R. Pool et. al. "Beam coupling impedance of fast stripline beam kickers" PAC 1999, US
[7] D. Boussard, "Schottky noise and BTF diagnostics", CERN Accelerator School on Advanced accelerator Physics (Rhodes, Greece, 1993) 749.

BPM (BEAM POSITION MONITOR) OF PAL LINAC AND BTL *

S. C. Kim#, D. T. Kim, W. W. Lee, H. J. Park, Y. J. Han, J. Y. Huang, J. H. Choi,
Pohang Accelerator Laboratory(PAL), San 31, Hyoja-dong, Pohang 790-784, KOREA

Abstract

In Aug. 2004, thirteen BPMs are installed at BTL(Beam Transport Line), and in Aug. 2005, three BPM installed at main linac for beam trajectory measurement and feedback. BPM of the Linac consist of 57mm strip-line electrodes in 100mm short chamber and SMA-R type feed-through. BPM of the BTL consist of 100mm strip-line electrodes in 150mm long chamber and used SMA-R type feed-through. These BPM electronics of Linac and BTL is adpoted 500MHz log-ratio signal processing circuits. BPM data acquisition system is developed as EPICS IOC by using NI S-series DAQ board and NI Lab-view 7.1. Maximum read-out accuracy of BPM system is measured as 20μm included BPM electronics. In this paper, we are describes on BPM characteristics of PAL Linac and BTL.

INTRODUCTION

The linac of the PAL is consists of 12 klystron-modulator systems, 11 pulse compressors, 44 accelerating columns. Pre-injector section of the linac has a 1-ns, 80 kV, 2 A thermionic electron gun, a pre-buncher, and a buncher. After passing through the pre-injector section, the beam is compressed as three μ-bunch. Operation frequency of the linac is 2,856 MHz. There are thirteen Beam Current Monitor (BCM), twelve Beam Profile Monitor (BPRM) and fifty-six Beam Loss Monitor (BLM) for diagnostics in the PLS linac and BTL. There are also two beam analysing stations in the linac. The delivery ratio of the beam current from Linac to SR is depends mainly on the beam optics. Thirteen BPMs were installed from Linac end to BTL end at Aug. 2004 and three BPM were installed main linac at Aug. 2005 for beam trajectory measurement and feedback. BPM of the linac consist of 57 mm strip-line electrodes in 100 mm long chamber, and BPM of the BTL consist of 100 mm strip-line electrodes in 150 mm short chamber beam signal pick-up is used SMA-R type feed-through. In this paper, we are describes on BPM characteristics of PAL Linac and BTL.

BEAM POSITION MONITOR(BPM) OF THE PAL

For stabilized beam injection from linac to storage ring (SR) beam trajectory measurement and energy feedback are very important and BPMs are necessary beam instrument.

BPM Chambers

A conventional strip-line type BPM was designed with a π/2 rotational symmetry. Length of strip-line was decided by BPM electronics frequency. The angular width of the electrode is 52 degree in order to avoid a strong electromagnetic coupling between electrodes and electrodes. Linac BPM consist of 57 mm strip-line electrodes in 100 mm chamber and diameter of strip-line to line is 20 mm. BTL BPM consist of 100 mm strip-line electrodes in 150 mm chamber and diameter of strip-line to line is 40 mm. A 50 Ω SMA-type feed-through is connected to the upstream side of each electrode, while downstream ends are short-circuited to the chamber. Fig 1 and 2 are show the strip-line type BPM for PAL Linac and BTL.

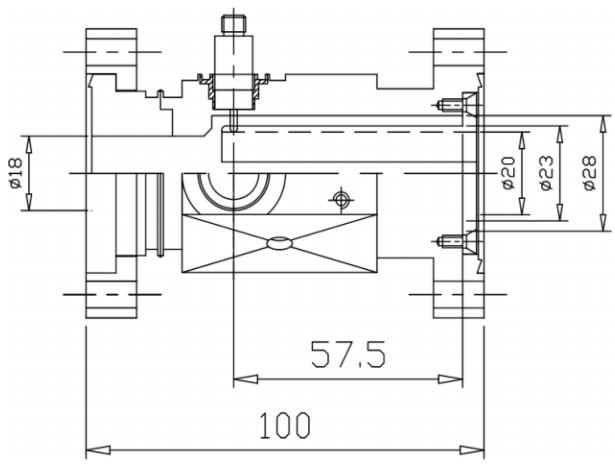

Figure 1: Strip-line type BPM for the PAL Linac

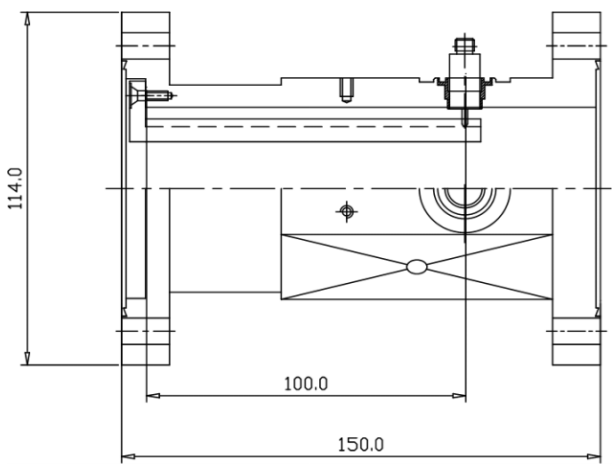

Figure 2: Strip-line type BPM for the PAL BTL

*Work supported by MOST, KOREA
#schkim@postech.ac.kr

Accuracy and calibration of the BPM

Accuracy and calibration of the BPM are measured by using 1ns pulse generator, and 500 MHz log-ratio BPM board at BPM test stand. Pulse applied at wire of the test stand, and X and Y output voltage of BPM board measure for each wire moving at BPM chamber inside. X and Y output voltage of BPM board each test beam position converted to real beam position. Fig. 3 is shows BPM test stand for accuracy and calibration measurement of the BPM.

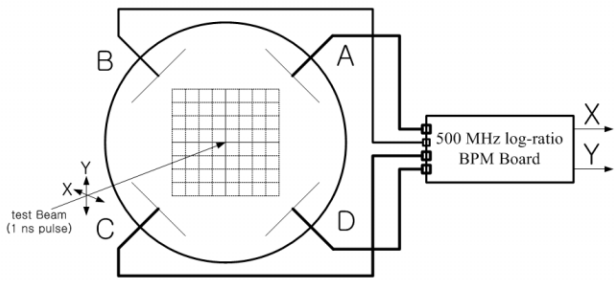

Figure 3: BPM test stand for accuracy and calibration measurement of the BPM

Calibration of the BPM calculates as factor between voltage and position. Accuracy of the Linac BPM is measure by X position change to 2.00 mm step up 0.01 mm at test beam position is X =2.00 mm and Y = 2.00 mm after BPM and BPM board calibration. Fig. 4 and 5 are accuracy measurement result PAL Linac BPM.

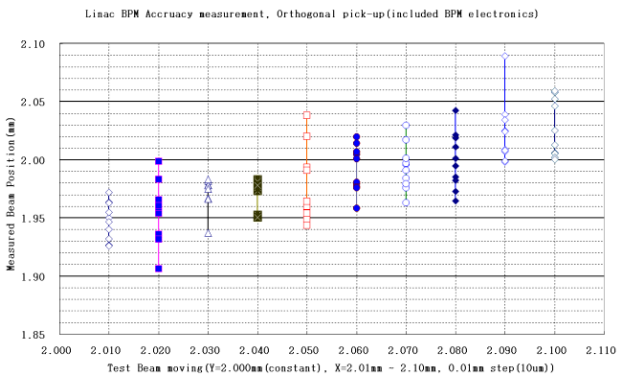

Figure 4: Accuracy measurement result PAL Linac BPM (10 times measurement)

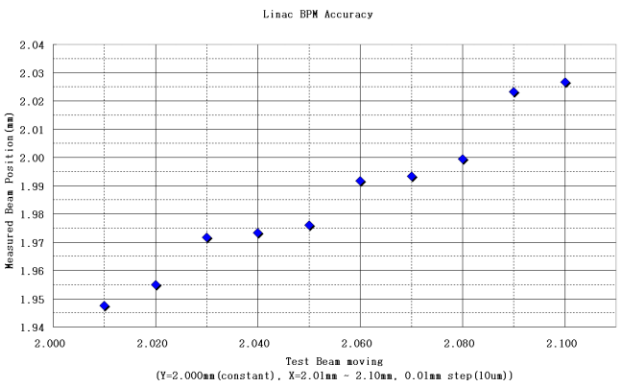

Figure 5: Accuracy measurement result PAL Linac BPM (averaged data of 10 times measurement)

Accuracy of the BTL BPM is measure by X position change to 2.00 mm step up 0.01 mm at test beam position is X =2.00 mm and Y = 2.00 mm after BPM and BPM board calibration.

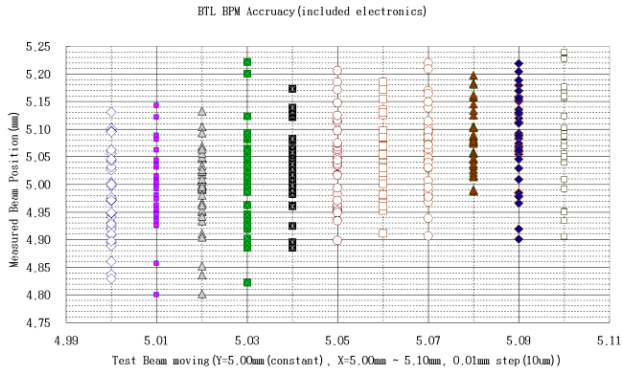

Figure 6: Accuracy measurement result PAL BTL BPM (20 times measurement)

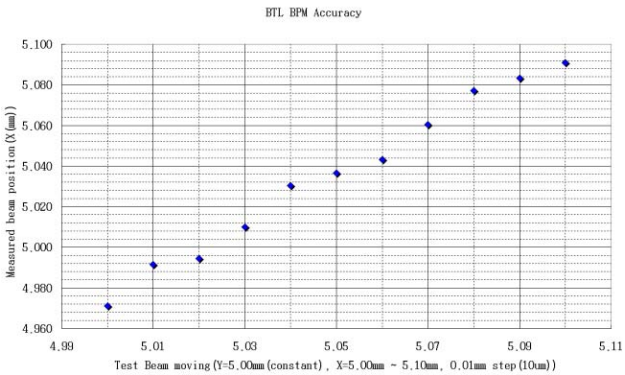

Figure 7: Accuracy measurement result PAL BTL BPM (averaged data of 20 times measurement)

Read-out accuracy of the PAL Linac and BTL BPM is measured 30 μm and 20 μm included BPM electronics, respectively. Table 1 lists BPM mainly specifications of the PAL Linac and BTL. Fig. 8 shows fabricated BPM of the PAL Linac BTL.

Table 1: Margin Specifications

BPM	Linac	BTL
Type	Strip-line	Strip-line
Electrode length (mm)	100	57
Chamber length (mm)	150	100
Diameter (strip-line) (mm)	20	40
BPM electronics	Log-ratio BPM Board (Berogoz)	
Accuracy (μm)	30	20
Installed no.	3	13

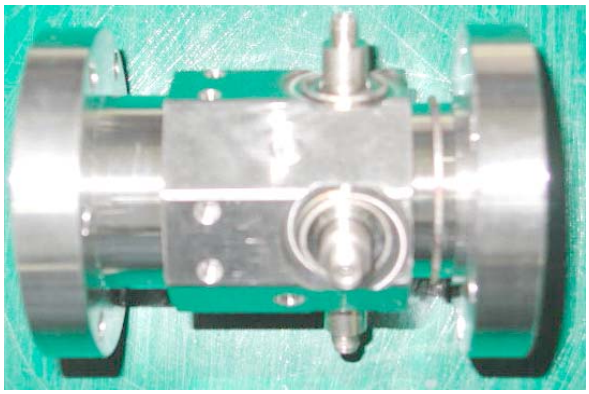

Linac BPM

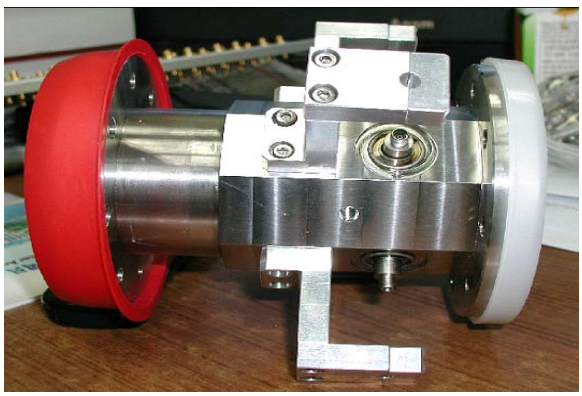

BTL BPM

Figure 8: Fabricated BPM of the PAL Linac and BTL

BPM Data Acquisition System

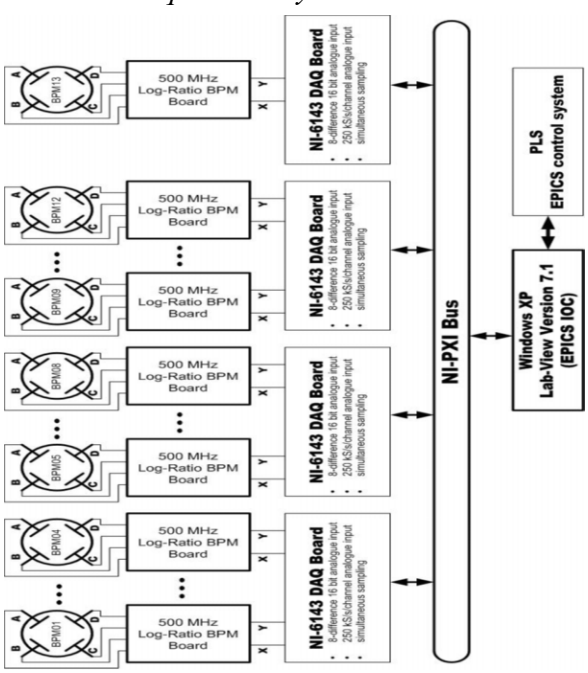

Figure 9: block diagram of BTL BPM data acquisition system.

Data acquisition board is adopted Nation Instrument (NI) S-series multifunction DAQ board NI6143 for data acquisition of the log-ratio BPM board beam signal(X Y). BPMs signal for beam occur almost simultaneously. Therefore all BPM value must measure simultaneously. NI6143 has capability simultaneously 16-bit, 250 kS/s/channel sampling for 8-independent analogue input. One DAQ board used for BPMs data acquisition of Linac, and four DAQ board used for BPMs data acquisition of BTL. All boards are simultaneously independent sampling for Linac beam trigger signal (10 Hz). Data acquisition system is consisted environment windows XP under NI-PXI. Using NI Lab-View programs data acquisition S/W. For monitoring of BPM data at EPICS control system, BPM data acquisition system is developed as EPICS IOC. Fig 7 shows block diagram of BTL BPM data acquisition system.

SUMMARY

At the PAL Linac and BTL, Thirteen BPM were installed from Linac end to BTL end at Aug. 2004 and three BPM were installed main linac at Aug. 2005 for beam trajectory measurement and feedback. BPM of the linac consist of 57 mm strip-line electrodes in 100 mm long chamber, and BPM of the BTL consist of 100 mm strip-line electrodes in 150 mm short chamber beam signal pick-up is used SMA-R type feed-through. To BPM data acquisition, 500 MHz Log-Ratio BPM board and NI S-series DAQ board (NI-6143) are adopted. Read-out accuracy of the PAL Linac and BTL BPM is measured 30 μm and 20 μm included BPM electronics, respectively. Using NI Lab-View programs data acquisition S/W. For monitoring of BPM data at EPICS control system, BPM data acquisition system is developed as EPICS IOC.

REFERENCES

[1] S. H. Nam, J. Y. Huang, Y. J. Ham, and M. Yoon, "Status of the PLS 2.5 GeV electron Linac," Linac 2002 proceeding pp. 617-619.

[2] I. S. Ko, M. H. Cho, J. S. Bak, J. Choi, H. S. Lee, and W. Namkung, "Operation status of the PLS 2-Gev electron Linac," Linac 96 proceeding pp. 617-619.

[3] S. C. Kim, W. W. Lee, Y. J. Han, J. Y. Huang, "Beam Position Monitor at the PLS BTL", PAC05 proceeding pp. 3289 – 3291.

DEVELOPMENT OF WIDE BAND FCT SYSTEM FOR BOOSTER SYNCHROTRON OF INDUS-1 & 2

Prashant Pareek*, Karan singh & R.S. Shinde
Raja Ramanna Centre For Advanced Technology, Indore, India.

Abstract

A precision, non-destructive type wide band FCT for measurement of electron current of Booster synchrotron for Indus-1 & 2 has been developed. This monitoring system is composed of fast and slow FCTs using NiZnCo ferrite toroids, pulse amplifiers and electromagnetic shields. The FCT shows fast rise time (60 ns) large time constant (38 ms), high sensitivity 25 mV/mA at 50 Ω and linearity within 1%. This paper focuses on FCT design, construction and pulse response.

INTRODUCTION

For the fine operation of accelerator it is important to measure beam current and pulse shape so a wide band FCT is required to measure electron beam turn to turn current and stored current accumulation during 1μs pulse injection into booster synchrotron. The parameters required for FCT are 1) fast rise time 2) large L/R ratio 3) high signal to noise ratio 4) good linearity. It is difficult to achieve above characteristics using single large ferrite toroid. So we have developed two FCTs using large Ni-Zn-Co ferrite toroids, housed in a single box with two outputs. One FCT measures the current from 60 ns to 15 μs and another measures from 12 μs to 1 ms. The spacing between two FCT is optimized to reduce mutual coupling .The two outputs are amplified, buffered and then transmitted through 50 Ω characteristic impedance coaxial cable to control room.

CIRCUIT DESCRIPTION

Principle

The FCT picks up the magnetic field generated by electron beam [1]. A simplified equivalent electrical circuit diagram is shown in fig 1.

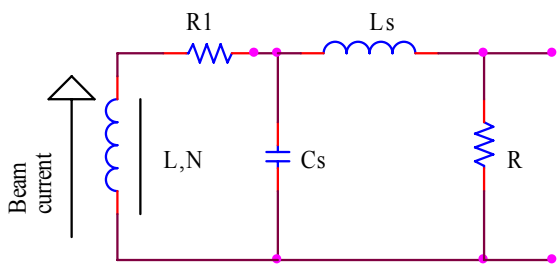

Figure 1: Equivalent electrical circuit diagram of FCT

where

- L, the pickup coil or secondary inductance
- N, the number secondary turns
- R, the load resistance
- R1, the resistance of cable of secondary circuit
- C_s, Stray capacitance between components
- L_s, stray inductance between the components

Due the combination of L_s & C_s results in overshoot and damped oscillation of the output signal. The stray inductance and capacitance influences the rise time. To get fast rise time 60 ns, numbers of turns are reduced in fast FCT and to get large time constant 38 ms, number of turns are increased. Secondary side reflected equivalent circuit diagram is shown in fig 2.

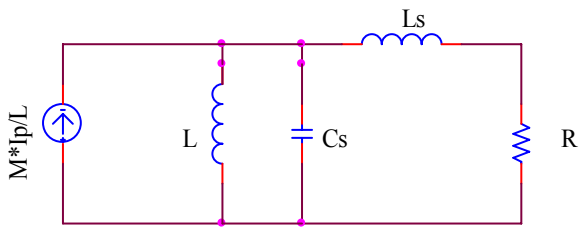

Figure 2: Equivalent secondary side reflected electrical circuit diagram of FCT

Fast FCT

Fast FCT has given 20 turns and terminated with 4.75 Ω resistance, which gives time constant 87 μs. The pickup coil wound on small region of the core, so the leakage inductance cannot be neglected. Therefore, the current transferred to secondary will be equal $M*I_{beam} / L_{pickup}$ instead of I_{beam} / N. M is the mutual inductance between pickup coil and I_{beam} acting as primary. The measured M and coupling coefficient K are 15 μH & 0.6 respectively . The signal across load resistance is amplified by differential video amplifier MC1733. A cable driver LH0033 is used to transmit the signal through 50 Ω characteristic impedance coaxial cable to control room. The electronic block diagram is shown in fig 3.

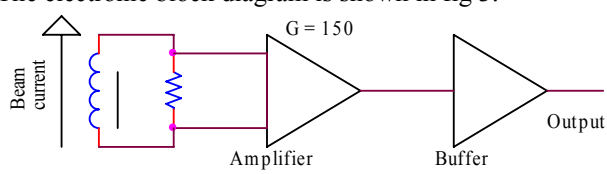

Figure 3: Electronic circuit block diagram for fast type FCT

Slow FCT

Slow FCT has given 350 turns and terminated with 3.2 Ω resistances, which gives time constant 38ms. Here the pickup coil wound on entire region of the core. The measured M and coupling coefficient K are 307 μH & 0.72 respectively. Due to large number of turns, high gain is required which is achieved in three stages using video amplifier and operational amplifier and cable driver LH0033 is used to transmit the signal through 50Ω characteristic impedance coaxial cable [2]. The electronic

*ppareek@cat.ernet.in

block diagram is shown in fig 4 and the parameters of FCTs are shown in table 1.

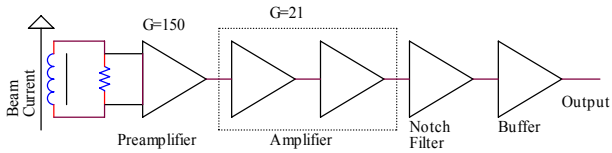

Figure 4: Electronic circuit block diagram for slow type FCT

Table 1: Parameters of FCTs

FCT	Number of Turns	Inductance	Load Resistance	Time constant
Fast	20	417µH	4.75Ω	87µs
Slow	350	124mH	3.2Ω	38ms

CONSTRUCTION

Fig 5 shows the photograph the wide band FCT. The current monitor composed of two ferrite toroids of dimension 120 mm (OD) x 100 mm (ID) x 15 mm thick. These toroids are cut using diamond wafer blade of 0.4 mm thick into two pieces. It is used as non-destructive type. These toroids are fitted into aluminium casing with spacing 10 mm between them to minimize mutual coupling between them. The electronic circuit is also enclosed in 3mm thick enclosure to reduce electromagnetic interference. The complete FCT system is enclosed in Mu-metal enclosure to reduce magnetostatic as well as electromagnetic interference.

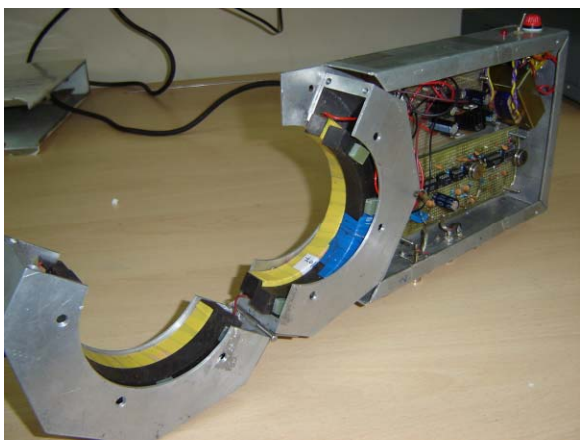

Figure 5: Photograph of Wide band FCT

CALIBRATION

The output voltage of the FCT will be given by, $V = G*R*M*I_{beam} / L_{pickup}$. There is nearly close agreement between measured voltage using calibration setup and voltage by formula. The FCT is calibrated by using pulse generator, single wire as a beam current, matching resistor 50Ω. Pulse current through single wire was measured by fast current probe (Tektronix TCP202) and output of FCT was measured by DSO (Tektronix TDS 540C,500MHz) [3]. Fig 5 and 6 shows the pulse response of the FCTs.

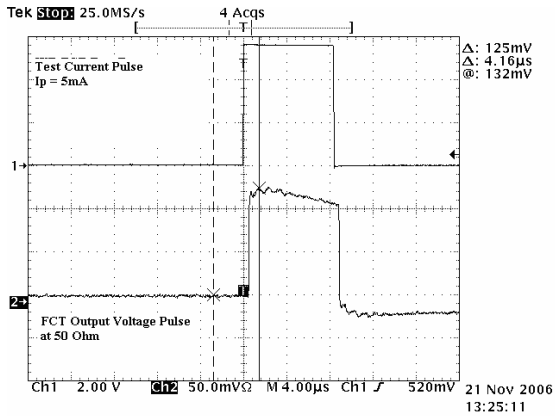

Figure 6: Pulse response of fast FCT

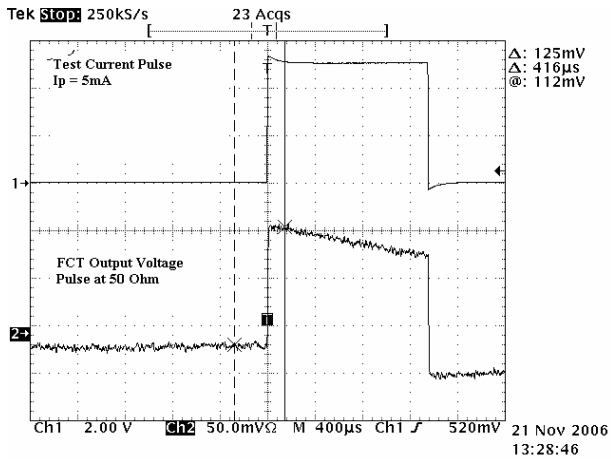

Figure 7: Pulse response of slow FCT

RESULTS

The sensitivity of both the FCTs is observed 25mV/mA with accuracy and linearity better then 1%. The observed droop is 2 %/µs for fast and 13 %/ms for slow type FCT. Large droop in slow FCT is due to notch filter in the electronic circuit. Stability of FCT over long period is measured in our laboratory. It is observed a stable & clean pulse. Now, FCT system is ready for its installation into Booster Synchrotron.

ACKNOWLEDGEMENTS

The authors would like to thank Shri.S. Kotaiah, PM (Indus-2) & Shri. Gurnam Singh, Head IOAPDD for their kind guidance, scientific & technical discussion during FCT developmental works. We express great thanks to Mr. Shiv Bachan & Mr. Lalchand Ghongde for their technical assistance throughout the fabrication of Wide Band FCT system.

REFERENCES

[1] R.S. Shinde "High precision current ferrite monitors", J.PHYS. IV FRANCE 7(1997) , p. C1-159
[2] P. Strehl "Beam Instrumentation and Diagnostics", Springer
[3] P. Pareek , K. Singh , etal "Pulse measurement of FCTs" RRCAT internal note , 2006.

PHOTON BEAM POSITION MONITOR WITH HYDRAULIC LEVEL SYSTEM

Y. J. Han, J. Y. Huang, S. N. Kim, Y. C. Kim, J. H. Choi, and I. S. Ko
Pohang Accelerator Laboratory, POSTECH, Pohang, 790-784, Korea

Abstract

In a synchrotron radiation source like the Pohang Light Source (PLS), a great effort has been made on beam stability improvements. For the beam line user-side orbit feedback, Photon Beam Position Monitor(PBPM) provides more practical information on the position and angle of the elector beam at the center of the bending magnet, compared the closed orbit data. For improvement of the orbit stability, PBPMs are used in PLS. However, the ground of PLS moves about 2mm every year. Therefore, we plan to measure the vertical orbit drift and angle variation considering the floor uneven settlement and the support thermal deformation by use of PBPM with Hydraulic Level System(HLS).

INTRODUCTION

Pohang Light Source (PLS) with beam energy of 2.5 GeV has provided the stable beam to the users during last 10 years. As the number of beamline requiring the micro-spot high resolution photon beam such as ID (Insertion Devices)has been increased, the stabilization of the electron beam orbit drift is strongly required. Therefore, in a synchrotron radiation source like PLS, a great effort has been made on beam stability improvement in various related field such as RF, magnet power supply, diagnostics, etc. For the beamline user-sided orbit feedback, PBPM provides more practical information on the position and the angle of the electron beam at the center of the bending magnet, compared the closed orbit data. For improvement of the orbit stability, PBPMs are used in PLS. However, the mechanical motions of main storage ring machine components such as girder, magnet, vacuum chamber, etc., have been known very important factors having potent influence on the beam trajectory. Therefore, it is necessary to measure and understand the real time movement behaviour of the storage ring components, the beamline components and their bases, i.e., the tunnel floor and the experimental hall floor. There has been a big amount of uneven settlement at the storage ring floor slab along its circumference at PLS. The amounts were almost 3mm per year at the beginning stage of measurement and it tends to converge to 2mm per year. These measurements were performed by the conventional optical surveying method at every machine shutdown period (2 times a year). To understand the real orbit drift, we have to consider the real impact of this floor uneven settlement on the beam operation. Therefore, we plan to measure the vertical orbit drift and angle variation considering the floor uneven settlement and the support thermal deformation by use of PBPM with HLS (Fogale, Nanotech, France).

SYSTEM

PBPM

Fig. 1 shows the wire type photon beam position monitor with hydraulic level system. Here, the material of the wire is tungsten with 0.5mm diameter and 90mm length. In order to improve the electric conductivity, the

Figure 1 : Installation of Photon Beam Position with Hydraulic Level System. HLS are installed on the floor and support.

wire for PBPM is coated with gold. There is a diaphragm with 60mm horizontal aperture which can block off the miscellaneous light. Additionally, the monitor can vertically move and the moving range is ±20mm. There is generally the cooling system in the blade type PBPM, but it is structurally impossible that the cooling system is installed in the wire type PBPM. Therefore, the heat transfer analysis is very important. We have studied the effects using heat-power theoretical method and ANSYS analysis code. These methods involved radiation for cooling method. PBPM are installed to diagnostic beamline about 14m away from source point. The source of diagnostic beamline is bending magnet and PBPM's wire size is 90mm x 0.5mm at 14m away from source. Then, total power become to about 9.57W. When the ration is involved by power-heat theoretical method, the temperature of the tungsten wire is saturated at 819^{o}K.

We also performed the heat-power analysis by ANSYS code. As the results, the maximum temperature of the tungsten wire is acquired about 1066^{o}K. This is a bit greater than the results of theoretical method. We can estimate the tungsten wire is under safe at this temperature. Another analysis with ANSYS code is performed in order to know the structure deformation by

heat-power. Therefore, we can get the results of structure deformation in X, Y direction. The maximum deformations of X-direction and Y-direction are 1.5um, and 2.1 um at temperature of 1066°K respectively. As the results of the heat-power analysis, we conclude that the wire type PBPM can be operated without the cooling system, because the ratio of $2x10^{-5}$ of the deformation length to the wire length can be acceptable for PBPM. The tungsten wire are not fixed in Z-direction to reduce equivalent stress.

HLS

As measurement principle of HLS, the sensor electrode and the targeted object make up a condensator the inverse capacitance of which is measured. Thus, according to used sensor, the electronics provides an output voltage proportional to displacement the potential of the target object is taken as reference. For the record of the real time of floor and support movement, 5 HLS are installed in the storage ring and experimental hall; 1 HLS is installed on the floor of the storage ring under beam source (bending magnet), 2 HLS are installed on the floor of the experimental hall under PBPM respectively, and 2 HLS are attached on the support of PBPM. The support material is used the granite in order to minimize the

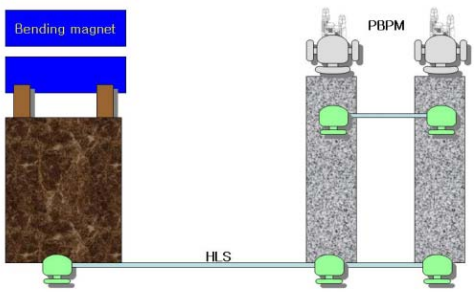

Figure : 2 HLS installation map

thermal deformation. The installation map is shown in Fig. 2. Therefore, we can measure the floor settlement between beam source and beamline. Furthermore, it is able to be monitored the deformation of the PBPM support which is caused by the temperature difference. According to installing HLS, we can analysis practical orbit drift considering the floor settlement and the support deformation.

STATUS AND RESULT

We measured the beam profile of the 1C diagnostic beam line with PBPM. As we expect, the profile of the beam is Gaussian except the edge. The photon current from each wires is detected by a picoammeter (keithly 6485). Two current signals from the top and below wires are then fed into a position processing system in order to obtain a signal proportional to the beam displacement and the angle variation. For the position and angle signals processing, we use the method of difference over sum[1]. We have calibrated the PBPM at the diagnostic beam line 1C1. When the monitor is calibrated, we move the vertical position and can acquire the position signals. According to the fitting curve, the sensitivity of PBPM is 0.276. As determining the sensitivity of PBPM, we begin to collect the data from PBPM. The resolution of PBPM signals is very important in order to measure precise displacement and angle variation. We plan to control the orbit stability of below 1 μm. Therefore, the resolution of PBPM requires the resolution of submicron in order to control the orbit stability of below 1μm. As the results of measurement, we get good values that the resolutions of the vertical displacement and the angle variation are 0.5μm and 0.01 μrad respectively. Although the beam motion at monitor is small at short period, the beam motion is a little large at long period. When we perform the measurement of the vertical displacement and angle variation during 24 hours, the vertical displacement is comparatively stable within 2 μm, but the angle variation of 8 μrad is fairly large compared to the vertical displacement. It is the first time to measure the angle variation at PLS. From these results, we can know that the measurement of angle is very important, because the angle variation of 8 μrad gives the vertical displacement of 160 μm to beamline user with 20 m long. Fig. 3 shows the vertical displacement and angle variation from Dec. 18 to Dec. 22. The both of the displacement and angle have the trend to decrease with time in general. But especially, there is the fluctuation per day in the angle variation. As shown Fig. 3, there is the vertical displacement of 12.4

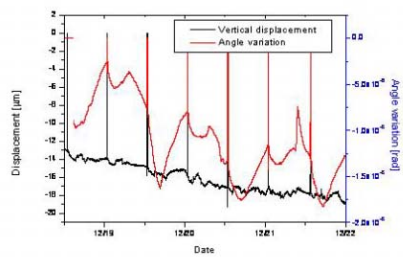

Figure 3 : The vertical displacement and angle variation from Dec. 18 to Dec. 22. There is the fluctuation per day in the angle variation.

μm during 5 days. Therefore, we can know there is averagely the vertical displacement of 2.5 μm per day. According to install HLS, we plan to analysis the practical orbit drift considering the floor settlement and the support deformation. But we have many problems after installing HLS at the beginning. During the operation of HLS, many factors were found to be harmful to the accuracy of the data, such as dirt or condensing water on the surface of sensor, water leakage in tube. With many efforts of removing harmful factors, we can perform the normal operation of the HLS. Fig. 4 shows

the variation of the floor on the basis of storage ring floor. When we measure the relative variation of the floor on based the storage

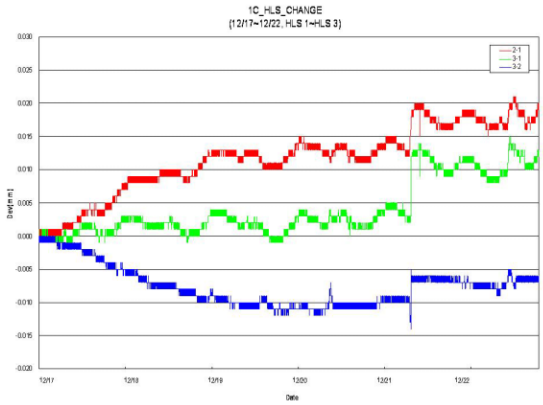

Figure 4 : The relative floor variation measured at 3 floors on based the storage ring floor. The maximum floor variation of 1'st PBPM(2-1) is 20μm, that of 2'nd PBPM is 15μm.

ring floor, the maximum floor variation of 1'st PBPM(2-1) is 20 μm, and that of 2'nd PBPM(3-1) is 15 μm. According to relative variation between 1'st PBPM and 2'nd PBPM, the floor settlement of 2'nd PBPM is less than that of 1'st PBPM. Fig. 5 shows the relative variation of the support. The maximum variation is 13 μm that contains both of the floor settlement and thermal deformation. Therefore, considering 10μm of the relative floor variation in Fig. 4, we can estimate the support variation of 3 μm to be pure variation by thermal deformation. Fig. 6 shows the temperature distributions at

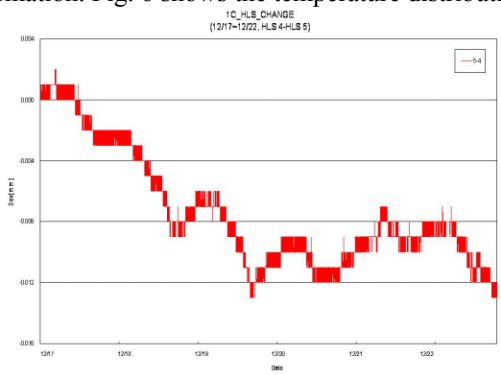

Figure 5 : The relative variation measured at 2 supports. The maximum variation is 13μm that contains both of the floor settlement and thermal deformation.

the spots where are installed HLS. As shown in Fig. 6, the temperature of storage ring is very stable, but other temperatures are a bit unstable. Especially, the temperatures of experimental hall repeat rise and fall per day. This is very similar pattern to the angle variation as shown in Fig. 3. Since the coefficient of expansion for granite to be the support material is 8.3 μm / ^{o}C-m, the temperature difference of 1^{o}C cause the angle variation of 4 μrad. Therefore, in order to measure the precise angle variation, we had to consider strict temperature control around PBPM.

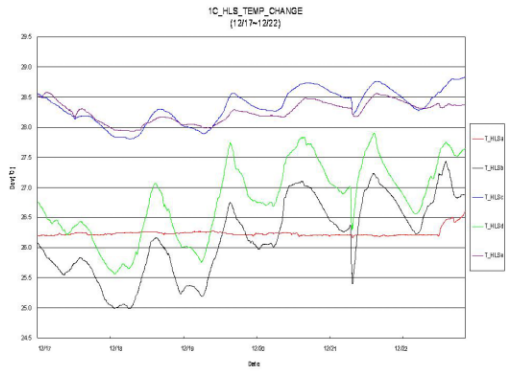

Fig. 6 The temperature variation around 5 HLS. HLS_a is the temperature around storage ring floor, HLS_b and HLS_c are the temperatures around 1'st PBPM and 2'nd PBPM floor respectively. HLS_d and HLS_e are the temperatures on 2 supports 1m away from the floor respectively.

SUMMARY

We will need to implement orbit feedback systems in order to achieve the orbit stability of <1 μm. For this, we need to analysis the data of PBPM with HLS carefully. According to the data above, the maximum floor variation is 20μm during 5 days. Therefore, the floor of PBPM averagely goes up 4 μm per day. If the floor rises, the orbit of beam seems to descend in appearance. As shown in Fig. 3, the orbit of beam goes down 2.5 μm per day averagely. However, the real orbit of beam goes up 1.5 μm per day because the floor goes up 4 μm per day. To make matters worse, the operator will try to descend the orbit of 1.5 μm per day. Then, the user of beam line will suffer worse photon beam position of 5.5 μm per day. Therefore, for the beam line user-side orbit feedback, we can conclude that PBPM with HLS provides more practical information on the position and angle of the elector beam compared the closed orbit data.

REFERENCES

[1] B. G. Sun, J. H. Liu, et al. "Development of a Split Photon Beam Position Monitor for HLS", High Energy Physics and Nuclear 2004, Vol. 28, No. 2, pp210-214.

TUNE AND LIFETIME STUDIES AT THE AUSTRALIAN SYNCHROTRON

M.J. Spencer, M.J. Boland, R.T. Dowd, G. LeBlanc, Y.E. Tan, ASP, Melbourne, Australia

Abstract

The 3GeV Australian Synchrotron [1,2] will begin operation in March 2007. This paper outlines the tune and lifetime measurement systems. It also provides a summary of a number of studies completed using these systems. Three different tune measurement systems have been tested. Lifetime measurements made using the DCCT were used to optimise the strengths of the harmonic sextupoles and the location of the tunes. The vertical aperture was determined using scrapers. Beta-function measurements have been completed by shunting individual quadrupoles and noting the resultant tune changes. Chromaticity measurements have been made by observing the change in tune as the RF frequency is varied.

TUNE MEASUREMENT

Spectrum Analyser with Tracking Generator

A Rohde and Schwarz FSL spectrum analyser with tracking generator is the current default tune measurement method. The input to the spectrum analyser is a signal from a stripline. The tracking generator output is amplified to around 10 Watts before being fed, in series, to the horizontal then the vertical excitation kickers.

A C-program was written to allow MATLAB to quickly obtain the positions of the peaks.

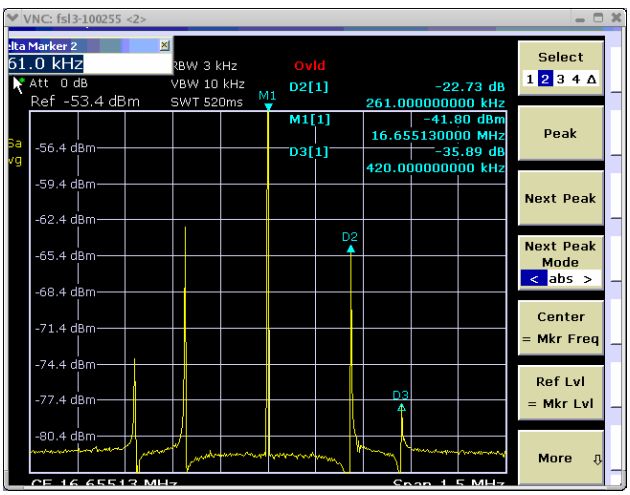

Figure 1: Tune measurement using a spectrum analyser with tracking generator.

Real-Time Spectrum Analyser in Conjunction with Arbitrary Waveform Generator

A Tektronix RSA3303A real time spectrum analyser was trialled as a tune measurement device. The stripline was used as a pickup. An Agilent 33220A arbitrary waveform generator was used to provide white noise up to 6 MHz. The signal from the noise generator was amplified and fed to the horizontal and vertical excitation kickers.

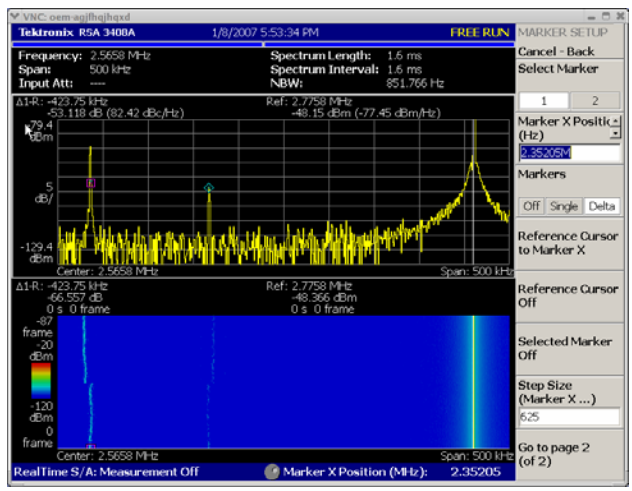

Figure 2: Tune measurement using a real time spectrum analyser and white noise generator. The waterfall plot shows a small jump in tune as a single quadrupole is shunted.

Injection Kicker with BPM Button Spectral Analysis

We have observed that our injection kickers provide a transient beam excitation in both the horizontal and vertical planes. To measure the tunes a single injection kicker is used, set to a low strength. Fourier analysis of the data from a triggered BPM button [3] reveals the tunes.

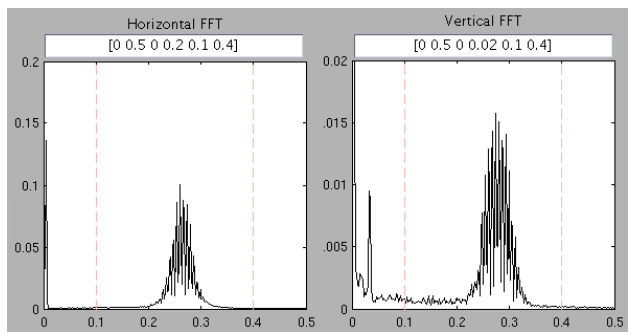

Figure 3: The tune peaks obtained by a fourier analysis of the BPM button data. Note that the large tune spread in this figure is due to the fact that the sextupoles were off.

LIFETIME MEASUREMENT

The Bergoz DCCT (Direct Current Current Transformer) provides a DC voltage proportional to the storage ring current. This is then fed to an ADC through an RC filter. The data is provided to MATLAB where the lifetime is determined using a gradient fit.

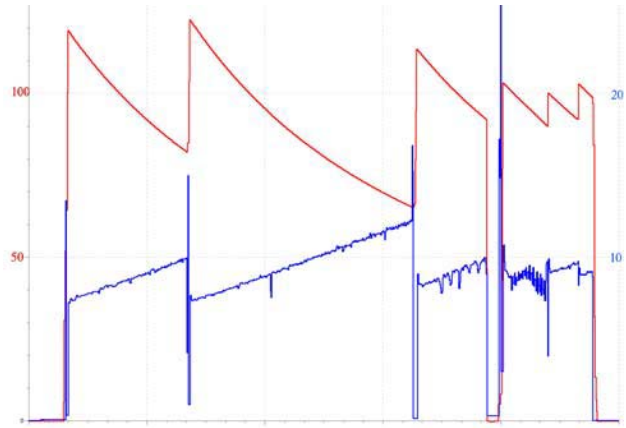

Figure 4: An example of a current (red) and lifetime (blue) measurements taken over 16 hours during commissioning activities.

A single tune or sextupole scan may require hundreds of lifetime measurements. Therefore, it is important that each lifetime measurement is completed as quickly as possible. To achieve this, it was important that the noise on the DCCT was reduced to the minimum achievable level.

STUDIES USING TUNE AND LIFETIME MEASUREMENTS

Harmonic Sextupole Optimisation

The lifetime was plotted as a function of the harmonic sextupole strength. It was found that the lifetime was maximised when the SDA family was set 15% higher than the SFA family.

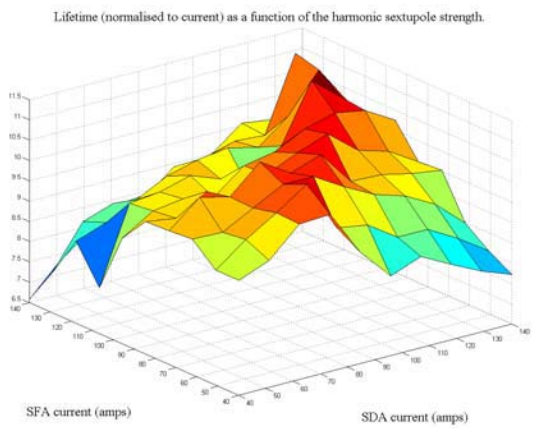

Figure 5: The change in beam lifetime as the harmonic sextupole families were varied.

Tune Space Optimisation

A tune scan was completed. With a ring symmetry of 14, the tune had very little effect on the lifetime. In order to see an effect, a single quadrupole was shunted to create a ring symmetry of 1. Figure 6 below shows that there was a clear effect on the lifetime as the tunes approached lines of resonance. This plot will become useful as wigglers are installed and the symmetry of the ring is affected.

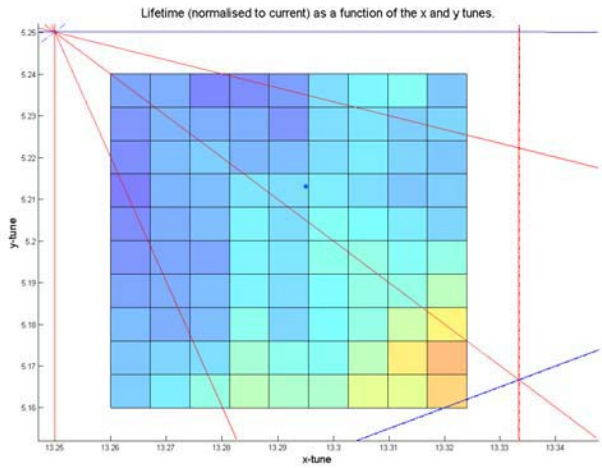

Figure 6: The change in beam lifetime as the horizontal and vertical tunes were varied (dispersion was kept constant).

Measurement of Vertical Aperture

The vertical aperture was measured at the position of the scrapers. Each scraper was moved in and the lifetime plotted versus scraper position. It was found that the scrapers are offset by 150 μm. In the plot below (figure 7) this offset has been removed.

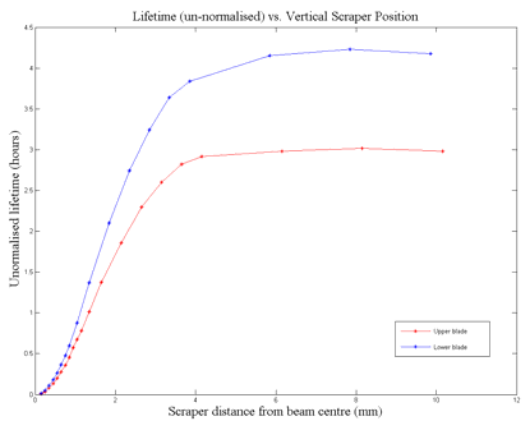

Figure 7: The lifetime as a function of the position of upper and lower vertical scrapers. Note that each data set was taken at different beam currents.

Beta function measurement

Beta functions are measured in two ways. Direct measurements are made by shunting individual quadrupole magnets and observing the change in the tune. The vertical beta function at a given QD is equal to

$$\beta_y = \frac{4\pi \cdot \Delta\nu_y}{\Delta k_l},$$

where β_y is the vertical beta function at the quadrupole, and $\Delta\nu_y$ is the change in tune resulting from the change in the quadrupole's integrated field strength, Δk_l.

The beta functions can also be calculated from a calibrated model. A calibrated model is a model which has been adjusted so that its behaviour resembles that of the real machine. Such a model can be created using the Linear Optics Closed Orbits (LOCO) [4] method. In this case the quadrupole strengths in the model are adjusted so that the model's orbit response matrix more closely resembles that of the real machine.

The calibrated model's vertical beta function is plotted with the experimentally determined vertical beta function at the QD magnets (figure 8). It can be seen that the two methods are in close agreement.

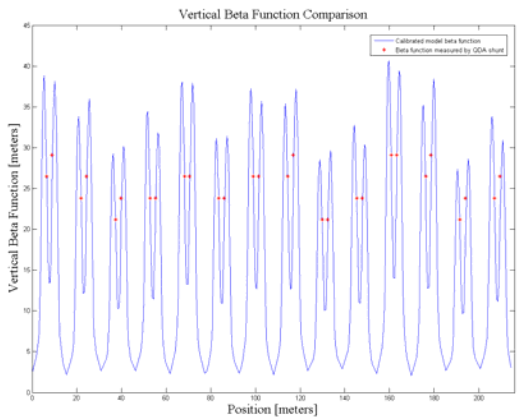

Figure 8: Comparison of calibrated model beta-functions with the experimentally determined beta-functions at the position of the QDs. Note that this data was taken in the early stages of commissioning before any adjustments were made to the optics.

Chromaticity Measurement

Chromaticity measurements are made by plotting the change in tune as a function of the momentum shift. The data is fitted with a second order polynomial. The coefficient of the linear term can be taken to be the chromaticity.

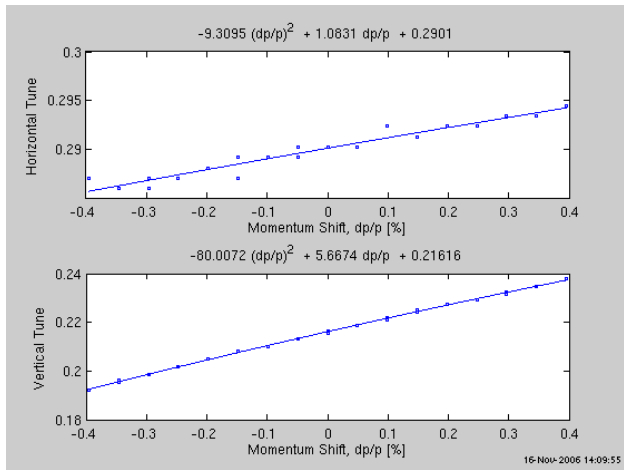

Figure 9: Tune versus momentum shift. In this case the chromaticity was measured as: $\xi_x = 1.08$ and $\xi_y = 5.67$.

REFERENCES

[1] G. LeBlanc, et.al. (ASP), "Status of the Australian Synchrotron", these proceedings.

[2] J. W. Boldeman, D. Einfeld, 2004 Nucl. Instr. And Meth. A **521**, 306

[3] E. Tan, et. al (ASP), "Commissioning of the Australian Synchrotron with EBPMs and Matlab", these proceedings.

[4] J. Safranek*, G. Portmann, A. Terebilo, SSRL/SLAC, Stanford, C. Steier, LBNL, Berkeley, "MATLAB-Based LOCO", EPAC'02, p. 1184.

COMMISSIONING OF THE AUSTRALIAN SYNCHROTRON WITH LIBERA EBPPS AND MATLAB

Y.-R. E. Tan, G. S. LeBlanc, M. J. Boland, R. Dowd and M. Spencer
Australian Synchrotron, Melbourne, Australia

Abstract

The Australian Synchrotron (AS) is equipped with a full compliment of 98 BPMs attached to Libera Electron Beam Position Processors (EBPPs) [1] that are capable of measuring turn-by-turn/first turn and averaged beam positions simultaneously. The BPM system coupled with Matlab applications has simplified the process of commissioning. This report will highlight how the various tools have been utilised and show the results of some studies.

INTRODUCTION

The Australian Synchrotron (AS) storage ring is a 14 cell, Chasman-Green type lattice with 3 families of quadrupoles, 4 families of sextupoles and a total of 42 horizontal correctors and 56 vertical correctors [2]. Each cell has been fitted with 7 BPMs, totalling 98 BPMs, all of which are connected to EBPPs.

EBPPs are being used at facilities such as Soleil and Diamond (just to name a few) and are versatile diagnostic tools. The specifications for the BPM system at the AS are RMS values of < 0.2 μm (slow, 1kHz BW) and < 6 μm (turn by turn, 1 MHz BW) between 10 and 200 mA. Additionally the beam current (10 – 200 mA) and thermal (±1°C) dependence needs to be < 2 μm. Many of these parameters have yet to be characterised.

On the control side over the last few years the use of a suite of applications written in Matlab at synchrotron facilities for accelerator physics studies and commissioning has grown. The core of this suite of applications now includes AT [3], MCA, LOCO [5] and Middle Layer [4]. The integrated system of programs and scripts has made it an ideal tool for us at the AS.

The sections below will outline the BPM system and its capabilities followed by some of the applications that have been used during commissioning and the results.

BPM GEOMETRY

The four BPM buttons (from Kyocera) are separated in the vacuum chambers by 20 mm (H) and 32 mm (V). Using POISSON it is possible to simulate the fields with the geometry of the BPM blocks. The results gave BPM coefficients of k_x = 14.60 mm and k_y = 14.66 mm (LOCO results later put these values closer to ~15.3 mm ±1%).

$$x = k_x\left(\frac{V_A - V_B - V_C + V_D}{\sum V_i}\right) \qquad y = k_y\left(\frac{V_A + V_B - V_C - V_D}{\sum V_i}\right)$$

The error estimates in the position due to the pincushion effect was also investigated (see Figure 1). Within a region of x = ±3 mm and y = ±2 mm the apparent position is accurate to < 5%. Given that most studies will not involve orbits > 1 mm, inverting the pincushion effect is not seen as necessary.

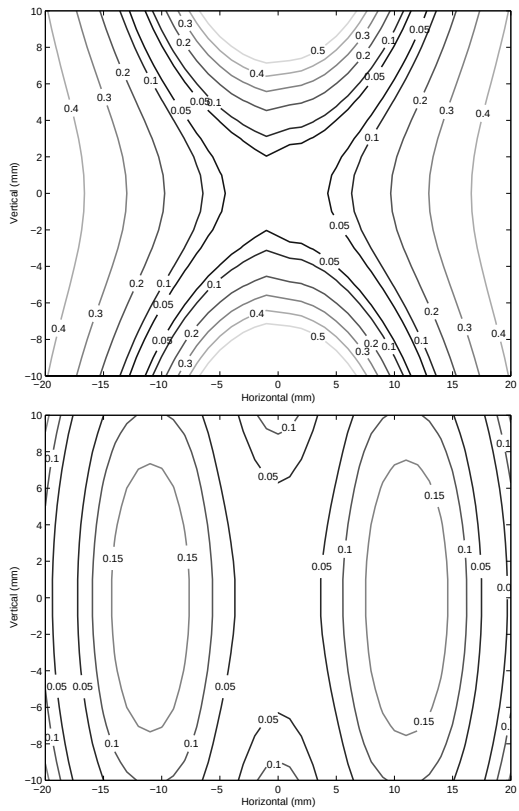

Figure 1 Relative error in the horizontal (TOP) and vertical (BOTTOM) position as a function of the actual beam position in x and y due to the pincushion effect.

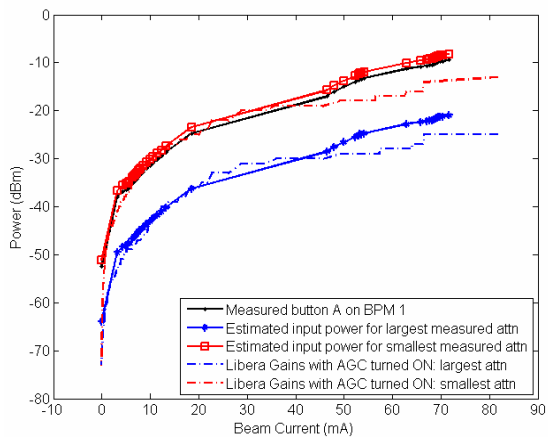

Figure 2 This plot shows a range of input power levels of the BPM signals going into the Libera based on measured signals (solid) and on gain settings of the EBPPs when Automatic Gain Control is turned on (dotted).

LIBERA

All 98 BPMs are connected to EBPPs with LMR200 cables rated at 0.25 dB/m. With cable lengths ranging from 18.7 to 64.0 m the expected dynamic range was 11.3 dB. However post installation measurements indicate that the attenuations were closer to 0.29 dB/m with a dynamic range of 12.8 dB. This is corroborated by the results in Figure 2 that show a dynamic range of 13 dB based on the gain settings of the EBPPs when the gain control is turned on. At the orbit interlock current threshold of 10 mA the power levels range from -42.4 dBm to -29.6 dBm. These are sufficient for accelerator physics studies.

The EBPPs are only supplied with the machine clock (revolution frequency of 1.388 MHz) to synchronise the AD converter and a trigger signal at a rate of 1 Hz. The EBPPs can also use other signals such as the system clock and a post mortem trigger [1] however they are not needed in the near future. A single set of the signals is generated by the timing system and is distributed via a series of fan-out units to the EBPPs. Ideally the BPM signals for a particular turn should arrive at the same time as the trigger at the EBPPs. In the current setup this is not possible for all the BPMs and the time difference between the signal and trigger can be as much as 1.1 μs. This means that without offsets in the data there is a 1.5 turn disparity between BPMs. The latest upgrade to the Libera will have features to compensate for this effect.

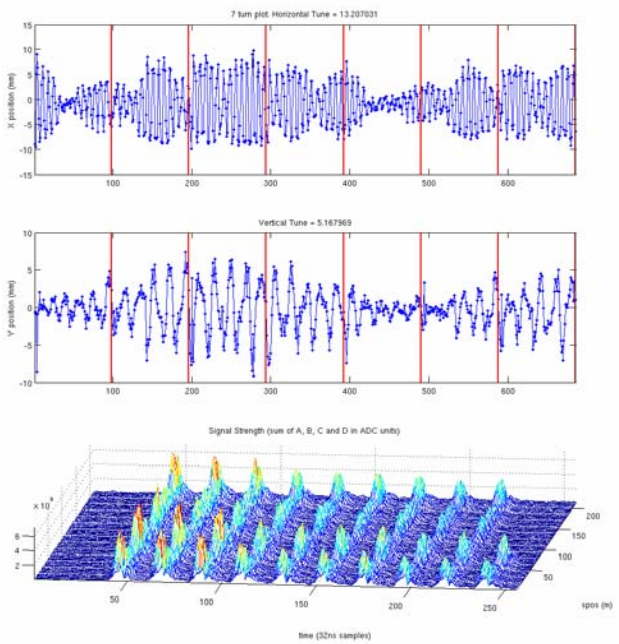

Figure 3 First turns plots showing the horizontal (top) and vertical (middle) orbit over 7 turns. Each section split by a vertical line is a snapshot of the orbit around the ring. The sum signal for 10 turns is shown in the bottom plot.

First Turns and Turn-by-Turn

Early in the commissioning when striving for first turns the initial version of the EPICS driver (developed at Diamond) for the EBPPs made it possible to effectively retrieve data sampled at 33.5 ns for first turn monitoring. Figure 3 shows one of the first turn plots after achieving ~30 turns. The data displayed has been offset to account for the timing issues mentioned before. The tunes in Figure 3 were obtained by a simple FFT over the 7 turn orbit, however due to the limited amount of data and noise the tunes were only used as a rough guide. Nonetheless they were close to the nominal tunes for the first day lattice (ν_x = 13.3 and ν_y = 5.2). The rise and fall of the peaks in the sum signal is due to the variation in the attenuations of the BPM cables around the ring. Comparisons between the strength of the sum signal and the cable attenuations showed near perfect correlation.

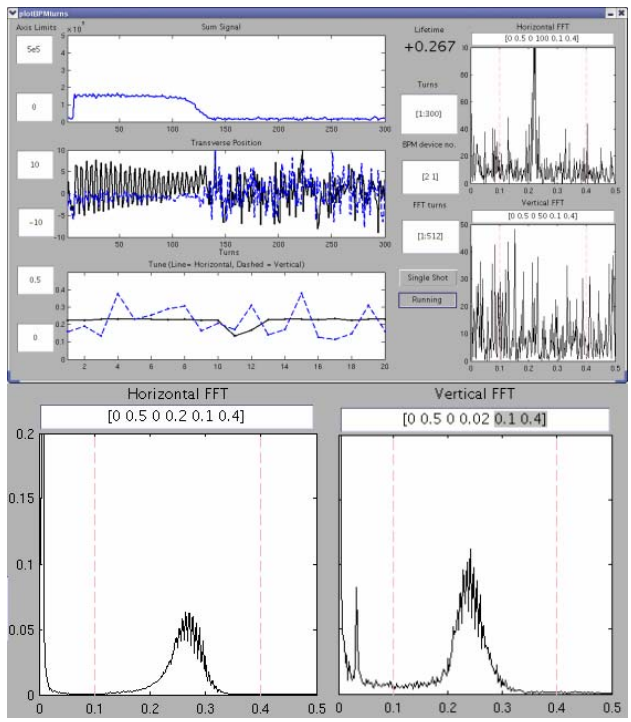

Figure 4 There are two GUIs here showing ~130 turns (top GUI) and the tunes (bottom). The GUIs developed in Matlab show the turn-by-turn sum signal (top left), position (middle left), fractional tune based on FFT peaks (bottom left) and an FFT on the horizontal (top right) and vertical (bottom right).

Shortly after achieving multiple turns, the beam was stored with no sextupoles and therefore at the natural chromaticity with a broad tune spread. The tune measurement system [7] was not sensitive enough to detect the tunes. It was however possible to use the injection kickers to excite the beam and apply an FFT on the turn-by-turn data to detect the tunes. This showed a tune spread of around 0.035 and 0.030, and with $\xi_{x,y} \approx$ -31,-24 the natural energy spread is therefore around 0.11% to 0.13%. This agrees quite well with the model of 0.10%. A simple display for the turn-by-turn data from the BPMs was developed in Matlab (screen shots are shown in Figure 4).

Slow Acquisition

The narrow band measurements for the EBPPs are referred to as the slow acquisition data (update rate of 10 Hz). Early measurements of the noise showed as much as 5 μm RMS however by detuning the machine clock PLL the noise level was reduced to ~0.2 μm RMS (see Figure 5). This is acceptable, however there is still room for improvement if we want μm level control of the orbit.

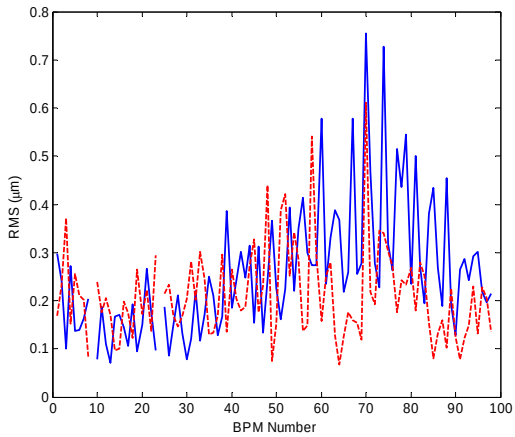

Figure 5 Noise measurement of the slow acquisition data in the horizontal (solid) and vertical (dotted) over 300 seconds at 85 mA (80% even fill pattern).

MATLAB SOFTWARE SUITE

Beam Based Alignment

Otherwise referred to as quadrupole centring in the code, this program only requires one to configure some initial scripts to define the groupings of BPM, corrector and quadrupole as well as the strength of the shunts. The algorithm is simple and involves taking a suitable corrector to sweep the beam through the BPM of interest. At designated points the nearest quadrupole to the BPM of interest is shunted and the change in the orbits around the Storage Ring is measured. Quadrupole field modulation with sinusoidal signals is not used. A complete run will take up to 3.5 hours using 4 points (8 measurements in total for a BPM). The current measured offsets do not show any systematic errors and has a max of 2.4 mm and deviation of 0.52 mm [6]. The current resolution is ~10 μm and requires further optimisation.

Response Matrices

This usually refers to corrector-BPM response matrices however as part of the suite of tools one can just as easily measure a sextupole-chromaticity response matrix as it is a program to measure linear maps from one parameter space to another. For example, a linear map was generated from a model to create a quadrupole-dispersion/tune map (3 by 3 matrix) that has since been used in an algorithm to globally fix the tunes and dispersion. Corrector-BPM response matrices take about 10 minutes to complete.

Orbit Correction

Orbit correction is typically done using "orbitgui" [8] that uses a measured response matrix and dispersion. The dispersion is used to distinguish the energy components in the orbit and corrector pattern. The program makes it easy to manipulate the orbit with ready access to the singular values. An RMS of the orbit of 16 μm has been achieved with corrector RMS values of 0.11 (H) and 0.06 (V) mrad (max of 1.5 mrad).

LOCO and Beta Function Measurement

With LOCO it is possible compute the lattice functions and calculate the necessary changes to reduce the beta beating and control the tunes and dispersion. The variations (deviation/mean) in the quadrupole power supply settings are QFA (0.1%), QDA (1.0%) and QFB (0.2%). Routine cycling of magnets has been in place to minimise hysteresis effects. Using LOCO the lattice has been configured for both zero and distributed dispersion (lower emittance). The quadrupole shunt measurement takes bout 15 minutes to complete and has shown strong correlations with the results from LOCO [7].

CONCLUSION AND REMARKS

The BPM system and tools for accelerator physics studies are in place and are well understood. The results shown have been promising however there remains a lot of work to be done to optimise the BPM system and improve the resolution.

ACKNOWLEDGEMENTS

Gunther Rhem, Michael Abbott and Yuri Chernousko at Diamond for their contributions to the BPM system.

REFERENCES

[1] A. Kosicek, "Libera Electron Beam Position Processor", PAC 2005, p. 4284.
[2] G. S. LeBlanc, M. J. Boland, Y.-R. E. Tan, "The Australian Synchrotron, Project Storage Ring And Injection System Overview", EPAC 2004, p. 2263.
[3] A. Terebilo, "Accelerator Modelling With Matlab Accelerator Toolbox", PAC 2001, p. 3203.
[4] G. Portmann, J, Corbett, A. Terebilo, "An Accelerator Control Middle Layer Using Matlab", PAC 2005, p. 4009.
[5] J. Safranek, G. Portmann, A. Terebilo, C. Steier, "Matlab-Based LOCO", EPAC 2002, p. 1184
[6] G. S. LeBlanc, "Status of the Australian Synchrotron", these proceedings.
[7] M. J. Spencer, M. J. Boland, R. Dowd, G. S. LeBlanc, Y.-R. E. Tan, "Tune And Lifetime Studies At The Australian Synchrotron", these proceedings.
[8] J. Corbett, A. Terebilo, "Interactive Orbit Control In Matlab", PAC 2001, p813.

MEASUREMENTS USING THE X-RAY AND OPTICAL DIAGNOSTIC BEAMLINES AT THE AUSTRALIAN SYNCHROTRON

M. J. Boland, J. Bergstrom, G. S. LeBlanc, Y.-R. E. Tan, R. Dowd and M. J. Spencer, Australian Synchrotron, Clayton, Victoria 3168, Australia.

D. J. Peake and R. P. Rassool, The University of Melbourne, Victoria 3010, Australia

Abstract

First Light has been achieved on the diagnostic beamlines at the Australian Synchrotron 3 GeV storage ring. The X-ray Diagnostic Beamline (XDB) has been used to measure the beam size, divergence and emittance, while the Optical Diagnostic Beamline (ODB) has been used the measure the bunch length and turn-by-turn stability. Both beamlines receive dipole radiation from a bend magnet and provide continuous diagnostic data to the control room. The beamlines compliment each other with the ODB providing mainly longitudinal (temporal) information, while the XDB measures predominantly transverse (spatial) information. A brief description is given of the equipment on each beamline and the commissioning results are presented.

X-RAY DIAGNOSTIC BEAMLINE

The x-ray diagnostic beamline provides mostly transverse beam information and is described in more detail in Ref [1]. Measurements made during the commissioning of the storage ring are presented here.

Image Array

A pinhole array generates 9 images of the bend magnet source point which is displayed in the control room via EPICS (see Fig. 1). The spots provide a qualitative as well as quantitative diagnostic of the status of the stored beam.

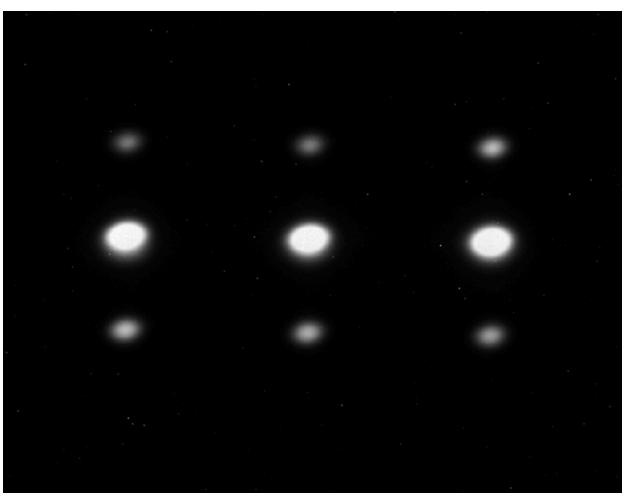

Figure 1: Array of beam spot images created by the x-ray pinhole array. The data is captured with a CCD camera viewing a YAG screen on the x-ray diagnostic beamline.

Beam Size and Emittance

The beam spot is measured from the YAG screen image and fitted with a Gaussian curve to obtain the horizontal and vertical beam sizes. The emittance was determined using the measured beam size and the beta-functions from the calibrated model that was fit using LOCO [2]. Fig. 2 shows the results of a measurement after the first correction to optics to remove beta-beating. The emittance of 17.5 nm is close to the design value of 15.8 nm for a lattice with zero dispersion in the straight sections.

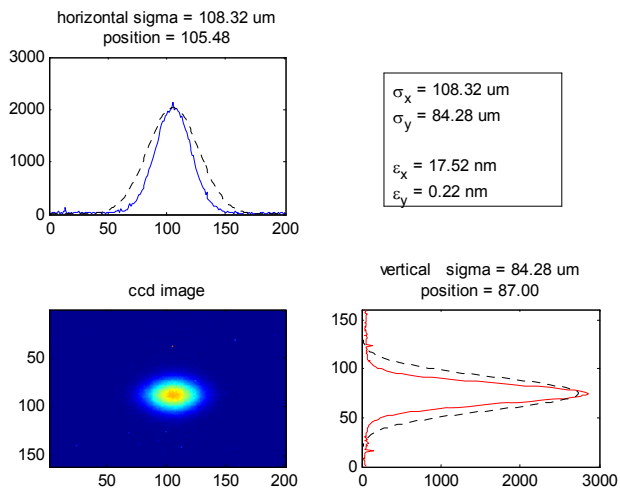

Figure 2: Emittance measurement from a single spot on the x-ray diagnostic beamline and beta-functions from a calibrated model.

Beam Stability

Using an EPICS driver to process the camera data from the Firewire CCD camera the x-ray beam centroid is monitored to track the beam stability. In order to get a good quality image the CCD integration time needs to be 50 ms or greater. With the CCD triggered at 1 Hz and a 50 ms integration time the beam stability is measured to be 2 μm rms.

Divergence

The multiple images from the pinhole array allows for divergence of the beam to be measured by fitting a Gaussian to the intensity distribution of the vertical beam spots. Fig. 3 shows the vertical profile and the Gaussian fit to the intensity distribution of the beam spot peaks.

The measurement is close to the $1/\gamma$ opening angle of 0.17 mrad.

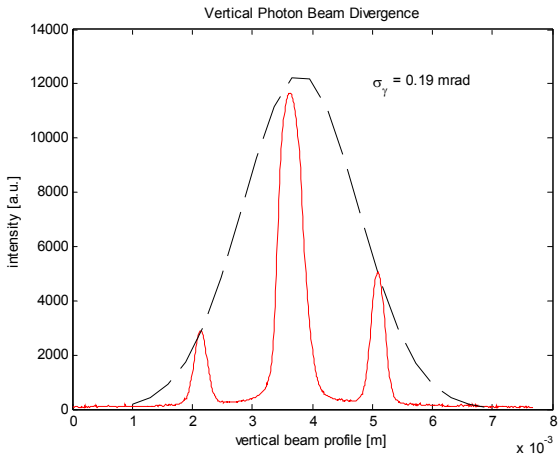

Figure 3: Vertical beam divergence measured by the x-ray pinhole array.

OPTICAL DIAGNOSTIC BEAMLINE

The optical diagnostic beamline provides mostly longitudinal beam information and is described in more detail in Ref. [1]. Results of the commissioning some of the optical instruments is presented here.

Dual Sweep Streak Camera

During the storage ring RF commissioning, the dual sweep streak camera was used to monitor the amplitude of the synchrotron oscillations while detuning the cavities. Fig. 4 shows the fast sweep on the vertical axis and the secondary sweep on the horizontal axis and the large amplitude synchrotron oscillation prior to detuning. After detuning the cavities there was no measurable amplitude modulation on the streak camera images.

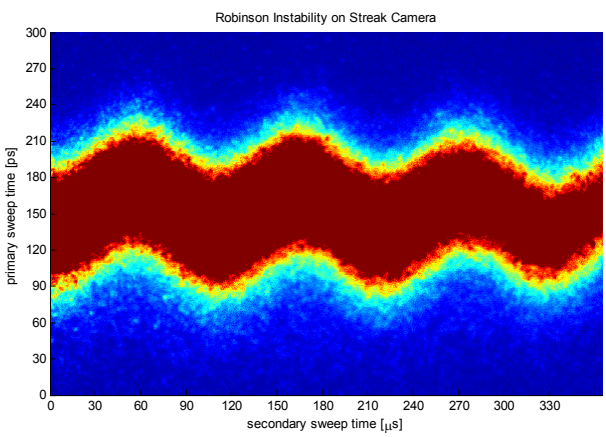

Figure 4: Dual Sweep Streak Camera image of a 9.19 kHz Robinson Instability during tuning of the storage ring RF cavities.

Beam Stability

A Position Sensitive Detector has been installed to measure the beam motion using visible light. A Hamamatsu S1300 2D photodiode connected to a C4757 controller board produces output voltages proportional to the horizontal and vertical beam position. The diode is biased by a PS2127 power supply from Oxford Electrical Products and has a stability of 1 mV RMS. The absolute position readout has not been calibrated since the beam is arbitrarily focused to as small a spot size as possible, but the frequency of the signal can be used to analyse the beam motion.

The voltage from the controller board it digitised using a Nation Instruments USB-6251 digitiser and LabView to EPICS software. Two different operational modes are used: slow and fast acquisition mode. In slow mode the systems outputs an average beam position at 1 Hz using a configurable number of samples and sample rate. This mode is used to monitor the long term stability of the beam. Using fast mode the system can output 1.4 MS/s with 16 bit resolution for up to 1.4 s to do more detailed analysis of transient beam motion.

Fig. 5 shows the beam motion during the RF commissioning when there was a large synchrotron oscillation due to the Robinson instability. The three plots of horizontal beam motion show some of the different ranges of data sampling that is possible with the system.

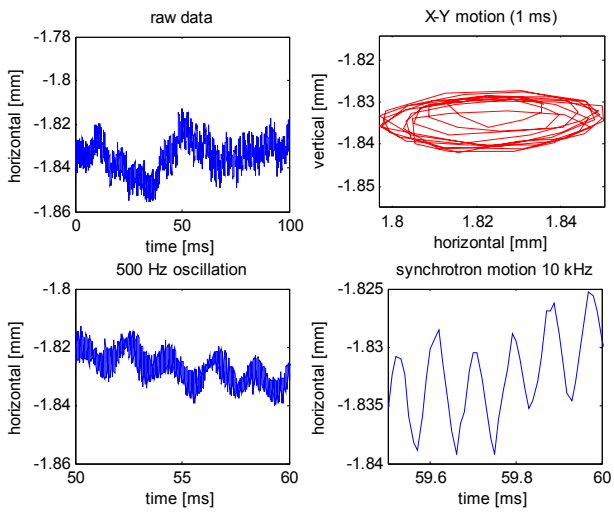

Figure 5: Beam stability measurements during RF cavity commissioning with a 2D position sensitive detector. At the maximum digitisation rate the synchrotron tune can be observed at approximately 10 kHz.

Bunch Length

During commissioning of the RF cavities, with only three of the four in operation, the storage ring was tested in single bunch mode. Using the streak camera the bunch length was measured while increasing the current in a single RF bucket. When the measurement was taken the cavities were still being conditioned and could not operate at full voltage. The theoretical bunch length at the design voltage is 22 ps, but with the commissioning settings a minimum bunch length of only 40 ps could be achieved.

Fig. 6 shows the bunch lengthening with increasing single bunch current as expected. The total current in one bunch was limited to 5 mA in this measurement as a precaution, but currents of up to 25 mA should be achievable in the future. More detailed studies will be conducted to determine the impedance of the vacuum chamber from the single bunch length, once the RF is fully operational.

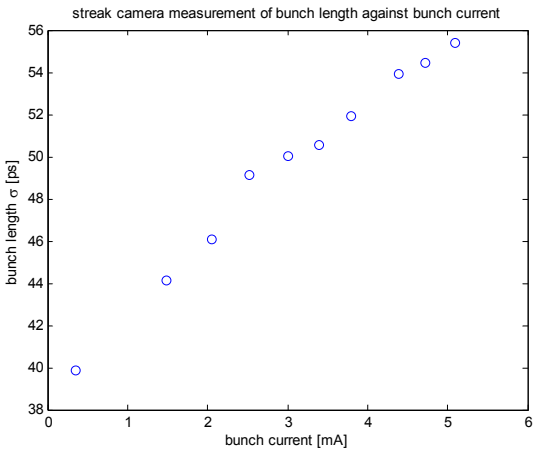

Figure 6: Bunch length measured by a streak camera for a range of single bunch currents.

Fill Pattern Monitor (FPM)

The electron bunch fill pattern in the storage ring is measured using an optical photodiode. The diode output is digitised and made available in EPICS. Fig. 7 shows a comparison between the FPM and a conventional measurement of the fill pattern using the signal from a stripline pickup on an oscilloscope. The measurements are in good agreement and the FPM is now in routine operation for controlling the filling of the storage ring.

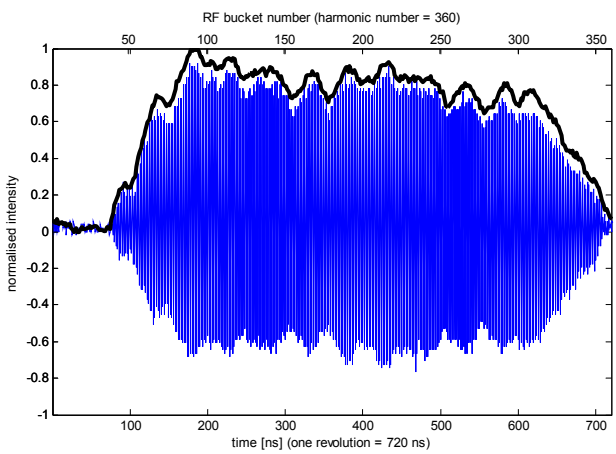

Figure 7: Comparison of the fill pattern measured on the optical monitor (thick black) and the stripline response on an oscilloscope (blue).

The system was sensitive down to less than 0.05 mA total current in the storage ring. Tests were also done with single bunch injection and the fill pattern was able to be flattened out and squared off. The fill pattern measurement was stable to less than 1 % of the maximum bunch current in an even fill, thus providing a reliable signal for injection efficiency and feedback systems. A system is under development using the FPM to provide automatic arbitrary pattern filling and can be used in a feedback loop for top up mode in the future.

SUMMARY

The diagnostic beamlines have been successfully commissioned and most of the instrumentation is now in routine operation. The x-ray diagnostic beamline has been providing stable and useful information from the first moment of stored beam in the storage ring. The optical diagnostic beamline has a powerful set of tools that have been used to tune the machine during commissioning and will be vital in the fine tuning required as we move into user operations in March 2007.

REFERENCES

[1] M. J. Boland et. al., EPAC 2006, Edinburgh, UK.
[2] J. Safranek et. al., EPAC 2002, Paris, France.

DIAGNOSTIC SUPPORTS FOR TOP-UP OPERATION AT TLS

K.H. Hu#, Jenny Chen, C.J. Wang, C.H. Kuo, K.T. Hsu
National Synchrotron Radiation Research Center, Hsinchu 30076, Taiwan

Abstract

The routine top-up operation of Taiwan Light Source (TLS) began in October 2005. The beam stability and integrated flux were drastically improved. Various diagnostics are needed to support the top-up operation. These tools include diagnostics for measuring beam charge and current and injection efficiency, as well as a filling pattern monitor, a tune monitor, and an instability and loss pattern monitor. This study summarizes design considerations, details and future plans.

INTRODUCTION

The accelerator system at the Taiwan Light Source (TLS) consists of a 140 keV thermionic gun, a 50 MeV linear accelerator (LINAC), a linac-to-booster (LTB) transport line, a 1.5 GeV booster synchrotron, a 70 m long booster-to-storage ring (BTS) transport line and a 1.5 GeV storage ring. The goals of the top-up mode operation are to provide high stability and a highly integrated flux photon beam and to keep the heat load of the optical components constant. A complete diagnostic of the accelerator system is required for routine monitoring and machine debugging, to support the requirements of top-up mode operation. Major diagnostics that support top-up operation include charge, transmission of transport line, current, injection efficiency, orbit stability, electron loss, profiles, tune and instability and others. Table 1 summarizes these diagnostics.

MAJOR DIAGNOSTICS SUPPORT FOR TOPUP OPERATION

Templates are provided for Microsoft Word (Mac and PC) and LaTeX. Authors are advised to use the templates provided. The JACoW Styles and Macros menu, available in the Microsoft Word .dot templates, is designed to help authors format their papers correctly. Please consult the individual conference help pages if questions arise.

LINAC and LTB Diagnostics

Diagnostic devices of the LINAC include several toroids, two fast gap monitors, and a screen monitor near the exit of LTB. These diagnostic devices can measure beam current, beam profile, energy and energy spread. A 60° bending magnet is adopted to bend the output of LINAC. An energy defining slit is located just before the last toroid to define the energy. Integrating the current waveform of this toroid monitor obtain the beam charge of the LINAC output. The energy and energy spectrum can be measured by scanning the bending angle of the bending magnet. A screen monitor is added behind the bending magnet, to measure the emittance of the LINAC by the quad-scan method when this bending magnet is turned off.

Table 1: Main diagnostics to support top-up operation

Accelerator system	Parameters should be monitor	Descriptions
Linac	Transmission	Toroid, gap monitor, oscilloscope
	Charge	Toroid and charge integrator
Booster synchrotron	Averaged beam current	MPCT
	Filling pattern	FCT, stripline with oscilloscope
BTS	Transmission	ICT and charge integrator
	Beam position	BPM
	Position, transverse profile	Screen monitor
Storage Ring	Averaged beam current	MPCT with 1 μA resolution
	Injection efficiency	$\Delta I_{avr,SR} * t_{rev,SR} / C_{ICT,BTS}$ per injection shot
	Filling pattern	Button pickups with oscilloscope
	Isolated bunch purity	Photon counting system – in planning

Note: $\Delta I_{avr,sr}$ is increment of beam current per injection shot, $t_{rev,SR}$ is the revolution period of the storage ring, $C_{ICT,\ BTS}$ is the beam charge pass the BTS per injection shot.

Booster Synchrotron Diagnostics

The booster synchrotron diagnostic consists of seven sets of screen monitors, MPCT, FCT, BPMs, and a synchrotron radiation monitor. The measured parameters include beam current, closed orbit, tune and beam profile. The averaged beam current is measured by the MPCT. The filling pattern is measured by the FCT. The synchrotron radiation monitor is upgraded using an IEEE-1394 camera with an external trigger and exposure time control functions. Several approaches have been applied during the last decade was to tune measurement. Figure 1

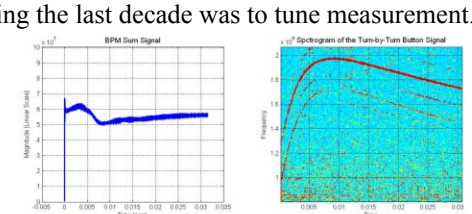

(a) (b)

Figure 1: (a) Beam intensity of the booster synchrotron; (b) tune variation during energy ramping.

#uka@nsrrc.org.tw

displays the Fourier analysis of the turn-by-turn beam position data captured by a Libera Electron.

BTS Diagnostics

Beam intensity, charge, trajectory and beam profile should be monitored routinely during top-up operation. The diagnostic devices of BTS consist of the FCT, ICT, BPMs and screen monitor. Bergoz's FCT and ICT is used to measure intensity and charge. Trajectory is measured using Bergoz's LR-BPM. Figure 2 plots the signal output of the charge amplifier to the timing waveform of Bergoz's charge integrator. In Fig. 3, the ICT signal suffers kicks the disturbance during injection. The solution to this problem warrants further study. The fired noise from injection kickers interferes with the baseline of the last ICT (ICT3) as shown in Fig.2. The ICT2 is located in the middle of BTS and located in the vertical bend. The charge measured by this ICT is accompanied with a charge increment per injection, enabling the injection efficiency of the storage ring to be computed.

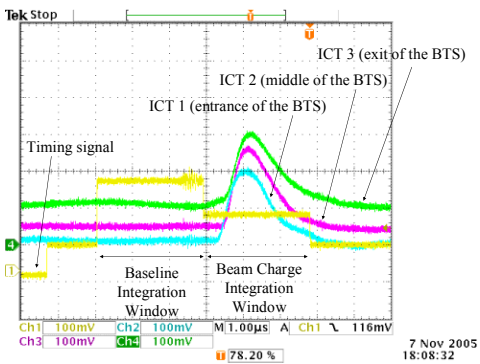

Figure 2: Signal output of the charge amplifier respectively to the timing signal of charge integrator.

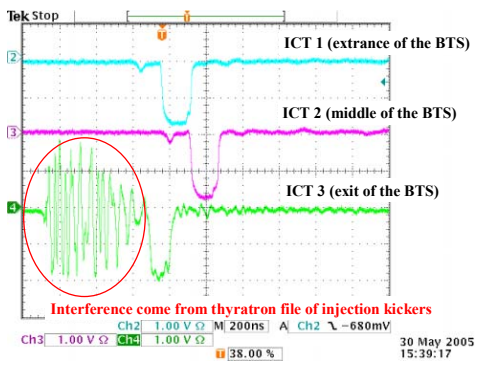

Figure 3: The ICT3 signal suffers the interference during injection kickers fired.

Storage Ring Diagnostics

The storage ring is equipped with the same standard diagnostics. The performance and functionality of the diagnostic system have been improved during the last decade. The new generation of BPM electronics are in their final integration phase. The synchrotron radiation monitor has been upgraded to include an IEEE-1396 digital camera, with drastic improvement in the dynamic range and linearity. The measurement parameter of the diagnostic system include closed orbit, beam current, tune, filling pattern, bunch current, beam loss, beam profile, emittance and beam energy. Several diagnostics are particular to the top-up operation and are addressed below.

The injection efficiency equals the increase in beam charge, measured by the DCCT of the storage ring, divided by the charge measured by the ICT2 of the BTS at the same injection cycle. Figure 4 plots the typical injection efficiency during top-up injection. An injection efficiency of over 70% is routinely achieved.

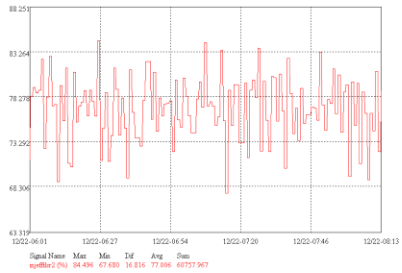

Figure 4: Typical injection efficiency of top-up mode operation.

The filling pattern of the storage ring drastically affects the operation performance. Control of the filling pattern is desirable. A dedicated filling pattern measurement system was set up as shown in Fig. 5, to satisfy the bunch current measurement requirements and possible filling pattern control in the near future. The sum of signal of BPM buttons is digitized by an Agilent 54832D oscilloscope with a bandwidth of 1 GHz, operated in equivalent sampling mode. The filling pattern server computer is connected to this oscilloscope via an Ethernet to the IEEE-488 adaptor. The ring clock triggers the oscilloscope. Performed analysis of the captured waveform can extract the relative bunch intensities of all bunches. The raw bunch intensity data normalized by the precision averaged beam current reading from DCCT is then obtain using a bunch-by-bunch current.

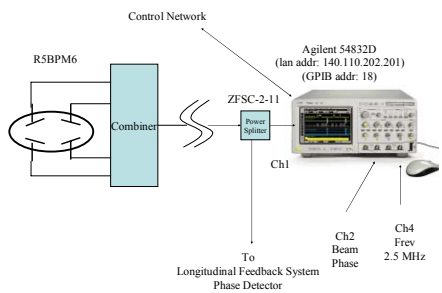

Figure 5: Setup for filling pattern measurement.

Figure 6 show the measured filling pattern with a stored beam current of 302 mA in a snapshot taken during top-up operation. This bunch current measurement has an accuracy of over 1%. The 16 nsec structure and bunch current variation are associated with the current injection scheme. A short bunch train of about 30 bunches is used to fill the storage ring at this moment, and the bucket is

jump 8 bunched for each injection. This process is repeated during the top-up operation scenario, which is the reason with this 16 nesc bunch current variation. Despite this fact, the filling pattern can be maintained within 5% during several days of continued top-up operation.

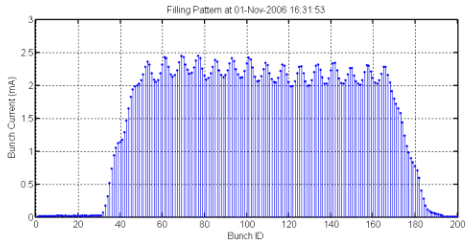

Figure 6: Measured bunch current of a snapshot during top-up operation. Total beam current is 302 mA.

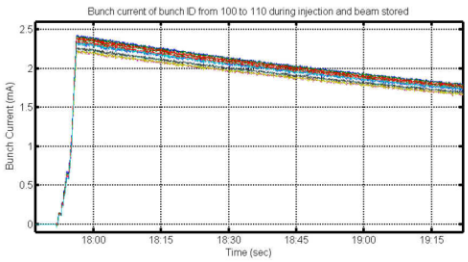

Figure 7: Bunch current of the decay mode operation.

The beam is perturbed in a fixed interval for top-up injection. This beam position oscillation caused by injection perturbation, can be captured by the new BPM electronics (Libera Electron). The Fourier analysis of the turn-by-turn data can extract the tune at every instance of injection. A Bergoz's type PIN diode beam loss monitor can acquire the radiation distribution. Several high counting rate scintillator type beam loss monitors are also installed to support various studies. A tune monitor and a beam loss monitor can support various studies and the monitoring of routine operation. Figure 8 plots the tune and beam loss as functions of the magnetic gap of a U9 undulator as an example.

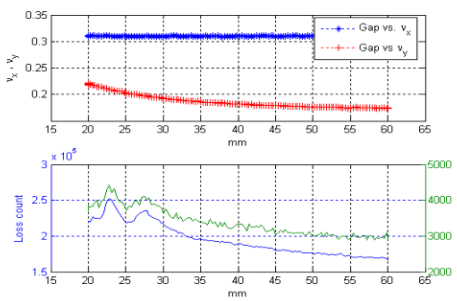

Figure 8: Bunch current of the decay mode operation. (tune vs. beam loss.)

An injection synchronization signal is available in all experimental stations, to deal with the beam perturbation caused by non-ideal injection local bump. This signal can help a user to gate out the signal when the beam is unstable upon injection, guaranteeing the quality of experimental data.

The stability of the beam position is important to the user. Figure 9 plots beam stability, measured by a tested Libera Electron at R4BPM5 during a top-up run. It is confirmed that 8 hours stability is around μm level.

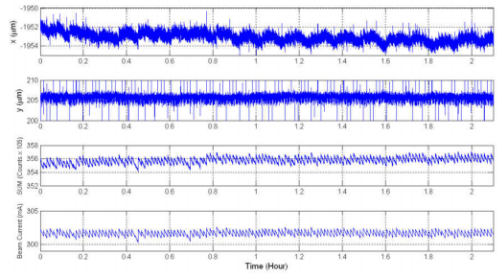

Figure 9: Eight hour position stability at R4BPM5 during top-up operation. The spike is due to the beam perturbation by the injection kick.

DISCUSSION

Diagnostics to support top-up operations of the TLS have been gradually improved over the last two years. Experience accumulated during the first year of top-up operation will support the next step improvement in coming year. Users require the injection of an isolated bunch in the multi-bunch filled-gap. The storage ring will be operated with a camshaft filling pattern is possible in the near future. Bunch purity diagnostics for this isolated bunch with photon counting technique is in planning. Study of the feasibility of purifying the single bunch at the booster synchrotron is under way.

REFERENCES

[1] M. Yoshioka, et. al., "Storage Ring Bunch Current Measurement", Proceedings of the 14th Symposium on Accelerator Science and Technology, Tsukuba, Japan, November 2003, pp. 428-430 (in Japanese).

[2] T. Ohshima, M. Takao, A. Yamashita, M. Yoshioka, "Top-up Injection Control Using Bunch Current Monitor at SPring-8", Proc. of the 2nd Annual Meeting of Particle Accelerator Society of Japan and 30th Linear Accelerator Meeting in Japan, Tosu, 2005, p.618.

[3] H. Tanaka, et al., "Stable Top-Up Operation at Spring-8", J. Synchrotron Rad. 13, 378-391 (2006).

[4] B. Kalantari, T. Korhonen, A. Ludeke, Ch. Quitmann, "Enhancements of Top-Up Operation at the Swiss Light Source", Proceedings of EPAC 2004, Lucerne, Switzerland, 309 (2004).

[5] B. Kalantari, V. Schlott, T. Korhonen, "Bunch Pattern Control in Top-Up Mode at the Swiss Light Source", Proceedings of EPAC 2004, Lucerne, Switzerland, 2885 (2004).

[6] Walter Barry, Mike Chin, David Robin, Fernando Sannibale, Tom Scarvie, Christoph Steier, "Diagnostic Systems Plan for the Advanced Light Source Top-Off Upgrade", Proceedings of 2005 Particle Accelerator Conference, Knoxville, Tennessee, 4066(2005).

EXPERIENCE OF BEAM DIAGNOSTIC SYSTEMS IN COMMISSIONING STAGE OF INDUS-2

T. A. Puntambekar#, Anil Banerji, L.K. Babbar, Akash Deep, Anil Holikatti, D.K. Joshi, A. Karnewar, S. Kotaiah, Mukesh Kumar, R.K. Nathwani, S.K. Suhane, Y. Tyagi, S.Yadav
Raja Ramanna Centre for Advanced Technology, Indore, India

Abstract

Indus-2 is a 2.5 GeV synchrotron radiation source under commissioning at this centre. Beam injection trials in the storage ring began in August 2005. Beam diagnostics systems played an important role during commissioning of the storage ring. Beam diagnostic systems installed in the machine include beam profile monitor, orbit measurement system, wall current monitor, DCCT, strip lines, tune measurement system and sighting beam line. This paper describes the diagnostic systems, experience of operation of these systems during commissioning, results obtained and the present status. During the initial stages of beam injection and circulation in Indus-2, wall current monitors, beam profile monitors and sighting beam line proved to be of utmost help. In the current stage of near routine beam operation, the main focus has shifted to the measurement of beam parameters with the objective of improving beam current and lifetime.

INTRODUCTION

Indus-2 is a 2.5 GeV energy dedicated electron synchrotron radiation source. The accelerator complex is composed of injector microtron, booster synchrotron and Indus-2 ring. Two bunches of 550 MeV are extracted from the booster synchrotron and injected in to Indus-2 through 88 m long transport line–3 (TL-3). The length of each bunch is about 1 ns and separation between them is 31.6 ns. The process of commissioning of Indus-2 started in August'05. Initially beam injection was carried out at 450 MeV energy, which was later on increased to 550 MeV to achieve higher accumulation rates. After successful beam accumulation in the storage ring, energy ramping to 2 GeV was done. Table 1 summarizes the diagnostic devices installed in Indus-2. Fluorescent screen type beam profile monitors, wall current monitors, septum hole monitors and sighting beam line were used to transport the beam effectively through the beam transfer line and achieve beam circulation and accumulation in the storage ring during the initial beam injection and commissioning stage. The main focus has shifted to the measurement of beam parameters with the objective of improving machine performance in the current stage of near routine beam operation. Measurement of betatron tunes (Horizontal and vertical) and closed orbit distortion (COD) has been carried out [1,7].

tushar@cat.ernet.in

Table 1: Beam diagnostic devices in TL-3 and Indus-2

S. No.	Name of diagnostic device	Total number
1	Beam Profile Monitor	19
2	Wall Current Monitor	5
3	DC Current transformer	1
4	Beam Position Indicator	56
5	Strip line Monitor	6
6	Sighting Beam Line	1
7	Horizontal and vertical Scraper	3
8	Thick and thin Septum Hole Monitors	2

BEAM DIAGNOSTIC SYSTEMS

An overview of the beam diagnostic systems installed in TL-3 and Indus-2, experience gained during beam commissioning and the results obtained so far are presented in the following sections.

Beam profile monitor

Fluorescent screen beam profile monitors (BPM) are installed in TL-3 and the storage ring for visual observation of beam profile and position in transport line and the storage ring [2]. The BPM uses a fluorescent screen made of chromium-doped alumina, which can be inserted into the beam path by a pneumatic cylinder based linear motion mechanism. The spot of fluorescent light generated by the beam can be viewed by a CCD camera placed vertically above the beam plane. Remote operation of BPM is achieved by BPM interface units kept near the device and video signal multiplexers. A PCI based frame grabber card is used to capture and digitise the image for further processing. Figure 1 shows photograph of a BPM and the inset shows a typical electron beam profile. One-turn beam circulation was confirmed by observing the beam spot at all eleven BPM placed in the storage ring. The septum hole monitor is used to view the position of the beam at the entrance apertures of the thick and thin injection septum. The beam passes through an opening in a fluorescent screen mounted just a few millimetres upstream of the septum aperture. It has been found to be very useful in steering the beam though the injection septum during initial beam injection into the storage ring.

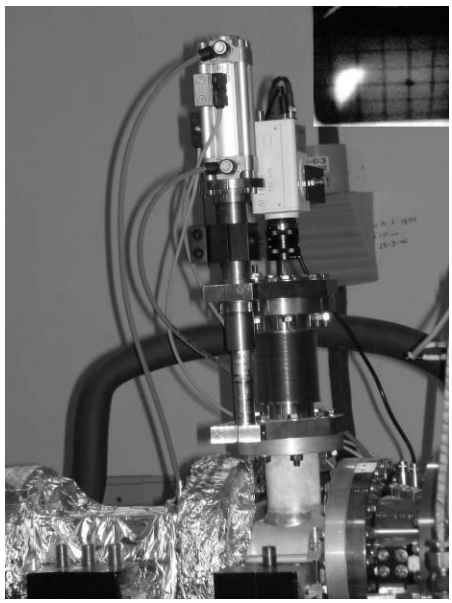

Figure 1: Photograph of beam profile monitor

Wall current monitor

Wall current monitor (WCM) is a non-interceptive beam diagnostic device, which monitors the image current flowing through the inner surface of the vacuum chamber. It is used to observe instantaneous bunch current signal. Four WCM are installed along the length of TL-3 to optimize the beam transport. Figure 2(a) shows typical bunch signals observed in TL-3. One WCM is installed in short straight section (SS-8) of the storage ring, which is used to observe beam injection and circulation in the ring. WCM proved to be very useful during commissioning to observe the circulation and survival of the beam in the ring. It was also used to optimize the timing of injection kicker magnet currents. Noise pickup from the pulsed magnets severely interfered with the bunch signal observation. The noise signal was reduced by using high pass filters at the input of the oscilloscope. Figure 2(b) shows three turn circulation of beam in the ring along with current waveform of one of the injection kickers. The spikes seen in the figure are the bunch signal. Also seen is the noise pickup from injection kickers. Figure 2(c) shows bunch pattern of the accumulated beam.

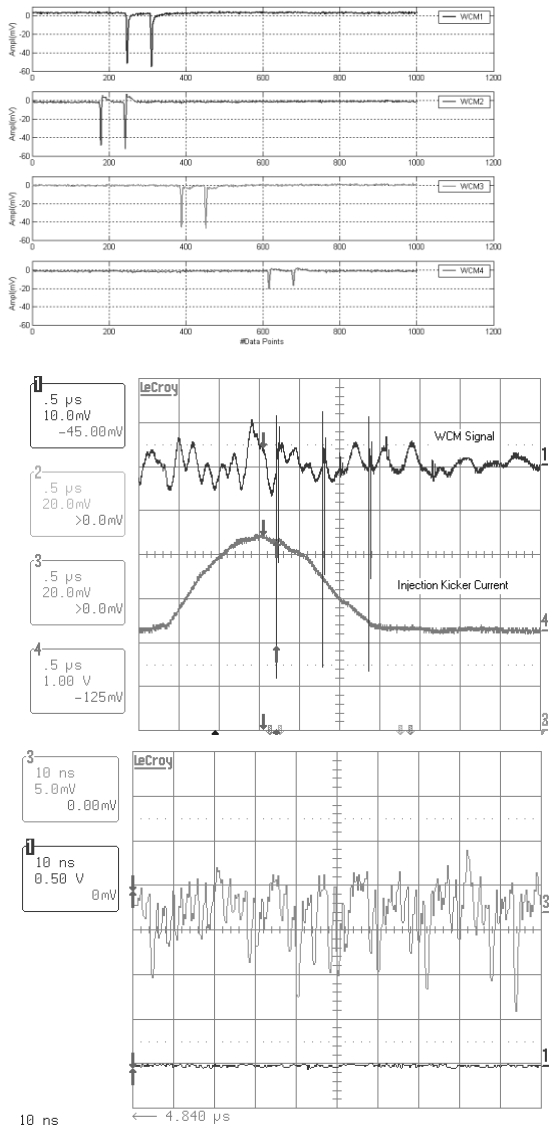

Figure 2 (Top to bottom): (a) Beam signals of TL-3 WCM (b) Three turn circulation of the beam in Indus-2 (c) Stored beam bunch pattern in Indus-2

Sighting beam line

Sighting Beam line (SBL) is primarily used to observe the synchrotron light spot during commissioning of the machine. It is installed at 10^{o} extraction port of beam-line BL-27 of Indus-2 dipole DP-11. SBL is completely situated inside the radiation-shielding wall. Beam line has a mirror chamber with a water-cooled gold plated copper mirror placed at 45^{o} to the beam path. Metallic mirror absorbs the x-rays and reflects the visible part of synchrotron radiation, which is observed with a CCD camera. First synchrotron light was observed on December 2, 2005 using sighting beam line.

Beam position measurement

Four-button electrode type beam position indicators (BPI) are used to measure closed orbit distortion in Indus-2. There are fifty-six BPI in the ring, seven in each unit cell. Out of these, forty BPI are of individual type, which are installed in the straight sections and sixteen are integrated type. One integrated type BPI is embedded in each dipole chamber. Individual type beam position

indicators were calibrated on a calibration bench before installing in the ring [3]. The BPI signal processing modules Bergoz MX-BPM[4] are installed in eight electronics racks distributed symmetrically on the equipment gallery. The output of the processing electronics is acquired by 4-channel, 16 bit ADC cards and the acquired data is transferred to the control room, where beam position is calculated by using position algorithm. Four-corrector compensated orbit bumps were created in eight long straight sections of the ring and the beam position observed by two BPI falling within the bump zone to study the performance of the BPI system. This study revealed a bug in the software and wrong cable connection of BPI electrodes at one place. Orbit correction was done in horizontal plane using the best correctors [1,7]. Figure 3 shows a typical display of beam orbit in the main control room.

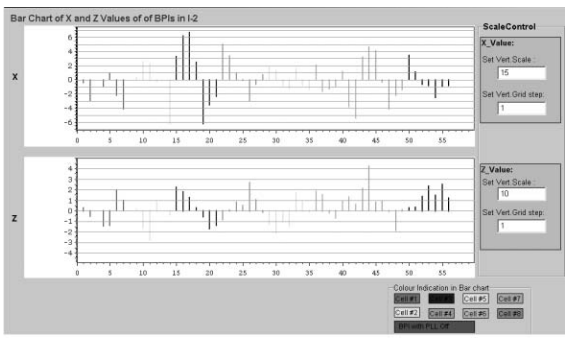

Figure 3: Beam orbit displayed in the control room

Betatron tune measurement

Betatron tune measurement system is based on continuous harmonic excitation method [5]. The measurement system employs a spectrum analyser equipped with a tracking generator. A VME bus based horizontal/vertical plane selector card allows the user to remotely select measurement of either horizontal or vertical tune. The tracking generator RF output, after splitting and amplification, is fed to a strip line kicker. Another strip line located downstream in the storage ring is used as a beam position monitor. The four strip line electrode outputs are used to produce real-time X and Z difference signals proportional to the beam position in horizontal and vertical plane. The position signal is then applied to the RF input of the spectrum analyser to observe the beam spectrum and betatron peaks. The betatron tunes in horizontal and vertical plane have been measured under various beam conditions [1].

Beam current measurement

Stored beam current is measured using parametric current transformer (DCCT) manufactured by M/s Bergoz [4]. A mounting system has been designed and fabricated for installation of PCT toroid [6], which includes features like ceramic gap, high frequency wall current bypass, thermal shield, temperature interlock system and a two layer magnetic shielding. A schematic of mechanical assembly is shown in fig. 4.

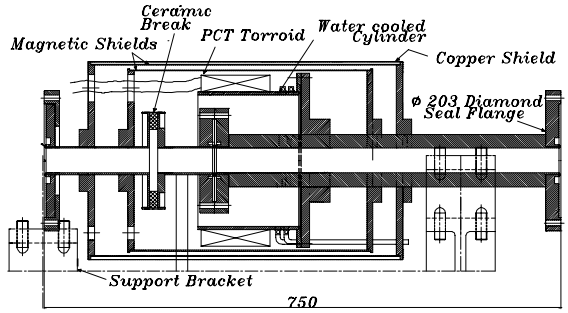

Figure 4: Schematic of DCCT Assembly

CONCLUSION

Beam diagnostic systems of Indus-2 have been commissioned. They have proved to be very useful during initial beam injection and commissioning phase of Indus-2. Exercises are currently being carried out to increase the beam current and energy and efforts are being made concurrently to study and improve the performance of diagnostic systems under different operating conditions. A preliminary exercise has been performed to correct the orbit in horizontal plane using beam position data, which has shown positive results.

ACKNOWLEDGEMENTS

Authors wish to thank colleagues of Accelerator Control Lab. for implementation of diagnostic system interfacing with the control system. Authors also wish to acknowledge the contribution of B.B. Sonawane in assembly and commissioning of the system.

REFERENCES

[1] G.Singh et al, “Indus-2: Machine Performance and Improvement Studies”,Proceedings of Indian Particle Accelerator Conference (InPAC) 2006, pp 94 -97
[2] T.A.Puntambekar et al, “Beam profile monitoring system for Indus-2”, National Symposium on Nuclear Instrumentation (NSNI) 2004, pp39-42
[3] Y.tyagi et al, “Analysis of Indus-2 beam position indicators calibration data”, Proceedings of InPAC 2006, pp247-248
[4] M/s Bergoz Instrumentation, France
[5] T.A.Puntambekar et al, “Betatron Tune Measurement System for Indus-2”, Proceedings of InPAC 2003, pp571-572
[6] S.K. Suhane et al,A set-up for installing parametric current transformer in Indus-2, Proceedings of InPAC 2005, pp193-194
[7] Riyasat Hussain et al, "Correction and Analysis of Measured COD in Indus-2", This conference

COMPARISON OF THE METHODS FOR BEAM ENERGY SPREAD MEASUREMENT AT THE VEPP-4M

V.A. Kiselev, N.Yu. Muchnoi, O.I. Meshkov, V.V. Smaluk, V.N. Zhilich, A.N. Zhuravlev
Budker Institute of Nuclear Physics, Novosibirsk 630090, Russia

Abstract

The VEPP-4M electron-positron collider is now operating with the KEDR detector for the experiment of precise measurement of tau-lepton mass. In this experiment, monitoring of beam energy spread is important to know the energy spread contribution into the total systematic error. Information about the energy spread gives an opportunity to reduce the error of the tau-lepton mass measuring. Several techniques for measuring the energy spread are described in the paper. Width of the ψ' resonance measured with the KEDR detector is used as a reference.

INTRODUCTION

The basic physical program of the VEPP-4M collider consists in precise measurements of mass of J/ψ, ψ', ψ'' narrow resonances and c-τ lepton mass on the threshold production. Value of beam energy spread σ_E is directly included into accuracy of the mass measurement. Knowledge of exact value of the beam energy spread enables us to reduce significantly a systematical error in the experiment of c-τ lepton mass measurement. It is also an essential supplement to the precise measurement of average beam energy.

Clear understanding of the reasons influencing the beam spread and the ability to control this value are important tasks for our experiments.

Energy spread of the beam can be increased with the 3-pole snakes and depends on strength of Robinson wigglers. Snakes have a length about 1 m and 1.8 T maximal strength of magnetic field. They were applied only during the beam energy spread measurements described below.

MODES OF THE VEPP-4M OPERATION

Table 1: Operation modes of the VEPP-4M used for energy spread measurements

Name	E, MeV	I_{WG}, A	I_{SN}, A	Comments
PNT4	1843	1055	0	$c-\tau$ lepton production. KEDR magnetic field is on.
PSIS	1843	1055	0	KEDR magnetic field is off.
ZMEJ	1843	1055	2000	KEDR magnetic field is off.
JPSI	1548	620	0	J/ψ meson peak. KEDR magnetic field is off

The target of our experiments was not only the definition of the beam energy spread for basic modes of the collider operation, but also the comparison of several procedures for measurement of relative energy spread $\delta_E=\sigma_E/E$. The experiments were carried out at the four modes of the collider operation (Tab. 1). The modes differ both in the energy E and in the energy spread σ_E value. Application of several methods to determine the energy spread for different modes of the VEPP-4M operation enables us to realize a cross-validation of the measurements and to compare the diagnostics considering convenience and efficiency.

METHODS

Spectrum of chromatic sideband peak of beam betatron oscillation (I)

Optical system [3] was applied to measure the beam dimensions $\sigma_{x,y,z}$ and spectrum of vertical betatron oscillations.

Chromaticity of a storage ring causes appearing of synchrotron sideband peaks in a spectrum of beam oscillation. The amplitude of the central betatron frequency and the synchrotron satellites is [4]:

$$R_m(y)=\frac{1}{y^2}\int_0^\infty J_m^2(x)e^{-\frac{x^2}{2y^2}}xdx,$$

$$y=\left(\frac{\omega_\beta\alpha}{\omega_s}+\frac{\omega_0 C_y}{\omega_s}\right)\delta_E\ ,$$

m is the number of harmonic, δ_E is the relative energy spread.

Determination of energy spread is based on the measurement of the ratio of synchrotron satellites to the main peak height.

Current dependence of energy spread (II)

The experiments with method (*I*) were carried out at the small beam current I_0 = 10–50 mkA, when collective effects are negligible. In the course of experiments with mesons mass measurements the beam currents were close to beam-beam effect threshold restriction. This value was from 1.5 to 3.5 мА depending on the beam energy spread. Radial and longitudinal beam dimensions σ_{xz} were taken to determine current dependence of the beam energy spread.

Energy spread of the beam was derived from the measured radial size σ_x and known amplitude functions

β_x=620 cm, η_x= 94 cm at the observation point. It was supposed that the main reason, which caused the growth of size σ_x and energy spread σ_E, was Touschek effect.

The experiments performed at [2] allowed us to obtain a semi-empirical formula to estimate the contribution of Touschek effect into beam energy spread. This formula (3) was used to adjust the energy spread dependence with the beam current:

$$\sigma_x = \left[\beta_x \varepsilon_x + (\eta_x \delta_{ET})^2\right]^{1/2} \quad (3),$$

where $\delta_{ET} \approx \frac{5.1\cdot 10^{-4}}{E[Gev]}\left(\frac{I_0[mA]\cdot \nu_s}{K}\right)^{\frac{1}{6}}$, $K = \sqrt{\frac{\varepsilon_y}{\varepsilon_x}}$ – coupling coefficient, $\varepsilon_y, \varepsilon_x$ – beam emittance,

$\delta_E = \sqrt{\delta_o^2 + \delta_{ET}^2}$, δ_0 - energy spread at $I_0 = 0$.

We must mention that all the data of method (II) were obtained under collider modes very similar to the modes listed in Table 1, but with the KEDR field switched on.

Compton Back Scattering (III)

VEPP-4M collider has a system of Compton Back Scattering for permanent measurement of average beam energy and energy spread [5].

The scattered photons with maximal energy W_{max} form a narrow edge in the spectrum. The value of W_{max} is strictly coupled with the average energy of the beam electrons by a simple equation:

$$W_{\max} \approx 4w_0 \cdot \left(\frac{E}{m_e c^2}\right)^2 .$$

The width of the edge is mostly determined by the resolution of the photons detector and the energy spread in the electron beam. Thus, direct measurement of the energy spectrum of scattered photons allows us to measure both the electron beam average energy and the energy spread.

At the VEPP-4M collider we use the infrared laser with w_0=0.117 eV. In this case, W_{max} is from 4 MeV to 7 MeV for the beam energy in the range from 1.5 GeV to 2 GeV.

The energy spectrum of backscattered photons is measured by High Purity Germanium (HPGe) coaxial detector Canberra GC2518 with the energy resolution around W_{max} about $\delta w/w = 4\cdot 10^{-4}$. The spectrum in Fig. 1 was gathered with the average electron beam current about Ie=1 mA and the electron beam energy ε =1842 MeV at the ZMEJ mode of the VEPP-4M. The resulting value of the measured energy spread is $\delta E = 1.13 \pm 0.04$ MeV.

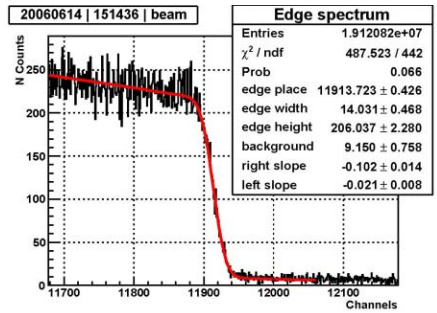

Figure 1: The edge of the energy spectrum of backscattered photons with fitting function.

EXPERIMENT

Method (I)

Beam oscillation was excited by a short kick with amplitude $b \geq \sigma_y$. Spectrum of betatron motion was derived with FFT. Frequency and amplitude of the peaks were defined more exactly with the approach proposed in [6]. Blackman-Harris window was also applied. All the measurements were made during 1024 beam turns following the kick. An example of measured spectrum is presented in Fig.2.

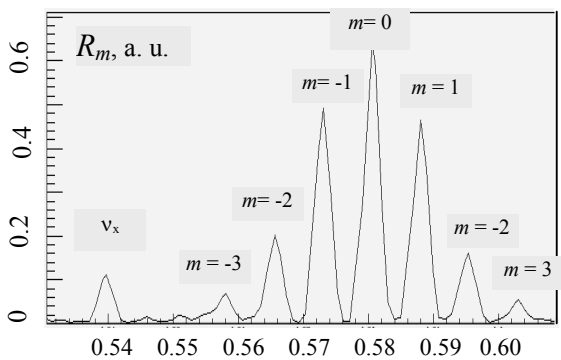

Figure 2: A spectrum of vertical betatron oscillations.

Three sideband satellites are clearly seen. The same measurements were made for various values of vertical chromaticity Cy=5÷20. Chromaticity was changed with sextupole magnets and was measured from the dependence of betatron tune on the rf frequency shift.

The best fit of experimental points corresponds to the energy spread δ_E=3.2·10^{-4} for JPSI mode, δ_E = 4.6·10^{-4} for PSIS mode and δ_E = 6.6·10^{-4} for ZMEJ mode.

Method (II)

Fit of radial size σ_x vs beam current I_0 with (3) is shown in Fig.3. The fit declines from the experimental points at the value of I_0 = 4 мА. Further dependence $\sigma_y(I_0)$ has a threshold behavior and requires additional studying. Declination might be caused by microwave instability with the threshold depending on accelerating voltage V_{rf}. Method (*I*) was applied with reduced value of

$V_{rf} = 150 \div 250$ kV to decrease a synchrotron frequency ν_s, which improves a resolution of the measurements described above. The collider runs in 2004-2006 were performed at $V_{rf} \geq 400$ kV and instability threshold was significantly higher than the currents of the operated beams restricted by the beam-beam effects.

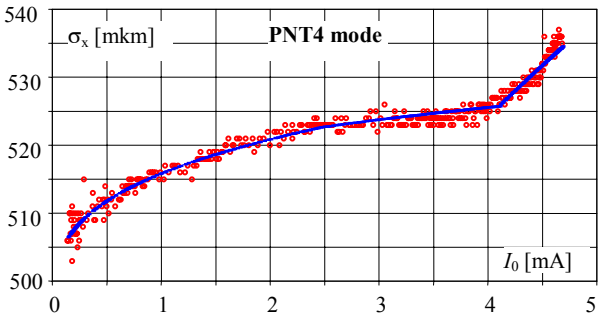

Figure 3: Dependence of beam radial size σ_x on beam current I_0 at PNT4 mode; O - CCD matrix measurement; — - derived with energy spread variation (3).

Measurement of the longitudinal beam size σz enables us to derive the energy spread at $I_0 = 0$. Further beam lengthening $\sigma z \; \alpha \; I_0^{1/3}$ is caused by the ring longitudinal impedance about 6 Om of an inductive type [2].

DISCUSSION

One can note that measurements by method (II) are in a good agreement with data of ψ' resonance scan at E_0=1843±10 MeV performed in 2006 (Tab. 2). This method has the same good agreement for J/ψ meson scan (Tab.2) with reduced wiggler current I_{WG} = 620A.

Table 2: Data of ψ' and J/ψ resonance scanning

	E, MeV	dW, MeV	$\sigma_{E'}$, 10^{-4}	I_{WG} [A]	I_0 [mA]	Year
ψ' width	1843	1.24	4.77	1135	2.0	2004
		1.15	4.42	1055	2.5	2005
		1.09	4.19	1055	2.5	2006
J/ψ width	1548	0.858	3.93	952	1.7	2002
		0.664	3.04	652	1	2002

Methods (*I*) and (*II*) demonstrate a good agreement for PSIS, ZMEJ and JPSI mode of the collider as well.

Fig. 4 represents the collected data of energy spread measurements of the beam for collider modes listed in Table 1. Unfortunately, we did not have enough time for machine study and did not perform the measurements with method (*II*) with the KEDR magnetic field switched off. Nevertheless, the data of all the three methods are in a satisfactory agreement.

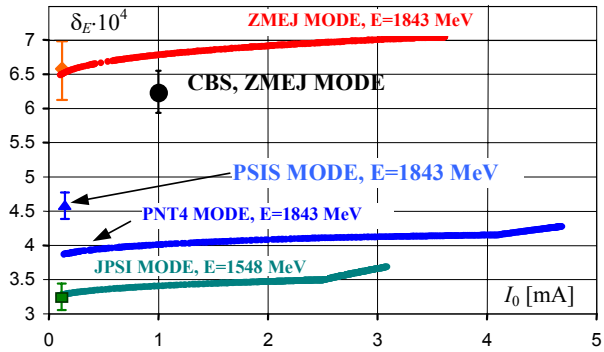

Figure 4: Data comparison of all the methods. Lines – data of (*II*); ■ - data of (*I*) for ZMEJ mode; ▲ - data of (*I*) for PSIS mode; ◆ - data of (*I*) for JPSI mode.

One can see the distinctions of ψ' resonance width obtained with the equal wiggler current (Tab.2). It indicates the necessity of radial orbit stability and the control of dispersion function in the wigglers because the value of energy spread depends on these parameters as well as on the current of the wigglers.

We suppose that variation of beam orbit could be the reason of distinction of energy spread for PSIS and PNT4 modes. It should be mentioned that reduction of δ_E by CBS data took place only during the run in 2006 and requires additional investigation. The data of (*II*) and CBS are in a good agreement with the runs in 2004/ 2005.

In conclusion we should admit that beam energy spread measurement is a nontrivial task and requires the comparison of data of several diagnostics.

SUMMARY

The measurements of the beam energy spread of the VEPP-4M collider have been done. The collider modes correspond to energy area of 1.5 – 1.8 GeV. Several experimental methods have been applied for each mode. The methods data are in a satisfactory agreement. The following experiments of precise measurement of tau-lepton mass should be performed with an accurate control of beam radial position as well as with the control of the dispersion function in the wigglers.

REFERENCES

[1] V. Anachin et.al. Proc. of the 6-th European Particle Accelerator Conference, Stockholm, 22-26 June, 1998, vol.1, p.400-402
[2] V. Kiselev, V. Smaluk. Proc. of the 6-th European Particle Accelerator Conference, Stockholm, 22-26 June, 1998,vol.2, p.1005-1007
[3] O. Meshkov et al. Proc. of EPAC 2004, Lucerne, Switzerland, pp. 2739-2741
[4] T. Nakamura et al. Proc. of the 2001 Particle Accelerator Conference, Chicago, p. 1972-1974.
[5] N. Muchnoi, S. Nikitin, V. Zhilich. Proc. of EPAC 2006, Edinburg, Scotland, TUPCH074
[6] V.V. Smaluk. PhD thesis (in Russian)

CONTROL OF THE MULTI-BUNCH INSTABILITIES AT TLS

C.H. Kuo, K.H. Hu, Demi Lee, Jenny Chen, S.Y. Hsu, K.T. Hsu
National Synchrotron Radiation Research Center, Hsinchu, Taiwan

Abstract

The goals of the recent superconducting RF upgrade and top-up operation at the Taiwan Light Source (TLS) are to increase stored beam current and provide stable beams. Suppressing multi-bunch instabilities caused by the resistive wall of the vacuum chamber and cavity-like structures and suppressing ion-related instability are essential to exploiting these upgrades. FPGA-based transverse bunch-by-bunch and longitudinal feedback systems were adopted. Multi-bunch instabilities were successfully suppressed at stored beam currents of over 400 mA. Chromaticity can be reduced using a transverse feedback system, which is essential to increasing the injection efficiency in the top-up operation mode. The status of the feedback systems and an analysis of the behavior of multi-bunch instability are presented.

INTRODUCTION

The Taiwan Light Source (TLS) at NSRRC is a 1.5 GeV storage ring. Two major upgrades of TLS have been completed - the superconducting RF cavity (SRF) upgrade in the late 2004 and the top-up operation in the late 2005. Both upgrades were intended to increase the stored beam current from 200 mA to over 400 mA, to eliminate strong instability that is caused by the high-order modes (HOM) with conventional RF cavities, and thereby continue to provide a constant heat load for high-quality photon beams. The threshold current of transverse multi-bunch instability is slightly less than 40 mA. The longitudinal instability is also a problem when the stored beam current exceeds 150 mA. The major source of the transverse instability is the resistive wall and the ion effects. The cavity-like structure of the vacuum duct is assumed to contribute in the source of longitudinal instability. These instabilities can be effectively controlled by the transverse feedback system and the longitudinal feedback system. This report will present the status of instability suppression at TLS.

MULTI-BUNCH FEEDBACK SYSTEM

FPGA-based bunch-by-bunch feedback applications are extensively adopted in numerous) laboratories. The SLAC/LNF-INFN/KEK collaboration G-board project [1] and Libera Bunch-by-Bunch projects for ESRF broadband feedback system are typical examples. The feedback processor in TLS was originally developed for the SPring-8 [2, 3]. A highly flexible feedback processor design led to easy adoption for TLS applications. Figure 1 presents the block diagram of a bunch-by-bunch feedback system. The system consists of a beam position monitor (BPM), an analog front-end (analog de-multiplexer for transverse feedback and phase detector for longitudinal feedback), a feedback processor, an SSB or QPSK modulator for a longitudinal feedback system, power amplifiers and kickers. The feedback processor is the key component of the feedback system, and is adapted from the SPring-8 design with minor modifications. The beam signals measured by the BPM are processed by an analog de-multiplexer or a phase detector into baseband signals and fed to the digital feedback processor, and converts the position or phase oscillation signal of each bunch into digital form which is filtered using the FIR filters. The filtered error signal drives the kicker to dampen the bunch motion. The latency of the system should be one or two periods of revolution of the storage ring plus the bunch propagation delay between the BPM and the kicker in the transverse feedback loop.

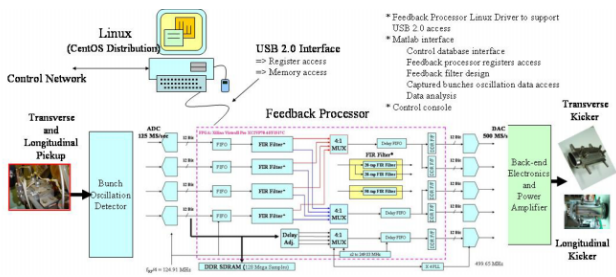

Figure 1: Block diagram of bunch-by-bunch feedback system. The feedback processor is shown in the center of the figure. The FIR filter inside the feedback FPGA consists of two 20-tap FIR filters in the transverse feedback and a 50-tap FIR filter in the longitudinal feedback.

Up to 32 sets of FIR filter coefficients can be stored in the internal register of FPGA and are selectable via a USB 2.0 interface or an external logic input control. The switching speed is about 10 ns in the latter case. This function makes the system very flexible for use in the grow-damp experiments**.** Up to 256 historic mega -samples of ADC are stored in the DDR memory of the feedback processor. Therefore, up to 256 ms of data can be stored in the memory. (One sample is two bytes.) The latency time of the feedback processor is about 300 ns. A favorable frequency response of the FIR filter can be easily achieved using a two-turn delay (800 ns) in the transverse feedback loop. The frequency multiplier supplies a DAC clock at the RF frequency with a cycle-to-cycle jitter of 50ps from the ADC clock. The processor with five DACs - four for the multiplexed FIR filter output and one for multiplexed raw ADC data - is used in diagnostics and tuning. The latency of the multiplexed FIR filter output can be controlled by adjusting the internal delay. Each DAC has

complementary outputs. These functions are very useful in the system tuning. For instance, the delay time and polarity of the individual kicker must be tuned when several kicker electrodes are used for feedback. A compact Flash (CF) card is used as an FPGA store and booting device. The USB2.0 interface is provided to control the processor and transfer captured data by Linux computer with kernel 2.4. The Matlab control software with this device driver was developed in the TLS to provide a convenient and integrated environment of the interface of the feedback processor. These scripts are compatible with the existing accelerator Matlab control interfaces; the environment effectively meets various needs in routine operation and accelerator studies.

The feedback processor has four parallel channels. Each channel has a 12-bit ADC and a FIR filter. The RF frequency f_{RF} is 499.654 MHz and the harmonic number is 200. In the four-ADC mode, the feedback processor and ADCs are operated with a clock frequency of $f_{RF}/4$.

Transverse feedback system

The SRF upgrade reduces the bunch volume by increasing the RF gap voltage. Severe transverse instability cannot be controlled by the compensation of chromaticity in a manner that is convenient in OR conveniently during) routine operation. The resistive wall and ion-related effects may contribute to such instability. The old analog transverse feedback system is very sensitive to the tuning [4]. The new FPGA based two-dimensional transverse feedback system with a single loop scheme, is proposed by Nakamura. This feedback loop comprises one pick-up and one kicker. The 20 taps FIR filter is linearly combined with vertical and horizontal responses. Bunch oscillation signals are multiplexed into four parallel channels in an analog manner. Delay lines align the four consecutive bunches in parallel. The differential output of the DACs drives two power amplifiers.

Longitudinal feedback system

TLS has suffered from severe longitudinal instabilities in during the last decade. The HOM of two conventional RF cavities are the main source of these instabilities. A second tuner has been introduced to adjust the HOM frequency and thus reduce the strength of instability. RF gap voltage modulation was adopted to eliminate the remaining instability at the cost of increased energy spread. Following the SRF upgrade, some residual longitudinal mode remained, possibly because of the impedance of beam ducts or some unknown sources. Extensive studies were performed during the operation of SRF in 2005. However, the aforementioned instabilities were not identified.

Because of limited space, the longitudinal kicker based on the SLS design was modified by fitting a beam tube into the TLS vacuum chamber, eliminating the request for a taper. The kicker was installed to storage ring in January 2006. The preliminary longitudinal feedback system was commissioned in early February 2006 after a long shutdown.

The BPM sum signals are fed into the I-Tech RF front-end detector [3], which is used as a bunch-by-bunch phase detector at three times f_{RF} (1.5 GHz). The baseband output is split into four channels with a suitable delay to align four consecutive bunches signals into four parallel channels at a data rate of 125 MHz. These signals are subsequently fed into feedback processor. The digitized signals are filtered through with 50-tap FIR filters. The corrected output is sent to the SSB modulator. The lower sideband is sent to the beam excitation amplifier and the kicker.

STATUS OF INSTABILITY CONTROL

Figure 2(a) shows betatron sidebands without feedback. These betatron sidebands are completely suppressed when the feedback is on, as shown in Fig. 2(b). A damping time less than 1 ms at an operating current of 300 mA is achieved. Beam blowup is caused by transverse instability when feedback is off can be easily identified using the synchrotron radiation profile monitor, as presented in Fig. 3(a). After the feedback is turned on, the beam becomes stable, as presented in Fig. 3(b).

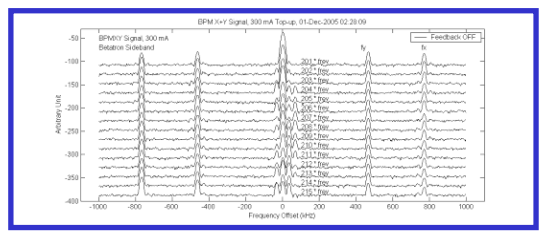

(a) Open feedback loop.

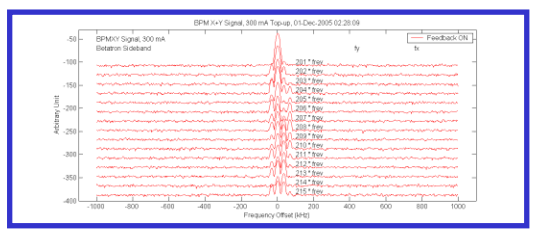

(b) Closed feedback loop.

Figure 2: Transverse spectrum from harmonic of revolution frequency 201 to 215 without longitudinal feedback. Strong synchrotron sidebands are observed near the harmonics of the revolution frequency.

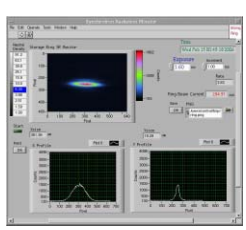

(a) Feedback on.

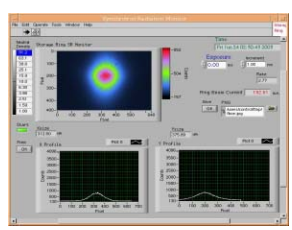

(b) Feedback off.

Figure 3: Measured transverse profiles of the synchrotron radiation monitor.

Figure 4 depicts the beam profile experiment between longitudinal feedback on and off. Since the synchrotron radiation monitor is located in the dispersion region, the energy oscillation contributes significantly to the horizontal beam size. After the feedback loop is turned on, the horizontal beam size is markedly reduced.

Figure 5 displays the image from a streak camera without and with feedback. A large oscillation is observed without feedback in (a). The energy oscillation is almost undetectable with feedback on in (b).

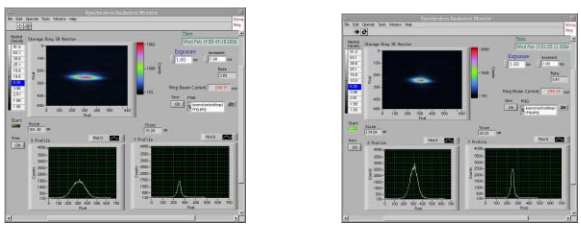

(a) Open Loop. (b) Closed Loop.

Figure 4: Transverse beam profile with and without longitudinal feedback. The source point of the synchrotron radiation is in the dispersion region ($\eta \approx 0.108$ m). The longitudinal feedback loop effectively reduces the horizontal beam size.

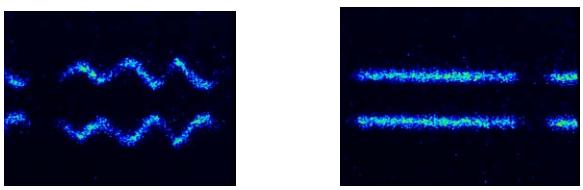

(a) Open loop (b) Closed loop

Figure 5: Snapshot of one-turn streak camera image. The vertical time span is 1.4 ns, and the horizontal time span is 500 ns in this dual scan configuration. The longitudinal feedback loop effectively suppresses the longitudinal motion.

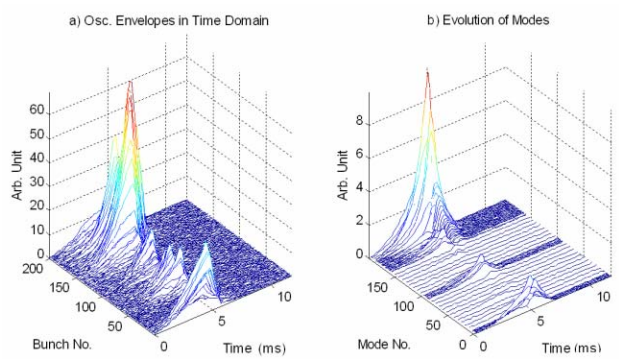

(a) (b)

Figure 6: The evolution of vertical oscillation envelops in transverse grow/damp experiments. (a) Evolution of oscillation envelope of bunches. (b) Evolution of modes.

Figure 6 shows the results of model analysis of the typical vertical grow/damp data measurements, and a corresponding modal analysis. A damping time of less than 1 ms and an operating current of 300 mA were obtained all modes in the vertical plane.

Figure 7 shows the growing/damping evolution of the envelopes and the mode pattern in the longitudinal feedback system. Only two modes dominate.

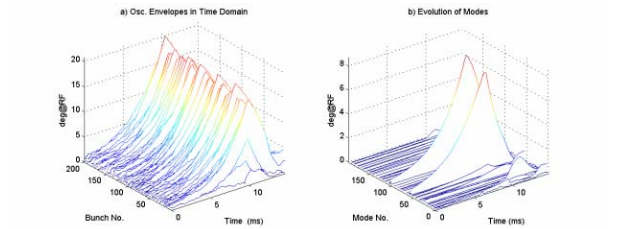

(a) (b)

Figure 7: Typical longitudinal grow/damp results. (a) Evolution of oscillation envelop of bunches. (b) Evolution of modes.

SUMMARY

This report summarizes the preliminary results of the newly commissioned transverse and longitudinal feedback systems. Both feedback loops are now in regular service. The transverse feedback system not only eliminates instability but also increases the injection efficiency because it supports low chromaticity operation, which is essential to the top-up injection. Longitudinal feedback increases the brilliance of the machine. The system performance and reliability of both loops are constantly being improved. The functionality of the feedback system will be improved.

REFERENCES

1. D. Teytelman, “Architectures and Algorithms for Control and Diagnostics of Coupled-Bunch Instabilities in Circular Accelerators”, SLAC-R-633, 2003.
2. T. Nakamura, et al., “Transverse Bunch-by-Bunch Feedback System for the Spring-8 Storage Ring”, Proceedings of EPAC 2004, Lucerne, Switzerland, pp. 2649-2651.
3. T. Nakamura, K. Kobayashi, “FPGA Based Bunch-by-Bunch Feedback Signal Processor”, Proceedings of ICALEPCA 2005, Geneva, Switzerland.
4. K.T. Hsu, et al., “Performance of the Transverse Coupled-Bunch Feedback System in the SRRC”, Proceedings of EPAC 1996, Barcelona, Spain, pp. 1920-1922.

THE DESIGN, FABRICATION AND PERFORMANCE TESTING OF THE ANALOG I/Q RF CONTROL SYSTEM AT NSRRC

M.S. Yeh#, L.H. Chang, F.T. Chung, Y.H. Lin, C.H. Wang, NSRRC, Hsinchu, 30076, Taiwan

Abstract

An analog low-level RF system, based on an I/Q modulator and demodulator, has been tested at NSRRC. The I/Q RF control system has the same function blocks as the digital low-level RF system, which we plan to develop for our proposed 3-GeV light source machine. This analog I/Q RF system provides a real function structure to verify the working principle, block functions and performance evaluation of the developing digital low-level RF system. This work presents the designed function diagrams, the measured results for the characteristics of the main RF components, and the performance testing of the analog I/Q RF control system with a dummy cavity.

INTRODUCTION

The existing low-level RF control system for the superconducting cavity of CESR-B type in NSRRC is based on analog feedback loops. It comprises four independent feedback loops, to control the gap voltage, the cavity phase, the klystron phase and the cavity frequency (tuner). These control loops ensure the required conditions of stability for operation of the superconducting cavity. Figure 1 shows a simplified block diagram of the analog low-level RF control system.

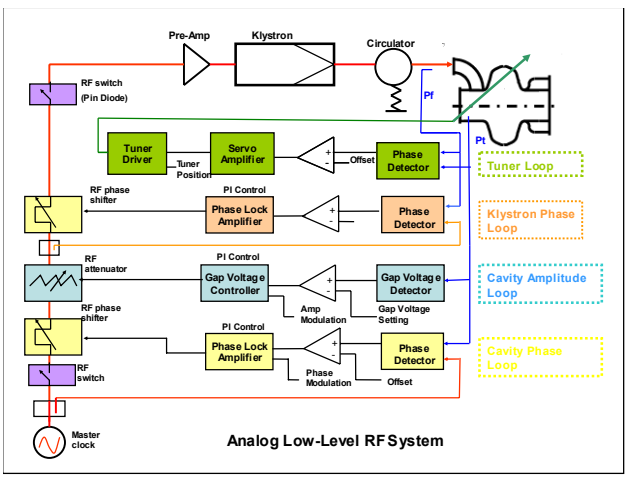

Figure 1: Functional block diagram of the analog low-level RF control system.

The fluctuations of amplitude and phase are controllable within ±1 % and ±2° respectively in routine operation with the current analog low-level RF system.

The present RF feedback control system is based on analog feedback loops for amplitude and phase. The I/Q (in-phase, quadrature) demodulation and modulator techniques are currently favoured in modern accelerating structures. A translation of the amplitude and phase information into IQ is advantageous because of the symmetry of the IQ signal paths. This analog I/Q RF system also provides a real function structure to verify the working principle, block functions and the performance evaluation for the developing digital low-level RF system. A new, FPGA-based, digital, low-level RF system is proposed for development of the new Taiwan Photon Source [1]. The analog I/Q and digital FPGA LLRF systems are conceptually similar, both being based on the IQ method and PID regulation.

This paper presents the designed function diagrams, measured results for the characteristics of the main RF vector components and the integration test of the analog I/Q RF control system

ANALOG I/Q CONTROL SYSTEM

The analog I/Q feedback control circuits are based on NIM modules and use in-phase (I) and quadrature (Q) signal components, commonly called an I/Q detection system [2-4]. Figure 2 shows a schematic of the analog I/Q RF control system.

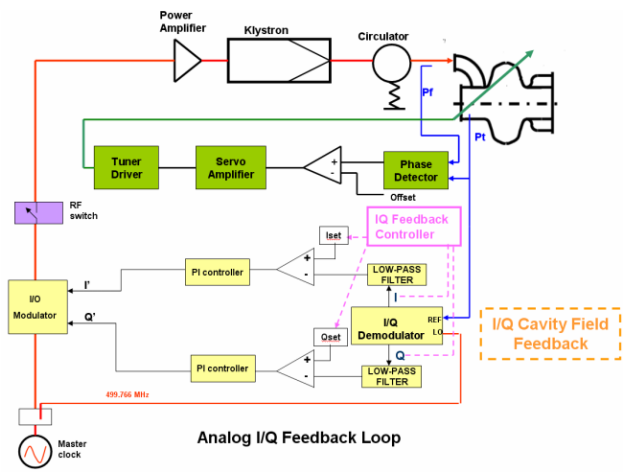

Figure 2: Function blocks of an analog I/Q control system.

The cavity field is directly down-converted to base-band signals, for which a vector demodulator performs I/Q detection. The resulting I/Q base-band signals that describe the cavity field are fed to a pair of Proportional & Integral (PI) controllers, one for the I signal and another for the Q signal. The set points for the I/Q channels are also fed to the PI controllers in which the cavity-field error signals are generated and processed. The outputs from the I/Q PI controllers are fed to an RF vector modulator, which modifies the I and Q components of the carrier frequency from the master reference clock

#msyeh@nsrrc.org.tw

to produce the specified RF for the klystron based on I/Q vector inputs from the analog I/Q feedback.

I/Q demodulator module

The AD8348 is a broad-band quadrature demodulator with an integrated intermediate frequency (IF), variable-gain, amplifier (VGA), and integrated base-band amplifiers [5]. It is responsible for converting the RF signal down to base-band differential I and Q components. To generate signal in-phase and quadrature data, the AD8348 requires an external LO signal of frequency twice the desired carrier frequency.

The I/Q demodulator module integrates the AD8348, manual phase shifter, manual attenuator and signal-adjustment circuit. Figure 3a shows a block diagram of the I/Q demodulator module. The 360-degree manual phase shifter is used to zero the initial loop phase for operation of the I/Q feedback control.

In Figure 3b, the performance measurement of the I/Q demodulator that covers 0 to 360 deg as shown with varied amplitude. The display mode of the oscilloscope is an XY mode.

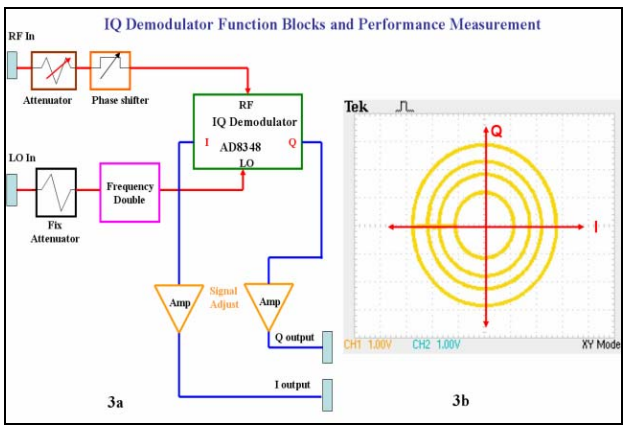

Figure 3: IQ demodulator function diagrams and performance measurement.

PI Controller module

The PI Controller module comprises an integrator with a proportional gain. The controller design consists of a front-end differential amplifier, followed by an integrator. The differential amplifier (or "error amplifier") amplifies the differences of the two single-ended inputs, the set point and measure, and multiplies the result by the proportional gain. An electronic switch is finally provided that opens the loop and switches a preset voltage at the I/Q modulator input; this mode of operation, called a "Tune Mode", allows a few kilowatts of RF into the cavity and is set by screw adjustment at the front panel of the module.

The frequency response of the PI controller was measured and the unit-gain point should be near 7 kHz.

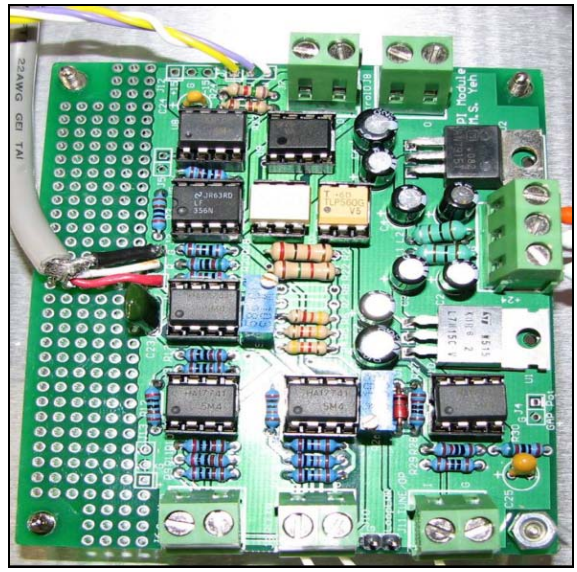

Figure 4: Circuit board of the PI controller.

I/Q modulator module

The vector modulator module modifies the I&Q components to produce the desired RF drive signal for the klystron according to the PI controller signal.

The AD8345 is used to perform I/Q up-conversion [5]. The component provides excellent specifications of amplitude and phase balance and sideband suppression.

I/Q Feedback-control module

The I/Q feedback-control module is the central controller of the feedback system, providing the following controls.

1. Two potentiometers adjust the operational set levels of I and Q for the cavity accelerating voltage; two panel meters display separately the I set and Q set values.
2. In the tune mode, the Tune/Operation mode manual switch turns the drive power on at a decreased level at which the cavity frequency-tuning loop can tune the cavity frequency to a resonant frequency. In the operation mode, the cavity-accelerating voltage becomes controlled by the set values of I and Q.

INTEGRATION TESTING

After development and construction of hardware for the analog I/Q control system, the integration bench testing of the I/Q control system is currently in progress. Figure 5 shows the configuration of system integration testing in operation with the NIM I/Q control module, rf signal source and oscilloscope.

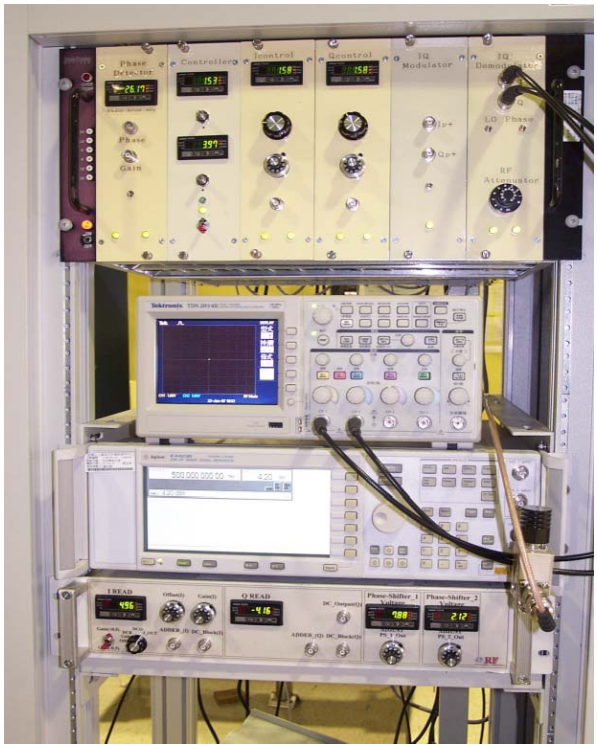

Figure 5: Photograph of analog I/Q control system.

To test the closed-loop response of the I/Q components to the set value, the I/Q components are recorded on the horizontal/vertical axes of the oscilloscope in persistence mode, shown in figure 6, as we vary the I component set value at a fixed Q set value, and vary the Q set value at a fixed I set value. Figure 6 shows that the RF I/Q components of the cavity field can be satisfactorily controlled independently.

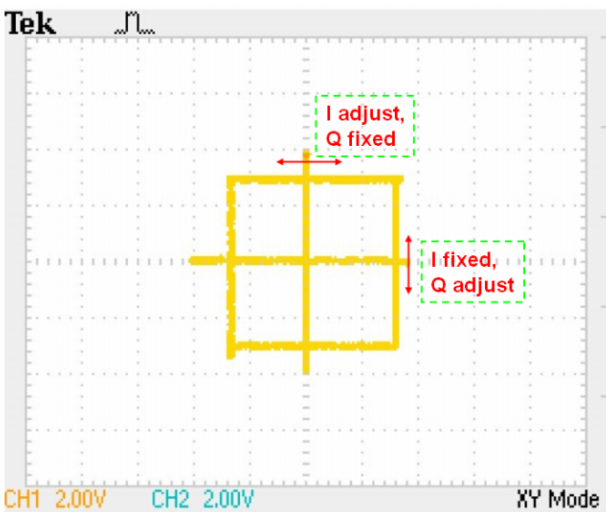

Figure 6: Measurement of I and Q components of the dummy cavity field in closed-loop bench testing.

CONCLUSIONS

Integration testing of the overall I/Q feedback system with a dummy cavity has been demonstrated to be successful. We expect to test the analog I/Q control system with the conventional Doris cavity in our booster. A campaign of tests will follow to assess finally the performances.

REFERENCES

[1] M. S. Yeh et al., ”Low-level RF System Development for the Superconducting RF cavity in NSRRC” in Proceedings of the 2006 European Particle Accelerator Conference, p. 1477.

[2] H. Hassanzadegan et al., “Analogue and Digital Low-level RF for the ALBA Synchrotron” in Proceedings of the 2006 European Particle Accelerator Conference, p. 1468.

[3] C. Ziomek et al., “Digital I/Q Demodulator” in Proceedings of the 1995 Particle Accelerator Conference.

[4] S. N. Simrock et al., ”State of the Art in RF Control” in Proceedings of Linac 2004, Lubeck, Germany.

[5] Analog Device Inc., homepage: http://www.analog.com.

CONTROL SYSTEM BASED ON PCS AND PLCS FOR THE L-BAND LINAC AT OSAKA UNIVERSITY

Ryukou Kato, Shigeru Kashiwagi, Tamotsu Yamamoto, Shoji Suemine, Goro Isoyama
ISIR, Osaka University, 8-1 Mihogaoka, Ibaraki, Osaka 567-0047, Japan

Abstract

A control system comprising of only personal computers and programmable logic controllers has been developed for the L-band electron linac at the Institute of Scientific and Industrial Research, Osaka University. The system has a simple structure consisting of a few PCs connected with Ethernet and PLCs with FL-net.

INTRODUCTION

The L-band electron linac at the Radiation Laboratory of the Nanoscience and Nanotechnology Center attached to the Institute of Scientific and Industrial Research (ISIR), Osaka University, was constructed in 1975-1978 [1] and has been used for radiation chemistry studies by pulse radiolysis technique. Recently, the linac has been extensively used for studies pertaining to nanotechnology, beam science as well as for basic studies in their related fields. In the advanced studies with the linac [2,3], stability of the electron beam and reproducibility of the linac operation are extremely important. The linac has been upgraded for higher stability and reproducibility of operation for advanced studies in beam science. A computer control system has been newly introduced for the linac not only to realize precise reproducibility of operation but also to make routine operation possible by even an unskilled operator.

In this paper, we present details of the control system and operational experiences.

HARDWARE IMPLEMENTATION

Configuration

The new control system is based on personal computers (PCs) and programmable logic controllers (PLCs). The PCs are used for operator consoles as human machine interfaces (HMIs), while the PLCs control various devices directly. The PLCs and their wiring terminals are installed in device control stations (DCSs). The DCS is the basic unit of the control hardware and all the devices of the linac except for those connected with GPIB are wired to the DCSs. The DCSs are placed at various places to form a distributed control system; three DCSs are in the control room and four in the linac room. In addition to these DCSs, the klystron modulator and the three SHB amplifiers, have their own PLCs for internal control. Network boards are added to each PLC, so that they can directly link to the control network. The schematic layout of the L-band linac and the present configuration of the control system are shown in Figures 1 and 2 respectively.

Networks

The PCs and the PLCs are connected to the networks using two different communication protocols. For the network connecting the PLCs, we have chosen FL-net, which is an open PLC network for factory automation. Protocol of FL-net is a vendor-independent open standard, and it works on compatible devices with Ethernet standard. Each PLC can share data through a common

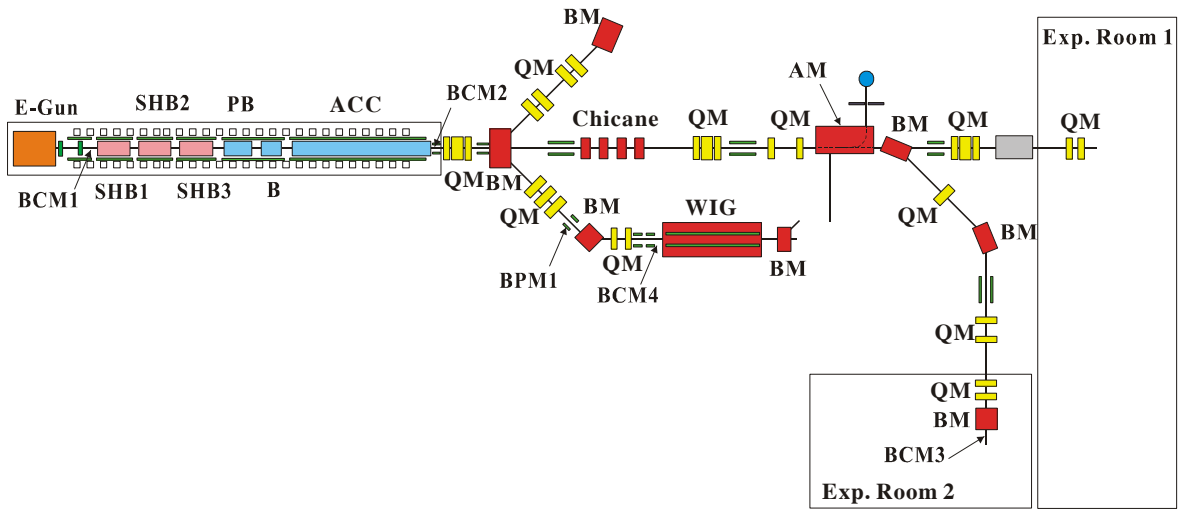

Figure 1: Schematic layout of the L-band linac. E-GUN: Electron gun, SHB1: 108MHz SHB cavity #1, SHB2: 108MHz SHB cavity #2, SHB3: 216MHz SHB cavity, PB: Prebuncher, B: Buncher, ACC: 1.3 GHz accelerating tube, BM: Bending magnet, QM: Q-magnet, AM: Analyser magnet, WIG: Wiggler, BCM1-4: beam current monitors, BPM1: beam position monitor.

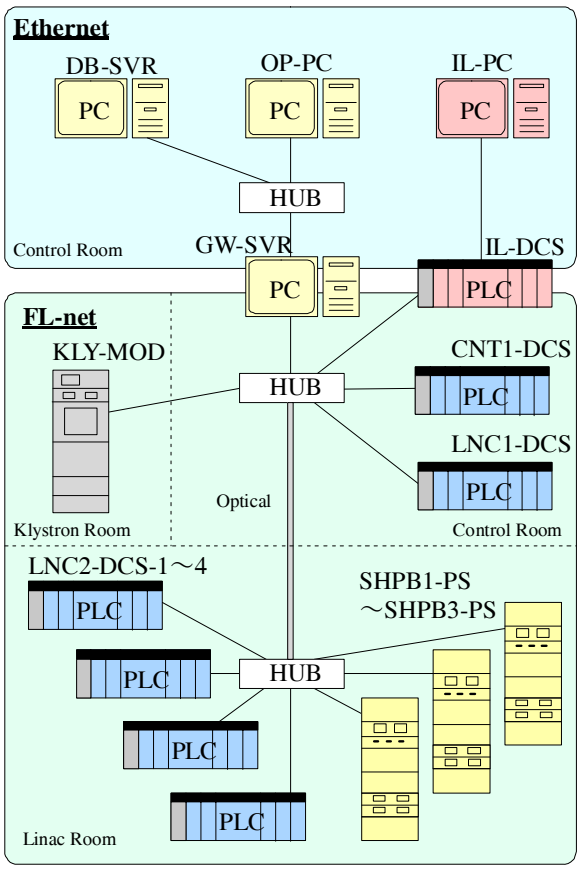

Figure 2: Schematic configuration of the hardware of the control system.

memory (also called link register) in the FL-net module. Data in the link register is sent at certain intervals (typically 10 ms/node) with cyclic transfer. On the other hand, the PCs communicate with each other by Ethernet. In order to transfer control information between these two networks with different protocols, one of the PCs is equipped with both FL-net and Ethernet and works as a gateway server. The PC converts data in the common memory in FL-net to the formats accessible to the other PCs and vice versa.

PLCs and Modules

A Programmable Logic Controller (PLC) is a device that was invented to replace the necessary sequential relay circuits for machine control. PLCs are widely used for factory automation (FA) such as control of machinery on assembly lines. They are recently also being used for control systems of accelerators, because they are more reliable and less expensive as compared to CAMAC, VME, VXI, etc. Since the PLCs are widely used in FA, stable supply of modules and spares over a long period of time can be expected.

Since PLC used in DCS is a key part of the control system, it is the important to select the model which has the maximum capability to be upgrade in future. Considerating the scale of the linac, the number of the control points, the processing speed, the extendability, easiness of the programming and so on, we selected the FA-M3 series maufactured by Yokogawa Electric.

Since the seven DCSs performed different roles, the number of desired modules and the requirement of the CPU abilities are not the same. However, taking maintenance and spare parts into account, we decided to use the same base module, power module, and the same CPU module in these DCSs. The list of the modules which were used is shown in table 1.

Devices and Interfaces

The most difficult part of the upgradation to the computer control system was that the old power supplies and devices had no computer interfaces. New and modified devices, such as the klystron modulator and the DC power supplies, were equipped with computer interfaces. Some of the old components without computer interfaces are still being used, and they would be upgraded in due corse.

The devices are connected to the PLCs with analog I/O, digital I/O, RS-232C, and RS-485 interface modules.The RS-485 serial interface is used for the computer interface of the power supplies. Since the Ladder language has no flexibility to control the serial devices, the BASIC CPU modules and language are used. Since up to 32 devices can be controlled with an RS-485 multipoint serial connection, much wiring is not necessary to introduce a digital control system with PCs and PLCs. The 58 new power supplies are installed in 6 racks and each rack is connected with a single line to an RS-485 controller in a PLC.

Table 1: Used modules

No	Module Name	Model	Qty
1	Base	F3BU13-0N/D2	7
2	Power Supply	F3PU30-0N	7
3	Sequence CPU	F3SP53-4S	7
4	BASIC CPU	F3BP20-0N	3
5	FL-net I/F	F3LX01-0N	7
6	Ethernet I/F	F3LE11-0T	1
7	DI	F3XD64-3F	5
8	DI	F3DX32-5F	3
9	DO	F3YD64-1F	3
10	AI	F3AD08-1N	7
11	AO	F3DA04-1N	3
12	Positioning	F3NC11-0N	14
13	RS232C	F3RS22-0N	4
14	RS422/485	F3RS41-0N	12

SOFTWARE

Hierarchical Structure and Data Flow

Figure 3 shows schematic diagram of the data flow in the hierarchical structure of the control system. DCSs capture the status or the response of the devices through the digital I/O, the analog I/O. As for the serial communication device, the program on the BASIC module does the sequence. The Ladder sequence of DCS transfers the data in the I/O register to the common memory in the FL-net module. Between the FL-net modules, communication is cyclic according to the given node number. The data on the common memory is updated at constant time intervals. GW-SVR updates the data on the shared memory based on the data which was written in the common memory by the FL-net communication and the data which was collected through GP-IB. OP-PC reads the latest data of the devices by accessing the shared memory and displays it on the operation screen. The operation which the user executed on the OP-PC is reflected in the devices by opposite flow.

Human Machine Interfaces

A virtual console panel on an operator PC is composed of : 1) the main control panel which was equipped with file menu and panel menu becomes the base operational panel, and does typical operation sequences such as the start-up, the shut-down, HV ON/OFF of the linac, etc, 2) the integrated operation panel which carries out individual operation sequences such as the LV ON/OFF, HV ON/OFF of the gun, the SHPB amplifiers and the klystron modulator, etc, 3) individual device panels to control each equipment connected to the PLC, 4) the trend monitor which graphically displays time-series analog values of the vacuum degree, the beam current, etc.

The linac can be started up or shut down by a few mouse clicks on the main control panel on the computer screen.

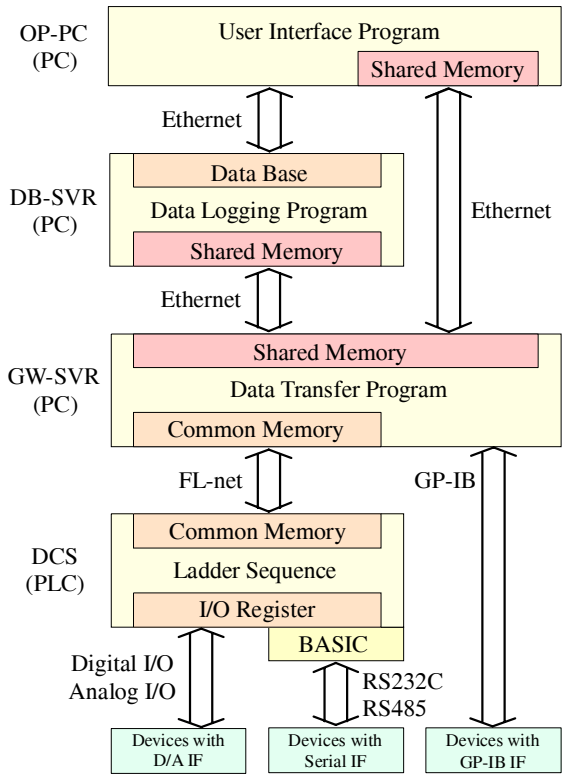

Figure 3: Schematic diagram of the data flow in the hierarchical structure of the control system.

SUMMARY

We developed the distributed control system for the L-band electron linac using the networked PCs and PLCs. The PLCs are used as the device controller and FL-net was selected as the network connecting the PLCs. Since RS-485 serial interface is used for the computer interface of the power supplies, much wiring is not necessary. A graphical user interface on the PC screen is employed as the operator interaction. Distributed computer control system, which has precise reproducibility of operation and user-friendly operation for an unskilled operator, has been realized.

REFERENCES

[1] S. Takeda, K. Tsumori, N. Kimura, T. Yamamoto, T. Hori, T. Sawai, J. Ohkuma, S. Takamuku, T. Okada, K. Hayashi and M. Kawanishi, IEEE Trans. Nucl. Sci. NS-32 (1985) 3219.

[2] T. Kozawa, Y. Mizutani, K. Yokoyama, S. Okuda, Y. Yoshida, S. Tagawa, Nucl. Instr. and Meth. in Phys. Res. A 429 (1999) 471.

[3] R. Kato, R. A. V. Kumar, M. Kuwahara, M. Fujimoto, Y. Nakamura, T. Igo, T. Konishi, S. Isaka, S. Mitani, S. Okuda, S. Suemine, G. Isoyama, Nucl. Instr. and Meth. in Phys. Res. A483 (2002) 46.

IMPROVEMENT OF WEB-BASED MONITORING OF EPICS-IOC FOR PAL CONTROL SYSTEM*

J. M. Kim#, K. M. Ha, E. H. Lee, J. H. Kim and H. S. Kang,
PAL, POSTECH, Pohang, Kyeongbuk, 790-784, Korea

Abstract

We are now operating a web-based monitoring system of PAL control system with MAC Power PC. In order to expand the IOC's web-based monitoring system, we are trying to use the X86/Linux platform. With the experience which we got in developing the web-based monitoring of EPICS-IOC based on MAC Power PC, a web-based monitoring system with an X86 Intel PC based on a new concept has been developed for lower costs, easier access and use. Its operating system employs Linux Fedora Core4. In order to drive the web-based monitoring system, EPICS Base 3.14.8 and MySQL 4.0 have been installed in the Linux Fedora Core 4. Archive engine with C language and EPICS channel access library are programmed to store the data. As a result of using the web-based monitoring system based on the X86 Intel PC, we have achieved its easier access and use, more convenient maintenance. Performance of the web-based monitoring system with an X86 Intel PC will be discussed.

INTRODUCTION

These days, web-based monitoring systems are on gradual increase. Required for the application of such systems are rapid application of newly added sub-systems and feasibility of maintenance. Currently, PAL EPICS IOC web-based monitoring system use MAC power PC G4 CPU based Linux Fedora Core 4 installed in it. By the time it was first developed in 2002, porting Linux OS in Mac system was not easy, because installation of Linux OS in Mac PC requires modification and complementation of the kernel to suit G4 CPU. Usually, Linux OS is distributed for free, and the OS kernel is seldom modified to fit any particular platform for installation. The OS kernel modification requires so specialized expertise that establishment of one system costs a great deal of time, efforts, and money. For such reason, the EPICS IOC Web Server to be newly developed adopted Intel/X86 CPU, which is easily accessible and facilitates comparatively easy system build-up.

The development experienced in MAC power PC was of great help in designing and developing new systems. The strong point of Intel/X86 PC compared to the current system is the simplicity of configuring and its low cost for the system establishment. For the operating system, Linux Fedora Core 4 was installed to maintain the compatibility with the current system. Archive Engine functioned to read data from EPICS IOC and store them in database. IOC web sub-systems developed in the new hardware platform are Beam Current, LINAC BCM, Temperature, and Modulator.

*Work supported by …
#jmkim@postech.ac.kr

SYSTEM ARCHITECTURE

Figure 1 shows the architecture of PAL EPICS IOC web monitoring system. EPICS IOC(Input Output Controller) consists of 19 components, and IOC Web Server is composed of three units of MAC and one unit of Intel/X86 System. The network interface is separated into two layers, Office-net and Control-net. Since SR BPM and MPS system are located in Control network, the data communication needs to be done via separate gateway. Each of the IOC Web Server system basically stores beam current data, and they are displayed as reference when the user requests a data plot from monitor screen. Each of IOC data are classified and stored through four units of IOC Web Servers. The systems which provide web service directly to users are accessed only by way of beam current web server.

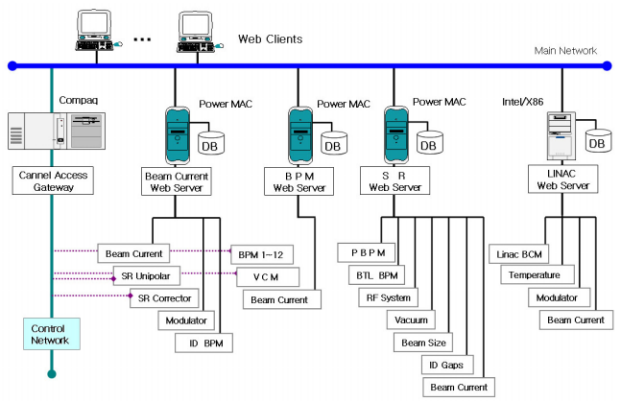

Figure 1: Architecture of IOC web monitoring system.

NEW HARDWARE SPECIFICATION

- CPU : Intel Pentium4 3.4GHz, Single.
- Memory : 2GB DDR PC400.
- Hard Disk : SATA 250GB x 2 Ea, 16MB Buffer.
- Chipset : Intel 865 + ICH5.
- Network Interface : 100Mbps.

INSTALL OF DEVELOPMENT TOOLS

In order to establish web based monitoring server, several software development tools have to be installed in advance. The tools installed are apache server for web service, EPICS 3.14.8 for channel accessing, MySQL Database for data storing, PHP Interpreter for web CGI programming, and gnuplot for tcl/tk and data plot. In

particular, cautions are needed when installing MySQL 4.0. InnoDB(Index) is installed as default from MySQL version 4.0, and this option needs to be taken out at Configure File while installing MySQL, since InnoDB requires a great deal of storage space. As PAL IOC PVs store data every three seconds or every ten seconds, disk storage space has to be spared as long as possible. And the reason why version 4.0 was chosen for MySQL is to keep the compatibility with the existing Mac system.

SOFTWARE STUCTURE

Figure 2 shows in a block diagram how data are processed in Web Server. As in the diagram, the PV data coming from all the IOCs are collected and first stored in MySQL database. Collecting the data from each IOC and storing them are operated by archive engine, which is created in C language by using EPICS channel access library. Archive engine collects raw data from IOC and periodically writes them in the applicable table of MySQL database every three seconds or ten seconds. In order to provide diverse data inquiry service to users, it is implemented using MySQL query instructions through PHP programming. Graphical display of data in the web client monitor is implemented with Gnuplot tool library.

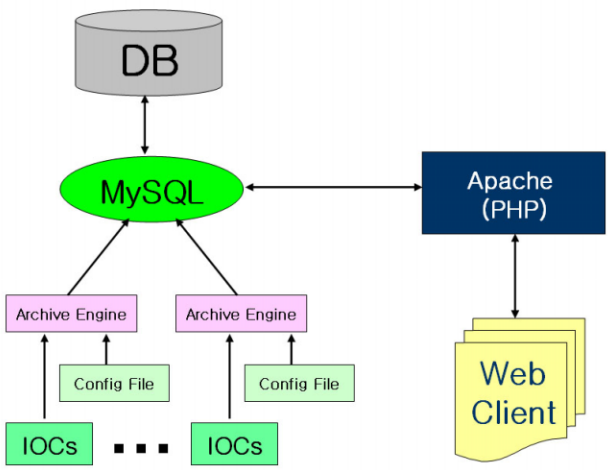

Figure 2 : Block diagram of Software Structure.

DATABASE DESIGNING

The purpose of PAL IOC web monitoring system database designing is to provide the service of rapid data inquiry in web client. To that end, one table is assigned to each PV of each IOC. That is done because web client can search out the temporary PV data stored in the database within 3 ~ 10 seconds through the assigned table. However, since such design involves too many simultaneously open tables, it has a shortcoming that too much computer memory resources are allocated. The reason the system is designed that way in spite of such weak points is for rapid data inquiry. This design lets the users temporarily store the current device value for all the IOC PV in a separate table(zPV), and display them real-time. And while the average values are calculated and stored every 30 minutes, they are named by attaching 'A' in front of the applicable PV table names. The inquiry times were greatly reduced by calculating and storing the values in separate tables when storing the average values. Figure 3 shows the PAL IOC Web Monitoring System homepage.

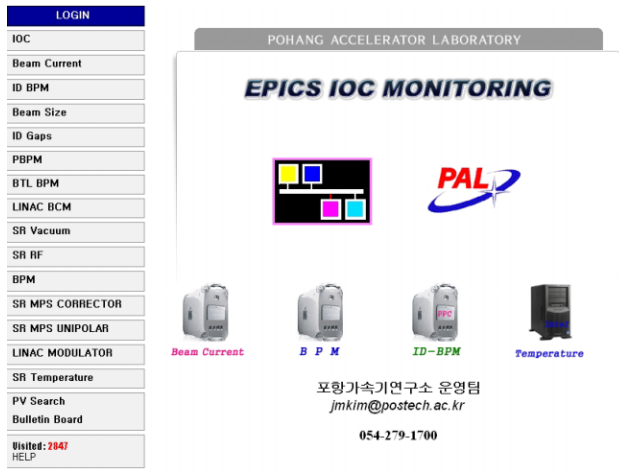

Figure 3 : PAL IOC Web Server Homepage.

STRUCTURE OF ARCHIVE ENGINE

Main Function
MAIN:main()
Engine:Begin()
A. create Archive for MySQL
B. ca_task_initialize()
C. ca_create_channel(pvArray,myChid)
D. Infinite loop (while)
a. ca_element_count(myChid)
b. pTD=malloc (nBytes)
c. ca_get(DOUBLE,myChid,pTD)
d. ca_pend_io(5.0)
e. call WriteFunction()
f. epicsThreadSleep(WaitTime)
E. Infinite loop (end)
MAIN:end()

WriteFunction:run()
a. CreateTableName()
b. ChannelInfo(archive, channel)
c. ArchiveMySQL(InsertPvValue)
d. VerifyMySQL(Name)
WriteFunction:return()

GRAPHICAL DATA PLOTTING

For visual display of the data to the users, a Gnuplot tool is utilized. Graphically expressing beam operation data in client computer screen required establishment in connection with PHP and Gnuplot. That is, PHP reads the data stored in MySQL and Gnuplot expresses the data in a more graphical way easier to understand. The interface between web program and Gnuplot displays the data in the client computer screen in HTML after temporarily storing them as PNG-type file. While inquiring data, diverse data search options are provided, such that several

PV data are inquired, one PV may be inquired during any arbitrary time or period, or Min value or Max value for the Y axis of the displayed values may be configured and displayed. It takes approximately 30 seconds to inquire the data for one month about one particular PV. Figure 4 is the screen to select data and Figure 5 is the picture of the plot for the actual data.

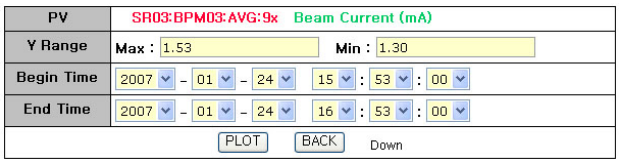

Figure 4 : Popup window for data select.

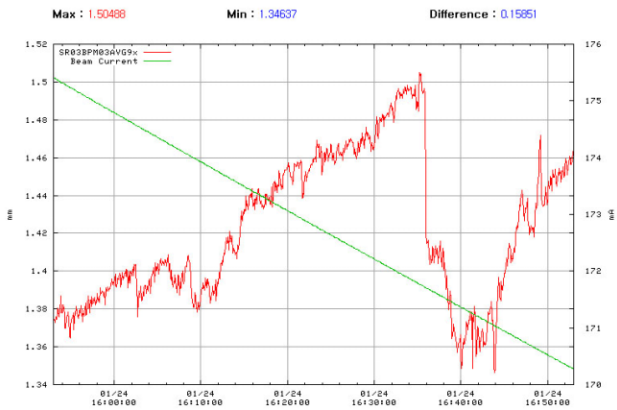

Figure 5 : Data Graph for One PV.

TEST RESULTS

Table 1 is the Bench Mark test results of the previous system and the new system. As for the test method, measurements were performed by using hdparm and time, the linux commands.

Table 1 : Performance comparison with the Existing System.

Items	New System	Exist System
CPU	3.4GHz Single	1Ghz Dual
Disk Access Times	60.47MB/sec	53.78MB/sec
Chche Buffer Reads	1995.3MB/sec	609.5MB/sec
DB Search Times (Data for one month)	3.109 Sec	6.446 Sec

CONCLUSION

In order to improve the performance of PAL EPICS IOC Web Monitoring System, Intel/X86 PC System was selected, and Linux Fedora Core 4 was successfully installed in Intel platform. Web-based IOC monitoring system should be interactively developed using various software tools, however though there are certain limitation in organizing diverse functions, IOC Web Monitoring System was successfully completed of its development. As for hard disk access time, SATA HDD demonstrated excellent performance not as good as SCSI though, and also regarding database access time, it has shown the processing speed nearly two times compared to the existing system. As for the future upgrade plan, we are considering to diversify the perspective on web monitoring system and develop systems using archive viewers provided in EPICS site that effectively reflects the characteristics of the acceleration devices.

REFERENCES

[1] http://epics.aps.anl.gov/epics.
[2] http://www.redhat.com/fedora.
[3] http://www.mysql.com/.
[4] K.M. Ha, “Development for PAL EPICS IOC Monitoring System”, PAL Report, 2003.

MONITOR AND ARCHIVE SYSTEM OF INSTRUMENTATION*

Z. D. Tsai#, J. C. Chang, T. S. Ueng, Y. H. Liu and J. R. Chen

Abstract

In the accelerator field, the instrumentation includes the vacuum, magnet, RF, utility, cryogenic, power, safety, optic device and so on. The highly complicate systems have many hybrid SCADA systems to ensure precise and optimum control. For the historical data integration and analysis of those signals, the monitor and archive system is introduced to provide a distributed multi-channel acquisition platform. The system possesses various connectivity of open database, communication protocols and commercial hardware. The signal data can be collected and delivered to the central storage area network (SAN) via fiber network without latency. Finally, the unique, friendly and fast trend logger and data analysis software is also developed to view, compare, and analyze relation between facility anytime and anywhere.

INTRODUCTION

Because most of accelerator control systems are highly hybrid systems with many VME based controllers and off-the-shelf industrial controllers, the integration of SCADA (supervisory control and data acquisition) system [1] is rather complicated. For fully handling the accelerator status, the data storage must be well processed [2-3]. In TLS, we has also investigated the related mechanism and developed a set of history program to access status of signals [4-5]. Furthermore, the users always want a unique, friendly and flexible interface to monitor, compare and analysis all available signals. This article presents a full architecture of our archive system from hardware to software. On the client side, an intuitive archive viewer program has provided related functions. On the server side, more and more channel accesses and industrial protocols are adapted to the archive system.

NETWORK ARCHITECTURE AND DATA STORAGE MECHANISM

For data transparency, the system has a hybrid network infrastructure as shown in Fig. 1. The network is divided into 5 layers, including a remote viewer level, data service level, data processing level, controller level and device level.

Both controller and device levels are hardware layers. The controller with algorithms takes over machine control. Besides, the distributed controllers often have a dedicated network protocol to communicate each other or delivery related data to the upper layer's central computer.

The central computer located on data processing level is responsible for data collecting, monitoring, alert and control. Generally, the user requires user friendly graphic interface to process the related parameters and control

algorithms. In the industrial SCADA systems, they always provide a set of corresponding software for their controllers and devices. A program to access the system signals via DDE (Dynamic Data Exchange), OPC(OLE Process Control) etc. must be developed. In the VME controller system or a simple data acquisition station, the process layer also needs a program to collect data via firmware. Each subsystem's central computer embedded with this channel access and time synchronous program is called an archive server. When the recorded data of the archive server excesses five minutes, the archive server will duplicate the same files into the data center sever located on the data service layer. This mechanism gives chances for data center server maintenance or avoids data loss in case of network failure. Moreover, the archive server also provides an alert with alarm and SMS (short message service) function.

The data center server located on the data service layer provides a common network service, FTP. Any client software can access the collected data from data center servers anytime and anywhere. The data center server always uses the server class computer to provide reliable service. Each component has the redundant part, such as cups, fans, powers, networks, array disks etc. These can guarantee the data center server with high reliability and robustness. Especially, the storage adopted fiber channel's array disks provides fast, reliable, extensible storage without latency. For avoiding the archive server shutdown, the data center server also takes charge of the alive monitoring of archive servers. While the archive server failure occurs, the data center server will give an alert via Email and GSM modem. This mechanism ensures the continue functioning of all archive servers. For internet security, all data center servers and archive servers are protected under firewall. A mirror server responsible for bridging and duplicating the data is also developed for outside user access.

On the top of remote viewer level, a set of archive viewer software has been used to grab data from data center server via FTP. The viewer program provides rich functions for monitoring, compare, analysis with a unique, friendly, flexible and intuitive interface. The signal data flow from IO devices to users is shown as Fig. 2.

*National Synchrotron Radiation Research Center, Hsinchu 30076, Taiwan, R.O.C.
*Department of Nuclear Science, National Tsing-Hua University, Hsinchu 300, Taiwan
ZDTsai@nsrrc.org.tw

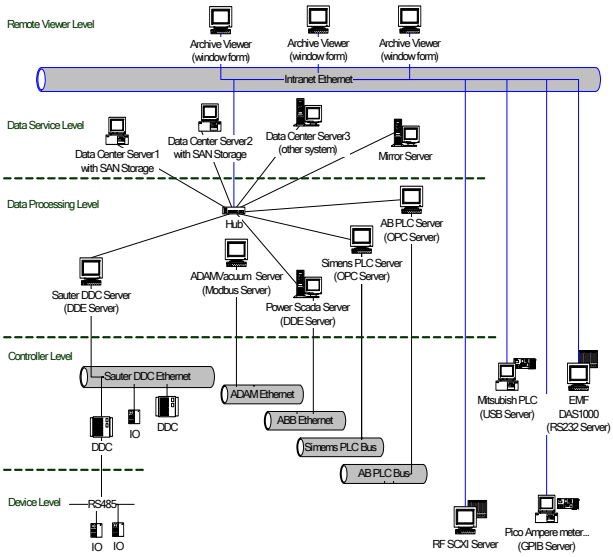

Figure 1 The network architecture of archive system

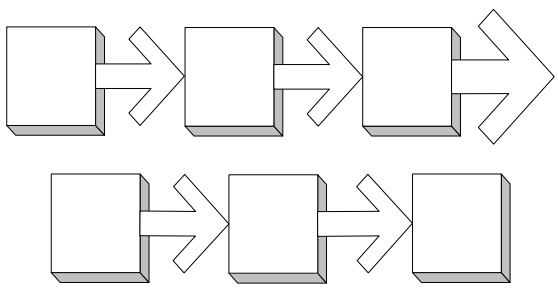

Figure 2 The data flow from hardware IO to users

DATA CONNECTIVITY OF SERVER

Owing to the hybrid network architecture, various controllers, devices or SCADA subsystems must be integrated in the archive system. However, each of hybrid systems always has its own protocol or driver to transmit data. The data collection faces a tough connectivity problem. So, the efforts devoted to the data connectivity on the archive server are significant. The hierarchy of channel access program for archive server connectivity is shown in Fig. 3.

The communication of the hardware involves Ethernet, RS485/RS232, 1394, GPIB, or specific DAQ card. The universal hardware vendors always provide various types of firmware or drivers to acquire the analog input/output or digital input/output data, such as DLL or ActiveX library. This method has more flexible and self-defined data acquisition and gives a fast sampling rate.

However, for well dedicated control and interlock, the subsystem often adopts a commercial SCADA system. The SCADA system is responsible for data collection, monitoring and alert. Most of them have their own closed loop hierarchy network for guarantee data streaming, such as DDC (direct digital controller), PLC (programmable logic controller), DCS (distributed control system) or RTU (remote terminal unit). The systems usually provide a DDE method to link the partial internal data for the third party software. Furthermore, the advance SCADA system provides a network communication method, such as OPC, Modbus, BACNet protocol or SQL (structure query language) database.

Currently, the archive server has successfully been developed with the ability of multi-channel access, via DDE, OPC, Modbus, BACNet, ODBC, DLL, ActiveX protocols etc. The archive server has unique interface to acquire data without extra procedure. The server manager just modify an Excel file to add signals for archive server to access. The archive server can automatically adapt to different SCADA system or data acquisition station, such as Johnson, Sauter DDC, AB, Simems, Mitsubishi, ABB PLC, NI, Advantech data acquisition device etc.

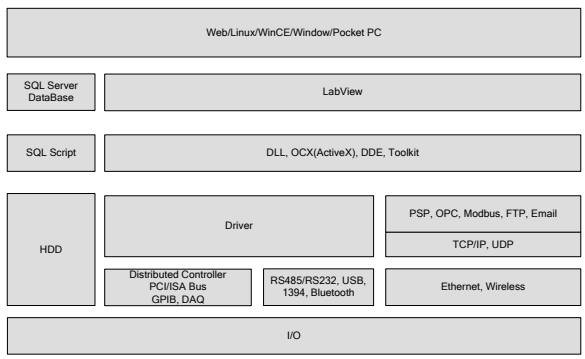

Figure 3 The hierarchy of data connectivity

USER FRIENDLY FUNTIONALITY OF VIEWER

For the purpose of unique monitoring and analysis interface, a novel viewer program called archive viewer is developed with LabVIEW. The program has various parsers to adapt all data format and can access all data center servers via FTP. The users can use a unique interface to access, compare, analyze and monitor the related data and find the abnormal condition of the system anywhere and anytime.

In intuitive aspects, the program uses the tree view to categorize all signals into subgroup systematically and provide a calendar form for the selection of view days. The program can display history data just clicking without learning or pre-knowledge. Besides, the zoom(in, out, pan), scale define(log/linear, auto scale, range scale), data filter(delete zero, delete negative, delete threshold), show cursor value, or plot type are also intuitive to operate as shown in Fig. 4.

In analysis aspects, the program presents some

comparison mechanism including overlap, normalize, two axes, eight drawings, moving mean, moving standard deviation, curve fitting etc. as shown in Fig. 5. These functions can be used to find correlation between signals. Furthermore, the program also has a customized mathematic function including algebra mathematics and script mathematics. The former let user define the symbolic algorithm and precede calculation instantly as shown in Fig. 6. The latter integrate with Matlab script function to implement the more complicated algorithms.

In output aspects, the archive viewer program can print out overall window and provide a periodic report. Just selecting intended or pre-defined signals, the periodic report can give graphic trend data in the self-defined day period. The raw data output is also provided in Excel or TXT logging file format.

CONCLUSION

This paper presents the architecture of monitor and archive system of instrumentation at NSRRC. On server sides, the system devote to multi-channel access to adapt different applications. On client sides, the system creates a user friendly monitoring and analysis platform. Moreover, the integration of hybrid network data acquisition is helpful for the more and more signal monitoring in the subsystem expansion. And the system will continue to be developed toward real-time data implementation and expert analysis system.

ACKNOLEDGEMENT

The authors would like to thank the colleagues of the utility group of NSRRC for their assistance.

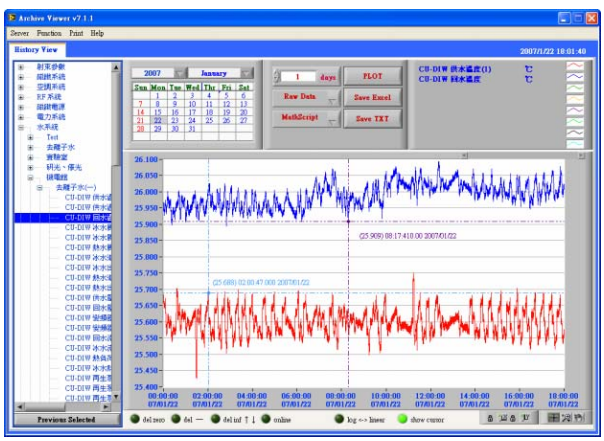

Figure 4 The show cursor function of Archive Viewer

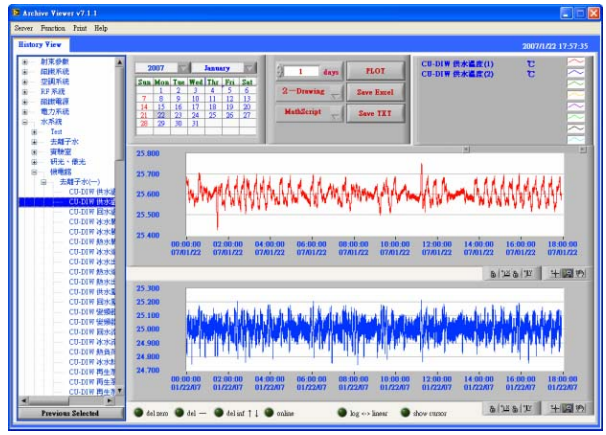

Figure 5 The two drawings function of Archive Viewer

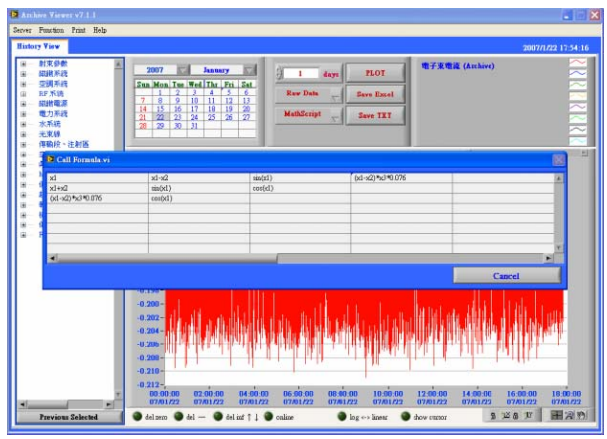

Figure 6 The algebra mathematics function of Archive Viewer

REFERENCE

[1] A. Daneels, W. Salter, "What is SCADA", International Conference on Accelerator and Large Experimental Physics Control System, 1999, Trieste, Italy.

[2] L. Sekolec, D. Vermeulen, "Data storage for the SLS", International Conference on Accelerator and Large Experimental Physics Control System, 1999, Trieste, Italy.

[3] T.Birke, R.Bakker, S. Bub, R. Miiller, " Logging of Supervisory Data At Bessy", International Conference on Accelerator and Large Experimental Physics Control System, 1999, Trieste, Italy.

[4] Y.K. Lin, G.H. Luo, C.C. Kuo, K.K. Lin, “Development of A Machine Status Program "History" And Its Application To Beam Stability Analysis”, Proceedings of EPAC2000, Vienna, Austria, pp. 648-650.

[5] Hsing-Chieh Li, Zong-Da Tsai, Feng-Zone Hsiao, Sheng-Hsiung Chang, Wen-Song Chiou, “The Cryogenic Supervision System in NSRRC”, Proceedings of 2005 Particle Accelerator Conference, May 16-20, 2005, Knoxville, Tennessee, USA.

HTS-ECRIS AND LOW ENERGY BEAM TRANSPORT SYSTEM OF THE HIGH CURRENT INJECTOR

G.Rodrigues, P.Kumar, P.S.Lakshmy, R.Ahuja, U.K.Rao, Y.Mathur, D.Naik, A.Mandal, D.Kanjilal and A.Roy
Inter University Accelerator Centre, Aruna Asaf Ali marg, New Delhi – 110067, India

Abstract

A new type of high performance electron cyclotron resonance ion source (ECRIS) called PKDELIS capable of operation at 14.5 and 18 GHz using high temperature superconducting (HTS) coils designed and developed jointly by IUAC, Delhi (earlier called NSC), Pantechnik, Caen and ISN, Grenoble is presently in operation. The source is very suitable for operation on a 400 kV high voltage platform for injecting beams from the High Current Injector (HCI) into the superconducting linear accelerator booster. Since the emittance of the source is large, the complete transport system is being made as short as possible, at the cost of some of the important beam diagnostics elements. A new type of extraction system is being developed in-house to improve the extraction conditions and better vacuum close to the beam formation region. A large aperture, 'third order' corrected analysing magnet has been fabricated for analysing the beams from the source. Typical axial and radial bremstraahlung spectra have been measured. The axial direction shows a single electron temperature component while the radial direction shows 'two electron' temperature components.

INTRODUCTION

The beam energy delivered by the 15 UD Pelletron accelerator at IUAC is above the Coulomb barrier for masses below 40. To augment the beam energy, a superconducting LINAC [2] is being installed to provide beams of ~ 5 MeV/A for the medium heavy ions. The input of LINAC demands high current, high charge state pulsed beam (150 ps). Since the pulsed beam available from the existing Pelletron is of low intensity (~ a few nA average current) and low charge state, an Electron Cyclotron Resonance (ECR) ion source based High Current Injector (HCI) is being installed to provide relatively high current (a few pμA) heavy ion beams for the LINAC.

A cryogen-free high temperature superconducting (HTS) coil based electron cyclotron resonance ion source has been developed and is being used as a part of high current injector for the superconducting linear accelerator at the Inter University Accelerator Centre. This kind of ion source is an off-shoot from the HYPERNANOGAN ECR ion sources developed by Pantechnik, France, where the resistive coils have been replaced using HTS coils [3]. By using HTS coils, the original injection field of 1.3 T has been increased to 1.8 T. The source is configured to be operated on a 400 kV high voltage platform. Power and cooling requirements for the sub-systems are designed to be minimal. Due to the use of HTS coils for the magnets, a reduction factor of 10 results in the power saving costs. In addition, the cooling requirements are also reduced tremendously. This type of ion source is first of it's kind designed to deliver highly charged ions ranging from a few keV to a few MeV depending on the extraction voltage and charge states extracted from the ion source. The source is designed to deliver A/q beams having a maximum value of 10 to be accelerated through the superconducting linear accelerator system of IUAC. A view of the high temperature superconducting ECR ion source is shown in figure 1.

DESIGN ASPECTS OF THE SOURCE

Unlike low temperature superconducting (LTS) materials, HTS coils do not require actively-cooled shields and the temperature can be controlled by standard industrial refrigeration systems. The systems are simpler to design, contruct and compact in form. LTS coils operate closer to their critical temperature as compared to HTS coils. Therefore, HTS coils can withstand wider temperature change without losing their superconducting properties. Also, the critical current density of HTS materials falls slowly as a function of temperature. In addition, the cooling costs are drastically reduced when compared to operation at lower temperatures of about 4 K. The requirements of cooling water on a high voltage platform is also negligible.

Figure 1. View of the High Temperature Superconducting ECR Ion Source, PKDELIS

The heart of the source is built using high strength Bi-2223 HTS tapes for the coils. High strength conductors were chosen instead of high current conductors to withstand the huge forces acting on the coils. Each coil consists of 10 pancakes connected in series wound on a

single copper former. The current capacity of the tape is rapidly reduced by the application of magnetic field, particularly in a direction perpendicular to the plane of the conductor. Since the performance of the tape is more critical when the magnetic field is perpendicular to the tape than when parallel to it, the maximum operating field of 1.8 T corresponding to a maximum current of 181 A determines the maximum radial field on the tape of about 1.4 T. This in turn determines that the maximum operating temperature of the coil which should be below 30 K.

SOURCE OPERATION

Figure 2 shows a schematic of the source coupled with the analysing system. The complete beamline is made as short as possible in order to minimise the beam losses due to the large emittances at the cost of a few diagnostic elements. During normal operations, we have observed beam losses due to space charge effects at low extraction voltages of 10 to 30 kV [4]. The transmission of these beams is being improved upon. In addition, x-ray measurements have been explored to understand the source performance. Typical axial bremstraahlung spectra measured at a distance of approximately one metre from the ECR plasma in the zero degree view port of the analysing magnet at a fixed rf power of 300 W is shown in figure 3.

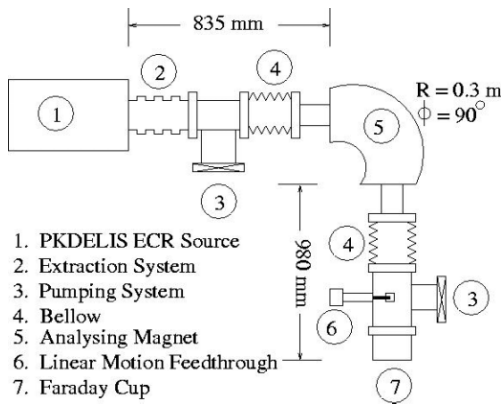

Figure 2: Schematic view of the source coupled with the analysing system.

A small Si pin diode detector (AMPTEK) was used with proper collimation to obtain the x-rays only from the plasma. From these measurements, we found that as the mirror ratio is increased on the injection and extraction sides, the slope of the distribution changed considerably. The legend in figure 3 shows the values of the injection and extraction coil currents used to change the mirror ratio at fixed rf forward power level of 300 W. This shows that a single electron temperature component is found to increase with higher mirror ratios. All measurements were performed for a fixed time period of 900 seconds. The energies of the x-rays which span from a few tens of keV to a few hundred keV show that at these power levels the energies of the x-rays correspond to the available electron energies. We expect that at higher power levels higher energy electrons would be produced, but these measurements could not be completed due to problems with the DC waveguide break at higher levels of RF power. We have also measured the bremstraahlung in the radial direction. These measurements however show a 'two-component' electron temperature. This requires more detailed measurements to further understand the behaviour of the plasma.

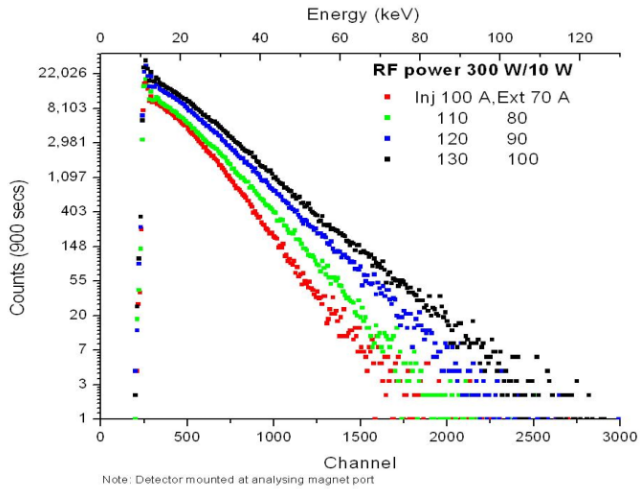

Figure 3. Axial bremstraahlung measurements from PKDELIS ECR plasma.

LOW ENERGY BEAM TRANSPORT

The LEBT of the High Current Injector consists of the High Temperature Superconducting ECR source PKDELIS, multi-electrode extraction system/solenoid/magnetic quadrupole doublet, 90° analysing Magnet, 400 kV high voltage accelerating column and a few focussing devices to transfer the beam from ECR to RFQ entrance. In the low energy beam transport (LEBT) system of the HCI, the beam extraction and transport becomes more and more challenging. From beam measurements, we have observed losses in the beam mainly due to beam blow-up at low extraction voltages of about 10 to 30 kV. From IGUN simulations, it has been found that the source beam emittance is of the order of ~ 200 π .mm.mrad and matches close to the measured values. In addition, due to the high currents (~ 10 mA) extracted, the extraction system needs proper cooling requirements and possibility of movement of the electrodes for tuning various A/q beams which have different focussing properties under the influence of a strong axial magnetic field. A new type of extraction system with movable electrodes and with provision for water cooling is being developed. A large acceptance analysing magnet has been designed to analyse ions from the ECR source. This magnet will be placed on the high voltage platform to reduce beam loading of the high voltage power supply. The combined function magnet has

been designed to incorporate higher order terms to reduce the higher order aberrations. Since the technical challenge of transporting low energy, high current ions lies mainly in the low energy section of the injector, utmost care has been taken in the design of the LEBT. The ions from the ECR source are first extracted around 30 kV and A/q analysed by a large acceptance analysing magnet and further accelerated using deck voltage with a maximum allowable voltage of 400 kV. The energy of this beam will be further accelerated by a Radio Frequency Quadrupole accelerator (RFQ), Drift Tube Linac (DTL) and low β cavity resonators to match the existing LINAC beam-input energy requirements. A new beam hall is being constructed on the east side of the present beam hall I to house these facilities. A schematic layout of the building and tentative layout of beam line is shown in figure 4. The ion optical design has been carried out considering the beam input parameters of maximum A/q = 10 and beam emittance of 200 π mm.mrad [5]. A second order corrected beam optics on the 400 kV high voltage platform and upto the RFQ entrance is shown in figure 5 for E/q= 380 kV.

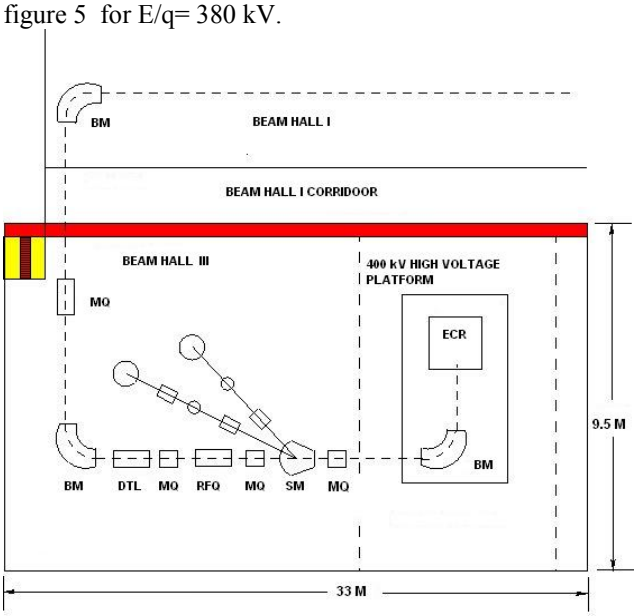

Figure 4: Schematic layout of new beam hall III.

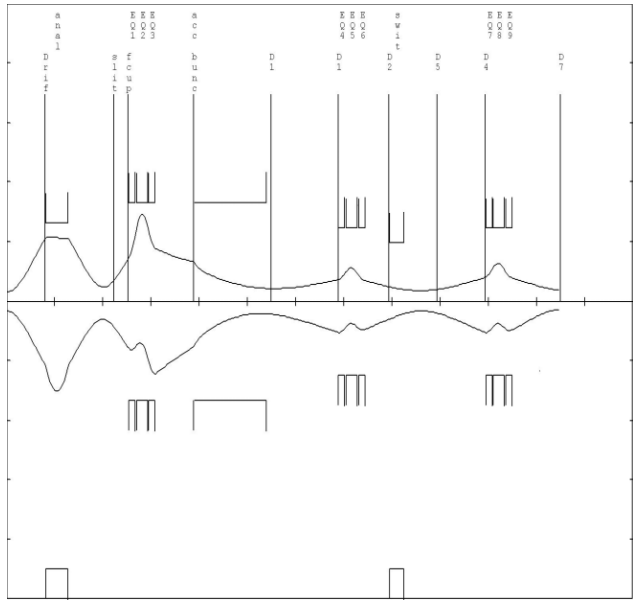

Figure 5: Second order corrected beam envelope from ECR source upto RFQ entrance for E/q = 380 kV.

REFERENCES

[1] D.Kanjilal, S.Chopra, M.M. Narayanan, Indira S. Iyer, V.Jha, R.Joshi and S.K.Datta, *Nucl.Instrum. Methods* A 328 (1993) pp.97

[2] A.Roy, Current Science, 76, 149 (1999)

[3] C.Bieth, S.Kantas, P.Sortais, D.Kanjilal, G. Rodrigues, S.Milward, S.Harrison, R.McMahon, *Nucl. Instr. and Meth.* B235 (2005) pp.498

[4] D.Kanjilal, G.Rodrigues, P.Kumar, A.Mandal, A. Roy, *Rev. Sci.Instrum.,77* (2006)03A317

[5] A.Mandal. G.Rodrigues, D.Kanjilal, A.Roy, Seventh International Conference on Charge Particle Optics, July 2006, Cambridge, England

CONTROL SYSTEM FOR THE BENGING MPS AT PLS LINAC*

J. H. Kim#, J. M. Kim, S. C. Kim, K. M. Ha, J. Y. Huang, H. S. Kang ,J. Choi and I. S. Ko,
Pohang Accelerator Laboratory, POSTECH, Pohang 790-784, Korea

Abstract

The former control system of the bending MPS (**M**agnet **P**ower **S**upply) was based on Supervisory Control and Data Acquisition (SCADA), RTworks[1]. It is changed based on EPICS as a framework for the full upgrade of the PLS control system. Also we have replaced the former VME 68K CPU boards with OS-9 to new Power CPU boards operated by VxWorks as IOC in the linac klystron gallery. The replaced bending MPS control system consists of a MVME5100 EPICS IOC core in the lower level control. It is implemented with the MEDM tool of EPICS to provide friendly Graphical User Interfaces. This paper describes the VME IOC and OPI and embedded local controller in MPS cabinet used for the bending MPS control in the PLS linac

INTRODUCTION

As of now, the bending MPS(Magnet Power Supply)control system have been well performed the mission to operate 2.5 GeV linac as the beam injector for the PLS storage ring. However, in early 2001, we have decided to convert the current control system into the EPICS based one because of its lack of flexibility and control speed [2]. We have been studied the key technology for EPICS control system during the development of EPICS based test-bed control system completed at the early of 2000.

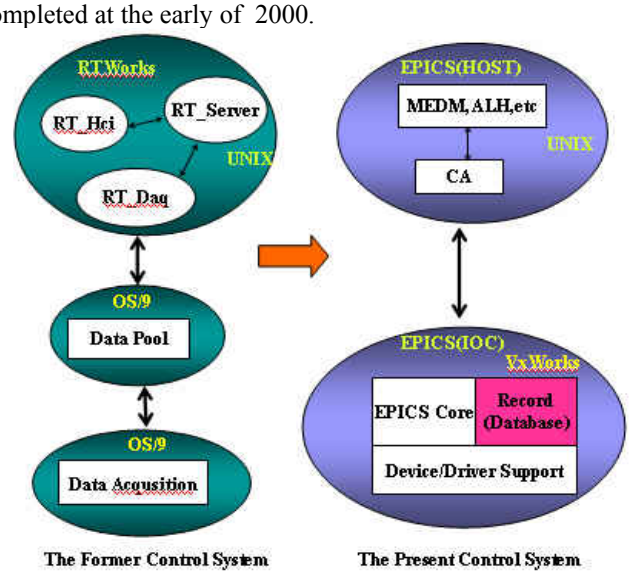

Figure 1: software structure of the former and present bending MPS control system.

*Work supported by Ministry of Science and Technology in Korea
#jihkim@postech.ac.kr

Originally, the former bending MPS control system has three layers of hierarchy; the operator interface computer, the supervisory control computer (SCC) for data processing and the device interface computer (DIC) for distributed data acquisition as shown fig. 1. The operator interface is designed configured on the commercial product, RTworks[1]. The VME systems under OS-9 are used for data processing and data acquisition. In order to provide EPICS structure, our bending MPS control system with three-layered architecture is changed.

Table 1 shows the difference between the former and present systems.

Table1: Comparison Table

	The former control system	The present control system
VME CPU	Eltec 16	MVME5110
I/O Board	TSVME500	TPMC866
Network	10base2	100base TX/FX
VME RTOS	OS-9	vxWorks
Core S/W	Homemade S/W	EPICSBase3.13.6
Device Interface	Serial	Serial

BENDING MPS CONTROL SYSTEM

There are 6 power supplies for bending magnet in BTL. These power supplies are placed in the BTL power supply room. A VME system for controlling them is installed in the nearest power supply [3].

As shown in fig. 2, this control system is based on the EPICS standard model. VME Systems as IOCs is used and connected via Ethernet for host and communicate with embedded controller of MPS using RS422 protocol.

This bending MPS control system has currently following features.

- All Current Set, Power/On, Off
- Individual Current Set, Power/On, Off
- Status Monitoring (Remote/Local, Polarity, Over-temperature, Over-current, etc)
- Degaussing for Bending Magnet
- Saving of individual set current value

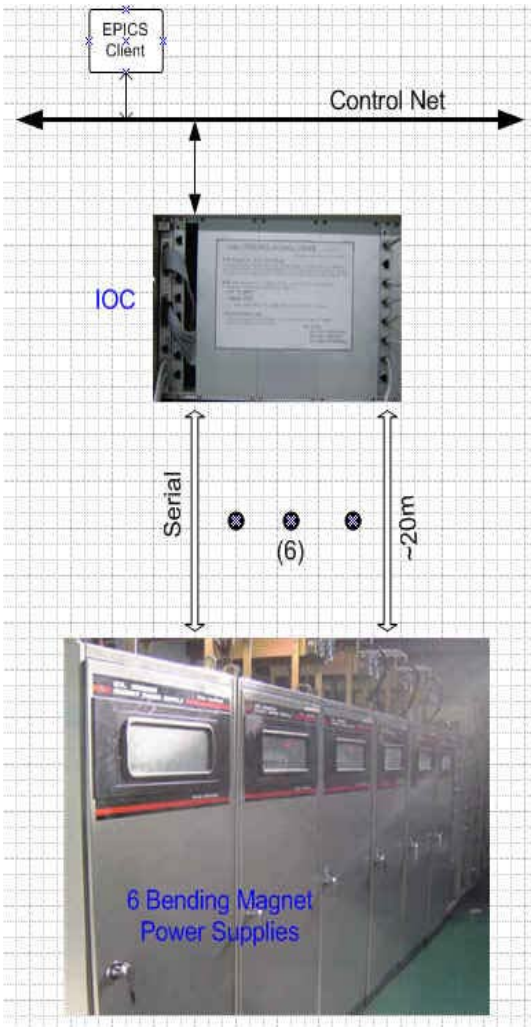

Figure 2: Structure of bending MPS control system.

Operator Interface

Sun Workstation with 2 CPUs and 1GB memory are selected as the console computer. The Motif Editor and Display Manager (MEDM) is chosen as the primary operator interface for MPS control system. Bending MPS operator windows are designed with schematic and user friend design concept as seen in fig. 3&4.

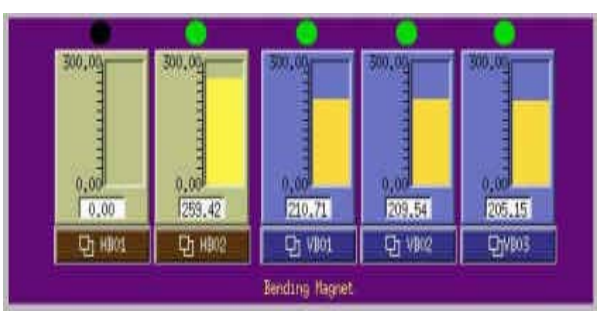

Figure 3: Monitoring panel of bending MPS.

There are two panels for monitoring of power supply parameters and for controlling individual power supply. The operator screen is designed for monitoring power supply data through bar graph object.

Figure 4: Control panel of bending MPS.

VME System as IOC (Input/Output Controller)

EPICS IOCs are implemented in VME bus system with MVME5100 CPU running the vxWorks real-time operating system. We selected the VME system under vxWorks to preserve our investment in hardware and to make much use of the existing EPICS resources for VME I/O boards. To interface the embedded controller of bending MPS with serial interface, serial PMC module (TPMC866) with 8 channels on PowerPC CPU Board is used. Also we can monitor the status of the working VME crate parameter (voltage, temperature, etc) remotely. The application tasks running IOC is developed by a SUN Workstation and vxWorks development environment.

Base Release3.13.6, EPICS Core S/W is configured and successfully installed. The device/record support was obtained from the community of the EPICS collaboration and is slightly modified to satisfy the in-house protocol of the power supply controller. Before constructing database for IOC, PV (Process Variable) list was defined by the rule of PLS naming convention.

For PLS EPICS, the Capfast schematic editor was chosen as the IOC database configuration tool in the initial development stage. But MPS IOC uses generic editor (vi etc) to construct the simple IOC function database as shown fig. 5.

The following functions are implemented using various records like Analog Input/Output, Binary Input, String Input/Output, Scalout, Sequence record etc.

- All Bending MPS Set Current Out, Current Out
- All Bending MPS Set Power On/Off, Power On/Off
- Individual Power O/OFF, Current Set
- Current Response Input
- Status Response Input

The configured IOC database is loaded into MPS IOC at start-up.

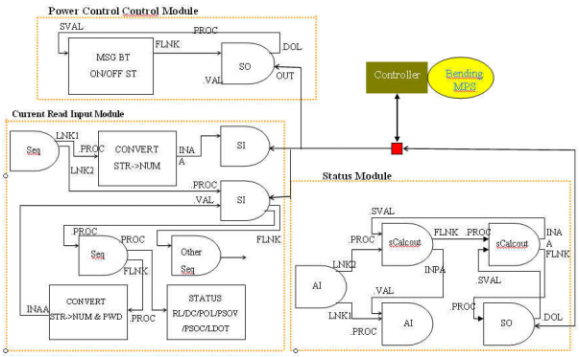

Figure 5: Schematic diagram of EPICS records for bending magnet power supply in IOC.

Embedded Controller in bending MPS

Local controller of bending MPS was developed in house member. The bending MPS has the capacity of handling the individual power supply.

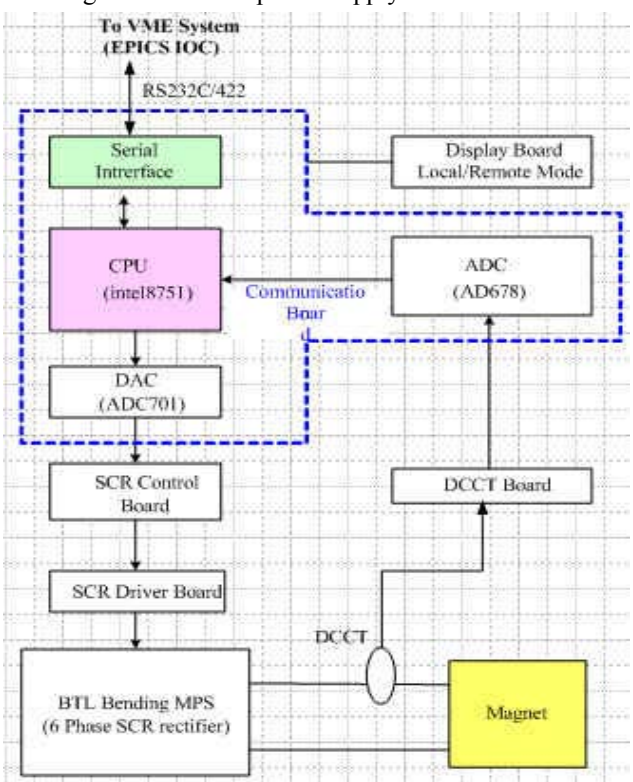

Figure 6: Block diagram of bending magnet power supply.

It is the embedded single board computer with serial interface and Analog to Digital, Digital to Converter in the custom crate. Also, it has self-diagnostic functions and with keypad on the front panel can adjust control and monitor power supply current locally without IOC intervention as shown fig. 6 & 7.

It is programmed in EPROM the execution code to handle the communication between the IOC and this controller via RS422 with in-house protocol.

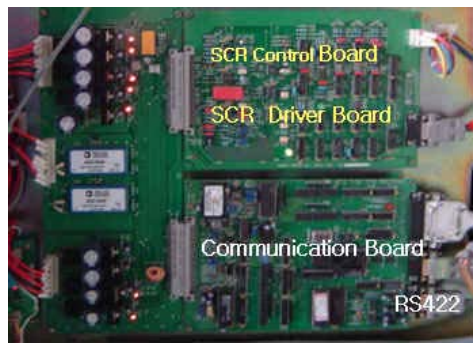

Figure 7: Electronic boards in bending MPS cabinet.

FUTURE PLANS

The EPICS based bending MPS control system has successfully operated since the beginning of installation in the linac field.

We have plan to upgrade bending MPS which have better performance and Ethernet interface connecting to upper level computer. If the local intelligent CPU on MPS is sufficient to load real-time operating system, like RTMES, EPICS IOCcore can run on the local intelligent CPU board and VME processing power can be off-loaded.

ACKNOWLEDGMENTS

This work is supported by Pohang Iron & Steel Co. and Ministry of Science and Technology, Korea.

REFERENCES

[1] http://www.talarian.com/rtworks.html

[2] J. H. Kim, K. M. Ha, J. M. Kim, I. S. Ko, et al., "Development Status of EPICS Application for PLS Computer Control System," ICALEPS2001, San Jose, USA (2001).

[3] I. S. Ko, J. H. Kim, J. Choi, and W. Namkung, "Control System of PLS 2-GeV Electron Linac," IEEE Trans. Nulc. Sci., 43, 25 (1996).

DESIGN OF C-BAND STANDING-WAVE ACCELERATING STRUCTURE*

S. H. Kim#, B. Park, H. R. Yang, S. D. Jang, Y. G. Son,
S. J. Park, J. S. Oh, M.H. Cho and W. Namkung
POSTECH, Pohang 790-784, Korea

Abstract

We design a C-band standing-wave accelerating structure for a compact electron linac. It is capable to produce electron beams with the beam energy of 4 MeV and the pulsed beam current of 50 mA. It is to be operated in the π/2 mode with the on-axis coupled structure. The beamline is composed of the E-gun and the accelerating column with 3 and half bunching cells and 9 and half normal cells. We design standing-wave RF cavities using the OMEGA3P code to implement the asymmetric magnetic coupling slots. For the beam dynamics study, we use the PARMELA code with the SUPERFISH fields configuration. Without the pre-buncher cavity and the focusing magnets, the lost beam power to the wall is 10 kW for the output beam power of 200 kW, while the transmission is 58%.

INTRODUCTION

The electron accelerator is widely used for industrial applications, for example, contraband detection, material processing, medical diagnosis and therapy, food sterilization, and environmental processing [1]. The environmental processing such as DeSOx or DeNOx and the sterilization processing requires the average beam power of several tens of kilowatts which depends on the processing speed. The contraband detection requires 5-10 MeV with the pulsed beam current of about 150 mA [2, 3].

We are developing an electron accelerator for an X-ray source. It uses a C-band 5-GHz RF source developed for the low-power tests on the LHCD system of KSTAR. With 1.5-MW input RF power, we designed an accelerating structure capable of producing 4 MeV at the 50-mA pulsed beam current. For compactness, a standing-wave bi-periodic structure is adopted with the π/2 mode. In this paper, we present design details of the RF cavity and the beamline with the beam dynamics.

ACCELERATOR SYSTEM

The accelerator uses a 5-GHz CPI magnetron as an RF source. It is capable of producing 1.5-MW RF with the 4-μs pulse length and the 200-Hz repetition rate. The WR187 waveguide network transports the RF power to the accelerating column. This waveguide is worked under atmospheric pressure SF6 gas except the pump-out-port waveguide which is connected to the input coupler of the accelerating column. The pulse modulator supplies the 40-kV and 90-A pulsed power to the magnetron with the 4-μs pulse length [4]. It also supplies the 40-kV pulsed voltage to the E-gun. The E-gun is a diode-type thermionic DC gun.

The accelerating column is attached to the E-gun directly as shown in Figure 1. For the compact structure, a pre-buncher cavity with a drift tube is omitted. Furthermore, any solenoids magnet is not used since the beam current is low enough to be focused by the intrinsic focusing effect of the standing-wave electric field [5].

Table 1: Accelerator Parameters.

Accelerator Parameters	
Operating Frequency	5 GHz
Input RF Power (pulsed)	1.5 MW
Pulse Length	4 μs
Repetition Rate	200 Hz
E-gun Voltage	40 kV
Output Beam Energy	4 MeV
Output Beam Current (pulsed)	50 mA
Beam Transmission Rate	58%
Output Beam Power (pulsed)	200 kW
Loss Beam Power (pulsed)	10 kW
Type of Structure	Bi-periodic, On-axis coupled
Operating Mode	SW π/2 mode
Aperture Diameter	10 mm
Average Accelerating Gradients	10.7 MV/m
Number of Cells	13
Inter-cell Coupling	6.2%
Quality Factor*	7500
Effective Shunt Impedance*	90 MΩ/m
Transit-time Factor*	0.81

*Values for normal cells.

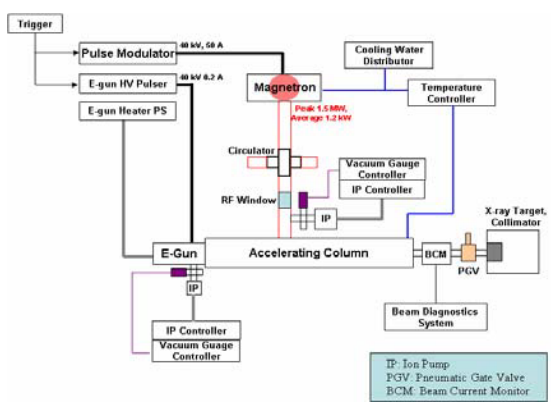

Figure 1: Block diagram of accelerator system.

*Work supported by PAL.
#khan777@postech.ac.kr

For the accelerating structure, a bi-periodic and on-axis coupled structure is adopted. Since the electric inter-cell coupling is too low due to the nose-cone, the magnetic coupling slot is bored on the wall between the accelerating cavity and the coupling cavity. The detailed design of the cavity is described in the next section and the accelerating structure in the BEAM DYNAMICS section.

CAVITY DESIGN

A bi-periodic accelerating structure has the following dispersion relation [6].

$$k_{AC}^2 \cos^2\varphi = [1-(\omega_A^2/\omega^2)+k_{AA}\cos 2\varphi] \times[1-(\omega_C^2/\omega^2)+k_{CC}\cos 2\varphi], \quad (1)$$

where ω is the resonance frequency of the coupled cavities at the φ mode, ω_A and ω_C are the resonance frequency of the accelerating cavity and the coupling cavity, and k_{AC} is the coupling coefficient between the accelerating cavity to the nearest coupling cavity, while k_{AA} for two neighbouring accelerating cavities and k_{CC} for two neighbouring coupling cavities. The design goal is to eliminate the stop band ($\omega_A - \omega_C$) and make k_{AA} and k_{CC} to be nearly zero. Also the resonance frequency at the π/2 mode should be the working frequency, 5 GHz [7].

The shape and significant dimensions of the normal accelerating cell is shown in Figure 2. The aperture diameter is 10.00 mm and the wall thickness is 3.00 mm. The gap distance between nose-cones is 16.67 mm. This model is simulated by the OMEGA3P code [8], a 3-D eigen-mode solver. The simulation is conducted for a normal cell, consisted of a coupling cavity and 2-half accelerating cavities, to find 0-, π/2-, and π-mode frequencies of the accelerating cavity. To find the π/2-mode frequency of the coupling cavity, the simulation is also conducted for a normal cell consisted of an accelerating cavity and 2 half coupling cavities.

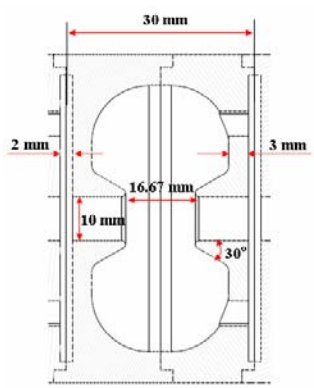

Figure 2: Crosssectional view of normal accelerating cell with significant dimensions.

With 290,000 mesh cells, the resonant frequency is 4999.88 MHz and the stop band is less than 0.5 MHz. The magnetic coupling slot on the wall is for the purpose of increasing the inter-cell coupling, since the electric coupling is not enough due to the nose-cone. Since the resonance frequency at the 0 mode is 5143.36 MHz and the frequency at the π mode is 4833.86 MHz, the k_{AA} and k_{CC} is nearly zero. The reason why the 0 mode frequency is larger than the π mode is due to the magnetic coupling slot [9]. With this mode separation, the inter-cell coupling coefficient is 6.2%.

BEAM DYNAMICS

For the beam dynamics study, the SUPERFISH and PARMELA codes are used. We assume that asymmetric fields due to the magnetic coupling slot do not affect the beam dynamics result significantly. Without any solenoid magnet and pre-buncher cavity, the beamline is composed of the E-gun and the accelerating structure with the bunching section as shown in Figure 3.

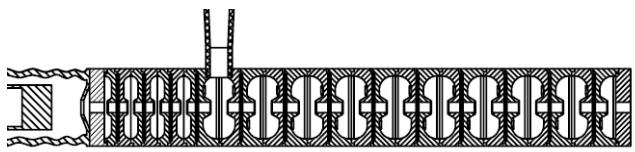

Figure 3: Accelerator column crosssectional view, position of the magnetic coupling slots are skewed to the plane of this crosssection.

The normal section is consisted of 9 and half identical normal cells with the phase velocity of c. The bunching section has 3 and half bunching cells with the phase velocity of 0.6c. For simple fabrications and measurements, the bunching cells are the same. When the phase velocity of bunching cell is 0.5c, there are significant loss at the position between the bunching section and the normal section. On the other hand, if the phase velocity is 0.7c, most of electrons can not be captured to the bunching section. The number of bunching cells is determined according to the result in Table 2, which shows that the second condition is for the optimum beam energy and transmission ratio with the acceptable beam loss power.

Table 2: Beam characteristics with number of bunching cells. The phase velocity of bunching cells is 0.6c.

	Loss Beam Power / Output Beam Power	Transmission Ratio	Beam Energy
2 & half	4.7%	50%	2.5 MeV
3 & half	4.9%	58%	4.0 MeV
4 & half	17.1%	53%	3.6 MeV

The beam dynamics simulation is conducted in consideration of the beam-loading effect. The average axial electric field is defined by

$$E_0 L = \sqrt{r_s P} - i_b r_s , \quad (2)$$

where r_s is the shunt impedance, P is the input RF power, i_b is the electron beam current, and L is the cavity length. Since the voltage, the electric field times the cavity length, is proportional to the shunt impedance of each cavity, the electric fields in the whole accelerating column is distributed as shown in Figure 4.

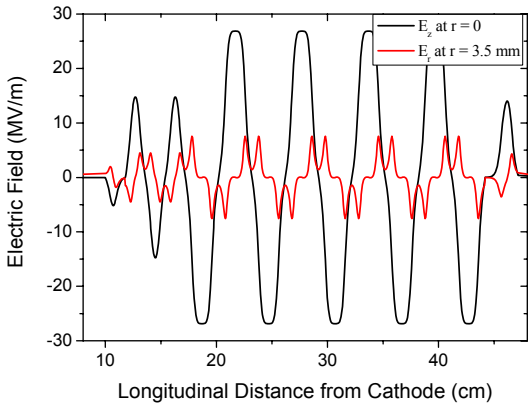

Figure 4: Electric fields in the accelerating column.

Since there is no focusing magnet, the electron beams are focused by the RF focusing effect induced by the standing-wave electric fields. In the low-energy region of Figure 5, including the bunching section, the RMS beam size is oscillating. The electron beams is still lost with the aperture in the end of accelerating column. But most of beam loss occurred in the bunching section. 91% of the lost beam has the energy lower than 1 MeV.

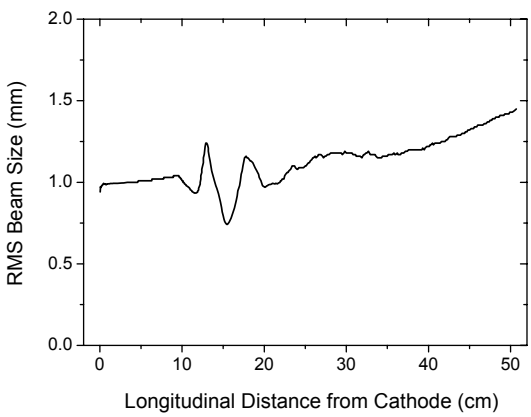

Figure 5: RMS transverse beam size, the entrance of the accelerating column is placed at 10 cm far from the cathode.

CONCLUSION

For the electron accelerator of 4 MeV and pulsed 50 mA with 1.5-MW RF source, the bi-periodic accelerating structure is designed with on-axis coupling. With the OMEGA3P code simulation, the cavity dimensions are determined for the π/2-mode frequency to be 5 GHz with 6.2% inter-cell coupling. In this geometry, the stop band is vanished. Without the pre-buncher and the solenoid magnet, this compact accelerator can make 4-MeV and 50-mA electron beams with 5% beam power loss. As the following step, cold tests for aluminium prototype of the bunching and normal cell are scheduled. Using these results, we will fabricate whole structure of the accelerating structure, braze it, and conduct fine tuning.

ACKNOWLEDGEMENT

This work is supported by PAL. The authors appreciate Dr. Luo Yingxiong at IHEP, Beijing for his advice on the accelerator system and the cavity design.

REFERENCES

[1] A. M. M. Todd, "Emerging Industrial Applications of Linacs," in *Proc. of Intl. LINAC Conf.* (Chicago, IL, August 23-28, 1998), 1036 (1998).
[2] V. Pirozhenko, et al. "Complex for X-ray Inspection of Large Containers," in *Proc. of EPAC 2006* (Edinburgh, Scotland, June 26-30, 2006), 2388 (2006).
[3] C. Hao, et al, "A New Type SW Linac Used in Industrial CT," in *Proc. of APAC 2004* (Gyeongju, Korea, March 22-26, 2004), 429 (2004).
[4] S. D. Jang, Y. G. Son, J. S. Oh, Y. S. Bae, H. G. Lee, S. I. Moon, M. H. Cho and W. Namkung, J. Korean Phys. Soc. **49**, 309 (2006).
[5] L. Auditore, R. C. Barna, De Pasquale, A. Italiano, A. Trifiro, and M. Trimarchi, Phys. Rev. ST-AB **7**, 030101 (2004).
[6] E. A. Knapp, B. C. Knapp, and J. M. Potter, Rev. Sci. Instr. **39**, 979 (1968).
[7] H. Euteneuer, A. Jankowiak, M. Negrazus, and V. I. Shvedunov, "The 4.9 GHz Accelerating Structure for MAMI C," in *Proc. of EPAC 2000* (Vienna, Austria, June 26-30, 2006), 1954 (2006).
[8] ANALYST with the OMEGA3P code is a trademark of STAR, inc.
[9] T. Shintake, "Analysis of the transient response in periodic structures based on a coupled-resonance model," in *Proc. of Joint US-CERN-Japan International School* (Hayama/Tsukuba, Japan, Sep. 9-18, 1996), 335 (1999).

IMPLEMENTATION AND EXPERIENCE OF ENERGY RAMPING FOR INDUS-2

R. K. Agrawal#, A. Chauhan, G. Singh, K. Saifee, M. Seema, P. Fatnani, R. Husain, Y. Sheth
Raja Ramanna Centre For Advanced Technology (RRCAT), Indore, India.

Abstract

Beam energy ramping in Synchrotron Radiation Sources (SRS) requires synchronous increase in power supply currents attached to various magnets and voltage of RF cavities. This paper describes the implementation at various layers of control system architecture, our experience of ramping beam energy from injection energy to 2.5 GeV. The total ramping system hardware and software for both magnet power supplies and voltage of RF cavities are described. The implemented ramping system provides a tracking uncertainty of better than 10 micro seconds in time.

INTRODUCTION

Indus-2 is a 2.5 GeV SRS under commissioning at Raja Ramanna Centre For Advanced Technology (RRCAT). The accelerator system at this centre has a 20 MeV Microtron as electron injector, a 450/700 MeV Booster synchrotron and a 2.5 GeV storage ring, Indus-2. The electron beam of 550 MeV from booster synchrotron is injected in the Indus-2 SRS ring from where it is ramped to energy of 2.5 GeV.

In Indus-2, the beam energy is increased from 550 MeV to higher levels by synchronously increasing the current in magnet power supplies and voltage in RF cavities (Devices). The ramp profile (sample) data is generated keeping tune and chromaticity fixed during beam energy ramp.

The ramping system is implemented in modular and distributed manner. A user interface built on PVSS SCADA layer allows the operator to send the ramp profile data to the lower layers of control system, which compute the final data. The computed data are sent sequentially to DAC on a common synchronising clock to provide a reference setting signal to interfaced ramping devices.

RAMP PROFILE DATA GENERATION

The integrated magnetic fields are calculated as per following equations:

$\int B.dl(T-m) = 3.3356.E(GeV).\theta(rad)$; for dipoles

$\int G.dl(T) = 3.3356.E(GeV).KL(m^{-1})$; for quadrupoles

$\int G'.dl(T/m) = (1/2)3.3356.E(GeV).SL(m^{-2})$; for sextupoles

where, θ is the bending angle which is 22.5 degree; KL and SL are the normalised integrated magnetic field strengths of the quadrupole and sextupole magnets.

#ragrawal@cat.ernet.in

The measured data of the dipole magnets for the excitation current and its first derivative versus energy and integrated magnetic field is shown in Fig. 1. The integrated magnetic field starts deviating from linearity well above 1.3GeV. The quadrupoles and sextupoles behave linearly with excitation current. The ramp profile data is generated using cubic-spline interpolation technique by fitting piece-wise cubic polynomial between two magnetic field data points. Fitting takes care of non-linear behaviour between excitation currents of dipoles, quadrupoles and sextupoles.

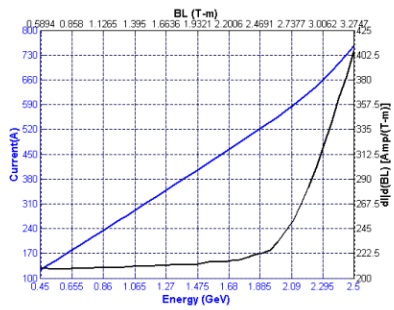

Figure 1: Measured magnetic filed data of dipole magnet.

THE SCHEME

The energy ramping process can be considered as a process in which the beam energy is changed from initial energy 'E_1' to final energy 'E_N' in '*N*' steps. Each energy level requires a set of current in magnet power supplies and voltage in RF cavities. Thus, for each device a setting is required corresponding to each energy level. This is named as **sample**. The samples are further linearly interpolated into **steps.** The number of steps between two samples is same for all the devices [3]. The samples are decided by the non-linearity of various ramping devices and steps are governed by the resolution requirements.

So, the ramping process can be seen as setting simultaneously the k^{th} samples ($1<k\leq N$) on the respective ramping devices, thus arriving to a higher beam energy.

IMPLEMENTATION

The above ramping scheme is implemented modularly in software and distributed hardware on Indus-2 control system.

The INDUS–2 control system is based on three-layer architecture namely the 'User Interface Layer' (UI), the 'Supervisory Control Layer' (SC) and the 'Equipment Interface Unit (EIU) Layer' [1].

The overall ramping system is composed of:

- User Interface module.

- Step data generation software module.
- Digital to Analog Converter (DAC) cards.
- Synchronisation system.

User Interface Module

The ramping system user interface has various GUI panels developed in PVSS SCADA. These panels sequence various operations and get & set data into PVSS DB [4]. The custom PVSS API manager provides the interface between PVSS SCADA and SC layer.

Ramping devices selection panel

This panel allows the user to select the devices to be ramped. This panel displays available devices in one pan and selected devices in the other pan. Facilities are provided for saving and loading the selected devices file. The DC mode setting & control of the devices selected for ramping are disabled from the main panel.

Ramp Data Entry panel

The panel, shown in Fig.2, allows the user to enter the samples for the selected devices. The first row displays the present settings of the devices. There is a support for 360 rows in this table to accept complex ramping profiles. Facilities to load and save the samples data are provided. The number of steps is automatically calculated normally considering dipole power supply as reference for best possible resolution supported by the hardware. Maximum number of steps allowed is limited to 64k which corresponds to 1 LSB change per step. A "Generate Ramp Button" is provided to start the ramp data generation process.

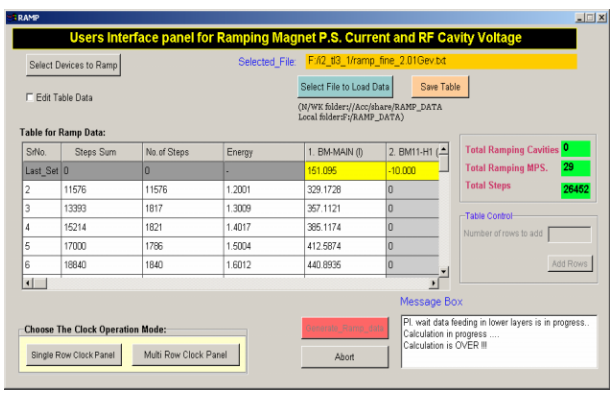

Figure 2: Ramp Data Entry Panel.

Clock Generation Panel

This panel allows the user to send the clock pulses to the DAC cards housed in the EIUs thus increasing the reference to the selected ramping devices. There are two type of panels, single-clock and multi-clock panel. In single clock panel, user can select number of steps and frequency. The frequency range allowed is limited from 1 to 1000 Hz and the maximum number of steps to be sent is limited to total number of generated steps. Multi clock panel (see Fig.3) supports multiple entries and delay between various entries. This panel provides a visual indication of last completed row. The ramp clock can be paused at any time in that case information is provided for the number of steps sent for the current command and total steps sent till pausing.

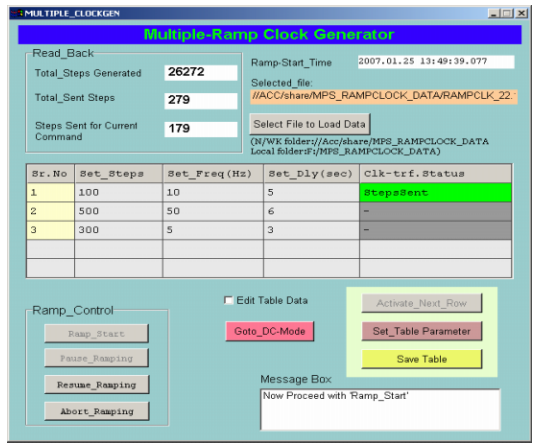

Figure 3: Clock Generator Panel.

API Managers

The PVSS SCADA communicates to the SC layer with the help of Application Programming Interface Manager (API) [4]. There is one API manager for sample data communication & controlling the final step data generation process and the other for communicating and controlling the ramp clock generator card. These API managers poll periodically the server process running at SC layer to get device read-back, current settings and mode data. Whenever any application program or user changes any parameter value, one message is generated by the PVSS SCADA Event manager. This invokes the API manager and corresponding value is sent to SC layer server process. SC layer in turn sends this data to the corresponding EIUs.

SC Layer Server Application

The SC layer has a VME bus based 68040 CPU with OS-9 Real Time Operating System (RTOS) running multiple processes. There is one socket server process which communicates with API manager at UI layer. There is another process implementing Profi master protocol that exchanges commands and data with EIUs distributed in the field over the Profi bus. The current status of EIUs is continuously polled. This layer also has a mapping of parameters and commands of various devices interfaced to EIUs.

Step data generation software at EIU Layer

The software at this layer receives the samples of the ramping curve. It then linearly interpolates the data in finer steps between successive samples to be filled in the DAC cards. It also updates data which indicates the progress of sample reception and step data generation process. There are 35 such EIU stations catering to 138 magnet power supplies and 4 RF cavities.

DAC Cards

DAC boards having 16-bit resolution are used to provide the analog reference to the interfaced devices. The interpolated steps data is stored in the DAC card memory. A 64k word memory buffer is provided on these cards for this purpose. These cards have a facility to scan the memory data on an external clock [2]. The scanned data is given sequentially to digital to analog converter chip on the card thus generating a programmed profile. The data scanning with each clock is implemented in hardware to minimise the tracking uncertainties between the reference signals for various ramping devices.

Synchronisation system

The transition to the next energy state requires synchronous setting of devices to avoid any undesirable deviation in the beam optics.

The synchronisation system can be software or hardware based but the software based system has a relatively poor tracking time uncertainty. Therefore we have selected a hardware based synchronising system. The synchronisation is achieved using an external common clock to all the DAC cards.

A custom made VME bus compatible programmable clock generator and driver board (CG) sitting at SC layer generates this common synchronisation clock. This card provides a programmable number of clock pulses at programmable pulse frequency to DAC cards housed in EIUs distributed in field over ~800 meters. The galvanic isolation is maintained while providing the common clock to various devices.

Data flow

User given sample data table is communicated to API manager of PVSS which communicates the data to SC layer. As this is a bulk data communication for all the ramping devices, it first stops the normal data polling from SC layer. The SC layer sends these samples data to EIUs in multiple Profi packets. The EIU puts the corresponding device in calculation mode after receiving the data. DC mode settings are not allowed in this mode. EIUs then linearly interpolate the sample data into steps and puts in DAC card memory buffers. This interpolation calculation goes on each of the EIUs in parallel. This distributed approach of calculation of the ramp data takes less time (typically 2 minutes for 60000 steps) due to parallelism. The EIUs put the DAC card in the Ramp mode after the interpolation is complete. Data interpolation completion status is reflected to the API manager at UI layer in its polling. API manager sends a "Ready to Ramp" signal to the GUI after all the EIUs have completed the interpolation operation. If any error occurs in this complete sequence, the GUI does not get the "Ready to Ramp" signal and times out. The GUI aborts the ramping operation and puts all the selected devices in DC mode again on time out.

EXPERIENCE AND RESULTS

Our experience show that beam loss occurs at low energy with normal ramping speed (130 Hz).This may be because of large dI/dt and excitation of larger beam oscillations at lower energy. It was possible to successfully ramp the beam energy with ramping speeds of 30 Hz up to 800MeV, 60 Hz up to 1.3 GeV and 130 Hz onwards.

In a typical beam energy ramp a 34mA beam current was stored and ramped to 2GeV. A beam current of 26mA survived at 2GeV as shown in Fig. 4.

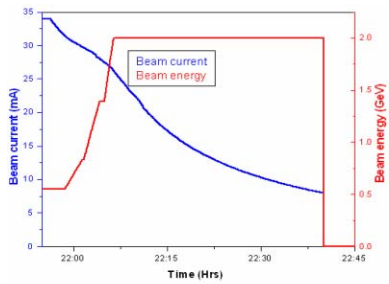

Figure 4: Beam intensity profile during energy ramp to 2GeV and stored condition.

CONCLUSION

The ramping scheme as implemented provides a user friendly GUI for machine operators with facilities to load and save data tables and increasing energy at required rates. The centralised synchronisation system based on hardware provides a very good tracking between various devices. The tracking uncertainty is less than 10 micro seconds.

Further improvements can be done in the implementation by providing a coherent interface between sample generation program (based on machine parameters) and ramping software.

The present ramping system has catered to the complex requirements of energy ramping in Indus-2 and found to be practically stable. With this ramping system accelerated beam of 2.4 GeV has already been achieved.

REFERENCES

[1] P. Fatnani et al, "INDUS-2 control system," PCaPAC'99, Tskuba, Japan.
[2] M. Seema et al, "Magnet Power Supply Control System for INDUS-2," InPAC'2003, Indore, India.
[3] R.K. Agrawal et al, "Synchronous Ramping Scheme for SRS Indus-2",ICALEPCS'2005 Geneva, Switzerland.
[4] R.K. Agrawal et al, "SCADA Functionality For Control Operations of Indus-2", ICALEPCS'2005 Geneva, Switzerland.

FIRST EXPERIENCES WITH CENTRAL WEB BASED FAULT INFORMATION SYSTEM

B. S. K. Srivastava#, P. Fatnani, RRCAT, Indore, India

Abstract

Indus Control System, which controls the Indus-1 and Indus-2 Synchrotron Radiation Sources at RRCAT, Indore, is a distributed computer system. It employs 8 VME Controllers, 300 interface modules, 7 Operator Computers for Indus-1 and approximately 100 Equipment Control VME stations, 10 Supervisory Controllers, 11 Operator Computers and 6 Server Machines for Indus-2. The machine is operated in shifts to provide synchrotron radiation from Indus-1 to users as well as carrying out commissioning experiments of Indus-2. To keep it up and running, the faults encountered during its operation are rectified at site and complete observations and rectifications of the faults are recorded electronically by the shift crewmembers in a central web based fault information system. This System is based on three tiers software architecture and has been developed using Java Servlets, HTML, JavaScript and SQL Database. Using relational database, facilities have been provided in the system for logging, e-mailing, acknowledging, exploring and analysing the fault information of various sub systems. This paper briefly describes experience, implementation aspects and functionalities provided by the system.

MOTIVATION

The main motivation of this project is to constantly monitor and improve the performance of Indus Control System. Indus-1 Control System Computers for different sub-systems are directly connected with their respective Equipment Controllers (ECs) through RS-232 serial link and these Equipment Controllers in turn are connected with different field devices e.g. Power Supplies, Vacuum Components, Radiation Monitors etc. Indus-2 Control System is based on three layer architecture for Controlling/Monitoring of various field devices. Operator Console Computers, which provide Graphical User Interface to operators, are connected with Supervisory Computers through 100 MBPS Ethernet link and Supervisory Computers are individually connected to EC Computers over RS-485 link. The EC Computers are finally interfaced to different field devices.

Seeing the complexities of different types of hardware and software involved in the control system, it was felt to have a system that would systematically track the information logged by machine crewmembers during operations of the machines.

#bsks@cat.ernet.in

REQUIREMENTS

Following basic requirements were considered before developing the system:

- It should be possible to use the system by multiple users simultaneously connected with CATNet (CAT Network).
- The system should be easy to use for especially non-computer experts.
- The information entered by the users should be precise and free of errors.
- It should be possible to send the entered information to concerned sub-system experts electronically.
- It should be possible to view the stored information in a structured way as per different search arguments e.g. system name, faulty device, time stamps, etc.
- It should be possible to acknowledge the stored faults by concerned sub-system persons.
- It should be possible to generate the system wise statistics of faults between a given periods of time.

It was realized that if web based system is designed then it would not only serve the above basic requirements but also offer many new features, which would not be possible with other non-web based systems. Thus this system was developed using Java, HTML, JavaScript and SQL Database. The first version of the system became operational in May 2004 and since then with various modifications and additions of new functionalities this system is being used continually by the crewmembers during operations of Indus-1 and Indus-2.

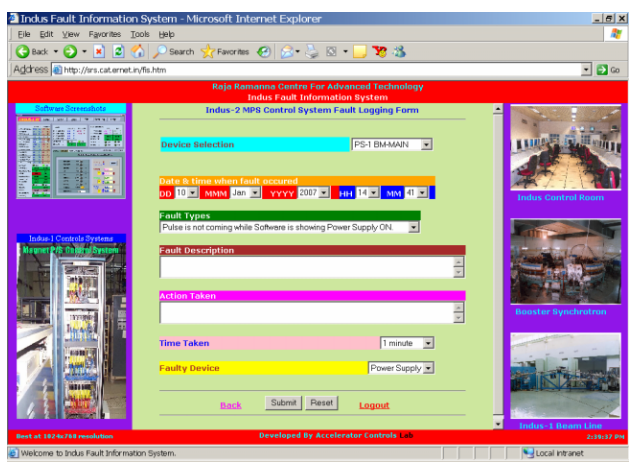

Figure 1: Fault Logger.

SYSTEM IN ACTION

Access to fault information system has been protected with password so that only authenticated users only could use the system. User interface part of the system has three sections namely Indus-1, Transfer Line-3 and Indus-2. All of these three sections have been divided into five sub-sections namely Fault Logger, Fault Acknowledger, Fault Explorer, Fault Analyser and Expert Info Viewer.

Fault Logger

This section provides option to log the entire fault related information from one point. Entries to be logged include subsystem name, device name, time stamp, fault type, fault description, action taken, time taken and name of the faulty device (Figure 1). To avoid the misspelling and confusion almost all the fields contain the drop down lists and masked with preset data so that user has to just select the value from the list. After logging the fault entries into database, system also asks users to opt for sending by e-mail the logged information to concerned persons. Names of the concerned persons are automatically displayed according to data filled in 'faulty device' field.

Fault Acknowledger

This section is meant only for persons concerned with the systems for acknowledging the faults. Users can retrieve (Figure 2) the list of unacknowledged faults by filling the query form.

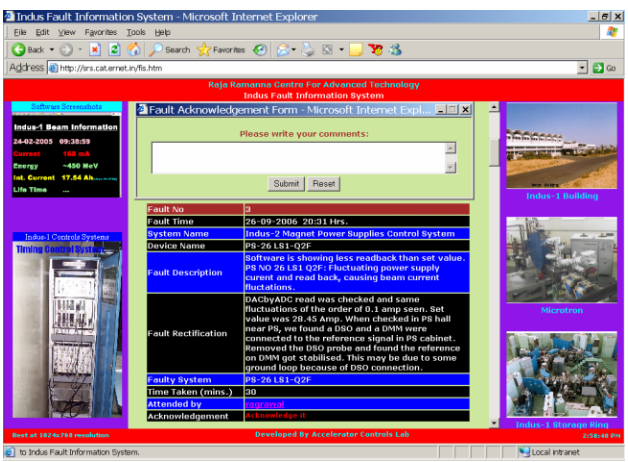

Figure 2: Fault Acknowledger.

Fault Explorer

This section provides facility to search the faults logged by crewmembers during operations of Indus-1 and Indus-2. By filling the query form user can search from the historical faults according to subsystem name, device name, faulty device and between given period of time. The historical faults are returned in a table, which contains the fault date & time, system name, device name, fault description, fault rectification, faulty system and logged by fields.

Fault Analyser

This section of the system (Figure 3) facilitates the users to view the statistics of devices found faulty out of any specific system in pie charts over a given period of time.

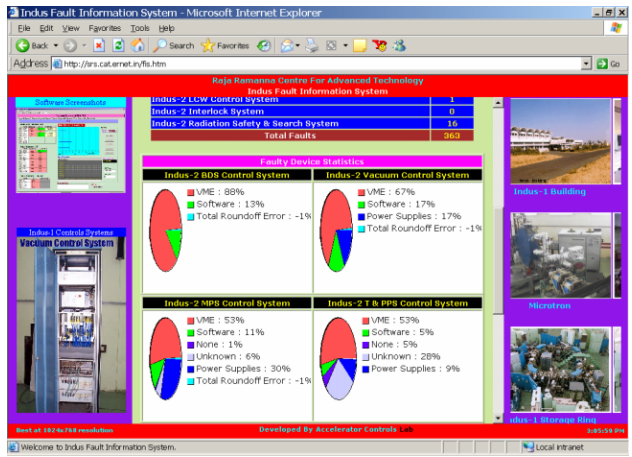

Figure 3: Fault Analyser.

VME, Power Supplies, Software, Computer, etc may be some of the faulty devices in case of fault related to any sub system controls.

Expert Info Viewer

This section of the system was added later and facilitates the users to only view the names of devices and concerned persons. Concerned persons listed in this table can acknowledge the faults and logged fault information is also mailed electronically to these concerned persons only.

Shift Summary

This special section of the system was added recently for logging, e-mailing and exploring the main activities done during the operations of Indus-1 and Indus-2. This section is very useful for group leaders and system experts.

CONCEPT

The system follows the three-tier software architecture where Web Browser, Java Servlets and DBMS Server reside on client, middle and data tier respectively. Java Servlets in middle tier connect clients built using HTML or applets to back-end servers.

Client Tier

For interacting with the system, the client tier (user interface part) has been designed using HTML and java

script. JavaScript codes have been incorporated in HTML query forms for validation of data filled by users at client end. A client communicates its requirements to the servlet, using HTTP and the business logic in the servlet handles the request by connecting to the DBMS Server.

Middle Tier

Java Servlets, which act between client and data tier were chosen to implement the middle tier that connects the client tier to data tier.

Java Applets were embedded in HTML pages (Figure 3) to plot the pie chart and bar chart for pictorially displaying the faults statistics of various sub systems.

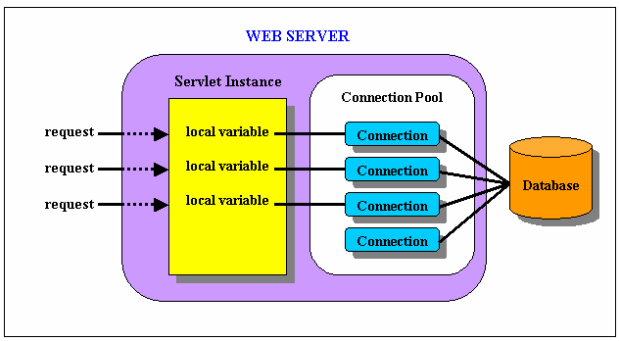

Figure 4: Servlets using a database connection pool.

Using JDBC Type4 Driver a database connection pool has been used to improve the performance. This servlet creates a pool of Connection objects in advance and hands them out as needed as shown in Figure 4. This servlet maintains a Hashtable, using Connection objects as keys and Boolean objects as stored values. The Boolean value indicates whether a connection is in use. If all the connections are in use, the class creates new one.

Data Tier

SQL Server 2000 based database was designed to implement the data tier, which stores the complete information in related tables. Device Information and concerned persons details were stored in the database so that logged fault information could be mailed electronically.

CONCLUSION

The first version of the system with only basic required functionalities was launched in May 2004. After that many new features were added as per the feedback from crewmembers, system experts and group leaders. The system is very useful for not only the accelerator crewmembers but also for machine/subsystem experts for improving the overall machine performance.

Presently, we are using Microsoft Windows 2000 based infrastructure and if we switch to Linux based infrastructure then very little modifications are required in codes of middle tier of the system during porting.

CONTROL SYSTEM FOR BEAM DIAGNOSTIC SYSTEM OF INDUS-2

Amit Chauhan#, Bhavna Merh, Pravin Fatnani, Sampa Gangopadhaya
Raja Ramanna Centre for Advanced Technology, Indore-452013, India.

Abstract

This paper presents the Beam Diagnostics Control System for Indus-2 that monitors and controls the parameters related to Beam Profile Monitors (BPM), Beam Position Indicators (BPI), Direct Current Transformer (DCCT) and XZ-selection for strip-lines. The system has three-layered architecture. The middle and lower layer have VME stations with CPU cards having RTOS OS-9. The lowest layer has nine stations that house various Analog and Digital I/O boards connected to the actual devices in the field. The boards include 4-channel 16-bit ADC cards developed for BPI interfacing. The middle layer collects the data from lower layer and passes to top layer and passes the commands from top layer to the lower layer. The top layer has the GUI for operator control built using a SCADA software PVSS. It provides various features to the user for graphical display, trending, configuring, controlling, data-logging and selective data monitoring of the parameters. This system finds use right from the beam injection stage to the Orbit correction stage in addition to the normal operation stage of the machine.

CONTROL SYSTEM OVERVIEW

The control system of Indus-2 has a three-layered architecture as shown in figure-1.

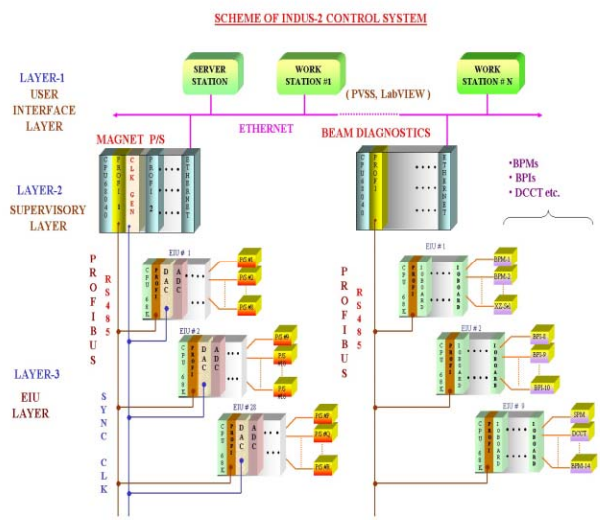

Figure 1: Scheme of Indus-2 Control system

At the lowest layer, Layer-3, known as Equipment Interface Unit (EIU) Layer there are VME stations that have various analog and digital I/O cards. These cards are interfaced with the devices in the field. The middle layer, Layer-2, is the Supervisory Layer where there are separate VME station controlling each sub-system of Indus-2 like Magnet Power supply system, beam diagnostic system, RF system, vacuum system etc. The top layer, Layer-1, is the User Interface Layer that provides the Graphical interface to the users for operating the machine.

The communication between Layer-1 and Layer-2 is on TCP/IP network using socket-based communication. Layer-2 and Layer-3 communicate using ProfiBus field-bus protocol where Layer-2 acts as the Profi Master and Layer-3 acts as Profi slave. Second and third layers make use of in-house developed Profi controller cards configured as master and slave respectively.

BEAM DIAGNOSTICS CONTROL SYSTEM

As the name suggests the Beam Diagnostics system is used for measuring the various parameters of the electron beam like its profile, position and the average current. For this various devices like BPIs, BPMs, DCCT etc. have been developed and installed in the machine by the Beam Diagnostic group at RRCAT. All the signals for controlling and monitoring of these devices are interfaced to the control system of Indus-2.

Like the control system for all other sub-system, the one for Beam Diagnostic system also has three-layer architecture as shown in Figure1.

Layer-3 has nine VME stations. Each station house a CPU card, a Profi salve card and the various digital and analog Input/output cards that are interfaced with the actual devices in the field. The OS-9 software at this layer implements Profi slave protocol, collects data from input cards and sets data on output cards.

Layer-2 has a single VME station that has one CPU card and one Profi master card. Layer-2 OS-9 software implements Profi master protocol and has socket programs for communication with Layer-1.It also holds the mapping of the various parameters of all the devices to the specific Layer-3 station, the I/O card and the channel number. So whenever a command from Layer-1 software is received, Layer-2 maps the command for the device at Layer-3 and sends it down.

Layer-1 software has been developed using PVSS, SCADA software. This software has two components. First is the API-manager written for PVSS that connects to Layer-2 on TCP/IP network and exchanges data and commands. It resides on a specific server machine. The second component is the Graphical User Interface (GUI) in the form of PVSS panels. These panels can be run on any PC on the Control Room network. Various panels have been developed for the various sections of the Beam-diagnostic sub-system like BPM, BPI, DCCT, etc

#amit@cat.ernet.in

BPM CONTROL

Beam profile Monitors (BPMs) have been developed by the Beam Diagnostic group. These are used to monitor the profile of the electron beam in the ring. A BPM typically consists of a CCD camera and a movable assembly to move a florescent screen in and out of the accelerator assembly. When the beam falls on the screen, an image is generated which is captured and transmitted by the CCD camera. There are 23 such BPMs in the system.

For operation of every BPM six signals are interfaced with control system. Two are control signals – activate and deactivate BPM interfaced with Relay-output cards. Four are status signal – screen in, screen out, selection/deselection status and remote/local status interfaced with opto-input cards. The video signals from all the BPMs are connected to a pair of Video-multiplexer cards. For the operation of a particular BPM, the corresponding relay channels and the video multiplexer channels are activated by the control system.

Figure 2 shown the control panel for BPM control system developed using PVSS.

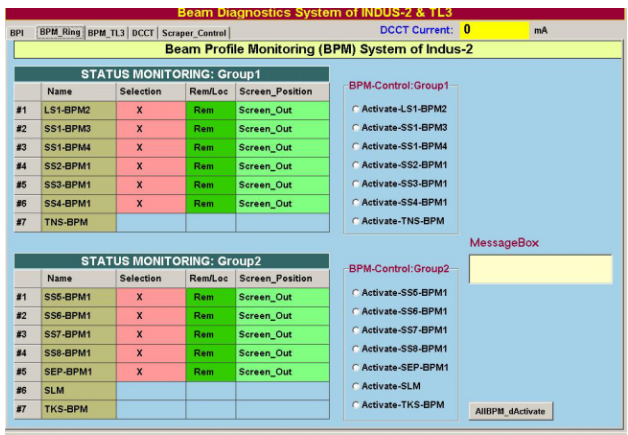

Figure 2: PVSS Panel for BPM control

BPI CONTROL

In Indus-2 the beam position is measured using Beam Position Indicators (BPI) that have 4-button electrodes each. There are a total of 56 BPI in the ring. Each BPI unit provided 4 analog signals and one digital signal. The analog signals are 0 to 10 volts corresponding to the charge induced on each button as per the beam position. The digital signal corresponds to the PLL status of the BPI unit.

The GUI panel shows all the individual readings as well as the calculated X-plane and Z-plane position of the beam under that particular BPI. The panel also shows the PLL and external trigger enable status for all BPIs.

Figure 3 shows the snapshot of the panel for BPI system.

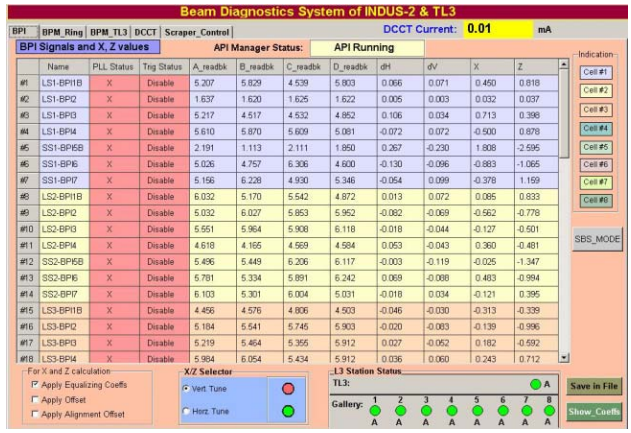

Figure 3: PVSS Panel for BPI control

4-channel 16-bit ADC card development

For the purpose of fast acquisition and conversion of the BPI signals, a VME based ADC card has been developed by the Controls group at RRCAT. The 4 analog signals from the BPI unit are connected to the 4 channels of this ADC card. The block diagram of this card is shown in figure 3.

The main features of this card are:

- 4-independent channels of 16-bit serial ADC with conversion time of 10 microseconds.
- 4- digital input channels
- Isolation between ADC front-end and VME logic circuit using DC-DC converters.
- Capable of interrupting VME controller on selectable level
- Full 24-bit selectable address
- 8-bit selectable interrupt vector
- External / Internal SOC selection by software. External SOC comes at the BNC connector and Internal SOC is generated by writing at an address location.
- Analog filters at the input with gain selection.
- ADC configuration has range selection through jumper setting (0 to 10 V or –10 to +10 V)
- Most of the logic implemented in CPLD

Presently there are 58 such cards used in the beam diagnostic control system

Features of Software

The Layer-2 API software for calculating the beam position uses various equations, offset data and calibration data to convert the button monitors readings into position values.

The overall software also provides the feature for averaging a number of sample readings of all the BPI data at Layer-3 station. The sample count is selectable from 2 to 20 per reading.

There is facility to selectively enable/disable particular BPIs from the panel. The software has the feature of periodically or on-demand archiving of the values of all the BPIs readings.

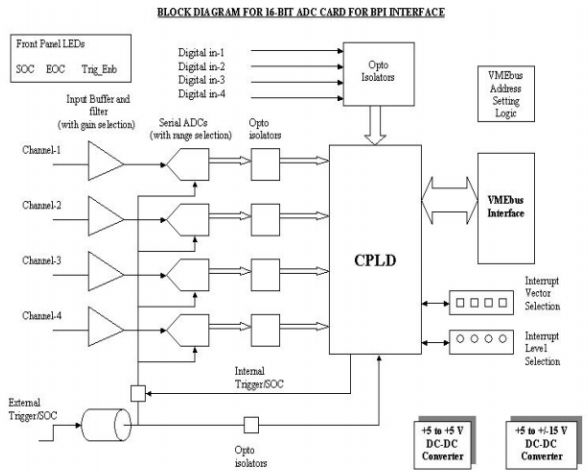

Figure 4: Block Diagram of ADC card

DCCT CONTROL

The Beam Diagnostic Group has installed a Direct Current Transformer (DCCT) in the Indus-2 ring to measure the average electron beam current.

The DCCT unit provides one analog signal to the control system that is digitised by the 16-bit ADC card (similar to the one used for BPIs). In addition to it there are five status-signals and five control-signals that are interfaced to the control system using opto-input and relay-output cards respectively. The status signals include calibration on/off, test on/off, Range A selection, Range B selection and temperature alarm. The control signals include test on/off, Range A/ Range B selection, put in calibration, Negative/positive calibration and temperature alarm reset.

Figure 5 shows the PVSS panel for DCCT. The panel has built in logic for automatically switching from Range A(0-1000 mA) to Range B(0-100 mA) and vice-versa depending on the present current value and the range limits. It also plots the current data and provided all the control and status information.

XZ-SELECTION CONTROL

There is a VME based XZ-selection card with RF-switch developed by Beam Diagnostic group. It is used to select the strip-lines in either X-plane (horizontal) or Z-plane (vertical). It is housed in one of the VME stations at layer-3 of control system. The logic to switch the plane and show the status of the presently selected plane has been incorporated in all the three layers of the control system. The PVSS panel for BPI system includes the XZ-selection control and display also as shown in Figure 3.

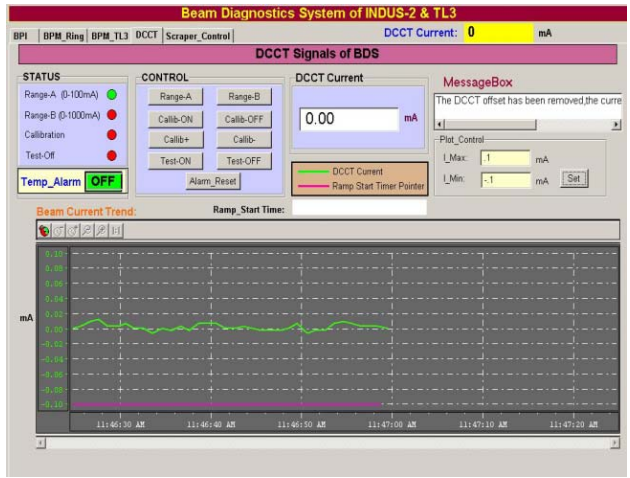

Figure 5: PVSS Panel for DCCT control

CONCLUSION

The control system for Beam Diagnostics is useful at all the stages of machine operation. During the injection process the various BPMs come in very handy to know the status of the electron beam. During the normal operation the DCCT data helps in knowing the beam current and BPIs data is used for displaying beam position. In near future during the orbit correction stage again the BPI data will be used to calculate the appropriate values to be applied to the various horizontal and vertical corrector magnets.

REFERENCES

[1] P.Fatnani et al, “Indus-2 Control System”, PCaPAC 1999, Tskuba Japan.

[2] T.A.Puntambekar et al, “Experiences of Beam Diagnostic System in commissioning stage of Indus-2”, APAC 2007, Indore, India.

[3] K.Saifee et al, “Profibus development for Indus-2 control system”, InPAC-2003, Indore, India

[4] Amit Chauhan et al, “Application of RTOS (OS-9) for Indus-2 Control System”, InPAC-2003, Indore, India

CONTROL AND INSTRUMENTATION FOR THE VEC SUPERCONDUCTING CYCLOTRON CRYOGEN DELIVERY SYSTEM

T. K. Bhattacharyya#, T. Das, C. Nandi, G. Pal and R. K. Bhandari
Variable Energy Cyclotron Centre, 1/AF Bidhan Nagar, Kolkata 700064

Abstract

The cryogen delivery system for the superconducting cyclotron supplies liquid helium to the superconducting main magnet coil and three cryopanels. It also supplies liquid nitrogen to the thermal shield of the liquid helium chamber housing superconducting coil and the thermal shield and baffles surrounding the cryopanels. A suitable efficient piping network comprising vacuum jacketed cryogenic transfer lines, liquid nitrogen shielded transfer line and distribution manifold is used in the superconducting cyclotron for distribution of cryogens. A liquid helium pump ensures the required flow of liquid helium through the cryopanels. The cryogen delivery system is fitted with necessary field instrumentation and controllers to monitor and automatically control certain important process parameters. This paper presents the overall control and instrumentation for the cryogen delivery system.

INTRODUCTION

The importance of cryogen delivery system [1] in the context of a superconducting cyclotron is immense and critical. The superconducting coils of the cyclotron are immersed in a pool of liquid helium. Liquid helium is supplied to the magnet from the liquid helium plant/refrigerator. The accelerating chamber of the superconducting cyclotron has to be maintained at high vacuum for proper acceleration of particles. Vacuum in the accelerating chamber is obtained by three cryopanels placed inside the cyclotron. These cryopanels are cooled by liquid helium. Liquid nitrogen is used to cool the thermal shields of the liquid helium chamber for the superconducting coil and the liquid helium cooled cryopanels. The delivery of liquid helium (4.2K) and liquid nitrogen (77K) from liquid helium plant and nitrogen dewars to the cryostat and cryopanels requires extreme caution, continuous monitoring and finest control. Considering its safety and control aspects an intensive data acquisition and control instrumentation has been designed, installed and successfully operated.

INSTRUMENTATION SCHEME

The system takes care of as many as hundred parameters which are extremely critical for operation of the superconducting cyclotron main magnet. The system is designed to operate in a harsh condition, without loosing its performance or speed. Each hardware component is selected considering fast action, appropriate range, continuous run and fail-safe operation. From the control point of view, the system is centralised. It employs a centralized approach to the tasks of control, monitoring, data acquisition and machine protection. The heart of the instrumentation hardware is a Schneider make level 3 premium processor based PLC. It has a three layer hierarchy with PLC at its centre. All duties related to process control, interlock generation are performed in this layer. The first layer consists of mostly field instruments of different make which acts as the gateway between process signals and the PLC. The top most layer is a supervisory control and data acquisition software, operating in two different computers in two distant locations for controlling, monitoring and data acquisition. The PC-based consoles employ Wonderware SCADA software for cryogen delivery system monitoring and control.

Hardware Layout

The first layer (Fig. 1) consists of mostly field instruments, viz. pressure transmitters, level monitors, temperature transmitters, multi-channel strain gauge scanner, vacuum gauge controllers, dewar pressurisers, valve controllers and positioners of different make. Processed analog signals from each of these transmitters/ instruments are taken to/ from the second layer (PLC) for data acquisition and control. The web server facility of the PLC has enabled all the other workstations connected in the dedicated LAN to monitor some of the important parameters. Dedicated control logic was developed to process digital and analog input channels, operate various controls, generate interlocks and communicate with the supervisory control. The control parameters [2] are operated through control loops operating independently on the PLC. The PLC continuously monitors values of all the cryostat and cryopanels parameters and primarily uses these signals to control the cryogen delivery system. This also generates a "PLC_OK" signal if all the parameters are healthy. If anything goes wrong in the system, it takes necessary actions for the cryogen delivery system and also "PLC_OK" signal is withdrawn. The PLC is powered from the on-line UPS for reliable operation.

tamal@veccal.ernet.in

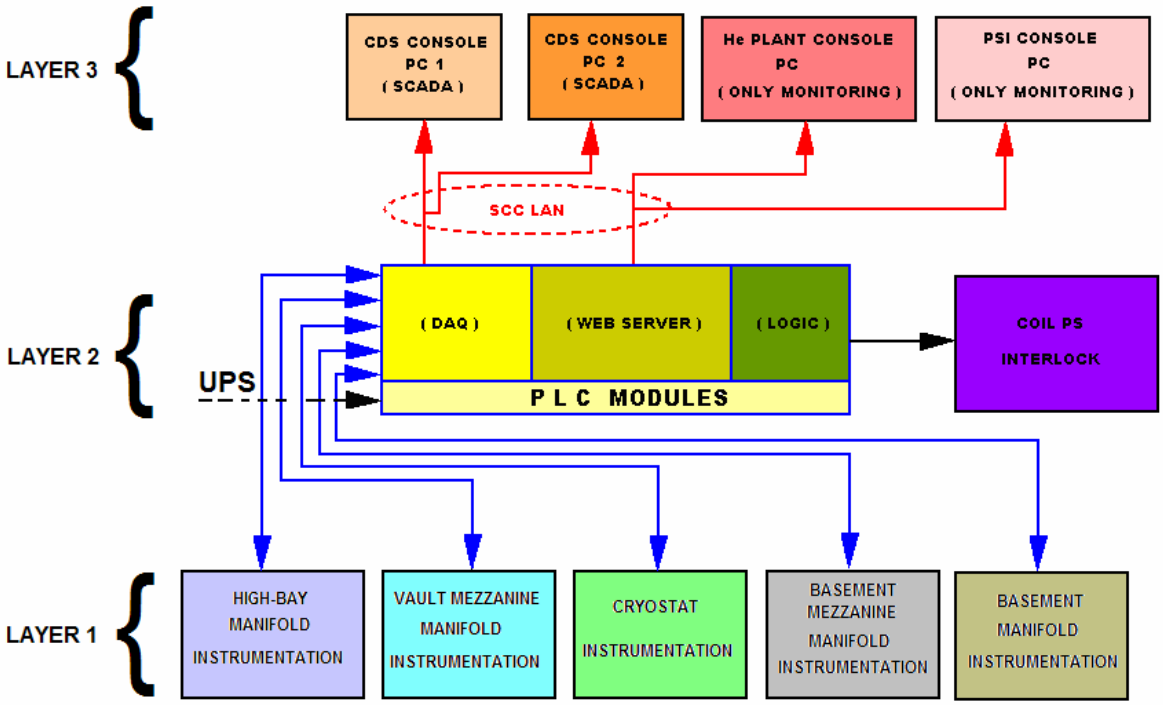

Figure 1: Hardware layout of cryogen delivery system instrumentation

Software

The supervisory control and data acquisition (SCADA) software monitors various system parameters, e.g. temperature, helium liquid level, condition of on-off valves, condition of control valves, etc. It has facility for remote control via Ethernet. It can control the parameters of the system by using PID or suitable control option. Special control panels for the different modes of operation are developed for the cryogen delivery system. The SCADA generates alarm on the console computer for the faulty conditions.

CONTROL SCHEME

The control system is a PLC based system. The SCADA communicates with the PLC through dedicated control LAN. It takes care of data acquisition and control in different operating modes through final control elements. In addition, this control system takes care of human as well as machine safety.

Monitoring and Data Acquisition System

Wonderware is used as SCADA. It allows the user to monitor, control, data logging and event monitoring. It also generates alarm as and when required and takes care of different mode of cryogen delivery system. Different access levels are provided for preventing unauthorised access. Modification is being carried out so that all the system requirements are met.

Control in Different Phases

This control system takes care of different modes of operation viz. cool down, steady state magnet standby, magnet ramp-up, steady state magnet energised, quench protection, magnet warm-up and power failure condition and generate alarm and interlock signals as and when necessary.

Safety features

Safety is one of the major aspects while operating with cryogens. Several safety interlocks, message displays and alarms are incorporated for human as well as machine safety.

- While energised, any reduction of helium level may cause severe damage to the superconducting magnet coils. To prevent this hazard, liquid helium level is constantly monitored and interlocked with the coil power supplies. Similarly, coil tank pressure and vacuum in the cryostat outer chamber are continuously monitored. ‘Slow dump’ and ‘fast dump’ interlocks are generated if any deviation is sensed.
- All the valves and actuators are installed such that they all remain in their respective fail-safe positions in case of any power or instrument air failure.
- Air-lock relays are used to maintain critical electro-pneumatic valves at their respective operating positions in case of sudden air failure.
- All the cryogen lines and dewars are equipped with safety valves, rupture discs to release the pressure in case of sudden pressure build-up.

CONCLUSION

The cryogen delivery system for the superconducting magnet was successfully commissioned in November 2004. It offered a hand full of complexities and technological challenges during the installation and commissioning. Cryopanel control was integrated with the magnet cryogen delivery system in the month of October, 2006. At present, this combined instrumentation and control system is running smoothly up to our satisfaction. Efforts are also being made to upgrade some of the field instruments with HART based smart transmitters.

ACKNOWLEDGEMENT

The authors are grateful to members of different subsystems of the superconducting cyclotron for their constructive remarks and feedbacks which helped us to define and integrate this system meeting all the requirements from different groups.

REFERENCES

[1] G. Pal, T.K. Bhattacharyya, C. Nandi, J. Pradhan, A. Dutta Gupta, J. Chaudhuri and R. K. Bhandari, “VECC Superconducting Cyclotron Cryogen Distribution System”, Proceedings of the Eighteenth International Cryogenic Engineering Conference (ICEC18), Mumbai, February 2000, p. 451.

[2] T. K. Bhattacharyya, C. Nandi, G. Pal, J. Chaudhuri and R. K. Bhandari, “Control System for Cryogen Delivery System of the Superconducting Cyclotron Magnet”, InPAC’03, Indore, February 2003, p. 594.

STATUS OF THE SUPERCONDUCTING INSERTION DEVICES CONTROL SYSTEM AT TLS

K.H. Hu#, Jenny Chen, Demi Lee, S. Y. Hsu, C.H. Kuo, K.T. Hsu
National Synchrotron Radiation Research Center, Hsinchu 30076, Taiwan

Abstract

Superconducting insertion devices installed at the Taiwan Light Source serve the rapidly growing community of X-ray users. The control system supports the operation of all these superconducting insertion devices. Control system coordinates the operation of the main power supply and the trimming power supply to charge/discharge the magnet and provide essential interlock protection for the coils and vacuum ducts. Quench detection and various cryogenic interlocks are designed to protect the system. A friendly user interface and control applications are developed to support routine operation. The diagnosis of the tripping of superconducting insertion devices related to machine operation is also addressed. Design considerations and details of the implementation will be summary in this report.

INTRODUCTION

Three superconducting insertion devices a superconducting wavelength shifter (SWLS), a superconducting wiggler (SW6) and an in-achromat superconducting wiggler (IASW-R6) have been installed. Two other such devices, IASW-R2 and -R4, will be installed in the future. These superconducting IDs are applied to enhance hard X-ray production to support diffraction, scattering, spectroscopy, EXAFS, imaging, and protein crystallography. The control system of superconducting insertion devices was designed implemented and commissioned to support the operation of these devices. This control system based on the VME crate system as a standard configuration; interlock protection and a graphical user interface (GUI). The interlock logic is implemented using a programmable logic controller (PLC) to protect the coils of the magnet. The user interface and various application programs enable routine operation.

Table 1:Parameters of Superconducting Insertion Devices

Device	No.	Parameters	Applications
SWLS	1	6 Tesla, 66 poles, 30 mm periods	X-ray Imaging, Diffraction, Scattering, EXAFS, Powder Diffraction
SW6	1	3.2 Tesla, 66 poles, 30 mm periods	Protein crystallography
IASW6 -R6, -R2, -R4	3	3.2 Tesla, 66 poles, 30 mm periods	X-ray Imaging, Diffraction, Scattering, Powder Diffraction

#uka@nsrrc.org.tw

INFRASTRASTRUCTURE OF THE CONTROL SYSTEM

The system can be controlled using a standard VME crate to accommodate various control modules. The crate includes a PowerPC-based CPU module, which runs a LynxOS 4.0 real-time operating system as a local controller of the superconducting IDs control system. The crate includes analog input/output modules, digital input/output modules and the RS-232 interface module. The control system of superconducting IDs depends on coordinating the operation of power supplies, cryogenic instruments and interlock protection logic. Figure 1 illustrates the infrastructure of the superconducting IDs control system. Control consoles communicate with the VME host module through the control Ethernet.

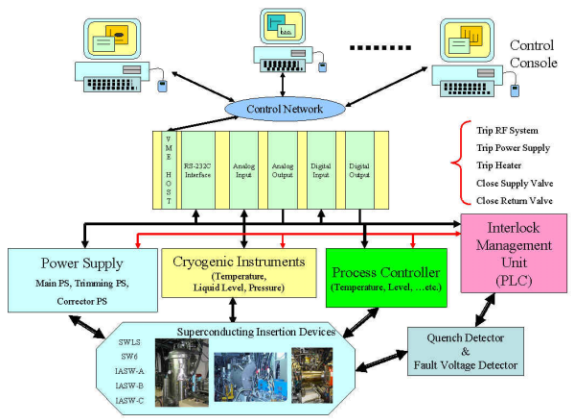

Figure 1: The control system infrastructure of the superconducting insertion devices.

Power Supplies

A precision bipolar main power supply is used to charge/discharge the magnet. The trimming power supplies are used to correct the field error. A low slew rate is used at the beginning because the inductance at low field is high when charging began. The slew rate is high after the field saturates the internal iron core, and the inductance is then considerably reduced. The control applications automatically control the slew rate. The trimming power supply can be set independently or follow the output of the main power supply, according to a predefined table. Two correctors are added upstream and downstream of all of the installed superconducting IDs. The control system coordinates the outputs of the corrector power supplies, to compensate for distortion of the beam orbit.

Cryogenic Instruments

Cryogenic instruments are used to monitor the parameters of the cryostat, which holds the magnets. The coil of the superconducting IDs is cooled by submerging it in liquid helium (LHe). Hence, the LHe level and He pressure in the vessel must be maintained in safe ranges. The instruments include a temperature monitor, level meters for LHe and liquid nitrogen (LN_2), pressure meters for He and N_2, and a vacuum gauge. The limiting high temperature, low level and high pressure can be set using these instruments. The pressure and the liquid level of the superconducting IDs control are also sent to the automatic filling system [4] to maintain the liquid level within the safe region automatically.

Quench Detector

The quench detector and interlock logic are used to protect the coil of superconducting IDs. The first layer of the hardware protection circuit consists of R620 diodes and 6 m stainless steel resistors. The protection circuit is connected in parallel to the coils of the magnet. This circuitry protects the coils form overheating during quenching. The voltage across the coils increases rapidly when a quench occurs. The quenched coil voltage is limited by the conducting diode. The resistors in series with the diodes help to dissipate the energy that was stored in the coils. The diodes provide a bypass route for the coil current. However, this scheme is only for short-term protection; the main power supply must be disabled after a quenching event. The power supply trip is triggered by the quench detector with a response time of less than 10 msec. Figure 2 shows the block diagram of the quench detector circuit and the interlock logic. The quench detector is in a VME form factor. A bridge circuit is used for quench detection. An imbalanced voltage in the bridge circuit implies the occurrence of a quench event. An imbalance between the voltages of the coil arm and the resistor arm cause the signal of the quench detector to trigger the protection logic of the PLC.

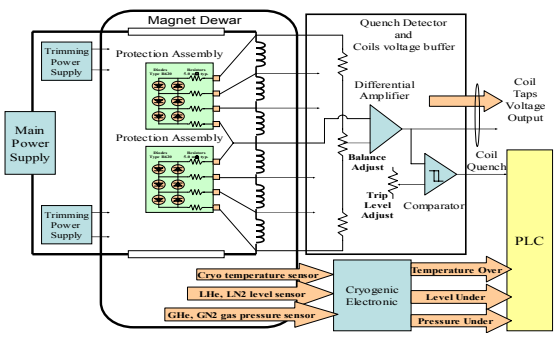

Figure 2 : The superconducting insertion devices protection scheme.

Interlock

The interlock logic is designed to protect the coils of the magnet. It is integrated in a fast scan PLC. The PLC manages the alarm signal from the cryogenic instruments, which measures the temperature, the LHe and LN_2 levels, and the pressures of He and N_2 in the vessel. The quench detector and the voltage tap monitor are also considered to generate hardware interlock signals. When the temperature is too high or the quench detector is triggered, the protective action is to shutdown the power supply, preventing excess heat from increasing the temperature, and dissipating LHe. The level meters and pressure meters are connected to the process controller of the valve box for an auto-fill system. If the pressure of He or N_2 exceeds the upper limit of the safety range, the PLC will immediately shutdown the power supply. The action of the PLC can make all decisions within 5 msec. The relief valve of the vessel is used to released when the pressure of the vapour of He and N_2 over its rate value. The reliability of the quench detector is important. The coils of the magnet are soaked in LHe, so the variation in the temperature of the magnet caused by quenching is very small. The quench detector is trigger by the large on/off transient of the main power supply. The interlock logic is disabled for 10 sec during the turning on of the power supply. It is safe because no output current flows from the power supply at that time, except up to 10 Amp current spike.

Trip Diagnostic

The trip event diagnostic is essential to obtaining information about the causes of the trip. Identifying the cause of quenching or tripping is helpful. One 16 channel transient recorder with a sampling rate of 100 kS/sec is installed to capture the event. The main coil current, the coil voltage, the quench detector output, and the interlock output of PLC continue to be monitored. The system was improved to help to identify several problems that arose during the last several months.

User Interface

The control system provides various application programs that support the routine operation of all superconducting Ids. They perform on/off control for the power supplies, charge/discharge control for the magnet and software protection for the magnet. The power supply cannot be enabled until the temperature of the magnet, the levels of LHe and LN_2 and the pressures of He and N_2 are all in safe ranges. These predefined protecting values are all stored in the control database. The control system has two types of archivers, which are supported by the control system. A long-term archiver record data every 10 sec. Another fast archiver with a lifetime of 1 week records data every 0.1 sec. The archiver records provide much useful information that can be used to improve the operation of the superconducting IDs. The user interface provides has two pages for all superconducting IDs to support normal operation. In the SW6 case, operators use the first page to monitor the status of the SW6 and set the output current and slew rate of the main power supply, as shown in Fig. 4 (a). The second page presents interlock information and the alarm limits of the SW6, as a temperature threshold, LHe and LN_2 levels and pressures of He and N_2, as shown in Fig. 4 (b). The operator can

reset the interlock status and set the alarm limit by software protection on this page. The user interface presents in real time information about the magnet and provides a convenient manipulation environment.

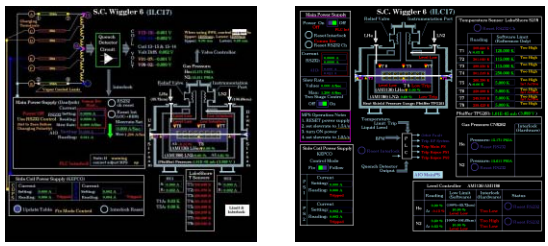

(a) Operation page (b) Maintenance page

Figure 4 : SW6 user interface for routine operation and user interface for interlock information.

SOME OPERATION SCENARIOS

Figure 5 plots a typical charge/discharge current history of the SW6. Figure 6 shows LHe level and pressure of Helium vapor variation. Figure 7 plots the voltage of the coils, the pressure of He vapor, and temperature variation when power supply is suddenly turned off. Trip diagnostics are very helpful for identifying the origins of problems. The main power supply of SWLS turn off occasionally was occurred during September and October 2006. Figure 8 provides trip diagnostic. Clearly, the power supply current decreases to zero before any interlock is activated. This problem was identified as having been caused by a bug in the power supply controller firmware. In Fig. 9, a charge current 270A flows upon occurrence quenching of the IASW during the measurement of the magnet field.

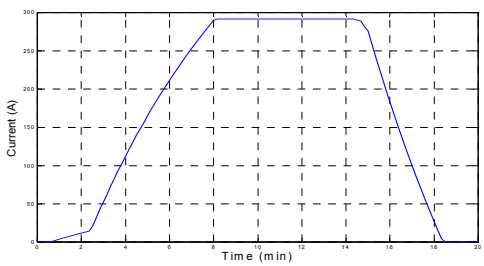

Figure 5 : T typical charge/discharge current history of the SW6.

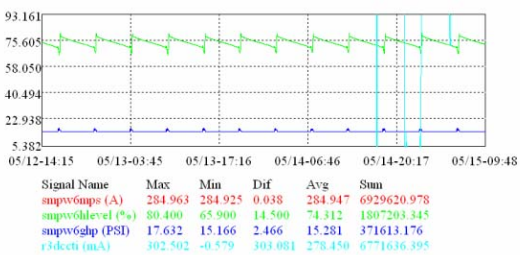

Figure 6 : Typical LHe level and pressure of Helium vapor.

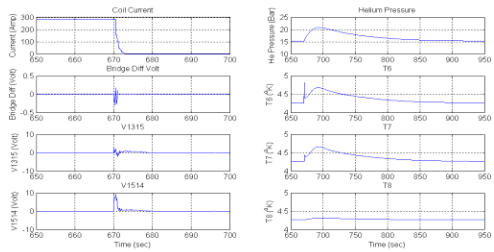

Figure 7 : Coils voltage, pressure of He vapor, and temperature variation when power supply is suddenly turned off.

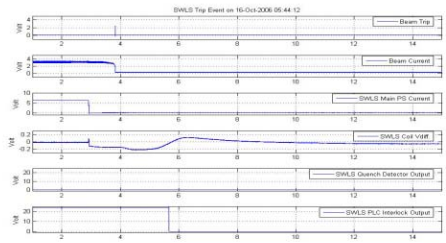

Figure 8 : Beam trip of the storage ring when main power supply trip of the SWLS.

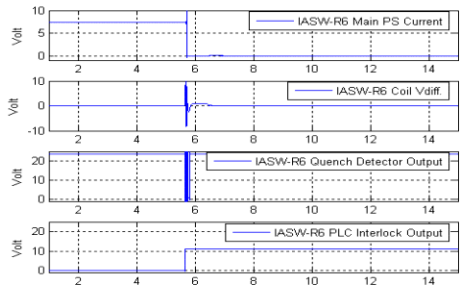

Figure 9 : A charge current history of the IASW when quench happened.

SUMMARY

The control system was implemented to support the routine operation of superconducting IDs. The same infrastructure is adopted, it will benefit to the operation and maintenance. Diagnostics of various trips are also included to elucidate the reasons; the reliability of the system can be improved after the tripping mechanism has been identified. Experiences accumulated during the last several years will help to improve the performance and the reliability of the control system.

REFERENCES

[1] C. S. Hwang, et al., "Design of a Superconducting Wiggler for Synchrotron Radiation", IEEE Trans. on Appl. Supercon, Vol. 13, No. 2, pp.1209-1212, 2003.

[2] C. S. Hwang, et al., "Superconducting wiggler with semi-cold beam duct at Taiwan Light Source", Nucl. Instr. and Meth. A 556, (2006) 607.

[3] F. Y. Lin, et al., "Auto-filling Cryogenic System for Superconducting Wiggler", Proceedings of EPAC 2004, Lucerne, Switzerland.

REJUVENATION OF LINAC CONTROL SYSTEM FOR TLS

C. Y. Wu#, S. Y. Hsu, Demi Lee, C. J. Wang, Jenny Chen,
K. H. Hu, C. H. Kuo, K. T. Hsu, K. K. Lin
National Synchrotron Radiation Research Center, Hsinchu 30076, Taiwan,
J. Y. Hwang, National Tsing-Hua University, Hsinchu, Taiwan

Abstract

The pre-injector control system is a turn-key system, which was deployed 15 years ago. It is complicated and out-of-date nowadays in terms of system integration and hardware upgrading. It must be modernized to ensure its performance and reliability, and most importantly, to facilitate system maintenance. Modernization involves upgrading to enhance functionality, to prevent obsolesce of out-of-date control modules, and to replace old parts. The purpose of the upgrade plan is to replace the pre-injector control system by a new unit which has the same control environment as that of the main control system of the NSRRC accelerator facilities. Thus, the control system maintenance, as a whole, will be made substantially easier than the original system.

INTRODUCTION

The pre-injector of the Taiwan Light Source (TLS) comprises a 140 kV thermionic electron gun and a 50 MeV traveling wave type linear accelerator (linac). The functional block diagram and layout of the pre-injector is depicted in figure-1. The electron beam emitted from the gun is accelerated through the linac with exiting energy of 50 MeV. Then, the electron beam is guided along the linac to booster (LTB) transfer line and is injected into the booster. Brief descriptions on elements in the LTB are also given in figure-1.

The control of the linac uses a dedicated programmable logic controller (PLC) equipped with 10 MB/sec Ethernet interface. It has been operated since 1990. Besides, the vacuum interlock logic of the booster is implemented using the PLC unit and is tightly coupled with the pre-injector control system. This integral arrangement causes difficulty in carrying out maintenance and replacement of some out-of-date devices in the pre-injector system. Consequently, the control system is being rejuvenated to improve its performance in the following aspects: decouple the vacuum interlock logic from the linac control system, provide better control functionality for top-up operation, and avoid lacking of out-of-date spare units. In order to achieve this goal, one VME crate system is dedicated to linac control. A new hardware unit with a high-resolution analog interface is installed to provide dedicated service of control tasks. Two separated PLCs are newly implemented to replace the "old" PLC. A compact PLC is used to deal with the interlock logic. The other PLC is used to be responsible for the remaining linac devices which require sequential control in routine operation. It includes: access interlock of high voltage (HV) and safety doors, delay process of klystron and electron gun warm-up etc. Both interlock and sequence control PLCs are controlled by using the VME crate. All other functions, without interlock or sequential requirement, are directly controlled by the VME crate. The upgrading linac control system is expected to provide better performance on control functionality and maintenance simplification.

#chunyiwu@nsrrc.org.tw

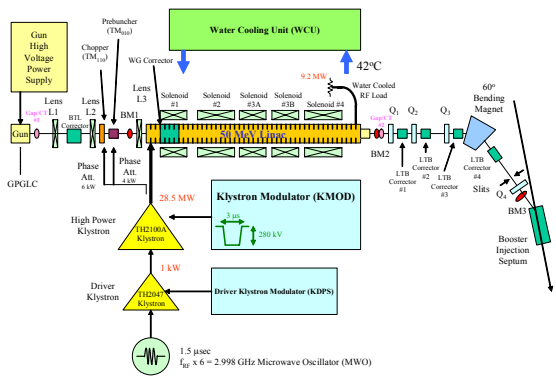

Figure 1. Synopsis of preinjector.

EVOLUTION OF THE LINAC CONTROL SYSTEM

The linac control system was embedded in the originally delivered turnkey control system of the injector, i.e. including pre-injector and booster. This system has been partly integrated with the NSRRC main control system in 1998 to enhance the operation efficiency. It reduced the resources of requirement in operating the injector and was directly benefited to performing the top-up operation. The remaining out-of-date PLC module has to be taken care of such that lacking of spare units would not jeopardize linac operation. Since top-up operation has been implemented in NSRRC in 2005, the accessible time for linac control upgrading is limited. Therefore, a long-lead transformation process toward a new control system is not avoidable. In dealing with this situation, a sideline in preparing the migration of the control environment has been exercised since July 2006 and its status is described in this report. It will become a new control system and is expected to be completed in June 2007.

Original Turnkey Control System

The original delivered injector control system was a turnkey design and was separated from the storage ring control system. Installing and replacing new devices as needed was not a straight forward task. The hierarchy of the system had three layers, as shown in figure-2. The first layer was a VAX/VMS workstation which was employed to provide an operational interface, such as system supervision, alarm management, communication with the computers in the second layer, and creation and maintenance of the system database.

The second layer was a PC which runs an iRMX-III operation system. It served as a master in the BITBUS network in communicating with the Siemens S5/135 PLC system, and processing the data.

The third layer had two subsystems: BITBUS network and PLC system. The BITBUS system connected all devices of the booster. The linac control function was attached to the PLC which also performed the vacuum interlock of the booster. The PLC was equipped with an IEEE-802.3 Ethernet interface communicating directly with the PC/iRMX-III system. The system was run in stand-alone mode, and must be operated separately from the storage ring control system.

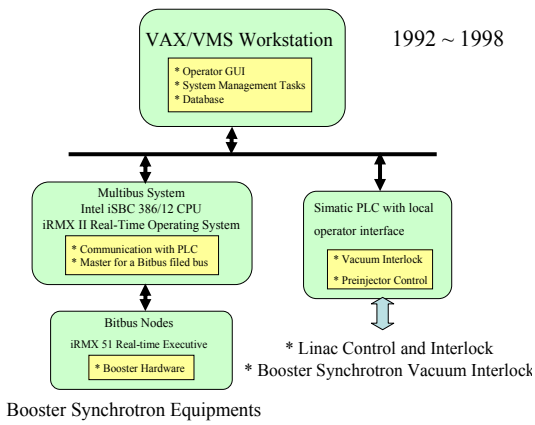

Figure 2. Functional block diagram of the original turnkey control system.

Integrated Control System

The major purpose of upgrading the control system is to: enhance the control efficiency and stability for light source operation; reduce the required maintenance resources, and prevent jeopardizing the system due to spare unit shortage. The first and partly upgrading of the control system of was carried out in 1998. As a result, it had improved system reliability and its response time. It also benefited to the upgrade project of the booster in raising electron beam energy from 1.3 to 1.5 GeV in 1999, since a number of major power supplies were replaced and was configured under the partly upgraded control system. Without the already prepared control system at that time, the booster 1.5 GeV upgrade would not be possible. Figure-3 shows the configuration of the partly upgraded control environment of the injector. The MULTIBUS system was replaced with VME crates. The BITBUS was eventually removed in 2000. The PLC system was retained due to the limited manpower available for the work.

PLC is the central core of the linac control system. It coordinates signals to and from the injector subsystem when it starts up and shuts down the linac. It communicates with the VME crate system via Ethernet network. The VME crate system runs a program to access the data of the PLC system. This VME crate functions as a protocol converter. The PLC is connected to the control network, and the VME crate communicates with the PLC over network connection.

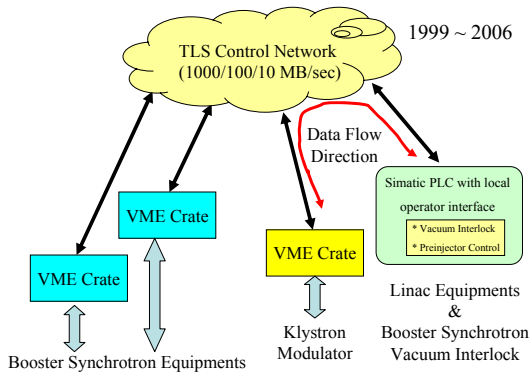

Figure 3. System block diagram of renewed control system in 1998. The signal flow between PLC and VME crate is highlighted.

New Control Environment

The partly upgraded system runs well since it was installed 1998. However, we have run into difficulty in maintenance of the PLC system. The existing system has all control and interlock functions in a large PLC. Separating functionality according to the hardware is not an easy task. The system is also complex because it combines all functionality in a single machine. The supports of this old PLC will soon become a problem. It is unavoidable that the old PLC has to be removed eventually and migrating to a full VME-based control system. The interlock logic is implemented using two simple PLCs. The new system utilizes one dedicated PLC to deal with the vacuum interlock logic while the other PLC handles the other interlock function of the linac system. Those functions without interlock requirement are connected directly to the VME.

A functional block diagram of the new control system is shown in figure-4. The new pre-injector control system consists of three parts. It includes the linac control interlock logic, the interlock for the booster vacuum system and the linac control subsystem. A proposed new hardware with a high-resolution VME analog interface provides better control flexibility. The alarm function of the digital panel meter generates a digital interlock signal to the PLC for analog alarm interlock. Accordingly, the PLC does not depend on the conversion of the analog signal to trigger analog alarm interlock The PLC runs only with digital input/output module. The two PLCs are

connected to the VME crate through simple digital interface. All functions of the linac control system are controlled using the VME crate.

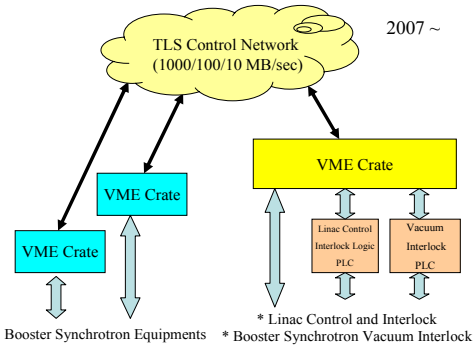

Figure 4. New control environment for LINAC system.

DISCUSSION

Three major changes of the LINAC control system have been made in the past 15 years for the following considerations: a) upgrade its functionality; b) replace out-of-date modules; c) integrate with the main control system. One of the major purposes of the upcoming upgrade tasks in 2007 is to improve its performance in terms of simplicity of device control. Its environment will be the same as the main control system of the NSRRC accelerator complex.

As a result, reducing the system delay of the communication between VME and PLC is one of the major improvements. In order to illustrate its effectiveness, the following top-up injection is taking as an example for demonstration purpose. During the process of top-up operation of the storage ring, both electron gun and the storage ring kickers have to be initiated simultaneously. It is because that the kickers disturb stored beam while adding electrons onto the beam. Consequently, it is important to minimize the disturbance as needed. However, observation shows that it is not the case in the "old" control system. The activating count of injection kickers is too high, 7 instead of 4, as shown in Fig. 5. It indicates that the delay between VME and PLC is more than 0.3 second. This delay causes the kickers lead extra cycles before gun does. The observed signals in figure-5 can be well understood as interpreted as follow. The top-up injection control program enables the injection kickers trigger and the gun trigger at the same time. However, due to the transmitting delay of the VME crate to PLC is about 0.3 second, it establishing unintentional three kicker cycles. After the beam current reaches the maximum level for top-up operation, the kicker trigger and gun trigger are immediately turned off. Again, due to the similar 0.3 second delay mentioned earlier, it produces three extra electron pulses without gaining to the stored beam. If the delay can be eliminated, both 3 leading kicker pulses and 3 following electron pulses will be eliminated as well. As a matter of fact, since these three extra pulses are found being loss nearby the injection septum of the storage ring producing undesirable radiation dosage. The cure of the signal delay can also improve the environment of health consideration. As shown in figure-6, the delay is reduced to 0.1 second in the new control environment. Only one extra cycle of the kicker pulse and gun pulse remains, respectively. The extra one cycle will be taking care of by modifying the timing system in June 2007.

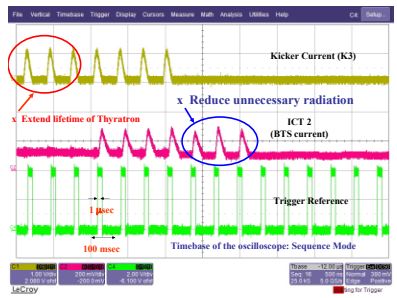

Figure 5. LINAC control system delay during injection control for top-up operation.

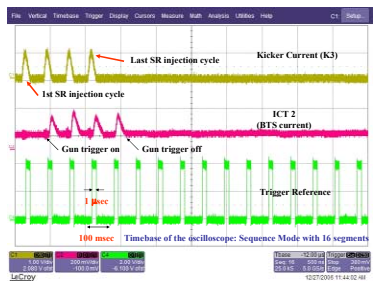

Figure 6. Reducing system delay of LINAC system during injection control in top-up operation.

SUMMARY

The migration of the LINAC control system started in July 2006 and is expected to be completed in June 2007. More than 60 % of the work has been done in 2006. This migrating process extends over one year due to the fact that only limited time slots are available while fulfilling top-up operation of the accelerator complex. All works are performed on every Monday morning of the weekly maintenance period. The new systems will simplify the overall control environment and equip with the required functionality. A drastic reduction in the system delay is a side benefit of this upgrade. This upgrade will also facilitate the control system in dealing with replacing out-of-date components and equipment associated with linac.

REFERENCES

[1]. C. S. Chen, Jenny Chen, J. S. Chen, K.T. Hsu, K. K. Lin, C. J. Wang, "Control Integration for the Injector in SRRC", Proc. of the 1998 EPAC, Stockholm, p. 1658.

[2]. C.S. Chen, C.J. Wang, Jenny Chen, J.S. Chen, S.H. Lee, K.H. Hu, K.T. Hsu, K. K. Lin, "Performance of the Rejuvenated Injector Control System in SRRC", Proc. of the 1999 PAC, New York, p. 682.

A NEW, PXI BUS BASED, PATTERN MEMORY SYSTEM FOR THE SIAM PHOTON SOURCE

George Garnet Hoyes
National Synchrotron Research Center (NSRC), PO Box 93, Nakorn Ratchasema, Thailand

Abstract

A new pattern memory system has been built from PXI bus modules to ramp the booster synchrotron magnet and RF power supplies, replacing an old and proprietary Toshiba system. The new system is compact, rugged, easy to program using LabVIEW, easy to repair and low cost.

INTRODUCTION

The SPS is a modified ring which was previously SORTEC [1]. The pattern memory system for the booster was the original and proprietary system custom made by Toshiba. This old system can be considered obsolete as finding any replacement parts if difficult if not impossible. As there are no spare parts available or detailed system description we were faced with a maintenance problem for this critical sub-system and we decided to look for a replacement system well before we had a failure. One of the main requirements was that it be easily repairable from commercially available replacement modules or components.

Most existing synchrotron facilities use many VME crates and modules and therefore historically VME based pattern memory systems have been used typically. We have no such history of using VME here and a lower cost modular PXI National Instruments based Pattern Memory System has been applied to replace the (much larger) Toshiba one. We believe that this is the first time that a synchrotron facility has utilized a PXI based pattern memory system.

DEVELOPMENT OF THE NEW PXI BASED SYSTEM

The old Toshiba system provides eight, 16 bit plus strobes, RS 422 differential outputs to the Bending Magnet power supply (3), Quadrupole power supplies (4) and RF power supply (1) of the booster synchrotron. To provide differential output at the RS422 levels to the power supplies we chose the National Instruments model PXI-6534 digital I/O waveform generator with 32 Mb onboard memory for pattern storage. This module has 32 single ended outputs which we configured as 16 differential outputs by programming. As each set of 16 bit outputs also needs a strobe signal one more 6534 module was used to provide the eight differential strobe outputs.

Initially the system concept was tested with just two 6534 modules, one outputting signals to the RF power supply, which only needed one set of 16 bit input signals, and another 6534 module for outputting the strobe signals and inputting the main trigger signal from our timing system. This test worked perfectly the first time. Figure 3 shows the input data stream and the output signals of the RF amplifier over one synchrotron injection and ramping cycle.

After the successful system concept test a complete new pattern memory system was purchased comprising of nine PXI-6534 modules, one 18 slot PXI-1045 19" chassis and one CPU controller module, a PXI-8186 P4 2.2 GHz running Windows XP. This controller has an Ethernet interface which was used to connect to our control system server for remote operation as well as for downloading the magnet and RF pattern data to the 6534 waveform generators.

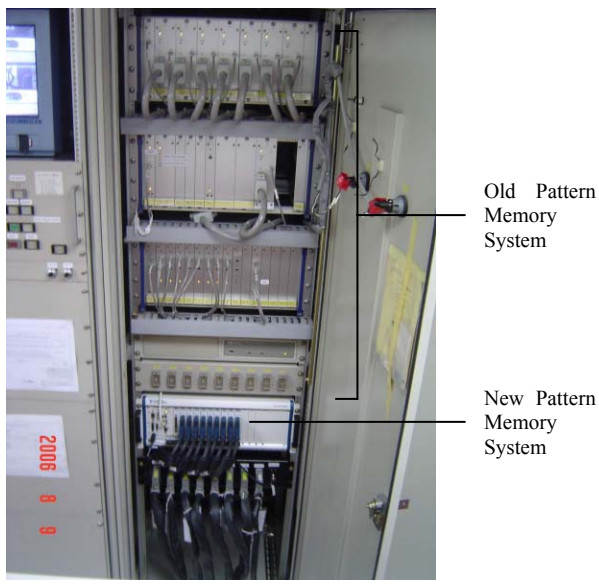

Figure 1 : Both old and new Pattern Memory Systems.

The whole system was configured, programmed and installed in the same Toshiba rack, see Fig. 1. Switching from the old system to the new system is done by simply unplugging the eight outputs from the Toshiba system and inserting them into the National Instruments system shown in Fig. 2. The Toshiba system is, for the time being, kept as a spare and eventually we shall remove it completely.

The ramping pattern is created and stored in the control server as 7001, 16 bit words for each power supply. The ramping time of the booster is 700.1mS so the data, after transfer to the digital I/O module memories, is sent during ramping to the power supplies at the rate of one word per 100 microseconds or 10kHz. This exactly emulates the old Toshiba timing although the new pattern memory can transfer data at much higher rates (up to 20MHz) allowing for the possibility of upgrading the system in the future.

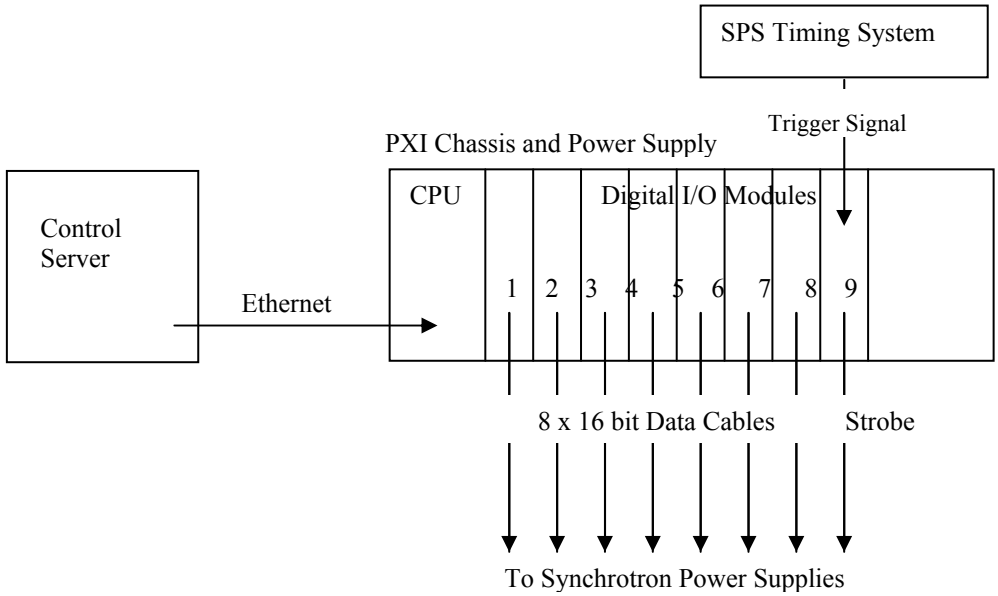

Figure 2: The NSRC built PXI Based Pattern Memory System.

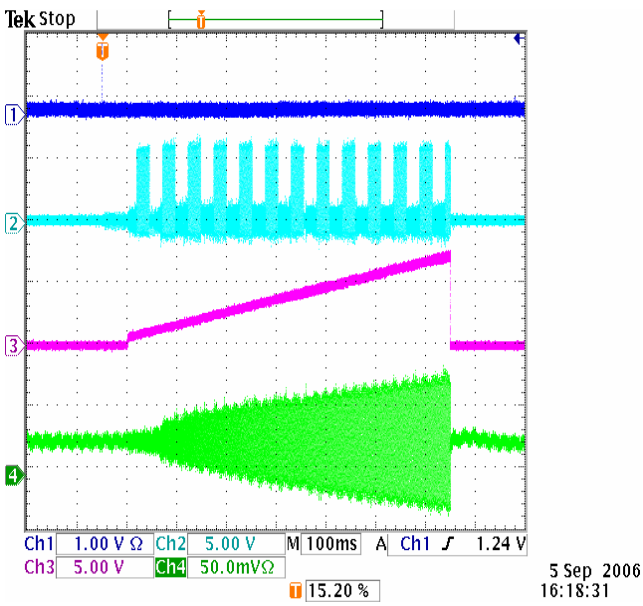

Figure 3: Input and output signals of the synchrotron RF amplifier system. Channel 1, the 1 cycle trigger signal. Channel 2, PM data output example. Channel 3 RF voltage envelope generated by the data. Channel 4, the RF signal at 118MHz.

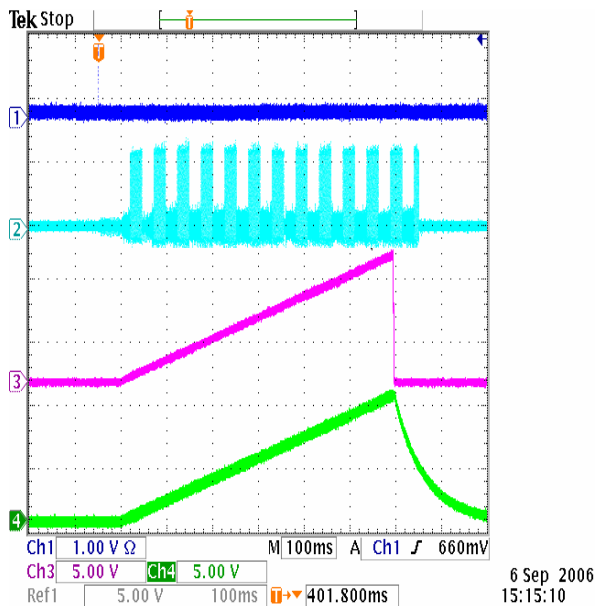

Figure 4: Input and output signals of the synchrotron bending magnet power supply. Channel 1, The 1 cycle trigger signal. Channel 2, PM data output example. Channel 3, Current reference envelope generated from PM data. Channel 4, Bending magnet current.

Table 1: Comparison of old and new pattern memory systems at NSRC.

System	Control & Data Bus	Memory	Programming	Cost ($)	Size (mm)
Toshiba 1985	Proprietary	100KB	Difficult	500,000	2000H 570W 850D
NSRC PXI-based 2006	PXI	32MB	Easy, LabVIEW	20,000	117H 446W 435D

The memory used, 14 Kbytes, is also much less than the 32 Mbytes capability of the new memory modules leaving ample for any upgrade. The ramp repetition rate is presently 0.5 Hz controlled by the SPS timing system trigger signal.

Figure 4 shows the input and output signals of the synchrotron bending magnet power supply. Table 1. is a comparison chart of the old and new pattern memory systems used at NSRC. The new system is a very cost effective solution to our potential maintenance problem.

SUMMARY

A new PXI bus based pattern memory has been commissioned for the SPS booster synchrotron. The new system is compact, rugged, easy to program using LabVIEW, easy to repair and low cost. It is now used as the primary pattern memory and has been used successfully continuously for the past six months.

ACKNOWLEDGEMENTS

Thanks to Mr. Chawalit Netsai for the LabVIEW programming and Mr. Nawin Junthong for the hardware configuration and to all engineers involved with the testing.

REFERENCES

[1] A New Timing System for the Siam Photon Source, Isoyama, G, Kawasima, Y., Hoyes, G., Attaphibarl, M., Pimol, P., Saguansak, N., Rujirawat, S., Apiwatwaja, R., Boonanan, L. and Pairsuwan, W. (2001). Proceedings of the 13th Symposium on Accelerator Science.

THE DESIGN AND PERFORMANCE OF THE PROTOTYPE DIGITAL FEEDBACK RF CONTROL SYSTEM FOR THE PLS STORAGE RING

I.H. Yu, D. T. Kim, S.C. Kim, H.S. Kang, I.S. Park, H.Y. Kim, J.Y. Huang,
PAL, Pohang, Kyungbuk 790-784, Korea.

Abstract

At the Pohang Light Source (PLS) Storage Ring, the low level RF system based on analog technique provides RF field control for the 4 RF stations, and each station drives each RF cavity at 500.082MHz. To achieve better control system stability and accuracy, the prototype digital feedback RF control has been developed in Pohang Accelerator Laboratory (PAL). In addition to RF field control, it provides cavity resonance control, and incorporates the personnel and machine protection functions. An accelerator electric field stability of ± 0.5% in amplitude and ± 0.5º in phase is required for the RF system. In order to accomplish these requirements, a digital feedback control technique is adopted for flexibility of the feedback and feed forward algorithm implementation.

INTRODUCTION

We are developing the digital RF feedback control (DRFC) system based on recent digital technology available for the better performance. One of the advantages of the on-going digital feedback control system is to take mainstream solution using a FPGA & an embedded processor. In DRFC system, an accelerator electric field stability of ± 0.5% in amplitude and ± 0.5º in phase is required for the RF system. The digital RF feedback control system using the FPGAs and DSP Embedded Processor is adapted in order to accomplish these requirements and flexibility of the feedback and feed- forward algorithm implementation. In addition to field control, it provides cavity resonance control, and incorporates the personnel and machine protection functions

FEEDBACK ALGORITHM & SIMULATION

Figure 1 shows the block diagram of DRFC system. Cavity pick-up RF signal is down-converted to about 10 MHz IF from 500.082MHz RF and the base-band is narrowed by analog low-pass filter, and then digitally sampled at about 40 MHz by a high speed ADC.

The sampled data is sequentially arrayed as I, Q, -I, -Q, I, Q, -I, -Q. Calibration factor *a* and θ is used to compensate the cable loss and delay of cavity pick-up RF signal with respect to RF cavity voltage using the vector rotator(XILINX CORDIC3.0). The arithmetic FIR Digital filter is applied to reduce the noise and make the appropriate bandwidth of the feedback. The digitally filtered output is compared with I set point table and Q set point table which are 10 MHz array data.

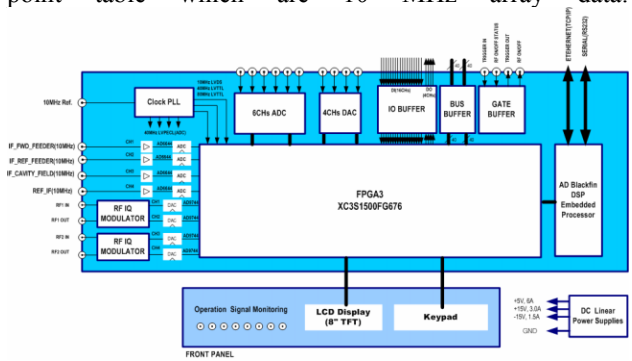

Figure 1: The block diagram of DRFC system.

The error output is passed to PI controller where the proportional gain and the integral gain are appropriately set based on cavity field simulation. Feedback variables such as calibration factor '*a*' and 'θ', the proportional gain and the integral gain, digital filter coefficient are set by remote control system.

A base band analysis, where only the bandwidth near the operation frequency is considered, enables a simplified state-space equation:

$$\frac{d}{dt}\begin{bmatrix} V_I \\ V_Q \end{bmatrix} = \begin{bmatrix} -\omega_{1/2} & -\Delta\omega \\ \Delta\omega & -\omega_{1/2} \end{bmatrix} \begin{bmatrix} V_I \\ V_Q \end{bmatrix} + \frac{\omega_{rf}}{2}\frac{R}{Q}\begin{bmatrix} I_I \\ I_Q \end{bmatrix},$$

Where $\omega_{1/2} = \omega_{rf}/2Q$ is the half width of the resonance, $\Delta\omega = \omega_0 - \omega_{rf}$ the cavity detuning, and ω_0 the resonance frequency of the cavity.

Since the RF amplifier has a wider bandwidth of about 1MHz, the dominant RF device to determine the FB characteristics is the cavity.

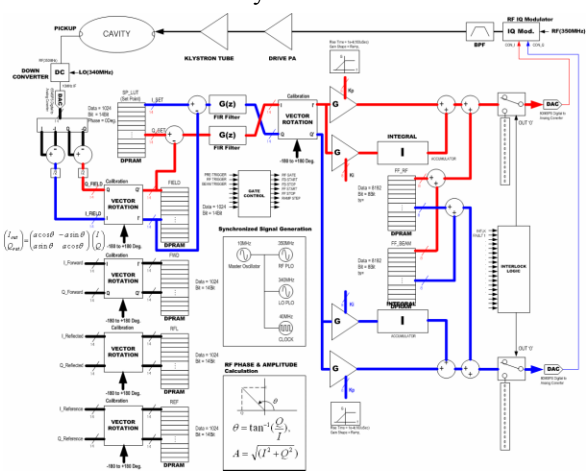

Figure 2: The detailed block diagram of the feedback algorithm.

The PI control transfer function in the system can be described as

$$G(s) = Kp(1+\frac{Ki}{s})$$

The added poles due to loop delay has created the possibility for instability to occur, and limited the maximum loop gain that can be used, and that in turn limited the control bandwidth and precision.

DIGITAL RF FEEDBAK HARDWARE

Most of the analog and digital processors including DSP embedded processor are included on the DRFC board as shown figure 3. We are developed the DRFC through three times changes in order to obtain good performance during last year. The four 14-bit ADCs(AD6644) operated at 40MS/s, and two 14-bit DAC(AD9744) operated at 80MS/s. Xilinx XC3S1500FG676 FPGA provides signal processing path, and connects to an 400MIPS DSP embedded processor(Analog Devices's Blackfin ADSP-BF532SBST400. The DRFC system relies on FPGA (Field Programmable Gate Array) and digital signal processors optimised for real-time signal processing. The digital feedback RF control system performs feedback and feed-forward algorithms on the field signal, resulting in control inphase and quadrature (I/Q) outputs, which are processing DSPs (Digital Signal Process) for slow and complicate processing.

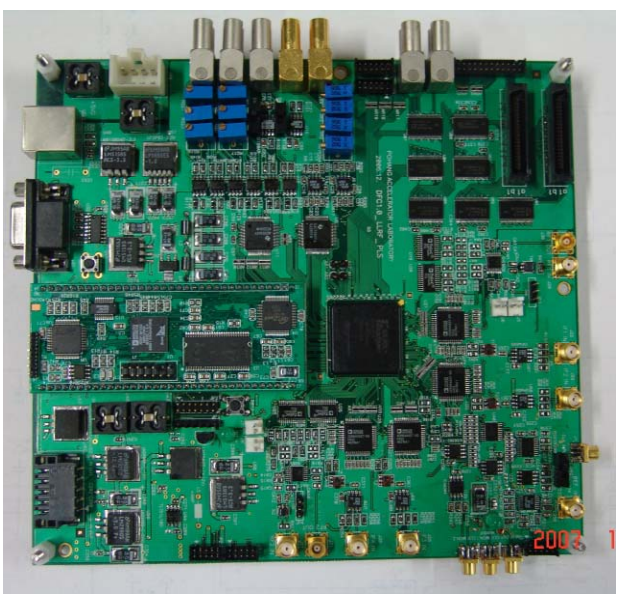

Figure 3: The photograph of the DRFC core board.

The total feedback loop delay is considered to be less than 1uS, including all of the RF components, cables, ADCs, DACs and FPGAs. The DRFC system is relatively complex as shown figure 1.

The phase lock loop circuitry, base on an PLL IC(Analog Devices's ADF4001) can lock the on-board voltage controlled crystal oscillator(VCXO, 80MHz Connor-Winfield VPLD54TE) to an external source. In our case, that source is a 10MHz master oscillator signal.

A synchronized clock signal (80MHz LVPECL) generation is serially-programmed to accommodate the optimised clock signal frequency. The RF amplitude and phase resolution depend on the ADC sampling clock jitter relative to the various RF sources in the system.

The control parameters are set through the MODBUS controller such as a single computer to set up the DRFC system. Registers on the module provide to access for all manners of control – set points, thresholds, mode selection, controller type, etc, and the DSPs provide the direct interface to the control register and hardware. Timing and interlocks are routed through an FPGA. Hard-wired interlocks provide positive cut off of the RF drive in case of external fault conditions. This feature is purposefully independent of the FPGA and DSP embedded processor.

DISPLAY AND CONTROL

Figure 4 shows the configuration of the display and control using ether-net. MODBUS TCP protocol is selected for communication at the DRFC system. The local test of the LLRF system was going to use lookout software at personal computer based on windows OS.

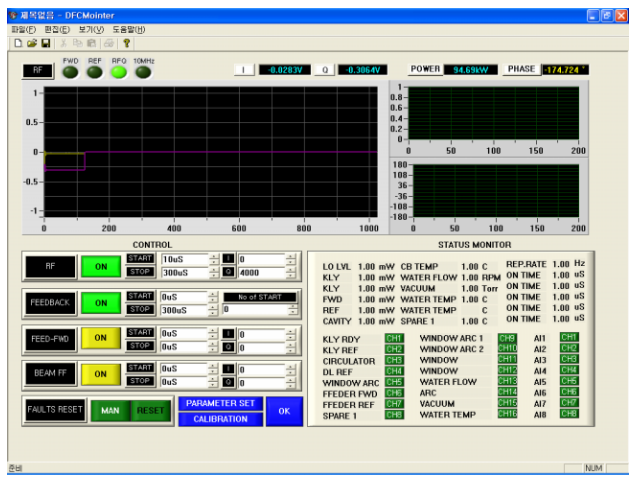

Figure 4: the configuration of the display and control using ether-net.

SUMMARY

In order to satisfy these requirements such as a fast digital feedback control and flexibility in the control algorithm and so on using FPGAs is adopted. FPGAs bring two key advantages to digital signal processing. First their architectures are well suited for highly parallel implementation of DSP functions, allowing for very high performance. Second, user programmability allows designers to trade-off device area vs. performance by selecting the appropriate level of parallelism to develop high-density FPGA devices that suited to the needs of high performance real-time signal processing.

The test with dummy cavity is successfully operated with a stability and accuracy of the ±1% in RF amplitude and ±1.0degree in RF phase was obtained at feedback region. And further improvement of the performance is being studied.

ACKNOWLEDGMENT

This work supported by MOST (Ministry of Science & Technology).

REFERENCES

[1] S. Park, et al., "Developmental Status of Beam Position and Phase Monitor for PEFP Proton Linac", BIW04, Knoxville, May 2004.

[2] L. Doolittle, et al., "Operational Performance of the SNS LLRF Interim System", PAC'03, Portland, May 2003.

[3] I. Yu, et al, "RFQ Low Level RF System for the PEFP 100MeV Proton Linac", EPAC04, Lucerne, July 2004

[4] L. Doolittle, et al., "Operational Performance of the SNS LLRF Interim System", PAC'03, Portland, May 2003.

[5] S. Michizono et al., "Digital Feedback RF Control System for 400-MeV Proton Linac of JAERI/KEK Joint Project" LINAC2002, Gyeongju, Aug. 2002, p.184.

[6] Hengjie Ma et al., "SNS Low-Level RF Control System: Design and Performance", PAC2005, Knoxville, May, 2005.

[7] I. Yu, et al, "The Digital Feedback RF Control System of The RFQ & DTL1 for 100MeV Proton Linac of PEFP

DRIVE SYSTEM INSTRUMENTATION FOR VEC SCC AXIAL-HOLE MAGNETIC FIELD MEASUREMENT

T K Bhattacharyya*, T Das, C Nandi, G Pal, C Mallik and R K Bhandari
Variable Energy Cyclotron Centre, 1/AF Bidhan Nagar, Kolkata 700064

Abstract

Characteristics of beam in the central region of the superconducting cyclotron are to a large extent influenced by the magnetic field it experiences during its passage through the axial-hole. Accurate knowledge of magnetic field in axial-hole is required in order to design the central region components and position the extraction elements. A probe drive with high resolution and repeatability was developed along with the required HMI to map the magnetic field through out this hole from median plane upto 3 meter above it. This paper describes the drive system, its control, data acquisition and instrumentation scheme.

DRIVE SYSTEM

The mechanical arrangement [1] for the measurement set -up can be divided into two parts: drive mechanism and probe holding mechanism. The drive mechanism has three lead screws and nuts. Lead screws of 1.5 m length are used to avoid complexity and to reduce fabrication problem and inaccuracy of the system. A stepper motor drives the lead screws. Rotational movement of the lead screws is restricted by two plates carrying hall probes, fixed at the top and the bottom ends of the lead screws. The stepper motor is fixed and the lead screws move up and down. Since the total required span of measurement is 3 m and the movement of the lead screws is restricted to 1.5 m, an extension of 1.5 m with bottom plate for mounting hall probes has been added. The plate at the end of the lead screw and extension form the probe holding mechanism. Two probes, one axial probe at the centre and one transverse probe at the outer radius, are fixed to each of the end plates. The end plates have provision to manually re-position the transverse probes at an angle of 90º. During one complete scan, the system can collect data over the complete required length of 3 m from the cyclotron median plane.

CONTROL AND DATA ACQUISITION

The axial-hole drive system can be broadly divided into two parts, the open-loop control of the drive system, and the magnetic field data acquisition system.

Control Scheme

The control scheme can be subdivided into following steps:

i. Optical limit switches are placed at both ends. At the start of each run, the drive is initialised by automatically moving it back till it touches the starting limit switch. As this operation is carried out in steps, an accuracy of 15 micron can be achieved.

ii. The system is then driven in steps upto 1500 mm. The heart of the control system is a stepper motor. It drives the three gear mounted lead screws which eventually move the hall probe assembly and position them correctly at 1.005 mm intervals. At this stage, the control software calculates the present absolute distance from the starting point and stores it in a file for ready reference. The control software confirms that the motor is powered (24VDC) before sending the drive pulses. In case of sudden power failure, the next drive signal is not sent and the last absolute position value is stored. When the mapping starts again after resumption of motor power, the software can easily recollect the last position value and starts scanning from that point.

iii. The motor stops after reaching the end point optical limit switch. The software scans the limit switch before each step. This results in end point detection at the theoretical accuracy of 15 micron. After reaching the end point, it shows mapping completion message on the human-machine interface (HMI) screen.

iv. After completion of a full length scan, the system automatically resets back to its initial position showing probe resetting message. It stops only if it reaches the starting point. Then it gives an option of another scan/ stop to the user.

Data Acquisition Scheme

The data acquisition scheme can be subdivided into following steps:

i. The data acquisition starts after the probe assembly stops at 1.005 mm interval. A delay of 5 seconds is given before each set of magnetic measurement to eliminate the chance of any kind of mechanical vibration.

ii. The control software communicates with the three channel FW Bell hall probe monitor through RS 232 serial port. Although four hall probes are installed in the assembly, the monitor can only read three of them at a time. Two successive scans give complete data for a fixed magnet current. The software initialises the serial port and sends command to measure the magnetic field for each channel. The hall sensors' data are collected from the read buffer of the monitor and channel-wise separated by the software. Ten sets of data are collected during the total measurement time of 5 seconds.

* tamal@veccal.ernet.in

iii. The ten magnetic field data are statistically processed to minimise the chances of error. They are averaged and the dispersion value is checked. If the value of dispersion is 0 or more than 30 gauss the system rejects the whole set of data and takes a new set. If the dispersion is not met for second time, it gives a message of field monitor error.

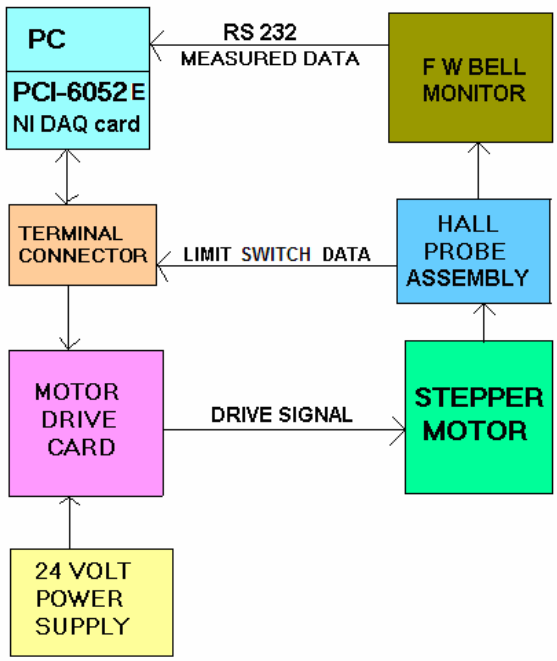

Figure 1: Basic Hardware Scheme of the System

INSTRUMENTATION SCHEME

Axial-hole drive system instrumentation can be described in two parts, its hardware and software.

Hardware

Figure 1 shows the basic hardware scheme. The system is controlled by a control software running on a dedicated computer (Fig. 2). The computer contains a PCI data acquisition card (NI PCI-6052E) for the digital I/Os and uses RS232 port for the magnetic field data acquisition. The DAQ card generates the digital pulse for the stepper motor and scans optical limit switches. External screw terminals board is used for easy access and connectivity of the various I/Os. This card takes the necessary 5V supply from the PCI slot itself. A separate control card for the motor is used to convert the pulse signal from PC (controlled by software) to necessary step signal for the motor. Software delay is incorporated in order to vary the time period of the pulse to adjust the speed of the motor. The Superior Electric make stepper motor (M111-FD-310) is a high torque (4.4 Nm) motor with 200 steps/rev. The motor runs at 24VDC and takes about 500mA current at its maximum speed (1000steps/sec). Holding current of 3A causes instantaneous stop and no further slippage. The motor has a very high resolution of 1.8º /step, thus offering very high sensitivity. To calculate x, linear movement/step, where p is screw pitch and r is gear ratio

$$x = \frac{p \times r \times 1.8^\circ}{360^\circ} = \frac{5 \times 0.6 \times 1.8^\circ}{360^\circ} = 0.015mm$$

The system has a resolution of 15 micron. As a result, any length interval can be set with certainty. The stepper motor has an accuracy of ±5% of a step and this error is non cumulative from one step to the next which allows the system to be accurate within 2% over 1 mm interval. The system uses an optical limit switch for initial and end position detection and it searches for these two interlocks before each step (15 micron), causing highly accurate starting at each run. The system has very high repeatability, (Table 1) as it takes exactly same number of steps to reach same distances (even for full span travel). The FW Bell monitor (Fig. 2) with an accuracy of ±0.05% of reading, acquires the analog signals via co-axial cables from hall sensors and processes it to display locally (channel wise) as well as provide digital signals for serial communication. This monitor accepts command from the control software through serial port for measuring magnetic field values (3 channels) and sends those back to PC.

Table 1: Repeatability of the data produced.

Position (mm)	1st run (gauss)	2nd run (gauss)	Difference (gauss)
89.91	-22270.4	-22254.1	-16.3
94.905	-22171.1	-22163.5	-7.6
99.9	-22154.9	-22152.5	-2.4
104.895	-22195.8	-22198.1	2.3
109.89	-22266.1	-22268.5	2.4
114.885	-22335.5	-22336.8	1.3
119.88	-22380	-22377.5	-2.5

Software

The HMI is developed on Labview. The program has all steps to automate each scan starting from initialisation of the probe assembly to the end of the scan and re-positioning for the next scan. The program calculates the distance travelled with respect to the reference point determined by the initial limit switch and stores the last position after every step in a file for ready reference while restarting from the power loss situation. The program checks for the motor power each time before sending the drive signal to the motor and in case of any power cut or stuck motor, the software can't send any false signal to the motor. While restarting after resumption of power, it takes the last saved position value. After completing each full scan, it stops and automatically resets to its original starting position. The field data are collected with

minimum cable connections to reduce noise. The processed data is plotted instantaneously as the scan progresses for visual interpretation. The program starts acquiring data only after a pre-defined delay of 5 seconds to avoid any kind of vibrations or mechanical disturbance.

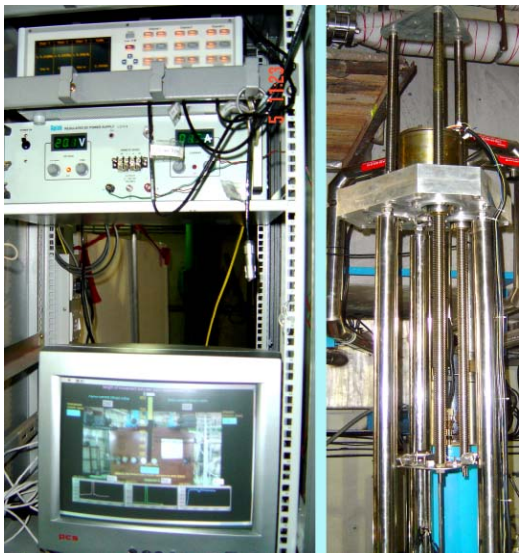

Figure 2: Basic Electronic and mechanical setup.

The HMI acquires multiple data for each specific position and discards any abnormal value, if collected, through a statistical process. It even can discard a whole set of data and take a new set, if required. Multiple rejections cause process to abort, showing error message. It also stores all the measured data in separate excel files for each scan with nomenclature containing date, time, current, probe positions etc. for user's convenience. All the operations are well informed to the user with consequent pop-up messages. In case of any error, the HMI shows first-up messages and can even abort whole measurement process, if required.

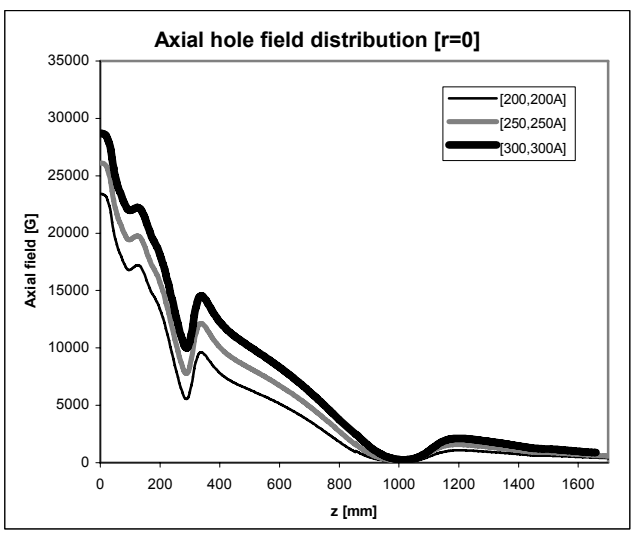

Figure 3: Axial-hole magnetic field distribution.

Conclusion

The well programmed HMI with open loop control, data acquisition system and the mechanical system was successfully used [2]. The performance of the drive was highly satisfactory and the axial-hole magnetic field mapping was completed within a few days. It produced useful data (Fig. 3) of axial-hole magnetic field measurement.

REFERENCES

[1] C. Nandi, S.K. Mishra, S. Gayen, R.N. Sharma, T.K. Bhattacharyya, G. Pal, C. Mallik and R.K. Bhandari, "Mechanical System for Magnetic Field Measurement through Central Axis and Inside Magnetic Channels for VEC K-500 Cyclotron", InPAC-2005, VECC, Kolkata, March 2005, p. 517.

[2] M.K. Dey, J. Debnath, U. Bhunia et al. "Magnetic Field Measurement and Correction of VECC Superconducting Cyclotron", InPAC-2006, Mumbai, November 2006, p. 285.

HIGH POWER TEST OF C-BAND ACCELERATING SYSTEM FOR JAPANESE XFEL PROJECT

K. Shirasawa#, T. Inagaki, H. Kitamura, T. Shintake, RIKEN,SPring-8 Harima, Hyogo, Japan
S. Miura, MHI, Hiroshima, Japan
H. Matsumoto, H. Baba, KEK, Ibaraki, Japan

Abstract

The C-band (5712 MHz) accelerating system will be used as the main accelerator for the SPring-8 Compact SASE Source project. In order to confirm the performance of the C-band accelerator for the 8 GeV XFEL machine, the same accelerating structure and RF system have been installed in the SCSS prototype accelerator. A high power test of all the accelerator components has been performed. A 35 MV/m accelerating field was achieved during the beam test.

INTRODUCTION

The X-ray free electron laser (XFEL) is one of the next generation light source. In Japan, SPring-8 has a single-pass XFEL project, the SPring-8 Compact SASE Source (SCSS). This project uses a 8 GeV linac to generate 1 $\AA$ coherent intense X-ray laser. The construction will start in 2007: 128 C-band accelerating tubes and 64 klystrons will be installed as the main accelerator.

Since the C-band accelerator generates a higher accelerating gradient than the traditional S-band accelerator, the machine is more compact and the cost is lower. However, the C-band accelerator is a new technology for an electron linac. In order to check the performance of the developed hardware components and to prove SASE amplification, the prototype accelerator for the XFEL was constructed. After the beam commissioning, the first SASE amplification was observed at 49 nm in June 2006 [1].

In the prototype accelerator, four 1.8 m long C-band accelerating structures are used to accelerate electrons from 45 MeV to 250 MeV. Normal operation, the accelerating gradient of the C-band accelerator is 28 MV/m with the klystron output power of 27 MW.

On the other hand, the C-band accelerator for the 8 GeV linac is designed to operate with the field gradient of 35 MV/m. Therefore, the accelerating filed measurement has been performed after the high power test at the prototype machine.

SCSS C-BAND ACCELERATOR

The C-band accelerator consists of two units; each unit has one 50 MW klystron, pulse compressor and two accelerating structures. A schematic diagram of the C-band accelerator is shown in Fig. 1.

#kshira@spring8.or.jp

Figure 2 shows the photograph of the C-band accelerator of the SCSS prototype machine. As shown in Fig. 1 and Fig 2, the stable support stands made from a low thermal expansion material, cordierite ceramic, are used for the accelerating structure [2]. Cordierite ceramic has a thermal expansion coefficient ten times lower than that of iron.

Klystron and HV Power Supply

The C-band klystron (Toshiba E3746A) [3] generates a maximum power of 50 MW with a pulse width of 2.5 μsec and a repetition rate of 60 Hz. In order to provide pulsed high voltage for the klystron, the inverter type high voltage power supply and the compact oil-filled modulator are used. [4]. The inverter type high voltage power supply charges the pulse forming network (PFN) circuit of the modulator. The charging voltage is 50 kV. A 1:16 step-up transformer is inserted between the PFN circuit and the klystron. Consequently, a pulsed high voltage of -350 kV is provided for the klystron.

C-band Choke-Mode Type Accelerating Structure

The first C-band choke-mode type accelerating structure was developed in 1998 for the linear collider project [5, 6]. A 1.8 m long structure was developed in 2002 for this project. The main parameters are listed in Table 1. The structure consists of 89 regular-cells with damping slots and input/output coupler-cells. In order to get enough space for the choke, the $3\pi/4$ mode was used. In this mode, the space which can be used for the choke is longer than in the conventional $2\pi/3$ mode by about 2mm. Therefore, this structure shows quite effective damping of HOMs over a wide frequency range. It makes possible to accelerate the multi-bunched beam with no wakefield instability [7].

Pulse Compressor

At the SCSS prototype machine, two types of pulse compressors, SKIP or SLED, has been adapted for research and development. The SKIP was developed by the KEK injector group [8]. On the other hand, the SLED was originally designed for linear collider [9]. Three-cavity design was introduced to improve energy efficiency. To make simple the system, the traditional SLED design (single cavity) has been chosen for the SCSS project. Parameters for each pulse compressors are listed in Table 2. The quality factor was measured with low level RF. The SKIP is installed on

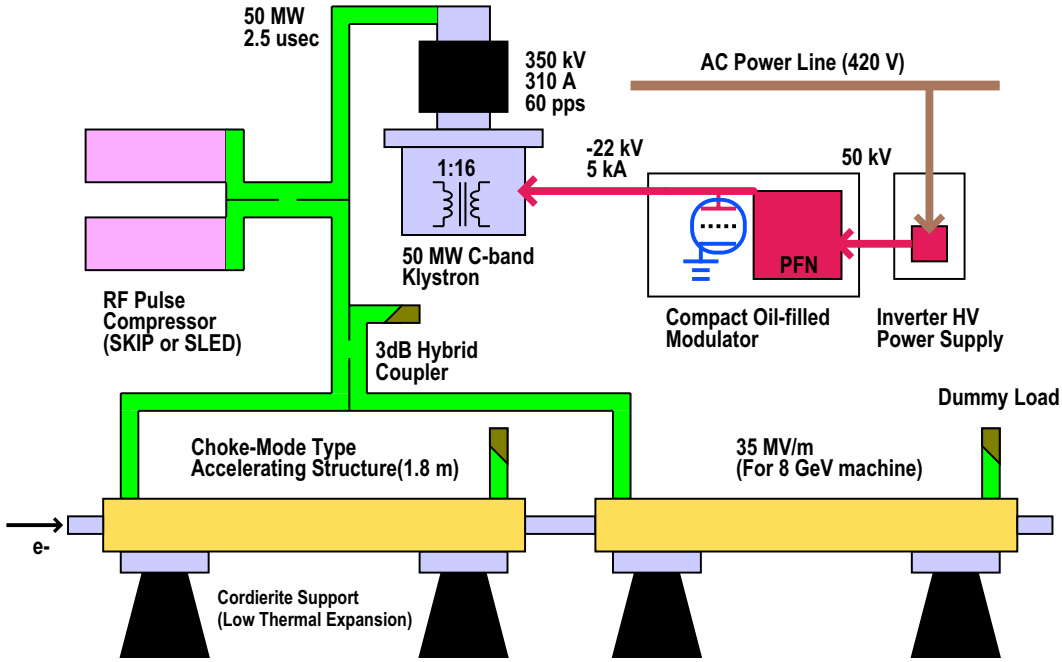

Figure 1: A schematic diagram of the C-band accelerator unit.

Table 1: Parameters of the C-band accelerating structure.

Frequency	5712 MHz
Phase shift per cell	$3\pi/4$
Field distribution	semi C.G.
Number of cells	89+2coupler cell
Active length	1791 mm
Disk thickness	4 mm
Q (measured)	10300∼10700
Group velocity (measured average)	0.019c
Attenuation parameter (measured)	0.52∼0.54
Filling time (measured)	308∼309 nsec

the upstream C-band accelerator, and the SLED is downstream. Each power gain, which is estimated from measured Q_0 and β, is almost same. A RF power gain above 3 is required for the 8 GeV machine.

Table 2: Parameters of the pulse compressors

	SKIP	**SLED**
Frequency	5712 MHz	
Q_0 (measured)	130000	170000
Mode	TE038	TE01,15
β (measured)	6.3	8.2

HIGH POWER TEST

A high power test has been performed to confirm the stability and reliability of all the components: klystrons, pulse compressors, accelerating structures, dummy loads and HV power supplies. After a 500 hours RF processing, the klystron output power was reached to 44 MW. The repetition during the processing was 60 Hz. The RF pulse width was started from 0.1 μsec. Finally, it was expanded to nominal value of 2.5 μsec, while the pulse width before phase inversion was 2.0 μsec. The vacuum pressure is monitored by cold cathode gauges (CCGs). The CCGs are used as trip signals of klystron modulators during RF operation to protect the structure from a breakdown. We carefully increased the klystron output power with monitoring the vacuum pressure. During the processing, the vacuum pressure around the pulse compressor was higher than at the other points, namely around the accelerator tube and the dummy

Figure 2: A photograph of the C-band accelerator. This view is from the downstream of the C-band accelerator.

load. However, after the klystron output power reached 40 MW, the vacuum pressure was as low as the other points. The typical RF wave form is shown in Fig. 3. To avoid RF discharge in the accelerator tube, a sharp peak at phase inversion has been suppressed by RF amplitude modulation. The modulation is applied by the low level RF system [10].

BEAM ENERGY MEASUREMENT

In order to find the energy gain of the accelerating structure, the beam energy was measured by the chicane magnets located downstream of the C-band accelerator. The beam timing and RF phase were optimized to obtain the maximum beam energy. Figure 4 shows the measured accelerating gradient as a function of the klystron output power. The maximum gradient was 35 MV/m. It corresponds to an average input power of 62 MW which is estimated from the measured shunt impedance. The operational repetition was 10 Hz at the beam energy measurement. Assuming the RF loss between the klystron and accelerating structure is 13 %, the RF power gain of SKIP was 3.2. The RF discharge was sometimes observed at 35 MV/m, even though the stable operation was possible up to 34 MV/m. Additional RF processing is considered to be necessary for the 35 MV/m operation.

CONCLUSION

As the result of the beam energy measurement, the achieved accelerating gradient is 35 MV/m. In this gradient, the klystron output power is 44 MW. Practical operation with an accelerating gradient above 35 MV/m seems feasible after a reasonable processing time. Total operation time of the C-band accelerator exceeds 1000 hours until the end of 2006. No serious problem has been observed for all the accelerator components.

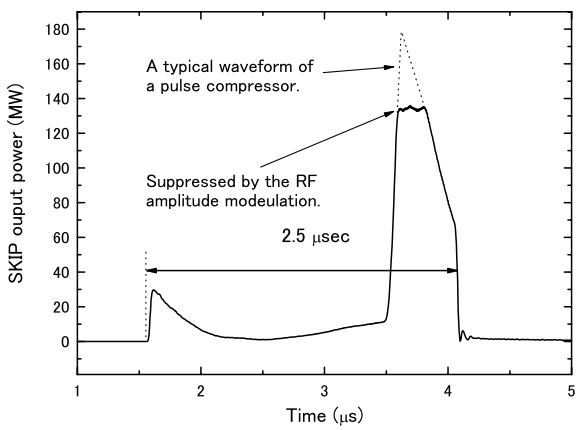

Figure 3: Typical RF waveform measured downstream of the SKIP. The klystron output was 42 MW.

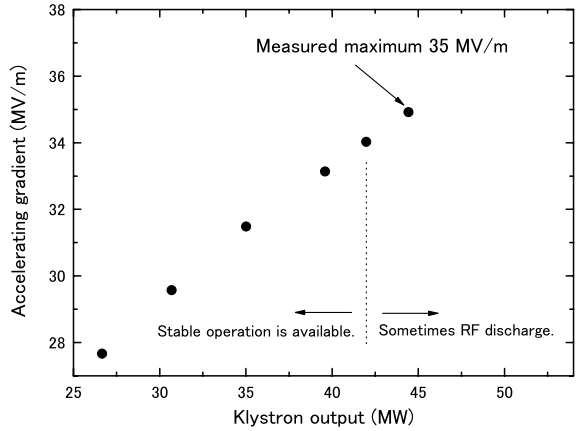

Figure 4: Measured accelerating gradient as a function of the klystron output power.

ACKNOWLEDGEMENT

The RF processing was performed with the help of many SCSS members.

REFERENCES

[1] T. Shintake, et. al., "Status of the SCSS Test Accelerator and XFEL Project in Japan", EPAC 06, to be published

[2] T. Saeki, et. al., "DEVELOPMENT OF A NEW SUPPORT-STAND WITH HIGH THERMAL-STABILITY FOR THE SCSS PROJECT", APAC 2004, 149-151, (2004)

[3] Y. Ohkubo, et. al., "The C-band 50 MW C-band Klystron Using Travelling-Wave Output Structure", LINAC 98, 932-934 (1998)

[4] T. Inagaki, et. al., "HIGH POWER TEST OF THE COMPACT, OIL-FILLED MODULATOR FOR THE C-BAND KLYSTRON", APAC 04, 654-656 (2005)

[5] H. Matsumoto et. al., "Fabrication for the C-band (5712 MHz) Choke-Mode Type Damped Accelerator Structure", LINAC 98, KEK Pre-print 98-143 (2004)

[6] T. Shintake, et. al., "HOM-Free Linear Accelerating Structure for e+e- Linear Collider at Cband", PAC 95, KEK-Preprint, 95-48 (1995)

[7] T. Shintake, et. al., "THE FIRST WAKEFIELD TEST ON THE C-BAND CHOKE-MODE ACCELERATING STRUCTURE", PAC 99, 3411-3413 (1999)

[8] T. Sugimura, et. al., "SKIP - A PULSE COMPRESSOR FOR SUPERKEKB", LINAC 2004, 754-756 (2004)

[9] T. Shintake, et. al., "A New RF Pulse-Compressor using Multi-Cell Coupled-Cavity System", EPAC 96, KEK Preprint 96-71, July 1996 A

[10] Yuji Otake, et. al., "SCSS RF CONTROL TOWARD A 5712 MHz PHASE ACCURACY OF ONE DEGREE", in this proceedings

POSITRON INJECTOR ACCELERATOR AND RF SYSTEM FOR THE ILC*

J. W. Wang#, C. Adolphsen, V. Bharadwaj, G. Bowden, E. Jongewaard, Z. Li, R. Miller, J.C. Sheppard
SLAC, Menlo Park, CA94025, U.S.A.

Abstract

Due to the extremely high energy deposition from positrons, electrons, photons and neutrons behind the positron target, and because a solenoid is required to focus the large emittance positron beam, the 1.3 GHz pre-accelerator has to use normal conducting structures up to energy of 400 MeV. There are many challenges in the design of the normal-conducting portion of the ILC positron injector system such as obtaining high positron yield with required emittance, achieving adequate cooling with the high RF and particle loss heating, and sustaining high accelerator gradients during millisecond-long pulses in a strong magnetic field. Considering issues of feasibility, reliability and cost savings for the ILC, the proposed design for the positron injector contains both standing-wave (SW) and traveling-wave (TW) L-band accelerator structures. A short version of the new type of the SW section is under fabrication and testing, an updated status report is given. This paper also covers the acceleration vs. deceleration for pre accelerator sections, SW vs.TW structures, as well as the longitudinal matching from target to linac and linac to damping ring.

INTRODUCTION

The positron source relies upon an intense source of high energy photons impinging upon a metal target. The photons must be of sufficient energy, typically of order 10 MeV, to generate electron-positron pairs that can escape from the target material and be captured and accelerated. The photons are generated by synchrotron radiation in a helical undulate through the interaction of relativistic electrons with a periodic, helical, magnetic field. The photon beam is incident on the rim of a rotating target of thickness 0.4 radiation lengths contained in a vacuum vessel. Approximately 24 kW of power from the photon beam is deposited in the target in a spot of ~ 1 mm rms. The resulting electron/positron particles emerging from the downstream side of the target are captured in a 0.09 m-rad transverse dynamic aperture. The energy of the beam coming out of the target is 2-10 MeV. The target is followed by the tapering magnetic field of an Optical Matching Device (OMD) which has a field which decays from 5-0.5 T over 20 cm. The OMD is used to match the beam phase space coming out of the target into the capture L-band RF. The capture RF is placed after the target and OMD and accelerates the beam to 125 MeV.

*Work supported by U.S. Department of Energy, contract DE-AC02-76SF00515 (SLAC).
#jywap@slac.stanford.edu

ACCELERATOR SYSTEM LAYOUT

The capture region is composed of two 1.27 m SW accelerator sections at 15 MV/m accelerating gradient and three 4.3 m TW accelerator sections at 8.5 MV/m accelerating gradient in order to capture and accelerate the electron beam to 125 MeV as shown in Figure 1.

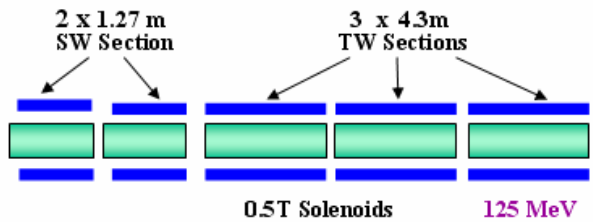

Figure 1: Schematic layout of the capture region.

The electrons are accelerated from 125 MeV to 400 MeV in a pre-accelerator region, which is composed of eight 4.3 m TW sections at 8.5 MV/m accelerating gradient. All accelerator sections are surrounded with 0.5 T solenoids as shown in Figure 2.

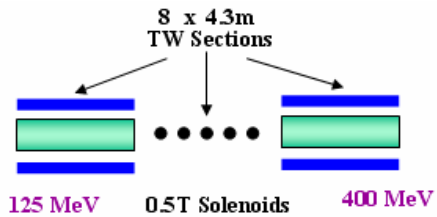

Figure 2: Schematic layout of the pre-accelerator region.

SW ACCELERATOR STRUCTURE FOR POSITRON CAPTURE

The high gradient (15 MV/m) positron capture sections have been designed to be simple π mode 11 cells SW type of accelerator structures. The advantages are a more effective cooling system, higher shunt impedance with larger aperture (60 mm), lower RF pulse heating, apparent simplicity and cost savings. The mode and amplitude stability under various cooling conditions for this type of structure have been theoretically verified. Figure 3 shows a cutoff view of the SW structure and Table 1 gives the important RF parameters.

Table 1: Parameters of SW stricture.

Structure Type	Simple π Mode
Cell Number	11
Aperture 2a	60 mm
Q	29700
Shunt impedance r	34.3 MΩ/m
E_0 (8.6 MW input)	15.2 MV/m

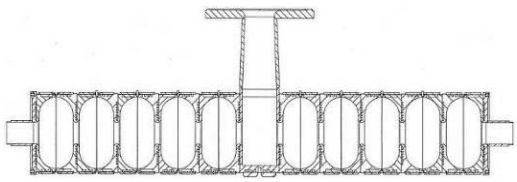

Figure 3: 11–cell SW structure.

TW ACCELERATOR STRUCTURE FOR PRE-ACCELERATOR REGION

All TW sections are designed to be 4.3 m long, 3π/4 mode constant gradient accelerator type of accelerator structures. The RF group velocity for traditional 2π/3 mode traveling wave structure is too high for our larger apertures (the radio of iris radius with wavelength a/λ~10%) to obtain a good RF efficiency. Therefore, to increase the "phase advance per cell" was used to optimize the RF efficiency for designing this type of large aperture TW structure. Comparing with some standing wave structures, the advantages are lower pulse heating, easy installation for long solenoids, no need to use circulators for RF reflection protection, apparent simplicity and cost saving. . Figure 4 shows the shapes for three typical cells of the TW structure and Table 2 gives the important RF parameters.

Table 2: Parameters of TW stricture.

Structure Type	TW 3π/4 Mode
Cell Number	50
Aperture 2a	46 mm
Attenuation τ	0.98
Q	24842 - 21676
Group velocity Vg/c	0.62% – 0.14%
Shunt impedance r	48.60 – 39.45 MΩ/m
Filling time T_f	5.3 μs
Power Dissipation	8.2 kW/m
E_0 (8.6 MW input)	8.0 MV/m

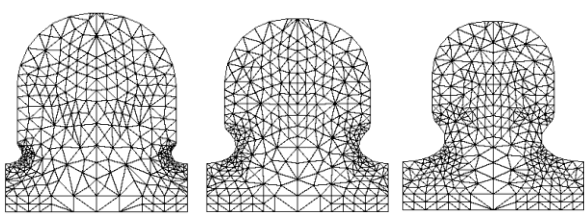

Figure 4: Profiles of the first, middle and last cell for 4.3m 3π/4 Mode TW structures.

RF SYSTEM

Each accelerator section is equipped with an individual RF station powered by a 1300 MHz, peak power 10 MW pulsed klystron. The RF station is composed of modulator, RF windows, phase shifters, RF loads, directional couplers and low-level RF system. For the SW structures, RF circulators are needed for reflection protection of the high-power klystrons.

TEST STRUCTURES AND EXPERIMENT PLAN

In order to gain the fabrication experience and make high power tests at full gradient and pulse length with an existing 5 MW peak power L-Band klystron, we have designed a 5-cell L-Band test structure with coupler cell at one end and all necessary features for positron capture section as shown in Figure 5.

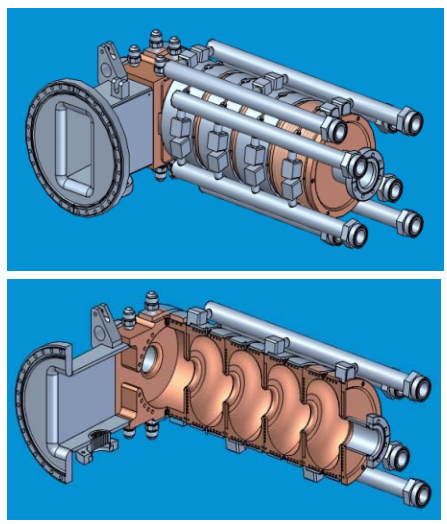

Figure 5: A 5-cell L-Band SW test accelerator section for the positron capturing structure - external view (top) and cut-away view (bottom).

At present, all structure components and sub-assemblies have been completed and microwave measured. The measurement accuracy and repeatability were carefully studied. The frequency tolerances are within 100 kHz. Two L-Band windows have been completed. They are checked, coated and delivered for high power test. The final assembly and high power test will be done in the first half of 2007. Figure 6 shows some important sub-assemblies.

Cooling channels are machined into the outer cylindrical surface and the planar end surface of the copper body. A copper cover is brazed over the planar end surface and a stainless steel cylinder brazed to the cylindrical outer surface of the copper body. A full cell is formed by brazing two of these half cell assemblies together at the cavity iris and the full accelerator section is assembled from these full cell subassemblies. To determine the operating temperature and the expected

tuning changes, an axisymmetric representation was modeled using the general purpose finite element code ANSYS. Cavity surface RF losses were calculated using the code Omega3P, a finite element parallel eigensolver developed at SLAC. A series of transient cases using the steady state temperature field as initial conditions were run to determine the temperature excursions during the RF pulse for the conditions of only RF heating and RF heating plus particle heating.

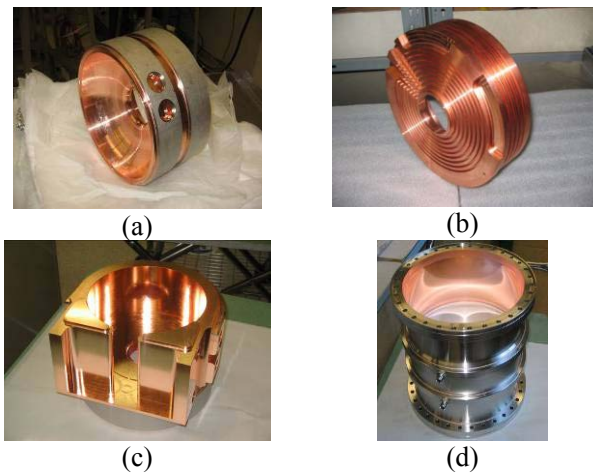

Figure 6: Some of the subassemblies for the 5-cell SW structure: a completed unit cell (a), a half cell to be brazed on the input coupler (b), coupler subassembly (c) and L-Band RF window (d).

SOME BEAM DYNAMICS STUDIES

A lot of beam dynamics studies were done for the design of conventional positron source. Their results may still be useful for the Keep Alive Source (KAS) for present undulator based reference design. The KAS is designed to deliver a low intensity (~10%) beam of positrons at 400 MeV to the positron booster linac in case the primary positron beam is unavailable. It uses a 500 MeV electron beam impinging on a tungsten-rhenium target to produced positrons in electromagnetic showers. The positrons are captured, separated and accelerated to 400 MeV using the same scheme as for the primary positron beam.

There are two approaches to the problem of capturing positrons: the acceleration capture and capture with initial deceleration. The traditional approach has been to arrange the phase and amplitude of the fields in the capture section(s) to accelerate the positrons as fast as possible. For this approach the higher the accelerator field the better because the higher the field, the more rapidly the velocity variation with energy becomes insignificant, and the less the beam debunches because of the initial energy spread of the positrons. At 1.3 GHz to get reasonable positron yield into a 15 degree bunch for acceleration in the linac requires an accelerating gradient of greater or order of 12 MeV/m.

In the 1970's at SLAC an alternative approach was discovered which significantly improved the yield of our positron source. This approach involved initially decelerating the positrons and arranging the phase and amplitude of the fields so that the distribution in longitudinal phase space of the incoming positrons lay along one of the orbits in longitudinal phase space as shown in Figure 7. Thus the positrons approached a small spread in asymptotic phase as their energy increased.

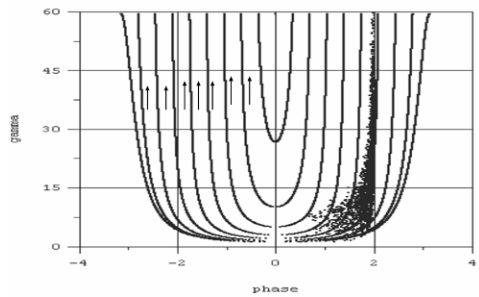

Figure 7: Phase space for positrons interring accelerator.

Simulations indicate that this approach can increase the yield of positrons into a 1% spectrum at 5 GeV by about 50%. These simulations were done without bunch compression. The optimum gradient in these capture-with-deceleration simulations was found to be about 6 MeV/m, a very comfortable gradient for the 1.3 GHz structure with ms long pulses inside a strong solenoid. With a gradient of 6 MeV/m a single 10 MW klystron can drive up to 6 meters of structure. Consequently, for deceleration capture, it makes sense to use a travelling wave structure for the capture section.

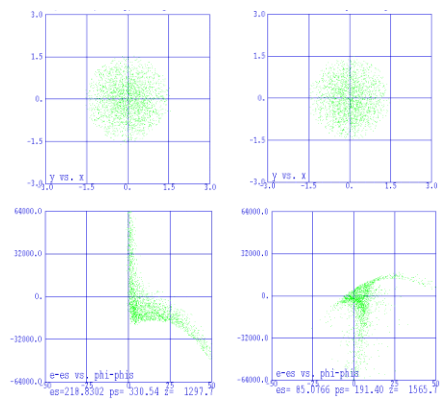

Figure 8: Plots to show transverse profile and phase space of captured beam for acceleration case (left) and deceleration case (right).

REFERENCES

[1] V. Bharadwaj, et. al. "Design issues for the ILC positron source", PAC2005, SLAC-PUB-11690.

[2] J.W. Wang, et. al. "Studies of Room Temperature Accelerator Structures for the ILC Positron Source", PAC05, SLAC-PUB-11767.

[3] B. Aune, R. Miller, "New Method for Positron Production at SLAC", LINAC1979, SLAC-PUB-2393.

DEVELOPMENT OF 100 KW RF AMPLIFIER FOR SUPERCONDUCTING CYCLOTRON AT VECC

S. Som#, Saikat Pal, A.K. Mukherjee, D.S. Bhattacharyay, P. Gangopadhyay, J.S. Prasad, Mondal, S. Seth, P.R. Raj, S.K.Manna, M. Banerjee, K.V. Krishnaiah, M.S. Saha, S. Biswas, S. Saha.
Variable Energy Cyclotron Centre, 1/AF, Bidhannagar, Kolkata-700064

Abstract

High power rf amplifiers (3 nos.) have been developed at our centre for feeding power to three nos. of coaxial rf cavities of the k500 Superconducting Cyclotron. Each of this amplifier can supply output power of 100 kW (max.) at 50 ohm impedance within the frequency range of 9 MHz to 27 MHz. The amplifier, based on Eimac 4CW 150,000E water-cooled tetrode, is tuned by moving the sliding short of the coaxial cavity within the said frequency range[1]. An inductive coupling loop is inserted along one side of the coaxial cavity through the sliding short and is matching the output impedance of 50 ohm. The four identical Bridge-T networks in the grid of the final amplifier are driven with equal power levels of up to 150 watts. The amplifier is operated in Class-AB mode with power gain of 22 dB. Anode Power supply of 20 KV@7.5A, Screen Power supply of 1.5 KV@1A, Grid Power supply of -500V, and Filament power supply of 15.5V@215A are applied to the terminals of the aforesaid tetrode. A PC-based stepper motor controlled sliding short movement system have been developed. The movement of the 3 transmitter cavities for tuning at different frequencies can be done from a computer located in the main RF control room through LAN. This system has been used for movement of the sliding shorts of the 3 transmitter cavities for different measurements including Q, shunt impedances etc at different resonating frequency at different length of the cavity. Limit switches are connected at the cavity for upper limit and lower limit. These limits are decided according to required cavity length at 9MHz (lowest freq) and 27 MHz (highest freq).The frequency response of the input circuit of the amplifier has been measured using Vector Network Analyzer.

POWER AMPLIFIER

The high power rf amplifier (Cross-sectional view as shown in Fig.1.) is based on Eimac 4CW 150,000E water-cooled tetrode[2] and the output tank circuit of the amplifier consists of a λ/4 type variable length coaxial cavity. The short-circuited coaxial cavity is tuned by the precise movement (minimum 50 μm corresponding to tuning accuracy of 19.35 Hz at the lowest frequency and 1.135 kHz at the highest frequency) of the sliding short within the operating frequency range of 9 MHz to 27 MHz under unloaded condition.

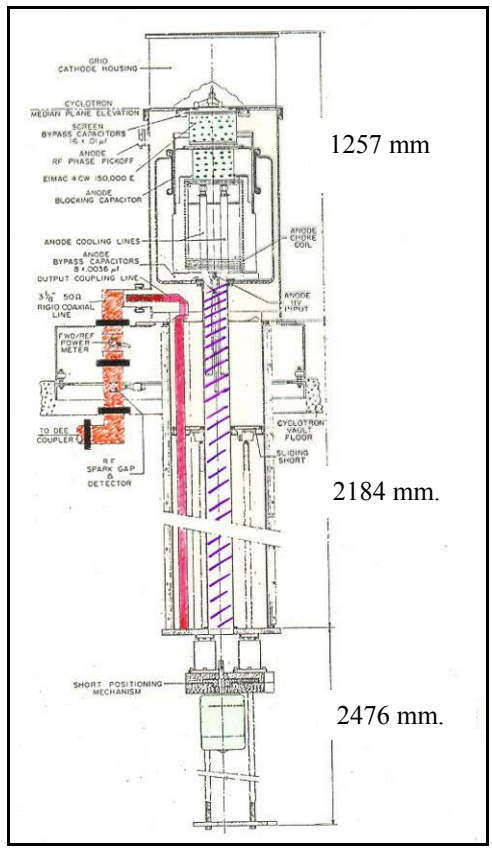

Figure 1: Cross-sectional view of high power rf amplifier.

The coaxial line is made of hexagonal outer conductor (with each side of hexagon 201.65±0.05 mm.) and circular inner conductor (with outer diameter 58.42±0.05 mm.). The sliding short plate is electrically connected to the outer and inner conductor of coaxial line by Be-Cu contact finger (as shown in Fig.2.) with sliver-graphite (99%Ag +1%C) contact ball at the tip. The sliding short contact must operate below the copper softening temperature (~460°k), since the softening could lead to fusion welding. The inner and outer conductors are aligned concentric preferably within ±0.25 mm., because large asymmetry may give rise to uneven stress on the contact finger. The contact resistance is of the order of 0.7mΩ per finger.

ssom@veccal.ernet.in

Figure 2: Sliding short contact fingers for amplifier

An inductive coupling loop is inserted along one side of the cavity (through the sliding short) at 1/5th voltage point to reflect nearly constant impedance at the anode of the tetrode. But as the length of the loop is comparable to operating wavelength, this assumption is not valid. So, by loop area trade-off it is kept in required range. Anode shell heavily loads the tank circuit, thus reducing the cavity length and shifting the cavity higher order modes beyond 66 MHz. The output rf power (~ 100 kW max) is taken out at 50Ω impedance through this inductive loop, which is matching the high cavity impedance to 50Ω.

The four identical Bridge-T networks (see Fig.3) in the grid of the final amplifier are driven with equal power levels of up to 150 watts each. VSWR of the input circuit of the amplifier has been measured using VNA (See Fig.4.) and obtained max of 1.14 at 18.18 MHz.

Figure 3: Input circuit (assembled) for amplifier

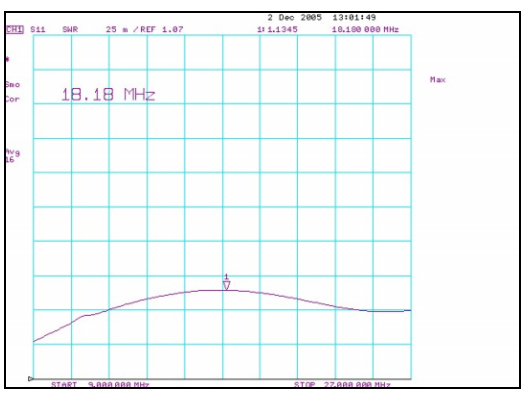

Figure 4: VNA measurement of input VSWR

The precise movement of the sliding short is accomplished by a PC-based Stepper motor controlled system (as shown in Fig.5.), that can be operated locally or from RF Control Room through LAN.

Figure 5: Stepper motor assembly with amplifier sliding short.

Limit switches (as shown in Fig.6.) are connected with the cavity for upper limit and lower limit of the movement. These limits are decided according to the required cavity length at 9 MHz (lowest freq) and 27 MHz (highest freq).

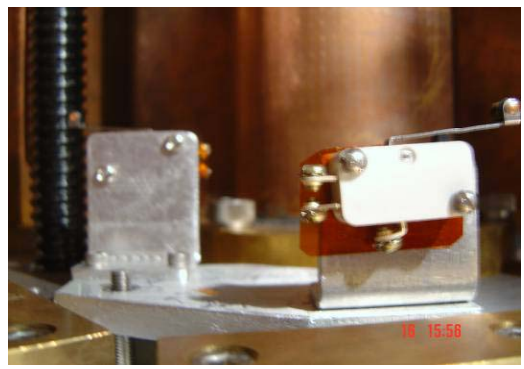

Figure 6: Limit switches assembly of the cavity

The anode of the tetrode is coupled to the cavity by a cylindrical Blocking capacitor (~ 3000 pF) as shown in Fig.7 & 8.

Figure 7: Anode Blocking Capacitor.

DC power supply (20kV@22.5A for 3 amplifier anodes) is fed to the anode through RF Choke (100 µH) and High Voltage Filter capacitors (3600 pF x 8 Nos. , 30 kV) as shown in Fig.9.

Figure 8: Tetrode assembled with anode blocking capacitor.

Figure 9: Assembly of RF Choke & HV Filter capacitors.

DC Power supply (1.5 KV@1A) is also made and fed to screen terminal. Screen by-pass capacitor (10000pF x 16 nos., 2.5kV) assembly is shown in Fig.10.

Figure 10: Assembly of Screen by-pass capacitors.

The measured unloaded Q of the cavity varies from 4300 to 1800 (as shown in Fig.11) and the measured loaded shunt impedance values vary from 5kΩ to 1kΩ for 9 MHz to 27 MHz as shown in Fig.12. Only for low frequency near 9 MHz presence of higher order modes is found[3]. But the values are significantly small. At 9 MHz, next higher order mode is found near 66 MHz with shunt impedance of 1.5k and at 10 MHz, next higher order mode is found near 81 MHz with shunt impedance of 1k.

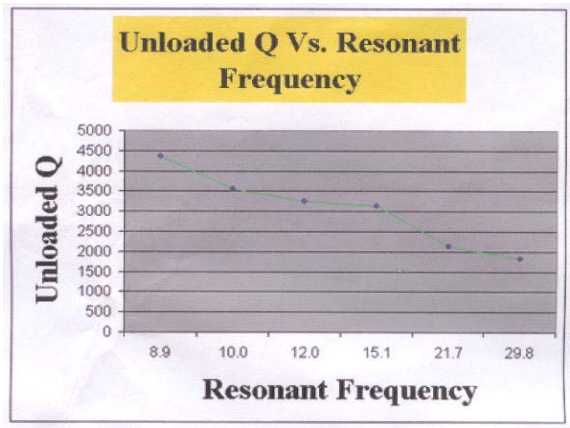

Figure 11: Unloaded Q vs. resonant frequency.

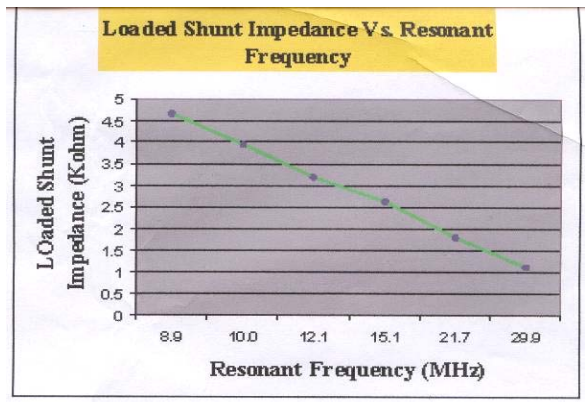

Figure 12: Loaded Shunt Impedance vs. resonant frequency.

CONCLUSION

Three nos. of 100 kW rf power amplifiers have been installed in the vault area of k500 Superconducting cyclotron building. The cold rf measurements of the amplifier cavity has been successfully carried out using Vector Network analyser (VNA). The warm rf measurements with dummy load are yet to be performed as cable laying are in progress and will be completed soon. The tetrode has been leak tested with 17 gpm of LCW flow at 80 PSI before assembly.

REFERENCES

[1] S. Som et. All, "An overview of the RF system of k500 Superconducting Cyclotron at VECC", InPac-2005, C-139.
[2] S. Paul et. All, "Overview of control and power electronics of k500 RF system". InPac-2005, C-141.
[3] S. Som et. All, "Present status of radiofrequency system of superconducting cyclotron at VECC", InPac-2006.

MECHANICAL ENGINEERING CHALLENGES IN THE DEVELOPMENT OF THE FEL AT RRCAT

Sanjay Chouksey#, S. Krishnagopal, Vinit Kumar, Shankar Lal, K. K. Kumar Pant, Vijendra Prasad; RRCAT, Indore (M.P.) 452013, India

Abstract

The Compact Ultrafast TErahertz Free-Electron Laser (CUTE-FEL) is being developed by BP&FEL Laboratory, RRCAT, which is designed to lase around 80 μm. Sub-systems like S-band high gradient accelerating structures, pre-buncher, buncher, pure permanent undulator etc. have already been developed and others are in advanced stage of fabrication/commissioning. In this paper we present the design, fabrication, measurements and status of various prototype developments of structures.

INTRODUCTION

The Compact Ultrafast TErahertz Free-Electron Laser (CUTE-FEL) is being developed by BP&FEL Laboratory, RRCAT for condensed matter research and chemistry applications. The FEL is designed to lase around 80 μm and will be driven by a 10 MeV Plane Wave Transformer (PWT) linac and will use planar, pure-permanent magnet (PPM) undulator with 5 cm period and 2.5 m length, developed in-house [1]. The major components needed

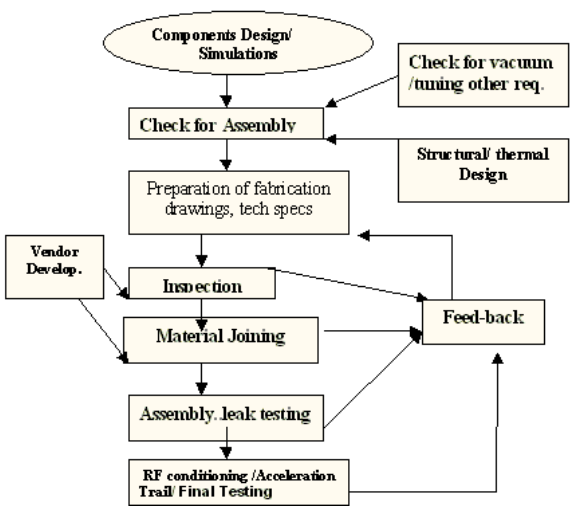

Fig.1 Process plan components development

for the development of the FEL are pre-buncher cavity, buncher, PWT linac and PPM Undulator. PWT linac and high brightness photo cathode guns are high gradient accelerating structures requiring an operational vacuum of better than 1x10-^{8} mbar. These devices require precise machining of components for accurate geometry on internal details with desired surface finish, and UHV quality leak tight joining. Development of these structures from simulation to final testing commissioning/ RF trials involves various levels of prototyping. In this paper we present the design, fabrication, measurements and status of various prototype developments of structures. Fig.1 shows our process plan for component development.

In the next section, we will review their engineering considerations, various prototype developments, results achieved and future plan.

COMPONENT DEVELOPMENTS

Pre-buncher cavity

In order to bunch low energy electron beam coming from thermionic electron gun, a sub-harmonic buncher cavity (476 MHz) was designed. Mechanical design considerations are:

- Fabrication of nose cone geometry cavity cell in two asymmetric halves with surface profile tolerance better than 0.05 mm for 350mm inner diameter.
- Accurate assembly of cavity cell in two asymmetric halves with various orthogonal ports.
- Requirements of vacuum sealing & tuning
- Structural and thermal requirements

Fig 2 Aluminium prototype of pre-buncher cavity

Current Status & future plans:

First, a true-to-scale prototype was made out of aluminium alloy T6061 to perform the low power RF test as shown in Fig 2. Inspection results done on CMM showed a tolerance of better than 0.04mm on inner profile. Final structure design was suitably modified based on the feedback received from cold test results. Critical design feature includes water-cooling channels on both sides for heat removal, tuner plungers for RF tuning, spring metal Helicoflex seal of dia 400 mm for UHV

#chouksey@cat.ernet.in

sealing. Final cavity structure made of AISI 304L is currently under fabrication at local vendor.

PWT linac structure

The PWT linac structure is a disk-washer loaded accelerating structure in which an array of disks (Ø90mm, 12mm, OFE copper), which is the periodic loading element that supports the slow-wave TM mode-like fields in the axial region used for particle acceleration. This is mounted inside a tank structure (AISI 304L) that serves as the outer boundary of the RF cavity and also as the vacuum envelope. The ports required for microwave power input, vacuum pumping, and diagnostics are also fitted onto the tank structure, while the array of disks is mounted on stainless steel (SS 304L) flanges using support tubes (Ø6mm, 1mm thick, SS 304L) that also carry cooling/heating water to the disks from a reservoir brazed to the flange. The beam entry/exit ports are mounted on the other side of these flanges (Fig. 3).

Mechanical design considerations are:

- Machining of components within surface profile tolerance of 0.03 mm Tool finish of better than 0.2 µm CLA on surfaces subjected to high field gradients
- Repeatable hole pattern on disk and supporting reservoir. This is to ensure assembly and required gap for vacuum brazing between disks to tube.
- Concentricity of the beam and disk axis better than 100 µm for complete length of 420mm
- Brazing of complete structure
- Vacuum requirement ~10^{-9} mbar (UHV)
- Structural and thermal requirements

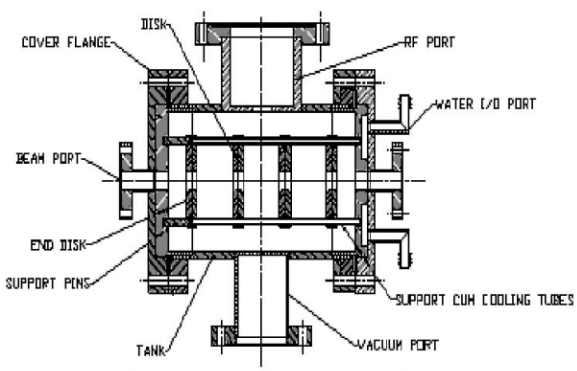

Fig. 3: PWT structure

Developments & present status:

We have built four prototype structures of the PWT linac. First & second prototypes (PWT1 & PWT2) have helped in fixing the parameters for brazing, machining, coating, chemical cleaning and handling of the components.

Machining: After initial trails, machining of the disk and other critical components was done at IGTR, Aurangabad on CNC machine (DECKEL-MAHO) using carbide tooling. Inspection done on CMM in scan mode showed better than 0.02mm profile tolerance and surface finish better than 0.2µm. Fabrication process using drilling jig on PCD ensured required positional accuracy and repeatable hole pattern. Initial prototypes with commercially available SS 304L tubes resulted improper assembly and failures of brazed joints. For 8-cell structure, cold drawn tubes were used.

Material joining: In the initial brazing trials, two-step brazing with 72 Ag - 28Cu (Cusil) & Incusil15 (Ag-Cu-In) was employed. Visual observations of the leak joints showed a poor fillet formation, and improper melting of filler wire at disk-tube junction [2]. Third prototype structure, after assembly was successfully leak-tested to a leak-rate of better than 1x10^{-9} Torr l/s, evacuated to a vacuum of 1x10^{-8} mbar, and acceleration of 3.5 MeV was observed. Another 4-cell structure PWT4 (that will actually used as the buncher) was made and tested. A brazing prototype of 8-cell structure was developed recently. Efforts are underway to build a. 8-cell structure for 10 MeV energy gain

Undulator:

A pure permanent magnet (NdFeB), variable-gap undulator period of 50mm period was designed and developed in two section of 2.5 m-long [3]. Mechanical design considerations are:

- Accurate positioning of mechanical structure jaws at different pole gaps.
- Errors in the physical dimensions of magnet block- < 20µm
- Parallelism of the surface formed by the array of the magnet blocks < 80 µm
- Vertical pole motion (gap) < 10µm.
- Pole gap variation mechanism to take variable magnetic force
- Magnet and frame structure should be rigid to keep minimum deflection within 0.01mm.
- Low magnetic permeability of the material during fabrication near magnet blocks.
- Ease in assembly.
- Provision for Alignment of the Undulator

Undulator was designed for above considerations. Magnets were assembled (Fig. 5) as per the arrangement calculated by the simulation.

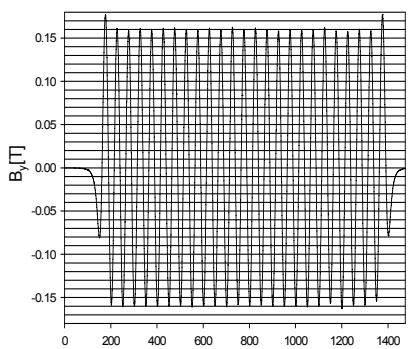

Fig 4: Plot of B_y along the undulator axis

A three-axis magnet field mapping system was developed and used to plot B_y along the undulator axis (Fig. 4). The mean of all the peak magnetic fields is 1.624 kG and the rms error is 0.9%, which is within the rather conservative 1% tolerance limit.

Fig. 5 Photograph of two Undulator segments with the field mapping system and corrector coil mounted

Photocathode gun:

We are developing a S-band, 1.6 cell, BNL/SLAC/UCLA type photoinjector. Electrons are extracted by shining a high power, high-stability Nd:VAN laser onto copper photocathode surface. Since the structure is used to accelerate electron beams to reasonably high energies over short distances, it is fed with high power microwaves to set up the high accelerating electric field gradients (~100MV/m) inside it. This imposes the requirement of precision machining with strict geometrical and dimensional tolerances. A complete gun structure has two accelerating cells (Body full cell & body half cell) and various ports for feeding the microwave power, vacuum pumping, laser entrance/exit and RF diagnostics.

Mechanical engineering considerations:

- Fabrication of accelerating cells with surface profile tolerance better than 0.02mm on internal cavity cell.
- Tool finish on surfaces subjected to high field gradients better than 0.1 micron CLA.
- Orientation between the various orthogonal and angular ports at component and assembly level.
- Concentricity of the oblong slot better than 0.02 mm
- Vacuum requirement ~10^{-9} mbar (UHV)
- Material Joining
- Support and assembly

Developments & present status:

We have successfully fabricated OFE Cu prototypes of the main accelerating cells to design specifications on high precision Schaublin lathe with polycrystalline diamond and cemented carbide tool.Inspection Results on 'Carl Zeiss' make CMM showed surface profile tolerance better than 0.02mm and surface finish of the order of 0.08 µm. We have also built two ETP Cu brazing prototypes using the eutectic filler alloy Cusil. With these technologies successfully demonstrated, we will now start fabricating four nos. of complete structure at Indo German Tool Room, Aurangabad.

CONCLUSIONS

While the initial trials of component development for the CUTE-FEL project were based on first principles, the actual realisation evolved after a large number of mock trials (Fig. 6). The real situation in fabrication & material joining is always more complex bringing into play a large number of variables. We have successfully built and tested two prototypes of PWT linac structure. We have also successfully built brazing & cold test prototypes and one full prototype of the laser photocathode gun.

.

The authors are highly grateful to Shri S. Kotaiah and Shri Gurnam Singh, for their support in implementation of this Project. We acknowledge the help rendered by Mr. S. Jafar Ali in finalizing the AutoCAD drawings for the structures. Authors also acknowledge the work done by Shri S.S. Parihar during prebuncher cavity development

REFERENCES

[1] S. Krishnagopal, et al., Current Science 87, 1066 (2004); S. Krishnagopal and V. Kumar, Rad. Phys. & Chem. 70, 559 (2004).

[2] S. Chouksey et al, "Vacuum brazing of an S-band electron linac & photo cathode gun," INVAC 2003, Nov 2003

[3] Vinit Kumar et al, "A Pure-Permanent Magnet Undulator for a Far-infrared FEL", International FEL Conference –2004

Fig 6: Evolution of prototype developments

THERMAL SIMULATIONS OF A PHOTOCATHODE R.F. GUN

B. Biswas#, Shankar Lal, K. K. Pant, Arvind Kumar and S. Krishnagopal
Beam Physics and FEL, Laboratory, Raja Ramanna Centre for Advanced Technology,
Indore 452013, India

Abstract

We are developing a photocathode linac, which uses a 2856 MHz r.f. gun, with a copper cathode driven by a 102 MHz, 266 nm laser at inclined incidence. The laser photocathode r.f. gun is a 1.6 cell BNL/SLAC/UCLA type III r.f. gun. In this paper we present the dynamic thermal cooling simulations to calculate the structural deformations and consequent frequency drift of the gun. We have done a complete r.f.-thermal-structural-r.f finite-element analysis (FEA) of the gun in that order, using ANSYS/MULTIPHYSICS. We find that with the present coolant channel design the gun can operate at up to 2 Hz without any significant change in resonant frequency and field balance.

INTRODUCTION

There is a wide range of normal-conducting photocathode guns working or under development all around the world as injectors for x-ray free electron lasers and colliders [1-4]. Typically the S-band laser photocathode normal conducting guns deliver up to 150 MV/m peak accelerating electric field.

The S-band photocathode gun we are developing is a BNL type III gun [5, 6]. It has a simple longitudinal cooling arrangement unlike the circular cooling channels in higher r.f. pulse repetition rate guns. We have done the complete r.f.-thermal-structural-r.f finite element analysis (FEA) of the gun in that order. We found that it is necessary to model the gun with all its ports, to capture the high heat flux spots around these port discontinuities. We also found that the resonant frequency in the 1.6 cell photocathode gun is very sensitive to geometrical deformations. Hence we re-simulated the heated-deformed gun for its r.f. properties. As deformations are of the order of microns we morphed the r.f. region's FE mesh boundary to absorb the surface displacements by using the structural solution. This approach is different from regenerating the deformed structure in a CAD package and remeshing it for simulation – as the new mesh may not be similar to the original one and mesh-to-mesh differences will overshadow the desired detuning result. We show that we can go up to 2 Hz operation at maximum gradient with modest cooling parameters and no degradation in r.f. parameters. Higher repetition rates will need modification of the coolant channel design. However operation at lower gradients and higher repetition rates will still be possible.

bbiswas@cat.ernet.in

THE ELECTROMAGNETIC SIMULATIONS

The RF parameters of the 1.6 cell BNL/SLAC/UCLA type photocathode gun, shown in Fig. 1, are given below in Table 1.

Table 1: Parameters of the photocathode gun.

Parameter	Value
Type	1.6 cell BNL/SLAC/UCLA type III
Frequency	2856 MHz
Bunch Charge	1nC
Field balance	~ 1.04
Peak accelerating field	147 MV/m
Rep. Rate	1 - 10 Hz
Laser pulse width	FWHM 12 ps
r.f. pulse width , power	4 μs , 8 –10 MW
Power dissipated at 10Hz, 4 μs r.f. pulse	0.5kW

We simulated the full model of the photocathode gun in FEA package ANSYS [7] to get the resonant π-mode at 2856.1 MHz and field balance of 1.042 as shown in Fig. 2. Copper and SS conductivity were applied at respective regions for calculation of heat loss/flux.

The average heat-flux obtained for an r.f. pulse of 4 μs and 2 Hz repetition rate obtained is shown in Fig. 3. The maximum heat flux, around the r.f./vacuum ports, is nearly three times the peak heat flux without ports (at full cell exit wall) when compared with SUPERFISH. The inner diameters of the two cells were fine tuned by up to 5 μm to get the required field balance. This is quite similar to the fabrication learning curve where final cuts of the order of 5-10 μm were taken on inner diameter of the two cells of prototype aluminium and then ETP copper gun.

THE THERMAL SIMULATIONS

The gun material comprises of OFE copper and some SS316L seal plates, beam and vacuum ports. For thermal (conduction) analysis all the metallic volumes were simulated. The o-ring was also modeled. The convection bulk temperature in the two channels for water flow is shown in Fig. 4 -for the 147 MV/m peak gradient at 4 μs r.f. pulse and 2 Hz repetition rate. For clarity only a one-fourth model is shown. The inlet water temperature is 30°C and the water flow is at 1.8 m/s. The ambient temperature is also 30°C.

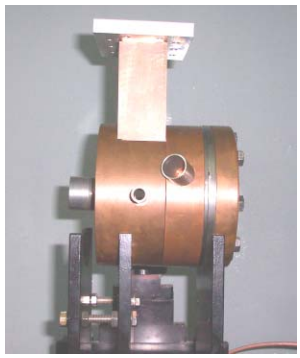

Figure 1: The 1.6 cell S-band photocathode gun OFE prototype .

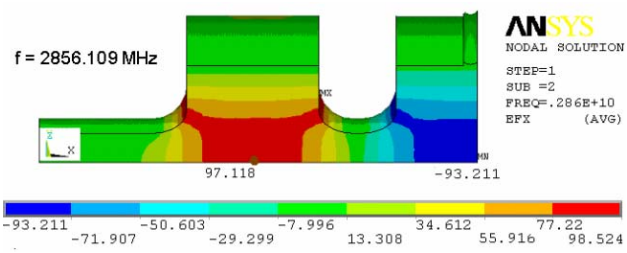

Figure 2: The axial electric field (not to scale) in photocathode gun.

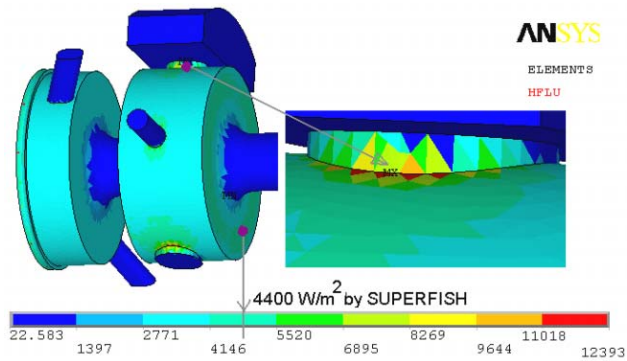

Figure 3: The heat flux for 147 MV/m peak field and 4 μs, 2 Hz, r.f. pulse.

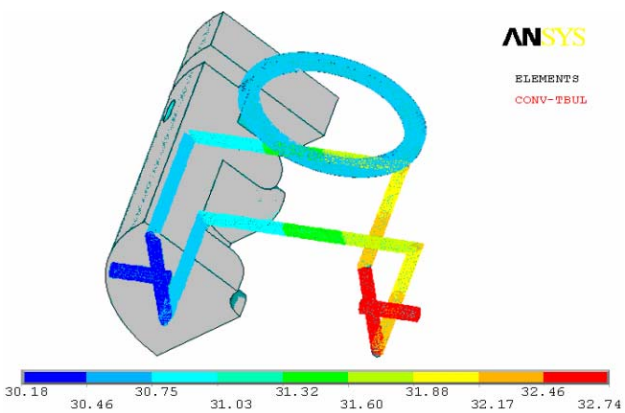

Figure 4: The coolant bulk temperature at 2 Hz r.f. cycle.

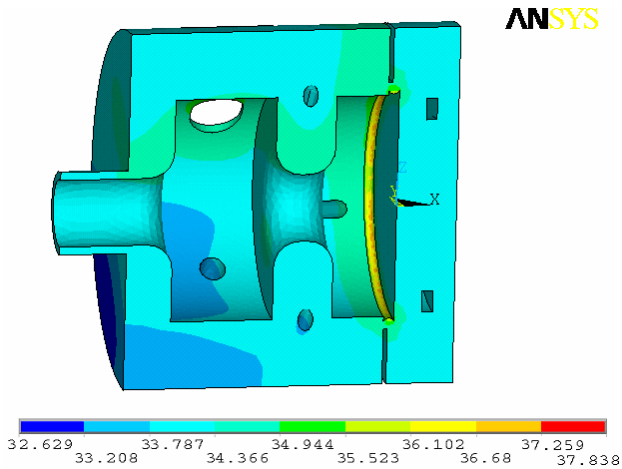

Figure 5: The temperature at 2 Hz r.f. cycle.

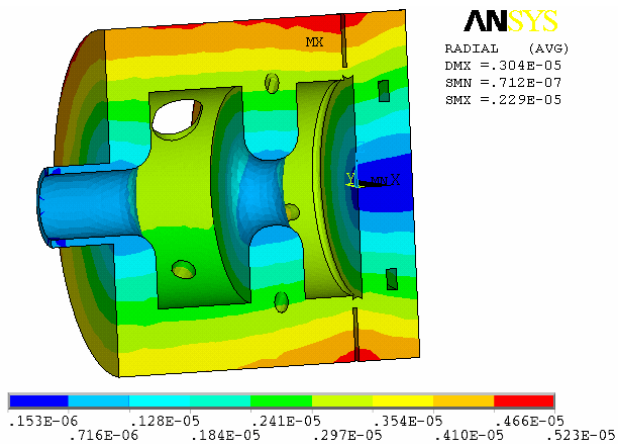

Figure 6: The radial deflections for 2 Hz r.f. cycle.

A fortran program was written to read the heat flux data from the surface faces of the outermost elements of the r.f. model into the common interface nodes of the structural model. The temperature distribution for the above 2 Hz case is shown in Fig. 5. The gun inner surface is quite *uniformly* heated by about 4°C. The o-ring is heated by 7.8°C because of poor thermal conductivity of SS and the small contact area.

THE STRUCTURAL SIMULATIONS

The full structure, including the vacuum region, was simulated for calculating the thermal strains. The thermal and electromagnetic elements were both changed to structural type. The temperatures from the thermal solution were read into the structure. The vacuum region was attributed dummy properties so that the structure was unaffected in solution. At cooling parameters of 2 Hz operation, the radial deflections are *uniformly* restricted to about 2 –3 *micron* as shown in Fig. 6. This reduces detuning and helps to preserve the field balance as is shown next.

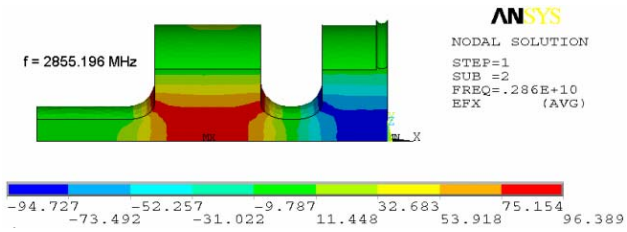

Figure 7: The axial electric field (not to scale) in photocathode gun and detuned frequency for 2 Hz r.f. cycle.

THE ELECTROMAGNETIC ANALYSIS OF THE DEFORMED CAVITY

The geometry of the vacuum region was *deformed* using the structural solution. Then the structural elements were reverted to electromagnetic high frequency type in ANSYS and an eigenmode solution was obtained. The frequency of the π-mode changed by –0.2 MHz to 2855.9 MHz and the field balance shifted from 1.042 to 1.044 as shown in Fig.7. The negligible change in field balance shows the uniformity of heating and hence optimization of the cooling layout. Thus the 2Hz repetition rate is just within the acceptable detuning range. The detuning is comparable with SUPERFISH which gives 46kHz/micron change of full cell inner diameter alone.

HIGHER R.F. DUTY CYCLES

We have simulated higher duty cycles of up to 10 Hz at 147 MV/m peak gradient and 4 μs r.f. pulse. The results show that we end up with larger deformations (+32 microns radially), temperature (57 degree) and detuning of - 0.9 MHz as shown in Fig.8, for unchanged cooling parameters (of 2Hz case). We do not wish to further push the water speed, as the channel diameter is only 6.5 mm and has many bends.

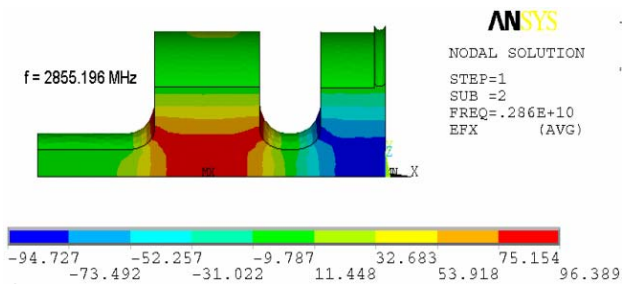

Figure 8 : The axial electric field (not to scale) in photocathode gun and detuned frequency for 10 Hz r.f. cycle at unchanged cooling parameters.

The present gun design does not allow annular cooling channels at the iris or full cell exit wall because of two component brazing assembly. In order to have annular channels, as for high repetition rate photocathode guns [8,9] the gun design will need complicated many component-brazing cycles. Instead we plan to increase the water channel diameter and reduce the path lengths to allow 10Hz operation.

CONCLUSIONS

The present coolant channel design in the 1.6 cell BNL/SLAC/UCLA type photocathode gun seems adequate for 2 Hz operation at 147 MV/m peak gradient and 4 μs r.f. pulse with 1.8 m/s water flow rate. The cooling is optimized to arrest deflections at the inner diameter to about 2-3 microns and a detuning of –200 kHz is seen. We have used a novel approach of complete r.f.-thermal-structural-r.f simulation cycle in the *same* FE mesh environment for the *full* model. Modeling ports in 3D helps to generate higher heat flux in regions around these ports which give temperature around these ports. rise than without ports as given by SUPERFISH. The cavity with deformed boundary was then re-simulated for resonant frequencies. This provides high sensitivity to r.f. detuning calculation as only boundary nodes are moved with the inner FE mesh unchanged. The technique developed could be used elsewhere also.

Higher water velocities are improper for a long, many-bend and narrow channel for water as it increases the pressure drop and pressure fluctuations due to flow round the corners. We are at present investigating the possibility of enhancing the flow rate by different methods to allow 10 Hz operations with minimal deformation and detuning.

ACKNOWLEGMENTS

One of us (BB) would like to thank Mr. Vikas Jain for useful discussions and providing fast computing resources for some runs.

REFERENCES

[1] J.S.Fraser, et al., IEEE Trans. Nucl. Sci. 32 (1985) 1791.
[2] S.Anderson, et al., Proc. of PAC'99, New York, p. 2006.
[3] Luca Serafini, NIMA 341 (1991) 341.
[4] Kirk T. McDonald, IEE Trans. Electron Devices 35 (1988) 2052.
[5] D.T.Palmer, Ph.D Thesis.
[6] Arvind Kumar, et al., PRSTAB 5 (2002) 103501.
[7] www.ansys.com
[8] F.Marhauser, et al., Proc. of FEL'06 , p.560.
[9] X.J.Wang, et. al., Proc. of PAC'01, Chicago, p.2233.

CONTROL CHARACTERISTICS OF THE PEFP RF SYSTEM*

H. J. Kwon#, Y. S. Cho, H. S. Kim, K. T. Seol, I. S. Hong, Y. G. Song
PEFP, KAERI, Daejeon 305-353, Korea

Abstract

A 20 MeV proton accelerator has been developed and tested at Proton Engineering Frontier Project (PEFP) as a front-end part of the 100 MeV accelerator. The initial test results showed that more stable RF operation was necessary to investigate the machine characteristics more comprehensively. A LLRF control system using commercially available digital board was newly developed and tested for this purpose. The goals of the RF control for 20 MeV accelerator are to achieve errors within 1% in amplitude and 1 degree in phase against external perturbations such as change of resonant frequency, fluctuation of klystron power supply voltage and also beam loading. In addition, the PEFP 20 MeV DTL has unique characteristics that single klystron drives four independent tanks simultaneously. In this paper, the initial test results of the RF system with digital controller are presented and its control characteristics are discussed.

INTRODUCTION

One of the missions of PEFP is to develop a 100 MeV proton linear accelerator. For this purpose, a 20 MeV accelerator was already fabricated and installed at KAERI test stand [1][2]. About two years later, the 20 MeV accelerator will be moved to be installed in Gyeongju city which was selected as an host city for PEFP 100 MeV accelerator. An initial test has been carried out at KAERI site to check the overall machine performance and tune the accelerator operating parameters. The test is being done with peak current of 1 mA at low duty, that is 50 μs beam pulse width and 0.1 Hz repetition rates, because of the improper radiation shielding for full beam power. The installed 20 MeV accelerator at KAERI site is shown in Figure 1. During the initial beam test, nearly 100 % beam acceleration was achieved through the four DTL tanks. But the pulse to pulse beam current fluctuation was observed. Moreover the beam current dependency on the tuning parameters such as RF power, RF phase, beam steering were not so obvious in the near 100 % beam transmission level. Therefore, more stable RF control system was necessary to investigate the machine performance more comprehensively. A digital control LLRF system was developed to satisfy the requirement [3]. Recently, the high power test using newly developed LLRF control system is being carried out to check the RF system characteristics and optimize the control parameters. In addition, the PEFP 20 MeV accelerator has unique characteristics, that is four independent tanks are driven by single klystron. Several methods were adopted to realize this scheme, and the DTL tank characteristics were investigated to obtain the basic parameters for the proper RF control.

* This work is supported by MOST of the Korean government
#hjkwon@kaeri.re.kr

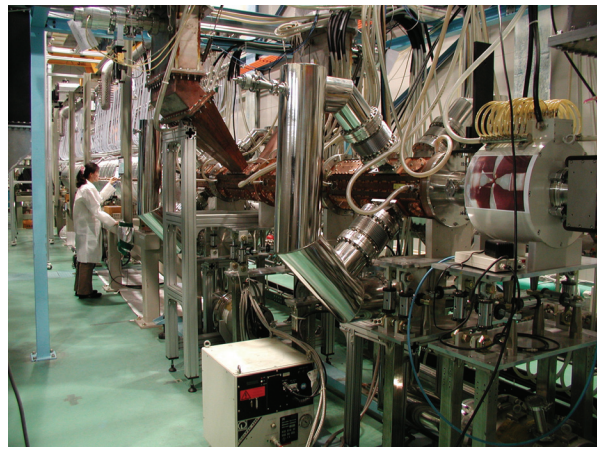

Figure 1: 20 MeV proton accelerator installed at KAERI test stand.

20 MEV ACCELERATOR TEST STAND

The main accelerator facilities at KAERI test stand are 20 MeV accelerator itself, two sets of 1 MW, 350 MHz RF system, two sets of –100 kV, 20 A DC high voltage power supply for the klystron, two sets of 2 MW cooling system for the cavity and RF system.

The ambient condition at KAERI test stand is not stabilized. Therefore the RF cavities should be stabilized against changing ambient conditions – especially ambient temperature. For this purpose, heater and heat shield were installed around the RFQ and DTL cavities. A 1 kW heating power per RFQ and a DTL tank was used. The heater was controlled by PID mechanism of the SCR power unit. By using this method, the frequency could be stabilized within ± 1 kHz.

The design duty of the 20 MeV accelerator is 24 % and two sets of 1 MW, 350 MHz klystron are used to drive a 20 MeV accelerator, one is for RFQ and the other is for DTL. All the other ancillary facilities such as klystron power supply and cooling system were designed for 100 % duty operation. During the low duty operation at KAERI test stand, the RF system is operating such that the electron beam of the klystron is CW whereas only the input RF signal is modulated for the low duty pulse operation.

Two sets of klystron power supply are used to drive two sets of 1 MW klystron. As mentioned above, the design duty of 20 MeV accelerator is 24 %, therefore, not modulator, but DC high voltage power supply is used as a klystron power supply. During test, the klystron power supply is operating in CW mode.

Two sets of cooling system are operating, one is for RFQ, the other is for DTL. One set of the cooling system at KAERI test stand supplies cooling water both to the

klystron and cavity simultaneously. With this cooling circuit configuration, the thermal load can be maintained nearly constant irrespective of the duty factor. Three-way valve is used to control the cooling water temperature during operation.

RF CONTROL CONCEPT OF THE 20 MEV DTL

The resonant frequencies of each DTL tank should be controlled independently. There are no frequency tuners in PEFP DTL. It is planned to adjust the resonant condition of each tank with cooling water temperature. Therefore the RF control concept is such that the RF system controls the RF amplitude and phase of the DTL tank with the signal from the reference tank (for example tank1), and the resonance control cooling system adjusts the frequency of each tank with the phase error signals between controlled tank and the reference tank. The cooling water unit for the resonance control (namely RCCS – Resonance Control Cooling System) will be installed for the control of each tank at Gyeongju site. Instead, the heater installed at each tank was used to adjust the resonant condition at KAERI site. One of the reasons to use the heater as a controller is that there is no test schedule requiring appreciable RF heat load at KAERI site.

The cooling water system is configured such that the klystron and four DTL tanks are connected in parallel at KAERI site. With this configuration, the main heat source is the klystron. The heat load from the DTL is only due to the quadrupole magnet cooling. A three-way valve was installed in the cooling loop to control the water temperature. During the test, the total heat loads was 1,330 kW, that was 1,200 kW from the klystron and 130 kW from the quadrupole magnet. With these conditions, the three-way valve could maintain the coolant temperature within ± 0.2 °C with standard deviation less than 0.1 °C.

HIGH POWER RF TEST OF DTL TANKS USING DIGITAL LLRF SYSTEM

After the low level test using dummy cavity [3], the high power RF test was done using newly developed digital LLRF system. As stated earlier, four independent DTL tanks were driven by single klystron. The power from the klystron is divided into four legs using magic tee. The mechanical phase shifter was installed to each waveguide leg to adjust the initial phase difference between waveguide legs. During initial test, the pickup signal from tank2 was used as a control signal instead of the vector sum signal of all four tanks. The pulse length was 200 μs and repetition rate 0.1 Hz during test. After adjusting the resonant conditions of each using heater, the high power RF test was carried out.

The loop gain and signal delay of the whole high power RF system were measured. The loop gain was about 0.76. The delay times with the reference to the system trigger were ~ 4 μs to the solid-state amplifier output, ~ 4.5 μs to the klystron output, and ~ 5.0 μs to the control board. The intrinsic delay due to the digital filter of the digital control board was ~ 2.5 μs, which was included in the ~ 4 μs delay to the solid-state amplifier output.

The forward power from the klystron and the tank power are shown in Figure 2. The P / I (Proportional / Integrate) gain values were 1.0 and 70,000 respectively. The set table was step function shape, and anti-windup scheme was used. As shown in the Figure, the klystron output power is overshooting as a response to the step function command. The typical reflected power from the tanks is shown in Figure 3. The tank is slightly over-coupled considering the beam loading effect.

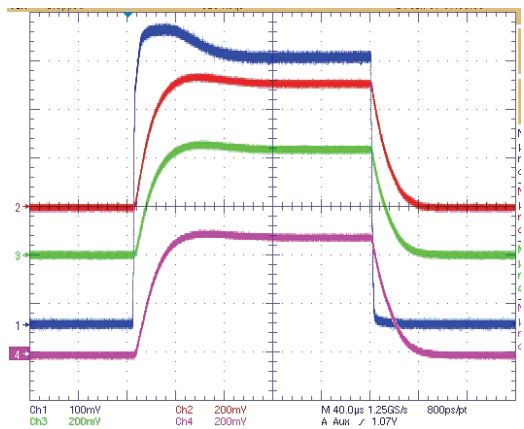

Figure 2: RF power profile (ch1 : klystron output power, ch2: tank1, ch3 : tank2, ch4 : tank3, horizontal : 40 μs/div.).

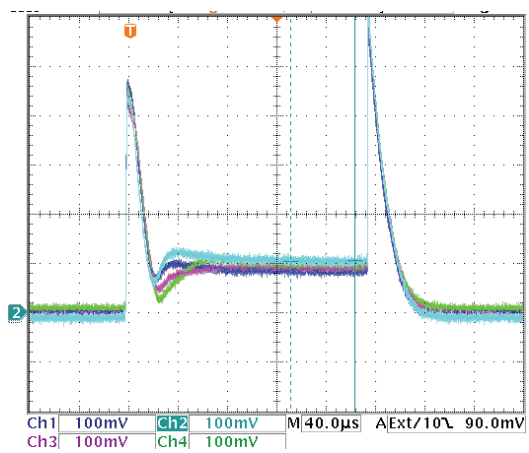

Figure 3: Reflected RF power profile (ch1 : tank1, ch2: tank2, ch3 : tank3, ch4 : tank4, horizontal : 40 μs/div.).

The phase and amplitude of the tank RF power were measured during test. The measured RF amplitude was scattered within 0.1 % of the set value and the standard deviation was about 0.02 %. The measured RF phase was scattered within 0.15 degree from the set value with standard deviation of 0.03 degree. The measured data

during 1 hour are shown in Figure 4 and Figure 5 respectively. The relative phase variations of each tank referenced to tank2 were also measured during test and the result is shown in Figure 6. The wall temperature of the tank1 is not stabilized during measurement, therefore the phase is monotonically increasing. As shown in the Figure, the phase of tank3 also showed some fluctuation, which results from the ± 0.1 °C temperature variation of the tank wall. Except tank1, the relative phase variations of all the other tanks with respect to the tank2 are within ± 0.5 degree with standard deviation less than 0.2 degree.

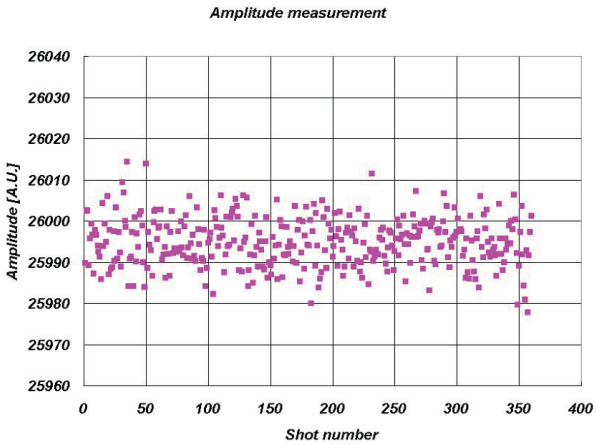

Figure 4: RF Amplitude fluctuation during feedback control (DTL tank2).

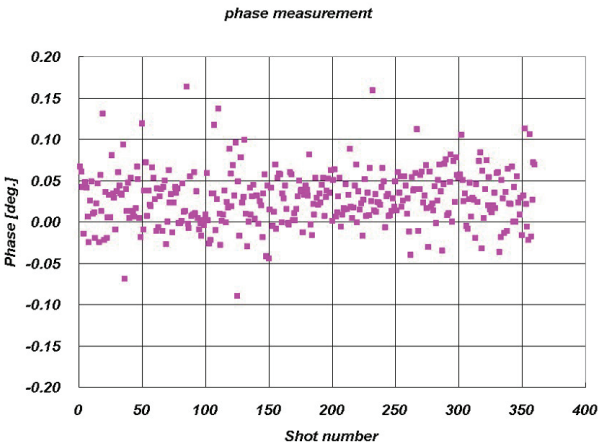

Figure 5: RF phase fluctuation during feedback control (DTL tank2).

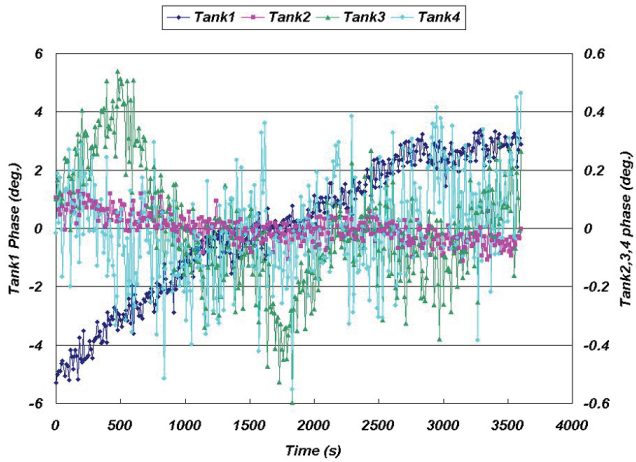

Figure 6: Relative Tank Phase Variation With Respect To Tank2 During High Power Rf Test.

CONCLUSION

The initial high power test of the PEFP DTL using newly developed LLRF system was carried out. To accomplish the proper RF control of four tanks driven by one klystron, heater at tank wall was used to control the resonance frequency of each tank and the global resonant condition was adjusted by the cooling water temperature. With this concept, the four independent tanks can be considered as a single tank. For the RF control test, system parameters such as loop gain and signal delays were measured. The three-way control valve could effectively stabilize the cooling water temperature. With this condition, the RF amplitude and phase could be maintained within required values. The relative phase variations also measured and tank1 needs re-adjustment of the control parameter of the wall temperature.

The control gain values need to be optimized from several criteria. In addition, the control system algorithm needs to include the feed-forward to compensate the beam loading effect. Before that, we should carefully check the stabilization of the tank parameters to distinguish the real RF control effect from the environmental noise and determine the control capability.

REFERENCES

[1] B. H. Choi, et al., “High Power Proton Accelerator Project in Korea”, in these proceedings.

[2] Y. S. Cho, et al., “100 MeV High-Duty-Factor Proton Linac Development at KAERI”, Proc. Of LINAC 2006, Knoxville, August, 2006.

[3] H. S. Kim, et al., “Development of the Digital RF Control System for the PEFP Proton Accelerator”, in these proceedings.

DEVELOPMENT OF THE DIGITAL RF CONTROL SYSTEM FOR THE PEFP PROTON ACCELERATOR*

H. S. Kim#, H. J. Kwon, K. T. Seol, I. S. Hong, Y. G. Song and Y. S. Cho
Korea Atomic Energy Research Institute, Daejeon 305-353, Korea

Abstract

The low level RF system is under development for the PEFP Proton Accelerator. The RF amplitude and phase stability requirements of the LLRF system are ±1% and ±1°, respectively. As a prototype of the LLRF, a simple digital PI control system based on commercial FPGA board is designed and tested. The main features are a sampling rate of 40 MHz which is four times higher than the down-converted cavity signal frequency, digital in-phase and quadrature detection, pulsed mode operation with the external trigger, and a simple proportional-integral feedback algorithm. The control logic is implemented in the Xilinx FPGA by using VHDL coding and the application program based on the VxWorks and VME platform is also developed. In this paper, the detailed design study and the test results of the prototype LLRF system are presented.

INTRODUCTION

In the 100 MeV proton linear accelerator for PEFP, the RF source will power an RFQ cavity and DTL tanks operated at a frequency of 350 MHz [1]. The low level RF(LLRF) system for 100 MeV proton linear accelerator provides field control including an RFQ and DTL tanks at 350 MHz. In our system, an accelerating field stability of ±1% in amplitude and ±1 deg. in phase is required for the RF system. The digital RF feedback control system using the FPGAs and PowerPC Embedded Processor is adopted in order to accomplish these requirements and flexibility of the feedback and feed-forward algorithm [2].

HARDWARE DESCRIPTIONS

The hardware components can be divided into the analogue parts and the digital parts. The analogue parts mainly deal with the signal mixing, IQ modulation and interlock system and the digital parts contain the control algorithm.

Analogue Components

The analogue parts consist of various components such as IQ modulator (Analog Devices AD8345), RF mixer, RF switch, RF amplitude detector, phase comparator and VSWR trip circuit along with many attenuators and power splitters. All of the analogue components are installed in the 19” subrack as shown in Figure 1. A 350 MHz cavity field pick-up signal is converted to 10 MHz IF signal in the analogue components subrack. The amplitude and phase of the cavity field can be measured by RF detector and phase comparator, therefore it is possible to compare the RF amplitude and phase measured by analogue system with those measured by digital system. The VSWR trip circuit and interlock system protect the machine in the event of an arcing or an RF full reflection.

Figure 1: Analogue components subrack

Digital Components

The main hardware components of the digital RF feedback system are ADC for sampling of the RF signal, FPGA for the signal processing and DAC for driving the IQ modulator. A ICS-572B commercial board which is shown in Figure 2 is adopted for the ADC/DAC and FPGA board. ICS-572B is a PMC module with 2-channel 105 MHz ADC, 2-channel 200 MHz DAC and with 4 million gate onboard Xilinx FPGA.

The board uses two 14-bit ADCs (Analog Devices AD6645) with a maximum sampling rate of 105 MHz. The sampling clock can be either internally or externally generated. The minimum ADC sample rate is 30 MHz. However, the board includes a programmable ADC output decimator that can reduce the output data rate by a factor of up to 32. Both input channels are simultaneously sampled. The input signals are connected via two front panel SMA connectors. The full-scale signal is 5.5 dBm into 50 ohms. The inputs are transformer-coupled with turn rato of 4:1.

The outputs of the ADCs are connected to a Xilinx FPGA for direct processing of the ADC data. The ICS-572B includes a Xilinx Virtex-II FPGA (XC2V4000) that can be programmed by the user via a JTAG port or PCI communication. On the standard ICS-572B board, the FPGA contains firmware that provides switch and data formatting functionality to route ADC and/or DAC data to the buffers. The user FPGA is connected to 64 MB

* This work is supported by the 21C Frontier R&D program in the Ministry of Science and Technology of the Korean government.
#kimhs@kaeri.re.kr

SDRAM and 16 MB QDR SRAM. The SDRAM clock rate is 133 MHz while the effective clock rate for the SRAM is 267 MHz.

On the output side, the ICS-572B uses two 14-bit high speed DACs (Analog Devices AD9857). The maximum simultaneous conversion rate is 200 MHz. The DAC has a built-in quadrature up-converter that allows the user to provide complex baseband input which is up-converted to a programmable IF (up to 100 MHz). For this purpose, the DAC includes the 32bit quadrature DDS. The DAC also provides a programmable clock multiplier.

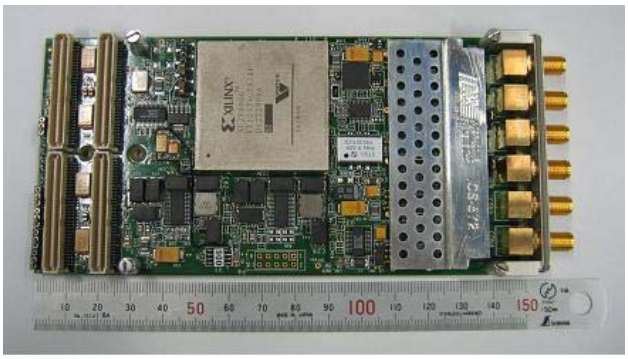

Figure 2: ICS-572B PMC Board

The communication between the ICS-572B board and host system is made using PCI bus. The QL5064 QuickPCI chip from QuickLogic is used for PCI interface solution. The performance of the QL5064 is 64 bit/66 MHz and automatically backwards compatible to 33 MHz or 32 bit

For the host system of the ICS-572B FPGA board, a Motorola VME processor module, MVME5100, is adopted. The main roles of the host system are the configuration of the FPGA board and the data acquisition.

SOFTWARE DEVELOPMENT

Cavity Model Feedback Simulation

The digital feedback algorithm has been simulated using MATLAB/Simulink as shown in Figure 3. Basically the control method is PI (proportional-integral) control. Figure 4 shows the feedback simulation results of the DTL tank with beam loading. The beam loading amounts to 20 mA and the cavity field can be maintained within 1% with the simple PI feedback control. If we assume that the total loop delay is about 1.6 μs, the gain margin is about 12 and if the loop delay is increased then the gain margin is decreased, which means that we should pay particular attention to the design of digital control logic.

FPGA Programming

The feedback logic based on the PI control is implemented in the FPGA by using VHDL. The I and Q component of the cavity field signal is fed into the FPGA using the ADC, which samples the RF signal four times during one period. The sampled I and Q components of the cavity signals are compared with the set value, which generates the error signal.

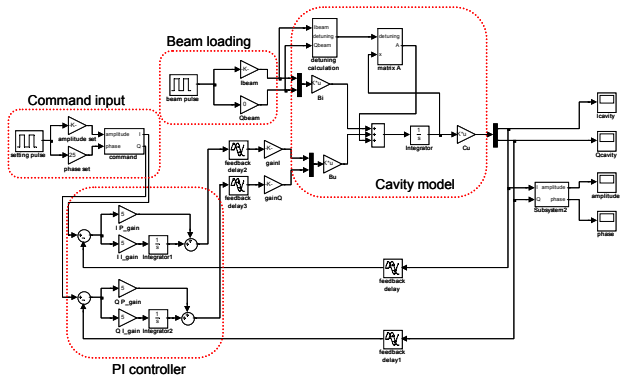

Figure 3: Feedback simulation schematics

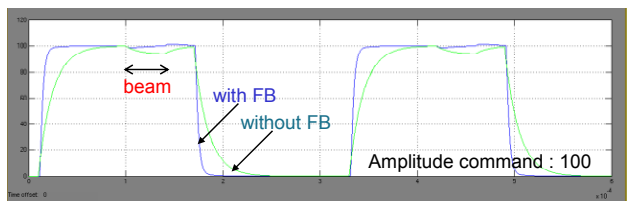

RF amplitude response
(P gain:3, I gain:200000, time delay:1614 ns)

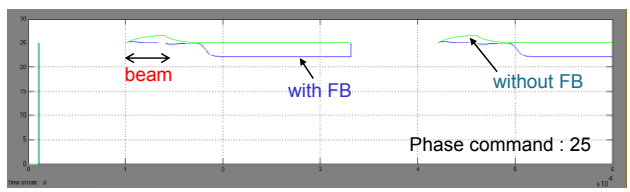

RF phase response
(P gain:3, I gain:200000, time delay:1614 ns)

Figure 4: Feedback simulation results

For a proportional control, the error signal is multiplied by the P gain. For an integral control, the error signal is multiplied by the I gain, and then integrated over time. The calculated proportional and integral control values are added then converted to an analogue signal by using DAC. The analogue signal from the DAC drives the IQ modulator. The set values and each gain value are written into the register in the FPGA by the host processor through a PCI communication. Therefore the set values and gains can be changed during the operation. The measured I and Q components of the RF signals are uploaded to the host board by using a PCI communication for monitoring and recording purposes.

The development environment for the FPGA coding is as follows.

- coding language: VHDL
- synthesis tool: XST in ISE 7.1i from Xilinx
- implementation: ISE 7.1i from Xilinx
- mapping and routing: ISE 7.1i from Xilinx
- logic simulation: ModelSim SE 6.1b from Mentor

The flash ROM download file can also be generated in the ISE environment. The flash ROM files are downloaded by using a PCI communication.

The developed logic was verified by using a ModelSim simulation before implementing it into the FPGA. Errors in the code can be found through this simulation and this process also makes it possible to predict the FPGA behaviour and save on the development time.

BASIC PERFORMANCE TEST

For the feedback test, we established the experimental setup by using a dummy cavity. The schematic of the experimental setup is shown in Figure 5. To observe the feedback effect, an intentional perturbation by using a step motor is applied to the dummy cavity. The perturbation is amount to 10% in RF amplitude and 12-degree in phase. The feedback stabilization effects of the RF amplitude and phase are shown in Figures 6 and 7, respectively. With the feedback control, there was no appreciable variation with a given perturbation. The shot-to-shot RF stability was measured for 60 shots and the results are shown in Figure 8. From the results we found that the feedback control improved the shot-to-shot stability by an order of a magnitude compared with an open loop control.

REFERENCES

[1] B. H. Choi, et al, "High Power Proton Accelerator Project in Korea", presented in this conference.
[2] M. E. Angoletta, "Digital Low Level RF", Proceedings of EPAC 2006, Edinburgh.

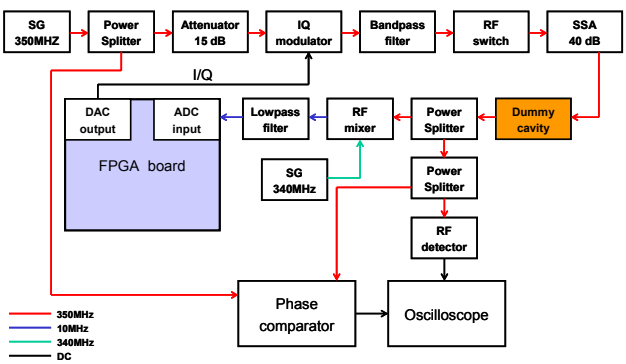

Figure 5: The schematic of the experimental setup

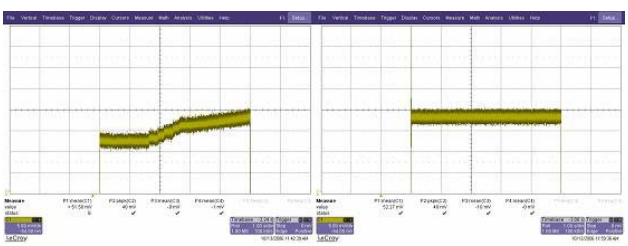

Figure 6: RF amplitude trace in the cavity, Left: Open loop case, Right: Closed loop case. With a feedback, a given perturbation of about 10% is fully suppressed. (vertical: 10% / div., horizontal: 1 s /div.)

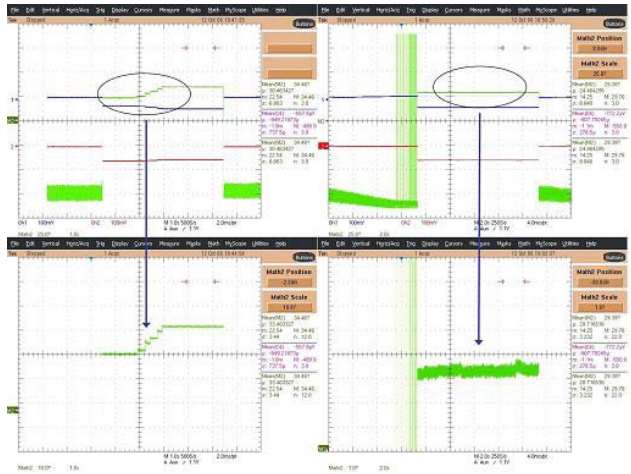

Figure 7: RF phase trace in the cavity. Left: Open loop case, Right: Closed loop case. With a feedback, a given phase perturbation of about 12°is fully suppressed. Note that the vertical scale of lower left figure is 10°/div., but that of lower right figure is 1°/div.

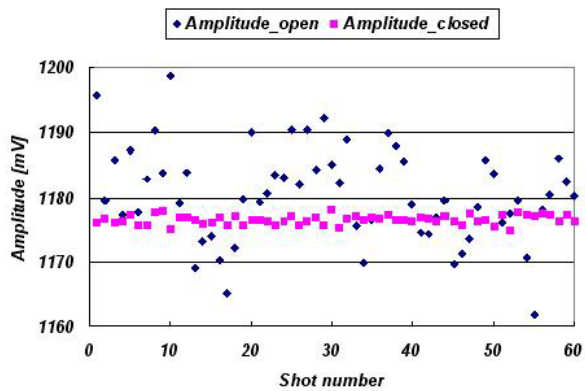

Figure 8(a): Shot-to-shot RF amplitude stability (diamond: without feedback, square: with feedback)

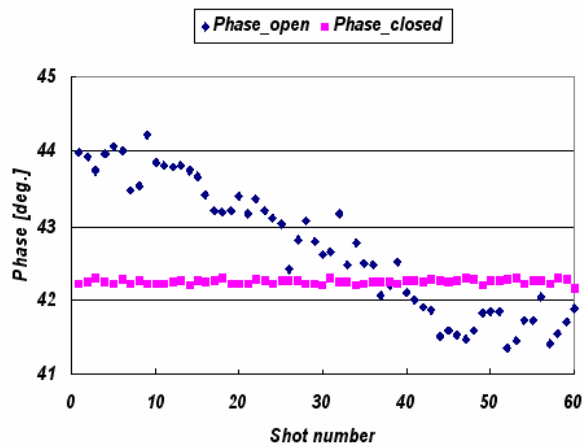

Figure 8(b): Shot-to-shot RF phase stability measurement (diamond: without feedback, square: with feedback)

DESIGN AND DEVELOPMENT OF 30 MEV, 3 KW RF ELECTRON LINAC

V.T.Nimje, D.Bhattacharjee, K.Dixit, D.Jayaprakash, K.C.Mittal and A. K. Ray
Accelerator & Pulse Power Division, BARC, Mumbai – 400 085.

Abstract

A 30 MeV, 3 kW on-axis coupled cavity RF electron linac is being designed, developed at BARC and will be installed at Vizag . It will be used as a neutron generator and will produce ~ 10^{12}-10^{13} n/sec. The design of the 94 cell RF structure, rf system, modulator for the electron gun and the Neutron generation target is in the advanced design stage . The design details of the linac are presented in this paper.

INTRODUCTION

Electron beams have played a key role in the field of basic sciences, applied sciences, medicine and agriculture. Over the last decade or so, the focus has shifted more towards industry. Depending upon the beam power and its energy, the electron beams have made tremendous impact in the area of food preservation, medicine, agriculture, biology, etc.[1]. Keeping in tune with the present and future scenario, the Accelerator and Pulse Power Division (APPD) of BARC has initiated the design and development of various types of electron accelerators. The project for Prototype Development of 30 MeV, 3 kW electron accelerator has been proposed based on the experience gained from 10 MeV RF Linac being commissioned at EBC, Kharghar, Navi Mumbai. This Accelerator can be used as a Prototype to study the Production of Medical Radioisotopes, Neutron rich Radioactive Nuclei, Energy Driver, Transmutation of Radioactive Waste, to study Electron beam based Nuclear physics including photonuclear reactions and target optimization for photoneutron production.

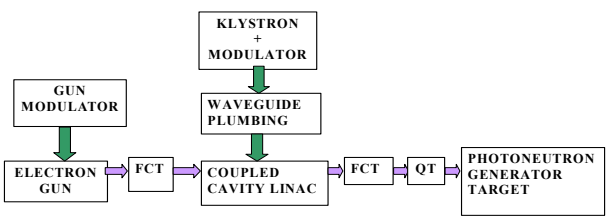

Figure 1: Schematic Diagram of 30 MeV, 3 kW Electron RF Linac System.

The linac is intended to deliver a beam with an average beam power of ~ 3 kW. It will be operated at a frequency of 2856 MHz. The duty cycle is chosen to be 0.1%, with a repetition rate (RR) of 100 Hz. The schematic of the linac is shown in Fig. 1. The electron gun (EG), will be directly coupled to the linac system, will inject a train of pulses into the linac at the rate of 100 pulses per sec, each having a pulse width of ~ 10 μsec. The beam will be accelerated to the required energy of ~ 30 MeV in the coupled cavity RF linac before being passed to the photoneutron generation target. The energy analysis will be done using the depth dose penetration method and the beam current will be monitored with the beam current transformer (ICT). A vacuum of ~ 4x10-7 torr will be maintained with the help of a turbo/sputter ion pump (TP/SIP) combination system. The RF power to the linac will be fed via a waveguide (WG) operated in the TE10 mode. The linac will have a horizontal configuration. The following sections give the brief details of the progress made in the design of various subsystems of the linac.

RF STRUCTURE

For the sake of simplicity of fabrication, constant impedance, on-axis coupled cavity linac configuration has been selected. It consists of two parts. Schematic of one of the part is shown in fig. 2. First part consists of 49 cells

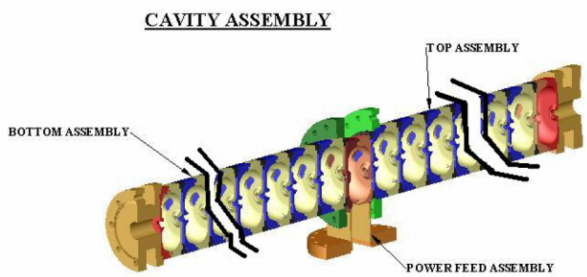

Figure 2: One part of On-Axis Coupled Cavity RF Linac

including 3 buncher cavities followed by 22 acceleration cavities and 24 coupling cavities. Second part consists of 45 cells, 23 acceleration cavities and 22 coupling cavities. These two parts will be separated by a drift space of ~ 15.7 cm. The length of the acceleration cavity is 52 mm, whereas the buncher cavities are 45, 48 and 50 mm respectively. A total length will be ~ 250 cm. An acceleration field gradient of 15 MV/m to 18 MV/m has been used for design considerations, leading to a Kilpatrick value of ~ 1.4, with a maximum field on the boundary as 62.712 MV/m. The corresponding maximum magnetic field is found to be 36.072 kA/m. The effective shunt impedance for the buncher cavities is ~ 80MΩ/m, while for the accelerating cavities, it is ~ 90MΩ /m. Some of the salient features of the two ½ accelerating cavity, sandwiching the coupling cavity, are shown in Fig. 3. The electric field distribution and profile are shown in Fig.4. The outer and inner nose radii have been optimised

to be 3 mm and 1 mm respectively. The electric field in the bore has been found to be uniform within 3.5%. Most of the design features of the linac have been worked out using SUPERFISH[2,3]. The total RF power dissipated into the structure at the operating frequency of 2856 MHz is estimated to be 5.083 MW (peak).

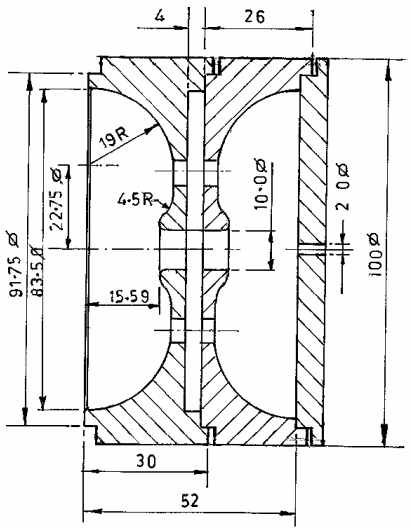

Figure 3: Two ½ Acceleration and one coupling cell

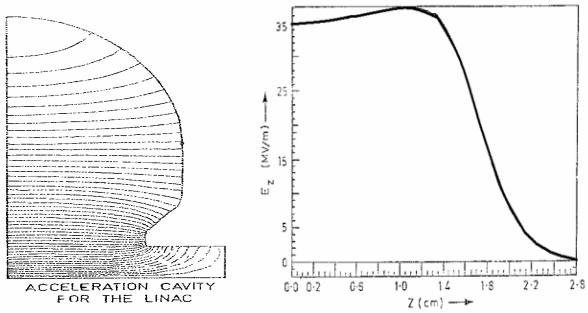

Figure 4: Electric field distribution and profile in the acceleration cavity

For the feedpoint at the central cell of the 49-cell (25 accelerating cells, 24 coupling cells) linac, the droop at the last cell works out to be 0.35%. Its variation along the cell is shown in Fig.5a and 5b. This would otherwise have been 1.40% if the feedpoint was chosen as the beginning or the end of the accelerator. The droop and phase shifts between the adjacent cells for a random frequency deviation of ± 1000kHz, due to fabrication errors etc., have been estimated and are shown in Fig. 5c. The annular aperture of size 10 mm width and 300 length along radius of 26 mm achieves rf coupling of ~ 4.6 % between adjacent accelerating and coupling cell. The RF preliminary tests have been done on the second part of the linac. The Q0 measured to be ~ 12000. The field flatness measured to be within ± 5%. The above parameters will be improved by acid cleaning of the cavities.

A rectangular waveguide operating in TE10 mode will be used to transfer power of 20 MW (peak), with duty cycle

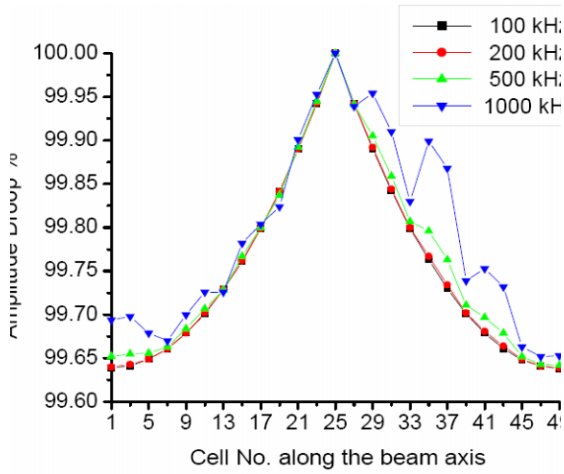

Figure 5 a: Electric field in accelerating cells

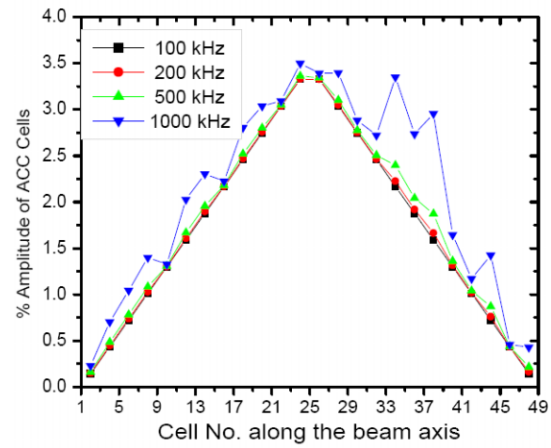

Figure 5 b: Electric field in coupling cells along the Beam Axis

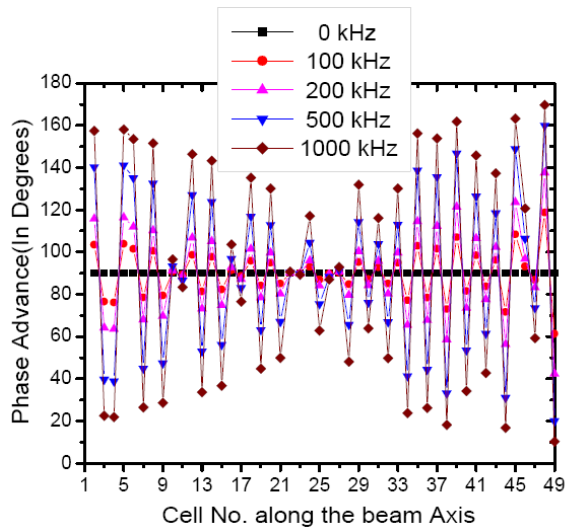

Figure 5c: Phase Advance between adjacent cells along the length of the linac.

of 0.1%, from klystron source to both the parts of the linac using 3 dB coupler. At a frequency of 2856 MHz,

with air as dielectric 72.14 mm x 34.04 mm waveguide has an attenuation coefficient of 0.0157 dB/m and power handling capacity of ~ 6.15 MW. By using SF6, at 1 bar pressure, the power handling capacity will be enhanced to ~ 24.61 MW.

STUDIES OF THE BEAM BEHAVIOUR

The beam behaviour in the linac has been studied by using the computer code PARMELA[3]. 6-dimensional phase space with random distribution have been taken for evaluation of the beam properties. The beam injection is done at 85 keV with an energy spread of 0.5 keV and emittance of 25 π mm-mrad. A phase width of 180o has been considered for the beam pulse. About 1000 particles

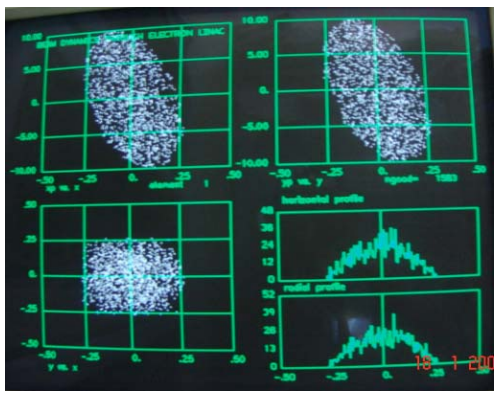

Figure 6: Phase space, Intensity distribution used as input for the linac.

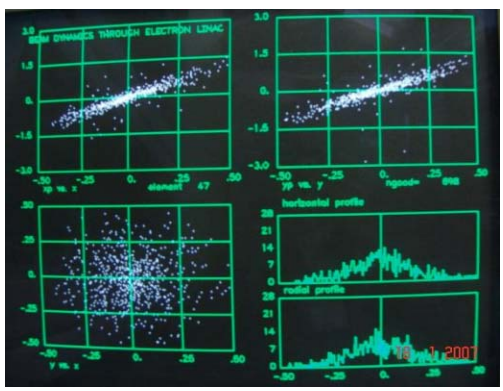

Figure 7: Phase Space, Intensity Distribution of the beam at the end of the Linac

are scanned. Optimum transmission of the beam is obtained at an injection phase of -35o. Since the linac does not use any solenoid or focussing element, the beam loss in the first five cavities is found to be 11.0%, 1.2%, 5.2%, 2.2% and 1.8% respectively. Using solenoids also the total beam losses comes out same. In the remaining cavities, the beam loss is found to be negligible. The total transmission through the linac is 73.4 % with an average energy of 30 MeV and a beam power of ~ 9.73 kW. The beam power lost to the linac structure is ~ 0.18 kW. The maximum energy of the beam is ~ 33.8 MeV with energy spread as ~ ± 3 MeV and a phase spread of ~ 90o. The output beam has a gaussian distribution with FWHM as ± 2.5 mm and maximum divergence as ± 1.5 mrad. Required input phase space and output beam emittance after 94 cells are shown in Figs. 6, 7.

INJECTOR

The electron gun, with a Diode/triode geometry, will deliver a pulsed 500 mA, 85 keV electron beam, with a width 10 μsec, at a RR of 100 Hz. The power for the injector will be derived from 230V, 50Hz AC mains. A solid-state modulator switching at ~ 1kV will be used to generate the required pulse output. The rise time targeted is less than 1μs. 1kV dc will be switched using an IGBT and a 1 : 85 pulse transformer will step up the primary voltage to 85 kV. The iron based METGLAS amorphous alloy cut C core will be used. The transformer will have bucket type geometry, to minimize the leakage inductance. The IGBT with V_{ce}s of 1700V and Ic = 220A(150A) at Tc = 25(80)oC will be used. The typical rise and fall time of these IGBT's is 100 ns and 40 ns respectively[4].

TARGET

Neutrons will produced in a water-cooled tungsten copper alloy (75% W and 25% Cu) target aligned horizontally in line with the electron beam. It will be Solid piece of ~ 9 cm long and ~ 7 cm diameter. It will be welded to the linac side by conflat flange to hold the vacuum. With a total beam power of ~ 3 kW, the face of the target which is inside the vacuum port, will heat up to several hundred ^{o}C. This will be conducted throughout the massive target (> 6kg.) and will be dissipated from its much lower temperature surface by circulation of water. The system will produce about $2x10^{-3}$ neutrons per electron, or $2x10^{10}$ n/s per μA of electron current at 30 MeV. With a projected time-averaged beam current of 100 μA and electron energy of 30 MeV, we expect to produce a driving source in excess of 10^{12} n/s. also, other targets will also be studied to have optimum neutron Source.

CONCLUSION

Design studies for the electron gun are in progress. Studies for coupling the waveguide to the linac are under way. By the end of 2007, we hope to complete the design of the 30 MeV linac Assembly.

REFERENCES

[1] Indo -USSR Seminar on Industrial Applications of Electron Accelerators, held at BARC, Mumbai, Nov.1988
[2] R.C.Sethi et. al., APAC 1998.
[3] Poisson-Superfish, Free distribution Code, LANL.
[4] Lloyd Young, AOTD, Los Alamos National Laboratory.
[5] A.R.Tillu, Private Communication.

COMPARATIVE ANALYSIS OF BLADE TUNER OPTIMIZATION OPTIONS FOR THE ILC

Carlo Pagani, Nicola Panzeri, INFN Milano, Italy

Abstract

Following the successful experience of the blade tuner concept for superconducting cavities, a full parametric analysis has been performed for ILC cost optimization. Different design details have been reconsidered and optimized on the basis of their impact on the ILC requirements and on production costs. Two different designs have been then developed for two options of fabrication material: titanium or stainless steel. The realization of two prototypes, one for each type, has been recently launched for the designs qualifications and comparison. In this paper we discuss the optimization rationales and the expected differences in cost and tuner integration and performances. Cold tests on cavities will be at the basis of the final choice for the ILC.

INTRODUCTION

For the ILC project more than 16000 coaxial tuner are required. The effort to optimize its design is widely justified by the subsequent enormous cost saving. Moreover the actual blade tuner version, although proved to fulfil the slow tuning requirements [1,2], it is far from being in the final design stage and some modifications are required in order to improve its reliability and reduce its total cost.

Two aspects have been considered in the optimization process here presented: first of all a whole design refinement of rings and blades has been performed. This has been obtained taking into account both the geometry and the material of the blade tuner, allowing to develop an unique geometrical solution that can be realized with the rings in titanium or stainless steel. This is very important in view of a possible future use of a steel helium tank when the technology will allow solving the problems in welding titanium to stainless steel. The second aspect considered concerns a major simplification of the driving mechanism and the moving of the motor from a central to a lateral position, thus freeing some space in correspondence of the invar rod of the ILC cryomodule.

The effectiveness of this solution has been proved by means of experimental tests and numerical simulations.

REVIEW OF THE TUNER DESIGN

The tuner review started from these considerations:

- the cost of materials (Ti) is steeply increasing;
- the cavity stability should have positive benefits from a lighter and more compact tuner design;
- the tuner strength and stiffness characteristics should be commensurate to the action on the helium tank and to the total stiffness of parts near the cavity.

By maintaining the original layout of the blade tuner [3-5] that assures a well symmetric behaviour, we optimized all the aspects, from the less relevant to the more important like the blades geometry and their distribution. The design of the optimized blade geometry has been driven by the following constraints:

- low cycle fatigue phenomena in the blades and a not reproducible tuner behaviour are unacceptable, therefore **no plasticity** has to occur in the blades in working conditions;
- the maximum **axial load** on the tuner occurs when the helium tank is under vacuum, and outside there is the atmospheric pressure. This compression force is equal to 4155 N;
- the reduction of the number of welds and machining steps leads to a total **cost reduction**.

Keeping in mind these constraints and the necessity to have at least the same tuning capabilities, different blade configurations have been analyzed: they have different materials and geometry, as reported in table 1 and table 2.

Table 1: Blade configurations taken into account

Combination	Geometry	Material
A	Original	TiGr5
B	Original	AISI 316
C	New	TiGr5
D	New	AISI 316
E	New thin	AISI 316
F	New	INCONEL 718

Table 2: different blade geometries considered

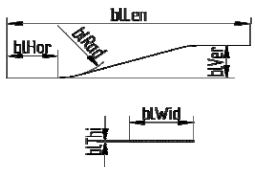

Geometry	blHor	blCla	blVer	blLen	blRad	blWid	blThi
Original	12	8	7.5	56	15	15	.5
New	12	8	10	66	15	16	.5
New thin	12	8	10	66	15	16	.2

Results

The choice of the best blade configuration has been based on the results of several finite element simulations that allowed the evaluation of the tuner strength in different work conditions.

An example of obtained results is pictured in figures 1 and 2, that report respectively the von Mises stresses and the axial load vs. displacement curve for the blade of configuration C. The values reported have been evaluated at the maximum admissible deformation, that has been assumed equal to 70% of blVer (see table 2).

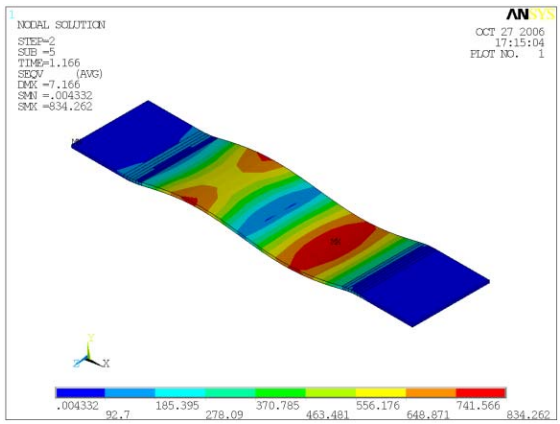

Figure 1: von Mises stresses after the applying of axial load at the maximum admissible deformation of the configuration C blade.

A summary of results is reported in table 3. It contains the loads obtained from limit or buckling analysis, that have been used for the definition of the best blade configuration. A critical comparison of the results point out that:

- configurations B and D are not allowable because of high stresses;
- configuration C has an higher tuning range with respect to the configuration A;
- configuration F can be the optimum solution if the inconel blades can be effectively connected to stainless steel rings by electron beam welding.

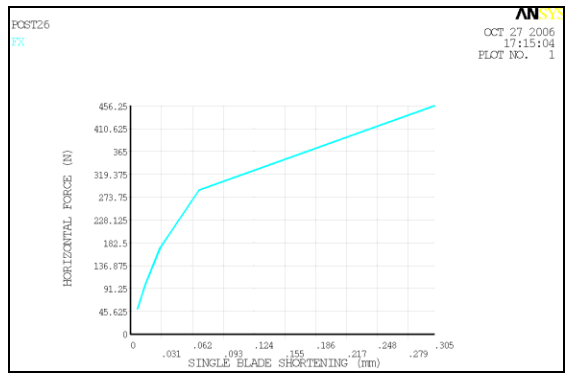

Figure 2: axial load vs. displacement for the configuration C blade at maximum deformation

Table 3: summary of finite element results

Combination	Limit load in stressed state (N)	Max load without plastic strains (N)	Limit load in non-stressed state (N)	Buckling load in undeformed state (N)	Tuning range at cavity (mm)
A	786	709	669	427	1.1
C	486	456	496	290	1.5
E	46	39	43	31	1.5
F	824	693	804	519	1.5

In order to evaluate the minimum required number of blades, the design force F_S = 4155 N is compared against the buckling value with a safety factor of 3.0 and against the limit load with a safety factor of 1.5. The possible choices are reported in table 4.

Because the final cost will depends from the machining operations, we plan to use a total number of 2x48 blades in configuration C or F. They will be grouped in 6 packs of 4 blades each, for any of the half rings (see figure 3), thus allowing a 75% reduction of welds respects to the original configuration A.

As a consequence of this choice we prefer to use the collinear blade position, and not the alternate one proposed in [6]. This will simplify the machining operations without a noticeable weight increase.

Table 4: minimum blade requirements

Blade conf.	Adm. blade load (N)	Blade stiffness (N/mm)	Minimum number of blade on 360°	
			For strength	For stiffness
A	223	6490	19	8
C	162	5432	26	10
E	14	990	290	51
F	268	10250	16	5

DRIVING SYSTEM SIMPLIFICATION

The existing driving system is composed of a stepping motor that, by means of a leverage arm, moves the two central rings pulling one side and pushing the other one such to have a perfect symmetric system. Unfortunately this solution is cumbersome and expensive. In particular the friction between rotating and translating parts makes them a weak point that has to be solved in a radically way. So that a simplified driving system has been designed, reducing drastically the number and complexity of parts. The new solution is pictured in figure 3 and it is mainly composed of a motor with its harmonic drive and a CuBe screw. The axial movement of the nut is directly transferred in the rotational one by the central rings.

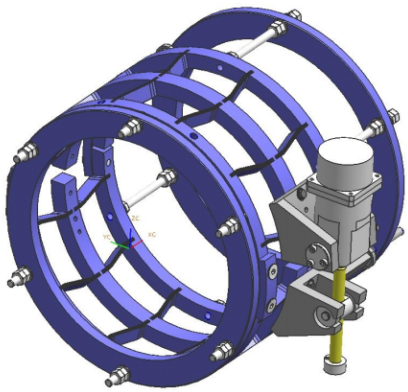

Figure 3: the optimized coaxial tuner for ILC

Although this arrangement simply push away the two central rings, therefore losing the complete symmetry, finite element computations and experimental test proved the effectiveness of the solution. The experimental test was performed in our laboratory by using a simplified mechanism in substitution of the motor (see figure 4). The displacement recorded at the free rings show the perfectly axial movement of them without any rotational or translation effects.

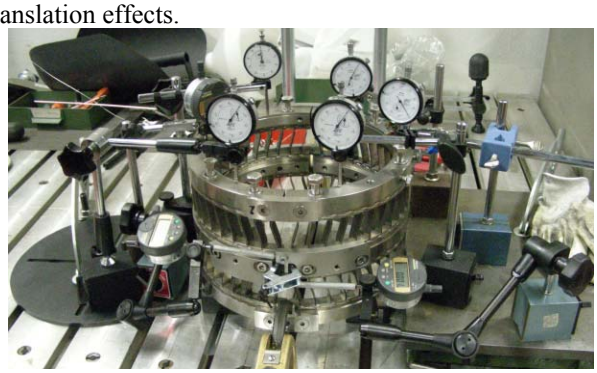

Figure 4: experimental setup to simulate the lateral motor solution.

This result has also been confirmed by finite element computations performed on the new tuner geometry. In particular figure 5 show the axial displacements at the maximum possible deformations of configuration C blades.

The maximum axial force on the motor has been evaluated in 400 N for titanium blades (configuration C) and 800 N for inconel blades (configuration F). These values are fully compatible with the motor and harmonic drive used as of today.

The only apparent drawback of the new design is the increase of the tuning step by a factor of 7. Nevertheless the proposed tuning step of 3 Hz is fully consistent with the experience gained with TTF operation.

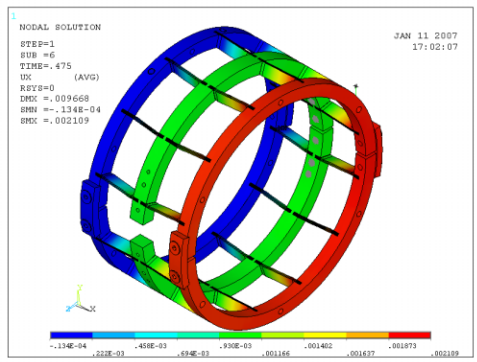

Figure 5: computed axial displacements from FE analysis for blade of configuration C

CONCLUSIONS

The tuner design has been deeply revisited obtaining a much less expensive configuration and the possibility to make it both with titanium and stainless steel rings. This is an important capability in view of future developments.

The new driving system solution is of course the simplest one possible, and it should also improve the overall tuner stiffness.

The estimated cost saving of stainless steel version with respect to the titanium version is of about 1000 €.

REFERENCES

[1] D. Barni, A. Bosotti, C. Pagani, R. Lange, H.B. Peters, "A New Tuner For TESLA", Proceedings of EPAC2002, Paris, France, p. 2205.

[2] J. Sekutowickz et al., "Test of Two Nb Superstructure Prototypes", in Phys. Rev. ST - AB, 7, 012002 (2004).

[3] C. Pagani, A. Bosotti, P. Michelato, N. Panzeri, P. Pierini, "Improvement of the Blade Tuner Design for Superconducting RF Cavities", Proceedings of PAC2005, Knoxville, TX, USA, p. 3456.

[4] C. Pagani, A. Bosotti, P. Michelato, N. Panzeri, R. Paparella, P. Pierini, "The Fast Piezo-Blade Tuner for SCRF Resonators", in Workshop on Superconducting RF, Cornell, USA, 2005.

[5] C. Pagani, A. Bosotti, P. Michelato, R. Paparella, N. Panzeri, P. Pierini, F. Puricelli, G. Corniani, CARE-Note-2005-021-SRF.

[6] C. Pagani, A. Bosotti, P. Michelato, N. Panzeri, R. Paparella, P. Pierini, "ILC Coaxial Blade Tuner", Proceedings of EPAC'06, Edinburgh, UK 26-30 June 2006, MOPCH171

PRELIMINARY DESIGN, ANALYSIS AND MANUFACTURING ASPECTS OF LOW BETA 350 MHZ REENTRANT SUPERCONDUCTING RF CAVITY

Deepak Mishra*, M.Prasad, V. Jain, M. Bagre, A M Puntambekar, G. Mundra, P. Shrivastava
Raja Ramanna Centre for Advanced Technology, PO: RRCAT, Indore, India

Abstract

A superconducting reentrant cavity for low beta, high intensity beam has been designed using SUPERFISH and MAFIA. The study has been done for cavity shape optimization. Further its structural design has been done and feasibility study of different manufacturing aspects has also been done. A full-scale mild steel model with copper coating has been fabricated. A twin arm mechanical tuner has been designed for slow tuning by elastic deformation. This was tested with low power RF to validate the design parameters and to check the tuning sensitivity. In this paper the design and development activity of the reentrant superconducting are discussed.

INTRODUCTION

It is proposed to build 100 MeV, high current H^+/H^- linac at RRCAT. The main components of linac are H^+/H^- ion source at 50 keV, low energy beam transport line, 4.5 MeV RFQ, MEBT, 100MeV injector linac. It is planed to use SFDTL structure after the RFQ from 4.5MeV to 100MeV. H^- linac will be used as an injector for 1Gev, 25Hz rapid cycling synchrotron, for the proposed Indian spallation neutron source (ISNS). Proton linac can be used as the low energy part of 1GeV linac, which will be used for accelerator driven subcritical systems (ADS).

As a technology development of superconducting cavity, we have started the work on reentrant low beta cavity. If we succeed in making the cavity to desired satisfaction, we will replace SFDTL structures with these re-entrant cavities.

CAVITY DESIGN CRITERIA

In designing the cavity, the criterion followed was to minimize the surface fields and maximize the R/Q. The cavity was optimized for beta equal to 0.20. All these issues are directly linked to shape of the cavity and the effects of the shape are different. The effects of shape on electric and magnetic fields compete and the optimization of the shape must be done wisely. Generally superconducting cavities are used to provide the high accelerating gradients (E_{acc}). But the linac beam dynamics design required relatively low energy gain per cavity in our case. The purpose of our design was not to achieve the maximum gradient but to operate it reliably and it must be capable of using the RF energy efficiently.

CAVITY SHAPE OPTIMIZATION

Fig.1 shows the quarter geometry and the cavity shape variables. The cavity optimization was done for frequency of 350MHz. The optimization was done step by step. The first variable was the gap length g. The frequency was adjusted with the help of R_{eq}. The gap length was optimized for the maximum R/Q. Fig.2a, 2b shows the variation of R/Q and E_{max}/E_0 Vs. gap length respectively. The value for R/Q shows a maximum for gap value of 1.7408cm. At this value the curve of Emax/E0 changes its direction. The second variable was the radius r1.This parameter was optimized for the minimum surface electric and magnetic field. During the whole optimization process the frequency was adjusted with the help of R_{eq}. The details of the cavity optimization can be found in refrence [1] [2] [3].

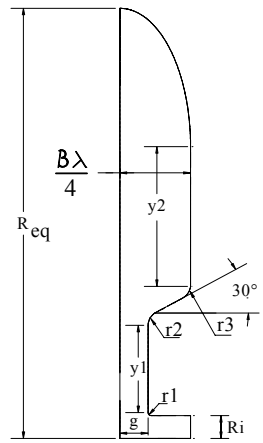

Fig.1 Cavity shape variables

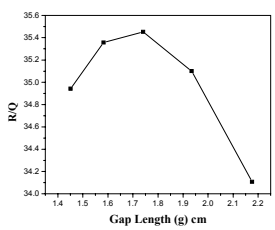

Fig2a R/Q Vs. Gap length

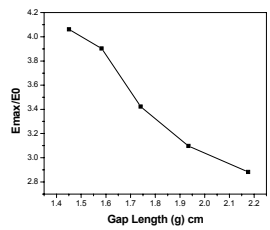

Fig.2b E_{max}/E_0 Vs. Gap length

Table-1 lists the basic parameter of the optimized cavity.

Table 1: Basic Shape Parameters of Reentrant cavity

Parameter	Value	Unit
g	1.7408	cm
Ri	1.5	cm
r1	5	mm
Y1	5.7564	cm
r2	2	mm
angle	30^0	degrees
r3	6	mm
Y2	10	Cm
R_{eq}	28.45	cm

* deepak@cat.ernet.in

As a comparison of the above calculation the same geometry was simulated with the help of MAFIA. During this simulation manual meshing was chosen in such a way as to produce the actual geometry. Geometry near the equator was not given due consideration. Fig.3 below shows the electric field of the TM_{010} mode. Table-2 shows the comparison of SUPERFISH and MAFIA, considering the cavity as normal conducting. The last column of the table lists the same parameters considering the superconducting cavity. The residual resistance used in this calculation was 100 nano-ohms. The results obtained in these calculations were encouraging. So we decided to make a full flagged model to validate the design.

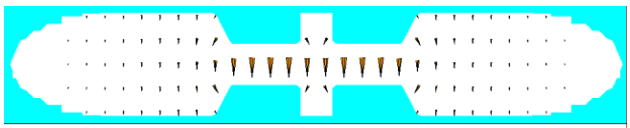

Fig.3 Electric field plot of TM_{010} mode

Table 2: Comparison of SUPERFISH and MAFIA

Parameter	SUPERFISH Normal conducting	MAFIA Normal conducting	SUPERFISH Super conducting
Freq (MHz)	350.02	349.85	350.02
Q	18384.4	18783.81	6.3656E+08
Z_{sh} MOhm/m	20.263	20.266	7.0160E+05
Emax/E0	3.6497	-	3.6497
Bmax/Emax mT/(MV/m)	0.7878	-	0.7878

ENGINEERING DESIGN

The basic design requirement of the accelerating structure is to provide the desired geometrical dimensions and surface characteristics at operating temperature. It is also required to maintain the same within allowable tuning bandwidth, typically within few KHz. Different factors considered during design are sensitivity of the structure due to various loads like LHe pressure fluctuation, Lorenz force detuning, microphonics, cool down distortions, RF power coupling etc [4].

The Mechanical design of reentrant cavity requires designing inner vessel, stiffeners and outer vessel along with ports and support operating at cryogenic condition. The design is considered for displacement and stresses evaluation for different loading condition during testing, cool-down to 4.5 K and certain fault conditions. The design is also considered for deforming the cavity elastically for tuning purpose. Two types of options, circumferential and radial stiffeners, are considered for stiffening purpose. FE model of both are shown in fig 4. Thickness of cavity is varied from 2 mm to 5 mm for Bulk Niobium structure by taking various combinations. All possible combinations of thickness for different components are tried for all load cases. Fig. 5 illustrates effect of thickness variation on stress and deformation using circumferential stiffeners at evacuation condition (here all the components are considered with uniform thickness). Further the results of thickness variation within the inner vessel, stiffeners and outer vessel evolves two safe designs for all loading situations. First design is 4-3-3 (Inner vessel 4mm, Stiffeners 3mm and Outer vessel 3 mm) having circumferential stiffeners and the other design is 3-3-3-45 (Inner vessel 3mm, Stiffeners 3mm welded at 45° and Outer vessel 3 mm) having total 8 radial stiffeners.

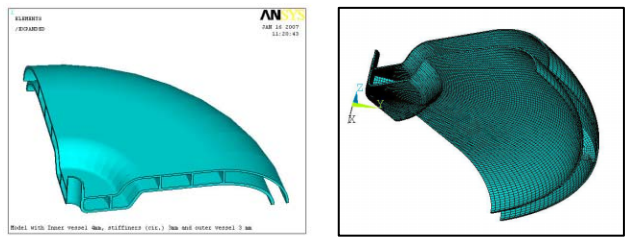

Fig.4 Re-entrant cavity model with circumferential stiffeners (Left) and with Radial stiffeners (Right).

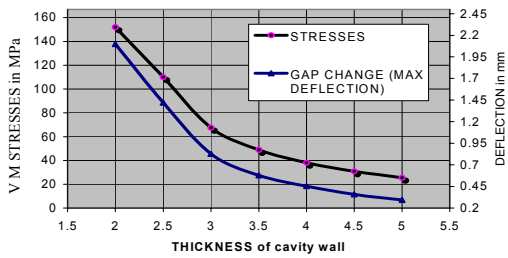

Fig.5 Effect of thickness change on maximum Von Misses stress and gap change due to evacuation of the Cavity with circumferential stiffeners

Since the cavities are fabricated and inspected at room temperature (300K) and operated at 4.5 K (LHe temperature), it is necessary to estimate and design dimensions of the cavity at room temperature. Fig.6a shows actual dimensions of the inner profile of the cavity, which is the basis for evolving manufacturing dimension of other parts.

Tuning force required to elastically deform the cavity for adjusting the fundamental frequency is estimated using a coupled approach between structural analysis and HF Emag analysis. Fig.6b shows the deformation pattern (profile) of the cavity of 4-3-3 model. HF Emag analysis using ANSYS is performed with HF119 element (taking second order accurate option) as shown in fig 7. Structural deformation sensitivity analysis yields 2.28 MHz /mm of gap change in 4-3-3 model.

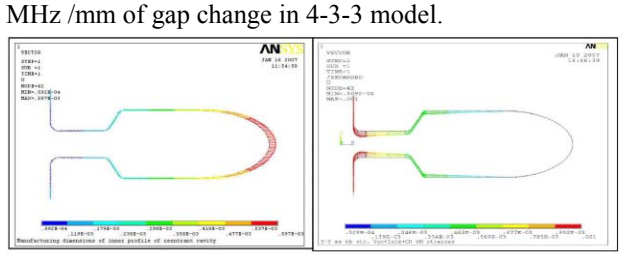

Fig.6a and 6b. Actual manufacturing dimensions (at room temperature) of inner profile (left) and Dimensions of inner profile for 1mm deformation (right).

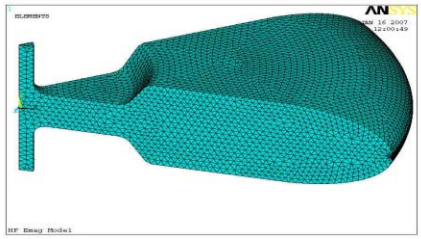

Fig. 7 HF Emag Model of deformed RF zone in ANSYS

DESIGN FOR MANUFACTURING

Input from FEM Analysis served as a basis for the design for manufacturing. In order to satisfy the design requirements careful study of the geometry, various possible options of forming & joining and different special process involved is necessary for designing for manufacturing, Apart from these the vacuum sealing techniques at low temperature, integration of tuners, RF power couplers in cryogenic enclosure along with cavity with proper alignment needs to be considered carefully. A detail feasibility study has been made for the manufacturing & processing of the RE cavity. Cavity fabrication requires variety of special infrastructure mainly Nb forming & EB welding, chemical cleaning & high pressure rinsing, heat treatment & finally assembly in to clean room. Necessary infrastructure as well as technology for the manufacturing of the SC Cavities is not readily available with domestic Industries.

Prototype activity

During the feasibility study a mild steel model was made & given 50 µm the copper coating. The two halves of the cavity were assembled by pressing the one half over the other. There was no welding done at the rim of the cavity. This model was used for the low power RF measurement. The quantities measured were frequency, quality factor and tuning range. Further as it is impracticable to use Niobium for initial development, it is planned to make the full scale copper/ ss prototype for the development of the manufacturing. Simultaneously different parameters for EB welding joining and cleaning will be first established over Nb samples.

Development of tuner

The slow tuner assembly under development consists of two levers and an actuating mechanism. There are two long parallel levers having ring at the center and pressing the cavity form both the ends at the center with the help of two buttons, on each levers in the plane perpendicular to that of the levers. These levers are connected with the help of two pins and a turn-buckle (for distance adjustment) at the bottom end and a motorized actuator at the top end. Fig. 8 shows the copper plated model under testing along with tuners (left) and tuner assembly (right). The design of the levers is optimized for the low weight and high rigidity. The tuning force required for the 1mm deflection of the cavity is calculated (~7500N).

The tuner was assembled along with stepper motor-based actuator. Two dial-indicators were installed to find the deflection of the cavity at the central portion. The cavity was made to resonate with low power RF then the tuner was made to press the cavity and the resonant frequency was measured both while pressing and retracting. The tuning frequency variation of 350.64 to 350.42 MHz was observed with total deflection of 84µm. Very high symmetry, linearity of deflection and the repeatability of tuning was observed. A tuning sensitivity of 2.619 MHz/mm was measured against a calculated value of 2.339 MHz/mm with SUPERFISH. Fig.9 shows the Tuning sensitivity test result. The measured Q of the cavity was 4700.

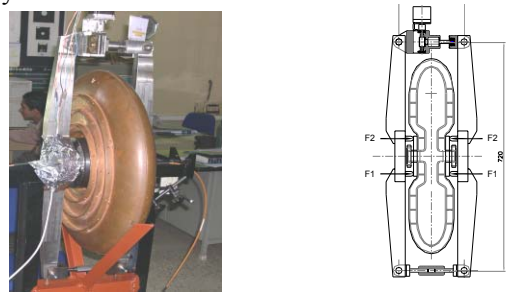

Fig.8 cavity with tuners on measurement bench (left) Tuner Assembly (right).

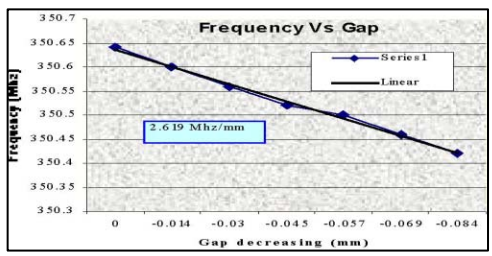

Fig.9 Frequency Vs. change in gap

CONCLUSION

We have build and tested the 350MHz copper coated mild steel Reentrant cavity. The RF tests and mechanical properties are consistent with calculation. The higher order mode analysis and multipacting study is in progress. The studies concerning the powering of the cavity is also in progress.

REFERENCES

[1] Deepak Mishra et al,"Design of low beta reentrant, superconducting cavity", InPAC-2006,151-152,India.

[2] Sang-ho Kim et al "Efficient design scheme of superconducting cavity", XX International Linac Conference, Monterey, California.

[3] Zhao shengchu et al. "Design study on 1.3 GHz scaled superconducting cavity for high intensity proton linac", Proc. Of 2nd Asian particle accelerator conference, Beijing, China, 2001

[4] A. M. Puntambekar et al," Feasibility study and related issues for technology development of 350 MHz bulk niobium SCRF cavities InPAC-2006, 361-362, India.

SUPERCONDUCTING NIOBIUM RESONATOR FABRICATION AND TESTING AT IUAC

P.N. Prakash, S.S.K. Sonti, K.K. Mistri, J. Zacharias, D. Kanjilal, A. Roy
Inter-University Accelerator Centre, Aruna Asaf Ali Marg, New Delhi - 110067, India

Abstract

Inter-University Accelerator Centre is currently constructing fifteen niobium quarter wave resonators for the superconducting linear accelerator project. The production is presently nearing its completion. In addition to building resonators for the in-house programmes, a project to build 325 MHz single spoke resonators for the proton driver linac for Fermi National Laboratory will begin soon. This paper presents details of the current resonator production work and future plans at IUAC.

INTRODUCTION

The Superconducting Resonator Fabrication Facility (SuRFF) consisting of an electron beam welding machine, surface preparation lab and high vacuum furnace, for constructing niobium quarter wave resonators (fig. 1) for the linear accelerator [1], has been operational at Inter-University Accelerator Centre (IUAC) since July '2002 [2]. In the first phase a single quarter wave resonator (QWR) was successfully fabricated and tested [3]. It has been installed in the rebuncher cryostat of the linac and operated at 3.3 MV/m with 6 W RF input power [4]. In the second phase two more completely indigenous QWRs were fabricated. Figure 2 shows one of the resonators along with its niobium slow tuner bellows [5]. In cold test at 4.5 K the low field Q_0 on this resonator was measured to be ~ 1.5×10^9, and with very little high power pulse conditioning it performed at 3.5 MV/m accelerating electric field with 3.5 W RF input power, exceeding the nominal design goal. Following the successful testing of the fully indigenously built resonators, production of fifteen more QWRs for the second and third linac modules began in July '2005 [6].

PRODUCTION OF QWRs

The resonator production is being done using both, the facilities setup at IUAC as well as commercial vendors. All the machining, forming, rolling and fitting of the niobium components and assemblies along with the fabrication of the outer stainless steel vessel are being done at a local vendor's site. Substantial amount of developmental work had been undertaken during the construction of the first two indigenous resonators to train the manpower in various machining and sheet metal works and in handling of the niobium material. This was done keeping the future resonator production and other projects in mind. All electron beam welding, electropolishing, heat treatment and testing are done using the SuRFF facilities setup at IUAC.

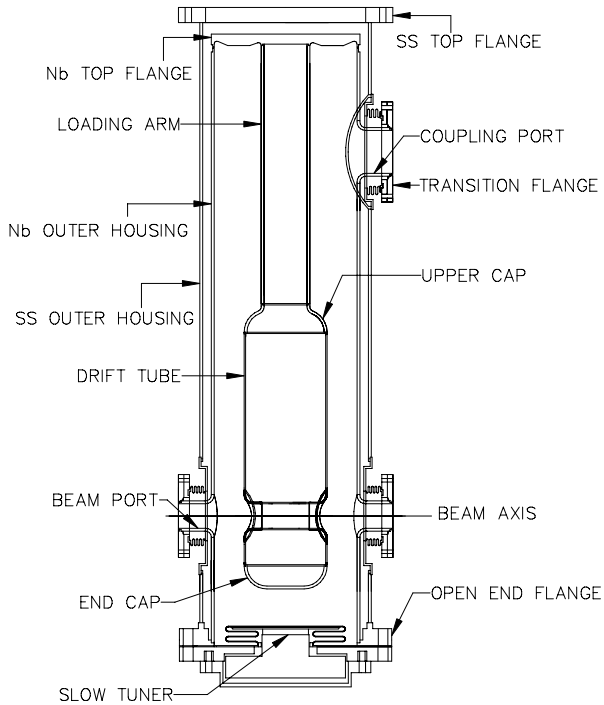

Figure 1: Schematic diagram of IUAC-QWR

Figure 2: One, of the two, fully indigenously built QWRs at IUAC along with its niobium slow tuner bellows.

The resonator production is being done with sufficient contingency of extra parts. Simultaneously the drift tubes of three existing resonators are also being repaired. Therefore the present effort can be considered equivalent to constructing eighteen complete resonators. For the production work the electron beam welding fixtures have been designed, wherever possible, to weld several pieces in a single pump down to increase productivity and save effort & time. Similarly the electropolishing work is planned so that several niobium assemblies can be polished in a single setup. Most of the tooling and fixtures for the production work is available from previous constructions. However, some additional tooling and fixtures have been made to replace the ones which had become unusable from wear and tear.

Figure 3 shows the niobium outer housings. The ports at the upper end of the cylinder are used for coupling and picking up RF power into/from the resonator. The beam ports are located at the lower end of the cylinders. Each outer housing assembly has seven electron beam welds. Figure 4 shows the loading arm and drift tube assemblies, made out of high RRR grade (>200) material. Each loading arm has two and each drift tube assembly has seven electron beam welds. The loading arm and drift tube form the inductive and capacitive part of the central conductor assembly respectively, which joins the outer housing through a niobium top flange.

Figure 3: Niobium Outer Housings.

In addition to the major assemblies shown in figures 3 and 4 machining of the niobium top flanges has started. Fabrication of the outer stainless steel vessels, which holds the liquid helium, has been completed. The stainless steel top flange of the resonator is being modified into a hemispherical dome to provide large buffer volume of liquid helium [7]. All the niobium-stainless steel flanges that provide the transition at the ports have been machined. SS bellows assemblies with appropriate end fittings for the same have been commercially procured, thermally shocked and pressure tested.

Figure 4: Loading Arm (below) and Drift Tube (top) assemblies.

The major assemblies shown in figures 3 and 4 are ready for electropolishing. Additional fixtures for this work have been made and the various acids required have been procured. As a quality control measure some critical welds will be radiographed before electropolishing is done. During the electropolishing work we plan to start the fabrication of the niobium slow tuner bellows. Niobium-copper explosion bonded material for the same has been received. Machining of the niobium-stainless steel open-end flanges, that provides the transition from the inner niobium housing to the outer stainless steel vessel at the slow tuner end of the resonator, will also be taken up during this period. We plan to complete all the fabrication work by the middle of this year.

RESONATOR REPAIRS

In addition to constructing resonators for the linac a variety of repairs on existing resonators have been successfully carried out. On several resonators the coupling and beam port transition flange bellows developed leak. A new design of the assembly has already been developed [3]. The leaking assemblies are machined out and replaced with the modified design. Prior to e-beam welding, the bellows as well as the complete assembly is thermally shocked and pressure tested.

The QWRs made for the first linac module had three coupling ports. Two of the ports were meant for coupling and picking up RF power into/from the resonator and the third port was kept for the VCX fast tuner system [8]. The

present resonator control system in the IUAC linac, however, uses dynamic phase control, which has made the third port redundant. It has been blanked off with a niobium flange on the resonators in the first linac module. On some QWRs the transition bellows assembly on this port developed leak. They have been permanently closed, instead of replacing with a new bellows assembly, by e-beam welding a niobium blankoff.

On three resonators the upper cap on the drift tube got punctured. The resonators were cut open and the punctured caps have been replaced. Figure 5 shows one of the repaired drift tubes.

Figure 5: A repaired Drift Tube assembly.

SINGLE SPOKE RESONATORS

In addition to constructing resonators for the in-house programmes, a project to build two single spoke resonators of β=0.22, operating at 325 MHz, for the proton driver linac for Fermi National Laboratory (FNL) is being taken up [9]. Figure 6 shows a view of the proposed spoke resonator which has been designed by FNL. Preliminary assessment of the tooling and fixtures required for the construction has started. The actual fabrication work is expected to begin towards the end of the production of the QWRs.

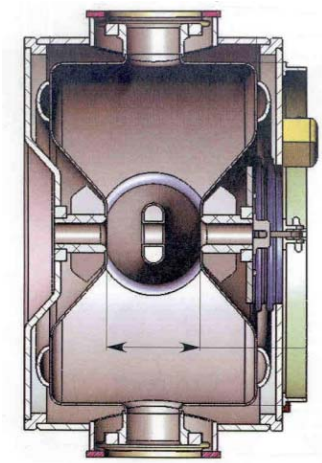

Figure 6: 325 MHz, β=0.22 Single Spoke Resonator.

CONCLUSIONS

The Superconducting Resonator Fabrication Facility at IUAC has been fully operational since July '2002. The facility is being used for constructing niobium resonators for the linac project. IUAC has successfully fabricated niobium quarter wave resonators and is currently in an advanced state of producing fifteen resonators for the second and third modules of the linac. One of the indigenously built resonators has been installed and tested in the rebuncher cryostat of the linac. Its online performance is inferior compared to the offline performance (4.5 MV/m @ 6 W). This could possibly be due to the slow cooling rate in the rebuncher cryostat, especially between 150 K and 80 K, which is known to produce Q-disease in niobium resonators. IUAC has also developed expertise in carrying out critical repairs on existing resonators. In addition to building resonators for the in-house projects construction of two single spoke resonators for FNL will also begin shortly.

ACKNOWLEDGEMENTS

The authors would like to thank the staff of Don Bosco Technical Institute, New Delhi, for their help in machining and sheet metal work of the niobium components. The authors thank the IUAC workshop, other members of the linac group and members of the cryogenics groups for their help.

REFERENCES

[1] P.N.Prakash et al., PRAMANA, Journal of Physics, Vol. 59, No. 5, p849
[2] P.N.Prakash et al., Proceedings of Indian Particle Accelerator Conference InPAC-2003, February 3-6, 2003, CAT, Indore, p148
[3] P.N.Prakash et al., Proceedings of Asian Particle Accelerator Conference APAC-2004, March 22-26, 2004, Gyeongju, Korea, p684
[4] S.Ghosh, IUAC, Private Communication
[5] P.N.Prakash et al., Proceedings of Indian Particle Accelerator Conference InPAC-2005, March 1-5, 2005, VECC, Kolkata, p477
[6] S.S.K.Sonti et al., Proceedings of Indian Particle Accelerator Conference InPAC-2006, November 1-4, 2006, BARC & TIFR, Mumbai, p139
[7] IUAC Annual Report 2005-06, p16
[8] N.Added et al., Proceedings of 1992 Linear Accelerator Conference, August 24-28, Ottawa, Canada, AECL-10728, p181
[9] G.Apollinari, FNL, Private Communication

EVALUATION OF EXTERNAL Q USING KROLL-YU METHOD WITH MICROWAVE STUDIO

A.S.Dhavale and K.C.Mittal
Accelerator and Pulse Power Division
Bhabha Atomic Research Centre, Mumbai 400 085

Abstract

Design and development of a superconducting cavity has been taken up as a part of Accelerator Driven Subcritical project(ADSS). An input coupler is designed for the same using Kroll-Yu method[1]. The evaluation procedure is optimised and the method has been successfully implemented for the evaluation of high external Q [2]. The validity of the Kroll-Yu method is tested with the external Q calculations by P. Balleyguier method for the Benchmark cavtity which is a pillbox cavity of diameter ~200 mm, length ~150 mm with semi-rigid coaxial line[3]. It is found that the careful choice of data points provide accurate results over wide range.

INTRODUCTION

BARC is involved in the development of technology for the Accelerator Driven Sub-Critical System (ADSS) that will be mainly utilized for the transmutation of nuclear waste and enrichment of U^{233}. The application demands a proton beam (30mA, 1 GeV) that will be generated by various stages of accelerator structures. Up to 100 MeV proton beam will be generated by the normal conducting accelerator structures whereas from 100 MeV to 1 GeV superconducting structure will be more efficient. It will be a coupled cavity structure made up of niobium cavities of elliptical shape. As an initial step single elliptical cavities operating at 700 MHz and 1.056 GHz were designed. [4, 5]

A co-axial type of input coupler has been designed for the same cavity. The power will be transferred efficiently from the coupler to the cavity only when the impedance of the coupler matches with the cavity impedance i.e. the coupling factor between cavity and transmission line is unity. Coupling factor, β is defined as,

$$\beta = Q_0 / Q_{ext} \quad \text{----------(1)}$$

where, Q_0 and Q_{ext} are the quality factors of the cavity and the transmission line respectively. Q_{ext} is the factor that depends solely on the geometry and can be evaluated by different computational methods with the help of 3-D electromagnetic codes.

COMPUTATION OF EXTERNAL Q

A number of computer programs viz., MAFIA, SUPERFISH, URMEL have been developed for the design of cavity resonators which give information about the field distribution, shunt impedance, Q-value but cannot calculate Q-value due to external coupling due to waveguide/ co-axial line. Thus, Kroll-Yu in 1990 developed a procedure to calculate external Q by using these codes. As this method is based on the frequency resonance differences, it was thought that it is better suited for the computation of low Q_{ext}. In 1997, Pascal Balleyguier developed a method based on the field calculations for the computation of high external Q. [3,6]

This paper presents results of the external Q calculation using both the methods with the help of computer code Microwave Studio[7]. The results indicate that Kroll-Yu method is also suitable for the high external Q calculation provided the data points near the resonant frequency of the cavity are chosen.

Kroll-Yu Method

Kroll-Yu suggested a method [1] that is easy to implement. A (cavity + waveguide) system terminated in a short (E_t=0, E_t----tangential electric field component) can be treated as two coupled resonators, cavity and waveguide.

The formulation deals with frequency, ω, as a function of phase change, ψ along the guide length that is given by $2\pi D/\lambda_g$ where λ_g is the guide wavelength and D is the guide length. A quantity $G \equiv -(1/2)\,(d\psi/d\omega)$ plotted as a function of ω exhibits a typical resonance curve with peak at the resonant frequency of (cavity + waveguide) system feeding into the matched load. When multiplied by the resonant frequency, the height of the curve is equal to Q_{ext}. The eigen modes of this system are complex in nature viz, u + i v. Also,

$$G = (1/2)\,(v/((w-u)^2+ v^2)) + (1/2)\,\chi'(u) \quad \text{----------(2)}$$

This is a resonant curve at frequency ω=u and $Q_{ext}=(1/2)(u/v) + (1/2)\chi'(u)$. The exact relation between ψ and ω is given by 4 – parameter formula,

$$\psi(\omega) = \tan^{-1}[v/(\omega-u)] - \chi(\omega) + n\pi \quad \text{---------(3)}$$

where , $\chi(\omega) \cong \chi(u) + \chi'(u)\,(\omega-u)$

By using simulation codes like MAFIA, Microwave Studio, HFSS one can obtain different ψ-ω pairs (data points) for different values of waveguide length, D. The essence of the method is to fit data points by 4 -parameter formula. The fitted values of u and v give information about the resonant frequency and external Q value.

Also it is observed that for Q_{ext} >20, choice of $\chi'(u)$ equal to zero is excellent [1]. Thus, for determination of u and Q_{ext} just three points are sufficient (3-parameter fit).

The implementation formulae are given by ,

$$u = \omega_2 + A\,B_{12} + \omega_1 A^2/(1+A^2) \quad \text{----------(4)}$$

$$v = (u-\omega_1)\,A - B_{12} \quad \text{--------(5)}$$

$$\chi(u) = \tan^{-1}[v/(\omega_i - u)] - \psi_i - \chi'(u)\,(\omega_i - u) \quad \text{----(6)}$$

Where, A, B_{12} and B_{23} are the quantities dependent on ω_i.

Setting $\chi'(u)$ to zero, three parameter fit of the resonance curve is obtained. Fitted values of frequency and Q_{ext} are calculated by using above implementation formulae for the given set of data points (ψ_i, ω_i). In the present analysis, external Q is obtained by 3- parameter fit of the data points.

Figure(1) shows the behaviour of (cavity + coupler) system as a function of position of the SHORT. As seen in the figure, the cavity mode (TM_{010}) frequency does not vary much whereas the coupler mode (TEM) frequency changes appreciably as a function of position of the SHORT. It was observed that the values of fitted parameters (f and Q_{ext}) were greatly affected by the choice of the data points.[2] It was observed that, the choice of data points in the vicinity of a point where cavity resonance frequency and the coupler frequency were nearly same, provided consistent results. Thus for Q_{ext} evaluation, points in the shaded portion indicated in the figure(1) were chosen.[2]

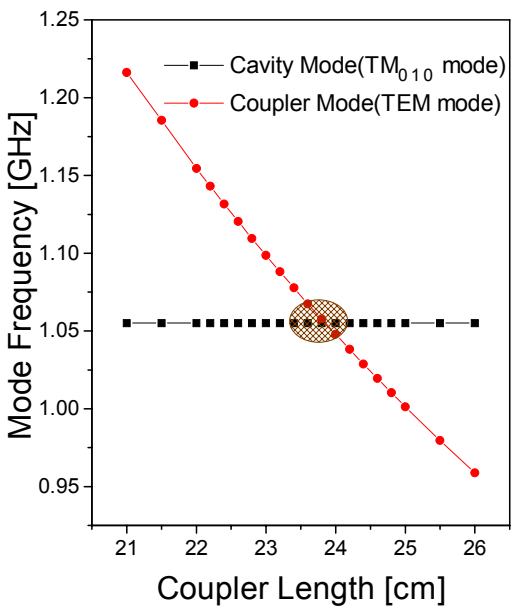

Figure 1: Study of Mode frequencies as a function of position of SHORT

Validation of Kroll-Yu Method

External Q was computed for the cavity operating at 1.056 GHz having beam pipe of radius 4.0 cm and a coaxial coupler of ID:ϕ 3.478 cm ; OD : ϕ 7.92 cm placed at a distance of 12 cm from the cavity centre using Kroll-Yu method and P. Balleyguier method.[3,6,8] (See Table 1).

Similar calculations were carried out for a cavity designed at a resonant frequency of 700 MHz, beam pipe radius of 5.0 cm having coaxial coupler of ID :ϕ 4.348cm; OD :ϕ 10cm connected at a distance of 12 cm from the cavity centre.(See Table 2)

Table 1

Penetration Depth (cm)	External Q, Q_{ext}	
	P.Balleyguier Method	Kroll-Yu Method
-2.0	3.69×10^7	5.13×10^7
-1.0	8.66×10^6	1.81×10^7
0.0	3.04×10^6	2.68×10^6
1.0	1.08×10^6	1.91×10^6
2.0	4.86×10^5	7.19×10^5

Table 2

Penetration Depth (cm)	External Q, Q_{ext}	
	P.Balleyguier Method	Kroll-Yu Method
-2.0	4.3×10^6	4.04×10^6
-1.0	1.31×10^6	1.45×10^6
0.0	5.95×10^5	6.37×10^5
1.0	4.0×10^5	2.72×10^5
2.0	2.21×10^5	1.06×10^5

To check the validity of Kroll-Yu method over the wide range of Q_{ext} values, the calculations were carried out for the Bench mark cavity that is a pill box cavity operating at 1146 MHz having diameter ~200mm, length ~150mm with semi-rigid coaxial line (ϕ in/out=1.65/5.35 mm). The penetration depth was varied from 0 to 5.5 cm [9]. Table 3 shows the calculated results.

Table 3

Penetration Depth (mm)	External Q, Q_{ext}	
	P.Balleyguier Method [9]	Kroll-Yu Method
0	6068050	3553030
2.5	407113	269016
5	81493	74439
7.5	23841	28111
10	10536	12086.1
12.5	5361	4449.1
15	2790	2660.16
17.5	1682	1709.18
20	1064	1061.46
25	455	482.99
30	207	232.46
35	106	118.52
40	56.5	61.87
45	33	34.15
50	19.9	20.36
55	13.1	13.87

For the penetration depth of 0 to 2.0 cm, data points near the resonance frequency of the cavity (as shown in Figure 1) were used whereas for the penetration depth from 2.5 cm to 5.5 cm points far away from the cavity resonance frequency give accurate answer.

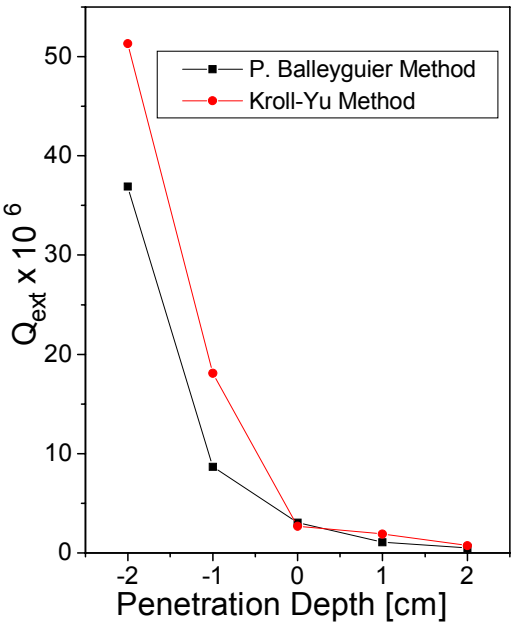

Figure 2 : Plot of Q_{ext} as a function of penetration Depth

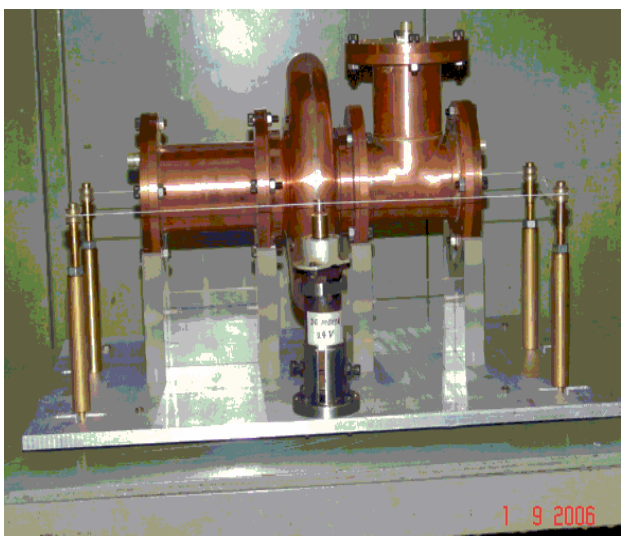

Figure 3 : Experimental Set-up (Copper mock-up)

CONCLUSION

Figure (2) shows the variation of Q_{ext} as a function of penetration depth calculated for the cavity operating at 1.056 GHz using P.Balleyguier as well as Kroll-Yu method. There is a discrepancy in the results at very high Q_{ext} ($> 10^7$) values while at lower values it is matching well.

From the results listed in Table 3 it is clear that Kroll-Yu method is also a suitable tool for the evaluation of external Q provided the data points are chosen carefully.

A comparison between the two techniques shows that P.Balleyguier method is very simple, straightforward and can be used efficiently for low as well as high external Q.

To get better insight of the subject a copper mock-up of the SC cavity with coaxial input coupler is fabricated at MDPDS Workshop, BARC, Mumbai (See Figure 3). The experimental study is under progress.

The author thanks P. Balleyguier, CEA Bruyeres le Chatel, France for his help in understanding the subject.

REFERENCES

[1] N.M.Kroll,D.U.L.Yu, "Computer determination of the external Q and resonant frequency of waveguide loadaed cavities", Stanford Linear Accelerator Centre Report No. SLAC-PUB-5171, Jan1990(A)

[2] A.S.Dhavale and K.C.Mittal,"Evaluation of external Q of the superconducting cavity using Kroll-Yu method", Review Of Scientific Instruments 77, 066101 (2006)

[3] P.Balleyguier, "A straightforward method for cavity external Q computation", Particle Accelerators, Vol.57, P.113-127, 1997

[4] A.Roy, A.S.Dhavale et.al., "RF Design of a Single Cell Superconducting Elliptical Cavity with Input Coupler", 12th Workshop on RF Superconductivity, Cornell University, USA, 2005

[5] A.Roy et.al., "Superconducting Elliptical 1050 MHz β=0.49 Cavity Design for High Current Proton Accelerator", Indian Particle Accelerator Conference (InPAC2006), Nov. 1-4, 2006, Mumbai, India

[6] P.Balleyguier, "External Q studies for APT SC-cavity Couplers", XIX Internaltional Linear Accelerator Conference, Chicago, IL, 23-28 August 1998, p.133-135

[7] "CST Microwave Studio™", Version 3, Tutorials

[8] V.Shemelin, S.Belomestnykh, "Calculation of the B-cell Cavity external Q with MAFIA and Microwave Studio", Cornell Publication:SRF020620-03, 2002

[9] P. Balleyguier, "External Q computation in cavities with MWS", CST User Meeting, Darmstadt, September 2004

MECHANICAL ANALYSIS AND DESIGN OF THE PEFP LOW BETA CAVITY*

Sun An#, Y. S. Cho and B. H. Choi
PEFP, KAERI, Daejeon 305-353, Korea

Abstract

The PEFP low beta superconducting RF cavity is the lowest beta elliptical cavity operating at pulse mode so far, the Lorentz force detuning control of the PEFP low beta cavity is a big challenge in cavity design. In this paper, a basic design consideration in the stiffening structure for Lorentz force detuning control has been presented. Based on this consideration, a new stiffening structure has been designed for the PEFP low beta cavity. The PEFP low beta cavity with this structure has low Lorentz force detuning coefficient K_L, reasonable cavity field flatness sensitivity, frequency sensitivity, tuning sensitivity and stable mechanical property.

INTRODUCTION

Superconducting RF (SRF) cavity is considered to accelerate a proton beam with repetition rate of 60 Hz at 700 MHz in the PEFP Linac being built at Gyeongju [1, 2]. The first section of the SRF linac is composed of 9 low beta cryomodules with three 5-cell elliptical cavities of β_g=0.42, and will accelerate a proton beam from 80 MeV to 178.6 MeV [3,4]. Table 1 lists the primary parameters of the PEFP Low beta cavity.

Table 1: Primary parameters of the PEFP Low beta cavity.

Parameters	Value
Frequency (MHz)	700
Geometrical beta β_g	0.42
E_{acc} (MV/m)	8.0
E_{pk}/E_{acc}	3.71
B_{pk}/E_{acc} [mT/(MV/m)]	7.47
R/Q (Ω)	102.30
Cell to cell coupling (%)	1.41
Geometrical Factor (Ω)	121.68

The cavity is deformed by the Lorentz radiation pressure, the tuner, the helium liquid pressure and the atmosphere pressure after pump-down. This deformation induces resonant frequency shift, field flatness change, ununiform stress distribution of the cavity. Therefore, mechanical stability of the SRF cavity is a fundamental consideration in the cavity design.

Generally, the lower beta cavities have stronger Lorentz force detuning than that of the higher beta cavities. For pulse SRF accelerators, the Lorentz force detuning is a more serious issue than that of CW accelerators. The PEFP low beta cavity is the lowest beta elliptical cavity operating at pulse mode so far. Its Lorentz force detuning control is a big challenge in the cavity design. In order to control Lorentz force detuning, a optimized stiffening structure is installed on the cavity normally. In this paper, a basic consideration to optimize the stiffening structure is presented. The stiffening structure design of the PEFP low beta cavity is introduced.

STIFFENING STRUCTURE DESIGN

The function of the stiffening structure is to control Lorentz force detuning and protect cavity. A good stiffening structure should:

- Effectively control the Lorentz force detuning.
- Have low cavity field flatness sensitivity.
- Have low tuning sensitivity.
- Have low peak stress in the cavity.

The PEFP stiffening structure design follows above rule.

In the superconducting RF cavity, the RF power produces radiation pressures on the inside cavity wall [5]. The pressures deform the cavity wall, that produces the cavity resonant frequency shift. RF system needs to supply a surplus RF power to compensate the cavity frequency shift for keepping the cavity voltage constant. It can be demonstrated the cavity frequency shift is negative, and can be expressed as:

$$\Delta f = -K_L E_{acc}^2 . \quad (1)$$

Here E_{acc} is the cavity accelerating gradient. K_L is the Lorentz force detuning coefficient, which strongly depends on the cavity shape and cavity wall's thickness. In order to reduce the RF system costs, usually a stiffining structure is used to control the Lorentz force detuning.

Stiffening structure design

The simulation method of combining Poisson Superfish with ANSYS is used to analyze PEFP cavity mechanical property [6]. The different stiffening structures have been simulated for PEFP low beta cavity, as shown in Fig. 1. Table 2 lists the Lorentz force detuning coefficient K_L with the cavity wall thickness of 4.3 mm for different stiffening structures at the best condition.

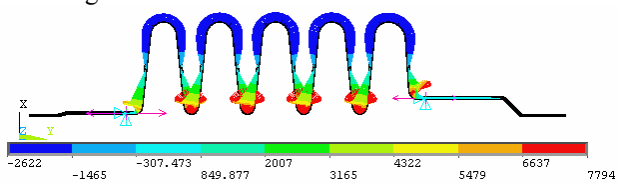

A. A PEFP low beta cavity without stiffening structure and the Lorentz pressure distribution on it.

* Work supported by the 21C Frontier R&D program in Ministry of Science and Technology of the Korean Government.
#sunan@kaeri.re.kr

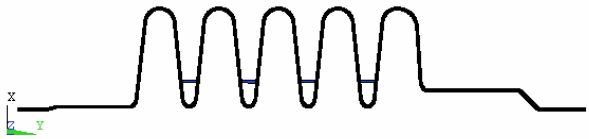

B. Single stiffening ring between inner cells.

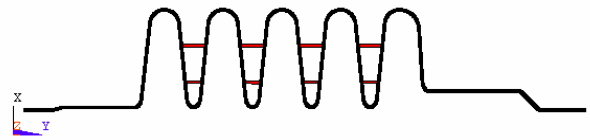

C. Double stiffening ring between inner cells.

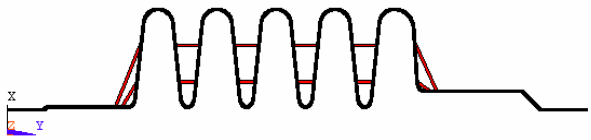

D. Double stiffening ring between inner cells and double stiffening cone on end cells.

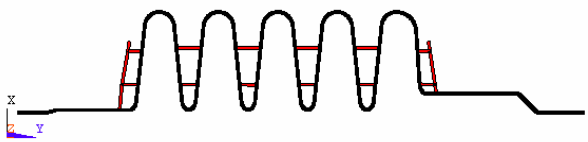

E. Double stiffening ring between inner cells and between end cell and end dish.

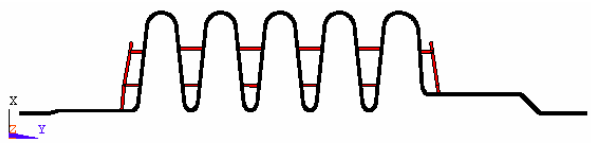

F. Double stiffening ring between inner cells and between Field Probe end cell and end dish, and single stiffening ring between FPC end cell and end dish.

Figure 1: Lorentz radiation pressure distribution and different stiffening structures of the PEFP low beta cavity.

Cavity field flatness sensitivity

The field flatness affects not only the accelerating voltage maximization and the peak surface electro-magnetic field minimization, but also the K_L and the external quality factors Q_{ext} of Field Probe and FPC [7]. Simulation shows that Lorentz pressures do not change cavity field flatness. PEFP cavity frequency tuning strucuture is a SNS type tuner located on the cavity Field Probe side to strecth or press the cavity in logitudinal direction. Measurements have indicated that the tuner's motion changes the cavity field flatness linearly when changing cavity frequency [7].

The cavity field flatness sensitivity due to tuner's motion depends on the cavity structure. Table 2 lists the field flatness sensitivity of a PEFP low beta cavity for different stiffening structures. Other parameters in the Table 2 will be obtained in following sections.

Table 2: Lorentz force detuning coefficient K_L, cavity field flatness sensitivity, frequency sensitivity and tuning sensitivity for different stiffening structures

Stiffening structure*	A	B	C	D	E	F
Min. K_L [Hz/(MV/m)^2]	25.90	19.20	7.60	0.4	0.1	-1.1
Field flatness sensitivity (%/MHz)	2.5	9.4	108	18.5	54.7	49.1
Frequency sensitivity (KHz/mm)	353	369	263	190	184	188
Tuning sensitivity (N/mm)	834	1123	2522	11766	4507	4498
Maximum Von Mises stress (MPa)	77.6	88.5	108	45	12.1	12.6

*Note: The stiffening structure A, B, C, D, E, F correspond to the structure in Fig. 1, respectively.

Cavity frequency sensitivity

The cavity frequency sensitivity is used to specify the tuner movement range and preload the tuner before cool-down. Low frequency sensitivity means a low tuner step resolution and a big tuner movement range for a given frequency range, which needs a heavy tuner-load. An ideal situation is low tuner load and low tuner step resolution. Because the cavity frequency sensitivity is strongly dependent on the mechanical prperty of the cavity and its stiffening structure, the cavity frequency sensitivity must be considered in the stiffening structure design. Table 2 lists the frequency sensitivity of a PEFP low beta cavity for different stiffening structures.

Cavity tuning sensitivity

Cavity tuning sensitivty stronly decides a specification of the tuner load. Higher tuning sensitivity means the heavier tuner load, which needs the biger-size tuner aims and thicker helium vesel wall. The tuning sensitivity depends on the cavity and cavity stiffening structrure. Table 2 lists the cavity tuning sensitivity of a PEFP low beta cavity for different stiffining structures.

Cavity stress distribution

After pump-down in the production, the cavity is deformed by the atmosphere pressure at the room temperature, and also deformed by the helium liquid pressure at the low temperature. Because the helium liquid pressure is much lower than the atmosphere pressure, and the niobium's yield strength at low temperature is higher than it at the room temperature, we only consider the inluence of the the atmosphere. Fig. 2 shows the cavity deformation and Von Mises stress distribution of a PEFP low beta cavity. The maximum Von Mises stress values in the cavity wall for different stiffening structures are listed in Table 2.

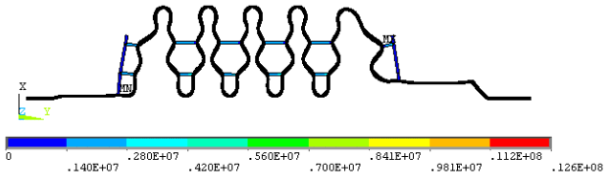

Figure 2: Cavity deformation and Von Mises stress distribution under atmosphere after pumped down.

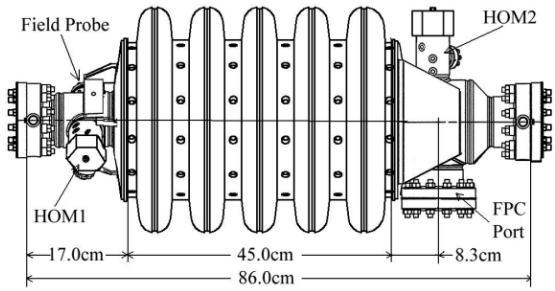

Figure 3: PEFP low beta cavity with the stiffening structure F and the support structures on the end sides.

Discussion

According to above discussions and simulations, structure C, D, E and F can get low Lorentz force detuning coefficient K_L. But structure C could induce very high stress in the cavity, the niobium yield strength is about 70 MPa, therefore, the cavity with structure C is not stable during pumping down. The cavity with th structure D has the highest tuning sensitivity, which increases the tuner design difficulty. The cavity with E. structure E or F has low stress, and its field flatness sensitivity is little higher, but it is acceptable. The structure F is easier to fabricate than structure Therefore, the best stiffening structure for the PEFP low beta cavity should be structure F. Fig. 3 shows a PEFP cavity with the stiffening structure F and the support structures on the cavity end sides.

MECHANICAL MODE ANALYSIS

For PEFP SRF cavities, the pulse repetition rate of 60 Hz means the Lorentz force shakes the cavities to vibrate with 60 Hz, and the cavity's mechanical mode, whose frequency is near the 60 Hz could be dangerous. Here the cavity's mechanical modes are calculated by using the ANSYS 2-D model and 3-D model.

The simulation results show that the mechanical mode with the lowest frequency is a longitudinal mode of 152 Hz, and the lowest frequency of the transverse mode is about 306 Hz. Normally the Dynamic Amplification Factor η is used to judge the resonance risk. The Dynamic Amplification Factor η of the first longitudinal and transverse modes is 1.0 approximately, as shown in Fig. 4. This means that PEFP Low Beta Cavity has no dangerous mechanical modes for 60 Hz pulse repetition.

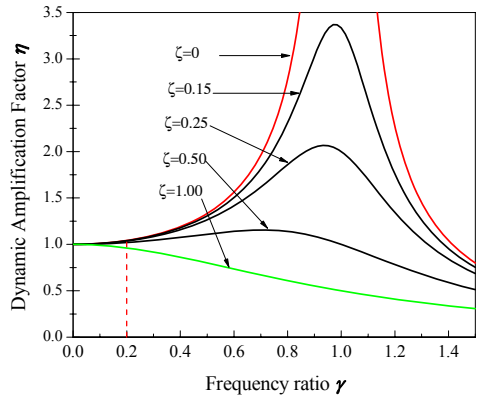

Figure 4: Dynamic Amplification Factor η curves of the frequency ratio γ. Here $\gamma=f_d/f_n$ (f_d is the driving frequency, for PEFP Cavity f_d =60 Hz; fn is the cavity mode's frequency). ζ is the damping ratio of the cavity.

CONCLUSION

The PEFP low beta cavity with the stiffening structure of double stiffening ring between inner cells and between Field Probe end cell and end dish, and single stiffening ring between FPC end cell and end dish has low Lorentz force detuning coefficient K_L, reasonable cavity field flatness sensitivity, frequency sensitivity, tuning sensitivity and stable mechanical property.

ACKNOWLEDGEMENT

The authors would like to thank H. Wang, E. Daly from JLab for their technical review, and all the PEFP members for discussing and support. This work is supported by the 21C Frontier R&D program in Ministry of Science and Technology of the Korean Government.

REFERENCES

[1] Y. S. Cho and K. Y. Kim, J. Korean Phys. Soc. 48, 721(2006).
[2] H. J. Kwon, H. S. Kim, K. T. Seol and Y. S. Cho, J. Korean Phys. Soc. 48, 726(2006)
[3] Sun An, Y. S. Cho, B. H. Choi and J. H. Jang, J. Korean Phys. Soc. 59, (2007).
[4] Sun An, Y. S. Cho and B. H. Choi, *Design of the PEFP Low Beta Cryomodule*, Proceedings of APAC2007 in Indore, January 29 to February 2, 2007, 2007, WEPMA127.
[5] R. Mitchell et al., *Lorentz Force Detuning Analysis of the SNS Accelerating Cavities*, Proceedings of SRF2001, SA010.
[6] Sun An, *Superconducting RF Cavity Frequency and Field Distribution Sensitivity Simulation*, Proceedings of PAC 2005, p4194.
[7] Sun An, H. Wang, G. Wu, Effect of the Tuner on the Field Flatness of SNS Superconducting RF cavities, Proceedings of LINAC 2004, p815.

DESIGN AND SIMULATION OF MULTIBEAM KLYSTRON CAVITY

Ashish Kumar Tiwari#, Rajiv Kumar Arora, P. R. Hannurkar
Raja Ramanna Centre for Advanced Technology, Indore, India.

Abstract

The design and simulation of a multibeam re-entrant type cavity with four beams is presented for a 350 MHz, 250 kW CW klystron. The simulation is carried out using electromagnetic code CST Microwave Studio. This klystron will be used for 100 MeV proton Linac for Spallation Neutron source (SNS). Important Simulation results are presented.

INTRODUCTION

Klystrons have the inherent capability to provide maximum gain per unit length among the conventional electron beam devices. With the practical limits on increasing the number of cavities for a higher gain, increasing the output power level in conventional klystrons means increasing either operating voltage or the beam current. For increase in current the perveance of the gun is to be increased which results in increased space charge forces and the reduced efficiency of the device. Further high magnetic field is required to keep the beam focused throughout the drift length. Increase in anode voltage is limited by thermal and voltage breakdown considerations. A number of klystrons may be paralleled to get more power output and increased redundancy but phase matching at output remains a troublesome part of any such arrangement. Further any such arrangement is bulky and requires room.

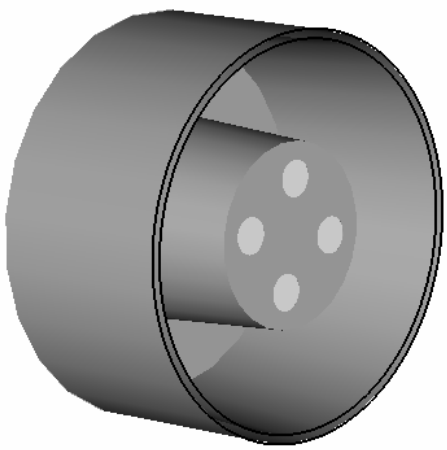

Figure 1: Cross-section of a multibeam cavity with four beamlets.

Another option is to parallel a number of beams within the same interaction structure. Since all the beams are accelerated through a common voltage and interaction takes place in a common structure namely multibeam cavity so the problem of phase matching no longer exists. This type of device is called the Multi-Beam Klystron (MBK). After the first experimentation in 1940's these klystrons have been developed and manufactured especially in Russia for past few decades. The multibeam klystrons are being looked into with renewed interest worldwide for their large scale application in accelerators. RRCAT has taken up the development of 350 MHz 250 kW CW klystrons for the accelerator applications. This paper presents the design and simulation of a multibeam cavity to be used as an interaction structure for the multibeam klystron.

#atiwari@cat.ernet.in

DESIGN OF RE-ENTRANT CAVITY WITH MULTI-BEAM CHANNEL

Analytical methods can be used for the estimation of parameters of the cavity having simple shapes but for the more complex shapes experimentation or computer simulation are the only resorts. Analytical methods are still required for initial estimation of input geometrical parameters in computer models to be further analyzed and optimized numerically. The parameters were determined from the coaxial line analogy and parallel resonant circuit. Figure 1 shows the cavity shape. The RF interaction circuit for MBK is re-entrant cavity operating in TM_{010} mode. The diameter of gap channel is much larger than that of single beam klystron cavity in order to hold more beam channels. Therefore the RF electric field in inner layer beam channels is stronger as compared to outer layer beam channels. It is found that the electric field is not constant and slightly asymmetrical over the cross section of four beams for slightest disparity in interaction gap and field is more at the central beam if it exists. Therefore the radial dimension of the cavities must be chosen in order to minimize the disparities between the interaction gaps.

Suitable choice of the diameter of the gap projection is important for MBK design as it will influence the beam wave interaction and hence the efficiency. The following relation between cavity diameter and the diameter of gap projection is to be satisfied according to calculation and experience [1]

$$\frac{D_p}{D} < \frac{3}{4} \quad (1)$$

$$\frac{D}{\lambda} < \frac{3}{4} \quad (2)$$

where D_p = Diameter of gap projection
D = Diameter of cavity
λ = Operating wavelength

Beam and tunnel diameter are decided so that it can be easily focused and radial beam coupling coefficient having less than 3% variation. Figure 2 shows the equivalent circuit of the cavity for the purpose of determining the parameters from the coaxial line analogy and parallel resonant circuit [2].

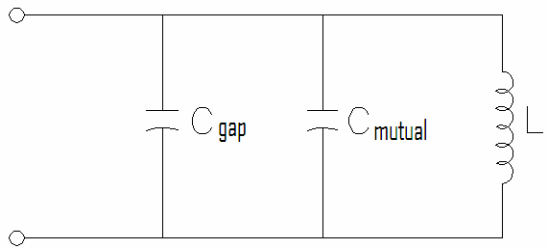

Figure 2: Equivalent Circuit of a multibeam cavity.

The inter gap capacitances C_{gap} plays the vital role in deciding the frequency of operation. In the drift tube inside the cavity the total area of cross section of annular portion is made to be equal to the area of its single beam counterpart. Gap capacitances are determined from it with gap distance estimation from beam coupling coefficient. The inductance value is considered as an inductance of a coaxial line where the diameter of the inner conductor as the diameter of the circle where the beams are placed. Beam position is kept such that the mutual interaction between them may be less pronounced. At a first approximation the mutual capacitances were neglected as these may be taken care by optimisation through computer simulation [3].

PHYSICAL MODEL AND COMPUTER SIMULATION

Being an asymmetric structure such a cavity need to be modeled in a 3D code. CST's microwave studio is used for the purpose. One such cavity, whose initial geometric parameters are calculated analytically as above, is modeled and analyzed using the CST Microwave Studio. Cavity is crossed by all the beams in parallel according to the figure 1. The resonant mode is the fundamental mode (TM_{010}).

CST Microwave Studio employs the combination of the proprietary perfect boundary approximation (PBA) with the Finite Integration Technique (FIT). It has a simple 3D figure input interface. According to the estimated geometrical parameters cavity was modeled using the template based GUI modeler in Microwave Studio [5]. The frequency for different modes with the associated Q value is listed below.

Table 1: Separation of modes

Mode Number	Frequency (MHz)	Q Value
1	350.00	9655
2	763.91	11908
3	991.97	16488

RESULTS AND DISCUSSION

Eigen-mode AKS solver is used with interpolated quasi Newton optimization routine. Table 1 indicates that the modes are sufficiently separated. From the field distribution inside the 4-gap cavity for different modes, mode 1 is clearly identified as dominant TM_{010} mode. R/Q for the geometry shown is found to be 68 with Q factor of about 9,655. R/Q is optimized by varying gap and subsequent cavity height for the resonant frequency. The R/Q factor of a conventional cavity is given by

$$\frac{R}{Q} = \frac{V^2}{2\omega U} \tag{3}$$

where V is the RF voltage across the gap and U the electrical energy stored in the gap. If C is the capacitance of the equivalent circuit, $U = CV^2/2$ and then $R/Q = 1/\omega C$. Now MBK cavity is made of 4 such capacitance so R/Q factor related to a single beam counterpart is $R/Q = 4/\omega C$. Therefore the instantaneous bandwidth is significantly large in this case. Effects of fabrication errors and geometrical changes are being investigated.

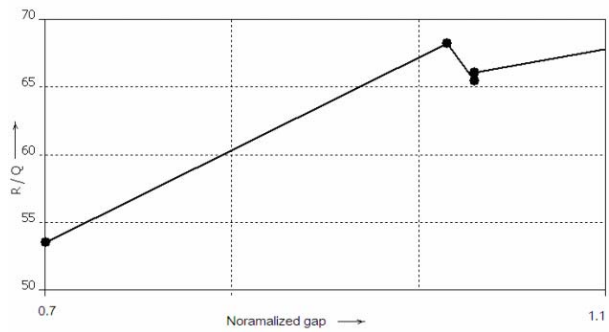

Figure 3: Variation of R/Q with normalized gap distance for dominant mode.

REFERENCES

[1] Ding Yaogen et al., Theortical and Experimental Research on Multi-beam Klystron, Proceedings of High Energy Density Microwaves Conference, Pajaro Dunes, California, 1998
[2] K. Fujisawa, General treatment of klystron reentrant cavities, IRE Trans. Microwave theory Tech., vol. 6, pp. 344-358, Oct. 1958
[3] A. Ghose et al, RF Cavity Design for A Multibeam Klystron, Proc. of National Symposium of Indian Vacuum Society, 1998
[4] E. A. Gelvich, The New Generation of High Power MBK, IEEE, MTT, Vol 41, No.1 Jan 1994
[5] CST Microwave Studio User's Manual.

DEVELOPMENT OF HIGH-POWER MICROWAVE DEVICES IN TOSHIBA

Kenichi Hayashi, Masao Irikura, Yoshika Mitsunaka, Setsuo Miyake, Yoshihisa Ookubo
Mitsunori Sakamoto, Hiroyuki Taoka, Katsuhiko Tetsuka, Hiroto Urakata
Toshiba Electron Tubes & Devices Co., Ltd.
1385, Shimoishigami, Otawara-Shi, Tochigi 324-8550, Japan

Vacuum microwave devices continue to be essential for high-power RF accelerator systems and plasma heating or current drive systems for fusion experimental devices. Klystrons are suitable for use in amplification at the frequency ranges from 300 MHz to X band, while gyrotrons are mainly utilized in the millimeter wave range. Input couplers also play an important role in the building of acceleration cavity systems. TETD (Toshiba Electron Tubes & Devices Co., LTD.) has been developing these vacuum microwave devices in collaboration with some Japanese research institutes.

Two kinds of long-pulse klystron for the J-PARC project were developed in collaboration with KEK and JAEA, which each have their operation frequencies, 324 MHz and 972 MHz as listed in Table 1. Both tubes output 3 MW with a pulse duration of 0.62 ms at a repetition frequency of 50 pps. They have a triode-type electron gun and the same beam parameters and operate with an anode-modulating mode to reduce the cost of the power supply system. The tubes have a different output structure optimized for the operating frequency.

The 324-MHz tube, E3740A is horizontally oriented as shown in Fig. 1. Its weight was trimmed by 35% compared with the same size klystron by unifying it with the focusing solenoids. The maximum power of 3.03 MW was achieved with an efficiency of 57% for a beam voltage of 110 KV after some problems such as oscillation caused by reflected electrons from the collector and instability probably due to the magnetic field distribution like mirror field were solved. Twenty of the tubes were already installed in the J-PARC linac system and successfully completed acceptance testing.

Table 1: Design parameters of klystrons for J-PARC

	E3740A	E3766
Frequency (MHz)	324	972
Output Power (MW)	3	
Efficiency (%)	50	
Gain (dB)	55	
RF Pulse Length (ms)	0.62	
Beam Pulse Length (ms)	0.7	
Repetition Rate (Hz)	50	
Beam Voltage (kV)	110	
Anode Voltage (kV)	94	
Beam Perveance ($I/V^{1.5}$)	1.37×10^{-6}	
No. of cavities	5	6
Window	Coaxial	Pillbox
Output Flange	WR-2300	WR-975
Tube Length (m)	4.55	2.93

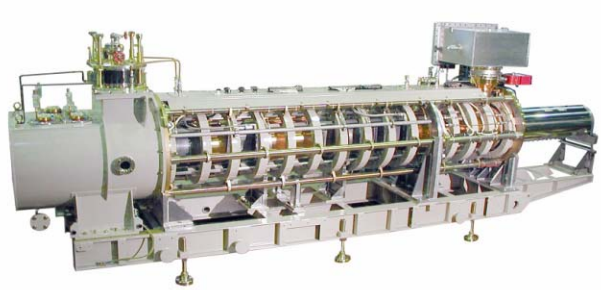

Figure 1: 324-MHz, 3-MW klystron E3740A

Figure 2 shows the 972-MHz tube, E3766. The second cavity incorporated in the first two prototypes had a relatively wide gap to meet a bandwidth of 10 MHz, and in addition, its RF electric field in the gap was symmetric with respect to the gap center, leading to TM011 and TM021-mode monotron oscillations. The 3-MW stable operation was obtained in the third tube with a new RF structure aimed at mass production.

TETD has been developing 1.3-GHz, 10-MW MBKs (multi-beam klystrons) for the Euro XFEL project in collaboration with KEK. A vertically-oriented MBK, E3736, the external view of which is shown in Fig. 3, already completed acceptance testing at DESY. Its design parameters are listed in Table 2. The MBK has six low-perveance beams operated at a relatively low voltage

Figure 2: 972-MHz, 3-MW klystron E3766

Figure 3: 1.3-GHz, 10-MW, MBK E3736

Table 2: Design parameters of 1.3-GHz, 10-MW MBK

Frequency	1.3 GHz
Peak Output Power	10 MW
Average Output Power	150 kW
Beam Voltage	115 kV
Beam Current	132 A
Efficiency	more than 65%
RF Pulse Duration	1.5 ms
Repetition Rate	10 pps
Gain	47 dB
Number of Beams	6
Number of Cavities	6
Cathode Loading	2.0 A/cm^2

of 115 kV and six ring-shaped cavities to enable a higher efficiency than a single-beam klystron for a similar power.

Figure 4 indicates dependence of the output power and the efficiency on the beam voltage, where the solid lines and the solid circles correspond to the design and the measured data, respectively. The difference between the two data at high voltage region is probably due to selecting a lower value than the optimum one obtained by calculation for an external Q factor of the output cavity to prevent instability from occurring for unmatched loads. We achieved a 10.2-MW average power over a 1.5-ms pulse with a repetition rate of 10 pps and demonstrated a stable 24-hour continuous operation under this condition. A horizontal version of the MBK has been designed. It will be tested this summer.

Figure 5: Test facility for E3762

Table 3: Specifications and Design parameters of 5-GHz klystron

	Specs	Design
Frequency (GHz)	5	
Output power (kW)	400	500
Pulse length (s)	10	CW
Beam voltage (kV)	< 70	68
Anode voltage (kV)	< 66	61
Beam current (A)	< 17.5	15.5
Efficiency (%)	> 30	> 50
Drive power (W)	< 30	< 20
Number of cavities		6
Dissipation (kW)	800	800
Length (m)	2.6	
Weight (kg)	800	
Number of windows	2	2 (BeO)

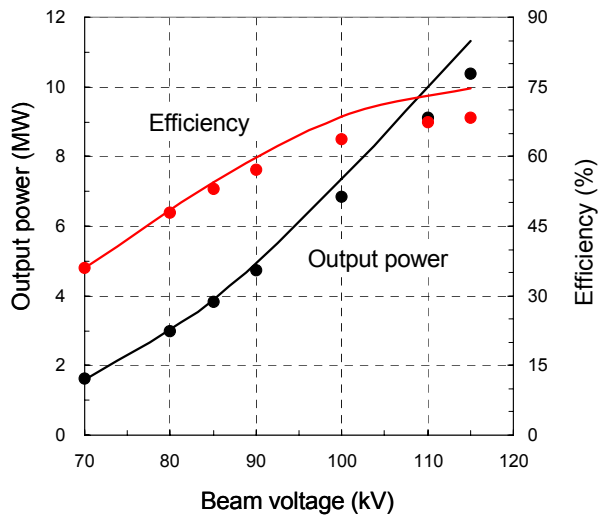

Figure 4: Output characteristics of E3736

A prototype of the 5-GHz, 500-kW CW klystron for KSTAR was completed. The klystron E3762 was designed with the aim of outputting continuous wave power of 500 kW with efficiencies above 50% as listed on Table 3. A 1.5-π three-cell output cavity was adopted to realize higher efficiency within an allowable heat load. Beryllium oxide disks, which have relatively high thermal conductivity and low tan delta, were selected to avoid window failure by thermal stress. Evaporative cooling was adopted as shown in Fig. 5.

Figure 6 shows dependence of the output power, the efficiency, and the drive power on the beam voltage. A maximum power of 510 kW with an efficiency of 50% was achieved for a beam voltage of 68 kV. We also demonstrated a continuous operation of 350 kW and a 10-s pulsed operation of 455 kW and confirmed that the measured losses of the body and the windows were similar as calculated. It can be expected from the test results that the continuous operation of 500 kW will be achieved in the next tube.

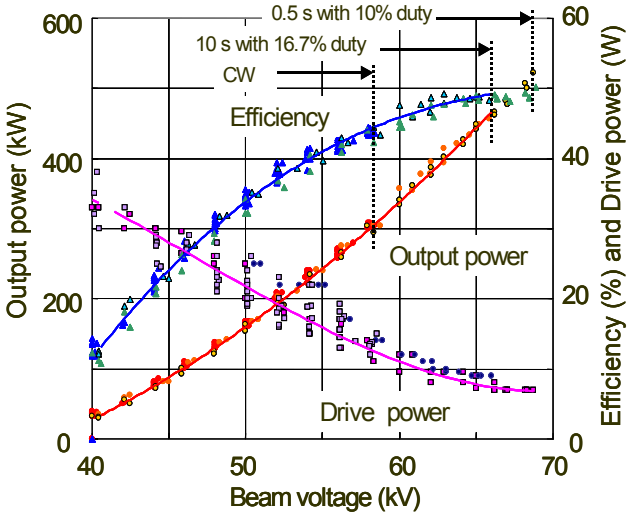

Figure 6: Output characteristics of E3762

JAEA and TETD have been jointly developing the 170-GHz, 1-MW long-pulse gyrotron for ITER, which is shown in Fig. 7. Tests is currently proceeding into the demonstration of high-power and long-pulse operation at the JAEA's test bench.

Figure 7: 170-GHz, 1-MW gyrotron E3993

DEVELOPMENT OF C-BAND MULTI BEAM SUB-BOOSTER KLYSTRON

M. Yoshida#, S. Fukuda, KEK, Ibaraki, Japan
V. E. Teryaev, BINP SB RAS, Novosibirsk, Russia

Abstract

A C-band small multi beam klystron (MBK) has been under development. It is designed for the sub-booster klystron which is required to drive multiple 50 MW C-band klystrons for the SuperKEKB injector upgrade plan. The designed output power is 150 kW in case of the applied voltage of 25 kV which is suitable for the existing pulse modulator for the S-band sub-booster klystron. At this operating condition, the designed micro-perveances of the total and the each beamlet are 2.0 and 0.25 respectively. The design overview will be presented.

MOTIVATION

KEKB attained the highest luminosity of 1.7×10^{34} cm^{-2} s^{-1} in the world. KEKB consists of an 8 GeV electron ring (HER) and a 3.5 GeV positron ring (LER). The KEKB Injector linac [1] has provided 8 GeV electrons and 3.5 GeV positrons to inject those rings directly.

To aim for a ten-times higher luminosity, the SuperKEKB project [2] is under consideration as an upgrade of KEKB. In the SuperKEKB project, energy exchange of beams has an important role to escape the influence of electron clouds for the positron ring (LER). To exchange the beam energy of the LER and the HER, the energy of a positron beam has to be raised from 3.5 GeV to 8 GeV. However the acceleration length after generating positrons is restricted because a positron is a secondary particle. One of solutions is to double an acceleration field. Thus the C-band (5712 MHz) accelerating unit [3] has been developed to obtain the higher acceleration field over 40 MV/m.

A C-band accelerating unit consists of one 50 MW klystron and four accelerating structures. In the present KEKB Injector linac, eight S-band klystrons, which is called as a sector, are driven by one 80 kW sub-booster klystron and its low RF power circuits. In case of the C-band acceleration, one sector consists of 16 accelerating units because a C-band accelerating unit has only half length compared with the present S-band accelerating unit. Thus the C-band sub-booster klystron has to drive 16 high power klystrons. The required output power of the sub-booster klystron becomes 150 kW considering the power loss of the waveguide.

DESIGN OUTLINE

Assuming the lower expected efficiency of 0.8 - 0.2 μP which is obtained from the general experience, the relation between the applied high voltage and the RF output power satisfies the following equation.

$$\mu P\left(0.8-0.2\mu P\right) = Pout/\mathrm{Vk}^{2.5}\times10^{6} \qquad (1)$$

Figure 1 shows the micro perveance (μP) and the expected efficiency versus the applied high voltage in case of the required RF output power (Pout) of 150 kW.

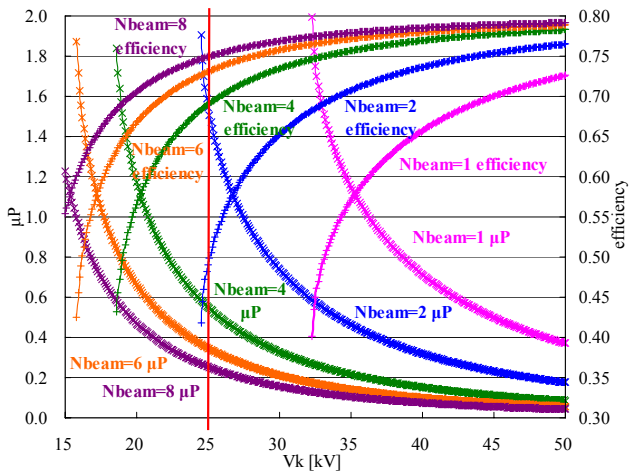

Figure 1: Micro perveance (μP) and Expected efficiency versus the applied high voltage in case of the required RF output power (Pout) of 150 kW.

The existing pulse modulator for the S-band sub-booster klystron is planned to use for the newly developed C-band sub-booster klystron. The operating high voltage (Vk) of the pulse modulator is 25 kV. From figure 1, more than 4 beamlets are required to obtain the RF output power of 150 kW.

Table 1 shows the klystron parameters corresponding to the number of beamlets.

The difficulty to construct the multi-beam klystron is the insertion of some iron plates to make the magnetic field parallel, even though the convergent electron gun is used. To avoid this difficulty, the immersed flow electron gun is chosen. Thus 8 beamlets are chosen for this C-band sub-booster klystron to make the cathode within the limited cathode beam loading (6 A/cm^2).

#mitsuhiro.yoshida@kek.jp

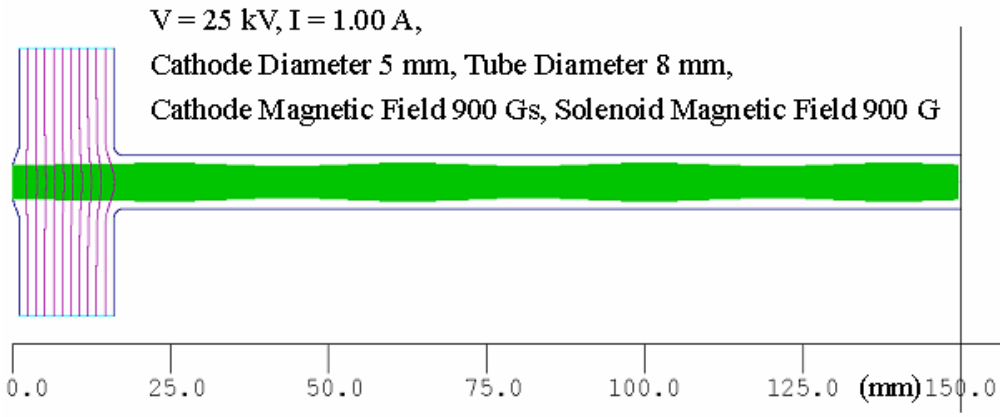

Figure 2: The beam trajectory of the electron gun.

Table 1: Klystron parameters corresponding to the number of beamlets.

Parameter	Value				
Frequency (MHz)	5712	5712	5712	5712	5712
Output Power (kW)	80	150	150	150	150
Beam Voltage (kV)	25	25	25	25	25
Beam Current (A)	7.88	6.11	2.17	1.37	1.00
μP per beamlet	1.98	1.55	0.55	0.35	0.25
Efficiency (%)	40.4	49.1	69.0	73.1	74.9
Number of Beams	1	2	4	6	8
Cathode Loading (A/cm^2)	6.00	6.00	6.00	6.00	6.00
Cathode Area (cm^2)	1.31	1.02	0.36	0.23	0.17

ELECTRON GUN

Figure 2 shows the beam trajectory of the electron gun determined by the simulation code DGUN [4]. Although the beam trajectory has periodic bulges in the immersed flow, the required magnetic field for enough small beam radius is 900 Gauss. The cathode beam loading is 5 A/cm^2 which is enough low for long life time in such a short pulsed klystron.

INTERACTION CAVITIES

The designed klystron consists of 6 interaction cavities. Those cavities are common for the 8 beams. Although the structure of cavities has to consider the 3D geometrical shape, the axial symmetric model is enough for the beam simulation after some translation to the electrical parameters: R/Q, Q, the frequency detuning and the distance of gaps etc. The parameters of those interaction cavities were optimized using the 1D and 2.5D PIC simulation code. Figure 3 shows the result of the 1D simulation. The simulations show that the efficiency is close to 60 % at a drive power of 5 W. The efficiency becomes lower than the ideal expected luminosity since the beam pipe radius comparatively becomes large due to the immersed flow. Thus the expected output RF power is 120 kW which is enough for the C-band system.

According to the optimization of the parameters of cavities, the 3D geometrical shape was determined by 3D electromagnetic wave solver. Figure 4 is 3-dimensional shape of the interaction cavity(left) and the output cavity(right).

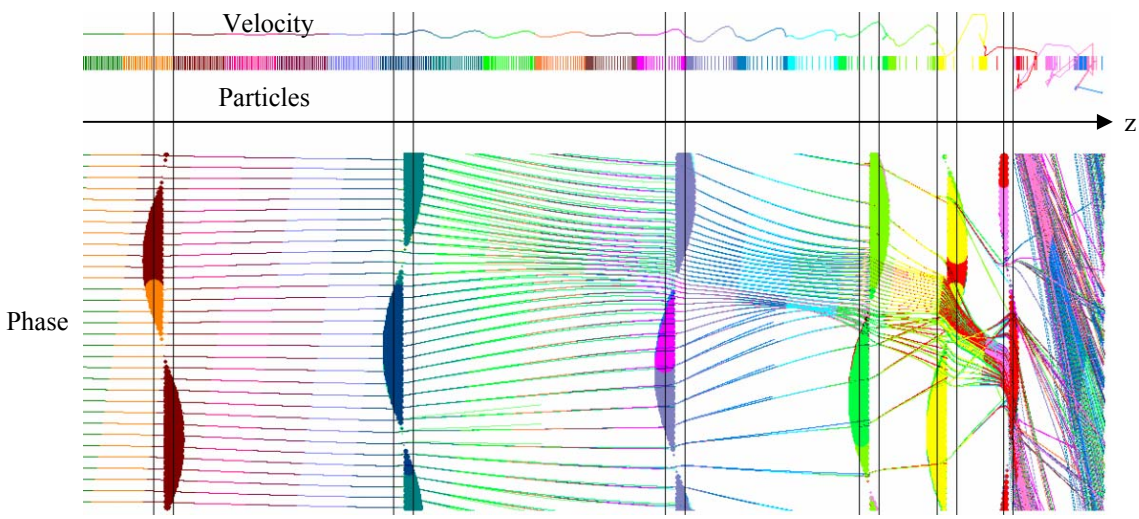

Figure 3: The result of the 1D simulation.

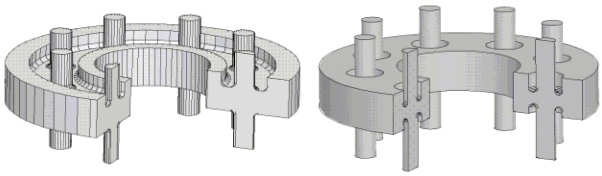

Figure 4: The interaction cavity(left) and the output cavity(right).

MECHANICAL DESIGN

Figure 3 shows the mechanical design of the klystron using the 3D CAD. Before testing the klystron, we will test the electron gun itself. Figure 4 shows the beam test tube to test the electron gun. The 8-beam cathode was made of Toshiba Electron Tubes & Devices Co., Ltd. In this design, the common type heater was adopted for easy fabrication.

CONCLUSION

The design of the C-band sub-booster klystron is completed and currently under construction. The klystron has 8 beamlets and its output power is over 120 kW expected by the simulation. We will test the klystron performance after the beam test tube will be tested. If we successed to operate this klystron, we will proceed to manifacture the L-band multi beam klystron for the ILC project by using the same design procedure.

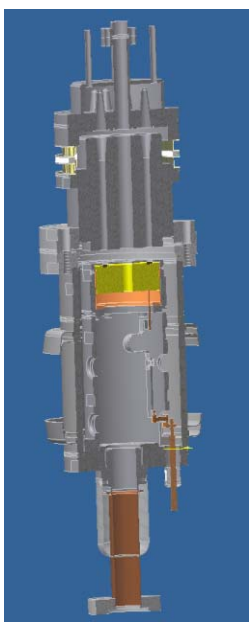

Figure 5: Design of the Beam Test Tube.

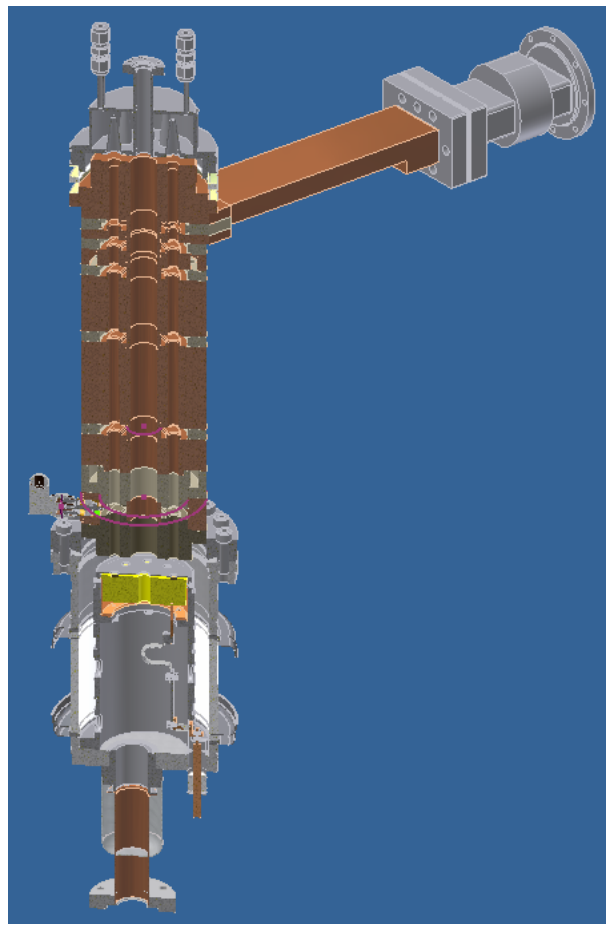

Figure 6: Mechanical design of the klystron.

REFERENCES

[1] I. Sato, et al., “Design report on PF Injector linac Upgrade for KEKB”, KEK Report 95-18, in Japanese.
[2] J. W. Flanagan, Y. Ohnishi, et al., “Letter of Intent for KEK Super B Factory”, Part III: Accelerator Design, KEK Report 04-4.
[3] S. Michizono, et al., “KEKB Injector Linac and Upgrade for SuperKEKB”, Proceedings of LINAC’04, Lübeck, Germany, August 2004, p. 549.
[4] A. Larionov, K. Ouglekov, “D-GUN for Simulation of Intensive Axial symmetric Electron Beam”.

COMMISSIONING AND OPERATIONAL EXPERIENCE WITH INDUS-2 RF SYSTEMS

M R Lad[#], M K Badapanda, Pritam Singh Bagduwal, Ashish Bohrey, R.K.Deo, P R Hannurkar, Akhilesh Jain, M K Jain, Narendra Kumar, Ramesh Kumar, Moonuku Prasad, Vikas Rajput D.Sharma, Nitesh Tiwari, R.Tyagi,
Raja Ramanna Centre for Advanced Technology (RRCAT), Indore-452013, India

Abstract

Indus-2 is a 2.5GeV/300mA third generation Synchrotron Radiation Source being commissioned at Raja Ramanna Centre For Advanced Technology, Indore. RF system provides sufficient voltage for boosting electron energy from 550 MeV to 2.5 GeV in addition to compensate for Synchrotron Radiation losses. 505.8 MHz Indus-2 RF systems is in operational state since April 2005. The beam injection into Indus 2 from Booster Synchrotron started in Aug. 2005.First beam accumulation was achieved on Dec.1st, 2005 with injected beam of 450 MeV.The injection energy was subsequently increased to 550 MeV. After achieving beam accumulation at the injection energy, the beam energy was ramped to 2 GeV. So far 38 mA of beam current has been stored at the injection energy and accelerated to 2 GeV at 26 mA.

During First commissioning phase of Indus 2 the RF system was switched on with one RF cavity and then for 2 GeV operation two RF cavities were energized. Modular RF system has been operating satisfactorily during machine operation. The low-level control system has been completely installed with optimization of phase & amplitude loop to the desired stability in progress; the tuning loop was installed in the beginning phase. For the stored beam of 38 mA.at 550 MeV no dangerous HOM frequencies were observed.

INTRODUCTION

Full description of Indus-2 RF system can be found in [1], but briefly it is composed of four numbers of bell shaped elliptical cavities (Fig.1) to generate 1500 kV accelerating RF voltage. 64 kW RF amplifier system powers each RF cavity. Each power plant can run independently of others. The power from Klystron amplifier is transmitted to RF cavity through 6 1/8" co-axial line. Two racks of low level & control electronics are installed for each plant. The RF module comprises of 64 kW klystron amplifier, 20 kV/5A HV power supply, 10 W solid-state driver amplifier, and low-level control. For fine regulation & stabilization of the cavity fields frequency, amplitude and phase loops are installed on each RF station. High precision cavity temperature control system is incorporated to control HOM. Protective equipment's interlock unit act directly to the RF switch, which cuts driving power to RF amplifier chain. The RF system is completely remote controlled from both RF & main control rooms

Figure 1

OPERATIONAL ASPECTS

RF cavity gap voltage requirement is 75 kV for injection and 375 kV at 2.5 GeV; correspondingly the wasted power on the cavity surfaces is 900 watts and 22 kW respectively. The power transferred to the beam is of the order of 50 kW per cavity at full beam current. Table1 shows the main parameters of Indus-2 RF system.

Initially with injection energy of 450 MeV few thousand turns were achieved without RF.Then the RF system was switched on by the end of Nov.2005.On 1st Dec 2005 first time SR was observed with **RF ON**. Only one RF cavity (Station 4) was switched on at 60 kV gap voltage. Later on injection energy was increased to 550 MeV & beam accumulation was observed in Feb 2006 with only one RF cavity at 60 kV gap voltage. Phase of RF signal was optimized for proper injection. With low beam currents stored the ramping trials were carried out. On 18th may 2006 the beam was ramped to 1.9 GeV at very low currents with only one RF cavity at around 350 KV of gap voltage. At 1.9 GeV the losses to restore were only ones due to bending magnets (no ID used at present) which are 210 keV, the beam power was very low. For these 3 months the machine was operated with RF cavity no.4 only. The cavity resonant frequency was set to 1.5 kHz below the generator frequency to avoid Robinson instability where as the remaining 3 cavities were detuned 100 kHz or more in order to avoid harmful interaction with the beam. The vacuum trip level was set at 10^{-7} mbar. The injection was tried at different gap voltages; at higher gap voltage injection rate was slightly lower.

ladm@cat.ernet.in

Table 1: Main RF Parameters

	Stage-I	Stage-II	
Operating Energy	2	2.5	GeV
Injection Energy	550	550	MeV
Beam Current	300	300	mA
Frequency	505.81227	505.81227	MHz
Energy Radiated per turn at Final Energy			
Bending magnets	255.02	622.613	keV
Wavelength shifter	14.33	22.390	keV
Multipole wiggler	17.33	27.080	keV
Total energy radiated per turn			
At injection energy	2.0635	2.0635	keV
At final energy	286.68	672.083	keV
Total Beam Power	86.03	201.62	kW
Total Voltage across cavities			
At injection energy	300	300	kV
At final energy	1.1	1.5	MV
Over-voltage factor (q)			
At injection energy	145.4	145.4	
At final energy	3.84	2.232	

For ramping to 2 GeV or above two cavities were switched on (Station no.4 & 1) in May 2006. Initially the gap voltages of both cavities were kept at lower values. The station phase of each plant were optimized for best injection. The cavity resonant frequencies were set to 1.5 kHz below the generator frequency & the remaining 2 cavities were detuned 100 kHz or more. In Aug-Sept.2006 beam was ramped to 2 GeV at 26 mA, Cavity #1 was operated at 500 KV max. (40 kW) & Cavity #4 was operated at 450 KV max. (30 kW). The cavity tuner loop was operative since start of commissioning, however the phase loop optimization was done for two stations to achieve +/- 1 deg.stability.Phasing between two RF cavities was performed by balancing the input power to cavities at max. gap voltage & full beam loading during operation. The operation was carried out in different combinations of gap voltages and sometimes with only one independent cavity; injection rates were also noted. Max. beam accumulation of around 38 mA was achieved. In the initial phase of commissioning low beam current operation was planned hence cavity main coupler coupling was adjusted to 1.09 (critical coupling) without beam for all four RF cavities.Each RF plant is independently controlled hence machine could be operated with any of two RF plants or with one RF plant also at lower beam energy.

At higher beam currents the beam induced voltages were measured & calibrated in RF control room. Also the HOM signals monitoring was done at each energy & current levels, no dangerous HOM were observed.
During the shutdown of the machine from Oct onwards the main coupler coupling was adjusted to 2.0 without beam for all four RF cavities. This will allow higher beam current operation in the machine.

Many components like Synthesized signal generator, fast electronic phase shifter, RF limiter, RF power monitors have been developed indeginously.

RF SYSTEM OPERATION

RF Power Amplifier

NDUS-2 RF amplifier (fig-2) is based on 64 kW multi-beam, integral-cavity type klystrons. The auxiliary power supplies for its filament, ion pump and modulating-anode are floating at beam supply voltage of 20 kV. The current and voltage signals floating at beam voltage are monitored through optical fibre interface. The RF power transmission system is realized using $6^{1}/_{8}$" EIA lines and coaxial-line components, which operate at normal atmospheric pressure. The power amplifier has operated well during operation. Initially the problem of cross talk between two amplifiers was there which was later on solved. The amplifier was operated from remote & calibration of analogue signals like Klystron beam voltage, beam current, body current was done.
The problem of spurious circulator arc trips happening during early phase of commissioning was observed & was solved.

Figure 2

RF Cavities

Once installed in the ring, the cavities were baked and RF conditioned. The careful procedures were followed during conditioning of the cavities and slowly power was

increased for each cavity. With many hours of operation at high RF power and also beam current good conditioning of the RF cavity occurred; hence cavity vacuum interlock trips happening during the first months of commissioning are not occurring. Vacuum in the cavities is now normally $2\text{-}10^{-9}$ mbar without beam at nominal RF power and with beam at higher energies vacuum degraded sometimes and also trips were observed (level of $1.0\text{-}10^{-7}$ mbar).

Low Level Electronics

The low level electronics has proved to be very reliable. It is of modular construction, which is easy for installation and maintenance. Except initial problems like signal level, signal noise and operation with remote no further problems came from this part of the RF system. All the required specifications have been met after the fine settings of the loops parameters. The frequency loop keeps the cavity resonant frequency to ±500Hz or ±100 Hz . Actually the frequency loops sensitivity is normally set to ±500 Hz, while the cavity resonant frequency is kept –1 to –1.5 kHz below the generator frequency to avoid Robinson instabilities. The amplitude loop keeps the cavity gap voltage stable to ±1% low beam loading, while the phase loop keeps the phase of the input power to the cavity within ±1.0 degrees (at 505 MHz) at any power level. During commissioning sometimes when phase error was higher the injected beam was getting lost. All the other components of the low level electronics (interlock switches, station phase shifter, Cavity RF signal distribution, power monitoring at all stages in amplifier chain etc.) have performed well within the required specifications.

Klystron Bias power supply

SCR primary controlled 20 kV, 5.5 Amp power supply has been built. It is designed to operate with wide input variation of –30 % to +10% to deliver rated power with output variation within 0.3%. An 800 kVAR-detuned filter is employed, not only to keep the input power factor near unity but also to keep the line harmonics within certain limit. A spark gap based crowbar protection system is used to protect the expensive klystron tube, which diverts the energy stored in the filter capacitor of the high voltage power supply. Except some trivial problem no major faults has been experienced in HV power supply during operation.

Solid State Driver Amplifier

Solid-state amplifiers operating at 505MHz have been developed to drive the klystron power amplifiers. Each of these solid-state amplifiers is capable of providing 10 Watt of RF power with a gain of 40dB.Except initial problems Solid-state amplifiers have worked satisfactorily. 1-Watt solid-state amplifier has also been used in main distribution rack.

CONCLUSION

All the RF cavities have been tested & two were set into operation. The whole system has worked reliably. For higher beam current operation remaining cavities will be energised depending on the requirement A study on the working temperature of the activities and its relation with HOM has been carried on. This will allow operating the system with no excitation of HOM by the beam.

For the moment the operation of the whole system is satisfactory but complete tests have to be performed on the mutual interaction among all the control loops of the plants at higher beam currents. On each RF plant four loops, the control of the reference temperature, the turning loop, the amplitude loop and finally the phase loop would be optimised for high beam loading.

ACKNOWLEDGMENT

Authors would like to thank Dr V.C.Sahni, Director, Raja Ramanna Centre for Advanced Technology, Indore, and Shri S. Kotaiah, Project Manager (I-2) Raja Ramanna Centre for Advanced Technology, Indore, for providing continued support and guidance.

REFERENCE

[1] P R Hannurkar, “Design and Commissioning of RF System for Indus-2”, *Proc. of InPAC-2005,* Mar. 2005 VECC, Kolakata.

[2] Mahendra Lad, Nitesh Tiwari, Ashish Bohrey, Narendra Kumar, P.R.Hannurkar, “The Low Level RF Systems For Indus 2 RF Plants”, *Proc. of InPAC-2003,* Feb. 2003 CAT, Indore.

HIGH-POWER, LOW-LOSS, RADIAL RF POWER DIVIDERS/COMBINERS

Akhilesh Jain, Deepak Kumar Sharma, Alok Kumar Gupta, P. R. Hannurkar
RRCAT, Indore INDIA

Abstract

Development of a 20 kW Solid State Power Amplifier (SSPA), at 352 MHz, is in progress at RRCAT. This design uses radial dividing and combining architecture. As a part of this system, two high power (4 kW) combiners have been designed and developed. First one is 8 way with output ports in opposite but parallel direction to input port. Second one is 16 way with radial output ports. This paper describes design and measured performance of these two structures. Predicted results are in good agreement with those measured results.

INTRODUCTION

With growing interest in high power solid state RF source for particle accelerator [1] [2], design of high Power Divider/Combiner (PDC) structures has received enormous attention. Among different combining approaches, radial combiners proved to be efficient for summing N (>2) amplifiers. The tree structures have simpler design, but they have disadvantage of using multitude of transmission line segments, which add losses. This significantly degrades overall performance, especially for higher N. Radial combiners on other hand, can lead to power combining efficiency over 90% and insertion loss less than 0.5dB. Being in phase structures, their phase and amplitude stability depends upon symmetry, which in turn can be achieved easily with good mechanical design. In this paper, using simplified design methodology, two type of PDCs (8 way and 16 way) have been designed with central feed (1-5/8" rigid line) and peripheral collecting ports (N type connector) structure. With these structures, combined RF power of the order of up to 4 kW can be achieved. Necessary vector and scalar measurements were carried out for testing these designs.

DESIGN

Radial power combiner offers low loss, excellent amplitude and phase balance, with high power handling capability [3]. Unlike corporate combining structures, radial structure permits placement of a large number of ports very close to central feed port, thus minimising combining path and losses. A careful optimisation of physical structure is essential to obtain low insertion loss and good isolation over desired bandwidth. Project design specifications, include 8 way and 16 way PDC with combining efficiency > 90%, 1 dB bandwidth of ± 5 MHz, at center frequency of 352 MHz. As total output power is within 5kW, 1-5/8" EIA flange at output port, has been selected. Similarly at combining port expecting maximum power of 300-400W, N type connectors were selected for these design. Overall design should have insertion loss (other than coupling) less than 0.5 dB between desired coupled ports.

Combiner/Divider model

Proposed combiner/divider structure consists of three parts: the launcher, combining path and N way peripheral ports (Fig. 1). The launcher is coaxial line, feeding radial transmission line. The combining path (the radial line) is a low loss parallel plate stripline type transmission structure, with a central point excitation. From central excitation, energy spreads uniformly outward in the dominant E mode with an axial electric field component. It is important to maintain mechanical stability in feeding power symmetrical in order to prevent propagation of higher order modes. Feed symmetry governs insertion loss and phase imbalance. Last part is N way peripheral port (usually 50 ohm) section, connected to circular combing path. Design methodology of complete structure is stated step by step in terms of these three parts.

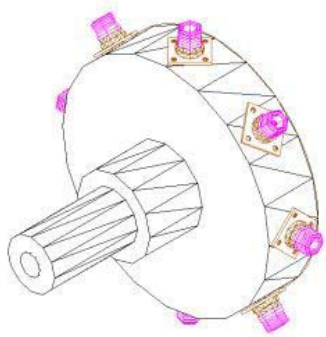

Figure 1: Radial combiner/divider structure

Designing Feed section

A 50 ohm input coaxial feed line is connected to radial line. In between these two lines, comes impedance matching section, realised in the form of coaxial lines having different characteristic impedance. Characteristic impedance of radial line is similar in nature to that of a TEM transmission line [4]. Hence, at feed point each dividing port can be thought as parallel connection of transformed impedance of port termination values. Transformation ratio can be deduced from formula for characteristic impedance of radial line. Problem is significantly complicated by the existence of complex characteristic impedance with spatial dependence, as well Bessel function arguments associated with radial line parameters. However, to simplify design, impedance of radial line at feed point can be assumed that of equivalent resistance of N port connected in parallel.

Using this formula we get approximate real value of radial line impedance, terminated by matched boundary at discrete ports. Coaxial impedance matching sections can be designed with this value for matching it to 50 ohms feed port. This initial step gives us idea for the design of coaxial sections. To improve this approximation and to

determine radial line and coaxial line junction dimensions, we need to account for the effect of coaxial/radial line junction discontinuity. This effect can be incorporated in the design using Williamson's [5] equivalent circuit. This calculation gives value of imaginary part at junction in the form of Bessel's and Neumann functions.

Designing combining path and peripheral ports

Design of combining path and peripheral ports was carried out by treating circular geometry as uniformly spaced circular array of coupled non uniform transmission line. [6] [7]. Each line impedance function is expanded in terms of Taylor's series. In this method, all distributed primary parameters of the line and also the voltage and current distribution along the line are considered as Taylor's series. Once V and I matrices are known, S matrix can be derived. For present design, we formulated the problem as circular array of 8 and 16 numbers of coupled linearly tapered transmission line, for 8 and 16 way PDCs respectively. This analysis gives us idea about return loss and isolation.

Placement of peripheral ports and radius of combining path is dictated by placement and dimension of N connector footprint, to accommodate all N connectors with some space for movement, while making cable connection. Due to this reason, N type connectors in 16 way PDC, were placed on periphery, unlike 8 way PDC, where combining ports are in line and opposite to Central feed.

Design Optimisation

During this simplified design approach, many real time discontinuities were ignored. These discontinuities include radial line to coaxial line discontinuity and discontinuities involved in step changes of inner conductor of different coaxial lines in impedance matching section and finite thickness of substrate and strip line. Hence for final optimisation, complete design was simulated using full wave EM simulator of HFSS. During this simulation, we computed first, impedance at feed port. This value was used for improving impedance matching section at central feed (1-5/8" rigid coaxial port) using circuit simulator. During this simulation care was taken to remove high electric field spots away from restricted regions, where possibility may exist for dielectric failure at full power. Fig. 2 and 3 shows completely assembled 8 way and 16 way PDCs.

Circular section radius is kept 80mm for both 8 way as well as 16 way PDC. Impedance matching from radial line to 50 ohm environment was carried out by different impedances' coaxial line sections having same outer conductor diameter. This matching section length is 95 mm in 8way PDC and 86 mm in 16 way PDC. Provision has been made for frequency tuning by placing Teflon rings.

Figure 2: 8 way power combiner/divider structures

Figure 3: 16 way power combiner/divider structure

MEASURED PERFORMANCE

Both of fabricated PDCs were measured at low and high power. At low power, measurement was carried out using vector network analyser E5071B. At high power scalar measurement was performed using R&S NRT power meter and FSP7 spectrum analyser. Insertion loss was measured as 0.2 dB and 0.4 dB for 8 way and 16 way PDC respectively. VSWR at the input port was measured as 1.05 and 1.15, while return loss measured at input feed was less than -35 dB and -22dB, for 8 way and 16 way PDC respectively. 90% bandwidth for 8 way and 16 way PDC was found to be in excess of 50 MHz. Figure 4 and 5 shows variation of return loss (S00) and feed port to dividing port coupling (S10) with frequency, for both of the structures. Measured performance of 8 way and 16 way PDC was satisfactory.

For phase imbalance measurement and power combining testing, two similar 8 way PDCs were connected back to back. Thus one PDC performs dividing action, while second one combines divided power. Ports connections were randomly changed several times. Total worst case insertion loss for this divider-combiner system was 0.43 dB. As each 8 way PDC has insertion loss of 0.2 dB hence loss due to phase mismatch is 0.03 dB which is very low. This measured value directly reflects control over phase stability in radial PDC. Combining efficiency calculated by measured data was better than 93% and 89% for 8 way and 16 way PDC.

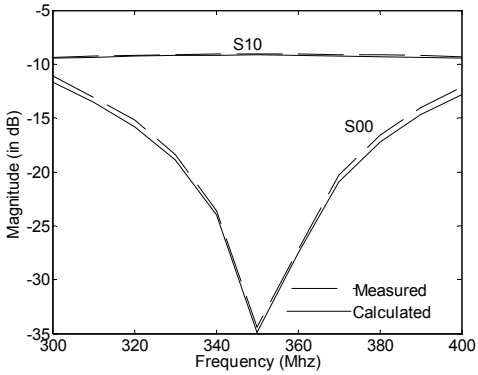

Figure 4: Comparison of measured and calculated results for 8 way Power Divider/Combiner

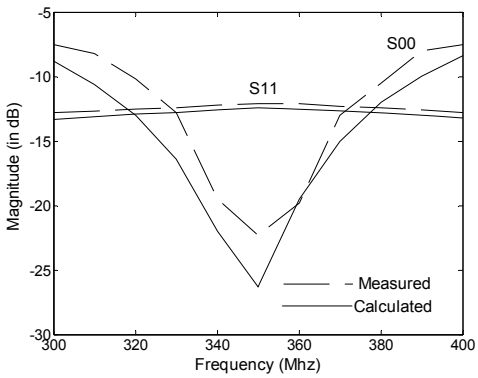

Figure 5: Comparison of measured and calculated results for 16 way Power Divider/Combiner

CONCLUSION

Using approximate design methodology, two different types of PDC at 352 MHz, were designed and tested. Zero Order structure design was further optimised using HFSS, full wave EM simulator. Measured and predicted results are in good agreement. Inspired by successful operation of Soleil 200 kW Solid state source and successful development of these PDC, another 8 way and 20kW power PDC design has been started. This successful development adds confidence for selecting solid state RF source in particle accelerator, among other tube based sources for few hundred kW of RF power regime.

ACKNOWLEDGEMENT

We are thankful to Mr. Ramesh Kumar and Mr. R K Arya for carefully preparing and assembling all of the combiner/ divider parts, with a special care from RF design point of view. For testing and measurement work, we are grateful to Ms Vasanti Sekhar. Mr D K Verma has carefully assembled all lines and testing rack with necessary electronics. We are also thankful to S. K. Jain for providing useful suggestions for mechanical assembly at various occasions during the course of this development. We are thankful to M/s Vistech Information system (P) Ltd. Banglore for providing us evaluation version of HFSS.

REFERENCES

[1] P. Marchand, et al, " High power (35 and 190 kW) solid state amplifiers at 352 MHz for synchrotron soleil", Proceedings of EPAC 2004, Lucerne, Switzerland

[2] Akhilesh Jain, Deepak Kumar Sharma, P R Hannurkar, "Solid state RF amplifier development at 350 and 700 MHz", 2006, Indian Particle Accelerator Conference InPAC-2006 BARC Mumbai, India

[3] Akhilesh Jain, P. D. Vyavahare, D. D. Bhawalkar, P. R. Hannurkar "A broadband High power 4-port power combiner at UHF" Journal of MANIT, 36, 1-7, 2004

[4] G. W. Swift, et al, "A comprehensive design technique for radial wave power combiner", 1988 IEEE MTT-S Int. microwave Symp Dig. Vol. 1 1988, pp. 279-281

[5] A G williamson, "Radial line/coaxial line stepped junction", 1986 IEEE Trans. Microwave Theory & Tech. Vol. 33 January 1985, pp. 1985

[6] A K Gupta, et al, "Full wave analysis of single and coupled stripline in multilayered cylindrical dielectrics using 3D TLM method", 2006 microwave and Optical Technology Letter Feb 2006, pp. 298-302

[7] M Khalaj-Amirhosseini, "Analysis of coupled or single non uniform transmission lines using Taylor's series expansion", Progress in Electromagnetic Research, PIER 60 2006 pp.107-117.

HIGH POWER MICROWAVE GENERATION FROM COAXIAL VIRTUAL CATHODE OSCILLATOR

A. Roy, J.Mondal, R. Menon, S. Mitra, D. D. P. Kumar, A. Sharma, K. C. Mittal
Accelerator and Pulse Power Division, BARC, Mumbai, INDIA

Abstract

A coaxial virtual cathode oscillator (VIRCATOR) has been designed to generate Relativistic Electron Beams and High Power Microwaves. Coaxial virtual cathode oscillators are known for better efficiency compared to the axial virtual cathode oscillators. This Coaxial VIRCATOR has been designed for the KALI-5000 (*1MeV, 60kA, 100 ns*) pulse power system. Provision for a large anode cathode gap has been kept to avoid the prepulse effect during the electron beam generation from the KALI-5000 system. Experimental studies are carried out to generate and characterize Relativistic Electron Beams and High Power Microwaves. Relativistic Electron Beams are generated by the Coaxial Explosively emitted graphite cathodes. Electron beam voltage has been measured by a copper sulphate voltage divider and beam current by a B-dot probe. High Power Microwaves are detected by the glow of neon lamps placed closed to the output window.

INTRODUCTION

Virtual Cathode Oscillators [1, 2] consist of an electron-beam diode and a waveguide. The electron beam is accelerated in the axial or coaxial direction and is injected into the waveguide. Electron beam is accelerated in the diode gap where pulsed high voltage is applied between the anode and the cathode. The beam passes through the anode, which is usually a thin foil or a mesh, and is injected into the area on the other side of the anode.

In the Vircator device the beam front forms a virtual cathode at a distance equal to the Anode Cathode (AK) gap if the injected current is greater than the space charge limiting current, I_l given by (for axial vircator)

$$I_l = \frac{4\pi\varepsilon_o m_o c^3(\gamma^{2/3}-1)^{3/2}}{e[1+2\ln(R/r_b)]} \qquad (1)$$

Where r_b is the beam radius and R is the drift column radius, (γ is the relativistic factor, and e and m_o are electron charge and rest mass respectively.

The virtual cathode reflects the electrons that follow the beam front. Thus electrons oscillate between the cathode and virtual cathode and cause microwave emission. The reflexing frequency is given by [3, 4]

$$f_r = \frac{v}{4d} \qquad (2)$$

where v is the velocity of the electrons.

The virtual cathode also emits radiation around the beam plasma frequency. The frequency at which maximum power emitted is given by [3, 4]

$$f_{vc} = 10.0\left(\frac{J}{\beta\gamma}\right)^{1/2} \qquad (3)$$

where J is the current density expressed in kA/cm^2.

Schematic of Coaxial Vircator is shown in Figure 1, it has a coaxial pair of cathode and anode that injects the electron beam radially into the circular waveguide. The interaction is between the electron beam current and the radial electric field of the waveguide mode.

COAXIAL DIODE DESIGN

Space charge limited current in a coaxial diode is given by [5],

$$j = \frac{4\in_o}{9}\left(\frac{2e}{m_e}\right)^{1/2}\frac{V^{3/2}}{d^{1/2}r_c^{3/2}}\left[\frac{1}{\ln\left(\frac{r_c}{r_a}\right)}\right]^{3/2} \qquad (4)$$

Coaxial diode impedance is given by

$$Z_d = \frac{68307}{V^{1/2}}\frac{(dr_c)^{1/2}}{h}\left[\ln\left(\frac{r_c}{r_a}\right)\right]^{3/2}\ \Omega \qquad (5)$$

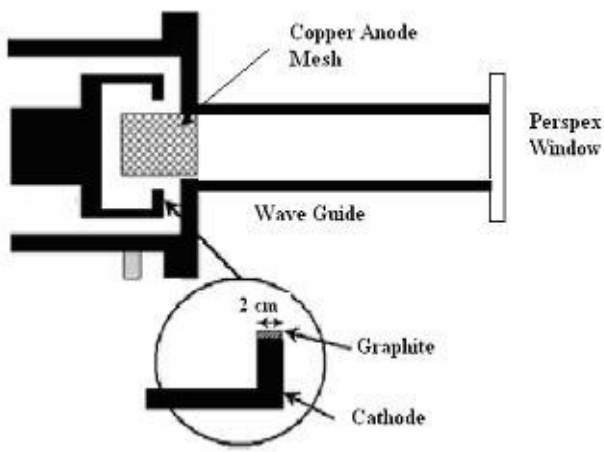

Figure 1: Schematic of Coaxial Vircator.

Table 1

Diode Voltage (kV)	Cathode Radius (cm)	Anode Radius (cm)	A K Gap (cm)	Cathode Width (cm)	Diode Impedance (ohm)
300	5.5	4.5	1.0	2	13
	5.9	4.5	1.4	2	25
	6.3	4.5	1.8	2	41
	6.9	4.5	2.4	2	71
400	5.5	4.5	1.0	2	11
	5.9	4.5	1.4	2	22
	6.3	4.5	1.8	2	35
	6.9	4.5	2.4	2	61

Table 2

Diode Voltage (kV)	Cathode Radius (cm)	Anode Radius (cm)	A K Gap (cm)	*fr* (GHz)	*fvc* (GHz)
300	5.5	4.5	1.0	5.8	4.8
	5.9	4.5	1.4	4.0	4.7
	6.3	4.5	1.8	3.0	4.5
	6.9	4.5	2.4	2.4	4.3
400	5.5	4.5	1.0	6.2	4.4
	5.9	4.5	1.4	4.4	4.3
	6.3	4.5	1.8	3.5	4.1
	6.9	4.5	2.4	2.6	3.9

Coaxial diode impedance for various anode cathode radiuses is given in the Table I.

Coaxial Vircator is constructed around KALI-5000 pulse power system. KALI-5000 [6] is capable of generating an Intense Relativistic Electron Beams of *1MeV, 60 kA, 100 ns* when connected to impedance matched electron beam diode. This indigenously developed pulse accelerator consists of a *1.5MV, 25 kJ* Marx generator, *1MV, 5kJ* Blumlein type transmission line and *60 kA* electron beam diode with voltage and current diagnostics.

Since Blumlein impedance is 18 ohm the diode impedance matches at 1.4 cm gap for 400 kV voltage. But the Prepulse voltage as shown in Figure 3 reduces the diode impedance significantly and perfect matching occurs at 1.8 cm diode gap. In this gap no reversal in the Marx out put (Figure 4) voltage confirms the impedance matching.

Coaxial Vircator microwave reflex and virtual cathode oscillation frequency are calculated from equations (2) and (3) respectively and listed in the Table II. Coaxial Vircator emits the maximum microwave power when the reflex and virtual cathode oscillation frequency are same.

For 400 kV diode voltage both the frequency are same for 1.4 cm diode gap and the calculated frequency is around 4.4 GHz. Figure 2 shows Beam Voltage and Current waveform from the Coaxial Vircator for 1.8 cm diode gap. Beam Voltage is measured by a resistive ($CuSO_4$) Voltage Divider and Current wave from is measured by a B-Dot probe and rogowski coil.

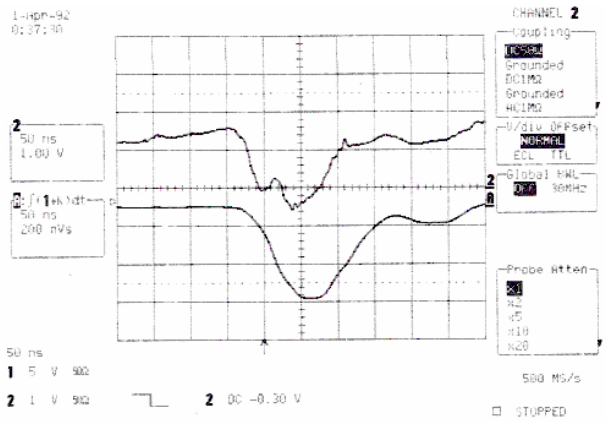

Figure 2: Coaxial Diode Voltage (top 200 kV/ Div) and Current (Bottom 10 kA/ Div) (Time 50 ns/Div).

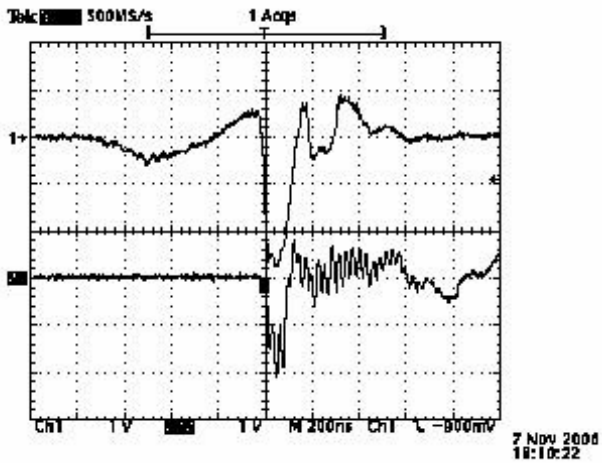

Figure 3: Coaxial Diode Prepulse voltage (Top 100 kV/Div) and diode current (Bottom 10 kA/Div) (Time 200 ns/Div).

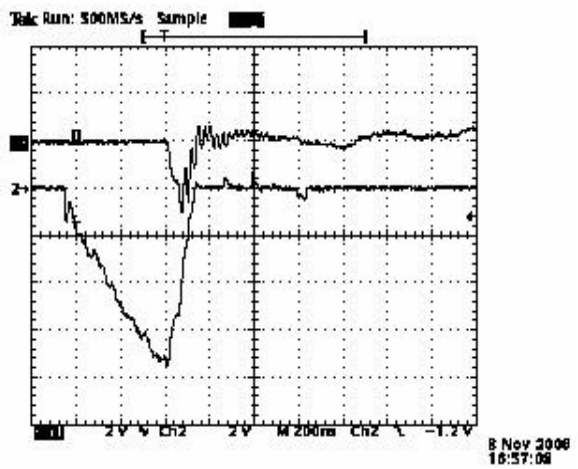

Figure 4: Marx out put voltage (Bottom 80 kV/Div) and diode current (Top 10 kA/Div) (Time 200 ns/Div).

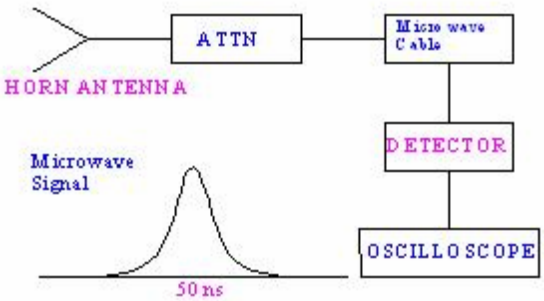

Figure 5: High Power Microwave Diagnostic Scheme.

EXPERIMENTAL RESULTS

Relativistic electron beam and HPM generation studies were carried out in the Coaxial Vircator for 1.8 cm and 1.2 cm AK gap. For 1.8 cm AK gap diode impedance matches exactly with the Blumlein impedance as can be seen from the Figure 4, there were no reversal in the Marx generator output pulse. But for 1.2 cm AK gap there is some reversal showing impedance mismatch. Prepulse voltages were recorded and for 300 kV diode voltage the Prepulse voltage was 50 kV. For 1.8 cm AK gap peak diode voltage obtained was 350 kV and the peak current was 25 kA. For 1.2 cm AK gap the peak diode voltage was 200 kV and the peak diode current was 40 kA.

The microwave pulse was measured by using the set up shown in Figure 5. The HPM radiation was received by a double-ridge horn antenna located a distance 4 meter away from the output window and after suitable attenuation given to a diode detector. The diode detector output is shown in the Figure 6. Also HPM discharge observed on Tube light and Neon Lamp placed a distance away from the output window.

For both the cases HPM generation was observed and microwave pulse recorded by the diode detector (Figure 6). For 1.2 cm diode gap HPM has got more peak power as the diode detector was getting saturated even when the antenna has been placed at around 4.5 meter distance from the vircator output window. At this place the measured HPM peak power was more than 20 dBm.

Also Neon Lamp Glow was observed at a distance of 10 cm from the output window and the power density required for HPM discharge is more than 1 kW/ cm^2. So the estimated peak power of the Coaxial Vircator was more than 1 MW. Further experiments are required to measure the HPM power more accurately. Also these experiments were carried out without a transmitting antenna from the vircator. With the transmitting antenna the measured HPM power is expected to be increased.

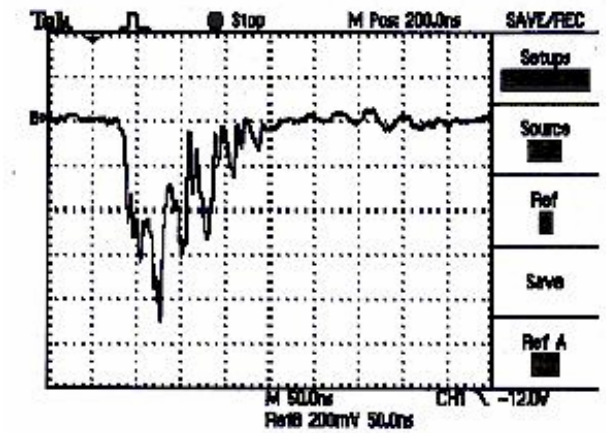

Figure 6: Microwave Signal recorded by Horn Antenna and Diode detector (200 mV/Div, 50 ns/ Div).

ACKNOWDGEMETS

We would like to express our sincere thanks to A. K. Ray, Director BTD group, for his constant encouragement and support. We are thankful to D. P. Chakravarthy, Head APPD and Dr. K.V. Nagesh for helpful discussions.

REFERENCES

[1] "High Power Microwave Generation by a Coaxial Virtual Cathode Oscillator" Weihua Jiang et al IEEE TRANSACTIONS ON PLASMA SCIENCE, VOL. 27, NO. 5, PP 1538- 1542, OCTOBER 1999.

[2] "A Diode Design Study of the Virtual Cathode Oscillator With a Ring-Type Reflector" Wook Jeon, et al IEEE TRANSACTIONS ON PLASMA SCIENCE, VOL. 33, NO. 6, PP 2011-2016, DECEMBER 2005.

[3] "High-Power Microwave Generation from an Axially Extracted Virtual Cathode Oscillator" E. H. Choi et al. IEEE Trans. Plasma Sci. 28, pp 2128-2134, (2000).

[4] "Effects of High Power Microwave Illumination on Electronic devices" G. V. Rao, A. Roy, A. S. Paithankar, P. H. Ron "Electro 2001", BHU, (2001).

[5] "Approximate analytical solutions for the space-charge-limited current in one-dimensional and two-dimensional cylindrical diodes" Xupeng Chen et al PHYSICS OF PLASMAS, VOLUME 11, NUMBER 6, PP 3278- 3283, JUNE 2004.

[6] "Intense Pulsed Power Electron Accelerators Developed at BARC" K. V. Nagesh, Archana Sharma, K. C. Mittal, G. V. Rao, NPSC P-866 (2004).

DEVELOPMENT OF 35 KW POWER AMPLIFIER AT 350 MHZ FOR RFQ BASED NEUTRON GENERATOR

Manjiri Pande, Atul Soni, Niranjan Patel, K.R.shinde, M.K.V.Rao, V.K.Handu
Vacuum Physics and Instrumentation Division,
Bhabha Atomic Research Centre, Mumbai-400085, India

INTRODUCTION

A 400 KeV, 1 mA (deuterium ion) radio frequency quadrupole (RFQ) based 14 MeV Neutron generator [1] is being developed in BARC to study physics of coupled neutron sources, sub-critical assembly and radio frequency (RF) coupling to accelerator. RFQ will accelerate the deuterium ion beam from 50 KeV to 400 KeV which will impinge upon a tritium target inside a sub-critical assembly to generate 14 MeV neutrons. Two RF systems of power around 35 KW each, are under development to feed the RF power at two ports of the RFQ. This paper describes the system design aspects, operating conditions and current status of the RF power system.

RF SYSTEM DESCRIPTION

Each 35 kW amplifier is a three-stage amplifier chain, comprising of a 100 W solid-state driver, a triode based intermediate power amplifier (IPA) of 1.5 kW and a tetrode based high power amplifier (HPA). Auxiliary power supplies, forced air/water cooling circuits and circulators are part of the associated electronics.

Driver

The solid-state driver [2] requires a maximum input of 20 dBm and provides up to 100W of power. It is coupled to Intermediate Power Amplifier (IPA) via a Y-junction circulator. The IPA uses EIMAC 8938 coaxial base triode. It is configured in cathode driven i.e. in grounded grid mode. Its input matching circuit uses 'L' type circuit using lumped components, output matching circuit uses a single ended half wave-length strip line (Fig. 1), capacitively loaded by the tuning capacitor at one end and by the tube output capacitance at the other end. This plate line is a short transmission line with characteristic impedance of 53 Ω. The triode is operated at an anode dc voltage between 1.5 kV to 3 kV by means of a variable 4 kV power supply.

Table 1: Test results of IPA at various frequencies.

Frequency (MHz)	Output power (W)	Efficiency (%)	Gain (dB)
343	500	25	8.3
350	200	12	4.0
368.8	740	34.3	10.2
368.8	420	60	7.25

A 47-Ω/50 W series resistance is inserted between the power supply and anode to dissipate energy in case of internal tube arc. Operating bias is established using 15 V zener. The test results of IPA are summarized in table 1. Efforts are being made to increase the rated output with better efficiency. Simultaneously a coaxial cavity based configuration for 8938 is being tried. Its design and simulation work is in progress.

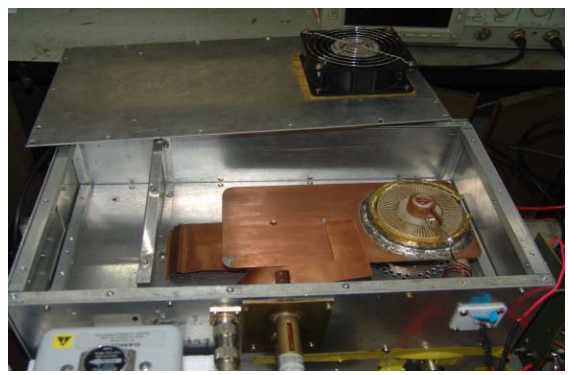

Figure 1: Intermediate Power Amplifier (IPA).

THE HIGH POWER AMPLIFIER (HPA)

DC Power Supplies

The HPA is powered by a variable 12 kV/10 A EHT supply (Fig. 2) and associated control grid and screen grid power supplies. EHT uses a 3 Phase, 6 Pulse thyristor based ac regulator on the primary low voltage (LV) side. The controlled output voltage is stepped up and rectified in a transformer unit. Suitable L-C filter is incorporated to keep output ripple within the desired limit of 1%. The power supply has been installed and tested at full load for a voltage regulation of 1%. Various protection circuits like over-voltage, over current, under voltage, phase failure, thermal overload, oil temperature sensor and its protection, spark/arc protection have been incorporated in this power supply. Various fault conditions were simulated in this power supply and all above-mentioned protection features were checked. Many LED indication features are provided in the front panel for quick detection and rectification of any fault condition. These include phase failure/phase reversal; fuse fail trip, thermal overload, oil temperature indicator, under voltage trip, over-volt trip, SCR over-volt, etc. A well regulated dc supply for screen grid (800 V / 500 mA) and control grid (-300 V/500 mA) has been bench tested and installed.

Figure 2: Anode power supply and its transformer unit.

Crowbar Protection

All the power grid tubes operate at high voltages that can cause severe damage in the event of an internal arc across the tube, unless it is properly protected. This damage becomes catastrophic when power supplies use large capacitor resulting in large stored energy or follow on current. Hence to protect the tetrode from the stored energy of output filter of the power supply, a fast acting crowbar circuit is incorporated across HV power supply and tetrode. If the output current of the tetrode increases above the set value around 7 A, an appropriate pulse is generated to trigger the crowbar circuit. When crowbar is fired, it behaves like a short circuit, thereby allowing the capacitor to discharge its stored energy through crowbar instead of the RF tube. The spark gap breakdown voltage is 18kV and operating voltage will be between 10 to 14 kV depending upon insitu operating conditions.

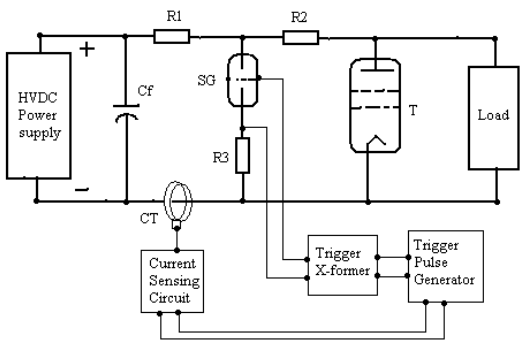

Cf: Filter Capacitor T: Tetrode
SG: Spark Gap CT: Current Transformer
R1, R2 & R3: High Energy Resistance

Figure 3: Crowbar protection circuit.

A high-energy series resistor R1 (10 Ω/1 kW) (fig 3) is inserted between the power supply and the crowbar to limit the peak current into the crowbar as well as limit the peak current demand on the transformer and rectifier of the power supply. Another high energy series resistor R2 (10 Ω/1 kW) is used between crowbar and the RF tube to insure the majority of the current flows through the crowbar after trigger. Both the resistor will also damp the circuit ringing sufficiently to prevent current reversal in crowbar which will cause it to open before fault conditions are cleared. Energy dumping resistor R3 is provided in series with spark gap.

Filament Supply

This is a variac controlled, current regulated power supply with a regulation of ± 1%. A control circuit (Fig. 4) in the power supply adjusts the variac, as the supply output current varies beyond its set value. This ac supply ramps up the voltage from 0 to 8 V in 5 minutes with a minimum step voltage of 0.025 V. A provision is made in the circuit to apply permanent backup heating voltage of 1.5 V ± 5 % during amplifier off time. Heater current will be approximately 180 A corresponding to 8 V.

Figure 4: Filament supply.

Interlock and Protection Circuit

All the auxiliary power supplies and two low power RF modules of HPA needs to be switched ON and OFF in a predefined timing sequence to prevent damage to the high power RF devices. Hence a suitable interlock circuit (Fig. 4) has been developed. It initializes certain sequence and logically checks the actual presence of each parameter at its respective location. These parameters include low conductivity water (LCW) flow and temperature, airflow, filament voltage, control grid voltage, anode voltage, screen voltage and driver RF power.

Figure 5: Interlock and Protection circuit.

The protection circuit performs two functions. In the absence of any bias voltage, the next consecutive sequence is not activated. It also senses faults signals, such as fault in power sources like over voltage, over current, arcing in transmission line etc and generates a trip signal, which in-turn switches off individual parameter in a controlled sequence. The unit has manual

reset switch, to reset the circuit after the trip condition. This unit provides indications for presence of all the voltages and trip condition on its front panel.

Tetrode Amplifier of HPA

The HPA (Fig.6) is designed [3] around TH571B tetrode in class-C mode. The tube is rated for 60 kW CW operation upto 400 MHz. It employs cavity configuration with λ/4 tuning circuit for anode and grid.

Table 2: Operating parameters of HPA.

Anode Voltage (kV)	10
Control Grid (Vg1) (V)	-300
Screen Grid-2 (Vg2) (V)	800
Power gain (dB)	14.6
Class of Operation	C
Efficiency (η)	74
Output RF Power (kW)	35

The operation of vacuum tube depends upon a number of interdependent parameters namely total cathode current, minimum instantaneous plate voltage, maximum grid voltage, plate and grid current conduction, which needs to be optimized to achieve high efficiency and high power gain. Hence behavior model [4] of TH571B is developed from its constant current curves using MATLAB. The code written in MATLAB uses asymptotic approximation method in order to get plate current, grid current and screen grid current as a function of grid and plate voltage.

Table 3: Optimized tube performance parameters given by the code.

Efficiency (η)	73.25 %
Power input (DC)	58.1 kW
Power output	42.56 kW
Total Peak Cathode current	40 A
Average anode current	5.81 A
Optimized anode conduction angle	94.96º

RF Transmission Line and Components

Coaxial line is used for transferring the RF power from source to accelerator in TEM mode. The HPA output is available on 6⅛" rigid coaxial line flange. Hence the RF transmission line was designed around 6⅛", 50-Ω rigid line of EIA standard. It comprises of 90º miter elbow bends, straight sections of various lengths, directional couplers and RF load. These silver brazed components are made up of ETP copper with electronic grade brass flange. Each individual component has been designed and tested on VNA. The layout of this RF transmission line has been made for two cases: one for testing the RF power supply across 50-Ω resistive load and other for feeding the RF power to accelerator. The layout of the complete transmission system in the latter case has been simulated [5] in the Microwave Studio version 6.2.

Table 4: VNA Results (RCTL 304.8mm).

SWR	1: 1.067
Attenuation	0.356 dB/m
Reflection co-efficient	-29.58 dB
Forward transmission co-efficient	-0.0426 dB
Reverse transmission co-efficient	-0.0386 dB

The simulation gives SWR, Port impedance, surface current density, S-parameters, electromagnetic field analysis, etc. The test setup (Fig. 6) includes 571 B tube, cavity, transmission line, direction coupler and RF load. It has been assembled and installed with necessary water-cooling arrangements.

Figure 6: Tetrode based high power amplifier.

CONCLUSION

Most of the above-mentioned subsystems of 35 kW amplifier have been developed and evaluated for their expected specifications. Mechanical installation of cavity and tube has been completed.

ACKNOWLEDGEMENT

Authors wish to thank Dr. V. C. Sahni, Director, Physics Group and Dr. S. Kailas, Associate Director, Physics Group for their constant support and encouragement.

REFERENCES

[1] R. Anand et al, "Design of RFQ based 14 MeV Neutron Generator" DAE symposium on nuclear physics, Mumbai, 2003.
[2] Rao B.V.R. et al, "Development of UHF solid state driver at 350 MHz", Indian Particle Accelerator Conference (INPAC-05), VECC, Kolkata-64.
[3] Data sheet of Thales TH571 B.
[4] T. R. Turlington, Behavioral Modeling of Nonlinear RF and Microwave Devices, Artech House, Inc.
[5] Atul soni et al,' Simulation of 6 1/8" Rigid Coaxial RF Transmission line' Indian Particle Accelerator Conference (INPAC-06), Mumbai-85.
[6] CST Microwave Studio software version 6.2.

LINEAR ACCELERATOR DESIGNS FOR THE UPGRADE OF THE CERN PROTON INJECTOR COMPLEX (LINAC4, SPL)

M. Vretenar, G. Bellodi, R. Garoby, F. Gerigk, K. Hanke, A. M. Lombardi, S. Maury, M. Pasini, C. Rossi, E.Z. Sargsyan, CERN, Geneva, Switzerland

Abstract

Looking beyond the commissioning of the LHC, which is expected to start at the end of 2007, CERN is setting up its scientific plan for the years to come. The concerns about the reliability of the old LHC injectors and the need to progressively remove the technical bottlenecks towards higher luminosity in the LHC have initiated a reflection on the design of the main elements of the LHC injection chain.

A plan under consideration foresees in the years 2007-2010 the construction of a 160 MeV H^- linear accelerator, Linac4, injecting into the old 1.4 GeV PS Booster (PSB). In a second stage, the PSB could be replaced by a superconducting linac, the SPL, at an energy between 3.5 and 5 GeV. The Proton Synchrotron (PS) would be in turn replaced by a new PS2 reaching a higher energy of 50 GeV. Linac4 and SPL can operate at a higher duty cycle than needed for LHC injection, allowing functioning as a high-intensity facility for neutrino or radioactive ion physics at a later stage.

This paper describes the design of the two linear accelerators involved in this upgrade strategy, Linac4 and SPL, and outlines some results of the R&D programme aimed at preparing the construction of Linac4.

INTRODUCTION

The present LHC injection chain (Fig. 1) consists of a 50 MeV proton linear accelerator (Linac2), followed by the 1.4 GeV PS Booster (PSB), the 26 GeV Proton Synchrotron (PS), and finally by the 450 GeV Super Proton Synchrotron (SPS), which injects into the LHC. While Linac2, PSB and SPS have been commissioned between 1972 and 1978, the first PS beam dates back to 1959.

The injection chain has been upgraded and partly modified in the years 1995-2000 [1] in preparation for the LHC. Beam tests following this upgrade have demonstrated that the nominal LHC beam can be provided at injection in the LHC. However, it is now clear that attaining and possibly exceeding the LHC ultimate luminosity of 2.3×10^{34} $cm^{-2}s^{-1}$ will require higher beam brightness (intensity/emittance) from the injector chain, which can only be obtained after a major upgrade of the injectors. Moreover, all of the scenarios that are currently being detailed for possible LHC upgrades [2] rest on the renovation of the present injection chain.

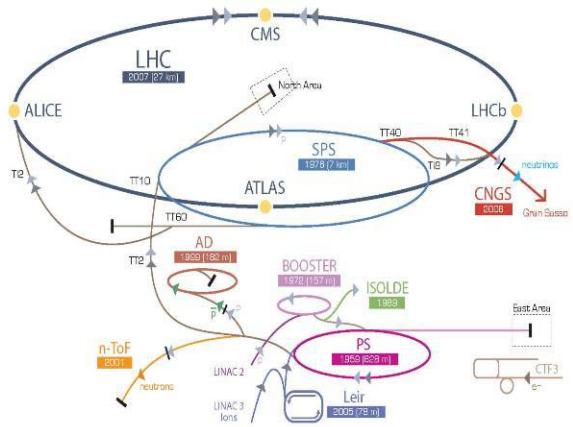

Figure 1: Scheme of the CERN Accelerator Complex

Another motivation for the reconstruction of the injectors concerns operational reliability of the present machines. The correct functioning of all the elements in the injection chain is essential for achieving the required LHC integrated luminosity. However, the past few years have shown recurrent reliability problems: radiation damage on the PS magnets, water leaks in the SPS magnets, failures of the PS main power supply, vacuum problems in the Linac2 tanks. An urgent consolidation programme has been launched, aimed at solving the most immediate problems to ensure a correct start-up and operation of LHC during its first years, but it is clear that some of the foreseen repairs are only temporary fixes and that more problems can be expected in the future.

A third argument for reconsidering the CERN injectors concerns possible future requirements for higher beam intensity from the CERN machines. For some of the presently planned experiments requiring intense secondary beams, ISOLDE for radioactive ion beam (RIB) physics and CNGS for neutrino physics, proton flux from the CERN machines is already at its limits, while both the neutrino and radioactive ion communities have presented ambitious long-term plans [3,4], which if approved would require significantly higher intensities from the CERN machines. Considering the relatively low beam energies required by these applications (~1 GeV for RIB, 5 to 10 GeV for neutrino production from pion decay), it appears attractive a scheme where the low energy accelerators in the new LHC injection chain are capable of a higher average beam current than what needed for the LHC, compatibly with the requirements of other physics experiments.

UPGRADE SCENARIO FOR THE LHC INJECTORS

A working group on "Proton Accelerators for the Future" (PAF) has been set up in May 2005 by the CERN management to elaborate a baseline scenario of the possible development and upgrade of the present Proton Accelerator Complex, working in close connection with the working group on "Physics Opportunities with Future Proton Accelerators" (POFPA) that has expressed recommendations on the physics programme.

Focused on the goal of maximizing the integrated luminosity for LHC experiments, a scenario of evolution has been proposed [5], subject to further refinement using the future experience of commissioning and running-in of the collider and its injector complex. The potential of this accelerator complex for producing high-intensity beams has been consequently analysed [6]. A renovated LHC injection chain would be composed of:

- Linac4, a 160 MeV H^- linear accelerator.
- An intermediate energy accelerator as the SPL, a 4 to 5 GeV superconducting H^- linac, or alternatively, a 5 GeV Rapid Cycling Synchrotron (RCS).
- A new Proton Synchrotron (PS2) up to an energy of 40 to 50 GeV.
- A renovated SPS (or in alternative a new superconducting SPS, SPS+, going to 1 TeV)

A scheme of the present and proposed future layout of the accelerator chain is presented in Fig. 2.

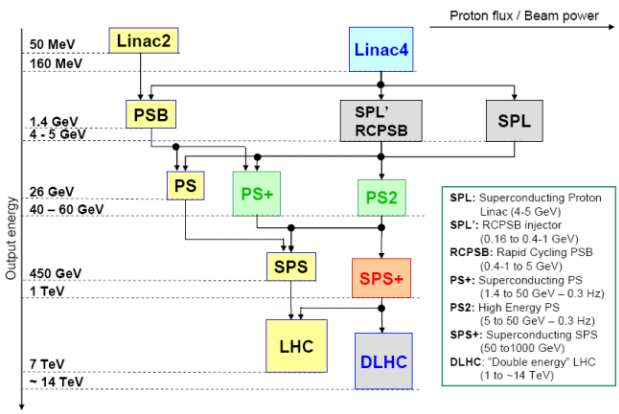

Figure 2: Present and proposed future CERN accelerators.

In the medium term, the new 160 MeV Linac4 should be built to overcome the space-charge bottleneck towards higher brightness at injection into the PSB [7]. This will allow the regular delivery of the ultimate beam to the LHC, reduce its filling time and improve the overall reliability of the injector complex. In order to benefit from these improvements already in 2011, Linac4 construction has to start in 2007-2008.

In the long term, the replacement of the PS is crucial for the reliability of the overall accelerator complex, and the replacement of the PSB has to be planned at the same time, to get the maximum benefit from the new PS. Although necessary to reach the expected luminosity from the LHC, the new intermediate energy accelerator will most probably be dimensioned in relation to the future needs of physics apart from LHC. A Superconducting Proton Linac (SPL) [8] is today the most promising accelerator for high-intensity applications in the CERN context, and if limited to low duty cycle operation can still be competitive in cost with a RCS. A decision in that respect will have to wait until the design is further refined and the future of high-intensity facilities at CERN is clarified.

The first stage of this scenario, which is consistent with the priorities set in 2006 by the CERN Council Strategy Group [9], was included in a proposal from the CERN Director to the Council for an update of the CERN medium-term plan. Together with measures for LHC consolidation and improvements and with urgent consolidation of the injectors, this programme envisages the construction of Linac4 and the detailed design of SPL and PS2 in 2008-2010. A decision on this additional programme is expected during 2007.

A preliminary study of the layout of the new injector complex on the Meyrin site is presently under way. This layout considers the staged construction of the different elements in what will be the future complex, by providing a coherent scheme for their final integration. A first option, presently under study, is shown in Fig. 3. In this layout, Linac4 is below ground level and connected to the PSB by a short transfer line. An underground tunnel housing the SPL can be subsequently built in the continuation of Linac4, with a parallel tunnel housing the SPL klystrons and equipment. Tangential to the SPL line will be the PS2, which will directly connect to the SPS.

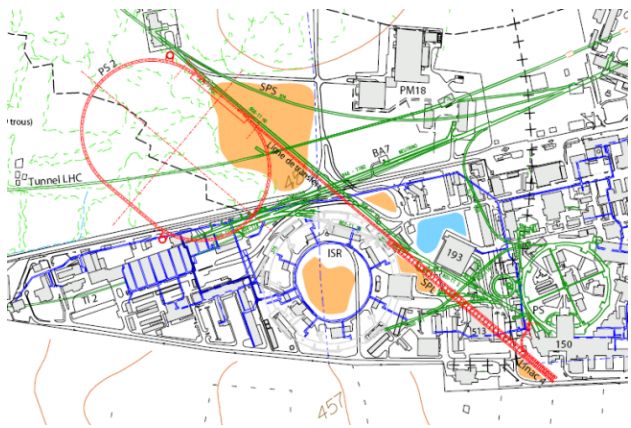

Figure 3: Possible layout of Linac4-SPL-PS2 on the CERN site.

LINAC4 IN THE PRESENT ACCELERATOR COMPLEX

Different schemes for increasing beam brightness out of the PS have been considered and several limitations to higher beam brightness have been identified [10]. The first bottleneck towards higher brightness is the space-charge dominated injection into the PS Booster.

Removing this restriction with the construction of a new higher energy linac replacing the 50 MeV Linac2 appears a solution offering many advantages in terms of reliability and flexibility already in the short term. The basic requirement for the new linac injector is to allow making the nominal LHC beam in a single PSB batch instead of the present double batch, which requires doubling the bunch population in the PSB within constant normalised transverse emittances. The incoherent transverse detuning at PSB injection being inversely proportional to the relativistic factor $\beta\gamma^2$, keeping the present tune shift while doubling the brightness is possible by increasing by a factor of 2 the value of $\beta\gamma^2$ at injection; this corresponds to an increase of the injection energy to 160 MeV. Going back to double batch injection should allow reaching and possibly exceeding the ultimate LHC luminosity. The flexibility allowed by using charge-exchange H^- injection for painting in the PSB acceptance should allow preserving the higher brightness during the acceleration process.

Apart from the benefits for the LHC beams Linac4 will also allow to increase the proton flux to the CNGS and ISOLDE experiments by a factor of 2. Furthermore, one can expect a reduction of beam loss in the high-energy accelerators by providing a beam with smaller transverse emittance.

LINAC4 DESIGN

The main Linac4 parameters are based on the requirements for PSB injection. Emittances are defined by the stringent needs of LHC while the maximum number of ions per pulse has been fixed at 1×10^{14} particles per pulse, in order to satisfy future needs of the ISOLDE experiment. The maximum repetition frequency for Linac4 is given by the limiting PSB frequency of 2 Hz.

Considering the present limits of ion source technology and the overall RF requirements, the average pulse current has been fixed to 40 mA. The required number of particles can then be provided with a 400 μs pulse length. The beam duty cycle for PSB injection is only 0.08%.

A chopping section allows low energy removal of a fraction of the linac bunches, thus avoiding beam loss during longitudinal capture in the PSB. With the selected parameters, the pulse current before chopping has to be as high as 64 mA. Taking reasonable margins for beam loss in the low-energy transfer line between ion source and RFQ and in the chopping line, the RFQ output current is nominally set at 70 mA and the source current, at 80 mA. The target value for the transverse emittance out of the source has been set to 0.2 π mm mrad, a value compatible with present source technology that will allow for about a factor 2 reduction in the emittance at PSB entrance with respect to the present Linac2. The overall Linac4 beam parameters are summarised in Table 1.

The operating frequency of Linac4 is dictated by the availability at CERN of 352.2 MHz klystrons, circulators and waveguides from the LEP RF system and by the use of the RFQ from the IPHI project from CEA and IN2P3 [11], which is intended to be sent to CERN for use in Linac4 after the beam tests at Saclay. It is foreseen to double the RF frequency to 704.4 MHz in the last section of Linac4, thus increasing efficiency and gradient.

Table 1: Linac4 Beam Parameters

Ion species	H^-	
Output Energy	160	MeV
Bunch Frequency	352.2	MHz
Max. Rep. Rate	2	Hz
Beam Pulse Length	400	μs
Max. Beam Duty Cycle	0.08	%
Chopper Beam-on Factor	62	%
Chopping scheme: 222 transmitted /133 empty buckets		
Source current	80	mA
RFQ output current	70	mA
Linac current	40	mA
N. particles per pulse	1.0	$\times 10^{14}$
Source transverse emittance	0.2	π mm mrad
Linac transverse emittance	0.4	π mm mrad

The overall architecture of Linac4 is shown in Fig. 4. The chosen sequence of accelerating sections is standard for modern pulsed linac designs. The ion source is followed by a Radio Frequency Quadrupole (RFQ), a chopping line and the accelerating structures. Three types of structures bring the energy up to 160 MeV: Drift Tube Linac (DTL) up to 40 MeV, Cell-Coupled Drift Tube Linac (CCDTL) up to 90 MeV and finally a Side Coupled Linac (SCL) to the final energy. A transfer line equipped with debunching and collimation sections connects Linac4 to the existing Linac2 transfer line.

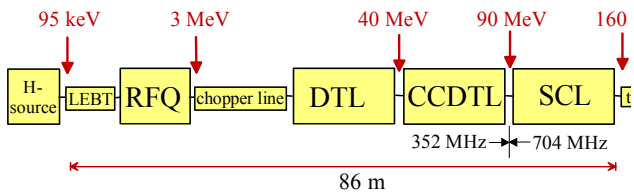

Figure 4: Scheme of Linac4.

Although the RF duty cycle of Linac4 will be only 0.1%, all the accelerating structures have been designed for a maximum duty cycle of 10%, to enable future operation of Linac4 as first part of the high-energy high-intensity SPL. As a way to minimise initial installation costs, all the hardware (accelerating structures, magnets, diagnostics, RF high-power components, etc.) of the linac will be built for future high-duty operation, whereas the electronics (power supplies, etc.) and the infrastructure will be dimensioned only for the low duty cycle required for the PSB.

The chopper line for Linac4 is being built at CERN, to be tested in a dedicated test stand presently in preparation. It includes two meander line fast chopping devices printed on an alumina substrate and water cooled, housed inside large aperture quadrupoles. The choppers have been assembled and successfully tested for RF, vacuum and thermal properties [12]. The fast rise and fall times

(2 ns) are provided by a solid-state driver presently under testing. Figure 5 shows the layout of the 3 MeV test stand, where first beam tests are expected for the end of 2008.

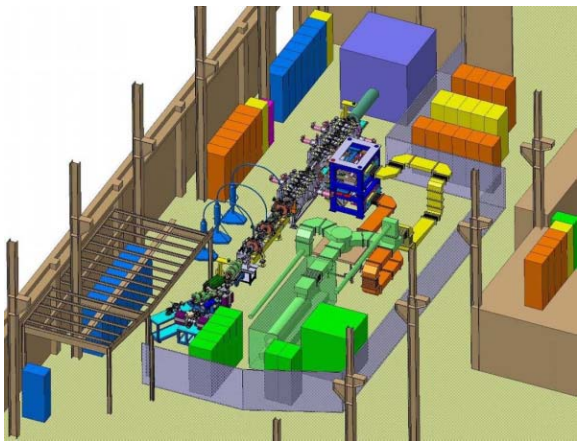

Figure 5: The 3 MeV test stand in preparation at CERN.

The Linac4 accelerating structures are based on a conservative design, required for reliability and for the future high-intensity operation of the SPL. Modern concepts for intertank coupling are used wherever possible. Accelerating gradients are relatively high, between 3 and 4 MV/m, allowing for a compact structure with peak surface fields still below 1.7 Kilpatrick. Large apertures (20 to 32 mm diameter) provide enough safety margins with respect to beam size when operating at high intensity.

The DTL is a standard Alvarez-type structure equipped with Permanent Magnet Quadrupoles (PM), while the CCDTL is a structure with external electromagnetic (EM) quadrupoles placed between short tanks. Sections of three tanks are coupled by coupling cells, thus forming a single resonator [13]. This design allows using EM quadrupoles above 40 MeV, with sufficiently high shunt impedance and simplified RF distribution. The construction cost is lower than for a DTL, whose cost is dominated by the tight tolerances required for positioning of the quadrupoles inside the drift tubes. A 3D schematic drawing of Linac4 is presented in Fig. 6.

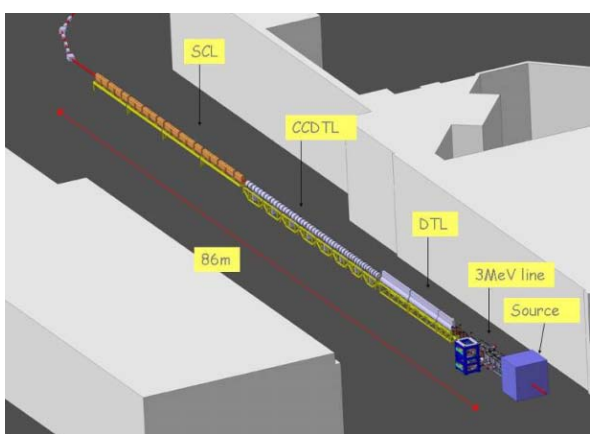

Figure 6: 3D view of Linac4.

The basic parameters of the Linac4 accelerating structures are reported in Table 2. Prototypes for the Linac4 accelerating structures are under construction at CERN (CCDTL) and in Russia (DTL, CCDTL, SCL). The R&D for Linac4 is part of a Joint Research Activity partially funded by EU.

Table 2: Parameters of Linac4 accelerating structures

	RFQ	Chopper line	DTL	CCDTL	SCL	
Energy	3.0	3.0	40	90	160	MeV
Frequency	352	352	352	352	704	MHz
Current	70	40	40	40	40	mA
RF Power	1.0	-	3.9	6.4	12.5	MW
Klystrons	1	-	5	8	4	-
No. tanks	1	-	3	24	20	-
Length	5.95	3.7	13.4	25.2	28.0	m

SPL DESIGN

The design of the Superconducting Proton Linac (SPL) started originally in 1996, with the idea to reuse the RF equipment (klystrons and superconducting cavities) from the decommissioned LEP collider. A first Conceptual Design Report (CDR) [14] was published in 2000, aimed at the specific needs of a Neutrino Factory based at CERN.

Since the first CDR, new techniques have been proposed for the production of intense neutrino beams (neutrino superbeam and beta-beams [15]), leading to a revision of the basic machine parameters. At the same time, the progress in superconducting cavity preparation techniques suggested to change the design from LEP-type 352 MHz sputtered Niobium cavities to 704 MHz bulk-Niobium cavities that allow a higher gradient. Moreover, more experience is presently available in the design and construction of long (10-15 m) cryomodules containing cavities as well as quadrupoles and diagnostics at cryogenic temperature, suggesting moving from a classic design with short cryostats spaced by warm quadrupoles to a new and more compact design with less cold to warm transitions. The new design is summarised in a second CDR published in 2006 [8]. Again, Linac4 makes the initial section of the SPL, followed by an additional normal-conducting module bringing the beam energy to 180 MeV, and then by two superconducting sections made of 5-cell 704 MHz cavities, designed for a nominal β of 0.65 and 1, respectively. The RF power is provided by 4 MW klystrons, and then split to 4 or 6 cavities. To avoid oscillations induced by Lorenz-force detuning, the cavities will be stiffened, and each arm of the RF splitting will be equipped with high-power phase shifters acting as fast phase and amplitude modulators [16]. Thanks to the higher gradients and longer cryomodules, the second version of the SPL is 340 m shorter than the initial one (430 m instead of 770 m length), even though it accelerates up to 3.5 GeV instead of 2.2 GeV. A schematic layout of the SPL (CDR2) is shown in Fig. 7.

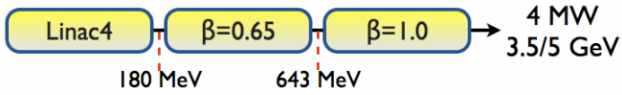

Figure 7: Schematic layout of the SPL.

Table 3 compares the SPL beam parameters for three cases, CDR1, CDR2 and a CDR2 design extended to 5 GeV. The parameters of the two superconducting sections of SPL are reported in Table 4.

Table 3: SPL Beam parameters for three configurations.

Design		CDR1 (2000)	CDR2 (2006)	CDR2+
Energy	GeV	2.2	3.5	5
Beam power	MW	4	4	4
Rep. frequency	Hz	75	50	50
Protons / pulse	10^{14}	1.5	1.4	1.0
Av. pulse current	mA	11	40	40
Chopping ratio	%	62	62	62
Pulse length	ms	2.2	0.57	0.4
Bunch frequency	MHz	352.2	352.2	352.2
Length	m	690	430	535
Peak RF power	MW	32	162	220

Table 4: SPL superconducting section parameters.

Design β	0.65	1	
Energy	180-643	643-3562	MeV
No. of cavities	42	136	
No. of klystrons	7	32	
No. of cryostats	7	17	
Gradient E_{acc}	19	25	MV/m
Length	85.8	256.1	m

It must be noticed that the CDR2 SPL design is specifically aimed at two high-intensity users, Radioactive Ion Beam physics and neutrino physics, which require a maximum beam power of 4 MW. However, a first implementation of the SPL for the needs of the LHC would be made at the reduced duty cycle required by the new injectors. The potential would be there for high-power operation, but it would be used only at a later stage, according to the programmes of the different communities. In case no future high-intensity application is considered, a Rapid-Cycling Synchrotron replacing the PS Booster could be a valid alternative to the SPL, although a cost analysis has to be made in detail to validate the economics of this solution.

ACKNOWLEDGEMENTS

This work has profited of the collaboration of many groups and services at CERN and of a large number of international partners. To all of them goes our gratitude. We acknowledge the support of the European Community-Research Infrastructure Activity under the FP6 "Structuring the European Research Area" Program (CARE, Contract No. RII3-CT-2003-506395).

REFERENCES

[1] LHC Design Report, Volume III, "The LHC Injector Chain", CERN-2004-003, http://cdsweb.cern.ch/record /823808.

[2] F. Ruggiero, W. Scandale, F. Zimmermann (eds.), "2nd CARE-HHH-ADP Workshop on Scenarios for the LHC Luminosity Upgrade - LHC-LUMI-05", Arcidosso, Italy, CERN-2006-008, http://cdsweb.cern.ch/record/886375.

[3] A. Baldini et al., "Beams for European Neutrino Experiments", CERN-2006-005, http://cdsweb.cern.ch/record/955252.

[4] EURISOL Design Study, http://eurisol.org.

[5] M. Benedikt, R. Garoby, F. Ruggiero, R. Ostojic, W. Scandale, E. Shaposhnikova, J. Wenninger, "Preliminary Accelerator Plans for Maximizing the Integrated LHC Luminosity", CERN-AB-2006-018-PAF.

[6] M. Benedikt, R. Garoby, F. Ruggiero, R. Ostojic, W. Scandale, E. Shaposhnikova, J. Wenninger, "Potential for Neutrino and Radioactive Beam Physics of the Foreseen upgrades of the CERN Accelerators", CERN-AB-2006-019-PAF.

[7] F. Gerigk, M. Vretenar (eds.), "Linac4 Technical Design Report", CERN-AB-2006-084 ABP/RF.

[8] F. Gerigk (ed.), "Conceptual Design of the SPL II", CERN-2006-006, http://cdsweb.cern.ch/record/975366.

[9] "The European Strategy for Particle Physics", http://council-strategygroup.web.cern.ch/council-strategygroup/Strategy_Brochure.pdf .

[10] M. Benedikt, R. Garoby (eds.), "Report of the High Intensity Protons Working Group", CERN-AB-2004-022 OP/RF.

[11] P.Y. Beauvais, "Recent Evolutions in the Design of the French High Intensity Proton Injector (IPHI)", EPAC'04, Lucerne, July 2004, http://www.jacow.org.

[12] F. Caspers, Y. Cuvet, J. Genest, M. Haase, M. Paoluzzi, A. Teixeira, "The CERN SPL Chopper concept and final layout", EPAC'04, Lucerne, July 2004, http://www.jacow.org.

[13] M. Vretenar, Y. Cuvet, F. Gerigk, M. Pasini, "High Power RF testing of a Cell-Coupled Drift Tube Linac Prototype for Linac4", this conference.

[14] M. Vretenar (ed.), "Conceptual Design of the SPL", CERN 2000-012, http://cdsweb.cern.ch/record/489425.

[15] P. Zucchelli, A novel concept for a neutrino factory: the beta-beam, Phys. Let. B, 532 (2002) 166-172.

[16] D. Valuch, H. Frischholz, J. Tückmantel, "First Results with a Fast Phase and Amplitude Modulator for High Power RF Application", EPAC04, Lucerne, July 2004, http://www.jacow.org.

.

CONSTRUCTION AND COMMISSIONING OF THE HIRFL-CSR*

J.W. Xia#, W.L. Zhan, Y.J. Yuan, Y. Liu, X.D. Yang, Y. He, J. C. Yang and CSR group
Institute of Modern Physics (IMP), Chinese Academy of Sciences (CAS)
P.O. Box 31, Lanzhou, 730000, P.R. China

Abstract

CSR is a new ion cooler-storage-ring system in China IMP, it consists of a main ring (CSRm) and an experimental ring (CSRe). The two existing cyclotrons SFC (K=69) and SSC (K=450) of the Heavy Ion Research Facility in Lanzhou (HIRFL) will be used as its injector system. The heavy ion beams from HIRFL will be first injected into CSRm, accompanying with the accumulation, e-cooling and acceleration, finally extracted to CSRe for many internal-target experiments. In 2005 the main construction of the CSR project was finished, and from that the preliminary commissioning of CSRm was started, including the first turn commissioning as a beam line, the stripping injection, and the zero-bumping orbit test, fixed-bumping orbit test with four in-dipole coils, bumping orbit test, C-beam accumulation and the investigation of the closed orbit with BPM. And now the correction of closed orbit, e-cooling and ramping test are just on going.

INTRODUCTION

From 1996 to 1998, a new ion accelerator plan was proposed [1] to upgrade the HIRFL with a multi-functional Cooling Storage Ring (CSR) forming an HIRFL-CSR accelerator system shown in Fig. 1. This will greatly enhance the performances of IMP for those researches by using Radioactive Ion Beams (RIB) and high-Z heavy ion beams in the fields of nuclear physics and atomic physics. In July of 1998 the Chinese center government approved this proposal, and at December 10 of 1999 the CSR project was started. The period from the beginning of 2000 to the summer of 2001 was the stage of the building construction, design optimization and prototype experiments. The machine fabrication was from 2001 to 2003, and the past two years of 2004 and 2005 were used for the machine installation and subsystem tests. The period from 2006 to 2007 will be the initial commissioning stage.

PROJECT DESCRIPTIONS

Outline

CSR is a double cooling-storage-ring system with a main ring (CSRm), an experimental ring (CSRe), and a radioactive beam line (RIBLL2) to connect the two rings, shown in Fig.1. The heavy ion beams with the energy range of 7~25 MeV/u from the cyclotron SFC or the cyclotron complex SFC+SSC will be accumulated, cooled and accelerated to the high-energy range of 100~500 MeV/u in the main ring CSRm, and then extracted fast to produce radioactive ion beams (RIBs) or highly charged heavy ions (high-Z beams). Those secondary beams will be accepted and stored or decelerated by the experimental ring CSRe for many internal-target experiments or high precision spectroscopy with beam cooling. On the other hand, the beams with the energy range of 100~1000MeV/u will also be extracted from CSRm by using slow extraction or fast extraction for many external-target experiments, and for the future development, the possibility of internal-target mode in CSRm was reserved for those high-energy proton experiments with the energy range of 2~2.8GeV.

Two electron coolers located in the long straight sections of CSRm and CSRe, respectively, will be used for beam accumulation and cooling.

The beam parameters and the major machine parameters of CSR are listed in table 1.

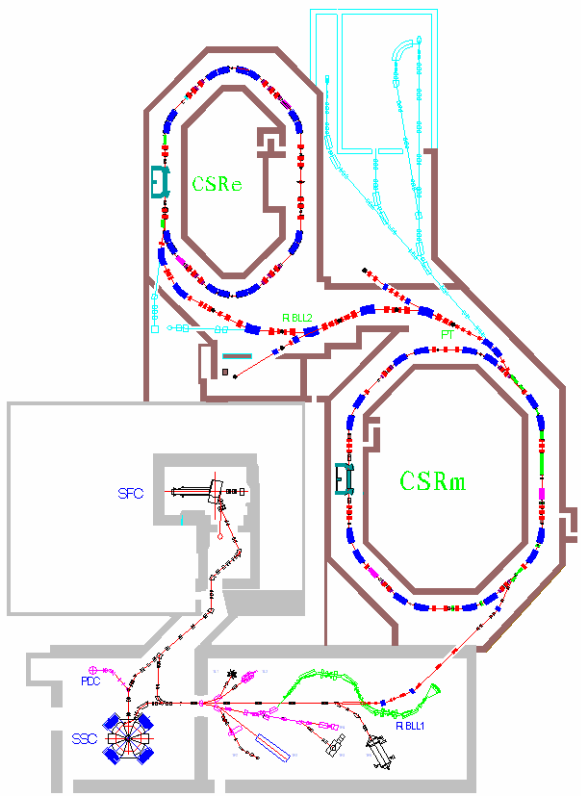

Figure 1: Overall layout of HIRFL-CSR.

Normal Operation Mode

CSR is a double ring system. The accumulation duration of CSRm is about 10s. Considering the ramping rate of magnetic field in the dipole magnets to be

*Work supported by the center government of China and NSFC
#xiajw@impcas.ac.cn

Table 1 Major parameters of the CSR

	CSRm	CSRe
Outline		
Circumference (m)	161.00	128.80
$B\rho_{max}$ (Tm)	12.05	9.40
B_{max} (T)	1.6	1.6
Ramping rate (T/s)	0.1--0.4	0.1--0.4
Beams		
Ion species	Stable nuclei: p -- U, RIBs: A<238	Stable nuclei: p -- U, RIBs :A<238
Max. energy (MeV/u)	2800(p), 1100 (C^{6+}), 500 (U^{72+})	2000(p), 750 (C^{6+}), 500 (U^{90+})
Intensity (Particles)	10^6---10^9 (stable nuclei)	10^{3--9} (stable nuclei, RIBs)
Lattice	Fast extraction mode	Normal mode
Transition gamma	γ_{tr} = 5.418	γ_{tr} = 2.629
Tune values	Q_x / Q_y = 3.64 / 2.61	Q_x / Q_y = 2.53 / 2.57
Max. β (m)	β_x/β_y =15.3/30.5	β_x/β_y =30.9/22.3
Dispersion (m)	$D_{max(x)}$=5.4 (β_x=9.9)	$D_{max(x)}$=7.8 (β_x=16.0)
Acceptance		
A_h (π mm-mrad)	200 (ΔP/P = ±0.15 %)	150 (ΔP/P = ±0.5%)
A_v (π mm-mrad)	40	75
ΔP/P (%)	1.4 (ε_h= 50 π mm-mrad)	2.6 (ε_h= 10 π mm-mrad)
Subsystem		
E-cooler		
Ion energy (MeV/u)	7---50	10---500
Length (m)	4.0	4.0
RF system	Acceleration Accumulation	Capture
Harmonic number	1, 2 16, 32, 64	1, 2
f_{min}/f_{max} (MHz)	0.24 / 1.81 6.0 / 14.0	0.4 / 2.0
Voltages (n × kV)	1 × 7.0 1 × 20.0	2 × 10.0
Vacuum pressure (mbar)	3.0×10^{-11}	3.0×10^{-11}

0.1~0.4T/s, the acceleration time of CSRm will be nearly 3s. Thus, the operation cycle is about 17s. The experimental ring (CSRe) can obtain the beams once for every operation cycle.

In CSRe, two operation modes will be adopted. One is the storage mode used for internal-target experiments or high precision spectroscopy with electron cooling. Another one is the deceleration-storage mode used for atomic-physics experiments. Fig. 2 shows the magnetic field exciting procedure of the two rings.

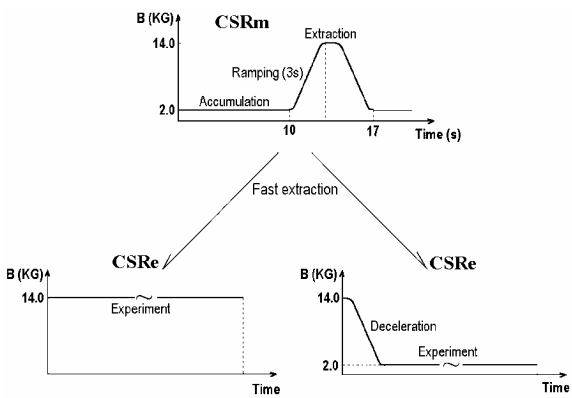

Figure 2: Magnetic field exciting procedure of CSR.

Beam Accumulation

Three modes will be used in CSRm to accumulate ions up to $10^{6\sim9}$ in a short duration of 10s. The first is the Stripping Injection (STI) for those light heavy ions (A<20) from SFC. The second is the Multiple Multi-turn Injection (MMI) in the horizontal phase space with the acceptance of 150π mm mrad for those very heavy ions (A>40) from SFC. The third one is the combination of the horizontal MMI and the RF Stacking (RFS) [3] in the momentum phase space for those heavy ions (20≤A≤40) from SFC+SSC. In the third one the horizontal acceptance is 50π mm mrad used for the multi-turn injection and the momentum acceptance is 1.25% for the RF stacking. During the accumulation, electron cooling will be used for the cooling of beam in order to increase the accumulation ratio and efficiency.

Magnets and Correlative Sub-systems

All magnet cores of CSR will be laminated of 0.5mm-thick sheets of electro-technical steel with high induction and cold-rolled isotropy. Coils will be made of T2 copper conductor with hollow and insulated with polyimide stick tape and vacuum epoxy resin impregnating. In order to reach the necessary field uniformity at the

different levels of the range of 1000Gs ~ 16000Gs, a so-called modified H-type dipole was designed for CSRm. In CSRe the C-type dipole with large useful aperture will be adopt for physics experiments.

All power supplies of the ring magnets need DC and pulse operation modes, and high current stability, low current ripple and good dynamic characteristic were required. Two types of supply, traditional multi-phase thyristor rectifier for dipoles and switching mode converter for quadruples, were adopted. Table 4 is the major parameters of magnets and its correlative power supplies and vacuum chambers.

Table 2 Major correlative parameters of the magnets

	CSRm	CSRe
Dipole		
Number×angle (deg.)	16×22.5	16×22.5
Bending radius (m)	7.6	6.0
Field range (T)	0.1--1.4	0.1--1.4
Ramping rate (T/s)	0.1--0.4	0.1--0.4
Air gap (mm)	80	84
Useful aperture (mm^2)	140×60	220×70
Homogeneity (ΔB/B)	$\pm1.5\times10^{-4}$	$\pm1.5\times10^{-4}$
Vacuum Chamber		
Inner aperture (mm^2)	156×61	236×70
Cross section	Rectangular	Rectangular
Supply of dipole		
Number	1	1
Feeding mode	Series	Series
Stability (at low cur.)	$\pm1\times10^{-4}$/8h	$\pm1\times10^{-4}$/8h
Ripple (at low cur.)	5×10^{-5}	5×10^{-5}
Tracking precision	$\pm3\times10^{-4}$	$\pm3\times10^{-4}$
Quadruple		
Number	30	22
Gradient range (T/m)	0.3—10.0	0.3—6.5
Bore diameter (mm)	170	240
Useful aperture (mm^2)	160×100	280×140
ΔK/K	$\pm1.5\times10^{-3}$	$\pm1.5\times10^{-3}$
Ideal length (m)	0.5, 0.65	0.65, 0.75
Vacuum. Chamber		
Aperture (mm^2)	180×110	285×150
Cross section	Octagonal	Octagonal
Supply of quadruple		
Number	30	22
Feeding mode	Independent	Independent
Stability (at low cur.)	$\pm1\times10^{-4}$/8h	$\pm1\times10^{-4}$/8h
Ripple (at low cur.)	5×10^{-5}	5×10^{-5}
Tracking precision	$\pm5\times10^{-4}$	$\pm5\times10^{-4}$

INITIAL COMMISSIONING OF CSRM

Subsystem Tests

The construction and installation of the two storage rings were finished in the end of 2004. Since that time many offline tests have been done. For example, e-cooler, RF station, power supply, Ultra-high vacuum, magnetic field measurement and ring alignment, etc. For the e-cooler, the hollow electron beam can be obtained to partially solve the problems due to space charge effect and reduce the effect of recombination between the ions and the e-beam. In CSRm the vacuum pressure already reached to 5×10^{-12} mbar.

First Beam Storage in CSRm

In the beginning of 2006, the main ring CSRm was under the preliminary commissioning. At January 18 of 2006, the single-turn stripping injection beam of C^{6+}-6.89MeV/u was stored successfully in CSRm with bumping orbit. Fig. 3 is the stored beam signal from a BPM. In this case the RF system of CSRm wasn't used, thus the bunched beam from the cyclotron SFC would be become as a costing beam gradually after the single-turn injection, and the beam signal from BPM also became weak turn by turn.

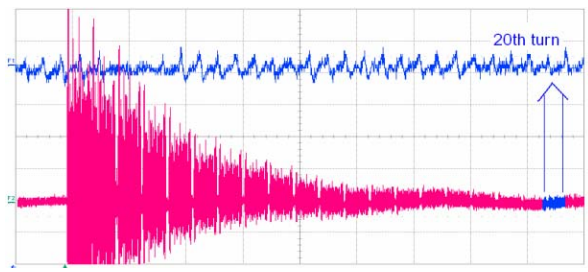

Figure 3: The stored beam signal from BPM.

From the result of the Fig.3, we can see that the beam signal of the 20th turn had already become very weak.

Based on the single-turn beam storage, at January 23 of 2006, the multi-turn stripping injection beam of C^{6+}-6.89MeV/u was stored successfully in CSRm with bumping orbit. Fig. 4 is the stored beam signal from the spectrum analyser connected with a BPM in the zero-span mode.

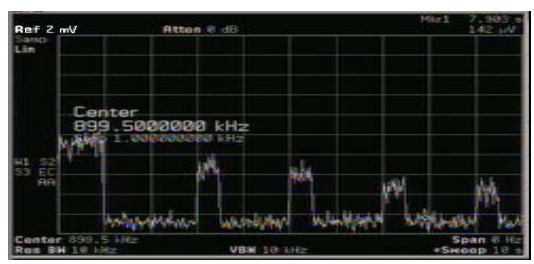

Figure 4: The stored beam signal from the spectrum analyser with 5 times of RF modulating.

In order to observe the stored beam signal from BPM in a long time, the stored costing beam should be re-bunched by the RF system of CSRm with the harmonic number of 4 and the RF voltage of 1.3KV. By the RF modulating, the stored beam signal can be obtained from the spectrum analyser connected with a BPM in the zero-span mode. As the showing in Fig. 4, after the multi-turn stripping injection, the stored beam was modulated by RF five times in 10 seconds. The first modulating period was 1 second, and after that every period was 0.5

seconds. According to Fig. 4, the 1/e life time of stored beam was about 10 seconds.

Preliminary Beam Accumulation of CSRm

In the spring of 2006, the new controller DSP developed by ourselves was used in the power supply control system of dipole, quadruple, bump and RF system. By using this new DSP, the synchronous times between the dynamic bumping orbit which used to cross the stripper, the period of injection beam and the RF system can be controlled accurately. Fig. 5 is the synchronous signal between RF, bumping orbit and injection beam.

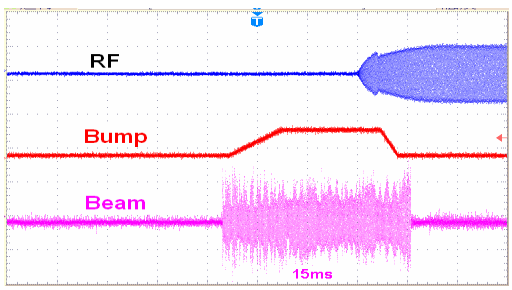

Figure 5: The synchronous signal between RF, bumping orbit and injection beam.

At April 20 of 2006, just after the bumping injection with the accumulation period of 15ms, the RF system switched on to capture the stored beam. In this case, the accumulated beam of C^{6+}-7.185MeV/u with a high intensity can be observed on the spectrum analyser. Fig. 6 is the stored beam signal from the spectrum analyser in the 5 seconds of RF modulation.

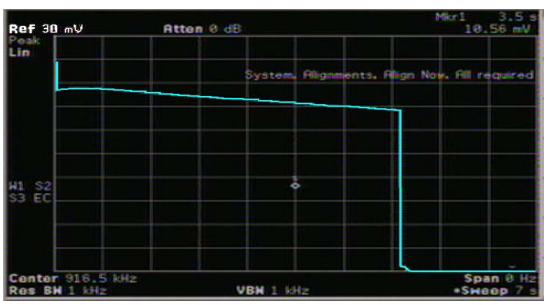

Figure 6: The stored beam signal from the spectrum analyser just after the bumping injection.

As the results shown in Fig. 6, the 1/e beam life-time is about 37 seconds with the RF capture in the first second, and the beam intensity is about 100eμA.

First Ramping Test of CSRm

In May of 2006, the dynamic scale for all quadruple power supplies was finished. After that a short acceleration test was done. In the test, the C^{6+} beam energy was increased from 7MeV/u to 14MeV/u. Fig.7 is the exciting currents of dipoles and quadruples, the RF voltage and frequency during the ramping test.

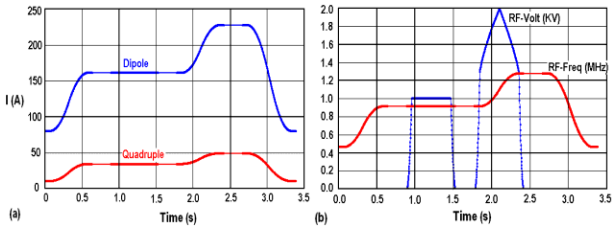

Figure 7: (a) The exciting currents of dipole and quadruple, (b) The curves of RF voltage and frequency.

The short ramping test consists of two steps, the first step is the ramping injection, and the second one is the accelerating. At June 16 of 2006, the first accelerated beam-signal was observed on the spectrum analyser with a wide-band range of 300 KHz. Fig.8 shows the beam signal of the ramping injection and acceleration from the spectrum analyser during the acceleration test.

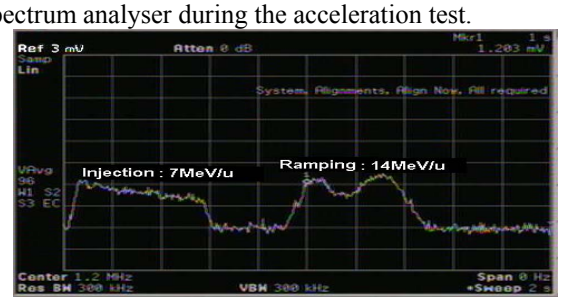

Figure 8: The beam signal of the acceleration test.

DCCT Diagnosis for the Beam Accumulation

In the summer of 2006, the new DCCT device was used to measure the beam current in CSRm. With this powerful diagnosis, the adjusting of the injection match orbit and the preliminary closed orbit correction can be done carefully. At June 29 of 2006, the accumulated beam current was first exceeded 200μA for the beam of C^{6+}-7MeV/u. Fig. 9 is the DCCT current signal for the stored beam in CSRm.

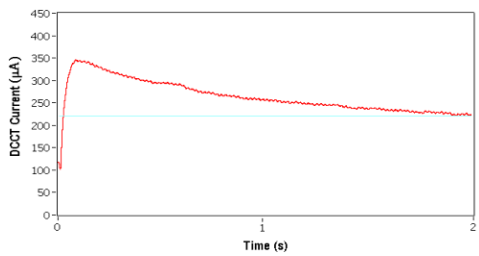

Figure 9: DCCT current of the stored beam in CSRm.

First Tune Measurement and Modification

In the autumn of 2006, the tune value of the machine can be measured first, and the initial tune (Q_x/Q_y) of CSRm is 3.44/2.75 that is far from the design value of 3.64/2.61. According to the analysis, this large tune shift was caused by the reason of the hysteresis of quadruple fields. After the modifying of the quadruple-field data, the machine tune was adjusted to the original design value, and the 1/e beam life-time in the first 3 seconds was became longer from 4s to 15s. Fig. 10 shows the stored beam with the tune value of 3.610/2.637.

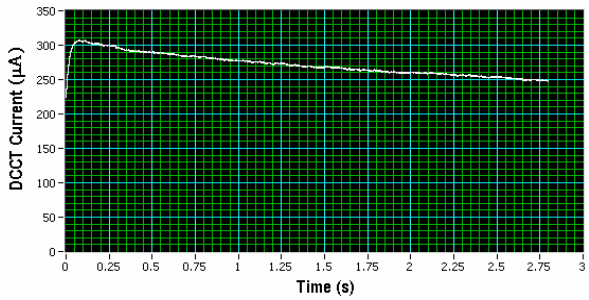

Figure 10: The stored beam with the tune of 3.610/2.637.

1GeV/u Ramping Commissioning

After the modification of tune value, the high energy acceleration experiment from 7MeV/u to 1000MeV/u for C^{6+} ions was done. Fig. 11 is the energy curve, the curves of RF voltage and frequency, and the exciting currents of dipoles and quadruples during the whole ramping period.

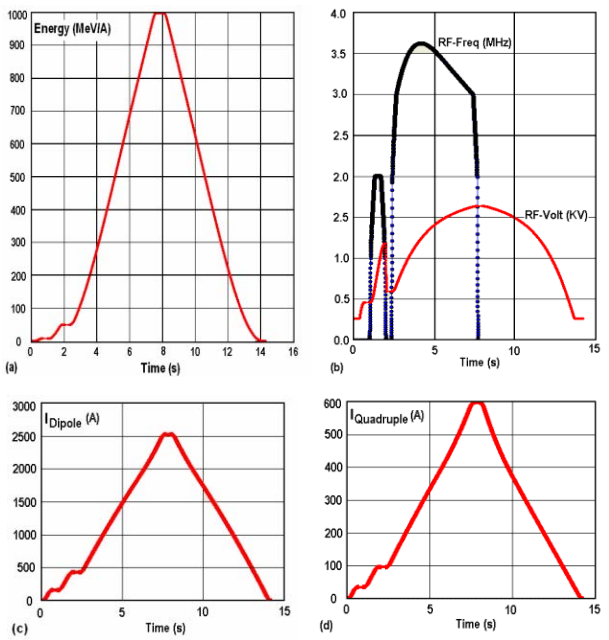

Figure 11: Curves of energy, RF and exciting currents during the ramping period from 7MeV/u to 1GeV/u.

During the 1GeV/u acceleration, the C^{6+} beam, which was injected by stripping injection from the small cyclotron SFC, will be accelerated from 7MeV/u to 1GeV/u, the magnetic rigidity of beam will be changed from 0.76T.m to 11.3T.m, the dipole field will be increased from 0.1T to 1.5T accompanying with the exciting current of power supply from 160A to 2500A, and the exciting currents of the 30 quadruples will be raised from nearly 20A to about 600A respectively.

For the 1GeV/u ramping, the RF harmonic number of frequency should be changed from 2 to 1 at the energy of 50MeV/u. Because the frequency region of the CSRm RF system is 0.25~1.7MHz, but the revolution frequency of the beam at the injection energy of 7MeV/u is only 0.227MHz, this can't reach to low limit of the frequency region. So, in the low energy section of the acceleration, the harmonic number of RF is adopted as 2, and the start frequency is 0.454MHz. After 50MeV/u the revolution frequency is more than 0.586MHz, than the harmonic number can be changed to 1 until the final energy of 1GeV/u. Fig. 12 shows the beam current during the 1GeV/u ramping.

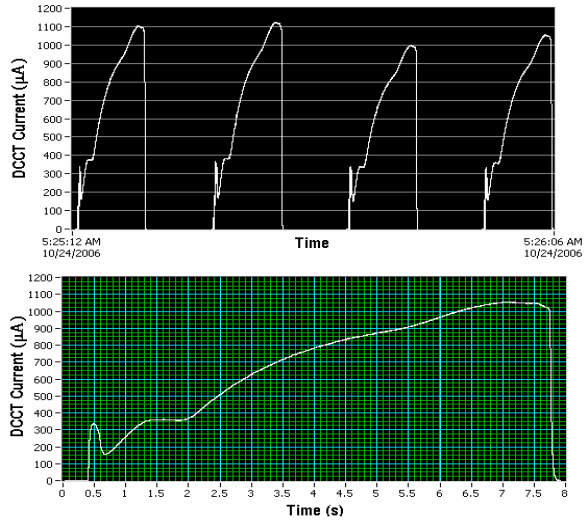

Figure 12: The beam current during the 1GeV/u ramping.

For the 1GeV/u acceleration, the whole ramping time is about 8s, including 200ms for the stripping injection, 200ms for the harmonic number changing, and 200ms for the 1GeV/u top. The whole acceleration efficiency of the beam is more than 90%, and in the final 1GeV/u top, the beam current also can be reach to 1mA, namely the particle number of the C^{6+} ions with the energy of 1GeV/u is more than 5×10^{8} in CSRm.

Commissioning Schedule of CSR

Before the summer of next year, the fast extraction, COC, e-cooling, and multiple multi-turn injection will be done in CSRm, and after that the second ring CSRe can obtain the first beam. The whole initial commissioning of CSR will be finished in the end of 2007.

REFERENCES

[1] J. W. Xia, et al., HIRFL-CSR Plan, Proc. of the 6th China-Japan Joint Symposium on Accelerators for Nuclear Science and Their App., Chengdu, China, Oct. 1996, 24pp.

[2] B. W. Wei, Results From Lanzhou K450 Heavy Ion Cyclotron, Proc. of 1989 Particle Acc. Conf., IEEE.

[3] Y J. Yuan et al., Simulation of RF Stacking and Multiple Single-Turn Injection and Multi-turn Injection, Proc. of the 14th Inter. Conf. on Cyclotrons and Their App., South Africa, 1995, 479pp.

KICKERS FOR INJECTION AND EXTRACTION IN DAMPING, COMBINER AND STORAGE RINGS

F. Marcellini, LNF-INFN, Frascati, Italy

Abstract

Injection and extraction kickers play a fundamental role in all the projects of new major accelerators at present under study. The feasibility of these accelerators depends also on the possibility to realize kickers based on unconventional design and new technologies. This paper describes the R&D carried out at LNF on two different types of deflecting devices. The first are the kickers for the Damping Ring (DR) of the International Linear Collider (ILC) and the Storage Rings (SR) of colliders like DAFNE. They require very low impedance, good field uniformity in a wide region around the beam axis and very short pulse duration for limiting the length and consequently the cost of the DR and for reducing the perturbation of the stored bunches in SRs. The tests made on stripline prototypes, fast high voltage pulsers and vacuum feedthroughs are presented. The second are the RF kickers for the CLIC Test Facility 3 (CTF3) for which an original SW structure has been designed and realized for the Delay Loop (DL) while a more conventional TW deflector allows the multiplication of bunch current and frequency in the Combiner Ring (CR). Results of their performances are described.

INTRODUCTION

An activity concerning the study, the design and the realization of devices for deflecting the trajectory of beams that must be extracted and/or injected in circular machines has been recently carried out at LNF.

The devices developed are different for typology and application and the motivations of the different choices are described in the following sections.

RF deflectors has been chosen in the two rings used for the bunch frequency multiplication in CTF3 [1][2]. In particular the RF deflector of the CR is a 10+2 cells TW structure operating in the TM_{11}, $2/3\pi$ mode [3][4], while the deflector for the DL is a system composed of a hybrid junction (HJ) coupler and two SW cavities which resonate in the TM_{110} deflecting mode [5][6]. The main differences between TW and SW RF deflectors are reported in Table I. All this characteristics are consequence of the different bandwidth between the two types of devices.

The possibility of using TW RF deflectors also for the DR of the ILC [7] has been investigated [8][9]. To get significant factors of bunch recombination in the DR, which means significant reduction of the DR circumference, groups of deflectors powered in multi-frequency mode are necessary.

However, an alternative solution looks now possible thanks to recent developments of new technologies in the field of high voltage (HV) pulse generators. The characteristics of the pulse (amplitude up to tens of kV, rise time from 100 ps to 1ns, pulse width from 5 ns to 50ns and repetition frequency up to hundreds of kHz) seem promising for the use of these fast pulsers to feed the kickers in the DR, where the bunch spacing must be strongly reduced.

Table 1: Comparison between TW and SW RF deflectors

main features	SW	TW
efficiency per unit length (deflection vs RF power)	high	low
filling time	proportional to the quality factor: generally slow.	~ to the group velocity and structure length: generally fast
deflecting field vs. n (# of cells)	scales as $\sqrt{n}$	scales as $n\left(1-e^{-\alpha n}\right)$ with α=attenuation
maximum number of cells	the maximum number of cells is limited because of mode overlapping	in principle there are no limitations to the number of cells.
temperature sensitivity	automatic tuning system or precise temperature stabilization	less temperature sensitivity.

People from several different laboratories are working on the design of stripline electrode kickers or on development of fast HV pulsers [10].

At LNF we have studied this solution for the upgrade of the DAFNE injection system. A special stripline kicker has been designed and its realization is in progress[11]. This activity is also a valid R&D of the injection and extraction kicker for the ILC Damping Ring.

THE CTF3 DELAY LOOP DEFLECTOR

The RF deflector allows the bunch frequency doubling process that takes place in the DL. Referring to the scheme illustrated in Fig. 1, the beam coming from linac is composed of an alternate sequence of so called even and odd trains, which differ for a 180° phase jump between each other. This sequence of 140ns long sub-trains is realized by a pre-bunching system. The RF deflector gives kicks of the same amplitude but opposite

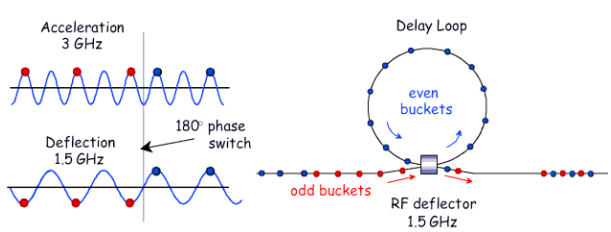

Figure 1: The bunch frequency multiplication scheme in the CTF3 Delay Loop.

sign to the incoming even and odd trains. Only the even trains are injected into the ring and, after a turn, they are extracted and interleave with the following odd train.

The RF deflector system deflects of ±15mrad beams with energy up to 300MeV. The total train length is 1.4μs and the deflection given to the bunches is uniform within 1%. Peak power and duration of the RF pulses feeding the RF deflector are 20MW and 5μs respectively.

The deflector has been conceived as two cavities fed by the same klystron through a 90° hybrid junction (see Fig 2).

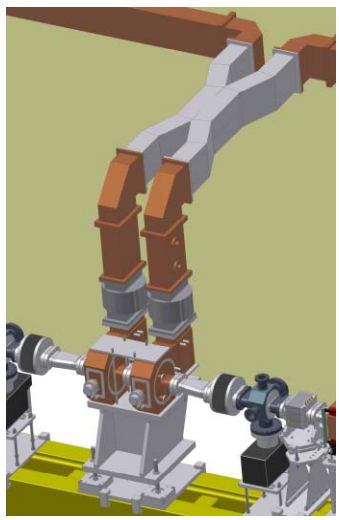

Figure 2: CAD drawing of the Delay Loop region with the RF deflector system.

Being the cavities $(1+1/4)\lambda_{RF}$ apart along the beam trajectory, where λ_{RF} is the free space wavelength at the RF frequency (1.499275GHz), the beam takes the same deflection in the two gaps. The Q is determined by proper dimensioning of the input coupler and the chosen value results from a compromise between the needs to have enough shunt impedance and sufficiently fast rise time as response to the RF pulse. Fig.3 shows the time domain signal monitored from one cavity when the 5 μs RF pulse is applied. The drop of the deflecting voltage in the last 1.4μs of the pulse, i.e. the spread of the kick amplitude along the train length is limited at less than 1%.

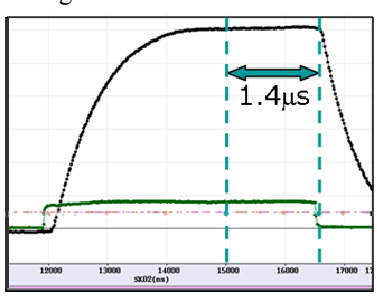

Figure 3: Cavity voltage vs. time with 5ns input pulse.

As it is shown in Fig. 4, the cavities reflect back the incident power both during the transients (the resonance has finite bandwidth) and the flat-top of the pulse (the input coupling coefficient is $\beta \neq 1$). However the HJ isolates the klystron from this reflected power, while it is dissipated in the load.

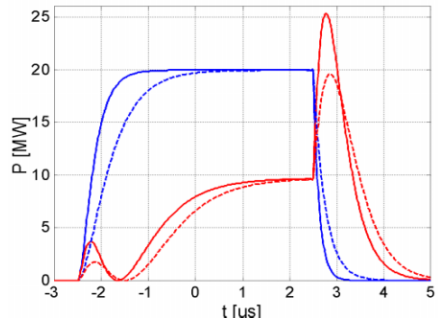

Figure 4: Time domain cavity response to a step input (Blue – RF input pulse. Red – cavity reflected power).

The klystron could be protected by a ferrite circulator as well, but the solution adopted presents two main advantages: the shunt impedance of the deflector is doubled by the use of two cavities and an expensive component like the circulator is avoided.

The deflector has been successfully used during the DL commissioning [12]. The train recombination was soon obtained and then improved in a few weeks of operation. Fig. 5 illustrates the results of recombination procedure. The beam current, equally distributed along the ten incoming sub-trains, results almost doubled where the trains are recombined and near to zero elsewhere.

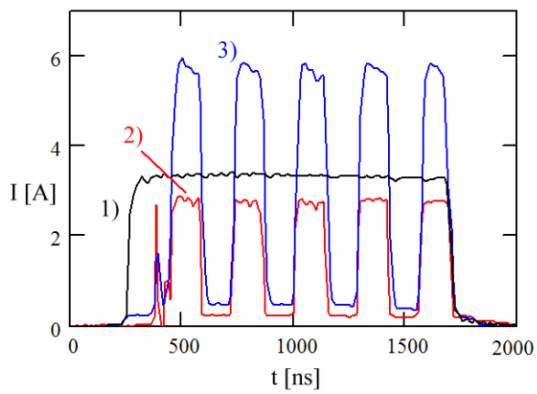

Figure 5: Beam current in the transfer line before the DL (black), in the DL (red) and after recombination (blue).

The deflector has been used also as a diagnostic device to measure the bunch length [13]: if the RF phase is 90 degrees shifted respect to normal condition of operation, the bunches cross the cavities when the field amplitude is zero and time derivative is maximum. The particles receive different transverse kicks, depending on their longitudinal position in the bunch. The streak camera measurement of the beam profile downstream the RF deflector gives direct information of the bunch longitudinal length before the kick.

THE COMBINER RING DEFLECTOR

In the DL take place the first stage compression by a factor of two of the bunch train. The CR is used in the second stage to further compress the pulse by a factor of five according to the scheme described in Fig 6. The bunches coming from the linac are on the crest of the deflector RF wave and take the kick to be injected in the

CR. The ring circumference differs for 1/5 respect to a multiple integer of the RF wavelength, so that in the following turns the already injected bunches pass in the RF deflector out of the phase of maximum field and their trajectory remains below the septa magnet. A second deflector has the function to compensate the residual kicks that the first one gives to the stored bunches.

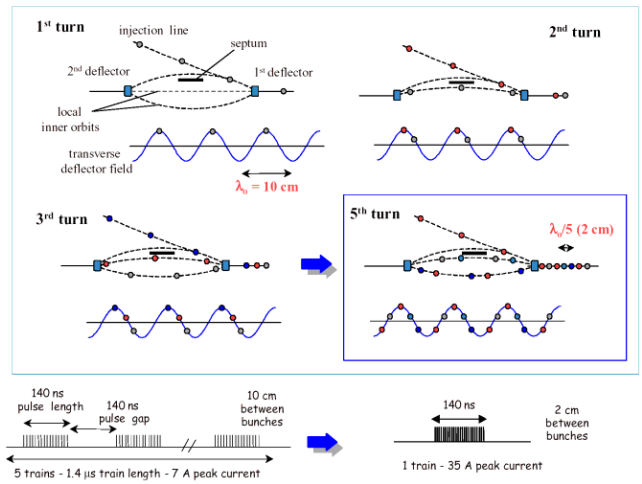

Figure 6: Bunch frequency multiplication in the CR.

The two RF deflectors working at 2.99855 GHz has been only just installed in the CR but they are already successfully tested in the CTF3 Preliminary Phase, a low current test of the bunch train combination in the EPA ring of the former LEP Pre-Injector (LPI) complex at CERN. The deflector parameters are reported in Table II.

Table 2: Combiner Ring RF Deflector Parameters

Frequency (f)	2.99855 [GHz]
Cell length (D)	33.33 [mm]
Cell radius (b)	56.01 [mm]
Iris internal radius (a)	21.43 [mm]
Iris thickness (t)	9.53 [mm]
Number of active cells (N_c)	10
Phase advance per cell (βD)	$2\pi/3$
Deflector length (L)	33 [cm]
Group velocity (v_g/c)	-0.0237
Filling time (τ_F)	47 [ns]
Shunt impedance per unit length (r_s)	18.1 [MΩ/m]
r_s/Q	1425 Ω/m
Input power (P_{in})	2 MW
Deflection (ϕ_D)	5 [mrad]

The design of the deflector has been done scaling to the CTF3 working frequency the dimensions of CERN RF separators (the so-called *Langeler structures*). These are disk-loaded backward waveguides working in the $2\pi/3$ EH_{11} hybrid mode already optimized for beam deflection [14][15]. The final 10 cells structure is shown in Fig. 7.

With 2D simulations the dimensions of each cell have been optimized. The $2\pi/3$ EH_{11} mode dipole degeneration of the two orthogonal polarities, has been removed by inserting 2 longitudinal rods crossing off-axis the cells (just like the CERN separators).

The structure has been characterized by simulating and measuring the dispersion curves of a stack of 8 cells (+2 half cells). Finally the coupler has been designed with the 3D code HFSS [16] and the reflection coefficient (S_{11}) at the device input port has been minimized. Measured dispersion curve and S_{11} fulfil design requirements.

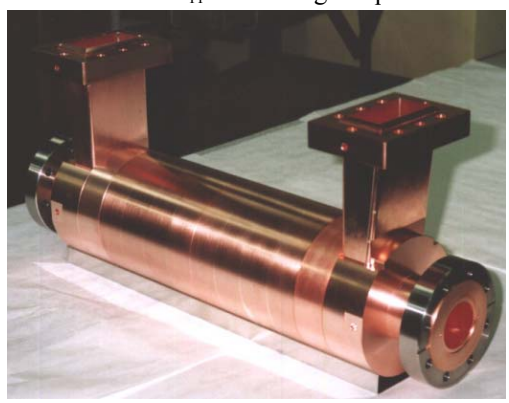

Figure 7: Picture of the CR deflector.

The deflectors have been made on OHFC high quality copper using hard soldering (brazing) technique. For simplifying the fabrication it has been decided to avoid a tuning system of the cells. The correct frequency and field phase advance has been obtained by performing different sets of measurements on prototypes and by carefully controlling the machining and soldering procedure.

The streak camera images of Fig. 8 show the results of the recombination process obtained during the CTF3 Preliminary Phase runs.

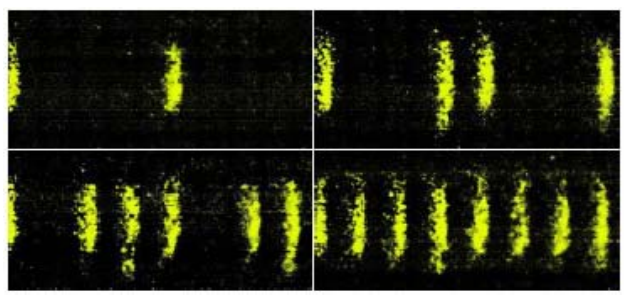

Figure 8: Bunch train combination of factor four, as observed with a streak camera. The images are taken for one to four bunch trains injected.

RF DEFLECTOR IN MULTIFREQUENCY MODE FOR THE ILC DAMPING RING

The scheme adopted for the CTF3 CR could be a good solution for the bunch injection and the extraction in the DR of ILC. The separation between the bunches in the linac should be strongly reduced in the DR unless to have a huge circumference of the ring. The original distance has to be restored between the bunches leaving the DR. Referring to Fig. 6, the injection process occurs as described for the CTF3 CR, while in the phase of extraction the two deflectors invert their roles. The second one kicks the beam for the extraction and the first corrects the orbit of the bunches not yet extracted.

As an example, to limit the CR circumference below 15km, the compression factor (F) should be at least F=20, which means to put at least 20 bunches in a period of the RF sinusoid, as represented in Fig. 9. But, for a given amplitude of the RF deflecting voltage, the difference ($\Delta\phi*$) between the deflection angle given to the injected or extracted bunch respect to the adjacent bunches becomes as smaller as F increases. If $\Delta\phi*$ is too small it is difficult to discriminate the bunches that have to pass above or below the septa magnets. An obvious solution to increase $\Delta\phi*$ consists in increasing the amplitude of the deflecting RF and this can be done with the use of a large number of deflectors in each of the two groups used for the injection or for the extraction.

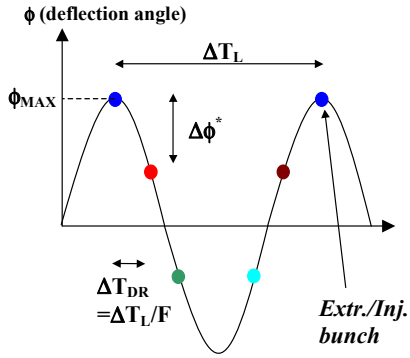

Figure 9: Bunch distribution over the RF voltage.

Alternatively, just two or three deflectors for each group are sufficient if they are powered with RF frequencies slightly different. With an optimal choice of these frequencies the ratio $\Delta\phi*/\phi_{MAX}$ can be significatively increased. Fig. 10 shows the situation for the case of 3 different frequencies and F=20.

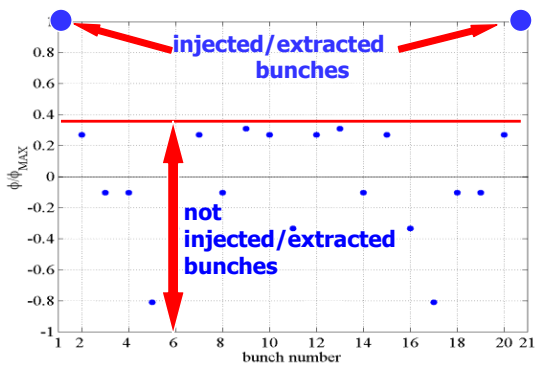

Figure 10: Deflection with 3 frequencies and F=20.

THE FAST PULSE KICKER FOR ILC DAMPING RING AND DAFNE

Recent developments of new technologies have made realistic the hypothesis of using fast HV pulse generators to feed kickers capable to give transverse momentum to the bunch injected in a ring without perturbing the orbit of the adjacent ones. With a kicker pulse duration sufficiently fast the bunch distance in the ring and therefore the ring circumference can be reasonably short. Groups from different laboratories are working on R&D programs concerning both fast pulser development and kicker design.

The injection and extraction kickers for the positron DR, which has a minimum bunch distance of 6.2 ns, should satisfy the following requirements:

- Ultra short rise and fall time (total pulse duration<12ns);
- High integrated strength;
- deflecting field uniformity within few percent over 90% of the beam stay clear;
- impedance of the structure as low as possible;
- 3MHz repetition rate.

The same fast pulse technology and similar kicker requirements are needed for the upgrade of the DAFNE injection system. Once installed in DAFNE, these new kickers will be an important test for the ILC project, since they should demonstrate, with beam measurements, the achievement of the kicker performances. These kickers could also be used to test new fast pulsers produced by different laboratories or industries. Compared to the present DAFNE injection kickers [17] the new ones have the following characterisics:

- much shorter pulse ($\approx$ 12 ns instead of $\approx$ 150 ns);
- better uniformity of the deflecting field;
- lower impedance;
- higher injection rate (max 50 Hz).

The much shorter pulse allows perturbing only the injected bunch and the two adjacent ones while, at present, a large fraction of the stored bunches (50/110 with 2.7 ns bunch spacing) are affected by the injection kick. This improvement, by reducing the perturbation of the kicker injection pulse on the stored bunches, can increase the current threshold of the transverse instability in the positron ring (as it has already been observed experimentally at DAFNE). The better uniformity of the deflecting field can increase the injection efficiency at high currents and reduce the background to experiments during injection. The broadband impedance, according to the calculations, is reduced by a factor 3 with respect to the present kickers. Moreover, since the new kickers have been designed with the same beam pipe cross section of the dipoles, no tapers are needed between the dipoles and the kicker and this also contributes to the reduction of the machine impedance. Finally, the possibility of injection at 50 Hz can be useful for future upgrades of the whole injection system.

The kicker has been designed as a conventional device with stripline electrodes. The peculiarity is in a proper shaping of the striplines, which allows to:

- reduce the broadband beam impedance of the structure;
- improve the deflecting field uniformity as a function of the transverse coordinate (horizontal in particular);
- obtain a better matching between the generator and the kicker structure at high frequency.

The kicker structure is sketched in Fig. 11. Each transverse section has constant 50Ω characteristic impedance matching the output impedance of the high

voltage pulse generator. The deflecting field configuration on the transverse plane of the structure varies according to the stripline coverage angle. Narrow striplines have stronger field intensity close to the electrode while for larger stripline the maximum intensity is in the center of the structure. Optimizing the relative length of the tapers respect to the straight section of the stripline, this property has been used to get a uniform deflection within few percent along the transverse coordinates.

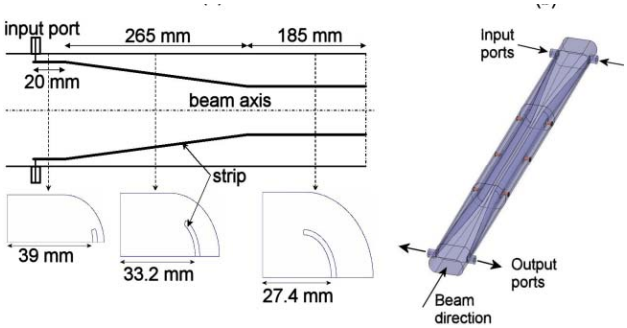

Figure 11: Sketch of the half kicker and HFSS 3D model.

The small dimensions of the stripline end sections assure well matched transition between the coaxial input/output lines and the stripline and reduce the longitudinal and transfer impedance of the structure. The longitudinal and transverse impedances have been calculated and Fig.12 shows the result obtained in the longitudinal case.

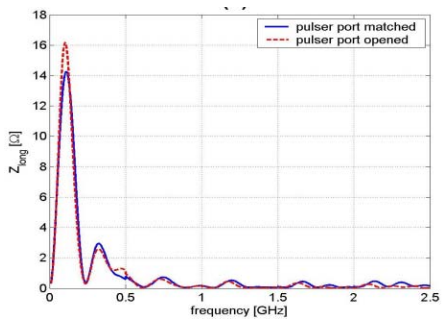

Fig. 12: Longitudinal beam impedance (HFSS simulation).

The needed deflecting voltage is obtained applying 45 kV to each electrode of the designed kicker. The German company FID GmbH [18] has developed a series of fast power generators which can produce trapezoidal voltage pulses with the characteristics needed for DAFNE (amplitude up to tens of kV, overall pulse width from 5 ns, no secondary pulses, pulse jitter limited to 20÷30ps). A 50 kV pulser has been commissioned to FID.

High voltage (HV) tests on prototypes are therefore necessary to verify if there are discharges on vacuum feedtrough, connectors or between the strip and the vacuum chamber. To this purpose a small prototype of the kicker has been constructed. The device has a uniform strip with the same section of the kicker stripline end section (the region with the higher field intensity). On the test device can be mounted different types of feedtroughs in order to perform measurements and tests on them and to pick out a suitable one. First high voltage tests have been carried out with a 24 kV 7ns pulse generator courtesy given by FID GmbH. No discharges have been registered in the stripline test structure.

CONCLUSIONS

Different typologies of devices for injecting and extracting the beam in combiner or damping rings has been studied, designed and realized in the last years at LNF. An original RF deflector system and a TW RF deflector have been constructed for the CTF3 DL and CR respectively. Both of them have been already and successfully commissioned. The possibility to use TW structures powered in a multi-frequency mode has been investigated for the ILC DR. Finally a stripline electrode fast pulse kicker has been designed for the upgrade of the DAFNE injection system and it is now under construction. The same design criteria are valid to implement a fast kicker for the ILC DR.

REFERENCES

[1] "CTF3 Design Report", CERN PS 2002-008 (RF), Geneve, (2002).
[2] J. Delahaye, et al., "CLIC, a 0.5 to 5 TeV e+/e- Compact Linear Collider",.EPAC, Stockholm 1998.
[3] D. Alesini, et al.,"RF Beam Deflectors for CTF3 Combiner Ring", EPAC'02, Paris.
[4] D. Alesini and A. Gallo, Phys. Rev. ST Accel. Beams 7, 059901 (2004)
[5] F. Marcellini, D. Alesini "Design Options for the RF Deflector of the CTF3 Delay Loop", EPAC'04, Lucerne.
[6] F. Marcellini, D. Alesini "The RF Deflector for the CTF3 Delay Loop", EPAC'06, Edinburgh.
[7] S. Guiducci, "Progress and Plans for R&D and the Conceptual Design of the ILC Injector. Systems", PAC05, Knoxville.
[8] D. Alesini, S. Guiducci, F. Marcellini, P. Raimondi, "TESLA Damping Ring: Injection/Extraction Schemes with RF Deflectors", TESLA Report 2003-26
[9] D. Alesini, F. Marcellini, P. Raimondi, "RF Deflectors for TESLA Damping Ring", TESLA Report 2003-27
[10] http://hirune.kek.jp/mk/ilc/kicker/
[11] D. Alesini, et al, DAFNE tech. note I-17, 2006.
[12] R. Corsini et al. "Commissioning Status of the CTF3 Delay Loop", EPAC'06, Edinburgh.
[13] D. Alesini, R. Corsini, D. Filippetto, A. Ghigo, F. Marcellini, B. Preger: "CTF3 Bunch Length Measurement with the 1.3 GHz RF Deflector ", CTFF3-010.
[14] Y. Garault, CERN 64-43, 1964
[15] Ph. Bernard et al., CERN 70-26
[16] http://www.ansoft.com/products/hf/hfss/
[17] S. De Simone and A. Ghigo, EPAC92, Berlin, 1992.
[18] http://www.fidtechnology.com/

PROGRESS IN UNDERSTANDING THE HIGH-GRADIENT LIMITATIONS OF ACCELERATING STRUCTURES

W. Wuensch, CERN, Geneva, Switzerland.

Abstract

CLIC main linac accelerating structures have an extremely demanding high-gradient requirement and an intensive research and development program to raise the achievable gradient is under way. The current understanding of the effects which both limit the ultimate accelerating gradient and fix the practical operating gradient is presented.

INTRODUCTION

One of the main objectives of the CLIC study is to demonstrate that an accelerating gradient of 100 MV/m or higher is feasible using realistic accelerating structures under practical operating conditions. There are two main effects which limit achievable accelerating gradient: rf breakdown and fatigue cracking due to pulsed surface heating. This report considers mainly the limit due to rf breakdown which is currently the most severe. Dark current capture may also become a limitation in a high-gradient accelerator.

There are a number of issues which define 'realistic' which are quite specific to accelerating structures for linear colliders. One issue is that the structures must produce an rf to accelerated-beam efficiency as high as possible since this is one of the key efficiencies which define the overall efficiency of a linear collider complex and the power capacity which must installed. Another issue is that the beam aperture be sufficiently large so that the beam emittance growth driven by short-range wakefields be limited to acceptable values. Yet another is that the accelerating structures must contain features which suppress long-range wakefields so that bunch-to-bunch driven instabilities do not create relative offsets which give a train emittance growth. These efficiencies and emittance growths can all be determined from the geometry of the accelerating structures through electromagnetic and beam dynamic simulations. On the other hand, the achievable gradient is strongly affected by the geometry and this dependence is only approximately known. This creates one of the principle complications in optimizing and demonstrating the feasibility of a linear collider design.

One of the most important aspects of the 'practical' operating conditions is that the breakdown probability of the individual accelerating structures must be of the order of 10^{-6} to 10^{-7}. Breakdowns in the accelerating structures induce random kicks on the beam which can lead to either emittance growth or even loss of the beam if the kick is large enough. The acceptable breakdown probability is a function of the emittance loss caused by an individual kick, the number of structures in the linear collider (in the range of tens of thousands) and the acceptable emittance loss budgeted for this effect. After conditioning to certain gradient, accelerating structures become more stable as the gradient is reduced. The breakdown probability falls exponentially with gradient but many tens of percent are typically required to make the structures sufficiently stable. The cause of the breakdown rate and its dependence on field is not well understood, but initial ideas are presented below. Other aspects of practical operating conditions include: sufficiently fast rf (surface and heat treatments during production are being studied to reduce this time to a minimum or even to eliminate it) conditioning, acceptable surface modification caused by the conditioning process and the accumulated number of breakdowns over the lifetime of the linear collider and a vacuum level inside the structure during the rf pulse which is sufficiently low. All of these conditions depend on the length of the rf pulse and a longer pulse is worse for all of them. However the rf pulse length also influences the rf to beam efficiency mentioned in the previous paragraph where for this the longer pulse is better,

This objective of this report is to elaborate on the some of the effects which have been mentioned in this introduction to give the reader an idea, and the motivation, of the areas which are being pursued by the CLIC accelerating structure development program.

THE EFFECT OF SRUCTURE GEOMETRY

Very generally it has been observed that different accelerating structure designs result in a different accelerating gradient potential, all other parameters such as material, preparation and conditioning strategy being equal – although there are statistical variations between structures. The aspects of the structure design which appear to be relevant for the high gradient performance include the transition region between the input (and output) waveguide and the periodic part of the structure, the periodic part of the structure itself and its profile and the geometry of damping features. With modern three-dimensional electromagnetic field solving programs, the complete fields patterns and functions of the fields, including electric and magnetic fields, local power flow group velocity, energy density, of the structures can be determined.

What is less clear, however, is exactly how the gradient depends on these quantities, or indeed if the gradient can even be determined from the field pattern calculated without considering the fields perturbed by the currents and plasmas that are known to form during a breakdown. In fact, it appears that a fairly accurate prediction of gradient can be determined from the unperturbed fields.

The accelerating gradient limit for traveling-wave accelerating structures has been observed to depend on

surface electric field, and lowering the peak surface electric field to accelerating gradient ratio has been used to improve the performance of structures [1]. There is clear evidence however, in data from both CLIC and NLC [2,3,4] which covers structures with a wide range of rf parameters, that a simple constant surface field limit is insufficient to predict the performances of different structures. In general the data shows that larger aperture and higher group velocity structures tolerate lower surface electric fields. They do on the other hand support much higher power flows. An attempt to explain this and to quantify the limit has led to the suggestion that traveling wave structures have a material dependent limit which is given by,

$$\frac{P\tau^{\alpha}}{C} < Const$$

where P is the power flow, τ is the pulse length, α gives the pulse length dependence (observed to be about 1/3 for copper and 2/3 for molybdenum) and C is the smallest circumference of the structure [2]. A refined physical explanation for this power limit scaling and expanded data is presented in this report. The subsequent arguments will be made for constant pulse length and the pulse length dependence will be addressed again below. The variation of the value of the constant with frequency is also considered.

The proposed limit is an extension of the ablation limit of $P\tau^{1/2}$ described in [4]. The physical reasoning for a power over *circumference* limit begins with the observation that the melted spots observed on structures after rf conditioning have a typical diameter of 100 μm independent of frequency and structure parameters, and are thus small with respect to the features of structures in the frequency range of 30 GHz and below. The power available to feed a discharge which produces such a small but fixed width spot is proportional to the power density, which is given by the total power flow through the structure divided by the circumference of structure.

During the conditioning process, the cumulative effect of breakdowns is to improve the field holding capacity of the structure surface. Above a certain threshold in discharge power however, the detrimental effect on surface geometry from a breakdown, surface roughening or even erosion and eventually 'damage', is greater than the improvement in field holding capacity. This surface roughening raises the local peak surface electric field. Conditioning saturates under these conditions and the power limit of the structure is reached. What is added by this proposed scaling is that the power available to the discharge is related to the geometry of the structure through the quantity P/C.

The pulse length dependence of the originally proposed $P\tau^{1/2}$ scaling is given by one dimensional heat diffusion during the breakdown. Observed pulse length dependencies, generally $\alpha \approx 1/3$ for copper [5] and $\alpha \approx 2/3$ [6] for molybdenum, differ somewhat. The lower value for copper may indicate that the heat diffusion is in more than one dimension or that another cooling process, such as radiation, is occurring. The higher value for molybdenum may be because of its lower thermal conductivity.

The validity of the scaling has been tested by considering data from a number of data sets for a series of very different geometry 30 GHz structures tested under comparable conditions, figure 1. The value of $P\tau^{1/3}/C$ for the three 30 GHz structures is remarkably consistent even though the values of group velocity differ by an order of magnitude, the surface electric field differs by over a factor of two and the total power flow differs by a factor of three in the opposite direction.

It is likely however that the parameter $P\tau^{1/3}/C$ is not the final word. Rather, the fundamental quantity must be a function of local electric and magnetic field which scales like $P\tau^{1/3}/C$ as the aperture is changed. If such a function is the true limit it would be frequency independent, and one would then expect that the limiting value of $P\tau^{1/3}/C$ would scale linearly with frequency. Using this assumption, 30 GHz and X-band data can be plotted together, as shown in figure 1. The data is plotted on a log-log scale, so if the quantity $fP\tau^{1/3}/C$ is the correct invariant, the data should lie on a straight line with a slope of one. The data indeed shows the validity of the constant for over an order of magnitude range in power. Deviation from the line indicates that other parameters than just circumference must be included. For example, the HDS (Hybrid Damped Structures which are assembled from quadrants and have slotted irises [7]) fall below the line and appear to have a reduced power handling capacity due to the damping features. Finding the correct function of local fields is being actively pursued.

Table 1: 30 GHz copper periodic structure data [8,9,10,11]. For structures at the conditioning limit. $2a$ refers to iris diameter.

	f [GHz]	V_g/c	E_{acc} [MeV/m]	E_{surf} [MeV/m]	P [MW]	τ [ns]	$2a$ [mm]	$\frac{P\tau^{1/3}}{C}$
Accelerating	30	0.047	116	253	34	70	3.5	13
CTF2 PETS	30	0.5			240	16	16	12
CTF3 PETS	30	0.40	30	116	100	50	9	13

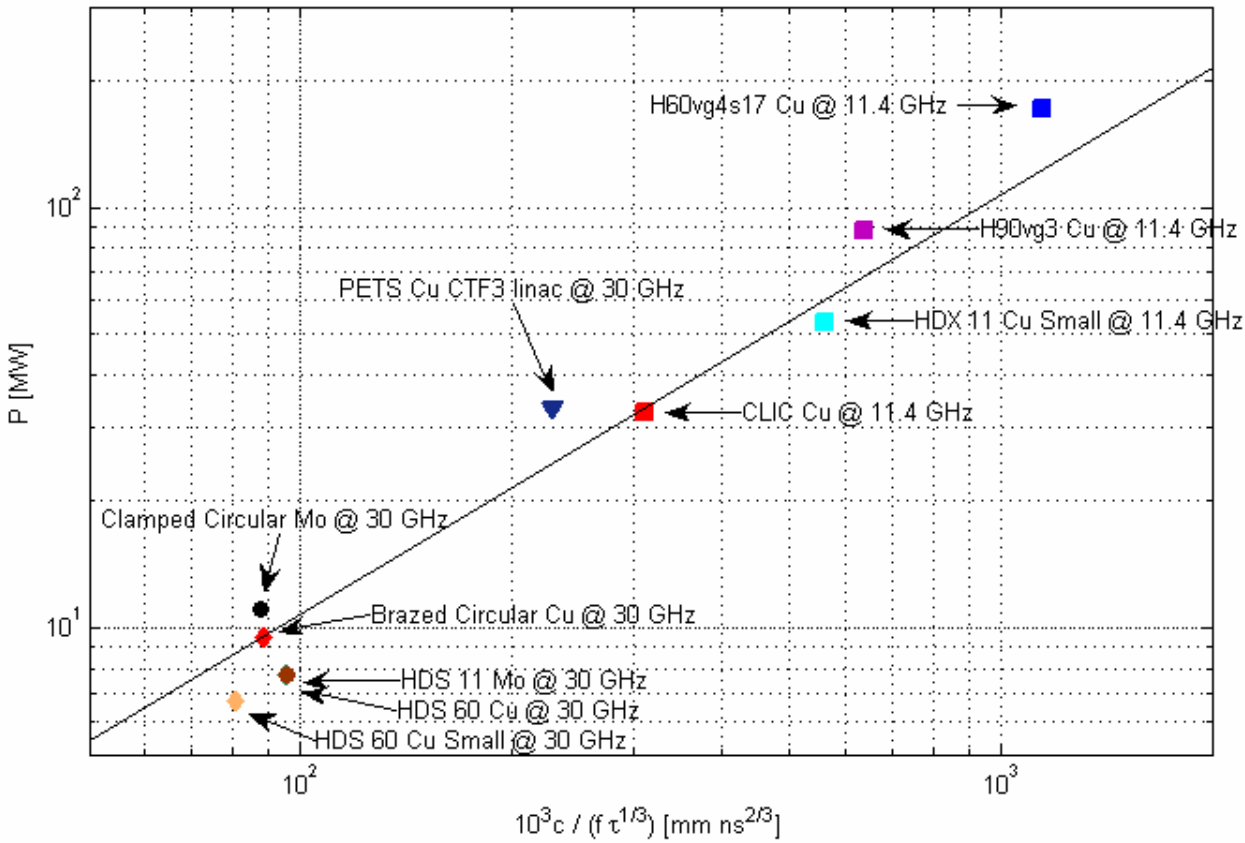

Figure 2: Data from 30 GHz and X-band structures [12]. In order to be able to compare the data from the different experiments, the power is given for a breakdown rate of 10^{-6} and a pulse length of 70 ns. The line has a slope of one.

The validity of the $P\tau^{1/3}/C$ limit applied to rectangular waveguide has been investigated using an experiment made at SLAC [13]. In the experiment two different width copper waveguides were investigated and data taken from the reference is presented in table 2. The circumference taken in the $TM_{0,1}$ structures has been replaced by twice the width of $TE_{1,1}$ mode of the rectangular waveguide, the part of the waveguide circumference with normal electric field. The relative consistency of the power over circumference limit for the waveguides is again remarkable despite the large differences between the other parameters.

Table 2: Copper waveguide data taken from [20]. *a* is the waveguide width.

	f [GHz]	V_g/c	E_{surf} [MeV/m]	P [MW]	τ [ns]	a [mm]	$\frac{P\tau^{1/3}}{2a}$
WR-90	11.424	0.82	60	56	750	22.9	11.2
Reduced width	11.424	0.18	45	32	750	13.3	10.8

MATERIAL AND BREAKDOWN PROBABILITY

Alternative materials to copper have been investigated by the CLIC study, initially in response to the observation of surface damage caused by the conditioning process. Early tests showed that refractory metals could be conditioned to significantly higher gradients than copper. These results have been duplicated in dc spark experiments. The question of material choice is significantly complicated when considerations of breakdown probability are included.

Breakdown induced transverse kicks have been measured to be about 10 KeV in X-band accelerating structures in the NLCTA [3]. A simple order of magnitude estimate for an acceptable breakdown probability for CLIC, based on the assumptions that all luminosity is lost on a pulse with a breakdown and that not more than 10% of total luminosity should be lost, gives that the breakdown probability for a structure

should be 10^{-6} since there will be approximately 10^5 accelerating structures in CLIC. This is a very low probability which has serious consequences on a practical operating gradient of a linear collider.

Breakdown probability data from tests of four structures is shown in fig. 1. The data are from an NLC structure [5] and a series of tests of identical geometry CLIC structures: a 30 GHz molybdenum iris structure [6], a 30 GHz copper structure [8] and an X-band molybdenum iris structure [14]. The data have been taken at different pulse lengths and also conditioning state in the case of the 30 GHz copper data. In all the three structures the breakdown probability at a given gradient could only be improved by conditioning the structure. No long term improvement in breakdown rate was observed during the low breakdown probability operation which lasted for about one hundred hours.

The breakdown probability of a structure appears in all cases to fall off exponentially as the gradient is reduced. The data are fit with two groups of lines on the linear/log plot in Fig. 1, one group for copper and another group for molybdenum. Each individual line is fit with a single parameter $E(10^{-1})$, the gradient giving 10^{-1} breakdown probability. The slope of each fit line, in units of decades of probability per MeV, is given by $1/0.09E(10^{-1})$ for molybdenum data and $1/0.06E(10^{-1})$ for copper data.

That the data can be fit in such a way gives insight into two major effects. One is that there appears to be a dependence of the slope on material. The other is that the breakdown probability, for a given pulse length, is determined entirely by the highest gradient at which the structure can be conditioned to, independent of frequency, structure geometry and conditioning state.

There are a number of consequences of these effects. The first is that while a material like molybdenum has a clearly higher peak gradient capability compared to copper, the lower breakdown probability slope means that at a certain probability it will be no better. Intriguingly the cross over point for copper and molybdenum appears to be at around 10^{-6}, which corresponds to the estimated requirement for CLIC. This implies that the dominant effect considered in material studies for linear colliders should be breakdown rate. On the other hand, other applications which do not require such a low breakdown probability may be able to profit from molybdenum. Another effect is that the breakdown probability is determined by the ultimate gradient, the value of which is explained by the arguments of and referred to in the previous section. The inverse proportionality of the slopes to gradient at fixed probability also implies that the pulse length dependence is constant for all breakdown probabilities – probability lines of different pulse length converge at lower gradient so as to maintain the same pulse length dependence.

Although the data provides very compelling evidence for the arguments which have been presented, the understanding emerged after the data was taken. As a consequence further tests are required to verify their validity and to address possible errors. One of the main questions is the effect clamped irises (rather than brazed) have on the molybdenum data, since both the 11 GHz and the 30 GHz were clamped iris structures. In addition the initial surface finish of the irises of both structures was quite poor. Another question is whether the breakdown probability dependence is really exponential down to low values. This will require long and stable running periods.

A possible explanation for the origin of a breakdown rate and its functional dependence is fatigue due to local cyclic tensile stress. It has been proposed that the ultimate gradient is determined when the electrostatic pull caused by the local electric field, including the Fowler-Nordhiem derived field enhancement factor β, exceeds the material tensile strength limit [15,16]. In this model rf breakdown is initiated when a the pulling force of a local electric field site exceeds the tensile strength of the material and a clump of material is broken off. A logical extension of this argument is that the breakdown probability below the ultimate gradient is given by fatigue, the accumulation of defects, under the cyclic tension. The curves of fatigue as shown for example in [17] give qualitatively the correct functional form to fit the breakdown probability data. Fatigue data of molybdenum is planned for the fatigue test to determine if the same relationship holds as for the rf breakdown probability data.

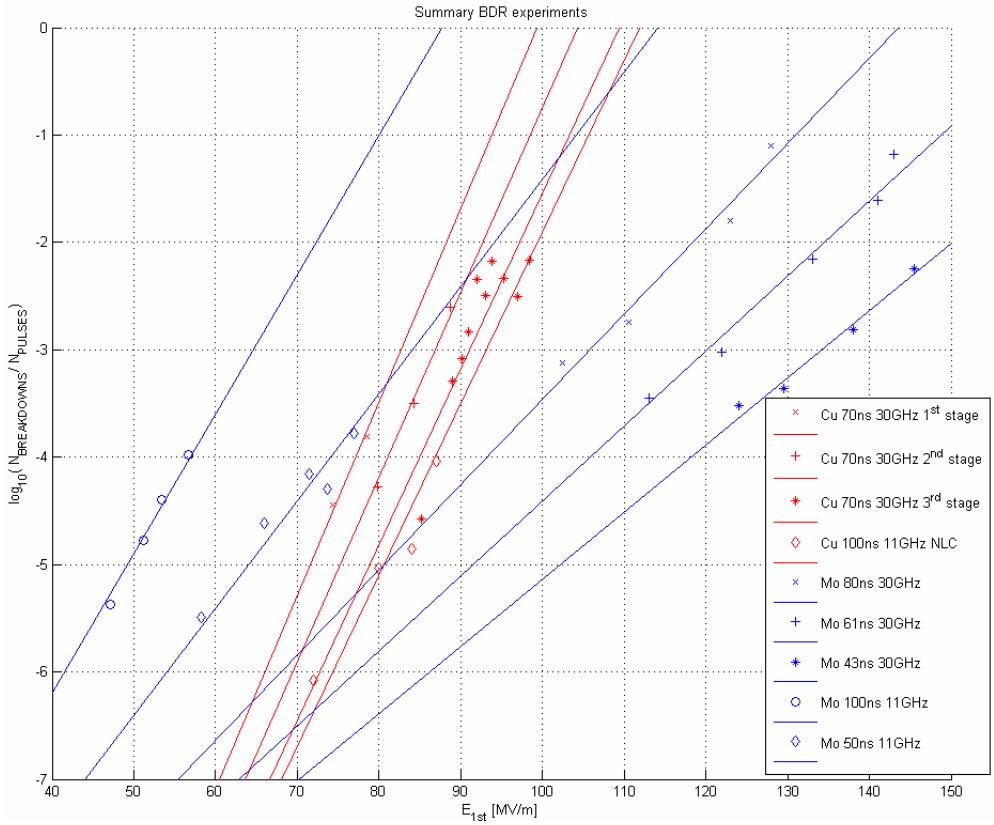

Figure 2: Breakdown rate measurements. The copper data is plotted in red and fit with $1/0.06E(10^{-1})$ and the molybdenum is plotted in blue and fit with $1/0.09E(10^{-1})$. The three 30 GHz copper data sets were taken at successive moments in the conditioning process, hence the improving breakdown probability at fixed gradient.

REFERENCES

[1] W. Wuensch, et.al. "A Demonstration of High-Gradient Acceleration", Proceedings PAC2003 and CERN-AB-2003-048-RF.

[2] W. Wuensch, "Observations About RF Breakdown From the CLIC High-Gradient Testing Program" Proceedings 12 Advanced Accelerator Concepts Workshop, Wisconsin.

[3] C. Adolphsen, "Advances in Normal Conducting Accelerator Technology From the X-Band Linear Collider Program", Proceedings PAC2005.

[4] V. Dolgashev, "Effect of Rf Magnetic Fields and Input Power on Rf Breakdown Limit", Workshop on High-Gradient RF, Argonne, October 2003.

[5] S. Döbert et. al., "High Gradient Performance of NLC/GLC X-Band Accelerating Structures", Proceedings PAC2005.

[6] W. Wuensch et. al., "A High-Gradient Test of an 30 GHz Molybdenum-Iris Structure", Proceedings EPAC06.

[7] A. Grudiev, W. Wuensch, "A newly designed and optimized CLIC main linac accelerating structure", Proceedings LINAC2004.

[8] R. Corsini et.al., "A High-Gradient Test of a 30 GHz Copper Accelerating Structure", to be published in proceedings LINAC06.

[9] W. Wuensch, et.al."30 GHz Power Production in CTF3", Proceedings PAC2005.

[10] S. Döbert, "Gradient Limitations for High-Frequency Accelerators" Proceedings LINAC2004.

[11] J.W. Wang et.al., "Progress Toward NLC/GLC Prototype Accelerator Structures", Proceedings LINAC2004.

[12] J.W. Wang, et.al. "SLAC/CERN High Gradient Tests of an X-band Accelerating Section", Proceedings PAC95 and CERN-SL-95-27 RF.

[13] V. Dolgashev, S. Tantawi, "RF Breakdown in X-Band Waveguides", Proceedings EPAC2002 and SLAC pub. 10355.

[14] W. Wuensch, et.al, "A High-Power Test of an X-Band Molybdenum-Iris Structure", Proceedings LINAC2004.

[15] A. Grudiev, private communication.

[16] J. Norem, Proceedings 12 Advanced Accelerator Concepts Workshop, Wisconsin.

[17] Sergio Calatroni, et.al "Status of the Fatigue Studies on the CLIC Accelerating Structures", Proceedings EPAC06.

COMMISSIONING EXPERIENCE OF SUPERCONDUCTING RADIO FREQUENCY SYSTEMS FOR THE TAIWAN LIGHT SOURCE

Ch. Wang#, L.H. Chang, M.C. Lin, M.S. Yeh, F. Z. Hsiao, F.T. Chung, T.T. Yang, S.S. Chang, M.H. Tsai, M.H. Chang, Y.H. Lin
National Synchrotron Radiation Research Centre, Hsinchu 30076, Taiwan

Abstract

An industrially manufactured SRF module of CESR type has been routinely operated at the Taiwan Light Source (TLS) in the National Synchrotron Radiation Research Centre (NSRRC) since 2005 early March. The original goals of doubling the electron beam current to increase the intensity of synchrotron light and to eliminate the instability caused by the interaction of electron beams with higher-order modes of the cavity have been successfully demonstrated. We report here our operational experience over the past two years of the SRF module at TLS at a large beam current toward a maximum beam current 400 mA (300 mA in routine operation) in top-up mode from originally 200 mA in decay mode. Together with digital feedback systems, fluctuations of the synchrotron light intensity (I_0) are less than 0.1 % for more than 95 % of user beam time on the average. We emphasize the diagnostic analysis of SRF trip events and the continuous improvements of the operational analogue low-level RF system against instability caused by heavy beam loading. The greatest challenge to the operational reliability, which is the brevity of the mean time between failures (MTBF), has been successfully overcome; a mean time between failures of the complete RF system of the TLS storage ring more than 200 hr has been demonstrated.

SRF PROJECT AT NSRRC

Since the successful commissioning of the TLS storage ring in 1993, the electron beam has suffered from strong coupled-bunch instabilities caused mainly by two existing room-temperature RF cavities designed in the 1970s. To improve significantly the electron beam stability, many attempts have been made, including the improvement of the cavity cooling water system, replacement of the cavity's damping antenna with a higher-order mode (HOM) tuner, and the application of an RF modulation technique. Various efforts to increase the photon flux and brightness have also been undertaken, but only a limited improvement was achieved. In 1999, a major accelerator upgrade project [1] was initiated with the objectives to double the TLS photon flux by increasing the electron beam current to 500 mA and to improve substantially the stability of the electron beam by replacing the two existing room-temperature cavities with one SRF module most recently developed of CESR-III design. Figure 1 shows the schematic drawing of the SRF module. The

#rfwang@nsrrc.org.tw

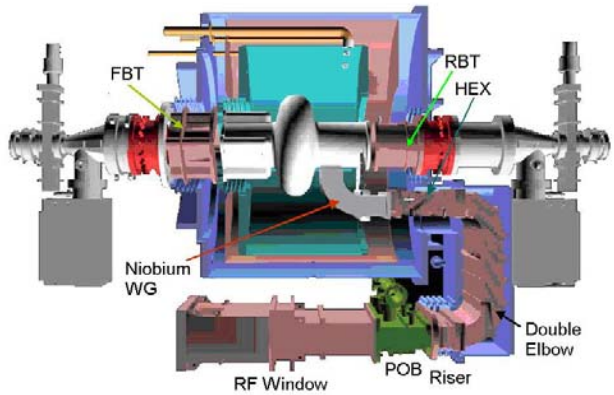

Figure 1: A schematic plot of the SRF module at TLS/NSRRC.

fabrication of the SRF modules was contracted to ACCEL after NSRRC arranged a technical transfer from Cornell University. Various difficulties were encountered during the production. Major faults were the buckling of the niobium waveguide during a warm high-pressure cryogenic safety test and the cracking of the RF ceramic window during high-power RF processing. The delivery of the repaired SRF module (named as S2) was again interrupted by an unexpected quenching at an extremely small field gradient due to indium contamination. An acceptable field gradient was radically achieved after an indium piece was removed from the cavity bottom.

A cryogenic plant has been built and installed by Air Liquide to support the operation of the SRF, according to NSRRC specifications and configurations. The final performance fulfils most design objectives and requirements for SRF operation at synchrotron light sources. These include (a) the capability of long-term continuous operation using a turbine cold box instead of a piston cold box, (b) isolating mechanical vibrations from the helium compressor by locating it remotely from the storage ring, (c) minimizing the two-phase mixture of the liquid helium supply and the diminution of return pressure drop of helium on locating the cold box near the SRF module, (d) convenience of operation on exploiting fully automatic control, (e) a large redundancy of helium cooling capacity by a safety factor 1.5, (f) a large redundancy of inventory of helium gas capable of sustaining once the loss of all helium in the SRF module, (g) capability of rapid cooling with the aid of a 2000-L main dewar, and (h) cryogenic load matching with a frequency driver in various operational modes to save electric power.

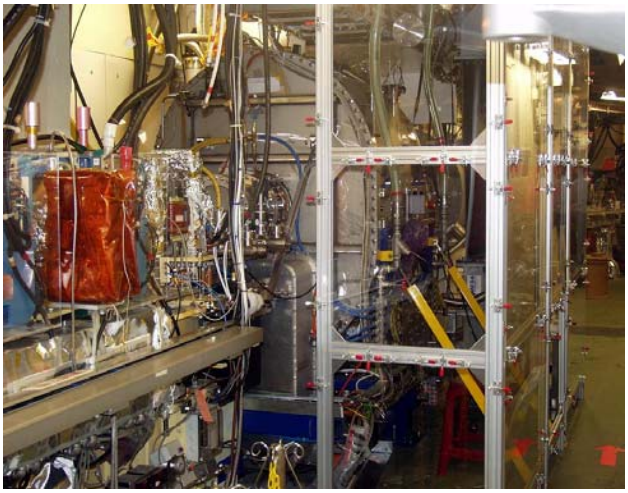

Figure 2: SRF module in routine operation at NSRRC [2].

Additional efforts are required to solve other problems, such as minimizing the large rate of consumption of LN2 through the long transfer line, stabilizing the LN2 supply pressure into the SRF module by installing a phase separator near the SRF module, preventing a surge in helium pressure caused by poor coordination between the main compressor and the helium gas manager during shutdown or failure, and using an effective motor bearing in the main helium compressor that is reliable when the cryogenic plant is operated at full power.

A new RF plant was developed internally and tested thoroughly for SRF operation concurrently with the production of the SRF modules. A new 100-kW RF transmitter of crowbar type was assembled internally, with emphasis on the attenuation of RF noise and operational reliability. Through this independent RF plant, the system integration and the high-power test run of the SRF module were completely independent of routine operation of the synchrotron before decommissioning of the room-temperature cavities. Most individual interface problems were solved during the test run without interrupting the synchrotron operation, significantly decreasing the duration required for commissioning the SRF module during installation in TLS.

Table I: Parameters governing operation of the CESR-III 500-MHz SRF module at TLS [1].

nominal machine energy	1.5 GeV
revolution frequency	2.49827 MHz
maximum beam current	< 500 mA
SR energy loss per turn	<164 keV
RF harmonic number	200
beam power	< 82 kW
RF frequency	499.654 MHz
RF voltage	1.6 MV
number of RF cavities	1
R/Q per cell (V^2/2Pc)	89/2
nominal external Q	250,000
cryogenic static load	< 30 W @ 4.5K

SRF OPERATION

After the SRF module was successfully installed and commissioned in 2004 November-December, NSRRC entered its new era of SRF operation [2]. Figure 2 shows the SRF module (named as S1) in operation at TLS. The parameters that control the operation of the 500-MHz SRF module at TLS appear in Table I. The storage ring was first operated at a maximum beam current 200 mA in decay mode. Doubling the integrated photon flux was first achieved on operating the storage ring in top-up mode at a beam current 300 mA in 2005 November [3]. Protracted (more than 8 h) reliable test runs at a beam current 400 mA in top-up mode were verified in 2006 September, after successfully increasing the available RF power from the RF transmitter. Routine operation at a beam current 360 mA in top-up mode is scheduled for 2007 after solving the problems of thermal loading at some beam lines.

The SRF module features heavily damped higher-order modes. No detectable effect of the coupled-bunch instability, caused by the SRF module, on the photon intensity has been observed. Transverse feedback is, however, absolutely required to stabilize the photon beam that is heavily perturbed by residual instabilities; those were fully suppressed by the coupled-bunch instabilities of the accelerating cavities before the installation of the SRF module. Without competition from the coupled-bunch instabilities driven by higher-order mode impedances of the accelerating cavities, the residual instabilities have become the dominant source of the photon beam turbulence. After those residual instabilities were properly damped, a highly stable photon beam with so-called I_0 fluctuations (dI_0/I_0) better than 0.08% became available for most scheduled user shifts. Further improvement of the I_0 fluctuations, to 0.06 %, has been achieved with the longitudinal digital feedback, as shown in Fig. 3. Few spontaneous spikes or glitches appear in the daily plot of I_0 fluctuations as Figure 3 shows, which is not a direct consequence of frequent injections for operation in top-up mode but somewhat resembling a turbulence of photon flux due to temporal over-excitation of residual instabilities.

Although the use of SRF technology at synchrotron light sources can fundamentally improve both the intensity and the stability of the photon flux, it also challenges the reliability and availability of machine operation, especially at higher operating beam currents. Figure 4 displays the statistics concerning the mean time between failures (MTBF) of the RF plant with SRF module over the past two years, in contrast to those with the room-temperature cavities. A comparable system reliability using an SRF module in comparison with that using a room-temperature cavity is obviously highly promising. A MTBF greater than 200 h is acceptable for the requirement of machine reliability for synchrotron users of TLS that has only one SRF module in operation, but not for the proposed 3-GeV light source, Taiwan

Photon Source (TPS), at NSRRC, which requires four sets of SRF modules for machine operation at its target current 400 mA (and beam power 720 kW). As a trip rate once per week for the completed RF systems is required, the SRF trip rate must be decreased to once per month on average per module.

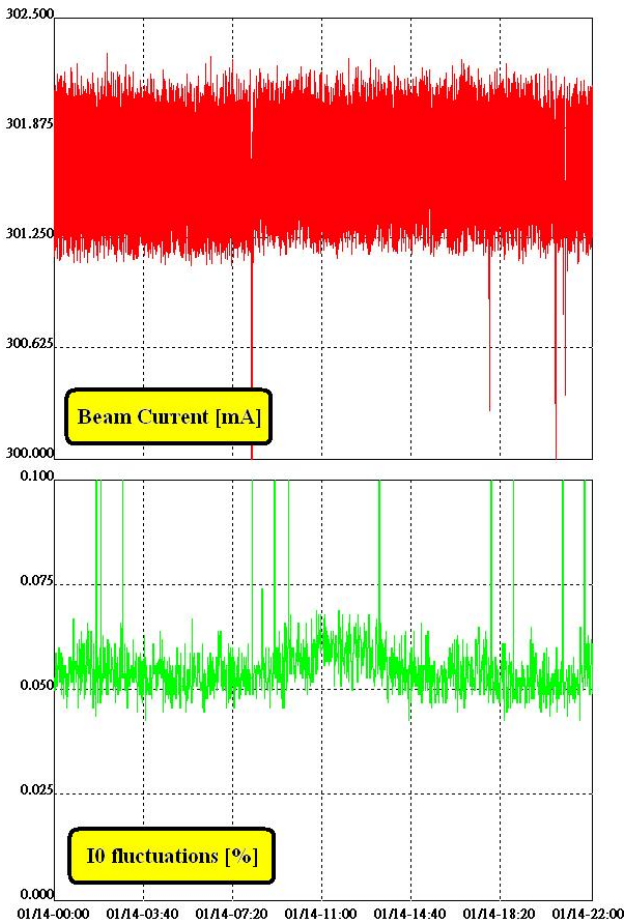

Figure 3: Plot of I_0 fluctuations for the TLS using the SRF module as an accelerating cavity.

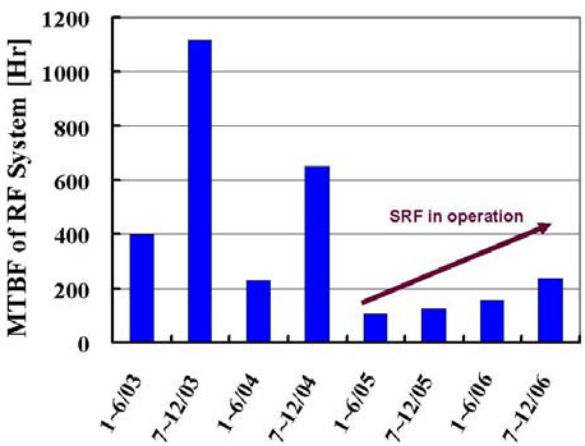

Figure 4: Mean time between failures of the complete RF plant with SRF module as accelerating cavity since 2005.

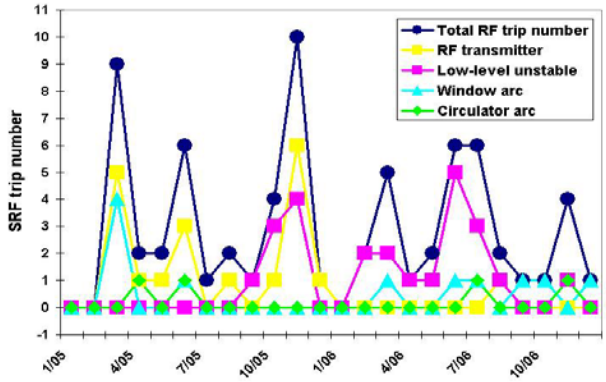

Figure 5: Trip distribution of RF plant with SRF module.

The most challenging trip events of the RF plant with the SRF module at TLS are due mainly to the instability of the feedback loops of the low-level RF system owing to heavy beam loading and false alarm of the window arcing occurring mostly during beam injection into the storage ring, as shown in Fig 5. An instability of the low-level RF feedbacks results in either an activation of the quench detector due to ringing of the RF gap voltage or an overdrive of the RF drive power of the low-level RF system to the klystron for maintenance of the RF gap voltage via an amplitude loop. Even though coherent synchrotron oscillations driven by Robinson instability are not observed at a beam current 360 mA, the insufficient phase margin against the DC Robinson instability occasionally caused ringing of the RF gap voltage that was regulated by the amplitude loop of the low-level RF system. As the ringing was not reproducible at the same beam current but became more frequently (once every few hours) at a higher beam current, it seems to be excited by some external turbulence.

With the increasing operational beam current, the feedback loops were first stabilized on decreasing the loop gains stepwise and then on applying a non-zero loading angle up to -5^{o} to extend the stable margin of Robinson instability. Later, a higher loop gain became available on broadening the bandwidth of the feedback loops. The detailed mechanism of instability of feedback loops of the low-level RF system under a heavy beam loading remains under investigation. Modeling of the feedback loops is in progress. The RF direct feedback has been prepared and will be applied to expand the stable margins of Robinson instability as required.

The tuner loop should ideally behave quietly for the machine operated in top-up mode because the temporal variation of beam current is minor, but the tuner loop is still busy compensating the slow drifts of the cavity resonance frequency in a time interval of about 20-30 min. mainly owing to large fluctuations of the LN2 temperature at the thermal transition flute beam tube (FBT) attached to the niobium cavity. Recent experiments strongly indicate that fluctuations of the LN2 inlet pressure might not be the only source that causes fluctuations of temperature or pressure of LN2 inside the

SRF module. Excellent regulation of LHe pressure with fluctuation less than 3 mbar has been achieved with a low-speed PID loop, but minor effects on the variation of the cavity resonance in a time interval of few seconds are still observable at a low tuner loop gain. Careful functional examination of the helium pressure compensator will be undertaken.

Microphonics might be intensely excited by individual driving pulses of the stepping motor, which was observed when the tuner loop was operated at high gain. A tuner loop with an extremely small gain, however, causes a slow drift of the resonance frequency of the cavity and therefore a temporal variation of the operational loading angle. After applying the micro-stepping controller to decrease the driven torque, the tuner loop is now re-operated at a much high gain without exciting intense microphonics resulting in quenching.

Window arcing is troublesome during operation in the top-up mode. AFT arc detectors are used to drive the interlocks of window arcing. Optical fibers sense the visible arcing and transfer the optical signal to a photo-diode in the circuit of the arc detector. When the photo-induced current increases above a specified threshold, the detector sends a TTL signal as a rapid interlock of SRF protection, regardless of the pulse duration of the photo-induced current. During kicker firing for beam injection, a false alarm of window arcing of the spare SRF module S2 was sometimes observed (the RF of S2 was off), even though the pulse duration of that arcing is of merely a few μs. An interlock mask of window arcing for an ultrabrief pulse of optical signal might be a plausible solution to avoid false alarms of this kind. More evidence for similar events is being collected for a final decision. Implementing dual arcing sensors on the individual view-ports provides a voting mechanism helpful to eliminate false alarms, when the false alarm is a consequence of EMI from high voltage pulse generators of the kickers. Clarification whether the source of false alarm of arcing arises from electronic noise or stray light is under study. The design of SRF modules in the next project will be considered accordingly.

The cavity vacuum is satisfactory: it attains 0.1 nTorr just after thermal cycling and as the vacuum of the cold cavity is isolated from other parts of the beam lines of the storage ring. The cavity vacuum increases to about 0.45 nTorr after opening the vacuum gate valves on both ends of the SRF module but with RF power off. The cavity vacuum is still better than 0.6 nTorr after continuous operation for one year in the top-up mode with a beam current 300 mA. A vacuum burst has been observed at an RF gap voltage 0.9-1.2 MV. Such a vacuum burst appears sometimes during initiation of the RF power to its nominal operational voltage 1.6 MV. We speculate that the vacuum burst is due to the excitation of multipacting near the coupling tongue of the waveguide coupler, but no tangible evidence supports this speculation. The appearance of such a vacuum burst is significantly decreased by rapid ramping of the RF gap voltage across this problematic zone. The condensed residual gases of cavity vacuum are mainly H_2, CO/N_2, and H_2O. The hydrogen has the worst vacuum in a short time interval during warm-up. It was up to 700 nTorr and 400 nTorr during the warm-up after one-year continuous operations in 2005 and 2006, respectively.

A rapid loss of beam current at a large beam current develops an enormous reflection of RF power and causes a great RF loading on the ceramic window of the SRF module. Arcing might be observed. The window vacuum deteriorates and might activate the interlock to close the vacuum gate valves. The RF system is used to terminating the RF after a sudden beam loss to protect the RF window. A super-rapid (TTL) interlock to limit the reverse RF power has been implemented to protect the window. In addition, a fault of the interlock ready chain automatically decreases the RF drive power of the RF transmitter. Abruptly curtailing the RF power on activating slow interlocks will cause a rapid loss of beam current, which is not necessary and can be avoided by a slow termination of RF power. A successful attempt can be made to allow survival of the RF system with warm cavity after a sudden beam loss, but such a design is difficult to implement when operating the SRF module with a quench interlock. A rapid decrease the RF drive power (RF gap voltage) to the RF transmitter corresponding to the increasing amount of reverse RF power is under investigation.

CRYOGENIC PROTECTION

The design philosophy for cryogenic protection of the SRF module operated at TLS is similar to what is used at CESR but with a few modifications. The SRF module is mainly operated as a refrigeration load for the cryogenic plant, with merely about 40 SLPM cold helium gas to cool part of the HEX waveguide section (as shown in Fig 1) to a temperature intermediate between that of LHe and that of LN2.

The cryogenic plant has faults of two types: a fault of the GHe main compressor and a fault of the cold box. A fault of the GHe main compressor automatically terminates the cold box, but the GHe main compressor continues to operate under a fault of the cold box. The fault of the cryo-plant from SRF module's point of view called as *cryo-area trip* is caused by the pressure in the suction line exceeding 4 psig (1.28 bara) for a nominal operational pressure 1.05 bara (15.35 psia) with the GHe main compressor. A cryo-area trip is detected when the GHe main compressor has a fault or is overloaded. A cryo-area trip causes the SRF module (and its cryogenic valve box) to be automatically isolated from other parts of the cryogenic system. Under this condition, the heater of the LHe bath and the RF power are terminated automatically. Meanwhile, the LHe bath pressure increases with time because of evaporation of LHe by the static cryogenic loss about 30 W. Within a few minutes,

the LHe bath pressure attains about 22 psia and an extra mechanical thermal-relief valve opens automatically. If the LHe bath pressure increases further, the spring relief valve opens for depressurization. We added a latch function for the opening of the spring relief valve to avoid oscillation of the LHe bath pressure between atmospheric pressure and its threshold pressure 9.0 psig (0.62 barg). Such a design risks contamination from impurity if manual reclosing the spring relief valve cannot be effected before the emptying of the LHe inside the LHe bath of the SRF module. The 1-barg mechanical burst disk is the ultimate safety protection for the SRF module with over-pressure. We twice experienced a broken burst disk before opening the spring relief valve at a pressure below its threshold. The reason is unclear: we speculated that the burst disk might become very fragile after several cycles of purging and pumping even at an extremely small rate, 1000 mbar/50 min. For the operating SRF module (S1), there is notably an additional burst disk at 1.4 bara to protect the cavity buckling when it is warm; this is bypassed when the cavity is cold.

With a fault of the cold box alone, the cold box becomes isolated from its loads, but the interlock of a cryo-area trip cannot be detected. The LHe supply valve becomes closed when the pressure at the cold return valve exceeds 1.4 bara, and the heater of LHe bath is terminated automatically. The cold return valve of the SRF module is expected to become close after fault of cold box but still open to the other cryogenic loads according to the original design to allow depressurization of LHe bath during a real quenching of the superconducting cavity. To solve this conflict, additional protection (without the latch function) was subsequently implemented to close the LHe supply valve and the cold GHe return valve of the SRF module immediately when their pressures at upstream of corresponding cryogenic valves exceed 21 psia and 19 psia, respectively. A cold-to-warm bypass valve on the intermediate switching valve box between the SRF valve box and the main dewar as well as the other cryogenic plant becomes opened automatically when its pressure exceeds about 1.28 bara, depending on the opening of its upstream manual valves.

There is experience with freezing of the readout from the AMI LHe level sensors at some specific levels. This condition causes full opening of the LHe supply valve of the SRF module. The LHe bath of the SRF module consequently becomes over-filled, and the static loss increases significantly. An additional interlock has been implemented to close the ready chain of the interlock of the SRF module when the opening of the LHe supply valve much exceeds its nominal opening (60 % vs. 23 % at 60 W dynamic loss and 30 W static loss of cryostat).

A GHe recovery compressor that has been installed for our cryo-plant becomes automatically actuated when the suction line pressure exceeds 1.2 bara, regardless whether the increase of suction line pressure is due to overloading or a fault of the GHe main compressor. Our SRF module benefits little from the GHe recovery compressor according to the design philosophy of the cryogenic protection. The cryogenic bypass valve from the cold GHe to the warm GHe line is closed as default. Operating the interlock of the cryo-area trip in a non-latched mode allows this bypass valve to open if the suction line pressure becomes small again – after full operation of the recovery compressor. Fully opening the bypass valve according to the current design using an OMEGA PID controller without a function of an upper bound of opening might, however, result in a rapid expansion of cold helium gas, and create a backward pressure to send the warm gas back to accelerate the evaporation of the LHe in the LHe bath. A PLC-based control loop to allow slow opening of the bypass valve with a second unlatched interlock of the cryo-area trip (to allow closing the LHe supply and the GHe cold return valve in a latched mode) will allow the SRF module to benefit the implementation of the recovery compressor.

Taiwan is located on the circum-Pacific seismic belt on which more than 70 % of all global earthquakes occur. Additional mechanical supports have been implemented on both sides of the cryostat of the SRF module. The LHe bath is suspended with four invar wires on the top of the cryostat alone. An earthquake will create rapid fluctuations of LHe pressure on the cavity and consequently rapid variations of the cavity resonance frequency. A similar phenomenon has been observed through a surge of helium pressure caused by malfunction of the cryo-plant. A restriction of the available RF drive power will activate the interlock to terminate the RF power.

CONCLUSION

In 1999, a bold decision was made at NSRRC to adopt SRF technology in a major TLS machine upgrade. The SRF cavity has become the preferred choice in building or planning new synchrotron lamps worldwide. As pioneers in using an SRF module as an accelerating cavity for a third-generation light source, we are pleased to report that our users are satisfied with the SRF performance. Mastering SRF technology internally is vital to the realization of highly reliable and optimal operation of the SRF module in an accelerator. Bridging the SRF technical gap quickly remains a major challenge for our technical staff and requires a continual intensive effort.

REFERENCES

[1] Ch. Wang et al., “Superconducting RF Project at the Synchrotron Radiation Research Center,” 10th SRF Workshop, Tsukuba, Sept. 2001, p. 34.

[2] Ch. Wang et al., “Successful Operation of the 500-MHz SRF Module at TLS Current” in Proceedings of the 2005 Particle Accelerator Conference, p. 3706.

[3] Ch. Wang et al., “Operational Experience of the Superconducting RF Module at TLS” PHYSICA C, 441, p. 277, 2006.

DEVELOPMENT OF QUARTER WAVE RESONATORS

Amit Roy
Inter University Accelerator Centre, Aruna Asaf Ali Marg
P.O.Box 10502, New Delhi - 110 067, India

Abstract

The accelerating structure for the superconducting linac booster for the 15 UD Pelletron at IUAC is a Nb QWR cavity, designed and fabricated as a joint collaboration between IUAC and ANL, USA. Initial cavities required for the first linac module were fabricated at ANL. For fabrication of cavities required for future modules a Superconducting Resonator Fabrication Facility has been set up at IUAC. Three quarter wave resonator (QWR) cavities have been fabricated and fifteen more resonators for the second and third linac modules are in advanced stage of completion. This facility has allowed us to undertake repairs on some of the resonators which sprung leaks. First experiment with the accelerated Si beam through the first linac module having eight resonators along with a superconducting solenoid have been conducted recently.

INTRODUCTION

The Pelletron accelerator at IUAC is capable of accelerating ions having mass up to 40 amu above Coulomb barrier. To augment the beam energy above Coulomb barrier for mass up to 100 amu, a booster Superconducting Linear Accelerator structure is being installed[1]. The first Linac module consisting of eight Niobium Quarter Wave Resonators (QWR) optimized for IUAC Pelletron and a solenoid as focussing device, has been installed at IUAC. The QWR was designed and fabricated as a joint collaboration between IUAC and Argonne National Laboratory (ANL), USA[2]. The other elements of the Linac which have been installed are a superbuncher (SB) cryostat consisting of a single QWR and a rebuncher cryostat consisting of two QWRs.

A Multiharmonic Buncher has been installed and tested as the pre-buncher before the Pelletron. The bunch width delivered by this buncher is ~ 1-2 ns[3]. One superconducting QWR cavity has been installed after the Pelletron and operated as the Superbuncher delivering <150 ps pulsed beams for injection into one Linac module with eight resonators. Cryogenics facilities consisting of a 600 W liquid helium plant, LN2 plant, several large cryostats to house the cavities are fully functional and the cryogen distribution lines have been installed to supply cryogen to superbuncher and superconducting linear accelerator modules[4]. The cavity resonators for the 2nd and 3rd modules are being fabricated in house and a full fledged superconducting resonator fabrication facility has been established consisting of Electron Beam Welding machine, High Vacuum furnace and a Surface Preparation Laboratory. Major effort has been expended also in areas of beam transport and rf electronics required to operate this linac. Most of the required hardware has been built indigenously.

QUARTER WAVE CAVITY RESONATOR

The Quarter Wave resonator is a coaxial structure operating in the TEM mode with beam accelerating gaps in a direction perpendicular to the symmetry axis. The central conductor is shaped with two different diameters to reduce the effective length of the cavity by capacitive loading. This helps in reducing the frequency jitter and thus in the control of the cavity. The resonator is formed entirely of niobium and is closely jacketed in a vessel of stainless steel which contains the liquid helium. A small amount of niobium-stainless steel bonded composite material is used to provide welding transitions where beam and coupling ports penetrate the stainless steel jacket. A novel pneumatic slow tuner in the form of a niobium bellow provides a tuning range of approximately 100 kHz, substantially larger than in any working quarter wave resonators. A picture of completed QWR along with the Nb slow tuner bellows is given in figure 1.

Figure 1: Indigenously built niobium quarter wave resonator with slow tuner bellows at IUAC.

The pnematic drive for the slow tuner bellows has been further modified with the experience of running the cavities in the linac cryostat.

The prototype QWR and twelve more resonators were fabricated in ANL and out of these, 8 resonators are used in the first linac module. In the off-line tests, all the resonators have exceeded the minimum design goal of 3 MV/m with 4 watts of input power. The best performance achieved was 5.0 MV/m at 4 watts of input power. In the on-line tests the performance has been slightly worse compared to the off-line tests, but the field levels exceeded 3 MV/m at 4 W.

In order to fabricate the resonators in house, a Superconducting Resonator Fabrication Facility (SuRFF)

at Inter-University Accelerator Centre (IUAC) has been set up and is fully functional. It consists of a 15 kW Electron Beam Welding machine, an automated Surface Preparation Laboratory for electro-polishing the cavities, a High Vacuum Furnace, and a dedicated test cryostat set-up.

Initially, a single QWR was successfully constructed and tested using this facility and then installed in the first module of the IUAC linac. Two more QWRs have been fabricated and the performance of the resonators were checked using the test facility, consistng of a test cryostat and associated equipment that include the RF electronics for powering the cavity, the thermometry for temperature monitoring and the vacuum system controller. The process for fabrication of fifteen resonators for the second and third linac modules have made good progress and is expected to finish by middle of 2007[5]. The measured Q curve for the first cavity is presented in figure 2.

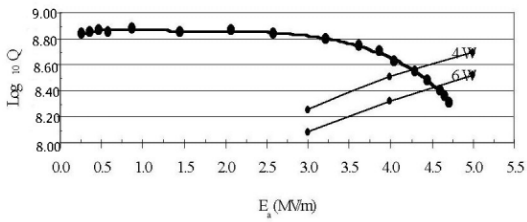

Figure 2: QWR-I1 cold test performance.

Repair Work on Existing QWRs

In addition to resonator fabrication for the linac modules several critical repair jobs have also been undertaken. For example, in the IUAC resonator the transition from the inner niobium housing to the outer stainless steel jacket is provided through niobium-stainless steel explosively bonded flange and edge welded stainless steel bellows. On several of the ANL built QWRs these assemblies leaked when the resonators were loaded in the cryostat and filled with liquid/gas helium. This problem had not been encountered during the prototype resonator testing. In order to avoid problems on future resonators we have modified the design of both the coupling and beam port transition flange assemblies using formed stainless steel bellows procured from a local vendor. Several transition flange assemblies have been fabricated, thermally cycled and pressure tested. The leaking assemblies on several cavities have been successfully repaired by machining them out and replacing with the modified design.

RF POWER & CONTROL

The amplitude and phase of the resonator were maintained constant with respect to the master reference using a resonator control module based on the principle of dynamic phase control, designed in collaboration with Electronics division, BARC, Mumbai. It is found that the control module can stabilize the phase of the super conducting resonator up to 0.5 degree accuracy and amplitude with accuracy of 1%. A Slow -tuner is used to bring the frequency of the resonator close to the master frequency and stabilize it there. The resonators are powered using a 400Watt, 97 MHz RF amplifier designed in house and tested with an RF circulator and load at the output to take care of the reflected power. The technology is transferred to M/s BEL, Bangalore for production of initially required ten amplifiers and the rest of the required units are being produced at IUAC.

The clock distribution system has been designed and developed to provide the master reference to the Linac and its subsystems which includes a multi harmonic buncher, High energy sweeper and phase detector. The circuit uses 6.0625 MHz as the fundamental frequency generated using a crystal oscillator specially made at M/s BEL, Bangalore and the other frequencies are generated by frequency multiplication. The clock distribution system is now being used with the Linac control. A phase meter input module has been developed which mixes the RF signal phase to be measured with some offset RF frequency within a few kHz and then extracts the AF signal for phase meter input.

Reduction of Microphonics frquency jitters

During on-line beam tests of niobium superconducting quarter wave resonators (QWR), it has been observed that due to presence of microphonics in the ambience of linac, rf power of about 300 watts is required to lock the resonators in over-coupled mode. The high rf power causes several operational problems like melting of insulation of RF power cable; excessive heating of drive coupler leading to other associated problems and increased cryogenic losses. To reduce the requirement of RF power, a novel technique of damping the mechanical mode of the resonator by inserting stainless steel balls of suitable diameter inside the central conductor (figure 3) of the QWR has been adopted.

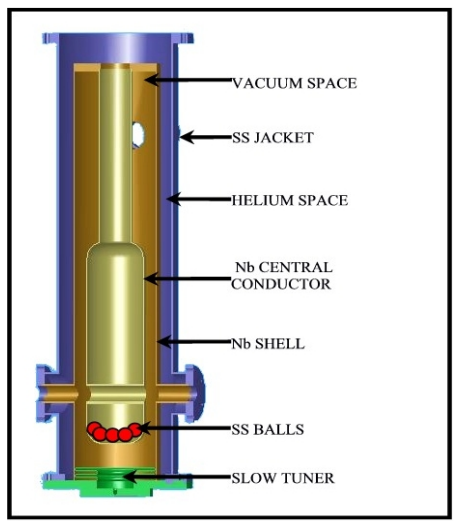

Figure 3. Schematic for the damping of vibrations of central conductor through stainless steel balls.

Due to dynamic friction between the balls and the niobium surface, the amplitude of the vibration of the central conductor excited by the mechanical mode has been reduced drastically. Microphonics measurement on

QWR at superconducting temperature has been performed without/with SS balls with the help of cavity resonance monitor in phase lock loop and a reduction of microphonics by a factor of 3 has been recorded with balls as damper. During phase and amplitude locking, a remarkable reduction of input rf power of about 50% (figure 4) has been achieved to lock the resonator[6].

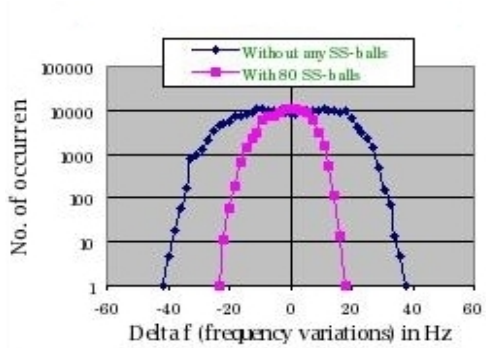

Figure 4. Damping in frequecy jitter with ss balls in central conductor of resonator.

ON-LINE TEST OF LINAC

After carrying out cold tests of the resonators in test cryostat, eight resonators and a superconducting solenoid has been installed and aligned in the first linac cryostat. The resonator assembly with a superconducting solenoid mounted on the support bars suspended from the top plate of the cryostat module is shown in figure 5. Initial off-line tests of the resonators in linac were carried out to understand the cool down times and check the field levels in the resonators.

Figure 5. Eight resonators and a solenoid in first linac module ready to be loaded for a cold test.

Finally, dc and pulsed beam were accelerated through resonators in Linac cryostat. Three runs with ^{28}Si beam from the Pelletron have been succesfully carried out. The beam bunching system of IUAC consists of a pre-tandem multiharmonic buncher (MHB) and a post tandem high-energy sweeper (HES). A phase detector has been placed after analyser magnet of the Pelletron to sense the phase of the beam bunch. The bunched beam was transported to the superbuncher located about 25 metres downstream from the phase detector. The point of time focus of the superbuncher is ~ 9 metres from it and coincides with the entrance point of the first linac cryostat.

During these tests, the resonators could be maintained in phase locked condition for several hours. The field levels in the first test were quite low (1-2 MV/m) although field levels > 4 MV/m have been reached in previous tests. The cause for the low field levels was coating of the resonator surface from overheated brass rack and pinion arrangement for movement of the rf coupler drive. The coupler design has been changed to avoid exposure of the brass portion to inside of the resonator and to provide better cooling through liquid nitrogen. After these modifications, two runs of the linac with Si beam were performed. In these runs the field levels > 3 MV/m were maintained and the field levels were locked for 3-4 days for experiments to be done with the accelerated ions. The transmission of the beam through Linac was close to 100%. The result of the energy gain is shown in figure 6.

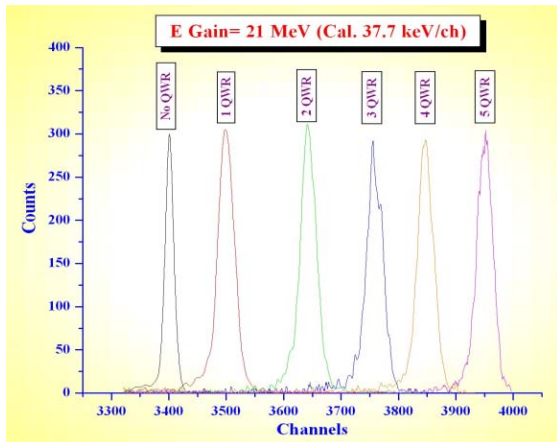

Figure 6. Energy gain by Si beam as resonators get turned on one by one.

MODIFICATIONS

New Drive Coupler

To change the coupling strength and couple the RF power into cavities we had a drive coupler based on rack and pinion design to facilitate linear motion of the loop. The Quarter Wave Resonators (QWR's) required nearly 300 Watts of RF power to generate field of ~4 MV/m in over coupled mode. Due to this high power requirement, in our first few tests, we found that the insulator of rf power cables were melting and a thin layer of material was deposited on to the cold surface of cavities. A detailed analysis of this thin film was done using Energy Dispersive X-Ray Analysis (EDX) at Solid State Physics Laboratory, Delhi. This showed Zn (96.5%)/Cu (2.49%) in atomic % as main peaks. The rack and pinion were made of brass and the excessive heating during powering of the cavities might have caused the coating. Two new designs of drive coupler were made to replace the rack

and pinion and to also incorporate LN_2 cooling. Salient features of one of the new drive probes(figure 7a) are:

1) The movement of drive probe is done using worm and worm wheel.
2) Liquid nitrogen cooled central conductor and outer conductor.

In the second design (figure 7b), the rack and pinion is kept outside of the cavity so that there is no chance of contamination.

(a)

(b)

Figure 7(a), (b) . Two different new drive couplers which avoids brass components inside and can be cooled with liquid nitrogen.

The performance of the new drive couplers were checked in cold tests in the test cryostat. High power pulse conditioning was done for long duration (4-5 hrs). Cavity was then locked at 2.2 MV/m @ 150-170 watts of input power for nearly 18 hrs. With successful completion of the tests it was decided to replace all old drives with the new design. To increase the coupling range a rotational motion was incorporated in one of the designs along with linear motion through a spiral groove. This enables the loop to have a linear travel of ~70 mm and 70 deg rotation.

Slow Tuner & Top Flange

During last few cold tests the original slow tuner bellows were observed to start leaking from welding joints. Though these leaks could be repaired, we decided to re-design the whole system of movement of the slow tuner. In new design, He gas in introduced in an stainless steel bellows and through a mechanical attachment linear motion is transferred to niobium bellows. The new design was successfully tested in STC for frequency range and response measurements. The new assembly is shown in figure 8.

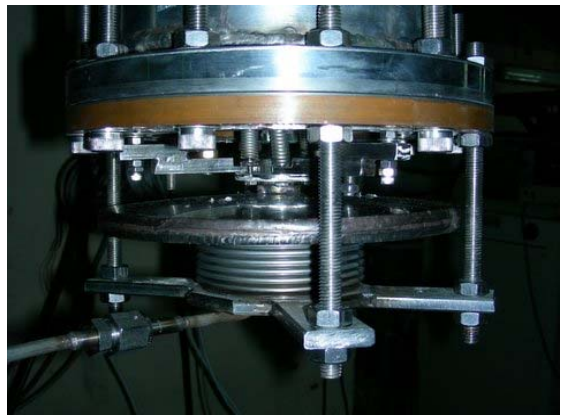

Figure 8. New slow tuner bellows with ss pnematic tuner mechanism.

The SS top flange of the resonator is flat and clearance between this flange and top niobium surface is about 1/2 inch. During boiling of liquid helium bubbles may get trapped in this region and reduce the cooling of the top flange. To overcome this, a hat like structure having slope for movement of bubbles and as well as a buffer volume is developed. The modified top flange is shown in figure 9. This hat structure gives two fold advantage, one it provides a buffer volume for LHe, secondly it does not allow bubble to be trapped, thus localized heating / insufficient cooling problem is removed. Results of performance tests with hat type structure showed marked improvement. At present all eight resonators in linac cryostat are connected to liquid helium dewar using this hat structure.

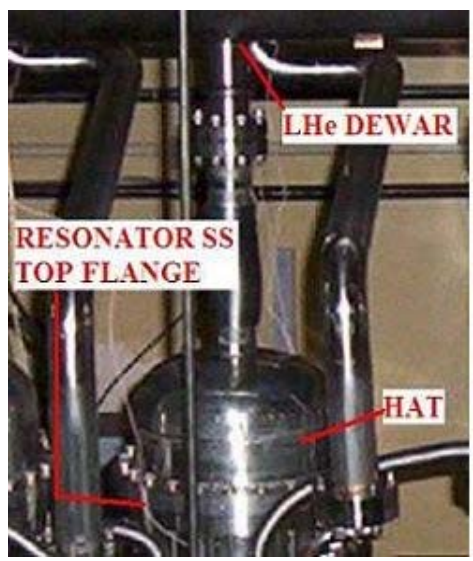

Figure 9. The stainless steel top flange of the resonator jacket in the form of a hat.

ACKNOWLEDGEMENTS

The work reported here is on behalf of the Phase II group of Inter-University Accelerator Centre.

REFERENCES

[1] A.Roy, Current Science, Vol 76, No 2, (1999) 149.
[2] K.W.Shepard, P.N.Potukuchi and A. Roy, Proc. of the 1993 Particle Accelerator Conference, 17-20 May, 1993, Washington, DC,1045.
[3] A. Sarkar et al., Ind J. Pure and Appl. Phys. Vol 39(2001)15.
[4] T.S.Datta et al., Proceedings of this conference. Contribution THPMA050.
[5] P.N.Prakash et al., Proceedings of this Conference, Contribution WEPMA132.
[6] S. Ghosh, P.NPatra, B.K.Sahu, A.Rai, G.K.Chaudhuri, A.Pandey, D.Kanjilal and A.Roy, Submitted to Physical Review ST.

LOW-LEVEL RF CONTROL SYSTEM DESIGN AND ARCHITECTURE*

Lawrence Doolittle†, LBNL, Berkeley, California

Abstract

Low-level RF (LLRF) control hardware and its embedded programming plays a pivotal role in the performance of an accelerator. Modern designs implement most of the signal processing in the digital domain. This reduces the size and cost of the hardware, but places the burden of proper operation on the programming. FPGAs (field programmable gate arrays) and communications-grade ADCs and DACs enable sub-microsecond delay for the LLRF controller feedback signal. Ancient concepts of the virtue of simplicity are easy to apply to the hardware, but more of a challenge in the context of programming. Digital signal processing, combined with dedicated hardware, can control and maintain cavity phase (relative to an absolute reference) unaffected by drift or $1/f$ noise of any long cables or active components. Developing and testing that programming is a very real challenge. This paper discusses approaches and techniques to make LLRF systems meet their goals in upcoming accelerators.

INTRODUCTION AND THEORY

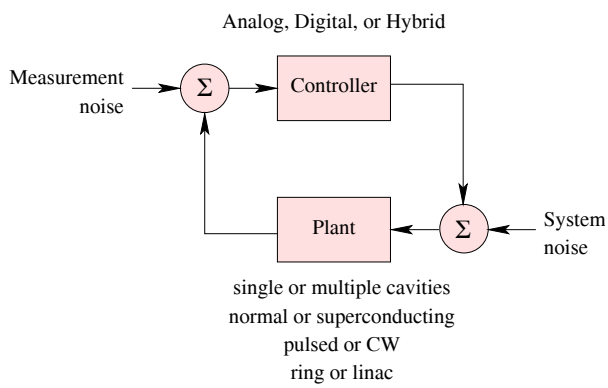

Figure 1: Textbook feedback topology.

At their simplest, modern LLRF control systems can be considered a combination op-amp and digital storage oscilloscope, with some additional built-in computational ability. An understanding of basic control theory, as diagrammed in figure 1, forms the starting point for a discussion of the signal processing needed to control cavity fields.

The feedback system is best understood in the rotating frame of the cavity resonance, so all signals are complex numbers. Cavity bandwidths can vary from 50 Hz to 1 MHz, although direct the direct feedback described here is only useful for cavity bandwidths up to 50 kHz. While any pulsed machine can use pulse to pulse feedback (also known as adaptive feedback), the shortest pulse machines (e.g., SLAC-style linacs) only permit pulse-to-pulse feedback. These are the machines with cavity bandwidths greater than 50 kHz.

The dominant limitation on feedback gain is the delay around the feedback loop, usually dominated by the controller, cables, and waveguides. 1 μs delay limits the gain-bandwidth product to about 100 kHz. A zero in the control system gain can cancel the cavity pole, giving a pure integrator (plus delay) feedback system response.

Narrow band (e.g., superconducting) cavities could sustain a broadband (up to 5 MHz) gain of up to 70 dB within that plan, but that is not practical: too much noise would be sent to Klystron. Figure 2 shows a set of plausible controller gain curves that limit the noise output of the controller, keeping proper phase margins and the basic pole-zero cancellation response.

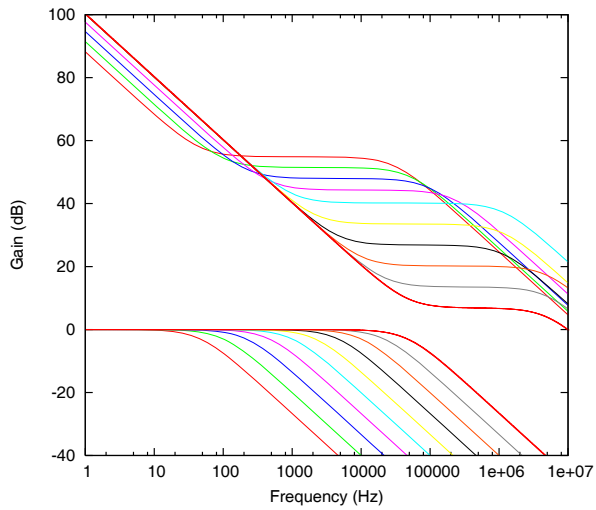

Figure 2: Frequency domain strategy for closing feedback loop.

For any given application, this control loop has to be thoroughly analyzed and/or simulated to understand its behavior under the stresses of

- beam loading
- ring dynamics
- microphonics
- ponderomotive tuning
- klystron nonlinearity

* Work supprted by the U. S. Department of Energy
† ldoolitt@recycle.lbl.gov

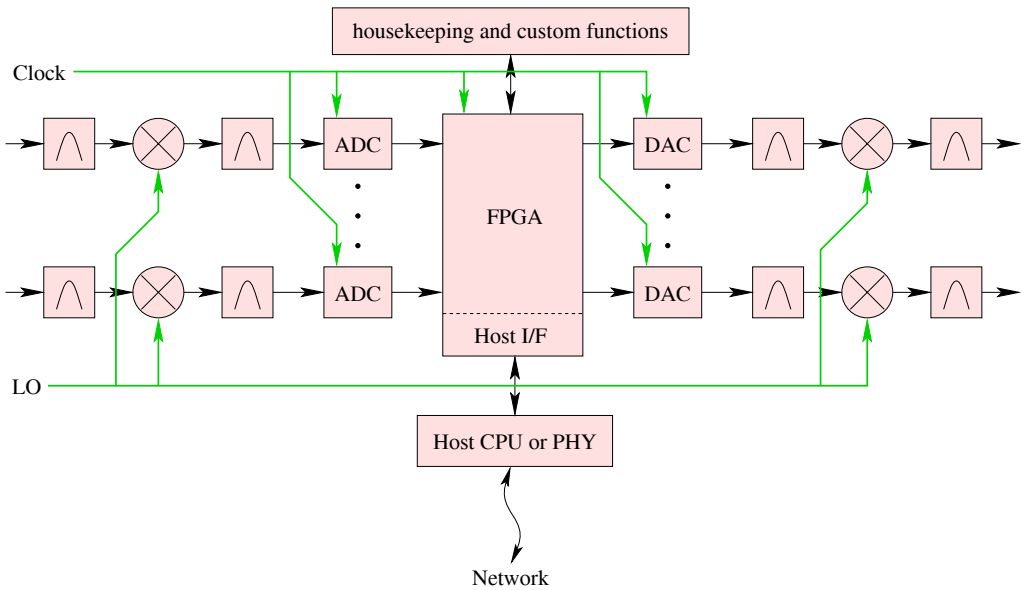

Figure 3: Familiar block diagram, including RF signal conditioning.

HARDWARE

All accelerator front-end measurement and control equipment should fit the general framework of figure 3, although the downconversion step shown here has to be generalized to "signal conditioning." In some circles a DSP or CPU is added as a separate block, but FPGAs are now big and fast enough to absorb that functionality.

An ADC will never compete with a mixer for phase noise (additive jitter), so a mixer is essential for RF above 100 MHz. Typical downconversion is to an IF in the 30 to 100 MHz range, placed in the second or third Nyquist zone of an ADC clocked at 40 to 100 MS/s. The DAC chain is less critical than ADC, because of its placement after the feedback gain.

Communication grade ADCs are now available and affordable for large scale use in the 12- to 14-bit range, 65 to 170 MS/s. Latency seems stalled in the 30 to 80 ns range, while power consumption is falling steadily.

Hardware concerns:

- mixer and ADC nonlinearity
- clock jitter
- crosstalk
- packaging and interfacing
- but not cable length variation, as will be explained

Figure 4 shows the hardware needed to transfer a phase standard to the cavity pickup probe, using a modulated calibration line. All drifts outside the highlighted section are corrected for with digital signal processing. The remaining cables, splitters, and summing junctions can be located close to the cavity, in the accelerator tunnel, and have their temperature regulated.

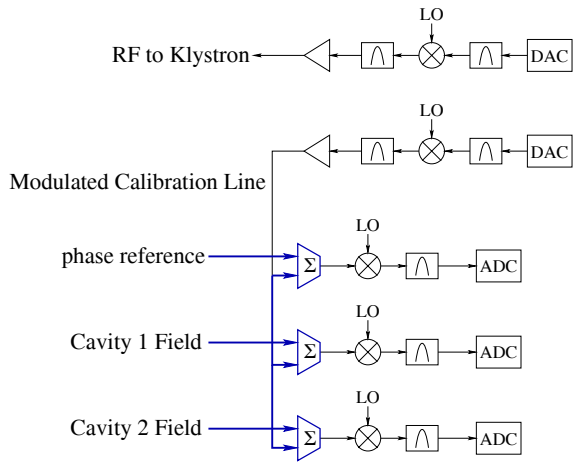

Figure 4: Insertion of phase calibration signal.

SIGNAL PROCESSING

An LLRF system always takes in a phase reference signal, that provides a reference against which to measure cavity phase. The signal processing architecture to accomplish that inside the FPGA is shown in figure 5.

The CORDIC[1] blocks are used to perform trigonometric calculations. The phase of the reference signal is used as the baseline from which the setpoint waveform is computed. Once the setpoint is subtracted from the measurement of cavity voltage, the feedback gain $K_P + K_I/s$ is applied. These coefficients are complex numbers, since a phase rotation has to be applied to correct for cable length.

While there is an option of taking the phase reference signal from a separate ADC (and mixer and filter), in a pulsed machine it is easy to take it from the same ADC as the cavity, just at a different time.[2] Using the RF hard-

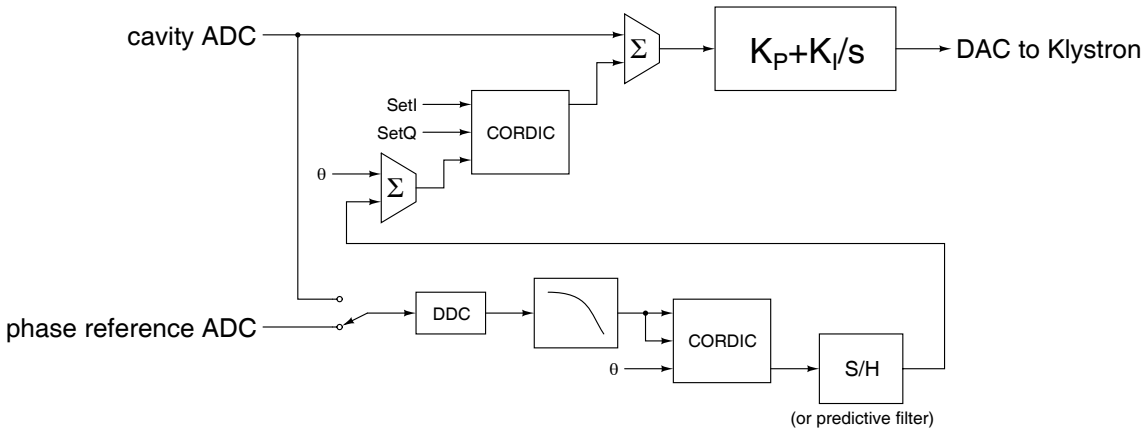

Figure 5: Digital signal processing of cavity and reference signals.

ware support as shown in figure 4, the phase calibration pulse is offset in time from beam pulse.

A CW machine can also passively combine a calibration signal with the cavity probe, but that calibration signal (diagnostics folk call it a pilot tone) has to be offset in frequency, not time. That case requires a little extra (digital) work to pull sideband modulation out of the cavity ADC signal. Those calibration tone sidebands need to be in-band for data acquisition chain, but out-of-band for the cavity. They will be suppressed (adaptive feedback) at the input of the main digital feedback amplifier.

Representing RF vectors in IQ form in the digital signal processing path makes it easy to give proper signal averaging behavior for low frequency gain (integration), without accumulating spurious rounding errors. Non-IQ sampling at the analog/digital boundary is really good for coaxing linearity from ADC and DAC.

The Digital Downconversion (DDC) step, that converts from non-IQ to IQ representations, takes two multipliers and two adders. It can absorb phase rotation and fine gain adjustment with no additional latency. The digital upconversion step is similar, and can be combined with an interpolating filter in the common case that the output DAC is run at a higher speed than the input ADC.[3]

A direct feedback path (no IQ conversion step) can be used for the highest bandwidth cavities, that need low latency but no controlled noise filtering in the K_I path.

Depending on configuration, the delay through the digital section can range from 8 to 16 clock cycles, or more if the bandwidth is purposely reduced.

Simulations are a key part of the signal processing design. The basic physics problem and its solution must be analyzed and understood (possibly using simulations) before meaningful progress can take place on the component design. Then each component can be simulated to check its intended operation. Ideally, these tests will carry forward to act as regression tests on production code.

Finally, the ensemble of signal processing code, physics models, and driver software can be simulated as a whole. The more complete the simulation, the more confident one can be in deploying new code into an accelerator. Note that there can be many orders of magnitude spread in relevant time scales for these simulations, which can make the simulations take extravagant amounts of time. Creative solutions are needed for that class of problems.

INTERFACES

The LLRF subsystem interacts in important ways with

- Beam Diagnostics
- High power RF
- Machine timing
- Phase reference
- Interlocks

and, like everything else, the global control system.

There are relationships and interactions not only between accelerator subsystem hardware, but also the communities that design, build, and commission them.

Design decisions and infrastructure assumptions made in any one of these subsystems can have profound affects on the quality of implementation achievable in connected subsystems. While that is a very general statement, the achievable phase noise and jitter of the LLRF is very sensitive to the choice, distribution, and synchronization of the LO (local oscillator) and beam timing.

Modern accelerators and their controls have grown so complex that they will materially benefit from having simulations built into the next generation of LLRF controller. A cavity simulator built in to the digital fabric will allow the machine to be virtually turned on (to test the controls) before high voltage is applied.

CONCLUSIONS

A modern LLRF control system performs sophisticated feedback and calibration techniques in the digital domain, where drift is nonexistent and noise can be made arbitrarily small. When properly integrated with the rest of the

accelerator, the overall performance of the RF system appears able to meet the performance goals of even the most demanding proposed accelerators.

Many of the ideas presented here have only seen laboratory or small-scale tests. It remains to be seen how perceptions will change as accelerator design comes to depend on them.

The hardware design for LLRF control systems has become conceptually quite simple. This potentially represents real progress in cost and reliability. The complexity of design is now buried in programming, especially with an FPGA. While simplicity of design is still a goal there (one which more powerful design languages can help reach), complexity in that design can at least be managed by traditional software development strategies, including extensive automated testing (simulation).

ACKNOWLEDGEMENTS

The author would like to thank Fermilab, SNS, FERMI@ELETTRA, and SSRF for challenging and productive collaborations.

REFERENCES

[1] Volder, J., "The CORDIC Trigonometric Computing Technique," IRE Trans. Electronic Computing, Vol EC-8, pp330-334, Sept. 1959.

[2] Piller, C., "Multiplexed Cavity RF and Reference RF Signal Processing for SNS LLRF," SNS Tech Note, March 7, 2003.

[3] "Plan for a 50 MHz Analog Output Channel," http://recycle.lbl.gov/∼ldoolitt/plan50MHz, August 8, 2002.

DESIGN OF THE PEFP LOW BETA CRYOMODULE*

Sun An#, Y. S. Cho and B. H. Choi
PEFP, KAERI, Daejeon 305-353, Korea

Abstract

A low beta elliptical superconducting RF cavity has been designed for the linac of Proton Engineering Frontier Project (PEFP). A double stiffening-ring structure is used to reduce Lorentz force detuning of the low beta cavity. Higher order mode (HOM) analysis has shown, for the low beta cavities, the HOM coupler's Q_{ext} needs to be lower than 3×10^5 for reducing the influence of the dangerous modes on the beam instabilities and HOM-induced power. A coaxial coupler is designed for PEFP cryomodules. The cooling system and the magnetic shielding structures shaped by two coaxial cylinders for the low beta cryomodules are described.

INTRODUCTION

Superconducting RF (SRF) cavity is considered to accelerate a proton beam with repetition rate of 60 Hz at 700 MHz in the PEFP Linac being built at Gyeongju in Korea [1, 2]. The first section of the SRF linac is composed of the low beta cryomodules with three 5-cell elliptical cavities of β_g=0.42, and will accelerate a proton beam from 80 MeV to 178.6 MeV [3].

Generally, the low beta cavities have stronger Lorentz force detuning than the high beta cavities. For pulse SRF accelerators, the Lorentz force detuning is a more serious issue than that for CW accelerators. The PEFP low beta SRF cavity is the lowest beta elliptical cavity operating at pulse mode so far. The Lorentz force detuning control of the PEFP low beta cavity is a big challenge in the cavity design [4].

Although the TTF HOM coupler has been used on many cavities successfully, there are two faults: notch frequency shift and feed-through tip melting of the capacitive coupling, which have been found during SNS cavity VTA, cryomodule testing at JLab and the SNS commissioning at ORNL. In order to satisfy PEFP HOM damping requirements, easily control the notch frequency shift and avoid the feed-through tip melting, a new HOM coupler is needed to design.

In this paper, the low beta cavity design, the HOM analysis of the PEFP low beta linac, the HOM coupler design, the cooling system and magnetic shielding of the PEFP low beta cryomodule have been introduced.

RF CAVITY DESIGN

Cavity design

Considering the cavity field sensitivity and the cavity production difficulty, we chose 5 as the PEFP low beta cavity's cell number, 6 degree as the wall angle α of internal cell, and 4220 as the field sensitivity that corresponds to the cell-to-cell coupling factor of 1.41%.

Based on the present SRF technology at KAERI, our choice was a reduction in the ratio of E_{pk}/E_{acc}, and a realization of the higher *R/Q* in the PEFP low beta cavity optimization.

After optimization design of the cavity shape in RF properties, a multipacting simulation code FishPact developed by Genfa Wu [4] is used to estimate the multipacting risk for the whole cavity. The calculations indicate the occurrence of the multipacting is unlikely, because the electrons can not gain sufficient energy to generate secondary electrons when impacting on the cavity surface. Table 1 lists the RF parameters of the PEFP low beta cavity.

Table 1: Primary parameters of the PEFP Low beta cavity.

Parameters	Value
Frequency (MHz)	700
Geometrical beta β_g	0.42
E_{acc} (MV/m)	8.0
E_{pk}/E_{acc}	3.71
B_{pk}/E_{acc} [mT/(MV/m)]	7.47
R/Q (Ω)	102.30
Cell to cell coupling (%)	1.41
Geometrical Factor (Ω)	121.68

Stiffening-ring structure design for reducing Lorentz force detuning

After optimization design of the stiffening structure regarding to the Lorentz force detuning control, cavity field flatness sensitivity, frequency sensitivity, tuning sensitivity and stability of the cavity mechanical property, a stiffening structure composed of double stiffening ring between inner cells and between Field Probe end cell and end dish, and single stiffening ring between FPC end cell and end dish has been designed for the low beta cavity. This structure can reduce Lorentz force detuning factor to -1.1 Hz/(MV/m)^2 for a wall thickness of 4.3 mm. Frequency sensitivity of the low beta cavity is 187.8 KHz/mm; the field flatness sensitivity of the cavity is 49.1%/MHz; and the tuning sensitivity is 4498 N/mm, and the maximum Von Mises stressin the cavity is 12.6 MPa [5]. Fig. 1 shows the stiffening structure and a PEFP low beta cavity with this structure.

HOM analysis [3]

Two main HOM related issues of the superconducting RF linac are the beam instabilities and the HOM-induced power. In order to understand the HOM issues regarding to beam stabilities and induced power in the PEFP low beta SRF linac, we have analyzed a normalized HOM-induced voltage, an induced power and a time-averaged

*Work supported by the 21C Frontier R&D program in Ministry of Science and Technology of the Korean Government.
#sunan@kaeri.re.kr

induced power especially from the TM monopole modes. The HOM trapping possibility has been established by considering a manufacturing deviation of the HOM frequency and by studying the spectra of the monopole, dipole and quadrupole modes in the low beta SRF cavity. The HOM-induced power in the PEFP cavity has been calculated for different Q_{ext}. The discussion about beam instabilities has shown the beam instabilities both in transverse and longitudinal directions are not issues in the PEFP low beta SRF linac. For the low beta cavities, the HOM coupler's Q_{ext} is lower than 3×10^5 for reducing the influence of the dangerous modes on the beam instabilities and HOM-induced power.

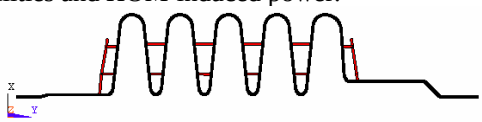

a. A 2-D PEFP low beta cavity with stiffening structure.

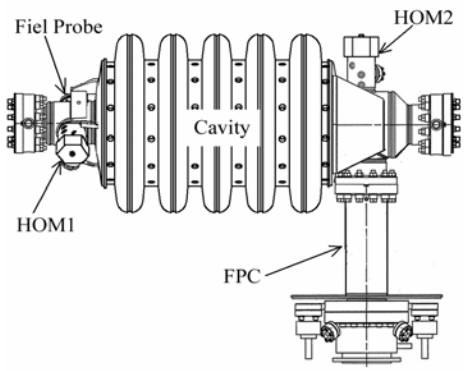

b. a low beta cavity with stiffening structures, HOM couplers, Field Probe and FPC.

Figure 1: PEFP low beta cavity and its stiffening structure.

HOM COUPLER AND FUNDAMENTAL POWER COUPLER

It has been designed a coaxial coupler with two stubs, one hook and one feed-through tip, which is directly installed on the inner conductor for the PEFP cryomodules, as shown in Fig. 2. The stick of the inner conductor is used to couple electric components of the HOMs, and the hook is for coupling magnetic components of the HOMs. The stubs are used to match capacitors of the notch filter and coupling feed-through, and to optimize the electromagnetic distribution in the coupler. The notch frequency filter is for tuning the notch position.

In order to control notch frequency shift, the frequency sensitivity has been reduced, and a nut tuner is designed.

PEFP Fundamental Power Coupler (FPC) is an antenna coaxial coupler, which is planed to copy and scale SNS FPC for PEFP cavities.

COOLING SYSTEM

PEFP cooling system includes cryogenic circulation, thermal insulation, cooling circuit of FPC, and detectors of temperature, pressure and helium liquid level. The design of the PEFP cryomodule cooling system is largely based on the SNS cryomodule cooling system. Table 2 lists the primary parameters of the PEFP low beta cryomodule.

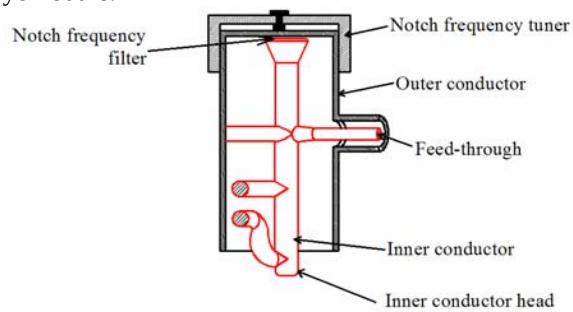

Figure 2: PEFP HOM coupler and its notch frequency tuner.

Table 2: Primary parameters of the PEFP low beta cryomodule cooling system.

Parameter name	Value
Cavities per cryomodule	3
Helium vessels per cryomodule	3
Primary circuit static heat load	24.8 W
Primary circuit dynamic heat load*	16.2 ~ 101.2 W
Pressure in Helium vessel*	0.032 ~ 1.0 Bar
Temperature in Helium vessel*	2.0 ~ 4.2 K
Pressure of the primary circuit helium liquid supply	3 Bar
Temperature of the primary circuit helium liquid supply	5 K supply
50 K shield heat load	163 W
Pressure of the 50 K shield supply	4.0 Bar
Temperature of the 50 K shield supply	35 K
Pressure of the 50 K shield return	3.0 Bar
Temperature of the 50 K shield return	55 K

Cryogenic circulation

As shown in Fig.3, there are three helium streams flowing in the PEFP cryomodule. A primary circuit produces 2.0 K to 4.2 K helium coolant in 3 helium vessels within the cryomodule. A secondary circuit provides coolant to 3 FPC flanges and outer conductors, and a third circuit provides coolant to the 50 K radiation shield. According to the testing and operating experience of the SNS cryomodules, the PEFP End Tank performs the function of the supply end tank and return end tank of the SNS cryomodule. The heat exchanger, Joule-Thomson (J-T) valves and auxiliary pipes are installed in the End Tank. The End Tank is not welded on the vacuum space, but sealed. This design is for easily repairing the cryomodule.

Thermal insulation

The thermal radiation shield is used to prevent the vacuum space and the other parts from transferring the thermal radiation to primary circuit. The thermal

insulation structures in the PEFP cryomodule are comprised of four parts, namely, thermal radiation shield (50K Shielding), multilayer insulation, space frame and vacuum space (see Fig.4). The multilayer insulation mitigates the heat transmission, heat convection and heat radiation to cold surface. The space frame reduces the heat transmission from the vacuum space to the primary circuit system. The vacuum space is used to decrease the heat convection in the cryomodule. The insulation is comprised of materials suitable for being used in a high radiation environment.

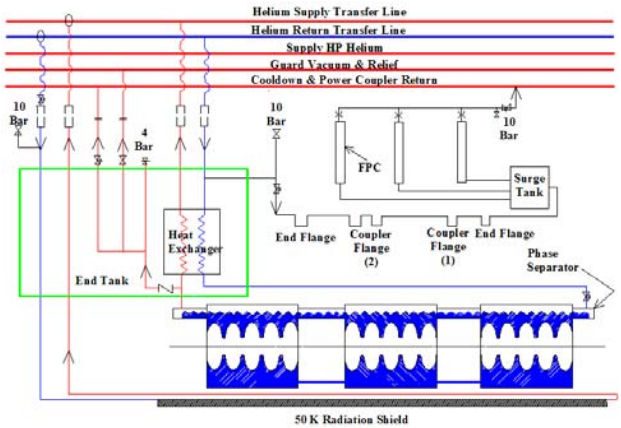

Figure 3: Cryogenic circulation schematic of the PEFP Low beat cryomodule. The blue color means the supply coolant or cold helium liquid; and red color means the return coolant.

FPC cooling circuit

The FPC flange and outer conductor are cooled by the secondary circuit. The inner conductor transfers the RF heat load to the inner conductor extension, which is cooled by DI water of 30°C with flux of 1 Gal per minute. The outer conductor extension is cooled by air.

Detectors of temperature, pressure and helium liquid level

There are four kinds of detectors for cooling system in the PEFP low beta cryomodule. Temperature detectors employ Temperature Diode (TD) and Thermocouple (TE) to pickup the temperature signal of helium liquid and helium gas within cryomodule and on FPC for control system; helium liquid level detectors send signal of the helium liquid level in helium vessel to the control system; pressure detectors transfer the helium stream pressure signal to the control system; and vacuum gauges measure the vacuum in the vacuum space, FPC vacuum side, and beam-pipe for the control system.

MAGNETIC SHIELDING

Because we did not find the serious cavity intrinsic quality factor Q_0 degradation due to trapped magnetic flux in the SNS cryomodules' testing and commissioning, we are going to copy and scale the SNS magnetic shielding for PEFP cryomodules (see Fig.4). The magnetic shielding structures of PEFP cryomodules are shaped by two coaxial cylinders. The Amumetal inner shield is attached on the helium vessels and covers the beam pipes between cavities and the end cavities. The effective working temperature of the inner shield is 9.2 K. The Amumetal outer magnetic shield is attached on the outside of the support frame and the end covers of the cryomodule. Its working temperature is almost the room temperature. If the Q_0 degradation due to trapped magnetic flux is found during prototype testing, we will choose the three-layer structure. The shielding effectiveness of the low beta cryomodules is: transverse shielding attenuation S_T=111.3 and axial shielding attenuation S_A=24.2.

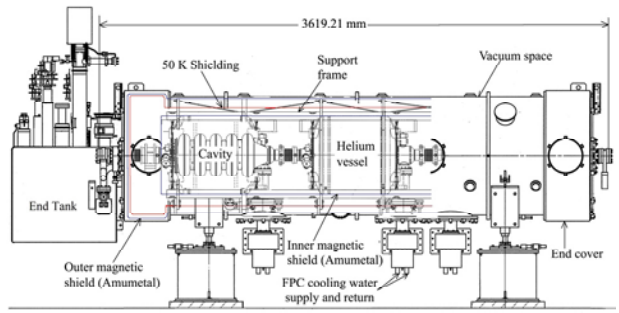

Figure 4: PEFP low beta cryomodule assembly.

CONCLUSION

The design of the PEFP low beta cryomodule is largely based on the successful design, construction and commissioning experience of the SNS project at JLab and ORNL. The comprehensive and competent analysis has been done for the fundamental electromagnetic and mechanical designs. Overall design is technically feasible.

ACKNOWLEDGEMENT

The authors would like to thank H. Wang, E. Daly from JLab for their technical review, and G. Wu and P. Kneisel from JLab, I. Campisi from ORNL, E. Pozdeyev from BNL and all the PEFP members for discussing and support. This work is supported by the 21C Frontier R&D program in Ministry of Science and Technology of the Korean Government.

REFERENCES

[1] Y. S. Cho and K. Y. Kim, J. Korean Phys. Soc. 48, 721(2006).
[2] H. J. Kwon, H. S. Kim, K. T. Seol and Y. S. Cho, J. Korean Phys. Soc. 48, 726(2006).
[3] Sun An, Y. S. Cho, B. H. Choi and J. H. Jang, J. Korean Phys. Soc. 59, (2007).
[4] Sun An, Y. S. Cho and B. H. Choi, Mechanical Analysis and Design of the PEFP Low Beta Cavity, Proceedings of APAC2007 in Indore, January 29 to February 2, 2007, 2007, WEPMA135.
[5] http://www.jlab.org/~genfa/fishpact/.

EXPERIENCES WITH THE MANUFACTURING, TESTING AND QUALITY CONTROL OF LARGE NUMBER OF SUPERCONDUCTING MAGNETS

A. Puntambekar, M. Bagre, Vikas Jain, Prashant Khare, M.G. Karmarkar, S. Kotaiah
Raja Ramanna Centre for advanced Technology, Indore, INDIA
R. Wolf, Guiseppe Mugnai, CERN, Geneva, Switzerland

Abstract

Raja Ramanna Centre for Advanced Technology has successfully completed the supply of nearly 1800 nos. Superconducting Corrector (SC) Magnets for the LHC project at CERN. Under the DAE-CERN collaboration agreement India through RRCAT, Indore was entrusted to manufacture, test & supply half of the total Sextupole Corrector (MCS) 1232 nos. and Decapole Octupole Corrector (MCDO) 616 nos. required for the LHC main dipole, while rest half were made in Europe. In this paper we describe the experience gained during technology development, prototyping and technology transfer to industry.

INTRODUCTION

The MCS & MCDO spool correctors consists of a coil assembly, glass fibre slit tube, steel laminations & aluminium shrinking cylinder for pre compression of coils, end plates for coil connection, parallel resistor for magnet protection (in case of MCS) and a magnetic shield also acting as a support. The coils have been wound using CERN supplied Nb-Ti SC wire in copper matrix.

Table 1: Main parameters of spool correctors

Parameters	MCS	MCD	MCO
Nominal strength	1970 T/m^2	1.2 X 10^6 T/m^4	8200 T/m^3
Length (mm)	160	110	
Aperture (mm)	58	63.6	58
Nom. current (A)	550	550	100
Working temp. (K)	1.9		
Turns per coil	2 x 13	2 x 20	1 x 43
Self ind. (mH)	0.8	0.4	
Quench current at 1.9K/4.2K (A)	1300/950	1250/915	297/195
Peak field (T)	1.9	2.4	2
Mass (Kg.)	~5.5	~5.0	

These corrector magnets require precision components and coils, accurate assembly procedure, elaborate testing plan and stringent quality control required for repeatable performance.

DEVELOPMENT CYCLE

Looking to the complexities and total quantum of work a two-fold strategy was adopted. All the technology was developed in-house at RRCAT in collaboration with CERN. The same was proved by way of making prototypes and elaborately testing them at 4.2 K at RRCAT & further at 1.9 K at CERN. Their large-scale production was planned at industries to make use of their infrastructure, expertise and efficiency under strict quality control from RRCAT.

Prototype Development

Prototype phase comprised of development of various critical components, tooling, coil winding & magnet assembly process and manual coil-winding machine. The coil former was CNC machined out of G-11 tubes. AISI M-45 grades Si steel laminations were punched using 0.5 mm thick sheet. Shrinking cylinder, its anodising treatment and different precision tooling for coil winding, magnet assembly & shrink fit tooling were developed at fabrication facility of RRCAT. Special bandage tooling was also developed for the application of B-stage semi cured glass epoxy tape over coil assembly, which was a messy affair. There were some troubles during assembly of hot shrinking cylinder over stacked laminations as it was getting stuck halfway. The inter coil connections were made using standard soldering. The individual modules were tested at 4.2 K in existing ϕ 200 mm bore cryostat & warm magnetic measurement (WMM) at 300 K was done at RRCAT on specially developed rotating coil vertical shaft bench. The 1.8 K training & also field quality test on these prototypes were done at CERN. The acceptance of prototype proved the tooling & process and gave confidence to proceed further [1].

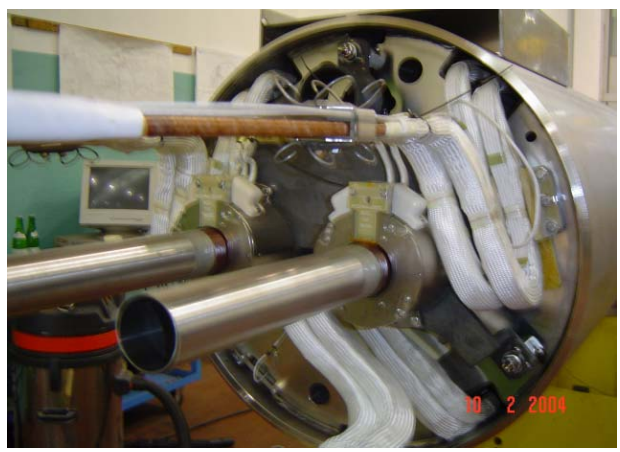

Figure 1: MCS fitted at one end of LHC Dipole.

Various Developments

The zero period due to design modifications was utilised in development of components & special machine requiring long development cycle time. Compression moulding for the Central island & end spacers were tried. The dimensional accuracies were achieved however the strength was not consistent due to variation in resin and glass content from batch to batch. Different concepts were

tried for automatic coil winding machine and finally cam guided twin arm type design fitted with torque motors was adopted. Similarly for low contact resistance & high productivity a 20 KHz, 4.5 kW ultrasonic welding machine was developed with the support of industries [2].

Large-scale Manufacturing

There was no industry, which had expertise & earlier experience of making SC magnet within the country. Market survey was conducted to explore the prospective manufacturer. Electrical motors manufacturer with ISO-9000 certification capable of handling large volume were pre requisite criteria.

Accordingly M/s Kirloskar Electric Co. Ltd, Bangalore was awarded order for making MCS magnet. Pre-series phase was introduced, during which the necessary technology was transferred for complete manufacturing cycle including tooling development & training personnel for various critical processes. Experience was also shared for the manufacturing of critical components with the vendors. The industrial partners were trained to adopt tolerances from tenth to hundredth of mm. As part of strategy the order for MCDO was awarded to another industry M/s Crompton Greaves, Bhopal, even though this required duplication of all infrastructure like clean room, special machine and imparting training etc.

Figure 2: Magnet production facility at Industry.

Process Modifications

Based on the experience of prototype certain modifications were also carried during series manufacturing. The semi cured 'B'-stage fibreglass tape was replaced by pre machined slit tube of G-11. Alternate use of open end & cross end coils with introduction of ultrasonic welding not only simplified the interconnections of coils but also resulted in very low contact resistance. Introduction of checking the lamination stack with a simulated hot dummy cylinder eased out the shrink fitting process to a very large extent. Initially the coil curing was tried by resistive heating by passing current through the coil itself however it was felt safe to cure the coil in the oven to avoid the risk of over burning of coil. The material of shrinking cylinder as per original specifications given by CERN was AA5082/5086 for its good mechanical strength. This material in the desired tube form was neither available nor the quantity was attractive to the manufacturer. As an alternate AA 6061 was introduced which has very good extrudability & the desired strength was achieved with temper T6. A marginal higher average compressive stresses (60-80 MPa) were maintained over the coil assembly, which resulted in excellent cold testing performance. Critical dowel holes were given suitable allowances for Electroless Nickel plating and assembly drilling were adopted for achieving tolerances of 0.01 mm. There was additional requirement of 516 MCO insert from CERN. Since the same was not agreed by the manufacturer to take up, they were made in-house at RRCAT through works contract, thanks to the infrastructure & expertise generated during prototype phase.

Figure 3: Magnets under preparation for cold testing.

TESTING & QUALITY CONTROL

Testing & quality control of nearly 2000 SC magnets being manufactured at different geographical locations nearly 1500 km away spreading over the duration of two to three years was a massive task.

Inspection and Quality Control at Industry

In pre-series magnets (a batch of ten) 100 % inspection was done. This was to prove the manufacturing cycle consisting of components & process. The philosophy of inspection during series manufacturing was based on sampling for batch control still keeping 100% inspection for identified critical parameters. Suitable gauges were employed for this. Trend monitoring was employed to keep the process within acceptable limits. The higher value of contact resistance in few lots was traced to worn out sonotrode, which was suitably repaired back. Periodic pre-despatch inspections were carried out at respective industries before despatch of each batch to RRCAT for dimensional control & electrical parameters. Magnetic measurement at warm for each magnet was also carried out on CERN built industrial magnetic measurement bench posted with each industry.

Inspection and Quality Control at RRCAT

All the SC magnets were also tested at 4.2K liquid He temperature. Since this required use of LHe and skilled manpower to handle cryogenic fluids, the cryogenic test facility was established at RRCAT [3]. The cold test plan for every magnet include training, measurement of contact resistance and ground insulation and retraining (after a thermal cycle to room temp) at 4.2 K. Starting with the capacity of testing 24 magnets per month and providing required training to the personnel the testing capacity was enhanced based on experience finally to more then 100 magnets per months to meet the schedule. Innovative technique of testing many magnets in 'series' using common current leads were also introduced for improvement of productivity & efficiency of testing with the help of sc switches specially designed & fabricated for this. Automated operation for powering & recording data using Desy-Lab based acquisition system were adopted. After the cold testing WMM was done on CERN built industrial test bench again to check for a possible variation change due to cold shock.

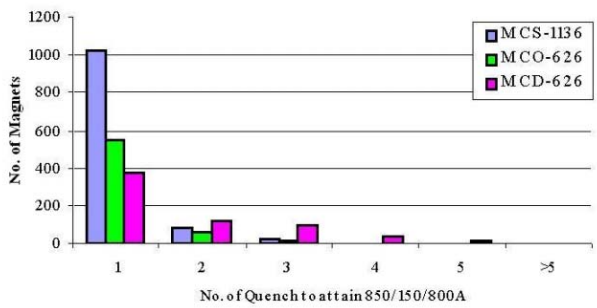

Figure 4: Training Performance of Corrector.

Table 2: Acceptance criteria for WMM & cold testing

	MCS	MCD	MCO
Axis Shift (mm) dX-dY *	0.1	0.1	0.1
Axis Shift (mm) dX-dY **	0.3	0.3	0.3
Mean & SD of Axis Shift lot of 50 (mm) dX-dY **	0.1	0.1	0.3
Axis twist (m-rad) dT *	1.5	2.5	3
Axis twist (m-rad) dT **	3	4	4
dB/B (%) mag. to mag.	<1	<1	<1
$I_{leakage}$ (300K) (μA)	<3	<3	<3
$I_{leakage}$ (4.2K) (μA)	<6	<6	<6
1 st Quench current (A)	550		100
In max 5 quench magnet to reach (A)	850	800	150
Contact resistance (nΩ)	< 35	<40	<50
No retraining Quench allowed below (A)	850	800	150

TEST RESULTS

All the magnets showed excellent cold testing result with more then 80 % reaching critical current in 1st quench itself and almost all reaching desired current with allowed 5 quenches (Fig-4). The rejection in cold testing was less then 0.5 %. For field quality at warm the main field variation was within ± 1 % (Fig-5). The limits set for axis shift & twist even though could be met during pre-series, were proving to be difficult & expensive to maintain during large series production on account of very tight tolerances (*-table-2). As the compensating errors average out & does not affect the machine performance a revised norms by keeping average & standard deviation still within original limits for a lot of 50 magnets allowing individual limits to higher values (**- table-2) was introduced. This reduced the rejection of magnets, which would not have affected the machine performance. Contact resistance was also successfully measured & was within limits with rejection below 1 %.

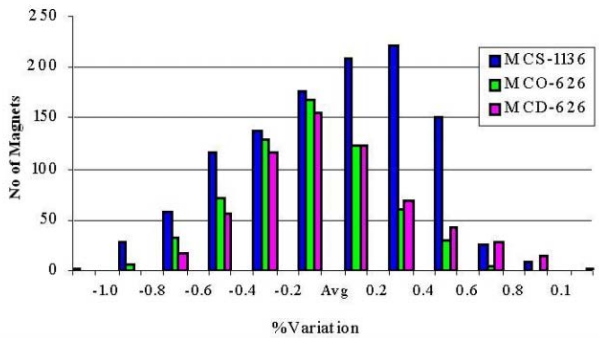

Figure 5: Main Field Variation of Corrector Magnets.

CONCLUSION

The complete project was accomplished with success with methodical planning, pre qualification by intensive testing and close monitoring on well-defined quality assurance plan. Splitting the order between Indian & Europe for each half quantity proved to be very wise. The short supply of Indian MCS magnet and long delayed supply of European MCDO magnets were compensated by their respective counterpart.

ACKNOWLEDGEMENT

The complete task was an effort of people from large number of groups. We acknowledge contribution from all the team members of AAMDDiv, erstwhile magnet division, power supply, cryogenic, IMA, computer div. & Fabrication facility RRCAT as well as team members of LHC-AT-MEL-MC group at CERN.

REFERENCES

[1] Salminen J. CERN Geneva, Puntambekar A., et al "Experience with the fabrication & testing of the sextupole Superconducting corrector magnets for the LHC". MT15, China 1997

[2] M. Allitt, A. Puntambekar, et al "Further development of Sextupole and Decapole corrector magnets for the LHC" MT-16 (1999).

[3] M. Bagre et al, "Development of cryogenic test facility and associated instruments for the testing of large number of superconducting spool corrector magnets at CAT" InPAC 2003.

DESIGN OF L-BAND SUPERCONDUCTING CAVITY FOR THE ENERGY RECOVERY LINACS

K. Umemori*, T. Furuya, S. Sakanaka, T. Suwada, T. Takahashi, KEK, Ibaraki, Japan
H. Sakai, K. Shinoe, ISSP/SRL, Chiba, Japan
M. Sawamura, JAEA/ERL, Ibaraki, Japan

Abstract

For the energy recovery linacs (ERLs), strong higher-order-mode (HOM) damping is indispensable to achieve high current operations. For this aim, we have designed L-band superconducting cavity which is optimized for the ERL operations. New cavity cell shape is designed. The HOMs are damped with microwave absorbers mounted on large beampipes. A new idea of eccentric fluted beampipe is proposed. Design concepts and estimated HOM characteristics are described in this paper.

INTRODUCTION

The ERLs are considered as promising future light sources which can provide excellent synchrotron radiation lights. The ERL project in Japan has been started with the cooperation of KEK, JAEA, ISSP and other SR institutes, with an aim to realize 5 GeV class ERLs [1]. For this aim, we have started to develop superconducting accelerating cavities for the main linacs, which are key components of the ERLs.

Accelerating gradient of 15 $\sim$ 20 MV/m is required to achieve high energy electron beams. For this purpose, multi-cell cavity is inevitable. A most challenging issue, which comes from a requirement of high current CW beams, is a strong suppression of HOMs excited in accelerating cavities. Dipole HOMs can cause current limitation due to the beam-breakup (BBU) instabilities. Even quadrupole HOMs can be problematic and lead to the quadrupole BBU instabilities. Typical simulation results, calculated by the Cornell university, show that the dipole and quadrupole HOMs should be damped to $(R/Q)Q/f < 1.4 \times 10^5$ ($\Omega\mathrm{cm}^{-2}\mathrm{GHz}^{-1}$) and $(R/Q)Q/f < 4 \times 10^6$ ($\Omega\mathrm{cm}^{-4}\mathrm{GHz}^{-1}$) respectively, for 100 mA operation [2], where f is the resonant frequency, Q is the quality factor, and R/Q is the ratio of the impedance and the quality factor. Monopole HOMs are also harmful. They are damped by HOM absorbers and could become significant heat load on cryo-modules. The frequencies of monopole HOMs should not be around multiples of 2.6 GHz to avoid resonant excitation.

The TESLA cavity is known as a representative L-band superconducting cavity. However, it is not adequate for the ERLs, because its HOM damping ability is not enough for high current operations. Furthermore, it is known that the loop-type HOM couplers, which are adopted for the TESLA cavity, have a heating problem for the CW operations [3]. Therefore, we decided to develop 1.3GHz superconducting cavity which is optimized for the ERL operations, especially for HOM damping. We have designed new cavity cell shapes, applied large beampipes on which microwave absorbers are mounted, and adopted a new idea of an eccentric fluted beampipe. Details of the design concepts and its HOM characteristics are discussed below.

* kensei.umemori@kek.jp

HOM SUPPRESSION BASED ON TESLA SHAPE CAVITY

At first, we start discussion based on the TESLA shape cavity. Subjects are concentrated on the effectiveness of the large beampipes and a number of cells

Large Beampipe

In order to investigate the HOM damping capability of the large beampipes with microwave absorbers, we designed the KEK-ERL model-1 cavity. In this model, cavity cell shapes are basically the same as the TESLA cavity, but one side of beampipe diameter is enlarged from 78 mm to 108 mm. All monopole and dipole modes, except TM010, propagate through the beampipe and are damped by the absorbers. From simulation results, it was found that the large beampipe damper is from several to ten times more effective than the loop-type HOM couplers, as shown later in Figure 4. Here, HOM impedances of the TESLA cavity are quoted from the data shown in [4, 5] and those of the KEK-ERL model-1 cavity are calculated using MAFIA. External Q (Q_{ext}) of the beampipe is estimated and used for the plot. For the KEK-ERL model-1 cavity, the value of $(R_t/Q)Q_{ext}/f$ is just below the 100mA threshold. Considering the fact that loaded Qs of absorber could be somewhat larger than the estimated Q_{ext}, further suppression of dipole HOMs is required.

Number of cells

One method to decrease the HOM impedances is to reduce number of cells per one cavity [6]. We attempted a seven-cell cavity with the KEK-ERL model-1 strategy. The HOM impedances are lowered around half, but the effect is not so drastic. The shunt impedance (R_{sh}) of the accelerating mode is also lowered more than 20 %. From this result, we decided to keep nine cells.

DESIGN OF THE KEK-ERL CAVITY

With the aim of strong HOM damping, we have designed a new cavity cell shapes which have larger iris diameter. As

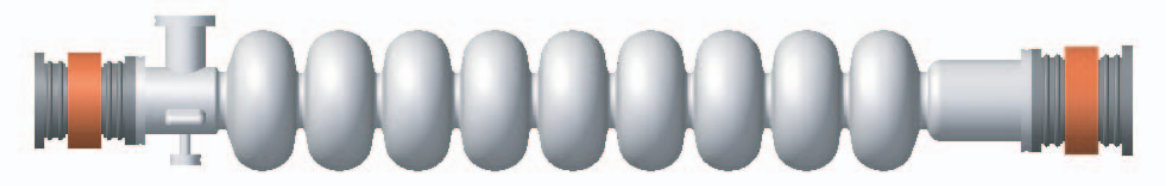

Figure 1: Conceptual view of the KEK-ERL model-2 cavity.

a measure against the quadrupole HOMs, the idea of eccentric fluted beampipe is introduced and its damping ability is discussed in this section.

Cavity Cell Shape

We have designed cavity cell shapes with the following strategy; impedances of dipole HOMs should be as small as possible, frequencies of monopole HOMs should be sufficiently far from multiples of 2.6GHz, and R_{sh}/Q of the accelerating mode should be kept as high as possible.

First, we investigated the possibility of a larger iris diameter, which strengthens the cell-to-cell couplings. It was found that it can significantly lower the impedances of HOMs even in the case of nine-cell cavity, but as expected it reduces that of the accelerating mode. In view of above strategy, we selected 80 mm as the iris diameter. Next, we considered about a cavity diameter. The frequency of TM020 mode is close to 2.6 GHz and depends on it. Therefore, we have to select cavity diameter carefully. Considering the characteristics of TM020 mode and a typical fabrication precision, we required that the all of frequencies of TM020 pass-band should be more than 40 MHz apart from 2.6 GHz. As a result, the cavity diameter was decided as 206.6mm, which was same with that of the TESLA cavity.

Large beampipes, whose diameters were chosen as 120 mm and 100 mm, were adopted so as to propagate TE111 and TM011 mode effectively. Microwave absorbers were mounted on both sides of beampipes. The eccentric fluted beampipe, which is described below, was attached to the side of the input coupler port. The cavity described above is called as the KEK-ERL model-2 cavity. The conceptual view is shown in Figure 1.

Table 1: Parameters of the accelerating mode for the KEK-ERL model-2 cavity and TESLA cavity

	KEK-ERL model-2	TESLA
Frequency [MHz]	1300	1300
Iris diameter [mm]	80	70
Cavity diameter [mm]	206.6	206.6
Rsh/Q [Ω]	897	1030
$Q_0 \times R_s$[Ω]	289	270
E_p/E_{acc}	3.0	2.0
H_p/E_{acc} [Oe/(MV/m)]	42.5	42.6
Coupling [%]	3.8	1.9

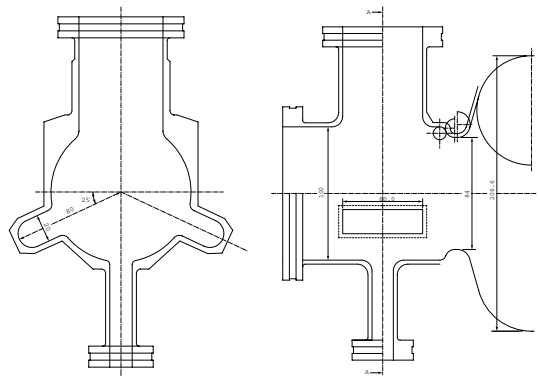

Figure 2: The schematic views of the eccentric fluted beampipe.

Main parameters of the accelerating mode are shown in Table 1. Since the cavity design is focused on the HOM damping, the accelerating mode is sacrificed to some extent. Its R_{sh}/Q is lowered around 900 and E_p/E_{acc} is raised to 3.0.

Eccentric Fluted Beampipe

Another challenge is the damping of the quadrupole HOMs. Because their cut-off frequencies are generally high, their damping is difficult. For this purpose, we propose the eccentric fluted beampipe. The schematic views are shown in Figure 2.

The eccentric fluted beampipe acts as a mode transformer. Due to its asymmetric shape, the quadrupole modes can be partly transformed into dipole modes. Then, they propagate through the beampipes and are absorbed by the dampers. The length of around 6 cm is enough to transform the modes. Angle of the flutes is chosen to couple with both polarizations of the quadrupole modes. The effect on acceleration mode was checked and found to be negligible.

HOM CHARACTERISTICS

The HOM characteristics of the KEK-ERL model-2 cavity were estimated using MAFIA. The results are shown below.

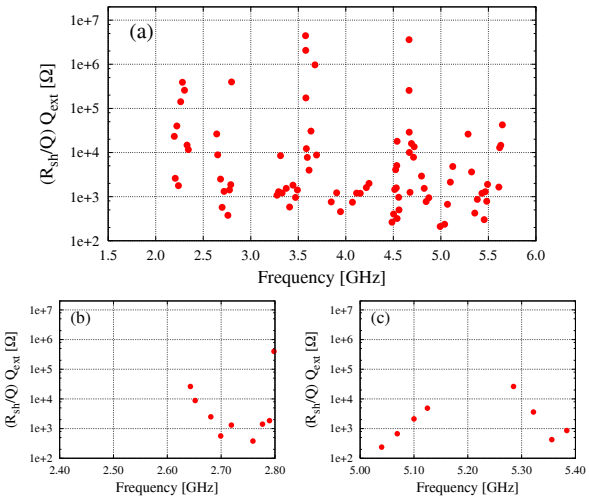

Figure 3: (a) Spectrum of the monopole HOMs and that for (b) around 2.6 GHz and (c) around 5.2 GHz for the KEK-ERL model-2 cavity.

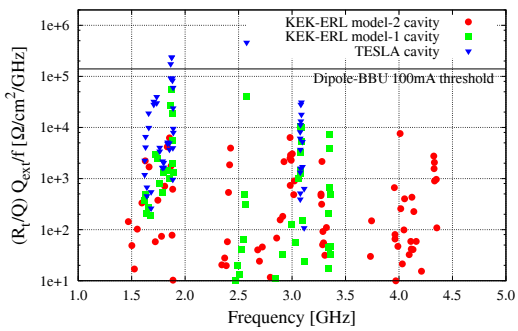

Figure 4: Spectrum of the dipole HOMs. The values of $(R_t/Q)Q_{ext}/f$ are plotted for the TESLA cavity, KEK-ERL model-1 cavity and model-2 cavity.

Monopole Modes

The impedances of monopole HOMs were calculated up to 5.6 GHz and shown in Figure 3. No HOMs exist around 2.6 GHz and 5.2 GHz. It is noted that when ERL is operated with lower frequency of beam repetition, its frequency should be selected carefully not to excite the monopole modes of high impedances.

Dipole Modes

The impedances of dipole modes were calculated up to 4.5 GHz. In Figure 4, the values of $(R_t/Q)Q_{ext}/f$ for KEK-ERL model-2 cavity are plotted and compared with the TESLA and KEK-ERL model-1 cavity. Impedances for the KEK-ERL model-2 cavity are about one order smaller than those for the model-1 cavity. The BBU simulations performed by JAEA indicate that the BBU threshold reaches to more than 600 mA for the KEK-ERL model-2 cavity even without randomization of HOM frequencies [7].

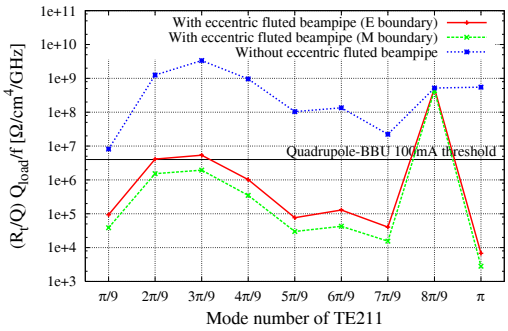

Figure 5: Impedances of the TE211 modes for the KEK-ERL model-2 cavity, for the case with and without the eccentric fluted beampipe. The results for both polarizations are plotted.

Quadrupole Modes

The impedances of the TE211 were calculated for KEK-ERL model-2 cavity with the eccentric fluted beampipe. The values of $(R_t/Q)Q_{load}/f$, assuming ideal absorbers, are plotted in Figure 5. At present, the design of the eccentric fluted beampipe is not yet optimized for the KEK-ERL model-2 cavity, but it shows a promising damping ability. High impedance of $8\pi/9$ mode results from an asymmetry of its field. After optimization, it is expected that 100 mA quadrupole-BBU threshold can be satisfied.

SUMMARY

We have designed the 1.3 GHz superconducting cavity, for the ERL main linacs, which is optimized for the ERL operations. With the goal of the strong damping of HOMs, we designed new cavity cell shape and adopted large beampipes with microwave absorbers. Quadrupole HOMs are damped with the eccentric fluted beampipe. Although some optimization is needed for the eccentric fluted beampipe, our cavity design satisfies the conditions for 100 mA CW operations. At the moment, nine-cell Nb KEK-ERL model-2 cavity is in production. Its performance will be evaluated in the near future. We also proceed the development of components such as an HOM damper, an input coupler and a frequency tuner.

REFERENCES

[1] T. Kasuga et al., in these proceedings

[2] M. Liepe, Proc. of the 11th Workshop on RF Superconductivity (SRF2003), Lübeck/Travemünde, Germany, 2003.

[3] P. Kneisel et al., PAC'05, p. 4012

[4] *TESLA Test Facility Linac Design Report*, edited by D. A. Edwards, DESY, 1995.

[5] *TESLA Technical Design Report*, edited by R. Brinkmann et al., DESY, 2001.

[6] R. Rimmer et al., PAC'03, p. 1389

[7] R. Hajima (JAEA), private communication

STATUS OF THE SOLEIL PROJECT

L. Nadolski, J.C. Besson, P. Brunelle, A. Buteau, L. Cassinari, M.E. Couprie, J.C. Denard, J.M. Filhol, C. Herbeaux, J.F. Lamarre, P. Lebasque, V. Le Roux, A. Lestrade, M.P. Level, A. Loulergue, A. Madur, P. Marchand, A. Nadji, R. Nagaoka, B. Pottin, J.B. Pruvost, F. Ribeiro, M.A. Tordeux,
Synchrotron SOLEIL, Gif-sur-Yvette, France

Abstract

SOLEIL, the 2.75 GeV new French Synchrotron Radiation Facility, located near Paris, is under commissioning. Here are reported the main results obtained especially on the storage ring. The beam dynamics characterisation of the 3.7 nm.rad optics is presented, as well as the first measurements of the instability thresholds. Furthermore comparison is made with expectations of the linear optics model and instability calculations. First experience with innovative devices and technologies is also presented: TANGO control system, BPM system, extensive use of NEG coated vacuum vessels, unconventional RF system (Solid state amplifiers and superconducting cavities). Seven insertion devices accommodating a wide energy range from 5 eV to 30 keV (in-vacuum, Apple II, large period electromagnetic types) are now installed on the machine and some of them are producing the first photon beams which are delivered to the beamlines. Finally a roadmap towards beam delivery to users will be presented.

INTRODUCTION

SOLEIL is designed as a 2.75 GeV third generation light source with 21 out of 24 straight sections (SS) dedicated for installing insertion devices (IDs). This very large ratio of straight sections (43% of the 354 m long circumference, with 29% for magnetic structures) is shared between 4x12 m long SS, suitable for accommodating long period IDs, 12x7 m medium SS, and 8x3.8 m short SS to accommodate in-vacuum undulators. With a small emittance and a target 500 mA beam intensity, the average brilliance will range from 10^{16} to 10^{20} ph/s/0.1%bw/mm^2/mrad^2 for respectively bending magnet and ID based beamlines. Table 1 sums up the main storage ring parameters.

A total of 24 beamlines have been approved by the SOLEIL council. The spectral range is equally shared above and below the energy of 1.3 keV, with a distribution of 6 beamlines on bending magnets (BM) and 18 on ID beamlines, plus 2 IR beamlines.

Here are reported the commissioning results from the Linac to the beamlines with a focus on the storage ring (SR) and the performances reached by the end of 2006.

INJECTOR COMMISSIONING

The injector is composed of two parts, a 100 MeV Linac and a full energy Booster, that were both commissioned in 2005.

The Linac HELIOS is a turn-key system provided by THALES whereas the transfer line from Linac to Booster was constructed by SOLEIL. The performances are better than specifications and have been reported extensively before [1]. In the long pulse mode, the Linac produces a 300 ns train of pulses with a total charge up to 9.3 nC with an energy spread below ± 0.5 % and normalized (4 $\gamma\varepsilon_{rms}$) emittances of 47 (± 10) and 52 (± 10) π mm.mrad respectively in horizontal and vertical planes. For temporal structure a short pulse mode provides 1 to 4 pulses of 1.3 ns with an energy spread of ± 0.6 % for 1 pulse and ± 0.8 % for 4 pulses.

The 3 Hz 157 m long Booster ring provides a 140-150 nm.rad beam emittance at 2.75 GeV. The tracking of the SLS-type digitally control power supplies (dipole and quadrupoles) of ± 0.2 % keeps the tunes within ± 0.05 giving an injection efficiency of 90-95% without further losses during the energy ramping up for different filling patterns. Beam extraction and guiding from Booster to SR transfer line occurred smoothly on May 8th 2006. Further details are given in references [2,3].

Parameter	Value
Energy (GeV)	2.75
Circumference (m)	354.097
Revolution period (μs)	1.18
Betatron tunes H/V	18.2/ 10.3
Energy spread	1.016 10^{-3}
H-Emittance (nm.rad), 1% coupling	3.7
Bunch length @ 4 MV (ps)	14
Damping times H/V/L (ms)	6.56/6.56/3.27
RF frequency (MHz)	352.2

Table 1: Storage ring main design parameters.

STORAGE RING COMMISSIONING

Challenges

Before injecting the first electrons, the storage ring was incorporating new technologies and challenges which potentially, could have jeopardized the commissioning schedule. Final 10 mm vertical aperture 5 m long ID vacuum chambers were installed from day one on the 10 medium straight sections. Moreover the ring was equipped with NEG coated aluminium chambers over 56 % of the circumference, with a SOLEIL designed super conducting cryomodule containing 2 HOM free SC RF cavities, new BPM digital electronics, and 4 insertion devices (1 Apple II type, 1 in-vacuum and 2 electro-

magnetic undulators). A new type of RF power sources based on solid state amplifiers was implemented to feed the RF cavities. Finally human resources from the support groups (computing, vacuum, alignment…) had to be shared with beamlines to get the first eleven beamlines receiving beam between 2006 and 2007.

Main Milestones

The first electron beam was injected into the storage ring on May 14th 2006 [4,5]. The progress was then very fast as 300 mA (maximum achievable beam current with the present RF configuration) were stored in ¾ filling pattern end of September, after only 8 effective weeks of commissioning. By the end of December 2006, a total current dose of 75 A.h was accumulated (see Fig. 1), and five beamlines had received the photon beam.

During this period, intensive commissioning of the main equipments was performed. Several shutdown periods were dedicated for installing new IDs, for installing and baking out front ends, for cleaning the cooling water circuit polluted accidentally with resin balls (6 weeks), and for replacing badly mounted RF fingers of bellows in some short straight sections.

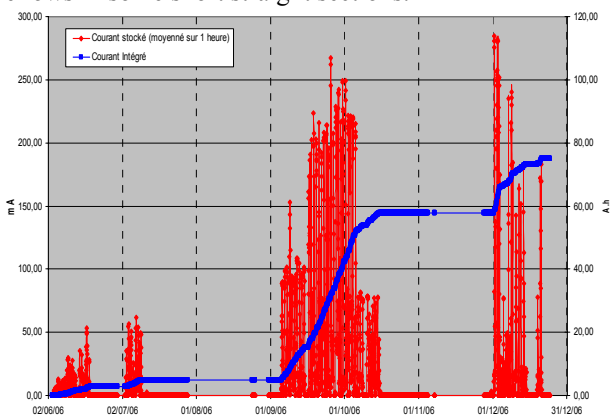

Figure 1: Beam current (red) and evolution of the integrated current (blue) during year 2006.

Closed Orbit

Thanks to very good magnetic measurements (quadrupoles: $\Delta x, \Delta z$ = 8.4, 7.5 µm rms , $\Delta\theta$ = 40 µrad rms) [6] followed by a very accurate equipment alignment (60 µm rms for horizontal and vertical quadrupole+girder assembly), the uncorrected rms beam orbit was 3.1 mm and 0.41 mm respectively in horizontal (H) and vertical (V) planes. After calibration of the offsets of the 120 BPMs by beam based alignment [7] and orbit correction, using the standard SVD method applied to the 56 H & V correctors, these values were reduced down to 68 and 58 µm rms. The rms corrector strengths are 0.9 (H) and 0.4 (V) A, *i.e.* below 10 % of their maximum capability.

Beam Position Stability

As reported in [4], to achieve beam stability at a level of 1/10th of the beam sizes, a careful girder design was done with a first resonance mode predicted at 40 Hz: it was determined to be 47 Hz through experimental modal analysing and confirmed by the beam noise spectrum (see Fig. 2). In a spectral frequency span of 0-100 Hz, the integrated beam noise is below 2 µm rms in both planes. Slow thermal drift of a few tens of micrometers will disappear as soon as the tunnel air conditioning is fully operational. Slow and fast orbit feedbacks will be implemented in 2007.

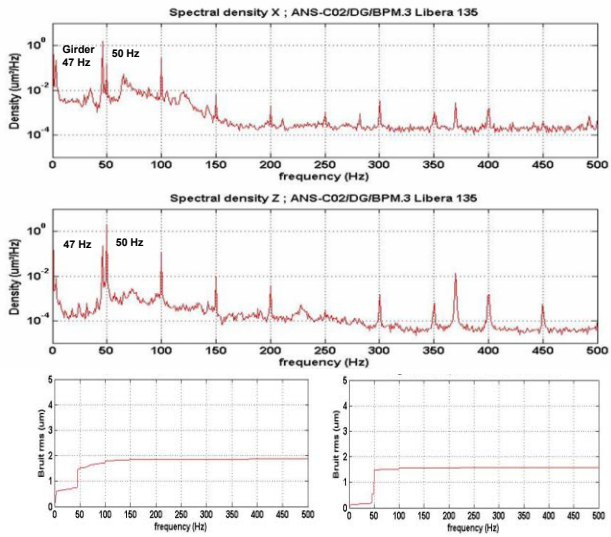

Figure 2: First measured beam noise spectrum using BPM turn by turn data showing an integrated noise less than 2 µm rms in both planes.

Linear Optics

The four-fold symmetry of the lattice has been restored by using the LOCO code [8]. The beta-beats were reduced from 6 (H) and 8 % (V) rms down to 0.8 (H) and 1.0 % (V). The amplitude of variations of the 160 individual quadrupole gradients are still to be understood, especially for defocusing quadrupoles with variation up to 3-4 %.

Natural total chromaticities (-52 and -19) are closed to the model (-53, -23). The main difference in the V-plane is coming from the energy dependence of the dipole fringe field not taken into account in our numerical model.

Betatron coupling deduced from the closest tune approach is about 0.08 % using Guignard formalism [9]. Beam emittance measurement was performed using a pinhole system on a 3.8° exit dipole port. The horizontal emittance was measured at 3.9 ± 0.25 nm.rad (for a design value of 3.7 nm.rad) and the vertical emittance at 11 pm.rad, giving a very low 0.08 % natural coupling (no skew quadrupoles powered on).

Tune shift variations with energy are also very close to the model (see Fig. 3). Minimum acceptance apertures are 5 mm (V-plane) and -15 mm (H-plane) in agreement with the size of the smallest vertical chamber and the horizontal position of the injection Eddy current septum.

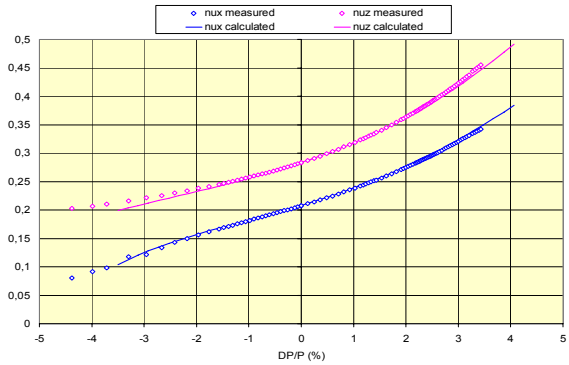

Figure 3: Comparison between measurement and modelling for tune shift with energy for nominal lattice.

High Current and Instabilities

No instability was observed in the longitudinal plane as expected with the superconducting RF cavities.

In multi-bunch mode, a mixture of resistive-wall and ion induced instabilities is observed in both H- and V-planes. The behaviour of the ions induced instability depends much on the beam filling pattern.

The vertical threshold at low chromaticity is in very good agreement with prediction (30 mA), but for larger chromaticity, it is not possible to conclude yet because of the ions. In the horizontal plane, the current threshold seems smaller than the one expected around 90 mA (see Fig. 4 and [10,11]), but the beam is still ion dominated.

Stable conditions up to 300 mA could be achieved with both a ¾ filling pattern and reasonable normalized chromaticities (ξ_H = 0.2, ξ_V = 0.4). For single bunch mode, current thresholds seem to be lower by a factor 2 with respect with the simulations. Further verification is underway.

To combat the transverse instabilities a digital bunch by bunch transverse feedback was installed. The SPring 8 bunch by bunch processor is used, enabling a single loop to correct both planes. For excitation, a dedicated stripline is under construction. First tests with a provisional stripline have shown that the beam can be kept stable up to the maximum current (300 mA) at zero chromaticity in both planes.

Diagnostics

SOLEIL developed BPM electronics in cooperation with Instrumentation Technologies [11]. The resulting electronic rack, called LIBERA, is in the final commissioning phase. The resolution of the BPM electronics for orbit feedback is below 0.2 µm rms within a 100 Hz bandwidth. It also provides turn-by-turn data for machine studies with 3 µm rms resolution (for a 4 mA beam) or 10 Hz data for slow orbit feedback with a 10 kHz data flow for simultaneous fast orbit feedback. Each LIBERA can deliver a position interlock signal. An additional LIBERA is accurately monitoring the tune.

A visible synchrotron monitor and an X-ray pinhole camera are operational for beam imaging enabling to follow beam motions, induced instabilities, and giving beam size measurements.

The first bunch length measurements with a Hamamatsu streak camera gave 45 ps FWHM with 2 MV RF accelerating voltage, a value close to the expected one at low current. The bunch length increases by a factor of two with a current up to 10 mA/bunch.

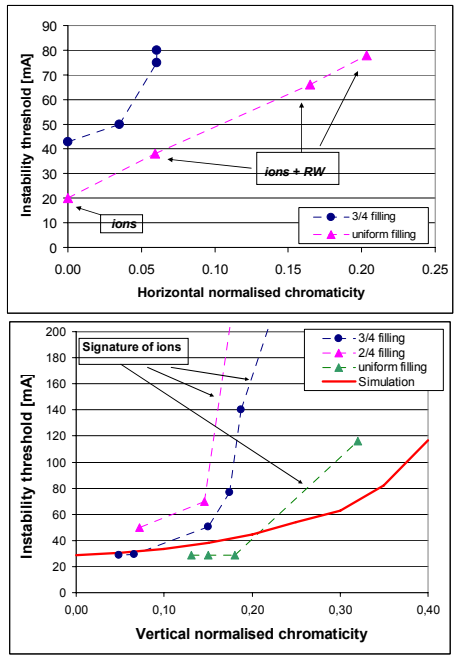

Figure 4: Observed transverse multibunch instabilities thresholds versus normalized chromaticity.

RF System

With the first cryomodule [13,14] the maximum current of 280 mA was reached in operation with no particular difficulties. Before installing the RF-feedback, the cavities were slightly detuned in order to push away the Robinson instability. Overall the RF system is very stable. Further RF conditioning of the cavity coupler will be necessary for continuous operation at 300 mA. No longitudinal instabilities (HOM) were observed on the beam. The two 180 kW solid state amplifiers are running very smoothly. A few transistors failures (18/1450) were observed over 1500 hours of operation but without interrupting the beam. The residual phase oscillation is about 0.1°. The cryogenics plant which maintains the cryomodule at 4 K (50 l/h liquefaction, 400 W refrigeration) is under very reliable operation.

Vacuum System

Average pressure before the first beam was 4 10^{-10} mbar after having baked out the whole ring except the injection section. All vacuum chambers but the dipole ones are in aluminium and coated with a NEG (Non Evaporable Getter) layer with thickness varying from 0.5 (centre) to 1.5 µm (vacuum chamber sides) over a total of 56 % of the ring circumference.

During the commissioning the maximum sustainable current was not limited by the pressure rise due to the photon stimulated desorption but mainly by obstacles in

the vacuum vessel reducing the vertical beam stay clear from 5 mm down to 1.5 mm. These obstacles were found to be the consequence of a systematic bad mounting of the RF shield of the bellow of the short straight sections.

In addition, reduction of water flow (presence of resin balls in the cooling water circuit) and bad brazing in the dipole absorber led to abnormal temperature rises. Figure 5 illustrates the average pressure normalized to beam current versus beam dose giving the vacuum conditioning. Radiation measurement downstream the 10 m long NEG coated chamber (14 mm of vertical aperture) showed that Bremsstrahlung rate is negligible at 250 mA.

Twelve front-ends (FE) are now installed inside the SR tunnel. Already 9 FEs are connected to the vacuum vessels in the optics hutches through the shield wall.

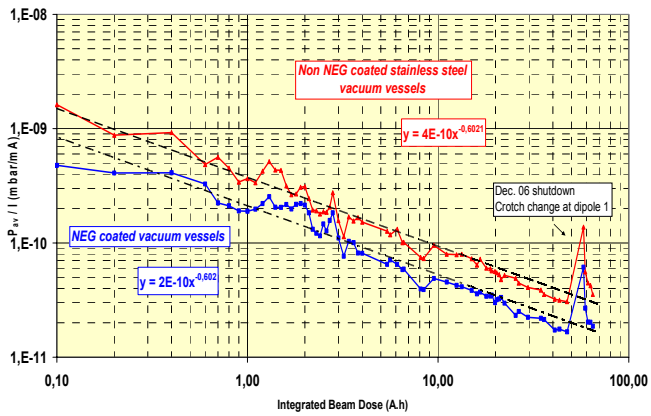

Figure 5: Average pressure of Cell 07 normalized to beam current versus beam integrated dose.

Machine Safety System

The machine protection is fully operational and based on PLCs interconnecting vacuum system and diagnostics.

Using the low latency LIBERA port, the position interlock has been commissioned based on the vertical position reading of all the BPMs upstream the 32 dipoles. Any vertical position larger than ± 1mm trips the beam in less than 10 ms if the stored current is above 20 mA.

For avoiding heating up the narrow part of the vacuum chamber, an instability interlock has been commissioned with success. It consists on a 4.4 mm vertical slit located on a beamport, and locked on the beam through thermocouples. If any large vertical instability occurs the beam is tripped off.

Insertion Devices

By the end of December 2006, seven insertion devices were already installed into the storage ring: 2 Apple II type (HU80), 2 hybrid in-vacuum undulators (U20, 5.5 mm minimum gap), 3 electromagnetic undulators (1xHU640, 2xHU256) [15]. These IDs are under heavy commissioning: beam effect characterization, feedforward table generation, and active compensation on the e-beam.

As the ID control will be partial or total by the beamlines, the full compensation of their effects on the beam (orbit distortion, focusing, emittance coupling) will be quite challenging.

First results are rather promising. For instance, for HU80 and HU256, the residual orbit motion is already around 1.5 µm rms in both planes with feedforward switched on (see Fig. 6). Both U20 were closed at minimum gap without beam losses and with focusing and orbit distortions as expected from magnetic measurements. Because of coil motions of the 10 m long HU640 during dis- and re-assembling of the upper and lower parts, coil repositioning was necessary to reduce large orbit distortions.

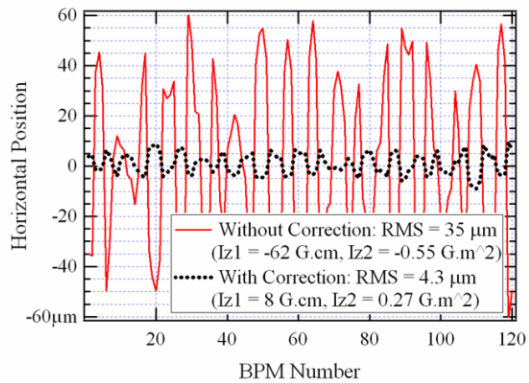

Figure 6: Horizontal orbit distortion without (red) and with (black) feedforward for HU80 tuned in linear horizontal polarization mode.

Control System

For the first time, the TANGO control system is used to control and supervise a full facility from the accelerators to the beamlines. Beam commissioning has been greatly accelerated by using the generic JAVA TANGO applications, and the GlobalSCREEN supervision panels written by operators. Accelerator commissioning has benefited from the Matlab Middle Layer applications fully integrated in the control system. More than 30 000 parameters are supervised from the control room. Use of electronic logbooks, archiving system, and monitoring tools makes all these tasks more manageable (see [16-17] for more details and references within). Main work now focuses on converting expert to daily control applications.

Day to Day Operation

A typical beam lifetime is 10 h for 100 mA stored in ¾ filling pattern with 0.3 % coupling and 2 MV as a total voltage of the RF cavities. Beam lifetime in multibunch mode is still dominated by vacuum pressure.

A total of 1 400 hours of beam was achieved from July to December 2006. Beam availability was close to 83.5 % with 11.2 % of failures (mainly water and power supplies), and 5.3 % including start-up, injection and equipment testing.

Operation group is now complete with 8 fulltime operators. For a 24h/24h and 7 day a week operation, part time operators coming from Machine, technical and computing division (around 70 people) will work up to 12 8 hour shifts per year.

BEAMLINE COMMISSIONING

Between 2006 and 2007, 11 beamlines (BL) will be opened. Energy spectrum extends from IR, VUV to Soft, and Hard X-Rays.

From September to December 2006, 5 BL opened their front-ends (3 on bending magnets, 2 on insertion devices). Thanks to a very good alignment, synchrotron beam was observed almost instantly on a beam screen. On bending magnet beamlines, qualification of the optics and calibration of the monochromator have started and first absorption spectra could be observed. For ID beamlines, the alignment of the first diaphragms and elements has been checked thanks to a so-called DIAGON diagnostics (CCD in case of HU256, multilayer mirror + CCD on HU80). Figure 7 shows the radiation ring pattern using HU80 undulator in case of the vertical linear polarization.

These beamlines are now either under intense commissioning or finishing installing the optics and equipments down to the optical and experimental hutches.

First beam on in-vacuum and IR beamlines are planned for beginning of February 2007. By April 2007, beam time will be allocated to the first users by the peer review committees.

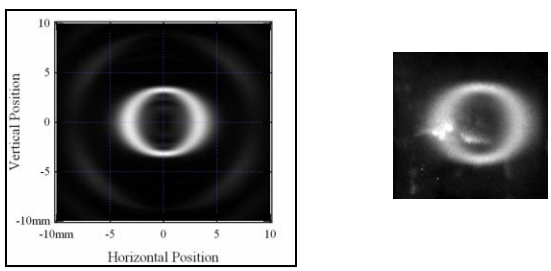

Figure 7: Comparison between SRW simulation (left) and measurement (right) of synchrotron radiation emitted from an elliptical undulator (HU80) at an 180 eV energy.

NEXT STEPS IN 2007

To improve beam stability, the slow, fast orbit feedbacks, XBPMs, and the multibunch transverse feedback will be set into operation.

Characterisation of instabilities, high current operation and studies of 1 and 8 bunch modes will continue.

A digital RF feedback is under development, the second cryomodule enabling to reach up to 500 mA is foreseen by fall 2007.

In parallel, another set of 7 IDs will be installed into the tunnel, and preparation for top-up operation will start.

Opening of the first 11 beamlines to expert or external users will occur in spring of 2007.

AKNOWLEDGEMENTS

Those rapid progresses and successes are mainly due to a strong and very productive interaction and support between the commissioning team and many groups such as the operation, magnetism and insertion, power supplies, RF, Linac, diagnostics, vacuum, alignment, mechanical and engineering, electronics and computer, infrastructure, and safety groups.

REFERENCES

[1] A. Setty et al., “Commissioning of the 100 MeV Preinjector HELIOS for the SOLEIL Synchrotron”, EPAC’06, Edinburgh, July 2006, pp. 1274-1276

[2] A. Loulergue, “Commissioning of the SOLEIL Booster”, EPAC’06, Edinburgh, July 2006, pp. 3281-3283.

[3] P. Gros et al., “The 3Hz Power Supplies of the SOLEIL Booster”, EPAC’06, Edinburgh, July 2006, pp. 2652-2654.

[4] J.M. Filhol et al., “Overview of the Status of the Soleil Project”, EPAC’06, Edinburgh, July 2006, pp. 2723-2727.

[5] A. Nadji et al, “First Results of the Commissioning of the Storage Ring”, EPAC’06, Edinburgh, July 2006, pp. 3284-3286.

[6] P. Brunelle et al., “Magnetic Measurement Results of the Dipoles, Quadrupoles and Sextupoles of the SOLEIL Storage Ring”, EPAC’06, Edinburgh, July 2006, pp. 3278-3280.

[7] A. Madur et al, “Beam Based Alignment for The Storage Ring Multipoles of Synchrotron SOLEIL”, EPAC’06, Edinburgh, July 2006, pp. 1939-1941.

[8] J. Safranek, “Experimental Determination of Storage Ring Optics using Orbit Response Measurements”, Nucl. Inst. And Meth. A388, 27 (1997).

[9] Guignard, “Betatron Coupling and related Impact of Radiation”, Yellow Report CERN 95-06, Geneva, pp. 43-76.

[10] R. Nagaoka, “Instability Studies using Evaluated Wake Fields and Comparison with Observations at SOLEIL”, EPAC’06, Edinburgh, July 2006, pp. 2847-2849.

[11] R. Nagaoka et al. “Recent Studies of Geometric and Resistive Wall Impedance at SOLEIL”, EPAC’06, Edinburgh, July 2006, pp. 2850-2852.

[12] J.C. Denard et al., “Preliminary tests of a new kind of BPM System for SOLEIL”, DIPAC’05, Lyon, 2005, pp. 39-41.

[13] P. Marchand et al., “Commissioning of the SOLEIL RF Systems”, EPAC’06, Edinburgh, July 2006, pp. 384-386.

[14] M. Diop et al., “Low Level RF System development for SOLEIL”, EPAC’06, Edinburgh, July 2006, pp. 1447-1449.

[15] F. Briquez et al., “Status of the SOLEIL Insertion Devices”, EPAC’06, Edinburgh, July 2006, pp. 3556-3558.

[16] L. Nadolski et al., “Control Applications for SOLEIL Commissioning and Operation”, EPAC’06, Edinburgh, July 2006, pp. 3056-3058.

[17] A. Buteau et al., “Status of SOLEIL Control Systems”, EPAC’06, Edinburgh, July 2006, pp. 3053-3055.

STATUS OF THE AUSTRALIAN SYNCHROTRON PROJECT

G. LeBlanc, Australian Synchrotron Project

Abstract

The Australian Synchrotron, a synchrotron light facility based on a 3-GeV electron storage ring, is currently being commissioned at a site in the Metropolitan District of Melbourne. On July 14, 2006 less than three years after earth moving machines started to prepare the site, beam was captured, accumulated and stored in the storage ring. Storage ring commissioning, and beamline installation and commissioning will continue through March 2007, after which the facility will become operational. In this paper we give a brief overview of the facility and its beamlines, followed by the latest results from accelerator commissioning activities.

FACILITY OVERVIEW

The Australian Synchrotron is located adjacent to Monash University in Clayton, Victoria. It has been built by a project team from Major Projects Victoria (MPV), a part of the Victorian State Government. The funding for the building and accelerators has been provided by the Victorian State Government. The beamlines are being funded by a group of interested parties, including universities, research organisations, other state governments, and New Zealand.

Staffing

The Australian synchrotron is being delivered with a relatively small staff of only 54 people, plus specialist contractors and consultants. Due to the relatively small number of staff, much of the responsibility for the design and project management has been placed on suppliers, with turn-key contracts. Contracts for the following systems included all design, engineering, project management, installation and commissioning:

- Injection system
- Storage ring RF system
- Storage ring vacuum vessels
- Beamline photon delivery systems
- Storage ring girders
- Front ends

Schedule

The original schedule milestones can be seen in Table 1. The project is currently on schedule and transition from the project stage to the start of operations will be in April 2007. All of the major schedule milestones have been achieved within days of the target dates, including the start of accelerator installation in April 2005, the completion of installation in May 2006 and first turns in the storage ring in June 2006.

Table 1: Schedule Milestones.

Design announced.	January 2003
Building contract placed	July 2003
Building complete	February 2005
Staff move into building	March 2005
Installation begins	April 2005
Injection system commissioning begins	October 2005
Storage ring installation complete	May 2006
Storage ring commissioning begins	June 2006
First turns in the storage ring	June 2006
Beamline installation begins	September 2006
Beamline commissioning begins	February 2007
Transition to operations	April 2007

ACCELERATOR SYSTEMS

The Australian Synchrotron accelerator systems are comprised of a 100 MeV linear accelerator, a 3 GeV booster synchrotron, and a 3 GeV storage ring. The entire injection system, from the electron source to the injection septa in the storage ring, was a single, turn-key contract. The storage ring equipment was provided by several different contractors and assembled using the local labour force with supervision from the different component contractors. A schematic of the layout of the accelerator systems is shown in Figure 1.

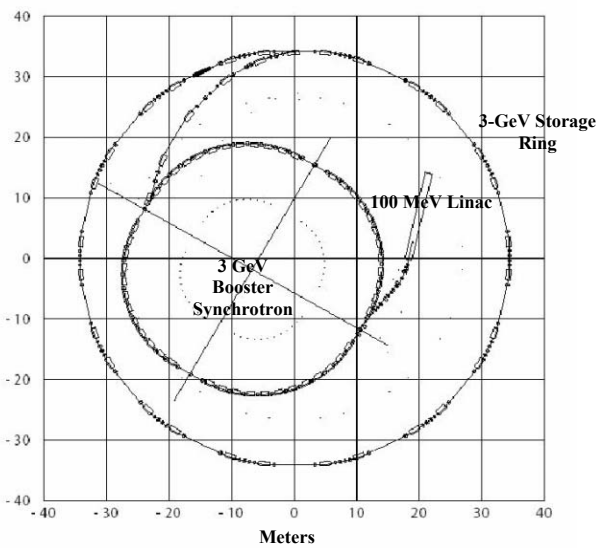

Figure 1: Layout of the accelerator systems.

The Linac

The electron source is a 90 keV thermionic gun that can run in both short pulse mode and long pulse mode. The operating frequency is 3 GHz. The short pulse mode is designed to deliver a single bunch into the 500 MHz

structure of the booster. There are two 5 m accelerating structures. The linac specifications can be seen in Table 2.

Table 2: Linac Specifications

Energy	0.1	[GeV]
RF Frequency	2997.92	[MHz]
Sub-harmonic Pre-buncher	499.654	[MHz]
Repetition rate	1-5	[Hz]
Normalised Emittance	<50π	[mm·mrad]
End charge (short/long)	>0.31/>3.1	[nC]

The Booster

The booster is based on a combined function lattice and is made up of four quadrants. Each of these quadrants has 8 vertically focussing dipoles and 7 horizontally focussing dipoles. The sextupole fields needed to get a positive chromaticity in both planes is integrated into the combined function dipoles. There are four quadrupoles for focussing correction as well as four sextupoles for chromaticity correction per quadrant. The booster specifications can be seen in Table 3.

Table 3: Booster Specifications

Energy	0.1 → 3.0	[GeV]
Circumference	130.2	[m]
RF Frequency	499.654	[MHz]
Harmonic Number	217	
Single Bunch Current	>0.5	[mA]
Multi-bunch Train	>5.0	[mA]
Betatron Tune (h/v)	9.2/3.25	
Natural Chrom. (h/v)	-8.8/-11.5	
Energy Spread (3GeV)	0.094	[%]
Horizontal Emittance	33	[nm·rad]

The Storage Ring

The machine functions of one of the 14 sectors of the storage ring are shown in Figure 2.

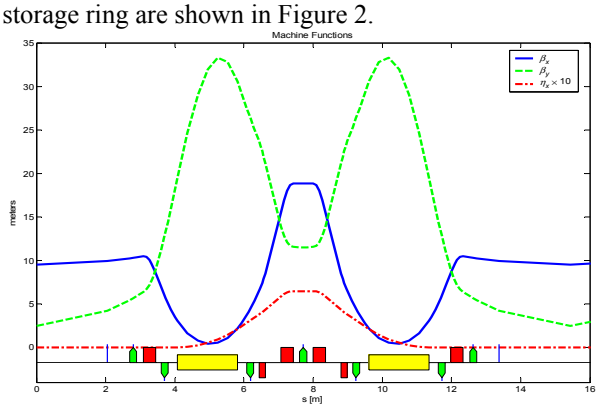

Figure 2: Machine functions for one cell of the ASP storage ring with zero dispersion in the straight sections.

The bending magnets are gradient dipoles with a focusing strength of $k = -0.335$ m^{-2}. There are three families of quadrupoles and four families of sextupoles. Horizontal and vertical corrector coils are wound into the sextupole magnets to make the lattice more compact.

The nominal lattice tunes are $\nu_x = 13.3$ and $\nu_y = 5.2$, but the machine can be tuned over a large range by using the outer two of the quadrupole families. The inner quadrupoles are used to distribute the dispersion to allow it to leak into the straight sections. Two of the straight sections are used for RF cavities; one for the injection septum and the remaining eleven will be available for insertion devices. It is possible to install two shorter insertion devices in the straight sections with the RF cavities. The design specifications are shown in Table 4.

Table 4: ASP Storage Ring Specifications.

Energy	3	[GeV]
Circumference	216	[m]
RF Frequency	499.654	[MHz]
Harmonic Number	360	
Peak RF Voltage	3.0	[MV]
Current	200	[mA]
Critical Photon Energy	7.8	[keV]
Betatron Tune (h/v)	13.3/5.2	
Momentum Compaction	0.002	
Natural Chromaticity (h/v)	-28/-27	
Radiation Damping (h/v/l)	3/5/3	[ms]
Energy Spread	0.1	[%]
Radiation Loss Per Turn	932	[keV]
Horizontal Emittance	7-16	[nm·rad]

Controls and Commissioning Tools

The control system for the Australian synchrotron uses EPICS. Different control systems have been delivered by different contractors with varying degrees of control, but in all cases it was specified that they had to be EPICS compatible.

In addition to the EPICS tools available, the Accelerator Toolbox [1] running in the Matlab environment is used. Using the Matlab Channel Access [2], all of the process variables in the control system are available in the Matlab environment making it possible to make measurements while changing settings and then perform calculations on the results. This has been an invaluable resource during the commissioning where a simple Matlab script could be written to automate a number of different measurements.

The Storage Ring Diagnostics

The storage ring is equipped with a host of diagnostics. The beam position monitor system provides first-turn, turn-by-turn, and slow acquisition position information simultaneously. There are seven beam position monitors in each sector.

The other diagnostic equipment is:

- Horizontal and vertical scrapers
- Horizontal and vertical stripline detectors
- A DCCT
- A beam loss monitor system

The beam position monitors and beam loss monitors are distributed around the ring. The rest of the diagnostic equipment is installed in a single straight section.

There are two diagnostic beamlines for machine studies. The first of these is an x-ray pinhole array beamline that is installed inside the storage ring tunnel. It

produces images of the beam from a dipole. The beam size and stability can be studied with the beamline. The layout of the beamline can be seen in Figure 3. The second is an optical beamline where the visible light from a dipole is sent through an optical chicane and led into an enclosure where there is a streak camera, an intensified CCD camera, a fill pattern monitor and a firewire camera.

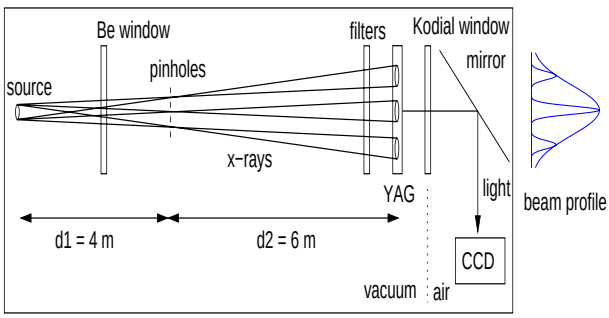

Figure 3: X-ray diagnostic beamline layout.

INITIAL BEAMLINES

The initial suite of nine beamlines is shown in Table 5.

Table 5: The initial suite of beamlines.

Beamline Identifier	Technique	Source
2IR	Infrared Spectroscopy	Bending Magnet
3BM	Protein Crystallography 1	Bending Magnet
3ID	Protein Crystallography 2	In-vacuum undulator
8ID	Imaging & Medical Therapy	Superconducting wiggler
9ID	Microspectroscopy	In-vacuum undulator
10BM	Powder Diffraction	Bending Magnet
12ID	X-ray Absorption Spectroscopy	Wiggler
13ID	Small & Wide Angle X-ray Scattering	In-vacuum undulator
14ID	Soft X-ray Spectroscopy	APPLE II Undulator

Five of these beamlines are expected to be in an advanced state of commissioning in April 2007 with the first user experiments being conducted. These are:

- Infrared Spectroscopy
- Protein Crystallography 1
- Powder Diffraction
- X-ray Absorption Spectroscopy
- Soft X-ray Spectroscopy

The other five beamlines will be built in the coming year, with the final one expected to be finished in the second quarter of 2008.

ACCELERATOR COMMISSIONING

The Injection System

The contract for the injection system included commissioning the systems. It was important for the ASP personnel to be involved in these activities in order to gain the operational knowledge of the systems needed in order to operate and maintain the systems when the commissioning was finished and the contractors left. Members of the accelerator group were present during all of the commissioning shifts and members of the mechanical, electrical, and controls teams also participated.

The linac klystrons were the first systems to be commissioned starting in September 2005. The first electrons from the gun were observed in the first week of October 2005. The first electron beam accelerated through the entire linac was observed in the transfer line in the middle of December 2005.

In February 2006, the first beam was injected into the booster. By the end of March 2006 the booster ramp was being developed and the first beam was accelerated to 3 GeV in the beginning of April 2006. The injection system routinely delivers the specified beam for injection into the storage ring.

The Storage Ring

Due to installation activities in the storage ring tunnel, the commissioning of the booster to storage ring transfer line (BTS) was not included in the injection system program, but was considered the start of the storage ring commissioning program. The first beam in the section of the BTS in the storage ring tunnel was observed on June 1 2006. The first turn in the storage ring was observed on June 8, 2006.

On July 14, 2006 the first beam was stored in the storage ring and the current was stacked to 1 mA. After a few days the storage ring could routinely be injected to 10 mA and all of the diagnostic equipment could be commissioned and the storage ring characterization began. To date, 200 mA has been stored with a lifetime of 6.5 hours after the first of the insertion device chambers has been installed. The first insertion device is installed and has been run with the minimum gap of 14 mm with 100 mA in the storage ring. A second insertion device chamber is installed and the lifetime at 200 mA remained the same as it was previously. The results of the storage ring characterization and performance demonstration will be presented in the next section.

STORAGE RING PERFORMANCE

Injection

The injection system runs at 1 Hz. The injection efficiency from the booster to the storage ring is now ~90%. This results in >2 mA per shot. It takes about 100 seconds to inject from 0 to 200 mA. A strip chart of the injection process can be seen in Figure 4.

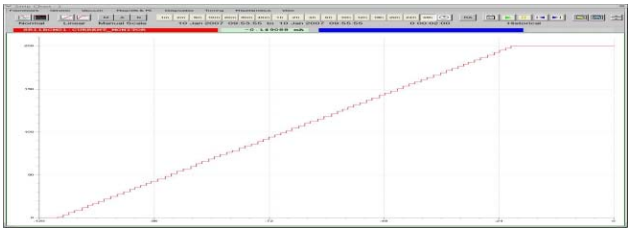

Figure 4: Injection from 0 to 200 mA.

Vacuum Conditioning

The vacuum conditioning has gone well. The lifetime-current product as a function of the integrated dose since the start of commissioning can be seen in Figure 5. The point at which the stored current was spread to ~300 bunches instead of 75 and the installations of the first two insertion device chambers are indicated. To date a total integrated current of 35 Ahrs has been accumulated.

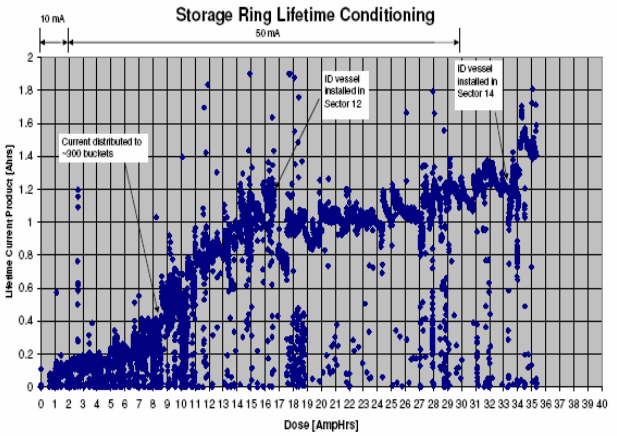

Figure 5: Current-lifetime product as a function of integrated current.

Orbit Correction

Beam based alignment has shown that the mechanical and electrical offsets of the beam position monitors were of the order of a few mm. The rms noise on the position signals is ~0.2 µm. The orbit has been corrected to an RMS deviation from zero of ~16 µm. Figure 6 shows the beam position offsets from the beam based alignment.

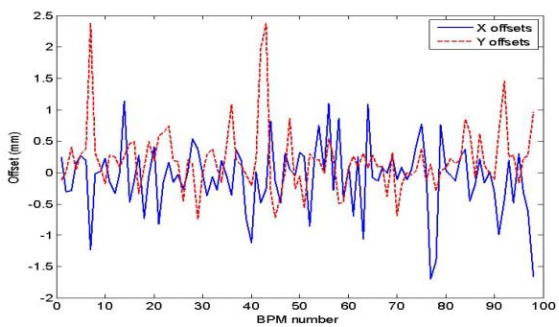

Figure 6: Measured BPM offsets.

Storage Ring Optics

LOCO [3] is used to get calibrated models of the storage ring. These models are then used to calculate corrections and changes to the optics. The first measured response matrix can be seen in Figure 7. There were some BPMS that had some coupling that was not correct as can be seen in the coupling quadrants of the matrix.

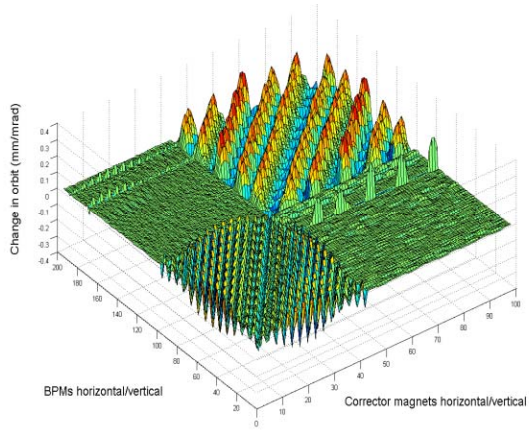

Figure 7: The first measured response matrix

Once the BPM signals were fixed the response matrix was used to correct the initial betatron beating. Figure 8 shows the measured and model vertical beta functions prior to correction. The corrections were applied and Figure 9 shows the results of a new LOCO run where the betatron beating has been corrected.

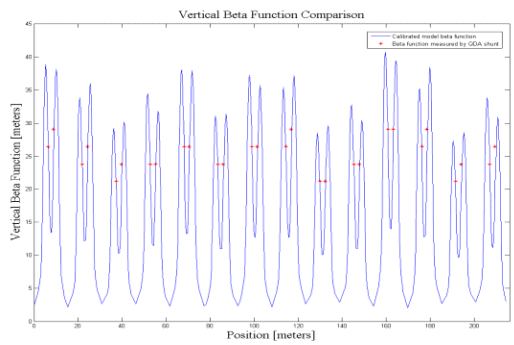

Figure 8: Measured and model vertical beta functions.

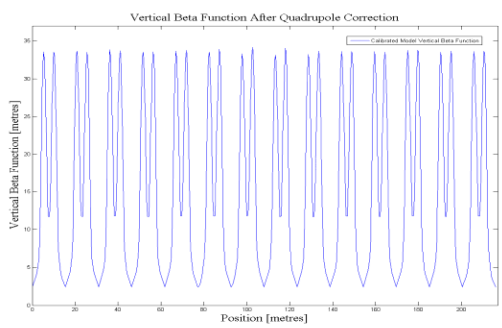

Figure 9: Corrected vertical beta functions.

Distributed Dispersion Optics

The commissioning lattice had zero dispersion in the straight sections. The final operating lattice will have a finite dispersion in the straight sections of ~0.1 m. A

calibrated model from LOCO was used to set the dispersion. The measured dispersion functions before and after the changes are shown in Figure 10 and Figure 11. As can be seen, there was a BPM in sector 3 that was not functioning at the time of the measurement.

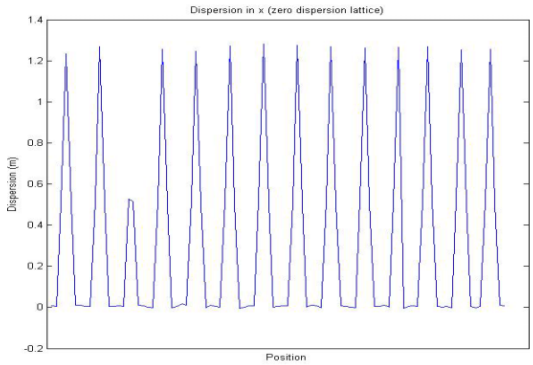

Figure10: Zero dispersion in the straight sections.

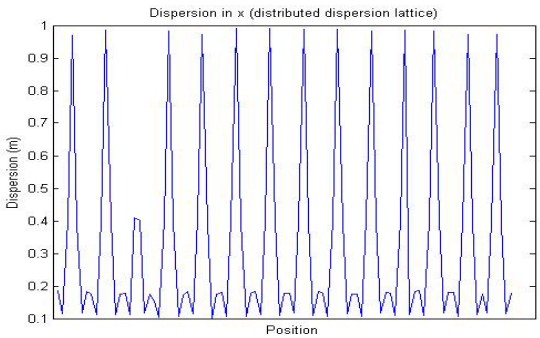

Figure 11: Distributed dispersion in the straight sections.

Emittance

The emittance has been measured using the x-ray diagnostic beamline. Using the beta functions from the model obtained using LOCO on the response matrix gives a horizontal emittance of 18.7 nm rad and a vertical emittance of 0.09 nm rad. Figure 12 shows the images from the pinhole array.

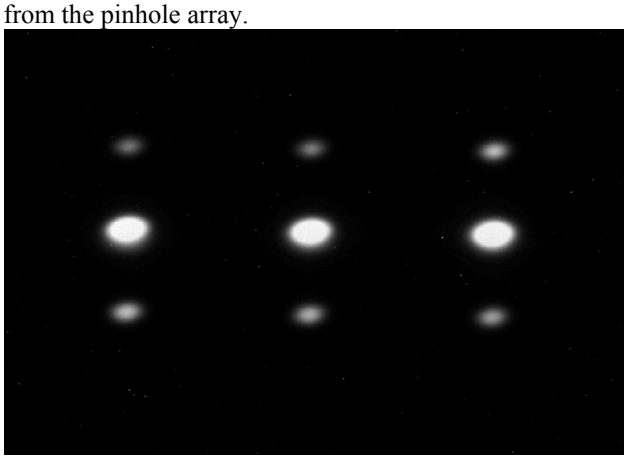

Figure 12: X-ray diagnostic beamline pinhole array image.

Bunch Length

Studies of the bunch length are under way. The streak camera on the optical diagnostic beamline is used to measure the length of a single bunch with increasing current. Figure 13 is an image showing a single bunch on two successive turns.

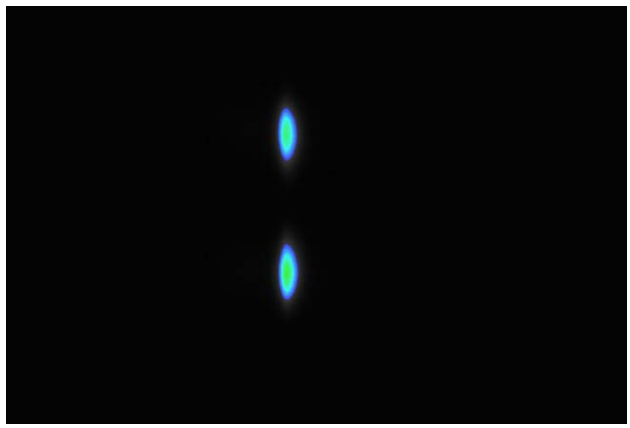

Figure 13: Streak camera image of a single bunch.

CONCLUSIONS

The Australian Synchrotron Project has been very successful. While there is still work to be done before becoming an operational facility, the small team of dedicated staff have done an excellent job of writing the specifications, working with the contractors and integrating all of the systems. This has led to a smooth commissioning according to the project schedule.

REFERENCES

[1] A. Terebilo, "Accelerator Modelling With Matlab Accelerator Toolbox", PAC 2001, p. 3203.

[2] G. Portmann, J, Corbett, A. Terebilo, "An Accelerator Control Middle Layer Using Matlab", PAC 2005, p. 4009.

[3] J. Safranek, G. Portmann, A. Terebilo, C. Steier, "Matlab-Based LOCO", EPAC 2002, p. 1184

CONSTRUCTION OF SHANGHAI SYNCHROTRON RADIATION FACILITY

Z. T. Zhao, H. J. Xu, H. Ding for the SSRF Project Team
Shanghai Institute of Applied Physics, Shanghai 201800, P. R. China

Abstract

The Shanghai Synchrotron Radiation Facility (SSRF), a third generation light source based on a 3.5GeV storage ring, is under construction at Zhang-Jiang Hi-Tech Park in Shanghai. The SSRF groundbreaking was made in December 2004 and the construction of the SSRF main and auxiliary buildings was basically completed in November 2006. The construction and installation of the SSRF accelerator components are under going with the target schedule of starting storage ring commissioning in April 2008 and the user operation in April 2009. This paper reports the construction progress of the Shanghai Synchrotron Radiation Facility.

INTRODUCTION

The SSRF complex in phase one consists of a 150MeV electron linac, a full energy booster, a 3.5GeV storage ring with a circumference of 432m and seven beamlines and experimental stations [1].

The SSRF project was fully approved by the central government in December 2004, and its groundbreaking was made a few days later on December 25. Since then the SSRF construction has been in progressing towards the target schedule of starting user operation from April 2009 [1, 2]. Constructions of SSRF buildings, including the main building housing accelerator tunnels and the experimental hall, two utility buildings, a technical building, an office building, a cafeteria and a guesthouse, have been basically completed, and they have been fully opened for utilization, such as utility installation and commissioning, machine pre-assembly and installation. Figure 1 shows the SSRF main building in January 2007.

Figure 1: The SSRF main building, January 2007.

The SSRF utilities, including electric power stations water cooling systems, air cooling systems, compressed air system and etc., have been installed and partly commissioned. The main power station has been in operation since October 2006. The piping and cabling from the main stations to the substations of the utility systems have been finished, and the engineering work in the main building is still going on. The commissioning of the SSRF utility systems is progressed on schedule, which is able to meet the requirements of various accelerator equipment testing and commissioning.

At this writing, most of SSRF accelerator components are under manufactures in domestic and foreign industries. At the same time, the machine installations, including linac, the booster RF power transmitter, a storage ring mechanical and electrical sector C10 and etc. are under way. The engineering design of the seven beamlines and experimental stations is in the final stage, and beamline components procurements are under going. The contracts of seven front-ends, four mono-chromators and etc. have been awarded.

STORAGE RING

The SSRF storage ring has 20 double bend lattice cells with four-fold symmetry, which incorporate four 12m long and sixteen 6.5m straight sections to accommodate injection magnets, SRF cavity modules and various insertion devices. With the finite dispersions leaking into the straight section, the storage ring natural emittance can be optimized to less than 4 nm·rad. Table 1 shows the main parameters of the SSRF storage ring.

Table 1: Main Parameters of the SSRF Storage Ring.

Energy (GeV)	3.5
Circumference (m)	432
Harmonic Number	720
Number of cells/Super-periods	20/4
Nature Emittance (nm·rad)	3.9
Beam Current, Multi-Bunch (mA) Single-Bunch (mA)	200~300 >5
Straight Lengths (m)	4×12.0, 16×6.5
Betatron tunes, Q_x/Q_y	22.22/11.32,
$\beta_x/\beta_y/D_x$ @12m straight (m)	10.0/6.0/0.15
$\beta_x/\beta_y/D_x$ @6.5m straight (m)	3.5/2.5/0.10
Momentum Compaction	4.2×10^{-4}
Relative Energy Spread	9.7×10^{-4}
RF Frequency (MHz)	499.65
Dipole Radiation per Turn (MeV)	1.448
Damping Times $\tau_x/\tau_y/\tau_s$(ms)	6.97/6.97/3.49
Bunch Length (mm)	4.0

Magnets and girders [3]

A total of 40 dipole magnets, 200 quadrupoles and 140 sextupoles, are being built for the SSRF storage ring. The dipole and quadrupole magnets are under fabrication at IHEP workshop, Beijing, and the magnetic measurements of the magnets for the first cell are completed. The first 10 dipoles achieved 3×10^{-4} variation in the integrated field across ±27mm, and their magnet to magnet integrated

field reproducibility is 1×10^{-3}. The first 20 quadruploes achieve 5×10^{-4} variation in the integrated field across the aperture radius 26mm. These dipoles and quadrupoles are qualified within the specifications. The sextupoles with skew quadrupole windings are being manufactured and measured at SINR Workshop, Shanghai. The first 20 magnets achieved 1×10^{-3} variation in the integrated field across the aperture radius 26mm, and the magnet to magnet integrated field reproducibility is 2×10^{-3}, these are within the required tolerance. The first static corrector magnet has been also manufactured and measured with qualified field parameters, and the rest 80 correctors are under fabrication at SINR workshop.

Figure 2: The storage ring cell C10 in the tunnel.

There are three steel girders and two concrete pedestals in each of the 20 storage ring arc cells, for supporting 10 quadrupoles, 7 sextupoles and 2 dipoles. The steel girders are 3.3 to 4.5m long each, and each one consists of a steel plate and a welded steel structure with rectangular section, supported by 3 ball bearing and wedge jack combined adjusters and 3 accessorial fixed sticks.

The 60 girders and 40 concrete pedestals are under manufacturing on schedule in Baoyie Engineering Technology Co. Ltd, Shanghai. The girders and pedestals for the first cell have been built and installed in the storage ring tunnel, and based on them the first cell of storage ring magnet and vacuum chamber assembly unit has been installed and aligned. Figure 2 shows the first mechanical storage ring sector in the ring tunnel.

Vacuum system [4]

The SSRF storage ring vacuum chamber is made of stainless steel 316LN, and it includes 20 arc cells and 20 straight sections. Each 14m long arc vacuum chamber cell consists of 6 sections of antechamber type vessels with lengths of about 1.42m to 2.97m each. In each arc cell, two DN150 RF shielded bellows are used to connect the two end chambers and the one middle straight chamber, each end chamber comprises two or three short stainless steel chambers with hard connection of rectangular flanges. The vacuum chambers are under manufacturing at Sanjing Vacuum Equipment Co. Ltd, Shanghai, the fabrication of the curved chambers for dipole magnets is completed while the fabrication of the straight chambers is still going on. Before being assembled, all these chambers will be annealed at above 900°C in vacuum furnace for lowering the magnetic permeability of their wielding line. The vacuum chamber sections will be pre-baked and pumped before installation since there is no in-situ baking employed.

There are totally 80 RF shielded bellows, 177 photon absorbers, 188 TSP pumps and 316 SIP pumps required for the SSRF storage ring in phase one. The RF shied bellows are manufactured at AnZ Co. Ltd, Korea, the first one passed the acceptance test in beginning of January, 2007, and now the batch production is under way. The fabrication of the photon absorbers for the arc vacuum chamber cell C10 is completed in December, 2006, and the rest ones are being fabricated at Hangzhou Dahe Thermo-magnetics Co. Ltd.

RF system

The storage ring RF system has five main components, three 499.65MHz SRF cavity modules, three 310kW klystron amplifiers, a 650W liquid helium refrigerator, low level RF control and cryogenic control systems. The SRF cavity modules are located in a 12m long straight section, it will provide 2~6 MV accelerating voltage and about 600kW RF power to the 300mA electron beam which circulates in the storage ring. The SRF cavity modules are under construction at ACCEL Instruments GmbH Germany. After vertical test, two niobium cavities are under chemical processing and baking now. And their cryostats are ready for final assembly. The first SRF module will be shipped to the SSRF site in April 2007 and the last one in August 2007. The first RF amplifier including the klystron and its power supply has been shipped into the SSRF RF building from THALES, France, the installation will start in the beginning of February, 2007 and its site acceptance is scheduled in April 2007. The RF waveguides, circulators and RF loads are all shipped to SSRF and to be installed from February, 2007. The digital low level RF control prototype achieved the required performance when tested on the high power RF system built in the SSRF R&D phase last October, then the first digital LLRF control system will be tested on the SSRF SRF cavity in the coming May.

The cryogenic plant with cooling power of 650W at 4.2K is under construction in collaboration with Institute of Physical and Chemical Technology, CAS, Beijing. The helium refrigerator manufactured at Air-Liquide, France, has been shipped into the SSRF cryogenics building, and its compressors have been installed into the SSRF utility building. The SSRF helium gas tanks and liquid nitrogen tank have been installed in the place close to the utility building, the transfer lines from compressors to the SSRF cryogenics hall have been constructed last December. The commissioning of the SSRF cryogenics plant is expected to be performed from February to April, 2007, and then it will be tested together with the first SSRF SRF module in May 2007.

Power supplies and injection system[5]

The SSRF storage ring requires a total of 520 power supplies in various types and ratings. These power supplies are all switched mode and digitally regulated. The 200 individual quadrupole power supplies rated at 280A/20-40V are being manufactured at Boxing Keyuan Electronic Tech. Co. Ltd., Beijing. A prototype with 5 choppers sharing a common DC link voltage source, which is for 5 quadrupoles, has been made and tested up to the current stability of 50ppm in 24 hours. The dipole magnet power supply rated at 850A/800V and sextupole magnet power supplies rated at 200-280A/100-290V are under fabrication at Xi'an Action Electronics Co. Ltd., Xian. A half scale dipole power supply and a full scale sextupole power supply have been constructed and tested up to the current stability of 20ppm and 100ppm in 24 hrs. Manufactures of all the power supplies will be completed in September 2007.

All the SSRF storage ring injection magnets, including two septum magnets and four kicker magnets, are located in one of the four 12m long straight sections. The kickers and the pulsed power supply are being manufactured at ACCEL Instruments GmbH and Puls-Plasmatechnik GmbH, Germany. The whole system is expected to be delivered to the SSRF site in August, 2007. The prototype of septum magnets and its pulser, manufactured at SKY Technology Development Co. Ltd, and COWEMV Wuhu, are under acceptance test at the SSRF lab. The whole septum system will be installed and tested at the SSRF site in July 2007.

Beam diagnostics

The SSRF storage ring beam instrumentation system includes 140 four button BPMs equipped with the digitalized electronic processor (Libera, Instrumentation Technologies in Slovenia), one synchrotron radiation diagnostics beamline, two beam scrapers, two stripline kickers, two DCCTs and two profile monitors. In addition, there are 12 BPMs for tune measurement, transverse feedback and backups. The BPMs are being manufactured in Kyocera Co. Ltd, Japan, the first 10 pieces will be received at SSRF in beginning of February 2007 and the rest will be delivered to SSRF in April. The Libera processors are scheduled to arrive at SSRF in the coming July. Two NPCTs are being fabricated at Bergoz, France, and will be delivered to SSRF in April 2007.

Installation and alignment [3]

A test installation of a storage ring sector, consisting of magnets, girders, vacuum chambers, photon absorbers, vacuum pumps, a front-end model and utility installations, was performed with the first components received from manufactures in summer 2006, the main purpose is to validate the engineering design and evaluate the cabling and piping techniques as well as installation procedures.

Based on this installation experience, the installation of the first storage ring sector C10 is being carried out in the SSRF storage ring tunnel and the inner technical gallery. The mechanical installation started last December has been completed this January, the utility and electrical installations of this ring sector are being performed and will be completed in February 2007. Along with the pre-assembly and pre-alignment of the ring mechanical sectors, the mechanical batch installation in the tunnel will start in May 2007, which will be followed by the utility and electrical installations as well as systematic equipment testing sector by sector. The SSRF storage ring installation is expected to be completed in a year, and its beam commissioning is scheduled to start in April 2008.

The horizontal and vertical alignment control network has been established in the storage ring tunnel and the linac and booster tunnels as well. For monitoring the deformation of the ring tunnel slab, the vertical control network has been measured twice in two months. And a re-checking of the global control network is in progress.

INJECTOR

Linac[6]

The 150MeV linac is consisted mainly of a 100kV electron gun, a 499.65MHz sub-harmonic buncher, a fundamental buncher, four 3m long/2.998GHz travelling wave accelerating sections, two 45MW klystrons and two 110MW modulators. Its designed performance parameters are reported in elsewhere [6].

All the main linac components have been delivered to the SSRF site for testing and acceptance, and the linac installation, started in November 2006, is being carried out in both the linac tunnel and the klystron gallery. Figure 3 shows the linac under installation in the linac tunnel. At time of this writing, the accelerating sections, focusing coils, magnets, girders and Farady beam dumps have been installed, and the waveguides and the sub-harmonic buncher are being installed. Two klystrons and two modulators have been installed and tested, and their high power acceptance is being performed on site. In addition, the beam diagnostics elements, including three Stripline BPMs, five profile monitors, four wall current monitors and one ICT will be installed in February 2007.

Figure 3: The SSRF linac under installation, January 2007.

The SSRF linac installation is planned to be completed before April, and the linac commissioning is scheduled to start in April 2007.

Booster[6]

The SSRF booster, ramping electrons from 150MeV to 3.5GeV, is a 2Hz synchrotron with a circumference of 180m. Its 48 dipole magnets, 56 quadrupole magnets and 46 sextupole magnets are being fabricated and measured at Kelin Shanghai and USTC Chuangxin Co. Ltd., Hefei, and they will be delivered to the SSRF site for unit cell pre-assembly and pre-aligned in February 2007. In the meantime, the manufactures of the booster stainless steel vacuum chambers including BPM sections will be finished in February, 2007.

The 180kW klystron power amplifier equipped at SSRF in 2001 is relocated and being re-commissioned at the SSRF site, and in the meantime, two 5-cell copper cavities and their associated LLRF system are under factory acceptance tests at ACCEL, Germany. These above equipment will be integrated for the RF system commissioning in April, 2007.

The main power supplies for dipole, quadrupoles and sextupoles, the injection and extraction kickers, septa and extraction bumpers as well as their pulsers are still under manufacturing and will be delivered to the SSRF site for acceptance testing in May 2007. Then they will be tested with the machine central control system from June 2007.

The main booster installation will be carried out from March to July 2007. It will be followed by equipment tests from July to September 2007. The booster beam commissioning is scheduled to start in October 2007.

INSERSION DEVICES

There are seven beamlines and one branch beamline funded as first beamlines in the SSRF project, and among them six are based on insertion devices [7].

Table 2: Main Parameters of first SSRF IDs.

	Type	Period mm	N	Min.Gap mm	Peak Field T
EPU100	PPM	100	42	32	0.6 (By) 0.33(Bx)
IVU25-1	Hybrid	25	80	6	0.94
IVU25-2	Hybrid	25	80	6	0.94
W79	Hybrid	79	19	14	1.2
W140	Hybrid	140	8	14	1.94

Based on the input from beamline specifications, the design of the five insertion devices has been finalized in 2006, table 2 shows their main parameters. The contract of the two in-vacuum undulators has been awarded to Advanced Design Consulting Inc., USA, and these two undulators are under construction and expected to be shipped to SSRF in March 2008. Two wigglers are under manufacturing at Lanzhou Kejin Taiji Technology Co. Ltd, China, they are expected to be delivered to the SSRF site in February 2008. The EPU undulator is being developed in house with the joint efforts of SSRF and Chinese industries [8], and its installation in the SSRF storage ring is scheduled to start in October 2008.

MACHINE CONTROL SYSTEM

The EPICS based machine control system is under development at SSRF [9]. The hardware and software environments have been established, and high level physical application environment has been set up and the online tests of device control using Matlab 2006 R2 with Accelerator Toolbox (AT) and middle layer have been carried out.

A prototype of the power supply control system has been developed, and with it the digital power supplies have achieved the required performance [10]. In the meantime, the timing system, the machine and personnel safety interlock systems are under construction to meet the schedule requirements of machine commissioning.

OUTLOOK

The SSRF project is in the beginning stage of the SSRF accelerator installation, the fast progress of the machine installation is expected in the following year, which creates many challenges in the construction quality and schedule of accelerator components. In the meantime, the linac commissioning and booster commissioning will be carried out and expected to be completed in 2007.

REFERENCES

[1] Z.T. Zhao H.J. Xu and H.Ding, “Construction status of the SSRF project”, Proc. EPAC06, Edinburgh, June 26 - 30, 2006.

[2] Z.T. Zhao H.J. Xu and H.Ding, “Status of the Shanghai Synchrotron Radiation Facility”, Proc. PAC05, Knoxville, May 16 - 20, 2005.

[3] L.X. Yin, H.W. Du, D.K. Jiang, and etal “Mechanical Prototype for the SSRF storage Ring”, these proceedings.

[4] D.K. Jiang, Y.L. Chen, L.P. Chen and etal, “The Vacuum System for the SSRF Storage Ring”, these proceedings.

[5] T.J. Shen, D.M. Li, R. Li and etal, “Construction of SSRF Magnet Power Supply System”, these proceedings.

[6] D.M. Li, M.H. Zhao, H.H. Li and etal, “Construction Progress of the SSRF injector”, these proceedings.

[7] Q.G. Zhou, N. Chen, L. Zhang and et al, “First Group of Insertion Devices for SSRF”, SRI2006, Daegu, May. 27- June 1, 2006.

[8] Q.G. Zhou, M.Zhang, Y. Li and etal, “An Apple-II Helical Undulator for SSRF”, these proceedings.

[9] D.K. Liu, L.R. Shen and Y.B. Leng, “The Status of Instrumentation and control for SSRF”, Proc. EPAC06, Edinburgh, June 26 - 30, 2006.

[10] J.G. Ding, H.J. Zhu, H. Zhao, and L.R. Shen, “A prototype of the SSRF Power supply system”, these proceedings.

STATUS AND FUTURE OF TAIWAN LIGHT SOURCE

Keng S. Liang, C.C. Kuo, J.R. Chen, D.J. Wang, G.H. Luo, and Y.W. Yang
National Synchrotron Radiation Research Center, No. 101, Hsin-Ann Road, Hsinchu, Taiwan

Abstract

The Taiwan Light Source of National Synchrotron Radiation Research Center (NSRRC) has reached a very stable operation condition and productive scientific outputs. The copper Doris RF cavities were replaced with a niobium Superconducting (SC) RF cavity in order to eliminate higher-order-modes and deliver higher beam current. Superconducting wigglers were installed to provide higher flux at higher photon energy. The storage ring is now operated at 300 mA top-up mode with better than 97 % of beam availability during users shifts. The original layout of the magnets has been greatly modified to accommodate one SC wavelength shifter at the injection section, one SC wiggler at the RF cavity section, and three SC wigglers in achromatic sections in addition to the original design of one wiggler and three undulators. In view of the future scientific demands, the NSRRC is proposing to construct a new synchrotron storage ring of 3.0~3.3 GeV and ultra low emittance, the Taiwan Photon Source (TPS). The TPS will provide brilliant X-rays at 10^{21} photons/s/0.1%BW /mm^2/mr^2 by SC undulator upon its completion, making it the brightest synchrotron light with the finest performance in the world.

TOP-UP INJECTION

Several major upgrades are integrated into routine operation in Taiwan Light Source (TLS) in recently years. Top-up injection mode was achieved after series upgraded of injector, transfer line and injection components. The operation current of Top-up injection reached 300 mA during users shift. The commissioning [1] of the first and second Superconducting RF cavities (SRF) was very smooth and exceeded the specification in several measures. The first In-Archromat-Superconducting-Wiggler (IASW) was installed and commissioned successfully. The associated beamlines will be commissioned in the first quarter of 2007.

To reach the ultimate goal of third generation light source, TLS prepared all the necessary steps to provide top-up operation to the users. To improve the thermal relaxing problem of dipole magnets and cure the orbit drift during the energy ramping era at TLS, the injector was upgraded to have the capability of full energy injection to the storage ring. This provided an essential tool to evaluate the feasibility of top-up injection at TLS.

The top-up mode [2, 3, 4, 5] provides the best solution to the thermal variation of beamlines' optical components and locks the launching condition of the synchrotron light to end-stations. This greatly benefits those superconducting wiggler x-ray beamlines which have large thermal load on the optical components and take relatively long time to reach thermal equilibrium. In addition, these beamlines generally have high demands on the photon energy stability after the monochromator, and top-up mode offers the best solution to the short beam lifetime of a storage ring. Top-up injection also opens new opportunities in probing better operation conditions, for example, the lower emittance, the lower gap of insertion device, and the increase of bunch current without the need to worry the impact of beam lifetime.

Figure 1 shows the stored beam current in user's shifts with top-up injection mode. The maximum stored current sets to 302 mA. The zoom-in to one-hour period of stored beam current is shown on top of Fig. 1. The intensity variation of the stored current can be maintained within ±0.25%. During users' shifts, the injection time interval was set to 60 seconds due to low lifetime, around 250 minutes, of stored current.

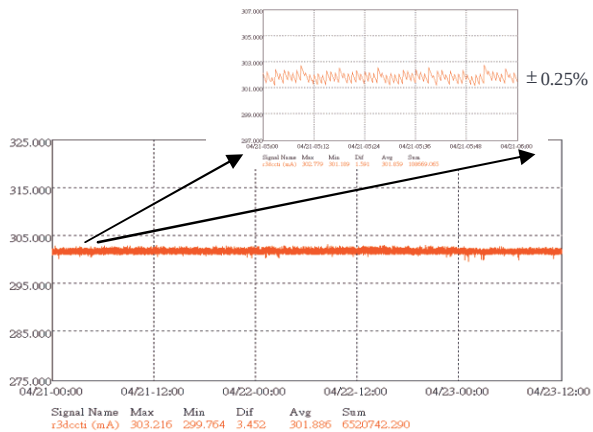

Figure 1: The standard operation of top-up injection and the zoom-in of current variation, ±0.25%.

To increase the transverse acceptance of the ring and have acceptable injection efficiency, the chromaticity is corrected to slight positive. Further help from the digital transverse feedback system, the transverse instability can be suppressed to the most minuscule range without scarifying the transverse acceptance and injection efficiency.

To ensure the radiation safety before switching to top-up operation, a series of radiation safety analyses including calculations and measurements were performed. Additional interlock logic has been integrated into the existing interlock system to prevent dipole failure, injection difficulty as well as excessive radiation exposure.

Six accumulation type dose meters were placed close to the shielding wall at straight sections, which tend to be the hot spots around the ring. The interlock system will be activated when the accumulated dose exceeds the threshold value, 4 μSv within 4 hours. All the

surveillance results and the TLD readings of the staff and users in NSRRC demonstrate that the radiation safety measures have been effective and radiological impact to the personnel and environment due to top-up operation is minimum.

SUPERCONDUCTING RF CAIVTY

A 500 MHz Superconducting RF cavity (SRF) of CESR-III design was installed and successful commissioned at the end of 2004. It started routine operation since February, 2005. The operational performance of the SRF module is impressive. The operating mode of storage ring also was upgraded from decay mode to top-up mode, and the beam current of routine operation was increased from 200 mA to 300 mA at the forth quarter of 2005. The RF system is operated under heavy beam loading with the loading factor of 4.2 at 300 mA. This results in feedback loops of low-level RF system potentially unstable for any change of the machine operational mode. The feedback loops of low-level RF system need to fine-tune to minimize the SRF trip due to potential unstable of feedback loop. The average trip rate, due to RF system fault, is once per week in the user beam shifts during 2005. It is an exceptional good record during the first year of SRF operation in accelerator community. The target of RF system reliability is less than one trip per month in average to fulfill the stringent requirement of TPS project.

The SRF module is powered by an in-house assembled 100kW RF transmitter. A 100 kW klystron, co-developed with manufacturer from standard 60 kW model, was installed into the RF transmitter. Theoretical estimation shows that there is sufficient RF power for storage ring operating at 400 mA of stored beam current. A 400 mA decay and top-up modes were demonstrated without any trips or instability during accelerator development shifts. The integrated RF plant did not experience any difficulty in operation with 400 mA.

The major R&D efforts of RF system are focused on the development of assembly capability of the SRF module, and the conceptual design of 2K cryo-plant for passive Landau cavity. In the meantime, the conceptual design of RF system for the proposing 3 GeV light source, with ultra-low emittance, at NSRRC has been conceived with emphasis on the impact of low momentum compaction factor and heavy beam loading on the performance and reliability of RF plant.

CRYOGENICS SYSTEM AND SUPERCONDUCTING INSERTION DEVICES

There are three Superconducting Insertion Devices (SCIDs) and one superconducting RF cavity installed in TLS. Additional two SCIDs will be installed in the storage ring. It is crucial to have very stable cryogenic operation parameters for the SRF cavity due to the very high quality factor, Q, of the cavity. Small variation of return pressure of cold He gas or liquid helium level will induce frequency change of SRF cavity in the cryo-module. It is not a desirable solution in sharing the cryogenic system between SRF and SCIDs. The second cryogenic system is installed and dedicates to the SCIDs. Figure 2 indicates the infrastructure of the installed cryogenic system in experimental hall. The first cryogenic plant, MCP1, is dedicated liquid helium plant to the SRF cavity and the second plant, MCP2, provides sufficient cryogenic capacity for the SCIDs. Either MCP1 or MCP2 can provide cooling capacity of 450 W at 4.5 K and serve as the backup system to each other.

Figure 2: The infrastructure of installed cryogenic system in the experimental hall.

The commissioning of the switch valve box and the nitrogen-shielding liquid-helium transfer line completed in February 2005. The shielded transfer line is 100 meters long and situated above the tunnel of storage ring to supply liquid helium to five SCIDs. The second sets of compressor, the oil-removal module, and the frequency driver are installed in a vibration isolated room and sit in remote utility hall to suppress the vibration transmission to the storage ring.

The refrigerator and Dewar are located on a platform at height 2.8 m in the experimental area as shown in Fig. 2. A 2.5-inch discharge pipe and a return suction pipe with diameter of 8-inch, each with length of 160 m, connect the main compressor and the refrigerator. The commission of MCP2 was smooth and reached the specifications in 2006.

User community demands for high flux of hard x-ray source in the field of protein crystallography and advance material research in recent years. A Superconducting (SC) wavelength shifter with 6-Tesla field strength and a 3.2-Tesla SC wiggler were installed at injection section and RF section respectively. The beamlines were fully subscript associated with above SC insertion devices.

A 16-pole, 6.1 cm period IASW with field strength of 3.1 T was constructed in-house and installed between the first and second bending magnets of a Triple-Bends-Archromat (TBA) arc section, , as shown in Fig. 3. The design of the IASW is similar to that of the SW6. The inner horizontal and vertical aperture of the UHV beam

duct is 100 x 11 mm to prevent the synchrotron radiation from heating the beam duct. The magnet gap is maintained at 19 mm to accommodate the thickening of UHV beam duct.

A 16-pole magnet was completed and tested in the vertical test dewar. A nominal field strength of 3.1 T was obtained at an excitation current of 264 A. The first and second integral field that is very consistent with the results of the 16-pole magnet measured in the vertical test dewar and the simulated field.

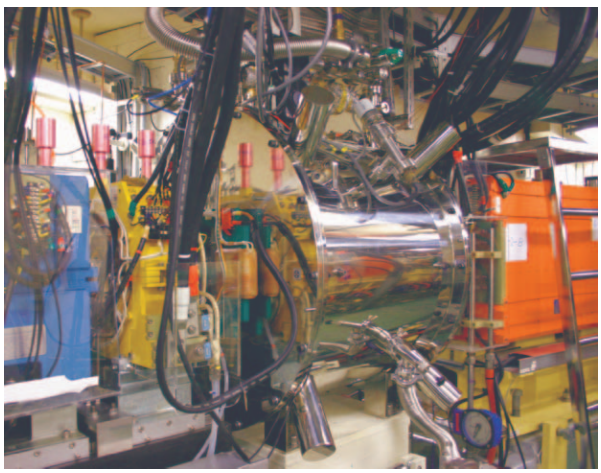

Figure 3: A superconducting wiggler installed between two bending magnets.

The first IASW was commissioned very successfully in March, 2006. The peak field was set to 3.13 Tesla during the measurement. Tune shift as function of excitation strength was measured and compared with theoretical model. Good agreement between measured and predicted values.

The excursion of closed orbit distortion from zero to maximum field (3.13 Tesla) is within acceptable range. There was no beam loss even when the IASW system tripped off. This indicates a very good field quality control during the manufacture process. Working tunes and the closed orbit distortions can be well corrected. The corrected user lattice of storage ring can successfully incorporate with the routine top-up injection mode without disturbing injection efficiency and beam stability. However, the IASW is installed in the dispersive region, which results in an increase of the beam emittance. From the synchrotron light monitor, the beam size information confirmed the prediction of the emittance growth.

TUNE MEASUREMENT SYSTEM AND FEEDBACK SYSTEM

Online tune measurement using digital Beam Position Monitor (BPM) was implemented. There are three potential application modes for tune measurement system, which include top-up mode, spontaneous excitation without transverse feedback, and continuous excitation. The turn-by-turn information from the digital BPM, after Fourier analysis, gives precise results of the betatron tunes of storage ring. The monitor system will be very helpful to identify occasional beam-loss or beam instability during the users shift.

The closed-orbit of stored beam is perturbed by injection septum and the unbalanced injection kickers in storage ring during injection. The trigger signal of the turn-by-turn BPM synchronizes with the injection signal. Hence, the betatron tunes can be extracted from the turn-by-turn BPM every sixty seconds as top-up mode in operation.

Transverse instability is excited as the stored current exceeds the threshold current, several tens mA in TLS. The turn-by-turn BPM can extract the betatron tunes from the turn-by-turn BPM due to the spontaneous excitation without the transverse feedback system. It is a powerful tool to study the dynamic behaviour of transient perturbation to the accelerator.

The continuous excitation mode, triggered by white noise with narrow bandwidth, provides an effective tool for betatron tunes scanning when the stored beam current lower than the threshold current in the storage ring. Any of measurement modes can provide very accurate tunes measurement and the turn-by-turn information for dynamic analysis in the experiment of accelerator physics.

Multi-bunch instabilities may deteriorate beam quality, increase beam emittance, and even cause beam loss in the synchrotron light source. The feedback system is essential to suppress multi-bunch instabilities caused by the impedances of beam ducts, and trapped ions. A new Field-Programmable Gate Array (FPGA) based transverse and longitudinal bunch-by-bunch feedback system has been commissioned. A single feedback loop is used to suppress the horizontal and vertical multi-bunch instabilities simultaneously. Longitudinal instabilities caused by cavity-like structures are suppressed by the longitudinal feedback loop. The same FPGA processor is employed in the transverse feedback and the longitudinal feedback system respectively. Diagnostic memory is included in the system to capture the bunch oscillation signal, which can be used to support various studies

RF AND PHOTOCATHODE GUN

Pre-Injectors with high brightness beam, especially RF guns, are critical sub-systems for new generation light sources. The superior performance and elegant configuration of a thermionic RF gun system made it an attractive option as a reliable pre-injector. In cooperate with an alpha-magnet as low energy bunch compressor, ultra-short electron beam pulses can be generated from an RF gun with thermionic-cathode. It can be used to generate intense and coherent short wavelength radiations, for example production of femto-second electron and ultra-fast X-ray pulses with tunable wavelength. Figure 4 shows the 3D assembly of a thermionic RF gun system.

The cathode assembly is installed at the end wall of the half-cell of the gun cavity and this cell is coupled to the full cell through a side-coupled cell. Klystron power will be fed into the cavity at the side wall of the full cell

through an iris. When the field amplitude of the full cell approximately equals to two times that of the half cell, the electron beam has a linear energy chirp that is ideal for bunch compression with alpha magnet. Unloaded Q of the π/2-mode under such cavity field ratio is about 9000.

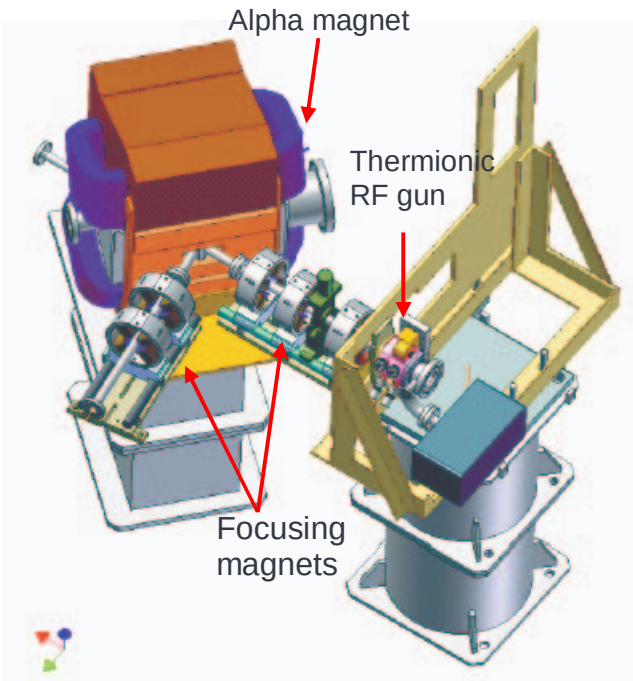

Figure 4: the 3D assembly of a thermionic RF gun system

An alpha magnet has been built and well tested by the magnet construction group. Field gradient at 450 G/cm has been achieved. The gradient of the magnet during normal operation will be at about 400 G/cm. The trimming of field near the beam entrance is in progress. The vacuum chamber of alpha magnet with momentum filter is to be built and put into the alpha. A beam transport system will be needed to guide the beam from RF gun exit to the entrance of alpha magnet, then from the alpha magnet to the S-band linac to reach the desired beam energy. The RF gun project intends to have a high brightness beam injector with future applications on (1) booster synchrotron pre-injector for TPS and (2) advanced accelerator and novel light source research.

TAIWAN PHOTON SOURCDE

An intermediate energy synchrotron light source has been proposed. The goal is to construct a high performance light source in complementary to the existing 1.5 GeV ring in Taiwan. A 3~3.3 GeV machine with 486 m and 6 super-period DBA/QBA lattice structure is considered and other options are also investigated.

NSRRC Board of Trustee endorsed a new synchrotron light source with energy around 3 GeV to increase the research capacity, especially in the X-ray range. To best use of existing resource, fit into the existing site and to satisfy the user requirements, several configurations of the accelerator systems as well as the size of the storage ring have been discussed. One of the attractive configurations is a 6 super-period's ring with its circumference in 486 m. The site planning of the new ring is shown in Fig. 5 which is coloured in navy-blue.

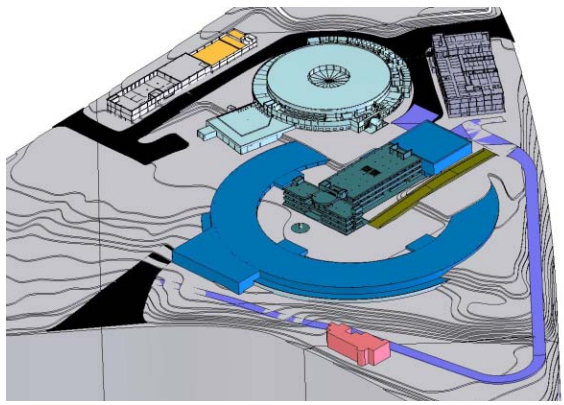

Figure 5: The planned construction site of the new storage ring which co-exists with the TLS.

A 24-cell Double Bend Achromate (DBA) [6] and 12-cell Quadruple Bend hybrid-Achromate (QBA) [7] structure will be the major focus in the coming optimization process. The linear lattice and frequency map analysis of non-linear effect of the DBA structure is shown in Fig. 6. By allowing slight positive dispersion in the long straights, the natural emittance of 1.7 nm-rad can be achieved. With a 6-fold symmetry configuration, the ring provides 6 long straights for injection, long IDs, and SRF modules. With different kind of insertion devices, the calculated brilliance with 1% emittance coupling is plotted in Fig. 7.

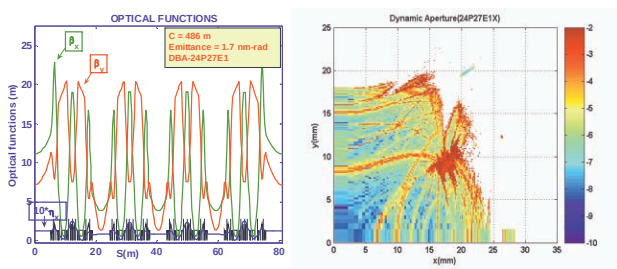

Figure 6: Optic functions of linear lattice and Frequency Map Analysis of a DBA lattice layout with 6-fold symmetry and 24-cells.

To correct chromaticity and to reduce the nonlinear effects we employ a sextuple scheme of 8 families. A sufficient large dynamic aperture, in both on-energy and off-energy particle cases, is obtained to ensure efficient injection and reasonable lifetime.

There will be more than 21 insertion devices in the ring and their effects on the beam dynamics are also investigated. We simulated beam dynamics effects with 21 planned insertion devices in the TPS. The beam dynamics effects such as tune shift, emittance changes, etc. are studied and the tracking results with these IDs

show there are significant impacts on the dynamic aperture, but still acceptable.

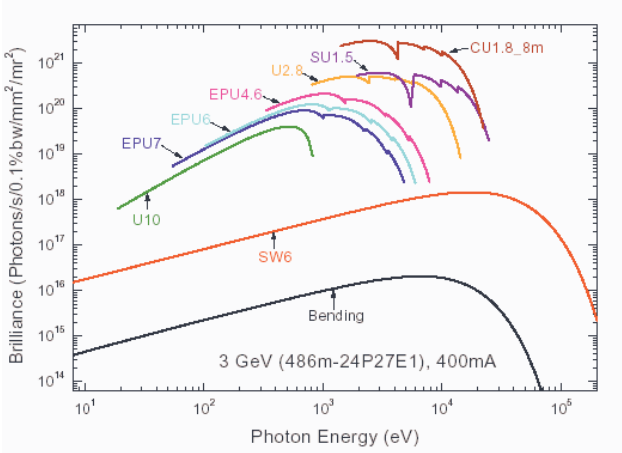

Figure 7: The calculated brilliance with 1% emittance coupling of a DBA lattice with distributed dispersion function.

Vertical beam size in the low emittance and small coupling ring can be less than 10 microns. Stringent request for small vertical beam orbit fluctuation within sub-micron range is necessary to keep the photon flux stable. One of these sources is the ground vibration. The maximum optics response to the plane ground wave in the vertical plane is less than 5 within 10 Hz and around 10 above 10 Hz with the help of girder supports. Careful ground motion control is needed in the facility construction planning. A sophisticated girder design is also necessary.

With the superconducting cavities, no coupled bunch instabilities are anticipated due to higher order modes from cavities. However, the small gap insertion devices can induce transverse instabilities and the impedance budget is also very low to avoid microwave instabilities. Lifetime is estimated to be larger than 10 hours for 5 mm vertical chamber size, 1% coupling, 1 nTorr vacuum, 0.6 mA bunch current and 3.5 MeV RF voltage.

An intensive study of QBA lattice was carried out. The optics function of linear lattice of QBA structure is shown in Figure 8 with the frequency map analysis. The QBA structure is an alternative dispersion and non-dispersion long straights configuration and the lengths of the inner dipoles is 1.5 longer than the outer dipoles such that the emittance can be further minimized. The dipole field strength of the QBA is lower than DBA so that the damping effect with high field IDs is stronger. It also means that the length for IDs of the QBA would be shorter than DBA. The natural emittance of the QBA is higher than DBA distributed-dispersion type but lower than DBA achromate type. With high field IDs, the effective emittance of the QBA in the dispersion-free straights can be smaller.

SUMMARY

In order to improve the thermal relaxing problem during the energy ramping era at TLS, the injector was upgraded to have the capability to be full energy injection to the storage ring. To reach the ultimate goal of third generation light source, TLS has prepared all the necessary steps to provide top-up operation mode to the users. The TLS operates in top-up mode 100% in users shifts at 302 mA of stored current. The installation of SRF cavity also makes the ring have the capability to provide more photon flux with better beam quality to the users. The installation of SCIDs pushes the delivered photons to hard x-ray range in a 1.5 GeV storage. NSRRC is pursuing a much better synchrotron facility, Taiwan Photon Source.

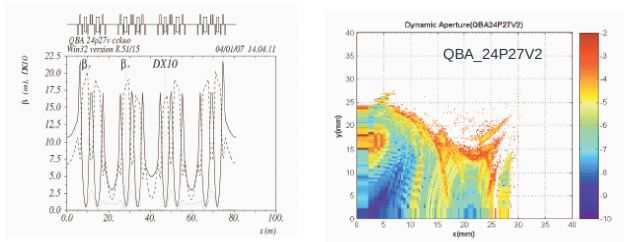

Figure 8: Optic functions of linear lattice and Frequency Map Analysis of a 12-cell QBA lattice layout with 6-fold symmetry.

There are several promising QBA configurations, which has been intensively studied, as alternations to DBA layout. In QBA configuration, the positions of quadrupole and sextupole magnets are almost identical to the DBA structure. Nonlinear optimization shows that the beam dynamic behaviour of the QBA lattices is similar to DBA. Further studies on the nonlinear effects and other beam dynamics issues are in progress.

REFERENCES

[1] C. Wang, et. al, "Commissioning experience of SCRF system at Taiwan Light Source," this proceeding.
[2] L. Emery and M. Borland, "Upgrade Opportunities at the Advance Photon Source Made Possible by Top-Up Operations,"EPAC'02, Paris, 2002, p.218
[3] L. Emery, M. Borland "Top-Up Operation Experience at the Advance Photon Source," PAC'99, 1999, New York, p. 200
[4] A. Ludeke, M. Munoz, "Top-up Operation Experience at the Swiss Light Source," EPAC'02, 2002, Paris, p.721
[5] H. Tanaka, et.al. "Top-up Operation at Spring-8," EPAC'04, 2004, Lucerne, p. 222.
[6] Proposal of Taiwan Photon Source, National Synchrotron Radiation Research Center, Oct. 2006.
[7] M.H. Wang, et.al, "Quadruple-bend achromatic low emittance lattice studies", submitted to PRSTAB.

REVIEW OF HADRON MACHINES FOR CANCER THERAPY

M. Kanazawa
National Institute of Radiological Sciences, 4-9-1 Aanagawa, Inage, Chiba, Japan 263-8555

Abstract

Particle cancer therapies with proton and light ion have been considered as excellent treatment for deep-seated tumors, which are due to excellent dose distributions with Bragg peak. To realize these therapies, dedicated accelerator facilities were constructed. With good clinical results in these frontiers, many plans of dedicated facility have been started in the both case of proton and light ion treatment facilities. In this paper, important types of accelerator facilities will be presented.

INTRODUCTION

Though radiotherapy of cancer patient is important treatment method, X-ray will be mainly used. This situation is from the low cost and compactness of the required hardware. If we can use charged particle beam like proton and light ion for deep seated tumor, depth dose distribution can be improved to concentrate the dose. This advantage is pointed out first by R.R Willson[1] in 1946. This comes from the existence of Bragg peak in the case of charged particle beam. We can adjust the depth position of Bragg peak at tumor to obtain high concentration of the particle dose.

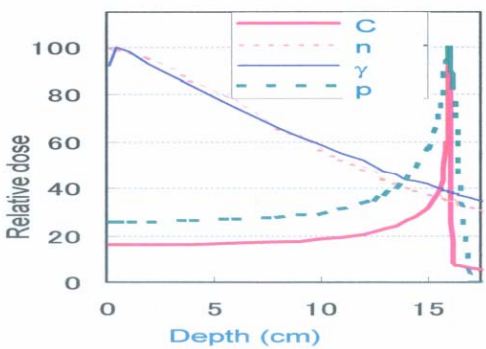

Figure 1: Depth dose distribution of X-ray, neutron, proton, and carbon ion.

In the actual treatment with charged particle, Bragg peak with different energies must be superimposed to fit on the tumor thickness. In Fig.2, calculated depth dose distributions[2] of several ions are compared with a SOBP (Spread Out Bragg Peak) width of 6cm. In these calculations, nuclear interactions of the incident beam with water and RBE (Relative Biological Effectiveness) are included. As seen from these calculations, entrance dose is less than 70% of the dose value at SOBP, which make the entrance dose on normal tissue low. In the cases of X-ray and neutron, the dose values are decrease gradually in the patient body, and this nature is demerit in the treatment of a deep seated tumor.

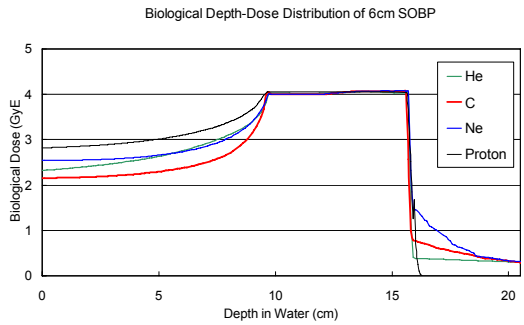

Figure 2: Calculated depth dose distributions of proton, helium, carbon, and neon beams with SOBP of 6xm.

In the case of light ion, there is another merit concerning biological effect. If we see the RBE as a function of a LET (Linear Energy Transfer), the RBE is maximum around 200keV/μ as shown in Fig.3. In the case of carbon, the RBE value at entrance is low with small LET value, and the value at SOBP region is high. This makes desired characteristic point that kill tumor effectively with light side effect on the normal tissue. With low OER (Oxygen Enhancement Ratio), carbon beam can well control the tumor of hypoxic cell that is considered as radio-resistant.

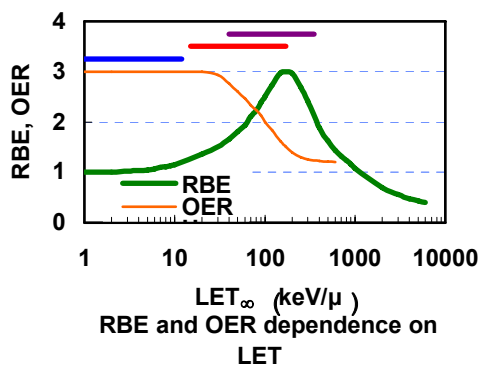

Figure 3: RBE and OER as a function of LET.

NEW IDEAS OF THE ACCELERATORS FOR RADIO-THERAPIES

Though there are already dedicated accelerators for cancer therapy that are used for routine treatments, several new ideas are presented. One is proposed by U. Amaldi[3], and is shown in Fig.4. In this system, beam is accelerated with cyclotron at the first stage, and is accelerated with linac up-to a required energy for therapy. To compact the linac, high frequency as 3 GHz is used, beam test was performed with one unit of this linac system. To verify the system as a dedicated accelerator for cancer treatment, further R&D is left.

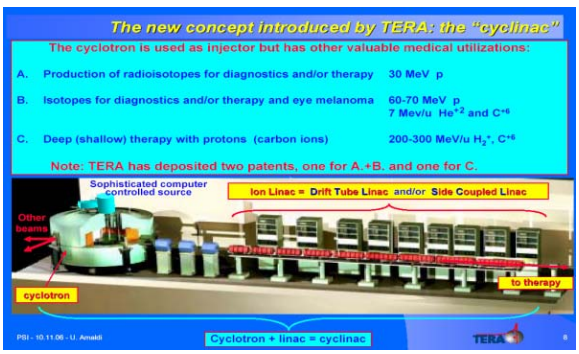

Figure 4: Accelerator concept of LIBO (Linac Booster).

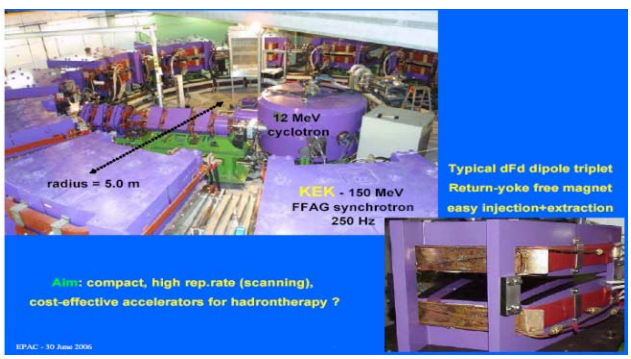

Figure 5: FFAG at KEK.

New type of accelerator is proposed by Mori et al[4], which is FFAG (Fixed Field Alternating Gradient synchrotron). They constructed a proton machine which has maximum design energy of 150 MeV. Though they could demonstrate the beam acceleration up-to 100 MeV, the size is larger than the dedicated synchrotron for proton therapy.

There is design study of super-conducting cyclotron for light ion radio-therapy by L.Calabretta et. al.[5]. In their design study, diameter of the cyclotron is as small as 5m. To realize the cyclotron that is used for cancer therapy, R&D is required.

PROTON FACILITIES

A dedicated proton facility (see Fig.6) with gantries was constructed at Loma Linda University (USA), and the treatment was started in 1990. A main accelerator is synchrotron, and there are three gantries and one horizontal fixed line. This is first hospital-based facility, and accumulated patient number was 10324 at July 2005. Another choice of accelerator is cyclotron. In Fig.7, normal-conducting cyclotron at NCC (Kashiwa, Japan) is shown that was constructed by IBA and Sumitomo. Accelerated beam energy is fixed, and required beam energy for therapy is obtained by use of a degrader. At PSI, super-conducting cyclotron was installed as shown in Fig.8, which was manufactured by ACCEL. In this facility, spot-scanning irradiation was adopted.

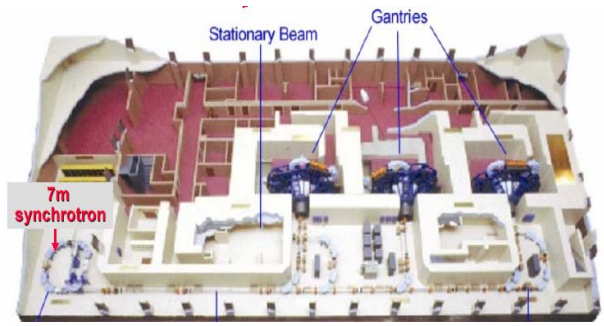

Figure 6: Lay-out of the proton facility at Loma Linda University.

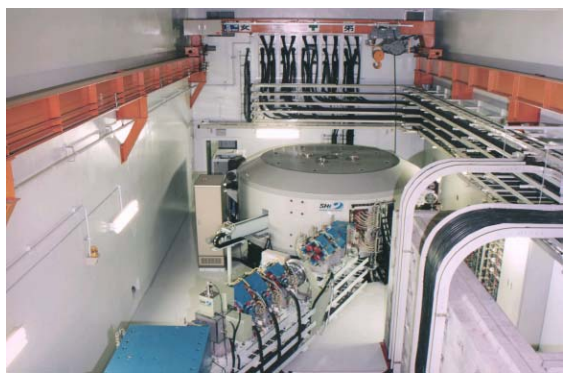

Figure 7: Normal conducting proton cyclotron by IBA at Kshiwa.

Figure 8: Super conducting cyclotron by ACCEL at PSI.

LIGHT ION FACILITIES

Firstly, ion beam was used for cancer therapy at LBNL (Lawrence Berkeley National Laboratory, USA) by use of the Bevalac, which was constructed for physical experiments. Following the pioneering works at LBNL in this field, a dedicated facility of HIMAC (Heavy Ion Medical Accelerator in Chiba) was constructed at NIRS (National Institute for Radiological Sciences; see Fig.9). The maximum beam energy is 800MeV/u in the case of e/m=0.5, and required ion species are from He to Ar. There are three treatment rooms. In one room, there are horizontal and vertical beam lines. In other rooms, we can use only horizontal or vertical beam line. Treatment was started in June 1994 with carbon beam, and more than 3000 patients have been treated until December 2006. In the clinical study, fractionations were reduced in the cases of lung and liver tumors, and now treatments with one and two fractions are practiced with better tumor controls, respectively. In the case of radio-resistive tumor like a bone and soft tissue sarcomas, good clinical results are obtained also. Following HIMAC, a dedicated facility was constructed at Hyogo in Japan, where proton beam can be used also. The gantry was equipped in the proton room as shown in Fig.10.

Figure 9: HIMAC facility.

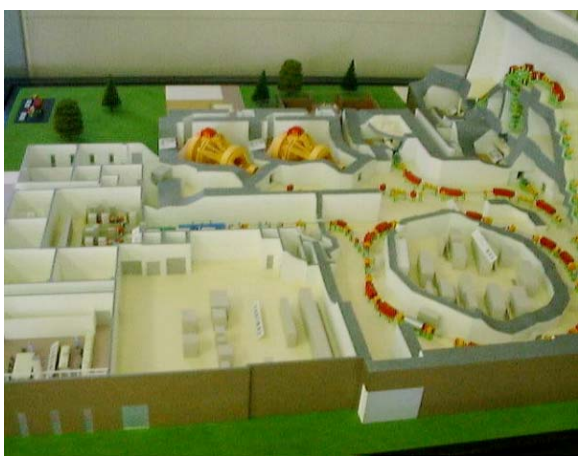

Figure 10: HIBMC at Hyogo.

At GSI (Gesellshaft fur Schwerionenforschung), treatment with carbon beam from a synchrotron of SIS18 was started in 1997. In this treatment, irradiation with raster scanning was developed, where beam energy is changed in the synchrotron during the irradiation. With this irradiation method, 198 patients have been treated successfully until December 2003. Based on the experiences with carbon ion radio-therapy, construction of a dedicated facility of HIT(Heidlberger Ionenstrahlen-Therapie; see Fig.11) was built at Heidelberg[6]. In this facility, there is one gantry room that is first one in the ion beam facility. In this facility, proton beam is also expected to use for therapy.

In Italy, there is a project of CNAO (Centro Nazionale di Adroterapia Oncologica) [7], which is under construction in Pave. Though the injector linac is expected to use same one as in HIT, there is no gantry in this facility as shown in Fig.12.

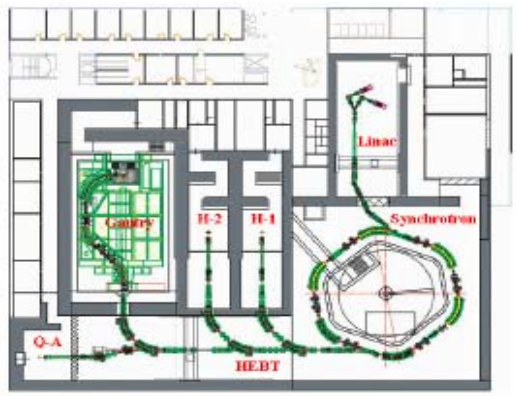

Figure 11: Layout of HIT (Heidlberger Ionenstrahlen-Therapie) at Heidelberg.

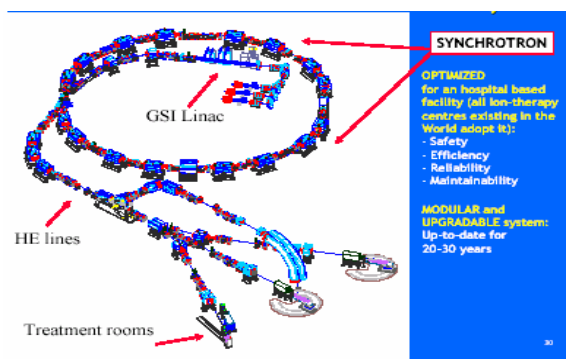

Figure 12: CNAO at Pave (Italy).

At Lanzhou in China, there is a plan to use carbon beam for cancer therapy of a deeply seated tumor at IMP (Institute of Modern Physics) with a newly constructed CSRm synchrotron that is shown in Fig.13. As a first step of this plan, superficially-placed tumors were treated last year[8] with carbon beam of 100 MeV/u that was accelerated in a cyclotron of SSC.

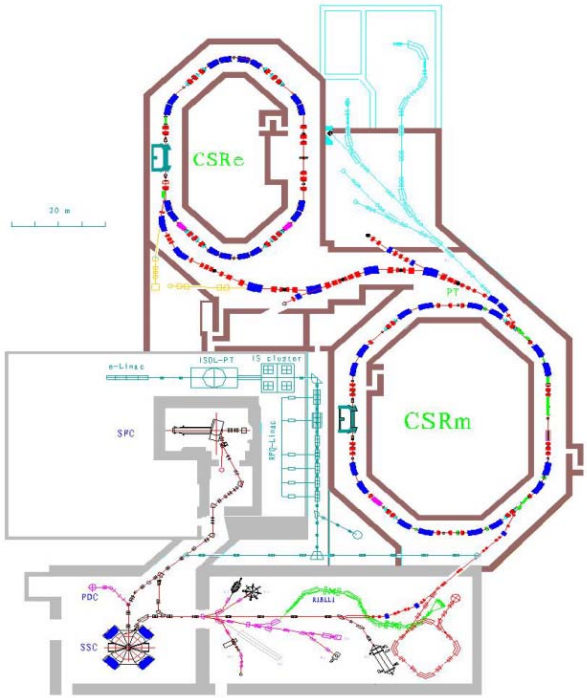

Figure 13: Accelerator facility at IMP.

At NIRS in Japan, design of a compact facility with carbon ion beam was performed, which must have good stability and reliability. These properties are important in the dedicated radio-therapy facility to treat many patients. The designed facility[9] consists of an ECR ion source with permanent magnet, an RFQ linac, an APF-IH linac with 4 MeV/u, and a synchrotron with maximum energy of 400 MeV/u. There are three treatment rooms. One is equipped with horizontal and vertical ports, and other two are equipped with horizontal or vertical port as seen in Fig.14. Concerning the important subsystem in this new design, beam tests of linacs, an acceleration cavity in the synchrotron, power supply for lattice quadropole magnet, and new irradiation devices have been performed. A tested injector system is shown in Fig.15, and the accelerated beam intensity was 490 eμA with fully stripped carbon beam. This beam intensity is twice the required value in the system design[10]. Based on these tested results of each component, the dedicated facility will be realized at Gunma University in 2009.

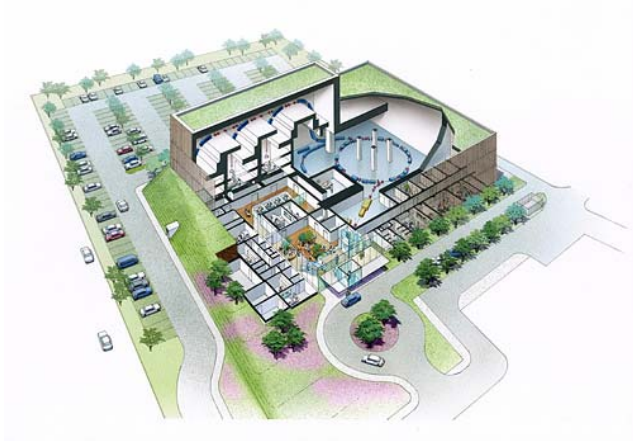

Figure 14: Image of the designed facility for Gunma University.

Figure 15: Tested injector system with an APF-IH linac.

REFERENCES

[1] R.R.Willson, Radiology 47(1946)487
[2] T.Kanai, private communication
[3] U.Amaldi, PTCOG Paris, June 2004
[4] T.Mori et al., private communication
[5] L.Calabretta et al., NIM A 562(2006)1009
[6] H.Eickhoff, Proceedings of EPAC 2002, Paris
[7] R.Rossi, Proceedings of EPAC 2006
[8] Q.Li, private communication
[9] K.Noda, Proceedings of EPAC 2006
[10] Y.Iwata et al., NIM A569(2006)685

USE OF MICROBEAM AT JAEA TAKASAKI

M. Fukuda#, K. Hatanaka, T. Yorita, RCNP, Osaka University, Osaka 567-0047, Japan
T. Kamiya, M. Oikawa, T. Satoh, T. Sakai, S. Kurashima, N. Miyawaki, S. Okumura, H. Kashiwagi, W. Yokota, Department of Advanced Radiation Technology, JAEA, Takasaki, Gunma 370-1292, Japan

Abstract

The TIARA facilities of JAEA in Takasaki is equipped with a several-MeV light-ion and a several-dozen-MeV heavy-ion microbeam formation systems of focusing type, and a several-hundred-MeV heavy-ion microbeam formation system of collimating type. The microbeams with a spot size of 1 μm or less in diameter are extensively utilized for the research in materials science and biotechnology. An in-air micro-PIXE analysis system using a 2 MeV proton microbeam is quite useful for medical science and dentistry to visualize two-dimensional distribution of very small quantities of elements in a microscopic area like cells with very high sensitivity. A single-ion hit system using a several-hundred-MeV heavy-ion microbeam is available for medical and biological applications such as elucidations of cellular radiation response. Highly stable ion beams with energy spread less than 0.02 % are required for the microbeam production. Improvements of accelerator performance are indispensable to realize the ion beams of high quality. A flattop acceleration system and a magnetic field stabilization system have been developed for the JAEA AVF cyclotron. These accelerator technologies are also required for very precise spectroscopic studies in nuclear physics. Ultrahigh energy resolution of 0.005 % has been achieved at the RCNP cyclotron facility of Osaka University.

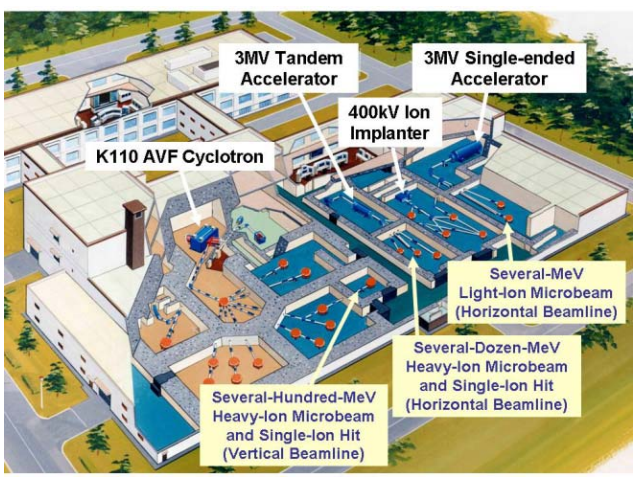

Figure 1: Bird view of the TIARA facility, equipped with four accelerators and three microbeam formation systems.

#mhfukuda@rcnp.osaka-u.ac.jp

INTRODUCTION

The ion beam irradiation research facility, TIARA (Takasaki Ion accelerators for Advanced Radiation Applications), was completed in 1993 at the Takasaki Radiation Chemistry Research Establishment of Japan Atomic Energy Research Institute(JAERI), the predecessor of the present Takasaki Advanced Radiation Research Institute of Japan Atomic Energy Agency (JAEA) [1]. Ion beam applications to the research and development in materials science and biotechnology have been fairly progressing after the full-scale operation of the ion accelerator complex facility. The bird view of the TIARA facility is shown in Fig. 1. A variety of ion beams are provided by a K110 AVF cyclotron, a 3 MV tandem accelerator, a 3 MV single-ended accelerator and a 400 kV ion implanter. The wide energy range from 20 keV through 1 GeV is covered by the accelerator complex.

Three kinds of light- and heavy-ion microbeams with a beam spot size of 1 μm or less in diameter are available at the TIARA facility. Use of the ion microbeam has greatly enhanced spatial and targeting resolutions of the ion irradiation in a finite area.

The micro-PIXE analysis has become widespread in various fields. Proton or helium ion beam with energies from 2 to 3 MeV is produced by the single-ended accelerator with acceleration voltage stability of the order of 10^{-5}. The helium ion microbeam with a spot size of 0.25μm has been produced using the high quality ion beam. The in-air micro-PIXE technique, first developed at TIARA, enables elemental analysis in cells without drastic change of the living cell condition by placing the frozen cell sample in atmosphere.

The tandem accelerator is equipped with a several-dozen-MeV heavy-ion microbeam formation system. The heavy-ion microbeam is useful for material processing and elucidation of radiation effects such as single-event upset of semiconductor devices used in space, caused by high LET(Linear Energy Transfer) irradiation. As the integration level of the semiconductor devices increases, higher spatial- and targeting-resolutions are required for the investigation of the radiation effects.

The LET range from 10 to 1000 keV/μm in water equivalent is covered by several-hundred-MeV heavy ions accelerated by the AVF cyclotron. The deposit energy is transferred in a localized area along the ion track. In case of the cell irradiation, the heavy ion causes high dose localization within the cell. A heavy-ion microbeam formation system of collimating type has been installed in a vertical beam line of the AVF cyclotron for

the elucidation of cellular radiation response. Targeting precision of 5 through 10 μm has been achieved, which is sufficient to hit the cell nucleus or cytoplasm.

The quality of the ion beam provided by the accelerators directly influences the microbeam production. The microbeam spot size is determined by a gap of slits and the chromatic aberration of the beam focussing lens. The chromatic aberration originates in the energy spread of the accelerated ion beam. In case of the electrostatic accelerator, the energy spread depends mainly on the stability of the acceleration voltage. In the case of the cyclotron beam, the energy spread can be minimized by a flattop acceleration technique. The flattop acceleration for the high quality beam production is also applied to the high energy resolution experiment in nuclear physics.

PRODUCTION OF THE MICROBEAM

A microaperture with a hole of 5 to 10 μm in diameter or a precisely manufactured slit is used in the microbeam formation system of collimating type. The minimum beam spot size was limited by the size of the microaperture or the slit gap. Contamination of particles scattered at the edge of the microaperture or the slit might bring deterioration of the microbeam spot size, in some case.

A beam focusing using a multiplet of quadrupole lenses is a sophisticated technique to reduce the beam size less than 5 μm [2]. A schematic image of the focusing system for microbeam production is shown in Fig. 2. The object of the primary beam is determined by the first slits. Divergence of the beam is defined by a series of the second slits. An image of these slits can be projected at a focal plane by the focusing lenses. The microbeam spot size is determined by the demagnification factor of the lens system. Spherical and chromatic aberrations in the lens system are also taken into account to minimize the beam size.

In order to measure the microbeam spot size, the microbeam is scanned on a silicon relief pattern, and the secondary electrons emitted from the silicon relief pattern are detected. The position of the microbeam can be known from the voltage supplied to an electrostatic beam scanner. We can estimate the beam spot size from the peak width of the secondary electron distribution obtained at the edge of the relief pattern. The beam spot size of 250 nm in diameter has been achieved for 2 MeV proton and helium ion beams.

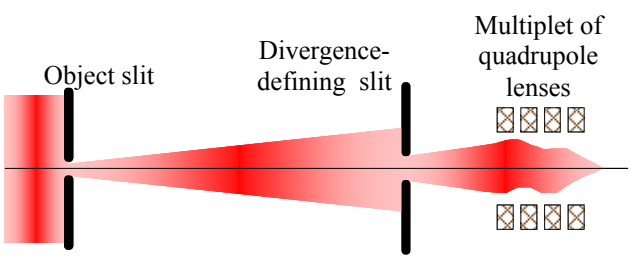

Figure 2: Image of the microbeam production.

APPLICATIONS OF THE MICROBEAMS

Several-Dozen-MeV Heavy Ion Microbeam

A heavy ion microbeam, such as a 15 MeV nickel ion accelerated by the 3 MV tandem accelerator, is utilized to investigate SEU(single event upset) of semiconductor devices used for space [3]. A single ion hit system, consisting of single-ion detectors and a fast beam switcher has been developed for observation of the SEU phenomena at a specific position of the micro device.

Several-MeV Light Ion Microbeam

The micro-PIXE analysis using the 2 MeV proton microbeam has an overwhelming advantage in analyzing very small quantities of elements in a microscopic aria with very high sensitivity. Two-dimensional distribution of elements included in cells can be visualized by the in-air micro-PIXE technique [4]. A schematic drawing of the in-air micro-PIXE system is shown in Fig. 3. A 4 μm thick Mylar film is used as a sample backing and a vacuum partition. The microbeam is focused on an experimental sample mounted on annular sample holder in the atmosphere. The X-rays emitted from the sample elements are measured by a Ge or Si(Li) detector placed upstream. The microbeam is scanned horizontally and vertically by the electrostatic beam scanner. The element species is identified by the X-ray energy. The in-air micro-PIXE system enables multi-elemental mapping of samples in atmospheric environment without drying the biological samples. The micro-PIXE analysis technique is widely applied to various research fields such as bio-medical research, dentistry, environmental science, and geology.

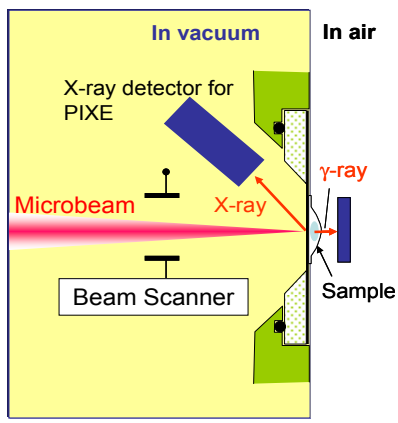

Figure 3: Schematic drawing of the in-air micro-PIXE system.

Several-Hundred-MeV Heavy Ion Microbeam

The high energy heavy-ion microbeam formation system, installed in a vertical beamline of the JAEA AVF cyclotron, is used for living biological cell irradiation. The single ion hit technique was also applied to the microbeam formation system to irradiate the specific part of individual cells [5]. Heavy ions are delivered to atmosphere through the microaperture with an inner

diameter of 10 μm. A sample stage is placed just after the microaperture. Single ions are detected with a plastic scintillation counter placed downstream of the sample stage. Every time a single ion is detected, the ion injection into the cyclotron is inhibited by kicking out the ion beam with a beam switcher installed on the injection line until the single ion detection system and a data processing system become ready for the next single ion event.

The heavy ion microbeam with energy of hundreds MeV, inducing high LET in substances, is extremely useful for the research in biology and biotechnology. The high energy heavy-ion microbeam is a fine probe for the investigation of the cell response by causing great damage to DNA without destroying the whole cell. The single ion hit technique using the high energy heavy-ion microbeam is indispensable for investigation of cell-to-cell communications like bystander effects, the analysis of cellular spatial sensitivity, the interaction of damages caused by individual irradiation, the cellular repair dynamics, and the intra-cellular process such as apoptosis.

DEVELOPMENT OF A NEW HIGH-ENERGY HEAVY-ION MICROBEAM FORMATION SYSTEM

A new microbeam formation system of focusing type, using a quadruplet of quadrupole lenses in combination of a series of slits, is under development to improve the special and targeting resolutions. The new microbeam formation system has been installed in another vertical beam line of the JAEA AVF cyclotron. The system is equipped with a magnetic beam scanning system to increase the speed of the single ion hit to 600 hits/min.

The spot size of the microbeam has been estimated by measuring the distribution of the secondary electrons emitted from a copper grid with sharp edges. The position of the single ion hit has been observed using a CR-39 film. Recently the beam spot size of 1 μm has been successfully obtained [6].

UPGRADE OF THE CYCLOTRON FOR GENERATION OF HIGH QUALITY BEAMS

In order to generate the high quality beam with the energy spread of $\Delta E/E = 0.02$ %, a flattop acceleration system has been developed for the JAEA AVF cyclotron. Reduction of the energy spread has been achieved by using the flattop acceleration voltage waveform, generated by superimposing the fifth-harmonic voltage waveform on the fundamental one.

In case of the flattop acceleration using the fifth-harmonics, the magnetic field fluctuation of the cyclotron magnet is required to be less than 2×10^{-5} FW to suppress the beam phase within 16 RF degrees [7]. The magnetic field fluctuation of conventional cyclotrons is of the order of 10^{-3} to 10^{-4}. The temperature control system of the cyclotron magnet has been improved to fulfil the tolerance of the magnetic field fluctuation causing the beam phase excursion.

Development of the Flattop Acceleration System

An additional co-axial cavity, called FT cavity, has been coupled capacitively to the middle part of the transmission line of the fundamental cavity to generate the fifth-harmonic voltage. The impedance matching between the two cavities is optimized by tuning the gap between the capacitive coupler electrode and the inner tube of the fundamental cavity. The fifth-harmonic resonant frequency range from 55 to 110 MeV is fully covered by the FT cavity. The rf power for the fifth-harmonic voltage generation is fed to the FT cavity from the 3 kW wide–band amplifier.

A demonstration of the flattop voltage waveform, observed with the capacitive pickup placed at the corner of the dee electrode near the extraction radius, is shown in Fig. 4. In the practical flattop acceleration, however, the pickup signal doesn't have such a flattop waveform, because the dee electrode has a spanning angle of 86 degrees and the fifth-harmonic voltage decreases with a radius due to the voltage variation of the standing wave along the transmission line of the cavity [8]. The ratio of the fifth-harmonic voltage to the fundamental one is required to increase from the theoretical value of 1/25. The voltage ratio depends on the resonant frequency and the acceleration harmonic number.

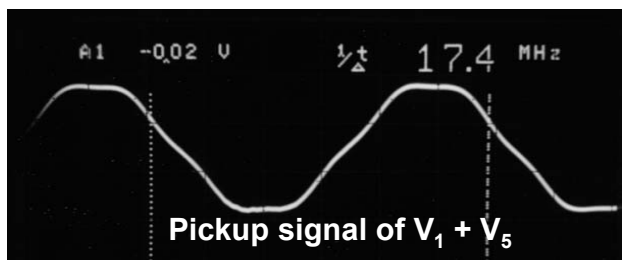

Figure 4: Flattop voltage waveform observed with the pickup of the dee electrode.

The flattop accelerated beam of 260 MeV $^{20}Ne^{7+}$ ions has been developed for the microbeam production. A clear turn pattern in the large radius region before extraction has been observed by the flattop acceleration. The energy spread of the extracted beam has been reduced to $\Delta E/E = 5 \times 10^{-4}$ or less.

Stabilization of the Cyclotron Magnet Field

The beam phase excursion out of the tolerable phase range for the flattop acceleration is caused by the error of isochronous field generation and by the fluctuation in the magnetic field. The magnetic field fluctuation originates in the temperature variation of a pole and a yoke of the cyclotron magnet.

On the basis of investigation of the correlation between the magnetic field and the yoke temperature changes, effective measures have been taken to stabilize the magnetic field. Water-cooled copper plates were installed between the main coil and the magnet yoke to control

thermal conduction from the main coil to the magnet yoke. Cooling water temperatures of the copper plates and trim coils were optimized to keep the pole and yoke temperatures constant according to the excitation level. The magnetic field fluctuation has been reduced down to $\Delta B/B = \pm 1 \times 10^{-5}$ by the stabilization measures [9].

PRODUCTION OF HIGH QUALITY BEAM AT RCNP CYCLOTRON FACILITY

The techniques of the flattop acceleration and the cyclotron magnet field stabilization are common to the generation of the high quality beams for high-resolution experiments in nuclear physics. The RCNP(Research Center for Nuclear Physics) cyclotron facility of Osaka University has been upgraded to improve the beam quality and transmission to the RCNP ring cyclotron[10].

The RCNP cyclotron facility is shown in Fig. 5. The K400 ring cyclotron, equipped with a flattop acceleration system and the magnet field stabilization system, provides the high quality beam with the energy spread of the order of 10^{-4}. The magnetic field of the ring cyclotron is stabilized at the order of 10^{-6}. Ultrahigh energy resolution of $\Delta E/E = 5 \times 10^{-5}$ has been achieved with the spectrometer "Grand Raiden" by a dispersion matching method applied to the beam transport from the ring cyclotron to the spectrometer.

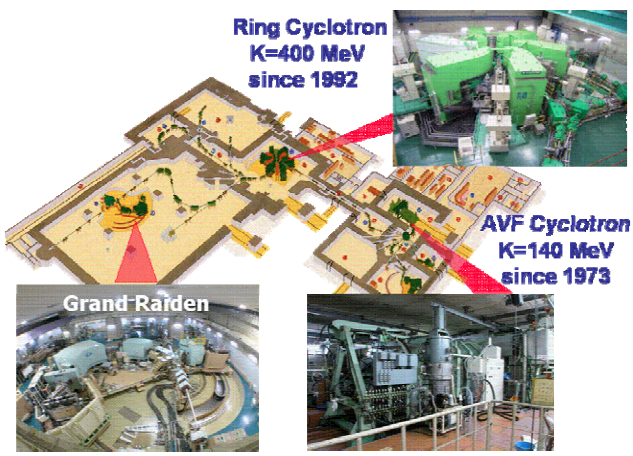

Figure 5: RCNP cyclotron facility.

A new flattop acceleration system using the fifth, seventh and ninth harmonics has been developed for the K140 AVF cyclotron to reduce the energy spread of the beam. The flattop acceleration voltage waveform has been successfully produced in the frequency range from 50 to 80 MHz. In order to improve the beam transmission to the ring cyclotron, the development of the flattop accelerated beam is now in progress.

REFERENCES

[1] R. Tanaka, et al., "JAERI AVF Cyclotron for Research of Advanced Radiation Technology", Proc. 12th Int. Conf. on Cyclotrons and Their Applications, Berlin, May 1989, p. 566.

[2] M.B.H. Breese, D.N. Jamieson, P.J.C. King, Materials Analysis Using A Nuclear Microprobe, 1996, (New York: Wiley-Interscience).

[3] T. Kamiya, N. Utsunomiya, E. Minehara, R. Tanaka, Nucl. Instr. and Meth. B 64 (1992) 362.

[4] T. Sakai, T. Kamiya, M. Oikawa, T. Sato, A. Tanaka, K. Ishii, Nucl. Instr. and Meth., B190 (2002) 271.

[5] Y. Kobayashi, M. Taguchi, T. Shimizu, S. Okumura, H. Watanabe, J. Radiat Res., 36 (4), 290 (1996).

[6] M. Oikawa, et al., "Design of a Focusing High-Energy Heavy Ion Microbeam System at the JAERI AVF Cyclotron", Nucl. Instrum. Methods B210 (2003)54.

[7] M. Fukuda, et al., "A Flat-top Acceleration System for the Variable-Energy and Multi-Particle AVF Cyclotron", Rev. Sci. Instrum., 74(2003) 2293.

[8] S. Kurashima et al., "Development of the Flat-Top Acceleration System for the JAERI AVF Cyclotron", Proc. 17th Int. Conf. on Cyclotron and Their Applications, Tokyo, Japan, 2004, p. 362.

[9] S. Okumura, et al., "Magnetic field stabilization by temperature control of an azimuthally varying field cyclotron magnet", Rev. Sci. Instrum., 76 (2005) 033301.

[10] K. Hatanaka, et al., "Upgrade Project of the RCNP AVF Cyclotron Facility", Proc. 17th Int. Conf. on Cyclotron and Their Applications, Tokyo, Japan, 2004, p. 115.

THE PROGRESS OF ACCELERATOR MASS SPECTROMETRY AND THEIR APPLICATIONS IN CHINA

Chen Jia-er, Guo Zhiyu, Liu Kexin, Institute of Heavy Ion Physics, Peking University and Key Laboratory of Heavy Ion Physics, Ministry of Education, Beijing 100871, China
Wu Xiaohong, Yuan Sixun, School of Archaeology and Museology, Peking University,
Jiang Shan,China Institute of Atomic Energy
Zhou Weijian, Xi'an AMS Centre

Abstract

The facilities and technologies developed for AMS at Peking University, China Institute of Atomic Energy and Xi'an AMS Centre are presented. Interesting results about Chronology frame of Xia-Shang-Zhou dynasties based on radiocarbon dating with PKU-AMS on serial samples from various sites like Tianma-Qucun, Xinzha sites etc and oracle bones from Yinxu site, are given as examples of the AMS application in the field of Archaeology. Applications in the fields of earth sciences, biomedical sciences are introduced as well.

INTRODUCTION

As a result of substantial development for more than a quarter of a century, the accelerator mass spectrometry (AMS) has become a leading technique for the detection of long-lived radio nuclides such as ^{10}Be, ^{14}C, ^{26}Al, ^{36}Cl and ^{129}I at isotopic ratios between 10^{-10} and 10^{-15} and has been applied extensively in the fields of archaeology, earth sciences, environmental sciences, biomedical sciences, nuclear safeguards, nuclear physics and astrophysics.

Comparing with the conventional mass spectrometers and radio decay measurement, the AMS has following merits:

- Ultra high sensitivity. For a number of radioactive nuclides, the measuring background of isotopic ratios could be reduced down to 10^{-15} or even less, which is much lower than traditional mass spectrometer.
- Small sample size. The sample amount of AMS measurement is usually in the order of mg elements, which are three orders lower than that needed for decay counting method. In the case of meteorite measurement even 10 μg carbon sample is still workable.
- High throughput. The time of direct atom counting is much shorter than that of decay counting for the same precision.

However, to carry out a precise abundance measurement of rare nuclides is really a challenging issue. Careful precautions have to be made to eliminate various interferences in the whole process starting from sample collection and preparation, beam generation, beam handling and acceleration, gas stripping and finally to the data acquisition and processing. Precautions have to be made to ensure AMS facilities operating under conditions with extremely low machine background, low isotopic fractionation, high beam transmission efficiency, and high resolution beam analysis as well as with high performance stability.

There are about 60 AMS facilities around the world and more new facilities are to be developed or constructed. In China, AMS technology has been developed at the China Institute of Atomic Energy and Peking University since 1980's. There are now 5 AMS facilities working. In the following paragraphs, only tandem based AMS facilities in China and their features will be presented followed by some discussion on typical applications.

AMS FACILITIES IN CHINA

The HI-13 Tandem at China Institute of Atomic Energy (CIAE) was the first facility in China that used for AMS measurements of mid or heavy nuclei like ^{10}Be, ^{26}Al, ^{36}Cl, ^{41}Ca and ^{129}I etc.[1] and the applications has been concentrated on geosciences, biomedical sciences, nuclear physics and astrophysics. The layout of the facility is shown on fig. 1.

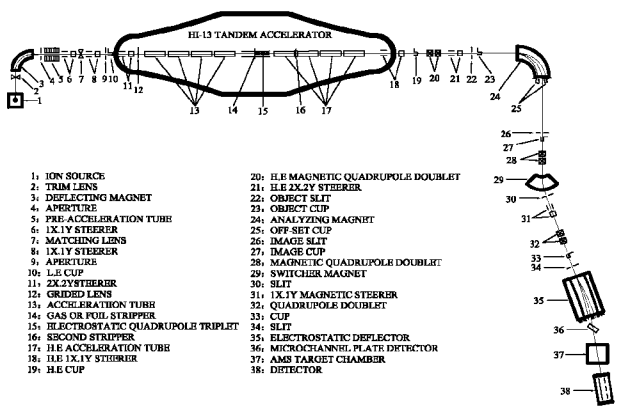

Figure 1: The layout of CIAE's HI-13 AMS system.

It consists of mainly a HI-13 Tandem accelerator, sputtering ion source, injection section with low energy beam analysis, post acceleration beam analyzing magnet and electrostatic deflector, as well as AMS target chamber and micro-channel plate detector. Typical parameters of the CIAE AMS used for measurements of ^{10}Be, ^{26}Al, ^{36}Cl, ^{41}Ca nuclides are listed in Table 1.

Various methods have been developed along with ΔE-E ionization chamber for the detection of rare nuclides and the elimination of their isotope and isobar interferences, as indicated in the Table 1. For instance to measure ^{10}Be, an absorber of 15.3mg/cm^2 Ni is added in front of the ΔE-E ionization chamber, and for the measurement of ^{129}I, TOF technique is adopted for isotope identification while for

Table 1: Main Parameters of CIAE AMS

Radio-isotopes	Negative ions	Terminal voltage	Detection method	Sensitivity
^{10}Be	BeO^-	8.4MV	Absorber +ionization chamber	11×0^{-14}
^{26}Al	Al^-,AlO^-	7.6MV	ionization chamber	11×0^{-14}-15
^{36}Cl	Cl^-	8.0MV	ionization chamber	2×10^{-15}
^{41}Ca	CaF_3^-,CaH_2^-	8.2MV	ionization chamber	3×10^{-14}
^{79}Se	Se^-	8.2MV	Projectile X-ray	2×10^{-11}
^{129}I	I^-	8.0MV	TOF	11×0^{-13}

^{79}Se, projectile X-ray method was developed for the isobar identification. Typical spectra of AMS measurements are shown in fig.2-3.

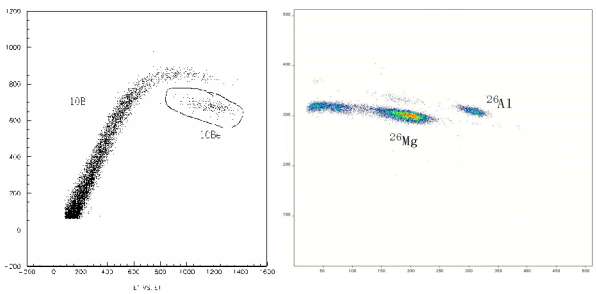

Figure 2: Two-dimensional spectra of standard sample ^{10}Be (10^{-11}), and standard sample of fully stripped ^{26}Al.

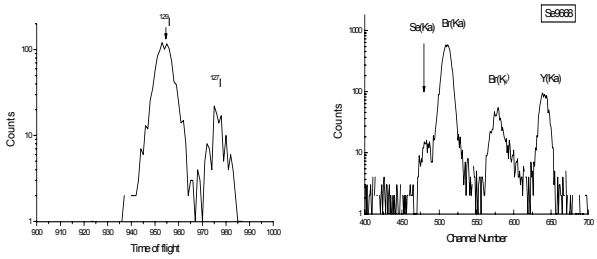

Figure 3: TOF spectrum of ^{129}I & projectile K_α ray of ^{79}Se.

The AMS facility at Peking University (PKU-AMS) is a user's facility mainly for ^{14}C, ^{10}Be and ^{26}Al measurements [2]. It is based on an EN tandem accelerator and the layout is shown in fig.4. It has been upgraded to a precision of 0.4%-0.5% for ^{14}C measurements, with a background corresponding to ^{14}C age of 50ka, since 1996, to meet the requirements of the Xia-Shang-Zhou Chronology Project. [3] The low energy injection part mainly consists of a NEC MC-SNICS ion source with 40 target positions, an Einzel lens and a 20kV pre-acceleration section. The power supplies for injection system, bending magnets as well as HV power supplies were replaced with high precision products. The charging belt and voltage-dividing resistors

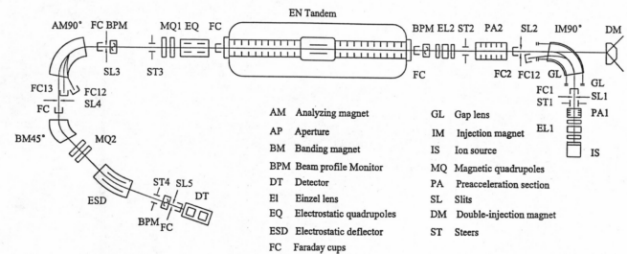

Figure 4: The layout of PKU-AMS.

in the EN tandem accelerator were upgraded too. Some instruments have installed to stabilize the humidity, temperature and AC voltage in the accelerator hall. Finally, a new control system for beam line was constructed, which is a distributing system contained 6 local control stations and one PC via a fibber-optical loop. The software for the system was developed on the LabVIEW platform. It has fine user interface and is easy to operate. The system is reliable and stable, with a control precision of 0.05% and a long-term stability of 0.1% for 8 hours [4]. A master PC is used to read the ^{14}C counts, the stable isotope beam current and to control the target changing in ion source as well as the sequential injection of isotopes.

To reach high accuracy, the measuring procedure has been designed carefully. One sample was distributed into multiple targets, which were measured individually and then the results were combined to see if they could pass the so called t or F test. The off-line data manipulation program (OLDMAP) has been developed, which can manipulate, analyze measured data and finally give ^{14}C age and its error. The measured ^{14}C age has to be converted into calendar date by using calibration curve and in order to minimize the error during the conversion, calibration of serial ^{14}C samples with Bayesian method has been studied and developed. [5].

A compact AMS system manufactured by NEC has been installed in 2004 at Peking University which is dedicated for ^{14}C measurements [6]. The system is based on Pelletron accelerator with a maximum terminal voltage of 0.6MV. The system has been strictly tested by using standard samples and the results clearly indicate that the precision and reproducibility of the system are better than 0.3% for modern samples and the machine background is 4×10-16, corresponding to ^{14}C age of 65ka. The system utilizes a NEC 40 sample Multi-Cathode SNICS ion source. The fast switching injection system injects the carbon ions ^{12}C-, ^{13}C-, ^{14}C- for 0.3, 1 and 100 ms sequentially with a repetition rate of 10 Hz. The terminal voltage is set to 0.46MV during routing operation. The high energy analyzing system includes a 90° double focusing magnet and a 90° electrostatic deflector. The final ion detector is a simple silicon surface barrier detector. A computer is used for data acquisition and control of the system while another one is used for off-line data analysis. At the terminal voltage of 0.46MV, the ion beam transmission of typically 43% (HE/LE ^{12}C particle current) has been reached at a range of stripper gas pressure from 14-16μτ. Since this machine is capable to measure 3000

^{14}C samples per year, EN tandem based AMS facility is now mainly used for measurements of ^{10}Be and heavier nuclides.

The Xi'an Center of Accelerator Mass Spectrometry (Xi'an AMS Center) was jointly established by the Institute of Earth Environment of the Chinese Academy of Sciences and the Xi'an Jiaotong University recently. The major equipment at this center is a 3 MV tandem-based accelerator mass spectrometer imported from High Voltage Engineering, Netherland. The equipments of sample preparation and set-up systems have been developed locally [7]. This spectrometer, in its present capability, is already able to make high quality measurement of nuclides such as, ^{10}Be, ^{14}C, ^{26}Al and ^{129}I. Its functionality can be further expanded to include several other nuclides such as ^{41}Ca, which also have important applications. It has the capacity of making routine high quality ^{14}C analyses with a precision better than 0.3% and a significant annual throughput. At the same time, it allows for a number of applications to be explored with ^{10}Be, ^{26}Al and ^{129}I, as well as the potential of the multi-element analysis offered by the facility. Its detection limit for ^{10}Be and ^{129}I is at the level of 10-15 and 10-14 respectively.

TYPICAL APPLICATIONS

A number of AMS applications have been carried out in China since 1990. Only some interesting examples are presented in this paper.

Archaeological Studies

The Chinese civilization has been lasting for several thousand years and has never been interrupted. The most authoritative book which gives a reliable chronicle of ancient Chinese history is Shi Ji, written by Sima Qian, an official historian of Han Dynasty in about 100 BC, which started from 841 BC in the later period of Western Zhou and is generally recognized. Shi Ji also gives all the King's names and their genealogy since Xia. However, the ancient Chinese chronology has not been well established so far. An important example is for the date of the conquest of Shang by King Wu of Zhou, there have been at least 44 different solutions offered spreading over a span of 112 years. Radiocarbon dating played an important role in Xia-Shang-Zhou Chronology Project. Nine series of samples were studied for this purpose [8], including 7 sites, one tomb series and a special series of oracle bone samples (Fig. 6). Most of the bones are from the final capital of the Shang Dynasty, they are important for establishing a chronology of late Shang Dynasty, since the inscriptions on oracle bones recorded the King's name, activities, war, sacrificial offerings and important astronomical phenomena. However, the ages of sites and cultural phases may have an offset compared with the ages of kings and dynasties. Furthermore, radiocarbon dating always has an error and sometimes it might be too large to be accepted by chronologists. For this reason, calibration of all the samples as a series with Bayesian method results much narrower confident intervals than that of the single sample calibration. Fig. 5 is an example, where boundaries were set at beginning and end corresponding to the beginning time of the Tianma-Qucun site and the end of Western Zhou. The results show that the end of Western Zhou is in 796−754 BC, which is consistent well with the historical record of 770 BC.

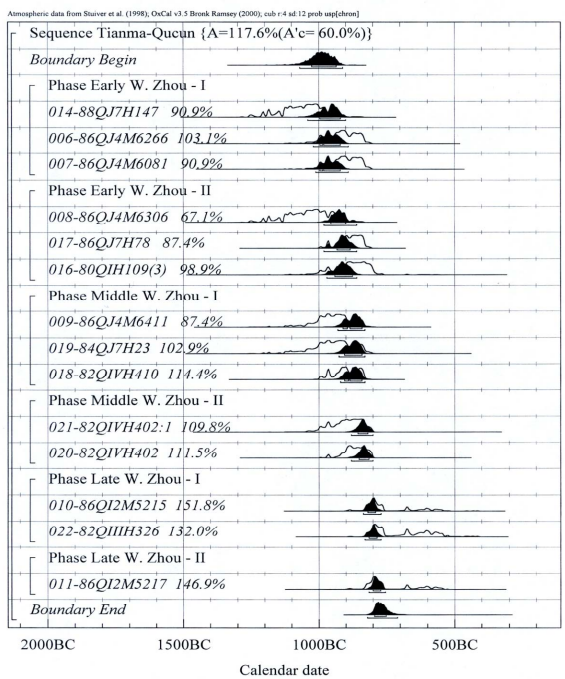

Figure 5: Calibration of sample series with Bayesian method.

Figure 6: Oracle bones with inscriptions.

Precise measurements of ^{14}C in oracle bones have been carried out on the compact NEC machine. The results obtained with OxCal 3.9 shows that the calendar ages of these oracle bones are from 1260 BC to 1050 BC. This indicates that the end of Shang Dynasty should be around 1050 BC. It is consistent with the ^{14}C dating result of serial bone samples from the Yinxu site and the result from the eclipse calculations according to the records in oracle bone inscriptions. So far, more than 100 oracle bone samples have been dated, among them more than 60 bone samples were measured with the new machine, and the results are consistent with the rest of the samples measured with EN based AMS system. The final results through the synthesis of various ways are listed in the Table 2.

Table 2

Dynasties	Dates
Xia	ca. 2070 BC – ca. 1600 BC
Shang	ca. 1600 BC – 1046 BC
Western Zhou	1046 BC – 771 BC

Another interesting example with ^{14}C dating is study on the chronology of Xia dynasty with serial samples from the cultures of Longshan, Xinzai and Er-li-tou. The cultural remains in Xinzhai site contain late Longshan, Xinzhai and early Er-li-tou. Bayesian method is used again for the calibration of the serial samples to reduce the calibrated ranges. Oxcal 3.9 Program was used for the calibration of ^{14}C ages of serial samples from Xinzhai. Samples were organized into three phases according to the layer sequence with an upper boundary and a lower boundary; boundaries are also added between the phases. To check the reliability, many samples were measured twice. The results show that the transition time from Longshan to Xinzhai was about 1840BC – 1820BC, Xinzhai culture lasted about 120a. The end age of Xinzhai (around 1720BC) is approximately the same with the beginning age of Er-li-tou [9]. Most archaeologists in China believe Xinzhai culture belongs to Xia, therefore the beginning of Xia dynasty was at least before 1820BC.

Recently Donghulin site which is located to the west of Donghuli village near Beijing city was discovered and excavated [10]. Tombs, ash-pits, fireplaces and other vestiges were found along with abundant objects including chipped stone implements, microliths, polished stone tools and potteries. More than 20 charcoal and bone samples were collected from this site and then dated with the AMS at Peking University. The results show that the Donghulin Man lived from 9000BC to 7000BC, the early Neolithic period. This is another very important archaeological discovery in Beijing area following the famous Peking Man site and Upper Cave Man site. Donghulin site has great significance to study the living style of the early Neolithic Man and the evolution of early Neolithic cultures in North China and the relationships between them.

Earth Science

^{10}Be produced in the atmosphere is soon attached to mineral aerosols and deposited on the earth surface by precipitation. It is a useful isotopic tracer for investigating the formation of Aeolian deposits and Quaternary climate evolution. The Matuyama-Brunhes polarity reversal which happened 0.78 Ma ago was recorded in loess L8 in Chinese loess sequence. This corresponds to a glacial period and is obviously different from the marine record where the same reversal boundary has been found in the sediments of Oxygen Isotope Stage 19, an interglacial period. One explanation is that the loess record of the Matuyama-Brunhes boundary (MBB) is displaced downwards by over 100 cm [11]. In order to determine the true position of the MBB in loess, ^{10}Be concentration in loess from Louchuan, Shanxi Province is investigating by AMS ^{10}Be measurements at Peking University based on the assumption that the increase of the ^{10}Be production rate due to the reduction of geomagnetic field intensity during the polarity reversal is significant and can be recorded in the loess sequence.

Bio-science

AMS is a powerful tool to study the adduction effect between the toxic material such as Nicotine, nitrobenzene, Methyl tart-butyl ether (MTBE) and acryl amide (AA) at environmental low dose levels and bio-macromolecules such as DNA and Hemoglobin (Hb). Recently this kind of research is extended to the study of the inhibition effects of adductions by dietary constituents [12].

Nicotine is a major alkaloid in tobacco products and has proven to be a potential geno-toxic compound. Many natural dietary products can suppress the DNA adduction, and hence act as inhibitors of cancer. The inhibitory effects of curcumin, garlic squeeze, grape-seed extract, tea polyphenols, vitamin C and vitamin E on nicotine-DNA adduction have been investigated using AMS. The results demonstrated that all these dietary constituents induced marked dose-dependent decrease in nicotine-DNA adducts as compared with the control. The reduction rate reached about 50% for all agents, except garlic squeeze (40%), even at its highest dose level. Amongst the six agents, grape-seed extract exhibited the strongest inhibition to the DNA adduct formation.

CONCLUSIONS

AMS technology has been well developed in China. Two of the AMS facilities are based on early developed HI-13 and EN tandem, while the other two are modern dedicated systems. Each of them performed successfully to meet their needs in the fields of archaeology, earth science, environmental sciences and biomedical sciences and etc. Meanwhile, all of them will be further upgraded according to the requirements of new applications.

REFERENCES

[1] S. Jiang, M. He et al., NIM. B 172(2000) 87-90
[2] Chen Chia-erh, Guo Zhiyu, Li Kun, Liu Kexin et al., NIM B92 (1994) P.47-50
[3] Guo Zhiyu, Liu Kexin et al., NIM B172 (2000) 724-31
[4] Liu Kexin, Guo Zhiyu et al., NIM B172 (2000) 70-74
[5] C.E. Buck, et al., Antiquity 65 (1991) 808-821.
[6] Kexin Liu, Xingfang Ding et al., to be published in NIM B (2007)
[7] Zhou Weijian et al., private communication Sep. 2006
[8] Guo Zhiyu, Liu Kexin et al., Proc. of 1st East Asia Symposium on AMS, Tsukuba, Japan, 26-28 Jan. 2006
[9] Kexin Liu, Baoxi Han et al., Radiocarbon, Vol. 47, Nr 1, 2005, p.1-5.
[10] Chaohong Zhao, Archeology, Nr 7, 2006, p 3-8 (in Chinese)
[11] K.X. Liu, L.P. Zhou et al., NIM B 223-224(2004) 168-171.
[12] Y. Cheng, H.L. Li, H.F. Wang et al., Food and Chemical Toxicology 41(2003) 1045-1050.

PAPER NOT YET RECEIVED

OPERATION AND RECENT DEVELOPMENTS AT THE SIAM PHOTON SOURCE

P. Klysubun#, S. Rugmai, S. Rujirawat, S. Cheedket, C. Kwankasem, G. Hoyes, and M. Oyamada, NSRC, Nakhon Ratchasima, Thailand

Abstract

The Siam Photon Source (SPS) is a dedicated synchrotron radiation facility located in Nakhon Ratchasima, Thailand. After successful commissioning and recent energy upgrade from 1.0 GeV to 1.2 GeV, the Siam Photon Source is currently well into user mode of operation. The light source is now providing routinely synchrotron radiation in the vacuum ultraviolet and soft x-ray spectral ranges to both internal and external researchers. In this report we describe the overview of the current machine performance including user availability, the progresses made recently, and the planned machine improvements, which emphasizes on improving beam stability and machine reliability. Plan to install two insertion devices, a permanent magnet planar undulator and a superconducting magnet wavelength shifter, is also discussed.

INTRODUCTION

The Siam Photon Source (SPS) is a synchrotron light source operated by the National Synchrotron Research Center (NSRC), and is located in Nakhon Ratchasima, Thailand. The accelerator complex consists of two 20-MeV injector linacs, a 1.0-GeV booster synchrotron, and an electron storage ring. The storage ring was originally designed to operate at 1.0 GeV and was later upgraded for 1.2-GeV operation in 2005 [1]. The lattice of the storage ring is a double bend achromat (DBA) lattice with four superperiods for a total of eight bending magnets. The ring is equipped with four straight sections for insertion devices. Currently the beam is injected to the storage ring at 1.0 GeV and then ramped up to 1.2 GeV. It is planned that the energy of the booster synchrotron will also be upgraded to 1.2 GeV for full energy injection and subsequently top-up mode of operation of the storage ring. Machine specifications of the SPS can be summarized as listed in Table 1. At present there are three photon beamlines in operation: a photoelectron spectroscopy (PES) beamline (BL-4) operated in the vacuum ultraviolet (VUV) spectral range, an x-ray lithography (XRL) beamline (BL-6), and an x-ray absorption fine-structure spectroscopy (XAFS) beamline (BL-8). All three are bending magnet beamlines.

Table 1: Summary of SPS machine specifications

Electron beam energy [GeV]	1.2
Beam current [mA]	120
Lattice	DBA
Superperiod	4
Horizontal emittance [nm·rad]	41
Coupling [%]	0.8
Circumference [m]	81.3
Number of straight sections	4 (7 m)
Betatron tunes ν_x, ν_y	4.75, 2.82
Synchrotron tune ν_s	2.33×10^{-3}
Natural chromaticities ξ_x, ξ_y	-9.40, -6.61
Momentum compaction	0.0170
RF frequency [MHz]	118
Harmonic number	32
RF voltage [kV]	120
RF power [kW]	14
Number of RF cavity	1
Energy loss per turn [keV]	65.94
Injection beam energy [GeV]	1.0
Number of beamlines	3

OPERATION AND MACHINE PERFORMANCE

In the year 2006 the SPS has been operated in user mode of operation, providing routinely synchrotron radiation in the VUV and soft x-ray spectral ranges to users. The weekly operation schedule has been such that Monday morning was reserved for weekly preventive maintenance, while Monday afternoon and every other Tuesday were designated for machine study. The rest of the week until 2 PM Friday was scheduled for user experiments. Since the beam lifetime in the storage ring was still comparatively short, the beam was injected four times a day. The time it took for beam injection and energy ramping was approximately one hour for each round of injection. At the beginning of the year the beam lifetime was around 2.5 hours at 100 mA beam current. As time passed vacuum condition in the ring was improved by continual photodesorption, which in turn increased the beam lifetime. At the end of the year the beam lifetime increased to around 4 hours at 100 mA stored current, and was still increasing.

Table 2 shows the comparison between the scheduled beamtime and the beamtime actually delivered to the users in 2006. In total 1865 hours of user beamtime were scheduled and 1571 hours were actually delivered, resulting in the user beam availability of 84.25%. There were several machine problems which contributed to unscheduled downtime in 2006. It has been found that the main cause of the machine downtime was the electrical instability of the 22-kV electrical line supplying the SPS which led to numerous machine trips. This was even more prevalent during the rainy season. The problem is being addressed with the construction of a new electrical

#pklysubun@nsrc.or.th

substation dedicated solely to the SPS. The construction was already finished and the station will be fully operational in 2007. Figure 2 shows the failure statistics in 2006, where the number outside the parentheses is the number of machine trips. The total number of machine trips occurred in 2006 was 117.

Table 2: Scheduled vs. delivered beamtime in 2006

Month	Scheduled beamtime (hours)	Delivered beamtime (hours)	Percentage (%)
January	175.0	149.5	85.4
February	180.0	168.5	93.6
March	155.0	130.0	83.9
April	65.0	43.2	66.5
May	265.0	198.8	75.0
June	210.0	173.0	82.4
July	175.0	119.3	68.2
August	265.0	250.4	94.5
September	200.0	171.5	85.8
October	175.0	167.0	95.4
November	Machine shutdown		
December			

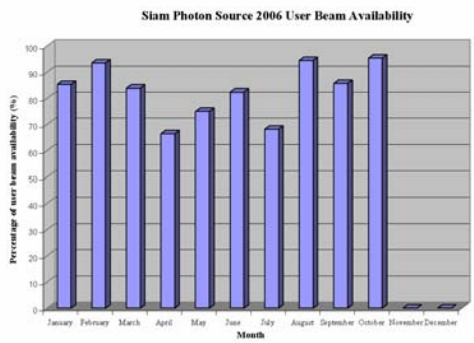

Figure 1: Percentage of the SPS 2006 user beam availability.

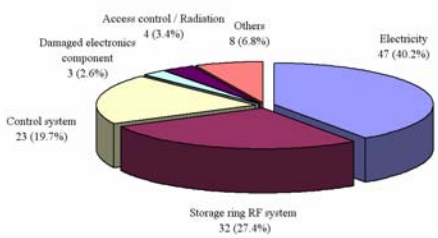

Figure 2: SPS 2006 machine failure statistics.

RECENT DEVELOPMENTS

In the first machine shutdown of 2006 the old and proprietary pattern memory system for the booster synchrotron was replaced with a new PXI-based digital I/O waveform generator [2]. The open PXI standard offers several advantages above the existing system. Most notably among them are improved reliability, easier programming, easier repair, and lower cost. The previous pattern memory system, custom-made by Toshiba, had occasionally experienced both software and hardware malfunctioning, which required system reset followed by pattern reloading and/or electronics board replacement altogether. Up to now the new PXI pattern memory has proved to be very stable and reliable.

A new data logging system for the SPS had also been developed [3]. The earlier data logging scheme was consisted of only simple Java applets that record the monitored data in a comma separated value (CSV) file format, without neither search nor retrieval capability. The new logging and retrieval systems were written entirely with MATLAB language and utilize MATLAB toolboxes, namely, the Open Process Control (OPC) Toolbox, the Data Acquisition Toolbox, and the Database Toolbox, to handle data communications and database interface, respectively. Since the MATLAB-based Accelerator Toolbox [4] is the most-used accelerator modelling tool at the SPS, the MATLAB-based retrieval module can be reused by accelerator physicists to easily import the logged data for accelerator optics studies.

During the second machine shutdown of 2006 at the end of the year the SPS storage ring was realigned. It had been found that before the realignment the ring was misaligned by as much as 3 mm in the vertical direction, which was primarily due to the effect of floor settlement. The situation was better in the horizontal plane, where the position of the magnets differed from the design values by less than 400 microns. However, the storage ring vacuum chambers were not aligned with the magnet centres. From the optical survey of the beam position monitors it was found that the position of the BPMs can be off by as much as 7 mm. The whole ring was then realigned. After the realignment the position of all the components were brought to within 200 microns with respect to the design values.

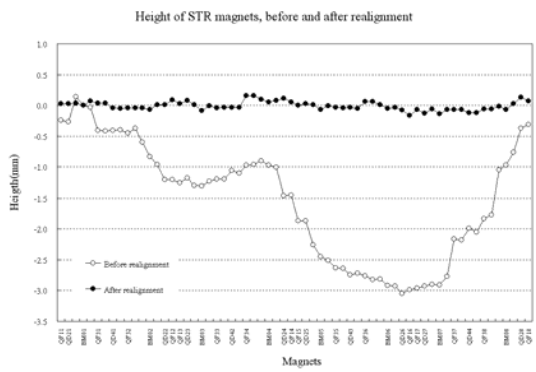

Figure 3: Height of SPS storage ring magnets, before and after the realignment.

After the realignment the SPS was successfully recommissioned. The first task carried out afterward was beam position monitor calibration, which was accomplished by using beam-based alignment [5] together with orbit response matrix measurement. After the BPMs were calibrated, closed orbit distortion (COD) correction was performed using Singular Value Decomposition (SVD) method. This was the first time the electron orbit in the SPS storage ring had been corrected.

The orbit rms errors were brought down from 3.13 mm. to 0.39 mm. in the horizontal direction and from 2.06 mm. to 0.85 mm. in the vertical direction [6].

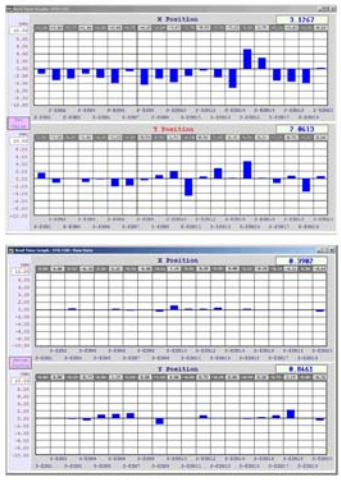

Figure 4: SPS uncorrected orbit (top) compared to the corrected orbit (bottom).

Currently a new beam profile monitoring system is being installed at the bending magnet 2. The previously employed monitoring system, which consisted of only a simple telescopic imaging optics, at the bending magnet 6 (BM6) was removed because of the plan to modify the beamline BL-6 for soft x-ray lithographic research and microstructure fabrication by LiGA technique [7]. The plan for the new beam profile monitor includes x-ray pinhole imaging employing a YAG crystal, x and y interferometers, and an optical beam profiler in the visible region. During the second machine shutdown in 2006 most of the components of this new system had been installed, and it is expected that the system will be fully functioning before the second quarter of 2007.

INSERTION DEVICES

Two insertion devices, a permanent magnet planar undulator (U60) and a 6.4T superconducting magnet wavelength shifter (WLS), will be installed in the SPS storage ring in the next two years. The U60 undulator, which has 41 magnetic periods with period length equal to 60 mm, will be installed in 2007. It will provide more intense synchrotron radiation with photon energy tunable from 30 to 900 eV to the users. At present the magnetic measurements of the magnet are being carried out [8].

For the installation of the WLS in 2008, matching calculations had been performed. It was found that the perturbations introduced by the WLS on the SPS storage ring optics can be corrected by adjusting three pairs of quadrupole magnets adjacent to the WLS. Three quadrupole magnet power supplies had been procured. Two superconducting magnet power supplies and a quench detector had been purchased from Danfysik A/S in 2006. A helium liquefying system for supplying liquid helium to the WLS had been purchased from Air Liquide and is now being installed. The installation is expected to be completed in July 2007, when the system will be commissioned. Currently the WLS cryostat is being modified to accommodate all the instrumentation and sensors. Vacuum chambers both downstream and upstream of the WLS including heat absorbers had been designed and analyzed for heat load tolerance using FEA software. Due to limited space the details of this preparation will be presented elsewhere [9].

SUMMARY

After successful commissioning and energy upgrade of the storage ring from 1.0-GeV to 1.2-GeV operation, the Siam Photon Source is now operated in the user mode of operation. There are currently three photon beamlines. The SPS operation still requires energy ramping in the storage ring; however, energy upgrade of the booster synchrotron is planned. In 2006 user beam availability in 2006 was around 84%, where the main problem was the electricity coming to the facility. A new electrical substation was already built and will be fully operational in 2007. Several machine improvements were carried out with further machine enhancements already planned. The main goal is to improve the machine reliability and beam stability. Two insertion devices, a permanent magnet undulator, and a 6.4T superconducting WLS, will be installed to increase the flux and energy range of the generated synchrotron radiation to the users.

ACKNOWLEDGEMENT

The authors would like to thank accelerator division staff for their support, and Prof. Helmut Wiedemann for invaluable suggestions and advices.

REFERENCES

[1] S. Rugmai et al., "Energy Upgrade of the Siam Photon Source", AIP Proceedings 879 (2007) 58.
[2] G. Hoyes, “A New, PXI Bus Based, Pattern Memory System for the Siam Photon Source”, these proceedings.
[3] P. Klysubun and C. Netsai, “Development of MATLAB-based Data Logging System at the Siam Photon Source”, EPAC’06, Edinburgh, June 2006, p. 3098.
[4] A. Terebilo, “Accelerator Toolbox for MATLAB”, SLAC-PUB-8732 (2001).
[5] G. Portmann et al., “Automated Beam Based Alignment of the ALS Quadrupoles”, PAC’95, Dallas, May 1995, p. 2693.
[6] S. Rugmai et al., “Beam Based Alignment and COD Correction for the Siam Photon Source”, these proceedings.
[7] P. Klysubun et al., “Soft X-ray Lithography Beamline at the Siam Photon Laboratory”, AIP Proceedings 879 (2007) 1490.
[8] S. Rugmai et al., “Soft X-ray Undulator for the Siam Photon Source”, AIP Proceedings 879 (2007) 335.
[9] P. Klysubun et al., “A 6.4 T Superconducting Wavelength Shifter for the Generation of Hard X-rays at the Siam Photon Source”, to be published.

SESAME STATUS

G. Vignola, A. Amro, M. Attal, H. Azizi, A. Kaftoosian, F. Makahleh, M. Shehab, H. Tarawneh, S. Varnasseri. SESAME, c/o UNESCO Amman Office, P.O. Box 2270, Amman 11181, Jordan

Abstract

An update of the status of SESAME* is presented. SESAME is a third generation light source facility, with an e-beam energy of 2.5 GeV, located in Allan, Jordan. The emittance is 26 nm.rad and 12 straights are available for insertion devices. The injector consists of a 22.5 MeV microtron and 800 MeV booster synchrotron, with a repetition rate of 1 Hz. The conceptual design of the accelerator complex has been frozen, and the engineering design is well advanced. The Phase I scientific program for SESAME has also been finalized, and it foresees 6 beam lines, including 2 IR ports. The construction of the SESAME building is in progress, and the beneficial occupancy is expected by late spring of 2007. The completion of the accelerators complex construction is scheduled for 2010.

INTRODUCTION

The technical evolution of SESAME is described in [1, 2]. The Building that will house SESAME is under construction with funds and site provided by Jordan (see Fig. 1), under the supervision of R. Al Sarraf, from Al-Balqa University. Its completion, including a 6.0 MVA dedicated Electrical Power Station, is scheduled by the first half of 2007.

Figure 1: A panoramic view of SESAME building during construction (Nov. 2006).

Fig. 2 shows the layout of the accelerator complex and beamlines in the experimental hall. The injector complex (800 MeV booster synchrotron and 22.5 MeV Microtron) is the one already used in Bessy I [3], with new power supplies and vacuum pumps. The 2.5 GeV Main Storage Ring is completely new.

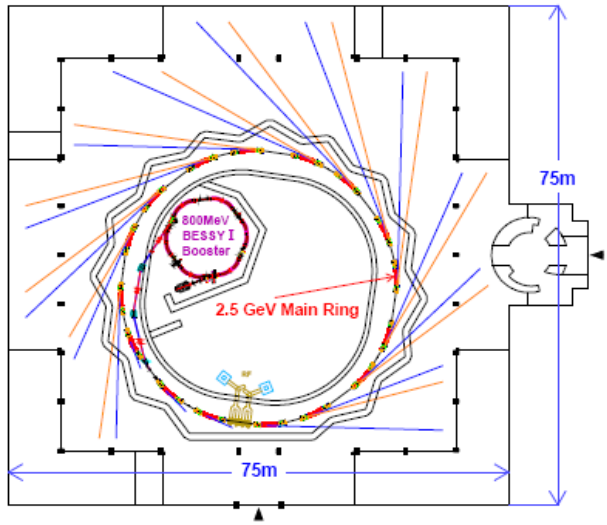

Figure 2: SESAME layout in the experimental hall.

THE MAIN STORAGE RING

The main storage ring parameters are given in Tab. 1. The storage ring is composed of 8 super periods with 16

Table 1: SESAME design parameters.

Energy (GeV)	2.5
Circumference (m)	133.12
N. of Periods	8
Dipole field (T)	1.455
Dipole field index	11
Q_x - Q_z	7.23 – 6.19
Mom. Compaction	0.00829
N. Emitt.(nm.rad)	26.0
U_0 (keV/turn)	589.7
τ_ε, τ_x, τ_z (ms)	2.80, 2.28, 3.77
RF freq. (MHz)	499.564
Harmonic Number	222
Peak Voltage(MV)	2.4
Synch. Freq. (kHz)	37.18
σ_L (cm)	1.15
Current (mA)	400
N. of bunches	200
1/e Lifetime(hrs)	16.9

*Synchrotron-light for Experimental Science and Applications in the Middle East is a cooperative venture by the scientists and governments of the region with founding members Bahrain, Egypt, Israel, Jordan, Pakistan, Palestine Authority, Cyprus and Turkey. Iran is in the process of finalizing its formal membership.

dipoles and 16 straights sections of alternate length of 4.44m and 2.38m respectively. 4 straights (2 Long and 2 Short) are allocated for Injection, RF cavities, beam diagnostic etc. Each dipole chamber is equipped with a port, to collect the synchrotron light, centered at 6.5^{O}. We will summarize in the following the main features of the Optics and of the main subsystems.

The Optics

For SESAME a Double Bend Achromat (DBA) lattice has been adopted with vertical focusing gradient inside the dipoles and dispersion distribution in the straights. The bare lattice has only 2 families of quadrupoles and 2 of sextupoles. The optical functions for a full period are shown in Fig. 3, while the dynamic aperture [4] is shown in Fig. 4.

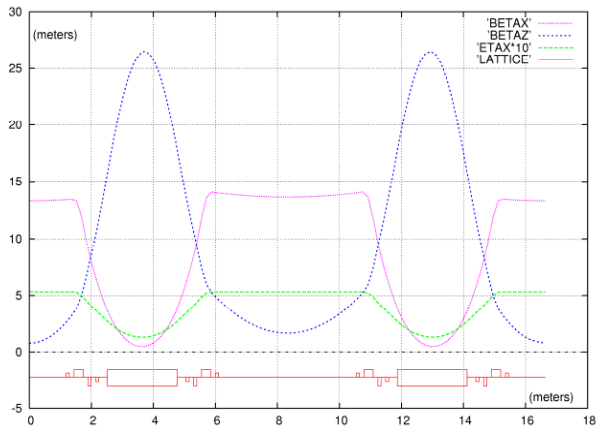

Figure 3: SESAME full period optical functions.

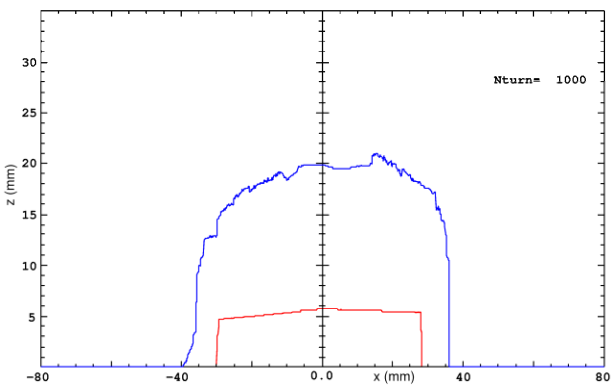

Figure 4: On momentum dynamic aperture (blue) and vacuum chamber limited one (red) in the middle of the Long straight section, taking in account the effect of all the high order multipoles in the magnets.

Injection Scheme

The injection scheme is based on using a four-kicker bump with 3 μsec pulse length. The thin septum exit is located in the centre of a long straight section [5], see Fig.4. The kicker strengths for 20 mm bump are given in Tab. 2, taking into consideration the effect of sextupole magnets. Many solutions have been found to achieve an injection efficiency of 100% taking into account some safety margin, i.e. the energy spread is three times larger and the emittance is 9 times larger than the nominal value at 800 MeV [5]. Fig 6 is an example of injecting into the storage ring with an angle.

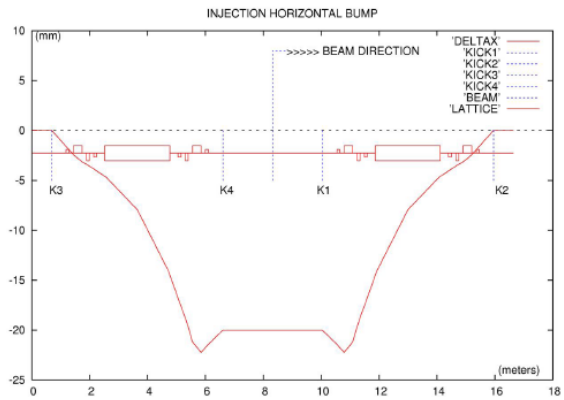

Figure 5: Layout of SESAME kickers and septum magnets.

Table 2: SESAME kicker's strengths in mrad.

Kicker strength	K1	K2	K3	K4
With sextupole	-2.936	-3.190	-3.190	-2.936
w/o sextupole	-2.872	-3.242	-3.242	-2.872

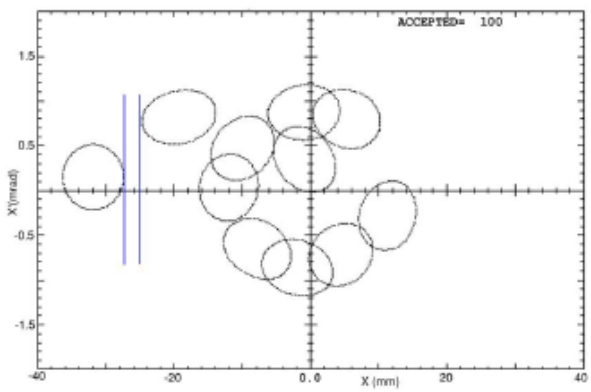

Figure 6: Tracking of 100 particles for 10 turns injected with 0.15 mrad angle.

The RF system

The RF system for the SESAME initial phase is based on four single-cell cavities of ELETTRA type, each one powered with an 80 kW CW IOT amplifier [6, 7, 8]. In Phase II the available RF power will be doubled by combining two 80 kW IOTs for each cavity to increase the stored beam current, the lifetime and to compensate the additional losses due to the insertion devices. The possible RF operating scenarios are listed in Tab. 3.

Table 3: Voltage and power for SESAME RF system.

P_{tot} (per cavity)	V_{RF} [kV] (4 cavities)	$P_{cav.}$ [kW] (each cavity)	P_{beam} [kW] (P_{tot}-P_{cav})	Max. I_{beam} [mA]
80 kW (Phase I)	2400	53	27	183
	2100	40	40	275
	1800	30	50	340
150 kW (PhaseII)	2400	53	97	658

The Magnets system

In SESAME there are 16 Dipoles, 32 F-quadrupoles with magnetic length of 30 cm, 32 D-quadrupoles with magnetic length of 10 cm, 32 F-sextupole and 32 D-sextupole with magnetic length of 10 cm. 4 additional coils inside each F(D) sextupole are used as horizontal (vertical) correctors. For quadrupoles and sextupoles a design identical (a part the length) to the one adopted for ANKA has been chosen [9], the max gradient is 19T/m for the quadrupoles and 300 T/m^2 for the sextupoles. The design of the other magnets is described in [10].

The Vacuum system

The design of the stainless steel vacuum chamber is based on the chamber-antechamber concept, with OFHC crotch absorber and a slot height of 12 mm. The full stay clear aperture in the chamber is 70mm in the horizontal plane and 30 mm in the vertical one. The chamber wall thickness is 3 mm, while the antechamber length in the transverse direction, depending on the position, is up to 25 cm. A 3D view of the Arc Vacuum Chamber is shown in Fig. 7.

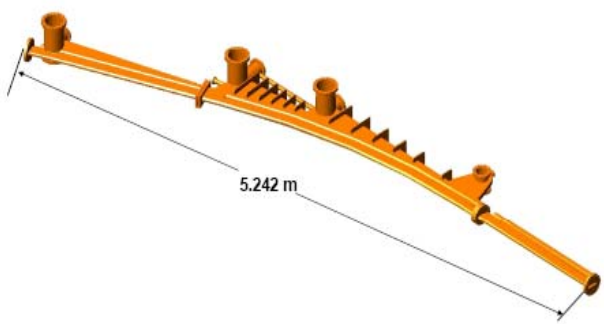

Figure 7: 3D view of the Arc Vacuum Chamber.

The SESAME vacuum system, with a total pumping speed of ~30.000 l/s, is dimensioned to reach after adequate beam conditioning (~100 Ampere-hours of stored beam) an average operating pressure of ~ 1 nTorr with 400 mA of circulating current.

Let us point out that we have adopted the ante-chamber concept in the entire storage ring: this allows, by properly positioning the 8 crotch absorbers of one super period, to intercept ~100% of the emitted synchrotron radiation while reducing the antechamber transverse size to a maximum of ~25 cm. The vacuum layout for one full period is shown in Fig. 8

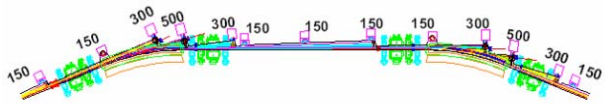

Figure 8: Vacuum Layout for one SESAME period: the numbers indicate the pumping speed in l/s of the vacuum pumps.

The dynamic pressure profile along one period is plotted in Fig. 9: the value of the average pressure is ~ 0.9 ntorr.

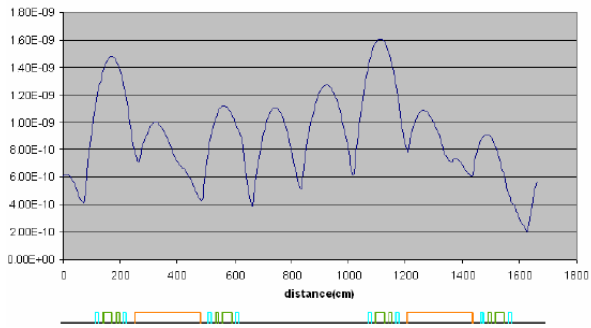

Figure 9: Dynamic pressure profile (mbar) at 400 mA along one full period, after a dose of 100 Ah.

ACKNOWLEDGMENTS

We acknowledge the importance of the contribution of D. Einfeld in developing and coordinating the conceptual design on which SESAME is based.

We are also indebted to the SESAME Technical Committee (A. Wruhlich, Chairman, A.A. Adly, E.E. Alp, C. Bocchetta, M. Eriksson, A. Nadji, S. M. Salman, and E. Weirheter) for the advice and the support given.

REFERENCES

[1] See www.sesame.org.jo.
[2] G. Vignola et al. – PAC 2005 Proceedings – p. 586.
[3] D. Einfeld, W. D. Klotz, G. Mülhaupt, T. Müller , R Richter – IEEE NS 26 (1979) 3801.
[4] M. Attal – SESAME Technical Note O-4, Aug. 2005.
[5] M. Attal – SESAME Technical Note I-2, Jun. 2006.
[6] A. Kaftoosian, H. Azizi – SESAME Technical Note RF-1, Aug. 2006.
[7] D. Einfeld et al. – PAC 99 Proceedings – p. 809.
[8] P.Craievich et al. – PAC 99 Proceedings – p. 1123.
[9] D. Einfeld et al. –EPAC 96 Proceedings – p. 2179.
[10] S. Varnasseri – EPAC 2006 Proceedings.

NSLS-II DESIGN: A NOVEL APPROACH TO LIGHT SOURCE DESIGN *

S.L. Kramer, J. Bengtsson, S. Krinsky, V.N. Litvinenko, and S. Ozaki for NSLS-II Design Team#
BNL/NSLS, Upton, NY 11973, U.S.A.

Abstract

The NSLS-II storage ring will be a replacement for the existing two NSLS light sources, which although innovative when proposed, have been exceeded by modern light source designs. NSLS-II design takes a new approach toward providing users with the very bright beams after commissioning and a strategy of evolving to higher brightness beams as more ID devices are installed during its operations. This is achieved not by pushing the basic lattice to lower emittance, an approach that hits severe limits in the control of the dynamic aperture of an ever increasing non-linear lattice. Our approach is rather to reduce the natural emittance using damping wigglers, in addition to damping from the user undulator's. Details on the lattice design are presented.

INTRODUCTION

NSLS-II is the proposed replacement of the NSLS light sources that have been operating for more that 23 years. The storage ring requirements of the lattice are:

Ultra-low horizontal emittance ε_x <1.0nm (achromatic),
Diffraction limited vertical emittance at 12KeV,
$I_o \geq$ 500mA, Top-off injection, and
More than 24 ID straight section ≥5m, for IDs,

After several years of study a DBA lattice with 30 cells has been selected. This lattice while not reaching the emittance goal by itself has been designed to achieve this goal using damping wigglers (DWs) rather than the lattice functions. This avoids the difficulty in dealing with high chromaticity and low dynamic aperture (DA) that limits ultra-low emittance lattice designs. The DA impact of the DWs and undulators must be handled for any lattice and have less impact on the DA than the strong sextupole of alternate lattice designs. Also the number of cells provides for sufficient beam ports for our current VUV and Xray ring users, when those ring are decommissioned.

LINEAR LATTICE CHOICE

The basic light source lattices that can be used are: double bend (DBA) and triple bend (TBA) achromatic lattices. For *M* cells the theoretical minimum emittance is given by [2]:

$$\varepsilon_{MEDBA} = \frac{\gamma^2}{M^3}(0.77\ pm-radians) \quad (1)$$

$$\varepsilon_{METBA} = \frac{\gamma^2}{M^3}(0.151\ pm-radians) \quad (2)$$

where γ is the relativistic energy and the horizontal partition factor J_x is assumed unity. For low emittance, the lowest possible energy is preferred, this is possible due to the advances with in-vacuum, small gap and short-period undulators pioneered at the NSLS [3]. The Xray energy range of 2-20 keV can now be achieved with ~3 GeV beam energy, lowering the RF power and shielding cost for either ring.

A 24-cell TBA, with a potentially factor of five lower emittance per cell, was initially preferred. Due to difficulties in achieving large DA, the emittance goal had to be relaxed [4]. At that time a bold suggestion was made by S. Krinsky [1], to provide the initial emittance with a DBA lattice and use the extra straight sections for DWs to lower the emittance. Although this was a novel approach for new 3rd generation light sources, this idea has been used in colliders [5,6] and previously proposed for light sources [7,8]. This is the approach taken for NSLS-II, using a 30 cell DBA lattice with alternating long and short ID straight sections, one cell is shown in Figure (1).

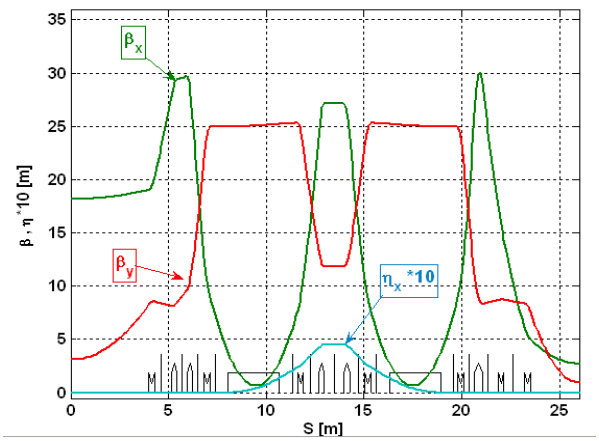

Figure (1) Twiss parameters for one cell of the DBA(15x2) lattice, with 8 and 5m ID lengths.

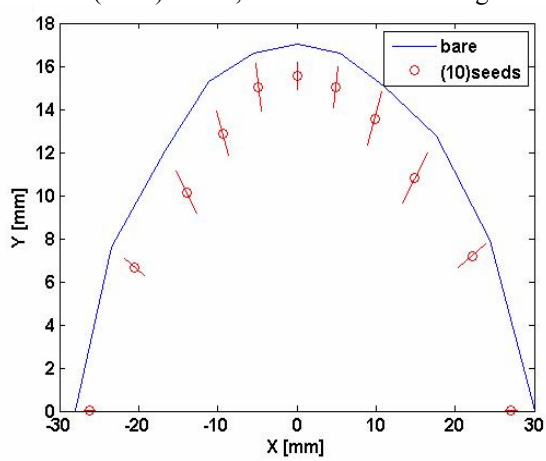

Figure (2) DA for the lattice with alignment tolerances (no field errors) and synchrotron oscillations (δ=0). Orbit distortions are corrected with beam based aligned BPMs.

This lattice was optimized for efficient use of the DWs for reducing the emittance, using weak dipole magnets

skramer@bnl.gov
*Work supported by U.S. DOE, Contract No.DE-AC02-98CH10886

with a bend radius of ρ_o = 25m. A quartet of quadrupoles is used in both the long and short ID straight sections to cancel the phase and beta function modulations from undulators and wigglers. Eleven families of sextupoles are powered to provide a large DA in the presence of realistic engineering and alignment errors. Figure (2) shows the DA for the bare lattice, as well as for the lattice (10 seeds) with alignment tolerances listed in Table I, with the resulting orbit distortions corrected using beam based aligned beam position monitors (BPMs).

Table I Lattice design parameters for NSLS-II

Energy [GeV]	3
Circumference [m]	780
Bending Radius [m] Dipole Energy Loss U_o [keV]	25.019 286.5
Bare Horizontal Emittance, ε_o /Vertical [nm]	2.05 / 0.01
Hor. Emittance w. 8-DWs, ε_{nat} /Vertical [nm]	0.51 / 0.008
Momentum Compaction	0.000368
Bare RMS Energy Spread / with 8- 7m DWs [%]	0.051 / 0.099
Tunes (Q_x , Q_y)	(32.35,16.28)
Chromaticity (ξ_x , ξ_y)	(-100, -41.8)
Peak Dispersion [m]	0.45
Long 8m ID (β_x, β_y) [m]	18/3.1
Short 5m ID (β_x, β_y) [m]	2.7/0.95
Alignment Tolerance Girder & Dipole (x, y, Φ) [mm, mrad]	(0.1, 0.1, 0.5)
Alignment Tolerance. Quad. & Sext.. (x, y, Φ)) [mm, mrad]	(0.03, 0.03, 0.2)

DW'S FOR EMITTANCE REDUCTION

The impact of damping wigglers added into an achromatic straight section is basically to enhance the damping of the lattice without significantly increasing the quantum excitation. The equilibrium values for the energy spread and the emittance depend not only on the wiggler peak field B_w,(bend radius ρ_w) and length L_w, but also on ρ_o , i.e. the dipole energy loss U_o= 7.17[MeV]/ρ_o[m]. The fractional change of the horizontal emittance ε_{nat} relative to the bare lattice emittance ε_o is given by

$$\frac{\varepsilon_{nat}}{\varepsilon_o} = \frac{1+f}{1+\frac{L_w}{4\pi\rho_o}\left(\frac{\rho_o}{\rho_w}\right)^2} \approx \frac{U_o}{U_o+U_w} \qquad (3)$$

where f in most cases is a small correction factor [1],
U_w is the energy radiated by the wigglers and
$U_w+U_o = U_T$ is the total radiated energy.

Thus the emittance can be reduced by increasing U_w or reducing U_o. Since RF power will limit U_T, the emittance reduction can be enhanced by reducing U_o. For undulator beam-lines, the brightness of the higher order harmonics will be reduced if the beam energy spread increases beyond 0.1%, further limiting the total emittance reduction. The fractional change of the beam energy spread, δ_W, relative to the bare lattice value δ_o, is given by

$$\frac{\delta_W}{\delta_o} = \sqrt{\left[U_o + \frac{8U_W}{3\pi}\left(\frac{\rho_o}{\rho_W}\right)\right][U_T]^{-1}} \qquad (4)$$

For $\rho_w < \rho_o$, δ_W will increase with U_w. Increasing ρ_o will have the added benefit of reducing δ_o, allowing lower values of ε_{nat} to be reached before the δ_W <0.1% limit. Figure (3) shows the dependence of these two parameters on the wiggler radiated power, for two values of ρ_o: 25 and 16.68m (1 and 1.5X NSLS-II dipole field). This clearly shows the advantage of the lower dipole field and shows a natural progression of the lattice to lower emittance as DWs or IDs increase U_w for the ring. Clearly a factor of 3-5 reduction is possible within the limitations listed above. A similar reduction is not easily achieved if one has to change the lattice functions, since the DA for strong sextupoles must to be solved.

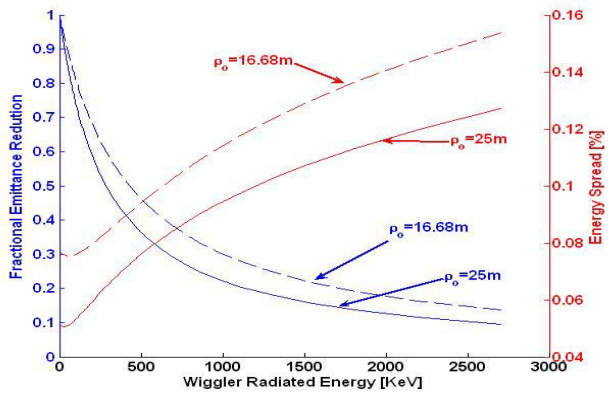

Figure (3) Change in ε_{nat} and δ_W with wiggler radiated energy for B_w = 1.8T and two values of dipole radius ρ_o.

The actual emittance will be limited by the bunch current dependent intra-beam scattering (IBS), a disadvantage of low beam energy. Increasing ρ_o or U_w beyond some point will become ineffective in further reducing the total emittance, $\varepsilon_{x,tot}$, as ε_{nat} approaches the IBS emittance value, ε_{IBS}. The value for $\varepsilon_{x,tot}$ is the emittance resulting from the equilibrium of the radiation damping rate and the quantum plus IBS diffusion rates given by

$$\varepsilon_{x,tot} = \tau_x < H \cdot D_{\delta,SR} > + \tau_x < H \cdot D_{\delta,IBS} > \qquad (5)$$

where τ_x is the horizontal synchrotron damping time,
H is the invariant dispersion amplitude and
$D_{\delta,SR}$ and $D_{\delta,IBS}$ are the radiation and IBS energy diffusion coefficients.

The first term in Eq. (5) is just ε_{nat} , from Eq.(3). The IBS energy diffusion term has been shown [9,10] to be inversely proportional to the equilibrium emittance, $\varepsilon_{x,tot}$ and proportional to a scattering integral of the small angle Möller scatter rate within the energy acceptance (at the scatter point). Factoring out $\varepsilon_{x,tot}$ from the 2nd term in Eq. (5) this term becomes $\varepsilon_{IBS}^2 / \varepsilon_{x,tot}$, where ε_{IBS} is the emittance when the damping reduces the ε_{nat} to zero. Eq. (5) can then be solved for the scaled total emittance

$$\frac{\varepsilon_{x,tot}}{\varepsilon_{IBS}} = \left[\frac{\varepsilon_{nat}}{2\,\varepsilon_{IBS}} + \sqrt{\left(\frac{\varepsilon_{nat}}{2\,\varepsilon_{IBS}}\right)^2 + 1} \right] \quad (6)$$

Reference [9] shows that ε_{IBS} can be estimated using the weak dependence of the diffusion term $D_{\delta,IBS}$, on the energy acceptance and the vertical beam emittance. The diffusion coefficient times H can be averaged over the NSLS-II lattice functions for an assumed maximum beam current of 500mA in 1000 bunches. This yields ε_{IBS} in the range of 0.2 to 0.25nm, which we take as a constant at the maximum value. Figure (4) shows the dependence of $\varepsilon_{x,tot}$ on ε_{nat} as expressed by Eq.(6). For fixed U_T, as the dipole field is reduced, U_o is reduced as does $\varepsilon_{nat}/\varepsilon_o$, Eq.(3). Figure (4) shows that as $\varepsilon_{nat} \rightarrow 0$, the fractional reduction of $\varepsilon_{x,tot}$ becomes less effective. The optimum value appears to be

$$\varepsilon_{nat} \approx (2\ to\ 3)\,\varepsilon_{IBS} \;\Rightarrow\; (U_o/U_T) \approx (2\ to\ 3)(\varepsilon_{IBS}/\varepsilon_o)$$

which for U_T= 1MeV and ε_{IBS} = 0.25nm yield the range ρ_o ~ (20-30)m, 25m was chosen for NSLS-II.

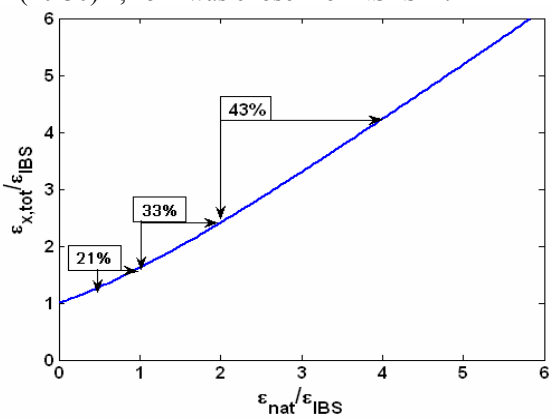

Figure (4) Total emittance reduction with IBS growth for 500mA ring current.

Table II Expected beam properties as the DWs are added

#-DW	ε_{nat} [nm]	$\varepsilon_{x,tot}$ [nm]	U_T [keV]	δ_W [%]	$\Delta\nu_y$
3	0.91	0.98	673.8	0.072	0.119
5	0.63	0.72	932.5	0.09	0.199
8	0.5	0.61	1320	0.1	0.318

The initial design for NSLS-II includes 3- 7m long DWs with B_W = 1.8T and λ_W =100mm. The beam parameters for this and future increases in number of DWs is shown in Table II. These simplified estimates are supported by calculations using computer codes that don't assume ε_{IBS} is constant [11]. Reducing the ρ_o further would make several properties of this lattice less desirable. The critical energy of the Xrays for ρ_o =25m is 2.4 keV, while not adequate for hard Xray beams, these will yield bright sources for our soft Xray and VUV users from NSLS. The DWs will provide high flux and brightness hard Xray beams, far exceeding beams from higher field dipoles. Another disadvantage is the reduced damping rate which could increase the impact of high current instabilities. This rate will increase as DWs are installed, helping to stabilize high current operations. Finally the increased cost for a slightly larger circumference (low uncertainty) needs to be balanced by the greater risk of achieving this performance with lattice changes that drive highly nonlinear lattices and small DA.

LATTICE EFFECTS OF DW

The impact of installing the DWs in the lattice will be similar to those of the user ID devices for which the ring is being designed. These include 1st and 2nd order tune shifts and the vertical betatron function modulation. The linear tune shift is large for this energy and long DW and is approximated by

$$\Delta\upsilon_y \approx <\beta_y> L_w/[4\pi\rho_w^2] \approx 0.038$$

While significant it can be locally corrected using a pair of quadrupoles. The beta function modulation is $\leq$ 8%[12] but this can also be locally corrected with another pair of quadrupoles. For this reason we have used four quads in the ID straight section to minimize these linear distortions and maintain the careful sextupole cancellation of higher order driving terms that yield the large and robust DA.

The nonlinear impact of the DWs can be estimated from

$$d\nu_y/d\,J_y \approx \pi <\beta_y^2> L_w/[2\lambda_w\rho_w]^2 \quad .$$

While significant, this term is only ~30% of the tune shift expected for the λ_w =19 mm undulators, that are planned for the NSLS-II beams. It has been show that by correcting for the linear tune and beta modulation with the four ID quads, this restores much of the DA of the lattice, including the effects of engineering tolerances [13].

There was concern that this large reduction of emittance would cause low Touschek lifetime, requiring too frequent injections to meet the ΔI/I goal. This proved not to be the case, since the scattering rate remains almost constant or slightly reduced, as was pointed out in Ref.[9].

CONCLUSIONS

The lattice design for NSLS-II has taken a novel approach toward achieving the ultra-low emittance goals with a natural progression to these values as DWs and IDs are added to the ring. This approach has been shown to be a less risky approach to the DA problem of these ultra-low emittance lattices and should keep NSLS-II at the fore of the emittance frontier for some time to come.

REFERENCES

[1] S. Krinsky et. al., EPAC'06, p. 3487 (2006).
[2] Accelerator Physics, S.Y.Lee, World Scien.(1999).
[3] P.M. Stefan et. al.,PAC'91, p. 1096(1992).
[4] S.L. Kramer and J.Bengtsson, EPAC'06,p.3481(2006)
[5] H. Weidemann, NIM **A266**, p.24 (1988).
[6] J.M. Jowett et. al., IEEE Tran.NS **30**, p. 2851(1983).
[7] J.L. Laclare, 17th Adv. Beam Dyn.Wksp., ANL (1999).
[8] K. Balewski, EPAC'06, p.3317 (2006).
[9] V.N. Litvinenko,17th Adv. Beam Dyn.Wksp., ANL (1999) and NSLS-II CDR (2006).
[10] J. LeDuff, CERN 95-06 II,p. 573 (1995).
[11] P. Podobedov, NSLS-II CDR (2006).
[12] R. Walker, CERN AccSch.,ST/M94/4,Rhodes(1994).
[13] T. Shaftan et. al., EPAC'06, p. 3490 (2006).

STATUS OF THE NOVOSIBIRSK HIGH POWER TERAHERTZ FEL*

S.V. Miginsky#, N.A. Vinokurov, D.A. Kayran, B.A. Knyazev, E.I. Kolobanov, V. V. Kotenkov, V.V. Kubarev, G.N. Kulipanov, A.V. Kuzmin, A.S. Lakhtychkin, A.N. Matveenko, L.E. Medvedev, L.A. Mironenko, A.D. Oreshkov, V.K. Ovchar, V.M. Popik, T.V. Salikova, S.S. Serednyakov, A.N. Skrinsky, O.A. Shevchenko, M.A. Scheglov, Budker INP, Novosibirsk, Russia.

Abstract

The first stage of Novosibirsk high power free electron laser (FEL) has been commissioned in 2003. It is based on the normal conducting CW energy recovery linac (ERL). Now the FEL provides electromagnetic radiation in the wavelength range 120 - 230 micron. The maximum average power is 400 W. The minimum measured linewidth is 0.3%, which is close to the Fourier-transform limit. Four user stations are in operation now. Manufacturing of the second stage of the FEL based on a four-track energy recovery accelerator is in progress.

INTRODUCTION

A new source of terahertz radiation was commissioned a few years ago in Novosibirsk [1]. It is a CW FEL based on a ERL. Its differences from other ERL-based FELs [2, 3] are: a low frequency non-superconducting RF system and longer wavelength operation range. A full-scale Novosibirsk FEL will be based on the four-track 40 MeV energy recovery accelerator (see Fig. 1). It will generate radiation in the range from 5 micrometer to 0.24 mm [4, 5] together with the first-stage FEL.

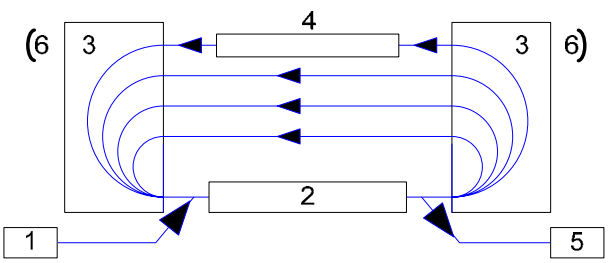

Figure 1: Scheme of an energy recovery accelerator based FEL. 1 - injector, 2 - accelerating RF structure, 3 - 180-degree bends, 4 – undulator, 5 – beam dump, 6 – mirrors of the optical resonator.

ACCELERATOR-RECUPERATOR

The first stage machine contains a full-scale RF system, but has only one track. The scheme of the ERL is shown in Fig. 2. A 2 MeV electron beam from an injector passes through the accelerating structure, gains 12 MeV energy there, and comes to an FEL, installed in the straight section. After interaction with radiation in the FEL the beam passes once more through the accelerating structure, returns the power, and comes to a beam dump at the injection energy. Main parameters of the accelerator are listed in Table 1. The electron source is a 300 keV DC gun with a gridded cathode. Maximum charge per bunch is 1.7 nC.

Table 1: Accelerator parameters (first stage)

RF frequency, MHz	180
Number of RF cavities	16
Amplitude of accelerating voltage at one cavity, MV	0.7
Injection energy, MeV	2
Final electron energy, MeV	12
Maximum bunch repetition rate, MHz	22.5
Maximum average current, mA	20
Beam emitance, mm·mrad	2
Final electron energy spread, FWHM, %	0.2
Final electron bunch length, ns	0.1
Final peak electron current, A	10

FEL

The FEL is installed in a long straight section of the backward track of the ERL. It consists of two undulators, a magnetic buncher, and an optical resonator. Both electromagnetic planar undulators are identical: the length is 4 m, the period is 120 mm, the gap is 80 mm, and the deflection parameter K is up to 1.2. The buncher is a three-pole electromagnetic wiggler. It is necessary to optimize the relative phasing of undulators and is used now at low longitudinal dispersion $N_d < 1$.

Both laser resonator mirrors are spherical, of 15 m curvature radius, made of gold-plated copper, and water-cooled [6]. There is a hole in the centre of each mirror. It is intended for mirror alignment (using the He-Ne laser beam) and output of small amount of radiation. The distance between the mirrors is 26.6 m. The forward mirror has the hole of the diameter 3.5 mm, while the rear one of 8 mm (see Fig.3). The calculated transparency of the 8-mm hole mirror is 1.5% at the wavelength 150 μm. The measured round-trip loss is near 7% at this wavelength. The output radiation passes through two windows which separate the FEL vacuum system from the atmosphere. An additional iris and a normal-incidence quartz window are installed after the forward mirror. A diamond window tilted at the Brewster angle is used for outcoupling behind the rear mirror.

* The work was partially supported by SB RAS grant N174/06 and by grant N2.1.1.3846 of Russian Ministry of Science and Education.
# S.V.Miginsky@inp.nsk.su

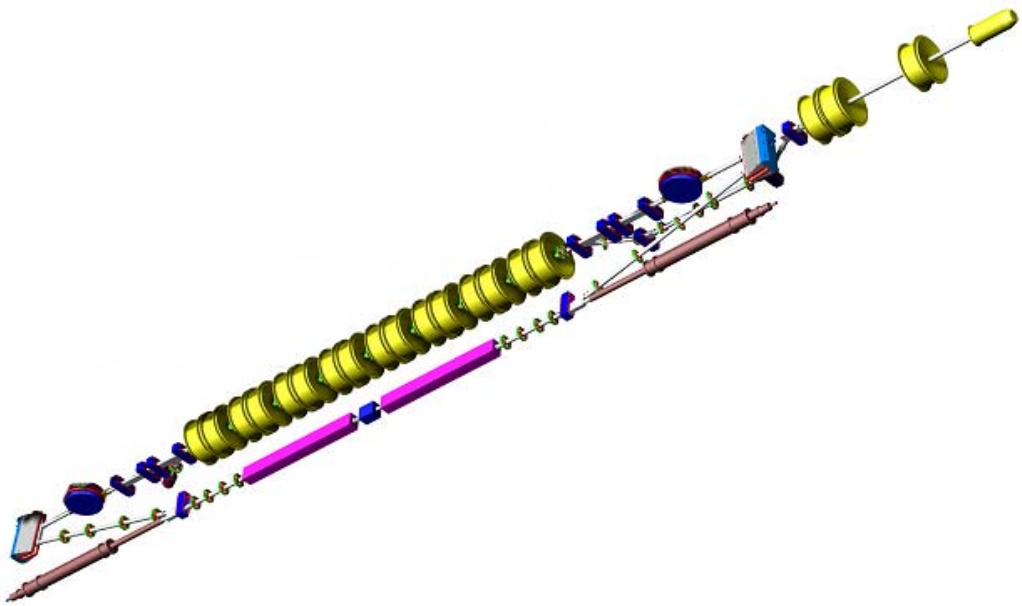

Figure 2: Scheme of the first stage of the Novosibirsk terahertz FEL. The loop lies in the vertical plain.

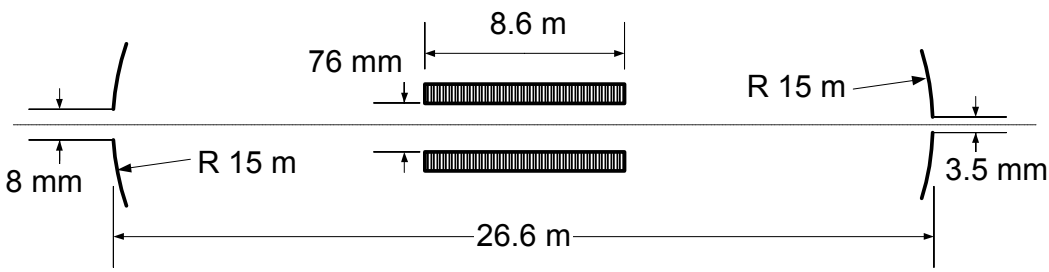

Figure 3: Scheme of the optical resonator.

RADIATION STUDY

First measurements of radiation parameters were reported before [1]. Instead of the fine tuning of the optical resonator length, we tuned the RF frequency. The tuning curve is shown in Fig. 4. The preliminary simulation results [7] demonstrated a reasonable agreement with the measured data. The experimental curve is wider, that may be explained by the shortening of the optical resonator due to heating of the mirrors.

The average radiation power passed through the hole at the rear mirror was about 400 W. Taking into account the 7% loss, one get approximately 2 kW of power, extracted from the electron beam. The electron beam power was 200 kW. Therefore, the electron efficiency was about 1%. The FEL radiation parameters are listed in Table 2.

Table 2: The radiation parameters

Wavelength, mm	0.12...0.23
Minimum relative linewidth, FWHM	$3 \cdot 10^{-3}$
Pulse length, FWHM, ps	50
Peak power, MW	1
Repetition rate, MHz	11.2
Maximum average power, kW	0.4

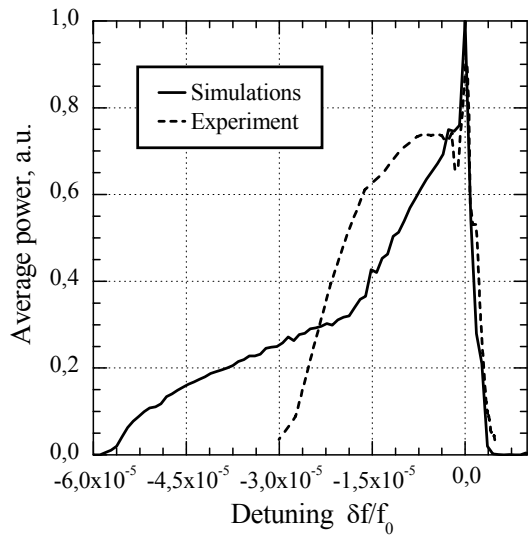

Figure 4: Dependency of the average power on the RF frequency detuning.

BEAMLINE AND USER STATIONS

An optical beamline from the accelerator hall to the user hall was built to transmit the radiation from the rear mirror hole to user stations. As the diffractional angular divergence $1.22 \cdot \lambda / D \approx 0.03$ (for 200 micron) is high, the spherical mirror is used to transform the radiation beam to almost parallel one. The incidence angle is only 7 degrees, therefore its astigmatism is negligible (see Fig. 5). Other 5 mirrors are flat. The beamline is filled by dry nitrogen. It is separated from the accelerator vacuum by the diamond window, and from the air by polyethylene windows. After installation of nitrogen dryer we obtained almost complete transparency of the beamline.

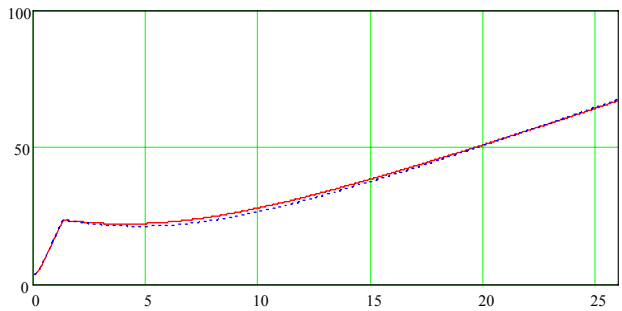

Figure 5: Calculated size of equivalent Gaussian beam (mm) vs. distance along the beamline (m).

Now radiation can be delivered to 5 stations. Two of them are used for measurement of radiation spectrum, and other three for users. In particular, selective terahertz ablation of DNA, proteins and other biologically relevant molecules was performed [8]. It was shown, that transfer from surface occurred without molecular destruction.

FURTHER DEVELOPMENTS

We plan to increase further the output power. The electron gun upgrade for the increase of the average current up to 0.1 A is in progress.

The design and manufacturing of the full-scale four-track accelerator is underway. An artistic view of the machine is shown in Fig. 6. The existing orbit with the terahertz FEL lies in the vertical plane. The new four tracks are in the horizontal one. One FEL will be installed at the fourth orbit (40 MeV energy), and the second one at the bypass of the second orbit (20 MeV energy).

REFERENCES

[1] E. A. Antokhin et al. NIM A528 (2004) p.15-18.
[2] G.R. Neil et al. Phys. Rev. Lett. 84 (2000), p. 662.
[3] E.J. Minehara. NIM A483, p. 8, 2002.
[4] N.G. Gavrilov et al. IEEE J. Quantum Electron., QE-27, p. 2626, 1991.
[5] V.P.Bolotin et al. Proc. of FEL-2000, Durham, USA, p. II-37 (2000).
[6] Kubarev V.V., Persov B.Z., Vinokurov N.A., Davidov A.V. NIM A528 (2004), No. ½, p. 199-202.
[7] O.A. Shevchenko, A.V. Kuzmin, N.A. Vinokurov. NIM A543 (2005), No. 1, p. 114-117.
[8] A. K. Petrov et al., Russian Dokl. Acad. Nauk, v. 404 (2005), No. 5, p. 1 – 3.

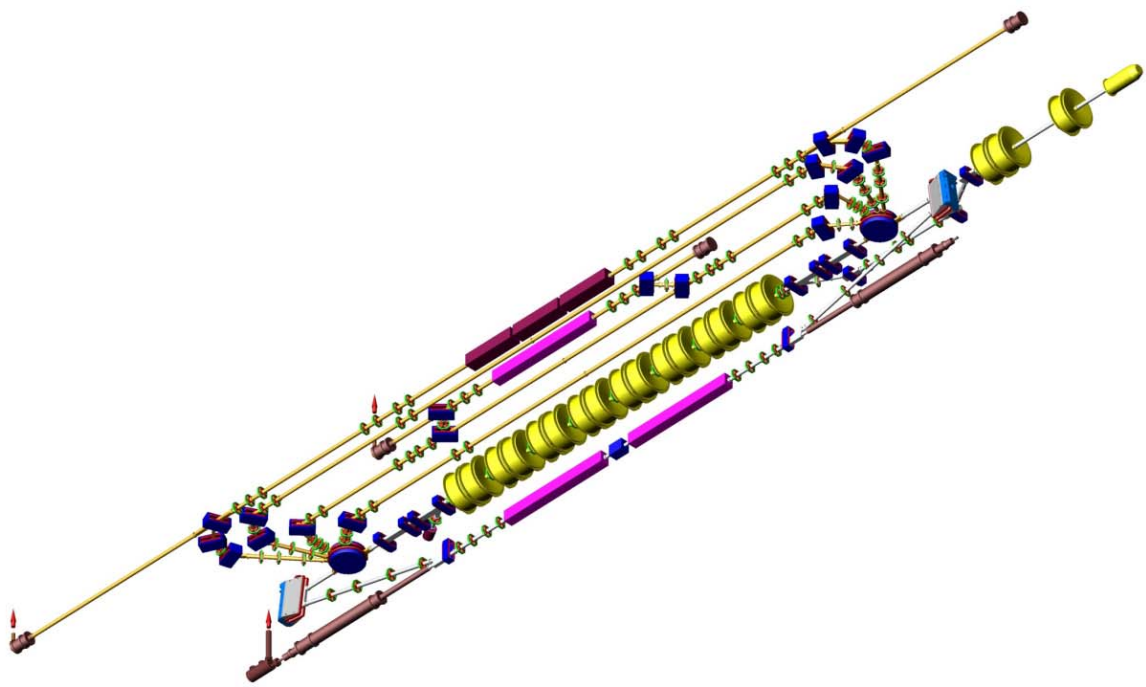

Figure 6: Scheme of the full-scale machine. The terahertz FEL track lies in the vertical plain while four others in the horizontal one.

BUNCH COMPRESSION USING THE TRANSPORT LINE AND SHORT BUNCH REVOLVING IN NEWSUBARU

S. Suzuki*, T. Asaka , JASRI/SPring-8, 679-5198, Japan
T. Matsubara#, T. Mitsui, Y. Hisaoka, Y. Shoji, LASTI, University of Hyogo, 678-1205 Japan

Abstract

The electron bunches was compressed to a few pico-seconds rms by the transport line from SPring-8 linac to NewSUBARU storage ring (NewSUBARU). And the compressed bunch was circurated for some tens of turns after injection while maintaining the short bunch length in the NewSUBARU. The NewSUBARU was set to a quasi-isochronous condition. Bunch length in the NewSUBARU was measured the streak camera and maicrowave detector. There data was not accord by the deformation of the bunch structure.

INTRODUCTION

The production of short bunches is an important technique, since bunches on a millimeter scale are necessary for time-resolved experiments and for stable production of coherent synchrotron radiation (CSR). Some methods have been proposed for producing a short electron bunch in a storage ring, like the laser-slicing method [1] and the quasi-isochronous (QI) operation of a storage ring [2]. The ring stores electron bunches as short as a few pico-seconds in a stationary state. These two methods produce more stable radiation than that produced by a linac. However, the beam charge in a short bunch is much smaller than in a bunch produced by a linac.

This paper reports a demonstration of another method, which is based on a combination of a linac and a storage ring. A short, high-current bunch is produced with a linac and a bunch compression system. The short bunch is injected into an isochronous ring, and circulates for many turns. The bunch length becomes longer even in an ideal isochronous ring because of the longitudinal radiation excitation, but this takes many turns [3]. This method has several merits: (1) a bunch with higher charge is possible in a storage ring than with the existing two methods; (2) one short bunch produced by the linac is reused at every turn of the ring that it makes; (3) the repetition rate of the radiation pulse can be very stable in an isochronous ring; (4) pulsed light is obtained in every beam line of the storage ring; (5) a few pico-seconds long pulse is possible with no special expense; and (6) future improvements of the linac beam quality would give better performance of this method.

The aims of this report are (a) to demonstrate the method, (b) to investigate the problems associated with it, and (c) to clarify the limitations of the present hardware, the SPring-8 linac, and the NewSUBARU. The results of our experiment provide suggestions for future light source projects with an energy recovery linac and a more sophisticated short-bunch circulator [4].

* shin@spring8.or.jp
# Present address: Sumitomo Heavy Industories Ltd.

EXPERIMENTS AND MEASUREMENTS

Bunch Compression of Linac Beam

Figure 1 shows the layout of the SPring-8 linac [5], the energy compression system (ECS) [6], the booster synchrotron, and the NewSUBARU [7]. Tables 1 and 2 show the main parameters of the linac and the NewSUBARU. In normal operation, the typical bunch length of the linac bunch was about 20 ps (full width), and the energy spread was 0.7% (full width) at 1 GeV. However, in this experiment, the chicane of the ECS was bypassed and the acceleration cavities of the ECS were used to compress the bunch as it passed through the transport line to the NewSUBARU. Figure 2 shows the simulation of the bunch length from the ECS to the injection point of the time profile and η-function.

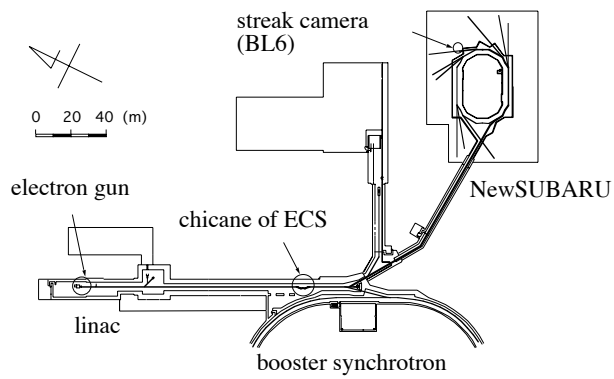

Figure 1: Layout of the SPring-8 linear accelerator, the energy compression system (ECS), the booster synchrotron, and the NewSUBARU. The streak camera is placed in beamline 6 (BL6) of NewSUBARU.

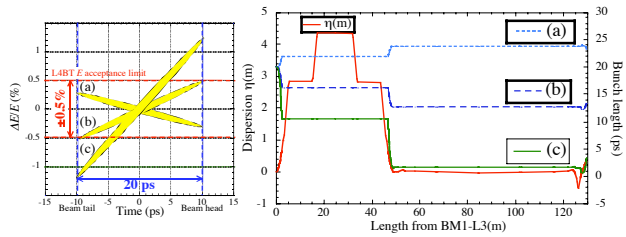

Figure 2: Simulation of the bunch length from the ECS to the injection point. Each line corresponds a difference of phase space of a left-hand figure.

Figure 3 shows the bunch length measured by a streak camera in beamline 6 (BL6) [8]. Stronger compression was in principle possible but the transport line would not

accept the larger energy spread of such a compressed bunch. The energy acceptance of the transport line is 1 % full width. The time profile was fitted to a Gaussian distribution for the subsequent analysis, although the fitting was not good.

Table 1: Main Parameters of the Linac with the ECS

RF frequency	2856 MHz
Transverse emittance at 1GeV	71π□nm
Micro bunch length (FWHM)	20 ps
Energy spread (full width)	0.6 %
Micro bunch charge	0.03-0.3 nC

Table 2: Main Parameters of NewSUBARU at 1 GeV

RF frequency	500 MHz
Harmonic number	198
Linear momentum compaction factor	0.0013
Natural energy spread (σ)	0.047 %

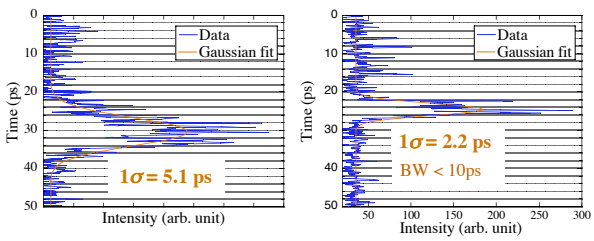

Figure 3: Time profile of the normal injection bunch (a) and the compressed bunch (b). Bunch length was measured at BL6.

Bunch Length Measurement

The NewSUBARU has six modified double bend achromat (DBA) cells with an 8° inverted bending magnet between two 34° normal bending magnets. These special cells facilitate control of the linear momentum compaction factor α_1 while maintaining the achromatic condition. The nth momentum compaction factor, α_n, is defined by

$$\Delta L/L_0 = \alpha_1\delta + \alpha_2\delta^2 + \alpha_3\delta^3 + \dots . \qquad (1)$$

Here L_0 is the circumference, ΔL is the change of the path length for one revolution, respectively, and δ is the relative energy displacement. At the NewSUBARU, α_1 and α_2 are adjustable but α_3 is not ($\alpha_3 \approx 0.5$).

Figure 4 shows the bunch length in the ring after injection for different values of α_1. A small negative value of α_1 is better for maintaining a short bunch because it reduces the spread caused by α_3. Figure 5 shows the evolution of the time profile in a quasi-isochronous ring for the best condition ($\alpha_1 = -6\times10^{-5}$). The injected beam charge was 24 pC/bunch in this case. The bunch length (σ of the fitted Gaussian) was still less than 3 ps after 50 turns (20 ps).

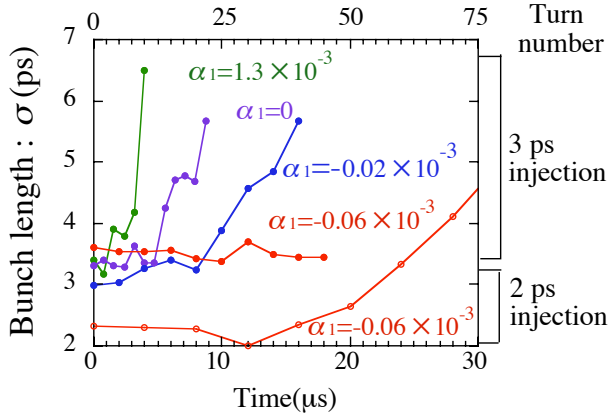

Figure 4: The elongation of the bunch length after injection for different values of α_1. The initial length was not the shortest, because the buncher phase of the linac was not optimized at that time.

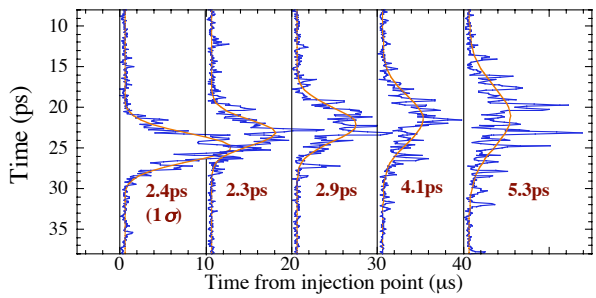

Figure 5: Evolution of the time profile of the bunch after injection, for $\alpha_1 = -6\times10^{-5}$.

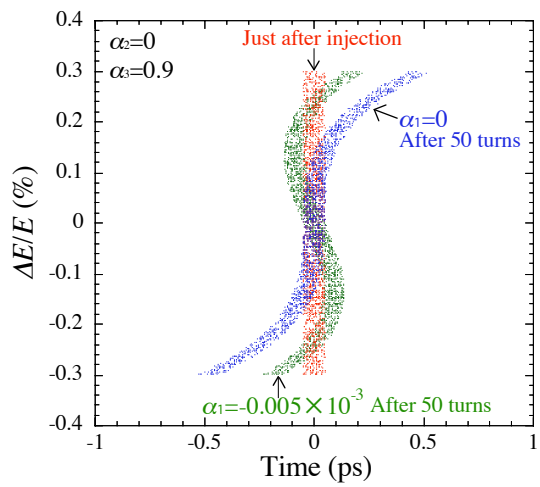

Figure 6: Tracking simulation of phase spece distribution for this experiments case.

In Figure 6, the tracking simulation results of phase spece distribution for this experiments case is shown. For higher order momentum compaction factor, the bunch length is grown up by α_1 = 0 lattice than $\alpha_1 = -6\times10^{-5}$ lattice.

CSR Power Measurement

The relative CSR power was measured by a Schottky diode detector, which was sensitive to radiation in the frequency range 90–140 GHz. The turn-by-turn change of the CSR power is shown in Fig. 7. The reduction of the CSR power was due to a reduction of $f(\omega)$. In the frequency range of the detector, f is sensitive to small changes in the length and shape of the bunch; the shape may be angular or a smooth Gaussian shape.

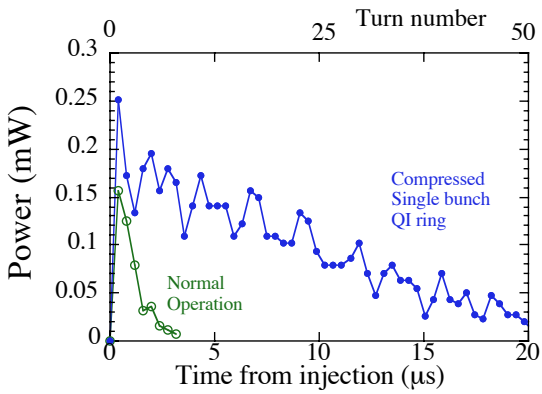

Figure 7: The turn-by-turn CSR power after injection. The bunch charge was about 20 pC/bunch in both cases, where there were three bunches in a pulse.

The radiation power $P_{tot}(\omega)$ from a short bunched beam containing N electrons is given by [9, 10]

$$P_{tot}(\omega) = p(\omega)[N + (N^2 - N)|f(\omega)|^2], \qquad (2)$$

where $p(\omega)$ is the power at a frequency ω radiated from one electron, and $f(\omega)$ is the form factor calculated from the azimuthal charge distribution $\rho(z)$ using

$$f(\omega) = \int \rho(z)\exp(i\omega z/c)dz. \qquad (3)$$

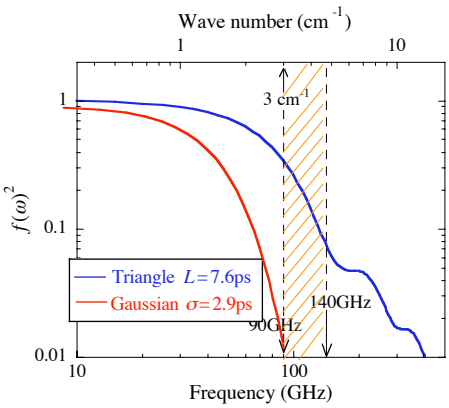

Figure 8: The form factor of the triangle bunch and the guassian bunch. Mesh area is the sensitive region of the Schottky diode detector.

DISCUSSIONS

The bunch was compressed by the transport line. And we have demonstrated that and the NewSUBARU could keep a bunch as short as 3 ps and with a charge of about 20 nC for 50 turns. Here we mention some additional results and problems encountered in the experiments:

(1) Adjustment of the higher-order α's was essential for keeping a short bunch in the storage ring. With a small value of α_2, we observed a considerable increase in the bunch length.

(2) The shot-by-shot fluctuation of the shape and charge of the injected bunch was also considerable.

(3) The CSR power from a short bunch comparable in length to the wavelength depends strongly on the form factor. This means that the bunch should be much shorter than the wavelength to obtain stable CSR.

The beam performance at present does not reach that achieved by the existing methods mentioned earlier. However the improvement of the bunch charge would not be difficult and more careful adjustment of the linear and higher order momentum compaction factor would keep the short bunch longer in the ring. In order to achieve much shorter pulses, we need to upgrade the hardware. In particular, the linac and the transport line were not originally designed for short-pulse injection and leave much room for improvement.

REFERENCES

[1] A.A. Zholents and M.S. Zolotorev, *Phys. Rev. Lett.* **76** (1996) 912.

[2] M. Abo-Bakr, *et al.*, *Phys. Rev. Lett.* **88** (2002) 254801.

[3] Y. Shoji *et al.*, *Phys. Rev. E* **54** (1996) R4556–R4559.

[4] H. Hama, Proceedings of the 27th International FEL Conference, Stanford, Jacow/eConf C0508213 (2005).

[5] H. Hanaki, *et al.*, Proceedings of APAC, Gyeongju, Korea, March 22–26, 2004, pp. 3585–3589.

[6] T. Asaka, *et al.*, Proceedings of the 2002 EPAC, Paris, pp. 10879–10881 (2002).

[7] A. Ando, *et al.*, *J. Synchrotron Radiat.* **5** (1998) 342–345.

[8] T. Matsubara, *et al.*, *Phys. Rev.* **ST-AB 9** (2006) 042801.

[9] J.S. Nodvic and D.X. Saxon, *Phys. Rev.* **96** (1954) 180–184.

[10] J. Schwinger, *Phys. Rev.* **75** (1949) 1912–1925.

STATUS OF THE INDUSTRIAL RF-ACCELERATORS IN BINP

D. Artamonov, V. Auslender, V. Bezuglov, A. Bryazgin, V. Gorbunov, V. Cheskidov, I. Gornakov, B. Faktorovich, V. Nekhaev, V. Podobaev, A. Panfilov, A. Sidorov, E. Shtarklev, V. Tkachenko, A. Tuvik, L. Voronin,
BINP, Novosibirsk, Russia

Abstract

The report describes ILU type industrial electron accelerators. It describes their main parameters, design, principle of action, electron beam extraction devices, wide set of auxiliary equipment for various technological processes and ways of their usage.

INTRODUCTION

The pulse nature of the generated electron beam (their main difference from the widely used high voltage accelerators generating continuous electron beam) permits to adapt ILU machines easily to technological processes requiring formation of an irradiation zone with a complex configuration. The most bright example of such process is the irradiation of polymer insulation of cables and thermoshrinkable tubes. In this case the usage of 4-sided irradiation permits sharply to raise the productive rate of process, to improve quality of production and to expand the nomenclature of treated products without increase of electron energy. The ILU machines designed and produced in the Institute cover the energy range from 0.6 MeV to 5 MeV, and the maximum beam power is 50 kW.

The main activity field of ILU Laboratory of BINP is the development, manufacturing and supply of the ILU accelerators for industry. Up till now more than 50 machines are installed, about 30 of them are installed worldwide. The ILU machines are successfully working in the industrial lines in Korea, China, India, Italy, Poland, and other countries.

Table 1: Main parameters of the ILU accelerators.

PARAMETERS	ILU-6	ILU-8	ILU-10	ILU-12 Proj.
Energy of electrons, MeV	1.2-2.5	0.6-1.0	2.5-5.0	4.0-5.0
Average beam power (max), kW	20	25	50	300
Average beam current (max), mA	20	30	15	60
Power consumption, kW	100	80	150	700
Accelerator weight, tons	2.2	0.6	2.9	5

- Single-resonator ILU type accelerators have simple design, hence they are reliable, have low cost, and is easy to maintain. The used generator scheme with self excitation and pre-excitation allowed us to provide the absolute stability of the RF system.
- Placing the electron gun directly into the accelerating gap with using the adjustable cathode voltage shift allows us to adjust the beam pulse current and so the average power within the wide range of values.
- In ILU 10 the additional RF voltage of the operating frequency with the phase shift relative to the accelerating voltage is applied to the cathode-grid gap, that allowed us to greatly decrease the accelerated beam energy spread.

ACCELERATOR ILU-6.

The base model of the family is ILU-6. This machine has rather high parameters at modest dimensions and can be used for wide spectrum of technological processes. A principle of high-voltage acceleration is used in majority of modern accelerators, i.e., the energy of electrons corresponds to the voltage generated by the rectifier. The industrial accelerators type ILU are the exception of this rule. A principle of acceleration of electrons in the gap of HF resonator is used in the ILU machines. Such accelerator does not contain details, potentials of which with respect to the ground is comparable to accelerating voltage. So the complex high-voltage units (accelerating tubes, sections of rectifiers and etc.) which are damaged by the occasional discharges are not used in ILU machines. And so there is also no necessity to use insulating gas and high-pressure vessels. Use of a principle of high-frequency acceleration has allowed to create rather simple design of the machine having modest dimensions and weight. As a result the machine can be placed inside the hall of the smaller dimensions compared to the halls for high-voltage accelerators having the same parameters. Figure 1 represents the accelerating system of the accelerator ILU-6 for explanation of a principle of action of the ILU machines. The accelerating system consists of copper toroidal resonator 1 placed inside the vacuum tank 2. The resonator consists of top and bottom halves, on the internal protrusions of which the electrodes forming an accelerating gap are installed. The top electrode has a built-in control grid. The cathode unit is mounted on this electrode on the insulator, and together with the grid it forms an electron injector (gun). The bottom electrode and the injector together form the accelerating system. The current of a beam of accelerated electrons is controlled by varying the value of positive bias on cathode concerning the grid. To suppress the high-frequency resonance discharge in resonator the bottom half of it is installed on insulators and the bias

voltage is passed on it through inductance 3. An axially symmetric magnetic lens is installed inside the protrusion of the bottom half of the resonator to form an electron beam in the channel of the accelerator and extraction device 6. The extraction device is connected to the flange of the magnet lens through the vacuum valve and bellows unit. The single-stage RF generator is installed directly on the vacuum tank of the resonator and is connected to the resonator by means of coupling loop. The generator is designed using the circuit with a common grid. It works in the self-excitation mode with frequency close to the specific frequency of the resonator.

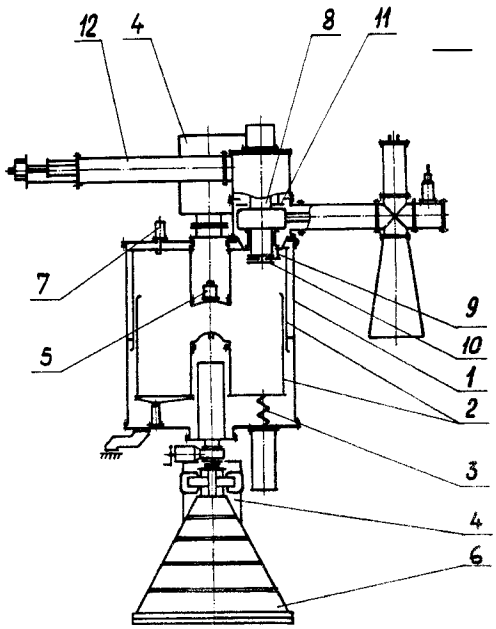

Figure 1 Main elements of ILU-6 electron accelerator:1 – vacuum tank; 2 – RF cavity divided into 2 halves; 3 – input of constant bias voltage for lower cavity half; 4 – high vacuum pumps; 5 – electron injector; 6 – scanning horn; 7 – measuring loop; 8 – RF generator; 9 – coupling loop; 10 – coupling vacuum capacitor; 11 – feedback circuit, 12 – cathode circuit tuning line.

ACCELERATOR ILU-8.

The ILU-8 machine is the result of ILU-6 further development. It is designed mainly for cables and tubes processing (Figure 2). This accelerator does not require construction of a special protected premise (hall) and can be placed in usual industrial shop. It can work inside the local biological shielding. The local shielding of the accelerator is a kind of a box made of steel plates. Inside the box is divided into two parts. The upper part is used to place accelerating system with HF resonator and fore-vacuum system. The beam extraction device, air pipes of ventilation system and technological equipment are placed in the lower part of the shielding. The back wall of the shielding has the channels (labyrinths) for input of cables, air and water pipes. The removable front wall serves as a door of a protective box. The thickness of radiation shielding in side walls part is 330 mm and in top is 240 mm. Gross weight of shielding is 76 tons.

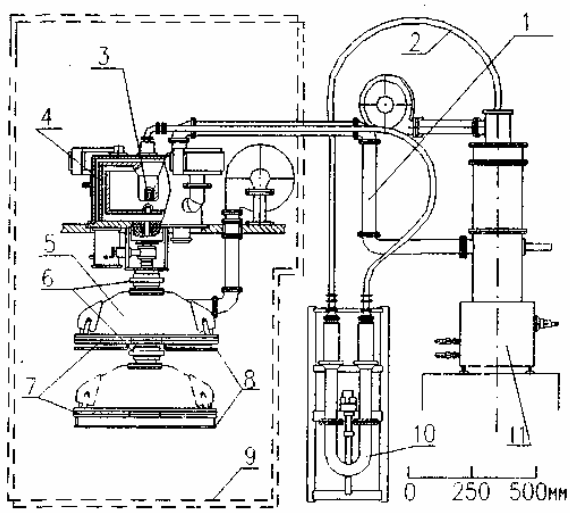

Figure 2. Main elements of ILU-8 electron accelerator**:**1 – RF cavity power supply feeder; 2 – feedback RF system cable; 3 – cathode unit with control electrode; 4 – RF cavity of the accelerator; 5 – output device; 6 – deflecting magnets; 7 – output windows; 8 – beam collectors; 9 – contour covering elements placed into the individual radiation protection; 10 – phase shifter; 11 – RF generator.

ACCELERATOR ILU-10.

The model ILU-10 is purposed mainly for processes requiring increased electron energy up to 5.0 MeV [1]. The dimensions of this machine are not sufficiently greater than the dimensions of ILU-6. For needs of processes requiring increased beam power the accelerator is supplied by two HF generators (Figure 3). Unlike ILU-6 machine, the resonator of ILU-10 machine is performed as a whole unit without separation on two halves as in ILU-6. As the result of the optimization work the resonator operates without discharges. Its shunt resistance is 9 Mohm, power, required for its excitation, is 1.4 MW, and the resulting beam pulse power is up to 2.5 MW.

The main application area for ILU-10 is industrial sterilization by electrons and X-rays (optionally, by using special electron-X-ray converter). ILU-10 has two times more energy than ILU-6 so thickness of irradiation material is also increased more than twice.

On the ILU-10 we have an experience of sterilization of single-use medical products like surgical dresses and instruments (electron mode) and massive medical devices like dialyzers, catheters etc.(X-ray mode). Also ILU-10 is suitable accelerator for irradiate PE pipes with diameter up to 140 mm for hot water supply networks.

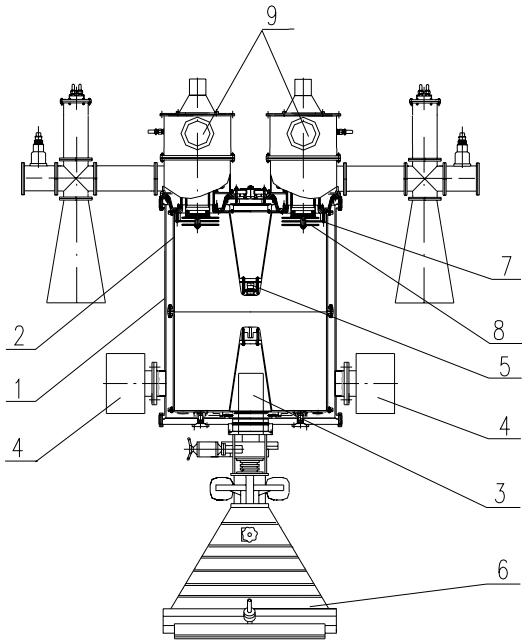

Figure 3: ILU-10 accelerator. 1 – vacuum tank, 2 – copper toroidal cavity, 3 – magnetic lens, 4 – ion pumps, 5 – grid-cathode unit, 6 – beam extraction device with linear scanning, 7–-coupling loop support, 8 – vacuum capacitor, 9 – RF generators.

PROJECT OF ACCELERATOR ILU-12.

New industrial accelerator with electron energy up to 5 MeV, and average beam power of up to 300 kW was designed basing on experience of work with the ILU accelerators [2]. The design of its accelerating system is shown in Figure 4. The accelerating structure consists of five modules and forms three complete accelerating cells, two accelerating half-cells and four coupling cells. The new machine is relatively simple in its production and adjustment. The electrons are accelerated in the low frequency multi-resonator standing wave structure with on-axis coupling resonators. This design makes it possible to decrease power losses in each resonator comparing with the single-resonator accelerator (at the same average beam power level) and to obtain the electron efficiency of the accelerator about 70%.

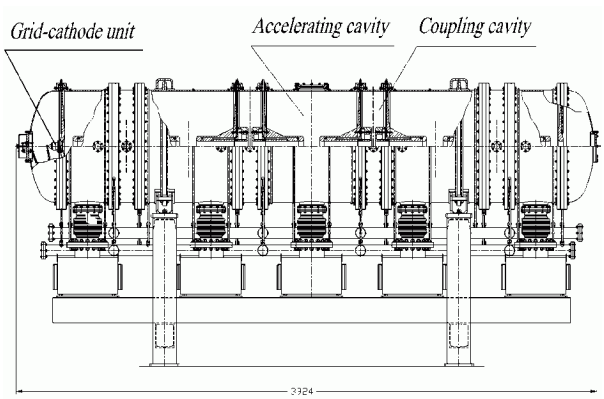

Figure 4. : General view of accelerating structure.

ELECTRON BEAM EXTRACTION

The pulse nature of electron beam generated by ILU machines permits to design the beam extraction devices for radiation technologies forming the irradiation zones for multilateral irradiation of objects having the various forms. It enables one to increase beam usage efficiency and in some cases to reduce the electron energy required for irradiation, or to expand the nomenclature of treated products.

The electron beam extracted into the air through foil. Usually three types beam extraction device can be used: linear scanning device for treatment of flat and complex form products, 3-window extraction device and beam extraction device with X-ray converter.

In the linear scanning device each pulse of the beam is scanned along the length of extraction window. The control of the current of the scanning magnet and using additional magnet lenses to allow forming complex dose distribution along the foil. Some applications requires the dose bumps on the ends of extraction widows. It allows to irradiate only separate parts of the products.

In the 3-window extraction device beam pulses are scanned sequentially along its upper windows and along the left and right parts of lower window (Figure 5). This type of extraction system is using for 4-sided tube or cable irradiation

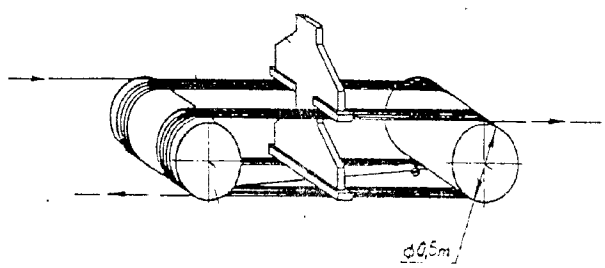

Figure 5: 4-side irradiation system.

To generate X-ray the electron beam can be directed to the X-ray converter. The technological process of the product treatment requires the certain type of the extraction device. For example, the beam bent at an angle of 90 grades enables a substantial simplification in the design of the vertical hanging conveyor system for subjecting the treated product to two-sided irradiation.

REFERENCES

[1] V.L. Auslender et al., “Electron accelerator for energy up to 5.0 MeV and beam power up to 50 kW specially designed for use in industrial applications”, IMRP 2006, Kuala-Lumpur, Feb 2006, p. 156.

[2] V.L. Auslender et al., “Project of high power linear accelerator for E-beam and X-ray processing”, IMRP 2006, Kuala-Lumpur, Feb 2006, p. 157

PRACTICAL CONSIDERATIONS IN THE DESIGN OF A HIGH CURRENT COMMERCIAL H-MINUS CYCLOTRON

M. Dehnel, T. Stewart, M. Roeder, J. Theroux, P. Jackle, Dehnel – Particle Accelerator Components & Engineering, Inc., P.O. Box 201, Nelson, B.C., Canada V1L 5P9

Abstract

High current H^- cyclotrons (>1000 μA) are being developed and implemented for radioisotope production, radioactive therapeutic implants and other applications. The beam dynamics and general physics design of these cyclotron systems must be well done. However, to not compromise an elegant and effective physics design, engineering practicalities must be carefully considered and then implemented. Based on our experience in the design, upgrading, and maintenance of commercial H^- cyclotron systems, we offer practical issues and solutions to be considered in the engineering design and implementation of such high current systems.

INTRODUCTION

Of the modern commercial 30 MeV H^- cyclotrons utilizing axial injection, over thirty Cyclone30s, and about a half-dozen TRIUMF technology TR30s are installed.

Given the large number of Cyclone30s, this paper uses the Cyclone30 design circa the late 1990s and earlier as a baseline reference, and discusses practical engineering improvements to be made to this cyclotron to enable reliable and consistent operation at high current. This would increase radioisotope production yields, and operational cost-effectiveness.

ION SOURCE & INJECTION SYSTEM

The Cyclone30 ISIS is mounted on the moveable upper half of the cyclotron on a cantilevered support. Beam injection is downwards as shown in the left hand side (LHS) of Figure 1. This is problematic because the ISIS is moved each "lid-up" maintenance, and with a springy cantilevered support structure the ISIS frequently becomes misaligned and requires correction as shown in the right hand side (RHS) of Figure 1. The solution is to use a permanently aligned ISIS mounted to the lower fixed half of the cyclotron with a sturdy support structure.

The ISIS vacuum is provided by a diffusion pump system (Figure 2 LHS), which introduces hydro-carbon molecules into the ion source chamber [1,2]. The hydro-carbons interfere with H^- production, reduce filament life-time to ~80 hours within months, and over this time scale deposits 2 to 3 mm of material on the chamber walls. With the ion source emitting the beam downwards, debris from the deposits falls onto the grounded plasma electrode as shown in Figure 2 RHS. Some of this debris falls through the lens aperture into the injection line buncher wires, and onto the inflector electrodes. Cleaning a thick coating with a blunt instrument requires a great deal of force risking micro-cracking of the source chamber and concomitant water leaks.

An ion source mounted on the lower fixed side of the cyclotron stops debris falling into the cyclotron. Thick deposition and debris can effectively be eliminated by the use of the TRIUMF source [3]. The TRIUMF source utilizes Cryo/Turbo pumping for a clean environment, and only a very thin deposition layer must occasionally be cleaned using fine grit sandpaper.

Figure 1: LHS shows ISIS on top of Cyclone30, and RHS shows ISIS out of alignment after several tank openings.

Figure 2: LHS shows Cyclone30 ISIS diffusion pump. RHS shows ion source with hydro-carbon debris.

Figure 3 LHS shows a hairpin tungsten filament with eroded supports due to exposure to the plasma, and RHS shows the backplate with two cusp magnet rows. The TRIUMF source utilizes tantalum ring filaments, recessed support posts, and four backplate cusp magnet rows for improved H^- performance. The absence of a filament induced magnetic field in the TRIUMF ion source centre contributes to a quiescent plasma [4].

The plasma lens (Figure 2 RHS) is at the same electric potential as the source body, whereas in the TRIUMF case it is electrically biased for optimized H^- production and a three-fold reduction in extracted electrons [1]. In addition, the TRIUMF puller lens utilizes a double-dipole magnetic electron filter with ($\int Bdl = 0$), whereas the Cyclone30 typically utilizes a single dipole magnetic field

($\int$Bdl ~ 4000 Gauss·mm). This means that the H^- beam is deflected after electron filtering and substantial beam loss occurs on the ground lens causing significant wear as shown in Figure 4 LHS. To compensate for the mis-steered beam a permanent magnet steering magnet is used internal to the vacuum (Figure 4 RHS). This structure requires several source ventings in order to be aligned correctly for centred beam. This can take several hours. The TRIUMF double-dipole magnet electron filter enables a centred beam to exit the ground lens, so no asymmetric wear is evident [4]. For steering corrections TRIUMF uses an in vacuum wire wound XY steering magnet for easy tuning through the control system [4].

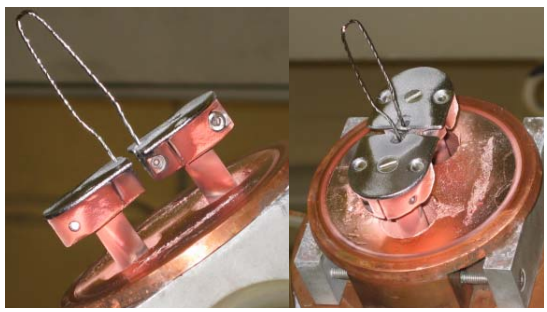

Figure 3: LHS shows hairpin tungsten filament and exposed support posts. RHS shows backplate with two cusp magnet rows used in the Cyclone30.

Figure 4: LHS shows wear in source ground lens. RHS shows permanent steering magnet in Cyclone30.

The typical Cyclone30 ion source of this era does not have a hydrogen flow controller. This device is required for optimizing the plasma density and beam production. The vacuum level in the injection line must be optimized at about the micro-Torr level for effective space-charge neutralization without excessive beam stripping [5].

The nominal Cyclone30 injection line utilizes an electrostatic einzel lens, XY steering magnets, a buncher, and a solenoid magnet. There is no asymmetric focusing. It is important to utilize rotate-able quadrupole magnets to ensure asymmetric focusing to de-couple the cross-plane coupling introduced by the inflector [7,8,9].

The typical Cyclone30 injection line provides little beam diagnostic information. An ion source Faraday Cup is typically provided, and a 1 MeV beamstop is optional (customers should select this option). It is our recommendation that 4-jawed collimators be located at the exit of the ion source vacuum box, at the entrance of the solenoid magnet and at the entrance to the inflector, so that beam focusing/centring can be easily carried out.

CENTRAL REGION

The Cyclone30's inflector electrodes are not enclosed in a grounded enclosure, nor is an electrically isolated collimator with beam current readback provided, as shown in Figure 5 LHS. This means that it is not straightforward to centre the beam at the inflector entrance, and ions or electrons from the source or injection line region strike and erode the inflector electrodes. It is our experience that inflector entrance collimators with beam current readback are useful, and it is important that the inflector insulators be properly shadowed, so that shorts due to sputtering do not occur. The inflector ground enclosure should only have a small opening at the entrance and exit, and the structure should be water-cooled to accommodate beam loss in the first turns. Figure 5 RHS shows the inflector electrode wires. The high voltage connection to the inflectors should be an automatic connection rather than a hand connection. In addition, inflector pieces should be mounted into the cyclotron in a manner which ensures a high tolerance fit, so there is no possibility of adjustable insertion available to maintenance personnel who likely have little training in the area of centre region optics. Figure 5 RHS also shows the bottom half of the Cyclone30 dees, as the top half are connected to the upper yoke of the cyclotron magnet. Separation of the dees introduces an unnecessary risk of misalignment error. It is our recommendation that the upper and lower dees be built as a single permanently aligned structure as in the TRIUMF 30 MeV cyclotron.

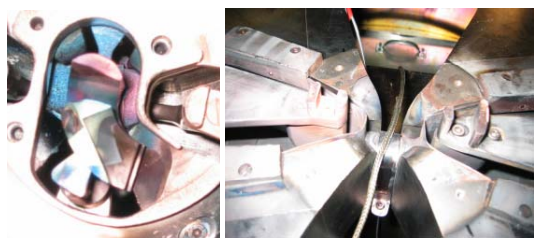

Figure 5: LHS shows inflector entrance with open ground enclosure. RHS shows dee bottoms in centre region.

A 1 MeV beamstop enables transmission to be determined between 1 MeV and the source Faraday Cup, and 1 MeV and the strippers. A neutral beam current measuring device is also useful.

MAIN CYCLOTRON SYSTEMS

Figure 6 shows the basic layout of the Cyclone30 magnet steel. O-rings are located throughout the magnet steel, and this is a very serious shortcoming of this design. When these o-rings harden and fail, it is a major operation first to locate the vacuum leak, and second to disassemble the magnet steel, particularly when an o-ring in the lower half fails. Magnet steel is relatively soft and can bind easily, ice baths have been used to permit concentric pieces to slide past each other. The TRIUMF 30 MeV

cyclotron technology avoids this problem by having double o-ring seals between the vacuum tank top/bottom and the magnet steel surfaces immediately above and below the median plane. In the TRIUMF technique only four o-rings are required, and these are easily accessible when the cyclotron is opened for maintenance.

Clean Cryo or Turbo pumping is recommended rather than diffusion pumping to prevent hydro-carbon contamination. Nickel-plated poles with pumping to achieve the low 10^{-7} Torr range is recommended.

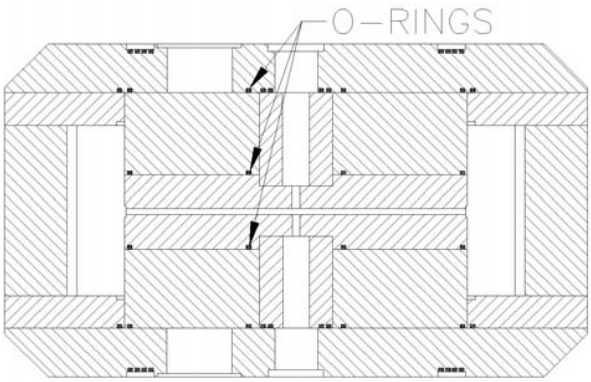

Figure 6: Cyclone30 magnet steel & o-ring arrangement. Fasteners/dowels are not shown. O-rings are not to scale.

TRIUMF 30 MeV cyclotron technology utilizes AISI 1006 as rolled annealed steel. This is electric furnace quality vacuum improved plate ultrasonically tested to ASTM Specification #A578/A 578M-85. Cast or forged steel, and voids of any sort are not permitted. In addition, the cyclotron magnet must be mapped and shimmed in an iterative procedure to ensure a high degree of isochronism is obtained. Phase excursions must be kept within ± 10° of the RF.

It is important that a magnet lid-up procedure is developed that ensures a level closure of the magnet. With the Cyclone30 RF dees separately attached to the upper and lower yokes, it is essential that these delicate structures re-connect in a controlled manner upon lid closure. We have observed damaged dee structures when such procedures are not adhered to. RF ground liners that are single contiguous copper pieces mounted to the hill edge steel rather than plated, as is done for some commercial cyclotrons, is highly recommended.

An extraction stripper that can be retracted for foil changes and sealed by a gate valve to avoid main tank venting is essential. Strippers with several TRIUMF long-life diamond like foils are recommended, as is radial, azimuthal and rotational degrees of freedom. The stripper must be water-cooled, and capable of capturing the stripped electrons for an accurate accounting of the extracted beam current. The beamline switching dipole magnet should not utilize a return yoke that is shared with the cyclotron magnet as is often done in Cyclone30 installations as shown in Figure 7. This introduces unwanted harmonics into the cyclotron magnetic field, and makes dual beam extraction tuning quite difficult.

The Cyclone30 beamlines are generally well made, but it is our recommendation additional water-cooled 4-jaw collimators with beam current readback be installed to facilitate easy beam tuning as described in [10,11,12].

Figure 7: Cyclone30 switching magnet.

CONCLUSION

This document presents practical improvements to the Cyclone30 for consistent reliable high-current operation.

REFERENCES

[1] M.P. Dehnel *et al*, "An Ion Source Upgrade for an Axial Injection Based Commercial Cyclotron", NIM B 241, 2005, p. 896.

[2] M.P. Dehnel et al, "An Industrial Cyclotron Ion Source & Injection System", 17th Int'l Conf. On Cyclotrons and their App's, Tokyo, 2004, p. 293.

[3] T. Kuo et al, "Injection Study for High Current H– Cyclotrons," Proc. 15th Int'l Conf. Cyc. & Apps., Caen, 1998, p. 381.

[4] T. Kuo et al, "A 15 mA DC H^- Multicusp Source for Cyclotron Injection," Proc. 14th Int'l Conf. Cyc. & Apps., Cape Town, 1995.

[5] R. Baartman and D. Yuan, "Space Charge Neutralization Studies of an H– Beam," EPAC'88, Rome, 1988, Vol. 2, p. 949.

[7] W. Kleeven and R. Baartman, "Beam Matching and Emittance Growth Resulting from Spiral Inflectors for Cyclotrons," Part. Acc. 41, 1993, p. 55.

[8] M.P. Dehnel et al, "Injection System Design and Tests for the TR13 Cyclotron," EPAC'94, London, 1994, Vol. 3, p. 2367.

[9] M.P. Dehnel et al, "The Experimental Characterization of a Compact H– Cyclotron's Spiral Inflector," NIMA, 396, 1997, p.35.

[10] M.P. Dehnel et al, "A Compact Cost-Effective Beamline for a PET Cyclotron", CAARI, in press, Fort Worth, Texas, USA, 2006.

[11] M.P. Dehnel et al, "Beamline Developments in Commercial Cyclotron Facilities", NIMB 241 2005, p. 655.

[12] M.P. Dehnel et al, "Industrial Beamline Design for Radioisotope Production", 17th Int'l Conf. On Cyclotrons and their App's, Tokyo, Japan, 2004, p. 486.

THE COMPACT INDUCTION CIRCULAR ACCELERATOR FOR RADIATION TECHNOLOGIES

G.V. Dolbilov#, Joint Institute for Nuclear Research, Dubna, 141980, Russia.

Abstract

The variant of the circular accelerator of electrons with energy up to 10 MeV is discussed. Acceleration is carried out by an induction electric field on a constant equilibrium orbit of radius about 50 cm. For reduction of reactive power of the accelerator the alternating magnetic fields are concentrated in small volume near to the equilibrium orbit. Use of high-frequency magnetic fields (tens or hundreds κHz) allows to increase power of the accelerated electron beam up to some tens kW or some hundreds kW.

INTRODUCTION

The wide range of possible parameters of a electron beam allows to use these accelerator for a wide spectrum of applications: protection of an environment (for example: clearing flue gases of the industrial enterprises from harmful impurity NOx, SOx, etc.), updating and reception of the new materials, new technologies without application of harmful chemicals (polymerization of various materials, etc.), sterilization of medical tools, disinfection of medical and other waste products. Researches have shown, that methods of radiating processing of foodstuff (radurisation) in many cases successfully solve the problem long storage of products without infringement of their flavouring and nutritious qualities. Small dimensions and low cost of the accelerator, will allow to use it on fishing seiners for sterilization of fish products.Manuscripts

For many radiation technologies electron beams with energy 0.5 – 10 Mev with average energy of a beam from $\sim 10^3$ to $\sim 10^5$ W are required. As to energy such beams can be received by acceleration of electrons in the circular induction accelerator – betatron. Essential feature of the betatron work consists in the fact that speed of change of the average magnitude of a magnetic field induction B_{aver} should exceed twice speed of change of an induction in an equilibrium orbit B_0. It is well-known a betatron condition «B_{aver}: B_0 = 2:1» when the radius of an electron orbit remains to constants in a magnetic field growing in time.

Betatron rate «2:1» limit an average power of an accelerated electron beam because magnetic flux inside an equilibrium orbit and magnetic energy are very high. The number of particles, accelerated in one cycle of acceleration, is limited to instability of an electron beam, and the increase of a repetition rate demands increase in average power of accelerator power supplies which has a limit too.

The radius of an equilibrium orbit can remain to constants at increase in a magnetic induction in an orbit at B_{aver}: $B_0 << 1$ if special ratio between amplitude-time characteristics of a magnetic induction in an orbit and an induced accelerating voltage are carried out. At $B_{aver} << B_0$ magnetic energy of the accelerator decreases and so both frequency of accelerating cycles and average capacity of the accelerated beam can be essentially increased. And use of rigid focusing by magnetic field B_0 with the high radial gradient (the module /n/>> 1) allows to increase number of electrons in the orbit and to reduce dimensions of magnetic system.

#dol@sune.jinr.ru

MAGNETIC SYSTEM

The magnetic field in an equilibrium orbit is formed by C-shaped electromagnets with the high parameter of the field $n_1 >> 1$ (Figure 1(a)) and $n_2 << -1$ (Figure 1(b)). The combination of such magnets allows to realize rigid focusing of electrons. Electromagnets are fed by a rectangular wave of a voltage V_0 (Figure 2(a)) and form the magnetic B_0 induction which form is shown on Figure 2(b). For reduction of energy losses at magnetic reversal of electromagnet cores the magnitude of induction chooses much less induction of saturation of a core material .

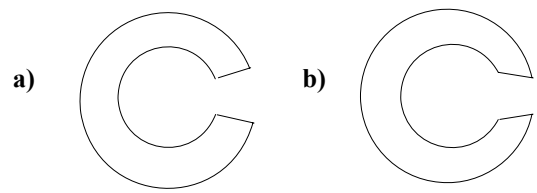

Figure 1: C-shaped cores of electromagnets: a) n >> 1, b) n <<-1.

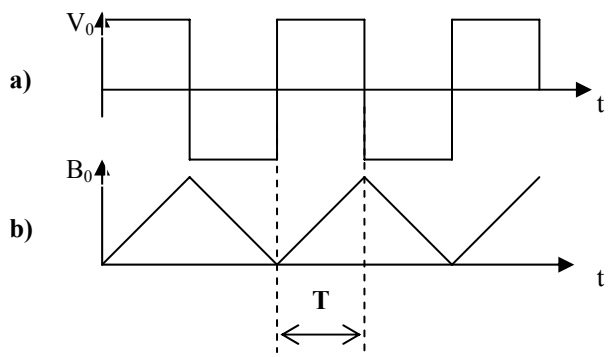

Figure 2: a) Square wave of Power System, produced by transistor converter, b) Form of magnetic induction B_0.

ACCELERATING SYSTEM

Electrons are accelerated by the electric field induced by O-shaped ferromagnetic cores which are located on

one or several azimuths of an electron orbit. To keep radius of an orbit to constants during acceleration, the gain of an electron energy $e\Delta U_{aver}$ for one turn should be equal

$$e\Delta U_{ac} = e\Delta B_0 v R_0 ,$$

where ΔB_0– the gain of a magnetic induction of C-shaped magnets during for one turn, R_0 – equilibrium radius of an orbit, v – speed.

At linear growth of an induction in time

$$B_0(t) = B_{0max} (t / T)$$

where T – time of increase of an induction, the amplitude of induced pulses of accelerating voltage ΔU_{ac} should be equal

$$\Delta U_{ac} = 2\pi R_0^2 (B_{0max} / T)$$

The form of a wave of accelerating voltage $U_{ac}(t)$ is shown on Figure 3.

Pulse duration τ of accelerating voltage U_{ac} is equal to half of time of a electron turn in an orbit

$$\tau = \pi R_0 / v$$

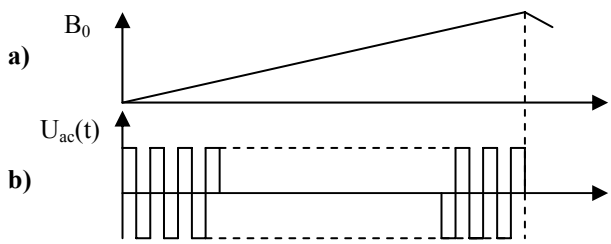

Figure 3: a) Magnetic Induction in equilibrium orbit. b) Waveform of accelerating voltage induced by O-shaped cores.

ACCELERATOR PARAMETERS

For an example we shall consider key parameters of the electron accelerator on energy E = 10MeV with radius of equilibrium orbit R_0 = 0.5m and time of induction increase T = 5μs.

The maximal size of a magnetic induction of C-shaped cores is equal

$$B_{0max} = m\gamma v / eR_0 = 0.067 \text{ T}$$

This magnitude is much less than induction of saturation of ferromagnetic cores, therefore losses of energy on their magnetic reversal will be small.

The amplitude of accelerating pulses is equal

$$\Delta U_{ac} = 2\pi R_0 (B_{0max} / T) = 42\text{kV}$$

If the magnetic induction O-shaped cores does not exceed B = 0.1T losses in cores will be small. At such magnitude of an induction the total section accelerating O-shared cores should be equal not less

$$S = \Delta U_{ac}\tau / B = 22\text{cm}^2$$

To realize such accelerating system the minimum of 10 ferromagnetic cores with the sizes 125 x 80 x 10 mm is required.

From all variants of the power supply system of the accelerator the transistor variant has preference. Transistor converters of a voltage from DC in AC have high reliability and efficiency. Creation of such converter for magnetic system of the suggested accelerator does not represent complexities. Now 1.5 MW converters with frequency of switching up to 150 kHz (T = 3.3 μs) are realized [1]. Development of converters with frequency of switching ~100 MHz represents more difficult task. From existing transistor RF switches DE475-102N21A RF Power MOSFET possesses the maximal frequency of switching 30 MHz. Average power of the switch – 1.8 kW. For increasing output frequency and output power are used special Converter Systems. The high output frequency is achieved using a phase-shifted gating of "n" converter modules [2].

Use of rigid focusing of electrons will allow to receive a steady current of a beam with number of particles $\sim 5 \cdot 10^{11}$ and an average current of the accelerated beam - 8 mA. At energy of electrons 10 MeV average power of the beam will make 80 kW.

The rapid progress in the field of semi-conductor switches allows to hope, that powerful devices with operating frequency up to 100 MHz in the near future will be developed.

SUMMARY

For reduction of magnetic energy of the induction circular accelerator (betatron) with the purpose to increase the cycles frequency and increase of average power of the accelerated electron beam it is offered to use the C-shaped electromagnets for formation magnetic field in an equilibrium orbit and the electric field induced by O-shaped ferromagnetic cores for electron acceleration.

Application of C-shaped cores of electromagnets allows to form magnetic fields with the high radial gradient and to realize rigid focusing of electrons.

REFERENCES

[1] H. Matthes, R. Jurgens "1.6 MW 150 kHz Series Resonant Circuit Converter incorporating IGBT Devices for welding applications". International Induction Heating Seminar, Padova, p. 25-31.

[2] Hammad Abo Zied, Peter Mutschler, Guido Bachmann "A Modular IGBT Converter System for High Frequency Induction Heating Applications", PCIM 2002, 14.-16.05., Nuremberg.

RF AMPLIFIERS AND STRUCTURES FOR ISAC/TRIUMF

A.K. Mitra, Z. T. Ang, Y. Bylinski, K. Fong, R.E. Laxdal , J. Lu, R. Poirier,
V. Zvyagintsev, TRIUMF, Vancouver, Canada

Abstract

The ISAC-I accelerator is comprised of two room temperature linacs; a 35MHz RFQ and a 106MHz separated function drift tube linac producing an accelerating voltage up to 4.5MV and 8.1MV respectively. In addition a pre-buncher, chopper and several re-bunchers are used in the accelerator chain to manipulate the longitudinal phase space. A heavy ion superconducting linac is being installed at ISAC/TRIUMF to increase the energy of ISAC-I from 1.5 MeV/u to 6.5 MeV/u for ISAC-II. A first stage, now in commissioning, consists of twenty medium beta cavities driven by twenty, 106MHz, tube amplifiers. In the second stage of ISAC-II, 20 high beta quarter wave superconducting cavities will be installed operating at 141 MHz. A transfer line connecting ISAC-I and ISAC-II has a room temperature buncher cavity at 35 MHz. This report will summarize rf amplifiers employed in ISAC facility and discuss the choice of amplifiers for the second stage of ISAC-II. Some of the re-furbishing and improvements that are done to ISA-I rf system will also be discussed.

INTRODUCTION

A heavy ion superconducting linac with a total accelerating voltage of 20 MV is being installed as a first stage of the ISAC-II upgrade as an addition to the existing room temperature linac ISAC-I. ISAC–I has the capability of maximum energy of 1.8 MeV/u for ions with A/q ≤ 6 [1]. For ISAC-II a beam of 1.5MeV/u is delivered from the exit of IH-DTL5 of ISAC-I to the entrance of the medium β section of the SC linac via a 25m transfer line. In the second stage of the ISAC-II upgrade, an additional 20 superconducting high beta cavities will be added in the same accelerating vault to produce an accelerating voltage of 20 MV for masses up to 150, with A/q ≤ 7. The medium beta cavities employ 106 MHz tube amplifiers whereas the rf amplifiers for the high beta cavities operating at 141 MHz will be decided soon.

ISAC

ISAC-I

The ISAC–I heavy ion linac is composed of room temperature rf structures operating at various rf frequencies [2]. Figure 1 shows the layout of the accelerator as well as the S-bend transfer line joining ISAC-I and ISAC-II. Table 1 shows the list of room temperature rf structures and rf amplifiers with power requirements for the accelerating voltages. ISAC-I has been operational since 2000 with excellent performance [3]. Some of the re-furbishing and improvements that were carried out are mentioned here. The RFQ which was operational since 1999 was opened in 2006 spring shutdown since the vacuum deteriorated to $2x10^{-6}$ from $5x10^{-7}$ Torr. Water leaks in two of the split ring resonators of the RFQ and cooling line brazing joints were the major cause for poor vacuum. They were replaced with two identical rings and joints were repaired.

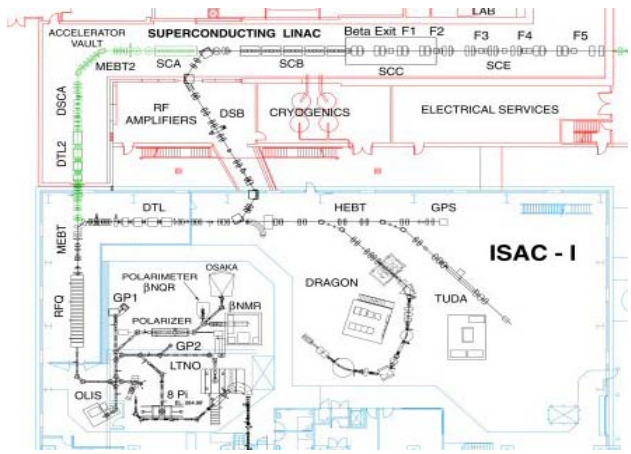

Figure 1: Layout of ISAC linear accelerator

Table 1: ISAC-I Room Temperature RF Structures

RF Device	RF Structure Type	Frequency	Electrode Voltage	Nominal Power
		MHz	V	P
Prebuncher	Parallel Plates	11, 23, 35	400 V	500 W
RFQ	Split Ring 4 Rod	35.36	74 kV	80 kW
Bunch Rotator	Split Ring	106.08	35.5 kV	3.5 kW
Chopper	Coil + Parallel Plates	5.89	5.5 kV	45 W
Chopper	Coil + Parallel Plates	11.78	7.4 kV	140 W
Rebuncher	Spiral	35.36	30 kV	1 kW
DTL Tank1	IH	106.08	47 kV	3.9 kW
Buncher 1	Split Ring	106.08	55 kV	8 kW
DTL Tank2	IH	106.08	69 kV	10 kW
Buncher 2	Split Ring	106.08	74 kV	10.2 kW
DTL Tank3	IH	106.08	97 kV	16 kW
Buncher 3	Split Ring	106.08	91 kV	11.6 kW
DTL Tank4	IH	106.08	109 kV	19 kW
DTL Tank5	Split Ring	106.08	116 kV	20.3 kW
Low Beta Buncher	Coil + Drift Tube	11.78	30 kV	1.5 kW
High Beta Buncher	Spiral	35.36	170 kV	12.6 kW
S-bend buncher	Spiral	35.36	170 kV	12.6 kW

The most probable cause is due the use of very aggressive flux which was applied for soldering of copper and

stainless steel joints. This material was excluded from the MS manufacturing process in 2002.
The DTL tank 1 cooling channels, drilled in the mild steel end plates and nickel plated, lately showed corrosion and water contamination. An external water-cooling on the end plate was designed and implemented to eliminate this problem. The DTL amplifiers also went through some modifications. All five DTL amplifiers were installed with a new high voltage proof circuit. In addition the amplifier status signals and DC voltage, current and rf parameters were incorporated in a new remote control system to facilitate operation.

Transfer Line

The transfer line buncher is identical to the HEBT 2-gap spiral buncher operating at 35 MHz. It's rf amplifier, built in-house, employs a power tetrode EIMAC 4CW25000A. The buncher-amplifier system has been tested up to 13 kW of power equivalent to 170 kV gap voltage. A fine tuner without finger stock was successfully installed in this buncher with a maximum temperature increase of 15^0C in the tuner parts. The same tuner modification has being implemented in DTL tanks 2-5.

ISAC–II

The medium beta cavities employed in ISAC-II are two-gap bulk niobium quarter wave structures. The first eight cavities are designed for particle velocity β = 5.7 % while the remaining 12 have a β of 7.1 % [4]. These cavities provide an average gradient of 7 MV/m with power dissipated, P_{cav}= 7 W exceeding the design gradient of 6 MV/m. The gradient corresponds to an acceleration voltage of 1.26 MV per cavity with a peak surface field of 35 MV/m. Figure 2 shows the accelerating gradients for all 20 cavities installed in the beam line.

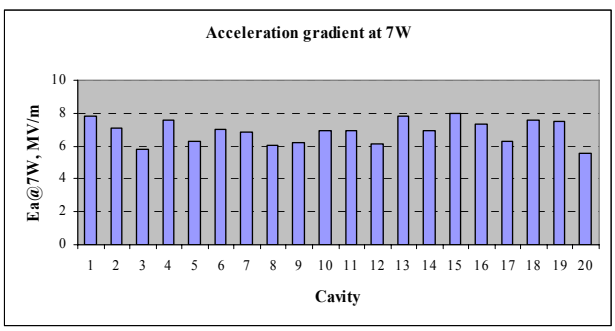

Figure 2: Gradients of 20 cavities with 7 W rf power

These 20 cavities are housed in five cryomodules with four cavities and one superconducting solenoid in each cryomodule. The equipments for cryomodule vacuum pumps and sensors, heater power supplies, rf power amplifiers and rf control system, cavity tuner motor drivers and control, dc power supplies for superconducting solenoid and xy-steer are installed in the power supply room which is adjacent to the ISAC-II accelerator vault. The arrangements of the equipments have been modular so that one row of equipment feed one cryomodule. At the end of each row, there is a BOP (break out panel) which houses the EPICS interface providing operation of the accelerator from the control room. Figure 3 shows the equipment layout in the power supply room. Two racks close to the wall house four rf amplifiers for each cryomodule.

Figure 3: Power supply room equipment layout

Medium Beta RF

The rf amplifiers for the medium beta linac, a total of 20, operate at 106.08 MHz and are interfaced with EPICS. Although rf power required for each cavity is 7 W, much more power is delivered from the rf amplifier. The movable coupling loop associated with each cavity is providing over coupling in order to increase the bandwidth and thus enabling rf controls to suppress the micro-phonics effects. The power required for nominal operation is 150 watts. The amplifiers are capable of delivering 800 watts for pulse conditioning of the cavities. ISAC safety requires that the rf amplifiers to be interlocked such that rf can not be turned on when the medium beta cavities are cooled to liquid helium temperature and the vault door is open. This safety interlock and remote operation has been fully established as a pre-condition to get a license to power the linac cavities

The rf control system for the medium beta superconducting cavities is a hybrid of analog and digital system. Each system consists of a self-excited feedback loop with phase-locked loops for stabilizing phase and frequency of the accelerating cavities. Amplitude and phase regulation is also performed by the rf control system by using digital signal processing. The gain linearity from 4 to 200 watts is specified to be within ± 0.5 dB and the phase stability to be < ± 5 degree. An important parameter is phase noise of the rf system within 1 - 200 Hz bandwidth. Figure 4 shows the measured phase noise of SCB1, cavity 4, where SCB stands for medium beta section. The integrated value of phase noise within the specified bandwidth meets the linac specification of < ±1 degree.

High Beta RF

The second stage of ISAC-II is to install 20 bulk niobium high beta quarter wave cavities operating at 141 MHz [5]. These cavities are divided into two modules of six cavities and one module of eight cavities with one

superconducting solenoid in each cryomodule. Table 2 summarizes the parameters of the 106 MHz medium beta cavities and 141 MHz high beta cavities. The power requirements from the rf amplifier is similar to the 106 MHz amplifier.

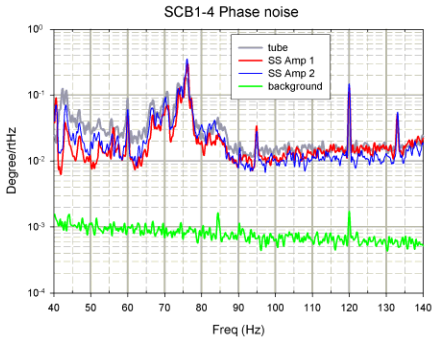

Figure 4: Phase noise spectra for SCB cavity with solid state and tube amplifiers

Table 2: ISAC-II Medium Beta and High Beta Cavities

		Medium Beta		High Beta
Parameters	unit	flat	round	round
f_0	MHz	106	106	141
Active length	mm	180	180	180
Ea	MV/m	6	6	6
U/Ea2	J/(MV/m)2	0.1	0.093	0.073
Bp/Ea	mT/(MV/m)2	10.3	10.1	10.3
Ep/Ea		5.2	4.7	4.7
Va @ 6MV/m	MV/m	1.08	1.08	1.08
Power @ 6MV/m	W	4.6	4.5	4.0
Mech. frequency	Hz	80	80	150

Tube and Solid State Amplifier

Considerable experience has been gained from running the installed tube amplifiers for ISAC-II medium beta linac. The rf performance of these tube amplifiers have been compared with solid state amplifiers operating at 200 Watts. Although both type of amplifiers satisfy the gain and the phase linearity requirement, phase noise for the solid state amplifier is lower in the 40 - 140 Hz band. This can be seen in figure 4. AC ripple at 60 Hz and 120 Hz of the high voltage dc power supply of the tube amplifier are the main contributors to the higher phase noise. Solid state amplifiers employ low dc voltage, high current switching mode power supplies hence low frequency AC ripple is non existent.

Long term phase drift of the grid tube amplifier poses a significant challenge to the control system. Both prototype tube amplifier and solid state amplifier have been tested for long term phase drift. The tube amplifier has a 15 degree phase shift for the first 15 minutes of rf start up at 250 Watts. The solid state amplifier produces only 2^0 phase drift in the first two minutes. Both tube and solid state amplifiers, however do not drift in phase after the initial worm up.

Tube life can be extended by employing filament power management for tubes with a thoriated tungsten emitter [6]. This is based on measured loss of carbon as a function of temperature. For 400 Watt output power for the 106 MHz rf amplifiers, tube anode current changes from 0.46 A to 0.45 A when the filament power is reduced from 100% to 80%. This produces relative life extension probability by a factor of two as shown in figure 5. This power management will be implemented in all the 20 power amplifiers to get extended tube life.

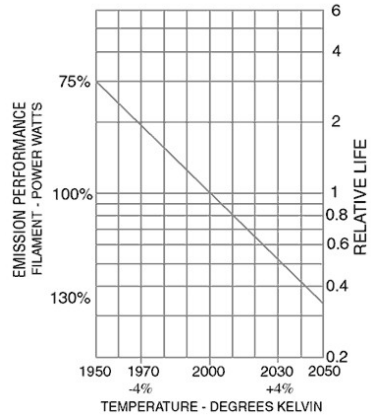

Figure 5: Extension of tube life by filament power management

Although the solid state amplifiers are more expensive than the tube amplifier, low phase noise, small phase drift, broad bandwidth and long device life make them an attractive choice for 141 MHz ISAC-II high beta linac.

CONCLUSIONS

The ISAC-I rf system worked very reliably since they were commissioned. ISAC-II medium beta rf amplifiers have just been installed and have worked in conjunction with the rf control to test and commission the medium beta linac. Steps are being taken to increase the tube life beyond their normal expected life. Although solid state amplifiers are more expensive than the tube amplifiers, they are being considered for high beta rf system.

REFERENCES

[1] P. Schmor, et al, "Development and Future Plans at ISAC", LINAC2004, Lubeck, Germany, Aug, 2004.

[2] A.K. Mitra, et al, " RF Test and Commissioning of the Radio Frequency Structures of the TRIUMF ISAC I facility", LINAC 2002, Gyeongju, Korea, August 2002

[3] I. Bylinskii, et al, "TRIUMF ISAC RF System Improvements After 2 Years of Operational Experience", PAC 2003, Portland, May 2003

[4] R. E. Laxdal, et al, "Commissioning of the ISAC-II Superconducting Linac at TRIUMF", EPAC 2006

[5] R.E. Laxdal, et al, "Recent progress in the superconducting RF Program at TRIUMF/ISAC", Physica C 441 (2006) 13-20

[6] Tech_no 54, Broadcast/Communications, "Extending the Life of Power Grid Electron Tubes", B-N "Bob" Alper, Pentalaboratories

SCSS RF CONTROL TOWARD 5712 MHz PHASE ACCURACY OF ONE DEGREE

Yuji Otake, Hirokazu Maesaka , Masanobu Kitamura , Tumoru Shintake, RIKEN, Harima Institute
1-1-1 Kouto, Sayo-tyou, Sayo-gun, Hyogo, 679-5148, Japan
Takashi Ohshima, Naoyasu Hosoda, Toru Fukui, Toru Ohata, Japan Synchrotron Radiation Research Institute (JASRI/SPring-8), Kouto, Sayo-tyou, Sayo-gun, Hyogo, 679-5198, Japan

Abstract

A 250 MeV prototype accelerator was built. Its low-level rf system, which mainly controls a 5712 MHz pulsed rf signal, was built to achieve very tight requirements: phase stability and a setting resolution of less than 1 deg.. These requirements correspond to a beam energy variation of 10^{-4} at the crest acceleration for the 5712 MHz rf. To realize the requirements, IQ-modulators/demodulators and arbitrary wave form generators/digitizers of VME modules (D/A, A/D) to handle an IQ-function were developed. The PID control method was employed to compensate for any time drift, such as an rf phase. We finally achieved phase setting and a detecting resolution of the IQ-modulators/demodulator of +/- 0.5 deg. at 5712 MHz. Decreasing the phase drift with in +/- 0.5 deg. was also achieved by a PID control program. By this control performance, a beam energy variation of 0.06% was achieved.

INTRODUCTION

To check the feasibility of X-FEL(SCSS),[1] the 250 MeV prototype accelerator was constructed at SPring-8 [2]. The construction was started from October, 2004, and finished in December, 2005. After construction, we confirmed 49 nm SASE light by the prototype accelerator with 250 MeV, 0.2 nC electron beams, and 10 Hz reputation [2,3]. This 60 m long accelerator comprises a 500 kV CeB6 mono-crystal thermionic electron gun with a beam deflector for making a 1ns (FWHM) beam pulse width, a 238MHz pre-buncher cavity and a 476 MHz booster cavity for bunching and accelerating beams, a 2856 MHz APS cavity and a 2856 MHz/2m long accelerator guide to obtain 50 MeV beams, four 1.8 m long/5712 MHz accelerator guides to make the beam energy up to 250 MeV, and two 3 mm gap in-vacuum undulators to generate 49 nm laser light. In the case of the prototype accelerator, the pulse width of the beams should be compressed to 1 ps by a magnetic bunch compressor to obtain about a 1 kA peak current for generating SASE [3]. Therefore, a low-level RF system of the accelerator was built to achieve very tight requirements, which were 5712 MHz phase stability and a resolution of less than +/-0.5 deg., as well as 5712 MHz amplitude stability and a resolution of less than 10^{-4} [4]. These requirements correspond to a beam energy variation of less than 10^{-4} at a crest acceleration of a 5712 MHz rf. This phase value corresponds to time stability and a resolution of less than 500 fs. Such stability and a resolution are necessary to achieve 100 μm pointing stability of electron beams and to generate laser light for the undulator section of about 10 m long [5]. This paper gives a summary and describes the performance of the low-level rf system and its key components, such as an IQ-demodulator and an IQ-modulator as well as the PID control method to obtain long-term phase and amplitude stability.

RF SYSTEM

The low level rf system of the prototype accelerator was built as shown in Fig. 1 [6]. CW signals of 238 MHz, 476 MHz, 2856 MHz, and 5712 MHz for acceleration are provided with a signal source having a very low noise level, which causes an rf phase jitter. These signals are transmitted to rf components through phase-stabilized coaxial cables having a temperature coefficient corresponding to an electrical length of 10 ppm/^{O}k.

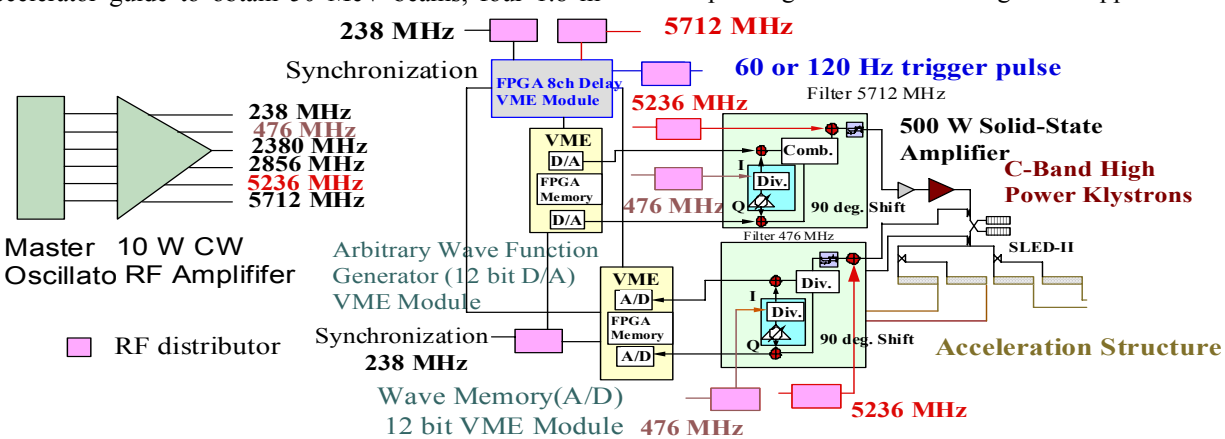

Figure 1: SCSS rf system. The system mainly comprise a very low-noise signal source, IQ-modulators/demodulators, A/Ds and D/As to control IQ- instruments, and 600 w solid state klystron driver amplifiers.

The signals drive rf components, such as a 5712 MHz klystron with 50 MW output power and a 2 µs pulse width. Because of using coaxial cables, we should take care of any rf loss. Therefore, 10 W rf amplifiers of these signals, stabilized by PLL (Phase Locked Loop) and ALC (Auto Level Control), should be used. To drive the C-band 50 MW klystron, the signals should be modulated to make a 2 µs pulsed rf, and rf phase and amplitude control to the signals is necessary. These signal manipulations are achieved with an IQ-modulator and a VME-D/A module. The output of the IQ-modulator is applied to a 600 W solid state amplifier to drive the klystron. The phase and amplitude of the output rf form the klystron are monitored with an IQ-demodulator and an VME-A/D modulse though an 60 dB rf waveguide directional coupler.

COMPONENTS OF LOW LEVEL RF SYSTEM

Master Oscillator

The master oscillator,[6] which generates 238, 476, 2380, 2856, 5236, and 5712 MHz stable rf signals, is a time reference source. The circuit configuration of the oscillator is shown in Fig. 2. It comprises a very stable reference generator (stability of 10^{-11}) of 10 MHz, which has a low-noise characteristic in the frequency region below 1 kHz measured from 10 MHz, a 2856 MHz signal generator having a low-noise characteristic in the frequency region over 1 kHz measured from 2856 MHz, a frequency doubler instrument to make 5712 MHz from 2856 MHz, and frequency dividers to generate the above-mentioned frequency signals. Both low-noise signal generators are connected by a PLL circuit to make the very low SSB (Single Side Band) phase noise over the whole frequency range, as shown in Fig. 3. The noise level is -140 dBc/Hz at 1 MHz, measured from 2856 MHz.

IQ-modulator and demodulator

The IQ-modulator and demodulator [6] employs a Gilbert Cell, which has a very good rf phase and amplitude stability to any temperature change as well as nice rf isolation, as a mixer. Figure 4 shows an example of a developed 5712 MHz IQ-demodulator. The IQ-modulator also uses a similar circuit. The cell can handle up to 2.7 GHz, because of technical limitation when we designed them. Therefore, the IQ-modulator and demodulator use detection in 476 MHz, which is the frequency of the booster cavity, and employ the heterodyne method to make 476 MHz by mixing 5712 MHz and 5236 MHz. An amplifier having a noise level of nV/Sqrt(Hz) is used at the input/output stage of the modulator/demodulator. To prevent the effect of external noise, a 100 ohm differential signal transmission is employed for connection between the modulator/demodulator and the A/D/D/A modules to read/write the IQ-data. Figure 5 shows the phase-detection characteristic of the IQ-demodulator. The phase-modulation characteristic of the IQ-modulator is also of comparable performance. The phase-detection resolution is about +/- 0.5 deg. at 5712 MHz, and the relative amplitude resolution is lass than 0.1%.

VME-A/D and D/A module

The VME-A/D, [6, 7] as shown in Fig. 6, was developed to digitize the IQ-detection signal. A VME-D/A [6,7] module was also developed to manipulate the IQ-modulator. Both modules have 12-bit resolutions, wave-data generation driven by 238 MHz clock, and a 30 MHz base band width at the input/output.

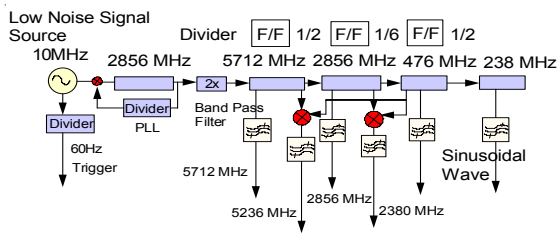

Figure 2: Circuit diagram of the master oscillator. The oscillator uses frequency dividing, a very low-noise power supply and PLL connection between the 10 MHz and 2856 MHz sources to achieve low noise.

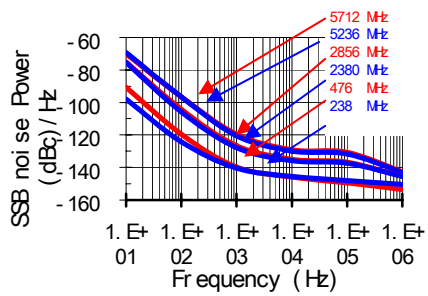

Figure 3: SSB noise power spectra of the master oscillator. The decreasing noise level at individual frequencies is proportional to the dividing ratio.

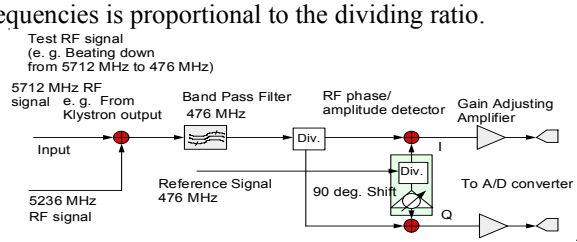

Figure 4: Block diagram of the IQ-demodulator. The demodulator uses the heterodyne method for detection at 476 MHz. The 476 MHz signal is made from mixing the 5712 MHz and 5236 MHz signals.

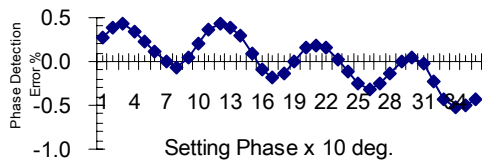

Figure 5: Phase Detection Error of the IQ-Demodulator. The detection error is within +/- 0.5 deg.

The D/A has functions that make a pulse of an arbitrary wave form such as 2 μs in a width, and a PSK(Phase Switch Keying) operation during the rf pulse to realize rf pulse compression with SLED. One set of the two output channels of the D/A module can manipulate the IQ-function to control the IQ-modulator. This D/A module each time generates the arbitrary shape pulse triggered by an external pulse synchronized to an accelerated electron beam. The A/D module is like an oscilloscope without a display to digitize an arbitrary wave form. The VME A/D module can detect an error wave form out of tolerance referred to a reference wave form that is memorized in advance. The tolerance is such as 10% defined in advance. For example, by this function, the module can automatically catch a large thyratron jitter that shows its replacement. We finally obtained a dynamic range devoid of noise in the A/D and D/A modules is about 11 bit (5 x 10^{-4} V resolution).

Stabilization of rf phase and amplitude

To stabilize the long-term rf phase and amplitude, PID (Proportional Integrate Differential) feedback control [8] of the rf phase and amplitude in the acceleration cavities was employed. The method uses the equation

$$y = K\left(e_n + \frac{\theta}{T_i}\Sigma e_n + T_d\left(e_n - e_{n-1}\right)\right), \qquad (1)$$

where K is the gain value, e_n and e_{n-1} are the deviation values between a target value and the output of equipment at each sampling time, θ is the sampling period, Ti is the integration factor, T_d is the differentiation factor, and n is the sampling number. Y is the output value to a control target (the equipment). This equation is a quantized equation to apply to computer control. This method was achieved with the A/D and D/A modules, and a LINUX computer connected vir Giga-bit Ethernet. The maximum response frequency of the method is about one tenth of the maximum repetition of the accelerator, because of the Nyquist Frequency. Figure 7 shows example stabilization data of an rf phase in the 238 MHz prebuncher cavity. The rf phase was controlled within 0.5 deg. for more than 2 hours. The control parameters of K, Ti, Td, and θ were , 0.1, 0.001, 0, and 1 s.

SUMMARY

We achieved generating non-linear amplification of a 49 nm VUV laser by the SCSS prototype accelerator using the above-mentioned low-level rf system. A pulse-by-pulse acceleration voltage (energy) jitter of 10^{-4}, which is caused by noise of the signal source, was estimated by integrating the noise spectrum (-140 dBc/Hz at 1MHz offset frequency) shown in Fig. 3 by applying a weight function described in Ref. [9]. The +/-0.5 deg. phase and amplitude resolutions of the IQ-detection and modulation were effective to satisfy our requirement to realize a beam energy stability of 10^{-4}. The PID control method stabilized the 238 MHz cavity rf phase within +/-0.3 deg. for a long period. This fact also satisfies our requirements. We finally applied this PID method to controlling the rf phase and amplitude of the 238 MHz and 476 MHz cavities, and the rf phase of the 2856 MHz cavities. All controls worked well. We finally obtained a beam energy variation of 0.06% (peak-to-peak) in the prototype accelerator.

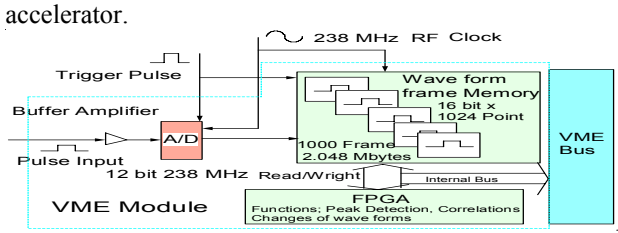

Figure 6: Schematic diagram of the A/D module. It has a 12-bit dynamic range, a data taking speed driven by a 238 MHz clock, and a 30 MHz input base bandwidth.

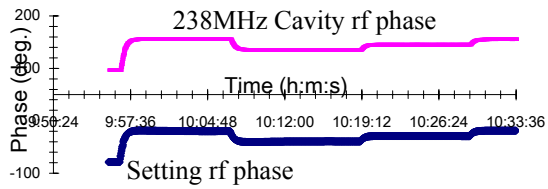

Figure 7: Example of PID feedback control performance of the 238 MHz cavity phase. This graph shows the cavity phase follows the setting phase purposely changed by an operator. The 238 MHz cavity phase is controlled within 0.5 deg. The phase difference between the cavity and setting phase is artificial.

REFERENCES

[1] SCSS X-FEL Conceptual Design Report, 2005.
[2] T. Shintake et al., FIRST LASING AT SCSS, Proc. of the 26th International Free Electron Laser Conference, http://www.bessy.de/fel2006/proceedings/ HTML /AU-THOR.HTM, in press, 2006.
[3] H. Tanaka et al., LOW EMITTANCE INJECTOR AT SCSS, Proc. of the 26th International Free Electron Laser Conference, http://www.bessy.de/fel2006/proceedings/ HTML /AUTHOR.HTM, in press, 2006.
[4] M .Cohlus et al., BUNCH COMPRESSION STABILITY DEPENDENCE ON RF PARAMETERS, Proc. of the 27th FEL conf., 250-253, USA, 2005.
[5] Dr. T. Tanaka, private communications.
[6] SCSS X-FEL Conceptual Design Report, pp 81-89,2005.
[7] T.Fukui et al., A Development of High-Speed A/D D/A VME Boards for a Low Level RF System of SCSS, Proc. of the 9th ICALEPCS 2005.
[8] J.J. D`Azzo and C. H. Houpis, *Feedback Control System Analysys & Synthesis*, Second Edition, 158-160 (McGRAW HILL, 1966).
[9] Y. Otake et al., Sub-pico-second trigger system for the SCSS prototype accelerator, Proc. of the 26th International Free Electron Laser Conference, http://www.bessy.de/fel2006/proceedings/HTML/AUTHOR.HTM, in press, 2006.

FIELD MEASUREMENT RESULTS OF THE QUADRUPOLE MAGNETS FOR ATF2

M.Masuzawa, R.Sugahara and Y.Suetsugu, KEK, Tsukuba, Japan

Abstract

ATF2 will be built at KEK as a test facility for the final focus system for the ILC. The specifications for the final focus system require transverse focusing of the electron beam to nearly 40 nm. The quadrupole magnets for the ATF2 magnets have to meet strict specifications on the multipole components, especially the sextupole components, in order to achieve the required small beam size. Preliminary measurement results of these magnets using a harmonic coil system will be reported in this paper.

INTRODUCTION

The Accelerator Test Facility (ATF) at KEK was built for R&D work for a future electron-positron linear collider [1]. The main goals of the ATF project are to produce, measure and control a very low emittance beam. The ATF is composed of an electron gun, a 1.5 GeV electron linac, a 1.5 GeV damping ring of 138 m circumference and an extraction line for beam diagnostics. The ATF2 project will extend the existing ATF extraction line with an ILC-type final focus system [2]. Most of the tolerances, such as the tolerances on magnetic field, jitter vibration and power supply stability, are common between the ATF2 and the ILC. ATF2 will be a very good model for the ILC final focus system and a successful commissioning of the ATF2 project will assist in the design of the ILC. The ATF2 beam line is shown in Fig. 1. The quadrupole magnets for the ATF2 extraction line are called the QEA magnets. The QEA magnets have been manufactured at IHEP in China. The basic mechanical and magnetic parameters are summarized in Table 1. Field error tolerances for the extraction quadrupole magnets are summarized in Chapter 3 in the ATF2 proposal [2]. Tolerances on the normalized sextupole amplitude to the quadrupole amplitude (B3/B2) for some of the quadrupole magnets are as tight as 0.04 % at r = 10 mm. The tolerance on the tilt is on the order of 0.1 mrad.

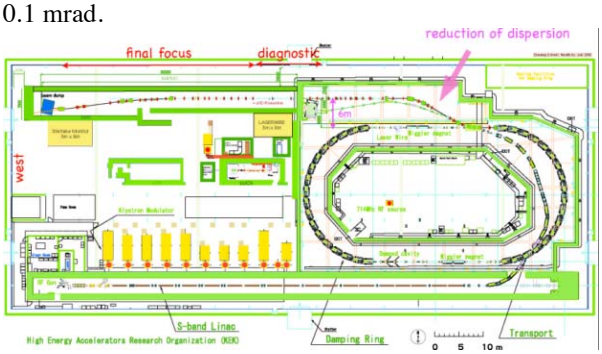

Fig.1. ATF and ATF2 layout.

Table 1

Bore diameter (mm)	32
Core length (mm)	180
# of turns per pole	48
Max. current (A)	150 or 50
Field gradient @115A (T/m)	54

MEASUREMENT SYSTEM

General

A harmonic coil system was used to measure the QEA magnets. The rod of the measurement coil, shown in Fig. 2, is made of ceramic (Alumina 99.5 %). The main and the additional bucking coils are mounted on the same frame made of Macor. Air bearings are used for smoother rotation. The number of turns and locations of the main and bucking coils are determined so that the dipole and quadrupole components are cancelled when two coils are connected in a certain configuration (bucking coil configuration). Polyurethane coated copper wire with a diameter of 0.1 mm is used for both coils. The field strength, magnetic center and the main quadrupole phase are measured by the main coil, without connecting the bucking coil (the main coil configuration). The sextupole component is evaluated by the bucking coil configuration. A coupling structure, shown in Fig. 3, is introduced in order to guarantee the relation between the coil and the encoder. When placing the magnet on the measurement system, the coil rod has to be removed from the encoder. With the coupling structure, the relative position of the coil to the encoder is expected to give good reproducibility.

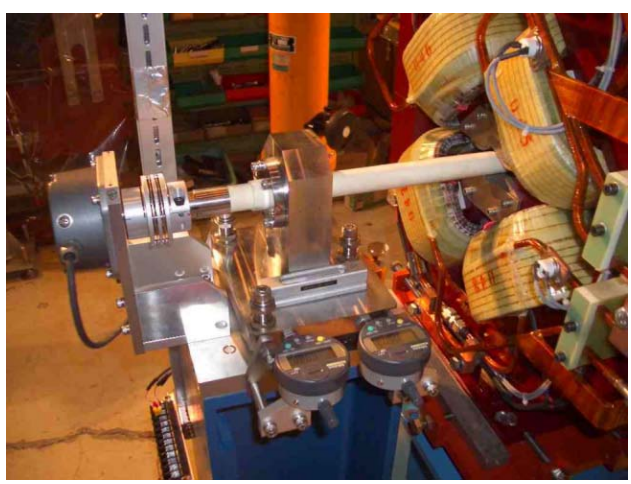

Fig.2. Harmonic coil system.

Fig.3. Coupling between the coil rod (left) and the encoder (right).

Measurement Reproducibility

In order to evaluate the stability of the measurement system and the reproducibility of the coupling detachment, a measurement was repeated 25 times. The measurement started ~30 minutes after the magnet was ramped up to I = 100 A. At each measurement, the harmonic coil was detached from the encoder. The measurement interval was ~5 minutes. Main quadrupole amplitude (integrated field strength) is normalized to the average value and plotted on the left side in Fig.4. The median plane angle, the tilt of the quadrupole magnet is plotted in the right side. The r.m.s. of the reproducibility of the strength and the tilt measurements are 1.2×10^{-5} and 0.01 mrad, respectively in the case where the measurement was repeated continuously.

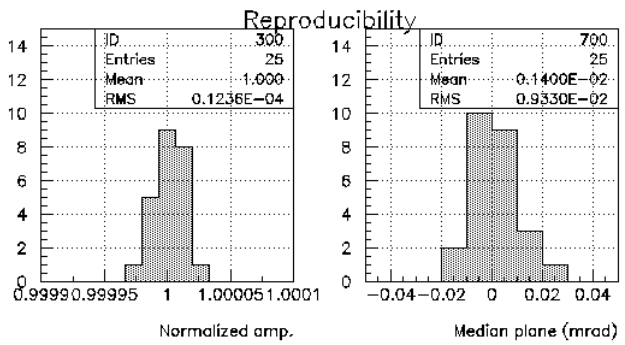

Fig. 4. Measurement reproducibility of the strength (left) and the tilt (right).

MEASUREMNT RESULTS

Twenty four QEA magnets, 13 high current magnets and 11 low current magnets, were measured in 2006. The magnets were divided into two groups, the “high current” group and the “low current” group. The “high current” magnets were allowed to ramp up to 150 A while the “low current” magnets were only up to 50 A. This requirement comes from the specification of the power supplies that will be connected to the magnets in the actual beam line. The magnets are standardized first and then ramped up to the measurement current from 0 A. In order to obtain excitation data the measurement was carried out at every 10 A step for the high current magnets and 3.33 A step for the low current magnets, respectively, with the main coil configuration. At each current, the measurement was repeated three times. The current on the power supply was monitored by DCCT all through the measurement. The temperature of the measurement hall and the cooling water were controlled within +/- 0.3 degree and +/- 0.1 degree, respectively.

Integrated Strength (B’L)

The distribution of the quadrupole strengths normalized to the average of the high current group magnets is shown in Fig. 5. It is seen that the strength varies by the order of 0.1 % among the magnets. This large spread can be explained by the thickness of the liner plates which were inserted between magnet quadrant cores in order to control the sextupole component by IHEP, as is shown in Fig. 6. Since each QEA magnet will have its own power supply, the large variation in the quadrupole strength is not a big concern.

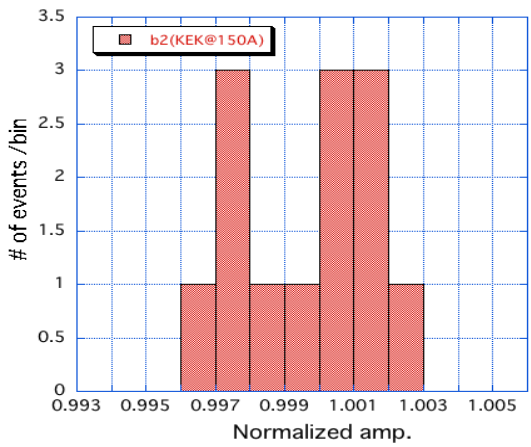

Fig. 5. B’L distribution.

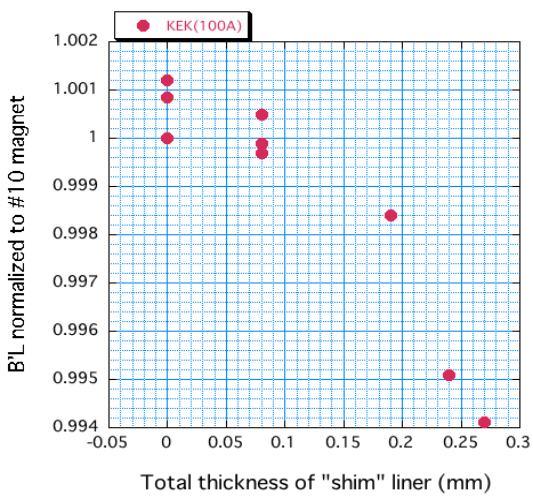

Fig.6. B’L vs. shim liner thickness.

Magnetic Center and Median Plane

The magnetic center, Δx and ΔY, when aligned using the reference plate placed on top of the magnets are plotted in Fig. 7 for all 24 magnets. A large offset was measured, especially in the horizontal direction, x. Fig. 8 shows the distribution of the median plane when the magnet is aligned using the reference plate. Some magnets are tilted as much as 1 mrad, which is larger than the measurement system error. The offset and the median plane data must be taken into account when aligning the magnets in the beam line.

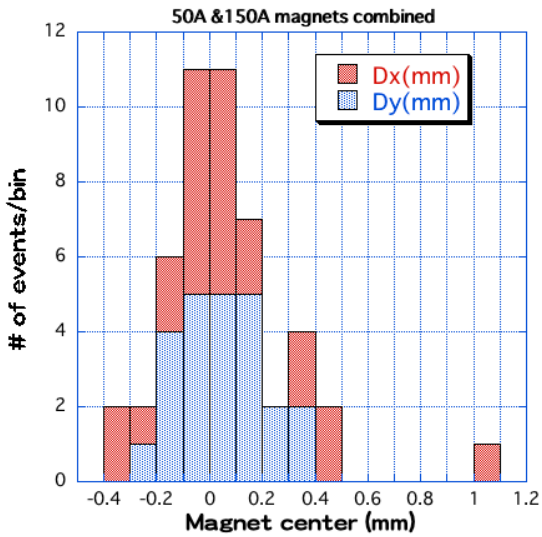

Fig. 7. Magnet center.

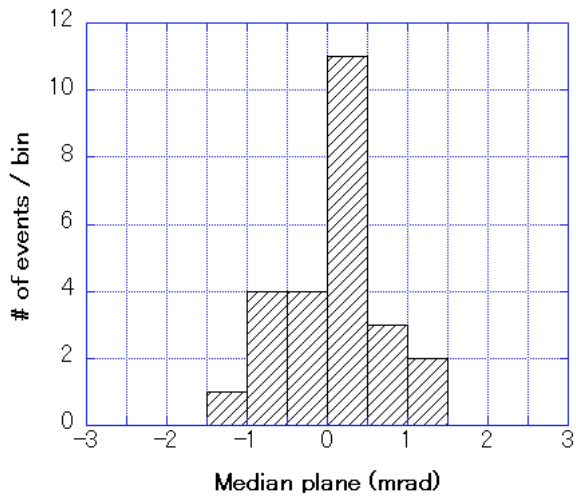

Fig. 8. Median plane distribution.

Sextupole Component

The sextupole component was measured with the bucking configuration. The magnets with shim correction, which are indicated by squares in Fig. 9. show small sextupole components. They satisfy the requirement from the optics design. Other magnets show 0.1% or larger sextupole components. Since the requirement for the sextupole component depends on the lattice position of the magnets, we can assign the magnets according to the sextupole component to a proper lattice position.

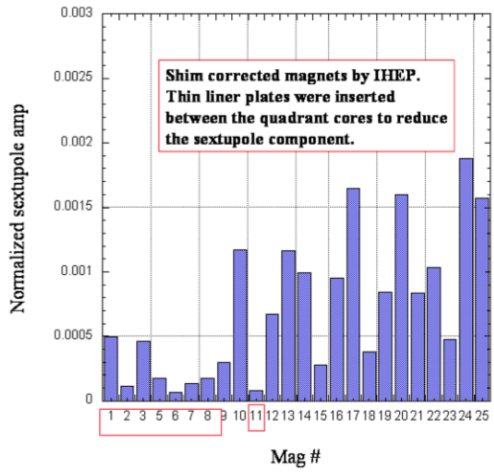

Fig. 9. Sextupole component vs magnet number.

CONCLUSIONS

The quadrupole magnets for the ATF2 extraction line have been measured at KEK using a harmonic coil system. Preliminary results from 24 QEA magnets have been presented in this report. We see a large variation in the integrated field strength, magnetic center and the median plane among the 24 magnets. The large variation of the strength is not a problem since each magnet will have its own power supply. The large offset and median plane (tilt) must be taken into account when aligning the magnets in the beamline. The reasons for the large offsets are under investigation. The sextupole components were controlled well by shim insertion performed at IHEP for some magnets. We did not require shim insertion for all of the magnets since the shimming process is time consuming.

Some more detailed analysis of the measurements will be reported somewhere else. We thank IHEP for their contributions in magnet production and measurement.

REFERENCES

[1] The ATF Group, "ATF Design and Study Report", KEK Internal 95-4, June 1995.

[2] The ATF2 Group, "ATF2 Proposal Vol.1",CERN-AB-2005-035, CLIC note 636, DESY 05-148, ILC-Asia-2005-22, JAI-2005-002,KEK Report 2005-2, SLAC-R-771,UT-ICEPP 0502.

STRUCTURES OF QUADRUPOLE MAGNET CORE

Nanyang Li, SLAC, USA , M/S18,2575 Sand Hill Rd., Menlo Park, CA 94025

Abstract

In general, there are two different quadrupole core designs: two pieces (up half and low half cores) and four pieces (four quarter halves). Both structures work on those quadrupole magnets in different accelerators around the world. There is no certain standard about which design is good for what machine, it is most likely defends on the engineer's preference and the coil size. There are advantages and disadvantages with both structures. However, the disadvantage of four pieces design is rather visible. It is the goal of this paper to study those advantages and disadvantages of two types of core structure from manufacturer's point of view and the perturbations of the magnet field.

RIGIDITY COMPARISON OF TWO STRUCTURES

Figure 1 below is the prototype of LEB, SSC quadrupole magnet which was built at LBL. Its core was built by four quarter cores and the quarter core was stacked and glued by laminations. In addition to gluing laminations together and tightening the pole by a bolt in a stacking fixture under the pressure, a tight bar was welded on the back of the core. This prototype was checked at LBL and then shipped to SSC by air. After the shipment, the gaps between the poles and the diameter of the aperture were all shifted and were out of the tolerances.

Figure 2 below is a quadrupole magnet of SPEAR3, SLAC. Its core was built by two half cores. The half core was glued by laminations as well. Rather than a tight bar, laminations were tightened by four bolts in addition to gluing laminations together and tight bolt at pole. The quadrupole magnets were built at IHEP, China and inspected and measured there and then shipped to SLAC by boat. Some of those magnets were re-measured at SLAC. The results were correspondent with what IHEP people obtained, which indicated that the quadrupole rigidity is very good and the structure of the core experienced all sorts of impact during the shipment.

These two examples mentioned above demonstrated that a two piece core is more rigid than a four piece core.

But one may notice that the coil dimension of LEB SSC quadrupole made it impossible to be installed into a two piece half core. An engineer must examine the size and the shape of the coil carefully and make sure it will be installed into the half core without trouble should a two piece core structure is selected.

Figure 1: SSC, LEB Quadrupole

Figure 2: SLAC, SPEAR3 Quadrupole

COMPARISON OF GLUED CORE AND WELDED CORE

Figure 3 below is a half core of SPEAR3 quadrupole magnet. It was glued by laminations. Figure 4 below is a half core of LER, PEPII quadrupole, it was laminated as well, but was welded as one piece by angle plate instead of gluing.

Glued Core

The first problem with a glued core is an environment issue. The workers smell epoxy directly which is different from the case of coil impregnation. The later one is processed under the vacuum. In most case, the workers do not feel comfortable to work under a strong smell working place. The second problem with a glued core is that the cleaning work after core curing is a quite involvement. The cleaning work actually can be limited when the thickness of the epoxy layer is adjusted very carefully. But it is not an easy task, if the gluing machine is old and the roller of it is not built with very tight tolerance. The third problem with a glued core is that it leaves almost no room for re-adjusting after curing if the dimension(s) shifted during the curing by some reason(s). The advantage of gluing procedure is that it will avoid from deformation caused by welding, especially for a

long core. A core longer than 750mm, usually it is difficult to control the welding deformation and its sugariness is very much rely on the skill of welder(s).

Welded Core

A welded core does not have those problems a glued core has. But it will involve solid end plates and angle plates in most cases. When an accelerator has a very tight placement, which leaves a very small room between magnets, additional solid end plate may cause problem. Also, the angle plate is a rather costly part, it will involve heating treatment, forming and machining. Sometimes, one maybe surprised by the cost of the angle plate comparing with other main components of a magnet.

An advantage of the welded core is that it can be re-adjusted almost as many times as it needed after welding until reach the tolerance requirement. A very skilled technician can pick up the right spot(s) of a welding seam based on the dimension that is out of the tolerance and hammer it (them) to release welding strength at point(s). The welding deformation will be then corrected sequentially. But this procedure involves high man skill and it can not always work if the core is very long and the deformation is big.

Figure 3: SPEAR3 Quadrupole Glued Half Core

Figure 4: PEPII LER Quadrupole Welded Half Core

Should a core be welded or glued, is a comprehensive decision. An engineer shall consider available fabrication fixture of the selected manufacturer, the environment code of the place where it located and also its workers' workmanship, allowed magnet dimension and cost, etc.

PERTURBATIONS [1]

In general, there are four factors which cause perturbations of a quadrupole magnet.

A. Excitation Error $\varepsilon_j=\Delta j/J$: caused by coil design position or fabrication and installation error or caused by length or magnetic property of half core.

B. Radial Offset $\varepsilon_{rd}=\Delta x/r$: caused by horizontal shift of the pole(s) (shown in figure 5).

C. Azimuthal Offset $\varepsilon_{az}=\Delta y/r$: caused by vertical shift of the pole(s) (shown in figure 5).

D. Pole Rotation $\varepsilon_{rot}=\Delta$Ang: pole(s) rotated (shown in figure 6).

The core assembly of four quarter structure involves three factors among those mentioned above: B. C and D. Furthermore, each pole of quarter core can be offset individually (shown in figure 7). While, a two half core structure, during the assembly can reduce the effort of adjustment of factor B, C and D significantly comparing to four piece core (shown in figure 8).

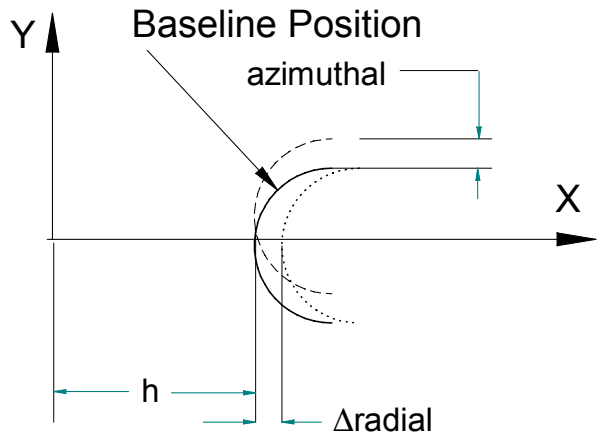

Figure 5: Case B and C

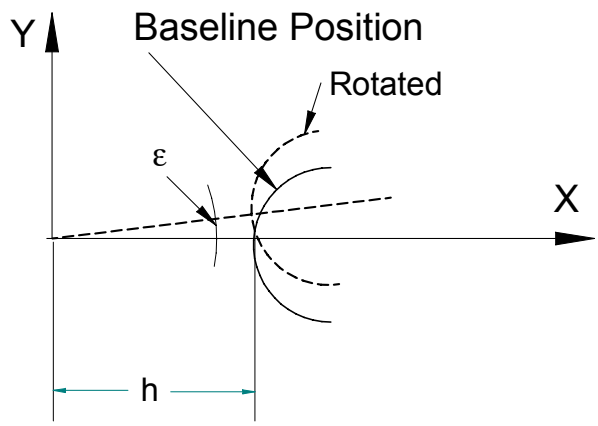

Figure 6: Case D

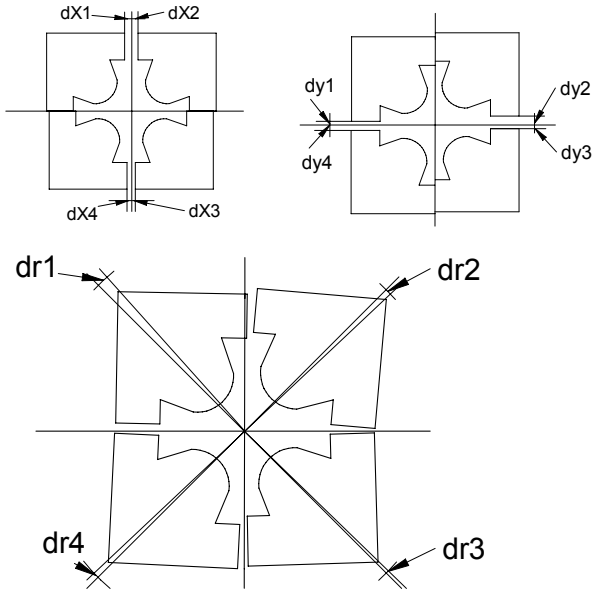

Figure 7: Four Piece Core Assembly Errors

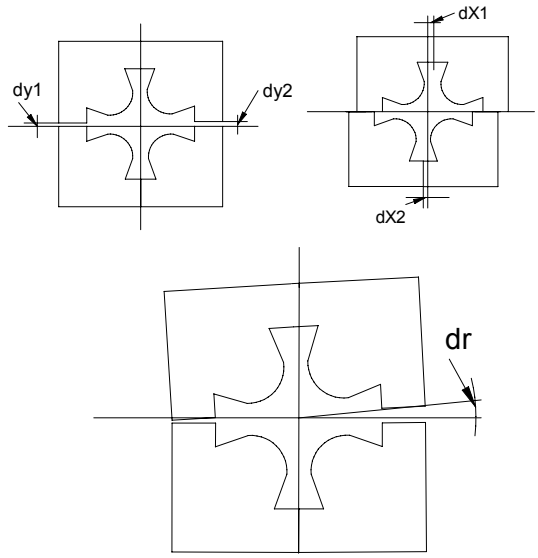

Figure 8: Two Piece Core Assembly Errors

CONCLUSIONS

Based on the discussions above, a core with two half cores shall be a first choice of an AC quadrupole magnet design. An engineer shall make the coil dimension easily install in between two poles. If the magnet shall be operated under DC current, usually, the core is built as a solid piece rather than laminated core. In this case, a four piece core is recommended, because that the machining tolerance is the direct proportion of the part dimension. A quarter half core will reduce machining cost significantly.

REFERENCES

[1] Jack T. Tanabe "Iron Dominated Electromagnets" Published by World Scientific Publishing Co. Pte. Ltd.

EFFECT OF EDDY CURRENT IN MAGNETIC LAMINATIONS ON PULSED SEPTUM MAGNET RESPONSE

R.S. Shinde#, R.K. Mishra, P. Pareek, M.M. Pandey, Vinod Gaud, S. Senthil Kumar, S. Kotaiah
Raja Ramanna Centre for Advanced Technology, Indore, Madhya Pradesh, India

Abstract

Pulsed Septum magnets have been developed for injection of 500 – 600 MeV, e beam into 2.5 GeV Storage ring (Indus-2). A Pulsed magnet system consists of a thin & thick passive type Septum magnets kept inside Vacuum Chamber & Kicker Magnets. Thin & thick septum magnets were excited using 50 μs & 100 μs half sine wave pulse respectively. A magnetic field homogeneity (ΔB/B) of the order of 10^{-3} & integrated stray fields ($\int B_{stray}.\ dl$) of nearly 0.7 Gm has been achieved.

This paper focuses on Pulse magnetization of Ni-Fe laminations; engineering challenges for septum magnets, Eddy current in lamination & their effects on pulse response of magnets.

INTRODUCTION

Injection of e beam into the Storage ring in the horizontal plane is carried out by combination of Thin & Thick Septum magnets & four kicker magnets. The Septa are used to deflect a beam coming from the transfer line-2 (TL-2) into a direction, which is parallel to that of the beam circulating in the Storage ring [1].

This method provides a smooth & continuous injection. Injection efficiency is the main requirements of the Pulsed Septum magnets. To this end we rely on the field produced by the magnet to have a maximum relative error (ΔB/B), below 10^{-3} in the useful aperture & time interval. There are several constraints on the development of these Septum magnets (Table-1). These are due to the accelerator geometry, the injection scheme and the materials used.

Table 1: Constraints on parameters of the Septum magnet

Parameters	Thin	Thick
Max. Septum Thickness (mm)	3.0	3.5
Deflection angle, degree	2	19
Magnet aperture (W X H), mm	28.5 x 10	26.5 x 10
Max. Stray magnetic field	< 2 G-m	--

In addition to the objectives & constraints, technology for development of the magnets taken into account the needs of low cost, HV insulations, Out gassing rates & easy maintenance.

#shinde@cat.ernet.in

MAGNET SYSTEM

Injection system of Indus-2 consisting of two Pulsed Septum magnets – thin & thick and Four Kicker magnets. In the injection scheme, a compensated bump (16 mm) produced by four Kicker magnets & the e beam is injected through two septum magnets. In order to minimize the thickness of septum magnets launching the e beam, thin & thick septum magnet combination has been adapted. Septum magnets are required to provide necessary deflection to the incoming beam to match the angle of the beam transfer line to the accelerator orbit. The design of such a system has to meet many requirements in order to achieve a high reliability injection operation, some of them are [2]:

(i) Septum sheet as thin as possible in order to enhance injection efficiency as septa isolates injected beam & circulating beam
(ii) High magnetic field (due to geometrical limitation)
(iii) Pulse magnetization of Ni-Fe lamination – high Pulse Permeability for stability & homogeneity of field greater than 100 ppm, high frequency response upto 100 KHz
(iv) Low out gassing rate, as magnets are to be placed in UHV environment
(v) Very low Stray fields (due to beam optics)

The magnet configuration, high pulse permeability & high Bknee on first magnetization curve of laminated yoke and Pulse power supply combinely determine the high performance of Septum magnet system

The main design criteria for the Pulsed Septum magnet are to produce Pulse magnetic field waveform with amplitude of ~ 1 T & pulse length ~ 50 μs & 100 μs. The requirement of magnetic field pulse shape for injection is half sine wave with field stability on top is of the order of (ΔB/B) ~ 1 X 10-3. As magnets have to keep inside vacuum, there are severe engineering challenges both in space & fabrications are involved [2].

PULSE MAGNETIZATION

Pulsed Septum magnets are to be operated at high field strengths, the magnetization rates (dB/dt) are involved are up to about ~ 1 T / μs & magnetization reverses in the order of μs. Also magnet performance greatly depending on magnetization of laminations. Therefore, it is necessary to know the behaviour of soft magnetic materials when its magnetization reverses in the order of μs.

The response of the magnetic field due to the time varying current in the septum coil is influenced by the

eddy current effects. The time delay and attenuation caused by eddy currents in the lamination of the yoke. This lead to inhomogenities in the field distribution.

The eddy current losses in the laminations were analytically computed [2]. Taking into account the skin effect in the thickness of the laminations has been choosen in such a way that to operate in linear region of B (H) curve & to avoid the magnetic saturation.

Pulse magnetization of Ni-Fe laminations has been measured by damping Sine B_{pulse} of first half peak of 100 μs [3,6]. Due to damped Sine wave, magnet comes into demagnetized state after every pulse. Measured pulse magnetization of Ni-Fe lamination is shown in fig1.

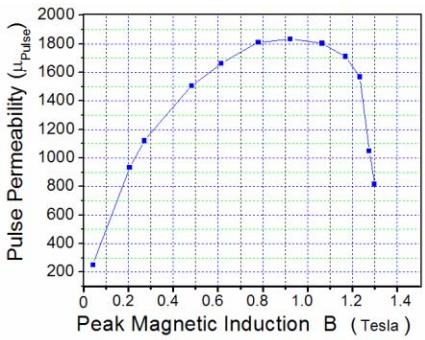

Figure 1: Pulse Magnetization Curve of Ni-Fe lamination

SEPTUM MAGNET

The magnet should produce a half sine wave field with a peak amplitude of ~ 8 KG and duration of t_d = 100 μs from zero field to zero field in the "inside" region. The stray field outside the septum edge should be < 2 G-m. At present time, the total septum thickness is 3 mm (Cu+Fe). The thickness of the lamination in the yoke is 0.1 mm. The stray field on the outside surface of the septum is calculated from [4],

$$B_{stray} = (2\sqrt{2}\tau / \sqrt{\pi e}\,\lambda_c d\sigma\mu_o)\,Bo \qquad (1)$$

Where, Bo is the amplitude of main field, τ is the pulse width of excited current, λ_c is the characteristics length of stray field decay outside the septum, d is the average thickness of septum, σ & μ_o are electric conductivity & magnetic permeability of the septum material respectively.

The time change curve of the stray field is analyzed using Flux-2D. In order to reduce the stray field further, a mu-metal shield of 1 mm thickness is placed along septum conductor. The mu metal has high magnetic permeability, which shield the stray field greatly.

The simulation results show that the stray field in front of the septum is much less than 0.1% at any position & at any time.

CONSTRUCTION

Thin & Thick septum magnets, being of Pulsed type, are constructed with laminated yoke. There are two issues considered carefully:

(i) Eddy current losses in Ni-Fe lamination. In order to reduce these losses, the core is made of 0.1 mm thick Ni-Fe lamination (36 % Ni). These laminations are annealed & then oxidized to get 10 μm oxidation thickness on both sides, which leads improvement in field quality.

(ii) The out gassing properties & the radiation resistance of the insulation material of the core and coil are crucial to the construction of the septum magnets.

The septum coil is made of Oxygen Free Copper Conductor & is insulated with Alumina by detonation process [1,6].

The cross section of the septum magnet is shown in fig 2.

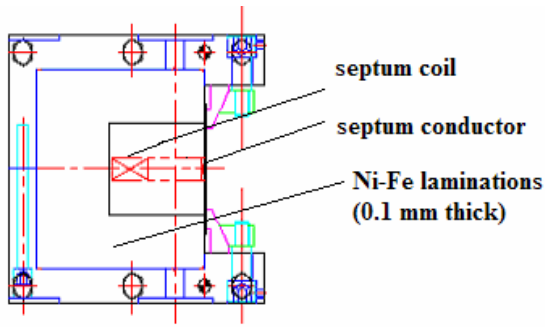

Figure 2: Cross sectional view of septum magnet

Table 2: Main Parameters of Septum magnet (600 MeV)

Parameters	Thin Septum	Thick Septum
1. Maximum Pulse magnetic field	4.190 KG	7.720 KG
2. Radius of Curvature	7162 mm	2594 mm
3. Deflection angle	2 °	19 °
4. Effective magnet length	250 mm	860 mm
5. Magnetic field Pulse shape	Half sine wave (50 μs)	Half sine wave (100 μs)
6. Effective Septum thickness	3 mm	3.50 mm
7. Maximum Exciting Current (Amp.)	3330	6140
8. Magnetic field homogeneity, (ΔB/B)	~ 5 x 10^{-4}	~ 5 x 10^{-4}

MAGNETIC PERFORMANCE

The main and stray magnetic fields are measured with integrated coil was realized with a strip of double sided PCBs & point coils. A 3-axis magnet measuring system was developed for pulsed field mapping. Magnetic field homogeneity with 100 ppm accuracy was measured using 16-bit digitizer system [5].

A Pulsed field homogeneity for thin & thick septum magnet is shown in figure 3 [6].

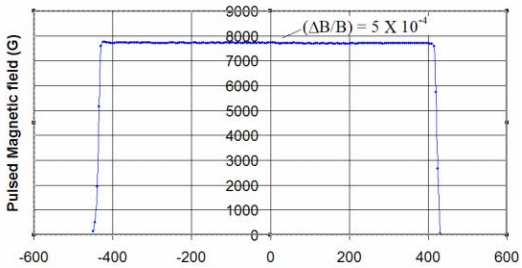

X (mm) - Along Beam direction (Thick Septum Magnet)

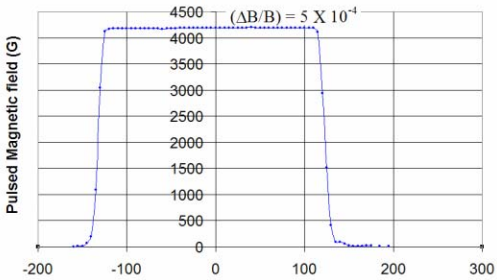

X (mm) - Along Beam direction (Thin Septum Magnet)

Figure 3: Pulsed field homogeneity for thin & thick septum magnet

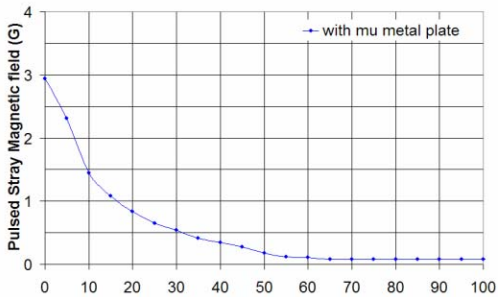

Distance from the Septum (in mm)

Figure 4: Distribution of stray field outside of the septum

The stray field at the edge of the septum to the outside region where circulating beam travels is shown in fig 4.

The distribution of stray field outside the septum, after adopting the measures of the magnetic screen, the maximum of the stray field is reduced down to 0.05% of the peak main field. The measured waveforms of stray field agree with the simulation results.

RESULTS & CONCLUSIONS

FEA, Flux-2D has successfully used to stimulate the Pulsed field of septum with & without magnetic screens. The simulated waveform of the stray field is similar to that of practically observed. The maximum stray field on the bump orbit is about 0.3 % of the peak of its main field. In order to reduce stray field further, a mu metal – magnetic screen was used. The effective thickness of the septum at the exist of the magnet controlled within 3.5 mm. The maximum stray field of 0.7 G-m was observed, which is less than the allowed 2 G-m value. The measured waveform of main & stray fields after magnetic screen is shown in figure 5 [2, 6].

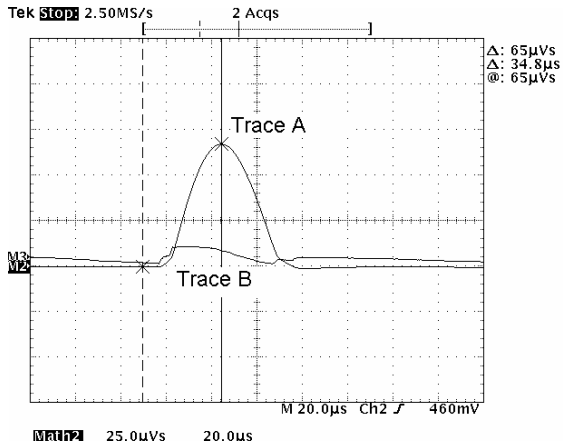

Figure 5: Integrated magnetic field along the e beam direction

Trace A: Main Pulsed Magnetic Field waveform
Trace B: Stray Magnetic Field waveform

ACKNOWLEDGEMENTS

The authors would like to thank Shri. S. Kotaiah, PM (Indus-2) & Shri. A.K. Jain, Head, ACEFD for their kind guidance, Scientific & Technical discussion during development of magnets. We indebted to thank Shri.Gurnam Singh, Head IOAPDD for Scientific discussion & encouragement. We are also greatful to Shri. Kelkar, Barothiya & Raikwar for Power Supply development. We express great thanks to Shri. R.R. Yadav & Karan Singh for Pulsed magnetic measurements of laminations & magnets. It is great pleasure to thank Shri. Shiv bachan & Lalchand Ghongde for magnet assemblies & installation into Indus-2 ring. A special thanks goes to Shri. L.V. Thorat, who made the 3-D drawings of Septum magnets.

REFERENCES

[1] R.K. Mishra, etal., "Proposed design report of Pulsed Septum Magnets for Indus-2 Ring", CAT Internal Report, May 2000.
[2] K.D. Metzmecher, "Technical discussion on Pulsed Magnets", at CERN, November 2001.
[3] R.S. Shinde, P. Pareek, V. Gaud, etal., "Pulsed Magnetization in Ni-Fe lamination – Measurements & Analysis", CAT Internal Report, October 2003.
[4] W.Kang, etal., "Development of eddy current Septum for the SSRF Storage ring", APAC 2001, Beijing, China.
[5] S.Kotaiah, etal., "Present Status of Synchrotron Radiation Source Indus-2", InPAC 2005, Kolkatta.
[6] R.S. Shinde, V.Gaud, etal., "Technical report on Pulsed Magnetic Measurements of Septum magnets" of Indus-2", CAT Report – FL, October 2005.

MECHANICAL STABILITY OF OPEN-TYPE QUADRUPOLE MAGNETS FOR A 2.5 GeV SRS (INDUS-2)*

K.Sreeramulu#, S. Das, Kailash Ruwali, M.G. Karmarkar, S.Kotaiah, P.K.Kulshreshta,
Raja Ramanna Centre for Advanced Technology, Indore, India
M.K.Ghosh, Banaras Hindu University, Varanasi, India

Abstract

The open type Quadrupole magnets (max. gradient: 16 T/m) for 2.5 GeV Indus-2 are made in C-configuration in which both of outer vertical sections of the steel are removed to take out the emerging synchrotron beam (SR) lines, in the region immediately adjacent to main dipole magnets of the ring. This induces engineering complexity relating to mechanical stability that critically controls the deviations in magnetic centre and field quality. To meet the stringent field quality requirements, the mechanical structure, which is precisely holding the magnet poles, is designed for minimum deflection at maximum gradient. The magnet is simulated with coupled magneto-structural analysis, using ANSYS. The measurement of deformation in prototype magnet assemblies with maximum excitation current is carried out and found within the acceptable limit. Measured magnetic centre shift with excitation is within 0.02mm. The magnetic measurement results show that the higher order multipoles are low and not changing with excitation current. The optimised open-type Quadrupole magnet design is implemented in series production of all 32 magnets for Indus-2. The mechanical assembly accuracies and stability of magnets with measurement results are discussed in this paper.

INTRODUCTION

The quadrupole magnets for Indus-2 are slowly ramped magnets (from 3.84 T/m to 16 T/m in 300 seconds). The main magnet design parameters are shown in Table 1. There are five families (Figure 1) in which Q1, Q2, Q5 families are of close type and Q3 (defocusing), Q4 (focusing) are of open type. The physical design of Indus-2 open-type quadrupole magnet is done using 2D POISSON group of magnet design codes [1]. Figure 2 shows 1/4th cross-section of the open type quadrupole

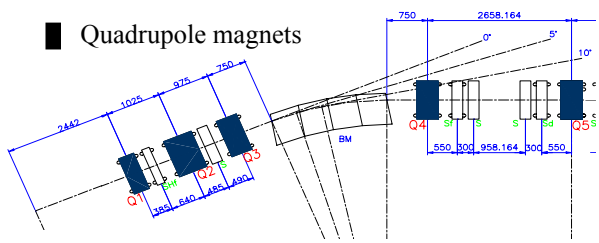

Figure 1: Half unit cell of Indus-2.

*Work supported by RRCAT, Department of Atomic Energy, India
#sreeram@cat.ernet.in

magnet. The design of Q4 magnet is a non-conventional 'open-sided' design, with upper and lower pole pairs not connected magnetically to take-out the emerging SR beam lines, which are located in the main dipole magnets of the ring and also to maintain symmetry. The design of

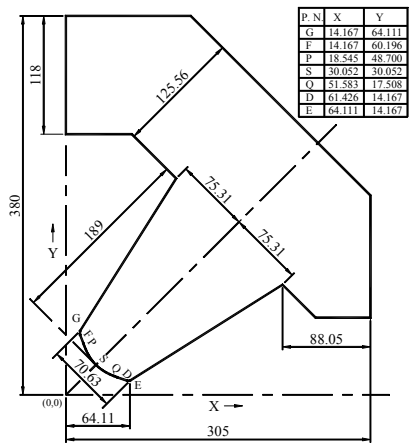

Figure.2: Magnet lamination (1/4th).

Q3 magnet is also kept same except supports at RHS (figures 4) to have symmetry in ring.

Table 1: Magnet Design Parameters.

Description	**Unit**	**Values**
Pole aperture diameter	mm	85
Steel & magnetic lengths	mm	362.50&400
Ampere turns/pole	AT	13,000
Good field region	mm	X=± 32, Z= ±17
Good field region field errors	Δk/k	± 1 x 10^{-4}
Allowed centre shift	mm	δX = δY ≤ 0.03
Allowed gradient errors over good field region		

c_1l/c_2l	c_3l/c_2l	c_4l/c_2l	c_5l/c_2l	c_6l/c_2l	c_7l/c_2l
2.35E-4	8.59E-4	1.33E-3	5.34 E-4	5.07 E-4	1.65 E-3

Where $c_n = \sqrt{(a_n^2 + b_n^2)}$ and a_n, b_n are skew and normal components for 2n-pole fields.

MECHANICAL DESIGN OF MAGNET

The magnet is an assembly of four laminated stacks in order to accommodate the required number of excitation coil turns in each pole. The design of mechanical assembly structure for holding four laminated poles is done after estimating the amount of magnetic forces from

2-D electromagnetic static analysis with magnetic vector potential (MVP) formulation using ANSYS1[2] and also consideration of gravity load of the magnet.

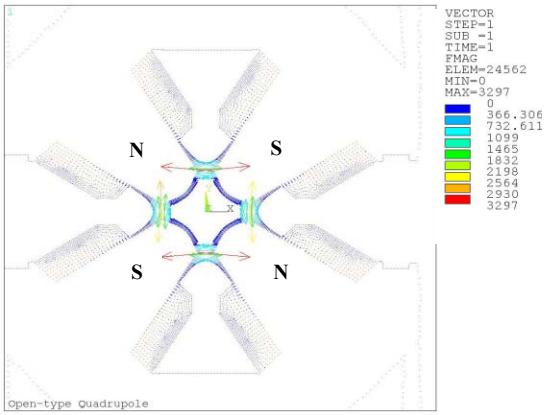

Figure 3: 2D-Magnetic nodal forces on poles in N/m.

The pulling force between top and bottom poles found from 2-D analysis is 39315 N/m. Considering the magnetic length of 0.4 m, the attractive force between the poles is 15726 N and the estimated weight of the magnet as 12,000 N. As the field uniformity of magnet is very much dependent on its geometry (pole geometry imperfection must be kept < 0.1mm from its ideal geometry), the sizing of various components for initial design of magnet assembly structure is done by considering the above mentioned forces and limiting the allowed deformation (0.01 – 0.02 mm) on critical magnet assembly components as per their functional importance. Therefore, the permissible stress level in various magnet components would be much below the proof stress of the material. The material for main assembly structural components is taken as nonmagnetic. The initial mechanical design of magnet assembly structure is further simulated with 3D magneto-structural analysis.

3-D magneto-structural analysis

The mechanical support structure of Q4 magnet is slightly weak (figure 5 - a C-clamp is asymmetrically placed on RH side due to space constraints) as compared to Q3 magnet. Therefore, Q4 magnet is taken for analysis and a 3D finite element model is made for sequentially coupled field static magneto-structural analysis using SOLID5 brick (eight nodded) elements. Scalar potential formulation is used for static magnetic analysis. SOURC36 elements are used to model racetrack coils. The vertical pulling force acting on the poles found from 3D- magnetic analysis is 15340 N. After the static magnetic analysis, structural analysis is carried out by directly imposing the magnetic forces from the static magnetic analysis. The gravity load is also applied at the centre of the FE modal during structural analysis. The $E_{lamination}$ (along magnet length) is taken as $E_{steel}/60$ [3] i.e. the properties on the magnet core is considered as orthotropic.

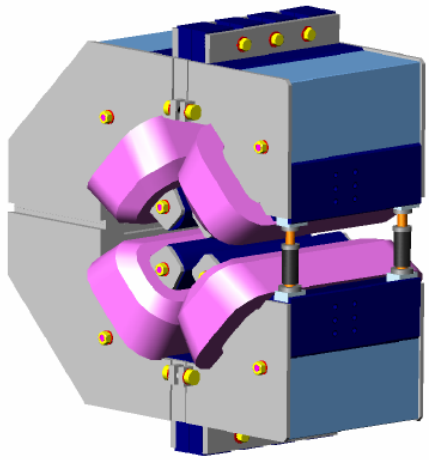

Figure 4: Open-type quadrupole (Q3) magnet.

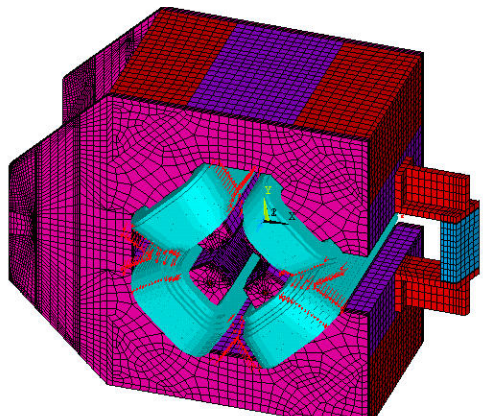

Figure 5: FE model of Q4 magnet (air region not shown).

The analysis shows that without any C-clamp or spacers at RH side of the magnet, under load, the top pole (in 1st quadrant of figure 5) displaced vertically downwards by ~ 0.1mm and horizontally by ~ 0.04 mm, which is not acceptable. The structural analysis with C-clamp shows (figure 6) the vertical displacement of 1st quadrant pole tip under load in the range of 0.020-0.025mm, which is quite acceptable. The horizontal displacement is found negligible (not shown).

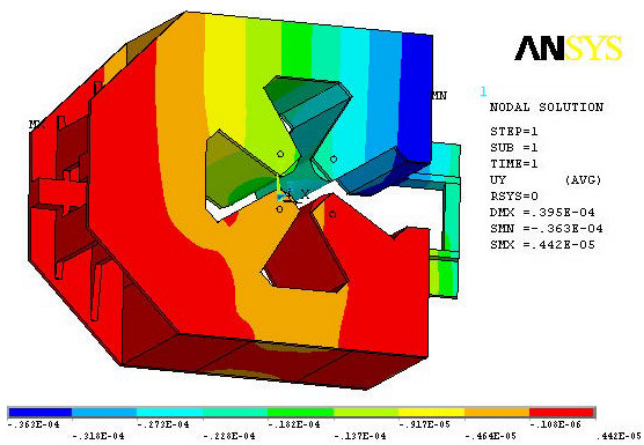

Figure 6: Vertical displacement plot of Q4 magnet.

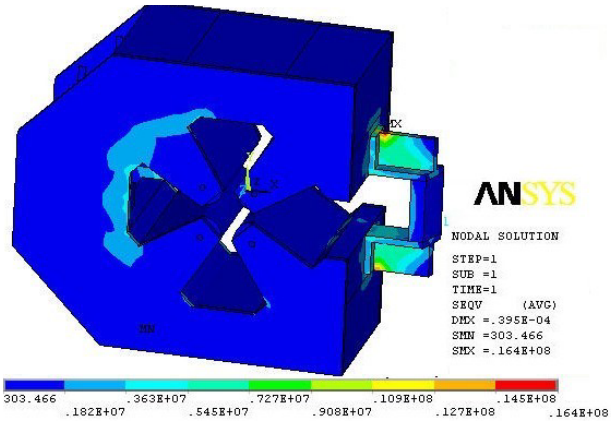

Figure 7: Stress plot of Q4 magnet.

Figure 7 shows the stress level in the structure which is found max. 16.4 MPa on C -clamp.

PROTOTYPES & CHARACTERISATION

Two prototype laminated cores (Q3 and Q4 types) are made by hybrid methods of laser cutting / wire-EDM and excitation coils from 7 x 7 x ϕ5 mm OFHC copper conductor [4]. The magnet assembly tolerances (on pole aperture diameter, angular spacing of poles) are maintained within in ± 0.05mm. The magnets are initially powered at rated excitation currents and measured the vertical displacement of core with precise mechanical dial gauges by placing them on outer surfaces of magnet core. The measured vertical displacement is found 0.04mm in the outer location (top edge), which is in good agreement with the 3D-ANSYS result (0.036 mm as shown in figure 6). The prototype magnets are tested using a rotating coil harmonic bench model 692 (Danfysik). The magnet is initially aligned with the magnetic centre at the operating gradient (16 T/m) and measured the changes in magnetic centre at injection to maximum operating currents (beam energies). Figure 8 shows the higher order harmonics present in Q3 and Q4 type magnets at 0.6 GeV and $c_n l/c_2 l$ does not change with various beam energies.

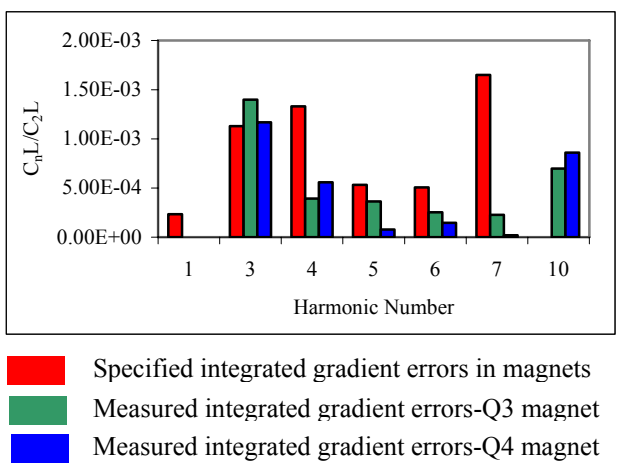

Figure 8: Higher order multipoles in Q3 and Q4 magnets.

Figure 9 and 10 show the magnetic centre shift of Q3 and Q4 types at various beam energies. Also, the opening and closing exercise on prototype magnets has been done few times for assembly of vacuum chambers and retested the magnets. We found that the magnetic centre is repeated within 0.02mm and also the multipole pattern does not change with opening and closing of magnets.

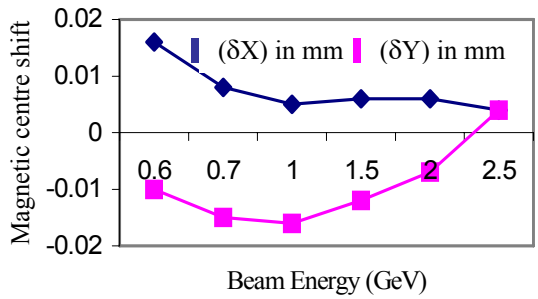

Figure 9: Magnetic centre shift of Q3 magnet.

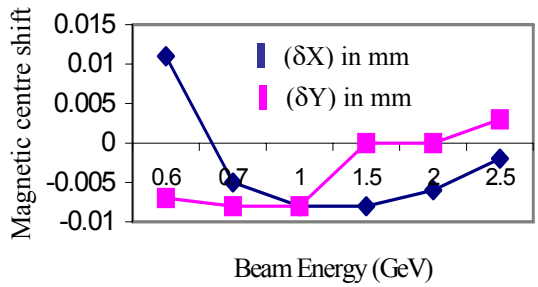

Figure 10: Magnetic centre shift of Q4 magnet.

Therefore, the same mechanical design is implemented in all series production of 32 units of magnets. We have magnetically characterized all the magnets after fabrication and are found acceptable.

CONCLUSIONS

The mechanical design of the assembly structure is rigid enough to satisfy the magnet design requirements. Repeatability of magnet is achieved during opening and closing of magnets for installation of vacuum chambers.

ACKNOWLEDGMENT

We acknowledge the efforts of M/s. CMTI, Bangalore for manufacturing of series magnet cores and M/s. D&S Electric works, Indore for completion of magnet coils.

REFERENCES

[1] Kailash Ruwali et.al, "Quadrupole magnets for Indus-2", MT'18, Japan, Nov. 2003.
[2] ANSYS Inc. ISO 9001:2000 company.
[3] Jack T. Tanabe, "Iron dominated magnets", World Scientific Publishing Co., 2005.
[4] Sreeramulu konjeti et.al, "Development & production of open-type Quadrupole magnets with advanced techniques for a 2.5 GeV SRS at CAT," MT'18, Japan, Nov. 2003.

PERFORMANCE OF 6MW PEAK, 25 KW AVERAGE POWER MICROWAVE SYSTEM FOR 10MEV, 10KW ELECTRON LINAC

Purushottam Shrivastava#, Jaikishan Mulchandani, Y. Wahnmode, P. Mohania
Pulsed High Power Microwave Section, Raja Ramanna Centre for Advanced Technology, RRCAT, Indore, India

Abstract

An S-Band microwave system with peak power capability of 6MW and average power capability of 25 kW was designed, constructed and commissioned at RRCAT. The in-house development of various microwave technologies and pulse modulator technologies was successfully achieved and the microwave system was interfaced to the 10MeV, 10kW electron LINAC. The electron LINAC could be tested to full rated energy and power using the present microwave system. The present paper highlights the details of the performance results.

INTRODUCTION

The microwave system for 10MeV, 10kW average beam power LINAC was designed and developed indigenously.

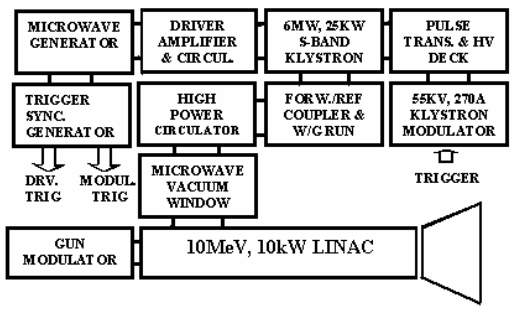

Figure 1: Schematic of 6MW S-band microwave system.

Table (1) shows the specifications of the Microwave system. The klystron needs 50-55kV, 270-300Amp beam voltage pulse to achieve the rated output power. The klystron modulator has been designed to give output pulse voltage of 15 microsec duration see fig 2.The specifications of the klystron modulator are listed in table (2). The klystron modulator and pulse transformer are designed to supply also the gun voltage up to 50kV. Challenging work on the technologies like droop compensation hyperboloidal tuneable pulse forming network, fast rise time long pulse high average power pulse transformer, pulse voltage and current measurement systems, short circuit protection, optically triggered command charging system, solid state trigger drives for thyratron, high voltage power supplies with fault protection systems which were developed in-house have performed to expectations.

#purushri@cat.ernet.in

Table 1: Microwave System Specifications Achieved

Peak o/p power	MW	6
Average o/p power	kW	25
Operating frequency	MHz	2856
Pulse duration	microsec	13/7
Pulse repetition rate	Hz	1-300
Pulse rise time	microsec	<2
Pulse top variation	%	<1
Pulse-pulse stability	%	<1
Frequency stability	/day / °C	$1X10^{-8}$ $1X10^{-8}$

Table 2: Modulator Specifications Achieved

Pulse output power	MW	15
Pulse voltage output	kV	50
Output impedance	Ω	180
Pulse duration	microsec	15
Rise time	microsec	~2
Fall time	microsec	<2
Flat top variation	%	< ±1
Mean output power	kW	70

SYSTEM DETAILS

The microwave system consists of a stabilized signal generator, circulator, 200W solid state microwave amplifier driver, circulator, directional coupler, 6MW klystron amplifier and waveguide system. The power from the signal generator is amplified up to 200W by the driver amplifier, which in turn is fed to a 6MW klystron. The power from the klystron is fed to the accelerator by means of a dual directional coupler, flexible waveguide, waveguide pressurizing system, circulator, dual directional coupler and vacuum ceramic window see fig. (1). The klystron modulator is line type construction see fig. 2. A high voltage regulated dc power supply rated for 16kV, 6 amp continuous duty with regulation better than 0.5% has been built for charging the pulse-forming network. An air core charging inductor with RC damping for high frequency ringing, occurring due to parasitic components, has been used. A command charging thyratron placed on a floating deck is triggered by an optical isolated triggering system. The necessary power to the trigger supplies, filament and reservoir is supplied by means of a high voltage isolation transformer. Pulse forming line consists of 16 sections Gullemin E type network in which the number of cells can be selected for desired pulse width from the modulator.

A shunt diode fault circuit protects the components from mismatched loads or load short circuit/arcing. The pulse-forming network is discharged through a high voltage high power thyratron, which is triggered by

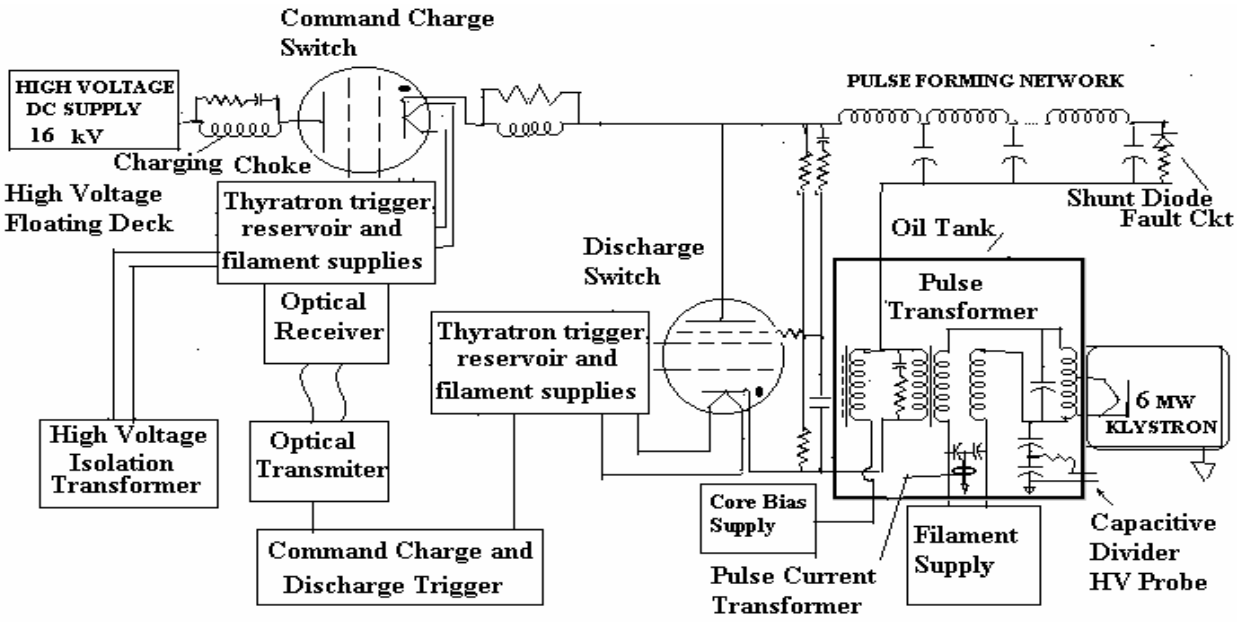

Figure 2: Schematic of the high power long pulse klystron modulator with command charging and pulse parameter measurement system.

means of a solid-state trigger drive. Cooling module as well as the gradient grid circuit for the discharge thyratron has been developed in-house. Sufficient care has been taken for reducing the parasitic components as well EMI, which is proven by the final test results of the modulator. Pulse transformer is oil insulated provided with water-cooling for high average power and thermal considerations. It is a 1:4 turns ratio, 2 mil CRGO ribbon core based transformer and has provision to provide the filament power to the klystron as well as the electron gun. Innovative design and fabrication techniques have been incorporated based on the previous experience to retain the good pulse characteristics. Separate windings on the secondary have been included to provide the gun voltage to the LINAC gun. The grid voltage for LINAC gun is tapped from the beam voltage pulse of the klystron.

Figure 3: Left - Klystron modulator showing discharge thyratron with associated supplies, command charge thyratron above the main thyratron. Middle- Tuneable Pulse Forming network Right up- klystron assembly on high voltage deck. Right lower- waveguide system connected to LINAC input.

PERFORMANCE DESCRIPTION

Operation Details

The Microwave system has been satisfactorily operating since more than 2 years with the rated specifications to deliver power to 10MeV Linac. During the period the system has been operated at different power levels up to 10kW for commissioning, qualification & radiation experiments for a total of 800 hrs. The Linac operation hours are over of ~600hrs. The microwave system has been operated for ~20 hrs. at max. Output power of 25kW and with Linac its recorded time is 15 hrs. for Linac mean beam power output of 9-10 kW.

Output performance

The beam pulse shape obtained is good & stability is within 1%. Initially the rise time of the cathode pulse was less than 1us. Later the gun cathode voltage at 50 kV was also supplied from the klystron along with grid voltage

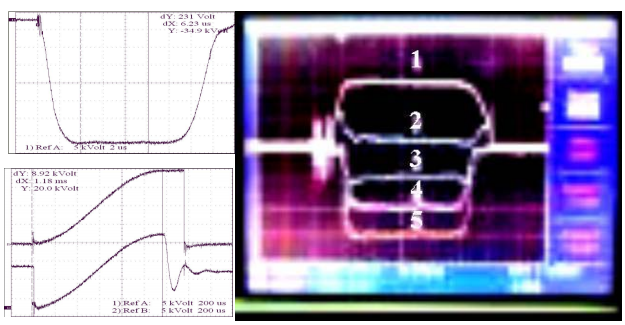

Figure 4: Left upper: Output of the klystron beam voltage @50kV, 2.5 µs/div loaded with LINAC gun and klystron, probe ratio is 1:1.47. Left lower: waveforms with command charging before and after charging diodes. Right- Traces from top 1) Forward power Pulse at 6MW peak. 2) Reflected power Pulse at 100kW in flat region. 3) & 4) Beam currents at first and second collecting electrodes 5) Total beam current @ 300mA. Horizontal scale @2.5 µs/div.

from a divider network. With this load the rise time has increased to 2us after tuning of the modulator for pulse top. The pulse top variations including the droop are less than ±1%. Fig (4) shows the cathode Pulse of klystron as measured from divider circuit, the measured microwave Forward/reflected power & Beam current pulses are shown.

Table 3: Interlocks & Limits Provided in the System

Interlock/Limit	Protection/value
Over voltage, overload, Transformer oil level/temperature, & Output short circuit Interlocks	To protect High voltage DC supply
Cooling water, vacuum, Waveguide gas pressure & Arcing interlocks / Pulse repetition & high voltage DC limit	For protection of Klystron / PRR 275Hz & High voltage limit 12kVDC
Air/water Cooling interlock	For protection of Thyratron/ klystron
Air changer, Door timer & Search 'N' Scram interlocks & Emergency stop switches	For personnel safety
Vacuum & beam scanner interlock	For Linac protection

Solid-state microwave driver amplifier

The solid-state microwave driver amplifier with capability upto 200 W output power was developed and interfaced with the klystron. At maximum gain of klystron with 50kV anode voltage the drive needed was only upto 30 W but at reduced anode voltages higher power from driver was required to be fed. The driver has worked satisfactorily.

Difficulties & Modifications

During the High Power operations of 10 MeV Linac with 6MW Peak power Microwave system a few of difficulties & breakdowns were faced. Initially during the time of arcing in Linac Gun, Pulse Forming Network capacitors leaked. These Capacitors are subjected to high mechanical stress during high power discharge and being plastic cased, they leaked during breakdown in Gun. All the capacitors were replaced & Pulse forming network was retuned. To overcome this loading problem of Pulse Forming Capacitors during any arcing inside the Gun, necessary circuit modifications were done to limit the short circuit current inside the Gun.

The connecting cable of Linac Gun was damaged partly during the time of arcing in Gun. Replacement of cable was difficult due to its narrow passage from Pulse transformer room to Linac room & requiring dismantling of waveguide line also. To overcome the problem Grid energising circuit was transferred near to Linac Gun.

The transformer to supply filament current to klystron Gun malfunctioned as its primary insulation failed during long heat run. The reason was found to be degradation of insulation over prolonged heat cycles. Filament transformer has been replaced with a taking into account the extra margins in and is kept dipped in oil inside the pulse transformer tank for with better cooling .

Besides these modifications extra interlocks & limits have been provided for protection of microwave system as well as Linac. Those include Beam Scanner & vacuum interlock to safeguard Linac, Pulse repetition & High voltage DC limit for Klystron safe operation. The complete list of Interlocks & Limits is shown in table (4) which stand for the safety of system & personnel.

CONCLUSION

The microwave system has been operated over long heat runs to produce 6MW peak and 25 kW mean power at 2856 MHz. Several modifications and upgrades resulted in higher reliability and reduced turn down time.

REFERENCES

[1] Purushottam Shrivastava, et.al., "Development of Indigenous 15MW peak 90kW average power Klystron Pulse Modulator and related technologies for 10MeV,10kW Industrial electron LINAC", Proceedings of InPAC 2005, RRCAT, Indore.

[2] Purushottam Shrivastava, et.al., "Development of 6MW Peak High Average Power Pulsed S-Band Microwave Source for 10MeV, 10kW LINAC", Proceedings of InPAC 2003, CAT, Indore.

[3] Purushottam Shrivastava, et.al., "Performance of 5MW Microwave system for 20MeV Pre-injector Microtron for INDUS-I SRS", Proceedings APAC 2001,Sept 17-21, 2001, Beijing, China.

MEDIAN PLANE MAGNETIC FIELD MAPPING FOR SUPER CONDUCTING CYCLOTRON (SCC) IN VECC

Anindya Roy#, Tanushyam Bhattacharjee, N. Chaddha, R. B. Bhole, M. K. Dey, J. Debnath, U. Bhunia, J. Pradhan, S. Paul, A. Dutta, Z.A. Naser, C. Nandi, G. Pal, C. Mallik, Sarbajit Pal
Variable Energy Cyclotron Centre, DAE, 1/AF Bidhannagar, Kolkata 700 064,

Abstract

The magnetic field at median plane of SCC Magnet (Peak field 5.8T) is measured over its operating range and upto 29 inch radius. The magnetic field is mapped at radial interval of 0.1 inch and angular interval of 1 degree. The complete map of 360 degree comprised of about 100K field points is obtained in less than 100 minutes. The field mapping system (MFM) is designed to minimise mapping time and human intervention. The control & data acquisition (DAQ) software (s/w) is developed to work as PC based TCP Client-Server mode to reduce the design complexity, system overload and debugging effort. The Server program is developed as windows console in 'C' and the Client is developed using LabView to provide a user friendly operation console along with online preliminary display and analysis of field data. This architecture provides a reliable and easily modifiable control s/w. The correctness of the magnet assembly is calculated from the acquired data, which in-turn represents the correctness of measurement system. A detailed study of the magnet characteristic is done. The first harmonics of the fields at different radii are obtained at all magnet excitation and corrected by coil-centering and shims placement. This paper also describes the major activities made during field mapping.

INTRODUCTION

The Magnetic Field Mapping (MFM) system comprises of a hardware system and a control & data acquisition software [1]. A search coil and Digital integrator combination are used to measure the difference in field between the center and any other point of the magnet [2]. The schematic diagram of the system is shown in Fig 1.

MFM DAQ HARDWARE

The hardware system consists of MFM jig, NMR Gauss meter, Digital integrator, DAQ Server PC and Client GUI PC. The MFM jig comprises of a centrally supported search-coil carrying arm, two Animatics smart motors, an angular encoder and a linear encoder. The schematic diagram of the jig is shown in Fig 2.

The radial movement range of the search coil is 29inch. An optical encoder system of 360 LPI was used to measure the search coil position. The angular position of the search coil carrying arm is measured by absolute rotary Inductosyn encoder (256/2 pole, 128/1 speed, 8.15 inch stator O.D.) associated with two dual channel preamplifier (219200) and AWICS converter board

#r_ani@veccal.ernet.in

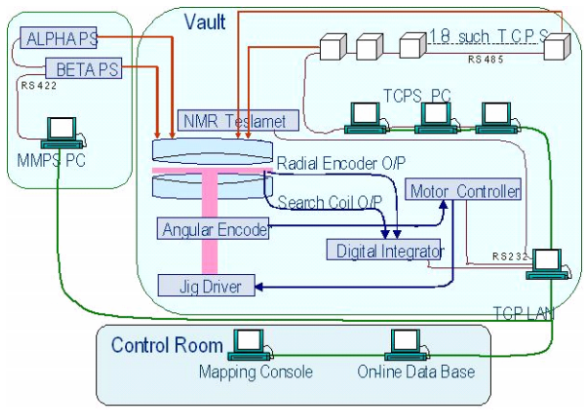

Fig 1: The schematic diagram of the system

(220500). A microcontroller based interface module was developed in house to read the angular position from the AWICS board online. The accuracy of the system was 1.7arc Sec.

The Measurement PC is placed at vault near the main magnet and connected by serial links with digital integrator, NMR Gauss meter, angular encoder and two smart motors. The Console PC is placed at the main control room. Both PCs are connected to the dedicated

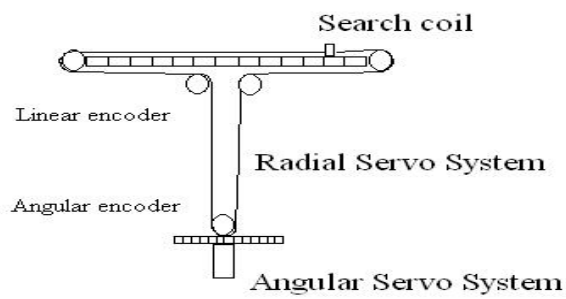

Fig 2: The schematic diagram of the jig

control LAN commissioned at Super-conducting cyclotron (SCC) building.

MFM DAQ SOFTWARE

The control & data acquisition software is designed in two independent modules i.e. Server Controller (SC) module and Client Graphical User Interface (GUI) module, to achieve distributed architecture, reduce system overhead, development and debugging effort. These two software modules incorporate the following features to satisfy the auto/manual mode of operation, minimum

human interventions and minimum measurement time requirement of the system.

- Multi-threaded architecture
- Faithful communication, control and acquisition of data from the individual hardware modules, i.e. Digital integrator, NMR Gauss meter, Smart motors and Angular encoder.
- User-friendly graphical interface for full remote control and monitoring of the MFM system from the SCC main control room in Auto/Manual mode.
- Generation of warning/error messages for unacceptable events during mapping
- Acquisition, display and storage of other sub-systems data.
- On-line analysis of the acquired data.

DAQ Server Controller Software

The server s/w, designed to communicate with Client gui having a predefined IP address in Ethernet TCP/IP protocol to prevent unauthorized access, developed in C using Windows API performs following three tasks simultaneously.

- Receive command from Client GUI and decode the command to invoke appropriate job.
- Execute one of the jobs. i.e. initialization of the system, radial data acquisition, setting azimuthal position and reading NMR gauss meter.
- Execute a watchdog timer independently to monitor any unacceptable event and notify Client GUI.

DAQ Client GUI Software

The Client GUI module developed in LabVIEW 6.1, enables users to control the complete process of field mapping comprises of acquiring, storing and on/off-line analysis of the data. This software performs following three tasks simultaneously [3].

- Communication with SC s/w for automatic and manual mode of operation, control and monitoring the MFM procedure and field data acquisition and storing.
- Transaction with a centralized Oracle Database server to read and display different subsystem parameters to ensure the magnetic field during the mapping.
- Online 2D visualization of the acquired field data for comparing the actual and theoretical profile the magnetic field.
- Offline Fourier analysis of MFM data stored in database for the analysis of azimuthal field modulation.

DAQ ACTIVITIES

The Magnetic field mapping of SCC magnet comprises of the following activities.

- The starting point of the search coil over radial movement is fixed at -1.28 inch beyond centre for reproducibility check of the measured data. This requires precise positioning of the optical scale of the encoder with respect to optical limit switches placed on the radial arm.
- The tuning of fine and coarse preamplifier of the angular encoder is repeated to reduce measurement error introduced by fringe field effect during the higher values of coil excitation. The tuning requirement was reduced for different coil excitation after providing proper magnetic shielding on encoder signal processing electronic modules. To maximize the accuracy, repetitive adjustment of phase and frequency of angular encoder system was done after installation of the jig inside SCC magnet and placement of associated electronics at vault.
- The digital integrator was adjusted repeatedly for various field magnitudes to optimize the gain and offset error value.
- The search coil (height 0.72 inch and o.d. 1 inch, 20,000 turns of 40 SWG wire [1]) and digital integrator assembly was calibrated by moving the search coil from centre and RF centre and measuring difference of the magnetic field by NMR gauss meter between these two points. The calibration factor was 0.4766 mGauss/ 10-8 volt-sec of digital integrator.

RESULT

Extensive magnetic field mapping has been carried out at different main coil excitations. The median plane magnetic field distribution is three-fold symmetry dominated due to three-sector geometry of the cyclotron. Deviation from perfectly three-fold symmetry arises out of manufacturing tolerances and assembly errors. The goal was to reduce the error harmonics to manageable proportions at the important places by adding iron shims, especially the 1st harmonics at the extraction region. The data analysis comprises of the following major activities: (i) processing of the measured raw data, (ii) reproducibility check up, (iii) finding the magnetic symmetry axis by minimization of second harmonic component, (iv) correction of average iron field distribution by adding iron shims and (v) minimization of first harmonic component by shimming of iron, which are completed successfully.

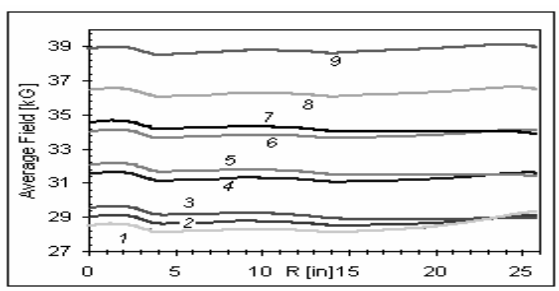

Fig 3: Average field for following main coil excitations (I_{alpha}, I_{beta}). 1: (475, 175), 2: (425, 225), 3: (375, 275), 4: (453, 290), 5: (403, 340), 6: (481, 356), 7: (509, 422), 8: (459, 472), 9: (537, 487)

The radial distribution of B_{av} for different current settings (I_α, I_β) is shown in Fig 3. Iron shims were added to remove unwanted dips in the average iron field at about 4", 7" and 14" radii (Fig 4). The distributions of 1st harmonic field at different stages of corrections are shown in Fig 5 by map1, map2 and map3. Finally, the 1st harmonic field is within 7 gauss near the extraction radius.

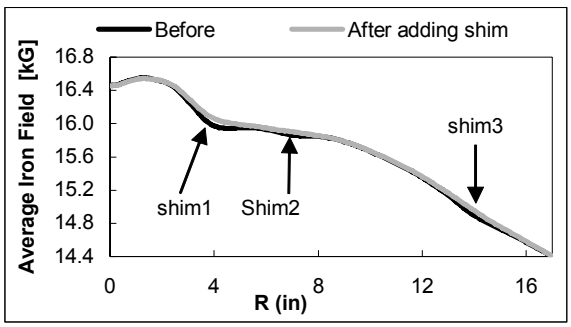

Fig 4: B_{av} correction by adding shim 1,2 and 3

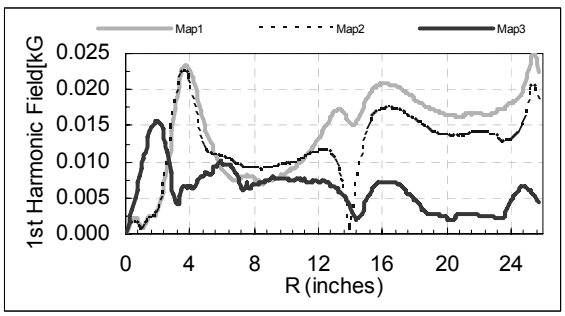

Fig 5: Minimization of 1st harmonic field profile

.

CONCLUSION

The MFM system is installed and complete field mapping at different coil excitation are performed successfully. The maximum radial and azimuthal field variations of SCC magnet are 4 KGauss/inch and 1 KGauss/deg respectively at maximum excitation. The objective i.e. to measure the field with the accuracy of 100 ppm i.e. 1 in 10^4 Gauss is achieved successfully using search coil of optimised dimension, digital integrator of 10^{-8} volt-sec resolution, 17 bit angular encoder with 1.7 arc-sec accuracy and linear encoder of 70 µm resolution with 10 µm accuracy. The analysis is done on measured field data and the subsequent corrections are incorporated on the magnet to improve the field quality by reducing the 1st harmonic content.

REFERENCES

[1] Sarbajit Pal, et al, Development towards magnetic field mapping system, Indian Particle Accelerator Conference-2003, Feb 3-6, 2003, Indore, India.

[2] L.H. Harwood and J. A. Nolen Jr, Plans for Magnetic Mapping of the NSCL K800 Cyclotron Magnet, CHI996-3/84/0000-0101.

[3] F. Marti and P. Jhonson, A LabView based Cyclotron Magnetic Field Mapping System, Proc Int. Conf. On Cyclotron and their Applications, Caen, 1998.

MATHEMATICAL MODEL FOR FAST AND SLOW DUMPING OF K-500 SUPERCONDUCTING CYLOTRON MAGNET

Anirban De, S.K. Thakur, S. Saha, VECC, 1/AF, Bidhan Nagar, Kolkata 700064, INDIA

Abstract

A superconducting cyclotron (K-500) is under construction at Variable Energy Cyclotron Centre. Two superconducting coils – named 'Alpha' and 'Beta' – generates the main magnetic field of the cyclotron. Subsequent to the in-house fabrication of the two coils, it was assembled into the cryostat and the magnet assembly completed. Immediately after the cool down, the superconducting coils were energized. Two dump resistors – slow and fast – serve to dissipate the energy stored in the coils externally depending upon the situation.

Various sets of data were collected during dumping and based on these an approximate mathematical model was constructed to simulate the dumping characteristics. This model took into account the lead drops, the cable and the joint resistances along with the dump resistor values and the self- and mutual- inductances (that varied with current) of the coil.

INTRODUCTION

The two coils are powered by M/S Danfysik make two power supplies rated 20V, 1000A, 10ppm stability class. Along with this, each of the magnet coils are always connected with two dump resistors, viz., fast dump and slow dump as shown in Figure 1.

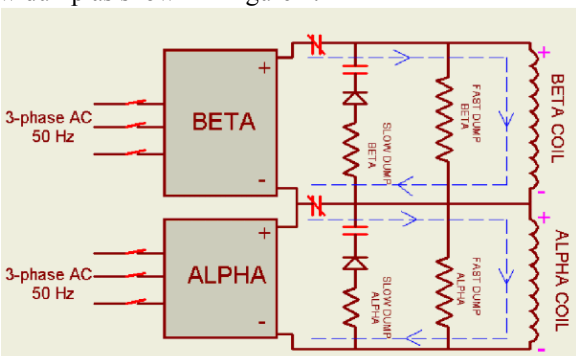

Figure 1: Schematic of Power Supplies with Superconducting Coils and Dump Resistors

The two dump resistors – slow and fast – serve to dissipate the energy stored in the coils externally depending upon the situation. For example, during power failure, the energy stored in the coils is slowly dissipated through the slow dump resistors. Slow dumping is also automatically triggered for the following conditions viz, He level in upper part of cryostat falling below 95%, He pressure rising to more than 306mbar, horizontal support link forces not within permissible range (1000lbs – 10000lbs), panic button operated manually, power supply tripped due to internal interlock failure. For a potentially catastrophic situation (like quench, lead voltage drop increasing above 160mV, He pressure in coil exceeding 680mbar, cryostat vacuum exceeding 10^{-1}mbar, He level sensor in upper half of cryostat reading less than 80%) the energy is quickly dumped through the fast dump resistors.

MATHEMATICAL MODEL

Theoretical Model

During dumping, the 3ϕ supply is withdrawn and the series contact gets automatically opened and the system shown in Figure 1 reduces to the circuit as shown in Figure 2.

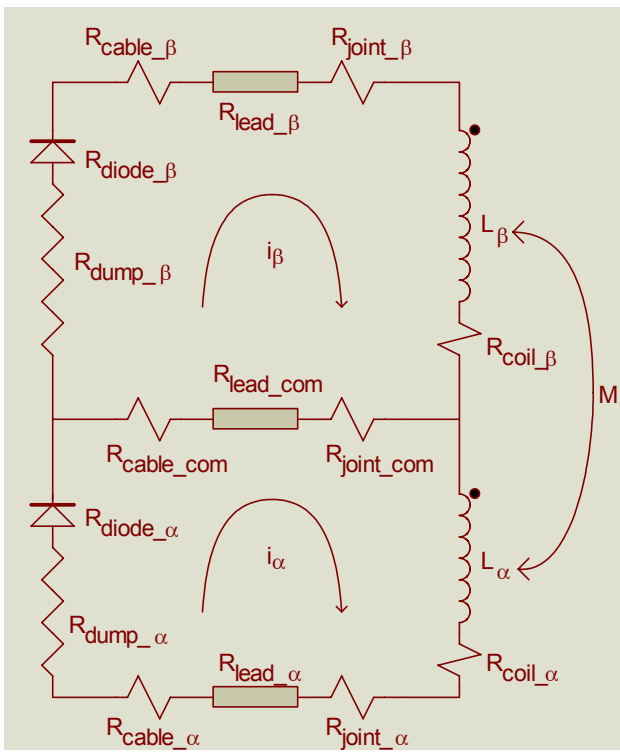

Figure 2: The dumping scheme

The governing differential equations for the model:

$$L_\beta \frac{di_\beta}{dt} + M\frac{di_\alpha}{dt} + R_\beta i_\beta + R_{com}(i_\beta - i_\alpha) = 0 \qquad (1a)$$

$$L_\alpha \frac{di_\alpha}{dt} + M\frac{di_\beta}{dt} + R_\alpha i_\alpha + R_{com}(i_\alpha - i_\beta) = 0 \qquad (1b)$$

where,

$M = k\sqrt{(L_\beta L_\alpha)}$

$R_\beta = R_{dump_\beta} + R_{diode_\beta} + R_{cable_\beta} + R_{lead_\beta} + R_{joint_\beta} + R_{coil_\beta}$

$R_{com} = R_{cable_com} + R_{lead_com} + R_{joint_com}$

$R_\alpha = R_{dump_\alpha} + R_{diode_\alpha} + R_{cable_\alpha} + R_{lead_\alpha} + R_{joint_\alpha} + R_{coil_\alpha}$

It is to be noted that during fast dump condition, the diode will be absent.

Neglecting the diode drop, cable resistances, joint resistances, lead resistances and considering the inductance values of the coils to be independent of current, the system reduces to

$$i_\beta = (0.62i_{\beta0} + 0.41i_{\alpha0})e^{-t/5065.92} + (0.38i_{\beta0} - 0.41i_{\alpha0})e^{-t/901.42} \quad (2a)$$

$$i_\alpha = (0.38i_{\alpha0} + 0.58i_{\beta0})e^{-t/5065.92} + (0.62i_{\alpha0} - 0.58i_{\beta0})e^{-t/901.42} \quad (2b)$$

during slow dumping

and

$$i_\beta = (0.60i_{\beta0} + 0.40i_{\alpha0})e^{-t/155.88} + (0.40i_{\beta0} - 0.40i_{\alpha0})e^{-t/25.97} \quad (3a)$$

$$i_\alpha = (0.40i_{\alpha0} + 0.60i_{\beta0})e^{-t/155.88} + (0.60i_{\alpha0} - 0.60i_{\beta0})e^{-t/25.97} \quad (3b)$$

during fast dumping

with

$L_\beta = 26H$, $L_\alpha = 13H$,

$R_{slowdump_\beta} = 7m\Omega$, $R_{slowdump_\alpha} = 4.9m\Omega$

$R_{fastdump_\beta} = 250m\Omega$, $R_{fastdump_\alpha} = 167m\Omega$

$k = 1/\sqrt{2}$

$i_{\beta0}$ = initial current in Beta coil

$i_{\alpha0}$ = initial current in Alpha coil

It can be observed that both the equations for slow dumping (2a &2b) and fast dumping (3a & 3b) have a fast decaying component and a slow decaying component.

The time constants for them are as follows:

For slow dump

Time constant for the slowly decaying component = 5065.92sec (~ 84.5min)

Time constant for the fast decaying component = 901.42sec (~ 15min)

For fast dump

Time constant for the slowly decaying component = 155.88sec (~ 2.5min)

Time constant for the fast decaying component = 25.97sec (~ 0.5min)

From the equation sets (3a) & (3b) and (4a) & (4b), it can further be observed that when the initial currents in both the coils are same (i.e., $i_{\beta0} = i_{\alpha0}$), the fast decaying component almost vanishes and the currents in the coils, in that case, will be monotonically decaying with a time period of 84.5min in the case of slow dump and 2.5min in the case of fast dump (Actually starting from equation 1a & 1b, if we make the self inductances of β exactly twice of that of α, the coupling coefficient = $1/\sqrt{2}$ and the ratio of the dumping resistance of β to that of α to be exactly 1.5, then it can be shown that for the same initial currents in both the coils, the fast decaying component vanishes altogether).

Results

During actual dumping, we have to consider all the sources of energy dissipations viz, the diode drops, the lead drops, the cable drops, the joint resistance and the coil resistance. These were measured by monitoring the voltages across the load, leads, power supply output leads at different currents and obtaining an average resistance from the results.

The results hence obtained are shown in Figures 3 & 4.

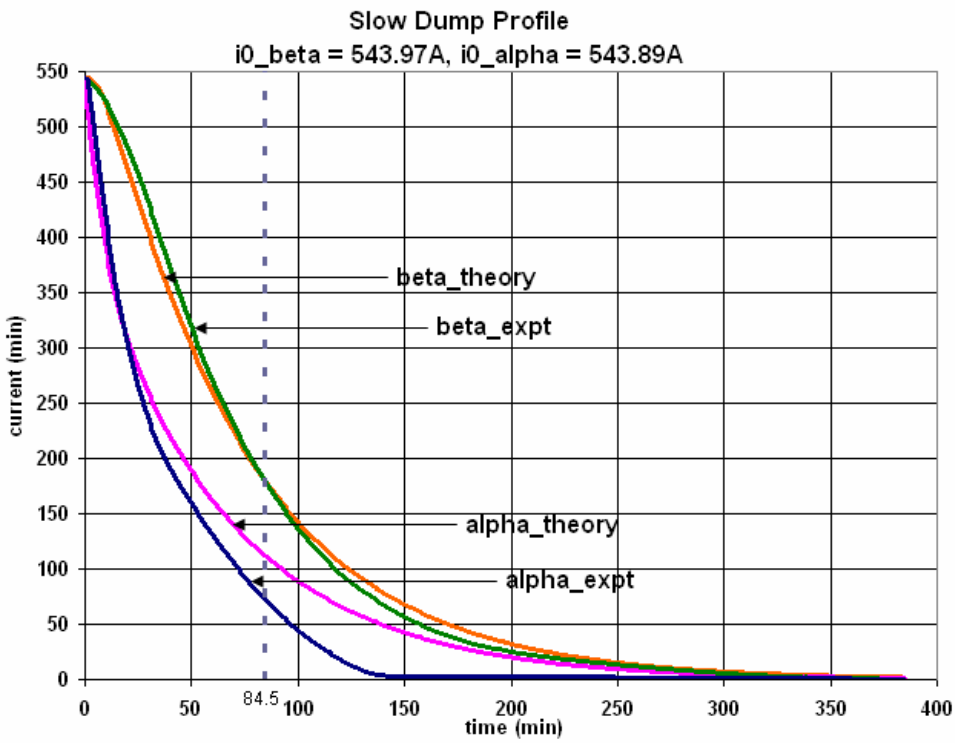

Figure 3: Comparison of the experimental and theoretical results during a Slow Dump

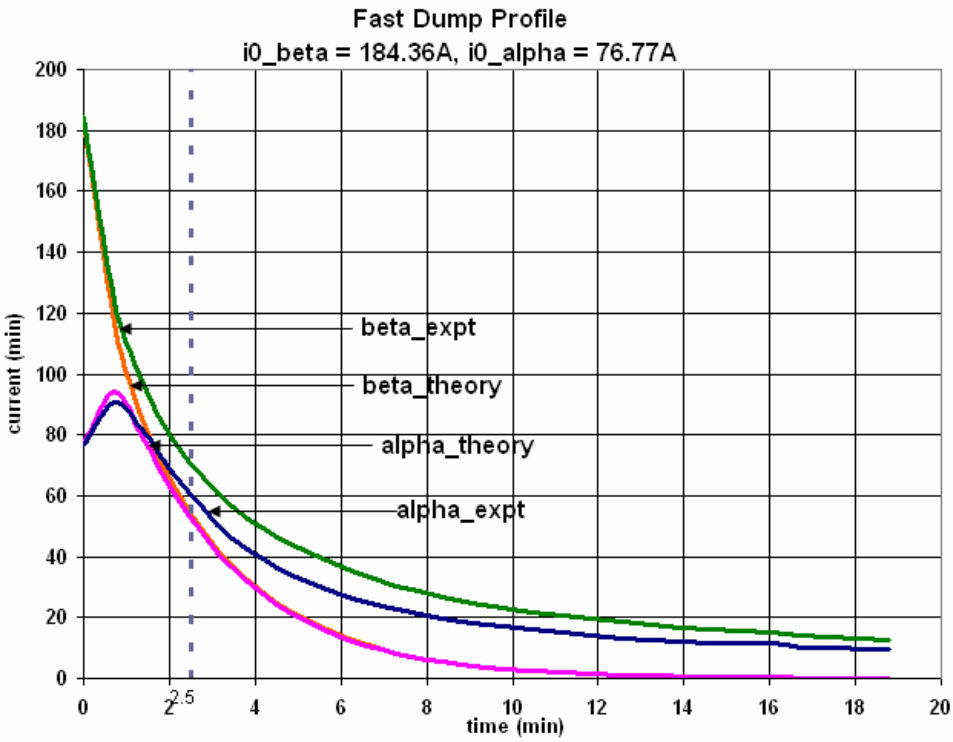

Figure 4: Comparison of the experimental and theoretical results during a Fast Dump

Discussion

From the above two plots it is fairly apparent that the model is useful in the higher current region and shows a marked error in the lower current region (current < 50A). The time of an overshoot occurring due to the difference in the coil currents can also be predicted from the model.

The main source of error in the lower current region is believed to be due to the fact that the inductances of the magnet coil are functions of current in the coil and the non-linearity is more pronounced near the low current zone. The inductance value is fairly constant when the iron part of the magnet gets saturated. The other deviations of the theoretical model from the experimental results arise from the non-linear nature of the diode and the resistance build up at the joints. Also since the dumping phenomenon is inherently slow, the resistances in the dumping path get ample time to get heated and hence may change their values.

ACKNOWLEDGEMENT

Sincere thanks are due to Mr. Biswajit Sarkar for developing the software to capture the data required for this study.

REFERENCES

[1]. D.P. May et. al. “Status of the Texas A & M University K-500 Superconducting Cyclotron”, Proc. 10th International Conference on Cyclotron and their applications April 30 – May 3, 1989.

IDEAL COIL-SHAPE FOR PERFECT FIELD IN SUPERCONDUCTING SEXTUPOLE MAGNETS

P. R. Sarma
VECC, 1-AF, Bidhannagar, Kolkata-700 064
email: sarma@veccal.ernet.in

Abstract

Superconducting magnets have become very essential components in high energy accelerators. The field in coil-dominated superconducting magnets depend mostly on the shape of the current-carrying coil. A coil shape generated by two overlapping ellipses produces the perfect dipole magnetic field. Similarly, a perfect quadrupole field can be produced with a coil shape generated by two perpendicular and concentric intersecting ellipses. For a sextupole, however, there is no mention of such coil shape in the literature. We have given here a coil shape for generating the perfect sextupolar magnetic field.

INTRODUCTION

In high energy accelerators like LHC at CERN [1,2], VEPP at Novosibirsk [3] etc. superconducting sextupole magnets are used as correctors of second order beam aberrations.

In these magnets the field quality depends on the coil shape. A cosθ azimuthal current distribution on a cylindrical surface produces a perfect dipole magnetic field inside. Similarly, a cos(3θ) azimuthal current distribution produces a perfect sextupole field. This, however, is not a practical way as one has to use a large number of power supplies for achieving the required current distribution. The practical way is to have a constant current pass through a coil winding whose number of turns varies azimuthally.

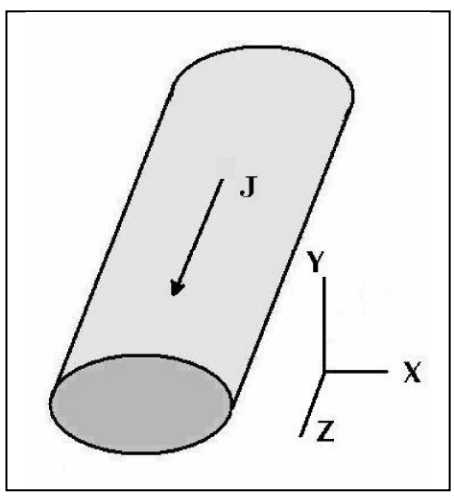

Figure 1. Coil cross-section and current direction.

It is well-known that a constant current flowing through a coil, whose shape is generated by two displaced overlapping ellipses, produces the perfect dipole field. Similarly, two perpendicularly intersecting and concentric ellipses produces a coil shape which generates the perfect quadrupole field [4-9]. However, for a superconducting sextupole no such ideal coil shape is available in the literature. In this work, we have worked out such an ideal coil shape for generating the perfect sextupolar field.

FIELD DUE TO LONG COIL

For a current I flowing along the z-direction through a point (x,y) in a thin strand of conductor of infinite length, the field B at a point (x_0,y_0) whose distance is r from the conductor, is given by the Biot-Savart law as

$$B(x_0, y_0) = \frac{\mu_0 I}{2\pi r} \tag{1}$$

where μ_0 is the permeability in air. The field B is perpendicular to both the radius vector r and the conductor. The field component in the y-direction is

$$B_y(x_0, y_0) = \frac{\mu_0 I}{2\pi} \frac{(x - x_0)}{(x - x_0)^2 + (y - y_0)^2} \tag{2}$$

For a coil of extended dimension the field is calculated by integrating the above over the cross-section of the coil. For a uniform current density J flowing along the length (z-direction) of the coil, i.e., perpendicular to the cross-section of the coil (Fig. 1), the field $B_y(x_0,y_0)$ is

$$B_y(x_0, y_0) = \frac{\mu_0 J}{2\pi} \int_y \int_x \frac{(x - x_0)}{(x - x_0)^2 + (y - y_0)^2} dx dy$$

$$= \frac{\mu_0 J}{4\pi} \oint \ln\left[(x(y) - x_0)^2 + (y - y_0)^2\right] dy \tag{3}$$

where $x(y)$ defines the boundary of the coil as a function of y, and integration is done for the closed path along the coil boundary. The x-component of the field is similarly

$$B_x(x_0, y_0) = \frac{\mu_0 J}{4\pi} \oint \ln\left[(x - x_0)^2 + (y(x) - y_0)^2\right] dy \tag{4}$$

The coil profile $x(y)$ (or conversely $y(x)$) defines the field type and its quality. For an elliptic shape with semi-axes a and b, and defined by the parametric equations

$$x(\varphi) = a\cos\phi, \qquad y(\varphi) = b\sin(\varphi) \tag{5}$$

eqs.(3) and (4) reduce to

$$B_y(x_0, y_0) = \mu_0 J \frac{bx_0}{(a+b)} \quad (6)$$

$$B_x(x_0, y_0) = -\mu_0 J \frac{ay_0}{(a+b)} \quad (7)$$

Thus there is a constant gradient of the field B_y along the x-axis, and of B_x along the y-axis. Actually, along any radial direction, the gradient of the field component perpendicular to that radius vector is constant.

This field is inside a conductor which is solid, a particle beam can not pass throught it. One requires a vacuum space for the beam to pass through. Superposition of positive and negative current distributions through two overlapping coil shapes creates a vacuum space and modifies the field inside that space. As has already been mentioned, two displaced elliptic current distributions produce the perfect dipole field, and two intersecting perpendicular elliptic coil shapes produces the perfect quadrupole field.

We point out that intersecting perpendicular elliptic shape is not the only shape which produces pure quadrupole field. Recently we showed that there exist coil shapes different from the above, which give perfect quadrupole field [10,11].

COIL FOR PERFECT SEXTUPOLE FIELD

Unlike a quadrupolar field, which is linear in form, the sextupolar field has a nonlinear nature along any direction. Since the field inside an elliptic coil produces linear field, one cannot use this field to produce a sextupolar field. One needs to produce a field which has second order spatial variation by using a suitable coil shape. Obviously, the parametric equations for x and y will have to be different from those for an ellipse. The following shapes for $x(y)$ and $y(x)$ have been tried.

$$x(\varphi) = a\cos\phi - c\sin(2\phi)$$
$$y(\phi) = a\sin\phi - c\cos(2\varphi) \quad (8)$$

where c is a constant which modifies the ellipse. With this shape eqs.(3) and (4) yield

$$B_y(x_0, y_0) = \mu_0 J\left[\frac{x_0}{2} + \frac{c}{a^2}x_0 y_0\right] \quad (9)$$

and

$$B_x(x_0, y_0) = -\mu_0 J\left[\frac{y_0}{2} + \frac{c}{2a^2}(x_0^2 - y_0^2)\right] \quad (10)$$

These fields are mixtures of a sextupolar field ($\propto x_0 y_0$, x_0^2-y_0^2) and a gradient field (x_0,y_0). Fig. 2 shows a typical coil shape given by eq.(8). Unlike the two-fold symmetric elliptic shape, this has a three-fold symmetry.

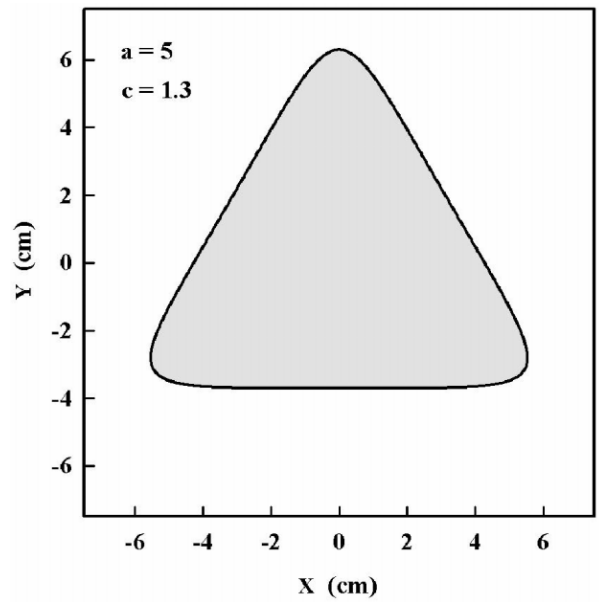

Figure 2. A three-fold symmetric coil shape which produces a second order magnetic field variation.

In order to produce a pure sextupolar field (and, of course, create a vacuum space) one has to superimpose two different current distributions.

$$B_y(x_0, y_0) = B_y(x_0, y_0, c, J) + B_y(x_0, y_0, -c, -J)$$
$$= \frac{2\mu_0 J}{a^2} x_0 y_0$$

$$B_x(x_0, y_0) = -\frac{\mu_0 Jc}{a^2}(x_0^2 - y_0^2)$$

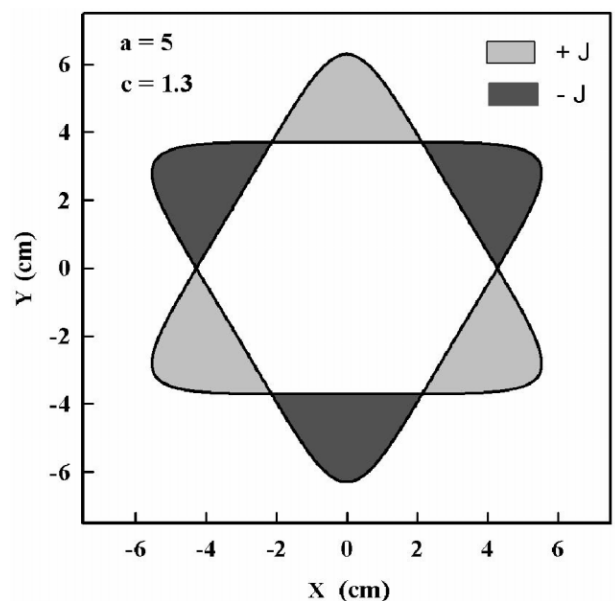

Figure 3. Superimposition of two opposite current distributions generates a perfect sextupole field.

These field values are valid within the overlapping region between the two current distributions. Fig. 3 shows the superimposed coil shape. This has a six-fold geometrical symmetry, the electrical symmetry is three-fold though. Fig.4 shows the lines of force obtained by POISSON calculation in this sextupole.

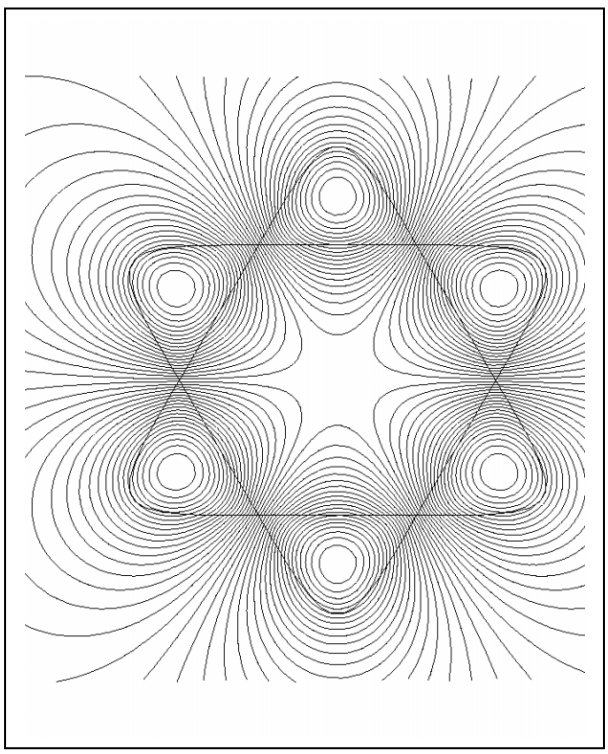

Figure 4. Lines of force in a sextupole of ideal coil shape.

CONCLUSIONS

It has been shown by us that just as coil shapes exist for producing perfect dipole and quadrupole magnetic fields, for a sextupole also there exists an ideal coil shape. This shape is generated by the superimposition of two opposite three-fold symmetric uniform current distributions given by eq.(8). This finding should be of help in designing practical superconducting sextupole magnets.

For canceling the linear part of the field it is not necessary that the two current distributions be of the same size (i.e., same a and c). For two shapes with a_1, c_1 and a_2, $-c_2$ as the parameters, the superposed field components are

$$B_y(x_0, y_0) = \mu_0 J \left[\frac{c_1}{a_1^2} + \frac{c_2}{a_2^2} \right] x_0 y_0 \qquad (11)$$

and

$$B_x(x_0, y_0) = -\mu_0 J \left[\frac{c_1}{2a_1^2} + \frac{c_2}{2a_2^2} \right] (x_0^2 - y_0^2) \qquad (12)$$

If the second distribution has a circular shape (i.e., a circular inner aperture for the sextupole) we have $c_2=0$, $c_1= c$ and therefore

$$B_y(x_0, y_0) = \frac{\mu_0 J c}{a^2} x_0 y_0 \qquad (13)$$

and

$$B_y(x_0, y_0) = -\frac{\mu_0 J c}{2a^2} (x_0^2 - y_0^2) \qquad (14)$$

A current distribution completely within the other will generate a shape where only three separate coils will be required. One can have an inner aperture of his choice by this method. This type of coil shape will be useful in constructing twin sextupoles in a common-coil configuration.

REFERENCES

[1] J.Salminen, A. Ijspeert and A. Puntambekar, Proc. 5th European Particle Accel. Conf. EPAC-96 (Barcelona, 1996) ed S. Myers, A. Pacheco, R. Pascual and Ch. Petit-Jean-Genaz, (Bristol: IOP Publishing) p. 2252.

[2] J. Salminen, A. Ijspeert, Z. Ang, J. Billan, L. Walckiers, S. Bapna, M. Karmarkar, A. Puntambekar, A. Thipsay and L. Garciá-Tabareś, LHC Project Report 263 (1999).

[3] L.G. Isaeva, B.A. Lazarenko, S.I. Mishnev, D.M. Nikolenko, S.G. Popov, I.A. Rachek, Yu V. Shestakov, D.K. Toporkov, D.K. Venovsky and S.A. Zevakov, Nucl. Instr. and Meth. in Phys. Res. **A411** (1998) 201.

[4] H. Brechna, Superconducting magnet systems (Berlin: Springer-Verlag) (1973) p. 30.

[5] R.A. Beth, IEEE Trans. on Nucl. Sci. **NS-14** (1967) 386.

[6] H. Shoaee and J.E. Spencer, Stanford Linear Accelerator enter Report No. SLC/AP-3 (1983).

[7] K.–H. Meß, CERN Report No. 89-04 ed S. Turner, (1989) p. 87.

[8] S. Wolff, Proc. CERN Accel. School, 5th General Accel. Phys. Course (Jyväskylä) Report No. 94-01 (1992) p. 758.

[9] P.R. Sarma, Nucl. Instr. and Meth. in Phys. Res. **A564** (2006) 81.

[10] P.R. Sarma, Rev. Sci. Instr. **76** (2005) 093303.

[11] P.R. Sarma, Nucl. Instr. and Meth. in Phys. Res. **A556** (2006) 443.

DESIGN OF THE PROPOSED 250 MEV SUPERCONDUCTING CYCLOTRON MAGNET

M. K. Dey#, A. Dutta Gupta, U. Bhunia, S. Saha, A. Dutta, J. Pradhan, S. Sur, S. Murali, J. Chaudhuri, C. Mallik and R.K. Bhandari
Variable Energy Cyclotron Centre, Kolkata

Abstract

VECC has proposed a project for the design and development of a 250 MeV superconducting proton cyclotron, which may be used in therapy. In this paper we describe the preliminary design calculations for the superconducting cyclotron magnet. Hard-edge approximation method has been adopted for finding the poletip geometry to meet the basic focusing requirements of the beam. The uniform-magnetization method has been applied to calculate the 3D magnetic field distribution due to saturated iron poletips, to verify the beam dynamical issues and optimize the poletip geometry. GM type closed cycle cryo-cooler technology is being considered for steady state liquefaction of evaporated helium gas from magnet cryostat.

INTRODUCTION

Basic design parameters are decided by the requirements for medical application of the cyclotron, i.e., for the treatment of deep seated cancerous tumors. Proton energy of 250 MeV corresponds to approximately 40 cm penetration range in water. The cyclotron is targeted to be designed for delivering a few hundreds of nano-amperes beam current.

The design of the cyclotron magnet is an iterative process. Approximate hard-edge formulas are used to determine the basic dimensions and geometry of the poletip sectors [1, 2]. The 3D software TOSCA has been used to calculate median plane magnetic field distribution (fig 1). Since the superconducting magnet is operated in high field level (peak hill field at median plane ~3.6T), the pole-tip iron is fully saturated. So the uniform-magnetization method is adopted to simulate the azimuthal variation of the field due to spiral hill-valley structure of the magnet [3]. This makes the iterative optimization of the poletip geometry faster. Orbit tracking codes are used to calculate the equilibrium orbit properties.

The cryogenic system primarily consists of helium reservoir, GM type cryo-cooler, magnet cryostat with multilayer insulation and 80 K radiation shield inside, conduction cooled current leads, etc. The cold mass can be slowly cooled down from room temperature to reach liquid helium temperature either by directly coupling the cryostat with helium refrigerator or initially by liquid nitrogen and then by liquid helium. The evaporated helium gas from the cryostat will be reliquefied by condensing it through the cold head of the multistage GM type cryo-cooler. This is a very new and economic technology compared with the conventional technique of coupling with liquid helium plant (as used in VECC K500 superconducting cyclotron magnet).

#malay@veccal.ernet.in

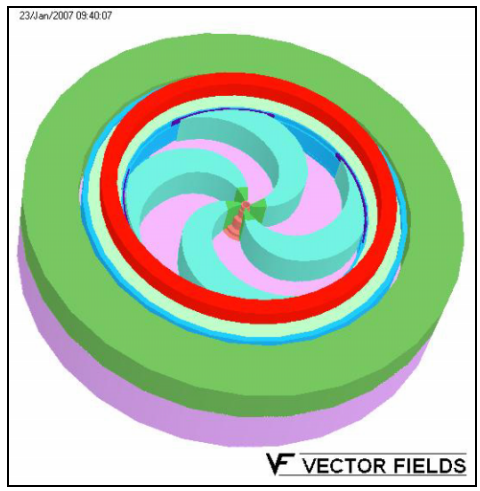

Figure1:TOSCA model of upper half of cyclotron magnet.

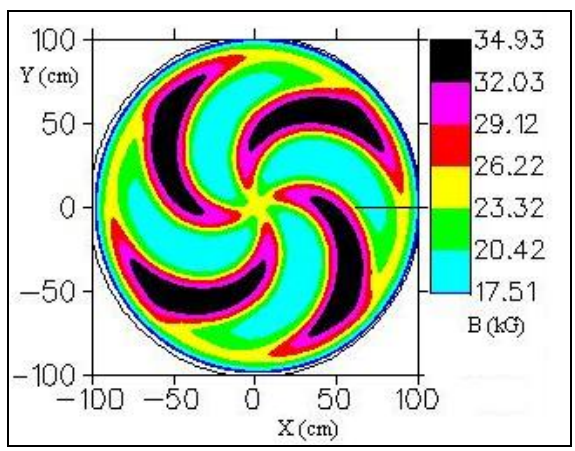

Figure 2: Contour plot of median plane magnetic field .

SECTOR GEOMETRY

To minimize the size and cost of the cyclotron it is desirable to operate at maximum possible magnetic field strength. But with stronger magnetic field, higher electric field is required at the deflector system to extract the beam, so making the extraction process very difficult and unstable. Moreover, since the fractional azimuthal variation of the field (flutter) decreases with increasing average field, stronger spiralling of the sector is required to compensate for the decrease in vertical focusing, causing manufacturing challenge. So an optimum value of

~2.37T is chosen for the central field B_o, for which the orbital rotational frequency is ~36.14 MHz. A four-sector cyclotron magnet is more suitable for 250 MeV proton beam than a three sector magnet like VECC K500 cyclotron, to avoid the proximity of $\upsilon_r = 3/2$ stop-band [4].

The average isochronous field is given by $B_{av} = B_o\ \gamma$, where, $\gamma = 1+T/E_o$, T is the kinetic energy and E_o is the rest mass energy. The average radius of the equilibrium orbit is given by $R = (T^2 + 2\ T\ E_o)^{0.5}/\ (300\ \gamma\ B_o\ q)$, where q is charge of the particle. Once the hill and valley fields (B_h, B_v) are decided, the required isochronous field determines the sector angles. The angular width of the sector angles are given by

$$\eta_h = \frac{2\pi}{N}\cdot\frac{(B_{av}-B_v)}{(B_h-B_v)} \quad \eta_v = \frac{2\pi}{N} - \eta_h$$

Then spiral angle is introduced to the hill-valley sectors to enhance the vertical focussing. In the initial design stage we rely on first order beam optics using hard-edge model. The transfer matrix for the cyclotron magnet can be composed, assuming it as a series of sector magnets with constant fields (B_h *or* B_v) and the edge matrices defined by spiral angles. Focusing frequencies are given by,

$\upsilon_r = (N/2\pi).cos^{-1}(Tr(M_r)/2)$, $\upsilon_z = (N/2\pi).cos^{-1}(Tr(M_z)/2)$, where Tr stands for trace of the matrix, M_r and M_z are transfer matrices for one sector of the cyclotron in radial and vertical planes respectively.

With the sector geometry, found by hard-edge model, magnetic field in the median plane of the cyclotron is calculated with TOSCA and uniform magnetization method (fig 2). Equilibrium orbit behaviour is investigated by orbit tracking (fig 3). At this stage, several iterations were required to optimise the sector geometry.

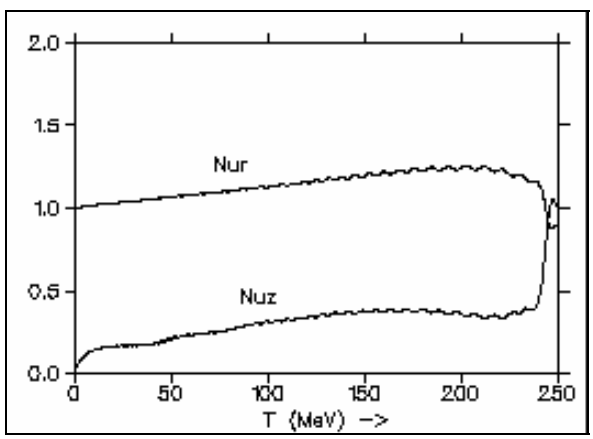

Figure 3: Radial and vertical tunes vs. kinetic energy.

COIL AND CRYOSTAT GEOMETRY

Cryostat for the proposed 250 MeV cyclotron has a stainless steel annular bobbin on which superconducting coil (Nb-Ti) will be wound at a pre-tension of about 80 MPa. The preliminary design of the cryostat looks like the one shown in figure 4.

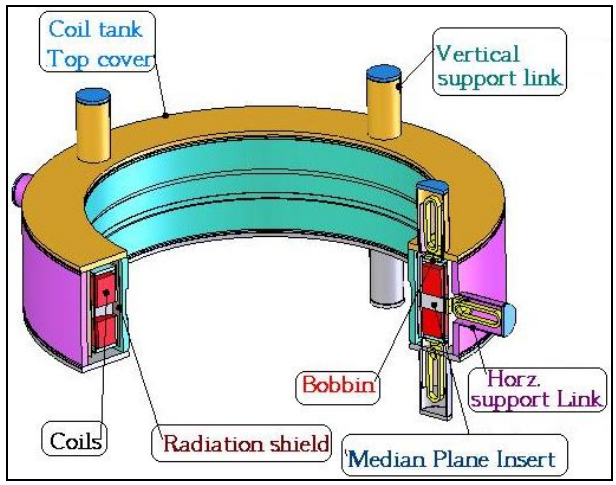

Figure 4: Preliminary design sketch of the cryostat.

Temperature distribution after cool down of magnet cryostat to liquid helium temperature is as shown in fig 5.

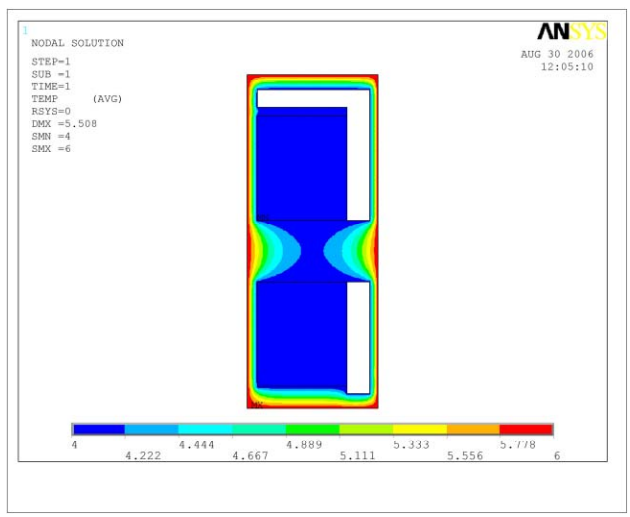

Figure 5: Temperature distribution in the coil & bobbin.

Figure 6 shows the magnetic field distribution in place of coil and cryostat. A preliminary one dimensional calculation was made and the radial and tangential stress distribution is plotted in the figure 7 and figure 8 [5].

The bobbin is made of stainless steel. It is estimated the heat load to the LHe could be kept below 6 watts. Hence, the cryocooler based cooling system may be considered instead of conventional LHe plant system. Both of direct conduction cooling or recondensing bath cooling may be considered before deciding over the methodology of operation. The second stage of the cryocooler is used to cool the copper radiation shields.

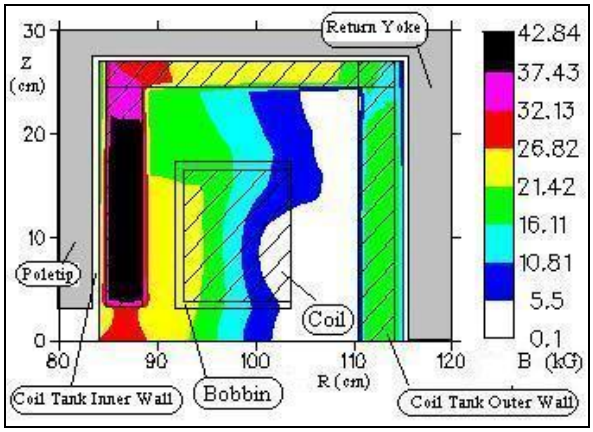

Figure 6: Magnetic field distribution in place of coil.

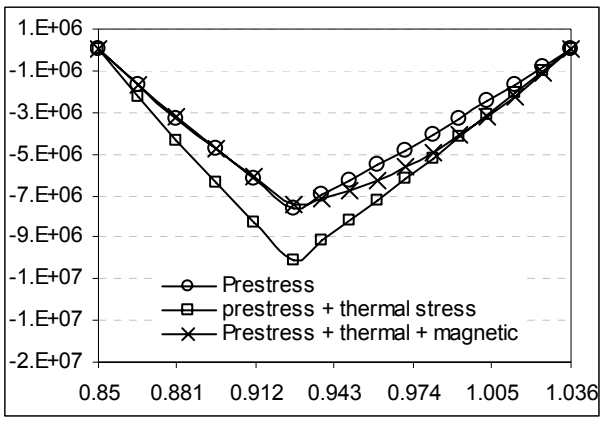

Figure 7: Radial stress distribution

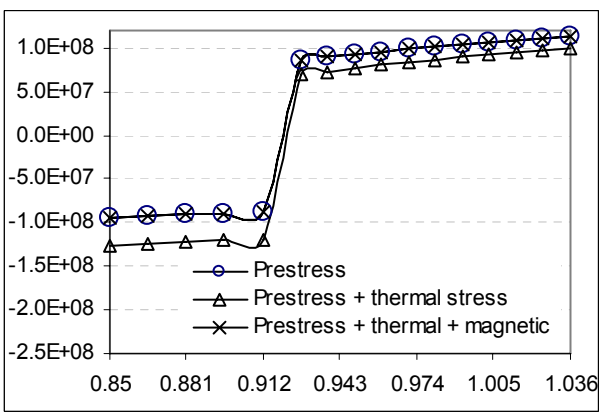

Figure 8: Tangential stress distribution

The 8 vertical and 4 horizontal support links of equal lengths support the liquid helium mass inside the vacuum chamber. The vacuum chamber is made of iron to reduce the return path iron requirements.

There is cooled radiation shield around the median plane penetrations to reduce the direct heat load to LHe from room temperature. All the supports and access pipes have intermediate temperature intercepts to reduce the conduction heat load.

CONCLUSION

The preliminary design study suggests the feasibility of developing such a cyclotron for therapeutic use. Detail design calculation is under progress. Primary design of superconducting magnet coil, cryostat, etc. has been completed. Cryo-condensation system of saturated helium gas at 4.5 K has to be practically demonstrated using multistage GM type cryo-cooler.

REFERENCES

[1] J.J.Livingood, Cyclic Particle Accelerator (Princeton, 1961). p. 42.
[2] K.G. Stephen, High Energy Beam Optics (New York, 1965), P. 100.
[3] M.M. Gordon and D.A. Johnson, Particle Accelerator, 1980, Vol.10, p.217-222.
[4] J. Kim and H. Blosser, International Conference on Cyclotrons and Their Applications, 2001, p345.
[5] Martin N. Wilson, Superconducting Magnets, Clarendon Press Oxford, 1983, p 41.

CONSTRUCTION OF SSRF MAGNET POWER SUPPLY SYSTEM

T.J. Shen, D.M. Li, R. Li, C.L. Guo, S.L. Lu, S.M. Zhu, H.G. Chen, R.N. Xu,
Z.M. Hu, D.X. Wang, W.F. Wu, H. Liu
Shanghai Institute of Applied Physics, Shanghai 201800, China.

Abstract

The Shanghai Synchrotron Radiation Facility (SSRF) is a third-generation synchrotron radiation light source under construction. In SSRF, there are 520 sets of magnet power supplies for the storage ring and 163 sets for injector. All of the power supplies are in PWM switched mode with IGBT. A high precision stable output power supply for 40 dipoles rated at 840A/800V with the stability of ±2E-5/8hrs will be used for storage ring. 200 sets of chopper type power supply will be used for exciting main winding of quadrupoles respectively. In booster ring, two sets of dynamic power supply for dipoles and two sets for quadrupoles will run at the biased 2Hz sinusoidal wave. All above power supplies will work with digital power supply controllers designed by PSI. All power supplies are being manufactured at professional power supply companies in China.

POWER SUPPLY CONTROLLER

A control solution of full digital control as Swiss Light Source(SLS) is adopted in large power supplies for dipoles of storage ring and booster. A pair of PSI controller (See Fig.1) are put inside the power supply cabinet as a master to control several analog slaves, to regulate the output current. There is a 60MHz DSP with 32/40 Bit floating point ALU, 8x16 bit electrically isolated AD converters (50ksps), 11 free memory units for 16,384 data points [2]. It can communicate with IOC through a pair of 5MB optical fibers. The main advantage of the full digital control is much better in stability, repeatability, and flexibility. At present, the long term stability for a sample power supply is up to 10ppm.

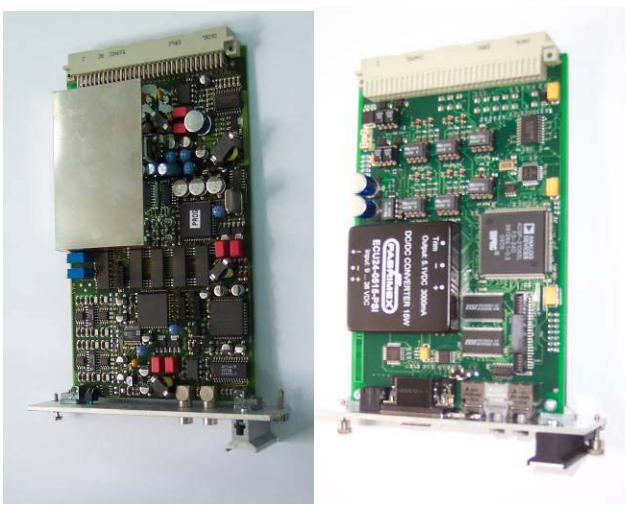

Figure 1: PSI power supply controllers

Additionally, in order to reduce the cost we have managed to develop a home-made power supply controller product. So far the stability is achieved 20ppm and this controller is expected to use in middle and small power supplies in SSRF linac after authentication.

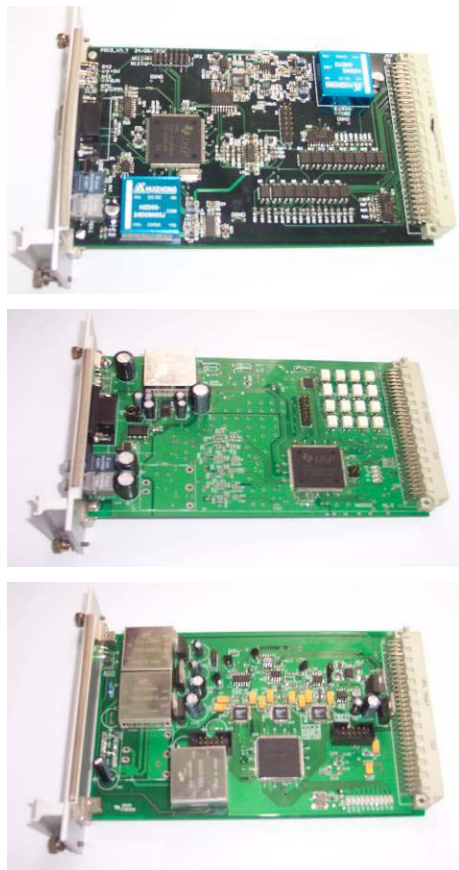

Figure 2: Home-made power supply controllers

LINAC POWER SUPPLY

SSRF is mainly composed of three parts: the 150MeV linac, the 3.5GeV booster and the full energy storage ring. In linac, unipolar power supplies adopted the circuit of chopper, full bridge (or half bridge), and bipolar power supplies adopted the circuit of H-bridge. The medial power supplies above 1kW adopted the full 19" width structure which put inside a standard 3U case. Other small power supplies shared the full 19" width by 2 to 3 units and used the common input DC module [3].

A LEM as a current sensor is adopted for those stability requirement larger than 1000ppm, a DCCT for those stability better than 100ppm, and a resistor for the bipolar power supplies, such as corrector power supplies.

The home made digital PWM controller can be adopted in linac, which communicate with EPICS via Ethernet and Serial port server.

Figure 3: ±10A25V bipolar power supply

BOOSTER POWER SUPPLY

In SSRF booster ring, two sets of dynamic power supply for 48 bending dipoles run at the repetition rate of 2Hz, which are in two quadrants topology with energy recover and rated of 1150A/1000V. A DC/DC booster chopper is staged in series, so that the voltage fluctuation on the power line could be reduced dramatically. A scaled prototype rated 600A/500V was built and tested, the topologic structure of power has been verified as well. A PSI digital PWM controller will be used in the dynamic power supply as a control master with global current feedback loop. Under digital commands from the central control system, PSI controller produces PWM outputs which be converted into analog voltage via a special circuit. This control voltage is then delivered to the analog PWM controllers, which has been designed to manipulate a power module with local feedback loop.

Figure 4: Booster power supply

STORAGE RING POWER SUPPLY

Most magnet power supplies in SSRF storage ring are static. High precision, stability and repeatability are important. The main power supply for 40 dipoles will be an IGBT type converter rated for 800A/840V. The long term stability requirement of this power supply is 20ppm (within 24 hours). Its scaled prototype rated for 400A/ 840V was built and tested with the stability of ±20ppm. The power supply will work with digital power supply controllers designed by PSI.

200 sets of chopper type power supplies are being manufactured to excite the main windings of quadrupoles respectively. Every 5 choppers share a common DC link voltage source. A prototype of power supplies with ratings of 280A/35V for 5 quadrupoles have been built and tested with the output current stability of ±50ppm for 24hrs.

140 sextupoles are divided into 9 groups. A chopper will be employed for the windings of each group in series. The scaled prototype rated of 400A/840V as mention above matches the demand of the sextupole power supplies.

Figure 5: Storage ring power supply

REFERENCES

[1] Shanghai Synchrotron Radiation Facility preliminary design, 2001, Shanghai Institute of Applied Physics.

[2] L. Tanner, F. Jenni, et al, Digital Control for Highest Precision Accelerator Power Supplies. Proceedings of PAC 2001, Chicago.

[3] T. SHEN, Development of power supply 061221, internal report, Shanghai Institute of Applied Physics

IMPLEMENTATION OF HIGH PRECISION MAGNET POWER SUPPLY USING THE DSP*

K. H. Park #, S. H. Jeong, D. E. Kim, J. H. Choi and C. W. Chung
Pohang Accelerator Laborator, POSTECH, Pohang, Kyungpook 790-784, Korea
B. K. Kang
Department of Electrical Engineering, POSTECH , Pohang, Kyungpook 790-784 Korea

Abstract

This paper presents an implementation of a precision magnet power supply (MPS) for the Pohang Light Source using the digitally controlled pulse width modulation method. The maximum output current of the power supply was 600 A at a precision of ~60 ppm. The digital control circuit of the power supply was implemented using two high speed 16-bit analog-to-digital converters and the TMS320F2808 digital signal processor. Three IGBTs are used at MPS with phase shifted parallel operation to increase the power rating and operating frequency. The duty ratio for IGBT control was determined using the PI control method. To reduce the output current ripple, the damped L-C filter was fabricated at both the DC link and output sides. Various experimental results, such as stability, drift, and controllability, are given to verify the characteristics of the DSP based magnet power supply.

INTRODUCTION

Many IGBT switching mode power supplies were implemented using a pulse width modulation controller such as UC1825 from Texas Instrument Co. This type of power supply can be a high precision MPS if the resolution and stability of the digital-to-analog converter, which generates an analog reference signal, is high. However, it requires many hardware components to implement the controller, and its output current is susceptible to variation of operating conditions.

A fully digital-controlled MPS has many advantages over the analog one. Its output characteristics are less sensitive to noise and less susceptible to parameter variations from thermal and aging effects. Also, it has a flexible and re-configurable control system [1]. We implemented and tested a fully digital-controlled MPS for the Pohang Light Source. The MPS used the phase shifted parallel operation [2] of three IGBTs to increase the power rating and operating frequency. The IGBTs were operated at a same duty ratio but 120° interleaved control phases. Because of this, the system operating frequency increased to three times higher than the one for a normal switching mode MPS, and the ripple content in output current could be reduced easily. The output of each IGBT was connected to a small separate inductor to reduce the size of inductor in the filter circuit. Digital control for MPS system was built on the DSP TMS320F2808 from TI Co. In this paper, we present the design details and measured results of the fully digital-controlled high precision MPS for the Pohang Light Source.

* Work supported by Ministry of Science and Technology of Korea.
# pkh@postech.ac.kr

AVERAGE CURRENT MODE CONTROL

The control of a switching mode power supply can be analysed using either the average current or peak current mode operations. For the peak current mode control, the instantaneous peak current of the inductor, which regulates the output current, is sensed and used to determine the duty ratio of the PWM. The duty ratio determined from the measured instantaneous peak current is quite fluctuating, and the peak current mode control is not suitable for a precision MPS for accelerator. For the average current mode (ACM) control [3], the load current is sensed and averaged for a given control loop duration, compared with the reference value to obtain the current error, and the current error is fed into the compensator in the control loop. Because the load current is averaged over the control loop duration, the noise immunity of the control loop is very high. A schematic diagram of buck mode MPS using the ACM control is shown in Fig.1. Here, D is the steady state duty ratio of the IGBT control signal, $H(s)$ is the gain of current sensor, and $G_c(s)$ is the proportional and integral (PI) compensator for load current regulation.

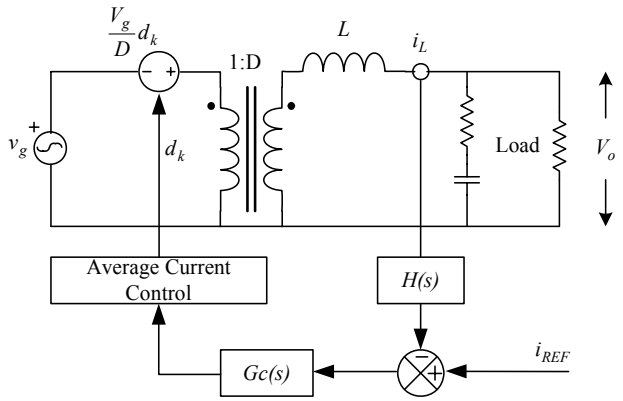

Figure 1: A schematic diagram of bucked mode MPS using the ACM control.

For an analysis of the MPS, we assume that the current through the filter capacitor is much smaller than the load current, and the converter operated at a continuous conduction mode. Then the inductor current is given by the following equations:

$$L\frac{di_L}{dt} = V_g - V_o \quad \text{for} \quad t_k \le t < t_k + d_k T_s \tag{1}$$

$$L\frac{di_L}{dt} = -V_o \quad \text{for} \quad t_k + d_k T_s \le t < t_{k+1} \tag{2}$$

Thus the initial inductor current at the $(k+1)th$ switching cycle can be written as

$$i_L(k+1) = i_L(k) + \frac{V_g(k) - V_o(k)}{L} d(k) T_s - \frac{V_o(k)}{L}(1 - d(k)) T_s \tag{3}$$

where d_k is the duty ratio function of the PWM and T_s is the switching period. In a steady state operation, the inductor current should follow the reference current $i_{REF}(k)$, i.e., $i_{REF}(k) = i_L(k)$.

From (3), the duty ratio in k th switching period is given by

$$d(k) = \frac{[i_{REF}(k+1) - i_{REF}(k)]L/T_s}{V_g(k)} + \frac{V_o(k)}{V_g(k)} \tag{4}$$

Then, the time averaged load current $< i_L >$ becomes

$$< i_L >= \frac{1}{T_s}\int_t i_L dt \quad \text{for} \quad t_k \le t < t_k + T_s . \tag{5}$$

During each switching period, the averaged load current $< i_L >$ was calculated in DSP using the digitized load current and the error from $i_{REF}(k)$ was fed into the PI compensator.

SYSTEM CONFIGURATION

The system configuration of the designed MPS is shown in Fig. 2. It used three IGBTs as switching elements. The IGBTs were operated at a same duty ratio but 120° interleaved control phases. Accordingly, the duty cycle of each IGBT was 1/3 of the converter duty cycle. This parallel operation mode also contributes to deal with the thermal problems of the switching components and inductors. Each IGBT output terminal was connected to a small separate inductor in the output filter circuits with reduced size of inductor.

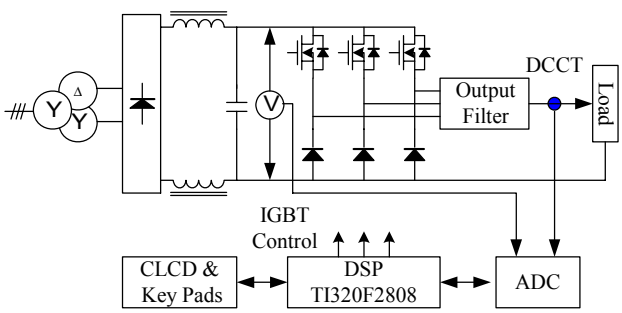

Figure 2: System configuration of MPS.

After each current of three IGBT were added up to output current of 600 A, the second stage output filter circuits were implemented to eliminate higher harmonics.

The output filter and load magnet were modelled as shown Fig. 3, where the load magnet was modelled with R_1 and L_1, and the filter circuit consisted of C_2, R_2 and L_3. The implemented output filter had more components in shown Fig. 3, and the values, which was not appeared components, are so small that the effects of these components could be ignored.

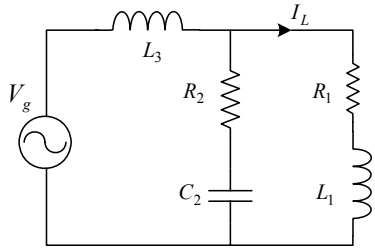

Figure 3: Equivalent circuit of output filter and load magnet.

The transfer function $G_p(s)$ of the circuit in Fig. 3 is

$$G_p(s) \equiv \frac{I_L(s)}{V_g(s)} = \frac{b_1 S + 1}{a_3 S^3 + a_2 S^2 + a_1 S^1 + R_1} \tag{6}$$

where $a_1 \equiv L_1 + L_3 + R_1 R_2 C_2$, $a_2 \equiv R_2 C_2 L_1 + L_3 R_1 C_2 + L_3 R_2 C_2$, $a_3 \equiv C_2 L_1 L_3$, and $b_1 = C_2 R_2$. The control loop for the designed MPS is given in Fig. 4. It does not contain any voltage feedback or reference feed-forward. The coefficients of PI compensator $G_c(s)$ were determined directly using the characteristic equation of the control loop.

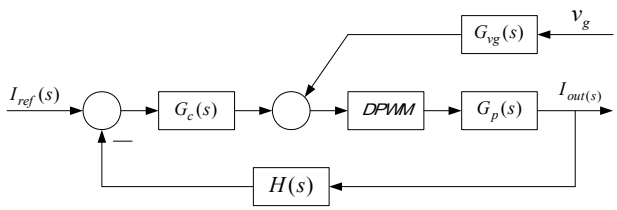

Figure 4: Block diagram of control loop of MPS.

For the diagram in Fig. 4, the output current is given by

$$I_{out}(s) = I_{ref}\frac{G_c(s)G_p(s)}{1+T(s)} + v_g\frac{G_{vg}(s)G_p(s)}{1+T(s)} \tag{7}$$

where $T(s) \equiv G_c(s)G_p(s)H(s)$ and $H(s)$ is the DC current transducer (DCCT) gain. Here the *DPWM* does not affect the loop equation. The step response of the control system is shown in Fig. 5, which shows a critical damp response and the rising time up to 600 A takes about 500 ms owing to the relatively large time constant of the magnet load.

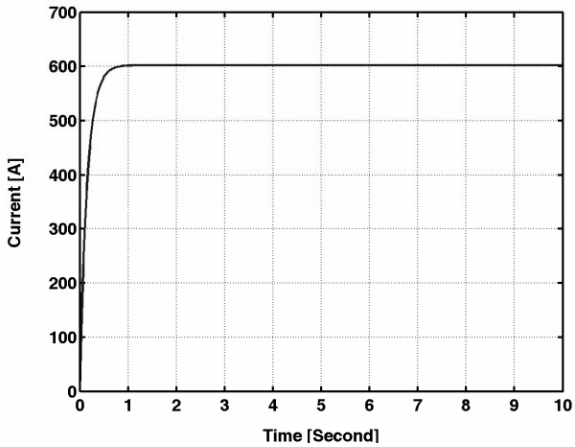

Figure 5: Step response of the overall control system.

We used the DSP TMS320F2808 to control the overall power supply system and the BSM300GB60DLC IGBTs from EUPEC Co. which can drive 300A at 600V link voltage. The controllability of the TMS320F2808 with the micro-edge positioning technology [4] was less than 10 ppm, which satisfied the required accuracy for the MPS. Since three IGBTs were connected in parallel with 120 ° interleaved control phases, the system operating frequency was tripled to 60 kHz and the MPS could drive up to 600 A.

For the control loop, the output current was measured using a DDCT and the output of DDCT was converted into a digital signal using two AD977A 16-bit analog-to-digital converters (ADCs) from Analog Devices. For control loop duration, each ADC digitised the output current ten times and the outputs of both ADCs were summed and averaged to reduce the system noise. The ADCs and EPWM duty control were executed at 20kHz using a real time interrupt routine. The overall control loop was updated for every 500 μs using the Timer Interrupt of the TMS320F2808. Both key scan and the LCD display operations were carried out at the base routine to avoid any serious control timer interrupt.

EXPERIMENTAL RESULTS

A 60 sec. short term current stability at different load current was measured using the HP3458A digital voltmeter from Agilent Co, and the results are given in Table 1 and Fig. 5. The stability of load current was less than 60 ppm at 550 A output current, and it decreased gradually to the 10 ppm at 50 A, as given in Table 1.

Table 1: The measured fluctuation of output current for 60 sec.

Load Current [A]	50	150	250	350	450	550
Stability [ppm]	10	20	30	40	50	60

The long term stability for two hours was also measured at 350A to check the system drift. The DC drift of output current was -10 ppm approximately and the peak-to-peak fluctuation increased to ~50 ppm. We confirmed that the current unbalance between IGBTs at a load current of 600 A was less than 1 A.

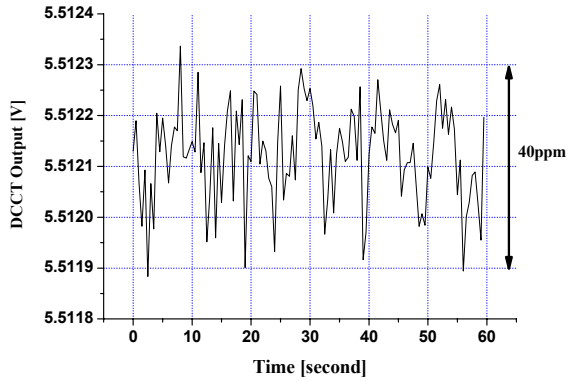

Figure 6: Current stability at load current of 550 A.

CONCLUSIONS

A fully digital-controlled high precision MPS for the Pohang Light Source was designed and tested. The maximum output current of the power supply was 600 A at a precision of ~60 ppm for a load inductance of 5 mH. Three IGBTs were connected in parallel with 120 ° interleaved control phases to increase the output current and system operation frequency. The duty factor for IGBT control was determined using the PI control method. The digital controller of MPS was implemented using two high speed 16-bit ADCs, the DSP TMS320F2808 and the other many components. The current unbalance between IGBTs at a load current of 600 A was less than 1 A. The temperature difference between the IGBTs was ~ 10 °C at the heat sink which was water-cooled to 45 °C for a load current of 580 A.

REFERENCES

[1] J. Carwardine and F. Lenkszus, “Trends in the use of digital technology for control and regulation of power supplies”, International Conf. on Accelerator and Large Experimental Physics Control System. Trieste, 1999, p. 171

[2] I. Cadirci, A. Yafavi and M.Ermis,”Untiy power factor boost converter with phase shifted parallel IGBT operation for medium power applications”, IEE Proc. Electr. Power appl. Vol. 149, No.3, May 2002. p. 237.

[3] G. Garcera, E. Figueres, M.Pascual and J.M. Benavent, “Analysis and design of a robust average current mode control loop for parallel buck DC-DC converters to reduce line and load disturbance”, IEE Proc. Electr. Power appl. Vol. 151, No.4, July 2004, p. 414.

[4] Texas Instruments Co., www.ti.com

REGULATION SCHEME FOR PRECISION MAGNET POWER SUPPLY

Samit Bandyopadhyay, Manoranjan Das
Variable Energy Cyclotron Centre, 1/AF Bidhannagar, Kolkata – 700064, India

Abstract

Accelerators require extremely precise high-current magnet power supplies to drive its magneto-optic devices for proper beam dynamics. The dc precision of the power supply, which generally defines the absolute tolerance of its current, can be split up into three distinct parts - ripple, short-term and long-term stability. To ensure that the output current is within an error-band of 10ppm or less, a three-loop regulation topology has been developed and implemented in a high current magnet power supply (750A/12V) that uses transistor bank as the series pass element.

INTRODUCTION

The component of the dc precision, which also defines the stability of the magnet power supply, is divided into three major parts- a. Long-term stability, b. Short-term stability and c. Output ripple. The major components /modules of the magnet power supply that needs to function simultaneously to meet its required stability components by taking necessary action in terms of power supply output is shown in Figure 1.

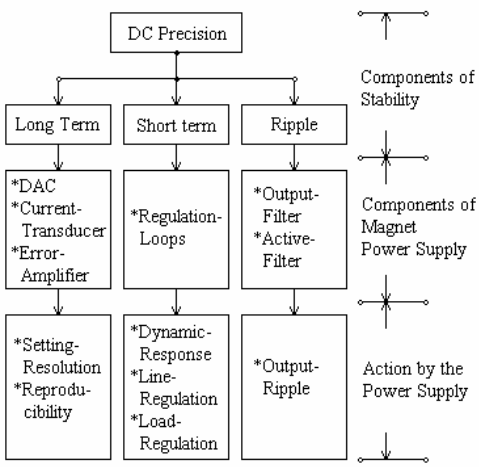

Figure 1: Components of stability of Magnet Power Supply

The factors that are responsible to affect the power supply stability are:

a. The input three-phase ac utility line, which may change in ramp or step.
b. The 12-pulse rectification of the ac signal gives an unregulated voltage, which contains an ac component of 600Hz and its harmonics.
c. Temperature, which affects semiconductor devices the most.
d. Load variation (Resistance of the load) with respect to temperature - a slow process.

REGULATION SCHEME

The implementations of close regulation highly stable low ripple magnet current require a special regulation scheme / topology [1]. The regulation scheme adopted for a high current 750A/12V, 10ppm magnet power supply using a series pass transistor bank is shown in Figure2.

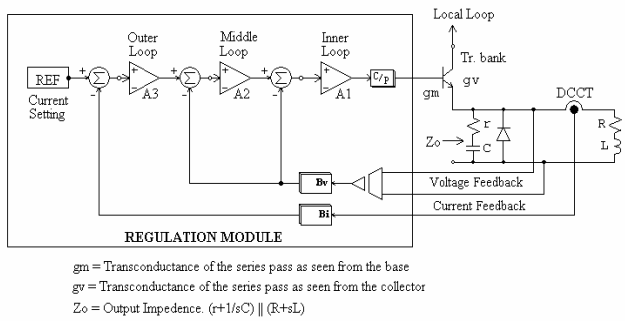

Figure 2: Regulation Scheme

The equivalent model of the designed regulation module along with the transfer function is shown in Figure 3.

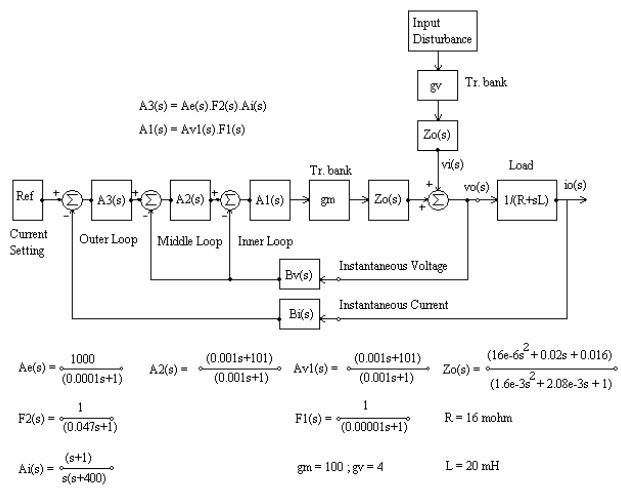

Figure 3 Equivalent model with transfer function

The underlying facts about this regulation topology are:

a. Precision low noise voltage reference source of very low drift and long-term stability for current setting.
b. Highly precise operational amplifiers with low offset voltage, exceptionally low TCV_{os}, high CMRR and PSRR used in the regulation module, increases the system accuracy over temperature.
c. Ultra-stable current sensor in the feedback loop. The current sensing for current regulation loop is done using DCCT [2] based on the zero flux principle. The

DCCT along with its associated electronics is made to give 10V output for primary current of 750A.

d. The regulation module consists of two fast inner voltage feedback loops ensuring short-term stability and an outer slow current loop for ppm stabilization that ensures the overall stability of the power supply.

e. The inner voltage feedback loop acts as an active filter [3] to reject the output voltage ripple. It also rejects the output voltage fluctuations due to float of input mains. The series–pass transistor bank, present as an element of this active filter, has the advantage of large control bandwidth that is considered to be infinity in the model. The output voltage change due to the change in the input voltage is given by the expression (1)

$$\frac{\Delta vo}{\Delta vi} = \frac{1}{1+(A1 \cdot gm \cdot Zo \cdot Bv)} \quad (1)$$

For $A1 \cdot gm \cdot Zo \cdot Bv >> 1$, the equation (1) reduces to

$$\frac{\Delta vo}{\Delta vi} \approx \frac{1}{(A1 \cdot gm \cdot Zo \cdot Bv)} \quad (2)$$

Thus to achieve $\frac{\Delta vo}{\Delta vi} \to 0$, for all disturbances (ripple and fluctuations) from the input, the gain and bandwidth of the denominator of equation (2) has to be made as large as possible. The trans-conductance gm is fixed for Darlington configuration used for the transistor bank. Hence large gain and compensation is done using $A1(s)$ to make the loop stable. The inner voltage loop is closed with respect to input at a frequency of 12.7KHz, and thus a 28db rejection is achieved at input ripple frequency of 600Hz.

f. Considering both the inner and middle loop, the output voltage fluctuation or ripple suppression with respect to the input is given by

$$\frac{\Delta vo}{\Delta vi} = \frac{1}{1+\{(A2+1) \cdot A1 \cdot gm \cdot Zo \cdot Bv\}} \quad (3)$$

For $\{(A2+1).\ A1.gm.Zo.Bv\} >> 1$, the equation (3) reduces to

$$\frac{\Delta vo}{\Delta vi} \approx \frac{1}{\{(A2+1) \cdot A1 \cdot gm \cdot Zo \cdot Bv\}} \quad (4)$$

The combined voltage loops (inner and middle) with proper compensation are closed with respect to the input at a frequency of 23kHz and thus a 52db rejection of 600Hz input ripple.

g. The magnet load with a large time constant (L/R) comes into the outer current control loop. Hence the loop is closed at a low frequency of 0.3Hz so that the pole introduced by the load is above the bandwidth of the circuit and does not affect the current loop stability. This slow outer type–1 (integrating type) current loop helps in getting a zero steady state error, which means that the output magnet current should perfectly obey the command that is the reference signal. This outer loop meets the required load regulation and tracks the reference for long-term current stability.

TEST RESULTS

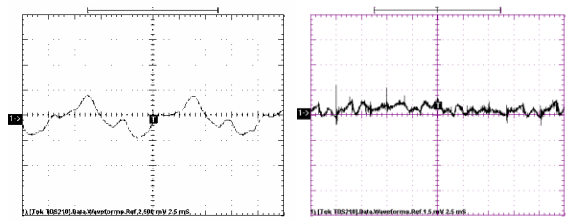

Figure 4. Input Voltage Ripple (left) = $1V_{p-p}$ and Output Voltage Ripple (right) < $5mV_{p-p}$

The input and output voltage ripples at full load current of 750A is shown Figure 4. The output current of the power supply is measured using standard test-bench [4] consisting of a precise ultra-stable DCCT with its associated electronics and 6-1/2-digit data logger for real time monitoring of the output current for obtaining its long-term stability.

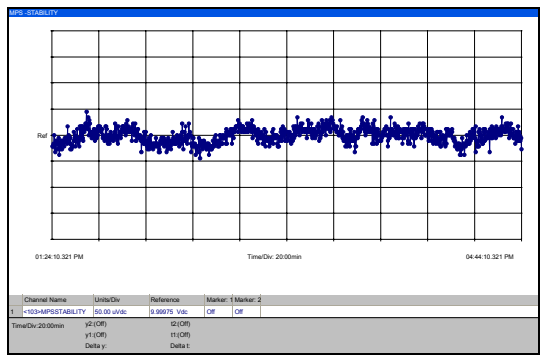

Figure 5. The current Stability Curve (Scale: y-axis: 1div=5ppm; x-axis: 1div=20min)

CONCLUSION

The design and the model of the regulation scheme adopted for the development of precision magnet power supply of 750A/12V comply well with its high stability specification of 10ppm.

ACKNOWLEDGEMENT

We sincerely thank Mr. Anirban De for his valuable help towards improvement of quality of the paper.

REFERENCES

[1] J.McCarthy, D.Wolff, "Very High Precision Current Regulated Power Supplies for the Fermilab Antiproton Source", IEEE Transaction on Nuclear Science, Vol.NS-32, No.5, June1985, Page3778-3780

[2] User's Manual "Ultrastab-866S", Danfysik, Denmark

[3] B.H.Kwon, J.H.Suh, S.H.Han, "Novel Transformer Active Filter", IEEE Transaction of Industrial Electronics, Vol.40, No.3, June1993, Page 385-388.

[4] Y-C Chien, C-Y Liu, J Chiou, K-B Liu, J-T Sheu, "Precision Current Monitor System For The Power Supplies At SRRC", Proceedings of the 2001 PAC, Chicago, Page 3690-3692.

ACTIVE FILTER FOR HARMONIC MITIGATION FOR MAGNET POWER SUPPLIES OF INDUS-II

Yash Pal Singh#, A.C.Thakurta, S.Kotaiah
Raja Ramanna Centre For Advanced Technology, Indore

Abstract

Power supplies used for powering of magnets in INDUS-I and INDUS-II use different type of power converters including SMPS and thyristorised power converters. Though considerations are given to keep the harmonic loading on a.c. mains low while designing these power supplies and selecting a suitable power converter for the required power, still they give a significant amount of harmonic loading on a.c. mains. In all the high power d.c. power supplies, wide variation in operating point leads to a considerable amount of reactive power generation and harmonic loading on ac mains.

In this work a study has been performed to know the variation of reactive power with time on some of the d.c. power supplies of INDUS-II. Various options to improve the power factor has been studied and their advantages & limitations for accelerator magnet power supplies have been highlighted. A combined system of a shunt passive and small rated series active filter has been proposed. The compensation principle is described and filtering characteristics are discussed in detail. A scaled down prototype of proposed series active filter has been developed in lab and experimental results produced.

INTRODUCTION

Harmonic interference problems generated by bulk thyristor converters become increasingly serious as they are widely used in industrial applications in general and accelerator power supplies in particular. So far shunt passive filters have been widely used to tackle this problem. However shunt passive filters have many problems to discourage their application. [6] Filtering characteristics of a shunt passive filter are determined by the impedance ratio of source and shunt passive filter. Fig 1 below shows the equivalent circuit of a shunt passive filter.

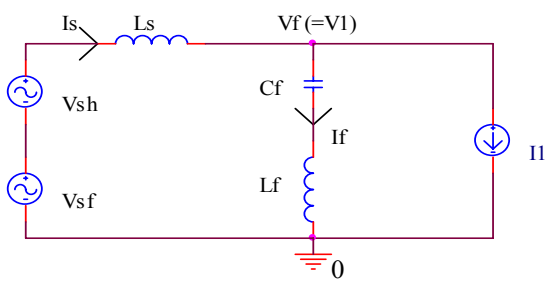

Figure 1: Basic principle of shunt passive filter

#ysp@cat.ernet.in

Therefore shunt passive filters have following problems.

(i) The source impedance, which is not accurately known and varies with the system configuration, strongly influences filtering characteristics of the shunt passive filter.

(ii) Shunt passive filter may fall in series resonance with source impedance for harmonic voltages in source voltage.

(iii) There is a possibility of parallel resonance between source impedance and shunt passive filter at a specific frequency at which even harmonic amplification may take place.

To solve the preceding problems of shunt passive filters, shunt active filters using PWM inverters have been used in recent years. A shunt active filter is controlled in such a way so as to actively shape the source current into sinusoid by injecting the compensating current. Fig 2 below shows the working principle of a shunt active filter.

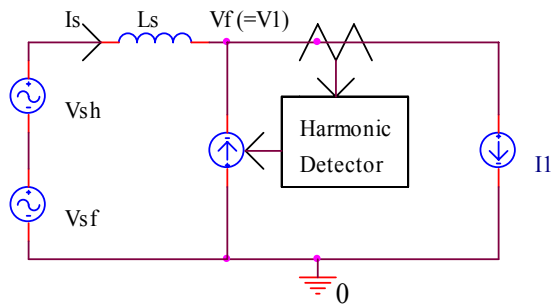

Figure 2 : Basic principle of shunt active filter

Difficulty in realising a large rated PWM current source inverter, high initial cost & low efficiency as compared to shunt passive filters and possibility of importing harmonics from other harmonic producing loads are the serious practical problems with the use of shunt active filters [5].

PROPOSED SCHEME

Conventional shunt passive and active filters have the aforementioned problems, which make their practical application difficult. As is already pointed out, filtering characteristics of a shunt passive filter partially depend on the source impedance which is not accurately known and is predominantly inductive. The impedance of the shunt passive filter should be lower than the source impedance at a tuned frequency to provide the attenuation required. Source impedance can be increased and thereby filtering characteristics of a shunt passive filter can be improved

by inserting an active impedance in series with the source impedance. Also series and parallel resonances in the shunt passive filter, which are partially caused by the inductive source impedance, can be eliminated by inserting an active impedance. This active impedance can be implemented by a series active filter using voltage source PWM inverter in automatic feedback loop.

The proposed scheme can supply a fixed amount of capacitive VARs only and the same has to be taken into account while designing the passive filters. Fig 4 below depicts the typical variation of reactive power for energy ramp time of 5 minutes in INDUS-II. Passive filters can be designed to supply an average KVAR between two extremities to maintain a reasonably good power factor over full range of operation.

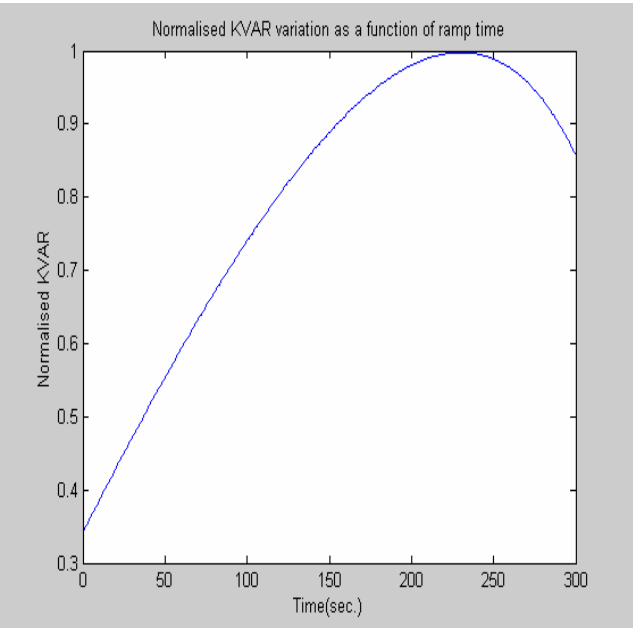

System Configuration and lab prototype

Figure 3 shows a system configuration of the proposed approach to harmonic isolation for generic harmonic producing loads. Figure 4 shows a detailed circuit of series active filter on a per phase basis. A small rating single phase diode rectifier is connected on dc side of inverter, supplying the energy corresponding to the switching and conducting losses in the inverter. The purpose of the transformer is not only to isolate the PWM inverter from the power system, but also to match the voltage and current rating of the PWM inverter with that of the power system.

The harmonic current flowing in the source which is produced because of, both the load harmonic current Ilh and the source harmonic voltage Vsh , is given as :

$$Ish = Ilh*Zf/(Zs+Zf+Rsf) + Vsh/(Zs+Zf+Rsf) \quad \ldots\ldots\ldots(1)$$

$$Ish \approx 0 \text{ if } Rsf >> Zs,Zf \quad \ldots\ldots\ldots\ldots (2)$$

Zs and Zf are source and passive filter impedances respectively. Rsf is the series active impedance introduced by series active filter. Thus a series active filter should maximise Rsf within practical limits to realise the approximation of equation 2. A lab prototype has been developed to test the effectiveness of series active filter in reducing harmonics. A 500VA 1ph diode rectifier, followed by LC filter and resistive load, has been taken as the source of harmonics. A 1ph PWM voltage source inverter has been designed to work as series active filter. The series active filter works on the harmonic current information of 1ph rectifier in an automatic feedback loop to deliver a suitably large value of Rsf as required by equation (2).

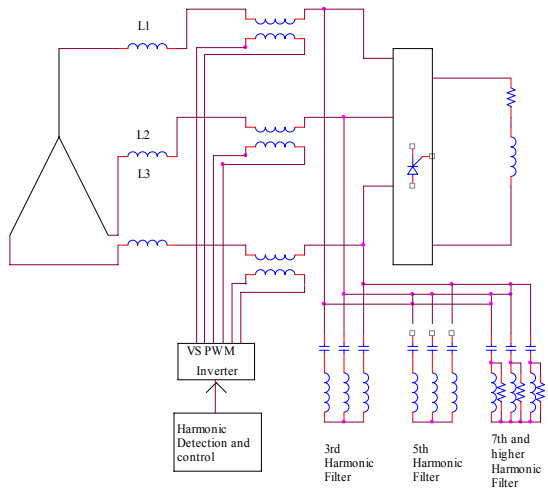

Figure 3: Harmonic mitigation using a combination of series active and shunt passive filters.

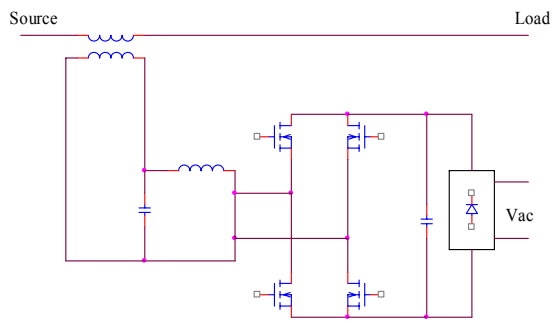

Figure 4 : Detailed circuit configuration of a series active filter on per phase basis

EXPERIMENTAL RESULTS

Figures 6,7 and 8 below shows the results of the proposed scheme on a lab prototype in three different conditions of operation. Results produced are for a source impedance of nearly 4%.Prototype used tuned filters for 3rd and 5th harmonics and a common filter for all higher order harmonics. Measured total harmonic distortion was found

to be nearly 6.0%. 3rd harmonic was found to be nearly 3.75%. For 3ph converters which do not load the line with 3rd harmonic currents, THD figures will be much better. This figure will improve further if a tuned filter is used for 7th harmonic also. Here active filter control works on the information of line current harmonics only. Source voltage was assumed to be purely sinusoidal. A DSP based control to retrieve the information of harmonics using the generalised theory of instantaneous reactive power in 3ph. circuits [1] is under development and results with the same are expected to be still better.

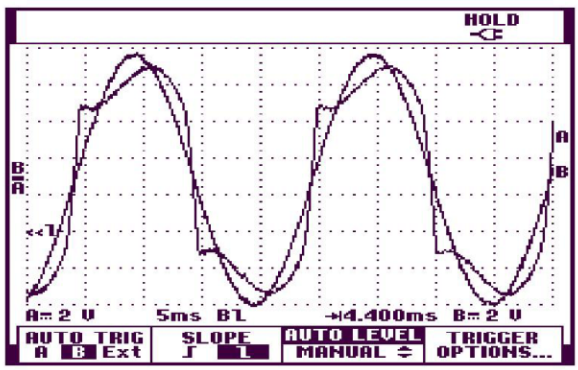

Figure 6: Load current on 1ph mains (Ch. A) and it's fundamental component (Ch. B)

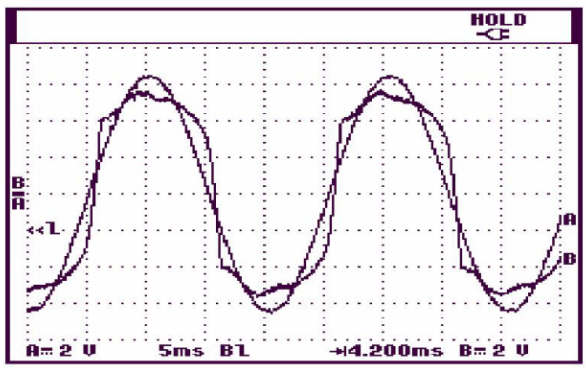

Figure 7: Load current on 1ph. mains (Ch. B) and it's fundamental component (Ch. A) with passive filter only.

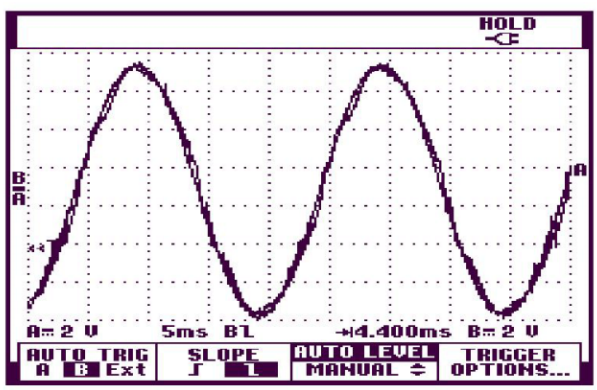

Figure 8: Load current on 1ph. Mains (Ch. B) and it's fundamental component (Ch. A) with both active and passive filters in operation

CONCLUSION

A combined system of shunt passive and small rated series active filter has been proposed in this paper. The compensation principle here is quite different from conventional shunt and series active power filters. The proposed scheme gives better filtering characteristics and offers lower initial and running cost. The proposed scheme is far superior in efficiency to conventional shunt active filters. However this scheme has few limitations listed below.

(i) This scheme in the present form can not supply variable reactive VARs. In our case reactive VARs vary in a wide range because of wide variation in displacement factor during the range of operation. Depending upon the design of passive filter, the present scheme at the most can improve the power factor in general across the range of operation. To get better results, switched capacitor scheme can be used but effect of the same on the dynamics of active filter should be studied.

(ii) Being a series element, active filter should have very reliable protection against overloads and short circuits.

Thus we see that a series active filter works as a harmonic isolator while a shunt active filter works as a harmonic compensator. The combination of shunt passive filter and a small rated series active filter is an efficient, simple and economic alternative to shunt active filters.

ACKNOWLEDGEMENT

The authors thank Shri Satyadav for technical assistance during assembly and testing of the proposed scheme on a lab prototype. We thank our colleagues Mr. Yogesh Kelkar and Mr. Ulhas Karandikar for their help in preparation of VAR curve and documentation of test results.

REFERENCES

[1] H. Akagi, Y. Kanazawa and A.Nabae, "Generalized theory of instantaneous reactive power in three phase circuits," in Proc. 1983 Int. power electronics conference, Tokyo, Japan 1983, pp 1375-1386.

[2] Simone Buso, Luigi Malesani et al, "Design and fully digital control of parallel active filters for thyristor rectifiers to comply with IEC-1000-3-2 standards" IEEE transactions on industry applications,Vol 34 ,No.3,May/June 1998,pp 508-517.

[3] J. van Wyk, " Power quality, power electronics and control" in Proc. 1993 European Conf. Power Electronics and Applications, Vol. 1,pp 17-32, 1993.

[4] M. Takeda, K. Ikeda and Y. Tominaga, " Harmonic current compensation with active filter", in Proc. 1987 IEEE/IAS annual meeting, 1987, pp 808-815.

[5] Hirofumi Akagi, , " New trends in active filters for power conditioning," in Proc. of IEEE transactions on industry applications, Vol. 32, No. 6, November/December 1996.

[6] Timothy L. Skvarenina, "The Power Electronics Handbook" , CRC Press

DIGITAL POWER SUPPLY DEVELOPMENT AT THE PLS*

K.M Ha#, S.C Kim, J.H Kim, J.Y Huang, H.S Kang, J Choi and I.S Ko
Pohang Accelerator Laboratory, Pohang 790-784, KOREA

Abstract

Digital power supply controller using the Digital Signal Processor (DSP) and Field Programmable Gate Array (FPGA) has been developed over the year at the Pohang Light Source (PLS). Recently, full digital buck type bi-phase PS development completed and tested using as the PSI card. A new digital controller is designed as 3 U euro-standard sizes and provides overall performance of the power supplies stability better than ± 5 ppm short-term stability (< 1 min) and ± 25 ppm long-term stability (< 12 hours). It is made use of the digital PI current controller which has one-pole digital filter and feed-forward voltage ripple compensation control algorithms. This paper presents the hardware and software structure of the developed digital controller and experimental results of digital power supply.

INTRODUCTION

Accelerator complex power supply application were increased to choose the based on digital technology [1],[3]. At 1999, the PSI developed the new digital control cards used DSP, FPGA and high precision AD. It was very successfully implemented to beam operation [2]. At 2005, PLS has been successfully replaced over 70 vertical correction PS sets same as PSI digital type, it has good performance and reliability for orbit feedback operation. At 2006, DLS facility commissioned digital type PS for BOOSTER, LINAC and even storage ring [3]. And SSRF in China also trying to develop digital controlled PS for the BOOSTER. PLS has the working experience of the digital PS since 2005 and had satisfactory experimental results. We choose the same type of digital controller for FIR solenoid PS. It is required single quadrant, 200 A, 25 ppm stability. The main topology has a phase shifted parallel operation mode. Practically bi-phase methods are complicated to have current balancing to each lags. But digital controller is capable of the fast cross-over frequency and 20 μs control loops for single feedback loops. This paper descries the implementation of the 20 V / 200 A bi-phase buck converters used full digital controller.

POWER SUPPLY SPECIFICATION

Hardware specification

Switch-mode power supply more advantages than linear type power supply. Switch-mode a buck type PS is common topology for single quadrant operation. The digital cards are simply provides single quadrant mode PWM for a buck converter driving. Fig. 1 shows the proposed bi-phase type buck converter. The maximum output current is 300 A, so we chosen bi-phase method implement more high current rating capability. IGBT device is twins 400 A Ic for parallel operation. Two independent switches were derived by 180 degrees phase shifted (delay) PWMs which makes them two-phase operation.

The FIR solenoid PS hardware specification is shown in table 1.

Table 1: The Specifications of the FIR solenoid PS

Parameters	Specifications
Output voltage/current	20 V / 200 A
Load resistance	0.1 Ohm
Operating quadrant	1 Q
Stability (0 sec to 60 sec)	± 5 ppm
Stability (> 12 hours)	± 25 ppm
Resolution of output current	> 17 bit
Reproducibility	± 10 ppm
Switching frequency	25 kHz bi-phase

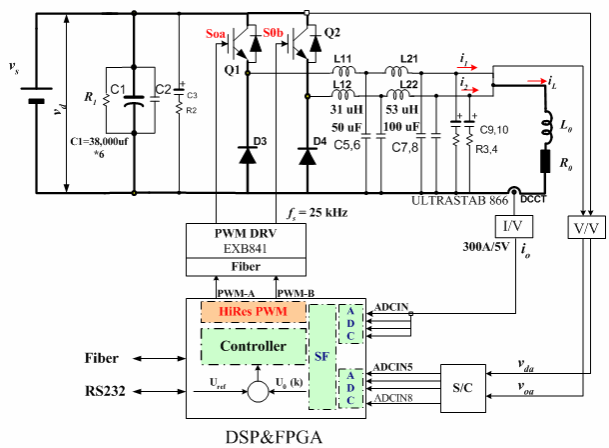

Figure 1: Hardware block diagram of the proposed switched-mode power supply

Controller description

Fig. 2 shows 3U size DSP and AD/DA cards for implementation of digital control power supplies. The core processor is Analog Device SHARC ADSP-21065L 66 MIPS floating-point capabilities with 66 MHz clock. FPGA are used for PWM generation and communication with 5 Mbps fibre channels and 115.2 Kbps serial as well

*Work supported by Ministry of Science and Technology in Korea
#hkm@postech.ac.kr

as 16 digital inputs and 8 digital outputs. For the accelerator control system, 5 Mbaud are applied with VME SBS for fast global control system. In addition to service mode support RS232 serial that is easily used for testing and diagnostics. DSP internal tasks are running every 20 µs (@ 25 kHz PWM frequency) for regulation of loops which perform calculation of error compensation and communication with AD/DA cards.

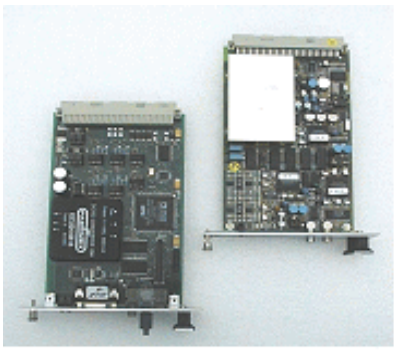

Figure 2: Digital control cards from DLS.

Left: DSP card, right: ADC card

Hardware Circuit Model

Matlab/simPowerSystem is widely using a power electronic circuit simulation. Fig. 3 shows the simplified model of Matlab/simulink for buck converter hardware characteristics of open-loop simulation. Voltage source is VCS (Voltage Controlled Source) DC 20V to 80 V step signals. Input LC and damping RC for DC-link voltage soothing filter the cut-off frequency is near to 45.6 Hz (L = 2 mH, C = 10 mF). Switch model is IGBTs and switching frequency is 25 kHz. In order to simulation buck-converter a power supply with the fallowing values were selected; L1 = 31 µH, L2 = 53 µH, C1 = 50 µF, C2 = 100 µF and magnet load is 10 mH 0.1 Ohm. Switching frequency is 25 kHz with filter order is 5th. Output filter cut-off frequency is the 100 Hz, It given by Fig. 4 (b).

Fig. 4 shows simulation result of load response and filter Bode plots by Fig 3. The output result waveforms are averaged continuance model. Output voltage oscillations are induced from Vin step transient. Input initial voltage is 20 V and final value is reaching up to 80 V.

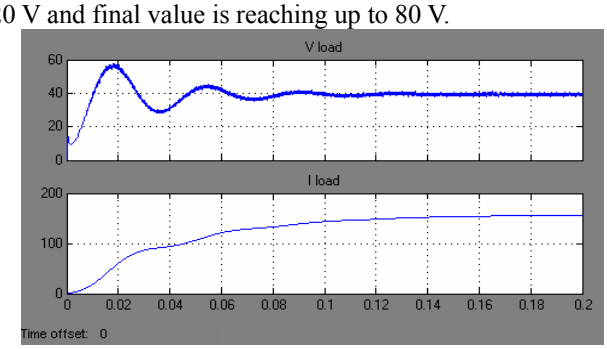

(a) Output voltage and current time constant

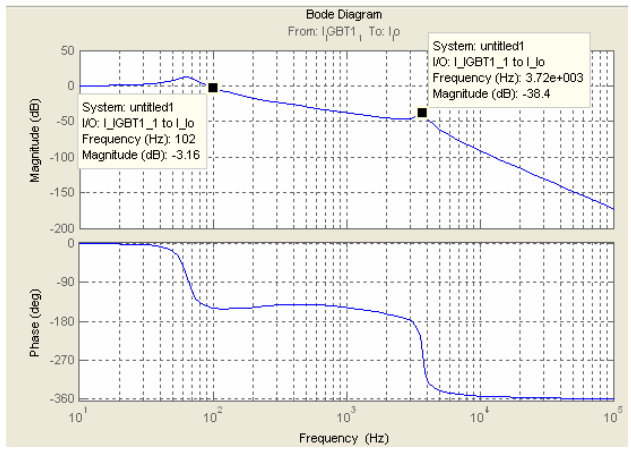

(b) Output filter Bode plots. Cut-off frequency: 100 Hz

Figure 4: Simulation result

EXPERIMENTAL RESULTS

Fig. 5 photograph shows a prototype was built and investigates for FIR solenoid PS. It housed 19" standard rack and divided into three parts; transformer, power stack, and output filter module. Experimental points are focused parallel mode IGBT operation, current stability and

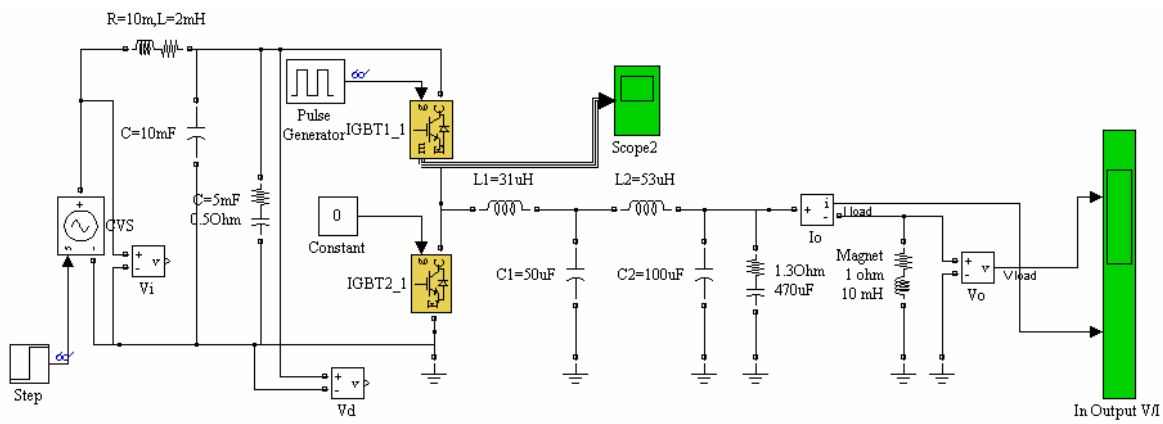

Figure 3: The simulink scheme of the buck converter model

current ripple.

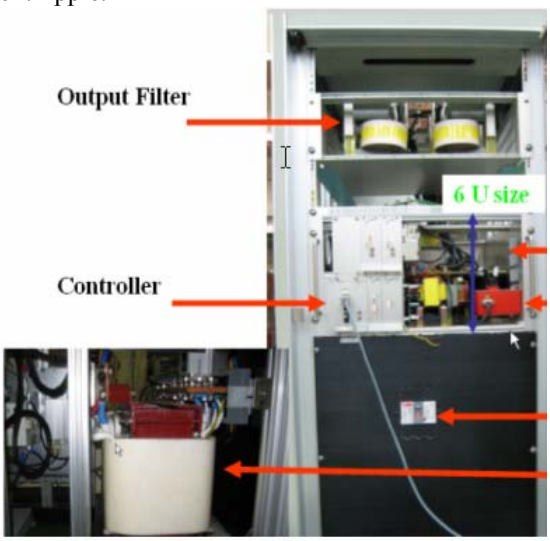

Figure 5: Photograph of completed PS

Fig. 6 shows the PWM signals for IGBTs gate drive and output current ripple waveforms. The PWM 1 and PWM 2 was 180 degree phase delayed due to the one periodic switching. The summing output current ripple is 50 kHz frequency.

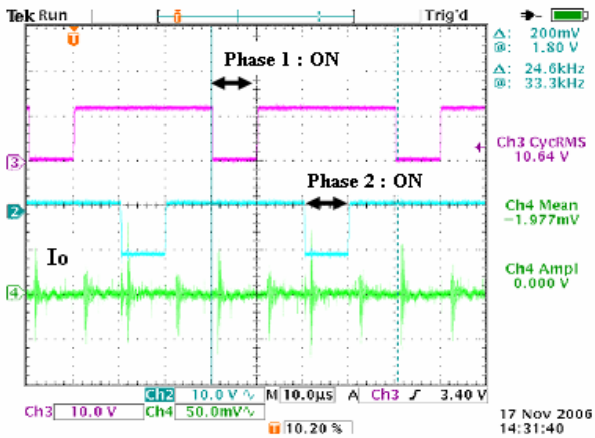

Figure 6: Experimental result of the PWM and current ripple waveform @ 150 A / 20 V. Up: Phase-1 PWM (10 V / div), Middle: Phase-2 (10 V / div), Bottom: Current ripple (50 mV / div), Horizontal time: 10 μs

Fig. 7 shows experimental result of output 5th order filter frequency characteristics. The SR780 Stanford Research Network Signal Analyser is used for the measurement. In the first, filter input have white source from instrument after measurement the response and secondly measurement with variable current 10 to 260 A. The practically attenuation is -70 dBVrms above the 1 kHz; the rejection value is -80 dBVrms at the switching frequency.

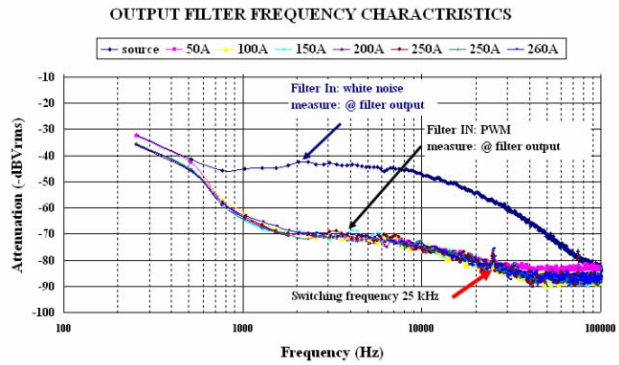

Figure 7: Experimental frequency response of the output LC filter. Upper trace: White source input, Lower trace: real current, horizontal scale is 100 Hz to 100 kHz; Vertical scale is -100 dBVrms to -10 dBVrms

Fig. 8 shows the one hour output current stability at 100 A. It means 3 ppm was very stable current regulation performance due to one hour.

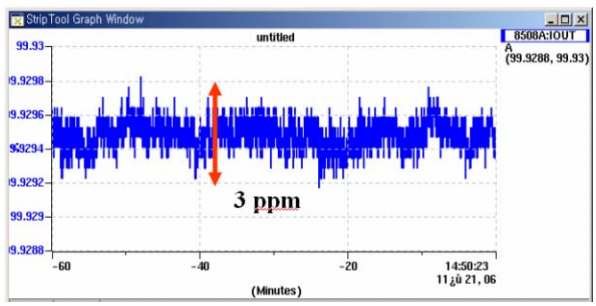

Figure 8: Current stability due to one hour

CONCLUSION

High precision bi-phase digital buck converter was successfully developed for PLS FIR solenoid. By the combination PSI digital cards an extremely flexible and fast prototype produced.

The current stability of the power supply is ± 25 ppm, the current reproducibility is ± 10 ppm and the current ripple is ± 100 ppm. Only single control loops are working well for two legs IGBT parallel operation.
This PS will be installed to the FIR machine by the Feb 2007.

ACKNOWLEDGEMENT

This work is supported by Ministry of Science and Technology in Korea.

REFERENCES

[1] F. Jenni, L. Tanner, M. Horvat, "A Novel Control Concept for Highest Precision Accelerator Power Supplies"
[2] L. Tanner, F.Jenni, “DIGITAL CONTROL FOR HIGHEST PRECISION ACCELERATOR POWER SUPPLIES”, PAC2001
[3] J. A. Dobbing, et al, “DIAMOND BOOSTER MAGNET POWER CONVERTERS”, PAC2006 Edinburgh, Scotland p2664

PAPER NOT YET RECEIVED

UTILIZING MULTIPLIER STACK'S REFLECTED PARASITIC CAPACITANCE TO ACHIEVE ZVS OPERATION OF RESONANT INVERTER FOR 750 keV DC ACCELERATOR

A. Kasliwal[#], R. Banwari, S. Kotaiah, T.G. Pandit, A. Upadhyay
Raja Ramanna Centre for Advanced Technology, Indore 452 013, India

Abstract

This paper presents the analysis and design of a high order LCLC resonant inverter that uses the reflected capacitance of the Cockcroft-Walton based multiplier stack as its tank circuit component. The inverter is being used for energizing the HV generator of the 750 keV dc accelerator developed at RRCAT, Indore. High frequency resonant inverters are replacing the conventional PWM counterparts due to high efficiency, reduced size, weight and cost. The operating characteristics and analysis of series resonant (SRC), parallel resonant (PRC) and series parallel (SPRC) resonant converters have been reported for fixed frequency operation. It has been shown that SPRC takes the advantage of both SRC and PRC curtailing their disadvantages. The inverter described feeds a high frequency, high voltage (HV) transformer isolation and utilizes the otherwise unwanted parasitic components to its advantage.

INTRODUCTION

Hard switching PWM inverters for high voltage application need to feed a very high voltage transformer. The HV transformer requires a relatively large spacing between the primary and secondary windings, which leads to a relatively large leakage inductance. In this case, it is generally difficult to employ a PWM type inverter due to output voltage lost during the reversal of current in the large leakage inductance of a high voltage transformer. On the other hand, an operating frequency higher than 30 KHZ is generally desired to avoid voltage drop across the capacitive column of the high voltage multiplier stack and to avoid any audio frequency noise that may be generated. This in turn improves the load regulation of the system. But it also enhances the effect of parasitic components. A sinusoidal voltage is desired as high frequency harmonics in the square wave voltage impose high dv/dt stress. For lower switching losses, high power density, better EMI characteristics and sinusoidal voltage and currents, resonant inverters have proved to be a better proposition. A series resonant inverter has the disadvantage of high circulating currents that increases the switching device ratings. Furthermore, a series resonant inverter cannot actually be developed due to the large parasitic capacitance generally existing in a high voltage transformer. Hence a series parallel LCLC combination has been used as it gives the advantage of low device currents and a better load regulation. The converter utilizes the leakage inductance and the inter-winding capacitance of the high voltage transformer it feeds to and the parasitic capacitance of the multiplier stack, for its resonant operation. This LCLC resonant tank functions to position zero voltage across the switching device prior to turn on, eliminating any power loss due to the simultaneous overlap of switch current and voltage at each transition.

The multiplier stack basically consists of several similar circuits containing diodes and capacitors, which are connected in series to achieve voltage multiplication. The high voltage rating demands the placement of components to be fairly apart to achieve required voltage isolation. The circuit is fed with a 40 kHz sine wave to achieve better regulation and minimum ripple at the DC output. Combined together, all these results in higher parasitic components. These capacitances are mostly contributed by parasitic capacitance between DC and AC columns of multiplier stack, diode capacitance etc. Moreover the stack is fed from a 45 kV-0-45 kV high voltage transformer with a very high step-up ratio, which is 150 in our case. The transformer secondary itself imposes high distributed capacitance

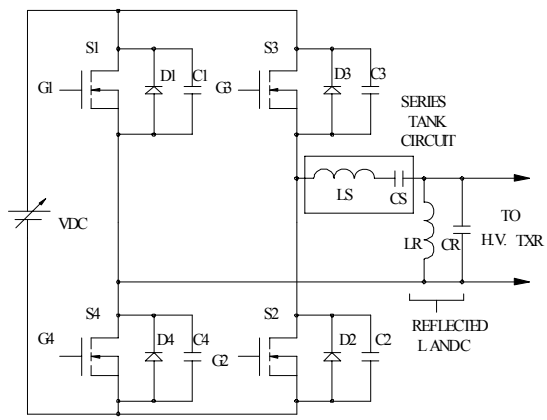

Figure 1: High frequency inverter.

OPERATION

When measured at the primary of the HV Transformer with the multiplier stack connected at its secondary, the reflected load at inverter output was found to be purely capacitive with a value of 4.1 μF. This could have been compensated by a parallel inductance on the primary side but it would have then resulted in high circulating currents in the transformer winding. Referred to the secondary side of the transformer, this capacitive reflection effectively comes out to be 0.177 nF.

[#]apollo@cat.ernet.in

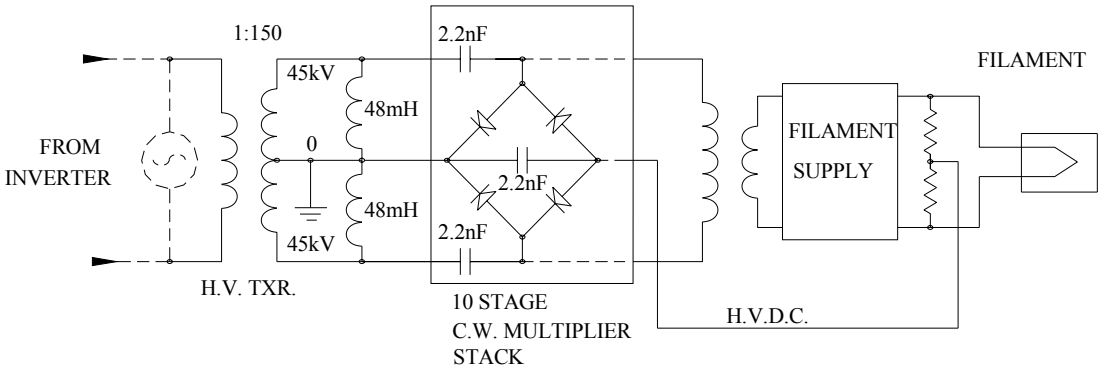

Figure 2: High voltage generator.

The compensating inductance required then was 96 mH to keep the resonating frequency very close to switching frequency of 40 kHz. This selection kept the no load circulating current demand at the switch end to the minimum possible.

A full bridge topology with fixed frequency operation is used in this inverter. The diagonal switches are driven together alternately to place an AC voltage across the resonant tank. Power is only transferred to the output section during the ON times of the switches. When the switch pair, which is currently on is switched off the primary current flows into the switch output capacitance causing the switch drain voltage to resonate to the opposite input rail. At the same time a current flows the output capacitance of the other pair of the switch discharging it to zero voltage enabling Zero Voltage Switching upon its turn on. An intentional dead time has been introduced in the power conversion cycle by using a higher value of resonant inductor, whereby the switch remains off and is clamped at zero voltage by the resonant tank. Rather than turn on the switch instantly when the zero voltage is attained, the switch is held off while the primary current circulates through the body diode. This has been done to achieve the ZVS condition for the full range of operation of the inverter. The minimum time available for the charged snubber capacitor placed across the off device was found to be 1.56 μS, under worst case of no load condition. The resonant inductive energy was sufficient to discharge the capacitor before the device was put on thus ensuring the ZVS operation.

The inverter output is varied by varying the input DC, which is tapped from a fully controlled 3-phase rectifier. The switching devices used are Mitsubishi make half bridge IGBT modules (CM200DY-24H). The switching frequency is kept at 40 KHZ. The series LC is tuned at 40 KHZ, which filters the higher harmonics to yield sinusoidal fundamental of 40 KHZ at the output. The parallel LC tank is tuned at 45 KHZ to limit the circulating current to 20% of the full load current at no load condition. This though impresses higher stress on switching devices, it yields the desired load regulation. The inverter operates under ZVS for the complete range of load variation. Thus a loss less snubber containing only a capacitor of 10 nF across each device has been used. This further improves the power transfer efficiency of the inverter. Complete discharge of the snubber capacitor has been assured under the worst case of no load condition to ensure ZVS operation of the inverter. The driver card designed for the switching device blocks the firing pulses in case the capacitor is not completely discharged by the load current avoiding lossy turn on of the device. The inbuilt anti-parallel diode of the IGBT module has been used to provide path for the freewheeling current.

CONCLUSION

The inverter has been tested up to 25 KW by using a water load and all the waveform have been found to be as stipulated. This inverter feeds a center tapped high voltage transformer with secondary peak voltage rating of 45kV-0-45KV. The transformer in turn feeds a 10-stage symmetrical voltage multiplier stack to generate the required DC high voltage of -750 kV.

REFERENCES

[1] J. R. Pinheiro, T. F. Pegoraro and J. E. Baggio, “Analysis and design of a DC/DC ZVS PWM off-line converter”, IEEE Applied Power Electronics Conference (APEC), 1998, pp.640-645.

[2] A. K. Bhat and V. Belaguli, “Analysis and design of hybrid parallel-series resonant converter” IEEE Trans. Circuits and Systems, Part-I: Fundamental Theory and Applications. Vol. 44, No. 8, Aug. 1997, pp. 705-711.

300 KV, 6 KW POWER SUPPLY SYSTEM FOR SELF-SHIELDED LOW ENERGY DC ACCELERATOR AT RRCAT INDORE

R. Banwari*, A. Kasliwal, Ajay Kumar, A. Upadhyay, P. R. Nath, S. Kotaiah and T. G. Pandit
Raja Ramanna Centre for Advanced Technology, Indore

Abstract

A compact, low energy, self-shielded dc accelerator for industrial applications requiring beam energy in the range of 100 to 300 keV is under development at RRCAT, Indore. The power supply and control system for this accelerator is discussed here in this paper. The high voltage source is a series fed cascade generator driven by a 30 kHz sine wave inverter. Two asymmetrical cascade generators are run in parallel to enhance the current capacity of the generator. A 15-0-15 kV, 30 kHz ferrite core transformer interfaces the cascade generators with IGBT based H-bridge inverter. A buck chopper controls the dc bus voltage of the inverter so as to control the terminal voltage of the high voltage generator. A low power high frequency inverter generates the filament power supply floating at terminal voltage of the accelerator through a capacitive isolation column. Control of the filament power supply is achieved by sensing the accelerator beam current and controlling the low power inverter in a closed loop. A PC based control system designed with Lab-View 7.0 software and ADuC812 Micro-converter cards monitors and displays the various parameters of the power supply and accelerator.

INTRODUCTION

Electron beam curing is an energy efficient process, which creates unique products and improves the existing ones. It occupies less space as compared to thermal ovens and cures all the colours equally with complete removal of solvents. Radiation curable inks and coatings can be employed essentially to any substrate imaginable including paper, wood, metal, leather, vinyl, plastic, glass and magnetic tape etc. Being radiant energy the electron beam directly converts reactive liquids into solids and do not have to rely on energy-intensive evaporation system to remove solvents or water.

Electron beams are currently being used in industries for the curing and cross-linking of coatings, inks and adhesives. An energy in the range of 100 to 300 keV is useful in many applications like heat shrinkable foils and tubes, hardening of coatings, wrinkle free textiles by graft polymerisation, surface sterilization of food materials and surface hardening of plastics. Keeping these applications in focus a compact, **S**elf-shielded, **L**ow **E**nergy dc **A**ccelerator (SLEA) is being developed at RRCAT. The operating energy of the accelerator is chosen as 100 to 300 keV with maximum beam power of 6 kW. The accelerator assembly is compact and light enough to be transported and installed at the site of demonstration or application. Design features and developmental aspects of the high voltage generator, filament power supply and control system for this accelerator is described in following sections.

*banwari@cat.ernet.in

HIGH VOLTAGE GENERATOR

The required accelerating voltage for this accelerator is generated using high frequency multi doubler circuits driven in parallel as shown in block schematic of Fig 1. A 30 kHz, 10 kW driver inverter feeds the power to the multiplier column through a centre-tap ferrite core high voltage transformer. A resistive voltage divider is used for measurement and control of the accelerator terminal voltage. A fast acting stabilization circuit operates the high voltage power supply either in a constant voltage or constant current mode. Both these functions can be controlled and monitored remotely through a PC that also displays the beam parameters.

For safety considerations the multiplier stack is designed for minimum stored energy. At the same time the ripple in the output voltage is kept low by selecting the high frequency operation. The power supply is short circuit protected by use of damping resistor and trip features of the chopper and inverter units. The filament power supply is generated through a capacitive isolation column, which is fed from a low power inverter. The beam current is stabilized by controlling this inverter in a closed loop with respect to emission current. The high voltage terminal of the multiplier stack is provided with a hemispherical dome and individual decks are fitted with equipotential rings so as to give electrostatic shielding to multiplier components and to control the external electric fields.

The multiplier stack embedded with high voltage divider and capacitive isolation column is fully contained in a SF_6 filled tank, which provides excellent insulation. The design aspect and constructional features of various subsystems of the high voltage generator are briefly described in following subsections.

Rectifier and Chopper Unit

The three-phase AC mains is rectified and filtered by an uncontrolled bridge rectifier and resultant DC voltage is fed to a buck-chopper, which regulates the inverter DC bus voltage in a closed loop. A half bridge IGBT module is chosen for this application where the first device is used as a chopping element and second one, with its gate-source shorted, serves as the freewheeling diode for the output stage thus reducing the size. The feedback signal for the chopper unit is derived from the terminal voltage of the HV generator through a resistive voltage divider. This means, controlling the chopper output voltage finally controls the beam energy of the accelerator.

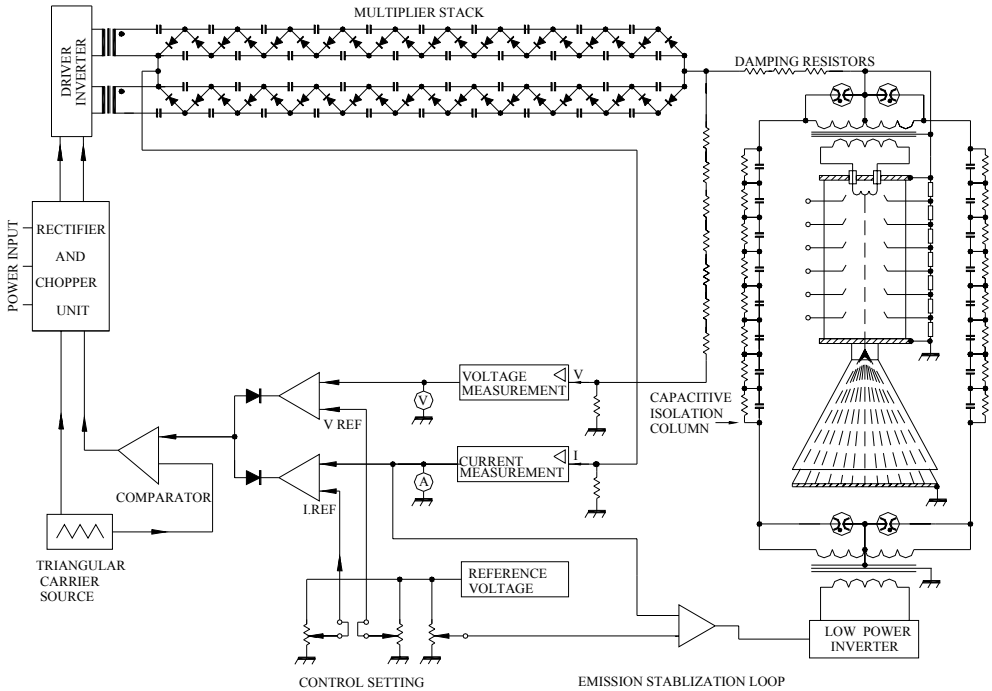

Figure 1: Block schematic of high voltage generator and filament power supply for 300 keV, 6 kW Self-shielded Low Energy DC Accelerator.

Driver Inverter

This IGBT inverter uses a high order LCLC resonant tank circuit to generate a sinusoidal voltage. For multiplier circuits a sinusoidal voltage is desired as high frequency harmonics in the square wave voltage impose high dv/dt stress resulting large peak currents in the components. A series parallel combination of LC

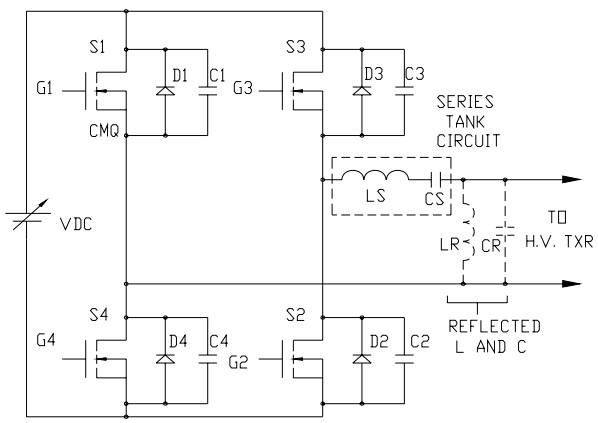

Figure 2: Schematic of the high frequency inverter.

tank circuits gives advantage of low device current and better load regulation. A full bridge topology is used for the inverter with fixed switching frequency of 30 kHz. The inverter output is controlled by controlling its DC bus voltage with the help of a buck chopper described earlier. The series arm of the LC tank circuit is tuned at 30 kHz, which filters the higher harmonics to yield a sinusoidal fundamental of 30 kHz at the output. The parallel LC tank circuit has been slightly detuned so as to limit the no-load circulating current to about 20% of the full load value. Complete discharge of the snubber capacitors has been ensured under the worst case of no load condition to maintain ZVS operation of the inverter. Thus a loss less snubber containing a capacitor of 10nF across each device has been used. Figure 2 shows schematic of the inverter.

High Voltage Transformer

The 30 kHz high voltage transformer is developed using U-93 ferrite cores. Two identical 400 V: 15 kV transformers with VA ratings of 6 kVA are made and connected in parallel. Secondary windings of the transformers are connected in series to realize a centre-tap configuration. The whole assembly is kept in oil filled tank and the high voltage terminals are brought out through Teflon bushings. Technical specifications and design parameter of individual transformers are listed below in Table 1.

Multiplier Stack Assembly

The 12-stage multiplier stack is realized using 2 kpF, 40 kV, high K, DC ceramic capacitors and 0.6 A, 30 kV, glass-passivated fast recovery avalanche diodes. Two asymmetrical voltage multiplier circuits fed from opposite phase secondary windings of the high voltage transformer run in parallel to improve upon ripple and regulation. Components of the multiplier circuits along with damping resistors are distributed and arranged

over 12 circular decks of glass epoxy. Each deck assembly corresponds to a single stage of the multiplier stack and they are fitted with equipotential rings. The equipotential rings are referred to DC potentials of the respective deck. A central space of 400 mm diameter is left clear for mounting of the acceleration column. A hemispherical dome fitted at the top of the multiplier

Table 1: Transformer Specifications

Specifications/ Design Parameters	Fabrication Details
Frequency : 30 kHz	Core : U-93 Ferrite Core (three pairs)
VA Rating : 6 kVA	
Primary Voltage : 400 V	Cross section : 2340 mm^2
Sec Voltage : 15 kV	Construction : Core Type
Flux Density : 0.120 T	Cooling : Oil Natural
Mag Inductance : 1 mH	No. of Pry turns : 8
Leakage Induct. : 8 µH	No. of Sec turns : 415
Core Loss : 57 W	Pri Wdg. : Cylindrical
Cu Loss (Pry) : 8 W	Pri Conductor: Litz wire
Cu Loss (Sec) : 3.5 W	Sec Wdg. : Cross-over
Regulation : 11%	Sec Conductor: 25 SWG

Figure 3: 300 kV multiplier stack assembly

stack provides a PD free termination of the accelerating voltage. The resistive voltage divider and the capacitive isolation column for feeding power to electron gun are also accommodated in the deck assembly. Figure 3 above shows a photograph of the 300 kV multiplier stack assembly.

FILAMENT POWER SUPPLY

The accelerator uses an indirectly heated LaB_6 disc type cathode of 4mm diameter as electron emitter. A power supply of 2.5 volts and 15 amperes is required to heat the filament for its full range of emission. The filament power supply has been designed and developed with a maximum rating of 5volts and 18 amperes, using series resonant scheme at a switching frequency of 30 kHz. The injector control unit of this accelerator comprises a 200-Watts, 30 kHz fixed frequency inverter, a ferrite core step up transformer, a 12-stage capacitive isolation column and a ferrite core step down transformer. The output voltage of the inverter is stepped up through a 10 kV high voltage transformer and fed to the isolation column, which provides required DC isolation of 300 kV between the inverter and electron emitter. The AC voltage available at the top of the isolation column is stepped down and fed to the cathode heater directly. An emission stabilising circuit controls the output of the inverter in a feed back loop so as to stabilise the emission current.

CONTROL SYSTEM

A PC based control and monitoring system is employed to automate the complete operation of the accelerator. Beam energy and current are regulated in real time by control loops of the HV generator and filament power supply against their set values. The PC is used to set these values and display the read-back signals. It is also used to control the on-off operation of different power supplies and subsystems of the accelerator and display their parametric values as well as status.

The control system uses Analog Device's 8051 core based micro-converter AduC 812 chip, which has inbuilt ADCs and DACs thus reducing the over-heads for both hardware and software drastically. Each power supply and subsystem is equipped with an AduC812 based micro-converter card and they are connected to the PC through a common RS485 multidrop line. The cards act as a slave with a unique address given to them. PC acts as a master and communicates with different power supplies and subsystems through this known address. The data communication takes place through well-framed packets, which contain the address of the source and the destination, the data and the checksum byte. The software for the PC operation is written using Lab-View 7.0, which is a dedicated standard industrial software development suit.

REFERENCES

[1] *R. Banwari, Apollo Kasliwal, Alok Tripathi, T. G. Pandit, S. Kotaiah,* "High Voltage Generator for 750 keV/ 20 kW DC Electron Accelerator"; Proc. Indian Particle Accelerator Conference, February 3-6, 2003 (InPAC-2003), CAT Indore; pp.277-280.

DEVELOPMENT OF 3 MeV, 30 kW DC ELECTRON ACCELERATOR AT EBC, KHARGHAR

K.C.Mittal, K.Nanu, A.Jain, K.V.Nagesh, S.Acharya, G.P.Puthran, R.I.Bakhtsingh, P.C.Saroj, D.K.Sharma, R.N.Rajan, Mukesh Kumar, S.K.Srivastava, A.S.Chawla, A.R.Chindarkar, S.R.Ghodke, D.Jayaprakash, Mahendra Kumar, Rajesh Barnwal, R.L.Mishra, Vijay Sharma, S.Dewangan, S.R.Barje, R.M Agarwal, M.K.Pandey, S.R.Raul, D.P.Chakravarthy and A.K.Ray
Electron Beam Centre, Accelerator and Pulse Power Division, Bhabha Atomic Research Center, Kharghar, Navi Mumbai, India

Abstract

A 3 MeV, 30 kW DC industrial electron accelerator has been designed and is in advanced stage of development at Electron Beam Center, Kharghar, Navi Mumbai. Electron beam at 5 keV is generated in electron gun with LaB_6 cathode and is injected into accelerating column at a vacuum of 10^{-7} torr. After acceleration, the beam is scanned and taken out in air through a 100 cm X 7 cm titanium window for radiation processing applications. The DC high voltage accelerating power supply is based on a capacitive coupled parallel fed voltage multiplier scheme operating at 120 kHz. The electron gun, accelerating column and high voltage multiplier are housed in accelerator tank filled with SF_6 gas insulation at 6 kg/cm^2. This paper describes about the design details and current status of the accelerator and its various subsystems.

INTRODUCTION

Electron beam accelerators are finding wide ranging applications like surface curing of coatings, cross-linking polymeric materials, sterilization of medical products, coloration of diamonds, disinfection and preservation of food products, purification of industrial and biological waste etc. Electron beam energy and dose rate for different application differs widely depending upon the type of product and the desired modification. The beam energy and dose rate requirement for these types of applications ranges between 0.15 MeV to 10 MeV and few kilowatt to hundreds of kilowatts. In view of the growing needs we have taken up indigenous development of industrial accelerators at APPD, BARC. A machine rated for 3 MeV, 30 kW beam power is now under development [1] which being commissioned at Electon Beam Centre, Kharghar, Navi-Mumbai. The 3 MV DC supply for this based on a parallel fed voltage multiplier scheme considering power efficiency, energy stability and reliability [2]. The accelerator is designed to operate with beam energies from 1 MeV to 3 MeV with beam current of 0 -10 mA.

ACCELERATOR DESIGN

Schematic of the accelerator is shown in Fig. 1. The accelerator and its high voltage power supply are housed in a pressure vessel filled with SF_6 gas as the insulation at 6 kg/cm^2. The accelerator is a vertical assembly housed in a concrete building where the accelerator is located in the upper cell and the product irradiation facilities in the lower cell. A triode electron gun using LaB_6 cathode generates the electron beam and injects into the accelerating column at 5 keV. This beam is accelerated through a 3.5 m long accelerating column assembly consisting of 10 numbers high gradient metal-ceramic diffusion bonded tubes made by NEC, USA. Potential grading of the accelerating column is accomplished by a resistive divider chain. Electron beam after acceleration is transported through a beam line, scanned and brought out to atmosphere through titanium window for radiation processing applications.

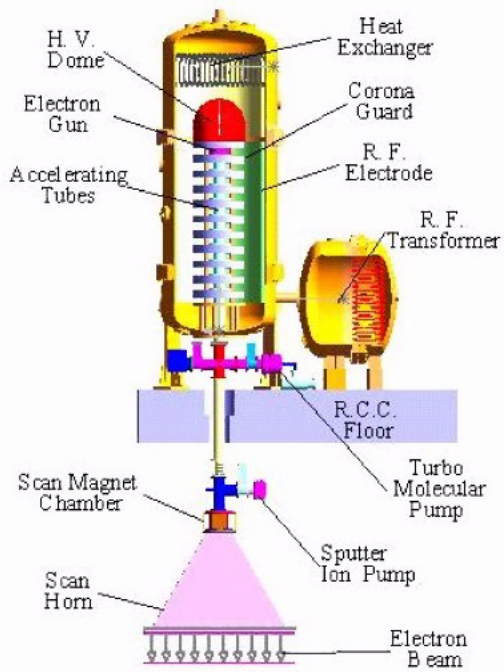

Figure 1: Schematic of 3MeV, 30kW Accelerator

High Voltage Supply System

The 3 MV, 10 mA DC supply for the accelerator is based on a 68 stage, capacitive coupled parallel fed voltage multiplier scheme operating at 120 kHz. The input to the voltage multiplier is 150 kV - 0 -150 kV (peak), 120 kHz which is fed to a pair of semi-

cylindrical feeder electrodes. The feeder electrode assembly supported on the insulators inside the pressure vessel is shown in fig.2. Power from the feeder electrodes is coupled to an array of semi-circular corona guards of the voltage multiplier column through the inter-electrode capacitances between each corona guard and the RF electrode. The coupled voltage between two opposite corona guard is about 50 kV (peak). These stage voltages are rectified using 68 numbers of high frequency rectifier stacks and cascaded to achieve 3 MV DC. Extra corona guard electrodes are provided for extracting auxiliary power at the high voltage terminal and for ripple filter.

Figure 2: Feeder Electrode Assembled inside the Pressure Vessel

Figure 3: 150kV-0-150kV/120kHz transformer

The 150 kV - 0 -150 kV (peak), 120 kHz source is generated [3] by class-C push pull vacuum tube oscillator operating in Colpits configuration and a resonant transformer. The self capacitance between RF electrodes and the secondary inductance of the transformer forms the tank circuit for the oscillator. Feedback for the oscillator is derived by configuring electrodes in between RF feeder electrodes and pressure vessel. The transformer is an air-core in toroidal geometry, made using 2464 strand, 40 AWG Litz wire has 5 mH inductance and no-load Q factor of 1500 at 120 kHz. A photograph of the transformer installed inside the transformer vessel is shown in fig.3.

The high voltage multiplier column is assembled around the accelerating column on an acrylic support structure. Height of the voltage multiplier column is made nearly equal to the accelerating column to minimize radial electric field stress between them. Components dimensions and geometries are designed to limit electric fields less than 160 kV/cm with 6kg/cm^2 SF_6 gas environment. For measurement of 3 MV DC a voltage divider chain made into 4 modules is attached on the high voltage column. A photograph of the voltage divider module is shown in fig.4.

Figure 4: 750kV Voltage Divider Module

Auxiliary Supply on 3 MV Terminal

For powering the devices which are floating at 3 MV terminal is provided by an alternator. The alternator is driven by a motor and an insulator shaft assembly supported on the high voltage column. The ratings of the power supplies at the high voltage terminal are 15V/20A, 5kV/15mA and 3kV/5mA for filament, anode and control electrode respectively of the electron gun, 24V/4A for sputter ion pump and 18V/1A for control electronics. Arrangements are also made for extracting power from the RF source itself at the terminal using a step-down transformer.

Beam Generation and Transport

A triode electron gun using indirectly heated LaB_6 material as cathode is the source of electron. Electrons beam is extracted with anode potential of 5 kV which is injected to in to the accelerating column. Magnitude of the beam current can be adjusted by controlling the heater temperature and the potential on the control electrode. Injected beam is accelerated under the applied potential and further transported through a 3.5 m long, 100 mm diameter beam line to the scan chamber. Vacuum pumping systems are attached on this beam line. Apart from vacuum system there is a thermal based beam locating aperture, a focus coil, and two sets of beam steering coils. Before the beam enters into the scan chamber it can be aligned by adjusting current in these coils. The beam is then scanned at 100 to 200Hz to cover over 1 m width uniformly using a bipolar magnet and brought out to the atmosphere through 120 cm x 7 cm, 50 micron thick titanium window for product irradiation.

Figure 5: High Voltage Assembly

Utility Systems

Other than the core systems described above there are many other sub-systems which are essential for reliable and safe operation of the accelerator. This includes radiation shielding, vacuum system, SF6 storage & transfer system, ozone removal system, product conveyor system and cooling systems. For radiation shielding the accelerator is housed in concrete building. Accelerator is located on the upper floor above the irradiation cell isolated one another with 1 m thick concrete slab to protect the sensitive components from high intensity X-Rays. Irradiation cell having 1.5 m thick concrete walls attenuate the estimated radiation of 4.6×10^8 mR/h at 1 m from source to a safe limit value of 0.1 mR/h in the occupational area. Separate conveyor arrangements are made for handling thick cables and products in trays. Two blowers of 11268 cfm capacity remove the ozone in the irradiation cell. This ensures ozone level in the cell below 0.1 ppm within 5 minutes of switching off the beam. Two chiller type heat exchangers, one at the top of the accelerator and the other in the RF transformer side tank removes heat generated within the accelerator tank. Cooling of scan horn, beam dump, vacuum system and oscillator components are with low conductivity water. Forced air cooling system is incorporated for the beam aperture. A SF_6 handling system consists of two storage tanks and a handling cart that can transfer the gas from accelerator tank to the storage tank and back to accelerator tank during maintenance. This system is also capable of evacuating the tanks up to 0.1 torr in either direction and also can remove dust, breakdown products and moisture through filters built in the handling cart.

Control and Protection Systems

A two level control scheme is adopted for the accelerator in which a centralized control system is for the normal operation and local control for each sub-system. This scheme allows easy testing and maintenance. All signals to and fro from the accelerator are brought on the respective local control. From local controls, the signals which are essential for regular operation is transferred to the control room for computer control. Control instrumentation has a number of interlocks for the personal and system safety. Most of this interlocks are ultimately linked with the high voltage power supply controls which inhibit operation in case of fault. A micro controller based annunciation panel is incorporated in the high voltage system local control which helps in fault identification. For protection of sensitive components hard wired fast acting interlocks are incorporated in the local control level. In order to minimize EMI, signal transmission between the accelerator and control system is through optical isolators.

STATUS AND SUMMARY

Fabrication of all the sub-systems of 3 MeV accelerator is completed. Most of the sub-systems like 50kW/120 kHz oscillator, RF feeders, 150kV – 0 – 150 kV transformer, SF_6 transfer system, cooling system, beam scan assembly, conveyor system, vacuum system are installed and tested. Installation and testing of the high voltage supply is in the advanced stage. It is expected that the accelerator will be commissioned shortly.

REFERENCES

[1] R. Majumder, K.C. Mittal, K.Nanu et al, “Design and Development and Status of 3 MeV, 30 kW DC Industrial Electron Accelerator at Electron Beam Centre, Kharghar”, Proc. InPAC-2003, CAT, Indore, Feb. 3–6, 2003, p-241.

[2] K. Nanu**,** D.K. Sharma, R.N. Rajan et al , “Design of 3MV, 10mA DC Power Source for E-Beam Accelerator”, Proc. InPAC-2003, CAT, Indore, Feb. 3–6, 2003, p-246.

[3] R.I.Bakhtsingh, S.K.Srivastava, P.C.Saroj et al, “Design of 50kW, 300kV RF Source for 3MeV, 10mA Industrial Electron Accelerator”, Proc. InPAC-2003, RRCAT, Indore, Feb. 3–6, 2003, pp-447.

ANALYSIS AND DESIGN OF A PARALLEL RESONANT NETWORK POWER SUPPLY FOR A RAPID CYCLING SYNCHROTRON

Sunil Tiwari[#], Mangesh Borage and Swarna Kotaiah
Raja Ramanna Centre for Advanced Technology, Indore 452 013, India

Abstract

Rapid Cycling Synchrotron (RCS) requires dc biased sinusoidal excitation for electromagnets. Power supplies based on resonant schemes are best suited for such applications, as only the losses of the resonant network are drawn from the mains and the magnets are energized by resonating its inductance with external energy storage elements. In this paper study of various options for powering the magnets and its excitation source is carried out. Optimization of network elements for parallel resonant network with respect to the operating and investment cost is carried out. Tolerance analysis of a high-*Q* resonant network with respect to variation in component values and its effect on amplitude and phase of magnet current, and the ac component reflected in the magnet current due to presence of ac and dc input source ripple is documented. Design of a parallel, continuous ac excited resonant network for the QF2 magnet for the proposed 1 GeV RCS is presented.

INTRODUCTION

A spallation neutron source which is an important tool for research in material science, life science, chemistry, fundamental and nuclear physics, earth and environment science is proposed at RRCAT. It mainly consists of a 1 GeV, 25 Hz RCS for production of high energy protons and a target which is bombarded with these protons to produce neutrons. This paper describes the analysis and design of a powering scheme for a family of quadrupole magnets of the proposed RCS. The requirements of a power supply for these electromagnets are quite different from conventional dc power supplies [1]. A method where the energy of the magnets, which is needed only for a short time during each period, can be stored is preferred. Therefore oscillatory circuits are used where the energy is stored in the capacitors and only the losses of the resonant network are drawn from the mains. A string of magnets energized with a single source develops a very high voltage with respect to ground. To overcome this problem, the circuit elements are connected in a configuration called White circuit [2]. The objective of this paper is to present a systematic approach for selection of circuit topology, to carry out tolerance analysis of the resonant network and finally to recommend a powering scheme for QF2 magnets.

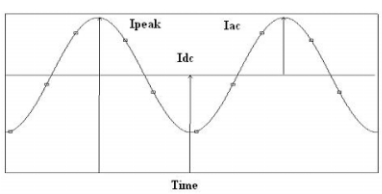

Figure 1: A dc biased sinusoidal current wave for excitation of RCS magnets.

[#]sunil@cat.ernet.in

SCHEMES

General specifications of the QF2 magnet are summarized in Table 1. The excitation frequency is 25 Hz and the peak current is 1230 A. Typical waveform of a dc biased sinusoidal current is shown in Fig. 1. I_{ac} is the peak current of the ac component and I_{dc} is the average current in the magnet. Parallel and series resonance circuits (PRC and SRC, respectively) are best suited for such applications. The PRC and SRC schemes are shown in Fig. 2. The comparison between PRC and SRC is as follows:

Table 1: Specifications of QF2 Magnet

Total Numbers	:8
I_{dc}	:1230 A
$I_{ac\ Peak}$	:730 A
I_{pk}	:1960 A
Inductance/magnet	:11 mH
Peak energy/magnet	:11kJ
DC resistance/Magnet	:2 mΩ
Resonant Frequency	:25 Hz

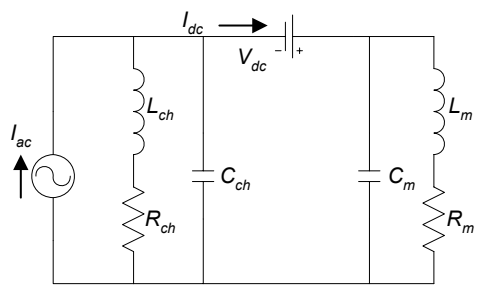

(a)

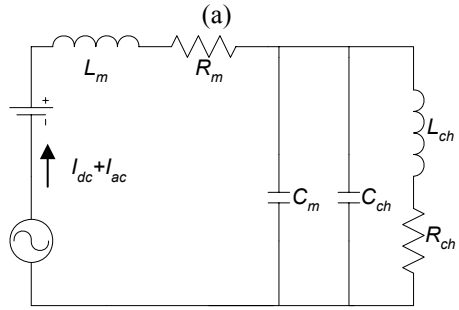

(b)

Figure 2: Resonant excitation schemes: (a) PRC (b) SRC.

In PRC two separate sources are required while in SRC the ac and dc source can be generated with a single power source. The current in SRC is directly driven in the magnet, while in the PRC the current is fed in the choke and is not directly fed to the magnet. PRC system is operated at low power as the peak power drawn during a cycle in SRC is more, while there is less variation in power drawn by PRC.

Further, the ac source can be either a continuous or a pulsed source. Continuous source is preferred as the pulsed sources lead to high percentage of harmonic component in magnet current and the waveform manipulations, in case of magnet saturation, is not possible in pulsed sources. In pulsed sources, an average dc current flows in the primary choke winding causing additional loss in primary winding of coupling transformer.

COST OPTIMIZATION OF PRC

The magnet current I_m (see fig. 1) can be expressed as:

$$I_m = I_{dc} - I_{ac}\cos wt \tag{1}$$

The current in the resonating choke L_{ch} is,

$$I_{ch} = I_{dc}(1 - m\alpha\cos wt) \tag{2}$$

where, $\alpha = (I_{ac}/I_{dc})$ and $m = (L_m/L_{ch})$. L_m is the total magnet inductance. The resonant frequency of the parallel resonant network is,

$$f = \frac{1}{2\pi}\sqrt{\frac{L_{ch}+L_m}{L_{ch}L_m(C_{ch}+C_m)}} \tag{3}$$

C_m and C_{ch} are the magnet and choke resonating capacitance, respectively. An index for the size of the choke in QF2 powering network can be computed as follows:

$$L_{opt_function} = 1/2 * Lch * Irms * Ipk \tag{4}$$

The choke investment cost (L_{ic}) normalized to the average stored energy in the magnet can be derived as:

$$\frac{L_{ic}}{0.5L_m{I_{dc}}^2} = \frac{0.376(1+m\alpha)C_l}{m}\sqrt{1+\alpha^2m^2/2} \tag{5}$$

C_l is the cost of transformer equivalent of the choke in Rs/kVA. The normalized choke operational cost, L_{oc} which depends on the Q factor of the choke (Q_{ch}) is:

$$\frac{L_{oc}}{0.5L_m{I_{dc}}^2} = \frac{\left(2+\alpha^2m^2\right)C_oN\omega_0}{1000mQ_{ch}} \tag{6}$$

where, N is the total operation time in hours, C_o is the electricity consumption rate in Rs/kWh, and,

$$Q_m = \frac{\omega_o L_m}{R_m} \qquad Q_{ch} = \frac{\omega_o L_{ch}}{R_{ch}} \tag{7}$$

Similarly the normalized capacitor investment (C_{ic}) and the operational (C_{oc}) cost can be derived as,

$$\frac{C_{ic}}{0.5L_m{I_{dc}}^2} = \frac{\alpha^2m\omega_oC_c}{1000} \tag{8}$$

$$\frac{C_{oc}}{0.5L_m{I_{dc}}^2} = \frac{2m\omega_0\beta C_0N}{10^6} \tag{9}$$

where, C_c is the cost of capacitor in Rs/kVAr, β is the loss factor of the capacitor in watts/kVAr.

Equations 5 through 9 are used for optimization of network. It can be seen that the total operating cost is minimum for a specific value of m .This is the optimum value of m. For the case of QF2 magnets, optimum value of m is 1.9. The maximum limit of m is decided by the ratio α, which is the limit for discontinuous current in the choke, the maximum limit for m is therefore 1/α. The optimum m is also a function of the quality factor However, this dependence is not very strong and for all practical purposes the optimum value for m can be taken as 1.5. Figure 3 shows the detailed cost break-up of QF2 magnet resonant network.

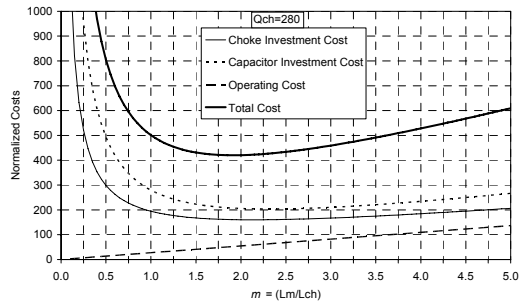

Figure 3: The cost break-up for QF2 as a function of m.

SOURCE HARMONICS AND TOLERENCE ANALYSIS

A high-Q resonant tuned circuit basically behaves like a band pass filter and dominantly passes the resonant frequency and attenuates significantly other frequencies present in the network. The ac and dc sources used in PRC are not ideal and contain unwanted frequency components. The expression for the ratio of the magnet current to the dc source current for calculating the allowable ripple current in the source is,

$$\left(\frac{I_m}{I_s}\right)_{dcsource} = \frac{1}{\left(1-{\omega_n}^2 + j\frac{\omega_n}{Q_m}\right)} \text{ where } \omega_n = \frac{\omega}{\omega_o} \tag{10}$$

Similarly, the expression for the ratio of the magnet current to the ac source current for calculating the allowable harmonics in the ac source is expressed as:

$$\left(\frac{I_m}{I_s}\right)_{acsource} = \frac{\left(q + j\omega_{nQ_m}\right)}{(m+q)-{\omega_n}^2(1+m)(1+q)+j\omega_n(1+m)\left(Q_m+\frac{q}{Q_m}-{\omega_n}^2Q_m\right)} \tag{11}$$

where $q = (Q_m/Q_{ch})$.The phase angle Φ in degrees, between the source and the magnet current can be calculated as follows,

$$\Phi = \tan^{-1}\frac{\omega_nQ_m}{q} - \tan^{-1}\left(\frac{\omega_n(1+m)\left(Q_m+\frac{q}{Q_m}-{\omega_n}^2Q_m\right)}{(m+q)-{\omega_n}^2(1+m)(1+q)}\right) - 180 \tag{12}$$

Various plots showing allowable per cent ripple in the dc current and voltage as a function of ripple frequency for QF2 network with specified allowable tolerance in magnet current and tolerable harmonic level in the ac source as a function of harmonic frequency for different specified tolerable variations in the magnet current can be generated using (10)-(12). Figure 5 shows the allowable

per cent ripple in the dc source current and voltage as a function of its ripple frequency for QF2 network with specified allowable tolerance in magnet current.

All passive components in PRC are subjected to variations due to manufacturing tolerances, aging, drift, temperature variations etc. All these variations results in change in the resonant frequency and/or Q which changes the gain and phase characteristics.

Figure 6 shows inverter current amplitude overdrive and phase overdrive for 0.25% variation in L_m and L_{ch}. Detailed analysis of the effects of component tolerances is reported in [3].

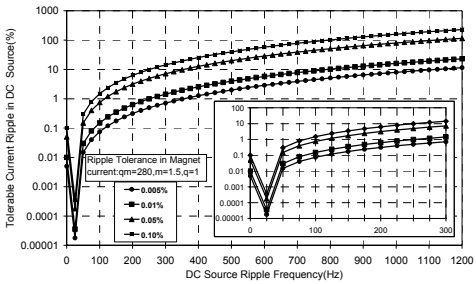

(a)

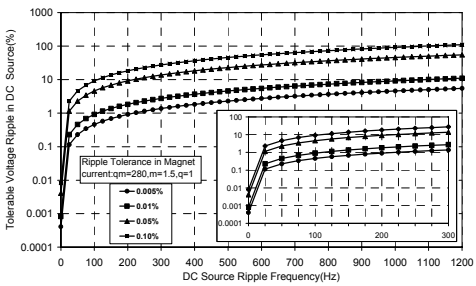

(b)

Figure 5: Allowable ripple in the dc source (a) current, and, (b) voltage with respect to ripple frequency for QF2.

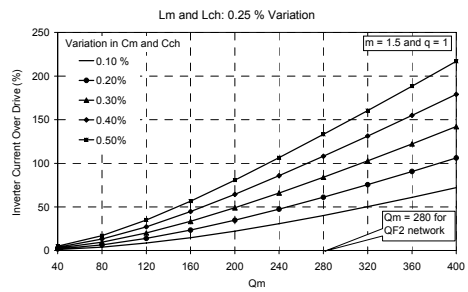

(a)

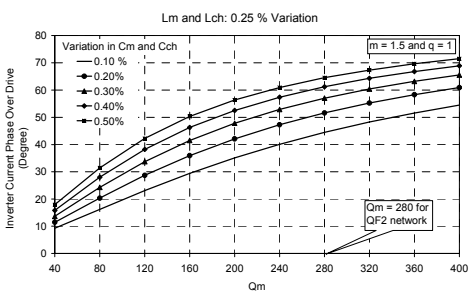

(b)

Figure 6: Inverter current (a) amplitude overdrive, and, (b) phase overdrive for 0.25% variation in L_m and L_{ch}.

Based on the above discussion the following recommendations are made for the powering scheme of QF2 magnet for the proposed RCS at RRCAT.

1) QF2 magnets should be energized with a single mesh, parallel resonant network powering scheme, excited by an ac excitation of continuous type.

2) Limits for ac and dc source harmonics for the QF2 network are as follows:

- Maximum tolerable 300 Hz current and voltage ripple in dc source for 0.01 % ripple in the magnet current is 0.8% and 3% respectively.
- Maximum tolerable 50 Hz current ripple in ac source for 0.01 % ripple in the magnet current is 10 %.

3) To limit the inverter amplitude overdrive to a reasonable 50% and phase to 45 degree, the tolerance in value of capacitances should be below 0.1%, and the inductances should be designed so that the tolerance in their values is below 0.25%.

CONCLUSION

A systematic approach to select a powering scheme for QF2 type quadrupole magnet for a 25 Hz, 1 GeV RCS is demonstrated. A single mesh parallel resonant network with a continuous ac excitation is deemed suitable for the purpose of powering all the 8 magnets in series. PRC is chosen and continuous ac source is preferred. The effect of variations and tolerances in the component values were reflected in graphical form. Also the effect of dc source voltage and current ripple components and ac source harmonics and its effect on output magnet current were studied. The ratings of the resonant network element and the power requirement of ac and dc source for QF2 magnet network were finalized. The study shows that to limit the current overdrive of the ac source of QF2 network to a lower level (50%), the tolerances in inductance should be as tight as 0.25% and the tolerance in resonating capacitors should be limited to 0.1%.

REFERENCES

[1] P. Bryant, "Performance requirements for accelerators" in Proc. CERN Accelerator School on Power Converters for Particle Accelerator, CERN 90-07, pp. 1-14.

[2] M.G. White, F.C.Shoemaker and G.K.O'Nell, "A 3 BeV high intensity proton synchrotron", CERN-Symposium, 1956, pp.525-529.

[3] Mangesh Borage, Sunil Tiwari and Swarna Kotaiah, "Component Tolerances Analysis of a Parallel Resonant Magnet Excitation Scheme for Rapid Cycling Synchrotron Using PSpice", Journal of Circuits, Systems and Computers, 14-3, (2005), pp. 439-452.

STUDY AND COMPARISON OF REACTIVE POWER COMPENSATION SCHEMES FOR AIR-CORE TRANSFORMER IN ELV-TYPE DC ACCELERATORS

Mangesh Borage#, Sunil Tiwari and Swarna Kotaiah
Raja Ramanna Centre for Advanced Technology, Indore 452 013, India

Abstract

The ELV-type accelerators use air-core, multi-secondary step-up transformer to generate the high voltage. The transformer has large leakage inductance and small magnetizing inductance. Suitable compensation scheme is required to minimize the reactive power loading on the source feeding the primary winding. The results of studies done to investigate suitability of various compensation networks are presented in this paper. Characteristics are studied and compared using simulation software PSpice, wherein normalized results suitable for comparison are directly obtained.

INTRODUCTION

The high-power ELV-type electron accelerators are widely used in industrial and research applications. The scheme for generating high voltage in these machines is based on air-core, multi-secondary step-up transformer. Each secondary has voltage doubler rectifier and filter, the outputs of which are connected in series to generate the high voltage. As opposed to the conventional transformer, the air-core transformer has large leakage inductance (L_s) and small magnetizing inductance (L_m). Moreover, the values of L_s and L_m are nearly the same [1]. A simplified equivalent circuit is shown in figure 1. The air-core transformer has poor regulation and draws a large reactive power from the source feeding the primary winding. Suitable compensation scheme must therefore be employed to minimize these undesirable effects. The compensation network (CN) should offer following benefits: (1) Near-unity power factor operation under all loading conditions. (2) Nearly load independent output voltage. (3) Minimum additional reactive components. (4) If possible, no additional compensating inductor.

The conventional compensation scheme [1] however can either achieve good voltage regulation or minimum reactive power depending on the operating frequency. Besides, the network uses an additional bulky inductor.

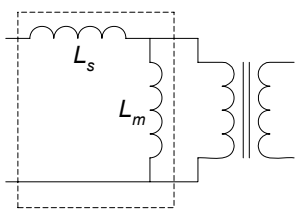

Figure 1: Simplified equivalent circuit of air-co re transformer in ELV-type accelerators.

#mbb@cat.ernet.in

Therefore, the possibility of using various other CNs is examined. In this paper, the results of studies done to investigate suitability of various CNs are presented. Characteristics of the CNs are studied and compared using PSpice [2].

COMPENSATION NETWORKS

The CNs considered for study and comparison are shown in Fig. 2. In the networks N1, N2 and N3, the inductive components of air-core transformer are compensated using one or more capacitors. The network N4 uses additional inductor (L_a) and is the conventional CN [1]. PSpice is used for analysis of these CNs. However, a method described in [3] is followed to obtain the normalized results for comparison directly from the simulation. Amplitude of input source V_{in} is assumed to be unity. The values of L_s and L_m are assumed to be the same [1]. Resonant frequency (f_o), characteristic impedance (Z_n) and circuit Q are defined as:

$$f_o = \frac{1}{2\pi\sqrt{(L_s + L_m)C}}, Z_n = \sqrt{\frac{(L_s + L_m)}{C}}, Q = \frac{R_{ac}}{Z_n} \quad (1)$$

where C is the compensating capacitor and R_{ac} is the resistive equivalent of secondary-side doubler-rectifier and load reflected on the primary side. Table 1 give the values of L_s, L_m and C making f_o and Z_n unity.

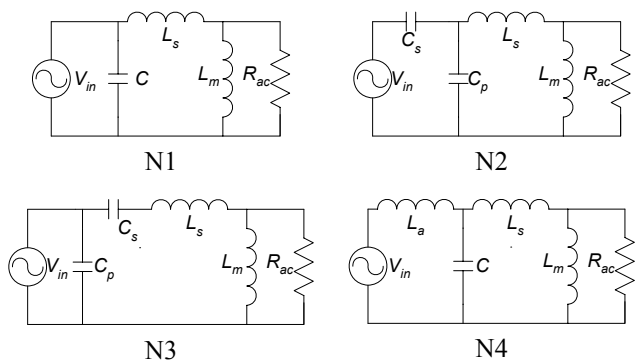

Figure 2: Compensation networks.

Table 1: Values of L_s, L_m and C used in simulation.

Component	Compensation Network			
	N1	N2	N3	N4
$L_s = L_m$	$\frac{(1/2\pi)}{2}$			
C	$(1/2\pi)$	—	—	$(1/2\pi)$
$C_s = C_p$	—	$(1/2\pi)=C$	$2(1/2\pi)=2C$	—

SIMULATION RESULTS

The CNs shown in Fig. 2 are simulated using PSpice to visualize their characteristics sweeping the operating frequency. With circuit parameters described in previous section, normalized results are directly obtained from the simulation. X-axis of the plots is operating frequency normalized to the resonant frequency. Circuit voltages and currents (displayed on Y-axis) are normalized with reference to V_{in} and (V_{in}/Z_n), respectively.

Compensation Network N1

The transformer and load is compensated by a capacitor C. Figure 3 shows the plots of load voltage (voltage across R_{ac}) and source current amplitude and its phase for different values of Q. Following observations are made at the resonant frequency:

1. The load voltage is a function of Q but remains nearly constant only for higher values of Q. The maximum voltage gain is 0.5.
2. The source current reduces as Q increases ensuring good part-load efficiency.
3. The phase angle between the source voltage and current (φ) depends on Q. They are nearly in-phase only for higher values of Q but φ changes steeply with slight shift in operating frequency.

Compensation Network N2

Two compensating capacitors C_s and C_p are used. Under the assumption that L_s and L_m are equal, if C_s and C_p are also chosen to be of the same value then load voltage becomes completely independent of Q at resonant frequency as shown by the plots of Fig. 4. Following observations are made at the resonant frequency:

1. The output voltage is independent of Q with voltage gain of 0.5.
2. The source current reduces as Q increases ensuring good part-load efficiency.
3. φ is zero, independent of Q.

Compensation Network N3

The network N2 has all desirable features required for a CN listed previously. However, the voltage gain is only 0.5 (see Fig. 4) necessitating a high-voltage input source.

In network N3, C_s and C_p are located in such a way that C_s compensates L_s and series combination of C_s and C_p compensates (L_s+L_m). The characteristics of N3 are plotted in Fig. 5. Similar to network N2, load-independent output voltage, in-phase source voltage and current waveforms and good part-load efficiency is observed for network N3 at resonant frequency. Moreover, the voltage gain of N3 is unity at resonant frequency.

Compensation Network N4

The network N4 with capacitor C and inductor L_a has been conventionally used for the compensation [1]. Figure 6 shows its typical characteristics for $L_a = (L_s+L_m)$. At operating point f_1, output voltage is independent of Q resulting in good voltage regulation but non-zero φ. At operating point f_2, φ is zero and independent of Q resulting in minimum reactive power loading but poor voltage regulation.

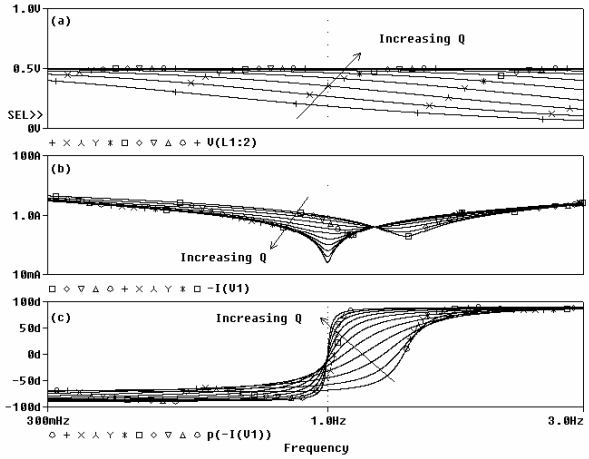

Figure 3: Characteristics of N1. (a) Load voltage, (b) source current amplitude and (c) source current phase.

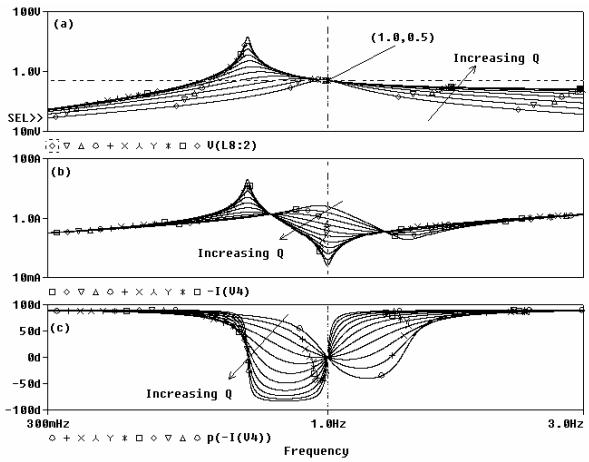

Figure 4: Characteristics of N2. (a) Load voltage, (b) source current amplitude and (c) source current phase.

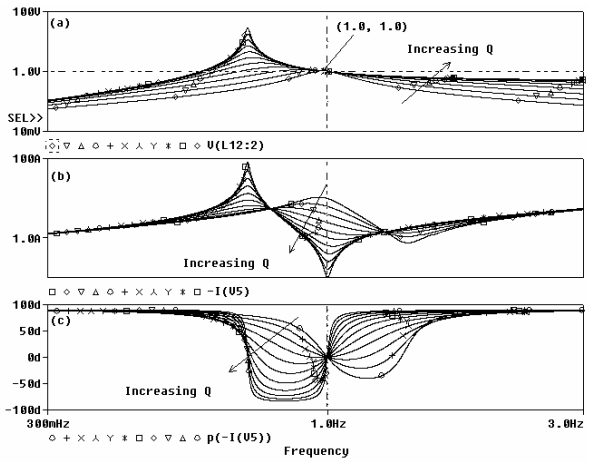

Figure 5: Characteristics of N3. (a) Load voltage, (b) source current amplitude and (c) source current phase.

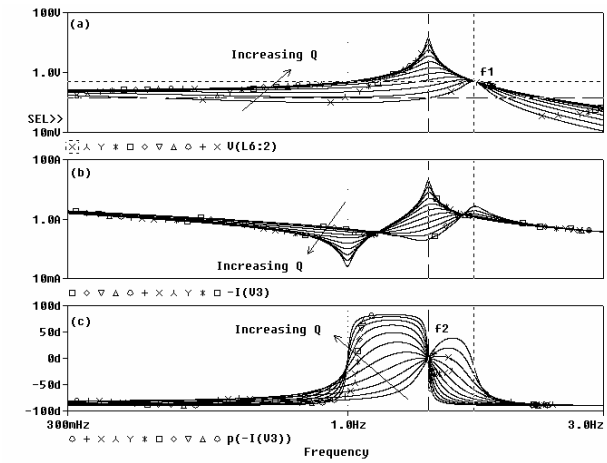

Figure 6: Characteristics of N4. (a) Load voltage, (b) source current amplitude and (c) source current phase.

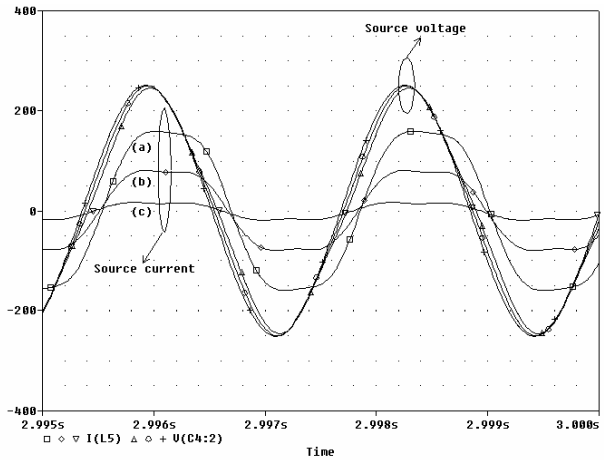

Figure 7: Source voltage and current waveforms of an air-core transformer compensated by network N3.

COMPARISON AND DISCUSSION

Based on the simulation results described in the previous section, following comparative observations can be made:

1. Network N1 neither provides constant output voltage nor in-phase source voltage and current under all loading conditions. Therefore, this CN is not advantageous for the present application.
2. Network N4 offers constant output voltage as well as in-phase source voltage and current under all loading conditions but at different operating frequencies. Therefore, depending on operating point either good voltage regulation or minimum reactive power can be achieved. Besides, the network uses an additional bulky inductor for compensation.
3. Adding another capacitor in network N1 at appropriate location results into the networks N2 and N3 which offer all desirable characteristics. These networks offer load-independent output voltage as well as the in-phase source voltage and currents simultaneously at one operating points. The only limitation of network N2 (that is, voltage gain of 0.5 at resonant frequency) is overcome in network N3. Therefore networks N2 and N3 can be advantageously used for the compensation.
4. Although the total value of capacitances in N3 is 4 times of that in N2, the capacitor voltage is also half. The stored energy and therefore approximately the total volume of capacitors in both the networks is the same.
5. While network N4 has been conventionally used with square-wave input source voltage, sinewave input sources need to be used with networks N2 and N3. Also the inherent protection of input source against the load short circuit offered by network N4 is absent in N2 and N3.

To confirm the observations made in the previous section, a air-core transformer with 31:2880 step-up turns ratio and having L_s=L_m=0.2 mH is simulated with different CNs studied. On the secondary side, the transformer has voltage doubler rectifier with 260 nF filter capacitors. The rectifier is loaded with 0.52 A (full-load) dc current source. The sine-wave input source is modeled as an ideal source of 250 V peak / 430 Hz in series with 75 μH inductance. Illustratively, the simulated waveforms for the source voltage and current waveforms are shown in Fig. 7 for network N3 with C_s=C_p=685 μF. Source current waveforms (a), (b) and (c) correspond to 100%, 50% and 10% loading condition, respectively. The non-sinusoidal source current and the slight phase lag is due to nonlinear load on the transformer secondary (instead of the resistive load approximated in the earlier results). More importantly, it is interesting to notice that the phase between source voltage and current does not change with the load. The output dc voltage is observed to increase only by 5 % from full-load (38 kV) to no-load.

CONCLUSION

Simulation results of different CNs required with air-core transformer in ELV-type accelerators are presented in this paper. As opposed to the network used conventionally (N4), two CNs (N2 and N3) are shown to offer load independent output voltage as well as unity power factor operation. These networks, being composed of only capacitors, are compact, light-weight and less noisy.

REFERENCES

[1] Yu. I Golubnko, N. K. Kuksanov, S. A. Kuznetsov, P. I. Nemytov, R. A. Salimov, S. N. Fadeev, M. E. Veis, “High power transistor frequency converter for supply of industrial transformer-type electron accelerators”, Vacuum, 62 (2001), pp. 251-256.

[2] “Orcad PSpice A/D – User’s guide”, Orcad Inc., 9300 SW Nimbus Avenu, Beavertron, OR 97008 USA. 1998.

[3] Mangesh Borage, Sunil Tiwari and Swarna Kotaiah, “Component Tolerances Analysis of a Parallel Resonant Magnet Excitation Scheme for Rapid Cycling Synchrotron Using PSpice”, Journal of Circuits, Systems and Computers, 14-3, (2005), pp. 439-452.

STAIR CURRENT OUTPUT POWER SUPPLY FOR SWITCHING MAGNET*

Seong-Hun Jeong #, Ki-Hyeon Park, Heung-Sik Kang, Dong-Eun Kim, Jin-Hyuk Choi,
PAL, Pohang, 790-784, Korea

Abstract

The switching magnet for beam distribution is served with Digital Signal Processor (DSP) controlled PWM switching-mode power supply (SMPS). This SMPS is employed phase-shifted parallel (PSP) operation of IGBTs. This technique allows ± 350 A, 2.5 Hz stair output, and ± 350 A at bipolar mode operation. Current feedback and input voltage feed-forward control schemes are applied to improve the output current stability. Experimental results showed that the implemented converter achieved a useful versatile power supply.

INTRODUCTION

High current sources are needed in accelerators to bend and focus of electron beam. For these application, the power supply demands several types of output. In some cases, high stability current source for stringent specification of load was required.

The DSP had been developed primarily for application in various high speed digital signal processing. Due to its fast computational speed nowadays, the DSP has replaced much of the complex control hardware. The applications of high-performance DSP in complicated power electronic systems have found great potential in synthesis of sophisticated control algorithms and PWM switching schemes [1].

In order to achieve requirements of accelerator current source, DSP based current-controlled PWM bipolar SMPS using the TMS320F2808 from the Texas Instrument was developed for universal purposes. This SMPS is possible to operate in two modes by program. The one mode is arbitrary waveform current source and the other is bipolar current source. Each mode use phase-shifted parallel operation of IGBTs, so, it is possible to increase power rating and operating frequency by a factor of 2 [2].

Conventionally, the regulation circuits of a SMPS are realized using analog circuit technique. Analog controller is easy to implementation and good for simple circuits. With a good DAC and the other fine circuits, a high stability SMPS can be archived. But, analog control technique also has its demits in complex circuit design, low reliability, non-flexibility, and higher manufacturing cost.

This paper describes the development of a programmable power supply (PPS) using a DSP-controlled phase-shifted parallel SMPS for accelerator magnet.

*Work supported by Ministry of Science and Technology of Korea.
#jsh@postech.ac.kr

SYSTEM DESCRIPTION

The simple diagram of the power supply with LC output filter and magnet load were shown in Figure 1. The SMPS scheme consists of two full bridge rectifiers followed by each full bridge inverter. Two DC-links of full bridge rectifiers are connected to each other to maintain same voltage. The topology is full bridge parallel inverter, which can be a dc-to-ac inverter. The basic concept of operation mode is phase-shifted parallel operation of IGBTs modules, where each IGBT has shared equal average current that is inherent in the PSP operation mode. This power supply has two operation modes. First mode is arbitrary current waveform generator and second is bipolar SMPS.

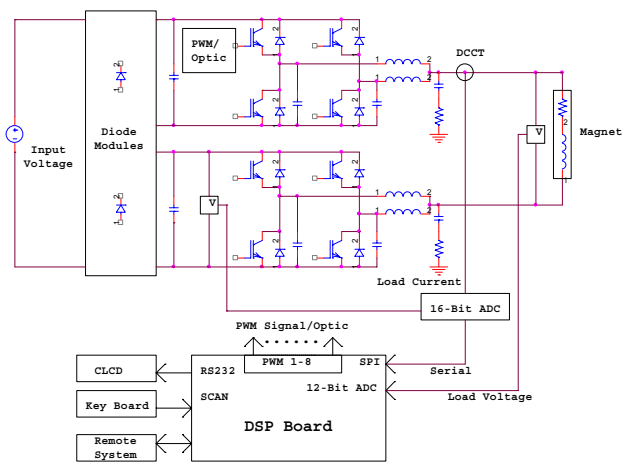

Figure 1: System Schematic Diagram.

Figure 1 shows control signal flow between the IGBT modules and the DSP and external devices.

This PPS was configured as a parallel full bridge type for driving higher load current, where each full bridge can drive 200A at 10 KHz switching frequency.

Owing to the PSP, the system operating frequency is doubled to 20 kHz and each IGBT current burden is one half of total current. Another advantage of PSP is one that the inductance value for output filter was reduced to one half comparing to the single full bridge type.

Current feedback and input voltage feed-forward control schemes are applied to improve the output current stability. The switching device is four dual packages of IGBT FF400R12KF4 from Eupec. The fiber optic connector HFBR series from Agilent Co. is used to interface from DSP to driver board for IGBT to improve system noise susceptibility and ground isolation. Two

external 16-bit ADCs AD977A from Analog Devices are used to digitize the output voltage of the 860R DCCT from Danfysik Co. for current feedback. The current errors which are differences between reference current and averaged load current is calculated every 0.5 ms, and duty ratio is updated to make error as small as possible. Output filter is composed of conventional L-R-C filter which includes an R-C damper circuit to make good filter response.

DSP CONTROLLER MODELING

The filter and magnet load part of the Figure 1 could be reduced to Figure 2, because the values of filter components are much smaller than that of the magnet model.

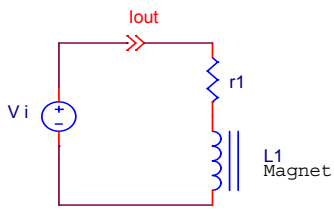

Figure 2: Simplified magnet model for digital controller design.

Thus the transfer function might be simplified as follow:

$$P(s) \cong \frac{1}{sL_1 + r_1} \quad (1)$$

A conventional PI controller is used for the PPS:

$$Gc(s) = \frac{Kps + Ki}{s} \quad (2)$$

Where, Ki and Kp are coefficients of integral and proportional gain, respectively. The PI coefficients are calculated directly using the characteristic equation of the control loop and compared to the result of the PSIM simulator [3]. Differences between two methods were in the order of range and the PI control loop worked very well. Then, the closed-loop control system for the PPS is given Figure 3.

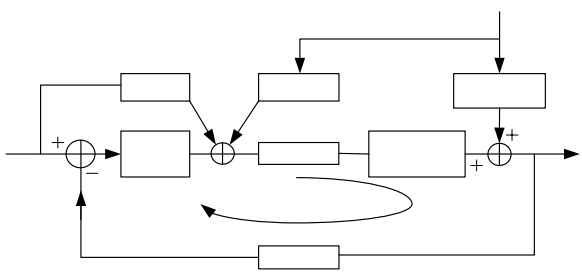

Figure 3: Block diagram of complete current loop system.

The closed-loop transfer function of the power supply is given by:

$$i_{out}(s) = i_{ref}(s)\left(\frac{G_c G_{id}}{1+T_c} + \frac{K_{FF} G_{id}}{1+T_c}\right) + v_g(s)\left(\frac{G_{iv}}{1+T_c} + G_v \frac{G_{id}}{1+T_c}\right)$$

while current loop gain, Tc is $Tc(s) = Gc(s) \bullet Gid(s) \bullet H(s)$.

The Bode plot was drawn with Kp=10 and Ki = 30 using the MATLAB in Figure 4. The shape of Bode plot was seen simple at a glance, but it really was a little more complicated one with complete output filter circuits. The sensed link voltage was used to modify the duty cycle. The updated duty cycle is expressed as

$d_{update}(k) = d(k) + G_v \Delta d(k)$, where $\Delta d(k) = (V_{ref} - v_{in}(k))/V_{ref}$

and G_v is the feed-forward gain.

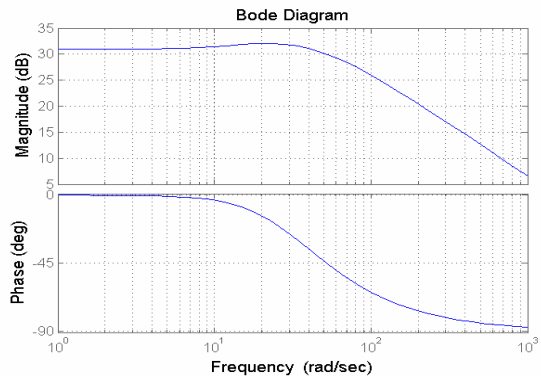

Figure 4: Bode plot of the given closed-loop control system.

CONTROL HARDWARE CONFIGURATION

The eight Enhanced Pulse Width Modulation (EPWM) signals are generated by the DSP. Four PWM signals of eights are generated with PWM control registers with updated PWM duty ratio according to the current direction, while the others are all off.

Four IGBTs in the first column in Fig.1, used as phase reference zero and the other in second column had phase shift of 180 Degree. Since PSP mode, the input voltage is subdivided into two pulse trains, the duty cycle of each IGBT is one half of the converter duty cycle.

After output current has been digitized ten times by two ADCs between control loops, the ADC values were added and averaged by divided by twenties to smooth the sensed load current value to keep the power system good control stability.

The rising or falling time of the current waveform depends on the time constant of the load magnet and DC input voltage. At the end of the rising mode of current or visa verse, the control loop should keep the load current constant for certain duration of 20ms for example, where PI control value was different from that of prior one. Thus, feed-forward compensation was necessarily required to archive fast output responses with changed control circumstances. The output current was increased in the fastest rate with applying the link voltage to the magnet without any PWM control for about 20 ms, while decreasing magnet current, all IGBTs are turned off so

that the stored energy of the magnet was discharged through the wheeling diodes of the IGBTs by the time constant of the magnet circuits itself.

ADC procedure and EPWM duty control are serviced by the each real time interrupt routine. And Timer Interrupt of the DSP was used for control loop. Both key scan and the LCD display were carried out at the base routine not to disturb the PWM interrupt.

The control program is composed using the CCS2000 from Texas Instrument. The object code of control program was simply loaded to developed home-made board through the JTAG.

EXPERIMENT RESULTS

A PPS has been implemented using the DSP, eights IGBTs and the other electric componenets. The quadrupole magnet of the PLS storage ring was used as a magnet load which inductance is 21 mH and resistance 25 mΩ. Figure 5 shows the phase-shifted voltage of each IGBTs. In this Figure, the Ch3 and Ch4 are forward voltages of PWM 1 and PWM 2. And the Ch1 and Ch2 are return voltages of PWM 1 and PWM 2 respectively, where we can see that PWM 1 and 2 are added. The Figure 6 shows the test results of PPS. This figure shows the output stair current. A measured magnet current is stair waveform, 2.5 Hz frequencies and ± 200A for 160 V of DC link voltages. Transient time between each stair is about 23 ms and flattop is 27 ms which are a little different from each stage because of time constant of magnet. Another experimental result is bipolar SMPS operation. The output current is ± 350 A at 160 V of DC link voltage. At this mode, the current stability is less than 80 ppm. The PSP mode was well worked. The current difference between parallel arms is less than 1 A at full current output. The surface temperature of output filter core rose to about 60 °C, but IGBT modules and rectifier diodes were under the 40 °C cooled by water.

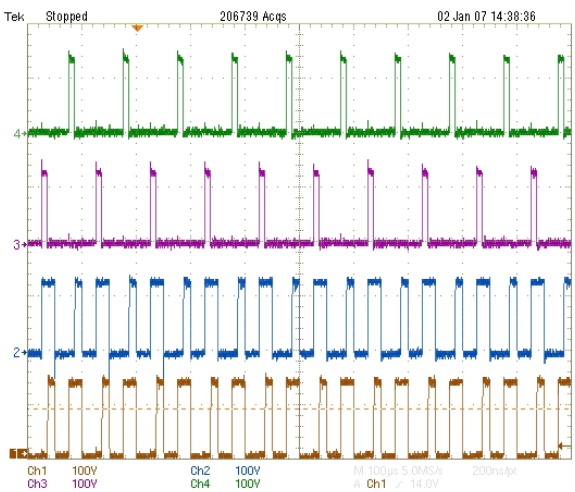

Figure 5: IGBT PWM voltage (Ch1: PWM-1 return, Ch2: PWM-2 return, Ch3: PWM-1 forward, Ch4: PWM-2 forward).

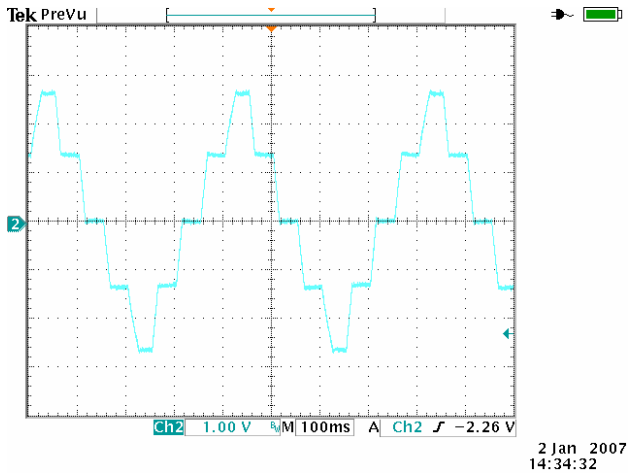

Figure 6: Actual load current of magnet (± 200A).

CONCLUSION

This paper deals with DSP-controlled PSP SMPS for accelerator magnet. This PPS is fully controlled by a DSP. From the experimental results with assembled power supply, output load current is well agreed with programmed arbitrary current waveform. In bipolar mode, the power supply output is ± 350 A with 160 V DC-link voltage. There was about 1 A difference between parallel arms at ± 350 A current output. The core temperature of output filter was about 60 °C, but IGBT modules and rectifier diodes were under the 40 °C cooled by water. The stability of this PPS is less than 80 ppm. It will be improve to 50 ppm in near future.

REFERENCES

[1] Shyh-Shin Liang, “DSP control of a resonant switching high-voltage power supply for X-ray generators,” PEDS’ 01, Indonesia, vol. 2, p. 522.

[2] Cadirci, I, “Unity power factor boost converter with phase shifted parallel IGBT operation for medium power applications” IEE Proc.-Electr. Power Appl., vol. 149, No. 3, p. 237, 2002.

[3] www.powersim.com POWERSIM, Powersim Inc. Andover, MA

STUDY OF VACUUM RELATED PROBLEMS DURING THE ENERGIZATION OF K-500 SUPERCONDUCTING CYCLOTRON

Md. Z.A.Naser[#], U.Bhunia, J. Pradhan, J Debnath, S. Paul, M.Dutta, A. Pole, D.L.Bandopadhaya, A. Sur, C. Mallik and R.K.Bhandari
Variable Energy Cyclotron Centre, 1/AF Bidhan Nagar, Kolkata-700 064, INDIA

Abstract

The K500 superconducting cyclotron main magnet has been commissioned successfully in VECC, Kolkata. During the process of energization, it has been observed that there is vacuum deterioration in the cryostat outer vacuum chamber (OVC). Detail studies have been carried out to examine the occurrence of such a situation. The electro-magnetic stress due to Lorentz force increases with current, and is more pronounced in the median plane region of cryostat having maximum number of welded joints. This could be the possible reason for the OVC vacuum degradation. The paper reports various observations on vacuum deterioration during energization. An extensive study has been carried out to understand and explain the situation.

INTRODUCTION

The K-500 Superconducting Cyclotron (SCC) main magnet consists of two superconducting coils (alpha coil and beta coil), which has been energized to different current levels for extensive magnetic field measurement. The superconducting coil inside the liquid helium chamber is suspended by nine number of support links; of which, three pulling up, three pulling down and three pulling radially out. This support system carries the whole weight of the coil and cryostat. An annular vacuum chamber, made of magnetic steel, referred as cryostat OVC, surrounds the stainless steel cryostat bobbin. Prior to cool-down of the cryostat, the force experienced on the support links is estimated theoretically, which is reported elsewhere [1] and compared with measured values. This is very crucial for the health of the support links, which is attached to the outer wall of the OVC. During higher excitations of superconducting coil, it is observed that the OVC vacuum degrades gradually. The mass spectrograph for helium leak detection (MSLD) is carried out and multiple leaks in the order of 10^{-4} mbar-lt/sec are found. Occurrence of such a situation is analysed in this paper. One of the basic reasons may be, that, during excitation a huge magnetic force develops on the OVC wall (coil tank) made of magnetic steel. This leads to a localised magnetic stress on coil tank, which is having several welded joints around the median plane. There is a possibility of mechanical failure on the defective welded joints (if any) of the coil tank at higher excitation. Another reason of failure may be due to the radial force experienced by the bobbin if the coil is off-centred with respect to surrounding iron yoke. This force propagates to the coil tank through support links.

[#]zamal@veccal.ernet.in

ANALYSIS

Experimental Observations

During cool-down of the superconducting coil a huge thermal force is developed as shown in figure 1 by the shrinkage of the cold mass and support links. Though the experimentally observed link force profile during cool-down matches with calculated value, there is mismatch between calculated and experimentally observed values. This is may be due to the differences of material property used during the calculation.

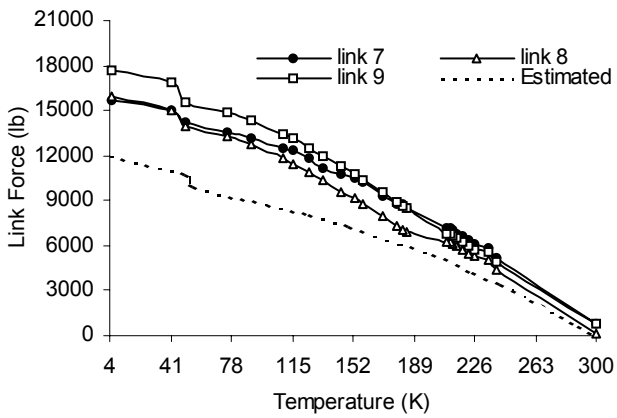

Figure 1: Support link force variation during cool-down of the superconducting coil.

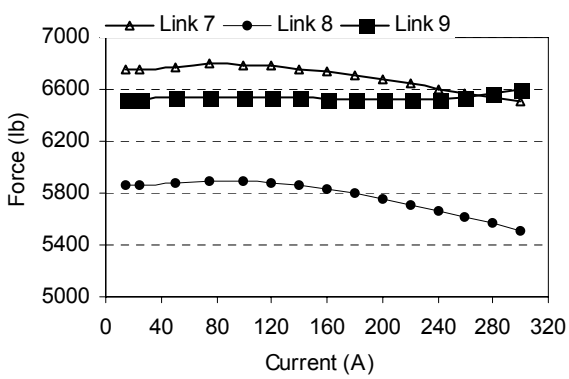

Figure 2: Support link force variation during energization of superconducting coil.

Tensile force on the radial support links decreases as the coil relaxes while energizing. The force recorded online during energization is shown in figure 2. The increase of tensile force on the radial support link indicates the centering error of the assembly.

It is observed that the OVC vacuum deteriorates with current as shown in figure 3. It is interesting to note that the degradation of OVC vacuum is dependent mainly on the current in alpha coil, which is nearer to the median plane. Being nearer to median plane, alpha coil has more contribution of magnetic field than beta coil, in the median plane region of OVC.

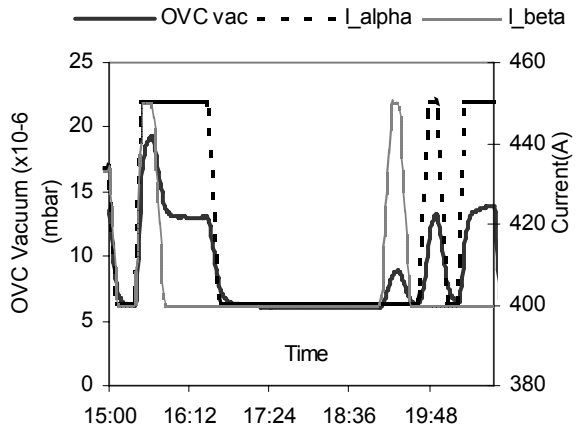

Figure 3: Variation of OVC pressure with alpha and beta coil current.

MSLD is carried out on the outer wall of the OVC with and without the current in the coils and existence of multiple real leaks is observed near the median plane. Figure 4 shows the temporal variation of the relative leak rates as well as OVC vacuum.

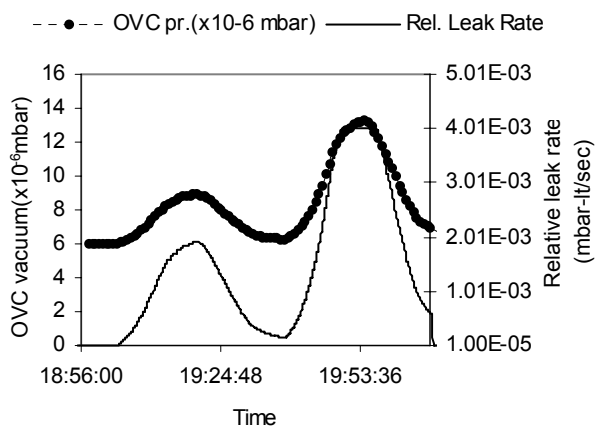

Figure 4: Temporal variation of leak rates and vacuum

The oscillating behaviour of the OVC vacuum with time may be due to the periodic bursting of condensed air molecules on various layers of multilayer insulation (MLI) as well as other cold surfaces inside the cryostat.

Theoretical Study

To analyze the fact that the OVC vacuum relates with the coil current, a 2-D model of the main magnet of K-500 SCC with iron yoke is simulated by Multiphysics ANSYS software. The magnetic stress near the median plane of the outer wall of coil tank is calculated at different coil excitations. Figure 5 shows the variation of the magnetic stress with the current level, and is fitted parabolically as

$$(S_X - 228.05) = -0.005(I + 145.57)^2 \quad (1)$$

$$(S_Z - 232.67) = -0.0093(I + 101.16)^2 \quad (2)$$

Here, S_Z S_X and I are axial stress (psi), radial stress (psi) and coil current (A) respectively.

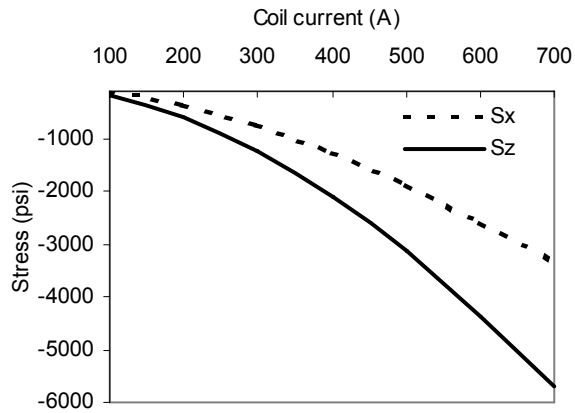

Figure 5: Magnetic stresses on the outer wall of OVC around the median plane at different coil excitations.

The magnetic stress at highest current level, as shown in the plot above is much lower than the yield strength of the carbon steel. But if there is any point defect especially in the welded part of the material, then there may be chance of mechanical failure due to the propagation of the defect.

The main magnet coil is placed at the center of the surrounding yoke with an accuracy of 0.1 mm. This ensures the magnetic center of coil and surrounding iron yoke aligned. If there is any centering error there will be a huge force on the coil that transfers to the OVC wall via support links. The radial unbalanced force is generated by $J_0 \times B_z$ interaction and is directed radially. The force is directly related to the gradient of z component of magnetic field at the coil region produced by the magnetic iron. The field gradient is calculated from ANSYS model.

The lines of force obtained from ANSYS model is shown in figure 6. For an infinitesimally small radial offset Δr of the coil w.r.t the iron assembly, the radial force developed is approximated as [3]

$$F \cong 4\pi\Delta r \int_r \int_z J \frac{\partial Bz[r,z]}{\partial r} r^2 dr dz \qquad (3)$$

The unstable force developed due to as small as 1 mil radial coil shift with respect to surrounding iron yoke at various excitations is calculated and shown in figure 7. The axial force developed due to vertical off-center of the coil median plane with respect to magnetic median plane is stable and is directed opposite to the direction of offset. Therefore, the centering of the coil by careful adjustment of support bolts in each link is necessary to minimize the magnetic force on the coil as well as outer vacuum chamber.

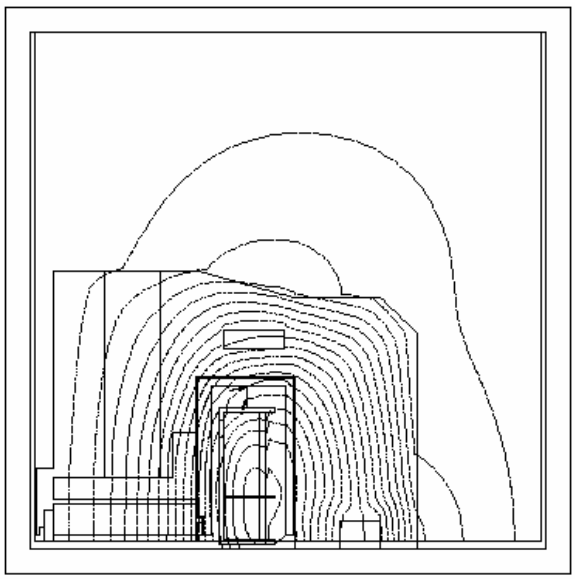

Figure 6: Magnetic lines of forces by ANSYS.

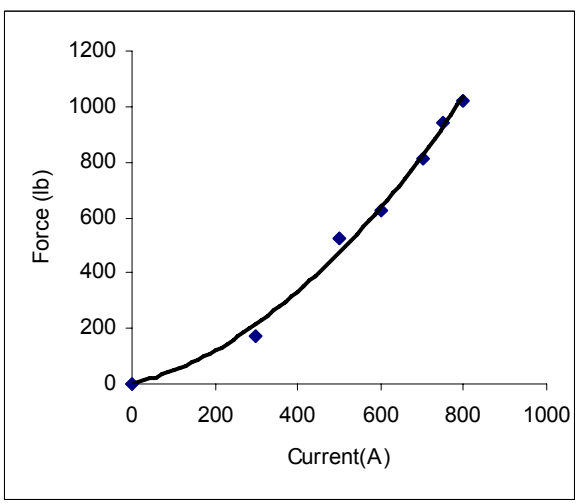

Figure 7: Radial unbalanced force w.r.t. current for 1 mil off-center.

CONCLUSIONS

Analysis establishes the fact that there is correlation between OVC vacuum and current, provided there is mechanical defect, void, or existence of any real leak on the wall of the OVC. It is extremely difficult to find out the real leak of OVC because of the non-accessibility in the assembly state of the K-500 Superconducting Cyclotron. Leaks have been identified carefully and repaired permanently by welding. Overall MSLD leak test (~ 10^{-8} torr-litre/sec) has been performed and it has been measured that OVC can now sustain very good vacuum level (~ 10^{-5} mbar). This will further improve during cryo-pumping by the cold surface in OVC. The radial off-centering force estimation suggests that the slight movement of the coil is very harmful to the OVC. During cool-down and energization the link forces are adjusted to keep the tensile forces much lower than the yield strength of the support link materials (glass epoxy). The abrupt change of the support link force during mechanical adjustment at higher excitation is very dangerous to the health of support link and OVC wall as well.

ACKNOWLEDGEMENT

Authors express their sincere gratitude to all colleagues who has directly or indirectly involved for successful completion of K-500 main magnet energization.

REFERENCES

[1] U. Bhunia et al, “Thermal Stress in the Support Link of K500 Superconducting Cyclotron Coil during Cool-down”, INPAC’05, VECC, March 2005, p. 509.

[2] J. Pradhan et al, “Studies of Magnetic Forces during the Energisation of K-500 Superconducting Magnet”, INPAC’05, VECC, March 2005,p.353.

[3] Iwasa, “Case Studies in Superconducting Magnets Design and Operational,” Plenum Press, New York, 1994.

PERFORMANCE OF CRYOMODULE AND CRYOGENIC NETWORK SYSTEM FOR THE SUPERCONDUCTING LINAC AT IUAC. DELHI.

T. S. Datta, J. Antony, S. Babu, J. Chacko, A. Choudhury, S. Kar, M. Kumar
R..S. Meena & A. Roy.
Inter- University Accelerator Centre. Aruna Asaf Ali Marg. New Delhi- 110067. India.

Abstract

The Superconducting Linear Accelerator as a booster of existing 15 UD Pelletron Accelerator is under construction at IUAC. The heart of superconducting linac is three cryomodules, each one housing eight quarter wave niobium cavities. In recent past two online tests with one linac module have been carried out and the beam (28 Si^{+10}) energy has been enhanced approximately from 130 MeV to 150 MeV with five effective cavities. The present paper highlights the operational experience of the cryogenic network system and its accessories during present run. Analysis of measured heat load at 4. 5 K from first Linac cryomodule is also presented

INTRODUCTION

To augment energy of heavy ion from 15 UD pelletron and to widen the mass range up to 80 to have energy above coulomb barrier, the Superconducting Linear Accelerator [1] is under development at IUAC, Delhi. Acceleration is achieved by using Superconducting quarter wave bulk niobium cavities operating at 97 MHz. The heart of linac is three cryomodules, each one is housed with eight cavities and one solenoid magnet. At present the first linac module along with superbuncher and rebuncher cryostats are installed in beam line and are integrated with helium and nitrogen refrigerator through indigenously developed cryogen distribution line. Except the portion of field joints connecting the cryomodules, the entire helium transfer line [2] is liquid nitrogen shielded, multilayer insulated and enclosed in a vacuum jacketed pipe of 8inches diameter. The Central VME based Cryogenics Data Acquisition System is developed to monitor and control operating parameters of cryostat, refrigerator and distribution system. Static and dynamic loads at 4. 2 K from all the cryomodules along with distribution line is met by a CCI make helium refrigerator of capacity 600 W at 4.2 K. The total load at 4.2 K on complete system as well as break up load in each cryomodule has been measured. Measured data with respect to vacuum, helium pressure, temperature of linac cryomodule related to the performance of cavities are analyzed and presented in this paper.

LINAC CRYOMODULE & COOLING METHODOLOGY

This is a rectangular cryostat [3] of dimension 3.0m x 1.2m x 1.9 m to house eight cavities and one solenoid magnet. A rectangular copper shield at 80- 100K is used to reduce the radiation load. Eight cavities and solenoid magnet are supported on two solid rectangular aluminum bar, which is supported from top plate with two SS sheet. Each cavity can be individually aligned in X – Y - Z direction. Total cold mass in one linac module is estimated to be ~ 600 kg. All RF accessories like drive coupler, slow tuner, liquid nitrogen cooled RF cable are assembled from top plate of cryostat.

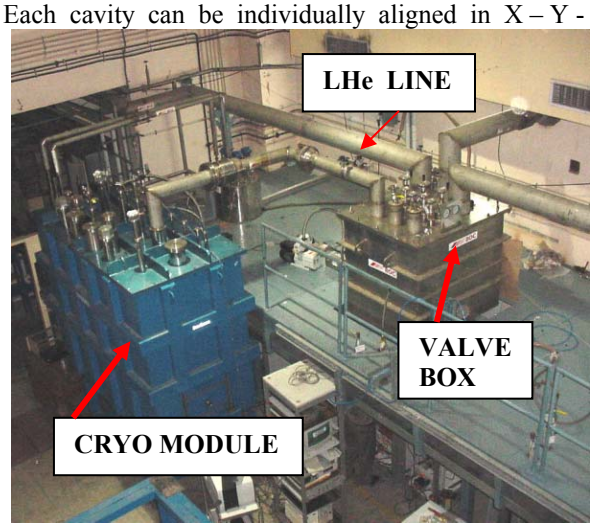

Figure 1 : Linac cryomodule with valve box

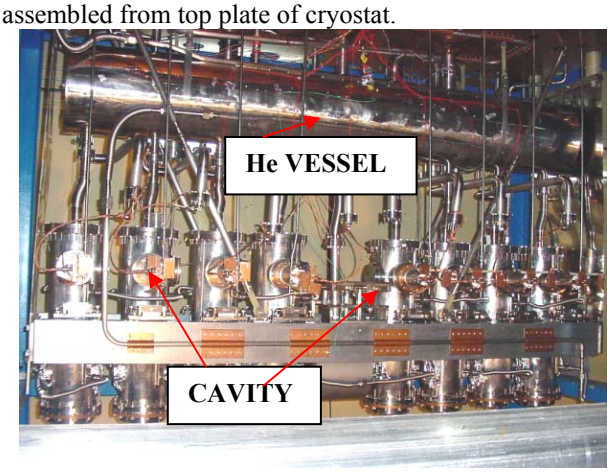

Figure 2 : Inside view of Linac cryomodule

Cool down of linac cavities [4] from 330 K to 4.2K is achieved in three steps, viz. inverse radiation cooling (330-220K) from shield, LN2 precooling (220- 140 K) and liquid Helium cooling (140 – 4.2 K). In-spite of slow cool down rate (15 K/ hr) in the critical zone, Q disease has not been reported. Minimum human interference is achieved by reducing final JT pressure with moderate liquid helium flow rate of 40 litres/hr. A complete cool down profile of linac module over three days is shown in figure 3.

PROBLEMS ENCOUNTERED AND SOLUTION

Vacuum

Earlier are reported [4] that the cryostat vacuum as measured by a Pfeiffer make cold cathod ionisation gauge did not show any improvement on Helium cooling. At the same time helium or nitrogen was not found by residual gas analyzer. Measurement was repeated with a Varian Nude ion gauge, which indicated better vacuum in the range of 10^{-7} to 10^{-8} Torr

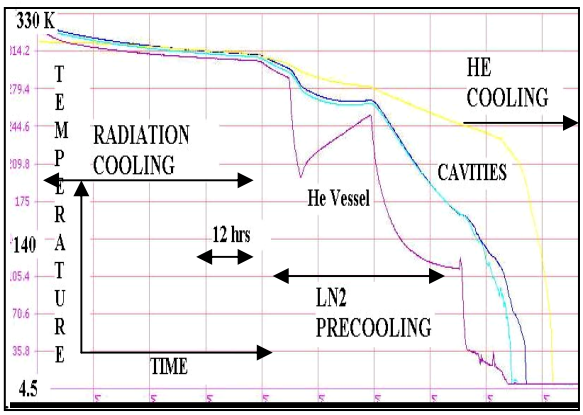

Figure 3: Cool down profile of linac cryomodule

Helium Pressure Stabilization

To evaluate the performance of slow tuner response time, measurement and analysis of helium pressure fluctuation in the cavity has been done in different modes

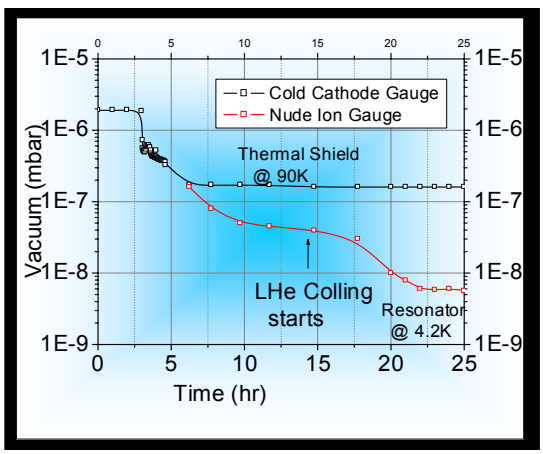

Fig 4 : Vacuum Profile of Linac module

of operation. It was observed that in normal mode, either in refrigeration or liquefaction mode, pressure fluctuation is less than 2 mbar/min and in case of power failure, the pressure fluctuation jumps to 6 mbar./min and lock invariably breaks. From recent observation, it may be concluded that rather than pressure fluctuations, vibration due to closing and opening of vacuum gate valve contributes more on breaking the resonator controller lock. Figure 5 and figure 6 explains the nature of pressure fluctuation in different modes of operation.

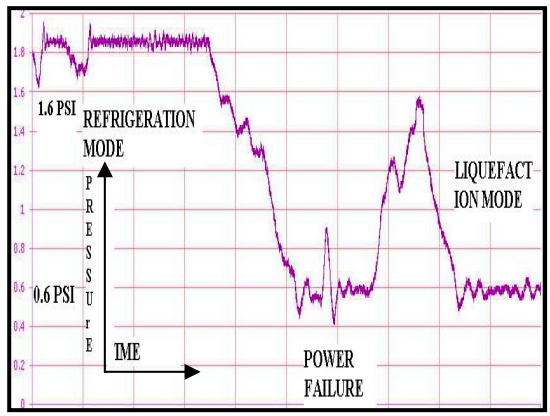

Fig 5 : Suction pressure of helium refrigerator

Temperature reading fluctuation

The temperatures at different locations in the cryostat were monitored by using Lake Shore make Silicon diode DT 470 thermometers. Earlier it was reported that temperature reading fluctuated with RF activity. To eliminate this noise, various steps like twisted double leads, cu shield on sensor as well as filter in the instruments is incorporated. Although fluctuation amplitude has been reduced significantly, it still exists. Fluctuations with high RF power through cables (200 W) without any field is bare minimum. Combination of high power with moderate field on poorly performing cavity contributes major fluctuation in the temperature reading.

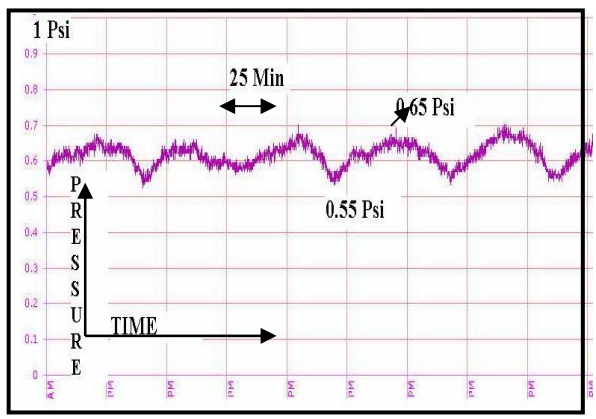

Figure 6 : Pressure fluctuation on Liquefaction mode

Control Shield Temperature

To avoid two phase flow in the suction side of nitrogen refrigerator and to have moderate constant shield temperature, automatic controller with two heaters of 600 W each and a feedback option from the LN2 level sensor has been developed and hooked up with CRYO DACS. The performance was found to be satisfactory.

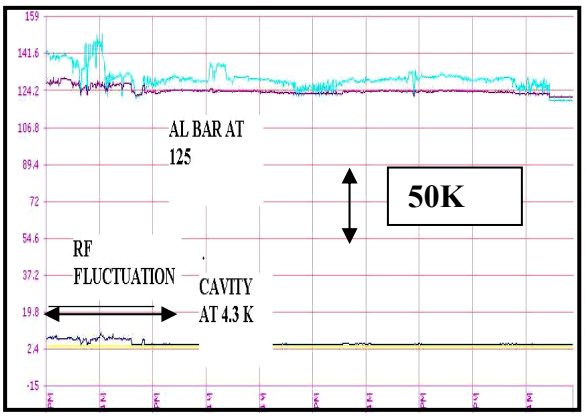

Figure 7: RF effect on temperature reading

Heat load in Linac module

An attempt has been made to measure total refrigeration load from linac, buncher and part of distribution line by isolating the linac system and simulating the same condition by an immersion heater in the master dewar. The static heat load measured at 4.5 K on linac module with cavity and RF accessories is 30- 35 W. The value is higher than the design value of 20 W. On thermal analysis, it is concluded that conduction from Al support bar at 125 K and drive coupler contributes about 10 W and 5 W loads respectively. Both these loads depend on number of cavities.

CONCLUSION

Cooling methodology is well established for one linac module with buncher and rebuncher. It is planned to have minor modification on 2 nd and 3rd linac cryomodule to have better cool down rate by using the cold enthalpy of helium gas efficiently. It is also planned to have intermediate UPS, backed by generator to have uninterrupted run of linac.

REFERENCES

[1] A. Roy et.al., Proceeding of 8th international conference on Heavy Ion Accelerator Technology, 1998, Argonne, USA p267.

[2] Auup Choudhury et.al " Cryogenic Distribution System" Indian Journal of Pure & Applied Physics, Vol 39,2001, p54

[3] Jacob Chacko et.al, " Cryostats for Superconducting Linac booster at NSC" Proceedings of 18 th International conference on Cryogenic Engineering, Mumbai. 2000, p131.

[4] T. S. Datta et.al., " Operation experience on cool down of superconducting linac" Proceeding of INPAC-2005,Calcutta, p 473.

CURE OF TEMPERATURE FLUCTUATIONS ON THE NITROGEN-COOLED SECTIONS OF A CESR-TYPE SRF MODULE

M. C. Lin#, Ch. Wang, M. H. Tsai, M. S. Yeh, F. T. Chung, T. T. Yang, M. H. Chang, L. H. Chang
TLS, NSRRC, Hsinchu 30076, Taiwan

Abstract

A strong correlation between tuner motion of the SRF module and the pressure fluctuation of the shielding liquid nitrogen flow is observed. The double elbow waveguide section with nitrogen cooling channels is one of the possible fluctuation sources. Thus it is tested along to investigate the mechanism of pressure and temerature fluctuations, whereas a phase separator with pressure regulation function is used to stabilize the supply pressure of liquid nitrogen. Also it is tried to stabilize the pressure fluctuation by optimizing and regulating the vent flow rate. System setup and primary test results are presented herein.

INTRODUCTION

As a major accelerator upgrade to increase the stored beam current and to eliminate the beam instability caused by higher-order modes of the cavity [1], an industrially manufactured superconducting radio-frequency module was installed into the storage ring at the Taiwan Light Source (TLS), in late 2004. The CESR-type SRF module[2], developed in the Newman Laboratory of Nuclear Studies, Cornell University, USA, was chosen for this project. During normal operation of the SRF module in 2005 and 2006, it is observed the cavity tuner motion has a strong correlation with the temperature variations of the thermal transition beam tubes of the SRF module [3].

The thermal transition beam tubes are located in between the room-temperature end plates and the nitrogen-cooled sections. Thus its temperature fluctuation must come from the temperature variation of liquid nitrogen shielding flow. As shown in Fig. 1, when the variation of helium vessel pressure is controlled within +/- 0.01 psia, correlations between the tuner motion, nitrogen supply pressure, nitrogen vent pressure, and the temperature at the thermal transition tube are observed.

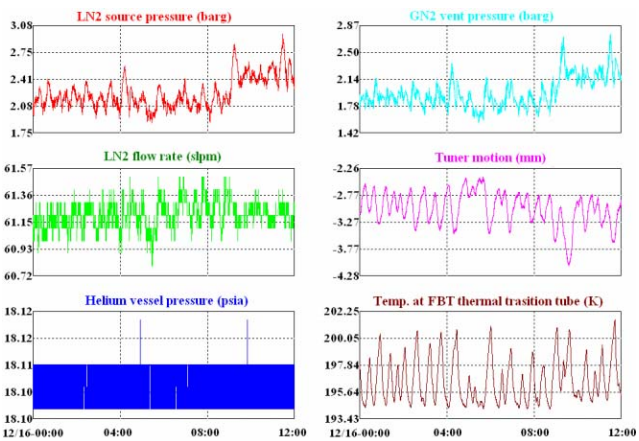

Figure 1: Tuner motion is correlated with the temperature of thermal transition tube and the nitrogen pressure, when the helium vessel pressure has a small variation.

#chyuan@nsrrc.org.tw

For the CESR type SRF module, liquid nitrogen cools not only the thermal shielding layers and the thermal transition tubes, but also a double elbow waveguide section. The double elbow waveguide section has much bigger cooling channels than the 1/2" copper pipes for thermal shielding. Thus it is highly suspected to be the source of pressure fluctuation. A spare double elbow waveguide section is used to study the fluctuation mechanism herein. With the help of a phase separator as liquid nitrogen supply source and a bypass flow control valve, the test results shows the cure of temperature and pressure fluctuations is promising.

EXPERIMENT SETUP

Layout

The layout of experimental setup is shown in Fig. 2. A phase separator with pressure regulation supplies liquid nitrogen to the double elbow waveguide through the inlet valve and a vacuum-jacketed flexible line. The double elbow waveguide section is wrapped with super-insulation layers and then installed into a vacuum sealed vessel. Its lower end section is connected to the vacuum vessel through a dummy waveguide section. Temperatures at 3 locations are monitored: T_u at upper end near the inlet cooling channel, T_{out} on the surface of cooling channel outlet, and T_b on the bottom end near thermal transition section. The vent nitrogen is warmed up to room temperature by a passive warmer.

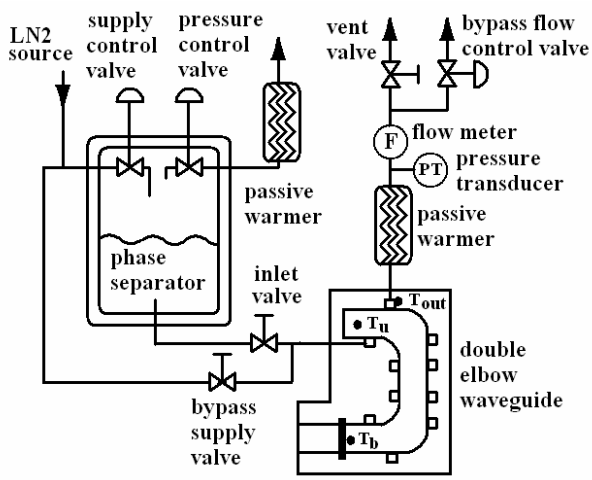

Figure 2: Layout of test setup, with a phase separator for supply pressure regulation.

Phase Separator (PS)

The phase separator is a 100-liter vessel with vacuum shielding. A bypass path for liquid nitrogen supply is constructed by ourselves for fail-safe operation. Liquid nitrogen comes from a huge outdoor container and flows through a 120-m transfer line and two valve boxes. Some small gas-vent devices have been installed along the long transfer path. But this 100-liter phase separator guarantees only liquid nitrogen is delivered to the downstream components, since the drain port is at its bottom. A pressure control valve, commanded by a PID controller, vents the gas out and regulates the vessel pressure to the setting value. With the supply control valve closed, the vessel pressure can achieve a variation of less than +/-5 mbar. A 500-W heater probe is installed inside. Note the safety devices, level sensor, and temperature probes are not shown in Fig. 2.

Passive Warmer

The passive warmer is constructed with finned tubes, with no active heater elements. A fan can raise the heat efficiency if necessary. The flow meter, pressure transducer, vent valve, and bypass flow control valve are all installed on the outlet port of the warmer, so that room-temperature devices can be used. The bypass flow control valve is commanded by a PID controller to regulate the warmer pressure by changing flow rate, while the vent valve guarantees a minimum flow rate.

TEST RESULTS AND DISCUSSIONS

Constant Flow Rate with PS Filled

The first try is to keep a constant flow rate of around 50 slpm at the warmer vent, while the phase separator is operated with setting pressure of 1.66 barg and level of 51%. To keep the liquid nitrogen level at 51%, the phase separator must be filled with liquid nitrogen occasionally. As shown in Fig.3, a pressure fluctuation of +/- 30 mbar happens at the phase separator during each filling. It is also shown that the temperatures T_u and T_b vary periodically from 98.5 K to 100.5 K and from 85 K to 85.6 K, respectively. Meanwhile the warmer pressure also varies periodically between 1.45 barg to 1.65 barg, and highly correlated with the temperature fluctuations.

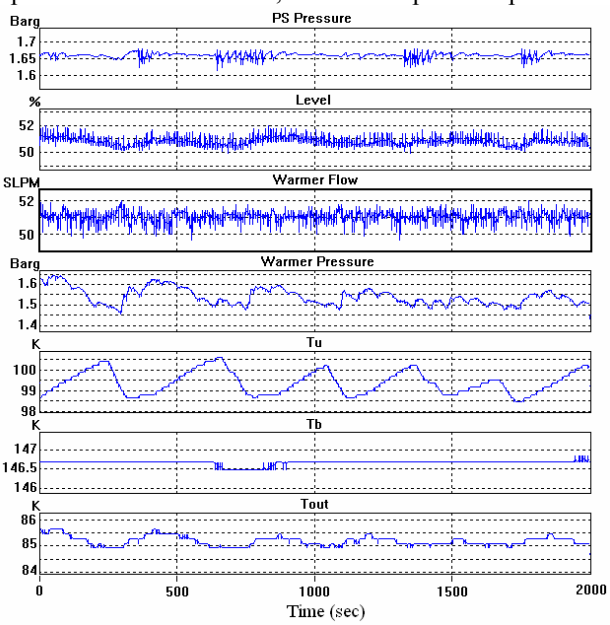

Figure 3: Variations of temperatures and warmer pressure at a constant warmer flow rate of about 50 slpm, while the liquid nitrogen level inside the phase separator is kept at +/-1% fluctuation by occasional filling.

Constant Flow Rate with PS Not Filled

To eliminate the possible disturbance from the pressure fluctuation of phase separator, the supply control valve is fully closed. As shown in Fig. 4, the level is thus decreased gradually. When the flow rate is kept at 50 slpm as the previous test, the pressure inside the phase separator has a fluctuation of +/- 15 mbar. Obviously this fluctuation is also correlated with the warmer pressure fluctuation.

Then the warmer flow is increase to 80 slpm and finally to 100 slpm. It is clearly shown in Fig. 4 that all monitored parameters including the PS pressure, warmer pressure, T_u and T_{out} are getting stable at 100 slpm. Though, T_u still has a fluctuation of +/- 0.3 K at 100 slpm. It is thus concluded that not only the temperature, but also the warmer pressure, can be stabilized at a high flow rate of 100 slpm. This result also hints that high flow rate eliminates the thermal breath inside the warmer structure.

Another interesting observation is that the periodical variation of warmer pressure is actually composed of two fluctuations. The first one has a period of 7 to 8 minutes, dominates at flow rate less than 80 slpm. The other one has a period of about 50 seconds, varies within +/- 20 mbar and dominates the pressure fluctuation at 100 slpm.

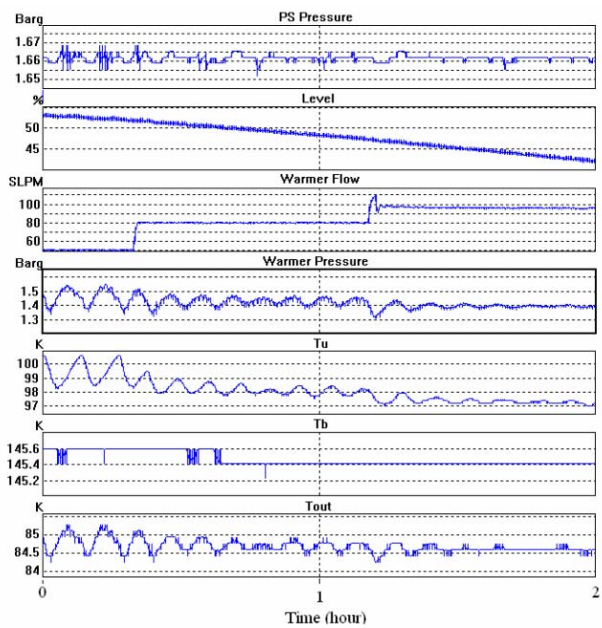

Figure 4: Variations of temperatures and warmer pressure at different warmer flow rates, while the phase separator is not filled with liquid nitrogen.

Unfortunately the real sources for these two periodical pressure variations can not be individually identified. Possible source structures are the double elbow waveguide section, passive warmer, and the vacuum jacketed flexible lines. Notice that a flow rate of 80 slpm equals a mass flow rate of 1.667 g/sec. The vacuum jacketed flexible lines have an inner pipe of diameter 0.5 inch. A calculation on the saturated nitrogen of 1.4 bar shows that the flow speed of pure liquid nitrogen and pure gas nitrogen is about 1.6 cm/sec and 210 cm/sec, respectively, inside the flexible line. Because only structures with slow flow speed are considered to induce pressure fluctuation, thus the double elbow waveguide section and the flexible line for liquid supply to it are suspected. But it needs more tests, like to use a flexible line of different length or a double elbow waveguide section with different cooling channel design, to prove this deduction.

Variable Flow Rate with PS Not Filled

Form the previous test results, it is shown the fluctuations of warmer pressure and T_u are correlated. This hints the temperature fluctuation on the double elbow waveguide section could be minimized by control the warmer pressure well. Thus the bypass flow control valve after the passive warmer is activated under a range of 10 to 40 slpm, while the vent valve guarantees a minimal flow rate of 65 slpm. The bypass flow control valve is set to maintain the warmer pressure at 1.47 barg. The bypass flow rate is increased as the warmer pressure grows up, and vice versa. Again the phase separator is not filled with liquid nitrogen to eliminate the possible disturbance from the vessel pressure of phase separator.

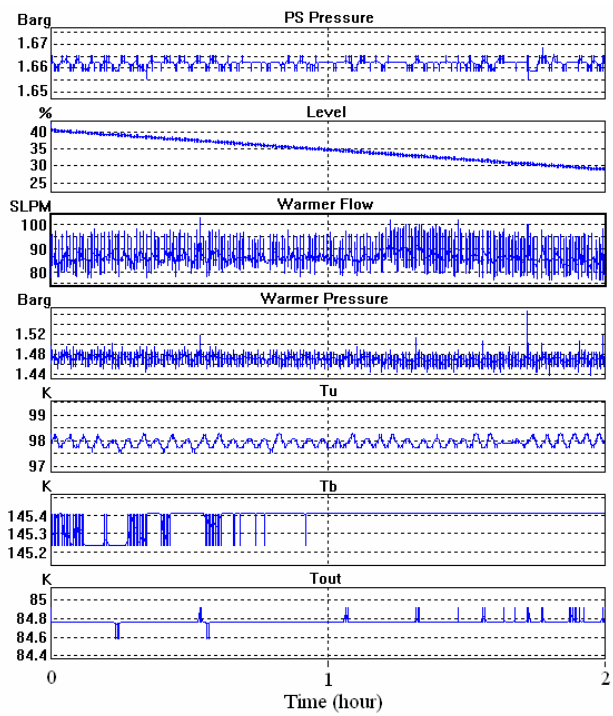

Figure 5: Variations of temperatures and warmer pressure at variable warmer flow rates to minimize the warmer pressure fluctuation, while the phase separator is not filled with liquid nitrogen.

As shown in Fig. 5, the warmer pressure is mostly kept in between 1.44 and 1.50 barg, and the temperature T_u varies within +/- 0.4 K. The spikes of warmer pressure have minor effect on the monitored temperatures. This test result shows the temperature fluctuation can also be minimized by regulating the warmer pressure with variable flow rate. Also it is noticeable that the time structure of the 50-second pressure fluctuation is terminated by the variable flow rate operation.

CONCLUSIONS

The test results prove the double elbow waveguide section is actually a source of temperature fluctuation. Thanks to the excellent performance of phase separator on pressure regulation, it is proven that the pressure and temperature fluctuations can not be cured by stabilizing the supply pressure only. Instead, increase of the vent nitrogen gas flow can reduce the temperature fluctuation. It is also proven that the warmer pressure fluctuation has a strong correlation with the temperature fluctuation. And a good regulation on the warmer pressure by the bypass flow control valve can also reduce the temperature fluctuation. However, a link between the cooling channel pressure of the double elbow waveguide section and the warmer pressure should be established to examine their correlation.

Based on the test results, a bypass flow control valve will be installed on the nitrogen vent port of the SRF module in operation. The nitrogen flow rate is currently 50 to 60 slpm, and it will be increase to 100 or 120 slpm. Both the effects of high flow rate and warmer pressure regulation will be tested. It is expected to stabilize the tuner motion by this simple modification. A further investigation is to modify the cooling channel of the double elbow section so that no temperature and pressure fluctuations will be induced at low flow rate.

REFERENCES

[1] Ch. Wang, L. H. Chang, S. S. Chang, F. Z. Hsiao, M. C. Lin, G. H. Luo, T. T. Yang, M. S. Yeh, C. C. Kuo, R. Sah, and C. T. Chen, "Superconducting RF project at the Synchrotron Radiation Research Center," in Proc. 10th Workshop on RF Superconductivity, Tsukuba, Japan, 2001, pp. 34-38.

[2] H. Padamsee, P. Barnes, C. Chen, W. Hartung, J. Kirchgessner, D. Moffat, R. Ringrose, D. Rubin, Y. Samed, D. Saraniti, J. Sears, Q.S. Shu, and M. Tigner, "Design challenges for high current storage rings," Part. Accel. Vol. 40, 1992, pp. 17-41.

[3] Ch. Wang, L. H. Chang, M. S. Yeh, M. C. Lin, F. T. Chung, S. S. Chang, T. T. Yang, and M H. Tsai, "Operational Experience of the Superconducting RF Module at TLS," Physica C, Vol. 441, 2006, pp. 277-281

DESIGN OF THE TPS BENDING CHAMBER

C. K. Chan, G. Y. Hsiung, C. C. Chang, Y. B. Chen, C. Y. Yang, C. L. Chen, H. P. Hsueh, S. N. Hsu, Y. H. Liu, NSRRC, Hsinchu, Taiwan.
Ivan Liu, NTHU, Hsinchu, Taiwan.
J. R. Chen, NSRRC, Hsinchu; NTHU, Hsinchu, Taiwan.

Abstract

This article describes the design, manufacture and treatment of the bending vacuum chamber (B-chamber) of the 3-GeV Taiwan Photon Source (TPS). The B-chamber is a aluminium-alloy chamber ~5 m long with an antechamber on the near side of the beam duct. The design of the B-chamber is aimed to diminish the power density and the photon-stimulated desorption (PSD) induced by synchrotron radiation. Simulations, by finite-element analysis, of the B-chamber deformation due to evacuation and pressure profiles of the vacuum systems of a unit cell by a Monte-Carlo method are also described.

INTRODUCTION

The TPS is a continuing project to construct a third-generation synchrotron source at the National Synchrotron Radiation Research Center (NSRRC) in Taiwan. The TPS storage ring, a 6-fold super-period of DBA structure with 24 unit cells, has an electron beam energy 3 GeV and a beam current 400 mA. Aluminium alloy is chosen as the B-chamber material because of its properties well known for the construction of accelerators, including large thermal conductivity, absence of magnetism, small rate of thermal outgassing, small residual radioactivity, and ease of machining. Because the latest lattice design alters the circumference of the storage ring from 518.4 m to 486 m, the design of the vacuum systems must be amended. The following sections update the design of the TPS B-chamber.

BENDING CHAMBER

Figure 1 shows the drawing of the TPS B-chamber, which consists of two pieces of aluminium plate (lower and upper halves); each has thickness 50 mm. The TPS B-chamber is designed to have the following features: (1) a large triangular aluminium chamber (~5 m) to confine almost outgassing sources induced by the PSD inside the B-chamber; (2) absorbers located as far from the beam source as possible to decrease the heat load on absorbers; (3) vacuum pumps arranged on the antechamber and near the outgassing sources to increase the effective pumping speed and to decrease the beam impedance generated by the pumping orifices.

Although many advantages can be gained, the compromise requires more complicated interfaces between the B-chambers and the magnets. Fig. 2(a) and 3(b) depict the cross-sectional views of the B-chamber combined with the quadrupole (Q-) and sextupole (S-) magnets, respectively. To attain a criterion of deformation < 0.1 mm in the beam duct, the outer profiles of the aluminium plates are machined according to the shape of the poles and coils of the Q-magnets and S-magnets. The clearance is generally maintained at 3 mm. The spaces with a clearance < 3 mm will be tested in the engineering with care taken during assembly. The channel between the beam duct and the antechamber has a height 10 mm. Figure 3 shows, by finite-element analysis, the deformation of half of the B-chamber due to evacuation. The result shows the maximum deformation at the coil of Q-magnet to be 0.13 mm, and the deformation in the beam duct is controllable within 0.1 mm.

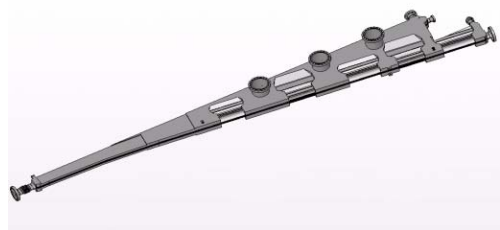

Figure 1: Assembly drawing of a TPS bending chamber 5 m long.

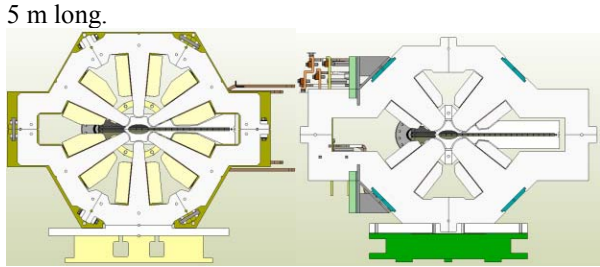

(a) (b)

Figure 2: Cross-sectional views of a B-chamber combined with a Q-magnet (a), and a S-magnet (b).

TREATMENTS

Some research reveals that ozone is effective to remove carbon on the surface and in the sputter-profiled passivation layer of aluminium alloys [1-3]. Treatments of three kinds, proposed to machining and to clean materials of the aluminium-alloy vacuum chambers for the TPS project, are listed below and evaluated by the techniques of thermal outgassing and PSD.

(A) Oil machining
-chemical cleaning with strong alkaline etching [4].
(B) Ethanol machining
- cleaning with ozonized water with a flow rate 5 L/h and a concentration 6.7~6.9 ppm at 24 ^{0}C for 30 min.
- drying with pure nitrogen gas (99.9999 %).
(C) Ethanol machining only

Thermal Outgassing

Figure 4 shows curves of the rate of thermal outgassing versus time measured with the throughput method [5]. Thirty aluminium alloy A6063 specimens, of size 50 mm × 70 mm × 5 mm, were fabricated according to each treatment mentioned above and placed into an aluminium alloy chamber with an orifice (φ=3 mm) for measurement. After pumping 10 h at room temperature, the outgassing rate of the samples with treatment A, q_{10}(A), is the least at ~ 9.7×10^{-11} Torr L s^{-1} cm^{-2} compared to q_{10}(B) ~ 5.3×10^{-10} Torr L s^{-1} cm^{-2} and q_{10} (C) ~ 5.9×10^{-10} Torr L s^{-1} cm^{-2}. The aluminium-alloy chamber containing the samples was baked at 120 ^{0}C for 24 h after pumping for 24 h. The rate of outgassing of the samples with treatment B measured after 24 h from bakeout, q_{72}(B), decreased to ~ 4.8×10^{-15} Torr L s^{-1} cm^{-2} less than q_{72}(A) ~ 9.5×10^{-14} Torr L s^{-1} cm^{-2} and q_{72}(C) ~ 1.4×10^{-14} Torr L s^{-1} cm^{-2}.

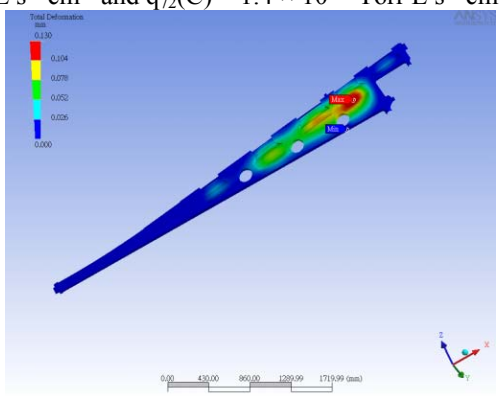

Figure 3: Deformation on the lower half of the B1 chamber due to evacuation, by finite-element analysis.

Photon-stimulated Desorption

A dedicated beam line of BL-19B at NSRRC used to study PSD is described elsewhere [6]. The design of aluminium samples with cooling channels can make the temperature increase < 0.5 ^{0}C to decrease noise from the thermal effect during exposure. The aluminium samples were baked in situ at 150 ^{0}C for 24 h before illumination with synchrotron radiation. Figure 5 shows the relation of the dynamic pressure rise per mA beam current vs. the accumulated beam dose. The PSD curves of aluminium samples subjected to treatments A, B and C are plotted in the figure with open squares, solid circles and open circles, respectively. It shows that treatment B is superior to the other treatments, especially at the beginning (beam dose < 10 mA h). At an accumulated beam dose 1000 mA h, ΔP/I of the samples with treatment B can even attain the range of 7×10^{-11} Torr/mA. The PSD data of treatment A are referred to our previous measurement for comparison in this paper [7].

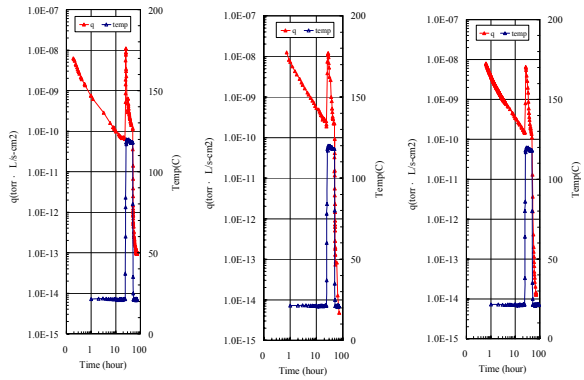

(a) (b) (c)

Figure 4: Curves of outgassing rate vs. time for aluminium samples with treatments A (a), B (b) and C (c) during 24 h pumping at room temperature, 24 h bakeout at 150 ^{0}C and after baking.

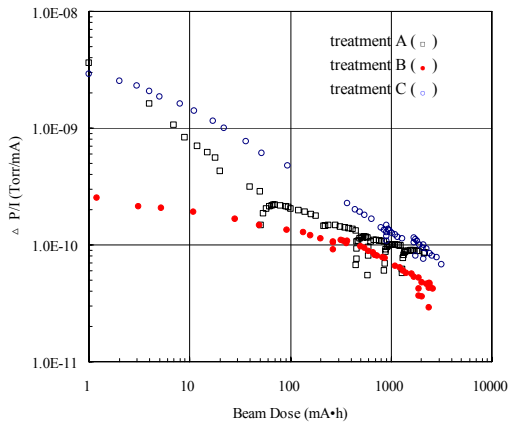

Figure 5: Total pressure rise per beam current as a function of the beam dose for aluminium samples according to three treatments.

PRESSURE PROFIE

In the storage ring of the synchrotron light source, a large gas load will be induced by synchrotron radiation from the vacuum chamber wall [8]. The dynamic pressure must be kept below a certain limit to meet the required beam lifetime. The design goal of the TPS vacuum systems is to achieve a dynamic pressure < 1×10^{-9} Torr for a beam lifetime 10 h for commission at 3 GeV, 400 mA. Figure 6 shows the vacuum system of a unit cell of the TPS storage ring, which comprises straight chambers, vacuum pumps, two gate valves and two B-chambers (B1, B2). For such a long triangular B-chamber, the photon span of synchrotron radiation emitted from the dipole magnet is almost (~92 %) contained inside the B-chamber, and we estimate a gas load ~2.3×10^{-6} Torr L s^{-1} induced by the PSD inside each B-chamber. Lumped NEG pumps and sputter-ion pumps (SIP) are employed as the principal pumps and placed near the gas source to prevent the conductance from limiting the pumping speed of the vacuum pumps. According to the pumping configuration in Fig. 6, the pressure profiles stimulated by the Monte-Carlo method for desorption coefficients η =

1×10^{-5}, 5×10^{-6} and 1×10^{-6} molecules/electron are shown in Fig. 7 [9-10]. The average pressures for these three cases are correspondingly 1.9×10^{-9}, 9.5×10^{-10} and 1.9×10^{-10} Torr. A conditioning period ~300 A h is estimated to decrease the desorption coefficient to 5×10^{-6} to satisfy an average pressure $<1\times10^{-9}$ Torr [11]. Two local pressure pumps near the downstream crotch absorbers of B1 and B2 reflect lack of space for installation of vacuum pumps.

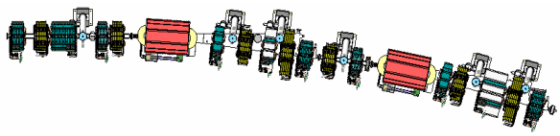

Figure 6: Layout of the vacuum system of a unit cell of the TPS storage ring.

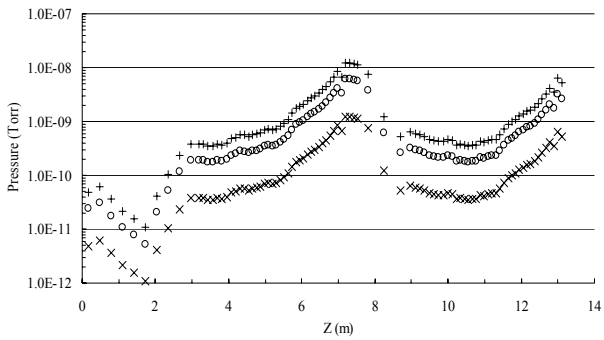

Figure 7: Pressure profiles for a unit cell of the TPS storage ring at $\eta = 1\times10^{-5}$ (+), 5×10^{-6} (○) and 1×10^{-6} (×) molecules/electron for an electron beam operated at 3 GeV, 400 mA.

CONCLUSIONS

The unique designs for the TPS bending chamber are reported in this paper. The simulation by finite-element analysis shows that deformation due to evacuation in the beam duct can be controlled within 0.1mm. A treatment with ethanol machining and ozonized-water cleaning is suitable for an aluminium-alloy material according to the thermal outgassing measurement and the PSD data. A calculation of the pressure with a Monte-Carlo method indicates that an average pressure 1×10^{-9} Torr can be achieved after a conditioning period 300 A h for electrons operated at 3 GeV and 400 mA.

ACKNOWLEDGMENTS

The author would like to thank Dr. Suetsugu at KEK for sharing his computer codes for pressure calculation

REFERENCES

[1] T. Momose, K. Asano, N. Ohta, Y. Kanda and H. Ishimaru, J. Vac. Sci. Technol. A13(2) (1995) 488.
[2] T. Momose, Y. Maeda, K. Asano and H. Ishimaru, J. Vac. Sci. Technol. A13(3) (1995) 515.
[3] T. Momose, E. Hayasaka, K. Saitou, K. Nagayama and S. Abe, J. Vac. Sci. Technol. A16(3) (1998) 961.
[4] A.G. Mathewson, J. –P. Bacher, K. Booth, R. S. Calder, G. Dominichini, A. Grillot, N. Hilleret, D. Latorre, F. LeNormand and W. Unterlerchner, J. Vac. Sci. Technol. A7(1) (1989) 77.
[5] J. R. Chen, K. Narushima and H. Ishimaru, J. Vac. Sci. Technol. A3(6) (1985) 2188.
[6] J. R. Chen, K. Y. Yang, J. Y. Yang and G. Y. Hsiung, J. Vac. Sci. Technol. A20(3) (2002) 859.
[7] G. Y. Hsiung, K. Y. Yang, Y. J. Hsu and J. R. Chen, J. Vac. Sci. Technol. A19(4) (2001) 1657.
[8] A. G. Mathewson, G. Horikoshi and H. Mizuno, KEK-78-9, 1978.
[9] C. K. Chan, G. Y. Hsiung, T. L. Yang and J. R. Chen, "Pressure Distribution for TPS Storage Ring", SRI'06, Daegu, Korea, May 2006.
[10] Y. Suetsugu, J. Vac. Sci. Technol. A14(1) (1996) 245.
[11] G. Y. Hsiung, J. R. Huang, J. G. Shyy, D. J. Wang, J. R. Chen, and Y. C. Liu, J. Vac. Sci. Technol. A12(4) (1994) 1639.

CYCLOTRON R.F. STRUCTURE'S LEAKS, CAUSES AND REPAIR

Deba Prasad Hajra, Debabrata Adak, Bidhan Chandra Mondal, Jayanta Chaudhuri,
Rakesh Kumar Bhandari,
VECC, DAE, 1/AF Bidhan Nagar, Kolkata-700064, India

SYSTEM DESCRIPTION

The room-temperature cyclotron (K-130) at VECC, Kolkata is delivering beam since June 16, 1977.The R.F. power of the cyclotron 'D' is passed through a cantilever type D-stem structure of 2750 mm long & 1350 wide. This structure has been fabricated by thin OFE grade copper sheet inside which has been reinforced by a structure made of light SS sections. The skin of the structure has been fabricated in a corrugated fashion to increase both surface areas for R.F skin current and mechanical strength (section modulus). A pair of moving panel has been assembled on both top and bottom side of the D-stem for frequency tuning of R. F. The whole system is functioning inside a big resonator tank of 3.1mx 2.4m x 2.1m which is under high vacuum of 10^{-7} m bar. LCW at pressure of 12.5kg/cm^2 flowing through 10mm OD and 1.1mm thick OFE copper tubes to remove the heat generated by the R.F. skin current. These tubes are brazed on the inner surface of corrugated copper sheets.

FABRICATION

Brazing in a vacuum furnace could provide uniform heating, no thermal distortion, uniform filler distribution, no oxidation and clean joint but it was not done because arge size facility was not available at that time. 10mm O.D copper tube to tube was joined by lap joint. Tube to copper strip of 25 mm wide and 1.6 mm thick of different lengths were brazed first. Then 25 mm strips were brazed with 2mm thick sheet of corrugated copper panel. This type of design has created some air gap (between strip and sheet) due to thermal distortion and this prevents efficient heat-transfer. Also it created a small under cut on the thin wall of the cooling tubes along the brazing line.

OBSERVATION OF LEAKS

Round the clock cyclotron operation for last 30 years, brazing joints of the cooling tubes and undercut of tube wall develops water leaks inside the resonator tank working under high vacuum. It is observe that the leaks are more near the 'D' region possibly due to the phenomenon like ion induced desorption, image current, nuclear scattering and high energy scattered beams. It also observe occurrence of leaks increases whenever the RF panels are kept open in atmosphere for considerable period of time. It is also noticed that after repair and during hydraulic testing at 15kg/cm^2 pressure numbers of new leak open-up. This indicates the existence of many other corroded weak points inside the tubes. As the cooling tubes are brazed inner surface of the structure and it is not easily accessible without dismantling. Repair of leak requires shut down of the cyclotron and takes a considerable loss of beam time.

dhajra@veccal.ernet.in

CAUSES OF LEAKS

The water leaks appear from the under-cut of thin walled of tubes. Because silver brazed alloys has very good compatibility with copper and forms continuous solid solution with copper at lower temperature of eutectic composition. Surface erosion occurred due to large mutual solubility resulting an undercut on the thin walled tubes. Brazing joints leaks of tube-to-tube, tube-to-sheet, SS couplings, bimetallic joint appear mainly due to electro chemical corrosion created over a time span of 30 years. The electrolyte for corrosion forms due to the following reasons.

1. Corrosion caused by spurious free chlorine ions from the irradiated halogen containing products like cable insulation, tapes.

2. Residue of brazing flux, trapped cleaning agents like tricholorethyline, carbon tetra chloride etc forms hydrochloric acid and highly toxic gases in contact with the brazing flame.

3. More than 60% relative humidity in vault atmosphere (when panels & R.T. is in air) is one of the causes of corrosion. The relative humidity is considerably higher close to the cooling tubes outer surface than the remaining vault areas this accelerates corrosion.

4. Presence of radioactivity enhances corrosion due to formation of free radical in the air, ozen, nitrogen oxide and subsequently form acids with surface moisture films.

5. Nitrogen oxide can also be formed by spurious discharge of high electric field.

6. Corrosion occurs in bimetal joints of aluminum &copper tubes in trimmer capacitator cooling tubes due to different electro-chemical potentials.

7. Corrosion also enhance by the speed of the cooling water and its residual impurities

8. Porosity will develop in the joint filler due to presence of low vapor pressure (less than 10^{-3} m bar) elements like zinc, cadmium, phosphorus in the filler alloy during brazing at high temperature. Micro-pores may appear under prolong high vacuum (10^{-7} m bar) and high

operating temperature. So the high vacuum service filler must be free from elements like Zn, Cd, P, Pb or they should be controlled below 0.010 Wt %.

REPAIR OF LEAKS

a) All invisible leaks have been detected by bubble emission tests at 1.5 atmosphere pressure and farther finer leaks are detected by MSLD after draining and drying the LWC from the tubes.

b) All the repair have been done by a design of lap type sleeve joint, with a joint-clearance of 20- 25 micron at brazing temperature. Strength of brazing joint reduces with the increase of filler metal film thickness. Length of lap joint has been made three times of the weaker section thickness to achieve good joint strength.

c) Through cleaning of the joint has been done without any chemical cleaning agent to avoid entrapping in the existing finer gaps.

d) The sheet and tubes materials are of OFE grade copper (C10200), which has high thermal and electrical conductivity. It will not produce any hydrogen embitterment during brazing in atmosphere. Since copper has high thermal conductivity and high thermal expansion brazing has been carried out with faster speed and high heat concentration produced by TIG process. Flow of filler by capillary forces has been achieved by manipulating heat of the TIG torch. Sufficient socking time has been provided for wetting molten filler on the joint surface.

e) No flux has been used to avoid residual contamination inside finer gap and corrosion thereafter. Self-fluxing brazing filler has been used.

f) Vacuum grade self-fluxing silver base eutectic alloy of filler wire diameter of 1.5mm has been used as per AWS designation BVAg-8a. This is an eutectic filler containing 72% Ag, 27.8%Cu and 0.2% Li ("Lithobraze" of Handy & Harman Co). Lithium helps to reduce refractory oxide at brazing temperature on the base metal surfaces while brazing at atmosphere. This filler has high electric conductivity of IACS 72%. This composition has the common solidus and liquidus temperature of 765^0C.

Brazing joints produced in this process gives vacuum leak tightness of 10^{-9} SCC /sec.

QUALITY PERFORMANCE TESTS

The performance of the brazing joint quality has been tested in the following steps.

1. Bubble emission test (1.25 ATM+10% excess pressure with air or N_2)- as per ASTM, E515-94

2. MSLD (mass spectrometer leak detector) test has done as per ASTM, E 499-94 to achieve a leak-tightness of $5x10^{-9}$ SCC/sec.

3. Hydraulic test has done with 1.25 times of delivery pressure, 15kg/cm^2 and if any new leak appear after this test and again repeat test no 1, 2 & 3 tests after repair.

4. Lastly MASLD test for gross/global leaks for all the joints in the panel up to a leak rate of $5x10^{-8}$ SCC /sec.

CONCLUSION

Cyclotron down time increases because of water-leaks in R.F. panel and this became a major concern for smooth cyclotron operation. Careful selection of brazing procedure, filler and necessity quality performance tests could minimize this type of down time.

REFERANCES

[1] CERN Accelerator School on Vacuum technology, '99 Materials on Accelerator Vacuum, Erhard Huttel, P-250.
[2] ASME Hand Book on welding, brazing &soldering Volume-6, P-686.
[3] Vacuum metallurgy, O. Winkler & R. Bbakish
[4] ASM Metals hand Book, P-781
[5] Vacuum Sealing Techniques, A. Roth, P-79, 82 &88

THE VACUUM SYSTEM FOR THE SSRF STORAGE RING

D.K.Jiang, Y.L.Chen, L.P.Chen, W.Li, Y.Lu, Y.Y.Liu
Shanghai Institute of Applied Physics, Chinese Academy of Sciences,
P.O.Box 800-204, Shanghai 201800, P. R. China

Abstract

SSRF is the first third generation light source in China. The storage ring vacuum system adopts SS316LN chambers with antechamber structure and discrete absorbers. Several chamber models using SS316L material were developed to confirm the fabrication technology. There are three types of absorber in the ring. TSP and SIP+NEG combined pumps are used for the system. The vacuum chambers with accessory components will be pre-baked before installation. RF shielded bellows with single finger structure have been designed and tested.

INTRODUCTION

The Shanghai Synchrotron Radiation Facility (SSRF) is the first third generation light source in China. The main part of the facility is a 3.5GeV, 300mA storage ring with a circumference of 432m. There are about 60 beam lines can be set to the ring and 7 beam lines are constructed at the first stage [1].

SYSTEM DESIGN

The main performance requirements for the storage ring vacuum system are as follows: (1) To keep the average pressure $<1\times10^{-7}$Pa for more than 10Hrs beam lifetime. (2) To design a reliable chamber with low impedance. (3) To extract the required SR beams and to absorb the rest part of the SR safely. (4) To enhance the mechanical stability for the chambers. The general design for the vacuum system was done under the detail consideration for all the above items. All the SR is stopped on discrete photon absorbers except to the beam lines. The photons will not irradiate the chamber inside wall directly. Large pumping speed pumps are located near the absorbers. There are 6 short section chambers in one cell. They are connected to 3 longer sections through 3 pairs of rectangular flanges with knife edge sealing structure. The 3 long chamber sections are connected by 2 DN150 RF shielded bellows. The location and structure of the absorbers are optimized to make the chamber narrow. The centre of the flange is designed offset to the centre of the beam channel in order to reduce the whole size of the bellows and valves. A standard cell vacuum chamber arrangement is shown in Fig.1.

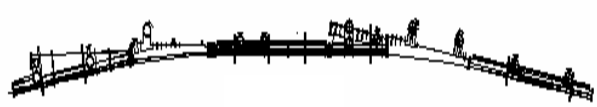

Figure 1: Layout of a standard cell

CHAMBER

The vacuum system for the storage ring adopts stainless steel chambers with antechamber structure. Stainless steel, aluminum and copper are all suitable materials for the medium energy storage ring. Stainless steel chambers are cheaper compared with the one made of aluminum alloys or copper. Stainless steel 316LN is used for the cell chambers in SSRF due to its higher yield strength and very low magnetic permeability after forming and welding. The beam position monitor blocks are used to connect short chamber sections by welding. The chamber pieces are formed by a deep-drawing die and cut by laser or wire cutting methods along the contour. TIG welding is used for the chamber. A section chamber is shown in Fig.2. There is no cooling channel design for the straight section of the chamber in quadruple and sextupole magnets region because of the space limited. The OFHC shielding bar inside of the chamber in dipole region, the absorbers, and the RF shielded bellows are designed with cooling water channel. All the chambers must withstand the power of synchrotron radiation emitted from dipole magnets up to 5mA without interlock operation.

To keep the BPM position stable is a key point for the support design. A stiff support is set to the BPM block as a fixed point for each chamber while other parts are supported on flexible SS plates. In order to avoid the chamber vibration generated by cooling water, smooth water channel and suitable valves are adopted and the flow velocity is limited below 2m/s in design.

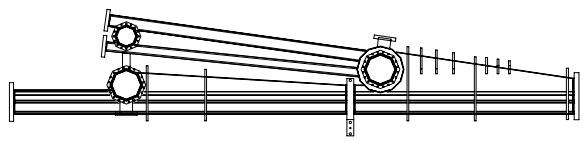

Figure 2: The section chamber structure

PUMPING SYSTEM

The required pressure in the storage ring is 1×10^{-7}Pa or less to get a beam lifetime of 10hrs or more. Assuming that the photon stimulated desorption coefficient $\eta=2\sim3\times10^{-6}$mol./ph. after 100Ah operation, the estimated total gas load is $Q=1.3\times10^{-2}$Pa.l/s. The required nominal pumping speed is about $2\sim3\times10^{5}$l/s in the ring. A sputter ion pump combined with NEG can increase the pumping speed at low pressure and the ratio of pumping speed to pump volume. Titanium sublimation pumps are used near absorbers for large gas load. The model for the combined pump has been tested and shown in Fig.3.Larger pumping speed is also necessary for the place where β_y is larger.

Movable units of TMP and piston dry pump will be used for start of the system.

The three chamber sections with its accessory components in one cell will be pre-baked before installation. They will be kept in vacuum condition while be carried to the tunnel and installed in their final location. The chambers will be vented to atmosphere pressure, connected by bellows and re-pumped as soon as possible because the in-situ bake out will not be performed for the chambers after installation. The vacuum chambers and absorbers will be scratched by photons during the beam cleaning period. As the beam cleaning effect can be memorized for the chamber surface, the pressure will be recovered quickly even if the system is exposed to atmosphere again during maintenance later.

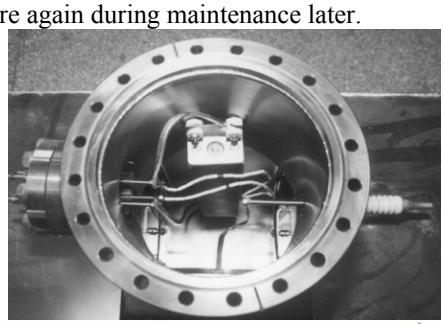

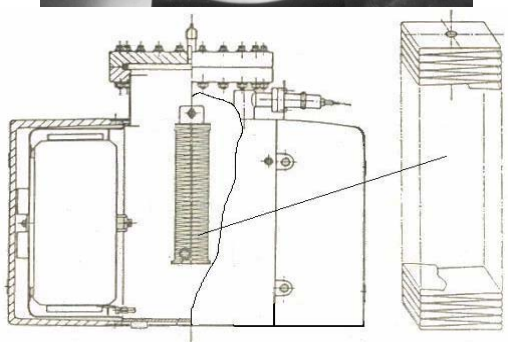

Figure 3: Model of a combined pump (SIP 200l/s+NEG WP1250)

ABSORBER

Absorbers are used to collimate the synchrotron radiation extracted to the beam lines and absorb the rest part of the photons to avoid direct impact of photons on the chamber. Two kinds of absorbers are designed due to the limited space in the ring, which are shown in Fig.4 and Fig.5.

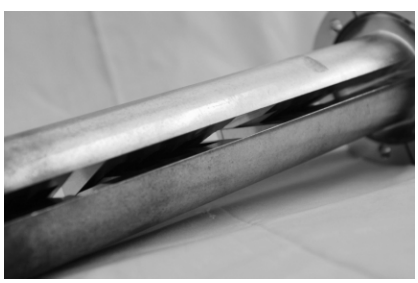

Figure 4: Vertical absorber

Figure 5: Horizontal absorber

To decide the dimension of absorbers and array the absorbers in the ring, many issues should be considered in detail including the radiation fan in a cell, the electron beam orbit shift, the chamber fabrication tolerance and deformation, as well as the chamber installation error. The shadow overlap between two neighbouring absorbers is around 10mm for safety. The absorbers are arranged with margin of 8mm between the chamber wall and the edge of the SR fan to avoid the damage of chamber. Some absorbers are inserted into the slot between beam channel and pumping channel because of the limitation in space. The beam current 400mA is used in the design analysis for the absorber in order to keep margin for safe operation. OFHC copper material is selected for all the absorbers in the ring.

RF SHIELDED BELLOWS

Many efforts should be made to make the total impedance of the beam chambers along the ring less than 1ohm. It is essential to design every component carefully. The inside wall of the beam channel should be as smooth as possible. The tapered transition in the channel should be <1/5. All the step height such as the connecting flange, the welding bead and so on should be less than 0.5mm. Most of the pumps and the vacuum gauges are set on pumping channel. Shielded structure must be designed for the opening on beam channel at the place where the direct connection can not be avoided.

Bellows and gate valves with RF shielding are used in the ring. A single finger structure is applied to the bellows because of its larger offset capacity up to 5mm. Three kinds of inner shape are designed to fit the channel size of neighbouring components. Fig. 6 shows the first group of products for each type of the bellows just after fabrication and test. The contact force between the finger and the inner tube is 60g/finger. Bellows are designed in each side of the high precision BPM block to isolate the movement of the long chambers. The BPMs are fixed on Invar material supports to decrease the thermal influence to the BPM.

Figure 6: RF shield bellows

INSTALLATION TEST

The first products for chambers, absorbers and bellows have been tested after fabrication. All the design specifications are achieved. The vacuum components are installed with other system hardware together. The components engineering design have been confirmed in the installation. Fig.8 to Fig.10 show the chambers in installation.

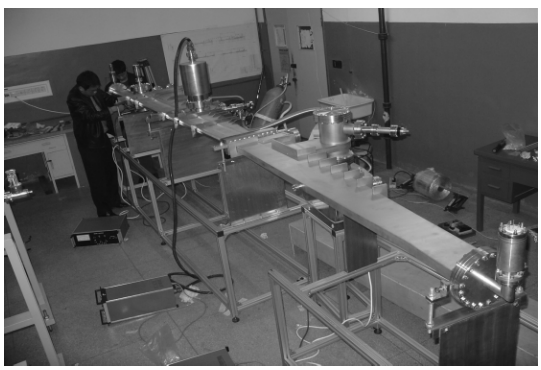

Figure 7: Vacuum test for the model of chambers

Figure 8: Suspend and install the chambers

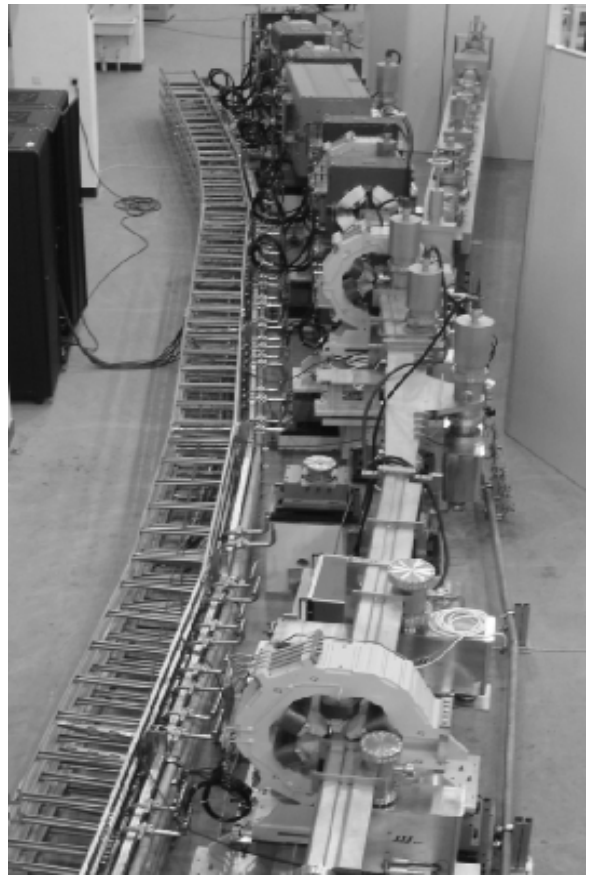

Figure 9: Chambers installed into magnets

SUMMARY

The engineering design for the SSRF vacuum system has been completed. The first products for each of the key components were fabricated and tested. All the specifications were achieved. The mass production for the hardware has been started and will be finished in this August.

REFERENCES

[1] Z.T.Zhao and H.J.Xu, et al, “Status of the Shanghai Synchrotron Radiation Facility”, PAC’05, p. 249

NUMERICAL STUDY OF FIELD ERRORS DUE TO MECHANICAL TOLERANCES IN SUPERCONDUCTING MINIUNDULATORS

C.Z. Diao, H.O. Moser, Singapore Synchrotron Light Source, National University of Singapore, 5 Research Link, Singapore 117603

Abstract

Using a wire model, analytical formulae are derived to describe the spatial distribution of the magnetic field of a superconducting miniundulator (supramini) as determined by the errors in positioning the wires. Semi-analytical numerical simulations are performed to estimate the tolerances of various errors required for a satisfactory function of the supramini, including the effects of systematic errors such as pitch, yaw and roll of a whole supramini coil, and random errors of the wire positions. These results can be used to help assess the minimal required mechanical tolerances.

INTRODUCTION

Superconducting miniundulators (supraminis) are believed to be a key component of 4th generation sources including FELs and Energy Recovery Linacs (ERL). Furthermore, they are expected to play an important role in the upgrading of 3rd generation sources [1-4].

In this paper, we evaluate the influence of the different potential mechanical errors on the quality of the magnetic field and specify acceptable tolerances. Based on a wire model introduced earlier [5], we derive analytical formulae to calculate the magnetic field including the mechanical errors. The effects of systematic errors are treated analytically, random errors are simulated numerically. The effects of these errors on the quality of the field are then graphically analyzed.

MODEL AND PROCEDURE

According to [5], the magnetic field that is produced by an array of wire pairs (wp) and that includes the effect of compensation coils can be written as

$$B_y(x,y,z) = B_y^u(x,y,z) + B_y^l(x,y,z) + B_y^c(x,y,z) \quad (1)$$

where B_y^u is the magnetic field produced by the upper part of coil, B_y^l is the magnetic field produced by the lower part of coil, and B_y^c is the magnetic field produced by the compensation coils. Explicit expressions for the first field contribution will be derived in the following while the other two will be taken from [5].

In our analysis of the mechanical errors of the supramini, we include systematic as well as random errors. To define coordinates, we call (x,y,z) the space frame where the (x,z)-plane is the midplane of the supramini without positional errors and z the direction of the electron beam. Coordinates (X,Y,Z) represent the body frame of the upper coil in which the (X,Z)-plane contains the wire axis and the current flow, X runs either along the axis of the central wire in the case of an odd number of wire pairs or along the equivalent straight line at half-distance between the two central wires in the case of an even number of wire pairs, Y is normal to the (X, Z)-plane through the center of the wire arrangement which is the origin of the coordinate frame as well.

Starting from the ideal position of the upper and lower coils, we construct the displaced error-causing position by translating and rotating the upper coil only while keeping the lower one in its ideal position. This is no restriction of the general validity. Translations are carried out along the space axes (x,y,z) and rotations according to the Euler angles as defined in fig. 1. We define, as shown in fig. 1,

- the pitch error when the upper coil is rotated by an angle θ about the x' axis,
- the yaw error when the upper coil is rotated by an angle α about the y_1 axis, and
- the roll error when the upper coil is rotated by an angle φ about the z_2 axis.

All rotations are in a counter-clockwise sense, i.e., right-handed in the mathematically positive sense. The transition from the space frame (x,y,z) to the body frame of the upper coil (X,Y,Z) is achieved by an initial translation along y by the distance from a wire centre to the midplane, three subsequent translations along x, y, z, and three rotations as defined in fig.1 where we adopted a convention as given in [6].

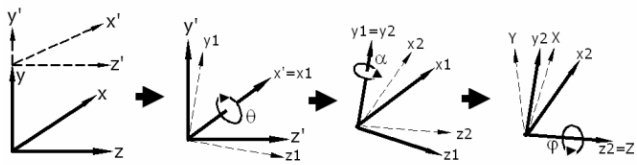

Figure 1: Coordinate transformations leading from the space frame to the body frame of the upper coil with positional errors. Translations of the (x',y',z') frame are not shown.

All error rotation angles θ, α, φ and translational errors $\bar{x}, \bar{y}, \bar{z}$ are supposed to be <<1 and <<g which is the gap, respectively. The magnetic field components produced by the upper coil in the coordinates X, Y and Z are written as $B_X^u(X,Y,Z)$, $B_Y^u(X,Y,Z)$ and $B_Z^u(X,Y,Z)$.

Assuming $B_X^u(X,Y,Z) = 0$, we obtain the magnetic field of the upper coil in the coordinates x, y, and z as

$$B_y^u(x,y,z) = B_Y^u(X,Y,Z)(\cos\varphi\cos\theta - \sin\theta\sin\alpha\sin\varphi) - B_Z^u(X,Y,Z)\cos\alpha\sin\theta$$

with

$$\begin{bmatrix} X \\ Y \\ Z \end{bmatrix} = \begin{bmatrix} \cos\varphi & \sin\varphi & 0 \\ -\sin\varphi & \cos\varphi & 0 \\ 0 & 0 & 1 \end{bmatrix} \begin{bmatrix} \cos\alpha & 0 & -\sin\alpha \\ 0 & 1 & 0 \\ \sin\alpha & 0 & \cos\alpha \end{bmatrix} \begin{bmatrix} 1 & 0 & 0 \\ 0 & \cos\theta & \sin\theta \\ 0 & -\sin\theta & \cos\theta \end{bmatrix} \begin{bmatrix} x-\bar{x} \\ y-\overline{G}-\bar{y} \\ z-\bar{z} \end{bmatrix}$$

where $\overline{G}$ is the distance from a wire centre to the midplane.

For random errors, we will introduce the mechanical errors of the position of the wires. We assume a random distribution of positional errors of the wires where $\Delta_z(1, i)$ and $\Delta_z(2, i)$ denote the positional error of the i^{th} wire in the z direction for the upper and the lower part of the undulator, and $\Delta_y(1, i)$ and $\Delta_y(2, i)$ accordingly for the y direction. As introduced above, the translational errors of the upper coil are $\bar{x}, \bar{y}, \bar{z}$ in the x, y and z directions, respectively.

Then, we will calculate the spatial distribution of the magnetic field from the zero-error wire model (see formula (1)) in combination with the mechanical errors as described above (we suppose the compensation field without mechanical error).

The random errors are assumed to be non-correlated, so that they can be treated separately. For a hypothetical supramini, a set of 2p (p is the number of wire pairs) random values was computer generated and then selected so that they followed a Gaussian distribution with standard deviation σ_1 for $\Delta_z(1, i)$ and $\Delta_z(2, i)$. Another set of 2p random values was generated following a Gaussian distribution with standard deviation σ_2 and for $\Delta_y(1, i)$ and $\Delta_y(2, i)$.

The random errors require many simulations with different seeds to get a statistical analysis. Careful selection of the simulation times is important for the analysis. In our statistical analysis, we will use 200 sets of random error distributions for each given standard deviation.

ERROR ANALYSIS

Next, we will focus on the effects of the field in the midplane due to the mechanical error on four parameters, namely, phase error, field zero, peak field, and the integral field. In the simulation, we use specifications of the prototype supramini at SSLS which are λ_u = 14 mm, N=50, I = 16 mm^2×1000 A/mm^2, g = 5 mm, a = 27 mm, and $\bar{x} = \bar{y} = \bar{z} = 0$.

Influence of integral coil positional errors

We will discuss the most general situation as one coil ideally aligned (in the simulation, we assume the lower one) and the other one rotated with respect to it.

From the simulation, we derive the influence of the pitch, yaw and roll errors on the magnetic field. The pitch error has a significant influence on the phase error, for example, the phase error will be larger than 8.2° when the pitch error is 0.1mrad. If we want to keep the phase error smaller than 1°, the pitch error should be restricted to less than 10 μrad. The effects on the integral field and the field zeros are not too strong.

For the yaw error, the effects on phase error, peak field, integral field and field zeros are not too strong. Assuming for example a yaw error of 200 μrad, the phase error equals 0.115° and the maximum change of field zeros is 0.01 μm.

The effects caused by the roll error only are not strong as the maximum change of field zeros is just 0.02 μm when the roll error reaches 200 μrad.

Taking pitch, yaw and roll errors together, obviously, the effects are mainly, i.e., to more than 90%, caused by the pitch error.

Influence of positional errors of wire windings

We will use 200 sets of random error distributions to do our statistical simulation. Every set of 2p random values was computer generated following a Gaussian distribution with standard deviation σ_1 for $\Delta_z(1, i)$ and $\Delta_z(2, i)$. Another set of 2p random values was generated with standard deviation σ_2 and for $\Delta_y(1, i)$ and $\Delta_y(2, i)$.

In the analysis of the effects on the phase error, peak field and the integral field, for a given standard deviation, we will derive results by averaging the data calculated by the 200 sets of random error distributions computer generated by 200 different seeds. For the field zero, there are many field zeros in one supramini (for example, there are 101 fields zeros for the supramini we used in the simulation). We will calculate the RMS for each field zero change caused by the errors over 200 distributions for a given standard deviation, and then average all RMS to get the effect on the field zero caused by the error with a given standard deviation.

The change of field zeros

Fig. 2 shows the change of field zeros versus the RMS errors in both, y and z direction. It can be seen that the change of field zeros grows almost linearly with the errors as described by the following approximate formulae.

Change by the error in z direction:

$$\delta z_0[\mu m] = 0.733385\sigma_1[\mu m]$$

Change by the error in y direction:

$$\delta z_0[\mu m] = 0.1926\sigma_2[\mu m]$$

The effect of errors in z direction is 3.8 times larger than in y direction.

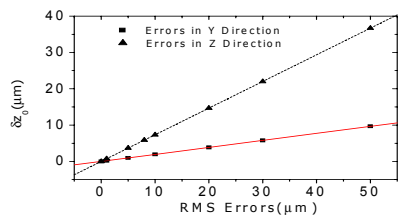

Figure 2: Change of field zeros versus positional error

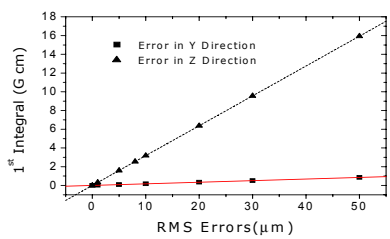

Figure 3: 1st field integral versus positional error

The change of field integrals

As shown in figs. 3 and 4, the field integrals also depend linearly on the RMS positional errors. The fit yields

- Change of the first field integral
  Errors in z direction: $I_z[Gcm] = 0.31877\sigma_1[\mu m]$
  Errors in y direction: $I_y[Gcm] = 0.01703\sigma_2[\mu m]$
- Change of the second field integral
  Errors in z direction: $II_z[Gcm^2] = 22.98\sigma_1[\mu m]$
  Errors in y direction: $II_y[Gcm^2] = 9.78\sigma_2[\mu m]$

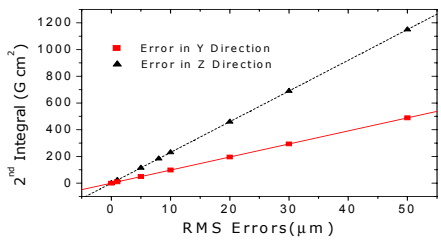

Figure 4: 2nd field integral versus positional error

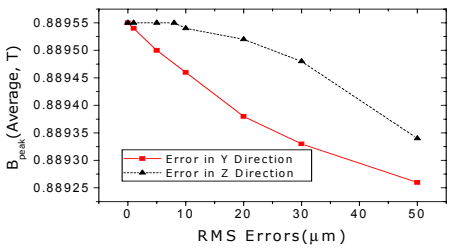

Figure 5: Average peak field versus positional error

The change of phase error and peak field

The average peak field and the RMS field error are also investigated, as in Fig. 5 and 6. In Fig. 5, $\sigma_{\Delta B} / B_{peak}(\%) = 0.42$ even for vanishing RMS error because of the influence of the finite length and of the end field structures on the field as discussed in [5].

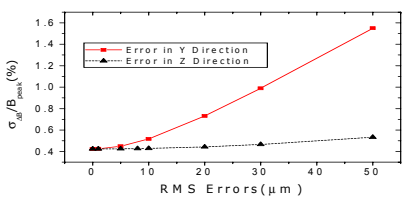

Figure 6: $\sigma_{\Delta B} / B_{peak}(\%)$ versus positional error

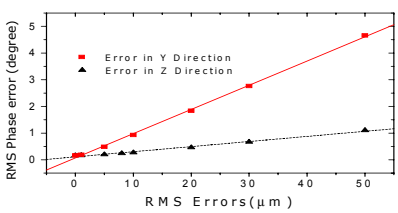

Figure 7: Phase error versus positional error

Fig. 7 gives the RMS phase error as a function of the error in y and z directions.

Errors in z direction: $\sigma_\varphi[\text{deg}] = 0.16 + 0.0187\sigma_1[\mu m]$

Errors in y direction: $\sigma_\varphi[\text{deg}] = 0.16 + 0.0889\sigma_2[\mu m]$

Discussion

From the above error study, the pitch error is found the most critical among the systematic errors pitch, yaw, and roll, As for the errors in wire positions, errors in z direction affect the field zeros and integrals more than those in y direction, while the phase error depends more strongly on errors in the y direction. These results can be used to help assess the minimal required positional tolerances, for example, if we want to construct an undulator with a phase error < 1.5°, the maximum change of field zero < 10 μm, $\sigma_{\Delta B} / B_{peak}$ < 1%, the required tolerances are a pitch error < 5 μrad, yaw error and roll error < 200 μrad, and positional errors of the wire < 4 μm in both directions.

CONCLUSION

In this paper, the influences of mechanical errors on the quality of the field of supraminis are investigated. Using analytical formulae including the effect of the errors in positioning the wires, semi-analytical numerical simulations are performed to estimate the tolerances of various errors. The pitch error was found the most critical error. Although the simulations are for a special specification of SSLS' prototype supramini, this method can be applied generally on other cases of such superconducting undulators.

REFERENCES

[1] H.O. Moser, B. Krevet, H. Holzapfel, "Mikroundulator", German patent P 41 01 094.9-33, Jan. 16, 1991.

[2] S. Casalbuoni, M. Hagelstein, B. Kostka, and R. Rossmanith, " Generation of X-ray radiation in a storage ring by a superconductive cold-bore in-vacuum undulator", Physical Review ST-Accelerator and Beams 9, 010702 (2006)

[3] Mikael Eriksson, Lars-Johan Lindgren, Erik Wallen, Sverker Werin, "A cascaded optical klystron on an energy recovery linac – race track microtron" Nucl. Instr. Meth. A 507 (2003) 470–474.

[4] G. Ingold , I. Ben-Zvi, L. Solomon, M. Woodle, "Fabrication of a high-field short-period superconducting undulator", Nucl. Instr. Meth. A375 (1996) 451-455

[5] H.O. Moser and C.Z. Diao, "Finite-length field error and its compensation in superconducting miniundulators". Nucl. Instr. Meth. A535 (2004) 606-613

[6] Olivier Chocron, Handout No 2, Course 2.05, October 2000. http://web.mit.edu/2.05/www/Handout/HO2.PDF

AN APPLE-II TYPE HELICAL UNDULATOR FOR SSRF

Q.G. Zhou, M. Zhang, Y. Li, Z.M. Qian, J.D. Zhang
Shanghai Institute of Applied Physics, Shanghai 201800, P.R. China

Abstract

Shanghai Synchrotron Radiation Facility (SSRF) is an intermediate energy (3.5GeV) light source under construction. Specially designed insertion devices will be required to realize the high brightness photon beams made possible by the low emittance of electron beam. The first insertion device being designed is a 4.2m long, 10 cm period, APPLE-II type helical undulator, EPU10.0. This device will use a pure permanent magnetic configuration corresponding to four standard Halbach-type magnet rows which consist of two pairs of planar permanent magnet rows above and below the electron orbit plane. The C-frame support structure is selected. The complete design for EPU10.0, including the magnetic structure, the backing beams, the support structure and the drive systems, is described**.**

INTRODUCTION

As the third generation of dedicated synchrotron light source, Shanghai Synchrotron Radiation Facility (SSRF) with 3.5GeV energy is scheduled for completion in 2009 [1]. Based on input from the user community, we are designing a set of insertion devices (IDs) and associated beam lines.

Table 1: Main Parameters of the EPU10.0

Magnetic structure	APPLE-II
Period length	100mm
Period number	42
Available gap range	30~85mm
Available phase shift range	-55~+55mm
Speed of gap motion	4mm/s
Speed of phase shift	1mm/s
Peak field for horizontal polarization	0.6 T
Peak field for vertical polarization	0.3 T
Peak field for circular polarization	0.3 T

An elliptically polarizing undulator for the SSRF has been designed and will be under construction recently. The EPU10.0 can generate a linearly (horizontal or vertical plane), an elliptically or a circularly polarized radiation by providing the phase position shifts to the magnet rows of the undulator. The EPU10.0 will produce very bright photon beams in the spectral range of 70eV to 2000eV. The magnetic design is a moveable quadrant pure permanent magnet structure featuring adjustable magnets to correct phase errors and on-axis field integrals. The support structure, backing beam, and positioning system are all designed to function comfortably with a maximum magnetic load of 2,100kg. Main parameters of the EPU10.0 are shown in Table 1.

MAGNETIC STRUCTURE

The four magnetic quadrants [2] [3] [4] are attached to separate backing beams which allow *a* and *d* to translate axially relative to *b* and *c*, which are fixed. The structure of the four magnetic quadrants is shown in Figure 1. Each quadrant has a magnetic structure length of 4.3m, including 42 full magnetic periods, the ends for achieving a gap-independent steering and displacement free entrance and exit, and magnetic trim sections for correction of integrated multipoles.

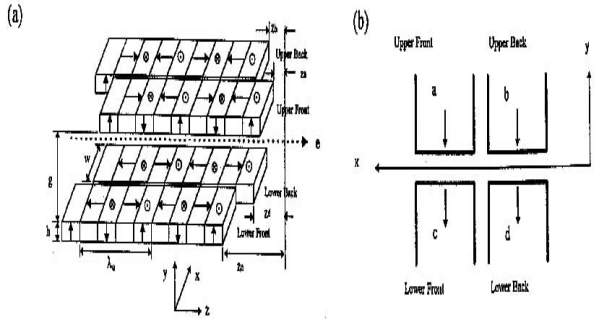

Figure 1: Four quadrants schematic of EPU10.0

Within each quadrant, the basic assembly unit is a 3, 5, or 7 blocks module. Each block within the module is bonded to an aluminium keeper which is mounted to the dove tail connector. Figure 2 shows the scheme of basic module with 5 blocks. Each magnet array consists of 173 blocks of NdFeB including six end blocks. The thickness of the end blocks are designed so as not only to make the first and the second integrals of fields (horizontal and vertical) along the axis of the undulator be zero but also to give no offset of oscillation axis from the axis of the undulator. The same dimensions of the width and the height (35mm × 35mm) of all blocks will give more freedom in the magnet sorting procedure. The magnet holder can be adjusted within ±0.25mm in horizontal and vertical positions by using different thickness shims for the magnetic field tuning. The clearance of 3.7mm between two magnet arrays provides the space for the magnet holder adjustment in horizontal direction.

The magnetic fields were calculated using the analysis formulae for each magnet then linearly superposed for all the magnets. Figure 3 and Figure 4 show the magnet fields on the axis of the undulator and the trajectories of the central electron in the horizontal linear polarization mode and the circular polarization mode with the permanent field of the magnet being 1.2 Tesla and the gap 32mm.

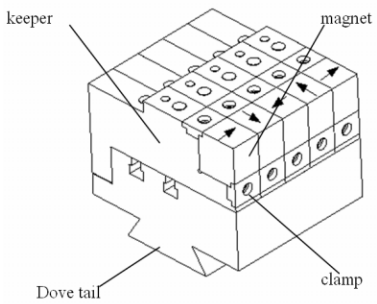

Figure 2: Scheme of basic module

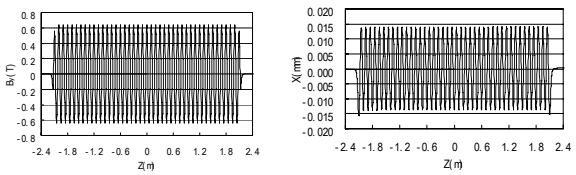

Figure 3: The fields on the axis and the trajectories of the central electron in the horizontal linear polarization mode

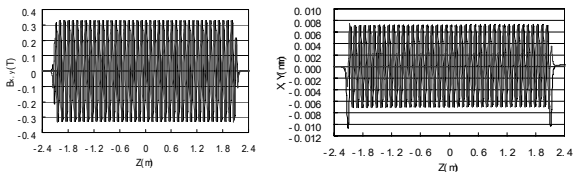

Figure 4: The fields on the axis and the trajectories of the central electron in the circular polarization mode

The magnetic force acting on the magnet arrays varies by phase shifting. It is important to estimate the force when the mechanical design is done. The result shown in Figure 5 indicates that the maximum vertical force (about 2,100kg) occurs when the shift is zero.

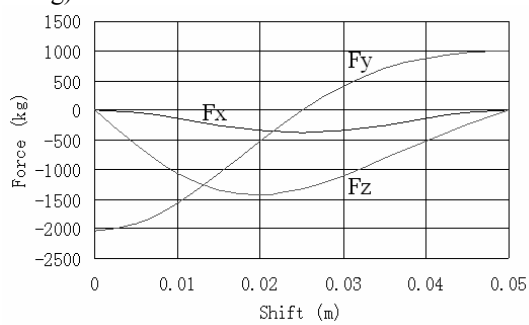

Figure 5: The magnetic force acting on magnet arrays with the gap 31mm

SUPPORT STRUCTURE AND DRIVE SYSTEM

Figure 6, an elevation and side view of the EPU10.0 structure, illustrate the support structure and drive systems. The support structure is a "C" frame design, which is convenient for the magnetic measurements and device installation. The adjusted base with 4 kinematics floor mounts is a welded steel structure, and the adjusted range for y direction is ±6mm, and ±10mm for x, z direction. Two vertical columns with two skew columns to strengthen the rigidity are mounted to the base. Four cube steel tubes, connecting base and vertical columns, further strengthen the stability of the support structure. The vertical columns support four roller screw assemblies which make the vertical moving of the upper and lower beams. The beam is composed of backing beam, stationary beam, and moving beam, which is shown in Figure 7. The backing beam is made of cast-Aluminium, and wrought-Aluminium for stationary, moving beam. The stationary beams support the moving beams via two set of crossed roller slides. The moving beam can move along the two guides mounted between backing beam and stationary backing beam.

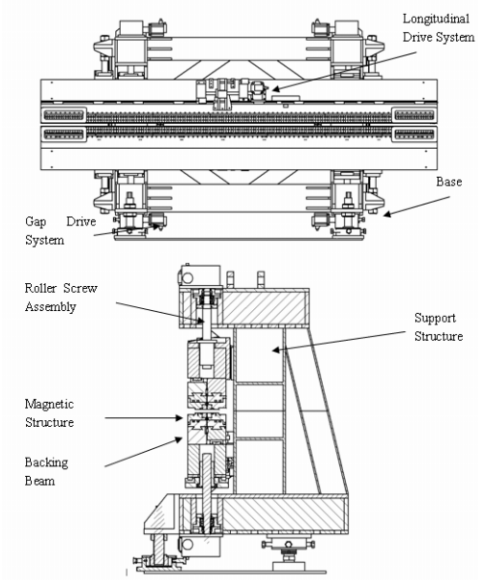

Figure 6: EPU10.0 elevation and side view

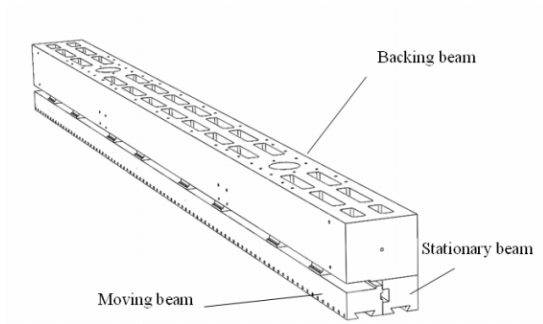

Figure 7: EPU10.0 backing beam

As shown in Figure 8, there are all 6 drive systems controlling the vertical and longitudinal movements. Each drive system consists of a motor, a drive train, an absolute encoder and a controller with digital readout. The vertical gap is moved via each chain drive system connecting a 60:1 worm gear reduction box and servo-motor to one of four roller screw assemblies. Four gratings are mounted to the vertical columns to provide direct feedback to the vertical gap drive system. The longitudinal drive system is a similar system using a smaller roller screw coupled

via a 40:1 gear box and servo-motor. There will be two longitudinal drive systems: one for the upper magnetic structure and one for the lower magnetic structure.

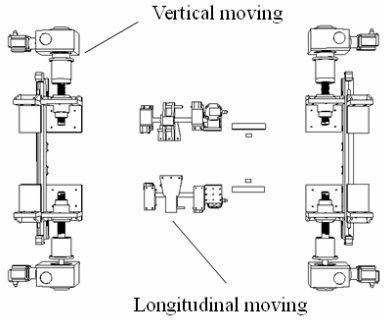

Figure 8: EPU10.0 dive systems

SUMMARY

The design of EPU10.0 for SSRF has been finished. The EPU10.0 will be manufactured recently, and will be completed in August 2008.

REFERENCES

[1] Z.T.Zhao and H.J.Xu, et al, "Status of the Shanghai Synchrotron Radiation Facility", PAC'05, p. 249.
[2] C.S.Hwang and Shuting Yeh, Nucl. Instr. Meth A420, 29-38(1999).
[3] S. Sasaki, Nucl. Instr. And Meth A304, 719(1991).
[4] R. Carr, Nucl. Instr. And Meth A360, 431(1994).

ENERGY STABILIZATION OF 2.5 GeV LINAC USING DEQING

S. H. Kim, S. S. Park, Y. J. Han, J. Y. Huang, S. H. Nam, S. C. Kim
Pohang Accelerator Laboratory, POSTECH, San 31 Hyoja-dong, Pohang, Kyeongbuk, 790-784, Korea

Abstract

The 2.5 GeV electron linac of Pohang Accelerator Laboratory (PAL) employs 80 MW klystrons with matching 200 MW modulators as RF sources. Beam voltage stability of the klystron is directly related to a PFN (pulse forming network) charging voltage of the modulator. Therefore, a good regulation of a PFN charging voltage is essential in the modulator. The regulation of the klystron pulse voltage amplitude is made by controlling the PFN charging voltage. In a conventional resonant charging pulse modulator, the regulation is usually achieved by using a deQing circuit. The required beam voltage regulation of less than +/- 0.5 %, without deQing circuit, has been achieved by using a SCR phase controller with a voltage regulator. For further improvement of the beam voltage stability for the PAL XFEL (x-ray free electron laser) linac, PAL is studying a deQing circuit aiming at the stabilization of less than 0.02%. A prototype deQing controller has been developed with a compensation function which can reduce a charge voltage fluctuation by about several times. The design concept and performance of the deQing circuit will be discussed.

INTRODUCTION

Without a deQing circuit, the beam voltage regulation of about 0.5% has been achieved by using a SCR phase controller with a DC feedback circuit. However, we have to study a deQing circuit aiming at the stabilization of about 0.02% due to getting further improvement of the beam voltage stability for the PAL XFEL linac.

A deQing system is a conventional method of regulating the PFN charging voltage [1]. The klystron beam voltage stability depends on the PFN charging voltage of the modulator. To keep a good regulation of PFN charging voltage in the modulator a deQing circuit is employed, and it can accomplish the required regulation. Finally the deQing unit controls the stability of PFN voltage. When the PFN charging voltage reaches desired level, the deQing SCR is triggered to remove energy remained in a charging inductor. The deQing unit consists of a deQing controller and deQing SCR switch assembly. The deQing should satisfy the following two most important conditions: (1) the peak voltage across primary of charging inductor during a period of deQing should be smaller than the PFN charging voltage. (2) The energy in the charging inductor should be removed by the deQing action before starting next charging cycle.

The prototype deQing controller has been tested in a test linac modulator that has a 150 MW peak power, and a HV divider is installed near the PFN inside of the modulator to use it for PFN charged voltage measurement. A signal coming from the divider will be compared with a DC reference voltage in the deQing controller, and according to the compared result, when the desired level of PFN voltage exceeds the DC reference voltage the comparator in the deQing controller generates an output pulse to trigger the SCR. The prototype deQing controller has a compensation function which can reduce E_{PEN} jitter and a charge voltage fluctuation of dV/dt.

POWER CONTROL SECTION

There are some voltage fluctuations in the input AC line. Since the AC line stability is not good and its amplitude is unstable, that makes fluctuated dV/dt. The dc power supply of the modulator is a conventional, three-phase full-wave bridge dc supply with choke input filter. In stead of using an induction voltage regulator (IVR), a phase-control system with six SCRs is used because the phase controller is more effective than IVR in terms of cost, space, and controllability. A SCR AC-AC voltage regulator controls primary 3-phase 480V AC power. The voltage regulator receives feedback signals from the primary AC voltage and the high voltage DC (HVDC) detector. The closed loop control of the AC-AC voltage regulator ensures stable HVDC output. Therefore, the phase control charging scheme has been used for control of full three phase primary power. Using a SCR phase controller with active feedbacks in a high voltage dc power supply can help us to get a stabilization of PFN charging voltage. We stabilized a high voltage charging power supply within 1% by a phase controlled SCR voltage regulator with AC feedback. We get about 0.5% variation of the PFN charging voltage by employing dc feedback circuit in the phase controller.

DEQING CRICUIT DESCRIPTION

The deQing SCR switch assembly is shown in Fig. 1. The amplitude of the PFN voltage is controlled by the deQing unit connected in parallel to a charging choke. The charging choke has a secondary winding to match the relatively low voltage components of the deQing unit to a high voltage charging circuit in the primary winding. When the desired PFN voltage exceeds the dc reference voltage coming from the prototype deQing controller, the comparator in the deQing controller generates an output pulse to trigger the SCR. The energy left in the charging chock at that time is dissipated in the secondary load resistors. The deQing circuit is normally adjusted to dissipate a few percent (about 3 ~ 5%) of the charge in each cycle. It can regulate the PFN voltage to 0.1% or more low levels.

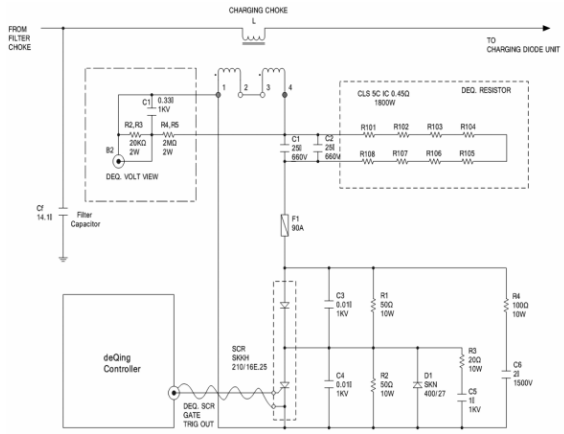

Figure1: Block diagram of SCR for deQing.

As shown in the figure 1, it consists of the secondary of the charging choke, a SCR switch with a diode in a series connection of RC parallel network for power dissipating resistors and energy storage capacitors in which R and C are 3.6Ω and 50μF, respectively. The values of R and C are determined by a simulation result. Various values of R and C in the deQing SCR switch assembly are tried to find optimum value. The function of these components is to regulate the charge placed on the PFN capacitors.

FUNCTION OF A DEQING CONTROLLER

Figure 2 and 3 show the picture of the controller and a simplified schematic of the deQing controller, respectively. It consists of a circuit of differentiating PFN charging voltage, sample and hold, a difference amplifier, ADC, digital delay, comparators, CPU for trigger control, LCD display, and a 0.01% high accuracy divider. The HV divider with an excellent performance is necessary to get a fine regulation of the PFN charging voltage. The HV divider, made by ROSS VD60-6.2Y-BD-KC-UJGA-F, placed on the modulator has acquisition bandwidth of 5Mhz, 0.01% DC, isolation voltage of 60KV dc, and a ratio of 10,000:1.

Figure 2: Picture of the deQing controller.

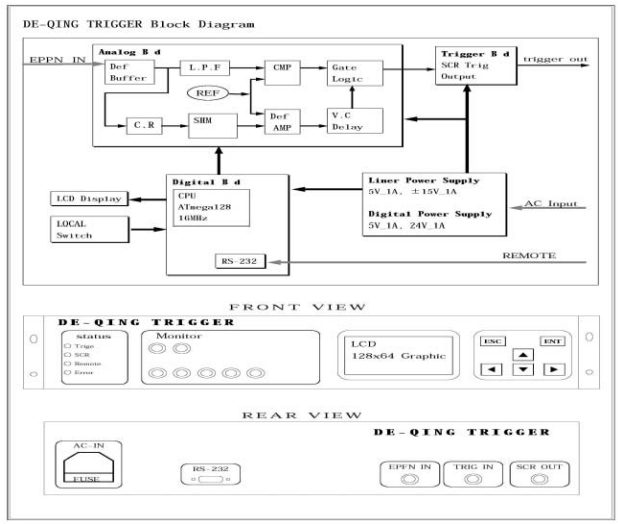

Figure 3: Block diagram of the prototype deQing controller.

As shown in the Fig. 3, the function of the circuit of differentiating PFN charging voltage is that it detects PFN charging voltage electrically from a difference buffer in the deQing controller. The sample and hold circuit picks up the peak value of the slope voltage coming from the differentiated charging waveform. The voltage selected from the sample and hold circuit and a dc reference voltage are compared with a difference amplifier. The difference amplifier outputs an error signal voltage compared with the reference which is coming from the deQing reference voltage which is calculated from the deQing controller. The role of the voltage control delay is that the error signal level obtained from the comparator is adjusted by the following amplifier and converted into a digital signal used for a deQing trigger delay. Its value makes the adjustment of the timing of a deQing trigger by the digital-delay circuit. The role of CPU is that displays a reference voltage and current high voltage, and condition of deQing on or off.

TEST RESULTS

The deQing controller has been tested in a test linac modulator that has a 150 MW peak power. The charged PFN voltage was 34KV with pulse duration of 6μs, and the pulse repetition rate is 30Hz. The HV divider which has 10,000:1 ratio is installed near the PFN inside of the modulator to measure PFN charging voltage. The charging voltage measured has been done using the digital oscilloscope (Tektronics DPO 7104).

Fig. 4 shows charging inductor secondary voltage waveforms that are measured by a 100:1 divider. The left trace is a waveform with 4.3% deQing, and the right trace is a waveform of over 5% deQing. At the measurement of a grade of deQing by using the deQing controller, the grade of 4.3% deQing is the best working. At the test of the grade below 3% deQing and over 4.5%, the stability of PFN charging voltage is more deteriorating. Thus, the

grade of the deQing is set about 4.3% of the full PFN charging voltage.

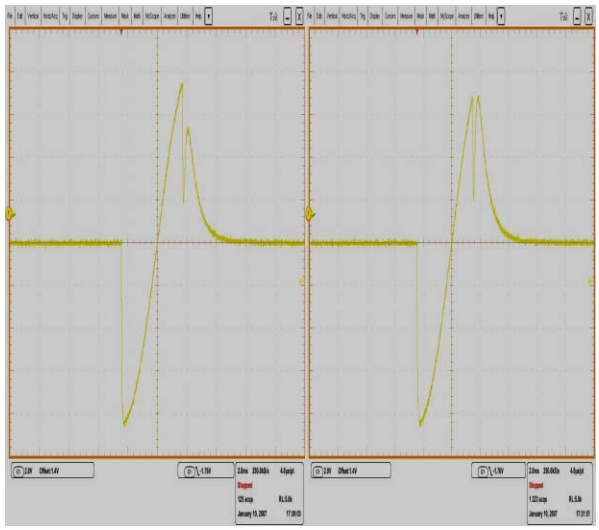

Figure 4: Waveforms of a charging chock secondary voltage. X: 2ms/div, and Y: 200V/div.

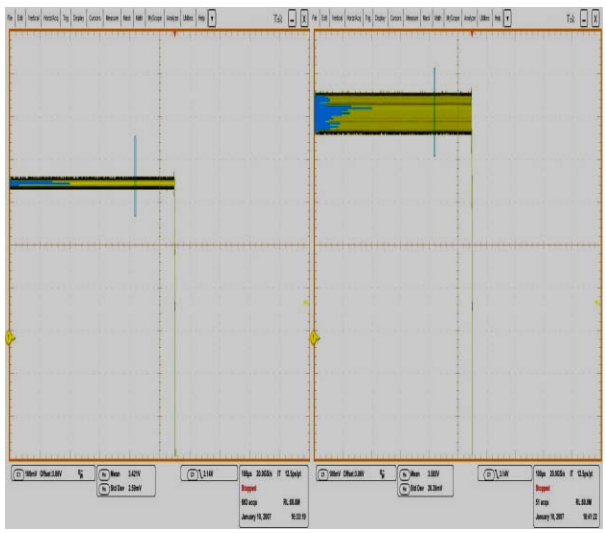

Figure 5: Accumulated waveforms of a PFN charging voltage. X: 100μs/div, and Y: 1kV/div.

PFN voltage waveforms that are measured by a 10,000:1 divider are shown in Figure 5 and 6. In the right Fig. 5 when the deQing controller is not activated, the stability accumulated for 10 minutes is about 0.57% (value of mean: 3.585(V) and value of standard deviation: 20.39(mV)). With the aid of deQing, as shown in the left Fig. 5, the variation measured for 1 hour is reduced to 0.076% (value of mean: 3.421(V) and value of standard deviation: 2.59(mV)) which is reduction of about 7.5 times from the previous value that is measured without the deQing.

As shown in the left Fig. 6, there are many noises remaining at the deQing controller PCB if the ground of the deQing controller PCB could not connect with a modulator ground. The left waveform shows occurring of noise by no connection with the modulator ground, and the right one does not remain noise at the waveform by connection with the modulator ground.

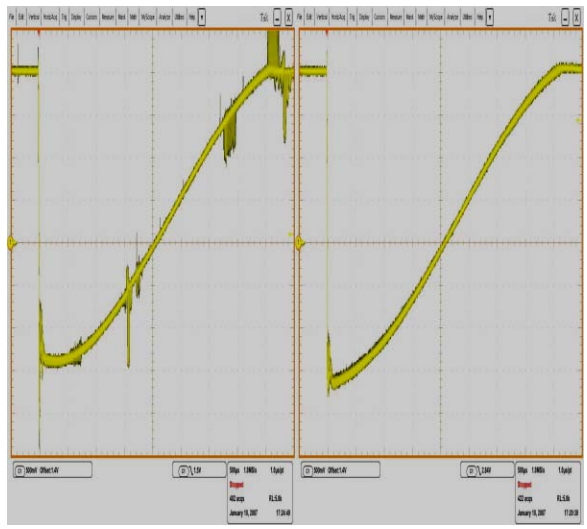

Figure 6: Waveforms of electrical noise and killing noise. X: 500μs/div, and Y: 5kV/div.

CONCLUSION

For improvement of the beam voltage stability for the PAL XFEL (x-ray free electron laser) linac, PAL has been studying a deQing unit aiming at the stabilization of less than 0.02%. The prototype deQing controller has been tested in the test linac modulator that has a 150 MW peak power. To get the required beam voltage stabilization of the modulator with a 65 MW SLAC 5045 klystron tube for PAL test linac, SCR AC-AC voltage reg ulators and the deQing controller are employed.

With the aid of deQing, the variation of PFN charging voltage is reduced to 0.076% which is about 7.5 times reduction from the value measured without the deQing. In the feature, the deQing controller will apply to the linac m ain modulator, and functions that adjust automatically a reference voltage of the deQing compared with a PFN voltage of the modulator may be added to the deQing controller at next upgraded one. Upgrades of the deQing controller will be continued to achieve performance characteristics of the modulator for the PAL XFEL linac.

ACKNOWLEDGEMENT

The authors would like to express our appreciation for useful discussion to Dr. Hayano who works for ATF in Japan.

REFERENCE

[1] R.B. Neal, ed., “The Stanford Two-Mile Accelerator,” W.A. Benjamin, New York, 1968.

DEVELOPMENT OF A 200KEV LINEAR INDUCTION ACCELERATOR

K.V.Nagesh, Archana Sharma, S.Acharya, Rehim N.Rajan, D.K.Sharma, P.C.Saroj, S.Mitra, D.P.P.Kumar, Senthil K, A.Roy, Ritu Agrawal, S.Raul, K.C.Mittal and D.P. Chakravarthy,
Accelerator and Pulse Power Division, Bhabha Atomic Research Centre, Mumbai-400085, India.

Abstract

Electron Linear Induction Accelerator (LIA) are for applications in high power microwaves (HPM), high gradient accelerators, flash X-rays radiography (FXR), flue gas clean-up, detoxification of chemicals, cross-linking of polymers, sterilization of food and medical waste/devices etc. The LIA-200 is being developed at APPD,BARC consists of mainly (i) solid state pulse modulator based on semiconductor devices, (ii) pulse compression and voltage amplifications stages, steps up to 200kV, 5μs and compresses these pulses to 75kV,10kA,50ns (FWHM) in five stage and (iii) three stage induction cavities in ADDER mode for relativistic electron beam generation, with matched load of 5Ω. Metglas cores have been used in transformers, switches and induction cavities. Deminearlised water capacitors and water pulse forming line have been used for low impedance energy storage and compactness. The complete system has been assembled and ready for commissioning. LIA-200 will be operated from a PLC based control system which is under testing.

INTRODUCTION

The principle of magnetic induction has often been applied to the acceleration of high-current beams in a variety of induction accelerators. The induction linac (IL) consists of a simple non resonant structure where the drive voltage is applied to an axially symmetric gap that encloses a toroidal ferromagnetic material. The change in flux in the magnetic core induces an axial electric field that provides particle acceleration. This simple non resonant (low-Q) structure acts as a single-turn transformer that can accelerate beams of hundreds of amperes to tens of kilo amperes, limited only by the drive impedance. The IL is typically a low-gradient structure that can provide acceleration fields of varying shapes and time durations from tens of nanoseconds to seve ral microseconds. The acceleration voltage available is simply given by the expression V = A*(dB/dt) Hence, for a given cross sectional area A of material, the beam pulse duration influences the energy gain. Following is th e details of LIA-200 configuration.

CIRCUIT DESCRIPTION

Fig.1 shows the photograph of the Linear Induction Accelerator and Fig.2 shows the simulated electrical equivalent circuit diagram in Orcad. Capacitor C1 is charged to 2.5kV with a constant current power supply. This is a Phase Shift Pulse Width Modulated (PS-PWM) power supply operating at 30 kHz. This topology has the capability to eliminate turn on losses and minimizes turn off losses of IGBTs present in the inverter. A Thyristor (X1) is placed to initiate the command resonance charging. T1 is a pulse transformer of 2.5kV / 20kV. L1 is the equivalent leakage inductance of the transformer T1. Diode D2 is placed to block the reverse pulses from the forward stages. Capacitor C2 gets charged to 20kV after the gate pulse to the Thyristor X1 is given. S1 is a magnetic switch to compress the pulse duration from 20μs to 5μs. Pulse transformer T2 steps up the voltage pulse of 20kV to 200kV. C3 and C4 are water capacitors of value 10nF. Magnetic switch S2 compresses the pulse from 5μs to 1μs and S3 from 1μs to 250ns. Deminaralized water Pulse Forming Line (PFL), is required to get a flat topped pulse of 50ns duration at the output. Magnetic switch S4 holds the output pulse from PFL for 250ns. It gives output pulse of 50ns with sharp rise time and is applied to an induction adder cavity. Each induction cell acts as a single turn 1:1 pulse transformer in co-axial configuration.

Pulse Transformers

Amorphous core toroids based pulse transformers are designed and developed with final parameters are tabulated in table-1. Each core has outer diameter, inner diameter and hight as 240mm, 160mm and 25mm respectively. Each transformer is kept in degassed transformer oil chamber for cooling and insulation. Teflon covered wires are used for winding with kepton tape and mylar as insulating layers. Perspex flanges were used to hold the full assembly.
Chokes are designed for DC resetting of cores at 20kV and 200kV side separately.

Table 1 : Parameters of pulse transformer 1 and 2

Main Parameters	Pulse Transformer-1	Pulse Transformer-2
Turns Np/Ns	22/176, parallel 6-cores (6P)	35 x 8P/50-on all 8-cores
Voltage Vp/Vs	2.5kV/20kV, 20μs	20kV/200kV,5μs
Current Ip/Is	15kA/1.8kA	8kA/800A
Leakage L	0.55 μH	3.5μH

OPERATION OF LIA

Magnetic pulse compression is the key in achieving the output of 200kV, 50ns pulse. The operation of Induction Linac is based on series magnetic pulse compressor as reported by D.Birx [1]. Three induction cells in parallel are driven by this output pulse from PFL. It is estimated that final output pulse to cavities will be of >75kV, 5kA, 100ns FWHM [2].

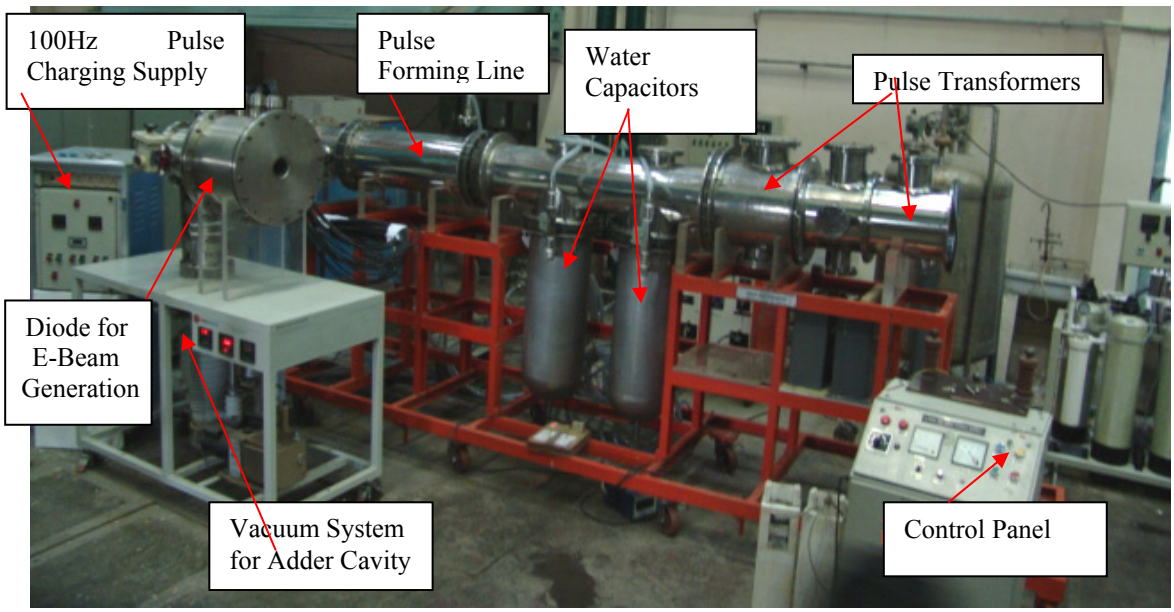

Figure 1 : Photograph of Linear Induction Accelerator

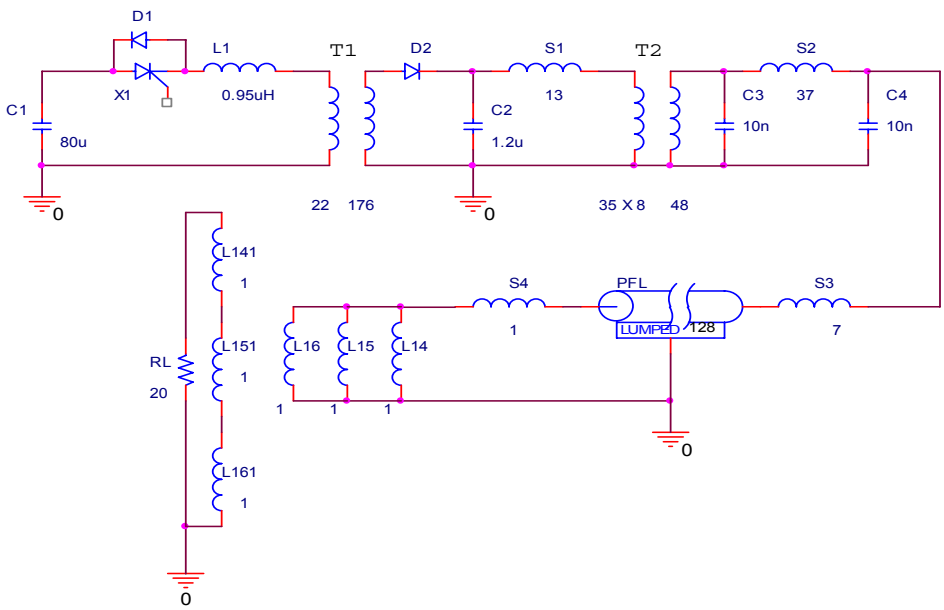

Figure 2 : Schematic showing the electrical equivalent circuit of LIA

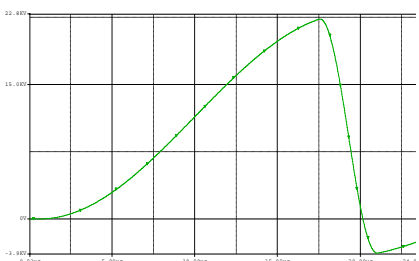

Figure 3 : Output of 20kV transformer

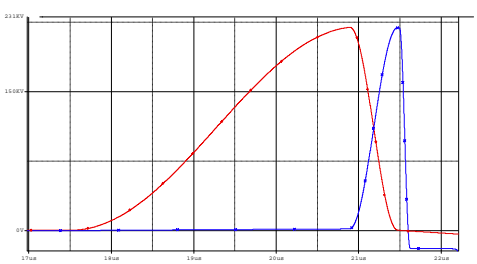

Figure 4 : Voltage across water capacitors 1& 2

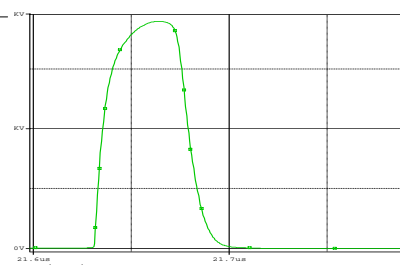

Figure 5 : Output pulse from the induction cell

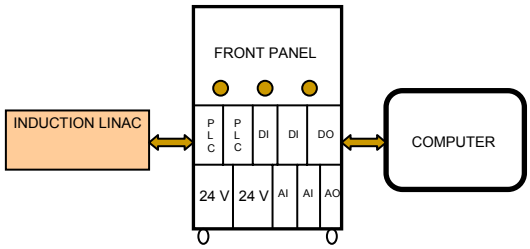

Figure 6 : Control of LIA showing front panel, PLC and data acquisition

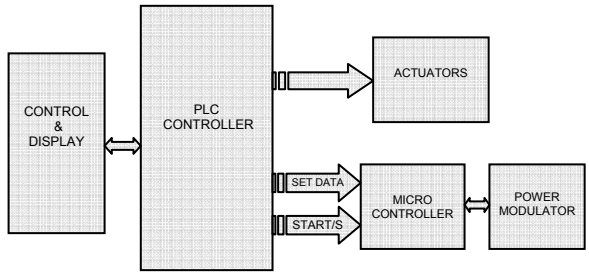

Figure 7 : Diagram showing PLC – Microcontroller interaction

ain pulse is getting reversed at the output of 20kV transformer, so that final output will be a negative pulse. Core resetting is done by applying a DC voltage in such a way that, resulted current flow should be in opposite direction to that of main pulse current [3]. Magnetic switch S1 and pulse transformers of 20kV /200 kV are reset by a 10mH blocking inductor in series with a DC supply of 0-40V/0-25A. Magnetic switches S2, S3, S4 and output induction cell are resetted by putting a reset circuit in parallel with the first water capacitor. This reset circuit consists of a blocking inductor of 10mH and current limiting resistor in series with a DC supply of 0-60V/0-60A.

SIMULATION RESULTS

OrCAD software has been used to simulate the circuit of Fig.2. Here a 3-stage induction cell is represented by three pulse transformers (L14 - L141, L15 - L151, and L16 - L161). Magnetic switch is modelled using Jiles & Atherton model and pulse forming line is modelled using a transmission line. Figure 3 shows the output of 20kV transformer charging capacitor C2. In Fig.4, the voltage across the two water capacitors are presented. Negative part of the pulse is due to oscillation with the previous stages and/or saturation of forward stage before the peak of the capacitor voltage. In Fig.5, the final output pulse, which is 280kV, 60ns has been illustrated. It is expected to get a 200kV, 100ns pulse with the experimental setup as the voltage drops with the forward stages and output switch and other stray inductances add to the duration of the pulse.

CONTROL OF LIA

For the purpose of controlling linear induction accelerator from remote position Programmable Logic Controller (PLC) based control system is used. 80C320 processor has been used for PLC system.

The PLC takes care of man-machine interaction through computer and control panel (front panel). Digital inputs from the computer or control panel (controlled manually) and from different sub-system parameters are given to PLC. Analog inputs from various sub systems are converted to 4-20mA signals and are carried to the PLC location through cables. These signals are converted to digital inputs using an Analog to Digital Converter (ADC), before being given to the PLC. The ladder logic present in the PLC processes these digital inputs and sends the required digital output through RS232 cable to microprocessor (80C535) present in the pulse modulator power supply. This microprocessor takes care of controlled DC voltage generation and triggering pulses to Thyristor. In case of any discrepancy in the process parameters like temperature rise or flow disruption, an interrupt signal goes from the PLC to the microprocessor and halts the whole system. All process parameters are sensed by the PLC as analogue and digital inputs. In EMI environment, S.S. conduits are used to shield the cables carrying various signals to PLC. These signals are filtered before being given to the PLC. PLC is encaged using thick copper strip, which is properly grounded to avoid any kind of interference. Analog signals like, oil temperature in transformer and switch chambers, water temperature at the outlet of water capacitor and PFL, water conductivity and pH, and current in the reset circuit are continuously monitored. Any variation from the preset value of these parameters will halt the system by sending the interrupt signal to the microprocessor. PLC can process 64 digital inputs and 32 analog inputs and can give a maximum of 16 analog and 96 digital outputs. Microcontroller is embedded in the power modulator. PLC will communicate to the microcontroller through RS232 for setting the charging voltage, charging current, repetition rate, number of pulses, and for sending the START/STOP signal.

CONCLUSIONS

Simulation for the induction accelerator has been performed and the results need to be checked with the experimental ones. PLC based remote control for the system was presented and it was installed at the site.

REFERENCES

[1] Danial Birx, “Induction Linear Accelerators” Physics of Particle Accelerators (AIP Conf. Proc.249) Vol.II, 1982, pp.1554-1613.

[2] Archana Sharma, S. Acharya, T.Vijayan , P. Roychoudhury & P.H. Ron, “ High frequency characterization of an amorphous magnetic material and its use in induction adder configuration”, IEEE-Transactions on Magnetics, vol.39,No.2, 2003, pp.1040-45.

[3] Design Report on Electron Linear Induction Accelerator (200keV, 5kA, 50ns, 10-100Hz); prepared by APPD, BARC, Mumbai, July, 2000.

THEORETICAL ANALYSIS OF THE RECOVERY TIMES IN LOW PRESSURE SPARKGAPS - POSITIVE ION DIFFUSION METHOD

K.V.Nagesh, Accelerator and Pulse Power Division, Bhabha Atomic Research Centre, Trombay, Mumbai, 400085, India.

Abstract

Presently there are no methods ideally suitable for the calculation of recovery times of low pressure sparkgaps. However an attempt has been made to calculate and analyze the recovery times of low pressure sparkgaps based on diffusion of positive ions here. The recovery times are calculated based on the reported data of plasma diffusion rates. The spherical ambipolar and free diffusion recovery times are generally in good agreement with the experimental recovery times at higher pressures. The cylindrical ambipolar and free diffusion recovery times are an order of magnitude lower than spherical diffusion recovery times. The recovery times are not in good agreement for positive polarity experimental recovery times. The theoretical calculation of recovery times, comparison of calculated & experimental recovery times and discussions are presented in this paper.

INTRODUCTION

The electrical breakdown and pre-breakdown characteristics of gases at atmospheric pressure and above, and at low pressures are widely investigated and there is reasonable agreement on the mechanism of growth of the current in the breakdown. But the recovery processes after the sparkgap breakdown are not studied extensively at low pressures. These are due to short duration {~100ns FWHM} of the present experimental voltage pulses leading to the lower plasma densities. The cross-sectional view of experimental setup and photograph of the system used for these studies are shown in Fig.1 and Fig.2 respectively. The recovery experiments are conducted at 10mm gap for argon gas, 10 and 2.5mm gaps for hydrogen gas and 2.5mm gap for deuterium gas with gap pressure varying from 1.1Pa to 34Pa at room temperature 295K [1, 2].

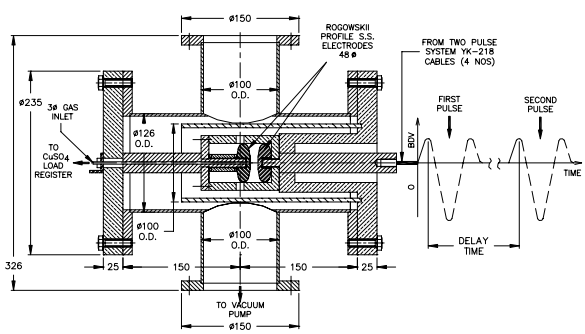

Figure 1. Cross-sectional view of experimental setup of Low Pressure Sparkgap

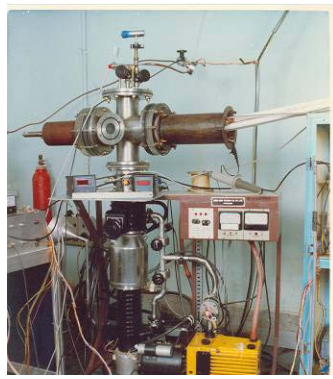

Figure 2. Photograph of the experimental setup of Low Pressure Sparkgap

The ratio of λ_e/d varies approximately from 40 for gap pressure of 1.5Pa to 1 at 23Pa and lower at higher pressures. Whenever the ratio λ_e/d is very much higher than 1, it indicates that the breakdown mechanism is initiated, developed and sustained by electrode mechanism. Here the recovery process mainly depends upon the anode temperature decay. Whenever the ratio λ_e/d is closer to 1 and lower, it indicates that the breakdown mechanism is initiated by electrode mechanism and developed and sustained by gas mechanism. Here the recovery process mainly depends upon the positive ion diffusion. Whenever the ratio λ_e/d is between these two extremes, the breakdown is initiated by electrode mechanism and sustained by gas discharge. Here the recovery process is a combination of anode temperature decay and positive ion diffusion with anode temperature decay being predominate at higher ratios and vice-versa. The recovery of the gap mainly depends upon diffusion of positive ions under the conditions of low gap current {<2.5kA}. The positive ion diffusion may be either spherical or cylindrical depending upon the discharge initiation. If the discharge is from a point then the diffusion is spherical. If it is diffuse discharge over a large surface area, then the diffusion is cylindrical. The spherical diffusion takes place when the discharge is due to pulses having risetimes in the microsecond range and above. The cylindrical diffusion is possible with applied pulses having rise times of 10 to 100ns. The positive ion diffusion may be classified as ambipolar or free diffusion, depending upon the Debye length of the plasma in the discharge. If the Debye length is less than characteristic diffusion length, then the diffusion is ambipolar and in other cases, it is free diffusion. Generally the diffusion is

ambipolar at high electron current densities and free diffusion at low electron current densities.

The free and ambipolar diffusion recovery times for spherical and cylindrical diffusions are calculated for hydrogen, argon and deuterium gases using the equations [3, 4] for the temperature range of 10K to 1000K. The general equation for diffusion of positive ions with no sources of electrons is given by

$$D \nabla^2 n = -\{n/\tau\} = -(1/D\tau)\, Dn \quad \ldots\ldots\ldots\ldots\ldots (1)$$

The solution to the above equations with a lowest mode (k=1) is given by

Cylinder. $n = n_0 \cos(a x) J_0(br)$, ...(2)

$$a^2 + b^2 = (1/D\tau) \quad \ldots\ldots\ldots (3)$$

With the boundary condition of n=0 at the walls of radius r and height h.

J_0 = Bessels function, $a = \pi/h$, $b = (2.405 / r)$

$$(1/\wedge)^2 = (\pi/r)^2 + (2.405 / r)^2 \quad \ldots\ldots\ldots (4)$$

Sphere $(1/\wedge)^2 = (\pi/r)^2$ or $\wedge = r/\pi$ .....(5)

where r = Sphere radius.

$\wedge_k^2 = D\tau_k$, $\wedge$ = Characteristics diffusion length,

τ = decay constant.

The free and ambipolar diffusion time constants are given by

(i) **Free diffusion time constant** = $\tau_F = \wedge^2 / D_+$ ..(6)

(ii) **Ambipolar diffusion time constant,** $\tau_a = \wedge^2 / D_a$ .... (7)

where D_+, D_-, = diffusion co-efficients for positive and negative ions,

D_a= ambipolar diffusion co-efficient = 0.1511 at NTP for hydrogen gas. For other temperatures and pressures,

$$D_a = \frac{[D_+ K_- + D_- K_+]}{[K_+ + K_-]} \quad \ldots (8)$$

K_-, K_+ = mobilities for negative & positive ions. Where D, T, P & D_0 T_0 P_0 = diffusion coefficient, temperature and pressure at temperature T and T_0 respectively. The diffusion coefficient at N.T.P. used in the calculation of recovery times are given in Table 1. The typical spherical diffusion recovery times (ambipolar) as a function of temperature for various gap pressures are plotted in Fig.3 for hydrogen gas. The spherical and cylindrical (ambipolar and free) diffusion recovery times as a function of gap pressure are plotted in Fig.4 to Fig.6 for a temperature of 295K {room temperature}, for hydrogen, deuterium & argon gases respectively. The corresponding experimental full recovery time characteristics are reproduced here for comparison [1, 2]. This calculated recovery time characteristic is a straight line in log-log scales. The recovery time increases with increase in gas pressure and decreases with increase in temperature. The spherical and cylindrical diffusion recovery times increase with molecular weight of the gas and pressure in the gap.

Table 1

Parameters	H_2 gas	D_2 gas	Argon gas
$D_+(m^2/s)$	123 x10^{-5}	108.1 x10^{-5}	32.2 x10^{-5}
D_- (m^2/s)	190 x10^{-5}	166.9 x10^{-5}	40.95x10^{-5}
K_+ (m2/s/V)	5.19 x10^{-4}	4.60 x10^{-4}	1.37 x10^{-4}
K-(m2/s/V)	8.15 x10^{-4}	7.10 x10^{-4}	1.70 x10^{-4}

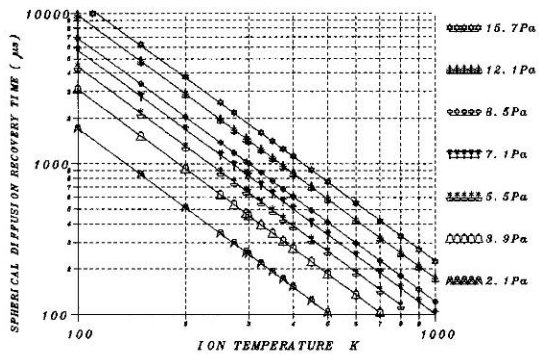

Figure 3. Spherical Ambipolar Diffusion Recovery Times vs +Ve Ion Temperature Characteristics. H_2 gas, 48mm Dia. S.S.Electrodes, 10mm Gap.

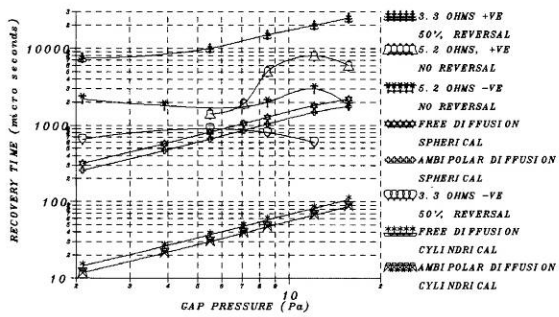

Figure 4. Hydrogen gas Diffusion Recovery Times vs Gap Pressure Characteristics, 48mm Dia., 2.5/10mm Gap.

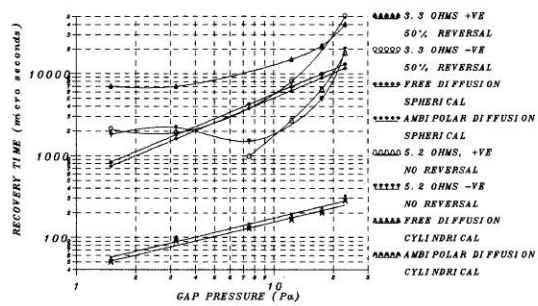

Figure 5. Argon gas Diffusion Recovery Times vs Gap Pressure Characteristics, 48mm Dia., 10mm Gap.

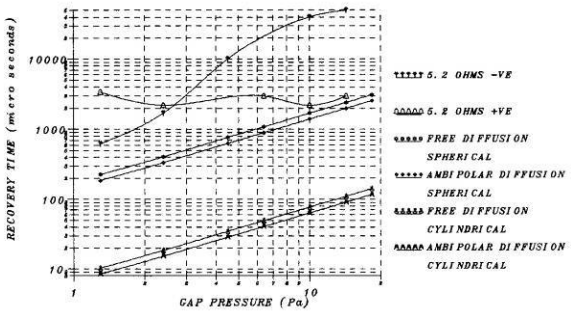

Figure 6. Deuterium gas Diffusion Recovery Times vs Gap Pressure Characteristics, 48mm Dia., 2.5mm Gap.

The cylindrical diffusion recovery times are only tens of microseconds at 295K. These are an order of magnitude lower than the spherical diffusion recovery times. The ambipolar diffusion recovery times are lower than free diffusion recovery times and the difference between them is small.

DISCUSSION

The recovery times are inversely proportional to the diffusion coefficients, which depends on the experimental temperatures. The diffusion coefficients increase with increase in temperature and decrease with increase in pressure. The recovery times decrease with increase in temperature and increase with increase in pressure and molecular weight of the gas. The volume discharge characteristics of cylindrical diffusion are an order of magnitude lower than the spherical diffusion times and not in good agreement with the experimental results. The spherical diffusion recovery times are in good agreement with the experimental recovery times. The difference between ambipolar and free diffusion recovery times is very small. The ratio of ambipolar and free diffusion recovery time is of the order of 0.8125 to 0.8136 in the pressure range of 1.2Pa to 34.7Pa. This small difference is due to lower current in the discharge. The diffusion process is a combination of free and ambipolar diffusion processes. At lower pressures and lower impedances ($<$5Pa & $\geq$5kA), the recovery due to anode temperature decay plays a major role. At slightly higher pressures (5-10Pa & 2-5kA), the recovery due to spherical ambipolar and free diffusion plays a major role. At pressures greater than 10Pa ($\leq$2kA) free diffusion plays a major role. The large difference in recovery times by spherical ambipolar and free diffusions compared to experimental recovery times at low pressures is partly due to metal vapour diffusion.

CONCLUSIONS

The cylindrical diffusion recovery times cannot explain the process of recovery in a low-pressure sparkgap for the present E/p range. It may be a suitable process for higher E/p range. The spherical ambipolar and free diffusion recovery process is suitable to analyze the experimental recovery times for negative polarity with current reversals but is not suitable for positive polarity in a low pressure sparkgap. Whenever the experimental recovery times are faster than ambipolar diffusion recovery times, the recovery of low pressure sparkgap may be a combination of spherical and cylindrical diffusion processes. The recovery time of a low-pressure sparkgap depends upon the anode temperature rise and decay (metal vapour diffusion) as well as free and ambipolar diffusion processes. At higher pressures, the recovery due to ambipolar and free diffusion plays a major role.

ACKNOWLEDGEMENTS

The author is thankful to staff members of Accelerator and Pulse Power Division for useful discussions and support. Grateful thanks are due to my guides, Dr.P.H.Ron, former Head, Accelerator and Pulse Power Division, BARC, Mumbai, and former Professor G.R.Nagabhushana and former Professor R.S.Nema, Department of High Voltage Engineering, Indian Institute of Science, Bangalore, for stimulating discussions and valuable guidance. Grateful thanks are also due to Dr. A.K.Ray, Director, Beam Technology Development Group, BARC and Shri D.P.Chakravarthy, Head, APPD, BARC, for their keen interest and encouragement.

REFERENCES

[1] K.V.Nagesh, A Study of Recovery Times of Low Pressure Sparkgaps, Thesis, Indian Institute of Science, Bangalore, July 1997.

[2] K.V.Nagesh, P.H.Ron, G.R.Nagabhushana, & R.S.Nema, Over Recovery in Low Pressure Sparkgaps, IEEE Trans. On Plasma science, Vol.27, No.1, Feb.1999, p-1-12.

[3] David.R.Lide, Handbook of Chemistry and Physics, 76th Edition, 1995-1996, CRC Press.

[4] J.M.Meek and J.D.Craggs, Electrical Breakdown of Gases, John Wiley and Sons, 1978.

THEORETICAL ANALYSIS OF THE RECOVERY TIMES IN LOW PRESSURE SPARKGAPS – ANODE TEMPERATURE DECAY METHOD

K.V.Nagesh, Accelerator and Pulse Power Division,
Bhabha Atomic Research Centre, Trombay, Mumbai, 400085, India

Abstract

The recovery characteristics of the low-pressure sparkgaps in the time interval of 300μs to 50ms, with stainless steel electrodes, in the pressure range of 1 to 40Pa, for gap spacings of 2.5mm & 10mm, have been determined experimentally for hydrogen, argon and deuterium gases. An attempt has been made to analyze the recovery times of low pressure sparkgaps by anode temperature rise and decay method based on liquid & solid vapour phases here. The liquid & solid phase recovery times, theoretical calculation of recovery times, comparison of calculated & experimental recovery times and discussions are presented in this paper.

INTRODUCTION

The recovery processes after the sparkgap breakdown are not studied extensively at low pressures with short duration pulses {~100ns FWHM} which do not allow sufficient time for the metal surface to melt. The cross-sectional view and photograph of the experimental setup are shown in Fig.1 and Fig.2 [1, 2]. The typical effects of electrodes after experiments, is shown in Fig.3.

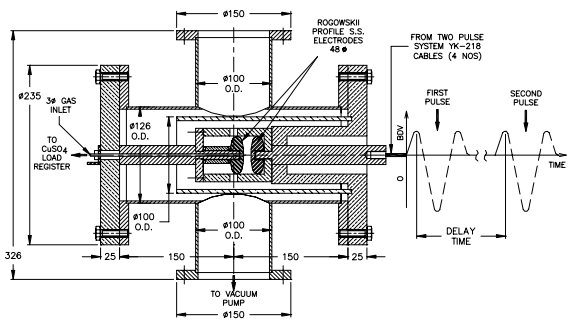

Figure 1. Cross-sectional view of experimental setup of Low Pressure Sparkgap.

Presently there are only three papers on calculation of recovery times of sparkgaps [3, 4, 5]. The experimental arc discharge times of Frind et. al. [3] are 300μs and 4500μs and currents in the range of 250A to 12kA. Since the discharges are in vacuum (1.3×10^{-4}Pa - 1.3×10^{-5} Pa) having longer pulse durations with higher currents, the anode spot has been observed in this case. The ionization potential (7.5V) is assumed to be equal to the anode drop with full recovery is assumed to be at 10^{-2} Torr with anode spot temperature decaying to 1200^{0}C for copper electrodes. However there is an order of magnitude difference between theoretical and experimental recovery times. Rich & Farrall [4] has assumed that recovery pressure is equal to twice the gap spacings as mean free path in the recovery of vacuum circuit breakers. There is good agreement in some cases and large difference in others. Tsuruta & Ebara [5] has calculated the recovery of air gaps based on gas temperature decay with the assumption as the gas temperature reduces to 300K at full recovery from peak discharge temperatures of 2000-5000K. There is good agreement at gap spacing of 3mm but the calculated recovery time is lower for 1mm and higher for 7mm than the experimental value.

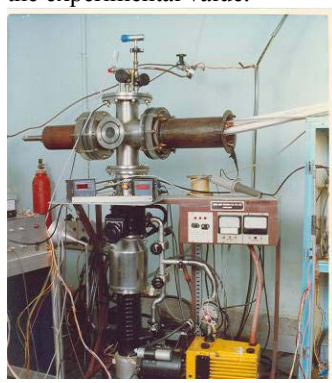

Figure 2. Photograph of the experimental setup of Low Pressure Sparkgap

Figure 3. Photograph of the typical effects of electrodes after experiments.

The recovery experiments of the present studies [1, 2] have been conducted for gases of hydrogen, deuterium and argon gases. The energy per pulse varies from 0.4 to 8J, which gives the peak power densities are of the order of 2×10^{11} W/m^2 which is lower than the critical power densities for melt zone. Presently there are no methods ideally suitable for calculation of recovery times of low pressure sparkgaps, however an attempt has been made to analyze the recovery times here by anode temperature rise and decay method based on Frind's work [3].

Recovery Time Calculation by Anode Temperature Rise and Decay Method

The rise in anode temperature for can be calculated using the following equation of Frind et. al. [3]

$$T = \frac{0.239.S.\Delta t}{\rho.C \ \{\alpha.\pi.t\}^{0.5}} e^{-\{x^2/(4.\alpha.t)\}} + 273 \quad (1)$$

Where T = Temperature in K.

Δt = Pulse Time Interval = 100ns & $\{\Delta t/(t)^{0.5}\}$ ..(2)
$= \Delta t^{0.5}$ for incremental calculation
S = Specific heat flux from arc to the surface
ρ = density gm/cm^3 = 7.54, C = Specific Heat = 0.115
α = Thermal diffusivity= 0.12
t = time since heat pulse is applied, s
x = depth below electrode surface, cm = 0.1mm
The factor 0.239 allows specific heat flux to be in watts/cm^2.

The temperature of the anode reduces due to cooling of the electrode as well of vaporization of the electrode during the initial period. This can be calculated using the equation of Frind et. al. [3]

$$T_F = \frac{0.239.WE(T).\Delta t}{\rho.C\ \{\alpha.\pi.t\}^{0.5}}\ e^{-\{x^2/(4.\alpha.t)\}} + 273 \quad ... (3)$$

For incremental calculations, this equation reduces to

$$T_F = \frac{0.239.WE(T).(\Delta t)^{0.5}}{\rho.C\ \{\alpha.\pi\}^{0.5}}\ e^{-\{x^2/(4.\alpha.\Delta t)\}} + 273 \ldots (4)$$

where $WE(T) = 16200.[T / 2000]^{9.91}$ .for copper electrodes .....(5)
$= 19970.[T / 2216]^{10.5}$ .for stainless steel electrodes .....(6)
with Δt = Pulse Time Interval = 100ns & $\{\Delta t/(t)^{0.5}\}$
$= \Delta t^{0.5}$ for incremental calculation
WE(T) = Anode temperature decay flux of the vaporization of anode surface in time Δt.
anode drop V_a = 25volts for H_2 at 26.7Pa
= 16-18 volts for D_2 at 133.3Pa-667Pa
= 15.3 volts for Argon at 66.7Pa

In the present work, the metal surface has been assumed to vaporize within the pulse duration time of 100ns due to high peak power density. Hence the discharge is assumed to be predominately gas discharge and for calculation of anode temperature rise and anode drop is assumed to be gas discharge anode drop. The recovery times are calculated based on the reported data of anode drops. The typical H_2 gas anode temperature decay as a function of Time Characteristics and peak anode temperature as a function of gap pressure characteristics are shown in Fig.4, and Fig. 5 respectively. The peak temperatures are lower than anode spot formation temperatures and higher than for anode foot-points. Hence it can be concluded that only the anode foot-points can be formed as per Gundersen [6] and Klapas et. al. [7]. Once the temperature decays to respective vapour pressure temperatures {1806K & 1612K at 1.2Pa for hydrogen, 1813K & 1617K at 1.3Pa for deuterium & 1819K & 1622K at 1.5Pa for argon gases for liquid & solid phases}, the sparkgap has recovered completely (full recovery).

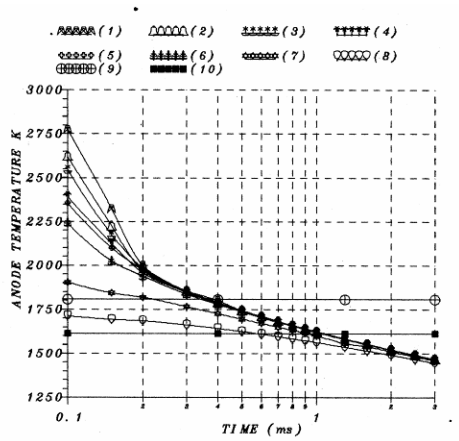

Figure 4. H_2 gas anode temperature decay vs Time Characteristics, 48mm Dia. S.S. Electrodes, 10mm Gap.
(1)- 2.1Pa, -Ve, (2)- 2.1Pa, +Ve, (3)- 5.5Pa, -Ve, (4)- 5.5Pa, +Ve, (5)- 8.5Pa, -Ve, (6)- 8.5Pa, +Ve, (7) 12.1Pa, -Ve, (8)-12.1Pa, +Ve, (9)- Liquid Vapour Phase Temperature-1806K, 1.2Pa, (10) Solid Vapour Phase Temperature-1612K, 1.2Pa.

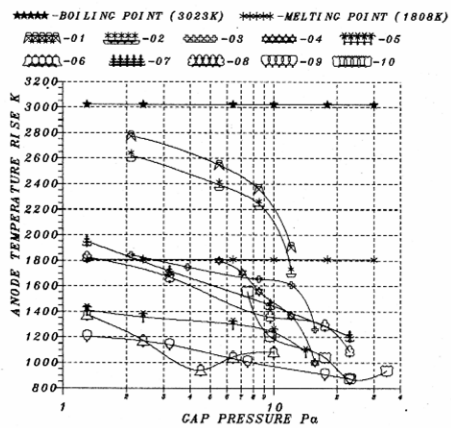

Figure 5. Anode temperature Rise vs Gap Pressure Characteristics, 48mm Dia. S.S. Electrodes, 10mm Gap.
H_2 gas, 50% Rev., 3.3Ohms, 10mm Gap-[01- -Ve, 02-+Ve] H_2 gas, 0% Rev., 5.2Ohms, 2.5mm Gap-[03- -Ve, 04-+Ve] D_2 gas, 0% Rev., 5.2Ohms, 2.5mm Gap-[05- -Ve, 06-+Ve] Ar gas, 50% Rev., 3.3Ohms, 10mm Gap-[07- -Ve, 08-+Ve] Ar gas, 0% Rev., 5.2Ohms, 10mm Gap-[09- -Ve, 10-+Ve].

RESULTS AND DISCUSSIONS

The typical estimated anode temperature decay full recovery times with gap pressure characteristics for hydrogen and argon gases are shown in Fig.6 and Fig.7. There is a small difference in recovery times of positive and negative polarities due to some difference in peak temperatures. This difference is not significant. The negative polarity recovery times are in good agreement with solid phase recovery times in case of hydrogen gas with 50% current reversals (gap currents of 5kA, Fig.6). The experimental recovery times are nearly two times

in case of 2.1Pa for hydrogen gas and 1.5Pa for argon gas. There is a large difference between experimental and solid phase recovery times for both argon and hydrogen gases under positive polarity with 50% current reversal. (seven times solid phase recovery time at 1.5Pa, argon gas and at 2.1Pa hydrogen gas). This process cannot explain this large difference between positive and negative polarities with large current reversals.

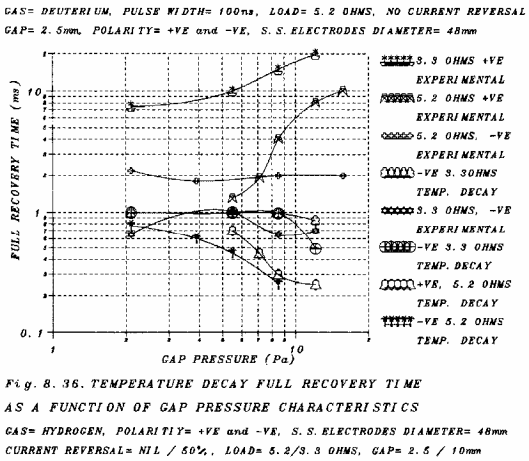

Fig. 8.36. TEMPERATURE DECAY FULL RECOVERY TIME AS A FUNCTION OF GAP PRESSURE CHARACTERISTICS
GAS= HYDROGEN, POLARITY= +VE and -VE, S.S. ELECTRODES DIAMETER= 48mm
CURRENT REVERSAL= NIL / 50%, LOAD= 5.2/3.3 OHMS, GAP= 2.5 / 10mm

Figure 6. Temperature Decay full recovery times vs Gap Pressure Characteristics, H_2 gas, 48mm Dia. S.S. electrodes, 2.5mm /10mm Gaps, Load=5.2 & 3.3 Ohms.

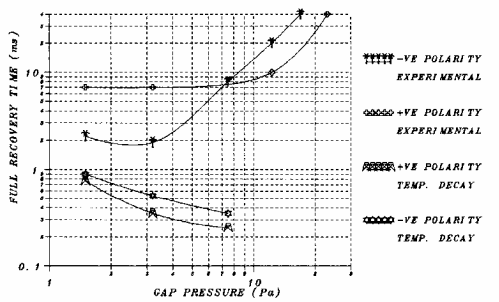

Fig. 8.37. TEMPERATURE DECAY FULL RECOVERY TIME AS A FUNCTION OF GAP PRESSURE CHARACTERISTICS
GAS= ARGON, POLARITY= +VE and -VE, S.S. ELECTRODES DIAMETER= 48mm
CURRENT REVERSAL= 50%, LOAD= 3.3 OHMS, GAP= 10mm, DYNAMIC PUMPING

Figure 7. Temperature Decay full recovery times vs Gap Pressure Characteristics, Ar gas, 48mm Dia. S.S. electrodes, 10mm Gap, Load= 3.3 Ohms, 50% Rev.

CONCLUSIONS

The anode spots cannot be formed but anode foot-points can be formed on anode for the present experimental currents. The anode temperature decay recovery time reduces drastically close to melting point temperature and increase in pressure. This does not fit well with the experimental recovery times. For short duration pulses and for anode temperatures greater than melting point, a combination of liquid and solid phase may be responsible for recovery of the gap. Generally the recovery of the gap depends upon the combination of these processes for temperatures between melting point and solid vapour pressure temperature.

ACKNOWLEDGEMENTS

The author is thankful to staff members of Accelerator and Pulse Power Division for useful discussions and support. Grateful thanks are due to my guides, Dr. P.H. Ron, former Head, Accelerator and Pulse Power Division, BARC, Mumbai, and former Professor G.R. Nagabhushana and former Professor R.S. Nema, Department of High Voltage Engineering, Indian Institute of Science, Bangalore for stimulating discussions and valuable guidance. Grateful thanks are also due to Dr. A.K. Ray, Director, Beam Technology Development Group, BARC and Shri D.P. Chakravarthy, Head, APPD, BARC, for their keen interest and encouragement.

REFERENCES

[1] K.V.Nagesh, A Study of Recovery Times of Low Pressure Sparkgaps, Ph.D. Thesis, I.I.Sc., Bangalore, July 1997.

[2] K.V.Nagesh, P.H.Ron, G.R.Nagabhushana, & R.S.Nema, Over Recovery in Low Pressure Sparkgaps, IEEE Trans. On Plasma science, Vol. 27, No.1, Feb.1999, p.199-210.

[3] G.Frind, J.J.Carroll and E.J.Tuohy, Recovery times of Vacuum Interrupters which have stationary Anode spots, IEEE Trans. on Power Apparatus and systems, Vol.PAS-101, No.4, April 1982, pp775-781.

[4] J.A.Rich and G.A.Farrall, Vacuum arc Recovery Phenomena, Proceedings of the IEEE, Vol.52, Nov. 1964, pp.1293-1301.

[5] K.Tsuruta and H.Ebara, Modeling of a Gas Temperature decay after Arc discharge in small Air Gaps, IEEE Trans. D and EI, Vol.27, No3, June 92, pp.451-456.

[6] G.Gundersen, Anode Spot formation in vacuum Arcs, Thesis, Norweg, Inst. Tech. Trondheim, Norway, 1971.

[7] D.Klapas and R.Holmes, Anode Spot Temperature in vacuum Arcs, Presented at XI Conf. Phen. Ion. Gases, 82, (Prague, Czechoslovakia) 1973.

STABILITY ANALYSIS OF A KLYSTRON-MODULATOR FOR PAL XFEL

J. S. Oh, S. D. Jang, S. J. Kwon, Y. G. Son, J. H. Suh, C. W. Chung, I. S. Ko, and W. Namkung
PAL/POSTECH, Pohang 790-784, Korea

Abstract

The PAL (Pohang Accelerator Laboratory) is persuading to construct a SASE-XFEL facility (PAL XFEL). The stable electron beam is essential for the single-pass free electron laser facility. The beam stability requirement for XFEL linac is determined from XFEL physics analysis. We need to find correlation between the beam parameters and related sub-system parameters to define the stability criteria of each sub-system. The beam stability is governed by an accelerating RF field, of which fluctuation is mainly caused by the modulation of a klystron voltage pulse. Therefore, it is directly determined by the charging stability of a modulator. This paper shows the detail analysis of the stability dependency of a klystron-modulator on the related parameters.

INTRODUCTION

PAL XFEL is a 4th generation light source that is a coherent X-ray free electron laser by utilizing an existing 2.5-GeV linac [1]. In order to provide reasonably stable SASE output, the RF stability of 0.02% rms is required for both RF phase and amplitude [2]. This is a technologically challenging issue for PAL XFEL.

The beam stability is given by the fluctuation of both RF power and phase driven by a klystron voltage pulse that is directly determined by the PFN (pulse forming network) charging voltage of a modulator. Therefore, it is useful to define the stability by using a sensitivity of the system parameters such as klystron voltage, RF phase and RF power by its relative stabilities to the one of a charging voltage. This paper analyzes the sensitivities of RF parameters and beam energy related to the PAL XFEL, in which Toshiba E3712 klystron (S-band, peak power of 80 MW) is to be used as main klystrons driving a XFEL linac [3].

MODULATOR SENSITIVITY

From the Ohm's law for a modulator and a klystron, $V_O = V_K + Z_{PFN} \times I_K$ and the klystron beam current, $I_K = k\, V_K^{1.5}$ with given klystron perveance k, we can define the sensitivity of a klystron voltage by

$$s_V = \left(\frac{dV_K}{V_K}\right)\Big/\left(\frac{dV_O}{V_O}\right) = \left(1+\frac{Z_{PFN}}{Z_K}\right)\Big/\left(1+1.5\frac{Z_{PFN}}{Z_K}\right) = \left(1+\sqrt{\frac{V_K}{V_{K,nom}}}\right)\Big/\left(1+1.5\sqrt{\frac{V_K}{V_{K,nom}}}\right) \quad (1)$$

where V_o is a PFN charging voltage, V_K is a klystron voltage, $V_{K,nom}$ is a nominal klystron voltage where the impedance is designed to be matched, Z_{PFN} is PFN impedance, Z_k is klystron impedance. Figure 1 shows the equation (1) with measured data of E3712 klystron for PAL XFEL. At the klystron voltage where the impedance is matched, the sensitivity of a klystron voltage is 0.8 and it is slowly varying over wide range of beam voltage.

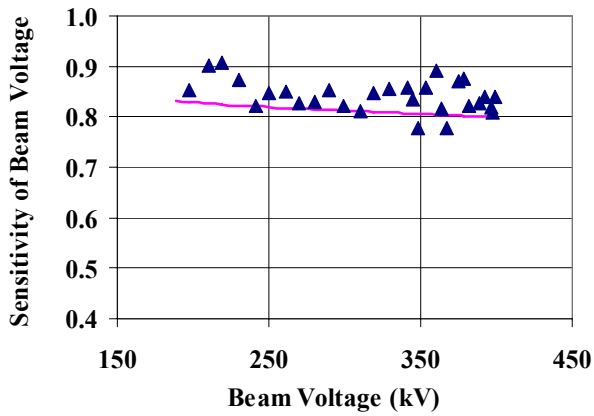

Figure 1: Sensitivity of klystron beam voltage (line: equation (1), triangle: measured data of E3712 klystron).

The sensitivity of a klystron beam current in the Figure 2 is given by

$$S_I = \left(\frac{dI_K}{I_K}\right)\Big/\left(\frac{dV_O}{V_O}\right) = \left(\frac{V_O}{I_K}\right)\Big/\left(\frac{dV_O}{dI_K}\right) = \left(1+\frac{Z_{PFN}}{Z_K}\right)\Big/\left(2/3+\frac{Z_{PFN}}{Z_K}\right) = \left(1+\sqrt{\frac{V_K}{V_{K,mon}}}\right)\Big/\left(2/3+\sqrt{\frac{V_K}{V_{K,mon}}}\right) \quad (2)$$

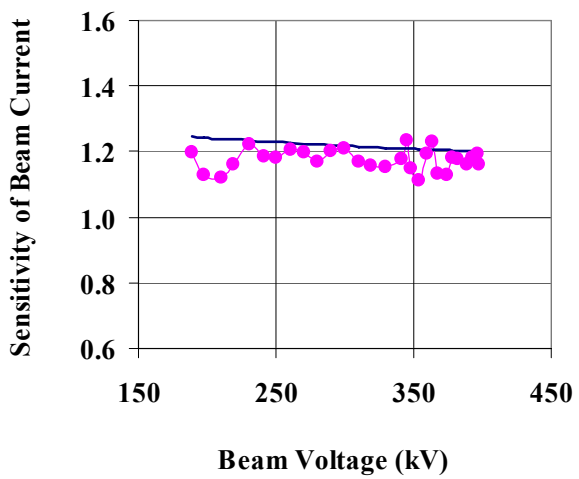

Figure 2: Sensitivity of klystron beam current (line: equation (2), circle: measured data of E3712 klystron).

*Work supported by the MOST and the POSCO, Korea
#jsoh@postech.ac.kr

At the klystron voltage where the impedance is matched, the sensitivity of a klystron current is 1.2 and it is also slowly varying over wide range of beam voltage.

KLYSTRON SENSITIVITY

The delayed RF phase ϕ_{RF} from a driving input RF phase ϕ_o of a klystron is given by

$$\phi_{RF} = \phi_o - 2\pi f t_{transit} = \phi_o - 2\pi\left(\frac{c}{\lambda_{RF}}\right)\left(\frac{L_{KLY}}{v}\right) \quad (3)$$

where $t_{transit}$ is the transit time of a drift length L_{KLY} between the input cavity and the output cavity of the klystron with an electron velocity v and λ_{RF} is a wavelength in a free-space, and c is the speed of light in vacuum [4]. Therefore, sensitivity of the RF phase is

$$s_\phi = \left(\frac{d\phi_{RF}}{2\pi}\right)/\left(\frac{dV_O}{V_O}\right) \approx \left(\frac{L_{KLY}}{\lambda_{RF}}\right)\left(\gamma^2-1\right)^{-1.5}\left(\gamma-1\right)\times s_V \quad . \quad (4)$$

where γ is the Lorentz factor of the electron. Figure 3 shows the phase shift and sensitivity of E3712 klystron of which the drift length of 64.6 cm. The sensitivity of the RF phase is slowly varying over wide range of beam voltage even though the phase change is large. The phase variation is 1.4°/kV and phase sensitivity is 1.53 at the beam voltage of 400 kV.

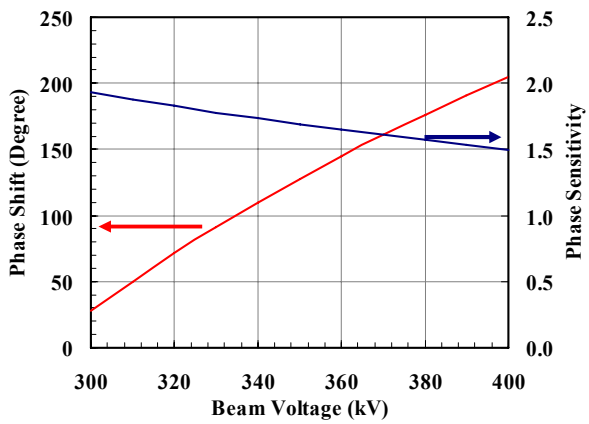

Figure 3: Phase shift and sensitivity of E3712 klystron.

The RF power of a klystron is given by $P_{RF} = \eta I_K V_K = \eta k V_K^{2.5}$ where η is the RF conversion efficiency. Therefore, the RF power fluctuation is

$$\left(\frac{dP_{RF}}{P_{RF}}\right)/\left(\frac{dV_K}{V_K}\right) = \left(\frac{d\eta}{\eta}\right)/\left(\frac{dV_K}{V_K}\right) + \left(\frac{dk}{k}\right)/\left(\frac{dV_K}{V_K}\right) + 2.5 \quad . \quad (5)$$

Figure 4 shows the relative fluctuations of RF power, efficiency and perveance of the E3712 klystron. The perveance dependency is relatively so small that it is neglected in the sensitivity of the RF power

$$s_P = \left(\frac{dP_{RF}}{P_{RF}}\right)/\left(\frac{dV_O}{V_O}\right) \approx s_\eta + 2.5\, s_V \quad (6)$$

where $s_\eta = (d\eta/\eta)/(dV_o/V_o)$ is the sensitivity of efficiency.

The efficiency variation of a klystron at low voltage has large effect on the sensitivity of RF power so that the power sensitivity is getting up from 3.1 at 400 kV to 8 at 250 kV for E3712 klystron. Therefore higher the beam voltage is, better the stability of RF power is.

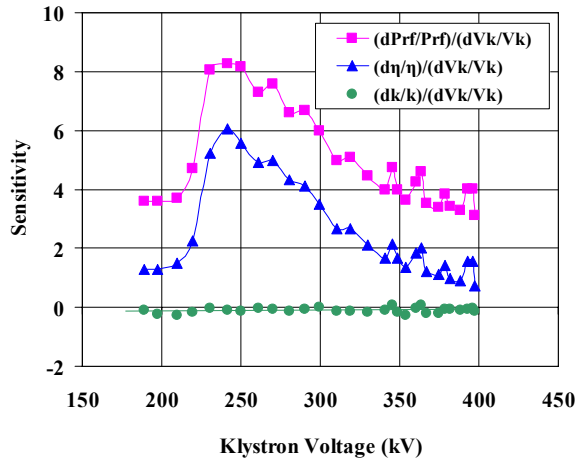

Figure 4: Sensitivity of RF power, efficiency, and perveance of E3712 klystron.

ENERGY GAIN SENSITIVITY

According to the energy gain of an accelerating unit $E \propto \sqrt{P_{RF}}\cos\phi_{RF}$, its relative fluctuation by a klystron is

$$\frac{dE}{E} = 0.5\times\left(\frac{dP_{RF}}{P_{RF}}\right) - \left(2\pi\times\tan\phi_{RF}\right)\left(\frac{d\phi_{RF}}{2\pi}\right) \quad . \quad (7)$$

Using Egs. (4) and (6), the sensitivity of energy gain is

$$s_E = \left(\frac{dE}{E}\right)/\left(\frac{dV_O}{V_O}\right) = 0.5\, s_\eta + 1.25\, s_V - 2\pi\tan\phi_{RF}\; s_\phi \quad . \quad (8)$$

Figure 5 shows the relative energy gain with charging voltage variations at the klystron voltage of 400 kV.

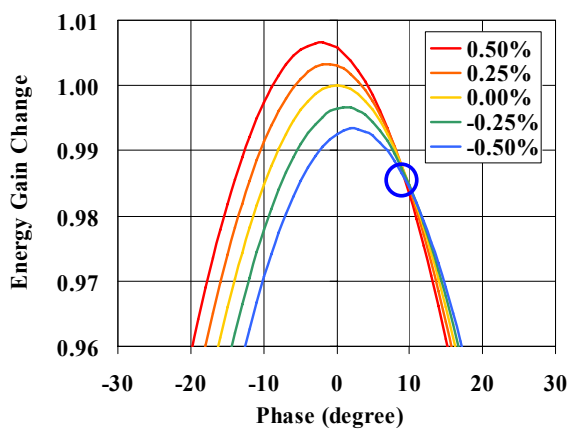

Figure 5: Relative energy change within 1% charging voltage variations at 400 kV level with E3712 klystron.

Around RF phase marked by the circle in the figure, the energy gain is almost same even though charging voltage is fluctuating. This RF phase is about +10 at the 400 kV level, which is given by following condition

$$\tan\phi_{RF} = \left(\frac{1}{2\pi s_\phi}\right)\left(0.5 s_\eta + 1.25 s_V\right) \quad . \tag{9}$$

Figure 6 shows the sensitivity of energy gain for the crest phase and the off-crest phase. The typical sensitivity of the energy gain at 400 kV is 1.3 for the crest operation and is getting larger up to 2.0 at the voltage lower than 350 kV. We can make the energy gain insensitive down to 350 kV at the off-crest phase of +10°. The loss of energy gain by the off-crest acceleration is 1.5%. We can increase the off-crest phase more to tune the energy gain insensitive lower than 350 kV level. For example, the off-crest phase of +12° makes the energy gain insensitive around 320 kV level with the energy loss of 2.2%.

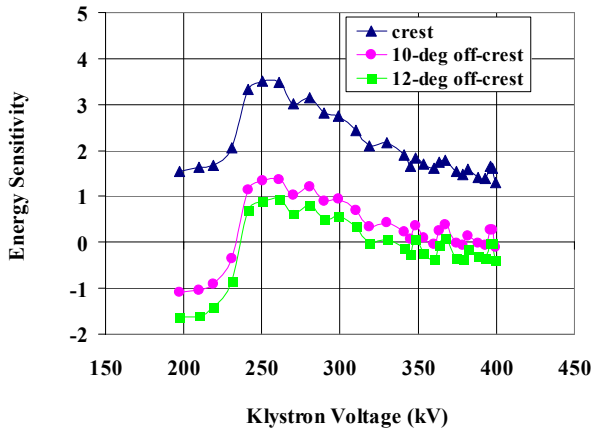

Figure 6: Sensitivity of beam energy gain for crest phase and off-crest phase of +10° and +12° with E3712 klystron.

If we consider the effect of relative phase jitter σ_ϕ between injected beams into the accelerating structures and corresponding klystron station, the sensitivity of energy gain becomes

$$s_E^2 = \left(0.5 s_\eta + 1.25 s_V - 2\pi \tan\phi_{RF} s_\phi\right)^2 + \left(2\pi \tan\phi_{RF}\right)^2 \left(\frac{\sigma_\phi}{2\pi}\right)^2 / \left(\frac{dV_o}{V_o}\right)^2 \quad . \tag{10}$$

SUMMARY AND DISCUSSION

The sensitivity of RF power is amplified at the lower klystron voltage due to the quick drop of conversion efficiency. Therefore, it is possible to provide better stability by tuning the RF system at the higher working voltage. The off-crest phase ranging from +10° to +12° provides better stability in case of the PAL XFEL linac. The reduction of beam energy due to off-crest acceleration is just less than 2%. The low-level RF control has to provide better stability than the one of a klystron modulator for this scheme to be effective.

The RF unit for bunch compressors is more sensitive to the RF fluctuation because the necessary off-crest phase is typically much larger than 10° to provide a necessary energy chirp. In this case, the RF unit has to satisfy more strict stability requirement than normal accelerating units.

REFERENCES

[1] I. S. Ko, "PAL XFEL project," Proc. FEL2005, Stanford University, USA, 2005
[2] Y. Kim, et al., "Start-To-End Simulation of the PAL XFEL Project," Proc. FEL2004, Trieste, Italy, 2004
[3] http://www.toshiba-tetd.co.jp/
[4] Linear Accelerators, P. M. Lapostolle and A. L. Septier, editors, North Holland Publishing Company, p322 (1970).

CHARACTERIZATION OF AMORPHOUS MAGNETIC MATERIAL WITH MULTIPLE PULSE EXCITATION

Archana Sharma, S. Acharya and K.V.Nagesh,
Accelerator and Pulse Power Division,Bhabha Atomic Research Centre, Mumbai - 400085
Uday Kumar and G.R. Nagabhushana,
High Voltage Engineering Department, Indian Institute of Science, Bangalore -560 012

Abstract

The magnetic characteristics of an amorphous magnetic material have been studied by applying multiple square voltage pulses to an inductor containing the magnetic material. The pulser is a 20 kV, 200 ns, 20 Ω source which drives the core of dimension 160/240/25 mm. Effect of the number of turns and the magnitude of the exciting voltage pulse on the saturation behaviour of the material are presented.

INTRODUCTION

The use of amorphous magnetic material in magnetic switches and induction cells has received widespread attention in the development of pulse power systems of high average power and high repetition rate. The physical dimension of these devices depend on the flux swing offered by the material when driven from remanence to saturation. [1,2]. It is well-known that the magnetic properties of amorphous material are influenced by several factors such as annealing, heat treatment, surface coating, rate of flux change dB/dt, toroidal radius and applied input power etc [3,4]. We are using the material 30 KCP obtained from Russia in the development of a 200 keV, 5 kA, 100 pps Induction Linac. Therefore, we studied the magnetic properties of cores available in standard sizes in the intended frequency regime of operation before designing the switches and induction cells

To emphasize the need for our investigation, we cite here a few problems which one may encounter while using a magnetic core as a switch. For example, when the input capacitor of a magnetic switch is getting charged, the magnetic switch is supposed to have practically infinite impedance. However, there is always a leakage current due to finite impedance, which charges the output capacitor to some extent. A crude design based upon only the flux swing data ignores this fact and one may start worrying why the input capacitor did not get charged to the estimated value.

Similarly the transition from high impedance to low impedance is not an instantaneous affair as one would like to have. Complete saturation means that the relative permeability of the material approaches the value in air. Depending on the material, this approach, say from μ_r = 10 to μ_r = 1 can be slow or fast. The charging time of the output capacitor of a switch is generally calculated by using μ = 1 in the saturated state of the switch. It is likely that the switch remains in the quasi-saturated state for quite sometime. Unless one knows this charging time, it will be difficult to design the switch for the next compression stage.

Besides this, the magnetic data provided by the manufacturers are obtained by experimenting with continuous sinusoidal power sources. The characteristics of the magnetic material differ considerably from the above situation when they are used as core material in switches and induction cavities. It is imperative to know the pulse characteristics of the material while designing these devices.

Thus, more insight into these limitations are needed for almost perfect designs of pulse transformers, magnetic pulse compression chain and induction cavities in Linear Induction Accelerators.

EXPERIMENTAL SET-UP

The amorphous core material used in our experiment was supplied to us by M/S Tukson Inc., Moscow, Russia, under the trade name 30KCP[5]. The chemical composition of the material is Fe(63.95%), Co(30%), Cr(3%), B(3%) and C(0.05%). The core is made from 25 μm thick tapes with SiO_2 insulation between layers and annealed in longitudinal field. The magnetic characteristics, provided by the manufacturer at 50 Hz, indicates that the core material has a flux swing around 3T ($-B_{max}$ to $-B_{max}$) and coercive field of 12A/m. The toroidal test core is taken to be of the same size as that to be used in the actual system i.e. inner diameter 160 mm, outer diameter 240 mm and height 25 mm.. Before using the core, it was cleaned with alcohol and then two layers of 2 mil semi-cured kapton tape were wound on it to prevent incursion of outside dirt and any damage during handling the material.

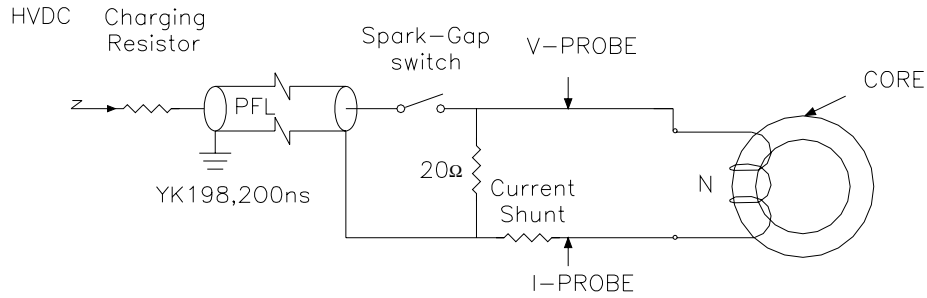

Fig.1 : Experimental set–up to study core characteristics

The core under test is connected in shunt with the matched load of a pulsed voltage source. The pulser consists of a YK198 cable of suitable length which is charged from a D.C supply through a resistor. At the other end, it is terminated through a spark gap switch to the matched resistive load (20 Ω) of copper sulphate solution and a pulse of 200 ns duration is realized when the spark gap fires. The experimental arrangement is shown in Fig. 1. Resetting is done before applying a series of pulses to the core. For resetting, 10 A D.C was passed through the turns of the core using a power supply of M/S Aplab make (Model 7317). The Voltage (V) across the core is measured by Tektronix voltage probe P6015A and current (I) through the turns of the core by a 10mΩ current shunt of T&M make (Model no. 8615). These V & I signals are displayed in a digital storage oscilloscope of Lecroy make (Model No.9350A). Voltage signal is captured, stored and integrated in this unit. The flux swing ΔB and the magnetizing field H during the pulse are calculated according to the following equations:

$$\Delta B(t)=\int V(t).dt/(N*A) \quad (1)$$

$$H(t)=N*I(t)/l \quad (2)$$

Here N denotes no. of turns, A the area of cross-section of core in m^2 and l the mean magnetic path length in meters. It has been assumed in the above equations that the magnetic induction is uniform throughout the core cross-section.

RESULTS AND DISCUSSION

While operating as a switch or as an induction cell, the magnetic core is driven from negative saturation to positive saturation by application of a single voltage pulse**.** In our experiment, we utilize low voltage pulses and observe the saturation after a series of pulses. The effect of number of pulses of peak magnitude (V_{pk}) 17.5 kV on the core with 7.5 turns is shown in Fig.2. When the first pulse was applied, voltage wave-shape showed no reversal as shown in Fig.2(A),. In the 2nd pulse, reversal is seen along with a voltage droop in the earlier flattop portion. The effect of exciting voltage (V_{pk})on the performance of the core was studied in the following manner. First, ΔB(t) was evaluated for a pulse at different times during the pulse using Eqn 1. At first, ΔB(t) rises with time and then remains steady, if the voltage pulse has no reversal. If it has reversal, it starts falling down from the peak value. For every pulse, ΔB(t) was evaluated and found to decrease after a few pulses. The test core has not been reset in between these shots. Resetting has been done in the beginning of each set of data. Effect of excitation level has been observed by changing the input charging voltage of the cable. The applied voltage to the core V_{pk} is varied from 7.5 kV to 17.5 kV and a range of dB/dt from 2.5T/μs to 6.5T/μs is obtained. As expected from equation 1, higher input voltage results in larger total flux swing ΔB. Also when pulses have been applied repeatedly without in-between resetting, the core moves closer and closer towards saturation and its impedance continually reduces. From Fig.4, it is observed that, for the same charging voltage, more current passes through the turns of the core in subsequent pulses. The value of the relative permeability μ_r defined by $\Delta B/ (H*\mu_0)$ can be estimated from the voltage and current pulse and one finds that it reduces from 1700 to less than 100 during this process. At lower excitation level, variation in ΔB is smooth but at higher excitation or near the saturation point, changes are drastic.

The effect of successive pulses on ΔB has been shown in Fig.4, for various number of turns keeping excitation voltage constant. As the no. of turns increases, ΔB decreases for the same charging voltage of the cable. When it approaches saturation, ΔB becomes minimum. At this point, the core will be at the knee of typical B-H loop. It has been observed that the core withstood large number of pulses (n) for more number of turns. This can be attributed to smaller flux value at each pulse as can be seen from eq.(1) i.e. ΔB will decrease with increase in N for fixed values of. V, t and A.

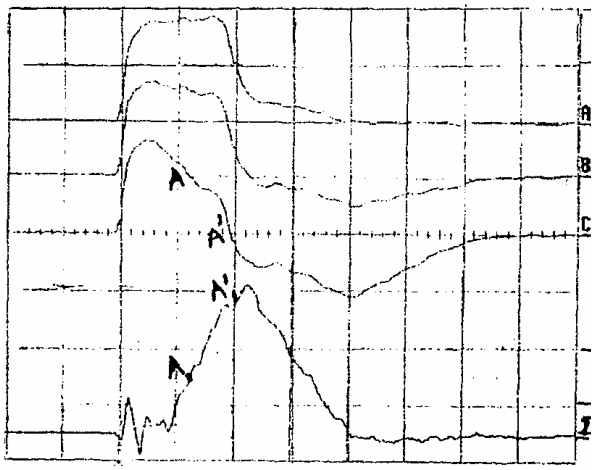

Figure 2 (A,B &C): Three successive pulses
Figure 2 (D): Current pulse for voltage pulse (C)
X-axis: 100ns/div, Y-axis:10kV/div, 200A/div.

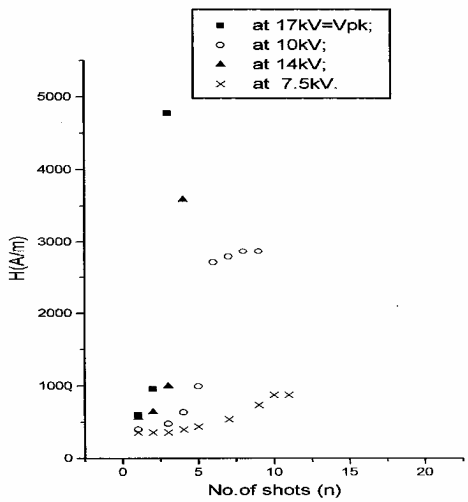

Figure 3: Core current with shot no.

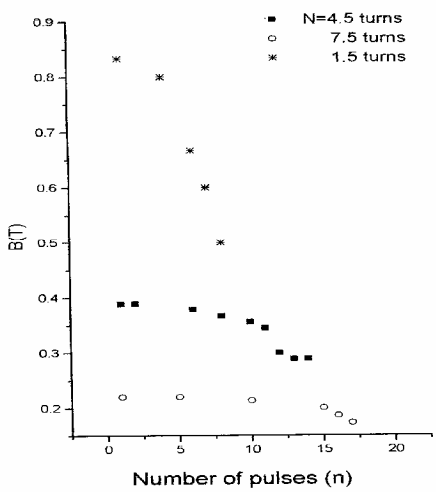

Figure 4: Effect of no. of turns.

Each pulse, of course, shows a departure from the previous one in terms of voltage drooping and the degree of reversal. At higher peak voltage, the difference in magnetic properties between the 1st (low dB/dt) pulse and last (saturated) pulse is significantly larger compared to that at low V_{pk}. Before saturation, H remains almost same irrespective of input excitation voltage, but ΔB is greater in case of higher V_{pk} or faster dB/dt. In the saturated state, H and ΔB increase with input level but μ_r remains almost constant. The relative permeability remained as high as 50 in this state of saturation. Possibly, very large current is necessary to achieve $\mu_r \approx 1$ and it can be realized in driving system of low impedance.

It is quite clear from the graphs that the core can be used for many pulses without resetting, either when input voltage is low, or the no. of turns are high. Thus an economic and efficient design for a specific application is possible by utilizing the core behavior.

CONCLUSION

These results show that few pulses of low voltage magnitude can be achieved at higher repetition rate, without having to reset the core. These results may be useful in applications such as design of pulse transformers and induction cavities where cores are to be used at multiple pulses without complex synchronized resetting unit. During the burst of pulses, the core will give reproducible results depending on the voltage and the number of turns used.

REFERENCES

[1] W.S. Melville, "The use of saturable reactors as discharge devices for pulse generators", Proc. I. E. E., London, England, Vol.98, pt.3, 1951, p.185.

[2] Induction Linear Accelerators, Daniel Birx, AIP Conference Proceedings, 11th March, 1992, (American Institute of Physics), p. 1554.

[3] M.H. Price and K.J. Overshott, "The variation of initial permeability of amorphous ribbons with frequency and annealing conditions", IEEE-transaction on Magnetics, vol.19, No.5, 1983, p.1931.

[4] G.E. Fish, V.R. Ramanan, R. Hasegawa and A.C. Diebold, "Stability of high frequency magnetic properties of metallic glasses", IEEE-transaction on Magnetics, vol.19, No.5, 1983, p.1937-39.

[5] Prof. Guennadi Mamaev, MRTI, Moscow, Russia, Private Communication.

STUDY OF INSULATION COORDINATION IN THE PRESENCE OF MULTIPLE DIELECTRIC MATERIALS

S. Mitra, D. Durga Praveen Kumar, Archana Sharma,
K. V. Nagesh and D.P. Chakravarty
Accelerators and Pulse Power Division, Bhabha Atomic Research Centre, Mumbai-400085.

Abstract

Use of various dielectric materials for insulation is inevitable in high voltage systems. Choosing a particular insulating material (solid, liquid, and gas) depends on various factors like the nature of the system, insulation level required, dielectric strength and thermal & mechanical stress handling capability of the material. Besides the surface break down strength of two material interfaces plays important role in the high voltage design considerations of the system. This paper critically analyses the field stress in high voltage points in presence of multiple dielectric media, in particular on the existing system of Kilo Ampere Linear Injector (KALI – 5000) system.

In this paper, local field enhancement phenomenon due to presence of different solid and liquid dielectrics is evaluated. Mathematical derivations of the percentage increment of field, at the critical point, due to presence of hybrid dielectric materials, are calculated for planar, spherical and cylindrical geometry of the high voltage elements. 2-d simulations of the same to support the mathematical calculations are done using MAXWELL SV software.

INTRODUCTION

This paper is all about local field enhancement of high voltage system due to lack of proper co-ordination of multiple dielectric materials instead of a single dielectric material. the work is inspired by some chronic corrosion leading to damage of a Perspex sheet inside MARX generator of KALI-5000 system. During investigation of the problem it has been found that use of multiple dielectric materials to avoid breakdown may lead to local field enhancement of any high voltage object of a high voltage system. The object can initiate to some other high voltage problems like corona discharge, higher leakage current, local heating etc. for the ease of analysis, some standard geometrical structures resembling to the practical situation is analyzed and simulated. Mathematical derivation is done to find out the range of enhancement of electric field stress at any particular point. The variation of per unit enhancement is also plotted against permittivity ratio of the multiple dielectric, their thickness and position. Simulation of similar structures is also done to support the mathematically derived results. Entire comparative and analytical study is reported in this paper.

THEORETICAL DERIVATIONS AND ANALYSIS

A mathematical approach to find out local field enhancement is attempted in this section. Let us assume that two points having high potential differences between them is separated by a dielectric of relative permitivity of ε_{r1}. Now, another dielectric material of higher relative permitivity value ε_{r2} is inserted in between the high voltage points without increasing the space between them. This is one of the very common practices for the high voltage engineers to avoid the bulk breakdown through the dielectric media. But, in this case, the metal boundary in contact with the lower relative permitivity value, experiences higher electric field stress than previous condition of single dielectric separation.

As far as bulk breakdown through the dielectric is concerned this method helps sometimes if the breakdown strength of the second dielectric is much higher than the previous one. The increased breakdown limit takes care of the added increment in field stress. But, if corona and all other high voltage unwanted phenomena are concerned then this method creates problem by local field enhancement. The above discussion is simplified considering two dielectric materials of different relative permitivity values. But the same inference is true for any number of dielectric materials used (two or more) two separate high voltage points. Below, it has been given, the mathematical explanation of the above mentioned conclusion in a generalized fashion.

Let us consider one object of voltage V is separated from the ground plane using a dielectric material of relative permitivity ε_r. The field experienced by the dielectric material at the metal dielectric juncture is E. Now, n number of dielectric materials of relative permitivity ε_{rn} and thickness t_n is inserted in between. Now the field at the same point of concern has changed to EM. For the ease of calculation let us replace the ground plane with the mirror reflection of the object and the dielectrics about the ground plane. The reflected object will be assigned a voltage of –V. Now, let us consider, the perpendicular distance between object and the ground plane is R and any point P is present on the line joining the object and its mirror image (same as the line perpendicular on the ground plane from the object) at a distance r. hence field strength at P can be defined as

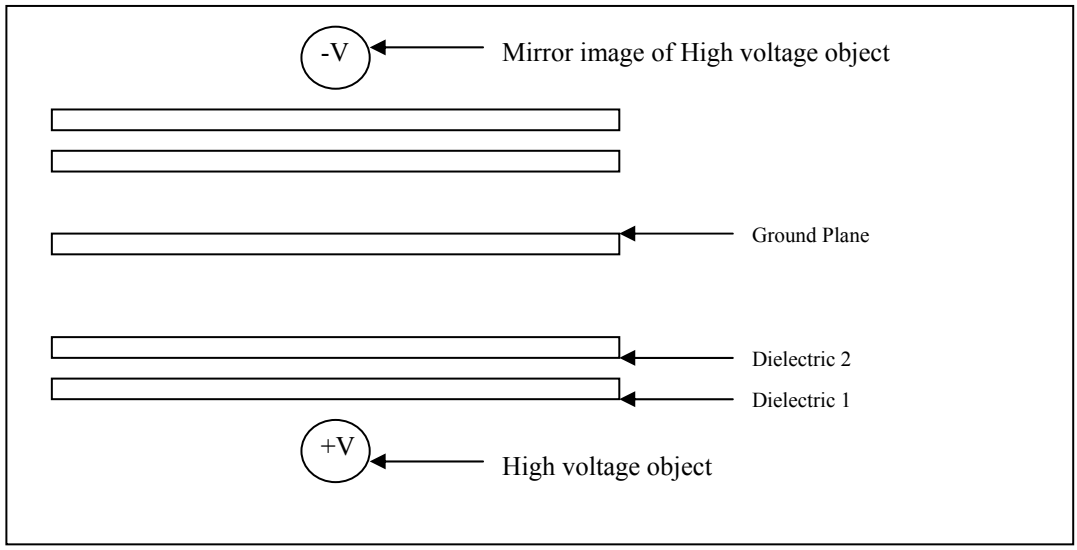

Figure 1: Schematic diagram of high voltage object and ground plane

$$E_r = E(r) - E(2 \cdot R - r) = Q \cdot \{F(r) - F(2 \cdot R - r)\} \quad (1)$$

Where, Q defines the charge accumulation in the high voltage conductor. Hence, we can further write,

$$V = Q_S \cdot \int_{r_c}^{R} F(r) \cdot dr \quad (2)$$

where, r_c is radius of curvature of the high voltage object. In presence of multiple dielectric materials this equation(2) can be re-written as

$$V = Q_M \cdot \left\{ \int_{r_c}^{r_1} F(r) \cdot dr + \int_{r_1}^{r_1+t_1} F_1(r) \cdot dr + \int_{r_c}^{r_2+t_2} F_2(r) \cdot dr + \ldots\ldots + \int_{r_c}^{r_n+t_n} F_n(r) \cdot dr + \int_{r_n+t_n}^{R} F(r) \cdot dr \right\} \quad (3)$$

Where, rn is the distance of the dielectric measured from the object. Considering at all the inter-dielectric boundaries electric field flux density will remain constant,

we can write $F_n(r) = \frac{\varepsilon_r}{\varepsilon_{r \cdot n}} \cdot F(r)$ and hence equation (3) can be rewritten as,

$$V = Q_M \cdot \left\{ \int_{r_c}^{R} F(r).dr + \sum_{p=1}^{n} \left(\frac{\varepsilon_r}{\varepsilon_{r \cdot n}} - 1 \right) \cdot \int_{r_p}^{r_p+t_p} F(r).dr \right\} \quad (4)$$

Therefore we can write that at the critical point at distance r_c field E_S with single dielectric of relative permitivity ε_r is

$$E_S = Q_S \cdot \{F(r) - F(2 \cdot R - r)\} = \frac{V \cdot \{F(r) - F(2 \cdot R - r)\}}{\int_{r_c}^{R} F(r) \cdot dr} \quad (5)$$

and the field stress at the same point with multiple dielectric materials E_M is

$$E_M = Q_M \cdot \{F(r) - F(2 \cdot R - r)\} = \frac{V \cdot \{F(r) - F(2 \cdot R - r)\}}{\left[\int_{r_c}^{R} F(r) \cdot dr + \sum_{p=1}^{n} \left(\frac{\varepsilon_r}{\varepsilon_{r \cdot n}} - 1 \right) \cdot \int_{r_p}^{r_p+t_p} F(r) \cdot dr \right]} \quad (6)$$

From equation (5) and (6) we can conclude that if $\varepsilon_{rn} > \varepsilon_r$, then $E_M > E_S$. i.e at the critical point the local field enhancement will take place at metal dielectric boundary.

Shape of the high voltage object is going to take significant part in the percentage increment of field enhancement at the most critical points. Considering some standard geometry like infinite plane, infinitely long cylinder and spherical object the calculation is extended. For an infinitely extended high voltage plane object $F(r) = 1/\varepsilon\varepsilon_r A$, for an infinitely long high voltage cylindrical object $F(r) = 1/2\pi\varepsilon\varepsilon_r r_c$, for a high voltage spherical object $F(r) = 1/4\pi\varepsilon\varepsilon_r r_c^2$,

SOFTWARE SIMULATION AND RESULTS

2-D simulations of the above mentioned objects are made using MAXWELL SV software. The enhancement of the electric field intensity at the critical point is observed due to presence of multiple dielectric materials. Simulation is done taking consideration of a practical situation, where high voltage object of 600kV potential is separated from the ground plane using transformer oil dielectric material ($\varepsilon_r \approx 2.3$). The field enhancement at metal dielectric boundary is observed when a perspex sheet ($\varepsilon_r \approx 3.2$) is inserted in between. The simulation window with field distribution is shown below.

DISCUSSIONS

The above analysis is done in context with MARX generator of KALI-5000 1.5 MV, 40 kA, 100 ns pulsed power system. The MARX generator is kept completely inside transformer oil. To further ensure any breakdown from high voltage points inside the MARX chamber, a Perspex sheet of 30 mm thickness is used in between high voltage point and ground. This had increased the breakdown strength of the system but, as a consequence, the high voltage points, having contact with transformer oil, have been subjected to higher electric field strength.

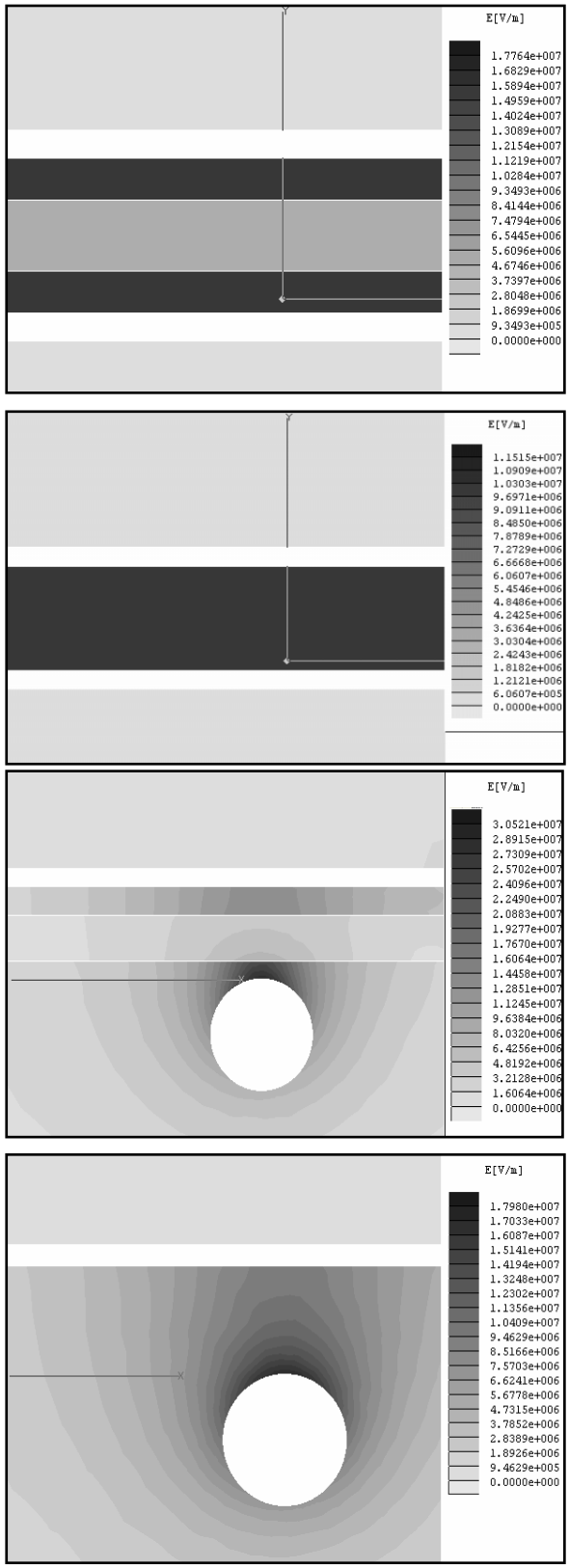

Figure 2: Comparative Field mapping of infinite plane object and infinitely long cylindrical object with single and multiple dielectric materials is shown.

This kind of situation may lead to increased possibility of corona discharge from the high voltage points inside the chamber. According to the above analysis percentage increment of the field stress at the concerned point is a function of thickness of the secondary dielectric material and its relative permittivity. Plot of increment of field with variation of thickness of dielectric and it's ε_r is plotted below for infinite plane and infinitely long cylindrical object.

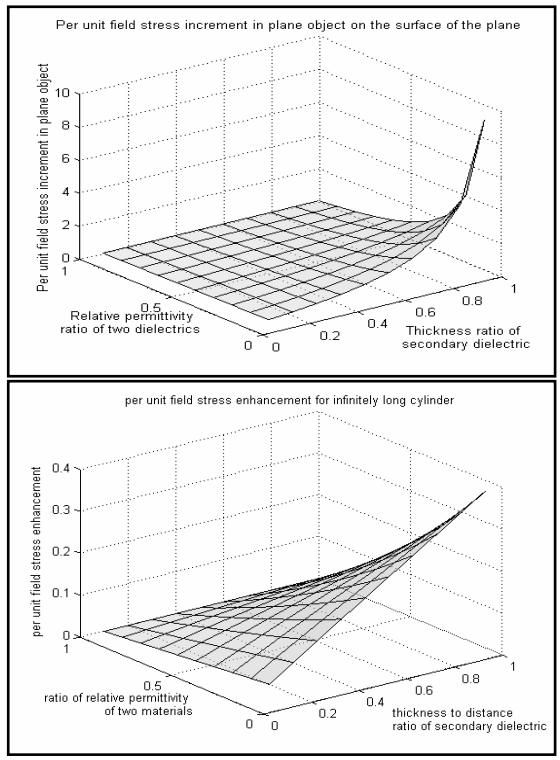

Figure 3: Field stress enhancement with change in permittivity and physical parameters of dielectric material

CONCLUSION

The above discussion leads to the conclusion that selection of dielectric material and their positioning is extremely critical in high voltage engineering point of view. The trades off between better breakdown strength and low relative permittivity, makes the selection further difficult. Position of the dielectric material is also very critical as it can enhance field at a particular point of a big structure. This local field enhancement can damage metallic and dielectric materials of the system leading to further chain breakdown of the total system.

ARTIFICIAL NEURAL NETWORK CALCULATES BACKWARD WAVE OSCILLATOR PARAMETERS RELIABLY FOR PULSED ACCELERATORS

Arti Gokhale, Archana Sharma and B. P. Dubey
Accelerator and Pulse Power Division Reactor Control Division, BARC, Mumbai-40085, INDIA
email:arti5_99@yahoo.com

Abstract

Backward wave oscillator (BWO) is a high power microwave-generating device, which is harmful for people and capable of damaging electronic equipments. It is mandatory to shield the critical control systems and instrumentation especially of strategic importance against such High Power Microwaves (HPM). To know the effects of HPM on human being and electronics, BWO is an efficient device, driven by pulsed accelerator electron beam of high power in Giga-Watt (GW) regime. These intense power electron beam pulses are obtained by an impulse generator followed by a pulse forming line and coupled to a field emission diode. Thereafter the electron beam interacts with electromagnetic modes of the wave-guide and produces microwaves in the frequency range of 1-20 GHz. Resultant frequency depends upon the wave-guide parameters, beam current, beam geometry etc. With analytical techniques, design optimization is cumbersome and slow. Every time the simulation program is run, it takes nearly 6 to 8 hours to generate a single result.Artificial Neural Networks (ANNs) have been used successfully in various applicatioins. A trained ANN generates its output in a fraction of a second. In this study ANN was used to calculate BWO frequency. The training of the ANN takes about half an hour. Once trained, the ANN takes plasma density, wave number and ripple amplitude as inputs and calculates the BWO frequency in a fraction of second. The frequencies calculated by ANN and that by simulation program differ at the most by about 2%. This shows that ANN is a reliable substitute for repeated run of simulation program.

INTRODUCTION

Accelerator driven Relativistic backward wave oscillators (BWO) are promising candidate as source of High Power Microwave (HPM) radiation. They were studied extensively in the last two decades and detailed overview of this research is presented in [1]. Microwave radiation in a relativistic BWO is produced by interaction between a pulsed accelerator relativistic electron beam and an electromagnetic field of a slow wave structure. Usually, the beam is generated by a field emission gun and guided by a strong homogeneous magnetic field. Metallic periodic structures are widely used as slow wave structure. In the construction of such device it is necessary to examine coupling coefficients of the electron beam with the fields of the slow wave structure (SWS), the solution of mode competition, and determination of the electrical strength of the SWS. The most complete analysis of theses problems is possible only for the dispersion description of the SWS.In the last two decades, significant research effort was directed in increasing output power and operating frequency. In most research and studies different wave-guide and beam parameters were assumed. In order to meet the requirement of maximum peak power, it is essential to explore accurate but fast technique of the dispersion relation's calculation for different wave-guide and beam parameters. This paper extends on our previous work and establishes a dispersion relation for a pulsed sheet beam driven backward wave oscillator in which a rectangular rippled wall wave-guide is used as SWS.

The generally believed superior cognitive capabilities of an Artificial Neutral Network (ANN) are being utilized these days for various event characterizations /classifications exercise in a wide range of fields. ANN had been used for estimating channel power distribution of a 220 MWe Pressurised Heavy Water Reactor [9]. An interesting and novel application of ANN is demonstrated in this work. It has been found that a properly trained ANN can be employed to reliably estimate the generating frequency of a BWO, depending upon the different wave-guide and pulsed accelerator beam parameters. A comparison of the results obtained by the ANN and the simulation program is presented at the end of this paper.

DISPERSION RELATION

Consider the interaction between pulsed accelerator sheet electron beam of density N_b in axially rippled infinitely long rectangular wave guide as considered in ref. [8]. The whole geometry of the slow wave structure (SWS) along with the sheet beam is immersed in a strong longitudinal magnetic field ideally having infinite magnitude.

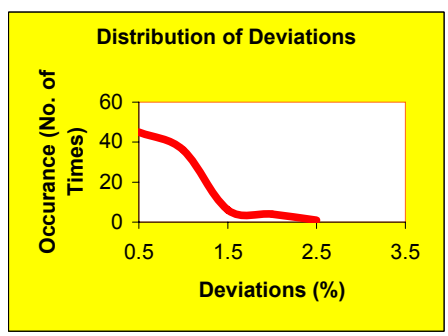

Figure 1: Deviations of the ANN calculated frequencies from the desired ones

Under this assumption the electron motions are 1-D in the axial direction. Using the Maxwell's equation and solving them by using the boundary conditions of waveguide we calculated the 3x3 matrix type dispersion relation as shown in Fig.1.

By substituting the values of waveguide parameters as width of the waveguide, ripple amplitude, thickness of the waveguide, plasma density inside the waveguide etc. we have got the data for resultant generating frequency.

In recent years, there has been a great deal of interest in artificial neural network (ANN) and its applications. The ability of ANN to handle non-linear data interpretations and their ease of implementation has encouraged their successful use in such diverse areas as physics, neurobiology, psychology, and computer research. ANN is basically a computation technique for recognizing data patterns. It consists of simple processing units called neurons or nodes, which bear resemblance to biological neurons. Each node is connected to the other nodes in the network by unidirectional connection of different strength, called weights.

COMPARISON OF NUMERICAL AND ANN DATA

The weighted inputs are summed and applied to a non-linear transfer function to produce an output. The nodes are usually arranged in a series of layers, which are bounded by input and output layers. Sandwiched between these two nodes, there are one or more hidden layers, which are provided with a structure compatible with the complexity of the problem at hand.

The ANN software package named BIKAS has been utilized for investigation of generating frequency for the BWO. The optimum performance was achieved with the following settings of various ANN parameters offered by this software. An input layer with 3 processing nodes, one hidden layers with 10 nodes and one output layer with one node. The training of the network was carried out by presenting plasma density, wave number and ripple amplitude to its 3 input nodes. There were 188 data sets. Half of them were used for training and the remaining half were used for testing.

The training and the test data were obtained by running the simulation program. During the training process, the interconnection weights of the network were iteratively adjusted until the network responded with minimum error, i.e. the ANN calculated frequencies closely matched with the frequencies obtained by simulation program. Following table-1 presents a sample of the results obtained by the ANN. Figure 2 shows the distribution of deviations of the ANN calculated frequencies from the corresponding desired frequencies.

The distribution of deviations is almost symmetrical around zero. Most of the deviations are around zero. The maximum deviation obtained in this study was ~3%. When the experiment of re-training and testing of the ANN was repeated, the deviations were of similar nature and magnitude. It shows the ruggedness and reliability of the ANN.

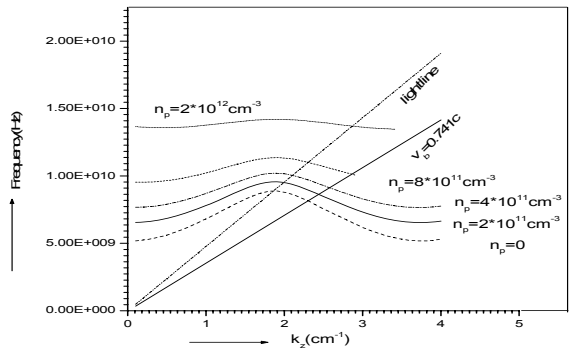

Figure 2: The calculated effect of varying the plasma density on the corrugatedWave-guide dispersion(y\-(0)=1.445cm, \g(e)=0.225cm,k\-(w)=3.76cm\+(-1))

CONCLUSION

A feasibility study has been carried out to access the potential of an Artificial Neural Network (ANN) for determining the generating frequency for a Backward Wave Oscillator (BWO) driven by pulsed accelerator sheet electron beams. The result obtained by ANN matched with those obtained with numerical technique and simulation program. A maximum deviation of ~3 % was noticed between the frequencies obtained by ANN and numerical technique. It is, therefore, concluded that ANN is reliable and suitable candidate for fast calculation of BWO frequencies.

ACKNOWLEDGEMENT

Authors acknowledge with thanks to CSIR New Delhi for financial support for this work.

Table 1: Comparison data obtained through numerical calculation and simulation through ANN

Plasma density n_p	Wave number K_z	Ripple amplitude h	Desired Frequency (Hz)	ANN Frequency (Hz)	Percentage Deviation (%)
0	2	0.225	$8.79*10^9$	$7.37*10^9$	0.5048
$2*10^{11}$	2	0.225	$9.51*10^9$	$9.206*10^9$	0.5525
$4*10^{11}$	2	0.225	$1.02*10^{10}$	$1.017*10^{10}$	0.4466
$6*10^{11}$	2	0.225	$1.42*10^{10}$	$1.379*10^{10}$	0.0307
$8*10^{11}$	2	0.225	$11.13*10^{10}$	$1.175555*10^{10}$	0.6827

OPERATIONAL ANALYSIS OF KLYSTRON-MODULATOR SYSTEM FOR PLS 2.5-GEV ELECTRON LINAC *

S. S. Park, S. H. Kim, S.C. Kim, J. Y. Huang,
Pohang Accelerator Laboratory/POSTECH, Pohang, Kyungbuk 790-784 S. Korea,
S. W. Park, K. T. Lee, Modulator & Klystron Technology Co., Ltd.
San 31, Hyoja-dong, Nam-ku, Pohang, Kyungbuk 790-784 S. KOREA

Abstract

The klystron-modulator(K&M) system of the Pohang Light Source (PLS) generates high power microwaves for the acceleration of 2.5 GeV electron beams. There are 12 modules of K&M system to accelerate electron beams up to 2.5 GeV nominal beam energy. One module of the K&M system consists of a 200 MW modulator and an 80 MW S-band (2856 MHZ) klystron tube. The total accumulated high-voltage run-time of the oldest unit among the 12 K&M systems has reached nearly 95,000 hours as of Dec. 2006. The overall system availability is well over 95%. In this paper, we review overall system performance of the high-power K&M system and the operational status of the klystrons and thyratron lifetimes, and overall system's availability will be analyzed for the period of 1994 to Dec. 2006.

INTRODUCTION

The Pohang Light Source is a third-generation synchrotron radiation facility composed of an injector Linac and a storage ring. The klystron-modulator(K&M) system of PLS Linac had been supplying high power microwaves for the acceleration of 2 GeV electron beams from 1994 to 2002. A 2.5 GeV full energy electron injection has been launched since on October 2002. The 2.5 GeV full energy electron beam from the linac is transported through a beam transfer line (BTL) to the storage ring. Total 12 units of high power klystron-modulator (K&M) systems are under continuous operation in the PAL linac. The peak powers of the modulator and the klystron are 200 MW and 80 MW, respectively. The klystron output frequency is 2856 MHz. Each klystron output is compressed with a SLED and supplied to four of three-meter long accelerating columns. The linac has been operated as a full energy injector for the PAL since December 1994. Annual operation hour of the K&M system is about 7,000 hours.

KLYSTRON AND MODULATOR

To satisfy PAL linac design requirements for peak power and maintainability, E3712 S-band klystron tube has been selected as a main microwave source. The tube is manufactured by Toshiba in Japan and SLAC in USA. A SLAC 5045 (65 MW peak) klystron is used for the pre-injection module and the following eleven klystrons are Toshiba E3712. The 200 MW modulator for the klystron tube is designed and manufactured inhouse by Pohang Accelerator Laboratory(PAL).

*Work supported by MOST(Korea Ministry of Science and Technology) and POSCO(Pohang Steel and Iron Company).

Klystron

Operational parameters of the Toshiba E3712 and SLAC 5045 klystron tube are listed in Table 1. The klystrons have two output ceramic windows to accommodate 80 MW and 60 MW peak power, respectively. The two outputs are combined after the window by a power combiner. The microwave power is compressed with a SLED to enhance accelerating field in the accelerating columns. Maximum accelerating field gradient of linac is 17 MV/m [2].

Table 1: Parameter of klystrons

Parameter	Toshiba E3712	SLAC 5045
Frequency	2,856 MHz	2,856 MHz
Pulse Width	4 μs	3.5 μs
Repetition Rate	60 Hz	180 Hz
Beam Voltage	400 kV	350 kV
Beam Current	500 A	420 A
μ-perveance	2.0	2.0
RF Output Power	84 MW	60 MW
Drive Power	500 W	600 W
Gain	53 dB	49 dB
Efficiency	42 %	40 %

Modulator

The specifications of the modulator are listed in Table 2. Maximum repetition rate of the modulator is 180 Hz as given in Table 1. However, the normal operating rate is 30 Hz. The injection rate of the electron beam to the PAL storage ring is further reduced 10 Hz. Fig. 1 shows a simplified modulator circuit. The modulator can be divided into four major sections: a charging section, a discharging section, a pulse transformer tank, and a klystron load. In the charging section, a SCR AC-AC voltage regulator controls primary 3-phase 480 V AC power. The voltage regulator receives feedback signals from the primary AC voltage and the high voltage DC (HVDC) detector as shown in Fig. 1.

Table 2: Modulator Specification

Description	Parameter
Peak Power	200 MW
Average Power	289 kW
	48 kW
Repetion Rate	180 Hz
	30 Hz
Peak Output Voltage	400 kV
Pulse Width(ESW)	7.5 μs
Flat-top Width(,±0.5 %)	4.4 μs
Charging Time	5.75 ms

The closed loop control of the AC-AC voltage regulator ensures stable HVDC output. The maximum HVDC is 25 kV. For the system and personal safety, the interlock has the static and the dynamic modes. The static mode has the interlock of doors, ground hooks, heater PS, flow and temperature of cooling water, over voltage and current, etc. The dynamic mode has an analog signal from the vacuum system and a digital signal of SCR ac over current. The pulse forming network (PFN) is resonantly charged from the HVDC filter capacitor through the charging inductor and diode. Pulse-to-pulse beam voltage regulation is less than ± 0.5% by using the closed loop control of the AC-AC voltage regulator that is SCRs. Two parallel, fourteen sections, type-E Guillemin networks [3] are used for the PFN. The PFN impedance is about 2.8 Ω. Each PFN capacitor has a fixed capacitance of 50 nF, and each PFN inductor can be varied manually up to 4.5 μH. By adjusting inductance of each PFN section, we can precisely tune the flattop of the modulator output voltage pulse. The end of line clipper (EOLC) shown in Fig. 1 removes excessive negative voltage developed after discharge on the PFN capacitors as well as the thyratron.

Two kinds of thyratrons have been installed in the modulator: ITT F-303 and LITTON L-4888. Forced air-cooling is used for the thyratron. Two triaxial cables in parallel are used to make electrical connections between the PFN and the pulse transformer. The pulse transformer has 1:17 turn ratio. Components in the pulse transformer tank are immersed in high voltage insulating mineral oil. The klystron sits on the pulse tank top cover and is connected to the high voltage output of the pulse transformer. The klystron impedance at the primary of the pulse transformer is 2.8 Ω, which matches with the PFN impedance. During fine-tuning of the PFN impedance, we intentionally produced about 5% positive mismatch to extend switch lifetime by reducing anode dissipation in the thyratron [4, 5]

Operation Status

The current status of the klystron tube is given in Table 3. Twelve klystrons have been failed and replaced so far since 1995 when they were installed in the Linac.

Table 3 : Status of The Klystron (as of Dec. 21, 2006)

Mod. No	Tube Type	Tube Serial No.	HTR Run(hr)	Replacement
M01	SLAC5045	622A	24,851	May 21, 03
M02	E3712	65023PLS	2,641	Aug. 1, 06
M03	E3712	64019PLS	16,020	Aug. 3, 04
M04	E3712	64020PLS	6,746	Dec. 26, 05
M05	E3712	79021PLS	6,746	Dec. 28, 05
M06	E3712	13024PLS	1,260	Dec. 6, 05
M07	E3712	77016PLS	23,431	Aug. 4, 03
M08	E3712	12022PLS	5,774	Feb. 24, 06
M09	E3712	96014PLS	26,608	Mar. 7, 03
M10	E3712	40018PLS	22,651	Oct. 17, 03
M11	E3712	65017PLS	23,465	Aug. 20, 03
M12	E3712	65008PLS/R	35,558	Dec. 26, 01

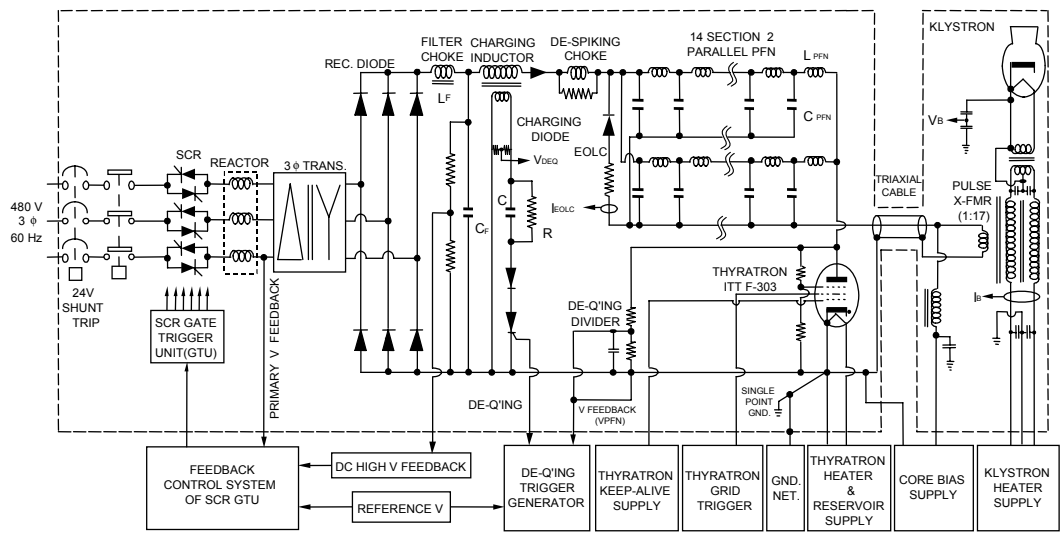

Figure 1: Schematic circuit diagram of the modulator.

The average heater run time of the failure klystron is about 61,700 hr. There are replaced of the klystron of all the modulator. Since the K&M system started its full operation in 1994, every klystrons installed in linac have been replaced once so far. The cases of the fifteen failed klystrons differ in failed ways. The klystron in the station 2 had damage of an electrode due to a focusing electromagnet shortage. The klystron in the station 6 showed bad internal vacuum and caused frequent internal arcing. Heater shortage occurred in the station 8 klystron. The klystron in the station 12 doesn't supply input cavity. And others are heater out of run time. The warranted lifetime of E3712 is 10,000 hours. However, the data listed clearly show that the real lifetime is much longer than the warranted lifetime. The klystron is very costly, and replacement of the klystron requires for a long shutdown time. Therefore, prediction of the klystron lifetime is important for the linac budget and maintenance schedule. But the data collected in the PAL linac are not enough to get a statistical lifetime which can be used for a reference.

The static and dynamic fault analysis of the K&M system during the period of January to December of 2006 is shown in Fig. 2 and Fig. 3. Fig. 2 shows that the MPS fault has the highest static fault count due to aged operation over 12 years old.

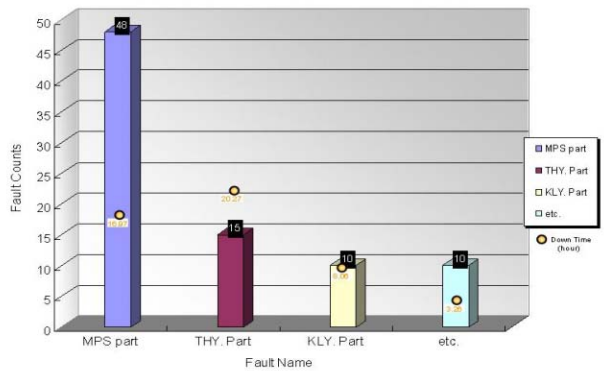

Figure 2: Static fault analysis of the klystron and modulator system (from January to December 21, 2006)

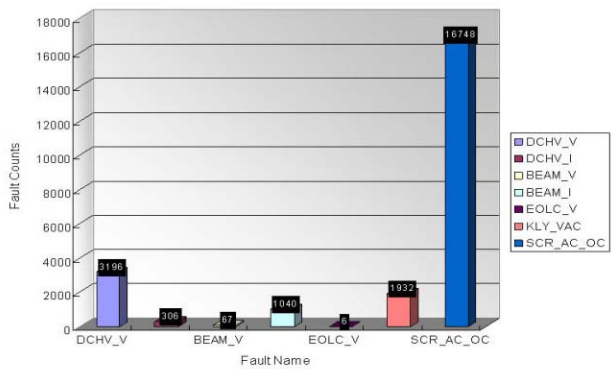

Figure 3: Dynamic fault analysis of the klystron and modulator system (from January to December 21, 2006)

In Fig. 3, The DCHV over-voltage and SCR ac over-current were caused by thyratron misfire due to misleading timing signals and electronic circuit malfunction due to electrical noises. The availability, down time, and fault count of modulator is shown in Fig. 4 during 1994 to 2006. In Fig. 4, we can see the availability reaches about 99.0 % in 2006. We are trying to further reduce the system failure in both dynamic and static count.

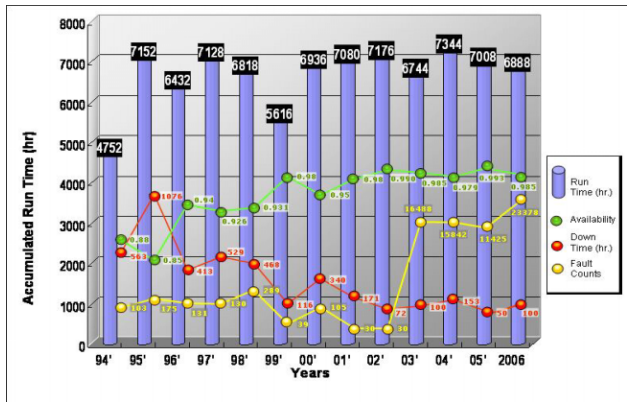

Figure 4: Availability, down time, and fault count of modulator during 1994 to 2006

SUMMARY

The K&M system is a key unit among linac facilities. PAL linac has 12 units of S-band K&M system. Since the K&M system started its full operation in 1994, every klystrons installed in linac have been replaced once so far. Fault and availability analysis of the K&M system shows that the system is running under a stable and reliable condition. The efforts are being made to improve continuously stability of the modulator system. Thanks to the efforts we can reduce faults in K&M system, and reviewed overall system performance of the high-power K&M system with accumulated operational data from 1994 to December 2006.

REFERENCES

[1] Z. D. Farkas et al., "SLED: A Method for Doubling SLAC's Energy," Proc. Of 9th Int. Conf. On High Energy Accelerators, SLAC, 1974, p. 576.

[2] W. Namkung et al., " PLS 2 GeV Linac," Proc. of 17th Int'l Linac Conf., Tsukuba, Japan, Aug. 21-26, 1994, pp. 14-16.

[3] G. N. Glasoe and J. V. Lebacqz, *Pulse Generators*, McGraw-Hill, 1948, Chapter 6.

[4] S. H. Nam, J. S. Oh, M. H. Cho, and W. Namkung, "Prototype Pulse Modulator for High Power Klystron in PLS Linac," IEEE Conf. Records of the 20the Power Modulator Symp., Myrtle Beach, SC, 1992, pp. 96-99.

[5] R. B. Neal, ed., *The Stanford Two-Mile Accelerator*, Q. A. Benjamin, New York, 1968.

[6] K. Kabayashi, et al., "Ba evaporation of Ir coated cathode impregnated cathode," Vacuum (Japanese), Vol. 29 (No. 3), 1989, pp 305-307.

DEVELOPMENT OF THE KLYSTRON MODULATOR USING A HIGH-VOLTAGE INVERTER POWER SUPPLY*

Y. G. Son#, S. J. Kwon, J. S. Oh, D. E. Kim, and C. W. Chung
Pohang Accelerator Laboratory

Abstract

The existing klystron modulator in the Linac use a 60 Hz high voltage power supply and adopt traditional L-C resonant charging scheme with De-Qing circuit. The stability of the output high voltage is not satisfactory especially when the AC line voltage fluctuations. If an inverter power supply is used as a HV generator, it will just meet the demands A high frequency inverter switching makes the overall system size small. The command-charging feature can guarantee the high reliability of switching function. In order to increase the stability, operating reliability and comply with the PLC (programming logic controller) and touch screen control system of PLS, an upgrading works is now in progress. This paper will discuss some inverter power supply design considerations and show the test results.

INTRODUCTION

The existing modulators of PLS 150 MW test lab began operation form 1991. The main component of high voltage charging power consists of a motorized 3-phase variable phase control (SCR), a high voltage step-up transformer, a rectifier assembly and charging inductance as show in Figure 1. After more than ten years' operation, some components are no longer in good condition and circuit failure occurred often. The stability of the output high voltage is not satisfactory especially when the AC line voltage fluctuations. The control of the modulators is based on manual method and therefore can not meet the requirement of new control system of PLS. Development of inverter power device was begun since 1996. In 2005, the modulator upgrade program using inverter power supply started. The upgrading includes two major parts. One is the replacing old HV powers with four 50 kV constant-current charging powers (Dong-A Hitec). The other is the addition of PLC in modulator as local machine controller. In the new control system, PLC achieves command control, status-monitor, safety interlock and real-time communication with the IOC.

SYSTEM DESCRIPTION

Klystron

The klystron currently used in the PAL linac is the Toshiba model E-3712, which was originally rated at 80 megawatts and 4 microseconds and 16 kilowatts average RF power. This tube is a pulsed cathode design with an oxide cathode. However, this new klystron station is designed to be easily adaptable to the other klystron tubes in the event it becomes necessary to change over. The nominal parameters of the klystron station are listed in Table 1.

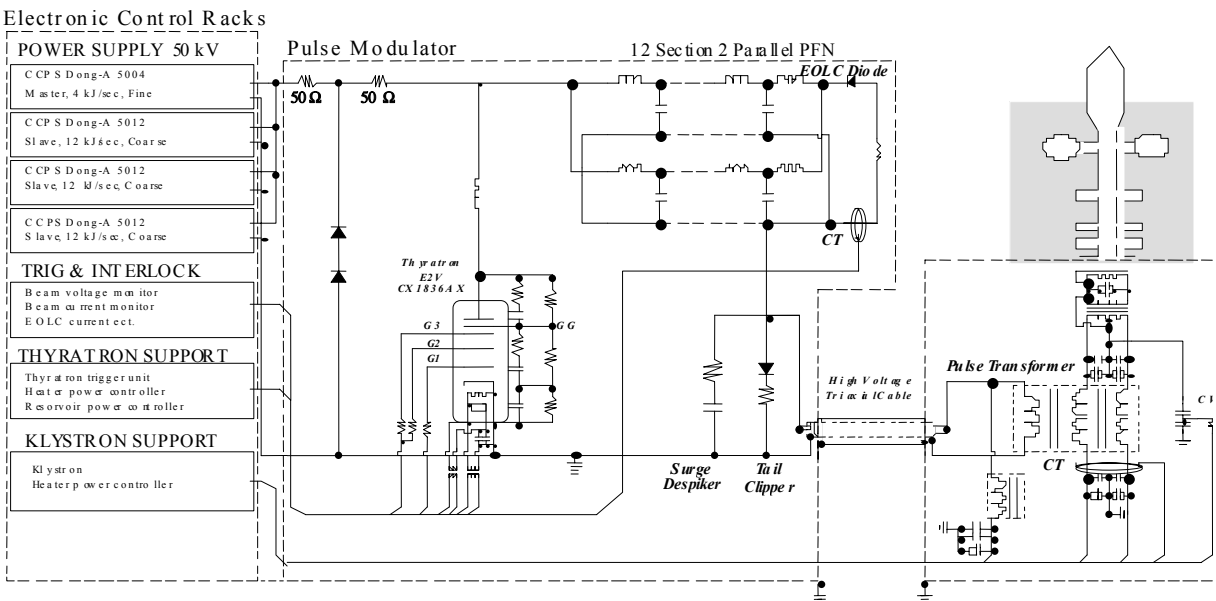

Figure 1: Simplified circuit diagram of line-type modulator for klystron station.

*Work supported by MOST and POSCO.
#ygson@postech.ac.kr

Table 1: Specifications of the klystron

Parameter	Value
Frequency (MHz)	2856
Peak power (MW)	80
Efficiency (%)	44
Gain (dB)	53
Pulse Length (us)	4
Pulse rate (pps)	50
Beam voltage (kV)	391
Beam current (A)	474
Weight (kg)	380
Height (m)	1.9

Modulator

The existing modulator uses a traditional resonant charging scheme. The charging voltage regulation of the linac is done by a de-Q'ing circuit. PAL modulators have a simple de-Q'ing controller and test results show a stability of 0.2% (rms). The essential modulator performance specifications are listed in Table 2.

The goals for the system are upgrade compact size, remote operation via computer and good reliability. The quest for compact size influenced all of the design choices in the system. Two of the major results of this quest are the use of high power density switching power supplies and compact high voltage PFN capacitors [1].
The modulator is a thyratron-switched, line-type, transformer coupled design. It is similar to standard practice for high power pulsed cathode klystron modulators.

Table 2: Specifications of the modulator

Parameter	Value
Max. peak power (MW)	150
Max. average power (kW)	29.3
Step-up ratio	1 : 17
PFN voltage (kV)	48
PFN impedance (Ω)	3.73
Flat top width (us)	4.0
High voltage pulse length (us)	6.5
Pulse energy (J)	975.5
Pulse repetition rate (pps)	30

Charging System

Pulse forming network (PFN) is energized with capacitor charging switch-mode power supplies. Four SMART 5015 power supplies (Dong-A Hitech model) are used in parallel. This combination can charge the pulse forming network (PFN) to 50 kV at 57.8 kJ per second. The charging voltage is going linear up to the desired PFN level V_{DC} with charging time T_C as shown in Figure 2. After dwell time T_D, a main switch is triggered to discharge the PFN. The next charging cycle of PFN starts with delay time T_I. This command charging provides safe operation for the thyratron recovery. The peak charging power P_O is given by E_O / T_C and the average charging power P_{AV} is given by E_O / T_P, where E_O is the PFN energy $C_O V_{DC}^2 / 2$ and T_P is the charging-discharging period [2].

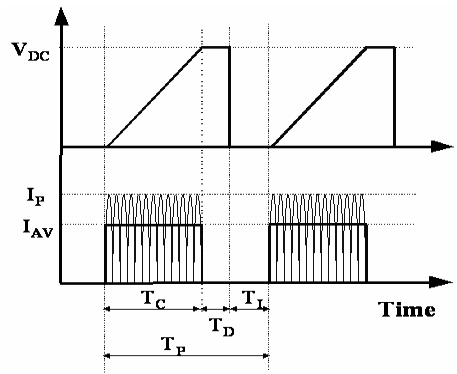

Figure 2: Charging voltage and current waveform of PFN.

The average current I_{AV}, the peak current I_P, and the resonant energy E_R are given by

$$I_{AV} = \frac{2}{\pi} I_P, \quad I_P = \frac{V_{DC}}{Z}, \quad E_R = \frac{1}{2} C_R (2V_{DC})^2$$

where V_{DC} is the source voltage driving the L-C circuit, Z is the resonant impedance, C_R is the capacitance of the resonant circuit. Then, the series resonant inverter can transfer maximum power P_O

$$P_O = \frac{1}{2} V_{DC} I_{AV} = \frac{1}{\pi} \frac{V_{DC}^2}{Z} = f_R E_R$$

where f_R is the resonant frequency. Therefore, a basic design parameter is C_R that is to be decided for the peak output power P_O with given parameters V_{DC} and f_R. If the switching frequency f_{SW} is smaller than the f_R, it is given by V_{DC} and f_{SW}. The supplies are based on a series-resonant, IGBT switched 50 kilohertz inverter. Careful attention was paid by the manufacture to thermal design of the inverter and transformer/rectifier to achieve 12 kW output power. The series resonant inverter power supply is developed for the capacitor charging application. The resonant frequency is 62.5 kHz with 4.4 μF capacitor and total series inductance 1.5 μH.

Pulse Forming Network

The PFN is made up of two parallel networks. Each of these is designed as a 12 sections, a type-E PFN with a nominal impedance of 3.73 ohms. The PFN is air insulated in a separate compartment of the modulator enclosure. Air insulation was chosen over oil or gas insulation in order to minimize and simplify maintenance time. The PFN inductors are simple solenoids wound of 11 turns from 0.4 inch diameter copper tubing on a 4 inch diameter, UHMW-PE, cylindrical support structure. A copper tuning slug is mounted on an axial, threaded rod for adjustment of the inductance. A slot in the end of

the tuning slug allows for insertion of a dielectric tuning wand to turn the slug and adjust the inductance during modulator operation. The tuning range of inductance is 2-4 μH [3]. Figure 3 shows PFN section (right side) of the modulator.

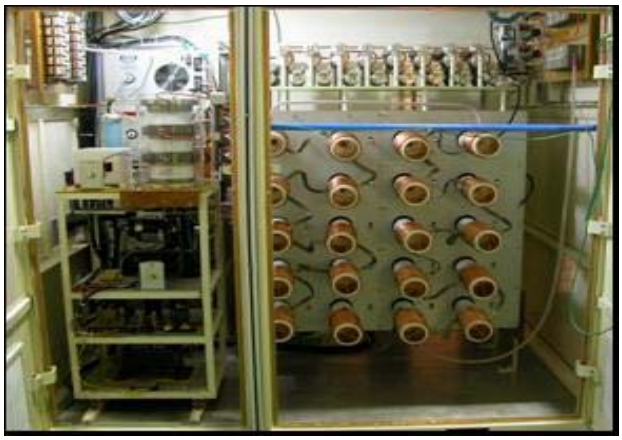

Figure 3: Photograph of PFN station and thyratron stand of modulator.

Thyratron

A thyratron switch was chosen because it is well proven in this type of modulator. The basic choices are the E2V CX1836AX and the Litton ITT F-303. The modulator was designed to accommodate any of these tubes, since all are available at PLS. However, the E2V CX-1836AX was chosen as the first choice because of its compact size and dispenser cathode. A thyratron support chassis supplies power to the cathode and reservoir heaters as well as grid bias and triggers. For the CX1836AX, both trigger grids are pulsed with solid state drivers manufactured by E2V (Model MA2709A). The second grid has an adjustable negative bias. An additional power supply is included to produce a keep-alive discharge for the F-303 in the event one of these tubes is installed.

Pulse Transformer

The pulse transformer is nominally rated at 400 kV output with 1 to 17 step-up ratio. It is designed to have less then 1% droops. Initial operation of the pulser indicated a substantial high frequency ringing on the leading edge of the pulse with an approximately 2 megahertz frequency. This was damped out with and resistor-capacitor snubber across the primary of the pulse transformer.

RESULTS AND SUMMARY

A compact klystron station has been designed to power the advanced PAL linac. Switching power supplies are used to achieve a compact size. Preliminary testing has achieved 310 kilovolt pulses with a klystron gun as the load. Figure 4 is showing modulator output voltage and current waveforms. Work is in progress to tune the pulse forming network for optimum fidelity.

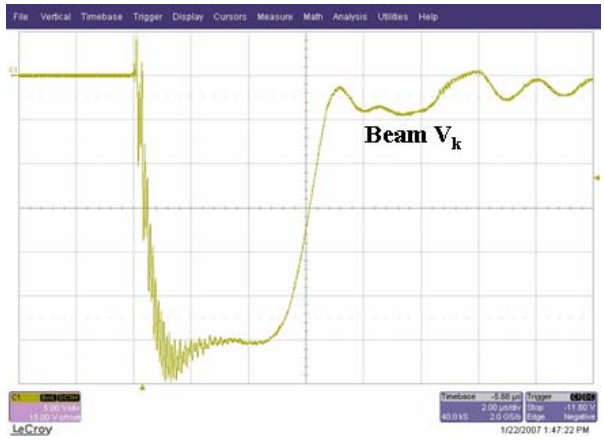

(a)

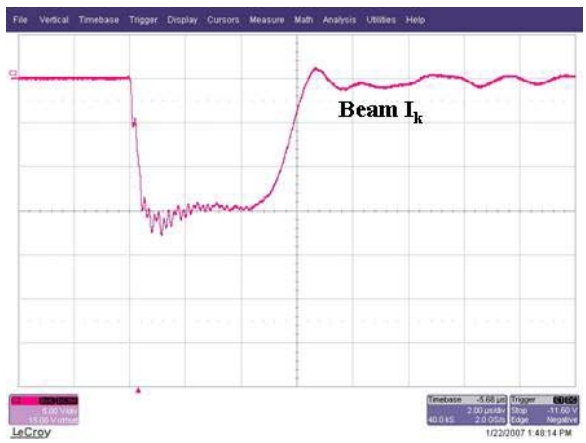

(b)

Figure 4: Modulator output voltage wave forms. (a) Beam voltage 310 kV (50 kV/div), (b) Beam current 300 A (0.05 V/A, 100 A/div)

REFERENCES

[1] John Kinross-Wright and John Plato, "Klystron station for the advanced free electron laser," Conference Record of the 1994 Twenty-First International Power Modulator Symposium, pp. 178-180, 1994.

[2] J. S. Oh, S. D. Jang, Y. G. Son, M. H. Cho, W. Namkung, "Development of a capacitor-charging power supply for a smart modulator." Proceedings of the second Asian Particle Accelerator Conference, Beijing, China, pp. 719-721, 2001.

[3] R. M. Ness, B. L. Thomas, and G. Schofield, "A 350 kW average power thyratron switched line type modulator," Conference Record of the 1994 Twenty-First International Power Modulator Symposium, pp. 34-38, 1994.

WIDEBAND CURRENT TRANSFORMERS FOR THE SURVEILLANCE OF THE BEAM EXTRACTION KICKER SYSTEM OF THE LARGE HADRON COLLIDER

C. Defrance, J. Bergoz, Bergoz Instrumentation, 01630 Saint-Genis-Pouilly, France
L. Ducimetière, E. Vossenberg, CERN, Geneva, Switzerland.

Abstract

The LHC beam dumping system must protect the LHC machine from damage by reliably and safely extracting and absorbing the circulating beams when requested. Two sets of 15 extraction kicker magnets form the main active part of this system. A separate high voltage pulse generator powers each magnet. Because of the high beam energy and the consequences which could result from significant beam loss due to a malfunctioning of the dump system the magnets and generators are continuously surveyed in order to generate a beam abort as soon as an internal fault is detected. Amongst these surveillance systems, wideband current transformers have been designed to detect any erratic start in one of the generators. Output power should be enough to directly re-trigger all the power trigger units of the remaining 14 generators.

The current transformers were developed in collaboration with industry. To minimize losses, high-resistivity cobalt alloy was chosen for the cores. The annealing techniques originally developed for LEP beam current measurement in collaboration between CERN and industry allowed to extend the frequency response beyond that of traditional core materials.

The paper shows the results obtained, exposes the problems encountered with shielding, conductor position sensitivity, load resistor technology and their solutions.

The know-how acquired during the collaboration was further applied by the industrial partner to cover a wider range of sensitivity, size and frequency.

INTRODUCTION

The LHC beam dump system is a safety system that must protect LHC machine components from damage due to excessive beam losses, or personnel from radiation hazards. Failing to respond to dump requests has severe consequences. The functional operation and the required reliability of functioning are described in the LHC design study [2]. An important ingredient in terms of reliability and safety is the dual branch generator with two parallel 30 kV semiconductor power switches. For a correct dump action the 15 generators are all fired at the same time and are synchronised with the 3 μs abort gap in the beam.

In case of an accidental un-triggered discharge of one of the generators beam would be deflected into the collider vacuum tube and cause severe damage to machine components. Therefore, in this event the other 14 generators are triggered automatically within 700 ns to deflect the beam into the extraction channel and dump it safely on the absorber block.

BEAM EXTRACTION KICKER SYSTEM

The circuitry of the dual branch generator is shown in Fig. 1.

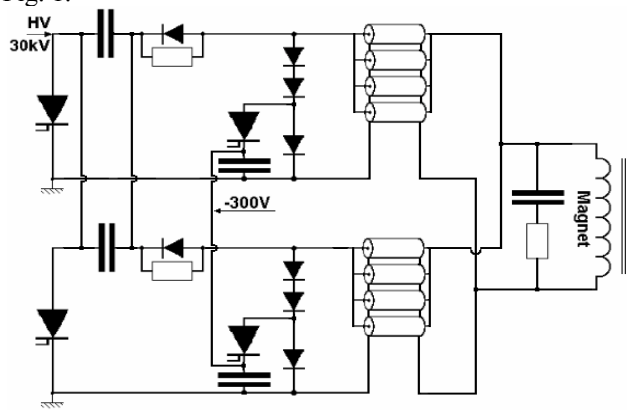

Figure 1: Dual branch generator circuit layout.

It consists basically of a discharge capacitor in series with a 30 kV semiconductor solid state switch, that produces in combination with a free-wheel diode stack parallel to the magnet a current pulse of 2.7 μs rise time and about 2 ms fall time, of which only 95 μs are used to empty the machine. After the magnet current has reached its peak amplitude the polarity of the generator inverses and the freewheel diode stacks start to conduct the magnet current. Simultaneously the 2.5 kV current droop compensation switch, which is connected in series with a 3.25 mF, -300 V capacitor, is closed and the current in the fast recovery diode is commutated. The 3.25 mF capacitor is then connected in series with the magnet inductance and oscillates with a superimposed half-sine wave, which compensates for the resistive losses of the magnet current freewheel circuit.

The generator capacitor voltages are tracked with the beam energy between 2.2 kV at 450 GeV and 30 kV at 7 TeV. The main parameters are listed in Table 1.

Table 1. Main generator parameters.

Voltage range	2.2-30	kV
Peak magnet current (7 TeV)	18.5	kA
Peak magnet current (450 GeV)	1.29	kA
Magnet current flat top 100-105%	95	μs
Current rise time 0-100%	2.7	μs
Repetition time, minimum	30	s

SPECIFICATIONS FOR THE CURRENT TRANSFORMERS

A re-trigger system (RTS) must immediately re-distribute a trigger request, arising from a spontaneous firing of one of the four solid state switches in one generator, to the remaining 14 generators. Therefore, a set of two redundant current transformers (CTs) is mounted in each of the 30 kV semiconductor power switches and 2.5 kV droop compensation switches. The CTs detect any un-triggered generator discharge by measuring the conduction of any of the switches. They have enough powering capabilities to trigger the power trigger modules of the 14 other generators.

Fig. 2 shows the re-trigger CTs in the 30 kV main switch and Fig. 3 the CTs in the compensation switch.

Figure 2: Re-trigger CTs in the main discharge switch.

Figure 3: Re-trigger CTs in the droop compensation switch.

The eight CTs of each generator are connected to a common re-triggering box, which is located in the same generator. The output of each re-triggering box is connected to the input of the trigger units of all other generators. A chained input/output system has been chosen instead of a star system because it is faster. Since each CT has enough energy to trigger all power trigger modules, there is no stored energy in the system itself. This minimizes the risk of creating spurious triggers, even when a cable is being disconnected or a trigger source is defective.

Due to the large dynamic range of the LHC beam energy and consequently also of the generator charging voltages, the re-triggering action of the CTs is particular critical at the lowest beam energy (450 GeV) and corresponding low charging voltages. For reliability reasons it was decided to use SMA output connectors. Droop specifications are not an issue; re-triggering takes place on the rising edge of the measured signal. The outer shield (case) of the CTs is only grounded at the input of the re-trigger box. The main specifications of the re-trigger CTs are listed in Table 2.

Table 2. Specification of the RTS current transformers (type CT1: main switch; type CT2: compensation switch).

Type	CT1	CT2	
Inner diameter	38		mm
Outer diameter	72		mm
Thickness	17		mm
Sensitivity, 50 Ω terminated	0.5	2.0	V/A
Accuracy, 50 Ω terminated	±1		%
Maximum CT current (7 TeV)	2400	177	A
Minimum CT current (450 GeV)	152	15	A
Minimum ampere-seconds	10	1	mAs
Maximum rise time response	50		ns
Repetition time, minimum	30		s

CT DEVELOPMENT

The development process was driven by requirements of the LHC: these being high reliability, small size, stability with respect to time and temperature variations, low loss, accuracy of the transfer function, independence of the core magnetic state left by a previous primary pulse. Cobalt-based alloy was chosen for its high electrical resistivity and modest annealing temperature. This choice was also based on the extensive experience with, and equipment for, this type of alloy by our industrial partner.

The annealing temperature, rate of cooling, magnetic field intensity and vector direction allow a full control over magnetic core parameters such as lower cut-off frequency (droop), higher cut-off frequency (rise time) and coercive field H_c. To achieve the same performances for unipolar and bipolar pulses, H_c has to be as low as possible, in order to keep the maximum I·t value constant and independent of the residual core state.

The high electrical resistivity minimises losses in the core and the modest annealing temperature allows alloy processing in a laboratory environment.

To minimize core memory effects due to a previous primary pulse, the cores were annealed above the alloy Curie temperature in a fixed magnetic field and cooled at a controlled rate. This keeps the coercive field to a minimum value.

The power rating and pulse withstanding requirement dictated the choice of film resistors for the 50 Ω internal load. Chip resistors with substantial pulse withstanding characteristics are now available in a wide range of sizes, tolerances and values. These resistors have been successfully tested at CERN with 7 kW peak power and energy >3 mJ.

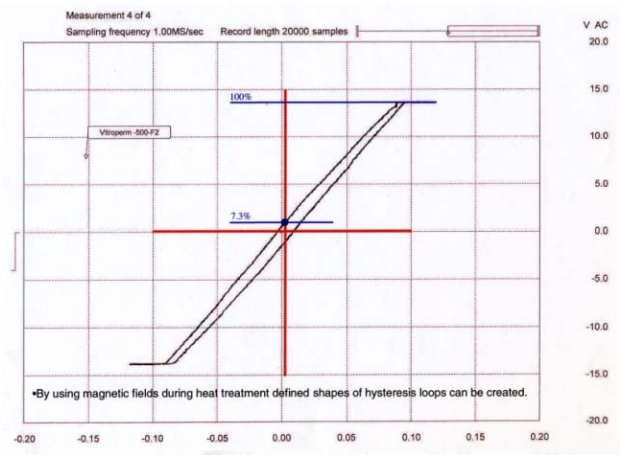

Figure 4: Magnetic core hysteresis cycle after annealing process and thermal treatment-Hc=7.3%.Bs.

The CTs are encased in a copper shield to minimise electrostatic pick-up and also to protect against interference from other sources. A gap is needed to avoid shorting the magnetic core. This gap presents a capacitance and acts as a low pass filter with a cut-off frequency inversely proportional to the gap width. To optimise the high frequency coupling, the gap width has been simulated and numerically analysed.

High frequency performance is obtained by keeping stray capacitance to a minimum. This implies the use of a small number of turns, yet enough to assure a uniform field distribution around the magnetic core.

A straightforward method to characterise CTs is to observe its transfer function in frequency domain. Calibration with an accuracy better than ±1% for the input/output ratio and ±0.1° for the phase is possible with a vector network analyser (VNA).

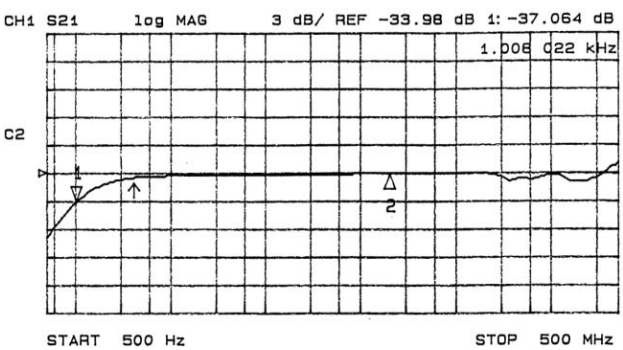

Figure 5:CT-36-2.0 V/A bandwidth (with 8751A Agilent VNA).

The nominal turns ratio value of CT-36-2.0 V/A is 25:1; this leads to 33.979 dB attenuation in the VNA 50 Ω input port. Hence, all values in the range 34.067 to 33.893 dB meet the +/-1% accuracy criteria. Ratio error is mainly due to the resistor precision. Rise time and droop of 700 ps and 0.63%/μs respectively are deduced from the -3 dB higher and lower cut-off frequencies; these being 500 MHz and 1.008 kHz respectively. In reality, the -3 dB higher cut-off frequency is well in excess of 500 MHz therefore not measurable with this VNA.

The last two years have yielded significant progress on CTs which can now be calibrated within ±0.5% accuracy. Their output dependency on the primary conductor position due to non-uniform field density distribution in the magnetic core has been considerably reduced. Sensitivity to high voltage has been also reduced by improving the electrostatic shielding.

CONCLUSION

A fault tolerant re-trigger system for the LHC Beam Dump System has been developed and built. It powers immediately all magnets in case of spontaneous discharge in one of the generators. Wideband current transformers form an essential part of this system.

Two different wideband current transformers have been developed, built and successfully tested for use as surveillance systems in the LHC beam dumping system. The main design criteria were reliability, minimum coercive field and case size.

The developments led to a range of technical solutions for current measurement from micro-amps to 20 kA, at frequencies from 0.5 Hz to 500 MHz and sensitivity from 0.05 V/A to 5 V/A, providing environmental application flexibility. These CTs can be used in various applications such as laser and plasma research, semiconductor gate switching, capacitor and electrostatic discharges, corona wire discharge or partial discharge measurement.

With sensitivities up to 5 V/A and assuring faithful rendering of fast transients, CTs overcome critical measurements as non-interceptive high frequency or low current monitoring. Close collaboration between CERN and industry allowed designing these new current transformers and achieving a performance level never reached before.

REFERENCES

[1] J.H. Dieperink, J.-L. Bretin, E. Carlier, L. Ducimetière, G.H. Schröder, E.B. Vossenberg : "Design aspects related to the reliability of the LHC Beam Bump Kicker Systems", PAC 1997, Vancouver, B.C., Canada.

[2] E.B. Vossenberg, L. Ducimetière, U. Jansson, J.H. Dieperink, J. Bonthond : "Dual Branch High Voltage Pulse Generator for the Beam Extraction of the Large Hadron Collider", Proc. 25th Int'l Power Modulator Symposium and High Voltage Workshop, 2002.

[3] K. Unser: "Toroidal AC and DC current transformers for beam intensity measurements", Atomkernenergie Kerntechnik, Vol.47(1985)N°1.

[4] Bergoz website: http://www.bergoz.com/products/CT.

PRECISE POSITIONING OF MAGNETIC FIELD CENTERS OF QUADRUPOLE MAGNETS ON THE GIRDER

Liren Tsai, Duan Jen Wang, Shen Yaw Perng, and Tai-Ching Fan
NSRRC, HsinChu, Taiwan

Abstract

Conventional alignment of quadrupole magnets on one girder was mainly based on the measurement from theodolite and fiducial. Most of the measurement errors came from human-eye resolution and fiducial precision. The resultant cumulative error could be in the order of 100μm. In this paper, vibrating wire method is proposed to align a group of quadrupole magnets concentrically on one girder to precision about 30μm. A short wire was adopted to reduce the sag. A laser PSD system was used to identify the position of the wire. Descriptions of the setup and test results are presented.

INTRODUCTION

The alignment of quadrupole magnets directly affects the closed orbit of electron beams in synchrotron light source. In past years, many efforts have been performed to accurately locate the magnetic center of quadrupole magnets, which include Hall probe measurement, pulsed wire technique, vibrating wire field measuring technique, moving wire technique, moving probe technique, and rotating coil technique, etc [1]. Through these techniques, individual quadrupole magnetic center could be identified with less than 50μm error. However, when aligning two or three quadrupole magnets on girder, the error generated from using fiducial and theodolite could be cumulative. Rotating coil can exam quadrupoles in detail, nevertheless it is extremely difficult to be used on nominal girders. Pulsed wire method has good resolution in narrow areas [2]; however it does not provide the information of quadrupole pitch and yaw. Moving wire method would be more effective in measuring high magnetic fields like superconducting quadrupoles [3]. In order to precisely align quadrupoles on girder, a new alignment system is developed in National Synchrotron Radiation Research Center, Taiwan. This technique adopted the advantages from both vibrating wire method and position sensitive detectors (PSD).

Vibrating Wire Method (VWM)

The vibrating wire method (VWM) is composed of a stretched wire in a magnetic field. By sending a sinusoidal current through the wire, the vibration of the wire induced by the Lorentz Force is observed [4] and the magnitude and orientation of this magnetic field can be determined. To precisely align quadrupoles on a girder, VWM has some clear advantages over other methods: (a) It can be fairly easily operated on a girder; (b) It requires no more than 10cm operating space beside a quadrupole; (c) It requires less operation time, however is as accurate as other techniques.

PSD Alignment System

The position sensitive detector (PSD) has been widely used in many engineering areas to precisely align multiple targets. It is composed of large area photodiodes to detect and record the position of an incident light beam. In this research, two PSDs were attached to the ends of the vibrating wire, as shown in Figure 1. When the laser position is fixed, one can literally "extend" the magnetic center of quadrupole Q1 to quadrupole Q2 by precisely reposition the wire using PSDs. Experiment setup and operation procedures were detailed in next section.

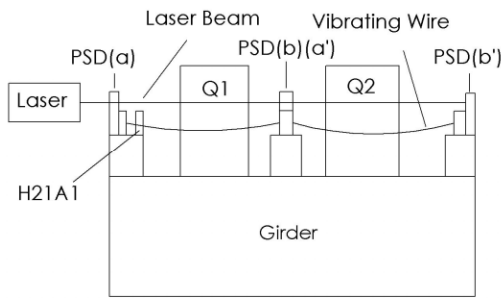

Figure 1: Experiment setup for vibrating wire method plus PSD system.

EXPERIMENT SETUP

Figure 1 shows the experiment setup of the vibrating wire and PSD systems. Two quadrupole magnets were pre-aligned on the girder using the traditional fiducial and theodolite method. The experiments took place in the following orders:

(1) The vibrating wire was tensioned around the ideal centerline of the first quadrupole magnet (Q1). The wire used in the experiment was 650mm length and 125μm diameter Be-Cu wire from GoodFellow™. In order to increase the repeatability of VWM, 100A constant current was applied to the testing quadrupole magnets while supplying the magnet coils with cooling water to keep their temperature at 20±0.5℃.

(2) HP 33120A function generator was connected to the wire to provide AC sine current. The frequency of the input current was carefully adjusted to match the fundamental mode frequency of the Be-Cu wire in order to maximize the vibration amplitude.

(3) The vibration amplitude was recorded by a pair of photo coupler H21A1, as shown in Figure 1. The magnetic center of the quadrupole was found by moving the vibrating wire along the horizontal and vertical directions to find the location with lowest vibration amplitude.
(4) The driving current was then tuned to the second harmonic frequency of the wire to find the magnetic center along pitch and yaw directions [4].
(5) A fixed laser, as shown in Figure 1, was utilized to match the position of the wire through the two PSDs mounted with the wire at PSD(a) and PSD(b). The PSDs in the experiments were ON-TRAK PSM 2-10. This 10mm x 10mm PSD module has typical resolution 250 nm. HP laser head 5517C was utilized as the light source. The distances between PSD center points and the two wire ends were measured using a microscope with 50 times magnification.
(6) The Be-Cu wire and PSDs were moved to PSD(a') and PSD(b') beside quadrupole Q2. The position of wire was carefully adjusted using PSDs and the fixed laser.
(7) The wire positioned at Q2 was taken as the extension of the magnetic center of Q1. By repeating step (1) through (4), the misalignment of magnetic centers between Q1 and Q2 can be determined and adjusted.

RESULTS AND DISCUSSION

Figure 2 shows the relationship between vibration amplitude and transverse location of the wire in a span of 550μm with 50μm increment. This experiment result showed good linearity between the vibrating amplitude (ordinate) and the transverse location (abscissa). When the wire moved from left hand side along horizontal axis towards the magnetic center, the vibrating amplitude decreased linearly and then increased linearly after the wire passed through the magnetic center. The approximated magnetic center in this measurement has location error 7.18μm (RMS). Figure 3 shows the relationship between vibration amplitude (ordinate) and yaw (abscissa) in an experiment. The approximated yaw measurement error is 0.012mrad.

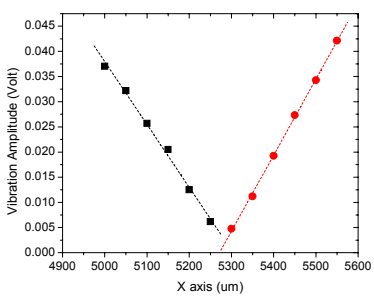

Figure 2: Vibration amplitude vs. transverse location in experiment 111006T.

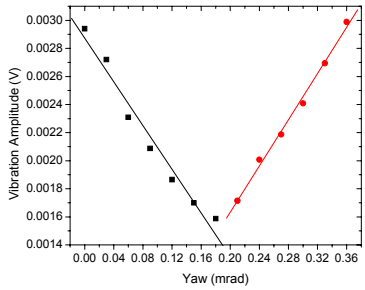

Figure 3: Vibration amplitude vs. yaw in experiment 012407T.

Error estimation

All wire methods suffer from the sag of wire and the temperature induced vibration frequency fluctuations. The sag-generated vertical position offsets were in the range of 25~100μm depending on its tension force. To estimate the sag of a vibrating wire, a simple relation between sag and the vibration fundamental mode frequency has been proposed by Temnykh [2]:

$$S = \frac{g}{32}\left(\frac{w_1}{2\pi}\right)^{-2} \quad (1)$$

In which S represents the sag of the stretched wire, g = 9.80665 m/s^2, and w_1 represents the fundamental mode frequency of the wire. In this project, the fundamental mode frequency of the vibrating wire was precisely controlled by means of carefully adjusting the tension force in the wire. The sag difference of the wire between location Q1 and Q2 was about 5μm.

Another error source is the drift of the laser which affects the PSD reading. Usual drift of the applied laser was 10μrad after warm up. To be certain about the amount of laser drift, the laser head was monitored and the results were displayed in Figure 4 and Figure 5.

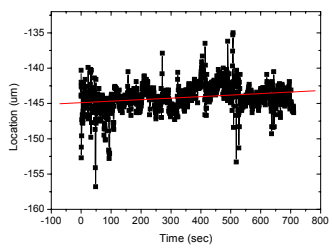

Figure 4: PSD reading along vertical axis with Standard Deviation = 1.77μm.

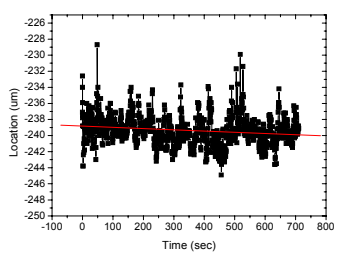

Figure 5: PSD reading along horizontal axis with Standard Deviation = 1.91μm.

Figure 4 and Figure 5 show the laser drift along vertical and horizontal axis, respectively. The abscissa represents the time from the beginning of the measurement, and the ordinate represents the position reading from PSD module. The data acquisition frequency was 1Hz and the durations of the experiments were 12 minutes. The laser drift induced positioning error was 1.91μm (RMS).

The sag of vibrating wire method is its main disadvantage because of the resultant dislocation of the whole wire to the magnetic centers. In this research, the sag problem was precisely controlled by adjusting the vibrating frequency of the wire. However, there were other error sources in this series of experiments. A summary of all the estimated errors is listed as following:

- VWM fitting: 7μm. The error came from the fitting process is about 7μm as discussed in the previous section.
- Wire parallelism: 15μm. In this research, PSD sensors were used as the coordinates of the wire, hence the parallelism between the PSD module and the wire is critical. To measure the parallelism between PSD and wire, a microscope with 50 times magnification was used. However, because of human eye resolution limit, error generated during this process is in the range of 15~20μm.
- PSD repeatability: 5μm. The drift of the laser was about 2μm plus the 3μm error from relocating the PSD module during the experiments.
- Sag difference: 5μm. Although the sag of the wire was carefully controlled by adjusting the tension in the wire, still, some error exists.

Table 1: Estimated Sources of RMS Error in VWM and PSD alignment method.

Error Sources	Current system error (μm)	Projected Future error (μm)
VWM fitting	7	5
Wire parallelism	15	5
PSD repeatability	5	5
Sag difference	5	5
Total error	32	20

Another VWM setting, which utilizes a stretched long wire through both quadrupole magnets, has also been planned to verify the accuracy of this proposed technique. The difference between using one long wire to this two-short-wire-segments technique is the sag issue. In the process of aligning both quadrupole magnetic centers, the sag of the short wire could be controlled by using the same wire with similar tension forces. When using a long wire, the sag of the wire become larger and requires precise inspections to determine its value. However, the precise transition of the short wire from one quadrupole magnet to another could be troublesome. The error sources were too many and could cause huge cumulative errors.

SUMMARY

This method can be used as a check method to align the magnetic center of multiple quadrupole magnets on a girder before installation of vacuum chambers. Although it has only been verified that the accuracy of this proposed method is better than the theodolite resolution, this novel method has the potential to align magnetic centers of multiple quadrupole magnets on one girder to 30μm.

REFERENCES

[1] N. A. Morozov, Review of the magnetic measurement technique (experience of the SLC, LEP, CEBAF), Workshop on the TESLA spectrometer, Dubna, 13-14 October 2003.

[2] J. G. Melton, M. J. Burns, D. J. Honaberger, Pulsed Taut-Wire Measurement of the Magnetic Alignment of the ITS Induction Cells, IEEE Particle Accelerator Conference Preceeding, 2944-2946, 1993.

[3] Z. Wolf, A Vibrating Wire System For Quadrupole Fiducialization, LCLS Document TN-05-11, May 2005.

[4] Temnykh, Vibrating Wire Field-Measuring Technique, Nuclear Instruments and Methods in Physics Research A 399, 1997.

THE MAGNET ALIGNMENT METHOD FOR THE J-PARC MAIN RING

M. J. Shirakata, K. Ishii, K. Niki, K. Okamura, T. Oogoe, E. Yanaoka and M. Yoshioka
KEK, Tsukuba, Japan

Abstract

In the J-PARC site, the infrastructure for the whole site measurement is planned for the global alignment of the accelerator components. For the neutrino experiments, the J-PARC main ring must be directed to the SUPER-KAMIOKANDE exactly. The global measurements from the Kamioka site to the J-PARC site are carried out by using GPS system on the ground level. Several measurement through-holes, in order to transport the coordinates from the ground level into the accelerator floor level directly, are prepared around the J-PARC accelerator complex. The beam-line definition and the magnet alignment method for the J-PARC main ring are reported with the present alignment status.

INTRODUCTION

The J-PARC accelerator complex [1] consists of a LINAC, RCS (Rapid Cycling Synchrotron) and MR (Main Ring). In the early stage of the J-PARC project, the through holes, which transfer the coordinates of GPS measurement on the ground level into the accelerator tunnel, were proposed on the MR construction plan because the MR has to be aligned precisely to have a direction to the SUPER-KAMIOKANDE which is 300 km away from the J-PARC site. Finally, this idea is adopted all over the site because it is convenient to grasp the relative positions of accelerator components. The whole site measurements is carried out every winter including these through holes in order to check the arrangement of accelerators.

The MR is composed of three straight lines (named as: INS-A, INS-B and INS-C) and three arcs (ARC-A, ARC-B and ARC-C). A schematic view of the J-PARC MR tunnel is shown in Fig 1. Six through holes are prepared MR_01 to MR_06. The 136 level target are distributed for the floor level measurement. Moreover, L-type and washer-type targets are placed on both walls among the level targets for the beam-line definition and magnet alignment.

BEAM-LINE DEFINITION AND MAGNET INSTALLATION

In usual, the beam-line is defined based on the whole ring measurement after the completion of the construction work. Unfortunately, we had to define the beam-line even the MR tunnel was under construction. The beam-line was defined in these four periods:

- The first stage: August 2005, (all 50BTHs, MHR01 to MHR56)
- The second stage: March 2006, (MHR57 to MHR74)
- The third stage: September 2006, (MHR75 to MHR103)
- The last stage: December 2006, (MHR104 to MHR124)

The parentheses indicate the corresponding areas. The on-wall targets (L-type and washer-type) are measured by laser-tracker (LT) system in the local coordinates. The LT measures the relative positions of the on-wall targets in the area of radius of 20 m at a time. By moving its location along the MR tunnel, the on-wall targets figure out the shape of MR tunnel. Measured position data of the on-wall targets are transformed to the KEK_J-PARC coordinates using GPS global measurement. The KEK_J-PARC coordinates are the right-hand system whose origin is set to the center of RCS ring and whose x-axis is parallel to the INS-C. The beam-line and central points of the magnet bases were drawn and marked on the floor by using the on-wall target coordinates. The magnets were installed on them.

Fig. 2 shows the floor levels of the MR tunnel. The vertical displacement is about $\pm$10 mm except for one section. At the MHR10, the 3NBT beam line which transfers the RCS beam to the neutron experimental hall is crossing above the MR tunnel. There is a largest vertical displacement of about 40 mm. The magnets were placed on high plane of 2.1 below the sea level considering the future subsidence. The magnets in the descended area were installed with spacers under their bases as shown in Fig 3 in order to compensate the floor subsidence.

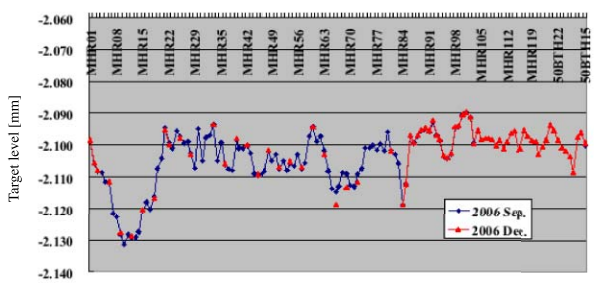

Figure 2: Measured target level of the MR tunnel from the sea level. The floor level is -13 mm from the target level. The floor level displacement is about -40 mm at the maximum.

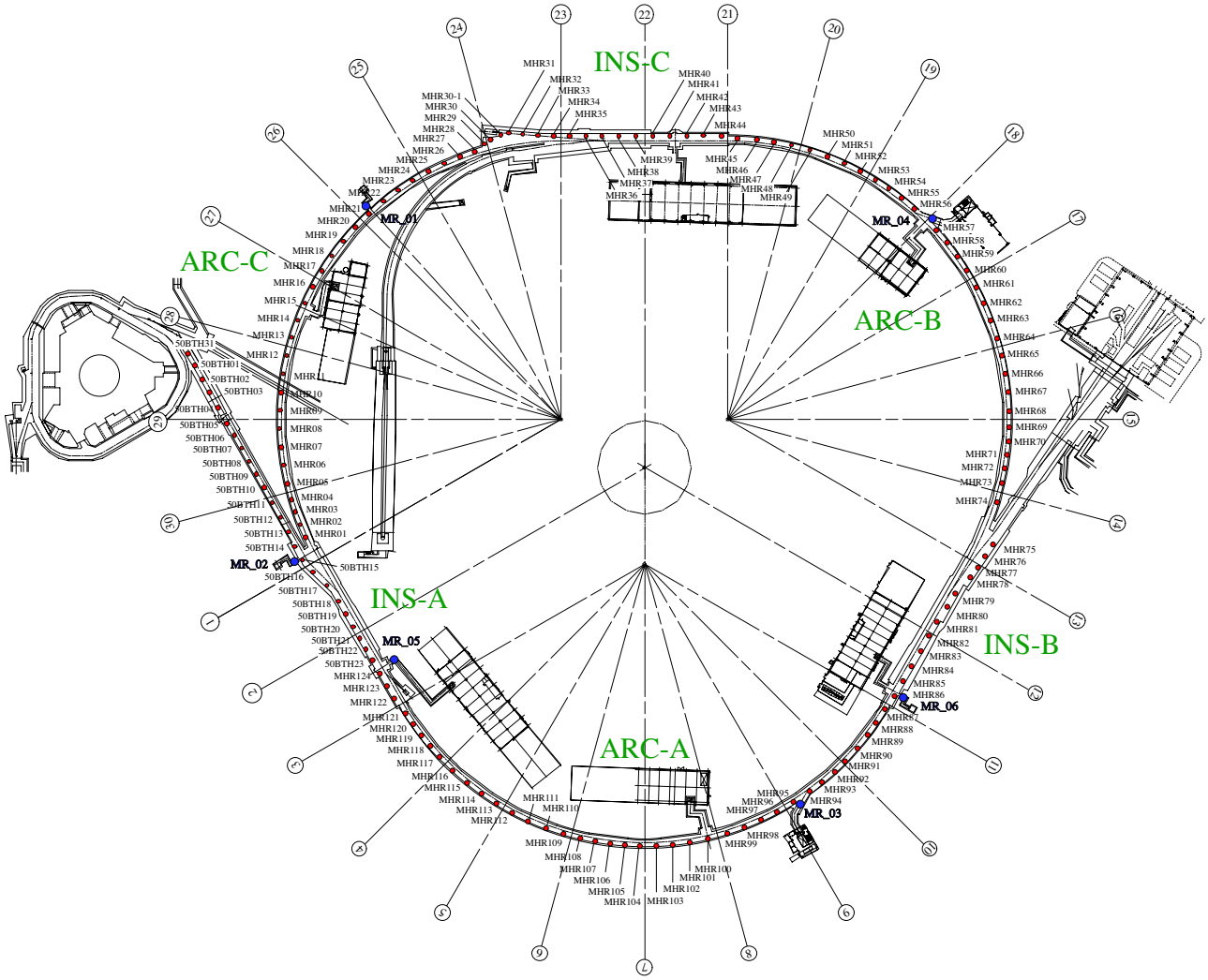

Figure 1: Distribution of the measurement targets for the floor level.

Figure 3: Magnet base spacer made of steel is installed to compensate the floor subsidence.

ALIGNMENT METHOD

The L-type and washer type targets are distributed on the walls in order to the horizontal position definition. As these targets have their own location data in the KEK_J-PARC coordinate system by the previous global measurements, the LT system represents the KEK_J-PARC coordinate by measuring four to six on-wall targets and fitting the results at any place. The magnets have the base plates with a target hole for their alignment. The bending magnet has three plates and the quadrupole and sextupole magnets have two plates. The position is measured by LT system and the rotation is measured by digital level. The required goal is less than 0.3 mm for the transverse displacement, and less than 1 mm for the longitudinal displacement as 1σ. The rotations have to be 0.3 mm/m for any direction also as 1σ. The maximum error has to be suppressed within 2σ.

As the weight of the bending magnets is about 35 ton, it is difficult to move it by the push-bolt mechanism. The alignment stage is prepared for the bending magnets which is the special tool consisting of the x-y slide stages and oil-jacks. Under the bending magnet, there are two large spaces for the air pallet system, Two alignment stages are inserted these area and handle the bending magnet as shown in Fig 4. The magnet position is monitored in real-

time by using the LT measurement system. People can adjust the magnet position directly watching the values. The

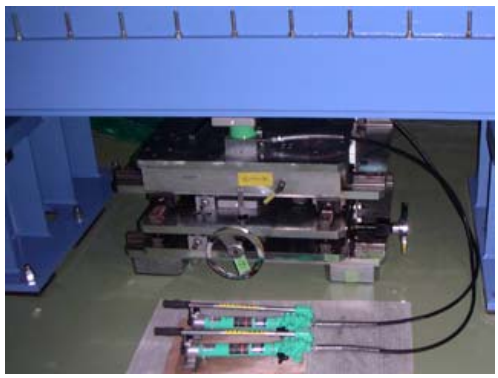

Figure 4: Alignment stage for the bending magnets consists of the two x-y stages and oil-jacks.

quadrupole magnets are adjusted by pull-bolt mechanisms for the horizontal alignment. Oil-jacks are used to assist the vertical alignment as shown in Fig 5. The sextupole mag-

Figure 5: Vertical alignment is assisted by oil-jacks for the quadrupole magnets.

nets are adjusted just using push-bolt system because they are light less than 1 ton. It was not difficult suppress the magnet displacement within 0.1 mm which was six times better than the alignment goal. On the other hand, the correction of rotations remained as the level of 0.2 mm/m due to the twist of magnets. As the bending magnets are long, they tend to be twisted around the beam-line and radial direction of the ring. The alignment efficiency which is defined as the average time needed for each magnet is about 60 minutes for the bending magnets, about 30 minutes for the quadrupole and sextupole magnets. The magnets in ARC-B and ARC-C sections have finished to be aligned.

FLOOR LEVEL FLUCTUATION OF THE TUNNEL

The short term subsidence of the floor level is shown in Fig 6 from target MHR01 to MHR103. Around MHR70, a fast subsidence of -1.8 mm/month is observed. The magnets involved in the corresponding area must be re-aligned. Generally, the fitting error of on-wall targets is large in the area with vertically large displacement. This indicates the horizontal displacement of the MR tunnel in some areas. The horizontal error at the closing point was found to be 11 mm by summing up the errors of traverse measurements along the ring tunnel, which spent more than one year. A round-trip measurement is necessary to figure out the present shape of the MR in this summer, and the continuous floor level observation is important.

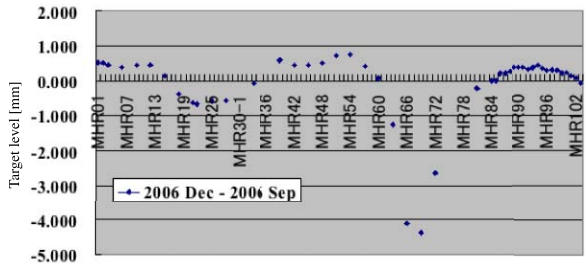

Figure 6: Observed subsidence of the MR tunnel during September to December in 2006.

SUMMARY

The magnet alignment of the J-PARC main ring carried out in 2006 is summarized as follows:

- Alignment procedure using LT system based on distributed on-wall targets is very effective.
- The floor level subsidence which requires the magnet re-alignment is still going on around the upstream of ARC-B.
- In the horizontal plane, it was found the shape of the ring is slightly distorted.
- A round-trip measurement of the MR shape is needed in this summer.
- Continuous floor level observation is necessary.

The magnet re-alignment work will be held before this December with the minimum modification case.

REFERENCES

[1] Acc. Group JAERI/KEK, "ACCELERATOR TECHNICAL DESIGN REPORT FOR J-PARC", KEK Report 2002-13, JAERI-Tech 2003-044, J-PARC 03-01, March 2003

A MECHANICAL INSTALLATION PROTOTYPE FOR THE SSRF STORAGE RING

L.X. Yin, H.W. Du, D.K. Jiang, Q.G. Zhou, Z.B. Yan, C.H. Yu, X. Wang
Shanghai Institute of Applied Physics, Shanghai 201800, P.R. China

Abstract

The engineering design of the mechanical system for SSRF storage ring was finished. The first group components in each system, such as the magnets, vacuum chambers, BPMs, girders and other hardware, were fabricated and tested, respectively. In order to check the overall design and the installation procedure, a lattice cell prototype was installed by using these components. Based on it, the related utility system was installed and checked. The dynamic properties of the girder-magnet assembly were also tested in this prototype. Most of the design was confirmed during the installation, but still some problems were found. The modification for the overall design and some components design has been made before their mass production. The detail design and installation of the cell prototype and the test results are described in this paper.

INTRODUCTION

The Shanghai Synchrotron Radiation Facility (SSRF) is a 3.5GeV, 300mA light source currently under construction [1]. The engineering design for the mechanical system was finished and the fabrication for the first group of components in each system, such as the magnets, vacuum chambers, BPMs, girders and others, was completed. The mass production for the components will be started. In order to check the overall design and the installation procedure, a lattice sector prototype was installed by using the first group of components in the tunnel.

MECHANICAL STRUCTURES FOR THE STORAGE RING

The physical study in the storage ring led to an optical design composed of four super-periods, each divided into five sectors. Each of the twenty sectors contains 10 quadrupoles, 7 sextupoles, 4 static correctors and 3 dynamic correctors distributed on three girders, as well as 2 dipoles isolated from the girders by its own supports. The structure of a typical sector in the storage ring is shown in figure 1.

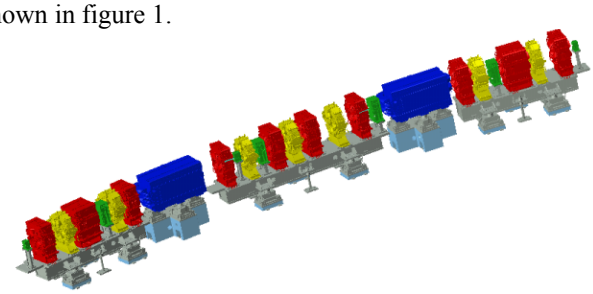

Figure 1: A typical sector in SSRF storage ring.

The support system for quadrupoles and sextupoles is composed of three parts, the girder, the adjuster unit and the concrete pedestal. Each girder is supported by three adjuster units on the pedestals. The girder is a box-structure welded from Q235A steel plates. Each adjuster unit contains a spherical bearing mounted on a wedge block adjuster, shown as figure 2. The bearing with flange is attached to the bottom of the leg in the girder. The flange can rotate 7 degrees maximum in any direction. The range of adjustment for the wedge block is ±7mm. There are two base plates under the adjuster unit to adjust the position in horizontal plane by blots. Self-lubricating plate is used in friction couple to reduce the force between slip surfaces. A concrete pedestal with damping effect is set on bottom of the adjuster unit. The pedestal can be set on the same height by adjusting the space to the floor. It is fixed on the floor tightly using the anchor bolts and a kind of non-shrinking concrete. For the dipole, the steel girder is eliminated and the magnet is supported on a higher concrete pedestal by the same adjuster unit.

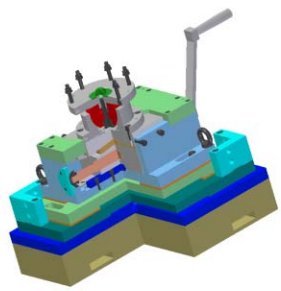

Figure 2: Girder adjuster.

The magnets are fixed on the girder by bolts. The precise position of the magnets on the girder is aligned by shimming in vertical direction and by bolt screw in horizontal direction.

There are three pieces of stainless steel vacuum chambers connected by two RF shielded bellows in one sector. The 6m bending chamber is supported on the first and the second girders, and the 5m bending chamber is on the second and the third girders. Only the 3m straight chamber is supported on the middle girder itself. Figure 3 shows the relation between chambers and girders. Each chamber is fixed on a stiff support near the downstream

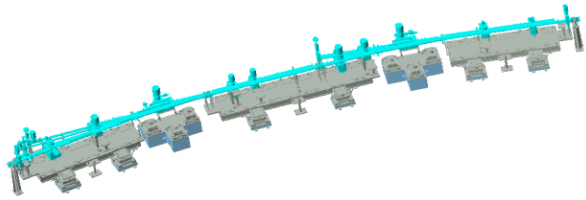

Figure 3: Vacuum chambers on girder.

BPM block and the other parts are supported by spring plates. It can let the chamber expansion easily along the longitudinal direction to the fixed point. Care should be taken during the girder re-alignment after the chamber is installed in order to avoid any damage to the chambers.

SECTOR INSTALLATION

In order to check the overall design for the machine and the fabrication quality for the system components, as well as confirm the installation procedures, it is decided to install a lattice sector prototype just after the first group of components finished. Based on the sector machine, the related utility system will also be installed to check the relation in machine, utility system and building. If any problems are found in this period, it is still possible to modify the related design and to correct the fabrication technique before the mass production started for hardware.

The installed components include the magnets (quadrupoles, sextupoles, dipoles and correctors), the vacuum chambers (with absorbers, bellows gauges and pumps) and the support components (girders, adjustment units, concrete pedestals and chamber supports) for one full sector. There is only one pare of BPMs welded on the chamber. A front end prototype for insertion device is also made and installed.

The installation procedure for the sector is as follows:

(1) Install the utility system in the tunnel, including the cooling water pipes and valves, the cable tray and the ventilation conduit. The cooling water pipes and the cable tray are pre-installed to fit the site condition and are moved out before the sector installation.
(2) Locate and fix the pedestals on the floor within the precision of 3mm in horizontal direction and 1mm in vertical direction, respectively. Mount the adjuster units on the pedestal.
(3) Position the quadrupoles and sextupoles on their own girders, align the magnets to the expected values within0.05mm in both horizontal and vertical directions.
(4) Move and position the girder-magnet assemblies to the tunnel using the 16T crane in the experimental hall. Align the assemblies to the expected values within 0.1mm in transverse direction and 0.5mm in longitudinal direction based on the control network in the tunnel.
(5) Disassemble the top side of the magnets. Position the vacuum chambers with all its attachments (absorbers, gauges, pumps and valves, etc) in vacuum condition using a dedicated hanging tool. Adjust the chamber location to the magnet.
(6) Vent the chambers with pure N_2. Connect the chambers using the bellows. Do leak check and start pumping.
(7) Disassemble the top side of the magnets. Position the vacuum chambers with all its attachments (absorbers, gauges, pumps and valves, etc) in vacuum condition using a dedicated hanging tool. Adjust the chamber location to the magnet.
(8) Vent the chambers with pure nitrogen. Connect the chambers using the bellows. Do leak check and start pumping.
(9) Position the dipoles using a dedicated tool and do alignment for them to the expected values.
(10) Reassemble the top pieces of the magnets.
(11) Survey for all the components. Adjust if necessary.
(12) Set the prototype of the front end to its location.
(13) Reset the cooling pipes and cable tray in the tunnel. Connect the plastic tubes and cables to the components.

Figure 4: The vacuum chamber installation.

Figure 5: The dipole installation.

All the above procedures are carried out and completed for the sector in one month. Figure 4 and figure 5 show a vacuum chamber and a dipole magnet in positioning. Figure 6 shows the sector in the tunnel after installation. All the magnets are positioned and aligned to its expected value smoothly. There is no leak be found after the chamber installed and adjusted under vacuum condition. The installation procedure has been confirmed in the work. There are still many problems be found during the installation period. One kind of problems is the miss position, such as the screw holes on the girder surface, the connection points on the bottom of the diploes, etc. Another kind of problems is the interface between hardware, such as between the chamber support and the magnet adjustment bolt, between the support of front end and the ring girder, between the chamber rib and the dipole coil, between the pump bake-out feedthrough and the chamber support, etc. All the problems have been solved by modifying the design and correcting the fabrication before mass production of the components. This test installation work ensures us that the engineering

design for the machine will fit the requirement and the mistakes will be leave as less as possible.

Figure 6: The sector machine in the tunnel.

DYNAMIC PERFORMANCES

The mechanical vibration of storage ring components is one of the critical issues to influence the beam orbit stability. The specification for the mechanical system in SSRF is that the first eigenfrequency should higher than 20Hz and the frequency response function should less than 30 in lateral direction and 10 in vertical direction, respectively. One of the efforts in the design of the support system is to decrease the amplification from floor to magnets through structure optimization. The first eigenfrequency for the girder-magnet assembly is about 30Hz after optimized in ANSYS. In order to confirm the dynamic performances, a serial of measurements were carried out on the girder-magnet assembly in the installed sector to characterize the system.

The tests are performed for the long girder in the sector. The length of the girder is 4m and the total weight is about 11T. The ambient excitation method is adopted in the test. Two sets of sensors (941B seismometers) are used for the test. One set is arranged on the floor while the other is located on the top of a quadrupole. The results are shown as figure 7 and figure 8. From figure 7 we can see that the first eigenfrequency in lateral direction for the girder-magnet assembly is 19.1Hz. The frequency response function is around 38 in the first eigenfrequency and there is no amplification in the low frequency range (less than 6Hz). There is no much response in vertical direction in figure 8. From the results we can see that the damping structure maybe necessary to suppress the vibration in the lateral direction. The damping pad as APS [2] and the damping link as ESRF [3] will be considered. Extensive testing for the structure will be carried out on the sector in next step.

CONCLUSION

Based on the first group of components, one standard sector for the SSRF storage ring has been installed according to the proposed procedure. The related utility system was also set in the tunnel. Most of the design for the sector was confirmed during the installation, but still some problems were found. Some necessary modifications for the overall design and for the components design have been made before the hardware mass production. The dynamic performance of the girder-magnet assembly was tested also. The damping structure maybe necessary to considered for the support system. From this work, the construction reliability for the ring is ensured. This sector will be used as a platform for the electrical test, control test and other test for the machine in the next several months.

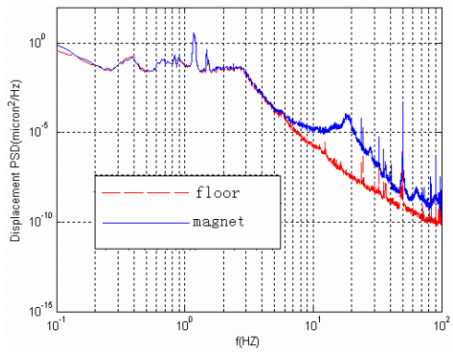

Figure 7: PSD curve for magnet to floor (Lateral direction).

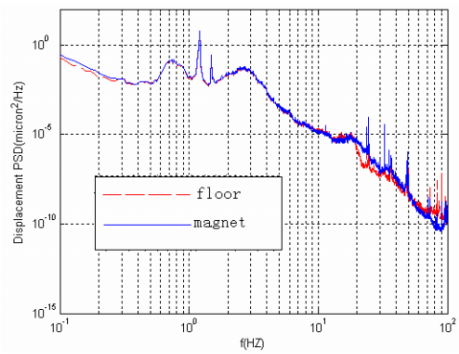

Figure 8: PSD curve for magnet to floor (Vertical direction).

ACKNOWLEDGEMENT

The authors would like to thank Mr. T. K. Chen, Mr. X. J. Cai and Mr. K. Qian in the Shanghai Installation Engineering Co. Ltd. for the discussion on the installation techniques. And also thank the colleges in SSRF for their assistance throughout the installation and the test.

REFERENCES

[1] Z.T. Zhao, "Construction of Shanghai Synchrotron Radiation Facility". These proceedings.

[2] C. Doose, S. Sharma; "Investigation of Passive Vibration Damping Methods for the Advanced Photon Source Storage Ring Girders", MEDSI02, APS, Chicago 2002, p 133-139.

[3] L. Zhang, "Vibration Damping Device Development for the ESRF Storage Ring Magnet-Girder Assembly", 22nd Advanced ICFA Beam Dynamics Workshop on Ground Motion in Future Accelerators, Stanford, November 2000.

MECHANICAL COUPLING BETWEEN THE LHC CRYOGENIC DISTRIBUTION LINE AND THE SHORT STRAIGHT SECTION HOUSING THE SUPERCONDUCTING QUADRUPOLE - THEORETICAL ANALYSIS AND EXPERIMENTAL VALIDATION

Subhajit Dutta#, Jishnu Dwivedi, Abhay Kumar, RS Sandha, HC Soni, SC Bapna and S Kotaiah
Raja Rammana Centre for Advanced Technology, Indore, India,
Alain Poncet , Blazej Skoczen and Cedric Garion, CERN, Geneva, Switzerland

Abstract

Liquid and Gaseous Helium are supplied to the superconducting magnets of the Large Hadron Collider (LHC), presently being assembled at CERN, by a cryogenic distribution line (QRL). The cryogenic module of the twin-quadrupole Short Straight Section (SSS) is supplied with these cryogens through a jumper connection linking the service module of the QRL and the SSS. The internal as well as external features of the jumper construction allow for relative displacements between the QRL and SSS with sufficient flexibility to reduce the reaction forces responsible for elastic deformations when the SSS is moved for alignment. The SSS is composed of a cold mass and of a vacuum vessel equipped with fiducials posted on the external vacuum vessel reinforcement rings allowing the precise alignment of the machine when the cryostat is finally closed. A deformation of the structure linking the cold mass and the external vacuum vessel resulting from reaction forces induced by relative displacements of the SSS and the QRL, if unpredictable, would result in an unacceptable misalignment of the quadrupole magnetic axis. A unified FE model was generated at RRCAT to study the elastic behavior of the SSS under the conditions of alignment. This model was validated using a 40 meter long dedicated test setup at CERN. Correlations in the matrix form were generated so that all displacements of the cold mass can be related to the corresponding movements done for alignment. This transfer function, linking the action on the SSS external alignment jacks and the position of the cold mass will be used to properly align the machine in operation.

INTRODUCTION

The SSS can be structurally divided into two main parts: the external cryostat and the internal cold mass of the magnet. The cryostat is an 8 mm thick cylindrical vessel made of carbon steel with a diameter of 1025 mm and a length of 6480 m. Large Sleeves having length of 840 mm and diameter of 1077 mm connect the cryostats of adjacent magnets. Two 'Glass Fibre Reinforced Epoxy (GFRE)' composite support posts, separated by 2.57 m, support the cold mass of the magnet. One of the composite supports is free to move in the longitudinal direction and is also free to move upwards. The other support is bolted to the cryostat. The three-ply magnet-to-magnet interconnection bellows carrying the superconducting bus bars are welded to the cold mass. The service module of the SSS is connected to the distribution line through a "jumper connection". The jumper connection consists of seven (for the Arc) helium carrying internal pipes enveloped by an external vacuum jacket. Each pipeline has one vertical and one horizontal metal hose. The vacuum jacket has one vertical double gimbal universal joint and one horizontal gimbal assembly.

#subhajit@cat.ernet.in

The Short Straight Section (SSS) of the Large Hadron Collider (LHC) may undergo relative displacements between the cold mass and the cryostat for the following two reasons:

- Manufacturing tolerances of in situ welding
- Global smoothing after pre-alignment
- Ground motion in a sector of the LHC tunnel

The forces responsible for such displacements stem from finite stiffness of interconnect bellows & metal hoses of the internal piping of the jumper connection and from relatively flexible composite supports of the cold mass. In addition, the vacuum jacket of the jumper connection and the large sleeves attached to both ends of SSS produce elastic deformations of the cryostat vessel. The cold mass also deforms when subjected to forces. The magnets after being transported to the tunnel are placed in their theoretical position. The welding of the interconnect bellows and the mounting of jumper and large sleeves are done at this stage. The interconnection bellows may be transversely deformed due to their deviation from the theoretical position in vertical or radial directions thus producing a relative displacement between the cold mass and vacuum vessel. Another reason for relative displacement is the fine alignment (global smoothening) done after initial cool down to 77 K, which may cause magnet movements up to ±2 mm. Some areas of the tunnel are prone to ground motion up to 1 mm per year. This displacement is the third reason for relative displacement between the cold mass and the cryostat. The knowledge of the absolute position of the cold mass for each jack movement in radial and vertical directions is essential. The maximum relative displacement for satisfactory machine operation is 0.1 mm.

FINITE ELEMENT MODEL

The major components that contribute to the analysis of the structural behaviour are: Cold Mass, Cryostat,

Jumper-connection, Large Sleeves and Magnet Interconnects.

The mapping of this SSS system behavior (in the simulation) is carried out by developing an application program. The application program has been written with-in ANSYS using the Ansys Programming Development Language (APDL). This application program includes the experimental hysteresis curves, operational condition specific data like hinge friction and Warm/Normal operating condition of magnet interconnect bellows, constraints of the jacks and free end conditions of the interconnections and large sleeves. The program uses an appropriate stiffness for each flexible members for a given load condition through its logical construction associative paradigm

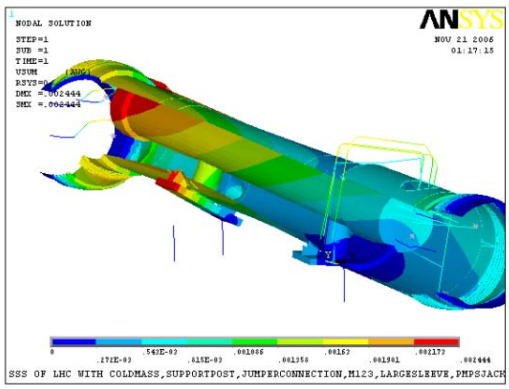

Figure 1: A view of the Short Straight Section Model

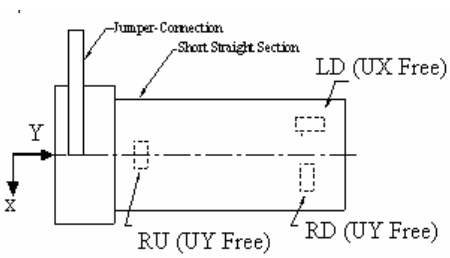

Figure 2: Kinematic arrangement of the jacks of SSS.

EXPERIMENT

An experiment was conducted to validate the unified FE model. . An experimental setup was erected with the help of prototype magnets, cryogenic distribution line and jumper connection,. At both ends of the SSS, the dipole magnets were assembled through the magnet-to-magnet interconnection bellows (M1, M2 and M3) and Large Sleeve. The other extremities of the dipoles was left free to satisfy the actual end condition of the SSS in the LHC ring.

Experiments were done in warm condition without creating vacuum. The erection of the huge experimental set up was planned and accomplished jointly by engineers from CERN, Geneva and RRCAT, Indore, India.

The first stage involved experiments with SSS along with jumper connection but without welding interconnection bellows and without clamping large sleeves at both ends of the SSS. All the measuring instruments and data acquisition system were mounted in this stage itself. The second stage involved experiments with SSS along with jumper connection and interconnection bellows welded at both ends but without clamping large sleeves. The third stage involved experiments with SSS with jumper connection, interconnection bellows welded & large sleeves clamped at both ends.

Figure 3:Experimental set up

FE MODEL TUNING WITH EXPERIMENTAL DATA AND TUNED STIFFNESS

The FE model of the Short Straight section is tuned with the experimented results conducted at CERN by CAT engineers. It was observed that the following stiffness were found to be most important for tuning the FE model:

- Stiffness of the cold mass,
- Stiffness of the column of the support post,
- Vertical and horizontal gimbals, and
- Stiffness of magnet-to-magnet interconnection bellows.

The fixed end conditions of the interconnection bellows were suppressed. Instead, the dipole extremities of the interconnection bellows were prescribed with the observed displacements. The final tuned parameters of the different components of the short straight section are listed in the table-1.

Table-1: Tuned values of important parameters.

Component	Tuned nominal stiffness
Cold mass	Equivalent Young's modulus = $0.61X10^{11}$ N/mm
Cold support post	Equivalent Young's modulus E=$0.24X10^{11}$ N/mm
Vacuum jacket of jumper	Angular stiffness: Bellows of Vertical Gimbal K1=17.8 N-m/grad K2=27.3 N-m/grad Bellow of Horizontal Gimbal K3=74.7N-m/grad
Interconnection bellows	Bending stiffness: 237 N/mm Axial stiffness: 183 N/mm
End conditions of Interconnects	Imposed movement of the dipole's dial readings.

RESULTS

The results are generated for the complete model of the Short Straight Sections in vacuum and normal operating condition. The elastic modulus of steel is increased by 10% for calculation at cold condition. The middle points between the centers of beam pipes on the adjoining faces of the cold mass are taken to demonstrate the result.

The final aim was to establish a relationship between given jack movements and relative displacements of cold mass with respect to cryostat as is given by;

$$\mathbf{d=K\,\Delta}$$

Where Δ, d and K are matrices of jack movements, cold mass absolute movements and proportionality constant respectively.

The first letter of the jack movement gives its jack's orientation, the second letter gives its location and the third letter gives the direction of movement.

The proportionality constants in radial and vertical directions are listed against the jack movement for all type of the movements in tables-2 and 3 for the two points. To get the absolute movement of the result points, the respective proportionality constant needs to be multiplied by the jack movement value.

Table2-Proportionality constant for X-direction (radial)

Jack movement	Location of the result node	Rigid part (K_{x1})	Flexible part (K_{x2})	*Total* $K_{x1}+Kx_2$
RUX	Upstream	1.272	-0.07	1.202
	Downstream	-0.62	0.14	-0.48
RUZ	Upstream	-0.0346	0.0172	-0.0174
	Downstream	0.0075	-0.0163	-0.0088
RDX	Upstream	-0.2113	-0.0112	-0.2225
	Downstream	1.4705	0.0001	1.4706
RDZ	*Upstream*	0.0000	-0.1722	-0.1722
	Downstream	0.0001	-0.5208	-0.5207
LDZ	*Upstream*	1.1558	-1.108	0.048
	Downstream	1.1557	-0.934	0.222

Table3: Proportionality constant for Z-direction (vertical)

Jack movement	Location of the result node	Rigid Part (Kz_1)	Flexible Part (Kz_2)	Total $K_{z1}+K_{z2}$
RUX	Upstream	0	-0.0027	-0.0027
	Downstream	0.00013	0.00212	0.00225
RUZ	Upstream	1.1799	0.0535	1.2334
	Downstream	-0.4954	-0.0002	-0.4956
RDX	Upstream	0.0001	0.0009	0.0010
	Downstream	-0.0004	-0.0015	-0.0019
RDZ	Upstream	1.2915	-1.3515	-0.0603
	Downstream	-0.6341	1.0108	0.3767
LDZ	Upstream	-0.1378	0.1066	-0.0312
	Downstream	0.8048	-0.616	0.1886

CONCLUSION

The experimental observations were sufficient to tune the unified FE Model of SSS. Although, the role of vacuum in the cryostat and the jumper have not been experimentally determined, the FE model has been tuned for warm and no vacuum condition and was extrapolated to predict coupling in cold and vacuum conditions.

The model is tuned within an accuracy of ±0.15 mm.

Table-4 summarises out the behaviour of elastic coupling in case of all five-jack movements.

Table-5 shows the displacements of both ends of the cold mass for 1mm movement of RU, LD and RD jack in radial and transverse direction.

Table-4.Behavior of the Elastic Coupling with respect to the rigid body displacements.

Jack move-ment	Location	Displacement in radial direction (x-direction)	Displacement in vertical direction (z-direction)
RuX	Upstream	REDUCTIVE	ADDITIVE
	Downstream	REDUCTIVE	ADDITIVE
RuZ	Upstream	REDUCTIVE	ADDITIVE
	Downstream	REDUCTIVE	ADDITIVE
RDX	Upstream	ADDITIVE	ADDITIVE
	Downstream	ADDITIVE	ADDITIVE
RDZ	Upstream	REDUCTIVE	REDUCTIVE
	Downstream	REDUCTIVE	REDUCTIVE
LDZ	Upstream	REDUCTIVE	REDUCTIVE
	Downstream	REDUCTIVE	REDUCTIVE

Table-5. The displacement of the beam pipe for 1mm movement of the jacks in transverse and radial direction.

Jack movement	Location	Displacement (in mm) in radial(x) and transverse(Z) direction	
		X	Z
1mm in RUX direction	Upstream	1.202	-0.003
	Downstream	0.048	0.002
1mm in RUZ direction	Upstream	0.017	1.23
	Downstream	0.009	-0.50
1mm in RDX direction	Upstream	-0.222	0.002
	Downstream	1.47	-0.060
1mm in RDZ direction	*Upstream*	-0.172	-0.06
	Downstream	-0.521	0.377
1mm in LDZ direction	Upstream	0.048	-0.031
	Downstream	0.222	0.189

REFERENCES

[1] S. Dutta, A. Kumar, J. Dwivedi and H.C. Soni, "Structural analysis for a unified model of SSS, service module, jumper connection and magnet interconnects of Large Hadron Collider of CERN", Internal Report, CAT Indore, India.

[2] C. Garion, B. Skoczen, "Forces in the LHC interconnections", CERN LHC-CRI Technical Note 2002-05, EDMS: 346011, May 2002.

[3] Structural Analysis of An Integrated Model of Short Straight Section, Service Module, Jumper Connection and Magnet Interconnects for the Large Hadron Collider; Subhajit Dutta#, Abhay Kumar, et al. EPAC-2004, Lucerne, Switzerland.

PRECISE SURVEY AND ALIGNMENT OF SYNCHROTRON RADIATION SOURCE INDUS-2

Vijendra Prasad#, R.K.Sahu, Dinesh Barapatre, M. Jagannath, K. P. Sharma & Gurnam Singh
Accelerator Programme, RRCAT, Indore-452013, India

Abstract

The 2.5GeV third generation synchrotron light source Indus-2 at RRCAT, which is in advance stage of commissioning, demanded a high precision of survey and alignment of all its components. In particular, we had to control the transverse and azimuthal positions of all quadrupoles and dipoles within a relative accuracy of 0.1 mm and overall circumference within 2.5 mm. This required a tight control over all the sources of errors starting from fiducializations, survey of networks, final alignment and smoothing. We have successfully accomplished this task by adopting the triangulation-trilateration technique of survey and alignment along with indigenously developed software for online survey data collection, least square adjustment of redundant measurements and error analysis. The accuracy of alignment was reflected from the successful circulation and storage of electron beam in the machine with a very small closed orbit distortion. This paper, in brief, presents the methodology adopted for survey and alignment and final accuracies achieved.

INTRODUCTION

Indus-2 with a circumference of 172.4743 meters consists of 16 dipole magnets, 72 quadrupoles, 32 sextupoles, 48 steering magnets, 56 beam position monitors and some special components like injection septums, kickers and RF cavities. The relative tolerances for alignment of magnets are given in table-1. These are the total error budgets in the placement of components including ambiguities in knowledge of the magnetic axis and errors in fixation of fiducials etc.

Table 1: Alignment tolerances.

Object name	δS mm	δX mm	δZ mm	θs mrad	θx mrad	θs mrad
Dipole	0.1	0.2	0.1	0.2	0.5	0.5
Quadrupole	0.1	0.1	0.1	0.2	0.5	0.5
Sextupole	0.5	0.1	0.1	0.2	1.0	1.0
Steering Magnet	1.0	1.0	1.0	2.0	2.0	2.0

Figure-1 shows the general layout of accelerators at RRCAT. The already existing Booster Synchrotron acts as injector for Indus-2. Hence before start of construction of building for Indus-2, it was necessary to mark the centre of building and fix the central monument with respect to Booster synchrotron.

#vijen@cat.ernet.in

During building construction the embedded plates for mounting girder jacks, embedded pipes for synchrotron beam lines, primary control network monuments etc. were fixed at their designed positions/orientations and elevations with in a fair accuracy. Since Indus-2 is housed in a narrow over-ground tunnel of 5.2meter width, the visibility of machine is limited to a very small zone. So we decided to adopt a network approach of alignment for controlling the overall shape and size of the machine and at the same time to align all components within specified tolerances [1]. For this we established three control networks, namely Primary Control Network, Secondary Control Network and Elevation Control Network.

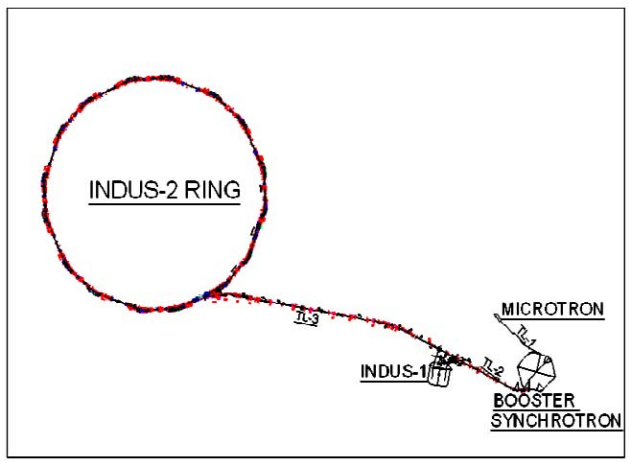

Figure 1: Layout of Accelerators at RRCAT.

SURVEY CONTROL NETWORKS AND FIDUCIALIZATION

Primary Control Network

The primary control networks are in the form of 400 mm diameter concrete pillars (monuments) with forced centering sockets over them for mounting survey instruments and optical targets [Figure 2]. Out of 11 monuments, the locations of 4, that lie in the tunnel, were decided in such a way that the whole machine is divided into four approximately equal parts. Holes have been provided in the inner wall of the tunnel, to facilitate direct measurements of distances and directions between them. The primary control network defines the coordinate system of Indus-2 and acts as a reference for the secondary control network. The coordinates of these monuments have been determined by least square adjustment of repetitive redundant distance and direction

measurements, using a Distinvar™ with calibrated invar wires and a Leica TDA5005™.

Secondary Control Network

The secondary control network is in the form of 42 uniformly distributed brackets fixed with the inner and outer wall of the tunnel [Figure 2]. These brackets are equipped with conical bases for mounting survey instruments and optical targets. Their locations were decided after considering the parameters like focusing (magnification) distances of theodolites, visibility of components, uniform positional strength (error ellipses) in all directions etc. The coordinates of these network points have been determined by repetitive distance and direction measurements [2] using a calibrated TDA5005™ and a TM5100™.

Elevation Control Network

The elevation control network is also in the form of wall brackets (24 no.) fixed with inner and outer wall of the tunnel. They are also equipped with conical bases for mounting optical targets. Elevation of each bracket has been determined by their repetitive survey using a Leica N-3™ optical level.

Fiducialization

All quadrupoles and sextupoles are fitted with two fiducial posts and one level plate. These fiducial posts were fixed during their magnetic characterization on harmonic bench using laser and quadrant diode. However for controlling the position along beam, reference with respect to mechanical mid section was established by using Axyz® system. All dipoles are fitted with four fiducial posts and one level plate. The magnetic measurements of dipole magnets were carried out by hall probe manipulating CNC machine and during this the fiducial posts were welded and their relationship with respect to magnetic axis was established by using Leica industrial measuring Axyz® system. For alignment in the tunnel, the coordinates of all these fiducials were transformed into Indus-2 machine coordinate system, based on the final sorted locations of dipoles and multipoles and axial as well as radial positions.

INSTRUMENTS AND SOFTWARES

Following measuring instruments are being used for survey and alignment of Indus-2:

- Angle measurement: Precision digital theodolites Leica TDA5005, TDM5000 and TM5100.
- Distance measurement: Distinvar® with calibrated invar wire, Laser Interferometer with self-aligning reflector, TDA5005 and TDM5000.
- Levelling and elevation: Wild N3 Optical Level.
- Tilt: Electronic Inclinometers Leica Nivel-20, Wyler precision spirit levels.
- Softwares: SNAAPS[3] (in-house developed) for survey data collection, their least square adjustment, on-line coordinate measurements, alignment error analysis, curve fittings, coordinate transformations, stake out, resection etc, Axyz™ for online coordinate measurements.

In order to ensure the accuracy of distance measurements by TDA5005, they were calibrated by using laser interferometer. Calibration files having the coefficients of Fourier fitting were prepared and used for online correcting the distances measured on site.

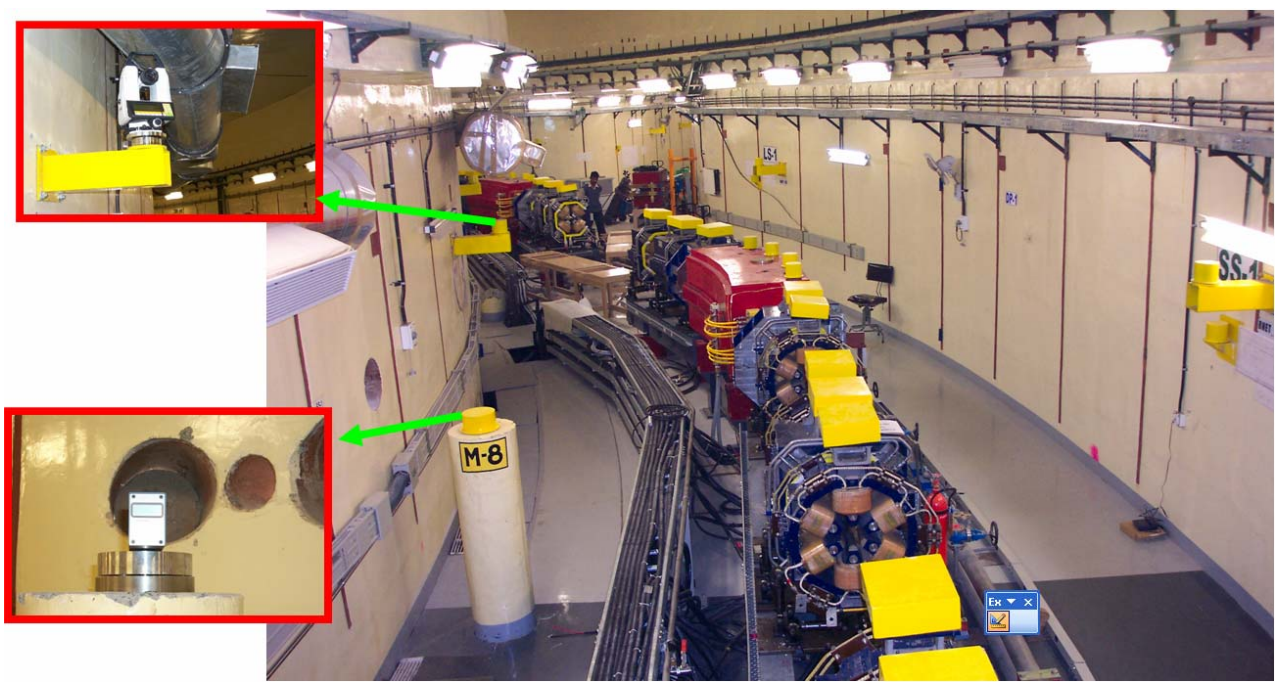

Figure 2: Indus-2 tunnel showing primary control network monument, secondary control network brackets and magnet fiducials protected by yellow coverings.

INSTALLATION AND PRE-ALIGNMENT

In order to have the full range of movement of girder jacks during final alignment, all jacks were fixed at their designed locations within ±5mm. Subsequently the straight sections and dipole girders were installed and aligned. Each straight section girder is supported on three precision movement jacks. The dipoles were first to install on their girders. All dipoles were individually aligned by taking reference from nearby network points. After completion of alignment of all dipoles individually, they were surveyed together to determine the relative positions and overall shape. Based on the results of this survey, 5 out of 16 dipoles were readjusted to obtain better relative alignment and smooth shape of the machine. After this all dipoles along with secondary control network points were resurveyed. The absolute error ellipses of this survey are shown in figure 3. The results of this survey were within acceptable limit and no further refinement in positions of dipoles was attempted. The Over the straight section girder, quardrupoles and sextupoles are supported on six strut support system for their individual alignment. The upper half of all the quadrupoles and sextupoles were required to open for assembly of vacuum chamber. Before removing the upper half, these magnets were pre-aligned within ±1mm to facilitate the assembly of vacuum chambers. The Beam position monitors (BPM) and beam position indicators (BPI) are part of vacuum envelope and required a precise alignment. So before connecting to adjacent vacuum chambers, they were aligned and fixed.

PRECISE ALIGNMENT

Precise alignment of multipoles started after completing the assembly of vacuum chambers and re-assembly of upper halves of multipoles. All quadrupoles and sextupoles on individual girder were first precisely aligned within the specified tolerances by using N-3 optical level, precision tilt level and two theodolites together, oriented in machine coordinate system by using the coordinates of nearby 5-6 secondary network points. For elevation control reference were taken from nearby elevation control network points. This helped us in not only controlling the relative alignment of multipoles on a girder within the specified tolerance but also the absolute position of girder in the machine. The same procedure was followed for all 16 straight sections. After this a full survey of the machine was carried out and approximately 1866 directions and 766 distances were measured by using motorized theodolite TDA5005. This data was processed by least square adjustment. During adjustment the coordinates of two primary control points, namely M1 and M3 which are in the tunnel, were assumed fixed. After adjustment the largest size error ellipse was found to have major axis of the order of 0.2 mm. The most probable coordinates obtained from this adjustment were used to analyze the overall shape of machine, orientation of straight sections with respect to each other and dipoles etc. Based on the result of this survey three girders were realigned and again a complete survey run was performed. The results of this survey were quite satisfactory and the calculated circumference was deviating by only an amount of 0.4 mm from designed. Therefore we did not need any further refinement in the alignment condition.

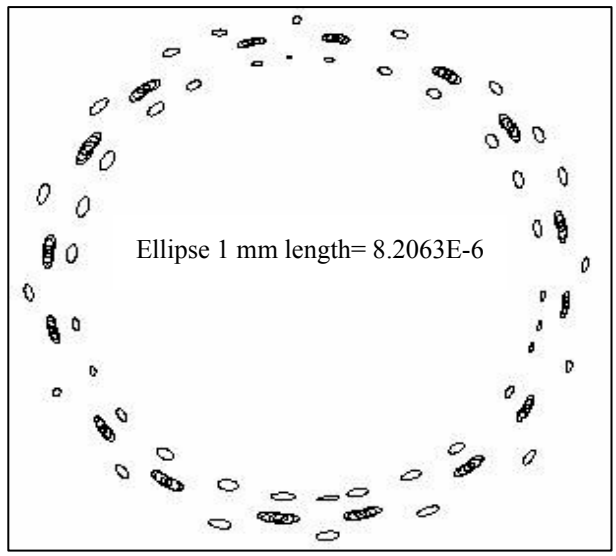

Figure 3: Absolute Error Ellipses (Dipoles & Secondary Control Network points).

CONCLUSION

The commissioning trials of the machine started with the above conditions of alignment. After a few days of injection trials it was possible to circulate and accelerate the beam. The successful circulation and acceleration of beam verifies that there is no gross error in alignment. Afterward closed orbit distortions were also measured and they were closely agreeing with the designed values. Further refinement in alignment will be based on the operating condition of the machine.

ACKNOWLEDGEMENT

We are highly thankful to Mr. S. Kotaiah, Project Manager, Indus-2 and Dr. V. C. Sahni, Director RRCAT, for their continuous support and coordination of alignment activities along with other activities during critical period of installation.

REFERENCES

[1] R.K.Sahu, Vijendra Prasad et. al, Methodology for Survey & Alignment of Indus-2, INPAC2003.
[2] Vijendra Prasad, R.K.Sahu et al., Survey, data adjustment and accuracy computation of Indus-2 alignment control networks, INPAC2005.
[3] Vijendra Prasad, Survey Network Adjustment Programs for adjustment and analysis of alignment data, INPAC2003.

PROTOTYPE BEAM DUMP FOR 10 kW LINAC

R.S. Sandha#, Jishnu Dwivedi, S.C. Bapna, V.C. Petwal, H.C. Soni
Raja Ramanna Centre for Advanced Technology, Indore (INDIA).

Abstract

A 10 MeV, 10 kW electron beam accelerator (Linac) has been developed at RRCAT, Indore for developing applications in the area of radiation processing of agricultural products and medical sterilization. This paper presents the functional requirements, design and manufacture of beam dump for this LINAC. Activation of beam dump, conversion of electron energy into primary bremsstrahlung and radiation damage are important parameters for selection of material. Other parameters considered are thermal conductivity, corrosion in ozone environment, manufacturability and mechanical strength. Thermal, hydraulic, structural and engineering design was done. FEM based analysis was performed for calculating temperature rise and stresses. The maximum temperature in beam dump is estimated to be about 325 K. A prototype beam dump was manufactured and installed and it is being tested in actual operating conditions.

INTRODUCTION

Beam dump is installed in front of scan horn after the product as shown in Figure 1. The pulsed electron beam obtained from Linac has a diameter of 30 mm. It is scanned in scan horn mounted at the end of beam transport line. The scanning system comprises of a scanning electromagnet that provides 600 mm wide radiation field at the product surface in its path. The electron beam will be dumped on beam dump in the absence of product. The scanned electron beam field has approximate size of 100 mm x 900 mm at the location of beam dump. Considering this, size of beam dump is kept as 120 mm by 1000 mm. The beam dump shall stop most of the electrons so that the electrons transmitted in nearby structure are minimised. Maximum power incident on beam dump will be 14 kW. Specifications of Linac are given in Table 1 [1].

Table 1: Specifications of Linac

Nominal energy of accelerated electrons	MeV	10
Maximum beam power	kW	14
Pulse current of accelerated electrons in nominal mode	A	0.33
Duration of beam current pulse	μs	14
Pulse repetition frequency	1/s	300

DESIGN FEATURES

Activation of beam dump and conversion of electron energy into primary bremsstrahlung are important parameters for selection of material. Radioactivity may be induced in beam dump irradiated by electron beam or bremsstrahlung beam due to γ-n reaction. The activity induced in beam dump depends on energy and power of incident beam. The threshold energy for γ-n reaction in copper, stainless steel and aluminium is 9.9 MeV, 10.57 MeV and 13 MeV respectively. Copper and stainless steel are susceptible to activation at 10 MeV energy while aluminium is insusceptible [2]. Keeping this in view, aluminium was selected. Other parameters are thermal conductivity, corrosion in ozone environment, manufacturability and mechanical strength. The thermal fatigue behaviour of the material is also an important consideration, which will be taken care of in design of regular beam dump. Practical range of 10 MeV electron beam in aluminium is 20 mm, hence beam dump thickness (including water) was kept as 30 mm.

#rssandha@cat.ernet.in

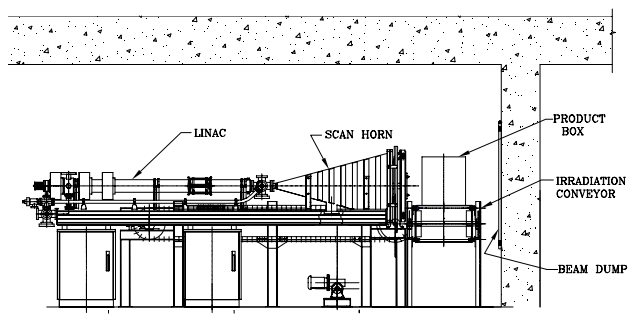

Figure 1: Location of beam dump

THERMAL AND STRUCTURAL ANALYSIS

Dittus-Boelter correlation [3] has been used for calculation of average heat transfer coefficient in the turbulent region over the cooling channels:

$$h = 0.023\ (k/d)\ (Re)^{0.8}\ (Pr)^{0.3}$$

Where h is average heat transfer coefficient, k is thermal conductivity of fluid, d is hydraulic diameter and Re is Reynolds number, Pr is Prandtl number.

Reference temperature was taken as 303K. Flow rate of 30 Litre/minute results in turbulent flow with water velocity of 3 m/s. Reynolds number of 40,000 and heat transfer coefficient of 8000 $W/m^2.K$ is achieved with this flow. The pressure drop in entire circuit is about 0.1 MPa. The beam dump cooling circuit can take a maximum pressure of 0.5 MPa, hence a separate coolant supply with low circuit pressure will be provided for beam dump. The normal cooling circuit in the building operates at a pressure of 1 MPa.

Finite element code ANSYS [4] was used for analysis. Second order quadrilateral element Plane77 were used to model the structure and obtain temperature rise in beam dump. Sequential coupled field analyses were performed to calculate thermal displacements and stresses.

Following properties were used for aluminium [5].

Thermal conductivity	= 231 W/m.K
Coefficient of thermal expansion	= 23×10^{-6}/K
Young's modulus	= 69 GPa
Yield strength	= 103 MPa

Assuming uniform distribution of power on beam dump due to scanning, the top surface of beam dump is exposed to heat flux of 11.6 W/cm^2. The heat is removed by water-cooling. Temperature contour due to power deposited is shown in Figure 2. The maximum temperature is estimated to be about 325 K. For the heat load of 14 kW and flow rate of 30 lpm, a 9K water temperature rise and aluminium-to-water temperature difference of 8 K are expected. Displacement contour and stress intensity contour due to temperature rise and water pressure are shown in Figure 3 and Figure 4. Maximum displacement of 0.2 mm and general stress intensity of 60 MPa is observed in beam dump due to thermal distortion and water pressure.

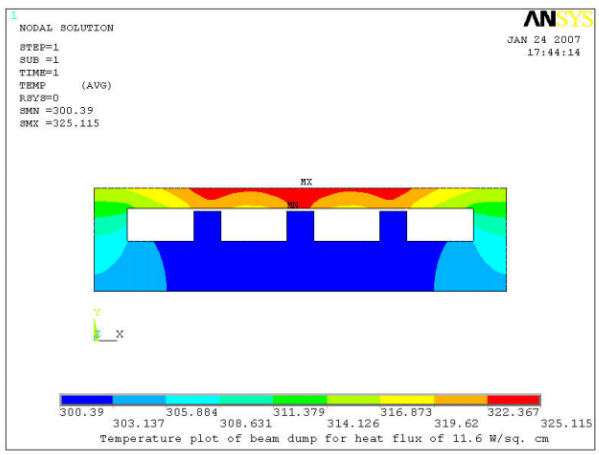

Figure 2: Temperature contour of beam dump

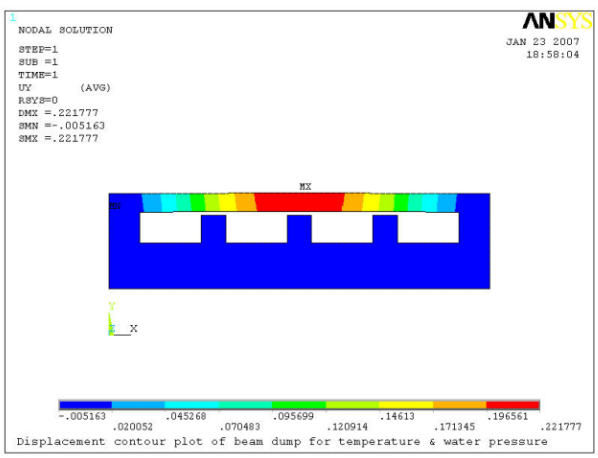

Figure 3: Displacement contour of beam dump due to thermal distortion and water pressure

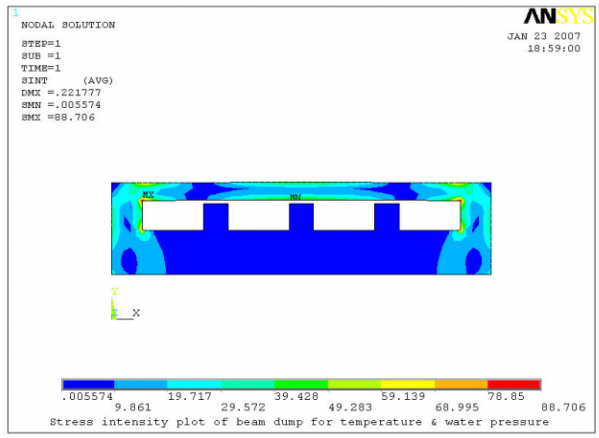

Figure 4: Stress intensity contour of beam dump due to thermal distortion and water pressure

FABRICATION

Beam dump consists of an aluminium block in which cooling channels are machined and a top plate that is welded to the block to create closed path for water flow. The machined components and assembled beam dump are shown in Figure 5 and Figure 6.

The material used in the fabrication of beam dump is commercial aluminium alloy as per ASTM B209. Filler alloy 4043 was used for Welding. Hydro test was carried out to ensure leak tightness of cooling circuit. The cooling circuit was pressurized at 0.5 MPa and kept at that pressure for 15 minutes. No leakage was observed. Care has been taken to select materials that are not far away in galvanic series. Stainless steel connectors are used to connect beam dump to braided hose. Polymers are avoided in beam dump assembly since the beam dump lies in region of high radiation dose. Radiation at location of beam dump is 1.1×10^8 kGy/year in electron mode [6]. Ozone level at beam dump location is ~1 ppm during operation. Beam dump is electrically isolated and is used to measure the beam current deposited on it. Mounting features are provided on beam dump to mount it on wall.

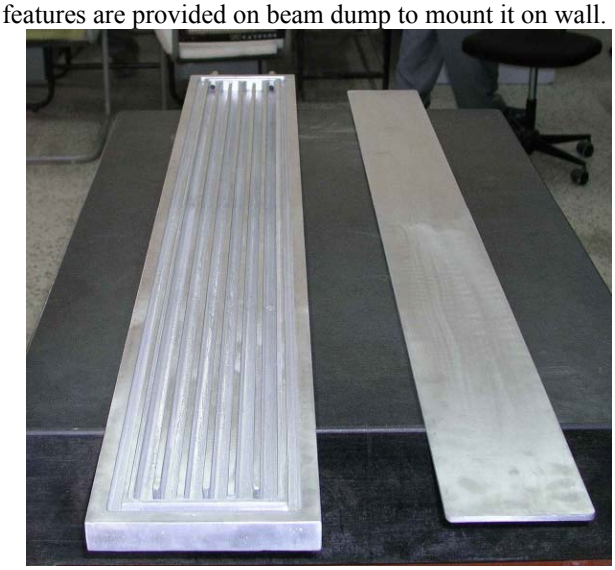

Figure 5: Components of beam dump before joining

Figure 6: Beam dump assembled in front of Linac

CONCLUSION

The beam dump has been designed, manufactured and installed in IMA Lab and is put to regular use. It is planned to develop another beam dump in near future for actual plant use, based on this experience of design, manufacturing and use.

ACKNOWLEDGMENTS

We are thankful to Mr. Abhay Kumar for useful discussions on thermal aspects of beam dump. We express our thanks to Mr. KC Arya and Mrs. TD Bindu for help in preparing drawings.

REFERENCES

[1] E.308.481 RE Linear Accelerator Structure Technical Description and Operator Manual
[2] Radiological safety aspects of electron Linear accelerators, IAEA report No. 188
[3] F.P. Incropera, D.P. Dewitt, “Fundamentals of Heat and Mass Transfer” V Ed. John Wiley And Sons Inc.
[4] Finite Element Code “ANSYS” version 8.1
[5] ASM specialty handbook: Aluminum and Aluminum alloys: Edited by J R Davis; ASM International Hand book Committee
[6] Shielding design calculation for Agricultural Radiation processing facility, Sept. 2003

BREMSSTRAHLUNG CONVERTER FOR HIGH POWER EB RADIATION PROCESSING FACILITY

V.C.Petwal#, S.C.Bapna, R.S.Sandha, Swarna Kotaiah, K.V.Subbaiah[1]
IMA Section RRCAT, Indore. [1]SRI, IGCAR. Kalpakkam, Tamilnadu

Abstract

A radiation processing facility based on 10 kW Linac is being set up at RRCAT for radiation processing of food products and sterilization of medical items. The facility is planned to operate in electron (10 MeV) and X-ray (5 & 7.5 MeV) mode. The required X-rays will be generated by bombarding an optimized target with 5 or 7.5 MeV electron beam. The composite target is made of Ta, water & SS. Monte Carlo simulation with MCNP has been performed to optimize the design of the target for maximizing the X-ray output. Characteristics of the emerging X-ray field e.g. photon energy spectrum, angular distribution, radial dose and depth dose distribution in unit density material have been simulated & compared for 5 & 7.5 MeV. Our simulation results show that for optimized design, the fraction of the energy transmitted and useful for radiation processing at 5 & 7.5 MeV is 9.3% & 14.2 % respectively. The most probable energy of the photons is 0.3 MeV for both 5 and 7.5 MeV electrons and the average energy is 0.84 MeV & 1.24 MeV respectively. Large fraction of electron beam power is dissipated as heat in the targets. Necessary data has been generated to carry out thermal design.

INTRODUCTION

Four types of ionizing energy have been approved by regulatory authorities for radiation processing of food products. These are gamma rays from Co-60 and Cs-137, electrons with energy up to 10 MeV and X-rays with energies up to 5 MeV. FDA has recently approved use of X-rays generated by 7.5 MeV electron beam for food processing (*Federal Register 2004).* The selection of the energy source for a particular application is usually based on practical considerations like product shape, size, density, average dose requirement, dose uniformity ratio, processing rate and cost. Treatment with direct electron beam provides the highest processing rate and the lowest unit cost but electron has relatively short range. X-rays have higher penetration quality and hence permits the treatment of dense objects in large packages.

TARGET MATERIAL

X-rays are produced when energetic electrons strike any target material. The intensity and efficiency of X-ray conversion increase with the energy of incident electron and the atomic no of the target material. In order to maximize the X-ray output, Ta, W, Au are the suitable choice for the target material. Tungsten has high brittleness, hence difficult for machining and fabrication, while Au is not cost effective, so both are not considered for target material. Tantalum is the suitable choice as a compromise between photon yield, residual radioactivity, physical properties, mechanical properties and fabrication simplicity for commercial environment. At 5 MeV no activation will arise from the Ta target as the threshold energy level for two common isotopes of tantalum (Ta-180 and Ta –181) are 6.6 and 7.6 MeV respectively. When operated at 7.5 MeV i.e. above the threshold for γ-n reaction in target material, two radio nuclide Ta^{180} and Ta^{182} are formed respectively by (γ-n) and (n-γ) reaction on naturally abundant Ta^{181}. The former has half-life of 8.1 h mostly β emitter, and the latter has half-life of 114 days emitting γ of 1.2 MeV. Also, the order of saturation dose rate (due to the induced activity) measured immediately after the shut down of the accelerator is reported about 1 mGy/h for Ta target at 7.5 MeV (*J. Mckeeown et.al, 1998*). Extensive study have been performed to investigate the induced activity in the irradiated product and concluded that the amount of induced activity created by 7.5 MeV X-rays in food product is negligible small. The IAEA report *(IAEA-TECDOC-1287*) says that the possible radiation exposure from induced radioactivity to human, consuming 40 kg/yr of beef irradiated by 7.5 MeV beam on Ta target for a dose of 30 kGy (a dose more than 6 times the maximum permitted dose level of 4.5 kGy) is 300 times less than the yearly dose due to the natural activity present in the food. Keeping these points in view Ta is suitable & acceptable for X-ray converter at 7.5 MeV. In order to make cooling channel SS is suitable as the threshold energy for γ-n reaction in Fe, Ni the major constuient of SS is more than 10 MeV.

TARGET GEOMETRY

To obtain the basic data for the study, multi-layered composite target geometry is considered (see Figure 1). The shape of target for simplicity is cylindrical (radius 5 cm) and is made of three layers, tantalum, water, and stainless steel. Tantalum is used to generate the bremsstrahlung radiation from incident electron beam, while water is used to remove the heat deposited on the tantalum. The SS is used to make the water channel and stop the unwanted electron contamination coming out with the bremsstrahlung radiation. The thickness of tantalum is varied in the range 0-20 mm while the thickness of water channel and SS; each, is taken judiciously 2 mm (for both 5 MeV and 7.5 MeV). A water phantom of size 40 cm x 40 cm x 40 cm, placed 10 cm away from target, is simulate to study the dose profile in unit density material.

#vikash@cat.ernet.in

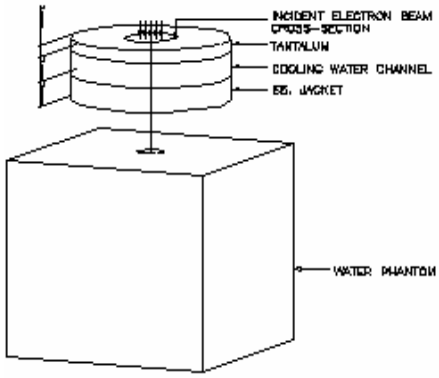

Figure 1. Target Geometry

METHOD OF CALCULATION

Three-dimensional photon and electron transport calculation is performed with MCNP. The MCNP uses continuous energy nuclear and atomic data libraries. The data in the photon/electron cross-section tables allow MCNP to account for coherent and in-coherent scattering, photoelectric absorption with the possibility of fluorescent emission and pair production.

The incident electron beam is taken to have a circular cross-section of diameter 25-mm ($\pm 2\sigma$) and is considered to fall normally on the target surface. The distribution of electrons in side the beam is taken Gaussian with mean at r = 0 and $\sigma = 6.25$. For electron sampling from 25-mm dia surface, the total surface is divided into 7 circular regions of radius 2 mm, 4 mm, 6 mm, 8 mm, 10 mm, 12 mm, and 12.5 mm. The sampling from different region is done to meet the requirement of Gaussian distribution. The probability of electron sampling from first region (i.e. encircled by 2mm-radius circle) is taken 0.251. For the successive annular region sampling probability is taken as 0.226, 0.185, 0.136, 0.091, 0.054, 0.029 respectively. The initial number of electron histories is taken 10^6, which reduces the statistical errors involved in the calculation below 2%. Contribution from electrons down to 10 keV and photons down to 20 keV has been included.

RESULTS AND DISCUSSION

Figure 2 shows the variation of the transmitted X-ray output with the Ta thickness. The optimum thickness of Ta for maximum bremsstrahlung yield at 5 MeV and 7.5 MeV is 0.9 and 1.4 mm respectively. As the thickness of Ta is increased beyond the optimum thickness the transmitted intensity decreases due to self-absorption in the target material. At 7.5 MeV the X-ray yield increases 50.3 % that of the yield achieved at 5 MeV. Useful data required for thermal analysis and throughput calculation are given in Table1 & Table 2. The cooling water and SS channel helps in reducing the electron contamination in the X-ray field by absorbing the low energy electrons (10% of incident energy) leaving the Ta target. The cooling water and the SS channel also absorb 5-8 % of the photon yield hence needs careful design consideration.

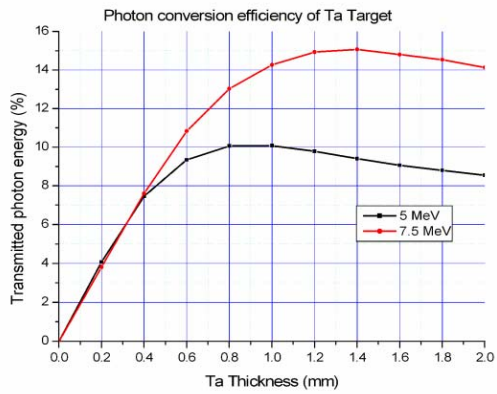

Figure 2. Transmitted X ray output as function of Tantalum thickness

Table 1. Data for 5 MeV electrons

Ta thick. (mm)	% of incident energy transmitted through various mediums in the form of photons				% of energy deposited in the Ta sheet
	Ta	Water	SS	10 cm air	
0.8	10.12	9.92	9.23	8.60	60.74
0.9	10.14	9.92	9.29	8.60	65.26
1.0	10.02	9.76	9.17	8.54	68.61
1.2	9.76	9.55	8.86	8.31	72.44
1.4	9.38	9.18	8.55	8.05	74.02

Table 2. Data for 7.5 MeV electrons

Ta thickness (mm)	% of incident energy transmitted through various mediums in the form of photons				% of energy deposited in the Ta sheet
	Ta	Water	SS	10 cm air	
0.8	13.52	13.40	13.72	12.82	40.12
1.0	14.69	14.49	14.16	13.26	50.66
1.2	15.20	14.94	14.17	13.30	58.92
1.4	15.24	14.97	14.18	13.33	64.92
1.6	15.02	14.74	13.88	13.10	68.98
1.4*	15.24	15.08	13.07	12.38	65.05

The conversion efficiency calculated above with MCNP agrees within 5% with the calculation done with the Integrated TIGER Series of Coupled Electron/Photon Monte Carlo Transport Code [*J. Meissner et al*].

The photon energy spectra transmitted from the target is shown in figure 3. The total number of photon and proportion of high-energy photons increases with electron energy. The most probable energy for both spectrums is at 0.3 MeV and the average photon energy ($\Sigma\, n_i\, E_i/n_i$) for 5, 7.5 MeV is 0.84 and 1.14 MeV respectively. The angular dose distribution of the photon beam is shown in figure 4, which is forward peaked in the direction of electron beam and this effect becomes more pronounced as energy

increase. FWHM for 5 and 7.5 MeV beam are 20° &13° respectively.

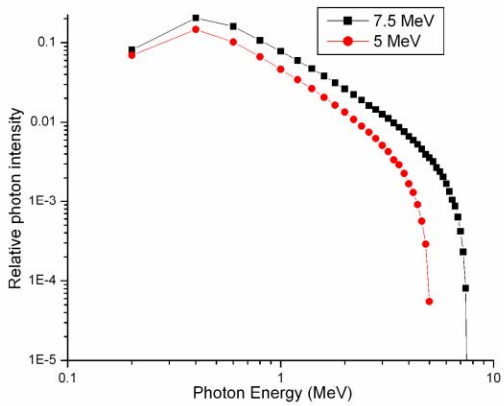

Figure 3. Spectrum of Photons Transmitted from optimised Ta Target

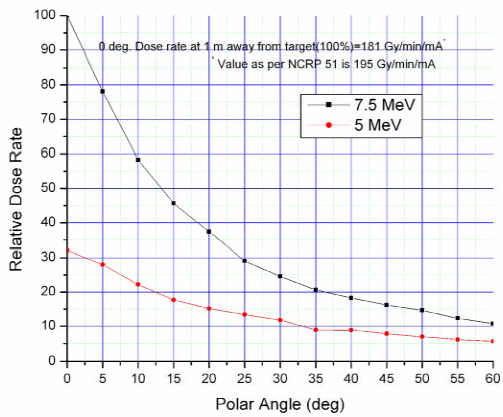

Figure 4. Angular dose distribution for 5 and 7.5 MeV X-rays

To calculate the radial dose distribution and depth dose distribution in product a water phantom of 30 cm x 30 cm x 30cm is simulated at 10 cm away from the target. Respective dose distributions are shown in figure 5 & 6. The depth dose fall rapidly in the initial part of the curve, which is due to the narrow beam geometry and soft energy x-ray components present in the beam. To improve the depth dose characteristics there is need to introduce some filter in the path of X-ray beam, which absorb the soft energy X-ray components and allow high energy component without much attenuation.

CONCLUSION

Tantalum is suitable target material to generate X-rays for radiation processing of food products. Optimum thickness of the Tantalum for 5 and 7.5 MeV beam is 1 mm and 1.4 mm corresponding to which the X-ray conversion efficiency is 10.1% and 15.2 % respectively. Analysis of photon spectrum shows that the most probable energy for both 5 and 7.5 MeV beam is 0.3 MeV and the average energy is 0.84 MeV and 1.24 MeV respectively. Due to the presence of low energy components surface dose to the products becomes severe, which cause poor dose uniformity ratio within the product. Hence to improve dose uniformity there is need to introduce a suitable filter, which absorb the low energy components from the X-ray field with least attenuation of high-energy components.

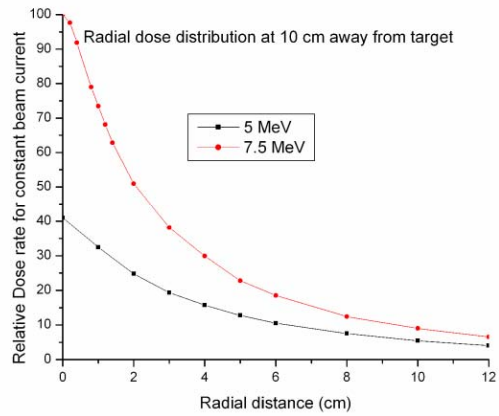

Figure 5. Radial dose distribution of 5 and 7.5 MeV X-rays

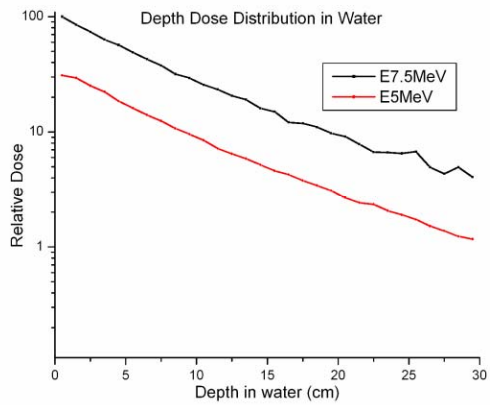

Figure 6. Depth dose distribution of 5 and 7.5 MeV X-rays in water

REFERENCES

[1] Photon energy limit for food irradiation: a feasibility study- J. Mckeown et al Radiation Physics & Chemistry 53 1998 55-61.
[2] IAEA-TECDOC-1287
[3] Federal Register Vol. 69 No.246 December 2004.
[4] X-ray treatment at 5 MeV & above- J.Meissner et al. Radiation Physics and Chemistry 57 2000. 647 – 651).
[5] MCNP A General Purpose Monte Carlo N-Particle Transport Code. Los Alamos National Laboratory. Briesmeister JF.

STUDIES OF METALLIC ION BEAMS USING ECRIS

P. Kumar, G. Rodrigues, P.S. Lakshmy and D. Kanjilal
Inter University Accelerator Centre, New Delhi 110067, INDIA

Abstract

Low energy (from a few keV to a few MeV) metallic ion beams have wide applications in various research fields especially in materials science, atomic and molecular physics. Several metallic ion beams have been developed successfully using all permanent magnet 10 GHz electron cyclotron resonance (ECR) ion source based low energy ion beam facility (LEIBF) at Inter University Accelerator Centre (IUAC), New Delhi. For the development of these metallic ion beams, different methods e.g. oven, sputtering, insertion and metal ions using volatile compounds (MIVOC) have been utilized. The charge state distribution (CSD) studies of two metallic ion beams are presented.

INTRODUCTION

To get the operational experience of ECR ion source [1] on high voltage platform and to provide the low energy ion beams from gaseous and solid species, the LEIBF [2] has been set up at IUAC. The most important feature of the facility (LEIBF) is that the ECR ion source and all its peripheral components including electronics (power supplies and RF power amplifier) and vacuum systems are on a high voltage (300 kV) platform. The various parameters of the source are controlled through fiber optics communications at 300 kV isolation. The regular operation of this facility provided us experience and expertise to design and build the world's first High Temperature Super-conducting ECR Ion Source (PKDELIS) [3] for use on a high voltage (400 kV) platform. The ion source has been tuned to get optimum intensities of metallic ion beams which are being used for research in emerging fields like nano science and spintronics. The high intensities of low energy metallic ion beams are suitable to engineer the optical, electrical and structural properties of materials via ion implantation and ion irradiation.

METALLIC ECR PLASMA PRODUCTION

The ions, inside the source, are produced by the impact of resonant electrons and are confined axially and radially by using permanent magnets (NdFeB). The desired vapors of materials are introduced into the source for ionization using micro-oven, sputtering system and MIVOC [4] method. A micro-oven, compact in size, is used for the heating of metallic elements in a temperature range of 100^0 - 1200^0 C. The heating is done using a 36 V, 4 A power supply. For micro-oven, a typical voltage of 14 volt is required in order to achieve a oven temperature of about 1000^0 C. A small cylindrical crucible (ceramic) filled with a few mg quantity of desired metallic element in powder or rod form is placed into the micro-oven. The micro-oven along with crucible, placed on a mounting system is injected into the plasma chamber from the injection side of the source. In order to have a continuous operation of the source to complete the experiments, the operational temperature is kept well below the melting point of the materials.

In the process of plasma sputtering, the sputtering target (high melting point > 1000^0C) in the form of a disc, wire or pellet is exposed to a background plasma. In regular operation of the source, the background plasma is developed using noble or inert gases. The ions lost from the plasma strike the sputtering target and the vapors of desired metallic species are released for the process of ionization. In MIVOC method, the vapors of volatile compounds are allowed to diffuse into the plasma chamber using a pressure control valve. The metal atoms in the structure of volatile compounds are released in the plasma. The ionization of these metal atoms then takes place by the impact of resonant electron.

ION EXTRACTION AND ANALYSIS

The extraction system consists of an extraction aperture (at high voltage (30 kV max.)) of 3 mm in diameter, puller electrode El1 in conical shape (at ground potential), a focus electrode El2 (at high voltage (15 kV max.)) and another electrode El3 at ground potential. The puller electrode, focus electrode and the last grounded electrode form two gaps (decelerating and accelerating gap) for the extraction and strong focusing of the ion beams. A rough sketch of the structure (plasma chamber and extraction) is shown in figure 1.

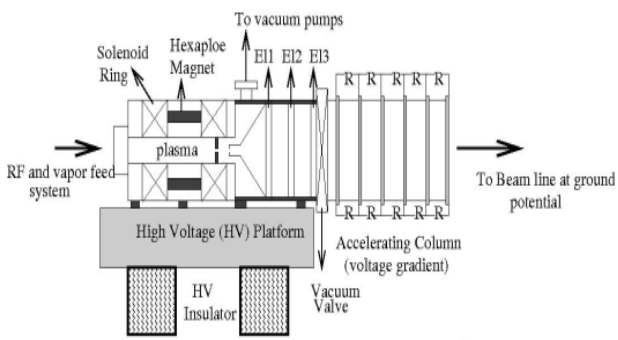

Figure 1: Schematic of source and extraction system

The ions extracted from the source can have maximum energy of 30 x q (charge state of ion extracted from source) keV with respect to high voltage platform voltage. A accelerating column placed between platform (at high voltage, max. 300 kV) and beam line (at ground potential) results in a further energy gain of 300 q keV (maximum). The beam coming out of Einzel lens is focused by voltage gradient along the accelerating column. The ions are analyzed in mass and energy using a high resolution dipole magnet having two bending ports ($90^0$and 15^0). The maximum beam rigidity (ME/q^2) of the dipole magnet for the 90^0 bend is 34 MeV amu. The analyzed beam currents/intensities are measured using a high power Faraday cup.

SOURCE OPERATION WITH METALLIC IONS AND RESULTS

Using LEIBF, various metallic ion beams e.g. Au, Ni, Fe, Sn, Eu, Zn and Cu of different energies suitable for experiments have been extracted and developed.

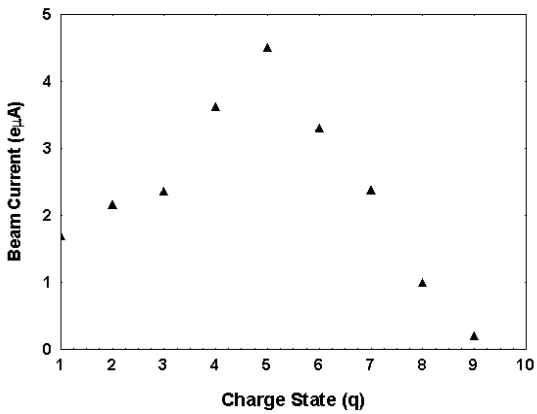

Figure 2: CSD of Ni optimized on +2 charge state

$^{58}Ni^{+2}$ and $^{56}Fe^{+}$ ions for total potential difference (E/q) of 100 kV and $^{63}Cu^{+8}$ for E/q = 160 kV, were produced using their volatile compounds ($(C_5H_5)_2Ni$, $(C_5H_5)_2Fe$ and $(C_5H_5)_2CuP(C_2H_5)_3$) respectively. The operating source pressure, in the case of Ni and Fe, was ~ $5x\ 10^{-6}$ mbar. Input microwave power of about 20 W was set to stabilize and populate the ECR plasma with low charge state ions. For $^{63}Cu^{+8}$ beam, the source was operated at $3x10^{-7}$ mbar. The ECR plasma has been produced using ~ 80 W of power. A typical CSD of Ni is shown in figure 2. The highest ion current/intensity of 4.7 μA was observed for q = 5.

^{120}Sn and ^{66}Zn ion beams were developed using the micro-oven. High purity Sn powder and Zn foil were kept in micro-oven to get the desired metallic vapors for the production of ECR plasma. In the case of Sn, the input microwave power was 47 W. The source was operated at a pressure of 6.5 x 10^{-7} mbar. The total potential difference (E/q), for the acceleration, was set at 100 kV. The oven temperature was kept ~ 2000C. The melting point of Sn powder is 231^0C. The CSD of Sn is optimized for m/q =9.23 (+13 charge state) and is shown in figure 3.

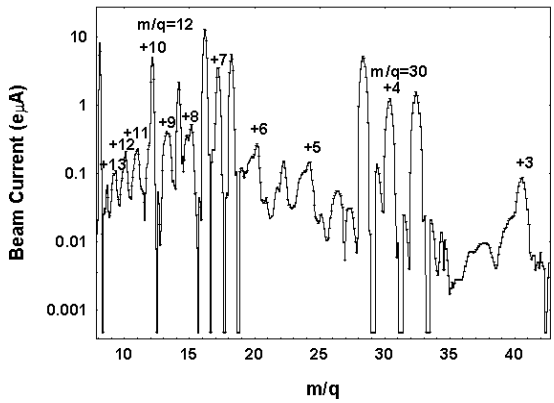

Figure 3: CSD of Sn optimized for m/q = 9.23

Although ^{64}Zn has the highest natural abundance, $^{66}Zn^{+2}$ ion beam was chosen to avoid the contamination with oxygen as $^{64}Zn^{+2}$ and molecular oxygen (O_2^+) have same m/q. The beams having same m/q can not be resolved using dipole magnet.

The sputtering process has been utilized to develop ion beams of ^{151}Eu and ^{153}Eu ion beams. In order to start the sputtering process, the argon gas has been used to generate the background plasma. ^{151}Eu and ^{153}Eu have natural abundance of 47.18% and 52.19% respectively. The E/q = 93.79 was set in this case and ions having charge states +4 are extracted to deliver 375 keV ion beam for experiment. With operating source pressure of $7x10^{-7}$ mbar and microwave power of 88 W, the source was tuned to extract the ion beam. The highest intensity/current of 8 μA was observed for q = 5 (mass 153). The optimized distance between sputtered target and background plasma was 7 mm.

DISCUSSION

The energy of ion beams can be increased by populating the ECR plasma with ions in high charge states. Lower pressure and the higher microwave power are essential to tune the source for such requirements. In fact with increasing q (beyond the most populated charge state), the intensity of ion beam decreases. For implantation, high intensity ion beams are needed. These beams are delivered by operating the source at high pressure and lower power levels of microwave. Using sputtering and micro-oven, ion beams of higher energy (higher q) are available at moderate intensities. The source tuning for better intensities over the full range of q can be achieved by using MIVOC system. The stability and intensity are two major issues which make metallic ion beams difficult to develop and optimize.

CONCLUSION

Various metallic ion beams are developed for experiments especially for implantation using LEIBF. The ECR ion source operated on high voltage platform is a unique feature of LEIBF and provides a choice of selection of energy in a wide range. The source performance is excellent for gaseous ion species. The ion beams from gases e.g. Ar, O_2, N_2, He, Ne, Xe, SO_2, CO_2, Kr, H_2 are regularly delivered for experiments. From last few years, various stable metallic ion beams have been developed for scheduled experiments by a large number of researchers.

REFERENCES

[1] R. Geller, Electron Cyclotron Resonance Ion Sources and ECR Plasmas, IOP, Bristol, (1996).

[2] D. Kanjilal, T. Madhu, G.O. Rodrigues, U.K.Rao, C.P. Safvan and A Roy, Ind. J. of Pure and Appl. Phys. 25 (2001) 39.

[3] C. Bieth, S. Kantas, P. Sortais, D. Kanjilal, G. Rodrigues, S. Milward, S. Harrison and R Mc Mohan, NIMB 498-503 (2005) 235.

[4] J. Arje, H. Koivisto and M. Nurmia, Proceedings of 11th Int. Workshop on ECRIS, Groningen, ed. A.G.Drentje, p. 27 (1993).

AIR TEMPERATURE ANALYSIS AND CONTROL IMPROVEMENT FOR THE INJECTION AREA AT TLS

Jui-Chi Chang#, Zong-Da Tsai, Yung-Hui Liu,
National Synchrotron Radiation Research Center, Hsinchu, Taiwan

Abstract

This paper presents the air temperature analysis and control improvement for the injection area at the Taiwan Light Source (TLS). The injector consists of a 50-MeV LINAC and a 1.5-GeV booster synchrotron. Because of insufficient cooling capacity, the air temperature was too high (> 27 °C) and the temporal temperature variation was more than 2 °C in one day. The air relative humidity was often higher than 60%. The problem of insufficient cooling capacity became more serious after the top-up mode operation. To cope with the above-mentioned thermal problem, the cooling capacity was increased and the PID parameter of the temperature control was also optimized. Totally 27 temperature sensors were distributed in this area to on-line record the air temperature history. The temperature control was improved to suppress temporal temperature variation within ± 0.1°C. The air humidity was also much improved than ever.

INTRODUCTION

We had studied the utility effects on beam quality [1] [2] to verify those effects on the stability of the electron beam orbit at TLS. According to those studies, thermal effect is one of the most critical mechanical factors affecting the beam stability. Accordingly, we had conducted a series of air conditioning (A/C) system improvements of the storage ring and applied the numerical simulation to analyze the flow field and temperature distribution. Those A/C improvements and analyses had been respectively conducted on the experimental hall [3], the storage ring tunnel [4] and the core area of technical equipment [5]. However, the cooling capacity of the injection area was insufficient to keep air temperature low and steady enough three years ago. This thermal problem would become worse after the project of the top-up injection mode was launched because waste heat generated by the top-up injection mode is steadier but much higher than that generated by the decay mode.

Figure 1 shows the 3D schematic drawing of the injection area, which includes the booster area and the transport line area. There are a 50-MeV LINAC and a 1.5-GeV booster synchrotron installed in the booster area. The booster synchrotron is mainly consisted of magnet system, rf system, and vacuum chambers. The transport line is not shown in this figure. Blue ducts and green ducts shown in Figure 1 are supply air ducts and return air ducts, respectively. Air exits and air exhausts are respectively distributed on the ceiling and side walls of the booster area. All air exits and air exhausts are distributed in the ceiling on the transport area.

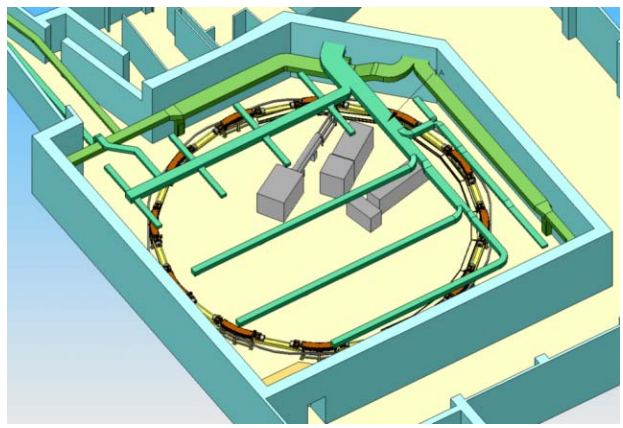

Figure 1: Schematic drawing of the injection area.

COOLING CAPACITY ENHANCEMENT FOR THE TOP-UP INJECTION MODE

As abovementioned, the cooling capacity of the injection area became insufficient while its A/C system was still kept as its original design of 13 years ago. The injection system had been upgraded from its original 1.3-GeV to 1.5-GeV and added some new air-cooled equipment in past decade. The air temperature was usually higher than 27 °C and the temporal temperature variation was more than 2 °C in one day even the valve of the cold water was fully opened. The air relative humidity was also often higher than 60% three year ago.

A new AHU was installed to replace the old one in 2004 accordingly. Specifications of both the old and new AHUs are list in the Table 1. The cooling capacity of the new AHU is about double that of the old one, as list in the table.

Table 1: Specifications of the old and new AHUs for the injection area.

AHU Specification			Old	New
Air Flow (CFM)			16900	30000
Fan	Total Static Pressure (in-WG)		3.5	3.5
	RPM		1485	914
	Motor (HP)		20	30
Cooling Coil		Enter air temp(°C DB)	24.8	24.8
		Enter air temp(°C WB)	18.3	18.3
		Face Area (FT^2)	40.4	71.9
		Energy (RT)	40	80

#jcchang@nsrrc.org.tw

EXPERIMENT MEASUREMENTS AND DATA ACQUISITION

To on-line control and monitor the air temperature of the injection area, we install total 27 temperature sensors of PT100 in this area, where 22 and 5 sensors are respectively distributed in the booster and the transport line areas, as shown in Figure 2. Those temperature sensors are also numbered in Figure 2.

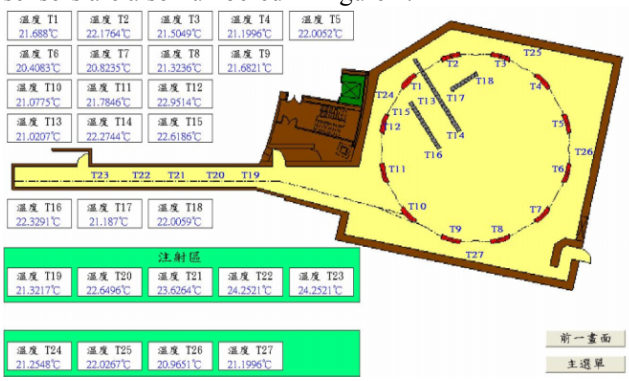

Figure 2: Injection area layout and temperature sensors distribution.

We had also developed a utility archive system to on line monitor thousands of utility parameters. Although each of the utility subsystem, such as the electrical power system, the cooling water system, the A/C system etc. is equipped with its own monitoring and control systems, the utility archive system still successfully integrates all those subsystems. The utility archive system is an integrated software written by the LabView language. This archive system consists of a remote viewer level, a data service level, a data processing level, a control level and a device level. The remote viewer level is opened for all in house and outside users. The archive viewer in the remote viewer level is a software of viewing for the whole archive system. Figure 1 is the network of the utility archive system for the A/C system.

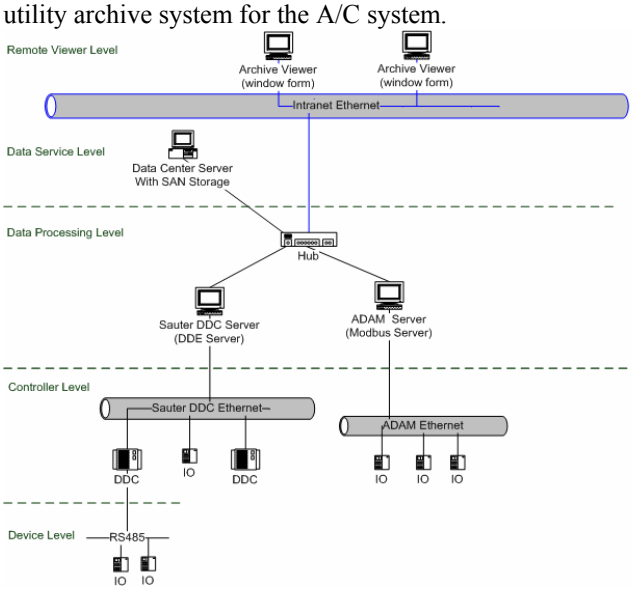

Figure 3: Network of the utility archive system for the A/C system.

TEMPERATURE AND HUMIDITY CONTROL SCHEME

Figure 4 demonstrates the control system of the AHU for the injection area. As shown in the figure, return air from the injection area is mixed with outdoor air then flows through a cold water heat exchanger, which is controlled by a cold water control valve to control the mixed air temperature to 13 °C, where the relative humidity of the air is near saturation and the air temperature is accordingly close to the dew point temperature. Cooled air then flows through a hot water heat exchanger, which is controlled by a hot water control valve to control the mixed air temperature to 17 °C. The relative humidity of the return air from the injection area is controlled within 45% ± 2%.

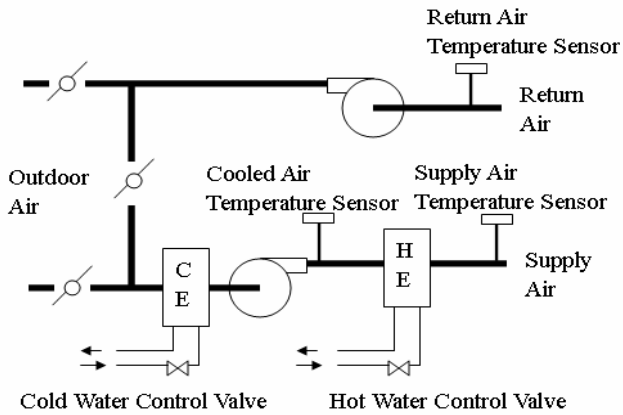

Figure 4: Control system of the AHU.

The basic structure of the controller of the cold water or hot water control valve includes an input variable, a set point variable and PID controller variables. The controller may also be defined as either direct or reverse acting.

The control histories of the new AHU are shown in Figure 5. The dew point temperature, supply air temperature and the return air temperature were stably controlled at 13 °C, 17 °C and 22 °C, respectively. The relative humidity was control at 44%. The openings of the cold water valve and hot water valve were operated at 28% ± 2% and 40% ± 10%, respectively.

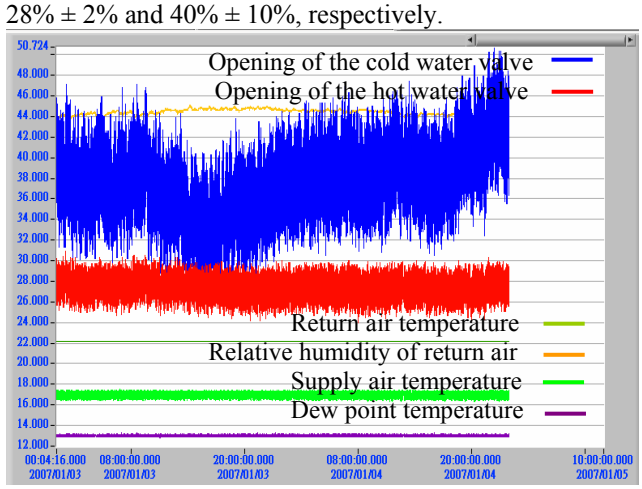

Figure 5: Control histories of the new AHU.

RESULTS AND DISCUSSION

Figure 6 shows the control histories, which were recorded in 2003, of the old AHU. As shown in the figure, the supply air temperature and the return air temperature were controlled at 13 °C, and 20 °C, respectively. However, the relative humidity was about 65% even the openings of the cold water valve was almost kept 100%. This phenomenon reveals insufficient of the cooling capacity of the old AHU.

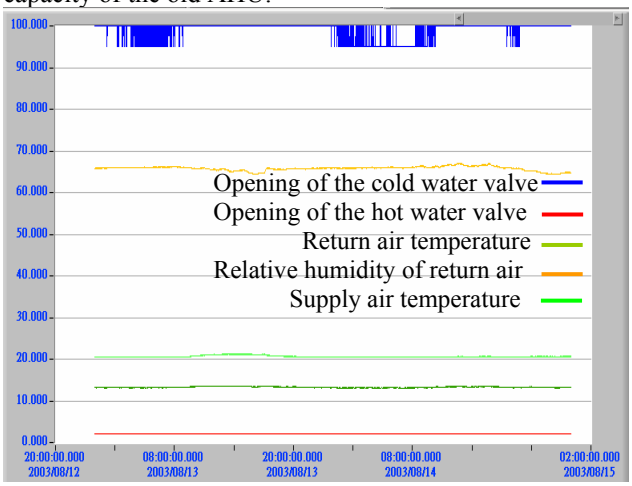

Figure 6: Control histories of the old AHU.

Figure 7 shows eight temperature histories of the injection area. These temperature histories were respectively recorded by sensors 4, 6, 8, 12, 14, 17, 19 and 21, whose locations are shown in Figure 2. Sensors 4, 6, 8 and 12 are respectively located on four sides of the booster synchrotron ring. Sensors 14 and 17 are located on the linac and sensors 19 and 21 are located on the transport line.

Data shown in Figures 5 and 7 were recorded in the same two day, i.e., Jan. 3rd to 5th, 2007. In those two-day temperature histories, almost all temperature variations along time were controlled within ± 0.1°C. Some of those temperature histories even varied less than ± 0.05°C. Those differences of temperature variations were basically influenced by local cooling loads, flow fields and noise to temperature sensors.

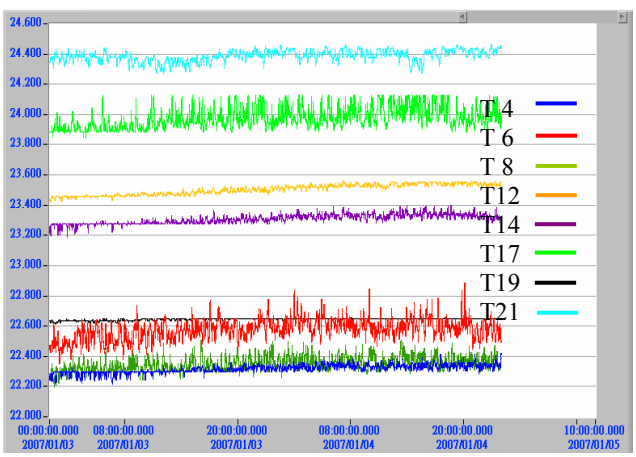

Figure 7: Temperature histories of the injection area.

CONCLUSION AND FUTURE WORKS

We have improved the A/C system by increasing about double cooling capacity of the AHU for the injection area, which includes the booster area and the transport line area. There were 22 and 5 temperature sensors respectively installed in the booster area and the transport line area to online monitor temperature variation. The dew point temperature, the supply air temperature and the return air temperature of the new AHU were stably controlled at 13 °C, 17 °C and 22 °C, respectively. The relative humidity of return air was also control at 45% ± 2%. The temporal temperature variation in the whole injection area is globally controlled within ± 0.1°C more than one day's operation.

However, the spatial temperature differences in the injection area are still more than 2 °C. Local temporal temperature variation is also effected by local cooling loads, flow fields and noise to temperature sensors. Therefore, to improve the local temperature variation, we will perform the numerical simulation to analysis temperature and flow fields in near future.

ACKNOWLEDGEMENT

Authors would like to thank colleagues in the utility group of NSRRC for their assistance.

REFERENCES

[1] J.R. Chen, H.M. Cheng, Z.D. Tsai, C.R. Chen, T.F. Lin, G.Y. Hsiung, and Y.S. Hong, "The Correlation between the Beam Orbit stability and the Utilities at SRRC", Proc. of 6th European Particle and Accelerator Conference EPAC98, Stockholm, Sweden, June 22-26, 1998.

[2] J.R. Chen, D.J. Wang, Z.D. Tsai, C.K. Kian, S.C. Ho, and J.C. Chang, "Mechanical Stability Studies at the Taiwan Light Source", 2nd Int'l Workshop on Mechanical Engineering Design of Synchrotron Radiation Equipment and Instrumentation (MEDSI02), APS, U.S.A., Sep 5-6, 2002.

[3] J.C. Chang, M. T. Ke, C.Y. Liu, and J.R. Chen, "Air Temperature Analysis and Control Improvement for the Large-Scale Experimental Hall" 2004 Asian Particle and Accelerator Conference (APAC), March 22-26, 2004, Gyeongiu, Korea.

[4] J.C. Chang, C.Y. Liu, and J.R. Chen, "Air Temperature Control Improvement for the Storage Ring Tunnel" 2003 Particle and Accelerator Conference (PAC), May 12-16, 2003, Portland, USA.

[5] J.C. Chang, M.T. Ke, Z. D. Tsai, and J. R. Chen, "Air Temperature Analysis and Control Improvement for the Technical Zone at TLS" 2006 European Particle and Accelerator Conference (EPAC), June 26-30, 2006, Edinburgh, Scotland, pp. 1825-1827.

VIBRATION EVALUATION FOR UTILITY INSTRUMENTS AND WATER PIPING SYSTEM IN TLS*

Yung-Hui Liu#, Duan-Jen Wang, Jui-Chi Chang, June-Rong Chen,
NSRRC, 101Hsin-Ann Road, Hsinchu Science Park, Hsinchu
30076, Taiwan.

Abstract

The purpose of this paper is to estimate the vibration source from water systems and the piping system in utility system. Analysis the vibration path from piping system is the first step. Then, propose the feasible proposals to eliminate the vibration source and reduce vibration propagation. The construction standards for water systems will be established before design. The test is based on TLS operating systems. Besides, the distance and path between utility building and storage ring is another factor for vibration propagation. Elimination the vibration source and propagation path in TLS will be the next step. The experimental results will be the guidline of TPS construction in the future.

INTRODUCTION

In order to design the new synchrotron light source in NSRRC, the vibration issue is more restrict. Vibration source from utility systems is one factor of instability. In 2004, ANL[1] studied the mechanical vibration control systems and the specifications for all rotational facilities. TLS has also investigated on water induced vibration[2] and ground vibration. In order to find out the vibration propagation from the utility systems, the dynamic signal analyzer also need to be studied.

LAYOUT AND PIPING SYSTEM IN UTILITY

The utility systems in 1st utility building (UT-1) are shown in Fig.1. There are air conditioning systems and de-ionized water (DIW) systems in the 1st utility building. The DIW systems and air conditioning systems are the two major cooling systems in the TLS. The DIW systems consist of three subsystems, the copper system, the aluminium system and the RF system.

The copper DIW system supplies DIW to magnets and magnet power supplies. The aluminium and RF DIW systems supply DIW to vacuum chambers and to RF transmitters and cavities, respectively. In each DIW loop, there are two heat exchangers in order to adjust the DIW flow temperature. After the heat exchangers, the DIW flow to the storage ring by the water pumps with variable frequency drive. The DIW piping is cross through the trench to the core area and was divided into 12 loops. Each DIW loop flows to half of the section in order to cool the half section. The inlet and outlet DIW were divided into subsystems here.

*Work supported by National Synchrotron Radiation Research Center
#iris@nerrc.org.tw

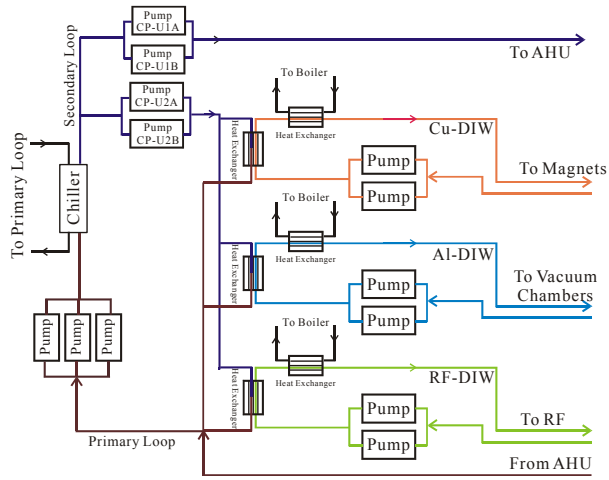

Figure 1: Layout of UT-1.

THE EXPERIMENTAL SETUP

The vibrations were measured by the portable spectrum analyzer COMMTEST VB2000 and piezoelectric type accelerometer IMI 603M56. The spectrum range is from 4 Hz to 200 Hz, and the resolution is 800 lines. The experiments were average for four times and recorded in displacement or accelerometer by the spectrum analyzer.

THE CHILLER VIBRATIONS

The chilled water is produced by three centrifugal chillers (YORK) in UT-1. Each capacity is 320 RT. The vibration on the top side of the chiller is much higher than the base of the chiller, which the significant frequency is ~60 Hz produced by the compressor. The cooling water side of chiller is connected to the cooling tower and the power for these 4 motors is 75 HP with fixed 1800 rpm. On the base of chillers, the rubber pad is located between the chiller and the ground. The experimental results show that the vibrations from 4 Hz to 200 Hz reduce for 2.1 to 4.5 times by using the rubber pad depends on the vibration amplitude.

VIBRATION PROPAGATION FOR DIW SYSTEMS

There are three DIW subsystems in UT-1, the copper system, the aluminium system and the RF system. Because of the DIW is delivered direct to the magnets and vacuum chambers, the vibration propagation is very important to the beam stability. The vibration propagation for the Al and Cu DIW systems are tested as follow.

Motors with Variable and Fixed Frequency Drive

The pumps with variable frequency drive (VF pump) are useful for auto adjust water pressure and stable the outlet and inlet water pressure. Its operation condition is depended on the local loading. The operation frequency for chilled water pump is about 43 Hz during testing. The DIW systems also use the VF water pump. The redundant pumps supply the DIW to the storage ring and avoid any accident from the pump incidents. It also helps to reduce the vibration effectively. The operation frequency for Al DIW pump is about 48.3 Hz. And the operation frequency for Cu DIW pump is about 50 Hz.

The pumps used in utility system were fixed frequency drive (FF pump) for several years ago. The fixed outlet water pressure was adopted by the by-pass system. Therefore the inlet water pressure and the local loading could not be adjusted. And the FF pump always operate in full energy output, it also produce larger vibration sources.

Vibration Propagation for Al DIW System

The measurement points for the vibration propagation for the Al DIW system is shown in Fig. 2. The first experimental point is located in Al DIW pump (P1), next located in the outlet pipe of the pump (P2). The DIW piping is connected through the trench (P3) and to the intersection point inside the storage ring R3-1 (P4). There are three quadrupoles, R3-Q1D (P5), R3-Q2F (P6), R3-Q3D (P7), in the first part of section3.

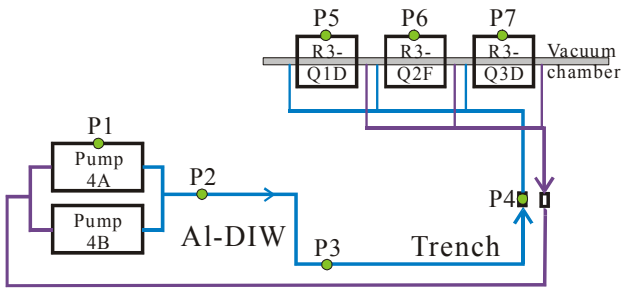

Figure 2: Layout of Al DIW System.

The experiments were recorded in acceleration from 4 Hz to 200 Hz with 0.25 Hz resolution and average for four times. Fig. 3 shows the vibration of P1 in vertical direction.

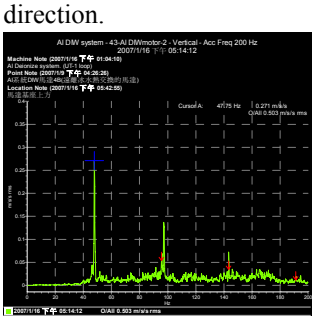

Figure 3a: Vibration of VFD motors (~48 Hz)

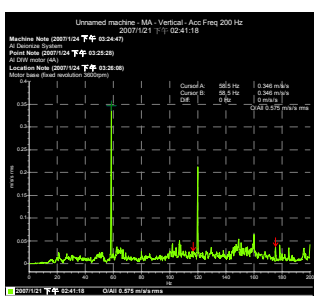

Figure 3b: Vibration of FFD motor (~58.5 Hz)

The frequency for VF pump (4B) is 47.75 Hz shown in Fig. 3a. The VF system used two 25HP (max. output) motors to maintain redundant, so the output power for each pump is less than 25HP. The frequency for FF pump (4A) is 58.5 Hz shown in Fig. 3b. The FF system used only one 25HP (max. output) motor with ~3600rpm, so the output power is almost 25HP. One 25HP power motor with maximum frequency drive is enough for outlet water pressure. The experimental results shows that the vibration produced by the VF pump is 271.32 mm/s^2(47.75 Hz), and he vibration produced by the FF pump is 346.16 mm/s^2(58.5 Hz).

The experimental results for vibration propagation are shown in Table 1. The left hand side of Table is vibration propagation for the VF pumps. The right hand side of Table is the vibration propagation for FF pump.

Table 1: Experimental results for Al DIW Vibration.

	Location	VF pump 4B Freq.(Hz) /a(mm/s^2)	VF pump 4A Freq.(Hz) /a(mm/s^2)	FF pump 4A Freq.(Hz) /a(mm/s^2)
P1	Base of pump	47.75 /271.32	48.25 /120.20	58.5 /346.16
P2	outlet side	47.75 /224.43	48.5 /80.05	58.5 /366.08
P3	Pipe in trench	47.75 /79.80		58.5 /104.20
P4	Intersect ion	47.75 /2.16		58.25 /10.90
P5	R3-Q1D	47.75/0.31		58.25/0.80
P6	R3-Q2F	47.75/0.68		58.5/1.04
P7	R3-Q3D	47.75/0.34		58.5/0.40

The two VF pumps operate in different frequencies, one is 57.75 Hz (pump 4B) and the other is 58.5 Hz (pump 4A). The vibration for the outlet water side is 224.43 mm/s^2 for 4B and 80.05 mm/s^2 for 4A. The spectrum is obvious in 47.75 Hz from P3 to P7, because of lower vibration source propagates less vibration. Compare with FF pump in 4A, the vibration produced by one pump with max. power is larger than two pumps for VF system. The vibration reduces 2.8 times from P3 to P2 for VF pumps and 3.5 times from P3 to P2 for FF pumps. There are bellows between P3 and P4, so the vibrations reduce 36.9 times and 9.6 times for VF and FF pump. From P4 to P5, the vibrations reduce 7.0 times and 9.6 times for VF and FF pump. The distance between P2 and P3 is ~50 m and the distance between P4 and P5 is ~ 10 m. Although P4 to P5 is shorter than P2 to P3, vibration decay is still larger. Because of the piping material is rubber from P4 to P5 and the piping material is stainless steel from P4 to P5. The vibrations decay through non-metal material. The experimental results show that the bellows and rubber piping material could reduce vibration propagation effectively.

Effects and Difference Between FFD and VFD Motors in Vibration Propagation

The advantages for the VFD motors are stable for the outlet water pressure, raise up the pressure while one of the pump failure, auto-adjust the local loading to maintain

the lower inlet water pressure for the pump itself. The most important reason is the lower generated vibration and propagation. Although there are two pumps operating for VF system and only one pump operating for FF system, the vibration produced in VF system is still less than FF system.

Vibration Propagation for the Cu DIW System

The measurement locations for the vibration propagation for the Cu DIW system are shown in Fig. 4. The first experimental point is from Al DIW pump (P1), next point is the outlet pipe of the pump (P2). The DIW piping is connected through the trench (P3) and to the intersection point inside the storage ring R3-1 (P4). There are three quadrupoles, R3-Q1D (P5 & P8), R3-Q2F (P6 & P9), R3-Q3D (P7 & P10), in the first part of section3. The Cu DIW piping was sent direct to the magnet to cool down the magnet temperature. The test points are applied to the piping inlet and top side of magnet.

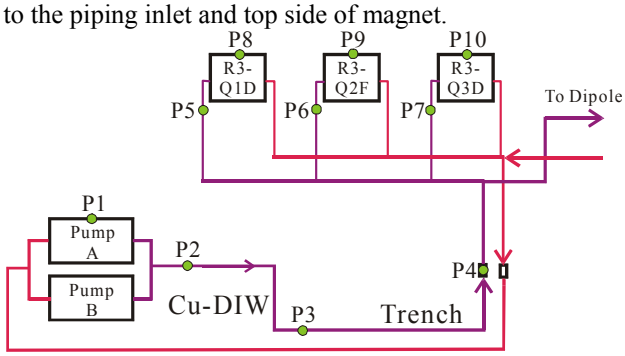

Figure 4: Layout of Cu DIW System.

The experimental results are shown in Table 2. The Cu DIW system used two 75HP motors to maintain redundant for fixing outlet water pressure. The frequencies of VF pumps are 50 Hz. Compare with the experimental results with the Al DIW system, the vibrations produced by Cu DIW pump (75HP) is less than Al DIW pump (25HP). This result indicates that the vibration for the pump is very important. Every motor should be calibrated before assembling in NSRRC, and the vibration specifications must be set. There is multiple frequency 100 Hz vibration around the pumps, and the vibration amplitude is even larger than 50 Hz (max. 197.76 mm/s^2). Vibrations about 100 Hz is vanished close to trench, so higher frequency vibration can not propagate for long distance.

Table 2: Cu DIW System. (Vibration peak @ 50 Hz)

	Cu DIW Location	Accel. (mm/s^2)
P1	Base of pump	107.18
P2	outlet pipe	91.45
P3	Pipe in trench	17.68
P4	Intersection point	1.26
P5	R3-Q1D (Piping)	1.78
P6	R3-Q2F (Piping)	3.72
P7	R3-Q3D (Piping)	3.10
P8	R3-Q1D (Magnet)	0.12
P9	R3-Q2F (Magnet)	0.52
P10	R3-Q3D (Magnet)	0.52

The vibrations for the water piping inlet point to the quadrupole are larger than magnet itself. This means that the vibration decay by different material and its intersection. There are some interest phenomena that the Al DIW frequency (~48 Hz) appeared in the piping system in the Cu system. It perhaps caused by the same piping girder and magnet girder.

VIBRATION FOR CHILLED WATER SYSTEMS

The vibration propagation for the chilled water system was also tested here. The frequency around 29.5 Hz was obvious existed everywhere in NSRRC before because almost all of the motors used FF pumps with 1800rpm. Now, the chilled water systems also changed to VF pump. In order to compare 29.5 Hz vibration propagation, the following experiments show the vibration propagation in piping for AHU loop and DIW loop in FF condition, shown in Table 3.

Table 3: Chilled Water System. (@ 29.5 Hz)

Location a(mm/s^2)	FF pump AHU loop	FF pump DIW loop
P1	36.88	154.12
P2	48.73	140.48
P3(Cu)	4.85	4.78
P3(Al)	7.39	4.54

Both water pumps to AHU and to DIW produce 29.5 Hz vibration in FF operation. The chilled water loop has no direct relation with DIW loop, so vibrations in P3 for Cu and Al system were not obvious. The vibration source from UT-2 and other pumps is not included.

CONCLUSIONS AND DISCUSSIONS

The advantages for the VF pumps are stable for the outlet water pressure and the lower vibration produced. The experimental results identify the vibration propagation from the utility system and give some clues about the modification for utility facilities and piping methods.

The vibrations (29.5 Hz) were larger during FFD operation. The vibration propagation almost vanished in the trench. The 29.5 Hz vibrations could be possibly produced by the local pumps or other systems.

Higher frequency vibrations can not propagate for long distance. The different frequency of vibrations could propagate by the same piping girder, magnet girder or ground.

REFERENCES

[1] W Zander, “Mechanical Vibration Controls”, sec. 15071, 2004, Department of Energy, Argonne National Lab., Argonne, Illinois.

[2] D. J. Wang, H. C. Ho, Jeremy Wang and Z. D. Tsai, “Water Induced Vibration in the NSRRC”, PAC’05, 2005, Knoxville, Tennessee, USA.

SF_6 GAS HANDLING SYSTEM FOR 3 MeV, 30 kW ELECTRON BEAM ACCELERATOR AT EBC, KHARGHAR, NAVI MUMBAI

Shyam Rao Ghodke, Rajesh Barnwal, Mahendra Kumar, D. Jayaprakash, Barje Supriya, Radhelal Mishra, Nagesh Lawangare, K. Nanu, G. Puthran, Vinod Sopan Veer, K. K. Abdullah, Kailash Chandra Mittal, Devi Pada Chakravarthy and Asish Kumar Ray (BARC, Mumbai), India.

Abstract

The 3 MeV Accelerator Project involves designing, fabrication, installation and commissioning of a 3 MeV, 30 kW Industrial Electron Beam Accelerator with a terminal voltage of 3 MV and is housed inside the Electron Beam Centre building at Kharghar, Navi Mumbai. The Accelerator has capability of delivering electron beam of 3 MeV energy for radiation processing applications. For ecological and economical reasons, the SF_6 gas is reincorporated into a closed cycle because gas should not be released into the atmosphere. The aim of the SF_6 gas handling system is to introduce the gas at high pressure to the accelerator tank after evacuation and to bring back into the storage tanks with minimum loss. The gas handling system also provides purification of gas, prevention from mixing with air or any other substances, which may contaminate and thus bring down the high voltage insulation characteristics of the gas. A heat load of 12 kW is coming due to high frequency transformer, electron gun, power supplies, motor alternator system, fan motor and blower etc. A radiator type heat exchanger with high-pressure blower and finned tube has been used for cooling the gas.

This paper discusses about mechanical design, fabrication, testing and safety of different components of SF_6 gas handling system such as gas piping, non lubricating compressor, dryer, vacuum pump, dust & oil filters, storage tanks etc. It also discusses about mechanical and thermal design of heat exchanger, which includes calculations of heat transfer coefficient, surface area, pressure drop, design and selection of high-pressure blower, 5-ton chiller unit, insulation and cooling tower.

INTRODUCTION

3 MeV Accelerator is an electrostatic accelerator in which terminal is floating at a voltage of 3 MV and the accelerator tank is at ground potential. As shown in the fig. 1, from voltage gradient point of view there is two geometries, coaxial cylindrical and spherical geometry. Design calculations show that SF_6 is the most suitable medium for insulation and cooling purpose. Apart from excellent electrical properties, SF_6 has good chemical stability, thermal properties and nontoxic. SF_6 Gas Handling System of 3 MeV project mainly covers SF_6 gas **transfer** system and SF_6 gas **cooling** system. The Accelerator Pressure vessel [1] is the main body of the 3 MeV Accelerator, which will house high voltage multiplier columns, RF electrodes, corona shields, high voltage terminals, electron gun, accelerating tubes, motor generator set, heat exchangers, RF transformer etc. All of these components require SF_6 gas insulation and efficient cooling. Hence there is a need of SF_6 gas and its handling system. Normal operating pressure inside the accelerator is 6 kg/cm^2. The accelerator tank has to be evacuated to vacuum of 10^{-1} torr before filling the gas.

Detail design [1] and fabrication [2] of the accelerator pressure vessel using ASME B&PV SEC-VIII, DIV-1 Code was carried out and reported earlier.

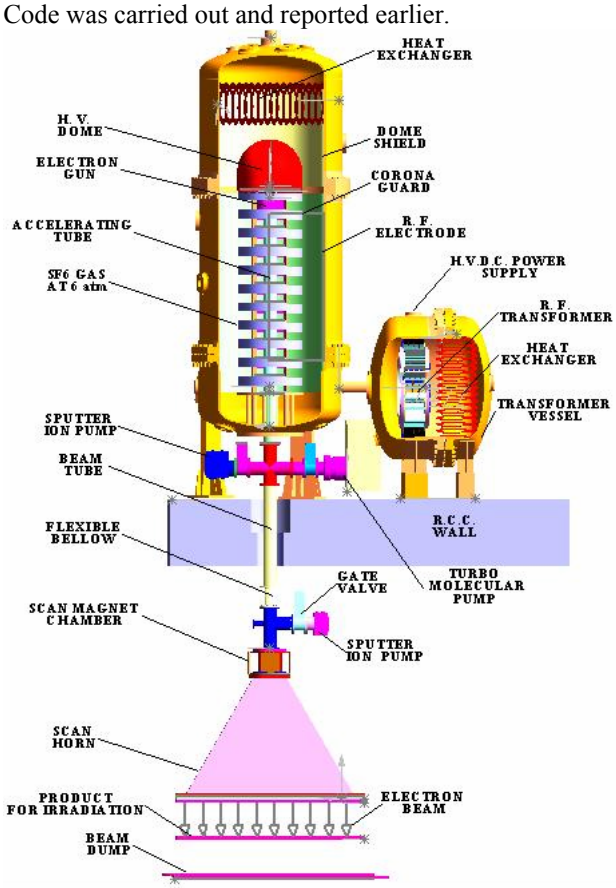

Figure 1: 3D Schematic of 3 MeV Electron Beam Accelerator

SF_6 GAS TRANSFER SYSTEM

The main objectives of SF_6 gas handling system is:

► Transfer of SF_6 gas from SF_6 cylinders to SF6 storage tank for storage.

►Transfer of SF_6 gas from Storage tank to accelerator tank while starting the accelerator

► Transfer of SF_6 gas from accelerator tank to storage tank for maintenance

► Recirculation of SF_6 gas during accelerator operation for removal of moisture and secondary products.

This 150-meter long pipe line is mainly comprises of 3" size pipeline, compressor, vacuum pump, dryer, filter, heater and blower. SF_6 **compressor** is a non lubricating type, vertical double acting, single stage air compressor de-rated for SF_6 use with a free air delivery of 83 CFM and a maximum discharge pressure of 125 psi (g). The compressor is used for transferring the gas from storage tank to accelerator and vice versa. The compressor is rated for a maximum discharge pressure of 125 psi (g) and a suction pressure of 1 atm. pressure. The 3000 lt capacity **rotary vacuum pump** is used to pump all the gas remaining in the tank after one atm pressure, which is supplied to compressor and then transferred to storage tank. About 0.5 Torr vacuum is achieved in the accelerator tank, storage tanks and pipeline.

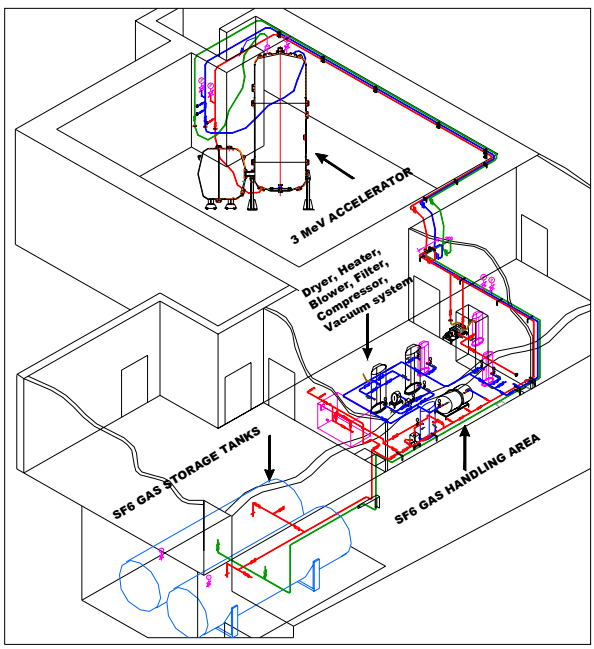

Figure 2: SF_6 Gas Transfer System

Vertical vessel twin column activated alumina filled **dryer** is used for removal of moisture and breakdown products. Activation of alumina balls is done by passing preheated air at 150^{0}C through alumina bed via blower & heater. Coarse and fine **filters** are provided to make sure that dust free gas is circulated through the accelerator column. Coarse filter is Pleated Bag type filter suitable for filtering 0.3-micron size dust particles. Fine filter is a cartridge type filter having borosilicate glass fiber cartridge mounted into a SS housing, suitable for filtering 0.01-micron size dust particles.

SF_6 GAS COOLING SYSTEM

This system is mainly comprises of 1.5" and 1" SS pipe line, radiator type heat exchanger and blower combination, 5 ton chiller unit, cooling tower, pressure transmitter, temperature sensors, safety interlocks, flow meter, pressure gauges and other instrumentation.

The high-pressure blower has been designed and commissioned to achieve special heat transfer requirements under 6-kg/cm^2 pressures of SF_6 gas. Ready made finned tube bundle with header have been purchased as per the area available inside the accelerator tank. Heat exchanger assembly is made of such four numbers of bundles and makes an enclosure of size 800x800x100 mm. High-pressure blower sits inside this enclosure and through SF_6 gas centrifugally outward direction. A design calculation for proper surface area of fin tubes and convective heat transfer coefficient in SF_6 environment at a pressure of 6-7 Kg/cm^2 for each bundle, have been calculated. Heat exchanger and blower combination along with 3 and 5 HP motors has been installed and tested for desired flow rate, pressure drop and motor current. Blower has sent for dynamic balancing after getting desired flow rate to reduce vibration.

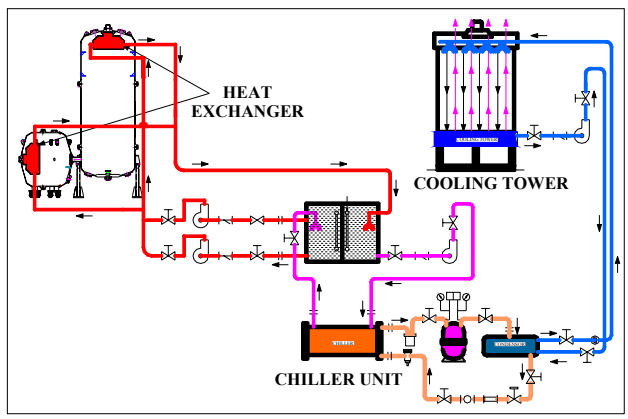

Figure 3: SF_6 Gas Cooling System

Figure 4: 5-Ton Chiller Unit and its Control System

Detailed chilled water flow and heat transfer calculations were done to make sure that high voltage RF Transformer, which is having a maximum heat load of 8 kW, is maintained within the permissible temperature limit. It was estimated that a total flow rate of 50 lpm of chilled water at 10^{0}C is required through the heat exchanger for cooling of transformer inside the accelerator tank. Similarly other accelerator components having a maximum heat load of 3 kW requires a flow rate of 20 lpm of chilled water at 10^{0}C. It was also estimated that a total pressure head equivalent to 3000 mm of water

column is required to maintain the above mentioned flow rate in the main chilled water process circuit. Valves and flow meters are provided to regulate and control the flow rate in the heat exchanger to meet variable heat loads.

Figure 5: Rectangular Radiator Type Heat Exchanger inside the Top Portion of Accelerator Tank

Freon-22 refrigeration pipeline of chiller unit was flushed with Nitrogen gas, evacuated and filled with Freon. Control panel of Chiller Unit checked and activated. Chiller plant along with heat exchanger & blower was run for eight hours to check its safety features, interlocks, trips and performance. We are getting chilled water of 100 lpm at 8°C, which is satisfactory. Fabricated pipeline pneumatically tasted at a pressure of 10 Kg/cm^2 and there was no drop in pressure recorded.

FABRICATION AND TESTING

Fabrication and testing of SF_6 gas transfer system and sf6 gas cooling system was similar. In this paper, it is mentioned for SF_6 transfer line. The material of the piping was stainless steel. The size of the Piping for SF_6 gas transfer line is 3" Sc 40. The length of this piping is approximately 150 meters along with 40 numbers of Audco make Butterfly valves, 10 numbers of pressure gauges, 4 numbers temperature gauges, 10 numbers flexible hose assembly, 70 numbers of weld neck flanges, 15 numbers of elbows, tee, rigid pipe supports with clamping etc.

Quality assurance plan was prepared by indicating various hold and witness stages of fabrication. Welding Procedure specifications, Welder Performance tests and Performance qualification records were prepared as per ASME SEC-IX.

Material Selection and Mechanical Testing: Raw Material [4] identified in the form of 3" pipe as per ASME SA 312 TP Gr-304L. Based on heat numbers involved, one sample per heat was analyzed for chemical and tensile properties. It also tested for Inter granular Corrosion test (IGCT) as per ASTM A 262, practice A and practice E and checked for seamless configuration as per microscopic analysis.

Welding Procedure Specification: WPS was carried out as per ASME SEC-IX, QW-482. Manual welding was carried out using GTAW welding process in pipe with 700 single V groove and internal gas purging. Non-consumable Electrode used was Tungsten and filler wire was ER308L as per specification number SFA-5.1. Size of the filler wire was 3.2/1.5 mm diameter and test has been taken in 6G position. Six numbers of coupons were given for mechanical testing in laboratory. Two numbers transverse tensile test and four numbers side bend tests were carried out and found satisfactory. In WPS 85-150A current, 18-24V, DC straight (EN) polarity, 160-170 mm/min speed was used.

Fabrication: Most of the pipe fabrication was carried out in 1G position. Insitu welding were carried out as per 2G and 5G position. Proper supports were provided for distortion control.

Non-Destructive testing: We have used "double wall double image" technique for radiography with X-ray and γ-rays source. In the radiographic film linear distortion like cracks, incomplete fusion, incomplete penetration, undercut etc, and rounded distortion like porosity, slag, tungsten inclusion was checked. 100% radiography was carried out on all butt weld joints including nozzle to shell joint. Dye penetrant testing was carried out on each layer of weld deposit and on pipe.

Pneumatic Test and Helium leak Test: Complete pipeline including all flexible hoses, valves, pressure gauges, etc was pneumatically tested at a pressure of 13.0 kg/cm2 (g) and found satisfactory. Pipeline was evacuated to a pressure of 1 X 10^{-4} Torr and 2 nos. of storage tanks was also evacuated to a pressure of 1 Torr. All the welded, flanged and threaded joints were helium leak tested to a leak rate of 2 x 10^{-7} std cc/sec and found satisfactory.

Fabrication of 3 numbers of coarse, fine and oil filter for SF_6 gas transfer system of size 300 mm diameter and 1500 mm height were completed. It was tested with helium leak detector and leak rate observed was less than 1 x 10^{-9} std.cc/sec. It was painted with one layer of red oxide primer and two layer of epoxy paint.

CONCLUSION AND STATUS

SF_6 Gas Cooling System has been fabricated, erected and commissioned. In SF_6 gas transfer system 150 meter long pipe line got fabricated and helium leak tested, Fabrication of course, fine and oil filter completed. Compressor and dryer system is under procurement.

REFERENCES

[1] Ghodke S. R, et. al. "Tank Design for 3 MeV, 30 kW Industrial Electron Accelerator", InPAC 2003, p-249.
[2] Ghodke S. R, et. al. "Development and installation of 'pressure vessel' for 3 MeV, 30 kW Industrial Electron Accelerator", InPAC 2005, p-118.
[3] ASME Boiler and Pressure Vessel Code SEC-VIII Div-1, SEC-IX, SEC-V, SEC-II (1998 Ed).
[4] Handbook of Piping Design by G. K. Sahu. (2002)
[5] Process Equipment Design, Brownell & Young. (1983)

INSTALLATION AND INTEGRATION OF INDUS-2

Sanjay Chouksey#, S. Kotaiah, S. S. Prabhu, Sridhar R, Vijendra Prasad,
S. K. Shukla, D. P. Yadav: R. R. C.A.T., Indore 452013, India

Abstract

The Synchrotron Radiation Sources consists of a large number of components of varying nature. Some components are light but highly delicate whereas some are big and heavy. However all components need a careful handling during their installation. Unit-cell mock-up assembly and virtual simulation of the installation process using software tools contributed significantly in visualizing various handling schemes, checking interferences and defining the assembly sequences. We have recently completed the installation and integration of 2.5 GeV Synchrotron Radiation Source, Indus-2, by adopting a set procedures of installation and pre-defined sequences. This paper presents an overview of procedures, sequences of assembly, equipments and toolings used for material handling and safety precautions taken during the whole task of installation and assembly.

INTRODUCTION

Indus-2 is a 2.5 GeV, 300mA electron storage ring designed for production of hard x-rays. It consists of 8 unit cells (or super periods) with a total circumference of 172.474 meter Each unit cell has two 22.5° bending magnets, a triplet of quadrupoles in the achromat section, two quadrupole in the long straight sections and four sextupoles in the achromat section..

Table 1: Components details for installation

Components	**Approx. size (meter), Weight (kg)**	
Dipole (16 Nos.)	2.2x1.35x0.88, 10000 kg	
Dipole vacuum chamber (16 Nos)	3.57x0.65x0.1, 300 kg	
Support Girders	Short straight section (8 Nos.)	6.5x0.92x0.37, 1500 kg
	Long straight section (16 Nos.)	3.25x0.92x0.37 1000 kg
	Dipole girder (16 Nos.)	1.83x0.84x0.47 1500 kg
	TL-3 Support (20 Nos)	3.0x0.58x0.8, 1000 kg
Quadrupole (72 Nos.)	0.56x0.86x0.8, 1500 kg	
Sextupole (32 Nos.)	0.78x0.3x0.75, 1000 kg	
Septum Magnets	1.3x0.6x0.6, ~1000 kg	

A total 27 number of beam lines are planned to tap the synchrotron radiation from Indus-2 for various purposes. (Ref.1). The electron beam from booster synchrotron is injected into Indus-2 through 65 meter long Transport line-3, which consists of 3 dipoles, 18 quadrupoles and 24 independent steering magnets (12 horizontal + 12 vertical). Major components for installation in Indus-2 with their critical features are given in Table 1.

The task of Installation of Indus-2 was much more complex due to narrow circular ring tunnel and severe restrictions on availability of space. The installation work started after the construction of the civil building (12000 Sq m) and was accomplished in stages (fig 3).

SEQUENCE OF INSTALLATION

Machine Component Installation

Installation of Indus-2 and Transport line-3 components can be broadly divided in two groups i.e. magnet and vacuum components. R.C.C. foundation is specially designed and constructed for this purpose with passive isolation of sensitive magnetic lattice from rest of the floor by using a sand blanket. Embedded Plate (MS) of 250 mm X 250 mm are provided in the ring floor to bear the large static loads of magnets and other components. After completion of the construction work, concrete floor adjacent to EPs was leveled to ensure uniform load distribution.

Installation of Support Girders & Alignment jacks

Threaded holes were drilled on the Floor Embedded plates (120 Nos.) for fixing the dipole girders and straight sections girder-jacks to make the machine foundation ready for installation. The positions of these holes were controlled by a combination of specially made template and theodolite equipped with distance meter. Afterward all dipole girders and straight section jacks were installed and anchored with these holes. Subsequently the straight section girders were installed on their jacks. References for drilling holes, for fixing of Transport line–3 support structures (20 nos.), were taken from the footprint marked as per designed location of TL-3. All support structures were first anchored to TL-3 RCC foundation.

Installation of Magnetic Components

Dipole magnets were the heaviest component for installation in the tunnel ring (fig 1). These magnets were transported by a truck in the Indus-2 building and there unloaded by 10 MT fixed hoist over a suitably designed transit trolley, used for transporting the magnets inside tunnel area. In the tunnel area they were transported to their designed locations by 10 MT EOT crane. A special fixture for handling and storing of multipoles was

#chouksey@cat.ernet.in

designed and fabricated. All the magnets were transported to tunnel area as per the procedure. Six-strut support

Figure 1: Installation of ring dipole at location.

system used for supporting multipoles were first doweled and bolted on straight section girders and afterward magnets were carefully fastened over them.

After installation of magnets, the machine was ready for pre-alignment. Dipoles were aligned with in their specified tolerances, whereas multipoles were aligned within 1 mm accuracy before opening the upper halves for installing vacuum chambers.

Maximum weight of the component in TL-3 was of dipole magnet (~1 MT) the installation was done using a single point hoist and hydraulic pallet.

Installation of Vacuum Components:

Ultra High Vacuum (UHV) components were installed in the ring and TL-3 subsequent to positioning & first alignment of magnets and beam diagnostic components. Major UHV components installed in the INDUS-2 ring are: dipole chambers, straight section chambers, pumps, and gauges. Aluminium alloy dipole chambers were filled with dry nitrogen gas before shifting to the ring. These dipole chambers are the heaviest & delicate components of UHV envelope and require high degree of safety in handling & transportation (fig.2). In order to install these large dipole chambers within available clearance of 3-4 mm in magnet pole gap, an adjustable placement trolley was designed & fabricated. This trolley has the necessary features of leveling, clamping & pushing the dipole chambers inside the dipole magnets. Straight Section chambers lighter in weight & were shifted manually and installed on pre-placed fixed and floating Aluminium supports at regular intervals in the ring. These chambers were also filled with Nitrogen gas & assembled with TSP bodies. Sputter Ion Pumps were installed manually due to limitation of space in the ring. Gauges & RGAs were last components to be installed before start of evacuation. Turbo molecular pumps for roughing were mounted on trolleys for their movement & installation.

RF-shielded SS316 bellows are used for compensating the misalignments during installation of the chambers, valves etc. and also to take care of the thermal expansion during bake-out and ring operation.

Final assembly and testing

After assembly of vacuum system, upper halves of the multipoles were positioned and machine was ready for precise alignment. A companion paper in these Proceedings gives details of the Alignment of Indus-2 machine. Assembly of ring (except injection system) and TL-3 assembly up to beam dump was completed by March 2005. Power and signal cabling was done and tested. Radiation system was installed. Final assembly & testing of other sub-systems with TL-3 was completed by July 2005. Trail experiment to store beam in Indus-2 started on August 14, 2005. Major milestones of installation are given in table2:

INSTALLATION CONSIDERATIONS

Component Design:

Lifting systems for the Indus-2 components has been designed as per relevant standards & specifications. Proper selection of lifting points with respect to C.G was also critical to avoid tilt less than 5º during installation. A proper support & transport system ensured the component and personnel safety.

Installation Process:

It is important to select efficient Installation process for the component installation Computer simulation contributed significantly in visualizing various handling schemes, checking and verifying interferences that helped in safe installation Footprint marking of the ring components helped in interference checking of various sub-systems before actual installation.

During Component Installation:

Sagging of the components due to self-weigh was minimized during handling by suitably supporting the components at suitable interval and other handling procedures. To prevent damage of the components due to sudden impact during handling & transportation, linear velocity was controlled.

RADIATION SHIELDING AND GENERAL SERVICES

A beam bump constitutes interlocking lead bricks (100mm Sq X 40mm thk) and Labyrinth made out of concrete blocks (300mmX300mmX 200mm) was installed at the end of TL-3.All the 27 Beam line holes are plugged with circular concrete plugs for biological shielding. These blocks are replaced by two part fabricated shielding to accommodated beam-lines.

For carrying cables of varying ratings like high current/low voltage for magnet power supplies, high voltage for power cables, signal, diagnostic and other instrumentation, a large cable tray system of more than 7 Km length was designed and installed in the Indus-2 building. At inner side of the ring, a separate four-tier cable tray system has been provided to feed the power to different magnets with separate rack for control cables.

Table 2: Major Milestones of Indus-2 Installation

Period	Activity
Dec 2003	First marking in ring begin
Jan-Feb 2004	Unit cell Mock up assembly
Feb-June 2004	Fixing of Jacks & girders
June-Nov 2004	Installation of ring magnets
1st Nov 2004	Last ring dipole magnet roll in
Nov 04- March 05	Installation of ring & Tl-3 vacuum components
March 05	TL-3 assembled & completed up to beam dump. Shielding maze assembled.
4th May, 2005	450 MeV beam was transported through TL-3 upto beam dump
6th June 2005	Last major installation for Indus-2 ring (Septum & Kicker magnet P/S)
Aug 26, 2005	Beam went first turn on Indus-2 ring

Access and crossover steel structures were designed and installed for quick access in ring and Transport line areas.

SAFETY DURING INSTALLATION

Ensuring safety during various phases of installation is always a difficult task. Strict safety guidelines (Ref. 2) and regulations are thus mandatory and their implementation need supervision and control. The building is provided with all the necessary material handling systems tested as per relevant codes to ensure personnel and component safety. Special care was taken in the handling of the vacuum components with dissimilar transition joint.

A Work Permit system was implemented for better coordination among the user group. This system also helped in monitoring the machine related activities and safe working culture.

Figure 2: Dipole Vacuum Chamber assembly with supports.

Figure 3: Beginning and completion of assembly.

CONCLUSIONS

The experience in installation and integration of Indus-2 components has shown that with a very systematic and careful approach in sequencing of the activities, planning, better coordination among sub-systems groups, the big challenge like this could be successfully met

Designing the support & transport system, mock-up trials, computer simulation of the installation process, checking and verifying interferences that helped in safe installation of the sub-system components in confined tunnel and other machine areas of the with severe restrictions on availability of space. A dedicated team coordinated the activities with a view to solve all interferences and to insure a smooth installation, which is the key to success.

ACKNOWLEDGEMENT

The authors are highly grateful to Dr. V.C. Sahani Director, RRCAT, for his constant support during all level of Installation of machine. Thanks are due to Shri S.K.Tiwari, Shri B.K. Sindhal, Shri K.K. Malviya, and his team for their active role during erection/installation of vacuum system. We also thank Shri V.K. Shrivastava, Shri K. Sreeramulu and Shri K. Veerabhadraiah for magnet system installation. Thanks are due to Shri R.Mehar, Shri J.S. Mahur, and his team for their active role during erection/installation. Thanks are due to Shri S. S. Parihar for supervising the activities.

The authors would like to thank all those who have contributed for the Indus-2 installation and integration.

REFERENCES

[1] Technical report of synchrotron radiation source, Indus-2 (Pub Sep 1998)
[2] Indus-2 Safety Report, (p133-141, clause10.0)

MULTIPACTING STUDY OF LINAC PREBUNCHER AT CAMD*

Y. Wang#, CAMD, Baton Rouge, LA 70806, USA.

Abstract

Multipacting currents can absorb RF energy and produce breakdown in the prebuncher cavity of CAMD linac. This phenomenon starts when the magnetic field to focus the electron beam is applied [1]. The multipacting has been studied in different magnetic field and RF electric field, and can be eliminated by RF processing. In the paper, the theoretical and experimental results of multipacting study will be presented; moreover, the operability of the system will be analyzed.

INTRODUCTION

A 500 MHz pillbox cavity in the linac [1] acts as the prebuncher, which is excited to a TM_{010} mode to produce an accelerating field. It can remove the unused electrons for the storage ring [2-3]. The cavity main specifications in operation are listed in Table 1.

Table 1: Prebuncher Specifications

Electron energy	50keV
Frequency	499.7MHz
Peak field	100kV
Cavity gap	9cm
Pulsed power	4.75kW
β	1
Q	4360
Filling time	5.6uS

EXPERIMENT SETUP

The prebuncher RF system in the linac is shown in Figure 1. In order to produce proper RF power for the cavity, there are a 500MHz, 54 dB, 250 W, pulsed amplifier and a 500MHz, 16 dB, 5 kW, pulsed amplifier to amplify the 500MHz, 0 dBm, CW signal coupled from storage ring master signal generator.

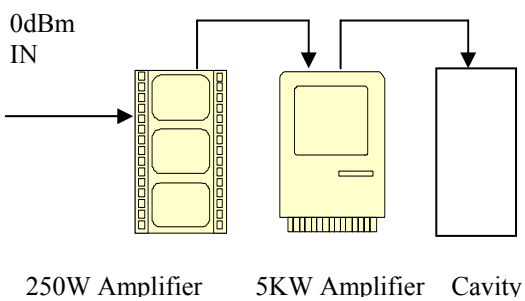

Figure 1: Diagram of the experiment.

The RF output waveforms from the two amplifiers are shown in Figure 2. The top one is the RF output of the 500MHz, 54 dB, 250 W, pulsed amplifier, and the bottom one is the RF output of the 500MHz, 16 dB, 5 kW, pulsed amplifier. The 30 μS pulse length is required by the cavity filling time in Table 1.

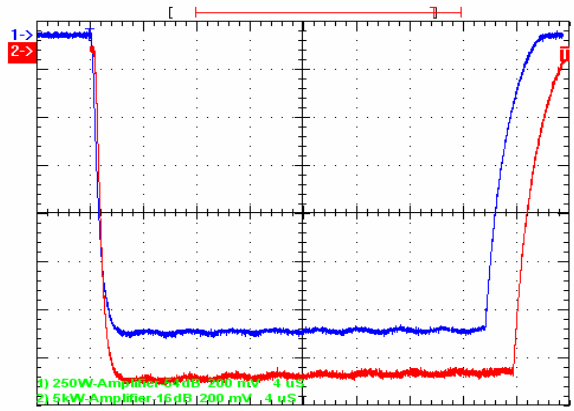

Figure 2: The RF output.

PRELIMINARY EXPERIMENT RESULTS

The RF system of prebuncher was tested and cavity was conditioned by RF power during recommissioning prebuncher. But when attending to operate the prebuncher work, multipacting in the cavity started when the power supplies for the focusing coils which generate magnetic field perpendicular to cavity surfaces in the buncher were turned on. In Figure 3, the signal is gotten by a coupler in the prebuncher cavity, the bottom waveform is without power supplies on, and the top one is with the power supplies on.

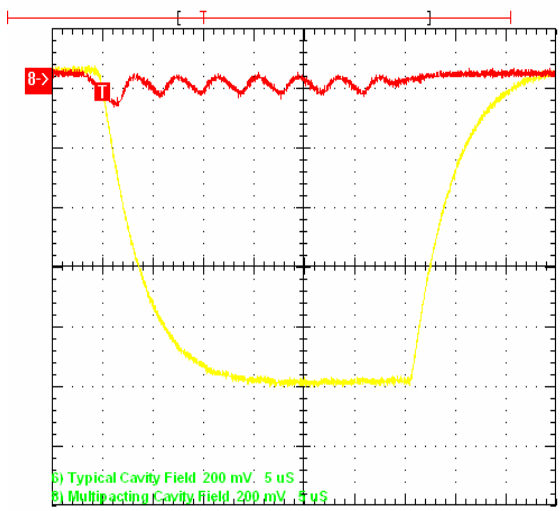

Figure 3: Cavity field.

In order to condition the cavity, the multipacting has been studied in RF power vs. magnetic field as shown in

*Work supported by the State of Louisiana, USA
#wangysh@lsu.edu

Figure 4. The multipacting happens between low boundary and upper boundary at different focusing coil magnetic field.

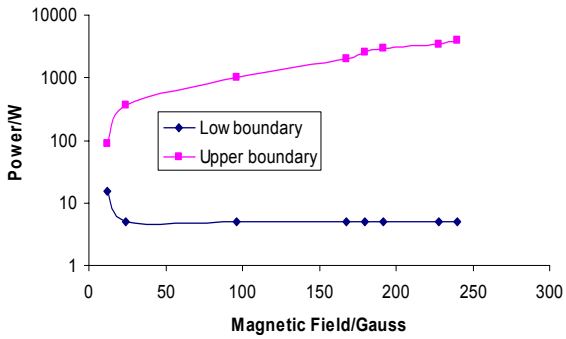

Figure 4: RF power vs. magnetic field in the cavity.

ANALYSIS

Through the experiment in Figure 5 and materials studied [3-8], the multipacting in the cavity is a half-cycle mode. The equation for an electron of mass m and charge e in a sinusoidal field of peak voltage V and frequency f of the cavity with gap d is [5-6]

$$V = \frac{4\pi^2 (fd)^2}{(e/m)\Phi} \qquad (1)$$

Where

$$\Phi = (\frac{k+1}{k-1})\pi\cos\varphi + 2\sin\varphi \qquad (2)$$

Where φ is the time phase angle at which secondary electrons are emitted, and k is the assumed constant ratio of electron arrival velocity to emission velocity.

There are four waveforms at magnetic field 24 Gauss in Figure 5 from multipacting beginning to the multipacting ending with RF power from 5 W to 360 W. In the Figure 5, there is a modulation with a frequency increase accompanying the RF power to the cavity increase. This modulation can help to pass the multipacting region described in [5] from equation (1) because the modulation is equivalent to the frequency decrease. From (a) to (d) in Figure 5, there is amplitude increase which is also required to pass the multipacting region.

In the experiment, the resonant frequency of the cavity is changed when multipacting occurred. As shown in figure 5 (d), the frequency is already about 300 kHz at very low magnetic level, but the bandwidth of the cavity is about ±50 KHz; therefore, it is impossible to eliminate multipacting by detuning cavity.

Figure 6 shows that there are high amplitude and high modulation frequency at high magnetic field because the higher magnetic field, the bigger the time phase angle; therefore, the larger multipacting region.

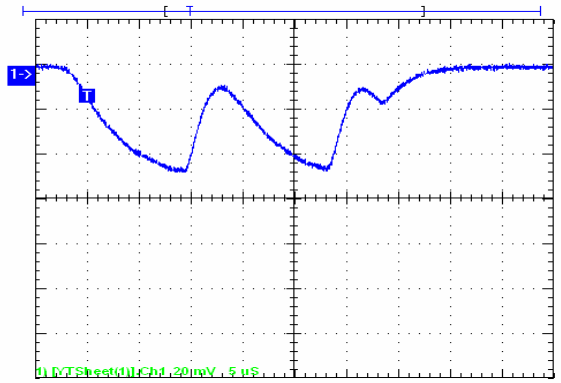

(a): 5W

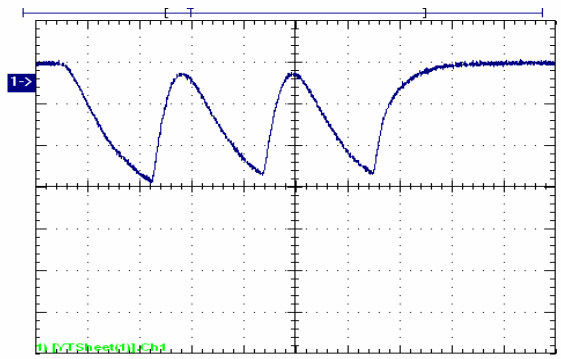

(b): more than (a) & less than (c)

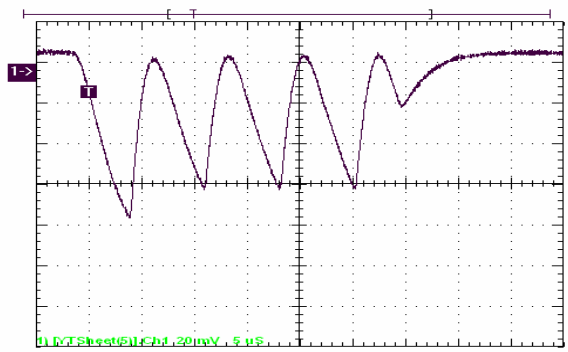

(c): more than (b) & less than (d)

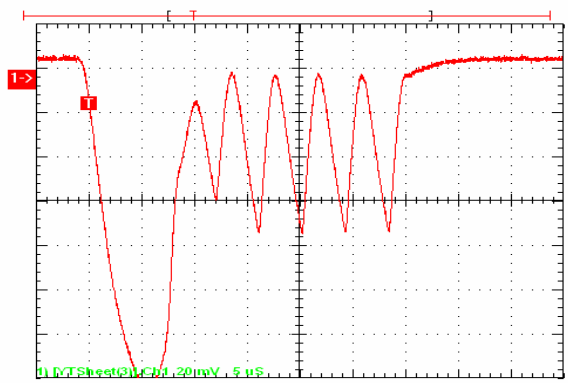

(d): 360W

Figure 5: Cavity field at magnetic field 24 Gauss with the power to cavity increase.

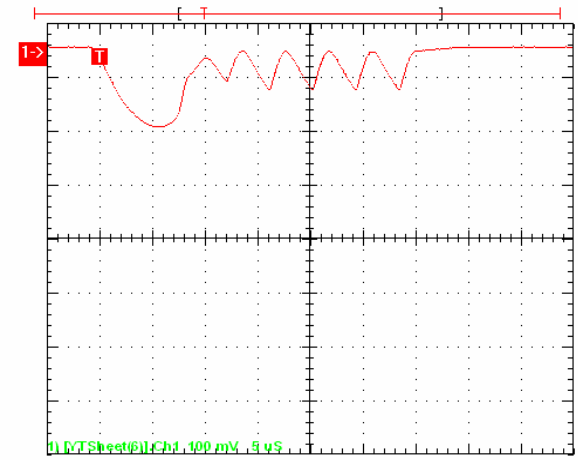

(a): RF power 360 W & magnetic field 24 Gauss

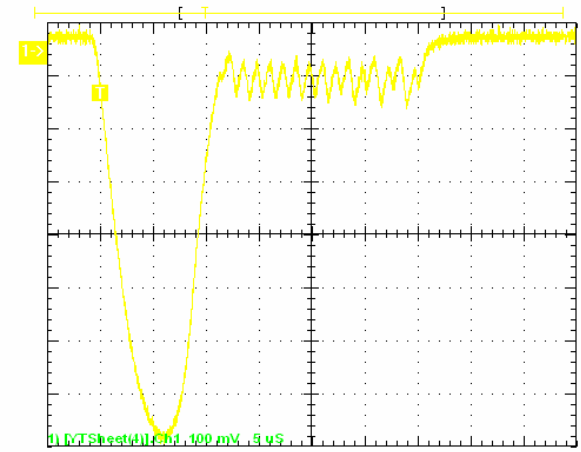

(b): RF power 2 kW & magnetic field 168 Gauss

Figure 6: Cavity field at upper boundary in Figure 4 at different magnetic field.

RF CONDITIONING

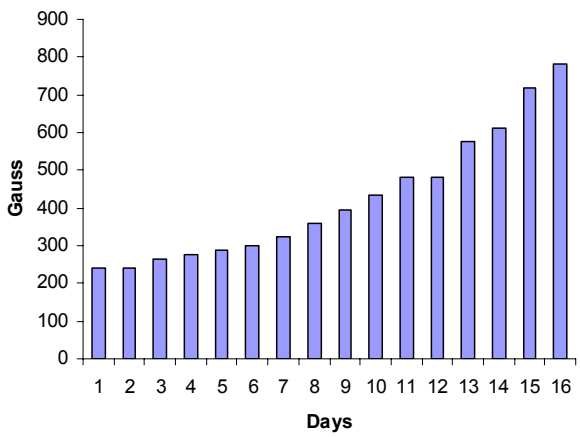

Figure 7: Magnetic field vs. days in commissioning

Commissioning the cavity begins after careful investigation by feeding reasonable RF power with focusing coil magnetic field increase in the upper boundary in Figure 4.

The very interesting results are shown in Figure 7. It takes 16 weekdays, about 12 hours per day, to reach the operation value at magnetic field 720 Gauss. The time is even longer if the investigation time is counted. The RF conditioning is very slow because the RF power duty cycle is very small (30 μs and 10 Hz, minus fill time of the cavity in Table 1), maybe, partly because the surface condition is poor.

CONCULSION & OPERABILITY

The RF conditioning makes the surface secondary ratio δ [9] big, and eliminate the multipacting in the prebuncher cavity.

When the RF conditioning reaches the operation value of magnetic field, the study to operation begins, the prebuncher is operated soon, and the multipacting does not affect operation afterward. A few months of operation later, this phenomenon totally disappears whenever the prebuncher RF system is maintained or checked.

ACKNOWLEDGEMENTS

The authors are grateful to Dr. M. Fedurin, Mr. P. Jines, Mr. D. Launey, Mr. T. Miller, Dr. V. Suller for their patience and support; to Mr. A. Crappell, and Mr. D. Dixon for their hard work in the prebuncher RF system upgrade; to the Machine Advisory Committee for CAMD/LSU for reviewing the project; to all other CAMD staff for the support and encouragement.

REFERENCES

[1] Y. Wang et al, Proc PAC2003, pp2892-2894.
[2] B. C. Craft et al., NIM B-40/41, p373, (1989).
[3] V. P. Suller et al., Proc EPAC2004, pp2424-2426.
[4] T. Wangler, Principle of RF Linear Accelerators, John Wiley & Sons, Inc., 1998, pp155-159.
[5] A. J. Hatch and H. B. Williams, J. Appl. Phys., 25, 47 (1954).
[6] A. J. Hatch and H. B. Williams, Physical Review, 112, 681 (1958).
[7] A. Chao and M. Tigner, Ed., Handbook of Accelerator Physics and Engineering, World Scientific, 1998, pp380-383.
[8] D. Proch et al., EPAC1998, pp1976-1978.
[9] M. J. Smith and G. Phillips, Power Klystron Today, Research Studies Press Ltd., Somerset, England, 1995, pp193-202.

THE PROTON AND ION LINEAR ACCELERATOR ILU-9

V.G. Abdulmanov, V.L. Auslender, A.A. Bryazgin, F.A. Emanov, E.S. Konstantinov, A.D.Panfilov, V.S. Podobaev, B.L. Faktorovich, V.G. Cheskidov
BINP, Novosibirsk, Russia

Abstract

The pulse RF ion linear accelerator of ILU-9-type is described. The accelerator is intended to use for various radiation-technological processes and investigations. The parameters of the accelerator and the ion beam measured during the tuning are given.

INTRODUCTION

The proton and ion linear accelerator ILU-9 was designed basing on experience gained in BINP SB RAS, Novosibirsk, during development, production and operation of single-resonator pulse radio frequency linear accelerators of ILU series. This machine is purposed for work as an injector for accelerating complexes for research, technological and medical application. The pulse duration required for synchrotron injection is 5 mks, energy – more than 2 MeV.

Figure 1: View of the vacuum tank and resonator inside it, RF generator is removed

Views of the ILU-9 vacuum tank and resonator inside it and RF generator with power input loop are shown in Fig.1 and Fig.2. Distinctive features of this machine are simplicity of design, convenience of operation and reliability at long work. The machine is designed to accelerate ion beams with Z/A = ½ up to energy 5.8 MeV per charge unit in the main channel, the other options are the possibility of proton beams acceleration up to energy 2.9 МэВ and ion beams with Z/A = 1/3 acceleration up to energy 8,7 MeV per charge unit at injection energy of 70 keV. After passage of magnetic turning system and acceleration in the additional channel the particles energy makes: 9.8 MeV per charge unit for ions with Z/A = ½, 14.7 MeV per charge unit for ions with Z/A = 1/3 and 4.9 MeV for protons.

Figure 2: RF generator with power input loop

ACCELERATING STRUCTURE

The design of the accelerator is shown in Fig.3. The machine is based on radio frequency (RF) resonator performed as an antiphase excited quarter wave asymmetrical shielded pair line. The upper sides of the double lines 1 are shortened by a disk 5, the other ends of the lines are loaded by capacity of drift tube 2. The main accelerating channel contains eight accelerating gaps and six drift tubes having the lengths determined by acceleration rate.

Lengths of accelerating gaps in the initial part of acceleration path are calculated so that the first gap transit angle is close to π at the given electric field tension. The drift tubes' lengths are growing along the beam line due to increase in particles' speed as passing the accelerating gaps with the acceleration period of $\beta\lambda/2$ ($\beta=v/c$, λ – length of a wave of the resonator) so the accelerating rate is decreasing. To keep the constant accelerating rate with the same accelerating electric field tension in all accelerating gaps it is necessary to increase the voltage on the last accelerating gaps by increasing their length. This problem is solved by a proper choice of double line design values.

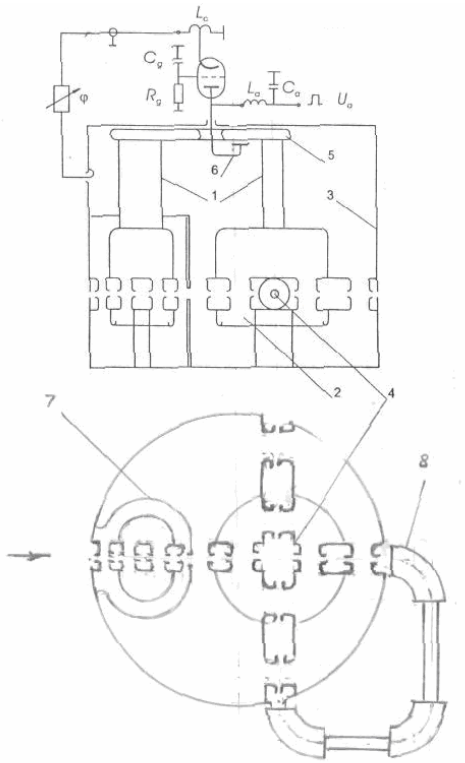

Figure 3: The basic circuit of the ILU-9 accelerator:1 - double lines; 2 – drift tube; 3 – outer drum of the resonator; 4 – drift tube; 5 – shortening disk; 6 – RF power input; 7 – screen; 8 – turning magnets.

Diameter of the resonator 3 is 1100 mm, height - 920 mm. The first conductor of a line having diameter of 156 mm is shifted from resonator's axis on 345 mm, the second having diameter of 75 mm is shifted on 153 mm in the opposite side. Length of accelerating gaps in the initial part of beam line is 40 mm, the last accelerating gaps have length of 73 mm. The beam channel aperture is 20 mm, diameter of drift tubes is 120 mm.

Drift tubes of the first conductor of a line are surrounded by the additional screen 7. This design of the shielded double line provides practically the same acceleration rate along the beam line at average electric field tension of 150 kV/cm for acceleration of ions with Z/A = ½. The RF voltage amplitude is 0.6 MV on drift tubes of the first conductor and 1.1 mV on the tubes of the second conductor.

The accelerator ILU-9 has an additional acceleration line 4 with three drift tubes. It can be used after ion beam turning through an angle of 270˚ by means of turning magnets 8. The use of the additional accelerating line allows to increase the ions energy without additional expenses on accelerating system. Drift tubes of the additional acceleration line are connected to the second conductor of a line and the external screen so that their longitudinal axis is perpendicular to the axis of the main beam line.

The line with drift tubes is insulated from the external screen and the constant bias potential of -7 kV is applied to them for suppression of high-frequency resonant discharge (multipactor). The bias voltage is applied to the point of minimum RF voltage in the middle of shortening disk 5.

RF GENERATOR

The resonator has eigen frequency of 42,66 МГц, Q-factor of $7*10^3$ and effective shunt resistance about 30 MOhm/m. The pulse power of 1.2 MW is required for its excitation to the working energy level.

The resonator is excited by the single stage autogenerator on triode GI-27AM having the external feedback through the resonator. The generator is placed directly on the resonator and is connected to it by means of an inductive loop 6 without an intermediate feeder.

The cathode contour is performed as RF ferrite autotransformer (see Fig.3) with turn ratio k = 1:2 to match the triode input resistance of 150 Ohm with cable impedance of 75 Ohm. The ring ferrite core is wound by one turn coil. The middle of a coil is connected directly to the cathode input of the triode, and the whole coil is fed by the voltage from the feedback loop through the phase changer. The cathode contour is tuned by the external magnetic field imposed on the ferrite core. The magnetic field is created by an electromagnet, the cathode contour is placed between its poles. The advantages of this design are: decrease in overall dimensions of cathode contour, matching of low input resistance of triode with feedback line impedance and the contactless contour tuning to the resonator's frequency is performed.

The RF generator operates in pulse mode. Duration of anode voltage pulse is up to 600 мкс, pulse repetition rate is 0.1÷50 Hz.

BEAM ACCELERATION DYNAMICS

The accelerating electric field distribution along the axis of the main channel drift tubes was calculated using error integral approximation. This distribution was checked using the probe body method, the measurement results are shown in Fig. 4. The electric field distribution data was used to calculate the beam dynamics. For the pulse beam current up to 10 mA the ion beam energy spread makes < ±0,25 %, calculated emittance – 10^{-3} cm*rad. The longitudinal and transverse beam stability is provided by the accelerating field due to variable phase focusing.

First time the ion beam was successfully accelerated in ILU-9 in 1991 with the drift tubes made of aluminum. The plasma proton source with the cold cathode was used.The proton beam was accelerated to the energy of 2.9 MeV, pulse current was 2 мА, pulse duration was 5 mks, pulse repetition rate was up to 50 Hz. The energy spread was < ±0,25 % at an angle of bite of 40˚.

The aluminum drift tubes did not permit to further increase the accelerating voltage up to the values required for acceleration of heavier particles. The drift tubes were replaced by the ones made of copper.

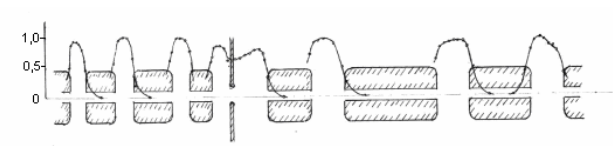

Figure 4: Accelerating field distribution along the axis of main channel drift tubes.

After replacement of the drift tubes and modernization of the feedback loop the H_2^{+1} ions beam is accelerated. The ions are generated by the plasm-arc discharge source.

The voltage on the accelerating gaps of the drift tubes was raised up to design size, practically twice exceeded the maximum voltage achieved during the acceleration of protons. The accelerated ion beam was fixed by the semiconductor detector after passage through a titanium foil having thickness of 35 micron. At last stage of experiments the accelerating voltage was raised in 1.5 times greater than the design value that allows to accelerate beams of ions with $Z/A = 1/3$.

CONCLUSION

For the nearest future we suppose to carry out measurement of phase volume and spectrum of the accelerated beams of protons and H_2^{+1} ions and also to study the possibility to accelerate the carbon ions C_{12}^{+4} using a carbon ion source along with the appropriate increase of voltage on the accelerating gaps of drift tubes without change of accelerating channel design.

REFERENCES

[1] V.G. Abdulmanov, N.I. Alinovskii, V.L. Auslender, A.F. Baidak, A.D. Panfilov, “Proton-ion linear accelerator ILU-9”, Sixth seminar on Problems of Theoretical and Applied Electron and Ion Optics. Moscow, 28-30 May 2003.

[2] V.G.Abdulmanov, N.I. Alinovsky, V.L. Auslender, A.F. Bajdak, A.D. Panfilov, “Proton-ion linear accelerator ILU-9”, Prikladnaya Fizika (Applied physics) 5-2004.

RF ACTIVITIES OF ACCEL INSTRUMENTS IN ASIA-PACIFIC

M. Pekeler, K. Dunkel, M. Peiniger, C. Piel, H. Vogel, P. vom Stein
ACCEL Instruments GmbH, D-51429 Bergisch Gladbach, Germany

Abstract

Since the foundation of ACCEL Instruments, Asia-Pacific has been an important market for RF, magnet and x-ray beam line devices. For the RF activities, pioneering work was done for JAERI, where complete superconducting RF modules where designed, built, tested and delivered. An important step for industrialization of superconducting RF modules was done, when NSRRC decided in 2000 as the first Light Source, to contract turn key superconducting 500 MHz modules of the Cornell design to ACCEL. Similar modules have been delivered in the meantime to CLS, Cornell and DLS and three more will be delivered to SSRF in Shanghai next year. Peking University is planning to use a Rossendorf design superconducting RF module housing two 1.3 GHz TESLA cavities for the operation of their FEL project. On the normal conducting RF systems, a complete 3 GHz 100 MeV linac has been delivered to ASP together with the 500 MHz booster cavities and the LLRF system. Booster cavities and LLRF system will be also delivered for SSRF. For SOREQ in Israel, ACCEL is developing a complete superconducting 40 MeV proton/deuteron linac. The first stage of this linac is currently under delivery and installation.

SUPERCONDUCTING 500 MHZ MODULES FOR JAERI

In the Asia-Pacific region, ACCEL is so far mostly supplying complete accelerator systems rather then single accelerator components like cavities or couplers. A good example already from the early 90's is the supply of turn key superconducting accelerator modules for JAERI.

Figure 1: Superconducting accelerator module housing one 5-cell 500 MHz module completely assembled and tested prior shipment to JAERI site.

JAERI decided in 1991 to order 4 superconducting 500 MHz modules, two modules housing a single cell cavity and two modules housing a 5 cell cavity. The complete design of the module was done in industry. As the modules are operated at a very low duty cycle of maximum 3 %, the RF losses are below 1 W and the modules were designed for as low as possible static losses. Two thermal shields at 20 K and 70 K were designed and each module is able to be cooled by a power of 4 W cryocooler at 4.5 K.

All modules were RF tested in house prior delivery and then shipped to JAERI site in 1993. The modules are still in operation at an operating gradient of 5 MV/m with Q values above 10^9. A RF coupler with external Q tunable from 10^5 to 10^9 was developed. Fig 1 shows one module prior delivery to JAERI site.

SUPERCONDUCTING 500 MHZ MODULES FOR LIGHT SOURCES IN TAIWAN AND SHANGHAI

In 2000 NSRRC decided as the first Light Source to take benefit of superconducting cavities. The decision finally was made to order two superconducting 500 MHz modules of the Cornell type design. ACCEL had agreed with Cornell University on a technology transfer and was thus able to produce those modules as a turn key system including the SRF electronics and the cryogenic valve boxes needed for helium bath pressure and level control In the same year also the Canadian Light Source and Cornell University itself ordered two more modules each. Diamond Light Source ordered three more modules in 2003 and Shanghai Light Source three more in 2005.

All modules are delivered with guaranteed values of about 2 MV accelerating voltage and can provide more than 250 kW of RF power to the beam. The cryogenic loss (static loss plus RF dissipation) is specified to be below 100 W. All modules for NSRRC, CLS, Cornell and Diamond are delivered; the first module for Shanghai Light Source will be shipped in the middle of 2007.

The cavities and the windows of the SRF module are tested separately prior assembly and have passed the acceptance test already. Figure 2 shows one of the NSRRC module prior shipment to Taiwan and during installation into the NSRRC storage ring.

During the last 6 years, the Cornell type module has developed into a product and the SRF electronic has been further improved and upgraded with state of the art data logging (S7) and interlock application. The installation, integration with helium plant and klystron and taking into operation of a module can be done within a time period of 4-6 weeks.

Figure 2: Completely assembled and tested first superconducting 500 MHz module with valve box and SRF electronics ready for shipment to NSRRC (above) and during installation into the NSRRC storage ring (bottom)

SUPERCONDUCTING 1.3 GHZ MODULES FOR FEL APPLICATION

For FEL application calling for a linac of about 100 MeV, Forschungszentrum Rossendorf developed [a] superconducting 1.3 GHz module based on TESLA technology developed within the TESLA collaboration for the Tesla Test facility (TTF) linac. In contradiction to the TTF modules, the Rossendorf module only hoses two TESLA cavities and can be operated in cw mode

Figure 3: Superconducting Rossendorf style 1.3 GHz module prior shipment to Daresbury. Peking University is planning to use this module for their FEL application.

ACCEL agreed with Rossendorf on a technology transfer and can deliver those modules with guaranteed voltage of 25 MV/module.

Two modules were delivered to Daresbury laboratory for the 4GLS test facility and are currently under commissioning. Peking University is considering using this module for their FEL. A decision is expected within this year. One of the two modules shipped to Daresbury is shown in Figure 3.

TURN KEY 3 GHZ INJECTOR LINAC AND BOOSTER CAVITIES FOR ASP

For the Australian Synchrotron project ACCEL has delivered in 2005 a turn key injector linac and the booster cavities including the LLRF control system.

Figure 4: Normal conducting 3 GHz linac (top) and 500 MHz booster cavity (bottom) installed at the Australian Synchrotron project.

The design of the 3 GHz linac is identical to the linac delivered for the Swiss Light Source and the Diamond Light Source. The accelerating structures were developed

at DESY within the development of the normal conducting version of a TeV linear collider in the early 90's. The main linac parameters are to be agreed upon at the beginning of the project and are to be demonstrated on site during the acceptance tests.

The normal conducting 500 MHz 5-cell booster cavities were originally also designed by DESY. ACCEL manufactures this cavity on a regular basis and has built so far more than 40 of such cavities. They can provide a voltage of up to 2 MV to the beam and are operated at about 50-70 kW RF power. The cavities are delivered on request with their own analogue LLRF system. A digital LLRF system is currently studied. The installations at the Australian Synchrotron project are shown in Figure 4.

TURN KEY 176 MHZ MODULE FOR CW PROTON/DEUTERON ACCELERATION

At the SOREQ research center in Israel, a linac is currently under construction and commissioning that was designed and built completely in industry. The linac will finally have an energy of 40 MeV and accelerate protons and deuterons in continuous wave mode and currents up to 4 mA.

Figure 5: ECR ion source (top) and RFQ (bottom) installed at the SARAF accelerator of the SOREQ institute in Israel

The project is divided into two phases. In the first phase, already contracted, a 7 MeV injector will be installed consisting out of an ECR ion source, a normal conducting 176 MHz continuous wave 250 kW RFQ and a first superconducting 176 MHz module housing 6 halfwave resonators and 3 superconducting focusing solenoids.

In case the first phase can be concluded successfully it is planned to install more superconducting modules to reach the final energy of 40 MeV.

Figure 5 shows the ECR source and the RFQ installed at the SARAF facility.

All six superconducting 176 MHz cavities were RF tested in a vertical bath cryostat at a temperature of 4.5 K at ACCEL prior integration into the module. All cavities safely exceeded the design specification of 25 MV/m peak electric surface field. The RF losses at those field levels were lower than the specified 10 W for each cavity. Also the superconducting solenoids were tested prior integration and a magnetic field of more than 6 T was demonstrated. The assembly of the module was done at the end of last year. Figure 6 shows the module at an intermediate assembly step. The module was shipped to the SARAF site and is currently being cooled down with the refrigeration plant. The high power RF test and the first beam operation are planned for spring 2007.

Figure 6: Assembly of the superconducting 176 MHz accelerator module for proton/deuteron acceleration. The module houses 6 halfwave resonators and 3 superconducting solenoids

STATUS OF BINP AMS FACILITY

M.V. Petrichenkov, A.D. Goncharov, V.F. Klyuev, S.G. Konstantinov, A.V. Kozhemyakin, A.M. Kryuchkov, V. V. Parkhomchuk, S.A. Rastigeev, V.B. Reva, BINP, Novosibirsk, Russia

Abstract

Present status of the accelerator mass spectrometer (AMS) facility at BINP is described. The AMS facility is dedicated for precise measurements of isotopes ratios. The scheme of the facility includes negative ion source, electrostatic tandem accelerator with accelerating voltage up to 2 MV and magnesium vapors stripper and also includes the high-energy and low-energy beam lines with analyzers. There is an additional beam separator (180°bend) with crossed electric and magnetic fields in high voltage terminal of tandem accelerator. The results of experiments on ion beams acceleration, stripping and selection are given.

INTRODUCTION

The accelerator mass spectrometry is a powerful method of isotopic analysis for archaeology, environment science, biomedical applications and etc.

The specialized building for AMS center is being prepared now. The accelerator will be placed in the underground room for radiation shielding. It will allow operation with accelerating voltage 0.5 MV and higher after May 2007.

The AMS is based on the electrostatic tandem accelerator. The AMS system consists of the negative ion source, low energy beam line, tandem accelerator and high-energy beam line. The low energy beam line is used for initial isotope selection. The tandem accelerator is used for molecular ions removal and, of course to obtain the required beam energy for the final detector.

The negative ion beam is horizontally extracted from the ion source. Then the beam is analyzed in low-energy beam line by 90° double-focusing magnet and injected vertically into the first accelerating tube. After acceleration negative ions are stripped into plus charge state in magnesium vapors stripper. The ions of 3+ charge state will be used for isotope analysis of Carbon–14. It requires 1.5-2 MV terminal voltage for necessary C^{3+} yield. Then they pass through the middle energy separator (180° combined bend with crossed fields) and are accelerated again in the second accelerating tube. The accelerated ions are analyzed in high-energy beam line by 90° double-focusing magnet and putted horizontally to the final detector.

The most distinguishing features of BINP AMS facility are the use of the middle energy separator (180° beam bend with crossed fields in HV terminal) of ion beams and the magnesium vapors target as a stripper. The aim of these innovations was described earlier [1].

LOW ENERGY BEAM LINE

Some modifications of low energy beam-line are to be made very soon. The gate valve will be installed just after the ion source to provide quick replacement of ion sources for their cleaning and samples change. Now the gate valve is located only at the exit of the bending magnet and vacuum conditions can be obtained during three-hour period after attachment of the ion source by 250 l/s turbo pump. In addition, the low-energy line will be equipped with a differential pumping system to decrease the gas flow from ion source to the beam line. The RGA system is installed after bending magnet for residual gas analysis in injection channel. At present time, the vacuum in the injection channel is $\sim 10^{-6}$ Torr with sputter ion source.

TANDEM ACCELERATOR

The AMS tandem accelerator is a folded type vertical machine with 180° bending system in the high voltage terminal where the beam is pre-selected at medium energy in crossed electric and magnetic fields. It consists of electrostatic 180° bending system with 40 cm orbit radius. The cylindrical electrostatic plates with 2.5 cm width and 1 cm pole gap are placed into vacuum chamber. The operation at required 30 kV/cm field of bending system has been demonstrated. The 180° dipole magnet with up to ~600 Gs field surrounds the vacuum chamber with electrostatic plates.

The magnesium vapors stripper has worked more than 600 hours in the BINP AMS facility under 450°C average temperature without refilling the magnesium. The precise system for magnesium target positioning developed in 2006 works well. The transverse position of the target is adjusted by the beam transmission. For this purpose, the bellows are placed at the entrance and exit of the magnesium target. The stripper channel has the inner diameter of 3 mm and puts the main limitation on the beam transfer.

The 500W gaseous turbine generates the power used in the terminal. The circuits of four electrostatic dipoles, 180° bend and three ion pumps are supplied by this turbine. Special unit for magnesium stripper temperature stabilization has been developed and tested. It allows to decrease significantly the pulse load on turbine and its circuits. The control and management of this electronics is realized through optical link by ADAM modules. The 15 l/s ion pump is installed just after 180° bend. The vacuum in tandem accelerator is kept better than 10^{-6} Torr. The gas pressure is measured by ion pump currents. The gate valve is placed after 180° bend. The

terminal equipment works without forced cooling, but it is possible by the turbine gas.

The accelerating voltage is generated by the symmetrical cascade generator with a resonant frequency ~ 20 kHz. The design value of terminal voltage is 2 MV. It is to be achieved with SF_6 insulating gas at 1.7 bar pressure. Now air at normal pressure is used as insulating gas. The maximum terminal voltage of 500 kV was achieved in previous experiments. The SF_6 gas system including gas transfer system, compressor and dryer have been prepared. A special radiation protected room is planned to be prepared by May 2007 in specialized centre for AMS operation with voltage >250 kV.

HIGH ENERGY BEAM LINE

The most part of the unwanted particles should be removed by magnet in low-energy beam line and 180° bending system with crossed electric and magnetic fields placed in the high voltage terminal of the accelerator. For the further background damping the 90° analyzing magnet is placed at the exit of the tandem accelerator. Finally, the Carbon-14 particles are measured by silicon detector placed at the end of high-energy beam line. [1]. Also we used scintillation detector (CsI and BGO crystals) in our experiments for the AMS system adjustment (see Fig. 3 below).

EXPERIMENTAL RESULTS

The previous experimental results have demonstrated, that the negative carbon beam can be accelerated and stripped into high voltage terminal of BINP AMS facility. The charge state fractions of carbon beam stripped in the magnesium vapors stripper were obtained [1,2]. Recently, the first accelerated beam has been observed at the exit of the BINP AMS tandem accelerator [2].

In this paper the first tests of isotopes selection are presented. During the experiments, the injection energy of carbon beam was 7.5 keV. The sputter ion source was used for negative carbon ions production. The terminal voltage was mainly 100kV and 250 kV in experiments with C^{3+} ions. The magnesium vapors stripper was heated for obtaining the equilibrium charge state distribution, but not more. The vacuum of the beam line was about 10^{-6} Torr. The current of accelerated beam was measured by "CsI" crystal. The ^{13}C enriched sample of graphite with $^{12}C/^{13}C \cong 1$ was used for clearness. The mass spectrums of the injected and accelerated beams for various fields of injection magnet are presented in Fig.1. There are $(^{12}C)_m(^{13}C)_n$ clusters in the beam.

The settings of tandem electrostatic bend system corresponded to charge state 1+. One can see that molecules and carbon clusters are not greatly destructed at these conditions. The comparison of transmissions of clusters and atoms show that about 90% carbon clusters are being destructed.

The current of accelerated ^{12}C beam as a function of terminal electrostatic bend field, where 1 (unit) of the field correspond to 1+ ions bend, is presented as curve #1 in the Fig.2.

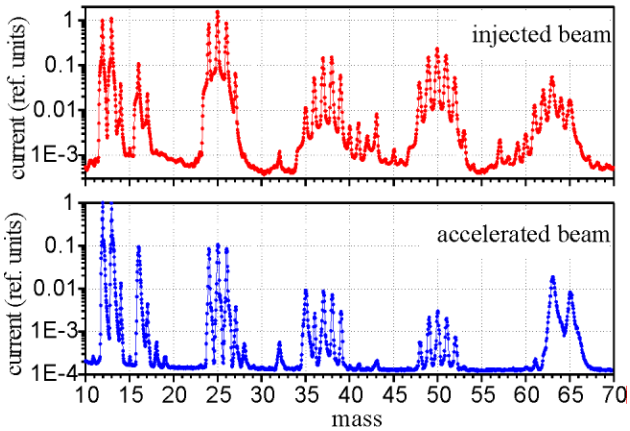

Figure 1: Mass spectrums of the ^{13}C enriched graphite with $(^{12}C)_m(^{13}C)_n$ clusters

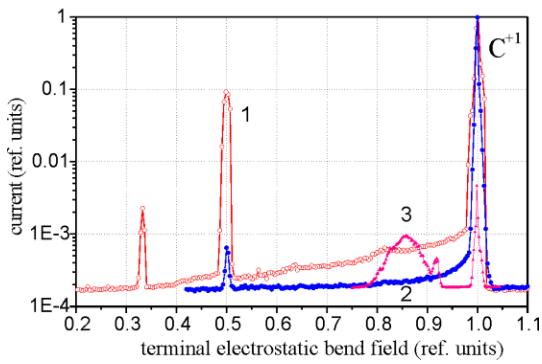

Figure 2: The currents of accelerated beams

One can see the large tail of beam intensity; this tail is caused by energy spread of ions recharged on residual gas in electric field of the first accelerating tube. The fractions 2+ and 3+ of the charge state distribution are also visible. Recently, the high-energy (HE) magnet for selection of accelerated beam was installed at the exit of the accelerator. One can see from curve #2 in Fig.2 that energy tail is cut after HE magnet. The peak at 0.5 value is caused by C^{2+} ions, which are exchanged to 1+ at the entrance of the HE tube on residual gas. The photo of 200kV carbon beam after HE magnet taken from CsI crystal and two transverse beam-profiles from wire monitor are presented in Fig. 3.

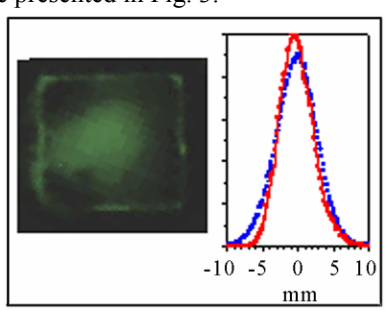

Figure 3: Beam photo from "CsI" crystal and profile at the exit of the AMS.

To test the terminal bend selection, the ^{13}C beam was accelerated and passed through HE magnet, which was set for $^{12}C^{1+}$ ions. As it is seen from curve #3 in Fig. 2, the peak of beam intensity exists at 0.85 of terminal bend value. It corresponds to energy of $^{13}C^{1+}$ and momentum is equal to the $^{12}C^{1+}$ ions. These low-energy ions are filtered by tandem bend at operational bend value + 1, and can not take part in charge-exchanging process in HE accelerator tube. The fragments of the destructed molecules are also filtered by tandem 180° bend system.

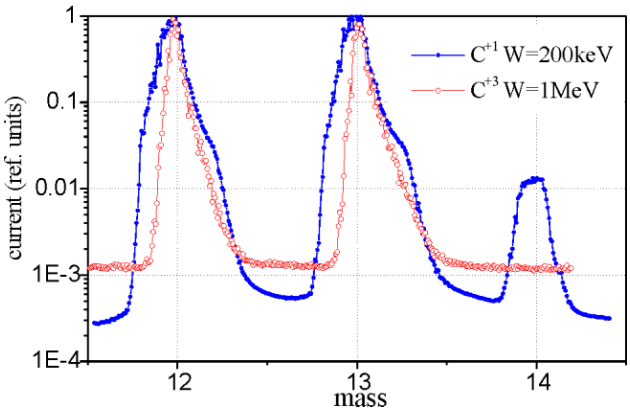

Figure 4: Mass spectrums of accelerated beams. The molecules of 14 mass are destroyed in stripper.

The mass spectrums of the accelerated ions in charge stages 1+ and 3+ are presented in Fig. 4. The HE magnet and low-energy (LE) magnet are being varied together for the desired mass passage. In order to increase 3+ ions output after magnesium stripper, the 250kV terminal voltage was used. The molecules (with mass M = 14) are destroyed in stripper. The intensity peaks at larger energy are narrower due to less ion scattering.

The scans of the HE magnet with ^{12}C and ^{13}C ions injected into the tandem accelerator are presented in Fig. 5.

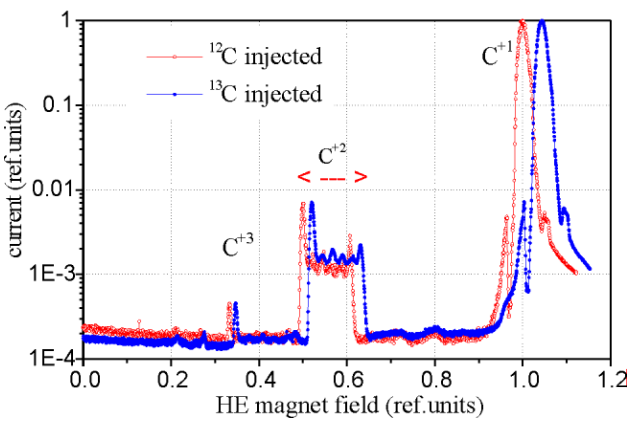

Figure 5: The scans of the HE magnet with 12C and 13C ions

The tandem 180° bend was set for 1+ charge state. The intensity peak from 0.5 to 0.6 ref. u. (HE magnet current) is caused by C^{1+} ions, which are charge exchanged to 2+ in the HE tube. The origin of 3+ state peak is the same. The peaks near the primary 1+ stage peak are also visible. These peaks are displaced about one unit of mass from the primary peak, but not precisely. It is not accountable from charge exchange or molecular breaking processes. Experiments when some of the pumps were turned off showed, what the values of these peaks are not correlated with pressure of residual gas. We assume that, these peaks appear due to scattering of the primary ion beam on vacuum chamber walls in the HE magnet when the primary beam is displaced from the central orbit. For reduction of such a background, the aperture collimator will be installed at the exit of HE magnet.

The detector and electronics for carbon ions counting will be prepared soon.

SUMMARY

- All the basic components of the AMS have been installed and now in operation.
- The magnesium vapors stripper was tested, it has shown 600 hours operation without magnesium refilling. The molecules destruction in stripping target has been observed.
- The first tests of isotopes selection were undertaken. The measurements of several samples (^{13}C enriched graphite, metallurgical silicon and others) have been performed at low energy.

ACKNOWLEDGEMENTS

This work is supported by FASIE Foundation# and by SB RAS*

REFERENCES

[1] N. Alinovsky et al., "Status of the Russian accelerator mass spectrometer, Proceedings of 10th European Particle Accelerator Conference (EPAC 06), June 26-30, Edinburgh, Scotland, p.2391, WEPCH195.

[2] N.I. Alinovsky et al., "Status of Accelerator Mass Spectrometer at BINP". Proceedings of XX Russian Accelerator Conference (RuPAC2006) Novosibirsk, Russia, September 10 - 14, 2006.

www.fasie.ru
* Integration Project #7

TARGET ASSEMBLY AND NEUTRONICS DESIGN STUDY FOR THE INDIAN SPALLATION NEUTRON SOURCE USING NMTC/JAM CODE*

V.K. Senecha[1#] and Masayoshi Kawai[2], [1]Power Supply Division, RRCAT, Indore, India;
[2]Institute of Material Structure Science, KEK, Ibaraki, Japan

Abstract

Target-moderator-reflector assembly (TMRA) design studies for the best neutronics performance of the proposed Indian Spallation Neutron Source (ISNS) have been carried out using high energy particle transport code NMTC/JAM. The issues relevant for TMRA design like selection of target material, effect of target shape and dimensions and placement of moderator, suitable material for reflector its size have been addressed using the code calculations. Code calculations have shown that the neutron yield per proton for thick Pb target and for varying target lengths are in good agreement within the error limit with the results reported by the experimental group and matching with the results of JAERI code calculations (JAERI –Data/code 2001-07). Different geometrical configurations for TMRA were attempted and resulted tallies for track-length, surface crossing, nuclide yield, heat deposition, and time for the neutrons have been calculated. It has been observed that wing type structure of moderator position with respect to the target is suitable for optimum neutron yield in the pulsed mode.

INTRODUCTION

Raja Ramanna Centre for Advanced Technology (RRCAT) is planning to establish a 1 GeV proton beam rapid cycling synchrotron (RCS) accelerator facility at Indore. The proton beam from the RCS will be directed towards the spallation target station which will produce intense pulsed neutrons as a complementary probing tool compared to x-rays from the synchrotron radiation source. Internationally, few such facilities are operational and efforts are being made towards development of advanced neutron sources that will revolutionize the future prospects in the basic science, material science, biology and new technologies. As next generation neutron sources are under advanced stages of construction at ORNL and JPARC which will exceed the neutron intensity level in the pulsed mode by nearly 1-2 orders of magnitude higher than the highest intensity available till date by the high flux nuclear power reactors (ILL). The neutron scattering experiments will be carried out at much higher resolution and efficiency level and in the wider range of wavelength and momentum to cover applications in almost all branches of science be it chemistry, physics, biology or material science. In the present study related to design of Indian Spallation Neutron Source (ISNS) the high energy proton beam interaction with the high atomic number solid targets have been performed using the NMTC/JAM code developed by the JAERI [1]. The TMRA design study involves evaluating best neutronics performance by selecting suitable target material its dimensions, position of moderators, reflector material its size and thermal energy deposition and related parameters that will be suitable for ISNS.

*Work supported by KEK, JAPAN and RRCAT, Indore
#senecha@cat.ernet.in

PROPOSED ISNS PARAMETERS

The conceptual design of the spallation neutron source is based on the 1 GeV proton beam extracted out of the RCS. Typical parameters of the system are as below:

RFQ Injection Energy (keV)	50 keV
DTL Injection	4.5 MeV
RCS Injection Energy (MeV)	100 MeV
Beam Energy on Target	1.0 GeV
RCS Repetition Rate	25 Hz
Average Beam Current	100 μA

NMTC/JAM CODE CALCULATIONS

NMTC/JAM can simulate transport of nucleons, mesons, baryons, leptons as well as their anti-particles through a given medium using Monte Carlo technique. It allows any target nucleus to be used for the material in the medium except the light ions like He^3 and α and heavy ions.

Maximum energy of the particle transporting in a medium is limited to 200 GeV for all transport particles, while the minimum energy is restricted to 20 MeV for neutrons and 0.1 MeV for other particles. The cut-off neutrons below the limit of nuclear models can be stored along with phase space information data of each such neutrons can be stored in a file for subsequent transport calculations using the MCNP4A code. A user supplied source routine is required to read the phase information data of individual cut off neutrons and photons in the MCNP4A code.

In order to check the validity and accuracy of various models used in the NMTC/JAM code, we have performed the simulations of a proton beam (12 GeV energy) interactions with the cylindrical lead target with 20 and 10 cm diameter and 60 cm length. These parameters were chosen so that it can be compared with the experimental results obtained at KEK using the Mn-bath moderation method. Neutron yields data are derived experimentally by changing the target length in steps of 10 cm. First we

tried to study the variation of neutron spectrum generated by the 12 GeV proton beam inside cylindrical Pb target of different dimensions ranging from 10 cm dia and 10 cm length to 20 cm dia and 60 cm length as shown in the Figure 1. It is noticed that the flux of neutrons along the length of the target in a given target volume will be highest for 10 x 10 cm cylinder and lowest for the 20x60 cm cylinder due to higher level of scatterings in larger volume and with pencil beam of proton being used to produce the spallation neutrons along the cylinder axis.

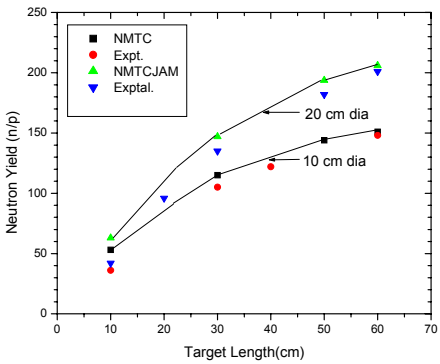

Figure 1: The neutron yields from lead target with 12 GeV protons striking the cylindrical target in units of neutrons per proton as a function of target length. The red symbols (10 cm diameter case) and blue symbols (20 cm diameter case) are experimental results and solid lines are the results of NMTC/JAM.

Then we compared the results of neutron yield from Pb cylindrical target of 10 and 20 cm diameter with length variation from 10cm to 60 cm, generated by 12 GeV proton beam and compared with experimental values. It is noticed that the neutron yield steadily increases with cylinder length and reaches a maximum value at 60 cm length. The experimental values are in close agreement with the NMTC/JAM code calculation values with in the error limit. The small difference in the calculation values is mainly due to the fact that the transport of neutrons below 20 MeV energy could not be carried out due to the non-availability of source code patch file for MCNP4A code.

Neutron production and leakage from the target

The neutron yield from the high-energy proton interaction with the target nuclei depends on the material type as well as its size for a given incident particle energy [2-4]. For practical purpose it is the number of neutrons obtained per incident proton. The axial distribution of leakage neutrons from the target depends on the target-moderator coupling (the best moderator position relative to the target). For thin target the cascade part of the spectrum can reach up to the energy of incident particle. It becomes strongly anisotropic with higher energies emerging mainly in the forward direction as expected from collision. The number of leakage neutrons from the cylindrical surface of a target depends on the target radius. Initially the number increases with increasing radius and then decreases.

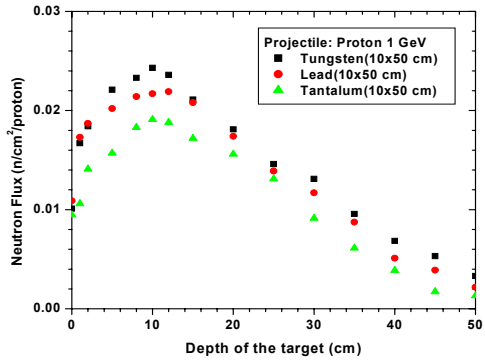

Figure 2: Neutron flux leakage from the tungsten, lead and tantalum targets (cylindrical with dia and length of 10 x 50 cm) as a function of target depth is shown for 1 GeV incident proton beam with Gaussian shape. Neutron flux consists of fast neutrons and has been obtained using NMTC/JAM code calculations.

This is due to the fact that probability of absorption of source neutron increases in the target. Therefore the 10 cm diameter is sufficient for optimum leakage of neutrons then the dependence on length of the cylinder has been calculated using the NMTC/JAM. As illustrated in Figure 2, the peak neutron flux is noticed near 10 cm depth of the target from the entrance surface of the target and this is the most suitable position for placement of the moderators in order to optimize the epithermal and cold neutron flux through the moderators. Further the neutron flux is higher for tungsten target compared to the lead and tantalum targets for 1GeV proton beam energy hence tungsten is chosen as a spallation target material.

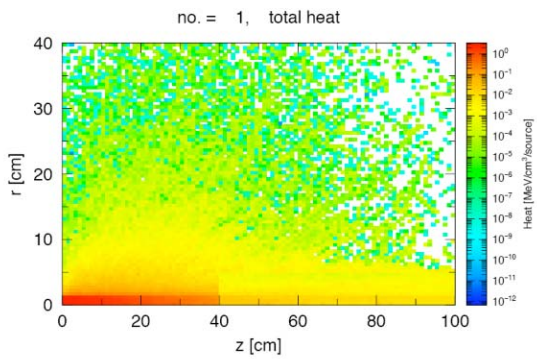

Figure 3: The heat deposition in bare tungsten target of cylindrical geometry by proton beam of 1 GeV energy with 7 cm diameter cylindrical shape.

For a cylindrical shape target the heat deposited in tungsten target is calculated for 1 GeV proton beam as shown in the Figure 3 gives a maximum value of 0.388 kW/cm^3. In the present studies we have performed using Tungsten as target, light water as moderator and Lead /Iron as reflector material. We have tried to study the TMRA configuration from neutronics point of view. We

performed the NMTC code calculations for fast neutrons that are emitted from the target are allowed to diffuse through the moderator and reflector materials. The arrangement of the TMRA is shown in the Figure 4.

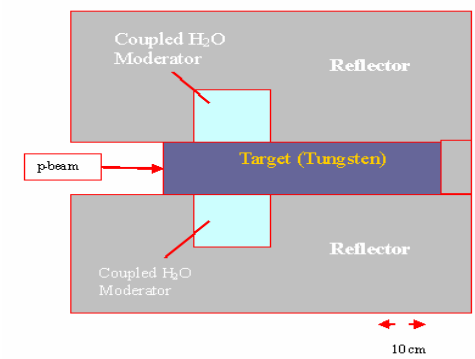

Figure 4: Target position near the centre of the reflector box is most suitable to obtain high neutron flux through the moderator. From the NMTC/JAM code calculations it appears that Pb can serve as a better reflector material compared to Fe.

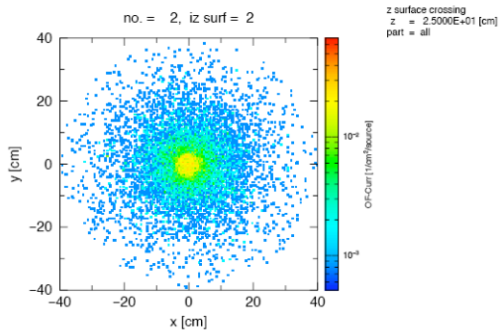

sum over track length flux value for all energies: 1.96×10^{-3}

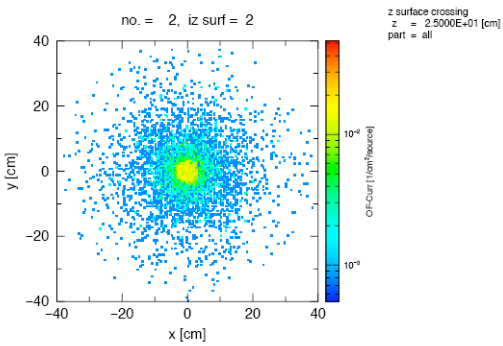

sum over track length flux value for all energies: 1.42×10^{-3}

Figure 5: Comparison of surface cross over current for the case of Tungsten (upper) and Pb (lower) target material through light water moderator at same z position suggest higher yield for tungsten target compared to Pb target.

The comparison of tungsten and lead target suggests that the surface cross over current is higher in case of tungsten target over the light water moderator surface than lead target case with sum over track length value for all energy bins of 1.96×10^{-3} for W compared to the value of 1.42×10^{-3} for Pb target, as shown in the Figure 5. Nearly similar comparison exists in the 3rd surface cross over current. The time profile of cut off neutron (20 MeV) obtained with NMTC/JAM shows that Pb can give better neutron yield of neutrons below 20 MeV energies compare to Fe as a reflector material. The escape neutron time profile also suggest that there are less number of escape neutrons in case of Pb reflector compared to Fe reflector case.

CONCLUSION

NMTC/JAM code calculations performed for the ISNS design studies of TMRA for 1GeV proton beam interaction with the heavy metal targets like W, Pb and Ta suggest tungsten to be the most suitable material. Further studies have shown that an elliptical cylinder target shape is suitable for the optimum neutron leakage from the surface of the target. The placement of moderator at a position around 10 cm from the start of the target surface gives maximum neutron flux with moderator at the top of the target in a wing type geometry suitable for better neutronics performance. The track length and surface cross over from the tungsten and Pb targets suggest that tungsten can give better neutron yield. The comparison of Pb and Fe as a reflector material shows that Pb offers superior properties in terms of the neutron time pulse profile giving higher numbers of cut off neutrons and lower number of escape neutrons. In order to make a detailed study of cold and epithermal neutrons generated in the pulsed mode from the TMRA the treatment of low energy neutrons below the energy of 20 MeV would be necessary.

REFERENCES

[1] Koji Niita, S.Meigo, H. Takada and Y.Ikeda , "High energy particle transport code NMTC/JAM", JAERI-Data/Code 2001-07, (2001).

[2] G.S. Bauer, "Physics and technology of spallation neutron sources",Nucl. Inst.& Methods in Phys. Res.A **463**, 505-543 (2001).

[3] M. Kawai, T. Ino, N. Torikai, S. Itoh, T. Kamiyama, M. Furusaka, Y. Kiyanagi, M. Ooi, T. Fukunaga, "Renewal of the KENS target–moderator–reflector assembly and its performance" Appld. Phys. **A 74** , S43-S45 (2002).

[4] Noboru Watanabe, "Neutronics of pulsed spallation neutron sources", Rev. Prog. Physics **66**, 339-381 (2003).

ACTIVITIES ON THE NUCLEAR DATA MEASUREMENT AT THE POHANG NEUTRON FACILITY BASED ON ELECTRON LINAC *

G.N. Kim#, A.K.M.M.H. Meaze, and M.U. Khandaker
Department of Physics, Kyungpook National University, Taegu 702-701, Korea
Y.D. Oh, H.S. Kang, M.H. Cho, I.S. Ko, and W. Namkung
Pohang Accelerator Laboratory, POSTECH, Pohang 790-784, Korea

Abstract

We report the present status of the Pohang Neutron Facility which consists of an electron linear accelerator, a water-cooled Ta target, and a 12-m time-of-flight path. We measured the neutron total cross-sections in the neutron energy range from 0.1 eV to few hundreds eV by using the neutron time-of-flight method. A ^{6}LiZnS(Ag) glass scintillator was used as a neutron detector. The neutron flight path from the water-cooled Ta target to the neutron detector was 12.1 m. The background level was determined by using notch-filters of Co, In, Ta, and Cd sheets. In order to reduce the gamma rays from bremsstrahlung and those from neutron capture, we employed a neutron-gamma separation system based on their different pulse shapes. The present measurements of Ta, Hf, Ag, and Mo samples are in general agreement with the evaluated data in ENDF/B-VI.

INTRODUCTION

The Pohang Neutron Facility (PNF) was proposed in 1997 and constructed at the Pohang Accelerator Laboratory on December 1998 [1]. It consists of a 65-MeV electron linac, water-cooled Ta neutron producing target, and a 12-m-long evacuated vertical flight tube leading to the detector location. The electron linac consists of a thermionic RF-gun, an alpha magnet, four quadrupole magnets, two SLAC-type accelerating sections, a quadrupole triplet, and a beam-analyzing magnet. The overall length of the linac is about 15 m. As a photoneutron target, we choose a tantalum, which has advantages of high density (16.6 g/cm^3), high melting point (3,017^{o}C), and high resistant against the corrosion by cooling water. The characteristics of PNF are described elsewhere [2].

We report the measured neutron total cross-sections of natural Ta, Hf, Ag, and Mo in the neutron energy range between 0.1 eV and 100 eV by using the neutron time-of-flight (TOF) method at the PNF. The results were compared with other measurements and the evaluated data in ENDF/B-VI.

*Work supported in part by the SRC program of KOSEF, and KAERI
#gnkim@knu.ac.kr

POHANG NEUTRON FACILITY

The Pohang Neutron Facility (PNF) consists of an electron linac, a water-cooled Ta target, and an 11 m long TOF path. The electron linac consists of standard subsystems: a thermionic RF-gun, an alpha magnet, four quadrupole magnets, two SLAC-type accelerating sections, a quadrupole triplet, and a beam-analyzing magnet. The overall length of the linac is about 15 m. The RF-gun is one cell cavity with a dispenser cathode of 6 mm diameter. The RF-gun produces electron beams of 1 MeV, 300 mA, and 1.5 μs [3]. The alpha magnet is used to match the longitudinal acceptance from the RF-gun to the first accelerating section. Electrons move along an alpha-shaped trajectory in the alpha magnet with the bend angle of 278.6^o. Four quadrupole magnets are used to focus the electron beam in the beam transport line from the thermionic RF-gun to the first accelerating section. The quadrupole triplet installed between the first and the second accelerating sections is used to focus the electron beam during the transport to the experimental beam line at the end of the linac.

A water-cooled Ta target was designed by the Electron Gamma Shower simulation code, EGS4 [4]. The Ta target was composed of ten Ta sheets, 49 mm in diameter and 74 mm in total length [5]. There was 1.5 mm water gap between Ta sheets in order to cool the target effectively. The target housing was made of 0.5 mm thick titanium. The calculated conversion ratio from a 100 MeV electron to neutrons was 0.032 obtained by using the EGS4. According to this result, the neutron yield per kW beam power for the electron energy above 40 MeV at the target was 2.0×10^{12} n/sec, which was about 2.5% lower than the calculated value based on the Swanson's formula, $1.21\times10^{11}\ Z^{0.66}$, where Z is the atomic number of the target material and the electron energy is above 40 MeV [6].

Since we have to utilize space and infrastructure at PAL, an 12 m long TOF path and a detector room were constructed vertically to the electron linac. The TOF tubes were made by stainless steel with two different diameters of 15 and 20 cm.

EXPERIMENTAL PROCEDURE

The experimental arrangement and data acquisition system for the transmission measurements are described in elsewhere [2]. The target is located in the position where the electron beam hits its center. This target was set at the center of a cylindrical water moderator contained in an aluminum cylinder with a thickness of 0.5 cm, a diameter of 30 cm, and a height of 30 cm. The water level in the moderator was 3 cm above the target surface, which was decided based on a measurement of the thermal neutron flux. The neutron collimation system was mainly composed of H3BO3, Pb and Fe collimators, which were symmetrically tapered from a 10-cm diameter at the beginning to a 5-cm diameter in the middle position where the sample changer was located, to an 8-cm diameter at the end of guide tube where the neutron detector was placed. There was 1.8-m-thick concrete between the target and the detector room. The sample changer consists of a disc with 4 holes; each hole is 8 cm in diameter, which matches the hole of the collimator in the neutron beam line. The sample changer is controlled remotely by the CAMAC module. The distance between centers of two opposite holes is 31 cm. The transmission samples were placed at the midpoint of the flight path and were cycled into the neutron beam by using the sample changer with four positions. The physical parameters of the samples used in the total cross-section measurements are given in Table 1. A set of notch filters of Co, In, and Cd plates with thickness of 0.5 mm, 0.2 mm, and 0.5 mm, respectively, was also used for the background measurement and the energy calibration.

Table 1: Physical parameters of the sample.

Sample	Purity (%)	Size (cm^2)	Thickness (mm)	Weight (g)
Ta	99.7	10×10	0.45	16.60
Hf	99.9	5×5	0.5	16.44
Mo	99.9	π×3.1×3.1	3.0	94.00
Ag	99.98	10×10	0.5	53.04

The neutron detector was located at a distance of 10.81m from the photo-neutron target. A ^{6}Li-ZnS(Ag) scintillator BC702 from Bicron (Newbury, Ohio) with a diameter of 127 mm and a thickness of 15.9 mm mounted on an EMI-93090 photomultiplier was used as a detector for the neutron TOF spectrum measurement.

During the measurement, the electron linac was operated with a repetition rate of 10 Hz, a pulse width of 1.5 μs and the electron energy of 60~65 MeV. The peak current in the beam current monitor located at the end of the second accelerator section is above 50 mA, which is the same as that in the photo-neutron target.

DATA TAKING AND ANALYSIS

Two different data acquisition systems were used for the neutron TOF spectra measurements: one for the NIM-based system and the other for the CAMAC-based system. The main purpose of the NIM-based system was neutron-gamma separation and the parallel accumulation of the neutron TOF spectra if necessary. The CAMAC-based system consists of a main data acquisition part and a control part of the sample changer. The 10-Hz RF trigger signal for the modulator of the electron linac was used as a start signal of the time digitizer. The details of data acquisition system are described in elsewhere [2].

The measurements were performed with two samples simultaneously. The two other positions of the sample changer were empty to collect the neutron TOF spectra without a sample (open beam). The positions of the samples were chosen in the following sequence: sample 1 – empty – sample 2 – empty. The exposition times for both sample 1 and sample 2 were 15 minutes (9000 pulses of PNF linac); for each empty position, it was 7.5 minutes. Thus, the durations for the samples were the same as those for the total open beam measurements. The interleaving sequence of free positions of the sample changer was chosen to minimize the influence of slow and/or small variation of the neutron beam intensity. If the beam intensity variations or its drift was fast and/or large, then these partial measurements were excluded from the total statistics. The total data taking times for Ta, Hf, Ag, and Mo were 21.75, 8.5, 65, and 48 hours, respectively, with the same times for the open beams.

We estimated the background level by using the resonance energies of the neutron TOF spectra of the notch-filters of Co, In and Cd. The magnitude of the background level was interpolated between the black resonances by using the fitting function, $F(I) = a + be^{-I/c}$, where a, b, and c are constants and I is the channel number of the time digitizer.

The neutron total cross-section is determined by measuring the transmission of neutrons through the sample. The transmission rate of neutrons at the i-th group energy E_i is defined as the fraction of incident neutrons passing through the sample compared to that in the open beam. Thus, the neutron total cross-section is related to the neutron transmission rate $T(E_i)$ as follows:

$$\sigma(E_i) = -\frac{1}{N}\ln T(E_i)$$

where N is the atomic density per cm^2 of the sample. Then, we have calculated the average total cross-sections for the same energy interval.

The total cross-sections of natural Hf , Ta, Ag, and Mo were obtained in the energy range from 0.1 eV to 100 eV by using the neutron TOF method as shown in Fig. 1. We only considered the statistical errors for the present measurements because the other sources of uncertainties, which include the detection efficiencies, the geometric factor for the sample, and the other systematic errors, are negligible.

RESULTS AND DISCUSSION

The present measurements for the neutron total cross-sections of Hf, Ta, Ag, and Mo are compared with the previous data measured by other groups [7, 8, 9, 10] and the evaluated data in ENDF/B-VI [11] as shown in Fig. 1. The present measurements without any corrections are generally in good agreement with other data and the evaluated ones in the energy range between 0.1 eV and 100 eV.

In addition to the measurements of neutron total cross-sections in the neutron energy range from thermal to several hundreds eV by using the neutron TOF method, we performed the activation measurements with photons produced by bremsstrahlung process and neutrons. We are also preparing gamma detectors with BGO crystals for the neutron capture cross-section measurement.

REFERENCES

[1] G. N. Kim *et al.*, in "Proceedings International Conference on Nuclear Data for Science and Technology" edited by G. Reffo *et al*. (Trieste, Italy, May 19-24, 1997), p. 556.

[2] V. Skoy *et al.*, J. Korean Phys. Soc. 41, 314-321 (2002); G. N. Kim *et al*., J. Korean Phys. Soc. 43, 479 (2003).

[3] H. S. Kang, G. N. Kim, M. H. Cho, W. Namkung, and K. H. Chung, IEEE Trans. Nucl. Sci. 44, 1639 (1997).

[4] W. R. Nelson, H. Hirayama and D. W. O. Rogers, "The EGS4 Code System," SLAC Report 265 (1985).

[5] W. Y. Baek *et al*., "Design of the Photoneutron Target for the Pulsed Neutron Source at PAL," Proc. Workshop on Nuclear Data Production and Evaluation (Pohang, Korea, Aug. 7-8, 1998).

[6] W. P. Swanson, "Radiological Safety Aspects of the operation of Electron Linear Accelerators," IAEA Tech. Rep. 188 (1979).

[7] S. Bernstein *et. al*., Phys. Rev. 87, 487 (1952); E. G. Joki *et. al*., J. Nucl. Sci. Eng. 11, 298 (1961); W. M. Moore, Bull. Am. Phys. Soc. 6, 70 (1961); R. Schermer, AEC reports to the NCSAG, WASH Progress Report-1031, 16 (1961); L. M. Bollinger *et. al*., Phys. Rev. 92, 1527 (1953); H. J. Cho *et al*., Ann. Nucl. Energy 27, 1259 (2000).

[8] E. Melkonian et al., Phys. Rev. 92, 702 (1953); R. L. Christensen, Phys. Rev. 92, 1509 (1953); J. A. Harvey et al., Phys. Rev. 99, 10 (1955); J. E. Evans *et al*., Phys. Rev. 97, 565 (1955); V. V. Vladimirskii *et al*., Proc. 1st Conf. on Peaceful uses Atomic Energy, Geneva, 4, pp 22 (1955); R. E. Schmunk *et al*., Nucl. Sci. Eng., 7, 193 (1960).

[9] W. W. Havens, Jr. and J. Rainwater, Phys. Rev. 70, 154 (1946); W. Selove, Phys. Rev. 84, 869 (1951); F. G. P. Seidi et al., Phys. Rev. 95, 476 (1954); R. G. Fluharty et al., Phys. Rev. 103, 1778 (1956); R. E. Wood, Phys. Rev. 104, 1425 (1956); K. K. Seth et al., Phys. Rev. 110, 692 (1958), J. B. Garg et al., Phys. Rev. 137, B547 (1965).

[10] J. R. Dunning et al., Phys. Rev. 48, 265 (1935); S. Wynchank et al., Phys. Rev. 166, 1234 (1968); E. R. Hodgson et al., Proceedings of the Physical society, London, 65A, 992 (1952); K. K. Seth et al., Phys. Rev. 110, 692 (1952); F. K. Moreno et al., Atomkernenergie, 31, 42 (1978); M. Salama et al., Atomkernenergie, 45, 282 (1984); Yu. V. Grigoriev et al., Ser. Yadernye Konstanty, 2002, 50 (2002).

[11] Evaluated Nuclear Data, ENDF/B-VI, Brookhaven National Laboratory (2004), http://www-nds.iaea.org/point2004/.

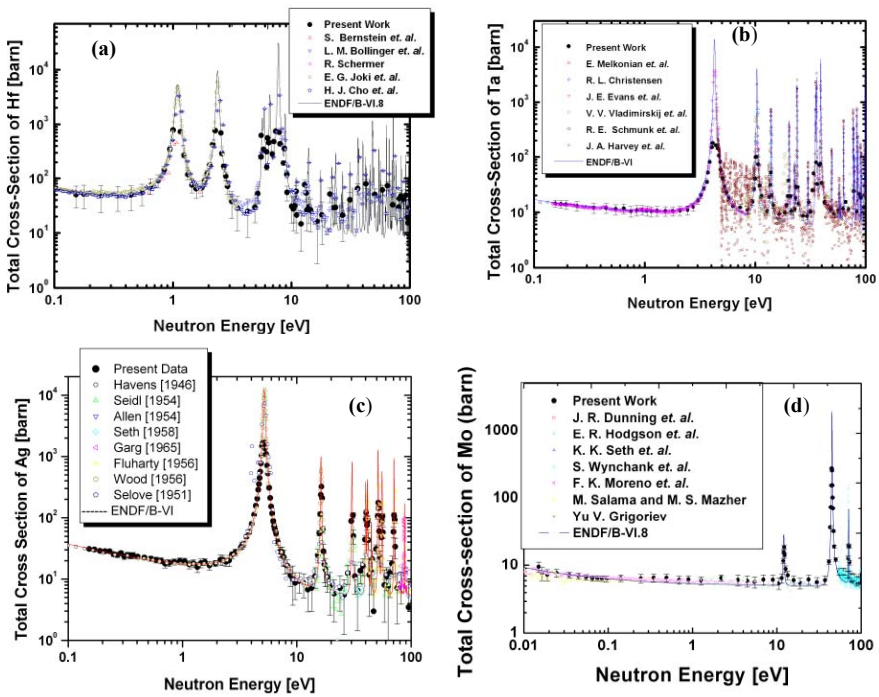

Figure 1: Comparison of the experimental total cross-sections of (a) Hf, (b) Ta, (c) Ag, and (d) Mo with the other experiments and the evaluated one from ENDF/B-VI in the neutron energy region between 0.01 and 100 eV.

PRESENT STATUS OF THE FFAG ACCELERATORS IN KURRI FOR ADS STUDY

M. Tanigaki*, Y. Mori, M. Inoue, K. Mishima, S. Shiroya
RRI, Kyoto University, Kumatori, Osaka 590-0494, Japan
Y. Ishi, S. Fukumoto, Mitsubishi Electric Corporation , Kobe, 652-8555, Japan
S. Machida, CCLRC/RAL, Chilton, Didcot, Oxon, OX11 0QX. UK

Abstract

KART (Kumatori Accelerator driven Reactor Test) project has started at Kyoto University Research Reactor Institute (KURRI) from the fiscal year of 2002. The purpose of this project is to demonstrate the basic feasibility of ADS, studying the effect of incident neutron energy on the effective multiplication factor of the subcritical nuclear fuel system. A proton FFAG accelerator complex as the neutron production driver for this project is now in the final stage of the test operation.

INTRODUCTION

As a substitute for the 5 MW reactor at Kyoto University (KUR), a neutron source based on the Accelerator Driven Sub-critical Reactor system (ADSR) concept has been proposed in 1996[1]. The conceptual design study on ADSR using the MCNPX code clarified the lack of reliable effective multiplication factor k_{eff} in the proton energy region between 20 MeV and 150 MeV. Since our current experimental studies are limited to those with a 300 keV Cockcroft-Walton accelerator[2, 3], a proton beam source which covers between 20 MeV and 150 MeV is required to extend our study on ADSR system.

A Fixed Field Altenating Gradient (FFAG) accelerator orignally proposed by Ohkawa 40 years ago[4] has a lot of advantages compared to synchrotrons such as a large acceptance, a possible fast repetition rate because of no active feed back in the acceleration. In ADS system, the stability of beam acceleration is directly connected to the stability of reactor itself. In such meaning, FFAG accelerators can be a good candidate for the neutron source driver in ADS system.

While an FFAG has a potential to a neutron source driver, there are still technical difficulties in FFAG accelerators, such as the lack of wide band high voltage RF cavity or the short straight section insufficient for beam injection and extraction. Mori has demonstrated that these difficulties can be overcome by recent developments [5], [6] with the successes of a 500 keV PoP FFAG and an 150 MeV FFAG with RF.

On such basis of our study and the technical developments on FFAG, KART project has been approved and started from the fiscal year of 2002. In this project, a practical proton FFAG accelerator complex of E_p = 20 $\sim$ 150 MeV as a proton driver for ADSR is constructed in KURRI and the basic feasibility of ADSR system and the multiplication factor k_{eff} in the energy region of $E_p = 20 \sim 150$ MeV will be studied.

* tanigaki@rri.kyoto-u.ac.jp

FFAG ACCELERATOR COMPLEX

The FFAG accelerator complex for KART project consists of one FFAG with an induction acceleration as the injector and two FFAG with RF as the booster and main accelerators, respectively. Basic specifications for this FFAG complex are summarized in Table 1. The layout of these FFAG accelerators in the accelerator room is shown in Fig. 1. All of these accelerators will be in pulse operation up to the repetition rate of 120 Hz. The beam energy of the current FFAG complex can be varied between 20 $\sim$ 150 MeV by the change of beam energy from the injector.

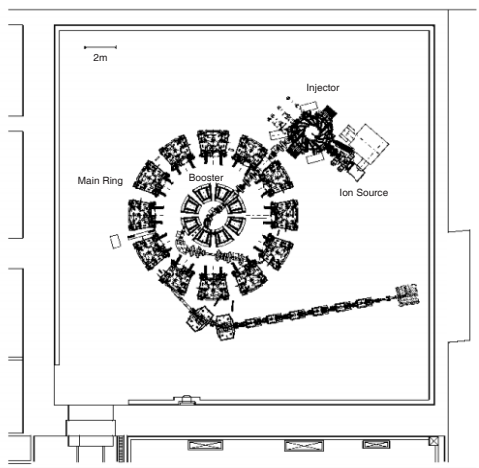

Figure 1: FFAG complex at KURRI.

Ion source and injector FFAG with induction acceleration

H^+ ions are extracted from the typical multi-cusp type ion source and accelerated to 100 keV, then transported to the injector. Since all of the FFAG complex are operated in the pulse mode, the ion source itself is also operated in the pulse mode for less power consumption. The arc voltage is pulsed at the duty of $\sim$ 10%, then the pulsed beam is

Table 1: Specification of the FFAG complex at KUR

	Injector	**Booster**	**Main**
Focusing	Spiral	Radial	Radial
Acceleration	Induction	RF	RF
k	2	2.45	7.5
E_{inj}	100 keV	2.5 MeV	20 MeV
E_{ext}	2.5 MeV	20 MeV	150 MeV
p_{ext} / p_{inj}	5.00	2.84	2.83
r_{inj}	0.60 m	1.27 m	4.54 m
r_{ext}	0.99 m	1.86 m	5.12 m

shaped to $\sim 50\mu$s at the beam chopper placed in the transport line between the ion source and the following injector.

The injector FFAG is a 2.5 MeV FFAG with induction acceleration scheme. 8 sprial sector magnets with the spiral angle of 42 degrees (Fig. 2) produces the FFAG magnetic field. The spiral sector type is chosen to this injector because of its rather long straight section and its higher packing factor. The index k for the FFAG field is determined by adjusting the currents of 32 trim coils placed on the pole face along the r direction (Fig. 3, 4). The beam energy of the current FFAG complex can be varied through the change of this k by supplying the proper current set for trim coils.

Booster FFAG with RF

The beam from the injector is then accelerated up to 20 MeV in this booster ring. This FFAG with RF is the radial sector type, consisting of 8 cells of DFD magnets. The FFAG magnetic field is produced by its pole shape with the half gap proportional to $(r/r_0)^k$. In this booster ring, $k = 2.45$ is chosen to minimize the beam excursion and the resonance variation. The window-frame type magnetic shield is attached to the both sides of the magnet to reduce the fringing field at the straight sections. The fringing field at the center of the straight section is confirmed to be less than 100 Gauss from the magnetic field measurement. The beam injection is performed by a septum magnet, an inflector electrode and a pair of bump magnets. Acceleration voltage is supplied by an RF cavity with very low Q (~ 1) for the flat output voltage over the acceleration frequency range. The beam extraction is performed by kicker and septum magnets. All the components for beam injection/extraction except the inflector for beam injection are in pulse operation. The booster ring under construction is shown in Fig. 5.

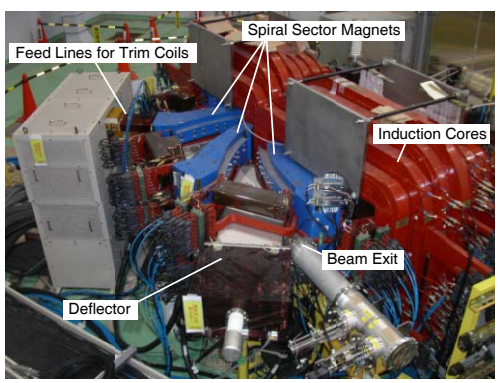

Figure 2: FFAG injector and ion source.

Figure 3: 32 trim coils attached to the pole piece of the injector.

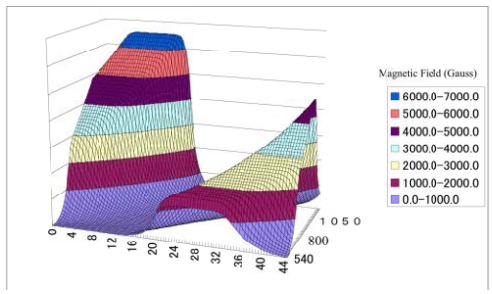

Figure 4: A typical FFAG magnetic field of the injector ring magnet with trim coils obtained by the field measurement.

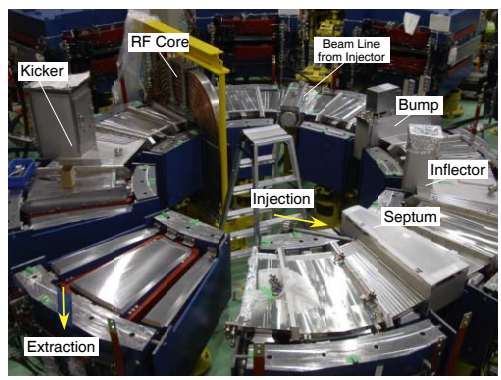

Figure 5: The booster FFAG under construction. DFD structure of the radial sector magnets can be seen in the front-left lattice. The remaining bump magnet and the septum for beam extraction are to be placed in the straight section before the lattice with beam extraction channel.

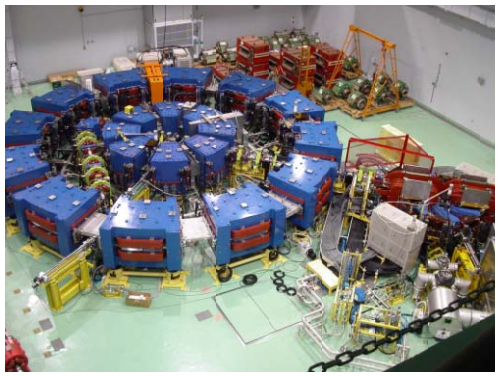

Figure 6: Current status of the accelerator room in "Innovation Research Laboratory".

Main FFAG with RF

The main accelerator is basically identical to the 150 MeV FFAG in KEK. Detailed discussions are available in ref. [6]. This time, the purity of iron in the magnets are increased to accept a high magnetic flux required for acceleration at 200 MeV, aiming the beam energy upgrade by the reinforcement of power supplies in near future. In our 150 MeV FFAG, a conventional amorphous core, not the finemet core, is used in the RF cavity. Then rather a larger size of the magnetic shield for the core is expected to be resulting in a COD source in our FFAG ring. A pair of dipole magnets are placed in both sides of RF cavity to minimize this effect.

CURRENT STATUS AND FUTURE PROSPECTS

The construction of FFAG accelerator complex is in progress since the construction of "Innovation Research Laboratory" was completed in March, 2004. This buliding is not only for FFAG accelerator complex, but also for the multipurpose usage of the beam from the FFAG complex in future, such as nuclear physics, chemistry, material science and cancer therapy. Currently, the construction of our accelerator complex are almost completed (Fig. 6). The basic studies for injector and booster are almost finished. Studies for beam injection and acceleration in the main ring are now in progress. The first beam from this FFAG complex is expected in the first quarter of 2007. The preparation of the subcritical core and the target for the neutron production are almost completed and the inspection for the actual operation will be held as soon as the accelerator complex is approved by the government.

This paper contains some results obtained within the task gFeasibility Study on ADSR Using Fixed Field Alternating Gradient (FFAG) Synchrotron as an Energy Amplifierh entrusted from the Ministry of Education, Culture, Sports, Science and Technology of Japan.

REFERENCES

[1] K. Kawase and M. Inoue, "Neutron Factory Project at KURRI", APAC 1998, Tsukuba, Japan, p. 104

[2] S. Shiroya, H. Unesaki et al., "Neutronics of Future Neutron Source Based on Accelerator Driven Subcritical Reactor Concept in Kyoto University Research Reactor Institute (KURRI)h, Int. Seminar on Advanced Nucl. Energy Systems toward Zero Release of Radioactive Wastes, 2nd Fujiwara Int. Seminar, Nov. 6-9, 2000, Shizuoka, Japan, *Abstracts* p. 58.

[3] S. Shiroya, H. Unesaki et al., Trans. Am. Nucl. Soc., 2001 Annu. Mtg., June 17-21, 2001, Milwaukee, Wisconsin, p. 78.

[4] T.Ohkawa, Proc. of annual meeting of JPS(1953)

[5] Y. Mori et al., "A new type of rf cavity for high intensity proton synchrotron using high permeability magnetic alloy", EPAC 1998, p. 299.

[6] T. Adachi et al., "A 150MeV FFAG SYNCHROTRON WITH hRETURN-YOKE FREEh MAGNET", PAC 2001, Chicago, the United States, p. 3254

[7] M. Aiba et al., "DEVELOPMENT OF A FFAG PROTON SYNCHROTRON", Proceeding of EPAC 2000, Vienna, Austria, p. 581

[8] M. Tanigaki et al., "Control System of a FFAG Complex for the ADSR Project in KURRI", Proceedings of the 5th International Workshop on Personal Computers and Particle Accelerator Controls, Hayama, Japan.

DESIGN AND FABRICATION OF ARUPS U6 UNDULATOR AT PLS

H.G.Lee, H.S.Suh, H.S.Han, Y.G.Jung, W.W.Lee, K.H.Park, D.E.Kim, C.W.Chung
Pohang Accelerator Laboratory, POSTECH, KOREA

Abstract

Pohang Accelerator Laboratory(PAL) had developed and installed U6 undulator recently to utilize brilliant undulator radiation for ARUPS (Angle Resolved Ultraviolet Photoemission Spectroscopy) beamline at Pohang Light Source (PLS). The U6 is a hybrid type device with period of 6 cm, minimum gap of 18 mm, maximum flux density of 0.902 Tesla and total magnetic structure length of 1830 mm. The support locations and structure of an insertion device are optimized to achieve a minimum deflection due to the magnetic loads. A Finite Element Analysis (FEA) is performed to find out the amount of maximum deflection and optimal support positions on the backing beam. The optimized maximum deflection is estimated to be about 11.6 μm, while the deflection before any optimization is 48.8 μm. In this report, all the mechanical design, fabrication and assembly details of the PLS U6 undulator are described.

INTRODUCTION

Pohang Light Source (PLS) is a 2.5GeV 3rd generation synchrotron light source [1]. The critical photon energy of the synchrotron radiation from bending magnet is about 5.48 keV at 2.5 GeV electron energy. U6 is designed for research on the electronic structure of solid surfaces and low dimensional nanostructures on surfaces. Using one sagittal focusing mirror and a specially designed chamber where a tube is passing through, brilliant UV and soft x-rays from two undulators can be efficiently delivered to the ARUPS system. The total energy resolution is about 10 meV at 20 eV photon energy.

The U6 consists of a magnetic structure, a support structure, and a drive and control system. Magnetic gap is adjusted by the drive system and the support structure, which includes the L-frame to support the magnetic structure. The L-frame structure is designed to allow for easy installation of the vacuum chamber and for easy magnetic field measurement. The U6 shown in figure 1 was designed with very rigid moment of inertia to length ratio resulting in minimum deflection. To reduce the deformation further, we designed and successfully implemented a Belleville washer springs system that counteracted the magnetic loads[2]. The compensation spring system will reduce the system friction, which gives better positional response from the drive system, reduced structure compression and no motor holding torque required at any magnetic gap. The drive system provides the gap adjustment mechanism to align the magnetic structure from gap 1.0 to 20.0 cm. The drive system includes two independent drive system in a standard structure. Each drive system is composed of step motor, gear reducer and absolutely rotary encoder. The positional accuracy is determined by two encoders attached on both ends of a ball screw. The measured gap repeatability is less than 7 μm. Five types of insertion device (U7, EPU6, U10, MPW14 and ARUPS U6) had been installed in the electron storage ring. The U6 described in this report is similar to other types of insertion device and built on the successful mechanical design concept, fabrication and assembly procedure

MAGNETIC STRUCTURE

The hybrid magnetic configuration consists of permanent magnets and ferromagnetic poles (vanadium permendur) to concentrate the magnetic flux to the poles. This hybrid scheme gives a higher peak field compared to pure permanent magnet structures. Using Radia developed in ESRF, magnetic geometry analysis have been carried out to study the optimal magnetic geometry. In the final design, the maximum magnetic field is 0.902 Tesla. Multiple trim magnets at the ends of the undulator will be installed to decrease the transverse multipole components and to correct the field integrals. The main parameters of U6 are listed in Table 1, and the schematic geometry configuration of half period is shown in figure 2.

The basic block of the magnetic structure is a half-period pole assembly which consists of an aluminium keeper, a Vanadium Permendur pole and six Nd-Fe-B magnetized blocks.

Table 1: Main parameters of the U6 based on 2.5GeV beam energy and 250mA beam current

Parameters	Value
Period length	6 cm
Number of full field poles	57
Peak field	0.902 Tesla
Total power	1.452 kW
Device length	1.83 m
Min. gap of magnetic structure	18 mm
Max. gap speed	10 mm/sec
Nominal gap speed	5 mm/sec
Max. magnetic load	2.4 Tons
Encoder type	Absolute rotating encoder
Encoder resolution	1.3 μm
Step motor	2-phase stepper motor
Motor resolution	< 1 μm/step

Figure 1: Photograph of ARUPS U6

The magnetic block has an average magnetization of 1.33 T and an intrinsic coercive force of 12.6 kOe. The variation of the magnetization (M_z) from block to block affects the pole-to-pole field error. Therefore, the block-to-block variation of the magnetization and the magnetization orientation error are limited to 1% and 1°, respectively. Flatness of the block surfaces shall be within 0.025 mm for the two surfaces perpendicular to the direction of magnetization and perpendicularity of the block surfaces to each other shall be within 0.002 mm/mm.

DESIGN AND FABRICATION OF SUPPPORT STRUCTURE

Deformation of backing beam

The structural deformation of the backing beam depends on the pole gap. The backing beam is designed to support a maximum magnetic load of 2.4 metric tons at minimum gap. The support point for the backing beam is determined to achieve minimum deflection. The backing beam is analysed using ANSYS [3], including the complicated geometry structure. A solid geometry is adopted for the backing beam, including girder, which is fixed at ball screw and a linear motion guide. The backing beam material is aluminium A6061-T6, and the girder is non-magnetic stainless steel 316L. For the study of the worst case for the backing beam, 2.4 metric tons magnetic loads were applied for estimation of the backing

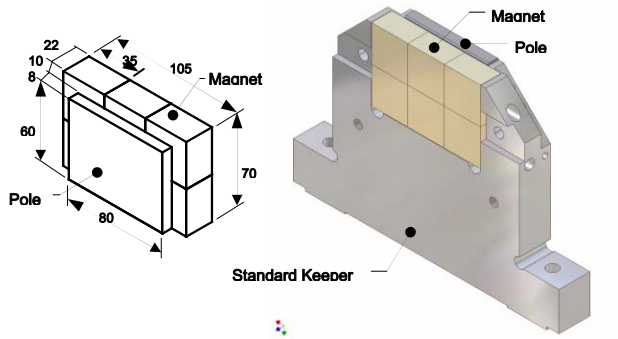

Figure 2: Geometry configuration of half period

beam deformation. ANSYS result for the backing beam in the vertical direction is shown in figure 3. The deformation of backing beam was analysed at no load, maximum magnetic load and maximum magnetic load with reaction force. The results are shown in figure 4. The minimum deformation at no load is 6 μm, and the maximum deformation at maximum magnetic load is 48.8 μm in the vertical direction without any compensating reaction force. This exceeds the specification and we need a mechanism to reduce the deformations. To reduce the deformations, we apply a reaction force from the compensation spring. The profile of the reaction forces is varied to find the optimum design parameter of the reaction spring system. The optimum occurs when 90% of the magnetic load is counteracted by the compensation spring system. In that case, the minimum deformation is 11.60 μm in the vertical direction, which meets our requirement. The deformation in the other two directions were negligible. The magnetic load compensation spring system will be provided for reacting the gap-dependent magnetic load. The magnetic load compensation spring system, as shown in Fig. 5, consists of several stacks of Belleville washers.

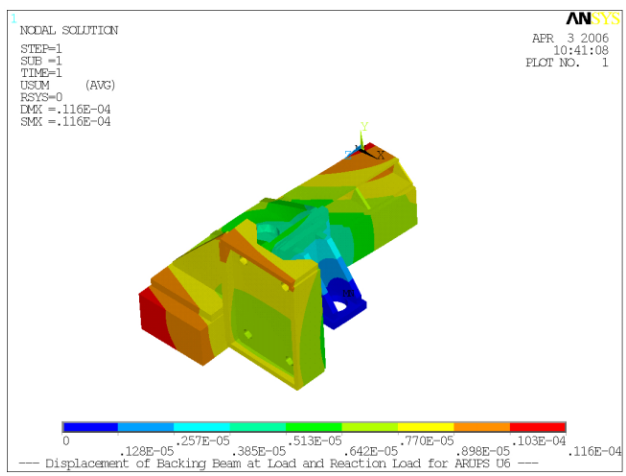

Figure 3: ANSYS result for the backing beam in the vertical (y) direction. The maximum deformation is about 11.60 μm for 2.4 metric tons of magnetic load and reaction

force with magnetic load compensation spring system are applied.

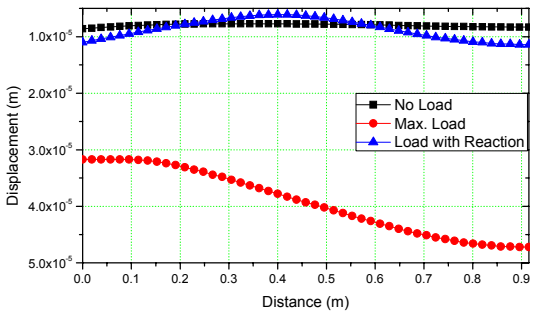

Figure 4: ANSYS results for the backing beam in the vertical (y) direction along Z-direction(beam pass) of backing beam at no load, maximum magnetic load and maximum magnetic load with reaction force.

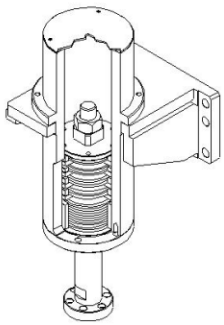

Figure 5: Design of magnetic load compensation spring system

Fabrication of magnetic structure

The magnetic structure will incorporate the hybrid magnetic configuration consisting of Nd-Fe-B magnetic block, vanadium permendur pole and aluminium keeper. The vanadium permendur (Fe 49%, Co 49%, Va 2%) pole is machined, heat treated, and then precision machined to the final geometry. Each pole is pinned to its keeper. The magnetic block is bonded into the pole assembly. The half-period pole assemblies and the end-pole assemblies are bolted to the backing beam by using a milling machine and assembly-holding fixture. The variation of pole heights from the lower surface of the backing beam is controlled to be within 25 μm, and the pole-to-pole longitudinal positioning accuracy is limited to be within ±25 μm.

Drive and control system

The drive and control system provides a gap adjustment mechanism to change the wiggler gap from 14 mm to 200 mm. Gap motion is achieved with a stepper motor, gear box, and left-handed & right-handed 5-mm-pitch ball screw at each side. The upper and the lower backing beams are attached to the ball screw and the load compensation spring system. The stepper motor is connected to a 20:1 reduction gear box unit. Two S106-250 stepping motors and AR-C absolute rotary encoders from Parker Co. are used to control the magnetic gap. The motor system has sufficient position accuracy to satisfy the specification. Test results show that the gap parallelism is better than ±5 μm and that the gap reproducibility is better than 7 μm, both of which exceed the specifications of 10 μm.

SUMMARY

PLS had developed 6 cm period ARUPS (Angle Resolved Ultraviolet Photoemission Spectroscopy) U6 for research on the electronic structure of solid surfaces and low dimensional nanostructures on surfaces. It features 0.902 Tesla, 57 poles at minimum magnetic gap of 18 mm. The maximum deflections of backing beams are estimated to be about 11.6 μm with the compensation spring under magnetic load of 2.4 metric tons and gap reproducibility of structures are 7 μm. The assembly tolerance of backing beam is 25 μm pole height and ±25 μm distance of pole to pole.

REFERENCES

[1] "PLS Conceptual Design Report", Pohang Accelerator Laboratory,(1992)
[2] "U5.0 Undulator Conceptual Design Report" LBLPUB-5256, (November 1989).
[3] Program ANSYS, a product of Swanson Analysis System, Inc., is a commercial available 3D code by using finite element method.

ELECTRON ACCELERATOR OF ELV-TYPE AND THEIR WORLDWIDE APPLICATION

Yu.I. Golubenko, N.K. Kuksanov, P.I. Nemytov, R.A. Salimov,
S.N. Fadeev, M.E. Veis, V.V. Prudnikov
Budker Institute of Nuclear Physics SB RAS Lavrentyev av. 11, Novosibirsk, 630090, Russia

Abstract

Beginning from 1971, the Budker Institute of Nuclear Physics Siberian Branch of Russian Academy of Science started its activity in the development and manufacturing of electron accelerators of the ELV-type for their use in the industrial and research radiation-technological installations. The ELV-type accelerators were designed with use of the unified systems and units enabling thus to adapt them to the specific requirements of the customer by the main parameters such as the energy range, beam power, length of extraction window, etc.. INP proposes a series of electron accelerators of the ELV-type covering the energy range from 0.3 to 2.5 MeV with a beam of accelerated electrons of up to 450 mA and maximum power of up to 400 kW. The design and schematic solutions provide the long term and round-the - clock operation of accelerators under the conditions of industrial production processes. The ELV accelerators are most popular accelerators not only in Russia, but in China, Korea, and etc.

INTRODUCTION

The main features of ELV-accelerators are as follows:

1. High power of electron beam in wide energy range, it means high productivity of EB processing;
2. High efficiency of conversation of electricity power to electron beam power. The efficiency is limited by frequency converter and in case of transistors frequency converter efficiency is increased up to 85-92%;
3. Simple procedure of accelerator control by operator due to control system based on IBM compatible computer. It allows operating accelerator in on-line mode.
4. Accelerator control system comprises a set of software and hardware covering all the accelerator units required an operative control and diagnostics.
5. Accelerator itself has simple design and high reliability. If some troubles appear our customers repair accelerator by themselves with our consulting by phone, as a rule.
6. After warranty service. It means we delivery spare parts or parts with limited lifetime or make any accelerator service after warranty period by separate contracts with the low price.
7. A set of additional equipment (such as transportation line, ring or double side irradiation system, 4-side irradiation system) increases the accelerator possibility.
8. ELV accelerators are stable in operation. The energy and beam current instabilities practically do not exceed +/-2%.

Basic parameters of the ELV-type accelerators are given below at the Table1. and ELV-4 is sown at Fig1.

Table1

	Energy range, MeV	Beam power, kW	Max. beam current, mA
ELV-0.5	0.4 - 0.7	25	50
ELV-1	0.4 - 0.8	25	50
ELV-2	0.8 - 1.5	20	25
ELV-3	0.5 - 0.7	50	100
ELV-4	1.0 - 1.5	50	50
ELV-6	0.8 - 1.2	100	100
ELV-8	1.0 - 2.5	90	50
ELV-6M	0.75 - 0.95	160	200
ELV-12	0.6 - 0.9	400	500

By now, over 100 accelerators had been delivered inside of Russia and abroad.

50 accelerators were delivered inside of former USSR
33 accelerators were delivered in China
12 were delivered in Korea
2 accelerators were delivered in Japan
2 accelerators were delivered in Poland
1 accelerators was delivered in Germany
1 accelerators was delivered in Chech Republic
1 accelerators was delivered in Bulgaria,
2 accelerators are delivering in India, and etc..

On international market we have strong competition with other firms producing accelerators. But number of delivered ELV accelerator during last 5 years is more than any others delivered accelerators. Many firms prefer to buy new ELV accelerator. So there are many plants where ELV accelerators are operating at same place and conditions with NHV and RDI accelerators.

Separate units and systems of ELV accelerators are widely used in installation for scientific research.

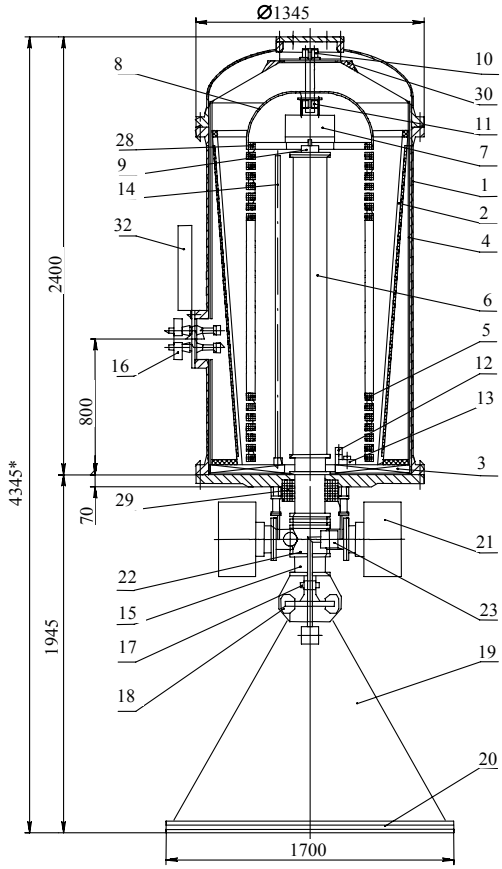

Figure 1 : General view of ELV-4 accelerator

1 - vessel, 2 - primary winding; 3,4 - magnitoguides; 5 - rectifier sections; 6 - accelerating tube; 7 - injector control unit; 8 - high voltage electrode; 9 - injector; 10,11 - optical channels for injector control; 12 - section divider; 13 - capacitor unit; 14 - energy divider; 15 - vacuum gate; 16 - primary winding terminals; 17,18 - scanning coils; 19 - extraction device; 20 - extraction window frame; 21 - vacuum pumps; 22 - cross head; 23 - vacuum gate; 28 - base of high voltage electrode; 29 - magnetic lens; 30 - high voltage shield; 32 - clamp set.

APPLICATION OF ELV ACCELERATORS

ELV accelerators are used practically in all technologies where electron beam is needed.

1 The main application of ELV-accelerators is modification of polyethylene insulation of cable and wires. The irradiation allows changing the properties of insulation: to make it thermo-, fire-, oil-, radiation- resists or with combined resistivity to these agents. The square of wire treated by ELV accelerator is from 0.1 to 120 mm2 . The productivity (depended on composition and properties) is up to 500 m/min.

We developed the system of 4-side irradiation for cable and pipes. This system increases the quality of irradiation, because improves the azimuth homogeneity of absorbed dose. Simultaneously it decreases required energy for irradiation, i.e. increase efficiency of treatment. 4-side irradiation system is especially effective for treatment of big diameter cables.

2 Another profitable application of ELV accelerators is production of thermo shrinkable pipes, films and bands. The productivity can be up to 1000 kg per hour.

As a rule the accelerators for cable and thermo shrinkable irradiation operate round-o-clock (24 hours per day). About 85% of accelerators are treating polyethylene.

3 The production of artificial leather. It means the polymerization by EB the several compounds for manufacturing leather-like material with heat-, fire-, oil-, cool, and etc. resistance. Radiation-chemical technology allows obtaining both non-base material and coats on the substances of different type. This material is for shelters, overalls, shoes, and bags. Productivity is up to 1000 m.sq. per hour.

4 The production of self-adhesion bands and rubberizing items. It is also the polymerization by electron beam.

5 Composite material for soft roofing. Intended for making roofs of residential, public and industrial buildings and structures. It is a roll polymerfabric formed of rubber mix based on rubbers of general application with subsequent vulcanization by EB.

6 One accelerator is used for manufacturing of polyethylene-oxide gel.

7 One accelerator is used for production of pre-pregs based on carbon fiber fillers and polymer binders.

8 Curing lacquer-paint coatings on different bases for the building industry with productivity of up to 500-m.sq./per hour. 2 accelerators for this purpose are in Russia (but they are not operated now).

9 Desinsectization of grain with productivity 200T/hour per accelerator in Ukraine, 2 accelerators with productivity 500 T/hour in China.

10 Waste water treatment. There was many lab scale installations using ELV accelerators for experiments. In 2005, in Taegu city (Republic of Korea) the full scale industrial installation for waste water treatment of dyeing textile center by an electron beam was put into operation. Installation productivity is up to 10000 cub. m/day. It is based on ELV-12 accelerator. The hall of irradiation treatment is shown on Fig.2

11 Purification of flue gases of coal thermal station from Sulfur oxide and Nitrogen oxide.

For waste water and flue gas treatment we developed high power accelerator ELV-12. It's design adapted to environmental application.

12 ELV accelerators can be equipped by system for extraction to atmosphere the concentrated electron beam. It allows using accelerator for other kind of application such as: production of catalysts for the ammonia synthesis; evaporation of any materials for

producing super fine powders; surfacing and hardening of metals; welding, melting and cutting of metals, producing the special types of ceramics

13 Eight accelerators are installed in research and irradiation centers. Accelerator here is not connected with determined technology but is used as multifunction device. ELV accelerator is very convenient for this purpose due to wide range and high stability of beam parameters and irradiation fields, simplicity of control. Practically, researchers (chemists or others specialists) operate with accelerator themselves without special training. Set of software allows obtaining required doze with high accuracy and repeatability.

Also in BINP we have special accelerator for investigation and developing of radiation processing. Our potential customer can make experiments with electron beam here. This accelerator has power up to 100 kW and beam energy 1.4 MeV.

In accordance with parameters and possibilities for users ELV accelerators are one of the best in the world.

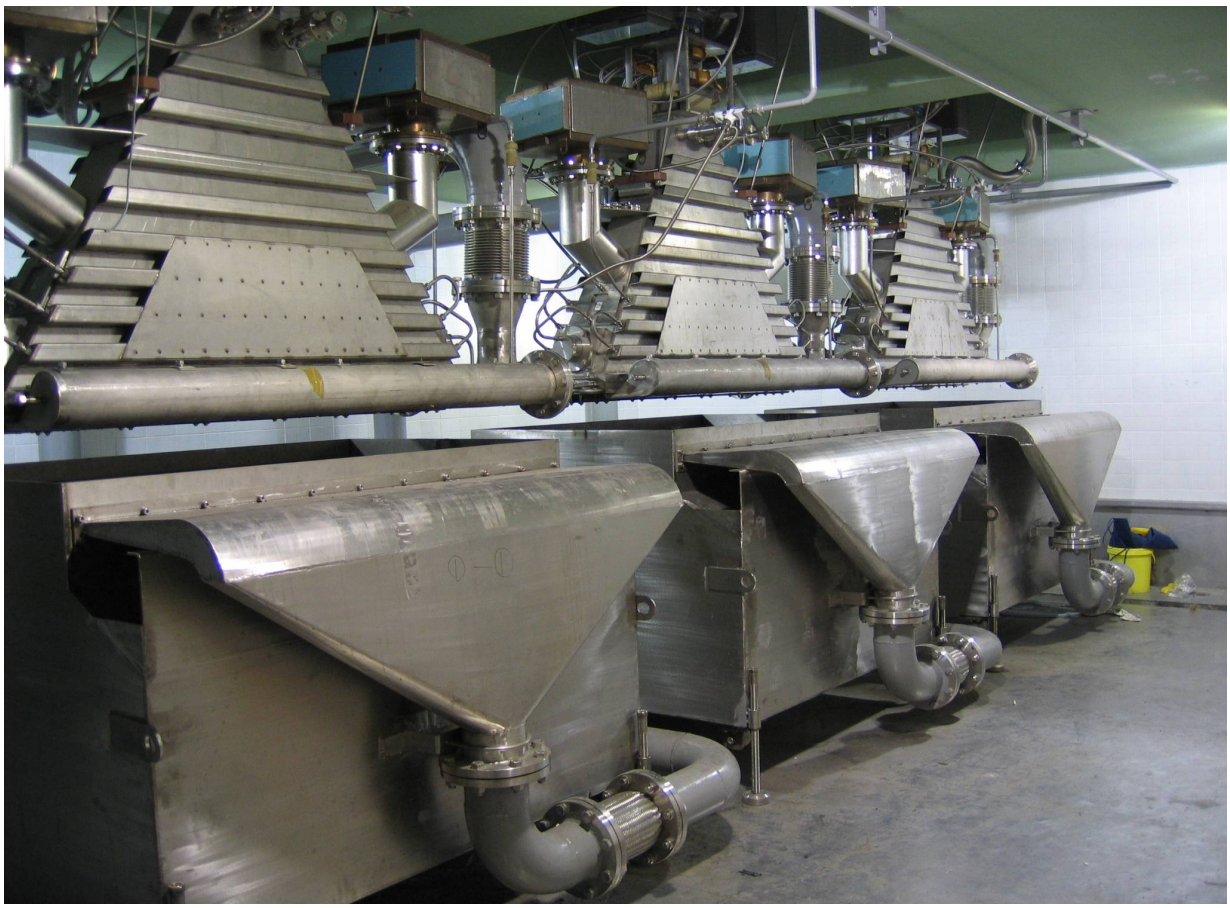

Figure 2 : The treatment of dyeing waste water by 400 kW electron beam. Taegu, Republic of Korea

ACCELERATOR BASED APPLICATIONS AT BARC-TIFR PELLETRON ACCELERATOR FACILITY

P.V.Bhagwat, P.Surendran, A.K.Gupta, J.P.Nair, S.C.Sharma, A.Shrivastava, N.G. Ninawe, M.L.Yadav, A. Shanbhag†, R.M.Kale*, S.K.Sarkar*, J.A. Gore, S. G. Kulkarni, N. Mehrotra, Ramlal, Q.N. Ansari, U.V. Matkar, Ramjilal, , R.N Lokare, M. Ekambaram, Hillary Sparrow, N.T.Jadhav, S.B.Salvi, M.B.Kurup*, R.K.Choudhury, S.Kailas and V.C.Sahni
Nuclear Physics Division,
†Radiation Safety Systems Division
Bhabha Atomic Research Centre, Mumbai-400 085.
*Tata Institue of Fundamental Research, Mumbai-400 005.

Abstract

The 14 UD Pelletron Accelerator, set up as a collaborative effort between Bhabha Atomic Research Centre and Tata Institute of Fundamental Research, has been operational since it's inception in 1989. Apart from basic research, various accelerator based programmes including accelerator mass spectrometry, production of track-etch membranes, production of radio isotopes, irradiation damage studies are being pursued. This contribution will describe the details of currently ongoing programmes.

ACCELERATOR MASS SPECTROMETRY

Accelerator mass spectrometry (AMS) is an ultra sensitive method of counting individual atoms having sufficiently long half life and available in low abundance. The medium energy tandem accelerator of this kind is an ideal machine to carry out AMS studies with heavy species like ^{36}Cl, ^{129}I etc. Cosmogenic radio isotope ^{36}Cl is widely being detected using AMS as it has got applications in ground water research, radioactive waste management, atmospheric ^{36}Cl transport mechanism studies of Arctic Alpine ice core etc [1]. As the interfering isobar in the ^{36}Cl detection is ^{36}S, a split anode ionization chamber, being the most suited one, was developed indigenously [2]. The detector was calibrated using very low yields of ^{35}Cl and ^{37}Cl (keeping source parameters low) from the natural sample. The source parameters were optimised and Mass 36 was injected and transported through the machine up to the detector. Background ^{36}S (coming from the ion source as an impurity or memory effect) is identified in the detector. Recently, a beam chopper required for this measurement has also been developed.

^{36}Cl was produced by irradiating sodium chloride (NaCl) with thermal neutrons at Apsara reactor, BARC by the nuclear reaction ^{35}Cl(n, γ)^{36} Cl. The irradiated sample was used to prepare the ion source sample.

The distinct peaks of ^{36}Cl and ^{36}S can be seen in the signals from anode 2 and Silicon detector (Fig.1). The yield of ^{36}Cl in the detector and the ^{35}Cl beam intensity in the Faraday cup located in close to the detector was measured. The ratio ^{36}Cl / ^{35}Cl in the sample is found to be ~ $1.5*10^{-10}$.

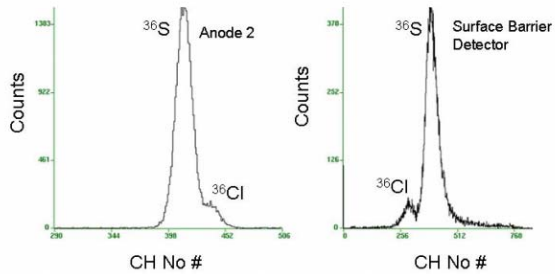

Figure 1: Spectra from Anode 2 and Silicon Detector.

PRODUCTION OF TRACK-ETCH MEMBRANES

Microporous membranes with features such as well defined and uniform pore size and pore density, uniform thickness, high tensile strength, inertness to toxic environments are in good demand for growing number of scientific and technological applications. Track Etch Membranes (TEMs) made by irradiating polymer films with heavy ions using accelerators are well known. Heavy ion accelerators provide greater flexibility to produce TEMs of a wide range as they can provide heavy ions of different atomic number (Z), kinetic energy (E) and particle flux. The damage size created by the heavy ions is of the order of 50 – 80 A^o. Chemical etching is essential to enlarge the pore size to micron range. Pore densities of the order of 10^6 to 10^8 pores/cm^2 and pore size of the order of 0.2 to 1.0 micron are required for many applications. Large scale industrial application needs membranes of large area and in bulk quantity.

The polymer films of 25 micron thickness were used. A magnet [3] was used to scan the heavy ions from the accelerator in horizontal direction and the polymer film was moved in vertical direction using a roller mechanism. The scanner magnet gives a peak magnetic field of 1.35 KGuass. To get larger deflection, higher charge states of

the desired ions are produced using post-stripper. The deflection, at the exit of the scanner is few centimeters which is then widened using a horn chamber of one metre length. At the end of the scanner, deflection up to 25 cms is achieved. The film is wound on a perspex shaft of 19 mm diameter and is continuously unwound on to another roller which is driven by a D.C motor from outside the chamber. Coupling is done using a vacuum rotary feedthrough. The linear speed of the film is kept at 60 cms/min. The beam is defocused in vertical direction to get almost uniform particle distribution. Fig. 2 shows scanning electron microscope (SEM) photograph of membrane.

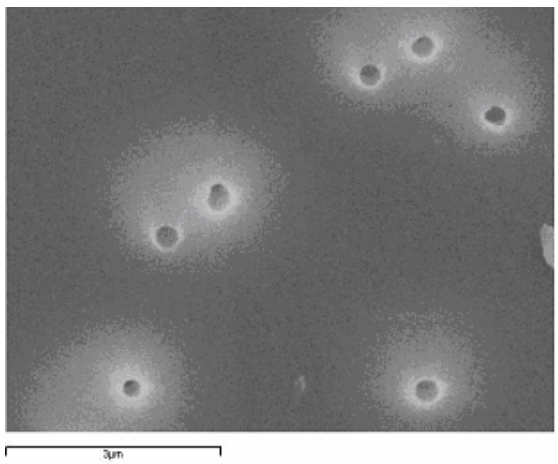

Figure 2: SEM Patograph of Membrane.

These membranes are being used to immobilize antibodies against specific analyte at Radiation Medicine Centre, Mumbai and for purification of gases at University of Rajasthan, Jaipur. Also, trial experiments are in progress at Desalination Division, BARC for water filtration. Besides these, the membranes were already used as Supported Liquid Membranes (SLM) in separating various Actinides and metals [4].

IRRADIATION SET UP

Drift space above analyzing magnet is modified to accommodate a Proton Beam Irradiation Setup at 6 meter level at this facility. This setup is capable of delivering proton beam in the energy range of 2 MeV to 26MeV and current in µA range. The shielding at this level is such that radiation is within permissible limit when proton beam with high energy and µA current is accelerated. In order to study radiation effects on metals at a higher temperature a hot target assembly is developed which can go upto 500 ^{0} C.

Radionuclides such as 52Mn, 67Ga, 96Tc, and 236Pu are produced for radiopharmaceutical applications. This setup is also being used for production of monoenergetic neutrons by Proton beam on Lithium Target. Same setup is being used to irradiate the target by a heavy ion beam having different charge states (which means essentially different energies corresponding to the terminal voltage) at the same time.

Figure 3: Proton Irradiation Set up.

This setup (Fig.3) is being used by various groups of BARC, TIFR, SINP and various universities to carry out experiments. The target assembly features can be modified/designed as per user's requirement.

LARGE AREA PROTON IRRADIATION SET UP

Large area Proton beam of diameter one inch and more is needed for irradiation of many devices e.g. electronic chips for space applications, which are of size more than 1 cm, need to be tested for their life time in radiation environment.

A large area proton beam of size 25 mm to 40 mm diameter in air was made available to ISRO for testing their on-line electronic devices. Proton beam flux of 10^{6} to 10^{10} particles/cm^{2} was achieved. The proton beam from the accelerator is focussed on to a gold foil of 1mg/cm^{2} thickness which scatters the proton beam. The scattered beam passes through a drift tube of length 1 metre at the end of which the size of the beam will be more than 50 mm diameter. A Titanium window of 12 mm diameter at the entrance of the drift tube isolates the high vacuum on the accelerator side from the rough vacuum in the drift tube. And, Titanium window of 50 mm diameter at the exit of the drift tube isolates the atmosphere from rough vacuum in the tube. This way even if the large titanium foil breaks accidentally the second titanium window will protect the accelerator vacuum. The thickness of the titanium film was 22 microns. The drift tube is maintained at a vacuum of 10^{-3} Torr. The size and energy

of the scattered beam was evaluated using SRIM 2003 program. The size of the beam was observed using a plastic scintillator (Fig. 4). The focussing of the beam was altered to get uniform distribution as far as possible. A current measuring device to monitor current as a function of distance from the centre of the scattered beam was made.

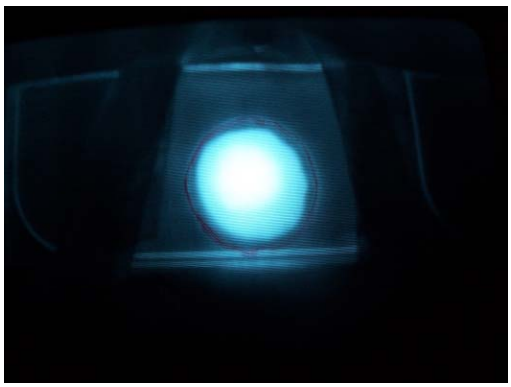

Figure 4: Scattered Proton Beam on Plastic Scintillator.

The experiment was conducted with 100 picoamps on 1cm^2 area in the centre as one cm^2 was the size of the chips to be irradiated (Fig. 4). More than 80 chips, mostly opto-couplers, were tested and found to be in agreement with the manufacturer's data.

RADIATION BIOLOGY

A thin window (20μ) of Titanium is placed at 30^0 N beam line to bring out ion beam in air. This facility has been used by users from BARC and TIFR.

REFERENCES

[1] L.K.Fifield, Rep. Prog. Phys. 62, 1223 (1999)
[2] A.Shrivastava et al. Xth ISMAS Symposium-2006, p.158.
[3] J.P.Nair et al, "Pilot Production of Track-Etch Membranes(TEMs) using Heavy Ion Beam Scanner", INPAC 2005, VECC, Kolkata.
[4] A. K. Pandey et al. Journal of Membrane Science, Volume 190, Issue 1, 31 August 2001, Pages 9-20.

ANALYSIS AND EVALUATION OF GAMMA AND NEUTRON DOSIMETRY FROM 48MeV 7Li ON NATURAL Cu AND ITS DOSE SIMULATION WITH MCNP

R. G. Sonkawade, Birender Singh, Pankaj. Kumar, S.P. Lochab, Inter University Accelerator Centre, Aruna Asaf Ali Marg, New Delhi-110 067, India
R. V. Kolekar, Radiation Safety System Division, Bhabha Atomic Research Centre, Mumbai-400 085, India

Abstract

Neutron and gamma radiation dose as a function of angle was measured from 48MeV, $^{7}Li^{3+}$ ion beam incident on thick natural copper target. The experiment is simulated keeping in view the health physics importance for monitoring the radiation environment in charged particle accelerator. The neutron dose observed in the forward direction is slightly higher compared to the lateral direction. Gamma energy of the same reaction is also monitored in the experimental setup with the HPGe-detector. The experimental results are compared with the calculated dose from empirical formulations. From the observed gamma spectrum, and PACE calculation, possible reactions were identified and correlated with the observed spectrum.

INTRODUCTION

In an accelerator, prompt secondary radiations such as gamma and neutrons are produced during the acceleration of ions, due to the interaction of the projectiles with the beam line materials. In a medium energy heavy ion accelerator, neutrons are the dominant prompt radiation. There are a number of low to medium energy accelerators utilized for research in various fields. In a heavy ion accelerator facility, neutron emission from thick targets are important, as they constitute the major component of prompt radiation environment owing to beam loss during normal operations or accidental situations. In this connection, energy and angular distribution of neutron and gamma dose distribution from thick targets are important for radiation protection point of view. The neutron dose in any direction is a function of the energy and angular distribution of neutrons, which in an accelerator environment vary depending upon the projectile, target and incident energy. Such measurements have been reported in the literature for protons and alpha particles but in the case of heavy ions, the experimental data are very few [1-5]. Moreover, most of the neutron yield data from heavy ion projectiles are in the energy region of 20MeV amu^{-1} and above. There are only few experimental measurements in the region of 10MeV amu^{-1} and below [6-7].

EXPERIMENTAL ARRANGEMENT

The experiment was performed at 15 UD Pelletron Accelerator Facility at the Inter University Accelerator Center (IUAC), New Delhi. The neutron energy spectrum and the radiation dosimetry were measured for $^{7}Li^{3+}$ ion beam accelerated through the Pelletron accelerator to 48MeV energy, stopped on thick Cu target of 1mm. Projectile ^{7}Li of 48MeV, has a range of 0.1026mm in Cu as calculated by SRIM [8]. The experiment is performed in the General Purpose Scattering Chamber (GPSC), which has the specially designed flanges of very small wall thickness to allow neutrons to emerge without much energy degradation . Spherical NDE meters are kept around 1.0m distance from the target at 0, 30, 60 and 90 degrees with respect to the beam direction. The neutron survey meter of make "Meridian" model 5085 is also used for monitoring the neutron dose level around the chamber. The gamma dose measurement is done with the gamma survey meter at one location at an angle of 90^{0}. The calibrated CR-39 sheet of thickness 500um procured from Pershore Moulding Ltd., UK and Lithium Borate radiators (Kodak, CA80-15 type B) of thickness 9.4$mgcm^{-2}$ were used in the experiment. CR-39 with 1mm polyethylene radiator and with Lithium Borate external radiator are used for discrimination of fast and thermal neutrons respectively. PACE is used to cross check the possible formation of compound nuclei from this reaction and to correlate with the observed gamma spectrum. MCNP simulation code is used for the simulation of gamma and neutron dose in the experiment. The high purity germanium detector from M/S EG&G, ORTEC, Oak Ridge, USA, Model MPX20P4 is used for gamma spectrum analysis from the Li projectile on Cu target. The detector has a resolution of 2.0 KeV at 1332 KeV and relative efficiency of 20%. A BC501 liquid scintillation detector of 5cm(ϕ)x5cm (thick) was kept at distance of 1.0m from the target at 30^{0} with respect to the beam. Time of Flight set up is used for the discrimination of neutron and gamma. This detector is shielded with the 9cm wax to minimize the contribution of the scattered neutrons during the experiment.

UNCERTAINTIES IN THE MEASUREMENT

Error or uncertainties in the measurement arises due to different factors including the uncertainty in overall beam current normalization which is estimated ~2%. For rem meters major contribution to error is from the pulsed nature of radiation fields, pile up (a random overlapping of pulses due to multiple events within a spill) can lead to large systematic errors [9]. The overall effect is due to possible underestimation of dose. Another source of error is due to pick up of radiofrequency (RF) pulses generated in accelerator. This is likely to add spurious

pulses to the rem meter. Further because of the large size of the rem meter it covers a relatively larger solid angle with respect to beam spot on the target and there can be uncertainty in the positioning of the detector. Divergent and anisotropic nature of the radiation field also adds to the uncertainty in the detector response[10], another possible non-negligible contribution to error is from the background scattered radiation.

RESULTS AND DISCUSSION

In the present work experimentally measured neutron ambient dose equivalents at the specified angles are compared with those calculated by Guo and Sunil [11,6]. Several researchers have developed empirical formalisms to estimate the total neutron dose, angular distribution of neutron dose equivalent and the yield [11-12]. Results shown by other researcher [6] using Clapier empirical relations are underestimated, which is quite un justified in the radiation dosimetry. Hence in the present study the Guo empirical relations are used, which are given as follows.

Formulations of Guo et. al.

Guo et al. has given an empirical relation for the neutron angular dose distribution (μSvh^{-1} $P\mu A^{-1}$) at 1 m) as follows :

$$D(\theta) = 2D_{AV}\left[\frac{(1+S)^2}{1+\exp^{S}}\right]\exp(-S\theta) \quad (1)$$

Where θ is defined in radians and S is defined as average center of mass (c.m.) velocity of the projectile while slowing down in the target as follows.

$$S = 0.5 \times \frac{A_b}{(A_b + A_t)} \times \sqrt{\frac{E_b}{A_b}} \quad (2)$$

and D_{AV} is defined in (μSvh^{-1} $p\mu A^{-1}$ at 1 m for P>0 i.e if the reaction is above Coulomb barrier).

$$D_{AV} = (33.4\,\bar{R}_b\,\bar{R}_t)^2 (P + 0.35)^2 \quad (3)$$

Values of the parameters $\bar{R}_b$ *and* $\bar{R}_t$ are defined by Guo et al for different Projectile and Target combinations and P is defined as follows.

$$P = \frac{E_b - CB}{A_b} \quad (4)$$

Where E_b is the projectile energy and CB is the coulomb barrier for a specific beam- target combination given by:

$$CB = 1.44 \times \frac{A_t + A_b}{A_t} \times \frac{Z_b Z_t}{\left[1.9 + 1.209\left(A_b^{1/3} + A_t^{1/3}\right)\right]} MeV \quad (5)$$

A_b, Z_b, A_t, Z_t are the mass and atomic numbers of projectile and target respectively.

Guo et al have given a conversion factor to estimate total neutron yield which can by expressed as follows :

$$Y = 1.41 \times 10^{-8}\, D_{AV}(proj)^{-1}$$

The neutron dose measured by using Neutron Radiation Detectors (NRD), rem detectors at 0, 30, 60, 90,120 degrees, are given in table.1 along with the calculated empirical relation of Guo [11]. All the results are given as dose rates in units of μSvh^{-1} per particle-nanoampere (pnA), the figures inside parentheses give (C/E) the ratio of calculated and experimental results. The results quoted by Sunil [6], with present work follows the same trend. No empirical relations are used for gamma dose equivalent. The values quoted for gamma dose equivalents are only experimental values and measured at an angle of 90 degree. The total neutron yield per projectile calculated by using the empirical formulae given by Guo is 2.89×10^{-3}, the same value is cross checked with the earlier published results for this projectile and target combination, the present results are in very good agreement with the earlier work [6]. The neutron energy input for the MCNP code is taken from the observed neutron spectrum from the BC501 detector. The observed neutron spectrum measured at angle 30^0 with respect to beam direction is shown in fig.1 and the time of flight spectrum is shown in fig.2. The neutron cumulative dose (mSv) measured by using CR-39 is shown in fig.3, the measured angular distribution is also following the same the trend, with the results of the empirical relations and the REM meters data. The observed gamma spectrum is shown in fig.4, the same is used for the MCNP simulation.

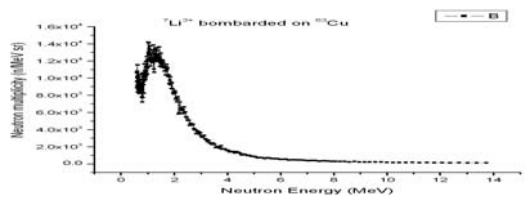

Figure 1 Neutron spectrum obtained with BC501A

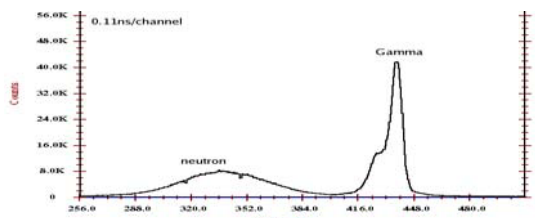

Figure 2 Time of flight spectrum

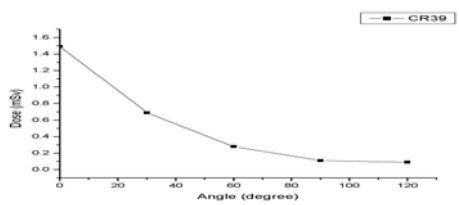

Figure 3 Dose response obtained by using CR-39

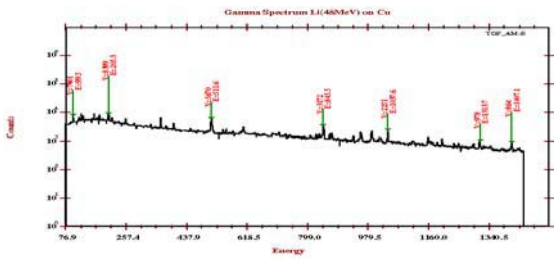

Figure 4 Gamma spectrum obtained by HPGe

MCNP and PACE simulation analysis:

MCNP simulation code is used to simulate the overall surface neutron and gamma dose equivalent, in the same the distributed energy of neutrons is taken assuming neutron as a isotropic source. PACE simulation code is used to cross check the possible cross sections of the nuclear reaction and the same is verified with the obtained gamma spectrum using HPGe-detector. From the PACE reaction cross section and the observed gamma spectrum it is seen that there is a possibility of (2p, 2n), (1p, 3n) and (α) channel reactions. The observed gamma spectrum is also very much useful for the radiation protection point of view for calculating the shielding calculations, etc

Table 1 Neutron Dose experimental values and with empirical relations of Guo at different angles

Lab Angle	**Dose Rate (μSv h^{-1} [pnA^{-1}])**		
	Gamma Expt.	Neutron Dose	
		Experimental REM meter	Calculated $D_{CAL}^{GUO}(\theta)$
0	-	290	245 (0.84)
30	-	242	229 (0.94)
60	-	220	214 (0.97)
90	9	207	199 (0.96)
120	-	193	186 (0.96)

CONCLUSIONS

The angular distribution of neutrons are very much important for the radiation shielding aspects of the accelerator as well it is very much useful to analyze the expected dose received by the radiation workers during the beam on condition in the beam area. Since, measurements are practically impossible for all targets and projectiles at various projectile energies, simple empirical relations are very useful tool for the purpose of first hand information for radiation protection. However, it is always better to have the experimental data as well so this study is done. The overall simulation codes used in this study are also very much useful for radiation protection aspects. This work presents the radiation environment around the heavy ion accelerator facility.

REFERENCES

[1]R. G. Sonkawade, S. P. Lochab, D. Sen, S. K. Datta, "Fast neutron dose equivalent rates for protons in 15UD Pelletron accelerator facility"Radiat. Prot. Dosi. , 1998, Vol 3 & 4, p.178-179.

[2]M. Nandy, T. Bandyopadhya and P. K. Sarkar, "Measurement and analysis of neutron spectra from thick Ta target bombarded by 7.2A MeV ^{16}O ions", Physical Review C, 2001, 63, p.34610-34616.

[3]M. Nandy, S. Ghosh and P. K. Sarkar, "Angular distribution of preequilibium neutron emission from heavy ion reactions", Physical Review C, 1999, 60, p.44607-44610.

[4]P. K. Sarkar, T. Bandyopadhya and G. Muthukrishnan, "Neutron production from thick targets bombarded by alpha particles: Experiment and theoretical analysis of neutron energy spectra", Physical Review C, 1991, 43, p.1855-1860.

[5]B. B. Back, "Radiation Safety at low energy heavy ion accelerators", Nuclear Instruments and Methods in Physics research B, 1993, 74, p.527-541.

[6] C. Sunil, M. Maiti, M. Nandy, P. K. Sarkar, "Thick target neutron dose evaluation for 19F+Al systems", Radiat. Prot. Dosi., 2006, p.1-6.

[7] C. Sunil, A. Saxena, R. K. Choudhary, L. M. Pant, "Neutron yield and dose equivalent from heavy ion interactions on thick target", Nuclear Instruments and Methods in Physics research A, 2004, 534, p.518-530.

[8] J. F. Ziegler, J. P. Biersack, U. Littmark, "The stopping and range of ions in solids" (NY:Pergamon press), 2000.

[9] S. Mayer, N. Golnik, J. KlloEnen, H.G.Menzel, Th. Otto, "Dose equivalent measurements in a strongly pulsed high energy radiation field", Radiat. Prot. Dosim., 2004, 110, p.759-762.

[10] R. J. Tanner, D. T. Bartlett, L. G. Hager, L. N. Jones, C. Molinos, N. J. Roberts, G. C. Taylor and D. J. Thomas "Modelling of neutron survey instrument performance and experimental validation of those calculated response data", Radiat. Prot. Dosim., 2005, 116, p.406-410.

[11] Z. Y. Guo, P. T. Allen, G. Doucas, H.R. Mck. Hyder, "Thick target fast neutron yields", Nuclear Instruments and Methods in Physics research B, 1987, 29, p.500-507.

[12] F. Clapier, C. S. Zaidins, "Neutron dose equivalent rates due to heavy ion beams" Nuclear Instruments and Methods in Physics research, 1983, 217, p.489-494.C.

BEAM OPTICS DESIGN FOR DC HIGH-VOLTAGE ACCELERATOR OF MW LEVEL

WANG Han-bin, XU Zhou, LI Ming, JIN Xiao, LIU Xi-san
Institute of Applied Electronics CAEP, P.O.Box 919-1014, Mianyang 621900, China.

Abstract

Here, we report on the working group ‘‘beam optics design’’ of MW levels dc high-voltage accelerator, that will be used in radiation technologies in large-scale industrial production (flue gas treatment, metallurgy, waste water treatment, etc.). This workshop also had working groups on ‘‘Electron Guns Designs and Beam control device’’, ‘‘MW level high-voltage power supply designs and fabrication’’, and ‘‘Beam scanning and extraction devices designs and fabrication’’. Comparing with existent high-voltage accelerators, our facility have higher average power of >500mA dc, which resulting in some technological challenges on beam production, power supply, and beam extraction. Here, we are concerned with several proposals that other laboratories have been working on. Subjects of concern are optics, accelerator design and modeling, stability requirements that connects the conventional DC high-voltage accelerators for round-the-clock operation. We describe the design, the projected performance and the status of our facility.

INTRODUCTION

We developed a series of RF accelerator whose electron beam is small in size, and they have been the driver of high energy industrial CT. To satisfy the requirement of radiation technologies in large-scale industrial production (flue gas treatment, metallurgy, waste water treatment, etc.), we have started the developmental program of MW level’s dc high-voltage accelerator.

This accelerator is designed with unified systems and units enabling them to be adapted to the specific requirements by varying the main parameters such as energy range, beam power, etc. The design is suitable to transmit high intensity current and realize the cathode of long lifetime, and can provide long term and round-the-clock operation of accelerators under the conditions of industrial production processes.

ACCELERATING TUBE STRUCTURE CHARACTERISTICS

A picture of the accelerating tube is shown in Fig 1. The cathode is single crystal LaB_6 and its best operating vacuum is less than 10^{-4}Pa. The channel aperture is 120 mm. This provides good vacuum conditions in the cathode region and consequently long time. The outer diameter of the insulator is 150 mm, its inner diameter is 130mm. A distance between the electrodes is 14mm. The ratio of the electrode’s thickness to the insulator’s height is 1/7. The 95 Al_2O_3 ceramic rings are connected to the 1Cr18Ni9Ti electrodes by thermodiffusion welding.

An accelerating tube is made up of seven sections, and a section includes ten electrodes, eleven insulators and two mounting flanges. Its rated voltage is 1.2 MeV, and the mean operation gradient in the tube is 11.13kV/cm. Operating experience indicates the tube can be safely running as high gradient as 20kV/cm in a steady state.

DESIGN OF POTENTIAL DISTRIBUTION

We introduce the paraxial movement track equation in electrostatic field:

$$r'' + \frac{V'(z)}{2V(z)} r' + \frac{1}{4V(z)}\left(V''(z) - \frac{I}{\pi\varepsilon_0 r_b^{\,2} v}\right) r = 0 \qquad (1)$$

the quantity V the generalized potential of charged particles, v equals to $\sqrt{\frac{2eV}{m}}$,r is the radial position of charged particle, and the prime symbol denotes a derivative taken with respect to z. The third term on the left hand side of Eq.1 represents the electrostatic focusing and defocusing progress of space charge force. Apparently, if want to have a beam form requisite, we must acquire some field gradient to counterbalance space charge force. Therefore ,we have to adjust the potential difference between adjacent electrodes. Now, for 0.5 ampere beam size of ϕ6, the required field gradient varies with generalized potential can be displayed in table 1.

Table 1: V & V'' for 0.5 ampere beam size of ϕ6

V (kV)	5	10	15	20	25
V''(kV/cm^2)	4.77	3.37	2.75	2.38	2.13

Cathode immerses in electrostatic field of accelerating tube. The beam current value is controlled by the cathode temperature, i.e. the gun is operated in a regime of full emission current take-off. Hence, the field on the cathode must be sufficiently strong, or it maybe in a space-charge-limited flow region. Considering the feasibility of beam current control, the quantity of field should be more than 7kV/cm on the surface of a ϕ6 cathode for 0.5 ampere. Table 2 lists the corresponding field for different current intensity of different size cathode.

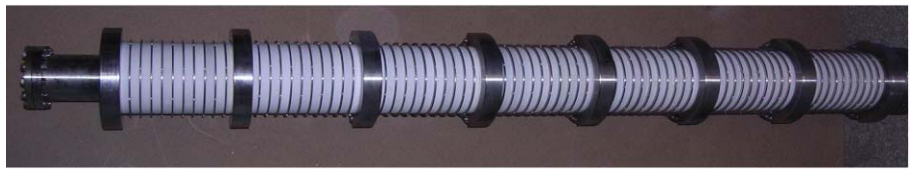

Figure 1: A picture of the accelerating tube.

Table 2: Extraction current and field intensity and cathode size.

Diameter of cathode(mm)	6	6	6	6	10	10	10	15	15
Surface field (V/cm)	8943	7336	5677	5262	6508	4555	3257	5063	2531
Extraction current (mA)	1106	765.3	523.2	469.0	1398	819.4	494.8	1669	590.8

If we try acquiring enough field gradient to balance space charge force by adjusting the difference between next electrodes, as a result, the field on some insulator-vacuum interface would approach or exceed 20 kV/cm, and this state must never be chosen for round-the-clock operation. So our design is the voltage distribution is homogeneous, but the voltage between cathode and anode is raised up to 45's kV.

ELECTRON GUN LAYOUT AND BEAM DYNAMICS SIMULATION

Figure 2 shows the electron gun layout. The slanted electrode adjacent to the source is pierce electrode and the cone angle is 20 degrees. This surface bends electric fields to generate focusing forces near the source. The electric force counteracts the defocusing beam-generated forces on the edge of the beam.

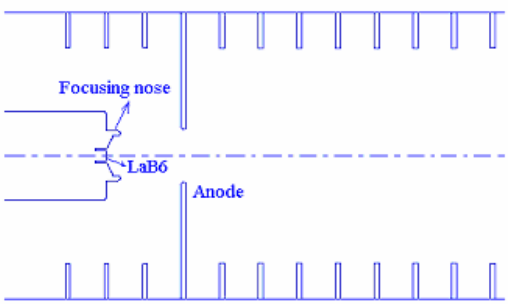

Figure 2: The layout of electron gun.

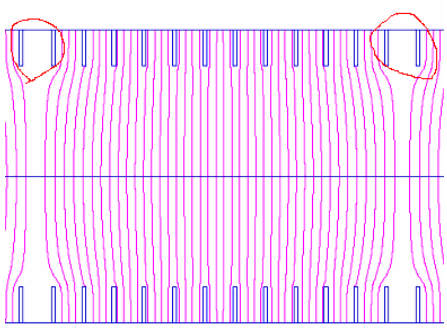

Figure 3: The equipotential lines distribution.

For the accelerating tube is made up of seven sections, the connecting flange region results in a large descent of axial field. Fig 3 shows the distortion of equipotential lines in or near the connecting flange region. The electrical field distribution was calculated using the computer program Poisson. Fig 4 displays the electric field distribution along axis from cathode to the accelerating tube exit. It clearly indicates the wide fluctuations of electric amplitude due to the effect of a connecting flange.

Beam dynamics studies were carried out from the cathode to the end of the accelerating tube using GPT code developed by Bas van der Geer and Marieke de Loos. Fig 5 displays the beam size at the end of the accelerating tube. The size is Φ30 including 86 percent of 5000 macro particles, and fig 6, which histogram represents radial distribution at the end of the accelerating tube, do approve that result. The envelope of 5000 macro particles can match the later beam propagation system, that is to say, our design can meet the requirement of customer.

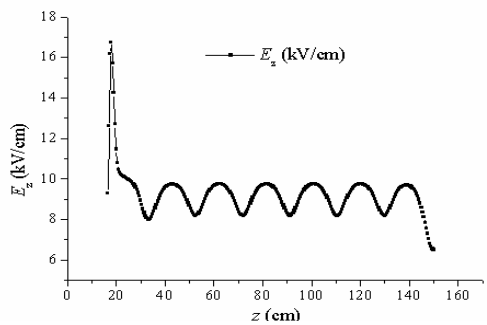

Figure 4: The axial electric field distribution.

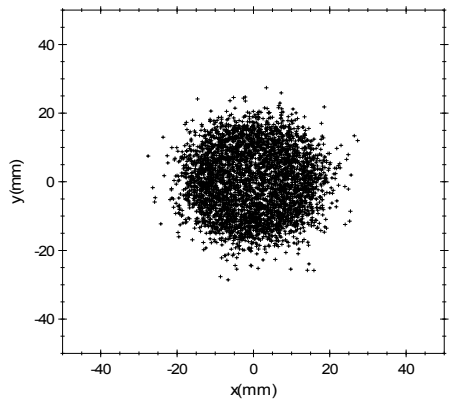

Figure 5: The beam size at the end of accelerating tube.

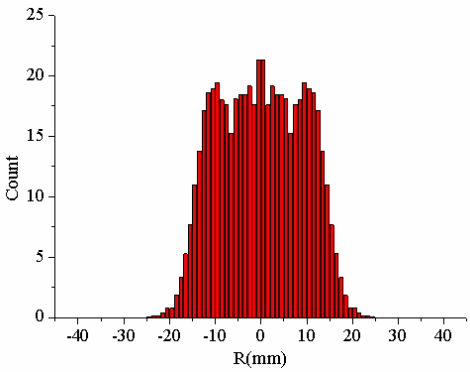

Figure 6: The radial distribution of particles at end of accelerating tube.

THE PRESENT CONDITION AND A WORK SCHEDULE

Based on the simulation we have conducted, we have performed the fabrication of the accelerating tube and accomplished the voltage hold-off capability test that voltages to 240 kV were applied to per section.

Now, we are ready to extracting beam from low to rated current step by step, at the same time, considering improvement of the measurement system to conduct a more complete exploration of all beam parameters, which are the constraint on the performance of this accelerator, relevant to the application.

REFERENCES

[1] H.B.Wang, et al. *High Power Laser and Particle Beams*, 2005, 17(6):930-934.

[2] X.J.Yin, *et al*. *High Power Laser and Particle Beams*, 2004, 16(2):246-250.

[3] S.F. Chen, et al. *High Power Laser and Particle Beams*, 2001, 13(4):513-516

DEVELOPMENT OF L-BAND ELECTRON ACCELERATOR FOR IRRADIATION SOURCE*

S. H. Kim#, S. I. Moon, B. Park, H. R. Yang, S. D. Jang, Y. G. Son,
S. J. Park, J. S. Oh, M.H. Cho, and W. Namkung

POSTECH, Pohang 790-784, Korea

Abstract

An intense L-band electron accelerator is under development for irradiation applications. It is capable of producing 10-MeV electron beams of 30 kW with the fully beam-loaded condition. The accelerator is powered by a pulsed klystron of 1.3 GHz and 25 MW with the 60-kW average power. The accelerating column, a traveling-wave structure, is operated with the 2π/3 mode and is installed vertically with other beam-line components. With the beam dynamics simulation, the beam transmission efficiency is over 90% and the beam size is enough to clear the apertures. Design details and the status of installation are presented for the L-band electron accelerator.

INTRODUCTION

Recently, the interests are increased in industrial applications of the electron linear accelerators [1]. The electron beam energy is limited by about 10 MeV due mainly to neutron production. For the clinical X-ray systems, low current and low repetition rate are required. The X-ray source for the container inspection requires 5-10 MeV with a few kilowatts of the average beam power [2]. On the other hand, the food or waste sterilization system requires relatively high average beam power since the process speed is proportional to it [3].

We are developing a high average-power electron accelerator for the grain sterilizing application by the institutional collaboration between the Korea Accelerator and Plasma Research Association (KAPRA) and Pohang Accelerator Laboratory (PAL) at POSTECH. The accelerator is required to provide an average beam power of 30 kW at the beam energy of 10 MeV. In order to achieve the beam power, we use a single L-band klystron with a matched pulse power supply. For an accelerating structure, the travelling-wave structure with 2π/3 mode is adopted in which the bunching section is included for compactness. Each component of the accelerator system is described in the next section. The design detail of the accelerating column follows.

SYSTEM OVERVIEW

The Thales TV2022D klystron generates the pulsed 25-MW and average 60-kW RF power at 1.3 GHz. It is transmitted to the accelerating column through the L-band waveguide network. These waveguides are filled with SF6 gas. Since the column is a travelling-wave structure, the extra RF power is exhausted in the high-power load as shown in Figure 1. For the pre-buncher cavity, the RF power is bypassed in the cross-coupled directional coupler and transmitted through the coaxial cable with the adjusted power and phase. The pulse modulator developed at PAL supplies 264-kV and 230-A pulse power to the klystron with the pulse length of 7 us and the repetition rate of 350 Hz. Due to the high average power requirement, 8 units of 30-kW high-voltage inverter stack connected in parallel are used for the PFN charging. E-gun high-voltage pulser supplies the 80-kV and 1.6-A pulse power between the cathode and the anode of the E-gun.

Table 1: Accelerator parameters.

RF Parameters	
Operating Frequency	1.3 GHz
Pulsed RF Power	25 MW
Pulse Length	7 μs
Repetition Rate	350 Hz
Averaged RF Power	60 kW
E-gun Parameters	
High Voltage	80 kV
Pulsed Beam Current	1.6 A
Pulse Length	6 μs
Repetition Rate	350 Hz
Beam Parameters	
Beam Energy	10 MeV
Pulsed Beam Current	1.45 A
Beam Transmission Rate	91%
Averaged Beam Power	30 kW
Accelerating Structure Parameters	
Type of Structure	Constant-impedance
Shape of Cell	Disk-loaded
Operating Mode	2π/3 mode
RF Filling Time	0.8 μs
Operating Temperature	40°C ± 1°C
Averaged Accelerating Gradients	4.2 MV/m
Beam Loading Factor	- 4.7 MeV/A
Temperature Shift Factor	- 2.3 MeV/1°C

*Work supported by KAPRA and PAL.
#khan777@postech.ac.kr

To evacuate the accelerating column and the beamline, two ion-pumps of 240 *l*/s are connected to the waveguide attached on the input and output couplers of the column. The E-gun also has a 20-*l*/s ion pump for strict vacuum condition on the cathode.

There are 5 solenoid magnets and a pair of steering magnets. To focus the electron beam by the solenoids, the first one requires 2000 A·turn while the rest requires 3-4.5×10^5 A·turn. The steering magnet tilts the beam direction up to 13° in the transverse direction with 500 A·turn.

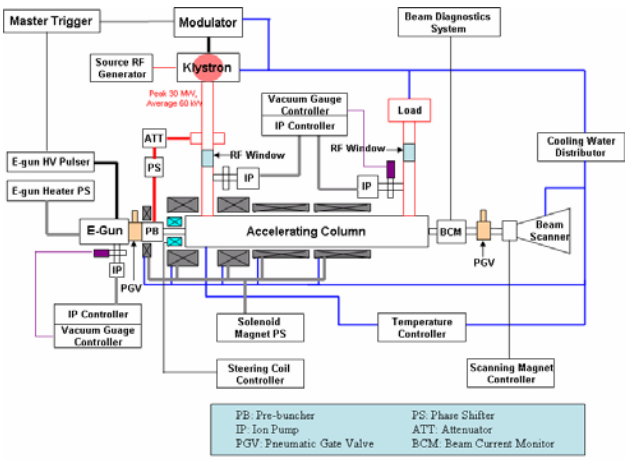

Figure 1: Block diagram of the accelerator system.

DESIGN OF ACCELERATING COLUMN

The accelerating column is consisted of 5 bunching cavities and 26 normal accelerating cavities. Since it is a travelling-wave accelerating structure, the first bunching cavity and the last normal cavity contain the input and output couplers, respectively. The phase velocity of each bunching cavity is determined as listed in Table 1.

Table 1: Phase velocity and attenuation coefficient

Cavity	Phase velocity / Speed of light	Attenuation Coefficient (Nep/m)
1st buncher	0.65	0.0538
2nd buncher	0.75	0.0489
3rd buncher	0.88	0.0442
4th buncher	0.92	0.0431
5th buncher	0.98	0.0415
Normal	1.00	0.0623

Since the RF power attenuates as passing through the accelerating column, the longitudinal electric field is defined by [3]

$$E(z) = E_0 \exp(-\alpha z)\sin\phi - Ir_s(1-\exp(-\alpha z)), \quad (1)$$

where r_s is the shunt impedance, $E_0 = \sqrt{2\alpha P_0 r_s}$, α is the attenuation coefficient listed in Table 1, P_0 is the input power from the RF source, and ϕ is the phase of the accelerating field. The last term represents the beam loading effect. The PARMELA simulation was conducted with the field amplitude of each cavity from Eq. (1). According to this equation, the electric field of the last cavity becomes almost zero as the beam current is increased. The accelerating column is operated with this condition, the fully beam-loaded condition.

To achieve the 10-MeV and average 30-kW electron beam, the beam energy and the beam power are calculated by the PARMELA code, with input beam current of 1 to 3 A. Figure 2 shows that the beam loading factor for the beam energy is –4.7 MeV/A. Figure 2 shows that the required beam are obtained with the input beam current of 1.6 A.

Since the beam current is high enough for the space-charge effect to be significant, the focusing magnet is required. With solenoids described in the previous section, the beam is focused effectively. The beam envelope in Figure 3 has no problem in the industrial applications.

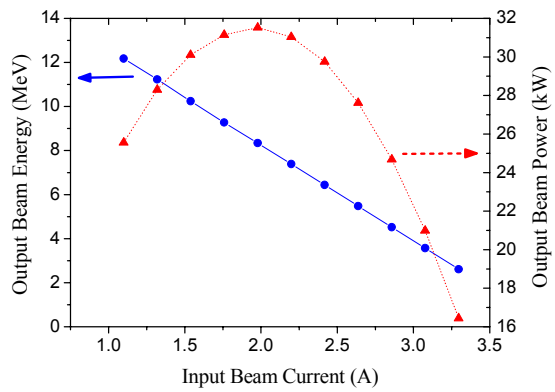

Figure 2: Output beam energy and power with the input beam current at the input RF power of pulsed 25 MW and average 60 kW.

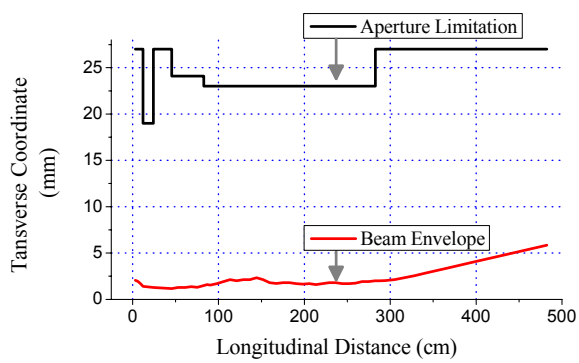

Figure 3: Beam envelope against the aperture limitation.

STATUS AND PLAN

The klystron tube with magnet was delivered from Thales, and it is installed in the klystron tank. The fabrication of the pulse modulator is finished and being tested at PAL. The accelerating column with the pre-buncher cavity, the E-gun assembly, the solenoid magnets are fabricated at IHEP, China. The waveguide components are fabricated at MEGA, US. Other components are being fabricated at POSTECH.

The accelerator system will be firstly installed at PAL for the beam commissioning. In this test, we will obtain the optimum condition of the pre-buncher input power and phase, and the magnetic field of the first solenoid, increasing the input beam current gradually. This accelerator will be finally installed at Cheorwon for the grain sterilization process as shown in Figure 4.

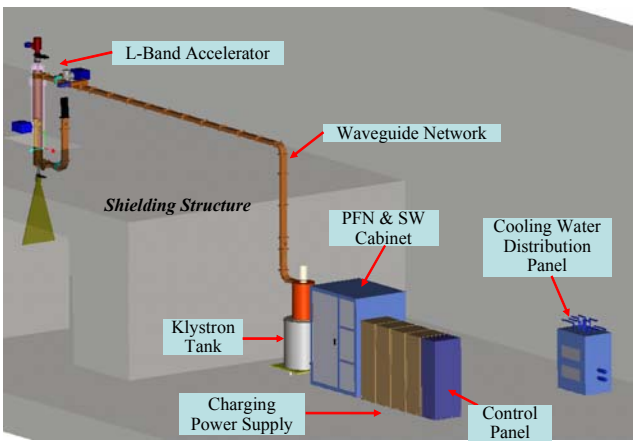

Figure 4: Drawing of accelerator setup at Cheorwon site.

ACKNOWLDEGEMENT

This work is supported by KAPRA and PAL. The authors are appreciated to Dr. Luo Yingxiong at IHEP, Beijing for his helpful discussion on general issues of the accelerator system and the design of the accelerating cavity.

REFERENCES

[1] A. M. M. Todd, “Emerging Industrial Applications of Linacs,” in *Proc. Intl. LINAC Conf.* (Chicago, IL, August 23-28, 1998), 1036 (1998).

[2] V. Pirozhenko, V. Belugin, A. Mischenko, N. Rozanov, B. Sychev, V. Vetrov, Y. Kokorovets, V. Ryzhikov, N. Shumeiko, S. Yatsenko, A. Korolev, K. Simonov, V. Eylan, “Complex for X-ray Inspection of Large Containers,” in *Proc. of EPAC 2006* (Edinburgh, Scotland, June 26-30, 2006), 2388 (2006).

[3] Y. Kamio, “10 MeV 25 kW Industrial Electron Linacs,” in *Proc. Int. Linac Conf.* (Geneva, Switzerland, Aug. 26-30 1996), 836 (1996).

[4] Y. Thiery, J. Gao, and J. Le Duff, "Design Studies for a High Current Bunching System for CLIC Test Facility (CTF3) Drive Beam,” in *Proc. Int. Linac Conf.* (Monterey, CA, Aug. 21-25, 2000), 95 (2000).

HIGH POWER INDUSTRIAL ELECTRON ACCELERATOR

S. C. Bapna, R. Banwari, M. Borage, A. Kasliwal, S. Kotaiah, Ajay Kumar, Pankaj Kumar,
R. Promod, Sunil Tiwari, S. V. Venkateswaran
RRCAT, Indore M.P.

Abstract

At RRCAT, we have a program of development of accelerators for Industrial applications. Under this, a 750 keV, 20 kW DC accelerator developed [1], is in operation since Nov. 2002. A 10 MeV, 10 kW electron linac is commissioned and is undergoing characterization. A 300 keV, 6 kW low energy accelerator is in advanced stage of development for curing applications. We have taken up development of a 2.5 MeV, 100 kW high power accelerator in collaboration with Budker institute of Nuclear Physics, Russia. In this paper we describe design details of the high power industrial accelerator

INTRODUCTION

The development of 2.5 MeV/ 100 kW air-core transformer type Industrial Accelerator is in progress in collaboration with Budkar Institute of Nuclear physics, Russia. Energy of the accelerator can be varied from 1 to 2.5 MeV with electron beam current up to 50 mA and maximum beam power up to 100 kW. The specifications are given in table 1. It is to be used for long term, round the clock continuous operation under industrial condition.

Table 1: Specifications of HPIA.

Operating Voltage	1 - 2.5 MeV
Max. beam Current	50 mA@ 2.0 MeV
Max. Beam Power	100 kW
Energy Dispersion	0.5 % at 2.0 MeV
Electron Gun	Indirectly heated triode electron gun with LaB_6 as emitter.
Maximum heater power	60 W
Accelerating Tube	PVA glued Accelerating tubes from BINP
HV Scheme	Air core transformer at frequency of 400-1000 Hz
Beam Scanning width	50 cm – 150 cms
Scanning frequency	50 Hz along the window and 1kHz in transverse direction.

DESCRIPTION

Figure 1 is a schematic of such an accelerator. The vessel is filled with an electrically insulating gas SF_6 and contains the primary winding, a high-voltage rectifier decks, electron gun, accelerating tube, a high- voltage electrode, and injector control unit. The elements of the vacuum unit with the output device are attached to the bottom of the vessel. The electron beam emitted by the cathode attached to the upper end of the accelerating tube is accelerated to the high voltage Uo and are transported through the beam line having vacuum pumps to the beam extraction window and is extracted into the atmosphere. The beam is scanned on the foil by X and Y scanning in order to increase the radiation field and also to distribute evenly the heat dissipated on to the foil. The irradiated material is conveyed under the beam exit window using a conveyor system.

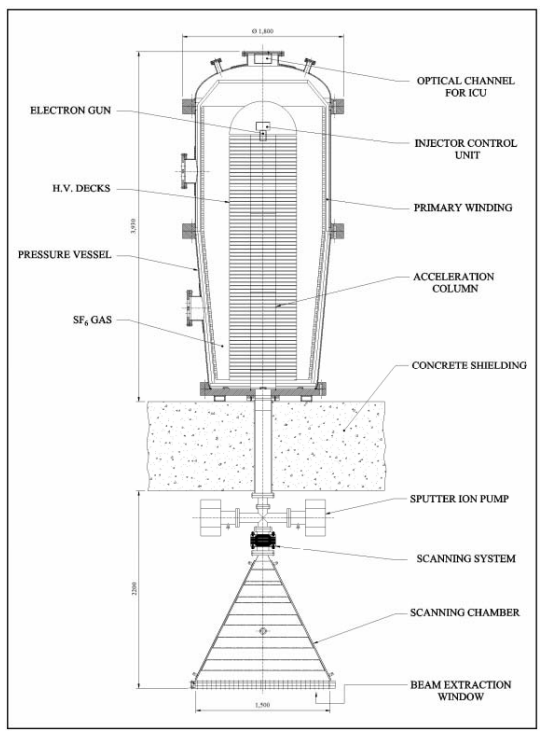

Figure 1: 2.5 MeV High Power Industrial Accelerator.

High-voltage rectifier

The HV scheme is based on Air Core Transformer (ACT), which has a water-cooled primary winding, and an epoxy molded multi-section secondary winding. Each section of the secondary winding is connected with a voltage doubler circuit and then they are stacked one upon another to build the complete high voltage column. The secondary modules are known as decks and their number in the system depends on the power supply voltage rating. Each deck generates a high voltage of 40 kilovolts and thus 64 number of such decks will be stacked in series for a total built up of 2.5 MV accelerating voltage.

The magnetic circuit consists of a tape wound yoke that surrounds the primary and secondary windings from the

sides and bottom. This yoke is terminated at the top near the high voltage dome and the return magnetic path is completed through air long the center of secondary decks.

The primary winding of the air core transformer will be excited with a 400 Hz, 180 kW solid-state inverter. The accelerating voltage at the high voltage terminal will be measured by a generating type voltmeter and a low voltage divider will monitor the first deck voltage to have a cross check over any abnormal condition.

The filament heating power will be derived from a low voltage secondary deck, which will be located at the top of the high voltage column. The 400 Hz ac voltage will be rectified and controlled in a solid state chopper to yield into a current controlled dc power supply for the filament. The control of this power supply from the control console at ground potential will be accomplished by optical means. The complete power supply along with the accelerating column will be housed in a pressure vessel filled with SF_6 at high pressure. The electron energy is regulated by changing the voltage across the primary winding.

Accelerating tube

The accelerating tube is located inside the high-voltage column. Provisions for shielding the electron beam from alternating magnetic field generated by primary winding and also to shield the HV decks from overvoltage which may appear in vacuum breakdowns in the accelerating tube is available in this design. The aperture size for the accelerating tube is 100 mm, which helps in achieving good vacuum in the tube and gun. The maximum operating gradient in the accelerating tube is 1 MV per m. A focusing lens is provided in the lower end of the tube to control the beam aperture The lens current is changed according to the beam energy and is controlled automatically.

We have also successfully developed an accelerating column rated at 300 kV at RRCAT. The ceramic to metal sealing was achieved by PVA. The column was subjected to leak test after thermal and pressure cycles and no leak was found in 10^{-10} mbar-litre/s order.

Pressure vessel

. The pressure vessel is designed as per the requirements of ASME Section VIII Div.1 The specifications are given in table 2.

Table 2: Specifications of Pressure vessel.

Design pressure: Internal External	 162 psi 15 psi
Design temp.: Minimum Maximum	 20°C 60°C
Inside diameter of cylindrical portion	1500 mm 1200 mm at small conical shell
Dimension of elliptical Head	Crown radius: 1350mm Knuckle radius: 255 mm
Allowable leak rate	10^{-6} mbar-litres/sec

BEAM SCANNING SYSTEM

The beam scanning system consists of a scanning chamber, two scanning magnets and two sets of correction coils. The two scanning magnets scan the beam in the mutually perpendicular directions which are transverse to the beam. Each magnet has a set of correction coils to correct the position of the beam by few rads in its scanning direction. Scanning chamber is triangular in shape having dimensions of 1.5m height and 1.5m base. For beam extraction, a 50 micron thick titanium foil with a clear opening of 70mm by 1500mm is used. The window flanges are water cooled and the foil is air cooled. The side walls of the chamber are suitably reinforced to minimize the weight of the chamber.

DEVELOPMENT OF INVERTER

Compensation Scheme

As opposed to the conventional transformer, the air-core transformer has large leakage inductance (L_s) and small magnetizing inductance (L_m). Therefore, the transformer has poor regulation and draws a large reactive power from the inverter feeding the primary winding. The conventional compensation scheme, as shown in Fig. 2(a), using shunt capacitor (C) and a series inductor (L_a) can either achieve good voltage regulation or minimum reactive power depending on the operating frequency. Besides, the network uses an additional bulky inductor. Therefore, the possibility of using various other schemes is examined and a network shown in Fig. 2(b) is chosen as it offers near-unity power factor operation and nearly constant output voltage under all loading conditions. Further, it is comparatively compact, light-weight and less noisy.

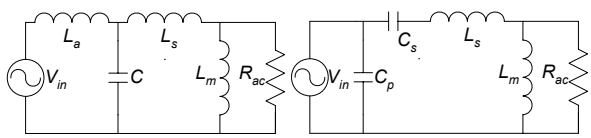

(a) (b)

Figure 2: Compensation schemes for the air-core transformer. (a) Conventional, and (b) proposed.

Inverter Scheme

Various schemes are available for the development of inverter. A simple scheme named as the dual half-bridge inverter is followed. Schematic diagram of the inverter is shown in Fig. 3. Three-phase ac mains is rectified and filtered using diode bridge rectifier and LC filter (Ldc-Cdc). The filter capacitors are split and the center point is used as the return of the following inverter stage. The inverting stage uses two active switches (IGBTs S1, S2) are two diodes (D1, D2). Since active switches are not directly connected in series, the scheme is free from the shoot-through (accidental simultaneous conduction of both the switches in the same leg) which is a potential failure mode in half-bridge and full-bridge inverters. The dual half-bridge inverter can be viewed as two buck

converters connected at the output through high-frequency filter inductors (Lf). Output inductor currents of two buck converters are opposite to each other, which doubles the effective output ripple frequency and reduces output ripple amplitude. In fact, there is a perfect ripple cancellation when the duty ratio of two buck converters is equal to 0.5. At this point effective output is zero. Thus zero-cross-over distortion (experienced in conventional inverters) is eliminated. Further, the paralleled inverters can be suitably phase shifted reducing input/output ripple amplitude and increasing ripple frequency. High-frequency filtering requirement (Lf- Cf) is thus reduced.

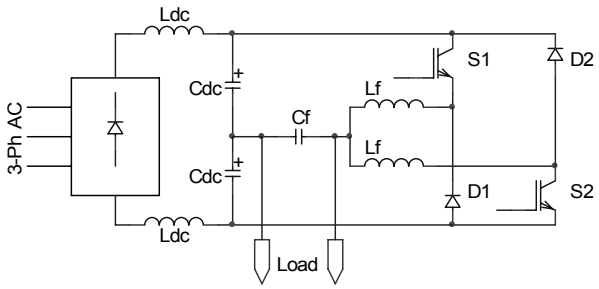

Figure 3: Schematic diagram of one inverter module.

Prototype 30 kVA Inverter

The first prototype inverter based on the dual half-bridge circuit is developed. The inverter is rated for 175 V/ 175 A rms output at 430 Hz. The IGBTs are switched at 20 kHz in sinusoidal PWM with unipolar voltage switching. Loss-less turns-off snubber is used to minimize the turn-off switching losses and stresses in the IGBTs. The module is currently tested up to 9 kVA output. Six such modules, each rated at 30 kVA, shall operate in parallel. In normal operation, when all 6 modules are healthy, each module will operate at 25 kVA. In case one module fails, rest five modules will continue to feed power to the accelerator structure without de-rating.

PC Based Control System

The PC based control and monitoring system of 2.5 MeV High Power Industrial Accelerator provides easier operation and better control and monitoring of different parameters of the accelerator and allied subsystems. The control scheme uses Analog Device's 8051 core based micro-converter AduC 812 chip. This micro-converter chip has inbuilt ADCs and DACs thus reducing drastically the over-heads for both hardware and software.

In this scheme each power supply and subsystem is equipped with a AduC812 based micro-converter card and all are connected on a common RS485 line to the PC. A RS485 to RS232 and RS232 to RS485 converter is used at subsystems and PC end. Each card will be allocated an address and will act as a slave. The PC will be the master and communicate with the power supplies and other subsystems through these known addresses. The data communication will take place through well-framed packets. Each packet will contain the address of the source and the destination, the data and the checksum byte.

The software for the PC operation is written using Lab-view 7.0 which is a dedicated standard industrial software development suit. The PC is used to automate the complete operation of the accelerator. It is also used to control the on-off operations or set references of different power supplies and display their parametric values as well as their status.

POTENTIAL APPLICATIONS OF 2.5 MEV / 100 KW ACCELERATORS IN INDIA

We list some of the applications of high power system:

- Sterilization e.g. urine specimen cards. 25000 cards per hour (1 MeV, 50 mA) and at 2 MeV, 20 kW this system and can sterilize disposable 2.5 ml syringes of about 100,000 per hour.
- Artificial leather for footwear production – 1.3 T/hr
- Paper pulp sheet for viscose yarn (10 kGy dose) at 50 kW power level 250 tonnes loads pulp per day.
- Grains irradiation (0.2 – 0.3 kGy). A 500 tonnes of material can be irradiated per hour with this system.
- Waste water treatment (0.4 kGy) – about 15000 M3/hr. throughput can be achieved.
- Cables – insulation thickness of 1mm to 5mm & cable outer diameter of 100mm can be cross linked using this system with a throughput of 100–1000 m/min.

In fact, in all these applications limitations will come from material handling point of view rather than the accelerator. The system can also be used in x-ray mode

CONCLUSION

The development of high power accelerator is under progress in collaboration with BINP, Novosobirsk, Russia. The equipment procured from them have been qualified and found satisfactory. Efforts are underway to interlink the equipment with indigenously developed systems e.g. Inverter, Vacuum system, extraction system, gas handling system, pressure vessel etc.

REFERENCES

[1] S.C.Bapna et.al., "Development of DC Accelerator at CAT, Indore", Invited Talk in InPAC-2005 held at Calcutta March 01 – 05, 2005.

INTRODUCTION OF EPICS IN VEC & SCC CONTROL SYSTEM

Tanushyam Bhattacharjee#, Anindya Roy, Biswajit Sarkar, R. B. Bhole, Samit Bandopahdyay, Anirban De, Jaydeep Mishra, Niraj Chaddha, K. Kundu, Sarbajit Pal
Variable Energy Cyclotron Centre, 1/AF Bidhannagar, Kolkata – 700064, India

Abstract

As a part of computerization of the VEC and SCC Control System, using a standard open-source software tool for designing distributed control system named as EPICS (Experimental Physics and Industrial Control System), several IOCs (Input Output Controller) are developed to control and monitor the Main Magnet Power Supply (MPS), Beam line MPS, Deflector Power Supply, Beam line instruments and LCW (Low Conductivity Water) system. The device layer of IOC, responsible for communication with MPS distributed over several multi-drop networks (RS485) ensures reliable and fast response while setting several MPS simultaneously. Process parameters e.g. water level, temperature and conductivity in different subsystems are measured using standard industrial sensors. An IOC is developed for acquiring process data form sensors using Modbus-TCP based distributed DAQ modules on Windows platform. An IOC is developed for affecting the necessary control for conditioning of the electrostatic deflector with facility for supervisory intervention. Application of EPICS in sub-systems will lead towards unified distributed control architecture for auto beam tuning of the machines.

INTRODUCTION

The subsystems like MPS, LCW, Cryogenic control, Beam line control, beam diagnostics etc for VEC/SCC are interdependent and most of the control subsystem often require handling of control/monitoring parameters from other subsystems. The control/monitoring parameters handling among the subsystems become difficult as different proprietary software solutions are used by each group responsible for designing and maintaining their subsystems. The unified open source accelerator control system s/w tools of EPICS provide rugged distributed architecture and implementation of it helps to overcome the control data sharing difficulties. Many developed open source drivers to control various devices are already available for EPICS and these drivers are extremely useful for the system designer to reuse by modifying and rebuilding as per the specific system requirements.

The portability of EPICS in different platform/processor [1] provides the advantage of distributing EPICS applications without changing existing OS/processor architecture. Several EPICS device drivers, OPIs (Operator Interface) and input output controllers are developed recently and integrated with the existing system. Input Output Controllers are also developed to run on arm based embedded systems and operator interface is developed for Windows and Linux on x-86 processor.

#btanu@veccal.ernet.in

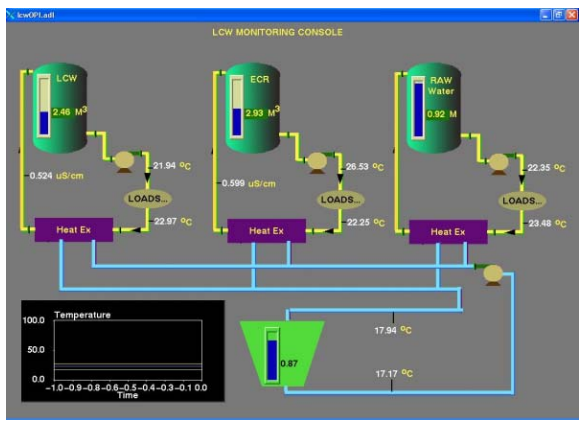

Figure 1: LCW OPI

CHANGE-OVER TO EPICS

Upgradation of LCW Monitoring for VEC

The web enabled modules with TCP connectivity are used for monitoring of plant parameters of Main LCW, ECR Cooling Water and Raw Water Systems. The gauge pressure type smart level transmitters are chosen to measure water levels in Raw-water storage tank, Main LCW Storage tank, ECR LCW Storage tank and Cooling-tower sump. The capacitance type level switches are also selected to provide HI & LOW level indications to initiate alarms. The temperatures at inlet and outlet headers of each subsystem by RTD and conductivities at different points are measured. EPICS asyn device support is used to develop the driver for DAQ modules having MODBUS-TCP connectivity.

The IOC uses the driver to communicate with the device and sends the channel data as Process Variables (PVs) to the client by Channel Access (CA) protocol. The LCW IOC loads the memory resident database which comprises of records contains several fields (variables). The bundled attributes of each record like scan rate, alarm limits etc. are defined according to the system requirements. The user interface as shown in Figure 1 is designed by MEDM (Motif Editor and Display Manager).Both the IOC and OPI is developed and running on win-x86 environment.

Upgradation of MPS system

The device driver for the commercially available magnet power supply (MPS) is developed using EPICS asyn device support routines. The device layer of IOC is responsible for communication with the Main Magnet and beam line power supplies having serial multidrop connectivity with ASCII protocol.

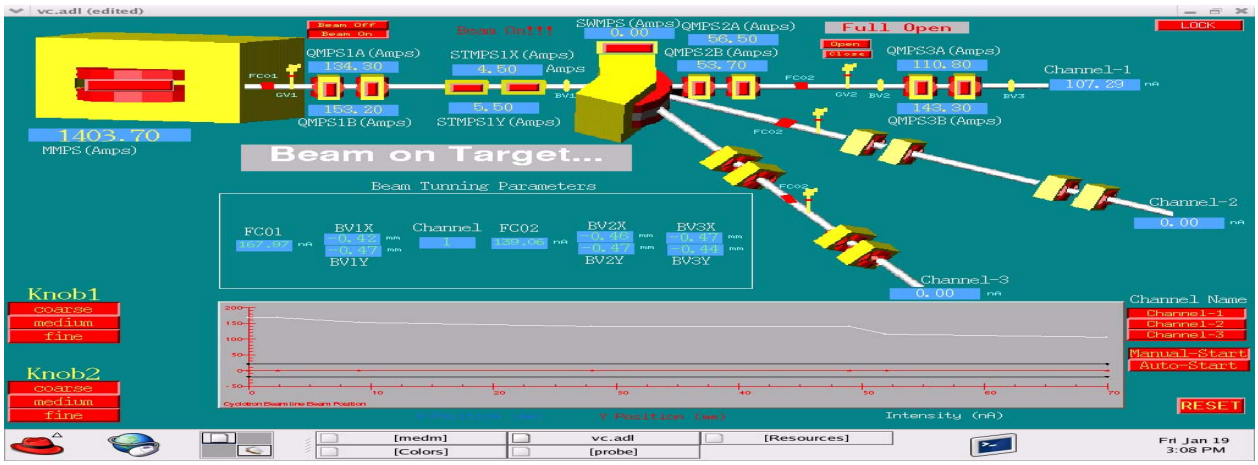

Figure 2: Virtual beam line control OPI

Asyn octet and asyn Int32 methods are mainly used in the driver source. Epics threads and mutex functions are used to ensure pseudo parallelism of the application. The scan rates of the channel are suitably chosen, so that the commands to the MPS do not repeat during single SET/READ action of a particular PV. The IOCs/drivers (compiled in both linux-x86 and Linux-arm environment) are tested with a virtual device simulates the field conditions.

Figure 3: IOC running on arm based embedded system

Development of Deflector System

Conditioning of the electrostatic deflectors for the machine is done by modulating the voltage applied across the deflectors to reduce the *dark current*. The distributed client/server architecture is adopted for this control as the operation is performed from control console located far away from the actual devices. EPICS IOC communicates with two deflector power supplies and one gas flow meter having RS 485 connectivity. Deflector voltage and dark current are measured using 16-bit serial ADC. A heterogeneous protocol driver routine is responsible for communication with two different devices from the single IOC. An embedded arm processor based controller as shown in Figure 3 is used as an input/output controller and is housed inside the deflector power supply. The operator interface communicates with IOC via channel access protocol developed using EDM (Extensible Display Manager).

Simulation of Beam line Control

A virtual beam line control is designed to validate the auto tuning of the beam line with the help of EPICS tools. Here all beam line objects are soft device and virtual device configuration routines are developed for such objects. The designed IOC can dynamically load the virtual object of interest during run time. All objects are presently considered as an ideal one which is to be replaced with suitable mathematical model to simulate the real one. The OPI shown in Figure 2 gives the facility of choosing Auto/Manual mode of operation. The operators set the parameters using encoder based soft-knob during manual mode of control. The integration of two soft-knobs for simultaneous control of two power supply parameters is done.

CONCLUSION

The change-over of LCW and MPS systems of VEC from existing control mechanism, development of Deflector conditioning system for SCC and simulation of accelerator beam line using EPICS are completed. EPICS R3.14.8 which does not support linux-arm architecture is used for these applications. A separate ‘patch’ file is used for needed cross compilation. Several other subsystems control for SCC and VEC which are partially developed or in final stage of development, are yet to be upgraded to EPICS. EPICS are also used as a SCADA (Supervisory Control & Data Acquisition) in PLC based systems where instead of channel archiver, Oracle DB integration is being incorporated for historical storage.

REFERENCES

[1] http://www.aps.anl.gov/epics

INDIAN PARTICIPATION IN LHC, SPL AND CTF-3 PROJECTS AT CERN, SWITZERLAND

V. Bhanage, J. Dwivedi, A.K. Jain, P. Khare, S. Kotaiah, P.K. Kush, Abhay Kumar, S.S. Prabhu, A.M. Puntambekar, A. Rawat, V.C. Sahni[#], A. Sharma, R. Shridhar, Purushottam Shrivastava, G. Singh, Raja Ramanna Centre for Advanced Technology, Indore, India,
R.K. Sadhu, Bhabha Atomic Research Centre, Mumbai, India

Abstract

India has contributed to the construction and commissioning of CERN's most ambitious particle accelerator project the "Large Hadron Collider" (LHC) and is now engaged in other activities, namely, CTF 3 and LINAC-4. The contributions to LHC span from hardware, software, expert manpower support for evaluation of some of the LHC sub-systems and commissioning support of various subsystems of LHC. India has developed and supplied a total of 7080 Precision Magnet Positioning Systems (PMPS) Jacks for supporting Cryo-dipole magnets of LHC, 1146 Superconducting Corrector Magnets (MCS), 616 Superconducting octupole-decapole correcting magnets (MCDO), 5500 Quench Heater Power Supplies(QHPS), 1435 Local Protection Units (LPUs) etc., for LHC. With the background of these contributions to CERN's satisfaction, India was invited to participate in CERN's upcoming Advanced Accelerator Projects, like, Superconducting Proton LINAC, SPL and Compact Linear Collider Test Facility, CTF 3. The present paper describes the highlights of the past, ongoing and future collaboration activities.

INTRODUCTION

CERN has started commissioning world's biggest particle accelerator the Large Hadron Collider (LHC) located over the Swiss-French border about 100m below ground. It would be colliding protons, each with 7 TeV energy during end 2007-2008 and will later collide lead nuclei, each of 1150 TeV energy. Indian involvement in LHC began in 1996. Earlier, after informally working for many decades with CERN, India formally signed a cooperation agreement in 1991 which was then followed by a protocol (signed in 1996) that led to Department of Atomic Energy's various laboratories to participate in the construction and utilization of LHC. The protocol provided a framework to deliver hardware and expert manpower envisaging an 'in kind' Indian contribution valued at 34 million Swiss Francs (i.e. US $25 million at 1994 rates). This was later raised to 60 MCHF under an agreement signed between DAE and CERN. Half of the value of this 'in kind' contribution is treated as India's contribution to LHC and other half is credited to 'Indian Fund' which was created to provide support to our scientists for their stay at CERN and also to meet essential expenses in foreign exchange required for some of the contributions. The lead DAE lab for this collaboration is RRCAT, Indore. After successful completion of LHC related contributions, CERN invited India to join in its Advanced Accelerator Projects like Super Conducting Proton LINAC (SPL) and Compact Linear Collider Test Facility CTF-3. For this an additional protocol has been signed between Prof. Robert Aymer, Director General, CERN and Dr. Anil Kakodkar, Chairman AEC, India. This envisages additional contributions up to 5 MCHF on similar lines as done before for LHC contributions.

CONTRIBUTIONS TO LHC

The in-kind contributions that DAE committed is described in detail elsewhere [1][2] and a summary of some of these is given in Table 1. All the equipments, components and devices have been designed, developed, tested and supplied to CERN and accepted.

Table 1: Major Contributions to LHC

Sr.	Details of Indian Contributions	Qty.
1	50000 litres Liquid Nitrogen tanks.	2
2	Superconducting corrector magnets i) Sextpole (MCS) ii) Decapole and Octupole (MCDO)	 1146 616
3	Precision Magnet Positioning System (PMPS) Jacks	7080
4	Quench Heater Protection Systems (QHPS)	5500
5	Integration of QHPS units into racks	6200
6	Control electronics for circuit breakers of energy extraction system	70
7	Local protection units (LPU)	1435
8	SC Dipole magnet tests/measurements, expert support in Man years	100
9	LHC Hardware Commissioning of Cryogenics, Power converters, Protection systems, Controls. Man years	20
10	Data management software upgrade, Data analysis software/documentation projects	41 Man years eq.
11	Development of JMT-II software	
12	Software development-slow control of Industrial Systems of LHC	
13	Design and calculations for Vacuum system for beam dump line	
14	Analysis of cryo-line jumper and magnet connections	

The items listed in table 1 were pursued with the help from different units of DAE with RRCAT acting as nodal

[#]vcsahni@cat.ernet.in, vcsahni@magnum.barc.ernet.in

agency. RRCAT was involved with (1), (2), (3) (7), (8), (10), (13) & (14); BARC was involved in(10), (11), (12); BARC and Electronics Corporation of India Ltd (ECIL) were associated with (4), (5), (6) and (7); BARC, VECC, IGCAR and RRCAT, provided necessary skilled engineers and physicists for (8). BARC, RRCAT and ECIL are providing expert manpower support for (9). A brief description of some important items listed in table 1 is given below:

Superconducting corrector magnets (MCS and MCDO

The main dipoles of LHC are equipped with sextupolar (MCS) and decapolar (MCD) superconducting corrector magnets. Each decapole corrector also has an octupolar insert (MCO), and together these are designated as MCDO. Each corrector magnet consists of a superconducting coil assembly, glass fibre slit tube, steel lamination, aluminum shrinking cylinder for pre-compression of coils, end plates for connection, parallel resistor for magnet protection and a magnetic shield also acting as a support. Fig 1 shows picture of finished MCS and MCDO assemblies before dispatch.

PMPS-jacks

The various cryo-magnets need to be precisely positioned in the tunnel to ensure proper beam trajectories of particles. The dipole magnet assemblies, each weighing more than 32 tons with a length of 15 m, need to be positioned with a precision of 50 μm all along the 27 km length. Jacks have to be capable of accommodating LHC tunnel slope of 1.4%. The main specifications of the jack are: (a) range of movement (i) in *X–Y* phase ± 10 mm (in both directions simultaneously), and (ii) in *Z* direction ± 20 mm; (b) load capacity 32 MT, and (c) maximum operating torque for lateral movement to be less than 60 Nm in nominal realignment operation. A total of 7080 units were made by the Indian industry and supplied to CERN under the supervision of RRCAT. Fig. 2 shows a picture of the PMPS jacks ready for shipment to CERN.

Quench Heater Protection Systems (QHPS)

The LHC superconducting dipole and quadrupole magnets are powered with current up to 13 kA. All superconducting magnets require protection in case of quench (resistive transition) or other failures. The main dipole is equipped with quench heater strips on magnet coils and cold bypass diodes. When the quench is detected (via a floating-bridge detection of voltage build-up above a certain threshold value across magnet coils), the protection system will power the quench heater strips and distribute the energy evenly in the entire magnet. Fig. 3. shows a picture of QHPS integrated racks.

Local Protection Units

These electronic devices detect quench occurring on the LHC superconducting magnet system and is made of local quench detector and the acquisition and monitoring controller put together in a 3U, 19″ crate. The local quench detector is attached to an LHC superconducting magnet and activates the respective protection systems in case a resistive transition occurs. Fig 4 shows a picture of the local protection units.

Expert Manpower for Magnetic Tests and Measurements

The LHC cryo-dipoles, quadrupoles and corrector elements required testing as part of a QA plan at super fluid helium temperatures of 1.9 K, as well as at room temperature (warm) at dedicated test stations. These involve cryogenic tests, power tests, quench behaviour analysis, protection test, precise magnetic measurements at injection and high fields, and warm measurements. The SM18 Hall at CERN was the home for conducting all such evaluations, where several test stations were installed for dipoles (MB test-station based on twin rotating units and long shaft), quadrupoles (SSS test-station using automated scanner and LTD with single harmonic coil and single stretched wire system) and two benches for warm measurements. Teams of Indian specialists worked at SM18 hall and performed complete tests and measurements on full series produced magnets.

PARTICIPATION IN LINAC-4 OF SPL

RRCAT has designed an all-solid state klystron bouncer modulator for 1MW klystron for 3MeV RFQ of LINAC-4. A prototype is being built at RRCAT. RRCAT submitted three designs 1) All solid-state modulator with active compensation using a fast acting power supply. 2) All solid-state bouncer compensated modulator. 3) Conventional line type modulator. After intensive discussions between RRCAT and CERN teams, scheme 2 was agreed for prototype development and scheme 1 would be incorporated later by changing the lumped bouncer with an active power supply for droop compensation by feedback loop. Table 2 and figure 5 give salient features of the modulator.

Table 2: Specifications for modulator for LINAC-4

Parameter	**Design Targets**
Klystron modulator type	Bouncer
High Voltage pulse amplitude	-10kV to –110 kV
Pulse width, 70% to 70 % of pk.	800 □sec
Minimum Flat top available	600□sec
Maximum current during pulse	24A
Pulse repetition rate	2 Hz
Acceptable voltage drop	≤ 1.0 %
Allowed ripple on flat top	≤ 0.1 %
Rise time/fall time	<100 μsec
Arc energy dissipated in klystron	<10J

PARTICIPATION IN CTF 3

Some items for collaboration were identified based on CERN's requirement. These are summarized in table 3. Design of TL-2 is nearly over and three prototype dipole

vacuum chambers have been built and qualified. Fabrication of dipole magnets has been initiated.

Table 3: Items for contributions to CTF 3

Description	Requirement
CTF 3 control system Software	5 Man months
Optics Design of TL-2	Design
Dipole Vacuum chambers for TL-2 Straight vacuum chambers (Round and racetrack profile)	5 Quantity based on optics design
Dipole Magnets for TL-2 Nominal Field 1.3 Tesla	5

Figure 1: MCS & MCDO

Figure 2: PMPS jacks.

Figure 3: Integrated QHPS.

Figure 4: LPUs.

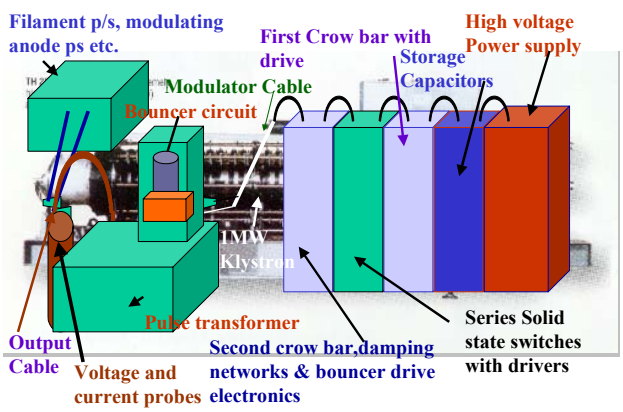

Figure 5: Prototype solid state modulator schematic.

Figure 6: Prototype dipole vacuum chamber for TL-2.

The Indian Team: Efforts of all DAE colleagues (listed institution- wise) are acknowledged as follows:

BARC: B.S. Arunkumar, G. Arvamutham, P.K. Awle, B.M. Barapatre, P.G. Behere, S. Chowdhury, V. Deodhar, K. Dube, V. Pharakiya, P.K. Gopalakrishnan, A. Govindan, G. Govindrajan, V. Goyal, P.K. Kavalan, A.P. Laddha, P. Lala, S. Malhotra, R. Mathu, B. Maurya, Y.S. Mayya, S. Mukhopadhyay, K.P.K. Nair, R. Narayanan, M. Patil, D.B. Perupayyikad, C.K. Pithawa, K. Premkumar, A. Roy, D.A. Roy, Shilpi Saha, V. Sanadhya, S.S. Shetty, D.K. Tyagi and C.C. Verghese.

RRCAT: R. Adbole, A. Amban, H. Ashoka, M. Bagre, S.C. Bapna, V. Bhatnagar, D.D. Bhawalkar, A.G. Bhujle, M.B. Borage, P.P. Deshpande, S. Dutta, P. Fatnani, M.L. Gandhi, A.D. Ghodke, S.G. Goswami, R.K. Gupta, R. Jain, V. Jain, M.R. Jathar, M. Joshi, M.G. Karmarkar, A. Kasliwal, K.M. Khare, A. Laxminarayan, R.G. Marathe, T. Maurya, J. Mulchandani, A. Pagare, S. Palod, P. Pareek, J. Patil, R. Pramod, M. Pravinkumar, A. Rahim, Alpana Rajan, M. Sharma, U. Sharma, S.K. Shukla, S.N. Singh, B.S.K. Srivastava, H.C. Soni, A.P. Thipsay S.S. Tomar, K.G. Vaishnav, A. Valecha, A. Yadav and A. Yedle.

DAE: Sudha Bhave, C.V.A. Bose, R.B. Grover and Anil Kakodkar.

ECIL: Md. Arifuddin, G. Balaiah, A.A. Hussain, Rajshekar Rao and G.P. Srivastava.

IGCAR: K. Palanisami, R. Dandapani, T. Selvakumaran and S. Sridhar.

VECC: T.K. Bhattacharya, R.B. Bhole, U. Bhunia, S. Pal and J. Pradhan.

Finally, We thank Mr. Vinod Chohan, CERN, for his support to Indian team members engaged in magnet tests and measurements at CERN.

REFERENCES

[1] V.C. Sahni, "Indian contribution to the Large Hadron Collider under construction at CERN, Geneva", Current Science, Vol. 87, NO. 4, 25 August 2004. p. 441.

[2] V.C. Sahni, "Cheers to Indian science and technology community engaged in building large research and development facilities and the challenges ahead", PRAMANA Journal of physics, Vol. 67, No. 1 July 2006, pp. 225-248.

PROGRESS OF THE LASER-PLASMA ACCELERATION RESEARCH AT KERI

H. Suk#, M.S. Hur, H.J. Jang, J. Kim, and S.H. Yoo
Center for Advanced Accelerators, KERI, Changwon, Republic of Korea

Abstract

An intense laser pulse can produce a plasma wake wave, which has an extremely strong electric field. This electric field can be used for electron acceleration with a ultrastrong high acceleration gradient (100 times or more compared with RF-based conventional accelerators). We have an experimental program on the laser-plasma acceleration research at KERI (Korea Electrotechnolgy Research Institute), where a 2 TW (700 fs in pulse duration) Nd:glass/Ti:sapphire lasser system and a 20 TW (30 fs in pulse duration) Ti:sapphire laser system (located at GIST-APRI) are used. In this paper, we present an overview of the experimental results for the laser-plasma acceleration research.

INTRODUCTION

RF-basedd conventional accelerators have a limited accelerating electric field of ~ 100 MV/m. Compared with this field, a focused laser beam has a much stronger electric field. For example, if the intensity is I=1018 W/cm2, which can be nowadays easily achieved with a table-top terawatt laser system, the field strength is E=3 TV/m. However, the laser electric field can not be directly used for particle acceleration because the electric field is transverse. This problem can be solved if the laser beam is sent into a plasma, so the laser field is converted into a strong longitudinal plasma wake field that is almost in the same order of magnitude as the laser field itself [1]. There are several ways to excite a strong laser-plasma wake wave. One way is to send a rather long (longer than the plasma wavelength) laser pulse, so the plasma wave can be resonantly excited by a pulse train from the Raman scattering instability. This is called the self-modulated laser wakefield acceleration (SM-LWFA). Another way is to send a short laser pulse (pulse duration ~ plasma wavelength) and this can excite the plasma wake wave almost resonantly as well. We have an experimental program on the SM-LWFA and resonant LWFA at KERI in collaboration with GIST-APRI (Gwangju Institute of Science and Technology-Advanced Photonics research Institute). In this paper, we show some experimental results from the SM-LWFA and LFWA research.

EXPERIMENTAL RESULT ON THE SELF-MODULATED LASER WAKEFIELD ACCELERATION

For the self-modulated laser wakefield acceleration experiment, we used the 2 TW (1.4J/700 fs) Nd:glass/Ti:sapphire hybrid type laser system at KERI. The experimental schematic is shown in Fig. 1. The 2 TW laser beam with a diameter of 5 cm is focused to a small spot (~ 10 μm in diameter) by the gold-coated parabolic mirror in the He supersonic gas jet (backing pressure ~ tens of bars, gas jet diameter=0.8 mm), so the He gas is ionized to a plasma by the strong electric field of the laser beam. Due to the interaction of the plasma and the laser beam, a self-modulated laser wakefield is generated and some background plasma electrons are randomly injected into the acceleration phase. The injected electrons are accelerated and the produced beam passes through the dipole magnet. And then it arrives at the LANEX film (a kind of phosphor film). This measurement gives an energy and energy spread of the generated electron beam. The beam charge is measured with an ICT (integrating current transformer) that is located after the thin LANEX film (made by KODAK). In this experiment, the generated electron beam has a continuous energy spectrum because plasma electrons are randomly injected into the acceleration phase. Hence, we used a very small pinhole-like collimator with a diameter of 1 mm to select only high energy electrons that are distributed mainly along the axis.

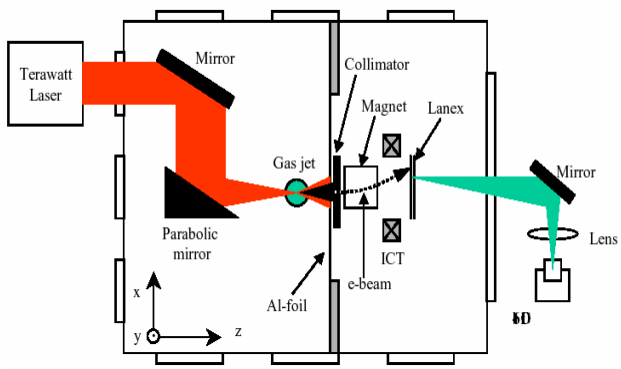

Figure 1: Schematic for the SM-LWFA experiment.

hysuk@keri.re.kr

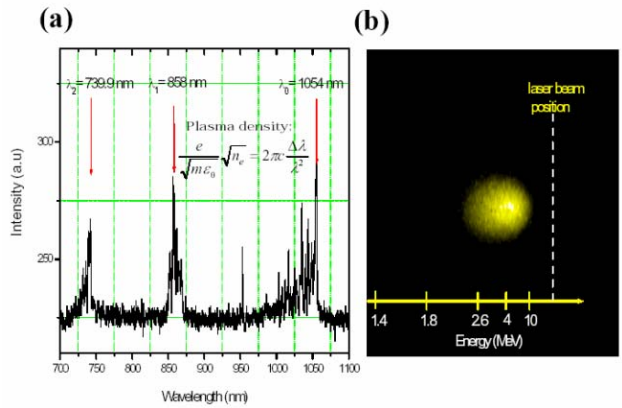

Figure 2: (a) Spectrum of the Raman forward-scattered light and (b) energy spectrum of the generated electron beam.

Interaction of the long laser pulse and the plasma produces the Raman forward scattered light and Fig. 2(a) shows its spectrum. It shows that the spectrum has a few side bands and analysis of the result gives the plasma density ($n_p = 10^{19} \sim 10^{20}$ cm-3). Our comparison of this result and interferometric measurement of the neutral gas density gave the same result, which implies that the He gas is almost 100 % ionized with the focused 2 TW laser beam. Figure 2(b) shows the energy spectrum of the generated electron beam from the SM-LWFA experiment, in which a 1-mm diameter collimator was used to select only high energy electrons along the axis. The measured result shows that the beam is quasimonoenergetic, reaching up to ~10 MeV in energy. Although this method is not a perfect way to generate a monoenergetic beam, it is a quite useful and practical way for quasimonoenergetic beam generation from the SM-LWFA.

EXPERIMENTAL RESULT ON THE RESONANT LASER WAKEFIELD ACCELERATION

In addition to the SM-LWFA experiment, a separate experiment for the resonant laser wakefield acceleration was performed with the 20 TW (30 fs) Ti:sapphire laser system of GIST-APRI. In this case, the plasma density is tuned for the plasma wavelength $\lambda_p \cong c\tau$, where c is the light speed and τ is the laser pulse duration. The used gas was also He and the gas jet has dimensions of 4 mm by 1.2 mm (the laser propagates along the 1.2 mm direction). We measured the generated electron beam with the same diagnostic tools as Sect. 2. By tuning the plasma and laser parameters carefully, we could sometimes generate quasimonoenergetic electron beams. One example is shown in Fig. 3, in which the energy spectrum of the electron beam (measured after a dipole magnet) is clearly quasimonoenergetic. It shows that the peak energy is around 35 MeV and the maximum energy

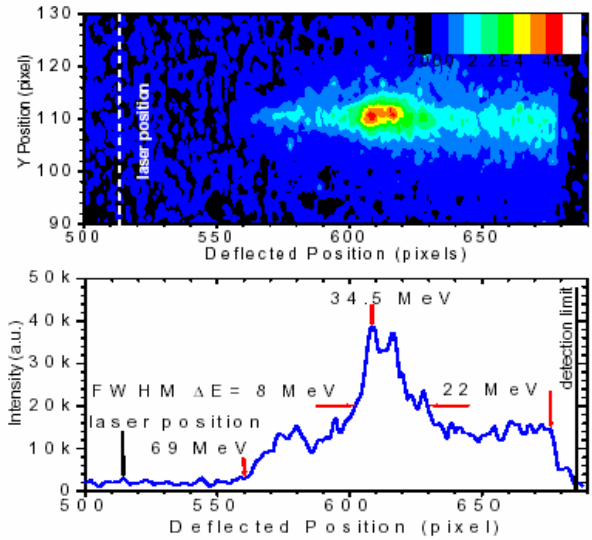

Figure 3: (a) Energy spectrum of the generated electron beam from the resonant LWFA experiment and (b) profile of the energy spectrum.

is about 70 MeV. However, it should be pointed out that generation of this kind of quasimonoenergetic electron beam is quite unstable, so it can not be repeated with high probability. This is probably due to highly nonlinear injection of the plasma electrons into the acceleration phase of the wake wave. Therefore, a good way for controllable injection is required for realization of the laser-plasma accelerators and this is one of the most important research issues in the laser-plasma accelerator community.

QUASIMONOENERGETIC ELECTRON-BEAM GENERATION FROM THE DENSITY TRANSITION

Several ideas were proposed to produce such beams using lasers [2,3]. One of them is to use a sharp downward density transition. According this idea, some background plasma electrons can be self-trapped by the laser wakefield when an intense laser beam pulse propagates through a sharp downward density transition. At the transition the wavelength of the wake wave increases suddenly so that some background plasma electrons are self-injected into the local acceleration phase of the wakefield and a small energy-spread beam can be generated. This was confirmed by particle-in-cell simulations before, and now we are doing an experiment to verify the idea. Although the experiment is still in the preliminary stage, we found a promising result already.

For this experiment, one needs a sharp downward density transition in the plasma and we produced it with an expanding plasma channel. In other words, the high power Ti:sapphire laser beam at GIST was split into two parts and then one of them was used to produce a plasma channel and the other was sent at right angle to cross the plasma channel. The laser pulse for the plasma channel was not compressed, so its pulse duration is rather long

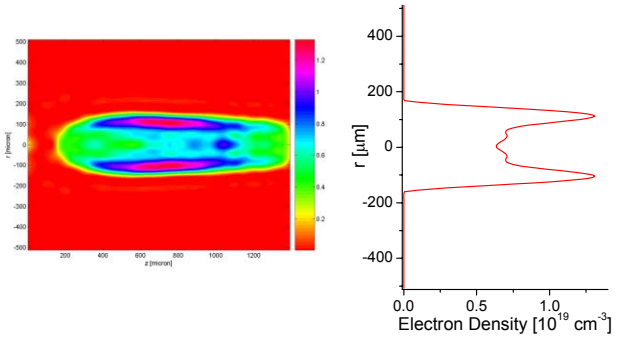

Figure 4: Generated plasma channel (left) and its density profile. In the left figure, the long (~300 ps) laser pulse propagates in the horizontal direction and the channel expands rapidly.

(~300 ps, 500 mJ). When it propagates in the He gas jet, it produces a plasma channel and it expands radially. In this process, the density profile becomes steep outward due to a nonlinear effect and the compressed high power laser beam is focused near the downward part of the second density peak, so a laser plasma wake wave passes through a sharp downward density transition. Here, it should be noted that the plasma channel of Fig. 4 is surrounded by a neutral He gas and this neutral gas is converted to a 100-%-ionized plasma as the high power laser beam propagates through the gas. So the overall plasma density profile has two density peaks with a flat plasma background and the trapped plasma electrons can be accelerated in the plasma with a flat density profile. Figure 5 shows one example of the results, where a quasimonoenergetic electron beam was generated. In this experiment, the time delay between the two laser pulses was fixed to 4 ns due to a technical problem and we could not optimize the situation. Nevertheless, the generated electron beam showed a quasimonoenergetic property. Of course, it should be remembered that this is a preliminary result and there are still quite many issues to clarify. Hence, we will continue this research to answer all questions and to optimize the result.

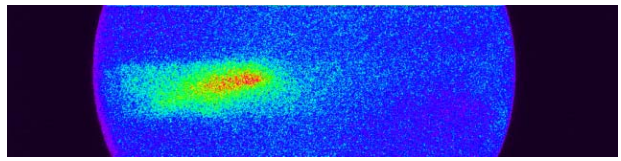

Figure 5: Energy spectrum of the generated electron beam from the density transition experiment.

CONCLUSIONS

Laser-plasma accelerator research has made an amazing progress around the world for the past several years. One of the most important achievements is production of quasimonoenergetic electron beams. We have also made a good progress in this direction at KERI. Although the methods for quasimonoenergetic beam generation are not perfect yet, we are going ahead for better achievement and we believe that the final goal will be achieved in the future.

ACKNOWLEDGMENT

This research was supported by the Creative Research Initiative Program of MOST/KOSEF. We would like to express deep thanks to staffs and Profs. D.K. Ko and J. Lee of GIST-APRI for the collaboration research.

REFERENCES

[1] T. Tajima and J. M. Dawson, Phys. Rev. Lett. 43, 267 (1979)
[2] D. Umstadter, J. Kim, E. Dodd, Phys. Rev. Lett. 76, 2073 (1996).
[3] E. Esarey, R. F. Hubbard, W. P. Leemans, A. Ting, and P. Sprangle, Phys. Rev. Lett. 79, 2682 (1997).
[4] H. Suk et al., J. Opt. Soc. Am. B 21, 1391 (2004); H. Suk et al. Phys. Rev. Lett. 86, 1011 (2001).

PAPER NOT YET RECEIVED

ACHIEVEMENT OF ATF AND ITS FUTURE PLANS *

Junji Urakawa for the ATF International Collaboration
High Energy Accelerator Research Organization(KEK), 1-1 Oho, Tsukuba-shi, Ibaraki, Japan

Abstract

The ATF (Accelerator Test Facility at KEK) International collaboration has been launched formally under the MoU (Memorandum of Understanding) from August 1, 2005, so as to maximally contribute to the world design and development efforts in the areas of particle sources, damping rings, beam focusing and beam instrumentation towards the International Linear Collider (ILC) project. I will give a talk on the achievement at ATF and its future plans, especially ATF2 project.

OUTLINE OF ATF AT KEK

The Accelerator Test Facility (ATF) at KEK comprises a multibunch-capable RF gun (with up to 20 bunches, spaced by 2.8ns, per pulse), an 1.3GeV S-band injector linac, a damping ring, and a beam diagnostic section(EXT)[1]. Each part directly contributes to the development of technologies relevant to high luminosity linear colliders. ATF at KEK is a research center for studies of issues concerning the injector, damping ring and beam delivery systems for ILC. Fig.1 shows a schematic plan view of ATF[2, 3, 4]. The multibunch scheme is essential to boost the rf-to-beam transfer power efficiency in the accelerator.

ATF generates, accelates, damps, and extracts a train of 20 bunches with $1x10^{10}$ electrons/bunch and 2.8ns spacing. The achievable normalized emittance is 3.8μm horizontally and 0.0125μm vertically, and an energy spread 0.08% and the bunch length 8mm for the multibunch beam. The small emittance from the damping ring has been achieved by special design of a strong focusing lattice with precise alignment of components and beam orbit control. The nonlinear behavior of the beam has to be well understood to provide enough dynamic aperture under such strong focusing conditions.

After the technology choice for ILC Main Linac, we proposed ATF2 project as a test beam line using very flat beam from the ATF damping ring to realize 37nm vertical beam size at the final focus point stably. Then, we have established an International Collaboration of ATF (including ATF2 project) with many institutes and it was launched on Aug. 1st 2005. Now several other institutes were added to join into this collaboration.

The International Collaboration of ATF is based on the Memorandum of Understanding (MoU) which defines the organization of the international collaboration to carry out the research programs at ATF and its extension ATF2, so as to maximally contribute to the world design and development efforts in the areas of particle sources, damping rings, beam focusing and beam instrumentation towards the ILC project. We are adding the MoU, the chart of the organization and related material into new ATF Web Site (http://atf.kek.jp/).

As evidence from this MoU, the construction and operation of ATF2 will be executed in the framework of the International Collaboration of ATF. The management of activities of ATF2 will be carried out under the supervising bodies as described in the later section.

I described the simplified explanation of the ATF MoU in the following sub-sections. Also, I explain the achievement of ATF and the plan of ATF2[5].

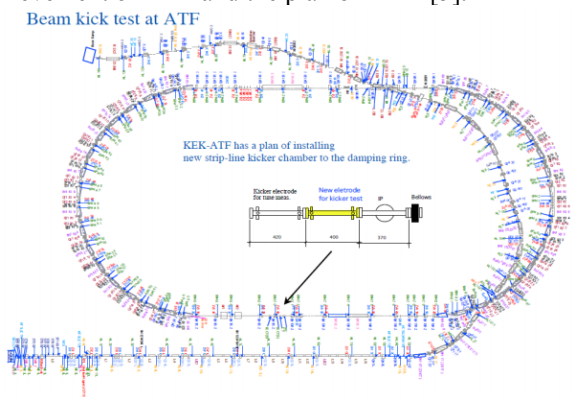

Figure 1: Schematic plan view of ATF.

MISSION OF ATF/ATF2

ATF is to establish the technologies associated with producing the electron beams with the quality required for ILC and to provide such beams to ATF2 in a stable and reliable manner.

ATF2 is effectively to use the beams extracted from ATF at a test final focus beamline which is similar to what is envisaged at ILC. The goal is to demonstrate the beam focusing technologies that are consistent with ILC requirements. For this purpose, ATF2 aims to focus the beam down to a few tens of nm (rms) with a beam centroid stability within a few nm for a prolonged period of time.

Both ATF and ATF2 is to serve the mission of providing the young scientists and engineers with training opportunities of participating in R&D programs for advanced accelerator technologies.

ORGANIZATION OF ATF/ATF2

To execute the scientific programs at ATF/ATF2, the following bodies were instituted:

- International Collaboration Board (ICB)
- Technical Board (TB)
- Spokesperson (SP) with his/her Deputies
- System/Group Coordinators (SGCs)

International Collaboration Board (ICB)

The International Collaboration Board (ICB) is the decision making body for executive matters related to the

* Work supported by "Grant-In-Aid for Creative Scientific Research of JSPS(KAKENHI 17GS0210)"

ATF collaboration. Each collaborating institute can delegate one member to the ICB. In addition, the ICB is joined by the three GDE Regional Directors, who represent Asian, North American and European regions.
One of the members of the ICB is to serve as the ICB Chair. The nomination of the ICB Chair is done through mutual voting by all of the ICB members.

According to the 1st ICB meeting at Snowmass 2005, an ICB meeting will be held approximately once per year. Research programs and near term schedules of the machine operation will be posted to the ATF Web Site, usually for the upcoming two weeks. If some collaborators have a need to change the schedule, SP or deputies have to coordinate it.

Technical Board (TB)

The TB consists of approximately 4~5 members from each of the Asian, North American and European regions. The members of the ATF Technical Board (TB) are nominated and appointed by the ICB. The TB serves the following tasks:

- At the request of ICB, assist the Spokesperson in formulating the ATF Annual Activity Plan, which outlines the activity plans of ATF/ATF2 including the budget and beam time allocation for each Japanese fiscal year.
- Assist the ICB in assessing the scientific progress that is being made by the ATF collaboration.

Usually schedule of ATF machine operation is divided to two blocks of operating time per year with about four months summer long shutdown. One block is from mid. of Oct. to Dec, and the other is from mid. of Jan. to mid. of June. Since there are many collaborators, we decided two meetings of TB per year in Dec. and May for review and recommendation of the research programs at ATF.

Spokesperson (SP)

The SP serves the following tasks:

- Direct and coordinate the work required at ATF/ATF2 in accordance with the ATF Annual Activity Plan.
- Report the progress made by the collaboration to the ICB and the director of KEK.
- Report the matters related to KEK budget and KEK properties to the director of KEK.

To carry out these tasks, the SP will

- Appoint, with an approval of ICB, up to three Deputies to assist his/her tasks in the areas of
  - Beam operation,
  - Hardware maintenance, and
  - Design, construction and commissioning of ATF2.
- Appoint, with an approval of ICB, the System/Group Coordinators (SGCs) on critical ATF subsystems and study programs.
- Organize a "Coordination Group" with the Deputies and System/Group Coordinators for coordinating the details of the operation and development at ATF/ATF2 on a daily (during the beam operation period) or weekly (during the maintenance and construction period) basis.

The report and the discussion are usually carried out through the ATF Web Site (http://atf.kek.jp/) with members of ICB, TB and SGCs.

System/Group Coordinators (SGCs)

- The System/Group Coordinators were appointed by the Spokesperson with an approval of ICB.
- The appointment of the System/Group Coordinators was made in a manner consistent with the ATF Annual Activity Plan.
- The System/Group Coordinators coordinate the tasks charged to the assigned Systems or Groups, and assist the Spokesperson and the Deputies coordinate the ATF/ATF2 research programs.

In case of small study groups with less than 5 members, the Spokesperson or the Deputies may assume the role of its Coordinator on an acting basis.
Simplified organization chart is shown in Fig.2.

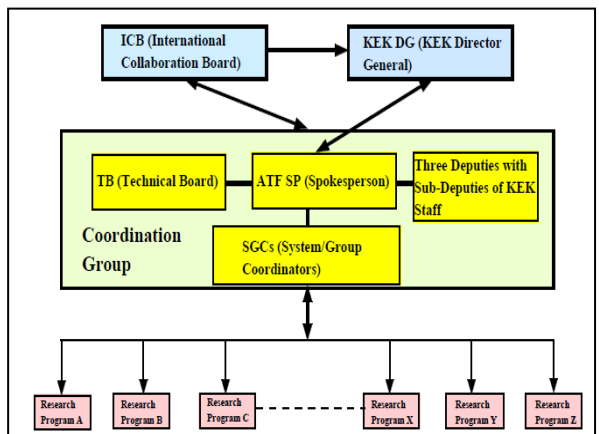

Figure 2: Simplified organization chart.

Execution of Research Programs at ATF/ATF2

The ATF Spokesperson (SP) supervises the construction and operation programs of ATF/ATF2 in accordance with the ATF Annual Activity Plan, as approved by the ICB. The ATF SP can delegate part of his/her tasks to the Deputies and System/Group Coordinators, as deemed appropriate. The planning and execution of the construction and operation programs of ATF/ATF2 must be conducted in a manner consistent with the Japanese laws, KEK internal regulations and other rules applicable in case of activities by non-KEK members of the collaboration. Details of the group structures are to be formulated in ways optimized in accordance with the technical nature of each program in question, e.g. activities such as design, simulation, testing, construction, commissioning, operation, and investigation.

Additional agreements concerning the matters related to execution of non-KEK budget, management of non-KEK properties at the premise of ATF, together with handling of KEK properties at the premises outside KEK, are to be individually dealt with in Annexes attached to the ATF MoU.

The detailed coordination of beam time allocation will be done by the Coordination Group.

An institute who has not signed on the ATF MoU may participate in part of the research programs at ATF, with an authorization of the ATF SP, in as much as the proposed activity is:

- within the ATF Annual Activity Plan,
- under the consent by the relevant Deputies or System/Group Coordinators, and
- promptly reported to the ICB.

Should a conflict of interests occur among the members or Work Groups within the collaboration, the Spokesperson will make the best efforts to resolve it in an amicable manner. When a suitable resolution cannot be reached, the Spokesperson will bring the matter to the ICB for further negotiation towards a resolution.

Membership of the Collaboration

Membership of new institutes for the ATF collaboration is subject to approval of the ICB. Institutes who desire to join the ATF collaboration shall submit a proposal to the Spokesperson, who will relay the matter to ICB.

Withdrawal of a member institute from the ATF collaboration is subject to acknowledgement by the ICB. Institutes who desire to withdraw from the ATF collaboration shall submit a notification to the Spokesperson, who will relay the matter to ICB.

ACHIEVEMENT OF ATF

There is a lot of developments on beam instrumentation at ATF since 1993. The detail report is given by reference of [6]. This report covers remained achievements.

Emittance Measurements at EXT

Intensive studies on the vertical emittance with the wire scanners in EXT have been ongoing since March(2000)[7]. An important observation we made during this time is that there appears to be a source of x-y cross plane coupling somewhere between the extraction point of the damping ring (DR) and the wire scanner region in EXT. The measured vertical emittance is approximately $(1.1+/-0.1)x10^{-11}$ m for the beam intensity of $(2.0+/-0.2)x10^{9}$ electrons per bunch. The emittance is found to grow to $(2.2+/-0.1)x10^{-11}$ m at the beam intensity of $(8.0+/-0.3)x10^{9}$ electrons per bunch, however. In these measurements, the x-y beam profile showed a tilting of a few degrees, as observed by using 10 degree wires. The quoted vertical emittance in these plots might be further reduced by re-optimizing the setting of skew magnets. Obviously, repeated measurements and careful studies are needed, and the results shown here should be considered preliminary. It appears that the following points play an important role.

1. Tuning with skew knobs in the arc sections of the DR for reducing the betatron coupling in the ring.
2. Careful corrections for residual dispersion in EXT.
3. Additional cross-plane coupling correction using a skew quadrupole magnet in EXT, upstream of the wire scanners.

Beam Tuning and Diagnostics in Damping Ring

COD and Dispersion: The program SAD is used in orbit and dispersion corrections, for calculating new setting of the steering magnets. The results of the COD correction in DR were 2mm (peak to peak) horizontally with 1mm expected from simulations and 1mm vertically. The dispersion in the DR is measured as difference of orbits with different RF frequencies. The dispersion correction in the ring worked and typical r.m.s. of the vertical dispersion after the correction was about 5 mm which is close to our target.

X-Y Coupling Corrections: To correct x-y coupling, trim coils of the all sextupole magnets are connected to produce skew quadrupole field. A global correction of the coupling is essential to achieve the smaller emittance. We tried a global coupling correction minimizing vertical COD response to horizontal steering. The orbit coupling was clearly reduced and some reduction of the vertical emittance was observed after the correction. We also tried a coupling correction by 4 dedicated skew quadrupoles and achieved some reduction in the vertical beam size at the SR source point.

Local orbit bumps were also used for low vertical emittance tuning. Setting many bumps one-by-one the vertical beam size was monitored using SR-interferometer.

We tried new coupling correction using orbit response matrix (ORM) analysis. It has been confirmed that ORM analysis is a technique used to diagnose and correct optics errors in storage rings. Recently, we achieved and confirmed the normalized vertical emittance of 0.015μm at a bunch charge of $(7.0+/-0.2)x10^{9}$ electrons in the ATF ring by ORM analysis and the laser wire monitor [8,9].

New Extraction Kickers with a Flat-top Longer than 300ns

A project to replace the extraction kicker system in the ATF damping ring was collaboration between KEK and SLAC. A SLAC epoxy kicker system was prepared. At the same time, a modification to the kicker pulse was introduced so that flat-top of pulse lengths 340ns was achieved. This allows us to experimentally examine the implications to the beam instrumentation hardware and component stabilization issues in conditions similar to ILC. A team of accelerator physicists from KEK and SLAC succeeded in extracting 3 bunches of electron beam at 154 ns duration and 2 bunches at 336 ns duration in Fall, 2005 (Fig.3), a milestone in realizing the beam control operation mode required in the ILC.

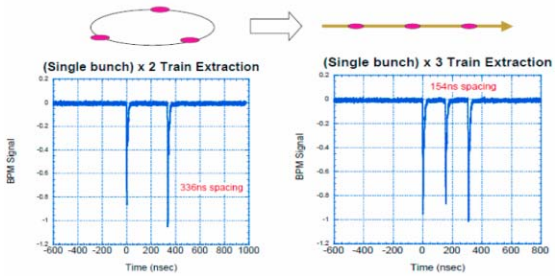

Figure 3: ILC-like beam extraction at ATF.

Polarized Positron Beam Generation

The proof of principle experiment for polarized positron beam generation based on backward-Compton scattering has been done at EXT. Almost 100% circular polarized gamma-ray was generated at about 56MeV with 2.2×10^7 photons/collision. The polarization of the positron beam which was generated through the process of pair-creation at the gamma-ray target has been measured by the transmission method of gamma-ray related Compton scattering in magnetized iron. Detail report was published soon[10].

Development of a Fast strip-line Kicker

In the present ILC design baseline, the damping rings must store up to ~5600 bunches in a ~6 km circumference and provide the main linacs with the bunches spaced apart by ~150ns or ~300ns. Thus, the injection and extraction kickers have to realize 3.0nsec rise and fall times at a repetition rate of 3MHz or 6MHz. A collaboration was formed among KEK, SLAC, DESY, LBNL and LLNL in the Fall of 2004 to address this issue. In Spring, 2005, three flavors of pulse circuits (built by DESY, SLAC/LLNL and KEK) were used to test-drive a stripline kicker (prepared by KEK), which was installed at the ATF damping ring. Fig.4 shows a beam kick angle measured with the BPMs while scanning the kicker timing with respect to the bunch arrival. It demonstrates the rise and fall times of 2.2 ns and 3.0 ns, respectively, as achieved with two commercially available 5kV fast pulses and with two 32.7cm long strip line kickers. This R&D program will continue and will attempt to demonstrate the beam extraction, to check the stability and reliability, and to check the effects on previous and following bunches.

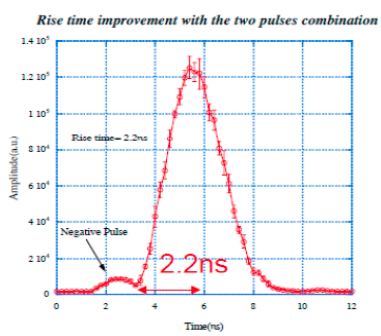

Figure 4: Beam kick amplitude vs timing.

Beam Position Monitors

Fig.5 shows the schematic design of a beam position monitor unit that has been used at the ATF damping ring. In 2005-2006, collaborators from SLAC tested a new signal processing circuit which average the BPM signals over a prescribed number of turns for improved resolution. Fig.6 overlays the measured beam position data from the BPMs with existing and test circuits. A dramatic improvement, close to a sub-micron level, has been demonstrated. We will improve all signal processing circuits of the damping ring BPM by the end of 2008 in order to reduce vertical emittance near 1pm.

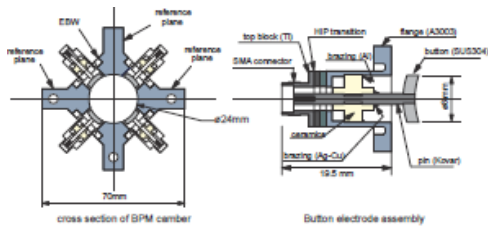

Figure 5: Schematic view of an ATF damping ring BPM.

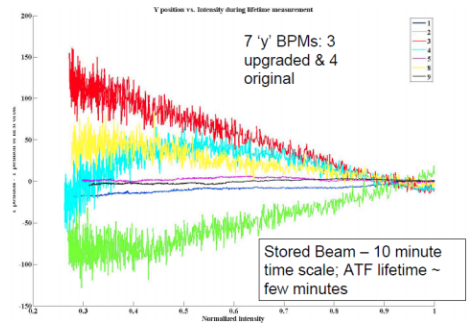

Figure 6: Position data of the stored beam, as function of the bunch intensity. Data from BPMs with the old, existing readout circuits and with new test circuits are overlaid.

FUTURE PLANS FOR ILC AT ATF/ATF2

ATF2

ATF2 is a scaled model of the ILC Beam Delivery System which transports, focuses and controls the low-emittance beam at an interaction point. Two major goals of ATF2 are: (1) to focus the beam vertically at 37nm with the local chromaticity correction scheme and (2) to control beam position with a few nm vertical jitter at the focus point, by taking advantage of the ultra-low emittance beam at ATF.

The ATF2 beam line in the latest design comprises 26 standard quadrupole magnets, a doublet of final quadrupole magnets, 5 sextupole magnets and 3 bending magnets. Fig.7 shows the layout of ATF2. Each of the quadrupole and sextupole magnets features a cavity type BPM (Beam Position Monitor, QBPM) with 100nm position resolution. In JFY2005-2006, 28 standard Q-magnets and 26 QBPM were produced by groups at IHEP (China) and PAL (Korea), respectively. The electronics

of QBPMs with digital readout have been designed at SLAC and are under construction there.

The schedule of ATF2 construction and beam commissioning/operation was fixed at 3rd ATF2 project meeting and approved by ICB and TB. Fig.8 shows the final schedule of ATF2. Both the ATF and ATF2 will be managed to serve the mission of providing the young scientists and engineers with training opportunities in R&D programs for advanced accelerator technologies.

Future plans of fast kicker R&D and beam instability studies

R&D on fast kicker is going to check the performance of the system with 2.8ns 20-bunch train. Preliminary results indicate the possibility of beam extraction without kick effect into adjacent bunch. We consider more detail study of the system is necessary.

The fast ion instability, micro-wave instability and non-linear beam dynamics studies are underway to obtain important information for the ILC damping ring design. Several international groups already proposed the plan and we are discussing the details on each study soon.

ACKNOWLEDGMENTS

The author would like to thank Professors A.Suzuki, F.Takasaki, Y.Kamiya, K.Yokoya, and S.Kurokawa for their encouragement. All members of KEK-ATF group and international collaborators for this research program are acknowledged. We also thank Professor E.Paterson of the ATF ICB Chair for supporting the ATF project as an international collaboration.

REFERENCES

[1] J.Urakawa, Results from DR and Instrumentation Test Facilities, PAC05, pp.305-309, Tennessee, 2005.
[2] J.Urakawa, KEK/ATF Damping Ring, PAC97, pp.444-448, Vancouver, May 1997.
[3] Edited by H.Hayano et al., KEK Internal 2000-6 A (2000).
[4] J.Urakawa et al., presented at 17th International Conference on High-Energy Accelerators (HEACC98), Dubna, Russia, 7-12 Sep. 1998. KEK Preprint 98-154.
[5] ATF2 Proposal, Volume 1, CERN-AB-2005-035, CLIC note 636, DESY 05-148, ILC-Asia-2005-22, JAI-2005-002, KEK Report 2005-2, SLAC-R-771, UT-ICEPP 05-02 (2005), Volume 2, KEK Report 2005-9, CERN-AB-2006-004, DESY 06-001, ILC-Asia-2005-26, JAI-2006-001, SLAC-R-796, UT-ICEPP-05-04
[6] Y.Honda, Proc. of this conference.
[7] J.Urakawa, H.Hayano and M.Ross, Proc. of Nanobeam 2002, p223.
[8] A.Wolski et al., ATF Reports-04-09, LBNL-57046, SLACPUB-11040, 2004.
[9] Y.Honda et al., Physical Review Letters, Vol.92, No.5, 054602-1 (2004).
[10] T.Omori, et al., Physical Review Letters, Vol.96, 114801-1 (2006).

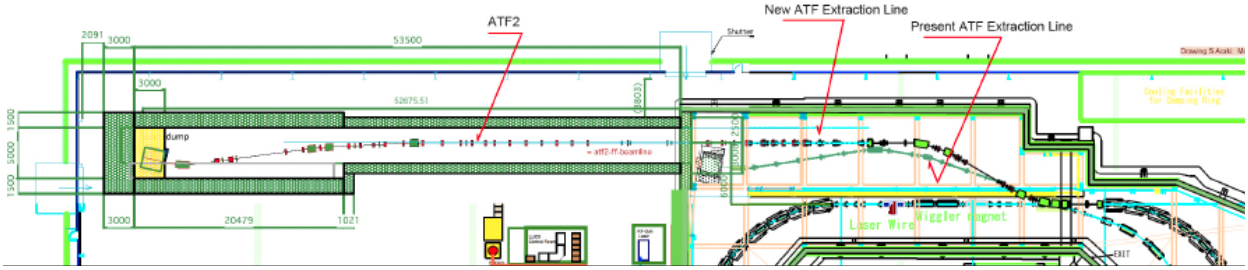

Figure 7: Layout of ATF2.

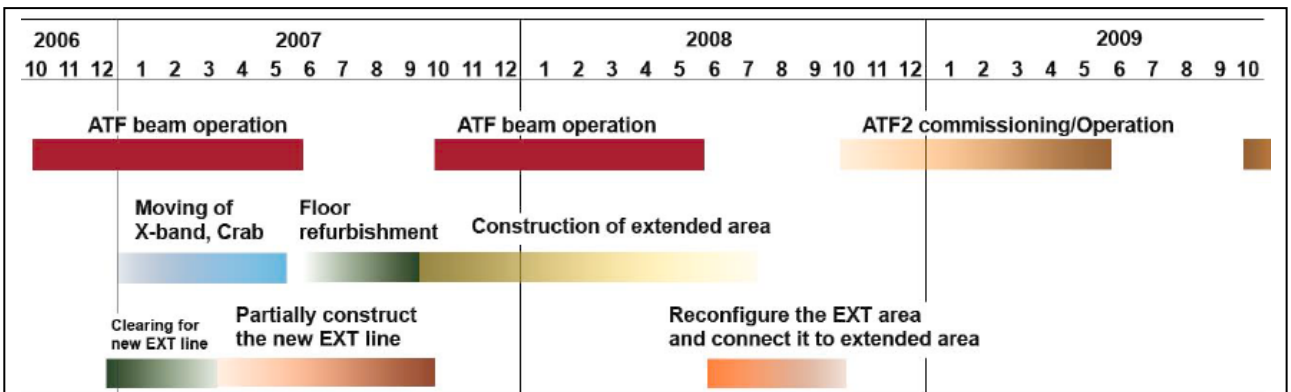

Figure 8: Schedule of ATF2 construction and commissioning/operation.

EXPERIENCE WITH THE HERA LEPTON-PROTON COLLIDER

F. Willeke, DESY, Hamburg, Germany

Abstract

A review of the experience of operating the HERA lepton proton collider with a high luminosity of up to $5 \cdot 10^{31} cm^{-2} s^{-1}$, a discussion of the important accelerator physics issues and a summary of the most important physics results of the lepton-hadron (ep) collider HERA is presented.

INTRODUCTION

Collisions of high energy leptons with hadrons reveal the structure and dynamics and the nature of the forces between the constituents of hadrons. Electron scattering experiments on protons were performed already fifty years ago when R. Hofstadter and co-workers measured the nuclear form factor by analysis of (200-600) MeV electrons scattered on protons [1]. As leptons with energies of several GeV became available, a series of lepton nucleon scattering experiment revealed an inner structure of the proton with point-like constituents [2, 3]. This discovery was followed by many experiments yielding a better understanding of the proton structure. The experiments E49-89 at SLAC [4] observed that the cross section for small x† remained constant in the range of $x \approx 1/3\text{-}0.01$. This result (among others) suggested that additional quarks-antiquark pairs are produced inside the proton by the strong force between the valence quarks and the gluons. A lepton-hadron collider with large centre of mass energy (E_{cm}) was expected to provide the ultimate experimental evidence for this model because it would provide access to small x with sufficient spatial resolution or high Q^2. At that time, the HERA ep collider with E_{cm} = 318 GeV was proposed [5]. HERA was expected to provide precision measurements of the proton dynamic structure function F_2, of electro-weak and strong interactions, and to provide experimental evidence of lepton quark resonances. HERA was approved in 1984 and the physics program was started in 1992.

HERA OVERVIEW

HERA consists of two 6.4 km long storage rings, one with 5T superconducting magnets for the 920 GeV protons and another with normal conducting magnets for the 27.5GeV electrons or positrons. The beams collide at two collision points (IP) denoted by North and South, where the detectors H1 and ZEUS are located. The interaction regions (IR) were upgraded for a high luminosity of $L > 5 \cdot 10^{31} cm^{-2} s^{-1}$ in 2001 [6]. The HERA lepton beam is spin polarized by the Sokolov-Ternov [7] effect. Three pairs of ppin rotator magnets [8] around each of the three experiments provide longitudinally polarized leptons for collisions with protons.

HERA ACCELERATOR PHYSICS ISSUES

The HERA injection energy for protons is only 40 GeV, 0.043 times the operation energy of 920 GeV. The corresponding large persistent current field errors of the superconducting magnets at injection [9] are the cause for a small dynamic aperture of only 3.8 RMS times the beam sizes $\sigma_{x,y}$ [10]. This serious issue is solved by strictly controlling the beam parameters. Emittance dilution at injection is avoided by correcting injection errors to < 1mm transversely and to $< 4 \cdot 10^{-4}$ in relative energy at each proton injection. The tunes during injection and the first part of acceleration must be kept to within a small window of $\Delta Q_{x,y} \leq 0.002$. They are controlled by a software-based feedback [11] with a non-destructive tune measurement [12]. Persistent and eddy current sextupole components of the guide fields must be suppressed dynamically to a level of 0.3% which is accomplished by a combination of continuous monitoring and correction via a reference magnet system, by look-up tables for correction of systematic errors and by manual fine tuning the chromaticity on analysis of the tune spectra. As a result, the chromaticities $\xi_{xy} = \Delta Q_{xy} \left(\Delta p/p\right)^{-1}$ are controlled to about one unit. The betatron-oscillations must be decoupled to levels of < 0.005 in the coupling strength. Failure to meet these requirements leads either to beam loss > 1% due to poor dynamic aperture, or multi-mode head tail instabilities. The head tail instability is driven by a conspiracy of coupling and small values of chromaticity [13]. Attempts to control the instabilities during acceleration by broadband dampers [14] have been abandoned because of significant emittance growth due to feedback noise and the then required PLL-type tune measurement, and, more importantly, due to the loss of information necessary to fine-tune the chromaticities based on analysis of the tune spectra for maintaining good lifetime. This part of HERA experience may be relevant for the LHC. High precision, non-destructive tune and chromaticity measurements in conjunction with low-noise damper systems are deemed necessary for the LHC.

The lepton beam tune working space is limited by strong 2nd and 3rd order synchro-betatron resonances. In the vicinity of these resonances the emittance of the leptons growth dramatically and the lifetime becomes very poor. These resonances are excited by accumulative effects around the long circumference of HERA. The widths of

†The parameter x is the fractional momentum of the interacting proton-constituent. It is related to the transfer of energy $\nu = E\text{-}E'$ and the transfer of 4-momentum $Q^2 = (k\text{-}k')^2$ from the projectile to the target by basic kinematics (neglecting terms with the proton rest mass M) by $x = Q^2 \cdot (2M\nu)^{-1}$ and is thus determined from the directly measured quantities Q^2 and ν. While Q^2 constitutes the parameter which controls the spatial resolution, x controls the dynamics of the proton structure.

the 2nd order resonances can be controlled by careful measurement and compensation of dispersion errors, by suppressing orbit oscillations to a level of 0.1 mm with a slow orbit feedback [18], by careful control of the angle of the beam orbit in the interaction point and by empirically optimized dispersion bumps. The 3rd order synchro-betatron resonances are generated as interference between synchrotron side bands of the integer and the half-integer resonance. They are controlled by compensation of higher-order chromatic effects by proper betatron-phasing of the high chromaticity interaction regions [19].

HERA is unique in colliding very different species of particles. In order to establish stable beam-beam operation, matching of the beam cross sections at the IP to ≤20% of the relative beam size is required. The bunch intensity of both beams is limited by the beam-beam effect suffered by the opposite beam. The vertical beam-beam tune shift parameters at two collision points reach levels of $\Delta\nu_{ye}$= 0.05 for leptons and around $\Delta\nu_{yp}$= 0.001 for protons. The proton beam-beam effect is a soft limit. Increasing beam-beam forces produce a gradual increase in experimental background by increased diffusion of protons into the beam halo. Orbit stability is therefore most critical. If the beam retracts from the collimators, diffusing particles fill the gap between beam edge and collimators and are lost on the subsequent approaches to the collimators [15]. The collimation system has a leakage of about 1% [16]. This causes a sudden increase in background which is not tolerable. Power supply ripple, magnet defects or mechanical vibrations enhance the diffusion. Mechanical vibrations of the IR magnets of more than a few μm are not tolerable. Cultural noise has been observed to have an impact on backgrounds.

The beam-beam limit for the lepton beam occurs at values of the vertical beam-beam tune shift of $\Delta Q_y \leq 0.1$. These are values which are typically achieved at conventional electron-positron colliders. However, the mechanism of limitation is quite different at HERA. The choice of betatron tunes is restricted to values close to the integer resonance in order achieve a high polarization of the lepton beam (see below). This region in tune space is governed by strong synchro-betatron resonances. The beam-beam limit of HERA thus occurs if the lepton beam tune spread overlaps with these resonances. The corresponding coherent motion leads to dramatic emittance growth of the proton beam emittance. This kind of indirect impact on the proton beam into itself has been predicted by simulations [17]. Due to the collision of different species and the restriction in choosing the betatron tunes of the leptons, HERA cannot exploit the focusing effects of the beam-beam force (dynamic beta) as in modern electron-positron colliders. A significant difference in specific luminosity is observed in HERA for positrons, $L_{sp}=1.5\cdot10^{30}mA^{-2}cm^{-2}s^{-1}$ and electrons, $L_{sp}>2\cdot10^{30}mA^{-2}cm^{-2}s^{-1}$ which is attributed to the fact the beam-beam force is focusing for electrons and defocusing for positrons. In order to mitigate this effect, the tunes for positron operation are chosen below the integer resonance (mirror tunes). In order to avoid lepton-proton orbital instabilities, the tunes for protons must be chosen below the integer resonance as well in this case. This way the luminosity with positrons can be improved significantly, but is still lower than with electrons (see Figure 1).

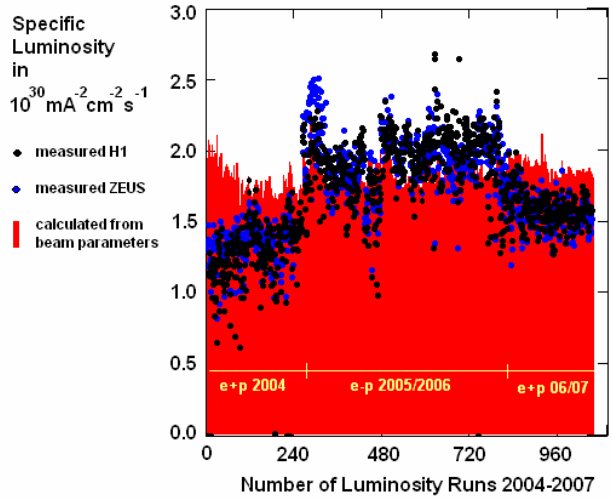

Figure 1: Specific Luminosity for HERA lepton proton collisions since 2004. The specific luminosity is significantly larger with electrons. Specific luminosity with positrons is recovered partly with tunes below the integer resonance in 2006/7.

Longitudinal spin polarization of the lepton beam is obtained by spin rotator magnets around the IRs, by spin transparent optics [20], by careful adjustment of the beam energy and by cancellation of detrimental harmonic content of spurious dipole errors [21] and by placing the betatron tunes as far as possible away from the half integer resonance. The polarization with three pairs of spin rotators reaches (50-60) % [22]. Colliding particles suffer a loss of (10-20) % of polarization. Optimum tunes for high luminosity conflict with high polarization and vice versa.

HERA OPERATIONAL ISSUES

Strong synchrotron radiation (30kW) in each interaction region, which is due to the magnetic separation of lepton and proton beams, generates considerable gas desorption and critical vacuum conditions. The desorbed gas particles become targets for the protons in the IR which causes critical background conditions. This is overcome by beam cleaning of the IR vacuum system, and good pumping in the IR, in particular also for high Z molecules such as Argon. Sufficient pumping is achieved by a combination of ion pumps, NEG pumps, Ti sublimation pumps, and pumping provided by the cold beam pipe of the superconducting separator magnets.

In order to control the high power synchrotron radiation beams of power, the beam orbits must be kept constant to sub-millimetre level during the entire operation cycle. The present HERA low beta quadrupole magnets, added during the 2001 upgrade are located inside the detector solenoid field and move by up to 1mm during the acceleration process. For this reason, a sophisticated orbit feedback has been implemented [30] that keeps the orbit within 0.1mm of a reference state which is interpolated between two reference states during acceleration and low beta squeezing and which recognizes and accommodates deliberate orbit changes for the sake of tuning. This sophisticated system is fully integrated in the automatic machine file handling system.

The availability of the large HERA accelerator complex was an important issue. In the last years HERA reached an availability of 72% of the scheduled time. The complicated injection, the slow acceleration and luminosity set up procedure required about 16% of the scheduled time so that the accelerator delivered luminosity for 56% of the time. These efficiencies have been achieved after high level of automatization of operations, and, more important, provisions of transient recording and long term archiving for all control points. This helps with quick trouble shooting and provides the base for error and performance analysis of the hardware components and for effective preventive maintenance. Preventive maintenance turned out to be particularly useful for increasing the availability of the more than 1200 power converters of HERA.

HERA STATUS AND PLANS

The HERA ep collider is presently operated with 920 GeV protons and 27.5 GeV positrons. The record peak luminosity with electron-proton operation is L_{peak} = $5.1 \cdot 10^{31} cm^{-2} s^{-1}$ and the average luminosity production is $\approx 1 \cdot pb^{-1} d^{-1}$. The peak luminosity in positron-proton operation is only 80% of the electron-proton operation, but the daily luminosity yield is about the same due to very stable conditions with positron running. Recent improvements include successful implementation and test of a broadband longitudinal damper system for the protons which provides proton bunch lengths of 12cm by suppressing coupled bunch instabilities [23]. A fast orbit feedback for the leptons has been implemented recently which is designed to reduce orbit oscillations with frequencies of up to 100 Hz to the 1 μm level at the IPs. The most important operating parameters are presented in Table 1. Figure 2 shows the HERA luminosity production in 2004-2006. After running with electrons since November 2004, positron-proton operation resumed in July 2006.

Before the end of HERA operation in June 2007, it is planned to operate HERA for three months with lower proton energy of 460 GeV for a luminosity of 10 pb^{-1}. In order to mitigate the stronger influence of the electron magnets on the proton beam and in order to achieve minimum beam-cross sections at the IP, the increased flexibility of the magnets for low energy operation has been fully exploited. As a result, low energy proton operation is possible without changing any magnet positions. A peak luminosity of $L = 1.47 \cdot 10^{31} cm^{-2} s^{-1}$ is expected for this mode of operation.

SELECTED HERA PHYSICS RESULTS

The HERA physics program started with a spectacular success. With a delivered luminosity of only 60 nb^{-1} in 1992, the total cross section of inelastically scattered 27.5 GeV electrons on 820 GeV protons plotted versus x revealed a dramatic increase of the density of proton constituents for x below 0.01 as shown in Figure 3 together with the data obtained by fixed target experiments ($x > 0.01$) for comparison. These results form the basis of our present understanding of the structure of the proton with a very large density of sea quarks and gluons which make up the 99% of the proton mass. Figure 4 summarizes the HERA measurements of the proton structure function F_2 versus Q^2 for fixed values of x.

Table 1: HERA Parameters in 2007

Parameter [Unit]	Electro	Protons
Beam Energy [GeV]	27.5	920 (460)
Particles per bunch [10^{10}]	≤ 3.68	≤8.75
Number of Bunches	184	180
Horiz./vert. Emittance [nm]	20 / 3	3.8 / 3.8
Bunch length [cm]	0.9	12
Vert./Hor. β at IP[cm]	26/62	18/245(36/490)
Beam Lifetime in collision	10-15	200
Longitudinal Polarization [%]	30-45	-
Peak Luminosity	5 (1.5) · $10^{31} cm^{-2} s^{-1}$	
Average Luminosity	1 (0.25)· $pb^{-1} d^{-1}$	

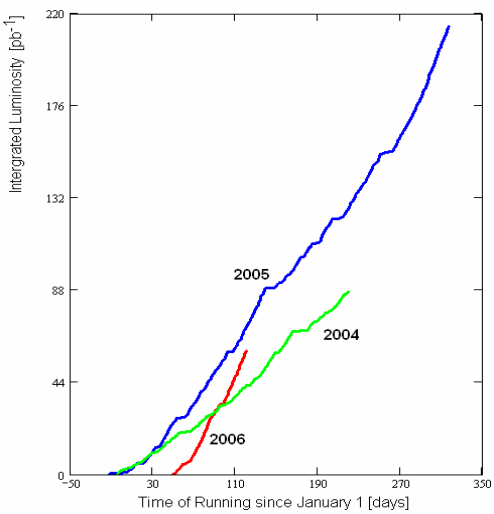

Figure 2: HERA luminosity accumulation 2004-2006

These measurements constitute the synopsis of the present understanding of the proton structure. The data reveal the spatial densities and the momentum distribution of quarks and gluons in the proton. The strong dependence on Q^2 (scaling violation) for small x is a consequence of short range quantum fluctuations of gluons into quark being resolved as the spatial resolution is increased.

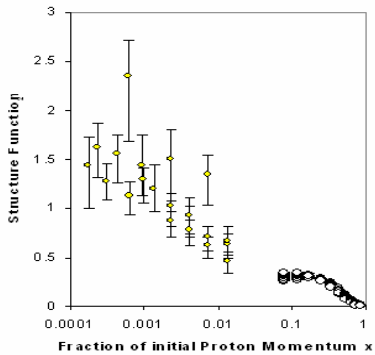

Figure 3: First measurement of ep scattering cross section versus x at HERA [24] including results of ref [4].

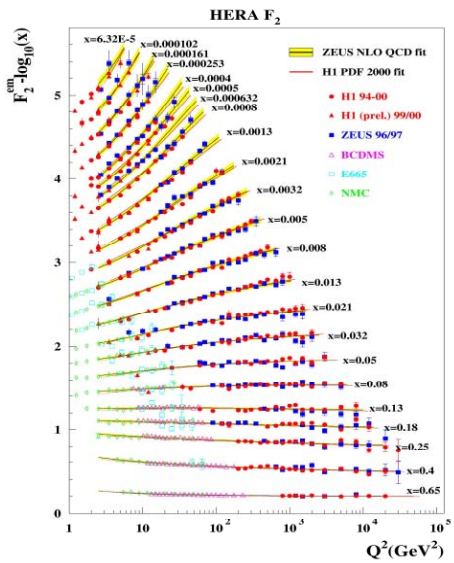

Figure 4: Proton structure function F_2 versus Q^2 in the range of (1-10^5) GeV^2 for fixed values of x in the range of 0.65-6·10^{-5} [25].

Another important part of the HERA physics program is measurements of the electro-weak interaction. According to electro-weak theory, electrons interact with quarks by exchanging either a photon, a neutral Z-boson or a charged W-boson. In ep scattering experiments, an electron is observed in the detector in the first two cases, also called neutral current events. The case of interaction via a W-boson, also called charged currents is characterized by the absence of an electromagnetic shower in the detector and missing transverse momentum because of an escaping neutrino. The scattering cross sections for Z and W exchange are proportional to $(Q^2+M_{W,Z}{}^2c^4)^{-2}$ thus are strongly suppressed by the large Z and W masses compared to electromagnetic exchange with a cross section proportional to Q^{-4}. HERA results on this topic are summarised in Figure 5. Plotted are the neutral and charged current cross sections versus Q^2 for proton electron and proton-positron scattering. All cross sections become comparable at $Q^2 \geq M_{W,Z}{}^2c^4$. Electron and positron cross sections for charged currents differ by a factor of two which is related to the u-d quark ratio of 2 and the helicity structure of the proton. Interfering γ and Z exchange reduces the cross section for proton-positron neutral current events as compared the proton-electron case. The measurements constitute a direct experimental verification of electro-weak theory.

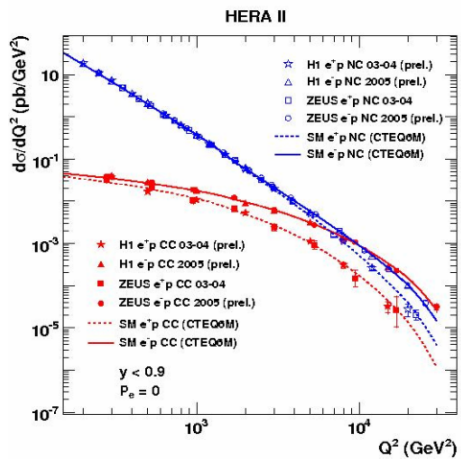

Figure 5: Charged (red) and neutral (blue) current cross sections of ep scattering at HERA [26] versus Q^2

At HERA, the coupling constant of the strong interaction α_s was measured with high precision. It can be extracted in numerous ways from ep scattering data, for example by detecting the relative cross section of ep scattering with one or two hadronic showers. The second hadronic shower arises from a decaying gluon emitted by the struck quark which has a probability proportional to α_s. The combination of all HERA data on α_s has yielded an error of less than 1% which is a significant improvement. Figure 6 shows a plot of α_s versus the energy $\mu = 1 / Q$. These data confirm the theory of asymptotic freedom, for which the Nobel Prize was awarded in 2004 [29] to David Gross, David Politzer and Frank Wilczek.

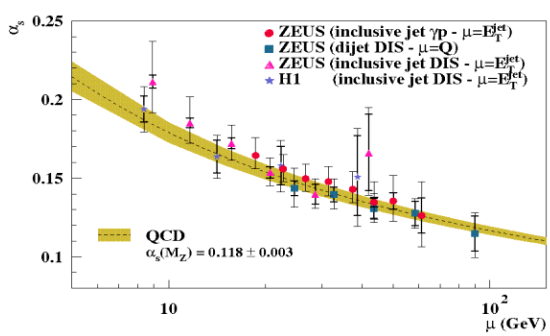

Figure 6: Measurements of α_s versus μ, the energy in the system of interacting quarks from HERA [27]

Electro-weak theory and the standard model predict that a W-boson will couple only to a left-handed electron. The polarization dependence of the charged current cross section for positrons has the opposite sign. Recent HERA data confirm these predictions with very high accuracy as shown in Figure 7 which depicts the charged current cross section for electron-proton and positron proton collisions as a function of polarization.

The examples given above represent only parts of the physics investigated at HERA. Note that the important results from the non-collider, fixed target experiments HERMES and HERA-B are omitted.

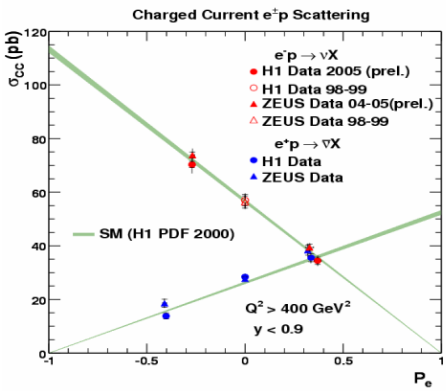

Figure 7: Measurements of the charged current cross section in HERA versus lepton beam polarization [28]

CONCLUSIONS

The HERA lepton proton collider which is being successfully operated since 1992 is soon coming to a conclusion. The achieved peak luminosity which was reached after an upgrade program exceeded the design luminosity by a factor of 3.4 and the luminosity production reached about 1 pb^{-1} per day. HERA is expected to produce a total luminosity of 850 pb^{-1} until July 2007. Most of the physics experiments which motivated the construction of this complicated machine were successfully addressed in the physics program. Some of the results obtained at HERA raised new questions which are considered to be investigated at a possible future lepton proton collider which needs a larger centre of mass energy such as the recently discussed lepton-hadron collider in the LHC tunnel [31].

REFERENCES

[1] E.E.Chambers, R.Hofstadter, Phys.Rev.103,1454(1956)
[2] J.I.Friedman, 14th Int. Natl. Conf. HEP,Vienna (1968)
[3] E.D. Bloom et al, SLAC PUB 796 (1968)
[4] See for example L.W. Whitlow, Thesis, SLAC-357(1990)
[5] HERA proposal, DESY (1981)
[6] U.Schneekloth (ed), DESY HERA 98-05 (1998)
[7] A.Sokolov, I.Ternov, Sov.Phys.Dokl.8, 1203 (1964)
[8] J.Buon, K.Steffen, Nucl.Inst.Meth., A245,248 (1986)
[9] F.Willeke, F.Zimmermann, PAC91, San Fran.(1991)
[10] O. Brüning et al, DESY HERA 95-05 (1994)
[11] S. Brinker et al, EPAC'06, Edinburgh, THPCH083 (2006)
[12] S. Herb, Kerntechnik, Carl Hanser, 1991.
[13] E. Metral et al, EPAC02, Paris (2002), p.1535
[14] D.Heins et al, EPAC96, Sitges (1996) p1857
[15] Mike Seidel, PhD Thesis, Univ.Hamburg (1992)
[16] P. Hahne, E. Lohrmann, DESY-HERA 87-26 (1987)
[17] J. Shi, PAC03, Portland (2003), WOAA009
[18] J. Keil et al, EPAC'06, Edinburgh, THPCH086 (2006)
[19] F. Willeke, EPAC04, Luzern (2004), MOPLT046
[20] A. Chao, K.Yokoya, KEK TRISTAN Report 81-7(1981)
[21] E. Gianfelice-Wendt, EPAC94 , London (1994), p.184
[22] D.P.Barber et al, EPAC2004, Luzern, (2004),
[23] M. Hoffmann et al, EPAC'06, Edinburgh, THPCH085
[24] replotted from Abt et al Nucl. Phys. B407 (1993) 515
[25] H1 and ZEUS preliminary
[26] H1 and ZEUS preliminary
[27] H1 and ZEUS preliminary
[28] H1 and ZEUS preliminary
[29] nobelprize.org/physics/laureates/2004/public.html
[30] J. Maass, S.W. Herb, P.K. Bartkiewicz (PCaPAC 2005), Hayama, Japan, 22-25 Mar 2005.
[31] J. Dainton, et al, JINST 1:P10001,2006. [2006]

TOWARDS A MULTI TEV LINEAR COLLIDER; DRIVE BEAM GENERATION WITH CTF3

H.H. Braun, CERN, Geneva, Switzerland for the CLIC team

Abstract

The 3 TeV compact linear collider, CLIC, foresees an RF source based on a high current drive beam running parallel with the main linac. To generate this drive beam of very high instantaneous power a sophisticated complex consisting of a fully beam-loaded linac and several stages of beam compression is used. Although this scheme is very promising in terms of cost and power efficiency, it needs demonstration in a scaled version before construction of CLIC can be envisaged. This is the aim of the CLIC Test Facility CTF3, built by an international collaboration. CTF3 is constructed and exploited in several phases. Here we report present status, experimental achievements and future plans for CTF3.

INTRODUCTION

The CLIC study develops the technology for a linear electron-positron collider with a centre of mass energy reach of $E_{CMS} = 3$ TeV [1]. This energy is chosen to complement the discovery potential of LHC Hadron collider with a Lepton collider capable to perform crucial precision measurements in the whole energy range accessible by LHC [2]. The luminosity requirement for these measurements is $L_1 > 3 \cdot 10^{34}$ cm^{-2} s^{-1}, where L_1 denotes the luminosity available in a 1% energy bin. To reach 3 TeV in a reasonable length high accelerating gradients are essential. These gradients are in excess of the fundamental limitations for superconducting RF at about 50 MV/m. Therefore normal conducting, high frequency RF is the technology of choice for CLIC. As a consequence of the high gradient, high peak RF power is required to feed the accelerating structures. This power is extracted from a second beam of high intensity and low energy, running parallel with the main beams. Such a two beam scheme provides the required RF peak power with good efficiency. Since the drive beam is produced in a central area no active high power components are required along the linacs and a single tunnel scheme with an inner diameter of 4.5 m as shown in fig. 1 can be used [3].

Recently combined results from RF structure testing [4], an overall optimisation of parameters [5] and the introduction of a scalable cost estimate in the optimisation lead to a major parameter revision for CLIC. The main modification are the reduction of the main linac RF frequency from the former value of 30 GHz to now 12 GHz and the reduction of accelerating gradient from 150 MV/m to 100 MV/m. This leads to an overall length including beam delivery system of 47 km for 3 TeV CLIC.

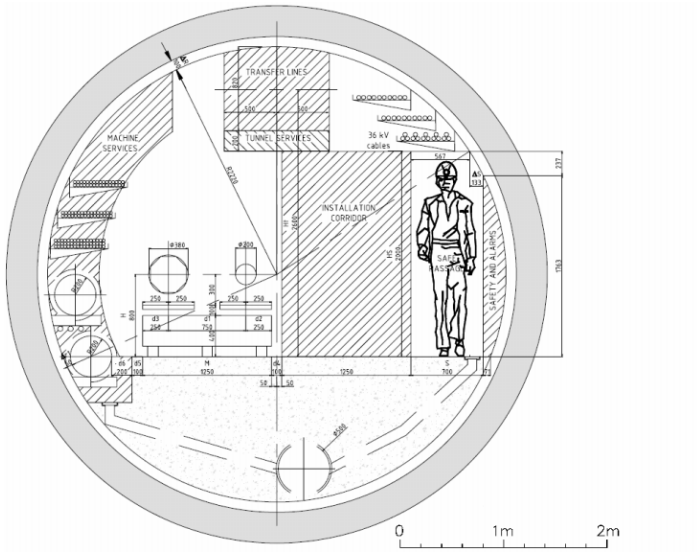

Figure 1: CLIC tunnel layout.

CLIC TEST FACILITY CTF3

The two beam scheme has been successfully demonstrated in the former CLIC test facility CTF II achieving accelerating fields of almost 200 MV/m [6]. However, in CTF II the drive beam was not produced in a manner representative for CLIC. In consequence the RF pulse length was limited to 16ns and the power efficiency of drive beam acceleration was poor.

The present CLIC test facility CTF3 aims to demonstrate the nominal CLIC drive beam production scheme [7] together with most other technical feasibility issues [8] as raised by the International Linear Collider Technical Review Committee ILC-TRC in 2003 [9]. CTF3 is build by a collaboration of institutes (table 1), with an organisation structure similar to large particle physics experiments.

The ILC-TRC issues addressed in CTF3 are:

a) *Demonstration of the CLIC accelerating structure at design gradient and pulse length*. CTF3 is already used as RF power source for 30 GHz testing. The 30 GHz CLIC accelerating structures are being tested in a well instrumented test stand. A vigorous development programme of accelerating structures is under way.

b) *Demonstration of the Drive Beam scheme.* The main issue here is the generation of the Drive Beam, i.e. acceleration of a long bunch train with conventional klystrons and subsequent bunch manipulations in order to increase the bunch repetition frequency, together with an increase in electron current in short, compressed bunch

trains. A very important feature of the Drive Beam acceleration is the operation of the accelerating structures under full beam loading. The other issue is the bunch train compression and frequency multiplication of the drive beam in isochronous delay loop and combiner ring with RF deflectors as injection kickers. CTF3 uses one delay loop with compression factor two and one combiner ring with a compression factor variable between one and five.

c) *Test of Power Extraction Structure (PETS) with on/off capability*. Special PETS are being used to provide the 30 GHz RF power for structure testing in the linac test stand, but 12 GHz PETS close to the CLIC design will be tested once the 35 A beam is available following completion of the Combiner Ring.

d) *Beam stability and beam loss control of the Drive Beam under deceleration for RF power production.* This will be tested in the Test Beam Line (TBL), where several PETS will decelerate the beam to a small fraction of its initial energy, converting the beam energy into RF power.

e) *Test of a relevant linac sub-unit with beam*. The full scheme will be tested with acceleration of a low-charge beam, the Probe Beam. Contrary to the CTF II, CTF3 allows tests with RF pulses in the 40-200ns range, covering the whole range of interest for CLIC.

As a consequence of these objectives, operation of the CTF3 facility is split between two main activities: Testing the Drive Beam generation complex and operation for high frequency RF power production for the development of CLIC accelerating structures. This second task uses presently the first part of the linac and a dedicated structure test stand. From 2008 on also the two beam test stand in the new CLEX (=CLIC EXperiment area) building will be used.

An overview of CTF3 is shown in figure 2. The drive beam is produced in a high current (10 A, 140 kV) thermionic gun. After bunching and a magnetic chicane for energy filtering a bunch train with maximum duration of 1.54μs and a beam current beam of up 5 A with a bunch repetition frequency of 1.5 GHz is accelerated in a fully loaded linac to 150 MeV. At half linac length a switch yard allows to take the beam either to a decelerating structure for 30 GHz RF power production or to keep it in the linac for full acceleration After passing the linac and a magnetic chicane which allows to adjust the bunch length, the beam is subject to a first frequency multiplication by a factor two using the 42m long isochronous delay loop. Afterwards the beam is transported with the isochronous transfer line TL1 to the combiner ring. This 84m circumference isochronous ring allows for frequency multiplication adjustable between two and five, leading to a maximum beam current of 35 A at extraction, with a train length of 140ns. Depending on the frequency multiplication factor bunch repetition, frequencies of 6, 9, 12 and 15 GHz can be obtained at extraction. Thus RF power at all these frequencies and their harmonics can be produced with the CTF3 drive beam. This flexibility allows easy adjustment of CTF3 to the new CLIC parameters. After frequency multiplication in the combiner ring, the high current beam is sent through tranfer line TL2, where bunch compression with R_{56} variable from -0.35 to +0.35m is applied. A sophisticated sextupole scheme keeps T_{566} at zero for the whole R_{56} range. A so called tailclipper kicker in TL2 allows to adjust the train length, by kicking an adjustable fraction of the train to a dump.

Table 1: Present members of CTF3 collaboration

Country	**Institute**
many	CERN
Finland	Helsinki Inst. of Physics
France	DAPNIA
	LAL
	LAPP
India	BARC
	RRCAT
Italy	LNF
Pakistan	NCP
Russia	BINP
	IAP
	JINR
Spain	CIEMAT
	IFIC
	UPC
Sweden	Uppsala University
Switzerland	PSI
Turkey	Ankara Universities
USA	NWU
	SLAC

In the CLEX building the drive beam can be switched either into the two beam test stand or into the decelerator test beam line (TBL). In TBL stability of the beam will be demonstrated under deceleration in a string of up to 16 PETS down to about 50% of its energy. In the two beam test stand the drive beam is sent through a PETS structure, producing 12 GHz RF power for feeding the 12 GHz accelerating structures in the probe beam. The probe beam is a low current beam of small emittance, delivered by a 180 MeV S-band linac named CALIFES. CALIFES uses a photo-injector and ballistic compression, to obtain short bunches of small emittance. The two beam test stand allows in addition to the two beam acceleration measurements, experiments on key aspects of RF breakdown phenomena and their effects on the beam and measurement of wakefield phenomena. For the probe beam there is a, not yet funded, option to add a beam line for beam instrumentation development (ITB= Instrumentation Test Beam).

The former CTF II building is used for high power RF testing and also for a test stand for a new photo injector, which will replace the thermionic injector of the drive beam. More detailed descriptions can be found in [10].

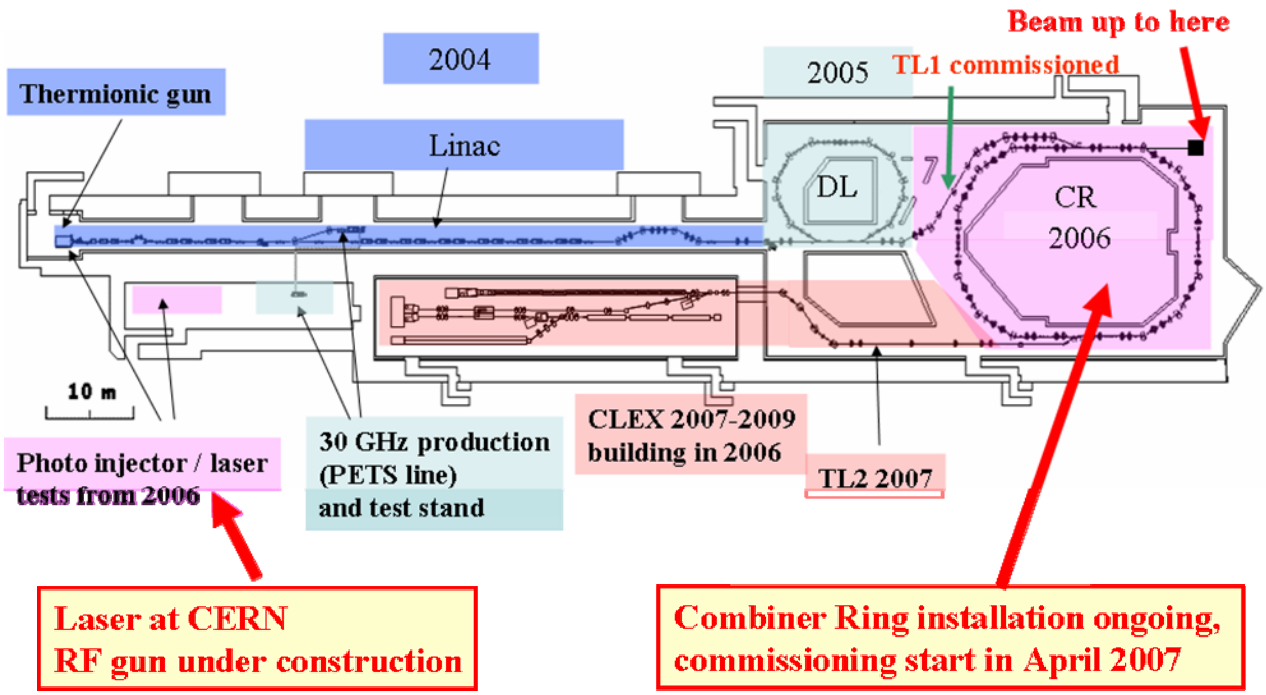

Figure 2: Overview of CTF3, indicating the present commissioning status and the different installation phases.

CTF3 STATUS AND ACHIEVEMENTS

So far the thermionic drive beam injector, the drive beam linac, the stretcher chicane, delay loop, TL1 and the injection region of the combiner ring have been commissioned with beam. Key achievements are:

- Nominal beam production and stable acceleration of a 3.5 A beam with full pulse length in the drive beam linac [11,12] without significant emittance growth. This demonstrates the stability of high current bunch trains in the presence of strong transverse and longitudinal wakefields. The wakefields are kept under control with Higher Order Mode (HOM) damping, HOM detuning and strong transverse focusing. The measured performance is consistent with predictions from beam dynamics simulations.
- Measured RF power to beam energy transfer efficiency of 95% in fully loaded operation for a normal conducting linac [13] ! This proves that drive beam production can be as efficient as predicted.
- Demonstration of frequency multiplication by a factor two with delay loop using RF deflector cavities and phase coding with rapidly phase switched subharmonic buncher cavities [14,15]. This is a key ingredient to achieve the bunch train compression.
- Routine 24h, 7 days a week operation of the fully loaded linac for 30 GHz production in the mid linac test stand [16], demonstrating that a fully loaded linac can be operated very reliable and stable.

CTF3 PROGRAM UNTIL 2010

Early in 2007 the combiner ring [17] will be completed and commissioning will start. Commissioning of the combiner ring and beam experiments will be interleaved with running for 30 GHz power production in the linac test stand. Many machine experiments and developments will be performed to get a good understanding and control of the longitudinal and transverse dynamics in the delay loop and combiner ring. The design [18] and construction of components for TL2 is proceeding, with installation of TL2 foreseen from late 2007 to spring 2008.

The already installed parts of CTF3 including the combiner ring use existing buildings, recuperated from the LEP pre-injector. For CLEX a new concrete surface building with inner dimensions of 42x8m has been constructed in 2006 to house all the CLEX beam-lines. Figure 3 shows the layout of the experimental beam-lines in CLEX. An equipment gallery on top provides rack space for all magnet power supplies and other electric equipment for the beam-lines in CLEX as well as klystrons and modulator for the probe beam injector CALIFES [19]. The assembly of CALIFES, transfer lines in CLEX and the two beam test stand [20] will start mid 2007, with the goal to get first beams to the two beam test stand in spring 2008. The test beam line (TBL) [21] will be build up in phases, for completion in 2009.

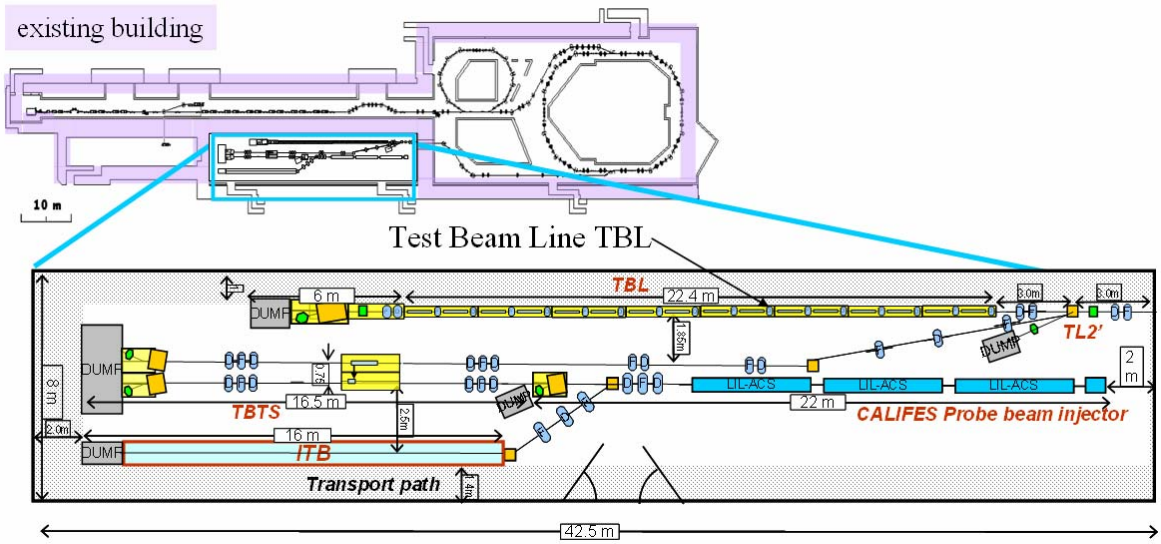

Figure 3: CLEX (=CLIC Experimental area) of CTF3
TBL=Test Beam Line
TBTS=Two Beam Test Stand
ITB=Instrumentation Test Beam

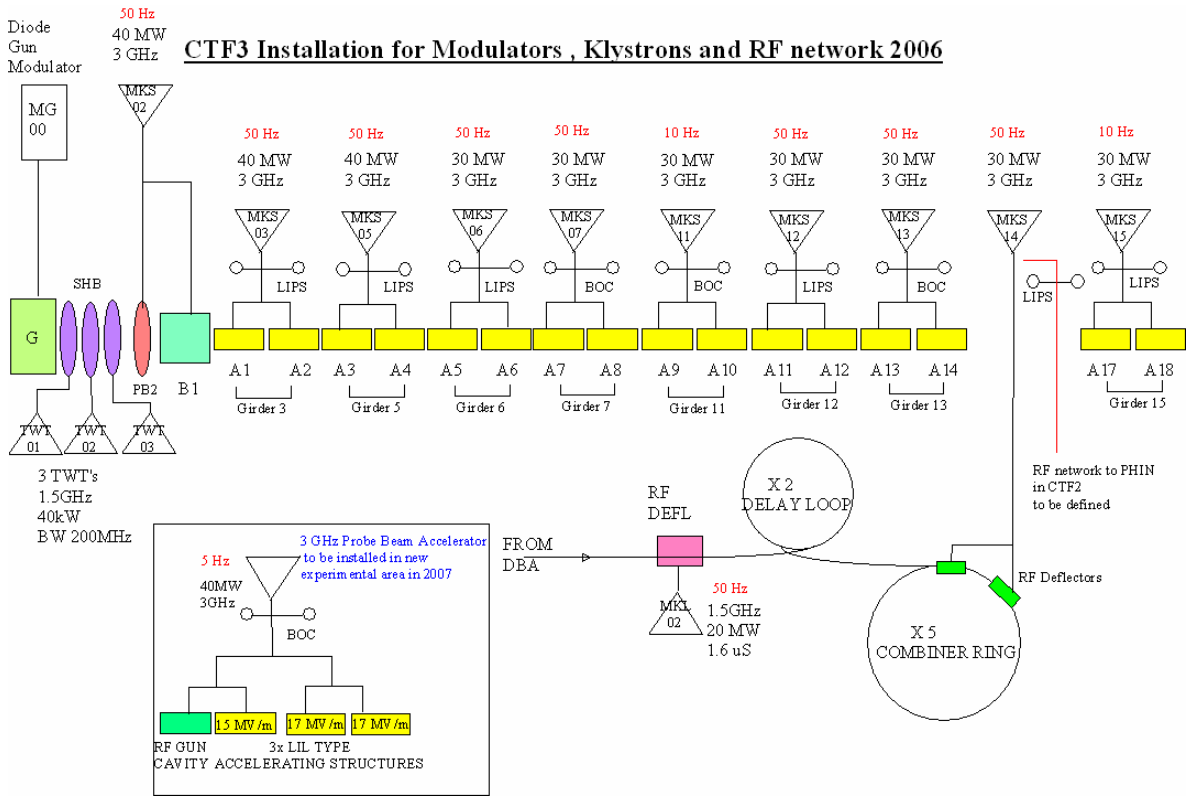

Figure 4: The 1.5 GHz and 3 GHz RF power plant for CTF3 drive beam linac and RF injector kickers.

Tests of the new drive beam photo-injector [22] consisting of a long train laser and a RF gun designed for very high beam loading will start in 2007. If successful, the present thermionic injector can be replaced with the photo injector in 2009. The laser system, however, is also used for the CALIFES RF gun and has therefore to operate from mid 2007 on. The drive beam photo-injector and its laser are financed by European Union in the framework of the joint research activity PHIN.

A key element to make all this work is the RF power plant feeding all the accelerating structures, bunchers, RF deflecting cavities and RF guns of CTF3. It consists of 11 S-band klystron modulators, one L-band klystron and three travelling-wave L-band tubes [23]. Fig. 4 shows the schematics of this power plant.

CONCLUSIONS

The program of the CTF3 collaboration to demonstrate key feasibility issues for a Multi TeV linear collider by 2010 is progressing according to schedule. Key targets like very power efficient high current drive beam acceleration without emittance growth, bunch frequency multiplication and stable long term operation in fully loaded mode have been achieved. Interleaved with commissioning and beam experiments the facility is routinely used as 30 GHz power source for accelerating structure development. The versatility of the drive beam generation scheme allows to adjust the facility readily for the new CLIC main linac frequency of 12 GHz.

REFERENCES

[1] H.H. Braun, "CLIC Progress Towards Multi-TeV Linear Colliders," proc. PAC'05 and CLIC note 628, 2005

[2] M. Battaglia, A. de Roeck, J. Ellis, D. Schulte (editors), "Physics at the CLIC Multi-TeV Linear Collider, rep. of the CLIC Physics Working Group," CERN report 2004-005

[3] C. Wyss, "Initial Considerations about the Cross-Section of a Tunnel for CLIC," CLIC note in preparation

[4] W. Wuensch et al., "Progress on the CLIC structures," this conference

[5] A. Grudiev, D. Schulte, W. Wuensch, "Optimum Frequency and Gradient for fhe CLIC Main Linac Accelerating Structure," proc. EPAC'06 and CLIC note 677, 2006

[6] H.H. Braun for the CLIC study team, "Achievements and Future Plans of CLIC Test Facilities," proc. HEACC 2001 and CLIC note 473

[7] R. Corsini (ed.), "The CLIC RF Power Source: a Novel Scheme of Two-Beam Acceleration for Electron-Positron Linear Colliders", CERN report 99-06, 1999

[8] A. Ghigo for CLIC collaboration, "CLIC Feasibility Study in CTF3," proc. EPAC'06, 2006

[9] "International Linear Collider Technical Review Committee, 2nd report," SLAC Report 606, 2003

[10] G. Geschonke for the CTF3 team, "Status Of The Clic Test Facility (CTF3)," proc. LINAC'06 and CLIC note 696, 2006

[11] H.H. Braun et al., "An Injector for the CLIC Test Facility (CTF3)," proc. LINAC 2000 and CLIC note 455, 2000

[12] R. Corsini et al., "First Full Beam Loading Operation with the CTF3 Linac", Proc. EPAC'04 and CLIC note 604, 2004

[13] P. Urschütz et al., "Efficient Long-Pulse Fully-Loaded CTF3 Linac Operation," proc. LINAC'06 and CLIC note 697, 2006

[14] D. Alesini et al., "Commissioning Status of the CTF3 Delay Loop", proc. EPAC'06 and CLIC note 675, 2006

[15] P. Urschütz et al., "Beam Dynamics and First Operation of the Subharmonic Bunching System in the CTF3 Injector," proc. EPAC'06 and CLIC note 683, 2006

[16] C. Achard et al., "30 GHz Power Production in CTF3," proc. PAC'05 and CLIC note 635, 2005

[17] C. Biscari et al., "CTF3: Design of Driving Beam Combiner Ring," proc. EPAC'2000

[18] A. Sharma et al., "Design of the Transfer Line-2 for the CTF3 at CERN," . this conference

[19] A. Mosnier et al., "The Probe Beam Linac in CTF3," proc. EPAC'06, 2006

[20] T.Ekelöf et al., "The Two Beam Test Stand in CTF3," proc. EPAC'06, 2006

[21] S. Döbert et al., "Progress on the CTF3 Test Beam Line," proc. EPAC'06 and CLIC note 690, 2006

[22] R. Losito, "The PHIN Photoinjector for the CTF3 Drive Beam," proc. EPAC'06 and CLIC note 684, 2006

[23] G. McMonagle, "Operational Performance and Improvements to the RF Power Sources, for the Compact Linear Collider Test Facility (CTF3) at CERN," proc. IVEC/IVESC 2006 , Monterey, and CLIC note 694, 2006

THE ACCELERATOR ACTIVITIES OF THE EUROTRANS PROGRAMME*

Paolo Pierini†, INFN Sezione di Milano, LASA

Abstract

The objective of the EC Integrated Project EUROTRANS is the design and feasibility assessment of an industrial accelerator driven system prototype dedicated to the transmutation of high level waste from nuclear power plants. A part of the program is dedicated to the further development of the high power proton accelerator needed for both the short term experimental demonstrator systems and the long term large scale industrial realizations. In particular the accelerator program addresses the issues of the qualification of the beam reliability with respect to the spallation target requirements, the development of the beam transport line to the subcritical reactor, and the demonstration of the key prototypical components of the proposed linear accelerator. This communication will present an overview and status of the accelerator activities carried out by the partners of the EUROTRANS project.

INTRODUCTION

The European Research Programme for the Transmutation of High Level Nuclear Waste in an Accelerator Driven System is a research program funded by the European Commission in the 6th Framework Programme, involving 31 partners between research agencies and nuclear industries and with the contribution of 16 universities. EUROTRANS is a 4 year program extending previous activities (PDS-XADS, Preliminary Design Study for an eXperimental Accelerator Driven System) and paving the road towards the construction of an eXperimental facility demonstrating the technical feasibility of Transmutation in an Accelerator Driven System (XT-ADS) in the next EC framework programmes.

The main objective of EUROTRANS is to work towards a European Transmutation Demonstration (ETD) in a step-wise manner:

- to provide an advanced design of all components of an XT-ADS system at significant power levels of the subcritical assembly (50 to 100 MWth), driven by conventional MOX fuel, in order to allow its realization in a short-term (~10 years),
- to provide a generic conceptual design of modular European Facility for Industrial Transmutation (EFIT), with power levels exceeding several 100 MWth and operated with new fuel loaded with reprocessed waste. The EFIT is the long-term objective of the program.

TRANSMUTATION IN AN ADS

Transmutation in an Accelerator Driven System (ADS) intends to address the problem of the long term disposal of the nuclear waste. In particular its objective are to reduce the radiotoxicity of the waste, to minimize the volume and the heat load of the nuclear waste sent to the deep geological storage in underground repositories.

The EU has (2001 data [1]) 145 reactors, providing more than 125 GW of electrical power, with an 850 TWh yearly production (covering 35% of the total), and producing an yearly amount of 2500 tons of spent fuel, among which 25 are Pu.

The strategy aimed at solving this problem relies on partitioning and transmutation, i.e. to separate chemically the waste fuel - that is, isolate Pu, the Minor Actinides (MA) and the Long Lived Fission Fragments (LLFF) – and to recombine the chemically pure elements obtained in this way in proper assemblies that could fuel dedicated transmuter systems, aimed at disposing of them in times much shorter than the natural decay times.

In order to deploy a solution for the waste disposal problem, two main technological ingredients are needed for a transmutation system:

- a **subcritical reactor** (with a criticality factor k substantially smaller than 1) where the fission chain reaction is not self-sustained, and operating with U-free fuel, in order to avoid nuclear proliferation problems
- an **intense neutron spallation source** (i.e. a high proton flux on a liquid lead target) that provides the "missing" neutrons that are needed to keep the reaction going. The neutrons produced by a high energy proton beam by spallation have also the broad energy spectrum which is needed to "burn" the MA components, that are otherways accumulated in conventional critical reactors operating with a thermal neutron spectrum.

The radiotoxicity of the spent fuel decreases to the level of the starting raw uranium ore used to produce the fuel elements only after a period greater than a million years. In order not to release these toxic elements in the biosphere it is thus necessary to dispose of the waste in deep and stable geological repositories, ensuring proper containment and surveillance for this extremely long period. The Partioning and Transmutation (P&T) goal is, via chemical separation and irradiation in a fast and intense neutron flux, to reduce this time to 700-1000 years (See Figure 1).

*Work supported by the EURATOM 6th framework program of the EC, under contract FI6W-CT-2006-516520.
†On behalf of the Accelerator Workpackage of the EUROTRANS Programme

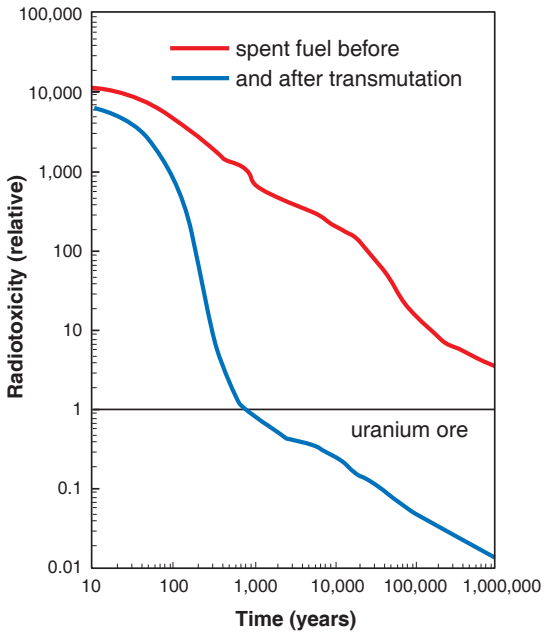

Figure 1: Ingestion radiotoxicity of spent nuclear fuel, before and after partitioning and transmutation, compared to the uranium ore level. From Ref. [1].

Within the EUROTRANS program the activities are carried in five main technical areas (called Domains):

- The first domain is dedicated to the **design** of the ADS systems (XT-ADS and EFIT), and subcomponents. The accelerator activities are carried in one workpackage of this domain.
- The second domain is devoted to experimental activities on the **coupling** of an accelerator, a neutron spallation target and a subcritical blanket. Experiments have been proposed using research reactors at low power levels driven by photofission generated neutrons by small electron accelerators.
- The remaining domains are concerned with the study of **advanced fuels** for transmuters, the investigation of structural materials for ADS systems and **heavy liquid metal technologies** (in particular the spallation target design), and nuclear data for transmutation.

EUROPEAN TRANSMUTATION DEMONSTRATION

EUROTRANS aims at proceeding towards the demonstration of the industrial transmutation through the ADS route, primarily with the design of the XT-ADS and EFIT systems. The first is intended to be as much as possible a test bench of the main components and of the operation scheme of the EFIT, but at the lower working temperatures allowed by the use of Lead-Bismuth Eutectic (LBE) as core coolant and spallation target material. The EFIT design will be detailed to a level which will allow a parametric cost estimate of the ADS-based transmutation process. The reactor coolant and the spallation target material will be pure lead. Both designs (XT-ADS and EFIT) share the same fundamental system characteristics in order to allow for scalability considerations.

The basic features of XT-ADS and EFIT

The EFIT is intended as a full-scale transmutation demonstrator system, loaded with transmutation dedicated fuel. The machine becomes operational many years after the XT-ADS (around 2040) and takes into account all the experience gained from the already running R&D programs on fuel and materials. On the other hand, the XT-ADS is meant to be built and tested in a near future (about 8-10 years from the start of the EUROTRANS project). The machine should be completely operational around 2017 – 2018 and fulfil three objectives: demonstrate the ADS concept (coupling of accelerator, spallation target and sub-critical core) and its operability, demonstrate the transmutation, provide an irradiation facility for the testing of different EFIT components (samples, fuel pin, fuel assembly).

Even though the EFIT and XT-ADS have different objectives, they share as many designs characteristics as possible. As EFIT is an industrial-scale transmutation facility, the characteristics were meant to maximize the efficiency of transmutation, the easiness of operation and maintenance, and the high level of availability in order to achieve an economical transmutation. For XT-ADS on the other hand, the characteristics have been defined to deploy a flexible testing facility. Despite those sometimes contradictory definitions, many characteristics remain identical in the EFIT and XT-ADS machines:

- A superconducting linac solution has been chosen for both systems. The main reasons for that choice are the perspectives of improvement of beam reliability at such levels of proton energy [2-4].
- The cores of both systems are significantly different, but some characteristics are still identical.
- The vessel designs, which integrate the primary cooling system, share many design features.

Besides these identical features, divergence has occurred in the choices of components or parameters of the two machines. The following table resumes the main differences in the two concepts.

Table 1: Main differences in the two European Transmutation concepts

	XT-ADS	EFIT
Objective	Irradiation facility and EFIT test bench	Industrial waste burner
Power range	50-100 MWth	100 MWth
Subcriticality	~0.95	~0.97
Beam characteristics	5 mA@350 MeV or 2.5 mA@600 MeV	20 mA@800 MeV
Fuel	Conventional MOX	Minor Actinides loaded
Coolant	Lead-Bismuth Eutectic	Lead (gas as backup)

The reference accelerator

The ETD requires a high power proton accelerator operating in CW mode, ranging from 1.5 MW (for XT-ADS operation) to 16 MW (for the EFIT). Additional requirements at the neutron spallation target are a 2% beam power stability and 10% beam size stability, in order to provide a sufficiently stable neutron flux [2,3].

The reference design for the accelerator has been developed during the PDS-XADS programme and is shown in Figure 2. For the injector, an ECR source with a normal conducting RFQ is used, followed by an energy booster section which uses either a normal conducting IH-DTL or superconducting CH-DTL structures up to a transition energy still under optimization, around 20 MeV. This first part of the linac is duplicated in order to provide good reliability perspectives [4]. Then a fully modular superconducting linac (based on different RF structure) accelerates the beam up to the final energy.

The design of such a linac configuration has been motivated by the specific reliability requirements imposed to the ADS accelerator, which are summarized in the following paragraphs.

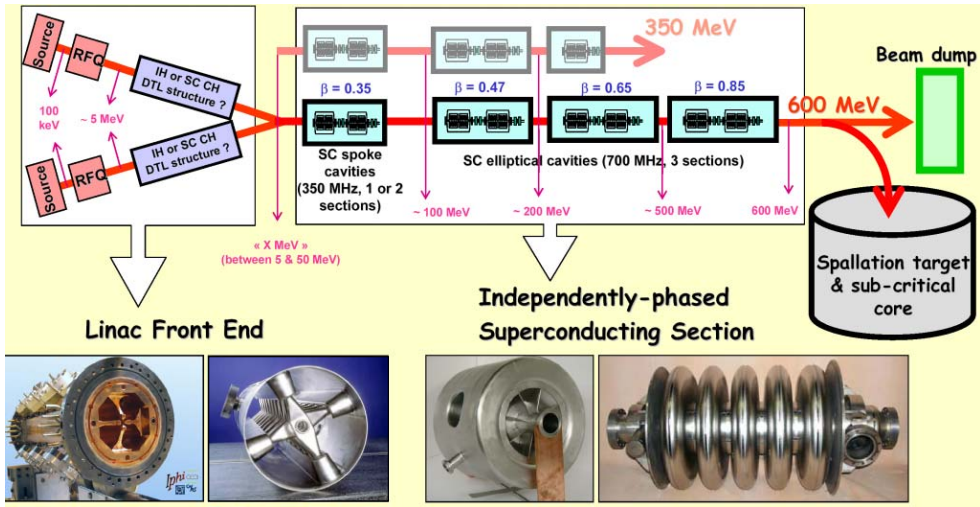

Figure 2: The reference accelerator scheme for the ETD/XT-ADS.

Issues and challenges for an ADS driver

The ADS accelerator is expected - especially in the long term EFIT scenario - to have a very limited number of unexpected beam interruptions per year which cause the absence of the beam on the spallation target for times longer than a second. This requirement is motivated by the fact that frequently repeated beam interruptions can significantly damage the reactor structures, the target or the fuel elements, and also decrease the plant availability. Therefore, it has been estimated that beam trips in excess of one second duration should not occur more frequently than five times per year (EFIT). To provide such an ambitious goal, which is lower than the reliability experience of typical accelerator based user facilities by many orders of magnitude, it is clear that reliability-oriented design practices need to be followed from the early stage of component design. In particular, "strong design" practices (based on component derating with respect to limiting performances) are needed, a rather high degree of redundancy needs to be planned and fault tolerance capabilities has to be introduced [4].

The chosen strategy to implement reliability relies on over-design, redundancy and fault-tolerance. Redundancy at the low energy stage has been obtained by duplicating the source, RFQ and booster stage, while a superconducting linac, with its modular and repetitive design, consisting in accelerating sections grouped in "cryomodules", naturally meets this reliability strategy.

A second requirement on the operation of the CW ADS linac comes from the requirement to perform on-line reactivity measurements of the subcritical assembly. For this reason, the accelerator, while the RF operates in CW, needs to provide zero current beam "holes" with durations up to 200 μs and sharp rise and fall times of few μs, at a very low duty cycle, with a repetition rate ranging from 10^{-3} to 1 Hz.

The accelerator workpackage of EUROTRANS is dedicated to the design, operation and experimental characterization of the reliability characteristics of each of the major linac component in the various energy sections.

Design for reliability

As previously mentioned, the fundamental reliability guidelines have been extensively used in the linac design, in terms of:

- component derating,
- inclusion of redundancies,
- capabilities of fault tolerance operation..

During the PDS-XADS program a preliminary bottom-up reliability analysis (Failure Mode and Effects Analysis, FMEA) has been performed [4] in order to identify the critical areas in the design in terms of impact on the overall reliability. This activity suggested to provide a second, redundant, proton injector stage (composed of the source, RFQ and low energy booster), with fast switching capabilities.

After the injector stage, the superconducting linac has a high degree of modularity, since the whole beamline is an array of nearly identical "periods". All components are operating well below any technological limitation in terms of potential performances, and therefore a high degree of fault tolerance with respect to cavity and magnets can be expected in the superconducting linac, where neighbouring components have the potential to provide the functions of a failing component without affecting the accelerator availability. Clearly this approach implies a reliable and sophisticated machine control system, and in particular a digital RF control system to handle the RF set points to perform fast beam recovery in the case of cavity failures.

THE ACCELERATOR ACTIVITIES

The accelerator workpackage is split in several tasks, focussed to identify the design of the main subcomponents of the ADS linac in the different energy areas and to identify their reliability characteristics.

Activities are dedicated to:

- the experimental evaluation of the proton injector reliability, performed at the CEA IPHI injector,
- the assessment of the reliability performances of the intermediate energy accelerator component, with particular attention to the comparison of different accelerating structures proposed,
- the design and the experimental qualification of the reliability performances of a high energy cryomodule tested at full power and nominal temperature,
- the design and testing of a prototypical RF control system intended to provide fault tolerance operation of the linear accelerator,
- the update of the accelerator design - including beam dynamics issues and investigation of control strategies for fault tolerance – and the development of further reliability analyses and cost estimations for the XT-ADS and EFIT.

Proton injector reliability tests

The IPHI injector (see Figure 3), developed in France by CEA and CNRS, fulfils the specifications of the ADS proton injector, with wide margins in term of beam current capabilities. IPHI is composed by the SILHI ECR ion source, a 3 MeV RFQ under completion, the associated beam lines and diagnostics, that are being assembled at Saclay. The IPHI injector, once completed, will be used for a long run test (several months), to demonstrate and assess, on a real scale, the reliability characteristics of this accelerator subcomponent.

In the past years the SILHI source has been successfully used for several week-long reliability tests at currents of 30 mA, showing no beam stops and occasional sparks in the extraction region, causing no beam interruptions. These tests will be extended to a few months and will include acceleration in the RFQ and propagation in the beam lines.

The possibility to achieve the sharp "beam holes" required for reactivity measurements, already tested at the source SILHI, will be extended to the full beam from the IPHI injector, at 3 MeV.

RF structures for intermediate energy

For the intermediate energy region after the RFQ and up to approximately 100 MeV, several cavity types are considered as valid "candidates". Studies and test of prototypes are being developed in order to evaluate their feasibility and assess their potential reliability performances.

In particular, activities concentrate on:

- high shunt impedance copper DTL structures of the IH type, with "Konus" focussing scheme, i.e. elements outside the drift tubes.
- superconducting multi-gap CH structures, with "Konus" focussing scheme.
- superconducting spoke cavities which can operate at very low energies (around 5 MeV), and can be efficiently used up to 100 MeV and more.

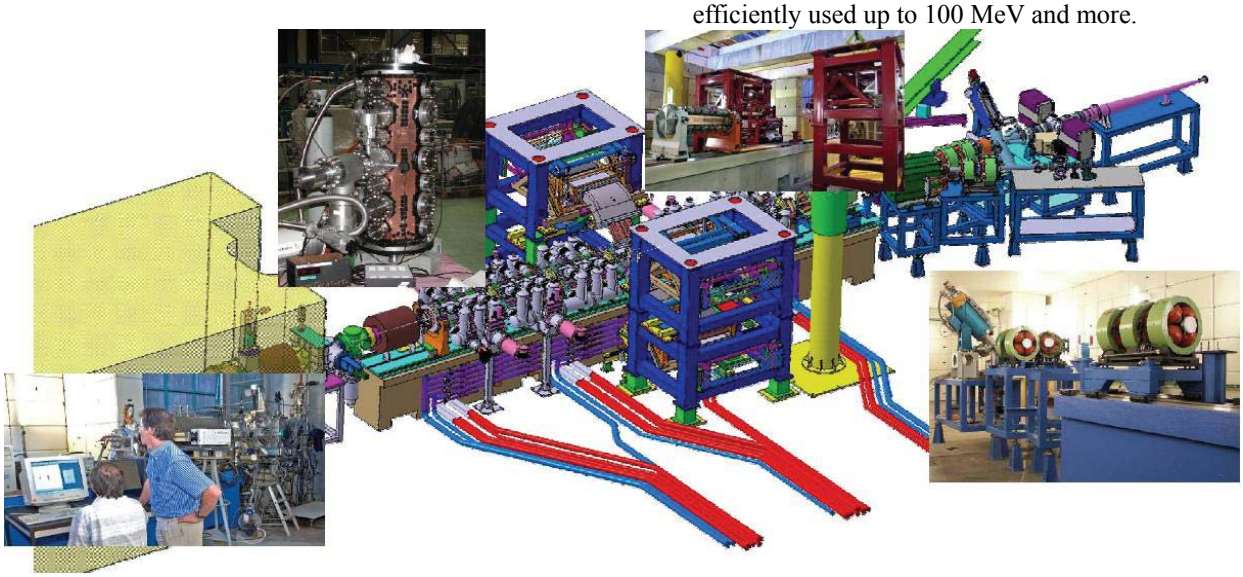

Figure 3: Scheme of the IPHI injector, and pictures of the components during their installation at Saclay.

The first activity is carried out at IBA, while the 19 gap SC CH structure has been successfully tested at IAP-Frankfurt and is ready to be installed in an existing cryostat, with an external driven mechanical tuner [5]. In addition, CNRS/Orsay is equipping an existing cryomodule with a β=0.15 spoke cavity, fully dressed with its stainless steel helium reservoir, the cold frequency tuning mechanism and the high power (20 kW) RF coupler [6]. The cavity, which has already reached the design goals in vertical tests, once completed with its ancillary RF components, will be operated at nominal operating conditions in long tests to determine the reliability characteristics of the components. Figure 4 shows the tests of the tuning mechanism on the cavity.

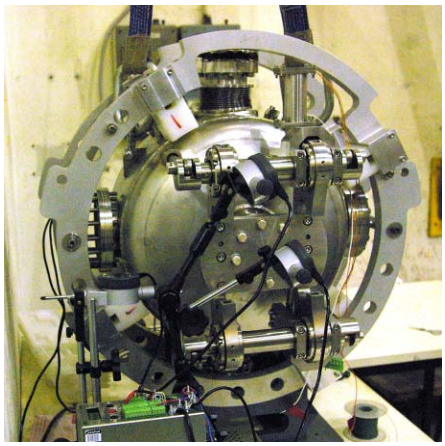

Figure 4: The spoke cavity equipped with the cold frequency tuner in the support frame of the cryostat.

The high energy cryomodule

For the high-energy part of the linac, using low beta elliptical cavities from an energy of approximately 100 MeV, one of the existing β=0.47 TRASCO cavities [7], equipped with a cold frequency tuner and a high power RF coupler, will be installed in a prototype cryomodule, under development at INFN and CNRS, to be tested in Orsay under nominal operating conditions. Figure 5 shows a conceptual layout of the module.

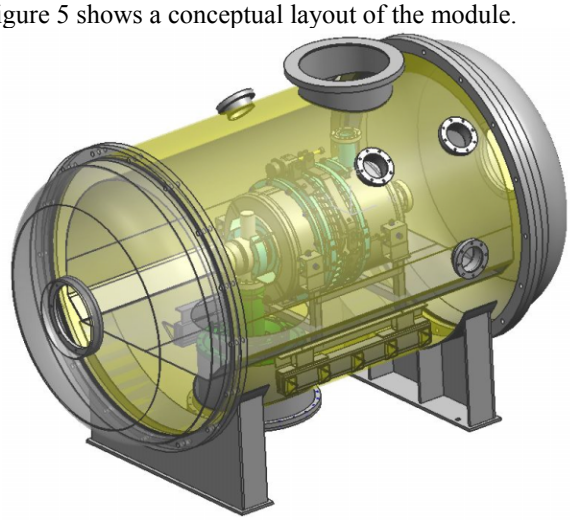

Figure 5: Conceptual layout of the single cavity module for the testing of the high energy components.

RF control system for fault tolerance

The scope of this activity, mainly carried out by CEA, CNRS and IBA is to develop a digital RF control system intended to provide the necessary field and phase stability and to identify and handle fast recovery scenarios for cavity failures in the superconducting linac, by means of local compensation at neighbouring cavities.

Accelerator design

The last task in the accelerator workpackage deals with the progress of the accelerator design and the characterization of its reliability goals. In particular, start to end beam dynamics simulations are performed for the different options for the intermediate energy structures. The modelling includes the effect of the beam transients induced by RF faults and explores the possible recovery scenarios needed to provide the necessary beam availability to the ADS application. Furthermore, an integrated reliability analysis is being performed to predict the reliability characteristics of the proposed accelerator, following the standard practices used in the nuclear energy applications (mainly failure mode and effects analysis and reliability block diagrams).

ACKNOWLEDGEMENTS

The principal institutions in the accelerator workpackage of EUROTRANS are CNRS, CEA (F), IBA (B); IAP-Frankfurt University (D) and INFN (I). Additional contribution, especially in issues with the coupling to the subcritical assembly, is provided from AREVA NP (D), ITN (P) and UPM (S). The program has the financial support of the European Commission through the contract FI6W-CT-2004-516520.

REFERENCES

[1] "The European Roadmap for Developing ADS for Nuclear Waste Incineration", European Technical Working Group, ISBN 88-8286-008-6, ENEA 2001.
[2] A.C. Mueller, "The PDS-XADS reference accelerator", International Workshop on P&T and ADS Development, Oct 2003, SCK•CEN, Belgium.
[3] J-L. Biarrotte et al., "A reference accelerator scheme for ADS applications", International Conference on Accelerator Applications, August 2005, Venice, Italy.
[4] P. Pierini, "ADS Reliability Activities in Europe", 4th OECD NEA International Workshop on Utilization and Reliability of HPPA, May 2004, Daejon, S. Korea.
[5] H. Podlech, "Development of Room Temperature and Superconducting CH-Structures", LINAC'04, p.28-32, Lübeck, Germany, 2004.
[6] G. Olry et al., "Recent developments on sc beta 0.35 and beta 0.15 spoke cavities at IPN for low and medium energy sections of proton linear accelerators", EPAC2004, Lucerne, Switzerland, July 2004.
[7] A. Bosotti et al., "RF Tests of the beta=0.47 five cell TRASCO Cavities", EPAC2004, Lucerne, Switzerland, July 2004.

PAPER NOT YET RECEIVED

List of Authors

Italic papercodes indicate primary authors

— A —

Abdullah, K.K. THPMA094
Acharya, S. THPMA043, THPMA064, THPMA070
Adak, D. THPMA058
Adolphsen, C. WEPMA109
Agarwal, R. THPMA043, THPMA064
Agoh, T.A. WEXMA01
Agrawal, R.K. *WEPMA085*
Ahuja, R. WEPMA078
Akai, K. MOOPMA04, WEXMA01
Akemoto, M. WEXMA01
Akiyama, A. WEXMA01
Akiyama, K. TUPMA049, TUPMA052, WEPMA038
Amro, A. THC3MA02
An, S. WEZMA03, *WEPMA135*, *THC2MA01*
An, W.M. TUPMA123
Ang, Z.T. THPMA004
Anghel, A. TUPMA036
Angoletta, M.-E. TUPMA085
Antokhin, E. TUPMA018, *TUPMA023*
Antony, J. THPMA050
Antoshin, A.V. TUPMA122
Arinaga, A. WEXMA01
Arora, R. K. WEPMA137
Asaka, T. TUPMA067, THC3MA05
Asaoka, S. TUPMA028
Attal, M. THC3MA02
Auslender, V. *THC3H101*, THPMA102
Avilov, M.S. TUC3MA03, TUPMA122
Azizi, H. THC3MA02

— B —

Baba, H. WEPMA105
Babbar, L.K. WEPMA065
Babu, S. THPMA050
Badapanda, M.K. WEPMA142
Baggiolini, V. TUPMA085
Bagre, M. WEPMA124, THC2MA02
Balewski, K. TUPMA016
Bandapadhaya, D. L. THPMA048
Bandyopadhyay, A.K. *TUPMA016*
Bandyopadhyay, S. *THPMA028*, THPMA130
Banerjee, M.B. WEPMA110
Banerji, A. WEPMA065
Banwari, R. THPMA036, *THPMA039*, THPMA120
Bapna, S.C. THPMA085, THPMA087, THPMA088, *THPMA129*
Barapatre, D. THPMA086
Barish, B.C. *MOZMA01*
Barnwal, R. THPMA043, THPMA094
Basak, T. WEPMA044, WEPMA045
Bellodi, G. THXMA02
Belochitskii, P. TUPMA085
Bengtsson, J. THC3MA03
Ben-Zvi, I. *TUXMA03*
Bergoz, J.F. THPMA078
Bergstrom, J.C. WEPMA060
Besson, J.C. THZMA01
Beuret, A. TUPMA084, TUPMA085
Bhagwat, P.V. *THPMA121*
Bhanage, V.B. THPMA131
Bhandari, R.K. TUPMA097, TUPMA113, TUPMA116, *WEZMA04*, WEPMA015, WEPMA089, WEPMA104, THPMA022, THPMA048, THPMA058
Bharadwaj, V. WEPMA109
Bhatnagar, V. TUPMA032
Bhattacharjee, D. WEPMA122
Bhattacharjee, T. THPMA016, *THPMA130*
Bhattacharya, S. TUPMA097
Bhattacharyay, D.S.B. WEPMA110
Bhattacharyya, T. *WEPMA089*, *WEPMA104*
Bhole, R.B. THPMA016, THPMA130
Bhunia, U. TUPMA097, THPMA016, THPMA022, THPMA048
Biscari, C. TUPMA075
Biswas, B. *WEPMA112*
Biswas, S.B. WEPMA110
Blas, A. TUPMA085
Blinov, M.B. TUC3MA03
Bohrey, A. WEPMA142
Boland, M.J. WEPMA058, WEPMA059, WEPMA060
Bolkhovityanov, D. TUPMA122
Borage, M. THPMA045, *THPMA046*, THPMA129
Borburgh, J. TUPMA084, TUPMA085
Bowden, G.B. WEPMA109
Braun, H.-H. *FRYMA02*
Brunelle, P. THZMA01
Bryazgin, A.A. THC3H101, *THPMA102*
Buteau, A. THZMA01
Bylinskii, I.V. THPMA004

— C —

Carli, C. TUPMA084, TUPMA085
Cassinari, L. THZMA01
Chacko, J. THPMA050
Chaddha, Chaddha, N. THPMA016, THPMA130
Chakravarthy, D.P. TUPMA076, WEPMA014, THPMA043, THPMA064, THPMA071, THPMA094
Chan, C.K. *THPMA056*
Chanel, M. TUPMA084, *TUPMA085*
Chang, C.-C. THPMA056
Chang, H.-P. TUPMA034
Chang, J.-C. WEPMA077, *THPMA091*, THPMA093
Chang, L.-H. WEPMA071, THYMA03, THPMA051

Chang, M.H. THYMA03, THPMA051
Chang, S.-S. THYMA03, THPMA051
Chao, H.C. *TUPMA059*
Chattopadhyay, S. FRXMA02
Chaudhuri, J. THPMA022, THPMA058
Chauhan, A. WEPMA085, *WEPMA087*
Chawala, A.S. THPMA043
Cheedket, S. THC3MA01
Chen, C. L. THPMA056
Chen, C.-T. TUPMA034
Chen, H.G. THPMA023
Chen, J. TUPMA034, WEPMA063, WEPMA070, WEPMA090, WEPMA096
Chen, J.-E. TUPMA070, *THZH103*
Chen, J.-R. TUPMA034, THZMA04, THPMA093, WEPMA077, THPMA056
Cheng, W.X. TUPMA028, *WEC3H101*
Cheskidov, V.G. THC3H101, THPMA102
Chindarkar, A.R. WEPMA011, THPMA043
Cho, M.-H. WEPMA083, THPMA114, THPMA127
Cho, Y.-S. *TUPMA119*, WEZMA03, WEPMA119, WEPMA120, WEPMA135, THC2MA01
Chohan, V. *TUZMA02*
Choi, B.H. TUPMA119, *WEZMA03*, WEPMA135, THC2MA01
Choi, J. TUZH102, WEPMA050, WEPMA054, WEPMA080, THPMA024, THPMA047
Choudhury, A. THPMA050
Choudhury, R.K. THPMA121
Chouksey, S. *WEPMA111*, *THPMA096*
Chu, P. TUPMA105
Chung, B.C. TUPMA119, WEZMA03
Chung, B.H. THPMA035
Chung, C.W. TUPMA057, THPMA024, THPMA067, THPMA076, THPMA117
Chung, F.-T. WEPMA071, THYMA03, THPMA051
Chung, K.-H. THPMA035
Colombet, T. TUPMA001
Cornelis, K. TUPMA085
Corsini, R. TUPMA075
Couprie, M.-E. THZMA01
Cox, B. TUPMA001
Cuvet, Y. TUPMA088

— D —

Das, M. THPMA028
Das, S. THPMA014
Das, T.D. WEPMA089, WEPMA104
Datar, V.M. *WEYMA02*
Datta, T.S. *THPMA050*
De, A. *THPMA017*, THPMA130
Debnath, J. TUPMA097, WEPMA015, THPMA016, THPMA048
Deep, A. WEPMA065
Defrance, C. *THPMA078*
Dehler, M. *TUPMA014*, *TUPMA036*
Dehnel, M.P. *THC3H102*
Delayen, J.R. *WEPMA024*, *FRXMA02*
Denard, J.-C. THZMA01
Denisov, Yu.N. TUPMA064
deo, R.K.DEO. WEPMA142
Dev, V. TUPMA015
Dey, M.K. TUPMA097, WEPMA015, THPMA016, *THPMA022*
Dhavale, A.S. *WEPMA133*
Diao, C. *THPMA061*
Ding, H. THZMA03
Ding, J.G. *TUPMA026*
Dixit, K. WEPMA122
Dixit, T.S. *TUPMA099*
Doebert, S. TUPMA075
Dolbilov, G. *THC3H103*
Domenico, D. TUPMA001
Doolittle, L.R. *THYMA05*
Dowd, R.T. WEPMA058, WEPMA059, WEPMA060
Drentje, A.G. TUPMA116
Du, H.W. THPMA084
Dubey, B.P. THPMA073
Ducimetière, L. THPMA078
Dumas, L.D. TUPMA084
Dunkel, K. THPMA104
Dutta, A. TUPMA097, WEPMA015, THPMA016, THPMA022
Dutta, M. THPMA048
Dutta, S. *THPMA085*
Dutta Gupta, A. THPMA022
Dwivedi, J. THPMA085, THPMA087, THPMA131

— E —

Ebihara, K. MOOPMA04, WEXMA01
Egawa, K. WEXMA01
Ego, H. WEPMA048
Enomoto, A. WEXMA01
Evans, L.R. *TUXMA01*

— F —

Fadeev, S. TUPMA122, THPMA118
Fakhri, A.A. *TUPMA053*, *TUPMA060*
Faktorovich, B.L. THC3H101, THPMA102
Fan, T.-C. THPMA081
Fang, J.X. TUPMA070
Fang, S.X. TUC3H101, WEZMA02
Fatnani, P. TUPMA032, WEPMA085, WEPMA086, WEPMA087
Fawley, W.M. TUPMA038
Feng, J. WEZMA02
Filhol, J.-M. THZMA01
Flanagan, J.W. WEXMA01
Fong, K. THPMA004
Fowler, T. TUPMA084, TUPMA085
Fu, S. WEZMA02
Fujino, T. TUPMA102

Fukuda, M. *THZH102*
Fukuda, S. WEXMA01, WEPMA140
Fukui, T. WEPMA048, THPMA005
Fukuma, H. *TUZH103*, WEXMA01
Fukumoto, S. THPMA115
Fukuyama, Y. TUPMA031
Funakoshi, Y. WEXMA01
Furukawa, K. WEXMA01
Furuya, T. MOOPMA04, TUPMA046, WEXMA01, THC2MA03

— G —

G, G. TUPMA113
Gangopadhyay, P.G. WEPMA110
Gangopadhyay, S. WEPMA087
Gao, J. TUC3MA01, TUPMA005, TUPMA006
Gao, S.L. TUPMA070
Garion, C. THPMA085
Garoby, R. THXMA02
Gaud, Gaud,V.K. THPMA013
Gerigk, F. TUPMA088, THXMA02
Geschonke, G. TUPMA075
Ghigo, A. *TUPMA075*
Ghodke, A.D. TUC2MA02, WEPMA013
Ghodke, S.R. THPMA043, *THPMA094*
Ghosh, M.K. THPMA014
Gokhale, A. *THPMA073*
Goncharov, A.D. THPMA110
Gorbunov, V. THC3H101
Gore, J.A. THPMA121
Gornakov, I.V. THC3H101
Goswami, A. WEPMA005
Gourber-Pace, M. TUPMA084, TUPMA085
Gubin, K. *TUPMA122*
Guo, C.L. THPMA023
Guo, J.F. TUPMA070
Guo, Z.Y. TUC3MA01, TUPMA005, TUPMA006, *TUPMA070*, THZH103
Gupta, A. WEPMA143
Gupta, A.K. THPMA121
Gupta, R.K. TUPMA032
Gvozdev, A. TUPMA018

— H —

Ha, K.M. WEPMA075, WEPMA080, *THPMA033*
Haba, J. WEXMA01
Haga, K. TUPMA028
Hajima, R. *MOYMA01*, *TUPMA047*, TUPMA046
Hajra, D.P. *THPMA058*
Hama, H. TUPMA049, TUPMA052
Han, H.S. THPMA117
Han, Y.J. WEPMA050, *WEPMA054*, THPMA063
Hancock, S. TUPMA084, TUPMA085
Handu, V.K. WEPMA145
Hanke, K. THXMA02
Hannurkar, P.R. WEPMA124, WEPMA137, WEPMA143
Hara, K. MOOPMA04, WEXMA01
Hara, T. *TUPMA042*
Harada, K. TUPMA028
Hatanaka, K. THZH102
Hayashi, K. *WEPMA139*
He, Y. THXMA03
Herbeaux, C. THZMA01
Higo, T. WEXMA01
Hill, C.E. TUPMA085
Hinode, F. TUPMA049, TUPMA052, *WEPMA038*
Hiramatsu, S. WEXMA01
Hisamatsu, H. MOOPMA05, WEXMA01
Hisaoka, Y. THC3MA05
Holikatti, A.C. WEPMA065
Honda, T. TUPMA028
Honda, Y. *WEZH102*, WEC3H102
Hong, I.-S. WEPMA119, WEPMA120
Hong, J.S. THPMA035
Honma, H. WEXMA01
Honma, T. MOOPMA04, WEXMA01
Hori, Y. TUPMA102
Hosoda, N. *TUPMA035*, WEPMA048, THPMA005
HOSOKAWA, M. TUPMA102
Hosoyama, K. MOOPMA04, TUPMA124
Hourican, M. TUPMA084, TUPMA085
Hoyes, G.G. *WEPMA099*, THC3MA01
Hsiao, F. Z. THYMA03
Hsiung, G.-Y. THPMA056
Hsu, K. T. WEPMA063, WEPMA070, WEPMA090, WEPMA096
Hsu, S-N. THPMA056
Hsu, S.Y. WEPMA070, WEPMA090, WEPMA096
Hsueh, H.P. THPMA056
Hu, K.H. *WEPMA063*, WEPMA070, *WEPMA090*, WEPMA096
Hu, Z.M. THPMA023
Hua, Hua,J.F. TUPMA123
Huang, J.Y. *WEC3H102*, WEPMA050, WEPMA054, WEPMA080, WEPMA103, THPMA063, THPMA074
Huang, W.-H. TUPMA123
Hur, M.S. FRXMA01
Husain, R. *WEPMA013*, WEPMA085
Hwang, J.-Y. WEPMA096
Hwang, W.H. WEC3H102

— I —

Ieiri, T. TUPMA028, WEXMA01
Igo, T. TUPMA068
Iida, N. WEXMA01
Ijima, H. TUPMA047
Ikeda, H. WEXMA01
Ikeda, M. WEXMA01
Inagaki, S. WEXMA01
Inagaki, T. WEPMA105

Inoue, I.Y. WEC3H102
Inoue, M. THPMA115
Irikura, M. WEPMA139
Isagawa, S. TUPMA028, WEXMA01
Ishi, Y. THPMA115
Ishii, H. WEXMA01
Ishii, K. TUPMA102, THPMA083
Isoyama, G. TUPMA067, *TUPMA068*, WEPMA071
Israel, B.S. THPMA043
Izawa, M. TUPMA028

— J —

Jackle, P.T. THC3H102
Jagannath, M. THPMA086
Jain, A. *WEPMA011*, THPMA043, WEPMA142, *WEPMA143*
Jain, A.K. THPMA131
Jain, M.K. WEPMA142
Jain, P. TUPMA076, *TUPMA093*, *WEPMA014*
Jain, V. WEPMA124, THC2MA02
Jang, J.-H. WEZMA03, FRXMA01
Jang, S. D. WEPMA083, THPMA067, THPMA127
Jayaprakash, D. WEPMA122, THPMA094, THPMA043
Jeon, D.-O. *TUPMA105*, *TUPMA108*, *WEC3MA01*
Jeon, J.H. *THPMA035*
Jeong, S.-H. THPMA024, *THPMA047*
Jiang, D.K. *THPMA059*, THPMA084
Jiao, Y. *TUC3H101*
Jin, X. THPMA126
Joestingmeier, A. TUPMA016
Jongewaard, E.N. WEPMA109
Joshi, D.K. WEPMA065
Joshi, S.C. TUPMA109
Jowett, J.M. TUPMA084
Jung, Y.G. THPMA117

— K —

Kabe, A. MOOPMA04, WEXMA01
Kadokura, E. WEXMA01
Kadyrzhanov, K.K. TUPMA023
Kaftoosian, A. THC3MA02
Kageyama, T. TUPMA028, WEXMA01
Kailas, S. THPMA121
Kakihara, K. WEXMA01
Kako, E. WEXMA01
Kamada, S. WEXMA01
Kamitani, T. TUPMA066, WEXMA01
Kamiya, T. THZH102
Kanazawa, K.-I. MOOPMA05, WEXMA01
Kanazawa, M. *THZH101*
Kanekiyo, T. MOOPMA04
Kang, B.-K. THPMA024
Kang, H.-S. TUZH102, WEPMA075, WEPMA080, WEPMA103, THPMA047, THPMA114
Kanjilal, D. WEPMA078, WEPMA132, THPMA088
Kar, S. THPMA050
Karmarkar, M.G. THC2MA02, THPMA014
Karnewar, A. WEPMA065
Kasamsook, K. TUPMA049, *TUPMA052*, WEPMA038
Kashiwagi, H. THZH102
Kashiwagi, S. *TUPMA067*, TUPMA068, WEPMA073
Kasliwal, A. *THPMA036*, THPMA039, THPMA129
Kasuga, T. *TUPMA046*, TUPMA028
Katagiri, H. WEXMA01
Kato, R. TUPMA067, TUPMA068, *WEPMA073*
Kato, S. WEXMA01
Kawai, M. TUPMA049, TUPMA052, THPMA111, WEPMA038
Kawamoto, T. WEXMA01
Kawashima, Y. TUPMA067
Kawata, H. TUPMA046
Kayran, D. THC3MA04
Kazakov, S. WEXMA01
Khare, P. THC2MA02, THPMA131
Kikuchi, M. TUPMA028, WEXMA01
Kikutani, E. WEXMA01
Kim, D.E. *TUPMA057*, THPMA024, THPMA047, THPMA076, THPMA117
Kim, D.T. WEPMA050, WEPMA103
Kim, G.N. *THPMA114*
Kim, H. S. WEPMA119, *WEPMA120*
Kim, H.Y. WEPMA103
Kim, J. TUPMA031
Kim, J.H. WEPMA075, *WEPMA080*, THPMA033
Kim, J.M. *WEPMA075*, WEPMA080
Kim, J.-U. FRXMA01
Kim, J-Y. WEZMA03
Kim, K. R. TUPMA119, WEZMA03
Kim, K.-J. *TUZH101*, TUPMA039
Kim, K.Y. TUPMA119, WEZMA03
Kim, S. N. WEPMA054
Kim, S.-C. *WEPMA050*, WEPMA080, WEPMA103, THPMA063, THPMA074
Kim, S.H. WEC3H102, *THPMA063*, THPMA074, *WEPMA083*, *THPMA127*
Kim, Y.-C. WEPMA054
Kim, Y.-H. TUPMA119
Kiselev, V. WEPMA068
Kitamura, H. TUPMA042, WEPMA105
Kitamura, M. THPMA005
Klysubun, P. TUPMA020, *THC3MA01*
Klyuev, V. THPMA110
Knyazev, B.A. THC3MA04
Ko, I.S. TUPMA057, WEPMA080, WEPMA054, THPMA067, THPMA114
Ko, S.K. THPMA035
Kobayashi, H. TUPMA102, TUPMA111
Kobayashi, Y. TUPMA046, TUPMA028
Koiso, H. WEXMA01
Kojima, Y. MOOPMA04, WEXMA01
Kolekar, R.V. THPMA123
Kolobanov, E.I. THC3MA04

Komada, I. WEXMA01
Kon, Y. TUPMA068
Konjeti, S. *THPMA014*
Konstantinov, E. THPMA102
Konstantinov, S.G. THPMA110
Koseki, T. *TUPMA111*
Kotaiah, S. TUPMA115, WEPMA065, THC2MA02, THPMA013, THPMA032, THPMA036, THPMA039, THPMA046, THPMA085, THPMA088, THPMA096, THPMA125, THPMA131
Kotenkov, V.V. THC3MA04
Kozhemyakin, A. THPMA110
Kramer, S.L. *THC3MA03*
Krinsky, S. THC3MA03
Krishnagopal, S. TUPMA038, WEPMA111, WEPMA112
krishnaiah, K.V. WEPMA110
Kryuchkov, A. THPMA110
Kubarev, V.V. THC3MA04
Kubo, T. TUPMA102, WEXMA01
Kuchler, D. TUPMA084, TUPMA085
Kudo, K. TUPMA028, WEXMA01
Kudo, N.K. WEXMA01
Kuksanov, N.K. *THPMA118*
Kulipanov, G. *TUPMA018*, TUPMA023, THC3MA04
Kulshreshtha, P.K. THPMA014
Kumagai, N. TUPMA049
Kumar, A . *TUPMA115*
Kumar, A. WEPMA039, WEPMA112, THPMA035, THPMA085, THPMA129, THPMA131
Kumar, Kumar,S. THPMA013
Kumar, M. THPMA050, WEPMA065
Kumar, M. K. THPMA094, THPMA043
Kumar, M.K. THPMA043
Kumar, N. WEPMA142
Kumar, P. WEPMA078, *THPMA089*, THPMA125
Kumar, P.K. THPMA123
Kumar, R. TUPMA093, WEPMA002
Kumar, U. THPMA070
Kumar, V. *TUPMA038*, *TUPMA039*, WEPMA111
Kundu, Kundu, K.C. THPMA130
Kuniyasu, Y. TUPMA102
Kuo, C.-C. TUPMA034, TUPMA059, THZMA04
Kuo, C.H. WEPMA063, *WEPMA070*, WEPMA096, WEPMA096
Kurashima, S. THZH102
Kurihara, A. WEPMA038
Kurokawa, S.-I. TUPMA123, TUPMA124, *WEYMA03*
Kurup, M.B. THPMA121
Kush, P.K. THPMA131
Kuzmin, A.V. THC3MA04
Kwankasem, C. TUPMA020, THC3MA01
Kwon, H.-J. WEZMA03, *WEPMA119*, WEPMA120
Kwon, S.J. THPMA067, THPMA076

— L —

Lad, M. *WEPMA142*
Lakhtychkin, A.S. THC3MA04
Lakshmy, P.S. WEPMA078, THPMA089
Lal, S. WEPMA111, WEPMA112
Lamarre, J.-F. THZMA01
Lawangare, N. THPMA094
Laxdal, R.E. THPMA004
Le Roux, V. THZMA01
Lebasque, P. THZMA01
Lebedev, N.N. TUPMA122
Lebedev, V.A. WEPMA010
LeBlanc, G. WEPMA058, WEPMA059, *WEPMA060*, *THZMA02*
Lee, D. WEPMA070, WEPMA090, WEPMA096
Lee, E.-H. WEPMA075
Lee, H.-G. *THPMA117*
Lee, S.-Y. TUPMA059
Lee, T.-Y. *TUZH102*
Lee, W.W. WEPMA050, THPMA117
Lee, Y.Y. TUPMA119, WEZMA03
Lestrade, A. THZMA01
Level, M.-P. THZMA01
Li, D. TUPMA039
Li, D.M. *TUPMA022*, THPMA023
Li, H.H. TUPMA022
Li, M. THPMA126
Li, N. *THPMA010*
Li, R. THPMA023
Li, W.G. TUPMA070
Li, Z. WEPMA109
Liang, K.S. TUPMA034, *THZMA04*
Lin, K.-K. WEPMA096
Lin, M.-C. THYMA03, *THPMA051*
Lin, Y.-H. WEPMA071, THYMA03
Litvinenko, V. THC3MA03
Liu, H. THPMA023
Liu, K.X. THZH103
Liu, X.S. THPMA126
Liu, Y. THXMA03
Liu, Y.-C. TUPMA034
Liu, Y.D. *WEPMA030*
Liu, Y.-H. WEPMA077, THPMA056, THPMA091, *THPMA093*
Lochab, S.P. THPMA123
Lockyer, N. *FRBMA01*
Logachev, P.V. *TUC3MA03*, TUPMA018, TUPMA122
Lombardi, A.M. THXMA02
Loulergue, A. THZMA01
Lu, J. THPMA004
Lu, S.L. THPMA023
Lu, Y.R. TUPMA070
Luo, G.-H. *TUPMA034*, THZMA04
Lyssukhin, S.N. TUPMA023

— M —

Machida, S. *MOZMA03*, WEPMA035, THPMA115
Madur, A. THZMA01
Maesaka, H. TUPMA035, *WEPMA048*, THPMA005
Maezawa, H. TUPMA028
Mahner, E. TUPMA084, TUPMA085
Makahleh, F. THC3MA02
Mallik, C. TUPMA097, TUPMA113, WEPMA015, WEPMA104, THPMA016, THPMA022, THPMA048
Mandal, A. WEPMA110, *WEPMA002*, WEPMA078
Manglunki, D. *TUPMA084*, TUPMA085
Manna, S.K. WEPMA110
Marathe, R.G. *TUPMA032*
Marcellini, F. TUPMA075, *THYMA01*
Marchand, P. THZMA01
Marinkovic, G. TUPMA014
Marque, S. TUPMA001
Marques Balula, J. TUPMA088
Martini, M. TUPMA084
Martyshkin, P. TUC3MA03, TUPMA122
Marutsuka, K. WEXMA01
Masuzawa, M. WEXMA01, *THPMA008*
Mathur, Y. WEPMA078
Matsubara, T. THC3MA05
Matsumoto, H. TUPMA102, TUPMA111, WEPMA105
Matsumoto, S. WEXMA01
Matsumoto, T. WEXMA01
Matveenko, A.N. THC3MA04
Maury, S. TUPMA084, TUPMA085, THXMA02
Medvedev, L.E. THC3MA04
Meena, R.S. THPMA050
Mehrotra, N. THPMA121
Menon, R. TUPMA113
Menon, RM. WEPMA144
Merh, B.N. WEPMA087
Merminga, L. *MOOPMA03*
Meshkov, I.N. TUPMA064
Meshkov, O.I. WEPMA068
Mezentsev, N.A. TUPMA018, TUPMA023
Michelato, P. TUPMA083
Michizono, S. WEXMA01
Miginsky, S.V. *WEPMA022*, *THC3MA04*
Mikawa, K. WEXMA01
Miller, R.H. WEPMA109
Mimashi, T. WEXMA01
Mironenko, L.A. THC3MA04
Mishima, K. THPMA115
Mishina, A. TUPMA028
Mishra, A. WEPMA039
Mishra, C.S. *WEYMA01*
Mishra, D.K. *WEPMA124*
Mishra, R. L. THPMA043
Mishra, R.K. THPMA013
Mishra, R.L. THPMA094
Misra, J. THPMA130
MISTRI, K.K. WEPMA132
Mitra, A.K. *THPMA004*
Mitra, S. WEPMA144, THPMA064, *THPMA071*
Mitsuhashi, T. TUPMA028
Mitsui, T. THC3MA05
Mitsunobu, S. MOOPMA04, WEXMA01
Mittal, K.C. TUPMA076, WEPMA011, WEPMA122, WEPMA133, WEPMA144, *THPMA043*, THPMA064, THPMA094
Miura, S. WEPMA105
Miyajima, T. TUPMA028
Miyake, M. Y. WEPMA139
Miyauchi, H. TUPMA028
Miyawaki, N. THZH102
Mohan, S. TUPMA113
Mohania, P. THPMA015
Monaco, L. TUPMA083
Mondal, B.C. THPMA058
Mondal, J. WEPMA144
Moon, S.-I. THPMA127
Morgan, J. P. WEPMA010
Mori, K. WEXMA01
Mori, Y. THPMA115
Morita, A. WEXMA01
Morita, Y. *MOOPMA04*, WEXMA01
Moser, H.O. THPMA061
Muchnoi, N.Yu. WEPMA068
Mugnai, G. THC2MA02
Mukherjee, A.K. WEPMA110
Mulchandani, J. THPMA015
Mundra, G. WEPMA124
Murali, S. THPMA022
Muto, T. TUPMA049, TUPMA052, WEPMA038
Myneni, G. *TUZMA03*

— N —

Nabhiraj, P.Y. *TUPMA113*
Nadji, A. THZMA01
Nadolski, L.S. *THZMA01*
Nagabhushana, G.R. THPMA070
Nagahashi, S. TUPMA028
Nagai, R. TUPMA047
Nagaoka, R. THZMA01
Nagaslaev, V.P. *WEPMA010*
Nagesh, K.V. *THPMA064*, *THPMA065*, *THPMA065*, *THPMA066*, *THPMA066*, THPMA070, THPMA071, THPMA043
Naik, D. WEPMA078
Nair, H. *TUPMA015*
Nair, j.p. THPMA121
Naito, F. *MOXMA01*
Nakagawa, T. TUPMA116
Nakai, H. MOOPMA04, WEXMA01
Nakajima, H. WEXMA01
Nakajima, K. TUPMA123
Nakamura, N. TUPMA046

Nakamura, T.T. TUPMA028, WEXMA01
Nakanishi, H. TUPMA028, WEXMA01
Nakanishi, K. MOOPMA04, WEXMA01
Nakao, K. WEXMA01
Nakayama, H. WEXMA01
Nam, S.H. THPMA063
Namkung, W. WEPMA083, THPMA067, THPMA114, THPMA127
Nanbu, K. TUPMA049, TUPMA052, WEPMA038
Nandi, C.N. WEPMA089, WEPMA104, THPMA016
Nanu, K. THPMA094, THPMA043
Naser, Z.A. TUPMA097, *THPMA048*, THPMA016
Nathwani, R.K. WEPMA065
Nayak, M.K. TUPMA015
Nekhaev, V.E. THC3H101
Nema, P.K. TUPMA093
Nemytov, P.I. THPMA118
Niki, K. THPMA083
Nimje, V.T. *WEPMA122*
Ninomiya, S. WEXMA01
Nishimori, N. TUPMA047
Nishitani, T. TUPMA047
Nogami, T. TUPMA028
Noh, S.J. THPMA035
Nonoshita, E. TUPMA031

— O —

Obina, T. TUPMA028, WEC3H101
Ogawa, H. TUPMA037
Ogawa, Y. WEXMA01
Oh, J.-S. TUPMA057, WEPMA083, *THPMA067*, THPMA076, THPMA127
Oh, Y. D. THPMA114
Ohata, T. TUPMA035, THPMA005
Ohmi, K. WEXMA01
Ohnishi, Y. WEXMA01
Ohsawa, S. WEXMA01
Ohsawa, Y. WEXMA01
Ohshima, T. *TUPMA031*, TUPMA035, WEPMA048, THPMA005
Ohuchi, N. WEXMA01
Oide, K. TUPMA028, WEXMA01
Oikawa, M. THZH102
Okamura, K.O. THPMA083
Oki, H. TUPMA102
Okubo, K. MOOPMA04
Okubo, Y. WEPMA139
Okumura, S. THZH102
Omar, A.S. TUPMA016
Ono, M. MOOPMA04, TUPMA028, WEXMA01
Oogoe, T. TUPMA102, THPMA083
Oreshkov, A.D. THC3MA04
Otake, Y. TUPMA035, WEPMA048, *THPMA007*
Ouyang, H.F. WEZMA02
Ovchar, A.V. THC3MA04
Oyamada, M. THC3MA01
Ozaki, S. THC3MA03
Ozaki, T. TUPMA028, WEXMA01

— P —

Pagani, C. *MOOPMA02*, TUPMA083, *WEPMA123*
Pak, C.O. TUPMA028
Pal, G.P. WEPMA089, WEPMA104, THPMA016
Pal, S. THPMA130, THPMA016
Pal, S.P. WEPMA110
Panchenko, V.E. TUPMA018, TUPMA023
Pande, M.M. *WEPMA145*
Pande, R. WEPMA044, WEPMA045
Pandey, M.K. THPMA043
Pandey, Pandey, M.M. THPMA013
Pandit, T.G. THPMA036, THPMA039
Pandit, V.S. *WEPMA005*
Panfilov, A.D. THC3H101, THPMA102
Pant, K.K. WEPMA111, WEPMA112
Panzeri, N. WEPMA123
Paoluzzi, M.M. TUPMA085
Pareek, P. *WEPMA051*
Pareek, Pareek,P. THPMA013
Park, B. WEPMA083, THPMA127
Park, H.J. WEPMA050
Park, I.S. WEPMA103
Park, J. W. WEZMA03
Park, K.-H. TUPMA057, *THPMA024*, THPMA047, THPMA117
Park, S.J. WEC3H102, WEPMA083, THPMA127
Park, S.S. THPMA063, *THPMA074*
Park, Y.J. WEC3H102
Parkhomchuk, V.V. THPMA110
Pasinelli, S. TUPMA084, TUPMA085
Pasini, M. TUPMA088, THXMA02
Pasternak, J. TUPMA085
Patel, N.R. WEPMA145
Pattalwar, S.M. *TUPMA001*
Paul, S. TUPMA097, *WEPMA015*, THPMA048, THPMA016
Peake, D. J. WEPMA060
Peiniger, M. THPMA104
Pekeler, M. *THPMA104*
Peng, S.X. TUPMA070
Perng, S.Y. THPMA081
Peteti, P.R. THPMA039
Petrichenkov, M. *THPMA110*
Petrov, V.V. *TUPMA008*
Petwal, V.C. THPMA087, *THPMA088*
Philipchenko, A.V. TUPMA018, TUPMA023
Piel, C. THPMA104
Pierini, P. *FRAMA01*
Plum, M.A. *MOXMA02*
Poirier, R.L. THPMA004
Pollet, P. TUPMA014
Polley, A. THPMA048
Poncet, A. THPMA085

Popik, V.M. THC3MA04
Potter, K.M. TUPMA001
Pottin, B. THZMA01
Prabhu, S.S. THPMA096, THPMA131
Pradhan, J. *TUPMA097*, WEPMA015, THPMA028, THPMA048, THPMA016
Prakash, P.N. *WEPMA132*
Prasad, J.S.P. WEPMA110
Prasad, M. WEPMA124, WEPMA142
Prasad, V. WEPMA111, *THPMA086*, THPMA090
Praveen Kumar, D.D. WEPMA144, THPMA064, THPMA073
Prior, C.R. *WEZMA01*
Promod, R. THPMA129
Prost, L.R. TUPMA094
Pruvost, J.B. THZMA01
Puntambekar, A. WEPMA124, *THC2MA02*, THPMA131
Puntambekar, T.A. *WEPMA065*
Puthran, G.P. THPMA043, THPMA094

— Q —

Qin, Q. TUC3H101, WEXMA02, WEZMA02, WEPMA037
Qu, H. WEZMA02

— R —

Rahim, A. TUC2MA02
Rahman, M.M. MOOPMA04, *TUPMA124*
Raich, U. TUPMA084, TUPMA085
Raj, P.R. WEPMA110
Rajan, R.N. THPMA064, THPMA043
Rajput, V. WEPMA142
Rakshun, Y.V. TUPMA018
Ramasubramanian, R. THPMA096
Rao, V. WEPMA145
Rassool, R.P. WEPMA060
Rastigeev, S. THPMA110
Raul, S.R. THPMA064, THPMA043
Rawat, A. THPMA131
Ray, A.K. TUPMA076, WEPMA014, WEPMA123, THPMA071, THPMA043, THPMA098
Ray, P.K. TUPMA116
Renaglia, T. TUPMA001
Reschke, D. *MOOPMA01*
Reva, V.B. THPMA110
Rey, A. TUPMA084
Ribeiro, F. THZMA01
Rinolfi, L. TUPMA075
Rodrigues, G. WEPMA002, *WEPMA078*, THPMA088
Roeder, M. THC3H102
Roncarolo, F. TUPMA085, TUPMA001
Roser, T. *TUZMA01*
Ross, M.C. *WEZH103*, WEC3H102
Rossi, C. TUPMA085, THXMA02
Roy, A. *WEPMA144*, *THPMA016*, THPMA138, WEPMA078, WEPMA132, *THYMA04*, THPMA050
Roy, S. WEPMA044, WEPMA045
Roychowdhury, P. *TUPMA076*, WEPMA014
Royer, J.-P. TUPMA084, TUPMA085
Royer, M. TUPMA085
Rugmai, S. *TUPMA020*, *TUPMA020*, THC3MA01
Rujirawat, S. THC3MA01
Ruwali, K. THPMA014

— S —

Sadhu, R.K. THPMA131
Saha, M.S. WEPMA110
Saha, S. WEPMA110, THPMA017, THPMA022
Sahni, V.C. *TUYMA02*, THPMA121, *THPMA131*
Sahu, R.K. THPMA086
Saifee, K. WEPMA085
Saito, K. WEXMA01
Saito, Y. TUPMA102
Sakai, H. TUPMA028, WEXMA01, THC2MA03
Sakai, T. THZH102
Sakamoto, Y. TUPMA028, WEXMA01
Sakanaka, S. *TUPMA028*, TUPMA046, THC2MA03
Salikova, T.V. THC3MA04
Salimov, R.A. THPMA118
Sandha, R.S. THPMA085, *THPMA087*, THPMA088
Sargsyan, E.Zh. THXMA02
Sarkar, B. THPMA130
Sarkar, P.K. TUPMA015
Sarma, P.R. TUPMA116, WEPMA005, *THPMA020*
Saroj, P.C. THPMA064, THPMA043
Sasaki, H. TUPMA028
Sato, M. WEXMA01
Sato, Y. TUPMA028, TUPMA102
Satoh, K. TUPMA046
Satoh, M. WEXMA01
Satoh, T. THZH102
Sawamura, M. THC2MA03
Scheglov, M.A. THC3MA04
Schilcher, T. TUPMA014
Schmor, P. *WEZMA05*
Schreiber, S. *MOYMA02*, TUPMA083
Scrivens, R. TUPMA084, TUPMA085
Seema, M. WEPMA085
Sei, N. *TUPMA037*
Senecha, V.K. TUPMA115, *THPMA111*
Sengoku, H. TUPMA031
Sennyu, K. MOOPMA04
Seol, K.T. WEPMA119, WEPMA120
Serednyakov, S.S. THC3MA04
Serio, M. TUPMA075
Sermeus, L. TUPMA084, TUPMA085
Sertore, D. *TUPMA083*
Seth, S. WEPMA110
Sharma, A. *TUC2MA02*, THPMA131
Sharma, A.S. WEPMA144, *THPMA070*, THPMA071, THPMA073, THPMA064
Sharma, D. WEPMA142, WEPMA143

Sharma, D.K. THPMA043, THPMA064
Sharma, D.N. TUPMA015
Sharma, K.P. THPMA086
Sharma, N.K. *TUPMA109*, *TUPMA109*
Sharma, S.C. THPMA121
Sharma, V. THPMA043
Shehab, M.M. THC3MA02
Shemyakin, A.V. *TUPMA094*
Shen, L.R. TUPMA026
Shen, T.J. *THPMA023*
Shen, Z.Q. TUPMA022
Sheppard, J. WEPMA109
Sheth, Y. M. WEPMA085
Sheu, R.J. TUPMA034
Shevchenko, O.A. THC3MA04
Shibasaki, Y. WEPMA038
Shibata, K. MOOPMA05, WEXMA01
Shidara, T. WEXMA01
Shilendra, R. THPMA043
Shimamoto, M. TUPMA102
Shimosaki, Y. TUPMA099
Shinde, K.R. WEPMA145
Shinde, R.S. WEPMA051, *THPMA013*
Shinoe, K. THC2MA03
Shintake, T. *MOYMA03*, TUPMA042, WEPMA048, WEPMA105, THPMA005
Shioya, T. TUPMA028
Shirai, M. MOOPMA05, WEXMA01
Shirakata, M.J. TUPMA102, *THPMA083*
Shirakawa, A. WEXMA01
Shirasawa, K. *WEPMA105*
Shirkov, G. TUPMA064
Shiroya, S. THPMA115
Shiyankov, S. TUPMA122
Shobuda, Y. *WEPMA035*
Shoji, Y. THC3MA05
Shridhar, R.S. THPMA131
Shrivastava, P. WEPMA124, *THPMA015*, THPMA133
Shukla, S.K. THPMA096
Sidorov, A.I. THC3H101
Sing Babu, P. WEPMA005
Singh, B.S. THPMA123
Singh, G. TUC2MA02, TUPMA032, TUPMA053, TUPMA060, WEPMA013, WEPMA039, WEPMA085, THPMA086, THPMA131
Singh, K. WEPMA051
Singh, P. TUPMA093, WEPMA044, WEPMA045
Singh, Y.P. *THPMA032*
Sinha, G. *WEPMA039*
Sinha, S.K. *THZH104*
Sissakian, A.N. TUPMA064
sista, V.L.SR. TUPMA093, *WEPMA044*, WEPMA045
Skoczen, B. THPMA085
Skrinsky, A.N. THC3MA04
Smaluk, V.V. WEPMA068
Som, S.S. *WEPMA110*
Son, Y. G. WEPMA083, THPMA067, *THPMA076*, THPMA127
Song, Y.-G. WEPMA119, WEPMA120
Song, Z.Z. TUPMA070
Soni, A. WEPMA145
Soni, H.C. THPMA085, THPMA087
Sonkawade, R.G. *THPMA123*
Sonti, S.S.K. WEPMA132
Spencer, M.J. *WEPMA058*, WEPMA059, WEPMA060
Srivastava, B.S. *WEPMA086*
Srivastava, S.C.L. WEPMA044, *WEPMA045*
Steinhagen, R.J. *WEZH101*
Stella, A. TUPMA075
Stephan, F. TUPMA083
Stewart, T.M. THC3H102
Subbaiah, K.V. THPMA088
Sudmuang, P. TUPMA020
Suemine, S. TUPMA067, TUPMA068, WEPMA073
Sueno, T. WEXMA01
Suetake, M. WEXMA01
Suetsugu, Y. *MOOPMA05*, WEXMA01, THPMA008
Sugahara, R. WEXMA01, THPMA008
Sugimura, T. WEXMA01
Suh, H.S. THPMA117
Suh, J.-H. THPMA067
Suhane, S.K. WEPMA065
Suk, H. *FRXMA01*
Suman, S.K. WEPMA002
Sun, Y. *TUC3MA01*, *TUPMA005*, *TUPMA006*
Suneet, S.K. THPMA043
Supriya, S.B. THPMA043, THPMA094
Sur, A. THPMA048
Sur, S.S. THPMA022
Surendran, P. THPMA121
Suryaprakash, D.P. THPMA043
Suwada, T. WEXMA01, THC2MA03
Suzuki, S. *THC3MA05*
Swarna, K. THPMA014, THPMA045
Swoboda, D.K. TUPMA001

— T —

Tadano, M. TUPMA028
Takahashi, S. WEPMA038
Takahashi, T. TUPMA028, THC2MA03
Takano, S. WEXMA01
Takasaki, S. TUPMA028, WEXMA01
Takayama, K. TUPMA099
Takenaka, T. WEXMA01
Takeuchi, Y. TUPMA102, WEXMA01
Taki, G.S. *TUPMA116*
Taki, R. *TUPMA123*
Tan, Y.E. WEPMA058, *WEPMA059*, WEPMA060
Tanaka, H. TUPMA042, TUPMA049
Tanaka, T. *TUPMA049*, TUPMA052, WEPMA038
Tanaka, Y.T. TUPMA031
Tang, C.-X. TUPMA123

Tang, J. WEZMA02
Tanigaki, M. *THPMA115*
Tanikawa, T. TUPMA042
Tanimoto, Y. TUPMA028
Tarawneh, H. *TUPMA058*, THC3MA02
Tauchi, T. WEC3H102
Tawada, M. WEXMA01
Tecchio, L.B. TUPMA122
Tecker, F. TUPMA075
Tejima, M. TUPMA028, WEXMA01
Teryaev, V.E. WEPMA140
thakkar, thakkar,k.k. TUPMA015, TUPMA032
Thakur, D.S. TUPMA032
Thakur, S.K. THPMA017
Thakurta, A.C. THPMA032
Theroux, J.E. THC3H102
Tiwari, A.K. *WEPMA137*
Tiwari, N. WEPMA142
Tiwari, S.R. *THPMA045*, THPMA046, THPMA129
Tkachenko, V.O. THC3H101
Tobiyama, M. WEXMA01
Togawa, K. TUPMA042, WEPMA048
Tokuda, N. WEXMA01
Tordeux, M.-A. THZMA01
Tranquille, G. TUPMA084, TUPMA085
Trubnikov, G.V. *TUPMA064*
Tsai, L. *THPMA081*
Tsai, M.H. THYMA03, THPMA051
Tsai, Z.-D. *WEPMA077*, THPMA091
Tsuchiya, K. TUPMA028
Tuvik, A.F.A. THC3H101
Tyagi, R.K. WEPMA142
Tyagi, Y. WEPMA065

— U —

Uchiyama, T. TUPMA028
Ueda, A. TUPMA028
Uehara, S. WEXMA01
Ueng, T.-S. WEPMA077
Umemori, K. TUPMA028, *THC2MA03*
Unnam, U. WEPMA078
Uno, S. WEXMA01
Uota, M. TUPMA102
Upadhyay, A. THPMA036, THPMA039
Urakata, H. WEPMA139
Urakawa, J. WEC3H102, *FRXMA03*
Urschütz, P. TUPMA075
Utkin, A.V. TUPMA018, TUPMA023

— V —

Vallet, J.L. TUPMA084
Vander Meulen, D. WEPMA010
Vandorpe, B. TUPMA084
Varnasseri, S. *WEPMA049*, THC3MA02
Veer, V.S. THPMA094
veis, M.E. THPMA118
Venkateswaran, S.V. THPMA129
Verma, V. TUPMA015
Vignola, G. TUPMA058, *THC3MA02*
Vinokurov, N. TUPMA018, THC3MA04
Vogel, H. THPMA104
vom Stein, P. THPMA104
Voronin, L.A. THC3H101
Vossenberg, E. THPMA078
Vretenar, M. *TUPMA088*, TUPMA085, *THXMA02*
Vsevolozhskaya, T.A. TUC3MA03

— W —

Wahnmode, Y.W. THPMA015
Walker, R.P. *TUYMA03*
Wang, Ch. WEPMA071, *THYMA03*, THPMA051
Wang, C.-J. WEPMA063, WEPMA096
Wang, C.-X. *TUPMA056*
Wang, D.-J. TUPMA034, THZMA04, THPMA081, THPMA093
Wang, F.W. WEZMA02
WANG, H.B. *THPMA126*
Wang, J.W. *WEPMA109*
Wang, N. *WEPMA037*
Wang, S. WEZMA02
Wang, Wang, J. Q. TUC3H101
Wang, X. THPMA023, THPMA084
Wang, Y. *THPMA100*
Wang, Z. TUPMA070
Wanzenberg, R. TUPMA016
Watanabe, Y. TUPMA102
Wei, J. *WEZMA02*
Werkema, S.J. *TUXMA02*
Willeke, F.J. *FRYMA01*
Wolf, R. THC2MA02
Wrulich, A.F. *TUYMA01*
Wu, C.Y. *WEPMA096*
Wu, J. WEPMA024
Wu, W.F. THPMA023
Wuensch, W. *THYMA02*

— X —

Xia, J.W. *THXMA03*
Xu, G. TUC3H101
Xu, H. THZMA03
Xu, R.N. THPMA023
Xu, X. WEZMA02
Xu, Z. THPMA126

— Y —

Yadav, D.P. THPMA096
Yadav, S. WEPMA065
Yamada, K. Y. TUPMA037
Yamamoto, N. WEXMA01
Yamamoto, S. TUPMA028
Yamamoto, T. TUPMA068, WEPMA073

Yamamoto, Y. MOOPMA04, WEXMA01, *TUPMA012*
Yan, Q.W. WEZMA02
Yan, X.Q. TUPMA070
Yan, Z.B. THPMA084
Yanaoka, E. THPMA083
Yang, H.R. WEPMA083, THPMA127
Yang, J.C. THXMA03
Yang, J.Y. THPMA056
Yang, T.-T. THYMA03, THPMA051
Yang, X.D. THXMA03
Yano, Y. WEXMA01
Yasuda, M. TUPMA052, TUPMA049, WEPMA037
Yasumoto, M.Y. TUPMA037
Yeh, M.-S. *WEPMA071*, THPMA051, THYMA03
Yin, L. *THPMA084*
Yokota, W. THZH102
Yokoya, K. MOZMA01, *MOZMA02*
Yokoyama, K. *TUPMA066*, WEXMA01
Yoo, S.H.Yoo. FRXMA01
Yorita, T. THZH102
Yoshida, M. *WEXMA01*, *WEPMA140*
Yoshida, Ma. WEXMA01
Yoshimoto, S.I. TUPMA028, WEXMA01
Yoshino, K. WEXMA01
Yoshioka, M. *TUPMA102*, TUPMA111, THPMA087
Yu, C.H. THPMA084
Yu, I.H. *WEPMA103*
Yu, J.X. TUPMA070
Yu, M.L. TUPMA070
yuan, Y. THXMA03

— Z —

Zacharias, J. WEPMA132
Zhan, W.-L. THXMA03
Zhang, C. *WEXMA02*, TUPMA070
Zhang, J. WEZMA02
Zhang, M. THPMA062
Zhang, Z. WEZMA02
Zhao, H. TUPMA026
Zhao, M.H. TUPMA022
Zhao, Z. TUPMA022, *THZMA03*
Zhilich, V.N. WEPMA068
Zhou, D.M. TUC3H101
Zhou, Q.G. *THPMA062*, THPMA084
Zhu, H.J. TUPMA026
Zhu, K. TUPMA070
Zhu, S.M. THPMA023
Zhuravlev, A.N. *WEPMA068*
Zolotarev, K. TUPMA023, TUPMA018
Zviagintsev, V. THPMA004

Institutes List

ACCEL
Bergisch Gladbach
- Dunkel, K.
- Peiniger, M.
- Pekeler, M.
- Piel, C.
- Vogel, H.
- vom Stein, P.

AIST
Tsukuba, Ibaraki
- Ogawa, H.
- Sei, N.
- Yamada, K. Y.
- Yasumoto, M.Y.

ANL
Argonne, Illinois
- Kim, K.-J.
- Wang, C.-X.

ASP
Clayton, Victoria
- Bergstrom, J.C.
- Boland, M.J.
- Dowd, R.T.
- LeBlanc, G.
- Spencer, M.J.
- Tan, Y.E.

BARC
Mumbai
- Abdullah, K.K.
- Acharya, S.
- Agarwal, R.
- Barnwal, R.
- Basak, T.
- Bhagwat, P.V.
- Bhattacharjee, D.
- Chakravarthy, D.P.
- Chawala, A.S.
- Chindarkar, A.R.
- Choudhury, R.K.
- Datar, V.M.
- Dhavale, A.S.
- Dixit, K.
- Ghodke, S.R.
- Gore, J.A.
- Gupta, A.K.
- Handu, V.K.
- Israel, B.S.
- Jain, A.
- Jain, P.
- Jayaprakash, D.
- Kailas, S.
- Kumar, M. K.
- Kumar, M.K.
- Kumar, R.
- Lawangare, N.
- Mehrotra, N.
- Menon, RM.
- Mishra, R. L.
- Mishra, R.L.
- Mitra, S.
- Mittal, K.C.
- Mondal, J.
- Nagesh, K.V.
- Nair, j.p.
- Nanu, K.
- Nema, P.K.
- Nimje, V.T.
- Pande, M.M.
- Pande, R.
- Pandey, M.K.
- Patel, N.R.
- Praveen Kumar, D.D.
- Puthran, G.P.
- Rajan, R.N.
- Rao, V.
- Raul, S.R.
- Ray, A.K.
- Roy, A.
- Roy, S.
- Roychowdhury, P.
- Sadhu, R.K.
- Saroj, P.C.
- Sharma, A.S.
- Sharma, D.K.
- Sharma, S.C.
- Sharma, V.
- Shilendra, R.
- Singh, P.
- Soni, A.
- Srivastava, S.C.L.
- Suneet, S.K.
- Supriya, S.B.
- Surendran, P.
- Suryaprakash, D.P.
- Veer, V.S.
- sista, V.L.SR.

BERGOZ Instrumentation
Saint Genis Pouilly
- Bergoz, J.F.
- Defrance, C.

BHU
Varanasi
- Ghosh, M.K.

BINP SB RAS
Novosibirsk
- Antokhin, E.

- Antoshin, A.V.
- Auslender, V.
- Avilov, M.S.
- Blinov, M.B.
- Bolkhovityanov, D.
- Bryazgin, A.A.
- Cheskidov, V.G.
- Fadeev, S.
- Faktorovich, B.L.
- Goncharov, A.D.
- Gorbunov, V.
- Gornakov, I.V.
- Gubin, K.
- Gvozdev, A.
- Kiselev, V.
- Klyuev, V.
- Knyazev, B.A.
- Kolobanov, E.I.
- Konstantinov, E.
- Konstantinov, S.G.
- Kotenkov, V.V.
- Kozhemyakin, A.
- Kryuchkov, A.
- Kubarev, V.V.
- Kuksanov, N.K.
- Kulipanov, G.
- Kuzmin, A.V.
- Lakhtychkin, A.S.
- Lebedev, N.N.
- Logachev, P.V.
- Martyshkin, P.
- Matveenko, A.N.
- Medvedev, L.E.
- Meshkov, O.I.
- Mezentsev, N.A.
- Miginsky, S.V.
- Mironenko, L.A.
- Muchnoi, N.Yu.
- Nekhaev, V.E.
- Nemytov, P.I.
- Oreshkov, A.D.
- Ovchar, A.V.
- Panchenko, V.E.
- Panfilov, A.D.
- Parkhomchuk, V.V.
- Petrichenkov, M.
- Petrov, V.V.
- Philipchenko, A.V.
- Popik, V.M.
- Rakshun, Y.V.
- Rastigeev, S.
- Reva, V.B.
- Salikova, T.V.
- Salimov, R.A.
- Scheglov, M.A.
- Serednyakov, S.S.
- Shevchenko, O.A.
- Shiyankov, S.
- Sidorov, A.I.
- Skrinsky, A.N.
- Smaluk, V.V.
- Teryaev, V.E.
- Tkachenko, V.O.
- Tuvik, A.F.A.
- Utkin, A.V.
- Vinokurov, N.
- Voronin, L.A.
- Vsevolozhskaya, T.A.
- Zhilich, V.N.
- Zhuravlev, A.N.
- Zolotarev, K.
- veis, M.E.

BNL
Upton, Long Island, New York
- Ben-Zvi, I.
- Bengtsson, J.
- Kayran, D.
- Kramer, S.L.
- Krinsky, S.
- Litvinenko, V.
- Ozaki, S.
- Roser, T.
- Wei, J.

Bengal Engineering and Science University
Howrah
- Ray, P.K.

Bhabha Atomic Research Center, Computer Division
Mumbai
- Dubey, B.P.

Bhabha Atomic Research Centre
Mumbai
- Kolekar, R.V.
- Sharma, D.N.

CAEP/IAE
Mianyang, Sichuan
- Jin, X.
- Li, M.
- Liu, X.S.
- WANG, H.B.
- Xu, Z.

CALTECH
Pasadena, California
- Barish, B.C.

CERN
Geneva
- Angoletta, M.-E.
- Baggiolini, V.
- Bellodi, G.
- Belochitskii, P.
- Beuret, A.

- Blas, A.
- Borburgh, J.
- Braun, H.-H.
- Carli, C.
- Chanel, M.
- Chohan, V.
- Colombet, T.
- Cornelis, K.
- Corsini, R.
- Cuvet, Y.
- Doebert, S.
- Ducimetière, L.
- Dumas, L.D.
- Evans, L.R.
- Fowler, T.
- Garion, C.
- Garoby, R.
- Gerigk, F.
- Geschonke, G.
- Gourber-Pace, M.
- Hancock, S.
- Hanke, K.
- Hill, C.E.
- Hourican, M.
- Jowett, J.M.
- Kuchler, D.
- Lombardi, A.M.
- Mahner, E.
- Manglunki, D.
- Marque, S.
- Marques Balula, J.
- Martini, M.
- Maury, S.
- Mugnai, G.
- Paoluzzi, M.M.
- Pasinelli, S.
- Pasini, M.
- Pasternak, J.
- Poncet, A.
- Raich, U.
- Renaglia, T.
- Rey, A.
- Rinolfi, L.
- Roncarolo, F.
- Rossi, C.
- Royer, J.-P.
- Royer, M.
- Sargsyan, E.Zh.
- Scrivens, R.
- Sermeus, L.
- Skoczen, B.
- Steinhagen, R.J.
- Swoboda, D.K.
- Tecker, F.
- Tranquille, G.
- Urschütz, P.
- Vallet, J.L.
- Vandorpe, B.
- Vossenberg, E.
- Vretenar, M.
- Wolf, R.
- Wuensch, W.

Candox Systems Inc.
Gyoda city, Saitama perfecture
- Nonoshita, E.
- Sengoku, H.

D-Pace
Nelson, British Columbia
- Dehnel, M.P.
- Jackle, P.T.
- Roeder, M.
- Stewart, T.M.
- Theroux, J.E.

DAE/VECC
Calcutta
- Adak, D.
- Bandapadhaya, D. L.
- Bandyopadhyay, S.
- Banerjee, M.B.
- Bhandari, R.K.
- Bhattacharjee, T.
- Bhattacharya, S.
- Bhattacharyay, D.S.B.
- Bhattacharyya, T.
- Bhole, R.B.
- Bhunia, U.
- Biswas, S.B.
- Chaddha, Chaddha, N.
- Chaudhuri, J.
- Das, M.
- Das, T.D.
- De, A.
- Debnath, J.
- Dey, M.K.
- Dutta Gupta, A.
- Dutta, A.
- Dutta, M.
- Gangopadhyay, P.G.
- Goswami, A.
- Hajra, D.P.
- Kundu, Kundu, K.C.
- Mallik, C.
- Mandal, A.
- Manna, S.K.
- Menon, R.
- Misra, J.
- Mondal, B.C.
- Mukherjee, A.K.
- Murali, S.
- Nabhiraj, P.Y.
- Nandi, C.N.
- Naser, Z.A.
- Pal, G.P.
- Pal, S.
- Pal, S.P.
- Pandit, V.S.
- Paul, S.

- Polley, A.
- Pradhan, J.
- Prasad, J.S.P.
- Raj, P.R.
- Roy, A.
- Saha, M.S.
- Saha, S.
- Sarkar, B.
- Sarkar, P.K.
- Sarma, P.R.
- Seth, S.
- Sing Babu, P.
- Som, S.S.
- Sur, A.
- Sur, S.S.
- Taki, G.S.
- Thakur, S.K.
- krishnaiah, K.V.

DESY Zeuthen
Zeuthen
- Stephan, F.

DESY
Hamburg
- Balewski, K.
- Reschke, D.
- Schreiber, S.
- Wanzenberg, R.
- Willeke, F.J.

Dankook University
Seoul
- Chung, B.H.
- Hong, J.S.
- Jeon, J.H.
- Noh, S.J.

Diamond
Oxfordshire
- Walker, R.P.

Fermilab
Batavia, Illinois
- Lebedev, V.A.
- Mishra, C.S.
- Morgan, J. P.
- Nagaslaev, V.P.
- Prost, L.R.
- Ross, M.C.
- Shemyakin, A.V.
- Vander Meulen, D.
- Werkema, S.J.

GUAS/AS
Ibaraki
- Dixit, T.S.
- Taki, R.

Hitachi Ltd., Hitachi Research Laboratory
Ibaraki-ken
- Kanekiyo, T.

IHEP Beijing
Beijing
- Fang, S.X.
- Fu, S.
- Gao, J.
- Jiao, Y.
- Liu, Y.D.
- Ouyang, H.F.
- Qin, Q.
- Qu, H.
- Tang, J.
- Wang, N.
- Wang, S.
- Wang, Wang, J. Q.
- Xu, G.
- Xu, X.
- Zhang, C.
- Zhou, D.M.

IISC
Bangalore
- G, G.
- Kumar, U.
- Mohan, S.
- Nagabhushana, G.R.

ILT
Suita, Osaka
- Li, D.

IMP
Lanzhou
- He, Y.
- Liu, Y.
- Xia, J.W.
- Yang, J.C.
- Yang, X.D.
- Zhan, W.-L.
- yuan, Y.

INFN-Torino
Torino
- Domenico, D.

INFN/LASA
Segrate (MI)
- Michelato, P.
- Monaco, L.
- Pagani, C.
- Panzeri, N.

- Pierini, P.
- Sertore, D.

INFN/LNF
Frascati (Roma)
- Biscari, C.
- Ghigo, A.
- Marcellini, F.
- Serio, M.
- Stella, A.

INFN/LNL
Legnaro, Padova
- Tecchio, L.B.

INP NNC RK
Almaty
- Kadyrzhanov, K.K.
- Lyssukhin, S.N.

IPHY
Beijing
- Feng, J.
- Yan, Q.W.
- Zhang, J.
- Zhang, Z.

ISIR
Osaka
- Igo, T.
- Isoyama, G.
- Kashiwagi, S.
- Kato, R.
- Kon, Y.
- Suemine, S.
- Yamamoto, T.

ISSP/SRL
Chiba
- Nakamura, N.
- Sakai, H.
- Shinoe, K.

IUAC
New Delhi
- Ahuja, R.
- Antony, J.
- Babu, S.
- Chacko, J.
- Choudhury, A.
- Datta, T.S.
- Kanjilal, D.
- Kar, S.
- Kumar, M.
- Kumar, P.
- Kumar, P.K.
- Kumar, R.
- Lakshmy, P.S.
- Lochab, S.P.
- MISTRI, K.K.
- Mandal, A.
- Mathur, Y.
- Meena, R.S.
- Naik, D.
- Prakash, P.N.
- Rodrigues, G.
- Roy, A.
- Singh, B.S.
- Sonkawade, R.G.
- Sonti, S.S.K.
- Suman, S.K.
- Unnam, U.
- Zacharias, J.

IUCF
Bloomington, Indiana
- Lee, S.-Y.

Institute of Physics, Chinese Academy of Sciences
Beijing
- Wang, F.W.

JAEA/ARTC
Takasaki
- Kamiya, T.
- Kashiwagi, H.
- Kurashima, S.
- Miyawaki, N.
- Oikawa, M.
- Okumura, S.
- Sakai, T.
- Satoh, T.
- Yokota, W.

JAEA/ERL
Ibaraki
- Hajima, R.
- Iijima, H.
- Nagai, R.
- Nishimori, N.
- Nishitani, T.
- Sawamura, M.

JAEA/FEL
Ibaraki-ken
- Hajima, R.

JAEA/J-PARC
Tokai-Mura, Naka-Gun, Ibaraki-Ken
- Shobuda, Y.

JASRI/SPring-8
Hyogo-ken
- Asaka, T.
- Ego, H.
- Fukui, T.
- Fukuyama, Y.
- Hosoda, N.
- Kawashima, Y.
- Kim, J.
- Kumagai, N.
- Ohata, T.
- Ohshima, T.
- Suzuki, S.
- Tanaka, H.

JINR
Dubna, Moscow Region
- Denisov, Yu.N.
- Dolbilov, G.
- Meshkov, I.N.
- Shirkov, G.
- Sissakian, A.N.
- Trubnikov, G.V.

Jefferson Lab
Newport News, Virginia
- Chattopadhyay, S.
- Delayen, J.R.
- Merminga, L.
- Myneni, G.

KAERI
Daejon
- An, S.
- Cho, Y.-S.
- Choi, B.H.
- Chung, B.C.
- Hong, I.-S.
- Jang, J.-H.
- Kim, H. S.
- Kim, J-Y.
- Kim, K. R.
- Kim, K.Y.
- Kim, Y.-H.
- Kwon, H.-J.
- Lee, Y.Y.
- Park, J. W.
- Seol, K.T.
- Song, Y.-G.

KAPRA
Cheorwon
- Chung, K.-H.

KEK
Ibaraki
- Agoh, T.A.
- Akai, K.
- Akemoto, M.
- Akiyama, A.
- Arinaga, A.
- Asaoka, S.
- Baba, H.
- Cheng, W.X.
- Ebihara, K.
- Egawa, K.
- Enomoto, A.
- Flanagan, J.W.
- Fujino, T.
- Fukuda, S.
- Fukuma, H.
- Funakoshi, Y.
- Furukawa, K.
- Furuya, T.
- Haba, J.
- Haga, K.
- Hara, K.
- Harada, K.
- Higo, T.
- Hiramatsu, S.
- Hisamatsu, H.
- Honda, T.
- Honda, Y.
- Honma, H.
- Honma, T.
- Hori, Y.
- Hosoyama, K.
- Ieiri, T.
- Iida, N.
- Ikeda, H.
- Ikeda, M.
- Inagaki, S.
- Inoue, I.Y.
- Isagawa, S.
- Ishii, H.
- Ishii, K.
- Izawa, M.
- Kabe, A.
- Kadokura, E.
- Kageyama, T.
- Kakihara, K.
- Kako, E.
- Kamada, S.
- Kamitani, T.
- Kanazawa, K.-I.
- Kasuga, T.
- Katagiri, H.
- Kato, S.
- Kawai, M.
- Kawamoto, T.
- Kawata, H.
- Kazakov, S.
- Kikuchi, M.
- Kikutani, E.
- Kobayashi, H.
- Kobayashi, Y.
- Koiso, H.
- Kojima, Y.

- Komada, I.
- Koseki, T.
- Kubo, T.
- Kudo, K.
- Kudo, N.K.
- Kurokawa, S.-I.
- Maezawa, H.
- Marutsuka, K.
- Masuzawa, M.
- Matsumoto, H.
- Matsumoto, S.
- Matsumoto, T.
- Michizono, S.
- Mikawa, K.
- Mimashi, T.
- Mishina, A.
- Mitsuhashi, T.
- Mitsunobu, S.
- Miyajima, T.
- Miyauchi, H.
- Mori, K.
- Morita, A.
- Morita, Y.
- Nagahashi, S.
- Naito, F.
- Nakai, H.
- Nakajima, H.
- Nakajima, K.
- Nakamura, T.T.
- Nakanishi, H.
- Nakanishi, K.
- Nakao, K.
- Nakayama, H.
- Niki, K.
- Ninomiya, S.
- Nogami, T.
- Obina, T.
- Ogawa, Y.
- Ohmi, K.
- Ohnishi, Y.
- Ohsawa, S.
- Ohsawa, Y.
- Ohuchi, N.
- Oide, K.
- Okamura, K.O.
- Oki, H.
- Ono, M.
- Oogoe, T.
- Ozaki, T.
- Pak, C.O.
- Saito, K.
- Saito, Y.
- Sakai, H.
- Sakamoto, Y.
- Sakanaka, S.
- Sasaki, H.
- Sato, M.
- Sato, Y.
- Satoh, K.
- Satoh, M.
- Senecha, V.K.
- Shibata, K.
- Shidara, T.
- Shimamoto, M.
- Shimosaki, Y.
- Shioya, T.
- Shirai, M.
- Shirakata, M.J.
- Shirakawa, A.
- Sueno, T.
- Suetake, M.
- Suetsugu, Y.
- Sugahara, R.
- Sugimura, T.
- Suwada, T.
- Tadano, M.
- Takahashi, T.
- Takano, S.
- Takasaki, S.
- Takayama, K.
- Takenaka, T.
- Takeuchi, Y.
- Tanimoto, Y.
- Tauchi, T.
- Tawada, M.
- Tejima, M.
- Tobiyama, M.
- Tokuda, N.
- Tsuchiya, K.
- Uchiyama, T.
- Ueda, A.
- Uehara, S.
- Umemori, K.
- Uno, S.
- Uota, M.
- Urakawa, J.
- Watanabe, Y.
- Yamamoto, N.
- Yamamoto, S.
- Yamamoto, Y.
- Yanaoka, E.
- Yano, Y.
- Yokoya, K.
- Yokoyama, K.
- Yoshida, M.
- Yoshida, Ma.
- Yoshimoto, S.I.
- Yoshino, K.
- Yoshioka, M.

KERI
Changwon
- Hur, M.S.
- Kim, J.-U.
- Suk, H.
- Yoo, S.H.Yoo.

KURRI
Osaka
- Inoue, M.
- Mishima, K.

- Mori, Y.
- Shiroya, S.
- Tanigaki, M.

KVI
Groningen
- Drentje, A.G.

Kyungpook National University
Daegu
- Kim, G.N.

LBNL
Berkeley, California
- Doolittle, L.R.
- Fawley, W.M.

LSU/CAMD
Baton Rouge, Louisiana
- Wang, Y.

MELCO SC
Tsukuba
- Kuniyasu, Y.

MHI
Hiroshima
- Miura, S.
- Okubo, K.
- Sennyu, K.

Melbourne
Melbourne
- Peake, D. J.
- Rassool, R.P.

Mitsubishi Electric Corp, Energy amp; Public Infrastructure Systems Center
Kobe
- Fukumoto, S.
- Ishi, Y.

NIRS
Chiba-shi
- Kanazawa, M.

NSRC
Nakhon Ratchasima
- Cheedket, S.
- Hoyes, G.G.
- Klysubun, P.
- Kwankasem, C.
- Oyamada, M.
- Rugmai, S.
- Rujirawat, S.
- Sudmuang, P.

NSRRC
Hsinchu
- Chan, C.K.
- Chang, C.-C.
- Chang, H.-P.
- Chang, J.-C.
- Chang, L.-H.
- Chang, M.H.
- Chang, S.-S.
- Chao, H.C.
- Chen, C. L.
- Chen, C.-T.
- Chen, J.
- Chen, J.-R.
- Chung, F.-T.
- Fan, T.-C.
- Hsiao, F. Z.
- Hsiung, G.-Y.
- Hsu, K. T.
- Hsu, S-N.
- Hsu, S.Y.
- Hsueh, H.P.
- Hu, K.H.
- Hwang, J.-Y.
- Kuo, C.-C.
- Kuo, C.H.
- Lee, D.
- Liang, K.S.
- Lin, K.-K.
- Lin, M.-C.
- Lin, Y.-H.
- Liu, Y.-C.
- Liu, Y.-H.
- Luo, G.-H.
- Perng, S.Y.
- Sheu, R.J.
- Tsai, L.
- Tsai, M.H.
- Tsai, Z.-D.
- Ueng, T.-S.
- Wang, C.-J.
- Wang, Ch.
- Wang, D.-J.
- Wu, C.Y.
- Yang, J.Y.
- Yang, T.-T.
- Yeh, M.-S.

NTHU
Hsinchu
- Chen, J.-R.

New Affiliation Request Pending
-TBS-
- Shinde, K.R.

NewSUBARU/SPring-8, Laboratory of Advanced Science and Technology for Industry (LASTI)
Hyogo
- Hisaoka, Y.
- Matsubara, T.
- Mitsui, T.
- Shoji, Y.

ORNL
Oak Ridge, Tennessee
- Chu, P.
- Jeon, D.-O.
- Plum, M.A.

Otto-Von-Guericke University
Magdeburg
- Bandyopadhyay, A.K.
- Joestingmeier, A.
- Omar, A.S.

PAL
Pohang, Kyungbuk
- Choi, J.
- Chung, C.W.
- Ha, K.M.
- Han, H.S.
- Han, Y.J.
- Huang, J.Y.
- Hwang, W.H.
- Jang, S. D.
- Jeong, S.-H.
- Jung, Y.G.
- Kang, H.-S.
- Kim, D.E.
- Kim, D.T.
- Kim, H.Y.
- Kim, J.H.
- Kim, J.M.
- Kim, S. N.
- Kim, S.-C.
- Kim, S.H.
- Kim, Y.-C.
- Ko, I.S.
- Kwon, S.J.
- Lee, E.-H.
- Lee, H.-G.
- Lee, T.-Y.
- Lee, W.W.
- Nam, S.H.
- Oh, J.-S.
- Oh, Y. D.
- Park, H.J.
- Park, I.S.
- Park, K.-H.
- Park, S.J.
- Park, S.S.
- Park, Y.J.
- Son, Y. G.
- Suh, H.S.
- Suh, J.-H.
- Yu, I.H.

PKU/IHIP
Beijing
- Chen, J.-E.
- Fang, J.X.
- Gao, S.L.
- Guo, J.F.
- Guo, Z.Y.
- Li, W.G.
- Liu, K.X.
- Lu, Y.R.
- Peng, S.X.
- Song, Z.Z.
- Sun, Y.
- Wang, Z.
- Yan, X.Q.
- Yu, J.X.
- Yu, M.L.
- Zhang, C.
- Zhu, K.

POSTECH
Pohang, Kyungbuk
- Cho, M.-H.
- Kang, B.-K.
- Kim, S.H.
- Ko, I.S.
- Moon, S.-I.
- Namkung, W.
- Park, B.
- Yang, H.R.

PSI
Villigen
- Anghel, A.
- Dehler, M.
- Marinkovic, G.
- Pollet, P.
- Schilcher, T.
- Wrulich, A.F.

RCNP
Osaka
- Fukuda, M.
- Hatanaka, K.
- Yorita, T.

RIKEN Spring-8 Harima
Hyogo
- Hara, T.
- Inagaki, T.
- Kitamura, H.
- Kitamura, M.
- Maesaka, H.
- Otake, Y.

- Shintake, T.
- Shirasawa, K.
- Tanaka, Y.T.
- Togawa, K.

RIKEN/RARF/CC
Saitama
- Nakagawa, T.

RRCAT
Indore (M.P.)
- Agrawal, R.K.
- Arora, R. K.
- Babbar, L.K.
- Badapanda, M.K.
- Bagre, M.
- Banerji, A.
- Banwari, R.
- Bapna, S.C.
- Barapatre, D.
- Bhanage, V.B.
- Bhatnagar, V.
- Biswas, B.
- Bohrey, A.
- Borage, M.
- Chauhan, A.
- Chouksey, S.
- Das, S.
- Deep, A.
- Dev, V.
- Dutta, S.
- Dwivedi, J.
- Fakhri, A.A.
- Fatnani, P.
- Gangopadhyay, S.
- Gaud, Gaud,V.K.
- Ghodke, A.D.
- Gupta, A.
- Gupta, R.K.
- Hannurkar, P.R.
- Holikatti, A.C.
- Husain, R.
- Jagannath, M.
- Jain, A.
- Jain, A.K.
- Jain, M.K.
- Jain, V.
- Joshi, D.K.
- Joshi, S.C.
- Karmarkar, M.G.
- Karnewar, A.
- Kasliwal, A.
- Khare, P.
- Konjeti, S.
- Kotaiah, S.
- Krishnagopal, S.
- Kulshreshtha, P.K.
- Kumar, A .
- Kumar, A.
- Kumar, Kumar,S.
- Kumar, M.
- Kumar, N.
- Kumar, P.
- Kumar, V.
- Lad, M.
- Lal, S.
- Marathe, R.G.
- Merh, B.N.
- Mishra, A.
- Mishra, D.K.
- Mishra, R.K.
- Mohania, P.
- Mulchandani, J.
- Mundra, G.
- Nair, H.
- Nathwani, R.K.
- Nayak, M.K.
- Pandey, Pandey, M.M.
- Pandit, T.G.
- Pant, K.K.
- Pareek, P.
- Pareek, Pareek,P.
- Peteti, P.R.
- Petwal, V.C.
- Prabhu, S.S.
- Prasad, M.
- Prasad, V.
- Promod, R.
- Puntambekar, A.
- Puntambekar, T.A.
- Rahim, A.
- Rajput, V.
- Ramasubramanian, R.
- Rawat, A.
- Ruwali, K.
- Sahni, V.C.
- Sahu, R.K.
- Saifee, K.
- Sandha, R.S.
- Seema, M.
- Sharma, A.
- Sharma, D.
- Sharma, K.P.
- Sharma, N.K.
- Sheth, Y. M.
- Shinde, R.S.
- Shridhar, R.S.
- Shrivastava, P.
- Shukla, S.K.
- Singh, G.
- Singh, K.
- Singh, Y.P.
- Sinha, G.
- Soni, H.C.
- Srivastava, B.S.
- Suhane, S.K.
- Swarna, K.
- Thakur, D.S.
- Thakurta, A.C.
- Tiwari, A.K.
- Tiwari, N.

- Tiwari, S.R.
- Tyagi, R.K.
- Tyagi, Y.
- Upadhyay, A.
- Venkateswaran, S.V.
- Verma, V.
- Wahnmode, Y.W.
- Yadav, D.P.
- Yadav, S.
- deo, R.K.DEO.
- thakkar, thakkar,k.k.
- Kush, P.K.

Ritsumeikan University
Kusatsu-City, Shiga
- Yamamoto, Y.

SESAME
Amman
- Amro, A.
- Attal, M.
- Azizi, H.
- Kaftoosian, A.
- Makahleh, F.
- Shehab, M.M.
- Tarawneh, H.
- Varnasseri, S.
- Vignola, G.

SINAP
Shanghai
- Chen, H.G.
- Ding, H.
- Ding, J.G.
- Du, H.W.
- Guo, C.L.
- Hu, Z.M.
- Jiang, D.K.
- Li, D.M.
- Li, H.H.
- Li, R.
- Liu, H.
- Lu, S.L.
- Shen, L.R.
- Shen, T.J.
- Shen, Z.Q.
- Wang, X.
- Wu, W.F.
- Xu, H.
- Xu, R.N.
- Yan, Z.B.
- Yin, L.
- Yu, C.H.
- Zhang, M.
- Zhao, H.
- Zhao, M.H.
- Zhao, Z.
- Zhou, Q.G.
- Zhu, H.J.
- Zhu, S.M.

SLAC
Menlo Park, California
- Adolphsen, C.
- Bharadwaj, V.
- Bowden, G.B.
- Jongewaard, E.N.
- Li, N.
- Li, Z.
- Miller, R.H.
- Ross, M.C.
- Sheppard, J.
- Wang, J.W.
- Wu, J.

SOLEIL
Gif-sur-Yvette
- Besson, J.C.
- Brunelle, P.
- Buteau, A.
- Cassinari, L.
- Couprie, M.-E.
- Denard, J.-C.
- Filhol, J.-M.
- Herbeaux, C.
- Lamarre, J.-F.
- Le Roux, V.
- Lebasque, P.
- Lestrade, A.
- Level, M.-P.
- Loulergue, A.
- Madur, A.
- Marchand, P.
- Nadji, A.
- Nadolski, L.S.
- Nagaoka, R.
- Pottin, B.
- Pruvost, J.B.
- Ribeiro, F.
- Tordeux, M.-A.

SSLS
Singapore
- Diao, C.
- Moser, H.O.

STFC/DL/ASTeC
Daresbury, Warrington, Cheshire
- Pattalwar, S.M.

STFC/RAL/ASTeC
Chilton, Didcot, Oxon
- Machida, S.
- Prior, C.R.

Safety Research Institute, Indira Gandhi Center for Atomic Research
Tamilnadu
- Subbaiah, K.V.

Suranaree University of Technology
Nakhon Ratchasima
- Rugmai, S.

TETD
Otawara
- Hayashi, K.
- Irikura, M.
- Okubo, Y.
- Urakata, H.

THK CO., LTD
Hitachinaka
- HOSOKAWA, M.

TIFR
Mumbai
- Kurup, M.B.

TRIUMF
Vancouver
- Ang, Z.T.
- Bylinskii, I.V.
- Fong, K.
- Laxdal, R.E.
- Lu, J.
- Mitra, A.K.
- Poirier, R.L.
- Schmor, P.
- Zviagintsev, V.

TUB
Beijing
- An, W.M.
- Hua, Hua,J.F.
- Huang, W.-H.
- Tang, C.-X.

Terna Collage of Engineering
Navi Mumbai
- Gokhale, A.

Tohoku University, School of Scinece
Sendai
- Akiyama, K.
- Hama, H.
- Hinode, F.
- Kasamsook, K.
- Kawai, M.
- Kurihara, A.
- Muto, T.
- Nanbu, K.
- Shibasaki, Y.
- Takahashi, S.
- Tanaka, T.
- Yasuda, M.

Toshiba
Yokohama
- Miyake, M. Y.

UCSD
La Jolla, California
- Sinha, S.K.

UMAN
Manchester
- Cox, B.
- Potter, K.M.
- Roncarolo, F.

University of Chittagong
Chittagong
- Rahman, M.M.

University of Hyogo
Hyogo
- Tanikawa, T.

University of Pennsylvania
Philadelphia, Pennsylvania
- Lockyer, N.

University of Ulsan
Ulsan
- Ko, S.K.